

COMPUMAG
2009
Florianópolis, Brazil



Proceedings of the
**17th Conference on the Computation of
Electromagnetic Fields**

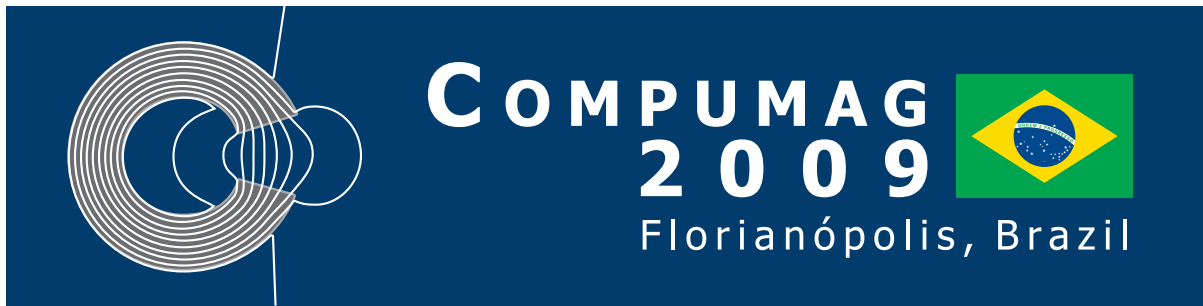
November, 22nd – 26th
Florianópolis, Brazil

ORGANISATION:



SPONSORING:





Proceedings

17th International Conference on the
Computation of Electromagnetic Fields

November 22-26, 2009

Florianópolis, Brazil

CHAIRMAN FOREWORD

It is a great pleasure and honour for us to welcome you all to COMPUMAG 2009, the 17th International Conference on the Computation of Electromagnetic Fields in our town, Florianópolis, state of Santa Catarina, Brazil.

It is the second time that COMPUMAG is held in Brazil. The first one was in 1997, in Rio de Janeiro. That event accomplished an important goal: it encouraged the Brazilian Community to maintain and expand their activities in the area of Electromagnetic Modelling. If today Brazil has a significant standing in this field of research, COMPUMAG 1997 contributed to this achievement. We believe that Compumag 2009 will assume a similar motivating role. In the same spirit, it is our sincere hope that this event will inspire our worldwide community.

At this point, we would like to provide you with some figures and facts about COMPUMAG 2009. The conference has attracted 622 valid submissions from 36 countries. About 220 reviewers of the Editorial Board, led by Nathan Ida, have worked diligently to select the accepted papers. The list of reviewers was enhanced with several new members mostly recommended by the ICS Board. COMPUMAG 2009 has 8 Oral Sessions and 25 Poster Sessions, with 548 accepted contributions, including 8 invited papers. The main criterion for the selection of invited papers was the technical and scientific quality of the papers. The first paper in each Oral Session is an invited paper.

The organisation of the conference started in 2005 when Florianópolis was chosen as the conference venue for 2009. Of course, the preparation activity became intense two years ago. The Brazilian community, especially our colleagues from *Universidade de São Paulo* and *Universidade Federal de Minas Gerais* were very active partners in our organization work. The *SBMag – Sociedade Brasileira de Eletromagnetismo* – was also very supporting since its financial participation was necessary in the conference preparation.

The Local Organizing Committee was formed mainly from members of *GRUCAD – Grupo de Concepção e Análise de Dispositivos Eletromagnéticos*, from the *Universidade Federal de Santa Catarina*, an amazing

team that allowed us to organize COMPUMAG 2009 in a consistent and systematic way. They are a very reliable group of people who worked with serenity and professionalism. All were very enthusiastic when taking up duties and fulfilling tasks to shape the most prestigious conference in our scientific area.

We hope that all of you will benefit from the excellent quality of technical presentations at COMPUMAG 2009, have fruitful discussions and pleasant moments through meeting friends and colleagues and establish new scientific relationships. A meeting of this size cannot be brought together without the dedicated efforts of many people and we would like to take this opportunity to thank everyone involved in the conference. Each attendee and each paper are very important to its success.

As organisers of COMPUMAG 2009 we were particularly keen to encourage young researchers to attend the conference and enjoy all available benefits. We trust we achieved this goal by offering a significantly reduced registration fee for full time students (lower than at any previous COMPUMAG). Additionally, it is fully inclusive (all lunches, conference dinner, social programme). We strongly believe that students should have the same networking opportunities as their supervisors and we hope that this will motivate our young colleagues to work vigorously in the fascinating field of computational electromagnetic.

Finally, we hope that the conference will give you a chance to visit and get to know this country of the South Hemisphere. Florianópolis is a small but beautiful place and you certainly should try to capture its charm. We wish you a pleasant stay in our island and a safe return home after the conference. We also hope that the atmosphere at COMPUMAG 2009 will inspire new friendships amongst engineers and scientists for the benefit of the society in the years ahead.

João Pedro Assumpção Bastos
Chairman

CONTENTS

CHAIRMAN FOREWORD	I
LOCAL ORGANISING COMMITTEE	V
INTERNATIONAL COMPUMAG SOCIETY	VII
PAPERS BY TOPICS	XI
PAPERS BY COUNTRY	XII
SPONSORING AND EXHIBITOR COMPANIES	XIV
VENUE	XV
GENERAL INFORMATION	XIX
AUTHOR INFORMATION	XX
SESSION CHAIRS	XXIII
SCHEDULE	XXV
TECHNICAL PROGRAM	XXVII
Monday, November 23rd	XXVII
Session OA1: Static and Quasi-static Fields	XXVII
Session PA1: Static and Quasi-static Fields I	XXVII
Session PA2: Static and Quasi-static Fields II	XXX
Session PA3: Coupled Problems I	XXXII
Session PA4: Static and Quasi-Static Fields III	XXXIV
Session PA5: Coupled Problems II	XXXVI
Session PA6: Electrical Machines and Drives I	XXXVIII
Session OA2: Coupled Problems	XL
Tuesday, November 24th	XLII
Session OB1: Wave Propagation and Nanomagnetism	XLII
Session PB1: Optimization I	XLII
Session PB2: Optimization II	XLV

Session PB3: Waves Propagation I XLVIII
Session PB4: Numerical Techniques I L
Session PB5: Optimization III LII
Session PB6: Waves Propagation II, Nanomagnetism, Photonics and Optoelectronics LVI
Session PB7: EMC – Electromagnetic Compatibility LVIII
Session OB2: Optimization LX

Wednesday, November 25th LXII

Session OC1: Material Modelling and Numerical Techniques LXII
Session PC1: Material Modelling I LXII
Session PC2: Electrical Machines and Drives II LXIV
Session PC3: Devices and Applications I LXVII
Session PC4: Numerical Techniques II LXIX
Session PC5: Material Modelling II LXXII
Session PC6: Electrical Machines and Drives III LXXIV
Session PC7: Numerical Techniques III LXXVII
Session PC8: TEAM, Education and Software Methodology LXXX
Session OC2: Devices and Applications and Electromagnetic Compatibility LXXXII

Thursday, November 26th LXXXIII

Session OD1: Electric Machines and Drives LXXXIII
Session PD1: Electrical Machines and Drives IV LXXXIII
Session PD2: Electrical machines and Drives V LXXXVI
Session PD3: Devices and Applications II LXXXVIII
Session PD4: Numerical Techniques IV XCI
Session OD2: Numerical Techniques and Software Methodology XCIII

ABSTRACTS 1

AUTHOR'S INDEX I

LOCAL ORGANISING COMMITTEE

The organising committee is composed of members of the three main Brazilian research groups in EM Modeling:

- **GRUCAD** (Grupo de Concepção e Análise de Dispositivos Eletromagnéticos), from the Universidade Federal de Santa Catarina (UFSC);
- **LMAG** (Laboratório de Eletromagnetismo Aplicado), from the Universidade de São Paulo (USP);
- **GOPAC** (Grupo de Otimização e Projetos Assistidos por Computador) from the Universidade Federal de Minas Gerais (UFMG).

Chairman

Prof. João Pedro Assumpção Bastos (GRUCAD, UFSC)

Vice-Chairman

Prof. Nelson Sadowski (GRUCAD, UFSC)

Committee Members

from GRUCAD/UFSC: R. Carlson, N. J. Batistela

from LMAG/USP: J. R. Cardoso, L. Lebensztajn, S.I. Nabeta, V. Silva, C.A.F. Sartori

from GOPAC/UFMG: R.C. Mesquita, J.A. Vasconcelos, R.R. Saldanha, J.A. Ramirez, E.J. da Silva

Secretariat (GRUCAD/UFSC)

Mauricio Valencia Ferreira da Luz

Walter P. Carpes Jr.

Celly D. Melo

Treasurer

Patrick Kuo-Peng (GRUCAD/UFSC)

Technical Support

Mauricio Rigoni

Tulio L. dos Santos



The Local Committee (left to right): Walter, Patrick, Mauricio, Renato, Celly, Nelson, João Pedro and Jhoe

Contact

compumag2009@grucad.ufsc.br

Address

GRUCAD / EEL / CTC, UFSC, CP 476
Florianópolis, SC, 88040-900, Brazil

Phone: +55 48 3721-9649

Fax: +55 48 3234-3790

website: www.compumag2009.com

INTERNATIONAL COMPUMAG SOCIETY

<http://www.compumag.co.uk>

ICS Board

President: Prof. Arnulf Kost (Germany)

Honorary President: Dr. Bill Trowbridge (UK)

Secretary: Prof. Jan Sykulski (UK)

Vice-President (The Americas): Prof. David Lowther (Canada)

Vice-President (Asia and Oceania): Prof. Norio Takahashi (Japan)

Secretary (The Americas): Prof. João Pedro Bastos (Brazil)

Secretary (Asia and Oceania): Prof. Dexin Xie (China)

Prof. Raffaele Albanese (Italy),

Prof. Piergiorgio Alotto (Italy),

Dr. Oszkar Biro (Austria),

Dr. Patrick Dular (Belgium),

Prof. Chang-Seop Koh (Korea),

Mr. Behzad Forghani (Canada),

Prof. Herbert de Gersem (Belgium),

Prof. Kay Hameyer (Germany),

Prof. Nathan Ida (USA),

Prof. Hajime Igarashi (Japan),

Prof. Hyung-Kyo Jung (Korea),

Dr. Jun Wei Lu (Australia),

Prof. Jaime Ramirez (Brazil),

Dr. Zhuoxiang Ren (USA),

Dr. Stephan Russenschuck (Switzerland),

Dr. Sheppard Salon (USA),

Dr. Viviane Cristine Silva (Brazil),

Prof. Jan Sykulski (UK),

Prof. Qingxin Yang (China),

Prof. Jianguo Zhu (Australia).

Editorial Board

Chairman: Prof. Nathan Ida (The University of Akron, USA)

Editorial Board Members

Abou El-Fadl, Ahmed	Albanese, Raffaele
Alfonzetti, Salvatore	Ali, Abakar
Alotto, Piergiorgio	Andjelic, Zoran
Antonopoulos, Christos	Arjona, Marco
Assumpção Bastos, João Pedro	Auchmann, Bernhard
Außerhofer, Stefan	Badics, Zsolt
Bandelier, Bernard	Bardi, Istvan
Barmada, Sami	Batistela, Nelson Jhoe
Belahcen, Anouar	Biro, Oszkar
Bouillault, Frédéric	Brandstaetter, Bernhard
Brauer, Hartmut	Brauer, John
Brosseau, Christian	Buchau, André
Burais, Noel	Buret, François
Campelo, Felipe	Canova, Aldo
Cardelli, Ermanno	Cardoso, Jose Roberto
Carlson, Renato	Carpentieri, Mario
Carpes Jr., Walter Pereira	Cavalcante, Gervásio P.
Cesar, Amilcar Careli	Chabu, Ivan
Chadebec, Olivier	Chan, Tze-Fun
Cheng, Zhiguang	Chiampi, Mario
Choi, Charles T. M.	Christopoulos, Christos
Ciuprina, Gabriela	Clemens, Markus
Clenet, Stephane	Coco, Salvatore
Codecasa, Lorenzo	Coulomb, Jean-Louis
Cranganu-Cretu, Bogdan	Cui, Xiang
d' Assunção, Adaildo Gomes	da Luz, Mauricio V. Ferreira
Davenport, Liz	De Gersem, Herbert
de Vasconcelos, João Antonio	Di Barba, Paolo
Di Rienzo, Luca	Dolinar, Drago
Duffy, Alistair	Dufour, Stephane
Dughiero, Fabrizio	Dular, Patrick
Dupre, Luc	Dyck, Derek
Dyczij-Edlinger, Romanus	Emson, Cris
Fahimi, Babak	Feliziani, Mauro
Fernandes, Paolo	Figueroa, Hugo E. H.

Florea, Hantila
Forghani, Behzad
Fresa, Raffaele
Geuzaine, Christophe
Golosnoy, Igor
Gratkowski, Stanislaw
Gyselinck, Johan
Hameyer, Kay
Henneron, Thomas
Hijazi, Toufic M.
Hu, Yan
Igarashi, Hajime
Ishibashi, Kazuhisa
Iwashita, Takeshi
Janssen, Rick
Kaltenbacher, Manfred
Kamitani, Atsushi
Kanayama, Hiroshi
Kasper, Manfred
Kettunen, Lauri
Kim, Chang Eob
Koh, Chang Seop
Kotiuga, P. Robert
Kuczmann, Miklós
Kurz, Stefan
Lebensztajn, Luiz
Lefevre, Yvan
Lesselier, Dominique
Liu, Xiaoming
Lu, Junwei
Maradei, Francescaromana
Marinova, Iliana
Matsuo, Tetsuji
Mazauric, Vincent
Melkebeek, Jan
Meunier, Gerard
Molinari, Giorgio
Morabito, Francesco Carlo
Muramatsu, Kazuhiro
Nervi, Mario

Flores Filho, Aly Ferreira
Formisano, Alessandro
Freschi, Fabio
Giannacopoulos, Dennis D.
Gonnet, Jean-Paul
Gyimothy, Szabolcs
Hafla, Wolfgang
He, Renjie
Henrotte, Francois
Hong, Jung-Pyo
Ida, Nathan
Iles-Klumpner, Dorin
Ishikawa, Takeo
Jacobs, Ralf
Jung, Hyun-Kyo
Kameari, Akihisa
Kanai, Yasushi
Kangas, Jari
Kawase, Yoshihiro
Kim, Hyeong-Seok
Kladas, Antonios
Kost, Arnulf
Krähenbühl, Laurent
Kuo-Peng, Patrick
Le Menach, Yvonnick
Lee, Jin-Fa
Leite, Jean Viane
Li, Lin
Lowther, David
Magele, Christian
Marchand, Claude
Martone, Raffaele
Mayergoyz, Isaak
McFee, Steve
Mesquita, Renato Cardoso
Mohammed, Osama
Monebhurrin, Vikass
Munteanu, Irina
Nabeta, Silvio
Nicolas, Alain

Nicolas, Laurent
Nishiguchi, Isoharu
Ostrowski, Jörg
Perugia, Ilaria
Piriou, Francis
Popovic, Milica
Premel, Denis
Raizer, Adroaldo
Rao, Liyun
Razek, Adel
Renhart, Werner
Resende, Ursula
Rischmueller, Volker
Rucker, Wolfgang M.
Sabariego, Ruth V.
Saguet, Pierre
Sartori, Carlos
Schlensok, Christoph
Schuhmann, Rolf
Shao, K.R.
Specogna, Ruben
Stumberger, Bojan
Sykulski, Jan
Takagi, Toshiyuki
Takorabet, Noureddine
Todaka, Takashi
Trlep, Mladen
Tsuboi, Hajime
van Rienen, Ursula
Verdeyme, Serge
Vollaire, Christian
Wang, Zanming
Webb, Jon
Xie, Dexin
Yang, Shiyou
Yatchev, Ivan
Zhou, Ping
Zou, Jibin

Nicolet, Andre
Noguchi, So
Perrussel, Ronan
Pichon, Lionel
Poeplau, Gisela
Preis, Kurt
Raffetto, Mirco
Ramirez, Jaime
Rapetti, Francesca
Ren, Zhuoxiang
Repetto, Maurizio
Reyne, Gilbert
Rodger, David
Russenschuck, Stephan
Sadowski, Nelson
Salon, Sheppard
Savini, Antonio
Schmidt, Erich
Scorretti, Riccardo
Silva, Viviane Cristine
Sterz, Oliver
Suuriniemi, Saku
Szücs, Áron
Takahashi, Norio
Tamburrino, Antonello
Trevisan, Francesco
Tsiboukis, Theodoros D.
Tsukerman, Igor
Vandavelde, Lieven
Villone, Fabio
Wakao, Shinji
Watanabe, Kota
Wurtz, Frederic
Yamazaki, Katsumi
Yang, Qingxin
Yoshifumi, Okamoto
Zhu, Jianguo

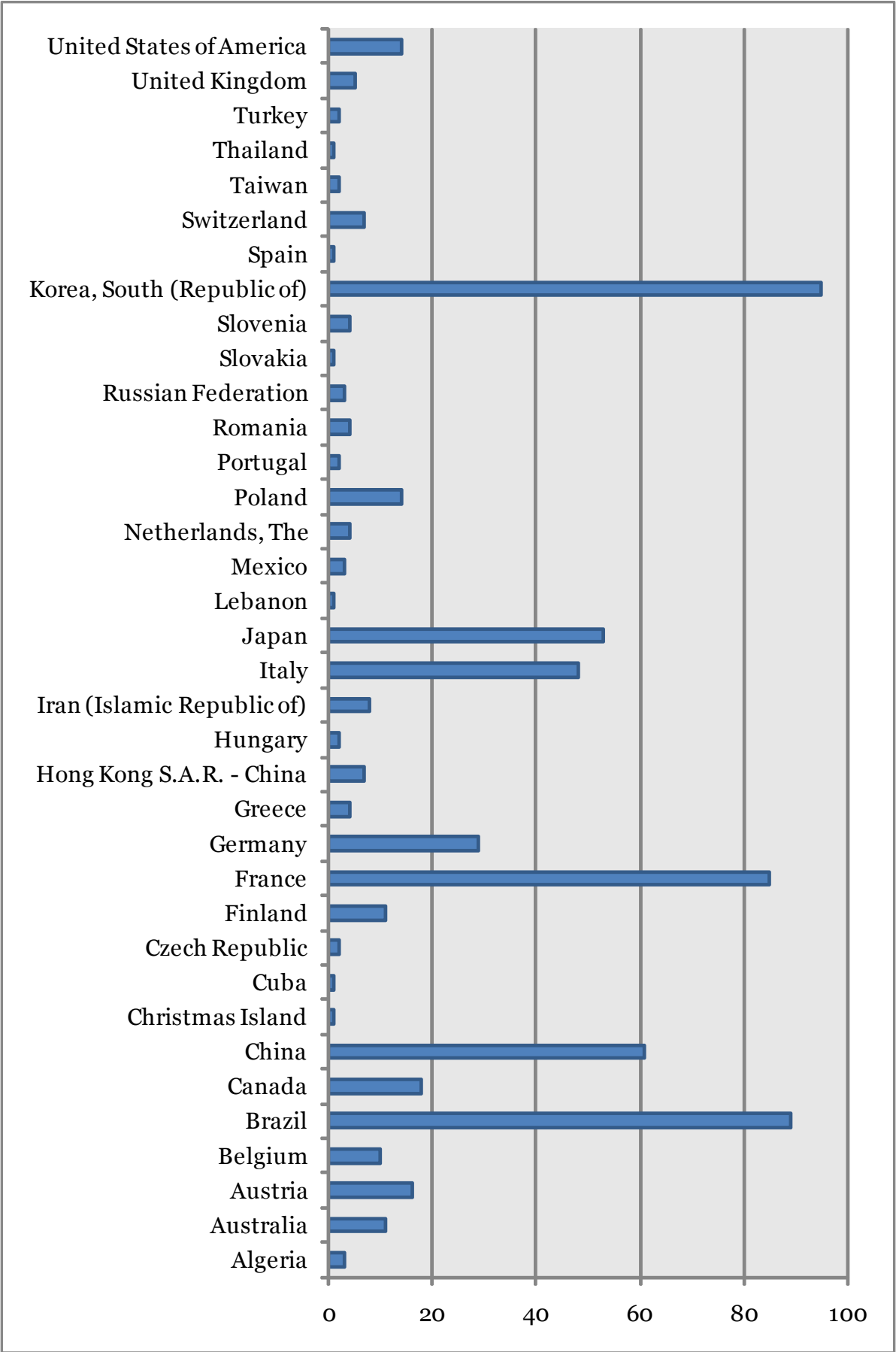
PAPERS BY TOPICS

Here you find a survey of the number of submissions for each conference topic. Notice that some papers were assigned by the authors on more than one topic.

Topics	No. of Submissions
Static Fields	35
Quasi-Static Fields	45
Wave Propagation	47
Electromagnetic Compatibility	35
Nanomagnetics and Applications	5
Optimization	97
Material Modelling	49
Coupled Problems	62
Numerical Techniques	176
Software Methodology	32
Electric Machines and Drives	164
Devices and Applications	101
Education	7
Benchmarking (TEAM)	9
Photonics/Optoelectronics	8

PAPERS BY COUNTRY

Algeria	3
Australia	11
Austria	16
Belgium	10
Brazil	89
Canada	18
China	61
Christmas Island	1
Cuba	1
Czech Republic	2
Finland	11
France	85
Germany	29
Greece	4
Hong Kong S.A.R. – China	7
Hungary	2
Iran (Islamic Republic of)	8
Italy	48
Japan	53
Lebanon	1
Mexico	3
Netherlands, The	4
Poland	14
Portugal	2
Romania	4
Russian Federation	3
Slovakia	1
Slovenia	4
Korea, South (Republic of)	95
Spain	1
Switzerland	7
Taiwan	2
Thailand	1
Turkey	2
United Kingdom	5
United States of America	14
TOTAL	622



SPONSORING AND EXHIBITOR COMPANIES

UFSC – Universidade Federal de Santa Catarina

ICS – International Compumag Society

PPGEEL – Programa de Pós-Graduação em Engenharia Elétrica

SBMag – Sociedade Brasileira de Eletromagnetismo

CNPq – Conselho Nacional de Desenvolvimento Científico e Tecnológico

CAPES – Coordenação de Aperfeiçoamento de Pessoal de Nível Superior

Electromagnetics Tecnologia e Informática Ltda

ESSS – Engineering Simulation and Scientific Software

CST – CST: Computer Simulation Technology AG

EM Software and Systems – SA (Pty) Ltd

JSOL Corporation

Schneider-Electric

Whirlpool S.A. – Unidade EMBRACO

VENUE

“Costão do Santinho” Resort and Spa is the venue of the conference.

- it is one of the best resorts in Brazil, recognized by Brazilians and foreign people as an outstanding hotel, offering an international quality level service
- it is the favourite place to hold conferences since it has several facilities to meet various needs
- the resort has a commercial center with stores, tourism agencies, banks, transportation, pharmacy, etc.
- inside the resort, there are several restaurants, cafes and meeting points located in different places
- several pools, gym rooms, sport and spa facilities are available for the guests
- the resort is located on the Santinho beach, one of the most beautiful of the island

The “Costão do Santinho” Resort is located at the north of the island, 40 km from downtown and 50 km from the airport. Typical prices for taxis to downtown are around 35 Euros (one way).



The Costão do Santinho is located at the Santinho beach



Resort, aerial view

Florianópolis

Overview

Florianópolis is the capital of the state of Santa Catarina, located in southern Brazil. It is located some 700 km south (about 1 hour flight) of São Paulo. Its population is around 450,000 inhabitants and is known as a calm city, with excellent quality of life.

The city of Florianópolis is located on an island called “Ilha de Santa Catarina”. Its dimensions are about 52 km (north-south) by 12 km (east-west). Three bridges connect the city to the continent but only two are operational (the third is a historical monument and a symbol of the city). The airport “Hercílio Luz” is located on the island. Florianópolis boasts 42 beaches, which are quite different from each other. The ones located between the mainland and the island, (Canasvieiras, Jurerê, Cachoeira do Bom Jesus, Ponta das Canas, etc) are calm and the water is warm. Those who prefer a little fresher water with waves would choose the beaches on the ocean side (Joaquina, Moçambique, Campeche, Costão do Santinho, Pântano do Sul, Barra da Lagoa, Mole). The latter beaches offer excellent surfing.

In the interior of the island there is a large lagoon connected to the ocean by a narrow channel, called the “Lagoa da Conceição”, an amazing environment, with alternating water and landscapes. Around this lagoon, there are many bars and restaurants offering international food, but the typical fish dishes are, of course, the most appealing.

In downtown there is the concentration of buildings and commerce. That is also the place where the bridges connect the island to the continent. Being an average size town, the downtown is calm and walking on its pedestrian street (Felipe Schmidt) or on the main plaza (Praça 15 de Novembro) is highly recommended. The old public market (1898) is also an interesting point to be visited.

History

The foundation of Florianópolis dates to **1726** by Azorean (Portuguese) colonization. Shortly afterwards, **Santo Antônio de Lisboa** (1751) and **Ribeirão da Ilha** (1803) were established. They are also located on the island and are now neighborhoods in the city. These two villages boast **old Portuguese colonial buildings** as well as very good restaurants and bars and an atmosphere quite different than the rest of the city. Visiting them is a very pleasant choice.

In **1823 Florianópolis became the capital of the state**. At that time, its name was “Nossa Senhora do Desterro”. The name of the town changed to Florianópolis in 1894 in homage to the **Marechal Floriano Peixoto**. Interestingly, this military man was, and still is considered, a nasty personage by the people of the town. He was instructed by the national government in Rio de Janeiro (at that time) to quell a rebellion after the republican revolution (Brazil was a monarchy until 1889). Many influential people of the town were executed in **this violent repression** by the federal government. As a result, the name **Florianópolis, imposed by Rio de Janeiro**, was never well accepted by the local people. Today, these sad memories have been slowly erased by the time, but, nevertheless, some people still reject this name and prefer to use expressions such as “capital of Santa Catarina” or “Desterro” and even avoid pronouncing the word “Florianópolis”.

Florianópolis was an **important and strategic place** for the Portuguese colonizers, since this land was constantly disputed by Spain. Indeed, the city of Laguna (100 km south of Florianópolis) was on the me-

ridian that **divided the lands of Portugal and Spain** (treatise of Tordesilhas, agreed upon in 1494 by the two countries). Therefore fortresses were built on the island and on the main land, to protect the land from the Spaniards. The most important is the “**Fortaleza da Ilha de Anhatomirim**” which was restored and is a nice place to visit. There are also two fortresses on two small islands called “Ilha de Ratonés Grande” and “Ilha de Ratonés Pequeno”, both easily reached by boat. For a long period, Florianópolis was mainly the administrative capital and, in terms of economy, the **town was far below the industrially developed Blumenau and Joinville** to its north. These two cities were established by **Germans and Italians in the XIX century**.

In the 1970s, with the establishment of the Federal University of Santa Catarina and Eletrosul (utility company for the South Region of Brazil) Florianópolis **became a more important town and a cultural center of the state**. Recently many other private universities were also established in the capital and its economy is flourishing. Because of its privileged nature and the quality of life, many people moved to Florianópolis in the 90s and the **city is constantly growing in population**. Residential and commercial buildings as well as hotels have been constructed regularly in these last years. Since it is the most touristy and demanded town in the South Region, its **population swells by about 50% each summer** only to revert to its normal size by the end February.

GENERAL INFORMATION

Conference Desk

The Conference Desk is located near the entrance of the Conference Area of the Hotel Costão do Santinho Resort. It will be open all day long, throughout the conference. Staff members will be available there to assist you in all matters related to the conference itself.

Açoriana Tourism Agency Desk

This tourism agency has a desk close to the Conference Desk. They will provide you information about tourist activities in Florianópolis, the post-conference tour, flight information, etc.

Welcome Reception

The Welcome Reception takes place on Sunday, November 22nd, between 19:30 and 21:30 in the hotel chalet by the Santinho beach. Finger food and refreshments will be served, in a convivial atmosphere, to celebrate the reunion of the COMPUMAG community and the beginning of the conference.

Lunches

All lunches are served in the Lunch room, between 12:10 and 13:30. Please, make sure to have with you, when presenting yourself at the restaurant's door, the appropriate lunch ticket for that day.

Conference Dinner

The Conference Dinner takes place on Wednesday, November 25th, from 20:00 to 23:30, in the Alameda Casa Rosa. A typical Brazilian music performance will be presented to the guests. The coaches will be ready at 19:00 at the Venue entrance. Make sure you have the appropriate ticket and, please, be on time for the buses departure.

AUTHOR INFORMATION

Guidelines for Oral Presentations

Timing

Oral presentations are allocated **15 minutes** for the talk and an additional **5 minutes** for questions and discussion. Session timings are listed in the technical program booklet. Session chairs will strictly enforce these time limits. A useful estimate is to allot approximately one minute for each transparency or slide prepared for the talk.

As for **invited papers**, the allocated times are **25 minutes** for presentation and **5 minutes** for questions and discussion.

Format

All oral presentations should be prepared in Microsoft Powerpoint format. There will be a number of computers available at the Conference Computer Room with the same version of Powerpoint installed as in the plenary room, in order to allow all speakers checking their presentation in advance (fonts, resolution, etc.). After this check, the presentation can be uploaded into the Conference media system. You are asked to hand in the file of your presentation, on a CD-rom or a USB Memory stick, **the day before** the session where it will be presented. An assistant will be present in Media Center, every day between 8:00-10:30 and 14:00-17:10 to receive your file and upload it on the system.

Presentation

The day of their oral presentation, all speakers should “check in” with the session chairman at least 10 minutes before the scheduled start of the session in order to confirm the name of the author (or co-author) who will present the talk. Talks will be called at the time scheduled in the technical program booklet. Session chairs have the responsibility of reporting “no-shows” to the Editorial Committee. No-show papers will not be considered for publication in the IEEE Transactions on Magnetics journal. All speakers are urged to prepare visuals in advance of the conference and to

practice their talk. The success of the conference depends on the quality of the technical work as well as their presentations.

Guidelines for Poster Presentations

Attendance

Please arrive at least 10 minutes ahead of the scheduled poster session to arrange your poster and check that all necessary supplies are present. One or more of the authors including a prime presenter should be present at the poster for most of session and be capable of explaining it. Session chairs have the responsibility of determining whether papers have actually been presented. Failure to attend or adequately explain your poster will result in your poster being deemed a “no show”. No-show papers will not be considered for publication in the IEEE Transactions on Magnetics journal.

Dimensions

Poster boards will be available for the presentation of poster papers. Before the session begins, the conference organizer will place the paper number on the top left of the board, as shown on the opposite picture. Prepare your poster in the format 90cm (width) x 130cm (height). Your paper title and author names, affiliations should be displayed prominently across the top of your poster. Push pins or stickers will be provided by the conference organization. Please, keep in mind that your poster will be seen by everyone at the conference. Pay very close attention to the visual appearance of your presentation, be clear and concise, and keep text to a minimum.

Removal

All poster materials must be removed promptly at the end of the session. Poster materials not collected immediately by an author will be removed and discarded by the organizers to allow preparation for the next poster session.

Software Companies Exhibits

During the conference, next to the Poster Session Room I, you have the opportunity to visit the stands of our software and industrial exhibitors,

presenting the latest innovations offered by state-of-the-art computational electromagnetic products available on the market.

Emerald Compel Award

This prize will be awarded to a young researcher, who is a participant of Compumag 2009 registered as a STUDENT. The paper may be co-authored, but the recipient must have contributed significantly, the evidence of this being demonstrated for example by the fact that he/she is listed as the first author. Finally, the paper must be presented by the young researcher in either an oral or a poster session. A special Awards Committee, working together with session chairs and the Board of the International Compumag Society, will select about 6 papers which will be commended and the authors will receive certificates on behalf of the ICS Board. One of these authors (in exceptional circumstances two for a joint award) will be identified as the recipient of the Emerald COMPEL award.

More information about the COMPEL journal can be found at:

<http://www.emeraldinsight.com/info/journals/compel/compel.jsp>.

Final submission

Papers presented at the conference will be considered for publication in 2010 special issue of the “IEEE Transactions on Magnetics” journal after a second peer-review process. The length of all extended papers is limited to **4 pages for regular** papers and **7 pages (minimum) for the invited** papers. Templates and general information on this topic can be found in the conference web site www.compumag2009.com.

SESSION CHAIRS

Alotto, Piergiorgio, Università di Padova, Italy **(OB2)**
Arkkio, Antero, Helsinki University of Technology, Finland **(PC2)**
Badics, Zsolt, Rhythmia Medical, Inc., USA **(PA4)**
Batistela, Nelson Jhoe, GRUCAD, Univ. Federal da Santa Catarina, Brazil **(PC1)**
Benabou, Abdelkader, L2EP-University of Lille, France **(PC3)**
Biro, Oszkar, IGTE, TU Graz, Austria **(OD2)**
Bottauscio, Oriano, Istituto Nazionale di Ricerca Metrologica, Italy **(PB7)**
Bouillault, Frédéric, LGEP, France **(PA2)**
Cardelli, Ermanno, University of Perugia, Italy **(PC5)**
Cardoso, Jose Roberto, Escola Politécnica, USP, Brazil **(OA1)**
Carlson, Renato, GRUCAD, Univ. Federal da Santa Catarina, Brazil **(PD2)**
Carpes Jr., Walter Pereira, GRUCAD, Univ. Federal da Santa Catarina, Brazil **(PB2)**
Clemens, Markus, Univ. Fed. Armed Forces Hamburg, Germany **(PC4)**
Clénet, Stéphane, L2EP/Arts et Métiers Paris Tech, ENSAM, France **(PB7)**
De Gersem, Herbert, Katholieke Universiteit Leuven, Belgium **(PD2)**
Demenko, Andrzej, Poznan University of Technology, Poland **(OD1)**
Di Rienzo, Luca, Dipartimento di Elettrotecnica, Politecnico di Milano, Italy **(PA4)**
Dlala, Emad, Helsinki University of Technology (TKK), Finland **(PD3)**
Dular, Patrick, University of Liège, Belgium **(OB1)**
d'Assunção, Adaildo Gomes, Univ. Federal do Rio Grande do Norte, Brazil **(PB3)**
da Luz, Mauricio V. Ferreira, GRUCAD, Univ. Federal de Santa Catarina, Brazil **(PA1)**
Flores, Aly Ferreira, UFRGS, Brazil **(PC2)**
Forghani, Behzad, Infolytica Corp., Canada **(PD1)**
Françoise, Rioux-Damidaou, U2R2M, France **(PD4)**
Freschi, Fabio, Politecnico di Torino, Italy **(PD4)**
Giannacopoulos, Dennis D., McGill University, Canada **(PA3)**
Hameyer, Kay, RWTH Aachen University, Germany **(PA1)**
Henrotte, François, RWTH Aachen University, Germany **(PB5)**
Ida, Nathan, The University of Akron, United States **(OB1)**
Kawase, Yoshihiro, Dept. of Information Science, Gifu University, Japan **(PC3)**
Kladas, Antonios, National Technical University of Athens, Greece **(PC6)**
Koh, Chang Seop, Chungbuk National University, South Korea **(OD1)**
Kost, Arnulf, TU Berlin, Germany **(OC2)**

Krähenbühl, Laurent, CNRS, Université de Lyon, France **(PB1)**
Le Menach, Yvonnick, L2EP-University of Lille, France **(PC4)**
Lebensztajn, Luiz, Escola Politécnica, USP, Brazil **(PA5)**
Lowther, David, ECE Dept., McGill University, Canada **(OB2)**
Lu, Junwei, Griffith University, Australia **(PC7)**
Marechal, Yves, G2ELAB, Grenoble, France **(PB1)**
Matsuo, Tetsuji, Kyoto University, Japan **(PC5)**
Mazauric, Vincent, Schneider Electric, France **(PD1)**
Mesquita, Renato Cardoso, Universidade Federal de Minas Gerais, Brazil **(OD2)**
Muramatsu, Kazuhiro, Saga University, Japan **(PB4)**
Nabeta, Silvio, Escola Politécnica, USP, Brazil **(PA6)**
Nicolet, André, Université Paul Cézanne, France **(PC8)**
Perrussel, Ronan, CNRS, Université de Lyon, France **(PA5)**
Piriou, Francis, L2EP-University of Lille, France **(OA2)**
Preis, Kurt, IGTE, Technical University Graz, Austria **(PB6)**
Raizer, Adroaldo, GEMCO, Univ. Federal da Santa Catarina, Brazil **(PB3)**
Ramirez, Jaime, Universidade Federal de Minas Gerais, Brazil **(PB2)**
Razek, Adel, LGEP, France **(PC6)**
Ren, DaQi, The University of Tokyo, Japan **(PC7)**
Ren, Zhuoxiang, Mentor Graphics Corporation, USA **(PD3)**
Sabariego, Ruth V., University of Liège, Belgium **(PC1)**
Saldanha, Rodney R., Universidade Federal de Minas Gerais, Brazil **(PB5)**
Sartori, Carlos, Escola Politécnica, USP, Brazil **(PB4)**
Scorretti, Riccardo, CNRS, France **(PC8)**
Silva, Elson J., Universidade Federal de Minas Gerais, Brazil **(PB6)**
Silva, Viviane Cristine, Escola Politécnica, USP, Brazil **(PA3)**
Sykulski, Jan, University of Southampton, United Kingdom **(OA2)**
Takahashi, Norio, Okayama University, Japan **(OC1)**
Tounzi, Abdelmounaim, L2EP-University of Lille, France **(PA2)**
Trowbridge, Bill, Honorary President of the ICS, United Kingdom **(OA1)**
Xie, Dexin, Shenyang University of Technology, China **(OC2)**
Yamazaki, Katsumi, Chiba Institute of Technology, Japan **(PA6)**
Zhu, Jianguo, University of Technology, Sydney, Australia **(OC1)**

SCHEDULE

	Monday, 23/Nov	Tuesday, 24/Nov	Wednesday, 25/Nov	Thursday, 26/Nov
08:30 10:20	Opening Session* and OA1	OB1	OC1	OD1
<i>Coffee Break</i>				
10:40 12:10	PA1 (PSR I) PA2 (PSR I) PA3 (PSR II)	PB1 (PSR I) PB2 (PSR I) PB3 (PSR II) PB4 (PSR II)	PC1 (PSR I) PC2 (PSR I) PC3 (PSR II) PC4 (PSR II)	PD1 (PSR I) PD2 (PSR I) PD3 (PSR II) PD4 (PSR II)
<i>Lunch</i>				
13:30 15:00	PA4 (PSR I) PA5 (PSR I) PA6 (PSR II)	PB5 (PSR I) PB6 (PSR I) PB7 (PSR II)	PC5 (PSR I) PC6 (PSR I) PC7 (PSR II) PC8 (PSR II)	OD2 (13:30-15:20)
<i>Coffee Break</i>				
15:20 17:10	OA2	OB2	OC2	Closing Session
20:00			Conference Dinner	

Oral sessions take place in the **Plenary Session Room**.

PSR I: Poster Session Room I

PSR II: Poster Session Room II

* The Opening Session takes place between 08:30 and 09:00 at the Plenary Session Room

Sessions

- OA1: Static and Quasi-static Fields
- OA2: Coupled Problems
- OB1: Wave Propagation and Nanomagnetism
- OB2: Optimization
- OC1: Material Modelling and Numerical Techniques
- OC2: Devices and Applications and Electromagnetic Compatibility
- OD1: Electric Machines and Drives
- OD2: Numerical Techniques and Software Methodology
- PA1: Static and Quasi-Static Fields I
- PA2: Static and Quasi-Static Fields II
- PA3: Coupled Problems I
- PA4: Static and Quasi-Static Fields III
- PA5: Coupled Problems II
- PA6: Electrical Machines and Drives I
- PB1: Optimization I
- PB2: Optimization II
- PB3: Waves Propagation I
- PB4: Numerical Techniques I
- PB5: Optimization III
- PB6: Waves Propagation II, Nanomagnetism, Photonics and Optoelectronics
- PB7: EMC – Electromagnetic Compatibility
- PC1: Material Modelling I
- PC2: Electrical Machines and Drives II
- PC3: Devices and Applications I
- PC4: Numerical Techniques II
- PC5: Material Modelling II
- PC6: Electrical Machines and Drives III
- PC7: Numerical Techniques III
- PC8: TEAM, Education and Software Methodology
- PD1: Electrical Machines and Drives IV
- PD2: Electrical machines and Drives V
- PD3: Devices and Applications II
- PD4: Numerical Techniques IV

TECHNICAL PROGRAM

Monday, November 23rd

Session OA1: Static and Quasi-static Fields

09:00-10:30 – Room: Plenary Session Room

OA1.1	1
(Invited) Surface-Impedance Boundary Conditions in Dual Time-Domain Finite-Element Formulations	
<i>Ruth V. Sabariego, Patrick Dular, Christophe Geuzaine, Johan Gyselinck</i>	
OA1.2	3
Kriging for eddy-current testing problems	
<i>Sandor Bilicz, Emmanuel Vazquez, Szabolcs Gyimothy, Jozsef Pavo, Marc Lambert</i>	
OA1.3	5
Adaptive Parabolic-Elliptic Time Integration Method for Electroquasistatic Problems	
<i>Zsolt Badiacs</i>	
OA1.4	7
Numerical experimentations on the coupling between PEEC and volume integral method	
<i>Le Duc Tung, Chadebec Olivier, Meunier Gerard, Lembeye Yves, Guichon Jean- Michel, Delinchant Benoit</i>	

Session PA1: Static and Quasi-static Fields I

10:40-12:10 – Room: Poster Session Room I

PA1.1	9
Electromagnetic Device Analysis using a Meshless Approach coupled to a Kohonen Network	
<i>Rajeev Das, David Lowther</i>	

PA1.2	11
Hysteresis Phenomenon Implementation in FIT: Validation with Measurements	
<i>Julien Korecki, Abdelkader Benabou, Yvonnick Le Menach, Jean Pierre Ducreux, Francis Piriou</i>	
PA1.3	13
Influence of a rough thin layer on the potential	
<i>Clair Poignard, Ronan Perrussel, Ionel Ciuperca</i>	
PA1.4	15
Shell's magnetization identification from very close magnetic measurements	
<i>Yannick Vuillermet, Olivier Chadebec, Jean-Louis Coulomb, Laurent Demillier, Laure-Line Rouve, Gilles Cauffet</i>	
PA1.5	17
Interaction Body Force Field and Total Force on Permanent Magnet by Virtual Air-gap Approach	
<i>Se-Hee Lee, Young-Sun Kim, Ho-Young Lee, Heung-Geun Kim, Hong-Soon Choi</i>	
PA1.6	19
Block-preconditioning for hybrid discretisations in combination with Lagrange-multiplier coupling	
<i>Stephan Koch, Herbert De Gersem, Thomas Weiland</i>	
PA1.7	21
MHD Convection of a Electrically Conductive Fluid with Variable Thermal Conductivity	
<i>Mohsen Pirmohammadi, Majid Ghassemi, Asghar Keshtkar</i>	
PA1.8	23
Introduction of a Direct Solver at Subdomains in Non-linear Magnetostatic Analysis with HDDM	
<i>Shin-Ichiro Sugimoto, Jian Zhao, Masao Ogino, Hiroshi Kanayama, Shinobu Yoshimura</i>	
PA1.9	25
A Discrete Geometric Approach to solving 2D non-linear magnetostatic problems	
<i>Paolo Bettini, Ruben Specogna, Francesco Trevisan</i>	

PA1.10	27
Optimal Selection of the Integration Surface in the Hybrid FEM-DBCI Method	
<i>Nunzio Salerno, Giovanni Aiello, Salvatore Alfonzetti</i>	
PA1.11	29
Periodic and Anti-periodic boundary conditions with the Lagrange multipliers in the FEM	
<i>Mathieu Aubertin, Thomas Henneron, Francis Piriou, Pierre Guerin, Jean Claude Mipo</i>	
PA1.12	31
Analysis of the Ionized Field under HVDC Transmission Lines Including Wind's Effect Based on Finite Element Method	
<i>Tiebing Lu, Han Feng, Xiang Cui, Zhibin Zhao, Lin Li</i>	
PA1.13	33
A new self-consistent 3D unbounded magnetic field FE computation for electron guns	
<i>Antonino Laudani, Salvatore Coco, Giuseppe Pollicino, Paola Tirrò</i>	
PA1.14	35
Using a direct field calculation method to solve magnetostatic design inverse problem	
<i>Raphael Vilamot, Carole Henaux, Bertrand Nogarede</i>	
PA1.15	37
Calculation of the Flux Linkage of a 12/8 Dual-Channel SRM Including Mutual Coupling and Saturation: From Magnetic Circuit Model to FEM Analysis	
<i>Wen Ding, Deliang Liang</i>	
PA1.16	39
Effects of Core Materials on Magnetic Bearing Parameters	
<i>Bronislaw Zbigniew Tomczuk, Jan Zimon, Andrzej Waindok</i>	
PA1.17	41
Optimization of Electrostatic Micromotor by a Non-linear Interior Point Method	
<i>Adriano Chaves Lisboa, Rodney Rezende Saldanha, Douglas Alexandre Gomes Vieira</i>	

PA1.18	43
A Modified FEM-DBCI Method for Static and Quasi-Static Electromagnetic Field Problems	
<i>Nunzio Salerno, Giovanni Aiello, Salvatore Alfonzetti, Giuseppe Borzi', Emanuele Dilettoso</i>	
PA1.19	45
Dynamic Simulation of Surge Corona with Time-dependent Upwind Difference Method	
<i>Wei Li, Bo Zhang, Jinliang He, Rong Zeng</i>	
PA1.20	47
Using Neumann Series for Reduction of Computational Effort of Quasistatic EM-Simulations	
<i>Carsten Potratz, Daniel Kluess, Robert Souffrant, Hartmut Ewald, Ursula van Rienen</i>	
PA1.21	49
Exposure of working population to pulsed magnetic fields	
<i>Aldo Canova, Fabio Freschi, Luca Giaccone, Maurizio Repetto</i>	

Session PA2: Static and Quasi-static Fields II

10:40-12:10 – Room: Poster Session Room I

PA2.1	51
Comparative Study Applying Constant Current Source and Constant Voltage Source to Treat Cancer Using Electrochemical Therapy	
<i>Marcos Telló, Luciana Oliveira Oliveira, Rosemari Teresinha Oliveira, Orlando Parise Jr., Antonio Carlos Buzaid, Rodrigo Zanella, Helio Radke Bittencourt, Augusto Cardona</i>	
PA2.2	53
Calculation of Poynting Vector and Analysis on the Energy Transfer of Transmission Line	
<i>Fan Yang, Wei He, Yuxin Yun, Dongping Xiao</i>	
PA2.3	55
A Particle Trajectory Code using the FEM approach: preliminary results	
<i>César Candido Xavier, Cláudio Costa Motta</i>	

PA2.4	57
Hierarchical Block Wavelet Compression for BEM Problems of Arbitrary Dimension	
<i>Christian Scheiblich, Remus Banucu, Jan Albert, Veronika Reinauer, Wolfgang M. Rucker</i>	
PA2.5	59
A quick and efficient method to compute radial flux density distribution in the airgap of a superconducting inductor	
<i>Gaël Malé, Smail Mezani, Renaud Moulin, Jean Lévêque, Abderrezak Rezzoug</i>	
PA2.6	61
Solution of Dual Stochastic Static Formulations Using Double Orthogonal Polynomials	
<i>Stephane Clenet, Nathan Ida, Roman Gaignaire, Olivier Moreau</i>	
PA2.7	63
Nonlinear Eddy Current Analysis by BEM Minimum Order Formulation	
<i>Kazuhisa Ishibashi, Zoran Andjelic, David Pusch</i>	
PA2.8	65
A perturbation method for the $T-\Omega$ eddy-current formulation	
<i>Ruben Specogna, Lorenzo Codecasa, Patrick Dular, Francesco Trevisan</i>	
PA2.9	67
Electromagnetic Inspection of Outer Side Defect on Steel Tube with Steel Support using 3D Nonlinear FEM Considering of Non-Uniform Permeability and Conductivity	
<i>Yuji Gotoh, Atsushi Kiya, Norio Takahashi</i>	
PA2.10	69
Discontinuous Galerkin method with T,Phi-Phi Formulation for 3D eddy current problems	
<i>Stefan Außerhofer, Oszkár Bíró</i>	
PA2.11	71
A Mesh-Free Model of Eddy-Current Losses for 2D Analysis of Ferromagnetic Laminations	
<i>Paavo Rasilo, Antero Arkkio</i>	
PA2.12	73
Boundary Element Modelling of Earth Effects on Railway Track Transmission Line Impedances	
<i>Luca Di Rienzo, Zichi Zhang</i>	

PA2.13	75
Integral Formulation and Genetic Algorithms for Defects Geometry Reconstruction using Pulse Eddy Currents	
<i>Gabriel Preda, Mihai Rebican, Florea I. Hantila</i>	

Session PA3: Coupled Problems I

10:40-12:10 – Room: Poster Session Room II

PA3.1	77
A Coupling Procedure for Plasma, Iron and 3D Eddy Currents in the JET Tokamak	
<i>Raffaele Fresa, Raffaele Albanese, Giovanni Artaserse, Guglielmo Rubinacci, Fabio Villone, Bruno Viola</i>	
PA3.2	79
Magnetic Saturation Modeling within Finite Volume Method	
<i>Loïc Rondot, Vincent Mazauric, Gerard Meunier</i>	
PA3.3	81
Weak Coupling between Electromagnetic and Structural Models for Electrical Machines	
<i>Siegfried Rainer, Oszkár Bíró, Bernhard Weilharter</i>	
PA3.4	83
Comparing Weak and Strong PEEC-MoM Coupling	
<i>MOKHTARI Lounes, DELINCHANT Benoit, CHEVALIER Thierry, COULOMB Jean Louis</i>	
PA3.5	85
Dynamic Electro-Flow-Thermal 2D Model of a Transformer Using the CBS algorithm	
<i>Marco Arjona, R.B.B Ovando-Martínez, C Hernandez</i>	
PA3.6	87
FEM for directly coupled magneto-mechanical phenomena in electrical machines	
<i>Katarzyna Anna Fonteyn, Anouar Belahcen, Reijo Kouhia, Antero Arkkio</i>	
PA3.7	89
3D Numerical Modeling of the Thermo-Inductive Technique Using Shell Elements	
<i>Brahim Ramdane, Didier Trichet, Mohamed Belkadi, Javad Fouladgar</i>	

PA3.8	91
Coupled Mechanical-Electrical-Thermal Modeling of Electric Contacts based on the Cell Method	
<i>Federico Moro, Carmelo Majorana, Massimo Guarnieri, Mazzucco Gianluca</i>	
PA3.9	93
Improvements to convergence of coupled nonlinear circuit modelling	
<i>Simon Taylor, Nick Robertson, John Simkin</i>	
PA3.10	95
Particular Electromagnetic Field Computation for Permanent Magnet Generator Wind Turbine Analysis	
<i>Charalampos Patsios, Antonios Chaniotis, Evagelos Tsambouris, Antonios Kladas</i>	
PA3.11	97
A Fully Coupled Three-dimensional Dynamic Model of Polymeric Membranes for Fuel Cells	
<i>Massimo Guarnieri, Piergiorgio Alotto, Federico Moro</i>	
PA3.12	99
Coupled 3D Fluid Flow-Thermal FEM Model for Power Transformer Temperature Analysis	
<i>Marina Antonios Tsili, Eleftherios Ioannis Amoiralis, Antonios Kladas, Athanassios Souflaris</i>	
PA3.13	101
Inductively Heated Incompressible Flow of Electrically Conductive Liquid in Pipe	
<i>Ivo Dolezel, Lenka Dubcova, Pavel Karban, Jakub Cerveny, Pavel Solin</i>	
PA3.14	103
Equivalent stress criteria for the effect of stress on magnetic behavior	
<i>Laurent DANIEL, Olivier HUBERT</i>	
PA3.15	105
Shape Formation of Ferrofluid Droplet in Magnetic Field and Gravity by FEA coupled with LSM	
<i>Young Sun Kim, Il Han Park</i>	

Session PA4: Static and Quasi-Static Fields III

13:30-15:00 – Room: Poster Session Room I

PA4.1	107
FEM/BEM Hybrid Method for Magnetic Field Evaluation Due to Underground Power Cables	
<i>Vitor Malo Machado</i>	
PA4.2	109
Voltage and current sources for massive conductors suitable with the $A-\chi$ Geometric Formulation	
<i>Ruben Specogna, Pawel Dlotko, Francesco Trevisan</i>	
PA4.3	111
Efficient Computation of Eddy Current losses in SMC PM machines with 3D Time-Harmonic FEA	
<i>Ahmed Chebak, Philippe Viarouge, Jérôme Cros</i>	
PA4.4	113
Decoupling of Nonequidistant Time Steps by Fixed Point Method for Nonlinear Eddy Currents	
<i>Gergely Koczka, Oszkár Bíró</i>	
PA4.5	115
Homogenization for periodical electromagnetic structure: which formulation?	
<i>Gerard Meunier, Vincent Charmoille, Christophe Guerin, Patrice Labie</i>	
PA4.6	117
Geometric interpretation of frequency-domain surface-impedance boundary conditions	
<i>Herbert De Gersem</i>	
PA4.7	119
Field Analysis for Thin Shields in the Presence of Ferromagnetic Bodies	
<i>Ioan R. Ciric, Florea I. Hantila, Mihai Maricaru</i>	
PA4.8	121
Evaluating the Guidance Force Capabilities of Flat Passive Maglev Guideway Topologies Using the A-phi Formulation	
<i>Jonathan Bird</i>	

PA4.9	123
Improved Accuracy of Electro-Quasistatic Simulations of Large-Scale 3D High Voltage Equipment Including Nonlinear Field-Grading	
<i>Daniel Weida, Thorsten Steinmetz, Markus Clemens</i>	
PA4.10	125
3-D Calculation of Surface Electric Field around Conductor of UHVAC Transmission Lines	
<i>Dongping XIAO, Wei HE, Mingyou CHEN, Fan YANG</i>	
PA4.11	127
Analytical Prediction of Eddy-Current Loss in Armature Windings of Permanent Magnet Brushless AC Machines	
<i>Yacine Amara, Pascal Reghem, Georges Barakat</i>	
PA4.12	129
Complementarity of Dual Eddy Current Formulations on Dual Meshes	
<i>Zhuoxiang Ren, Hui Qu</i>	
PA4.13	131
Numerical Model of Transient Electromagnetic Field around the Grounding System by FEM	
<i>Anton Habjanic, Marko Jesenik, Mladen Trlep</i>	
PA4.14	133
A New Formulation Using Differential Permeability Based on the Source-Field Method	
<i>Nelson Sadowski, João Pedro Assumpção Bastos, Jean Viane Leite</i>	
PA4.15	135
Homogenization of Form-Wound Windings in Finite Element Modelling of Electrical Machines	
<i>Johan Gyselinck, Ruth V. Sabariego, Patrick Dular, Nelson Sadowski, Patrick Kuo-Peng</i>	
PA4.16	137
Electrokinetic Model Refinement via a Perturbation Finite Element Method – From 2-D to 3-D	
<i>Mauricio Valencia Ferreira da Luz, Patrick Dular, Ruth V. Sabariego, Patrick Kuo-Peng, Nelson Jhoe Batistela</i>	
PA4.17	139
Magneto-convection in an Enclosure with Partially Active Vertical Walls	
<i>Mohsen Pirmohammadi, Majid Ghassemi</i>	

PA4.18	141
Comparison between BEM + ACA and classical FEM for 3D low-frequency eddy-current analysis	

David Pusch, Jasmin Smajic, Zoran Andjelic

PA4.19	143
An Energy-Based Error Criterion for Eddy Current Transient Analysis	

Loïc Rondot, Dimitrios Ladas, Vincent Mazauric

PA4.20	145
Magneto-Mechanical effects under low fields and high stresses - Application to a ferromagnetic cylinder under pressure	

Antoine Viana, Laure-Line Rouve, Gilles Cauffet, Jean-Louis Coulomb

Session PA5: Coupled Problems II

13:30-15:00 – Room: Poster Session Room I

PA5.1	147
Large-Scale Analysis of Magnetic Beads Behavior in Magnetic Field with Fast Multipole Method	

Takuya Tatsuishi, Yasuhito Takahashi, Masahiko Miwa, Shinji Wakao

PA5.2	149
Dynamic Analysis Method of Linear Resonant Actuator with Multi-Movers Employing 3-D Finite Element Method	

Yasuyoshi Asai, Katsuhiko Hirata, Tomohiro Ota

PA5.3	151
New FEM Approach for Multi Physics Problems Modeling in EPM Applications	

Yves Du Terrail Couvat, Annie Gagnoud

PA5.4	153
Analysis of Transient Eddy Current and Conductor Motion in an Electromagnetic Repulsion Mechanism with Meshless Collocation Method	

Guangyuan Yang, K.R. Shao, Youguang Guo, Jianguo Zhu

PA5.5	155
Coupled Magneto-Thermal FEM Model of Direct Heating of Ferromagnetic Bended Tubes	

Michele Forzan, Alexandr Aliferov

PA5.6	157
Streamer Simulation based on Discontinuous Galerkin Method and Hierarchical Reconstruction	
<i>Chijie Zhuang, Rong Zeng, Bo Zhang, Shuiming Chen, Jinliang He</i>	
PA5.7	159
Buoyancy Force Evaluation on Nonmagnetic Solid Object Submerged in Magnetic Liquid Subjected to Non-uniform Magneto-static Field	
<i>Hong Soon Choi, Young Sun Kim, Il Han Park</i>	
PA5.8	161
Field-circuit Co-simulation of Controllable Reactor using Integral Equation Method	
<i>Yang Xiaobo, Zoran Andjelic, Cherry Yuen</i>	
PA5.9	163
Steady and Transient Electromagnetic-thermal Fields Analysis for Induction Machines Using FEM and FVM	
<i>Shuhong Wang, Qiuwang Wang, Zhe Ren, Wei Sun, Dan Liao, Jie Qiu, Limin Zhou, Youming Jiang, Jian Guo Zhu, Youguang Guo, Yi Wang, Wei Xu</i>	
PA5.10	165
Electromagnetic-Structure-Acoustic Coupled Analysis Method of GMM Transducer Speaker	
<i>Katsuhiro Hirata, Byungjin Yoo, Atsurou Oonishi</i>	
PA5.11	167
3D Transient Field-Circuit Modeling of Inductive Fault Current Limiters	
<i>Dalibor Cvoric, Domenico Lahaye, Sjoerd W.H. de Haan, J. Abraham Ferreira</i>	
PA5.12	169
Hybrid Analytical-FEM Method for Microwave Heating Analysis in a Single Mode Cavity	
<i>Diogo Batista Oliveira, Elson Jose Silva</i>	
PA5.13	171
Distributed Models for Air-Core Ethernet Transformers	
<i>Isaak Mayergoyz, David Bowen, Charles Krafft</i>	
PA5.14	173
Dynamic simulation of an electromechanical energy scavenging device	
<i>Aldo Canova, Elvio Bonisoli, Fabio Freschi, Sandro Moos, Maurizio Repetto, Stefano Tornincasa</i>	

PA5.15	175
Accurate Control of Position by Induction Heating-Produced Thermoelasticity	
<i>Ivo Dolezel, Pavel Karban, Petr Kropik, David Panek</i>	
PA5.16	177
Physics Based High Frequency Transformer Modeling by Finite Elements	
<i>Osama A Mohammed, Nagy Y Abed</i>	
PA5.17	179
Permanent Magnet Motor Damping Analysis by using a particular 2D FEM technique	
<i>Minos E. Beniakar, Themistoklis D. Kefalas, Antonios G. Kladas</i>	
PA5.18	181
Performance Investigation of Canned Induction Motor for Coolant Pump in Nuclear Reactor	
<i>Jian Li, Jungtae Song, Yunhyun Cho</i>	
PA5.19	183
Field-Circuit Method for the Non-Steady State Analysis in the Active Magnetic Bearings	
<i>Bronislaw Zbigniew Tomczuk, Jan Zimon, Andrzej Waindok</i>	
PA5.20	185
Study of a double-star synchronous machine fed by a dual Voltage Source Inverter	
<i>André de Andrade, Meynard, Thierry:Nelson Sadowski, Patrick Kuo-Peng</i>	
PA5.21	187
Magneto-elastic finite element modeling based on a multiscale approach	
<i>Xavier Mininger, Laurent Daniel, Laurent Santandrea, Laurent Bernard, Frédéric Bouillault</i>	

Session PA6: Electrical Machines and Drives I

13:30-15:00 – Room: Poster Session Room II

PA6.1	189
Novel Design Method of a Single-phase Induction Motor considering Magnetic Balance	
<i>Myoung-Hyun Choi, Byung-Taek Kim</i>	

PA6.2	191
Finite-Element Analysis for a Rolling-Rotor Electrical Machine	
<i>Antero Arkkio, Grzegorz Kaminski, Asko Niemenmaa, Pawel Staszewski</i>	
PA6.3	193
Numerical Modelling of Transformer Inrush Current	
<i>Ermanno Cardelli, Vincenzo Esposito, Antonio Faba</i>	
PA6.4	195
Gaussian Modulated Pulse Excitation for SM Parameter Estimation Using a 2D-FE Model	
<i>Marco Arjona, Concepcion Hernandez, Merit Cisneros-Gonzalez</i>	
PA6.5	197
Efficient FEA Identification of Equivalent Circuit Inductances for DFIM Design	
<i>Davide Aguglia, René Wamkeue, Philippe Viarouge, Jérôme Cros</i>	
PA6.6	199
Comparison of Analytical and Finite Element Calculation of Eddy-Current Losses in the Solid Back-Iron of PM Machines with Concentrated Fractional Pitch Windings	
<i>Anoop Jassal, Henk Polinder, Domenico Lahaye</i>	
PA6.7	201
Numerical Analysis of the Induced Current in an XY-Actuator with Soft Magnetic Composite	
<i>Nolvi Francisco Baggio Filho, Ály Ferreira Flores Filho</i>	
PA6.8	203
Least Square Support Vector Machine Network-Based Modeling for Switched Reluctance Starter/Generator	
<i>Wen Ding, Deliang Liang</i>	
PA6.9	205
An Accurate Magnetic Field analysis for Estimating Motor Characteristics Taking Account of Elasto-Plastic Deformation in the Magnetic Core	
<i>Shinichi Yamaguchi, Akihiro Daikoku, Yoshihiro Tani, Toshinori Tanaka, Chiyo Fujino</i>	
PA6.10	207
Calculation of Radial Forces in Cage Induction Motors at Start – the Effect of Rotor Differential	
<i>David George Dorrell</i>	

PA6.11	209
Eddy-current Losses and Temperature Rise in the Form-wound Stator Winding of an Inverter-fed Cage Induction Motor	
<i>Mohammad Jahirul Islam, Huynh Van Khang, Anna-Kaisa Repo, Antero Arkkio</i>	
PA6.12	211
Semi-Analytical Solution of Cogging Torque in SMPMM	
<i>Frédéric Dubas, Christophe Espanet</i>	
PA6.13	213
Interactive Postprocessing Formulations in 3D	
<i>Martin Hafner, Marc Schöning, Marcin Antczak, Andrzej Demenko, Kay Hameyer</i>	
PA6.14	215
Comprehensive Magnetic Model of Surface Mounted PM Machines Incorporating Saturation Saliency	
<i>Yi Wang, Jianguo Zhu, Youguang Guo, Shuhong Wang, Wei Xu</i>	
PA6.15	217
Magnetic Field in an Axial-Flux Permanent-Magnet Synchronous Generator	
<i>Tze-Fun Chan, Weimin Wang, Loi Lei Lai</i>	
PA6.16	219
Unified Scheme for Implementing the Fixed-Point and Newton-Raphson Methods in Finite-Element Programs of Electromagnetic Field Problems	
<i>Emad Dlala, Antero Arkkio</i>	
PA6.17	221
Parametric Design Coupled with Dynamic Equation of the BLDC Motor for Electric Vehicle	
<i>YoungKyoung Kim, Se-Hyun Rhyu, Jung-Pyo Hong</i>	

Session OA2: Coupled Problems

15:20-17:10 – Room: Plenary Session Room

OA2.1	223
(Invited) Discrete Magneto-Elasticity: A geometrical approach	
<i>Alain Bossavit</i>	
OA2.2	225
Nonlinear coupled FE-circuit model for th optimization of hybrid motors	
<i>Nouredine Takorabet, Eric D. Kenmoe-Fankem, Farid Meibody-Tabar, Francois. M. Sargos</i>	

OA2.3	227
Co-Simulation as Multirate Time Integration of Field/Circuit Coupled Problems	
<i>Sebastian Schoeps, Andreas Bartel, Herbert De Gersem</i>	
OA2.4	229
Efficient Numerical Modelling of Field Diffusion in High-Temperature Superconducting Wires	
<i>Igor O. Golosnoy, Jan K. Sykulski</i>	
OA2.5	231
Unipolar and Bipolar Charge Injection and Transport in Dielectric Liquid by Finite Element Method	
<i>Se-Hee Lee, Il-Han Park, Francis O’Sullivan, Markus Zahn</i>	

Tuesday, November 24th

Session OB1: Wave Propagation and Nanomagnetism

08:30-10:20 – Room: Plenary Session Room

- OB1.1** 233
(Invited) Masking with Generalized Cloaking
Andre Nicolet, Frederic Zolla, Christophe Geuzaine
- OB1.2**235
Micromagnetic Analysis of a Shielded Write Head Using Symmetric
Multiprocessing System
*Yasushi Kanai, Kazuya Koyama, Manabu Ueki, Toshio Tsukamoto, Kazuetsu
Yoshida, Simon Greaves, Hiroaki Muraoka*
- OB1.3**237
Efficient implementation of UPML in the finite integration technique using
hexahedral and prismatic elements
Ruben Torrado, Laurent Bernard, Lionel Pichon
- OB1.4** 239
An Electromagnetic Field Computation Using Space-Time Grid and FIT
Tetsuji Matsuo
- OB1.5**241
Solution of the frequency domain Maxwell equations by a high order non-
conforming discontinuous Galerkin method
Stéphane Lanteri, Mohamed El Bouajaji, Victorita Dolean, Ronan Perrussel

Session PB1: Optimization I

10:40-12:10 – Room: Poster Session Room I

- PB1.1** 243
Identification of Hidden Ferrous 3D Objects Using a GMR Sensor Array
*Alice Köstinger, Michael Jandl, Markus Kienesberger, Christian Magele, Werner
Renhart, Gunter Winkler*
- PB1.2** 245
Multiobjective Particle Swarm Approach for the Design of a Brushless DC
Wheel Motor
Leandro dos Santos Coelho, Leandro Zavarez Barbosa, Luiz Lebensztajn

PB1.3	247
Coupling Particles Swarm Optimization for Multimodal Function Optimization	
<i>Minh-Trien Pham, Baatar Nyambayar, Chang Seop Koh</i>	
PB1.4	249
Automatic Differentiation Applied for Optimization of Dynamical Systems	
<i>Petre Enciu, Laurent Gerbaud, Frederic Wurtz</i>	
PB1.5	251
Influence of Sensor Variations on the Condition of the Magnetostatic Linear Inverse Problem	
<i>Roland Eichardt, Jens Haueisen</i>	
PB1.6	253
The application of topological gradients to defect identification in magnetic flux leakage-type NDT	
<i>Min Li, David Lowther</i>	
PB1.7	255
Grid-enabled Tabu Search for Electromagnetic Optimization Problems	
<i>Sara Carcangiu, Alessandra Fanni, Anna Mereu, Augusto Montisci</i>	
PB1.8	257
An Exact Optimization Code Combined with a Hybrid Model for Magnetic Couplings Design	
<i>Julien Fontchastagner, Frederic Messine, Yvan Lefevre</i>	
PB1.9	259
Electromagnetic Device Design Based on New Sequential Optimization Strategies	
<i>Gang Lei, Keran Shao, Youguang Guo, Jianguo Zhu, J. D. Lavers</i>	
PB1.10	261
A Metaheuristic Algorithm for Multiobjective Designs of Inverse Problems	
<i>S.L. Ho, Shiyong Yang</i>	
PB1.11	263
The Use of Feature Selection to Create a Compact Prototype for Electromagnetic Device Optimization	
<i>Jun Ouyang, David Lowther</i>	

PB1.12	265
Optimization of Electromagnetic and Magnetic Shielding using ON/OFF Method	
<i>Norio Takahashi, Shunsuke Nakazaki, Daisuke Miyagi</i>	
PB1.13	267
Reducing the Design Space of Standard Electromagnetic Devices using Bayesian Response Surfaces	
<i>Linda Wang, David A. Lowther</i>	
PB1.14	269
Nonlinear Filtering on Mesh Discretization Errors by Neural Networks	
<i>Douglas Alexandre Gomes Vieira, Adriano Chaves Lisboa, Vasile Palade, Rodney R. Saldanha</i>	
PB1.15	271
Particle Swarm Optimization of Coupled Electromagnetic-Electromechanical Systems	
<i>Nizar F. Al-Aawar, Toufic M. Hijazi, Abdul Rahman A. Arkadan</i>	
PB1.16	273
Self-Adjoint Material Sensitivity Analysis for Solving Inverse Problems in RF Domain	
<i>Dong-Hun Kim, Jin-Kyu Byun, Hyang-Beom Lee, Hyeong-Seok Kim</i>	
PB1.17	275
Spatio-temporal reconstruction of magnetic nanoparticle distributions	
<i>Daniel Baumgarten, Jens Haueisen</i>	
PB1.18	277
Non-Iterative Methods for Locating Inclusions in Electrical Impedance Tomography	
<i>Flavio Calvano, Guglielmo Rubinacci, Antonello Tamburrino</i>	
PB1.19	279
A Research of PTP MRAM about Shape Optimization for High Gb/Chip	
<i>Hyuk Won, Gwan Soo Park, Dong Sok Kim, Jae Min Kim</i>	
PB1.20	281
Brain source localization: a MILP approach	
<i>Fabio Freschi</i>	

PB1.21	283
A Hybrid Design of Distribution Transformers Using 2D-FE and a Conventional Method	
<i>Marco Arjona, Concepcion Hernandez</i>	
PB1.22	285
Inverse Magnetic Field Calculation For Underground Grid Condition Monitoring	
<i>Sheppard Salon, MVK Chari, J. Braunstein, J. Selvaggi</i>	
PB1.23	287
A Practical Approach to Robust Design of an RFID Triple-Band PIFA Structure	
<i>Jae-Hyeong Ko, Dong-Hun Kim, Hyang-Beom Lee, Hyeong-Seok Kim</i>	
PB1.24	289
Parameter Extraction and Optimal Design of Spiral Inductor Using Evolution Strategy and Sensitivity	
<i>Jae-Hyeong Ko, Jin-Kyu Byun, Hyeong-Seok Kim</i>	

Session PB2: Optimization II

10:40-12:10 – Room: Poster Session Room I

PB2.1	291
Optimization of perfectly matched layer parameters for finite element modeling of grounding systems	
<i>Luiz Lebensztajn, Viviane Cristine Silva, Lucas Blattner Martinho</i>	
PB2.2	293
Corrosion diagnosis of a ship mock-up from near electric field measurements	
<i>Arnaud Guibert, Jean-Louis Coulomb, Olivier Chadebec, Corinne Rannou</i>	
PB2.3	295
Dynamic Multiobjective Clonal Selection Algorithm for Engineering Design	
<i>Lucas de Souza Batista, Diogo Oliveira, Frederico Gadelha Guimaraes, Elson Jose Silva, Jaime Arturo Ramirez</i>	
PB2.4	297
Stochastic uncertainty quantification of the conductivity in EEG source analysis by using polynomial chaos decomposition	
<i>Roman Gaignaire, Guillaume Crevecoeur, Luc Dupré, Christophe Geuzaine, Patrick Dular</i>	

PB2.5	299
The EMC Method Applied to the Design of Local and Asymmetric Gradient Coils for MRI	
<i>Hector Sanchez Lopez, Michael Poole, Feng Liu, Stuart Crozier</i>	
PB2.6	301
Two complementary methods to face with convexity issues in topology optimization problems	
<i>Thibaut Labbé, François Glineur, Bruno Dehez</i>	
PB2.7	303
A Multiobjective Gaussian Particle Swarm Approach Applied to Electromagnetic Optimization	
<i>Piergiorgio Alotto, Leandro dos Santos Coelho, Helon Vicente Hultmann Ayala</i>	
PB2.8	305
Magnetic Field Synthesis in the Design of Inductors for Magnetic Fluid Hyperthermia	
<i>Fabrizio Dughiero, Paolo Di Barba, Elisabetta Sieni</i>	
PB2.9	308
Stochastic Finite Element Analysis for Parasitic Extraction of Interconnects with Material Parameter Variations	
<i>Xiaoyu Xu, Hui Qu, Li Kong, Zhuoxiang Ren</i>	
PB2.10	310
Kriging assisted design of a synchronous superconducting generator with YBCO windings	
<i>Bartosz Lukasik, Kevin Goddard, Mihai Rotaru, Jan K. Sykulski</i>	
PB2.11	312
Multiobjective Efficient Global Optimization – A Win-win Approach to Optimal Design and Model Development	
<i>Alexandru Claudiu Berbecea, Sangkla Kreuawan, Frédéric Gillon, Pascal Brochet</i>	
PB2.12	314
Parallel hybrid algorithms based on Artificial Life for Multimodal Optimization	
<i>Francesco Riganti Fulginei, Alessandro Salvini, Antonino Laudani, Salvatore Coco</i>	
PB2.13	316
Two-level refined direct method for electromagnetic optimization and inverse problems	
<i>Guillaume Crevecoeur, Ahmed Abou-Elyazied Abdallah, Luc Dupré</i>	

PB2.14	318
Application of Response Surface Methodology to Electric Machine Design with Multivariate Adaptive Regression Splines	
<i>Kenta Takayasu, Asuka Otake, Masahiko Miwa, Shinji Wakao, Tamio Okutani, Yasuhito Takahashi, Masahiro Tanai, Kazuhiko Onda</i>	
PB2.15	320
A Research on the Optimm Design of Magnet Structure for Improving Measurement Accuracy in the Dual Magnetic Float Type Level Gauge	
<i>Dong Sok Kim, Jae Min Kim, Gwan Soo Park</i>	
PB2.16	322
Examination of Optimal Design of IPM Motor using ON/OFF Method	
<i>Norio Takahashi, Takaya Yamada, Daisuke Miyagi</i>	
PB2.17	324
Optimization of Inductors Using Evolutionary Algorithms and Its Experimental Validation	
<i>Kota Watanabe, Felipe Campelo, Yosuke Iijima, Kenji Kawano, Tetsuji Matsuo, Takeshi Mifune, Hajime Igarashi</i>	
PB2.18	326
Multiobjective Optimization of Electrooptic Modulators with Floating Electrodes	
<i>Ademar Muraro Jr, André Cortes, Angelo Passaro, Nancy Mieko Abe, Airam J. Preto, Stephan Stephany</i>	
PB2.19	328
A Multi-frequency Strategy for Reconstruction of Deep Stress Corrosion Cracks from ECT Signals of Multiple Liftoffs	
<i>Li Wang, Zhenmao Chen</i>	
PB2.20	330
Accelerating Evolution Algorithm Using Kriging Metamodel	
<i>Dong-kung Woo, Jang-Ho Seo, Chany Lee, Hyun-Kyo Jung</i>	
PB2.21	332
Topology Optimization of Electrostatic Actuator Using Level Set Method and Shape Design Sensitivity	
<i>Young Sun Kim, Il Han Park</i>	

PB2.22	334
Electromagnetic Characterization of Biological Tissues with Particle Swarm Optimization	
<i>Nicolas Siauue, Corine Lormel, Romain Marion, Julien Dardenne, Fabien Sixdenier</i>	

Session PB3: Waves Propagation I

10:40-12:10 – Room: Poster Session Room II

PB3.1	336
Analysing the Relevant Features of GPR Scattered Waves in Time- and Frequency-Domain	
<i>Lucas Travassos, D. A. G. Vieira, V. Palade, N. Ida</i>	
PB3.2	338
Recent developments on a DGTD method for time domain electromagnetics	
<i>Stéphane Lanteri, Hassan Fahs, Loula Fezoui, Victorita Dolean, Francesca Rapetti</i>	
PB3.3	340
Detection of Defects in Wiring Networks using Time Domain Reflectometry	
<i>Smail Mostafa Kamel, Pichon Lionel, Olivas Marc, Auzanneau Fabrice, Lambert Marc</i>	
PB3.4	342
Finite Element Multiharmonic Modelling for Nonlinear Optics	
<i>Pierre Godard, Frederic Zolla, Andre Nicolet</i>	
PB3.5	344
An Amplitude Finite Element Formulation for Multiple-Scattering by a Collection of Convex Obstacles	
<i>Christophe Geuzaine, Patrick Dular, Roman Gaignaire, Ruth Sabariego</i>	
PB3.6	346
Finnite element analysis of electromagnetic scattering using p-adaption and an Iterative absorbing boundary condition	
<i>Prakash Paul, Jon Webb</i>	
PB3.7	348
Investigation on the shading effect of reinforced concrete construction to lightning radiation field based on TDIE method	
<i>Zhibin Zhao, Mingxia Zhang, Xiang Cui, Lin Li, Tiebing Lu</i>	

PB3.8	350
2D Scattering Integral Field Equation Solution through a IMLS Meshless-Based Approach	
<i>Williams Lara Nicomedes, Renato Cardoso Mesquita, Fernando José da Silva Moreira</i>	
PB3.9	352
Numerical Techniques for Multi-Objective Synthesis of an Inverted-S Antenna	
<i>Lei Liu, Junwei Lu, Shiyong Yang, Guangzheng Ni</i>	
PB3.10	354
Blending PSO and ANN for Optimal Design of FSS Filters with Koch Island Patch Elements	
<i>Rossana M. S. Cruz, Paulo H. da F. Silva, Adaildo Gomes d'Assunção</i>	
PB3.11	356
Coefficients of Finite Difference Operator for Rectangular Cell NS-FDTD Method	
<i>Tadao Ohtani, Kenji Taguchi, Tatsuya Kashiwa, Yasushi Kanai</i>	
PB3.12	358
Investigation of UHF Circular Loop Antennas for RFID	
<i>Kurt Preis, Thomas Bauernfeind, Oszkar Biro, Igor Ticar</i>	
PB3.13	360
Full Wave Analyses of Electromagnetic Fields with an Iterative Domain Decomposition Method	
<i>Amane Takei, Shin-ichiro Sugimoto, Masao Ogino, Shinobu Yoshimura, Hiroshi Kanayama</i>	
PB3.14	362
A New Waveguide Design Based in Thin Films of Niobium and Tantalum	
<i>Marcílio Nunes Freire, José Patrocínio da Silva</i>	
PB3.15	364
Analysis of Simple FSS Cascading With Dual Band Response	
<i>Antonio Luiz Pereira de Siqueira Campos, Robson Hebraico Cipriano Maniçoba, Lincoln Machado de Araújo, Adaildo Gomes d'Assunção</i>	
PB3.16	366
A broadband symmetric surface integral equation based on Calderón projector	
<i>Annalisa Buffa, Guglielmo Rubinacci, Antonello Tamburrino</i>	

PB3.17..... 368
Local Timestepping Techniques Using Taylor Expansion for Modeling
Electromagnetic Wave Propagation with Discontinuous Galerkin - FEM
Steffen Schomann

PB3.18 370
Safety Assessment of UWB Radio Systems for Body Area Network by the
FDTD Method
Valerio De Santis, Mauro Feliziani, Francescaromana Maradei

Session PB4: Numerical Techniques I

10:40-12:10 – Room: Poster Session Room II

PB4.1.....372
Computation Method for Transients in Underground Cables with Lossy Earth
Return Path
Xose M. Lopez-Fernandez, Casimiro Alvarez-Mariño, Vitor Malo Machado

PB4.2374
FDTD Analysis of a Metamaterial with Particles Having Oh Point Group
Symmetry
Tiago Carvalho Martins, Victor Dmitriev

PB4.3376
Discrete Constitutive Relations for the Discrete Geometric Approach over
Hexahedral Grids
Ruben Specogna, Lorenzo Codecasa, Francesco Trevisan

PB4.4 378
Domain Decomposition Methods with Second Order Transmission Conditions
for Solving Multiscale Electromagnetic Wave Problems
Zhen Peng, Vineet Rawart, Jin-Fa Lee

PB4.5 380
Improving the Mixed Formulation for Meshless Local Petrov–Galerkin
Method
*Alexandre Ramos Fonseca, Bruno Carvalho Corrêa, Elson José da Silva, Renato
Cardoso Mesquita*

PB4.6 382
Effectiveness of Higher Order Time Integration in Time Domain Finite
Element Analysis
Yoshifumi Okamoto, Koji Fujiwara, Yoshiyuki Ishihara

PB4.7	384
Extended Meshfree Point Collocation Method for Electromagnetic Problems with Layered Singularity	
<i>Young-Cheol Yoon, Do Wan Kim</i>	
PB4.8	386
Strategies for accelerating non-linear convergence for T- Ω formulation	
<i>Ping Zhou, Dingsheng Lin, Bo He, Sameer Kher, Zoltan Cendes</i>	
PB4.9	388
Shape Optimization of Rotating Machines Using Time-Stepping Adaptive Finite-Element Method	
<i>Katsumi Yamazaki, Yuji Kanou</i>	
PB4.10	390
Algorithmically Efficient Ray Tracing for the Simulation of Wall Heating in Particle Accelerator Structures	
<i>Eike Michael Scholz, Markus Clemens, Martin Dohlus</i>	
PB4.11	392
Hierarchical Sparsified Models for the Substrate of Integrated Circuits	
<i>Daniel Ioan, Gabriela Ciuprina</i>	
PB4.12	394
SUPG 3D vector potential formulation for electromagnetic braking simulations	
<i>François Henrotte, Enno Lange, Holger Heumann, Kay Hameyer</i>	
PB4.13	396
Robust FEM-BEM Coupling for Magnetostatics on multi-connected Domains	
<i>David Pusch, Joerg Ostrowski</i>	
PB4.14	398
Edge element multigrid solution of time-harmonic 3-D non-linear eddy- current problems	
<i>Chao Chen, Oszkár Bíró</i>	
PB4.15	400
FE Analysis of Magnetic Particle Dynamics on Fixed Mesh with Level Set Function	
<i>Young Sun Kim, Myung Ki Baek, Il Han Park</i>	

PB4.16	402
A Step Forward in Wavelet-Based Algebraic Multigrid Method Using the Lifting Technique	
<i>Fabio Henrique Pereira, Silvio Ikuyo Nabeta</i>	
PB4.17	404
Solution of Static Field Problems with Random Domains	
<i>Stephane Clenet, Duy Hung Mac, Jean-Claude Mipo, Olivier Moreau</i>	
PB4.18	406
Quality Evaluation of Automatically Generated Hexahedral Mesh for FEA	
<i>Yuichiro Motooka, So Noguchi, Hajime Igarashi</i>	
PB4.19	408
Parallel Sparse Matrix Solver on the GPU Applied to Simulation of Electrical Machines	
<i>Wendell O. Rodrigues, Frédéric Guyomarc'h, Jean-Luc Dekeyser, Yvonnick Le Menach</i>	

Session PB5: Optimization III

13:30-15:00 – Room: Poster Session Room I

PB5.1	410
Design of Conventional C-core Magnets Using a Multi-Step Optimization Procedure	
<i>Felipe Campelo, Jaime Arturo Ramirez, Hajime Igarashi</i>	
PB5.2	412
Self-consistent Optimization of Multi-Quantum Well Structures by a Genetic Algorithm	
<i>Angelo Passaro, Roberto Yuji Tanaka, Ademar Muraro Jr., Gustavo S. Vieira, Nancy Mieko Abe</i>	
PB5.3	414
Impact of Wave Propagation Effects in Electrical Tomography	
<i>Markus Neumayer, Gerald Steiner</i>	
PB5.4	416
Optimal Design of Electromagnetic Valve Actuator using Generic Algorithm	
<i>Jinho Kim, Junghwan Chang, Kyuyoung Han</i>	

PB5.5	418
Niched Pareto-Archived Evolutionary Programming for Multi-Objective Electromagnetic Optimization	
<i>Nunzio Salerno, Emanuele Dilettoso, Santi Agatino Rizzo</i>	
PB5.6	420
Optimization of Vibratory Behavior of Electromagnetic Devices through Material Properties Evaluation	
<i>Ferkha Nassira, Mekideche Mohamed Rachid, Miraoui Abdellatif, Djerdir Abdesslem</i>	
PB5.7	422
An Improved Continuous Genetic Algorithm for Electromagnetic Optimization	
<i>Paulo H. da F. Silva, Rossana M. S. Cruz, Adaildo Gomes d'Assunção</i>	
PB5.8	424
Differential Evolution-based Technique for Thermal Parameters Identification of a Transformer FEM model	
<i>Adnan Glotic, Joze Pihler, Nermin Sarajlic, Mensur Kasumovic, Majda Tesanovic</i>	
PB5.9	426
Multi-objective Optimization of an Axial Flux Wind Generator	
<i>João Antônio Vasconcelos, Selênio Rocha Silva, Laís Martins Araújo, Claret Laurente Sabioni, Jonas Alves de Almeida Pereira, Moisés Ferber de Vieira Lessa, Bruno Marciano Lopes</i>	
PB5.10	428
GA-based optimized design of the novel compact transversal-type UWB bandpass filter	
<i>Sungtek Kahng, Eunchul Shin, Koon-Tae Kim, Hyeong-Seok Kim</i>	
PB5.11	430
Software Methodology for Optimization of Weakly Coupled Multiphysical Problems using Object Oriented Programming	
<i>Michael Jaendl, Alice Köstinger, Ralph Kutschera, Christian Magele, Werner Renhart</i>	
PB5.12	432
Sensitivity based generation of optimized data set for ECT inversion	
<i>Szabolcs Gyimothy, Imre Kiss, Jozsef Pavo, Sandor Bilicz</i>	

PB5.13	434
Dynamic Multilevel Optimization of Machine Design and Control Parameters for PMSM Drive System Based on Correlation Analysis	
<i>Shuhong Wang, Xiangjun Meng, Jie Qiu, Jian Guo Zhu, Yi Wang, Youguang Guo, Dikai Liu, Wei Xu</i>	
PB5.14	436
Variational Level Set Methods in the Roentgen Images Segmentation	
<i>Tomasz Rymarczyk, Stefan Franciszek Filipowicz, Jan Sikora, Marek Tymburski</i>	
PB5.15	438
Numerical tool for the design of magnetic sensors based on GMI effect	
<i>Lena ABI RACHED, Francisco ALVES, Yann LE BIHAN</i>	
PB5.16	440
Harmony Search with Cauchy Operator Applied to the Hysteresis Modeling of a Transformer	
<i>Leandro dos Santos Coelho, Viviana Cocco Mariani</i>	
PB5.17	442
Automatic Design of Insulation Structure of Power Transformer Based on Sensitivity Analysis	
<i>Liu Yang</i>	
PB5.18	444
The Use of Case-Based Reasoning in Creating a Prototype for Electromagnetic Device Optimization	
<i>Jun Ouyang, David Lowther</i>	
PB5.19	446
Slot Shape Optimization for Permanent Magnet Synchronous Machines by Evolution Strategy and Time-Stepped Finite Element Analysis	
<i>Yang Zhan, Andrew M. Knight</i>	
PB5.20	448
Numerical-analytical coupled optimization of a echatronic system with particular attention to the embedded linear machine	
<i>Alexander Thomas Oswald</i>	
PB5.21	450
3-D Optimal Design of Laminated Yoke of Billet Heater for Rolling Wire Rod using ON/OFF	
<i>Norio Takahashi, Shunsuke Nakazaki, Daisuke Miyagi, Naoki Uchida, Keiji Kawanaka, Hideyuki Namba</i>	

PB5.22	452
Multiobjective Differential Evolution Approach for the TEAM Workshop Problem 25	
<i>Luiz Lebensztajn, Leandro dos Santos Coelho</i>	
PB5.23	454
A Populational Particle Collision Algorithm Applied to Electromagnetic Optimization	
<i>Piergiorgio Alotto, Leandro Dos Santos Coelho</i>	

**Session PB6: Waves Propagation II, Nanomagnetism,
Photonics and Optoelectronics**

13:30-15:00 – Room: Poster Session Room I

PB6.1	456
Microstrip Ring Antennas on Double-Layered Ferrimagnetic Substrates	
<i>Christianne F. L. Vasconcelos, Sandro Gonçalves Silva, Maria Rosa M. L. Albuquerque, José de Ribamar S. Oliveira, Adaildo Gomes d'Assunção</i>	
PB6.2	458
CFL Conditions for Finite Integration Methods Using Parallelogram and Parallelepiped Grids	
<i>Tetsuji Matsuo</i>	
PB6.3	460
A hybrid model for path loss calculation in urban environment	
<i>Leandro Carísio Fernandes, Antonio José Martins Soares</i>	
PB6.4	462
Temperature Dependence of Optical Fiber	
<i>Jose Patrocínio da Silva, Vitaly Felix Rodriguez Esquerre, Diego Souza Bezerra, Hugo Enrique Hernandez Figueroa</i>	
PB6.5	464
Analysis of the Effects of Irregular Terrain on Radio Wave Propagation Based on a Three-dimensional Parabolic Equation	
<i>Marco Aurélio Nunes da Silva, Emanuel Costa, Markus Liniger</i>	
PB6.6	466
Determination of Electromagnetic Sources Through Field Measurements	
<i>Ibrahim Akduman, Hulya Sahinturk, Ali Yapar</i>	
PB6.7	468
Improved FE-mesh truncation by surface operator implementation to speed up antenna design	
<i>Werner Renhart, Christian Magele, Christian Tuerk</i>	
PB6.8	470
Application of Method of Moments for Near Field Optics with Metal Nanoparticles	
<i>Karlo Queiroz Costa, Victor Dmitriev</i>	

PB6.9	472
Eigenvalue analysis of lossy waveguide structures using hybrid H(curl) second order finite elements	
<i>Christian Scheiber, Oszkàr Bíró</i>	
PB6.10	474
Efficient Interface Conditions for Finite Difference Time Domain Methods	
<i>Dirk Schulz</i>	
PB6.11	476
FDTD Analysis of UHF-band RFID for Metallic Objects	
<i>Yuta Watanabe, Kota Watanabe, Hajime Igarashi</i>	
PB6.12	478
The Auxiliary Problem For Transient Lossy Transmission Lines With Non-Matched Loads	
<i>Turhan Karaguler</i>	
PB6.13	480
A low cost parallel and distributed architecture for full micromagnetic numerical codes	
<i>Carlo Ragusa, Bartolomeo Montrucchio, Maurizio Repetto, Vittorio Giovara, Fabio Freschi, Baochang Xie</i>	
PB6.14	482
A Research of Various MRAM Design for High Gb/Chip on Perpendicular Pole System	
<i>Hyuk Won, Gwan Soo Park, Kang Seo, Il hwan Park</i>	
PB6.15	484
Theoretical Analysis of Field Distribution and Attenuation in a Ag/GaN Periodic Plasmon Waveguide	
<i>Anderson Oliveira Silva, Victor Dmitriev</i>	
PB6.16	486
Model for Antenna Positioning in Indoor Environments Using 2-D Ray-Tracing Technique Associated to a Particle Swarm Optimizer	
<i>Stevan Grubisic, Emanuela Cabral, Walter Pereira Carpes Junior</i>	
PB6.17	488
Accurate Transmission-Path Ray-Tracing Computation for Indoor EM Field Prediction	
<i>Antonino Laudani, Salvatore Coco, Giuseppe Pollicino</i>	

Session PB7: EMC – Electromagnetic Compatibility

13:30-15:00 – Room: Poster Session Room II

PB7.1	490
Study of the Parasitic Effect Caused by Vias in High-Frequency Circuit	
<i>Adaildo Gomes D’Assunção Jr, Glauco Fontgalland, Henri Baudrand</i>	
PB7.2	492
A 3D PEEC Method for the prediction of radiated fields from automotive cables	
<i>Yahyaoui Wissem, Pichon Lionel, Duval Fabrice</i>	
PB7.3	494
Simulation of a Real Overvoltage Transient in a TLM-Modeled Grounding Mesh	
<i>Luiz Henrique Alves de Medeiros, Marcos T. de Melo, Fabio R. L. Silva, Andre A. Almeida, Fabio. N. Fraga</i>	
PB7.4	496
Conservativeness of the Head Tissue Equivalent Liquid for Body-Worn SAR Assessments	
<i>Vikass Monebhurrun</i>	
PB7.5	498
Investigation of Electronic Stirring Chamber Phase-shifting Excitation and Load Effects	
<i>Mario Alves dos Santos Jr, Damien Voyer, Carlos Antonio França Sartori, Djonny Weinzierl, Ronan Perrussel, Christian Vollaire, Laurent Krahenbuhl, Jose Roberto Cardoso</i>	
PB7.6	500
3D Near-field Reconstruction from PCBs by Equivalent Sources Using Legendre Functions	
<i>Lotfi Beghou, Lionel Pichon, Adroaldo Raizer, François Costa</i>	
PB7.7	502
Evaluation of Shielding Effectiveness within Operating Room Using TLM Method	
<i>Wilson Valente Jr., Luciana Firmino, Adroaldo Raizer</i>	
PB7.8	504
Full Wave Solution for Intel CPU with a Heat Sink for EMC Investigations	
<i>Junwei Lu, Boyuan Zhu, David Thiel</i>	

PB7.9	506
Conductor Positions Optimization of a Transmission Line Excitation Chamber	
<i>Avila Sérgio, Santos Jr Mario, Lebensztajn Luiz, Sartori Carlos, Krahenbuhl Laurent, Cardoso José, Weinzierl Djonny</i>	
PB7.10	508
Magnetic Shielding of Apertures Loaded by Resistive Coating	
<i>Marcello D'Amore, Valerio De Santis, Mauro Feliziani</i>	
PB7.11	510
Numerical FEM models for the evaluation of EM fields exposure near welding machines	
<i>Fabrizio Dughiero, Michele Forzan, Elisabetta Sieni</i>	
PB7.12	512
Identification of equivalent multipolar electromagnetic sources by space filtering	
<i>Benjamin Vincent, Olivier Chadebec, Jean-Luc Schanen, Kévin Berger, Ronan Perrussel, Laurent Krähenbühl</i>	
PB7.13	514
Pre-evaluating a SAR Measurement System Performance by Numerical Simulations	
<i>Carlos Antonio França Sartori, Marcelo Perotoni, Antonio Marini de Almeida, José Kleber Cunha Pinto, José Roberto Cardoso, Sérgio Mühlen, Alberto Lisboa Dantas, Mário Leite Pereira Filho</i>	
PB7.14	516
Computer Analysis of Electromagnetic Transients in Grounding Systems	
<i>Rafael Silva Alípio, Marco Aurélio de Oliveira Schroeder, Márcio Matias Afonso</i>	
PB7.15	518
Proposal of Computational Model Validation for EMC Automotive Tests in Vehicles	
<i>Leonardo Lopes Santos Alvarenga, Ricardo Luiz Adriano, José Osvaldo Paulino, Joao Antônio Vasconcelos, Arnaud Christophe Pierre Marie Colin, Claudio Henrique Gomes Santos</i>	
PB7.16	520
Effect of grounding system on Electromagnetic Fields around Building Struck by Lightning	
<i>Bo Zhang, Jinliang He, Rong Zeng, Shuiming Chen</i>	

PB7.17	522
Conservativeness of the SAM Phantom for the SAR Evaluation in the Child's Head	
<i>Vikass Monebhurrun</i>	
PB7.18	524
3D-Modelling of an Aperture Illuminated by HF Electromagnetic Source for EMC Application	
<i>Mohammed djennah, Françoise Rioux</i>	
PB7.19	526
The Dynamic Circuit Model of the Spark Plug for EMI Prediction	
<i>Ya-li ZHENG, Ji-hui YU, Quan-di WANG, Jin JIA</i>	
PB7.20	528
Steady-state Inductive Coupling to the Underground Pipeline Parallel to Overhead Transmission Line above Two-layer Soil	
<i>Lei Qi, Yan Wu, Xiang Cui</i>	
PB7.21	530
A New Stochastic LPP Model for studying ELF Bioelectromagnetic Interaction	
<i>Antonino Laudani, Enrica Calà, Salvatore Coco</i>	

Session OB2: Optimization

15:20-17:10 – Room: Plenary Session Room

OB2.1	532
(Invited) An Enhanced Ellipsoid Method for Electromagnetic Devices Optimisation and Design	
<i>Douglas Alexandre Gomes Vieira, Adriano Chaves Lisboa, Rodney R. Saldanha</i>	
OB2.2	534
Robust Optimization Utilizing the Second-order Design Sensitivity Information	
<i>Dong-Hun Kim, Giwoo Jeung, Dong-Wook Kim, Heung-Geun Kim, David A. Lowther, Jan K. Sykulski</i>	
OB2.3	536
Adapted Output Space-Mapping Technique for a Bi-Objective Optimization	
<i>Stephane Brisset, Tuan-Vu Tran, Pascal Brochet, Fouzia Moussouni</i>	

OB2.4	538
Niching Evolution Strategies for Simultaneously Finding Global and Pareto Optimal Solutions	
<i>Christian Magele, Alice Koestinger, Michael Jaindl, Werner Renhart, Bogdan Cranganu-Cretu, Jasmin Smajic</i>	
OB2.5	540
Design Optimization of Waveguide Filters Using Continuum Design Sensitivity Analysis	
<i>Dong-Hun Kim, Nak-Sun Choi, Giwoo Jeung, Joon-Goo Park, Jin-Kyu Byun</i>	

Wednesday, November 25th

Session OC1: Material Modelling and Numerical Techniques

08:30-10:20 – Room: Plenary Session Room

- OC1.1** 542
(Invited) Evaluation of Electromagnetic Inspection of Hardened Depth of Spheroidal Graphite Cast Iron using 3-D Nonlinear FEM
Yuji Gotoh, Nobuya Sasaguri, Norio Takahashi
- OC1.2** 544
Modelling of Vector Hysteresis in Si-Fe Magnetic Steels and Experimental Verification
Ermanno Cardelli, Edward Della Torre, Antonio Faba
- OC1.3** 546
Size Is in the Eye of the Beholder: Technique for Non-destructive Detection of Parameterized Defects
Flavio Calvano, Pasi Raunonen, Saku Suuriniemi, Lauri Kettunen, Guglielmo Rubinacci
- OC1.4** 548
An Improved Jacobi-Davidson Method for the Computation of Selected Eigenmodes in Waveguides
Bastian Bandlow, Denis Sievers, Rolf Schuhmann
- OC1.5** 550
GPU Accelerated Adams-Bashforth Multirate Discontinuous Galerkin FEM Simulation of High Frequency Electromagnetic Fields
Nico Gödel

Session PC1: Material Modelling I

10:40-12:10 – Room: Poster Session Room I

- PC1.1** 552
Determination of Induction Motor End-Winding Leakage Inductances Using 3-D Non-Conforming FE Meshes
Andrej Stermecki, Oszkár Bíró, Kurt Preis Preis, Siegfried Rainer, Klaus Krischan Krischan, Georg Ofner Ofner

PC1.2	554
Neural FEM for Hysteretic Materials Unbounded Magnetic Field Analysis	
<i>Alessandro Salvini, Salvatore Coco, Antonino Laudani, Francesco Riganti Fulginei</i>	
PC1.3	556
Homogenization of anisotropic laminated stacks taking into account eddy currents	
<i>Slawomir Jan Wiak, Ewa Napieralska-Juszczak, Nabil Hihat, Jean Philippe Lecoq, Krzysztof Komez, Piotr Napieralski</i>	
PC1.4	558
An Anisotropic Vector Hysteresis Model Using Isotropic Vector Play Model	
<i>Tetsuji Matsuo</i>	
PC1.5	560
Influence of Material Dynamic Hysteresis Modelling in Losses Computation	
<i>Thai Phuong Do, Fabien Sixdenier, Laurent Morel, Eric Morin, Laurent Gerbaud, Frederic Wurtz</i>	
PC1.6	562
Interlamination Shorts in Transformer Cores: Estimation of Local Power Dissipation	
<i>Carl A. Schulz, Daniel Roger, Stéphane Duchesne, Jean-Noël Vincent</i>	
PC1.7	564
Modeling of Magnetolectric Effect: A Comparison between Homogenization and Finite Element Techniques	
<i>Romain Corcolle, Laurent Daniel, Frédéric Bouillault</i>	
PC1.8	566
Simple Numeric Modelling of Anomalous Eddy Current Taking Account of Domain Wall Motion in Steel Plate	
<i>Yanhui Gao, Kazuhiro Muramatsu, Koji Fujiwara</i>	
PC1.9	568
Inclusion of Eddy Currents in Laminations in Two-Dimensional Finite Element Analysis	
<i>Jenni Elina Pippuri, Anouar Belahcen, Emad Dlala, Antero Arkkio</i>	
PC1.10	570
Electromagnetic Multi-scale Homogenization of Carbon Fiber Composite Materials	
<i>Guillaume Wasselynck, Didier Trichet, Javad Fouladgar</i>	

PC1.11572
The Effects of Steel Lamination Core Losses on 3D Transient Magnetic Fields	
<i>Dingsheng Lin, Ping Zhou, Qingming Chen, Zol Cendes</i>	
PC1.12574
Analytical calculation of the interactions between two cylinder-shaped magnets	
<i>Jean-Paul Yonnet, Hicham Allag, Benoit Delinchant</i>	
PC1.13576
Numerical Modelling of Superconducting Filaments for Coupled Problem	
<i>Thitipong Satiramatekul, Frederic Bouillault</i>	
PC1.14578
Improved Accuracy of the Classical Eddy-Current Loss-Computation Technique	
<i>Anouar Belahcen, Emad Dlala, Jenni Pippuri</i>	
PC1.15	580
A New 2D Magnetic Reluctivity Model for Rotating Magnetic Fields and Its Application to FEM	
<i>Hee Sung Yoon, Sun-ki Hong, Chang Seop Koh</i>	
PC1.16	582
Measurement and Analysis of Magnetic Properties of Soft Magnetic Composite Material Considering 3-D Reluctivity Tensor	
<i>Yongjian Li, Qingxin Yang, Jianguo Zhu, Youguang Guo</i>	
PC1.17	584
A Model for Specific Losses in Grain-Oriented Steel	
<i>Oszkár Bíró, Ulrike Baumgartner, Yu Chen, Gerald Leber</i>	

Session PC2: Electrical Machines and Drives II

10:40-12:10 – Room: Poster Session Room I

PC2.1	586
Transient Performance of an Induction Motor with the Smith Connection	
<i>Tze-Fun Chan, Loi Lei Lai, Lie Tong Yan</i>	
PC2.2	588
Multi-objective Shape Optimal Design of PMLSM Utilizing Response Surface Method and Grid Computing	
<i>Chang Seop Koh, Hee Sung Yoon, Nyambayar Baatar, Hong-soon Choi</i>	

PC2.3	590
End-Effect Equivalent Method for back-EMF of High Speed SPMSM	
<i>Ki-Yong Nam, Soon-O Kwon, Jeong-Jong Lee, Jung-Pyo Hong</i>	
PC2.4	592
A performance model of an induction motor for transient simulation with a PWM drive	
<i>Derek Dyck, Geoff Gilbert, David A. Lowther</i>	
PC2.5	594
Design of a Dual-Rotor Dual-Output Radial-Flux Motor for Variable Speed Air Conditioners	
<i>Min-Fu Hsieh, Yu-Han Yeh, David G. Dorrell, Samsul Ekram</i>	
PC2.6	596
Vibration Synthesis for Electrical Machines based on Force Response Superposition	
<i>Matthias Boesing, Timo Schoenen, Knut A. Kaper, Rik W. De Doncker</i>	
PC2.7	598
Torque Ripple Analysis Method for Permanent Magnet Synchronous Reluctance Motor	
<i>Ki-Chan Kim, Ju Lee</i>	
PC2.8	600
On the Importance of Incorporating Iron Losses in the Magnetic Field Solution of Electrical Machines	
<i>Emad Dlala, Anouar Belahcen, Antero Arkkio</i>	
PC2.9	602
Efficiency Evaluation of PMASynRM Vs. SynRM Using Coupling FEM & Preisach Modeling	
<i>Tae Won Yun, Yong Hyun Kim, Jung Ho Lee</i>	
PC2.10	604
Optimization of Magnetic Bearing applied to a Ventricular Assist Device	
<i>Luiz Lebensztajn, Everton S. Yoshida</i>	
PC2.11	606
Design of High Performance Line Start Permanent Magnet Synchronous Motor with High Inertia Load	
<i>Jian Li, Byongkuk Kim, Yunhyun Cho</i>	

PC2.12	608
Slit Effect of Laminated Stator Core in Transverse Flux Rotary Machine	
<i>Ji-Young Lee, Seung-Ryul Moon, Do-Hyun Kang, Jung-Pyo Hong</i>	
PC2.13	610
Design and Analysis of a Written-pole Motor Using a Symmetric Field and FE Methods	
<i>Byung-Taek Kim, Dae-Kyong Kim, Byung-Il Kwon</i>	
PC2.14	612
Inductance Calculation and Measurement of Interior Permanent Magnet Synchronous Motor	
<i>Tao Sun, Soon-O Kwon, Jeong-Jong Lee, Geun-Ho Lee, Jung-Pyo Hong</i>	
PC2.15	614
Shape Optimization of a Thomson-coil Actuator for Fast Response Using Topology Modification	
<i>Wei Li, Jiang Lu, Young Woo Jeong, Chang Seop Koh</i>	
PC2.16	616
Optimized Axially Magnetized Permanent Magnet Tubular Actuator: Pole-Piece Shaping	
<i>Laurentiu Encica, Johan Paulides, Koen Meessen, Bart Gysen, Jorge Duarte, Elena Lomonova</i>	
PC2.17	618
Permanent Magnet Wheel Motor for Electric Vehicle Applications	
<i>Konstantinos I. Laskaris, Anastasios G. Vichos, Antonios G. Kladas</i>	
PC2.18	620
Optimized geometrical parameters of a SRM by numerical-analytical approach	
<i>Ammar Bentounsi, Redem Rebbah, Fares Rebbahi, Hind Djeghloud, Hocine Benalla, Soltane Belakehal, Bachir Batoun</i>	
PC2.19	622
Methods for efficient computation and visualization of magnetic flux lines in 3D	
<i>Martin Hafner, Marc Schöning, Marcin Antczak, Andrzej Demenko, Kay Hameyer</i>	
PC2.20	624
Calculation of Copper Losses in Intercell Transformers by 2D FEM simulation	
<i>Bernardo Cougo, Thierry Meynard, François Forest, Eric Labouré</i>	

PC2.21	626
Loss Analysis and Efficiency Evaluations of Synchronous Reluctance Motor Using Coupled FEM & Preisach Modelling	
<i>Il Kyo Lee, Yung Hyun Kim, Jung Ho Lee</i>	

Session PC3: Devices and Applications I

10:40-12:10 – Room: Poster Session Room II

PC3.1	628
A Novel Calculation Method of Distributed Parameters in Transformer Winding	
<i>Chun Zhao, Zhiye Du, Jiangjun Ruan, Ying Peng, Liang Chen</i>	
PC3.2	630
Optimal Regularization for MEG Source Reconstruction by Inverse Methods	
<i>Feng Luan, Chany Lee, Jong-Ho Choi, Hyun-Kyo Jung</i>	
PC3.3	632
Dynamic Force Analysis of Saturated Core HTS FCL under Short-Circuit Operation	
<i>Xu Fang, Jie Qiu, Shuhong Wang, Hongli Xiao, Weizhi Gong, Ying Xin, Jian Guo Zhu, Youguang Guo, Yi Wang, Wei Xu, Xiaoyang Zhang</i>	
PC3.4	634
Adaptive Ablation Treatment Based on Impedance Imaging	
<i>Alessandro Formisano, Ida Maria Vincenza Caminiti, Fabrizio Ferraioli, Raffaele Martone</i>	
PC3.5	636
A contactless dielectrophoretic handling of diamagnetic levitating water droplets in air	
<i>Paul Kauffmann, Pascale Pham, Alain Masse, Thibault Honegger, David Peyrade, Vincent Haguet, Gilbert Reyne</i>	
PC3.6	638
Compact Electromagnetic Bandgap Structures for Notch Band in Ultra-Wideband Applications	
<i>Mihai Dragos Rotaru, Jan K. Sykulski</i>	
PC3.7	640
Microwave Characterization using Least-Square Support Vector Machines	
<i>HACIB Tarik, Acikgoz Hulusi, Le Bihan Yann, Meyer Olivier, Pichon Lionel</i>	

PC3.8	642
Electromagnetic disruption loads on ITER blanket modules	
<i>Maurizio Furno Palumbo, Raffaele Albanese, Roberto Palmaccio, Guglielmo Rubinacci, Pietro Testoni, Fabio Villone</i>	
PC3.9	644
Fast Computations Technique of Forces Acting on Moving Permanent Magnet	
<i>Marek Ziolkowski, Hartmut Brauer</i>	
PC3.10	646
A model to relate SAR to surface field measurements in human phantoms	
<i>Oriano Bottauscio, Mario Chiampì, Luca Zilberti</i>	
PC3.11	648
Design of Railway Wheel Detector Insusceptible to Electromagnetic Noise	
<i>Asuka Otake, Kenta Takayasu, Shinji Wakao, Tamio Okutani, Yasuhito Takahashi, Masahiko Saito, Akihisa Toyoda</i>	
PC3.12	650
Simulation of Internal Myocardium Defibrillation using Macroscopic Anisotropy Models and Finite Element Analysis	
<i>Steve McFee, Maryam Golshayan</i>	
PC3.13	652
Novel Applications of Inductive Method for Measuring Critical Current Density	
<i>Atsushi Kamitani, Teruou Takayama, Soichiro Ikuno</i>	
PC3.14	654
Hybrid generation of subject specific head models	
<i>Robert Szmurło, Jacek Starzyński, Bartosz Sawicki, Stanisław Wincenciak</i>	
PC3.15	656
Modeling a “flying carpet” stable in both the positive and negative z-directions	
<i>Mikhail Kustov, Orphée Cugat, Gilbert Reyne</i>	
PC3.16	658
3D Voltage Driven Finite Element Analyses of Eccentric Rotor Positions of a Novel Hybrid Radial Active Magnetic Bearing	
<i>Erich Schmidt, Matthias Hofer</i>	

PC3.17	660
Contact Parameter Computation and Analysis of Air Circuit Breaker with Permanent Magnet Actuator	
<i>Shuhua Fang, Heyun Lin, Siu-lau Ho, Xianbing Wang, Ping Jin</i>	
PC3.18	662
Reduction of Repulsion Forces on Current-Carrying Contact using 3-D FEM	
<i>Tomohiro Ota, Satoshi Suzuki, Katsuhiro Hirata</i>	
PC3.19	664
Dynamic Analysis Method for Electromagnetic Artificial Muscle Actuator under PID Control	
<i>Yoshihiro Nakata, Hiroshi Ishiguro, Katsuhiro Hirata</i>	
PC3.20	666
Controllable Reactor Simulation using Integral Equation Method	
<i>Zoran Andjelic, David Pusch, Xiaobo Yang</i>	
PC3.21	668
SAR Calculations Using Realistic Phone Models: Uncertainty Due to Positioning	
<i>Vikass Monebhurrun, Azzedine Gati, Man-Fai Wong, Joe Wiart</i>	
PC3.22	670
Antenna Modeling for Inductive RFID Applications Using the PEEC Method	
<i>Peter Scholz, Wolfgang Ackermann, Thomas Weiland, Christian Reinhold</i>	
PC3.23	672
Design and Implementation of a High Frequency Flyback Converter Using New-developed Polymer-bonded Magnetic Cores	
<i>Kai Ding, K.W.E Cheng, Yang Shiyou</i>	
PC3.24	675
Evaluation of Discharge Current by Generalized Energy Method and Integral Ohm's Law	
<i>Se-Hee Lee, Il-Han Park, Francis O'Sullivan, Markus Zahn</i>	

Session PC4: Numerical Techniques II

10:40-12:10 – Room: Poster Session Room II

PC4.1	677
On the equivalence of Finite Element and Finite Integration formulations	
<i>Andrzej Demenko, Jan Sykulski, Rafal Wojciechowski</i>	

PC4.2	679
A Fast Numerical Analysis of Electromagnetic Fields in Large Grounding Systems	
<i>Hongxia Huang, Lin Li</i>	
PC4.3	681
Overlapping Finite Elements for Arbitrary Surfaces in 3D	
<i>Stephane Clenet, Guillaume Krebs, Igor Tsukerman</i>	
PC4.4	683
Basis functions for divergence constraints in the finite element method	
<i>C. M. Pinciuc, A. Konrad, J. D. Lavers</i>	
PC4.5	685
Agglomeration-based algebraic multigrid for linear systems coming from edge-element discretizations	
<i>François Musy, Laurent Nicolas, Ronan Perrussel</i>	
PC4.6	687
A 2D robust FE-FV mixed method to handle strong nonlinearities in superconductors	
<i>Abelin Kameni, Smail Mezani, Frédéric Sirois, Denis Netter, Jean Lévêque, Bruno Douine</i>	
PC4.7	689
A Posteriori Error Estimation and Adaptive Mesh Refinement Controlling in Finite Element Analysis of 3D Steady State Eddy Current Fields	
<i>Jinbiao Li, Dexin Xie, Xiaoming Liu</i>	
PC4.8	691
Auto adaptive interface treatment for the EFGM in electromagnetic problems	
<i>Carlos Alex Sander J. Gulo, Jose Marcio Machado, Gleber Nelson Marques</i>	
PC4.9	693
Automatic treatment of multiply connected regions in Integral Formulations	
<i>Guglielmo Rubinacci, Antonello Tamburrino</i>	
PC4.10	695
Complex Adjoint Variable Method for Finite Element Analysis of Eddy Current Problems	
<i>Hajime Igarashi, Kota Watanabe</i>	

PC4.11	697
New Method Analysis of Non-rotating Magnetoacoustic Tomography with Magnetic Induction	
<i>yang zhang</i>	
PC4.12	699
Combined Spectral-Element, Finite-Element Discretization for Magnetic- Brake Simulation	
<i>Herbert De Gersem</i>	
PC4.13	701
Weight Function Control of Moving Least-Squares Interpolants: Application to Axisymmetric Shielding Current Analysis in HTS	
<i>Soichiro Ikuno, Teruou Takayama, Atsushi Kamitani</i>	
PC4.14	703
Interior Penalty Discontinuous Galerkin Method for the Time-Domain Maxwell's Equations	
<i>Stylianos Dosopoulos, Jin-Fa Lee</i>	
PC4.15	705
A FEM Approach for Analyzing the Corona Ionized Field of Bipolar Bundled Conductors	
<i>Haiyan Yuan, Zhengcai Fu, Junwei Lu</i>	
PC4.16	707
The Solution of Electromagnetic Field Problems using a Sliding Window Gauss-Seidel Algorithm on a Multi-Core Processor	
<i>Hussein Moghnieh, David Lowther</i>	
PC4.17	709
Speeding Up the Process of Building High-Quality Finite-Element Meshes	
<i>Cássia Regina Santos Nunes, Renato Cardoso Mesquita, David Alister Lowther</i>	
PC4.18	711
Extended Boundary-Node Method: Application to Potential Problem	
<i>Ayumu Saitoh, Taku Itoh, Atsushi Kamitani</i>	
PC4.19	713
Reduction of Eddy Current Losses by several Cuts in Conductors	
<i>Arnulf Kost, Matthias Ehrich</i>	

PC4.20	715
Fields and Current Formulation for Radiofrequency Antennas	
<i>Nabil El Alami, Bernard Bandelier, Françoise Rioux-Damidou</i>	
PC4.21	717
A New Method to Solve 3D Magnetodynamic Problems without Assembling an $Ax = b$ system	
<i>João Pedro Assumpção Bastos, Nelson Sadowski</i>	
PC4.22	719
Multiphysics problems via the Cell Method: the role of Tonti diagrams	
<i>Piergiorgio Alotto, Fabio Freschi, Maurizio Repetto</i>	
PC4.23	721
Time--domain geometric eddy--current SA formulation for hexahedral grids	
<i>Ruben Specogna, Lorenzo Codecasa, Patrick Dular, Francesco Trevisan</i>	
PC4.24	723
A finite element method for structures defined by a regular 3D grid of material properties	
<i>Huanhuan Gu, Jean Gotman, Jon Webb</i>	

Session PC5: Material Modelling II

13:30-15:00 – Room: Poster Session Room I

PC5.1	725
Hysteresis Losses' Calculation of Magnetostrictive Ultrasonic Transducer with Jiles-Atherton Hysteresis Model	
<i>Jianbin Zeng, Baodong Bai, Haiquan Zeng</i>	
PC5.2	727
Implementation of an Advanced Eddy-Current Model for Non-Linear Laminated Media	
<i>Anouar Belahcen, Emad Dlala, Jenni Pippuri</i>	
PC5.3	729
Vector Magnetic Hysteresis Modeling of Soft Magnetic Composite Material	
<i>Youguang Guo, Haiyan Lu, Jianguo Zhu, Zhiwei Lin, Jinjiang Zhong, Shuhong Wang</i>	

PC5.4	731
On the Use of Multi-Direction Si-Fe Sheet Sample Magnetic Properties Measured by Epstein Frame in Finite Element Analysis	
<i>Dexin Xie, Qilin Liu, Zhiqiang Ren, Xiaoyan Wang, Yanli Zhang, Zhiguang Cheng</i>	
PC5.5	733
A Study for Harmonic Iron Loss for Electrical Steel under Alternating Magnetic Field	
<i>Sun-Ki Hong, Chang Seop Koh</i>	
PC5.6	735
An Improved Reluctivity Model for Vector Magnetic Properties of Silicon Steels under Distorted Magnetic Flux Density	
<i>Yanli Zhang, Jingguo Yuan, Dexin Xie, Chang Seop Koh</i>	
PC5.7	737
Inrush Currents in a Three-Phase Transformer Taking Into Account Vector Hysteresis	
<i>Jean Vianei Leite, Abdelkader Benabou, Nelson Sadowski</i>	
PC5.8	739
Study of Different FEM Models to Analyze Homogenized Iron Lamination with Electrical Fault	
<i>Juliana Luisa Müller, Abdelkader Benabou, Thomas Henneron, Francis Piriou, João Pedro Assumpção Bastos, Jean-Yves Roger</i>	
PC5.9	741
Three-Phase Transformer Modelling Using the Vector Hysteresis Model and Including the Eddy Current and the Anomalous Losses	
<i>Mauricio Valencia Ferreira da Luz, Jean V. Leite, Abdelkader Benabou, Nelson Sadowski</i>	
PC5.10	743
Iron-Loss Modeling for Rotating Machines: Comparison between Bertotti's Three-Term Expression and 3-D Eddy-Current Analysis	
<i>Katsumi Yamazaki, Noriaki Fukushima</i>	
PC5.11	745
Effect of Temperature Dependence of Magnetic Properties on Heating Characteristics of Induction Heater	
<i>Norio Takahashi, Hiroyuki Kagimoto, Hiroaki Kurose, Daisuke Miyagi, Naoki Uchida, Keiji Kawanaka</i>	

PC5.12	747
Evaluation of Electromagnetic Inspection of Retained Austenite in High Chromium Cast Iron using 3-D Nonlinear FEM Considering Non-Uniform Permeability	
<i>Yuji Gotoh, Akira Nishishita, Nobuya Sasaguri, Norio Takahashi</i>	
PC5.13	749
3-Dimensional Modelling of Magnetostriction in Iron Core with Equivalent Nodal Forces	
<i>Yanhui Gao, Kazuhiro Muramatsu, Koji Fujiwara, Yoshiyuki Ishihara, Shigemasa Fukuchi, Tetsumi Takahata</i>	
PC5.14	751
Tolerance Analysis of NMR Magnets	
<i>Alessandro Formisano, Raffaele Martone</i>	
PC5.15	753
homogenization in electromagnetism: a thermodynamic insight	
<i>Vincent Mazauric</i>	
PC5.16	755
FE Analysis of Plasma Discharge and Sheath Characterization in Dry Etching Reactor	
<i>Gwang-Jun Yu, Young Sun Kim, Se-Hee Lee, Il Han Park</i>	

Session PC6: Electrical Machines and Drives III

13:30-15:00 – Room: Poster Session Room I

PC6.1	757
Permanent-Magnet Synchronous Generator Supplying an Isolated Load	
<i>Tze-Fun Chan, Weimen Wang, Loi Lei Lai</i>	
PC6.2	759
Development of Flux Reversal Linear Synchronous Motor with Multiple Auxiliary Salient Poles	
<i>Shi-Uk Chung, Hong-Ju Lee, Byung-Chul Woo, Ji-Won Kim, Seung-Ryul Moon, Sang-Moon Hwang</i>	
PC6.3	761
Reduction of Cogging Torque for Axial Flux Generator Applied to Small Wind Turbine	
<i>Min-Fu Hsieh, Yu-Han Yeh, David G. Dorrell, Samsul Ekram</i>	

PC6.4	763
Comparison of Magnetic Characteristics according to Stator Core Composition in Transverse Flux Rotary Machine	
<i>Ji-Young Lee, Ji-Won Kim, Byung-Chul Woo, Sang-Ho Lee, Jung-Pyo Hong</i>	
PC6.5	765
Design of the Cage-bars for Single Phase LSPMSM considering the Starting Torque and Magnetic Saturation	
<i>Seung Joo Kim, Won Ho Kim, Kwang Soo Kim, Jong Bin Im, Ju Lee</i>	
PC6.6	767
Analysis of Very Fast Transient Overvoltages and Electric Field Stresses in Conventional Tesla Transformers Using FDTD Method	
<i>Edris Agheb, Ehsan Hashemi, Kaveh Niayesh, Ali Mousavi, Mohsen Faridi</i>	
PC6.7	769
Computational Analysis of Fringing Fields and Forces in the Cylindrical Coordinate System	
<i>Bart. L.J. Gysen, Koen J. Meessen, Johannes J.H. Paulides, Elena A. Lomonova</i>	
PC6.8	771
Field Calculation in the Innovative Transformers with Amorphous Modular Cores	
<i>Dariusz Koterak, Bronislaw Tomczuk, Kazimierz Zakrzewski</i>	
PC6.9	773
Automated Optimization in the Design Process of a Pending Workbench	
<i>Jan Albert, Remus Banucu, Alexander Hafla, Veronika Reinauer, Christian Scheiblich, Wolfgang M. Rucker, Alexander Huf</i>	
PC6.10	775
Effects of Load Variation on Eccentricity Fault Diagnosis in Round Rotor Synchronous Motors	
<i>Bashir Mahdi Ebrahimi, Mohammad Mohammad Etemad Rezaie, Jawad Faiz</i>	
PC6.11	777
Dynamic Characteristics Analysis of Spherical Resonant Actuator Using 3-D FEM	
<i>Satoshi Suzuki, Yoshihiro Kawase, Tadashi Yamaguchi, Shuhei Kakami, Katsuhiro Hirata, Tomohiro Ota</i>	

PC6.12	779
Finite Element Processing Methods to Peripheral Flux Leakage in Axial Field Flux-Switching PM Machines	
<i>Mingyao Lin, Lei Zhang, Xin Li, Haitao Yu</i>	
PC6.13	781
Slotted and Torus PM Generators for Low Speed Direct Drive Applications using an Analytical/Static 2D FEA Design Technique	
<i>David George Dorrell</i>	
PC6.14	783
A General Cuboidal Element for Three-Dimensional Thermal Modeling	
<i>Rafal Wrobel, Phil Mellor</i>	
PC6.15	785
Time-Stepping Finite Element Analysis of a Salient-pole and Round-Rotor Synchronous Generators under Dynamic Eccentricity Fault	
<i>Jawad Faiz, Mojtaba Babaie, Bashir Mahdi Ebrahimi, Jalal Nazarzadeh</i>	
PC6.16	787
Magnetic Forces and Displacement Analysis of Large Scale BLDC Motor by Magneto-Mechanical Formulation	
<i>Pan Seok Shin, Hee Jun Cheong, Sung Hyun Woo, Chang Seop Koh</i>	
PC6.17	789
Optimized Coil Position for Improvement of Holding Torque of the PM - Spherical Motor	
<i>Sung-Hong Won, Dong-Woo Kang, Won-Ho Kim, Sung-Chul Go, Cheol-Jick Ree, Ju Lee</i>	
PC6.18	791
Comparative study of the inductances of an induction motor with rotor eccentricities	
<i>Elkin Ferney Rodriguez Velandia, Jose Andres Santisteban Larrea, Antonio Carlos Ferreira</i>	
PC6.19	793
Development of a Flexible Phase Variable Model for Two-Phase Hybrid Stepping Motor Using Virtual Magnetic Gateway based FEA	
<i>Jiixin Chen, Youguang Guo, Jianguo Zhu, Weinong Fu</i>	

PC6.20	795
Novel Modeling of Flux-barriers in Interior-type PM Synchronous Motor For Pulsation Torque Reduction: Part I. Various Flux-barrier Designs	
<i>Liang Fang, Jeong-Jong Lee, Jung-Pyo Hong</i>	
PC6.21	797
Parametric Finite Element Analyses of a Permanent Magnet Synchronous Machine with an External Rotor	
<i>Erich Schmidt, Marko Susic</i>	
PC6.22	799
2D Exact Analytical Solution of Open Circuit Magnetic Field in Slotted Surface Mounted PM Radial Flux Synchronous Machines	
<i>Yacine Amara, Jacques Raharijaona, Georges Barakat</i>	
PC6.23	801
Quasistatic Electromagnetic Field Computation by Conformal Mapping in Permanent Magnet Synchronous Machines	
<i>Martin Hafner, David Franck, Kay Hameyer</i>	
PC6.24	803
Calculation of Inductances in Intercell Transformers by 2D FEM simulation	
<i>Bernardo Cougo, Thierry Meynard, François Forest, Eric Labouré</i>	

Session PC7: Numerical Techniques III

13:30-15:00 – Room: Poster Session Room II

PC7.1	805
Study on Analysis Method for Ferrofluid	
<i>Yu Okaue, Gaku Yoshikawa, Fumikazu Miyasaka, Katuhiro Hirata</i>	
PC7.2	807
Isogeometric analysis for electromagnetic problems	
<i>Annalisa Buffa, Rafael Vázquez</i>	
PC7.3	809
Nonoverlapping and overlapping decomposition methods in 3D BEM multilayered model for Optical Tomography	
<i>Tomasz Marek Grzywacz, Jan Sikora</i>	

PC7.4	811
Galerkin Projection Method for Sliding Interfaces in Finite Element Analysis of Electrical Machines	
<i>Enno Lange, François Henrotte, Kay Hameyer</i>	
PC7.5	813
Convergence Acceleration of Time-Periodic Electromagnetic Field Analysis by Singularity Decomposition-Explicit Error Correction Method	
<i>Yasuhito Takahashi, Tadashi Tokumasu, Akihisa Kameari, Hiroyuki Kaimori, Masafumi Fujita, Takeshi Iwashita, Shinji Wakao</i>	
PC7.6	815
Efficient Block Gauss-Seidel Preconditioner for 3D Full-Wave Finite Element Analysis	
<i>Toshio Murayama, Shinobu Yoshimura</i>	
PC7.7	817
Numerical Convergence of Method of Moments in the Analysis of Bodies of Revolution	
<i>Ursula Resende, Fernando Moreira</i>	
PC7.8	819
A 3-D FE Particle-in-Cell Parallel code with adaptive load balancing	
<i>Antonino Laudani, Salvatore Coco, Giuseppe Pollicino, Paola Tirrò</i>	
PC7.9	821
Parallel Computing of Magnetic Filed for Rotating Machines on the Earth Simulator	
<i>Tomohito Nakano, Yoshihiro Kawase, Tadashi Yamaguchi, Masanori Nakamura, Noriaki Nishikawa, Hitoshi Uehara</i>	
PC7.10	823
An efficient algorithm for planar circuits design	
<i>Alexandre Serres, Glauco Fontgalland, José Ewerton P. De Farias, Henri Baudrand</i>	
PC7.11	825
MPI Parallelization for Large Electromagnetic Simulations using Curvilinear Finite Elements	
<i>Wolfgang Ackermann, Galina Benderskaya, Thomas Weiland</i>	

PC7.12	827
Multicore Acceleration of CG Algorithms using Blocked-Pipeline-Matching Techniques	
<i>David M. Fernández, Dennis D. Giannacopoulos, Warren J. Gross</i>	
PC7.13	829
A New Approach to the Impedance Method	
<i>Airton Ramos, Daniela O.H. Suzuki</i>	
PC7.14	831
A simplified T- ϕ formulation for eddy current computation in thin CFRP plates	
<i>Hocine MENANA, Mouloud FELIACHI</i>	
PC7.15	833
Preconditioned BICGSTAB Algorithm and its Application to a Moving Linear Electric Motor	
<i>Haitao Yu</i>	
PC7.16	835
An Efficient Two-Level Preconditioner for FEM-BEM Equations based on Lifting	
<i>Fabio Henrique Pereira, Marcio Matias Afonso, Silvio Ikuyo Nabeta</i>	
PC7.17	837
A Comparison of Parallel Finite Element Analysis Using Domain Decomposition	
<i>Kota Watanabe, Kenji Yoneta, Hajime Igarashi</i>	
PC7.18	839
Kernel Regularization for Volume Integral Equations	
<i>Michael V. Davidovich</i>	
PC7.19	841
Error Estimators based on Kriging Interpolation	
<i>Vanessa Gomes Cruz, Luiz Lebensztajn</i>	
PC7.20	843
Investigations on the Accuracy of Maxwell Stress Tensor based Force Calculations	
<i>Ghislain Remy, Guillaume Krebs, Francois Henrotte</i>	

PC7.21	845
Determination of Uniform Magnetizing Current Density With Stable ICCG Convergence Using Simple Technique and Regularization	
<i>Yoshifumi OKAMOTO, Koji FUJIWARA, Yoshiyuki ISHIHARA, Tetsuji MATSUO</i>	
PC7.22	847
Parallel Direct Solver For The Finite Integration Technique in Electrokinetic Problems	
<i>Abdellatif TINZEFTE, Yvonnick Le Menach, julien korecki, Frédéric Guyomarch, francis piriou</i>	
PC7.23	849
Computation of forces using mean and difference potentials	
<i>Antônio Flavio NOGUEIRA</i>	
PC7.24	851
Numerical algorithms for the image reconstruction in electrical impedance tomography	
<i>Stefan Franciszek Filipowicz, Tomasz Rymarczyk, Jan Sikora</i>	

Session PC8: TEAM, Education and Software Methodolgy

13:30-15:00 – Room: Poster Session Room II

PC8.1	853
The Application of System Dynamics in Learning Electromagnetic Contactor Operation	
<i>Paulo Irineu Koltermann, Jéferson Meneguín Ortega, Valmir Machado Pereira, Éder Rodrigues Martins, Luiz Antônio Righi</i>	
PC8.2	855
Educational Software for the Numerical Correction of the Experimental Magnetization Curves	
<i>Valentin IONITA, Emil CAZACU</i>	
PC8.3	857
Application of the Method of Residues in Comparison to TLM Method in a Practical Case	
<i>Sérgio Henrique Lopes Cabral, Sávio Leandro Bertoli</i>	
PC8.4	859
Semi-Analytical Solution of 2-D Rotor Eddy-Current Losses due to the Slotting Effect in SMPMM	
<i>Frédéric Dubas, Christophe Espanet</i>	

PC8.5	861
Effect of Source Replacement on both Iron Loss and Flux in Solid and Laminated Steel Configurations	
<i>Zhiguang Cheng, Norio Takahashi, Behzad Forghani</i>	
PC8.6	863
An Adaptive Equivalent Circuit Method for TEAM Problem 28: An Electrodynamic Levitation Device	
<i>Wei Li, Jiang Lu, Chang Seop Koh</i>	
PC8.7	865
Proposal of a Benchmark for Multi-Level Optimization with 3D Finite Element Model	
<i>Stephane Brisset, Tuan-Vu Tran, Pascal Brochet</i>	
PC8.8	867
Visualization Method of Magnetic Flux Lines with Accurate Allocation Applying Tube System	
<i>So Noguchi, Hideo Yamashita</i>	
PC8.9	869
A Weakly Coupled Parallel 2D Delaunay Refinement Algorithm	
<i>Mauro Massayoshi Sakamoto, José Roberto Cardoso Cardoso, Marcelo Facio Palin Palin, Fabio Henrique Pereira Pereira, Maurício Barbosa de Camargo Salles Salles</i>	
PC8.10	871
The Broad Sense Chain-Making and Chain-Coupling Theorems of Element Grid in 2-D Problems	
<i>Nan Xiong, Kexun Jiang</i>	
PC8.11	873
Analyse of different programming solutions adapted to block matrix type in electromagnetic modelling	
<i>Laurent Santandrea, Yahya Choua, Alejandro Ospina, Yann Le Bihan, Claude Marchand</i>	
PC8.12	875
Simulation of Electric Field Distribution in Polymeric Insulators	
<i>Rosemeri C Fagundes, Walmor C Godoi, Marco A A Vasco, Vitoldo Swinka-Filho, Klaus de Geus, Andre E Lazzaretti</i>	
PC8.13	877
The Cross-Entropy Method and its Application to Inverse Problems	
<i>S.L. Ho, Shiyong Yang</i>	

PC8.14	879
Scalability of Higher-Order Discontinuous Galerkin FEM Computations for Solving Electromagnetic Wave Propagation Problems on GPU Clusters	
<i>Markus Clemens, Nico Gödel, Tim Warburton, Nigel Nunn</i>	

Session OC2: Devices and Applications and Electromagnetic Compatibility

15:20-17:10 – Room: Plenary Session Room

OC2.1	881
(Invited) EMC Modeling of an Industrial Variable Speed Drive with an Adapted PEEC Method	
<i>Vincent Ardon, Jérémie Aimé, Olivier Chadebec, Édith Clavel, Jean-Michel Guichon, Enrico Vialardi</i>	
OC2.2	883
Calculation of Equivalent Circuit Parameters for a High-Frequency RFID Transponder	
<i>Thomas Bauernfeind, Kurt Preis, Oszkar Biro, Florian Hämmerle</i>	
OC2.3	885
Planar Coil Model using Shell Elements Applied to an Eddy-Current Non-Destructive Testing	
<i>Alejandro Ospina, Laurent Santandrea, Yann Le Bihan, Claude Marchand</i>	
OC2.4	887
Numerical Field Calculation in Support of the Hardware Commissioning of the LHC	
<i>Bernhard Auchmann, Stephan Russenschuck</i>	
OC2.5	889
Fault Classification and Detection by Wavelet Based Magnetic Signature Recognition	
<i>Francisco Xavier Sevegnani, Carlos A.F. Sartori</i>	

Thursday, November 26th

Session OD1: Electric Machines and Drives

08:30-10:20 – Room: Plenary Session Room

- OD1.1**891
(Invited) Modeling the dynamic behavior of magnetostrictive actuators
Oriano Bottauscio, Paolo E. Roccato, Mauro Zuca
- OD1.2** 893
Determination of d-q Axis Parameters of Interior Permanent Magnet Machines
Ping Zhou, Dingsheng Lin, Georg Wimmer, Zoltan Cedens
- OD1.3** 895
Simulation of the Winding Overhangs in Permanent Magnet Synchronous Machines
Bogdan Funieru, Andreas Binder
- OD1.4** 897
Dynamic Analysis Method of Spiral Resonant Actuator Using 3-D FEM
Satoshi Suzuki, Yoshihiro Kawase, Tadashi Yamaguchi, Shuhei Kakami, Katsuhiko Hirata, Tomohiro Ota
- OD1.5** 899
Field Reconstruction Method in the Optimal Design of Doubly Fed Induction Generators
Wei Wang, Babak Fahimi

Session PD1: Electrical Machines and Drives IV

10:40-12:10 – Room: Poster Session Room I

- PD1.1**901
Analysis of Harmonic Iron Losses for IPMSM Considering the Rotating Field
Jang-Ho Seo, Hyun-Kyo Jung
- PD1.2** 903
Characteristic Analysis & Optimum Design of Permanent Magnet Assisted Synchronous Reluctance Motor for Premium Efficiency Performance
Tae Won Yun, Sung Ju Mun, Jung Ho Lee

PD1.3	905
Characteristic Analysis Method of Irreversible Demagnetization in Single-phase LSPM Motor	
<i>Byeong-Hwa Lee, Soon-O Kwon, Jeong-Jong Lee, Liang Fang, Jong-Pyo Hong, Hyuk Nam</i>	
PD1.4	907
Pre-Processing of Inductances for Intercell Transformer Optimization	
<i>Bernardo Cougo, Thierry Meynard, François Forest, Eric Labouré</i>	
PD1.5	909
Hysteresis Torque Analysis of PM Motor Using Initial B-H curve and Tested Core Loss	
<i>Jeong-Jong Lee, Soon-O Kwon, Jung-Pyo Hong, Hong-Soon Choi</i>	
PD1.6	911
Contactless Torque Transmission by a Magnetic Gear	
<i>Veronika Reinauer, Jan Albert, Remus Banucu, Wolfgang Hafla, Christian Scheiblich, Wolfgang M. Rucker</i>	
PD1.7	913
Tests and simulation results of the static torque characteristics of a brushless DC permanent magnet motor	
<i>Pedro Pereira de Paula, Paulo Sérgio Ulian</i>	
PD1.8	915
An Improved Calculation Model for Core Losses of Soft Magnetic Composite Motors	
<i>Yunkai Huang, Jianguo Zhu, Youguang Guo</i>	
PD1.9	917
An Extended B-H Curve Modeling of 2D Magnetic Properties of Silicon Steel and Its Influences on Motor Performances	
<i>Hee Sung Yoon, Pan-seok Shin, Chang Seop Koh</i>	
PD1.10	919
Computation on Electromagnetic Torque of Solid Rotor Induction Motor	
<i>Yan Hu</i>	
PD1.11	921
Dynamic Characteristics Analysis in A Pole Changing Memory Motor Using Coupled FEM & Preisach Modeling	
<i>Yong Hyun Cho, Il Kyo Lee, Jung Ho Lee</i>	

PD1.12	923
Improvement in accuracy of thermal FEM model partition wall with the use of optimization algorithm	
<i>Peter Kitak, Igor Ticar, Joze Pihler, Oszkar Biro, Kurt Preis</i>	
PD1.13	925
Field Computation and Performance of a Series-Connected Self-Excited Synchronous Generator	
<i>Tze-Fun Chan, Weimin Wang, Loi Lei Lai</i>	
PD1.14	927
Power Factor Calculation by the Finite Element Method	
<i>Claudia Andréa da Silva, Francis Bidaud, Philippe Herbet, José Roberto Cardoso</i>	
PD1.15	929
Comprehensive Research on Stator Shapes and Frames in Switched Reluctance Motor: Electromagnetic, Thermal and Vibration Analyses	
<i>Jian Li, Xueguan Song, Dawoon Choi, Yunhyun Cho</i>	
PD1.16	931
Investigation of System Efficiency in Nd-Fe-B and Ferrite Magnet Synchronous Motors with Coupled Field-Circuit Analysis	
<i>Tao Sun, Soon-O Kwon, Jung-Pyo Hong</i>	
PD1.17	933
Minimizing Torque Ripple of a BLDC Motor by Offsetting Cogging Torque with Voltage Control	
<i>Jin seok Jang, Byung teak Kim</i>	
PD1.18	935
A novel transverse flux linear motor for direct drive applications	
<i>Junghwan Chang, Jiwon Kim, Dohyun Kang, Deokje Bang</i>	
PD1.19	937
Design Strategy of Interior Permanent Magnet Synchronous Motor for Electric Power Steering Considering Cogging Torque and Torque Ripple using Current Harmonics	
<i>Soon-O Kwon, Jeong-Jong Lee, Tao Sun, Young-Kyun Kim, Geon-Ho Lee, Jung-Pyo Hong</i>	
PD1.20	939
Calculate the Parameters of IPMSM according to distance of PM and Magnetic saturation.	
<i>Ik Sang Jang, Chang Sung Jin, Seung Joo Kim, Ju Lee</i>	

PD1.21941
Axial Magnetic Flux and Eddy-Current Loss in Core Ends of a Large Induction Machine

Ranran Lin, Ari Haavisto, Antero Arkkio

PD1.22 943
Double-layer Interior-PM Design in Single-Phase Line-Start Motor For Reducing Magnet

Liang Fang, Byeong-Hwa Lee, Jung-Pyo Hong, Hyuk Nam

Session PD2: Electrical machines and Drives V

10:40-12:10 – Room: Poster Session Room I

PD2.1..... 945
Study on Partial Discharge Location in Oil Based on Ultrasonic Phased Array and Wideband Array Signal Processing

Qing Xie, Yan-qing Li, Fang-cheng Lu, Cheng-rong Li, Nna Wang

PD2.2947
A Study on the Relation between Deformation of Stator Yoke and Acoustic Noise in Interior Permanent Magnet Motor

DoJin Kim, SangHo Lee, JeongJong Lee, JiMin Kim, JungPyo Hong

PD2.3 949
Analysis of Vibration and Music Scale of Brushless DC Motor with Surface Permanent Magnets

Takeo Ishikawa, Satoshi Azami, Ryo Ataka

PD2.4951
Internal Faults Simulation and Analysis for Linear Synchronous Motor

Haitao Yu

PD2.5 953
Effects of Magnetic Saturation on Spindle Motor Characteristics

Jaenam Bae, Seung-Joo Kim, Sung-Chul Go, Dong-Woo Kang, Sang-Hwan Ham, Ju Lee

PD2.6955
The Optimal Design of the Secondary Reaction Plate Shape of Single-Sided Linear Induction Motor for Urban Maglev Train

Sang-Hwan Ham, Sung-Gu Lee, Su-Yeon Cho, Chang-Sung Jin, Ju Lee

PD2.7	957
The impact of static eccentricity on rotor bar current distribution in case of one broken bar in Induction Motor	
<i>Hubert Razik, François-Michel Sargos</i>	
PD2.8	959
Optimum LIM Interval Selection of Vector Controlled Moving Secondary Plate Conveyor System Using FEM & SUMT	
<i>TaeHoon Lee, YongHyun Cho, JungHo Lee</i>	
PD2.9	961
Novel method for analyzing the Permanent Magnet Motors	
<i>Sung-Hong Won, Cheol-Jick Ree, Ju Lee</i>	
PD2.10	963
Design of copper die-cast rotor bar of single phase induction motor for high starting torque	
<i>Kwangsoo Kim, Jong Bin Im, Seung Joo Kim, Won Ho Kim, Ju Lee</i>	
PD2.11	965
A Study on Performance Simulation of Interior Permanent Magnet Synchronous Motor for Electric Vehicle considering Nonlinearity	
<i>Ki-Chan Kim, Ju Lee</i>	
PD2.12	967
Characteristics Analysis & Optimum Design of Anisotropy Rotor SynRM Using Coupled	
<i>Il Kyo Lee, Yong Hyun Cho, Jung Ho Lee</i>	
PD2.13	969
Irreversible Demagnetization on Permanent Magnet Motors	
<i>Flavio Jorge Haddad Kalluf, Luiz Von Dokonal, Rodrigo Stanzola Teixeira</i>	
PD2.14	971
Improved FE Post-Processors for Design of PM Fractional-Slot Machines	
<i>Jérôme Cros, Mehdi Taghizadeh, Philippe Viarouge</i>	
PD2.15	973
Novel DTC Based on SVM with Adaptive stator Flux Observer for Induction Motors	
<i>Zhifeng Zhang, Renyuan Tang, Baodong Bai</i>	

PD2.16	975
A New Anisotropic Bonded NdFeB Permanent Magnet and Its Application to a Small DC Motor	
<i>Chang Seop Koh, Hyo Jun Kim, Hee Sung Yoon</i>	
PD2.17	977
Optimum Design For Premium Efficiency of 250 kW Traction Induction Motor Using Response Surface Methodology & FEM	
<i>SUNG JU MUN</i>	
PD2.18	979
Optimal PM Design of PMA-SynRM for Wide Constant-Power Operation and Torque Ripple Reduction	
<i>WonHo Kim, KwangSoo Kim, SeungJoo Kim, JongBin Im, Ju Lee</i>	
PD2.19	981
Study of Static and Dynamic Eccentricities of a Synchronous Generator Using 3D FEM	
<i>Bruno Akihiro Tanno Iamamura, Yvonnick Le Menach, Abdelmounaïm Tounzi, Nelson Sadowski, Eilin Guillot</i>	
PD2.20	983
FE-Circuit Coupled High Frequency Model of Electric Machines for Simulation and Evaluation of EMI Issues in Motor Drives	
<i>Osama A Mohammed</i>	

Session PD3: Devices and Applications II

10:40-12:10 – Room: Poster Session Room II

PD3.1	985
A New Scheme for Detecting Longitudinal Defects in Conductive Tubes by EC Testing	
<i>Alessandro Formisano, Raffaele Martone, Francesco Iacotucci, Fabrizio Ferraioli</i>	
PD3.2	987
A Study on the FE Analysis of a Flux-Reversal Machine under 4-switch converter	
<i>Tae Heoung Kim, Hyun-Soo Kang, Byoung-Kuk Lee</i>	
PD3.3	989
EEG inverse problem solution with minimal influence of the conductivity	
<i>Bertrand Russel Yitembe, Guillaume Crevecoeur, Luc Dupré, Roger Van Keer</i>	

PD3.4	991
Modeling and Extraction of Parasitics in IGBT Modules	
<i>Zarife Cay, Olaf Henze, Stephan Koch, Thomas Weiland</i>	
PD3.5	993
Modelling Motion, Stiffness and Damping of a Permanent-Magnet Shaft Coupling	
<i>Antero Arkkio, Asko Niemenmaa, Lauri Salmia, Juha Saari</i>	
PD3.6	995
Discrete geometric approach to modeling the cathodic region in a PEM fuel cell	
<i>Paolo Bettini, Ruben Specogna, Andrea Stella, Francesco Trevisan</i>	
PD3.7	997
Modeling of a current sensor with a FE-tuned MEC: Parameters identification protocol	
<i>Fabien Sixdenier, Marie-Ange Raulet, Bruno Lefebvre</i>	
PD3.8	999
Study of Three Dimensional Flux Distribution in Nonlinear Core of Power Transformers Based on 3-D FEM Modeling	
<i>Seyed Ali Mousavi, Mohsen Faridi, Vahid Nabaei, Hashemi Ehsan</i>	
PD3.9	1001
Wideband Equivalent Circuit Model for Automotive Ignition Coil	
<i>JIA Jin, YU Ji-hui, WANG Quan-di, ZHENG Ya-li</i>	
PD3.10	1003
Factors Affecting Eddy Current Losses of Segmented Nd-Fe-B Sintered Magnets without Insulation	
<i>Norio Takahashi, Hirofumi Shinagawa, Daisuke Miyagi, Yuhito Doi, Koji Miyata</i>	
PD3.11	1005
Electromagnetic Analysis of Umbilical Cables with Complex Configurations	
<i>Mauricio Barbosa de Camargo Salles, Mauricio Caldora Costa, Mario Leite Pereira Filho, Jose Roberto Cardoso, Giuseppe Renato di Marzo</i>	
PD3.12	1007
Signal-to-noise ratio analysis of radio frequency coils in low-field MRI systems	
<i>Ye Li, Xiaohua Jiang</i>	

PD3.13	1009
Time Domain Analysis Of Compact Lumped Element Circulators	
<i>Dirk Schulz</i>	
PD3.14	1012
Determination of a correction factor due to joints for core losses in power transformers by 2D FEA	
<i>Wilerson Venceslau Calil, Viviane Cristine Silva</i>	
PD3.15	1014
Effects of a remanent magnetization on the detection signals of the metal loss in Magnetic Flux Leakage type NDT	
<i>Kang Seo, Gwan Soo Park</i>	
PD3.16	1016
Force Computation in a MEMS Structure Using Adaptive Mesh Refinement	
<i>Francisc Attila Bölöni, Abdelkader Benabou, Guillaume Krebs, Abdelmounaim Tounzi</i>	
PD3.17	1018
A methodology for applying three-dimensional constrained Delaunay tetrahedralization algorithms on MRI medical images	
<i>Feras Abu Talib, Dennis D. Giannacopoulos</i>	
PD3.18	1020
Analysis of copper losses in resistance spot welding transformer windings with Dowell method and numerical approach	
<i>Jelena Popović, Drago Dolinar, Gorazd Štumberger, Igor Tičar, Beno Klopčič</i>	
PD3.19	1022
Lightning Induced Voltage on the Underground Pipeline near Overhead Transmission Line	
<i>Lei Qi, Xiang Cui, Yan Wu, Zhaonan Luo</i>	
PD3.20	1024
A Development on the Analysis Method of Synchronous Reluctance Motor Using FEM Coupled Electromagnetic Field of Thermal Field	
<i>TaeHoon Lee, SungJu Mun, JungHo Lee</i>	

Session PD4: Numerical Techniques IV

10:40-12:10 – Room: Poster Session Room II

- PD4.1** 1026
Novel Preconditioning in Finite Element Analysis of Electromagnetic Field:
A- ϕ Block IC Preconditioning
Yasuhito Takahashi, Takeshi Mifune, Takeshi Iwashita
- PD4.2** 1028
H-Matrix Based Operator Preconditioning For Full Maxwell At Low
Frequencies
Jörg Ostrowski, Mario Bebendorf, Ralf Hiptmair, Florian Krämer
- PD4.3** 1030
The hybrid numerical integration algorithm of Hankel transform for magnetic
induction tomography
He wei, Luo haijun, Xu zheng, Li qian, Wang junfeng
- PD4.4** 1032
A New Multilevel Smoothing Method for the Wavelet-Based Algebraic
Multigrid
Fabio Henrique Pereira, Silvio Ikuyo Nabeta
- PD4.5** 1034
Analysis of Omnidirectional Compact Dual-reflector Antenna
José Ricardo Bergmann, Sandro Rogério Zang
- PD4.6** 1036
Mixed Fault Diagnosis of Squirrel Cage Induction Motor by Winding Function
Approach
Kyungil Woo, Daesuk Joo
- PD4.7** 1038
Simple Parallelization Strategy for Mesh Refinement Algorithms
Thiago Emanuel Alves Macêdo, Adriano Chaves Lisboa, Renato Cardoso Mesquita
- PD4.8** 1040
Magnetic Field Analyses of Architectural Components Using Homogeneous
Technique
*Shunya Odawara, Yu Haraguchi, Kazuhiro Muramatsu, Keita Yamazaki,
Shigetaka Hirosato*

PD4.9	1042
Finite element method coupled with Delaunay refinement for curved geometries	
<i>Adriano Chaves Lisboa, Renado Cardoso Mesquita, Rodney Rezende Saldanha, Ricardo Hiroshi Caldeira Takahashi</i>	
PD4.10	1044
Impact of Tetrahedral Mesh Quality for Electromagnetic and Thermal Simulations	
<i>Julien Dardenne, Nicolas Siauve, Sébastien Valette, Rémy Prost, Noël Burais</i>	
PD4.11	1046
Parallel Computing of Magnetic Field for Rotating Machines on PC Cluster	
<i>Tomohito Nakano, Yoshihiro Kawase, Tadashi Yamaguchi</i>	
PD4.12	1048
Mesh Refinement in Eddy Current Testing with Separated T-R probes	
<i>Yahya Choua, Laurent Santandréa, Yann Le Bihan, Claude Marchand</i>	
PD4.13	1050
Demagnetized Permanent-Magnet Fault Recognition in Synchronous Motors	
<i>Bashir Mahdi Ebrahimi, Jawad Faiz</i>	
PD4.14	1052
Induction motor analysis using optimal torque predictor and massive conductor approach	
<i>Slawomir Stepien</i>	
PD4.15	1054
FD-TD Calculations of SAR validated through measurements	
<i>Ana de Oliveira Rodrigues, Juliano Junio Viana, Alisson Henrique Quemel de Souza, Eduardo Aparecido dos Santos</i>	
PD4.16	1056
Finite Element Method Model Improvement for the Conducted Emission Analysis of a Lighting Fixture	
<i>Yoshihiko Namba, Tomoyuki Kida, Katsuhiko Hirata, Shohei Ikejiri, Fuminao Obayashi</i>	
PD4.17	1058
Reduced Thermal Model for Stator Slot	
<i>Idoughi Laïd, Mininger Xavier, Bouillault Frédéric, Hoang Emmanuel</i>	

PD4.18	1060
Distributed Processing Management using ROME	
<i>Nancy Mieko Abe, Claudio Dias Marins, Angelo Passaro</i>	
PD4.19	1062
Evaluation of Solution Accuracy on Finite Element Analysis using Magnetic Flux Lines	
<i>So Noguchi, Hideo Yamashita</i>	
PD4.20	1064
Performance Analysis of Inductive Coil Gun Based on Field-Circuit Method	
<i>Liu Shoubao, Ruan Jiangjun, Zhang Yu, Peng Ying, Du Zhiye</i>	
PD4.21	1066
Finite Element Magnetic Models via a Coupling of Subproblems of Lower Dimensions	
<i>Patrick Dular, Ruth V. Sabariego, Christophe Geuzaine, Mauricio V. Ferreira da Luz, Patrick Kuo-Peng, Laurent Krähenbühl</i>	
PD4.22	1068
Improved Bacterial Foraging Strategy Applied to TEAM Workshop Benchmark Problem 22	
<i>Piergiorgio Alotto, Leandro dos Santos Coelho, Camila da Costa Silveira, Cezar Augusto Sierakowski</i>	
PD4.23	1070
A Population Based Incremental Learning Method for Robust Optimal Solutions	
<i>S.L. Ho, Shiyong Yang</i>	
PD4.24	1072
Krylov-based algebraic multigrid for edge elements	
<i>François Musy, Artem Napov, Yvan Notay, Ronan Perrussel, Riccardo Scorretti</i>	

Session OD2: Numerical Techniques and Software Methodology

13:30-15:20 – Room: Plenary Session Room

OD2.1	1074
(Invited) A p-adaptive scheme for scalar fields, using high-order, singular finite elements	
<i>Jon Webb</i>	

OD2.2	1076
A Discrete (2+1)-D Formulation for 3-D Field Problems with Continuous Symmetry	
<i>Bernhard Auchmann, Bernd Flemisch, Stefan Kurz</i>	
OD2.3	1078
Electromagnetic Field Computation in 2D Using the Discrete 1D Green's Function	
<i>Do Wan Kim, Young-Cheol Yoon</i>	
OD2.4	1080
Load Scheduling for Power Aware Matrix Multiplication on CPU-GPU Multiprocessing Platform	
<i>DaQi Ren, Reiji Suda</i>	
OD2.5	1082
Finite element sparse matrix vector multiplication on graphic processing units	
<i>Maryam Mehri Dehnavi, David M. Fernández, Giannacopoulos, Dennis D.</i>	

Surface-Impedance Boundary Conditions in Dual Time-Domain Finite-Element Formulations

R. V. Sabariego ¹, P. Dular ^{1,2}, C. Geuzaine ¹ and J. Gyselinck ³

¹ Dept. of Electrical Engineering and Computer Science, University of Liège, Belgium, r.sabariego@ulg.ac.be

² Fonds de la Recherche Scientifique - FNRS, Belgium

³ Dept. of Bio-, Electro- and Mechanical Systems (BEAMS), Université Libre de Bruxelles (ULB), Belgium

Abstract—This paper deals with time-domain surface-impedance boundary conditions in computational magnetodynamics considering both magnetic-vector potential and magnetic-field formulation. Based on the resolution of the 1-D eddy-current problem in a semi-infinite slab, the massive conducting region is accounted for by choosing a number of exponentially decreasing trigonometric basis functions covering the relevant frequency range. Herein the method is elaborated for the magnetic-field formulation. Results for both formulations are compared and validated on a two-dimensional test case.

I. INTRODUCTION

SURFACE-impedance boundary conditions (SIBCs) are widely applied in frequency-domain eddy-current problems for considering massive conducting regions. The approach is based on the relation between the tangential components of the electric and the magnetic field at the surface of the conducting region and allows to avoid the discretisation of its volume. The few time-domain extensions proposed to date are mostly based on the fast Fourier transform [1], [2], or on the iterative coupling between the main 3-D finite element (FE) model and a large number of 1-D FE calculations (with classical nodal basis functions) [3].

In [4], the authors proposed a time-domain approach based on the magnetic-vector-potential formulation. This approach is herein extended for the magnetic-field formulation. Results of both formulations will be compared and validated on a 2-D test case.

II. 1-D EDDY CURRENT PROBLEM IN SEMI-INFINITE SLAB

Let us consider a low-frequency eddy-current problem in a bounded domain $\Omega = \Omega_c \cup \Omega_c^C \in \mathbb{R}^3$ with boundary Γ . The conductive and non-conductive parts of Ω are denoted by Ω_c and Ω_c^C , respectively. We are only concerned with linear and homogeneous media, i.e. the conductivity σ (resistivity $\rho = 1/\sigma$) and the permeability μ (reluctivity $\nu = 1/\mu$) are constant scalars in Ω .

The following Maxwell equations and constitutive laws are taken into account:

$$\operatorname{div} \underline{b} = 0, \quad \operatorname{curl} \underline{h} = \underline{j}, \quad \operatorname{curl} \underline{e} = -\partial_t \underline{b}, \quad (1 \text{ a-c})$$

$$\underline{j} = \sigma \underline{e}, \quad \underline{b} = \mu \underline{h}, \quad (2 \text{ a b})$$

where \underline{b} is the flux density (or induction), \underline{h} the magnetic field, \underline{j} the current density and \underline{e} the electric field.

This work was partly supported by the Belgian Science Policy (IAP P6/21).

A. 1-D eddy-current problem and FE model

The 1-D eddy-current problem in a semi-infinite slab ($0 \leq x \leq \infty$, $b(x, t)$ and $h(x, t)$ parallel to the z -axis, $j(x, t)$ and $e(x, t)$ parallel to the y -axis) can be expressed in terms of the z -component of $\underline{h}(x, t)$ denoted by $h(x, t)$:

$$\partial_x^2 h = \sigma \mu \partial_t h \quad \text{with} \quad h(x = \infty, t) = 0, \quad (3)$$

where the boundary condition at infinity ($x = \infty$) ensures the uniqueness of $h(x, t)$. The sinusoidal steady-state solution of (3) at frequency f (pulsation $\omega = 2\pi f$), with boundary condition $h(x = 0, t) = \hat{h} \cos(\omega t + \phi)$, reads

$$h(x, t) = \hat{h} \cos(\omega t + \phi) e^{-x/\delta} \cos(x/\delta) + \hat{h} \sin(\omega t + \phi) e^{-x/\delta} \sin(x/\delta), \quad (4)$$

with δ the skin depth and ϕ an arbitrary phase angle.

The FE discretisation of (3) by means of N basis functions $\alpha_i(x)$, $0 \leq x < \infty$, $1 \leq i \leq N$, leads to a system of first-order differential equations. It reads

$$[S][H(t)] + [M] \partial_t [H(t)] = [V(t)], \quad (5)$$

where $[H(t)]$ is the column matrix that comprises the N degrees of freedom of $h(x, t)$; the only non-zero element (first) of column matrix $[V(t)]$ equals the electromotive force; the elements of $[S]$ and of $[M]$ are given by

$$S_{ij} = \rho \int_0^\infty \partial_x \alpha_i(x) \partial_x \alpha_j(x) dx, \quad (6)$$

$$M_{ij} = \mu \int_0^\infty \alpha_i(x) \alpha_j(x) dx. \quad (7)$$

The associated positive-definite quadratic forms are the instantaneous magnetic energy density $w(t)$ and the instantaneous eddy-current loss density $p(t)$:

$$w = [H]^T [M] [H] \quad \text{and} \quad p = [H]^T [S] [H]. \quad (8)$$

B. Dedicated basis functions

The choice of basis functions is motivated by the solution of the 1-D eddy-current problem (4) [4]. For a given time-domain problem, a set of skin depths δ_k can be preset accounting for the frequency content of the magnetic fields and the accuracy required. We define thus the following $2n$ basis functions:

$$\alpha_{c1}(x) = e^{-x/\delta_1} \cos(x/\delta_1), \quad (9)$$

$$\alpha_{ck}(x) = e^{-x/\delta_k} \cos(x/\delta_k) - \alpha_{c1}(x), \quad 2 \leq k \leq n, \quad (10)$$

$$\alpha_{sk}(x) = e^{-x/\delta_k} \sin(x/\delta_k), \quad 1 \leq k \leq n. \quad (11)$$

Note that all basis functions vanish at the boundary except the first one, i.e. $\alpha_{c1}(x = 0) = 1$.

III. INTEGRATION IN FE MODEL

The SIBC method is applied to a massive subdomain Ω_m of Ω_c . The weak form of the Faraday law (1c) is written as:

$$\partial_t(\mu \underline{h}, \underline{h}')_{\Omega \setminus \Omega_m} + (\rho \text{curl } \underline{h}, \text{curl } \underline{h}')_{\Omega_c \setminus \Omega_m} + \langle n \times e, h' \rangle_{\partial \Omega_m} = 0, \quad (12)$$

where $(\cdot, \cdot)_{\Omega}$ and $\langle \cdot, \cdot \rangle_{\partial \Omega_m}$ denote a volume integral in Ω and a surface integral on $\partial \Omega_m$, respectively, of the scalar product of their arguments; \underline{n} is the outward normal on $\partial \Omega_m$. At the discrete level Whitney edge elements are adopted for (12).

Ignoring the finite depth of Ω_m and the curvature of $\partial \Omega_m$, we can consider a local coordinate system and write the magnetic field in Ω_m as $\underline{h} = \underline{h}_t(y, z) p(x, t)$, with \underline{h}_t tangential to $\partial \Omega_m$ and $p(x, t)$ differentiable with respect to x ($0 \leq x < \infty$). With our time-domain approach, the two volume integrals considered in Ω_m are thus reduced to the following surface integrals:

$$\partial_t(\mu \underline{h}, \underline{h}')_{\Omega_m} = \partial_t \langle \underline{h}_t, \underline{h}'_t \rangle_{\partial \Omega_m} \cdot \mu \int_0^{\infty} p p' dx, \quad (13)$$

$$(\rho \text{curl } \underline{h}, \text{curl } \underline{h}')_{\Omega_m} = \langle \text{curl } \underline{h}_t, \text{curl } \underline{h}'_t \rangle_{\partial \Omega_m} \cdot \rho \int_0^{\infty} \partial_x p \partial_x p' dx, \quad (14)$$

Considering $\alpha_{ck}(x)$ and $\alpha_{sk}(x)$ for the space discretisation of $p(t)$ and $p'(t)$, the integration along the x -axis in (13) and (14) produces the elements of the matrices $[S]$ and $[M]$.

IV. APPLICATION EXAMPLE

The 2-D application example concerns a non-magnetic conducting cylinder (radius $R = 10$ cm; $\sigma = 6 \cdot 10^7$ S/m) inside an inductor (rectangular cross-section) with imposed current. Only one quarter of the geometry is modeled (see Fig. 1). The

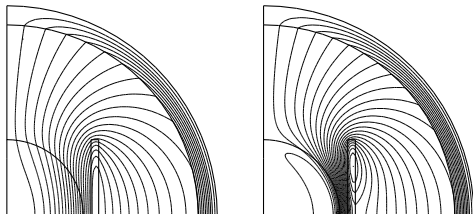


Fig. 1. Flux pattern (in phase with imposed sinusoidal current) with $\delta/R = 0.5$ (left) and $\delta/R = 0.1$ (right)

classical magnetic-field (h-)formulation and magnetic-vector-potential (a-)formulation with a very fine discretisation of the cylinder near its surface provide an accurate reference solution. Two typical flux patterns obtained with the a-formulation are depicted in Fig. 1. When applying the SIBC, only the mesh outside the cylinder is effectively considered. A trapezoidal current varying between 1 and -1 at 1 kHz is considered. We adopt a low order approximation of the SIBC with $f_1 = 1$ kHz and further discrete frequencies being odd multiples of f_1 . The induction and the current density in a point at the surface of the cylinder are shown in Fig. 2 for the first fundamental period. Note that the results obtained with the low-order SIBC converge faster ($n = 1$) for the induction with the h-formulation and for the current with the a-formulation.

The magnetic energy and the joule losses in the cylinder have been calculated during the first period with the fine model

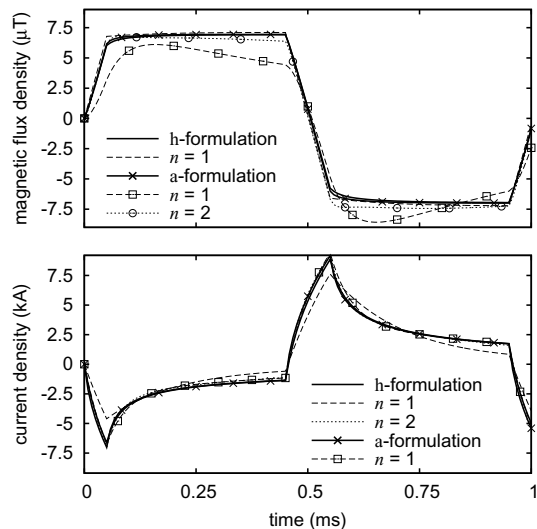


Fig. 2. Induction and current density in a point at the surface of the cylinder versus time obtained with dual fine models and time-domain SIBC approaches

(without SIBC) and the low-order SIBC (n equal to 1 and 2). A good convergence of the SIBC results towards the reference results for both formulations is observed in Fig. 3.

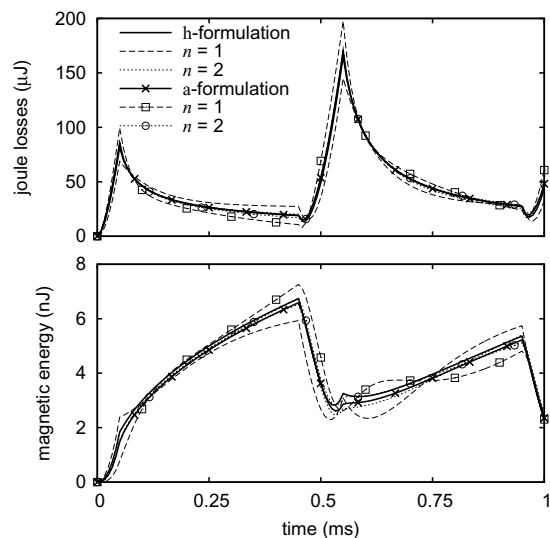


Fig. 3. Joule losses and magnetic energy in the cylinder versus time obtained with dual fine models and time-domain SIBC approximations ($n = 1, 2$)

Further results obtained with the two dual formulations on a 3-D application will be included in the full paper.

REFERENCES

- [1] S. Barmada, L. Di Rienzo, N. Ida and S. Yuferev, "The use of surface impedance boundary conditions in time domain problems: numerical and experimental validation," *ACES Journal*, vol. 19, pp. 76–83, July 2004.
- [2] K.R. Davey and L. Turner, "Transient eddy current analysis for generalized structures using surface impedances and the fast Fourier transform," *IEEE Trans. Magn.*, vol. 26, pp. 1164–1170, May 1990.
- [3] D. Rodger and H.C. Lai, "A surface impedance method for 3D time transient problems," *IEEE Trans. Magn.*, vol. 35, pp. 1369–1371, May 1999.
- [4] J. Gyselinck, P. Dular, C. Geuzaine, R. V. Sabariego, "Surface-impedance boundary conditions in time-domain finite-element calculations using the magnetic-vector-potential formulation," *IEEE Trans. Magn.*, vol. 45, pp. 1280–1283, March 2009.

Kriging for eddy-current testing problems

S. Bilicz ^{*†}, E. Vazquez [‡], Sz. Gyimóthy [†], J. Pávó [†], M. Lambert ^{*}

^{*} Département de Recherche en Électromagnétisme, Laboratoire des Signaux et Systèmes UMR8506 (CNRS-SUPELEC-Univ Paris-Sud), 91192 Gif-sur-Yvette cedex, France

[†] Budapest University of Technology and Economics, Egrý J. u. 18, H-1521 Budapest, Hungary,

[‡] SUPELEC, 91192 Gif-sur-Yvette cedex, France

E-mail: bilicz@evt.bme.hu

Abstract: Accurate numerical simulation of eddy-current testing (ECT) experiments usually requires large computational efforts. To avoid time-consuming computations, a natural idea is to build a cheap approximation of the expensive-to-run simulator. In this paper, a kriging-based approximation of an ECT simulator is presented. Kriging is widely used in other domains, but is still quite unexplored in the ECT community. The kriging approximation is built using a random process model of the simulator and a set of simulation results obtained for a number of different input configurations. The resulting approximation might yield almost the same results as those of the simulator.

Keywords: Eddy-current testing; Kriging; simulator approximation

I. INTRODUCTION

Eddy-current testing is well-known for a long time and is applied in a wide range of industrial problems. However, the accurate numerical simulation of the physical phenomenon is still challenging. Finite element and/or integral equation methods are able to provide acceptable accuracy, at a quite high price however, since these methods are implemented using technically complex computer programs that generally necessitate advanced hardware and long computation times. Nowadays, more and more emphasis is put on the *emulation*, or *surrogate modeling* of EM phenomena [1]. This trend leads the electromagnetic community to consider new methods based on mathematical tools from other domains.

Our paper presents an application of *kriging* to eddy-current testing problems. The proposed method provides a way to construct a cheap approximation for a *specific* ECT problem. The main idea is to build a database of ECT configurations, i.e. a set of pairs consisting of a vector of the parameters of a defect and the corresponding output signal, and then to use kriging to predict the output signal at any untried vector of defect parameters. Once the database is built, one does not need the expensive simulator any longer, but only a cheap kriging model.

Kriging is a prediction method appeared in the 60s in the domain of geostatistic. By now, several variants of the method have been developed and a comprehensive literature deals with kriging (see, e.g. [2]). For a recent review of the topic, see [3]. Some applications in electromagnetics are presented for instance in [4]. Also the authors have applied kriging to solve ECT inverse problems in [5]. However, the approach of [5] focuses on the kriging prediction of a *cost-function* (to be minimized in an optimization loop) – now the present paper deals with the use of kriging *directly* on the output signal.

II. THE PROPOSED METHOD

A. The forward prediction problem

The cheap input-output approximation will be built from a database of computer simulations of the ECT problem. To simplify the notation, let us suppose that a vector of output parameters \mathbf{y} is related to a vector of input parameters \mathbf{x} through

$$\mathbf{y} = \mathbf{f}(\mathbf{x}), \quad (1)$$

\mathbf{f} representing the underlying physical phenomena. For eddy-current testing application \mathbf{x} might be the geometrical parameters describing a defect affecting a plate and \mathbf{y} the measured data (coil impedances at different locations above the plate). A possible realization \mathbf{f} is a numerical solution of the corresponding Maxwell's equations.

The proposed method is a two-step approach.

- 1) Compute some corresponding $(\mathbf{x}_i, \mathbf{y}_i), i = 1, \dots, n$ pairs (“samples”) using (1) and store them in a *database* that one will use at the stage 2.
- 2) Fit a kriging interpolator to the samples stored in the database and predict the sought \mathbf{y} output at any arbitrary \mathbf{x} input point.

B. Basics of kriging

The main idea of kriging is to model a real-valued function f by a Gaussian process, the latter being characterized by its mean and its covariance function. The covariance function describes the statistical dependence between two values of the process and it is a scalar function of one parameter under the hypothesis of a *stationary* modeling process. However, the covariance function is not known before f has been observed. Generally, one chooses a class of parameterized covariance functions and tunes the parameters in order to fit the modeling process to the pointwise observations of f .

Once an appropriate covariance function is determined, the prediction $\hat{f}(x)$ of $f(x)$ at any arbitrary x is written as a linear combination of the observations:

$$\hat{f}(x) = \sum_{i=1}^n \lambda_i(x) f(x_i).$$

The $\lambda_i(x)$ weights are computed using the covariance function, by solving a linear system of n equations. The prediction is an *interpolation*, since $f(x_k) = \hat{f}(x_k)$ holds for all $k = 1, 2, \dots, n$. Note that beyond the mere interpolation, kriging provides additional information about the *uncertainty* of the prediction as well.

C. Application to the ECT problem

In (1), the output \mathbf{y} is a vector of size q . It is then appropriate to use an extension of kriging called *co-kriging*

[2] to obtain a prediction model, which takes into account, not only the statistical dependence between the inputs and each component of the vector-valued output, but also the dependence *between* the components of the output vector. Formally, the kriging prediction is

$$\hat{\mathbf{y}}(\mathbf{x}) = \sum_{i=1}^n \Lambda_i(\mathbf{x}) \mathbf{y}_i, \quad (2)$$

with the weighting matrices $\Lambda_i(\mathbf{x})$ of size $q \times q$. The use of n pre-computed samples ($\mathbf{y}_i = \mathbf{y}(\mathbf{x}_i)$, $i = 1, 2, \dots, n$) leads to a linear system of $n \times q$ equations to solve which can be computationally demanding. The hypothesis that all entries of \mathbf{y} have similar statistical behaviour leads to a simpler problem of q distinct kriging models (one for each entry of \mathbf{y}). Due to the assumed statistical similarity of entries, the models are the same and one can then write

$$\hat{\mathbf{y}}^*(\mathbf{x}) = \sum_{i=1}^n \lambda_i(\mathbf{x}) \mathbf{y}_i, \quad (3)$$

using the weighting scalar $\lambda_i(\mathbf{x})$ obtained through the solution of a system of only n linear equations. The common covariance (describing the behaviour of all entries of \mathbf{y}) can be either chosen “by hand” or fitted by maximum likelihood to an appropriate one-dimensional representation of \mathbf{y} (e.g. the first principal component).

The (3) expression is a convenient and computationally cheap interpolator. Beyond the introduction of the method, the main aim of our paper is to examine the validity of the assumptions (leading from the exact (2) to the treatable (3) predictions).

III. ILLUSTRATIVE ECT PROBLEM

In the studied ECT configuration, a volumetric defect (with a $\sigma(\mathbf{r})$ variable conductivity) takes place within a homogeneous, non-magnetic conductive plate (with σ_0 conductivity). An air-cored pancake type coil (probe) scans above the damaged zone, in a plane parallel to the plate. The coil is driven by sinusoidal current and the variations of its impedance at different locations are measured. These locations are placed at the nodes of a rectangular grid, i.e. a surface scan is performed. The defect is assumed to be cuboid-shaped of volume Ω , thus, can be described by a small number of geometrical parameters, such as sizes and positions. The solution of the forward problem is obtained by the classical *volume integral approach* [6]. The electric field at a position \mathbf{r} in the plate is written as a sum of two terms: $\mathbf{E}(\mathbf{r}) = \mathbf{E}^i(\mathbf{r}) + \mathbf{E}^d(\mathbf{r})$ where \mathbf{E}^i is the *incident field* (in a flawless plate), and \mathbf{E}^d is the *defect field*, i.e. the distortion of the field due to the flaw. The current dipole densities \mathbf{P} and \mathbf{P}^i are defined by $\mathbf{P}(\mathbf{r}) = (\sigma(\mathbf{r}) - \sigma_0) \mathbf{E}(\mathbf{r})$ and $\mathbf{P}^i(\mathbf{r}) = (\sigma(\mathbf{r}) - \sigma_0) \mathbf{E}^i(\mathbf{r})$. The interaction of the EM field of the coil with the flaw can be described by an integral equation given by

$$\mathbf{P}(\mathbf{r}) = \mathbf{P}^i(\mathbf{r}) - j\omega\mu_0\sigma_0\chi(\mathbf{r}) \int_{\Omega} \mathcal{G}(\mathbf{r}|\mathbf{r}') \mathbf{P}(\mathbf{r}') dV'. \quad (4)$$

The so-called defect description function $\chi(\mathbf{r})$ is defined as $\chi(\mathbf{r}) = [\sigma(\mathbf{r}) - \sigma_0] / \sigma_0$. $\mathcal{G}(\mathbf{r}|\mathbf{r}')$ is nothing but the classical dyadic Green’s function. Once (4) is solved, the variation

of the coil impedance can be expressed as

$$\Delta Z = -\frac{1}{I_0^2} \int_{\Omega} \mathbf{E}^i(\mathbf{r}) \cdot \mathbf{P}(\mathbf{r}) dV, \quad (5)$$

based on the reciprocity theorem. Here, I_0 denotes the current of the probe coil.

A simple case with two input parameters is chosen to illustrate the method. An OD-type defect (having $\sigma(\mathbf{r}) = 0$ everywhere in Ω) with a known position and width takes place within the plate. The defect is characterized by its length (L) and depth (D , given in % of plate thickness) leading to a 2-dimensional input parameter vector \mathbf{x} . The surface scan of the probe coil is centered on the crack and contains $q = 841$ measurement points and the corresponding q ΔZ complex values (5) are stored in the output parameter vector \mathbf{y} .

The region of interest in the input domain is $0.5 \text{ mm} < L < 3.5 \text{ mm}$ for the length and $10\% < D < 90\%$ for the depth, respectively. In Fig. 1, one can see the input samples (5×5 regularly spaced) and the normalized error of the prediction by (3).

The result is promisingly nice: a very small ($\approx 2\%$) prediction error, by using only $n = 25$ samples (which means that the kriging prediction is made in no time).

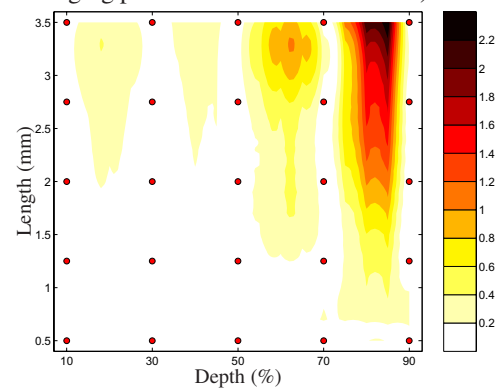


Figure 1. Normalized interpolation error (%) in the example. The normalizing term is $\|\mathbf{y}\|_2$ of the largest ($L = 3.5 \text{ mm}$, $D = 90\%$) defect.

IV. CONCLUSION AND FUTURE WORK

A kriging-based approach as a cheap approximation for ECT problems is presented. In the light of the preliminary results, the method is promising. However, a precise examination of the validity of the simplifications is the main task for the future.

Though no theoretical limitation restricts the method to the domain of ECT problems, we described and formalized our approach in the context of a given ECT configuration. However, generality is not narrowed in this way, one can also easily imagine other applications.

REFERENCES

- [1] J. K. Sykulski, “New trends in optimization in electromagnetics,” *Przegląd Elektrotechniczny*, vol. 83, no. 6, 2007.
- [2] J. Chiles and P. Delfiner, *Geostatistics, Modeling Spatial Uncertainty*. Wiley, 1999.
- [3] J. P. Kleijnen, “Kriging metamodeling in simulation: A review,” *European Journal of Operational Research*, vol. 192, no. 3, 2009.
- [4] L. Lebensztajn, C. A. R. Marretto, M. C. Costa, and J. L. Coulomb, “Kriging: a useful tool for electromagnetic device optimization,” *IEEE Transaction on Magnetics*, vol. 40, no. 2, 2004.
- [5] S. Bilicz, E. Vazquez, M. Lambert, S. Gyimóthy, and J. Pávó, “Characterization of a 3D defect using the Expected Improvement algorithm,” in *Proc. of the 13th IGTE Symposium*, Austria, 2008.
- [6] J. Bowler and S. Jenkins, “Eddy-current probe impedance due to a volumetric flaw,” *Journal of Applied Physics*, vol. 70, no. 3, 1991.

Adaptive Parabolic-Elliptic Time Integration Method for Electroquasistatic Problems

Zsolt Badics*

Rhythmia Medical, Inc.

111 South Bedford Street, Burlington, MA 01803, U.S.A.

badics@ieee.org

Abstract—An adaptive parabolic-elliptic time-integration algorithm based on a singly diagonal implicit Runge-Kutta (SDIRK) scheme is described for the FE solution of nonlinear electroquasistatic (EQS) problems. The algorithm uses the nodal charge as the dynamic variable in addition to the scalar potential, thereby achieving superior stability and performance compared to schemes using only the scalar potential. High-order integration is achieved by incorporating the Jacobian into the time integration formula.

I. BACKGROUND

We can often utilize electroquasistatic (EQS) computational models when the inductive effects are negligible compared to the capacitive and conductive phenomena [1]. A brilliant analysis of how to decide if an EQS model is applicable can be found in [2]. There is a wide range of application areas of EQS models: high voltage problems [3], semiconductor substrate coupling modeling [4], thermistor modeling [5], electroquasistatic MEMS micro-machine modeling [6], and biomedical applications [7].

The EQS approximation allows the representation of the electric field by a scalar potential

$$\mathbf{E} = -\text{grad } \Phi \quad (1)$$

and thus yields the following governing equations:

$$\dot{\rho} = \frac{\partial \rho}{\partial t} = -\text{div } \mathbf{J}(\Phi) \quad (2)$$

$$0 = \rho - \text{div } \mathbf{D}(\Phi) \quad (3)$$

$$\mathbf{J}(\Phi) = \bar{\sigma}(\mathbf{E}(\Phi), \mathbf{x}) \mathbf{E}(\Phi) \quad (4)$$

$$\mathbf{D}(\Phi) = \bar{\epsilon}(\mathbf{E}(\Phi), \mathbf{x}) \mathbf{E}(\Phi) + \mathbf{P}_0 \quad (5)$$

We allow anisotropic, nonlinear and spatially varying conductivity $\bar{\sigma}$ and permittivity $\bar{\epsilon}$. It is an algebraic exercise to incorporate permanent polarization, \mathbf{P}_0 , into the algorithm. Therefore, we assume $\mathbf{P}_0=0$ for the rest of the discussion.

The most common solution approach is to eliminate the volumetric charge distribution by plugging (3) into (2)

$$\frac{\partial}{\partial t} [\text{div}(\bar{\epsilon} \text{grad } \Phi)] + \text{div}(\bar{\sigma} \text{grad } \Phi) = 0 \quad (6)$$

and derive a time integration scheme for (6). The main downside of this approach is that the EQS model allows temporal discontinuity in the excitation potential, which can seriously degrade the performance of adaptive variable-step time integration methods. It is also difficult to model problems by (6) when perfect insulator regions or high conductivity contrasts are present.

We find advantageous to develop a time integration scheme directly for the parabolic-elliptic system (2), (3).

II. FORMULATION

For the sake of simplicity, let us derive the time integration method for the Dirichlet problem depicted in Figure 1. (The generalization to more complex arrangements, boundary conditions and excitations is straightforward.) Since the two domains have different material properties, a surface charge density q appears on the interface Σ [2] satisfying

$$\dot{q} = \frac{\partial q}{\partial t} = -(\hat{\mathbf{n}} \cdot \mathbf{J}^+ - \hat{\mathbf{n}} \cdot \mathbf{J}^-) \quad (7)$$

$$0 = q - (\hat{\mathbf{n}} \cdot \mathbf{D}^+ - \hat{\mathbf{n}} \cdot \mathbf{D}^-) \quad (8)$$

Let us split $\Phi = v + v_D$, where $v = 0$ and $v_D = \Phi_D$ on the boundary Γ_D as usual. Thus the weak form of the parabolic-elliptic system (2), (3), (7) and (8) is

$$\int_{\Omega} v' \dot{\rho} + \int_{\Sigma} v' \dot{q} ds = \int_{\Omega} \text{grad } v' \cdot \mathbf{J}(v) + \int_{\Omega} \text{grad } v' \cdot \mathbf{J}(v_D) \quad (9)$$

$$0 = \int_{\Omega} \rho' \rho + \int_{\Sigma} \rho' q ds + \int_{\Omega} \text{grad } \rho' \cdot \mathbf{D}(v) + \int_{\Omega} \text{grad } \rho' \cdot \mathbf{D}(v_D) \quad (10)$$

where v' and ρ' are the weighting functions. We can write the abstract differential algebraic equation (DAE) system (9), (10) in the concise form of an abstract Cauchy problem

$$H\dot{y} = Ky + K_D v_D(t) = F(t, y), \quad y(0) = y_{initial} \quad (11)$$

where $y = [\rho \quad q \quad v]^T$.

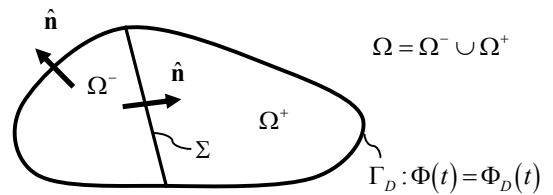


Fig. 1. Dirichlet problem with two regions having different materials

III. TEMPORAL DISCRETIZATION

We discretize (11) in time first by utilizing a one-step SDIRK (singly diagonal implicit Runge-Kutta) method. The application of DIRK schemes for electromagnetic problems is proved to be very efficient, especially when the problem is stiff [8], [9], [10]. We follow the Rosenbrock type SDIRK discretization scheme discussed in detail in [11].

Suppose that at time step t_n y is y_n and the selected time step is τ_n . Then, the M -stage SDIRK scheme estimates y_{n+1} at the next time step $t_{n+1} = t_n + \tau_n$ in the form

*The author was with Ansoft Corp. when this research was pursued.

$$y_{n+1} = y_n + \sum_{s=0}^{M-1} m_s Y_{n,s}; \quad Y_{n,s} = [R_{n,s} \quad Q_{n,s} \quad V_{n,s}]^T \quad (12)$$

where the stage variables $Y_{n,s}$ are computed recursively by

$$\begin{aligned} \left[\frac{1}{\tau_n \gamma} H - F_y(t_n, y_n) \right] Y_{n,s} &= F(t_s, y_s) \\ &+ \tau_n \gamma_s F_t(t_n, y_n) - \sum_{j=0}^{s-1} \frac{c_{sj}}{\tau_n} H Y_{n,j}; \quad s = 0, 1, \dots, M-1 \end{aligned} \quad (13)$$

Here F_y is a linear operator representing the Fréchet derivative of F and

$$t_s = t_n + \alpha_s \tau_n, \quad y_s = y_n + \sum_{j=0}^{s-1} a_{sj} Y_{n,j} \quad (14)$$

The coefficients m_s , γ , γ_s , c_{sj} , α_s , and a_{sj} are selected to obtain desired properties [11]. In order to choose optimal time steps adaptively we employ the time step control algorithm described in [11]. Notice that Newton iteration is not required in the nonlinear case when solving (13) because the Jacobian is incorporated directly into the time integration formula.

IV. SPATIAL DISCRETIZATION

We discretize the scalar variables ρ , q , and v of the boundary value problem (13) in space by the finite element method. One troublesome issue is that we have to introduce the surface variable q for all the interfaces where the conductivity is discontinuous. This significantly increases the complexity of the implementation. Fortunately, there is remedy for this problem. The idea is to introduce nodal charges [12] analogously to the nodal forces in mechanical FE models.

Consider the volumetric and surface charge density terms in the weak form (9) and (10). The corresponding charge density terms in the FE discretization of (13) can be replaced by

$$\eta_m = \int_{\Omega} \alpha_m \rho + \int_{\Sigma} \alpha_m q ds \quad (15)$$

where α_m is the shape function and η_m is the nodal charge associated with the FE node m . By utilizing (15) the finite element y vector contains only the nodal charges and the nodal values of the electric scalar potential. Similarly, we can introduce nodal charge stage variables in (12) instead of $R_{n,s}$ and $Q_{n,s}$.

V. VERIFICATION

The method and its efficiency are verified by solving a benchmark problem introduced in [1]. The physical model is depicted in Figure 2.(a) where 100V is switched between the central and ground electrodes. Figure 2.(b) and 2.(c) show potential and electric field plots at $t=0$ and $t \gg \tau_e$, respectively. ($\tau_e = \epsilon/\sigma$ is the charge relaxation time.) The temporal behavior shows good agreement with the control results in [1]. The full paper will present and analyze the performance of the variable time stepping procedure similarly as presented for thermal problems in [11]. The full version will also demonstrate further advantages of our time integration technique by presenting additional examples.

VI. REFERENCES

- [1] K. Preis, "Numerical computation of transient quasistatic electric fields," (<http://www.igte.tugraz.at/de/forschung/ExtendedInternetVersionBourne-mouth.html>) *Proc. CEM 2002*, 2002.
- [2] H. A. Haus and J. R. Melcher, *Electromagnetic Fields and Energy*, Englewood Cliffs, Prentice-Hall, 1990.
- [3] D. Weida, T. Steinmetz, and M. Clemens, "Electro-Quasistatic High Voltage Field Simulations of Large Scale Insulator Structures Including 2-D Models for Nonlinear Field-Grading Material Layers," *IEEE Trans. on Magnetics*, 45(3), 2009, pp. 980-983.
- [4] G. Manetas, V. N. Kourkoulos, and A. C. Cangelaris, "Investigation on the Frequency Range of Validity of Electroquasistatic RC Models for Semiconductor Substrate Coupling Modeling," *IEEE Trans. on Electromagnetic Compatibility*, 49(3), 2007, pp. 577-584.
- [5] K. Preis, O. Biró, P. Supancic, and I. Ticar, "FEM simulation of thermistors including dielectric effects," *IEEE Trans. on Magnetics*, vol. 39(3), 2003, pp. 1733-1736.
- [6] J. L. Steyd, et al, "Generating electric power with a MEMS electroquasistatic induction turbine-generator," *MEMS 2005, 18th IEEE International Conference on MEMS*, 2005, pp. 614-617.
- [7] A. Barchanski, T. Steiner, H. De Gerssem, M. Clemens, and T. Weiland, "Local Grid Refinement for Low-Frequency Current Computations in 3-D Human Anatomy Models," *IEEE Trans. on Magnetics*, 42(4), 2006, pp. 1371-1374.
- [8] A. Nicolet and F. Delincé, "Implicit Runge-Kutta methods for transient magnetic field computation," *IEEE Trans. on Magnetics*, 32(3), 1996, pp. 1405-1408.
- [9] F. Cameron, R. Piché, and K. Forsman, "Variable Step Size Time Integration Methods for Transient Eddy Current Problems," *IEEE Trans. on Magnetics*, 34(5), 1998, pp. 3319-3322.
- [10] M. Clemens, et al, "Transient Electro-Quasistatic Adaptive Simulation Schemes," *IEEE Trans. on Magnetics*, 40(2), 2004, pp. 1294-1297.
- [11] Z. Badics, B. Ionescu, Z. J. Cendes, "High-Order Adaptive Time-Domain Solution of Nonlinear Coupled Electromagnetic-Thermal," *IEEE Trans. on Magnetics*, 40(2), 2004, pp. 1247-1277.
- [12] M. Gyimesi, I. Avdeev, and D. Ostergard, "Finite-Element Simulation of Micro-Electromechanical Systems (MEMS) by Strongly Coupled Electromechanical Transducers," *IEEE Trans. on Magnetics*, 40(2), 2004, pp. 557-560.

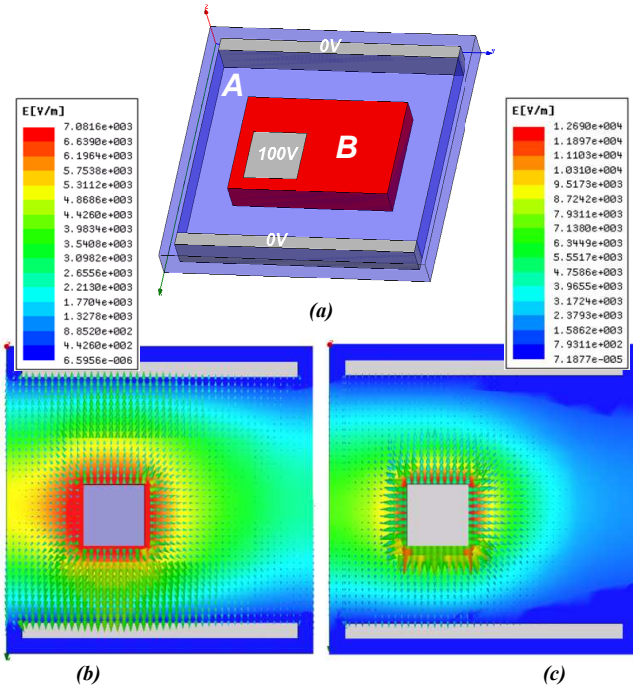


Fig. 2. (a) The 3D model of a 2D benchmark problem from [1] is analyzed. The properties of material A are $\epsilon_r = 10$, $\sigma = 2E-6 S/m$, and $\tau_e = 44.3 \mu s$. Material B 's are $\epsilon_r = 20$, $\sigma = 1E-6 S/m$, and $\tau_e = 177.0 \mu s$. (b) and (c) depict potential (contour) and electric field (arrow) plots at $t=0$ and $t \gg \max(\tau_e^A, \tau_e^B)$, respectively. The potential contour plot is from 0 to 100V.

Numerical experimentations on the coupling between PEEC and volume integral method

Tung Le Duc, Olivier Chadebec, Jean-Michel Guichon, Gérard Meunier, Yves Lembeye
Grenoble Electrical Engineering Laboratory, Grenoble-INP / Université Joseph Fourier / CNRS
ENSE³, BP46, 38402 Grenoble, France

Abstract — In order to model ferromagnetic material in quasi-static PEEC method, a coupling with a volume integral equation is proposed. This coupling enables to take advantage of the strong points of each method. The modeling of complex conductor geometry is achieved thanks to PEEC method and magnetic materials are taken into account thanks to a volume integral equation. The coupling is carried out by introducing an impedance matrix (computed with PEEC method in the vacuum) within an integral magnetostatic equation solved by moment method.

I. INTRODUCTION

The PEEC method (Partial Element Equivalent Circuit) is mainly used for the modeling of complex interconnections and can be applied to a large range of devices where the air region is dominant [1] (printed circuits, bus bars...). However, the classical PEEC method does not enable the 3D modeling of ferromagnetic materials widely present in devices (ferromagnetic shielding, disruptive magnetic masses, and cores of inductance). The magnetostatic moments method is well-known and derives from a volume integral equation solved by a point matching approach. It is particularly well adapted to model lightly very simple magnetic materials volume. Like the PEEC method, it does not require the meshing of the air region; on the other hand, it is limited to modeling of magnetostatic effects. Both methods are complementary. A strong coupling of them can be accomplished by modeling non conductive magnetic regions with a method of moments, while PEEC method allows the modeling the contributions of the inductors fed with alternative currents.

II. COUPLING PRINCIPLE

A. Magnetostatic moment method

Let us consider a non conductive magnetic material placed in an inductor field \mathbf{H}_0 . The total magnetic field \mathbf{H} is the sum of \mathbf{H}_0 and \mathbf{H}_{red} , the reaction of the material. A well-known integral volume equation links the local field to the magnetization of the whole material volume V_{mat} :

$$\mathbf{H} = \mathbf{H}_0 + \frac{1}{4\pi} \int_{V_{\text{mat}}} \left(3 \frac{(\mathbf{M} \cdot \mathbf{r})}{r^5} \mathbf{r} - \frac{\mathbf{M}}{r^3} \right) dV \quad (1)$$

where \mathbf{r} is the vector linking the integration point to the point where the field is expressed, V_{mat} the ferromagnetic volume and \mathbf{M} its magnetization. Usually, this integral is solved with a numerical technique. The easier way is to mesh the volume into n elements and to consider that the magnetization is uniform on each of them. Then, thanks to a point matching approach of the linear magnetic material's law at the center of

each element, a linear matrix system is obtained. It remains to solve it, to obtain the magnetization of the whole volume V_{mat} . This method is usually called magnetostatic moment method. This formulation is known to suffer of some inaccuracies in some specific configurations [2]. However, the purpose of this paper is the coupling and very similar methodology can be applied to more sophisticated volume integral formulations.

Let's now assume that the inductor field is created by m unknown alternative currents I flowing in m conductors. In a very similar way to the previous one, we can get a linear system of equations. For instance, the equation associated to magnetic element k is:

$$\frac{\mathbf{M}_k}{\mu_r - 1} = \frac{1}{4\pi} \sum_{i=1}^n \int_{V_{\text{mat}_i}} \left(\frac{(\mathbf{M}_i \cdot \mathbf{r})}{r^5} \mathbf{r} - \frac{\mathbf{M}_i}{r^3} \right) dV_i + \frac{1}{4\pi} \sum_{j=1}^m \int_{V_{\text{cond}_j}} \frac{d\mathbf{l} \times \mathbf{r}}{r^3} I_j dV_j \quad (2)$$

where μ_r is the relative permeability of the material. The second integral term correspond to the Biot and Savart's law integrated on each conductor volume V_{cond_j} . The global matrix system obtained has $6n$ equations (a vector complex equation per element) and $6n+2m$ unknowns (a vector complex magnetization per element plus m complex currents).

B. Inductive PEEC method

Let us consider m volume conductors fed with alternative sources placed in a surrounding air region without any magnetic materials. The well-known PEEC method is particularly reliable to solve this kind of problem. It is based on the determination of partial voltage generated on each conductor by electromagnetic sources. To compute these voltages volume integration on the conductor of the magnetic vector potential created by all the others conductor is provided. For instance, for the conductor k , the expression is [1]:

$$V_{k_cond} = \frac{\mu_0}{4\pi} \frac{j\omega}{s_k} \int_{V_k} \left(\sum_{i=1}^m \frac{I_i}{s_i} \int_{V_i} \frac{1}{r} dV_i \right) dV_k \quad (3)$$

where ω is the angular frequency and S_i is the section of the i -th conductor. This equation links partial voltages of conductors to currents flowing in them. If we write this equation for all conductors, we get a matrix system known as impedance matrix system. By combing these electromagnetic equations with the circuit ones representative of the conductors wiring and adding resistance source effect, it is possible to get a simplified system representative of the device which can be easily coupled with a standard circuit simulator. This inductive PEEC method has already shown its efficiency for the modeling of complex conductor geometries in comparison with FEM.

Let us now consider that linear ferromagnetic materials are present in the surrounding air region. Equation (3) has to be

modified by taking into account the influence of the field created by the material. In fact, like in the first approach, we have to integrate the magnetic vector potential on the volume conductor k . A new voltage has to be added to the previous one, not generated by the current but by the magnetization [3].

$$V_{k_mat} = \frac{\mu_0}{4\pi} \frac{j\omega}{s_k} \int_{V_k} \left(\sum_{i=1}^n \int_{V_i} \frac{\mathbf{M}_i \times \mathbf{r}}{r^3} dV_i \right) \cdot \mathbf{u}_k dV_k \quad (4)$$

Finally, equations (3), (4) and (5) are brought together in a global square $(6n+2m) \times (6n+2m)$ matrix system:

$$\begin{bmatrix} \mathbf{MoM} & \mathbf{BS} \\ \mathbf{L}_M & \mathbf{L}_{standard} \end{bmatrix} \times \begin{bmatrix} \mathbf{M} \\ \mathbf{I} \end{bmatrix} = \begin{bmatrix} \mathbf{0} \\ \mathbf{V} \end{bmatrix} \quad (5)$$

where \mathbf{MoM} is the standard moments matrix (first two rearranged term of equation (2)), \mathbf{BS} is the Biot and Savart integral term (last term of (2)), \mathbf{L}_M is the influence of magnetization on conductors in PEEC approach (equation (4)) and $\mathbf{L}_{standard}$ the classical inductive and resistive PEEC matrix. By taking into account circuit equations, it is possible to reduce (5) to get a lighter system and to solve it to get magnetizations and currents in conductors.

III. NUMERICAL EXAMPLES

We consider two numerical examples (Fig.1.). For both, three numerical methods are compared. The first one is the scalar magnetic potential FEM coupled with circuit equations. In this modeling, a special care is given to the mesh around both conductors to ensure accurate results. The second one is a coupling between PEEC to model inductances and FEM to take into account the ferromagnetic material. This approach has already shown its good accuracy with a reduced number of elements in comparison with standard FEM [4]. The last one is the considered coupling.

In the first example, two conductors are considered with a ferromagnetic bar ($\mu_r = 1000$, linear) placed between them (Fig.1, left). The first conductor is fed by a voltage source (1V, 1 kHz). The second one is in short circuit mode. To compare different approaches, we focus on the computed current in the second conductor with different meshes for the three approaches (see table I).

TABLE I. Currents values obtained (A)

FEM			
Nb of elements	230.000	600.000	1.000.000
Current values	-36.25+6,00i	-32.47+7,94i	-32.61+7.87i
FEM/PEEC			
Nb of elements	60.000	150.000	
Current values	-32.60+8,38i	-32.50+8.34	
MoM/PEEC			
Nb of elements	32	126	392
Current values	-35.97+8,95i	-32.94+8.34i	-32.70+8.32i

Whereas the convergence is quickly reached with the FEM/PEEC method, the problem needs a very fine mesh to be accurately solved with FEM. We can see a small difference between both computed values. It can be explained by a small difference in the modelling method used to represent conductors. Results provided by our coupling are very encouraging, the convergence being reached with a very few

number of elements (around 200). Of course, the obtained matrix is fully dense, but the computation time is divided per one hundred in comparison with FEM and ten with FEM/PEEC. Moreover, no specific mesh refinement has been needed.

The second test case is an inductance of microphone converter. It is composed of a complex-shaped conductor and of two ferrite parts (Fig.1. right). In our study, the conductor is fed by a voltage source (1V, 10 kHz) and the ferrite is considered as linear with a permeability of 1000. Values of currents are still compared.

TABLE II. Currents values obtained (A)

FEM 100.000 elements	FEM/PEEC 30.000 elements	MoM/PEEC 2000 elements
14,36 – 1,97i	14,39 – 1,85i	14,43 – 1,68i

Results seem to be not so good for the coupling MoM / PEEC especially if we have a look to the imaginary part of the current. This inaccuracy is mainly due to the small distance between conductors and the magnetic material, leading to important variation of magnetization in the neighborhood of currents. This configuration benefits FEM in comparison with our coupling. A good improvement would certainly be to couple PEEC with a more sophisticated implementation of the volume integral equation.

IV. CONCLUSION

In this paper, we have presented a coupling between PEEC and an integral volume equation. Our approach can be very fast and accurate and enables the introduction of linear magnetic material in PEEC methodology. It is particularly capable for the modeling of complex shapes conductors and relatively simple magnetic material geometry.

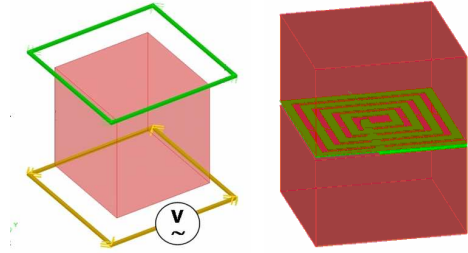


Fig.1. Geometry of both tested numerical cases.

V. REFERENCES

- [1] A.E. Ruehli, "Equivalent circuit models for three dimensional multiconductor systems", IEEE transaction on microwave theory and techniques, Vol. 22, No 3, 1974.
- [2] K. Forsman, L. Kettunen, "Influence of the Discrete Spaces an Integral Equation Formulations," , IEEE Transactions on Magnetics, , Vol 22, No 2, 1997
- [3] G. Antonini, M. Sabatini, G. Miscione, "PEEC Modeling of Linear Magnetic Materials", IEEE International Symposium on Electromagnetic Compatibility 2006, EMC 2006., Vol. 1, pp 93- 98, 2006.
- [4] T-S. Tran, G. Meunier, P. Labie, Y. Le Floch, J-M. Guichon, J. Roudet, "FEM-PEEC coupled method for modeling solid conductors in the presence of ferromagnetic material", Compel Journal, Vol. 27, No 4, pp 904-910, 2007

Electromagnetic Device Analysis using a Meshless Approach coupled to a Kohonen Network

Rajeev Das and David A. Lowther,
 Department of Electrical and Computer Engineering, McGill University
 3480 University Street, Montreal, H3A 2A7, Canada
 E-mail: rajeev.das@mail.mcgill.ca, David.Lowther@McGill.ca

Abstract— The paper describes a novel adaptive solution system for electromagnetic field problems. The solution method is based on a meshless approach and thus the pre-processing effort is minimized. The positions of the nodes used for this solution are determined adaptively using a Kohonen Neural Network. The objective of the proposed approach is to obtain an optimal placing of the nodes before adding any new degrees of freedom to reduce the error.

I. INTRODUCTION

The numerical solution of electromagnetic field problems has been a subject of research for almost half a century and it is now possible to simulate the real device to a very high level of accuracy. The most commonly used methods for low frequency electromagnetic systems are based around the finite element technique which has been steadily improved in all its aspects over many years. However, the computational cost is still relatively high and can lead to long execution times, especially if an adaptive system is used to reduce the error. One of the problems with the finite element approach is that it requires the solution domain to be meshed. While great gains have been made in reducing the complexity of solving the resulting linear equations, the mesh generation process is still costly and can be the most time consuming part of certain classes of problems. When adaptation is included, and is implemented by modifying the mesh to add new degrees of freedom, this cost becomes significant. For this reason, attention has been paid to alternate differential approaches usually known as “meshless methods”. These systems, as the name implies, do not need to generate a mesh and thus bypass this drawback of the finite element system. Adaptation can also be implemented in such a system by adding new nodes at points of high error. However, this approach increases the size of the problem and thus the solution time. A better, initial approach to adaptation might be to consider an optimal placement of the starting node set such that the global and local errors in the solution are minimized. This paper proposed that this might be done by considering the nodes of a meshless system to be part of a Kohonen Self Organizing Feature Map – a form of neural network. Using this approach, the nodes of the system can be repositioned to minimize the errors before any new degrees of freedom are added.

II. MESHLESS SOLUTION SYSTEMS

In a meshless system, the field solution is approximated by local shape functions, often, but not always, a form of radial basis function. Each node, through its shape function, is considered to have a domain of influence which could cover the entire problem space or might be limited to a local

neighborhood [3]. The field value at any point in space is then given by summing the contributions of all the nodes within whose domain of influence the point lies. Boundary and interface conditions can be handled through a collocation technique.

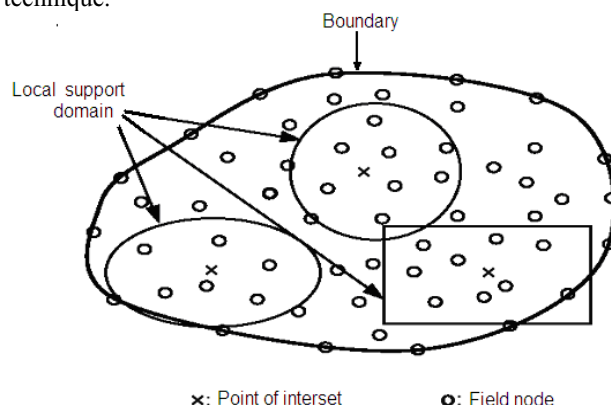


Fig.1. A meshless discretization of an arbitrary domain

A typical radial basis function is the Gaussian given by

$$\Psi(r) = e^{-(\epsilon r)^2} \quad r \in \mathfrak{R} \quad (1)$$

The radius, r , can be expressed in terms of the distance from the center of the function, $x-x_k$. [4]

III. KOHONEN NEURAL NETWORKS

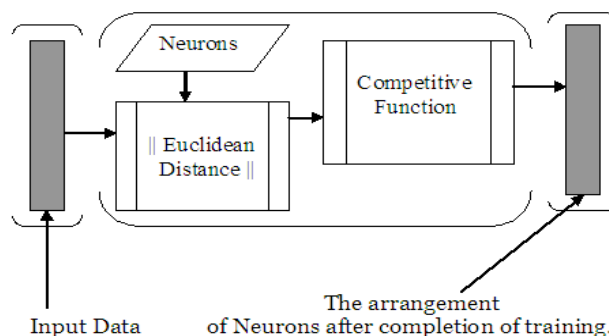


Fig.2. The Kohonen Architecture.

The Kohonen network, also known as self-organizing map is a two-layer unsupervised neural network and has fully interconnected processing units that compete among themselves to be activated or fired[1][2]. It has a strong self-organizing ability, because of which after the training procedure the predefined network grid will follow the structure and distribution of the input points. It is trained iteratively. In each training step one vector x from the input data set is chosen

randomly and the distances between it and all the weight vectors of the Kohonen nodes are calculated using the Euclidean distance. The neuron whose weight vector is the closest to the input vector x is called the Best Matching Unit (BMU) denoted here by b

$$\|x - m_b\| = \min_{i \in N} \{\|x - m_i\|\} \quad (2)$$

N represents the set of Kohonen nodes and $\|\cdot\|$, the Euclidean distance. After this the BMU along with its topological neighbors are moved closer to the input vector in the input space using the following relation.

$$m_i(s+1) = m_i(s) + \alpha(s)h_{bi}(s)[x(s) - m_i(s)] \quad (3)$$

where s denotes time or iteration steps, x is an input vector drawn from the input data set during s , $h_{bi}(s)$ is the kernel function around the winning neuron b and $\alpha(s)$ is the learning rate during s .

IV. THE PROPOSED ALGORITHM

Based on the above, the meshless adaptive algorithm is as shown in Fig. 3.

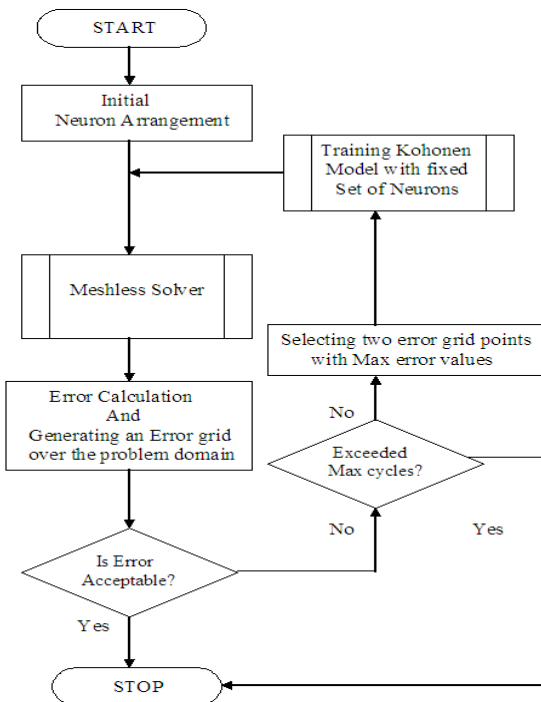


Fig. 3. Flow chart of the proposed algorithm.

The error criterion being used in the present work is relatively simple. The error is estimated by taking the average value of the potential around a particular point and comparing it with the potential computed at that point. Thus an error map is created covering the entire problem domain. The points of maximum error are then identified and the coordinates are used to “train” the Kohonen network and, in the process, the nodes are moved towards the high error positions.

V. INITIAL TESTS

The algorithm has been tested on a very simple problem in order to check out the overall performance and convergence characteristics. The device considered is a parallel plate capacitor. Fig. 4.

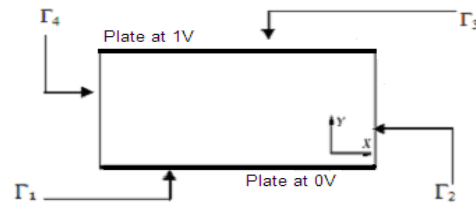


Fig.4. A simple parallel plate capacitor

The solution space was populated with 16 nodes which formed the basis of both the meshless solution and the Kohonen network. At each iteration, the problem was solved using the meshless system and the error computed. The nodes were then moved by using the Kohonen network and the process repeated. The results are shown in Fig. 5.

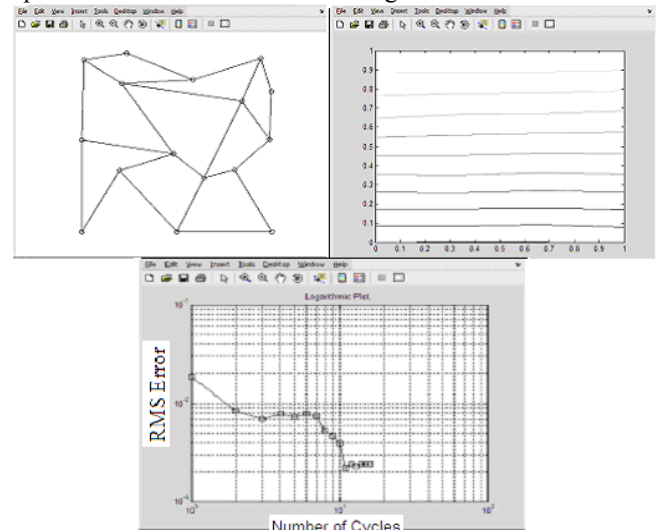


Fig.5. Final positions of the 16 nodes and the field solution and the convergence plot at the bottom.

VI. CONCLUSIONS

An adaptive meshless algorithm using a Kohonen network has been proposed and initial results are shown. The system appears to optimize the positions of the nodes and thus provides the most accurate solution that can be obtained with the given degrees of freedom. The full paper will provide an analysis of the performance of the algorithm and give examples on more complex geometries.

VII. REFERENCES

- [1] Simon Haykin “Neural Networks a Comprehensive Foundation”. Prentice Hall 1999 Pages 58, 443- 476.
- [2] Christopher M Bishop “Neural Networks for pattern recognition” Oxford Univ Press 1995. 1-17,116-126.
- [3] G.R. Lui “Meshfree Methods Moving beyond the Finite Element Method” CRC Press 2003 Pages 15, 19-24, 67-107.
- [4] Martin D Bhuman “Radial Basis Functions”. Cambridge Univ Press 2003 1-5, 48-65, 99-108.

FIT applied to a magnetostatic case with hysteresis phenomenon

J. Korecki¹, A. Benabou¹, Y. Le Menach¹, F. Piriou¹, J-P. Ducreux²
¹Université Lille1, LAMEL L2EP, Bât. P2, 59655 Villeneuve d'Ascq, France
²LAMEL EDF R&D, 1 avenue du Général de Gaulle, 92141 Clamart, France
 Julien.korecki@ed.univ-lille1.fr, abdelkader.benabou@univ-lille1.fr

Abstract — The presented work is about the implementation of a vectorial hysteresis model in a Finite Integration Technique (FIT) computation code. This is achieved in the magnetostatic case using the vector potential formulation and with the external electric circuit coupling. The used behaviour law model is the vectorized Jiles-Atherton model with the magnetic flux density as input variable. The proposed approach is illustrated by modelling a coil made of Soft Magnetic Composite (SMC) magnetic core. Comparison with measured global quantities is also done.

I. INTRODUCTION

The numerical study of electromagnetic devices requires knowing the geometrical as well as the physical parameters of the involved system. Geometrical parameters can be easily obtained, whereas the magnetic behaviour law is often approximated as linear or non linear using an average model from the experiment and the hysteresis effect is often neglected. Most of the electrical devices can be studied without the hysteresis phenomena. Nevertheless, for more accuracy, a numerical implementation of the hysteresis phenomena can be required to study specific systems, for example hysteresis motors or systems where the remnant flux has an influence on the global behaviour.

Several hysteresis models exists in the literature, such as the Preisach [1] and the Jiles-Atherton (J-A) [2] models. In this work, we use the vectorized J-A model [3] in its inverse form, i.e. with the magnetic flux density as input variable. The numerical technique used to discretize the mathematical model of the Maxwell's equations is the Finite Integration Technique (FIT) [4]. As the vectorized J-A model provides naturally the differential reluctivity tensor, the magnetic vector potential formulation is written using an Euler approximation of the magnetic behaviour law including the differential reluctivity tensor. The coupling with the external circuit is also presented in order to study a coil with a SMC magnetic core and comparison with the experiment is realised.

II. VECTOR HYSTERESIS MODEL

To take into account rotational fields and anisotropy, a vectorization of the J-A scalar direct model, i.e. with the magnetic field as input variable, has been proposed in [5]. An inverse vector generalisation of the J-A model, proposed in [3], is used in this paper as the vector potential formulation is considered for the numerical model. The input variable of the hysteresis model is the magnetic flux density vector \mathbf{B} and the main equation is [3],

$$d\mathbf{M} = \frac{1}{\mu_0} \left[\mathbf{I} + \bar{\chi}_f \left| \bar{\chi}_f \right|^{-1} \bar{\chi}_f (\mathbf{I} - \bar{\alpha}) + \bar{c} \bar{\xi} (\mathbf{I} - \bar{\alpha}) \right]^{-1} \cdot \left[\bar{\chi}_f \left| \bar{\chi}_f \right|^{-1} \bar{\chi}_f + \bar{c} \bar{\xi} \right] d\mathbf{B} \quad (1)$$

where $\bar{\chi}_f$ is given by $\bar{\chi}_f = \bar{k}^{-1} (\mathbf{M}_{an} - \mathbf{M})$. Vectors \mathbf{M}_{an} and \mathbf{M} are, respectively, the anhysteretic magnetization and the total magnetization. The parameters of the model are described by the third rank tensors \bar{k} , $\bar{\alpha}$ and \bar{c} which terms must be obtained experimentally. \mathbf{I} is the diagonal unity matrix and $\bar{\xi}$ is the diagonal matrix of the anhysteretic functions derivatives with respect to the effective field components [3].

Using $d\mathbf{M}$ obtained from equation (1) and $d\mathbf{H} = \frac{1}{\mu_0} d\mathbf{B} - d\mathbf{M}$, one can write $d\mathbf{H} = \|\partial v\| d\mathbf{B}$, where $\|\partial v\|$ is the differential reluctivity tensor.

III. NUMERIC MODEL

In the magnetostatic case, the Maxwell equation to be solved is,

$$\begin{aligned} \mathbf{Curl} \mathbf{H} &= \mathbf{J} \\ \mathbf{Div} \mathbf{B} &= 0 \end{aligned} \quad (2)$$

where \mathbf{J} is the current density. The constitutive relationship, i.e. the magnetic behaviour law, is such as $\mathbf{H} = \mathbf{f}(\mathbf{B})$. To take into account the vector hysteresis model, the magnetic field is written using the Euler scheme to introduce the differential reluctivity tensor,

$$\mathbf{H}_{t_i} = \|\partial v\| (\mathbf{B}_{t_i} - \mathbf{B}_{t_0}) + \mathbf{H}_{t_0} \quad (3)$$

with t_i and t_0 the current and previous time calculation steps. Using the magnetic vector potential \mathbf{A} , such that $\mathbf{B} = \mathbf{curl} \mathbf{A}$, and using equation (2), we can write the magnetic vector potential formulation. To impose the voltage u , we consider the coupling with the external circuit [6-7]. The coil winding density field \mathbf{N} is defined such as $\mathbf{J} = \mathbf{N}i$ and the voltage expression, using \mathbf{A} and \mathbf{N} , becomes,

$$u = Ri + \frac{d\phi}{dt} = Ri + \mathbf{N} \frac{d\mathbf{A}}{dt} \quad (4)$$

The density field vector \mathbf{N} is constructed with help of sections and numbers of turns of the coil winding [6]. Then, the magnetic vector formulation is,

$$\mathbf{Curl} \|\partial v\| \mathbf{Curl} (\mathbf{A}_{t_i} - \mathbf{A}_{t_0}) = \mathbf{N} i_{t_i} - \mathbf{Curl} \mathbf{H}_{t_0} \quad (5)$$

The finite integration technique [4] is used here to

discretize and solve the problem. The space is discretized using orthogonal elements. For the time discretization, the implicit Euler scheme is used. The operator “*Curl*” became an incidence matrix $[C]$. To construct the material matrix $[dv]$ the series reluctances notions were used by considering field tubes. For each facet, the relation between magnetic induction fluxes through a facet and the field circulation on the dual edges is established. For each time step, the system is solved until the error convergence criterion on A is reached.

IV. SIMULATION RESULT

The studied system consists in a coil with SMC iron core [8]. The current evolution in the winding is calculated using the numerical scheme presented previously. Dimensions of the system and its mesh are reported on figure 1. As the system is axisymmetric, a 2D approach is considered. The mesh is constituted of 480 elements with 525 nodes. By considering the boundary conditions, the number of unknowns is 438.

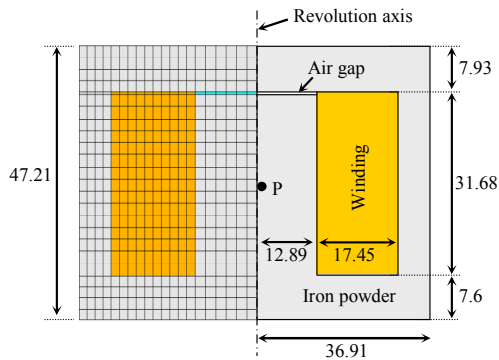


Fig. 1. Dimensions of the studied system (mm) and its mesh.

The coil winding is supplied by a voltage of 90 V RMS at 60 Hz. The system was simulated during 20 periods with 100 time steps per period. The inrush current, due to the magnetic core saturation, is clearly emphasised in figure 2. Figure 3 shows the steady state of the calculated current and the measured one. Despite the small number of elements in the mesh, good accuracy is observed between calculation and measurement.

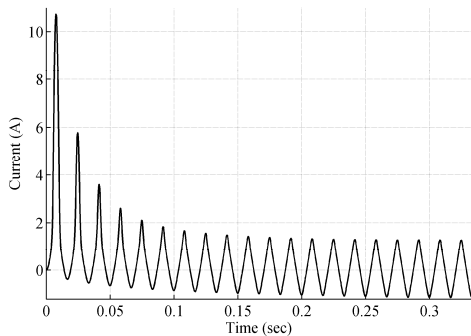


Fig. 2. Computation inrush current.

The hysteresis loops at three different moments (1st, 10th and 20th periods) at point P (see figure 1), are given in figure 4. During the first period, the hysteresis loop presents the saturation shape due to the inrush current. At the 20th period,

the steady state is reached and the hysteresis loop becomes symmetric.

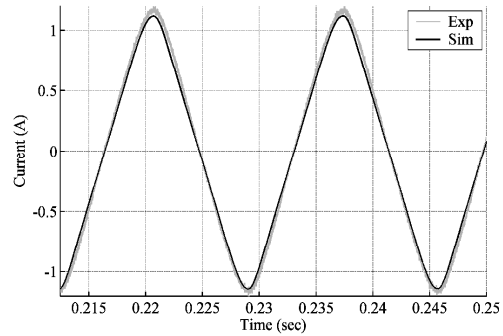


Fig. 3. Simulated and measured current evolutions.

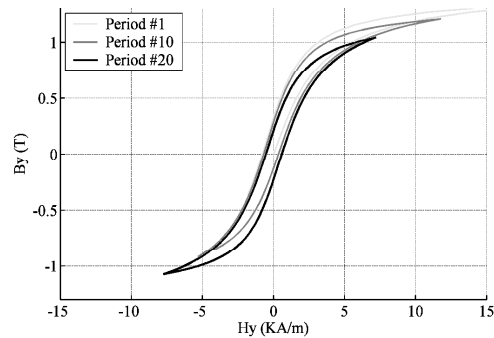


Fig. 4. Hysteresis loops at P.

V. CONCLUSION

A vector hysteresis model has been implemented in the FIT. To validate the numerical model, a coil with SMC core has been studied. The model shows good agreement with the measure for a global quantity, i.e. the current in the winding. The system will be studied in detail to compare the calculated iron losses with the measured ones.

VI. REFERENCE

- [1] F. Preisach, “Über die magnetische nachwirkung”, *Zeitschrift für Physik* 94, pp. 277-302, 1935.
- [2] D.C. Jiles, D.L. Atherton, “Theory of ferromagnetic hysteresis”. *Journal of Magnetism and Magnetic Materials* 61, pp. 48-60, 1986.
- [3] J.V. Leite, N. Sadowski, P. Kuo-Peng, N.J. Batistela, J.P.A. Bastos, A.A. de Espndola. “Inverse Jiles-Atherton Vector Hysteresis Model”, *IEEE Trans. On Magn.*, vol. 40, No. 4, p. 1769-1775, 2004.
- [4] T. Weiland, “A discretization method for the solution of Maxwell’s equations for six-component fields,” *Electronics and Communications AEÜ*, Vol. 31, No. 3, 116–120, 1977.
- [5] A.J. Bergqvist, “A Simple Vector Generalization of the Jiles-Atherton Model of Hysteresis”, *IEEE Trans. on Magnetics*, Vol. 32, No. 5, pp. 4213-4215, 1996.
- [6] F. Piriou, A. Razek, “Finite element analysis in electromagnetic systems accounting for electric circuit equations”, *IEEE Trans. on Magnetics*, Vol. 28, pp. 1295-1298, 1992.
- [7] G. Albertier, Y. Le Menach, J.P. Ducreux and F. Piriou, “Consideration of the coupling of the magnetic and electric equations with Finite Integration Technique (FIT)”, *EPJ*, Vol. 30 No. 1, April 2005.
- [8] J. Cros, A.J. Perin, P. Viarouge, “Soft Magnetic Composites for Electromagnetic Components in Lighting Applications”. *IAS 2002*, Pittsburgh, Pennsylvania USA, October 13-18.

Influence of a rough thin layer on the potential

I. Ciuperca*, R. Perrussel†, and C. Poignard‡;

*Université de Lyon, ICJ UMR CNRS 5208, Lyon, F-69003;

†Laboratoire Ampère UMR CNRS 5005, Université de Lyon, École Centrale de Lyon, F-69134 Écully, France

‡INRIA Bordeaux-Sud-Ouest, Team MC2, IMB UMR CNRS 5251, Université Bordeaux1, Talence 33405, France
mail to: clair.poignard@inria.fr

Abstract—In this paper, we study the behavior of the steady-state voltage potentials in a material composed by an interior medium surrounded by a rough thin layer and embedded in an ambient bounded medium. The roughness of the layer is supposed to be ε -periodic, ε being the small thickness of the layer. We present and validate numerically the rigorous approximate transmissions proved by Ciuperca *et al.* in [1]. This paper extends previous works in which the layer had a constant thickness.

I. INTRODUCTION

In the domains with a rough thin layer, numerical difficulties appear due to the complex geometry of the rough layer when computing the steady-state potentials. We present here how these difficulties may be avoided by replacing this rough layer by appropriate transmission conditions. Particularly, we show that considering only the mean effect of the roughness is not sufficient to obtain the potential with a good accuracy.

A. Statement of the problem

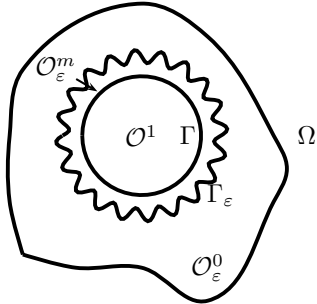


Fig. 1. Geometry of the problem.

Let Ω be a smooth bounded domain of \mathbb{R}^2 with connected boundary $\partial\Omega$. For $\varepsilon > 0$, we split Ω into three subdomains: \mathcal{O}^1 , $\mathcal{O}_\varepsilon^m$ and $\mathcal{O}_\varepsilon^0$. \mathcal{O}^1 is a smooth domain strictly embedded in Ω (see Fig. 1). We denote by Γ its connected boundary. The domain $\mathcal{O}_\varepsilon^m$ is a thin oscillating layer surrounding \mathcal{O}^1 . We denote by Γ_ε the oscillating boundary of $\mathcal{O}_\varepsilon^m$: $\Gamma_\varepsilon = \partial\mathcal{O}_\varepsilon^m \setminus \Gamma$. The domain $\mathcal{O}_\varepsilon^0$ is defined by: $\mathcal{O}_\varepsilon^0 = \Omega \setminus (\mathcal{O}^1 \cup \mathcal{O}_\varepsilon^m)$. We also denote by $\mathcal{O}^0 = \Omega \setminus \mathcal{O}^1$. Two piecewise-constant conductivities on the domain Ω have to be defined:

$$\sigma(z) = \begin{cases} \sigma_1, & \text{if } z \in \mathcal{O}^1, \\ \sigma_m, & \text{if } z \in \mathcal{O}_\varepsilon^m, \\ \sigma_0, & \text{if } z \in \mathcal{O}_\varepsilon^0. \end{cases} \quad \tilde{\sigma}(z) = \begin{cases} \sigma_1, & \text{if } z \in \mathcal{O}^1, \\ \sigma_0, & \text{if } z \in \Omega \setminus \mathcal{O}^1. \end{cases}$$

where σ_1, σ_m and σ_0 are given positive constants¹.

Let u^ε and u^0 be defined by:

$$\begin{cases} \nabla \cdot (\sigma \nabla u^\varepsilon) = 0, & \text{in } \Omega, \\ u^\varepsilon|_{\partial\Omega} = g, \end{cases} \quad \begin{cases} \nabla \cdot (\tilde{\sigma} \nabla u^0) = 0, & \text{in } \Omega, \\ u^0|_{\partial\Omega} = g, \end{cases} \quad (1)$$

where g is a sufficiently smooth boundary data. We present how to define the potential u^1 such that u^ε is approached by $u^\varepsilon = u^0 + \varepsilon u^1 + o(\varepsilon^{3/2})$ for ε tending to zero².

II. HEURISTICS OF THE DERIVATION OF THE CONDITIONS

Suppose Γ is a smooth closed curve of \mathbb{R}^2 of length 1 and parameterize it by the curvilinear coordinate $\Gamma = \{\Psi(\theta), \theta \in [0, 1]\}$. Let n be the (outward) normal to $\partial\mathcal{O}^1$. Γ_ε is described by

$$\Gamma_\varepsilon = \{\Psi(\theta) + \varepsilon f(\theta/\varepsilon)n(\theta), \theta \in [0, 1]\},$$

where f is a smooth 1-periodic and positive function, which describes the roughness of the layer.

A. Boundary layer corrector in the infinite strip

The key-point of the derivation of the equivalent transmission conditions consists in taking advantage of the periodicity of the roughness. This is performed by unfolding and upscaling the rough thin layer into the infinite strip $\mathbb{R} \times [0, 1]$.

Define the closed curves \mathcal{C}_1 and \mathcal{C}_0 , which are trigonometrically oriented by

$$\mathcal{C}_0 = \{0\} \times [0, 1], \quad \mathcal{C}_1 = \{(f(y), y), \forall y \in [0, 1]\}.$$

The outward normals to \mathcal{C}_0 and \mathcal{C}_1 equal

$$n_{\mathcal{C}_0} = \begin{pmatrix} 1 \\ 0 \end{pmatrix}, \quad n_{\mathcal{C}_1} = \frac{1}{\sqrt{1 + (f'(y))^2}} \begin{pmatrix} 1 \\ -f'(y) \end{pmatrix}. \quad (2)$$

According to [1] there exists a unique couple (A^0, a^0) where A^0 is a continuous vector field and a^0 is constant such that

$$A^0 \text{ is 1-periodic in } y, \quad \Delta A^0 = 0, \text{ in } \mathbb{R} \times [0, 1], \quad (3a)$$

$$\sigma_0 \partial_n A^0|_{\mathcal{C}_1^+} - \sigma_m \partial_n A^0|_{\mathcal{C}_1^-} = (\sigma_m - \sigma_0) n_{\mathcal{C}_1}, \quad (3b)$$

$$\sigma_m \partial_n A^0|_{\mathcal{C}_0^+} - \sigma_1 \partial_n A^0|_{\mathcal{C}_0^-} = -(\sigma_m - \sigma_0) n_{\mathcal{C}_0}, \quad (3c)$$

$$A^0 \rightarrow_{x \rightarrow -\infty} 0, \quad A^0 - a^0 \rightarrow_{x \rightarrow +\infty} 0, \quad (3d)$$

where the convergences at infinity are exponential. We emphasize that a^0 is not imposed but is a floating potential.

¹The same following results hold if σ_0, σ_1 , and σ_m are given complex numbers with imaginary parts (and respectively real parts) with the same sign.

²The notation $o(\varepsilon^{3/2})$ means that $\|u^\varepsilon - (u^0 + \varepsilon u^1)\|$ goes to zero faster than $\varepsilon^{3/2}$ as ε goes to zero. We refer to Theorem 1.1 of [1] for a precise description of the involved norms and the accuracy of the convergence.

B. Approximate transmission conditions

Our transmission conditions are then obtained with the help of the constant vectors D_1 and D_2 defined by:

$$\begin{aligned} D_1 &= (\sigma_0 - \sigma_m) \left[\int_0^1 f(y) dy n_{C_0} + \int_0^1 A^0(f(y), y) dy \right] \\ &\quad + (\sigma_m - \sigma_1) \int_0^1 A^0(0, y) dy - \sigma_0 a^0, \\ D_2 &= (\sigma_m - \sigma_0) \left[\int_0^1 A^0(f(y), y) f'(y) dy \right. \\ &\quad \left. - \int_0^1 f(y) dy \begin{pmatrix} 0 \\ 1 \end{pmatrix} \right]. \end{aligned}$$

The potential u^1 is then defined by³:

$$\begin{cases} \Delta u^1 = 0, \text{ in } \mathcal{O}^0 \cup \mathcal{O}^1, & u^1|_{\partial\Omega} = 0, \\ [\tilde{\sigma} \partial_n u^1]_{\Gamma} = -\kappa D_1 \cdot \begin{pmatrix} \partial_n u^0|_{\Gamma^+} \\ \partial_t u^0|_{\Gamma^+} \end{pmatrix} + D_2 \cdot \partial_t \begin{pmatrix} \partial_n u^0|_{\Gamma^+} \\ \partial_t u^0|_{\Gamma^+} \end{pmatrix}, \\ [u^1]_{\Gamma} = a^0 \cdot \begin{pmatrix} \partial_n u^0|_{\Gamma^+} \\ \partial_t u^0|_{\Gamma^+} \end{pmatrix}, \end{cases}$$

where ∂_t and ∂_n denote the tangential and the normal derivatives along Γ and κ is the curvature of Γ .

We emphasize that our conditions are different than if we would only consider the mean effect of the roughness. In this case, denoting by \bar{f} the mean of f , the conditions would be (see [1], [3], [4]):

$$[\tilde{\sigma} \partial_n \tilde{u}^1]_{\Gamma} = (\sigma_0 - \sigma_m) \bar{f} \partial_t^2 u^0|_{\Gamma}, \quad [\tilde{u}^1]_{\Gamma} = \frac{\sigma_0 - \sigma_m}{\sigma_m} \bar{f} \partial_n u^0|_{\Gamma^+}.$$

III. NUMERICAL SIMULATIONS

In order to verify the convergence rate stated in Section I, we consider a problem where the geometry and the boundary conditions are ε -periodic. The computational domain Ω is delimited by the circles of radius 2 and of radius 0.2 centered in 0, while \mathcal{O}^1 is the intersection of Ω with the concentric disk of radius 1. The rough layer is then described by $f(y) = 1 + 1/2 \sin(y)$. One period of the domain is shown Fig 2(a). The Dirichlet boundary data is identically 1 on the outer circle and 0 on the inner circle.

The mesh generator *Gmsh* [2] and the finite element library *Getfem++* [5] enables us to compute the four potentials u^ε , u^0 , u^1 and \tilde{u}^1 .

The rough thin layer is supposed slightly insulating. The conductivities σ_0 , σ_1 and σ_m respectively equal to 3, 1 and 0.1. The computed coefficients⁴ issued from Problem (3) are given in Table I.

TABLE I
COEFFICIENTS ISSUED FROM THE SOLUTION TO PROBLEM (3). 3
SIGNIFICANT DIGITS ARE KEPT.

a_1^0	a_2^0	D_1^1	D_2^1	D_1^2	D_2^2
19.3	0	0	0	-0.0499	-3.87

³We denote by $[w]_{\Gamma}$ the jump of a function w on Γ .

⁴The convergences at the infinity in Problem (3) are exponential hence we just have to compute problem (3) for $|x| \leq M$, with M large enough to obtain a^0 with a good accuracy.

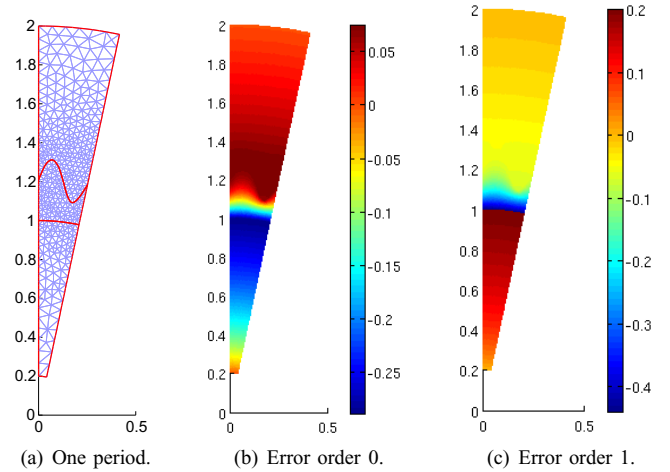


Fig. 2. Representation of one period of the domain and the corresponding errors with approximate solutions u^0 and $u^0 + \varepsilon u^1$. $\varepsilon = 2\pi/30$. Do not consider the error in the rough layer because a proper reconstruction of the solution in it is not currently implemented.

The numerical convergence rates for the H^1 -norm in \mathcal{O}^1 of the three following errors $u^\varepsilon - u^0$, $u^\varepsilon - u^0 - \varepsilon u^1$ and $u^\varepsilon - u^0 - \varepsilon \tilde{u}^1$ as ε goes to zero are given Figure 2. As predicted by the theory, the rates are close to 1 for the order 0 and for the order 1 with the mean effect, whereas it is close to 2 for the “real” order 1 equal to $u^\varepsilon - u^0 - \varepsilon u^1$.

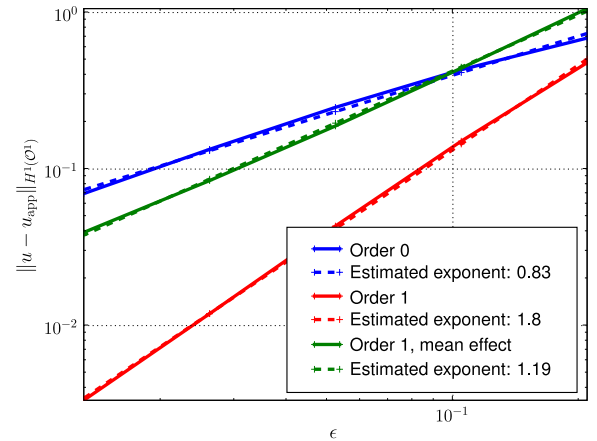


Fig. 3. H^1 -Error in the cytoplasm vs ε for three approximate solutions.

REFERENCES

- [1] S. Ciuperca, M. Jai, and C. Poignard. Approximate transmission conditions through a rough thin layer. The case of the periodic roughness. Research report INRIA RR-6812. <http://hal.inria.fr/inria-00356124/fr/>.
- [2] C. Geuzaine and J. F. Remacle. Gmsh mesh generator <http://geuz.org/gmsh>.
- [3] C. Poignard. Approximate transmission conditions through a weakly oscillating thin layer. *Math. Meth. App. Sci.*, 32:435–453, 2009.
- [4] C. Poignard, P. Dular, R. Perrussel, L. Krähenbühl, L. Nicolas, and M. Schatzman. Approximate conditions replacing thin layer. *IEEE Trans. on Mag.*, 44(6):1154–1157, 2008.
- [5] Y. Renard and J. Pommier. Getfem finite element library. <http://home.gna.org/getfem/>.

Shell's magnetization identification from very close magnetic measurements

Y. Vuillermet^{1,2}, O. Chadebec¹, J.L. Coulomb¹, L. Demilier², L.L. Rouve¹, G. Cauffet¹

¹Grenoble Electrical Engineering Lab (CNRS, Grenoble INP, UJF), Université de Grenoble
ENSE3, BP 46, 38402 Grenoble, France

²DCNS, 2 rue Sextius Michel, 75732 Paris cedex 15, France

Abstract — This paper presents an algorithm dedicated to the determination of shells unknowns magnetization. Thanks to magnetic measurements realized on sensors located very close to ferromagnetic material, an inverse problem is solved enabling the determination of the whole magnetic state of the device. The method is experimentally validated on a mock-up of submarine, the purpose of the study being the prediction of its magnetic anomaly form onboard measurements.

I. INTRODUCTION

Most part of submarines are made of steel. One of the drawbacks using such material is that steel is ferromagnetic. The hull of the submarine, placed in the earth's magnetic field and subjected to important pressure effect, get a static magnetization. This phenomenon is well-known and called magnetostriction. This magnetization creates a local static magnetic anomaly around the submarine and can lead to its detection or localization by magnetic sensors embedded in airplanes or even worse in mines. Therefore, for decades, worldwide marines are looking for reducing this magnetic anomaly by setting up large coils in the whole ships feeding them with adapted currents. Before achieving the reduction of anomaly, it is necessary for the ship to evaluate its own magnetic anomaly. The key point of such system is the identification of the magnetization of the ship's hull and this problem is quite difficult to solve. Indeed, the magnetization can be divided in two parts: an induced one, due to the reversible reaction of the material in the inductor field, and a remanent one due to the magnetic history of the material (which depends on hysteresis, mechanical and thermal constraints). The computation of the induced magnetization is now a well-known problem, however, the remanent part is impossible to evaluate with a deterministic calculation because we have no access to the magnetic past of the material. Moreover, even if we had such knowledge, existing models would be too complex to be applied to 3D geometries. It is then necessary to use magnetic measurements to determine the total magnetization of the hull. Thus, the main goal is to solve an inverse problem (i.e. determination of the sources by knowing the effects) with magnetic sensors placed in the air region closed to the hull.

This problem has already been studied and the magnetization identification has already been achieved when sensors could be located far enough from the sheets and with a simplified mock-up of a surface ship [1], [2]. Some of main results of this problem will be reminded in this paper. However, this method has not been tested yet on realistic

mock-up of a double-hull submarine with an important magnetic sensors number placed between the two hulls.

II. BACKGROUND THEORY

A. Forward modeling

Let us consider a device composed of a ferromagnetic sheet S with a thickness e and placed in an inductor magnetic field \mathbf{H}_0 (the earth's magnetic field, for instance). This sheet has an unknown static magnetization \mathbf{M} which contributes to the global magnetic field. Therefore, field \mathbf{H} is the sum of the inductor field and the field created by the shell itself. The field generated by the ferromagnetic material is directly linked to its magnetization by a classical volume integral equation. For a sheet configuration, it is standard to assume that the magnetization is tangential to the shell and constant through it, its permeability being high and its thickness e being low in comparison with other dimensions. Therefore, the integral equation can be written as follows:

$$\mathbf{H} = \mathbf{H}_0 + \frac{e}{4\pi} \nabla \int_S \frac{\mathbf{M} \cdot \mathbf{r}}{r^3} dS \quad (1)$$

where \mathbf{r} is the vector between the point where \mathbf{H} is expressed and the integration point on the S surface of the shell. For complicated geometries, this equation has of course no analytical solution, it is then necessary to discretized it to get a numerical expression. Lets us consider that surface S is meshed into n surface patches with a uniform magnetization \mathbf{M}_i associated to each of them. Equation (1) becomes:

$$\mathbf{H} = \mathbf{H}_0 + \frac{e}{4\pi} \sum_{i=0}^n \nabla \int_S \frac{\mathbf{M}_i \cdot \mathbf{r}}{r^3} dS_i \quad (2)$$

This equation is a vector one and depends linearly from the \mathbf{M}_i values. Let us remember that the magnetization is tangential to the surface S . Each patches magnetization has then two degrees of freedom. Therefore, equation (3) can be represents as a system of equations:

$$[\mathbf{H}] = [\mathbf{H}_0] + [\mathbf{A}][\mathbf{M}] \quad (3)$$

where \mathbf{H}_0 and \mathbf{H} are vectors of 3 components (each component of the inductor and total field), \mathbf{A} is a $3 \times 2n$ matrix which represents the interaction linking the sources to the field and \mathbf{M} is the $2n$ magnetization vector (2 components per meshed element).

B. Inverse modeling

Let us now imagine that we want to determine \mathbf{M} vector (an image of the magnetization of the sheet projected on it

mesh). A solution is to place magnetic sensors around the shell to have a measurement of \mathbf{H} at a given point of the air region. Let us consider that m tri-axis magnetic sensors are placed around the shell, (3) leads to a Matrix system where \mathbf{H} is measured, \mathbf{H}_0 is known (the position of the device in the earth's magnetic field is known), \mathbf{A} is a $3m \times 2n$ matrix (the coefficient of the matrix can be computed with numerical integration techniques) and \mathbf{M} is searched. To get \mathbf{M} , it remains to solve this system. Unfortunately, this task is not so simple and several aspects can lead to very uneasy resolution process:

-*The system is underdetermined:* If the shell geometry is complicated and the magnetization has important local variations, a very fine mesh is needed to accurately represent the real device. The sensors number being limited, we are faced to a linear system with fewer equations than unknowns.

-*The system has a poor condition number:* This mathematical property leads to an unstable solution. In fact, the measurement vector is associated with a non negligible range of noise and a poor condition number will amplify it during the resolution process to give a divergent solution.

This Inverse problem is said ill-posed. In order to solved it, [1] proposes to add others equations representative of the magnetic behavior of the shell. In our case, it enables to write $2n$ additional equations and to add them to the previous system. The dimension of the research space is therefore considerably reduced and a standard single value decomposition, which returns the solution with the minimal norm generally, succeeds. Let us notice that this approach is efficient if sensors are located sufficiently far enough to ensure a global magnetic observation of the whole device. However, in a real naval application, magnetic sensors have to be placed very close to the hull to get a sufficient signal level and to avoid magnetic disturbance. In this configuration, the solution proposed by [1] failed, returning a non satisfying solution. It is then necessary to use additional a-priori information to select the good solution. It is done by combining the classical approach to a regularization method like proposed in [3]. This kind of method ensures the stability of the solution and improved magnetization identification process.

III. EXPERIMENTAL VALIDATION

A submarine double-hull mock-up of about 3.5 meters long has been designed, built and placed on a railway in a field simulator. It has been instrumented with 75 bi-axis fluxgate sensors and 5 tri-axis ones placed very close to the hull. Above the mock-up, another fluxgate sensor has been placed. By moving the submarine over it, we get a measurement of the anomaly to compare it with the predicted one. Then, the accuracy of the inversion process can be evaluated (Fig.1). Pictures of the experimental set-up are shown on figure 2. The mock-up has been placed in a realistic magnetic state with a strong permanent magnetization.

The whole geometry of the mock-up is meshed into more than 4000 surface elements. So, about 8000 unknowns, fully describing the magnetization, have to be determined. From

sensors; 165 measurement equations are get, the system is then strongly over-determined. To reduce the size of the research space, 4000 equations, representative of the intrinsic magnetic material behavior are added. Then, the matrix system is regularized to finally get a magnetization distribution which seems to be satisfying (Fig.3.). From this magnetization distribution, it is possible, by applying a matrix relation similar to (3) to compute a predicted field on a reference line located outboard the submarine. As it is shown on figure 4, the predicted and the measured field present a very good adequacy.

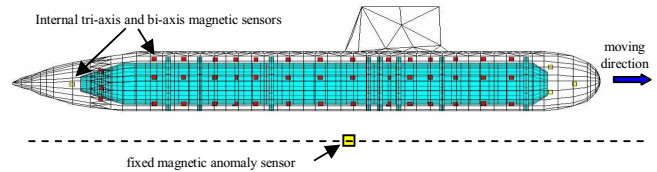


Fig 1: Mock of a double hulls submarine with the mesh, internal fluxgates sensors (bi-axis in red and tri-axis in yellow) and anomaly measurement line.



Fig 2: Pictures of the experimental set-up Experimental results

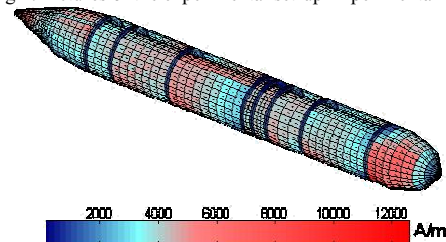


Fig 3: Reconstructed hull's magnetization

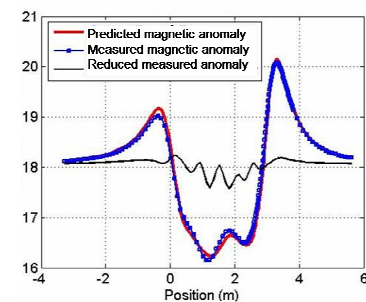


Fig 4: Results of the experimental set-up (measured, predicted and reduced magnetic fields)

IV. REFERENCES

- [1] O. Chadebec, J.L. Coulomb, J.P. Bongiraud, G. Cauffet, P. Le Thiec, "Recent improvements for solving inverse magnetostatic problem applied to thin hulls", IEEE Trans. Magn., vol.38, pp.1005-1008, 2002.
- [2] Yang, C.-S., Lee, K.J., Jung, G., Chung, H.-J., Park, J.-S., Kim, D.-H., "Efficient methodology for solving an inverse magnetostatic problem by utilizing material sensitivity", Journal of Applied Physics, Volume 103, Issue 7, 2008
- [3] A. N. Tikhonov, V. Y. Arsenine, "Solution of ill-posed problem," Wiston/Wiley, Washington , 1977.

Interaction Body Force Field and Total Force on Permanent Magnet by Virtual Air-gap Approach

Se-Hee Lee,¹ Young-Sun Kim,² Ho-Young Lee,¹ Heung-Geun Kim,¹ and Hong-Soon Choi³

¹School of Electrical Eng. and Computer Science, Kyungpook National University, Daegu 702-701, Korea

²School of Information and Communication Eng., Sungkyunkwan University, Suwon 440-746, Korea

³School of Electronic and Electrical Engineering, Kyungpook National University, Sangju 742-711, Korea
tochs@naver.com

Abstract — The interaction body force density and total force were evaluated in permanent magnets by using the virtual air-gap scheme incorporating the finite-element method. Until now, the virtual air-gap concept has been successfully applied to calculate a contact force and a body force density in soft magnetic materials. For permanent magnets, however, there have been few research works on a contact force and a force density field. When the generalized methods, methodologies with virtual air-gap scheme, are introduced, one can have an actual total force, but their distribution has an irregularity, which seems to be random distribution of body force density. Inside permanent magnets, however, a smooth pattern was obtained in the interaction body force density, which represents the interacting force field among magnetic materials. To evaluate the interaction body force density, the intrinsic force density should be withdrawn from the total force density. Several analysis models with permanent magnets were tested to verify the proposed methods evaluating the interaction body force density and the contact force, in which the permanent magnet contacts with a soft magnetic material.

I. INTRODUCTION

Virtual air-gap method has been successfully applied to soft magnetic materials for evaluating the force density and global force, especially contact force [1]-[2]. These force calculating methods employing the virtual air-gap scheme have been called as generalized methods such as the generalized magnetic charge force density method (GMC), the generalized magnetizing current force density method (GCM), and the generalized Kelvin force density method (GKV).

Unlike the soft magnetic materials, there have been few research works related to force density and global force in permanent magnets [3]. One might have a difficulty in dealing with permanent magnet because of its permanent magnetization, which is linked to the energy after magnetizing process. To deal with this energy consideration, the intrinsic and interaction forces between a magnet and exterior media were introduced incorporating the virtual work principle [3].

By the same analogy, here, we calculated the interaction body force field inside permanent magnet and contact force, sliding force between a magnet and soft magnetic material, by using the virtual air-gap method. The resultant interaction body force field was quite interesting and seemed to be interpreted as an actual interaction body force density field between a magnet and magnetic materials. In addition to this, the global force including sliding contact force was also successfully evaluated and verified by the conventional magnetic charge and magnetizing current methods.

II. GENERALIZED FORCE CALCULATING METHODS

To model the permanent magnet, the magnetic flux density \mathbf{B} including permanent magnetization can be expressed as

$$\mathbf{B} = \mu_0(\mathbf{H} + \mathbf{M}_i + \mathbf{M}_0) \quad (1)$$

where μ_0 is the magnetic permeability in air, \mathbf{H} the magnetic field intensity, \mathbf{M}_i the magnetization in soft magnetic materials due to an applied magnetic field, and \mathbf{M}_0 the permanent magnetization in hard magnetic materials.

The GMC, GCM, and GKV were derived by multiplying the equivalent magnetizing sources such as magnetic charge, magnetizing current and magnetic dipole by external applied fields, respectively [1]-[2]. It is important to point out that those external fields have to be obtained after insertion the virtual air-gap at common edge. The resultant external applied fields, \mathbf{H}_{ext} and \mathbf{B}_{ext} , acting on the equivalent sources, therefore, should be included the additional fields and can be expressed as

$$\mathbf{H}_{ext(1\ or\ 2)} = (\mathbf{H}_1 + \mathbf{H}_2) / 2 + \mathbf{H}_{\sigma_m(2\ or\ 1)} \quad (2)$$

$$\mathbf{B}_{ext(1\ or\ 2)} = (\mathbf{B}_1 + \mathbf{B}_2) / 2 + \mathbf{B}_{J_m(2\ or\ 1)} \quad (3)$$

where \mathbf{H}_1 and \mathbf{H}_2 are the magnetic field intensity, and \mathbf{B}_1 and \mathbf{B}_2 are the magnetic flux density acting at the edge of material 1 and 2, respectively. \mathbf{H}_{σ_m} and \mathbf{B}_{J_m} are the magnetic field intensity and flux density produced by the adjacent magnetic charge σ_m or magnetizing current J_m after insertion of the virtual air-gap, respectively.

III. INTERACTION BODY FORCE DENSITY

Energies and force densities of permanent magnet can be divided into three different categories: total magnetic energy and total force density, intrinsic magnetic energy and intrinsic force density, and interaction magnetic energy and interaction force density [3]. The intrinsic force density is obtained when a single magnet in the air and its distribution is supposed to represent the force density on the magnet due to its intrinsic magnetization. The interaction force density represents that the pure interaction force between a magnet and exterior materials. To evaluate the interaction body force density, therefore, the intrinsic force density should be withdrawn from the total force density.

Because the generalized force density methods were calculated in each element inside material, the resultant force field represents a body force density, but this total force density has an irregular pattern [2]. On the contrary, the interaction body force density was obtained in regular pattern after subtracting the intrinsic force density from the total force density.

IV. NUMERICAL RESULTS

Figs. 1(a) and 1(b) represent the effect of different interaction forces between two magnets with x direction of magnetization. The intrinsic body force field has an irregularity as shown in Fig. 2(a), but the interaction body force field, a regularity, which seems to represent an actual body force density field inside the magnet as shown in Fig. 2(b) and Fig. 3.

To verify the sliding contact force, two magnet systems were tested as shown in Figs. 4(a) and 4(b), of which the magnetization had a horizontal and vertical directions, respectively. While the permanent magnets slides into x direction, the resultant forces can be correctly calculated by using the magnetic charge force density method for Model III and the magnetizing current force density method for Model IV. Figs 5(a) and 5(b) show well the trends of solution as we mentioned above. Figs 6(a) and 6(b) represent the resultant distributions of interaction force.

In extended paper, we will present more numerical examples including mechanical deformation and discuss about its physical meanings in detail.

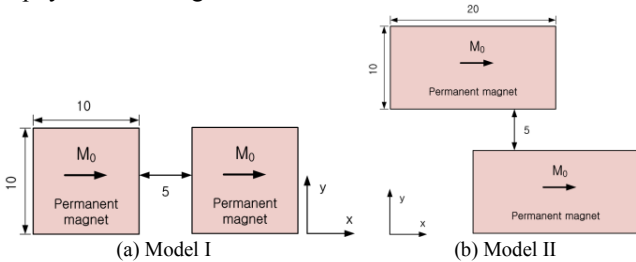


Fig. 1. Analysis models with two permanent magnet systems (Unit: [mm]).

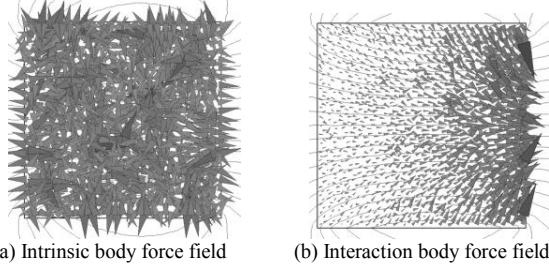


Fig. 2. Distributions of electromagnetic body force field for model I.

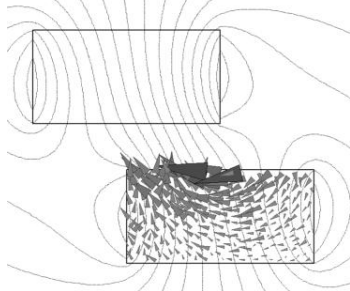


Fig. 3. Distribution of interaction body force field for model II.

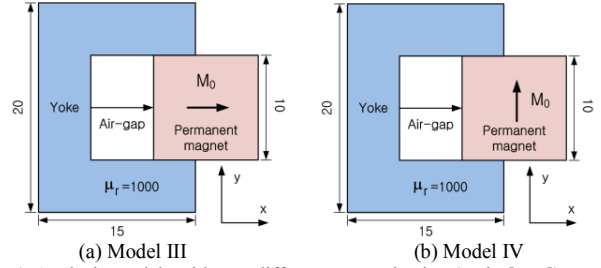
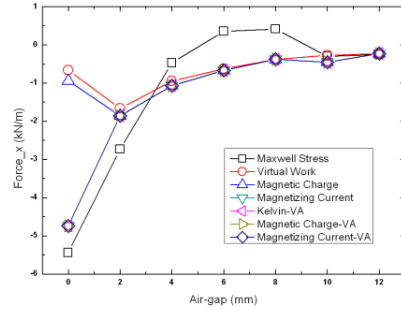
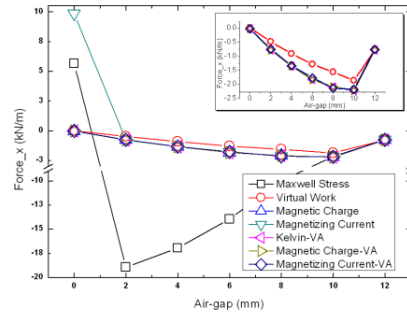


Fig. 4. Analysis models with two different magnetization (Unit: [mm]).

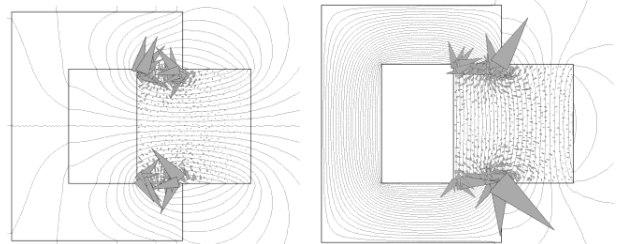


(a) Sliding forces for model III



(b) Sliding forces for model IV

Fig. 5. Comparisons of sliding contact forces with air-gap.



(a) Interaction force field for model III (b) Interaction force field for model IV
Fig. 6. Distributions of interaction body force fields with the air-gap of 6 mm.

Acknowledgement: This work was supported by the Korea Science and Engineering Foundation (KOSEF) grant funded by the Korea government (MEST) (No. 2008-0062032).

V. REFERENCES

- [1] Hong-Soon Choi, Se-Hee Lee, and Il-Han Park, "General formulation of equivalent magnetic charge method for force density distribution on interface of different materials," *IEEE Trans. on Magnetics*, vol. 41, no. 5, p. 1420-1423, May 2005.
- [2] Se-Hee Lee, Hong-Soon Choi, and Il-Han Park, "Introducing the virtual air-gap scheme to the Kelvin force densities with external and total field," *IEEE Trans. on Magnetics*, vol.43, no. 4, pp. 1457-1460, April 2007.
- [3] L. H. De Medeiros, G. Reyne, and G. Meunier, "A unique distribution of forces in permanent magnets using scalar and vector potential formulations," *IEEE Trans. on Magnetics*, vol. 36, no. 5, pp. 3345-3348, September 2000.

Block-preconditioning for hybrid discretisations in combination with Lagrange-multiplier coupling

Stephan Koch¹, Herbert De Gersem², and Thomas Weiland¹

¹Technische Universität Darmstadt, Institut für Theorie Elektromagnetischer Felder,

Schlossgartenstrasse 8, D-64289 Darmstadt, Germany, koch/thomas.weiland@temf.tu-darmstadt.de

²Katholieke Universiteit Leuven, Faculty of Science, Kortrijk B-8500, Belgium, Herbert.DeGersem@kuleuven-kortrijk.be

Abstract—The linear systems of equations arising from hybrid discretizations, e.g., by coupling finite elements (FE) with spectral elements (SE), are sparse and symmetric. However, the use of a saddle-point formulation leads to indefinite algebraic equations. Their solution requires, therefore, the application of appropriate iterative solvers and preconditioners. In order to achieve an acceptable solution time, in particular for transient simulations requiring repetitive solves, an adapted block-preconditioner based on approximations of the Schur complement is applied. The performance regarding the number of iterations of the Krylov subspace method as well as the solution time is compared for different types of preconditioners.

I. INTRODUCTION

In case of technical devices featuring large subdomains in which a particular symmetry holds, such as according to rotation or translation, the application of an anisotropic discretization can lead to a beneficial reduction of the number of degrees of freedom in the numerical model [1]. This approach is based on domain decomposition, whereas the actual model is separated into parts exhibiting symmetry and the surrounding region lacking symmetry (Fig. 1(a)). While for formulations involving scalar potentials the systems of equations remain regular, as, e.g., in [2], introducing the magnetic vector potential to the magnetostatic approximation of the Maxwell equations leads to a consistently singular system due to the nullspace of the curl-operator. This inhibits the use of direct solution strategies, e.g. by LU-factorization. Therefore, iterative methods are required in order to solve the system of equations [3].

II. HYBRID DISCRETIZATION

The magnetostatic formulation in terms of the magnetic vector potential \mathbf{A} introduced in order to represent the magnetic flux density \mathbf{B} as $\mathbf{B} = \nabla \times \mathbf{A}$ reads

$$\nabla \times (\nu \nabla \times \mathbf{A}) = \mathbf{J} \quad (1)$$

with the reluctivity ν and the impressed current density \mathbf{J} . Based on the decomposition of the computational domain into parts with and without symmetry (Fig. 1), discretization is carried out for the respective subdomains separately. While in the non-symmetric region, standard 3D-FE shape functions \mathbf{w}_j^{3D} are applied to discretize \mathbf{A} in the weak formulation of (1), special shape functions accounting for the symmetry present in the model are used for the translatory symmetric region. In contrast to a scalar potential formulation as, e.g., in [1], two sets of vectorial shape functions, $\mathbf{v}_{i,j,q}^{xy}$ and $\mathbf{v}_{i,q}^z$, based

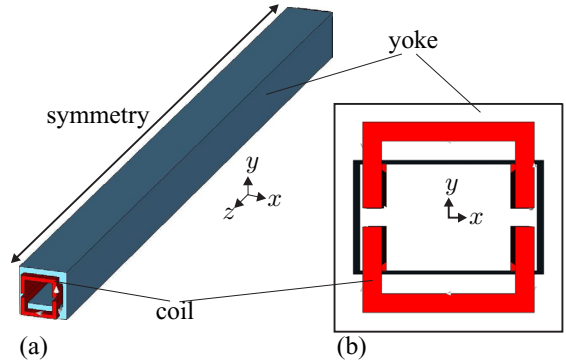


Fig. 1. (a) Idealized model of a long dipole magnet featuring a large domain of symmetry; (b) Cross-section of the magnet serving to establish geometric modeling of reduced order.

on triangular prisms defined by the triangulation of the cross-section in Fig. 1(b) are required to discretize the weak form of (1) inside the domain of symmetry. These are introduced in [2] for the representation of the source field in combination with a magnetostatic formulation in terms of the magnetic scalar potential. Here the two sets of shape functions are used to approximate the primary unknown \mathbf{A} . The discretization leads to two independent systems of equations for the separate domains. These are combined by means of Lagrange multipliers \mathbf{v}_{lg} which guarantee a symmetric coupling by ensuring the tangential continuity of the magnetic field strength \mathbf{H} as well as the normal continuity of the magnetic flux density \mathbf{B} across the interface between both regions. The coupled system reads

$$\begin{pmatrix} \mathbf{K}_{3D} & 0 & -\mathbf{B}_{3D} \\ 0 & \mathbf{K}_{fese} & \mathbf{B}_{fese} \\ -\mathbf{B}_{3D}^T & \mathbf{B}_{fese}^T & 0 \end{pmatrix} \begin{pmatrix} \mathbf{a}_{3D} \\ \mathbf{a}_{fese} \\ \mathbf{v}_{lg} \end{pmatrix} = \begin{pmatrix} \mathbf{j}_{3D} \\ \mathbf{j}_{fese} \\ 0 \end{pmatrix} \quad (2)$$

with the vector of degrees of freedom \mathbf{a} and the vector \mathbf{j} corresponding to the excitation for the non-symmetric part (3D) and the translatory symmetric part (fese), respectively.

III. BLOCK-PRECONDITIONING

In order to ensure an efficient numerical solution of the system (2), an appropriate preconditioner is required, as the condition number of the system matrix is very large especially due to the anisotropic discretization with respect to the direction of symmetry. The approach chosen here accounts for the blockwise structure of the matrix making use of the property

$$\begin{pmatrix} \mathbf{A} & \mathbf{C}^T \\ \mathbf{C} & 0 \end{pmatrix}^{-1} = \begin{pmatrix} \mathbf{T} & -\mathbf{A}^{-1}\mathbf{C}^T\mathbf{S}^{-1} \\ -\mathbf{S}^{-1}\mathbf{C}\mathbf{A}^{-1} & \mathbf{S}^{-1} \end{pmatrix} \quad (3)$$

TABLE I

COMPARISON OF THE ACHIEVED ACCURACY AND THE REQUIRED SOLUTION TIME IN COMBINATION WITH DIFFERENT PRECONDITIONERS USING THE GMRES METHOD LIMITED TO 3000 ITERATIONS WITHOUT RESTARTING. THE DIMENSION OF THE SYSTEM MATRIX IS 30952.

precond type (for \mathbf{A}/\mathbf{S})	iterations	time / s	rel. residual
no precond / -	(3000)	4873	1.7e-1
global Jacobi / -	(3000)	5567	6.7e-3
Jacobi/Jacobi	401	178	2.4e-5
Gauss-Seidel/Gauss-Seidel	187	66	1.7e-5

with $\mathbf{T} = \mathbf{A}^{-1} + \mathbf{A}^{-1}\mathbf{C}^T\mathbf{S}^{-1}\mathbf{C}\mathbf{A}^{-1}$ and the Schur complement $\mathbf{S} = -\mathbf{C}\mathbf{A}^{-1}\mathbf{C}^T$. Taking the upper left (2×2) -block of the system matrix in (2) as \mathbf{A} and $\mathbf{C} = (-\mathbf{B}_{3D}^T, \mathbf{B}_{fese}^T)$, different approximations of the inverse of \mathbf{A} and \mathbf{S} , respectively, are sought. Even though the system matrix is symmetric, the generalized minimal residual method (GMRES) is used in combination with an approximation of the inverse in (3) as a preconditioner. In the full paper the algebraic symmetry will be exploited by using the computationally more efficient minimal residual method (MINRES) which is more efficient with respect to memory consumption due to the three-term recursion scheme. In that case, however, a symmetric positive definite preconditioner must be used [4], [5].

An approximation of the inverse of \mathbf{A} is required to form the sub-blocks of the preconditioning matrix in (3). Moreover, the inverse of the Schur complement \mathbf{S} needs to be built using an appropriate representation of \mathbf{A}^{-1} . Two possibilities are investigated here: First, the exact inverse of \mathbf{A} in (3) is replaced by the reciprocal of the main diagonal, yielding a Jacobi-type preconditioning. The dimension of \mathbf{S} corresponds to the number of degrees of freedom allocated at the interface between the separate domains. Therefore, the size of this matrix remains moderate and explicit inversion can be carried out for sufficiently small numerical models. Secondly, an additive splitting of \mathbf{A} into upper and lower triangular parts leads to Gauss-Seidel preconditioning. Now, the action of the particular blocks of the preconditioning matrix on a given vector is provided by forward and backward substitution at the corresponding occurrences of \mathbf{A}^{-1} .

IV. COMPARISON OF DIFFERENT PRECONDITIONERS

The performance of different types of preconditioners is investigated by solving the system matrix resulting from the hybrid discretization of the schematic magnet model in Fig. 1(a). For the matrix dimension of 30952 the maximum number of GMRES iterations is set to 3000. The results in terms of the achieved accuracy and the required solution time are summarized in Table I. In order to compare the performance to common approaches, the results without any preconditioning as well as for global Jacobi preconditioning are also included. For the latter, the zeros present on the main diagonal of the system matrix are replaced by unity during the construction of the preconditioner. Therefore, the coupling blocks \mathbf{C} are not considered in the preconditioning process. As a consequence, only a slight benefit compared to the absence of any preconditioning is observed as shown

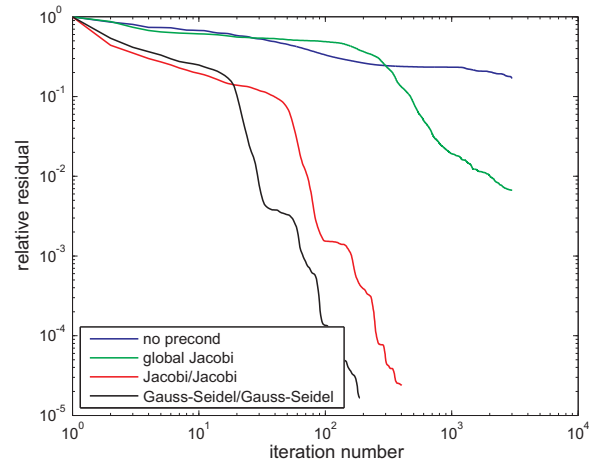


Fig. 2. Convergence history for different types of preconditioners in terms of the relative residual in each iteration step of the GMRES method.

in Fig. 2. In both cases achieving the prescribed accuracy of $1e-6$ is virtually impossible due to the increasing amount of memory for each additional iteration step. Restarting the GMRES iteration discarding the previous search directions does not generally change the situation. However, a significant improvement is observed by considering the coupling blocks of the inverse in (3) in terms of blockwise Jacobi and Gauss-Seidel approximations for \mathbf{A} as a part of \mathbf{T} and \mathbf{S} , respectively. Even though the time required for each iteration is larger in case of the Gauss-Seidel procedure due to the forward and backward substitutions, the number of iterations as well as the solution time is decreased. This is very important especially when considering the hybrid discretization scheme in the time-domain, where the system matrix is solved repeatedly.

V. CONCLUSION

The saddle-point problem resulting from a hybrid discretization in combination with Lagrange multipliers is solved by means of the preconditioned GMRES method. Accounting for the particular structure of the system matrix, superior convergence results in terms of the number of iterations as well as in the solution time are observed using blockwise preconditioning. The beneficial approximation properties of the anisotropic discretization using vectorial shape functions can be exploited in combination with appropriate preconditioners as proposed in this paper.

REFERENCES

- [1] S. Koch, H. De Gersem, and T. Weiland, "Hybrid Finite-Element, Spectral-Element Discretization for Translatory Symmetric Model Parts," *IEEE Transactions on Magnetics*, vol. 44, no. 6, pp. 722-725, June 2008.
- [2] S. Koch, H. De Gersem, and T. Weiland, "Magnetostatic Formulation with Hybrid Finite-Element, Spectral-Element Discretizations," *IEEE Transactions on Magnetics*, vol. 45, no. 3, pp. 1136-1139, March 2009.
- [3] R.E. Bank, B.D. Welfert, and H. Yserentant, "A class of iterative methods for solving saddle point problems," *Numerische Mathematik*, vol. 56, pp. 645-666, 1990.
- [4] D. Silvester and A. Wathen, "Fast iterative solution of stabilised Stokes systems, part II: using general block preconditioners," *SIAM Journal on Numerical Analysis*, vol. 31, no. 5, pp. 1352-1367, October 1994.
- [5] G. Gatica and N. Heuer, "A preconditioned MINRES method for the coupling of mixed-FEM and BEM for some nonlinear problem," *SIAM Journal on Scientific Computing*, vol. 24, no. 2, pp. 572-596, 2002.

MHD Convection of a Electrically Conductive Fluid with Variable Thermal Conductivity

M. Pirmohammadi¹, M. Ghassemi², and A. Keshtkar³

¹ Research Management of R & D Deputy, Mapna Group, Tehran, Iran

² Mechanical Engineering Department, K. N. Toosi University of Technology, Tehran, Iran

³ Engineering and Technology Department, Imam Khomeini International University (IKIU), Ghazvin, Iran

Pirmohammadi@Mapna.com

Abstract— The effect of temperature-dependent thermal conductivity on the magneto-convection in a low Prandtl number liquid is investigated numerically. The liquid is contained in a closed square enclosure with isothermal vertical walls kept at different temperatures. The top and bottom walls are assumed to be insulated. To solve the governing non-linear differential equations (mass, momentum and energy) a finite volume code based on SIMPLER algorithm is utilized. The results for different Rayleigh and Hartmann numbers show that the strength of the magnetic field has significant effects on the flow and temperature fields. The convection becomes stronger as the Rayleigh number increases while the magnetic field suppresses the convective flow and the heat transfer rate. The heat transfer is found to decrease appreciably across the cavity with a decrease in thermal conductivity.

I. INTRODUCTION

The Lorentz force acts against the buoyancy force. This phenomenon is used in material manufacturing industry and turbine blade casting as a control mechanism. Employment of an external magnetic field has increasing applications in material manufacturing industry as a control mechanism since the Lorentz force suppresses the convection currents by reducing the velocities. Study and thorough understanding of the momentum and heat transfer in such a process is important for the better control and quality of the manufactured products. The Garandet et al. [1] proposed an analytical solution to the governing equations of magneto hydrodynamics to be used to model the effect of a transverse magnetic field on natural convection in a two-dimensional enclosure. Al-Najem et al. [2] used the power law control volume approach to determine the flow and temperature fields under a transverse magnetic field in a tilted square enclosure with isothermal vertical walls and adiabatic horizontal walls at Prandtl number of 0.71 and showed that the suppression effect of the magnetic field on convection currents and heat transfer is more significant for low inclination angles and high Grashof numbers. Recently, Pirmohammadi et al. [3] studied the effect of a magnetic field on buoyancy-driven convection in differentially heated square enclosure. They showed that the heat transfer mechanisms and the flow characteristics inside the enclosure depend strongly upon both the strength of the magnetic field as well as the Rayleigh number. It was concluded that the magnetic field considerably decreases the average Nusselt number.

In previous studies the dependency of thermal conductivity on temperature has not been considered. The present study considers laminar natural convection flow in the presence of a longitudinal static magnetic field in a square enclosure heated

from the left wall and cooled from the right wall while the other walls are kept adiabatic. The enclosure is filled with an electrically conducting fluid which its thermal conductivity varies with temperature. The object of the study is to obtain numerical solutions for the velocity and temperature fields inside the enclosure and to determine the effects of the magnetic field strength on the transport phenomena.

II. BASIC EQUATIONS

The geometry and the coordinate system are schematically shown in Fig. 1.

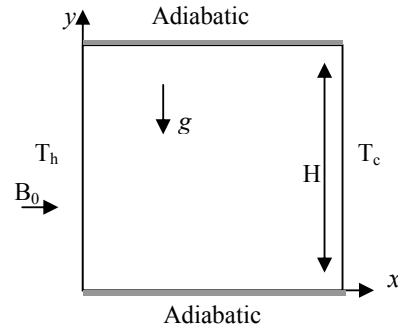


Fig. 1. Geometry of enclosure configuration with magnetic effect.

The non-dimensional governing equations in this study are based on the conservation laws of mass, linear momentum and energy are given as:

$$\frac{\partial U}{\partial X} + \frac{\partial V}{\partial Y} = 0 \quad (1)$$

$$U \frac{\partial U}{\partial X} + V \frac{\partial U}{\partial Y} = -\frac{\partial P}{\partial X} + \text{Pr} \left(\frac{\partial^2 U}{\partial X^2} + \frac{\partial^2 U}{\partial Y^2} \right) \quad (2)$$

$$U \frac{\partial V}{\partial X} + V \frac{\partial V}{\partial Y} = -\frac{\partial P}{\partial Y} + \text{Pr} \left(\frac{\partial^2 V}{\partial X^2} + \frac{\partial^2 V}{\partial Y^2} \right) + Ra \text{Pr} \theta - Ha^2 \text{Pr} V \quad (3)$$

$$U \frac{\partial \theta}{\partial X} + V \frac{\partial \theta}{\partial Y} = \frac{\partial}{\partial X} \left(k^* \frac{\partial \theta}{\partial X} \right) + \frac{\partial}{\partial Y} \left(k^* \frac{\partial \theta}{\partial Y} \right) \quad (4)$$

In the above equations, the primary non-dimensional parameters, the Rayleigh number and the Prandtl number, are defined as:

$$\text{Pr} = \frac{\nu}{\alpha}, \quad Ra = \frac{g\beta(T_h - T_c)H^3}{\alpha\nu}, \quad Ha = B_0 H \sqrt{\frac{\sigma}{\rho\nu}}, \quad k^* = \frac{k}{k_0} \quad (5)$$

Where, ρ is the density, g is the gravitational acceleration, ν is the cinematic viscosity, β is the coefficient of thermal

expansion, k_0 is thermal conductivity in reference temperature and B_0 is the magnitude of magnetic field and σ is the electrical conductivity. Also U , V and θ are non-dimensional velocity components and temperature, respectively. The non-dimensional thermal conductivity of the liquid is assumed to vary linearly with temperature as $k^*=1-\eta\theta$ where η is the temperature coefficient of thermal conductivity.

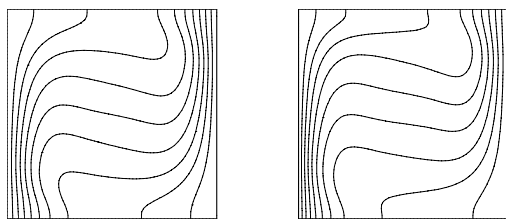
The local Nusselt number $Nu = -\frac{\partial\theta}{\partial X}$ is computed at the hot wall (Nu) and cold wall (Nu_c). The average Nusselt number is expressed as $\overline{Nu} = \int_0^1 Nu dY$.

III. RESULTS

The accuracy of results is verified with that of Rudraiah and is presented in Pirmohammadi et al [5].

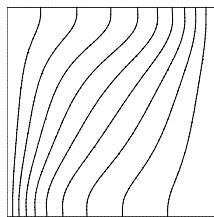
The computations have been done for $Ra = 10^4$ and 10^5 , $\eta=0, 0.25$ and 0.5 , $Ha=0, 15, 30$ and 90 and Pr is fixed at 0.054 corresponding to liquid sodium– potassium alloy. Fig.2 shows the effect of magnetic field and variability of thermal conductivity on temperature field.

It is observed that in the case $\eta=0$ (constant k , i.e. $k = k_0$) and $Ha=0$, as the left wall is maintained at a higher temperature, the adjoining liquid particles experience a drop in their local densities and hence a clockwise rotating buoyancy-induced cell appears and the upper region of the isotherms are pushed towards the cold wall and the lower region towards the hot wall. This results in a simple clockwise rotating convection cell. When η is increased to 0.5 (varying k , i.e. $< k_0$) the isotherms are attracted towards the hot wall as such without any change in their qualitative shape and the formation of thermal boundary layer is clear [4], showing that smaller quantity of heat is propagated from the hot wall to the cold wall across the cavity compared to $\eta=0$ case. By applying



(a) $\eta=0$ and $Ha=0$

(b) $\eta=0.5$ and $Ha=0$



(c) $\eta=0.5$ and $Ha=90$

Fig.2 isotherms for $Ra=10^5$

magnetic field ($Ha=90$) the Lorentz force acts against the buoyancy force and convection heat transfer suppresses. Also it is shown that the temperature stratification in the core diminishes and the thermal boundary layers at the two side walls disappear. This is due to the retarding effect of the Lorentz force. For a sufficiently large Ha , the convection is completely suppressed as in the case of a small Ra .

We observe that the effect of η is to increase the \overline{Nu} from Table I. \overline{Nu} gives the relative measure of the total heat transfer rate to the conductive heat transfer rate. This shows that the retardation of conductive mode of heat transfer is more compared to that of convective mode near the hot wall, even though the heat transfer across the cavity from the hot to cold wall gets reduced by both conduction and slower convection for an increasing η . Also it can be seen that \overline{Nu} decreases with an increase of Hartmann number. This shows that the convection in the enclosure is suppressed due to the introduction of the magnetic field.

TABLE I
EFFECT OF η AND Ha ON AVERAGE NUSSLETT NUMBER

Ra	η	Ha	\overline{Nu}	\overline{Nu}_c
10^4	0.	0	1.93	1.93
		15	1.54	1.54
		30	1.17	1.17
	0.25	0	2.33	1.77
		15	1.88	1.42
		30	1.40	1.05
	0.5	0	3.01	1.56
		15	2.46	1.27
		30	1.83	0.93
10^5	0.	0	3.26	3.26
		30	2.65	2.65
		90	1.30	1.30
	0.25	0	3.91	2.99
		30	3.21	2.45
		90	1.57	1.19
	0.5	0	5.03	2.67
		30	4.18	2.21
		90	2.08	1.07

IV. REFERENCES

- [1] J.P. Garandet, T. Alboussiere, R. Moreau, "Buoyancy driven convection in a rectangular enclosure with a transverse magnetic field", *International Journal of Heat and Mass Transfer*, 35:741–748, 1992.
- [2] N.M. Al-Najem, K.M. Khanafer, and M.M. El-Refae, "Numerical study of laminar natural convection in tilted enclosure with transverse magnetic field", *International Journal of Numerical Methods in Heat and Fluid Flow*, 8: 651–672, 1998.
- [3] M. Pirmohammadi, M. Ghassemi, and G.A. Sheikhzadeh, "Effect of magnetic field on buoyancy driven convection in differentially heated square cavity", *IEEE Trans. on magnetics*, 45(1):407-411, 2009.
- [4] S.Sarvanan and P.Kandaswamy, "Buoyancy convection in low prandtl number liquids with large temperature variation", *Meccanica*, 37:599-608, 2002.

Introduction of a Direct Solver at Subdomains in Non-linear Magnetostatic Analysis with HDDM

Shin-ichiro Sugimoto¹, Jian Zhao², Masao Ogino², Hiroshi Kanayama² and Shinobu Yoshimura¹

¹School of Engineering, The University of Tokyo
7-3-1 Hongo, Bunkyo-ku, Tokyo 113-8656, Japan
sugimoto@sys.t.u-tokyo.ac.jp, yoshi@sys.t.u-tokyo.ac.jp

²Faculty of Engineering, Kyushu University
744 Motoooka, Nishi-ku, Fukuoka 819-0395, Japan
zhao@cm.mech.kyushu-u.ac.jp, ogino@mech.kyushu-u.ac.jp,
kanayama@mech.kyushu-u.ac.jp

Abstract — This paper deals with large-scale 3D non-linear magnetostatic analysis by Hierarchical Domain Decomposition Method (HDDM). In magnetostatic numerical analysis, the computational object is always made in a complicated way at a large scale, and computational time is always very large. But, with the development of computational capabilities, it is now possible to focus our attention on the computational time without worrying about the amount of memory. In this paper, we reexamine the solution strategy for Finite Element Analysis (FEA) in the subdomain problems. Because the finite element equation of the A method that neglects the Lagrange multiplier p is singular, it has been solved by the Conjugate Gradient (CG) method in past researches. To solve it by the direct method, the A method that doesn't neglect the Lagrange multiplier p is considered. In this method we can expect to analyze more complex objects in relatively short time.

I. INTRODUCTION

There are many machines or devices where the electromagnetic phenomena are applied such as a computer, a cell phone, a transformer, and an MRI, etc. In order to analyze these engineering or physical phenomena, computer simulation is a reliable and yet economical approach.

Moreover, a computational object tends to be large and complicated for numerical analysis recently. In addition, subdivision of the mesh is performed for the improvement of accuracy. Therefore, large-scale computations are increasingly important in electromagnetic field problems. To meet this requirement, we have already introduced Hierarchical Domain Decomposition Method (HDDM) [1][2] together with the data handling type "Parallel processor mode (P-mode)" [3][4] to 3D non-linear magnetostatic problems using the Newton method to solve the simultaneous non-linear equations and the A method with the continuity of the electric current density that uses the magnetic vector potential A as an unknown function [5]. To verify the accuracy of our analysis, Testing Electromagnetic Analysis Methods (TEAM) Workshop Problem 20 was analyzed changing its Degrees of Freedom (DOF) several times up to 50 million DOF. The computations were performed with a PC cluster that consists of 32 PC. As a result, a non-linear magnetostatic problem with 50 million DOF was successfully solved in about 8.5 hours [6].

The possibility of large-scale analysis in 3D non-linear magnetostatic problems has been shown. However, we have to reduce the number of iterations and computation time. In this paper, to reduce computation time, the solution strategy of Finite Element Analysis (FEA) in subdomains is reexamined.

Usually, FEA in subdomains is performed by the direct method. However, because the finite element equation that we employ is singular, it is solved by the ICCG method, namely

Conjugate Gradient method that uses the shifted incomplete Cholesky factorization as the preconditioner. If the direct method is applied for solving FEA in subdomains, the computation time seems to be reduced by storing matrices that are results of the LU decomposition on main memory. Moreover, because the accuracy of the solutions in subdomains is improved by solving with the direct method, the characteristic of convergence of the interface problem can be improved, too. Therefore, to solve FEA in subdomains by the direct method, we consider the A method that doesn't neglect the Lagrange multiplier p in subdomains.

II. ITERATIVE DOMAIN DECOMPOSITION METHOD

We consider 3-D non-linear magnetostatic problems using the A method and the Newton method, see [5]. Then, we introduce an iterative domain decomposition method to this method. Let us denote the finite element equations of the A method by the matrix form as follows:

$$Ku = f \quad (1)$$

where K denotes the coefficient matrix, u the unknown vector, and f the known vector.

The polyhedral domain Ω is partitioned into the non-overlapping subdomains. Then the linear system (1) is rewritten as follows:

$$\begin{pmatrix} K_{II} & K_{IB} \\ K_{IB}^T & K_{BB} \end{pmatrix} \begin{pmatrix} u_I \\ u_B \end{pmatrix} = \begin{pmatrix} f_I \\ f_B \end{pmatrix} \quad (2)$$

where the subscripts I, B correspond to the nodal points in the interior of subdomains and on the interface boundary.

At first the unknown vector u_B is obtained from the algorithm based on the CG method to (2), see [5]. After solving u_B , the unknown u_I is obtained from:

$$K_{II}u_I = f_I - K_{IB}u_B. \quad (3)$$

The vector u_I can be solved independently in each subdomain. Hence we can get the unknown u in the whole domain.

In the past, the vector u_I was solved by the ICCG method, because the finite element equation of the A method that neglects the Lagrange multiplier p is singular. In this paper, to solve FEA in subdomains by the direct method, the A method that doesn't neglect the Lagrange multiplier p is considered in subdomains.

In the actual parallel computing in the next section, we adopt HDDM with "Parallel processor mode (p-mode)".

III. NUMERICAL EXAMPLES

In this section, TEAM Workshop Problem 20 [7] is considered, which consists of a center pole, a yoke and a coil.

The center pole and the yoke are made of SS400, and the coil is made of polyimide electric wire. The electric current in the coil is 1,000 [A]. The magnetic reluctivity is a positive constant in each element such that in the region of air and coil, the value is $1/(4\pi \times 10^{-7})$ [m/H]. TABLE I shows numbers of elements, DOF and subdomains.

TABLE I
NUMBERS OF ELEMENTS, DOF AND SUBDOMAINS

	elements	DOF
Model (1)	440,634	527,319
Model (2)	1,033,404	1,227,859
Model (3)	1,786,748	2,114,436
Model (4)	38,052,061	44,440,020
Model (5)	50,254,629	58,650,613

TABLE II
COMPUTATION TIME, SPEED-UP RATIO AND AMOUNT OF MEMORY PER CPU

	method	computation time [s]	speed-up previous/new	memory per CPU [MB]
Model (1)	previous	230	1.60	25.3
	new	144		60.7
Model (2)	previous	715	1.49	59.3
	new	481		142
Model (3)	previous	1,402	1.52	102
	new	920		246

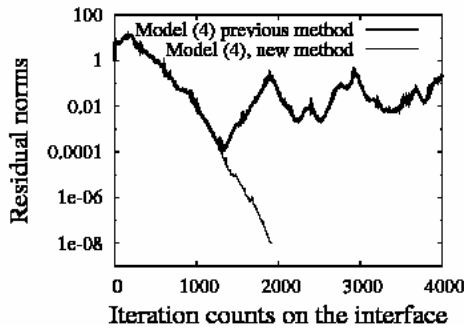


Fig. 1. History of residual norms (Model (4)).

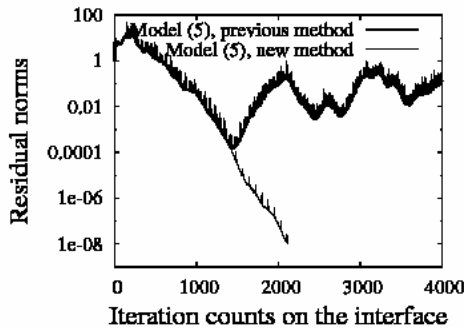


Fig. 2. History of residual norms (Model (5)).

A. Comparison the new method with the previous method

In this section, we compare the new method (solving by the direct method with Lagrange multiplier p) with the previous method (solving by ICCG method) by solving Model (1)-(3). A simplified block diagonal scaling is used as the preconditioner in the CG procedure on the interface. Each process is stopped when the residual norm becomes less than 10^{-4} . The Newton iteration is stopped by $\|u_b^{n+1} - u_b^n\| / \|u_b^{n+1}\| < 10^{-5}$.

FEAs in subdomains of the previous method are solved by the shifted ICCG method (the shift value is 1.2) and it is stopped when the preconditioned residual norm becomes less than 10^{-9} . Computations were performed by a PC cluster that consisted of 8 CPUs of Intel Core2Duo E6600 (2.4GHz). TABLE II shows computation time, speed-up ratio and amount of memory per CPU versus method cases. In any Model (1)-(3), the new method needs much memory than the previous method by about twice, because the matrices that are results of the LU decomposition are stored on main memory. However, the computation times of the new method are reduced and speed-up ratios are 1.5-16.

B. Characteristics of convergence of the interface problem

To investigate characteristics of convergence of the interface problem, the CG procedure on the interface is iterated up to 4,000 times or is stopped when the relative residual norm become less than 10^{-8} . In this section, Model (4) and (5) are computed. Computations were performed by a PC cluster that consisted of 28 CPUs of Intel Core2Duo E6600. Fig. 1 and Fig. 2 show the histories of residual norms. It is clear that the characteristic of convergence of the new method is better than that of the previous method. Moreover, the residual norms of the previous method have diverged after reaching the minimum residual nom. However, those of the new method have become small smoothly.

IV. CONCLUSIONS

To solve FEA in subdomains by the direct method, the A method that doesn't neglect the Lagrange multiplier p is considered in subdomains. Because the direct method is used in subdomains, the amount of memory of the new method is about twice as much as that of the previous method. However, the computation time of the new method is about 0.65 times as long as that of the previous method by storing matrices that are results of the LU decomposition on main memory. Moreover, the characteristic of convergence of the interface problem is improved. As present work, we are trying to analyze the model with 100 million DOF.

V. REFERENCES

- [1] A. Quarteroni and A. Vali, *Domain Decomposition Methods for Partial Differential Equations*, CLARENDON PRESS · OXFORD, 1999.
- [2] R. Shioya and G. Yagawa, "Iterative domain decomposition FEM with preconditioning technique for large scale problem", *ECM'99 Progress in Experimental and Computational Mechanics in Engineering and Material Behaviour*, pp.255-260, 1999.
- [3] A.M.M. Mukaddes, M. Ogino, H. Kanayama and R. Shioya, "A scalable balancing domain decomposition based preconditioner for large scale heat transfer problems", *JSME International Journal Series B*, 49-2, pp.533-540, 2006.
- [4] H. Kanayama and S. Sugimoto, "Effectiveness of A-phi method in a parallel computing with an iterative domain decomposition method", *IEEE Trans. Magn.*, Vol.42, No. 4, pp.539-542, 2006.
- [5] H. Kanayama, H. Zheng and N. Maeno, "A domain decomposition method for large-scale 3-D nonlinear magnetostatic problems", *Theoretical and Applied Mechanics*, 52, pp.247-254, 2003.
- [6] S. Sugimoto, S. Yoshimura and H. Kanayama, "Non-linear magnetostatic analysis of a 50 million DOF problem by hierarchical domain decomposition method", *Proceedings of the 26th Japan Simulation Conference*, (in Japanese), pp.175-178, June 2007.
- [7] IEEJ, *IEEJ Technical Report No.486*, IEEJ, (in Japanese), 1994.

A Discrete Geometric Approach to solving 2D non-linear magnetostatic problems

Paolo Bettini, Ruben Specogna, and Francesco Trevisan

Dipartimento di Ingegneria Elettrica, Gestionale e Meccanica, Università of Udine,
Via delle Scienze 208, 33100 Udine, Italy,
bettini@uniud.it, ruben.specogna@uniud.it, trevisan@uniud.it

Abstract—The aim of this paper is to introduce a **Discrete Geometric Approach to solving 2D non-linear magnetostatic problems**. In particular, an efficient algorithm will be presented to solve magnetostatics in isotropic non-linear media by means of a Newton-Raphson scheme, in which the Jacobian is calculated analytically. Results on a reference configuration (TEAM Workshop Problem 25) are reported and discussed.

Index Terms—Discrete Geometric Approach, Non-linear Magnetostatics, TEAM Workshop Problem 25

I. INTRODUCTION

We focus on a Discrete Geometric Approach (DGA) based on the geometric structure behind Maxwell's equations [1], [2] to solving non-linear magnetostatic problems in two-dimensional domains. An efficient Newton-Raphson scheme will be presented in which the elements of the Jacobian matrix can be calculated analytically in the case of isotropic non-linear media. As an application, the optimal design of a die press model (TEAM Workshop Problem 25 [3]) is carried out.

II. DISCRETE GEOMETRIC APPROACH

In a 2D domain of interest D , a pair of interlocked cell complexes (\mathcal{K} , $\tilde{\mathcal{K}}$) [1], [4] is introduced, where \mathcal{K} is simplicial and $\tilde{\mathcal{K}}$ is obtained from it using the barycentric subdivision, see Fig. 1. The interconnections between the pairs (edge e , node n), (face f , edge e) of \mathcal{K} are described by the incidence matrices \mathbf{G} , \mathbf{C} respectively; we denote with $\tilde{\mathbf{C}}$ the incidence matrix between pairs (dual faces \tilde{f} , dual edges \tilde{e}) of $\tilde{\mathcal{K}}$ and $\tilde{\mathbf{C}} = \mathbf{C}^T$ holds. The edge and face vectors will be denoted in roman type.

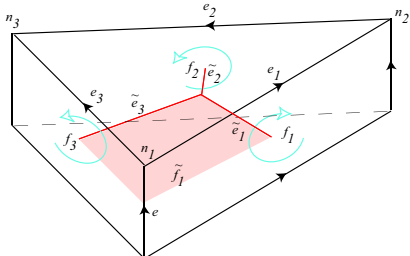


Fig. 1. A restriction of the primal and dual cell complexes is shown within a single volume v .

Next, we consider the integrals of the field quantities involved in the magnetostatic problem with respect to the

oriented geometric elements of $\mathcal{K} - \tilde{\mathcal{K}}$, yielding the Degrees of Freedom (DoF) arrays. There is a precise association between the DoFs and the geometric elements of \mathcal{K} and $\tilde{\mathcal{K}}$ [5]. We denote by Φ the array of magnetic fluxes associated with primal faces f , by \mathbf{F} the array of magneto-motive forces (m.m.f.s) associated with dual edges \tilde{e} , by \mathbf{I}_s the arrays of electric source currents across dual faces \tilde{f} , and by \mathbf{A} the array of circulations of the magnetic vector potential on primal edges e .

Maxwell's laws can be written *exactly* as topological balance equations between DoFs arrays, as

$$(\mathbf{C}^T \mathbf{F})_e = (\mathbf{I}_s)_e, \quad e \in D \quad (1)$$

$$(\Phi)_f = (\mathbf{C}\mathbf{A})_f, \quad f \in D \quad (2)$$

where (1) is the Ampère's Law, (2) involves the array \mathbf{A} in such a way that Gauss' Law $\mathbf{D}\Phi = 0$ is satisfied identically (since $\mathbf{D}\mathbf{C} = 0$). The discrete counterpart of the constitutive law $\mathbf{H} = \nu\mathbf{B}$ can be written as

$$\mathbf{F} = \nu \Phi, \quad (3)$$

where the matrix ν is a square symmetric matrix which can be efficiently constructed in a pure geometric way. In fact, considering the cell v_k , the Gauss' law, since $f_1 + f_2 - f_3 = 0$, is always verified for an element-wise constant field \mathbf{B}

$$\Phi_1 + \Phi_2 - \Phi_3 = \mathbf{B} \cdot \mathbf{f}_1 + \mathbf{B} \cdot \mathbf{f}_2 - \mathbf{B} \cdot \mathbf{f}_3 = 0. \quad (4)$$

The three fluxes are dependent and only two are used to produce the \mathbf{B} field by

$$\begin{bmatrix} f_{1x} & f_{1y} \\ f_{2x} & f_{2y} \end{bmatrix} \begin{bmatrix} B_x \\ B_y \end{bmatrix} = \begin{bmatrix} \Phi_1 \\ \Phi_2 \end{bmatrix}. \quad (5)$$

Inverting this linear system and using the fact that $f_{iy} = e_{ix}$ and $f_{ix} = -e_{iy}$

$$\mathbf{B} = \frac{1}{2S} \begin{bmatrix} e_{2x} & -e_{1x} \\ e_{2y} & -e_{1y} \end{bmatrix} \begin{bmatrix} \Phi_1 \\ \Phi_2 \end{bmatrix}, \quad (6)$$

where S is the area of v_k . The local constitutive matrix ν^k , for an isotropic medium, can be obtained by

$$\mathbf{F}^k = \nu^k \Phi^k = \begin{bmatrix} \tilde{e}_1 \\ \tilde{e}_2 \\ \tilde{e}_3 \end{bmatrix} \nu \frac{1}{2S} \begin{bmatrix} e_{2x} & -e_{1x} & 0 \\ e_{2y} & -e_{1y} & 0 \end{bmatrix} \Phi^k, \quad (7)$$

Substituting (2) and (3) in (1), the set of algebraic equations governing the magnetostatic problem can be derived

$$\mathbf{C}^T \nu \mathbf{C} \mathbf{A} = \mathbf{I}_s. \quad (8)$$

A. Non linear case

In the presence of non-linear (ferromagnetic) media, the following set of non-linear equations has to be solved

$$\mathbf{C}^T \boldsymbol{\nu}(\mathbf{A}) \mathbf{C} \mathbf{A} = \mathbf{I}_s. \quad (9)$$

An iterative scheme is needed to nullify the vector

$$\mathbf{f}(\mathbf{A}) = \mathbf{C}^T \boldsymbol{\nu}(\mathbf{A}) \mathbf{C} \mathbf{A} - \mathbf{I}_s. \quad (10)$$

At the n -th step of the iterative process we get

$$\begin{aligned} \mathbf{W}^n \mathbf{h}^n &= -\mathbf{f}(\mathbf{A}^n) \\ \mathbf{A}^{n+1} &= \mathbf{A}^n + \mathbf{h}^n \end{aligned} \quad (11)$$

where \mathbf{h}^n is the correction vector used to determine the new estimate \mathbf{A}^{n+1} and \mathbf{W}^n is the Jacobian matrix or a non-singular matrix which approximates it, if a Newton-Rapshon or a Broyden method are adopted respectively. The advantage of the Broyden method is that the Jacobian matrix needs not to be recomputed at each iteration; on the other hand the order of convergence is lower (in between 1 and 2).

B. Computation of the Jacobian

The element (i, j) in the Jacobian matrix can be written as

$$\mathbf{W}_{i,j} = \frac{\partial \mathbf{f}_i}{\partial A_j} = [\mathbf{C}^T \boldsymbol{\nu}(\mathbf{A}) \mathbf{C}]_{i,j} + \left(\mathbf{C}^T \frac{\partial \boldsymbol{\nu}(\mathbf{A})}{\partial A_j} \mathbf{C} \mathbf{A} \right)_i. \quad (12)$$

For the primal edges e not belonging to the ferromagnetic region the second addendum of (12) vanishes while the first one is independent of \mathbf{A} . It is convenient to compute the contribution \mathbf{W}^k to the Jacobian \mathbf{W} due to the cell v_k . For isotropic non-linear media, the reluctivity matrix is scalar and the constitutive matrix $\boldsymbol{\nu}^k$ can be rewritten as $\boldsymbol{\nu}^k(\mathbf{A}) = \mathbf{m}^k \nu^k(\mathbf{A}^k)$, where \mathbf{m}^k is the matrix $\boldsymbol{\nu}^k$ calculated by swapping the reluctivity ν^k with the pure number 1. The contribution of v_k to the Jacobian becomes

$$\mathbf{W}_{i,j}^k = [\mathbf{K}^k]_{i,j} \nu^k(\mathbf{A}^k) + (\mathbf{K}^k \mathbf{A}^k)_i \frac{\partial \nu^k(\mathbf{A}^k)}{\partial A_j^k}, \quad (13)$$

where $\mathbf{K}^k = \mathbf{C}^{kT} \mathbf{m}^k \mathbf{C}^k$ is a constant matrix. The derivative in (13) becomes

$$\frac{\partial}{\partial A_j^k} \left(\frac{1}{\mu^k(\mathbf{A}^k)} \right) = -\frac{1}{(\mu^k)^2} \frac{\partial \mu^k}{\partial B^k} \frac{\partial B^k}{\partial A_j^k}, \quad (14)$$

where B^k is the amplitude of the induction field in v_k , $\frac{\partial \mu^k}{\partial B^k}$ is the slope of the permeability curve. By substituting (2) in (6) with $f = \{1, 2\}$, we write the components of \mathbf{B} in terms of \mathbf{A}^k by defining two vectors \mathbf{k}_x and \mathbf{k}_y , such that

$$B_x = \mathbf{k}_x \cdot \mathbf{A}^k, B_y = \mathbf{k}_y \cdot \mathbf{A}^k \quad (15)$$

holds. The amplitude B^k can thus be computed by

$$B^k = \sqrt{(\mathbf{k}_x \cdot \mathbf{A}^k)^2 + (\mathbf{k}_y \cdot \mathbf{A}^k)^2}. \quad (16)$$

Using these equations, the $\frac{\partial B^k}{\partial A_j^k}$ term can be calculated analytically as

$$\frac{\partial B^k}{\partial A_j^k} = \frac{(\mathbf{k}_x \cdot \mathbf{A}^k) k_{xj} + (\mathbf{k}_y \cdot \mathbf{A}^k) k_{yj}}{\sqrt{(\mathbf{k}_x \cdot \mathbf{A}^k)^2 + (\mathbf{k}_y \cdot \mathbf{A}^k)^2}}, \quad (17)$$

where k_{xj} and k_{yj} represent the values in the j -th column of \mathbf{k}_x and \mathbf{k}_y respectively. Finally (17) can be rewritten as

$$\frac{\partial B^k}{\partial A_j^k} = \frac{B_x k_{xj} + B_y k_{yj}}{B^k}, j = 1, \dots, 3. \quad (18)$$

III. PROBLEM DESCRIPTION AND RESULTS

As a test problem, the TEAM Workshop Problem 25 [3] has been considered. A detail of the two-dimensional benchmark geometry is shown in Fig.2. The die molds are set to form a radial flux density distribution. The shape of the inner die mold is assumed as a circle; the inside shape of the outer die mold is represented by an ellipse and a line parallel to the x -axis. Then, the radius R_1 of the inner die, the long and short axes (L_2, L_3) of ellipse and the dimension L_4 are chosen as design variables with specified upper and lower bounds.

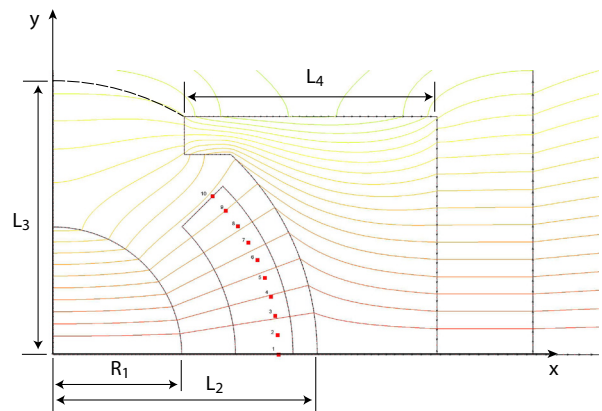


Fig. 2. TEAM Workshop problem 25: enlarged view of the die press model.

The developed 2D numerical code based on the DGA is coupled to a hybrid optimization approach which combines parallel genetic algorithms for global minimum search and a deterministic algorithm for local refinement.

In Fig.2 the magnetic flux density distribution is shown, evaluated for the final (optimal) shape of die molds obtained using the numerical code developed based on the proposed DGA. The maximum errors of the of the flux density in P_i are $\varepsilon_B^{max} = 0.87\%$ in terms of amplitude and $\varepsilon_\theta^{max} = 1.1$ deg in terms of direction.

The main features of the hybrid search algorithm and the results of the investigations on number of mesh elements, iterations, CPU time, accuracy, will be described in detail in the full paper.

REFERENCES

- [1] E. Tonti, "Finite Formulation of the Electromagnetic Field", IEEE Trans. Magn. Vol. 38, No. 2, pp. 333-336, 2002.
- [2] A. Bossavit, L. Kettunen, "Yee-like schemes on staggered cellular grids: a synthesis between FIT and FEM approaches", IEEE Trans. Magn., Vol. 36, pp. 861-867, 2000.
- [3] N.Takahashi, K.Ebihara, K.Yoshida, T.Nakata, K.Ohashi and K.Miyata, "Investigation of simulated annealing method and its application to optimal design of die mold for orientation of magnetic powder", IEEE Trans. Magn., Vol. 32, N. 3, pp. 1210-1213, 1996.
- [4] E. Tonti, "Algebraic topology and computational electromagnetism", 4-th International Workshop on Electric and Magnetic Fields, Marseille (Fr) 12-15 May, pp. 284-294, 1988.
- [5] E. Tonti, "On the formal structure of physical theories", Quaderni dei Gruppi di Ricerca Matematica del CNR, 1975.

Optimal Selection of the Integration Surface in the Hybrid FEM-DBCI Method

Giovanni Aiello, Salvatore Alfonzetti, and Nunzio Salerno

Dip. Ing. Elettrica, Elettronica e dei Sistemi, Università di Catania – Viale A. Doria, 6 – I-95125 Catania– Italy

Abstract — In this paper the optimal placement of the integration surface for the integral equation in the hybrid FEM-DBCI method is achieved by selecting it as lying in the middle of the tetrahedral or hexahedral finite elements. Better accuracy is obtained with respect to the case in which the integration surface lies along the element faces. Some numerical examples are provided.

Index Terms— Finite Element Method, Integral Equations, Open Boundary Problems.

I. INTRODUCTION

FEM-DBCI (Finite Element Method - Dirichlet Boundary Condition Iteration) is a numerical method devised by the authors to solve a variety of static and quasi-static electromagnetic field problems in unbounded domains [1-4]. FEM-DBCI, like the well-known FEM-BEM (Boundary Element Method) [5-6], is a hybrid method in which the differential equation, which governs the interior problem, is coupled with an integral one which expresses the unknown boundary condition on the fictitious truncation boundary Γ_F .

The integral equations of the two methods make use of the free-space Green function, but while the integration surface and truncation boundary coincide in FEM-BEM, FEM-DBCI uses another closed surface, say Γ_M , strictly enclosed by Γ_F and containing all relevant parts of the system. The resulting global algebraic systems are partly sparse and partly dense; however, the FEM-DBCI integral equation is explicit with respect to the boundary unknowns and this property allows a simple iterative solution of the global system: assuming an initial guess for the Dirichlet condition on the truncation boundary Γ_F , the sparse FEM equations are solved by means of the conjugate gradient (CG) solver; the dense equations are then used to improve the Dirichlet condition on Γ_F ; the procedure is iterated until convergence is reached. This solution strategy is efficient because the CG is only applied to the sparse equation, and the dense equation is only used a few times. An improvement on this solving method is obtained by means of the Generalized Minimal Residual (GMRES) method, as described in [7]. A detailed comparison between FEM-BEM and FEM-DBCI is made in [8], concluding that the former is more accurate than the latter but more time-consuming.

Recently the authors showed that a notable improvement in the accuracy of FEM-DBCI is obtained in a mesh of triangular elements by selecting the integration curve as constituted by segments connecting the middle points of triangle sides [9]. The improvement is obtained with respect to the standard

selection of the integration curve as made of triangular element sides.

In this paper it is shown that a similar improvement is obtained in a mesh of tetrahedral elements. The paper is organized as follows: In the next section a brief description of the FEM-DBCI method is given, by referring, for sake of simplicity, to a simple electrostatic problem. In Section III the proposed improvement is highlighted. A simple system is numerically analyzed in Section IV.

II. FEM-DBCI FOR ELECTROSTATIC PROBLEMS

Consider a three-dimensional electrostatic system made of distributed and/or lumped charges, voltage conductors and non-homogeneous objects embedded in air. In order to compute the electrical potential v , a closed truncation boundary Γ_F is introduced enclosing all the conductors, all the dielectric objects and some distributed charges, but possibly leaving out some other distributed and/or lumped charges (external charges). In the bounded domain D delimited by $(F$, the Poisson equation holds:

$$-\nabla \cdot (\epsilon \nabla v) = \rho \quad (1)$$

where ϵ is the electric permittivity and ρ the charge density. The unknown Dirichlet condition on Γ_F is expressed through:

$$v(\mathbf{r}) = v_{\text{ext}}(\mathbf{r}) + \iint_{\Gamma_M} \left(v(\mathbf{r}') \frac{\partial G(\mathbf{r}, \mathbf{r}')}{\partial n'} - G(\mathbf{r}, \mathbf{r}') \frac{\partial v(\mathbf{r}')}{\partial n'} \right) dS' \quad (2)$$

where Γ_M is a closed surface enclosing all the conductors and dielectric non-homogeneities but strictly enclosed by Γ_F , \mathbf{n}' is its outward normal unit vector and v_{ext} is due to the external charges. By discretizing the domain D by means of tetrahedral finite elements, equations (1) and (2) read as follows [1]:

$$\mathbf{A}\mathbf{V} = \mathbf{B}_0 - \mathbf{A}_F \mathbf{V}_F \quad (3)$$

$$\mathbf{V}_F = \mathbf{V}_{F0} + \mathbf{H}\mathbf{V} \quad (4)$$

where \mathbf{A} is a standard FEM matrix (symmetric and positive definite), \mathbf{V} is the vector of unknown nodal values inside the domain, \mathbf{B}_0 and \mathbf{V}_{F0} are due to source and conductor potentials, \mathbf{A}_F is a rectangular matrix of coefficients similar to \mathbf{A} , \mathbf{V}_F is the vector of nodal field values on Γ_F , and \mathbf{H} is a rectangular matrix in which null entries appear for the nodes of the elements not adjacent to the integration surface Γ_M . The integrals in (2) are performed by means of the Gauss method with a variable number of Gauss points according to ratio of the distance of the node on Γ_F from a point on Γ_M to the mean radius of the subpart of Γ_M . The system (3)-(4) is solved iteratively. Starting with an initial guess for the potential on Γ_F (for example $\mathbf{V}_F = \mathbf{0}$), equation (3) is solved for \mathbf{V} . Equation (4)

is then used to improve V_F . The procedure is iterated until convergence takes place.

III. SELECTING THE INTEGRATION SURFACE

The most simple way to select the integration surface Γ_M in a tetrahedral mesh is to build it by means of triangular faces of tetrahedral elements (see triangles ABD and BCD in Fig. 1, where capital letters denote the element vertices and small letters denotes the middle points of edges). In this way, however, accuracy is not well balanced between v and $\partial v/\partial n$ in (2). No accuracy problems arise in evaluating G and $\partial G/\partial n$, because the Green function is known analytically. In fact, the first term is much more accurate than the second one, since the numerical derivative $\partial v/\partial n$ is maximally erroneous on the tetrahedral faces, where v is maximally correct because of the presence of several nodes on the element face itself.

To improve the accuracy of the integral equation, one can select the integration surface as constituted by sub-surfaces internal to the tetrahedra and connecting the middle points of their edges (see fig.1). Note that two kinds of sub-surfaces arise: triangles and quadrangles (it is simple to show that the four points b, d, f, and h in fig. 1 are coplanar).

In this way the accuracy of the derivative $\partial v/\partial n$ is maximized, whereas the accuracy of the field variable v is not greatly decreased, so that a global improvement in the accuracy of the integral equation and the whole solution is expected. In order to verify this, in the next sections an example is provided for which analytical solutions is known.

IV..A VALIDATION EXAMPLE

The example concerns the computation of the electrostatic potential v near a conducting sphere of radius R , voltaged at V_0 , embedded in a homogeneous unbounded dielectric medium of permittivity ϵ_0 . By selecting the origin of a Cartesian reference frame in the center of the sphere, the problem exhibits the analytical solution:

$$v^*(x, y, z) = \frac{R}{\sqrt{x^2 + y^2 + z^2}} V_0 \quad (5)$$

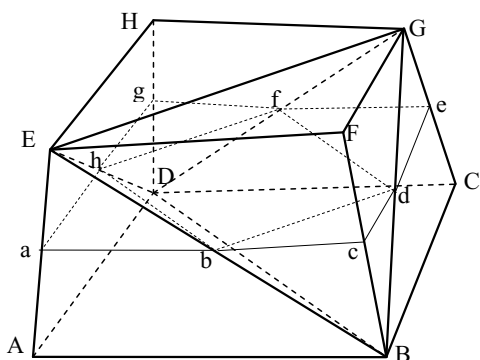


Fig. 1- Two different choices for the integration surface Γ_M in a tetrahedral mesh (tetrahedra: ABDE, CDBG, FGBE, HGED, EGBD); first choice: triangles ABD and BCD; second choice triangles abh, bcd, def, fgh and quadrangle bdfh.

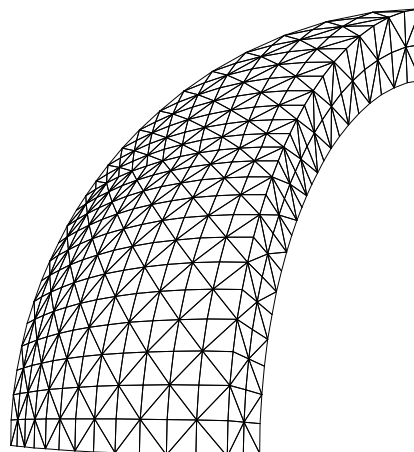


Fig. 2- Tetrahedral mesh of the example.

The analysis can be restricted to the first octant only, by imposing homogeneous Neumann conditions on the coordinate planes. The unbounded domain is truncated by a spherical fictitious boundary Γ_F of radius $R+d$, with $d=1.2 R$. The mesh was made of 8640 first-order tetrahedra, with two layers of elements in the radial direction (see Fig. 2). Selecting Γ_M coinciding with the conductor surface, the relative error between the computed solution and the analytical one is 2.8 per cent, having set the convergence tolerance to 0.1 per cent. Selecting Γ_M at a distance of $d/4$ from the conductor (that is in the middle of the first layer of tetrahedra), the relative error decreases to 0.8 per cent. More details and examples will be provided in the full paper.

REFERENCES

- [1] G. Aiello, S. Alfonzetti, and S. Coco, "Charge iteration: a procedure for the finite-element computation of unbounded electrical fields," *Int. J. Numer. Methods Eng.*, vol. 37, pp. 4147-4166, Dec. 1994.
- [2] G. Aiello, S. Alfonzetti, S. Coco, N. Salerno, "A theoretical study of charge iteration," *COMPEL*, vol. 15, pp. 22-46, Sept. 1996.
- [3] G. Aiello, S. Alfonzetti, S. Coco, and N. Salerno, "Finite element iterative solution of skin effect problems in open boundaries," *Int. J. Numer. Modelling: Electr. Net., Dev. and Fields*, vol. 9, pp.125-143, January-April 1996.
- [4] G. Aiello, S. Alfonzetti, E. Diletto, "Finite element solution of eddy current problems in unbounded domains by means of the hybrid FEM-DBCI method," *IEEE Trans. Magn.*, vol. 39, no.3, pp. 1409-1412, March 2003.
- [5] C. A. Brebbia, J.C.F. Telles, and L. C. Wrobel, *Boundary Element Technique*, Springer-Verlag, Berlin, 1984.
- [6] S. J. Salon, and J. D'Angelo, "Applications of the hybrid finite element - boundary element method in electromagnetics," *IEEE Trans. Magn.*, vol. 24, no. 1, pp. 80-85, January 1988.
- [7] G. Aiello, S. Alfonzetti, G. Borzi, "A generalized minimal residual acceleration of the charge iteration procedure," *Journal de Physique III*, vol. 7, n. 10, pp. 1955-1966, October 1997.
- [8] G. Aiello, S. Alfonzetti, G. Borzi, E. Diletto, N. Salerno, "Comparing FEM-BEM and FEM-DBCI for open-boundary electrostatic problems", *European Physical Journal - Applied Physics*, vol. 39, no. 2, pp 143-148, August 2007.
- [9] G. Aiello, S. Alfonzetti, E. Diletto, N. Salerno, "Improving the accuracy of the integral equation in the hybrid FEM-DBCI method for open boundary electrostatic problems", *IEEE Trans.Magn.*, vol. 42, no. 4, pp. 579-582, April 2006.

Periodic and Anti-periodic boundary conditions with the Lagrange multipliers in the FEM

M. Aubertin¹, T. Henneron², F. Piriou², P Guérin³ and J-C. Mipo¹

¹Valeo Electrical System, 94017 Créteil, France

²LAMEL-L2EP, USTL, 59655 Villeneuve d'Ascq, France

³EDF R&D, 92141 Clamart, France

thomas.henneron@univ-lille1.fr

Abstract — In this paper, an approach based on the double Lagrange multipliers is developed in the finite element method in order to impose complex periodic or anti-periodic boundary conditions. The magnetostatic equations are solved using the vector or scalar potential formulations. In order to show the possibilities of the proposed approach, an example of application is studied and the results are discussed.

I. INTRODUCTION

To model an electromagnetic device, the finite element method is currently used today. In order to reduce the mesh of the studied domain, the geometric symmetries of the system are generally considered. Then, only one part of the device is modelled. The reduction of the domain can introduce periodic or anti-periodic conditions on the fields. To impose these conditions, a simple method consists to build a same mesh on the boundaries where the conditions are applied. In the device with a simple geometry, same meshes on two boundaries can be easily fixed. In the case of complex structures, this method is not rather flexible and becomes difficult to implement. In order to avoid this difficulty, a technique based on the double Lagrange multipliers method can be used [1][2]. By using this approach, the meshes on the boundaries with periodic or anti-periodic conditions can be different. The continuity of the fields is obtained by imposing supplementary relations.

In this communication, the double Lagrange multipliers approach is introduced in the case of magnetostatic problems. In first, the magnetostatic problem is presented. Then, the double Lagrange multipliers approach is developed in the scalar and vector potential formulations to impose the periodic or anti-periodic boundary conditions. At last, an application based on the simplified structure of a claw pole electrical machine is analyzed.

II. MAGNETOSTATIC PROBLEM

Let's consider a domain D with its boundary Γ divided into four parts such that $\Gamma = \Gamma_{S1} \cup \Gamma_{S2} \cup \Gamma_B \cup \Gamma_H$ and $\Gamma_{S1} \cap \Gamma_{S2} \cap \Gamma_B \cap \Gamma_H = \emptyset$ (Fig. 1). In the case of a magnetostatic problem, Maxwell's equations and the behaviours law are given by:

$$\text{div } \mathbf{B} = 0 \quad \text{with } \mathbf{B} \cdot \mathbf{n}|_{\Gamma_B} \quad (1)$$

$$\text{curl } \mathbf{H} = \mathbf{J} \quad \text{with } \mathbf{H} \times \mathbf{n}|_{\Gamma_H} \quad (2)$$

$$\mathbf{B} = \mu \mathbf{H} \quad (3)$$

with \mathbf{n} the outward normal of Γ , \mathbf{B} the magnetic flux density, \mathbf{H} the magnetic field, \mathbf{J} the current density supposed to be known in stranded inductors and μ the magnetic permeability. The boundaries Γ_{S1} and Γ_{S2} are used to impose

a periodic or anti-periodic condition on the fields. These conditions can be expressed such that:

$$\mathbf{B} \cdot \mathbf{n}|_{\Gamma_{S1}} = \alpha \mathbf{B} \cdot \mathbf{n}|_{\Gamma_{S2}} \quad \text{and} \quad \mathbf{H} \times \mathbf{n}|_{\Gamma_{S1}} = \alpha \mathbf{H} \times \mathbf{n}|_{\Gamma_{S2}} \quad (4)$$

with α a scalar value equal to 1 or -1 . This one depends on the periodic or anti-periodic condition between Γ_{S1} and Γ_{S2} .

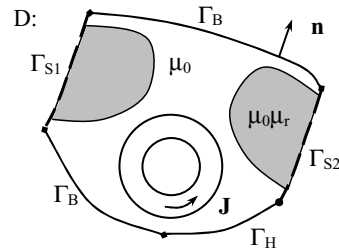


Fig. 1 Definition of the studied domain

III. POTENTIAL FORMULATIONS

In the scalar potential formulation, a source field \mathbf{H}_s is introduced such that $\text{rot } \mathbf{H}_s = \mathbf{J}$ with $\mathbf{H}_s \times \mathbf{n} = 0$ on Γ_H , Γ_{S1} and Γ_{S2} . From (2.a), a scalar potential Ω can be introduced and the magnetic field can be rewritten such that $\mathbf{H} = \mathbf{H}_s - \text{grad } \Omega$ with $\Omega = Cst$ on Γ_H . Equation to solve in the studied domain is given by the weak formulation of (1.a) such that:

$$(\mu \text{ grad } \Omega, \text{ grad } \psi)_D + \langle \mathbf{B} \cdot \mathbf{n}, \psi_{S1} \rangle_{\Gamma_{S1}} + \alpha \langle \mathbf{B} \cdot \mathbf{n}, \psi_{S2} \rangle_{\Gamma_{S2}} = (\mu \mathbf{H}_s, \text{ grad } \psi)_D \quad (5)$$

with ψ a test function chosen in the same space than Ω and ψ_{S1} and ψ_{S2} the restriction of ψ on Γ_{S1} and Γ_{S2} . On Γ_B and Γ_H , the surface integrals vanish by (1.b) and (2.b). To impose a periodic or anti-periodic condition on Γ_{S1} and Γ_{S2} , the double Lagrange multipliers method can be introduced. The Lagrange multipliers can be expressed on Γ_{S1} or Γ_{S2} . We define the multipliers λ_{B1} and λ_{B2} on Γ_{S1} such that $\mathbf{B} \cdot \mathbf{n}|_{\Gamma_{S1}} = \lambda_{B1} + \lambda_{B2}$ [1]. The test function associated with the multipliers is chosen equal to ψ_{S1} . The geometric transformation T between Γ_{S1} and Γ_{S2} is defined in order to project the test function ψ_{S2} on Γ_{S1} . The final equation system to solve can be written such that:

$$\begin{aligned} & (\mu \text{ grad } \Omega, \text{ grad } \psi)_D + \langle \lambda_{B1}, \psi_{S1} \rangle_{\Gamma_{S1}} + \langle \lambda_{B2}, \psi_{S1} \rangle_{\Gamma_{S1}} \\ & + \alpha \langle \lambda_{B1}, T\psi_{S2} \rangle_{\Gamma_{S1}} + \alpha \langle \lambda_{B2}, T\psi_{S2} \rangle_{\Gamma_{S1}} = (\mu \mathbf{H}_s, \text{ grad } \psi)_D \\ & \langle \Omega_{S1} + \alpha T\Omega_{S2}, \psi_{S1} \rangle_{\Gamma_{S1}} + \langle \lambda_{B1} - \lambda_{B2}, \psi_{S1} \rangle_{\Gamma_{S1}} = 0 \\ & \langle \Omega_{S1} + \alpha T\Omega_{S2}, \psi_{S1} \rangle_{\Gamma_{S1}} + \langle -\lambda_{B1} + \lambda_{B2}, \psi_{S1} \rangle_{\Gamma_{S1}} = 0 \end{aligned} \quad (6)$$

with Ω_{S1} and Ω_{S2} the restriction of Ω on Γ_{S1} and Γ_{S2} . The two last equations are introduced to insure the continuity of

the scalar potential on Γ_{S1} and Γ_{S2} . For a periodic condition, these last relations impose the equality of Ω on Γ_{s1} and Γ_{s2} . To discretize Ω , ψ , λ_{B1} and λ_{B2} , nodal shape functions are used.

In the vector potential formulation, a potential \mathbf{A} is introduced by using (2.a) and the magnetic flux density can be rewritten such that $\mathbf{B} = \text{curl } \mathbf{A}$ with $\mathbf{A} \times \mathbf{n} = 0$ on Γ_B . From (2.a), the weak formulation is given by:

$$(\mu^{-1} \text{curl } \mathbf{A}, \text{curl } \psi)_D + \langle \mathbf{H} \times \mathbf{n}, \psi_{s1} \rangle_{\Gamma_{s1}} + \alpha \langle \mathbf{H} \times \mathbf{n}, \psi_{s2} \rangle_{\Gamma_{s2}} = (\mathbf{J}, \psi)_D \quad (7)$$

with ψ a test function and ψ_{s1} and ψ_{s2} its restriction on Γ_{S1} and Γ_{S2} . A similar approach to the scalar formulation is used to impose a periodic or anti-periodic condition. Then, we define λ_{H1} and λ_{H2} the Lagrange multipliers on Γ_{S1} such that $\mathbf{H} \times \mathbf{n}|_{\Gamma_{s1}} = \lambda_{H1} + \lambda_{H2}$. The final equation system to solve is given by:

$$\begin{aligned} & (\mu^{-1} \text{curl } \mathbf{A}, \text{curl } \psi)_D + \langle \lambda_{H1}, \psi_{s1} \rangle_{\Gamma_{s1}} + \langle \lambda_{H2}, \psi_{s1} \rangle_{\Gamma_{s1}} \\ & + \alpha \langle \lambda_{H1}, \mathbf{T} \psi_{s2} \rangle_{\Gamma_{s1}} + \alpha \langle \lambda_{H2}, \mathbf{T} \psi_{s2} \rangle_{\Gamma_{s1}} = (\mathbf{J}, \psi)_D \\ & \langle \mathbf{A}_{s1} + \alpha \mathbf{T} \mathbf{A}_{s2}, \psi_{s1} \rangle_{\Gamma_{s1}} + \langle \lambda_{H1} - \lambda_{H2}, \psi_{s1} \rangle_{\Gamma_{s1}} = 0 \\ & \langle \mathbf{A}_{s1} + \alpha \mathbf{T} \mathbf{A}_{s2}, \psi_{s1} \rangle_{\Gamma_{s1}} + \langle -\lambda_{H1} + \lambda_{H2}, \psi_{s1} \rangle_{\Gamma_{s1}} = 0 \end{aligned} \quad (8)$$

with \mathbf{A}_{s1} and \mathbf{A}_{s2} the restriction of \mathbf{A} on Γ_{S1} and Γ_{S2} . Edge shape functions are used to discretize the vector potential and the Lagrange multipliers.

IV. APPLICATION

The studied structure is based on a simplified claw pole electrical machine (Fig. 2). The rotor is composed by two half claws and the stator by three windings. These ones are supplied by a three phase current source. The mesh is constituted by 5663 nodes and 28786 tetrahedrons. An anti-periodic condition, according to an axis, is applied on two boundaries (Fig. 3). This structure has been solved by both potential formulations. For the scalar and vector formulation, the number of unknowns is equal to 6525 and 36090. In Fig. 4, the distribution of the magnetic flux density trough a section obtained by the scalar potential formulation is presented for a given time step. In Fig. 5, the magnetic energy waveform in function of time obtained by both formulations is presented. The shapes of the curves are similar. The different between the maximal values is due to the discretization of the mesh in the air gap [3]. In term of solution, the matrix systems are solved by the minimum residual method with a SSOR (Successive Over Relaxation) preconditionner. The iteration method requires 3% of unknown number to obtain the solution with the scalar formulation and 12% with the vector formulation.

V. CONCLUSION

The double Lagrange multipliers method has been introduced in the scalar and vector potential formulations in order to impose the periodic and anti-periodic conditions. The studied example shows the possibilities of the proposed model for a complex geometry with anti-periodic conditions.

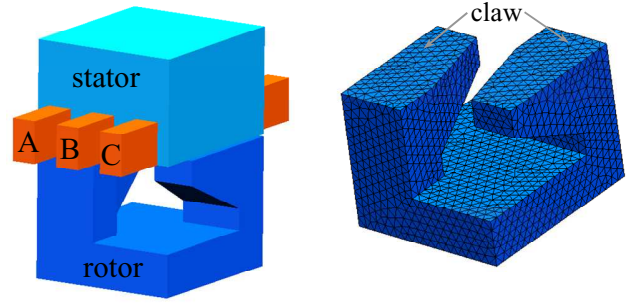


Fig. 2. Application example (a- structure, b- mesh of the rotor)

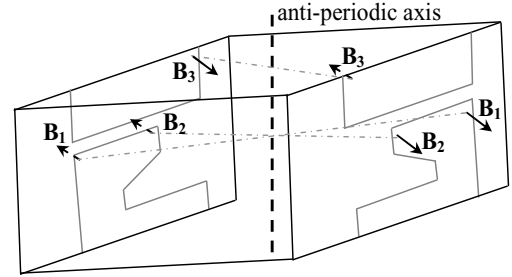


Fig. 3. Definition of the anti-periodic condition

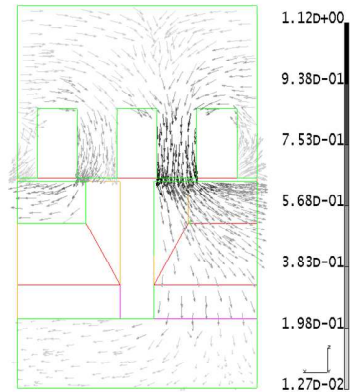


Fig. 4. Distribution of the magnetic flux (T) through a section of the machine

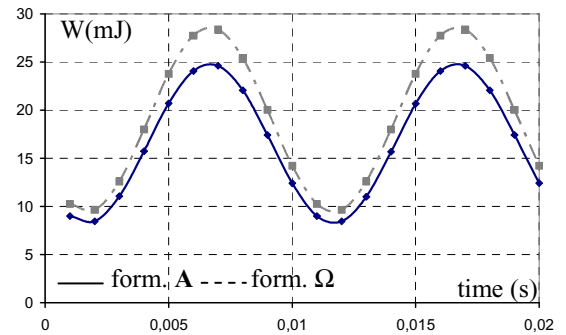


Fig. 5. Magnetic energy

VI. REFERENCES

- [1] T. Charras, A. Millard and P. Verpeaux "Solution of two-dimensional and three dimensional contact problems by means of Lagrange multipliers in the CASTEM 2000 finite element program", Proceeding of Contact Mechanics, Computer Mechanics Publication, 1993.
- [2] D. Rodger, H. C. Lai, P. J. Leonard, "Coupled elements for problems involving movement", IEEE Trans. on magnetics, 26(2), 548-550, 1990.
- [3] G. Marques, S. Clénet, F. Piriou, "Error Estimators in 3D Linear Magnetostatics", IEEE Trans. on Magnetics, 36, 1588-1591, 2000.

Analysis of the Ionized Field under HVDC Transmission Lines Including Wind's Effect Based on Finite Element Method

Tiebing Lu, Han Feng, Xiang Cui, *Senior Member, IEEE*, Zhibin Zhao, Lin Li
School of Electrical and Electronic Engineering, North China Electric Power University
Baoding, 071003, Hebei, China
E-mail: tiebinglu@yahoo.com

Abstract: The corona generated from HVDC transmission lines can affect the environment nearby. Based on the upstream finite element method, an iterative algorithm to analyze the ionized field and the ion current density at the ground level generated from the bundled conductors of bipolar lines is modified. The algorithm is proved to be convergent efficiently. The effect of wind is taken into account. A unipolar line in the presence of wind is calculated and the validities are testified by comparing with measurement results. Finally, bipolar lines can be analyzed by the method.

I. INTRODUCTION

In order to set up a strong and steady power system in China, ± 800 kV ultra HVDC transmission lines system is building. But the ionized field and the ion current density at the ground level due to the corona have to be analyzed in advance to make sure the environment friendly.

Because of the ions existing in the space, the ionized field is very difficult to be calculated [1]. However, the problem has been considered by a number of researchers over the past several decades [2-6]. Based on Deutsch's assumption, Sarma et al. [2] firstly proposed an analytical equation to solve the ionized fields of unipolar line. Obviously, it is not valid when wind is present. Janischewskyj and Gela [3] proposed a numerical method by using the finite element method. Furthermore, Takuma et al. [4] proposed the upstream finite element method. The stability and convergence can be improved effectively. They assumed that the space charge density remains constant around the surface of the conductors. As a matter of fact, the assumption of the constant charge density is not quite true, especially in the presence of wind. Z.Al-Hamouz [5] suggested a method to solve the ion current density based on a finite element mesh which fits the flux tubes of the field. Fortin et al. [6] proposed a similar approach to calculate the ionized electric field of bundled bipolar conductors by treating the conductors in the bundles individually.

In this paper, an iterative method based on upstream FEM is modified to analyze the ionized electric field and the ion current density under the HVDC lines and the effect of wind is included. Different from [4], the assumption that the space charge density remains constant around the surface of the conductors is waived to avoid empirical factor. The algorithm is proved to be convergent efficiently. The effect of wind is taken into account. The validities of the method are testified by comparing with measurement results.

II. METHODOLOGY OF BIPOLAR LINES

Under some assumptions, for the bipolar lines with the effect of wind, the potential φ , the ionized field \vec{E}_s , the space charge density ρ_+ and ρ_- , the current density \vec{j}_+ and \vec{j}_- are defined by the following equations [1]:

$$\nabla^2 \varphi = -(\rho_+ - \rho_-) / \varepsilon_0 \quad (1)$$

$$\vec{j}_+ = \rho_+ (K_+ \vec{E}_s + \vec{w}) \quad (2)$$

$$\vec{j}_- = \rho_- (K_- \vec{E}_s - \vec{w}) \quad (3)$$

$$\nabla \cdot \vec{j}_+ = -R_i \rho_+ \rho_- / e \quad (4)$$

$$\nabla \cdot \vec{j}_- = R_i \rho_+ \rho_- / e \quad (5)$$

$$\vec{E}_s = -\nabla \varphi \quad (6)$$

where K is the ionic mobility within the corona area, R_i is the ion recombination coefficient. The subscript + is for positive and - for negative, and \vec{w} is the wind velocity vector and e is the charge of the electron.

Because FEM only can be applied in a limited region, an artificial boundary far from the lines must be placed, where the potential is equal to the value of the charge-free field obtained by Charge Simulation Method (CSM).

The iterative process is started by assuming initial values of charge density at grid nodes. The space-charge density at the conductor surface can be gained from [7]. Equations (1) and (6) are used to compute values of ionized field. Based on (2)-(5), we can get:

$$\nabla \rho_+ \cdot \vec{v}_+ = -\frac{K_+}{\varepsilon_0} \rho_+^2 + \left(\frac{K_+}{\varepsilon_0} - \frac{R}{e} \right) \rho_+ \rho_- \quad (7)$$

$$\nabla \rho_- \cdot \vec{v}_- = -\frac{K_-}{\varepsilon_0} \rho_-^2 + \left(\frac{K_-}{\varepsilon_0} - \frac{R}{e} \right) \rho_- \rho_+ \quad (8)$$

where $\vec{v}_+ = K_+ \vec{E}_s + \vec{w}$, $\vec{v}_- = -K_- \vec{E}_s + \vec{w}$ are the mobility velocity vector of positive and negative ions, respectively.

In order to calculate (7) and (8), the upstream FEM is applied [4]. The nodes are calculated one by one from their upstream elements from the surface of the conductor until all of the nodes have been calculated.

The charge density in the element ijm can be described by the following interpolating function:

$$\rho(x, y) = N_i \rho_i + N_j \rho_j + N_m \rho_m = [N] [\rho] \quad (9)$$

If b, c are functions of corresponding coordinates:

$$\begin{aligned} b_i &= y_j - y_m & b_j &= y_m - y_i & b_m &= y_i - y_j \\ c_i &= x_m - x_j & c_j &= x_i - x_m & c_m &= x_j - x_i \end{aligned}$$

we can obtain:

$$\frac{\partial \rho}{\partial x} = \left[\frac{\partial N}{\partial x} \right] [\rho] = \frac{1}{2\Delta} \begin{pmatrix} b_i & b_j & b_m \end{pmatrix} [\rho] \quad (10)$$

$$\frac{\partial \rho}{\partial y} = \left[\frac{\partial N}{\partial y} \right] [\rho] = \frac{1}{2\Delta} \begin{pmatrix} c_i & c_j & c_m \end{pmatrix} [\rho] \quad (11)$$

$$\begin{aligned} \nabla \rho_{i+} \cdot \vec{V}_{i+} &\approx \frac{\partial \rho}{\partial x} V_{x+} + \frac{\partial \rho}{\partial y} V_{y+} \\ &= \frac{1}{2\Delta} (b_i \rho_{i+} + b_j \rho_{j+} + b_m \rho_{m+}) V_{x+} + \frac{1}{2\Delta} (c_i \rho_{i+} + c_j \rho_{j+} + c_m \rho_{m+}) V_{y+} \end{aligned} \quad (12)$$

Equation (7) and (8) can be changed as:

$$A_+ \rho_{i+}^2 + B_+ \rho_{i+} + C_+ = 0 \quad (13)$$

where

$$\begin{aligned} A_+ &= \frac{K_+}{\epsilon_0}, \\ B_+ &= \frac{(b_i V_{x+} + c_i V_{y+})}{2\Delta} - \left(\frac{K_+}{\epsilon_0} - \frac{R}{e} \right) \rho_{i-}, \\ C_+ &= \frac{(b_j V_{x+} + c_j V_{y+}) \rho_{j+}}{2\Delta} + \frac{(b_m V_{x+} + c_m V_{y+}) \rho_{m+}}{2\Delta} \\ \Delta &= \frac{1}{2} (b_i c_j - b_j c_i) \end{aligned}$$

The larger solution can be looked as the final result, thus the calculation is stable. Next, the obtained charge density is used to calculate the ionized field in (1), so the iteration continues until the satisfied result is obtained.

III. VALIDITY

Fig. 1 shows the calculated results of a $\pm 200\text{kV}$ unipolar test line in the presence of wind with 0.25cm in radius and 2m in height. The relevant measurements in [8] are also shown in Fig. 1 as separate stars and circles. The star * is for the results without wind, and the circle o is for the results with 8m/s wind velocity. The calculated curves agree reasonable with measurement results.

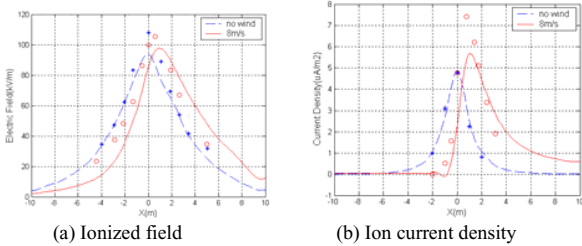


Fig.1 Comparison between the measurement and calculation

IV. APPLICATIONS

The proposed method is applied to an operating HVDC lines in the present of wind of 1m/s and 3m/s respectively. The unipolar line is energized at 500kV with a $4 \times 1.185\text{cm}$ and a 45cm spacing conductor bundle at height of 12.5m . The distributions of ionized electric field and the ion current density at the ground level are shown in Fig. 2. The results show that the ionized field can be influenced by wind

obviously. Both of the maximum of electric field and current density shift to the downwind side, increasing down the wind and decreasing against the wind. And the effect of wind on ion current density is stronger than that on ionized field. Both of the field and current curves became wider down the wind. This trend is visible when wind velocity increases from zero to 3m/s . However, if the velocity is increased to 6m/s or more, the field strength almost doesn't increase any longer. The explanation of the results and the case of bipolar lines will be included in the final version

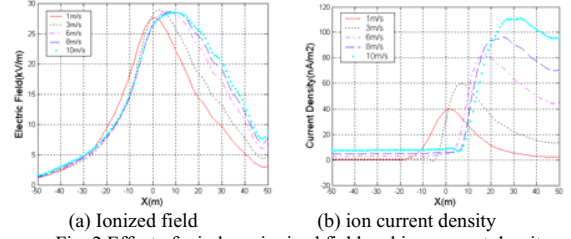


Fig. 2 Effect of winds on ionized field and ion current density

V. CONCLUSIONS

The charge generated from corona conductors of HVDC transmission lines can enhance greatly the electric field in the space and on the ground plane. An upstream FEM-based approach can effectively calculate the ionized field and ion current density e . The influence of wind can be taken into account. The validity of the method is testified. And the rapidity of convergence is satisfying. Then, the influence of wind on one unipolar line is analyzed. The tendency can be explained corresponding to the physical fact.

This project is partly supported by National Nature Science Foundation of China under grant No. 50677016.

VI. REFERENCES

- [1] P Sarma Maruvada. Corona performance of High-Voltage Transmission lines. Reseach studies press Ltd., Baldock, Hertfordshire, England. 2000.
- [2] M.P.Sarma, W.Janischewskyi, Analysis of Corona Losses on DC Transmission Lines, Part I—Unipolar Lines, IEEE Trans.on PAS, Vol.PAS-88, No.5,1969
- [3] W.Janischewskyi, et al., Finite Element Solution four Electric Fields of Coronaing DC Transmission Lines, IEEE Trans. On PAS,Vol.PAS-98,No.3,May/June 1979
- [4] Tadasu Takuma,et al.. A Very Stable Calculation Method For Ion Flow Fields of HVDC Transmission Lines , IEEE Trans. On Power Delivery, Vol. PWRD-2, No.1, 1987
- [5] Z. Al-Hamouz. Corona power loss, electric field, and current density profiles in bundled horizontal and vertical bipolar conductors. *IEEE Trans. on Industry Applications*, Vol. 38(5), 2002, pp: 1182 - 1189
- [6] S. Fortin, H. Zhao, J. Ma, and F. P. Fawalibi, "A New Approach to Calculate the Ionized Field of HVDC Transmission Lines in the Space and on the Earth Surface", 2006 International Conference on Power System Technology
- [7] Tiebing Lu, Han Feng, Zhibin Zhao, Xiang Cui, "Analysis of the Electric Field and Ion Current Density under Ultra High-voltage Direct-current Transmission Lines Based on Finite Element Method", IEEE Tran. On Magn., 2007, 43(4): 1221-1224
- [8] M. Hara, N. Hayashi, K. Shiotsuki, and M. Akazaki, "Influence of wind and conductor potential on distribution of electric field and ion current density at ground level in DC high voltage line to plane geometry ", IEEE Trans. On Power Apparatus and Systems, Vol. 101, No. 4, April 1982, pp. 803-811

A new self-consistent 3D unbounded magnetic field FE computation for electron guns

S. Coco, A. Laudani, G. Pollicino and P. Tirrò

DIEES, University of Catania
V.le A. Doria 6, Catania, I-95125, Italy
alaudani@diees.unict.it

Abstract — An innovative 3-D Finite Elements approach for the computation of the self-consistent unbounded magnetic field of electron beams is presented for the analysis of electron guns. The solution of the whole problem is obtained by solving iteratively a Vlasov-Maxwell equation together with the relativistic dynamical equations of motion, by assuming stationary conditions. The self-consistent unbounded magnetostatic field is computed by using an edge elements curl-curl formulation for the magnetic vector potential \mathbf{A} , and by adopting a fictitious boundary iterative algorithm to overcome the problem of boundary conditions assignment. An example of application to the spread of relativistic beam is given in order to better illustrate the procedure.

I. INTRODUCTION

In the design process of electron guns the electromagnetic analysis is a critical issue in order to achieve the desired electron beam characteristic. In fact, the adoption of more complex geometries and the insertion of appropriate control grids allow the designer to obtain a better performance, but, on the other hand, require the use of dedicated tools to carry out the electromagnetic analysis. For this reason some numerical analysis tools, most of them based on the Finite Element Method (FEM), have been set up [1], but they do not address satisfactorily the self-consistent magnetic field (SCMF). In fact, although high focusing magnetic fields (about 100 times the self consistent component) are usually used for these devices in the focusing region, the influence of SCMF is important above all in the electron gun region, where the focusing magnetic fields vanish. Several approaches were developed to model self-consistent magnetic field: some apply directly the Ampere's law to obtain only the angular component (in a cylindrical symmetric system) of the magnetic field, others solve numerically the whole magnetic problem by using the magnetic vector potential, taking into account all the three components (angular, radial and axial) of the magnetic field. In the latter case a tricky problem is the assignment of the boundary conditions for the magnetic vector potential \mathbf{A} .

In this paper we present an innovative scheme for the treatment of the self-consistent unbounded magnetic field in 3D Finite Elements code for the analysis of electron guns. The solution of the whole problem is obtained by solving iteratively a Vlasov-Maxwell equation together with the relativistic dynamical equations of motion [2], by assuming stationary conditions. In particular in order to model efficiently the self-consistent unbounded magnetostatic field a curl-curl formulation for the magnetic vector potential \mathbf{A} has been employed, and a fictitious boundary iterative algorithm has been adopted to overcome the problem of boundary conditions

assignment. On the fictitious boundary the \mathbf{A} components are initially guessed and successively updated according to the magnetic vector potential and current density distributions obtained in the preceding iteration step. This treatment closely follows an analogous approach, successfully used for the solution of uncoupled electromagnetic problems in unbounded domains [3].

II. 3-D FE ANALYSIS OF ELECTRON GUN

The dynamics of a set of charged particles subject to an electromagnetic field in collisionless conditions can be described by means of the Vlasov equation for the particle distribution function $f(t, \mathbf{x}, \mathbf{p})$, defined in the phase space $(\mathbf{x}, \mathbf{p}) \in \mathfrak{R}_x \times \mathfrak{R}_p$ and time t ,

$$\frac{\partial f}{\partial t} + \frac{\mathbf{p}}{m} \cdot \nabla_x f + q(\mathbf{E} + \frac{\mathbf{p}}{m} \times \mathbf{B}) \cdot \nabla_p f = 0 \quad (1)$$

where \mathbf{p} is the particle momentum, m and q are the particle mass and charge respectively. The electric field \mathbf{E} and magnetic field \mathbf{B} satisfy the Maxwell equations, for which the charge and current densities

$$\rho(t, \mathbf{x}) = q \int_{\mathfrak{R}_p} f(t, \mathbf{x}, \mathbf{p}) d\mathbf{p}, \quad \mathbf{J}(t, \mathbf{x}) = q \int_{\mathfrak{R}_p} \frac{\mathbf{p}}{m} f(t, \mathbf{x}, \mathbf{p}) d\mathbf{p} \quad (2)$$

are the source terms.

The Vlasov equation together with the Maxwell equations constitutes a system of coupled equations called Vlasov-Maxwell system. This coupled problem is usually solved by using Particle-in-Cell (PIC) approaches, in which the electron beam is represented by a reasonable number of macro-particles, subject to the dynamic equations and sources of the electromagnetic field. In addition, it is often possible to consider a stationary solution for this particle model: in this case the self consistent electric field \mathbf{E} is the solution of a Poisson equation, including the space-charge density as a source, while the self-consistent magnetic field \mathbf{B} can be calculated from the field equations for the magnetic vector potential, including the beam current density as a source. In particular we use a FE approach to perform the fully 3-D steady-state analysis. The resulting discretized problem consists of three set of equations: the first is an FE linear algebraic system regarding the spatial distribution of the unknown potential values originated by a nodal formulation of the Poisson equation for the electrical scalar potential, the second is an FE linear algebraic system regarding the spatial distribution of the unknown magnetic potential vector \mathbf{A} originated by an edge element discretization of a curl-curl

formulation for the magnetostatic problem; the other regards the trajectories computation of all the discrete particles used in the model. The solution of the whole system is carried out by following an iterative scheme which alternates the tracing of the electron trajectories and the computation of space charge distribution with the solution of the electrostatic and magnetostatic problems. These steps are repeated until convergence is reached, when the “distance” between two consecutive solutions is less than a user-specified end-iteration tolerance: in this situation a fixed point for the solution is approached and the current flow and electromagnetic field distribution can be assumed self-consistent.

Hereafter, we discuss briefly the aspects concerned with the solution of the unbounded magnetic problem, the solution of the other problems have been illustrated in [3]. A curl-curl formulation for the magnetic vector potential \mathbf{A} in an unbounded domain is used:

$$\nabla \times \nabla \times \mathbf{A} = \mu_0 \mathbf{J} \quad (3)$$

This equation is considered in a bounded domain Ω_M delimited by a fictitious boundary and enclosing all the magnetic sources (that is all particles current-carrying), which might be the same domain Ω of the electrical problem or smaller ($\Omega_M \subseteq \Omega$), since the electron beam usually does not sit in the whole electron gun geometry. In this way the solution of the unbounded problem is converted into the iterative solution of a sequence of bounded Dirichlet magnetic problems. In Ω_M the discretized vector potential is expressed inside each mesh element by using edge elements, in order to avoid spurious solutions. A congruent distribution of 3-D current density is a fundamental aspect for the convergence: the source current density is obtained directly after tracing the electron trajectories by following a suitable deposition and accumulation scheme. As regards the boundary conditions on the fictitious boundary, they are initially guessed and successively updated according to the magnetic vector potential and current density distributions obtained in the preceding iteration step. In particular the boundary values of magnetic potential field can be derived by exploiting its Laplacian behaviour in a region not containing sources by means of the Green's function. In fact, for a generic harmonic function H in the external homogeneous unbounded region one has:

$$\mathbf{H}(\mathbf{r}_F) = - \int_{\Gamma} \left[\frac{\partial \mathbf{H}(\mathbf{r})}{\partial \mathbf{n}} G(\mathbf{r}, \mathbf{r}_F) - \frac{\partial G(\mathbf{r}, \mathbf{r}_F)}{\partial \mathbf{n}} \mathbf{H}(\mathbf{r}) \right] ds \quad (4)$$

where: Γ is an arbitrary surface contained in Ω_M enclosing the whole electron beam; \mathbf{n} is the unit vector normal to Γ , oriented toward Ω_M ; \mathbf{r} and \mathbf{r}_F are point vectors relative to Γ and $\partial\Omega_M$, respectively and G is the 3-D Green's function for free space. Since in the FEM approximation, the surface curve Γ is conveniently selected as constituted by finite element sides, equation (5) can be rewritten for each boundary “unknown” \mathbf{A}_F in the form:

$$\mathbf{A}_F = \mathbf{R}_M \mathbf{A} \quad (5)$$

where \mathbf{R}_M is a rectangular matrix of purely geometrical coefficients. The solution of the discretized equations (3) and (5) are well suited to be solved iteratively, arbitrarily guessing at the beginning the magnetic vector potential on the boundary $\partial\Omega_M$.

III. AN EXAMPLE OF APPLICATION TEST

In order to evaluate the accuracy and the computational performance of the proposed procedure a test regarding the spreading of a relativistic beam is hereafter presented. In particular we consider the evolution of an axisymmetric relativistic laminar electron beam inside a cylindrical drift tube of radius 2m and length 10 m [4]. The self consistent solution of this problem has been computed by means of the last version of the COLLGUN code [2], including the above described computational facility for SCMF. A relativistic beam carrying a current of about 170 and having an energy of 212 kV ($\gamma\beta = 1$, $\beta=v/c$, $\gamma = 1/(1-\beta^2)^{1/2}$) was injected at one end of the drift tube. Three unstructured tetrahedral meshes have been employed for this problem, generated by imposing a constraint to the maximum element volume (less than $2^{1/2}h^3/12$, where h assumes the values 0.5m, 0.25m and 0.125m respectively): the rough mesh has about 16k elements, the fined one has about 1M elements. The beam having a radius of 1m was discretized according to mesh size by spacing the particles of about $h/5$ (about 300, 1300 and 5500 particles respectively for the three setup problems). In all the three tests performed 4 iterations were needed to reach the desired accuracy of 0.1 %. The obtained results show a very good agreement with the analytical ones available in literature [5]. Fig. 1 shows the axisymmetric relativistic beam expanding in the cylindrical drift tube (for the intermediate mesh) and the computed magnetic field surrounding the electrons.

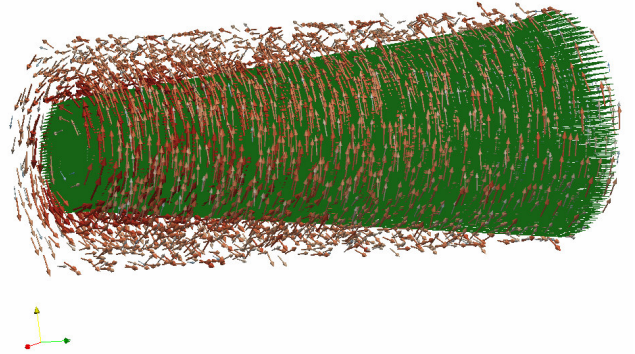


Fig.1. The relativistic beam expanding in the drift tube and the compute magnetic field surrounding the electrons

IV. REFERENCES

- [1] E. M. Nelson and J. J. Petillo, “Current Accumulation for a Self Magnetic Field Calculation in a Finite Element Gun Code, IEEE Trans. on Magnetics, vol. 41, No. 8, pp. 2355-2361, August 2005.
- [2] S. Coco, S. Corsaro, A. Laudani, G. Pollicino, R. Dionisio, and R. Martorana, “COLLGUN: A 3D FE simulator for the design of TWT’s electron guns and multistage collectors,” in Scientific Computing in Electrical Engineering: Proc. SCEE-2004 Conf., Berlin, Germany: Springer-Verlag.
- [3] S. Coco and A. Laudani, “Iterative FE Solution of Unbounded Magneto-Thermal Problems”, Proceedings of the 10th International IGTE Symposium on Numerical Field Calculation in Electrical Engineering, September 16-18, 2002 Graz, AUSTRIA
- [4] E. M. Nelson and J. J. Petillo, “Test of a 3D Self Magnetic Field Solver in the Finite Element Gun Code MICHELLE”, Proceedings of 2005 Particle Accelerator Conference, Knoxville, Tennessee, USA.
- [5] M. Raiser, *Theory and Design of Charge Particle Beams*, Wiley, 1994 (pag. 196).

Using a direct field calculation method to solve magnetostatic design inverse problem

R. Vilamot, C. Henaux, and B. Nogarede

Laboratoire Plasma et Conversion d'Energie (LAPLACE),
Université de Toulouse-CNRS, BP 7122,31071 INPT-ENSEEIH, Toulouse Cedex 7, France
nogarede@laplace.univ-tlse.fr

Abstract— This paper deals with an inverse problem methodology devoted to the automated definition and design of electromagnetic structures. Then, using a statistical approach, a discussion on the existence and the uniqueness of the problem solution is led. The last part focuses on the behaviour of the solving algorithm for several case studies.

I. INTRODUCTION

Optimal electromagnetic systems design can nowadays be understood and formulated as an inverse problem, i.e., from characteristic values given by the specifications, obtaining the dimensions and material for a previously chosen structure.

Optimal design procedures are often based on analytical modelling considering an idealized structure. It gives satisfying results thanks various optimization methods [1]. Whatever the character stochastic [2] or deterministic [3] of the employed algorithm, the available solutions field is seriously limited by the preliminary choice of a given structure.

This paper presents an inverse problem methodology devoted to the automated definition and design of electromagnetic structures, in the context of quasi-static fields. The ability to reproduce a prescribed 2D magnetic field pattern with a distribution of out of plane conductors is analysed. Such a problem is ill-posed according to Hadamard's definition [4]. Indeed, existence and uniqueness of the obtained solution, which are not guaranteed, is taken into account in the paper.

II. PROBLEM STATEMENT

A. Assumptions

The aim of the proposed inverse problem methodology consists in finding a current distribution which generates a given magnetic field map in free space of μ_0 permeability. The current distribution will be defined by a set of infinite parallel to the z axis conductors and the field map will be described by tests points on xOy plane. Consequently the resulting system is invariant by translation along the z axis and the analytical calculation can be carried on the xOy plane.

B. Magnetostatic equations

To solve the inverse problem, the field at the test points will be analytically calculated thanks to Biot-Savart's law (1) [3]:

$$\vec{B}(M) = \frac{\mu_0}{4\pi} \int_D \frac{\vec{Idl} \wedge \vec{SM}}{\|SM\|^3} \quad (1)$$

So, considering a set of current elements oriented along z axis, the magnetic flux density $\vec{B}_W(M)$ produced by a single conductor located in W (in the xOy plane), and carrying a current I, at a given point M in the plane perpendicular to z axis is given by (2):

$$\vec{B}_W(M) = \frac{\mu_0 I}{2\pi} \begin{pmatrix} \frac{-(y_M - y_W)}{(x_M - x_W)^2 + (y_M - y_W)^2} \\ \frac{(x_M - x_W)}{(x_M - x_W)^2 + (y_M - y_W)^2} \end{pmatrix} \quad (2)$$

Consequently, the global problem to solve can be formulated as a coupled matrix system (3):

$$\begin{cases} \mathbf{A}_x \mathbf{I} = \mathbf{B}_x \\ \mathbf{A}_y \mathbf{I} = \mathbf{B}_y \end{cases} \quad (3)$$

With

$$\mathbf{A}_x = \left[\frac{-(y_{Mi} - y_{Wj})}{(x_{Mi} - x_{Wj})^2 + (y_{Mi} - y_{Wj})^2} \right]_{[i, j] \in [1, n_{meas}] \times [1, n_{fils}]}$$

$$\mathbf{A}_y = \left[\frac{(x_{Mi} - x_{Wj})}{(x_{Mi} - x_{Wj})^2 + (y_{Mi} - y_{Wj})^2} \right]_{[i, j] \in [1, n_{meas}] \times [1, n_{fils}]}$$

Components of \mathbf{I} vector corresponds to the various current elements.

\mathbf{B}_x and \mathbf{B}_y are the vectors of the expected magnetic flux density values on each test point, projected on x and y axes.

The inverse electromagnetic problem can be linear or not depending on the investigated quantities (conductor position, and current value). So the problem is linear only when the conductor position is fixed.

III. DISCUSSION ON EXISTENCE AND UNIQUENESS OF THE SOLUTION

A. Existence

The linear and non-linear problems are solved by a least-square optimization method. Existence and uniqueness of solution are analysed by statistic approach on test cases depending on number of test points and conductors. Concerning the existence of solution we can observe that:

- In a linear case (position fixed), a configuration in which the test points number is twice conductors number leads to a well-posed problem according to Hadamard's definition.

- In the non-linear case (position and current value are not fixed), the solutions domain is significantly increased (as illustrated in Fig.1).

A more precise sensitive analysis on bounded values of investigated quantities will be described in the final paper.

B. Uniqueness

The magnetostatic inverse problem methodology can be applied on underdetermined or overdetermined systems. In the case of underdetermined systems, it is interesting to determine the initial conditions (i.e. number and bounded values of conductors and test points) which guarantee a set of available solutions. This set must be wide enough to allow an optimization procedure. In this context, from a given field map generated by a known conductors distribution, the convergence of the solving inverse problem is studied. It can be observed for example on Fig.2 that when the number of conductors is sufficient, this method does not only converge on the initial known conductors distribution.

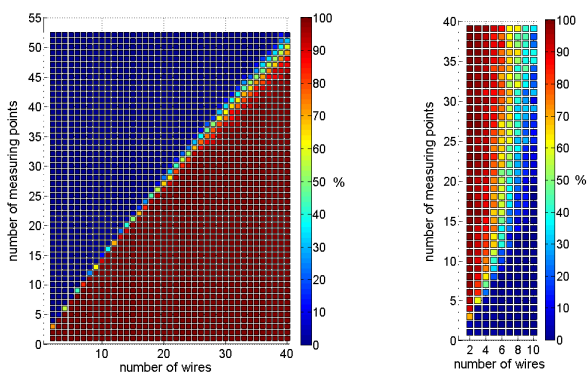


Fig 1. Convergence rate on a solution (100 resolutions per case).
Random B field value on test points.

3 degrees of freedom per conductor (coordinates and current value)
Fig. 2. Convergence rate on the initial solution (100 resolutions per case).

IV. CASE STUDIES

The final paper will present several cases in order to study the behaviour of the resolution algorithm and the resulting solution for a strongly constrained problem (conductors excluded from domain of test points, and/or bounded current value). As example, the Fig.3 shows a linear case with a very high number of conductors. The comparison between the initial magnetic field test point and the magnetic field resulting from inverse problem solving gives satisfying results with a difference lower than 0.7% (cf. Fig.4).

Let us underline that from Fig.3 it is possible to easily characterize patterns in the current distribution. Those patterns could be used in a postprocessing inverse problem solving for the design of a magnetic structure.

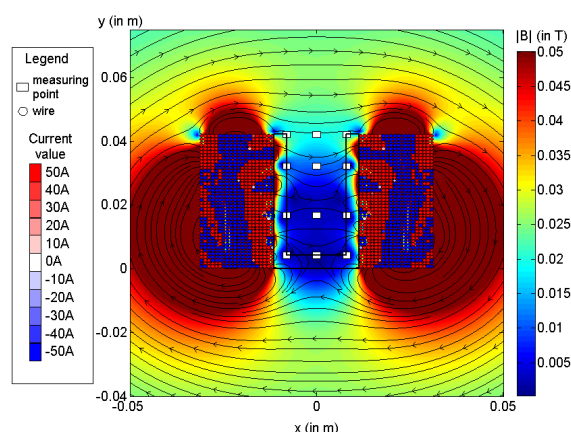


Fig. 3. Example of current values distribution obtained after resolution.
12 test points, 840 current values.

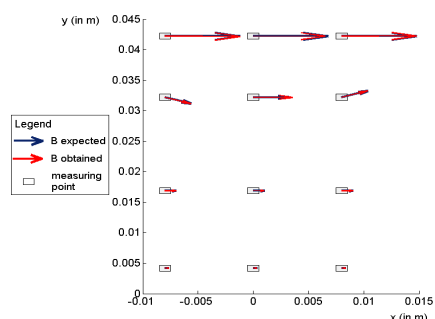


Fig. 4. Comparison of B values on the test points for the same example.

V. CONCLUSION

The authors have presented an inverse problem methodology devoted to the optimal design of electromagnetic structures. This methodology is based on an analytical description of the static fields thanks to Biot and Savart equation. Considering a generic multi-conductor distribution makes it possible to discuss existence and uniqueness of the solution by using a statistical approach. This analysis led to a rational definition of the required conductor number considering the number of test points. Case studies have been done to explore the limits of the solving method. The results presented in this last part open a new field of investigation in the magnetostatic inverse problem methodology.

VI. REFERENCES

- [1] E. Fitan, F. Messine, B Nogarède "The electromagnetic actuator design problem: a general and rational approach", *IEEE Trans. Magn.*, vol.40(3) 2004.
- [2] N. Bianchi, S. Bolognani, "Brushless Dc motor design: an optimisation procedure based on genetic algorithms" *Electrical Machines and Drives*, 1997, pp 16-20
- [3] J. Fontchastagner, F. Messine, Y. Lefèvre "Design of electrical rotating machines by associating deterministic global optimization algorithm with combinatorial analytical and numerical models," *IEEE Trans. Magn.*, vol.43(8), 2007.
- [4] E. Durand, *Magnétostatique*. Paris: Masson/Dunod, 1968.
- [5] P. Neittaanmaki, M. Rudnicki, and A. Savini, "Inverse problems and optimal design in electricity and magnetism," in *Monographs in Electrical and Electronic Engineering 35*. Oxford, U.K.: Clarendon, 1996.

Calculation of the Flux Linkage of a 12/8 Dual-Channel SRM Including Mutual Coupling and Saturation: From Magnetic Circuit Model to FEM Analysis

Wen Ding and Deliang Liang

Department of Electrical Machines and Drives, Xi'an Jiaotong University
28 West Xian Ning Road, Xi'an 710049 P. R. China
Tel:029-826-73409, fax:029-826-75306
e-mail: stiwen@163.com

Abstract — The dual-channel switched reluctance machine (SRM) is driven by two independent sets of power electronic circuits with dual control channels, so a fault tolerated operation mode can be used in this system for high reliability. This paper presents a magnetic analysis of a 12/8 dual channel SRM in order to compute the nonlinear magnetization curves including mutual coupling. The proposed analysis implements the magneto-motive force (mmf) sources and consists of the equivalent magnetic circuit, the analytical saturable airgap permeances and nonlinear yoke permeances. Then the performance of this dual channel SRM including self flux and mutual flux have been determined using the two-dimensional finite-element (2D-FE) method under different rotor positions (fully aligned to fully unaligned) for varying exciting current conditions. The effectiveness of this proposed magnetic circuit analysis is verified by comparing with 2D-FE method in terms of the analytical accuracy.

I. INTRODUCTION

With the development of the power electric and control technology, the switched reluctance machine (SRM) is becoming more and more attractive for many applications. However, it is rather difficult to design the machine and develop the drive performance because of the magnetic nonlinearity of the motor [1]-[2]. The 12/8 novel dual-channel SRM is a dual three phase motor and its configuration is shown in Fig.1. Dual channel SRM control system can work as dual channel mode or single channel mode. When a power circuit is failure, the system is transferred into single channel mode which is called fault-tolerant operation.

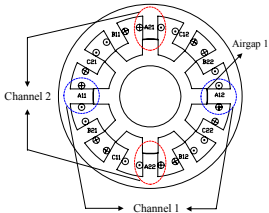


Fig.1 Structure of dual-channel SRM

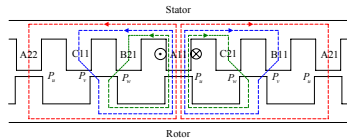


Fig.2 Flux paths ($\theta=0^\circ$)

This paper presents a magnetic circuit model for calculating the self and mutual flux linkage of a 12/8 dual channel SRM including saturation effects. The model determines the flux linkage of one channel in each phase for any geometry, phase count, rotor position, and combination of phase current. The model presented in this paper does not require time consuming data entry and meshing. And the results presented can be obtained in a matter of minutes. Then the results of this modeling method are verified against the Ansoft/Maxwell 2D finite element solver.

II. THE MAGNETIC CIRCUIT MODEL

As the channel one of A-phase is only excited, the equivalent magnetic circuit and flux path diagram are shown in Fig.2. The rotor angular position θ is defined as $\theta = 0^\circ$ at the aligned position and $\theta = 22.5^\circ$ at the unaligned position.

III. AIRGAP PERMEANCES

There are three different permeances which are included in the airgap model: overlap; fringing; and nonoverlapping.

A. Overlap and fringing permeance

Fig.3 shows the case of overlap and fringing flux path in airgap 1. In this paper, the stator and rotor pole arcs are assumed $\pi/12$ respectively.

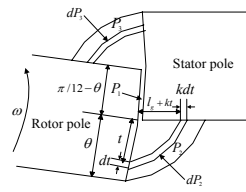


Fig.3 Partially overlapping poles

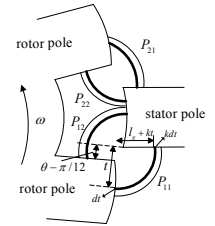


Fig.4 Nonoverlapping poles

The overlap and fringing permeance P_a of airgap 1 can be divided into three parts of permeances $P_1 \sim P_3$.

$$P_a = P_1 + P_2 + P_3 \quad (1)$$

$$= \frac{\mu_0 h (\pi/12 - |\theta|) (r_{sp} + r_{rp})}{l_g} + \frac{2\mu_0 h}{\pi} \ln \left(\frac{l_g^2 + 2l_g r_{rp} |\theta| + 2r_{rp}^2 |\theta|^2}{l_g^2} \right)$$

B. Nonoverlapping permeance

Fig.4 shows the situation being considered and outlines the appropriate flux tubes to approximate the path.

The nonoverlapping permeance P_a of airgap can be divided into three parts of permeances $P_{11} \sim P_{22}$.

$$P_a = P_{11} + P_{12} + P_{21} + P_{22} = 2P_{11} + 2P_{21} \quad (2)$$

$$= \frac{2\mu_0 h}{\pi} \left[\ln \frac{l_g + l_g r_{rp} \pi/6 + r_{rp}^2 \pi^2/72}{l_g + 2l_g r_{rp} (|\theta| - \pi/12) + 2r_{rp}^2 (|\theta| - \pi/12)^2} + \ln \frac{l_g + l_g r_{rp} \pi/6 + r_{rp}^2 \pi^2/72}{l_g + 2l_g r_{rp} (\pi/6 - |\theta|) + 2r_{rp}^2 (\pi/6 - |\theta|)^2} \right]$$

IV. YOKE PERMEANCES

Fig.5 shows the flux path in the stator yoke, the permeance of stator yoke between adjacent poles

$$P_{sy} = \frac{u_r A}{L_{sy}} = \frac{12u_r L_{syd} h}{(r_s + r_{sy})\pi} \quad (3)$$

where u_r is steel permeability.

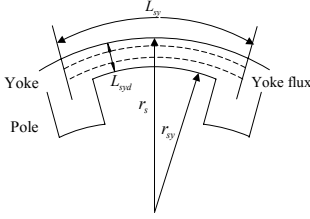


Fig.5 Flux paths at stator yoke

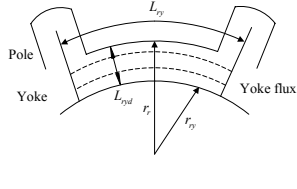


Fig.6 Flux paths at rotor yoke

Fig.6 shows the flux path in the rotor yoke, similarly the permeance of rotor yoke between adjacent poles can be derived as

$$P_{ry} = \frac{8u_r L_{ryd} h}{(r_r + r_{ry})\pi} \quad (4)$$

V. NONLINEAR SOLUTION

To obtain the static characteristics of the SRM, the rotor position should be changed in small decrements to cover half an inductance cycle. With a change in rotor position, the flux pattern in the poles and airgap changes. Once all of the various airgap permeances have been determined for a give rotor position, they must be incorporated into the model. The complete set of closed loops equations is a system which can be represented in matrix form

$$[R][\Phi] = [F] \quad (5)$$

Where Φ is the vector of branch fluxes, F is the vector of magneto motive forces and R is matrix of magneto resistance. Gauss-Siedel method with an accelerating factor for faster convergence has been used to solve the nonlinear problem. Once the fluxes have been calculated form (5), the flux linkage can be calculated.

V. FINITE ELEMENT ANALYSIS

In this section, a finite element analysis using Ansoft/Maxwell 2D is performed to obtain the magnetic characteristics of the machine, considering the saturation and mutual coupling effects.

1) *Flux lines*: One and two channels of A -phase are excited in the aligned and unaligned positions. Flux contours at these two positions are shown in Fig.7, respectively.

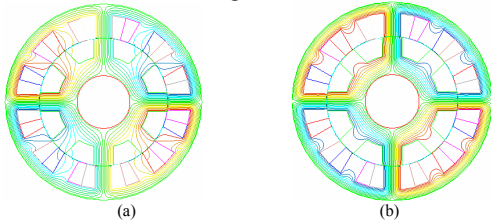


Fig.7 Magnetic field distribution of dual-channel SRM: (a) one channel is excited; (b) two channels are excited.

2) *Self flux linkage and inductance*: The self flux linkage and inductance in channel one of A -phase as a function of rotor position and excitation current as obtained by finite

element method analysis are shown in Fig.8 along with the magnetic circuit analysis results.

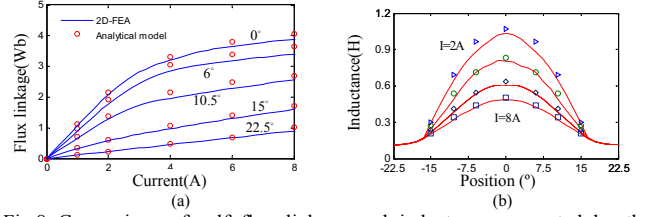


Fig.8 Comparison of self flux linkage and inductance computed by the analytical and FE methods: (a) flux linkage, (b) inductance

3) *Mutual flux linkage*: In Fig.9-10, the mutual magnetic flux linkage obtained by FE method is compared with the results of the analytical model.

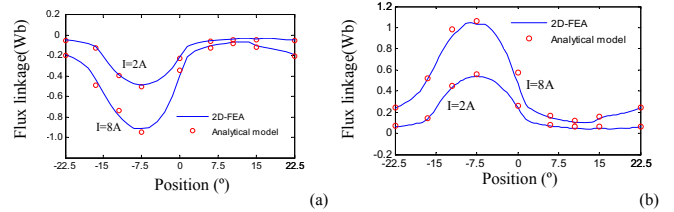


Fig.9 Mutual flux linkage in (a) B1 and (b) B2 when A1 is excited

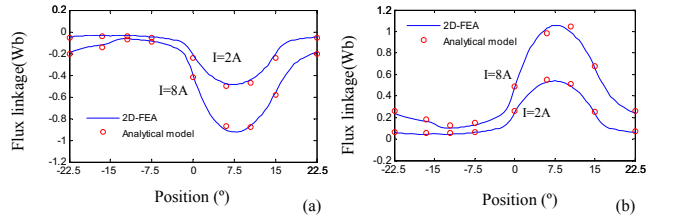


Fig.10 Mutual flux linkage in (a) C1 and (b) C2 when A1 is excited

VI. CONCLUSION

This paper has described the electromagnetic characteristics including mutual coupling and saturation for a dual-channel 12/8 switched reluctance machine (SRM) from its magnetic circuit model analysis and compares the two-dimensional finite element method (2D-FE) analysis results by using Ansoft/Maxwell. The magnetic circuit model presented airgap permeance including the stator and rotor poles overlap and nonoverlapping and the nonlinear yoke permeance. The magnetic characteristics results show that the self flux linkage and mutual flux linkage in the two channels of the same phase are not the same. The magnitude of mutual coupling in neighboring channels is almost identical but the direction is not the same. The model approach presented here is also suitable for conventional SRM geometries that require consideration of mutual coupling effects. Additional numerical algorithms can translate model flux solutions to motor torque predictions.

REFERENCES

- [1] A. Radun, "Analytically computing the flux linked by a switched reluctance motor phase when the stator and rotor poles overlap," *IEEE Trans. Magn.*, vol. 36, no. 4, pp. 1996-2003, July. 2000.
- [2] S. M. Jang, J. H. Park, J. Y. Choi, and H. W. Cho, "Analytical prediction and measurements for inductance profile of linear switched reluctance motor," *IEEE Trans. Magn.*, vol. 42, no. 10, pp. 3428-3450, Dec. 2006.

Effects of the Core Materials on Magnetic Bearing Parameters

B. Tomczuk, J. Zimon, *IEEE Member* and A. Waindok, *IEEE Member*
 Department of Industrial Electrical Engineering, Opole University of Technology
 ul. Luboszycka 7, 45-036 Opole, Poland
 b.tomczuk@po.opole.pl, j.zimon@po.opole.pl

Abstract— Magnetic field in an active magnetic bearing has been analyzed with Finite Element Method (FEM). Influence of the magnetization characteristics on the field distribution and values of the device static parameters has been studied. The investigations have been done for the physical model of the magnetic bearing, as well. Selected parameters of the device have also been measured and compared with the calculation results.

I. INTRODUCTION

Rotary magnetic bearing, like other electric motors and generators, is a composite of interacting subsystems: stators and rotors [1], [3]. Each stator is assembled from horse-shoe electromagnets, which form a multipole system (Fig.1). So far, rotor and stator magnetic cores were stacked from silicon-steel sheets. We simulated parameters of the bearing with magnetic core made of amorphous magnetic alloy, as well [1], [2].

Magnetic field, arisen in the stator, is passing to the rotor and generates forces supporting rotating shaft of a drive without any mechanical suspension [3]. They are produced by the bias and control currents which supply the stator coils (Fig.1) in response to the signals from sensors [4]. Disturbing of the balance in the control currents brings that the rotor is attracted (along a radius) towards the stator. It indicatives of the stator and rotor axes are out of alignment [5]. The magnetic forces depend not only on the stator currents, but the magnetic material characteristics, as well.

II. GEOMETRY OF THE BEARING AND THE FIELD PROBLEM

The eight-pole magnetic bearing, pictured in Fig.1, has been considered. The laminated stator and rotor stacks are 10 and 20 mm in thickness, respectively. We supposed thin (0.35mm) sheets, which are made from silicon steel M55 in our prototype. Small air gap between the rotor lamination and the set of stator teeth is amount of 0.2 mm.

The considered bearing has basic and control windings. They are situated so that four, horse-shoe electromagnets are created. The $N_1=40$ turn basic coil and $N_2=100$ turn control one are situated on each pole of the magnets. The I_b and I_s currents are forced in the coils, respectively. Both, bias and control windings are located separately, and generate the flux crossing two stator poles.

The simplified shapes of the coils in Fig.1 slightly differ from the physical object ones [6]. It is due to limiting the number of elements in the field simulation with FEM [7]. One should add that more exact approximation does not change the resulting field significantly.

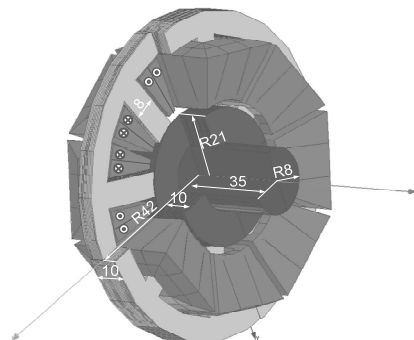


Fig. 1. Magnetic bearing outline with stator cutting out

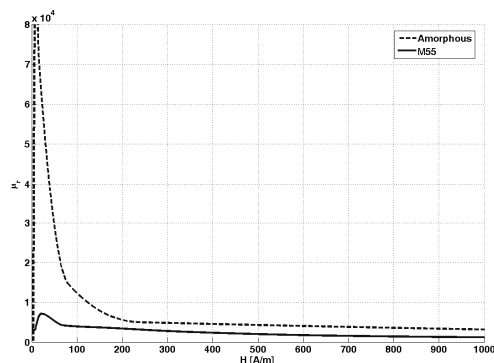


Fig. 2. Permeability curves $\mu_r(H)$ of silicon steel and amorphous alloy

Including, in the field analyses, the nonlinearity of the magnetization curves (Fig.2), $T-\Omega$ method has been used for the solutions of the boundary problems [4].

$$\nabla^2 \vec{T} = j\omega\mu\gamma \vec{H}_s \quad (1)$$

$$\nabla \cdot (\mu(H)\nabla\Omega) = 0 \quad (2)$$

The electric vector potential T is used, in Eq. (1) for regions contain currents. The field intensity H_s , excited by currents is governed by Biot-Savart law. In other regions, e.g. occupied by the magnetic material, the equation (2) governs the field distribution. After solution of the nonlinear equations above, magnetic flux density distribution has been calculated for the conducting and other regions, respectively:

$$\vec{B} = \mu_r(H) \mu_0 [\vec{H}_s - \nabla\Omega] \quad (3)$$

$$\vec{B} = -\mu_r(H) \mu_0 \nabla\Omega \quad (4)$$

III. COMPUTATIONAL RESULTS OF THE FIELD ANALYSIS

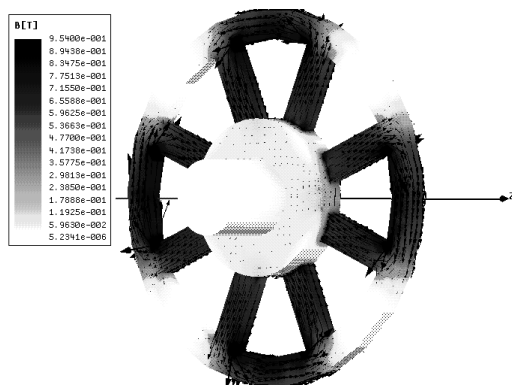


Fig. 3. Flux density distribution under the bias current excitation of $I_b=0.8A$

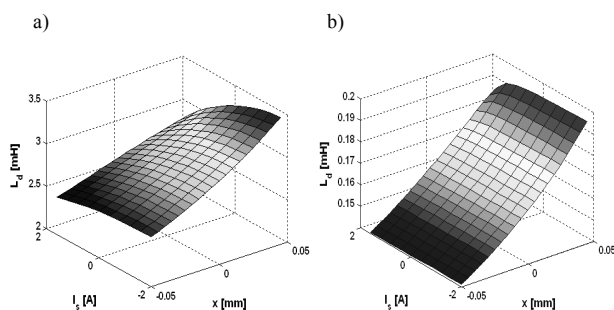


Fig. 4. Dynamic inductances vs. control current I_s , and shaft position x for:
a) M55 steel b) amorphous material

The flux distribution in the prototype of the bearing under bias excitation is shown in Fig. 3.. In this case, the shaft was centrally positioned. Although the prototype magnetic circuit is made of M55 steel [8], we also considered other modern materials. We see from Fig. 2 that at $H < 200$ A/m the permeability curves are strongly nonlinear, for both considered materials. Due to brevity we did not present the distributions of the magnetic flux densities for other materials.

TABLE I. STATIC INDUCTANCE OF THE WINDING FOR TWO MATERIALS OF THE CORE

Material	L_s [mH]
Amorphous	16,4
M55 calculations	3,72
M55 measurements	3,7

The field distribution is used to estimate the electromagnetic force, which acts on the moving bearing shaft, as well as to determine the dynamic L_d (Fig.4) and static L_s (Tab.1) inductances of the stator winding.

In the calculation model the control current has been superposed on the bias excitation. Its magnitude varied from up to 2 A, and the shaft center was moved from the middle position by $x=0.05$ mm. For calculation of the static inductance, the bias current $I_b=0.8A$ has been assumed.

We presented the force values for the shaft extracted from the central position up to $|x|=0.05$ mm. The control current magnitude altered up to 2 A, (Fig. 5).

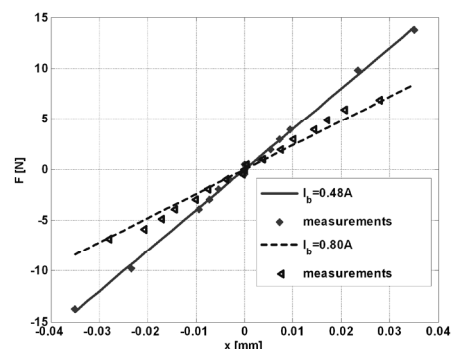


Fig. 5. Magnetic force vs. the shaft center locus

The variation of the magnetic forces is slightly nonlinear respect to the rotor position x (Fig. 5). However, the force generated by the interaction between rotor and stator, strongly depends on the rotor position and sense of the control current, which is opposite to the bias current direction. Thus, the force value is greater when the bias current I_b is lower (Fig. 5). Differences between calculated and measured parameters are attributed to the simplifications of the field modeling and the measurement errors, as well.

IV. CONCLUSIONS

Bearings with the core laminations which are made up of different materials have been considered in 3D field analyses. Small air-gap between the stator and rotor as well as slight displacement of the shaft was included. Additional benefits of the computer simulations, is that different coils and their dimensions can be tried.

The integral parameters of the magnetic field were calculated and compared with the measured ones. The calculated errors occur also due to eddy currents and anisotropy neglecting. Estimation with their including is very difficult. However, they are not as profitable as expected. Despite the simplifications in the mathematical modeling, the measured results confirm acceptability of the computer simulations.

V. REFERENCES

- [1] B. Tomczuk, J. Zimon, "Field determination and calculation of stiffness parameters in an active magnetic bearing (AMB)", *Solid State Phenomena*, Zurich, Vols. 147-149, 2009, pp. 125-130.
- [2] R. Albanese, G. Rubinacci, "Numerical Procedures for the Solution of Nonlinear Electromagnetic Problems", *IEEE Trans. on Magnetics*, Vol.28/2, 1992, pp.1228-1231.
- [3] G. Schweitzer, A. Traxler, H. Bleuler, *Magnetlager*, Springer Verlag, Heidelberg, Germany, 1993.
- [4] M. Antila, "Electromechanical Properties of Radial Active Magnetic Bearings", *Acta Polytechnica Scandinavica*, 1998, pp. 1-45.
- [5] J. Zimon, "Field Analysis and Parameters Computation in the Active Magnetic Bearings", Doctoral Thesis, Opole, Poland, 2008.
- [6] B. Tomczuk, J. Zimon, "Numerical field analysis in the magnetic bearing", *Computer App. in Electr. Eng. ZKwE'05*, Poznan, Poland, 7-9 April, 2005, pp. 91-92.
- [7] C.F.R. Lemos Antunes, "Force Calculations with T- Ω Method", *IEEE Trans. on Magnetics*, Vol. MAG-21/6,1985, pp. 2432-2.
- [8] Catalog of cold rolled electrical sheets and strips, Bochnia, Poland, 2008.

Optimization of Electrostatic Micromotor by a Non-linear Interior Point Method

Adriano C. Lisboa, Rodney R. Saldanha, and Douglas A. G. Vieira
 Department of Electrical Engineering, Universidade Federal de Minas Gerais
 Av. Antônio Carlos 6627, 31270-901, Brazil
 adriano@cpdee.ufmg.br, douglas@cpdee.ufmg.br

Abstract—This paper applies optimization techniques to design electromagnetically feasible optimal micromotors, considering torque characteristics and electrical breakdown. Furthermore, it tries to bring the non-linear interior point method to the optimization of electromagnetic devices.

I. INTRODUCTION

Microtechnology and nanotechnology have become new important fields of research with wide range of applications, including medicine and electronics. In very small scales, simple geometries are highly desirable due to fabrication constraints. Under this conditions, electrostatic motors are truly competitive.

Unfortunately, the torque ripple of an electrostatic micromotor is typically large [1]. Another important issue about micromotors is the electrical breakdown due to high electric field magnitudes. Much effort has been devoted to improve feasibility of micromotors, since the very beginning [2], which is closely related to materials science and development of new technologies. Some micromotors have also been optimized, specially with the objective of minimizing the torque ripple [1]. This paper investigates the optimization of electromagnetically feasible micromotors, considering torque and electrical breakdown.

The optimization algorithm in focus at this paper is the interior point method in its non-linear version. Despite it has been largely applied to many real-world problems [3], [4], there are few works on optimization of electromagnetic devices. The most constraining feature seems to be the need of second order derivatives from the objective and constraint functions. This paper proposes to take this information from iterative techniques.

II. ELECTROSTATIC MICROMOTOR

The electrostatic micromotor is formed by electric conducting rotor and stator, as shown in its geometry in Fig. 1. The rotor is a contiguous piece tied to ground. The stator teeth are mutually electrically isolated, so that each one can be tied to arbitrary electric potentials. The electrostatic micromotor is typically build on a dielectric board and surrounded by air.

In this work, the electrostatic micromotor is analyzed with a finite element method (FEM) derived from a bi-dimensional

This work was supported by FAPEMIG under grants 13180 and 13348, Brazil.

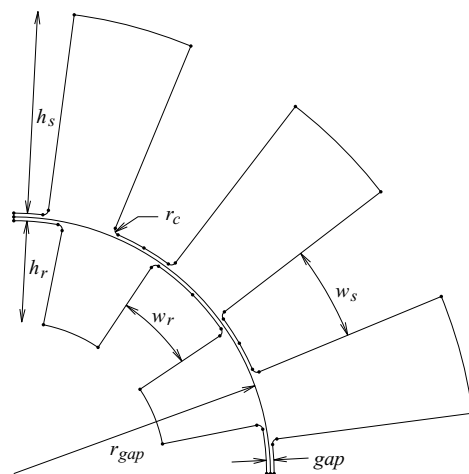


Fig. 1. Geometry of the micromotor and its parameters.

electrostatic formulation. The rotor and stator are modeled as perfect electric conductors, so that only their boundaries are considered. The FEM is then applied to the meshed air region between rotor and stator, where the electric potential is known in some nodes, from where the torque is calculated using Maxwell stress tensor.

The torque is calculated for each rotor position. In order to reduce the computational cost, it is considered the electrical symmetry of the problem, leaving natural boundary conditions at split interfaces. For instance, only a quarter of a motor with 8 rotor teeth and 12 stator teeth, as shown in Fig. 1, can answer for the whole motor. Furthermore, a uniform segmentation at the middle gap region is guaranteed by the mesh generator, so that the mesh can be split into two and doubled nodes are reconnected by boundary conditions. Hence, every rotor position can be simulated using the same mesh.

III. INTERIOR POINT METHOD

The primal-dual interior point method used in this work [3], [4], [5] considers optimization problems in the form

$$\begin{aligned} \min_x \quad & f(x) \\ \text{s.t.} \quad & g(x) \leq 0 \\ & Ax = b \end{aligned} \quad (1)$$

where $x \in \mathbb{R}^n$ is the vector of parameters, $f(x) : \mathbb{R}^n \mapsto \mathbb{R}$ is a twice continuously differentiable objective function, $g(x) : \mathbb{R}^n \mapsto \mathbb{R}^m$ is the vectorial twice continuously differentiable constraint function, $A \in \mathbb{R}^{p \times n}$ is a full row rank equality constraint matrix, and $b \in \mathbb{R}^p$ is the equality constraint vector. The interior point method then approximate, in the neighborhood of point x_k at iteration k , the non-linear objective and constraint functions by quadratic functions in the form

$$\tilde{f}(x) = f(x_k) + \nabla^T f(x_k)x + \frac{1}{2}x^T \mathcal{H}f(x_k)x \quad (2)$$

where $\nabla f(x_k) \in \mathbb{R}^n$ denotes the gradient vector of f at x_k , and $\mathcal{H}f(x_k) \in \mathbb{R}^{n \times n}$ denotes the Hessian matrix of f at x_k . To avoid calculating second order derivatives of a numerical evaluated problem, the Hessian of objective and constraint functions are iteratively approximated by the Broyden-Fletcher-Goldfarb-Shanno (BFGS) method.

The primal-dual search direction d_k is given by

$$d_k = -H_k^{-1}r_k \quad (3)$$

where

$$r_k = \begin{bmatrix} \nabla f(x_k) + \nabla g(x_k)\lambda_k + A^T \nu_k \\ -\text{diag}(\lambda_k)g(x_k) - 1/t_k \\ Ax_k - b \end{bmatrix} \quad (4)$$

is the residual, $\eta_k = -\lambda_k^T g(x_k)$ is the dual gap, $t_k = (\mu m)/\eta_k$ is the barrier parameter, μ is an algorithm parameter (typically 10), λ_k and ν_k are Lagrange multipliers, and

$$H_k = \begin{bmatrix} L_k & \nabla g(x_k) & A^T \\ -\text{diag}(\lambda_k)\nabla^T g(x_k) & -\text{diag}(g(x_k)) & 0 \\ A & 0 & 0 \end{bmatrix} \quad (5)$$

where

$$L_k = \mathcal{H}f(x_k) + \sum_{j=1}^m \lambda_{kj} \mathcal{H}g_j(x_k) \quad (6)$$

A backtracking line search algorithm is then applied to find a step $\alpha_k \in (0, 1)$ towards d_k such that $\lambda > 0$ and $g(x) < 0$. The iterative update is then given by

$$\begin{bmatrix} x_{k+1} \\ \lambda_{k+1} \\ \nu_{k+1} \end{bmatrix} = \begin{bmatrix} x_k \\ \lambda_k \\ \nu_k \end{bmatrix} + \alpha_k d_k \quad (7)$$

IV. OPTIMIZATION

The optimization problem is to minimize the torque ripple constrained to a maximum electric field to prevent breakdown. It can be written as

$$\begin{aligned} \min_x & \frac{\max_{\theta}(\tau(\theta, x)) - \min_{\theta}(\tau(\theta, x))}{\text{mean}_{\theta}(\tau(\theta, x))} \\ \text{s.t.} & \max_{\theta}(E_{\max}(\theta, x)) \leq 75\text{V}/\mu\text{m} \\ & x_{\min} \leq x \leq x_{\max} \end{aligned} \quad (8)$$

where $x \in \mathbb{R}^n$ is the vector of variables, θ is the rotor position, $\tau(\theta, x)$ is the torque, $E_{\max}(\theta, x)$ is maximum electric field in the air. The stator teeth potentials switch between 0 and 100V.

Two parameters of the electrostatic micromotor (see Fig. 1) are variables of the optimization problem: the rotor w_r and stator w_s teeth width. The remaining parameters are set

constant: gap radius $r_{gap} = 50.75\mu\text{m}$, rotor to stator gap $gap = 1.5\mu\text{m}$, stator teeth height $h_s = 40\mu\text{m}$, rotor teeth height $h_r = 20\mu\text{m}$, and rounding radius $r_c = 1\mu\text{m}$. As a preliminary result, the optimal parameters for problem (8), with constraints not yet considered, are shown in Table I. The respective optimal torque is shown in Fig. 2, with optimal ripple of about 20%.

TABLE I
LOWER BOUND, UPPER BOUND AND OPTIMAL PARAMETERS.

parameter	min	max	optimal
w_r ($^{\circ}$)	4.50	40.50	21.23
w_s ($^{\circ}$)	3.00	27.00	19.79

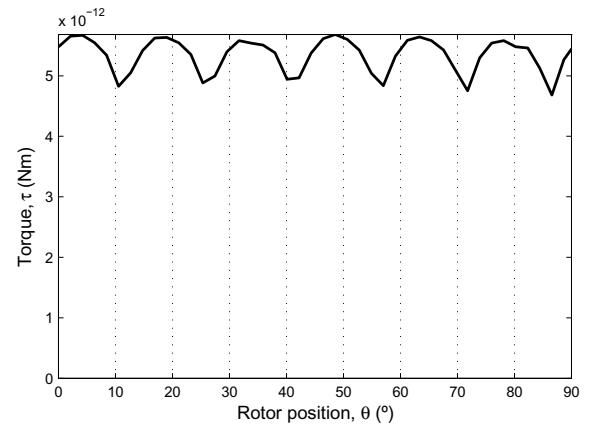


Fig. 2. Optimal torque.

Results considering more parameters of the electrostatic micromotor as variables, as well as more optimal solutions of variations of problem (8), will be shown in the final paper. Further details about the primal-dual interior point method used in this work will also be given.

ACKNOWLEDGEMENT

This work was supported by CNPq under grant n^o 305265/2005-9, and by FAPEMIG under grants n^o 13348 and 13180, Brazil.

REFERENCES

- [1] V. Behjat and A. Vahedi, "Minimizing the torque ripple of variable capacitance electrostatic micromotors," *Elsevier Journal of Electrostatics*, vol. 64, pp. 361–367, 2006.
- [2] J. H. Jang and S. F. Bart, "Toward the design of successful electric micromotors," *IEEE Technical Digest*, pp. 127–130, 1988.
- [3] S. Boyd and L. Vandenberghe, *Convex optimization*. Cambridge University Press, 2004.
- [4] H. Hindi, "A tutorial on convex optimization ii: duality and interior point methods," *Proceedings of the 2006 American Control Conference*, pp. 686–696, 2006.
- [5] P.-A. Absil and A. Tits, "Newton-KKT interior-point methods for indefinite quadratic programming," *Computational Optimization and Application*, vol. 36, no. 1, pp. 5–41, 2007.

A Modified FEM-DBCI Method for Static and Quasi-Static Electromagnetic Field Problems

G. Aiello⁽¹⁾, S. Alfonzetti⁽¹⁾, G. Borzi⁽²⁾, E. Dilettoso⁽¹⁾, and N. Salerno⁽¹⁾

(1) Dip. Ing. Elettrica, Elettronica e dei Sistemi, Univ. di Catania – Viale A. Doria, 6 – I-95125 Catania – Italy

(2) Dipartimento di Ingegneria Civile, Università di Messina – Salita Sperone, 31 – I-98166 Messina – Italy

Abstract — This paper presents a modified version of the hybrid FEM-DBCI method to solve static and quasi-static electromagnetic field problems in open boundary domains. The modification consists of overlapping the fictitious truncation boundary with the integration one, as in the FEM-BEM method. The global algebraic system obtained is solved iteratively by means of the GMRES solver, applied virtually to a reduced system in which the unknowns are those relative to the potential on the truncation boundary only. Some validation examples are provided.

Index Terms— Finite element method, boundary element method, integral equations, electrostatic field.

I. INTRODUCTION

The well-known hybrid FEM/BEM (Finite Element Method - Boundary Element Method) method [1], [2] is probably the most widely used numerical method to solve static and quasi-static electromagnetic field problems in open-boundary domains. Recently the authors have devised another hybrid method, called FEM-DBCI (Dirichlet Boundary Condition Iteration), to solve electrostatic [3], [4], time-harmonic skin effect [5], [6] and eddy current [7] problems.

Both FEM-BEM and FEM-DBCI couple a differential equation, which governs the interior problem, with an integral one which makes use of the free-space Green function and expresses the unknown boundary condition on the fictitious truncation boundary.

The differences between the two methods are the following.

In FEM-BEM the integration surface coincides with the truncation one, whereas in FEM-DBCI the integration surface is another surface strictly enclosed by the truncation boundary; note that this characteristic allows us to avoid singularities in the integral equation and to obtain it in explicit form with respect to the potential values in the nodes of the truncation boundary. Nevertheless FEM-BEM requires less mesh than FEM-DBCI (typically one or two layers of elements are inserted between the integration surface and the truncation one);

In FEM-BEM the normal derivative of the potential on the truncation boundary is introduced and treated as an independent unknown, so that the interior problem is very often a pure Neumann one. In FEM-DBCI the normal derivative is not explicitly defined, but a numerical derivative is performed in the integral equation, so that the interior problem is a Dirichlet one;

Both the resulting global algebraic systems are partly sparse and partly dense. The FEM-DBCI system can be efficiently solved in an iterative way: assuming an initial guess for the Dirichlet condition on the truncation boundary, the sparse FEM equation is solved by means of the

conjugate gradient (CG) solver; the explicit dense equation is then used to improve the Dirichlet condition; the procedure is iterated until convergence is reached; this solution strategy is efficient because the CG is applied to the sparse equation only, and the dense equation is used only a few times. An improvement on this solving method is obtained by means of the Generalized Minimal Residual (GMRES) method, as described in [4]. Recently the authors have shown that a similar GMRES-based solving strategy can also be used for the solution of FEM-BEM algebraic systems [8].

A comparison was made in [9] between the two methods, concluding that FEM-BEM is more accurate than FEM-DBCI, but requires more computing time: FEM-DBCI appears more appropriate for applications which require a shorter computing time, for example in the stochastic optimization of electrical devices, where some thousands of analyses must be performed to obtain satisfactory results. Conversely, FEM-BEM is more appropriate in cases in which a high level of precision is required in a single computation.

This paper presents a modified version of the FEM-DBCI method in order to alleviate its major drawback, that is, the insertion of some meshes between the integration and truncation surfaces. The paper is organized as follows: in Sect. II the modified FEM-DBCI formulation is described for a simple- electrostatic problem; in Sect. III the iterative solution of the resulting global system is outlined; in Sect. IV a numerical example is given which validates the method.

II. THE MODIFIED FEM-DBCI FOR ELECTROSTATICS

Consider a system of voltaged conductors, dielectric bodies and charges embedded in an unbounded vacuum. A fictitious truncation boundary Γ_F is introduced, enclosing all the conductors and dielectric bodies, but possibly leaving out some (lumped or distributed) charges. In the bounded domain D thus obtained, the Poisson equation holds:

$$-\epsilon_0 \nabla \cdot (\epsilon_r \nabla v) = \rho \quad (1)$$

where ϵ_0 is the vacuum electric permittivity, ϵ_r the relative permittivity and ρ the charge density. Equation (1) is subject to Dirichlet conditions on the conductors, whereas an unknown Dirichlet condition is assumed on Γ_F .

Discretizing the domain D by means of simplex finite elements, (1) is rewritten in matrix form as:

$$\mathbf{A}\mathbf{v} + \mathbf{A}_F \mathbf{v}_F = \mathbf{b}_0 \quad (2)$$

where: \mathbf{v} and \mathbf{v}_F are the vectors of the unknown values of the potential v in the nodes inside the domain and on the boundary Γ_F , respectively, \mathbf{A} and \mathbf{A}_F are sparse matrices of geometrical coefficients, \mathbf{b}_0 is due to the conductor potentials and internal (distributed) charges.

The integral equation at node P_i on Γ_F is:

$$c_i v(P_i) + \iint_{\Gamma_F} v(P) \frac{\partial G(P, P_i)}{\partial n} dS =$$

$$= v_{\text{ext}}(P_i) + \iint_{\Gamma_F} \epsilon_r \frac{\partial v}{\partial n} G(P, P_i) dS \quad (3)$$

where $G=1/4\pi r$ is the free-space Green function, v_{ext} is due to the external (lumped or distributed) charges, and the normal derivative is evaluated internally to D . In numerical form, equation (3) reads

$$c_i v_i + \sum_k \sum_n v_n \iint_{T_k} \alpha_n(P) \frac{\partial G(P, P_i)}{\partial n} dS =$$

$$= v_{\text{ext}}(P_i) + \sum_k \epsilon_k \sum_n v_n \iint_{T_k} \frac{\partial \alpha_n(P)}{\partial n} G(P, P_i) dS \quad (4)$$

where T_k is the triangular face of tetrahedron E_k lying on Γ_F ; index n refers to the nodes of the tetrahedron E_k , α_n are the nodal shape functions, ϵ_k is the relative permittivity of E_k , c_i is the normalized solid angle of the domain at P_i . In matrix form we obtain:

$$\mathbf{H} \mathbf{v}_F = \mathbf{G} \mathbf{v} + \mathbf{v}_{\text{ext}} \quad (5)$$

where \mathbf{H} and \mathbf{G} are dense matrices of geometrical coefficients. Note that \mathbf{H} is square by construction, whereas \mathbf{G} may be rectangular. Note also that null columns appear in \mathbf{G} for the nodes of the tetrahedra not lying on Γ_F .

III. SOLUTION OF THE GLOBAL SYSTEM

In order to solve the global system (2)-(5):

$$\begin{bmatrix} \mathbf{A} & \mathbf{A}_F \\ -\mathbf{G} & \mathbf{H} \end{bmatrix} \begin{bmatrix} \mathbf{v} \\ \mathbf{v}_F \end{bmatrix} = \begin{bmatrix} \mathbf{b}_0 \\ \mathbf{v}_{\text{ext}} \end{bmatrix} \quad (6)$$

a simple approach is the direct use of an iterative CG-like solver for non-symmetric systems of linear algebraic equations. This approach suffers from the fact that in each step of the solver the matrix-by-vector multiplication is very costly, due to the presence of dense parts in the global matrix, and the number of steps is high (typically several hundreds).

Now consider the reduced system:

$$\mathbf{M} \mathbf{v}_F = \mathbf{k} \quad (7)$$

where formally:

$$\mathbf{M} = \mathbf{H} + \mathbf{G} \mathbf{A}^{-1} \mathbf{A}_F \quad \mathbf{k} = \mathbf{G} \mathbf{A}^{-1} \mathbf{b}_0 + \mathbf{v}_{\text{ext}} \quad (8)$$

The matrix \mathbf{M} and vector \mathbf{k} are not directly available. However, the vector \mathbf{k} is simply built as follows: 1) assume a zero initial guess $\mathbf{v}_F=0$; 2) solve (2) by means of the CG solver to obtain \mathbf{v} ; 3) compute $\mathbf{k}=\mathbf{G}\mathbf{v}+\mathbf{v}_{\text{ext}}$. Similarly, matrix \mathbf{M} can be used to perform matrix-vector multiplications $\mathbf{M}\mathbf{v}_F$, as follows: 1) given the vector \mathbf{v}_F ; 2) solve (2) with $\mathbf{b}_0=0$ by means of the CG solver to obtain \mathbf{v} ; 3) compute $\mathbf{M}\mathbf{v}_F=\mathbf{H}\mathbf{v}_F-\mathbf{G}\mathbf{v}$.

Then several non-stationary CG-like solvers for non-symmetric matrices, such as BiCG (BiConjugate Gradient), QMR (Quasi Minimal Residual), CGS (Conjugate Gradient Squared), BiCGstab (BiCG stabilized) and GMRES could be used to solve (7). However, GMRES should be preferred because it performs a true minimization of the residual and thus minimizes the number of matrix-vector multiplications.

IV. A VALIDATION EXAMPLE

In order to validate the modified FEM-DBCI method a

simple two-wire transmission line is considered. The line is constituted by two parallel conducting circular cylinders of radius R whose centers are separated by a distance of $D=2.4R$, voltaged with opposite potentials $V_0/2$ and $-V_0/2$. This problem exhibits a well-known analytical solution v_a [10]. A FEM-DBCI solution is pursued in this paper by selecting the truncation boundary as constituted by two circumferences of radius $1.1R$ centered at the cylinder centers. For symmetry reasons the analysis is restricted to the first quadrant only. The domain is filled with 2 layers of elements (a total of 360 triangles). An accuracy indicator is defined as:

$$\zeta = 100 \sqrt{\iint_D (v - v_a)^2 dx dy} / \iint_D v_a^2 dx dy \quad (9)$$

where D is the domain of the FEM analysis. The end-iteration tolerances are set to 10^{-2} per cent for the GMRES and 10^{-4} per cent for the CG. Three analyses are performed using triangular elements of orders 1, 2 and 3. Curved elements are used at the conductor surface for orders 2 and 3. The accuracy indicators are $5.05 \cdot 10^{-1}$, $3.17 \cdot 10^{-1}$ and $2.85 \cdot 10^{-1}$, for the three analyses, respectively.

More details will be provided in the full paper.

REFERENCES

- [1] C. A. Brebbia, J.C.F. Telles., and L. C. Wrobel, *Boundary Element Technique*, Springer-Verlag, Berlin, 1984.
- [2] S. J. Salon, and J. D'Angelo, "Applications of the hybrid finite element - boundary element method in electromagnetics," *IEEE Transactions on Magnetics*, vol. 24, pp. 80-85, Jan. 1988.
- [3] G. Aiello, S. Alfonzetti, and S. Coco, "Charge iteration: a procedure for the finite element computation of unbounded electrical fields," *International Journal for Numerical Methods in Engineering*, vol. 37, pp. 4147-4166, Dec. 1994.
- [4] G. Aiello, S. Alfonzetti, G. Borzi, "A generalized minimal residual acceleration of the charge iteration procedure", *Journal de Physique III*, vol. 7, pp. 1955-1966, Oct. 1997.
- [5] G. Aiello, S. Alfonzetti, S. Coco, and N. Salerno, "Finite element iterative solution of skin effect problems in open boundaries," *International Journal of Numerical Modelling: Electronic Networks, Devices and Fields*, vol. 9, pp. 125-143, Jan.-April 1996.
- [6] G. Aiello, S. Alfonzetti, G. Borzi, and N. Salerno, "An improved solution scheme for open-boundary skin effect problems," *IEEE Transactions on Magnetics*, vol. 37, pp. 3474-3477, Sept. 2001.
- [7] G. Aiello, S. Alfonzetti, E. Dilettoso, "Finite element solution of eddy current problems in unbounded domains by means of the hybrid FEM-DBCI method" *IEEE Transactions on Magnetics*, vol.39,pp.1409-12, May 2003.
- [8] G. Aiello, S. Alfonzetti, G. Borzi, E. Dilettoso, N. Salerno, "Efficient solution of skin-effect problems by means of the GMRES-accelerated FEM-BEM method" *IEEE Transactions on Magnetics*, vol. 44, no. 6, pp. 1274-1277, June 2008.
- [9] G. Aiello, S. Alfonzetti, G. Borzi, E. Dilettoso, N. Salerno, "Comparing FEM-BEM and FEM-DBCI for open-boundary electrostatic problems", *The European Physical Journal - Applied Physics*, vol. 39, no. 2, pp 143-148, Aug. 2007.
- [10] E. Durand "*Electrostatique*," Masson Ed., Paris, 1968

Dynamic Simulation of Surge Corona with Time-dependent Upwind Difference Method

Wei Li, Bo Zhang, Jinliang He, Fellow, IEEE, Rong Zeng
 Department of Electrical Engineering, Tsinghua University
 Beijing 100084, China
 lwei@mails.tsinghua.edu.cn

Abstract— A method to simulate the surge corona of power transmission line is introduced. The charge simulation method (CSM) and the finite element method (FEM) are applied to calculate the electric field, while a time-dependent upwind difference (TDUD) algorithm is applied to calculate the migration of space charges. The Q-V (charge-voltage) curves of impulses applying on bundle conductors in a cage having a square cross-sectional shape are calculated. The simulation results are supported by the published experiments.

I. INTRODUCTION

Corona on overhead transmission lines is one of the key factors for the propagation characteristics of overvoltage occurring in electric power systems. When the applied voltage exceeds a certain value, corona discharge occurs and space charges are formed in the vicinity of transmission lines. Then, the space charges migrate with the electric field force and in turn affect the electric field. In the case of surge overvoltage, the corona discharge process appears as a dynamic capacitance of the transmission lines and is usually investigated by the Q-V (charge-voltage) diagrams which indicate the derivative of the charge towards the voltage.

Several computer simulation models have been proposed to reproduce the dynamic process of surge corona. Most of the models are constructed in 1-D. Menegozzi and Feldman [1] simulated a single ionizing burst in the wire-cylinder geometry. Sekar [2] used the idea of charge shells to simulate the pulsed corona discharges in the wire-cylinder geometry. Jesus [3] introduced dynamic radius of the ionization layer to explain the delay effect. In sum, the applicability of 1-D models is restricted in coaxial geometries. 2-D models are needed to deal with the practical complex geometries.

Rajanikanth [4] and Buccella [5] reported 2-D methods with uniform meshing. However, the uniform meshing leads to a huge amount of calculation with large scale geometry as line-to-ground geometry. Zhang and Adamiak [6] presented a new numerical algorithm for the simulation of the dynamic corona discharge in the 2-D point-to-plane geometry. The space charge distribution was considered as a steady state in each time step. However, the steady state is hardly reached in the transient process of surge corona.

In this work, the process of surge corona of transmission line is simulated in 2-D. The charge simulation method (CSM) and the finite element method (FEM) are applied to calculate the electric field, while a time-dependent upwind difference (TDUD) algorithm is applied to calculate the migration of space charges. The space charge distribution is calculated in a dynamic process rather than a steady state.

II. CALCULATION METHOD

A. Overview of the method

The computational process of surge corona is separated in several parts. Firstly, the corona onset field E_c is calculated with Peek's formula. Secondly, the time lag t_0 of the surge corona is calculated with the critical volume theory proposed in [7]. Then, corona inception time t_c is decided with E_c and t_0 for the given surge waveform. Thirdly, mesh of triangular elements is generated. After that, at each time step, the Laplacian field is solved with CSM; the space charge density is calculated with TDUD; the field caused by space charges is calculated with FEM; the space charge density boundary condition in the vicinity of conductor surfaces is calculated as Clade [8] suggested. These processes are executed iteratively until the last time step has been solved.

B. The governing equations

The equations that constitute the mathematical description of the surge corona are as follows. Overvoltage of positive polar is presented as example here.

Poisson's equation:

$$\nabla^2 \Phi(t) = -\rho^+(t)/\epsilon_0 \quad (1)$$

The positive and negative current density vectors:

$$\mathbf{J}(t) = -k^+ \cdot \rho^+(t) \cdot \nabla \Phi(t) \quad (2)$$

The current continuity condition:

$$\frac{\partial \rho^+(t)}{\partial t} = -\nabla \cdot \mathbf{J}(t) \quad (3)$$

where, $\Phi(t)$ is the total electric potential (V); $\rho^+(t)$ is the positive charge density (C/m^2); ϵ_0 is the permittivity of air; k^+ is the positive ion motility (m^2/Vs); $\mathbf{J}(t)$ is the ion current density vector (A/m^2).

CSM and FEM are applied to solve the Laplacian field and the field caused by the space charges. The space charge density $\rho^+(t)$ is calculated with TDUD method described as follows.

C. Time-dependent upwind difference method

By combining the equations (1) to (3), equation for solving the space charge density is obtained

$$\frac{\partial \rho^+(t)}{\partial t} = -k^+ \nabla \Phi(t) \cdot \nabla \rho^+(t) - \frac{k^+}{\epsilon_0} (\rho^+(t))^2 \quad (4)$$

In (4), the migration of space charge is solved dynamically, which is different from the stationary solution proposed in [6].

Triangular meshes are applied to discrete the calculating region. Fig. 1 illustrates the node i and the triangular mesh elements around it.

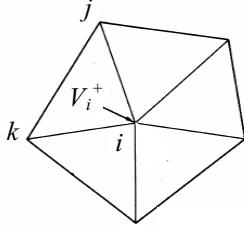


Fig. 1. Triangular mesh elements around node i .

In Fig. 1, $V_i^+(t) = -k^+ \nabla \Phi_i(t)$. $V_i^+(t)$ serves as the kinematic velocity of the positive charges. The field caused migration dominates the motion of the charges. So, the charge density of node i is mainly decided in the element opposite to the velocity direction of the positive charge. This element is called upwind element. The upwind element of node i is Δijk in Fig. 1. Then, the first-order discretized form of (4) based on upwind scheme is derived as (5).

$$\frac{\rho_i^+(t_{n+1}) - \rho_i^+(t_n)}{\Delta t} = k^+ \cdot \nabla \rho_{\Delta ijk}^+(t_n) \cdot \nabla \Phi_{\Delta ijk}(t_n) - \frac{k^+}{\epsilon_0} (\rho_i^+(t_n))^2 \quad (5)$$

Where, t_n and t_{n+1} are two adjacent points in time, Δt is the time interval between them; $\Phi_{\Delta ijk}(t_n)$ is the electric potential in Δijk on time t_n ; $\rho_{\Delta ijk}^+(t_n)$ is the charge density in Δijk on time t_n .

III. APPLICATION ON CONDUCTOR BUNDLES

The simplification of equivalent sectional radius is usually employed to deal with the conductor bundles. This may produce errors because of the change of the actual geometric boundary. Subconductors can be considered in the simulation with the method in this work. Q-V curves for positive surge corona of 4×15.25 mm radius conductor bundle in a 5.5 m square cage were presented in [9]. Impulses of 260/2300 μ s with peak voltage of 520, 610, and 700 kV were applied. The experimental and calculating results are illustrated in Fig. 2. The time step is 1 μ s. The total calculation time is 10 ms.

Fig. 2 shows that the simulation reproduces the experimental results well for voltage of 700 kV and 610 kV. However, the simulated charge quantity is lower than the experiment for voltage of 520 kV because of the overvalued inception voltage.

The meshes and the charge density distribution on the moment of 10 ms under voltage of 610 kV are illustrated in Fig. 3. It can be seen that the space charges are forced to migrate in the direction departs from the bundle center. And the migration distance of the space charges is very limited.

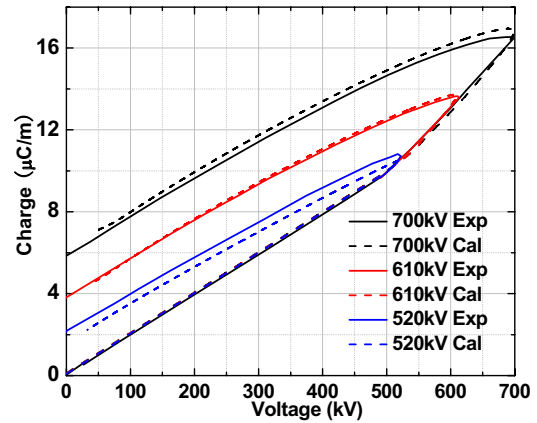


Fig. 2. Q-V curves of surge corona on conductor bundle.

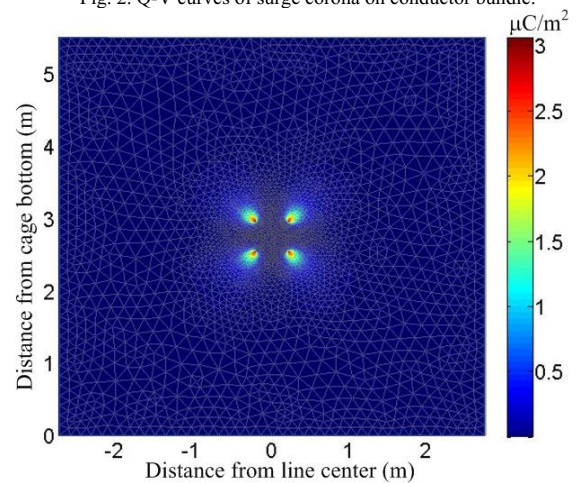


Fig. 3. Meshes and charge density distribution on the moment of 10 ms under voltage of 610 kV.

IV. REFERENCES

- [1] L. N. Menegozzi and P. L. Feldman, "The physics of pulse energization of electrostatic precipitators", *Proc. 3rd Symp. Transf. Utilization Particulate Control Technol.*, Orlando, FL, Mar. 9-13, 1981.
- [2] S. Sekar, "An investigation of pulsed corona in cylindrical and wire-plate geometries", *J. Electrostat.*, 13: 29-41, 1982.
- [3] C. Jesus and M. Barros, "Modelling of corona dynamics for surge propagation studies", *IEEE Trans. on Power Delivery*, 9(3): 1564-1569, 1994.
- [4] B. S. Rajanikanth and B. R. Prabhakar, "Modeling of prebreakdown VI characteristics of a wire-plate electrostatic precipitator operating under combined dc-pulse energization", *IEEE Trans. Dielectr. Electr. Insul.*, 1(6): 1058-1067, 1994.
- [5] C. Buccella, "Computation of V-I characteristics in electrostatic precipitators", *J. Electrostat.*, 37(4): 277-291, 1996.
- [6] J. C. Zhang and K. Adamiak, "A Single-Species Pulsed Model of Negative Corona Discharge in Air", *IEEE Trans. on Industry Applications*, 44(2):494-500, 2008.
- [7] N. Harid, R.T. Waters, "Statistical study of impulse corona inception parameters on line conductors", *IEE Proc. - Science, Measurement and Technology*, 138(3):161-168, 1991.
- [8] J. J. Clade, C. H. Gary and C. A. Lefevre, "Calculation of Corona Losses Beyond the Critical Gradient in Alternating Voltage", *IEEE Trans. on Power Apparatus and Systems*, 88(5):695-703, 1969.
- [9] P. S. Maruvada, H. Menemenlis and R. Malewski, "Corona characteristics of conductor bundles under impulse voltages", *IEEE Trans. on Power Apparatus and Systems*, 96(1):102-115, 1977.

Using Neumann Series for Reduction of Computational Effort of Quasistatic EM-Simulations

Carsten Potratz, Daniel Kluess, Robert Souffrant, Hartmut Ewald, Ursula van Rienen

Abstract—In this paper we present an approach using magnetostatic simulations and a generalized geometric series to solve a low-frequency quasistatic problem. This is applicable for systems of inductively coupled coils within the simulation domain. With this approach the discretization may be coarsened significantly thus reducing the simulation time significantly. Consequently, setups which might be beyond computational equipment at hand get computable. This proposal describes the basic theory. The final paper will furthermore include a comparison of results obtained by this approach and conventional simulations. We will also give an analysis of possible deviations.

Index Terms—Inductive coupling, simulation, reduction, numerical effort

I. INTRODUCTION

THE simulation of systems of coils in time-harmonic low frequency magnetic fields is accompanied by an increased computational effort. Especially for coils with many turns and small volumes compared to the computation domain's volume, the discretization effort and the simulation time increase significantly. In 2008 we proposed [1] the usage of an intracorporeal system of electrodes embedded in a total hip revision endoprosthesis to stimulate the growth of new bone after a failed total hip endoprosthesis has been replaced. Different studies suggested that this treatment with a low frequency electric field increases the bone proliferation rate. Aaron et al. [2] analyzed different preclinical and clinical electrostimulation studies. Most of these attest the improvement of bone healing during an electrostimulation therapy. This is applicable for different bone healing dysfunctions, especially for large bone defects caused by osteolysis around a loose, failed implant. The proposed revision cup system is equipped with numerous stimulation electrodes with embedded coils. By applying an extracorporeal oscillating magnetic field an electric field is generated in the vicinity of the endoprosthesis. However, the inherent complexity of both the acetabular region and the endoprosthesis require numerical simulations to compute the generated electric field distribution for a subsequent optimization process. Due to the low stimulation frequency (Kraus [3], 20 Hz) and small volumes of the stimulation electrodes, several hundred turns are needed for the secondary coils to induce a suitable voltage. For numerical reasons the total volume of the computational domain inhibits appropriately fine discretization of the coils unless a very powerful computer system is at hand. Therefore we developed an approach to circumvent the discretization problems and reduce the complexity by replacing the secondary coils by current sources. The amplitudes have to be modeled according to the induced voltage under consideration of the self and mutual induction effects. By applying a generalized geometric series

known as Neumann's series a reaction matrix, incorporating the induction effects, can be created. This matrix maps flux vectors from static simulations to their quasistatic counterparts. Based on these mapped fluxes, suitable current sources and short circuited induction rings are calculated. This results in the reduction of discretization effort by several magnitudes and allows for the quasistatic simulation of a problem that otherwise would be hardly computable. We present the theory as well as practical modeling examples and conclude with a comparison of results of conventional modeling and our approach under aspects of accuracy and necessary simulation/preparation time.

A. Methods

The coils within the stimulation electrodes are comprised of several hundred turns wrapped upon a ferromagnetic core. Therefore, the scattering flux of the secondary coils is minimal. The flux in the i^{th} coil generated by the primary coil is:

$$\Psi_i(t) = \hat{\Psi}_i \cos(\omega t) = \iint_{A_i} \mathbf{B}(t) \cdot d\mathbf{a}, \quad (1)$$

with \mathbf{B} denoting the primary magnetic flux density. By neglecting the reaction field of the induced current, the amplitude of the induced voltage is given by the induction law:

$$\hat{u}_i = \hat{\Psi}_i \omega n. \quad (2)$$

Here n denotes the number of coils turns and ω denotes the circular frequency. The induced current \hat{i}_i generates a reaction flux in the coil proportional to n and \hat{i}_i :

$$\hat{\Psi}_{re,i} = \alpha \hat{i}_i n, \quad (3)$$

with a scaling factor α representing the coils geometry. For identical secondary coils α has the same value for all coils. The ratio of the induced voltage and current is given by Ohm's law:

$$|Z_i + R_w n + j\omega L| = \frac{\hat{u}_i}{\hat{i}_i} \quad (4)$$

with Z_i denoting the outer impedance created by the conductive tissue. R_w and $j\omega L$ denote the coils ohmic resistance and self inductance respectively. The self inductance is proportional to n^2 with the proportionality factor l depending on the geometry of the coil:

$$L = l n^2. \quad (5)$$

A ratio expressing the reaction of the coil to a primary flux can be derived from (2) and (3):

$$c_{ii} := \frac{\hat{\Psi}_{re,i}}{\hat{\Psi}_i} = \frac{\alpha \omega n^2}{|Z_i + R_w n + j\omega l n^2|}. \quad (6)$$

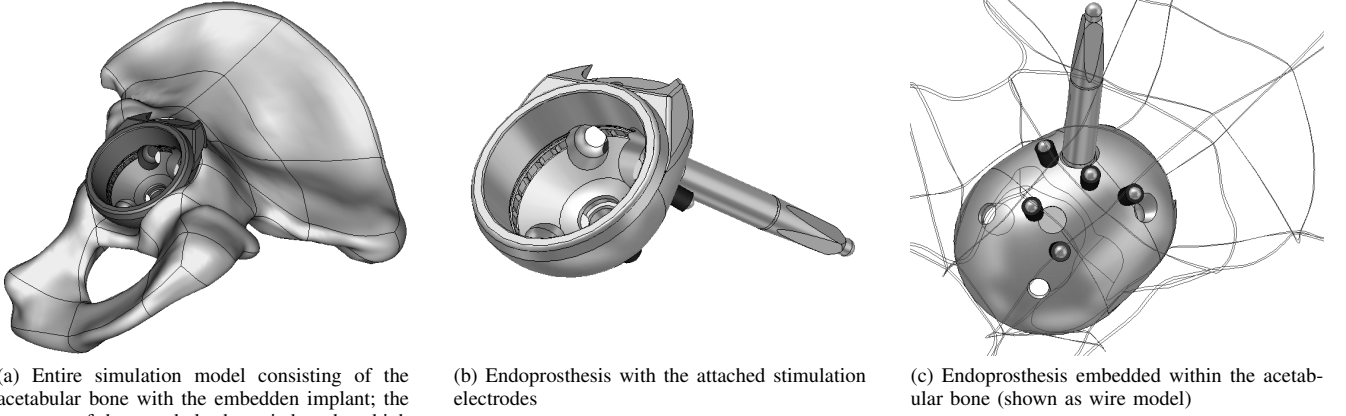


Fig. 1. Simulation model for the optimization process

Similarly a mutual reaction factor can be defined using the i^{th} coil for magnetic excitation:

$$c_{ji} := \frac{\Psi_{re,j}}{\Psi_i}. \quad (7)$$

This ratio describes the reaction of the j^{th} coil to the current flowing through the i^{th} coil. All reaction factors defined above form a matrix:

$$\mathbf{C} = \begin{pmatrix} c_{11} & \dots & c_{1N} \\ \vdots & \ddots & \vdots \\ c_{N1} & \dots & c_{NN} \end{pmatrix}. \quad (8)$$

With this matrix the self and mutual induction effects can be expressed as infinite series:

$$\Psi_{\mathbf{S}} := \begin{pmatrix} \Psi_{S1} \\ \vdots \\ \Psi_{Sn} \end{pmatrix} \quad \Psi_{\mathbf{Q}} := \begin{pmatrix} \Psi_{Q1} \\ \vdots \\ \Psi_{Qn} \end{pmatrix} \quad (9)$$

$$\Psi_{\mathbf{Q}} = \Psi - \mathbf{C}\Psi_{\mathbf{S}} + \mathbf{C}^2\Psi_{\mathbf{S}} - \dots + = \sum_{i=0}^{\infty} (-1)^i \mathbf{C}^i \Psi_{\mathbf{S}}$$

with $\Psi_{\mathbf{S}}$ and $\Psi_{\mathbf{Q}}$ denoting the fluxes through the secondary coils extracted from a magnetostatic simulation and the expected fluxes of a quasistatic simulation respectively.

Due to conservation of energy the norm of \mathbf{C} has to be less than one. Therefore partial sum of eq. (9) is given as:

$$\sum_{i=0}^{\infty} (-1)^i \mathbf{C}^i = (\mathbf{I} - \mathbf{C})^{-1} \text{ while } \|\mathbf{C}\| < 1 \quad (10)$$

The resulting fluxes $\Psi_{\mathbf{Q}}$ are given by:

$$\Psi_{\mathbf{Q}} = (\mathbf{I} - \mathbf{C})^{-1} \Psi_{\mathbf{S}} \quad (11)$$

Based on the flux vector $\Psi_{\mathbf{Q}}$ and eq. (2), the secondary coils in the simulation model are replaced by current sources. They generate the same current density in the electrode's vicinity while the discretization effort is highly reduced.

The secondary coils cannot be omitted entirely. The distortion of the primary magnetic field due to the secondary

coils and the generated eddy current distribution has also to be accounted for. Equation (3) states that the reaction flux is proportional to the current flow and the number of turns. Therefore, the turns wrapped around the ferromagnetic core were replaced by a conductive hollow cylinder. The conductivity of the used material has to be adapted, such that the induced eddy currents equals n times the current of the equivalent current sources. This guarantees that the distortion of the primary magnetic field is similar to that of the original problem.

II. CONCLUSION

The presented approach requires a series of simulations to extract the necessary geometric parameters and reaction ratios. Yet, the discretization of the simulation model may be rather coarse and the overall numerical effort is acceptable. Main advantage of this procedure is that the whole setup of the endoprosthesis within the acetabular bone and the surrounding tissue may be simulated without the need for a high-performance supercomputer.

ACKNOWLEDGMENT

The authors would like to thank Dr. Hans-Walter Glock and Dr. Gisela Pöplau for helpful discussion.

REFERENCES

- [1] C. Potratz, H.-W. Glock, R. Souffrant, R. Bader, H. Ewald, U. van Rienen, "Periprosthetic Fields and Currents of an Electrostimulative Acetabular Revision System." *IFMBE Proceedings*, no. 22, pp. 1808–1811, 2008.
- [2] R. Aaron, D. Ciombor, B. Simon, "Treatment of nonunions with electric and electromagnetic fields." *Clinical Orthopaedics and Related Research*, no. 419, pp. 21–29, 2004.
- [3] W. Kraus, "Magnetfeldtherapie und magnetisch induzierte Elektrostimulation in der Orthopädie," *Orthopädie*, vol. 13, pp. 78–92, 1984.

Exposure of working population to pulsed magnetic fields

Aldo Canova, Fabio Freschi, Luca Giaccone, Maurizio Repetto
 Dipartimento Ingegneria Elettrica
 Politecnico di Torino
 I-10129 Torino, Italy
 Email: name.surname@polito.it

Abstract—Reference values of exposure for working population at extremely low frequency electromagnetic fields have been stated in ICNIRP Guidelines of 1998, and accepted by European Parliament in 2004. Nevertheless, quantification of coupling mechanism under pulsed field conditions is still an open question. The effect of complex non-sinusoidal or non-periodic waveforms is not univocally defined and several ways of estimating it have been proposed. This paper compares different ways of assessing effects of pulsed electromagnetic fields with frequency spectrum below 100 kHz and compare them to the eddy currents induced in one realistic model of human body by a resistance spot welding system supplied by in pulsed medium frequency direct current mode.

I. INTRODUCTION

Protection of working population against the possible effects of extremely low frequency (ELF) electromagnetic fields is a concern of European Community which has published in 2004 Directive 2004/40/EC [1]. The Directive refers to the risk to the health and safety of workers due to known short-term adverse effects in the human body caused by the circulation of induced currents and by energy absorption as well as by contact currents. One of the most important points stated in the Directive is the rationale of exposure at low frequency which is defined in accordance with ICNIRP 1998 guidelines [2]. These Guidelines report that in the ELF frequency range, the risk to the health and safety of workers is due to known short-term adverse effects caused by the circulation of induced currents in the human body. The evaluation of eddy currents is not an easy task, involving the electromagnetic study of a complex system like the human body.

While continuous wave mode of exposure is strictly defined in ICNIRP guidelines, the evaluation of eddy currents induced in human body by pulsed or non-sinusoidal magnetic field waveforms is still an open question. In 1998 ICNIRP guidelines, the problem of non-sinusoidal waveforms was tackled by means of superposition of harmonic values. This approach, even if possible, has been highly criticized afterwards because of an excessive conservative estimates of exposure levels. Due to the increasing importance of non-sinusoidal sources of magnetic fields, in 2003 ICNIRP has published a new guideline for pulsed and complex non-sinusoidal waveforms [5]. This document addresses the exposure evaluation in non-sinusoidal conditions by means of proper weighting factors to be applied to different harmonic components of the waveform

spectrum and by focusing more precisely the time derivative of magnetic flux density as the most important cause of biological interaction. Notwithstanding this correction to the previous 1998 Guidelines, also this approach has been considered not particularly effective for the representation of the real interaction mechanism with nervous stimulation caused by induced eddy currents. In 2007 Heinrich [3], in fact proposes a new set of weighting coefficients more strictly related to the process of electrostimulation of nervous tissues. By resorting to a biomedical equation which states the inverse relation between duration of eddy currents and cell membrane excitation, very short pulses, even with relatively high amplitudes, are considered less effective in causing dangerous nervous excitations.

Even if all these techniques address in depth the interaction between source magnetic flux density and tissues, they consider only very rough models of the human body. All considerations are in fact related to simple circular loops representing the path of eddy currents inside the body, considered as homogeneous in electrical conductivity.

The use of electromagnetic analysis tools for assessing the exposure levels is possible and this fact opens an opportunity of application to this topic of numerical tools. Several difficulties are present at this stage: modelling of external magnetic fields and of the human body are not an easy task. In the following the main simplification hypotheses that can be adopted in the computation of eddy currents are described and then the application of numerical evaluation tools to an industrial case of resistance spot welding, which is working in a pulsed way, is presented and discussed.

II. EVALUATION OF INDUCED EDDY CURRENTS IN HUMAN BODY

The Scalar-Potential Finite-Differences (SPFD) method for the calculation of induced current densities inside the human body has been introduced in [6]. This approximated approach is valid when the magnetic field created by induced currents is small with respect to the one created by source currents. Under this hypothesis, the magnetic field distribution is not perturbed by eddy currents and so it can be computed independently on the conducting body. By making reference to the standard notation for discrete operators introduced in [7] the problem can be formulated in algebraic form as follows.

Solenoidality of eddy currents (since displacement currents are neglected) imposes that:

$$\tilde{\mathbf{D}}\mathbf{i} = \mathbf{0} \quad (1)$$

where $\tilde{\mathbf{D}}$ is the discrete expression of divergence operator and \mathbf{i} is the vector of induced eddy currents. Electromagnetic induction law can be expressed in terms of magnetic vector potential:

$$\mathbf{u} = -\mathbf{G}\varphi - \frac{d\mathbf{a}}{dt} \quad (2)$$

where \mathbf{G} is the discrete expression of gradient operator, \mathbf{u} are induced electro-motive forces, φ is the vector of electric scalar potential and \mathbf{a} is the array of magnetic vector potential. Electrical constitutive equation can be written as:

$$\mathbf{i} = \mathbf{M}_\sigma \mathbf{u} \quad (3)$$

where \mathbf{M}_σ is the discrete expression of Ohm's law. By inserting (3) in (1) and using (2) together with duality relations $\tilde{\mathbf{D}} = -\mathbf{G}^T$ [7]:

$$\mathbf{G}^T \mathbf{M}_\sigma \mathbf{G} \varphi - \mathbf{G}^T \mathbf{M}_\sigma \frac{d\mathbf{a}}{dt} = \mathbf{0} \quad (4)$$

Finally, by exploiting the hypothesis that magnetic flux would not be modified by eddy currents, magnetic part of (4) is a known term so that previous equation can be rewritten as:

$$\mathbf{G}^T \mathbf{M}_\sigma \mathbf{G} \varphi = -\mathbf{G}^T \mathbf{M}_\sigma \frac{d\mathbf{a}_s}{dt} \quad (5)$$

where \mathbf{a}_s is the magnetic vector potential due to imposed current sources.

Under sinusoidal steady-state (with angular frequency ω), previously defined variables become phasors and (5) becomes:

$$\mathbf{G}^T \mathbf{M}_\sigma \mathbf{G} \hat{\varphi} = -j\omega \mathbf{G}^T \mathbf{M}_\sigma \hat{\mathbf{a}}_s \quad (6)$$

III. HUMAN BODY MODEL

The choice of a suitable human model is not a standardized task. In fact, possible 3D models may have different spatial resolutions and tissue properties are not well assessed. A realistic model is the "Hugo" 3D anatomical data set which is a discretization of the body of a 38 year old man of about 180 cm height [8]. Many resolutions are available from $8 \times 8 \times 8$ mm down to $1 \times 1 \times 1$ mm voxels and 31 tissues with their electrical properties are defined.

IV. RESISTANCE SPOT WELDING SYSTEM

Welding systems are characterised by high values of currents and by non-sinusoidal waveforms, thus their effects of exposure must be evaluated by means of particular techniques [4]. Resistance spot welding system supply system is often based on medium frequency direct current (MFDC). In MFDC technique, the primary current is regulated by a three phase inverter and the secondary current is rectified by a diode bridge.

The welding gun was placed at a distance of 1.5 m from the body. Supply current value was set to a maximum value of 20 kA rms with the waveform shown in Fig. 1. Evaluation

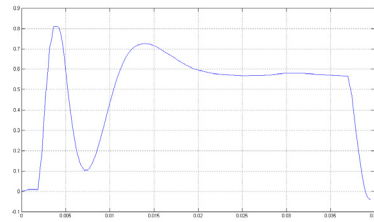


Fig. 1. Behavior of the secondary transformer current with MFDC supply: abscissas in seconds and normalized.

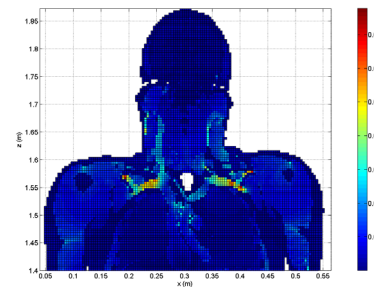


Fig. 2. Detail of induced eddy currents in Hugo model using the 4 mm voxel model.

of eddy currents has been performed by means of harmonic summation, as proposed in [2], using its frequency spectrum and by means of time-stepping technique as previously proposed in (5). In Fig. 2, the color map of induced eddy currents at the highest value of eddy current is shown. An accurate comparison of results will be presented in the full paper.

REFERENCES

- [1] Directive of the European Parliament, of the Council of 29 April 2004, "On the minimum health and safety requirements regarding the exposure of workers to the risks arising from physical agents (electromagnetic fields)"
- [2] The International Commission on Non-Ionizing Radiation Protection, "Guidelines for limiting exposure to time-varying electric, magnetic, and electromagnetic fields (up to 300 GHz)", Health Physics, April 1998, Vol. 74, No. 4, pp. 494-522.
- [3] H. Heinrich, "Assessment of non-sinusoidal, pulsed or intermittent exposure to low frequency electric and magnetic fields", Health Physics, June 2007, Vol.92, No. 6, pp. 541-546.
- [4] D. Desideri, A. Maschio, P. Mattavelli, "Human exposure to pulsed current waveforms below 100 kHz", EMC Europe Proceedings, Sept 8-12, 2008.
- [5] The International Commission on Non-Ionizing Radiation Protection, "Guidance on determining compliance of exposure to pulsed and complex non-sinusoidal waveforms below 100 kHz with ICNIRP guidelines", Health Physics, March 2003, Vol. 84, No. 3, pp. 383-387.
- [6] T. Dawson, K. Caputa, "Evaluation of eddy currents in human beings", Physics in Medicine and Biology 47, 2561 (2002)
- [7] E. Tonti, "Finite Formulation of Electromagnetic Field", IEEE Trans. Magnetics, Vol. 38, No. 2, March 2002, pp. 333-336
- [8] F. Sachse, C. Werner, C. Waarden, O. Dossel, Computerized Medical Imaging and Graphics 24, 165 (2000)

Comparative Study applying Constant Current Source and Constant Voltage Source to Treat Cancer using the Electrochemical Therapy

M. Telló¹, L. Oliveira², R.T. Oliveira³, O. Parise⁴, A. C. Buzaid⁴, R. Zanella³, R. H. Bittencourt¹, A. Cardona¹

¹Pontifical Catholic University of Rio Grande do Sul, Porto Alegre, RS, Brazil

²Veterinary Teaching Hospital, Federal University of Rio Grande do Sul, Porto Alegre, RS, Brazil

³Federal University of Rio Grande do Sul, Porto Alegre, RS, Brazil

⁴Sirio Libanês Hospital, SP, Brazil

Av. Ipiranga 6681, 90619-900, Brazil

E-mail: tello@puers.br

Abstract - Electrochemical Therapy (in short EChT) is a technique used to treat cancer by applying a small constant electric current or low level constant voltage. The EChT treatment effectiveness depend on Dose (charge) imparted into the cancer region [Dose (Coulomb) = Current (Ampère) x time (second)], beyond the accuracy of electrodes insertion (vertical or parallel electrodes direction into the cancer region), the number and the distribution of electrodes into cancer area. Our researches indicate that Doses greater than 20 C/cm³ are desirable to treat cancer using EChT. The principal aim of this paper is to show the studies done applying Constant Current Source (CCS) and Constant Voltage Source (CVS) in *ex-vivo* experiments of canine mammary cancer. We performed *ex-vivo* experiments using CCS and CVS for EChT 'standard', monopolar and cerclage electrodes disposition. This study was basically designed to evaluate what scheme (CCS or CVS) increase the delivered charge to the cancer region during EChT, enhancing the treatment efficacy. CCS has been used by our group since 2001, applying EChT *in vivo*. There have been no investigations comparing CCS and CVS to treat cancer using EChT. We investigate the amount of dose deposited at each electrode disposition using CCS and CVS. In the cerclage electrode disposition connected to a CVS; there is a highest amount of dose imparted into cancer area compared with other electrodes disposition and electrical sources schemes.

I. INTRODUCTION

EChT procedures involve placing electrodes into cancer region and connecting the electrodes to CCS or CVS. Current flowing through electrodes into the cancer starts an electrolytic process[1], [2]. Electrochemical products of electrolysis are formed destroying cancer cells by creating toxic products in the vicinity of the electrodes. The important advantage of this treatment is that the electric current is applied locally, with no systemic side effects.

Our research group in October of 2001 started the EChT studies. The EChT experiments were conducted *in vivo* (animals that acquired the malignant tumor during their life, that means, spontaneous cancer). Indeed, we use CCS for *in vivo* experiments. We perform a statistical analysis of our EChT experiments. So, the software SPSS – version 11.5 was used. The total number of animals

statistically evaluated (animals submitted to the EChT) was 79 (147 tumors), having different types of neoplastic disease. It's important to point out that in the number of animals statistically evaluated the spontaneous head and neck tumors of cats and dogs are not included. Statistical analysis of head and neck tumors was done in previous paper [3]. Sensitivity and Specificity are statistical measures well known in scientific area. The sensitivity is the proportion of actual "positives" which are correctly identified as such, and the specificity is the proportion of "negatives" which are correctly identified. Having these concepts in mind, the sensitivity for the Dose k was defined as the proportion of cases with dose $\geq k$ among patients cured and the specificity was the proportion of cases with dose $< k$ among patients not cured. Graph showing the sensitivity and specificity is called Receiver Operating Characteristic curve or simply ROC curve. The ROC curve allows to identify the doses (or other parameter of interest) cut points that maximize the estimated probability of cure. For the *in-vivo* experiments conducted by our research group since 2001, Fig. 1a and 1b shows the obtained ROC curves for EChT Response x Applied Dose and for EChT Response x Cancer Volume, respectively.

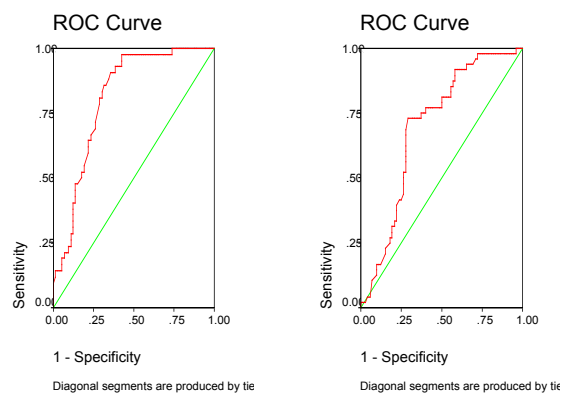


Fig. 1. EChT Response x Dose.

Fig.1b – EChT x Volume.

Fig. 1. EChT Statistical Analysis.

According ROC Curve the "ideal/optimum" dose is situated among 20.8 and 23.9 C/ cm³ (Fig. 1a). Indeed, volumes smaller than 6.35 cm³ the Sensibility is

approximately 73% (Fig. 1b). That means, among all cured tumors 73% shown volume smaller or equal than 6.35 cm³. About Specificity, our evaluation indicates that among all non-cured tumors, 70% had volume greater than 6.35 cm³. Results shown in Fig. 1 were obtained using CCS scheme. However, doubts arise: what is the difference in EChT treatment effectiveness using CCS or CVS schemes? Reminding, EChT treatment effectiveness depend of the Dose (charge) imparted into the cancer region [Dose (Coulomb) = Current (Ampère) x time (second)], beyond the accuracy of electrodes insertion (vertical or parallel electrodes direction into the cancer region), the number and the distribution of electrodes into cancer area.

II. EChT EX-VIVO EXPERIMENTS

EChT *ex-vivo* experiments were performed using equipment which constant electric current and constant voltage modes are possible. So, current (CCS) and voltage (CVS) operations modes can be adjusted in the equipment. With this equipment, the range of electric current and voltage are 0-100.0 mA and 0-30V, respectively. In this study, *ex vivo* fresh mass of different types of dog's mammary cancer were used. The cancer mass was obtained by surgical resection of dog's mammary glands. Each mammary cancer mass was divided in six small pieces. The volume of each piece is approximately 4.2 cm³. So, fresh cancer mass was divided in six samples. It's important to say that samples with necrosis were discarded. Samples 1, 3 and 5 (odd samples) forms the *group 1*, which electrodes dispositions are connected to a CCS. Samples 2, 4 and 6 (even samples) forms the *group 2*, connected to a CVS. The electrodes dispositions used in these experiments were: (a) 'Standard' EChT electrode disposition: Anodic and Cathodic electrodes into the tumor, 1.0cm apart (samples 1 and 2); (b) EChT monopolar: Anodic electrode into the tumor and Cathodic electrode outside the tumor (samples 3 and 4) and (c) EChT Cerclage: Anodic electrode connected to the wire and Cathodic electrode outside the tumor (samples 5 and 6). In the 'Standard' and monopolar EChT electrodes schemes Platinum (90%) and Rhodium (10%) electrodes were used. Steel wire was used in EChT cerclage scheme. Fig. 2 shows the electrodes dispositions. In this figure, the number after the letter N indicates the fresh masse under test following the sample number. For example, N2.6 represents the second fresh mass under test, EChT cerclage electrode disposition is been evaluated and we are using the CVS scheme.



Fig. 2a – 'Standard' EChT electrode disposition: Anode and Cathode into the tumor (Samples 1 & 2).
 Fig. 2b – Monopolar electrode disposition: anode into the tumor and Cathode outside (Samples 3 & 4).
 Fig. 2c – Cerclage disposition: anode connected to the wire and cathode outside the tumor (Samples 5 & 6).

Fig. 2. Electrodes dispositions for groups 1 and 2.

Applying CCS scheme to samples of group 1, the equipment was adjusted to produce an initial voltage of 5 Volts. The electric current obtained with 5Volts is the Constant Current (DC current) flowing into the cancer samples during the experiment. The voltage was recorded every 1 min for 10 min during electrochemical therapy. On the other hand, applying CVS scheme to samples of group 2, the equipment was adjusted to produce a constant voltage of 5Volts during the experiment. The electric current was recorded every 1 min for 10 min during EChT. The charges (doses) delivered to the samples were calculated by integration of the electric current versus treatment time (10 min). After the experiment, the sample was sent for pathological examination.

III. RESULTS

Distinct behavior was verified applying CCS and CVS schemes to the samples. In all fresh mass of group 1 (CCS), the voltage between electrodes decreased gradually during the experiment. On the other hand, using the CVS scheme (group 2) the current flowing by the all cancer samples increased during the experiment. The EChT efficacy is enhanced maximizing the charge delivered to the cancer region. Table 1 shows for the second fresh mass under test some obtained results. Similar results were obtained for all fresh cancer mass evaluated.

TABLE I
DOSE COMPARATIVE RESULTS.

SOURCE TYPE/ SAMPLE (*)	CCS/ 1	CVS/ 2	CCS/ 3	CVS/ 4	CCS/ 5	CVS/ 6
TUMOR RESISTANCE VARIATION (Ω)	25.0	116.4	27.9	147.0	121.7	129.4
DOSE (C)	4.8	3.1	4.7	4.9	5.5	17.75

(*) **Samples 1 & 2:** Anode and Cathode Electrodes into the tumor; **Samples 3 & 4:** Monopolar Electrodes disposition, **Samples 5 & 6:** Cerclage electrode disposition.

IV. CONCLUSION

We agree that up to now there have been no investigations comparing CCS and CVS schemes to treat cancer using EChT. Important conclusion is that the EChT cerclage electrode configuration applying CVS scheme increase the treatment efficacy, because the charge delivered (dose) is greater than the others tested electrodes dispositions and sources of electrical energy.

V. REFERENCES

- [1] Telló, M., Dias, G. A. D., Cardona, A. V., Raizer, A., "Tumor Compression Due Application of DC Current", IEEE Transactions on Magnetics, 37, 2001, pp. 3753-3756.
- [2] Telló, M., Oliveira, L. O., Parise, O., Buzaid, C. A., Oliveira, R. T., Zannela, R., Cardona, A., "Electrochemical Therapy to Treat Cancer (in vivo Treatment)", 29th IEEE EMBS Annual International Conference of IEEE, Lyon, France August 23-26, 2007, pp. 3524-3527.
- [3] Parise, O., Oliveira, L. O., Telló, M., Gioso, M. A., Buzaid, A. C., "Electrolysis and Electrochemical Therapy in the Treatment of Spontaneous Head and Neck Tumors of Cats and Dogs", Annual Meeting & Research Workshop on the Biology, Prevention and Treatment of Head and Neck Cancer, August, 2006.

Calculation of Poynting Vector and Analysis on the Energy Transfer of Transmission Line

Fan Yang¹, Wei He¹, Yuxin Yun² and Dongping Xiao¹

1. State Key Laboratory of Transmission and Distribution Equipment and System Security and New Technology,
Chongqing 400044, China

2. Shandong Electrical Power Research Institute,
Jinan 250002, China

E-mail: yangfancqu@gmail.com

Abstract—A novel method to analyze the energy transfer efficiency of the HV transmission lines is presented in the paper based on the Poynting Vector (PV) distribution around the transmission lines, which can avoid the calculation of the circuit parameters of the transmission lines. The charge simulation method and current simulation method were used to compute the distribution of the PV distribution around the transmission lines, and the influence on the PV distribution caused by the distance of the phase conductors was investigated.

I. INTRODUCTION

With the installed capacity of electric power system around the world, many new techniques have been investigated for the transmission lines [1], such as compact transmission lines, FACTS, and UHV DC transmission lines. In the investigation of new type transmission lines, analysis on the energy transfer efficiency is necessary, and all the analysis on the energy transfer efficiency were carried out from the view of circuit at present, which need to compute the circuit characteristics parameters, and the load of the transmission lines should be given.

The Poynting Theory indicates that the energy is transferred by the electromagnetic field around the transmission lines, and the transmission lines only determine the direction of the energy transfer [2]. In addition thermal loss rises up inside the transmission lines.

In the paper a novel method to analyze the energy transfer efficiency of the transmission lines is presented based on the PV distribution around the transmission lines, and the charge simulation method and current simulation method were used to compute the distribution of the PV around the transmission lines. In addition, the influence on the PV distribution caused by the distance of the phase conductors was investigated.

The numerical calculation on the PV distribution around a 500 kV double-circuits was carried out firstly, and results indicate that the PV distribution changes with the distance between the phase conductors. When the distance between the phase conductors reduces to a certain degree, the average longitudinal component of the PV reduced from 2.347×10^3 to 2.196×10^3 W/m², even the maximum value change from 2.59×10^5 W/m² to 3.23×10^5 W/m². Therefore for the design of HV transmission lines, the PV distribution around the transmission lines can be computed to analyze the energy transfer efficiency, based on which measures to increase the energy transfer efficiency can be obtained.

II. COMPUTATIONAL METHOD

According to the definition of PV, $\mathbf{S}=\mathbf{E} \times \mathbf{H}$, the PV \mathbf{S} can be computed in the following way: Firstly in the Cartesian coordinate system, the three components E_x , E_y , E_z of the electric field strength \mathbf{E} and the three components H_x , H_y , H_z of the magnetic field strength \mathbf{H} around the transmission lines can be computed, then with the calculated E_x , E_y , E_z and H_x , H_y , H_z , \mathbf{S} can be calculated.

For the calculation of E_x , E_y , E_z and H_x , H_y , H_z , the charge simulation method can current simulation method were adopted respectively.

According to the charge simulation method and the geometry characteristics of transmission lines, the electric field strength in the vicinity of them can be calculated according to equation (1).

$$\begin{aligned} [P][Q] &= [U] \\ [E_x] &= [f_x][Q] \\ [E_y] &= [f_y][Q] \\ [E_z] &= [f_z][Q] \end{aligned} \quad (1)$$

Where $[P]$ is potential coefficient of matching points; $[Q]$ is size of the simulation charges; $[U]$ is potential at matching points; $[f_x]$, $[f_y]$ and $[f_z]$ are electric field strength coefficient along x , y , z axis. $[E_x]$, $[E_y]$ and $[E_z]$ are the corresponding electric field strength.

According to the current simulation method, the magnetic field strength around the transmission lines can be computed according to equation (2).

$$\begin{aligned} [\beta][I] &= [A_m] \\ [A] &= [\beta][I] \\ \mathbf{H} &= \frac{1}{\mu}(\nabla \times \mathbf{A}) \end{aligned} \quad (2)$$

Where $[\beta]$ is the magnetic coefficient, $[A_m]$ is the magnetic vector at the matching points, and $[A]$ is the magnetic vector at measuring points.

III. RESULT AND ANALYSIS

A 500kV double-circuits transmission lines as shown in Fig.1 was taken as an example for the calculation of the PV distribution firstly, then the influence on the PV distribution around the transmission lines caused by the distance between the phase conductors was investigated.

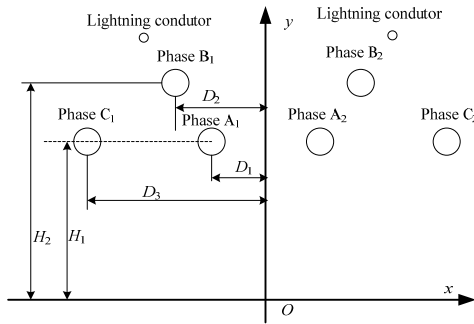


Fig.1 Cross section of a 500kV double-circuits transmission lines

The parameters of the model in Fig.1 are as follows: D_1 , D_2 , D_3 are the distance between the phase conductors and y -axis, and $D_1=4.5\text{m}$, $D_2=5.5\text{m}$, $D_3=11.5\text{m}$. H_1 and H_2 are the height of the phase conductor, and $H_1=20\text{m}$, $H_2=25\text{m}$. For each phase conductor, 4 bundle conductors were used, and the radius of the sub-conductor $r=0.0148\text{m}$, the split radius $R'=0.323\text{m}$, and the radius of the lightning conductor $R'_L=0.0054\text{m}$. To simply the calculation, the influence caused by the arc sag was ignored, hence the electric field and magnetic field produced by the transmission lines can be solved as two dimensional field.

Firstly the PV distribution around the transmission lines when the y -coordinate of each phase conductor are 20m, 25m, 20m, 20m, 25m, 20 m, 30m, 30m respectively. As mentioned above, the E_x , E_y , E_z and H_x , H_y , H_z were calculated firstly, then PV S was computed, and Fig.2 shows the longitudinal component of PV S_z around the transmission lines, it can be seen that the main power energy is transferred near the transmission lines. The maximum value of the S_z is $2.59 \times 10^5 \text{ W/m}^2$, and with the increase of the distance of the measuring points between the transmission lines, the value of S_z decreases.

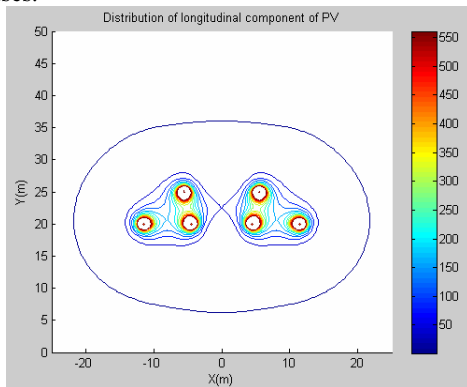


Fig.2 Distribution of S_z when the y -coordinate of each phase conductor are 20m, 25m, 20m, 20m, 25m, 20 m, 30m, 30m

To investigate the influence on the PV distribution and energy transfer efficiency caused by the change of the distance between the phase conductors, the PV distribution around the transmission lines were calculated when the distance between the phase conductors was changed, for which the y -coordinates of each phase conductors are 20m, 22.5m, 20m, 20m, 22.5m, 20m, 30m, 30m, and Fig.3 shows

the distribution of the S_z , and the maximum value of the $3.23 \times 10^5 \text{ W/m}^2$.

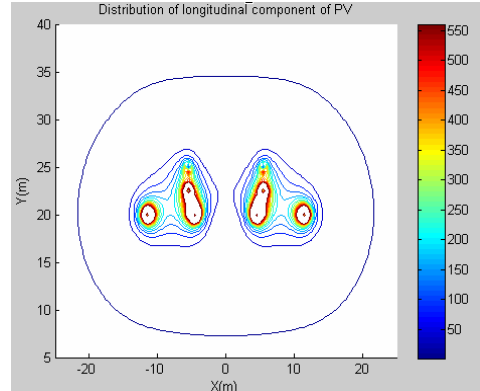


Fig.3 Distribution of S_z when the y -coordinate of each phase conductor was changed

To evaluate the energy transfer efficiency of the transmission lines, an average value of the longitudinal component is set as S_{zav} , which is the average value of 10201 points in the vicinity of the transmission lines shown in Fig.1, and the $S_{zav1}=2.347 \times 10^3 \text{ W/m}^2$ for the first case, and $S_{zav2}=2.196 \times 10^3 \text{ W/m}^2$ for the second case, which means that the energy density around the transmission lines decreases, even though the maximum value of longitudinal component of PV S_z increases from $2.59 \times 10^5 \text{ W/m}^2$ to $3.23 \times 10^5 \text{ W/m}^2$. Therefore the energy transfer efficiency of the transmission lines decreases. Therefore for the design of the HV transmission lines, to increase the energy transfer efficiency, the distance between the phase conductors can be analyzed according to the PV distribution around the transmission lines.

IV. CONCLUSION

A novel method to analyze the energy transfer efficiency of the HV transmission lines is presented in this paper based on the PV distribution around the transmission lines, which can avoid the calculation of the circuit parameters of the transmission lines. The PV distribution around a 500 kV double-circuits was computed, and results indicate that the PV distribution changes with the distance between the phase conductors. When the distance between the phase conductors reduces to a certain degree, the average longitudinal component of the PV reduced from 2.347×10^3 to $2.196 \times 10^3 \text{ W/m}^2$, which means that the energy transfer efficiency decreases.

V. REFERENCES

- [1] Zhou Xianzhe; Liu Guangye. Survey on New Technologies of Electric Power Transmission and Transformation. Guangxi Electric Power. 2006, 2, pp. 5-11. (In Chinese).
- [2] Emanuel, A.E. Poynting Vector and the Physical Meaning of Nonactive Powers. IEEE Transactions on Instrumentation and Measurement, 2005, vol.54 (4), pp.1457-1462.

A Particle Trajectory Code using the FEM approach: preliminary results

¹César C. Xavier and ²Cláudio Costa Motta

¹Instituto de Pesquisas Energéticas e Nucleares/CNEN-SP and ²Universidade de Sao Paulo
Av. Lineu Prestes 2242 – Cid. Universitária - Sao Paulo – 05508-000 – Brazil

¹cesarcx@usp.br, ²ccmotta@usp.br

Abstract—A numerical code based on Finite Element Method (FEM) developed to study the focusing properties of electrostatic lenses for non-relativistic electrons trajectories on a two-dimensional electron gun with cylindrical symmetry is presented. In order to apply the FEM, the Galerkin Weak Formulation was used. A Delaunay triangulation of the domain was built, and using FEM, the sparse system was solved for the scalar potential associated to the nodes. To solve the non-linear second order electron path differential equation, a fourth-order Runge-Kutta integrator is used. It's shown that absolute paths errors were below $1.5 \times 10^{-4}\%$, even with a modest discretization of the total space domain.

Index Terms—Finite Element Method, electron path, electron gun.

I. INTRODUCTION

The focusing properties of electron guns to be used in power microwave tubes can be investigated analysing the charge-particle path equation. The particle paths in electron gun are important because they establish the beam edge, the beam waist and beam waist distance from the anode. For this purpose many gun codes, such as [1]-[3], were developed.

In this work it is proposed a methodology to solve the electron steady-state self-consistent space-charge on electron guns from path instead of the equations of motion in axially symmetric field.

The finite element formulation and the derivation of the second order differential equation for non-relativistic charged-particle path are described. The code has been benchmarked and the most relevant results are also presented.

II. THE THEORETICAL PHYSICAL PROBLEM DESCRIPTION

A. Physical Formulation

Starting with the Lorentz force and energy conservation equations, the charged-particle path is obtained by elimination of the time variable. In order to obtain the scalar potential, a code using FEM with first order triangle elements was developed. The axially symmetric electron path steady-state flow can be described by the Poisson equation for the scalar potential $V(r, z)$:

$$\nabla^2 V = \frac{1}{r} \frac{\partial}{\partial r} \left(r \frac{\partial V}{\partial r} \right) + \frac{\partial^2 V}{\partial z^2} = -\frac{q}{\epsilon_0} \sum_i \frac{\delta(r - r_i) \delta(z - z_i)}{2\pi r_i} \quad (1)$$

were the right hand side is due to the space-charge, i.e, q represents the macro particle charge transported by the beam

current of the electron gun located at (r_i, z_i) position, and $\delta(r - r_i)$ and $\delta(z - z_i)$ denote the Dirac delta function.

From the scalar potential, the electric field \vec{E} , is given by:

$$\vec{E} = -\nabla V = -\left(\frac{\partial V}{\partial z} \hat{z} + \frac{\partial V}{\partial r} \hat{r} \right) = -E_z \hat{z} - E_r \hat{r} \quad (2)$$

The charged-particle path is obtained using the Lorentz force, under condition $\frac{v}{c} \ll 1$ and energy conservation law:

$$\frac{d^2 r_i}{dz_i^2} = \left[\frac{1 + \left(\frac{dr_i}{dz_i} \right)^2}{2V_i} \right] \left(E_{r_i} - E_{z_i} \frac{dr_i}{dz_i} \right) \quad (3)$$

where subscript i represents the i -th particle path of the problem.

In order to solve (1)-(3), a FEM code with first-order triangle elements was developed, and for the second-order differential equation for the path a fourth-order Runge-Kutta integrator was used.

B. Finite Element Formulation

Due to accuracy and versatility associated with weighting residual methods, such as Galerkin method, the finite-element method (FEM) [4]-[5], has been adopted as a standard on solving electromagnetic problems. The triangular finite element scalar potential V_e is written as $V_e(z, r) = \sum_{i=1}^3 \phi_i V_i$, where V_1 , V_2 and V_3 be the unknown potential at nodes 1, 2 and 3 and $\phi_i = \phi_i(z, r)$ represents the basis/shape function. This leads to the following system of equations:

$$[S][U] + [g] = 0 \quad (4)$$

where:

$$S_{ij} = \int_{\Omega} \nabla \phi_i \cdot \nabla \phi_j d\Omega \quad (5)$$

$$U_i = V_i \quad (6)$$

and,

$$g_i = \frac{1}{\epsilon_0} \int_{\Omega} \phi_i \rho_i d\Omega \quad (7)$$

where ρ_i is the right-hand side of Eq. (1).

This system can be solved for the N unknown equations and coefficients. To use the Galerkin method the weighting

functions must be set as the same as shape functions. A Gaussian Elimination solver was developed to solve the global system matrix.

C. Self-Consistent Algorithm

All electron gun codes, used to design intense beam guns, are said to be self-consistently if their solvers take into account the space-charge contribution to the static fields and the static fields forces contribution that act on the particles.

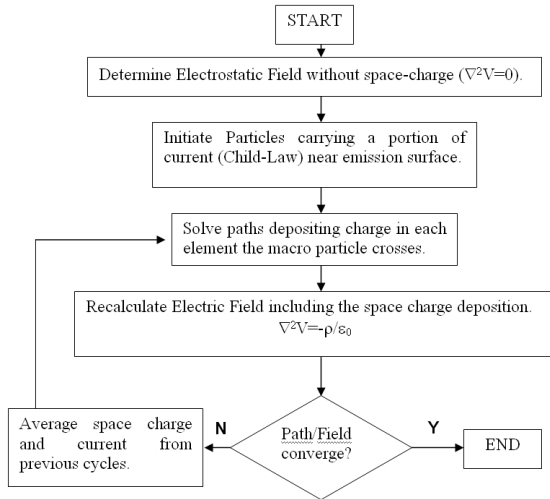


Fig. 1. Flowchart of the method of successive approximation.

The flowchart at Fig. 1 presents the successive approximation method to be implemented. At the first approximation, only the electrostatic field without the space-charge field is used to trace the particle paths. These paths establish a distribution of space charge. The second approximation takes into account that charge contribution to calculate the new electrostatic field which in turn is used to calculate the paths of the second approximation. This procedure is repeated several times until the convergence criterion is reached.

III. RESULTS

In order to validate the code, five axial-symmetric rectangular regions, with length equals five times height, were evaluated. The number of nodes and finite elements vary from 12 up to 3000 and 14 up to 4790, respectively. It was used 20 paths and was observed an absolute error radial position at the final point of integration lower than $1.5 \cdot 10^{-4}\%$.

It was also evaluated the charged-particle trajectory for the ideal Pierce diode structure. This model, Fig. 2, has 2996 nodes and 5731 finite elements. As expected, due to the focusing electrode, the paths curved down to the axis of symmetry according to Fig. 3. Under space-charge limited condition, the paths have to be parallel [6].

IV. CONCLUSION

It was described the FEM formulation to solve Poisson equation for the scalar potential and the non-linear second order differential equation for non-relativistic electrons path, which was integrated using the fourth-order Runge-Kutta integrator

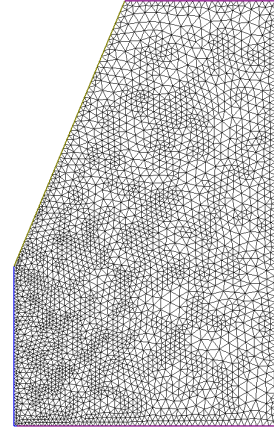


Fig. 2. A Pierce structure domain subdivided into 5731 finite elements.

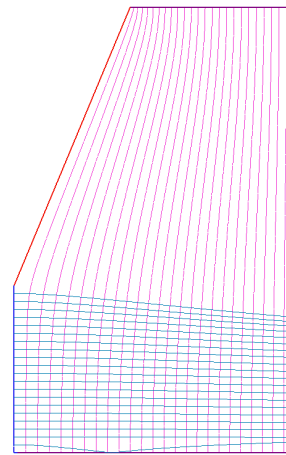


Fig. 3. Output solution shown for the ideal Pierce diode structure. Equipotentials are represented by the red lines and the trajectories by the light-blue.

method to obtain the electrons paths. Path absolute errors were below $1.5 \times 10^{-4}\%$ on a rectangular model, and on a Pierce diode structure, without space-charge deposition yet, paths presented a consistent behavior which indicates that the code is ready to evolve in order to work under space-charge limited condition. The next objective is solve the paths taking into account the space-charge limited condition and solve complex geometries, such as electron guns with grids and shadow-grids.

A complete set of results will be presented in the final paper.

REFERENCES

- [1] Herrmannsfeldt, W. B., Stanford Linear Acc. Center, SLAC-331 1988 (unpublished).
- [2] Humphries Jr., S., "TRACK", *Computational Accelerator Physics*, edited by R. Ryne (Am. Inst. of Phys., New York 1994), p.597; "Integrated Software System for High-Power Beam Design", in *Beams 94: Proc., 10th Conf. High Power Particle Beams*, p. 568.
- [3] Petillo, J. Eppley, et al., "The MICHELLE electron gun and collector modeling tool: Theory and design", *IEEE TPS*, vol. 30, pp. 1238-1264, Jun. 2002.
- [4] J. P. A. Bastos and N. Sadowski, *Electromagnetic Modeling by Finite Element Methods*, New York: Routledge, 2003
- [5] P. P. Silvester and R. L. Ferrari, *Finite Elements for Electrical engineers*, 3rd ed. Cambridge:Cambridge University Press, 1996
- [6] J.R.Pierce, *Theory and Design of Electron Beams* (Van Nostrand, Princeton, NJ, 1949).

Hierarchical Block Wavelet Compression for BEM Problems of Arbitrary Dimension

Christian Scheiblich, Remus Banucu, Jan Albert, Veronika Reinauer, and Wolfgang M. Rucker
 Institute for Theory of Electrical Engineering
 Pfaffenwaldring 47, 70569 Stuttgart, Germany
 christian.scheiblich@ite.uni-stuttgart.de

Abstract — Today’s computer hardware developments offer a complete and powerful parallel shared memory system (multi core CPUs) for a price of a home office system. To deliberate these developments on compression techniques for numerical applications using a Boundary Element Method (BEM), techniques are of first choices which are easy to parallelize by offering state of the art compression rates. The latest development of our Wavelet based compression technique fulfills these requirements. Its efficiency should be presented, discussed, and proven by numerical examples investigating the numerical accuracy related to different compression rates.

I. INTRODUCTION

To compute numerical applications using a BEM, one has to establish a compression technique for the fully populated system matrix (SM) of the system of linear equations (SLE). If a compression technique is not used, even nowadays available hardware capacities are rapidly limited, due to the fact of quadratic memory consumption while applying a BEM.

Several widely used compression techniques, like the well-known Fast Multipole Method, the Adaptive Cross Approximation (ACA) and algorithms working with a Singular Value Decomposition, reduce this memory consumption to a nearly linear dependency. All those techniques are established and selected by their advantages relying on the chosen numerical BEM application.

Furthermore, following in aspects of computer hardware developments a compressions technique offering an easy to handle parallelization becomes more and more important. This highlights techniques, like the ACA, that are exclusively dealing with the SM for compression. Whereas, the ACA uses a block structure for splitting the system matrix into several parallel computable blocks.

These blocks represent by their different sizes the importance of the expectant entries for the numerical accuracy of the BEM SLE. So, it is a good idea to pick up such a useful block structure called Hierarchical Matrices (HM) and bases a new development called Hierarchical Block Wavelet Compression (HWC) on it.

II. FAST WAVELET TRANSFORM AND COMPRESSION

Another well-know compression technique for BEM SMs of different formulations is based on the Fast Wavelet Transform (FWT). This technique applies a 2-D FWT to the SM for a selected wavelet, e. g. the Haar wavelet or one of the Daubechie wavelet family.

If only one dimension is considered, a 1-D FWT can be represented as a recursively applied filter bank:

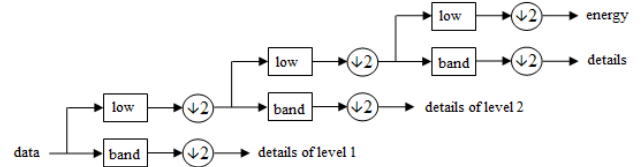


Fig. 1. 1-D FWT displayed as a recursively applied filter bank

By Fig. 1 all data are split into half parts by every filter level; low pass (energy) coefficients and band pass (detail) coefficients. To receive the requested 2-D FWT, two 1-D FWTs can be applied horizontal and vertical over all entries.

For a compression of the BEM SM one has to thin out smaller detail coefficients by artless setting those to zero, e. g. using the average magnitude of all detail coefficients. Finally, not storing those zeros, normally around 60% percent, by a Compressed Row Storage fulfills the physical compression in memory. An advantage for orthogonal wavelets is that the right hand side (RHS) of the BEM SLE can also be transformed by a 1-D FWT and the matrix vector operation (MVO) can be directly applied at compressed state. The found solution vector (SV) has to be reverse transformed by a 1-D FWT and discloses the requested solution of the BEM SLE.

But an enormous disadvantage is the applicability of the described compression technique. It claims that data are always of length to the power of two while splitting it into halves by each transform level. Assigning this fact to a BEM SM, the dimension N subjects to $N = 2^p \mid p \in \mathbb{N}_0$. Whereas, the FWT is not applicable for other dimensions without extending the BEM SM by empty entries to the next possible dimension $N + 1 \Rightarrow 2^{p+1}$. For common numerical applications this is a knock-out criterion due to the fact of a growing to $2^{p+1} \times 2^{p+1}$.

III. BLOCK WAVELET COMPRESSION

The basis technique to overcome this knock-out criterion was introduced by setting up a Block Wavelet Transform [1].

A. Block structure for selected dimensions

Therefore, the BEM SM is split into blocks of the same size allowing for still the same procedure of compression as described above, but now applied block by block.

The dimension N extends to $N = k \cdot 2^p \mid (k, p) \in \mathbb{N}_0$ for the number of k^2 blocks picturing the BEM SM. Reapplying the example from above, the overhead reduces to

$N+1 \Rightarrow (k+1)2^p$ and results in $2 \cdot k - 1$ nearly zero filled blocks as a necessary extension of the BEM SM [1].

B. Block structure for arbitrary dimensions

To finally tackle an arbitrary dimension N by absolutely no overhead, our achievement was to apply an adaptive block structure [2] combined with a modification of the used wavelet coefficients (Haar, Daubechie, Coiflet coefficients) [3].

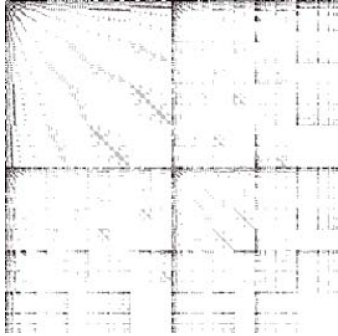


Fig. 2. SM at compressed state for an adaptive block structure

Fig. 2 displays these modifications; a calculated, transformed and compressed BEM SM of worst case dimension $N = 511$ split by an adaptive block structure.

C. Modification of the 2-D FWT for arbitrary dimension

To handle stretched or squeezed blocks, each dimension of the 2-D FWT has to be matched to each dimension of a treated block. For example, a block of size $2^p \times 2^q$ ($p, q \in \mathbb{N}_0$) claims a 2-D FWT of p recursive steps in vertical and q recursive steps in horizontal dimension (see Fig. 2).

Another indispensable modification regards the coefficients of the mandatory orthogonal wavelet. Those have to be normalized concerning the energy to allow for a block by block MVO at compressed state. Therefore, the MVO can be fulfilled by the matching and transformed parts of the RHS and the SV for each block multiplied by a selectable solver. In our case a GMRES or a BICG solver [2][3] is used.

The given example of $N+1$ is tackled in mathematical manner by absolutely no overhead and results in a dimension of $N+1 \Rightarrow k \cdot 2^p + 2^0$ for the BEM SM.

IV. HIERARCHICAL BLOCK WAVELET COMPRESSION

Within this work, our aim is to present an innovation of the already established [2] and parallelized BWC [3] towards Hierarchical Matrices.

A. Renumbering Degree of Freedom

For using HM in an efficient way, it is necessary to renumber the Degree of Freedom (DoF) to achieve a bandwidth minimization of the BEM SM. This is done by a kd-tree using a bounding box based algorithm in 3-D [2].

B. Hierarchical Matrices

Afterwards, an estimator function, derived from the kernel function of the BEM problem, splits the base structure of k^2 blocks into smaller hierarchical blocks. Fig. 3 was directly

generated from data output of our software ELFE++ and displays HM by a comprehensible example:

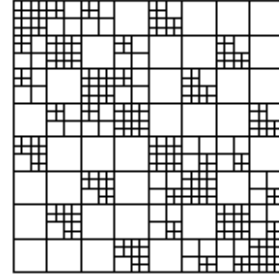


Fig. 3. HM of an applied HWC for an example of dimension $N = k \cdot 2^p$

C. Modified Wavelet Packet Transform for tackling HM

To attain the same advantages as described within the BWC, a MVO at compressed state, a modified 2-D Wavelet Packet Transform (WPT) [3] instead of a 2-D FWT has to be applied. A normal 1-D WPT displays an extension of the filtering scheme of the FWT (Fig. 1) by also recursively filtering details of each level. Our modification of the WPT interchanges the filtering scheme completely and, therefore, matches to the zoning of hierarchical blocks as shown (Fig. 3).

D. Push and pull functions for MVO

For a MVO at compressed state with no overhead, so called push and pull functions were particular developed for the HWC. Those functions change the hierarchical representation of the matching parts of the RHS and the SV for a hierarchical block. Both functions can be seen as a single matching transform step to lower (push) or higher (pull) hierarchy. For example, two smaller parts of the RHS of length 2^{p-1} are combined to match a block vertical length 2^p by only one call to the pull function with negligible linear effort of 2^p multiplications and 2^{p-1} additions.

V. NUMERICAL APPLICATIONS

In general, the HWC is applicable to any compressible SLE. Therefore, typical numerical applications demanding an electrostatic BEM problem in 3-D will be investigated for an arbitrary number of DoFs. The applications will be presented in detail and proven by numerical accuracy for different compression rates.

VI. ACKNOWLEDGEMENTS

This work was supported in part by the Deutsche Forschungsgemeinschaft (DFG) under Grant RU 720/6-2.

VII. REFERENCES

- [1] H. F. Buchner, L. C. Wrobel, W. J. Mansur, and C. Magluta, "On the block wavelet transform applied to the boundary element method," *Eng. Analys. with Boundary Elements*, vol. 28, no. 6, pp. 571-581, 2004.
- [2] C. Scheiblich, V. Kolitsas, and W. M. Rucker, "Compression of the radiative heat transfer BEM matrix of an inductive heating system using a block-oriented wavelet transform", *IEEE Transactions on Magnetics*, vol. 45, no. 3, pp. 1712-1715, March 2009.
- [3] C. Scheiblich, V. Reinauer, J. Albert, V. Kolitsas, A. Buchau, W. M. Rucker, "Parallelization of the block wavelet compression for a radiative heat transfer BEM matrix of an inductive heating system," *The 13th International IGTE Symposium, Graz*, vol. 13, pp. 72-77, Sept. 2008.

A quick and efficient method to compute radial flux density distribution in the airgap of a superconducting inductor

G. Malé, S. Mezani, R. Moulin, J. Lévêque
 GREEN-UHP, Faculté des Sciences
 BP. 239, 54506, Vandoeuvre-lès-Nancy, France
 Email: smail.mezani@green.uhp-nancy.fr

Abstract — The paper describes a quick method to calculate the radial flux density in the air gap of a superconducting inductor. This original topology uses superconducting bulks to shield the magnetic field created by two solenoids. Hence, the obtained airgap field is multipolar as in conventional AC machines. We propose a simple method based on the determination of the modulating function associated with the radial flux density distribution resulting from the introduction of the superconducting bulks. In a first step, a 2D magnetostatic finite element (FE) analysis allows the calculation of the modulating function. The later is used in a second step together with the field produced by the two solenoids to calculate the radial flux density distribution in the airgap of the considered inductor. Comparisons to 3D FE results show the validity of the proposed approach.

I. INTRODUCTION

In some types of electrical machines (claw pole, Lyndell machines...) ferromagnetic materials are used to modulate and concentrate the magnetic field to obtain a multipolar wave in the airgap from a constant excitation. In superconducting (SC) applications, ferromagnetic materials are heavily saturated since they are subjected to high magnetic fields. Hence, they can not be used for modulation purposes.

The use of the shielding properties of superconducting bulks allows flux concentration. An original topology of inductor, Fig.1, has been proposed [1] and a SC synchronous motor has been designed, built and successfully tested [2].

Fundamental to the operation of this inductor is the modulation of the magnetic field produced by two solenoids supplied by dc currents in contra-direction. In so doing, the radial flux density in a circle of the airgap is multipolar as in conventional ac machines. This flux density is minimal above the SC bulk and maximal above the bulks interspace.

Three dimensional finite elements as well as Monte Carlo methods [3, 4] can be used to compute the magnetic field distribution but this leads to high computation time. In this study, we propose a simple and quick method based on the determination of the modulating functions associated with the radial flux density distribution resulting from the introduction of the superconducting bulks.

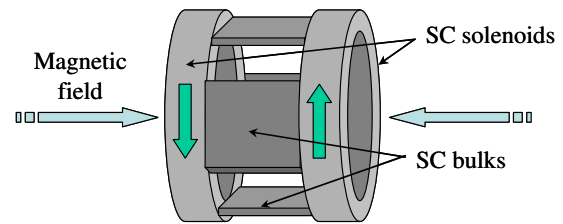


Fig. 1. Schematic of the flux concentration superconducting inductor

II. PRINCIPLE OF THE METHOD

At a given axial position in the air above the SC bulks, the radial flux density distribution at a radial distance r produced by the two solenoids can be written in the following form:

$$B_r(r, \theta) = B_{r0}(r) \cdot \Lambda_r(r, \theta) \quad (1)$$

where θ is the angular position, B_{r0} is the radial flux density created by the solenoids without the SC bulks and Λ_r is the modulating function. Because of axial symmetry, B_{r0} has no azimuthal component and it can be computed analytically using the Biot-Savart law.

It has to be noticed that the modulating function only depends on the geometry and the magnetic permeability of the system as far as the linearity of the materials is assumed. In the present work, the superconducting materials are considered almost diamagnetic so their relative permeability is much smaller than unity (a value of 10^{-3} is found to be enough for the numerical simulations).

The modulating function can be written as follows:

$$\Lambda_r(r, \theta) = \Lambda_{r0}(r) + \sum_{k=1,2,3,\dots} \Lambda_{rk}(r) \cos(kN_b \theta) \quad (2)$$

where Λ_{rk} are the Fourier coefficients for the modulating function and N_b is the number of the superconducting bulks. From (1) and (2):

$$B_r(r, \theta) = B_{r0}(r) \Lambda_{r0}(r) + \sum_{k=1,2,3,\dots} B_{r0}(r) \Lambda_{rk}(r) \cos(kN_b \theta) \quad (3)$$

1. StaticFields

From (3), it can be seen that the radial flux density exhibits a dc component which doesn't create any emf.

Since the highest space harmonic is obtained for $k=1$, the number of pole pairs of the device is $p = N_b$.

A. Determination of the modulating function

To calculate the A_{rk} coefficients, we consider a 2D domain corresponding to the median cross section of Fig.1 where the radial flux density distribution is maximal.

We proceed in two steps:

Firstly, at a radius R_0 , Fig. 2.a, we impose a radial flux density by imposing a magnetic vector potential (mvp) of the form:

$$a(R_0, \theta) = A_0 \cos(p\theta) \quad (4)$$

The mvp A_0 can take any value and the magnetic field distribution can be computed analytically in this configuration where the SC bulks are removed. From this computation, the radial flux density at a radius R has the following form:

$$B_{ra}(R, \theta) = B_0 \sin(p\theta) \quad (5)$$

In a second step, the SC bulks are introduced, Fig.2.b. A 2D magnetostatic FE analysis is carried out with the same condition on R_0 as in (4). The radial flux density resulting from the introduction of the SC bulks is called $B_{rb}(R, \theta)$.

The modulating function can be obtained by simply dividing $B_{rb}(R, \theta)$ by $B_{ra}(R, \theta)$. This straightforward method leads to some indeterminations due to divisions per zero in some points. The preferred method is to proceed to a Fourier series expansion of $B_{rb}(R, \theta)$, then to use (2) and (5) to obtain the A_{rk} coefficients. Indeed, the harmonic analysis allows a better understanding of the modulation process.

III. APPLICATION EXAMPLE

The dimensions of the considered inductor [2] are given in Table I. We have tested the proposed method to determine the radial flux density on a circle of the airgap.

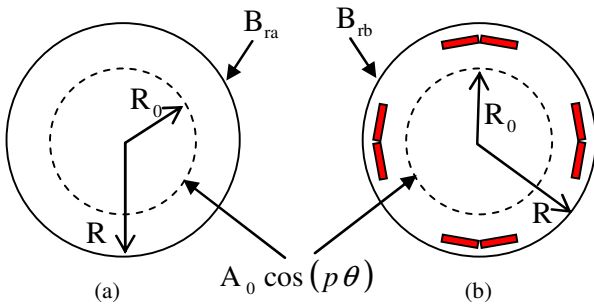


Fig. 2. Studied domains for the determination of the modulating function (a) without SC bulks (b) including SC bulks

TABLE I
PARAMETERS OF THE SUPERCONDUCTING INDUCTOR

Solenoid SC material (wires)	NbTi
Number of solenoids	2
Inner radius of solenoid, mm	75
Outer radius of solenoid, mm	105
Axial length of solenoid, mm	50
Bulk SC material	YBCO
Number of bulks ($N_b = p$)	4
Bulk thickness, mm	5
Bulk axial length, mm	50
Bulk angular opening, deg.	45

Because of the cryostat wall, the magnetic airgap is large in SC machines (typically 15 to 20 mm). Hence, for a radius $r=124$ mm and a current density in the solenoids of about 70 A/mm², we have compared, Fig.3, the results obtained by the presented method and these issued from a 3D FE analysis. The results are in good accordance. Furthermore, the computation time is about 5 minutes when using the FE method whereas it is only 5 seconds for the proposed approach.

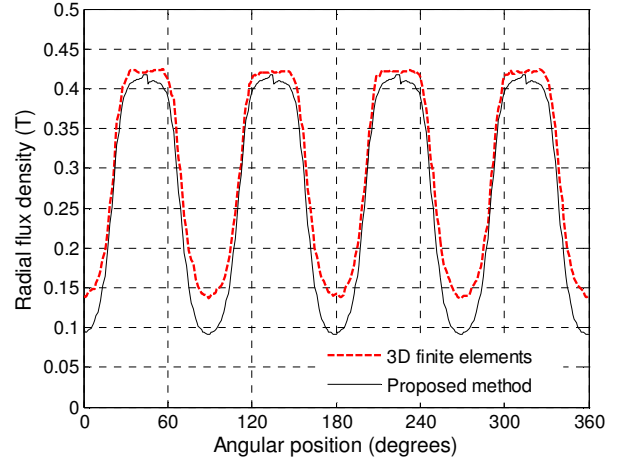


Fig. 3. Comparison of radial flux densities at $r = 124$ mm

IV. CONCLUSION

A simple and quick method to compute the radial flux density created by an original topology of a superconducting inductor has been presented. Comparisons to 3D finite element calculations show the validity of the proposed approach with the benefit of huge savings in computation time.

V. REFERENCES

- [1] P. Masson, J. L ev eque, D. Netter, A. Rezzoug, "Experimental study of a new kind of superconducting inductor," *IEEE Trans. on App. Supercon.*, 13(2), 2239-2242, 2003.
- [2] E. Ailam, D. Netter, J. L ev eque, B. Douine, A. Rzzoug, P. Masson, "Design and testing of a superconducting motor," *IEEE Trans. on App. Supercon.*, 17(1), 27-33, 2007.
- [3] S. Mandayam, L. Udpa, S. S. Udpa and W. Lord, "Monte Carlo methods for modelling magnetostatic NDE phenomena: A feasibility study," *IEEE Trans. Mag.*, 32(3), 1425-1428, 1996.
- [4] P. Masson, J. L ev eque, D. Netter, A. Rezzoug, "Magnetic field concentration: Comparison between several shapes of superconducting shields," *IEEE Trans. on App. Supercon.*, 11(1), 2248-2251, 2001.

Solution of Dual Stochastic Static Formulations Using Double Orthogonal Polynomials

S. Clénet^{†,*}, N. Ida^{*}, R. Gaignaire[&] and O. Moreau[°]

[†]L2EP/AMPT Lille, 8, Bd Louis XIV, 59046 Lille Cedex, France

^{*}Department of Electrical and Computer Engineering, The University of Akron, Akron, OH 44325-3904, United States

[&]Bât. B28 Applied and Computational Electromagnetics (ACE), Grande Traverse 10, 4000 Liège 1, Belgique

[°]Electricité de France, R&D Division, 1 Avenue du Général de Gaulle, 92141 Clamart, France

E-mail: stephane.clenet@lille.ensam.fr

Abstract— The solution of stochastic PDEs using the Stochastic Finite Element Method (SSFEM) can lead to a very large linear system. If the random input data are independent, it can be shown that the initial linear system can be split into smaller independent linear systems by using double orthogonal polynomials. In this paper, we propose to apply this approach in the case of the dual potential formulations in electrokinetics and to compare the two.

I. INTRODUCTION

The Spectral Stochastic Finite Element Method can be used to solve the stochastic static electromagnetics problem. This method has been proposed originally in mechanics by Ghanem [1] in the early 90's and has recently been applied to solve stochastic static electromagnetics problems [2][3]. This method is very accurate but requires the solution of a large linear system. The number of unknowns in the system is equal to the product of the number of Degrees of Freedom (DoFs), N required to discretise the spatial dimension (spatial mesh) and the number of DoFs, P_{out} required to discretise the random dimension. Even though the system to solve has special properties, its solution can be tricky when the number of random input variables is greater than about a dozen. If the randomness is in the behaviour laws and the input random variables are independent it has been shown by Babuska et al. [4], that using special polynomials (so called double orthogonal polynomials) as basis to discretise the random dimension, the SSFEM yields P_{out} independent equation systems of size N . The double orthogonal polynomials have been previously used to solve the scalar potential formulation in static electromagnetics [5]. Here, we propose to solve the two dual potential formulations using double orthogonal polynomials and to compare them on an example.

II. DESCRIPTION OF THE STOCHASTIC PROBLEM

On a contractible domain D with a boundary S , the electrokinetic problem can be written as:

$$\text{div } \mathbf{J} = 0 \quad (1)$$

$$\text{curl } \mathbf{E} = 0 \quad (2)$$

Boundary conditions are imposed on S . To simplify the problem, we will assume that we have only two disjoint surfaces S_{E1} and S_{E2} ($S_E = S_{E1} \cup S_{E2}$) on which:

$$\mathbf{E} \times \mathbf{n} = \mathbf{0} \quad (3)$$

with \mathbf{n} the outward unit vector on S . On the complement of S_E , denoted S_J , we have:

$$\mathbf{J} \cdot \mathbf{n} = 0 \quad (4)$$

The behaviour law can be written on D as:

$$\mathbf{J} = \sigma(\mathbf{x}, \theta) \mathbf{E} \quad (5)$$

$\sigma(\mathbf{x}, \theta)$ is the random field conductivity. We will assume that the conductivity is equal to a random variable $\sigma_q(\theta)$ on M disjoint subdomains D_q of D :

$$\sigma(\mathbf{x}, \theta) = \sum_{q=1}^M \sigma_q(\theta) I_q(\mathbf{x}) \quad (6)$$

With $I_q(\mathbf{x})$ is the function that is equal to 1 on the subdomain D_q and 0 elsewhere. Since the conductivity is random, \mathbf{E} and \mathbf{J} are random fields. To solve the previous problem, two potential formulations can be used. Since, $\mathbf{E}(\mathbf{x}, \theta)$ is curl free, it can be written as the gradient of a scalar function $\varphi(\mathbf{x}, \theta)$. The equation to solve is then:

$$\text{div}[\sigma(\mathbf{x}, \theta) \mathbf{grad} \varphi(\mathbf{x}, \theta)] = 0 \quad (7)$$

We have Neumann boundary conditions on S_J and Dirichlet type on S_E with:

$$\varphi(\mathbf{x}, \theta) = 0 \text{ on } S_{E1} \quad \varphi(\mathbf{x}, \theta) = V \text{ on } S_{E2} \quad (8)$$

To obtain an unknown with homogeneous boundary conditions, we consider a function $\boldsymbol{\beta}(\mathbf{x})$ on D such that $\boldsymbol{\beta}(\mathbf{x})$ satisfies (2), (3) and such that the circulation of $\boldsymbol{\beta}(\mathbf{x})$ from S_{E1} to S_{E2} is equal to 1. We now consider the new problem with the scalar potential $\varphi'(\mathbf{x}, \theta)$ and with homogenous boundary conditions on S_E :

$$\text{div}[\sigma(\mathbf{x}, \theta) \mathbf{grad} \varphi'(\mathbf{x}, \theta)] = -V \text{div} \sigma \boldsymbol{\beta}(\mathbf{x}) \quad (9)$$

If we denote I the current flowing through S_{E1} and S_{E2} , this current can be calculated as:

$$I(\theta) = - \int_D \mathbf{J}(\mathbf{x}, \theta) \cdot \boldsymbol{\beta}(\mathbf{x}) dD \quad (10)$$

Since $\mathbf{J}(\mathbf{x}, \theta)$ is divergence free, $\mathbf{J}(\mathbf{x}, \theta)$ can be written as the curl of the vector potential $\mathbf{T}(\mathbf{x}, \theta)$. The equation to solve is then:

$$\text{curl}[\sigma^{-1}(\mathbf{x}, \theta) \text{curl } \mathbf{T}(\mathbf{x}, \theta)] = \tilde{0} \quad (11)$$

$\mathbf{T}(\mathbf{x}, \theta)$ has nonhomogenous boundary conditions on S_J . We therefore introduce a field $\mathbf{N}(\mathbf{x})$ satisfying (1) and (4) such that the flux of $\mathbf{N}(\mathbf{x})$ through the surface S_{E2} is equal to 1. It can be shown that the problem to solve is then:

$$\text{curl}[\sigma^{-1}(\mathbf{x}, \theta) \text{curl } \mathbf{T}'(\mathbf{x}, \theta)] = -I \text{curl}[\sigma(\mathbf{x}, \theta) \mathbf{N}(\mathbf{x})] \quad (12)$$

With \mathbf{T}' the unknown with homogeneous boundary conditions. The voltage $V(\theta)$ can be calculated using the following equation:

This work is supported by the IAP IPOLFE (Belgium government) and also by the French American Commission (Fulbright Program)

$$\mathbf{V}(\theta) = - \int_D \mathbf{E}(x, \theta) \cdot \mathbf{N}(x) dD \quad (13)$$

III. APPROXIMATION OF THE POTENTIALS USING DOUBLE ORTHOGONAL POLYNOMIALS

In the following, we detail the solution of the vector potential formulation. In the deterministic case, the vector potential \mathbf{T}^* is approximated using edge shape functions. Let us denote N_1 the set of edges, N_1^0 the sets of edges not located on S_j , $\mathbf{w}_a(x)$ the function associated with the edge a . The cardinal of the set N_1^0 will also be denoted N_1^0 . We will denote $W_1^0(D)$ the space generated by the functions associated with the edges belonging to N_1^0 . Functions in $W_1^0(D)$ have naturally homogeneous boundary conditions (3) on S_E .

Let us denote Ω the space of outcomes θ , consider the space of functions X depending on the random variables $\sigma_1(\theta), \dots, \sigma_M(\theta)$ such that the variance exists. To approximate this space, we will consider a set of P_{out} orthogonal polynomials $(H_i(\sigma_1(\theta), \dots, \sigma_M(\theta)))_{1 \leq i \leq P_{\text{out}}}$ (these polynomials will be denoted $H_i(\theta)$ to simplify the notations in the following):

$$E[H_i(\theta)H_j(\theta)] = 0 \text{ if } i \neq j \quad (14)$$

With $E[\cdot]$ the expectation. We will denote $W_{\text{Pout}}(\Omega)$ the space generated by this set of polynomials. Various methods have been proposed to define these polynomials. The most common polynomials used are the multivariate polynomial based on the Askey Scheme. We are looking for an approximation of the vector potential \mathbf{T}^* in the space $W_0^0(D) \otimes W_{\text{Pout}}(\Omega)$, so that \mathbf{T}^* can be written as:

$$\mathbf{T}^*(x, \theta) = \sum_{a=1}^{N_1^0} \sum_{j=1}^{P_{\text{out}}} T'_{ij} \mathbf{w}_a(x) H_j(\theta) \quad (15)$$

where T'_{ij} are the degrees of freedom we need to determine. Applying the Galerkin method to a weak form of (11) leads to $N_n^0 \times P_{\text{out}}$ linear equations:

$$\mathbf{S} \mathbf{T}^* = \mathbf{F} \quad (16)$$

where \mathbf{S} is a $(N_1^0 \times P_{\text{out}}) \times (N_1^0 \times P_{\text{out}})$ square matrix and \mathbf{F} a $(N_1^0 \times P_{\text{out}})$ vector. The vector \mathbf{T}^* is the vector of DoFs T'_{ij} . Using the expression **Erreur! Source du renvoi introuvable.** for the conductivity allows us to rewrite the equation system in a different way [3]. We denote the matrices \mathbf{S}_q and \mathbf{D}_q , the vectors \mathbf{F}_q and the Σ_q with the coefficients:

$$\begin{aligned} s_{ni}^q &= \left(\mathbf{I}_q(x) \mathbf{curl} \mathbf{w}_i(x), \mathbf{curl} \mathbf{w}_n(x) \right)_D \quad q \in [1, M] \quad (i, n) \in [1, N_1^0]^2 \\ d_{mj}^q &= E \left[\sigma^{-1}_q(\theta) H_j(\theta) H_m(\theta) \right] \quad q \in [1, M] \quad (j, m) \in [1, P_{\text{out}}]^2 \\ f_n^q &= \mathbf{I} \left(\mathbf{I}_q(x) \mathbf{N}(x), \mathbf{curl} \mathbf{w}_n(x) \right)_D \quad q \in [1, M] \quad n \in [1, N_1^0] \\ \Sigma_m^q &= E \left[\sigma^{-1}_q(\theta) H_m(\theta) \right] \quad q \in [1, M] \quad m \in [1, P_{\text{out}}] \end{aligned}$$

Then, using the Kronecker product \otimes , the system (16) can be written in the form [3]:

$$\mathbf{S} = \sum_{q=1}^M \mathbf{D}_q \otimes \mathbf{S}_q \quad \mathbf{F} = \sum_{q=1}^M \Sigma_q \otimes \mathbf{F}_q \quad (17)$$

The size of the linear system (17) can become very large even with a coarse mesh. If the random variables $\sigma_q(\theta)$ are independent, we can take advantage of this property by using double orthogonal polynomials $H_i(\theta)$ which enables us to get a

diagonal matrix \mathbf{D}_q . In that case, we have to solve P_{out} linear systems of size $N_1^0 \times N_1^0$ instead of the whole system (16). The multivariate double orthogonal polynomial $H_i(\theta)$ are constructed from $(p_{\text{out}}+1)$ univariate polynomials $h_q^n(\theta)$ of order p_{out} that satisfy the following relations:

$$E[h_q^n(\sigma_q[\theta]) h_q^m(\sigma_q[\theta])] = \delta_{nm} \quad (6.a)$$

$$E[\sigma_q[\theta] h_q^n(\sigma_q[\theta]) h_q^m(\sigma_q[\theta])] = 0 \text{ if } m \neq n \quad (6.b)$$

The polynomials are orthogonal to each other according to the first relation and the second relation is related to their double orthogonality property.

IV. APPLICATION

We consider a device with three subdomains where the conductivity is assumed to be random. We calculate the expectation of energy for both formulations and for 4 meshes (M1, M2, M3, M3). We consider an approximation of the first, second, third and fourth order ($p_{\text{out}}=1, 2, 3$ and 4) for the multivariate polynomials $H_i(\theta)$ which lead to the calculation of $P_{\text{out}}=8, 27, 64, 225$ "deterministic" problems. The evolution of the energy expectation as a function of the number of elements is given figure 1. The difference between the energy expectation given by both formulations is an image of the numerical error. Therefore, the closer the energies are, the more accurate the model. According to that statement, we can see that whatever the order of interpolation the error decreases with the number of elements. But we can see also that up to an order two the accuracy does not improve much.

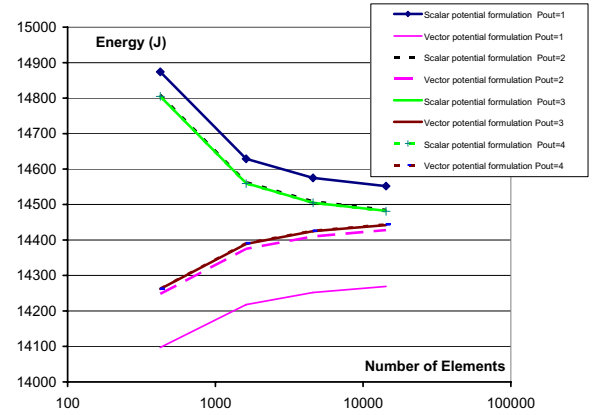


Figure 1: Evolution of the energy expectation for both formulations and for different order of approximation and different meshes.

V. REFERENCES

- [1] R. G. Ghanem and P. D. Spanos, *Stochastic Finite Element: a spectral approach*, Springer-Verlag (1991)
- [2] R. Gaignaire, S. Clénet, O. Moreau, B. Sudret, "3D Spectral Stochastic Finite Element Method in Electromagnetism", IEEE Trans. on Magnetics, vol. 43, no. 4, pp. 1209-1212, 2007.
- [3] R. Gaignaire, F. Guyomarc'h, O. Moreau, S. Clénet, B. Sudret, "Speeding up in SSFEM Computation using Kronecker tensor Products", CEFC 2008, Athen, 2008
- [4] I. Babuska, R. Tempone, G. E. Zouraris, "Galerkin Finite Element Approximations of Stochastic Elliptic Partial Differential Equations", SIAM J. Numer. Anal. Vol. 42, No. 2, pp. 800-825, 2004
- [5] S. Clénet, N. Ida, R. Gaignaire, O. Moreau, Polynômes doublement orthogonaux pour la résolution de problème en électromagnétisme stochastique », Conférence NUMELEC, Liège (Belgique), 2008

Nonlinear Eddy Current Analysis by BEM Minimum Order Formulation

Kazuhiisa Ishibashi, Zoran Andjelic, and David Pusch

Corporate Research, ABB Switzerland Ltd

Baden-Daettwil, CH-5405, Switzerland

isibasi@keyaki.cc.u-tokai.ac.jp, zoran.andjelic@ch.abb.com, david.pusch@ch.abb.com

Abstract — Nonlinear eddy currents induced in a steel plate are formulated with the help of the boundary integral equations of minimum order for the calculation of three-dimensional eddy current problems. The integral equations for the nonlinear analysis are derived by considering nonlinear terms as fictitious sources. Since the periodic electromagnetic fields in the steel are distorted, these fields are expressed with the help of Fourier series, whose fundamental and harmonic fields are determined by solving the corresponding integral equations with the surface magnetic fields given as the boundary values. The internal and surface electromagnetic fields are obtained numerically one after the other until convergence by a simple iterative method.

I. INTRODUCTION

Nonlinear eddy current is formulated by considering nonlinear terms as fictitious sources in BEM. Recently an efficient nonlinear analysis by BEM has been proposed [1]. With the help of the rapid attenuation of the electromagnetic field in the conductor, the nonlinear eddy current is analyzed with negligible few additional computer-memory. Mayergoyz has proposed minimum order eddy current formulation [2]. Since the minimum order formulation gives the magnetic field in the conductor with only the surface electric current, the nonlinear eddy current may be formulated easily. Hence, employing the minimum order formulation and utilizing the procedure given in [1], we derive boundary integral equations to solve the nonlinear problems and check effectiveness.

II. FORMULATION OF EDDY CURRENT

A. Electromagnetic fields in steel

The electromagnetic fields in the steel with the conductivity σ satisfy Maxwell's equations as:

$$\nabla \times \mathbf{E}_i + \partial \mathbf{B}_i / \partial t = 0, \quad (1)$$

$$\nabla \times \mathbf{H}_i - \sigma \mathbf{E}_i = 0, \quad (2)$$

$$\nabla \cdot \mathbf{B}_i = 0, \quad (3)$$

$$\nabla \cdot \sigma \mathbf{E}_i = 0, \quad (4)$$

where \mathbf{E}_i is the electric field, \mathbf{H}_i is the magnetic field and \mathbf{B}_i is the magnetic flux density. The permeability is affected by the magnetic field. Thus, in order to apply Green's theorem, we introduce a fictitious permeability μ_f , and with the help of Fourier series we rewrite (1)-(4) for the k -th harmonic electromagnetic fields as:

$$\nabla \times \mathbf{E}_k + j\omega_k \mu_f \mathbf{H}_k = -j\omega_k (\mathbf{B}_k - \mu_f \mathbf{H}_k), \quad (5)$$

$$\nabla \times \mathbf{H}_k - \sigma \mathbf{E}_k = 0, \quad (6)$$

$$\nabla \cdot \mu_f \mathbf{H}_k = -\nabla \cdot (\mathbf{B}_k - \mu_f \mathbf{H}_k), \quad (7)$$

$$\nabla \cdot \sigma \mathbf{E}_k = 0. \quad (8)$$

where ω_k is the k -th angular frequency of the fundamental one ω , and the subscript k denotes the k -th harmonic. Hence, (5)-(8) are regarded as linear equations by considering the right sides of (5) and (7) to be fictitious magnetic current \mathbf{K}_k and charge m_k sources, which are defined as:

$$\mathbf{K}_k = j\omega_k (\mathbf{B}_k - \mu_f \mathbf{H}_k), \quad m_k = \nabla \cdot \mathbf{K}_k / (j\omega_k). \quad (9)$$

B. Magnetic field given by minimum order formulation

Following the minimum order formulation [2], we derive the integral equation for the nonlinear magnetic field inside the steel. From (5) and (6), we get

$$\nabla \times \nabla \times \mathbf{H}_k - j\omega_k \mu_f \sigma \mathbf{H}_k = \sigma \mathbf{K}_k. \quad (10)$$

Green's theorem gives the integral representation of \mathbf{H}_k with the subscript p denoting an observation point P_o as:

$$\mathbf{H}_{kp} = \mathbf{H}_{kep} - \int_S \mathbf{J}_{sf} \times \nabla G_k dS \quad (11)$$

where S is the surface of the steel, \mathbf{J}_{sf} is the fictitious surface electric current, G_k is fundamental solution of (10) defined as $G_k = \exp(-\gamma_k r) / (4\pi r)$ with $\gamma_k = \sqrt{j\omega_k \mu_f \sigma}$ and the distance r from an integration point on S to P_o , and \mathbf{H}_{kep} is the magnetic field produced by \mathbf{K}_k at P_o defined as:

$$\mathbf{H}_{kep} = -\int_V \left[\sigma \mathbf{K}_k G_k - \frac{\nabla \cdot \mathbf{K}_k}{j\omega_k \mu_f} \nabla G_k \right] dV \quad (12)$$

where V is the volume of the steel.

C. Nonlinear eddy current formulation

The magnetic field \mathbf{H}_o at an observation point P_o in the free space is given from scalar potential Φ produced by the fictitious surface magnetic charge m_{sf} , see [2]:

$$\mathbf{H}_{op} = -\nabla \Phi = \mathbf{H}_{ep} + \int_S \frac{m_{sf}}{\mu_0} \nabla G_o dS \quad (13)$$

where $G_o = 1/(4\pi r)$ and \mathbf{H}_{ep} is the exciting magnetic field at P_o .

The boundary integral equations for nonlinear eddy current analysis are derived as follows. Firstly, we shall obtain the magnetic fields, \mathbf{H}_i and \mathbf{H}_o , at an observation point P_o on the surface of the inside and outside steel by employing (11) and

(13), respectively. Next, we obtain the tangential magnetic fields, H_{it} and H_{ot} , and also the normal magnetic flux densities, B_{in} and B_{on} . Applying the boundary conditions, we get the surface integral equations to analyze the nonlinear eddy current. From the continuity of the tangential magnetic fields, $H_{it}=H_{ot}$, we get

$$-\frac{\mathbf{J}_{sf}}{2} + \mathbf{n}_p \times \int_S \left[\mathbf{J}_{sf} \times \nabla G_k + \frac{m_{sf}}{\mu_0} \nabla G_o \right] dS = -\mathbf{n}_p \times [\mathbf{H}_{oep} + \mathbf{H}_{kep}] \quad (14)$$

and from the continuity of the normal magnetic flux densities, $B_{in}=B_{on}$, we get

$$\frac{m_{sfp}}{2\mu_0} + \mathbf{n}_p \cdot \int_S \left[\frac{\mu_f}{\mu_0} \mathbf{J}_{sf} \times \nabla G_k + \frac{m_{sf}}{\mu_0} \nabla G_o \right] dS = -\mathbf{n}_p \cdot \left[\mathbf{H}_{oep} + \frac{\mu_f}{\mu_0} \mathbf{H}_{kep} \right]. \quad (15)$$

III. NONLINEAR EDDY CURRENT ANALYSIS

We shall solve the eddy current induced in a steel plate when the plate is placed in the uniform magnetic field. The plate dimension is much larger than the skin depth and its thickness is 0.5 cm. The conductivity is $\sigma=64850$ S/cm and the relation between \mathbf{B}_i and \mathbf{H}_i is given as:

$$\mathbf{B}_i = \frac{1000}{0.194 + 0.0734|H_i|} \mu_o \mathbf{H}_i \quad [\text{Wb/cm}^2]. \quad (16)$$

The strength of uniform magnetic field parallel to the plate surface is given as function of time t [s] as:

$$H_{oep} = 20\sqrt{2} \sin(100\pi t) \quad [\text{A/cm}]. \quad (17)$$

As the electromagnetic fields are attenuated rapidly in conductive materials such as steel, (14) is rewritten by taking the same procedure given in [1] as:

$$-\frac{\mathbf{J}_{s1fp}}{2} + \frac{\mathbf{J}_{s2f}}{2} e^{-\gamma_k d} - \frac{\sigma}{2\gamma_k} \int_0^d \mathbf{n}_{1p} \times \mathbf{K}_k e^{-\gamma_k z} dz = -\mathbf{n}_{1p} \times \mathbf{H}_{oe1p} \quad (18)$$

$$-\frac{\mathbf{J}_{s2fp}}{2} + \frac{\mathbf{J}_{s1f}}{2} e^{-\gamma_k d} - \frac{\sigma}{2\gamma_k} \int_0^d \mathbf{n}_{2p} \times \mathbf{K}_k e^{-\gamma_k(d-z)} dz = -\mathbf{n}_{2p} \times \mathbf{H}_{oe2p} \quad (19)$$

where the subscripts 1 and 2 denote the face-to-face plate surfaces shown in Fig.1, z is the distance from S_1 and d is the plate thickness. Substitution of (12) into (11) leads to:

$$\mathbf{H}_{kp} - \frac{\sigma}{2\gamma_k} \int_0^d \mathbf{K}_k e^{-\gamma_k|z-z_p|} dz = \frac{\mathbf{J}_{s1f} \times \mathbf{n}_1}{2} e^{-\gamma_k z_p} + \frac{\mathbf{J}_{s2f} \times \mathbf{n}_2}{2} e^{-\gamma_k(d-z_p)} \quad (20)$$

Since the fictitious surface electric currents \mathbf{J}_{sf1p} , \mathbf{J}_{sf2p} are affected by the fictitious magnetic current \mathbf{K}_k , we can't adopt them as the boundary values. And so, regarding the boundary values as $\mathbf{J}_{s1p}=\mathbf{n}_1 \times \mathbf{H}_{oe1p}$ and $\mathbf{J}_{s2p}=\mathbf{n}_2 \times \mathbf{H}_{oe2p}$, which are defined by the actual surface magnetic fields on the plate-space boundaries, we solve (20) by modifying (18) and (19) as:

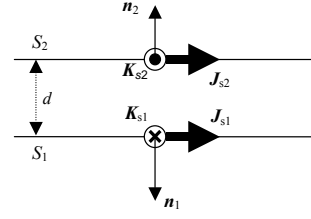


Fig. 1. Actual surface electric and magnetic currents defined respectively as $\mathbf{J}_s=\mathbf{n} \times \mathbf{H}_s$ and $\mathbf{K}_s=-\mathbf{n} \times \mathbf{E}_s$ with surface magnetic and electric fields \mathbf{H}_s and \mathbf{E}_s .

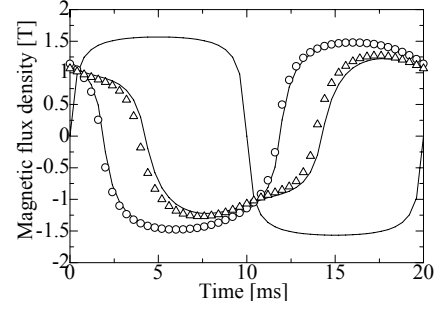


Fig.2. Computed results of magnetic flux density in steel plate

$$\frac{\mathbf{J}_{s1fp}}{2} - \frac{\mathbf{J}_{s2f}}{2} e^{-\gamma_k d} + \frac{\sigma}{2\gamma_k} \int_0^d \mathbf{n}_1 \times \mathbf{K}_k e^{-\gamma_k z} dz = \mathbf{J}_{s1p} \quad (21)$$

$$\frac{\mathbf{J}_{s2fp}}{2} - \frac{\mathbf{J}_{s1f}}{2} e^{-\gamma_k d} + \frac{\sigma}{2\gamma_k} \int_0^d \mathbf{n}_2 \times \mathbf{K}_k e^{-\gamma_k(d-z)} dz = \mathbf{J}_{s2p} \quad (22)$$

where \mathbf{J}_s with the subscript 1 or 2 is the actual surface electric current shown in Fig.1 defined with the magnetic field \mathbf{H}_s as:

$$\mathbf{J}_{sp} = \mathbf{n}_p \times \mathbf{H}_{sp} = \mathbf{n}_p \times \left[\mathbf{H}_{oep} + \int_S \frac{m_{sf}}{\mu_0} \nabla G_o dS \right]. \quad (23)$$

In the numerical analysis, the plate thickness is divided into 20 virtual volume elements (layers). Fig.2 shows the computed results of the magnetic flux density inside the steel plate at 0.5 mm (shown by \circ) and 1 mm (shown by Δ) from the surface with the solid lines obtained by the method given in [1]. The magnetic flux density obtained from sinusoidal magnetic filed on the surface is shown also by the solid line.

IV. CONCLUSIONS

Following the minimum order eddy current formulation, we have derived the boundary integral equations and solved the eddy current induced in the thin steel plate to check adequacy of the nonlinear formulation. The computed results are almost the same as those by the formulation given in [1], which have been confirmed to give adequate solutions. The analysis of the full model is given in the full paper.

V. REFERENCES

- [1] H. Fujita and K. Ishibashi, "Nonlinear Eddy Current Analysis of Thin Steel Plate by Boundary Integral Equations," *IEEE Trans. Magn.*, Vol.44, No.6, pp.758-761, 2008.
- [2] I.D. Mayergoyz, "Boundary Integral Equations of Minimum Order for the Calculation of Three-Dimensional Eddy Current Problems," *IEEE Trans. Magn.*, Vol.18, No.2, pp. 536-539, 1982.

A perturbation method for the $T - \Omega$ eddy-current formulation

Lorenzo Codecasa¹, Patrick Dular², Ruben Specogna³, and Francesco Trevisan³

¹Dipartimento di Elettronica e Informazione, Politecnico di Milano, I-20133 Milano, Italy,

²Département d'électricité, électronique et informatique, Université de Liège, B-4000 Liège, Belgium,

³Dipartimento di Ingegneria Elettrica, Gestionale e Meccanica, Università di Udine, I-33100 Udine, Italy, ruben.specogna@uniud.it.

Abstract—A perturbation method for the $T - \Omega$ geometric formulation to solve eddy-current problems is introduced. The proposed formulation is applied to the feasibility design of a non-destructive evaluation device suitable to detect “long” longitudinal flaws in hot steel bars.

Index Terms—Cell Method (CM), Finite Integration Technique (FIT), Discrete Geometric Approach (DGA), eddy-currents.

I. INTRODUCTION

The so called “Discrete Geometric Approach” (DGA) [1], similarly to the Finite Integration Technique (FIT) [2] or the Cell Method [3], allows to solve Maxwell equations in an alternative way with respect to the classical Galerkin method in Finite Elements.

The domain of interest D of the eddy-current problem, has been partitioned into a source region D_s and in a passive conductive region D_c . The complement of $D_c \cup D_s$ in D represents the air region D_a .

We cover the domain D with a tetrahedral mesh represented by the simplicial complex \mathcal{K} . The barycentric subdivision is used to obtain the interlocked dual complex \mathcal{B} [1]. For the simplicial complex \mathcal{K} , we denote by \mathbf{G} the incidence matrix between edges e and nodes n , by \mathbf{C} between faces f and edges e and by \mathbf{D} between cells v and faces f . The matrices $\mathbf{G}_{\mathcal{B}} = \mathbf{D}^T$, $\mathbf{C}_{\mathcal{B}} = \mathbf{C}^T$ and $\mathbf{D}_{\mathcal{B}} = -\mathbf{G}^T$ describe the mutual interconnections of the dual barycentric complex \mathcal{B} .

Next, we consider the integrals of the field quantities with respect to the oriented geometric elements of the mesh, yielding the Degrees of Freedom (DoF) arrays [3]:

- Φ is the array of magnetic induction fluxes associated with $f_{\mathcal{B}} \in D$; \mathbf{F} is the array of magnetomotive forces (m.m.f.s) associated with $e \in D$; \mathbf{I} is the array of induced electric currents associated with $f \in D_c$; In D_s the array \mathbf{I}_s of known source currents is defined; \mathbf{U} is the array of e.m.f.s on edges $e_{\mathcal{B}} \in D$.
- \mathbf{T} is the array of the circulations of the electric vector potential T along $e \in D_c$. In D_s the array \mathbf{T}_s of impressed electric vector potential is introduced; Ω is the array of magnetic scalar potential Ω associated to the nodes $n \in D$.

Using the incidence matrices, Maxwell’s laws can be written exactly as balance equations between Dofs arrays as

$$\mathbf{G}^T \Phi = 0 \quad (\text{a}), \quad \mathbf{C}^T \mathbf{U} = -i\omega \Phi \quad (\text{b}), \quad (1)$$

where (1a) is the Gauss’ magnetic law at discrete level and (1b) is the Faraday’s Law. The array \mathbf{T} is defined such that the Ampere’s balance law $(\mathbf{C}\mathbf{F})_f = (\mathbf{I})_f$, $\forall f \in D_c$, holds

$$\begin{aligned} (\mathbf{F})_e &= (\mathbf{G}\Omega)_e & \forall e \in D_a, \\ (\mathbf{F})_e &= (\mathbf{G}\Omega)_e + (\mathbf{T}_s)_e & \forall e \in D_s, \\ (\mathbf{F})_e &= (\mathbf{G}\Omega)_e + (\mathbf{T})_e & \forall e \in D_c - \partial D_c. \end{aligned} \quad (2)$$

In fact one has $\mathbf{C}_c \mathbf{T} = \mathbf{I}$ and $\mathbf{C}_s \mathbf{T}_s = \mathbf{I}_s$, where the subscripts c and s refer to the corresponding sub-array or sub-matrix relative to geometric elements in D_c and D_s respectively. This implies that the continuity law $\mathbf{D}_c \mathbf{I} = 0$, where \mathbf{D}_c is the sub-matrix of \mathbf{D} relative to the volumes and faces in D_c , is identically satisfied, since $\mathbf{D}\mathbf{C} = 0$. The interface conditions that avoid the current flow outside the region D_c are taken into account by considering $T = 0$, $\forall e \in \partial D_c$. In this way, in fact, $(\mathbf{I})_f = 0$, $\forall f \in \partial D_c$ holds.

The discrete counterpart of the constitutive laws can be written using the constitutive matrices [3]

$$\Phi = \mu \mathbf{F} \quad \text{in } D \quad (\text{a}), \quad \mathbf{U}_c = \rho \mathbf{I} \quad \text{in } D_c \quad (\text{b}). \quad (3)$$

The square matrices μ and ρ can be efficiently calculated in a pure geometric way for a mesh composed by tetrahedra as described in [6].

For sake of simplicity, D_c is considered as a union of simply-connected conductive regions. In case of multiply-connected regions, the m.m.f.s along cycles contained in D_a cannot be described completely by the magnetic scalar potential alone. In this case the *thick cuts* [5] have to be found and for each thick cut a non-local Faraday’ law [5] has to be written. One additional unknown per thick cut is added and all of them represent a set of linearly independent currents in D_c .

By substituting (3a), (3b) and (2) in (1a), the algebraic equations corresponding to the nodes in D are obtained. By substituting (3a), (3b) and (2) in (1b) the algebraic equations corresponding to edges in D_c are derived. The final algebraic system, having \mathbf{T} and Ω as unknowns Dofs arrays, can be written as

$$\begin{aligned} (\mathbf{G}^T \mu \mathbf{G} \Omega)_n &= 0 & \forall n \in D_a, \\ (\mathbf{G}^T \mu \mathbf{G} \Omega)_n &= -(\mathbf{G}_s^T \mu_s \mathbf{T}_s)_n & \forall n \in D_s, \\ (\mathbf{G}^T \mu \mathbf{G} \Omega)_n + (\mathbf{G}_c^T \mu_c \mathbf{T})_n &= 0 & \forall n \in D_c, \\ (\mathbf{C}_c^T \rho \mathbf{C}_c \mathbf{T})_e + i\omega (\mu_c (\mathbf{T} + \mathbf{G}_c \Omega_c))_e &= 0 & \forall e \in D_c. \end{aligned} \quad (4)$$

The system (4) is singular and, to solve it, a conjugate gradient method without gauge condition is used.

II. DISCRETE PERTURBATION METHOD FOR $T - \Omega$

Let us suppose that the resistivity of a tetrahedron $v_k \in D_c$ is perturbed from ρ to $\rho + \rho^p$, where ρ^p is a perturbation of the resistivity due to for example a defect in the conductive domain D_c ; this configuration is the defected configuration denoted with a superscript d . From (3b), the e.m.f. associated with edge $e \in v_k$ in the unperturbed configuration is $(\mathbf{U}_c)_e = (\rho \mathbf{I})_e$, where \mathbf{I} is the array of eddy currents in D_c in the unperturbed configuration; it can be equivalently written as

$$(\mathbf{U}_c)_e = ((\rho + \rho^p) \mathbf{I} - \rho^p \mathbf{I})_e = ((\rho + \rho^p) \mathbf{I} + \mathbf{U}_g)_e, \quad (5)$$

where the term $\mathbf{U}_g = -\rho^p \mathbf{I} = -\rho^p \mathbf{C}_c \mathbf{T}$ can be interpreted as an array of compensation e.m.f. generators connected in series to each primal edge e of v_k . By applying the superposition of effects, we consider the following configurations, see Fig. 1:

- \mathbf{I}_s is active, \mathbf{U}_g is switched off. This is the defected configuration, where the resistivity is $\rho + \rho^p$ and the eddy currents \mathbf{I}^d account for the presence of the defect; we have that $\mathbf{U}_c^d = (\rho + \rho^p) \mathbf{I}^d$ holds, where \mathbf{U}_c^d is the array of e.m.f.s in this configuration.
- \mathbf{I}_s is switched off, \mathbf{U}_g is active. This is the perturbed configuration, where $\mathbf{U}_c^p = (\rho + \rho^p) \mathbf{I}^p + \mathbf{U}_g$ holds, where \mathbf{U}_c^p , \mathbf{I}^p are the corresponding arrays of e.m.f.s and currents in this configuration.

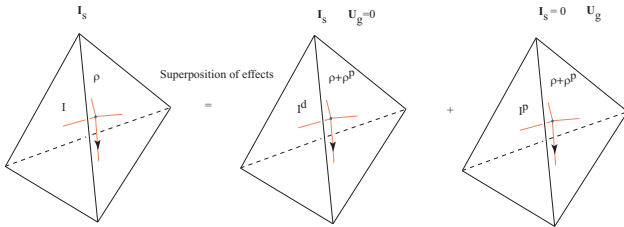


Fig. 1. Superposition of effects for the tetrahedron v_k .

A. Analysis of the perturbed configuration

From the above described superposition of effects, an eddy-current analysis of the perturbed configuration, yields e.m.f.s or currents arrays which are opposite to the difference of e.m.f.s or currents arrays between the defected and the unperturbed configuration. For edges belonging to tetrahedra v_k where resistivity has been changed, we introduce the e.m.f. generators $\mathbf{U}_g = \rho_p \mathbf{C} \mathbf{T}$ in the equations in (4) associated with those edges, obtaining

$$\mathbf{C}^T (\rho + \rho_p) \mathbf{C} \mathbf{T}_p + i\omega \boldsymbol{\mu} (\mathbf{T}_p + \mathbf{G} \boldsymbol{\Omega}_p) = \mathbf{C}^T \rho_p \mathbf{C} \mathbf{T}. \quad (6)$$

III. APPLICATION TO NON-DESTRUCTIVE TESTING

The application concerns the design of a device for the detection of long longitudinal defects that can be present during the hot mill rolling process of the steel bars with circular cross-section [7].

The geometry of the problem, depicted in Fig. 2 and described in detail in [7], consists of a conducting steel bar,

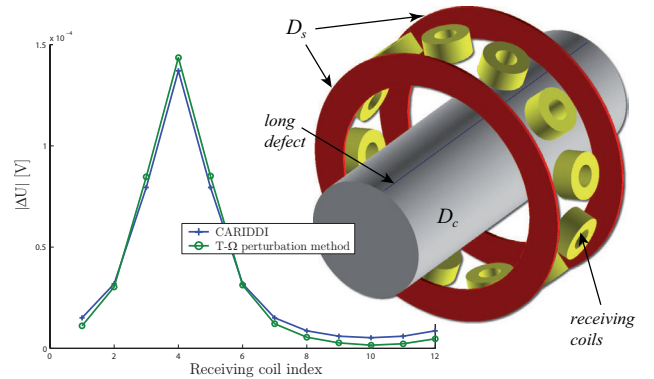


Fig. 2. Geometry of the problem and the comparison on the perturbation in the induced e.m.f. due to the defect over the receiving coils between the proposed formulation and an integral formulation.

modeled as a conducting cylinder D_c . A longitudinal perfectly insulating defect is assumed, 0.5 mm deep from the surface of the cylinder and 0.2 mm thick.

A mesh consisting of about 1 million of tetrahedra is used for the computations. The value of the perturbation in the induced voltages over the receiving coils due to the defect calculated with the proposed formulation is compared to the ones computed with the CARIDDI code [8], which implement an integral formulation.

IV. CONCLUSIONS

The perturbation method, reducing the cancellation error, produces accurate results also for small variations in the solution. This is especially required when the tool is used as a forward solver for an inverse problem. Moreover the method yields also a considerable speed-up: The mesh used in the perturbed problem can in fact be reduced [9], considering only a limited region surrounding the defect, at a small fraction of the initial mesh.

REFERENCES

- [1] A. Bossavit, L. Kettunen “Yee-like Schemes on Staggered Cellular Grids: A synthesis Between FIT and FEM Approaches”, IEEE Trans. Mag., Vol. 36, 2000, pp. 861–867.
- [2] T. Weiland, “A discretization method for the solution of Maxwell’s equations for six-component fields”, Electron. Commun. (AEU), Vol. 31, No. 3, 1977, p. 116.
- [3] E. Tonti, “On the geometrical structure of electromagnetism”, in Gravitation, Electromagnetism and Geometrical Structures, Ed. Bologna, Italy: Pitagora Editrice, 1995, pp. 281–308.
- [4] R. Specogna, F. Trevisan, “Eddy-currents computation with $T - \Omega$ discrete geometric formulation for a NDE problem”, IEEE Trans. Magn., Vol. 44, No. 6, 2008, pp. 698–701.
- [5] R. Specogna, S. Suuriniemi, F. Trevisan, “Geometric $T - \Omega$ approach to solve eddy-currents coupled to electric circuits”, Int. J. Num. Meth. Eng., Vol. 74, No. 1, 2008, pp. 101–115.
- [6] L. Codecasa, R. Specogna, F. Trevisan, “Symmetric positive-definite constitutive matrices for discrete eddy-current problems”, IEEE Trans. Magn., Vol. 43, No. 2, 2007, pp. 510–515.
- [7] R. Specogna, F. Trevisan, “Advanced Geometric Formulations for the Design of a Long Defects Detection System”, Nondestructive Testing and Evaluation, Vol. 24, No. 1, 2009, pp. 192–207.
- [8] R. Albanese, G. Rubinacci, F. Villone, “An Integral Computational Model for Crack Simulation and Detection via Eddy Currents”, Jour. Comput. Phys., Vol. 152, 1999, pp. 736–755.
- [9] R. V. Sabariego, P. Dular, “A Perturbation Approach for the Modeling of Eddy Current Nondestructive Testing Problems With Differential Probes”, IEEE Tran. Mag., Vol. 43, 2007, pp. 1289–1292.

Electromagnetic Inspection of Outer Side Defect on Steel Tube with Steel Support using 3D Nonlinear FEM Considering of Non-Uniform Permeability and Conductivity

Yuji Gotoh¹, Atsushi Kiya¹, and Norio Takahashi², *Fellow, IEEE*

¹Department of Mechanical and Energy Systems Engineering, Faculty of Engineering, Oita University, 700 Dannoharu, Oita 870-1192, Japan, goto-yuuji@cc.oita-u.ac.jp

²Department of Electrical and Electronic Engineering, Graduate School of Natural Science & Technology, Okayama University, 3-1-1 Tsushima, Okayama 700-8530, Japan, norio@elec.okayama-u.ac.jp

Abstract — Steel tubes are used in the heat exchanger in the petrochemical plant. Since these steel tubes are grouped in a bundle by the support steel plate (the baffle), it is necessary to inspect the existence of defects from the inside of each tube. In these steel tubes, the corrosion or the defects are generated by the friction with baffle at the outer side of steel tube.

In this paper, problems in applying the ac flux leakage testing method using an inner coil of low exciting frequency (about 60Hz) for the inspection of the outer side defect on steel tube with baffle are examined using 3-D nonlinear FEM. Moreover, the detecting property of the magnetic noise is investigated by 3-D FEM considering the non-uniformity of the permeability and conductivity in the steel tube and the baffle.

I. INTRODUCTION

The steel tubes of heat exchanger in petrochemical plant etc. are stored as a bundle. Moreover, these steel tubes are covered with the steel plates (baffle). In a heat exchanger, a large friction is generated between the baffle and the steel tube by the flow of the fluid inside or outside of the tube. Therefore, the corrossions or the defects are generated on the outer side of the steel tubes. It is necessary to inspect outer side defects on these tubes from the inside of the tube.

In this paper, the ac flux leakage testing method using an inner coil at a low frequency for detecting outer side defects on steel tube with baffle is proposed [1]. Since the permeability and conductivity of the steel tube and the baffle are usually non-uniform, the signal of the electromagnetic inspection may contain a large magnetic noise [2]. Then, the property of the inspection method of the outer side defect on the steel tube with baffle, and the effect of the non-uniformity of the permeability and conductivity on the large magnetic noise are investigated using the 3-D nonlinear FEM. In addition, the experimental verification is also carried out.

II. NON-UNIFORMITY OF PERMEABILITY AND CONDUCTIVITY IN STEEL TUBE AND BAFFLE

The non-uniformity of permeability and conductivity in the steel tube (SUS430) and baffle (SS400) were measured. Fig.1 shows the maximum non-uniformity of permeability in the steels of SUS430 and SS400, respectively. The dispersion rate ε_μ of relative permeability μ_r is defined by

$$\varepsilon_\mu = \frac{\mu_r(\text{each position}) - \mu_r(\text{average})}{\mu_r(\text{average})} \times 100 \quad (\%). \quad (1)$$

The figure denotes that the non-uniformity (ε_μ) of permeability is increased when the magnetic field is small. When the magnetic field is increased, both ε_μ s are decreased, because the direction of each magnetic moment becomes nearly the same. The non-uniformity of conductivity in SUS430 and SS400 is measured using two column specimens (diameter: 9mm, length: 2m) by the double bridge circuit. The conductivity of the column specimen between two points of 10cm distance was measured. The dispersion rate ε_σ of conductivity σ is defined by

$$\varepsilon_\sigma = \frac{\sigma(\text{each position}) - \sigma(\text{average})}{\sigma(\text{average})} \times 100 \quad (\%). \quad (2)$$

Fig.2 shows the non-uniformity of conductivity at each steel position, respectively. The figure denotes that the non-uniformities of conductivity of SUS430 and SS400 are within about 1.5%, respectively.

III. MODELS AND METHOD OF ANALYSIS

Fig.3 shows the inspection model for outer side defect of steel tube with baffle. The proposed inner inspection probe is also shown in the figure. The inspection probe is composed of a yoke, an exciting coil and a search coil for detecting the perpendicular component $|B_x|$ of leakage flux due to the outer side defect. The outer diameter of the inspection steel tube is 25mm, and the thickness is 1.5mm. B-H curves of steel tube (SUS430) and baffle (SS400) are shown in Fig.4. These curves are the average of non-uniform curves of which the non-uniformity of permeability is shown in Fig.1. The outer

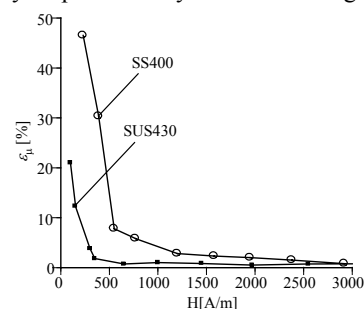


Fig.1. Dispersion rate ε_μ of permeability in steels (SUS430 and SS400).

2. Quasi-Static Fields

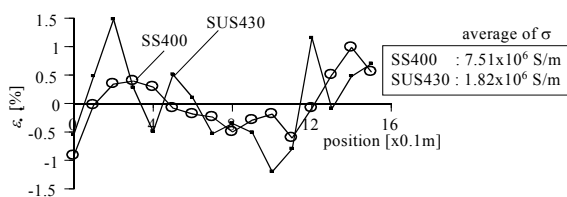


Fig.2. Dispersion rate ε_σ of conductivity in steels (SUS430 and SS400).

side defect is a circumferential one. The defect width (z-direction, Dw) and the defect depth (x-direction, Dd) of the steel tube are 2mm and 0.5mm, respectively. The distance (Lift-off, Lo) between the search coil and the inner surface of steel tube is 0.2mm. The frequency is chosen as 60Hz. The exciting current is 5A(rms). The magnetization curve and the conductivity of steel tube and baffle are used in the 3-D

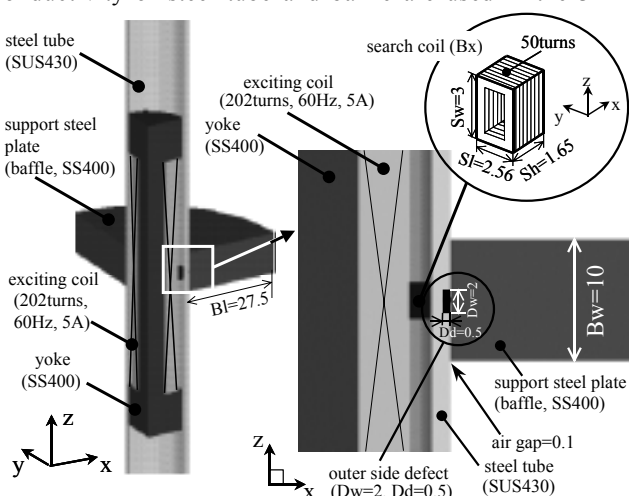


Fig.3. Inspection model for outer side defect of steel tube with the baffle (60Hz, 5A(rms)).

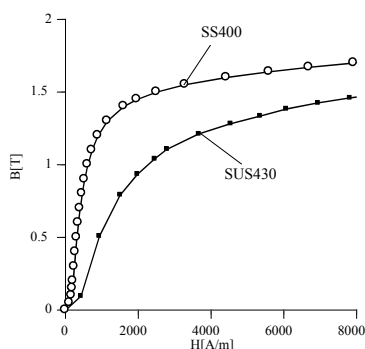


Fig.4. B-H curves of baffle (SS400) and steel tube (SUS430).

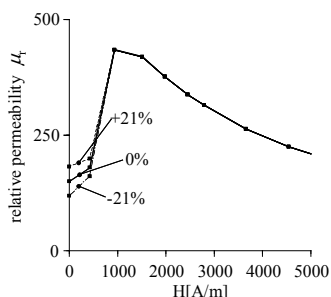


Fig.5. Dispersion of μ_r -H curves (SUS430).

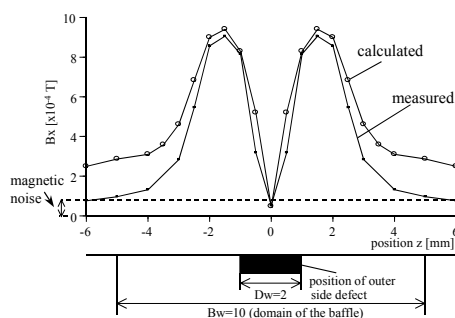


Fig.6. Detected $|B_x|$ (60Hz, 5A).

nonlinear FEM using the 1st order hexahedral edge element. The example of non-uniformity of magnetic characteristic of steel tube (SUS430) is shown in μ_r -H curve of Fig.5. As for the dispersion ε_μ of the steel tube (within $\pm 21\%$) and the baffle (within $\pm 47\%$), twenty curves with initial permeability are created, respectively. A curve is chosen at random among twenty μ_r -H curves following the normal random number (standard deviation: 5.0), and the selected curve is given to each finite element in the steel tube region. Similarly, the conductivity is generated according to a normal random number (standard deviation : 0.5 ($\times 10^6$)).

Fig.6 shows the distribution of the calculated value of $|B_x|$ in a search coil when there is the steel tube with baffle. Moreover, the experimental investigation is also carried out. $|B_x|$ is obtained by moving the inspection probe in the z-direction inside the steel tube. The calculated result is in agreement with measurement. The figure shows that each peak value is obtained near two edges of an outer side defect. Moreover, the magnetic noise from non-uniformity of permeability and conductivity is generated about 1×10^{-4} T. Since the signal from the outer side defect is larger than the magnetic noise about 10 times, the outer side defect in the steel tube with baffle is detectable using this proposed inspection method. In the full paper, the optimal magnetization condition for the inspection is examined using the 3-D edge-based hexahedral FEM. In addition, the experimental verification is also carried out.

IV. CONCLUSIONS

The results obtained are summarized as follows:

- (1) The ac flux leakage testing method using an inner coil at the low frequency (about 60Hz) is possible for detecting the outer side defect in steel tube with support steel plate (baffle).
- (2) In this inspection method, the magnetic noise due to the non-uniformity of permeability and conductivity in the steel tube and the existence of baffle is negligible.

V. REFERENCES

- [1] N.Kasai • K.Sekine, and H.Maruyama, " Non-destructive evaluation method for far-side corrosion type flaws in oil storage tank bottom floors using the magnetic flux leakage technique", *J. Jpn. Petrol. Inst.*, vol.46, no.2, pp.126-132, 2003.
- [3] Y.Gotoh and N.Takahashi, "3D FEM analysis of electromagnetic inspection of outer side defects on steel tube using inner coil-", *IEEE Trans. Magn.*, vol.43, no.4., pp. 1733-1736, 2007.

Discontinuous Galerkin method with \mathbf{T}, Φ - Φ Formulation for 3D eddy current problems

Stefan Außerhofer and Oszkár Bíró

Institute for Fundamentals and Theory in Electrical Engineering
Graz University of Technology, Austria
Email: stefan.ausserhofer@tugraz.at

Abstract—In this paper a method is proposed where discontinuous shape functions are used in eddy current problems to describe the quantities in the conducting region. Using these shape functions, the application of Galerkin’s method leads to a block-diagonal mass-matrix. Hence, if an explicit time stepping method is used, the solution of the first-order differential equation system can be solved with minimal computational effort. In the non-conducting region traditional continuous basis functions are used. The eddy current problem is formulated with the current vector potential \mathbf{T} and the reduced magnetic scalar potential Φ . In the two domains different time steps are used whereas the time steps in the conducting region have to be chosen small enough to ensure stability.

Index Terms—Discontinuous Galerkin method, Explicit time stepping, Time domain analysis, Eddy currents

I. INTRODUCTION

Discontinuous shape functions are used for several applications in technical science. One motivation for using these basis functions is the ease of handling non-matching meshes (e.g. [1]) and another reason is the ease of solving large algebraic equation systems if an explicit time stepping is used (e.g. [2]). Since the mass matrix becomes block-diagonal in the latter case, only small blocks of the mass-matrix have to be inverted which needs less computational effort. In [3] and [4] the Discontinuous Galerkin Method was introduced for two dimensional eddy current problems using the magnetic vector potential \mathbf{A} .

In this paper, the method is applied to the \mathbf{T}, Φ - Φ formulation and similarly to [3] and [4], discontinuous shape functions are used in the conducting region only because this is the region with a diffusion equation. The support of the basis functions belonging to a finite element in the conducting region is limited to this element only. Therefore, the mass-matrix in the eddy current region becomes block-diagonal and, to take advantage of this structure, explicit time stepping is used. This avoids having to solve the notoriously ill-conditioned system resulting from the discretization of the diffusion equation valid in eddy current regions. Due to the explicit time stepping, the time steps have to be chosen small enough to avoid instability.

In the eddy current free domain, where the fields are static, traditional basis functions are used which leads to a well-conditioned equation system. The time step in this region can be chosen higher compared to the time step in the

conducting domain. The combination of the two methods leads to potentially fast solutions for eddy current problems.

II. \mathbf{T}, Φ - Φ FORMULATION AND GALERKIN’S EQUATIONS

The problem is split up into two regions whereas the conducting region is denoted by Ω_c with boundary $\partial\Omega_c$ and the non-conducting region is denoted by Ω_n with boundary $\partial\Omega_n$. The interface between the two regions is Γ_{nc} .

A. Conducting region Ω_c

Multiplying Faraday’s law by \mathbf{N}_i and multiplying the time derivative of $\text{div}\mathbf{B} = 0$ by f_i , integrating over the k^{th} finite element and summing over all k yield:

$$\sum_k \int_{\Omega_k} \text{curl}\mathbf{N}_i \cdot \rho\mathbf{J}d\Omega - \sum_k \int_{\partial\Omega_k} (\mathbf{N}_i \times \rho\mathbf{J}) \cdot \mathbf{n}d\Gamma = - \sum_k \int_{\Omega_k} \frac{\partial\mu\mathbf{H}}{\partial t} d\Omega, \quad (1)$$

$$- \sum_k \int_{\Omega_k} \text{grad}f_i \cdot \frac{\partial\mu\mathbf{H}}{\partial t} d\Omega + \sum_k \int_{\partial\Omega_k} f_i \frac{\partial\mu\mathbf{H}}{\partial t} \cdot \mathbf{n}d\Gamma = 0. \quad (2)$$

In (1) and (2) the material equations $\mathbf{E} = \rho\mathbf{J}$ and $\mathbf{B} = \mu\mathbf{H}$ have been used, where ρ is the resistivity and μ is the permeability of the conductive material. \mathbf{N}_i and f_i in (1) and (2) denote the basis functions to approximate the potentials \mathbf{T} and Φ :

$$\mathbf{T} \approx \mathbf{T}_n = \sum_j t_j \mathbf{N}_j, \quad (3)$$

$$\Phi \approx \Phi_n = \sum_j \phi_j f_j. \quad (4)$$

Since $\text{div}\mathbf{J} = 0$ and $\text{curl}\mathbf{H} = \mathbf{J}$, these two potentials can be introduced as

$$\mathbf{J} = \text{curl}(\mathbf{T} + \mathbf{T}_0) \quad \text{and} \quad (5)$$

$$\mathbf{H} = \mathbf{T} + \mathbf{T}_0 - \text{grad}(\Phi), \quad (6)$$

where $\mathbf{J}_0 = \text{curl}\mathbf{T}_0$ represents the imposed current density and, therefore, \mathbf{T}_0 is known.

From (1) and (2), a first-order differential equation system can be obtained if \mathbf{J} and \mathbf{H} are replaced by (5) and (6) and if the approximations (3) and (4) are used:

$$\mathbf{M} \cdot \begin{Bmatrix} \dot{t}_i \\ \dot{\phi}_i \end{Bmatrix} + \mathbf{S} \cdot \begin{Bmatrix} t_i \\ \phi_i \end{Bmatrix} = \mathbf{f}. \quad (7)$$

In (7), \mathbf{M} is the mass-matrix, \mathbf{S} is the stiffness-matrix and \mathbf{f} includes terms with the known quantity \mathbf{T}_0 . Using appropriate basis functions (see Section III), the mass-matrix can be made block-diagonal.

B. Non-conducting region Ω_n

In the non-conducting region there are no induced currents and, therefore, only the known vector potential \mathbf{T}_0 and the unknown scalar potential Φ need to be introduced:

$$\mathbf{J}_0 = \text{curl}\mathbf{T}_0, \quad (8)$$

$$\mathbf{H} = \mathbf{T}_0 - \text{grad}(\Phi). \quad (9)$$

As a differential equation, the time derivative of $\text{div}\mathbf{B} = 0$ is used. The unknown scalar potential Φ in Ω_n is approximated by traditional continuous basis functions f_j (see Section III).

III. BASIS FUNCTIONS \mathbf{N}_j AND f_j

A. Conducting region Ω_c

The basis functions \mathbf{N}_j and f_j in Ω_c are chosen so that each of the basis functions is non-zero in one finite element only and zero in all other elements:

$$\mathbf{N}_j^k(\mathbf{r}) = \mathbf{0} \text{ if } \mathbf{r} \notin \Omega_k \text{ for } j = 1, \dots, N_k, \quad (10)$$

$$f_j^k(\mathbf{r}) = 0 \text{ if } \mathbf{r} \notin \Omega_k \text{ for } j = 1, \dots, M_k. \quad (11)$$

In (10) N_k is the number of edge basis functions \mathbf{N}_j^k for the k^{th} finite element Ω_k and in (11) M_k is the number of node basis functions f_j^k for the finite element Ω_k . Using these functions, the mass-matrix in (7) becomes block-diagonal with one block for each finite element. The finite elements are coupled by the surface integrals in (1).

B. Non-conducting region Ω_n

In Ω_n traditional continuous basis functions are used, i.e. each basis function f_j belonging to a global node is non-zero in all elements sharing this node and zero in all other elements.

IV. TIME DISCRETIZATION AND COUPLING

For the two regions Ω_c and Ω_n , two different time steps are used. The time step in Ω_c is denoted by Δt_c and in Ω_n the time step is Δt_n . To discretize the differential equation system in Ω_c an explicit time scheme is used:

$$\dot{\mathbf{x}} \approx \frac{\mathbf{x}_{k+1} - \mathbf{x}_k}{\Delta t_c}, \quad (12)$$

$$\mathbf{M} \cdot \frac{\mathbf{x}_{k+1} - \mathbf{x}_k}{\Delta t_c} + \mathbf{S} \cdot \mathbf{x}_k = \mathbf{f}. \quad (13)$$

The index k in (12) and (13) refers to the k^{th} time step and \mathbf{x} stands for the vector of the unknown variables t_i and ϕ_i in (3) and (4). In (13) the solution at step $k+1$ can be obtained from the previous solution at time step k by inverting \mathbf{M} . As a consequence of the block structure of \mathbf{M} , this can be easily done. However, the explicit scheme requires smaller time steps Δt_c in order to ensure stability. The time step in Ω_n can be chosen larger since the fields in the non-conducting region have a static character. The two time steps have been chosen

so, that the condition $\Delta t_n = L \Delta t_c$ holds. This means that the time step Δt_n is subdivided into L smaller time steps Δt_c .

For the coupling of the two domains it is assumed that the boundary conditions on Γ_{nc} for the differential equation in Ω_c are given by the boundary values obtained from the solution in Ω_n . The solution in Ω_n and hence the boundary values on Γ_{nc} are available at the time steps:

$$t = r_n \Delta t_n \quad (r_n = 1, 2, 3, \dots). \quad (14)$$

To calculate the solution in Ω_c for the time instant

$$t = r_n \Delta t_n + r_c \Delta t_c \quad (r_c = 0, \dots, L), \quad (15)$$

the boundary values from the solution in Ω_n at the time step $t = r_n \Delta t_n$ are used.

The conditions on the surface Γ_{nc} are the continuity of the normal component of \mathbf{B} and the continuity of the tangential component of \mathbf{H} :

$$\mathbf{B}_c \cdot \mathbf{n}_c + \mathbf{B}_n \cdot \mathbf{n}_n = 0, \quad (16)$$

$$\mathbf{H}_c \times \mathbf{n}_c + \mathbf{H}_n \times \mathbf{n}_n = 0. \quad (17)$$

In (16) and (17), \mathbf{n}_c and \mathbf{n}_n denote the normal vector out of the region Ω_c and Ω_n .

V. CONCLUSION

The combination of using discontinuous basis functions in the conducting region and continuous ones in the non-conducting region leads to potentially fast solutions for eddy current problems. The advantage of having a block-diagonally structured mass-matrix and using an explicit time stepping permits to solve the equation system very fast because only small blocks of the mass-matrix have to be inverted. The disadvantage of the method is the higher number of degrees of freedom in the eddy current domain and the higher number of time steps.

A possibility to improve the stability of the method is to introduce a term which penalizes the continuity of the potentials on the interface between finite elements in the conducting domain. This approach will be described in the full paper.

ACKNOWLEDGMENT

This work was supported by the Christian Doppler Laboratory for Multiphysical Simulation, Analysis and Design of Electrical Machines.

REFERENCES

- [1] P. Houston, I. Perugia and D. Schötzau, "Nonconforming mixed finite-element approximations to time-harmonic eddy current problems", *IEEE Transactions on Magnetics*, vol. 40, no. 2, pp. 1268-1273, March 2004.
- [2] J. S. Hesthaven and T. Wartburton, "Nodal higher-order methods on unstructured grids. I. Time-domain solution of Maxwell's equations", *Journal of Computational Physics*, vol. 181, pp. 186-221, 2002.
- [3] S. Außerhofer, O. Bíró and K. Preis, "Discontinuous Galerkin Finite Elements in Time Domain Eddy-Current Problems", *IEEE Transactions on Magnetics*, vol. 45, no. 3, pp. 1300-1303, March 2009.
- [4] S. Außerhofer, O. Bíró and K. Preis, "Discontinuous Galerkin Formulation for Eddy-Current Problems", *The International Journal for Computation and Mathematics in Electrical Engineering (COMPEL)*, vol. 28, no. 4, to be published, 2009.

A Mesh-Free Model of Eddy-Current Losses for 2D Analysis of Ferromagnetic Laminations

Paavo Rasilo, Antero Arkkio

Department of Electrical Engineering, Helsinki University of Technology
P.O. Box 3000, FI-02150 TKK, Finland
paavo.rasilo@tkk.fi

Abstract — A numerical model to include the effect of eddy-currents and associated losses into time-discretized 2D finite-element analysis of ferromagnetic laminations is presented. The flux-density distribution in the lamination is approximated by a truncated Fourier cosine series, and the corresponding components for the 2D nodal values of the vector potential are solved at each time step from the resulting system of equations. The eddy-current losses obtained with the model are compared with losses calculated by solving the 1D diffusion equation for the flux density in the lamination.

I. INTRODUCTION

2D finite-element (FE) analysis is commonly used in the design and analysis of electrical machines with laminated iron cores. One of the major simplifying assumptions of the 2D model is that the eddy-currents in the core regions are assumed to be zero and have thus no effect on the magnetic field to be solved. Although this assumption may be reasonable for the axial component of the currents in thin laminations, the currents flowing parallel to the cross-sectional plane of the machine may have a damping effect on the inducing field, especially at higher frequencies. Thus a method to include the eddy-current effects into the field analysis is needed for accurate loss calculation of variable-speed drives in which high-frequency flux-density harmonics commonly occur.

The in-plane eddy-currents in the laminations can be included into the 2D field calculation by coupling the 2D model to a 1D FE model of the lamination [1]. However, this approach may encounter convergence problems, especially if Newton-Raphson iteration is used, since analytical formulation of the equations needed in the iteration is difficult.

Another method to include eddy currents in laminations into the field calculation was presented in [2]. Originally implemented for homogenization of lamination stacks in 3D FE calculation, the method was based on approximating the flux-density distribution in the lamination by orthogonal polynomial basis functions, without actually discretizing the lamination. The coefficients of these functions were solved from a system of equations resulting from the error between the actual and approximated magnetic field strengths. These equations are relatively easy to form analytically and should thus lead to better convergence.

In this paper, a modified version of the latter method is applied to include the effect of eddy-currents in non-hysteretic ferromagnetic laminations into 2D FE calculation. The lamination model and the 2D model are presented, and the results of calculation are compared with a 1D FE lamination model.

II. THE LAMINATION MODEL

The mesh-free model of the flux-density distribution in a lamination with thickness d and conductivity σ is developed in detail in [1]. The time-dependent behavior of the magnetic field is described by the system of N_F equations

$$\begin{bmatrix} h_s(t) \\ 0 \\ \vdots \end{bmatrix} = \mathbf{C}_1(\nu) \begin{bmatrix} b_0(t) \\ b_1(t) \\ \vdots \end{bmatrix} + \sigma d^2 \mathbf{C}_2 \frac{\partial}{\partial t} \begin{bmatrix} b_0(t) \\ b_1(t) \\ \vdots \end{bmatrix}, \quad (1)$$

where $h_s(t)$ is the magnetic field strength on the lamination surface and $b_n(t)$ with $n = 0, \dots, N_F - 1$ are coefficients of selected basis functions $\alpha_n(z)$ used to approximate the flux-density distribution in the lamination depth $z \in [-d/2, d/2]$ as

$$b(z, t) = \sum_{n=0}^{N_F-1} b_n(t) \alpha_n(z). \quad (2)$$

The matrix coefficients are obtained by integration over the lamination thickness as

$$C_{1,lm}(\nu) = \frac{1}{d} \int_{-d/2}^{d/2} \nu(z) \alpha_{l-1}(z) \alpha_{m-1}(z) dz \quad (3)$$

$$C_{2,lm} = \frac{1}{d} \int_{-d/2}^{d/2} \alpha_{l-1}(z) \beta_{m-1}(z) dz, \quad (4)$$

where $\nu = \nu(b)$ is the reluctivity of the material and functions $\beta_n(z)$ are defined so that $\beta_n(\pm d/2) = 0$ and

$$\alpha_n(z) = -d^2 \frac{\partial^2 \beta_n(z)}{\partial z^2}. \quad (5)$$

Here, instead of polynomial basis functions, the flux-density is approximated by a truncated Fourier cosine series with $\alpha_n(z) = \cos(nkz)$, $k = 2\pi/d$. These Fourier terms fulfill the orthogonality requirement of the basis functions by definition, and make it possible to integrate coefficients (3) analytically also in nonlinear cases, if a discrete Fourier transform is first performed for the reluctivity in the lamination. Linear cases and integrations (4) can be fully handled analytically.

The eddy-current loss density in the lamination can be calculated from the time-varying flux-density distribution as

$$p(z, t) = \sigma \left[\int_0^z \frac{\partial b(z, t)}{\partial t} dz \right]^2. \quad (6)$$

III. THE 2D MODEL

The 2D finite-element electrical machine model used in this work solves the Ampere's circuital law

$$\nabla \times \mathbf{H} = \nabla \times (\nu \nabla \times \mathbf{A}) = \mathbf{J} \quad (7)$$

combined with required circuit equations in the cross-sectional xy-plane of the machine using the axial magnetic vector potential $\mathbf{A} = A(x, y, t)\mathbf{u}_z$ as the variable [3]. In the core regions, the axial component of the current density \mathbf{J} is assumed to be zero, and (7) reduces to

$$-\nabla \cdot (\nu \nabla A) = 0. \quad (8)$$

Discretizing the cross-section into elements with N nodes in total and applying the Galerkin weighted residual method results into a system of N equations for the nodal values $\mathbf{a} = (a_1 \dots a_N)$ of the vector potential.

The effect of the in-plane eddy-currents can be accounted for in the model by requiring the magnetic field strength \mathbf{H} in (7) to be equal to the surface field strength $\mathbf{h}_s = h_{sx}\mathbf{u}_x + h_{sy}\mathbf{u}_y$ obtained from the lamination model (1) and (2) for both x and y components of the magnetic field strength and flux density. This is equivalent with expressing the dependency of the vector potential on the axial coordinate z as

$$A(x, y, z, t) = \sum_{n=0}^{N_F-1} A_n(x, y, t)\alpha_n(z). \quad (9)$$

Now, instead of one single equation as in (7) and (8), a system of N_F equations is obtained for the vector potential coefficients A_n . The spatial discretization of each equation is performed as before, and the time derivatives can be discretized using e.g. the Crank-Nicolson approximation. The resulting system consists of $N_F N$ equations for the nodal values of the vector potential coefficients $\mathbf{a}_n = (a_{n,1} \dots a_{n,N})$, with $n = 0, \dots, N_F - 1$. These equations can be solved by using a suitable linear system solver and Newton-Raphson iteration in case of nonlinear materials.

IV. APPLICATION AND RESULTS

The presented model was applied to calculate eddy-current losses in a rectangular homogeneous steel lamination with a thickness of 2 mm, area of 0.06 m² and conductivity of 8 MS/m supplied by an alternating average flux density $\mathbf{B}_0(t) = B_{y0m} \sin(2\pi ft)\mathbf{u}_y$. Using $N_F = 10$ cosine terms to approximate the flux density distribution, the eddy-current losses at each time step were calculated from (6) by integrating over the volume of the lamination.

For comparison, the eddy-current losses and flux-density profiles in the lamination were calculated by a 1D FE lamination model similar to the ones presented in [1] and [4]. The magnetic vector potential in one half of the lamination was approximated by 20 linear shape functions.

Eddy-current losses obtained from the two models for a frequency range of $f = 50 \dots 5000$ Hz and amplitudes of $B_{y0m} = 0.5, 1.0$ and 1.5 T are presented in Fig. 1. Flux-density

profiles in the lamination at 1.5 T, 1000 Hz excitation are presented in Fig. 2. The results show good agreement.

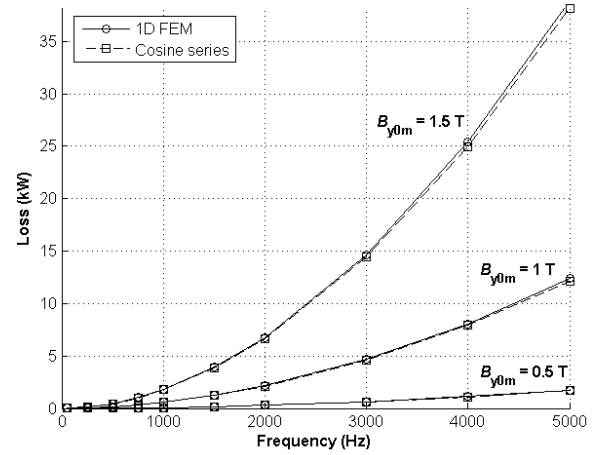


Fig. 1. Comparison of eddy-current losses from the two models

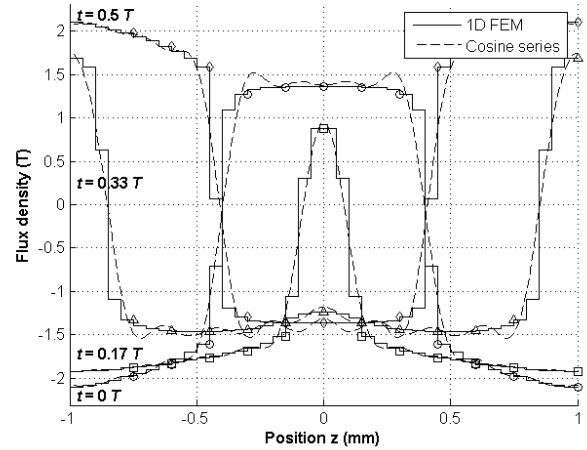


Fig. 2. Comparison of flux-density profiles from the two models with $B_{y0m} = 1.5$ T, $f = 1000$ Hz (period $T = 1$ ms)

V. CONCLUSION

A mesh-free eddy-current loss model of ferromagnetic laminations for 2D field analysis was presented. The model is able to approximate the eddy-current losses equally to a FE model. In the upcoming paper, the power balance of the model is studied and the model is applied to calculate losses in a synchronous machine.

VI. REFERENCES

- [1] O. Bottauscio, M. Chiampi, D. Chiarabaglio, "Advanced Model of Laminated Magnetic Cores for Two-Dimensional Field Analysis", *IEEE Trans. Magn.*, vol. 36, no. 3, pp. 561-573, May 2000.
- [2] J. Gyselinck, R. V. Sabariego, P. Dular, "A Nonlinear Time-Domain Homogenization Technique for Laminated Iron Cores in Three-Dimensional Finite-Element Models", *IEEE Trans. Magn.*, vol. 42, no. 4, pp. 763-766, April 2006.
- [3] M. V. K. Chari, P. Silvester, "Analysis of Turboalternator Magnetic Fields by Finite Elements", *IEEE Trans. PAS*, vol. 90, no. 2, pp. 454-464, March 1971.
- [4] R. M. Del Vecchio, "The Calculation of Eddy Current Losses Associated with Rotating Magnetic Fields in Thin Laminations", *IEEE Trans. Magn.*, vol. 18, no. 6, pp. 1707-1709, November 1982.

Boundary Element Modelling of Earth Effects on Railway Track Transmission Line Impedances

Luca Di Rienzo¹ and Zichi Zhang^{1,2}

¹ Dipartimento di Elettrotecnica - Politecnico di Milano – Milano - Italy
e-mail: luca.dirienzo@polimi.it

² State Key Laboratory of Electrical Insulation for Power Equipment, Xi'an Jiaotong University
Xi'an - P. R. China
e-mail: zichi.zhang@mail.polimi.it

Abstract — This work deals with the efficient computation of per-unit-length impedances of a railway line. Under the quasi-TEM approximation, valid in a frequency range up to some MHz, in this paper a boundary element formulation based on the magnetic vector potential is proposed, which leads to a straightforward calculation of the per-unit-length impedance matrix. The computational burden is dramatically reduced by implementing appropriate impedance boundary conditions on the rails and on the aerial lines and by substituting in the boundary integral equations the fundamental solution with a Green's function satisfying the boundary conditions at the air-earth interface, avoiding the discretization of the lossy ground.

I. INTRODUCTION

In order to increase the level of accuracy of multiconductor transmission line (MTL) models of railway lines, a key issue is the correct computation of per-unit-length (p.u.l.) impedances, taking into account the real geometry of the rail track and the property of the earth. Under the quasi-TEM approximation, which for typical values of the earth conductivity and geometrical dimensions of the railway track system holds in a frequency range up to 1 MHz [1], the computation of p.u.l. parameters of the rail track equivalent MTL can be carried out using different approaches.

The classical analytical method is based on the Carson's formula, that is valid under the assumption of filamentary conductors and homogeneous earth [2]. In order to take into account the real geometry of the rails and the multilayer nature of the earth, in [3] the finite element method (FEM) was applied. The FEM model of the ground must be sufficiently large to enclose all the eddy current distribution, which means that the current density must be reduced to practically zero before reaching the boundaries. Since the earth is characterized by low conductivity, the FEM model of the ground must have a characteristic linear dimension some orders of magnitude higher than the typical dimensions of the conductors, because it must be equal to some skin depths (in the order of 10^2 m at 50 Hz and in the order of 10 m at 100 kHz). Hence, the computational problem has a multiscale nature and the FEM model requires a mesh of a very large number of elements (of the order of 10^4). Furthermore, the presence of contact lines, some meters far from the earth, requires that a large area of the open space must also be meshed.

In this paper a different numerical approach is proposed, based on the boundary element method (BEM). The adopted

BEM formulation uses the magnetic vector potential (MVP). Following [4], a source component is introduced for the MVP which leads to a straightforward calculation of the p.u.l. impedance matrix of the MTL under analysis. The formulation taken from [4] is enriched by the implementation of the surface impedance boundary condition (SIBC) with the Leontovich approximation [5] on the rails and with its exact expression for circular wires [6] on the aerial lines, dramatically reducing the computational burden. The formulation is also further improved substituting in the boundary integral equations the fundamental solution with a Green's function satisfying the boundary conditions at the air-earth interface: in this way discretizing the lossy ground is not needed any more.

II. BOUNDARY ELEMENT FORMULATION

For the sake of simplicity and without loss of generality, the BEM formulation will be presented here referring to the geometry of Fig. 1, consisting of a MTL constituted by the two rails, the contact line, and the earth.

Under the hypothesis of a time-harmonic regime with angular frequency ω , vector fields are represented using phasors: from here on all field quantities are assumed to be complex. We also assume that displacement currents can be neglected.

Introducing the magnetic vector potential (MVP) as in [4] and expressing it as the sum of a "source" and an "eddy" components $\vec{A}(\vec{r}, t) = \vec{A}^s(\vec{r}, t) + \vec{A}^e(\vec{r}, t)$, the electric field in the conductors can be expressed as $\vec{E} = -j\omega\vec{A}^e$.

A Cartesian coordinate system is introduced, with the z -axis parallel to the conductor's axis. Currents flowing in the conductors are z -directed. Under the hypothesis that the problem is two-dimensional in the plane of the conductor's cross sections, the vectors \vec{H} , \vec{E} , \vec{A} , \vec{A}^s , \vec{A}^e can be written as $\vec{H} = H_x\vec{e}_x + H_y\vec{e}_y$, $\vec{E} = E\vec{e}_z$, $\vec{A} = A\vec{e}_z$, $\vec{A}^s = A^s\vec{e}_z$, and $\vec{A}^e = A^e\vec{e}_z$.

Application of the Coulomb's gauge $\nabla \cdot \vec{A} = 0$ to MVP leads to the Laplace equation for the MVP in air

$$\nabla^2 A = 0. \quad (1)$$

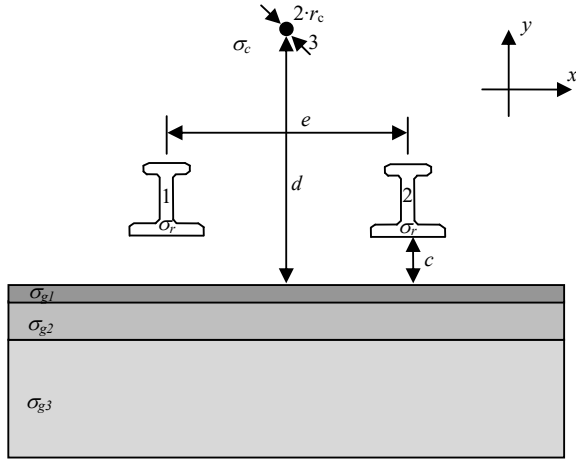


Fig. 1. The geometry of the system: conductor 1 and 2 are the rails, conductor 3 is the contact line. The geometrical dimensions are: $c=0.1$ m, $d=6$ m, $e=1.435$ m, and $r_c=6$ mm.

The boundary integral equation method yields the following integral equations

$$\frac{1}{2}A - \int_C \left(A \frac{\partial g}{\partial n} - g \frac{\partial A}{\partial n} \right) dl - \left(\frac{1}{2}A_k^s - A_1^s \int_{C_1} \frac{\partial g}{\partial n} dl - A_2^s \int_{C_2} \frac{\partial g}{\partial n} dl - A_3^s \int_{C_3} \frac{\partial g}{\partial n} dl \right) = 0, \quad (2)$$

where C_1 , C_2 , and C_3 are the conductors contours and $C = \bigcup_{k=1}^3 C_k$.

The function g is the Green's function of an infinite line current over the earth

$$g(x, y; x', y') = -\frac{1}{2\pi} \left[\log \sqrt{\frac{(x-x')^2 + (y-y')^2}{(x-x')^2 + (y+y')^2}} + \int_{-\infty}^{+\infty} \frac{e^{-\lambda(y+y')}}{\lambda + F(\lambda)} \cos \lambda(x - x') d\lambda \right], \quad (3)$$

where the first term represents the presence of a perfectly conductive plane and the second term takes into account the presence of the earth. The complex function $F(\lambda)$ can have different expressions, depending on the chosen model, which can assume the earth as homogeneous or made of two or three layers [7]. Thanks to the adopted Green's function (3), only the surface integral equations on the contours of the conductors have to be solved, without the need of discretizing the ground.

The entries of the impedance matrix can be computed by means of the following formulas

$$Z_{hh} = \frac{j\omega A_h^s}{I_h} + \text{Re}\{Z_{hh}^{an}\}, \quad (4a) \quad Z_{hk} = \frac{j\omega A_k^s}{I_h} + \text{Re}\{Z_{hk}^{an}\}, \quad (4b)$$

where $\text{Re}\{Z_{hh}^{an}\}$ and $\text{Re}\{Z_{hk}^{an}\}$ are the contribution to the self and mutual resistances from the ground return path, that can be calculated using the convenient analytical expressions of a filamentary current over a homogeneous or multilayer earth [7].

III. COMPARISON WITH FEM AND ANALYTICAL RESULTS

Numerical results given by the BEM formulation are compared with analytical solutions and with FEM simulations obtained with the help of a commercial software [8]. The contact line and the ground are considered of unitary relative permeability, while the rails have $\mu_{r1} = \mu_{r2} = 20$. The following values of conductivities are used: $\sigma_1 = \sigma_2 = 4.44 \cdot 10^6$ S/m, $\sigma_3 = 5 \cdot 10^6$ S/m. In preliminary simulations a homogeneous earth has been considered, so that $\sigma_{g1} = \sigma_{g2} = \sigma_{g3} = 0.01$ S/m. The rails are discretized using 40 constant elements per rail, while the contact line is discretized with 30 constant elements. The integral in (3) is calculated as suggested in [7].

Taking as the reference values those provided by Vance's formula [9], that is an approximation of Carson's formula [2], the maximum relative error of BEM simulations of p.u.l. self-resistance is 4% and of p.u.l. self-inductance is 1%, in a frequency range between 10 kHz and 1 MHz. On the other hand, the maximum relative error of FEM simulations of p.u.l. self-resistance is 15% and of p.u.l. self-inductance is 4.5% in the same frequency range. The errors of FEM results are mainly attributed to the finite size of the earth model and the BEM model gives more accurate results.

The analytical computation of p.u.l. self and mutual impedances of the rails is not possible, since Carson's formulae and their approximations are valid only for filamentary conductors. Anyway, BEM results are in good agreement with FEM results.

IV. REFERENCES

- [1] R. Cella, G. Giangaspero, A. Mariscotti, A. Montepagano, P. Pozzobon, M. Ruscelli, and M. Vanti, "Measurement of AT electric railway system currents at power-supply frequency and validation of a multiconductor transmission-line model," *IEEE Trans. on Power Delivery*, vol. 21, pp. 1721-1726, 2006.
- [2] J. R. Carson, "Wave propagation in overhead wires with ground return," *Bell Syst. Tech. J.*, vol. 5, pp. 539-555, 1926.
- [3] R. J. Hill, S. Brillante, and P. J. Leonard, "Railway track transmission line parameters from finite element field modelling: series impedance," *IEE Proc. - Electr. Power Appl.*, vol. 146, no. 6, pp. 647-660, Nov. 1999.
- [4] M. Cao and P. P. Biringer, "BIE formulation for skin and proximity effect problems of parallel conductors," *IEEE Trans. Magn.*, Vol. 26, No. 5, September 1990.
- [5] L. Di Rienzo, S. Yuferev, and N. Ida, "Computation of the impedance matrix of multiconductor transmission lines using high order surface impedance boundary conditions," *IEEE Trans. Electromagn. Compat.*, Vol. 50, No. 4, November 2008, pp. 974-984.
- [6] S. Ramo, J. R. Whinnery, and T. van Duzer, *Fields and waves in communication electronics*. New York: Wiley, 1994.
- [7] G. K. Papagiannis, D. A. Tsiamitros, D. P. Labridis, and P. S. Dokopoulos, "A Systematic approach to the evaluation of the influence of multilayered earth on overhead power transmission lines," *IEEE Trans. on Power Delivery*, vol. 20, No. 4, pp. 2594-2601, 2005.
- [8] Maxwell 2D v. 11, Ansoft Corporation, 1984-2006. [Online] Available: <http://www.ansoft.com>.
- [9] E. F. Vance, *Coupling to Shielded Cables*, R. E. Krieger, Melbourne, FL., 1988.

Integral Formulation and Genetic Algorithms for Defects Geometry Reconstruction using Pulse Eddy Currents

Gabriel Preda, Mihai Rebican and Florea I. Hantila
Electrical Engineering Department, Politehnica University of Bucharest,
Splaiul Independentei 313, Bucharest 060042, Romania
preda@elth.pub.ro

Abstract — A method for reconstruction of defects, buried deep under material surface, using pulse eddy currents, is proposed. Both an integral-FEM method for simulation of transient eddy-currents and genetic algorithms, as a model-free inversion technique are proposed. Numerical results for the inversion of the eddy-currents signals, using genetic algorithms, are shown.

I. INTRODUCTION

Pulse eddy currents technique is proposed as a method to detect cracks in conductive materials with large thickness. For thin structures, Eddy Currents Testing (ECT) using harmonic mode was used extensively in the past for detection of cracks in steam generator (SG) tubing of pressurized water reactors (PWR) of nuclear power plants. Although its advantages, as high speed and reliability for the routine inspections, skin effect limits this method only to thin and nonmagnetic structures. Pulse eddy currents has multiple advantages: its rectangular pulse profile accounts for a multi-frequency analysis, the lower harmonics penetrating deeper in the material, while limiting the heating exposure of the coil-probe system to only the short duration of a signal allows an increase in the power [1], [2]. Multiple industrial applications were reported, such as detection of cracks in multiple layered plates around fasteners for aeronautics industry [3], crack detection and thickness and conductivity evaluation in structural steels [4]. Current study investigates the possibility to reconstruct defects geometry using simulated pulse eddy currents signals. For the inverse problem, we apply genetic algorithms.

II. FORMULATION FOR THE FORWARD PROBLEM

The proposed method is based on application of \mathbf{T} - electric vector potential to the integral equation of eddy currents, like in [5]. Starting from Maxwell equations in quasi-stationary form and the constitutive relationship:

$$\mathbf{E} = \rho \cdot \mathbf{J}, \quad (1)$$

where \mathbf{J} is the current density, \mathbf{E} is the electrical field and ρ is the resistivity in the conductive domain Ω_c . We suppose that the field sources motion relative to the conductive domain is slow and therefore the component of the induced field through motion is very small and negligible. In the laboratory frame, the electrical field is:

$$\mathbf{E} = -\frac{\partial \mathbf{A}}{\partial t} - \nabla V, \quad (2)$$

where V is the electric scalar potential and \mathbf{A} is magnetic vector potential. The magnetic vector potential can be calculated using Biot-Savart formula:

$$\mathbf{A} = \frac{\mu_0}{4\pi} \int_{\Omega} \frac{\mathbf{J}}{r} d v + \mathbf{A}_0, \quad (3)$$

with \mathbf{A}_0 being the magnetic vector potential due to the impressed current sources:

$$\mathbf{A}_0 = \frac{\mu_0}{4\pi} \int_{\Omega_0} \frac{\mathbf{J}_0}{r} d v \quad (4)$$

and Ω_0 being the air. Only conductive media are meshed. The current density is expressed in terms of shape functions associated to the edges in the inner co-tree [5] [6]:

$$\mathbf{J} = \sum_{k=1}^n \mathbf{N}_k \nabla \times \mathbf{T}_k. \quad (5)$$

Applying Galerkin approach, the following equation system is obtained:

$$[\mathbf{R}]\{I\} + [\mathbf{L}] \frac{d\{I\}}{dt} = \{U\}, \quad (6)$$

where the terms of matrices $[\mathbf{R}]$ and $[\mathbf{L}]$ and the right-hand term $\{U\}$ are detailed in [5], [6].

In order to model 2D, zero-thickness defects, from the set of inner co-tree edges are eliminated those edges placed in the defect surface. The procedure is equivalent to zeroing the circulation of scalar electric potential \mathbf{T} on those co-tree edges [6].

All the coefficients in the system matrix are unchanged through time integration and, therefore, the resulting matrix system is formed and inverted only once. This results in considerable speed-up of overall computational process. The time step is adapted to each particular problem, in order to simulate accurately the fast variable transient regime of pulse eddy currents. Also, the rich harmonic components of a pulse impose adaptation of mesh size to the smallest skin depth, corresponding to the largest harmonic component to be taken into account [4].

III. INVERSION PROCEDURE USING GENETIC ALGORITHMS

A genetic algorithm first presented in [7] is used to solve the inverse problem of inferring the geometry and position of a zero-thickness outer defect. In order to speed-up the numerical solution, the parallel version, using Message Passing Interface (MPI), available at [8] is adopted. The optimization problem consists in finding the extreme of a fitness function, describing how accurate the simulation using the set of the actual estimated parameters approximate the original signal. Each chromosome corresponds to one parameter to be evaluated, like in [9]. The chromosome length is correlated to the parameters variation space. In our implementation, the maximum chromosome dimension is set to 7, to describe a maximum of 128 discrete values, while in a first set of tests its dimension is limited to 4. We set the following options for the genetic algorithm: variable mutation mode, mutation rate varying between 0.001 and 0.25, evolution plan: steady state with replace worst, elitism being allowed.

IV. NUMERICAL RESULTS AND CONCLUSIONS

The simulation setup for the test problem consists in a conductive plate, a pancake coil used to energize the specimen and a Hall sensor to pick-up the signal. The pancake coil – Hall sensor system is less sensitive to frequency variation than the classical auto-induction pancake used in AC testing, which in turn can be optimized for a single frequency; for pulse excitation, such an optimization is not possible [1][2][9]. The plate is 16 cm \times 16 cm, with 10 mm thickness and having conductivity $\sigma = 10^6$ S/m. Coil dimensions are inner radius $R_{min} = 2$ mm, outer radius $R_{max} = 5$ mm, axial length $l_z = 4$ mm, liftoff $z = 0.4$ mm. The pickup sensor measures the magnetic flux density and is placed in the coil axis, at $z = 0.4$ mm. The coil signal used is a 70 μ s, trapezoidal shaped pulse, and with additional rise and fall intervals of 10 μ s each, with amplitude $I_{max} = 2000$ AT, and with a repetition frequency of 50 Hz. 55 time steps are simulated for a single pulse.

In Fig. 1 we show the difference between signal with crack and signal without crack (difference signal) of z -component of magnetic flux density, measured at $x = 0$, $y = 0$, $z = 0.4$ mm (centered over the plate) for a 12 mm length, 40%, 60% and 80% outer, 0-thickness defect. The peak of the difference signal is obtained earlier for larger defects (80%) and at a later moment for the smaller defects (40%). Selecting the sampling moment according to this observation, we can increase the method sensitivity to one specific class of defects [9].

The difference signals are used as input in the inverse problem, for estimation of the defect geometry. In the first set of experiments, we aim to reconstruct the position, length and depth of a rectangular, with zero-thickness, longitudinal outer defect. The sampling moment used is $t = 30$ μ s. The three parameters to reconstruct are set as following: defect length: 0.4 from maximum 10 mm or 4 mm, defect thickness 60% or 6 mm, from maximum of 10 mm and defect position 0.8 or 4 mm from maximum or 5 mm.

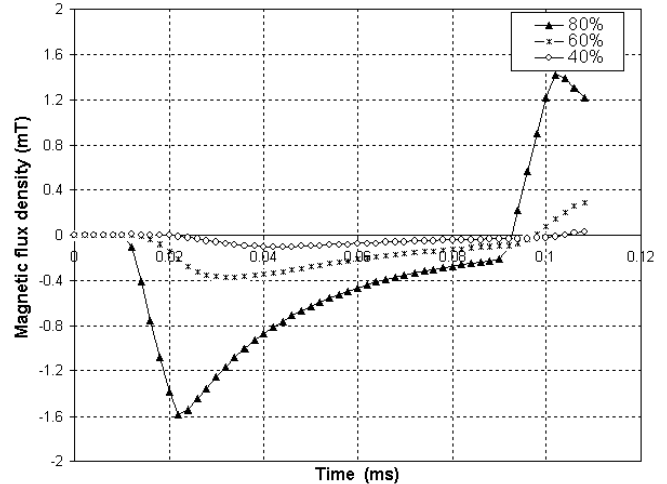


Fig. 1. Difference signals plotted against time. Defects are with zero-thickness, 12 mm long, open on outer side, ranged from 40% to 80%. The signal is the z -component of magnetic flux density, at 0.4 mm over the plate.

In this set of tests, each individual in the population is modeled with 3 chromosomes (one for each parameter to reconstruct), with a dimension of 4 bits per chromosome (to model discrete values from 0 to 1 with a 0.1 resolution). A population with 25 individuals evolves over a maximum of 120 generations. The parallel implementation for genetic algorithm described in [8] was used. The final estimation for the three parameters of (0.4, 0.6, 0.8) is approximated as (0.5, 0.6, 0.7). In the full paper we will extend the results for more complex defect geometries reconstructions, using a matrix-like representation of the defect zone, each cell corresponding to one chromosome.

V. REFERENCES

- [1] M. Gibbs and J. Campbell, "Pulsed eddy current inspection of cracks under installed fasteners", *Materials Evaluation*, Vol. 46, 1991, pp. 51-59.
- [2] J. Bowler and M. Johnson, "Pulsed eddy-current response to a conducting half space", *IEEE Trans. on Magn.*, Vol. 33, 1997, pp. 2258-2264.
- [3] B. Lebrun, Y. Jayet and J.-C. Baboux, "Pulsed eddy-current signal analysis: Application to the experimental detection and characterization of deep flaw in highly conductive materials", *NDT&E Int.*, Vol. 30, No. 3, 1997, pp. 163-170.
- [4] G. Preda, B. Cranganu-Cretu, F.I. Hantila, O. Mihalache and K. Miya, "Nonlinear FEM-BEM Formulation and Model-Free Inversion Procedure for Reconstruction of Cracks using Eddy Currents", *IEEE Trans. on Magn.*, Vol. 38, No. 2, 2002, pp. 1241-1244.
- [5] R. Albanese, F.I. Hantila, G. Preda and G. Rubinacci, "A nonlinear eddy current integral formulation for moving bodies", *IEEE Trans. on Magn.*, Vol 34, Issue 45, 1998, pp. 2529-2535.
- [6] G. Preda, F.I. Hantila, M. Rebian, "Eddy Current Solver for Nondestructive Testing using an Integral-FEM Approach and Zero-Thickness Flaw Model", *Proceedings of 13th Biennial IEEE Conference on Electromagnetic Field Computation-CEFC 2008*, Athens, Greece, 2008, pp 98.
- [7] P. Charbonneau, "Genetic Algorithms in Astronomy and Astrophysics", *The Astrophysical Journal (Supplements)*, 101, 309, 1995.
- [8] <http://whitedwarf.org/parallel/>, Parallel Pikaia Homepage.
- [9] B. Cranganu-Cretu, G. Preda, O. Mihalache, Z. Chen and K. Miya, "B-H curve reconstruction from MFL signals based on Genetic Algorithms", *Applied Electromagnetics and Mechanics*, 15, IOS Press, 2002, pp. 283-289.

A Coupling Procedure for Plasma, Iron and 3D Eddy Currents in the JET Tokamak

R.Albanese¹, G.Artaserse¹, R.Fresa¹, G. Rubinacci¹, F.Villone¹, B.Viola¹ and JET-EFDA Contributors*
JET-EFDA, Culham Science Centre, OX14 3DB, Abingdon, UK

¹Assoc. EURATOM-ENEA-CREATE, DIEL, Univ. Federico II, V. Claudio 21, 80125 Napoli, Italy

*See the Appendix of M.L.Watkins et al., Fusion Energy 2006 (Proc. 21st Int. Conf. Chengdu, IAEA, 2006)
raffaele.fresa@unibas.it

Abstract — The coupling strategy between linear MHD solvers and 3D electromagnetic codes based on the control surface concept, initially developed for the analysis of the non-axisymmetric resistive wall modes in air core fusion devices, is extended to the problem of shape and position control in the JET tokamak. This case is characterized by the presence of a ferromagnetic iron core, and the main objective of the study is the axisymmetric component of the plasma motion.

I. INTRODUCTION

The design and operation of effective control systems requires predictive models of the evolution of the plasma in the presence of complex 3D conducting structures. In [1] a linearized, non-rigid, MHD consistent model of the plasma vertical displacements is presented. It is in practice a perturbed equilibrium model, which is accurate and can be used for open loop analysis, sensor location optimization and controller design. Similar models have been proposed for the analysis of non-axisymmetric resistive wall modes [2]. For the modelling of the complex 3D structures, an integral formulation of the eddy current problem [3] was developed and successfully applied to the analysis of several cases of interest. A challenging problem is still related to a self consistent description of the MHD plasma models coupled to a detailed description of the passive structures. Although in some cases this coupling has been already efficiently modelled [4], this complex interaction still require a deeper analysis not only in future devices but also in the present tokamak experiments like the Joint European Torus (JET) tokamak, for which the effect of the bellows in the vacuum vessel has been already analyzed in a previous paper [5]. This effect is enhanced by the presence of the vacuum vessel ports and should be carefully analyzed since the time constant of the saddle currents, due to the presence of the ports, could be significant. Another important source of 3D field perturbation is represented by the combined influence of the in-

vessel components, the mechanical structure and the iron core.

The method proposed in this paper uses the coupling strategy between linear MHD solvers and 3D electromagnetic codes based on the control surface concept, initially developed for the analysis of the non-axisymmetric resistive wall modes in air core fusion devices [2, 6]. This technique is extended to the problem of shape and position control in the JET tokamak, characterized by the presence of a ferromagnetic iron core, for which the main objective of the study is to provide a linearized response model of the axisymmetric plasma motion in the presence of 3D structures.

II. THE COUPLING PROCEDURE

The coupling procedure used for the derivation of a linearized plasma response model in the presence of 3D magnetic and conducting structures requires the solution of three auxiliary problems. A suitable coupling surface, the virtual ideal wall (VIW), is chosen. This closed surface divides the domain Ω in two parts, namely the internal domain Ω_{mhd} , where the plasma dynamics is described by the ideal MHD model, and the external region Ω_{em} , in which the 3D eddy current model is used for the description of circuits, 3D magnetic media, and 3D conducting structures.

Problem 1

The first problem is defined in Ω_{mhd} , where the ideal MHD equations hold. The terms related to plasma mass are neglected [1-2]. Being interested to magnetic axisymmetric control, we solve:

$$\begin{cases} L_i^* \delta\psi_{i1} = \delta s_i \text{ in } \Omega_{mhd} \\ \text{with } \delta\psi_{i1} = 0 \text{ on VIW} \\ \text{with } \delta\psi_{i1} = 0 \text{ on } \Omega_{em} \end{cases} \quad (1)$$

where L_i^* is the linearized form of the left hand side of the axisymmetric Grad-Shafranov equation:

$$-\frac{\partial}{\partial r} \left(\frac{1}{\mu r} \frac{\partial \psi}{\partial r} \right) - \frac{\partial}{\partial z} \left(\frac{1}{\mu r} \frac{\partial \psi}{\partial z} \right) - J_\phi(\psi, s) = 0 \quad (2)$$

where μ is the magnetic permeability, ψ the poloidal flux per radian, J_ϕ the toroidal component of the current density, and s a set of plasma parameters, e.g. total plasma current, poloidal beta and internal inductance. Due to the lack of continuity of the tangential field, an artificial surface current distribution J_{s1} arises on the VIW.

Problem 2

The second problem is defined in the external domain Ω_{em} . In the presence of an iron core the problem is non-linear and a linearization procedure is needed. We use the formulation described in [5], i.e., the standard eddy currents equations in the time domain with the assumption that the magnetization \mathbf{M} is nonlinearly related to the magnetic flux \mathbf{B} :

$$\mathbf{B} = \mu_0(\mathbf{H} + \mathbf{M}), \quad \mathbf{M} = G(\mathbf{B}) \quad (3)$$

We solve the above stated problem using an integral formulation, well established for the analysis of the complex 3D structures. The solenoidality of the current density is warranted by the introduction of the electric vector potential \mathbf{T} (such that $\mathbf{J} = \nabla \times \mathbf{T}$) with a two-component gauge condition [5] to guarantee its uniqueness. We give a finite element discretization of iron and conductors, using edge elements \mathbf{N}_k to approximate \mathbf{T} , so that:

$$\mathbf{T} = \sum_k I_k \mathbf{N}_k \Rightarrow \mathbf{J} = \sum_k I_k \nabla \times \mathbf{N}_k \quad (4)$$

while the magnetization vector is supposed to be piecewise constant (\mathbf{P}_k 's are unit vector pulse functions):

$$\mathbf{M} = \sum_k M_k \mathbf{P}_k \quad (5)$$

The degrees of freedom in problem 2 are the coefficients I_k . The average axisymmetric component of the poloidal magnetic flux on the VIW is set to zero by adding a magnetostatic field in the whole domain generated by suitable axisymmetric surface currents J_{s2} located on the VIW. Suitable distributions of non axisymmetric surface currents can also be added to cancel other harmonic $n > 0$ components of the field on the VIW [2]. The resulting field inside Ω_{mhd} is then zero.

Problem 3

The last step is needed to restore continuity of the tangential field on the VIW. For each degree of freedom of the linearized problem, i.e., $\delta \underline{x}$ and $\delta \underline{l}$, we superpose the contribution due to a surface current density opposite to the previous ones computed in steps 1 and 2:

$$\left\{ \begin{array}{l} \text{linearized GS equation for } \delta \psi_{i3} \text{ in } \Omega_{mhd} \\ \text{linearized magnetostatic for } \delta \psi_{e3} = 0 \text{ in } \Omega_{em} \\ \text{with} \\ \text{poloidal flux continuity on VIW} \\ J_{sVIW} = -J_{sVIW1} - J_{sVIW2} \end{array} \right. \quad (6)$$

Dynamic model

The superposition of the three contributions can be used to derive the plasma response model by calculating the flux linked with each voltage driven circuit as well as the magnetic vector potential in the eddy current region, obtaining:

$$\underline{L}^* \frac{d\delta \underline{I}}{dt} + \underline{R} \delta \underline{I} = \delta \underline{V} - \underline{L}_s^* \frac{d\delta \underline{s}}{dt} \quad (7)$$

where \underline{L}^* is the modified inductance matrix taking account of plasma contribution [1-2, 6], \underline{L}_s^* is a similar term related to the plasma parameters, and \underline{V} is the set of applied voltages.

Acknowledgements:

This work was carried out within the framework of the European Fusion Development Agreement. The views and opinions expressed herein do not necessarily reflect those of the European Commission.

References

- [1] R. Albanese and F. Villone, "The linearized CREATE-L plasma response model for the control of current, position and shape in tokamaks", *Nuclear Fusion*, 38: 723-738, 1998.
- [2] R. Albanese, Y. Q. Liu, A. Portone, G. Rubinacci, F. Villone, "Coupling Between a 3-D Integral Eddy Current Formulation and a Linearized MHD Model for the Analysis of Resistive Wall Modes", *IEEE Trans. On Mag.* 44: 1654-1657, 2008.
- [3] R. Albanese, G. Rubinacci, "Integral Formulation for 3D Eddy Current Computation Using Edge Elements", *IEE Proceedings*, 135(7A): 457-462, 1988.
- [4] R. Albanese, R. Fresa, G. Rubinacci, F. Villone, "Time evolution of tokamak plasmas in the presence of 3D conducting structures", *IEEE Trans. on Magnetics* 36: 1804-1807, 2000.
- [5] R. Albanese, G. Rubinacci and F. Villone, "Electromagnetic Analysis of the 3D Effects of the Metallic Structures in JET Tokamak", *IEEE Trans. On Mag.* 40: 589-592, 2004.
- [6] P. Bettini, M. Cavinato and A. Portone, "Derivation of free-boundary equilibrium linear models by a flux perturbation method", *Nucl. Fusion* 49: 1-8, 2009.

Magnetic saturation modeling within finite volume method: Circuit Breaker Application

L. Rondot¹, V. Mazauric² and Gerard Meunier³

¹CEDRAT, 15 chemin de Malacher, 38246 – Meylan, France, E-mail: loic.rondot@cedrat.com

²Schneider Electric, Innovation Dept., 38TEC, 30050 – Grenoble Cedex, France

³Grenoble Electrical Engineering Lab, 38402 – Grenoble, France

Abstract — A magnetodynamic formulation is developed within the Finite Volume Method to address specific multiphysic issues involved in circuit breaker modeling. The coupling of various methods is described. Attention is paid on the non-linear magnetostatic problem. It is shown that the magnetic saturation effects have to be taken into account to correctly assess the force acting on the electric arc and, henceforth, not to jeopardize the modeling of the breaking process.

I. COUPLED ELECTROMAGNETISM AND FLUID DYNAMICAL MODELING

Various multi-physic modeling, and more particularly the current breaking modeling, requires fluid dynamics and electromagnetic models [1]. Whereas conventional Finite Volume Method (FVM) is usually dedicated to Computational Fluid Dynamics (CFD) and enforces the *local* conservation of mass, momentum and energy [2]; low-frequency electromagnetic resolutions minimize *global* energy functionals from which is derived the Finite Element Method (FEM) [3]. Hence, magneto-hydrodynamics problems are currently resolved using either:

- a FE dedicated-CFD code, which is not competitive for compressible flow with high Mach Number; or
- a hybrid method combining a FVM and a FEM, thereby sacrificing the high level of integration and the accuracy achieved with a single mesh [4].

Thus, the search for a common, effective and integrated model calls for a single numerical method for the two phenomena. In this work, an electromagnetic model based on the FVM is adopted to keep both numerical efficiency and accuracy for the CFD side.

II. ELECTROMAGNETISM WITH THE FINITE VOLUME METHOD

Previous studies established the finite volume method capabilities to (i) model the stationary current flow; (ii) determine the field in the vacuum; and (iii) characterize the field deformation around ferromagnetic pieces [5]. In order to progress towards a fully electromagnetic FVM package, a specific formulation should be developed to take into account non-linear magnetostatic properties.

A. Formulation

For 3D magnetostatics using a \mathbf{T} - ϕ formulation, the magnetic field reads $\mathbf{H}=\mathbf{T}_0-\nabla\phi$, and the magnetic flux density divergence-free is expressed as a diffusion equation with a source term resulting from the field \mathbf{T}_0 obtained in the vacuum case:

$$\underbrace{\operatorname{div}(-\mu_r \nabla \phi)}_{\text{diffusive term}} = \underbrace{\operatorname{div}(-\mu_r \mathbf{T}_0)}_{\text{source term}} \quad (1)$$

where μ_r is the non-linear magnetic permeability.

Among the various choices to describe the non-linearity [6], an “arctang” law with two parameters is used. After the vacuum magnetostatic resolution and the set-up of the relative magnetic permeability μ_r – typically the half-value of the relative magnetic permeability at the origin μ_{r_init} –, the computation is performed with an updating of μ_r at each iteration. To avoid the oscillation around the solution, an over-relaxation on μ_r is used.

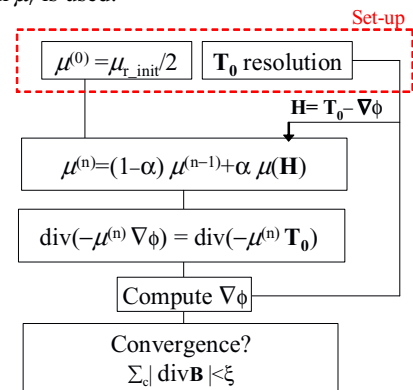


Fig. 1. Algorithm chart for the resolution of a non-linear magnetostatic problem.

The inspection of the flux density conservation provides a criterion to check the convergence.

B. Application to saturation modeling

The previous formulation is used in a 2D case where two circular conductors supplied by steady opposite currents excite a non-linear ferromagnetic plate (Fig. 2).

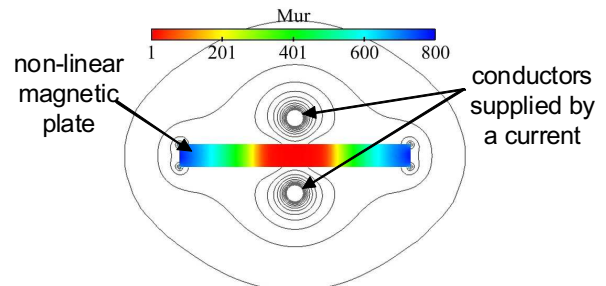


Fig. 2. Refraction of the \mathbf{H} -lines around a non-linear ferromagnetic plate excited by two conductors supplied in opposition.

The saturation is observed qualitatively and the numerical comparison with finite element computations – achieved with Flux2D[®] software – show that the relative error in energy deviates less than 5% (Fig. 2).

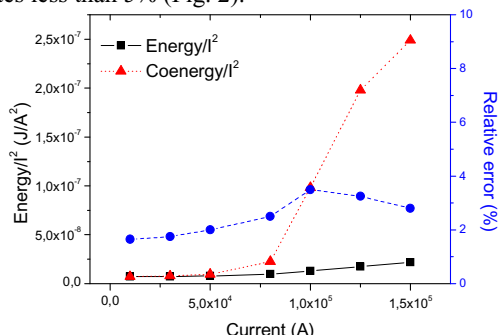


Fig. 3. Energy and co-energy curves reduced by squared current (left) and the maximum relative error computed with FEM (right) vs. supplied current.

Hence, the extension of the $\mathbf{T}\text{-}\phi$ formulation in 3D is quite straightforward [7].

III. CIRCUIT BREAKER MODELING

In the breaking process, the transient effects can be neglected in a first approach [8]. Therefore it is possible to model the whole breaking process within the previous FV electromagnetic developments.

A. The framework of the resolution procedure

The figure 4 describes the resolution procedure for each iteration. The previous formulation was implemented within the plasma physics-dedicated Schneider Electric software [9].

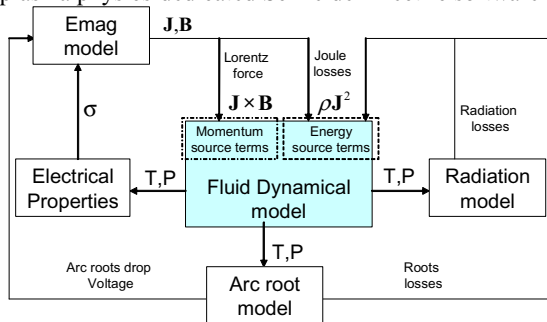


Fig. 4. Chart of the resolution procedure for the breaking process modeling (T temperature, P pressure, σ electrical conductivity)

All the models (real gas, radiation, root model and electromagnetism) are driven by the fluid dynamic based core [10]. These models are the inputs of source terms in energy and momentum. In the case of electromagnetism, the Lorentz forces and the Joule losses are introduced in fluid dynamical solver (Fig. 4).

This resolution with the CFD *Fluent*[®] code is achieved thanks to its explicit solver, which uses a Gauss-Seidel method with a multi-grid resolution.

B. Circuit Breaker Modeling

The figure 5 shows an experimental mock-up, composed of two feeders, three ferromagnetic splitters plates, and a far

pressure outlet. The mesh has 400.000 cells and the unknown solving are $(\rho, \mathbf{v}, H, V, \mathbf{T}_0, \phi)$, respectively density, velocity, Gibbs' energy, electrical potential, field in the vacuum and magnetic scalar potential. The computational time for a breaking process modeling is about 3 weeks on Pentium Xeon 2 GHz -2Go RAM.

The figure 5 also provides three iso-values of the current density when the arc enforces the ferromagnetic splitter plates.

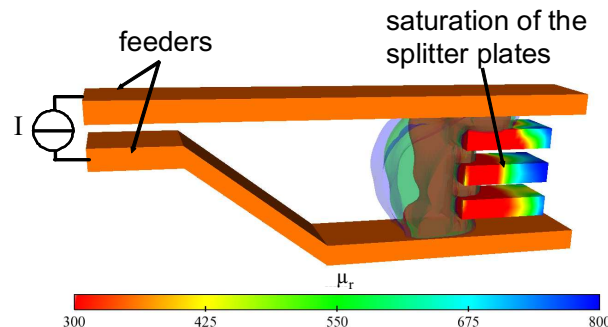


Fig. 5. Modeling of the breaking process: While the electric arc is displayed with three iso-values of the current density ($1.5 \cdot 10^7$; $8.0 \cdot 10^6$; $5 \cdot 10^6$ A·m⁻²), the saturation of the splitter plates is effective and represented with the relative magnetic permeability μ_r .

As a result, the saturation of the splitter plates is effective during the breaking process, showing that a non-linear treatment of the field is required to avoid an over-estimation of the driving force acting on the electric arc [11].

IV. REFERENCES

- [1] Carlo A. Borghi, Andrea Cristofolini, "A Hybrid Implicit Numerical Method for the Analysis of the Magneto-Plasmodynamics in a Gas Discharge," *IEEE Transactions on Magnetics*, vol. 40, 2004.
- [2] Patankar S.V. "Numerical Heat Transfer and Fluid Flow," *Hemisphere Publishing Corporation*, New York U.S.A., ISBN 0-89116-522-3, in Computational Methods in Mechanics and Thermal Sciences.
- [3] V. Mazauric, "From thermostatics to Maxwell's equations: A variational approach of electromagnetism," *IEEE Transactions on Magnetics*, vol. 40, pp. 945-948, 2004.
- [4] Ian J. Lytle "Use of MPCCI to Perform Multidisciplinary Analyses for Electrical Distribution Equipment," American Institute of Aeronautics and Astronautics, paper 0122, 2005.
- [5] L. Rondot, V. Mazauric, Y. Delannoy, G. Meunier, "Dedicating Finite Volume Method to Electromagnetic Plasma Modeling: Circuit Breaker Application", *International Symposium on applied Electromagnetics and Mechanics 2007*, paper 1– Lansing MI.
- [6] W. Thompson, P. Munk, "Mathematical model of nonlinear magnetic cores", *Magnetics, IEEE Transactions on* vol 6, p 523, Sep 1970.
- [7] Ian O.Biro et al., "Computation of 3D Current Driven skin effect Problems Using a Current Vector Potential", *IEEE Trans. AP*, vol. 29, pp. 1325-1332, 1993.
- [8] O. Chadebec, G. Meunier; V.G. Mazauric, Y. Le Floch, Y. Labie, "Eddy-current effects in circuit breakers during arc displacement phase"; *IEEE Transactions Magnetics*, vol. 40, pp 1358-1361, 2004.
- [9] P. Chevrier, M. Barrault, and C. Fiévet, "Hydrodynamic mode for electrical arc modeling", *IEEE Transactions on Power Delivery*, vol. 11, pp. 1824-1829, 1996.
- [10] F. Kareta and M. Lindmayer, "Simulation of the gasdynamic and electromagnetic processes in low voltage switching arcs", *IEEE Transactions on components, packaging, and manufacturing technology-Part A*, vol. 21, pp. 96-103, 1998.
- [11] M. Springstube and M. Lindmayer, "Three-Dimensional-Simulation of Arc Motion Between Arc Runners Including the Influence of Ferromagnetic Material", *IEEE Transactions on component and packaging technologies*, vol. 25, p. 409, 2002.

Weak Coupling between Electromagnetic and Structural Models for Electrical Machines

S. Rainer¹, O. Bíró^{1,2} and B. Weilharter^{2,3}

1- Institute for Fundamentals and Theory in Electrical Engineering, Graz University of Technology
Kopernikusgasse 24, 8010 Graz Austria
siegfried.rainer@tugraz.at

2- Christian Doppler Laboratory for Multiphysical Simulation, Analysis and Design of Electrical Machines
3- Institute for Electrical Drives and Machines, Graz University of Technology

Abstract — A weak coupling technique for an electromagnetic and a structural dynamic model for the finite element method (FEM) is presented. The algorithm fits the needs for acoustic simulations of electrical machines, and additionally offers an interface to any analytical treatment of the electromagnetic part. The algorithm will be applied to simulate vibrations of a skewed induction machine using FEM.

I. INTRODUCTION

For the numerical calculation of audible noise generated by electrical machines, it is necessary to simulate the mechanical vibrations of the stator. Based on the results of an electromagnetic simulation, the periodic reaction forces acting on the stator core stack at the air gap of the machine are estimated first. In a second step, the mechanical displacements caused by these forces on the surface of the stator are calculated by a FEM structural analysis. Displacements obtained in this way present one of the main sources of the audible noise in electrical machines. An example for this procedure can be found in [1].

Normally, the electromagnetic simulation has to be performed in the time domain for taking into account the rotor movement, and therewith the force- and field harmonics, relevant for the acoustic computation. Depending on the machine type, 2D, so called multi slice or if necessary also 3D models are conceivable.

For the mechanical part, the steady state vibrations are of interest, therefore, the structural simulation is usually done in the frequency domain by a linear time harmonic FEM computation. For the consideration of the often complex structural behaviour and boundary conditions, a 3D model is usually needed. In this case, 2D models represent quite a simplification and are therefore seldom used.

So the two models for the electromagnetic and structural simulation take care of quite different aspects and hence, apart from the underlying geometry, they have few common features. Especially the very small element size of the electromagnetic mesh near the air gap is inappropriate for a direct adoption into the structural model. As a result, the meshes of the two models are generally nonconforming with respect to each other and a coupling algorithm accounting for this has to be implemented. Usually, for acoustic concerns, the structural and the electromagnetic part can be handled independently (so called weak coupling), since the very small vibrations compared to the air gap length cause only a negligible fluctuation of the magnetic fields.

The coupling task consists mainly of a transformation of the electromagnetic forces from one mesh to the other. An important special case is the mapping from a 2D electromagnetic model to a 3D structural one. The procedure will be outlined for this case first, and then extended for multi slice and 3D electromagnetic models in the final paper.

II. EXPRESSION OF DISTRIBUTED SURFACE LOADS BY THE MEANS OF EQUIVALENT NODAL FORCES

The force output of the electromagnetic simulation is usually given in form of an electromagnetic surface force density σ (N/m²), acting on the iron core stack. From a mechanical point of view, σ is therefore a distributed force load on the surface of the structure.

The displacement based FEM formulation for a linear undamped structural dynamic problem can be stated as (see e.g. [2])

$$M \frac{d^2 u}{dt^2} + K u = f^N, \quad (1)$$

where M denotes the mass matrix, K the stiffness matrix, and u as well as $d^2 u/dt^2$ represent the unknown displacements respectively their second time derivate. f^N on the right hand side corresponds to the input load vector of equivalent concentrated nodal forces. To apply distributed surface force loads to this formulation, they need to be expressed in form of such equivalent concentrated nodal forces. Using the principle of virtual displacements (see [2]) this can be accomplished by the term

$$f_{m,\Gamma_i}^N = \int_{\Gamma_i} (H_{m,\Gamma_i})^T f_{m,\Gamma_i}^{sf} d\Gamma, \quad (2)$$

stated for a single element m with a distributed force f_{m,Γ_i}^{sf} acting on the surface Γ_i of the element. H_{m,Γ_i} denotes the part of the elemental displacement interpolation matrix contributing to any displacements on the element surface Γ_i . Therewith, f_{m,Γ_i}^N corresponds to the vector of equivalent concentrated nodal forces representing the surface load on the element m .

III. TRANSFORMATION OF THE ELECTROMAGNETIC FORCES

As the electromagnetic computation has to be performed in the time domain, $\sigma(t_n, x)$ is given in dependence of the time instant t_n and the position vector x on the iron surface. On the

other hand, the structural steady state computation is done by a time harmonic simulation and $\sigma(t_n, x)$ has to be expressed therefore by its equivalent (see e.g. [3])

$$\sigma(\omega_k, x_m) = \frac{1}{N} \sum_{n=0}^{N-1} \sigma(t_n, x_m) e^{-j(\frac{2\pi\omega_k n}{\omega_{\max}})} \quad (3)$$

in the continuous frequency domain. With the indices n and k , for the time- respective frequency index, the time period T and the total number of time samples per period N , the discrete angular frequency ω_k in (3) can be expressed as

$$\omega_k = \frac{2\pi}{T} k, \quad k = 0 \dots N-1. \quad (4)$$

Furthermore, ω_{\max} corresponds to

$$\omega_{\max} = \frac{2\pi}{T} N \quad (5)$$

in this case. Equation (3) basically results from the standard discrete Fourier transform (DFT) algorithm which is mapped into the continuous frequency domain used for the time harmonic computation of the structure. The factor $1/N$ therefore accounts for the fact that the DFT algorithm weights the resulting spectral lines with the number of time samples N .

For the transformation of the electromagnetic forces from one mesh to the other, an interpolation of the force density over the position coordinates is helpful, since it delivers a mesh independent description of the force distribution for the integral in (2). Due to the very fine mesh near the air gap, there are usually enough sample points to get a smooth function. Although this would be already sufficient for the force mapping onto the structural mesh, for acoustic computations, an additional step accounting for the periodicity of the angular position coordinate of a rotating machine, is often useful. In consequence of this periodicity, a second transformation of the forces into the spatial frequency domain is possible. Considering a 2D electromagnetic model with, apart from the slotting, constant radius of the iron - air gap interface, the general force density $\sigma(t_n, r_m, \varphi_m, z_m)$, given in a cylindrical coordinate system, reduces to a description of the form $\sigma(t_n, \varphi_m)$, neglecting any forces in the slots. The index m denotes the interpolated equidistant spatial sample points. Given this, a second DFT can be applied, leading to

$$\sigma(\omega_k, p_l) = \frac{1}{M} \sum_{m=0}^{M-1} \sigma(\omega_k, \varphi_m) e^{-j(\frac{2\pi p_l m}{M})}, \quad p_l = 0 \dots M-1, \quad (6)$$

where M denotes the number of spatial samples. Thus $\sigma(\omega_k, p_l)$, besides the angular frequency ω_k , is now given also in dependence of a spatial frequency p_l . For acoustic computations, this form is more intuitive than the form given in (3), as it is very close to the formulation an analytical treatment of the acoustic computation for the electrical machine would deliver (e.g. [4]). Additionally, only a small part of the information present in $\sigma(\omega_k, \varphi)$ respective $\sigma(\omega_k, p_l)$, in particular the parts with small spatial frequencies, produces any noise relevant mechanical vibrations. So, for an acoustic

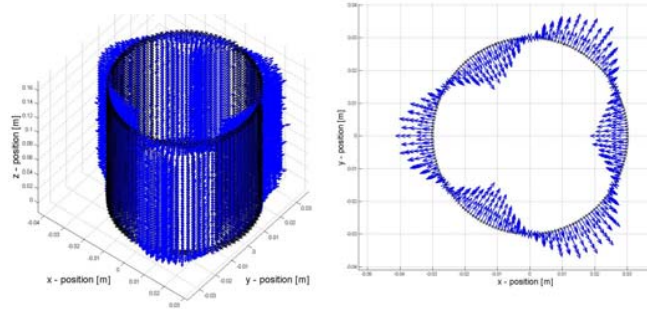


Fig. 1. Vector plot of the resulting equivalent nodal forces f^N on the cylindrical surface of an iron ring. On the surface, a radial directed, distributed force with a single spatial frequency of $p_l = 3$, constant along the z -axis, was applied. As the surface elements are not equally distributed and are varying in size, the amplitude of the nodal forces is varying too, along the axial direction.

analysis, the force description (6) depicts more clearly the source and cause of any audible noise. Furthermore it offers the possibility to investigate single spatial spectral lines, delivering in this way a better insight into the structural reaction due to specific parts of the entire excitation.

As already indicated, the description with spatial frequencies is really near to the analytical description of the machine, so it offers also a simple interface to any analytical force calculations. On the other hand, due to the totally decoupled meshes, the force distribution can be applied not only to the real structure, but also to more or less arbitrary simplifications of it, like e.g. iron rings used for analytical computations, see [4].

If due to more complex electromagnetic models, the surface forces are not constant along the axial direction, as it is the case for multi slice or 3D models, the axial force behavior has to be interpolated, too.

IV. PRELIMINARY RESULTS

The procedure has been implemented so far for a 2D electromagnetic model of an induction machine. The force transformation onto the structural mesh has been tested on a freely meshed 3D iron ring structure. Fig. 1 shows a vector plot of the estimated nodal forces for a radial surface force density with a single spatial frequency of 3 and constant behavior along the axial z -axis. For the final paper, the coupling mechanism will be implemented in order to compute vibrations of a skewed induction machine for a multi slice electromagnetic and a 3D structural machine model.

ACKNOWLEDGMENT

This work is supported by the Christian Doppler Research Association (CDG) and by the ELIN EBG Motoren GmbH.

V. REFERENCES

- [1] C. Schlensok, D. van Riesen, T. Küest, and G. Henneberger, „Acoustic simulation of an induction machine with squirrel-cage rotor,” *COMPEL*, vol. 25, no. 2, pp. 475-486, 2006.
- [2] K.-J. Bahte, “*Finite element procedures*” Upper Saddle River : Prentice-Hall, 1996, pp. 153-166.
- [3] A. V. Oppenheim, R. W. Schaffer, and J. R. Buck, “Discrete-time signal processing,” Upper Saddle River : Prentice-Hall, 1999.
- [4] H. Jordan, “*Der geräuscharme Elektromotor*”, Verlag W. Giradet, Essen, 1950.

Comparing Weak and Strong PEEC-MoM Coupling

L. Mokhtari, B. Delinchant, T. Chevalier, and J.-L. Coulomb

Grenoble Electrical Engineering Lab
BP: 46, 38402 Saint-Martin d'Hères, France
lounes.mokhtari@G2ELab.grenoble-inp.fr

Abstract. The aim of this paper is to compare strong and weak coupling of the PEEC and MoM methods applied to the modeling of magnetodynamic problem, and to generalize the weak coupling approach. MoM and PEEC are dedicated to the modeling of specific parts of the overall device. As an example of validation, we chose the modeling of a simple transformer. Resolutions of several weak couplings are compared to the strong coupling approach. Both linear and non-linear problems are treated.

Index terms. PEEC method, MoM method, weak/strong coupling, iterative methods.

I. INTRODUCTION

The PEEC (Partial Elements Equivalent Circuit) approach can model many ranges of cabling and interconnections in electric structures. The MoM method (Method of Moments) is employed to solve ferromagnetic materials interactions. Couplings have been developed [1]-[2] to take into consideration the influence of electric circuits and magnetic regions to the modeling of electric devices. This study compares coupling strategies.

II. PEEC AND MOM METHODS

A. The PEEC method

The principle of the PEEC method is to decompose a closed circuit into several parts, then calculate the mutual between them also the contribution of each of these elementary circuits to the total inductance. Inductance formulas (1) can be solved for different geometries [1]

$$l_{tot} = \frac{1}{I} \oint_C \vec{A} \cdot d\vec{l} \quad (1)$$

\vec{A} is the vector potential obtained with Biot-Savart's law, C is the whole contour of the conductor circuit which can be decomposed in N segments, and I the electric current in the conductor. We can also express the global inductance as follows (2)

$$L_{tot} = \sum_{n=1}^N \sum_{m=1}^N M p_{nm} \quad (2)$$

$M p_{nm}$ is the mutual partial between segment n and segment m calculated taken into account the shape, disposition and distance of the N conductors between them.

B. The MoM method

The MoM is an integral approach. It is well adapted to the modeling of radiating devices with simple geometries [3] The global elements magnetic field is given by (3)

$$H = H_{ext} + H_{red} \quad (3)$$

The discretization of the material gives us the magnetic field in any point P of the material (4)

$$H(P) = H_{ext}(P) + \frac{1}{4\pi} \iiint_{V_{mag}} \left(\frac{3(M \cdot r)}{r^5} \vec{r} - \frac{M}{r^3} \right) dv \quad (4)$$

H_{ext} and H_{red} are respectively the excitation magnetic field and the reaction of the material to the source field, and M is elements magnetizations.

III. PEEC-MOM COUPLING

The coupling of PEEC and MoM method can be carried out strongly by the expression of a unique linear system to solve [2], or weakly by iterations over both the two methods.

A. Strong PEEC-MoM

The strong PEEC-MoM coupling developed in [2] aimed at grouping in one global matrix the overall modeling (5),

$$\begin{bmatrix} A_{11} & A_{12} \\ A_{21} & A_{22} \end{bmatrix} \times \begin{bmatrix} M \\ I \end{bmatrix} = \begin{bmatrix} 0 \\ V \end{bmatrix}^T \quad (5)$$

$[A_{11}]$ is the MoM interaction matrix, $[A_{12}]$ gives the influence of conductors on magnetic region with Biot-Savart's law. The opposite influence is given by $[A_{21}]$ using Maxwell-Faraday's law, and finely $[A_{22}]$ is the impedance matrix obtained from PEEC method.

The resolution of the system (5) gives $[M \ I]^T$ vector composed by magnetizations of the material elements and the electric current in the conductors, according to the sources $[0 \ V]^T$.

B. Weak PEEC-MoM coupling

Each method is available separately; the coupling proposed is then based on iterative methods. The First weak coupling uses a linear system solving method for both PEEC and MoM as presents the algorithm in Fig. 1.

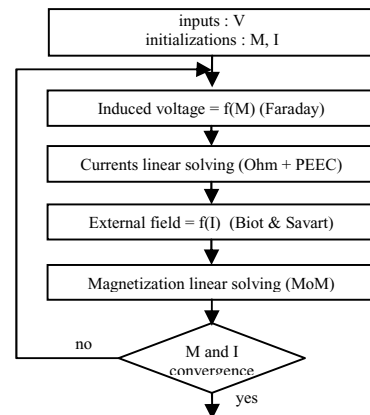


Fig. 1. Algorithm of weak coupling iterative approach

The Second and Third weak couplings use iterative methods (Jacobi or Gauss-Seidel) in order to solve linear systems, taking advantage of the existing loop.

C. Influence of non linear effects

Here we try to introduce the effect on the coupling of a non linear magnetic material. Reader must be aware that only MoM magnetization maximal value is affected by our basic non-linear modeling, PEEC solving has been kept with pure sinusoidal currents. The main idea is to linearize ferromagnetic material to solve iteratively linear systems with an equivalent permeability, taking advantage of the existing loop. Then we will see convergence properties of the coupling, even with temporary approximated currents.

IV. APPLICATION

The application example is the modeling of a simple transformer (Fig. 2). Two square conductors are placed on two parallel planes and a magnetic core is placed through their centers. The first conductor is powered by an alternative source voltage (1V, 1kHz). The second conductor is short-circuited.

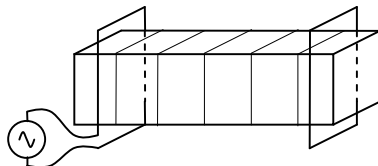


Fig. 2. Geometry of the test device

For the same results of currents and magnetizations, the resolution time between the strong and weak couplings are compared.

A. Results

Three comparisons have been made on system solving time, iterations number, computer memory, regarding the number of unknowns; one for a linear modeling, and two with non-linear iterations with and without saturation.

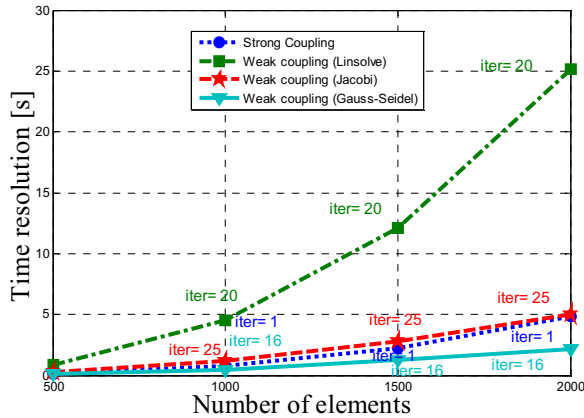


Fig. 3. Linear modeling methods comparison

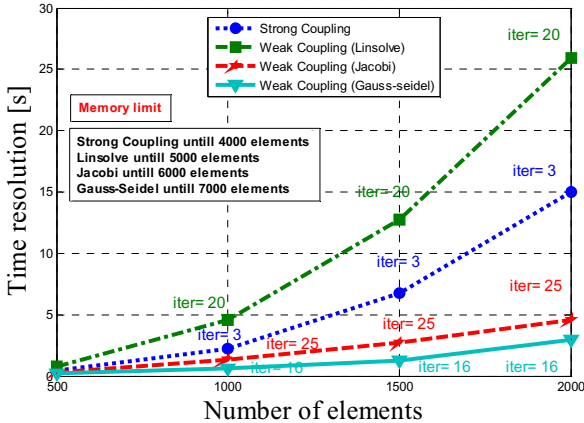


Fig. 4. Comparison with non-linear treatments without saturation

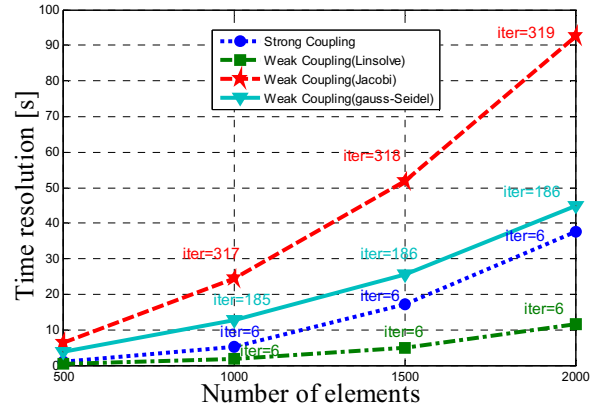


Fig. 5. Comparison with non-linear treatments with saturation

B. Comments

- linear case (Fig.3): the strong coupling reaches the result without iterations since it is a pure linear solving method, but time for high number of unknown is greater than weak coupling using GS. The case of weak coupling with direct linear solving is particular here since oscillations appear during convergence.

- non-linear material without saturation (Fig. 4): iterations of non linear solving are totally hidden by weak coupling solving. Only strong coupling results change compared to Fig. 3 to reach non linear convergence. It can be noticed that memory limitations have been compared with a limit about two times greater for weak coupling GS comparing to strong coupling.

- non-linear material with saturation (Fig. 5): weak coupling using iterative method shows slow convergence surely due to the interaction between iterative linear solving with approximated permeability. Here weak coupling with direct linear solving is the best (approximated permeability seems to act as a relaxation).

V. CONCLUSION

Different strategies of weak coupling of the PEEC and MoM methods have been compared with the strong coupling. It appears that weak coupling is better in term of time resolution and memory saving but for different method depending cases. An interesting improvement can be realized for both GS method in the case of saturated material, and direct linear solving in non saturated case to respectively speed up and relax convergence.

Adding to the gain on time and memory, the weak coupling presents other advantages like, easy understanding because it repeats faithfully the evolution of physical phenomena in system, more flexible and parallelizable tasks, and also reusability of the codes developed.

Perspectives are the modeling of more realistic non linear MoM-PEEC coupling. And then we try to establish interface specifications on MoM and PEEC methods to be easily coupled.

VI. REFERENCES

- [1] M.Troscher, U.Jakobus, Steinmair, G, « Combined PEEC/MoM solution technique for efficient electromagnetic emission calculations of PCBs in metallic enclosures », International Symposium on Electromagnetic Compatibility, 2004. EMC 2004.
- [2] T. Le Duc, O.Chadebec, J-M.Guichon, and G.Meunier, « Couplage de la méthode moment magnétique avec la méthode PEEC pour la résolution des problèmes magnétodynamique », NUMELEC 2008, Liège (Belgique) 8-9-10 décembre 2008.
- [3] O.Chadebec, J-L Coulomb, and Fleur Janet « A Review of Magnetostatic Moment Method », IEEE Transactions on Magnetics, vol. 42, no. 4, april 2006.
- [4] Antonini, G.; Sabatini, M.; Miscione, G. "PEEC modeling of linear magnetic materials", IEEE International Symposium on Electromagnetic Compatibility, EMC 2006. Vol. 1, n°14-18 Aug. 2006, pp: 93 – 98.

Dynamic Electro-Flow-Thermal 2D Model of a Transformer Using the CBS algorithm

M.A. Arjona, *IEEE Senior Member*, R.B.B. Ovando-Martínez and C. Hernández, *IEEE Member*
 Instituto Tecnológico de la Laguna, División de Estudios de Posgrado e Investigación
 Blvd. Revolución y Calz. Cuauhtémoc, 27000, México
 Email: marjona@ieee.org

Abstract — The paper presents the thermal and fluid dynamics prediction of a distribution transformer. The model is based on the solution of the Navier-Stokes equations and the Maxwell equations which are solved sequentially. The thermal-fluid equations are solved using first-order finite elements and the characteristic-based-split scheme was used. The model results are compared against those obtained with commercial CFD software.

I. INTRODUCTION

In the design of electrical equipment, i.e., motors, generators and transformers, one design aim of the engineers is the minimization of the losses to increase efficiency and to avoid high temperatures within it. Thermal prediction is important because it allows assessing the dissipation of losses in the equipment. In addition, the insulation damage is directly linked to the hot-spot winding temperature; most of the transformers are immersed in mineral oil which has the functions of acting as a coolant and as an insulator. The cooling of transformers can be achieved by force-air (dry-type), natural and forced convection (oil-filled) or a combination of them. Conduction, convection and radiation are the forms of heat transfer in the transformer. The Navier-Stokes equations can model the thermal and fluid dynamics of oil-filled transformers [1]. In this paper, two-dimensional (2D) Finite Elements (FE) are used to solve the Maxwell and Navier-Stokes partial differential equations. The loss density in a distribution transformer are computed under no-load and load conditions using two FE models; the loss density is then employed in the Navier-Stokes equations which are solved using the Characteristic-Based-Split (CBS) scheme to compute the transient behavior of temperature and velocity fields within the transformer. The mathematical formulation was coded in C and the thermal results were validated using commercial software. The paper presents initial results of a project to couple the fluid dynamics and electromagnetic phenomenon in order to have a model for the integral analysis of transformers.

II. ELECTROMAGNETIC FIELD MODEL

The electrical losses generated within a transformer are: winding (dc and eddy), core and stray losses; the latter are neglected because its small numerical values. A 1500 kVA, 13200/220 V, delta-wye transformer was used in this paper [2]. The induced eddy current loss was calculated simulating

the load test, and its governing equation for the axi-symmetric model is [3]

$$\frac{\partial}{\partial z} \nu \frac{\partial (rA)}{r \partial z} + \frac{\partial}{\partial r} \nu \frac{\partial (rA)}{r \partial r} + \frac{j\omega\sigma}{r} (rA) = J_s \quad (1)$$

where ν represents the reluctivity, ω is the angular frequency, σ is the electric conductivity, A is the complex magnetic vector potential, J_s is the source complex current and r is radius.

The winding eddy current loss is calculated with

$$P_w = \iiint_{\Omega_w} \left(\frac{J^2}{\sigma} + \frac{\pi^2 \sigma f^2 b^2 B^2}{6} \right) d\Omega_w \quad (2)$$

where P_w stands for the winding losses, f is the rated frequency, b is the dimension of copper strip in the flux density B directions (x and y), J is the current density and Ω_w is the winding region volume.

The no-load core-loss is computed with the 2D Cartesian expression for the non-linear Poisson equation coupled to an external voltage source and after discretizing it using first order finite elements, it can be expressed as

$$\begin{bmatrix} S + j\omega N & -P \\ j\omega Q & R + j\omega L \end{bmatrix} \begin{bmatrix} A \\ I_w \end{bmatrix} = \begin{bmatrix} 0 \\ V_e \end{bmatrix} \quad (3)$$

where S is the FE stiffness matrix, P and Q are weighting winding matrices, R is the external resistance, L external inductance, I_w a vector of winding currents, V_e denotes the external potential sources and A represents a vector of complex potentials.

The core loss is calculated using the computed flux density with (3) and the core-loss information given by the core manufacturer as

$$P_{fe} = \iiint_{\Omega_c} m_c \rho_c f(B) d\Omega_c \quad (4)$$

where $f(B)$ is the specific iron loss, m_c denotes the core weight, ρ_c is the density of core oriented steel and Ω_c is the core volume.

III. THERMAL FIELD MODEL

The fluid and thermal behavior for oil-filled transformers with natural cooling are described by the continuity, momentum and energy equations, they are also known as the Navier-Stokes equations [4]. For incompressible fluids and constant density, the set of equations are:

a) Continuity equation (or mass conservation)

$$\frac{\partial U_i}{\partial x_i} = 0 \quad (5)$$

where $i=1,2$ denotes the components of U_i in 2D, $U_i=\rho u_i$, u denotes the velocity, ρ is the mass density and x_i are space variables.

b) Momentum equation

$$\frac{\partial U_i}{\partial t} = -\frac{\partial(u_j U_i)}{\partial x_j} + \frac{\partial \tau_{ij}}{\partial x_j} - \frac{\partial P}{\partial x_i} - \rho g_i \quad (6)$$

where

$$\tau_{ij} = \mu \left(\frac{\partial u_i}{\partial x_j} + \frac{\partial u_j}{\partial x_i} \right)$$

and $i=1,2$; $j=1,2$, P is the pressure, μ represents the kinematics viscosity, g is the gravity, τ is the viscosity tensor, and t represents time.

c) Energy equation

$$\begin{aligned} \frac{\partial(\rho E)}{\partial t} = & -\frac{\partial(u_j \rho E)}{\partial x_j} + \frac{\partial}{\partial x_i} \left(k \frac{\partial T}{\partial x_i} \right) - \frac{\partial}{\partial x_j} (u_j P) \\ & + \frac{\partial}{\partial x_i} (\tau_{ij} u_j) \end{aligned} \quad (7)$$

where E is the stored energy per unit mass, T denotes the absolute temperature and k is the thermal conductivity.

After applying the characteristic Galerkin procedure to the discretization of (5-7), and applying the Characteristic-Based-Split scheme, where in the first step, the pressure term is dropped and an intermediate velocity is calculated. In the second step, the pressure is calculated and at step 3, the velocities are corrected [4]. The set of discrete equations to solve are,

$$\begin{aligned} [M] \frac{\{\Delta U_1^*\}}{\Delta t} &= [C] \{U_1^n\} + [K_m] \{U_1^n\} + [K_s] \{U_1^n\} \\ [M] \frac{\{\Delta U_2^*\}}{\Delta t} &= [C] \{U_2^n\} + [K_m] \{U_2^n\} + [K_s] \{U_2^n\} + \text{gravity forces} \\ [K_m] \{\Delta P\} &= [M] \{U_1^*\} + [C] \{U_2^*\} + [K_s] \{P^n\} \end{aligned} \quad (8)$$

$$[M] \{U_1^{n+1}\} = [M] \{U_1^*\} + [C] \{P^n\} + [C] \theta_2 \{\Delta P\}$$

$$[M] \{U_2^{n+1}\} = [M] \{U_2^*\} + [C] \{P^n\} + [C] \theta_2 \{\Delta P\}$$

$$[M] \frac{\{\Delta T\}}{\Delta t} = [C] \{T_n\} + [K_i] \{T_n\} + [K_s] \{T_n\} + \frac{qA}{3C_p \rho} [I] + \frac{\mathfrak{I}q}{2} [I^1]$$

where M , C , K_s , K_m and K_i are matrices that contain material properties and domain geometry. U_1^* and U_2^* denote velocity related terms in the first step of the CBS scheme. T is the temperature, C_p is the specific heat, A is area, q is the heat source, \mathfrak{I} represents the distance between nodes at a boundary and \bar{q} denotes power density dissipated in a surface

boundary. The parameter θ_2 are related to the time discretization of the equations. The identity vectors I and I^1 are used for the heat source and boundary regions.

IV. SIMULATION RESULTS

A first order FE mesh was constructed to compute the transformer losses [5]. Using the same mesh, with the proper classification of regions (solid and fluid), the Navier-Stokes equations were solved. The thermal distribution obtained with the formulation presented here and from the commercial software are shown in figs. 1-2 [6]. Good results were also achieved for the velocity field of the transformer oil. Dirichlet boundary condition was used, but the model can handle convective and radiation boundary conditions. More results will be presented in the full paper version.

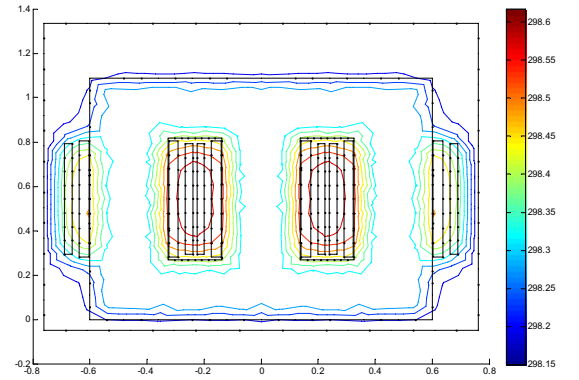


Fig. 1 Temperature distribution (°K) calculated at 60s using the model.

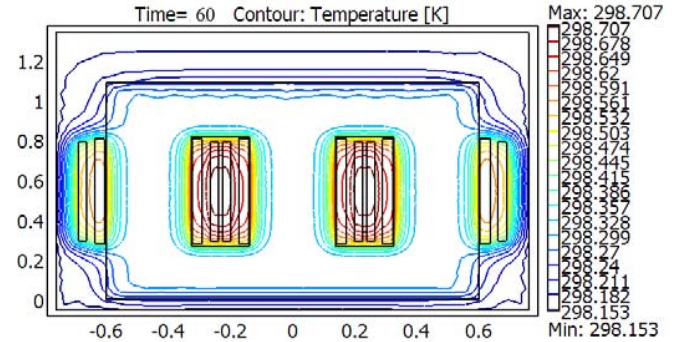


Fig. 2 Temperature distribution (°K) at 60s using the commercial software.

V. REFERENCES

- [1] C. Rosas, N. Moraga, V. Bubnovich and R. Fisher, "Improvement of the cooling process of oil-immersed electrical transformers using heat pipes," *IEEE Trans. on Magnetics*, 20(3):1955-1961, 2005.
- [2] C. Hernández and M.A. Arjona, "Design of distribution transformers based on a knowledge-based system and 2D finite elements," *Journal of Finite Elements in Analysis and Design*, 44:659-665, 2007.
- [3] J.P.A. Bastos and N. Sadowski. *Electromagnetic Modeling by Finite Element Methods*, Marcel-Dekker, Inc. 2003, pp. 283-339.
- [4] O.C. Zienkiewics and R.L. Taylor. *The Finite Element Method, Vol. 3 Fluid Dynamics*, Butterworth Heinemann, 2000, pp 64-85.
- [5] SLIM, user manual 2008.
- [6] COMSOL user manual 2009.

FEM for directly coupled magneto-mechanical phenomena in electrical machines

Katarzyna Fonteyn¹, Anouar Belahcen¹, Reijo Kouhia² and Antero Arkkio¹

¹Department of Electrical Engineering,

²Department of Structural Engineering and Building Technology,

Helsinki University of Technology, P.O.Box 3000, FI-02015 TKK, Finland

¹katarzyna.fonteyn@tkk.fi

Abstract—A fully coupled magneto-mechanical model is proposed for simulating the effect of the magnetostrictive and magnetic forces in iron and applied to electrical machines. The model is based on the general balance laws of electromagnetism, mechanics, and continuum thermodynamics and it is implemented in 2D by using a conforming finite element method for the magnetic vector potential and the displacement field. The simulated results are in accordance with measurements on a test device.

I. INTRODUCTION

In non-linear magnetic media, the magnetic permeability depends on the magnetic, mechanical and thermal behavior. The magnetostriction depends on the field and on the stress state of the material. Previous research mainly treats the magneto-mechanical coupling problem as an indirect strongly or weakly coupled problem [1], [2]. In the weak coupled problem, local magnetic forces and local forces due to magnetostriction are calculated and the displacement is evaluated from those. The magnetic flux density updating is realized through measured permeability curves dependent on stress as in [3]. However, the more complex direct coupling requires a formulation of the interaction of different factors on the behavior of the material. This paper reports on a numerical implementation of a model for isochoric magneto-elastic deformation describing the coupled behavior of magnetic and mechanical properties of the material.

II. MODELING MAGNETOELASTIC DEFORMATION

The constitutive equations coupling the magnetic and elastic properties of the material are derived from a suitable form of the Helmholtz free energy presented in [4]. The material is supposed to be isotropic and isochoric. The model is extensively justified in [4] and [5]. The magnetic field strength vector \mathbf{H} is related to the total strain tensor $\boldsymbol{\varepsilon}_{\text{tot}}$ and flux density vector \mathbf{B} by

$$\mathbf{H}(\mathbf{B}, \boldsymbol{\varepsilon}_{\text{tot}}) = \mu_0^{-1} \mathbf{B} + \mathbf{M}(\mathbf{B}, \boldsymbol{\varepsilon}_{\text{tot}}). \quad (1)$$

The total stress tensor, $\boldsymbol{\tau}$ for iron is defined as the contribution of the Cauchy stress tensor $\boldsymbol{\sigma}$ and the electromagnetic stress tensor $\boldsymbol{\tau}_{\text{em}}$

$$\boldsymbol{\tau}(\mathbf{B}, \boldsymbol{\varepsilon}_{\text{tot}}) = \boldsymbol{\sigma}(\mathbf{B}, \boldsymbol{\varepsilon}_{\text{tot}}) + \boldsymbol{\tau}_{\text{em}}(\mathbf{B}, \boldsymbol{\varepsilon}_{\text{tot}}). \quad (2)$$

The necessary 6 parameters of the model are identified from unidirectional magnetostrictive stress measurements from a

modified Epstein frame [5]. Figure 1 shows the measured magnetostrictive strain and corresponding results from the model for both cases of compressive (curves 2-4) and tensile (curves 5-9) mechanical pre-stresses. The best fitted curve (curve 1) corresponds to no mechanical pre-stress.

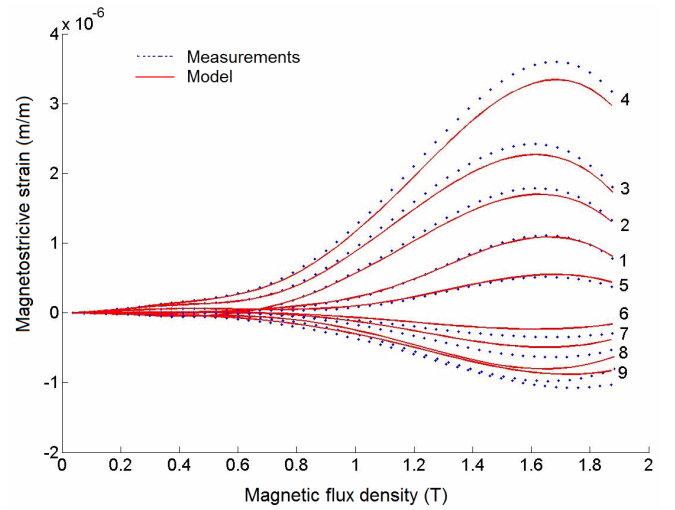


Fig. 1. Magnetostrictive strain vs. magnetic flux density in the presence of tensile and compressive pre-stresses.

III. PROPOSED FINITE ELEMENT METHOD

The magnetic flux density and the displacements are solved at the element level by a coupled 2-D FEM approach and the Galerkin weighted residual weak form is implemented. The first order linearization of \mathbf{H} and $\boldsymbol{\tau}$ for the Newton's iteration are written as

$$\mathbf{H} = \mathbf{H}_0 + (\partial_{\mathbf{B}} \mathbf{H}) \delta \mathbf{B} + (\partial_{\boldsymbol{\varepsilon}} \mathbf{H}) \delta \boldsymbol{\varepsilon} \quad (3)$$

$$\boldsymbol{\tau} = \boldsymbol{\tau}_0 + (\partial_{\boldsymbol{\varepsilon}} \boldsymbol{\tau}) \delta \boldsymbol{\varepsilon} + (\partial_{\mathbf{B}} \boldsymbol{\tau}) \delta \mathbf{B}. \quad (4)$$

The iterative changes of the magnetic flux density, magnetic vector potential, strain, and displacements are denoted as $\delta \mathbf{B}$, $\delta \mathbf{A}$, $\delta \boldsymbol{\varepsilon}$ and $\delta \mathbf{u}$, and they are related by:

$$\delta \mathbf{B} = \nabla \times \delta \mathbf{A} \quad (5)$$

$$\delta \boldsymbol{\varepsilon} = \frac{1}{2} (\nabla \delta \mathbf{u} + \nabla \delta \mathbf{u}^T). \quad (6)$$

The nodal displacements \mathbf{u}_i and \mathbf{v}_i in x and y directions and the nodal values of the magnetic vector potential \mathbf{a}_i are the quantities solved according to (5) and (6). The Jacobian

matrix for the system of equation is expressed from (3) and (4). Through this formulation, the effect of the magnetic field on the elastic field is accounted for as well as the effect of the elastic field on the magnetic field. The procedure is outlined in Figure 2.

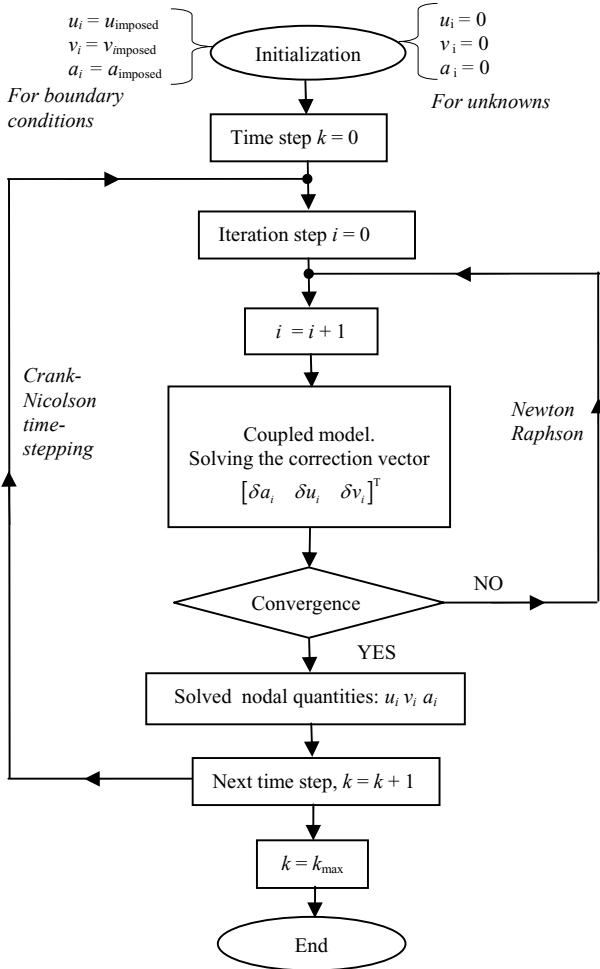


Fig. 2. Simplified flowchart illustrating the magneto-mechanical directly coupled finite element method.

IV. RESULTS AND VERIFICATIONS

The method is applied to a 4-pole 15 kW induction machine and also validated by comparing measurements and simulations from a test device. In the first case, the displacements in the rotor shaft are set to be zero in all directions. The outer surface of the stator can move in the radial direction only and all the other nodes are free. The contribution of magnetostriction and magnetic forces in iron, only, tends to expand the shape of the machine as seen in Figure 3. The simulation was performed under the rated voltage of 380 V and a slip of 3.2%. The amplitude of the maximum magnetic flux density in some parts of the machine (in some of the stator and rotor teeth, for instance) was 2 T. The distribution of the magnetic flux density is presented in Figure 4.

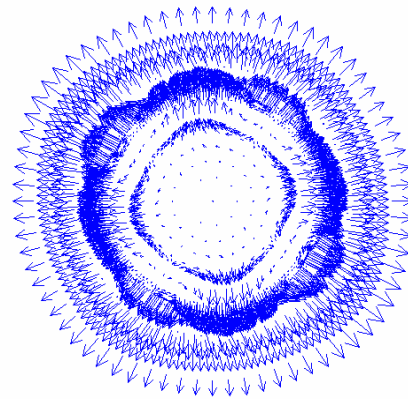


Fig. 3. Deformation of 15 kW induction motor due to magnetostriction and magnetic forces in iron, (Scale x 500 000)

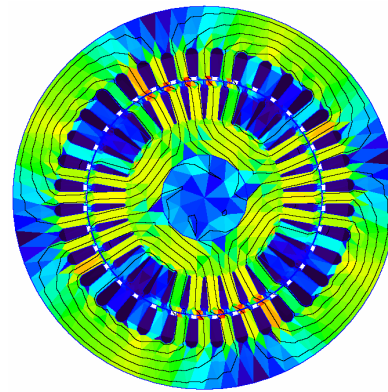


Fig. 4. Geometry of the studied machine for the non-deformed state and distribution of the magnetic flux density, cross section.

V. CONCLUSION

This study focuses on the suitability of a coupled magneto-mechanical technique for vibrations analysis in electrical machines. The 2-D magnetic field and displacement are solved simultaneously without using the common “equivalent forces” approach. It enables an efficient computation as the different single valued stress-dependent magnetization curves do not need to be evaluated one by one as in the previous methods.

VI. REFERENCES

- [1] Ch. Body, G. Reyne and G. Meunier, “Finite Element Modeling of Magneto-Mechanical Phenomena in Giant Magnetostrictive Thin Films” *IEEE Transactions on Magnetics*, Vol. 33, no. 2, pp. 1620-1623, 1997.
- [2] K. Delaere, W. Heylen, R. Belmans, and K. Hameyer, “Computational and Experimental Analysis of Electrical Machine Vibrations Caused by Magnetic Forces and Magnetostriction”. *IEEE Transactions on Magnetics*, Vol. 38, No.2, pp. 969-972, 2002.
- [3] A. Belahcen, "Magnetoelastic coupling in rotating electrical machines", *IEEE Transactions on Magnetics*, Vol. 41, No.5, pp.1624-7, 2005.
- [4] A. Belahcen, K. Fonteyn, A. Hannukainen, R. Kouhia, “On numerical modeling of coupled magnetoelastic problem”, *Proceedings of the 21st Nordic Seminar on Computational Mechanics*, Trondheim, 2008, pp. 203-206.
- [5] S. Fortino, R. Kouhia, A. Belahcen, K. Fonteyn, “A coupled model for magnetostriction in ferromagnetic materials”, *International Conference on Computational Methods for Coupled Problems in Science and Engineering Coupled Problems II*, Barcelona, Spain, 2007, 483-486.

3D Numerical Modeling of the Thermo-Inductive Technique Using Shell Elements

B. Ramdane, D. Trichet, M. Belkadi and J. Fouladgar

Institut de Recherche en Electrotechnique et Electronique de Nantes Atlantique (IREENA)

37, Boulevard de l'université – BP 406 – 44600 Saint Nazaire Cedex, France

Brahim.ramdane@univ-nantes.fr

Abstract—Thermo-inductive testing is a new technique used for health investigations on different components of automotive and aeronautic industries. In this technique, eddy current deviation around the default creates local heating which can be detected by an infrared camera. The purpose of this work is to develop an original 3D finite element model as a support tool and to study the reliability of the technique. To reduce the number of unknowns, shell elements are introduced to model the defects. Inspected materials are classified into magnetic, non-magnetic and composites. Investigations on various parameters of the technique and crack dimensions are performed in order to optimize the method. Experimental and simulation results show that the method is well suited.

I. INTRODUCTION

Cracks constitute one of the major problems threatening the security of systems subjected to mechanical, thermal or chemical constraints. In order to detect and characterize these defects, many methods of NDT are used and they are in a constant development according to applications and investigation fields. In this context, we propose a new method called thermo-inductive technique which combines the advantages of both eddy current and infrared thermography techniques. The relevance and the feasibility of the technique have been shown in previous papers [1-2].

Numerical modeling of cracks involves difficulties due to their small thickness compared to other dimensions. This is expressed by mesh problems such as high density or deformed elements leading to a prohibitive computing time or ill-conditioned matrix systems. In literature, many researches have been carried out to model thin regions. Among the various proposed methods, the shell elements one which derives from degeneration of Whitney prism elements is well suited for our problem [3].

The ability of thermo-inductive method to detect the defects depends on electromagnetic and thermal properties of the material under investigation. In automotive and aeronautic industry, three principal groups of material are used: ferromagnetic metals, non magnetic metals and carbon fibre composites. The first group has a non linear magnetic permeability and a typical small electromagnetic skin depth compared to the thermal depth. The second group has linear characteristics but the same constraint on electromagnetic and thermal penetration and the third group has non isotropic physical properties but a high skin depth.

To consider all these constraints, we have developed a 3D finite element method based on Whitney's elements under Matlab environment as a support tool to model the different phenomena involved in this technique. This model takes into

account the anisotropy, the non-linearity of materials and cracks modeled by the shell elements.

The new technique is applied to defects detection in typical pieces used in automotive and aeronautic industries. Due to their anisotropic properties and scale factor, composite materials are modeled after a preliminary homogenization stage. Investigations on various parameters such as inductor geometry, defect characteristics and field and thermal frequencies have been carried out for each material in order to optimize the defect detection.

II. PROBLEM DESCRIPTION

A typical measurement installation for the thermo-inductive method is shown in Figure 1. In this technique, the electromagnetic and thermal penetrations have a great influence on the defect detection. These two parameters depend on the field and thermal frequencies as well as the material physical properties. This is why the optimal field and thermal frequencies depend on the material under investigation. The induction frequency may vary from 50 Hz to 2 MHz and the thermal frequency from 0.1 Hz to 20 Hz.

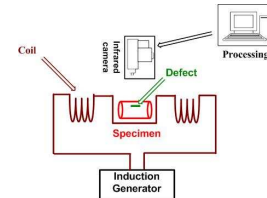


Fig. 1. Schematic of experimental system

A numerical modeling allows a good understanding of the influence of these properties on the current flow and the temperature distribution, and therefore on the defect detection.

III. NUMERICAL MODELING

The electromagnetic problem defined by Maxwell's equations is solved with the 3D finite element method. Using T- Φ formulation, the weak formulation T- Φ used in the harmonic state is [4]:

$$\int_{\Omega_C} \left(\left[\frac{1}{\sigma} \right] \text{curl } \mathbf{W}_{e_i} \cdot \text{curl } \mathbf{T} + j\omega[\mu] \mathbf{W}_{e_i} \cdot (\mathbf{T} - \text{grad}\Phi) \right) d\Omega = - \int_{\Omega_C} \left(\left[\frac{1}{\sigma} \right] \text{curl } \mathbf{W}_{e_i} \cdot \text{curl } \mathbf{T}_0 + j\omega[\mu] \mathbf{W}_{e_i} \cdot \mathbf{T}_0 \right) d\Omega \quad (1)$$

$$- \int_{\Omega_C} j\omega[\mu] \text{grad } \mathbf{W}_{n_i} \cdot \mathbf{T} d\Omega + \int_{\Omega} j\omega[\mu] \text{grad } \mathbf{W}_{n_i} \cdot \text{grad } \Phi d\Omega = \int_{\Omega} j\omega[\mu] \text{grad } \mathbf{W}_{n_i} \cdot \mathbf{T}_0 d\Omega \quad (2)$$

Where \mathbf{T} is the electric vector potential, Φ is magnetic scalar potential, $[\mu]$ represents the tensor of equivalent magnetic permeabilities, and $[\sigma]$ the tensor of electric conductivities and \mathbf{T}_0 is the source field. \mathbf{W}_{e_i} and \mathbf{W}_{n_i} are the edge and nodal shape functions respectively. Ω and Ω_C are respectively the whole and the conducting domains.

In order to take into account of the nonlinearity of magnetic materials, the iterative calculation using the Newton-Raphson method is adopted. Different algorithms to obtain optimal relaxation factor are introduced in our model to get faster and stable convergence [5].

In the thin regions like defects, similar elements to the prismatic elements are introduced. In the discrete formulation of the problem, the volume integrals are replaced by surface integrals using shell elements. The scalar and vector fields are approximated by nodal and edge elements which are developed specifically for thin regions. The formulation will be detailed in the full paper.

The thermal problem is defined by heat transfer equation:

$$\int_{\Omega} \left[\rho C_p \frac{\partial T}{\partial t} - \text{div}([\lambda] \cdot \text{grad } T) \right] \cdot \mathbf{W}_n \cdot d\Omega = \int_{\Omega} \mathbf{P} \cdot \mathbf{W}_n \cdot d\Omega \quad (3)$$

Where ρ , C_p , λ , \mathbf{P} are respectively, the specific mass, the specific heat, the thermal conductivity, and the electromagnetic induced power density. Ω is the studied domain.

Both electric and thermal formulations have been solved using finite element method based on Whitney's elements.

In order to study the defect detection and the influence of various parameters of the system on the characterization of the cracks, thermal and phase contrast are introduced as a discriminating parameter. They provide a good indication of the defect characteristics. The thermal contrast consists to compute the relative surface temperature difference between regions with and without defect. The phase contrast is calculated from the discrete Fourier's transform of the surface temperature $s(t)$ [2, 6]:

$$F(f) = \Delta t \cdot \sum_{n=0}^{N-1} s(t) \cdot \exp(-j2\pi f n \Delta t) = R(f) + jI(f) \quad (4)$$

Where Δt is the sampling time step. $R(f)$ and $I(f)$ are respectively, the real and imaginary components of $F(f)$.

IV. APPLICATIONS AND RESULTS

Numerical models developed for NDT by thermo-inductive technique allow the prediction of the defect detection depending on the parameters of the method and the physical properties of inspected materials. The validation of the finite element model by comparison with experimental data will be detailed in the extended paper.

The investigations show that depending on the nature of material, the induction and thermal frequencies and defect dimensions, the defects are more or less detectable.

Figure 2.b shows the cartography of the thermal contrast of a ferromagnetic material. The calculated temperature is more contrasted around the crack. The defect is appearing as a line with two hot spots in extremities. In the extended paper, the

behavior of the other groups of materials will be detailed and will be explained as function as the physical properties.

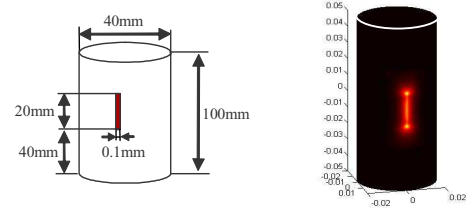


Fig. 2. (a) Modeled piece with crack and (b) Image of thermal contrast distribution (fr=100kHz)

Figures 3(a) and 3(b) present the thermal and phase contrasts for ferromagnetic materials calculated from the numerical model. The thermal contrast is inversely proportional to the heating duration. There is also an optimal induction frequency (27 kHz in this case) which corresponds to the maximum of both thermal and phase contrast. The results show that the use of both thermal and phase contrast allow a good and reliable detection of defects.

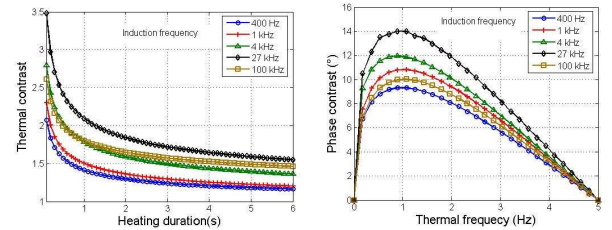


Fig. 3. (a) Thermal contrast as function of the heating period and (b) Phase contrast versus the thermal frequency for different induction frequencies

V. CONCLUSION

The results have demonstrated the relevance of the thermo-inductive technique and the efficiency of 3D model which takes into account the nonlinearity, the anisotropy of and introduces the shell elements for modeling defects.

In the full paper, the FEM models using shell elements will be detailed. Classification of materials according their properties will be specified. Investigation on various parameters of the method using optimization algorithms will be proposed with a goal function based on the contrast.

VI. REFERENCES

- [1] B. Ramdane, D. Trichet, M. Belkadi, J. Fouladgar "3D Numerical modeling of NDT by thermo-inductive technique" in *Proc of 13th IEEE CEEFC*, Athens, Greece, May 11-15, 2008, p. 418.
- [2] B. Ramdane, D. Trichet, M. Belkadi, J. Fouladgar "Modélisation numérique 3D de la technique thermo-inductive de contrôle non destructif de pièces conductrices" in *Proc Numelec2008*, Liege, Belgium, December 8-10, 2008, p. 68-69.
- [3] Z. Ren, "Degenerated whitney prism elements – general nodal and edge shell elements for field computation in thin structures", *IEEE Trans. on Magnetics*, 34(5): 2547-2550, 1998.
- [4] O. Biro, "Edge element formulations of eddy current problems," *Comput. Methods Appl. Mech. Engrg.*, vol. 169, pp. 391-405, 1999.
- [5] K. Fujiwara, Y. Okamoto, A. Kameari, "The Newton-Raphson method accelerated by using a line search – comparison between energy functional and residual minimization", *IEEE Trans. on Magnetics*, 41(5): 1724-1727, 2005.
- [6] X. Maldague, S. Marinetti, "Pulse Phase Infrared Thermography", *Eur. Appl. J. Appl. Phys.*, 79(5): 2694-2698, 1996.

Coupled Mechanical-Electrical-Thermal Modeling of Electric Contacts based on the Cell Method

Massimo Guarnieri*, Carmelo Majorana†, Gianluca Mazzucco†, and Federico Moro*

*Dipartimento di Ingegneria Elettrica, Università di Padova, Via Gradenigo 6/A, I-35131, Padova, Italy

†Dipartimento di Costruzioni e Trasporti, Università di Padova, Via Marzolo 9, I-35131, Padova, Italy

E-mail: moro@die.unipd.it

Abstract—A three-dimensional numerical method for solving mechanical-electrical-thermal coupled problems and suitable for analyzing electric connectors is presented. The analysis of electric connector performance is a typical multiphysics problem involving mechanical, electrical, and thermal coupled effects. In the proposed approach contact interfaces are analytically modeled in order to account for the surface roughness causing a random distribution of conducting spots. According to the Cell Method mechanical, electrical, and thermal problems in the bulk regions are directly expressed in terms of integral variables allowing for an easily coupling with the analytical contact interface model.

I. INTRODUCTION

Separable connectors are among the most widely used electric components, in a wide range of appliances, starting from signal applications (e.g. micro-connectors and fast-on) up to power applications (e.g. switch-gears). These components ensure the electric continuity between different circuits. The performance of electrical connectors relies on both mechanical and electrical properties of contact materials in order to ensure low and stable contact resistance over the expected service life. Connectors must fulfill tight requirements in terms of maintenance, reliability, and stability of material properties. Other desirable properties are: compact size, rugged construction, durability (capable of many connect/disconnect cycles), rapid assembly, simple tooling, and low cost.

Cost minimization is based on proper numerical design tools which should take care of multiple physics phenomena occurring in connectors. Mechanical, electrical, and thermal effect have to be coupled for a realistic modeling of the electric connector. The contact strength depends either on the applied stress or on the mechanical material response, which is affected by the local temperature distribution. A non-uniform distribution of current density around the contact may lead to hot spot formation, causing a thermal aging of materials. Moreover, the heat generated by Joule's losses determines a local flattening of the contact area and a contact pressure reduction [1].

II. NUMERICAL MODEL

In the following a three-dimensional numerical model accounting for multiple coupled physics phenomena related to electric contacts is discussed.

The analytical contact interface model is used for coupling the discrete models of the bulk connector domains. Bulk

regions are discretized according to the Cell Method (CM), which can be used effectively for coupling different formulations [2] [3]. The electro-thermal model is based on the discrete formulation presented in [4] and coupled to a non-linear elastic discrete formulation for analyzing the effects of the beam deformation on the connector performance.

Fig. 1 shows the reference geometry taken into account in the analysis: a hemisphere (1.2 mm radius, brass) is compressed with a 2 N applied load; the contact beam (0.4 mm thick, 1.4 mm width, iron and brass) is constrained to a hexaedron (1.5 mm edge).

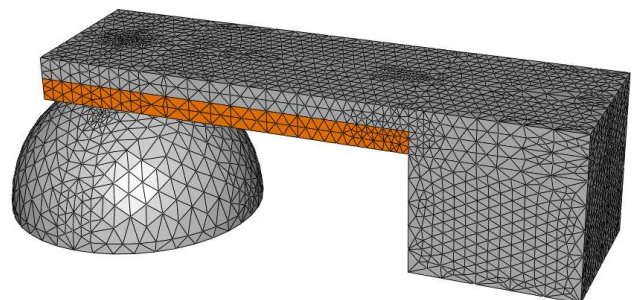


Fig. 1. Three-dimensional model of the electric connector (the brass region is shaded in gray, while the iron region is shaded in orange).

A. Contact interface model

The electric contact is established in correspondence of the mechanical contact surface, which depends on the applied force and the surface roughness. It is assumed that flux lines of the electric current density are concentrated on separated micro contact spots (*a*-spots). The conventional treatment of electrically heated contacts assumes that Joule's losses, concentrated at the *a*-spots, are dissipated only by conduction through bulk conductors [5]. In these conditions, according to Kohlraush's theory, the voltage drop at the contact interface can be expressed as a function of the maximum temperature T_m at the contact interface as:

$$U_c = \left(2 \int_{T_1}^{T_m} \lambda_1 \rho_1 dT \right)^{1/2} + \left(2 \int_{T_2}^{T_m} \lambda_2 \rho_2 dT \right)^{1/2} \quad (1)$$

where λ and ρ are respectively the thermal conductivity and the electrical resistivity of two contact elements, the subscripts

refers to the materials in contact, and T_1 and T_2 are the temperatures in bulk conductors. The coupling interface area can be estimated according to Hertz's theory. The contact surface is approximated locally as a discoidal region, accounting on average for the random distribution of a -spots. In the case of purely elastic deformation and a sphere-plane geometry, the a -spot radius can be approximated as:

$$a_e = \left(\frac{3}{4} F R \left(\frac{1 - \sigma_1^2}{E_1} + \frac{1 - \sigma_2^2}{E_2} \right) \right)^{1/3} \quad (2)$$

where F is the contact force, R is the sphere radius, E_1 and E_2 are the Young's elasticity modulus, and σ_1 and σ_2 are the Poisson's ratios. A similar empirical expression holds for plastic deformation [6].

B. Discrete conduction problem

In CM-based formulations field problem domains are discretized into primal and dual staggered cell complexes, where arrays of degrees of freedom (DoFs) are defined. For a steady state conduction problem the DoFs are voltages \mathbf{u} defined on primal edges and the electric currents \mathbf{j} defined on dual faces. Electric currents include both impressed and ohmic contributions computed by the discrete Ohm's law:

$$\mathbf{j} = \mathbf{j}_s + \mathbf{M}_\sigma \mathbf{u}. \quad (3)$$

where \mathbf{M}_σ is the electric constitutive operator. This operator can be constructed positive definite by a proper choice of shape functions [4]. The array of currents must comply with the div free condition:

$$\tilde{\mathbf{D}}\mathbf{j} = 0. \quad (4)$$

where \mathbf{D} is the discrete div operator and the tilde indicates the dual operator. The source current distribution \mathbf{j}_s is constructed in such a way that $\tilde{\mathbf{D}}\mathbf{j}_s = 0$ is automatically enforced.

In steady state conditions the electric scalar potential \mathbf{v} can be introduced, i.e., $\mathbf{u} = -\mathbf{G}\mathbf{v}$, where \mathbf{G} is the discrete gradient operator. By using the topological relationship $\tilde{\mathbf{D}} = -\mathbf{G}^T$ and by taking into account (3) and (4), the following semi-definite system of linear algebraic equations is obtained:

$$\mathbf{G}^T \mathbf{M}_\sigma \mathbf{G} \mathbf{v} = 0. \quad (5)$$

C. Discrete thermal problem

The transient thermal problem can be modeled by using the discrete Fourier equation [4]:

$$\mathbf{G}^T \mathbf{M}_\lambda \mathbf{G} \mathbf{t} + \mathbf{M}_{\rho c_p} \dot{\mathbf{t}} = \mathbf{w} \quad (6)$$

where \mathbf{t} is the array of temperatures on primal nodes, \mathbf{M}_λ is the discrete thermal conductivity operator, $\mathbf{M}_{\rho c_p}$ is the mass matrix, \mathbf{w} is the array of electric powers generated in dual volumes, and the dot indicates the time derivative. This system of linear differential-algebraic equations describing the propagation of heat in time and space can be integrated by the θ -method, which ensures both accuracy and stability with a proper choice of the parameter θ .

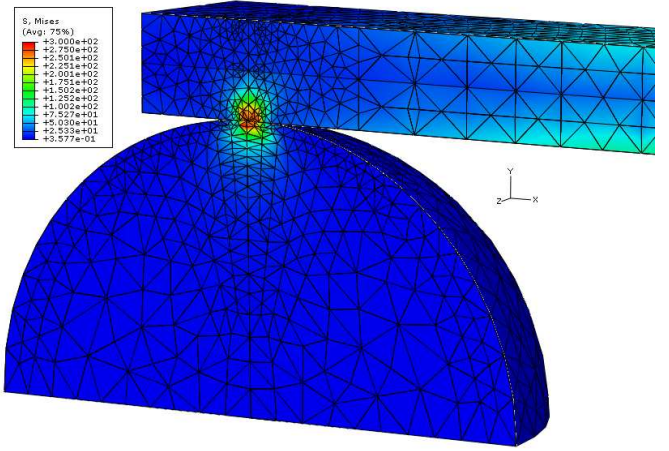


Fig. 2. Stress map σ [N m²] in proximity of the contact region.

D. Discrete non-linear elastic problem

The connector deformation due to thermal and mechanical effects is analyzed in the discrete non-linear elastic problem. By using a small strain approach the total strain array ϵ can be decomposed into elastic ϵ_e and plastic ϵ_p arrays [7]. Discrete Hooke's law accounts for mechanical properties of materials:

$$\boldsymbol{\sigma} = \mathbf{M}_e (\boldsymbol{\epsilon} - \boldsymbol{\epsilon}_p) \quad (7)$$

where \mathbf{M}_e is elastic constitutive operator. By using the Von Mises criterion the yield domain is defined by the plasticity function $f(\boldsymbol{\sigma}, k) = \sqrt{3}\bar{\sigma} - Y(k) \leq 0$ (k is the kinematic hardening parameter, $\bar{\sigma}$ is the Von Mises equivalent stress) and the material behaves elastically when $f < 0$.

Fig. 2 shows the Von Mises equivalent stress distribution around the contact interface.

III. DISCUSSION

The electro-thermo-mechanical coupling of previous equations is realized through constitutive matrices and the right hand sides (e.g., the array \mathbf{w}). For instance constitutive matrices depend on the temperature distribution and the node displacements obtained from the non-linear elastic problem. A more detailed description of the model and simulation results for the main physical quantities will be reported in the paper.

REFERENCES

- [1] P. G. Slade, *Electric Contacts: Principles and Applications*, New York: Marcel Dekker Inc., 1999.
- [2] P. Alotto, G. Gruosso, F. Moro, M. Repetto, "A Boundary Integral Formulation for eddy current problems based on the Cell Method," *IEEE Trans. Magnetics*, vol. 44, pp.770-773, June 2008
- [3] P. Dular, R. Specogna, F. Trevisan, "Coupling between circuits and A- χ discrete geometric formulation," *IEEE Trans. Magnetics*, vol. 42, pp. 1043-1046, April 2006.
- [4] P. Alotto, M. Bullo, M. Guarnieri, F. Moro, "A coupled thermo-electromagnetic formulation based on the Cell Method," *IEEE Trans. Magnetics*, vol. 44, pp.702-705, June 2008.
- [5] R. Holm, *Electric Contacts: Theory and Applications*, 4th ed. New York: Springer, 2000.
- [6] A. Monnier *et al.*, "A mechanical, electrical, thermal coupled-field simulation of a sphere-plane electrical contact," *IEEE Trans. Comp. and Packaging Technologies*, vol. 30, pp. 787-795, December 2007.
- [7] J.C. Simo, T.J.R. Hughes, *Computational Inelasticity*, New York: Springer, 1998.

Improvements to convergence of coupled non-linear circuit modelling

S.Taylor, N.Robertson and J.Simkin
Cobham Technical Services, Vector Fields Software
24 Bankside, Kidlington, OX5 1JE, UK
VectorFields.Info@cobham.com

Abstract— The finite element solution of electromagnetic problems often requires coupling into electric circuit equations. These circuits are often coupled to power electronic or control systems, where non-linear components, such as diodes are regularly used. The standard non-linear techniques used within finite element solutions are applicable to the coupled equation system, but tend to struggle to converge to the required accuracy due to the extreme nature of the non-linearity of these components. This paper describes an improvement to the non-linear solution of circuit equations containing diodes, using the Opera-3d finite element analysis software, though the method is equally applicable to other non-linear components.

I. INTRODUCTION

The use of finite element solutions for non-linear problems is common. A formulation for the electromagnetic solution can be found using the magnetic vector potential such that

$$\nabla \times \frac{1}{\mu} \cdot \nabla \times \mathbf{A} = \mathbf{J} \quad (1)$$

The permeability, μ , is a non-linear function of the local magnetic flux density. The standard technique used is an iterative solution process, where the best solution available at the present time is used to update the estimate of the non-linear permeability. For simple cases this technique will converge, but slowly.

Highly nonlinear material characteristics will cause simple update methods to oscillate wildly. The addition of over/under relaxation to the iterative process can be used to control these oscillations and ensure convergence. Typically, the matrix solution requires a significant solution time. By scaling the change in solution vector by a relaxation factor, it is possible to test and select a better estimate of solution. Finding a suitable relaxation factor is still a problem. This can be a particular problem when the current solution lies close to a local minimum. In this case it may be necessary to move away from this area before the convergence can find the true solution.

The use of a Newton-Raphson update is also a common technique for improving solution convergence. By using derivative information representing the change in non-linear property with terms in the solution vector, the equation solution matrix is augmented to give improved convergence properties. Within the capture radius this technique will converge quadratically; however with strong nonlinearities the capture radius is small and the use of Newton-Raphson techniques can slow convergence.

The application of both of these techniques [1,2] within the same system provides a robust solution.

II. COUPLED CIRCUIT EQUATIONS

When solving for the time variation of magnetic fields in a model domain, the use of a time varying current provides the standard input to drive the finite element formulation.

For many applications, the drive is provided by a voltage source rather than a prescribed current. Additionally, such a voltage will operate as part of an electric circuit. The use of a voltage drive requires a close coupling to be modeled as the voltage, current and magnetic fields are all tightly linked.

This can be achieved by including extra equations in the finite element matrix [3] to give a solution for the currents within the electric circuit.

$$\nabla \times \frac{1}{\mu} \cdot \nabla \times \mathbf{A} - \sigma \frac{d\mathbf{A}}{dt} - \mathbf{I} = 0 \quad (2)$$

$$\int n \cdot \frac{d\mathbf{A}}{dt} + \mathbf{I}\mathbf{R} = \mathbf{V} \quad (3)$$

Using Galerkin integration over the finite element mesh, and applying suitable scaling to equations, gives a symmetric matrix of the form

$$\begin{bmatrix} \mathbf{M}_{AA} & \mathbf{M}_{AI} \\ \mathbf{M}_{IA} & \mathbf{M}_{II} \end{bmatrix} \begin{bmatrix} \mathbf{A} \\ \mathbf{I} \end{bmatrix} = \begin{bmatrix} \mathbf{J} \\ \mathbf{V} \end{bmatrix} \quad (4)$$

For most problems $\text{rank}(\mathbf{M}_{AA}) \gg \text{rank}(\mathbf{M}_{II})$.

III. DIODE MODELLING

A typical non-linear characteristic of the diode can be seen in the Shockley description

$$I = I_s \left(e^{V_D / (nV_T)} - 1 \right) \quad (5)$$

where

- I is the diode current,
- I_s is the reverse bias saturation current,
- V_D is the voltage across the diode,
- V_T is the thermal voltage,

The diode can be represented as a non-linear resistor or using equivalent circuits to represent an approximate model at its current operating point. However, the non-linearity is extreme, as can be seen by the exponential variation of current through the diode.

A nonlinear circuit equation must be solved to determine the operating point of the diode. The same techniques used in the non-linear permeability updates can be applied.

IV. IMPROVED DIODE MODELLING

The method proposed uses a sub domain iterative solution of the circuit equations, as part of the relaxation procedure used to improve the convergence of the full solution. Rather than relax the solution to the circuit equations through the use of a single relaxation factor, an approximate solution to the circuit matrix, \mathbf{M}_{II} , can be found, given an updated relaxed magnetic vector potential.

$$\mathbf{I} = (\mathbf{M}_{II})^{-1} \left(\mathbf{V} - \mathbf{M}_{IA} \frac{d\mathbf{A}}{dt} \right) \quad (6)$$

- (1) Solve for full matrix using current estimate.
- (2) Calculate error in solution:
 - If the error is low, convergence has been achieved, exit.
 - If the error is reduced significantly, repeat (1).
- (3) Relax change in magnetic vector solution by new relaxation factor σ .
- (4) Converge the non-linear solution for equation (6).
- (5) Repeat from (2)

The relative rank of the circuit current sub matrix, \mathbf{M}_{II} , means that the independent solution to this sub matrix is very inexpensive compared to the full matrix solution and non-linear updates. By reducing the number of non-linear iterations, (1) in the loop above, we can achieve a reduced overall solution time.

V. RESULTS

The method has been implemented within the Opera-3d finite element module, ELEKTRA.

A model of a transformer and full wave rectifier has been created. Fig. 1 shows a quarter model of the device. Fig. 2 shows the circuit used to drive the model including the full wave rectifier.

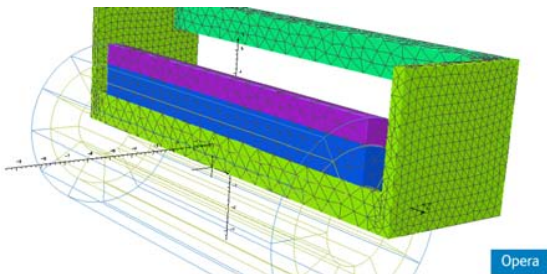


Fig. 1. Quarter model of transformer

The total CPU time for analysis using the standard non-linear updates and using the implemented method are detailed in Table I.

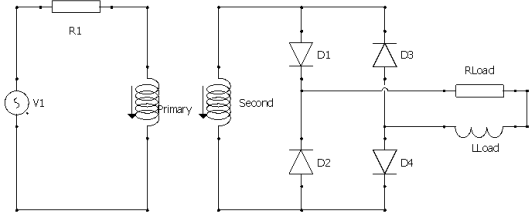


Fig. 2. Circuit of transformer and full wave rectifier

The CPU time as a function of simulation time is shown in Fig. 3. It can be seen that using the standard ELEKTRA, the analysis was successful, but as the voltages driving the rectifier switched sign, the analysis struggled to converge the non-linear solution. Using the updated method, the non-linear convergence characteristics are significantly improved as the solution at the switch positions.

TABLE I
CPU Time for analyses

Method	CPU Time (s)
Standard ELEKTRA	1713 s
Updated ELEKTRA	963 s

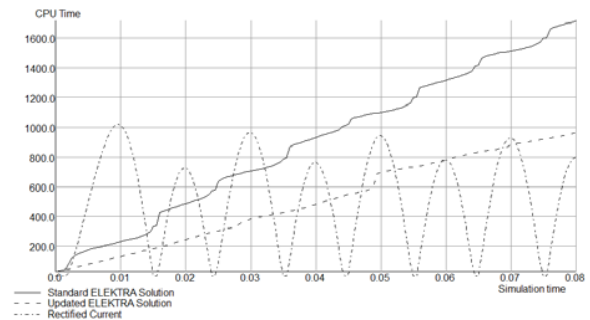


Fig. 3. CPU time required for analysis time, and resulting rectified current

VI. CONCLUSION

The updated method has been described and implemented within Opera-3d. A significant improvement for the solution of a transformer with full-wave rectifier can be seen. The application of the improved non-linear update algorithm will be tested further on more complex models.

VII. REFERENCES

- [1] C.A.Magele, K.Preis and W.Renhart, "Some Improvements in 3D Nonlinear Magnetostatics", IEE Transactions on Magnetics, 26(2): 375, 1990.
- [2] T.Nakata, N.Takahashi, K.Fujiwara and N.Okamoto, "Improvements of convergence characteristics of Newton-Raphson method for non-linear magnetic field analysis", IEEE Transactions on Magnetics, 28(2): 1048-1051, March 1992
- [3] P.Dular, F.Henrotte, W.Legros, "A General and Natural Method to Define Circuit Relations Associated with Magnetic vector Potential Formulations", IEEE Transactions on Magnetics, 35(3): 1630-1633, May 1995

Particular Electromagnetic Field Computation for Permanent Magnet Generator Wind Turbine Analysis

C. Patsios, A. Chaniotis, E. Tsambouris, A. Kladas
National Technical University of Athens

Faculty of Electrical and Computer Engineering, Laboratory of Electrical Machines and Power Electronics,
9 Iroon Polytechniou st., 15773 Zografou, Athens, Greece, Tel.: +30-210-772 2336, Fax: +30-210-772 2336
Email: hpatsios@central.ntua.gr, achan@cc.ece.ntua.gr, etsab@central.ntua.gr, kladasel@central.ntua.gr

Abstract— Precise permanent magnet generator modeling requires a complex electromagnetic field analysis in order to account for motor eccentricity and end zone leakage field. The paper presents a particular technique enabling to consider such phenomena through convenient 2D and 3D finite element models and incorporate the respective electromotive force distributions including space harmonics in real time control systems. The proposed methodology has been validated by measurements on a permanent magnet generator prototype.

I. INTRODUCTION

In wind generator (WG) systems, the generator holds a key role, both actual, in sense of efficiency as well as insubstantial, in sense of modeling and simulation [1]-[5]. This paper focuses on appropriate modeling of the characteristics of permanent magnet generator (PMG) by employing results of particular FEM analysis and producing harmonic representation of electromotive force and electromagnetic torque with loading and rotor speed. Such a model enables efficient real time generator representation for control purposes. The proposed methodology's accuracy has been verified by measurements on a prototype shown in Fig. 1, under transients as well as under three WG different control techniques which aim at maximizing the WG's output power through load variation.

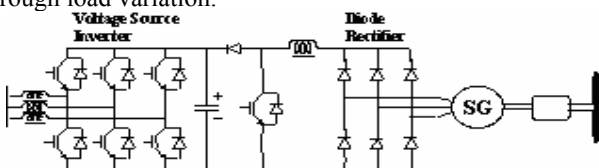


Fig. 1. Typical permanent magnet variable speed wind turbine system

II. GENERATOR MODELING

A. Permanent Magnet Material Optimization

Due to large cost of permanent magnets, it is necessary to minimize magnet material, given the output effective voltage. A 2D FEM is used to choose the best values for permanent magnet dimensions, in conjunction with sensitivity analysis technique [1] – [3]. In the above analysis it is important to account for rotor eccentricity, simulated through air gap variation as shown in Fig. 2. Eccentricity effects in conjunction with appropriate modeling of the end zone machine parts are then represented by using a convenient hybrid 2D-3D FEM model shown in Figs. 2 and 3.

In order to predict and accurately simulate the voltage waveforms and equivalent circuit components of the generator the 3D representation as well as the eccentricity consideration are necessary. The computed electromotive force waveforms for different eccentricities are shown in Fig. 4.

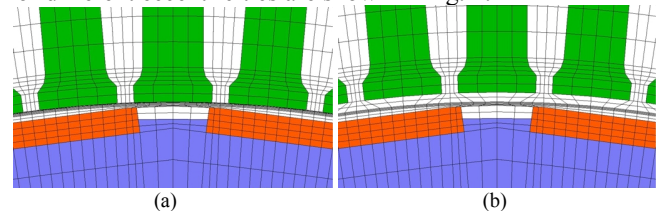


Fig. 2. 2D FEM model a) Region of reduced air-gap in b) region of increased air-gap

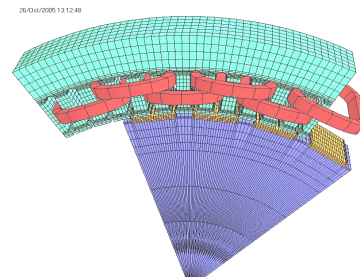


Fig. 3. 3D FEM model

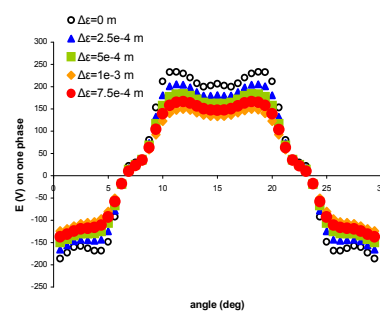


Fig. 4. Induced voltage variation for different air gap eccentricity values Δe

B. Non-linear system behavior

The FEM analysis enables to compute the electromotive force waveforms, varying with the loading and rotor speed as well as the equivalent circuit parameters of the generator. Such an analysis can be easily incorporated in the control algorithm of the system by calculating the electromotive forces e_n shown in Fig. 4 and electromagnetic torque T_{el} . Using these values it is possible to both simulate transient

response and calculate steady-state operation. Since the generator is used with a rectifier, average values sufficiently describe most interesting parameters, such as the rectified current that is charging the DC bus capacitor as well as the electromagnetic torque. In practice look-up tables have been used including a number of points adequate to interpolate the data without significant error, as shown in Fig. 5.

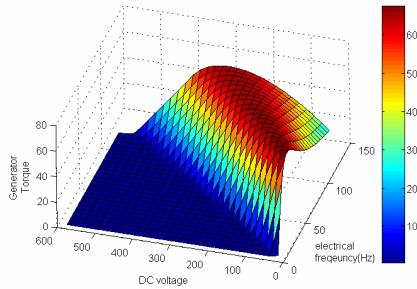


Fig. 5. Generator electromagnetic torque versus electrical frequency and load voltage

III. RESULTS AND DISCUSSION

A. Steady State Operation

When accurate data of voltage and current waveforms are available, it is possible to calculate power, the electromagnetic torque and associated losses with little error, therefore predict and fine tune the system behavior. Figures 6a,b show the computed and experimental phase voltages of the generator, respectively. The waveforms are in very good agreement, in both form and amplitude.

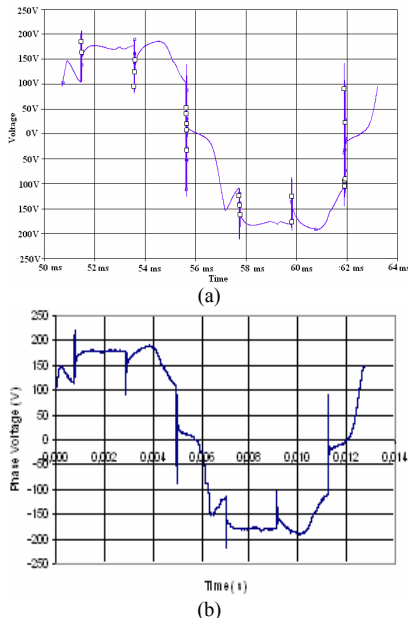


Fig. 6. Generator phase voltage waveform a) Simulation result b) Experimental result.

B. Dynamic Operation

Accurate prediction of operating points allows fine tuning of control parameters, which in turn results in optimal dynamic performance. Fig. 7a shows the simulation result for the rectified generator current for a nearly instant change of input mechanical torque from 4.9 Nt.m to 39.2 Nt.m, while Fig. 7b

shows the measured current for the same input. A good agreement is observed.

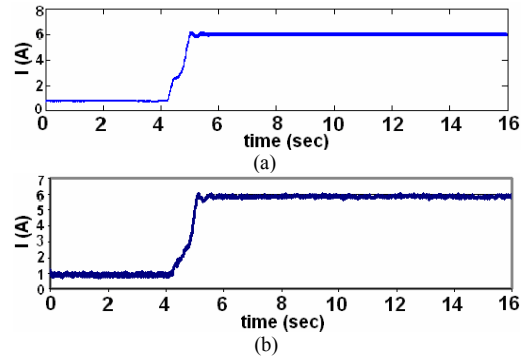


Fig. 7. Rectified generator current for input mechanical step torque variation from 4.9Nt.m to 39.2Nt.m a) Simulation results b) Experimental results

C. Operation under Variable Wind Speed

Further validation of the proposed model calls for operation under realistic stresses. The prototype system is tested under a specific measured wind time variation. Simulated and measured WG output power P_g are in conformity as can be seen in Fig. 8.

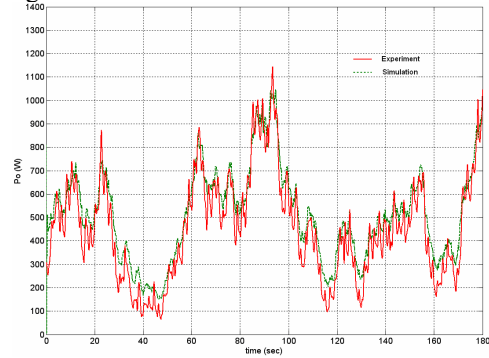


Fig. 8. Simulated and measured WG output power time variation, P_g .

IV. CONCLUSION

A new methodology has been proposed providing an appropriate model for the PMG representation. The method is based on particular field analysis considering higher harmonics of electromotive forces and taking into account both rotor eccentricity and winding end zone parts. It gives very good accuracy for both steady state and transient system response. Experimental validation on a prototype illustrated the method suitability for wind power applications.

V. REFERENCES

- [1] T. Higuchi, J. Oyama, E. Yamada, E. Chiricozzi, F. Parasiliti, M. Villani, "Optimization procedure of surface permanent magnet synchronous motors", *IEEE Trans. on Magnetics*, Vol. 33, no 2, 1997.
- [2] G. Tsekouras, S. Kiartzis, A. Kladas, J. Tegopoulos, "Neural Network Approach compared to Sensitivity Analysis based on Finite Element Technique for Optimization of Permanent Magnet Generators", *IEEE Trans. on Magnetics*, Vol. 37, no 5/1, 2001, pp. 3618-3621.
- [3] A. J. G. Westlake, J. R. Burnby, E. Spooner, "Damping of power-angle oscillations of a permanent magnet synchronous generator with particular reference to wind power applications", *IEE Proceedings - Electric Power Applications*, Vol. 143, No 3, 1996, pp. 269-280.
- [4] S. Urata, M. Enokizono, T. Todaka, and H. Shimoji, "Magnetic Characteristic Analysis of the Motor Considering 2-D Vector Magnetic Property", *IEEE Transactions on Magnetics*, Vol. 42, No. 4, April 2006.
- [5] Krebs, G.; Tounzi, A.; Pauwels, B.; Willemot, D.; Piriou, F. "Modeling of A Linear and Rotary Permanent Magnet Actuator", *IEEE Transactions on Magnetics*, Vol. 44, Issue 11, Part 2, Nov. 2008. pp.:4357 – 4360.

A Fully Coupled Three-dimensional Dynamic Model of Polymeric Membranes for Fuel Cells

Piergiorgio Alotto, Massimo Guarnieri, and Federico Moro
 Dipartimento di Ingegneria Elettrica, Università di Padova
 Via Gradenigo 6/A, 35131, Padova, Italy
 alotto,guarnieri,moro@die.unipd.it

Abstract— The proton exchange membrane is a key component in presently widely studied Proton Exchange Membrane Fuel Cells. In this paper a fully coupled three-dimensional dynamic numerical model of the membrane including ion transport, hydration-dependent conductivity and thermal effects is presented. The highly non-linear model is discretized by means of the Finite Element Method.

I. INTRODUCTION

Fuel Cells (FCs) are considered a very promising energy source for a number of different applications, ranging from small units for portable electronic devices to mid-size generators for the automotive industry and to large stationary power supply systems. The proton exchange membrane (PEM) is a key component in all so-called Proton Exchange Membrane Fuel Cells (PEMFCs). It is the component where most Ohmic losses occur, since ionic conduction is orders of magnitude lower than electron conduction in the anode and cathode current collectors. It also limits the operational temperature of the FC and presents fuel cross-over effects, which reduce fuel efficiency, increase electrochemical kinetics losses and causes cathode catalyst poisoning. An accurate modeling of the membrane is therefore needed for studying its electrical and physical behaviour. In this paper a three-dimensional model which includes all the most relevant physical phenomena (ion transport, hydration-dependent conductivity and thermal dependency) is developed and discretized with the help of the Finite Element Method.

II. COUPLED MODEL

A thorough description of the derivation of all equations is beyond the scope of this paper, further details can be found in [1]. All units are S.I. unless otherwise stated.

A. Polymeric conductivity model

The polymeric conductivity σ can reach values as high as 20 S/m at 100 °C, but strongly depends on the temperature T and on the membrane hydration λ , which varies from point to point being the ratio between the water concentration c_w and the sulfonic acid concentration $c_{sa}=1970$ mol/m³, according to the following semi-empirical expression:

$$\sigma(\lambda, T) = (51.93\lambda)e^{\frac{W_a}{k}\left(\frac{1}{303}-\frac{1}{T}\right)} \quad (1)$$

with W_a the activation energy and k the Boltzmann's constant. In our case $W_a/k = 1268$ K. Measurements show that λ is in the range [0,0.22]. Unfortunately, λ cannot be measured directly at the membrane's surface and therefore must be

expressed as a function of more readily measurable quantities. This can be achieved by following empirical relationship:

$$\lambda = \begin{cases} 4 \cdot 10^{-5} + 0.18a_w - 0.4a_w^2 + 0.4a_w^3 & a_w \in [0,1] \\ 0.14 + 1.4(a_w - 1) & a_w \in [1,3] \end{cases} \quad (2)$$

where a_w is the relative humidity, i.e. is the ratio between the partial water steam pressure p_w and the saturation value p_{ws} [bar] which depends on the temperature T according to:

$$a_w = \frac{p_w}{10^{(-20+0.11T-2.1 \cdot 10^{-4}T^2+1.4 \cdot 10^{-7}T^3)}} \quad (3)$$

The partial water steam pressure p_w , which can be measured at the membrane interface, is determined at the catalyst layers according to the electrochemical semi-reactions (fuel oxidation at the anode and oxygen reduction at the cathode) and the mass transport in the diffusion layers. The distribution of λ inside the membrane thickness depends on two effects, namely electro-osmotic drag and back-diffusion. The water molar flow due to the former effect can be expressed as:

$$N_{we} = \nu_w J_{prot} = \frac{\nu_w J}{F} \quad (4)$$

where $\nu_w = r_w = 2.5$ is the electro-osmotic drag coefficient and F is Farady's constant. Based on Fick's first law, water molar flow due to the back-diffusion effect is:

$$N_{wd} = -D_w c_{sa} \nabla \lambda \quad (5)$$

where D_w is the water diffusivity in the membrane which can be expressed by following semi-empirical expression:

$$D_w(\lambda, T) = (2.6 - 33\lambda + 264\lambda^2 - 671\lambda^3)e^{2416\left(\frac{1}{303}-\frac{1}{T}\right)-23} \quad (6)$$

The total water molar flow N_w across the membrane is therefore:

$$N_w = N_{we} + N_{wd} = \frac{\nu_w J}{F} - D_w c_{sa} \nabla \lambda \quad (7)$$

Its dynamic behavior conforms Fick's second law, expressed in terms of λ :

$$\nabla \cdot N_w + c_{sa} \partial_t \lambda = 0 \quad (8)$$

that, together with (7), gives the following diffusion equation:

$$\nabla \cdot D_w \nabla \lambda - \partial_t \lambda - \nabla \cdot \frac{\nu_w}{F c_{sa}} J = 0 \quad (9)$$

The current density \mathbf{J} of (9) is the same one appearing in Maxwell's equations so that, introducing the electric scalar potential V , (9) can be rewritten as:

$$\nabla \cdot D_w(\lambda, T)\nabla\lambda - \partial_t\lambda + \nabla \cdot \frac{\nu_w}{Fc_{sa}}\sigma(\lambda, T)\nabla V = 0 \quad (10)$$

B. Current flow model

The electric scalar potential of (10) must obey the charge conservation equation:

$$\nabla \cdot \sigma(\lambda, T)\nabla V = 0 \quad (11)$$

where the conductivity σ depends upon the temperature and the hydration according to (1). This equation allows to eliminate the last term in (10).

C. Thermal model

Since most quantities appearing in the polymeric conductivity model and the current flow model depend on the temperature it is also necessary to solve the transient heat equation

$$\rho c_p \partial_t T - \nabla \cdot k(\lambda)\nabla T - \sigma(\lambda, T)(\nabla V)^2 = 0 \quad (12)$$

where the last term on the left hand side represents the Joule losses. It has been shown in [3] that the thermal conductivity in (12) can be represented by $k = 0.12 + 0.81\lambda$.

D. Coupled multi-physics model

The complete model to be solved is assembled from (10), (11) and (12) together with nonlinearities (1) and (6) and with appropriate boundary (time-dependent Dirichlet and homogeneous Neumann) and initial conditions. The peculiarities of the set of equations and the very small thickness of the membrane with respect to its planar extension result in a very badly conditioned system of equations which is one side too large to be handled with a direct solver and on the other hand very difficult to precondition. Furthermore, the kind of nonlinearities in the model are such that the Newton-Raphson algorithm does not converge without strong underrelaxation. All these difficulties make it unadvisable to try and solve the full problem with naïve tools and call for the use of extremely robust nonlinear and linear solvers. Therefore the coupled model has been implemented with the help of the COMSOL Multiphysics environment [4].

III. RESULTS

The coupled model has been used to study a typical laboratory 2cm x 2cm x 200 μ m membrane. Fig. 1 shows the relative magnitude of the electro-osmotic and back-diffusion flows, while Fig.2 shows the behavior of the electrical conductivity across the membrane during a 10 minute transient (one line per minute).

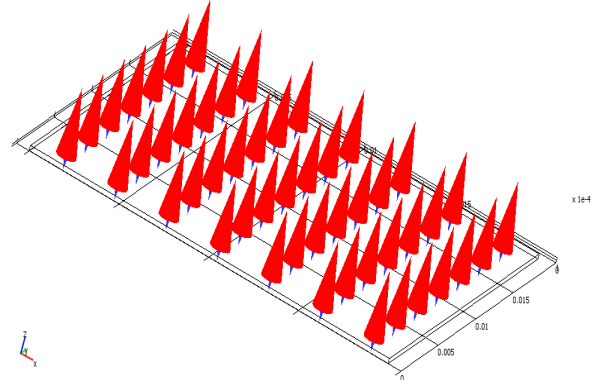


Fig. 1: Electro-osmotic drag (red cones) and back-diffusion (blue cones)

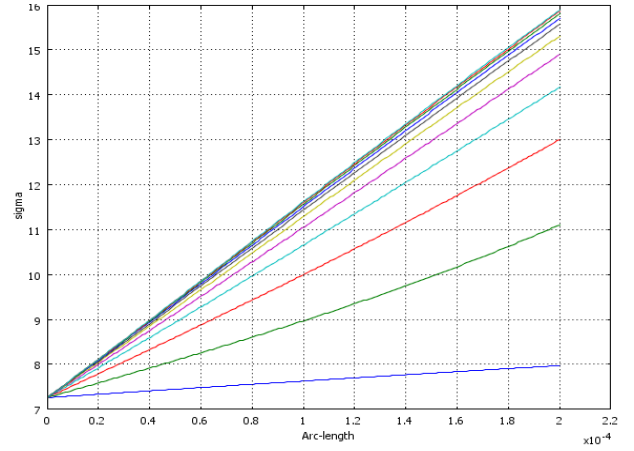


Fig. 2: σ across the membrane during transient

IV. CONCLUSIONS

The presented fully coupled three-dimensional dynamic model of polymeric membranes for fuel cells has been used to simulate the transient behavior of a PEMFC membrane under realistic operating conditions. In ongoing work the model will be coupled with other fuel cell components and will be used to study the influence of localized defects on the membrane's performance and. In the full paper more details regarding the model and its numerical implementation will be presented.

ACKNOWLEDGMENTS

This work was supported by the Italian Ministry for Instruction, University and Research under a PRIN 2006 grant.

V. REFERENCES

- [1] T. E. Springer, T. A. Zawodzinski and S. Gottesfeld, "Polymer Electrolyte Fuel Cell Model", *J. Electrochem. Soc.*, 138(8): 2334-2341, 1991.
- [2] C-Y. Wang, "Fundamental Models for Fuel Cell Engineering", *Chem. Rev.*, 104: 4727-4766, 2004.
- [3] M. Khandelwal and M.M. Mench, "Direct measurement of through-plane thermal conductivity and contact resistance in fuel cell materials", *J. of Power Sources*, 161:1106-1115, 2006.
- [4] COMSOL Multiphysics, <http://www.comsol.com>

Coupled 3D Fluid Flow-Thermal FEM Model for Power Transformer Temperature Analysis

Marina A. Tsili¹, Eleftherios I. Amoiralis², *Member IEEE*, Antonios G. Kladas¹, *Member IEEE*, and Athanassios T. Souflaris³

¹Faculty of Electrical and Computer Engineering, National Technical University of Athens, 9 Iroon Polytechniou Street, 15780 Athens, Greece

²Department of Production Engineering and Management, Technical University of Crete, 73100, Greece

³Schneider Electric AE, Elvim Plant, 32011, Inofyta, Greece
mtsili@central.ntua.gr

Abstract—Thermal performance in oil-immersed power transformers is governed by the flow of oil, acting both as an electrical insulator as well as a medium for the transport of heat generated in the core and windings towards the tank and the surrounding air. In our previous work, a two-dimensional hybrid analytical-numerical technique for ONAN transformer thermal analysis was presented, able to predict thermal performance at a low computational cost for optimization purposes. The present work expands thermal analysis in three dimensions, taking into account detailed transformer geometrical parameters and coupling with fluid flow dynamics. The proposed methodology provides an integrated tool for thermal simulation, able to predict detailed thermal distribution in a specific transformer, without requiring prior knowledge of nodal temperature or temperature gradient values.

I. PROPOSED METHODOLOGY

Thermal finite element method (FEM), as well as other numerical methods, has been extensively applied in thermal analysis of electric machines and transformers, providing enhanced representation of the geometrical configuration of the considered devices, in an effort to replace semi-empirical methods involving analytical formulas and constants deriving through experimental results. However, such an analysis requires correct definition of heat convection coefficient constants and boundary conditions [1], which are influenced by the oil flow in the transformer tank. For the accurate calculation of these parameters, the coolant flow distribution must be modeled, therefore necessitating the incorporation of computational fluid dynamics (CFD) tools to the analysis [2] [3]. The proposed methodology combines three-dimensional (3D) thermal and fluid flow FEM analysis, for the derivation of the transformer temperature distribution under different loading conditions. The coupling of fluid flow equations with heat equations is necessary in order to model the oil flow within the transformer tank. Therefore, the thermal conditions at the boundaries between the transformer active part and tank components and the cooling medium are calculated by the proposed method and there is no need to externally predefine them in the thermal finite element model.

Apart the aforementioned methodology, accurate prediction of transformer thermal performance is enhanced by:

- Detailed geometry representation of transformer active

part and tank: special consideration is given to the representation of design details of particular importance to thermal analysis, such as the existence of cooling ducts in the coils and the tank corrugated panels geometry.

- Accurate estimation of the transformer heat sources, i.e. the core and coils loss density, which are determined through an appropriate design methodology [4].

A. Thermal FEM Equations

The 3D thermal transformer analysis is governed by the equation:

$$K_x \cdot \frac{\partial^2 T}{\partial x^2} + K_y \cdot \frac{\partial^2 T}{\partial y^2} + K_z \cdot \frac{\partial^2 T}{\partial z^2} = q \quad (1)$$

where T is the temperature at each point of the considered domain ($^{\circ}\text{C}$), K_x , K_y and K_z are the materials thermal conductivity in the x -, y - and z - direction ($\text{W}/(\text{m}^{\circ}\text{C})$) and q is the heat source in the transformer conductors and cores (W/m^3), corresponding to the respective loss density. The proper solution of (1) involves correct definition of the boundary conditions between the transformer active part and tank components and oil (heat convection conditions).

B. CFD FEM Equations

In solid and liquid materials, heat transfer and viscous fluid flow are governed by Navier-Stokes equations, deriving from the basic principles of conservation of mass, momentum and energy:

$$\rho \left(\frac{\partial \vec{u}}{\partial t} + (\vec{u} \cdot \nabla) \cdot \vec{u} \right) - \nabla \cdot (2 \cdot \mu \cdot \bar{\varepsilon}) + \nabla p = \rho \cdot \vec{g} \quad (2)$$

$$\nabla \cdot \vec{u} = 0$$

where ρ stands for the fluid mass density (kg/m^3), \vec{u} is the fluid velocity (m/s), $\bar{\varepsilon}$ is the strain rate tensor, p denotes the pressure (N/m^2) and \vec{g} is the gravitational acceleration (m/s^2).

The thermal flow of incompressible fluids is governed by the Boussinesq approximation, i.e. that the density of the fluid depends linearly on temperature, through the equation:

$$\rho = \rho_o \cdot (1 - \beta \cdot (T - T_o)) \quad (3)$$

where β is the thermal expansion coefficient ($1/^{\circ}\text{C}$), while ρ_o and T_o represent reference values of mass density (kg/m^3)

and temperature ($^{\circ}\text{C}$), respectively.

C. Coupled 3D Fluid Flow-Thermal FEM model

Fig. 1 illustrates the transformer 3D FEM model, consisting of the one fourth of its real geometry, i.e. half of the transformer width and length, due to symmetry, which is taken into account by the imposition of appropriate Dirichlet as well as Neumann conditions. For the derivation of the transformer thermal distribution, the thermal and fluid flow equations (1) and (2) are solved iteratively, for a prescribed loss density in the transformer core and windings, derived by the loss values of the considered design. Fig. 2 illustrates the flowchart of the proposed method, describing the coupling of the thermal and fluid flow equations. Only an initial guess for the transformer temperature and oil velocity has to be defined, providing the initial condition for the coupled FEM solver.

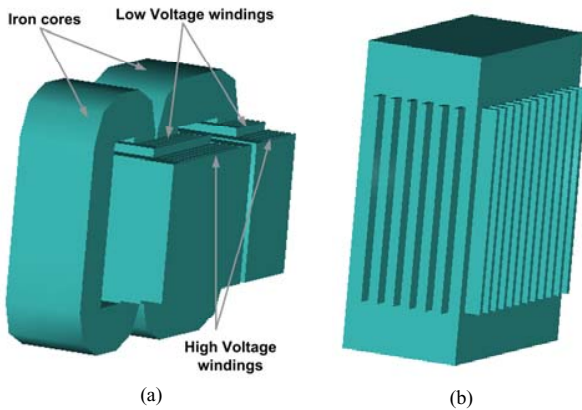


Fig. 1. Perspective view of 3D transformer FEM model: (a) active part, (b) oil tank.

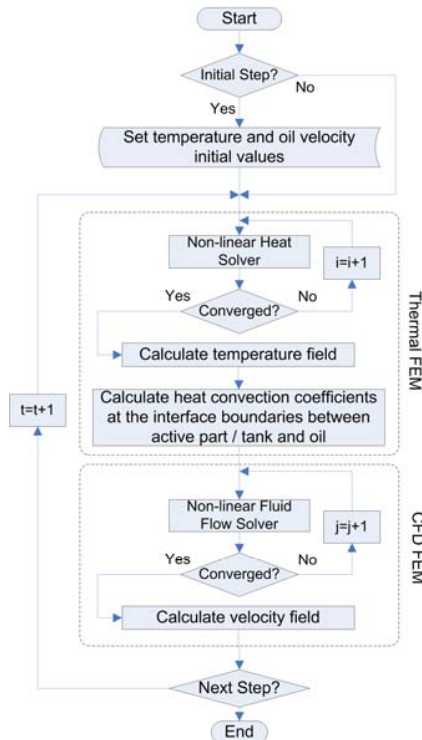


Fig. 2. Flowchart of the proposed coupled method.

II. RESULTS AND DISCUSSION

Figs. 3 and 4 illustrate the results of the method in a 400 kVA, 20-0.4 kV transformer, operating under nominal load, at an ambient temperature equal to 30°C . Fig. 3 comprises the thermal distribution results inside the active part and the tank walls in half of the FEM model (the rest of the wireframe model edges are kept in the figure for better representation purposes) Fig. 4 shows the arrow plot of the transformer oil velocity around the transformer active part, providing an aspect of the oil flow around the winding cooling ducts. These results are in good agreement with the measured ones and show the proposed methodology suitability for hot spots investigation in power transformers.

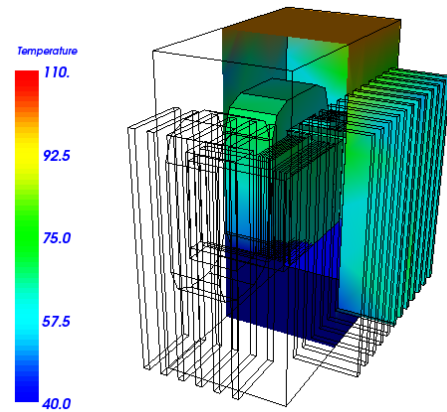


Fig. 3. Temperature distribution at the 400 kVA transformer active part and tank walls.

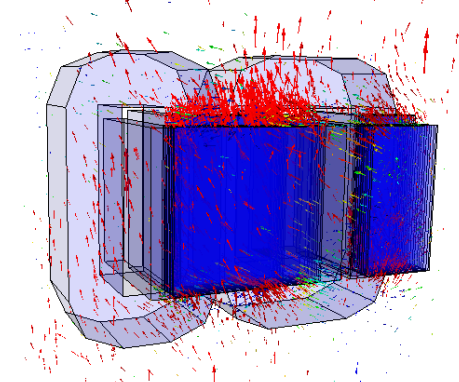


Fig. 4. Arrow plot of oil velocity around the the 400kVA transformer active part.

III. REFERENCES

- [1] M. A. Tsili, E. I. Amoiralis, A. G. Kladas, A. T. Souflaris, "Hybrid Numerical-Analytical Technique for Power Transformer Thermal Modeling," *IEEE Trans. on Magnetics*, 45(3): 1408-1411, 2009.
- [2] E. J. Kranenborg, C. O. Olsson, B. R. Samuelsson, L-Å. Lundin, R. M. Missing, "Numerical Study on Mixed Convection and Thermal Streaking in Power Transformer Windings," in *Proc. 5th European Thermal-Sciences Conference*, The Netherlands, 2008.
- [3] J. M. Mufuta, E. van den Bulck, "Modelling of the mixed convection in the windings of a disc-type power transformer," *Applied Thermal Engineering*, 20: 417-437, 2000.
- [4] E. I. Amoiralis, P. S. Georgilakis, M. A. Tsili, A. G. Kladas, "Global Transformer Optimization Method Using Evolutionary Design and Numerical Field Computation", *IEEE Trans. on Magnetics*, 45(3): 1720-1723, 2009.

Inductively Heated Incompressible Flow of Electrically Conductive Liquid in Pipe

I. Dolezel¹, L. Dubcova², P. Karban³, J. Cerveny², and P. Solin^{2,4}

¹Faculty of Electrical Engineering, Czech Technical University

Technicka 2, 166 27 Praha 6, Czech Republic, E-mail: dolezel@fel.cvut.cz

²Institute of Thermomechanics, Academy of Sciences of the Czech Republic

Dolejskova 5, 182 02 Praha 8, Czech Republic, E-mail: {dubcova, cerveny, solin}@it.cas.cz

³Faculty of Electrical Engineering, University of West Bohemia

Univerzitni 26, 306 14 Plzen, Czech Republic, E-mail: karban@kte.zcu.cz

⁴University of Nevada, Dept. Mathematics and Statistics, Reno

1664 N. Virginia St., Reno, NV 89557-0208, U.S.A., E-mail: solin@unr.edu

Abstract – A novel computer model of inductively heated incompressible flow of electrically conductive liquid in a pipe is presented. The numerical solution of this multiply coupled problem is realized by a higher-order finite element method using the code Hermes2d developed and written by the authors that contains a number of original features (i.e., hanging nodes of any order or dynamically changing mutually independent meshes for the evaluation of particular time-dependent field quantities). The methodology is illustrated by an example whose results are discussed.

I. INTRODUCTION

Numerous industrial technologies working with electrically conductive liquids (e.g., molten metals, acids, or solutions of salts) are based on the force and thermal effects of electromagnetic field. We can mention pumping, dosing, stirring, heating, and other similar processes.

The computer modeling of such processes is still a challenge. These tasks represent multiply coupled nonstationary and often nonlinear problems, characterized by interaction of several physical fields. Even when a considerable attention is paid to the topic (the books and papers in the domain abound, see, e.g., [1], [2]), a lot of tasks still remain unresolved.

The paper deals with the problem of heating a conductive liquid flowing slowly in a ceramic pipe. Its numerical solution is carried out (unlike former classical FEM and FVM-based algorithms) by our own code Hermes [3], [4] based on the *hp*-FEM.

II. FORMULATION OF THE PROBLEM

Consider the arrangement depicted in Fig. 1. It shows a ceramic pipe with electrically conductive liquid that flows from the left to the right and is warmed up by a time-variable magnetic field generated by a harmonic current carrying inductor. The arrangement is considered axisymmetric.

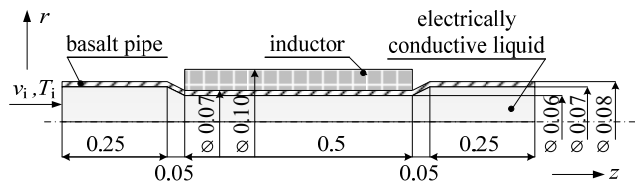


Fig. 1. The investigated arrangement

The task is to map the time evolution of all relevant physical fields in the system, namely magnetic field, temperature field, field of the radial and axial velocities of flow, and field of pressure. The physical parameters of the liquid, pipe and inductor are known as well as the initial and boundary conditions of the problem, and also the parameters of the field current (its amplitude I and frequency f).

III. MATHEMATICAL MODEL AND ITS SOLUTION

The mathematical model of the problem is given by three partial differential equations describing the distribution of the magnetic field, the temperature field and the field of flow.

The magnetic field is expressed in terms of the magnetic vector potential \underline{A} . Since the system contains no nonlinearities, its distribution may be described in terms of its phasor \underline{A} that is governed by the Helmholtz equation

$$\text{curlcurl}\underline{A} + \mathbf{j} \cdot \omega \gamma \mu \underline{A} = \mu \underline{\mathbf{J}}_{\text{ext}}, \quad (1)$$

where μ denotes the magnetic permeability, γ is the electric conductivity, ω is the angular frequency, and $\underline{\mathbf{J}}_{\text{ext}}$ stands for the phasor of the external harmonic current density in the inductor. The axis of the arrangement and sufficiently distant artificial boundary are characterized by the Dirichlet condition $\underline{A} = \mathbf{0}$

The heat transfer equation in the liquid continuum reads:

$$\text{div}(\lambda \cdot \text{grad}T) = \rho c \cdot \left(\frac{\partial T}{\partial t} + \mathbf{v} \cdot \text{grad}T \right) - p_J, \quad (2)$$

where λ is the thermal conductivity, ρ is the specific mass, c denotes the specific heat, and \mathbf{v} stands for the velocity. Finally, the symbol p_J denotes the time average internal sources of heat (the specific Joule losses) determined from the formula $p_J = \omega^2 \gamma |\underline{A}|^2$. The temperature field is calculated only in the liquid and also in the pipe, where the term $\mathbf{v} \cdot \text{grad}T$ vanishes. The boundary condition along the external surface of the pipe only respects the convection (basalt is a poor thermal conductor, thus the temperature of this surface is low and radiation from it can be neglected). The temperature of the liquid at the inlet of the pipe is supposed to be known.

The field of incompressible flow obeys the Navier-Stokes equation

$$\rho \cdot \left[\frac{\partial \mathbf{v}}{\partial t} + (\mathbf{v} \cdot \text{grad}) \mathbf{v} \right] = -\text{grad } p + \eta \cdot \Delta \mathbf{v} + \rho \mathbf{g} + \mathbf{f} \quad (3)$$

together with the equation of continuity
 $\text{div } \mathbf{v} = 0.$

Here \mathbf{v} denotes the velocity, p is the pressure, η is the dynamic viscosity, and \mathbf{f} stands for the internal volume Lorentz forces (produced by the time variable magnetic field). For practical computations, we neglected term $\rho \mathbf{g}$ in (4) in order to preserve the axial symmetry of the flow. The boundary conditions are classical—the velocity along the internal wall of the pipe vanishes, due to symmetry its radial component vanishes along the z -axis and the derivative of its axial component with respect to the radius r vanishes here, too.

After transforming (1)–(4) into cylindrical coordinates (respecting the axisymmetry), the numerical solution of the model was realized by a higher-order finite element method. Computation of the electromagnetic field was carried out once at the beginning and independently of the temperature and flow fields. Magnetic vector potential was solved on an automatically adapted higher-order finite element mesh. The obtained solution was subsequently used in a time-dependent computation of fluid-temperature interaction, where the Lorentz forces acted on the fluid flow and average Joule losses caused heating. In the fluid flow, the underlying meshes can generally be different from the hp -mesh used for the electromagnetic field, since they can differ both in polynomial orders and in geometry. Computation of the time-dependent fluid flow was carried out on dynamically changing meshes, where meshes for time level t_n are obtained automatically by our adaptive algorithm and, moreover, the mesh for temperature T can be different from the meshes for the flow fields—radial and axial velocities (v_r, v_z) and the pressure p . This approach leads to a significant reduction of the size of the discrete problem; therefore it speeds up the whole computation. Our own numerical software Hermes2d was used for the computation. It is capable of all the features mentioned above, such as the higher-order finite element method, automatic adaptivity on hp -meshes or assembling of the stiffness matrix on geometrically different meshes.

IV. ILLUSTRATIVE EXAMPLE

For an illustration, the following figures present a few interesting results obtained for molten sodium (for geometry of the pipe see Fig. 1). The inlet velocity of sodium is $v_i = 0.02 \text{ ms}^{-1}$ and the temperature $T_i = 150 \text{ }^\circ\text{C}$. The parameters of the field current are $J_{\text{ext}} = 8 \times 10^6 \text{ Am}^{-2}$ and $f = 50 \text{ Hz}$. Fig. 2 shows the convergence for the magnetic vector potential A (our hp -adaptivity versus the classical h -adaptivity) and Fig. 3 depicts the corresponding hp -mesh. Fig. 4 shows the distribution of the module of magnetic flux density B , particularly in melt. Finally, Fig. 5 shows the distribution of temperature T in melt after $t = 0.4 \text{ s}$ and Fig. 6 depicts the distribution of the module of velocity \mathbf{v} (and the visible vortices at the places where the pipe is getting narrow) for the same time.

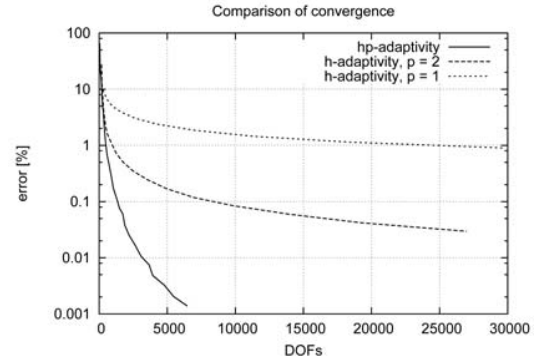


Fig. 2. Comparison of the convergence for magnetic vector potential A

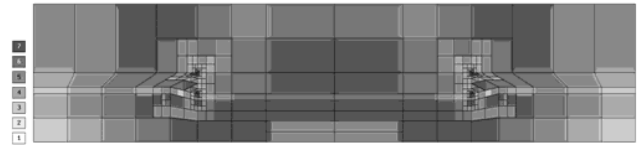


Fig. 3. Adaptive hp -mesh for computation of magnetic vector potential A (white—elements of the 1st order, black—elements of the 7th order)

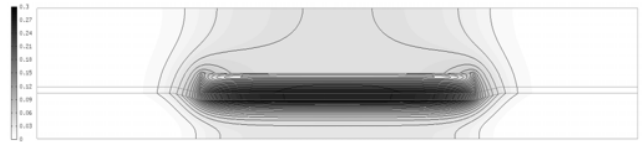


Fig. 4. Distribution of the module of magnetic flux density B in the arrangement (white color – 0 T, black color – 0.3 T)



Fig. 5. Distribution of temperature T (in $^\circ\text{C}$) in melt for $t = 0.4 \text{ s}$ (grey color – 150 $^\circ\text{C}$, black color – 200 $^\circ\text{C}$)



Fig. 6. Distribution of the module of velocity \mathbf{v} in melt for $t = 0.4 \text{ s}$ (white color – 0 ms^{-1} , black color – 2 ms^{-1})

V. ACKNOWLEDGMENT

Financial support of the Research Plan MSM6840770017 and Grant projects GA CR 102/07/0496 and GAASCR IAA100760702 is gratefully acknowledged.

VI. REFERENCES

- [1] P.A. Davidson, *An Introduction to Magnetohydrodynamics*, Cambridge University Press, Cambridge, 2001.
- [2] A. Alemany, P. Marty, and J.P. Thibault, *Transfer Phenomena in Magnetohydrodynamic and Electroconducting Flow*, Kluwer Academic Publishers, 1999.
- [3] <http://hpfem.org/>.
- [4] <http://hpfem.math.unr.edu/>.

Equivalent stress criteria for the effect of stress on magnetic behavior

L. Daniel^a and O. Hubert^b

^aLGEP (CNRS(UMR 8507) ; SUPELEC ; Univ Paris-Sud ; UPMC Paris 6)
Plateau de Moulon, 11 rue Joliot-Curie ; F-91192 Gif sur Yvette Cedex ; France

^bLMT-Cachan (CNRS (UMR 8535) ; ENS Cachan ; UPMC Paris 6)

61 avenue du Président Wilson ; F-94235 Cachan Cedex ; France

laurent.daniel@supelec.fr, olivier.hubert@lmt.ens-cachan.fr

Abstract—A main limitation of most models describing the effect of stress on the magnetic behavior is that they are restricted to uniaxial, tensile or compressive, stress. An idea to overcome this strong limitation is to define a fictive uniaxial stress, the equivalent stress that would change the magnetic behavior in a similar manner than a multiaxial one. Several authors have tried to define such a criterion. We propose in this paper to compare several equivalent stress definitions, and to apply them in the case of uniaxial and biaxial mechanical loadings for which experimental results are available.

Index Terms—Magneto-elasticity, effect of stress, equivalent stress, multiaxiality

I. INTRODUCTION

In most of practical electromagnetic applications, magnetic materials are submitted to multiaxial stress inherited from forming process or appearing in use. These stress states can change significantly the magnetic behavior of materials [1]. However, the few available models describing the effect of stress on the magnetic behavior are usually restricted to uniaxial (tensile or compressive) stress. A solution to introduce the multiaxiality of stress into modeling tools is the definition of an equivalent stress criterion. An equivalent stress for the magnetic behavior is a (fictive) uniaxial stress that would change the magnetic behavior in a similar manner than the multiaxial one. Some authors proposed such an approach in the past years [2]–[6]. We propose in this paper to compare these proposals. Experimental results carried out under biaxial mechanical loading will help to validate these criteria.

II. SEVERAL EQUIVALENT STRESS DEFINITIONS

Several authors tried to define an equivalent stress for magneto-elastic behavior, usually thanks to energetic considerations and experimental observations of magnetic behavior of materials submitted to biaxial mechanical loadings.

Kashiwaya (K) [2] proposed the following definition for the equivalent stress $\sigma_{\text{eq}}^{\text{K}}$:

$$\sigma_{\text{eq}}^{\text{K}} = K(\sigma_1 - \sigma_{\text{max}}) \quad (1)$$

with K a constant, σ_1 the eigenstress aligned with the magnetic field direction and σ_{max} the maximal value of the

stress tensor eigenvalues. This equivalent stress is always negative or null. Iso-values are parallel lines in the (σ_1, σ_2) plane. If the magnetic field is applied along the direction of the maximum eigenstress, the equivalent stress is zero, so that a tensile stress or an equi-biaxial tension or compression are supposed to have no effect on the magnetic behavior.

Schneider and Richardson (SR) [3] proposed the following definition for the equivalent stress $\sigma_{\text{eq}}^{\text{SR}}$:

$$\sigma_{\text{eq}}^{\text{SR}} = \sigma_1 - \sigma_2 \quad (2)$$

σ_1 and σ_2 are the eigenstresses in the sheet plane, the magnetic loading being aligned in the direction of σ_1 . The main difference with K definition is that the area of the stress plane where $\sigma_1 > 0$ and $\sigma_2 < 0$ defines a positive equivalent stress. But an equibiaxial stress is still supposed to have no effect on the magnetic behavior.

Sablik and co-workers (S) [4] proposed the following definition for the equivalent stress $\sigma_{\text{eq}}^{\text{S}}$, based on previous magneto-mechanical measurements by Langman [7]:

$$\begin{cases} \sigma_{\text{eq}}^{\text{S}} = \frac{1}{3}(2\sigma_1 - \sigma_2) & \text{for } \sigma_1 < 0 \\ \sigma_{\text{eq}}^{\text{S}} = \frac{1}{3}(\sigma_1 - 2\sigma_2) & \text{for } \sigma_1 \geq 0 \end{cases} \quad (3)$$

σ_1 is still the stress aligned with the magnetic field. Equi-bitraction and equi-bicompression do not lead to the same result, that is a significant difference with K and SR approaches. But S model is discontinuous for $\sigma_1 = 0$.

Pearson and co-workers [5] also proposed an equivalent stress for a biaxial mechanical loading. In its simplest form this equivalent stress corresponds to SR proposal. The more refined form is a polynomial interpolation that reveals complicated to use because the parameter identification is sample dependent.

Daniel and Hubert (DH) [6] proposed the following definition $\sigma_{\text{eq}}^{\text{DH}}$, based on an equivalence in magneto-elastic energy:

$$\sigma_{\text{eq}}^{\text{DH}} = \frac{3}{2} {}^t \vec{h} \mathbf{s} \vec{h} \quad (4)$$

\vec{h} is the direction parallel to the applied magnetic field and s is the deviatoric part of the stress tensor σ ($s = \sigma - \frac{1}{3}\text{tr}(\sigma)\mathbf{I}$). It can be noticed that the equivalent stress is zero when the stress is hydrostatic, meaning that a hydrostatic pressure has no effect on the magnetic behavior. A main advantage of this criterion is that it can be applied to a fully multiaxial mechanical loading, whereas the previous proposals only refer to biaxial stress state.

As a first analysis, these equivalent stress criteria can be compared in the case of a uniaxial mechanical loading (intensity σ_o). The result is presented in figure 1.

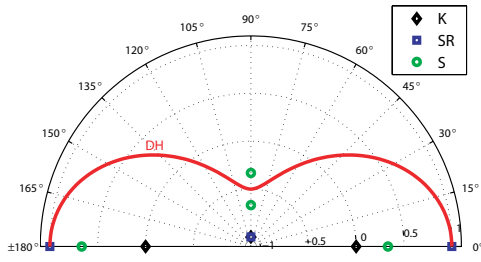


Fig. 1. Equivalent stress σ_{eq}/σ_o in the case of a uniaxial stress σ_o applied in a direction $\theta \in [0, \pi]$ with respect to the magnetic field (direction 0°).

K, SR and S criteria can only be applied in the case when the direction of the magnetic field is a principal direction for the stress. DH criterion can be applied whatever the relative orientation between stress and magnetic field. In the uniaxial case, σ_{eq}^{DH} can be written :

$$\sigma_{eq}^{DH}(\theta) = \frac{3}{2}\sigma_o \left(\cos^2\theta - \frac{1}{3} \right) \quad (5)$$

It can be noticed that in the case of an uniaxial stress applied in the direction of the magnetic field, the equivalent stress is the applied stress only for SR and DH proposals. The discontinuity of S model for $\theta=\pi/2$ ($\sigma_1=0$) is highlighted.

III. APPLICATION IN THE CASE OF BIAxIAL MECHANICAL LOADINGS

Experiments have been performed on iron-cobalt laminations [8]. They consist in anhysteretic magnetic measurements carried out under biaxial mechanical stress in homogeneous magnetic and mechanical conditions, for stress levels varying from -60MPa to +60MPa.

The expected susceptibility according to K, SR, S and DH criteria has been estimated (the experimental data for the susceptibility under uniaxial mechanical loading have been extracted from the measurements with $\sigma_2 = 0$). The experimental conditions correspond to biaxial stress (σ_1, σ_2) with the magnetic field applied along eigendirection 1 (DH equivalent stress is then defined by $\sigma_{eq} = \sigma_1 - \frac{1}{2}\sigma_2$). Figure 2 shows a map of the relative error between predicted χ_p and measured χ_e susceptibilities ($e = 100 \times |\chi_p - \chi_e|/\chi_e$). For all criteria, the errors observed in equibicompaction (-60 MPa, -60 MPa) for $H=2500$ A/m are very high, with a level of 635% for K and SR, 371% for S and 238% for DH.

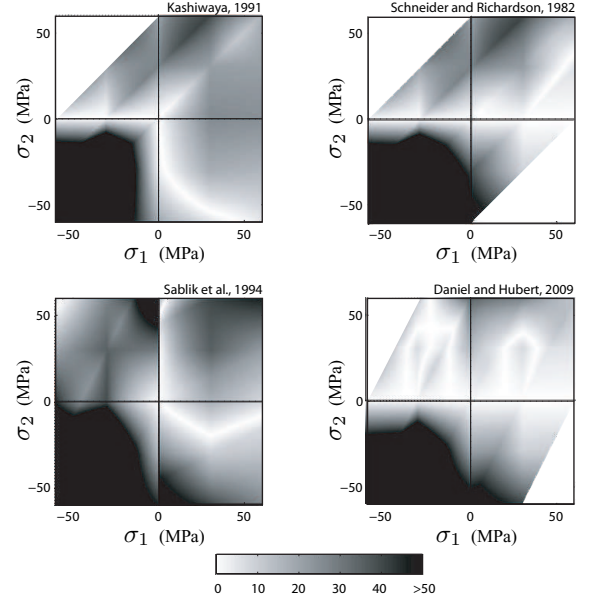


Fig. 2. Relative error (percent) for the predicted susceptibility ($H=250$ A/m) according to several equivalent stress proposals. (a) K ($K=1$), (b) SR, (c) S, (d) DH.

In Figure 2, the error values have been truncated at 50% for reading convenience. DH criterion appears to be closest to experimental results.

IV. CONCLUSION

Several equivalent stress for magneto-mechanical behavior are compared. The main weakness of these models is their inability to describe the effect of a bicompression stress on the magnetic behavior. Only one equivalent stress (DH) can describe fully multiaxial stress state, without any hypothesis concerning the relative orientation of the magnetic field direction in the principal stress coordinate system. This latter proposal is also the closest to experimental results obtained in biaxial configurations. A detailed comparison to experimental results will be discussed in the full paper.

REFERENCES

- [1] R.M. Bozorth, *Ferromagnetism*, ed. D. Van Nostrand Company, N.Y. 1951.
- [2] K. Kashiwaya, *Jpn J. Appl. Phys.*, 30 (1991), pp. 2932.
- [3] C.S. Schneider and J.M. Richardson, *J. Appl. Phys.*, 53 (1982), pp. 8136.
- [4] M.J. Sablik, L. Riley, G. Burkhardt, H. Kwun, P. Cannel, K. Watts and R. Langman, *J. Appl. Phys.*, 75 (1994), pp. 5673.
- [5] J.Pearson, P.T.Squire, M.G.Maylin, and J.G.Gore, *IEEE Trans. Magn.*, 38 (2000), pp. 3251.
- [6] L. Daniel, O. Hubert, *J. Appl. Phys.*, 105 (2009), 07A313.
- [7] R.A. Langman, *IEEE Trans. Magn.*, 26 (1990), pp. 1243.
- [8] O. Hubert, *Przedgląd Elektrotechniczny*, 83 (2007), pp. 70.

Shape Formation of Ferrofluid Droplet in Magnetic Field and Gravity by FEA coupled with LSM

Young Sun Kim, and Il Han Park

School of Information and Communication Engineering, Sungkyunkwan University
300, Cheoncheon-dong, Jangan-gu, Suwon, 440-746, Korea
youngsun@skku.edu, ihpark@skku.ac.kr

Abstract— This paper presents a numerical method for calculating shape of ferrofluid droplet that undergoes three influences: external magnetic field, gravitational force and surface tension. The shape is calculated using an equilibrium energy condition in the coupled system of electromagnetic field and ferrofluid in the presence of gravity and surface tension on the ferrofluid boundary. The shape of the ferrofluid is traced using level set method(LSM), where the continuum shape sensitivity of the material derivative concept is used for the velocity field on the boundary. The presented algorithm is implemented with standard finite element procedure and tested in a shape problem of ferrofluid droplet placed above an electromagnet.

I. INTRODUCTION

In this paper we present a method of numerical simulation for calculating shape of ferrofluid with considering the effects of external magnetic field, surface tension and gravitational field. The different physical phenomena have mutual influence and they are put together to set a nonlinear-coupled system. This paper aims to analyze the coupled system equation and calculate the ferrofluid shape. The numerical algorithm for shape calculation is developed by using an equilibrium energy condition of the coupled system of electromagnetic fields and surface tension in the presence of gravitational field. It is too difficult to calculate the shape using fluid dynamics driven by magnetic force, gravity and surface tension. Thus in this work we make use of the energy equilibrium condition at the final shape. We also employ level set method(LSM) to easily capture varying interface between the ferrofluid and the surrounding air. The physical model consists of magnetostatic equations, surface tension condition and an advection equation for the level set function. Each model is numerically implemented and coupled using a standard finite element procedure. The shape derivative of continuum sensitivity by the material derivative concept is used for the velocity field that is required for the level set technique. The proposed method is numerically tested and validated in a shaping problem of ferrofluid droplet placed above a DC electromagnet.

II. LEVEL SET METHOD

The basic idea of the level set method is to represent domains and their boundaries not via parameterization, but as level sets of a continuous function, the so-called level set function. It is expressed in an implicit form of a high dimensional function, and then the boundary changes are traced by the deformation of this function [1], [2]. In this

shape problem, the interface boundaries are varied in order to minimizing or maximizing the total system energy.

III. ALGORITHM FOR SHAPE FORMATION OF FERROFLUID

A. System Energies of Ferrofluid Droplet

The energy functions of magnetic, gravitational systems and surface tension are respectively expressed as

$$W_m = \int_{\Omega} \frac{1}{2} \mathbf{B}(\phi) \cdot \mathbf{H}(\phi) d\Omega \quad (1)$$

$$W_g = \int_{\Omega} \rho g y d\Omega \quad (2)$$

$$W_s = \int_{\Gamma} 2\sigma H d\Gamma \quad (3)$$

where, ρ is material density, g is material density and y is position of surface. σ and H denote coefficient of surface tension and curvature of boundary.

In magnetic system with current source the shape of ferrofluid varies to maximize its field energy W_m . On the contrary, in the gravitational system its shape varies to minimize its potential energy W_g . Surface tension changes also the shape to minimize the surface tension energy W_s . Therefore, this shape problem can be formulated as a kind of optimization problem with an objective function of energy functional as

$$\text{Maximize : } W_m - W_g - W_s$$

subject to two equality constraints of magnetostatic field equation and constant area as

$$\nabla^2 A = -\mu(\phi)J \quad (4)$$

$$\int_{\Omega} H(\phi)d\Omega = S^* \quad (5)$$

where the design variable is represented by Ω .

B. Velocity Fields and Constraint of Constant volume

Design variables are the movable boundary between ferrofluid and free space. The design boundary $\partial\Omega$ is represented using the level set function such that $\phi(\mathbf{x},t)=0$ for any time. Since the level set function holds at any time t , its total derivative is expressed by using an Eulerian formulation of the boundary variation as

$$\frac{d\phi}{dt} = \frac{\partial\phi}{\partial t} + V_n |\nabla\phi| = 0 \quad (6)$$

where the velocity field determines shape variation, that also causes change the objective function. Thus, calculation of

appropriate velocity field for increasing the energy functional is an important part for the shape problem.

When the constraint of constant area is imposed on the shape problem, the velocity field is modified from V_n to \hat{V}_n using Lagrange multiplier technique as

$$\hat{V}_n = (V_{n1} + V_{n2} + V_{n3}) - V_0 \quad (7)$$

$$V_0 = \frac{\int_{\gamma} (V_{n1} + V_{n2} + V_{n3}) d\Gamma}{\int_{\gamma} d\Gamma} \quad (8)$$

where V_{n1} , V_{n2} and V_{n3} are the normal components of the velocity field vectors in the magnetic system, the gravitational system and surface tension condition, respectively.

C. Continuum Sensitivity Analysis for Velocity Fields

The total derivative of objective function in electromagnetic systems can be derived using the material derivative concept of continuum mechanics and an adjoint variable technique. Here we call it continuum sensitivity for shape derivative. The continuum sensitivity formula in magnetostatic systems is represented as

$$\frac{dW_m}{dt} = \int_{\gamma} \frac{1}{2} \left(\frac{\mu_r - 1}{\mu_0 \mu_r} \right) \left(B_n^2 + \frac{1}{\mu_r} B_t^2 \right) V_{n1} d\Gamma \quad (9)$$

where, V_{n1} the normal component of the velocity field vector, γ design boundary [3].

The sensitivity formula is the relation of the objective function and the velocity field in (9). If the velocity field is taken as

$$V_{n1} = \frac{1}{2} \left(\frac{\mu_r - 1}{\mu_0 \mu_r} \right) \left(B_n^2 + \frac{1}{\mu_r} B_t^2 \right) \quad \text{on } \gamma, \quad (10)$$

the objective function is increased.

The potential energy of gravitational system depends on only the y-coordinate position and the fluid shape varies to minimize the gravitational potential energy. According to Reynolds' transport theorem for differentiating a volume integral, the material derivative of the potential energy is given by

$$\frac{dW_g}{dt} = \int_v \frac{\partial}{\partial t} (\rho g y) dv + \int_s (\rho g y) V_{n2} ds \quad (11)$$

where V_{n2} is the normal component of the velocity field vector and the integrand in the second term is zero since

$$\frac{\partial}{\partial t} (\rho g y) = \rho g \frac{\partial y}{\partial t} \Big|_{y=const.} = 0 \quad (12)$$

That is, the gravitational sensitivity has only surface integration. If the velocity field is taken as

$$V_{n2} = -\rho g y \quad \text{on } \gamma, \quad (13)$$

the objective function of gravitational system is decreased on the contrary to the magnetostatic system.

The surface tension energy depends on the radius of curvature at the material surface. The derivative of surface tension energy is expressed as

$$\frac{dW_s}{dt} = \int_{\gamma} 2\sigma (\nabla H \cdot \mathbf{n} + H^2) V_{n3} d\Gamma \quad (14)$$

where V_{n3} is the normal component of velocity field vector and the second term is zero. Thus, the sensitivity of surface tension energy is taken in order to decrease the energy as

$$V_{n3} = 2\sigma H \quad \text{on } \gamma. \quad (15)$$

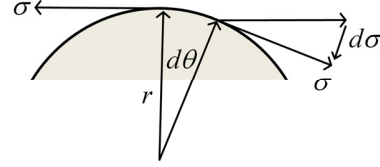


Fig. 1. Schematic of surface tension on ferrofluid surface.

The velocity field of sum of the magnetic velocity, the gravitational velocity and surface tension with constant area constraint is inserted into the level set equation of Hamilton-Jacobi equation in order to obtain shape evolution for maximization of the objective function.

$$\frac{\partial \phi}{\partial t} + (V_{n1} + V_{n2} + V_{n3}) |\nabla \phi| = 0 \quad (16)$$

The iterative procedure for optimization is transformed into a time domain problem of a Hamilton-Jacobi equation. The time in the partial differential equation (PDE) has no physical meaning. Thus, it is called "pseudo time" for optimization procedure.

IV. NUMERICAL TEST

To validate the algorithm, we tested a shape problem of Fig. 2. Its numerical results showed that the level set method coupled with physical systems of magnetic field, gravitational force and surface tension is feasible and effective for capturing its shape variation.

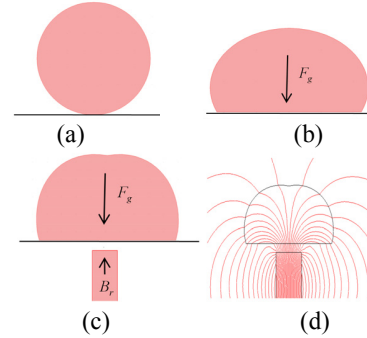


Fig. 2. Shape variation of ferrofluid droplet. (a) only with surface tension, (b) gravitational force added, (c) magnetic fields added and (d) distribution of magnetic field

V. REFERENCES

- [1] Osher, S. and Fedkiw, R., *Level Set Methods and Dynamic Implicit Surfaces*, Springer, New York, 2003.
- [2] Young Sun Kim, Se-Hee Lee, Hong Soon Choi, and Il Han Park "Shape formation of ferrofluid under external magnetic fields using level set method", *Journal of Applied Physics* 105, 07D539, 2009.
- [3] Il-han Park, Jean Louis Coulomb and Song-yop Hahn, "Design Sensitivity Analysis for Nonlinear Magnetostatic Problems by Continuum Approach," *Journal de Physique III*, Vol.2, No.11, November 1992, pp.2045-2053.

FEM/BEM Hybrid Method for Magnetic Field Evaluation Due to Underground Power Cables

V. Maló Machado

Centre for Innovation in Electrical and Energy Engineering (CIEEE)
 Instituto Superior Tecnico, Technical University of Lisbon
 Av. Rovisco Pais, 1049-001-Lisbon, Portugal
 malo.machado@ist.utl.pt

Abstract — This paper is a contribution to the electromagnetic field evaluation due to underground power cables. Open boundary 2D problems may be treated combining the finite element method (FEM) inside a region surrounded by a regular (cylindrical) fictitious surface with a semi-analytical boundary element method (BEM) to describe the field outside this region. For the outside region, a generalization of Pollaczek's solution is applied, taking into account eddy currents in the soil and the proximity effect between the soil/air plane surface and the cylinder fictitious surface with finite radius. The method is validated by using typical underground power cables where analytical methods may be applied accurately.

I. INTRODUCTION

Spreading of urban centres, and ever increasing demand for electrical power within them, is leading to the use of underground cable systems at high voltage. The growing use of cable systems makes the analysis of wave propagation characteristics and transients an important task. On the other hand, danger to human health has been a matter of concern and controversy particularly for magnetic fields produced by underground power transmission systems.

All these aspects have demanded great efforts in the research on methods to evaluate accurately magnetic field quantities, either related to the constitutive parameters, namely the series-impedance, or even to the magnetic induction field, particularly on the soil surface.

In the past, analytical methods [1]-[5] have been experimented to evaluate magnetic field quantities due to underground power cables. However, analytical methods can not be used always accurately. Those are the cases, for instance, where cables are buried inside underground pipes or galleries with irregular cross sections.

This paper is a contribution to the electromagnetic field evaluation of open boundary problems combining the finite element method (FEM) inside a region surrounded by a regular fictitious surface with a semi-analytical boundary element method (BEM) to describe the field outside this region. Hybrid methods have already been applied [6], [7] in order to adapt the FEM to treat open boundary field problems. In this paper, a two-dimensional (2D) periodic time-harmonic electromagnetic field problem is considered for the underground transmission system in which eddy currents inside phase conductors, sheaths and the soil are taken into account. A fictitious cylindrical surface located in the soil is considered in a way that the open space is partitioned into two regions: the inner region containing power cables and other apparatus eventually with irregular shapes; and, the outer

region composed by the soil and air separated by a surface taken as a plane.

A FEM formulation is used for the inner region [8]-[9].

For the outside region, a generalization of Pollaczek's solution [5] is applied, like the one described in [1], taking into account eddy currents in the soil and the proximity effect between the soil/air plane surface and the cylinder fictitious surface with finite radius. In this way, the outside field description is based on a Fourier series development over the cylinder fictitious surface for the potential and for its normal derivative values. These quantities, discretized and organized into finite dimension vectors, are related by using formulae derived analytically and expressed as a square coefficient matrix. A Discrete Fourier Transform (DFT) is then used to transform the relationship to the space domain where it assumes the form of another coefficient matrix relating the actual potential values with their normal derivatives over a set of discrete nodes on the fictitious separating surface. These nodes are coincident with the discrete nodes of the FEM mesh taken for the inner region.

Finally, the method is validated by using typical underground power cables where analytical methods may be applied accurately [1], [2]. Series-impedance as well as magnetic induction field values are evaluated and compared with results obtained by using those analytical methods. Excellent accuracy is found for the set of considered configurations and examples.

II. FIELD FORMULATION

The magnetic field for the internal region may be established, as described in [6], [8], by using an appropriate variational formulation where the magnetic vector potential appears as the primary quantity. The FEM is the adequate method for the corresponding numerical solution. The FEM formulation may be expressed, as done in [6], involving both the unknown potential values of the FEM nodal points as well as the potential normal derivative values on the nodes of the fictitious surface. The relationship allows boundary conditions on the above referred surface to be matched with the field formulation for the outer region.

For the outer region an analytical formulation is used based on the development presented in [1]. In this way, the matrix relating the actual phasor values over a finite set of points over the fictitious boundary of the magnetic vector potential with those of its normal derivative, similarly as done in [6], may be derived.

III. MAGNETIC INDUCTION FIELD

The magnetic induction field, $\mathbf{B} = B_x \vec{u}_x + B_y \vec{u}_y$, at any point (x,y) in the air, over the soil, originated by an underground cable involved by a fictitious cylindrical surface buried at the depth h , is given by

$$B_x = \int_{-\infty}^{+\infty} -|a|U(a) e^{jax} da, \quad B_y = \int_{-\infty}^{+\infty} -jaU(a) e^{jax} da \quad (1)$$

where

$$U(a) = \frac{1}{\pi} \frac{2j}{\mu_r |a| + \sqrt{a^2 - q^2}} e^{-h\sqrt{a^2 - q^2}} \sum_{m=-\infty}^{+\infty} G_m \left(\frac{a - \sqrt{a^2 - q^2}}{jq} \right)^m \quad (2)$$

with

$$q^2 = -j\omega\mu_r\mu_0\sigma \quad (3)$$

ω being the angular frequency, where μ_r , σ are the relative permeability and the conductivity, respectively, of the soil, and G_m are the coefficients, adopted in the development presented in [1], determined from the magnetic vector potential at the FEM nodal points over the fictitious surface whose values are obtained from the numerical solution of the matrix equation built by using the FEM/BEM hybrid method.

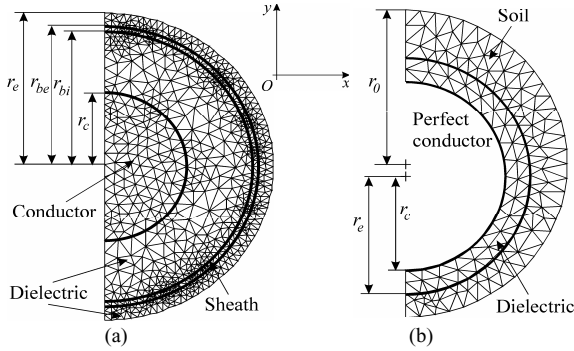


Fig. 1 – FEM mesh in the plane (x,y) for the inner region corresponding to the two underground cables considered in the paper.

IV. NUMERICAL RESULTS

Numerical results were obtained for two problems with analytical solution. The purpose is to compare results obtained with the FEM/BEM hybrid method used in this paper with analytical results obtained with the method described in [1]. The first problem, indicated in Fig. 1-a), considered in [2], consists in a 50 Hz underground cable buried at a depth 1,5 m in a soil with conductivity $\sigma=0,01$ S/m where $r_c=36$ mm, $r_{bi}=65$ mm, $r_{be}=67,6$ mm, $r_e=74$ mm taking the conductivity of the conductor and the sheath respectively equal to $5,8 \times 10^7$ S/m and $4,76 \times 10^6$ S/m. For this problem the fictitious surface coincides with the cable outer surface. The second problem, Fig. 1-b), considered in [1], consists in a underground cable buried at a depth 112,5 mm in a soil with conductivity $\sigma=1$ S/m for a working frequency 10 MHz, assuming the phase conductor as a perfect conductor where $r_c=45$ mm and $r_e=56,25$ mm. In this problem the fictitious surface located in the soil with radius $r_0=73,08$ mm and the cable are not coaxial where the distance between their axes is equal to 5,91 mm.

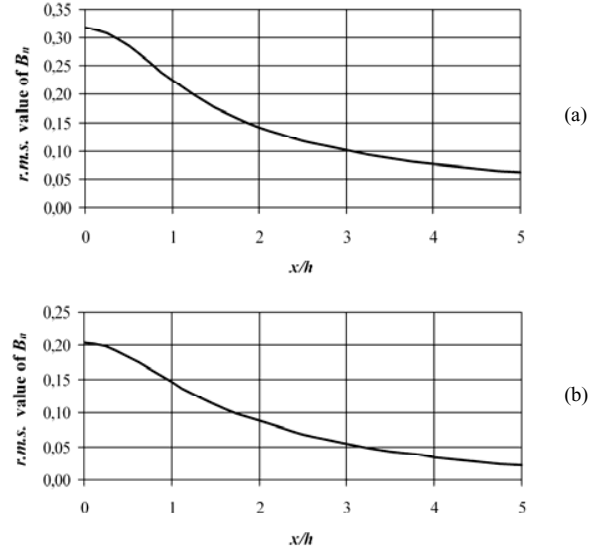


Fig. 2 – Normalized *r.m.s.* values of the magnetic induction field at the soil/air plane surface: (a) for the problem of Fig. 1-a); (b) for the problem of Fig. 1-b).

Fig. 2 shows results for the normalized *r.m.s.* value of the magnetic induction field at the soil/air plane, taking $\mu_0 I_{r.m.s.}/h$ as the normalizing factor, $I_{r.m.s.}$ representing the *r.m.s.* value of the cable current. These results mean that, comparing with analytical results, a deviation less than 1% is obtained for the first problem (Fig.1-a) and a deviation less than 2% is obtained for the second problem (Fig. 1-b)). Results were derived for $M \leq 5$, where M is the truncation order of the series development in (2).

Series-impedance elements per unit length were also obtained for the described cables. Relative deviations less than 0,3 % were found, again in comparison with analytical results.

V. REFERENCES

- [1] V. M. Machado, J. B. Silva, "Series-Impedance of Underground Transmission Systems", *IEEE Trans. on Power Delivery*, 3(2): 417-423, 1988.
- [2] V. M. Machado, M. E. Almeida, M. G. Neves, "Accurate Magnetic Field Evaluation Due to Underground Power Cables", *European Transactions on Electrical Power*, DOI: 10.1002/etep.296, Published Online: Nov. 2008.
- [3] L. M. Wedepohl, D. J. Wilcox, "Transient Analysis of Underground Power-Transmission Systems", *Proc. IEE*, 120: 253-260, Feb. 1973.
- [4] A. Ametani, "A general Formulation of Impedance and Admittance of Cables", *IEEE Transactions on Power Apparatus and Systems*, 99: 902-910, 1980.
- [5] F. Pollaczek, "Über das Feld einer unendlich langen wechselstromdurchflossenen Einfachleitung", *Elektrischen Nachrichten Technik*, 3: 339-360, 1926.
- [6] J. B. Silva, V. M. Machado, "Time-Harmonic Electromagnetic Field using a Hybrid FEM/BoundaryMethod for Open Transmission Line Systems", *IEEE Trans. on Magnetics*, 34(5): 3315-3318, 1998.
- [7] M. Chari, et al, "Solution of Open Boundary Problems by Differential and Integral Methods", *IEEE Trans. on Magnetics*, 22: 1037-1039, Sept. 1986.
- [8] V. M. Machado, "Eddy Current and Impedance Evaluation Using a Two Dimensional Finite Element Method", *IEEE Trans. on Energy Conversion*, 8: 362-368, Sept. 1993.
- [9] O. C. Zienkiewicz, K. Morgan, *Finite Elements and Approximation*, Singapore : John Wiley & Sons, 1983.

Voltage and current sources for massive conductors suitable with the $A - \chi$ Geometric Formulation

Paweł Dłotko¹, Ruben Specogna², and Francesco Trevisan²

¹Jagiellonian University, Institute of Computer Science, Lojasiewicza 4, 30348 Kraków, Poland,

²Università di Udine, Via delle Scienze 208, 33100 Udine, Italy, ruben.specogna@uniud.it.

Abstract—The aim of the paper is to present an automatic and general technique, suitable with the $A - \chi$ geometric eddy-current formulation, to impose sources over massive conductors of any shape. For this purpose, the *localized source approach* is used, which does not require the solutions of steady-state conduction problems in the pre-processing stage. Nevertheless, this approach needs a *thick cut* in each active conductor, which is usually found “by hand”. In this paper, an automatic and general algorithm to compute such thick cuts is introduced. Some benchmark problems are presented to demonstrate the generality and the robustness of the algorithm.

Index Terms—Cell Method, Finite Integration Technique (FIT), Discrete Geometric Approach (DGA), eddy-currents, current and voltage sources, thick cuts.

I. INTRODUCTION

The so-called “Discrete Geometric Approach” (DGA) [1], similarly to the Finite Integration Technique (FIT) [2] or the Cell Method [3], allows to solve directly Maxwell’s equations in an alternative way with respect to the classical Galerkin method in Finite Elements.

In this paper, an automatic technique to enforce sources on massive conductors, suitable with the eddy-current $A - \chi$ geometric formulation [4], is introduced. In particular, the localized source approach [5], [6] is considered here. It presents many advantages with respect to the distributed source approach [6]; For example it does not require steady-state conduction problem solutions in the pre-processing stage. Furthermore, the localized source approach is based on global quantities –voltages and currents– which enable a straight-forward coupling between the eddy-current formulation and electric circuits.

The domain of interest D of the eddy-current problem has been partitioned into an active conductive region D_s , a passive conductive region D_c and a non-conductive region D_a . We assume that the region D_s –where sources are enforced– consists of the union of N disjoint conductors D_s^j , $j = 1, \dots, N$, which are homeomorphic¹ to a torus and such that $D_s = \bigcup_{j=1}^N D_s^j$; No assumption are given about the conductors belonging to D_c .

The domain D is covered by a finite element mesh of tetrahedra; The corresponding simplicial complex [3] is denoted as \mathcal{K} . From \mathcal{K} , the barycentric dual complex \mathcal{B} is also introduced [3]. The incidence matrix between edges e and nodes n is

¹From the topological viewpoint, they are the same. This assumption is not restrictive, since sources can be imposed only on torus-like conductors. Thus, the active conductor can also be knotted.

denoted by \mathbf{G} , by \mathbf{C} is denoted the incidence matrix between faces f and edges e and by \mathbf{D} the incidence matrix between tetrahedra v and faces f . The matrices $\tilde{\mathbf{G}} = \mathbf{D}^T$, $\tilde{\mathbf{C}} = \mathbf{C}^T$ and $\tilde{\mathbf{D}} = -\mathbf{G}^T$ describe the mutual interconnections of the dual barycentric complex (dual volumes \tilde{v} , dual faces \tilde{f} , dual edges \tilde{e} , dual nodes \tilde{n}) [3].

The localized source approach needs a *thick cut* [6] for each active conductor, which is usually found “by hand”. When dealing with complicated geometries or a big number of active conductors, an automatic technique to find such thick cuts can be very useful. This is the reason why we propose a completely automatic and general topology-based algorithm to construct thick cuts, which does not require any prior knowledge about the geometry of the active conductors.

II. THICK CUTS FOR THE TORI

For each edge e belonging to the j -th torus D_s^j , an integer is specified. The values are specified in such a way that the sum (with incidence) of the values of the edges belonging to a generic cycle is equal to n (or $-n$) if and only if the cycle goes n times around the torus, inside it (all trivial cycles go around the torus zero times)². The integer values relate to each edge $e \in D_s$ are stored into arrays $(\mathbf{c}^j)_e$, $j = 1, \dots, N$, one for each torus. The array \mathbf{c}^j is by definition a thick cut³ for D_s^j .

On the left of Fig. 1, an example of torus-like conductor is considered. On the right of Fig. 1, the black edges are the edges e having non-zero value in the thick cut $(\mathbf{c}^1)_e$. Considering the union of dual faces one-to-one with edges belonging to the thick cut, a surface S^j which “cuts” the torus is obtained on the dual complex⁴, see for example on the right in Fig. 1.

In the full paper, a fast and robust algorithm to automatically compute the thick cuts in D_s^j will be described in detail.

²Formally speaking, since the 1-st homology group $H_1(\mathcal{K}_s^j) = \mathbb{Z}$ [7] then there exists one generator $[g] \in H_1(\mathcal{K}_s^j)$, where \mathcal{K}_s^j is the sub-complex of \mathcal{K} containing entities in D_s^j . For a given cycle c the sum of $(\mathbf{c}^j)_e$ with incidence is equal $n \in \mathbb{Z}$ if $c \in [ng]$, where $[ng]$ indicates the homology class of the cycle ng .

³More precisely, the thick cut is a generator of the 1-st cohomology group $H^1(\mathcal{K}_s^j)$ [7].

⁴Thanks to the Poincaré-Lefschetz duality $H^1(\mathcal{K}_s^j) \cong H_2(\mathcal{B}_s^j, \partial\mathcal{B}_s^j)$ [7], thus the 1-st cohomology group of \mathcal{K}_s^j can be reinterpreted as the 2-nd relative homology group in the dual complex \mathcal{B}_s^j . The generator of this group consist of triangles that form a surface S^j on dual complex having the boundary on ∂D_s^j and which is not itself boundary of any volume in D_s^j .

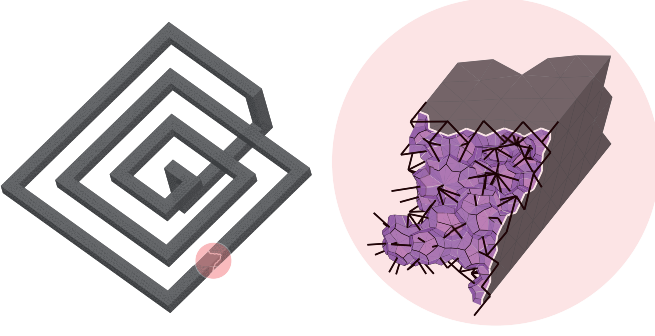


Fig. 1. On the left, an example of torus-like conductor. On the right, a zoom on a portion of the conductor in the neighborhood of the non-zero valued edges in the thick cut (the thick black edges). The collection of dual faces, dual to non-zero valued thick cut edges, form a surface S^j on the dual complex that “cuts” the conductor.

III. LOCALIZED VOLTAGE SOURCES

The localized voltage source approach [6], also referred to as “generalized source potential” in [5], is now recalled. Defining the array \mathbf{U}_s as

$$(\mathbf{U}_s)_e = \sum_{j=1}^N U_{tot}^j (\mathbf{c}^j)_e, \forall e \in D_s, \quad (1)$$

where U_{tot}^j is the enforced voltage on the j -th torus. Then the $A - \chi$ formulated eddy-current problem in the frequency domain becomes [6]

$$\begin{aligned} (\mathbf{C}^T \boldsymbol{\nu} \mathbf{C} \mathbf{A})_e &= 0 & e \in D_a \\ (\mathbf{C}^T \boldsymbol{\nu} \mathbf{C} \mathbf{A})_e + i\omega(\boldsymbol{\sigma}_s \mathbf{A}_s + \boldsymbol{\sigma}_s \mathbf{G}_s \boldsymbol{\chi}_s)_e &= (\mathbf{i})_e & e \in D_s \\ (\mathbf{C}^T \boldsymbol{\nu} \mathbf{C} \mathbf{A})_e + i\omega(\boldsymbol{\sigma}_c \mathbf{A}_c + \boldsymbol{\sigma}_c \mathbf{G}_c \boldsymbol{\chi}_c)_e &= 0 & e \in D_c \\ i\omega(\mathbf{G}_s^T \boldsymbol{\sigma}_s \mathbf{A}_s)_n + i\omega(\mathbf{G}_s^T \boldsymbol{\sigma}_s \mathbf{G}_s \boldsymbol{\chi}_s)_n &= (\mathbf{G}_s^T \mathbf{i})_n & n \in D_s \\ i\omega(\mathbf{G}_c^T \boldsymbol{\sigma}_c \mathbf{A}_c)_n + i\omega(\mathbf{G}_c^T \boldsymbol{\sigma}_c \mathbf{G}_c \boldsymbol{\chi}_c)_n &= 0 & n \in D_c, \end{aligned} \quad (2)$$

where $\boldsymbol{\nu}$, $\boldsymbol{\sigma}_x$, $x \in \{s, c\}$, are the discrete counterparts of the constitutive relations [4]; The subscript s, c denote the sub-arrays or sub-matrices relative respectively to entities belonging to D_s or D_c . Moreover we set $\mathbf{i} = \boldsymbol{\sigma}_s \mathbf{U}_s$.

The term $(\mathbf{G}_s^T \mathbf{i})_n, \forall n \in D_s$, assures that the continuity law is satisfied, therefore the ungauged $A - \chi$ formulation can be used [4], [6] to solve (2).

Finally, the total current I_{tot}^j flowing in the j -th active conductor can be easily determined in a post-processing stage as

$$I_{tot}^j = -i\omega \mathbf{c}^{jT} \boldsymbol{\sigma}_s (\mathbf{A}_s + \mathbf{G}_s \boldsymbol{\chi}_s) + (\mathbf{c}^{jT} \boldsymbol{\sigma}_s \mathbf{c}^j) U_{tot}^j. \quad (3)$$

IV. LOCALIZED CURRENT SOURCES

In the $A - \chi$ geometric formulation, I_{tot} can only be specified using (3), which also gives a relationship between I_{tot} and U_{tot} . The symmetric algebraic system of equations, having also U_{tot} as unknown, becomes

$$\begin{aligned} (\mathbf{C}^T \boldsymbol{\nu} \mathbf{C} \mathbf{A})_e &= 0 & e \in D_a \\ (\mathbf{C}^T \boldsymbol{\nu} \mathbf{C} \mathbf{A})_e + i\omega \boldsymbol{\sigma}_s (\mathbf{A}_s + \mathbf{G}_s \boldsymbol{\chi}_s)_e + (\mathbf{v})_e &= 0 & e \in D_s \\ (\mathbf{C}^T \boldsymbol{\nu} \mathbf{C} \mathbf{A})_e + i\omega \boldsymbol{\sigma}_c (\mathbf{A}_c + \mathbf{G}_c \boldsymbol{\chi}_c)_e &= 0 & e \in D_c \\ i\omega(\mathbf{G}_s^T \boldsymbol{\sigma}_s (\mathbf{A}_s + \mathbf{G}_s \boldsymbol{\chi}_s))_n + (\mathbf{w})_n &= 0 & n \in D_s \\ i\omega(\mathbf{G}_c^T \boldsymbol{\sigma}_c (\mathbf{A}_c + \mathbf{G}_c \boldsymbol{\chi}_c))_n &= 0 & n \in D_c, \\ -\mathbf{c}^{jT} \boldsymbol{\sigma}_s (\mathbf{A}_s + \mathbf{G}_s \boldsymbol{\chi}_s) + (\mathbf{c}^{jT} \boldsymbol{\sigma}_s \mathbf{c}^j) \frac{U_{tot}^j}{i\omega} &= \frac{I_{tot}^j}{i\omega} & j = 1, \dots, N, \end{aligned} \quad (4)$$

where $(\mathbf{v})_e = -\sum_{j=1}^N (\boldsymbol{\sigma}_s \mathbf{c}^j)_e U_{tot}^j$ and $(\mathbf{w})_n = -\sum_{j=1}^N (\mathbf{G}_s^T \boldsymbol{\sigma}_s \mathbf{c}^j)_n U_{tot}^j$.

Both the localized voltage sources and the localized current sources are easily generalized when a general external circuit is connected to the port of some active conductor. In this case, both U_{tot} and I_{tot} of that conductor have to be added as unknowns of (4). Correspondingly, an equation describing the external circuit has to be written into the linear system of equations (4).

V. NUMERICAL RESULTS

The localized voltage and current source approach was tested on many examples of massive conductors. For example, on the left of Fig. 2, the resulting current density in a planar inductor is shown. On the right of Fig. 2, another example consisting of a knotted torus is presented.

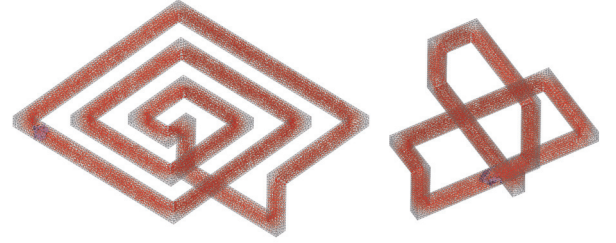


Fig. 2. On the left, the current density in a planar inductor. On the right, the current density in a knotted torus.

In the full paper, a number of benchmark problems will be presented and the results will be compared with the ones obtained by both the complementary $T - \Omega$ geometric formulation and with a Finite Element code.

VI. CONCLUSIONS

An automatic and robust algorithm to impose voltage or current sources on massive conductors suitable with the $A - \chi$ geometric eddy-current formulation was presented. The algorithm was tested on a number of real-sized three-dimensional finite element meshes, showing its utility for practical applications.

REFERENCES

- [1] A. Bossavit, “How weak is the Weak Solution in finite elements methods?”, IEEE Trans. Magn., Vol 34, No. 5, 1998, pp. 2429–2432.
- [2] T. Weiland, “A discretization method for the solution of Maxwell’s equations for six-component fields”, Electron. Commun. (AEÜ), Vol. 31, No. 3, 1977, p. 116.
- [3] E. Tonti, “Algebraic topology and computational electromagnetism”, 4-th International Workshop on Electric and Magnetic Fields, Marseille (Fr), 12–15 May 1988, pp. 284–294.
- [4] R. Specogna, F. Trevisan, “Discrete constitutive equations in $A - \chi$ geometric eddy-currents formulation”, IEEE Trans. on Magn., Vol. 41, No. 4, 2005, pp. 1259–1263.
- [5] P. Dular, F. Henrotte, W. Legros, “A general and Natural Method to Define Circuit Relations Associated with Magnetic Vector Potential Formulations”, IEEE Trans. Magn., Vol. 35, No. 3, 1999, pp. 1630–1633.
- [6] R. Specogna, F. Trevisan, “Voltage sources with $A - \chi$ discrete Geometric Approach to eddy-currents”, Eur. Phys. J.–Appl. Phys. 33, 2006, pp. 97–101.
- [7] J.R. Munkres, “Elements of algebraic topology”, Perseus Books, Cambridge, MA, 1984.

Efficient Computation of Eddy Current Losses in SMC PM Machines with 3D Time-Harmonic FEA

Ahmed Chebak¹, Philippe Viarouge², and Jérôme Cros²

¹Department of Mathematics, Computer Science and Engineering, University of Quebec at Rimouski, Rimouski (QC), G5L3A1, Canada

²Department of Electrical and Computer Engineering, Laval University, Quebec (QC), G1K7P4, Canada
ahmed_chebak@uqar.qc.ca, philippe.viarouge@gel.ulaval.ca, jerome.cros@gel.ulaval.ca

Abstract— The paper presents an efficient method for computing the no-load eddy current losses in the soft magnetic composite (SMC) stator of high speed slotless permanent magnet (PM) machines by using a fast 3D time-harmonic FEA avoiding time consuming 3D time-stepping transient FEA. The magnets are modeled as equivalent surface current sheets with time-varying sinusoidal current densities. This method is used to perform a correction mechanism that is embedded in the optimal CAD process of slotless SMC PM machines to take into account the influence of the 3D end effects on the full-load stator eddy current losses computed from 2D analysis. The proposed method improves the efficiency and convergence of the global design optimization process of the machine.

I. INTRODUCTION

The stator yoke of high-speed slotless PM machines can be made of soft magnetic composite material (SMC) instead of conventional laminated steel to minimize the eddy current losses due to high operation frequency, and to reduce production steps and manufacturing costs for high volume applications. If the conductivity of SMC materials is not negligible, the distribution of the magnetic losses is not independent of the magnetic circuit geometry as in laminated iron core, because the eddy currents not only circulate in the iron particles but also in the whole SMC core. The design methodology of such machines is a complex task because it needs an accurate knowledge of the eddy current circulation that is influenced by the machine structure, dimensions and supply [1]. There are also 3D end-effects on the eddy current distribution that become more significant when the axial length to pole pitch ratio of the SMC stator yoke is decreasing [1]-[2]. In such a case, the 2D assumption does not provide a good accuracy of the eddy current losses prediction required to perform an optimal motor design. A solution has been proposed by the authors in [2] where the 2D analytical design model of slotless machines is associated to an optimization procedure and an iterative correction mechanism performed by 3D Finite Element Analysis (FEA) to take into account the influence of the 3D end effects on the full-load stator eddy currents losses that are computed from the 2D analytical analysis (cf. Fig.1). For each intermediate optimal solution, a 3D time-stepping FE simulation is performed for no-load operation to quantify the 3D effects on the eddy current losses. A suitable correction factor that represents the 3D to 2D no-load eddy current losses ratio is derived and implemented in the analytical design model before the next optimization step. Because 3D time-stepping transient FEA with magnet rotation is time consuming, an alternative is

proposed in this paper that is based on a fast 3D time-harmonic FEA. The rotating magnets are modeled as fixed equivalent surface current sheets with time-varying sinusoidal current densities. The proposed method highly improves the efficiency of the iterative 3D correction mechanism.

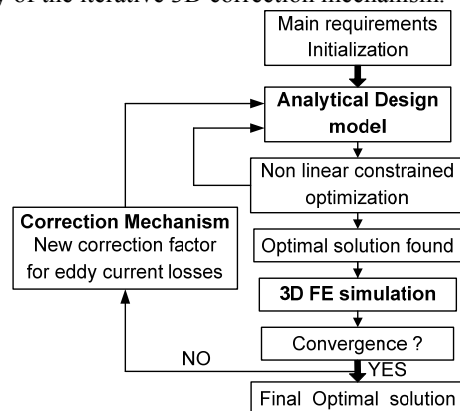


Fig. 1. Design optimization method with eddy current losses correction mechanism [2]

II. EDDY CURRENT LOSSES COMPUTATION WITH 3D TIME-HARMONIC FEA

The stator magnetic losses under full load operation can be predicted by an analytical model derived from the distribution of the electromagnetic field [1]. The field computation is based on the 2D solution of the Maxwell's equations in the magnets/air-gap/windings/stator core regions, for two different sources: the rotating magnets and the armature currents. The model takes into account the eddy currents induced in the conductive homogeneous SMC material and the time and space harmonics of the magnetic field. The representation of the magnet magnetization vector is applicable to radial or parallel magnetized magnets and discrete Hallbach arrays. In the radial case, the spatial magnetization distribution can be expressed by a complex Fourier series:

$$M_{r,rot}(\theta_s, t) = \sum_{k=-\infty}^{+\infty} \bar{M}_{r,k} e^{j(kp\theta_s - kp\Omega t)} \quad (1)$$

p is the number of pairs of rotor poles, $\bar{M}_{r,k}$ is the complex Fourier coefficient of the magnetization vector and Ω is the rotor speed. The no-load eddy current losses in the SMC stator yoke can be derived from the integration of the eddy current density [1]:

$$P_{ec,rot} = \frac{-2\pi L}{\mu_0 \mu_{rs}} \sum_{k=-\infty}^{+\infty} kp\Omega \text{Imag} \left[r \frac{\partial \bar{R}_{m,k}^{(4)}(r)}{\partial r} \bar{R}_{m,k}^{(4)*}(r) \right]_{R_{si}}^{R_{so}} \quad (2)$$

$$\bar{R}_{m,k}^{(4)}(r) = \bar{A}_{m,k}^{(4)} I_\alpha(\bar{\tau}_{m,k} r) + \bar{B}_{m,k}^{(4)} K_\alpha(\bar{\tau}_{m,k} r) \quad (3)$$

Imag is the imaginary part of the complex variable, R_{si} and R_{so} are the inner and outer radius of the stator core. I_α and K_α are modified Bessel functions of the first and second kind of order $\alpha=|k|p$, with $\bar{\tau}_{m,k}^2 = -jkp\Omega\mu_0\mu_{rs}\sigma_s$. $\bar{A}_{m,k}^{(4)}$ and $\bar{B}_{m,k}^{(4)}$ are constants coefficients in the stator core region ($i=4$) that can be determined by using the boundary conditions.

If one represents the rotating magnets as motionless magnets with time-varying sinusoidal magnetization at an angular frequency $\omega=p\Omega$, the new spatial magnetization distribution can be expressed as:

$$\begin{aligned} M_{r,st}(\theta_s, t) &= \sum_{k=-\infty}^{+\infty} \bar{M}_{r,k} \cos(p\Omega t) e^{jkp\theta_s} \\ &= \sum_{k=-\infty}^{+\infty} \frac{\bar{M}_{r,k}}{2} \left(e^{j(kp\theta_s - p\Omega t)} + e^{j(kp\theta_s + p\Omega t)} \right) \end{aligned} \quad (4)$$

Each pulsating magnet field harmonic of order k is equivalent to the superposition of two counter rotating field harmonics $H_{d,k}$ and $H_{i,k}$ with an amplitude proportional to $\bar{M}_{r,k}/2$ and respective angular speeds $+\Omega/k$ et $-\Omega/k$. The stator eddy current losses are then equal to the sum of the losses associated to each counter rotating field because there are no losses due to their interaction:

$$\begin{aligned} P_{ec,st} &= P_{ec,st,d} + P_{ec,st,i} = 2.P_{ec,st,d} \\ &= \frac{-4\pi L}{\mu_0 \mu_{rs}} \sum_{k=-\infty}^{+\infty} p\Omega \text{Imag} \left[r \frac{d\bar{R}_{m,d,k}^{(4)}(r)}{dr} \bar{R}_{m,d,k}^{(4)*}(r) \right]_{R_{si}}^{R_{so}} \end{aligned} \quad (5)$$

$$\begin{cases} \bar{R}_{m,d,k}^{(4)}(r) = \bar{A}_{m,d,k}^{(4)} I_\alpha(\bar{\tau}_{m,d,k} r) + \bar{B}_{m,d,k}^{(4)} K_\alpha(\bar{\tau}_{m,d,k} r) \\ \bar{\tau}_{m,d,k}^2 = -jp\Omega\mu_0\mu_{rs}\sigma_s \end{cases} \quad (6)$$

On can notice from (2) and (5) that for $k=1$ the stator no-load eddy current losses due to the rotating magnets are equal to twice the losses due to the equivalent motionless pulsating magnets ($P_{ec,rot}=2.P_{ec,st}$) because $\bar{R}_{m,k}^{(4)}$ et $\bar{R}_{m,d,k}^{(4)}$ are respectively dependant of $\bar{M}_{r,k}$ and $\bar{M}_{r,k}/2$. It is different for $k \neq 1$ because the field harmonics are rotating at $+\Omega$ in the case of the real rotating magnets and at $\pm\Omega/k$ in the case of the motionless pulsating magnets ($\bar{\tau}_{m,k}^2 \neq \bar{\tau}_{m,d,k}^2$). But this difference is negligible in the case of slotless machines because their relatively large effective magnetic air-gap highly limits the contribution of harmonics of order $k>1$ to the no-load losses. In such machines, it is then possible to compute the eddy current losses due to the real rotation magnets by computing twice the losses due to equivalent motionless pulsating magnets with time-harmonic FEA.

III. PM EQUIVALENT MODEL IN 3D TIME-HARMONIC FEA

The pulsating magnets can be implemented in 3D time-harmonic FEA by using equivalent surface current sheets with time-varying sinusoidal current densities at $\omega=p\Omega$ [3]. Such a representation is illustrated on Fig.2 in the case of radial and parallel magnetized magnets.

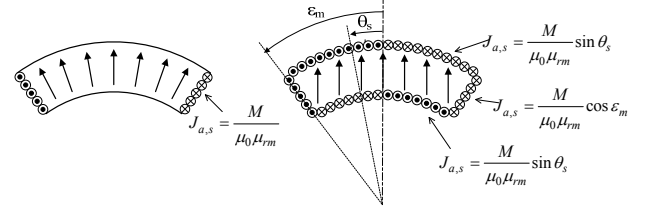


Fig. 2. PM equivalent models with (a) radial and (b) parallel magnetization

IV. VALIDATION AND COMPARATIVE ANALYSIS

The method has been applied to the optimal design of a 500W 20000rpm 3-phase 2 poles slotless PM motor with radial magnets. Fig.3 presents the variations of the correction factor that represents the 3D to 2D no-load eddy current losses ratio computed respectively by 3D time-stepping transient FEA as in [2] and by 3D time-harmonic FEA according to the proposed method, when the axial length of the motor varies. The correction factor obtained with 3D time-harmonic FEA is slightly higher but it has no influence on the optimal motor design solution. But the efficiency of the global design optimization process is highly improved in terms of computing time because the evaluation of the 3D losses correction factor is much faster.

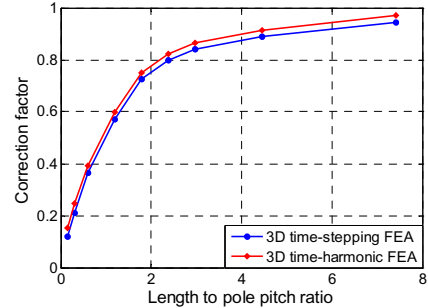


Fig. 3. Variation of correction factors with axial length to pole pitch ratio

V. CONCLUSION

The implementation of equivalent motionless pulsating magnets modeled as equivalent surface current sheets with time-varying sinusoidal current densities in 3D FE solvers is an interesting feature to compute eddy current losses in slotless SMC PM machines by fast 3D time-harmonic FEA.

VI. REFERENCES

- [1] A. Chebak, P. Viarouge and J. Cros, "Analytical computation of the full load magnetic losses in the soft magnetic composite stator of high-speed slotless PM machines," *IEEE Trans. on Magnetics*, 45(3): 952-955, 2009.
- [2] A. Chebak, P. Viarouge and J. Cros, "Design of high-speed slotless permanent magnet motors with soft magnetic composite stators," *IEEE Conf. on Electrical Machines & Systems*, Wuhan, China, Oct. 2008.
- [3] N. Boules, "Prediction of no-load flux density distribution in permanent magnet machines," *IEEE Trans. Ind. Appl.*, IA-21, 633-643, 1985.

Decoupling of Nonequidistant Time Steps by Fixed Point Method for Nonlinear Eddy Currents

Gergely Koczka, Oszkár Bíró

Institute for Fundamentals and Theory in Electrical Engineering
Kopernikusgasse 24/3, A-8010 Graz, Austria
gergely.koczka@tugraz.at

Abstract— A method is presented to get the steady state solution of nonlinear eddy current problems with periodic excitation using the \mathbf{T}, ϕ formulation in the time domain. The fixed point method is used to linearize the equations. A new decoupling technique is introduced for the case of nonequidistant time steps. The results are compared to the solution obtained by equidistant time steps and by a transient time stepping method in a three-dimensional example.

I. INTRODUCTION

Obtaining the steady-state solution of nonlinear eddy current problems with periodic excitation is very time consuming by stepping through transients in the time domain. An algorithm based on the fixed point technique has been presented in [1] and [2] for decoupling the equations of equidistant time steps using the \mathbf{A}, \mathbf{v} - \mathbf{v} formulation both in two (2D) and three dimensions (3D). It has been extended in [3] for the \mathbf{T}, ϕ method. With this approach, half as many complex linear equation systems have to be solved as there are steps within a period. The efficiency of the algorithm can be improved by decreasing the number of time steps without loss of accuracy. This can be achieved by using a nonequidistant time discretization which is capable of approximating the wave form of the excitation with less time steps. The aim of this paper is to generalize the method of [1], [2] and [3] for variable time steps. The equations of the \mathbf{T}, ϕ formulation are used. The results of the time periodic methods are compared to a transient time stepping approach for a 3D problem.

II. FIXED POINT METHOD USING THE \mathbf{T}, ϕ FORMULATION

The quasi static Maxwell's equations using the \mathbf{T}, ϕ formulation lead to

$$\nabla \times \rho \nabla \times \mathbf{T} + \frac{\partial}{\partial t} (\mu \mathbf{T} - \mu \nabla \phi) = -\nabla \times \rho \nabla \times \mathbf{T}_0 - \frac{\partial}{\partial t} (\mu \mathbf{T}_0) \quad (1)$$

$$\frac{\partial}{\partial t} \nabla \cdot (\mu \mathbf{T} - \mu \nabla \phi) = -\frac{\partial}{\partial t} \nabla \cdot (\mu \mathbf{T}_0) \quad (2)$$

where \mathbf{T} is the reduced electric vector potential, ϕ is the magnetic scalar potential, \mathbf{T}_0 is the impressed electric vector potential, ρ is the resistivity and μ is the permeability. The permeability is non-linear, i.e. it depends on \mathbf{T} and ϕ . The excitation is periodic i.e. $\mathbf{T}_0(t) = \mathbf{T}_0(t+T)$, and the periodic solution has to be determined ($\mathbf{T}(t) = \mathbf{T}(t+T)$, $\phi(t) = \phi(t+T)$), with $T > 0$. To achieve symmetry, the time derivative of the equation $\nabla \cdot \mathbf{B} = 0$ has been used in (2).

Introducing the fixed point permeability (μ_{FP}), linearizing (1) and (2), as shown in [3] and using Galerkin method for

discretizing the partial differential equations, the following iterative method is obtained:

$$S(\rho)x^{(s+1)} + \frac{d}{dt} M(\mu_{FP}^{(s)})x^{(s+1)} = f + \frac{d}{dt} g + \frac{d}{dt} M(\mu_{FP}^{(s)} - \mu^{(s)})x^{(s)}, \quad (3)$$

where $S(\rho)$ is the stiffness matrix depending on the resistivity, $M(\mu)$ is the mass matrix depending on μ , $x^{(s)}$ contains the unknowns \mathbf{T} and ϕ in the s -th iteration step. f and g contain the excitations, $\mu^{(s)}$ is the permeability and $\mu_{FP}^{(s)}$ is the fixed point parameter in the s -th iteration.

III. THE TIME PERIODIC METHOD

An ordinary differential equation system with periodic conditions has to be solved in all fixed point iterations. These equation systems have a general form:

$$Ax(t) + B \frac{d}{dt} x(t) = f(t) + \frac{d}{dt} g(t). \quad (4)$$

In contrast to [1]-[3], a time periodic method using the general time discretization $0 = t_0 < t_1 < \dots < t_n = T$ will be employed. The time derivatives are discretized by the implicit Euler scheme

$$dx(t_k)/dt \approx (x_k - x_{k-1})/(t_k - t_{k-1}) \quad (5)$$

where x_k is the approximate value of $x(t_k)$. With this discretization, (4) becomes

$$Ax_k + B \frac{x_k - x_{k-1}}{t_k - t_{k-1}} = f_k + \frac{g_k - g_{k-1}}{t_k - t_{k-1}}. \quad (6)$$

The discrete derivative operator in (5) can be represented as a multiplication by a matrix D , due to the periodic condition ($x_0 = x_n$). D is a block structured matrix. The entries of the k -th block-row of D are $I(t_k - t_{k-1})$, $-I(t_k - t_{k-1})$ and zeros, where I is the identity matrix with the same size as A or B . Equation (6) has a closed form:

$$\{Ax\} + D\{Bx\} = \{f\} + D\{g\}, \quad (7)$$

with the notation $\{Cx\} := [x_1^T C^T \quad x_2^T C^T \quad \dots \quad x_n^T C^T]^T$ and

$\{x\} := [x_1^T \quad x_2^T \quad \dots \quad x_n^T]^T$ where C is an arbitrary matrix.

The following relationship is a property of these notations:

$$D\{Bx\} = \{B(D\{x\})\}. \quad (8)$$

Since all blocks in D are constants times the identity matrix, the $n \times n$ matrix \tilde{D} can be defined so that its elements are the same as the multipliers in the blocks of D .

To solve (7) efficiently, an eigenvector decomposition of D ($DV = V\Lambda$) is needed, where the matrix V contains the eigenvectors and Λ is a diagonal matrix containing the eigenvalues of D , similarly as in [1]. The matrix V and Λ share a similar block structure with D , and they can be determined from the eigenvectors and eigenvalues of \tilde{D} . This decomposition and the use of the property (8) brings (7) to the following form:

$$\{Ay\} + \Lambda\{By\} = \{F\} + \Lambda\{G\}. \quad (9)$$

where $y = V^{-1}\{x\}$, $F = V^{-1}\{f\}$, $G = V^{-1}\{g\}$. Since Λ is diagonal, (9) can be solved decoupled for each time instant:

$$Ay_k + \lambda_k By_k = F_k + \lambda_k G_k \quad k = 1, 2, \dots, n, \quad (10)$$

where λ_k is the k -th eigenvalue of \tilde{D} . D being a real matrix, all complex eigenvalues of D have a complex conjugate pair, so the number of equations to be solved is half as many as there are time steps in a period.

IV. CONVERGENCE ANALYSIS

With the results of the previous section, the whole fixed point iteration can be described as follows:

$$x^{(s+1)} = V \left\{ \left(S(\rho) + \lambda_k M(\mu_{FP}^{(s)}) \right)^{-1} \left((V^{-1}\{f\})_k + \lambda_k (V^{-1}\{g\})_k + \lambda_k \left(V^{-1} \left\{ M(\mu_{FP}^{(s)} - \mu_i^{(s)}) x_i^{(s)} \right\} \right)_k \right) \right\}, \quad (11)$$

where the superscript (s) denotes the value of a variable in the s -th iteration step. $\{M(\mu_{FP} - \mu_i) x_i\}$ denotes the vector

$\left[x_1^T (M(\mu_{FP} - \mu_1))^T, \dots, x_n^T (M(\mu_{FP} - \mu_n))^T \right]^T$. $(V^{-1}\{f\})_k$ is the k -th transformed time step of $V^{-1}\{f\}$. The following theorem is used to prove the convergence:

The sequence $x_{k+1} = Bx_k + c$ is convergent, if and only if $\rho(B) < 1$, where $\rho(B)$ is the spectral radius of B .

The spectral radius of the linear operator in (11) can be estimated as:

$$\rho(\bullet) < C \text{cond}_\rho(V) \left\| \frac{\mu_{FP} - \mu}{\mu_{FP}} \right\|. \quad (12)$$

where \bullet represents the operator, $\text{cond}_\rho(V) = \rho(V)\rho(V^{-1})$ is the spectral condition number (this is not the same as $\text{cond}_2(V) = \|V\|_2 \|V^{-1}\|_2$, which is sometimes called spectral condition number), $\|\bullet\|$ is a corresponding norm, C is a constant independent of μ , μ_{FP} and V . It follows from (12) that the convergence of the fixed point method strongly depends on the transformation V , and the choice of the fixed point permeability. The fixed point permeability can be chosen similarly as the fixed point parameter in [1].

V. ANALYSIS OF THE TRANSFORMATION

The choice of the transformation matrix (V) is an important part of this method, since if its condition number is higher than one, then the fixed point algorithm will not be able to converge. Since V contains the eigenvectors of D , the

matrix $V\Gamma$ will contain the eigenvectors also, if Γ is a diagonal matrix, because the eigenvectors are unique only up to a constant multiplier. Tests with different transformation matrices have shown that a simple scaling with a diagonal matrix is not enough to get a well conditioned transformation matrix. The transformation matrix can be decomposed as a product of two matrices as

$$V = QW \quad (13)$$

where Q is a real matrix with the condition number 1, and W is an unitary matrix. The transformation can be done in two steps:

$$y = Wx, z = Qy. \quad (14)$$

This decomposition will be shown in the full paper.

VI. RESULT

The geometry of the 3D example is defined in [3]. The B - H curve is the same as in [1], the conductivity of the cube is 10^6 S/m and the highest value of the current density is 10^8 A/m² in the coil. The excitation has a half period sinusoidal form, and a half period zero value (Fig. 1.).

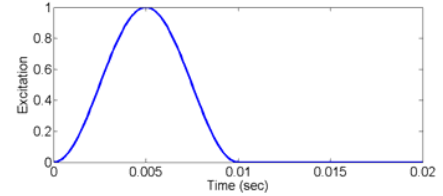


Fig. 1. The time function of the excitation.

Fig. 2. a. shows the results of the different methods. Fig. 2. b. illustrates the convergence of the nonequidistant time periodic method (NEqTPM) with a well conditioned and an ill conditioned transformation.

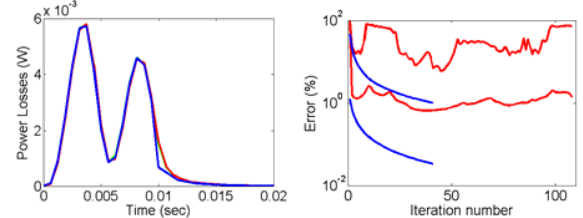


Fig. 2. a.: Comparing the results of the NEqTPM (blue line, 22 TS/per) with an equidistant discretization (red line, 32 TS/per) and a transient time stepping method (4-th period, 32 TS/per) (green line). b.: Maximal, and average material changes of the NEqTPM with well- (blue) and ill- (red) conditioned transformation.

VII. ACKNOWLEDGMENT

This work was funded by the Austrian Science Fund (FWF) under Project P18479-N07.

VIII. REFERENCES

- [1] G. Koczka, S. Außerhofer, O. Bíró and K. Preis, "Optimal convergence of the fixed-point method for nonlinear eddy current problems", *IEEE Trans. on Magnetics*, 45(3): 948-951, 2009.
- [2] G. Koczka, S. Außerhofer, O. Bíró and K. Preis, "Optimal fixed-point method for solving 3D nonlinear periodic eddy current problems", *COMPEL*, 28(4): in press, 2009.
- [3] G. Koczka, O. Bíró, "Fixed-Point Method for Solving Nonlinear Periodic Eddy Current Problems with T,Φ-Φ Formulation", to be presented at EMF 2009, May. 26-29. 2009, Mondovi (Italy).

Homogenization for periodical electromagnetic structure: which formulation?

G rard Meunier*, Vincent Charmoille**, Christophe Gu rin**, Patrice Labie

* Grenoble Electrical Engineering Laboratory, Grenoble-INP / UJF / CNRS, **Cedrat, Meylan, France

ENSE³, BP46, 38402 Grenoble, France

E-mail: Gerard.Meunier@g2elab.grenoble-inp.fr

Abstract— This paper proposes a general approach for the frequency-domain homogenization of electromagnetic periodical structures. This method allows us to calculate macroscopic equivalent properties including local effects. Based on a local resolution with adapted formulation we can find respectively the equivalent permeability and conductivity. An example of the modeling of eddy current losses in windings is presented.

I. CONTEXT

Eddy current losses can be directly taken into account by a finite element resolution. However meshing every elementary conductor by respecting the skin effect is required. Such modeling is very expensive and generally impossible to accomplish in three-dimensional cases.

In cases of periodical structures (as the windings) a methodology of homogenization can be set up. Then materials are represented with equivalent magnetic and electric properties [1], [2], [3].

In this paper, we describe our homogenization method for periodical structures, in the case of linear problems feed by sinusoidal sources (frequency domain). It is based on a local finite element resolution taking into account any shape of elementary structure. Equivalent complex macroscopic reluctivity and conductivity can then be computed in order to represent local effects. This technique has been applied to compute eddy current losses in windings.

II. METHODOLOGY

Our method is based on the resolution of local Maxwell equations, on an elementary cell of the periodical structure. Local fields are linked with macroscopic fields to find equivalent properties.

A. Local and macroscopic fields

At local level, assuming that properties of materials (resistivity ν and reluctivity ρ) are linear, we have:

$$\begin{aligned} \text{curl } \mathbf{e} &= -j\omega \mathbf{b} & \text{div } \mathbf{b} &= 0 \\ \text{curl } \mathbf{h} &= \mathbf{j} & \text{div } \mathbf{j} &= 0 \\ \mathbf{h} &= \nu \mathbf{b} = \frac{1}{\mu} \mathbf{b} & \mathbf{e} &= \rho \mathbf{j} = \frac{1}{\sigma} \mathbf{j} \end{aligned} \quad (1)$$

At macroscopic level, electric and magnetic fields \mathbf{H} and \mathbf{E} also verify Maxwell equations. Our goal is to determine macroscopic equivalent behavior laws from local periodical

effects. For this, we suppose that the macroscopic field has very few variations on a great number of elementary cells. So, the calculation at local level can be performed on an elementary cell of the periodical structure with periodical conditions. In practice, we write local fields as follows:

$$\begin{aligned} \mathbf{h} &= \mathbf{H} + \mathbf{h}_\mu & \mathbf{b} &= \mathbf{B} + \mathbf{b}_\mu \\ \mathbf{e} &= \mathbf{E} + \mathbf{e}_\mu & \mathbf{j} &= \mathbf{J} + \mathbf{j}_\mu \end{aligned} \quad (2)$$

where \mathbf{h}_μ , \mathbf{b}_μ , \mathbf{e}_μ and \mathbf{j}_μ are periodical fields. We can notice that these fields also verify the Maxwell equations, without any relationship between \mathbf{h}_μ and \mathbf{b}_μ or \mathbf{e}_μ and \mathbf{j}_μ . They represent local effects (difference with the macroscopic field) and are at the origin of additional losses. Since the macroscopic magnetic flux is obtained through the integration of local flux on any surface, we can link \mathbf{j} and \mathbf{J} , \mathbf{b} and \mathbf{B} by:

$$\langle \mathbf{b} \rangle = \mathbf{B} \quad \langle \mathbf{j} \rangle = \mathbf{J} \quad (3)$$

Where $\langle \mathbf{j} \rangle$ represent the average field of \mathbf{j} on the cell. It is important to notice that it is not possible to express directly \mathbf{H} and \mathbf{E} from their average values $\langle \mathbf{h} \rangle$ and $\langle \mathbf{e} \rangle$ on the cell. In practice, local curls of current \mathbf{j}_μ can produce a macroscopic field $\langle \mathbf{h}_\mu \rangle \neq 0$. As a result, \mathbf{H} differs from $\langle \mathbf{h} \rangle$.

To find macroscopic behavior we consider uniform field \mathbf{B} and \mathbf{J} at the local level. From Maxwell-Ampere Maxwell-Faraday equations, the macroscopic fields \mathbf{H} and \mathbf{E} can then be expressed in the following form:

$$\begin{aligned} \mathbf{H} &= \mathbf{J} \wedge \frac{\mathbf{x}}{2} + \mathbf{H}_c \\ \mathbf{E} &= -j\omega \mathbf{B} \wedge \frac{\mathbf{x}}{2} + \mathbf{E}_c \end{aligned} \quad (4)$$

where the components of \mathbf{x} are the coordinates (x, y, z) and \mathbf{H}_c , resp. \mathbf{E}_c , are the value of the macroscopic field at $\mathbf{x}=\mathbf{0}$, that we can choose at the center of the local domain of study. This allows us to define macroscopic equivalent properties such as:

$$\begin{aligned} \langle \mathbf{H} \rangle &= \mathbf{H}_c = [\nu_{eq}] \mathbf{B} \\ \langle \mathbf{E} \rangle &= \mathbf{E}_c = [\rho_{eq}] \mathbf{J} \end{aligned} \quad (5)$$

B. Local fields resolution

The first and natural way consists of applying \mathbf{J} and \mathbf{B} on the cell to solve the problem at the local level [2]. Then, \mathbf{h} and \mathbf{e} on the cell are determinate. Unfortunately, we do not obtain \mathbf{H} and \mathbf{E} . The solution for finding equivalent properties can be achieved by equalizing electromagnetic powers, from the local and macroscopic level. Globally this methodology requires some precautions (for applying \mathbf{B} and \mathbf{J}) and needs more simulations than the second approach presented below.

The alternative way we propose consists to apply the macroscopic field \mathbf{H} (resp. \mathbf{E}) on the cell. Then the knowing of local fields \mathbf{b} (resp. \mathbf{j}) allows to determine \mathbf{B} (resp. \mathbf{J}) from equation (3) and finally to establish equivalent properties.

For example, the tensor of permeability $[\mu_{eq}] = [v_{eq}]^{-1}$, can be obtained by solving local problem on the cell with a \mathbf{t} - ϕ formulation. Starting from (1), we solve the cell problem:

$$\begin{aligned} \text{curl}(\rho \text{curl} \mathbf{h}) + j\omega \mu \mathbf{h} &= 0 \\ \text{div} \mu \mathbf{h} &= 0 \end{aligned} \quad (6)$$

We introduce \mathbf{t}_μ and ϕ_μ from:

$$\begin{aligned} \text{rot} \mathbf{h}_\mu = \mathbf{j}_\mu &\Rightarrow \mathbf{j}_\mu = \text{rot} \mathbf{t}_\mu \\ \text{div} \mathbf{j}_\mu = 0 &\Rightarrow \mathbf{h}_\mu = \mathbf{t}_\mu - \text{grad} \phi_\mu \end{aligned} \quad (7)$$

Using equations (2) and (4) with $\mathbf{J} = \mathbf{0}$ we obtain:

$$\begin{aligned} \text{curl}(\rho \text{curl} \mathbf{t}_\mu) + j\omega \mu \mathbf{t}_\mu - \text{grad} \phi_\mu &= -j\omega (\mu \mathbf{H}_c) \\ \text{div} \mu (\mathbf{t}_\mu - \text{grad} \phi_\mu) &= \text{div} (\mu \mathbf{H}_c) \end{aligned} \quad (8)$$

with periodical boundary conditions for \mathbf{t}_μ and ϕ_μ on the cell problem. Applying \mathbf{H}_c along the three directions of the cell allows us to obtain easily $[\mu_{eq}]$. For example, with an applied field $\mathbf{H}_c = \{ H_{cx}, 0, 0 \}$ along the x direction, and after calculating \mathbf{B} from $\langle \mu (\mathbf{h}_\mu + \mathbf{H}_c) \rangle$ after solving (8), we have:

$$\mu_{xx} = \frac{B_x}{H_{cx}} \quad \mu_{xy} = \frac{B_y}{H_{cx}} \quad \mu_{xz} = \frac{B_z}{H_{cx}} \quad (9)$$

We can notice that with the previous \mathbf{t}_μ - ϕ_μ formulation the equivalent properties $\mathbf{J}(\mathbf{E})$ can not be determined. In practice, to apply a field \mathbf{E} , we choose an \mathbf{a} - v formulation. In this case, the following system is solved:

$$\begin{aligned} \text{curl}(v \text{curl} \mathbf{a}_\mu) + \sigma(j\omega \mathbf{a}_\mu + \text{grad} v_\mu) &= j\omega (\sigma \mathbf{E}_c) \\ \text{div} \sigma(j\omega \mathbf{a}_\mu + \text{grad} v_\mu) &= \text{div} (\sigma \mathbf{E}_c) \end{aligned} \quad (10)$$

with periodical conditions for \mathbf{a}_μ and v_μ . \mathbf{J} can be obtained after resolution from $\langle \sigma (\mathbf{e}_\mu + \mathbf{E}_c) \rangle$.

III. EXAMPLE

We have applied our method in order to determine macroscopic equivalent properties for a coil. Windings are the seat of losses due to the presence of eddy currents. These have as origin two effects: effect of each conductor

on itself (skin effect) and proximity effect (influence of the magnetic field on the neighboring conductors).

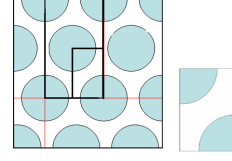


Fig. 1. Representation of the coil arrangement with associated elementary cell.

To determine the equivalent reluctivity tensor, as proposed, a \mathbf{t}_μ - ϕ_μ formulation with periodic condition (8) is used. Thanks to the imaginary part of the equivalent reluctivity, we can obtain a representation of the local eddy current losses due to proximity effects [1], [3]. To validate it, we have modeled a coil (with 80 elementary conductors) exposed to an external field (Fig. 1.). Then we have compared the active and reactive part in the domain of study in two cases:

- when each conductor is described (reference),
- when the coil is homogenized.

The obtained results (Fig. 2.) are very satisfactory considering the small number of conductors in the winding.

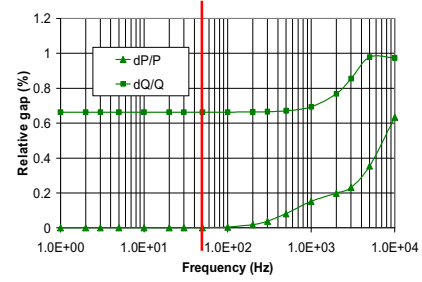


Fig. 2. Comparison (in %) of the active and reactive power between the homogenized model and the reference model. (The frequency which correspond to a skin depth equal to the diameter of the wire is represented with a vertical line.)

The method has been used to determine equivalent conductivity by solving (10). In the case of a coil, it allows to take into account skin effect.

IV. CONCLUSION

A general methodology for determining equivalent properties for electromagnetic periodical structure has been proposed. The importance of the choice of the formulation has been highlighted. The proposed method can be applied to any case of electromagnetic periodical structure, in two and three dimensions.

REFERENCES

- [1] A. T. Phung, P. Labie, O. Chadebec, Y. Lefloch, G. Meunier, "High frequency proximity losses for rectangular cross section conductors", in IEEE Transactions on Magnetics, Vol. 43, No. 4, April 2007, pp 1205-1208
- [2] M. El Feddi, Z.R Ren, A; Razek, A. Bossavit, "Homogenization Technique for Maxwell Equations in Periodic Structure" in IEEE Transaction on Magnetics, Vol. 33, N°2, March 1997, pp 1382-1385
- [3] J. Gyselinck, P. Dular, "Frequency-domain homogeneization of bundles of wires in 2D magnetodynamic FE calculations", in IEEE Transactions on Magnetics, Vol. 41, No. 5, April 2005, pp 1416-1419.

Geometric Interpretation of Frequency-Domain Surface-Impedance Boundary Conditions

Herbert De Gersem

Katholieke Universiteit Leuven, Wave Propagation and Signal Processing Research Group

Etienne Sabbelaan 53, 8500 Kortrijk, Belgium

herbert.degersem@kuleuven-kortrijk.be

Abstract—Lowest-order frequency-domain surface-impedance boundary conditions are reformulated as a finite-element approach with particular shape functions and as a finite-integration technique with a particular geometry.

I. INTRODUCTION

When the skin depth is expected to be small compared to the wire diameter, it may be convenient to model the eddy-current effect in a wire by a *surface-impedance boundary condition* (SIBC), thereby omitting the volumetric discretization of the inner wire geometry [1]. The relation between the tangential components E_γ and H_β of the electric and magnetic field strengths, assuming an infinite half-plane ($\alpha \geq 0$) of material with permeability μ and conductivity σ is then

$$E_\gamma = -\frac{1+j}{2}\omega\mu\delta H_\beta; \quad \delta = \sqrt{\frac{2}{\omega\mu\sigma}} \quad (1)$$

where ω is the angular frequency and δ the skin depth [2]. Higher-order SIBCs accounting for the curvature of the boundary and for field variations along the boundary have been proposed [3] and have been applied to a variety of problems (e.g. [4]). SIBCs have been combined with the finite-element (FE) method, the boundary-element method and the finite-integration technique (FIT) [5], [6] and have been formulated in frequency and time domain. This paper focuses on reformulating the SIBC using the typical mechanisms of the FE method and of the FIT. The idea is to come to a geometric interpretation for the Leontovich SIBC in the frequency domain.

II. INTERPRETATION AS A BOUNDARY INTEGRAL TERM

The weak form of the time-harmonic magnetoquasistatic formulation in terms of the magnetic vector potential \mathbf{A} reads

$$\int_{\Omega} (\nu \nabla \times \mathbf{A}) \cdot (\nabla \times \mathbf{w}_i) dV + \int_{\partial\Omega} (\mathbf{H} \times \mathbf{w}_i) \cdot d\mathbf{A} + j\omega \int_{\Omega} \sigma \mathbf{A} \cdot \mathbf{w}_i dV = \int_{\Omega} \mathbf{J}_s \cdot \mathbf{w}_i dV \quad (2)$$

with $\nu = 1/\mu$ the reluctivity, \mathbf{w}_i belonging to an appropriate set of edge shape functions, Ω the computational domain and \mathbf{J}_s the applied current density. The boundary integral term originates from partial integration and vanishes in the case of homogeneous Dirichlet or Neumann boundary conditions. In the case of SIBCs, the boundary integral term combined with (1) simplifies to

$$\int_{\partial\Omega} \nu \xi \mathbf{A} \cdot \mathbf{w}_i dA \quad (3)$$

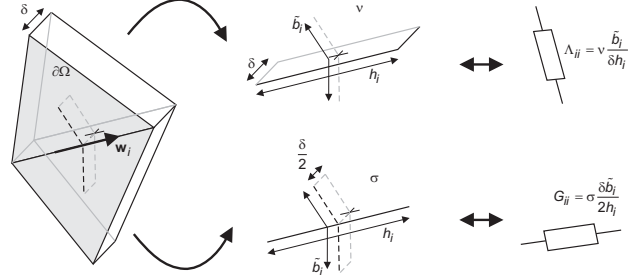


Fig. 1. Circuit equivalent of the SIBC for the 3D FE case: Reluctance Λ_{ij} perpendicular to edge i and conductance G_{ij} along edge i in function of reluctivity ν , conductivity σ , skin depth δ , edge length h_i and dual edge length \tilde{b}_i .

with $\xi = (1+j)/\delta$. With discretization by $\mathbf{A} = \sum_j \tilde{\mathbf{a}}_j \mathbf{w}_j$ and some rearrangement, the boundary integral terms resembles

$$\sum_j \tilde{\mathbf{a}}_j \underbrace{\int_{\partial\Omega} \nu \frac{\mathbf{w}_i \cdot \mathbf{w}_j}{\delta} dA}_{\Lambda_{ij}} + \sum_j j\omega \tilde{\mathbf{a}}_j \underbrace{\int_{\partial\Omega} \sigma \frac{\delta}{2} \mathbf{w}_i \cdot \mathbf{w}_j dA}_{G_{ij}}. \quad (4)$$

Λ_{ij} has the unit of a reluctance (1/H), whereas G_{ij} has the unit of a conductance (S). Both add up with already existing reluctance and conductance terms in the discretized partial differential equation. The meaning of both becomes very clear when mass lumping would be applied. Then,

$$\int_{\partial\Omega} \mathbf{w}_i \cdot \mathbf{w}_j dA = \begin{cases} \frac{\tilde{b}_i}{h_i} & \text{if } i = j \\ 0 & \text{if } i \neq j \end{cases}. \quad (5)$$

Here h_i is the length of edge i and \tilde{b}_i is the length of a dual edge lying in $\partial\Omega$ and crossing edge i . The entries become

$$\Lambda_{ij} = \nu \frac{\tilde{b}_i}{\delta h_i}; \quad (6)$$

$$G_{ij} = \sigma \frac{\delta \tilde{b}_i}{2 h_i}. \quad (7)$$

Hence, Λ_{ij} is the reluctance of the flux path perpendicular to edge i with length \tilde{b}_i and cross-section $h_i \delta$, whereas G_{ij} is the conductance of the current path along edge i with length h_i and cross-section $\tilde{b}_i \frac{\delta}{2}$ (Fig. 1). This interpretation becomes even more clear when considering the 2D case (Fig. 2).

III. INTERPRETATION AS A SPECIAL FE DOMAIN

Another interpretation is obtained by considering the highly conductive domain Ω_c as part of the computational domain $\Omega \cup \Omega_c$. Additional prism elements are constructed by lifting

the triangles at $\partial\Omega$ into Ω_c . In theory, these prisms extend from $\alpha = 0$ up to $\alpha = \infty$. Moreover, when $\partial\Omega_c$ is convex, the prisms are partially overlapping, whereas when $\partial\Omega_c$ is concave, the prisms do not span Ω_c completely. For every edge j incident to $\partial\Omega$, special shape functions are defined. Inside Ω , \mathbf{w}_j keeps its useful form whereas inside Ω_c , the complex-valued decaying function $\hat{\mathbf{w}}_j e^{-\xi\alpha}$ with $\hat{\mathbf{w}}_j$ the trace of \mathbf{w}_j at $\partial\Omega$, is used. These functions guarantee the tangential continuity at $\partial\Omega$. The expressions in (2) have to be integrated in $\Omega \cup \Omega_c$. The Ritz-Galerkin approach consists in using test functions which are conjugate to the trial functions. Hence, the test functions in Ω_c are $\hat{\mathbf{w}}_i e^{-\xi^*\alpha}$ where ξ^* denotes the conjugate of ξ . The contribution of Ω_c is

$$\sum_j \left(\Lambda_{ij} + \hat{\Lambda}_{ij} + j\omega \mathbf{G}_{ij} \right) \hat{\mathbf{a}}_j \quad (8)$$

where $\hat{\Lambda} = \hat{\mathbf{C}}^T \hat{\mathbf{M}}_\nu \hat{\mathbf{C}}$,

$$\hat{\mathbf{M}}_{\nu,pq} = \frac{\delta}{2} \int_{\partial\Omega} \nu \mathbf{z}_q \cdot \mathbf{z}_p \, dA, \quad (9)$$

\mathbf{z}_i are lowest-order face functions and $\hat{\mathbf{C}}$ is the discrete curl matrix restricted to $\partial\Omega$. Eq. (9) simplifies to

$$\hat{\mathbf{M}}_{\nu,pq} = \begin{cases} \frac{\nu\delta}{2A_p} & \text{if } p = q \\ 0 & \text{if } p \neq q \end{cases} \quad (10)$$

with A_p the cross-section of face p . This extra term does not appear in the interpretation of the SIBC as a boundary integral term. Although not relevant for the convergence of the method, $\hat{\Lambda}$ is important to obtain a complete geometric interpretation of the SIBC.

IV. INTERPRETATION BY THE FINITE INTEGRATION TECHNIQUE

The finite-integration technique (FIT) considers a staggered grid pair [7]. The discrete counterparts of the curl, divergence and gradient operators are incidence matrices and do not involve any discretisation. The Hodge operators are discretized into material matrices. The reluctance matrix \mathbf{M}_ν models the magnetic paths formed by primary faces and dual edges whereas the conductance matrix \mathbf{M}_σ considers the electric paths formed by primary edges and dual faces. Closely similar methodologies are described in [8] and [9]. In the particular case where an orthogonally intersecting grid pair is considered, \mathbf{M}_ν and \mathbf{M}_σ are diagonal matrices. The SIBC is easily introduced in FIT by considering an additional layer of primary grid cells of thickness δ , with conductivity σ and reluctivity ν (Fig. 2). Dual grid lines are present at a distance $\frac{\delta}{2}$. The generic construction of FIT material matrices leads to the same additional contributions Λ_{ij} , $\hat{\Lambda}_{ij}$ and \mathbf{G}_{ij} as described in the previous sections. Here, only the simplest case where the primary grid resolves the geometry, is considered. The non-matching case is treated in [6]. An additional difficulty arises when the SIBC is excited from the outside. In that case, one additional unknown $\hat{\mathbf{a}}_s$ is introduced per SIBC region and connected with the externally applied voltage [4].

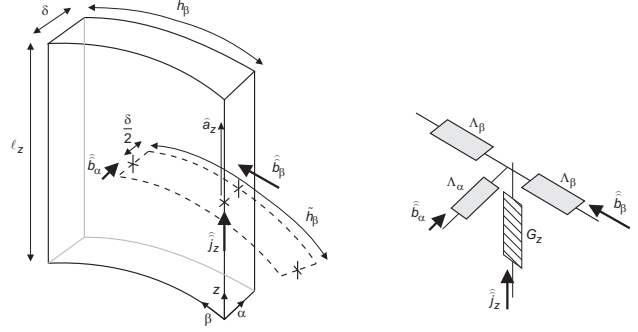


Fig. 2. Circuit equivalent of the SIBC for the 2D FIT case: Reluctance Λ_α perpendicular to the boundary, reluctance Λ_β and conductance \mathbf{G}_z parallel to the boundary, grid fluxes $\hat{\mathbf{B}}_\alpha$ and $\hat{\mathbf{B}}_\beta$, grid current $\hat{\mathbf{J}}_z$, skin depth δ , primary grid lengths ℓ_z and h_β , dual grid length \hat{h}_β , line-integrated magnetic potential $\hat{\mathbf{a}}_z$.

V. EXAMPLE

As an example, the transmission-line parameters of a winding are calculated [4]. The convergence of the formulations with and without $\hat{\Lambda}$ are the same, indicating the inferior importance of $\hat{\Lambda}$. The SIBCs replace the volume discretizations of the individual wires. After assembling, the system matrices are reduced by algebraic manipulation in order to obtain the transmission-line impedance matrix.

VI. CONCLUSIONS

The lowest-order frequency-domain SIBC can be interpreted within the framework of the FIT as an additional layer of primary cells with the skin depth as thickness. The typical FE formulation of the SIBC as a boundary integral term can also be found by considering specialized shape functions in the highly conductive domain.

REFERENCES

- [1] G. Smith, "On the skin effect approximation," *Am. J. Phys.*, vol. 58, no. 10, p. 9961002, 1990.
- [2] M. A. Leontovich, "On the approximate boundary conditions for the electromagnetic field on the surface of well conducting bodies," in *Investigations of Radio Waves*, B. Vvedensky, Ed. Moscow: Academy of Sciences of USSR (in Russian), 1948, p. 512.
- [3] S. Yuferev and N. Ida, "Selection of the surface impedance boundary conditions for a given problem," *IEEE Trans. Magn.*, vol. 35, no. 3, p. 14861489, May 1999.
- [4] L. Di Rienzo, S. Yuferev, and N. Ida, "Computation of the impedance matrix of multiconductor transmission lines using high-order surface impedance boundary conditions," *IEEE Trans. on Electromagnetic Compatibility*, vol. 50, no. 4, pp. 974–984, Nov. 2008.
- [5] S. Yuferev, L. Di Rienzo, and N. Ida, "Surface impedance boundary conditions for the finite integration technique," *IEEE Trans. Magn.*, vol. 42, no. 4, pp. 823–826, 2006.
- [6] R. Mäkinen, H. De Gersem, T. Weiland, and M. Kivikoski, "Modeling of lossy curved surfaces in 3-D FIT/FDTD techniques," *IEEE Trans. Antennas Propagat.*, vol. 54, no. 11, pp. 3490–3498, Nov. 2006.
- [7] T. Weiland, "Time domain electromagnetic field computation with finite difference methods," *Int. J. Num. Mod.*, vol. 9, no. 4, pp. 295–319, July–August 1996.
- [8] E. Tonti, "A direct discrete formulation of field laws: the cell method," *Computer Modeling in Engineering & Sciences*, vol. 2, no. 2, pp. 237–258, 2001.
- [9] A. Demenko, "Three dimensional eddy current calculation using reluctance-conductance network formed by means of FE method," *IEEE Trans. Magn.*, vol. 36, no. 4, pp. 741–745, Jul. 2000.

Field Analysis for Thin Shields in the Presence of Ferromagnetic Bodies

Ioan R. Ciric¹, Florea I. Hantila², and Mihai Maricaru²

¹ Department of Electrical and Computer Engineering, The University of Manitoba, Winnipeg, MB R3T 5V6, Canada

² Department of Electrical Engineering, Politehnica University of Bucharest, Spl. Independentei 313, Bucharest, 060042, Romania, hantila@elth.pub.ro

Abstract — A highly efficient method based on the current sheet integral equation is extended to thin metallic shields operating in the vicinity of nonlinear magnetic media. The polarization fixed point technique is applied, with the magnetic media replaced by a linear medium of permeability equal to that of free space and a distribution of magnetic polarization which depends nonlinearly on the magnetic induction. In a periodic regime, the integral equation is solved for each harmonic separately.

I. INTRODUCTION

For thin conducting shields, when their thickness is smaller than the depth of penetration corresponding to the harmonics involved, the analysis of the periodic electromagnetic field can be simplified by considering an equivalent surface distribution of the electric current induced in the shields. A surface impedance which takes into account the relationship between the field quantities on the two sides of the shield was introduced in [1]. An original solution for very thin shields was proposed in [2], where the surface density of the current induced is expressed in terms of unknown scalar quantities associated with the nodes of the surface discretization grid. In [3], simple vector functions are employed, such that the current continuity is preserved everywhere, the unknowns to be determined being scalar coefficients associated with the interior nodes of the grid and with only one unknown for each hole contour in the case of multiply connected shields. These unknowns are computed by applying a Galerkin technique to the current sheet integral equation.

The computation of the currents induced in the shields is drastically complicated when there are ferromagnetic bodies in their neighbourhood. A static magnetic permeability that is iteratively corrected by various criteria has been used in [4], which allows a phasor representation of the field quantities. Since the time constants involved in the electromagnetic shielding problems are relatively small, only a reduced number of harmonics is required and, thus, the harmonic balance method [5] could also be applied efficiently. Unfortunately, these methods do not allow the construction of an integral equation for the current induced in the shield in the presence of nonhomogenous media that have a permeability that is iteratively modified.

In this paper, the solution of the periodic electromagnetic field problem is obtained by using a surface integral equation for the currents induced in the shield even in the presence of nonlinear ferromagnetic materials. As in [6], a model is used where the nonlinear materials are replaced by a free space, but with a fictitious distribution of magnetization. The current

sheet integral equation is written for each harmonic and, at each iteration, we first determine the magnetic induction in the ferromagnetic material and, then, the magnetization is corrected in time domain in terms of the corresponding magnetic induction. The computation process is started by only considering the fundamental harmonic, with the results being afterwards improved by including higher harmonics. At most, three harmonics are sufficient for practical structures.

II. NONLINEARITY TREATMENT BY THE FIXED POINT METHOD AND ITERATIVE ALGORITHM

For ferromagnetic media we use the constitutive relation

$$\mathbf{B} = \mu_0 \mathbf{H} + \mathbf{I} \quad (1)$$

where the magnetic polarization \mathbf{I} is corrected iteratively in terms of the magnetic induction \mathbf{B} [7],

$$\mathbf{I} = \mathbf{B} - \mu_0 \mathbf{F}(\mathbf{B}) \quad (2)$$

$\mathbf{H} = \mathbf{F}(\mathbf{B})$ being the constitutive relation for the magnetic medium.

An initial value of polarization is arbitrary chosen. We use the representation

$$\mathbf{I}(t) = \sum_{n=1,3,\dots} (\mathbf{I}'_n \sin(n\omega t) + \mathbf{I}''_n \cos(n\omega t)) \quad (3)$$

with only the first N harmonics retained. For each harmonic n of polarization, written in phasor form as

$$\mathbf{I}_n = \mathbf{I}'_n + j\mathbf{I}''_n \quad (4)$$

we solve the field problem in the presence of the shield and determine the harmonic n of magnetic induction,

$$\mathbf{B}_n = \mathbf{B}'_n + j\mathbf{B}''_n \quad (5)$$

The time domain expression of \mathbf{B} is derived in the form

$$\mathbf{B}(t) = \sum_{n=1,3,\dots,2N-1} (\mathbf{B}'_n \sin(n\omega t) + \mathbf{B}''_n \cos(n\omega t)). \quad (6)$$

Then, at each time step, (6) is used to correct the magnetic polarization. The computational effort is substantially reduced if one starts with only the fundamental and, then, the solution accuracy is increased by adding a few more harmonics.

III. INTEGRAL EQUATION FOR THE SHIELD CURRENT SHEET AND ITS NUMERICAL SOLUTION

For each harmonic n of the surface density of the current induced over the surface S of the thin shield we have

$$\begin{aligned} & \rho_s \mathbf{J}_s(\mathbf{r}) + j\lambda_n \int_S \frac{\mathbf{J}_s(\mathbf{r}')}{R} dS' \\ & = -j2\pi f(A_0(\mathbf{r}) + \mathbf{A}_I(\mathbf{r})) - \nabla V(\mathbf{r}) \end{aligned} \quad (7)$$

where $\rho_s = \rho/\Delta$ is the surface resistivity of the shield, with Δ the shield thickness, $j \equiv \sqrt{-1}$, $\lambda_n \equiv nf\mu_0/2$, $R = |\mathbf{r} - \mathbf{r}'|$ with \mathbf{r} and \mathbf{r}' , respectively, the position vectors of the observation point and of the source point, A_0 is the magnetic vector potential due to the given sources, and \mathbf{A}_I is the magnetic vector potential due to the harmonic n of polarization in the region Ω occupied by ferromagnetic bodies,

$$\mathbf{A}_I = \frac{1}{4\pi} \int_{\Omega} \frac{(\nabla' \times \mathbf{J}(\mathbf{r}'))}{R} dS'. \quad (8)$$

The scalar potential term $-\nabla V$ in (7) can be ignored.

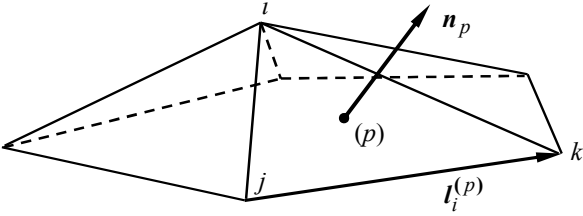


Fig. 1. Surface elements associated with the node i

Equation (7) is solved numerically as shown in [3]. S is approximated by a polyhedral surface with plane triangular surface elements. To each node i we associate a surface vector function \mathbf{U}_i , having the value $\mathbf{U}_i^{(p)} = \frac{1}{2S_p} \mathbf{I}_i^{(p)}$ for each

element (p) containing the node i (Fig. 1), and a zero value for all the surface elements which do not contain the node i . The surface current density is written as a linear combination of the functions \mathbf{U}_i as

$$\mathbf{J}_s(\mathbf{r}) \approx \sum_{i=1}^N \alpha_i \mathbf{U}_i(\mathbf{r}). \quad (9)$$

The unknown coefficients α_i are determined by taking the inner products of the two sides of (7) with \mathbf{U}_n , $n = 1, 2, \dots, N$, over the shield surface.

IV. CORRECTION OF MAGNETIC POLARIZATION

The region Ω with ferromagnetic material is discretized in polyhedral volume elements Ω_k of an arbitrary shape. In each Ω_k the magnetic induction is taken to be constant, namely,

equal to its average value over the element,

$$\tilde{\mathbf{B}}_k = \tilde{\mathbf{B}}_{0k} + \tilde{\mathbf{B}}_{Jk} + \tilde{\mathbf{B}}_{Ik} \quad (10)$$

where $\tilde{\mathbf{B}}_{0k}$ is due to the given sources, $\tilde{\mathbf{B}}_{Jk}$ is due to the shield's current sheet,

$$\tilde{\mathbf{B}}_{Jk} = -\frac{\mu_0}{4\pi v_k} \int_S \oint_{\partial\Omega_k} \frac{\mathbf{J}_s(\mathbf{r}') \times \mathbf{n}_k}{R} dS_k dS', \quad (11)$$

with v_k being the volume of Ω_k , and $\tilde{\mathbf{B}}_{Ik}$ is due to the magnetic polarization. Each element Ω_m with its polarization \mathbf{I}_m contributes to $\tilde{\mathbf{B}}_{Ik}$ by

$$\tilde{\mathbf{B}}_{Ikm} = -\frac{1}{4\pi v_k} \left(\oint_{\partial\Omega_k} \oint_{\partial\Omega_m} \frac{(\mathbf{n}_k \cdot \mathbf{n}_m) \bar{\mathbf{1}} - (\mathbf{n}_k \mathbf{n}_m)}{R} dS_m dS_k \right) \cdot \mathbf{I}_m \quad (12)$$

where $\bar{\mathbf{1}}$ is the identity dyadic and $(\mathbf{n}_k \mathbf{n}_m)$ is the dyad of the unit vectors \mathbf{n}_k and \mathbf{n}_m normal to the boundaries $\partial\Omega_k$ and $\partial\Omega_m$ of the elements Ω_k and Ω_m , respectively. Analytical expressions can be obtained for the integrals in (11), (12) over the closed surface of one of the volume elements since this surface has plane sides. Details regarding the numerical computation and illustrative examples will be presented at the Conference.

ACKNOWLEDGMENT

The authors are grateful to Prof. Oskar Biró who challenged them to perform the analysis presented in this paper.

REFERENCES

- [1] A.Tugulea and C.Fluerasu, "The complex surface conductivity and permeability in the study of a.c. in thin wall conductors," *Rev. Roum. Sci. Techn.-Electrotechn. et Energ.*, vol. 27, no.4, pp.395-398, 1974.
- [2] A. Kameary, "Transient eddy current analysis on thin conductors with arbitrary connections and shapes," *J.Comput.Phys.*, vol. 42, pp. 124-140, July 1981.
- [3] F.Hantila, I.R.Ciric, A.Moraru, and M.Maricaru, "Modelling eddy currents in thin shields," *The 13th IGTE International Symposium on Numerical Field Calculation in Electrical Engineering*, Sept. 22-24, 2008, Graz, Austria, p. 104.
- [4] G. Paoli, O. Biró, and G. Buchgraber, "Complex representation in nonlinear time harmonic eddy current problems," *IEEE Trans. Magn.*, vol. 34, pp. 2625-2628, Sept. 1998.
- [5] R. Pascal, Ph. Conraux, and J. M. Bergheau, "Coupling between finite elements and boundary elements for the numerical simulation of induction heating processes using a harmonic balance method," *IEEE Trans. Magn.*, vol. 39, pp. 1535-1538, May 2003.
- [6] I. R. Ciric and F. I. Hantila, "An efficient harmonic method for solving nonlinear time-periodic eddy-current problems," *IEEE Trans. Magn.*, vol. 43, pp. 1185-1188, April 2007.
- [7] F. I. Hantila, G. Preda, and M. Vasiliu, "Polarization method for static fields," *IEEE Trans. Magn.*, vol. 36, pp. 672-675, July 2000.

Evaluating the Guidance Force Capabilities of Flat Passive Maglev Guideway Topologies Using the $\mathbf{A}-\phi$ Formulation

Jonathan Bird

University of North Carolina - Charlotte
9201 University City Boulevard, Charlotte, NC, 28223, USA
jbird4@uncc.edu

Abstract— When a Halbach rotor is rotated and translationally moved over a flat conductive sheet guideway eddy currents are induced that can create simultaneous lift and thrust forces. This technique could enable Maglev cost to be reduced significantly since the guideway construction costs would be minimized. This paper investigates different flat guideway and rotor topologies that also create lateral re-centering forces.

I. INTRODUCTION

Despite high-speed maglev (magnetic levitation) vehicles being commercially available, city and intercity urban planners throughout the world continue to balk at the immense capital cost associated with installing currently available high-speed maglev designs. Rather, high-speed rail or more reliance on highways and aircraft continue to be the typical chosen path. This is unfortunate because maglev has some unique and beneficial characteristics, such as low pollution emissions, low maintenance and high-speed.

If the maglev guideway costs can be brought radically down in cost, to that which is typically incurred when constructing rail or high-ways, then perhaps maglev would be more frequently implemented. In order to reduce construction costs to the minimum the maglev guideway needs to be passive (non-electrified) and preferably horizontally flat. By using a horizontal flat passive guideway maglev could be more easily integrated into existing transportation infrastructure. Flat guideways can make use of electromagnetic directional switching [1] rather than impractical mechanically moving guideways. They are also less likely to accumulate debris and snow compared to vertically mounted guideways and they create less aerodynamic vehicle drag. However, using a flat guideway mandates that the magnetic forces alone create sufficient vehicle restorative forces to ensure stability.

Three possible flat aluminum sheet guideway topologies are considered in this paper and are shown in Fig. 1, Fig. 2 and Fig. 3. Only one side of the guideway track is shown. Using these flat guideways it is proposed that a vehicle could create simultaneous suspension and thrust forces by electromechanically rotating the magnetic rotors, shown above the guideways. The simultaneous thrust, lift and guidance forces are created by the induced eddy currents in the guideway [2-4]. The thrust is highly dependent on the slip, s

$$s = \omega_m r_o - v_x, \quad (1)$$

where ω_m = rotor mechanical angular velocity, r_o = rotor outer radius and v_x = translational velocity. The lift force is less

dependent on slip, especially at high translational velocity [5]. All three models use a 4 pole-pair Halbach rotor, with magnets arranged as illustrated in Fig. 4. The guideway and rotors are configured so that additional lateral re-centering (z-axis) forces are created when the magnetic rotors are offset. This re-centering is dependent on the relative difference between the flux impinging on either side of the guideway.

Numerous magnetic wheels would be needed for a full size vehicle and dynamic control would be essential. An onboard power source or power transfer to the vehicle will be needed and the vehicle will need to run on wheels at low speeds. Relatively high efficiency is achieved when using multiple wheels in series [3]. This paper focuses on determining which, if any, proposed guideway can create sufficient lateral re-centering guidance forces whilst not seriously deteriorating the thrust and lift forces.

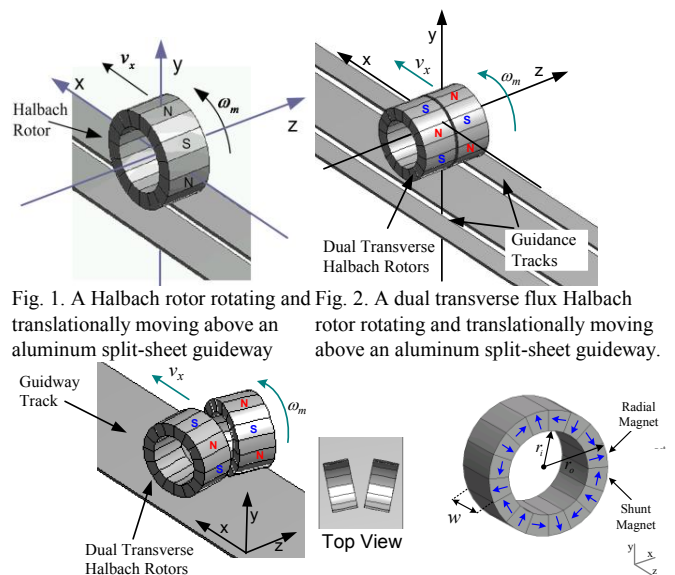


Fig. 1. A Halbach rotor rotating and translationally moving above an aluminum split-sheet guideway

Fig. 2. A dual transverse flux Halbach rotor rotating and translationally moving above an aluminum split-sheet guideway.

Fig. 3. A single guideway sheet with dual angled Halbach rotors simultaneously rotating and translational moving above an aluminum guideway.

Fig. 4. A four pole-pair Halbach rotor

II. MODEL FORMULATION SUMMARY

A novel 3D finite element $\mathbf{A}-\phi$ steady-state convective diffusion model presented in [4] was used to calculate the forces. The formulation used for the conducting and non-conducting regions is given in (2) and (3) respectively. The boundary conditions and more model details are provided in [4,5]. The Halbach rotor's field $\mathbf{B}_{\text{rotor}}$ is calculated semi-

analytically and incorporated into the model formulation via the guideway boundary conditions. The x-axis translational motion is model using a convective term in (2) while the rotation of the rotor(s) is modeled in steady-state using the electrical frequency, ω_e , term in (2). The, ω_e , is related to the mechanical rotor frequency by $\omega_e = (P/2)\omega_m$, where P =number of pole pairs. The problem space is illustrated in Fig. 5.

$$\nabla^2 \mathbf{A} = \mu_0 \sigma \left(j\omega_e \mathbf{A} + v_x \frac{\partial \mathbf{A}}{\partial x} \right), \text{ in } \Omega_c \quad (2)$$

$$\nabla^2 \phi = 0, \text{ in } \Omega_{nc} \quad (3)$$

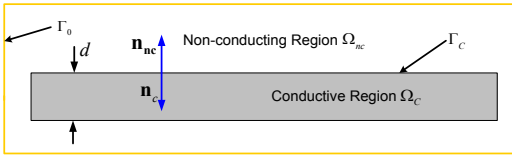


Fig. 5. 2D schematic of the finite element model.

TABLE I SIMULATION AND EXPERIMENTAL PARAMETERS

Rotor:	Outer radius, r_o	50 mm
	Inner radius, r_i	34.2 mm
	Width, w	175 mm
	Magnet (NdFeB), B_r	1.42
	Magnet relative permeability	1.055
	Pole-pairs, P	4
Guideway:	Conductivity (Al)	$2.459 \times 10^7 \text{ Sm}^{-1}$
	Single sheet width	77 mm
	Thickness, d	6.3 mm
	Airgap between rotor and guideway, g	9.5 mm

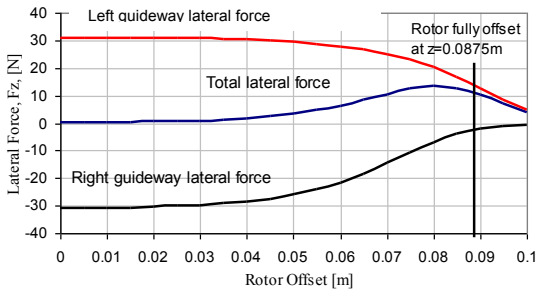


Fig. 6 Lateral restorative forces created by induced current on the left and right sides of the split-sheet guideway as the rotor is laterally offset. Rotor width is 175mm. The lateral forces on either side of the guideway cancel out for most of the rotor offset distance.

III. RESULTS AND DISCUSSION

The parameters shown in Table I have been used in this analysis. These parameters were chosen in order to agree with future experiment scale model measurements. Initially the split-sheet topology shown in Fig. 1 was studied [4,5] however, since the lateral forces are dependent on the difference between the flux seen on either side of the split-sheet guideway the lateral restorative forces are relatively small; particularly so if the rotor width is large (see Fig. 6). However, a large rotor width is necessary in order to create sufficient lift force, as shown in Fig. 7.

In order to improve lateral re-centering forces the guideway and dual magnetic rotor designs shown in Fig. 2 and Fig. 3 have been proposed. The guideway topology shown in Fig. 2 is more complex. Hence, the configuration shown in Fig. 3 may

be more desirable from a cost perspective. But this design will come at the price of a reduced thrust and thrust efficiency.

An illustration of the induced A_z vector potential field on the guideway surface is shown in Fig. 8 for the dual rotor design. The full paper shows that the dual design creates greater re-centering guidance force. It does this by utilizing the lateral field difference created by the transverse magnetic flux, (Fig 9)

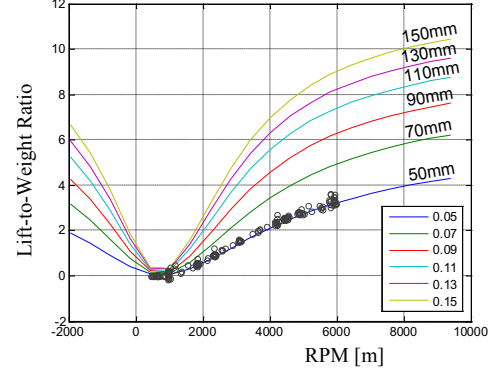


Fig. 7 The effect of the rotor width on the lift-to-weight ratio as a function of RPM for the case when the Halbach rotor is at the center of the split-sheet guideway. A 5 ms^{-1} translational velocity and 9.5mm air gap was used. Numerical results calculated using the $\mathbf{A}-\phi$ coupled finite element analytic model discussed in [4,5]. Experimental results discussed in [4, 5] also shown.

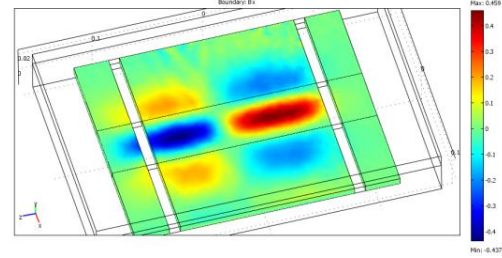


Fig. 8 Magnetic vector potential field on the guideway surface when the Dual Halbach rotors (175mm total width) are offset and rotated and translationally moved. The Halbach rotor is modeled analytically thus not shown in figure.

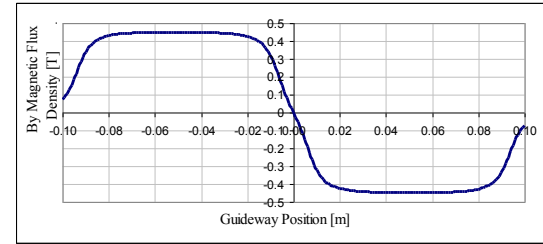


Fig. 9 The Analytically Calculated B_y magnetic flux density component on the guideway surface for the dual Halbach rotor topology (shown in Fig 2).

IV. REFERENCES

- [1] J. L. He and D. M. Rote, "Double-row loop-coil configuration for EDS maglev suspension, guidance, and electromagnetic guideway directional switching," *IEEE Trans. Magn.*, vol. 29, pp. 2956-2958, 1993.
- [2] N. Fujii, G. Hayashi, and Y. Sakamoto, "Characteristics of magnetic lift, propulsion and guidance by using magnet wheels with rotating permanent magnets," *Industry Applications Conference*, pp. 257-262, 2000.
- [3] J. Bird and T. A. Lipo, "Characteristics of an electrodynamic wheel using a 2-D steady-state model," *IEEE Trans. Magn.*, vol. 43, pp. 3395-3405, 2007.
- [4] J. Bird and T. A. Lipo, "Modeling the 3D Rotational and Translational Motion of a Halbach Rotor above a Split-Sheet Guideway," *IEEE Trans. Magn.*, 2009.
- [5] J. Bird and T. A. Lipo, "A 3D steady-state magnetic charge finite element model of an electrodynamic wheel," *IEEE Trans. Magn.*, vol. 44, pp. 253-265, 2008.

Improved Accuracy of Electro-Quasistatic Simulations of Large-Scale 3D High Voltage Equipment Including Nonlinear Field-Grading

Daniel Weida¹, *Graduate Student Member, IEEE*, Thorsten Steinmetz^{1/2}, Markus Clemens¹ *Senior Member, IEEE*

¹Helmut-Schmidt-University, University of the Federal Armed Forces Hamburg, Faculty of Electrical Engineering,

Chair for Theory of Electrical Engineering and Computational Electromagnetics, P.O. Box 700822, D-22008 Hamburg, Germany

²ABB Switzerland Ltd., Corporate Research, CH-5405 Baden 5 Dättwil

daniel.weida@hsu-hh.de

Abstract—Finite element method (FEM) simulations are analyzed for high voltage equipment featuring resistive field grading. In such simulations, the order of the used mesh and the polynomial order of the ansatz functions is varied. The resulting effects on the accuracy and the simulation time is developed. Simulation results of a simplified benchmark geometry and applications to large scale 3D high voltage equipment are presented herein.

I. RESISTIVE FIELD GRADING MATERIAL MODELING

Resistive field grading materials, such as provided with SiC or ZnO microvaristor polymer compounds, have a modifiable effect on the electric field both in and close to them [1]. First applications with ZnO μ -varistors can be found in [2], on the simulation of nonlinear stress grading materials in [3] and [4]. The effect of higher order elements on the accuracy of mechanical stress simulations is discussed in [5] and for electrostatic simulations in [6]. In this paper, it is enhanced for nonlinear electro-quasistatic simulations.

The electric field in the computational domain Ω is assumed to be electro-quasistatic [7]. From Maxwell's equations, the partial differential equation for the scalar electric potential φ can be derived which reads

$$\operatorname{div}(\kappa(\operatorname{grad} \varphi) \operatorname{grad} \varphi) + \partial_t \operatorname{div}(\varepsilon \operatorname{grad} \varphi) = 0. \quad (1)$$

It considers capacitive (ε) and field-dependant i.e. nonlinear resistive ($\kappa(\operatorname{grad} \varphi)$) effects. Equation (1) is discretized in time via a higher order implicit Runge-Kutta scheme and in space with the help of a strongly modified Whitney-FEM C++ library [8].

II. BENCHMARK PROBLEM

A simplified geometry setup described in [6] is employed. It is a eighth of a sphere capacitor. The mesh with first geometric order elements is plotted in Fig. 1 and contains 1 400 tetrahedra. Simulations for first and second order polynomial ansatz functions are performed for geometric elements of first and second order, respectively. A nonlinear resistive material is used in such a way that there is a known analytic solution for a static electric flow field simulation. The difference between elements of first and second geometric order is shown in Fig. 2.

This work is supported by the "Arbeitsgemeinschaft industrieller Forschungsvereinigungen e.V." (AiF) under Grant 15455 N/2.

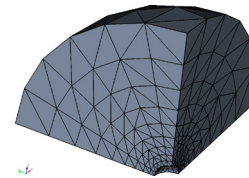


Fig. 1. Mesh with first order tetrahedra of the CAD model of the eighth sphere capacitor. It has an inner radius of 0.1 m and an outer radius of 1.0 m.

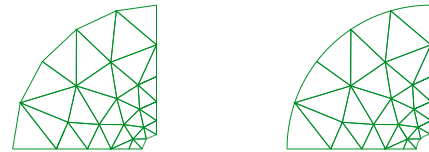


Fig. 2. Spatial discretization of the boundary surface of a eighth sphere capacitor. Quadratic triangulars on the right with curved edges allow for better geometry approximation than linear triangles on the left hand side.

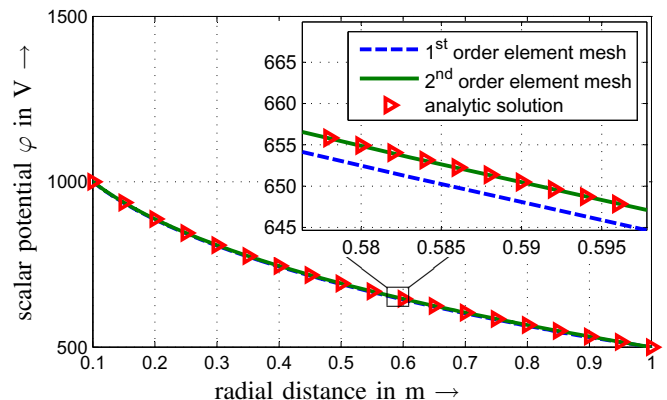


Fig. 3. Scalar potential φ of first and second order element mesh simulations and analytic solution for the sphere capacitor benchmark.

In Fig. 3, the simulation results using nonlinear resistive material behavior are plotted against the radial distance for second order ansatz functions. In the zoomed view it can clearly be seen that the solution of the second order element mesh agrees with the known analytic solution, but the solution of the first order element mesh is off.

Relative errors of the scalar potential are presented in Fig. 4 and Fig. 5 using geometric elements of both first and second order. In Fig. 4, first order ansatz functions are used for the simulations whereas second order ansatz functions are used for the simulations shown in Fig. 5. The results show that the geometric element order should not be greater than the polynomial order of the ansatz functions in order to improve the accuracy using a higher order mesh.

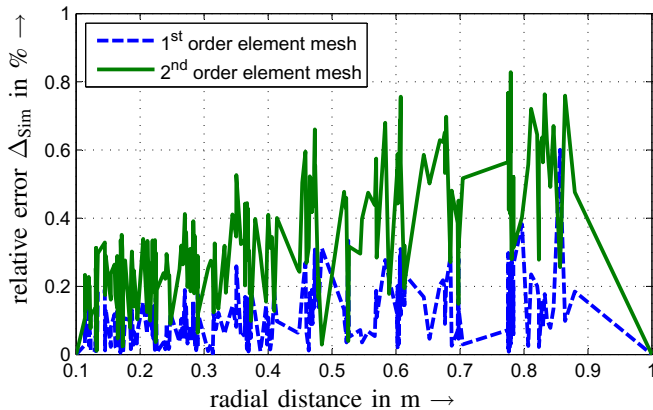


Fig. 4. Relative error of the scalar potential for the sphere capacitor benchmark with first order ansatz functions. The errors of simulations using geometric elements of first and second order are shown.

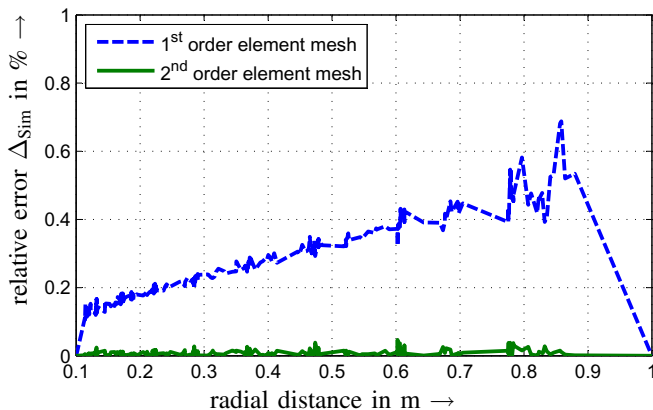


Fig. 5. Relative error of second polynomial order with first and second order element mesh for the sphere capacitor benchmark.

The computational times for running electro-quasistatic simulations are compared in Table I. They confirm the results of the static electric flow simulation. For ansatz functions of first and second order (poly. order), the number of degrees of freedom (DoF), of linear systems (lin.sys.) and the computational times (solver time) are listed for the same mesh with first and second order elements (geom. order). Since the results with same order of geometric elements and ansatz functions are less error-prone, less Newton-iterations have to be performed and thus less linear systems have to be solved. This results in less simulation time.

III. LARGE SCALE 3D HIGH VOLTAGE EQUIPMENT

The effects of the use of higher order elements are shown in the benchmark problem. This is applied to realistic large scale

TABLE I
EFFICIENCY OF TRANSIENT SIMULATIONS FOR THE SPHERE BENCHMARK.

poly. order	geom. order	# DoF	# lin.sys.	solver time
1	1	286	474	25 s
	2	286	1 207	62 s
2	1	2085	1 057	321 s
	2	2085	887	256 s

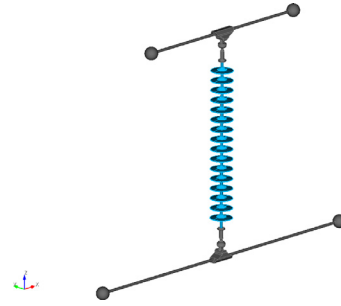


Fig. 6. Insulator test configuration. The lateral dimensions of the configuration are 2.6 m x 0.17 m x 1.824 m, of its bounding box 5 m x 5 m x 8 m.

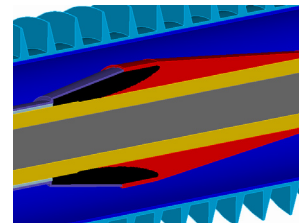


Fig. 7. Zoomed view of the stress cone of a high voltage cable terminator.

3D high voltage equipment in the full paper. A composite insulator example is presented in Fig. 6. Its first shed is made of silicon filled with field grading material. A cable terminator example is presented in Fig. 7. The simulation setup and results for those models will be presented in the full paper.

REFERENCES

- [1] D. Pearce, "Characteristics of non-linear doped zinc oxide for electrical stress grading," *ETG-Fachbericht Vol. 110*, VDE Verlag, Berlin 2008.
- [2] L. Donzel, T. Christen, R. Kessler, F. Greuter, H. Gramespacher, "Silicone Composites for HV Applications based on Microvaristors," *2004 Int. Conf. Solid Dielectrics.*, Toulouse, France, July 5-9, 2004.
- [3] L. Egiziano, V. Tucci, C. Petrarca, M. Vitelli, "A Galerkin model to study the field distribution in electrical components employing nonlinear stress grading materials," *Dielectrics and Electrical Insulation, IEEE Transactions on*, vol.6, no.6, pp.765-773, Dec 1999.
- [4] D. Weida, T. Steinmetz, M. Clemens, "Electro-Quasistatic High Voltage Field Simulations of Large Scale Insulator Structures Including 2D Models for Nonlinear Field-Grading Material Layers," *Magnetics, IEEE Transactions on*, vol.45, no.3, pp.980-983, March 2009.
- [5] A. Entekin, "Accuracy of MSC/NASTRAN first- and second-order tetrahedral elements in solid modeling for stress analysis," *MSC 1999 Aerospace Users' Conference Proceedings*, 1999.
- [6] D. Weida, T. Steinmetz, M. Clemens, "Benefits of Higher Order Elements for Electrostatic Simulations of Large-Scale 3D Insulator Structures," *IEEE DEIS Electrical Insulation Conference, Proceedings of the 2009*, accepted for publication, 01.-03.06.09.
- [7] H. A. Haus, J. R. Melcher, *Electromagnetic Fields and Energy*, Prentice Hall, Englewood Cliffs, New Jersey, 1989.
- [8] P. Castillo, R. Rieben, D. White, "FEMSTER: An object oriented class library of discrete differential forms," *Tech. Report UCRL-JC-150238-ABS*, Lawrence Livermore National Laboratory.

3-D Calculation of Surface Electric Field around Conductor of UHVAC Transmission Lines

Dongping XIAO, Wei HE, Mingyou CHEN, Fan YANG

State Key Laboratory of Power Transmission Equipment & System Security and New Technology (Chongqing University), Chongqing 400030, China
xiaodongping@cqu.edu.cn

Abstract—A 3-dimension model and a improved computational technique are proposed for calculating the surface electric field generated by the sagged conductors of UHVAC transmission lines, by taking advantage of the fact that the equation of the catenary exactly describes the line sag. This method is suitable for analyzing the effects of various factors on the surface electric field around bundle conductors, including the span, conductor type and meteorological condition, which have not been mentioned by available literatures. The results of a sample calculation for 1000kV compact transmission lines are given for variation in line parameters. It is hoped that the work will be useful to the transmission line engineer.

I. INTRODUCTION

With the ever-increasing need to electrical energy in China, ultra-high voltage alternating current (UHVAC) transmission lines are being constructed, and more projects are in programming. Advancing voltage degree induces the increase of surface electric field around conductor, and thereby corona disadvantages enhance [1].

When the conductor surface electric field exceeds the corona onset electric field, a partial breakdown ensues in the surrounding air near the conductor surface and it is called corona discharge [2]. Electric field at the surface of conductor and its adjacent is the direct factor resulting discharge activity. A crucial task of transmission line engineer is to select the optimum conductor size and bundle conductors' configuration to yield as low a surface potential gradient and electric field as possible.

In the case of field distribution around conductor in three phase AC transmission lines, analytical or numerical computations have been handled as 2-D model in which conductor is regarded as infinitely long and straight cylindrical electrode [1],[3]-[4]. The simple model neglects sag of overhead lines and induces some error, especially for UHV transmission lines. In order to obtain more accurate results, a 3-D model based on charge simulation method (CSM) is proposed in this paper. Then the field distribution around the surface of any subconductor in a bundle can be calculated accurately. The model is mainly optimized from the following improved aspects:

- 1) Considering the sag of overhead transmission lines and calculating the 3-D electric field;
- 2) Adopting adaptive optimization algorithm to determinate the location of simulation charges in subconductor.

II. METHODOLOGY OF CALCULATION

A. Overhead transmission line Equation

The conductor suspended between two towers of equal height can be described by equation of overhead catenary [5]:

$$z = \frac{\sigma_0}{g} \left(\cosh \frac{gx}{\sigma_0} - \cosh \frac{gL}{2\sigma_0} \right) + H \quad (1)$$

where L and H are the distance and the height of the points of suspension, g and σ_0 are the load and horizontal stress of conductor.

It is worth mentioning that most are: g and σ_0 are changing with altitude, temperature, velocity of wind, thickness of ice-coating, etc. Even for identical configuration of the transmission lines in different geographic environment and meteorological condition, there are different sags which will affect the electric field surrounding bundle conductor. The problem has not been discussed in available literatures.

B. Surface Electric Field Calculation

For the UHVAC conductors, the potential coefficient p , the potential ϕ and the electric field E can be defined as follows:

$$[\phi] = [P][\tau] \quad (2)$$

$$p_{ij} = \frac{1}{4\pi\epsilon_0} \int_{l_i} \left(\frac{1}{r_{ij}} - \frac{1}{r'_{ij}} \right) dl_i \quad (3)$$

$$\vec{E} = \sum_i -\nabla \phi_i \quad (4)$$

where τ is the simulating line charge density which can be calculated based on CSM. r_{ij} and r'_{ij} are the distance from the line charge i and its image to the j th field point, respectively. They are the function of coordinate x , y and z .

Currently available equations for p_{ij} are difficult to use directly in 3-D model, and require both a fundamental knowledge of electromagnetics and computer aided drawing skills.

In order to obtain accurate results, as well as to consider compute time-consuming, the following need to be accounted:

- 1) the amount and position of the simulating charges in the bundle conductors;
- 2) the numerical integral arithmetic of (3) combining with (1).

C. Adaptive Optimization Algorithm for Simulating Charges

It is logical to assume that one simulating line charge in each subconductor, and it is initially located in the center of

the subconductor. The optimization position, representing with the parameter d , is at somewhere among the connection direction of the equivalent phase center and subconductor center as indicated in Fig.1. It can be determined by adaptive optimization algorithm to satisfy the boundary condition [6]. The computational error for the potential of checking points can less than 0.1%, or even lesser.

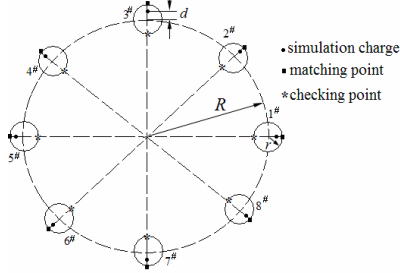


Fig.1 Configuration of simulating charge, matching and checking points for one phase line

D. Numerical Integral

Combining (1) with (3), the potential coefficient p_{ij} is merely the function coordinate x :

$$p_{ij} = \frac{1}{4\pi\epsilon_0} \sum_{k=-K}^{k=K} \int_{(k-\frac{1}{2})L}^{(k+\frac{1}{2})L} \left(\frac{1}{\rho_{ij}} - \frac{1}{\rho_{ij}'} \right) \cosh \frac{a(x_i - kL)}{L} dx_i \quad (5)$$

$$= \frac{1}{4\pi\epsilon_0} \sum_{k=-K}^{k=K} \int_{(k-\frac{1}{2})L}^{(k+\frac{1}{2})L} f(x_i) dx_i$$

where L is the length of span and K is the numeral of spans.

The integral interval is divided into elementary segments, then equation (5) can be calculated by the compound Simpson integration. The intervals are properly partitioned to improve analysis precision and recede time-consuming:

$$\int_{k-\frac{1}{2}L}^{k+\frac{1}{2}L} f(x_i) dx_i = \frac{h}{3} \left[f\left(k-\frac{L}{2}\right) + f\left(k+\frac{L}{2}\right) + 2 \sum_{n=1}^{m-1} f(x_{i2n}) + 4 \sum_{n=0}^{m-1} f(x_{i(2n+1)}) \right]$$

where h is the step size of discretization.

III. RESULTS AND CONCLUSION

The present 3-D model and improved computational technique can be used to calculate the surface electric field of any bundle conductor.

Fig.2 is an example of outputs for 1000kV (line-line) compact transmission lines operating in good weather. The bundled conductors of phase A is showed as Fig.1. GJ-500/45 with 30mm in diameter is adopted and the span length is 400m.

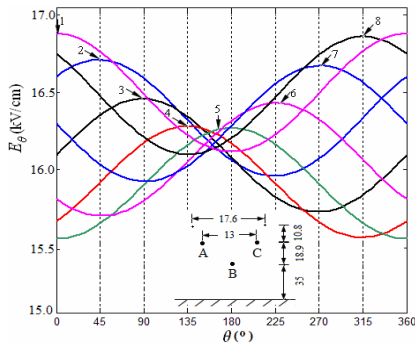


Fig.2 E distribution curves of bundle conductors of phase A

The curve of electric field distribution along the circumference of a subconductor is similar to sinusoid. The maximum electric field E_{\max} is located on the external surface of subconductor, as for the connection of the phase and the subconductor centers. And the minimum is located on the internal surface.

There are numerous factors that influence the surface electric field distribution. Energized line voltage, tower configuration, the number of conductors per bundle, bundle spacing and phase spacing has been discussed by literatures. However, the previous methods are invalid to be used to analyze the effects of different electric field distribution along conductors, the influence of span, different types of conductors and meteorological condition upon the surface electric field. The proposed 3-D model can solve the problem.

1) The overhead conductor suspended equal height is symmetrical with respect to the center of a span. Hence, E_{\max} varying along a subconductor is also symmetrical with respect to the center of a span. A 15m sag corresponds to about 5% increase or decrease in surface electric field. The center phase and outer phase conductors have inverse change characteristic.

2) The fields around the surface of subconductors increase as the span length increases. The calculations show when the span length extends from 400m to 450m the E_{\max} should increase approximately 6.5% for the center phase conductors and 8.1% for the outer phase conductors. The center phase is more affected by the changes in span length. Span length is an important factor in surface electric field.

3) If bundle conductors are replaced by 8×LGJ-500/45 (with 34.32mm in diameter) or 8×ACSR-720/50 (with 36.2mm in diameter), the fields on the surface of subconductors decrease beyond 20%. As such, conductor sector is recognized as a most significant factor in surface electric field.

4) The effect of air temperature upon the surface electric field is more distinct than other meteoric factors, such as velocity of wind, thickness of ice-coating, etc. The increase in air temperature reduces the surface electric field on outer phase conductors but increases it on center phase conductors for compact transmission lines.

IV. REFERENCES

- [1] M.S. Abou-seada and E.Nasser, "Digital Computer Calculation of the Potential and Its Gradient of a Twin Cylindrical Conductor", *IEEE Trans. on Power Apparatus and Systems*, 88(12):1802-1814, 1969.
- [2] S. K. Nayak and M. Joy Thomas, "An Integro-Differential Equation Technique for the Computation of Radiated EMI Due to Corona on HV Power Transmission Lines", *IEEE Trans. On Power Delivery*, 20(1):488-593, 2005.
- [3] IEEE Corona and Field Effects Subcommittee Report, Radio Noise Working Group. "A survey of methods for calculating transmission line conductor surface gradients", *IEEE Trans. on Power Apparatus and Systems*, 98(6):1996-2007, 1979.
- [4] Abdel-Salam M, El-Mohandes M Th, El-Kishky H. "Electric Field Around Parallel DC and Multi phase AC Transmission Lines". *IEEE Trans on Electrical Insulation*, 1990, 25(6):1145-1152.
- [5] A. V. Mamishev, R. D. Nevels, B. D. Russell, "Effects of Conductor Sag on Spatial Distribution of Power Line Magnetic Field", *IEEE Trans. on Power Delivery*, 11(3):1571-1576, 1996.
- [6] C.H. Sun, W Zong, S.Q. Li, *et al*, "A More Accurate Calculation Method of Surface Electric Field Intensity of Bundled Conductors", *Power System Technology*, 32(4): 92-96, 2006(in Chinese).

Analytical Prediction of Eddy-Current Loss in Armature Windings of Permanent Magnet Brushless AC Machines

Y. Amara, P. Reghem and G. Barakat

Groupe de Recherche en Electrotechnique et Automatisme du Havre - EA 3220, Department of Electronic and Electrical Engineering, University of Le Havre
25 rue Philippe Lebon - B.P. 1123 - 76063 Le Havre cedex, France

Abstract — This paper presents an analytical model for prediction of eddy current loss in armature windings of permanent magnet brushless AC machines. The developed model can either be used in the case of internal or external rotor radial-field machines topologies. First, a 2D exact analytical solution of armature reaction magnetic field distribution in a actual geometry of slotted surface mounted PM radial flux synchronous machines is established. It involves solution of Maxwell's equations in slots, airgap and PM's region. Then, magnetic vector potential solution in the slots is used for prediction of resistance limited eddy current in armature windings. Finally, results from this analytical model are compared to corresponding finite element analyses. This analytical model is then used to estimate eddy current loss in armature windings.

I. INTRODUCTION

This paper attempts to provide analytical tools to facilitate the analysis and design of a class of radial flux PM synchronous machines (fig. 1). The developed model gives exact magnetic field distribution due to armature reaction in the slots (radial slots) [1]. The developed model embraces both internal and external rotor topologies (fig. 1). The permanent magnet supporting armature can either be made of magnetic or non-magnetic material. The slotted stator has a classical configuration with radial teeth. The slots and teeth can be equally distributed or not [2], [3]. They can be arranged to accommodate any winding configuration (overlapping and non overlapping windings).

The developed model is then used to estimate resistance limited eddy current in armature windings and corresponding loss. It is also used to quantify the effect of segmenting armature windings conductors as means of reducing the loss. The validity of the developed model is verified by time-stepped transient finite element analysis.

II. ARMATURE REACTION FIELD ANALYTICAL SOLUTION

In order to establish the exact analytical solution, two concentric regions are considered (Fig. 2) (slots (I), airgap, permanent magnets and region under magnets (II)) Region under magnets is only considered in case of a non-magnetic permanent magnets supporting armature. Permeability of all ferromagnetic parts is assumed to be infinite. The permeability of permanent magnets is assumed to be equal to that of air. The governing field equations, in terms of the Coulomb gauge, $\nabla \times \mathbf{A} = 0$, are:

$$\begin{cases} \nabla^2 \mathbf{A} = -\mu_0 \mathbf{J} & \text{in region I} \\ \nabla^2 \mathbf{A} = 0 & \text{in region II} \end{cases} \quad (1)$$

\mathbf{A} (the magnetic vector potential) only has A_z component which is independent of z (infinitely long machine in axial direction). \mathbf{J} is the current density vector.

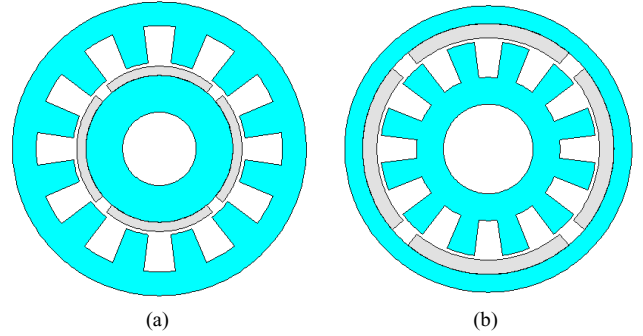


Fig. 1. Radial-field PM machines topologies: internal rotor (a) and external rotor (b).

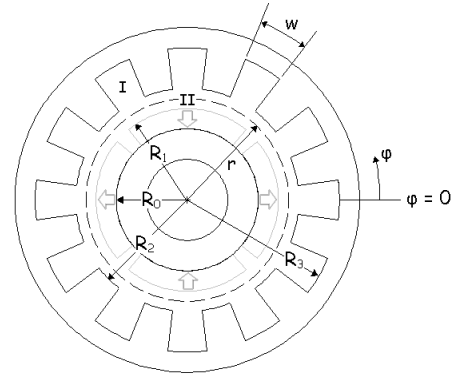


Fig. 2. Polar coordinates system.

Combining equations (1) with boundary conditions, and using separation of variables method, help establish a set of linear equations ($N_H \times N_H$) (where N_H is the number of considered harmonics), where coefficients of magnetic vector potential solution in region II are the unknown. Solving these linear equations and using interface conditions give coefficients of magnetic vector potential in the slots. Obtained linear system is solved using Gaussian elimination method. The developed model takes into account rotor movement.

The general solution of equation (2), in a slot 'i', can be written as follows:

$$A^{(i)} = \left[a_0^{(i)} + \sum_{m=1}^{+\infty} \left[F_m^{(i)} \left(\left(\frac{r}{R_1} \right)^{\left(\frac{m\pi}{w} \right)} + \left(\frac{r}{R_1} \right)^{-\left(\frac{m\pi}{w} \right)} \right) \cos \left(\frac{m\pi}{w} (\varphi - \varphi_i) \right) \right] \right. \\ \left. + \frac{\mu_0}{2} J^{(i)} \left(R_1^2 \ln(r) - \frac{r^2}{2} \right) \right] \quad (2)$$

where $J^{(i)}$ is the current density of slot 'i'.

III. ANALYTICAL PREDICTION OF EDDY CURRENT

The time dependence of magnetic vector potential solution in a slot ‘ i ’ is proportional to the time dependence of current density in this slot. If the current density is sinusoidal, the time harmonic content of induced eddy current will be limited to the fundamental component. Since armature windings conductors are always designed to have dimensions smaller than the skin depth, the induced eddy current density can be obtained from the following:

$$J_e(r, \varphi, t) = -\sigma \cdot \frac{\partial A^{(i)}(r, \varphi, t)}{\partial t} + C(t) \quad (3)$$

$$C(t) = C_0(t) + \sum_{m=1}^{+\infty} C_m(t) \quad (4)$$

where σ is the electric conductivity of the windings material (copper). $C(t)$ is a function of time which is introduced to insure that the total current flowing in each conductor is equal to the source current.

IV. COMPARISON WITH FINITE ELEMENT ANALYSIS

Table I presents the machine’s parameters used for the exposed results in this digest. A time-stepped transient finite element analysis was made to calculate the eddy current distribution in the armature windings for frequencies ensuring that the conductor dimensions are smaller than the skin depth. Figure 3 shows eddy current density distribution along the radial direction collinear with a slot axis at a given instant. Figure 4 compares the analytically predicted variation of J_e with time and the corresponding finite element results at a point situated in the middle of a conductor. It can be seen that, in both cases, the analytical predictions agree very well with the finite element simulations. Figure 5 shows a slot conductor eddy current loss calculated by finite element simulation on one hand, and on the other hand, the corresponding limited resistance eddy current loss predicted by the developed analytical model. It should be noticed that the eddy current loss at 35 Hz is about 8% of Joules losses due to source current. This comparison clearly shows the accuracy of the developed analytical model and validates by the way its effectiveness in the adequate frequency domain.

In the final paper, a study of the effect of segmenting armature windings conductors as means of reducing the loss will be presented and discussed.

V. CONCLUSION

This paper presents a general analytical solution of the armature reaction magnetic filed distribution in an actual geometry of radial flux permanent magnet brushless AC machines. The developed analytical solution of magnetic vector potential in the slots is used to predict the resistance limited eddy current losses in the armature windings.

TABLE I – MACHINE’S PARAMETERS

Pole number	6
Slot number	18
Number of slots per pole per phase	1
Number of turns	2
R_0, R_1, R_2 and R_3 (mm)	50, 58, 60 and 84
w (rad)	$\pi / 18$

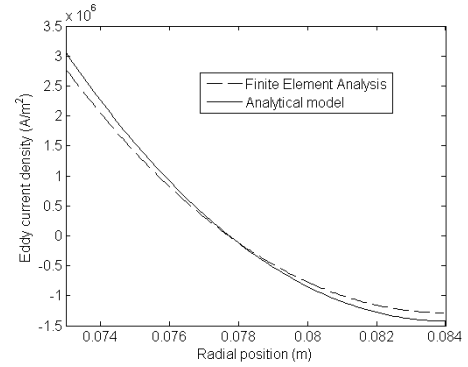


Fig. 3. Current density along a radius aligned with a slot axis.

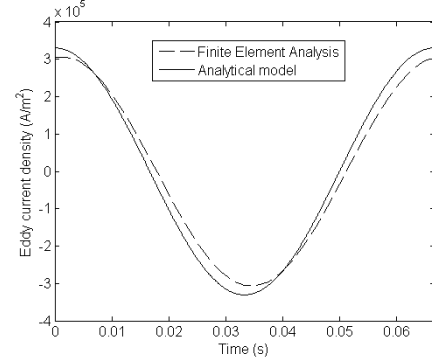


Fig. 4. Current density versus time at a point in the middle of a slot.

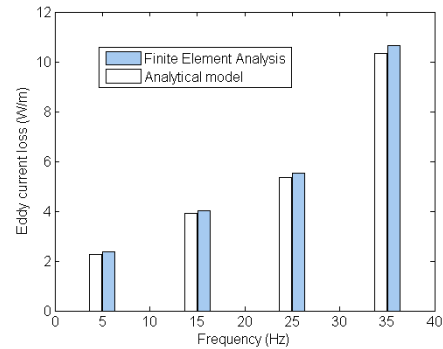


Fig. 5. Eddy current loss in a slot conductor versus frequency.

The obtained results have been validated by a time-stepped transient finite element analysis.

Developed model capabilities will be more deeply presented in the full paper and, in particular, the segmenting armature windings conductors effect on the loss reduction.

VI. REFERENCES

- [1] A. Bellara, Y. Amara, G. Barakat and B. Dakyo, “2D exact solution of armature reaction field in slotted surface mounted PM radial flux synchronous machines,” to be presented at *IEEE International Magnetics Conference*, Session BV (Actuators), Sacramento, California, May 4-8, 2009.
- [2] Z. Q. Zhu, S. Ruangsinchaiwanich, D. Ishak and D. Howe, “Analysis of cogging torque in brushless machines having nonuniformly distributed stator slots and stepped rotor magnets,” *IEEE Trans. Magn.*, vol. 41, no. 10, pp. 3910–3912, October 2005.
- [3] J. Azzouzi, G. Barakat and B. Dakyo, “Quasi-3-D analytical modeling of the magnetic field of an axial flux permanent-magnet synchronous machine,” *IEEE Trans. Energy Convers.*, vol. 20, no. 4, pp. 746–752, December 2005.

Complementarity of Dual Eddy Current Formulations on Dual Meshes

Zhuoxiang Ren and Hui Qu *

Mentor Graphics Corporation, 1001 Ridder Park Drive, San Jose, California 95131, USA

*Institute of Electrical Engineering, Chinese Academy of Sciences, Beijing, China

Email: zhuoxiang_ren@mentor.com

Abstract— The dual formulations of finite element method (FEM) and the finite integral technique (FIT) using dual meshes for eddy current problems are studied. Based on the algebraic discretization of Maxwell equations on dual meshes, two sets of dual formulations are derived. A rational comparison between these formulations is performed. The complementary energy bounds are illustrated through an example.

I. INTRODUCTION

The dual finite element formulations are traditionally obtained from the variational method in solving, respectively, one of the governing equations (e.g. Faraday's law and the Ampere's theorem) in strong sense and the other in weak sense. Advances in computational electromagnetics show the interests of differential forms and working with the global variables. The magnetic field computation is more suitably studied in the framework of discrete geometry, algebra and networks. By associating the field quantities with the edges and facets of the primal and dual meshes, the matrix equation systems can be derived pure algebraically from the differential equations. Such a procedure has the advantages of showing the algebraic and topology properties of the field computation methods [1][2], and their analogy to the circuit analysis.

The difference and the similarity of the two frequently used methods, the finite element method (FEM) and the finite integral technique (FIT), are also clearly drawn in the framework of discrete geometry. They differ only by the Hodge discretization. We have hence a better understanding of the material matrices resulted from the edge elements and facets elements. They have in fact a tight relation to the circuit elements on the dual circuit networks.

The complementarity of dual formulations of FEM and FIT on dual meshes has been studied in a previous work [3], where the study focuses essentially the cases of static fields. The present work extends the study to the case of eddy current problems. We will show that the dual formulations can be established on the dual sets of the meshes; and illustrate that the complementary energy bounds exist for both set of dual formulations and they are due to the geometry discretization.

II. DUAL FORMULATIONS OF EDDY CURRENT PROBLEMS

Let \mathcal{M}_p and \mathcal{M}_D are the two interlocked (primal and dual) meshes on the solution domain of the field problem. Let us denote by \overline{W}_p^p ($p=0, 1, 2, 3$) the spaces of DoFs on nodes, edges, facets and volumes of \mathcal{M}_p ; and \overline{W}_D^p ($p=0, 1, 2, 3$), the spaces of DoF on nodes, edges, facets and volumes of \mathcal{M}_D . The

incident mappings between \overline{W}_p^{p-1} and \overline{W}_p^p are expressed by the incident matrices G , C and D ; and the mappings between \overline{W}_D^{p-1} and \overline{W}_D^p are their transposes D^T , C^T and G^T .

By working with global variables, and replacing the differential operators by incident mappings, the governing equations of the eddy current problems can be written in algebraic forms. According to the assignment of the Faraday's law and the Ampere's theorem on the primal or dual sequences of the dual meshes, we can get two sets of equations:

$$\begin{aligned} C \bar{e}_p &= -d_t \bar{b}_p, & C^T \bar{h}_d &= \bar{j}_d, \\ \bar{h}_d &= M_{1/\mu} \bar{b}_p, & \bar{j}_d &= M_\epsilon \bar{e}_p \end{aligned} \quad (1)$$

and

$$\begin{aligned} C^T \bar{e}_d &= -d_t \bar{b}_d, & C \bar{h}_p &= \bar{j}_p, \\ \bar{b}_d &= M_\mu \bar{h}_p, & \bar{e}_d &= M_{1/\sigma} \bar{j}_p \end{aligned} \quad (2)$$

where $\bar{e}_p, \bar{h}_p \in \overline{W}_p^1$; $\bar{b}_p, \bar{j}_p \in \overline{W}_p^2$ and $\bar{h}_d, \bar{e}_d \in \overline{W}_D^1$; $\bar{j}_d, \bar{b}_d \in \overline{W}_D^2$. They are respectively, the circulations of electric or magnetic field along the edges of the primal or dual meshes and the magnetic flux or electric current across the facets of the primal or dual mesh. The matrices $M_{1/\mu}$, M_σ and M_μ , $M_{1/\sigma}$ are the metric dependent material matrices corresponding to the Hodge discretization of the constitutive laws.

The field variables can be represented by the combined vector-scalar potential pairs. Their discrete relations on the primal mesh are:

$$\bar{e}_p = -d(\bar{a}_p + G \bar{\psi}_p)/dt \quad \text{and} \quad \bar{h}_p = \bar{t}_p + G \bar{\phi}_p$$

where $\bar{\psi}_p, \bar{\phi}_p \in \overline{W}_p^2$ and $\bar{a}_p, \bar{t}_p \in \overline{W}_p^1$. They are, respectively, nodal values of the primitive in time of the electric scalar potential and of the magnetic scalar potential, circulation along edges of the magnetic vector potential and of the current vector potential. Replacing \bar{e}_p of (1) and \bar{h}_p of (2) by their respective potential pairs, and eliminating the variables on the dual mesh, we get two dual matrix equation systems:

$$\begin{aligned} C^T M_{1/\mu} C \bar{a}_p + \frac{d}{dt} M_\sigma \bar{a}_p + \frac{d}{dt} M_\sigma G \bar{\psi}_p &= \bar{j}_{0d} \\ \frac{d}{dt} G^T M_\sigma \bar{a}_p + \frac{d}{dt} G^T M_\sigma G \bar{\psi}_p &= 0 \end{aligned} \quad (3)$$

where \bar{j}_{0d} represents the current excitation. And

$$C^T M_{1/\sigma} C \bar{t}_p + \frac{d}{dt} M_\mu \bar{t}_p + \frac{d}{dt} M_\mu G \bar{\phi}_p = -\frac{d}{dt} M_\mu \bar{t}_{0p}$$

$$\frac{d}{dt}G^T M_\mu \bar{t}_p + \frac{d}{dt}G^T M_\mu G \bar{\phi}_p = -\frac{d}{dt}G^T M_\mu \bar{t}_{0p} \quad (4)$$

where \bar{t}_{0p} is the circulation of the current vector potential on the edges of the primal mesh.

Algebraically, the two well known methods FEM and FIT lead to the same form of dual matrix equations as (3) and (4). They differ only on the Hodge discretization, i.e. the obtaining of the material matrices. In the context of FEM, the matrices M_σ , $M_{1/\mu}$ and M_μ , $M_{1/\sigma}$ are calculated with the Galerkin approach by using, respectively, Whitney edge and facet elements on the primal mesh. Whereas in the case of FIT, the elements of material matrices are calculated algebraically by taking the ratio of the mean edge DoF and average of facet DoF of the primal-dual mesh doublets [2]. No shape function is required. In the particular case of an orthogonal mesh, the matrices M_σ , $M_{1/\mu}$ and M_μ , $M_{1/\sigma}$ are diagonal.

Making the analogy to the circuit network, M_σ (resp. M_μ) and $M_{1/\mu}$ (resp. $M_{1/\sigma}$) correspond to the conductance (resp. permeance) network on the primal mesh and the reluctance (resp. resistance) network on the dual mesh. This analogy is clearly observed in the FIT because the elements of the material matrices are nothing else but the circuit elements on the branches of the primal and dual circuit networks.

III. DUAL SET OF DUAL EDDY CURRENT FORMULATIONS

The dual formulations (3) and (4) are derived by working, respectively, with the electric field and magnetic field on the edges of the primal mesh. However, nothing prohibits us from working with the field variables on the edges of dual meshes. Let us use again the potential variables by writing

$$\bar{e}_d = -d(\bar{a}_d + D^T \psi_d)/dt \quad \text{and} \quad \bar{h}_d = \bar{t}_d + D^T \bar{\phi}_d$$

on the dual meshes, with $\bar{\psi}_d$, $\bar{\phi}_d \in \bar{W}_D^2$, \bar{a}_d , $\bar{t}_d \in \bar{W}_D^1$. By introducing the above potential pairs in (1) and (2) respectively, we obtain a new set of dual formulations:

$$C \tilde{M}_{1/\mu} C^T \bar{a}_d + \frac{d}{dt} \tilde{M}_\sigma \bar{a}_d + \frac{d}{dt} \tilde{M}_\sigma D^T \bar{\psi}_d = \bar{j}_{0p}$$

$$\frac{d}{dt} D \tilde{M}_\sigma \bar{a}_d + \frac{d}{dt} D \tilde{M}_\sigma D^T \bar{\psi}_d = 0 \quad (5)$$

and

$$C \tilde{M}_{1/\sigma} C^T \bar{t}_d + \frac{d}{dt} \tilde{M}_\mu \bar{t}_d + \frac{d}{dt} \tilde{M}_\mu G \bar{\phi}_d = -\frac{d}{dt} \tilde{M}_\mu \bar{t}_{0d}$$

$$\frac{d}{dt} D \tilde{M}_\mu \bar{t}_d + \frac{d}{dt} D \tilde{M}_\mu D^T \bar{\phi}_d = -\frac{d}{dt} D \tilde{M}_\mu \bar{t}_{0d} \quad (6)$$

Note that the material matrices in (5) and (6) are nothing else but the inverses of which in (4) and (3). In the context of FEM, the matrices cannot be derived because of the lack of interpolation basis functions on the dual mesh. On the contrary, in the case of FIT, the task becomes feasible since no shape function is needed to derive the matrices. In fact, in case of orthogonal mesh, the matrices are easily computed by just inverting diagonal terms.

Comparing (6) to (3), we solve in reality the same type of

equations from the circuit network point of view, even though we use different working variables. In fact, in (3), we solve the conductance network on \mathcal{M}_p and the reluctance network on \mathcal{M}_D . While in (6), we have the resistance network on \mathcal{M}_p and the permeance network on \mathcal{M}_D . They are just the inverse of the one from each other. To the equations (4) and (5), we have the similar observations.

IV. COMPLEMENTARY ENERGY BOUNDS

The theoretical prove of the energy bounds for eddy current problem is difficult because the no-conservative nature of the problem. There were in depth discussions about this subject (refs will be provided in full paper). It was observed that the complementary energy bounds of dual FEM formulations do exist numerically and pointed out that they could be due to the numerical discretization [4].

From the similarity between FEM and FIT, we expect that the complementary energy bounds exists as well for the dual FIT formulations. To illustrate this, we solved an eddy current problem which consists of a cross form of conductor place in a uniform time harmonic magnetic field. Fig. 1 shows the joule losses convergence with respect to the mesh finesses inside of conductor, obtained respectively, by the FEM and FIT. The energy bounds are clearly observed. Since FIT is purely based on the algebraic discretization. The study supports the idea that the complementary energy bounds are due to the numerical discretization.

In addition, if we look at the dual set of dual formulations (5) and (6), since (6) (resp.(5)) solves the same networks as (3) (resp.(4)). We expect (6) and (5) provides the same energy bounds as (3) and (4). Even tough the two set of equations work with opposite working variables.

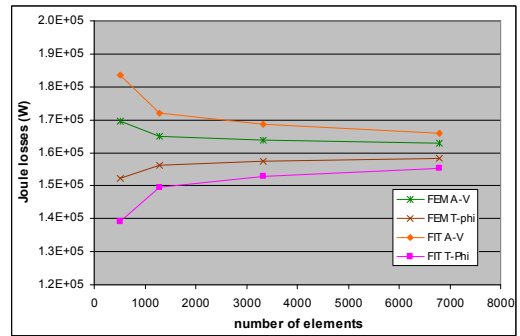


Fig. 1. Joule losses in function of mesh finesses.

REFERENCES

- [1] A. Bossavit, L. Kettunen, and T. Tarhassari, "Some realizations of a discrete Hodge operator: a reinterpretation of the finite element technique," *IEEE Trans on Mag.*, Vol. 35, 1494–1497, May 1999.
- [2] M. Clemens and T. Weiland, "Discrete electromagnetism with the finite integration technique", *Progress In Electromagnetics Research, PIER* 32, 65–87, 2001
- [3] Z. Ren, "On the complementarity of dual formulation on dual meshes", *IEEE Trans. Magn.* Vol.45, No 3, March 2009, pp.1284-1287
- [4] C. Li, Z. Ren and A. Razek, "Complementarity between the energy results of H and E formulations in eddy current problems," *IEE Proc. Sci. Meas. Technol.*, Vol. 1, No 1, 1994, pp25–30.

Numerical Model of Transient Electromagnetic Field around the Grounding System by FEM

Anton Habjanic, Marko Jesenik, and Mladen Trlep
Faculty of Electrical Engineering and Computer Science, University of Maribor
Smetanova ul. 17, 2000 Maribor, Slovenia
anton.habjanic@uni-mb.si

Abstract — A new program solution is presented to analyze the transient performance of grounding systems. In contrast to recently known numerical procedure based on the finite element method (FEM) in frequency domain, in this new methodology for the first time the differential equations of the electromagnetic field have been solved using the FEM directly in time domain. The results of calculations have been verified by comparison with the results of measurements found in the literature.

I. INTRODUCTION

The primary goal of grounding systems is to ensure the safety of personnel and prevent damage of installations while their secondary goal is to provide common reference voltage for all interconnected electrical and electronic systems. To optimize the design of grounding systems, as well as to minimize the disturbance level in the protected area, the program tool able to simulate the transient performance of grounding systems is fundamental. For that very reason, the goal of this work was to develop the methodology (the proper numerical model) which allows a complete three-dimensional (3-D) electromagnetic study of grounding systems by using the finite element method (FEM).

So far, three basic concepts have been used to simulate the transient performance of grounding arrangements: the circuit approach [1], the transmission line approach [2], and the electromagnetic field approach [3]. In this paper, the solution to analyze the transient behavior of grounding system is based on the electromagnetic field theory and on the implementation of the FEM. The validity of the suggested method of analysis has been verified by the comparison of obtained results with the results found in [4].

II. NUMERICAL MODEL OF TRANSIENT ELECTROMAGNETIC FIELD BASED ON FEM

A. Mathematical Background

The governing partial differential equation for transient problems can be derived from Maxwell's equations. In terms of the magnetic vector potential \mathbf{A} and the electric scalar potential φ , it can be formulated as:

$$\nabla \times \frac{1}{\mu} \nabla \times \mathbf{A} - \nabla \frac{1}{\mu} \nabla \cdot \mathbf{A} + \sigma \frac{\partial \mathbf{A}}{\partial t} + \sigma \nabla \varphi = 0, \quad (1)$$

where μ is the permeability and σ the electrical conductivity.

By applying the finite-elements procedure, the soil and the air domain of the problem are discretized by the prismatic elements of the first order and the conductors of the grounding system are discretized by the line elements of the first order.

Thereby, the unknowns \mathbf{A} and φ in arbitrary point within the prismatic and line finite elements are approximated between the computed values of the corresponding potentials in the finite element's nodes (A_{xi} , A_{yi} , A_{zi} , and φ_i) in terms of interpolation functions (polynomials) N_i respectively as:

$$\mathbf{A} = \sum_{i=1}^6 (\bar{1}_x A_{xi} N_i + \bar{1}_y A_{yi} N_i + \bar{1}_z A_{zi} N_i), \quad \varphi = \sum_{i=1}^6 \varphi_i N_i, \quad (2)$$

$$\dot{\mathbf{A}} = \sum_{i=1}^2 (\bar{1}_x \dot{A}_{xi} N_i + \bar{1}_y \dot{A}_{yi} N_i + \bar{1}_z \dot{A}_{zi} N_i), \quad \dot{\varphi} = \sum_{i=1}^2 \dot{\varphi}_i N_i. \quad (3)$$

To obtain the symmetry of the finite element's matrix (as it will be shown in the full paper), the special modified electric scalar potential V is introduced as:

$$\varphi = \frac{\partial V}{\partial t} = \dot{V}. \quad (4)$$

Regarding (4), the application of the FEM and the Galerkin's formulation of the weighted residual method to (1) result in the following matrix equation:

$$[\mathbf{K}] \{\mathbf{A}, V\} + [\mathbf{C}] \{\dot{\mathbf{A}}, \dot{V}\} = \{\mathbf{R}\} \quad (5)$$

where $\{\mathbf{A}, V\}$ is the column vector of the unknown nodal potentials; $\{\dot{\mathbf{A}}, \dot{V}\}$ is the column vector of the time derivatives of $\{\mathbf{A}, V\}$; $[\mathbf{K}]$ is the stiffness matrix which is associated with the potentials \mathbf{A} and V , and the Laplacian operator Δ ; $[\mathbf{C}]$ is the damping matrix which represents the contribution of the induced current term $\sigma \partial \mathbf{A} / \partial t$ to the system; whereas $\{\mathbf{R}\}$ is the forcing function column vector.

For the time integration, the Euler's method is used in which the derivative of the potential is substituted by the difference of the potentials, as follows:

$$\dot{\mathbf{A}}^{(n)} = \frac{\mathbf{A}^{(n)} - \mathbf{A}^{(n-1)}}{\Delta t}, \quad (6)$$

$$\dot{V}^{(n)} = \frac{V^{(n)} - V^{(n-1)}}{\Delta t} = \varphi^{(n)}. \quad (7)$$

If we introduce (6) and (7) into (5), the following expression for the calculation of the potential in the new time step (n), depending on the preceding time step ($n-1$), is obtained:

$$\left[\mathbf{K} + \frac{\mathbf{C}}{\Delta t} \right] \{\mathbf{A}^{(n)}, V^{(n)}\} = \{\mathbf{R}^{(n)}\} + \left[\frac{\mathbf{C}}{\Delta t} \right] \{\mathbf{A}^{(n-1)}, V^{(n-1)}\}. \quad (8)$$

Finally, the obtained set of linear algebraic equations is solved by the algebraic multi-grid (AMG) method [5].

B. Implementation of the Numerical Model

The developed program for the 3-D calculation of transient electromagnetic field, which has been written in Fortran, consists of three modules: the pre-processor, the processor,

and the post-processor. In the pre-processor, where first of all the 3-D mesh of the prismatic and line finite elements of the first order is built by the automatic mesh generator [6], also the geometrical and physical input data, as well as the forcing (injected) potential function, are defined. In the processor, the transient calculation is carried out, as shown in Fig. 1.

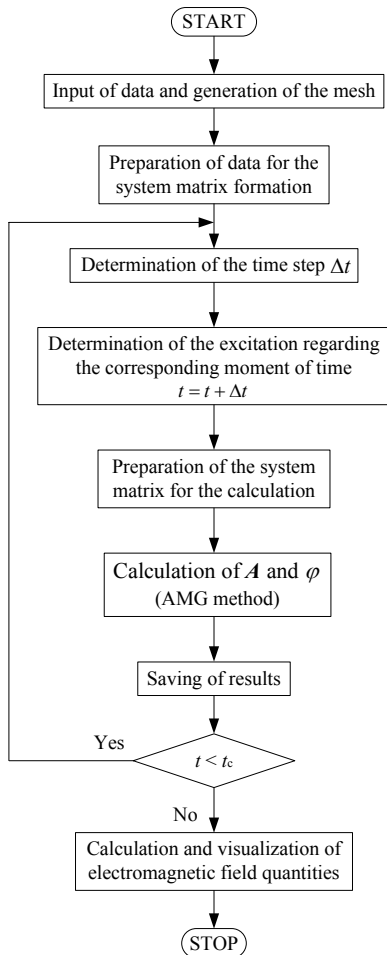


Fig. 1. Flow chart of the electromagnetic transient calculation

Finally, the post-processor allows interactive calculation and visualization of any desired quantity of electromagnetic field (e.g., current I , electric field intensity E , magnetic flux density B , etc.).

III. APPLICATION AND DISCUSSION

Following up Geri's research work [4], concerning the development of the mathematical model based on a circuit approach, in this paper, the program solution (the numerical model based on the FEM) is presented to analyze the transient behavior of the grounding rod when fed by an injected time variable potential function. The steel grounding rod with the length of 6 m, the diameter of 20 mm, and the conductivity of $5,88 \times 10^6$ S/m is buried vertically into the uniform soil with the resistivity of $40 \Omega\cdot\text{m}$, as shown in Fig. 2, where also the defined boundary conditions on the outer planes of the problem are presented.

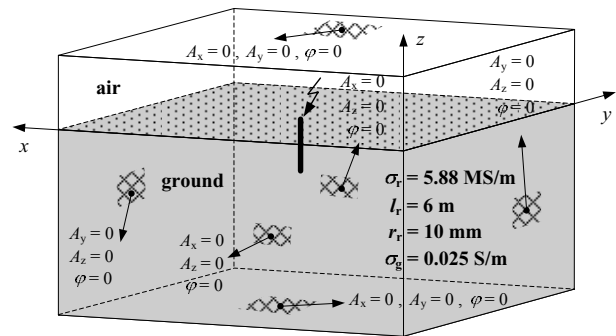


Fig. 2. Schematic view of the vertical grounding rod under analysis

In order to verify the reliability of the program solution, in Fig. 3, the comparison of the current variation, obtained as a response to the shape of the injected potential function, with the current variation from [4] is presented.

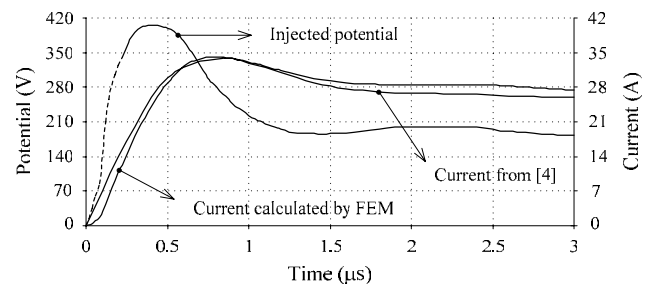


Fig. 3. The transient voltage and currents of the grounding rod

A detailed description of the actual implementation of the model will be given in the full paper where also the application of the model to horizontal grounding wire will be presented.

IV. REFERENCES

- [1] A. P. Meliopoulos and M. G. Moharam, "Transient analysis of grounding systems," *IEEE Transactions on Power Apparatus and Systems*, vol. 102, no. 2, pp. 389-399, February 1983.
- [2] F. E. Menter and L. Grcev, "EMTP-based model for grounding system analysis," *IEEE Transactions on Power Delivery*, vol. 9, no. 4, pp. 1838-1849, October 1994.
- [3] L. Grcev and F. Dawalibi, "An electromagnetic model for transients in grounding systems," *IEEE Transactions on Power Delivery*, vol. 5, no. 4, pp. 1773-1781, October 1990.
- [4] A. Geri, "Behaviour of grounding systems excited by high impulse currents: the model and its validation," *IEEE Transactions on Power Delivery*, vol. 14, no. 3, pp. 1008-1017, July 1999.
- [5] U. Trottenberg, C. Oosterlee, and A. Schüller, *Multigrid*, Academic Press, A Harcourt Science and Technology Company, London, 2001.
- [6] M. Jesenik, M. Trlep, and B. Hribernik, "Algorithm for automatic 2D discretization with variable mesh density for numerical methods," in *Proceedings of 6th International IGTE Symposium*, Graz, pp. 132-137, September 1994.
- [7] O. Biro and K. Preis, "On the use of the magnetic vector potential in the finite element analysis of the three dimensional eddy current," *IEEE Transactions on Magnetics*, vol. 25, no. 4, pp. 3145-3159, July 1989.
- [8] B. Nekhoul, C. Guerin, P. Labie, G. Meunier, and R. Feuillet, "A Finite element method for calculating the electromagnetic fields generated by substation grounding systems," *IEEE Transactions on Magnetics*, vol. 31, no. 3, pp. 2150-2153, May 1995.
- [9] A. Habjanic, *Numerical Model of Transient Electromagnetic Field around the Grounding System by the Finite Element Method (in Slovene)*, Ph.D. Thesis, FERi UM, Maribor, Slovenia, 2008.

A New Formulation Using Differential Permeability Based on the Source-Field Method

N.Sadowski, J.P.A. Bastos and J.V. Leite
GRUCAD/EEL/CTC, Universidade Federal de Santa Catarina
CP. 476, Florianópolis, SC, 88040-900, Brazil

nelson@grucad.ufsc.br, jpab@grucad.ufsc.br and jean@grucad.ufsc.br

Abstract — The source-field method is a very effective way to treat 3D magnetostatic and magnetodynamic cases for linear and non-linear studies. In this work, we propose a variation of this method based on the concept of differential permeability. With this new approach, it is possible to handle non-linear cases and also more complex hysteretic materials. The electric circuit is coupled with the magnetic structure and a time stepping technique is used.

I. INTRODUCTION

We have been intensively working with the “source-field” method for solving static and dynamic cases. This formulation is very effective and robust [1][2]. Additionally, we have good experience with the concept of differential permeability. We performed some implementations of this latter but it was applied to the magnetic vector potential [3][4]. According our experience, the hysteresis phenomenon can be adequately solved by a differential permeability approach. Non-linear cases (non-hysteretic) can be also treated with such an approach, with fast convergence. Therefore, in this paper we propose the use of this concept in conjunction with the source-field method. Some preliminary and encouraging results are already presented here.

II. THE SOURCE-FIELD METHOD

Let us recall the basic principles of the source-field method. With this formulation, the magnetic field \mathbf{H} can be divided in two parts, as:

$$\mathbf{H} = \mathbf{H}_s - \text{grad}\Omega \quad (1)$$

where \mathbf{H}_s is the field created solely by the imposed currents of the exciting coils and Ω is the reduced scalar magnetic potential. This potential is related to the field produced by magnet dipoles, induced of permanent. We define now the relationship between the imposed current density \mathbf{J} and the field \mathbf{H}_s : We have $\text{rot}\mathbf{H} = \mathbf{J}$ which can be expressed as

$$\text{rot}(\mathbf{H} - \mathbf{H}_s) = \text{rot}\mathbf{H} - \text{rot}\mathbf{H}_s = 0$$

and we have

$$\mathbf{J} = \text{rot}\mathbf{H}_s \quad (2)$$

Therefore, the “influence” of \mathbf{J} is replaced by the magnetic field \mathbf{H}_s spread in the calculation domain. To do so, \mathbf{H}_s is defined through its circulations on the edges of the tetrahedron first order finite elements. Having these circulations, shape functions of edge elements are used to easily define the vector \mathbf{H}_s . Tree and co-tree technique are necessary to properly find the source-field. More detailed text is given in [1][5].

III. USING THE DIFFERENTIAL PERMEABILITY

Using the proposed approach, we have

$$\Delta\mathbf{B} = \mu_d\Delta\mathbf{H} \quad (3)$$

where μ_d is the differential permeability and $\Delta\mathbf{B}$ and $\Delta\mathbf{H}$ are, respectively, the magnetic induction and field variations. For linear materials $\mu = \mu_d$. Using a time stepping discretization we consider that $t+1$ and t are respectively the current calculation step and the previous one. Then

$$\Delta\mathbf{B} = \mathbf{B}^{t+1} - \mathbf{B}^t \quad \text{and} \quad \Delta\mathbf{H} = \mathbf{H}^{t+1} - \mathbf{H}^t$$

With (3)

$$\mathbf{B}^{t+1} - \mathbf{B}^t = \mu_d(\mathbf{H}^{t+1} - \mathbf{H}^t) \quad (4)$$

or

$$\mathbf{B}^{t+1} = \mathbf{B}^t + \mu_d(\mathbf{H}^{t+1} - \mathbf{H}^t) \quad (5)$$

With (1), equation (5) becomes

$$\mathbf{B}^{t+1} = \mathbf{B}^t + \mu_d(\mathbf{H}_s^{t+1} - \text{grad}\Omega^{t+1} - \mathbf{H}_s^t + \text{grad}\Omega^t) \quad (6)$$

where \mathbf{B}^t is known from the previous step. The main equation on this development is

$$\text{div}\mathbf{B}^{t+1} = 0 \quad (7)$$

Applying the Galerkin method on equation (7), we have

$$\int_V N \text{div}\mathbf{B}^{t+1} dv = 0 \quad (8)$$

$$\int_V N \text{div}\mathbf{B}^{t+1} dv = \oint_{s(v)} N \mathbf{B}^{t+1} \cdot d\mathbf{s} - \int_V \text{grad}N \cdot \mathbf{B}^{t+1} dv = 0 \quad (9)$$

where N is the nodal shape function of the finite element. The first term of the right hand side of (9) is related to the classical boundary conditions for scalar potential [4]. The second one will be active to the numerical implementation, and, using (6), it becomes:

$$-\int_V \text{grad}N \cdot [\mathbf{B}^t + \mu_d(\mathbf{H}_s^{t+1} - \mathbf{H}_s^t) + \mu_d(\text{grad}\Omega^t - \text{grad}\Omega^{t+1})] dv = 0 \quad (10)$$

In order to couple the above equation to the feeding electrical circuit we need to define two new quantities \mathbf{K} and \mathbf{N} as follows [1][2]:

$$\mathbf{H}_s = \mathbf{K}I_0 \quad (11)$$

where I_0 is the current flowing in a conductor; \mathbf{K} is, therefore the corresponding source-field for a unitary current. Using the vector \mathbf{N} as:

$$\text{rot}\mathbf{H}_s = \mathbf{N}I_0 \quad (12)$$

we have then $\text{rot}\mathbf{K}I_0 = \mathbf{N}I_0$ and

$$\text{rot } \mathbf{K} = \mathbf{N} \quad (13)$$

Now we consider the electric circuit equation coupled to the magnetic structure.

$$V_m = R_m i_m + \frac{d\Phi_m}{dt} \quad (14)$$

where V_m , R_m , i_m and Φ_m are, respectively, the voltage, the resistance, the established current and the magnetic flux linkage in a generic electric circuit m . From [1], it can be shown that the magnetic flux can be expressed by:

$$\Phi^{t+1} = \int_{V_b} \mathbf{B}^{t+1} \cdot \mathbf{K} dv \quad (15)$$

and for the time step $t+1$ we have:

$$V_m^{t+1} = R_m i_m^{t+1} + \frac{d}{dt} \int_{V_b} \mathbf{B}^{t+1} \cdot \mathbf{K} dv \quad (16)$$

With the derivative time discretization, it gives:

$$\begin{aligned} \Delta t V_m^{t+1} &= \Delta t R_m i_m^{t+1} + \int_{V_b} \Delta \mathbf{B}^{t+1} \cdot \mathbf{K} dv \\ \Delta t V_m^{t+1} &= \Delta t R_m i_m^{t+1} + \int_{V_b} (\mathbf{B}^{t+1} - \mathbf{B}^t) \cdot \mathbf{K} dv \end{aligned} \quad (17)$$

Using the equation (6) in (17) we obtain:

$$\begin{aligned} \Delta t V_m^{t+1} &= \Delta t R_m i_m^{t+1} + \int_{V_b} (\mu_d (\mathbf{H}_s^{t+1} - \mathbf{H}_s^t + \\ &+ \text{grad } \Omega^t - \text{grad } \Omega^{t+1})) \cdot \mathbf{K} dv \end{aligned}$$

For alleviating the notations and equations writing, the above equation, considering (11), can be expressed as

$$\begin{aligned} \Delta t V_m^{t+1} &= \Delta t R_m i_m^{t+1} + \\ &+ (K^T M_{\mu_d} K i_m^{t+1} - K^T M_{\mu_d} K i_m^t - \\ &- K^T M_{\mu_d} G \Omega^{t+1} + K^T M_{\mu_d} G \Omega^t) \end{aligned} \quad (18)$$

where the numerical integrations are taken into account.

Here, $\text{grad } \Omega^t$ is written as $G \Omega^t$ and M_{μ_d} stands for μ_d . As

for the equation (10) we have, with the same notations:

$$\begin{aligned} -G^T \mathbf{B}^t - G^T M_{\mu_d} G \Omega^t + G^T M_{\mu_d} G \Omega^{t+1} - \\ -G^T M_{\mu_d} K i_m^{t+1} + G^T M_{\mu_d} K i_m^t = 0 \end{aligned} \quad (19)$$

Arranging equations (18) and (19) in matrix form, the resulting system is:

$$\begin{bmatrix} G^T M_{\mu_d} G & -G^T M_{\mu_d} K \\ -K^T M_{\mu_d} G & \Delta t R_m + (K^T M_{\mu_d} K) \end{bmatrix} \begin{bmatrix} \Omega^{t+1} \\ i_m^{t+1} \end{bmatrix} = \begin{bmatrix} G^T M_{\mu_d} G & -G^T M_{\mu_d} K \\ -K^T M_{\mu_d} G & (K^T M_{\mu_d} K) \end{bmatrix} \begin{bmatrix} \Omega^t \\ i_m^t \end{bmatrix} + \begin{bmatrix} G^T \mathbf{B}^t \\ \Delta t V_m^{t+1} \end{bmatrix} \quad (20)$$

This final system is quite similar to the one obtained for the more classical formulation using directly μ . It means that its implementation is relatively easy, since it is based in another one already known and, in our case, available in our calculation system Feecad [5]. Also, the previous \mathbf{B}^t act as a

permanent magnet. Hysteresis can be considered without particular difficulties since μ_d is always positive.

IV. EXAMPLE AND RESULTS

The magnetic circuit of Fig. 1 is used as an example. At this first stage of our development, we just considered a classical non-linear material.

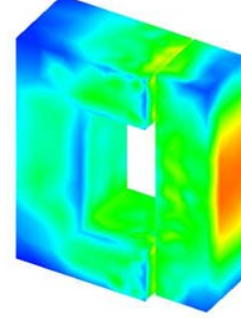


Fig. 1. Magnetic circuit (8247 elements, 1691 nodes)

A ten time steps field calculation was performed by the classical method and the proposed one, using the differential permeability. Of course, as first test, the materials were considered as linear and we obtained strictly the same result. Then, we enforced the non-linearity by a relatively high voltage. Here the two methods provide similar results with small differences. The relative errors for the magnetic energy and co-energy are 0.69% and 0.65%, respectively. The total number of iterations (for the ten steps) for the classical method is 52 and 41 for the proposed one. The corresponding computational times differ on the same proportion.

V. CONCLUSION

We presented in this work a new method for 3D field evaluation based on the concept of differential permeability applied on the source-field method. The magnetic structure is coupled with the electrical circuit and a time stepping technique is used. This formulation can handle, without difficulties, the hysteretic behavior of soft materials, which will be more detailed in the extended version of the paper.

VI. REFERENCES

- [1] Le Menach, Y., Clénet, S., Piriou, F., "Determination and utilization of the source-field in 3D magnetostatic problems", *IEEE Trans. on Magnetics*, 1998, Vol. 34 (5).
- [2] Dular, P., Robert, F., Remacle, J.F., Umé, M., Legros, W., "Computation of the source current density in inductors of any shape using a mixed formulation", *3rd International Workshop on Electrical and Magnetic Fields*, 1996, pp 107-112.
- [3] J. V. Leite, A. Benabou, N.Sadowski, M. V. Ferreira da Luz, "Finite element three-phase transformer modeling taking into account a vector hysteresis model", *Proceedings of IEEE CEFC 2008*, Athens, Greece, Mai 2008 (also accepted for publication in *IEEE Trans. On Magn.*).
- [4] J.P.A.Bastos, N.Sadowski, *Electromagnetic modeling by finite element methods*, Marcel Dekker Inc., New York, 2003.
- [5] J.P.A.Bastos, N.Sadowski, J. L. Müller, B. A. T. Iamamura, Y.Le Menach, F. Piriou, S. Clénet, "A tree construction technique for the Feecad electromagnetic 3D System", *Proceedings of MOMAG2008*, pp. 841-845, Florianópolis, Brazil, September 2008.

Homogenization of Form-Wound Windings in Finite Element Modelling of Electrical Machines

Johan Gyselinck¹, Ruth V. Sabariego², Patrick Dular^{2,3}, Nelson Sadowski⁴, Patrick Kuo-Peng⁴

¹ Dept. of Electrical Engineering, Université Libre de Bruxelles (ULB), Belgium, johan.gyselinck@ulb.ac.be

² Dept. of Electrical Engineering and Computer Science, University of Liège, Belgium

³ Fonds de la Recherche Scientifique, F.R.S. – FNRS, Belgium

⁴ GRUCAD/EEL/CTC, Universidade Federal de Santa Catarina, Brazil

Abstract— In this paper the authors deal with the FE modelling of eddy-current effects in form-wound windings of electrical machines using a previously proposed general homogenization method. The skin and proximity effect in one stator conductor is first quantified by means of a simple low-cost FE model, leading to a complex and frequency-dependent reluctivity for the homogenized winding. This reluctivity is next adopted in a model of a single slot. Resistance and inductance values obtained with the latter model agree well with those obtained with a brute-force approach (modelling and finely discretizing each conductor).

I. INTRODUCTION

Multi-turn windings in electromagnetic devices may be subjected to considerable skin and proximity effect, leading to higher losses and hot spots, and affecting the global characteristics of the device. In principle these effects can be taken into account in a FE simulation of the device by modelling and finely discretizing each separate conductor (with additional electrical circuit equations to connect the so-called massive conductors [1]). For most real-life applications the huge computational cost of such a brute-force approach cannot be justified. Most often the eddy-current effects are thus simply ignored in the resolution stage of the FE simulation (considering winding regions with uniform current density, so-called stranded conductors [1]), after which the eddy-current losses may be estimated *a posteriori*.

Accurate frequency and time domain homogenization methods for windings have recently been proposed in [2], [3]. For the winding type in hand (e.g., round wires with hexagonal-like packing or rectangular conductors with rectangular packing), an elementary FE model is used for determining frequency-domain coefficients regarding skin and proximity effect. These frequency-dependant coefficients can next be straightforwardly translated into constant time-domain coefficients and associated differential equations thanks to the introduction of additional unknowns for the homogenized winding (current components for the skin effect, and induction components for the proximity effect). The number of additional unknowns required and the computational cost depend on the frequency content of the application [3].

The above frequency and time domain methods have so far been applied to inductor-like devices [2], [3]. In this paper we consider the form-wound double-layer stator winding of a 50 Hz 1250 kW three-phase six-pole squirrel-cage induction machine [4]. Flux and current harmonics in the machine are due to the stator and rotor slotting, saturation and PWM supply

This work was partly supported by the Belgian Science Policy (IAP P6/21), F.R.S. – FNRS and the Brazilian National Council for Scientific and Technological Development (CNPq).

(at 2 kHz switching frequency). Compared to previous applications, the flux situation is *a priori* simpler, slot leakage being essentially governed by a 1D differential equation. However, the parallel connection and transposition of the conductors, if any, complicates the analysis. In this digest, a simple series connection of the conductors is supposed.

II. SKIN AND PROXIMITY EFFECT IN ONE CONDUCTOR

The two-layer stator winding of the machine is distributed in 72 rectangular and fully-open slots (width $w_s = 14$ mm, total height 80 mm), each slot comprising 2×9 copper bars of rectangular cross-section (height $h_c = 3.3$ mm, width $w_c = 10.6$ mm) [4]. The vertical insulation space between two conductors of the same group is $h_i = 0.5$ mm. The stack length is $l = 810$ mm (see Fig. 1). Taking as conductivity $\sigma = 6 \cdot 10^7$ S/m, the skin depth $\delta = \sqrt{2/(\omega\mu\sigma)}$, at pulsation ω , varies between 9.2 mm (at 50 Hz) and 1.45 mm (at 2 kHz), and the conductor height to skin depth ratio, h_c/δ , between 0.35 and 2.27.

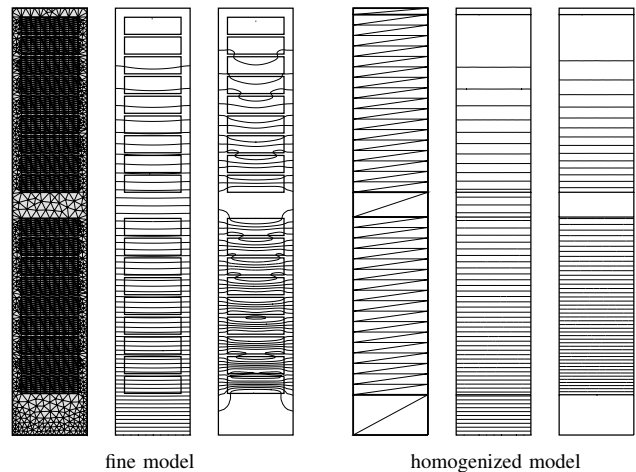


Fig. 1. FE mesh and flux lines (flux component in phase and in quadrature, respectively, with the same imposed 50 Hz current in all 18 conductors), fine model (for brute-force approach) and homogenized model

A. Elementary FE model and frequency-domain calculations

We consider an elementary FE model comprising one copper bar (modelled as a massive conductor) and the insulating space around it. Frequency-domain calculations are carried out in terms of the complex single-component magnetic vector potential \mathbf{a} (in bold), with adequate current and boundary conditions [1].

The complex power \mathbf{S} is then calculated from the local flux density \mathbf{b} and local current density \mathbf{j} :

$$\mathbf{S} = P + \imath Q = \frac{l}{2} \int_{\Omega} (j^2/\sigma + \imath \omega \nu_0 b^2) d\Omega, \quad (1)$$

with P and Q the active and reactive power, \imath the imaginary unit, and $j^2/2 = \mathbf{j}\mathbf{j}^*/2$ and $b^2/2 = \mathbf{b}\mathbf{b}^*/2$ r.m.s.-values squared. Equation (1) can be rewritten considering the average current density \mathbf{j}_{av} and flux density \mathbf{b}_{av} (averaged over the complete model, i.e. copper plus insulation):

$$\mathbf{S} = \frac{l}{2} \int_{\Omega} (j_{av}^2/\sigma_{skin} + \imath \omega \nu_{prox} b_{av}^2) d\Omega, \quad (2)$$

and we thus define the complex skin-effect conductivity σ_{skin} and the complex proximity-effect reluctivity ν_{prox} .

B. Proximity effect

Following the approach developed in [2], [3], a pure proximity-effect excitation is obtained by imposing a unit horizontal flux (with $\mathbf{a} = 0$ and $\mathbf{a} = 1$ on lower and upper boundaries, and the implicit Neumann condition $\partial\mathbf{a}/\partial n = 0$ on left and right slot walls) and zero net current. See the flux patterns in Fig. 2.

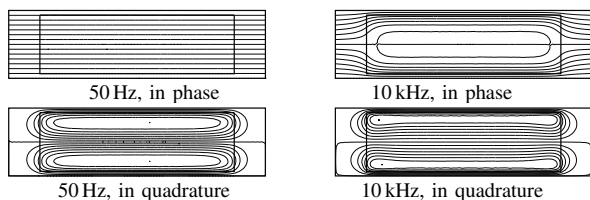


Fig. 2. Proximity-effect flux lines at 50 Hz and 10 kHz, with flux component in phase and in quadrature with imposed flux

The complex proximity-effect reluctivity ν_{prox} can also be estimated on the basis of the well-known analytical solution of the 1D diffusion problem (net current or flux in a conducting sheet of thickness h_c [5]) and considering the flux tubes connected in series or in parallel with the copper bar:

$$\nu_{prox} = \nu_0 \left(\left(\frac{w_c}{h_c} \mathbf{Y} + \frac{w_s - w_c}{h_c} \right)^{-1} + \frac{h_i}{w_s} \right)^{-1} \quad (3)$$

$$\text{with } \mathbf{Y} = \frac{1 + \imath}{2} \frac{h_c}{\delta} \cotanh\left(\frac{1 + \imath}{2} \frac{h_c}{\delta}\right). \quad (4)$$

Fig. 3 shows that the analytical approach produces excellent results thanks to the correction (3) for the insulation on all four sides of the conductor.

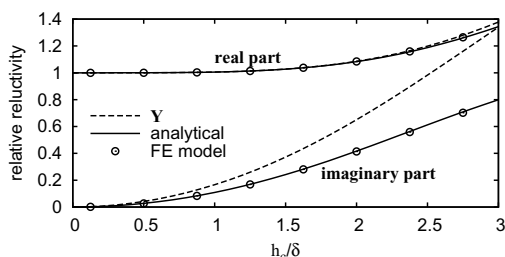


Fig. 3. Real and imaginary part of the relative permeability $\nu_{prox,rel} = \nu_{prox}/\nu_0$ versus h_c/δ

C. Skin effect

A pure skin-effect excitation is obtained by imposing a sinusoidal current (of unit amplitude, e.g.) in the bar, with condition $\mathbf{a} = 0$ on the complete boundary. The relative

increase in joule losses, i.e. the ratio R_{AC}/R_{DC} minus 1, is found to vary between 0.01% at 50 Hz ($h_c/\delta = 0.35$) and 12% at 2 kHz ($h_c/\delta = 2.27$).

III. HOMOGENIZATION OF A COMPLETE SLOT

We now carry out frequency-domain calculations with a FE model of a complete slot, with either fine discretisation of each conductor (18 massive conductors) or homogenization of the two groups of 9 conductors each (two stranded conductors). See Fig. 1 for the two meshes used (totaling 3618 first-order triangular elements versus 74). The complex reluctivity ν_{prox} is adopted in the homogenized winding regions, together with an imposed uniform current density. Two cases are further considered, the two conductor groups belonging either to the same phase or to different phases, and with either zero or 120 degree phase shift between the respective currents (of same unit amplitude, $I = 1$). See Fig. 1 for some flux patterns (with all conductors belonging to the same phase).

Using (1) and (2) we obtain the complex power and thus the equivalent resistance $R_{AC} = P/(2I^2)$ and inductance $L_{AC} = Q/(2\omega I^2)$ at a given pulsation ω . Fig. 4 shows the ratios R_{AC}/R_{DC} and L_{AC}/L_{DC} as a function of the h_c/δ . For the one-phase case, e.g., at 50 Hz the resistance increases by 34%, and at 2 kHz by a factor of 300. Clearly, the skin-effect losses are negligible compared to the proximity-effect losses. Notice in Fig. 4 the excellent agreement between the results obtained with the brute-force approach and with the homogenized model.

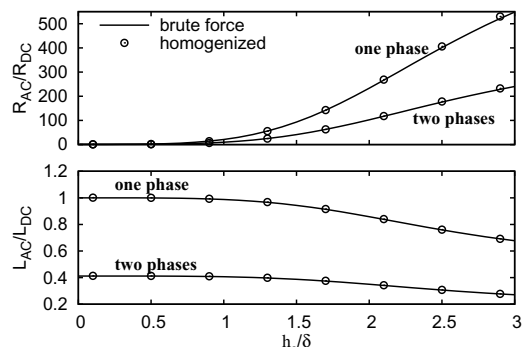


Fig. 4. Equivalent resistance and inductance (relative to DC values) versus h_c/δ

In the full paper the time-domain modelling will be detailed [3], and the parallel connection and transposition of the conductors considered.

REFERENCES

- [1] P. Lombard and G. Meunier, "A general purpose method for electric and magnetic combined problems for 2D, axisymmetric and transient systems", *IEEE Trans. on Magn.*, vol. 29, pp. 1737–1740, March 1993.
- [2] J. Gyselinck and P. Dular, "Frequency-domain homogenization of bundles of wires in 2D magnetodynamic FE calculations," *IEEE Trans. on Magn.*, vol. 41, pp. 1416–1419, April 2005.
- [3] J. Gyselinck, R. Sabariego and P. Dular, "Time-domain homogenisation of windings in two-dimensional finite element models", *IEEE Trans. on Magn.*, vol. 43, pp. 1297–1300, 2007.
- [4] M. Islam and A. Arkkio, "Effects of pulse-width-modulated supply voltage on eddy currents in the form-wound stator winding of a cage induction motor," *IET Electr. Power Appl.*, vol. 3, pp. 50–58, 2009.
- [5] O. Moreau, L. Popiel, and J. L. Pages, "Proximity losses computation with a 2D complex permeability modelling," *IEEE Trans. on Magn.*, vol. 34, pp. 3616–3619, September 1998.

Electrokinetic Model Refinement via a Perturbation Finite Element Method – From 2-D to 3-D

Mauricio V. Ferreira da Luz¹, Patrick Dular^{2,3}, Ruth V. Sabariego², P. Kuo-Peng¹ and N. J. Batistela¹

¹ GRUCAD/EEL/CTC, C.P. 476, 88040-900, Florianópolis, SC, Brazil.

² ACE, Dept. of Electrical Engineering and Computer Science, ³ FNRS, University of Liège, Belgium.

E-mail: mauricio@grucad.ufsc.br

Abstract — Counterpoise wires improve the reliability of overhead power transmission lines. This paper presents an electrokinetic model refinement via a perturbation finite element (FE) method to calculate the grounding resistance of counterpoise wires. The perturbation FE method is herein developed for refining the electric field distribution in soil starting from simplified models, based on electric field distribution from 2-D model, that evolve towards 3-D accurate model. The analysis of the distribution of the electric field and of the electric potential around the tower footing allows accurately determining the tower footing resistance. Computational results will be compared with measurements in the extended paper.

I. INTRODUCTION

For evaluating the behaviour of transmission lines in case of lightning strike the accurate modelling of tower footing resistance is crucial. In particular, the decrease of the earth resistance observed for high values of the current flowing from the tower to earth has to be accurately considered [1].

The complete system comprises e.g. four counterpoise wires, as shown in Fig. 1. Continuous counterpoise reduces the resistance of each tower ground and provides a parallel path with the overhead ground wire for the return of fault currents. Fig. 1 closely represents some towers used in Brazil, especially for 138 kV systems [1]. This problem demands a 3-D modelling. However, as the soil dimensions are much bigger than counterpoise wire dimensions, the problem becomes computationally expensive.

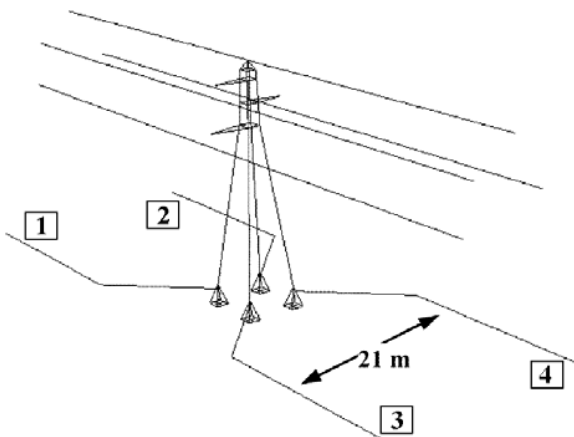


Fig. 1. Transmission tower, aerial cables, tower-footing and four counterpoise wires.

This paper analyses the behaviour of electric field and of electric potential on a counterpoise wire. The purpose of

this analysis is to calculate the grounding resistance of this wire. The electrokinetic model refinement is done via a perturbation finite element (FE) method from 2-D to 3-D.

The perturbation FE method is herein developed for refining the electric field distribution in soil starting from simplified models, based on electric field distribution from 2-D model, that evolve towards a 3-D more accurate model. It is an extension of the method proposed in [2]-[4]. The developments are performed for the electrokinetic scalar potential FE electrokinetic formulation, paying special attention to the suitable discretisation of the constraints involved in each sub-problem.

II. REFERENCE AND MODIFIED PROBLEMS

A. Canonical electrokinetic problem

A electrokinetic problem p is defined in a bounded domain Ω_p , with boundary $\partial\Omega_p = \Gamma_{e,p} \cup \Gamma_{j,p}$, of the two or three-dimensional Euclidean space.

A problem, defined with subscript p , is first considered. Its equations and material relations in Ω_p are:

$$\text{curl } \mathbf{e}_p = 0, \quad \text{div } \mathbf{j}_p = 0, \quad \mathbf{j}_p = \sigma \mathbf{e}_p, \quad (1a-b-c)$$

with boundary conditions (BCs) and interface conditions (ICs).

$$\mathbf{n} \times \mathbf{e}|_{\Gamma_{e,p}} = 0, \quad \mathbf{n} \cdot \mathbf{j}|_{\Gamma_{j,p}} = 0, \quad (1d-e)$$

$$[\mathbf{n} \times \mathbf{e}_p]_{\gamma} = \mathbf{e}_{su,p}, \quad [\mathbf{n} \cdot \mathbf{j}_p]_{\gamma} = \mathbf{j}_{su,p}, \quad (1f-g)$$

where \mathbf{e} is the electric field, \mathbf{j} is the electric current density, σ is the electric conductivity and \mathbf{n} is the unit normal exterior to Ω . The notation $[\cdot] = \cdot|_{\gamma^+} - \cdot|_{\gamma^-}$ refers to the discontinuity of a quantity through any interface γ (of both sides γ^+ and γ^-) (see Fig. 3(a)), which is allowed to be non-zero; the associated surface fields $\mathbf{e}_{su,p}$ and $\mathbf{j}_{su,p}$ are usually unknown, i.e., parts of the solution [4]. It is intended to solve successive problems, the solutions of which being added to get the solution of a complete problem [4]. At the first step, a simplified problem p is solved with the 2-D FE method. Its solution is called reference or source solution. In both cases, it is based on particular assumptions that aim to simplify its solving but that are to be further corrected.

Portions of a 3D structure satisfying a translational or rotational symmetry can be first studied via 2-D models. This consists in neglecting some end effects, zeroing $\mathbf{n} \times \mathbf{e}|_{\Gamma}$ or $\mathbf{n} \cdot \mathbf{j}|_{\Gamma}$. Furthermore, if the field is chosen to be zero out of Ω_p , a discontinuity of one of its faces is then voluntary defined through Γ_p .

With such assumptions, two sub-problems 1 and 2 with adjacent non-overlapping sub-domain Ω_1 and Ω_2 share a connexion interface $\Gamma_{p1} = \Gamma_{p2}$ through which a field discontinuity occurs. The 3-D problem is used to correct the field distribution in a certain neighbourhood Ω_2 on both sides of the interface γ . This is done via ICs

$$[\mathbf{n} \times \mathbf{e}_2]_\gamma = \mathbf{e}_{su,2}, \quad [\mathbf{n} \cdot \mathbf{j}_2]_\gamma = \mathbf{j}_{su,2}, \quad (2a-b)$$

where the so-defined volume source $\mathbf{e}_{su,2}$ is obtained from the reference solution (2D FE method) as

$$\mathbf{e}_{su,2} = [\mathbf{n} \times \mathbf{e}]_\gamma - \mathbf{e}_{su,1}. \quad (3)$$

Given that each solution is calculated on a different mesh, mesh-to-mesh projections of solutions are required [4]. This is a key point of the method for ensuring continuity and will be detailed in the extended paper.

III. APPLICATION

The experimental example considered for validation of the proposed approach is a 10 m length counterpoise wire with 0.1 m of diameter. It is embedded in the soil at a depth of 1.0 m.

Fig. 2 shows the 2-D calculation domain and its mesh. Fig. 3 shows the 3-D calculation domain and its mesh.

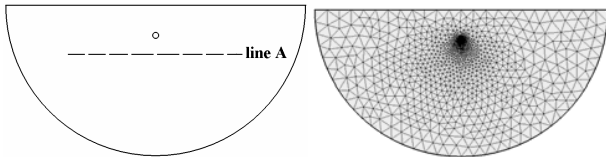


Fig. 2. The 2-D studied domain (left) and its 2-D mesh (right).

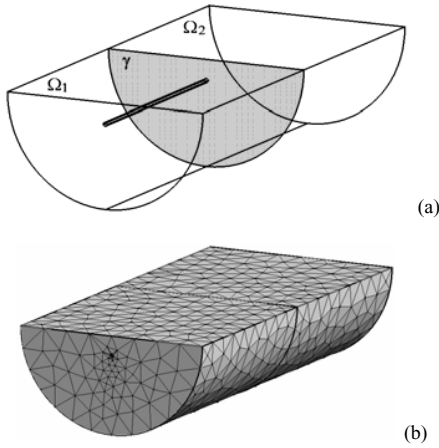


Fig. 3. (a) The 3-D studied domain and (b) The 3-D mesh.

The wire and the soil are first studied (Fig. 2). Its cross section in the XY plane initially defines an initial 2-D model, with the solution shown in Fig. 4. This 2-D solution is considered to be invariant in the Z direction up to a certain distance. Beyond this distance, the electric field is chosen to be zero, which results in a particular IC to be further corrected. This solution then serves as source for a perturbation problem allowing electric leakage flux in 3-D. The 3-D model allows accurately calculating the electric field in the vicinity of the end of the wire (see Fig. 4), with

its own adapted mesh. This way, they gain in accuracy for the benefit of more accurate grounding footing resistance.

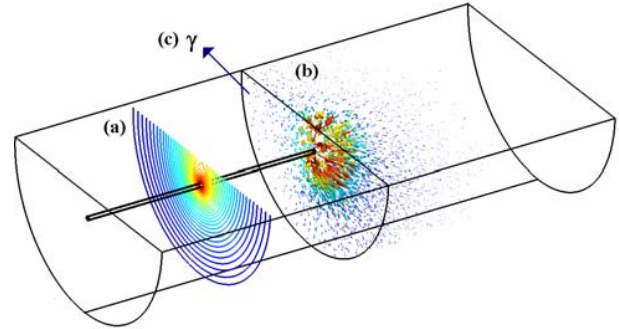


Fig. 4. (a) Electric scalar potential: solution of the 2-D model in XY plane, (b) Electric field: solution of the 3-D model - part of the 3-D correction in the region of the counterpoise wire extremity and (c) Interface γ of the studied domain.

Fig. 5 shows the module of electric field along the line A depicted in Fig. 2(left).

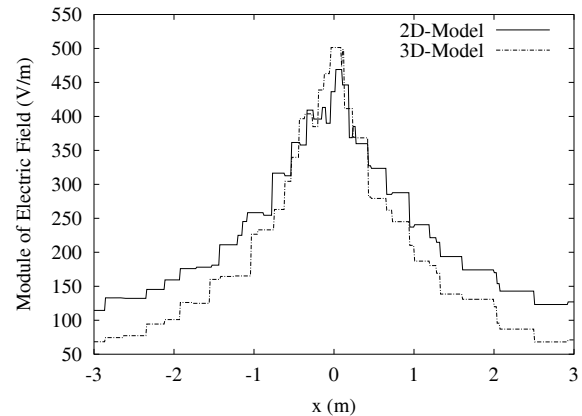


Fig. 5. Module of electric field along the line A (see Fig. 2(left)): solution of the 2-D model (implicitly extended as a constant up to $z = 10$ m) and 3-D solution (in $z = 10$ m) after correction in the vicinity of the surface γ .

The results on the grounding resistance of the counterpoise wire measured and calculated will be compared and presented on the extended paper.

IV. REFERENCES

- [1] A. Soares, M. A. O. Schroeder, S. Visacro, "Transient voltage in transmission lines caused by direct lightning strikes", *IEEE Transactions on Power Delivery*, Vol. 20, No. 2, pp. 1447-1452, 2005.
- [2] P. Dular and R. V. Sabariego, "A perturbation finite element method for modeling moving conductive and magnetic regions without remeshing," *COMPEL International Journal for Computation and Mathematics in Electrical and Electronic Engineering*, vol. 26, no. 3, pp. 700-711, 2007.
- [3] P. Dular and R. V. Sabariego, "A perturbation method for computing field distortions due to conductive regions with h-conform magnetodynamic finite element formulations," *IEEE Transactions on Magnetics*, vol. 43, no. 4, pp. 1293-1296, April 2007.
- [4] P. Dular, R. V. Sabariego, M. V. Ferreira da Luz, P. Kuo-Peng and Laurent Krähenbüh, "Perturbation finite element method for magnetic model refinement of air gaps and leakage fluxes", *IEEE Transactions on Magnetics*, vol. 45, no. 3, pp. 1400-1403, 2009.

Magneto-convection in an Enclosure with Partially Active Vertical Walls

M. Pirmohammadi¹, M. Ghassemi²

¹ Research Management of R & D Deputy, Mapna Group, Tehran, Iran

² Mechanical Engineering Department, K. N. Toosi University of Technology, Tehran, Iran

Pirmohammadi@Mapna.com

Abstract— Effect of longitudinal magnetic field on natural convection heat transfer in an enclosure with partially active vertical walls is numerically investigated. The active part of the left side wall is at a higher temperature than the active part of the right side wall. The top, bottom and the inactive parts of the side walls are thermally insulated. The governing equations are discretized by the control volume method with Hybrid scheme and solved numerically by SIMPLER algorithm for the pressure-velocity coupling together with under relaxation technique. The results are obtained for Rayleigh numbers (Ra) between 10^4 and 10^6 , Hartmann numbers (Ha) between 0 and 100 and Prandtl number 0.71. The heat transfer characteristics are presented in the form of streamlines and isotherms. Results show that the average and local Nusselt number decreases as Hartmann number increases because Lorentz force interacts with the buoyancy force and suppresses the convection flow by reducing the velocities. Also as Rayleigh number increases the temperature gradient and in fact the Nusselt number increases. In addition, it is shown that generally the local Nusselt number decreases along the left side active wall.

I. INTRODUCTION

The Lorentz force acts against the buoyancy force. This phenomenon is used in material manufacturing industry and turbine blade casting as a control mechanism. Employment of an external magnetic field has increasing applications in material manufacturing industry as a control mechanism since the Lorentz force suppresses the convection currents by reducing the velocities. Study and thorough understanding of the momentum and heat transfer in such a process is important for the better control and quality of the manufactured products. The Garandet et al. [1] proposed an analytical solution to the governing equations of magneto hydrodynamics to be used to model the effect of a transverse magnetic field on natural convection in a two-dimensional enclosure. Al-Najem et al. [2] used the power law control volume approach to determine the flow and temperature fields under a transverse magnetic field in a tilted square enclosure with isothermal vertical walls and adiabatic horizontal walls at Prandtl number of 0.71 and showed that the suppression effect of the magnetic field on convection currents and heat transfer is more significant for low inclination angles and high Grashof numbers. Recently, Pirmohammadi et al. [3] studied the effect of a magnetic field on buoyancy-driven convection in differentially heated square enclosure. They showed that the heat transfer mechanisms and the flow characteristics inside the enclosure depend strongly upon both the strength of the magnetic field as well as the Rayleigh number. It was

concluded that the magnetic field considerably decreases the average Nusselt number.

The present study deals with the natural convection in a square enclosure filled with an electrically conductive fluid with partially thermally active vertical walls in the presence of external magnetic field. The hot and cold regions are located at the middle of vertical walls. The results are displayed graphically in the form of streamlines and isotherms, which show the effect of magnetic field on temperature and flow field.

II. BASIC EQUATIONS

The geometry and the coordinate system are schematically shown in Fig. 1.

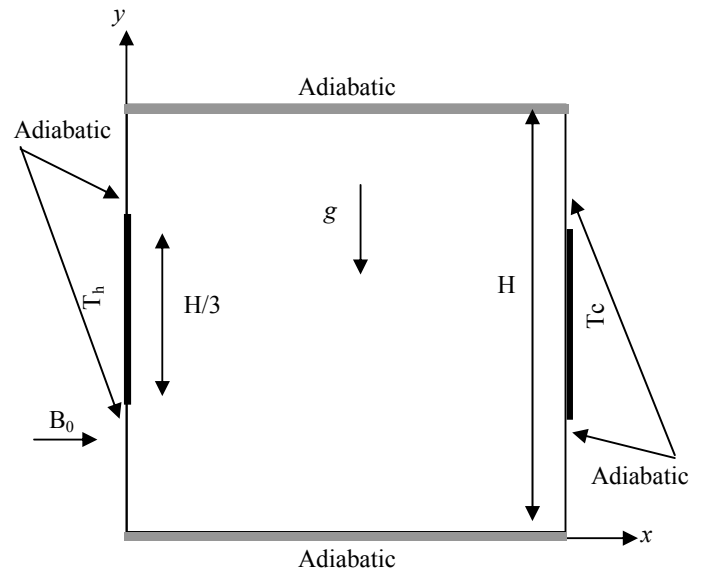


Fig. 1. Geometry of enclosure configuration with magnetic effect.

The non-dimensional governing equations in this study are based on the conservation laws of mass, linear momentum and energy are given as:

$$\frac{\partial U}{\partial X} + \frac{\partial V}{\partial Y} = 0 \quad (1)$$

$$U \frac{\partial U}{\partial X} + V \frac{\partial U}{\partial Y} = -\frac{\partial P}{\partial X} + \text{Pr} \left(\frac{\partial^2 U}{\partial X^2} + \frac{\partial^2 U}{\partial Y^2} \right) \quad (2)$$

$$U \frac{\partial V}{\partial X} + V \frac{\partial V}{\partial Y} = -\frac{\partial P}{\partial Y} + \text{Pr} \left(\frac{\partial^2 V}{\partial X^2} + \frac{\partial^2 V}{\partial Y^2} \right) + Ra \text{Pr} \theta - Ha^2 \text{Pr} V \quad (3)$$

$$U \frac{\partial \theta}{\partial X} + V \frac{\partial \theta}{\partial Y} = \left(\frac{\partial^2 \theta}{\partial X^2} + \frac{\partial^2 \theta}{\partial Y^2} \right) \quad (4)$$

In the above equations, the primary non-dimensional parameters, the Rayleigh number and the Prandtl number, are defined as:

$$\text{Pr} = \frac{\nu}{\alpha}, \quad Ra = \frac{g\beta(T_h - T_c)H^3}{\alpha\nu}, \quad Ha = B_0 H \sqrt{\frac{\sigma}{\rho\nu}} \quad (5)$$

Where, ρ is the density, g is the gravitational acceleration, ν is the cinematic viscosity, β is the coefficient of thermal expansion, and B_0 is the magnitude of magnetic field and σ is the electrical conductivity. Also U , V and θ are non-dimensional velocity components and temperature, respectively.

The local Nusselt number $Nu = -\frac{\partial \theta}{\partial X}$ is computed at the hot wall (Nu). The average Nusselt number is expressed as

$$\bar{Nu} = \frac{3}{H} \int_0^{H/3} Nu_y dY.$$

III. RESULTS

The accuracy of results is verified with that of Rudraiah[4] and is presented in Pirmohammadi et al [3].

Figure 2 depicts the vertical velocity component for various Hartmann number for $Ra=10^5$. It is shown that as magnetic field (Ha) increases, the vertical velocity component decreases so that it approaches zero at about $Ha = 100$.

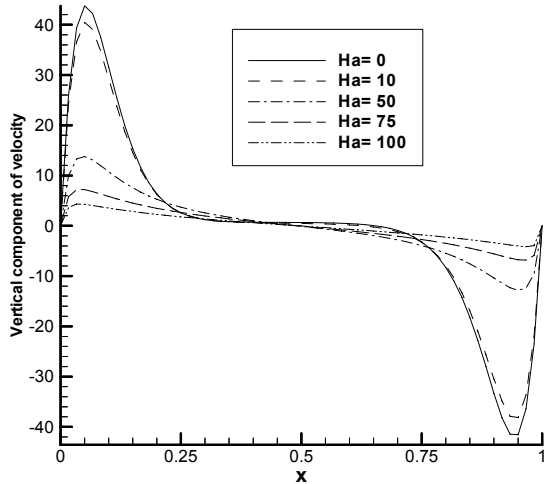
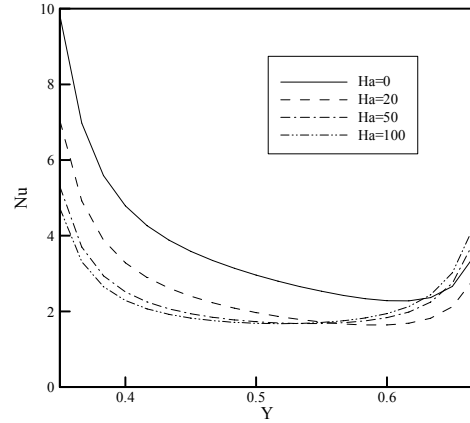
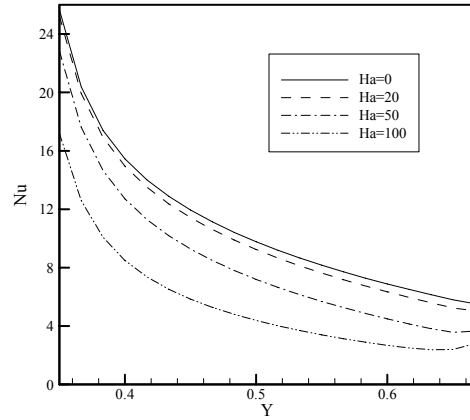


Fig.2 Vertical velocity component for various Ha at $Ra=10^5$

Local Nusselt number (Nu) along the thermally active left side wall for Rayleigh numbers 10^4 and 10^6 and various Hartmann numbers is shown in Fig. 3. As shown the Nu varies directly with Rayleigh number and inversely with Hartmann number. This means that Nu number increases with Rayleigh number and decreases as magnetic field (Ha) increases.



(a) $Ra=10^4$



(b) $Ra=10^6$

Fig.3 Local Nusselt number for various Ha and Ra

Because Lorentz force interacts with the buoyancy force and suppresses the convection flow by reducing the velocities. Also as Rayleigh number increases the temperature gradient and in fact the Nusselt number increases. In addition, it is shown that generally the local Nusselt number decreases along the left side active wall. Also it is shown that for low Rayleigh and high Hartmann numbers the local Nusselt profile along the wall is nearly symmetric and its value decreases.

IV. REFERENCES

- [1] J.P. Garandet, T. Alboussiere, R. Moreau, "Buoyancy driven convection in a rectangular enclosure with a transverse magnetic field", *International Journal of Heat and Mass Transfer*, 35:741-748, 1992.
- [2] N.M. Al-Najem, K.M. Khanafer, and M.M. El-Refaei, "Numerical study of laminar natural convection in tilted enclosure with transverse magnetic field", *International Journal of Numerical Methods in Heat and Fluid Flow*, 8: 651-672, 1998.
- [3] M. Pirmohammadi, M. Ghassemi, and G.A. Sheikhzadeh, "Effect of magnetic field on buoyancy driven convection in differentially heated square cavity", *IEEE Trans. on magnetics*, 45(1):407-411, 2009.
- [4] N. Rudraiah, R.M. Barron, M. Venkatachalappa, and C.K. Subbaraya, "Effect of a magnetic field on free convection in a rectangular enclosure", *International Journal of Engineering. Society*. 33: 1075-1084, 1995.

Comparison between BEM + ACA and classical FEM for 3D low-frequency eddy-current analysis

D. Pusch, J. Smajic and Z. Andjelic

ABB Switzerland Ltd., Corporate Research, CH-5405 Baden 5 Dättwil
e-mail: {david.pusch}{jasmin.smajic}{zoran.andjelic}@ch.abb.com

Abstract—In this paper we are concerned with eddy-current analysis based on fast boundary element methods. A novel compression and preconditioning technique adaptive cross approximation is used to benefit from several advantages when computing problems with highly permeable materials. Several numerical experiments have been performed with the aim to investigate the performance compared to commercial finite element solvers. The results are validated on the TEAM benchmark problem P21.

I. INTRODUCTION

In many industrial applications the electromagnetic physical phenomenon of eddy currents is playing an important role. Following the eddy-current approximation scheme proposed by Mayergoyz [1] we end up with a reduced Maxwell equation system which neglects the displacement currents of the problem. Hence, this leads to Fredholm integral equations of the second kind on the boundary of the investigated domain. Moreover, the applied Galerkin discretization yields a system of matrix equation with four unknowns per node in the space of complex numbers. In fact, we obtain a dense system matrix which is a major bottleneck in using boundary element methods (BEM). In the last decades several methods were developed in order to ensure fast BEM, like the fast multipole technique, hierarchical matrices, panel clustering or wavelet compression, see e.g. [5], [6], [2]. Since in industrial applications we are usually faced with a large number of unknowns, an iterative solution procedure has to be established. In our case we are using a preconditioned generalized minimal residual (GMRES) solver due to the non-symmetry of the system matrix. It turns out, that for bodies with high permeable materials the application of a proper preconditioning is essential.

The paper is organized as follows. In Section II we give a brief explanation of the $\mathbf{H} - \varphi$ formulation. A description of the approximation and preconditioning properties of the adaptive cross approximation method (ACA) for a Galerkin discretization is given in Section III. In the last Sections IV we show numerical results and additional final conclusions.

II. $\mathbf{H} - \varphi$ FORMULATION

Let us consider a simply connected conducting domain Ω with the boundary Γ . Considering the proposed Mayergoyz [1] formulation we have an integral representation for the magnetic field \mathbf{H}^{in} in the inner domain and a potential φ

representation in the unbounded outer air domain

$$\mathbf{H}^{in} = \frac{1}{4\pi} \operatorname{curl}_x \int_{\Gamma} \mathbf{j}^v(\mathbf{y}) K(\mathbf{x}, \mathbf{y}) ds_y \quad \mathbf{x} \in \Omega \quad (1)$$

$$\varphi(\mathbf{x}) = \frac{1}{4\pi} \int_{\Gamma} \sigma^v(\mathbf{y}) G(\mathbf{x}, \mathbf{y}) ds_y \quad \mathbf{x} \in \mathbb{R}^3 \setminus \bar{\Omega}. \quad (2)$$

In equations (1) and (2) we are concerned with the integral kernels $G(\mathbf{x}, \mathbf{y}) = |\mathbf{x} - \mathbf{y}|^{-1}$ and $K(\mathbf{x}, \mathbf{y}) = \exp(-\sqrt{2\pi f \mu \sigma} |\mathbf{x} - \mathbf{y}|) G(\mathbf{x}, \mathbf{y})$. Among the frequency f the integral kernel $K(\mathbf{x}, \mathbf{y})$ includes also the material information, both the conductivity σ and the magnetic permeability μ .

Taking into account the boundary conditions at the interface (continuity of tangential component of \mathbf{H} -field and normal component of \mathbf{B} -field) we finally have to find a solution (\mathbf{j}^v, σ^v) that solves the system of equations:

$$\begin{aligned} \frac{1}{2} \mathbf{j}^v(\mathbf{x}) + \frac{1}{4\pi} \int_{\Gamma} \mathbf{n}(\mathbf{x}) \times [\mathbf{j}(\mathbf{y}) \times \operatorname{grad}_x K(\mathbf{x}, \mathbf{y})] ds_y - \\ \frac{1}{4\pi} \int_{\Gamma} \sigma^v(\mathbf{y}) [\mathbf{n}(\mathbf{x}) \times \operatorname{grad}_x G(\mathbf{x}, \mathbf{y})] ds_y = -\mathbf{n}(\mathbf{x}) \times \mathbf{H}_0(\mathbf{x}) \end{aligned} \quad (3)$$

$$\begin{aligned} \frac{1}{2} \sigma^v(\mathbf{x}) + \frac{\mu}{4\pi \mu_0} \int_{\Gamma} \mathbf{n}(\mathbf{x}) [\mathbf{j}^v(\mathbf{y}) \times \operatorname{grad}_x K(\mathbf{x}, \mathbf{y})] ds_y + \\ \frac{1}{4\pi} \int_{\Gamma} \sigma^v(\mathbf{y}) [\mathbf{n}(\mathbf{x}) \operatorname{grad}_x G(\mathbf{x}, \mathbf{y})] ds_y = -\mathbf{n}(\mathbf{x}) \mathbf{H}_0(\mathbf{x}) \end{aligned} \quad (4)$$

for $\mathbf{x} \in \Gamma$. Note, that \mathbf{H}_0 is a prescribed excitation field and \mathbf{n} the outward unit normal vector.

III. ADAPTIVE CROSS APPROXIMATION

After Galerkin discretization of (3) and (4) we find the following discrete matrix equation system

$$\begin{pmatrix} A_1 & B_1 \\ \frac{\mu}{\mu_0} B_2 & A_2 \end{pmatrix} \begin{pmatrix} \underline{j}_h \\ \underline{\sigma}_h \end{pmatrix} = \begin{pmatrix} \underline{b}_1 \\ \underline{b}_2 \end{pmatrix}. \quad (5)$$

Note, that the system consists of complex submatrices A_1, B_1 and B_2 , which becomes dominant for high permeability. It is well known, the straight forward application of BEM leads to fully populated matrices, which immediately shows the bottleneck of the BEM approach: The demand of memory as well as the evaluation time of a single matrix-times-vector multiplication will behave $\mathcal{O}(N^2)$, where N denotes the number of unknowns in the matrix system (5).

In our calculation we use the adaptive cross approximation technique [2] which provides a hierarchical matrix (\mathcal{H} -matrix).

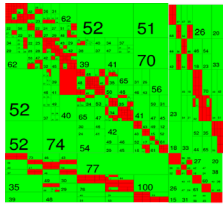


Fig. 1. \mathcal{H} -matrix structure, red: full blocks, green: low-rank blocks

A rigorous mathematical theory for \mathcal{H} -matrices can be found in [6], a typical structure is sketched in Fig. 1. One advantage of ACA is that an explicit knowledge of the kernel is not necessary, but only pure algebraic transformations on the matrix are needed. More precisely, selected matrix entries have to be evaluated, thus, the algorithm can relatively easily be implemented in an existing software code. The idea to obtain a hierarchical matrix $A_{\mathcal{H}}$ is to split the system matrix into far-field and near-field contributions depending on geometrical information of the considered basis functions and test functions

$$A_{\mathcal{H}} = A_h + \sum_{i=1}^{N_B} u_i v_i^{\top}. \quad (6)$$

The near-field blocks accumulate to a sparse matrix A_h , the separated N_B far-field blocks of the matrix are approximated by low-rank expressions $u_i v_i^{\top}$ up to a certain prescribed accuracy ε . We are now able to apply an efficient data-sparse \mathcal{H} -LU decomposition which is used as preconditioner for the ill-conditioned problem (5), see [2], [3]. Another realization of a preconditioner is a Schur-complement preconditioner, for more details and numerical results we refer to [7].

IV. NUMERICAL RESULTS

For numerical validation we calculate the TEAM problem P21^a-0, see Fig. 2. The problem specification and measure-

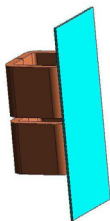


Fig. 2. TEAM benchmark problem P21^a-0

ment results can be found in [4]. The first test case considers non-magnetic steel, for which measurements for the total power losses as well as the B -field in x -direction exist. In order to test the BEM approach also for existing magnetic materials in the model, we replace the non-magnetic steel plate with magnetic steel, $\sigma = 6.66 \cdot 10^6 S/m$ and a relative permeability $\mu_r = 200$. Due to the lack of measurements, we compare our results with a commercial 3D FEM solver for electromagnetics.

For the non-magnetic steel plate we have a measured total power loss of $9.17W$, see [4]. In comparison to our simulation, which gives $9.54W$ on a relatively coarse mesh (3576 boundary elements).

Furthermore, the results for magnetic steel are shown in Fig. 3. It can be observed, that for convergence of the total

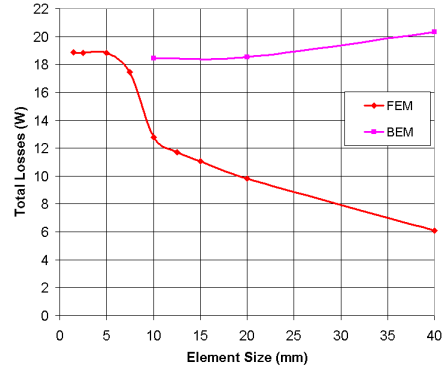


Fig. 3. Total losses, magnetic steel

power losses we need a fine FEM mesh in order to achieve a satisfying accuracy. On the other hand, the BEM approach gives already very good results even for coarser meshes. Note, that the penetration depth here is $\delta = 1.95$ mm. The corresponding memory consumption for the system matrix for both methods are listed in Table I. The second quantities

TABLE I
MEMORY CONSUMPTION

h [mm]	BEM-ACA [MB]	FEM [MB]
40	25 (58)	134
20	378 (782)	180
10	1523 (10680)	701

in the BEM column are the theoretical memory demands, which would be needed for fully populated matrices. It is obvious, that only the usage of compression techniques yields a reasonable BEM approach.

REFERENCES

- [1] I.D.Mayergoyz, 3-D Eddy current problems and the boundary integral equation method, Computational Electromagnetics, North-Holland: Amsterdam, 1996, 163–171
- [2] M. Bebendorf, Hierarchical LU decomposition-based preconditioners for BEM, Computing, No. 74, pp. 1–24, 2003
- [3] J. Smajic, Z. Andjelic and M. Bebendorf, Fast BEM for Eddy-Current Problems Using H-Matrices and Adaptive Cross Approximation, IEEE Trans.Magn., Vol. 43, No. 4, pp. 1269–1272, April 2007.
- [4] Z. Cheng and N. Takahashi et.al., Loss spectrum and electromagnetic behavior of Problem 21 family, COMPUMAG Senyang, 2005. Vol.11, pp. 266–267
- [5] L. Greengard and V. Rokhlin, A Fast Algorithm for Particle Simulations, J. Comp.Phys., 1987, pp. 325–348
- [6] S. Börm, L. Grasedyck and W. Hackbusch, Introduction to hierarchical matrices with applications, Eng. Anal. Bound. Elem. Vol. 27, 2003, pp. 405–422.
- [7] G. Schmidlin, U. Fischer, Z. Andjelic and C. Schwab, Preconditioning of the second-kind boundary integral equations for 3D eddy current problems, Int.J.Numer.Meth.Eng., Vol. 51, No. 9, pp.1009–1031, 2001.

An Energy-Based Error Criterion for Eddy Current Transient Analysis

Loïc Rondot¹, Dimitrios Ladas² and Vincent Mazaauric²

¹CEDRAT, 15 chemin de Malacher, 38246 – Meylan, France, E-mail: loic.rondot@cedrat.com

²Schneider Electric, Innovation Dept., 38TEC, 30050 – Grenoble Cedex 9, France

Abstract — In order to evaluate the accuracy of FEM modeling of transient-induced macroscopic eddy-currents in magnetic devices, a quadratic energy-based error criterion is proposed. It is suitable for 2D and 3D applications, independent of the formulation, and supporting the body motion. A validation is given on a Thomson effect device.

I. INTRODUCTION

Eddy currents are at the origin of losses and signal distortions in power electrical devices. In order to address their considerable impacts on both the energy efficiency and the performance requirement, eddy currents modeling and its accuracy are discussed from a thermodynamic approach. While this approach was successfully used in [1] to derive a quadratic energy-based error criterion suitable for magneto-harmonic cases, an extension to transient regime should be investigated.

While some former attempts, *e.g.* [2][3], are focused on the consistency of the magnetostatic resolution, the proposed error criterion is fully dedicated to the evaluation of the dynamic aspect in massive conductor where the skin effect occurs. It is independent of the formulation, and allows to take body motion into account.

A presentation of the variational approach of electromagnetism is first proposed. Then the error criterion is naturally derived. Finally, some numerical results obtained by Finite Element computation on a Thomson's effect device are presented.

II. VARIATIONAL FORMULATION

Classically, thermodynamic approaches of electromagnetism do not consider any extension towards time-varying regimes [4][5][6]. Whereas some improvements are summarized in [7] for steady states regimes, no general contribution is available for transient. For this purpose, the magnetodynamic behavior of any electrical system is derived from the functional [8]:

$$P_{\text{mech}} - \frac{dG}{dt} = \min_{H,E} \left(\int_C \sigma^{-1} (\text{curl} H)^2 d^3r + \frac{d}{dt} \int (\mathbf{B} \cdot \mathbf{H} + \mathbf{D} \cdot \mathbf{E}) d^3r \right) \quad (1)$$

where the functional in the RHS exhibits:

- the magnetic field \mathbf{H} related to free and displacement currents according to the Maxwell-Ampere equation. The quasi-static approximation enforces $\mathbf{D} = \mathbf{0}$ in conductors;
- the Joule losses P_J monitored in conductors. This term is even to respect invariance of losses with inversion of time inversion (σ^{-1} is the resistivity);

- the variation with time of the electromagnetic energy coupling the field with the generator I and the mass V_0 ;
- the magnetic $\mathbf{B}(\mathbf{h})$ and electrostatic $\mathbf{D}(\mathbf{e})$ behavior laws derived from thermostatic equilibrium of the Gibbs potential

$$G(T, I, V_0) = \int d^3r \left(\int_0^H (-\mathbf{B}) \cdot d\mathbf{h} + \int_0^E (-\mathbf{D}) \cdot d\mathbf{e} \right) \quad (2)$$

Extending the electric field in the conductor according to Ohm's law $\mathbf{E} = \sigma^{-1} \mathbf{J} - \mathbf{V} \times \mathbf{B}$, Faraday's law $\text{rot } \mathbf{E} = \partial_t \mathbf{B}$ may be viewed as acting locally to check globally a tendency towards reversibility [9]. This striking property provides a thermodynamic oriented insight of the variational theory of electromagnetism [10]. Hence, the functional (1) balances the variations with time of the co-energy ($-G$) and the mechanical power supplied to the whole system P_{mech} .

In order to consider sub-systems for design purpose, it is convenient to introduce the electrical power

$$P_{\text{elec}}(\Omega) = - \oint_{\partial\Omega} (\mathbf{E} \times \mathbf{H}) \cdot \mathbf{n} d^2r \quad (3)$$

After some calculations, it follows

$$P_{\text{elec}}(\Omega) = - \int_{\Omega} (\text{curl} \mathbf{E} + \partial_t \mathbf{B}) \cdot \mathbf{H} d^3r + \int_{\Omega} (\text{curl} \mathbf{H} - \mathbf{J} - \partial_t \mathbf{D}) \cdot \mathbf{E} d^3r + \int_{C \subset \Omega} \mathbf{J} \cdot (\mathbf{E} - \sigma^{-1} \mathbf{J} + \mathbf{V} \times \mathbf{B}) d^3r + P_J(\Omega) + \frac{dF}{dt}(\Omega) \quad (4)$$

$$- \sum_i \oint_{\partial\Omega_i} \left([\mathbf{E} \times \mathbf{H}] \cdot \mathbf{n} - \left[\int_0^B \mathbf{H} \cdot d\mathbf{b} + \int_0^D \mathbf{E} \cdot d\mathbf{d} \right] (\mathbf{V}_i \cdot \mathbf{n}) \right) d^2r + \int_{C \subset \Omega} \mathbf{V} \cdot (\mathbf{J} \times \mathbf{B}) d^3r$$

where F is the Helmholtz's potential and $[\cdot]$ denotes the discontinuity occurring at the interfaces $\partial\Omega_i \subset \Omega$.

At the minimum of the functional (1), the Maxwell equation set and Ohm's law are checked so that:

- the first three residual terms vanish in (4). After some tedious calculations on the motion induced-conductor interface discontinuities, the two last terms provide the mechanical power
- $$-P_{\text{mech}}(\Omega) = \sum_i \oint_{\partial\Omega_i} (\mathbf{n} \cdot \mathbf{V}) [\mathbf{D} \times \mathbf{B}] \cdot \mathbf{V}_i d^2r + \sum_i \int_{C_i} (\mathbf{J} \times \mathbf{B}) \cdot \mathbf{V}_i d^3r + \sum_i \oint_{\partial\Omega_i} \left([(\mathbf{B} \cdot \mathbf{n})\mathbf{H} + (\mathbf{D} \cdot \mathbf{n})\mathbf{E}] - \left[\int_0^H \mathbf{B} \cdot d\mathbf{h} + \int_0^E \mathbf{D} \cdot d\mathbf{e} \right] \cdot \mathbf{n} \right) \cdot \mathbf{V}_i d^2r \quad (5)$$

where the first term denotes a vanishing "impulsion" term within the quasi-static approximation; the second one is related to the power of the Laplace's force; and

the third one gathers the switching reluctance effects occurring at the various interfaces of the domain Ω . For conductors with linear magnetic behavior law, these three contributions may be lumped in the Maxwell's stress tensor. As a result, the relation (4) matches the integral form of the Poynting's conservation equation. Hence,

- the contribution of Ω to (1) reads

$$P_{\text{mech}}(\Omega) + P_{\text{elec}}(\Omega) - \frac{dG}{dt}(\Omega) \quad (6)$$

The Finite Element Method consists in building an approximation of (1),(2) but with a finite number of degrees of freedom chosen on a mesh. In the following, an evaluation of the local power conservation (4) is assessed to introduce the accuracy of any numerical solution.

III. NUMERICAL RESULTS

Whereas the stationary conditions expressed on (1),(2) provide an approximation of the fields, the consistency of the solution with energy conservation may be assessed through the local deviation of the Poynting's equation

$$\varepsilon(\Omega) = P_{\text{elec}}(\Omega) - P_j(\Omega) - \frac{dF}{dt}(\Omega) + P_{\text{mech}}(\Omega) \quad (7)$$

Strictly enforcing two relations among Maxwell-Ampere or Maxwell-Faraday equations and Ohm's law, the error criterion (7) highlights the elements where the third one is ill-checked.

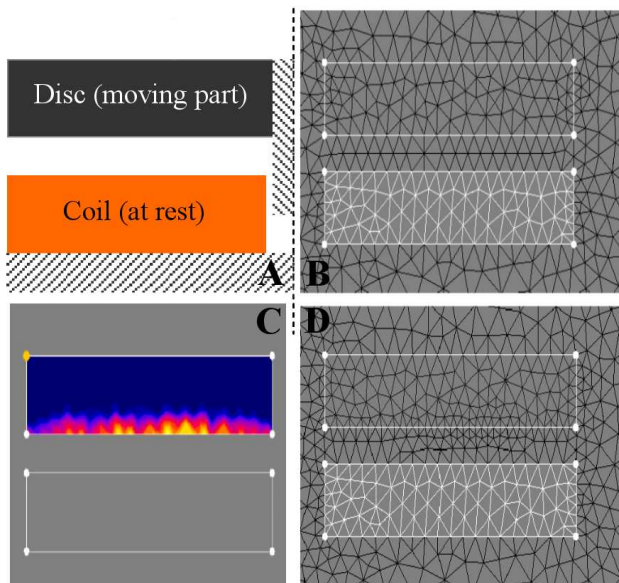


Fig. 1. Thomson effect actuator excited by a voltage source: Left: (a) axisymmetric cross-section, (b) initial mesh at the second time step, (c) error criteria assessed from (7) in the moving part: notice its confinement in the skin depth, (d) mesh enhancement at the second time step: notice the refinement in the skin depth and the related decline of (6) in table 1.

An iterative "bubble" remeshing technique [11] is coupled with the criterion (7) and applied to a Thomson's effect device (Fig.7). While the mesh is improved *locally*, the convergence of the *global* quantities is observed.

TABLE I. Convergence of the functional (1),(2) under mesh refinement. Notice the reduction of the G by Γ^2 to take meshing-induced current variation into account.

Δt (s)	Number of time step 2	Number of time step 3 (before remeshing)	Number of time step 3 (after remeshing)
U (V)	$3.1 \cdot 10^{-1}$	$5.9 \cdot 10^{-1}$	$5.9 \cdot 10^{-1}$
I (A)	$7.3 \cdot 10^{-4}$	$2.1 \cdot 10^{-3}$	$1.4 \cdot 10^{-3}$
G (J)	$-1.61 \cdot 10^{-9}$	$-1.34 \cdot 10^{-8}$	$-5.89 \cdot 10^{-9}$
G/P ($J.A^{-2}$)	$-3.05 \cdot 10^{-3}$	$-3.06 \cdot 10^{-3}$	$-3.09 \cdot 10^{-3}$
$P_{\text{mech}} - dG/dt + P_{\text{elec}}$	-	$2.5 \cdot 10^{-2}$	$9.4 \cdot 10^{-3}$

IV. CONCLUSION

The energy-based error criterion allows to refine the conducting regions where the mesh is not enough refined, with respect to the skin effect occurring therein. In addition to the error criterion, the thermodynamic approach provides the functionals from which the global convergence should be evaluated.

Hence an adaptive meshing strategy compliant with energy efficiency and performance requirements can be addressed.

V. REFERENCES

- [1] D. Ladas, V. Mazauric, G. Meunier, O. Chadebec, M. Ebene-Ebene, Y. Maréchal, and P. Wendling, "An energy based approach of electromagnetism applied to adaptative meshing and error criteria," *IEEE Transactions on Magnetics*, vol. 44, pp. 1246-1249, 2008.
- [2] C. Li, Z. Ren and A. Razek, "An Approach to Adaptive Mesh Refinement for Three-dimensional Eddy-Current Computations" *IEEE Transactions on Magnetics*, vol 30, number 1, January 1994, pp. 3482-3485.
- [3] S. Dufour, G. Vinsard, and B. Laporte, "Mesh Improvement in 2-D Eddy-Current Problems", *IEEE Transactions on Magnetics*, vol. 38, pp. 377-380, 2002.
- [4] S. Bobbio, "The use of energy and co-energy for the evaluation of forces in non-linear, anisotropic dielectric solids," *The European Physical Journal B*, vol. 16, pp. 43-48, 2000.
- [5] F. Delfino, R. Procopio, and M. Rossi, "Evaluation of forces in magnetic materials by means of energy and co-energy methods," *The European Physical Journal B*, vol. 25, pp. 31-38, 2002.
- [6] L. D. Landau and E. M. Lifschitz, *Electrodynamics of continuous media*. New York, NY, USA: Pergamon, 1960.
- [7] T. Christen, "Application of the maximum entropy production principle to electrical system," *Journal of Physics D: Applied Physics*, vol. 39, pp. 4497-4503, 2006.
- [8] V. Mazauric, "From thermostatics to Maxwell's equations: A variational approach of electromagnetism," *IEEE Transactions on Magnetics*, vol. 40, pp. 945-948, 2004.
- [9] V. Mazauric and N. Maïzi, "A global approach of electromagnetism dedicated to further long-term planning," *Proceedings in Applied Mathematics and Mechanics*, vol. 7, pp. 2130003-2130004, 2007.
- [10] P. Hammond, *Energy methods in electromagnetism*. New York, USA: Oxford University Press, 1981.
- [11] K. Shimada and D.C. Gossard "Automatic triangular mesh generation of trimmed parametric surfaces for finite element analysis", *Computer Aided Geometric Design*, vol. 15, pp. 199-222, 1998.

Magneto-mechanical effects under low fields and high stresses - Application to a ferromagnetic cylinder under pressure

A.Viana, L-L. Rouve, G. Cauffet, J-L. Coulomb

Grenoble Electrical Engineering Lab (CNRS UMR5269), Université de Grenoble, ENSE³, BP 46

38402 Saint Martin d'Hères, France

Antoine.viana@g2elab.grenoble-inp.fr

Abstract: This study focuses on the effects that a ferromagnetic material undergoes when subjected to high stresses under low magnetic fields. In order to predict the magnetic signature, we show that the Jiles law of approach can be used and applied to the induction measured by external sensors, and an analytical solution is derived in the case of our prototype, a ferromagnetic cylinder subjected to an internal pressure up to 100 Bars. Measurements were led at the LMMCF (Laboratory of Magnetic Metrology in Weak Fields – Grenoble France). Comparison between model predictions and measurements shows an error lower than 1%.

I. INTRODUCTION

Magnetic signatures expose all ferromagnetic vessels to risk from mines. Given the risk to seamen, the military handicap borne when a defense vessel is hit, and the economical costs, magnetic signature reduction for warships is essential. Determing methods and degaussing systems are used, but may be inefficient for vessels undergoing a high level of stresses, such as submarines: because of magnetostriction, pressure drastically changes the magnetization.

In order to investigate such effects, a simplified mockup has been built and subjected to internal pressures in a 0-100 Bars range. Magnetic signature has been measured and analyzed under various conditions.

Our aim is to model the magnetic signature variation due to pressure to describe magnetization changes due to strain. Several models can be found in literature. Nevertheless, the magnetostriction model developed by Jiles [1] seems particularly well suited to our approach in terms of level of stress (high) and of applied field (low field, around 50μT). This model clearly states that under strains, magnetization tends towards the anhysteretic magnetization.

In this paper, we propose to apply this model to a complex geometry: a hollow cylinder is used instead of usual rods. In order to achieve this, we extend the original Jiles equation, describing the evolution of magnetization \mathbf{M} inside a ferromagnetic material undergoing stresses. We demonstrate that this law is applicable to the magnetic induction \mathbf{B} measured by magnetic sensors outside the ferromagnetic body. An analytical solution is then found for the cases where the inductor magnetic field is vertical. Measurements show a good correlation with the expected results (error < 1%).

II. THE JILES LAW OF APPROACH

Jiles [1] postulated a law describing the behavior of magnetization \mathbf{M} for a ferromagnetic material undergoing stresses. This law can be expressed as:

$$\frac{\partial \mathbf{M}}{\partial \sigma} |_{\mathbf{H}_0} = \frac{\sigma}{\xi E} (\mathbf{M}_{\text{anh}} - \mathbf{M}) + c \frac{\partial \mathbf{M}_{\text{anh}}}{\partial \sigma} |_{\mathbf{H}_0} \quad (1)$$

where σ denotes the stress, ξ is a coefficient with dimension of energy per unit volume, E the Young modulus, c a unitary coefficient, describing the flexibility of the domain walls, \mathbf{H}_0 is the external applied magnetic field, and \mathbf{M}_{anh} the anhysteretic magnetization, function of stress. This equation requires:

- The knowledge of coefficients c , ξ (E is usually known)
 - The law of evolution of the anhysteretic magnetization with stress $\mathbf{M}_{\text{anh}}(\sigma)$ under the constant applied field \mathbf{H}_0 .
- This law is given in terms of magnetization \mathbf{M} , and thus can be depicted as an intrinsic law. Using results derived in [2] for thin ferromagnetic shells, we show that (1) can be formulated as

$$\frac{\partial \mathbf{B}}{\partial \sigma} |_{\mathbf{B}_0} = \frac{\sigma}{\xi E} (\mathbf{B}_{\text{anh}} - \mathbf{B}) + c \frac{\partial \mathbf{B}_{\text{anh}}}{\partial \sigma} |_{\mathbf{B}_0} \quad (2)$$

where \mathbf{B} is the external measured induction. Equation (2) is the expression of the Jiles law, expressed in terms of measured external induction, rather than in magnetization.

III. EXPERIMENTAL PROTOCOL

Measurements were conducted at the LMMCF (Laboratory of Magnetic Metrology in Weak Fields) is located in Grenoble, France [3]. The used prototype is a ferromagnetic hollow cylinder. The cylinder, filled with hydraulic oil, is subjected to an internal pressure up to 100 Bars, driven by an external pump. Applied field is generated by a system of triaxial coils, in the range of $\pm 80\mu\text{T}$, over a volume of $27 \times 2 \times 2 \text{ m}^3$. Magnetization variations due to stress are measured on external magnetic sensors, located under the cylinder.

Two series of measurements were conducted. The first one was dedicated to the determination of the anhysteretic curves under a constant stress. Anhysteretic curves were plotted for vertical applied inductions \mathbf{B} , ranging from 20 to 80 μT , with increasing steps of 20 μT , and for internal pressures ranging from 0 to 100 Bars, with increasing steps of 20 Bars. Results

7. Material Modelling

show that the anhysteretic inductions for vertical applied fields do not depend upon pressure.

The second series of measurements consisted in recording the evolution of the external induction \mathbf{B}_{mes} on the sensors while the cylinder was subjected to a stress cycle $0 \rightarrow P_{max} \rightarrow 0$ MPa under a given applied vertical inductor \mathbf{B}_0 . Then, the internal pressure was increased to its maximum value, and then set back to zero. The whole cycle was recorded, allowing plotting of \mathbf{B} vs. P curves.

IV. ANALYTICAL SOLUTION TO THE JILES-ATHERTON LAW OF APPROACH FOR A VERTICAL APPLIED FIELD

Given that for a vertical inductor field, measurements showed that $\mathbf{B}_{anh}(\sigma, \mathbf{B}_0) = \mathbf{B}_{anh}(\mathbf{B}_0)$, (2) can be simplified and an analytical solution to this equation is:

$$\mathbf{B}(\sigma, \mathbf{B}_0) = \mathbf{B}_{anh}(\mathbf{B}_0) + [\mathbf{B}_{m0} - \mathbf{B}_{anh}(\mathbf{B}_0)]e^{-\sigma^2/2E\xi} \quad (3)$$

where \mathbf{B}_{m0} is the initial measured induction under zero stress in T, $\mathbf{B}_{anh}(\mathbf{B}_0)$ the anhysteretic value obtained from anhysteretic induction measurements. The only parameter to determine in order to fully explicit the analytical solution is ξ . The value ξ is approached to fit a first HPP cycle with a least-square algorithm. Subsequent measured HPP cycles are then compared to the analytical solution.

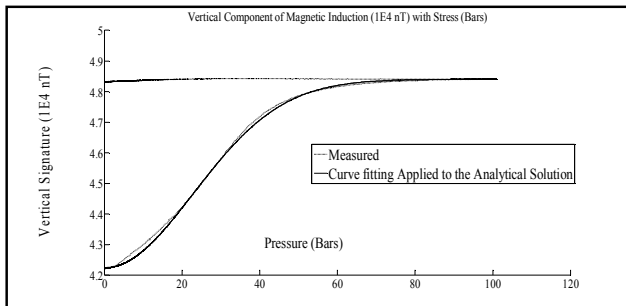


Fig. 1. Identification of parameter ξ required for analytical solution: a fitting method based on least square algorithm is used on vertical component variation of induction due to stress, on centered sensor B1.

For fitting, initial magnetization corresponds to the following state: the anhysteretic magnetization (at zero stress) under a vertical inductor field $\mathbf{B}_1 = -41 \mu\text{T}$ is achieved. Then, the applied field was then set to $+40 \mu\text{T}$. The initial measured value of the vertical component of induction on a centered magnetic sensor B1 was $\mathbf{B}_{m0} = 42300 \text{ nT}$. The stress was then raised to 100 Bars.

A least-square algorithm applied to the curve describing the induction variation when stress increases from 0 to 100 Bars provides the value $\xi = 2.55 \cdot 10^{-9}$ (for P expressed in Bars, and $E = 2.05 \cdot 10^{11} \text{ Pa}$). Figure 1 shows the measurements, and the fitted curve obtained by using the identified value ξ with the analytical solution.

To test our analytical solution, and the identification of the parameter ξ , 3 other cycles were measured under different vertical inductor fields. Figure 2 shows comparison between the analytical predicted induction and the measured induction

variation during one of these cycles. The maximum error is lower than 0.34%.

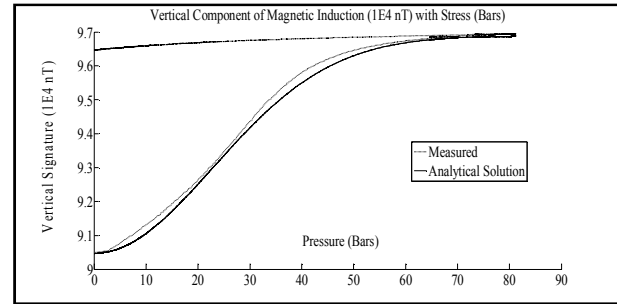


Fig. 2. Comparison between the analytical solution and the measurements for a vertical inductor field $\mathbf{B}_v = 80 \mu\text{T}$ and a given initial magnetic state.

V. CONCLUSION

In this paper, we demonstrated that the law of approach of Jiles could be applicable to model the measured external induction created by a magnetic source. For our application, a more complex geometry was used that the one usually found in literature. A hollow cylinder was tested instead of typical rods. The main difference is that with our geometry, shape factor is not negligible, especially when the inductor field is applied vertically.

Measurements established that, for vertical inductor fields, the anhysteretic curves were not a function of stress, the unfavourable shape effect acting like a mitigating factor for the effects of pressure. This result leads to a great simplification of the Jiles equation, and an analytical solution could be derived. In order to fully explicit this solution, the knowledge of a physical parameter was required, and a fitting method based on a first series of measurements led to determination of this constant.

Comparison between the analytical solution and others series of measurements showed the results were excellent, and the error between the predicted induction and the measured one was lower than 1%.

The inverse problem, i.e. the determination of magnetization in the cylinder by knowledge of the magnetic induction measured on the sensors is under work. It will allow the determination of the intrinsic law of magnetization of the material as a function, not only of the inductor field, but also of the stresses the material is undergoing.

VI. REFERENCES

- [1] D.C Jiles, "Theory of the Magnetomechanical Effect", *J. Phys. D: Appl. Phys.*, 28(1995), pp. 1537-1546.
- [2] Olivier Chadebec, Jean-Louis Coulomb and Fleur Janet "A review of Magnetostatic Moment Method", *IEEE Transaction on Magnetics* 42, NO. 4, April 2006
- [3] J-P Bongiraud, G.Cauffet, C. Jeandey, Ph. Le Thiec, "An optimization Method for Magnetic Field Generator", *Marelec 1999, Conference Proceedings*, 161-168

Large-Scale Analysis of Magnetic Beads Behavior in Magnetic Field with Fast Multipole Method

Takuya Tatsuishi¹, Yasuhito Takahashi², Masahiko Miwa¹, and Shinji Wakao¹

¹Waseda University, 3-4-1 Ohkubo Shinjuku-ku, Tokyo 169-8555, Japan

²Kyoto University, Yoshida-Honmachi, Sakyo-ku, Kyoto 606-8501, Japan
e-mail: wakao@waseda.jp

Abstract — This paper describes the large-scale analysis of magnetic beads' behavior in magnetic fields by developing a novel method combining the discrete element method (DEM) and the magnetic interaction calculation with the fast multipole method (FMM). Some numerical examples of large-scale magnetic-bead chain analysis are reported for confirming the effectiveness of the proposed method.

I. INTRODUCTION

The huge numbers of magnetic beads are utilized in the printing process of laser printers, in which the beads form chains and play a brush role in toner transfer. Due to the difficulties of actual measurement, when comprehending the magnetic beads' behavior in forming chains in magnetic field, it is indispensable to carry out the numerical analysis, i.e., a coupled magnetic and contact force analysis. However, the required computational cost to deal with the beads is of $O(N^2)$, where N is the number of beads. Therefore, it is also difficult to apply the numerical analysis to the large-scale problems of magnetic beads.

With the above background, in this paper, we develop a novel method combining the discrete element method (DEM) and the magnetic interaction calculation with the fast multipole method (FMM) [1]. Some numerical results, which demonstrate the effectiveness of the proposed method from the viewpoint of CPU-time, are presented. Finally, the large-scale magnetic-bead chain analysis is also carried out as a practical example.

II. METHOD OF ANALYSIS

A. Magnetic Force Analysis by Using FMM

The magnetic flux density \mathbf{B} generated by magnetic moment \mathbf{m}_j at the center of particle i is given by

$$\mathbf{B}_{ij} = \frac{\mu_0}{4\pi} \left(\frac{3(\mathbf{m}_j \cdot (\mathbf{r}_i - \mathbf{r}_j))(\mathbf{r}_i - \mathbf{r}_j)}{|\mathbf{r}_i - \mathbf{r}_j|^5} - \frac{\mathbf{m}_j}{|\mathbf{r}_i - \mathbf{r}_j|^3} \right), \quad (1)$$

where r_i and r_j are the positions of center of particle i and j , respectively, and μ_0 is the permeability of vacuum. The magnetic moment \mathbf{m}_i at the center of a magnetic particle i in homogeneous magnetic field \mathbf{B} is evaluated as follows:

$$\mathbf{m}_i = \frac{4\pi}{\mu_0} R^3 \frac{\mu_r - 1}{\mu_r + 2} \mathbf{B}, \quad (2)$$

where R is the radius of the particle and μ_r indicates the relative permeability. The magnetic moments corresponding

to each magnetic particle are obtained by updating \mathbf{m}_i with (1) and (2) until they converge to its steady state.

The magnetic particle with magnetic moment \mathbf{m} in the homogeneous field \mathbf{B} is subject to magnetic force expressed as

$$\mathbf{F} = (\mathbf{m} \cdot \nabla) \mathbf{B}. \quad (3)$$

On the other hand, \mathbf{B} can be written by using the local expansion as follows:

$$\mathbf{B} = -\frac{\mu_0}{4\pi} \sum_{n=0}^{\infty} \sum_{m=-n}^n L_n^m \nabla (Y_n^m(\theta, \phi) r^n), \quad (4)$$

where L_n^m is the local expansion coefficient, Y_n^m is the spherical harmonic function of degree n and order m , and (r, θ, ϕ) is its spherical coordinates. The second-order derivative of $Y_n^m(\theta, \phi) r^n$ is necessary for the calculation of magnetic force between magnetic beads by (3).

In order to calculate the second-order derivative of $Y_n^m(\theta, \phi) r^n$ at high speed while maintaining the accuracy in the FMM process, we propose the novel formulae derived from the local-to-local (L2L) translation in the same cell [2] as follows:

$$\begin{cases} \partial B_x / \partial x = -\mu_0 (L_2^0 - \sqrt{6} L_2^2 \cdot re) / 4\pi \\ \partial B_x / \partial y = \partial B_y / \partial x = -\mu_0 \sqrt{6} L_2^2 \cdot im / 4\pi \\ \partial B_x / \partial z = \partial B_z / \partial x = \mu_0 \sqrt{6} L_2^1 \cdot re / 4\pi \\ \partial B_y / \partial y = -\mu_0 (L_2^0 + \sqrt{6} L_2^2 \cdot re) / 4\pi \\ \partial B_y / \partial z = \partial B_z / \partial y = -\mu_0 \sqrt{6} L_2^1 \cdot im / 4\pi \\ \partial B_z / \partial z = \mu_0 L_2^0 / 2\pi \end{cases}. \quad (5)$$

These formulae have advantages that these equations are quite simple and it is not necessary to consider the singularity of Y_n^m .

B. Contact Force Analysis by Using DEM

In the DEM, all the particles are regarded as elastic body to take into account the deformation of the particles due to the collision. The equations of motion are set up by assuming the dashpots, frictions, and springs at the points of contact. The DEM is suitable for the case that a large number of particles are tightly-packed because it can treat the contact force from several particles at one time. The contact model of the particles in the DEM is shown in Fig. 1 and the corresponding equations of motion are given by

$$\begin{cases} f_n = -K_n \delta_n^{\frac{3}{2}} - \eta_n \dot{\delta}_n \\ f_s = -K_s \delta_s - \eta_s \dot{\delta}_s - \mu f_n \end{cases}. \quad (6)$$

Here, f is the force, δ is the displacement, μ is the friction coefficient, and the subscript means the normal and tangential components, respectively. K and η are the spring constant and the dashpot, which are derived from the Hertz's elastic theory of contact.

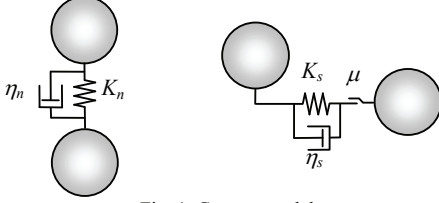


Fig. 1. Contact model.

C. Procedure of Particle Behavior Analysis Taking Account of Magnetic Force

The flowchart of the analysis of magnetic beads' behavior in magnetic field is shown in Fig. 2. In Fig. 2, Δt_{con} and Δt_{mag} indicate the time interval for contact force analysis and magnetic force analysis, respectively. The magnetostatic interactions are recalculated when the magnetic field around the magnetic particles varies to some extent because of their displacement.

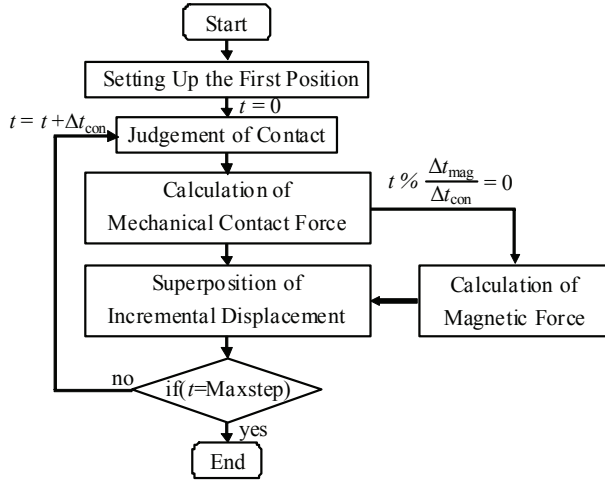


Fig. 2. Flowchart of behavior analysis of magnetic beads taking into account magnetic and contact force.

III. NUMERICAL RESULTS

Here, we investigate the model of 6125 magnetic beads with radius of 100 μm in the gradient magnetic field which is applied at $t = 0$ as a step function. The beads are enclosed in the rectangular solid space consisting of the wall with Young's modulus and Poisson's ratio of 100 GPa and 0.3, respectively. The volume density, relative permeability and Young's modulus of beads are 4900 kg/m^3 , 10.0, and 10 GPa, respectively. As for the time intervals, $\Delta t_{\text{con}} = 1.0 \times 10^{-7}$ s and $\Delta t_{\text{mag}} = 1.0 \times 10^{-5}$ s.

In this paper, we utilized the FMM based on diagonal forms for translation operators [1]. The orders of multipole and local expansions are 15 and 16, respectively. The

maximum order of exponential expansion for diagonal translation in the multipole-to-local conversion is 26.

The computational result at $t = 150$ ms is shown in Fig. 3 [3]. The figure indicates the beads' behavior reaches a steady state and the magnetic-bead chains are successfully simulated, which demonstrates the validity of the proposed method.

The comparison of CPU-time between the direct calculation and the proposed method with FMM is shown in Table I. All the computations were performed on a workstation with Xeon5365, 3.0 GHz, and 12 GB of RAM. The CPU-time in the table corresponds to the computational cost spent on magnetic force calculation for beads in a single step. The numerical value in a parenthesis stands for the CPU-time ratio of the direct calculation to the proposed method. In the case of more than about 5800 beads, the CPU-time reduction is achieved by using the proposed method, which concludes its effectiveness from the viewpoint of large-scale analysis of the magnetic beads' behavior.

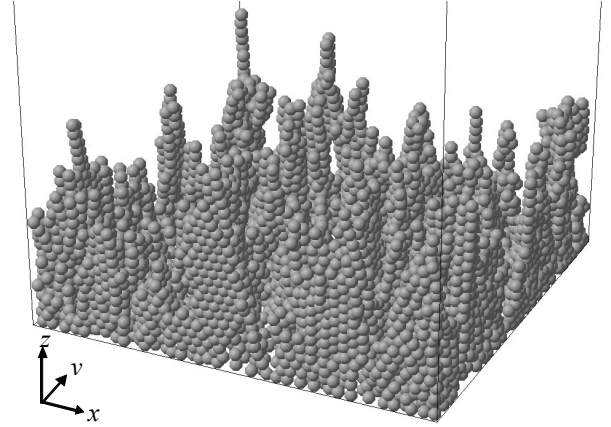


Fig. 3 Chains of magnetic beads.

TABLE I
ELAPED TIME FOR BEHAVIOR ANALYSIS

Number of Particles	Direct Calculation (s)	FMM (s)
1331	0.09 (0.14)	0.66
4096	0.87 (0.60)	1.45
4913	1.25 (0.81)	1.54
5832	1.77 (1.09)	1.62
9261	4.47 (1.25)	3.57
29791	56.98 (4.36)	13.07
68921	423.79 (11.85)	35.77

IV. REFERENCES

- [1] H. Cheng, L. Greengard, and V. Rokhlin, "A Fast Adaptive Multipole Algorithm in Three Dimensions," J. Comput. Phys., Vol. 155, pp. 468-498 1999.
- [2] S. Hamada, O. Yamamoto, and T. Kobayashi, "Analysis of electric field induced by ELF magnetic field utilizing generalized equivalent multipole-moment method," IEEE Trans. on Fundamentals and Materials, Vol. 125, No. 6, pp. 533-543, 2005.
- [3] <http://www.photon.t.u-tokyo.ac.jp/~maruyama/pvwin/pvwin.html>.

Dynamic Analysis Method of Linear Resonant Actuator with Multi-Movers Employing 3-D Finite Element Method

Yasuyoshi Asai¹, Katsuhiro Hirata¹, and Tomohiro Ota²

¹Department of Adaptive Machine Systems, Osaka University, Osaka 565-0871, Japan

E-mail: k-hirata@ams.eng.osaka-u.ac.jp

²Panasonic Electric Works, Ltd., Osaka 571-8686, Japan

E-mail: t_oota@panasonic-denko.co.jp

Abstract — This paper proposes the dynamic analysis method of a linear resonance actuator with multi-movers under PWM (Pulse Width Modulation) feedback control employing the 3-D finite element method (FEM). The effectiveness of this method is shown by the comparison with the experimental results. Furthermore, the effect of a link-spring on each mover motion is clarified.

I. INTRODUCTION

Recently, linear resonant actuators (LRA) have been used in a wide range of applications because they have a lot of advantages; high efficiency, simple structure, easy control, and so on, however, they have a problem that the amplitude severely decreases in response to an external load. To control this, a feedback control is adopted where the back EMF of the coil is detected to control the current duty [1].

In this paper, we propose the numerical analysis method for predicting dynamic characteristics of LRA with two movers under PWM feedback control [2] employing the 3-D FEM. The effectiveness of the method is confirmed through the comparison with the measurement. And, the effect of a link-spring on each mover motion is clarified when a single mover is operated with load.

II. ANALYSIS METHOD

A. Magnetic Field Analysis

The equations of the magnetic field and the electric circuit are coupled using the 3-D FEM, which are given by the magnetic vector potential \mathbf{A} and the exciting current I_0 as follows:

$$\text{rot}(\nu \text{rot } \mathbf{A}) = \mathbf{J}_0 + \nu_0 \text{rot } \mathbf{M} \quad (1)$$

$$E = V_0 - RI_0 - \frac{d\Psi}{dt} = 0 \quad (2)$$

$$\mathbf{J}_0 = \frac{n_c}{S_c} I_0 \mathbf{n}_s \quad (3)$$

Where ν is the relativity, \mathbf{J}_0 is the exciting current density, ν_0 is the relativity of the vacuum, \mathbf{M} is the magnetization of permanent magnet, V_0 is the applied voltage, R is the resistance, Ψ is the interlinkage flux of exciting coil, n_c and S_c are the number of turns and the cross-sectional area of the coil respectively, \mathbf{n}_s is the unit vector along with the direction of exciting current.

B. Coupled Analysis with Motion Equation

This actuator is composed of two movers linked together, and the motion equations are given as follows:

$$M_1 \frac{d^2 z_1}{dt^2} + C_1 \frac{dz_1}{dt} + F_{k_1} = F_{z_1} \quad (4)$$

$$M_2 \frac{d^2 z_2}{dt^2} + C_2 \frac{dz_2}{dt} + F_{k_2} = F_{z_2} \quad (5)$$

Where M_1 and M_2 is the mass of movers, z_1 and z_2 are the displacement of movers, F_{z_1} and F_{z_2} are thrust, F_{k_1} and F_{k_2} are spring force, and C_1 and C_2 is the viscous damping coefficient.

Two movers are linked by link-springs described later, and the spring forces are given as follows:

$$F_{k_1} = k_m z_1 + k_l(z_1 - z_2) \quad (6)$$

$$F_{k_2} = k_m z_2 + k_l(z_2 - z_1) \quad (7)$$

Where k_m is main spring constant, k_l is link-spring constant.

The thrust of each mover is calculated using the Maxwell stress tensor method, and is substituted for the equations (4) and (5). The position of each mover is calculated by the time step. PWM feedback control is taken into consideration in this analysis. Fig. 1 shows the flowchart for this coupled analysis.

III. BASIC STRUCTURE AND OPERATING PRINCIPLE

The basic structure of the LRA in this study is shown in Fig. 2. This actuator mainly consists of two movers, a common

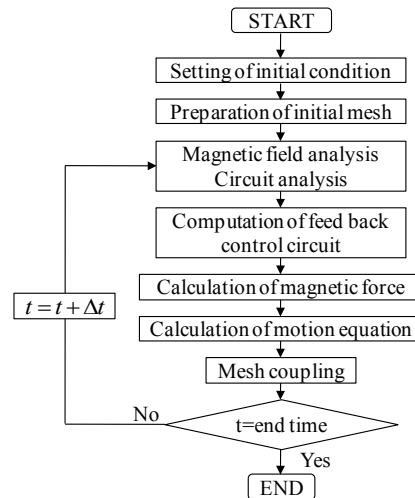


Fig. 1 Flowchart for analysis

stator and resonance springs that support the air-gap (0.36mm). Two parallelly arranged movers are composed of two opposite pole magnets fixed on the back yoke. The common stator is composed of E-type laminated yoke with an exciting coil of 68 turns at its midleg. The resonance spring is composed of main-springs and link-springs which link two movers. Two movers move to reverse direction by exciting the coil. The operation frequency of the LRA is substantially determined by the spring constant and the mass of the mover. This actuator is operated under PWM feedback control, and excitation time (duty) is decided by detecting the back EMF while the coil is not excited.

IV. VERIFICATION OF ANALYSIS METHOD

A. Analyzed Model and Condition

Fig. 3 shows the FEM model. The number of tetrahedron elements is about 670,000, the number of edges is about 790,000, and unknown variables are about 770,000. Table I shows the analysis conditions. The number of steps is 1,300, time division is 10μs, and total CPU time is about 300 hours.

B. Comparison Analyzed Results and Measured Results

Figs. 4 and 5 show the computed and measured waveforms of the amplitude, voltage, and current with no load. As can be seen, both results are well in good agreement, especially, influences of the back EMF and coil inductance on waveforms of voltage and current are accurately expressed, respectively.

V. EFFECT OF LINK-SPRING

This actuator has two link-springs in addition to main resonance springs which protect from the amplitude decreasing owing to the motion of the other mover when the amplitude of one mover is decreased by an external load. In order to verify the effect of link-springs, dynamic analysis is executed under the same conditions as no load. The horizontal load of 0.4N is applied to a single mover from the unloaded steady-state condition. Figs. 6(a) and (b) show the computed amplitude of unloaded and loaded movers without link-springs. From these figures, it is found that the amplitude of the loaded mover is greatly decreased by the load, and current duty is increased by the feedback control, and the amplitude of the unloaded mover is greatly increased.

Figs. 7(a) and (b) show the computed amplitude of unloaded and loaded movers with link-springs. From these figures, on the other hand it is found that a decrease in the amplitude of the loaded mover is controlled, and an increase in the amplitude of unloaded mover is also well controlled. As the results, the amplitude of both movers becomes steady and nearly the same.

From these results, it is clarified that link-springs are very effective in this LRA feedback control system.

VI. CONCLUSION

In this paper, we proposed the dynamic analysis method of a linear resonance actuator with multi-movers under PWM control employing the 3-D FEM. The effectiveness of this method was shown by the comparison with the measured

results. Moreover, the effect of link-springs on amplitude control was clarified.

TABLE I
ANALYSIS CONDITIONS

Input voltage (V)	3.6	Mass of mover (g)	6.95
Magnetization of magnets (T)	1.42	Viscous dumping coefficient (N·s/m)	0.14
Resistance(on) (mΩ)	350	Resistance(off) (mΩ)	290
Main-spring constant (N/mm)	6.93	Link-spring constant (N/mm)	3.22
Diode voltage (V)	0.5		

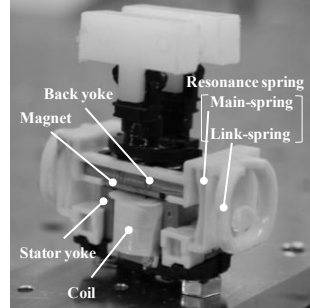


Fig. 2 Basic structure of the LRA

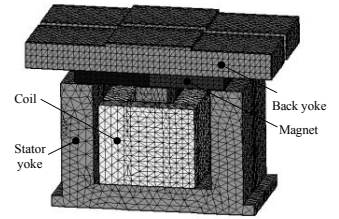


Fig. 3 FEM model

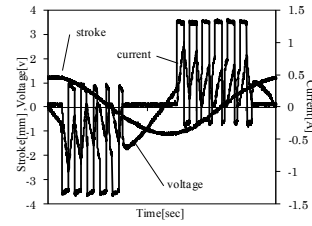


Fig. 4 Measured results

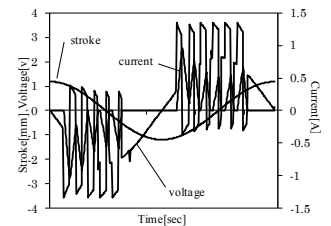
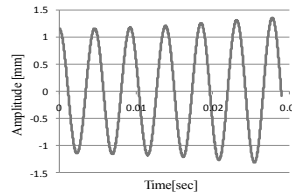
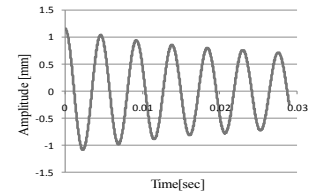


Fig. 5 Computed results

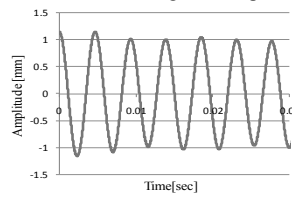


(a) Unloaded

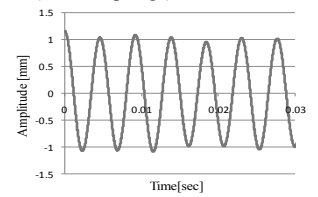


(b) Loaded

Fig. 6 Computed result (no link-springs)



(a) Unloaded



(b) Loaded

Fig. 7 Computed result (link-springs)

VII. REFERENCES

- (1) A. Yoshitake, K. Harada, T. Todaka, Y. Ishihara and K. Hirata, "Dynamic Analysis of A Linear Oscillatory Actuator Under Feedback Control", IEEE Transaction on Magnetics, VOL.33, No.2, pp.1662-1665,1997
- (2) K. Matsui, K. Hirata, and T. Ota "Dynamic Characteristics Analysis of Linear Resonant Actuator under PWM control employing the FEM", Papers of Technical Meeting on Linear Drive, IEE Japan, LD-07-17, pp.81-85,2007.

New FEM Approach for Multi Physics Problems Modeling in EPM Applications

Y. Du Terrail Couvat, A. Gagnoud
SIMaP/EPM Laboratory
ENSEEG, BP 75, 38402 Saint Martin d'Herès cedex, France
Yves.duterrail@simap.grenoble-inp.fr

Abstract — A FEM modeling tool based on multi equations and multi meshes coupling is presented. Data Structures of a DBMS, allow to program and manage sequentially or simultaneously multiple meshes and systems for multiple FEM formulations of physical equations. Principles of mesh coupling for multi physics, for numerical zoom or for different kind of meshes interconnection are detailed. The specific FEM integration algorithm is improved for calculating interpolation relations between coupled regions. Some Electromagnetic applications are presented : strong coupling with induction heating and numerical zoom of eddy current region. A very good agreement of results compared with industrial codes shows the robustness of the proposed modeling. Drawbacks and advantages will be discussed.

I. INTRODUCTION

Electromagnetic Processes of Materials (EPM) systems are typically applications where multi physics problems are always present. Some new interesting ways of investigation appear in modeling coming from other physics thematic and from computer science. This is the case of using multiple, non conformal grids during the simulation as presented by C.Rome in fluid mechanics problems [1] or in domain decomposition techniques as presented by [2]. The topic concerned here is the extension of such methods to multi physics simulations, based on the superposition of different grids adapted to each physical phenomena. The originality of the work proposed here is to realize the coupling of such grids inside a unique matrix system in place of classical data file exchanges between multiple codes. It appears also that the multiple mesh coupling is interesting for other applications like:

- . modeling local problems with a numerical zoom technique (eddy currents, front tracking and segregation defaults during solidification, NDT,...),
- . movements of groups of objects during time (surface heat treatment, particles movements, bubbling,...)
- . connection between different meshes, mixing of different types of finite element.

We have developed a toolbox called AEQUATIO composed of a programmable DBMS, a mesh generator and a finite element solver which allows designing numerical simulators based on multi-equations and multi-mesh coupling.

II. METHODOLOGY

The general form of a PDE equation treated in AEQUATIO is a discretized finite element weak form equation in which each term is the following:

$$\int_{\Omega} C * L * W \quad (1)$$

where C is the coefficient expression constant or variable, for example a physical property, L is the Interpolation polynomial expression, and W the differential weight.

A. Multiple Mesh Coupling

Two methods of mesh coupling are implemented, one for local Zoom and one for multi-physics coupling. Meshes must be associated to one or more FEM weak form equations. Two different meshes are necessarily linked to two different equations.

1) Multi-physics coupling

Considering two or more physical equations, one can construct adapted meshes for each phenomenon with the mesh generator. All data for meshes are stored in virtual memory and accessible everywhere during the simulation process. The coupling between two meshes is done by localizing Gauss integration points of each finite element in the coupled corresponding regions. Localization data, which are the index of the containing element and the reduced coordinates in that element are stored in element data structure.

2) Non conformal mesh coupling

That technique is applied on two or more meshes for local refinement (called here numerical zoom) and also for object movement. A hierarchical rule is applied. For example a zone in a mesh 'M1' may be zoomed by a 'zooming mesh 'M2'. A zone in the latter can also be zoomed by a following higher level mesh 'M3', etc... The principal constraints imposed are that meshes must overlap. Their intersection cannot be a frontier, excepted on domain external boundaries. The coupling between two meshes 'M1' and 'M2' is done by localizing boundary nodes of zooming mesh 'M2' inside zoomed mesh 'M1' and localizing all nodes of 'M1' inside 'M2'. Localization data are stored in the node data structure.

B. Solver algorithms

The coupling between 2 meshes is always done by order 1 or 2 Lagrange interpolation techniques as in [1]. The general management of data matrices and vectors during system construction, and a general integration algorithm have been developed. Also, when boundaries are coupled, boundary nodes equations are replaced by the interpolation law on the coupled state variable. Integrant calculation which contains a coupling term concerning element e1 on 'M1' and element e2 on 'M2' is expressed as follows :

Do for each element $e1$
 Do for each Gauss integration point in the element $e1$
 Localize the integration point in coupling element $e2$
 Do for each node i of the element $e1$
 Do for each node j of the element $e2$
 Calculate integrant expression
 Store integrant value in i,j index of the local rectangular matrix
 end.

III. APPLICATIONS

A. Strong physical coupling in Induction Heating Process

A cylindrical iron ingot of 3 m high and 6 cm diameter is moving vertically inside a 2m high and 10 cm diameter cylindrical coil as represented in figure1. In AEQUATIO, 2 independent meshes are coupled for electromagnetic and thermal equations. For electromagnetism, Maxwell equations in harmonic axi-symmetric form and for thermal transfer Diffusion-transport equation have been coupled [4]. The strong coupling is due to the temperature dependency of electrical conductivity and to the eddy currents thermal sources. AEQUATIO results have been compared with Comsol Multiphysics [5] and Flux-Expert [3] codes (figures 1,2 and Table).

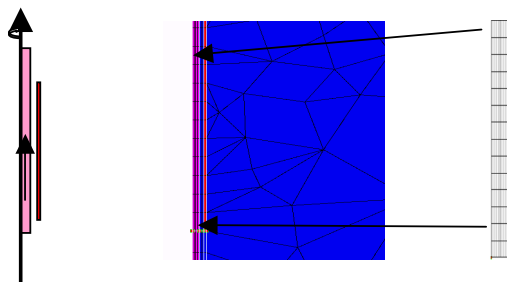


Fig. 1 Induction heating Device and multiple meshes

TABLE I: COMPARATIVE RESULTS

Models	Variables r^*AR max	Q max	T max
Aequatio $V=0$	0.177e-3	6.92e5	352.0
Comsol	0.185e-3	6.9e5	351.3
Flux-Expert	0.19e-3	6.9e5	-
Aequatio $V=1\text{cm/s}$	0.177e-3	6.92e5	314
Aequatio $V=10\text{cm/s}$	0.177e-3	6.92e5	301.8

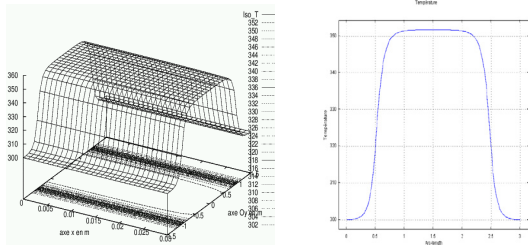


Fig. 2 Thermal distribution in the load with AEQUATIO (left) and Comsol (right)

B. Numerical Zoom on eddy current region

The 2D Magneto dynamic equation expressed in complex vector potential Az is applied on a domain composed of a coil and a rectangular iron load. The interior border of the load is covered on conductor and air regions by a second mesh whose role is to zoom the skin depth region (see Fig 3). Comparisons are done with Comsol code and give excellent agreement (figure 4). Very fine skin depths may be reached with AEQUATIO.

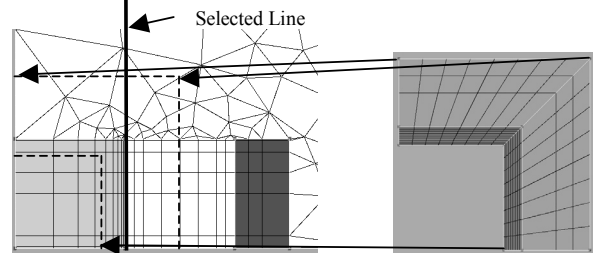


Fig. 3 Electromagnetic mesh Device (detail) and zoom mesh on skin depth

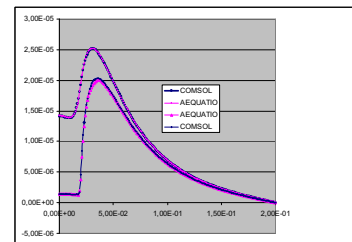


Fig. 4 Az calculations along selected line for frequency 10 kHz and 1MHz

IV. ADVANTAGES AND DRAWBACKS

As the general assembling of numerical integrants is done in a unique system matrix, Newton non linear algorithms may be used for strong coupling with different and adapted meshes for each physical phenomena. In the case of numerical Zoom, one controls easily the number of unknowns, some scale factors may be reached with hierarchical zooms, and movements of meshes may be introduced without changing the number of unknowns. Principal drawbacks are relative to the implementation of such algorithms on industrial codes and on the user interfaces for pre and post processing which have not been studied here.

V. REFERENCES

- [1] C. Rome, "methode de raccordement de maillages non-conformes pour la resolution des equations de Navier-Stokes ", PHD thesis., University of Bordeaux, France, June 2006.
- [2] J.L. Lions, O. Pironneau, "Domain decomposition methods for CAD", C.R.A.S., 328, pp73-80, Paris 1999.
- [3] J.Morandini, Y. Du Terrail Couvat, Ph. Massé, A. Gagnoud , "Modeling of coupled thermo-electro-magneto-hydrodynamic phenomena" *Int. J. of Computer Applications in Technology*, vol. 7, no. 3-6, pp 176-184, 1994.
- [4] M. Feliachi, J. Fouladgar, "Magneto-thermal Coupling", *The Finite Element Method for Electromagnetic modeling*, Edited by G. Meunier, Wiley, pp 405-428, 2008.
- [5] Comsol Multiphysics, <http://www.com>

Analysis of Transient Eddy Current and Conductor Motion in an Electromagnetic Repulsion Mechanism with Meshless Collocation Method

Guangyuan Yang¹, K.R. Shao¹, Youguang Guo², and Jianguo Zhu²

¹Huazhong University of Science and Technology, 430074, China, kkyanggy@126.com, krshao@hust.edu.cn

²University of Technology, Sydney, NCW 2007, Australia, youguang@eng.uts.edu.au, joe@eng.uts.edu.au

Abstract—This paper applies the radial basis function (RBF) collocation method in the moving coordinate systems for the first time to analyze the eddy current magnetic fields and conductor motion in an electromagnetic repulsion mechanism. The magnetic field in the solving domain is considered a superposition of two fields created by the excitation current and eddy current respectively. The governing equations are decoupled with the RBF and solved with time domain iteration. Moving coordinate systems in which the separate fields are calculated are constructed to avoid the model reconfiguration and simulate the motion process. The influence of model parameters to the field and motion is analyzed. The numerical result agrees well with the experiment data.

I. INTRODUCTION

Efficient method to solve the eddy current problem with moving conductors has attracted much attention in engineering applications. This paper presents a novel radial basis function (RBF) collocation method in moving coordinate systems to compute the transient eddy current magnetic field in an electromagnetic repulsion mechanism. Motion process of the conductor in the mechanism is also analyzed and compared with the experiment data.

II. ELECTROMAGNETIC REPULSION MECHANISM

The electromagnetic repulsion mechanism could also be named as electromagnetic switch system and its rotational symmetry structure is shown in Fig. 1.

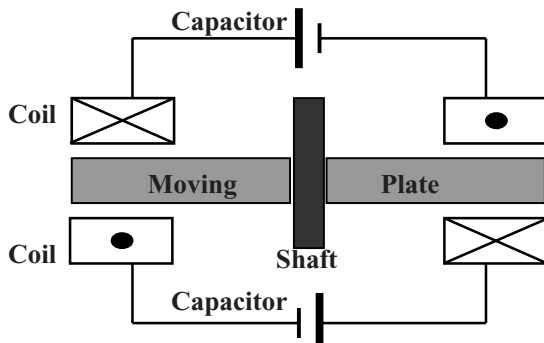


Fig. 1. Cross-section of the electromagnetic repulsion mechanism.

The switch is a round aluminium plate which could move along an insulated and nonmagnetic shaft. Two hollow cylinder-shaped excitation coils are wound with the same outer radius on the shaft to drive the motion. The millisecond level fast-rising excitation current in the coil is created by the discharge of a capacity. The time-variable magnetic field generates eddy current in the plate and force the plate to move

according to Ampere's force law. There is an initial 3000 (N) resisting spring force imposed by the shaft axle on the plate.

Because the upward and downward motions are driven by circuits with the same parameters, we only analyze the upward motion process excited by the coil below the plate. The numerical model could be simplified as a two dimensional problem. The model parameters of the solving domain are shown in Fig. 2.

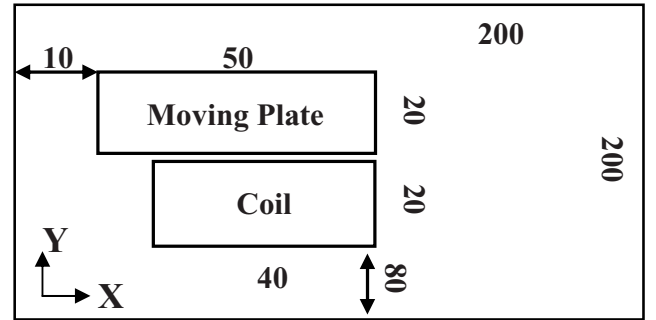


Fig. 2. 2D numerical model of the electromagnetic repulsion mechanism. (Unit: mm)

The solving domain Ω is considered homogeneous and isotropic and with a boundary $\partial\Omega$. The cross-section of the plate, which is also the eddy current area Ω_e , is moving with a speed $\mathbf{v} = \mathbf{v}_y$. The initial distance between the plate and the coil is 3 (mm) and the required distance is 7 (mm). The vector potential A , excitation current density \mathbf{J}_s and eddy current density \mathbf{J}_e exist only in the z -direction. Assuming that $A = A_z$, $\mathbf{J}_s = \mathbf{J}_{sz}$ and $\mathbf{J}_e = \mathbf{J}_{ez}$, we could get the governing equations as:

$$\sigma\mu \frac{\partial A}{\partial t} - L(A) = \mu J_s \quad \text{in } \Omega_e \quad (1a)$$

$$\nabla^2 A = -\mu J_s \quad \text{in } \Omega_h \quad (1b)$$

$$A = 0 \quad \text{on } \partial\Omega \quad (1c)$$

where σ is the conductivity, μ is the permeability, $\Omega_h \in (\Omega \cap \overline{\Omega_e})$ and the operator $L(\cdot)$ means

$$\nabla^2(\cdot) - \sigma\mu v \frac{\partial(\cdot)}{\partial y}.$$

III. RBF COLLOCATION TIME DOMAIN ITERATION IN MOVING COORDINATE SYSTEMS

The theory of RBF collocation method could be seen in [1]. Consider $A = A_s + A_e$ and establish two coordinate systems ξ_s and ξ_e where the subscript s and e means the excitation current field and eddy current field respectively. In each coordinate system, $N_I + N_B = N$ collocation nodes are set in Ω and on $\partial\Omega$ to form the RBF. Specially, we assume that nodes $1 \cdots N_P$ are in Ω_e . Using RBF to approximate A_s and A_e in ξ_s and ξ_e , we get:

$$A(\mathbf{x}, t) = \mathbf{Q}_s^T(\mathbf{x})\mathbf{a}_s(t) + \mathbf{Q}_e^T(\mathbf{x})\mathbf{a}_e(t) \quad (2)$$

where \mathbf{Q} is the RBF vector and \mathbf{a} is the unknown coefficient vector. Time domain iteration is constructed to solve \mathbf{a}_s and \mathbf{a}_e . In ξ_s , A_s in Ω satisfies the Poisson equation everywhere. With a known J_s , we could solve \mathbf{a}_s from:

$$\nabla^2(\mathbf{Q}_s^T(\mathbf{x}_{si}))\mathbf{a}_s^{k+1} = \mu J_s^{k+1}(\mathbf{x}_{si}) \quad i = 1, \cdots, N_{Is} \quad (3a)$$

$$\mathbf{Q}_s^T(\mathbf{x}_{si})\mathbf{a}_s^{k+1} = 0 \quad i = N_{Is} + 1, \cdots, N_s \quad (3b)$$

where k means the iteration steps and we have $t_k = t_0 + k\Delta t$.

Consider \mathbf{x}'_e to be the coordinates of nodes of \mathbf{Q}_e in ξ_s . Substituting (2) and (3) into (1) and using Crank-Nicolson time matching scheme to deal with the time differential, we get:

$$\begin{aligned} & \left(\frac{\sigma\mu}{\Delta t} \mathbf{Q}_e^T(\mathbf{x}_{ei}) - \frac{1}{2} L(\mathbf{Q}_e^T(\mathbf{x}_{ei})) \right) \mathbf{a}_e^{k+1} = \left(\frac{\sigma\mu}{\Delta t} \mathbf{Q}_e^T(\mathbf{x}_{ei}) + \right. \\ & \left. \frac{1}{2} L(\mathbf{Q}_e^T(\mathbf{x}_{ei})) \right) \mathbf{a}_e^k - \left(\frac{\sigma\mu}{\Delta t} (A_s^{k+1}(\mathbf{x}'_{ei}) - A_s^k(\mathbf{x}'_{ei})) \right. \\ & \left. + \sigma\mu v^k \frac{\partial A_s^{k+1}(\mathbf{x}'_{ei})}{\partial y} \right) \quad i = 1, \cdots, N_{Pe} \quad (4a) \end{aligned}$$

$$\nabla^2(\mathbf{Q}_e^T(\mathbf{x}_{ei}))\mathbf{a}_e^{k+1} = 0 \quad i = N_{Pe} + 1 \cdots N_{Ie} \quad (4b)$$

$$\mathbf{Q}_e^T(\mathbf{x}_{ei})\mathbf{a}_e^{k+1} = 0 \quad i = N_{Ie} + 1 \cdots N_e \quad (4c)$$

During the motion, the RBF model in each coordinate system is unchanged.

IV. ANALYSIS OF EDDY CURRENT AND MOTION

On the basis of the magnetic field, the distribution of eddy current and driving force imposed by the magnetic field could be obtained to analyze the motion. The parameter v in each iteration steps could be solved with kinetic equations. Besides, the influence of the eddy current magnetic field to the excitation circuit parameters is computed to modify J_s . Motion processes with different model parameters are also analyzed for a further optimization design. Fig. 3 shows the distribution of eddy current density in the plate section at time $t=1$ (ms) from which we could see the skin effect clearly.

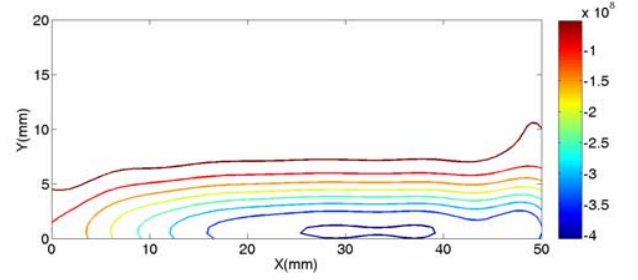


Fig. 3. Isopotential lines of eddy current density in the plate section at $t=1$ (ms).

We choose four observation points from Fig. 3 as: P1(30,0), P2(30,2.5), P3(30,5.0), P4(30,7.5) to analyze the variety of eddy current in different parts of the plate. The result is shown in Fig. 4.

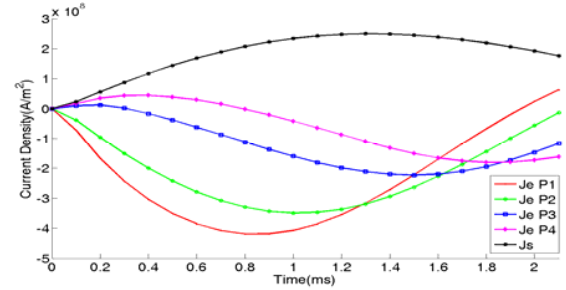


Fig. 4. Time-variation curve of the current densities.

The motion process is shown in Fig. 5.

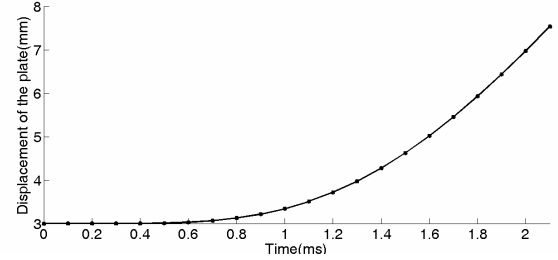


Fig. 5. Variation curve of the moving displacement of the plate.

Fig. 6 shows the influence of the initial voltage of the capacitor U_0 to the electromagnetic force of the plate.

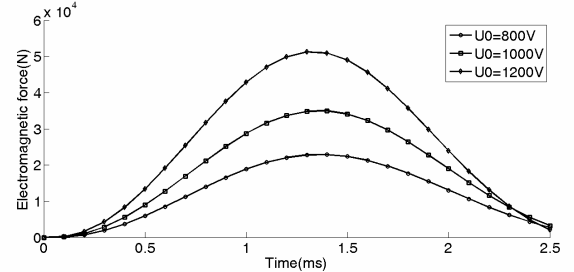


Fig. 6. Time-variation curves of Electromagnetic force when the initial voltage of the capacitor U_0 changes.

V. REFERENCES

- [1] C. Franke and R. Schaback, "Solving partial differential equations by collocation using radial basis functions," *Appl. Math. Comp.*, vol. 93, no. 1, pp. 73-91, 1998.

Coupled Magneto-Thermal FEM Model of Direct Heating of Ferromagnetic Bended Tubes

M. Forzan¹, A. Aliferov²

¹University of Padova, Dept. of Electrical Engineering, via Gradenigo 6/a, 35131 Padova, Italy

²Novosibirsk Technical State University, Novosibirsk, Russia

E-mail: michele.forzan@unipd.it

Abstract — Scalar and vector magnetic formulations have been applied to solve the current distribution in a 50 Hz direct resistance heating system of ferromagnetic tubes. The scalar formulation driven via an external circuit has been also applied to solve the Time-Harmonic EM part of the problem coupled with the thermal transient: the computed warm up curves have been compared with experimental data.

I. INTRODUCTION

Direct resistance heating of steel tubes is industrially achieved by supplying strong 50 Hz currents directly to the workpiece by means of suitable contact systems. The current density distribution inside a straight tube depends upon the skin effect, while for bended tube it is influenced also by the ring effect. The thermal sources for the heating are the Joule losses, which depend on the square of the current density: consequently the unbalanced distribution of the current density due to the ring effect produces a significant overheating in the inner part of the curved zone. In previous investigations the possibility of balance the ring effect by means of properly designed laminated cores has been analyzed [1]. The proposed solution has been realized in a laboratory set-up and experimental measurements have been used to verify the reliability of the numerical models. Numerical models have been developed to solve the electromagnetic problem by means of 3D finite element solution: because there is only one conductor carrying the source current, the A-AV formulation has been implemented applying Dirichlet conditions for the scalar electric potential on the edges of the conductor. The solution of the EM problem has been also implemented by means of a magnetic scalar coupled with the electric vector potential formulation. This formulation reduces substantially the computational requirements so that also the 3D coupled electromagnetic thermal solution can be achieved in reasonable times. Moreover the scalar formulation can be more efficiently driven by an external electrical circuit, allowing to feed a constant current in the model instead of an applied voltage [2, 3]. Some comparisons between the results obtained by means of the A-AV formulation with the ones made with T-T₀- ϕ are presented as well as some comparisons between the computed temperature distribution and the experimental measurements resulting from some warm up processes carried out controlling the current intensity during the heating transients.

II. COMPUTATION MODELS

The model represents the laboratory set-up built in NSTU (Novosibirsk State Technical University) and it is constituted by a ferromagnetic tube, a laminated yoke and a thermal insulator that envelops the tube (fig.1).

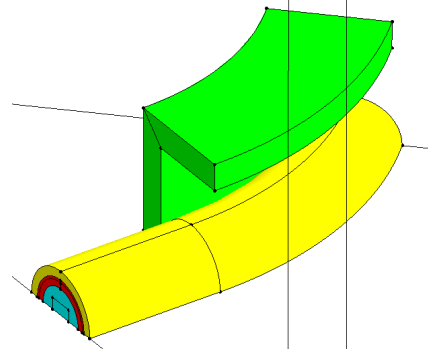


Fig. 1. Schematic of the bended tube laboratory set-up. The ferromagnetic tube (red region) is surrounded by a thermal insulator (yellow). The C yoke, placed to minimize the ring effect, is represented by the green region.

Only a part of the real system has been considered, applying tangential magnetic field conditions on the boundaries, represented in Fig.2 by the red and green lines. On these boundary faces there are also the terminals of the tube conductor.

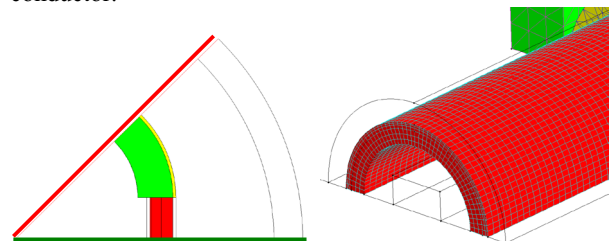


Fig. 2. On the left, the boundaries of the model are represented by the red and the green lines; the terminals of the conductive tube are located on the same boundaries. On the right the finite element model of the tube has been realized with a 3D mapped mesh to subdivide the skin depth layer.

As mentioned above, the electromagnetic solution, in particular the distribution of the current density inside the tube, has been obtained by means of two different numerical formulations. The magnetic vector potential \mathbf{A} coupled with the scalar electric potential V formulation leads to a very accurate solution for the current distribution, that can be obtained, in the hypothesis of a time harmonic field of angular frequency ω , directly from the solved nodal state variables:

8. Coupled Problems

$$\dot{\mathbf{J}} = -\sigma (j \omega \dot{\mathbf{A}} + \text{grad } \dot{V}) \quad (1)$$

where σ is the electrical conductivity and the dot over the \mathbf{A} , V potentials indicates the phasor representation. The model has been solved by applying a constant voltage drop between the two terminals of the tube. However, the vector formulation has some drawbacks: it requires huge computational resources, it badly describes the non linear magnetic properties when $\mu_r \gg 1$, and finally, when an iterative algorithm like Newton-Raphson is applied to non linear models, the computation time becomes very high and the convergence is usually poor. For these reasons, the electromagnetic solution has been obtained also by means of the $\mathbf{T}-\mathbf{T}_0-\phi$ formulation with an imposed current driven by an electrical circuit directly coupled with the FEM solver. The electric vector potential \mathbf{T} is defined since in quasi-static hypothesis the divergence of the current density must be 0; in this situation the current density can be computed from:

$$\dot{\mathbf{J}} = \text{rot } \dot{\mathbf{T}} + \text{rot } \dot{\mathbf{T}}_0 \quad (2)$$

and the field \mathbf{H} in the conducting region can be described as:

$$\dot{\mathbf{H}} = \dot{\mathbf{T}} + \dot{\mathbf{T}}_0 - \text{grad } \dot{\phi} \quad (3)$$

while in the air and the magnetic yoke, the field can be computed as the gradient of the scalar magnetic potential [3,4].

III. NUMERICAL AND EXPERIMENTAL RESULTS

The EM solutions obtained with the two different formulations have been compared, verifying the resulting current density distribution in the bended part of the tube.

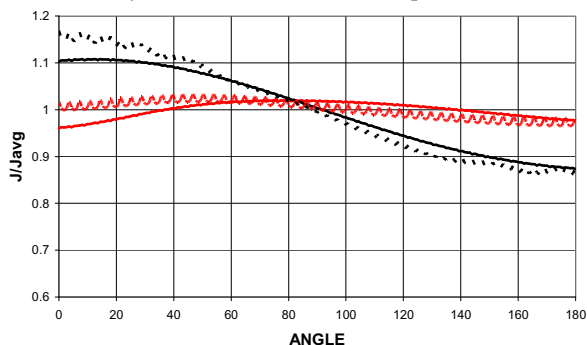


Fig. 3. Comparison between the current distribution, normalized to the average value, as a function of the azimuthal position obtained with the A-AV formulation (continuous lines) and the $\mathbf{T}-\mathbf{T}_0-\phi$ formulation. The black lines represent the solution without yokes while the red curves are with the laminated yoke.

In fig.3 the current distribution is represented as the ratio between the averaged value and the actual values along a curvilinear path located in the central section of the bended zone. The two calculated distributions are in good agreement; it can be noticed that the current densities, resulting from the curl operation (2) applied on the \mathbf{T} values as resolved on a 2nd order mesh, presents an oscillation due to the derivative operation that is not performed when the A-AV formulation is applied.

The coupled electromagnetic and thermal solution has been done taking into account the dependence of the material properties, i.e. electric conductivity, magnetic permeability, thermal conductivity and specific heat with temperature, while the non linear magnetic property of the steel with magnetic field intensity has been considered constant to avoid the excessive computation time required by the non linear solvers. The EM-thermal solution has been performed with a classic iterative procedure, where the temperature distribution and the joule losses represent the coupling terms. The total transient period, 3600 s, has been subdivided into 40 time steps of 90 s. The entire solution required roughly 20 days of calculation on a Xeon X5355, 2,66 GHz, with 32 GB of RAM.

The numerical transient is compared with the experimental data in the diagrams of Fig.4.

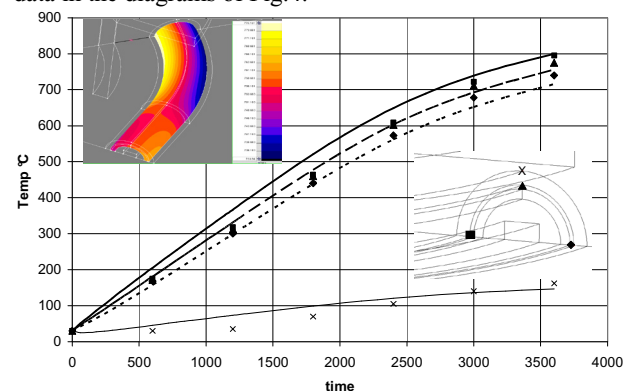


Fig. 3. Comparison between computed thermal transient and experimental measurements. Experimental data are obtained from three thermocouples placed on the tube, as shown in the sketch in the right part of the figure. The same symbols indicate the measured temperature on the diagrams, while the numerical results are represented by lines. A fourth measured point, indicated with X, is located on the thermal insulator.

IV. CONCLUSIONS

The scalar formulation coupled with the circuit equations has been proved to be suitable for the solution of the electromagnetic part of a coupled magneto thermal problem, allowing a faster process in comparison with the one achievable by means of A-AV formulation. Nevertheless, the 3D coupled MT problem requires still a very long computation time: further investigations will be devoted to the development of a parallel solver that will allow a significant speedup of the calculation process.

V. REFERENCES

- [1] Aliferov A., Lupi S., Forzan M.: "Electromagnetic and Thermal Processes in Direct Resistance Heating of Curvilinear Tubes", Int. Conf. IFOST, Novosibirsk-Tomsk (Russia), June 23-29, 2008,
- [2] G.Meunier, Y.LeFloch, C. Guérin, "A Nonlinear Circuit Coupled t-0-f Formulation for Solid Conductors", IEEE Tran.Mag., vol.39, No.3, 2003.
- [3] G.Meunier, H.T. Luong, Y. Maréchal, "Computation of Coupled Problems of 3D Eddy Current and Electrical Circuit by using $\mathbf{T}-\mathbf{T}_0-\phi$ Formulation", IEEE Tran.Mag., vol.34, No.5, 1998.
- [4]. O. Biro, K. Preis, G. Vrisk, K.R. Richter, I. Tigar, "Computation of 3-D magnetostatic fields using a reduced scalar potential", *IEEE Trans. Magn.*, pp. 1329-1332, 1993
- [5] <http://www.cedrat.com>

Streamer Simulation based on Discontinuous Galerkin Method and Hierarchical Reconstruction

Chijie Zhuang*, Rong Zeng**, Bo Zhang, Shuiming Chen and Jinliang He
 State Key Lab of Power Systems, Department of Electrical Engineering,
 Tsinghua University, Beijing 100084, People's Republic of China
 Email: zhuangcj02@mails.tsinghua.edu.cn*, zengrong@tsinghua.edu.cn**

Abstract—This paper renders a discontinuous Galerkin method combined with hierarchical reconstruction to simulate the fluid model of streamer discharges. This method generates little numerical diffusion and oscillations. It is of high resolution and high order accuracy and hence suitable to simulate streamer discharges. A simulation of a parallel-plate discharge using 1.5 dimensional fluid model is presented as an example.

I. INTRODUCTION

Numerical simulations help scientists achieve a better theory on the physics of the streamer formation and propagation. The simplest fluid model for streamer discharges consists of two convection-diffusion-reaction equations coupled with a Poisson's equation[1]:

$$\begin{aligned} \frac{\partial n_e}{\partial t} + \frac{\partial(n_e v_e)}{\partial x} - D_e \frac{\partial^2 n_e}{\partial x^2} &= \alpha n_e |v_e| + S_{ph}, \\ \frac{\partial n_p}{\partial t} + \frac{\partial(n_p v_p)}{\partial x} &= \alpha n_e |v_e| + S_{ph}, \\ \Delta u &= -\frac{e}{\epsilon}(n_p - n_e), E = -\nabla u. \end{aligned}$$

where n_e and n_p are the density of electrons and positive ions, v_e and v_p are their velocity, respectively. D_e is the diffusion coefficient, α is the collision ionization coefficient and S_{ph} is the photo-ionization. u is the voltage and E is the electric field. ϵ is the dielectric coefficient and e is the net charge of a unit electron. v_e, v_p and α are locally decided by the electric field[2].

Due to the convection term in the streamer simulation model, traditional numerical schemes would often generate much numerical diffusions or oscillations and lead to non-physical results. Flux-corrected-transport(FCT) technique combined with finite difference method(FD-FCT) or finite element method(FEM-FCT), finite volume method(FVM) with slope limiters were introduced to overcome this problem[1], [3], [4]. But on the other hand, FD and FVM cannot handle complex geometries easily and need wide stencils to construct high order schemes; FEM does not enforce the local conservation which is preferred for convection problems.

Discontinuous Galerkin method(DG) can overcome these shortages[5]. It uses a finite element space discretization by discontinuous approximations and can easily handle complicated geometries. It incorporates the ideas of numerical fluxes and slope limiters from the high-resolution FD and FV schemes. The DG methods not only enforce the local conservation, but also are very compact. Combined with hierarchical

reconstruction(HR)[6], which can generate essentially non-oscillatory solutions while keeping the resolution and desired order of accuracy for smooth solutions, the resulting DG scheme is of high resolution and high order accuracy.

II. THE SCHEME

Take the following notations:

$$\begin{aligned} n &= (n_e, n_p)^T, f(n) = (n_e v_e, n_p v_p)^T, g(n) = (D_e n_e, 0)^T, \\ q &= g_x, h(n) = (\alpha n_e |v_e| + S_{ph}, \alpha n_e |v_e| + S_{ph})^T. \end{aligned}$$

The convection-diffusion-reaction equations read:

$$n_t + (f - q)_x = h, q = g_x. \quad (1)$$

A. Space discretization

Suppose $I_j = (x_{j-1/2}, x_{j+1/2}), j = 0, 1, 2, \dots, N$, is a partition of the computational domain, $\Delta x_j = x_{j+1/2} - x_{j-1/2}$. The finite-dimensional computational space is

$$V = V_h^k = \{\psi : \psi|_{I_j} \in P^k(I_j)\},$$

where P^k denotes the polynomials of degree up to k defined on I_j . We choose Legendry Polynomials as the basis functions and re-scale them over $[-1, +1]$:

$$v_0^{(j)} = 1, v_1^{(j)} = \xi, v_2^{(j)} = 0.5(3\xi^2 - 1),$$

where $\xi = 2\frac{x-x_j}{\Delta x}$. The numerical solution can be written as:

$$n^h(x, t) = \sum_{i=0}^2 n_i^{(j)} v_i^{(j)}, \text{ for } x \in I_j.$$

Multiply equation (1) by a test function $\psi \in V_h^k$, integrate by parts, replace n, q by n^h, q^h , and choose suitable numerical flux \hat{f}, \hat{q} at the interface $x_{j+1/2}$, one gets:

$$\begin{aligned} \int_{I_j} n_t^h \psi dx - \int_{I_j} (f(n^h) - q^h) \psi dx + (\hat{f} - \hat{q})_{j+1/2} \psi_{j+1/2}^- \\ - (\hat{f} - \hat{q})_{j-1/2} \psi_{j-1/2}^+ = \int_{I_j} h(n^h) \psi dx, \quad (2) \end{aligned}$$

$$\int_{I_j} q^h \psi dx = \hat{g}_{j+1/2} \psi_{j+1/2}^- - \hat{g}_{j-1/2} \psi_{j-1/2}^+ - \int_{I_j} g(n^h) \psi_x dx. \quad (3)$$

where $-$ and $+$ means the left and right side values of the interface, respectively. Numerical flux \hat{f} is chosen according to the upwind principle because the directions of v_e and v_p are

easy to obtain. \hat{q} and \hat{g} are chosen according to the alternating principle.

In fact, the solutions are allowed to have jumps at the interface $x_{j+1/2}$, the cell size Δx_j and degree k can be changed from element to element, which leads to easy adaptivity.

B. Time discretization

Locally solve the auxiliary variable q in equation (3) from element to element, and substitute it into equation (2), one gets an ODE:

$$\frac{dn^h}{dt} = L(n^h) \quad (4)$$

For most cases, equation (1) is convection dominated, an explicit Total Variation Diminishing 3-order Runge-Kunta scheme can be used to solve the ODE[7].

$$\begin{aligned} n^{(1)} &= n^n + L(n^n)\Delta t, \\ n^{(2)} &= \frac{3}{4}n^n + \frac{1}{4}(n^{(1)} + L(n^{(1)})\Delta t), \\ n^{(3)} &= \frac{1}{3}n^n + \frac{2}{3}(n^{(2)} + L(n^{(2)})\Delta t), \\ n^{n+1} &= n^{(3)}. \end{aligned} \quad (5)$$

C. Hierarchical reconstruction

HR computes cell averages of various orders of derivatives of a polynomial, and uses them to reconstruct the non-oscillatory linear polynomial hierarchically. The coefficients of the reconstructed polynomial are used to update the corresponding ones of the original polynomial, see [6] for details. The HR process is applied after every sub-step of the Runge-Kunta scheme. In this way, the scheme guarantees non-oscillatory results.

III. APPLICATION

A simulation of a positive streamer was performed in pure N_2 at atmospheric pressure using 1.5D fluid model. Two infinite large parallel plate electrodes are placed perpendicular to the axis of symmetry. The origin of the cylindrical coordinates is located at the anode. The applied voltages on the anode($x=0$ cm) and cathode($x=1$ cm) are 52 kV and 0, respectively. The charges are assumed to uniformly distributing on a disc perpendicular to the axis of symmetry[8]. The disc radius is assumed to be 0.05 cm. The initial charge has a gaussian shape:

$$n_e(x)_{t=0} = n_p(x)_{t=0} = n_b + n_0 \times \exp\left(-\left(\frac{x-x_0}{\sigma_x}\right)^2\right),$$

where $x_0 = 0.03$ cm, $\sigma_x = 0.027$ cm, $n_0 = 10^{14}$ cm $^{-3}$, and S_{ph} is simplified by the background preionization $n_b = 10^8$ cm $^{-3}$. Neumann boundary conditions are applied for the convection-diffusion equations. The Poisson's equation is solved by the disc method[8].

Fig.1 shows that the electric field in front of a streamer is severely enhanced and is more than 100kV/cm. The streamer propagation velocity is about of the order of 10^8 cm/s. Fig.2 shows that there is a thin layer about 0.1mm thick at the head of a stream, which has a larger net charge density, and the

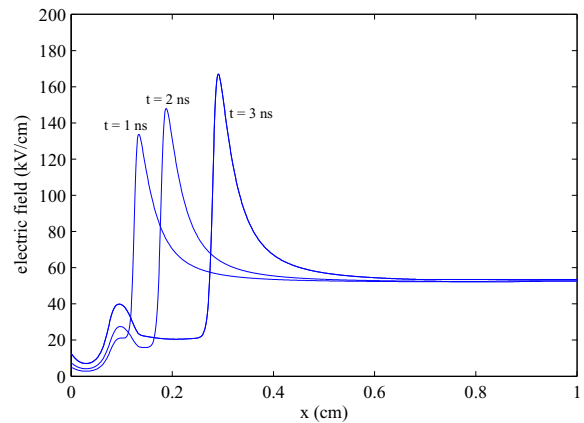


Fig. 1. electric field distribution along the axis

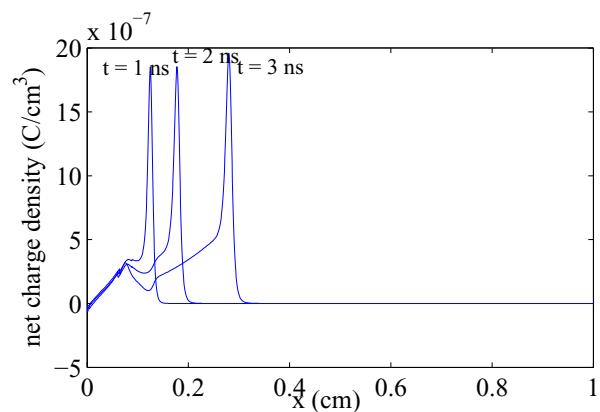


Fig. 2. net charge distribution along the axis

net charge density is of the order of 10^{-6} C/cm 3 . The sharp gradient of charge density profile was caught by the proposed scheme well.

REFERENCES

- [1] C. Montijn, W. Hundsdorfer, U. Ebert, An adaptive grid refinement strategy for the simulation of negative streamers, *J.Comput.Phys.*, 219, 2006, 801-835.
- [2] C. Wu, E.E. Kunhardt, Formation and propagation of streamers in N_2 and N_2 -SF $_6$ mixtures, *Physical Review A*, 37(11), June 1988,4396-4406.
- [3] R. Morrow and J. J. Lowke, Space-charge effects on drift dominated electron and plasma motion, *J. Phys. D: Appl. Phys.*, 14(11),1981,2027-2034.
- [4] Olivier Ducasse, Liberis Papageorghiou, Oliver Eichwald, etc., Critical analysis on two-dimensional point-to-plane streamer simulation using the finite element and finite volumn methods, *IEEE Trans. Plasma Sci.*, 35(5), 2007, 1287-1300.
- [5] Bernardo Cockburn,Chi-Wang Shu, Runge-Kutta Discontinuous Galerkin Methods for Convection-Dominated Problems, *Journal of Scientific Computing*, Vol. 16, No. 3, September 2001
- [6] Y.-J. Liu, C.-W. Shu, E. Tadmor, M.-P. Zhang, Central discontinuous Galerkin methods on overlapping cells with a non-oscillatory hierarchical reconstruction, *SIAM J. Numer. Anal.* 45 (2007)2442-2467.
- [7] Chi-Wang Shu,TVD time discretizations, *SIAM J. Sci. Stat. Comput.*, 9, 1988, 1073-1084.
- [8] A. J. Davies, C. J. Evans, and F. Llewellyn Jones, Electrical breakdown of gases: The spatio-temporal growth of ionization in fields distorted by space charge, *Proc. Roy. Soc.*, 281(1385),164-183.

Buoyancy Force Evaluation on Nonmagnetic Solid Object Submerged in Magnetic Liquid Subjected to Non-uniform Magneto-static Field

Hong Soon Choi*, Young Sun Kim, and Il Han Park

*School of Electrical Eng., Kyungpook National University, Sangju 742-711, Korea,
tochs@knu.ac.kr

School of Information and Communication Eng., Sungkyunkwan University, Suwon 440-746, Korea,
youngsun@skku.edu, ihpark@skku.ac.kr

Abstract — In this paper, the problem of magnetic buoyancy force on nonmagnetic solid object submerged in magnetic liquid is presented and discussed. It is shown that there are contradictions in the understanding and calculation of the buoyancy force using only the conventional Maxwell stress. On the other hand, the approach of Rosensweig's ferrohydrodynamics was also criticized by Rinaldi. For the calculation of buoyancy force of the submerged nonmagnetic object, a new approach of hydrostatic equilibrium considering magnetic body force is proposed.

I. INTRODUCTION

As in Fig. 1, a mutual repulsion force, which is generated between a magnet and a nonmagnetic object when they are submerged in magnetic liquid, is presented. The mutual force is not due to a direct interaction between the two bodies; the force arises because of the magnetic fluid attracted into the space between them. In the previous work [1] by Rosensweig, a magnetic force expression of the nonmagnetic body based on ferrohydrodynamics, including the gravitational effect, was presented. He recognized, though, the fact that there is an arbitrariness of the grouping of magnetic terms in his derived expressions [2] and there have been controversies and confusions for the magnetic force distribution for a hundred years. In a recent research by Rinaldi [3], an assertion, in which Maxwell stress is not a true mechanical stress, was shown and the Rosensweig's electromagnetic force derivations and applications of those were strongly criticized.

In Fig. 2, a hydrostatic model is presented for numerical study and discussion. In this model, a nonmagnetic solid object (solid-A) is submerged in a magnetic liquid subjected to non-uniform magneto-static field. Solid-A has a slightly bigger mass density than that of the magnetic liquid. Solid-A sinks to the bottom of the vessel when there is no permanent magnet under the vessel. On the other hand, if a magnet is put under the vessel, solid-A soars to the height at which the hydrostatic equilibrium is satisfied. Firstly, let's consider this model using only the conventional Maxwell stress. If we choose a closed integral surface path inside solid-A, which has air permeability, for the magnetic force calculation, the result is obviously negligible because there is no magnetic material within the closed surface. If we adopt the alternative point of view in which the integral path is taken on the magnetic liquid surface adjacent to solid-A for the calculation of pushing force, the path is, consequently, the same as the previous one except

the surface-normal direction. This also leads to a meaningless force value because the integration of this is just negative to that of solid-A. Here, there is another conceptual hole in Maxwell stress approach. From a mechanical viewpoint, the total magnetic buoyancy force should be the summation of solid-A's force itself and the pushing force of the magnetic liquid. As seen above, the summation is simply zero because of the opposite integration value. That is, the approach using only the Maxwell stress fails in explaining the mechanics of the magnetic buoyancy force of solid-A. This conclusion also supports the Rinaldi's assertion.

For evaluating the buoyancy force, in this paper, a new approach of hydrostatic equilibrium with consideration of magnetic body force [4] is presented. By using the magnetic body force, the above mentioned criticism can be avoided; not using the Maxwell stress itself but using an equivalence of divergence of the Maxwell stress tensor. For calculating the net uprising force, both of gravitational forces of the magnetic liquid and the solid-A should be considered as well as magnetic body force of the liquid. The proposed hydrostatic approach is made relatively simple than that of Rosensweig because both gravitational and magnetic body forces are dealt with in a same way. If the integration of hydrostatic pressure on the surface of solid-A, which makes the upward buoyancy, is bigger than gravitational downward force of solid-A, the net uprising force can be obtained. As well as detailed hydrostatic procedure, experimental and numerical tests will be presented in the full paper.

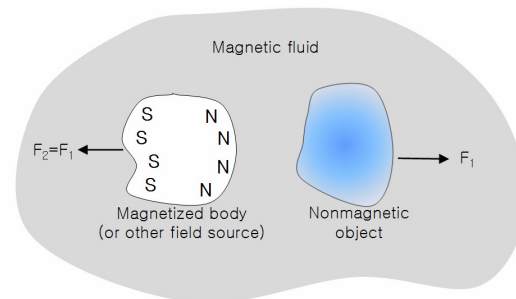


Fig. 1. Mutual repulsion of a magnet and a nonmagnetic object when both are submerged in a magnetic fluid.

II. HYDROSTATIC APPROACH WITH BODY FORCE

The momentum equation of hydrodynamics including magnetic body force is as follows,

$$\rho \frac{D\mathbf{v}}{Dt} = -\nabla \cdot \mathbf{T}_{mech} + \rho \mathbf{g} + \eta \nabla^2 \mathbf{v} + \mathbf{f}_m \quad (1)$$

where D/Dt is the substantial or Lagrangian derivative which is defined to trace the liquid motion, ρ is mass density of the liquid, \mathbf{v} is velocity of motion, \mathbf{T}_{mech} is mechanical stress tensor, \mathbf{g} is acceleration vector of gravity, η is viscosity, and \mathbf{f}_m is the magnetic body force. By applying the virtual air gap scheme to the Kelvin's formula [4][5], the magnetic body force can be expressed as

$$\mathbf{f}_m = \frac{\mu_0 + \mu}{2} (\mathbf{M} \cdot \nabla) \mathbf{H} \quad (2)$$

where \mathbf{M} is magnetization and \mathbf{H} is total field intensity. This force density can be regarded as an equivalence of divergence of Maxwell stress tensor. When the liquid is in static state, the hydrostatic momentum equation is reduced to,

$$\nabla p = \rho \mathbf{g} + \mathbf{f}_m \quad (3)$$

where p is the isotropic mechanical pressure with the relation of $\nabla \cdot \mathbf{T}_{mech} = \nabla \cdot p \mathbf{I} = \nabla p$. From (3), a pressure on the surfaces of solid-A can be obtained as follows,

$$p = \int_{L_0}^L (\rho \mathbf{g} + \mathbf{f}_m) \cdot d\mathbf{l} + p_0 \quad (4)$$

where L_0 is an arbitrary fixed position on the free surface of the liquid, p_0 is the atmospheric pressure, L is a position on the surfaces of solid-A [6]. By integrating the pressures along the surfaces of solid-A, total buoyancy force, which is generated by the liquid, can be obtained with consideration of both gravity and magnetic field. Finally, the net uprising force can be obtained by subtracting the weight of solid-A from the total buoyancy force. The assumptions used in this model are two-dimensional geometry, incompressibility of the liquid, neglecting the deformation of the free surface, and material linearity.

By applying the density of the magnetic liquid as 1 g/cm^3 , that of nonmagnetic object as 1.1 g/cm^3 , and the paper normal depth as 1 m , the final net uprising force is calculated as 2.8 N in the specified height from the bottom of the vessel. This resultant value means that the equilibrium height will be higher than the specified position. The final floating height

can be obtained iteratively. At the equilibrium height, the net uprising force should be zero. In Fig. 3, the calculated magnetic body force distribution in the magnetic liquid is shown.

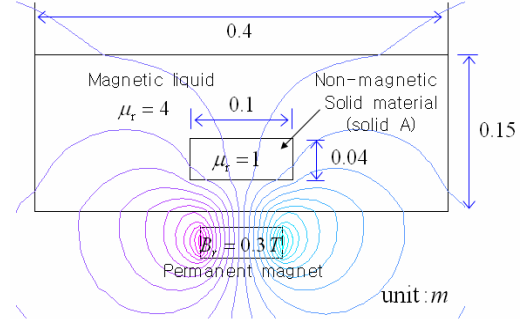


Fig. 2. A hydrostatical model: non-magnetic solid object submerged in magnetic liquid subjected to non-uniform magneto-static field produced by a magnet under a vessel. The field was solved by a finite element analysis.

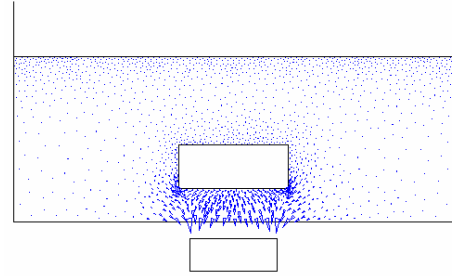


Fig. 3. Magnetic body force distribution using Kelvin's formula and virtual air gap scheme.

III. REFERENCES

- [1] R. E. Rosensweig, *Ferrohydrodynamics*, New York: Dover, pp. 150-158, 1997.
- [2] See Ref. [1], pp. 100-112.
- [3] C. Rinaldi and H. Brenner, "Body versus surface forces in continuum mechanics: Is the Maxwell stress tensor a physically objective Cauchy stress?," *Physical Review E*, vol. 65, 036615, 2002.
- [4] H. S. Choi, S. H. Lee, and I. H. Park, "Electromagnetic body force calculation based on virtual air-gap," *Journal of Applied Physics* 99, 08H903, 2006.
- [5] H. S. Choi, I. H. Park, and S. H. Lee, "Force calculation of magnetized bodies in contact using Kelvin's formula and virtual air-gap," *IEEE Trans. Appl. Supercond.*, vol. 16, no. 2, pp. 1832-1835, June 2006.
- [6] H. S. Choi, Y. S. Kim, K. T. Kim, and I. H. Park, "Simulation of hydrostatical equilibrium of ferrofluid subjected to magneto-static field," *IEEE Trans. on Magnetics*, Vol.44, No.6, pp.818-821, June 2008.

Field-circuit Co-simulation of Controllable Reactor using Integral Equation Method

X. Yang¹, Z. Andjelic², C. Yuen³

¹ ABB Corporate Research, Beijing, China, China (xiaobo.yang@cn.abb.com)

² ABB Corporate Research, 5405 Baden-Daettwil, Switzerland (zoran.andjelic@ch.abb.com)

³ ABB Corporate Research, 5405 Baden-Daettwil, Switzerland (cherry.yuen@ch.abb.com)

Abstract – For reactive power compensation of EHV/UHV lines, the controllable reactor has more advantages than the fixed value reactor. Among various controllable reactors schemes, the orthogonal flux type controllable reactor is remarked for its low harmonics and fast response time. In this paper, to verify the performance of the controllable reactor, we present an efficient approach for the field-circuit co-simulation of such controllable reactors using Integral Equation Method (IEM) and Simulink.

The indirect coupling procedure is based on exchanging of source variables i.e. current and voltage sources between field IEM simulation and Simulink based circuit simulation. With this method, the dynamic behavior of the controllable reactor can be simulated and analyzed with more accuracy. By using this co-simulation approach, the more complex system level simulation can be applied by using accuracy field model.

The field model of the controllable reactor is established firstly by IEM method and the circuit model is established in the Simulink environment. The simulation results are compared with the results obtained by mathematical model of the controllable reactor.

I. CONTROLLABLE REACTORS

In most of the existing power system, the switchable low voltage reactors/capacitors on tertiary winding of transformer or SVC are used to regulate the voltage, and the temporary over-voltage suppression widely adopts line shunt reactor, which is a fix value reactor. The appearance of controllable reactor gives an alternative of normal shunt reactor, as shown in Fig. 1. As the substitute of line shunt reactor, the functions of controllable reactor are 1) voltage regulation, 2) temporary over-voltage suppression and 3) dynamic voltage support.

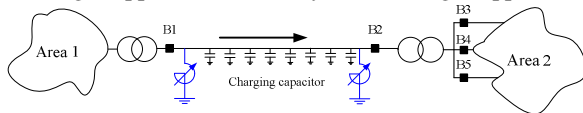


Fig. 1 The controllable reactor in the power system

In this paper, the orthogonal flux type controllable reactor^[1] is employed for the co-simulation, which is a kind of saturable reactor with 2 windings: AC winding (main winding), and DC winding (control winding). The respective DC flux and AC flux of the windings are orthogonal in the iron core of the controllable reactor. The equivalent circuit of the controllable reactor is as shown in Fig. 2, where U_{AC} is the input AC voltage of the main winding and I_{AC} is the AC current; U_{DC} is input DC voltage of control winding and I_{DC} is the DC current.

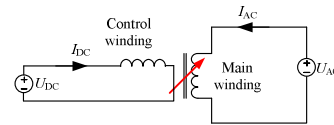
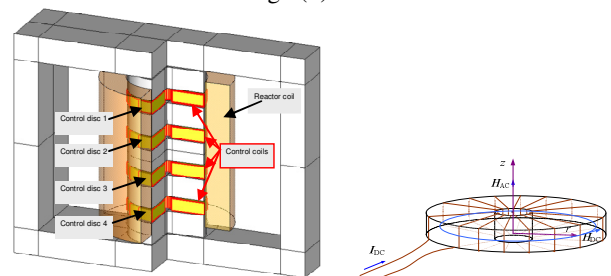


Fig. 2 The equivalent circuit of the controllable reactor

In this paper, the field-circuit co-simulation of such controllable reactors using Integral Equation Method (IEM)^[2] is presented. The filed simulation model considers the impact of the non-linear magnetizing behavior of the iron core and the leakage flux and thus is a closer approximation to the physical model. By coupling this field simulation model with the power system circuit model, the performance of the controllable reactor can be verified with higher accuracy and the parameters of the controllable reactor can be optimized.

II. THE FIELD SIMULATION MODEL OF THE CONTROLLABLE REACTOR

The characteristic of controllable reactor is achieved by the control of the saturation level of the “control discs” in the reactor’s central limb. Fig. 3(a) shows the structure of controllable reactor with air-gaps between the control discs and uncontrolled discs. By adding air-gaps, the control range can be adjusted and thus decrease the total cost of the controllable reactor. The main reactor coil is excited by the AC voltage. The control discs are excited by the auxiliary DC coils wound around each of them. The structure of the control disc is shown in Fig 3(b).



(a) The structure of controllable reactor (b) the control disc
Fig. 3 Structure of the controllable reactor with air-gaps between the discs

III. COUPLING MECHANISM

A. The coupling of the softwares

The circuit model in Simulink is based on the state space approach. The transmission line, the generators and the loads are described in the circuit model by the SimPowerSystem

blocks in the Simulink. The field model described by IEM is presented as a function block, in which the currents of the main winding and control winding of the controllable reactor are the input variables, which are measured from the circuit model; the voltage of the main winding and control winding (the EMF values) are calculated by the IEM and returned as output variables. The structure diagram of the co-simulation is shown in Fig. 4.

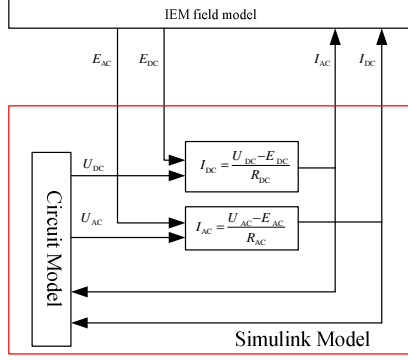


Fig. 4 The structure diagram of co-simulation

B. The Data Transfer

The input and output data that transferred between Simulink and IEM software are exchanged by ASCII format files. The data transfer mechanism can be described as follows:

At the beginning simulation time $t_0 = 0$, outputs of IEM field model are initialized as $E_{AC}^{(0)} = 0$ and $E_{DC}^{(0)} = 0$; the output variables of the Simulink are initialized as $I_{AC}^{(0)} = 0$ and $I_{DC}^{(0)} = 0$. At the time $t_1 = t_0 + \Delta T$, where ΔT is the simulation time step, the output variables of the Simulink $I_{AC}^{(1)}$ and $I_{DC}^{(1)}$ are calculated as:

$$\begin{cases} I_{AC}^{(1)} = \frac{U_{AC}^{(1)} - E_{AC}^{(0)}}{R_{AC}} \\ I_{DC}^{(1)} = \frac{U_{DC}^{(1)} - E_{DC}^{(0)}}{R_{DC}} \end{cases} \quad (3.1)$$

where R_{AC} and R_{DC} are the resistance of the main winding and control winding respectively.

The output variables $E_{AC}^{(1)}$ and $E_{DC}^{(1)}$ of the IEM field model at time t_1 are calculated as:

$$\begin{cases} E_{AC}^{(1)} = n_{AC} \frac{\Phi_{AC}^{(1)} - \Phi_{AC}^{(0)}}{\Delta t} \\ E_{DC}^{(1)} = n_{DC} \frac{\Phi_{DC}^{(1)} - \Phi_{DC}^{(0)}}{\Delta t} \end{cases} \quad (3.2)$$

Where n_{AC} and n_{DC} are the turns number of the main winding and control winding respectively; Φ_{AC} and Φ_{DC} are the AC flux and DC flux respectively.

By employing the calculation procedure in (3.1) and (3.2) at each time steps, the co-simulation can be carried on. The detailed co-simulation diagram is shown in Fig. 5.

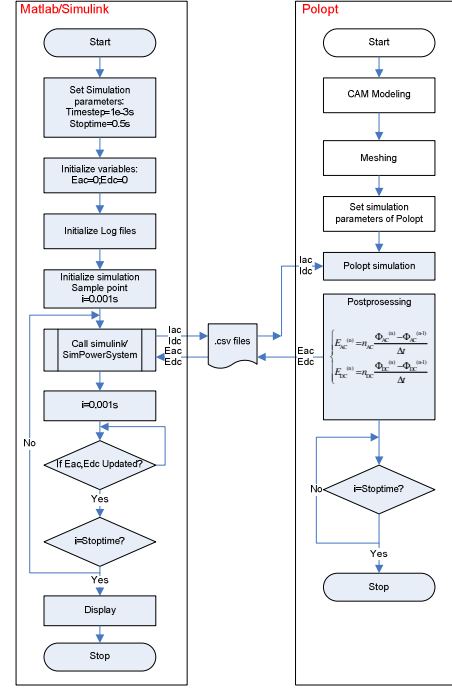


Fig. 5 The detailed co-simulation diagram

IV. APPLICATION EXAMPLES

A. The co-simulation results

The example is a 500kV/50MVA single phase controllable reactor with control system. The circuit diagram of the controllable reactor for the co-simulation is shown in Fig. 6. The breaker will trip the line when fault occurs at the load side, and the resulting overvoltage of the line caused by the load rejection will be suppressed by the controllable reactor, which is simulated by the IEM model.

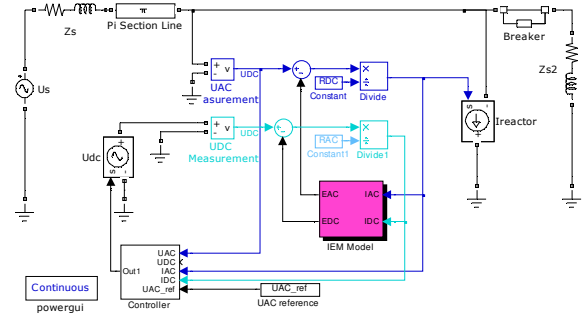


Fig. 6 Circuit diagram of 288kV/50MVA controllable reactor in the transmission grid system

Detailed co-simulation results will be presented in the full paper.

V. REFERENCES

- [1] Torbjörn Wass, Sven Hörmfeldt, Stefan Caldemarsson: *Magnetic Circuit for a Controllable Reactor*, IEEE Tran. on Mag, Vol. 42, No.9, Sep. 2006.
- [2] B. Krstajic, Z. Andjelic, S. Milojkovic, S. Babic, S. Salon: *Nonlinear 3D Magnetostatic Field Calculation by the Integral Equation Method with Surface and Volume Magnetic Charges*, IEEE Tran. on Mag., vol.28, No.2, March 1999.

Steady and Transient Electromagnetic-thermal Fields Analysis for Induction Machines Using FEM and FVM

Shuhong Wang, Qiuwang Wang, Zhe Ren, Wei Sun, Dan Liao, Jie Qiu

Xi'an Jiaotong University, Xi'an 710049, China

shwang@mail.xjtu.edu.cn

Limin Zhou, Youming Jiang

Zhuzhou CSR Electric. Co. Ltd, Zhuzhou 412001, China

Jian Guo Zhu, Youguang Guo, Yi Wang, Wei Xu

School of Electrical, Mechanical and Mechatronic Systems, University of Technology, Sydney, NSW 2007, Australia

Abstract — This paper presents a steady and transient analysis for magnetic and thermal field of induction machines (IM). The electromagnetic performances, such as magnetic field distribution, winding current and eddy currents flowing in conductor bars, are simulated by using field-circuit coupled method. The losses including of core loss, conducting loss of windings and rotor bars are evaluated during startup and steady operation. Excited by the losses, the transient and steady thermal fields are investigated by using finite volume method (FVM). The axial structural meshing is applied to simulate the temperature rise under ventilation case. The simulated electromagnetic performances and temperature rise are validated by experiment. The thermal field distribution of induction machine at both startup and steady states are discussed.

I. INTRODUCTION

The thermal conditions of induction machine (IM) are one of the main factors that limit the lifetime and the reliability of IM. Thermal analysis is very important for electrical machine designing, manufacturing, fault diagnosis and detection. One of the most effective methods to estimate the IM heating process is with the help of an equivalent thermal circuit, in which an IM is simulated as a system of heat sources that are interconnected to each other and connected to the environment by means of thermal conductivities [1]. A transient 2-D thermal analysis of switched reluctance motor by Finite Element Method (FEM) has been presented in [2], in which some thermal parameters are obtained by measurement.

The electromagnetic losses play a very important role as the sources of the temperature rise of electrical machines. Precise electromagnetic analysis of induction machines is necessary during steady and startup operation. FEM coupled with drive circuit is a powerful method to calculate the electromagnetic field distribution and the electromagnetic losses.

In this paper, the time-step field-circuit coupled method is applied to analysis of the electromagnetic field and current distribution of IM during startup and steady operation. The transient and steady thermal field is calculated by FVM after determination of the conduction and the convective heat transfer coefficients.

II. ELECTROMAGNETIC FIELD ANALYSIS OF IM

A two-dimensional (2D) FEM is applied for the IM, where the magnetic vector potential has only the z -component.

The Maxwell's equations applied to IM can be expressed as

$$\nabla \cdot (\nu \nabla A) - \sigma \frac{\partial A}{\partial t} + \frac{d_f N_f}{S_f a p} i_f + \frac{d_f a \sigma}{N_f l} u_{bar} = 0 \quad (1)$$

where A is the component of magnetic vector potential in the z axis, ν is the reluctivity of materials. i_f is the winding current, S_f is the total cross-sectional area of the region occupied by this winding in the solution domain, p is the symmetry multiplier which is defined as the ratio of the original full cross-sectional area to the solution area, d_f is the polarity to represent forward path or return path, a is the number of parallel branches, and N_f is the total conductor number. u_{bar} is the voltage difference between the terminals of solid conductor, and l is the model depth in the z axis.

The branch equations of the stranded windings and solid conductors are coupled with field equations. The loop method is applied to describe the circuit equations of the stranded windings, the solid conductors and the external circuits. The currents flowing in stranded winding and solid conductors are regarded as branch currents which may be expressed as a function of loop currents according to KCL. In loop method, the variables are chosen as loop current.

From above the field-circuit coupled equation can be established. The magnetic vector potentials of the nodes and the loop currents are chosen as unknowns.

The air gap of IM is re-meshed at each time step and the electromagnetic torque is calculated by using the Maxwell stress tensor. The angular speed and the rotor displacement at each time interval can be determined.

Core loss is evaluated by a traditional loss calculation approach. Because the current density is not uniform over the cross-section of the rotor bar, the loss on the rotor bar is expressed as the volume integration of current density of rotor bars.

III. THERMAL FIELD ANALYSIS USING FVM

Considering the computational accuracy and complexity of thermal field, the thermal model of IM such as end cover, end winding, end ring, bearing and shaft, etc., should be simplified. Fig. 1 illustrates the axial simplified models of IM.

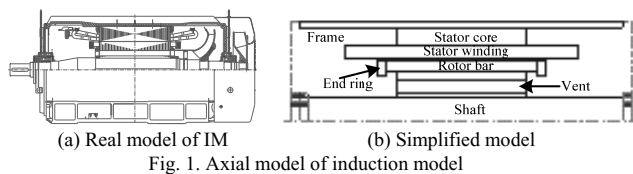


Fig. 1. Axial model of induction motor

The heat conductivity and convective heat transfer coefficients are determined by ventilation calculation and the bearing losses are evaluated. Those will be presented in detail in full paper.

In cross-section of the IM, the same triangular meshes are used in both electromagnetic FEM and thermal FVM. The structure grid is constructed in axial direction and an equivalent thermal circuit is applied to calculate the axial temperature distribution.

In FVM, the discrete equation is an integration of the conservation heat transfer equation over each control volume. In this paper, cell-centered method is used. For triangular mesh, the control volume is regarded as the element, also called the cell. The discrete temperature equation associated with one cell is expressed as

$$a_o T_o = \sum_{i=1}^3 a_i T_i + b_o \quad (2)$$

where, a_o and a_i are the convection and diffusion coefficients of a cell center and its adjacent points. b_o is the source associated with electromagnetic losses. T_o and T_i are temperatures of this cell center and its adjacent points. The boundary condition will be presented in full paper.

IV. STEADY AND TRANSIENT ANALYSIS OF ELECTROMAGNETIC-THERMAL FIELDS FOR IM

The simulation code of steady and transient coupled magnetic and thermal fields for IM is carried out. Due to the different time constants between the electromagnetic and the thermal systems, during every predefined time interval which including several time steps in electromagnetic computation, the thermal analysis is executed once.

A 3-phase four-pole asynchronous generator, a kind of IM, is used to evaluate the developed simulation code. The rated output power is 750 kW, the output voltage is 690 V and the frequency is 50 Hz. The finite element mesh is shown in Fig. 2. Fig. 3 pictures the current flowing in one rotor bar. The magnetic field distribution at startup operation is illustrated in Fig. 4 and the steady losses are shown in Fig. 5. Fig. 6 (a) and (b) show the temperature rise distributions at both startup and steady operations.

The axial temperature rise distribution is pictured in Fig. 7. The simulated temperature rise of stator winding, 106.4°C, is much closed to experimental result, 104.2°C, at steady operation. More simulation results and evaluation of developed code will be presented in full paper.

V. CONCLUSION

This paper develops a simulation code of electromagnetic-thermal field for IM. The transient electromagnetic losses are

calculated by FEM and temperature distribution is computed by FVM and equivalent thermal circuit. The simulation temperature rise of stator winding is verified by experimental ones. The temperature rise of the rotor bars is great than that of other parts at startup operation. At steady operation, the stator windings possess the greatest temperature rise. The detailed discussion will be presented in full paper.

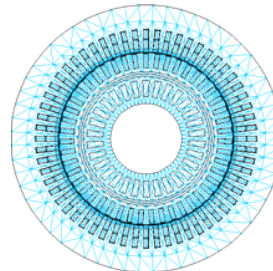


Fig. 2. FE meshes of IM

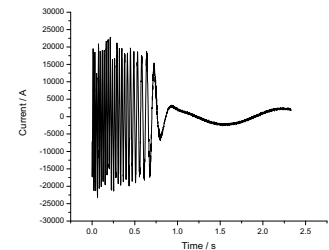


Fig. 3. Current flowing in rotor bar



Fig. 4. Magnetic field at startup

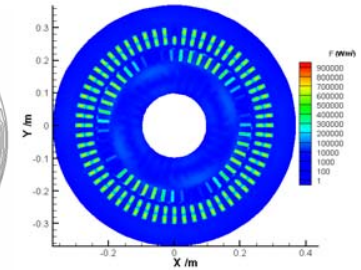


Fig. 5. Electromagnetic loss at steady

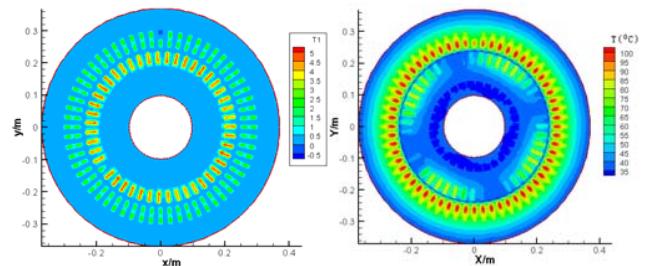


Fig. 6. Temperature rise distribution of IM

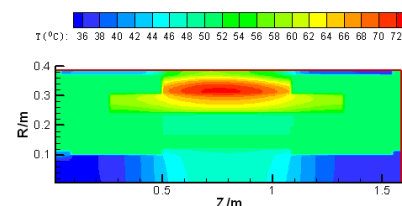


Fig. 7. Axial temperature rise distribution of IM

VI. REFERENCES

- [1] A. Shenkman, M. Chertkov and H. Moalem, "Thermal behaviour of induction motors under different speeds", *IEE Proc.-Electr. Power Appl.*, 152(5): 1307-1310, 2005
- [2] W. Wu, J. B. Dunlop, S. J. Collocott and B. A. Kalan, "Design Optimization of a Switched Reluctance Motor by Electromagnetic and Thermal Finite Element Analysis", *IEEE Trans. on Magn.* 39(5): 3334-3336, 2003.

Electromagnetic-Structure-Acoustic Coupled Analysis Method of GMM Transducer Speaker

Byungjin Yoo¹, Katsuhiko Hirata¹, and Oonishi Atsurou¹

¹Department of Adaptive Machine Systems, Osaka University
Yamadaoka 2-1, Suita-city, Osaka, 565-0871, Japan
{byungjin.yoo, k-hirata, atsurou.oonishi}@ams.eng.osaka-u.ac.jp

Abstract — This paper deals with a coupled analysis method of electromagnetic-structural-acoustic coupled fields for flat panel speaker driven by giant magnetostrictive materials (GMM) transducer using finite element method (FEM). This method is applied to predict the sound pressure level (SPL) of flat panel speaker at audio frequency. The validity of the analysis method is verified by the measurement of a prototype.

I. INTRODUCTION

Giant Magnetostrictive Materials came to attract attention because of great magnetostriction, strong force, high response speed and so on [1]. Recently, the flat panel speaker system driven by this smart material based transducer has been released. Whereas other standard speaker systems with enclosure create acoustic field, which only spread forward, one of the obvious advantages of speaker system like this is creation of 360-degree acoustic field by vibrating a rigid panel with a GMM transducer. However, by vibrating a rigid panel as principle of operation, it is difficult to optimize the SPL at audio frequency range. The SPL relies on the vibration of rigid panel occurred by GMM transducer, it is necessary to grasp not only the vibration of GMM transducer and rigid panel but also acoustical phenomenon at a time.

In this paper, we present the numerical analysis method of electromagnetic-structural-acoustically coupled system at frequency domain employing FEM. Moreover, the validity of the analysis method is verified through the comparison with the measurement of a prototype.

II. THEORY

A. Magnetic field analysis

The governing equation of the magnetic field can be indicated in frequency domain as follows

$$\text{rot}(\dot{\nu} \text{rot } \dot{A}) = \dot{J}_0 + \dot{J}_e = \dot{J}_0 - \sigma(j\omega \dot{A} + \text{grad } \dot{\phi}) \quad (1)$$

where $\dot{\nu}$ is the magnetic reluctivity, \dot{J}_0 is the exciting current density, \dot{J}_e is the eddy current density, σ is the electric conductivity, ω is the angular frequency, \dot{A} is the magnetic vector potential and $\dot{\phi}$ is the electric scalar potential. Dot ($\dot{\cdot}$) means complex number.

B. Structure analysis

For the modeling of vibration of GMM transducer and panel, the following equation of motion is used.

$$\nabla \cdot (\mathbf{T}_{mech} + \mathbf{T}_M) + \mathbf{b}_{mech} = \rho \frac{d^2 \mathbf{u}}{dt^2} \quad (2)$$

Where \mathbf{T}_{mech} is the stress tensor induced by deformation, \mathbf{T}_M is the Maxwell stress tensor, \mathbf{b}_{mech} is the mechanical body force, ρ is the mass density and \mathbf{u} is the displacement vector. Since GMM are magnetizable magnetic materials, \mathbf{T}_M can be described as [2]

$$\mathbf{T}_M = \mathbf{H} \otimes \mathbf{B} - \frac{\mu_0}{2} (\mathbf{H} \cdot \mathbf{H}) \mathbf{I} \quad (3)$$

where \mathbf{H} is the magnetic field intensity, \mathbf{B} is the magnetic flux density, the operator \otimes is the dynamic tensor product, μ_0 is the permeability matrix of vacuum and \mathbf{I} is the unit matrix.

C. Constitutive equations of GMM [3]

Although the constitutive equations that describe the phenomenon of magnetostriction are nonlinear formulation, they can be approximated to linear system under small changes of electromagnetic and mechanical quantities. The linearized constitutive equations of GMM can be expressed in the d -type form as follow

$$\mathbf{S} = \mathbf{s}^H \mathbf{T}_{mech} + \mathbf{d}^T \mathbf{H} \quad (4)$$

$$\mathbf{B} = \mathbf{d}^T \mathbf{T}_{mech} + \boldsymbol{\mu}^T \mathbf{H} \quad (5)$$

where, \mathbf{S} is the strain tensor, \mathbf{s}^H is the compliance matrix, \mathbf{d} is the magneto-mechanical coupling coefficient, $\boldsymbol{\mu}$ is the permeability and the superscript 't' indicates the transpose of the matrix. The superscript H and T mean that the value inside the matrix reflects condition under constant.

D. Acoustic field analysis

In this analysis, to deal with the structure-acoustic coupled field, the Eulerian approach [4] is used that the governing equation can be written as a wave equation in terms of pressure. In this case, the governing equation of the acoustic field can be indicated using Helmholtz equation as

$$\nabla \cdot \left(-\frac{1}{\rho_0} \nabla \mathbf{P} \right) - \frac{\omega^2 \mathbf{P}}{\rho_0 c^2} = 0 \quad (6)$$

where ρ_0 is the fluid density, \mathbf{P} is the pressure, c is the speed of sound and ω is the angular frequency.

III. ANALYSIS MODEL AND CONDITIONS

A. Analysis Model

The structure of GMM transducer is shown in Fig. 1. The transducer mainly consists of two GMM rods (TDK, PMT-1, $\phi 5$ -mm and 14-mm length), permanent magnet (Ferrite, 0.4T, supplying 18kA/m bias magnetic field to GMM rods) and

wound coil of 700 turns for driving. As a rigid panel, $\phi 200$ -mm and 1.5-mm thickness aluminum panel is used. Because these structures are axial symmetric, the analysis is conducted using 2-D axial symmetric model. Fig. 2 shows the entire analyzed model including air domain for SPL calculation. The air domain extends to one meter around panel and perfectly matched layer (PML) is constructed around the outside of the fluid domain for avoiding the reflection of sound pressure.

The input voltage is 1 V, in the frequency range from 400 Hz to 20 kHz. The discretization is listed in Table I.

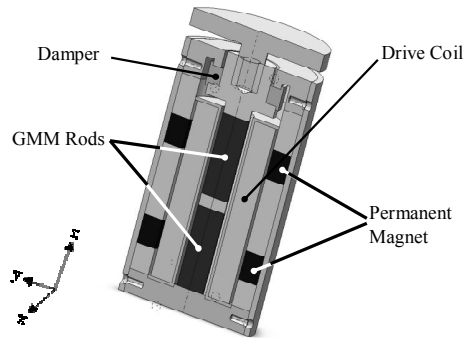


Fig. 1. Structure of GMM actuator.

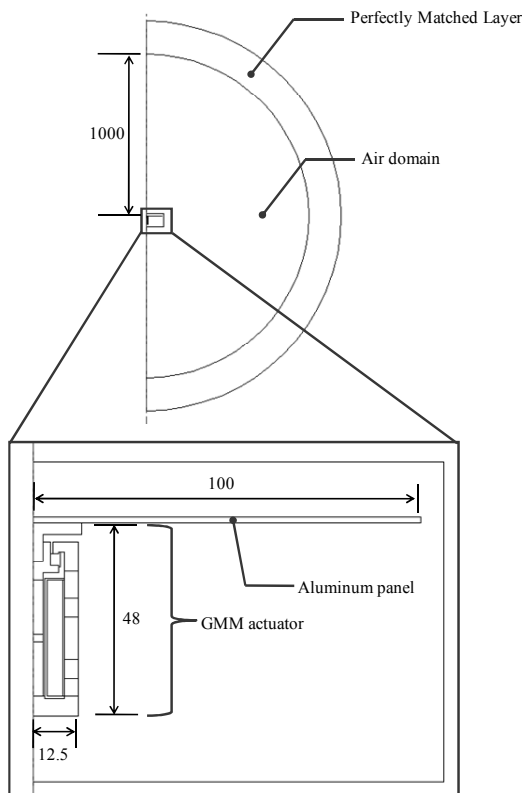


Fig. 2. Analyzed model.

TABLE I
DISCRETIZATION AND CPU TIME

Number of elements	402, 943
Number of nodes	201, 893
CPU time (hours)	2.5

Used computer: Xeon (3.0 GHz)

IV. VERIFICATION BY MEASUREMENT

The SPL measurement of flat panel speaker driven by GMM transducer is conducted in an anechoic room. The input AC voltage for driving the speaker is 1 V (peak-to-peak), and the frequency range is swept from 400 Hz to 20 kHz as well as analyzed conditions. Fig. 3 shows the SPL comparison positions between analysis and measurement. Fig. 4 shows the comparison results between analysis and measurement at above positions. As can be seen, analyzed results agree well with the measured ones.

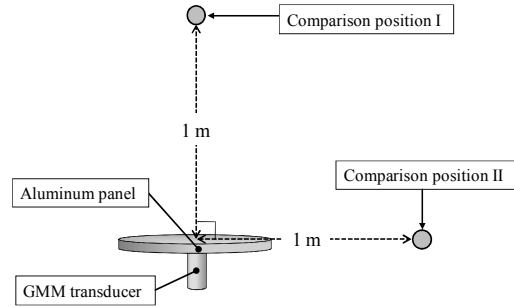
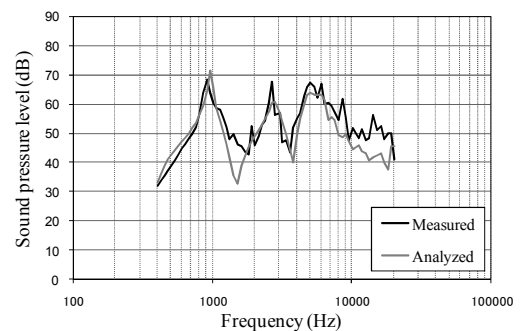
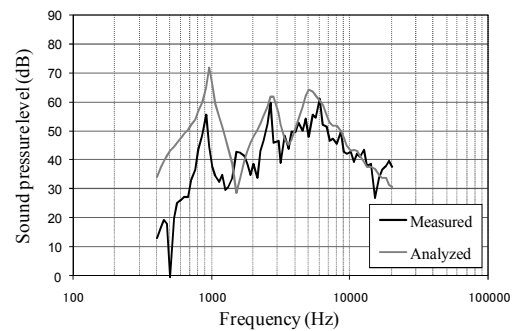


Fig. 3. SPL measurement points of flat panel speaker.



(a) Comparison position I



(b) Comparison position II

Fig. 4. SPL comparison between analyzed and measured results at each comparison position.

V. REFERENCES

- [1] Jiles D, *Introduction to Magnetism and Magnetic Materials*, London: Chapman and Hall, chapter 5, 1991.
- [2] J. Clerk Maxwell, *A Treatise on Electricity and Magnetism*, 3rd ed., vol. 2. Oxford: Clarendon, 1892, pp. 68-73.
- [3] J. G. Benatar, "Fem implementations of magnetostrictive-based applications", Master thesis, University of Maryland, 2005.
- [4] Zienkiewicz. O. C, Bettess. P, "Fluid-structure dynamic interaction and wave force", An introduction to numerical treatment *Int. J. Number. Methods Eng.* 13, 1-16, 1978.

3D Transient Field-Circuit Modeling of Inductive Fault Current Limiters

D. Cvoric**, D. Lahaye*, S. W. H. de Haan** and J. A. Ferreira**

Affiliation: ** Power system protection, power electronics, * Numerical Analysis Unit

**Electrical Energy Conversion Unit

*Delft Institute of Applied Mathematics

Department of Electrical Engineering, Mathematics and Computer Sciences

TU Delft, Mekelweg 4, 2628 CD Delft, The Netherlands

{d.cvoric,d.j.p.lahaye}@tudelft.nl

Abstract—Due to increasing levels of the fault currents, Fault Current Limiters (FCLs) are expected to play an important role in protection of future power grids. Inductive saturable FCL are particularly interesting due to their inherent reaction on the fault. Many different configurations have been proposed in literature. Being difficult or impossible to create accurate analytical models of some FCL configurations, the development of finite element (FE) FCL models is required. This paper presents 3D transient FE model of two configurations of inductive FCL: so called open-core and three-leg FCLs. The model has been validated by comparing simulation results with lab measurements. Results show very good agreement. The model is valuable tool for design, optimization and verification of inductive FCLs.

I. INTRODUCTION

Fault Current Limiters (FCLs) are expected to play an important role in the protection of future power grids. They are capable of preventing the fault currents from reaching too high levels and, therefore, reducing the mechanical and thermal stress of all power system components.

The FCLs can be classified on passive, solid-state and hybrid FCLs [1]. Passive FCLs are particularly interesting due to their merit to inherently react on the fault. Inductive FCLs based on the core saturation is type of the passive FCLs. They comprise magnetic cores and windings. Different configurations of inductive FCL are proposed in literature [1]-[4]. It is difficult, or in some cases impossible, to derive accurate analytical model of different FCL designs.

The goal of this paper is to introduce the 3D transient finite element (FE) model of the inductive FCL. The model presents a valuable tool for verification and optimization of the inductive FCL. The operation of the designed FCL can be verified precisely, with the possibility to vary all design parameters. The experiment with both FCL configurations, three-leg [2] and open-core [3], is done in lab in order to provide reference data for verification of the models. The simulation results of both 2D and 3D FCL models are presented. The 2D model is not sufficiently good for modeling of the FCL. The 3D simulation results show good matching with the experimental results.

II. PRINCIPLE OF OPERATION OF INDUCTIVE FCL

A. Three-Leg Core FCL Configuration

A single core is used per phase, with three vertical legs [2], see in Fig.1(a). Each outer leg contains one ac and

one dc winding. Dc windings provide circular dc flux flow, saturating the outer legs. Upon the fault inception, outer legs are alternately de-saturated, increasing in that way the impedance of the ac windings. The ac flux closes its path through the left (in another half cycle right leg) and the middle core legs.

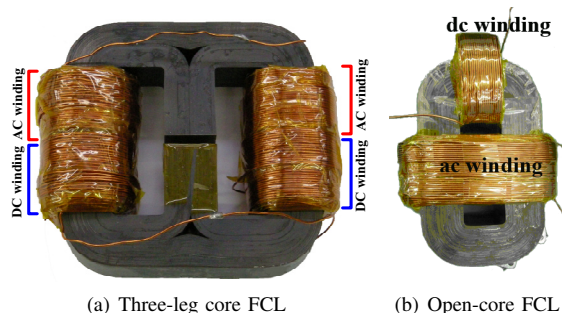


Fig. 1: FCLs used in the experiment

B. Open-Core FCL Configuration

FCL comprises single core per-phase with one ac and one dc winding [3], see in Fig.1(b). The dc winding is connected to a dc current source and saturates the core. The ac winding is connected in series with line. During a fault, core remains saturated and the inductance of the ac winding is very low. In a fault stage, left and right legs of the core are alternately de-saturated by the fault current, imposing large impedance into the line.

Detailed explanations of both configuration will be given in the full paper.

III. MATHEMATICAL BACKGROUND OF THE MODEL

The developed mathematical model consists of a partial differential equation for the magnetic field in the structure of the FCL, coupled with an ordinary differential equation for the current in the ac coil. Both are coupled by the magnetically induced voltage in the ac coil. We introduce the so-called coil winding function t , in such a way that the applied current density in the coils can be written as:

$$J_e = \frac{N_w I(t)}{S} t, \quad (1)$$

where $I(t)$, N_w and S are the applied current, the number of coil turns and the cross-sectional area, respectively. The magnetic field equation in the magnetic vector potential A can then be written as [5]:

$$\sigma \frac{dA}{dt} + \nabla \times \mu_0^{-1} \mu_r^{-1} (\nabla \times A) = J_e \quad (2)$$

The circuit relation for the current in the ac coil is an algebraic relation that ensures that at all times the sum of resistive and induced voltage V_{ind} is equal to the externally applied voltage:

$$(R_{load} + R_{ac}) I + V_{ind} = V_e \quad (3)$$

In this relation V_{ind} is computed as the following integral over the volume of the ac coil:

$$V_{ind} = \frac{N_w}{S} \int_{\Omega_{ac}} E t d\Omega \quad (4)$$

The fault is modeled by allowing $R_{load}(t)$ to suddenly drop to a very low value at a particular time instance. The Comsol Multiphysics package [6] offers an easy to use interface to implement this field-circuit coupled model.

IV. SIMULATION AND EXPERIMENTAL RESULTS

In this section the representative numerical and experimental results are presented. Fig.2 shows the close match between the 3D model and the experimental results for the open-core FCL, indicating that the 3D model can indeed be used to predict the behavior of the FCL. If a 2D model is used, the results are considerably different from those obtained in the experiment (see in Fig.2).

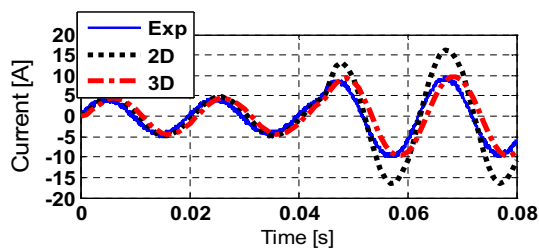
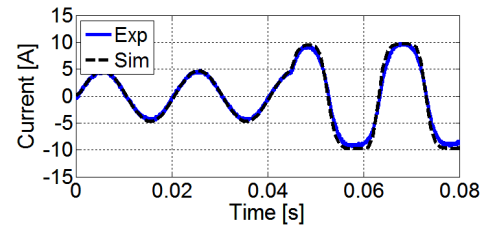


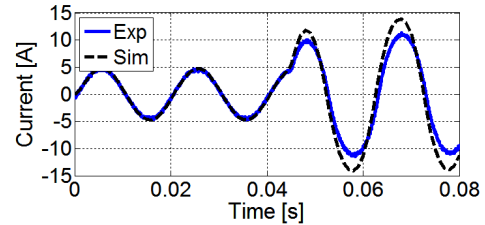
Fig. 2: Simulation and experimental current waveforms for open-core FCL

Fig.3 presents simulation and experimental results for the three-leg core FCL. They are derived for two cases: FCL without a gap in the middle leg and with the 3.5mm gap length. The shown results are for 2D FE model. In the case when there is no gap, results match very well. However, difference between results appears if the gap is inserted in the middle leg, see in Fig.3(b).

The results of the 3D model will be presented in the final paper. Just as in the case of the open-core FCL model, it is expected that 3D results will show much better matching with the experimental one.



(a) Without gap



(b) With 3.5mm gap

Fig. 3: Simulation and experimental current waveforms for the three-leg core FCL

V. WHAT WILL BE PRESENTED IN THE FINAL PAPER

All the sections will be further developed. The presented experiments will be described in detail and additional simulation results for both FCLs will be depicted. The results will clearly show the operation principles of both FCL configurations.

VI. CONCLUSION

FE modeling is required for accurate design of inductive saturable FCL. Although 2D model considerably saves simulation time, it cannot provide sufficiently accurate results.

Derived 3D model presents a valuable tool for design, optimization and verification of inductive FCL. 3D FE model was verified for two FCL configurations: open-core and three-leg core FCLs. Simulation results from 3D model match very well those from the lab experiments.

ACKNOWLEDGEMENT

This project is partially funded from the Energy Research program EOS by the Ministry of Economic Affairs.

The authors gratefully acknowledge the feedback provided by Prof. Herbert De Gerssem and by the Comsol Multiphysics support team.

REFERENCES

- [1] D. Cvoric, S.W.H. de Haan, J.A. Ferreira: "Improved configuration of the inductive core-saturation fault current limiter with the magnetic decoupling", Industry Applications Society Annual Meeting, 2008. IAS '08. IEEE, 2008, pp. 1-7.
- [2] D. Cvoric, S.W.H. de Haan, J.A. Ferreira: "New saturable-core FCL topology with reduced core size", IEEE ECCE Asia (IPEMC), 2009, to be published.
- [3] S. Wolfus and A. Friedman and Y. Yeshurun and V. Rozenshtein and Z. Bar-Haim, "Fault current limiters (FCL) with the cores saturated by superconducting coils", International Application Published Under the Patent Cooperation Treaty, WO 2007/029224 A1, March 2007.
- [4] Francis Anthony Darmann, Frank Darmann: "Superconductor current limiting system and method", US 2007/0115598 A1, May 2007.
- [5] J. Jin: "The finite element method in electromagnetics", John Wiley & Sons
- [6] www.comsol.com

Hybrid Analytical-FEM Method for Microwave Heating Analysis in a Single Mode Cavity

D. B. Oliveira and E. J. Silva

Department of Electrical Engineering, Federal University of Minas Gerais
Av. Antônio Carlos, 6627, 31270-901, Belo Horizonte – MG – Brazil
{diogo,elson}@cpdee.ufmg.br

Abstract — In this paper an approach to solve the thermal-electromagnetic problem of microwave heating a thin load inside a single mode applicator is presented. A direct problem solving methodology that takes into account the temperature dependence of the electrical permittivity is very time-consuming. By using a hybrid analytical finite element method we can speed up the determination of the electromagnetic field. Also the hybrid method provides an easy way of tuning the cavity coupling. To validate the approach the heating of a thin ceramic cylinder inside a WR-340 single mode cavity is presented.

I. INTRODUCTION

The single mode cavity is an applicator very common for processing small and low loss samples through microwave heating, Fig. 1.

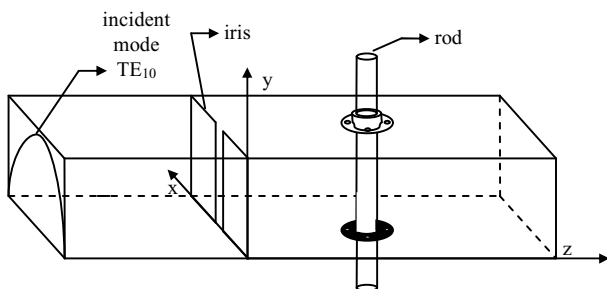


Fig. 1 – Description of single mode cavity.

The determination of the electromagnetic fields inside the cavity using the standard finite element method, even if the electrical permittivity is independent of the temperature, is a difficult task [1]. The iris presence makes the modal composition of the electromagnetic fields very complex leading to a very slow convergence rate to obtain an accepted solution. Also the FEM global matrix is usually ill-conditioning making the inversion very hard. Hence, the electromagnetic solution is very time consuming.

This work presents a methodology to solve the thermal electromagnetic problem in the single mode cavity. To overcome the drawbacks above a hybrid analytical finite element method is used in the computation of the electromagnetic fields. The analytical technique is based on the scattering matrix theory.

As a by product of this method, a tuning technique that allows the iris aperture and the end short to move during the heating process is obtained. It allows analyzing efficient working conditions of the highly resonant cavity.

The thermal problem is solved using the standart FEM in time domain with Crank-Nicolson time discretization.

II. METHODOLOGY

A. Electromagnetic Problem

Fig. 2 shows three planes z_1 , z_2 e z_3 through which is assumed to propagate only TE_{10} modes. It is a valid assumption if evanescent modes excited by the load and the iris have negligible amplitudes there.

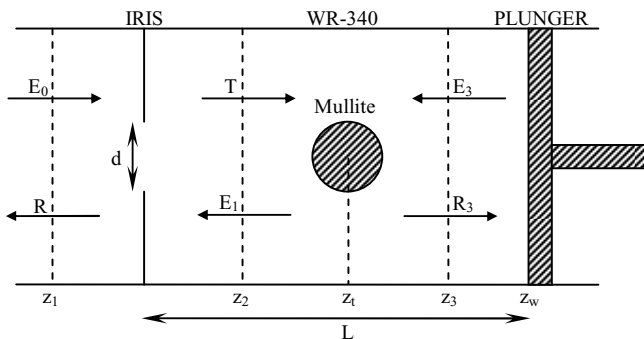


Fig. 2 – Top view of the applicator and the propagating modes.

Using the scattering matrix theory the ceramic sample region is modeled by the following matrix system

$$\begin{bmatrix} \bar{E}_1 \\ \bar{R}_3 \end{bmatrix} = \begin{bmatrix} r_c^l e^{-j2k_{10}z_l} & t_c^r \\ t_c^l & r_c^r e^{+j2k_{10}z_l} \end{bmatrix} \begin{bmatrix} \bar{T} \\ \bar{E}_3 \end{bmatrix} \quad (1)$$

where k_{10} is the propagation constant of TE_{10} mode, r_c and t_c are respectively the reflection and transmission coefficients of the load. The superscripts l and r mean that these coefficients are calculated considering the TE_{10} incident mode propagating in $+\hat{z}$ and $-\hat{z}$ direction. This distinction must be done since the temperature dependence of the permittivity makes the ceramic a non-symmetric load.

These coefficients are calculated numerically using the FEM [2]. Note that to calculate these coefficients we have to solve two simple problems as shown in Fig. 3.

Two other relations are needed for expressing analytically the modes amplitudes in the cavity. One to define the reflection coefficient (γ) of the structure composed by waveguide, load and short and another to relate the modes E_3 and R_3 .

$$E_1 = \gamma T \quad \text{and} \quad E_3 = -e^{+2jk_{10}z_w} R_3 \quad (2)$$

From (1) and (2) we can write the amplitudes of the modes R, T and E_3 and of the coefficient γ by analytical expressions

$$\gamma = r_c^l e^{-j2k_{10}z_l} + \frac{t_c^r t_c^l}{\left(\frac{-1}{e^{-j2k_{10}z_w}} - r_c^r e^{+j2k_{10}z_l} \right)} \quad (3)$$

$$R = r_1 E_0 + \frac{t_1^2 \gamma E_0}{1 - r_1 \gamma} \quad \text{and} \quad T = \frac{t_1 E_0}{1 - r_1 \gamma} \quad (4)$$

$$E_3 = \frac{t_c^l T}{\begin{pmatrix} -1 \\ e^{-j2k_{10}z_w} - r_c^r e^{+j2k_{10}z_t} \end{pmatrix}} \quad (5)$$

The coefficients r_1 and t_1 are the reflection and transmission coefficients of the iris [3].

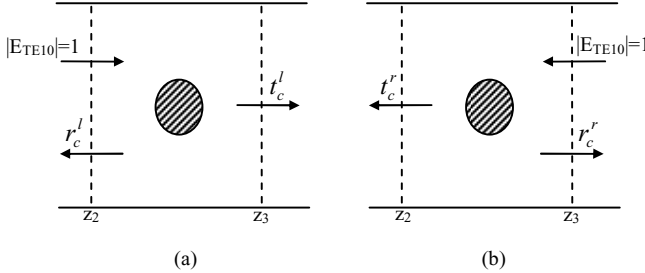


Fig. 3 – Reflection and transmission coefficients for TE₁₀ incidence, (a) from left and (b) from right.

As next step the length z_w and the iris aperture d are determined by what is called tuning process.

Finally, the electric field solution in the load region $z_2 \leq z \leq z_3$ can be found. It is done by multiplying the field distribution in Fig. 3(a) and Fig. 3(b) by T and E_3 respectively and then summing the distributions.

B. Coupled Problem

The source of heat due to the microwave is given by the power density absorption in the material

$$p = \frac{1}{2} \omega \epsilon_0 \epsilon_r''(T) |E|^2 \quad (6)$$

The complex electrical permittivity of the ceramic (mullite) changes with the temperature according to Fig. 4.

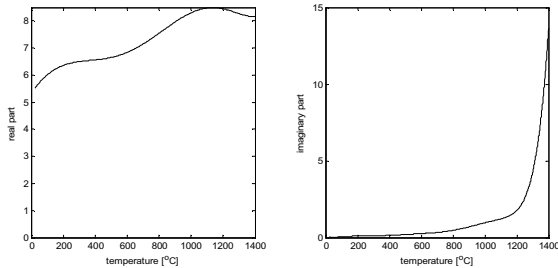


Fig. 4 – Mullite relative electrical permittivity.

In the simulation process the thermal problem is solved during some time steps until the temperature is sufficient to produce significant change in the permittivity. If significant changes are detected the heat source is updated by computing a new electromagnetic field distribution.

C. Tuning Technique

Most papers, tuning the cavity means to adjust the plunger position. In [4], the authors proposed an experimental device where an adjustable iris aperture is used for optimal coupling. This idea is modeled numerically in this work.

In the tuning process we search the aperture value and the plunger position that minimize the energy of the R mode every time the electromagnetic problem is solved.

This tuning technique is easily implemented by the methodology presented in this paper. In a standard finite element method we would have to re-mesh the problem every time that the plunger position or iris aperture changes.

III. RESULTS

To validate our approach we analyze the microwave heating of a mullite ceramic sample inside the heater. It is a rod of radius 0.01m.

The Fig. 5 shows the temperature distribution on the external surface of the rod. The total processing time was 1800s. In this case the electromagnetic problem was solved 58 times. The time step was 6s and the electrical permittivity was corrected when the real part or the imaginary part changed more than 5% in relation to the last value.

Although we have to solve two electromagnetic problems they are much simpler than the original one. By using a mesh parameter $h_{\max} = \lambda/25$, the tetrahedral mesh used in the hybrid method has 13727 elements while the original problem requires 90854 elements. This is due to the difference in the length of the domains. Also the mesh is more uniform in hybrid method since the iris is not present once it is taken into account in the analytical part.

Note that since the two electromagnetic problems in the hybrid method are independent we can use parallel multithreading processing in multi-core computer to determine the electric field. Another improvement can be obtained by optimizing the number of times the power density need to be re-calculated [5].

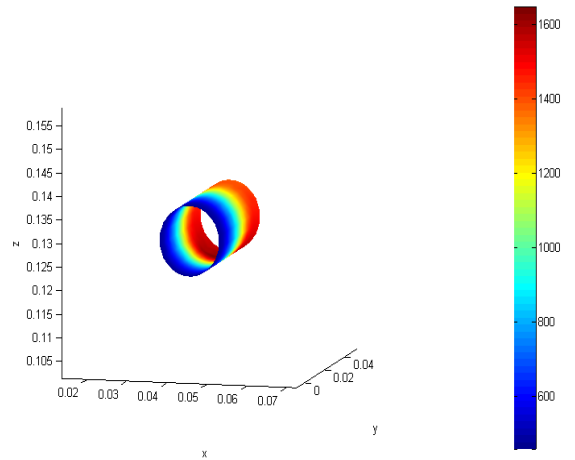


Fig. 5 – Temperature distribution on the external surface.

IV. REFERENCES

- [1] Cheryl V. Hile, Gregory A. Kriegsmann, "A Hybrid Numerical Method for Loaded Highly Resonant Single Mode Cavities", *Journal of Computational Physics*, 142(CP985951): 506-520, 1998.
- [2] Kiyoshi Ise, Kazuhiro Inoue, Masanori Koshiba, "Three-Dimensional Finite Element Method with Edge Elements for Electromagnetic Waveguide Discontinuities", *IEEE Trans. On Microwave Theory and Techniques*, 39(8): 1289-1295, 1991.
- [3] Robert E. Collin, *Field Theory of Guided Waves*, IEEE Press: NJ, 1991.
- [4] A. C. Metaxas, "Rapid Feasibility Test Using a TE_{10n} Variable Aperture Resonant Applicator," *Journal of Microwave Power and Electromagnetic Energy*, 2(1):16-24, 1990.
- [5] A. A. Rabello, E. J. Silva, R. R. Saldanha, C. Vollaire and Alain Nicolas, "Adaptive Time-Stepping Analysis of Nonlinear Microwave Heating Problems", *IEEE Transaction on Magnetics*, 41(5):1584-1587, 2005.

Distributed Models for Air-Core Ethernet Transformers

Isaak D. Mayergoyz¹, David Bowen¹, Charles Krafft²

¹ECE Department and UMIACS, University of Maryland, College Park, Maryland 20742, USA

²Laboratory for Physical Sciences, College Park, Maryland 20740, USA

Abstract— Ethernet transformers are widely used for isolation in computer networks in the high frequency range (0.1 MHz – 1GHz). It turns out that it is the cross-winding capacitance that supports the flat pass band of these transformers above 50MHz. Size reduction for fabrication of these transformers motivates the development of a capacitance coupled air-core device. In this paper, novel models of air-core Ethernet transformers that take into account the distributed nature of cross-winding and intra-winding capacitances will be discussed. Differential-mode signal transfer characteristics will be computed for different transformer parameters. The computation of cross-winding capacitance will be discussed as well along with the symmetry considerations which appreciably simplify its computation.

Ethernet transformers are widely used as interfaces between communication networks and computers. For this reason, these transformers are designed to suppress common-mode signals (noise), induced as a results of electromagnetic interference, and at the same time pass through with minimal distortion differential-mode signals, which carry transmitted information. To achieve this performance, the primary and secondary windings have the same turn numbers and are wound together (in bifilar manner) around ferrite cores [1]-[3]. This bifilar winding arrangement is done on purpose to minimize leakage inductances of these windings in order to get flat transfer characteristics of these transformers in the desired high frequency range (0.1 MHz – 1GHz). The close proximity of the primary and secondary windings results in the appreciable cross-winding capacitance. This cross-winding capacitance is beneficial to the Ethernet transformers bandwidth. However, this capacitance also serves as a channel for common-mode signals. To suppress this channel, the midpoints of the primary and secondary windings are grounded.

It is known (and has been confirmed in our experimental research) that magnetic permeability of ferrite cores appreciably and rapidly degrades at frequencies above 1MHz. This clearly suggests that the differential-mode signal pass band of Ethernet transformers for frequencies above 50 MHz is by and large supported by the cross-winding capacitance. This has prompted the idea that the air-core designs of Ethernet transformers must be possible. These designs are compatible with the existing silicon fabrication technologies and may result in planar miniaturized structures of Ethernet transformers.

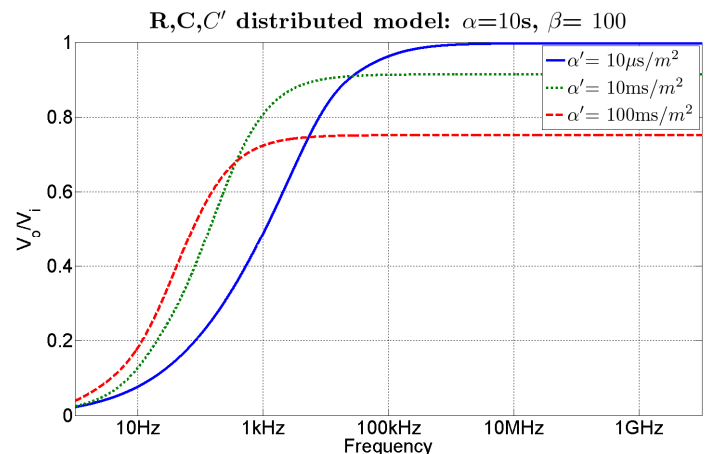


Figure 1. Transfer Characteristics of Distributed transformer model: varying α' .

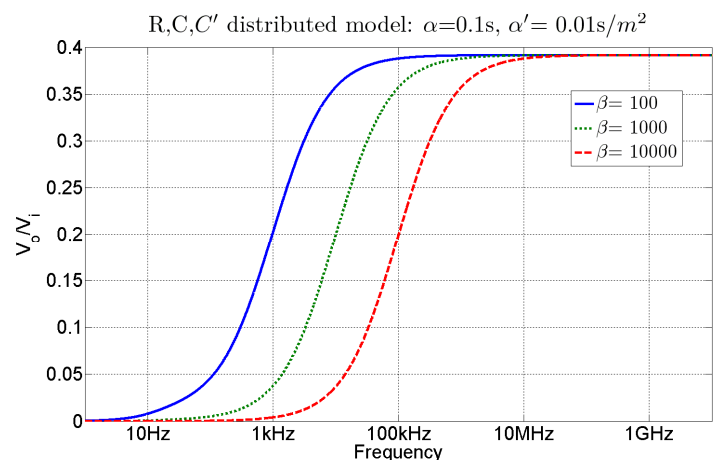


Figure 2. Transfer characteristics of distributed transformer model: varying β .

In the talk, novel distributed models of air-core Ethernet transformers will be discussed. These models take into account the distributed nature of cross-winding and intra-winding capacitances. Mathematically, these models are described by boundary value problems for specific differential equations. It turns out that separate distributed models are needed for differential-mode and common-mode signals. The main distinction between these models lies in the boundary conditions which are used for differential-mode and common-mode signals. The main goal of the analysis is the calculation

of the transfer characteristics of air-core transformers. These transfer characteristics depend on five variables (R, R_L, C, C' , and l) which can be combined into three parameters (α, α', β) (see below). In other words, these transfer characteristics can be fully encoded in terms of α, α' and β . Extensive numerical computations of transfer characteristics of air-core Ethernet transformers will be presented in the talk. An example of such computations is given in Figures 1 and 2. In these figures, the differential-mode signal transfer characteristics of Ethernet transformers are computed for different values of three parameters

$$\alpha = RC, \quad (1)$$

$$\alpha' = \frac{RC'}{l^2}, \quad (2)$$

$$\text{and } \beta = \frac{R}{R_L}. \quad (3)$$

Here, R is the resistance of the primary (or secondary) winding, C and C' are cross-winding and inter-winding capacitances, respectively, R_L is a load resistance, while l is

the length of each winding. It is apparent from Figures 1 and 2 that various designs of air-core Ethernet transformers encoded by the same values of α, α' , and β result in the same (and acceptable) differential-mode transfer characteristics. It is apparent that the values of cross-winding and intra-winding capacitances determine properties of Ethernet transformers. For this reason, the computation of these capacitances will be discussed in the talk along with the symmetry considerations which appreciably simplify the computation of these capacitances. These symmetry considerations allow one to reduce the calculation of capacitances of line conductors placed on dielectric substrate to the calculation of capacitances of the same conductors in free space.

REFERENCES

- [1] M. Xu, T. M. Liakopoulos, and C. H. Ahn, "A microfabricated transformer for high-frequency power or signal conversion," *IEEE Trans. Magn.*, vol. 34, pg 1369, 1998
- [2] H. Kurata, K. Shirakawa, O. Nakazima, and K. Murakami, "Study of thin film micro transformer with high operating frequency and coupling coefficient," *IEEE Trans. Magn.* vol. 29, pp. 3204-3206, 1993.
- [3] D. Bowen, I. Mayergoyz, C. Krafft, D. Kroop, and M. Beyaz, "On design of air-core Ethernet transformers," *J. Appl. Phys.*, vol. 105, 2009

Dynamic simulation of an electromechanical energy scavenging device

Aldo Canova^a, Elvio Bonisoli^b, Fabio Freschi^a, Sandro Moos^b, Maurizio Repetto^a, Stefano Tornincasa^b

^aDip. Ingegneria Elettrica, ^bDip. dei Sistemi di Produzione ed Economia dell'Azienda

Politecnico di Torino

I-10129 Torino, Italy

Email: name.surname@polito.it

Abstract—This paper presents the model of an electromechanical energy scavenging device whose energy conversion is due to the motion of a permanent magnet inside a magnetic circuit. Magnet acceleration is created by tyre deformation during car motion along the road. Small dimensions (less than one cubic centimeter) and relatively high power output (more than one milliwatt), requires an accurate modeling of the energy conversion device. A nonlinear magnetic modeling is carried out and its outcomes are coupled to a dynamic model developed inside the Simulink environment. A good agreement is found in the comparison between theoretical model and experiments.

I. INTRODUCTION

A recent concept being implemented to power circuits is using energy scavenging or energy harvesting. This makes use of energy diffused in the system to be collected by some energy conversion devices like solar cells, piezoelectric generators, or others like electromechanical structures. These devices take energy from diffuse sources, convert it to electricity, and, by means of a proper electronic signal conditioning, use it to supply isolated users, for instance remote wireless controlled sensors.

Among the main difficulties of the design phase of this class of devices, there is the need to reach high values of power density cell and very high global efficiency of the whole process since the diffuse power which primarily feeds the scavenger is usually low. This fact calls for an accurate simulation of the integrated energy scavenger component made up of converter and electronic circuit.

In the following, the design process of an electromechanical energy scavenger, aimed at taking power from tyre deformation during the movement of a car, is described. The main design constraints are related to the volume occupied by the converter which should be less than 1 cm³, by power which should be more than 1 mW in average over one wheel revolution and by voltage which should not be lower than 1.3 V and not exceeding 4 V.

II. SCAVENGER MODEL

An accurate model of the energy scavenger requires the study of different phenomena, in particular:

- magnetic circuit and interaction with magnet movement, taking into account nonlinearities of materials;
- interaction with external electric load and definition of a scavenger equivalent circuit;

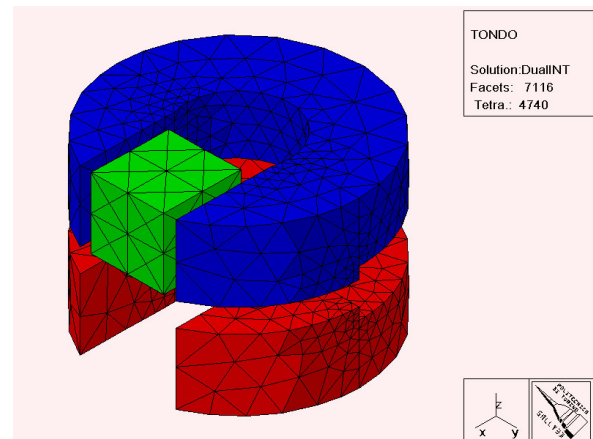


Fig. 1. Magnetic circuit of the energy scavenger without coils wound on cores

- dynamic simulation of the moving mass as a response from external acceleration;
- definition of the energy dissipations present in the system like dry friction and pneumatic forces arising from mass motion.

A. Magnetic simulation

The magnetic system is made by two ferromagnetic cores, with two coils wound on them, and by a brick shaped moving permanent magnet traveling between them. Ferromagnetic cores are made by Soft Magnetic Composite (SMC) material. The reasons for this choice are: the time-varying flux conditions and thus the need to reduce eddy currents and losses and the good machinability of the material that allows to obtain complex three dimensional core shapes. Magnetic analysis of the structure (reported in Fig. 1), should give as results: the magnetic flux linked with the coils and the forces acting on the magnet as function of the coordinate of the magnet z .

The nonlinear magnetic analysis is performed by a hybrid magneto-static code based on the coupling of a cell method volume discretization technique with a Green function integral approach [1]. Due to its mesh-less treatment of air, the code gives accurate results in term of force values computed by means of integration of the Maxwell stress tensor [2] and this fact is here very important since reluctance forces, caused

by ferromagnetic salient poles, largely influence the dynamic behavior of the moving mass.

B. Circuit model

The lumped parameter model of the converter is used to interface it with the external load and is made by an electromotive-force generator depending on magnet velocity $e = e(\dot{z})$ being z magnet position, by the ohmic resistance and by the inductance of the winding. The second parameter is varying because of core saturation and so the value of inductance is sampled at different magnet positions obtaining then a $L = L(z)$.

C. Dynamic simulation

The dynamic model is developed in Matlab/Simulink environment by means of a block-oriented approach that allows to interconnect both mechanical and electrical subsystems [3]. It takes into account external forces acting on the moving permanent magnet due to radial, longitudinal and transversal accelerations imposed by the tyre dynamic.

For the experimental comparison the electromechanical energy scavenging device is tested on a shaker. Thus, each mechanical or electrical subsystem coupled to the magnet is modelled in a relative system reference in order to transmit direct or reactive forces proportional to the displacement or velocity of the structure containing the moving magnet. The considered mechanical interactions on the moving magnet are adhesion or friction phenomena (dependent on the relative magnet velocity) inside the vertical box-runner. At both ends of the magnet stroke, rubbery bumpers are designed to protect magnet impacts. Their mechanical effect is a typical dead-band of the elastic-dissipative characteristic. Their lumped properties are assumed on a Kelvin-Voight model. Due to the finite volume of air inside the magnet box-runner, also pneumatic forces arising from the relative magnet motion are taken into account. Their effects are modelled with an equivalent lumped series of spring and damper.

The electromechanical coupling consists of a conservative elastic magnetic force due to reluctance effects and a dissipative proportional to the relative velocity between magnet and coils. Their nonlinear properties are mapped in function of the relative magnet position and velocity. For the experimental comparison on the shaker, a simple adapted resistive load circuit is adopted.

D. Comparison with experiments

In Fig. 2 the electromechanical energy scavenging prototype is shown. For the experimental tests on shaker or for tyre applications, the device is consolidated with potting fluid. The reported comparison between experimental data and simulations of Fig. 3 presents the voltage dynamic behaviour between the resistive load during impulsive testes related to tyre excitations. The second-order dynamic behaviour of the magnet has typical dissipative effects due to friction effects coupled to the desired power flow generated by the electromechanical energy scavenging device. A good agreement between model

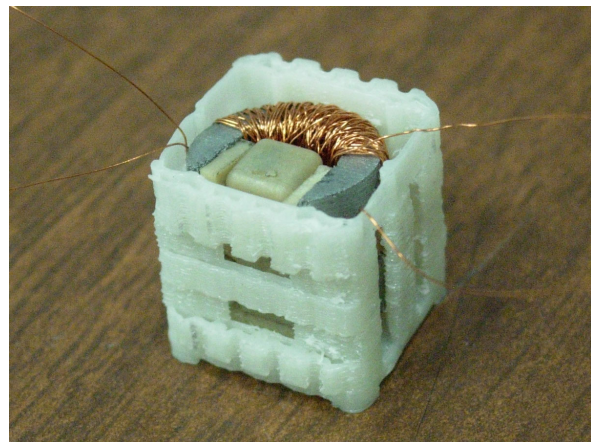


Fig. 2. Magnetic circuit of the energy scavenging prototype.

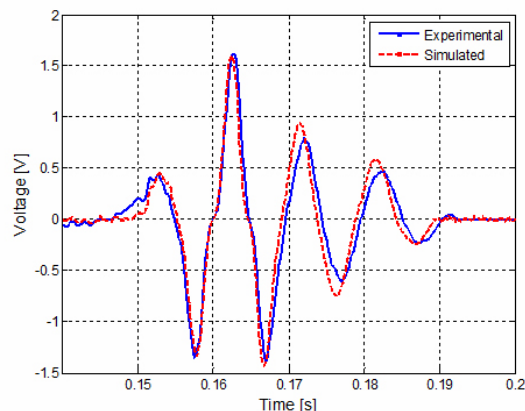


Fig. 3. Experimental and simulated voltage during impulsive test.

predictions and experimental outcomes is evinced. In the full paper a complete test of the energy conversion device under realistic tyre acceleration profiles will be presented.

ACKNOWLEDGMENT

The authors would like to thank Dr. Federico Mancosu from Pirelli for his enthusiasm and driving force in the project and Dr. Riccardo Crosa of Hoganas Italia Srl, for supplying Somaloy SMC material for prototype construction.

REFERENCES

- [1] G. Giuffrida, G. Grusso and M. Repetto, "Finite formulation of nonlinear magneto-statics with integral boundary conditions," *IEEE Transactions on Magnetics*, vol. 42, no. 5, pp. 1503–1511, May 2006.
- [2] F. Freschi, G. Grusso, M. Repetto, "Force Computation by Hybrid Cell Method" *IEEE Transactions on Magnetics*, vol. 44, no. 6, pp. 1198–1201, June 2008.
- [3] M. Velardocchia, N. D'Alfio, E. Bonisoli, E. Galvagno, F. Amisano, A. Sornioti, "Block-oriented models of Torque Gap Filler devices for AMT transmissions", SAE Technical Paper 2008-01-0631, pp. 1-10, April 2008.

Accurate Control of Position by Induction Heating-Produced Thermoelasticity

I. Dolezel¹, P. Karban², P. Kropik², and D. Panek²

¹Institute of Thermomechanics, Academy of Sciences of the Czech Republic
Dolejskova 5, 182 02 Praha 8, Czech Republic, E-mail: dolezel@iee.cas.cz

²Faculty of Electrical Engineering, University of West Bohemia
Univerzity 26, 306 14 Plzen, Czech Republic, E-mail: {karban, pkropik, panek50}@kte.zcu.cz

Abstract – An alternative possibility of highly accurate control of position is suggested, realized by a simple device with a cylindrical dilatation element that works on the principle of thermoelasticity produced by induction heating. The paper describes the device, presents its complete mathematical model in common with the methodology of its numerical solution, and also the algorithm of the control process. The theoretical analysis is illustrated by a typical example, whose results are discussed.

I. INTRODUCTION

Control of position can be realized on several different principles. We can mention, for example, sophisticated mechanical or hydraulic systems with 3D kinematic structures, devices with pneumatic elements, and also elements working on principle of magnetoelasticity. In the above cases, the accuracy of control usually reaches $10^{-5} - 10^{-4}$ m.

For a unidirectional control (e.g., tuning of the laser head for laser cutting or welding or regulation of position of elements in some optical systems) working with accuracy on the order of $10^{-6} - 10^{-3}$ m, the authors suggest an alternative methodology based on the principle of thermoelasticity produced by induction heating. The corresponding device works with a cylindrical element, whose longitudinal dilatation is controlled by the appropriate time evolution of the field current.

The papers in the domain are rather rare. Some applications based on thermoelasticity produced by induction heating (with a very limited possibility of control) were described in [1] and [2]. A time-variable magnetic field produced by harmonic current carrying field coil induces eddy currents in the dilatation element. These currents generate in it the Joule (and when the dilatation element is ferromagnetic, also hysteresis) losses that produce heat and, consequently, thermoelastic strains and stresses resulting in the corresponding displacements. The task is characterized by the interaction of three physical fields (electromagnetic field, temperature field, and field of thermoelastic displacements) influencing one another.

II. FORMULATION OF THE PROBLEM

The basic arrangement of the device (that may be considered axisymmetric) is depicted in Fig. 1. The dilatation element **2** made of a suitable metal is inserted into a harmonic current-carrying coil **3** fixed in frame **4**. The whole system is placed in a Teflon insulating shell **1**. The device is clamped by its bottom part **5** (Teflon front) in basement **6** that is supposed to be perfectly stiff. The time-variable magnetic field generated by field coil **3** induces in the dilatation element **2** eddy

currents that produce heat and consequent geometrical changes (mainly in its longitudinal direction z) of the thermoelastic origin.

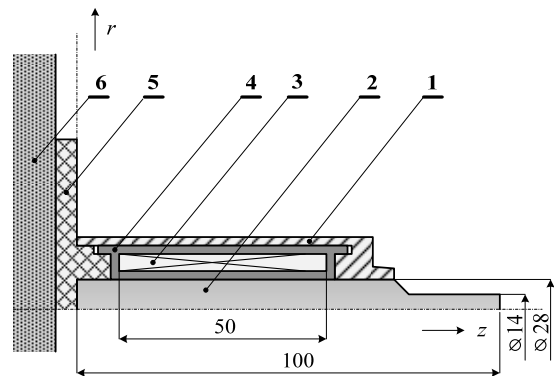


Fig. 1. The basic arrangement of the device
1 – Teflon shell, 2 – dilatation element, 3 – field coil, 4 – fixing frame,
5 – Teflon front, 6 – stiff wall

Now it is necessary to reach a prescribed dilatation u_d of element **2** in the shortest time possible, while the temperature of the system must remain within the allowed range. The situation is indicated in Fig. 2.

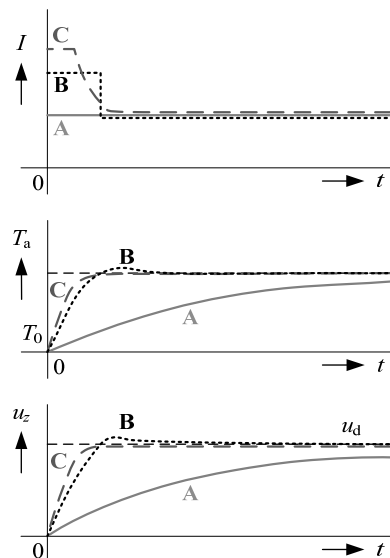


Fig. 2. Possible time evolutions of amplitudes of the field current I and corresponding time evolutions of the average temperature T_a of the dilatation element **2** and its dilatation u_z

The upper part of Fig. 2 contains three different time evolutions of the amplitude I of the field current (that is supposed to be controlled using the pulse-width modulation). The central and lower parts then show the corresponding time evolutions of the average temperatures T_a of the dilatation element (its initial temperature being T_0) and displacement u_z in the direction of the z axis. For current **A** the time of reaching the prescribed dilatation u_d is unacceptably long. A step change of the field current (line **B**) is more favorable, but still the time of reaching the steady state could be substantially shorter. Further shortening of this time can be achieved by using higher current for the first period of the process that is later decreased continuously to its steady-state value (line **C**). The main feature of the steady state is the balance between the heat produced in the system and heat loss due to convection and radiation.

The aims of the paper are:

- to optimize the envelope of the field current with respect to maximum possible shortening of the time of reaching the required dilatation u_d and
- to propose an approximate algorithm that would allow a very fast (on-line) and sufficiently accurate computation of this multiply coupled problem.

III. FUNDAMENTAL MODEL AND ITS SOLUTION

The task represents a nonstationary multiply coupled problem, combined with the optimization of the time evolution of the envelope of the field current. The computations were realized by a combination of the professional code Comsol Multiphysics and a lot of own procedures and scripts. The algorithm consists of the following items:

- Computation of the steady-state dilatation $u_{z,t \rightarrow \infty}$ as a function of the applied field current density $|\mathbf{J}|$ (for the methodology, mathematical model, boundary conditions, and other particulars, see [2]).
- Approximation of this function by a polynomial $f(|\mathbf{J}|)$ of a reasonable order using the least square method. The steady state field current density $|\mathbf{J}_d|$ necessary for dilatation u_d then follows from the solution of equation $f(|\mathbf{J}_d|) = u_d$.
- The model of dilatation is supposed to have the form $\ddot{u}_z = g(u_z, \dot{u}_z, f(|\mathbf{J}|))$ (but even more complicated forms with higher derivatives bring about no serious problems), where $|\mathbf{J}|$ is defined as $|\mathbf{J}| = J_{\max}$ for $t \in (0, \tau)$ and $|\mathbf{J}| = J_d + (J_{\max} - J_d)e^{-\lambda(t-\tau)}$ for $t > \tau$ (corresponding to line **C** in Fig. 2 left denoted by **3**). For a selected value of J_{\max} the quantities τ and λ are subject to optimization.
- The objective function respects the demand on the minimum time necessary for obtaining the dilatation u_d .
- The optimization of parameters τ and λ is carried out using the Nelder-Mead nonlinear simplex method.

IV. ILLUSTRATIVE EXAMPLE

The algorithm was tested on several arrangements. The computation of function $u_{z,t \rightarrow \infty}(|\mathbf{J}|)$ for any particular arrangement takes several hours. But once the results are available, the approximate determination of the envelope $|\mathbf{J}|$ for any required dilatation u_d takes only several seconds.

Figure 3 shows, for example, two graphs obtained for the device in Fig. 1 with zinc dilatation element. The dependence $u_{z,t \rightarrow \infty}(|\mathbf{J}|)$ was approximated by a polynomial of the second order and the model of dilatation had the form $\ddot{u}_z = \alpha(u_z + f(|\mathbf{J}|))$. The upper part of Fig. 3 depicts the time evolution of the current density optimized in accordance with the above algorithm. The lower part contains the corresponding time evolution of the dilatation u_z obtained by the solution of the coupled problem in Comsol (tens of minutes) and by the approximate method proposed by the authors (tens of seconds).

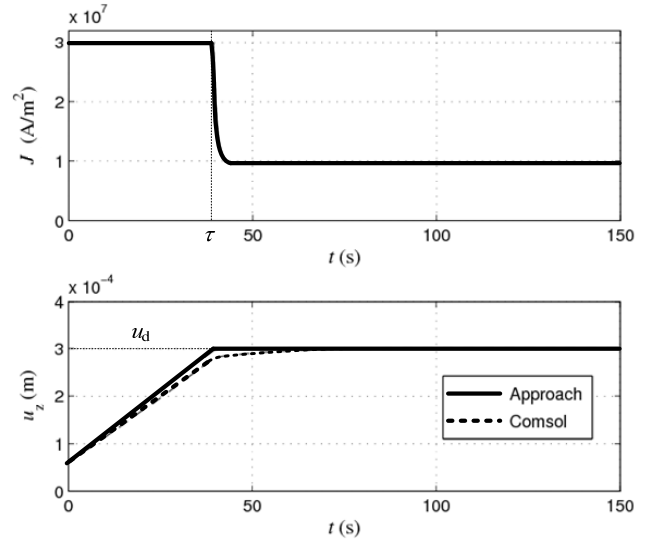


Fig. 3. Optimized time evolution of the field current density $|\mathbf{J}|$ for the arrangement in Fig. 1 (upper part) and time evolution of the corresponding dilatation u_z obtained by the complete calculation (Comsol) and by approximate algorithm suggested by the authors

V. ACKNOWLEDGMENT

This work has been financially supported from the Academy of Sciences of the Czech Republic (Institutional Research Plan Z20570509) and project GA CR 102/09/1305 of the Grant Agency of the Czech Republic.

VI. REFERENCES

- [1] M. Skopek, B. Ulrych, and I. Dolezel, "Optimized Regime of Induction Heating of a Disk Before its Pressing on Shaft," IEEE Trans. Magn. 37, 2001, No. 5, pp. 3380–3383.
- [2] I. Dolezel, P. Karban, B. Ulrych, M. Pantelyat, M. Matyukhin, P. Gontarowskiy, and M. Shulzhenko, "Limit Operation Regimes of Actuators Working on Principle of Thermoelasticity," IEEE Trans. Magn. 44, 2008, No. 6, pp. 810–813.

Physics Based High Frequency Transformer Modeling by Finite Elements

O. A. Mohammed and N. Y. Abed

Florida International University

ECE Department, Energy Systems Research Laboratory, Miami, FL, USA

mohammed@fiu.edu

Abstract— This paper proposes a physics based high frequency transformer model. The model can be used for setting edge rates, selecting switching algorithms, predicting over voltages at terminals, and predicting transformer harmonic behavior. The model is constructed by connecting the conventional power frequency transformer model in parallel with a frequency dependent branch (FDB). The FDB represents the transformer's high frequency behavior over wide frequency range while the power frequency model represents the transformer at low frequency. The model inductances, resistances, and capacitances were obtained by finite element (FE) analysis. The self and mutual capacitances of each conductor were calculated by electrostatic FE analysis. The order of capacitances is reduced by using a reduction technique. The transformer frequency response was obtained by coupling the transformer time harmonic FE model and external circuit simulations. The frequency response was then fitted with rational function approximation. The rational functions are then realized with RLC networks to form the FDB. The model simulation results show the ability of the developed model to predict transformer high frequency behavior during the design and development stage.

I. INTRODUCTION

Modeling of power transformer is challenging especially at high frequencies. In this case, numerical models become complicated and require various levels of details in order to include many effects such as core saturation, hysteresis, ferroresonance, and insulation issues in addition to geometric, and construction features. FE modeling can include all of these effects and provide an efficient way for analysis, simulation, and optimization for transformers. In this paper, the FE analysis has been coupled to driving electric circuit simulations in order to include the operating conditions of the transformer with the real power supply and load connections.

High-frequency modeling is essential in the design stage of transformers to study impulse voltage and switching surge distribution. It is also necessary for winding integrity and insulation diagnosis and most often frequency effects for high-fidelity models in bandwidths up to 10 MHz are required for condition monitoring purposes [1]. The study of the high-frequency part of the spectra is necessary due to the resulting stray capacitances shunting the series inductances and dominating the response.

In this paper, a high frequency model of transformers is developed by connecting a high frequency branch in parallel with the power frequency transformer model. The high frequency branch enables the presentation of the series and parallel resonance from mid to high frequency caused by winding-to-winding and winding to ground stray

capacitance. The Low and high frequency parameters of the windings were obtained from the FE solutions on a turn-to-turn basis. The model is then reduced to a lower order by using a reduction technique. The transformer frequency response was then obtained from coupled circuit-time harmonic FE analysis. The frequency response is curve fitted using vector fitting (VF). Vector Fitting is a robust numerical method for rational approximation in the frequency domain.

The proposed high frequency model and was used to demonstrate the primary current harmonic behavior and terminal overvoltage when the transformer is connected through a long cable to the power source with spikes in the current waveforms are present. Therefore, the model presented here can be used for evaluating electromagnetic interference issues for product development.

II. THE HIGH FREQUENCY FE MODEL

Simulations were carried out on a 60-Hz single-phase, shell type transformer with sandwich coils. The primary and the secondary windings were represented by rectangles of corresponding materials in the FE domain. The magnetic core is an isotropic non-linear magnetic material defined by analytic saturation curve. The FE model contains 11254 second order elements with 22541 nodes.

The transformer magnetic field is governed by the following nonlinear partial differential equations:

$$\vec{\nabla} \times ((\nu) \vec{\nabla} \times \vec{A}) = \vec{J} \quad (1)$$

$$\nabla \cdot \sigma \left(\frac{\partial \vec{A}}{\partial t} + \nabla V \right) = 0 \quad (2)$$

Where all the symbols have their usual meaning.

The current in the circuit domain is governed by:

$$[E_m] = [R_m][I_m] + [L_m] \frac{d}{dt} [I_m] + [C_m^{-1}] \int [I_m] dt + [\gamma_m] \quad (3)$$

Where, E_m , I_m , R_m , L_m , C_m^{-1} , and γ_m represent the vector of voltage sources in each electric mesh m, the vector of the mesh currents, the resistances matrix, inductances matrix, the matrix of the reciprocal of the capacitance, and the matrix of the non-linear voltage drop, respectively.

A. Capacitance Calculation

The transformer capacitance matrix is obtained from an FE electrostatic analysis by energy principles. It is assumed, in this paper, that both the electric permittivity of the materials and the electric field energy are constant with the frequency and, therefore, the value of the transformer capacitances are a function of geometry rather than the

frequency. The model considers three types of stray capacitances, winding to ground, winding to winding, and turn-to-turn capacitances.

A distributed parameter winding circuit is formed using the high frequency parameters obtained from the FE analysis. To reduce the computational burden, the model capacitances order needs to be reduced. We move the capacitance connected to internal nodes to the external nodes. In this technique, all the nodes other than terminal nodes are eliminated.

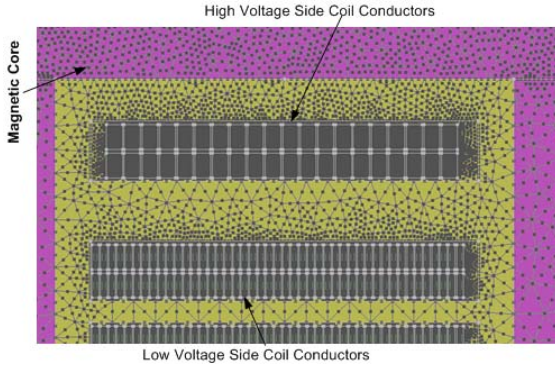


Fig. 1 the transformer mesh details

B. Resistance and Inductance Calculation

The transformer inductance and resistance values will change with a change supply frequency. The transformer resistances increase with an increase in the supply frequency. The inductances value decrease with the supply frequency increase. This change in the transformer parameters is due to the skin and proximity effects. The size of the mesh elements used is selected in coordination with the skin depth. Fig.1 shows the mesh details used to calculate the transformer frequency response. When the supply frequency changes from 60-Hz to 50-kHz, the transformer resistance increase by 300%, while the primary inductance decreased by 50%

III. VECTOR FITTING

The transformer admittance $Y(s)$ frequency response is obtained from harmonic coupled circuit- FE analysis by varying the primary voltage source frequency while the secondary is short circuited. The frequency response is curve fitted using vector fitting (VF). VF takes as input a column of $Y(s)$ and approximates all of its n elements simultaneously using an identical set of N poles. Each element, Y_j , in $Y(s)$ becomes [2]:

$$Y_j(s) \approx Y_{fitj}(s) = \sum_{i=1}^N \frac{c_{ji}}{s - a_i} + d_i + se_i \quad j=1, \dots, n \quad (1)$$

Where c_{ji} and a_i denote the residues and the poles, respectively. The terms d_i and e_i may be specified as zero, if desired. The poles and residues are real or complex conjugate, whereas d_i and e_i are real. The rational functions can then be represented by the electrical network shown in Fig.2.

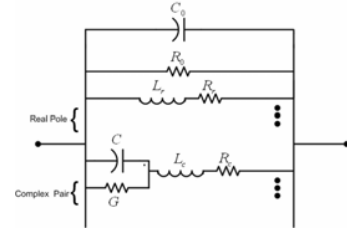


Fig. 2 Frequency dependent branch equivalent circuit

IV. IMPLEMENTATION AND SIMULATION RESULTS

The developed high frequency physical phase variable model of the transformer is tested with constant frequency inverter and cable to study the effect of different switching frequencies. The high frequency transformer primary current profile is shown in Fig. 3. It can be seen that the proposed HF model can reflect the spikes due to the PWM excitation. The pulsations in the waveforms are the result of PWM action while spikes are the result of high PWM switching speeds. The number of spikes within the current waveforms is increased with an increase in switching frequency. This is obvious as the spikes appear at every transition of PWM supply. These results are difficult to predict without the proposed model. Further details on the simulation and laboratory testing results will be presented in the full paper.

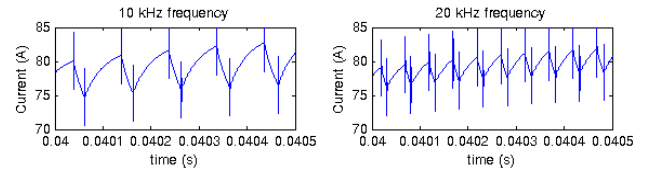


Fig. 3 Primary current profile at different switching frequencies

V. CONCLUSION

A new technique is described in this paper to obtain a high frequency phase variable transformer model from coupled circuit-FE analysis. The model has both frequency dependence and distributed effects. The model allows the analysis of high and low frequency phenomena simultaneously. The model takes into account the electromagnetic field effects which cause the change in the transformer frequency behavior. Thus this model can represent the transformer under non-sinusoidal operating condition. The model can be used for setting edge rates, selecting switching algorithms and predicting overvoltages at terminals. The study can be utilized to evaluate various transformer designs, diagnose the incompatibilities of the transformer with other components, and insulation issues.

VI. REFERENCES

- [1] F. de Leon, and A. Semlyen, "Complete Transformer model for Electromagnetic Transients", IEEE Transactions on Power Delivery, Vol: 9, NO: 1, Jan. 1994
- [2] B. Gustavsen and A. Semlyen, "Rational approximation of frequency domain responses by vector fitting", IEEE Trans. Power Delivery, vol. 14, no. 3, pp. 1052-1061, July 1999.

Permanent Magnet Motor Damping Analysis by using a particular 2D FEM technique

Minos E. Beniakar, Themistoklis D. Kefalas and Antonios G. Kladas, *Member, IEEE*,
Faculty of Electrical and Computer Engineering; National Technical University of Athens
9 Iroon Polytechniou Street, 15780 Athens, Greece
beniakar@central.ntua.gr

Abstract—This paper develops a particular 2D FEM model for iron loss analysis in permanent magnet machines during rotor speed oscillations. Hysteresis and saturation effects in solid rotor iron parts are considered and rotor skew is accounted by using a particular special air-gap element combined with standard 2D finite elements. Internal and surface permanent magnet rotor topologies are compared. The results obtained have been validated by measurements of rotor speed damping, consisting an important phenomenon of the respective drive.

Index Terms—Analytical solutions, finite element method, permanent magnets, rotor skew, speed oscillations.

I. INTRODUCTION

Permanent magnet (PM) motors are widely used in variable speed drive applications, due to their inherent advantages of high efficiency, high reliability and robustness [1]. However, the small damping effects of the rotor constitute an important constraint requiring adequate control techniques in order to avoid speed oscillations [2]. The present paper develops particular methodologies enabling to evaluate iron loss [3], [4] and the respective damping during oscillatory operation through convenient 2D finite element analysis. The method has been applied in order to compare damping effects of surface (SPM) and internal permanent magnet (IPM) rotor configurations.

II. FORMULATION

In order to enable a flexible time discretization and rotor skew consideration, the air gap of the machine has been represented by analytical solutions combined with standard 2D FEM techniques for stator and rotor simulation [1]. Such a methodology involves a particular coupling of the two methods across the boundary, obtained as follows:

A. 2D Hybrid FEM-Macroelement Formulation

In the air-gap of electrical machines, the magnetic field distribution is governed by Laplace equation as the magnetic permeability is constant and there are no current sources. The proposed technique involves shape functions α_i determination based on the general solution of Laplace equation in terms of the vector potential in two dimensional cylindrical coordinate system.

Generally the system of equations to be solved can be written in matrix form:

$$[S] [A] = [F] \quad (1)$$

where $[S]$ is the stiffness matrix, A is the matrix of unknown vector potential nodal values and $[F]$ the source matrix.

The standard finite element stiffness matrix is band while the nodes surrounding the air-gap (macroelement part) form locally a full coefficient sub-matrix with terms of the form:

$$s_{ij}^g = \frac{1}{\mu_0} \int_{\Gamma_g} \alpha_i \frac{\partial \alpha_j}{\partial n} d\Gamma_g \quad (2)$$

Such a technique enables consideration of rotor skew by convenient constitution of the respective integrals as well as flexible representation of the rotor rotation.

B. Coupled Electromagnetic-Mechanical Problem

The coupled mechanical-electromagnetic problem of rotor speed oscillations can be solved [5], by conveniently combining the above mentioned formulation for the field analysis with the one governing the rotor motion, expressed as follows:

$$T_{el} - T_m = J \frac{d^2\theta}{dt} + D \frac{d\theta}{dt} + k\theta \quad (3)$$

For this reason a step by step time discretization is employed. The relative movement of the rotor to the stator, in a time-transient analysis can be modeled by applying variable time step techniques and considering the relative geometry variation with rotor rotation. In a first step the 2D FE problem is solved and the electromagnetic torque is evaluated. Then, electromagnetic torque value, and the value of the rotor angle is obtained, providing feedback to the FE model. The problem is solved for the new rotor position and the new current values. The flowchart of the described algorithm is depicted in Fig. 1.

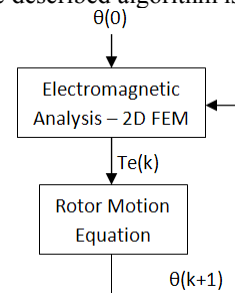


Fig. 1. Flowchart of the implemented algorithm

The time step is continuously adapted to the variation of electromagnetic quantities as the mechanical time constants are considerably greater.

III. RESULTS AND DISCUSSION

The proposed methodology has been applied in order to compare the damping effectiveness of rotor oscillations in case

of two different rotor configurations, SPM and IPM, respectively. The eddy current losses distributions for the SPM machine under maximum oscillation speed for two rotor positions are given in Fig. 2. Figure 3 shows the same results in case of IPM rotor configuration. The respective iron loss density and eddy current density distributions in the radial direction are presented in Figs. 4 and 5. These figures equally show the respective iron loss density and eddy current density distributions in the respective cases involving rotor skew. The total iron loss values for the different rotor configurations are tabulated in table I, illustrating that the IPM configuration provides six times greater damping than the SPM one. It may be noted that the calculated damping effects are in good agreement with the respective mechanical time constants derived by the measured current and speed oscillations shown in Fig. 6.

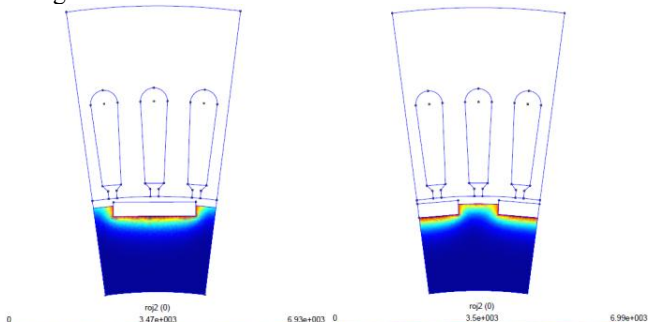


Fig. 2. Eddy losses distribution in the rotor body of the surface pm motor for two rotor positions during maximum oscillation speed

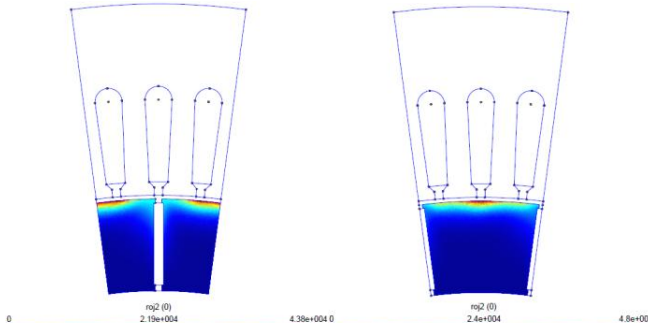


Fig. 3. Eddy losses distribution in the rotor body of the internal pm motor for two rotor positions during maximum oscillation speed

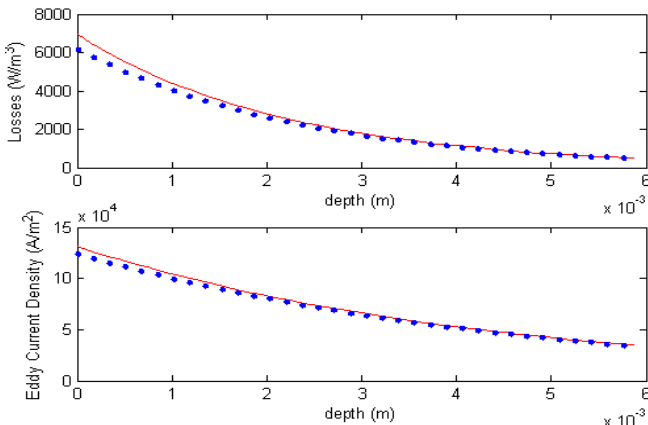


Fig. 4. Radial variation of eddy current density and iron loss density (SPM machine, * * * : without skew, — : with skew)

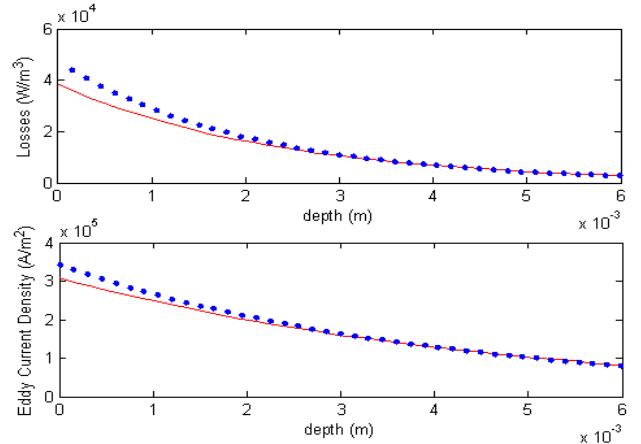


Fig. 5. Radial variation of eddy current density and iron loss density (IPM machine, * * * : without skew, — : with skew)

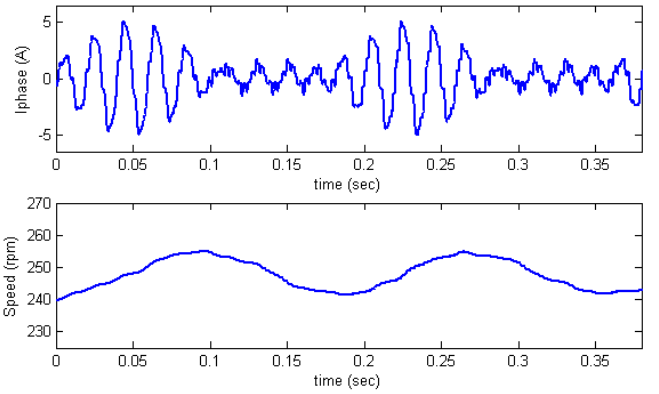


Fig. 6. Experimental waveforms of phase current and speed time variations (SPM machine)

TABLE I
TYPES SIZES FOR CAMERA-READY PAPERS

Type	Losses (W)
Surface (with skew)	0.419
Surface (without skew)	0.464
Internal (with skew)	2.5
Internal (without skew)	2.6

IV. REFERENCES

- [1] G.D. Kalokiris, T.D. Kefalas, A.G. Kladas, J.A. Tegopoulos, "Special air-gap element for 2-D FEM analysis of electrical machines accounting for rotor skew", *IEEE Trans. on Magnetics*, vol. 41, 2005, pp. 2020 - 2023.
- [2] K. Atallah, Z. Q. Zhu, D. Howe, "An Improved Method for Predicting Iron Losses in Brushless Permanent Magnet DC Drives", *IEEE Trans. on Magnetics*, vol. 28, 1992, pp. 2997 - 2999.
- [3] Chai Feng, Xia Jing, Guo Bin, Cheng Shukang, and Zhang Jiange, "Double-Stator Permanent Magnet Synchronous in-Wheel Motor for Hybrid Electric Drive System", *IEEE Trans. on Magnetics*, vol. 45, No 1, 2009, pp. 278 - 281.
- [4] W.N. Fu, Z.J. Liu, "Estimation of Eddy-Current Loss in Permanent Magnets of Electric Motors Using Network-Field Coupled Multislice Time-Stepping Finite-Element Method", *IEEE Trans. on Magnetics*, vol. 45, No 2, 2002, pp. 1225 - 1228.
- [5] G. Parent, P. Dular, J.-P. Ducreux, and F. Piriou, "Using a Galerkin Projection Method for Coupled Problems", *IEEE Trans. on Magnetics*, vol. 44, No 6, 2008, pp. 830 - 833.

Performance Investigation of Canned Induction Motor for Coolant Pump in Nuclear Reactor

Jian Li, Jungtae Song, and Yunhyun Cho

Dong-A University

Hadan 2 Dong, 840#, Saha-gu, 604-714, Busan, South Korea

E-mail lijian613@gmail.com

Abstract— This paper describes modeling and analysis of canned induction motor for coolant pump used in nuclear reactor. The electromagnetic field of a canned motor was analyzed by using the time-step finite element method, and the eddy loss was obtained. Equivalent circuit considering can loss was developed and the equation to calculate can loss was derived from theory of conventional motor. Using the loss from electromagnetic analysis as heat source of temperature field, thermal analysis was conducted by using Computational Fluid Dynamics (CFD) analysis. The simulation results show good agreement with experiment data, which indicates that this method has good accuracy and reliability for dealing with thermal behavior of canned motor.

I. INTRODUCTION

The main coolant pump used in system-integrated modular advanced reactor is an axial flow type, and it is constructed vertically because of the space limitation of building of reactor. A 200Kw three phase induction motor was designed and analyzed for application. Three journal bearings and one thrust bearing are used to hold rotor. The materials of bearings are black lead and silicon to endure high temperature and high pressure in reactor. For lubrication and cooling of bearings, pure water is forced to flow through airgap between stator and rotor. Therefore, the stator and rotor are welded by sealed can to prevent them from the lubricating water. The can is made of stainless steel SUS316L, which has resistivity of $74 \mu\Omega\cdot\text{cm}$ and relative permeability of 1.004. Eddy currents will be produced in the can and eddy current loss decreases efficiency of motor.

II. EQUIVALENT CIRCUIT OF CANNED INDUCTION MOTOR CONSIDERING CAN LOSS

In canned induction motors, the airgap is usually wider compared with conventional induction motors because cans are attached to the surfaces of stator and rotor. Eddy currents generated in the can also increases iron loss of the motor. Fig. 1 shows the characteristics of current produced in can. Similar to the currents in rotor bar and end ring of cage, the currents are denoted as I_{canb} and I_{canr} , which are the currents generated in can bars and ring respectively. The length of can bar l_{can} is same as length of core l_s , l_{can} is the total length of can bar and can ring.

The stator can Derived from the calculation of eddy current loss in cage at startup [1], the formulas to calculate eddy current losses in stator can and rotor can are as follows,

$$P_{canbar} = \left(\frac{I_{canb}}{\sqrt{2}} \cdot \frac{1}{4} \right)^2 \frac{\rho_{can} \cdot l_{canbar}}{A_{canbar}} \cdot 4 = I_{canbar}^2 \frac{\rho_{can} \cdot l_{canbar}}{2 \cdot A_{canbar}} \quad (1)$$

$$P_{canring} = \left(\frac{I_{canr}}{\sqrt{2} \cdot \pi \cdot p} \right)^2 \frac{\rho_{can} \cdot \pi \cdot D_{canr}}{A_{canring}} \cdot 2 \\ = I_{canbar}^2 \frac{\rho_{can} \cdot D_{canr}}{\pi \cdot p^2 \cdot A_{canring}} \quad (2)$$

where ρ_{can} is the resistivity of can, p is number of poles, D_{canr} is average diameter of ring and $A_{canring}$ is the cross area of can ring. The can does not have an inductive effect [2], only the resistances of the stator can and rotor can are represented in the equivalent circuit as shown in Fig. 2. Where r_1 is stator winding resistance per phase, x_1 is stator leakage reactance per phase, x_M is the magnetizing reactance per phase, I_1' is rotor current per phase referred to stator, r_2/s is rotor resistance per phase referred to stator, the r_{fe} is the resistance of iron loss, r_{can} is resistance of can, I_{1can} is the current in can referred to stator

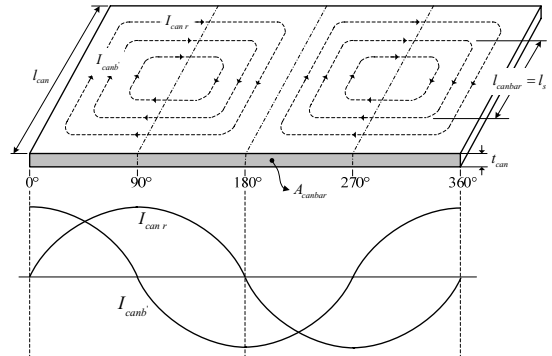


Fig. 1. Characteristics of currents in can.

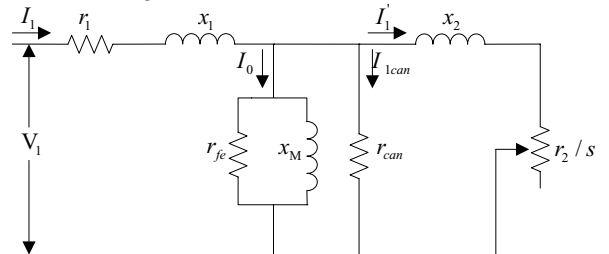


Fig. 2. Equivalent circuits of induction motor considering can loss

III. NUMERICAL SIMULATION

A. Electromagnetic Analysis

Time-step finite element analysis is used to study the performance of motor. Two models with and without can were simulated and compared. One model has cans made of stainless steel and in the other mode, the can is replaced with vacuum. Flux density distribution canned motor is given in Fig. 3. The stator can has a much higher current density than rotor can. Because magnet field traverses through stator can at frequency of f and through rotor at frequency of $s \cdot f$, where f is the frequency of magnetic field and s is slip factor. Due to eddy current effect in can, the peak value of phase current increases from 130A to 194A at same load condition, and the phase is also a little delayed as shown in Fig. 4.

B. Thermal Analysis Using CFD

Figure 5 gives the cooling system of canned induction motor. Because stator core as well as windings is enclosed by the can, the heat caused by core and copper loss was mainly conducted to the shell and stator can. The cooling water flows through airgap and the rotor rotates at a high speed. Conventional thermal analysis can't simulate this phenomenon, thus Computational Fluid Dynamics (CFD) was used to simulate fluid flow and heat transfer. Flow analysis involves solving of the Navier-Stokes equation using numerical tools. Thermal simulation involves solving of energy equations and can simulate distribution patterns of variables like temperature, heat loss/gain, thermal energy etc. The 3-D model of prototype is shown in Fig. 6, and the temperature distribution of stator core and coil at full load is given in Fig. 7. Experiment was also set for load and thermal test as shown in Fig. 8.

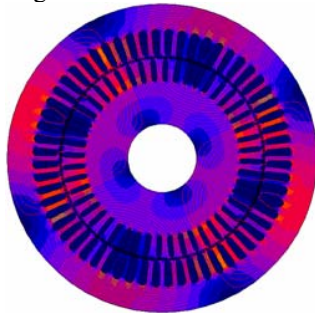


Fig.3. (a) Flux density distribution of canned induction motor.

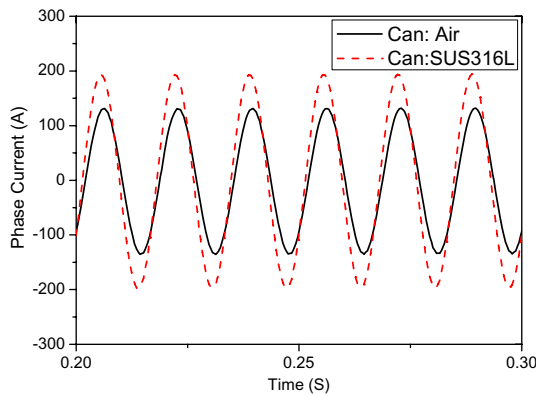


Fig. 4. Phase currents of motor with and without can.

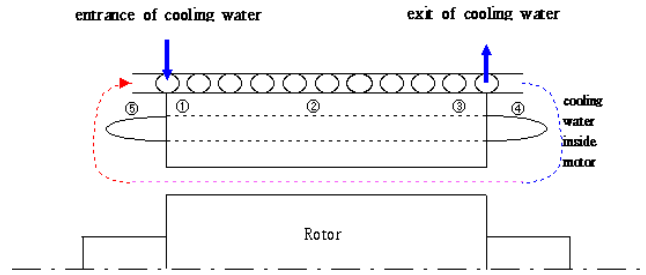


Fig. 5. Cooling system of canned induction motor.

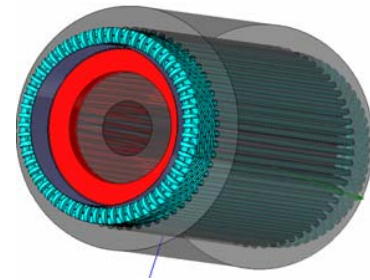


Fig. 6. Three dimensional model of canned induction motor used in CFD analysis.

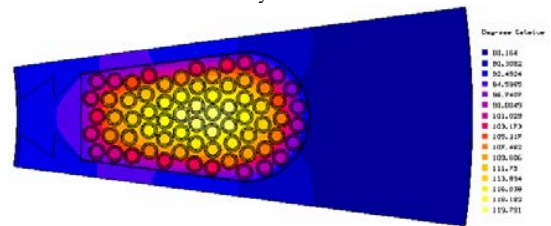


Fig. 7. Temperature distribution of stator core and coil at full load.

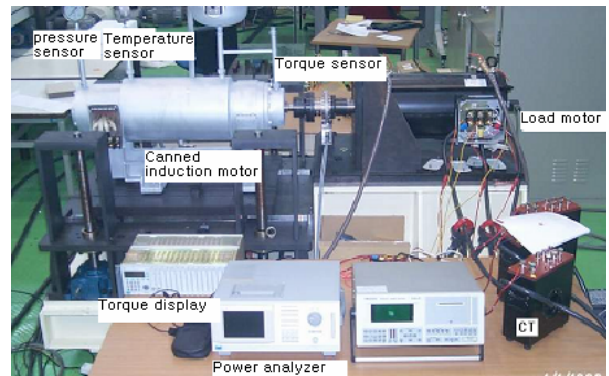


Fig. 8. Experimental setup of load test and thermal test.

IV. ACKNOWLEDGEMENT

This work is the outcome of a Manpower Development Program for Energy & Resources supported by the Ministry of Knowledge an Economy (MKE)

V. REFERENCES

- [1] C. G. Veinott, *Theory and Design of Small Induction Motor*, Mgraw-hill Book Company, Inc, New York, 1959.
- [2] L. T. Ergene, S. J. Salon, "Determining the equivalent circuit parameters of canned solid-rotor induction motors", *IEEE Trans. on Magnetics*, vol. 41: 2281-2286, Jul. 2008.

Field-Circuit Method for the Non-Steady State Analysis in the Active Magnetic Bearings

B. Tomczuk, J. Zimon, *IEEE Member* and A. Waindok, *IEEE Member*
 Department of Industrial Electrical Engineering, Opole University of Technology
 ul. Luboszycka 7, 45-036 Opole, Poland
 b.tomczuk@po.opole.pl, j.zimon@po.opole.pl

Abstract— A method for computer simulation of the radial active magnetic bearing (AMB) dynamic characteristics is presented. An implicit 3D finite element method (FEM) has been involved into the field-circuit model. Lagrange's equations, which contain the electrical and mechanical equations of motion, have been implemented. Some parameters of the AMB have been measured and compared with the calculated ones. Especially, for the moving and current characteristics, the calculation and tests results comparison yields a good agreement.

I. INTRODUCTION

Computer aided design (CAD) of an active magnetic bearing (AMB) can be done in two steps, mostly [1]. The first one includes the field-circuit model, and the second one concern the testing on the selected prototype [2], [6]. Finite element method (FEM) to the field analysis [3], [7] and Lagrange's equations for numerical modeling of the dynamic characteristics can be coupled in an implicit procedure [1]. The magnetic field integral parameters such as flux density distribution, winding inductances, and magnetic forces have been internally calculated with the procedure [4]. Inside this algorithm we have created the AMB dynamics characteristics.

II. THE DRIVE SYSTEM UNDER CONSIDERATION

We have considered the high-speed drive system with tree magnetic bearings. One of them, so-called radial AMB, was analyzed and tested in this work. The rated speed and torque of the motor are $n=40\,000$ RPM and $T_N=0.065$ Nm, respectively. The rotor mass of $m=1.2$ kg is suspended due to magnetic force arisen from both main flux, by the bias current of $I_b=0.8$ A, and additional flux by the control current. For the unstable rotor position, the controller should change all of the excitation currents, so that it is well kept, especially when their rotational speed is close to the critical banding mode [5].

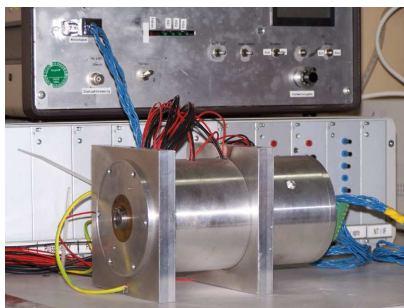


Fig. 1. Magnetically suspended, high speed electric motor.

III. MODELING OF THE AMB DYNAMIC CHARACTERISTICS

To simulate the AMB dynamic characteristics, Lagrange's differential equations should be formulated and solved.

$$\begin{cases} u_x = R_x i_x + L_{dx} \frac{di_x}{dt} + k_{ix} \frac{dx}{dt} \\ u_y = R_y i_y + L_{dy} \frac{di_y}{dt} + k_{iy} \frac{dy}{dt} \end{cases} \quad (1a)$$

$$\begin{cases} F_{ex}(\tilde{I}, x) = m \frac{d^2 x}{dt^2} + k_{sx} x + mg + F_{ox} \\ F_{ey}(\tilde{I}, y) = m \frac{d^2 y}{dt^2} + k_{sy} y + F_{oy} \end{cases} \quad (1b)$$

The voltage and current-balance equations (1a) with u_x , u_y voltages as well as i_x , i_y currents, taken together their stiffness coefficients k_{ix} , k_{iy} , govern electrical behavior of the AMB system. Dynamic inductances L_{dx} , L_{dy} of the coils in the stator electromagnets have been calculated with the field model [4]. The resistances R_x , R_y have been determined previously in the course of the coil design.

Relocations x and y of the bearing shaft center depend on the electromagnetic forces F_{ex} , F_{ey} as well as displacement stiffness coefficients k_{sx} , k_{sy} . They are included in the mechanical equations of motion (1b). The applied forces, which are time dependent functions of the currents I and shaft displacements, have been calculated with the field model.

The transfer function of the bearing shaft can be expressed including the control currents and external forces F_{ox} , F_{oy} in each displacement directions of the rotor [5]. After Laplace's transformation the equations can be expressed:

$$\begin{cases} x(s) = \frac{2k_{ix}}{ms^2 - 2k_{sx}} i_x(s) + \frac{1}{ms^2 - 2k_{sx}} F_{ox}(s) \\ y(s) = \frac{2k_{iy}}{ms^2 - 2k_{sy}} i_y(s) + \frac{1}{ms^2 - 2k_{sy}} F_{oy}(s) \end{cases} \quad (2)$$

Regarding the PID controller, the transformed function of the current, referring the control error e , is given:

$$i(s) = G_{PID}(s)e(s) = \left(\frac{K_d s^2 + K_p s + K_i}{s} \right) e(s) \quad (3)$$

The gain parameters K_p , K_d , K_i are proportional, derivative, and integral coefficients of the PID controller, respectively. The system of equations (1) is often characterized by its input-output (IN-OUT) relationships [5]. An alternative way of their representing is the simplified block diagram (Fig.2) where the control currents are coupled with the shaft displacements.

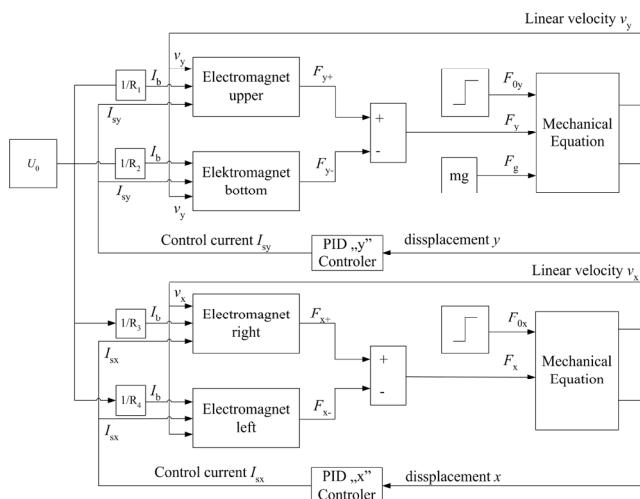


Fig. 2 Block diagram for the analysis of the AMB dynamics.

The blocks „Electromagnet” (Fig.2) have been realized in the FEM solution. After the field analysis, the magnetic forces F_{ex} , F_{ey} and other field parameters were obtained. Determination of the characteristics of the AMB operation has been included in the algorithm implemented in Matlab/Simulink application.

The blocks PID “x” and PID “y” (Fig.2) denote the controllers for two main directions of the shaft displacement. Regarding the algorithm of PID controllers, the functions $i(t)$ for control current are executed inside the block-diagram. As force-position and force-current characteristics are nonlinear, linearization of their segments has been implemented in the controlling procedure.

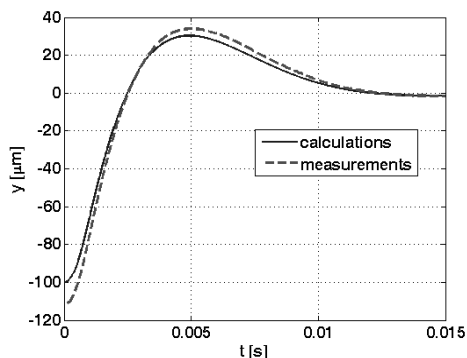


Fig. 3 Shaft positioning concerning the vertical symmetry axis.

Owing to the field-circuit method, we created characteristics of the shaft positioning and the control currents under non-steady states. The locus of the shaft center and the excitation currents have been measured, as well. One should add that the assumed vertical y -axis is perpendicular to the symmetry axis of the drive.

For the presented example, the shaft center is assumed to be replaced to the initial position: $x=0.3\mu\text{m}$, $y=-100\mu\text{m}$. The shaft locus changes abruptly within length of time $t=4$ ms, (Fig. 3). After $t=15$ ms, the shaft displacement nearly vanish, and we have the steady state.

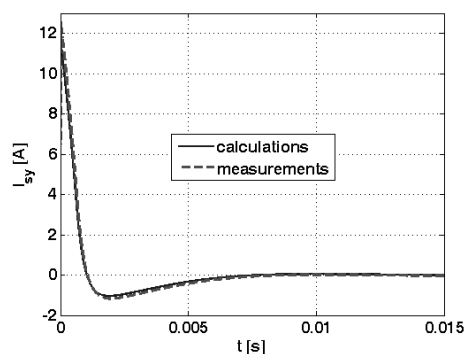


Fig. 4 Control current vs. time.

The transients of the control currents I_s in the coils have been calculated and compared with the measurement values. The wave of the current corresponding the y -axis is presented in (Fig. 4).

IV. CONCLUSIONS

We have studied transients of the active magnetic bearing (AMB). Many numerical examples have been executed with our field-circuit method, where the variation of the shaft center is governed by the mechanical as well as electrical nonlinear equations with changeable coefficients. Diagrams of the rotor axis locus as well as the control currents in the stator coils have been also created, which is not presented in this short version of the paper.

The control current highly influences the magnetic forces and displacements of the bearing shaft. As the bearing is a structurally unstable object, the fast control system is indispensable for its operating. Some measured waves, at the time of the AMB starting, were compared with the computer simulation results. The experiments have been done for the step response of the bearing, especially. The calculation and measurement errors have opposite signs. Thus, the curves are close each other. The field-circuit method presented in this paper has greatly assisted in computer aided design (CAD) of the magnetic bearings.

V. REFERENCES

- [1] B. Tomczuk, J. Zimon, “Field determination and calculation of stiffness parameters in an active magnetic bearing (AMB)”, Proceedings of Mechatronic Systems and Materials MSM’08, Bialystok, Poland, 14-17.07, 2008, pp. 52-53.
- [2] G. Schweitzer, A. Traxler, H. Bleuler, *Magnetlager*, Springer Verlag, Heidelberg, Germany, 1993.
- [3] C.F.R. Lemos Antunes, “Force Calculations with T-Ω Method”, *IEEE Trans. on Magnetics*, Vol. MAG-21/6, 1985, pp. 2432-2434.
- [4] J. Zimon, “Field Analysis and Parameters Computation in the Active Magnetic Bearings”, Doctoral Thesis, Opole, Poland, 2008.
- [5] Z. Gosiewski, K. Falkowski, J.T. Sawicki, “Introduction to smart magnetic bearing design”, VII International Symposium on Magnetic Bearings, Zurich, 2000, pp. 531-536.
- [6] J. D. Knight, H. Z. Xia, and E. B. McCaul, “Forces in Magnetic Bearings, Nonlinear Computation and Experimental Measurement”, Proc. of Third Int. Symposium on Magnetic Bearings, Technomic Publ., Lancaster-Basel, 29-31.06, 1992, pp. 441-450.
- [7] M. Antila, E. Lantto, and A. Arkkio, “Determination of forces and linearized parameters of radial active magnetic bearings by finite element technique”, *IEEE Trans. on Magnetics*, 1998, Vol. 34/3, pp. 684-694.

Study of a double-star synchronous machine fed by a dual Voltage Source Inverter

A. de Andrade¹
T. Meynard^{1,2}

¹Université de Toulouse INPT, UPS, LAPLACE
(Laboratoire Plasma et Conversion d'Énergie), ENSEEIHT

2, Rue Charles Camichel, BP 7122, F-31071
Toulouse Cedex 7, France

²CNRS; LAPLACE; F-31071 Toulouse – France

N. Sadowski³
P. Kuo Peng³

³GRUCAD (Grupo de Concepção e Análise de
Dispositivos Eletromagnéticos), UFSC

Campus Universitário
BP 476 CEP: 88040 – 900
Florianópolis – Brazil

Contact author: andre.deandrade@laplace.univ-tlse.fr

Abstract — The internal and external magnetic couplings within a double-star permanent magnet synchronous machine (DS-PMSM), the influence of the switching frequency and of interleaved control are studied. An architecture with external coupling devices allowing to phase-shift the control signals of the two inverters is proposed; it allows reducing the current ripples and the total losses of the converter-machine assembly. Obtaining the same effect within a special machine with no external magnetic coupling is also possible and will be presented in the final paper.

I. INTRODUCTION

Today, the power of electrical systems onboard aircraft increases and minimizing the weight and mass by means of global optimization is critical. Of course, in this field, safety is also a crucial requirement which must be taken into account in the optimization process. One solution is to change the architecture of the energy conversion chain by segmenting the power in the components with a high risk of failure [2]; for example, a multi-star machine can be supplied by several independent three-phase voltage source inverters (VSIs). However, the magnetic couplings between the different stars influence the harmonic content of the current flowing through each winding and this phenomenon needs to be studied.

Previous work concluded that because of these interactions the switching frequency voltage applied across the different sub-machines should be in phase, which brings us back to the behaviour of a single star machine supplied by a single VSI: no benefit in terms of current ripple in the windings and no reduction of the input filter.

This paper analyzes the mechanisms of interaction between the machine and the VSIs. Understanding these phenomena allows us to modify these interactions by means of InterCell Transformers (ICTs) [3]. In a second step, we show that it is even possible to modify the machine so that it incorporates the desired coupling characteristic and allows operation with a 180° phase-shift between the control signals of the two VSIs, thus bringing almost the same advantages as ICTs.

II. DOUBLE-STAR SYNCHRONOUS MACHINE – MODEL SUMMARY

The machine at stake is a double-star synchronous machine with permanent magnet and non-salient poles. In its general

form, the stator consists of two stars shifted by an electric angle γ [Fig. 1].

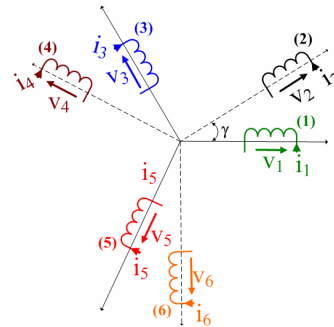


Fig. 1. Windings of the double-star synchronous machine

The machine is supposed to be unsaturated and the back EMF of the two stars is sinusoidal. The double-star machine has 6 coils, defining an inductance matrix with 36 parameters: 6 inductances and 30 mutual inductances. For reasons of symmetry, only 5 independent parameters are in general needed to define the magnetic couplings of such a machine.

The aim of this paper is to obtain a compensation of the harmonics at the switching frequency between the different subsystems; it is thus necessary to have the same harmonic amplitude, which requires equal duty cycles in corresponding phases. For this reason only the case $\gamma = 0^\circ$ is considered here and we will show that in this case, the machine is characterized by 4 parameters only: L_{11} , M_{12} , M_{13} , and M_{14} . Fig. 2 shows the simplified single-phase equivalent diagram of the double-star synchronous machine.

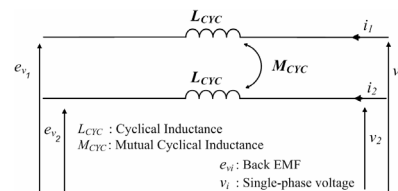


Fig. 2. Simplified equivalent circuit single-phase of the DS-PMSM

The voltage equation is expressed as follows:

$$\begin{bmatrix} v_1 \\ v_2 \end{bmatrix} = \begin{bmatrix} L_{Cyc} & M_{Cyc} \\ M_{Cyc} & L_{Cyc} \end{bmatrix} \cdot \begin{bmatrix} di_1/dt \\ di_2/dt \end{bmatrix} + \begin{bmatrix} e_{v_1} \\ e_{v_2} \end{bmatrix} \quad (1)$$

$$L_{CYC} = L_{11} - M_{13} = L_{11} - M_{15} \quad (2)$$

$$M_{CYC} = M_{12} - M_{14} = M_{12} - M_{16} \quad (3)$$

III. EXISTING STRUCTURES

The system studied in this paper is shown in Fig. 3. Considering the harmonic content at the input of the *VSI*s, it was first concluded that phase-shifting the control signals of the two *VSI*s by 180° is advantageous, because the input current harmonics of the two *VSI*s cancel out partially. In this case, the phase currents are as shown in Fig. 4.

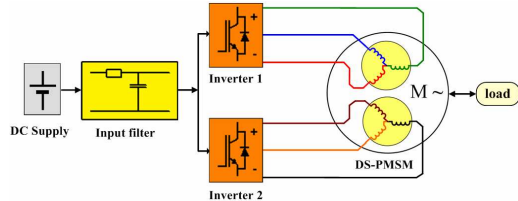


Fig. 3. Global system (inverters + machine) with internal magnetic coupling

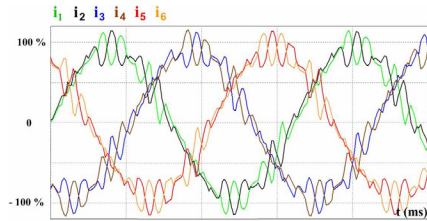


Fig. 4. Phase currents with inverter commands 180 degrees out of phase

Compared to the ideal sinusoidal supply, the relatively high current ripple generates extra conduction losses in the windings and higher stator and rotor losses. If the two *VSI*s are in phase, which means they operate as a single *VSI*, the current waveforms become those of Fig. 5. It can directly be seen that the current ripple is lower in this case, and a deeper study comes to the conclusion that the total losses in the machine are reduced very significantly with the *VSI*s in phase. By the way, this is in agreement with the conclusions presented in [1].

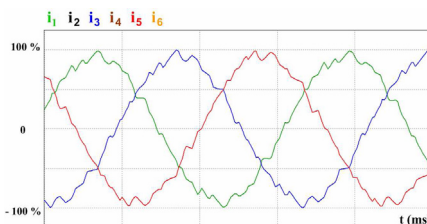


Fig. 5. Phase currents with inverter commands no shifted.

On the other hand, another study [3] showed that using external *ICT*s (Fig. 6), it is possible to use *VSI*s controlled with a phase-shift of 180 degrees and to obtain simultaneously two benefits that seemed incompatible until then:

- improving the input current *THD*;
- reducing the phase current ripple.

The first benefit is obtained as a well-known consequence of phase-shifting the control signals of the *VSI*s, and the second benefit can be explained as follows. The very strong coupling brought by the *ICT*s imposes quasi-equal currents in corresponding phases of the two inverters and their waveform is the same as if it was fed by a 3-level *VSI*: the current ripple

is at twice the switching frequency and the amplitude is roughly four times smaller than in the case of Fig. 5. Such waveforms will be shown in the final paper.

The price to pay for these important benefits is the addition of new components on the whole system, thus increasing the weight and price.

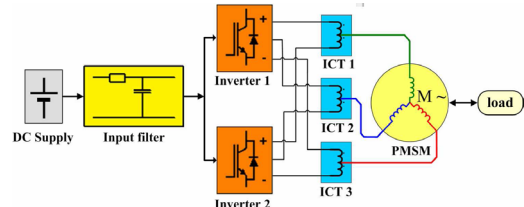


Fig. 6. Global system (inverters + *DS-PMSM*) with external magnetic coupling

IV. PROPOSED STRUCTURE

The innovation described in this paper allows obtaining the same effect within a machine which is slightly modified to provide the appropriate magnetic couplings without any external component (Fig. 3). Such a machine has been studied with the finite element software *EFCAD* (Fig. 7).

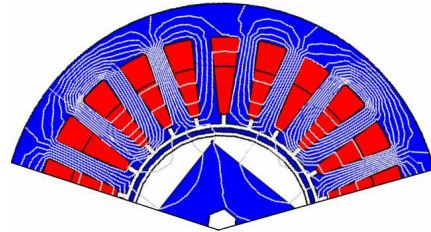


Fig. 7. Example of field map for the determination of magnetic couplings

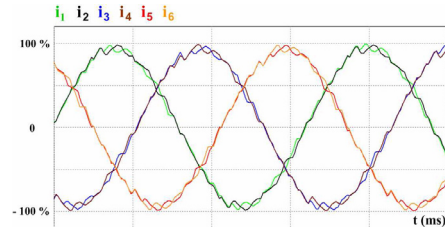


Fig. 8. Phase currents with internal magnetic couplings (proposed structure)

V. CONCLUSION

As will be shown, such internal couplings allow operation with *VSI*s 180 degrees out of phase thus providing multi-level operation, creation of a higher apparent frequency, reduction of the phase current ripples (Fig. 8) and of the input filter, as well as a significant reduction of the overall losses (inverters + machine).

VI. REFERENCES

- [1] N. Moubayed, F. Meibody-Tabar, B. Davat, "Alimentation par deux onduleurs de tension d'une machine synchrone double étoile", *Revue Internationale de Génie Electrique*, vol. 1, n° 4, 1998, pp. 457-470
- [2] F. Meibody-Tabar, B. Davat, R. Meuret, S. Vieillard, "Architectures segmentées d'alimentation à convertisseurs modulaires pour les actionneurs d'avion ; fonctionnement en modes dégradés", *Journées 2004 de la section électrotechnique du club EEA*, 18 -19 mars 2004, Cergy-Pontoise.
- [3] D. E. Baker, B. R. Mehl, "Parallel inverter motor drive with improved waveform and reduced filter requirements", *United States Patent*, US 7.109.681 B2, 19 Septembre 2006.

Magneto-elastic finite element modeling based on a multiscale approach

X. Mininger, L. Daniel, L. Santandrea, L. Bernard and F. Bouillault
LGEP (CNRS(UMR 8507) ; SUPELEC ; Univ Paris-Sud ; UPMC Paris 6)
Plateau de Moulon, 11 rue Joliot-Curie ; F-91192 Gif sur Yvette Cedex ; France
xavier.mininger@supelec.fr, laurent.daniel@supelec.fr

Abstract—The design of electromagnetic devices submitted to mechanical stress is a growing issue and requires appropriate modeling tools. We propose in this paper to implement a multiscale model for magneto-elastic behavior in a finite element code.

Index Terms—Magneto-elasticity, multiscale modeling, finite element method.

I. INTRODUCTION

Magnetic materials in electrical machines or actuators are submitted to multiaxial mechanical loadings. These stress states significantly modify their magnetic and magnetostrictive behavior [1]. The design of electromagnetic systems consequently requires appropriate modeling tools. A possible choice is the introduction of coupled constitutive laws into finite element modeling. Unfortunately, most of magneto-elastic models are restricted to uniaxial mechanical loadings [2], [3]. A fully multiaxial magneto-elastic model, based on a multiscale energetic approach has been proposed recently [4]. The implementation of this model into a finite element simulation still leads to dissuasive computational times for engineering design applications. We propose in this paper to define a simplified version of the multiscale approach and to implement it into a coupled magneto-mechanical code.

II. LOCAL MAGNETO-ELASTIC CONSTITUTIVE LAW

The local constitutive law is derived from a multiscale approach [4], [5] and gets very close to Armstrong model [6]. The model has been simplified considering fully isotropic materials. The local potential energy W_α of the material is then written as the sum of magneto-static energy and elastic energy.

$$W_\alpha = -\mu_0 \vec{H} \cdot \vec{M}_\alpha - \boldsymbol{\sigma} : \boldsymbol{\varepsilon}_\alpha^\mu \quad (1)$$

$$\vec{M}_\alpha = M_s \vec{\alpha} = M_s \begin{bmatrix} \alpha_1 \\ \alpha_2 \\ \alpha_3 \end{bmatrix},$$

$$\boldsymbol{\varepsilon}_\alpha^\mu = \frac{3}{2} \begin{pmatrix} \lambda_{100}(\alpha_1^2 - \frac{1}{3}) & \lambda_{111}\alpha_1\alpha_2 & \lambda_{111}\alpha_1\alpha_3 \\ \lambda_{111}\alpha_1\alpha_2 & \lambda_{100}(\alpha_2^2 - \frac{1}{3}) & \lambda_{111}\alpha_2\alpha_3 \\ \lambda_{111}\alpha_1\alpha_3 & \lambda_{111}\alpha_2\alpha_3 & \lambda_{100}(\alpha_3^2 - \frac{1}{3}) \end{pmatrix} \quad (2)$$

\vec{H} and \vec{M}_α are the magnetic field and the magnetization. $\boldsymbol{\sigma}$ and $\boldsymbol{\varepsilon}_\alpha^\mu$ are the stress and magnetostriction strain

second order tensors. The unknown of the problem is the local magnetization direction $\vec{\alpha}$. M_s is the saturation magnetization of the material, λ_{100} and λ_{111} its magnetostriction constants. Assuming an isotropic behavior, we will consider $\lambda_{100} = \lambda_{111} = \lambda_s$ (macroscopic saturation magnetostriction of the material). The probability f_α for the magnetization to be in the direction $\vec{\alpha}$ is calculated using a Boltzmann type relation:

$$f_\alpha = \frac{\exp(-A_s \cdot W_\alpha)}{\sum_\alpha \exp(-A_s \cdot W_\alpha)} \quad (3)$$

A_s being a material parameter linked to the initial anisotropic susceptibility χ_o [4]:

$$A_s = \frac{3\chi_o}{\mu_o M_s^2} \quad (4)$$

Once the probability f_α is defined, the macroscopic magnetization \vec{M} and magnetostriction $\boldsymbol{\varepsilon}^\mu$ are obtained thanks to an averaging operation over all possible directions:

$$\vec{M} = \langle \vec{M}_\alpha \rangle = \int_\alpha f_\alpha \vec{M}_\alpha d\alpha \quad (5)$$

$$\boldsymbol{\varepsilon}^\mu = \langle \boldsymbol{\varepsilon}_\alpha^\mu \rangle = \int_\alpha f_\alpha \boldsymbol{\varepsilon}_\alpha^\mu d\alpha \quad (6)$$

III. FINITE ELEMENT IMPLEMENTATION

The static finite element model (FE) is based on classical mechanical and magnetic formulations. Considering the mechanical problem with the decomposition of the total strain $\boldsymbol{\varepsilon}$ into elastic strain $\boldsymbol{\varepsilon}^e(\boldsymbol{\sigma})$ and magnetostriction strain $\boldsymbol{\varepsilon}^\mu(\vec{H}, \boldsymbol{\sigma})$ ($\boldsymbol{\varepsilon} = \boldsymbol{\varepsilon}^e + \boldsymbol{\varepsilon}^\mu$), the mechanical formulation contains an additional term $F^\mu(\vec{H}, \boldsymbol{\sigma})$, corresponding to an equivalent force due to the magneto-elastic coupling. After discretization with nodal elements, this term is expressed with:

$$F^\mu(\vec{H}, \boldsymbol{\sigma}) = \int_\Omega \nabla^s [C] \boldsymbol{\varepsilon}^\mu(\vec{H}, \boldsymbol{\sigma}) d\Omega \quad (7)$$

∇^s is the symmetrical gradient of the shape functions, $[C]$ the usual stiffness tensor, Ω the study domain. $\boldsymbol{\varepsilon}^\mu(\vec{H}, \boldsymbol{\sigma})$ is the magnetostriction strain obtained with the multiscale model (MSM). Similarly, the magnetic scalar potential (Φ with $\vec{H} = -\text{grad}\Phi$) formulation contains an additional term equivalent to a magnetic charge. The magnetic flux

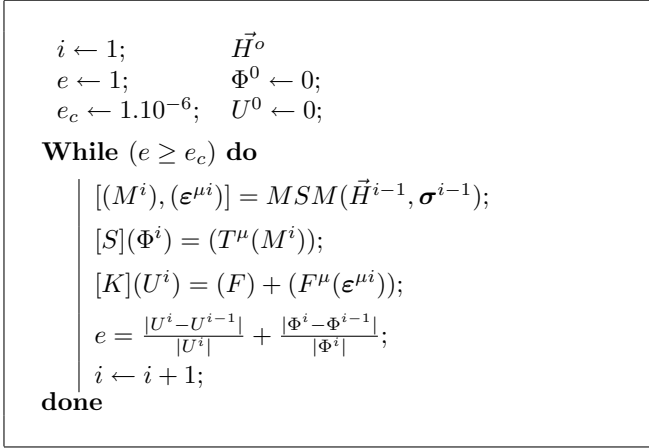


Fig. 1. Fixed-point algorithm; i represents the iteration number, MSM corresponds to the multiscale model.

density \vec{B} is defined from the magnetization \vec{M} ($\vec{B} = \mu_0(\vec{H} + \vec{M})$). Maxwell's flux conservation is written:

$$\text{div}(\text{grad}\Phi) = \text{div}(\vec{M}(\vec{H}, \sigma)) \quad (8)$$

where Φ corresponds to the magnetic scalar potential, and $M(\vec{H}, \sigma)$ to the magnetization obtained with the MSM. Thus, the coupling term in the magnetic formulation is finally obtained:

$$T^\mu(\vec{H}, \sigma) = \int_{\Omega} \nabla^m M(\vec{H}, \sigma) d\Omega \quad (9)$$

with ∇^m the gradient of the shape functions. The coupled system is then defined by:

$$\begin{cases} [S](\Phi) = (T^\mu(\vec{H}, \sigma)) \\ [K](U) = (F) + (F^\mu(\vec{H}, \sigma)) \end{cases} \quad (10)$$

with S and K respectively the magnetic and mechanical stiffness matrices, U the displacement field and F the external forces. Due to the non linearity of the problem introduced by the MSM model, an iterative algorithm based on the fixed point method is chosen for the resolution (Fig. 1). Values of magnetization and magnetostriction strain are updated using the MSM model at each step i for each element of the mesh, until the error criterion e falls down e_c .

IV. APPLICATION TO A SIMPLE STRUCTURE

In order to validate the finite element implementation, the first study concerns a rectangular FeCo sample placed in an uniform magnetic field and with uniform applied stress (here compression). For such a homogeneous configuration, the analytical MSM model provides the magnetization and the magnetostriction strain directly, allowing the comparison with the FE results (Fig. 2 and 3).

Considering these figures, the effect of the stress and of the magnetic field on the magnetic and mechanical behavior are obvious. Moreover, these results validate the implementation in the FE simulation.

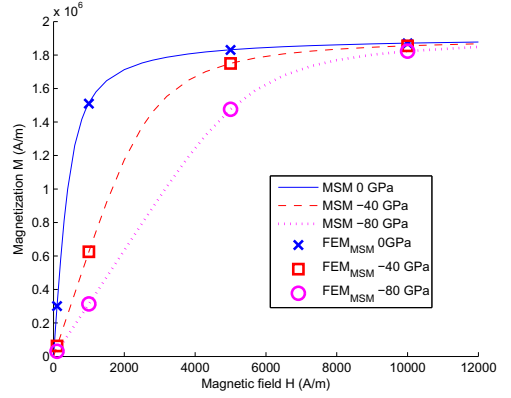


Fig. 2. Magnetization as a function of applied field and stress

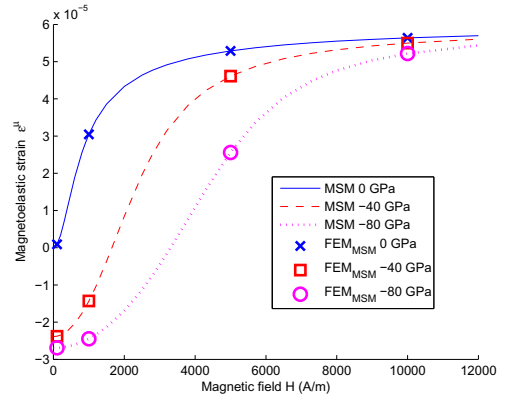


Fig. 3. Magneto-elastic strain as a function of applied field and stress

V. CONCLUSION

In this paper, the implementation of a multiscale magneto-elastic model in a finite element analysis has been detailed. This implementation is validated considering an iron-cobalt rectangular sample submitted to a homogeneous magneto-mechanical loading. The interest of this modeling tool concerns structural analysis for the design of electromagnetic devices. An illustration of a coupled calculation on the rotor structure of an electrical machine will be presented in the final paper.

REFERENCES

- [1] R.M. Bozorth, *Ferromagnetism*, ed. D. Van Nostrand Company, N.Y. 1951.
- [2] M.J. Sablik and D.C. Jiles, *IEEE Trans. Magn.*, 29, (1993) pp. 2113.
- [3] X.J. Zheng and X.E. Liu, *J. Appl. Phys.*, 97 (2005), pp. 053901.
- [4] L. Daniel, O. Hubert, N. Buiroon and R. Billardon, *J. Mech. Phys. Solids*, 56 (2008), pp. 1018.
- [5] L. Daniel, N. Galopin, *Eur. Phys. J. Appl. Phys.*, 42 (2008), pp. 153.
- [6] W.D. Armstrong, *Mater. Sci. Eng. B.*, B47 (1997), pp. 47.

Novel Design Method of a Single-phase Induction Motor considering Magnetic Balance

Myoung-Hyun Choi and Byung-Taek Kim, *IEEE, member*
 Dept. of Electrical Eng., Kunsan National University
 San68, myrongsong, 573-701, Korea
 cancmh@kunsan.ac.kr

Abstract — In this paper a design condition for magnetically balanced operation in a single phase induction motor is induced in analytic forms. In addition, a condition for minimal stator copper loss is also induced under the balance conditions. Using these conditions, an induction motor is designed by a proper optimization algorithm, and its loss characteristics are investigated. The validity of the proposed method is verified from the results.

I. INTRODUCTION

Single-phase induction motors (SPIMs) are used in various applications such as household applications, tooling machines and industry applications [1]. SPIMs are driven with a ‘single’ phase voltage source; therefore it is split to both a main and an auxiliary winding in order to develop start-up torque. However, the magneto-motive forces (MMFs) produced by both the windings of a SPIM are generally in a magnetically unbalanced state, thereby resulting in a backward field which deteriorates performances such as efficiency, vibration and noise etc. If the backward field can be artificially removed, the magnetic field of the motor gets in balanced state, improving efficiency [2]. In this paper, a new design method for the perfect balanced operation and the minimal copper loss is suggested.

II. OPTIMAL DESIGN OF A SINGLE-PHASE INDUCTION MOTOR

A. Conditions for the Balanced Operation

For a SPIM with a main winding in arbitrary angle ξ with respect to an auxiliary winding, magneto-motive forces (MMF) produced by both windings are shown in Fig. 1(a). To get a balanced state, the MMFs should satisfy

$$\mathbf{F}_m = -a\mathbf{F}_a e^{j\xi}. \quad (1)$$

The SPIM equivalent circuit considering the angle ξ in Fig. 1(a) can be deduced from its classical circuit model [3], [4] and shown in Fig. 1(b). Since a MMF is a product of the current and turn number of each winding, (1) is changed with

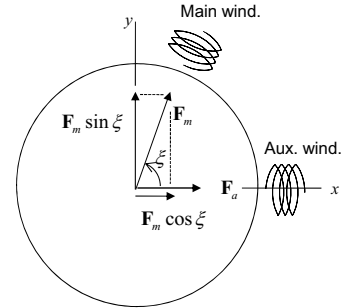
$$\mathbf{I}_m = -a\mathbf{I}_a e^{j\xi} \quad (2)$$

, where a is the effective turns ratio. By calculating the currents of the circuit of Fig. 1(b) and using (2), the balance conditions are induced as follows;

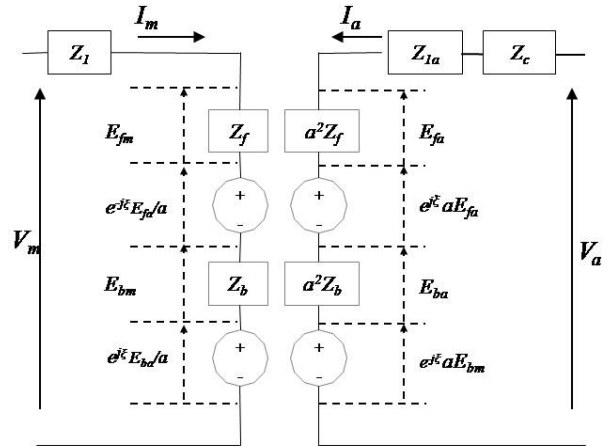
$$R_{1a} = f_1(a, \xi, R_1, \mathbf{Z}_f) \quad (3)$$

$$X_c = f_2(a, \xi, R_1, X_1, X_{1a}, \mathbf{Z}_f) \quad (4)$$

, where \mathbf{Z}_f is the forward impedance of a rotor circuit. The function f_1 and f_2 will be given in the full paper.



(a) Diagram of magnetic forces



(b) Equivalent circuit of a SPIM

Fig. 1. A single-phase induction motor

B. Conditions for the Minimal Copper Loss

Provided that the balance condition of (2) is satisfied, the conditions for minimal stator copper loss can be also induced as follows; Let the slot area for each winding be S_m , S_a and their total area be S_{tot} . The copper loss in a stator winding is given by (5), where n_m and n_a are each turn number, and l_c is stack length.

$$\begin{aligned}
W_{CS} &= R_1 I_m^2 + R_{1a} I_a^2 = I_a^2 (R_1 a^2 + R_{1a}) \\
&= I_a^2 \frac{L_c}{\sigma} a n_m n_a S_{tot} / \left(\left(S_m - \frac{S_{tot}}{2} \right)^2 + \left(\frac{S_{tot}}{2} \right)^2 \right)
\end{aligned} \quad (5)$$

By differentiating (5) a condition for minimal copper loss can be obtained by (6).

$$R_{1a} = a^2 R_1 \quad (6)$$

C. Optimal Design Strategy

By using the proposed design method, a given commercial SPIM for an instance is optimized. The optimization algorithm in Fig. 2 is applied to improve the given previous model. The turn number of each winding and the spatial angle ξ are selected as design variables. The total slot area of the designed model is same as that of the previous model. With variance of the design variables, all the combinations satisfying (3), (4) and (6) are founded and the best one is finally determined as shown in Fig. 2. The designed motor is compared with the previous one in Fig. 3 in which the determined angle ξ is 77.1° , not in quadrature.

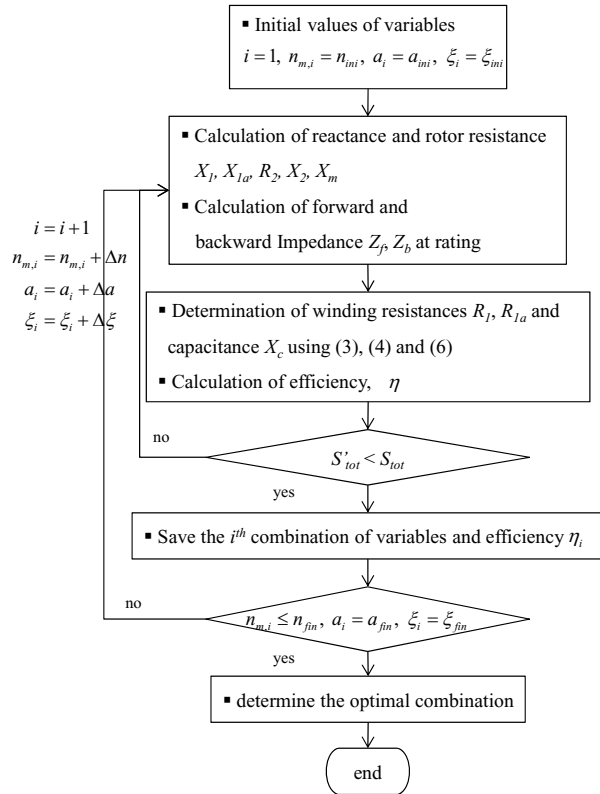


Fig. 2. Optimal design algorithm

Figs. 4-6 show the analysis results performed by the time-stepped FEA for the previous and optimized motors. From current waveforms in Fig. 4, it is noted that magnitudes of both MMFs become similar through the proposed design, getting into more balanced state. Magnetically balanced states lead to decrease of the torque ripple and ohmic losses in rotor

as shown in Fig. 5. The efficiency is improved by 0.8% at a rated load (110W) as shown in Fig. 6.

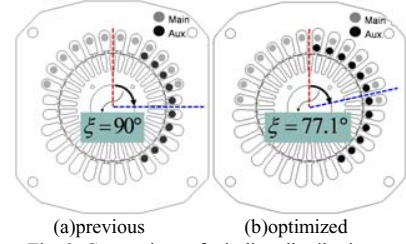


Fig. 3. Comparison of winding distribution

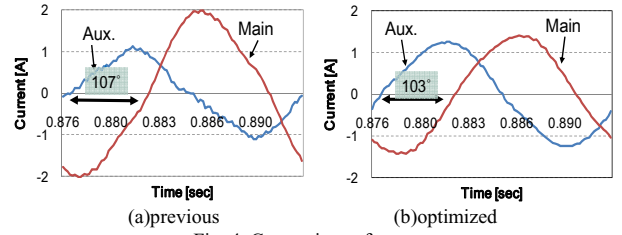


Fig. 4. Comparison of current

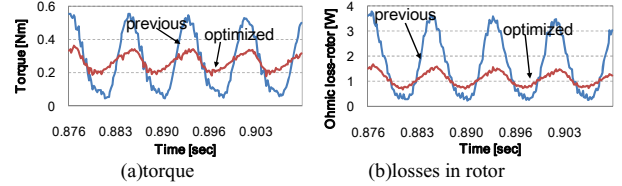


Fig. 5. Comparison of torque and ohmic loss in rotor

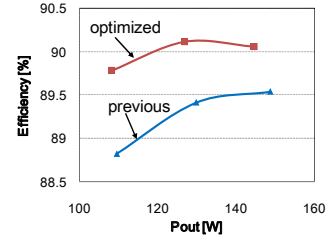


Fig. 6. Comparison of efficiency

ACKNOWLEDGMENT

This work is the outcome of a Manpower Development Program for Energy & Resources supported by the Ministry of Knowledge and Economy (MKE) and a second stage BK21 project of Korean Research Foundation.

III. REFERENCES

- [1] Aldo Boglietti, Andrea Cavagnino, Luca Ferraris, Mario Lazzari, and Giorgio Luparia, "No Tooling Cost Process for Induction Motors Energy Efficiency Improvements", *IEEE Trans. on Industry Applications*, 41(3): 808-816, 2005.
- [2] S. W. Baek, et al., "Design methodology for minimal stator copper loss in a single-phase induction motor", *Transactions of KIEE*, 57(9): 1536-1545, 2008.
- [3] Cyril G. Veinott, *Theory and design of small induction motors*, McGRAW-HILL, pp207-215, 1959.
- [4] P. H. Trickey. "Design of capacitor motors for balanced operation" *Transactions of the AIEE*, 51(3): 780-785, 1932.

Finite-Element Analysis for a Rolling-Rotor Electrical Machine

A. Arkkio¹, A. Biernat², B. Bucki², G. Kaminski², A. Niemenmaa¹, A. Smak², P. Staszewski²

¹Helsinki University of Technology, P.O. Box 3000, FIN-02015 TKK, Finland

²Warsaw University of Technology, pl. Politechniki 1, 00-661 Warszawa, Poland
antero.arkkio@tkk.fi

Abstract — A method for finite-element analysis of a rolling-rotor electrical machine was developed. The conventional moving-band technique for modelling motion was replaced by an element structure of radial bands in the air gap. This finite-element scheme allows a large distortion of the elements at the contact point of stator and rotor without suffering of problems in the convergence of numerical solution or the accuracy of results.

I. INTRODUCTION

Fig. 1 presents the operation principle of a rolling-rotor machine. The machine has no bearings, and the rotor rolls along the stator bore. A winding in stator produces a magnetic field and force F_{em} that causes the rotary motion and maintains the contact between the stator and rotor. The support forces on the contact line balance the electromagnetic force. The friction between the bodies has to be large enough to prevent slipping.

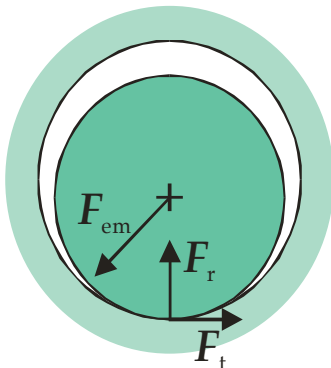


Fig. 1. Operating principle of the rolling-rotor machine.

The torque per volume ratio of a conventional radial-flux electrical machine remains small as the magnetic stress for the torque is proportional to the product of the radial flux density and circumferential flux density that is typically small. In the rolling-rotor case, the torque arm acts from the contact point of the rotor and stator, and the magnetic stress for the torque is proportional to the radial flux density squared. A large local force density can be obtained for torque production.

The contact line on the stator bore may move at a relatively large speed but the rotation speed of the rotor remains small. Thus, the potential applications of rolling-rotor machines are in low-speed high-torque drives. A rolling-rotor machine was first described by a Russian engineer A. I. Moskowitin in 1944 [1]. Later on, these machines have been studied by Viviani [2] and Kaminski&Wrotek [3], among others.

If finite-element analysis (FEA) and the commonly used moving-band technique [4] are applied for the rolling motion, problems arise related to the quality of the finite elements in the air gap. The elements become distorted, especially, close to the contact point. Refining the mesh may bring some relief but this easily leads to very large numbers of finite elements and long simulation times. Further more, as a rotor eccentricity is present, the finite-element mesh has to be constructed for the whole cross-section of the motor. There is no symmetry that could be used to reduce the solution region. Other possible ways of modelling the rolling motion within FEA could be the technique of overlapping meshes [5] or a hybrid method of FEM and BEM [6].

The aim of the present study is to develop the means to design and analyse rolling-rotor machines. The method should be computationally efficient and reliable enough to be used for structural optimisation of these machines. A small prototype of this machine was built and tested for the validation of the methods of analyses and for verifying the torque production ability of this type of a machine.

II. MODELLING MOTION AND TORQUE

The rotor of a rolling-rotor machine is typically a homogeneous cylinder made of electrical steel sheets. If the core losses of the rotor are neglected, more freedom is obtained for modelling the motion. The rotor can be just pushed against the stator at the successive time steps in such a manner that the contact point moves exactly as in the rolling motion but the rotor does not rotate. If using this semi-rolling approach, adjusting the finite-element mesh in the air-gap becomes easier.

To model the semi-rolling motion and avoid dense finite-element meshes, the circumferential element bands in the air gap were replaced by radial bands (Fig. 2a). The idea is to keep the thickness of a radial band relatively constant from the rotor to the stator. When the rotor approaches the stator, such an element band is gradually reduced to two elements, which cover an almost rectangular area (Fig. 2b). When the motion proceeds, the rectangle is gradually reduces to almost a line segment, however, still including the two elements. A right-angled triangular element seems to allow large distortions. Using this approach for a 2D time-discretised analysis, the process can be performed without convergence problems even if the length-to-thickness ratios larger than 1000 are allowed for the air-gap elements at the contact point.

The torque was computed from the air gap using the method developed by Coulomb [7]. No special treatment was used for the distorted elements close to the contact point.

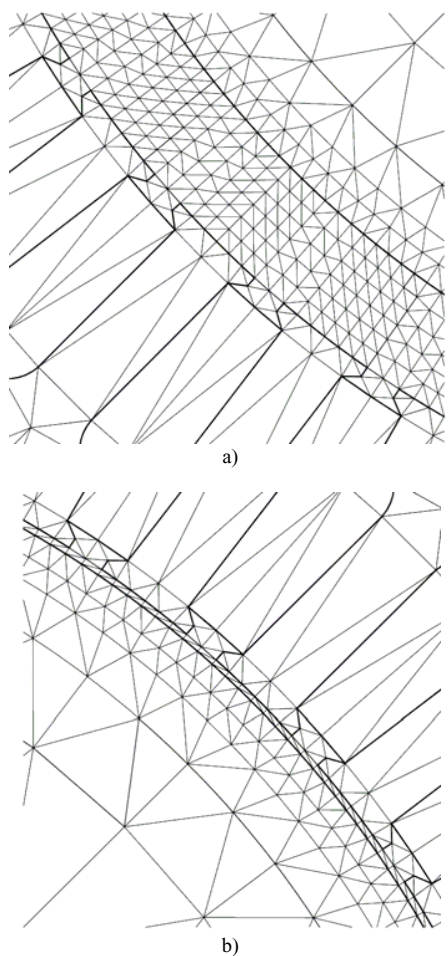


Fig. 2. Second-order isoparametric elements are used. Regions where the rotor and stator are a) relatively far from each other and b) close to each other.

III. RESULTS

Fig. 3 shows the geometry and magnetic field of the prototype rolling-rotor machine equipped with a five-phase stator winding, when the first phase is excited by a dc current. The definition of the load angle is also shown. Table I gives the main dimensions of the machine.

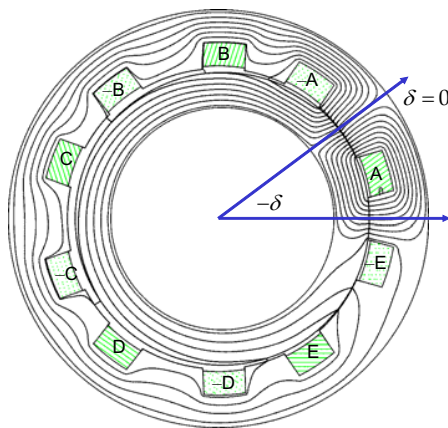


Fig. 3. Geometry of the rolling-rotor prototype motor. The eccentricity is 99% of the average air gap. The load angle δ defines the phase of the excitation with respect to the rotor position.

TABLE I
DIMENSIONS OF THE ROLLING-ROTOR MACHINE STUDIED

Outer diameter of the stator [mm]	160
Inner diameter of the stator [mm]	115
Outer diameter of the rotor [mm]	112
Inner diameter of the rotor [mm]	85
Core length [mm]	100

Fig. 4 shows the power versus load-angle curve of the machine, when the rotor is rolling and the phases are excited successively one by one with current pulses of amplitude 7 A.

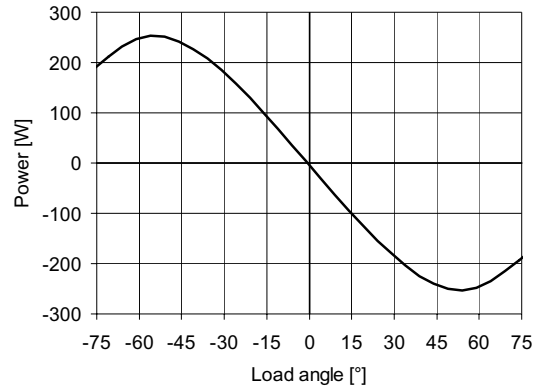


Fig. 4. The shaft power versus load angle for the rolling-rotor machine.

IV. CONCLUSION

Using the methods described above, it is possible to model cases with full stator-rotor contact, i.e. 100% eccentricity. No convergence problems were encountered when analysing machines supplied from current sources. When voltage-fed machines with full contact were studied, the time-stepping process was not completely reliable suffering from problems in convergence every now and then.

The operation characteristics computed and measured for the prototype machine, i.e. the validation of the method of analysis is presented in the full paper.

V. REFERENCES

- [1] Bertinov A.I., "Electrical Machines with Asymmetrical Rotors," *Energia*, 1969. (in Russian)
- [2] Viviani A., "Experimental and theoretical study of hypocycloidal motors with two-harmonic field windings," *IEEE Trans. Power Systems*, 99(1): 292-300. 1980.
- [3] Kaminski G., Wrotek H., "Magnetic circuit analysis of switched reluctance motor with rolling rotor," *Archives of Electrical Engineering*, L(4): 339-350. 2001.
- [4] Davat B., Ren Z., Lajoie-Mazenc M., "The movement in field modeling," *IEEE Trans. Magnetics*, 21(6): 2296-2298. 1985.
- [5] Lai H.C., Coles P.C., Rodger D., Leonard P.J., "Transient analysis of an electromagnetic actuator using an overlapping finite element scheme," *IEEE Trans. Magnetics*, 36(4): 1462-1467. 2000.
- [6] Kurz S., Fetzer J., Lehner G., Rucker W.M., "A novel formulation for 3D eddy current problems with moving bodies using a Lagrangian description and BEM-FEM coupling," *IEEE Trans. Magnetics*, 34(5): 3068-3073, 1998.
- [7] Coulomb J.L., "A methodology for the determination of global electromechanical quantities from a finite element analysis and its application to the evaluation of magnetic forces, torques and stiffness". *IEEE Trans. Magnetics*, 19(6): 2514-2519. 1983.

Numerical modelling of Transformer Inrush Currents

Ermanno Cardelli, Vincenzo Esposito, Antonio Faba
 Dipartimento di Ingegneria Industriale, 67 Via G. Duranti, 06124 Perugia, Italia
 ecar@unipg.it

Abstract — This paper presents an application of a vector Hysteresis model to the prediction of the inrush current due the arbitrary initial excitation of a transformer after a fault.

The approach proposed seems promising in order to predict the optimal time to close the circuit after the fault.

I. INTRODUCTION

Inrush currents are high value transient currents generated when a magnetic core is driven into saturation during initial excitation. They have many undesirable effects, such as damage or reduction of life of the transformer, opening of the power circuit by means of protective relays, and this fact can strongly reduce the quality and the continuity of the power systems, especially in the case of uninterruptible power supplies. The effects of inrush currents can be mitigated by using suitable late-closing relays, over-size fuses, or other passive components. Although reduction in inrush currents magnitudes has been achieved with this hardware, active controls, such as controlled closing ones, seem to be promising in order to reduce the complexity and the cost of the power system. An open question is about their complexity, that means how much must they have memory of the power system parameters, in order to ensure the desired degree of reliability and robustness of the protection system. Usually the control strategies are based on the prediction of the residual magnetic flux acting in the transformer in order to avoid a transient overshoot in the current, by selecting the closing time correspondent to the given residual flux [1], [2], [3],[4], [5]. The evaluation of the residual flux with accuracy is a very difficult and complex problem to solve, for the two following reasons: the effects of the eddy currents in the laminated cores is in general considerable; the hysteresis in the magnetic materials must be taken into account.

In this paper we approach the general problem of the prediction of the optimal closing time in a single-phase transformer, introducing a model of hysteresis in the transient during the transformer initial excitation.

II. NUMERICAL MODELLING

In this first approach to the problem, we postulate that magnetic hysteresis as a rate-independent phenomena and that the magnetic induction is uniform in the cross section of the magnetic core of the transformer. So, in the following, the eddy current effect will be neglected. The experiments reported in the extended version of the paper in order to help the discussion about the numerical modeling approached will be addressed to cases in which the eddy current effect seems to be negligible *a priori*. This paper is mainly focused to the introduction of vector models of static magnetic hysteresis in the simulation of inrush currents in order to discuss the improvement in accuracy achieved. The modelling of magnetic Hysteresis used is based on the rule of a phenomenological vector hysteresis operator recently defined

in the H -space. The vector hysteresis operator is defined by means of a convex surface, called critical surface, which is the locus of the values of H where there is discontinuity of the magnetization and a Barkhausen-like jump. This jump is represented in the model by the fact that the unit magnetization is frozen in the direction that it had just before it entered the critical surface for fields inside the critical surface, it remains constant until it is internal to the critical surface, and is then suddenly oriented along the direction normal to the critical surface when the applied vector field it exits the critical surface. These rules allow the model to intrinsically obey to the saturation and the static loss property [6], [7], [8]. The vector model of hysteresis above has been implemented as circuital block in the equivalent network of the transformer at industrial frequency (See Fig.1). The magnetic and electric equilibrium equations have been solved in time domain via a suitable finite difference scheme.

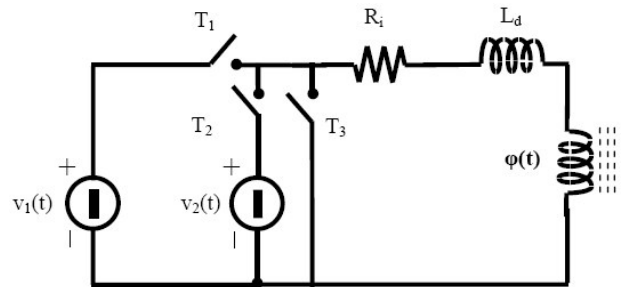
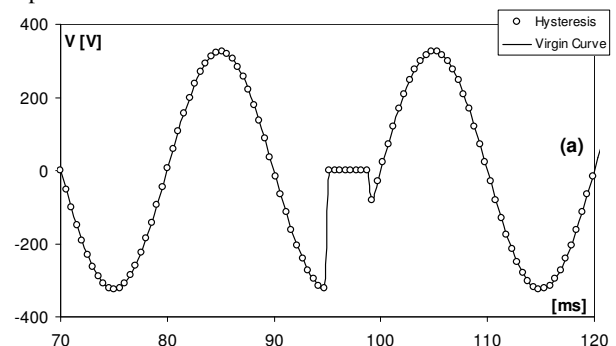


Fig. 1 – Equivalent circuit used for the simulation of the inrush of the no-load transformer.

III. PRELIMINARY RESULTS

In this section are reported preliminary data about the numerical simulations presented in the full paper.

The figures below refer to the initial excitation of a single-phase transformer respectively after a short circuit fault (see Fig.2) and an open circuit fault (see Fig. 3). Simulations of the example are made either by using the virgin curve or the complete hysteresis path. In Fig. 4 are reported the experimental data.



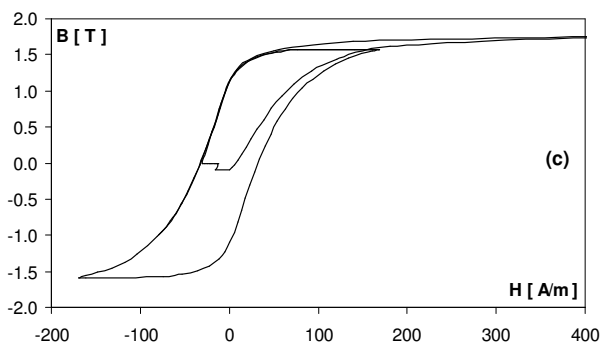
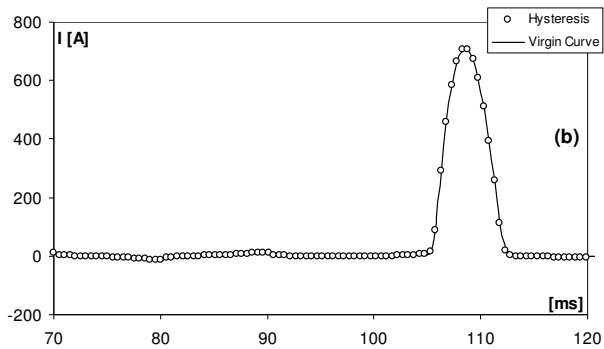


Fig. 2 – Voltage and current vs time (a)(b), and magnetization path (c) in the core of the transformer calculated for a single phase short-circuit.

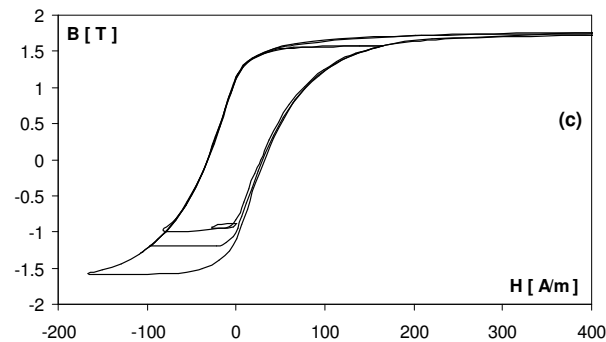
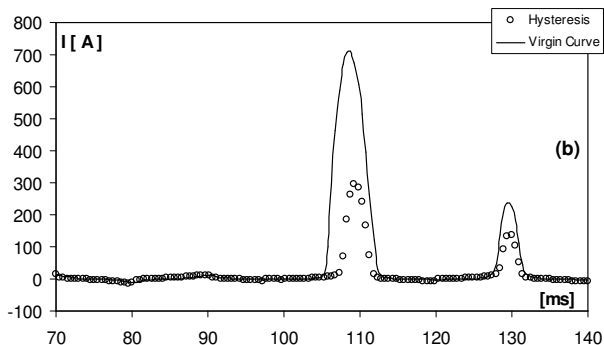
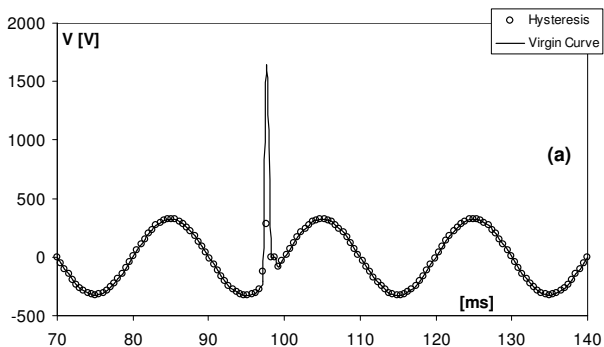


Fig. 3 - Voltage and current vs time (a)(b), and magnetization path (c) in the core of the transformer calculated for an open-circuit fault.

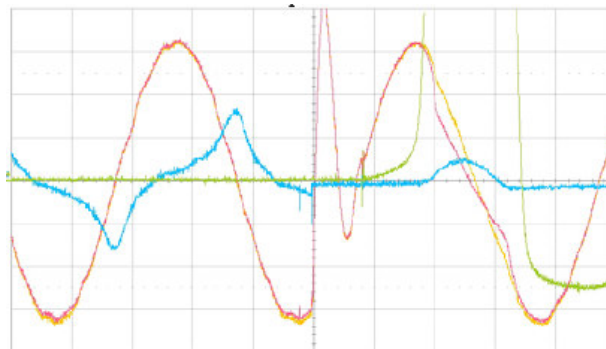


Fig. 4 – Experimental data recorded for the example of fig. 3.

REFERENCES

- [1] P.C.Y. Ling, A. Basak, "Investigation on magnetizing inrush current in single-phase transformer", *IEEE Trans. Magn.*, Vol. 24, NO.6, pp. 3217-3222, November 1988.
- [2] John H. Brunke, Klaus J. Frölich "Elimination of Transformer Inrush Currents by Controlled Switching – Part I: Theoretical Considerations", *IEEE Trans. on Power Delivery*, Vol. 16, NO.2, pp. 276-280, April 2001.
- [3] John H. Brunke, Klaus J. Frölich "Elimination of Transformer Inrush Currents by Controlled Switching – Part II: Application and Performance Considerations", *IEEE Trans. on Power Delivery*, Vol. 16, NO.2, pp. 281-285, April 2001.
- [4] Y. Cui, S. G. Abdulsalam, S. Chen, W. Xu "A Sequential Phase Energization Method for Transformer Inrush Current Reduction – part I: Simulation and Experimental Results", *IEEE Trans. on Power Delivery*, Vol. 20, NO.2, pp. 943-949, April 2005.
- [5] S. G. Abdulsalam, W. Xu "A Sequential Phase Energization Method for Transformer Inrush Current Reduction – Transient Performance and Practical Considerations", *IEEE Trans. on Power Delivery*, Vol. 22, NO.1, pp. 208-216, January 2007.
- [6] E. Cardelli, E. Della Torre, E. Pinzaglia, "Numerical implementation of the Radial Vector Hysteresis Model", *IEEE Trans. on Magn.*, Vol. 42, NO.4, pp. 527-530, April 2006.
- [7] E. Cardelli, E. Della Torre, A. Faba, "Properties of a class of vector hysterons", *Journal of Applied Physics* 103, 07D927, 2008.
- [8] E. Cardelli, E. Della Torre, and A. Faba, "Numerical Implementation of the DPC Model", *IEEE Transaction on Magnetics*, VOL. 45, NO. 3, March 2009.

Gaussian Modulated Pulse Excitation for SM Parameter Estimation Using a 2D-FE Model

M.A. Arjona, *IEEE Senior Member*, C. Hernández, *IEEE Member* and M. Cisneros-González
 Instituto Tecnológico de la Laguna, División de Estudios de Posgrado e Investigación
 Blvd. Revolución y Calz. Cuauhtemoc, 27000, México
 Email: marjona@ieee.org

Abstract — A 2D Transient FE model is used to evaluate a new excitation signal in the estimation of synchronous generator equivalent circuit parameters. Traditionally, step, dc flux decay, sinusoidal perturbations have been used for obtaining off-line data, which are then used to estimate the machine parameters. This paper presents the results of applying a Gaussian Modulated Pulse Signal into the d - q axes of the machine. The FE simulation results are used to estimate the equivalent circuit parameters with genetic algorithms, and the resulting parameters are then validated by applying a sudden three-phase short-circuit to a 7 kVA, 220V, 60 Hz, four-pole synchronous generator.

I. INTRODUCTION

Equivalent circuits of electrical machines are a lumped representation of its complex electromagnetic behavior. They have been used since several decades ago for predicting the performance of synchronous generators, induction motors and transformers; their main advantages are their simplicity and acceptable accuracy. Lumped models are represented by a set of nonlinear ordinary differential equations; its parameters have traditionally been obtained by standard methods: standstill and online tests. Standstill tests are attractive because by applying a small perturbation signal along each magnetic axis, the complete set of parameters can be estimated, and furthermore it avoids a possible damage to the generator. Step voltage, dc flux decay and frequency response are the perturbations commonly employed; recently new signals have been explored [1]. A Finite Element (FE) model offers the ability of evaluating new excitations signals, which can be of interest to manufacturers of large generators. In this paper, the Gaussian Modulated Signal Pulse (GMSP) excitation is investigated, a two-dimensional FE model is used to simulate the test. The data obtained is then used to estimate the machine parameters by using a Genetic Algorithm (GA) and they are fine tuned by using a deterministic method. To evaluate the estimated parameters from FE data, the model is compared with a real sudden short circuit of a 7 kVA, 220V, and 60 Hz salient pole generator.

II. MACHINE MODEL

The electromagnetic behavior of synchronous machines is governed by the time-domain diffusion equation.

$$\frac{\partial}{\partial x} \left(\nu \frac{\partial A}{\partial x} \right) + \frac{\partial}{\partial y} \left(\nu \frac{\partial A}{\partial y} \right) + \sigma E - \sigma \frac{\partial A}{\partial t} = 0 \quad (1)$$

where σ is the electric conductivity, E is the electric field intensity and ν is the magnetic reluctivity.

To couple the field and circuit equations fed by an external voltage source, it is necessary to consider the winding currents as one degree of freedom and solve simultaneously with (1), as it can be expressed by following set of equations [2]-[3]:

$$SA + N \frac{dA}{dt} - PI = 0 \quad (2)$$

$$Q \frac{dA}{dt} + RI + L \frac{dI}{dt} = V \quad (3)$$

where S is the stiffness matrix, N represents eddy current regions, P represents machine windings, Q are induced voltages, R are dc resistances, L are end-winding inductances and V are source voltages.

The synchronous generator, even though is of a salient-pole type, it has solid poles where eddy currents are present. The GMSP is applied to the d or q axes while the alternator is at standstill with the field winding in short-circuit. This kind of excitation has been applied to transient electromagnetic wave propagation and it is given by [4]:

$$v(t) = V_m e^{-\frac{(t-T_{delay})^2}{A}} \sin(\omega(t - T_{delay})) \quad (4)$$

where V_m is the amplitude of the signal, ω is the operational frequency, t is time, A and T_{delay} are the shape parameters.

The vector potential distribution while the machine is at the d -axis position is illustrated in Fig. 1, it can be seen the effect of the field produced by the eddy currents.

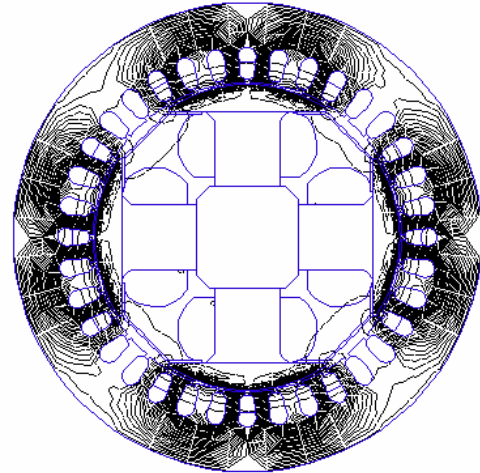


Figure 1. D -axis field distribution with the GMSP excitation at $t=0.15$ s.

III. PARAMETER ESTIMATION AND MODEL VALIDATION

The set of state-equations are derived using the electric equivalent circuit of the machine. One-damper winding is selected for both axes, and the equations for the d -axis are:

$$\dot{\mathbf{I}}_d = \omega_0 \mathbf{X}_d^{-1} \mathbf{V}_d - \omega_0 \mathbf{X}_d^{-1} \mathbf{R}_d \mathbf{I}_d \quad (5)$$

where \mathbf{I}_d , \mathbf{R}_d , \mathbf{V}_d and \mathbf{X}_d are vector of d -axis currents, resistance matrix, voltage vector and d -axis reactance matrix, respectively, ω_0 is the rated angular speed.

The q -axis state-space equations are,

$$\dot{\mathbf{I}}_q = \omega_0 \mathbf{X}_q^{-1} \mathbf{V}_q - \omega_0 \mathbf{X}_q^{-1} \mathbf{R}_q \mathbf{I}_q \quad (6)$$

where \mathbf{I}_q , \mathbf{R}_q , \mathbf{V}_q and \mathbf{X}_q stand for q -axis current vector, resistance matrix, voltage vector and q -axis reactance matrix, respectively.

The estimation of the fundamental parameters for each equivalent circuit was made using the least squares approach where the objective function can be expressed as:

$$\min J(\theta) = \frac{1}{2} \sum_{i=1}^N (y_i - \hat{y}_i)^2 \quad (7)$$

where $J(\theta)$ is the objective function, y_i is the set of experimental data, \hat{y}_i is the set of estimated responses from the proposed mathematical model, N is the number of the experimental points and θ is the parameter vector.

In this paper, a genetic algorithm was used to solve (7). A GA is a stochastic method that employs probabilistic and non-local search heuristics that simulate natural evolution, which works on the chromosomes [5]. The final results were determined using a deterministic algorithm (Gauss-Newton). The obtained set of parameters are shown in Table I. Fig. 2 illustrates the comparison of FE model and equivalent circuit for the d -axis current, where a good accuracy can be seen.

To validate the estimated set of parameters from FE data, a sudden three-phase short-circuit was applied to the generator which has special instrumentation features. The non-linear model of the synchronous machine under short-circuit conditions is represented by (8).

$$\dot{\mathbf{x}} = \mathbf{A} \mathbf{x} + \mathbf{F}(\mathbf{x}) + \mathbf{B} \mathbf{z} \quad (8)$$

where \mathbf{x} denotes the flux linkage state-variables, \mathbf{F} is a function of nonlinear terms, \mathbf{A} is the system matrix, \mathbf{B} is the input vector and \mathbf{z} is the input variable vector.

Fig. 3 shows the comparison of the lumped model against experimental data for the field current in the short-circuit fault. It can be seen that field current is reproduced with an acceptable accuracy. The line currents are also reproduced accurately. In the full paper version more validation results will be given.

TABLE I
ESTIMATED PARAMETERS FOR THE GENERATOR

Parameter	Value (pu)	Parameter	Value (pu)
X_{md}	1.44018595	X_{mq}	1.28136182
X_a	0.19250433	X_{kd}	0.23907052
X_f	0.27719480	r_{kd}	0.14906767
X_{kd}	0.01671623	r_a	0.05251969
r_{kd}	0.16033241	r_f	0.01304253

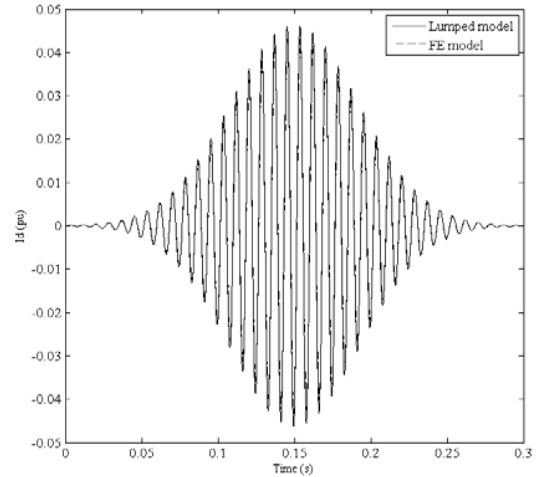


Fig. 2. Comparison of model and FE model for the d -axis current with a 6V GMSP amplitude.

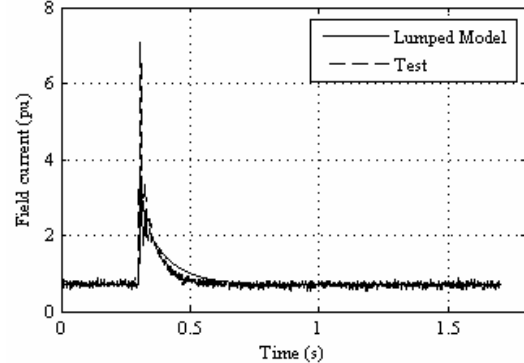


Fig. 3. Field current in the sudden three-phase short-circuit.

IV. CONCLUSION

The 2D FE ability as a data source for parameter estimation using the Gaussian Modulated Signal Pulse was demonstrated. A Genetic Algorithm was used to obtain the parameters which were then employed in a non-linear time-stepping lumped model to simulate the sudden three-phase short-circuit where good results were achieved.

V. REFERENCES

- [1] O. Makela, A.K. Repo and A. Arkkio, "Parameter Estimation for Synchronous Machines Using Numerical Pulse Test within Finite Element Analysis," *Proceedings of the 2008 International Conference on Electrical Machines*, pp. 1-5, 2008.
- [2] J.P.A. Bastos and N. Sadowski. *Electromagnetic Modeling by Finite Element Methods*, 2003, pp. 283-339.
- [3] SLIM, user manual 2008.
- [4] E. Bařaran, H. A. Serim, S. Aksoy, "The Distortion Analysis of Pulse Propagation along a Rectangular Waveguide which is Partially Filled with a Dispersive Dielectric Film," *Fourth International Workshop on Electromagnetic Wave Scattering*, pp. 9-14, 18-22 Sept., 2006, Gebze Institute of Technology, Kocaeli, Turkey.
- [5] J.A. Hageman, R. Wehrens, H.A. van Sprang, and L.M.C. Buydens, "Hybrid genetic algorithm-tabu search approach for optimizing multilayer optical coatings," *Analytica Chimica Acta*, vol. 490, pp. , June 2003, 211-222.

Efficient FEA Identification of Equivalent Circuit Inductances for DFIM Design

Davide Aguglia¹, René Wamkeue², Philippe Viarouge¹, and Jérôme Cros¹

¹ L.E.E.P.C.I. Lab., Electrical & Computer Eng. Dept., Laval University Quebec (Qc), G1K 7P4 Canada.

²Electrical Eng. Dept., Abitibi-Témiscamingue Quebec University (UQAT), (Qc), J9X 5E4 Canada.

E-mails: davide.aguglia@gel.ulaval.ca, rene.wamkeue@uqat.ca, viarouge@gel.ulaval.ca, cros@gel.ulaval.ca.

Abstract — This paper presents a new efficient method for finite-elements identification of the equivalent circuit inductances of doubly-fed induction machines (DFIM). The method can be easily integrated in a computer aided optimization design of DFIM, since it allows good precision combined with a fast magnetostatic analysis. The magnetizing inductance estimation is performed by a FFT of the spatial distribution of magnetic field measured in the air gap. The variable reluctance effect produced by the double slotting of the machine yokes is taken into account as well as magnetic saturation effect. An analysis of results precision versus mesh size is presented as well.

I. INTRODUCTION

During the design process of an electrical machine, Finite Elements Analysis (FEA) is widely used for precision increase of performance prediction. FEA offers the possibility to perform a simulation of experimental tests of an electrical machine. This can be considered as a validation step of the final structure, performed at the end of the design process. However, FEA can also be used for intermediate performances validations of the electrical machine structure during the iterative optimal design process. In this case the selected numerical analysis should optimize the balance between precision and time cost. Analytical design models of DFIM can be used in combination with FEA in order to increase the design optimization precision. The detailed method presented in [1], is illustrated by Fig.1.

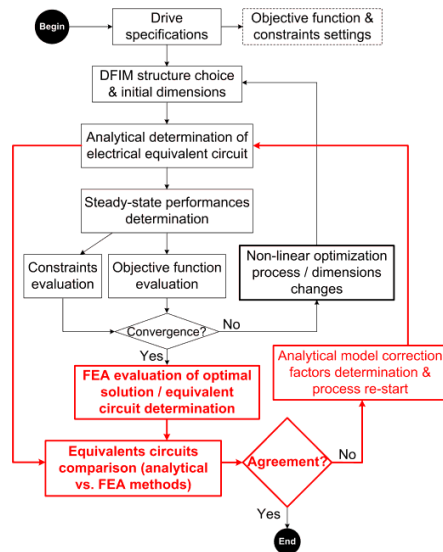


Fig.1 : Optimal DFIM design process in combination with a correction process thank to FEA.

In a first step a non-linear optimization process is used to find the optimal dimensions of the DFIM for a given

specification. The design models treated by the numerical optimization program are fully analytical based. In a second step the optimal dimensional solution is considered for FEA. In this process the goal is to determine the equivalent circuit parameters (inductances) by use of FEA and compare them with the ones determined by analytical methods. In case of unacceptable differences between analytical and FEA methods, correction factors are computed and inserted in the analytical models to improve their accuracy. The process last until the analytical model provides the same results as FEA method. These correction iterations should be as efficient as possible in terms of time cost (design time minimization) and precision.

This paper presents an efficient method to determine the DFIM equivalent circuit inductance with FEA, in order to be easily implemented in the correction process described above.

II. MAGNETOSTATIC ANALYSIS FOR EQUIVALENT CIRCUIT IDENTIFICATION

A. Cyclic inductances identification

For cyclic inductances determination by magnetostatics methods one has to take into account the slotting effect. Indeed, for different relative angular positions of the rotor with respect to the stator, the cyclic inductances may result to be different because of variable reluctance. The presented solution consists in performing several magnetostatic flux computations for n different relative angular positions and by considering the mean value of the measured magnetic flux. In the case of a three-phase balanced sinusoidal supply, one considers the time instant where one phase is supplied by a current with an amplitude value I and where the other two phases are supplied by a current with an amplitude $-I/2$. When magnetic saturation is taken into account, the peak current value must be selected in order to produce the specified maximal magnetic induction level. The rotor or stator cyclic inductance L_s or L_r are derived from the measured magnetic fluxes Ψ for each relative angular position θ , as showed in (1).

$$L_{(s,r)} = \frac{\sum_{\theta=1}^n \Psi_{\theta(s,r)}}{n \cdot I_{(s,r)}} \quad (1)$$

n is the number of relative angular positions. L_s and L_r' are defined in (2), and $L_{\sigma s}$, $L_{\sigma r}$ and L_m are presented in Fig. 2.

$$\begin{aligned} L_s &= L_m + L_{\sigma s} \\ L_r' &= L_m + L_{\sigma r} \end{aligned} \quad (2)$$

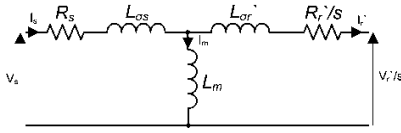


Fig.2 : Steady-state equivalent circuit of a DFIM.

Notice that $L_r' = L_r a^2$, where a is the stator to rotor voltage ratio defines as:

$$a = \frac{N_s \cdot k_{ws(h=1)}}{N_r \cdot k_{wr(h=1)}} \quad (3)$$

Where N_s and N_r are the number of turns in series per phase of the stator and the rotor windings respectively. Factors $k_{ws(h=1)}$ and $k_{wr(h=1)}$ are the stator and rotor winding factors with respect to the first spatial harmonic h .

B. Magnetizing inductance identification

Since the early 20th century the magnetizing inductance was defined as the one representing the induced voltage by the fundamental space harmonic of the magnetic flux in the air gap [2]. Since then this definition has not changed as it can be noticed by the analytical formulations in [3]. Therefore, the best way to determine such inductance by finite elements is to measure the air-gap radial magnetic field and perform a *FFT* in order to get the amplitude of its fundamental harmonic. Figure 3 shows the result of such a procedure, for a small DFIM with 48 stator slots and 36 rotor slots presented in Fig.4.

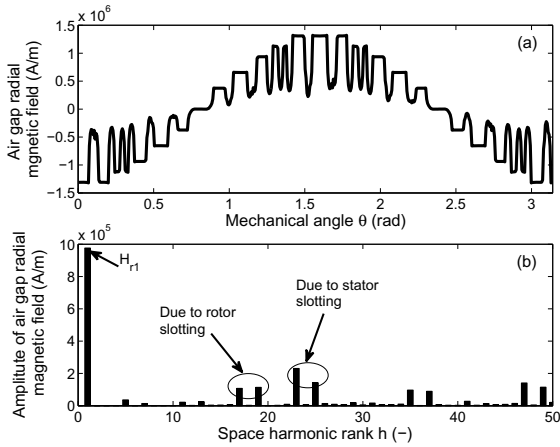


Fig.3 : (a) Radial magnetic field in the air-gap; (b) Harmonics spectrum amplitude of radial magnetic field in the air-gap.

Knowing the fundamental space harmonic amplitude of the radial magnetic field H_{r1} it is possible to derive the associates flux amplitude (4).

$$\hat{\psi}_m = \frac{2}{\pi} \mu_0 H_{r1} \frac{\pi DL}{2p} N_s k_{ws(h=1)} = \mu_0 H_{r1} \frac{DL}{2p} N_s k_{ws(h=1)} \quad (4)$$

D , L and p are the stator bore diameter, the axial length and the poles pair number whereas μ_0 is the vacuum magnetic permeability. Therefore the magnetizing inductance is determined as follows:

$$L_m = \frac{\hat{\psi}_m}{I_s} \quad (5)$$

Notice that the result is correct for any relative position between stator and rotor. The space harmonics of higher order cannot be used to compute the differential leakage inductances because of slotting effects (not rotating at the right speed).

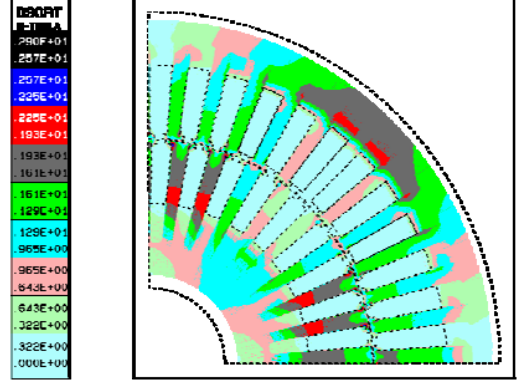


Fig.4 Geometry and induction distribution of the considered DFIM.

C. Leakage inductances & mesh size sensitivity analysis

The leakages inductances are derived by subtraction from (2). However the subtraction between two similar numbers could lead to precision errors. Table I shows that the leakage inductance value (showed for stator) is stable for different elements number n_e in the considered domain. Notice that n_e used for L_s estimation must be equal to n_e used to estimate L_m to avoid unacceptable errors in the leakage inductance value.

 TABLE I
EQUIVALENT CIRCUIT IDENTIFICATION SENSIBILITY VS. NUMBER OF ELEMENTS

Circuit element	$n_e = 5497$	$n_e = 7409$	$n_e = 11129$	$n_e = 14849$
L_s (mH)	3.67317	3.75544	3.79632	3.81714
L_m (mH)	3.65310	3.7350	3.77550	3.7970
L_{gs} (mH)	0.020074	0.020439	0.020818	0.020142

III. CONCLUSION

The presented method is efficient in terms of computing time and precision. The result sensibility against the chosen finite elements number demonstrates the stability of this method and makes it suitable for an implementation in a optimization design environment.

IV. REFERENCES

- [1] J. Cros, L. Radaorozandry, J. Figueroa and P. Viarouge, "Influence of the magnetic model accuracy on the optimal design of a car alternator ", *COMPEL – International Journal for Computation and Mathematics in Electrical and Electronics Engineering*, Vol. 27 (1), 196-204, 2008.
- [2] C. A. Adams, "The design of induction motor: With special reference to magnetic leakages", *AIEE Transactions*, Vol. 24, 649-687, June 1905.
- [3] M. Liwschitz-Garik, C. C. Whipple, *Alternating-current machines, Second ed.*, D. Van Nostrand Company, Inc, Princeton (NJ), 1961

Comparison of Analytical and Finite Element Calculation of Eddy-Current Losses in the Solid Back-Iron of PM Machines with Concentrated Fractional Pitch Windings

A. Jassal, H. Polinder, D. Lahaye*

a.k.jassal@tudelft.nl, h.polinder@tudelft.nl, domenico.lahaye@cw.nl
 Electrical Energy Conversion Group, *Numerical Analysis Group
 Faculty of Electrical Engineering, Mathematics and Computer Science,
 Delft University of Technology, Mekelweg 4, 2628 CD Delft, The Netherlands

Abstract—Permanent magnet (PM) machines with concentrated fractional-pitch stator windings are interesting because of their cost-effectiveness. However, in machines with fractional-pitch windings, the eddy-current losses, specifically in solid back-iron of the rotor are considerable and depend strongly on the combination of number of teeth and number of poles. This paper presents a comparison between analytically calculated eddy current losses and the loss calculation by Finite Element (FE) method. The software COMSOL is used for FE calculations. The model is applied to calculate the losses in the solid back-iron of the linear PM generator of the Archimedes Wave Swing (AWS) for different combinations of numbers of poles and numbers of teeth.

Index Terms—eddy currents, permanent-magnet machines, back-iron, fractional-pitch concentrated windings, finite element model.

I. INTRODUCTION

Permanent magnet (PM) machines with concentrated fractional-pitch stator windings are increasingly used because of their cost-effectiveness. The objective of this paper is to compare and bring out differences between an analytical model and a finite element model for calculation of eddy-current losses in the solid back-iron of these machines. If there is sufficient agreement between the results of each method, validation for the analytical method can be proved. The machine used for modeling is the linear PM generator of the Archimedes Wave Swing (AWS)*. Details about AWS are available in [1].

Currently, a PM machine with distributed full-pitch stator windings is applied. It has one slot per pole per phase as illustrated in Fig. 1. The winding is a two-layer winding, which makes it rather expensive. This is where fractional pitch concentrated windings come into picture.

*This work was supported in part by a Marie Curie Early Stage Research Training Fellowship of the European Community's Sixth Framework Programme under contract number MRTN-CT-2004-505166, the WAVETRAIN program.

PM generators with concentrated fractional pitch windings may be much cheaper because they have simple windings around one tooth which can be wound automatically and hence economically.

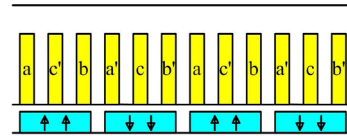


Fig 1: A Full pitch distributed winding (currently used in AWS)

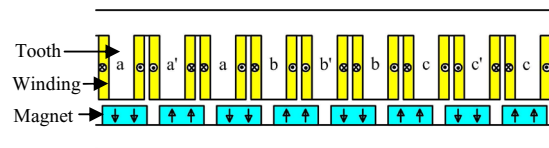


Fig 2: A fractional pitch concentrated winding

However, the magnetic field of fractional pitch concentrated windings has more space harmonics, including sub-harmonics (harmonics with a wave length larger than twice the pole pitch). This leads to additional eddy-current losses in the magnets and the back-iron, which is made of solid steel to make a cheap and strong construction. If these losses are high, the magnets may become so hot that they demagnetize. The contribution of this paper comes from validation of the analytical model used for calculation of these losses [5] by modeling the machines with different pole-teeth combination in a FE program.

II. TOPOLOGIES SELECTED

The combinations of number of poles and teeth affect the eddy current losses that occur in the solid conductive parts of the machine [5]. This section gives an overview of the type of winding arrangement selected and the combinations of poles and teeth used for analysis. The pole-teeth combinations are

selected in such a way that winding factor is comparable to that of a full pitch distributed winding. The table below shows the winding types considered for analysis

TABLE I
WINDING TYPES CONSIDERED

	WINDING TYPES CONSIDERED
I	Full pitch with 1 slot per pole per phase
II	Fractional pitch with 3 teeth with 3 coils per 2 poles
III	Fractional pitch with 3 teeth with 3 coils per 4 poles
IV	Fractional pitch with 9 teeth with 9 coils per 8 poles
V	Fractional pitch with 9 teeth with 9 coils per 10 poles
VI	Fractional pitch with 12 teeth with 12 coils per 10 poles
VII	Fractional pitch with 12 teeth with 12 coils per 14 poles
VIII	Fractional pitch with 6 teeth with 3 coils per 4 poles
IX	Fractional pitch with 6 teeth with 3 coils per 8 poles
X	Fractional pitch with 12 teeth with 6 coils per 10 poles
XI	Fractional pitch with 12 teeth with 6 coils per 14 poles

III. ANALYTICAL CALCULATIONS

The method for calculation of eddy current losses is fully described in [5]. The Method consists of the following steps:

- a) First of all, using Ampere's law, we estimate the flux density distribution in air gap.
- b) We decompose this flux density waveform into Fourier components.
- c) Then using relative position of rotor, we evaluate the space harmonics of this flux density waveform.
- d) Eddy Current losses can then be calculated from this data.

A three layer model [6-7] for calculation of eddy current losses was selected. The eddy-current losses per square meter of surface area P_A are given by

$$P_A = \frac{\hat{B}_0^2 v^2 \delta}{4\rho_{Fe}}$$

where

\hat{B}_0 is the amplitude of the flux density wave

v is the speed of the flux density wave

ρ_{Fe} is the resistivity of iron

δ is the skin depth

TABLE II
EDDY CURRENT LOSSES CAUSED BY THE SPACE HARMONICS (W)

	1	2	4	5	7	8	10	11	total
I	0	0	0	8	2	0	0	1	11
II	0	85	5	6	2	2	1	1	102
III	1369	0	15	2	3	1	1	1	1392
IV	104	98	0	211	0	0	0	0	415
V	296	35	516	0	2	0	0	0	849
VI	741	0	0	0	169	0	0	0	911
VII	741	0	0	651	0	0	0	1	1393
VIII	7301	0	242	12	16	15	18	3	7606
IX	10326	5476	0	86	4	61	9	8	15969
X	11067	0	0	0	182	0	0	1	11249
XI	11067	0	0	698	0	0	0	4	11769

IV. FINITE ELEMENT CALCULATION

A model for FE calculations has been prepared in COMSOL and the results will be included later in the full

paper.

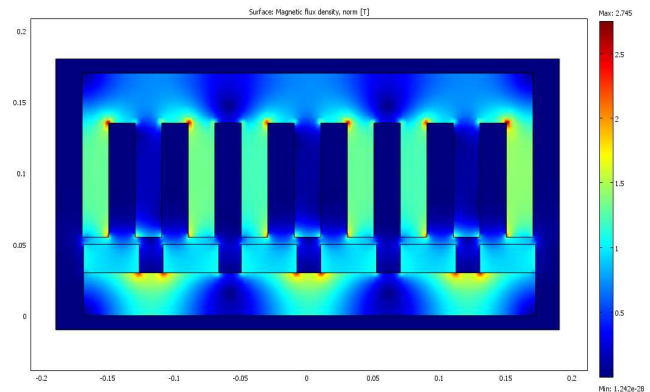


Fig 3: Flux Density Plot for a geometry

The results will include FE modeling of eddy current losses in the machine with motion included.

V. CONCLUSIONS

The following conclusions may be drawn from the paper:

- a) The analytical results for the eddy current loss model have been presented.
- b) The paper presents a comparison between analytical method and a Finite Element method to estimate eddy current losses.
- c) Validity of the analytical method and the error range has been estimated.
- d) Reasons for differences between FE results and analytical calculations have been summarized.

REFERENCES

- [1] H. Polinder, M.E.C. Damen, F. Gardner, "Linear PM generator system for wave energy conversion in the AWS," *IEEE Transactions on Energy Conversion*, vol. 19, pp. 583-589 (2004).
- [2] J. Cros, P. Viarouge, "Synthesis of high performance pm motors with concentrated windings," *IEEE Transactions on Energy Conversion*, vol. 17, pp. 248-253 (2002).
- [3] A.M. El-Refaie, T.M. Jahns, D.W. Novotny, "Analysis of surface permanent magnet machines with fractional-slot concentrated windings," *IEEE Transactions on Energy Conversion*, vol. 21, pp. 34-43 (2006).
- [4] F. Magnussen, C. Sadarangani, "Winding factors and Joule losses of permanent magnet machines with concentrated windings," in *Proc. of the 2003 IEEE International Electric Machines and Drives Conference*, 2003, pp. 333 - 339, vol.1.
- [5] H. Polinder, M.J. Hoeijmakers, M. Scuotto, "Eddy-current losses in the solid back-iron of permanent-magnet machines with concentrated fractional pitch windings," in *Proc. of the 2006 IEE International Conference on Power Electronics, Machines and Drives*, Dublin, 4-6 April 2006, pp. 479-483.
- [6] P.J. Lawrenson, P. Reece, M.C. Ralph. "Tooth-ripple losses in solid poles", *Proceedings of the IEE*, vol. 113, pp. 657-662 (1966).
- [7] K. Oberretl. "Eddy current losses in solid pole shoes of synchronous machines at no-load and on load", *IEEE Transactions on Power Apparatus and Systems*, vol. 91 pp. 152-160 (1972).

Numerical Analysis of the Induced Current in an XY-Actuator with Soft Magnetic Composite

Aly Ferreira Flores Filho, and Nolvi Francisco Baggio Filho

Post-Graduate Program in Electrical Engineering, Federal University of Rio Grande do Sul

Av. Osvaldo Aranha, N. 103, CEP 90035-190, Porto Alegre, RS, Brazil

E-mail Address: aly.flores@ufrgs.br

Abstract — Velocity induced eddy currents appear in the ferromagnetic core of an XY-actuator when the mover, equipped with permanent magnets responsible for the generation of the magnetic field of the primary circuit, moves over its working plan. The effect produces a damping force on the mover that affects its dynamics. Furthermore, the magnetic field in the air-gap is modified owing to the secondary magnetic field produced by the induced eddy currents. The induction of electrical current is investigated for different armature core materials, i.e. solid steel and a grain-insulated soft magnetic composite (SMC). The figures show a reduction the velocity-induced eddy current by the use of a SMC core instead of a steel core.

I. INTRODUCTION

The XY-actuator in study comprehends a ferromagnetic slotless core on the top of which two sets of planar windings are placed. The former are orthogonal with respect to each other and have four sections each. The mover is the moving part of the actuator, and holds two high energy product permanent magnets and a back iron that are above the working plane of the actuator across the air-gap, Fig. 1 [1].

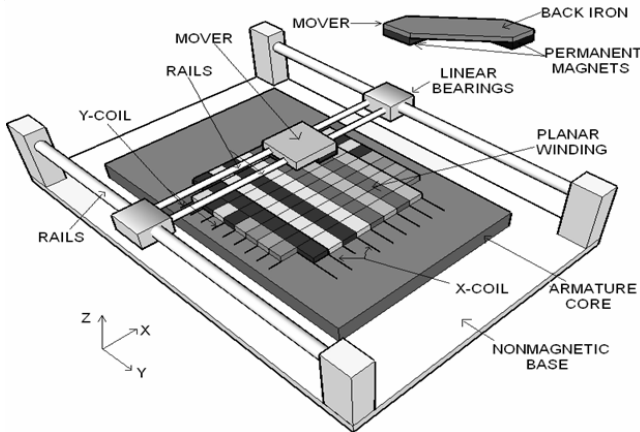


Fig. 1. Perspective view of the actuator and its parts.

II. FEATURES OF THE XY-ACTUATOR

The movement over its working plane, with two degrees of freedom, occurs when the coils of the armature phases located under the permanent magnets are properly fed with currents. The actuator relies also on a 3D distribution of the magnetic flux density in its magnetic circuit [1]. Owing to the velocity of the mover that moves the excitation field over the armature core, an electromotive force is produced on that core. As a result, currents are induced in the ferromagnetic core. These currents and their distribution depend on the resistivity and on

the permeability of the core material. One effect of such induced currents will be a breaking force acting on the car to oppose its movement. Additionally, the core will be heated by them. These two aspects can determine the performance of the actuator. The reduction of the velocity-induced currents as described and their effects can be obtained by employing an isotropic grain-insulated composite magnetic material as material core. Hence, a soft magnetic composite, i.e. Somaloy 500, is considered [3]. For comparison, two different slab-type cores are tested: one made of AISI 1020 steel, and other of Somaloy 500, Table I.

TABLE I
PARAMETERS OF THE ARMATURE CORES UNDER TEST [2]

Quantity	AISI 1020	Somaloy 500
Maximum relative permeability	3,800	500
Resistivity ($\mu\Omega\text{m}$)	0.1862	40.03823
Density (g/cm^3)	7.85	7.3356

III. VELOCITY-INDUCED EDDY CURRENT

The motion of the mover over the top face of the armature core causes the appearance of magnetically induced eddy currents in that core. Besides heat, the effect produces a second planar force that opposes the movement of the mover. The equation that sets the density of the induced eddy current, \vec{J} , may be given by (1) [3].

$$\vec{J} = \sigma (\vec{E} + \vec{v} \times \mu_0 \vec{H}) \quad (1)$$

In (1) σ is the electrical conductivity of the armature core, \vec{E} is the electric field, \vec{v} is the velocity of the mover with respect to the armature core, μ_0 is the permeability of the air and \vec{H} is the excitation magnetic field produced by the permanent magnets. In order to reduce those currents and, at the same time, maintain the benefit of the 3D distribution of the magnetic field, the use of an isotropic grain-insulated such as soft magnetic composite is taken into account.

A dynamic analysis carried out by means of a finite element analysis allowed to compute the distribution of the density of the induced current, J , in the core, as a function of the velocity of the mover. The region under the mover analyzed is where the structure has the largest concentration of magnetic flux density and can be visualized in the fig. 2.

Table II shows the results gathered from the numerical analysis for the velocity-induced current under the same air-gap flux distribution for both cores employed one at a time. That current is considered through the cross section of the

armature core defined in between the projected centers of permanent magnets and the thickness of the slab core.

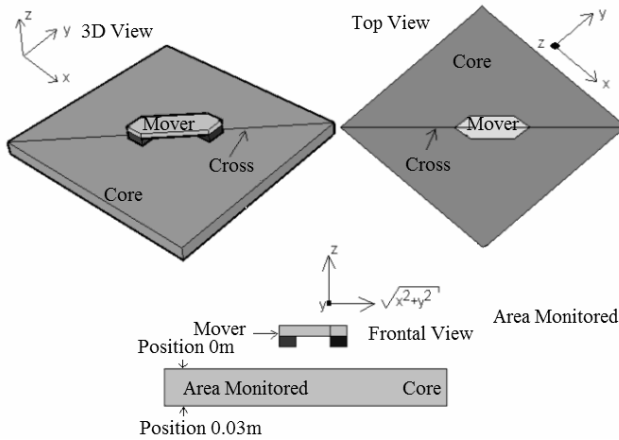


Fig. 2. View of the area monitored to show the electrical current density.

TABLE II
COMPUTED VELOCITY-INDUCED ELECTRICAL CURRENT

Mover velocity (m/s)	Computed induced current (A)	
	AISI 1020	Somaloy 500
0.05	1.61004	0.07837
0.10	2.37128	0.11274
0.15	3.24823	0.16762

Another important detail is that the depth the induced currents penetrate the core are affected by the frequency of flux variation, the electrical conductivity and the magnetic permeability of the material. It decreases when the frequency increases, or the magnetic permeability increases, or when the electrical conductivity rises.

These results are computed a velocity of 15m/s for the mover. Figure 4 shows the results for the two different materials [1]. The values presented in the fig. 3 are RMS figures for the electrical current density.

It is important to observe two important aspects. It is possible to see that the current density is much larger when the AISI 1020 is used in the armature core; that happens once its electrical resistivity is lower than the one for the Somaloy 500. Another aspect that deserves comment is that, due the higher magnetic permeability of the AISI 1020 steel, the closer to the air-gap, the larger the concentration of induced current in the core; however, when Somaloy 500 is used the current is less concentrated in the region close to the top of the armature core. That is explained by the skin effect.

IV. CONCLUSION

For the sake of a comparative study, AISI 1020 steel and Somaloy 500 were separately employed in the armature core of an XY-actuator. Although both allow a quite similar static propulsion force, the braking force resulting from velocity-induced eddy currents is smaller in the XY-actuator with

Somaloy 500. That is explained by a larger resistivity of that core material. An overall friction coefficient that takes into account the mechanical friction and the electromagnetic braking force produced by the velocity-induced eddy currents is proposed and shows coherent figures. Moreover, the SMC, as an isotropic material, favours a 3D flux density distribution which the XY-actuator relies on.

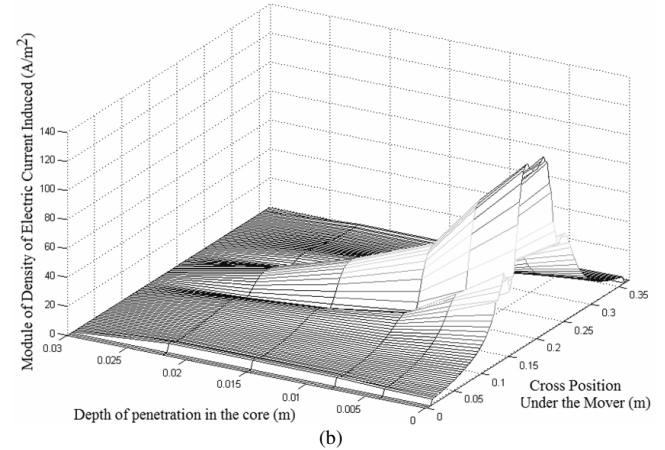
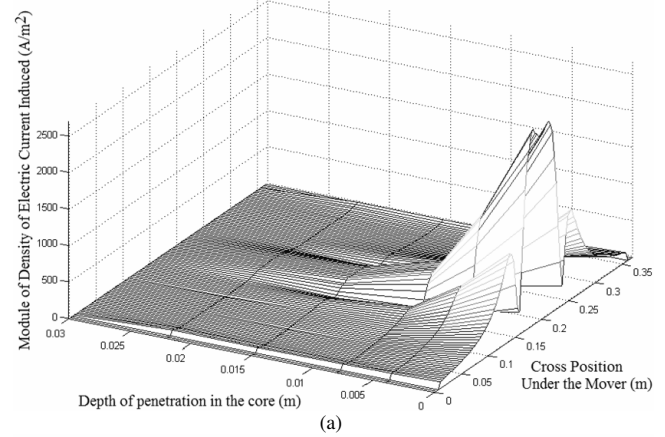


Fig. 3. Distribution of the induced current density in the armature core composed when the mover is movement with velocity of 0.15m/s with core material: (a) AISI 1020 and (b) Somaloy 500.

V. REFERENCES

- [1] BAGGIO FILHO, N. F. Study and Development of an XY-Actuator With Planned Windings and Ferromagnetic Core with Soft Magnetic Composite. Porto Alegre, RS, Brazil, 2008. MSc. Thesis, Federal University of Rio Grande do Sul.
- [2] PERSSON, P. Jansso. Soft Magnetic Composite Material – Use for Electrical Machines. The University, Newcastle Upon Tyne, UK, 1999.
- [3] MELCHER, James R. Continuum Electromechanics. Cambridge: MIT Press, 1981.
- [4] FLORES FILHO, A. F., BAGGIO FILHO, N. F., SILVEIRA, M. A. Dynamic Analysis of XY-Actuator Applying Soft Magnetic Composite (SMC) in the Armature Core. Magnetism and Magnetic Materials Conference. Tampa, Florida, 2007.

Least Squares Support Vector Machine Network-Based Modeling for Switched Reluctance Starter/Generator

Wen Ding and Deliang Liang

Department of Electrical Machines and Drives, Xi'an Jiaotong University
28 West Xian Ning Road, Xi'an 710049 P. R. China
Tel:029-826-73409, fax:029-826-75306
e-mail:dingwen_1981@163.com

Abstract- This paper presents least squares support vector machine (LS-SVM) neural networks as a new tool to develop the model of the Switched Reluctance Starter/Generator (SRS/G). The basic premise of LS-SVM regression is that it forms a very efficient mapping structure for the nonlinear phase flux linkage and torque characteristics of SRS/G. The LS-SVM models are comprised of magnetization data with rotor position and phase current as input, and the corresponding flux linkage and torque as output. A LS-SVM current-flux-linkage-position model and a LS-SVM torque model are then used to simulate the dynamic performance of SRS/G, and the accuracy of the model is tested via comparison to the measurements of steady state waveforms. Both the simulation and experimental test results for a 0.55kW 6/4 SRS/G system on a digital platform at the starting and generating modes are also presented along with useful guidelines for electric starter/generator implementation.

I. INTRODUCTION

The simply structure, low cost, and the absence of windings and permanent magnets on the rotor of a switched reluctance machine (SRM) makes it a viable candidate for various general purpose adjustable speed and operation in harsh environments as a generator. The development of a SRS/G system demands a good computer simulation model to reduce the expensive and time consuming experimental stage. This paper presents Least Squares Support Vector Machine (LS-SVM) as a new tool to develop the flux linkage current position and torque current position characteristics of the SRS/G. The sampled data sets obtained from experimental SRS/G by measurement and calculation via co-energy method, are comprised of magnetization data with position and current as inputs and the corresponding flux linkage and torque as outputs. Compared with the models based on artificial neural networks (ANN) methods, the proposed model has better capability of generalization and better convergent speed. The accuracy of the model is tested via comparison to the laboratory measurements of the machine's steady state current waveforms and torque-speed characteristics.

II. MATHEMATICAL MODEL OF SRS/G

This section firstly describes the basic operation principle of SRS/G and then gives an indirect method of obtaining the flux linkage and torque by experimental test calculation. The schematic diagram of the experimental setup to obtain the instantaneous voltage and instantaneous current for flux linkage determination is shown in Fig.1. The flux linkage versus different rotor positions and phase current, obtained are shown in Fig.2(a). Then, the static torque-current-position

characteristic can be calculated by derivative of co-energy via the principle of virtual displacement, which is shown in Fig.2(b).

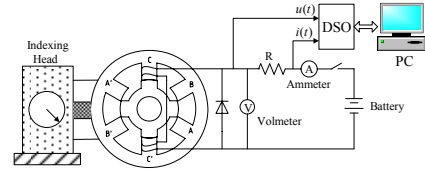


Fig.1 Experimental setup to obtain flux linkage of SRS/G

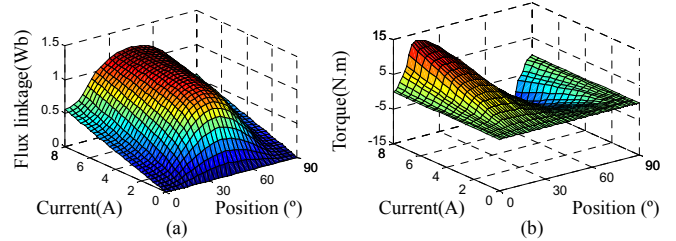


Fig.2 Flux linkage and torque characteristics of SRS/G: (a) flux linkage; (b) torque

III. MODELING FOR SRS/G BASED ON LS-SVM

This section presents least square support vector machine (LS-SVM) as a new toll to develop the model of flux linkage-current-position and torque-current-position models for the SRS/G.

A. Least Square Support Vector Machine

The discriminant function of LS-SVM classifier is constructed by solving the following minimization problem:

$$\min J = \frac{1}{2} \langle w \cdot w \rangle + \frac{1}{2} \gamma \sum_{i=1}^n e_i^2 \quad (1)$$

$$\text{s.t. } y_i = \langle w \cdot \phi(x) \rangle + b + e_i, \quad i=1, \dots, n \quad (2)$$

where γ is the regularization factor and e_i is the difference between the output y_i and $f(x_i)$. Using Lagrange function, the estimation function becomes:

$$f(x) = \sum_{i=1}^n \alpha_i K(x, x_i) + b \quad (3)$$

B. Application of LS-SVM for SRS/G modeling

The LS-SVM approximates the nonlinear function using the equation (3). The Gaussian radial basis function (RBF) kernel is

$$K(x, x_i) = \exp\left(-\|x - x_i\|^2 / 2\delta^2\right) \quad (4)$$

The LS-SVM has adapted for calculation of the flux linkage and torque of SRS/G. For the LS-SVM, the inputs are rotor position θ and current i , and the output are flux linkage

ψ and torque T . The LS-SVM model used for calculating the phase flux linkage and torque are shown in Fig.3.

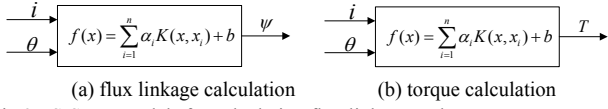


Fig.3 LS-SVM models for calculation flux linkage and torque

In this paper, the measurement flux linkage data and calculation torque data were used to generate sample data for training the LS-SVM and the data were shown in Fig.2. After the training is completed, the LS-SVM models of flux linkage and torque surface versus the rotor position and phase current are shown in Fig.4. The comparison of simulation results by ANN and LS-SVM models are shown in table I.

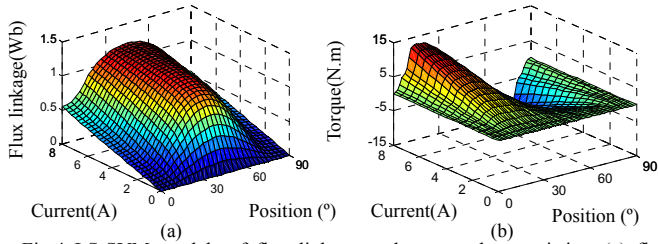


Fig.4 LS-SVM models of flux linkage and torque characteristics: (a) flux linkage; (b) torque

TABLE I COMPARISON OF SIMULATION RESULTS BY ANN AND LS-SVM MODEL FOR FLUX LINKAGE

Number of sample data	Modeling methods and parameters	$\varepsilon_{mae}/\text{Wb}$	$\varepsilon_{rms}/\text{Wb}$	CPU/s
248	ANN($\varepsilon=0.001, \delta=0.4$)	0.0487	0.0258	23.66
	LS-SVM($\varepsilon=10000, \delta=0.4$)	0.0085	0.0046	2.38
496	ANN($\varepsilon=0.001, \delta=0.4$)	0.0102	0.0076	58.37
	LS-SVM($\varepsilon=10000, \delta=0.4$)	0.0013	0.00045	4.12

V. SIMULATION AND EXPERIMENTAL RESULTS

In order to validate the accuracy of this model, this section uses machine variable waveforms and several characteristic curves predicted by the model for comparison with the actual machine data. Fig.5 shows the schematic diagram of the systematic simulation. The simulation algorithm includes an LS-SVM current-dependent inverse flux linkage model $i(\psi, \theta)$ to estimate current from flux linkage and rotor position, and an LS-SVM torque model $T(i, \theta)$ to estimate the torque from phase current and rotor position.

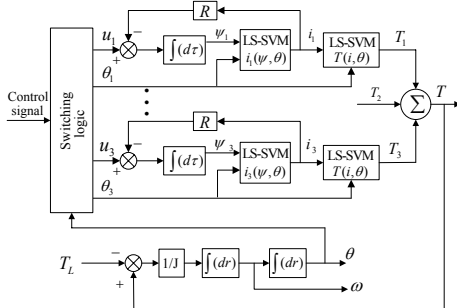


Fig.5 Schematic diagram of the systematic simulation

1) *Steady state waveforms*: Fig.6 shows a comparison of measured current and simulated phase current at the starting mode. Fig.7 shows a comparison of measured current and

simulated phase current when the machine was operated at the generating mode.

2) *Average torque versus speed*: Accurate prediction of the average torque versus speed characteristics of the SRM is crucial. Measurements were taken for dc voltages of 90V and 150 V at speeds ranging from 600 to 1200 r/min. Fig.8 depicts torque-speed data at the two dc voltages. The maximum deviation between the simulated and measured curves is lower than 10%.

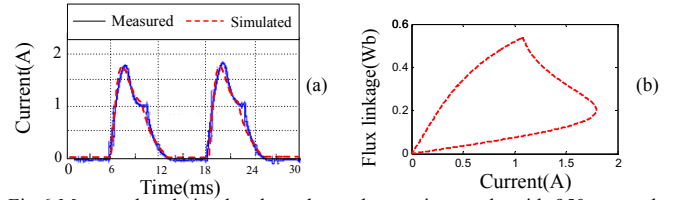


Fig.6 Measured and simulated results at the starting mode with 950rpm and 120V: (a) phase current; (b) energy conversion loop

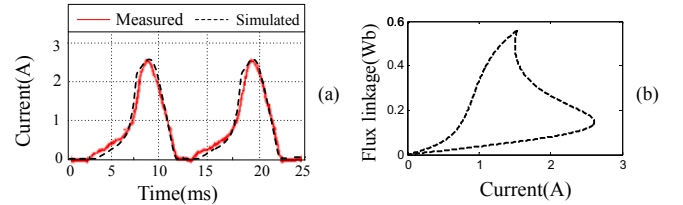


Fig.7 Measured and simulated results at the generating mode with 1100rpm and 100V: (a) phase current; (b) energy conversion loop

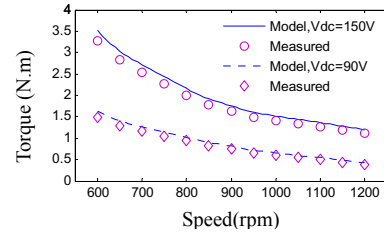


Fig.8 Average torque versus speed

VII. CONCLUSION

This paper has presented a new idea and the procedure to use least squares support vector machine (LS-SVM) networks to model SRS/G. The LS-SVM models are comprised of magnetization data with rotor position and phase current as input, and the corresponding flux linkage and torque as output. Compared with the models based on artificial neural networks (ANN) methods, the proposed model has better capability of generalization and better convergent speed. Using the LS-SVM current model and LS-SVM torque model, a dynamic performance model for 6/4 SRS/G is constructed. The simulation and experimental results are presented to verify the effectiveness of the proposed modeling method. In addition, the experimental results are shown to demonstrate that the proposed method can be ideal for practical implementation of SRS/G system.

REFERENCES

- [1] A. D. Cheok and Z. F. Zhang, "Fuzzy logic rotor position estimation based switched reluctance motor dsp drive with accuracy enhancement," *IEEE Trans. Pow. Elec.*, vol. 20, no. 4, pp. 908-921, Jul. 2005.

An Accurate Magnetic Field analysis for Estimating Motor Characteristics Taking Account of Elasto-Plastic Deformation in the Magnetic Core

Shinichi Yamaguchi^{*1}, Akihiro Daikoku^{*2}, Yoshihiro Tani^{*3}, Toshinori Tanaka^{*4} and Chiyo Fujino^{*5}

^{*1-4}Advanced Technology R&D Center, Mitsubishi Electric Corporation, Amagasaki 661-8661, Japan

^{*5}Nara Women's University, Nara 630-8506 Japan and also Diamond Personnel Company Ltd. Amagasaki 661-8661, Japan

E-mail Address: ^{*1}Yamaguchi.Shinichi@dp.MitsubishiElectric.co.jp, ^{*2}Daikoku.Akihiro@ab.MitsubishiElectric.co.jp,

^{*3}Tani.Yoshihiro@dy.MitsubishiElectric.co.jp, ^{*4}Tanaka.Toshinori@ak.MitsubishiElectric.co.jp,

^{*5}Fujino.Chiyo@zd.MitsubishiElectric.co.jp

Abstract — This paper discusses an accurate magnetic field analysis that elasto-plastic deformation in the magnetic core by using the finite-element method (FEM) to estimate motor characteristics. This analysis method consists of the following steps: 1) measurement of the magnetic characteristics of electrical steel sheets in a state where plastic strain and elastic stress are added; 2) calculation of strain distribution and stress distribution using structural analysis; 3) preprocessing of the magnetic field analysis, which generates the FEM mesh taking account of the changes of the magnetic properties in each of the core elements corresponding to strain and stress distribution; and 4) magnetic field analysis using the data measured in step 1) and the FEM mesh generated in step 3). As an example, a result of a permanent magnet motor's cogging torque calculation is shown, focusing on elasto-plastic deformation due to stamping electrical steel sheets when the stator core of motor is manufactured

As a result, the cogging torque waveform was shown to differ depending on the strain and stress in the magnetic core when the electric steel sheets of motor core are stamped by metal mold.

I. INTRODUCTION

The permanent-magnet synchronous motor (PM motor) is widely used in industrial drives, automotive applications, and traction machines for elevators due to its high performance. The electric steel sheets of PM motor are often stamped by metal mold in order to raise the productivity. On the other hand, the magnetic characteristics of electrical steel sheets in the strain and stress condition due to stamping are known to be inferior to those in the normal condition [1], but few examinations have reported on the relationship between stress and motor characteristics; up until now, quantitative analysis of the cogging torque or the torque ripple arising from strain has not been seen.

In this paper, we discuss an accurate finite-element analysis for estimating motor characteristics, focusing on elasto-plastic deformation in the magnetic core. First, we measured the magnetic characteristics of a single sheet specimen under a strain and stress condition, and using these data we conducted a magnetic field analysis concerning the distribution of the magnetic characteristics resulting from strain and stress. As an example, we showed a result of the cogging torque calculation of a PM motor, examining strain and stress in the electrical steel sheets when the stator core of motor is manufactured.

II. DEVELOPED COMBINED SYSTEM OF STRUCTURAL ANALYSIS AND MAGNETIC FIELD ANALYSIS

Taking strain and stress distribution into account, we developed a combined system of structural analysis and magnetic field analysis. Fig. 1 shows the flow of the developed motor analysis system. This method consists of the following four steps:

- 1) measurement of the magnetic characteristics of the electrical steel sheets in the condition where strain and stress is added;
- 2) calculation of strain and stress distribution using structural analysis when the electric steel sheets of motor core are stamped by metal mold;
- 3) preprocessing of the magnetic field analysis, in which the finite-element method (FEM) mesh is changing the properties of each mesh in the stator core corresponding to the strain and stress distribution;
- 4) magnetic field analysis using the measured data obtained in step 1) and the FEM mesh generated in step 3).

Several expressions of stress value can be used in the stress-mapping process of this system, e.g., principal stress, which means the vector value, or the von Mises stress, which expresses the stress in each element as a scalar value. In this paper we use the von Mises stress.

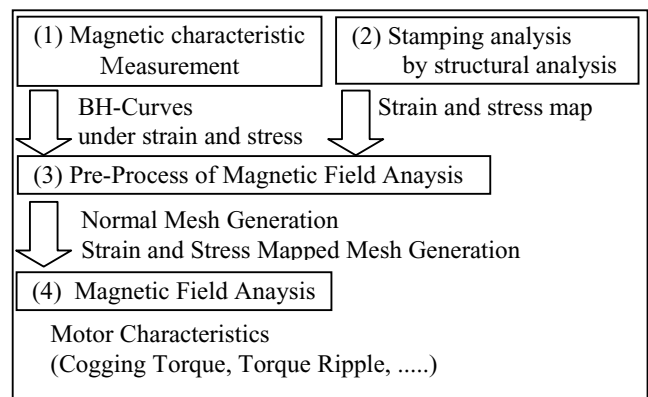


Fig. 1 Flow of motor characteristic analysis considering strain and stress distribution in stator core

III. MEASUREMENT OF MAGNETIC CHARACTERISTICS UNDER ELASTO - PLASTIC STRAIN AND STRESSED CONDITION

In order to add a uniform strain distribution to electric steel sheets, we prepared the tensile test piece in Fig 2. And a single sheet test pieces is produced by wire cut after the tensile test. A single sheet test pieces is add an elasto-strain of 0% and 5% by the tensile test. Fig. 3 and 4 show the example of the measured data. Fig. 3 shows BH-Curve versus applied strain, Fig. 4 shows relative permeability versus applied stress at magnetic flux density 1.0 T. The core grade of the magnetic steel sheet is 35A230 (JIS C 2552), and the measured frequency is 50 (1/s). These figures show that the BH-Curve and relative permeability under a strain and stressed condition is inferior to the normal (unstrain and unstress) condition; in particular, the characteristics under compressive are worse rather than those under tensile stress. For a combined analysis, we need to measure more data for different magnetic flux densities.

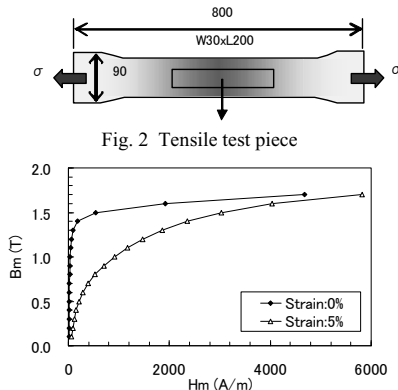


Fig. 3 Measured results of BH-Curve of magnetic steel with strain.

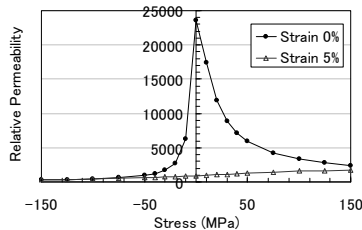


Fig. 4 Measured results of the relative permeability of magnetic steel with applied stress.

IV. SPECIFICATION OF ANALYSIS MODEL AND CALCULATION RESULTS

In this paper, we tried to estimate the cogging torque resulting from strain and stress, when the stator core is stamped by metal mold. The verification model is shown in Fig.5. We examine the PM motor having 8 poles and 12 sator slots.

Firstly, we calculate the strain and stress distribution of the motor core due to stamping using structural analysis. The calculated result is shown in Fig.6. The figure indicates that the stress of the motor core is growing in the edge of core. Secondly, the FEM mesh for the magnetic field analysis was generated using the result of structural analysis i.e., the properties of each of the core elements were changed according to the distributed elastic strain and plastic stress

value. The calculated results of cogging torque by magnetic field anaysis are shown in Fig. 7. This figure indicate the cogging torque with strained and stressed core due to stamping is greater than that with the normal (unstrain and unstress) core.

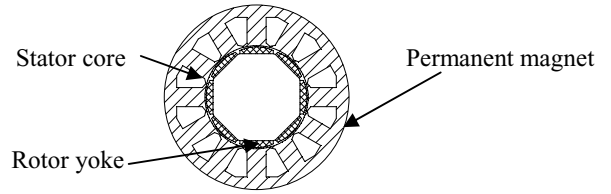


Fig.5 Verification model

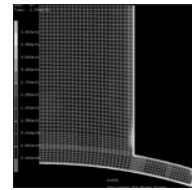


Fig.6 Calculation result of contour map of stress distribution in stator teeth

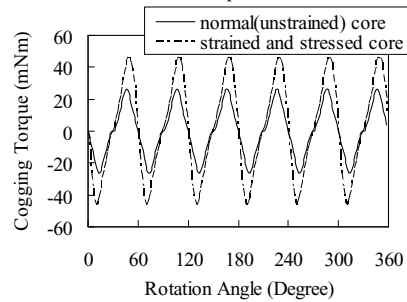


Fig. 7 Calculation Results of Cogging Torque

V. CONCLUSION

In this paper, we proposed an accurate finite-element analysis for estimating motor characteristics, focusing on elasto-plastic deformation in the magnetic core. Taking strain and stress distribution into account, we developed a combined system of structural analysis and magnetic field analysis. And, we then measured the magnetic characteristics of the electrical steel sheets under a strain and stressed condition. Using this method, we tried to estimate the cogging torque of a PM motor resulting from strain and stress generated in the stator core at stamping. As a result, we showed that the cogging torque waveform differed depending on the strain and stress in the stator core when electric steel sheets of motor core are stamped by metal mold.

VI. REFERENCES

[1] Y. Kashiwara, H. Fujimura, K. Okamura, K. Imanishi, H Yshiki, "Estimation model for magnetic properties of stamped electrical steel sheet (in Japanese)" presented at the IEEJ technical Meeting on Magnetics, Aichi, Japan, MAG-07-57.

[2] Akihiro Daikoku, Masatsugu Nakano, Shinichi Yamaguchi, Yoshihiro Tani, Yukari Toide, Takashi Yoshioka, Hideaki Arita, Chiyo Fujino, "An Accurate Magnetic Field Analysis for Estimating Motor Characteristics Taking Account of Stress Distribution in the Magnetic Core", IEEE TRANSACTIONS ON INDUSTRY APPLICATIONS, VOL. 42, NO. 3, MAY/JUNE 2006,p668-p674

Calculation of Radial Forces in Cage Induction Motors at Start – the Effect of Rotor Differential

David G. Dorrell

School University of Technology Sydney, Broadway, Sydney, Australia
ddorrell@eng.uts.edu.au

Abstract— In this paper the radial forces in an induction motor are calculated using finite element analysis. These radial forces (or unbalanced magnetic pull - UMP) are generated when the rotor is eccentric. The work illustrates the importance of higher winding harmonics and rotor differential leakage in the starting UMP. Examples of a 6 pole machine with 26 and 40 bar rotors show that increasing the bar number and air-gap length will reduce the UMP.

I. INTRODUCTION – CAUSES OF RADIAL FORCE

Radial forces, or unbalance magnetic pull (UMP) is caused by the concentration of air-gap flux so that it is asymmetrical. If the rotor is eccentric (not centered) then the flux will be concentrated around where the air-gap is narrowest. In terms of mathematical breakdown it was shown in [1] that in a cylindrical machine this concentration can be represented by flux waves with pole-pair numbers differing by one. There is much literature that focuses on the calculation of UMP, both in terms of analytical calculation and finite element analysis [2][3][4]. The standard approximation considers only the radial air-gap flux to produce normal stress where

$$\sigma = \frac{b_n^2}{2\mu_0} \quad (1)$$

However Binns and Dye [5] suggested that, while the tangential components are small, there is still up to a 10 % UMP component due to the tangential stress. More accurately, the shear and tangential stresses are

$$\sigma = \frac{b_n^2 - b_t^2}{2\mu_0} \text{ and } \gamma = \frac{b_n b_t}{\mu_0} \quad (2)$$

where b_t is the tangential air-gap flux density. Dorrell [6] has shown that there is up to 10 % variation of UMP due to the tangential components using finite element analysis (FEA). These can be used to calculate the UMP in orthogonal directions using stress integrals around the air-gap:

$$F_d = L \int_0^{2\pi r} (\sigma \cos(ky) - \gamma \sin(ky)) dy \quad (3)$$

$$F_q = L \int_0^{2\pi r} (\sigma \sin(ky) + \gamma \cos(ky)) dy \quad (4)$$

This assumes that y is the tangential direction, x is the radial direction, b_t is positive in the counter-clockwise direction and b_n is positive when flowing out in the radial direction; k is the inverse of the mean air-gap radius while L is the axial core length. In this paper a finite element analysis is carried out and (1) is implemented (first terms of (3) and (4) integrals) in a step-wise fashion since it is a valid approximation.

The literature contains little about UMP in cage induction motors when starting. Dorrell gave some results for a 10-pole machine at low voltage [7]. This is an analytical simulation and dates from 1994 when FEA of this problem was difficult. This simulation includes higher winding harmonic flux waves

but did not include the rotor differential flux waves in the UMP calculation. The machine had 90 stator slots (18 slots per pole-pair – which is the same as the 6-pole machines investigated here) and 80 rotor bars (which is 16 rotor bars per pole-pair, which is a very popular bar number per pole-pair; this compares to 8.67 bars per pole-pair for a 6-pole 26-bar rotor machine and 13.33 bars per pole-pair for a 6-pole 40-bar machine – these arrangements are investigated here).

Different types of eccentricity need to be addressed. Static eccentricity is where the rotor rotates on its own axis but is off-centre from the stator bore. This can be caused by misplaced bearings or alignment. Dynamic eccentricity is where the rotor is not rotating about the rotor centre but is rotating on the stator bore centre. This could be caused by a bent shaft. Obviously static and dynamic eccentricity can exist together and Burakov and Arkkio [2] studied eccentricity (with FEA analysis) in general terms of a rotating eccentricity which does not correspond to rotor speed. However, this only really becomes relevant at higher speed and rated load. This was illustrated by Dorrell [8]. At low speed the air-gap is dominated by the higher winding harmonic flux waves (which are undamped by the rotor because the bar number is usually close the harmonic number) and also the rotor differential flux waves (which increase with slip and tend to saturate the tooth tips of the stator and the rotor surface).

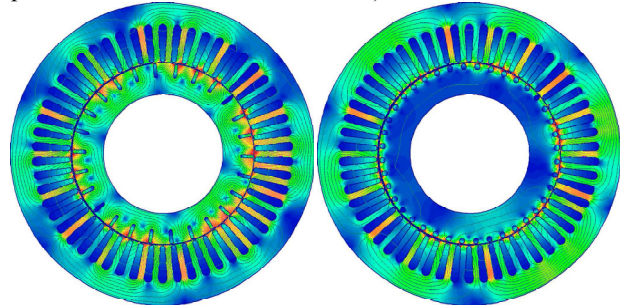


Fig. 1 Flux plots for 26 bar and 40 bar rotor at 75 % eccentricity.

II. 6-POLE MOTOR ARRANGEMENT

Some induction machines have marked differences from normal power drive machines. High-voltage submersible machines exist with hydrodynamic bearings for underwater operation. One of the properties of the hydrodynamic bearings is that there is a large degree of inherent rotor eccentricity compared to standard drive motors which means the air-gap has to be larger. In this paper an initial 26 bar rotor (air-gap of 1.7 mm) is studied – this had excessive UMP; while a further 40 bar rotor is studied with an increased 2 mm air-gap. This will give lower UMP because, for a given rotor movement, the per-unit eccentricity is less and UMP is more a function of the per-unit eccentricity.

Fig. 1 gives the UMP simulations for these machines when the rotors are up to 75 % eccentricity (1.5 mm for 40 bar rotor and 1.275 mm for 26 bar rotor). The aim of this work is to identify the UMP that will cause hard pull-over of the rotor against the stator. At start there is no differentiation between static and dynamic eccentricity. The 40 bar and 26 bar machines were studied under locked rotor conditions using magneto-static FEA (with the current in the rotor calculated using an analytical calculation tool) and an analytical algorithm [1]. It is possible to develop full transient time-stepped FEA models [2]; these are very time consuming both in terms of development and run. While magneto-static FEA should be used with prudence for an induction machine. The analytical calculation tool calculates a good value for the rotor current vector, even under locked and saturated conditions, which makes it suitable for carrying forward for use as the rotor current vector in a magneto-static FEA. In addition, the rotor damping currents of the main 6-pole MMF-sourced flux waves will be limited because the main 6-pole flux wave is small at start.

The initial results, which compare the FEA, analytical algorithm and a typical rotor deflection line for rotor with hydrodynamic bearings, are summarized in Fig. 2 with the 26 bar rotor having much higher UMP. The reasons for the different UMP characteristics are due to the increase in rotor bars, which will increase the damping of the lower pole number air-gap flux waves [7] and also decrease in rotor differential waves (which dominate the flux waves – this has not been reported in the literature before), and the increase in air-gap length. In Fig. 3, it can be seen that for both the 26 bar and 40 machines there are harmonics due to the stator winding at 15, 21, 51 and 57. For the 26 bar machine there are substantial harmonics due to rotor differential at 23, 29, 49 and 55. This is also further modulation of the first slot passing frequencies and differential to give 25 (51-26) and 31 (57-26). For the 40 bar machine there are first rotor differentials are 37 and 43 harmonics while there is first modulation of the slot passing frequencies at 11 (51-40) and 17 (57-40). There are several other harmonics for the machines which may be due to further modulations or possibly from numerical variance. When the rotor becomes eccentric additional flux waves either side of the main flux waves appear.

Further air-gap flux waves can be analyzed which illustrate the flux variation over speed and voltage. This shows the air-gap flux to be very variable in terms of harmonic make-up and hence the UMP is difficult to calculate, susceptible to continual variation and a function of core saturation. Hence there is variation between the FEA and analytical method from [1] in Fig. 2.

III. CONCLUSIONS

This paper assesses the UMP in a 6-pole induction motor with either 26 and 40 bar rotors with rotor eccentricity. It illustrates that at start the air-gap flux is dominated by the higher flux waves including the rotor differential waves. Hence increasing the bar number will decrease the UMP. This paper presents some new information on UMP in cage induction machines that has not appeared in the literature.

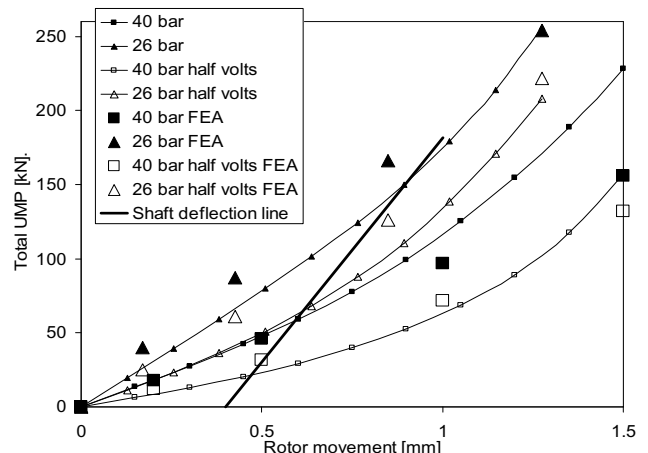


Fig. 2. UMP calculation for 26 bar and 40 bar rotors at start including half-voltage calculations – 26 bar rotor liable to rotor pull over since UMP higher.

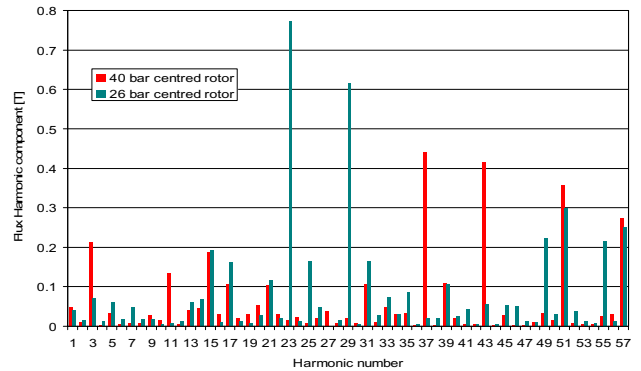


Fig. 3. Flux wave harmonics in air-gap for 26 and 40 bar rotors (centered) – from FEA at full voltage – the 6-pole main winding is harmonic 3.

IV. REFERENCES

- [1] D. G. Dorrell, "Experimental Behaviour of Unbalanced Magnetic Pull in 3-Phase Induction Motors with Eccentric Rotors and The Relationship with Tooth Saturation", *IEEE Transactions on Energy Conversion*, Vol. 14, No. 3, Sept. 1999, pp 304-309.
- [2] A. Burakov and A. Arkkio, "Comparison of the unbalanced magnetic pull mitigation by the parallel paths in the stator and rotor windings," *IEEE Trans. Magn.*, Vol. 43, No. 12, 2007.
- [3] A. C. Smith and D. G. Dorrell, "The calculation and measurement of unbalanced magnetic pull in cage induction motors with eccentric rotors. Part 1: Analytical model," 1996 Proc. IEE Electric Power Applications, Vol. 143, No. 3, pp 193-201.
- [4] Z. Q. Zhu, D. Ishak, D. Howe, and J. Chen, "Unbalanced magnetic forces in permanent-magnet brushless machines with diametrically asymmetric phase windings," *IEEE Trans. on Industry Applications*, Vol. 43, No. 6, Nov/Dec 2007.
- [5] K. J. Binns and M. Dye, "Identification of principal factors causing unbalanced magnetic pull in cage induction motors," 1973 Proc. IEE Vol. 120, pp. 349-354.
- [6] D. G. Dorrell, M.-F. Hsieh and Y. Gao, "Unbalanced Magnet Pull in Large Brushless Rare-Earth Permanent Magnet Motors with Rotor Eccentricity", submitted for consideration to INTERMAG 2009 special edition of the *IEEE Transactions on Magnetics*.
- [7] D. G. Dorrell and A. C. Smith, "The calculation and measurement of unbalanced magnetic pull in cage induction motors with eccentric rotors. Part 2: Experimental investigation", 1996 Proc. IEE Electric Power Applications, Vol. 143, No. 3, pp 202-210.
- [8] D. G. Dorrell, "The sources and characteristics of unbalanced magnetic pull in cage induction motors with either static or dynamic eccentricity", *Stockholm Power Tech, IEEE Int. Symp. on Elec. Power Eng., Stockholm, 18-22 June 1995*, Vol. Elec. Mach. and Drives pp 229-234.

Eddy-current Losses and Temperature Rise in the Form-wound Stator Winding of an Inverter-fed Cage Induction Motor

M.J. Islam, H.V. Khang, A-K. Repo, A. Arkkio
 Team of Electromechanics, Helsinki University of Technology
 P.O. Box 3000, FI-02015 TKK, Finland
 E-mail: huynh.khang@tkk.fi

Abstract— Temperature rise of the form-wound multi-conductor stator winding of a 1250-kW cage induction motor was analyzed resulting from the eddy currents in the winding. The eddy current was modeled using time-discretized finite-element analysis (FEA). The resistive losses in each of the conductor obtained from the FEA are used as input for thermal modeling. The distance from the air gap to the topmost bar in the stator has a significant effect on the eddy-current loss as well as temperature rise in the winding. An acceptable distance for winding design was recommended. By using magnetic slot wedges the eddy-current losses can be reduced.

I. INTRODUCTION

The eddy-current losses increase with the high-frequency harmonics of power supply. The loss determination has an important role in both design and use stages. The heating sources in a motor come from the losses. The consideration of the temperature rise is necessary to check whether the motor design is suitable or not. Numerical methods have been used to compute the losses, and then analyze the temperature rise in the electrical machines in recent years [1-2]. The time-stepping finite element analysis (FEA) is required to estimate the losses due to high-order harmonic fields [3].

In this paper, the eddy-current losses in a multi-conductor stator winding of an inverter-fed cage induction machine are modeled. Secondly, the thermal analysis is performed on the basis of the average loss density of each stator bar. The installment of the magnetic wedges at the slot opening is a simple way to reduce the temperature rise.

II. EDDY-CURRENT LOSSES IN STATOR WINDINGS

The two-dimensional (2-D) electromagnetic model is used to model the eddy currents in a cage induction machine [3]. The electromagnetic field in the multi-conductor winding is

$$\nabla \times (\nu \nabla \times A) + \sigma \frac{\partial A}{\partial t} - \left(\frac{1}{l} \sum_{j=1}^{Q_b} \sigma \eta_j u_j \right) e_z = 0 \quad (1)$$

where ν , σ – reluctivity and conductivity of conductor, A – magnetic vector potential, l – effective length of stator, Q_b – number of bars in stator winding, u_j – the potential difference of stator bar j , η_j is defined as follows

$$\eta_j = \begin{cases} 1 & \text{if the point belongs to stator bar } j \\ 0 & \text{otherwise} \end{cases}$$

A separate voltage equation is considered for the bar. This voltage equation strongly couples the field and circuit equation of the phase. The equations are discretised in time using backward Euler method. These equations are solved using Newton-Raphson method.

The stator resistive loss P_t includes the resistive loss of stator bar P_{sb} and the end-winding resistive loss P_{ew} . The eddy-current loss P_{eddy} is the difference between the total resistive loss and DC resistive loss.

$$P_t = P_{sb} + P_{ew} \quad (2)$$

$$P_{sb} = \frac{Q_l}{\sigma} \sum_{j=1}^{Q_b} \int_{\Omega} n_j J^2 d\Omega \quad (3)$$

$$P_{ew} = \sum_{j=1}^m R_e i_j^2 \quad (4)$$

$$P_{eddy} = P_t - \sum_{j=1}^m R_s i_j^2 \quad (5)$$

J – current density, i_j – phase current in stator bar j , Q_s – number of symmetry sectors. R_s and R_e are one phase DC resistances of the end-winding region and stator bar.

III. THERMAL ANALYSIS OF STATOR WINDING

The heat conduction of the solid conductor bars in the stator winding at the steady state obeys Gauss' law [4].

$$-\nabla \cdot (\lambda \nabla T) = p_{\text{loss}} \quad (6)$$

where p_{loss} – power loss density, λ – thermal conductivity.

A 2-D finite element model is built to consider the heat flow in the stator slot. The temperature T over a solution domain solved from (6) shows the thermal distribution in the stator winding. The heating sources are the average resistive losses in each conductor of the stator winding.

IV. RESULTS

A PWM inverter fed three-phase cage induction motor 690V, 1250 kW is used to consider the eddy-current losses and thermal distribution in the stator winding. The simulations are performed according to the distances from air gap to the conductor h_{sb} (the radial positions of the stator bar) in the

case of with and without the magnetic slot wedges installed at the slot opening. The stator bars are systematically transposed to reduce the effect of the circulating currents.

A. Eddy-current losses

The AC resistive losses decrease dramatically when the radial position h_{sb} is increased from 0.8 to 11.8 mm as shown in Fig. 1. This variation mainly comes from the dependence of eddy-current losses on h_{sb} in Fig. 2.

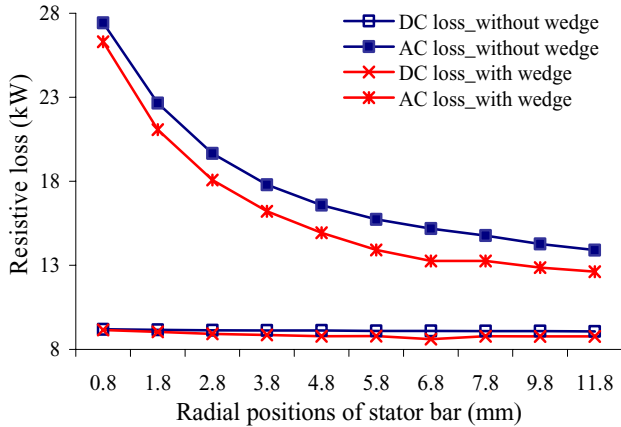


Fig. 1. AC and DC stator resistive losses at different radial positions.

The eddy-current losses in the stator slots can be reduced by installing the magnetic wedges at the slot opening. The thickness of magnetic slot wedges is varied from 0.5 to 5 mm when h_{sb} is increased from 0.8 to 5.8 mm. The thickness of wedges 5 mm is kept constant when h_{sb} is larger than 5.8 mm.

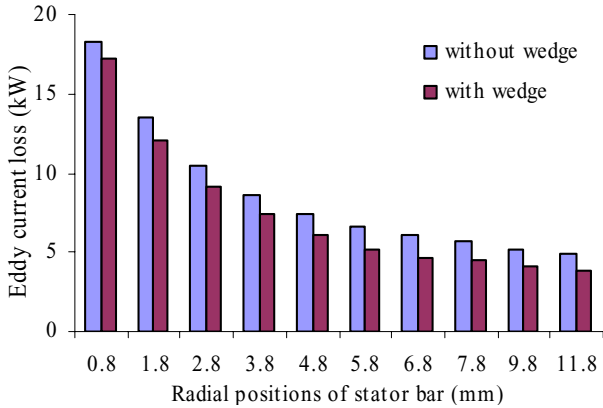


Fig. 2. Eddy-current losses at different radial positions.

B. Temperature rise

The temperature-rise analysis is performed by using public domain software FEMM [4]. The volume heat generation is calculated from the average AC resistive-loss density in each stator bar. The temperature-rise distributions in the stator slot without and with the magnetic wedge are shown in Fig. 3.

Fig. 4 shows the maximum and average temperature rise in the stator slot according to the radial position of stator bars. The design of the stator winding is reasonable when the difference between the maximum and average temperature rise is smaller than 10 K. The presence of magnetic wedges helps reducing the maximum temperature rise or this

difference. The radial position has to be larger than 5.8 mm or larger 4.8 mm in case of without or with the magnetic slot wedges installed.

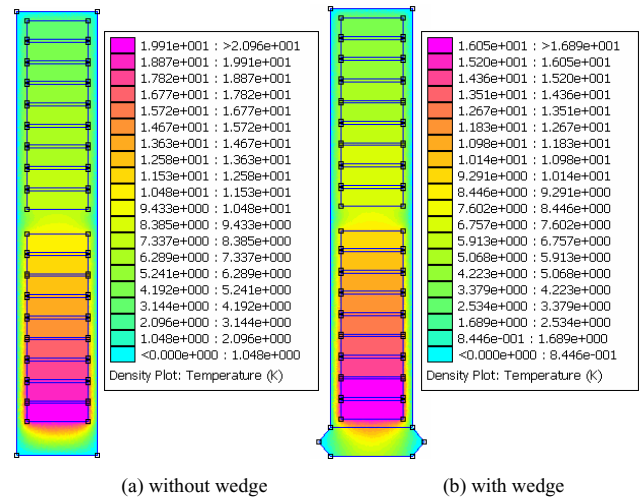


Fig. 3. Temperature-rise distribution in the stator slot at $h_{sb} = 5.8$ mm.

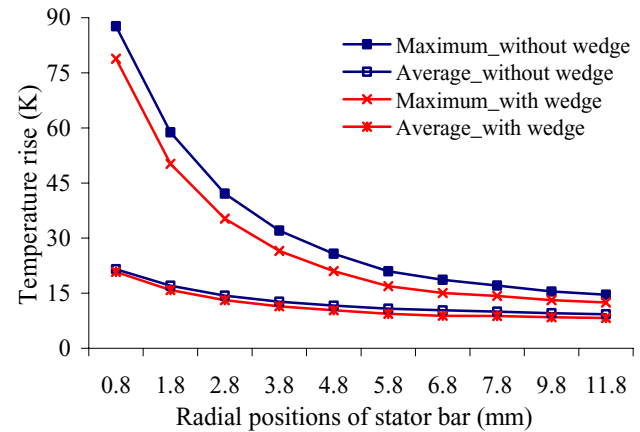


Fig. 4. The maximum and average temperature rise in the stator slot.

V. CONCLUSIONS

The eddy-current losses strongly depend on the distance from air gap to the stator bars. The magnetic wedges installed at the slot opening make it possible to reduce the eddy-current losses or heating dissipation in the stator windings. The goodness of winding design for an inverter-fed large induction machines can be pre-examined via a coupled electromagnetic and temperature-rise analysis.

VI. REFERENCES

- [1] Shingo Inamura; Sakai, T.; Sawa, K "A temperature rise analysis of switched reluctance motor due to the core and copper loss by FEM ", Magnetics, IEEE Transactions on, 2003, 39,(3), pp.1554 – 1557.
- [2] Chang-Chou Hwang; Wu, S.S.; Jiang, Y.H, "Novel approach to the solution of temperature distribution in the stator of an induction motor", Energy Conversion, IEEE Transaction on, 2000, 15,(4), pp. 401 – 406.
- [3] Islam, M. J.; Arkkio, A. "Effects of pulse-width-modulated supply voltage on eddy currents in the form-wound stator winding of a cage induction motor", IET Electr. Power Appl., 2009, 3, (1), pp. 50–58.
- [4] David Meeker, "Finite Element Method Magnetics", Version 4.2, User's Manual, 2009.

Semi-Analytical Solution of Cogging Torque in SMPMM

F. DUBAS and C. ESPANET

ENISYS Department, FEMTO-ST Institute, CNRS UMR 6174, F90010 Belfort, France

E-mail: FDubas@gmail.com

Abstract — In this abstract, the authors present a cogging torque determination by a new two-dimensional (2-D) semi-analytical solution of the magnetic field taking into account the slotting effect in surface mounted permanent-magnet (PM) motors (SMPMM). The cogging torque waveforms is compared with the finite element analysis (FEA) for radial and parallel magnetized PMs. The analytical results are in very good agreement with those obtained by the FEA, considering both amplitude and waveform.

I. INTRODUCTION

In a PM Brushless motor which consists of the magnet poles and slotted stator core, there exists the cogging torque. It can be the sources of speed pulsation, vibration, and acoustic noise...[1]. As electromagnetic forces result from the interaction between the rotor and the stator through the no-load magnetic field in the air-gap, an accurate prediction of the instantaneous local magnetic field taking into account the slotting effect is essential. In [2], Zhu *et al.* presents and compares six alternate analytical models for cogging torque prediction. In this paper, the authors propose another alternative approach for cogging torque evaluation by using the results of a new 2-D semi-analytical solution [3], which determines the no-load magnetic field distribution in the air-gap taking account into the slotting effect. The cogging torque waveforms predicted by this new approach of the slotting effect (and calculated for both radial and parallel magnetization) have been compared with the FEA [4]. The semi-analytical results are in very good agreement with those obtained by the FEA, considering both amplitude and waveform.

II. A 2-D NEW SEMI-ANALYTICAL SOLUTION [3]

A. Problem Description and Assumptions

Fig. 1 shows the geometric representation of the multi-pole SMPMM for the new 2-D semi-analytical solution used to study the effect of the stator slotting. The main parameters of this geometry are: the radius of the stator yoke surface, R_{sy} , the radius of the stator surface, R_s , the radius of the PMs surface, R_m , the radius of the rotor yoke surface, R_r , the mechanical angle of PMs, θ_m , the mechanical angle of a stator slot-opening, θ_o , the mechanical angle of a stator tooth-pitch, θ_t , and the mechanical angle of a pole-pitch, θ_p .

The authors make the following assumptions which are usual in many models of the literature: i) End-effects are neglected; ii) The stator and rotor back-iron is infinitely permeable (i.e., the magnetic saturation is neglected); iii) The electrical conductivity of the PMs is assumed to be null to

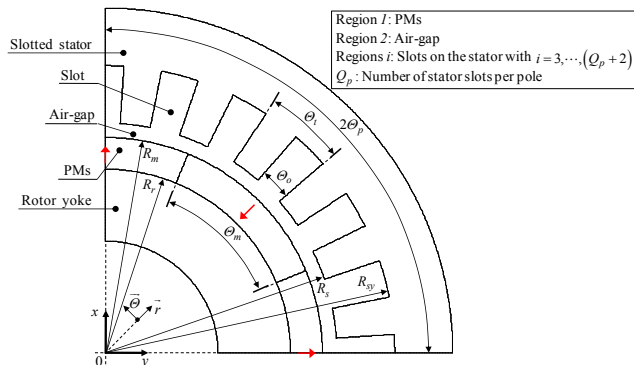


Fig. 1. Cross section of one pole pitch of the multi-pole SMPMM.

calculate the no-load magnetic vector potential (i.e., no resolution of Diffusion's equations); iv) The PMs are assumed to be nonoriented (with no particular direction of magnetization), isotropic, and having a linear demagnetization characteristic (rare earth magnets); v) Radial slot faces on the stator.

B. No-load Vector Potential Determination

The new semi-analytical solution is based on 2-D analysis in polar coordinates, and involves the solution of Laplace's equations in the air-gap (i.e., concentric region) and in the slots on the stator (i.e., non-concentric regions) and the solution of Poisson's equations in the PMs (i.e., concentric region) [see Fig. 1] with constant magnetic permeabilities. The no-load magnetic field solutions with the slotting effect are obtained by using the Fourier's series and the method of separating variables. However, it now caters for i) internal rotor motor topology; ii) radial and parallel magnetization; iii) curvature effect; iv) depth of the slots.

The no-load flux density, in each region, has been compared to the FEA calculations, and the agreement was quite satisfying (considering both amplitude and waveform). The no-load vector potential can be expressed in the PMs, i.e., in Region 1, by

$$A_{z1} = B_{rm} \cdot R_m \cdot f_{z1n}(E_{1n}, G_{1n}, r, \theta_s), \quad (1)$$

in the air-gap, i.e., in Region 2, by

$$A_{z2} = B_{rm} \cdot R_m \cdot f_{z2n}(E_{2n} \sim H_{2n}, r, \theta_s), \quad (2)$$

in the slots on the stator, i.e., Regions i , by

$$A_{zi} = B_{rm} \cdot R_s \cdot f_{ziv}(F_{iv}, r, \theta_s), \quad (3)$$

where B_{rm} is the remanent flux density of PMs; r and θ_s are respectively the radial position and the mechanical angular

position of the stator; f_{z1n} , f_{z2n} and f_{ziv} are the functions in Fourier's series which depend respectively on the integration constants E_{1n} & G_{1n} in Region 1, $E_{2n} \sim H_{2n}$ in Region 2, and F_{iv} in Regions i . In these equations, n and v represent respectively the spatial and the slotting harmonic orders.

The integration constants in each region are determined by numerically solving the linear equations (i.e., the Cramer's system) for each Θ_{rs} (with Θ_{rs} the mechanical angular position between the rotor and the stator). The Cramer's system, detailed in [3], for each Θ_{rs} is based on $6 \cdot (n_{max} + 1) + Q_p \cdot (v_{max} + 1)$ equations and unknowns with n_{max} and v_{max} terms in the Fourier's series for the computation of A_{z1} , A_{z2} and A_{zi} .

III. COGGING TORQUE CALCULATION

The cogging torque is calculated by multiplying the Maxwell stress tensor at the stator surface by R_s and integrating it over the stator surface, i.e.,

$$T_C = -\frac{p \cdot R_s \cdot L}{\mu_0} \cdot \int_{-\Theta_p}^{\Theta_p} \frac{\partial A_{z2}}{\partial r} \Big|_{r=R_s} \cdot \frac{\partial A_{z2}}{\partial \Theta_s} \cdot d\Theta_s, \quad (4)$$

where p is the number of pole pairs, μ_0 is the vacuum permeability, and L is the effective axial length of the motor.

By using (2), the cogging torque can be defined by

$$T_C = V_{cyl} \cdot \frac{B_{rm}^2}{\mu_0} \cdot f_T, \quad (5)$$

where $V_{cyl} = \pi \cdot R_s^2 \cdot L$ is the exchange volume of the stator, and

$$f_T = \sum_{n=1,3,5,\dots}^{n_{max}+1} f_{Tn} \cdot (E_{2n} \cdot H_{2n} - F_{2n} \cdot G_{2n}) \quad \forall np, \quad (6a)$$

$$f_{Tn} = 2 \cdot \left(np \cdot \frac{R_m}{R_s} \right)^2. \quad (6b)$$

It can be noted that the harmonic function f_T is equal to zero for the slotless motors equipped with surface mounted PMs and in this case the cogging torque does not exist.

IV. COMPARISON WITH FINITE ELEMENT SIMULATIONS

The cogging torque evaluation has been applied to a SMPMM, whose main characteristics are given in the Table I. Fig. 2 shows the cogging torque waveforms, under a tooth-pitch, with radial and parallel magnetized PMs. The semi-analytical results are in very good agreement with those obtained by the FEA, considering both amplitude and waveform. The new semi-analytical solution takes significantly less computing time than the FEA. In this comparison, the Cramer's system in [3] has 486 elements (i.e., with $n_{max} = 49$ and $v_{max} = 30$) which is much smaller than the FEA having 6,000 surfaces elements for the studied SMPMM.

TABLE I
PARAMETERS OF SURFACE MOUNTED PM MOTOR

Parameters	Values	Unit
Number of pole pairs, p	1	—
Total number of slots, Q_s	12	—
Magnet pole-arc to pole-pitch ratio, $\alpha_p = \Theta_m / \Theta_p$	100	%
Stator slot opening to tooth-pitch ratio, $\zeta_o = \Theta_o / \Theta_t$	33.33	%
Radius of the stator yoke surface, R_{sy}	37	mm
Radius of the stator surface, R_s	20	mm
Radius of the PMs surface, R_m	19	mm
Radius of the rotor yoke surface, R_r	14	mm
Axial length, L	45	mm
Remanent flux density of the PMs, B_{rm}	1.13	T
Relative magnetic permeability of the PMs, μ_{rm}	1.029	—

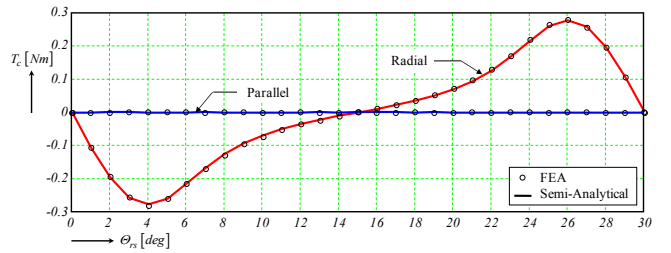


Fig. 2. Comparison of the cogging torque waveforms calculated numerically by FEA and semi-analytically by 2-D new approach of the slotting effect.

V. CONCLUSION

A new 2-D semi-analytical solution of the magnetic field taking into account the slotting effect has been used to determine the cogging torque in SMPMM. This general approach is mathematically more rigorous than the method based on the Schwarz-Christoffel transformation [5] which gives a 2-D complex permeance functions. Moreover, the semi-analytical solution can be a useful tool for design and optimization of multi-pole SMPMM, for example to minimize the cogging torque.

VI. REFERENCES

- [1] Z.Q. Zhu, and D. Howe, "Analytical Prediction of the Cogging Torque in Radial-Field Permanent-Magnet Brushless Motor," *IEEE Trans. on Magn.*, Vol. 28, No. 2, pp. 1371-1374, March 1992.
- [2] L. Zhu, S.Z. Jiang, Z.Q. Zhu, and C.C. Chan, "Comparison of Alternate Analytical Models for Predicting Cogging Torque in Surface-Mounted Permanent Magnet Machines," in *Proc. IEEE VPPC*, Sept. 03-05, 2008, Harbin, China.
- [3] F. Dubas, and C. Espanet, "Analytical Solution of the Magnetic Field in Permanent-Magnet Motors Taking Into Account Slotting Effect: No-Load Vector Potential and Flux Density Calculation," *IEEE Trans. on Magn.*, Accepted paper (Vol. 45, No. 5, Part. 1, June 2009).
- [4] Flux2D, "General operating instructions – Version 9.3.2.", Cedrat S.A. Electrical Engineering, 2006, Grenoble, France.
- [5] D. Zarko, D. Ban, and T.A. Lipo, "Analytical Calculation of Magnetic Field Distribution in the Slotted Air Gap of a Surface Permanent-Magnet Motor Using Complex Relative Air-Gap Permeance," *IEEE Trans. on Magn.*, Vol. 42, No. 7, pp. 1828-1837, July 2006.

Interactive Postprocessing Formulations in 3D

Martin Hafner¹, Marc Schöning¹, Marcin Antczak², Andrzej Demenko² and Kay Hameyer¹

¹ - Institute of Electrical Machines – RWTH Aachen University

² - Institute of Electrical Engineering and Electronics – Poznan University of Technology

E-mail: Martin.Hafner@IEM.RWTH-Aachen.de, Marcin.Antczak@doctorate.put.poznan.pl

Abstract—Nowadays, the postprocessing and visualization of finite element solutions is performed by means of static formulations and methods. Dynamic modifications and interactive exploration of 3D solution data are only possible in a very limited way. In this paper, an interactive postprocessing approach is introduced, allowing for a dynamic modification of finite element solutions, a simplified mesh cutting and data exploring as well as new ways of exploring complex solutions.

I. INTRODUCTION

The exploration and interpretation of a large amount of solution data is the most important part of a typical design process when using the finite element approach. Important decisions are made on basis of solution visualizations and next design steps are planned in dependency of the ongoing understanding of the device under research. Therefore, effective postprocessing algorithms handling large amount of finite element data and the usability of such methods in an interactive way allows a faster and optimized design with finite elements. Today, typical visualizations of finite element solutions are static colored representations of a field distribution, which map a computed value to a specific color. Additionally, vector fields can be visualized by colored cones or arrows, indicating the direction of the solution in every element. In this paper, further postprocessing methods and visualization techniques are introduced to enhance the exploration of finite element solutions. These are mainly mathematical modifications of the visualized solutions, simplified placing of cutting geometries like planes or spheres, and dynamic changing of display objects. For all mentioned aspects, examples are given to underline the usage possibilities of the proposed postprocessing formulations.

II. COMPUTER GRAPHICS SOFTWARE

3D finite element analysis (FEA) leads to a large amount of solution data. In general, developers of electrical devices need to analyze the electromagnetic behavior in certain critical machine parts, such as teeth or teeth heads, or identify local magnetic hot spots. An intuitive method for the evaluation of such simulation data is the interactive exploration in virtual reality [1], which provides a direct visual impression of the field characteristic. This ability supports the machine designer to recognize the points of design interest quickly and allows to perform further interactions and operations on the solution data directly. Therefore, in this paper a software methodology is presented to extend [2] by interactive postprocessing abilities.

The graphical package VTK [3] has been applied to visualize (static) 3D finite element solutions. The Visualization Toolkit (VTK) is an open source, platform independent, software library for 3D computer graphics, image processing

and visualization including an interface layer for several interpreted languages, such as Tcl/Tk, Python. The object oriented design of this software is characterized by general, easy to use data structures, whose versatility encourages a modular use of algorithms acting as filter objects. The working principle of VTK is based on visualization pipelines (see fig. 1).

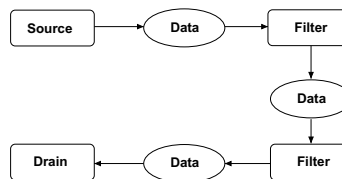
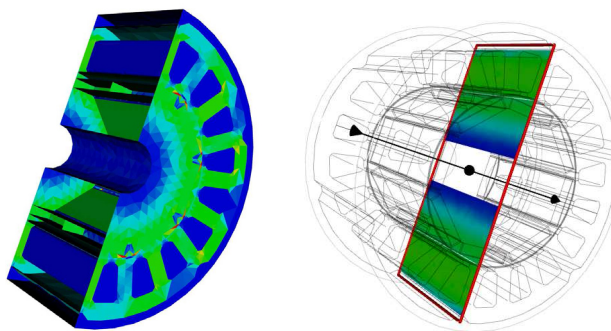


Fig. 1. Visualization pipeline of VTK.

III. APPLICATION

A. Interactive Cutting

Due to performance issues, the solution data of meshes is generally mapped to its surface in 3D visualization, so that mesh geometry and colored solution appear correlated. The corresponding visualization is restricted to the surface mesh of the data object, so that no information of the internal structure is available and cutting methods lead to an opened hollow representation, compare. fig. 2(a). In these situations,



(a) Hollow cutting through a flux density distribution of a PMSM. (b) Interactive cutting of the flux density distribution in a PMSM.

Fig. 2. Different cutting types for the visualization of the flux density distribution.

a cutting filter chain is required, that provides an insight into the electromagnetic behavior within the simulated devices. Since this exploration is data and user depended (direct user interaction), an intuitive cutting method is required which provides an interaction with the model, previewing the cutting surface and the solution.

The necessary filter procedure is shown in fig. 3. First,

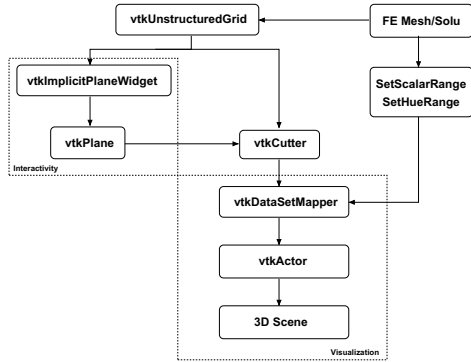


Fig. 3. VTK filter chain for interactive cutting.

the finite element mesh and solution are converted into a `vtkUnstructuredGrid` data set for each material. A `vtkImplicitPlaneWidget`, an interactively placeable infinite plane, is bounded to these grids. The mathematical representation of the cutting surface, in this case a `vtkPlane`, can be obtained from the 3D widget, so that the `vtkCutter` filter can generate a cutting mesh along that surface. The resulting grid is mapped to graphics primitives by the `vtkDataSetMapper`, who also maps the scalar range of the finite element solution to a given color range, specified by `SetHueRange`. The next element of the filter chain is the `vtkActor` representing an entity of the rendering scene. In particular, `vtkActor` combines object properties (color, shading type, etc.), geometric definition, and orientation in the world coordinate system. Since visualization, model interaction and cut-mesh generation are separated objects in the filter chain, other widgets types, such as point-, line-, plane-, sphere- and spline-widgets, can be applied for further purposes.

The cutting plane of fig. 3, can be moved, resized or rotated within the model boundaries and is computed in real time. Fig. 2(b) exemplifies this cutting interaction on a permanent magnet synchronous machine (PMSM) to illustrates the flux density distribution inside.

B. Direct Model Interaction

To improve the interactivity in 3D visualizations of finite element data, possibilities for a direct model interaction are required. The idea of a direct model interaction is to give the users an intuitive direct access to the visualized solution data. By this, any kind of operation, e.g. mathematical integration or multiplication, can be performed on the input, so that the modification of the visualization can directly be observed. Since 3D visualizations are scalable on different display systems (from normal desktop pc up to virtual reality systems like cave style systems [2]), an intuitive model interaction, controllable by various 3D input devices that directly operate in the 3D scenes, is required. To fulfill the mentioned criteria, a software methodology is required, that analyses the actual 3D scene to distinguish between different visualization types like a geometry, a mesh or a scalar or vectorial field solution plot. The methodology needs to returns the corresponding original data sets from the FE meshes and solutions. The generalized VTK filter chain for direct model interaction is

shown in fig. 4. As mentioned before, the finite element mesh

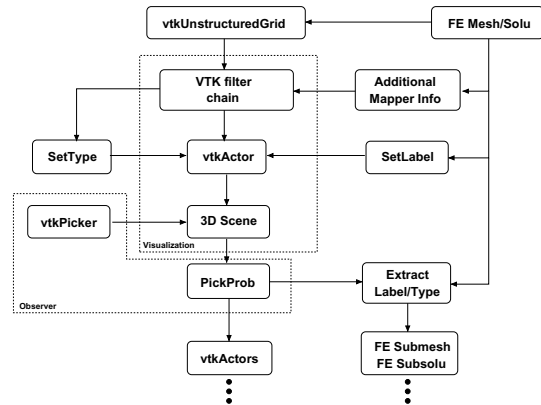


Fig. 4. VTK filter chain for interactive cutting.

and solution are filtered by an arbitrary VTK filter chain and stored in a `vtkActor` placed in a 3D scene, conf. sec. III-A. To identify the `vtkActors` in the further processing, each object gets additional information about the visualization type (`SetType`) and the submesh label identification (`SetLabel`). In the 3D scene, `vtkPicker`, controlled by a 3D input device, can be applied to grab `vtkActor` objects (`PickProb`). Type and label characteristics of the latter class objects can be used to extract the corresponding input data from the FE solution. These data sets are returned to the user interface. The same control pattern enables a direct access to the properties of single visualization objects.

Therewith, a combination of the interactive cutting geometries (cmp. section III-A) with the direct model interaction presented here is possible, to calculate the flux in various positions in an electrical machine for example.

IV. CONCLUSION

Efficient methods for the visualization of finite element solutions are essential for the evaluation of electromagnetic devices under research and development. In present, FE data is illustrated by means of static visualization formulations and methods. In this paper, an interactive postprocessing formulation is introduced, that extends the static process to provide dynamic modifications within the visualization and an intuitive 3D data exploration. Generalized techniques for this postprocessing approach are proposed and described by means of visualization patterns for interactive cutting and direct model interaction. A first application example is given to demonstrate the benefit of the presented 3D postprocessing formulation.

Since interactive visualization enables other illustration facilities, further applications, examples and details will be given in the full paper.

REFERENCES

- [1] W. R. Sherman and A. B. Craig, *Understanding Virtual Reality: Interface, Application, and Design*, 1st ed. Morgan Kaufmann, 2003.
- [2] M. Schoning and K. Hameyer, "Applying virtual reality techniques to finite element solutions," *Magnetics, IEEE Transactions on*, vol. 44, no. 6, pp. 1422–1425, 2008.
- [3] I. Kitware, *VTK User's Guide Version 5*, 5th ed. Kitware, Inc., Sep. 2006.

Comprehensive Magnetic Model of Surface Mounted PM Machines Incorporating Saturation Saliency

Yi Wang¹, Jianguo Zhu¹, Youguang Guo¹, Shuhong Wang², Wei Xu¹

¹School of Electrical, Mechanical and Mechatronic Systems, University of Technology
Sydney, NSW 2007, Australia

²Faculty of Electrical Engineering, Xi'an Jiaotong University, Xi'an 710049, China

Abstract— In this paper a comprehensive magnetic model of surface mounted permanent magnet synchronous machine (SPMSM) is proposed considering both the structural and the saturation saliencies to enable the numerical simulation of new rotor position detection algorithms. With an identifiable parameter matrix, a numerical nonlinear inductance model is developed, in which the rotor position and the stator current are taken as two independent variables. Furthermore, the stator current frequency is taken as another variable of the inductances and the inductance variation against the frequency is discussed. After experimentally identifying out all the parameters, a nonlinear mathematic model of SPMSM is built up based on the new magnetic inductance function. Simulation and experiment results are used to verify the proposed nonlinear magnetic model. The performance of proposed model is compared with the linear model provided in SIMULINK library.

I. INTRODUCTION

The permanent magnet (PM) machines, such as permanent magnet synchronous motor (PMSM), have been widely used and a number of techniques for position sensorless and initial rotor position detection have been proposed based on tracking the rotor magnetic saliency. The rotating magnetic saliency inside a PMSM can be classified as structural saliency that mainly comes from the interior structure, and saturation saliency induced by the magnetic saturation effect of the stator core [1]. Most of the existing sensorless control and initial rotor position detection schemes are designed mainly based on the structural saliency incorporated with the saturation saliency for identifying the polarity of magnetic pole. However, these sensorless strategies can only achieve good performance for interior PMSM (IPMSM). They are not suitable for surface mounted PMSM (SPMSM), which has little structural saliency.

Furthermore, the stator current frequency can also influence the values of the winding inductances, which are essential for rotor saliency tracking. The frequency should be counted in as a factor when performing the widely reported high frequency signal injection schemes for sensorless drive.

The conventional PMSM model does not incorporate the saturation saliency. When developing a new scheme for the rotor position detection, it is not possible to numerically simulate the proposed scheme, and the experimental trial and error method has to be employed, which is time-consuming and uncertain.

In this paper, a comprehensive mathematical model of SPMSM is built up considering magnetic saturation saliency

and the influence of the stator current frequency. A numerical nonlinear inductance model is proposed based on the stator currents and rotor position variation with all the parameters experimentally identified. The simulation and experiment results are used to verify the machine model. The comprehensive nonlinear machine model is built up in SIMULINK and this model can be further used to develop, simulate and evaluate the rotor position detection strategies.

II. MAGNETIC MODEL OF SPMSM WITH SALIENCIES

In an SPMSM, the observable total flux linkage λ_t inside the air-gap is contributed by both the stator currents and the permanent magnet on the rotor and it is the link of the stator and the rotor magnetic fields. The three-phase flux linkages λ_{abc} are here defined as the projection of λ_t on the stator reference frame and not only induced from the stator current. Therefore, the inductance of the stator is a function of both the stator currents and the rotor position, which are linear independent [2].

Then a composite function of both the current and rotor position is defined to express the inductance:

$$L(i, \theta) = I(i) \cdot A \cdot C(\theta) \quad (2)$$

where $I(i) = [1 \ i^1 \ i^2 \ \dots \ i^m]$ is obtained from the magnetization curve, indicating that the inductance is a polynomial function of current for a fixed rotor position; $C(\theta) = [1 \ \sin(\theta) \ \cos(\theta) \ \dots \ \sin(n\theta) \ \cos(n\theta)]^T$ is obtained from the Fourier Series expression, indicating that the inductance is a periodic function of rotor position for a fixed stator current; and A is an identifiable parameter matrix with $(m+1) \times (2n+1)$ dimensions.

An experiment platform is carried out on an SPMSM to identify the parameters and test the inductances. During the test, the stator currents are fixed at several different levels from 0 to 6A at which the magnetic circuit is fully saturated. For each current offset, by applying a smaller AC current component the incremental inductance at a particular rotor position is measured. By changing the rotor position with a dividing head, a series of inductance is recorded with a resolution of 6 electrical degrees. Fig. 1 shows the inductance curves at different current offset levels. The magnetic saturation effect can be found and the rotor polarity is

observable when the core is fully saturated with a large current offset.

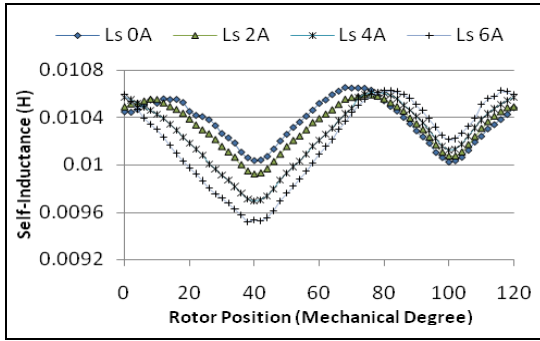


Fig. 1. Measured self-inductance curves at different current offset levels.

Based on the order of the magnetization curve and the FFT of the tested inductance values at different current offset levels, the dimension of matrix A is set to (7×17) , by setting $m=6$ and $n=8$ to acquire an accurate enough surface regression.

To obtain better regression results, the Least Relative Residual Sum of Square (LRRSS) method is employed.

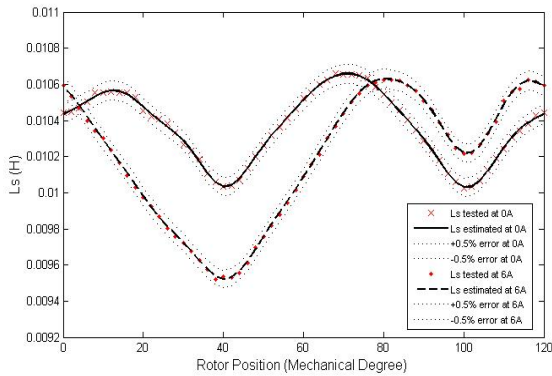


Fig. 2. Measured and estimated self-inductance at different current offsets.

Fig. 2 is the comparison between the tested and estimated self-inductance of phase A at 0A and 6A current offsets, where $\pm 0.5\%$ error bands are added. It can be found that the relative errors of the inductances are very small and the regressed objective function can be used to describe the variable self-inductance. The same regression method is applied to the mutual-inductance coefficient identification. Then a nonlinear inductance model is built up for this three-phase machine. An accurate inductance matrix can be calculated for given stator currents and rotor position. This model incorporates both the machine structural and the saturation saliencies.

III. INDUCTANCE VARIATION VERSUS FREQUENCY

As shown above, the inductance of the SPMSM is related to the stator current amplitude and the magnet rotor position. On the other hand, the inductance values are also variable with the stator current frequency, which is always varying in the machine drive system. In most of the proposed initial rotor position detection schemes, the injection signal frequency is set at a much higher value in order to keep the rotor at stand still and to amplify the inductance variation.

On the same experiment platform, the inductance tests are carried out on different frequencies. Fig. 3 shows the inductance curve at different current frequencies. The current offset level is set at 6A and the rotor angle varies. It can be found that the self-inductance varies against the current frequency.

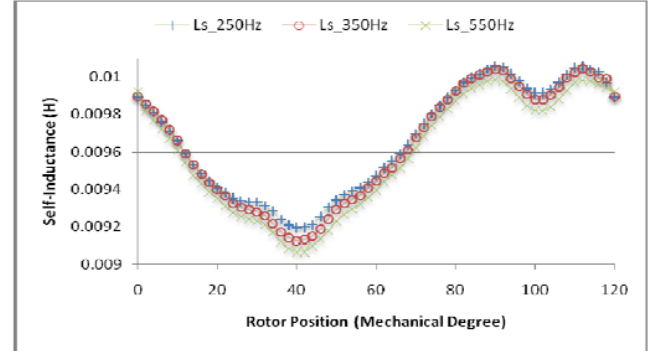


Fig. 3. Measured self-inductance curves at different current frequencies.

IV. MACHINE PERFORMANCE

A non-linear SPMSM model is built up in SIMULINK and simulated under open loop operation to compare the performance with the linear PMSM model in SIMULINK library. No-load and loaded tests are simulated with the same machine parameters except the inductance model. The unsaturated inductances are chosen and input into the linear model as the linear part of the magnetization curve. As an example, Fig. 4 shows the speed and torque curves by using the proposed non-linear model and the existing linear model. After adding a load torque on the rotor shaft, there is some ripple on the non-linear model speed and torque output, which results from the non-linear saturated inductances.

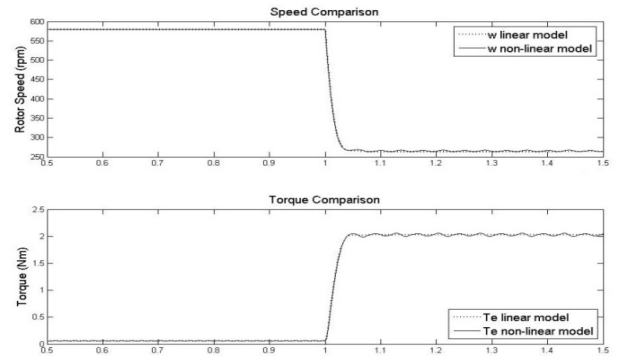


Fig. 4. Comparison of speed and torque at no-load and load change

More details about the model and the machine performance prediction using the new model will be presented in the full paper.

V. REFERENCES

- [1] Y. Yan, J. G. Zhu, Y. Guo and H. Lu, "Modeling and simulation of direct torque controlled PMSM drive system incorporating structural and saturation saliencies," in *Proceedings of the 41st IEEE Industry Application Society Annual Meeting*, Tampa, FL, Oct 2006, pp. 76-83.
- [2] P. Cui, J. G. Zhu, Q. P. Ha, G. P. Hunter, and V. S. Ramsden, "Simulation of non-linear switched reluctance motor drive with PSIM," in *Proceedings of the 5th International Conference on Electrical Machines and Systems*, Vol. 1, Aug. 2001, pp. 1061-1064.

Magnetic Field in an Axial-Flux Permanent-Magnet Synchronous Generator

T. F. Chan¹, Weimin Wang¹ and L. L. Lai²

¹Department of EE, the Hong Kong Polytechnic University, Hung Hom, Hong Kong, China

²Energy Systems Group, School of Mathematics and Engineering Sciences, City University London, UK
eetfchan@polyu.edu.hk

Abstract— The magnet field in a single-sided axial-flux permanent-magnet synchronous generator is analyzed using three-dimensional finite element method (3-D FEM). The flux that flow in radial planes, particularly that crossing the rotor back plates via the ferromagnetic rotor spacer, is accounted for. A time-stepping technique enables the output voltage to be determined to a good accuracy. The computed results have been verified by experiments on a small prototype generator.

I. INTRODUCTION

Two-dimensional analysis is often used for studying the field distribution in an axial-flux permanent-magnet synchronous generator (AFPMSG) [1],[2],[3]. In most the methods the rotor back plates that serve as the yoke are assumed to be physically separate. When the number of poles is large and the radial length of the magnets is large, a two-dimensional (2-D) analytical or finite element analysis gives quite accurate prediction of the machine performance. A 2-D analysis however is valid only when the field region has a uniform cross section, which is not the case with the AFPMSG. The effect of the fringing flux at the inner and outer radii cannot be accounted for. Besides, the end winding leakage is difficult to model accurately. In this paper, a time-stepping, coupled field-circuit, three-dimensional finite element method is used for analyzing an outer-rotor, single-sided, 16-pole, 60-Hz axial-flux permanent-magnet synchronous generator. The computed results have been verified by experiments on an experimental generator.

II. ANALYSIS

The three-dimensional (3-D) finite element transient solver of ANSYS Version 11 SP1 was used as the analysis tool For computation of the no-load magnetic field quantities a static field solution is sufficient. For computation of the generator performance on load, a time-stepping analysis is needed. The time-stepping field-circuit solution procedure is outlined as follows:

- Construct the geometric model of the AFPMSG
- Construct the circuit model of the AFPMSG, coupling with the field region being accomplished by defining appropriate nodes in the winding element and the corresponding field element.
- Construct the sliding surface for time-stepping analysis.
- Select solver, boundary conditions, and size of time-step.
- Execute program to obtain field/circuit solution.

It should be noted however that 3-D FEA is computationally intensive, hence a compromise has to be made with regard to the computational accuracy required and the solution time.

Fig. 1 shows a radial section of the AFPMSG and Fig. 2 shows the geometric model developed for 3-D FEA. The rotor magnet is embedded in the rotor surface and the armature winding is embedded in the stator surface in Fig. 2. Non-essential regions are not modeled in order to reduce the scale of the problem.

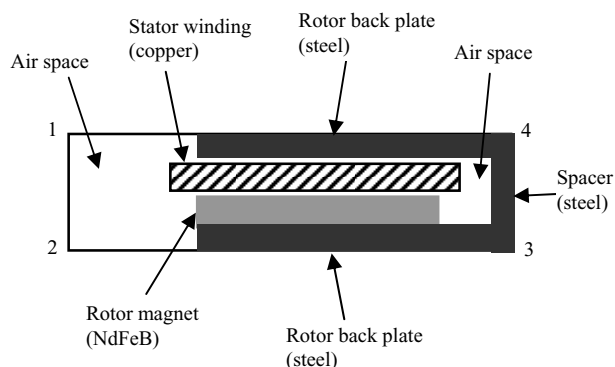


Fig. 1 Cross-section of experimental AFPMSG.

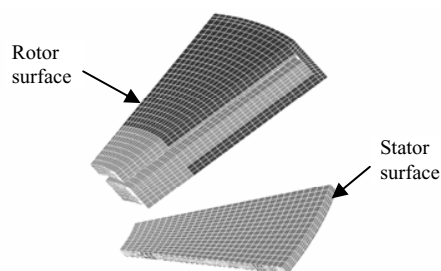


Fig. 2 Geometric model of AFPMSG for 3-D FEA.

III. RESULTS

A. Surface Plots of Air Gap Flux Density

In the subsequent discussion x , y and z denote, respectively, the radial, circumferential and axial directions of the AFPMSG. Fig. 2 shows the computed surface plots of the air gap flux density components in the AFPMSG under no load conditions, where circumferential distances 0° and 180° coincide with the interpolar axes. The value of B_x is small under a magnetic pole, but due to fringing flux in the radial directions at the inner and outer radii there are two

conspicuous peaks at $x = 0.055$ m and $x = 0.011$ m (Fig. 2a). At a given radial position, the value of B_y is zero at the pole centre, but it increases progressively towards the interpolar axis (Fig. 2b). Fig. 2c shows that the axial flux density component B_z decreases significantly at the inner and outer radii of the AFPMSG. This is due to fringing and results in reduction in the flux per pole. The use of 3D analysis is therefore justified as this phenomenon results in errors in a 2D analysis.

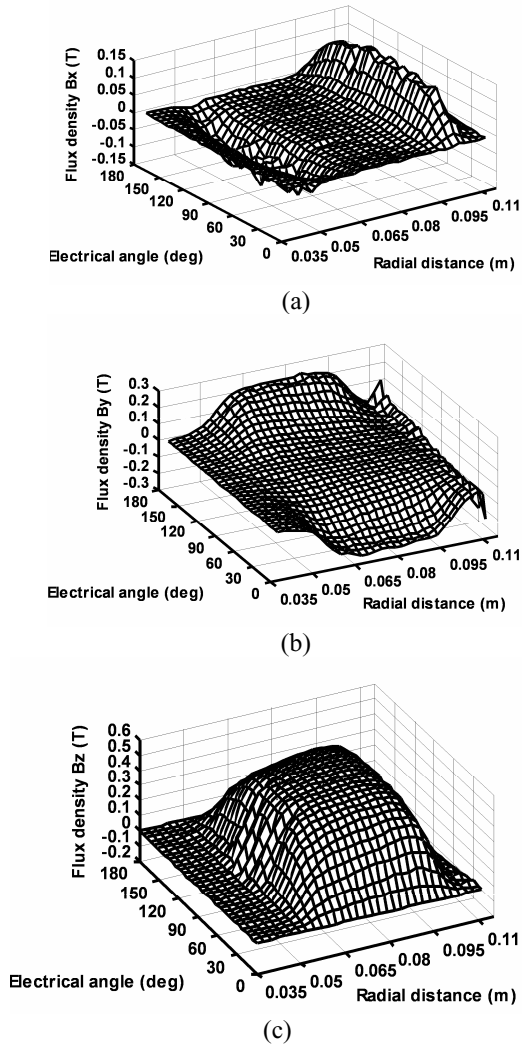


Fig. 3 Surface plots of no-load flux density components at mid-plane of armature winding: (a) radial; (b) circumferential; (c) axial.

B. Effect of Axial Position on Flux Density

Figs. 4 shows the circumferential and radial variations of B_z . The variation of B_z in the circumferential direction affects principally the magnitude and waveform of the generated emf. At $z = 12$ mm (1 mm above the surface of magnet), the B_z waveform is approximately trapezoidal but as z increases the waveform gradually becomes more rounded and become closer to a sinusoid and the magnitude decreases (Fig. 4a). The resultant waveform in the armature winding, however, depends on the axial thickness and radial length of the conductor as different sections of the conductor is cut by a

different value of B_z . As shown in Fig. 4b, the variation of B_z along the radial direction is not symmetrical about the mean radius and the maximum value occurs at a radial position closer to the outer radius. In the ferromagnetic spacer ($0.11\text{m} < x < 0.1135$ m) B_z is negative showing the effect of the spacer on the flux at the outer radius.

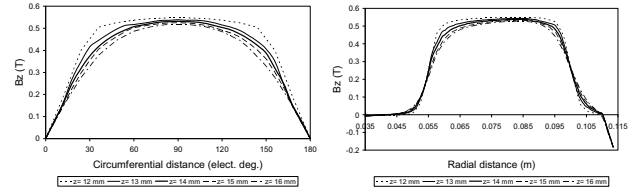


Fig. 4 Variation of B_z with axial position in the air gap region: (a) along circumferential direction at mean radius; (b) along radial direction at pole center.

C. Line and Phase Voltage Waveforms

Fig. 5 shows the computed waveforms of the phase and line voltages when the AFPMSG is supplying a resistive load of 1.75Ω per phase at rated speed. It is found that the phase voltages are flat-topped, due mainly to third harmonic contents in the air gap flux density B_z . The line voltages, however, are sinusoidal since a three-phase three-wire star-connected load is being supplied. Convergence of the 3D FEA computations is very fast: in less than 4 steps the computed values are already very close to those at steady state.

There is a slight imbalance in the line voltages and line currents, mainly due to the asymmetry introduced in the geometric winding model for 3D FEA.

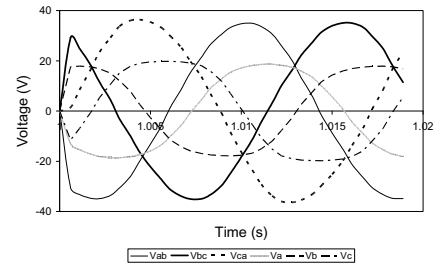


Fig. 5 Computed waveforms of line voltages and phase voltages for a load resistance of 1.75Ω per phase.

IV. ACKNOWLEDGMENT

The work described in this paper was fully supported by a grant from the Research Grants Council of the Hong Kong Special Administrative Region, China (Project No. PolyU 5121/06E).

V. REFERENCES

- [1] J. R. Bumby, R. Martin, M. A. Mueller, E. Spooner, N. L. Brown and B. J. Chalmers, "Electromagnetic design of axial-flux permanent magnet machines," *IEE Proc. - Elect. Power Appl.*, 151(2), pp. 151-159, 2004.
- [2] J. Azzouzi, G. Barakat and B. Dakyo, "Quasi-3-D analytical modelling of the magnetic field of an axial-flux permanent-magnet synchronous machine," *IEEE Trans. Energy Convers.*, 20(4), pp. 748-752, 2005.
- [3] T. F. Chan and L. L. Lai, "An axial-flux permanent-magnet synchronous generator for a direct-coupled wind turbine system," *IEEE Trans. Energy Convers.*, vol. 22, no. 1, pp. 86-94, 2007.

Unified Scheme for Implementing the Fixed-Point and Newton-Raphson Methods in Finite-Element Programs of Electromagnetic Field Problems

Emad Dlala and Antero Arkkio

Helsinki University of Technology, P.O. Box 3000 FI-02015 TKK, Finland

Email: emad.dlala@tkk.fi

Abstract—This paper proposes a unified scheme for implementing the fixed-point method (FPM) and the Newton-Raphson method (NRM) in finite-element (FE) analysis of nonlinear magnetic problems. As the NRM and FPM have advantages and disadvantages, the aim is to make both methods available in FE programs and use them in a convenient manner. It is shown in this paper that the FPM can be implemented using the same scheme of the NRM that is commonly applied in FE programs. The idea is simple and straightforward, and can be applied to a wide variety of magnetic problems. As an example, the unified scheme is applied here to a magnetic field problem formulated by the magnetic vector potential. Numerical results for two-dimensional FE simulations of an electrical machine are also presented.

I. INTRODUCTION

Taking into account magnetic nonlinearity is crucial to the investigation and design of electrical devices. The associated difficulties with nonlinearity, however, have restricted the methods that can handle the problem to the Newton-Raphson method (NRM), and less commonly, the fixed-point method (FPM). The NRM has gained monumental popularity, thanks mainly to its high convergence rate and its ability to solve nonlinear functions with several variables [1]. Today, the NRM is extensively applied to solve nonlinear electromagnetic field problems in finite-element (FE) software packages, whereas the FPM is scarcely employed. Popularity, however, can be a somewhat deceiving indicator for measuring success. Most of the NRMs, if not all, use the derivative to find the solution. Therefore, they can easily fail to solve a nonlinear magnetic problem, sometimes even with the simplest B - H curve, such as the normal magnetization curve, not to mention hysteretic field problems.

The FPM can also be applied to solve nonlinear functions with several variables, and because its convergence is not based on finding the derivative, the method is very stable and, hence, proved to be the best candidate to solve complicated nonlinear problems. Recently, the FPM has undergone an excellent improvement in accelerating its convergence, making it even a more attractive choice [2].

Although the FPM is reliable, the method should be regarded as an alternative and not a replacement to the NRM. Researchers and developers of FE software in the area of electrical engineering have become so familiar with the NRM so that they cannot afford to abandon it easily, a credit also goes to the method's quadratic convergence. On the other

hand, the different formulation the FPM imposes is perceived as a barrier towards the method's prevalence. Because most of the existing codes use the NRM formulation, switching to the FPM would obviously require laborious work.

It is therefore expedient to make both the NRM and FPM available in an FE package without augmenting or modifying the entire equations. Accomplishing this desirable situation will be the goal of this paper.

II. SOLUTION OF NONLINEAR EQUATIONS

The purpose of the NRM and FPM is to find the solution of the nonlinear system

$$\mathbf{r}(\mathbf{u}) = \mathbf{0} \quad (1)$$

iteratively in a systematic manner.

An iterative system like (1) can be put as

$$\mathbf{u}^{(k+1)} = \mathbf{g}(\mathbf{u}^{(k)}) \quad (2)$$

where \mathbf{g} is a real function with several variables. The solution of (2), if one exists, is a *fixed-point* vector $\mathbf{u}^* = \mathbf{g}(\mathbf{u}^*)$, which starts at a specified initial iterate $\mathbf{u}^{(0)}$.

The convergence criterion of (2) depends on the contraction mapping principle. A function \mathbf{g} is a contraction at a point \mathbf{u}^* if there exists a constant $0 \leq \beta < 1$ such that

$$\|\mathbf{g}(\mathbf{u}) - \mathbf{g}(\mathbf{u}^*)\| \leq \beta \|\mathbf{u} - \mathbf{u}^*\|. \quad (3)$$

In general, if $\|\mathbf{g}'(\mathbf{u}^*)\| < 1$, then \mathbf{g} is a contraction at \mathbf{u}^* .

The fixed-point iteration is the most basic technique for solving nonlinear equations and is the essence of all other methods. The Newton-Raphson iteration is a special case and consequence of the fixed-point iteration. The goal of the NRM is to construct an efficient iterative scheme that converges rapidly (quadratically) to the solution of (1). Now if (3) is utilized to enforce $\mathbf{g}'(\mathbf{u}^*) = \mathbf{0}$, the following result is obtained from (2) and (3) after simple mathematical manipulations

$$\mathbf{g}(\mathbf{u}^{(k)}) = \mathbf{u}^{(k+1)} = \mathbf{u}^{(k)} - \mathbf{r}'(\mathbf{u}^{(k)})^{-1} \mathbf{r}(\mathbf{u}^{(k)}) \quad (4)$$

which can be also written as

$$\mathbf{u}^{(k+1)} = \mathbf{u}^{(k)} - \mathbf{P}^{-1} \mathbf{r}(\mathbf{u}^{(k)}) \quad (5)$$

where

$$\mathbf{P} = \mathbf{r}'(\mathbf{u}^{(k)}) = \frac{\partial \mathbf{r}}{\partial \mathbf{u}}.$$

Equation (5) represents the *Newton-Raphson* iteration in which the iterates converge quadratically. The Jacobian matrix \mathbf{P} is, however, never explicitly inverted in practical computations. It is more efficient to solve the correction $\Delta \mathbf{u}^{(k+1)}$ from the linear systems of equations as

$$\mathbf{P} \Delta \mathbf{u}^{(k+1)} = -\mathbf{r}(\mathbf{u}^{(k)}) \quad (6)$$

hence

$$\mathbf{u}^{(k+1)} = \mathbf{u}^{(k)} + \Delta \mathbf{u}^{(k+1)}. \quad (7)$$

It is clear that the use of (6) instead of (5) is inevitable and (2) must be therefore modified to unify the scheme of implementing the NRM and FPM. Substituting (7) in (2) results in

$$\Delta \mathbf{u}^{(k+1)} = \mathbf{g}(\mathbf{u}^{(k)}) - \mathbf{u}^{(k)} \quad (8)$$

which ensures that the FPM is also based on solving $\Delta \mathbf{u}$ rather than \mathbf{u} , a straightforward but very useful achievement for solving magnetic field problems.

III. APPLICATION TO MAGNETIC PROBLEMS

The ideas introduced in Section II are general and can be applied to a wide variety of FE problems. The conventional FE formulations of the NRM and FPM are well reported in the literature (see e.g. [1]–[3]). Therefore, only the relevant equations will be shown here without introducing the details. As an example, Maxwell equations will be formulated by the magnetic vector potential \mathbf{A} .

The nonlinear magnetic equation can be put in a convenient way in order to solve it by the NRM as

$$\nabla \times \nu(\nabla \times \mathbf{A}) = \mathbf{J}. \quad (9)$$

For the FPM, the nonlinear magnetic equation is conveniently written as

$$\nabla \times \nu_{\text{FP}}(\nabla \times \mathbf{A}) = \mathbf{J} - \nabla \times \mathbf{M} \quad (10)$$

where \mathbf{J} is the electric current density and ν is the magnetic reluctivity, which is a nonlinear function of \mathbf{B} (or \mathbf{A}). ν_{FP} is a reluctivity-like quantity and is, for now, a positive constant. \mathbf{M} , which is a nonlinear function of \mathbf{B} (or \mathbf{A}), is resulting from enforcing the following constitutive equation

$$\mathbf{H} = \nu_{\text{FP}} \mathbf{B} + \mathbf{M}. \quad (11)$$

Applying the FE method to (9) and (10) results, respectively, in the following two systems of equations

$$\mathbf{S}(\mathbf{a}) \mathbf{a} = \mathbf{f} \quad (12)$$

$$\mathbf{S} \mathbf{a} = \mathbf{f} - \mathbf{q}(\mathbf{a}) \quad (13)$$

where the independent variable \mathbf{a} is a vector of the nodal values of the magnetic vector potential, \mathbf{S} is the assembly matrix, \mathbf{f} is a vector associated with the source \mathbf{J} , and \mathbf{q} is a vector associated with $\nabla \times \mathbf{M}$, which transforms the nonlinearity to the right hand side. (See [1]–[3] for more details about these FE matrices and vectors).

Solving (12) by the NRM, as $\mathbf{S} \mathbf{a} - \mathbf{f} = \mathbf{r} = \mathbf{0}$, leads to

$$\mathbf{P} \Delta \mathbf{a}^{(k+1)} = \mathbf{f}^{(k)} - \mathbf{S} \mathbf{a}^{(k)} \quad (14)$$

where

$$\mathbf{P} = \frac{\partial \mathbf{r}}{\partial \mathbf{a}} = \mathbf{S} + \frac{\partial \mathbf{S}}{\partial \mathbf{a}} \mathbf{a}. \quad (15)$$

On the other hand, solving (13) by the FPM leads to

$$\mathbf{S} \mathbf{a}^{(k+1)} = \mathbf{f}^{(k)} - \mathbf{q}(\mathbf{a}^{(k)}) \quad (16)$$

and since

$$\mathbf{a}^{(k+1)} = \mathbf{a}^{(k)} + \Delta \mathbf{a}^{(k+1)} \quad (17)$$

then (16) can be rewritten as

$$\mathbf{S} \Delta \mathbf{a}^{(k+1)} = \mathbf{f}^{(k)} - \mathbf{q}(\mathbf{a}^{(k)}) - \mathbf{S} \mathbf{a}^{(k)} \quad (18)$$

It is evident that (14) and (18) are analogous in several ways; the main one concerning this paper is that they are both leading to the solution of $\Delta \mathbf{a}$. Therefore, to switch between the NRM and FPM, one only needs to consider the terms of \mathbf{P} and \mathbf{q} when assembling the matrices and vectors within the FE equations. The significance of having a unified scheme for implementing the NRM and FPM will be even more appreciated when dealing with more complex problems, such as rotating electrical machines, for example.

IV. SIMULATION OF ELECTRICAL MACHINES

The developed methods are applied to the modeling of electrical machines using a two-dimensional, time-stepping FE method [3]. The voltage equations of the stator windings and rotor circuits are coupled with the FE equations and solved together, resulting in a strongly coupled system of equations. Therefore, similarly, the stator currents are solved for $\Delta \mathbf{i}$ and the rotor voltages for $\Delta \mathbf{v}$, a consequence that highlights the importance of the proposed scheme. FE simulations were carried out using the NRM and FPM applying the same stopping criterion. To speed up the convergence of the FPM, the locally convergent method was used [2]. Some numerical results carried out for a 380-V, 15-kW induction motor are presented in Table I. The quantities of the motor computed by the NRM and FPM are basically the same and the computation times are close to each other. Although the FPM required more iterates in average, the method was faster because it kept the assembly matrix constant during iteration [2].

TABLE I
NUMERICAL RESULTS OF THE NRM AND FPM

Quantity	NRM	FPM
Terminal current [A]	28.802	28.801
Shaft power [kW]	15.353	15.352
Air-gap flux density [T]	0.937	0.937
Electromagnetic losses [kW]	1.721	1.721
Power factor	0.8739	0.8740
Average number of iterates	5	13
Computation time [sec]	174.32	169.04

REFERENCES

- [1] P. P. Silvester and R. L. Ferrari, *Finite elements for electrical engineers*, 3rd ed., Cambridge University Press, 1996.
- [2] E. Dlala and A. Arkkio, "Analysis of the convergence of the fixed-point method used for solving nonlinear rotational magnetic field problem," *IEEE Trans. Magn.*, 44(4), 473-478, 2008.
- [3] E. Dlala, "Comparison of models for estimating magnetic core losses in electrical machines using the finite-element method," *IEEE Trans. Magn.*, 45(2), 716-725, 2009.

Parametric Design Coupled with Dynamic Equation of the BLDC Motor for Electric Vehicle

Young-kyoun Kim, Se-Hyun Rhyu, Jung-Pyo Hong
Korea Electronics Technology Institute
Yatap-Dong, Bundang-Gu, Seongnam-Si, Korea
ensigma@hitel.net

Abstract — The drive-train component of the electric vehicles is frequently using Brushless Permanent Magnet DC (BLDC) motor because that the motor have the advantages of high power density and high efficiency. The BLDC motor, owing to their restrictive field weakening range, is designed to be not as easy for vehicle application. Therefore, this paper presents a design procedure of BLDC motor for electric vehicle. Especially, the study focused to the decision method of the suitable scope of the BLDC motor parameters.

I. INTRODUCTION

Recently, owing to environmental concerns and energy conservation, electric and hybrid vehicles are receiving the significant interest. Hybrid electric vehicles are more interesting than electric vehicles powered only by batteries because they have a limit at cost and size as present technology [1]-[2]. Despite this fact, the electric vehicles (EV) are employed in the urban areas as small electric passenger cars. Because of the reason the advantages of high power density reducing weight and high efficiency giving longer ranges for a given battery size, the drive-train component of EV is frequently using Brushless Permanent Magnet DC motor (BLDC motor) [3].

This paper deals with a parametric design and verification of BLDC motor for an EV propulsion applications. Because that BLDC motor has a restrictive field weakening range, the parametric design of BLDC motor is applied in the design procedure to ensure the required specifications, which are instant rated power and continuous rated power of EV propulsion. The proposed parametric design is accomplished by coupling between the dynamic equation of EV and the voltage equation of BLDC motor.

II. SPECIFICATION OF ELECTRIC VEHICLE PROPULSION

Specifications of the EV, which is small electric passenger car, are as follows;

- EV top speed : 65 kph
- Instant rated power of the traction motor : 25 kW
- Continuous rated power of the traction motor : 10 kW
- EV mass included passengers : 900 kg
- Frontal area of EV : 1.2 m²
- Tire radius of EV : 0.27 m
- Rolling resistance coefficient : 0.013
- Aerodynamic drag coefficient : 0.75

BLDC motor power is required by an acceleration performance of EV. The vehicle acceleration performance is

evaluated by the tractive effort on the level ground, which is consists of two components as follows;

$$\text{Aerodynamic drag force: } F_a = 0.5\rho AC_d v^2 \quad (1)$$

$$\text{Rolling resistance: } F_r = \mu_r mg \quad (2)$$

where ρ is the air mass density 1.205 kg/m³, A is the frontal area of the EV, C_d is aerodynamic drag coefficient, v is the EV speed, μ_r is the rolling resistance coefficient, m is the EV mass. The total tractive effort required to reach the acceleration a is as follows;

$$F_t = ma + F_a + F_r \quad (3)$$

From above equation, the power required by acceleration can be estimated by [3].

$$P_{acc} = \mu_r mgv + 0.625AC_d v^3 + 1.05mv dv/dt \quad (4)$$

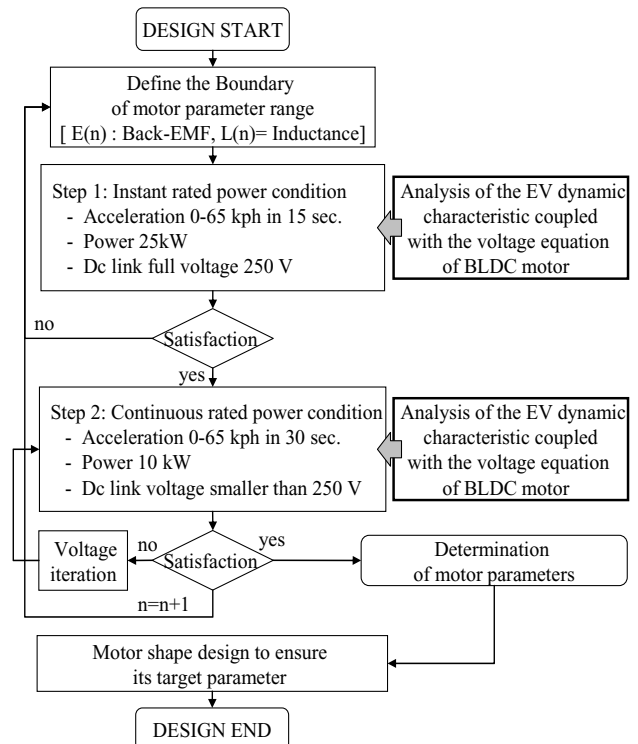


Fig. 1. Proposed parametric design process of BLDC motor

III. PARAMETRIC DESIGN OF TRACTION MOTOR

The important required condition of the traction motor in the EV is the capability for the extended speed range.

The speed and torque of the BLDC motor can be obtained by the voltage equation as follows [4];

$$V_{abc} = i_{abc}R + L \frac{di_{abc}}{dt} - M \frac{di_{abc}}{dt} + E_{abc} \quad (5)$$

$$T = \frac{i_a E_a + i_b E_b - i_c E_c}{\omega_m} \quad (6)$$

From the equation, it is realized that the characteristics of BLDC motor is totally depended on its parameters, such as back EMF, inductance, and resistance. Therefore, in order to design the BLDC motor, it is very important to decide the suitable scope of the BLDC motor parameters, which is corresponding to the given specifications of the EV propulsion, and it is accomplished by computing the dynamic acceleration (4) coupled with the electrical equation (5) and (6). The Proposed parametric design process is consists of two steps and the concept of this process is shown in Fig. 1.

IV. RESULT AND DISCUSSION

Characteristic analysis according to the change of the induced voltage and inductance is illustrated from Fig. 2 to Fig. 5. At the condition of instant rated power, the EV velocity in 15 second is shown in Fig. 2 and the armature current is illustrated like as Fig. 3.

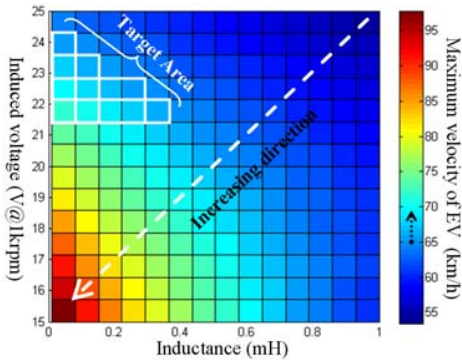


Fig. 2. Velocity map in 15 sec. at instant rated power

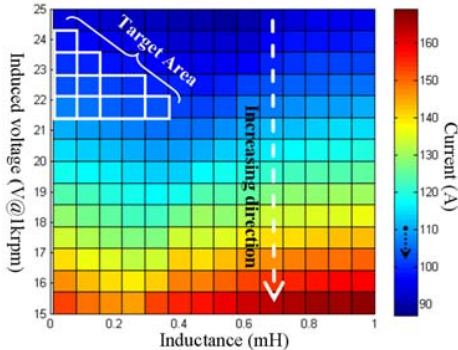


Fig. 3. Armature current map at instant rated power

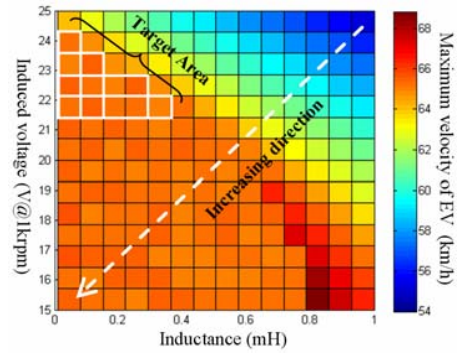


Fig. 3. Velocity map in 30 sec. at continuous rated power

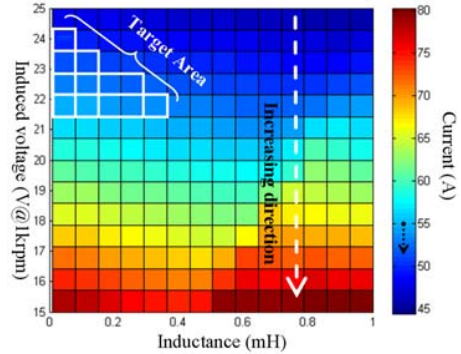


Fig. 5. Armature current map at continuous rated power

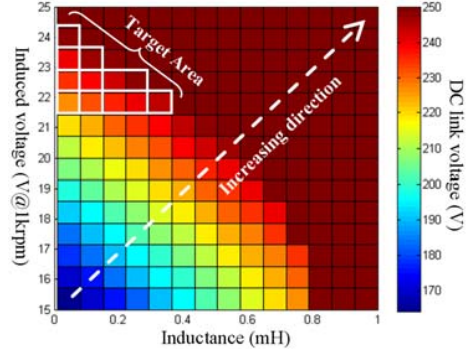


Fig. 6. DC link voltage at continuous rated power

At the condition of continuous rated power, the EV velocity in 30 second is shown in Fig. 4 and the armature current is described in Fig. 5. Fig. 6 shows the minimum voltage, which will be able to operate at the continuous rated power. The target area on the figures is estimated by considering the condition of EV top speed and the limitation of armature current. From now on, the BLDC motor should be design within the target area of its parameters, and the design results will be described in the full paper.

V. REFERENCES

- [1] P. Joshi and A. P. Deshmukh, "Vector Control: A New Control Technique for Latest Automotive Applications (EV)", ICETET '08. Conference on, 2008, pp. 911-916.
- [2] Y. Gao and M. Ehsani, "Parametric design of the traction motor and energy storage for series hybrid off-road and military vehicles," Power Electronics, IEEE Trans. On, Vol. 21, Issue 3, 2006, pp. 749 – 755.
- [3] J. Larminie and J. lowry, *ELECTRIC VEHICLE TECHNOLOGY EXPLAINED*, John Wiley & Sons, Ltd., 2003.
- [4] J. R. Hendershot Jr and T. Miller, *DESIGN OF BRUSHLESS PERMANENT-MAGNET MOTOR*, OXFOD MAGNA PHYSIS, 1994.

Discrete Magneto-Elasticity: A geometrical approach

Alain Bossavit

LGEP, CNRS & Univ. Paris-Sud
11 Rue Joliot-Curie, 91192 Gif-sur-Yvette CEDEX, France
Bossavit@lgep.supelec.fr

Abstract— We show that magnetism and elasticity have very similar mathematical structures when fields are considered as differential forms of adequate nature. The same discretization principles and techniques that succeeded in electromagnetism, notably the use of edge elements, then lead to a manageable form of coupled elasto-magnetic problems.

I. INTRODUCTION

Given a steady current density J and a spatial distribution of reluctivity ν , magnetostatics consists in finding fields B and H such that

$$\operatorname{div} B = 0, \quad H = \nu B, \quad \operatorname{rot} H = J \quad (1)$$

(plus boundary conditions that we shall ignore here). In terms of differential forms b , h and j for which B , H and J stand proxy, this becomes

$$db = 0, \quad h = \nu b, \quad dh = j, \quad (2)$$

where ν is a Hodge operator. The differential geometric framework in which (2) makes sense is pictured in the Tonti diagram of Fig. 1, which displays the underlying structure and how to fit magnetostatics in it. Its *discrete* counterpart, left aside in this Digest, will be addressed in the full-length version.

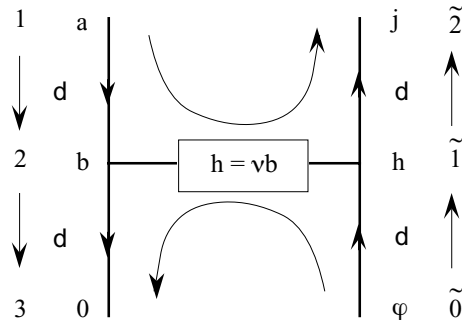


Fig. 1. The Tonti diagram of magnetostatics.

Our purpose here is to enlarge the framework, both at the continuous and discrete level, to make it home also to Elasticity, in order to fit coupled problems in magnetoelasticity into a diagram similar to Fig. 1. But in spite of meaningful analogies [1], the parallel between magnetism and elasticity is fraught with obvious difficulties: For instance, though the strain tensor ϵ derives from a potential u (displacement) like b derives from a , and must satisfy a compatibility condition

($\operatorname{rot}^t \operatorname{rot} \epsilon = 0$) somewhat reminiscent of $db = 0$, the analogy is weak, since d is a first order, instead of second order, differential operator. Finding a usable analogy requires some conceptual changes about "stress" and "strain", as follows. (We work in 3D affine space A_3 , not oriented, not metricized. Vectors we may mention are elements of the 3D real vector space V_3 , covectors are elements of its dual.)

II. THE GEOMETRY OF STRESS AND STRAIN

Let us start from the equality $\partial_t q + dj = 0$, or in integral form, $d_t \int_{\Omega} q + \int_{\partial\Omega} j = 0$ for all volumes Ω , that expresses (electric) charge conservation. We shall write this, using a Dirac-like bracket notation, $d_t \langle \Omega ; q \rangle + \langle \partial\Omega ; j \rangle = 0 \forall \Omega$, or as well, $\langle \Omega ; \partial_t q + dj \rangle = 0 \forall \Omega$, which shows how d and ∂ are dual to each other. There, q and j are *twisted* differential forms, of respective degrees 3 and 2, which means their integrals make sense over submanifolds (volumes and surfaces, respectively) with *outer* orientation. (In the case of $\partial\Omega$, this means providing it with a crossing direction. By convention, this direction is inside out with respect to Ω .)

Next, *momentum* (of a particle, say), being the integral in time of force, is a covector, since applied force—which linearly maps virtual displacements, i.e., vectors, to virtual work, a real number—is a covector itself. So we naturally represent the distribution of momentum in a continuum by a density of covectors, that is, a covector-valued twisted 3-form, denoted p . (Thus, the integral $\langle \Omega ; p \rangle$ is a covector, expressing total momentum inside Ω . Observe how the existence of *distant parallelism*, between vectors or covectors at different points, in affine space, is essential to give sense to this integral.)

Now, momentum also is a conserved entity, like charge, with the only difference that it is covector-valued: The rate of change $d_t \langle \Omega ; p \rangle$ of total momentum inside Ω plus the momentum flux across $\partial\Omega$ must add up to the rate at which momentum is poured into Ω by applied forces. We therefore introduce a twisted 2-form s , similar to j , but covector-valued, to represent this flux, hence the relation $\partial_t p + ds = f$, where the twisted 3-form f represents the applied force field, to encode momentum conservation. (The relation between this form s and the standard stress tensor σ^{ij} is a bit involved: As it happens, σ^{ij} is a *proxy* (when V_3 is equipped with a scalar product) for $-s$, the same way J, H , etc., are proxies

for j, h , etc. The minus sign results from a historically established convention about stress, to which we shall conform by setting $\sigma = -s$, and calling this the "stress $\tilde{2}$ -form".) The full version will give the discrete form, with edge-based covector-valued degrees of freedom.

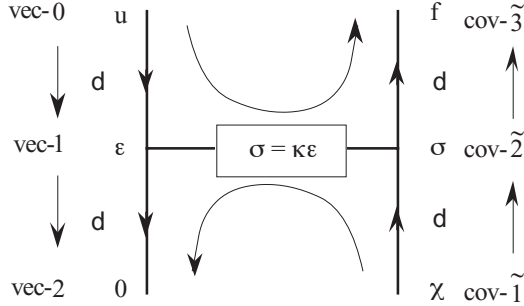


Fig. 2. The Tonti diagram of elasticity. Potentials, here, are the Beltrami one χ and the displacement u . The latter, being a point-to-vector map, is indeed a vector-valued 0-form.

Strain is more of a problem, even in the context of small deformations to which we shall restrain. We have a *material manifold* M , representing the deformable bodies. This deformation is often described by a map u from M into A_3 , called a *placement*. Instead of that, we shall prescribe the placement of material *vectors* (i.e., the vectors tangent to M , that form the tangent bundle TM) in physical space A_3 . So we have a map β_0 from TM to TA_3 for which *compatibility* is assumed, i.e., there is a point-to-point map $u_0 : M \rightarrow A_3$ the gradient of which is β_0 . This is the *reference placement*. Now, consider β from TM to TA_3 again, close to β_0 , but not necessarily compatible, since it need not preserve material continuity. Vectors $\beta(v_x)$ and $\beta_0(v_x)$, though not anchored at the same point, can be compared thanks to distant parallelism, so let's set $\epsilon_x(v_x) = \beta(v_x) - \beta_0(v_x)$: This is a linear map from $T_x M$ to $T_{u(x)} A_3$, hence a vector-valued 1-form ϵ , the "strain 1-form", that describes deformation with respect to the reference placement. [Again, the relation between this ϵ and the traditional tensor ϵ^{ij} is not simple: To say it briefly, the symmetric ϵ^{ij} proxy is obtained by "quotienting rotations out" of ϵ , as justified by the universal constitutive law according to which any material chunk can be rotated without deformation work.]

Since β is not a priori compatible, a compatibility condition must be imposed on ϵ . This is easily seen to be $d\epsilon = 0$ (for a simply-connected M), and we shall give the discrete form, in which degrees of freedom are vectors, one for each edge. Discretization, to say it briefly, consists in describing how *edges* of the mesh are displaced by ϵ . Interpolation will be done by using Whitney 1-forms.

It remains to link ϵ and σ by a constitutive law. This is done by assuming an energy functional (similar, in the isotropic case, to the standard $\lambda/2 \text{tr}(\epsilon)^2 + \mu|\epsilon|^2$, but expressed, as we shall show, in terms of the present strain 1-form ϵ), hence a linear relation $\sigma = \kappa\epsilon$ and equations similar to (2),

illustrated by the Tonti diagram of Fig. 2,

$$d\epsilon = 0, \quad \sigma = \kappa\epsilon, \quad d\sigma = f. \quad (3)$$

At this stage, one sees that the desired parallelism between magnetism and elasticity has been achieved, but (2) and (3) are still independent from each other, unless—and this is what coupling is about— v in (2) depends on ϵ – σ and/or κ in (3) depends on b – h .

III. COUPLED CONSTITUTIVE LAWS

Such dependences are best expressed in variational form, for which (non-hysteretic) magnetostatics gives a model: One introduces magnetic energy $\Psi_{\text{mag}}(b)$ and coenergy $\Phi_{\text{mag}}(h)$, Legendre–Fenchel transforms of each other, one sets $\mathcal{F}_{\text{mag}}(b, h) = \Psi_{\text{mag}}(b) + \Phi_{\text{mag}}(h) - \int b \wedge h$ (integrating over the whole domain of interest), and one requires $\mathcal{F}_{\text{mag}}(b, h) = 0$ (instead of ≥ 0 , which holds for *any* pair $\{b, h\}$ by definition of the L–F transform). This equality is equivalent to $h = \partial\Psi_{\text{mag}}(b)$ and $b = \partial\Phi_{\text{mag}}(h)$, so it's a way to state the behavior law. Problem (2) then becomes (see [2] for details) *find a pair $\{b, h\}$ that minimizes $\mathcal{F}_{\text{mag}}(b, h)$ under the linear constraints $b \in B^s$, $h \in H^s$, where B^s and H^s are functional spaces that account for source conditions such as $db = 0$ and $dh = j$, and for boundary conditions.*

Similarly, (3) consists in finding a pair $\{\epsilon, \sigma\}$ that stationarizes the quantity $\mathcal{F}_{\text{ela}}(\epsilon, \sigma) = \Psi_{\text{ela}}(\epsilon) + \Phi_{\text{ela}}(\sigma) - \int \epsilon \wedge \sigma$ under suitable linear constraints, $\epsilon \in E^s$, $\sigma \in \Sigma^s$, where Ψ_{ela} is elastic energy (an example of which was given in the previous Section) and Φ_{ela} its Legendre transform. (The wedge product $\epsilon \wedge \sigma$, a *real*-valued twisted 3-form, thanks to the vector-covector pairing, is a density of deformation work, just as $b \wedge h$, in magnetics, is a density of energy.) Introducing the total energy $\Psi(b, \epsilon) = \Psi_{\text{mag}}(b) + \Psi_{\text{ela}}(\epsilon)$ and its Legendre transform $\Phi(h, \sigma)$, we may set the two problems simultaneously, as the stationarization of $\mathcal{F}(b, \epsilon, \sigma, h) = \mathcal{F}_{\text{mag}}(b, h) + \mathcal{F}_{\text{ela}}(\epsilon, \sigma)$ under suitable linear constraints. So far, this only describes a parallel treatment of two independent problems. But this form of the problem allows one to grasp what a truly coupled problem is: *Coupling* occurs when $\Psi(b, \epsilon)$ *cannot* be written as a sum $\Psi_{\text{mag}}(b) + \Psi_{\text{ela}}(\epsilon)$ of distinct energy terms. The constitutive laws are then $h = \partial_b \Psi(b, \epsilon)$ and $\sigma = \partial_\epsilon \Psi(b, \epsilon)$, with now *partial* derivatives, and the variational form of the coupled problem has

$$db = 0, \quad d\epsilon = 0, \quad h = \partial_b \Psi, \quad \sigma = \partial_\epsilon \Psi, \quad d\sigma = f, \quad dh = j \quad (4)$$

as its "strong" counterpart. Discretization is then easy.

How one can know the energy functional $\Psi(b, \epsilon)$ in concrete situations, and why one should associate b and ϵ , instead of (say) b and σ , will be discussed in the full paper.

IV. REFERENCES

- [1] F.A. Firestone, "A new analogy between mechanical and electrical systems", *J. Acoust. Soc. Am.*, 4: 249-67, 1933.
- [2] A. Bossavit, "Complementarity bilateral bounds on forces in magnet systems", *COMPEL*, 26(4): 932-940, 2007.

Nonlinear Coupled FE-circuit model for the optimization of 3D Saturated Hybrid Motors

E. D. Kenmoe Fankem, N. Takorabet, F. Meibody-Tabar and F.M. Sargos
 Nancy University, INPL - GREEN
 2, av. de la Forêt de Haye 54516 Vandoeuvre lès-Nancy, France
Noureddine.Takorabet@ensem-inpl-nancy.fr

Abstract — This paper presents a coupled Finite Element – Reluctance Network model for a hybrid motor. The equivalent permeances of the air-gap are determined by two dimensional (2D) nonlinear finite element (FE) computations. The 2D results are used for setting up a 3D analytical model. Spectral decomposition and a nonlinear fitting of the amplitudes of the permeance harmonics is performed to account for both saturation and high order harmonics effect. The method is validated with a 2D FE computation and then applied in the case of a highly saturated 3D hybrid stepping motor.

I. INTRODUCTION

Three dimensional Finite Element (FE) method is a useful tool for the modelling of axial flux machines such as hybrid motors. However, this method requires a very long CPU time and a large space memory especially when the saturation phenomenon should be taken into account. The use of 2D finite element method coupled with nonlinear circuit model can be an alternate solution which combines accuracy, precision and fastness. Analytical models using reluctance networks have been developed which include the effect of saturation in well designed machines [1,2]. Various approximations and simplifications are often used which can be justified by FE computations.

The authors present a coupled FE – analytic model for a highly saturated hybrid stepping motor that can be applied for the design and the optimization of such devices. The main idea is based on the use of 2D FE parameter identification and a spectral analysis of the permeance function that can easily achieve the computation of the torque waveforms.

II. HYBRID MOTOR: DESCRIPTION AND EQUIVALENT MODEL

The general architecture of the hybrid motor is shown on Fig. 1 where the case of a 4-phase motor supplied by unidirectional currents is considered. The axial flux is provided by a cylindrical magnet axially magnetized located in the rotor. The number q of stator phases and N_r of rotor teeth allow determining the period of the permeance function motor according to:

$$\tau = 360^\circ / (q N_r) \quad (1)$$

The two slotted half-rotors are shifted by 180 electrical degrees and separated with an axial gap x . A reluctance network model, which is shown on Fig.2, is developed. It includes two circuits of 4 parallel branches representing the two half-machines. These two circuits are series connected via a circuit corresponding to the magnet and the yoke. According to the winding mode and the angular shift between the two rotors, there are permutation relationships between the permeances P_k on one hand, and equality relationships between the MMF sources V_k , $k = 1..8$ on the other hand.

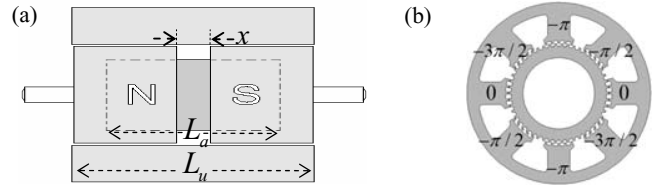


Fig. 1. (a) Longitudinal view of the hybrid machine, (b) Axial view

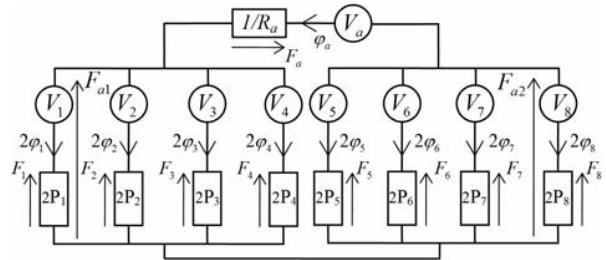


Fig. 2. reluctance network equivalent model.

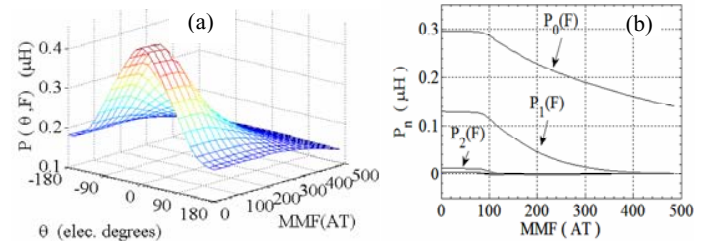


Fig. 3. Permeance function and its Fourier's coefficients.

III. FE IDENTIFICATION OF THE MODEL PARAMETERS

The principle of the proposed model consists firstly on a numerical computation of the phase fluxes with a nonlinear 2D FE code [3]. Then a numerical post-processing of the FE results is performed for setting up the circuit model. The flux-ampere turn curves of each coil are determined over one electrical period of the rotor, which allows determining the permeance $P(\theta, F)$ as a function of the ampere turns and position which is shown on Fig. 3-a. The spectral decomposition of this function is performed and expressed with the following expansion:

$$P(\theta, F) = \sum_n p_n(F) \cos(nN_r \theta) \quad (2)$$

where F is the magnetomotive force (MMF). The functions $p_n(F)$ are shown in Fig.3-b. According to some permutation rules corresponding to the winding arrangement, the Fourier coefficients of the 8 permeances (p_n^k , $k = 1..8$) are easily

determined. Therefore, p_n^k is the Fourier coefficient of order n of the the k^{th} branch permeance.

A nonlinear resolution of the flux equations of the circuit model is performed for different positions of the rotor thanks to an iterative process. A rigorous convergence criterion is adopted to ensure the correct final solution of the problem. Indeed, due to the high saturation level of the teeth, the nonlinearity of the permeances is important as illustrated on Fig. 4. The saturation level is represented by the position of the points $\varphi_i(F_i)$ in the flux-ampere turn diagram. The general structure of the algorithm is based on the following steps:

- a) F.E. identification of the parameters
- b) For a given position θ
 - b.1 : Initialize the permeances P_0^k
 - b.2 : Solve nonlinear circuit equations
 - b.3 : Compute the fluxes $\varphi_i^k(F_i^k)$
 - b.4 : Deduce the new values of permeances P_{i+1}^k
 - b.5 : Test the convergence and go to b.2 or B.6
 - b.6 : $\theta = \theta + \delta\theta$ go to b)
- c) Compute external performances energy and torque

According to the saturation level of the different permeances P^k , the convergence of the resolution process is reached after less than 9 iterations. The algorithm is tested in different situations and changing starting point does not disturb the convergence process. Indeed, on Fig. 4 two different starting points which are represented by (*) are considered. The two figures show the trajectories of the points

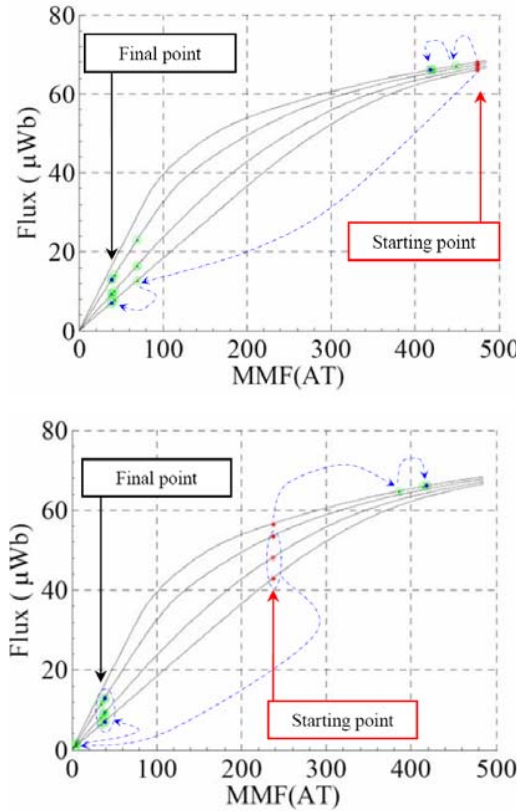


Fig. 4. Trajectories of the points $\varphi_n^k(F_n^k)$ during the iterative process

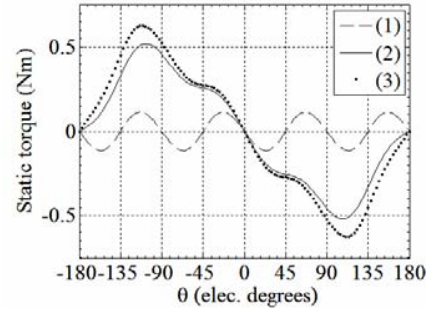


Fig. 5. Some static torques

$\varphi_i^k(F_i^k)$ that converge to the same final point $\varphi_\infty^k(F_\infty^k)$ after few iterations.

IV. EXTERNAL PERFORMANCES CALCULATION

The virtual works theorem is applied to compute the static torque of the motor for a given supply and for different positions. According to the spectral analysis of the permeance functions, we have:

$$T(\theta) = \partial_\theta \tilde{W}_m(\theta) = \partial_\theta \tilde{W}_m(\theta) - 2N_r \sum_{\substack{k=1:8 \\ n=1:\infty}} n \sin(n(N_r\theta + \alpha_k)) \int_0^{F_k} p_n^k(F) F dF \quad (3)$$

where: \tilde{W}_m is the coenergy in the magnet branch, F_k and α_k are the total ampere-turns and the phase shift of the permeances of the k^{th} branch respectively. Fig.5 shows the static torque waveforms obtained in different supplying modes: (1): the cogging torque (no current), (2): the phase 1 is supplied with a direct current i , (3): the phases 1 and 3 are supplied with the currents $i/2$ and $-i/2$ respectively.

The coupling between the results of numerical FE computation and the permeance network model is ensured by the good representation of $\mathbf{P}(\theta, F)$ functions, which takes into account the locals high saturation levels and high harmonic ranks of the MMF.

The developed model allows calculating the torque waveforms for any supplying mode. For high speed motors, the optimization of the supply according to the motor parameters is a serious problem that can be solved with such model. The computation of the optimal current waveforms can be performed with a minimal CPU time.

V. CONCLUSION

A nonlinear coupled Finite Element – circuit model is developed for the study and optimization of a hybrid motor.

The model is based on 2D FF results which are applied to simulate the 3D behaviour of the electromagnetic field in such devices. The use of nonlinear spectral analysis of the permeances allows determining the torque waveforms with an easy formulation. The model can be used for the optimization of the supply of such motors for high speed applications.

VI. REFERENCES

- [1] K.C. Lim, J.P. Hong, G.T. Kim, "Characteristic analysis of 5-phase hybrid stepping motor considering the saturation effect", *IEEE Trans. on Magnetics*, 37(5): 3518-3521, 2008.
- [2] T. Raminosoa, I. Rasoanarivo, F. Meibody-Tabar, F.M. Sargos, "Time stepping simulation of synchronous reluctance motors using nonlinear reluctance network method", *IEEE Trans. on Magnetics*, 44(12): 4618-4625, 2008.
- [3] Meeker, D. Finite Element Method Magnetics (FEMM): a free magnetics finite element package for windows. <http://femm.foster-miller.net>. 2007.

Co-Simulation as Multirate Time Integration of Field/Circuit Coupled Problems

Sebastian Schöps¹, Herbert De Gersem², and Andreas Bartel¹

¹ Bergische Universität Wuppertal, Gaußstraße 20, 42119 Wuppertal, Germany
 {schoeps,bartel}@math.uni-wuppertal.de

² Katholieke Universiteit Leuven, Campus Kortrijk, 8500 Kortrijk, Belgium
 Herbert.DeGersem@kuleuven-kortrijk.be

Abstract— This paper demonstrates how to take advantage of multirate behavior in the time-integration of electromagnetic field problems coupled to lumped electric circuits. The necessity of multiple time step sizes in different parts of the model according to their dynamics is explained and corresponding methods like the co-simulation are introduced to reduce the computational effort. This becomes especially important in cases where large field models are unnecessarily evaluated at a high frequency.

I. INTRODUCTION

The electromagnetic field is mathematically described by Maxwell's set of partial differential equations (PDEs), but in many applications simplified models of devices are accurate enough and one models them as a lumped electric circuit using a network approach. This leads to a time dependent system of differential algebraic equations (DAEs).

The coupling of both the field PDEs and circuit DAEs results in a system of partial differential algebraic equations that avoids the computationally expensive field simulation where possible, but allows particular devices to be given by field models. Finally, the spatial discretization of the field models yields a system of coupled DAEs, which leads to an efficient simulation scheme.

A. Multirate Phenomenon

The numerical solution of the coupled DAE system is obtained by integration schemes based on time discretization. This discretization has to resolve the dynamics of the system as a whole and thus yields a series of time steps that matches the dynamics of the most active component (respectively the one working at the highest frequency).

In coupled systems considering multiphysical behavior (e.g. heating) one can easily split the equation corresponding to their time constants since this is determined by the propagation speed of the effects. In contrast to this, the field and circuit equations are more describing the same effects, hence the same time constants occur. Anyhow due to switches, filters or high integration there may only be a small number of devices active at a time, while the others remain latent. In either case the time integrator will resolve parts of the model with an unnecessarily high resolution and hence higher computational costs than the problem requires are caused. Therefore a splitting w.r.t. the activity level is beneficial.

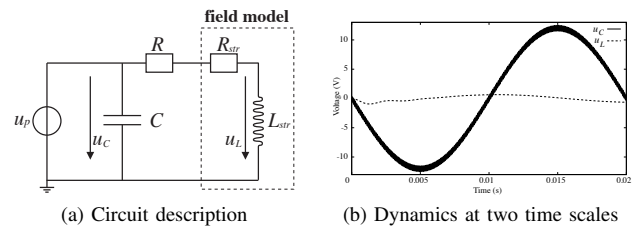


Fig. 1. A simple field/circuit configuration requiring different time constants in the time integration. The parameters are $R = 10\Omega$, $C = 100\mu\text{F}$ and $u_P(t) = 12 \sin(2\pi f_1 t) \text{V} + 0.5 \sin(2\pi f_2 t) \text{V}$ composed of two voltages with frequencies $f_1 = 50\text{Hz}$ and $f_2 = 10\text{kHz}$. The field model is approximately given by an equivalent circuit with $R_{\text{str}} = 0.07\Omega$ and $L_{\text{str}} = 1.7\text{mH}$.

B. Demonstration Example

The configuration shown in Fig. 1 demonstrates the phenomenon of different time constants within one circuit. Let $u_P(t)$ represent a simplified circuit model and the boxed inductor part is given by a stranded conductor model that is described by a large non-linear system of equations. Then the application of an adaptive time integration scheme would yield time step sizes in the order of $h_C = 10^{-5}\text{s}$, although step sizes of $h_L = 10^{-3}\text{s}$ would be sufficient to render the dynamics of the field model.

II. COUPLING

A. Electric Circuit

Electric circuits are commonly simulated by using the modified nodal analysis, this yields an DAE due to redundant coordinates, where voltages e and currents i are the unknowns

$$F_1\left(\frac{dx}{dt}, x, i_\lambda, t\right) := A \frac{dq}{dt}(x) + f(x, t) + A_\lambda i_\lambda = 0 \quad (1)$$

with incidence matrices A , the unknown $x := (e, i)$, charge and resistance functions q and f ; currents i_λ through field devices as modeled below, [1].

B. Magnetoquasistatic Field

The electromagnetic field is described by Maxwell's equations. We assume their spatial discretization based on the finite element method with lowest order Whitney elements or by the finite integration technique, [2, 3]. Then all equations can be combined such that one obtains the *curl-curl* equation (2)

$$M_\varepsilon \frac{d^2 \bar{a}}{dt^2} + M_\sigma \frac{d \bar{a}}{dt} + C^T M_\nu C \bar{a} = \hat{j}, \quad (2)$$

with the unknown magnetic vector potential (MVP) \bar{a} , the discrete curl operator C , the electric current density due to external sources \hat{j} ; the material matrices M_ν , M_ϵ and M_σ represent the reluctivities, permittivities and conductivities, with M_σ singular in general.

C. Coupling with Conductor Models

In [4] the solid, stranded and foil conductor models have been proposed for the usage in circuits. In all those cases the coupling is established by relating circuit currents i_λ and voltages $u_\lambda = A_\lambda^T x$ as defined in (1) to derivatives of the field's MVP \bar{a} in (2). The curl-curl equation is excited by currents that are derived from the coupling equation

$$\hat{j} = Q i_\lambda \quad \text{and} \quad R i_\lambda + Q^T \frac{d\bar{a}}{dt} = A_\lambda^T x, \quad (3)$$

where Q is the coupling matrix that imposes the circuit currents and voltages onto edges of the grid; R contains the dc resistances of all conductor models.

Finally, the field problem is given abstractly by the DAE

$$F_2\left(\frac{d^2}{dt^2}\bar{a}, \frac{d}{dt}\bar{a}, \bar{a}, A_\lambda^T x, i_\lambda\right) = 0 \quad (4)$$

III. SIMULATION

A. Monolithic Simulation

The DAE (4) defines a current/voltage relation and hence can be used as an element stamp in a circuit simulation package. This *monolithic* (or strongly coupled) approach will use the time integrator of the circuit simulator and serves as reference solution.

Typical circuit integrators do not yet use multirate techniques and thus the integration may become unnecessarily expensive because of the different time constants. Furthermore they focus on first order DAEs and hence one is forced to rewrite the curl-curl equation to first order with the drawback of doubling the number of unknowns or to disregard the displacement current at all. The latter approach is known as the *magnetoquasistatic* approximation and is the valid for low frequencies, but is numerically cumbersome due to the singularity of the conductivity matrix M_σ .

B. Waveform Relaxation

Instead of stamping the equations into one combined system, both subproblems can be simulated independently from each other by a *waveform relaxation scheme*, typically either of Jacobi or Gauß-Seidel type, [5]. We suggest the Gauß-Seidel scheme (5) that states the iteration in one time frame and is employed to further frames according to Fig. 2.

The scheme starts from given initial values and an additional initial guess for the current $i^{(0)}$. It iterates for $k = 1, \dots, N$ and in each iteration the circuit is computed first and the field afterwards. The first circuit solution $x^{(1)}$ is based on the initial guess $i^{(0)}$, while later computations ($k > 1$) rely on the previous field solution $i^{(k-1)}$. In Gauß-Seidel's scheme

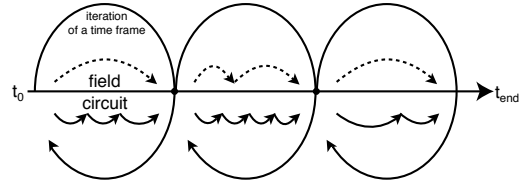


Fig. 2. Integration of three time frames using a waveform relaxation schemes

the field computation always utilizes the latest available field solution $x^{(k)}$:

$$\begin{aligned} \text{Circuit:} \quad & F_1\left(\frac{dx^{(k)}}{dt}, x^{(k)}, i_\lambda^{(k-1)}, t\right) = 0 \\ \text{Field:} \quad & F_2\left(\frac{d^2\bar{a}^{(k)}}{dt^2}, \frac{d}{dt}\bar{a}^{(k)}, \bar{a}^{(k)}, A_\lambda^T x^{(k)}, i_\lambda^{(k)}\right) = 0. \end{aligned} \quad (5)$$

This approach allows the usage of problem-specific software packages for the field and circuit equations („*co-simulation*”) and therefore supports the full Maxwell case including the displacement current. The convergence of this scheme is not trivial due to the algebraic parts of the DAE, but convergence has been shown in [6].

The co-simulation uses different time integrators and thus supports different time steps towards each subproblem. But this will not unlock all possible benefits of the multirate phenomenon: different time scales within one subproblem are not exploited and one may need too many iterations of one time frame. Furthermore the consistency of the time integration is only ensured on the subproblems. Therefore one has to pick up the idea of multirate methods as they were proposed in [7].

C. Implementation

A demonstration code for simulating the field/circuit coupled problem is implemented within the CoMSON demonstration platform: the package FIDES for field devices is coupled to the CoMSON circuit integrator (OCS). The results of Fig. 1 are obtained by the monolithic approach using a field model discretized by FEMM.¹

Acknowledgements: This work was partially supported by the European Commission within the framework of the COMSON RTN project and the post-doc program of the "FG Mathematik and Informatik" of the Bergische Universität Wuppertal.

REFERENCES

- [1] U. Feldmann and M. Günther, "CAD-based electric-circuit modeling in industry I: mathematical structure and index of network equations," *Surv Math Ind*, vol. 8, no. 2, pp. 97 – 129, 1999.
- [2] A. Bossavit, *Computational Electromagnetism: Variational Formulations, Complementarity, Edge Elements*. San Diego: Academic Press, 1998.
- [3] M. Clemens, "Large systems of equations in a discrete electromagnetism: formulations and numerical algorithms," *IEE Proc Sci Meas Tech*, vol. 152, no. 2, pp. 50 – 72, March 2005.
- [4] H. De Gersem and K. Hameyer, "A FEM for foil winding simulation," *IEEE Trans. Mag.*, vol. 37, no. 5, pp. 3472 – 3432, September 2001.
- [5] K. Burrage, *Parallel and sequential methods for ordinary differential equations*. Oxford University Press, 1995.
- [6] S. Schöps, A. Bartel, H. De Gersem, and M. Günther, "DAE-index and convergence analysis of lumped electric circuits refined by 3-D MQS conductor models," *IEEE SCEE 2008 Proc*, to be published
- [7] C. W. Gear and D. R. Wells, "Multirate linear multistep methods," *BIT*, vol. 24, no. 4, pp. 484 – 502, 1984.

¹see www.comson.org and femm.foster-miller.net

Efficient Numerical Modelling of Field Diffusion in High-Temperature Superconducting Wires

Igor O. Golosnoy and Jan K. Sykulski, *Senior Member IEEE*

University of Southampton

School of Electronics and Computer Science, Southampton, SO17 1BJ, UK

ig@ecs.soton.ac.uk, jks@soton.ac.uk

Abstract—Multidimensional field diffusion problems with front-type behaviour, moving boundaries and non-linear material properties are analysed by a finite volume front fixing method. Advantages and implementation challenges of the method are discussed with special attention given to conservation properties of the algorithm and achieving accurate solutions close to the moving boundaries. The technique is validated using analytical solutions of diffusion problems with cylindrical symmetry.

I. INTRODUCTION

Design and development of modern devices based on High Temperature Superconductors (HTS) requires numerical modelling since electromagnetic and thermal parts of the problem are coupled together via high sensitivity of HTS material properties to temperature [1, 2]. Both field variation and heat flow can be formulated in terms of diffusion. This allows utilising a standard modelling approach on fixed grids and thus simplifying the equipment design. But such approach often fails to deliver appropriate balance between accuracy and efficiency, especially when modelling pulse events or shallow field penetration. Special methods, such as adaptive meshes, front fixing and level sets methods [3], offer advantages in such applications but they have to be assessed and probably adapted for each particular problem. The paper focuses on the analysis of the front fixing technique [3] since it requires only a small modification of the computational algorithm in comparison with models based on fixed grids [4, 5]. The major challenges are an implementation of conservation laws and achieving accurate solutions close to the moving curved boundaries. The paper uses analytical solutions of common front type problems to evaluate the performance of the numerical method. Two types of the problem are considered, namely a current pulse and an imposed external magnetic flux.

II. PROBLEM FORMULATION

A. Governing equation and material properties

It is possible to describe the problem in terms of either magnetic or electric field diffusion [6, 7]. The electric field formulation is preferred for HTS materials with non-linear properties as it provides much more stable solutions [7]. The governing equation takes the diffusion-like form

$$\text{curl} (\text{curl} \mathbf{E}) = -\mu_0 \frac{\partial \mathbf{J}}{\partial t} \quad (1)$$

expressed in terms of the electric field \mathbf{E} and current density \mathbf{J} . HTS materials exhibit strong flux creep E - J behaviour often

described by Rhyner's power law [6], $E_c^{-1}E = (J_c^{-1}J)^\alpha$, where the critical current density $J_c \approx 10^9 \text{ A m}^{-2}$ corresponds to a critical electric field $E_c \approx 10^{-4} \text{ V m}^{-1}$. For practical HTS materials the power exponent α could be as high as 20. Substitution of the material properties into (1) results in a formulation of the problem in terms of the electric field only.

B. Boundary and initial conditions

A HTS wire with a round cross section of radius R is considered. For the first test, a pulse $I_z(r, t) = I_0 \delta(r) \delta(t - t_0)$ of current is applied along the z axis at an instant $t = t_0$. The second test case assumes an external magnetic flux B_z to be switched suddenly in the centre of the wire and maintained at a constant value afterwards.

C. Analytical solutions

The existence of an axi-symmetric analytical solution provides an opportunity to evaluate the performance of the algorithm on curved boundaries using the Cartesian coordinate system. The dimensionless solution for (1) in the case of cylindrical symmetry under the conditions of the current pulse can be derived as shown in [8]

$$\frac{E(\rho, \tau)}{E_c} = \frac{1}{(\alpha\tau)} \left[\left(\frac{i_0}{4} \right)^{\frac{\alpha-1}{\alpha}} - \frac{\rho^2(\alpha-1)}{4\alpha(\alpha\tau)^{1/\alpha}} \right]^{\alpha/(\alpha-1)}, \quad (2)$$

$$\rho = \frac{r}{R}, \quad \tau = \frac{(t-t_0)E_c}{\mu_0 J_c R^2}, \quad i_0 = \frac{I_0}{J_c \pi R^2}. \quad (3)$$

The electric field and the current gradually spread from the centre of the wire towards the edges and there is a sharp interface between the region with a non-zero field and the outside part of the wire. A similar solution exists for the second test case of the applied external magnetic flux [9].

III. THE FRONT FIXING METHOD

The spatial transformation uses new positional variables [3] adjusted to the front position and, generally, introduces a co-ordinate system in which all of the spatial boundaries are fixed to 0 or 1. As a result, the new computational domains remain the same with an additional advection term in diffusion equation plus an implicit non-linear equation for the boundary motion. This allows treating the nodes close to the interface as being independent of the motion, which gives higher accuracy for the same number of nodes used [4, 5]. In practical applications it is often sufficient to apply the transformation in

only one direction, resulting in additional simplification [3]. Equation (4) is an example of the transformed (1) in notations (3) for the case of cylindrical symmetry:

$$\frac{\partial(us^2e^{1/\alpha})}{\partial\tau} = \frac{ds}{d\tau} \frac{\partial(su^2e^{1/\alpha})}{\partial u} + \frac{\partial}{\partial u} \left(\frac{\partial e}{\partial u} \right), \quad e = (E_c^{-1}E). \quad (4)$$

with a boundary at $s(t)$ and a new coordinate $u = \rho/s(t)$. A divergent form of (4) ensures that there are no artificial energy sources [5].

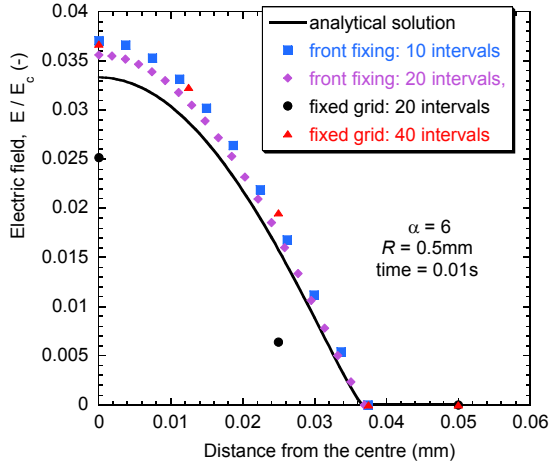


Fig. 1. Analytical and numerical predictions for a wire with $I_0 = 2A$, $R = 0.5mm$ and $\alpha = 6$: mesh size effects. Dimensionless electric field $E_z(r)$ at $t = 0.01s$ (time step $0.1ms$).

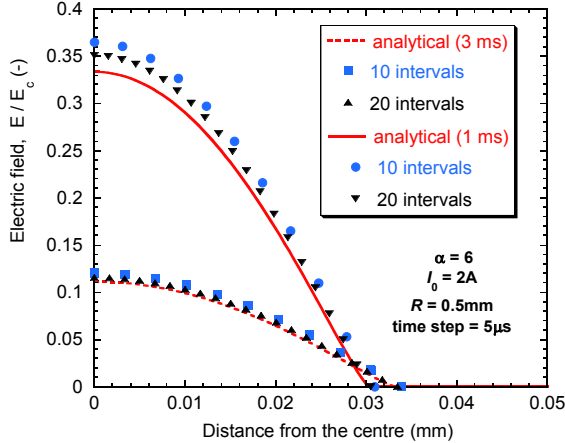


Fig. 2. Front-fixing method predictions of electric field inside the HTS wire after different times. Modelling conditions are similar to those in Fig. 1.

IV. COMPARISON OF COMPUTATIONAL TECHNIQUES

Predictions from fixed grid calculations and the front-fixing method are summarized in Figs. 1-3. Fixed nodes cannot adequately describe the field profile in the case of a shallow penetration (Fig. 1). At least 4 nodes per penetration depth are required, which could be computationally expensive for large devices. Placing nodes close to the boundary does not always solve the problem because the front propagates further into the material at later stages of the process. In contrast, the front fixing automatically adjusts the nodes towards the front boundary, Fig. 2, and good accuracy is achieved even by only 10 nodes in total. The particular

advantage of using a front-fixing method for modelling of superconductivity phenomena is that the high accuracy can be obtained with a small number of grid points. The interface motion can also be accurately predicted on a coarse moving mesh, Fig. 3.

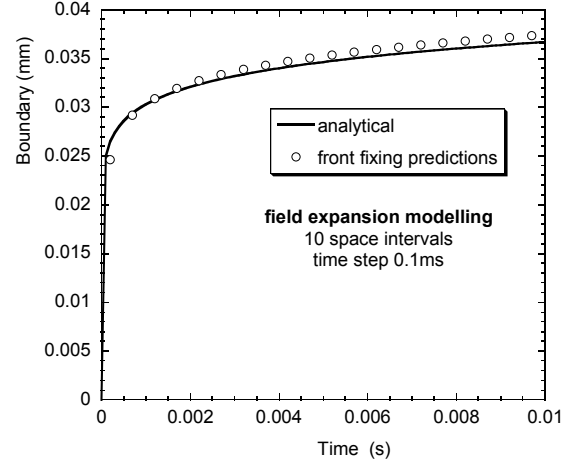


Fig. 3. Interface position as a function of time. Modelling conditions are similar to those on Fig. 1.

V. CONCLUSIONS

The application of a front-fixing method for modelling of shallow field penetration into HTS materials is demonstrated for 2D geometry cases. Efficient techniques for incorporating conservation laws are suggested and potential problems with complex boundary conditions are considered. It is shown that high accuracy can be achieved on a coarse mesh since the interface is fixed in new coordinates. The analysis of errors and further implementation details will be given in the extended version of the paper. The finite volume method has been utilised in the paper as an example; the finite element scheme can also be used for successful discretisation of space and time in the transformed equations.

VI. REFERENCES

- [1] K. Berger, J. LeVeque, D. Netter, B. Douine and A. Rezzoug, "AC Transport Losses Calculation in a Bi-2223 Current Lead Using Thermal Coupling With an Analytical Formula," *IEEE Trans. on Applied Superconductivity*, 15, pp. 1508-1511, 2005.
- [2] N. Schonborg and S. Hornfeldt, "Model of the temperature dependence of the hysteresis losses in a high-temperature superconductor," *Physica C*, 372, pp. 1734-1738, 2002.
- [3] J. Crank, *Free and Moving Boundary Problems*. Oxford: Clarendon Press, 1984.
- [4] I.O. Golosnoy and J.K. Sykulski, "Evaluation of the front-fixing method capabilities for numerical modelling of field diffusion in HTS tapes," *IET Science, Measurement & Technology*, 2, pp. 418-426, 2008.
- [5] T.C. Illingworth and I.O. Golosnoy, "Numerical Solutions of Diffusion-Controlled Moving Boundary Problems which Conserve Solute," *Journal of Computational Physics*, 209, pp. 207-225, 2005.
- [6] J. Rhyner, "Magnetic properties and AC-losses of superconductors with power law current-voltage characteristics," *Physica C*, 212, pp. 292-300, 1993.
- [7] J.K. Sykulski, R.L. Stoll and A.E. Mahdi, "Modelling HTc Superconductors for AC Power Loss Estimation," *IEEE Trans. on Magnetics*, 33, pp. 1568-1571, 1997.
- [8] G.J. Pert, "A class of similar solutions of the non-linear diffusion equation," *J. Phys. A: Math. Gen.*, vol. 10, pp. 583-593, 1977.
- [9] J. Gilchrist, "Flux diffusion and the porous medium equation," *Physica C*, 291, pp. 132-142, 1997.

Unipolar and Bipolar Charge Injection and Transport in Dielectric Liquid by Finite Element Method

Se-Hee Lee,¹ Il-Han Park,² Francis O'Sullivan,³ Markus Zahn,³

Leif Pettersson,⁴ Rongsheng Liu,⁴ Olof Hjortstam,⁴ Albert Jaksts,⁴ Tommaso Auletta,⁴ and Uno Gafvert⁴

¹School of Electrical Eng. and Computer Science, Kyungpook National University, Daegu 702-701, Korea

²School of Information and Communication Eng., Sungkyunkwan University, Suwon 440-746, Korea

³Department of Electrical Eng. and Computer Science, Massachusetts Institute of Technology, Cambridge, MA 02139, USA

⁴ABB Corporate Research, Sweden

shlees@knu.ac.kr

Abstract — In a dielectric liquid, unipolar and bipolar space charge injection and propagation were analyzed under simplified linear and Fowler-Nordheim charge injection conditions for parallel plane or needle-sphere electrodes stressed by a step voltage. Especially, here, the numerical aspects for solving space charge analysis were explored in a dielectric liquid by the Finite Element Method (FEM) employing the artificial diffusion scheme as a stabilization technique. We first tested parallel plane electrodes with a simplified linear charge injection law for unipolar space charge propagation that showed good agreement with older closed form with space charge limited condition. And tip-sphere electrodes, where the radius of tip was 40 μm , were also tested for bipolar space charge propagation including Langevin recombination.

I. INTRODUCTION

Dielectric liquids are widely used for many electrical insulation technologies such as transformer oil. When compared to gaseous or solid insulation, dielectric liquids generally offer greater electrical insulating strength, superior thermal conductivity, higher performance, and greater ease of use. One of the key issues for insulating liquids is to predict the electrical breakdown which is the final stage in the electrical breakdown process including several pre-breakdown stages.

This breakdown is basically based on the charge injection and transport phenomena between electrode and dielectric liquid. To analyze these mechanisms, charge continuity equations and Poisson's equation for the electric scalar potential must be self consistently satisfied [1]-[2]. The distributions of space charge in streamer propagating channel might have a shock-wave pattern, which causes severe numerical instabilities, due to the abrupt injection and propagation of space charge.

We briefly verified our numerical method by comparing analytic solutions earlier obtained by using the method of characteristics in the previous proceeding [3]. To stabilize this numerical difficulty, we, here, tested and discussed in the artificial diffusion technique incorporating the Finite element Method (FEM) considering the Peclet number in detail. The terminal current during discharge was calculated by using the principle of energy conservation for the electric field. Finally, we successfully applied the analysis to a tip-sphere electrode system, where the radius of tip was 40 μm , for analyzing bipolar space charge propagation in a dielectric liquid medium.

II. NORMALIZED GOVERNING EQUATIONS FOR UNIPOLAR SPACE CHARGE PROPAGATION

To deal with numerical aspects, we tested the parallel plane electrodes with the lower electrode as anode at $x=0$ and the upper electrode as cathode at $x=d$, the distance between two electrodes. To employ the normalized forms, we took the normalized variables as

$$\begin{aligned}\tilde{\nabla} &= d\nabla, \tilde{t} = t\mu V_0 / d^2, \tilde{V} = V / V_0, \tilde{\rho} = \rho d^2 / \varepsilon V_0, \\ \tilde{\mathbf{J}} &= 2\mathbf{J}d^3 / \varepsilon\mu V_0^2, \tilde{\mathbf{E}} = \mathbf{E}d / V_0, \tilde{A} = \tilde{A}d / \varepsilon\end{aligned}\quad (1)$$

where the tilde denotes non-dimensional variables, t the time, μ the charge mobility, V_0 the applied voltage, ρ the volume charge density, ε the dielectric permittivity, \mathbf{J} the current density, and V the electric scalar potential related to the electric field intensity as $\mathbf{E} = -\nabla V$. Then, the normalized governing equations can be expressed as

$$\tilde{\nabla} \cdot (-\tilde{\nabla} \tilde{V}) = \tilde{\rho} \text{ in } \Omega \quad (2)$$

$$\text{with } \tilde{V}(\tilde{x} = 0) = 1 \text{ and } \tilde{V}(\tilde{x} = 1) = 0 \text{ on } \partial\Omega$$

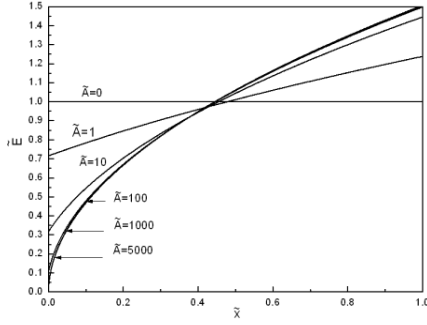
$$\frac{\partial \tilde{\rho}}{\partial \tilde{t}} + \tilde{\nabla} \cdot (\tilde{\rho} \tilde{\mu} \tilde{\mathbf{E}}) = 0 \text{ in } \Omega \quad (3)$$

$$\text{with } \tilde{\rho}(\tilde{x} = 0, \tilde{t}) = \tilde{A} \tilde{E}(\tilde{x} = 0, \tilde{t}) = \tilde{A} \tilde{E}_0 \text{ on } \partial\Omega$$

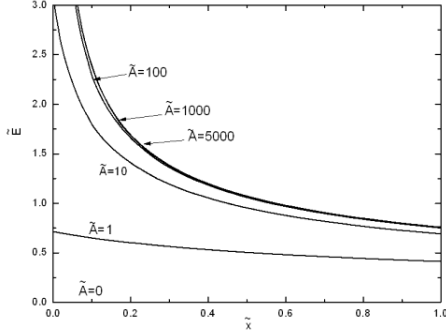
where \tilde{E}_0 is the non-dimensional electric field at $x=0$ and Ω is the domain region between electrodes. This governing equation for space charge propagation belongs to the hyperbolic-type PDE of which solution has a pattern of steep change in solution space resulting in numerical instabilities.

III. STEADY-STATE SOLUTIONS BY DIFFERENT LINEAR INJECTION AND SPACE CHARGE LIMITED CONDITION

In simple charge injection condition, when $\tilde{A} \rightarrow \infty$, then $\tilde{E} \rightarrow 0$. This condition is the same as the space-charge limited condition. Figs. 1(a) and 1(b) show the dc steady-state distributions of the normalized electric field and the normalized space charge distributions. These all trends are match well with Zahn's results published in [1]. The maximum value, therefore, $\tilde{A} = 5000$ can be regarded as the case of space charge limited condition as shown in Fig. 1.



(a) Normalized electric field distributions vs. normalized position



(b) Normalized charge density distributions vs. normalized position

Fig. 1. DC steady-state distributions with respect to normalized charge injection constant, \tilde{A} .

IV. NUMERICAL ASPECTS OF TRANSIENT ANALYSIS WITH ARTIFICIAL DIFFUSION SCHEME

The governing equation, (3), strongly depends on the convective term and the discretization of convective-dominated transport problems can introduce numerical instabilities in the solution. In this case, these instabilities might be noted as oscillations and non-convergence in the field solutions, primarily where steep gradients are present such as at the fronts of moving charge. The oscillations can even be large enough to prevent the solution from converging. To check this instability, the Peclet number at each element, $P_{e_{cell}}$, can give a useful information related to a numerical stability, which can be expressed as [4]

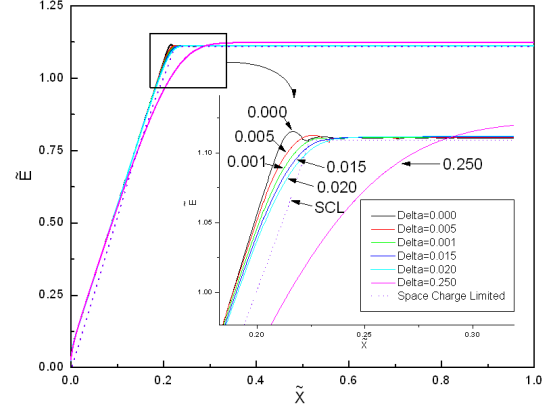
$$P_{e_{cell}} = h |\beta| / c \quad (4)$$

where h is the local mesh diameter, β the magnitude of the convective velocity, and c the diffusivity. Numerical solution will be unstable when the Peclet number exceeds two [4]. For our problem, because there is no diffusion term ($c=0$), $P_{e_{cell}} \rightarrow \infty$. To resolve this numerical instability, an artificial diffusion technique was adopted, which yield more reliable results, as

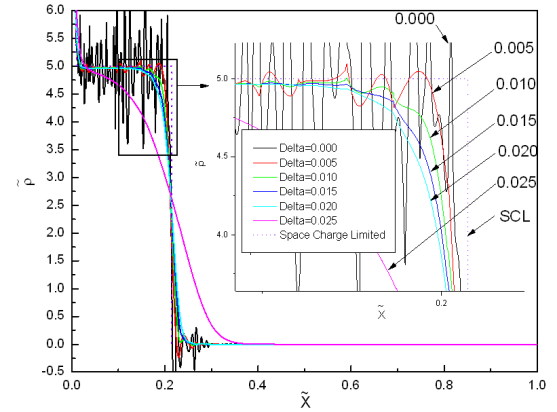
$$\frac{\partial \tilde{\rho}}{\partial \tilde{t}} + \tilde{\nabla} \cdot (\tilde{\rho} \tilde{\mu} \tilde{\mathbf{E}}) - \tilde{D} \tilde{\nabla}^2 \tilde{\rho} = 0 \quad (5)$$

where \tilde{D} is the non-dimensional artificial diffusion coefficient.

Figs. 2(a) and 1(b) show the transient solutions of electric field intensity and space charge propagation with the different artificial diffusion factors at normalized time $\tilde{t} = 0.1$ comparing to those from analytic approach with space charge limited condition [1].



(a) Normalized electric field distributions vs. normalized position



(b) Normalized charge density distributions vs. normalized position

Fig. 2. Electric field and charge density with respect to different artificial diffusion factors (Delta) in case of space charge limited condition (SCL) and simple charge injection condition ($\tilde{A} = 1000$) at normalized time $\tilde{t} = 0.1$.

In extended paper, more results will be presented in detail including the Fowler-Nordheim field emission condition and a tip-sphere electrode system, where the radius of tip was $40 \mu\text{m}$, for analyzing bipolar space charge propagation in a dielectric liquid medium.

V. REFERENCES

- [1] Markus Zahn, Cheung Fung Tsang, and Shing-Chong Pao, "Transient electric field and space-charge behavior for unipolar ion conduction," *Journal of Applied Physics*, pp. 2432-2440, Vol. 45, No. 6, June 1974.
- [2] Markus Zahn, "Solid, Liquid, and Gaseous Electrical Insulation," *Encyclopedia of Applied Physics*, VCH Publishers, American Institute of Physics, Vol. 18, pp. 431-466, 1997.
- [3] S.-H. Lee, F. O'Sullivan, I.-H. Park, and M. Zahn, "Analysis of charge transport in a dielectric liquid by employing the coupled finite element method," *Proc. IEEE Conf. Electr. Insulation Dielectr. Phenomena*, pp. 129-132, 2006.
- [4] J. C. Heinrich, P. S. Huyakorn, and O. C. Zienkiewicz, "An 'upwind' finite element scheme for two-dimensional convective transport equation," *International Journal for Numerical Methods in Engineering*, Vol. 11, pp. 131-143, 1977.

Masking with Generalized Cloaking

André Nicolet

Aix-Marseille Université
Ecole Centrale de Marseille
CNRS, Institut Fresnel UMR 6133
F-13397 Marseille cedex 20, France
Email: <http://www.fresnel.fr/perso/nicolet/>

Frédéric Zolla

Aix-Marseille Université
Ecole Centrale de Marseille
CNRS, Institut Fresnel UMR 6133
F-13397 Marseille cedex 20, France

Christophe Geuzaine

University of Liège
Dept. of Electrical Engineering
and Computer Science (ACE)
B-4000 Liège, Belgium

Abstract—In this paper, a generalization of cloaking is presented: instead of an empty region of space, an inhomogeneous structure is transformed via Pendry’s map in order to give, to any object hidden in the central hole of the cloak, a completely arbitrary appearance.

I. INTRODUCTION

In 2006, it was suggested by Pendry et al. [1] that an object surrounded by a coating consisting of an exotic material becomes invisible to electromagnetic waves. This device was named “invisibility cloak” in reference to Harry Potter, the popular character of J.K. Rowling. Beside his famous cloak, the little wizard has other spells to go unnoticed. Among the most spectacular is the “polyjuice potion” that is able to turn somebody into anybody else’s appearance [2]. In this paper, we do not present a potion but rather an optical device able to accomplish the same task, i.e. to give an arbitrary optical response chosen in advance to any other object placed inside the device. In fact, the principle is here very similar to the design of Pendry’s invisibility cloak but, instead of geometrically transforming an empty domain, it is a region containing the object to be imitated that is transformed leading thus to a generalization of cloaking.

II. GENERALIZED CLOAKING

In this section, we present a generalization of cloaking able to arbitrarily transform the electromagnetic appearance of an object. The basic principle is to obtain the constitutive relations of the cloak by application of a space transformation to a non-empty region.

A geometric transformation is given by a map φ from a space N to a space M . For all our practical purposes, M and N will be here the whole or parts of \mathbb{R}^3 . Given a Cartesian coordinate system \mathbf{x} on M and an arbitrary coordinate system \mathbf{x}' on N , $\varphi : N \rightarrow M$ is described by $\mathbf{x}(\mathbf{x}')$, i.e. \mathbf{x} given as function of \mathbf{x}' . All the useful information, i.e. necessary to transform differential forms and other covariant tensors, is contained in the Jacobian matrix field $\mathbf{J}(\mathbf{x}') = \partial\mathbf{x}(\mathbf{x}')/\partial\mathbf{x}'$.

The basic principle of transformation electromagnetics is that, when you have an electromagnetic system described by the tensor fields $\underline{\underline{\epsilon}}(\mathbf{x})$ for the dielectric permittivity and $\underline{\underline{\mu}}(\mathbf{x})$ for the magnetic permeability in the space M , if you replace your initial material properties by equivalent material

properties given by the following rule [3], [4]:

$$\begin{aligned}\underline{\underline{\epsilon}}'(\mathbf{x}') &= \mathbf{J}^{-1}(\mathbf{x}')\underline{\underline{\epsilon}}(\mathbf{x}(\mathbf{x}'))\mathbf{J}^{-T}(\mathbf{x}')\det(\mathbf{J}(\mathbf{x}')), \\ \underline{\underline{\mu}}'(\mathbf{x}') &= \mathbf{J}^{-1}(\mathbf{x}')\underline{\underline{\mu}}(\mathbf{x}(\mathbf{x}'))\mathbf{J}^{-T}(\mathbf{x}')\det(\mathbf{J}(\mathbf{x}')), \end{aligned} \quad (1)$$

(\mathbf{J}^{-T} is the transposed of the inverse of \mathbf{J}), you get an equivalent problem on N . Here, an equivalent problem means that the solution of the new problem on N , i.e. electromagnetic quantities described as differential forms, are the pulled back of the solution [4], [5] of the original problem on M and that the same Maxwell’s equations (i.e. as if we were in Cartesian coordinates or, more accurately, having the same form written with the exterior derivative) are still satisfied.

In the case of the cylindrical Pendry’s map [1], [6], described by the transformation of the 2D cross section, the plane \mathbb{R}^2 minus a disk D_1 of radius R_1 is mapped on the whole plane \mathbb{R}^2 in such a way that a disk D_2 of radius $R_2 > R_1$, concentric with D_1 , is the image of the annulus $D_2 \setminus D_1$ by a radial transformation. In cylindrical coordinates, this transformation is given by:

$$\begin{cases} r = (r' - R_1)R_2/(R_2 - R_1) \text{ for } R_1 \leq r' \leq R_2, \\ \theta = \theta', \quad z = z'. \end{cases} \quad (2)$$

As for the outside of the disk D_2 , the map between the two copies of $\mathbb{R}^2 \setminus D_2$ is the identity map.

The material properties given by rule (1) corresponding to this transformation provide an ideal invisibility cloak: outside D_2 , everything behaves as if we were in free space, including the propagation of electromagnetic waves across the cloak, and is completely independent of the content of D_1 .

Now, rule (1) may be applied to D_2 containing objects with arbitrary electromagnetic properties so that a region cloaked by this device is still completely hidden but has the appearance of the objects originally in D_2 . We may call this optical effect masking [7] or “polyjuice” effect.

III. NUMERICAL MODELING

Figs. 2 and 3 shows the effect of masking on a scattering structure. On Fig. 2, a cylindrical TM wave emitted by a circular cylindrical antenna is scattered by a conducting triangular cylinder (the longest side of the cross section is 1.62λ and $\epsilon_r = 1 + 40i$). The field map represents the longitudinal electric field $E_z(x, y)$ and the outer boundary of

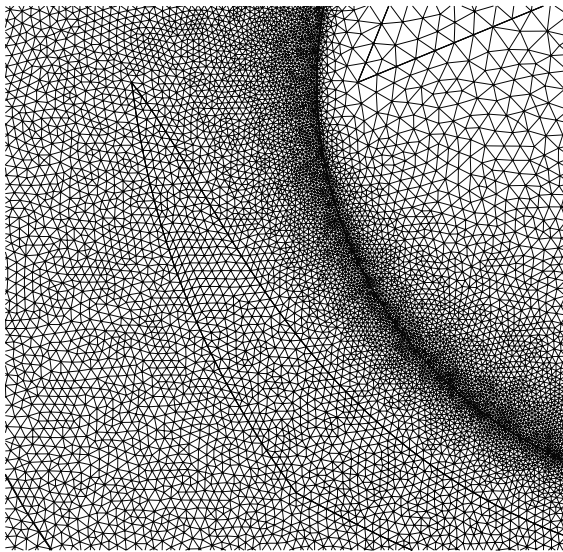


Fig. 1. This figure shows a part of the triangular mesh used for the finite element modeling of the scattering problem of Fig. 3. The singular behavior of the permittivity and of the permeability requires a very fine mesh along the inner boundary of the cloak in order to achieve a satisfactory accuracy with the numerical model.

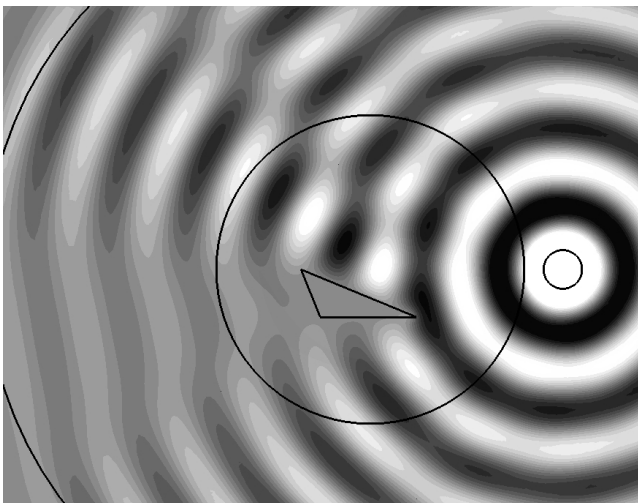


Fig. 2. A conducting triangular cylinder is scattering cylindrical waves.

the cloak is shown to ease the comparison with the masked case. On Fig. 3, the same cylindrical TM wave is scattered by a masked triangular cylinder. This triangular cylinder is the symmetric of the previous one with respect to the horizontal plane containing the central fibre of the cylindrical antenna. This bare scatterer would therefore give the Fig. 2 image inverted upside-down but, here, this object is surrounded by a cloak in order to give the very same scattering as before. Indeed, on both sides, the electric fields outside the cloak limit are alike.

The numerical computation is performed using the finite element method (via the GetDP freeware [8]). The mesh is

made of 148,000 second order triangles. The singularity of ϵ

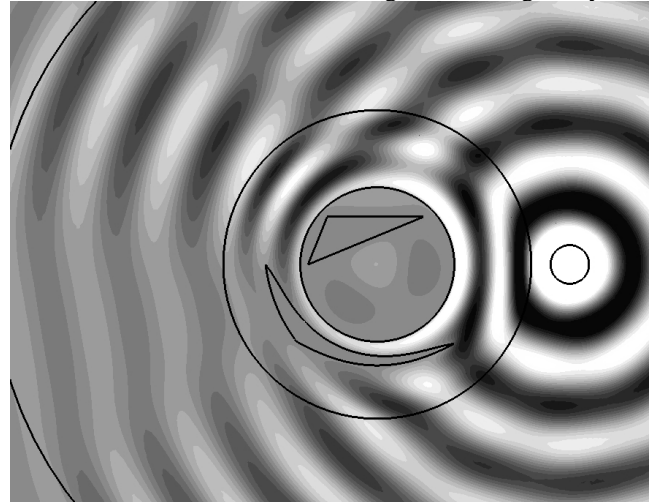


Fig. 3. A triangular cylinder different from the one on Fig. 2 is surrounded by a cloak designed to reproduce the scattering pattern of the Fig. 2 triangular cylinder in spite of the change of diffracting object.

and μ requires a very fine mesh in the vicinity of the inner boundary of the cloak and is also responsible for the small discrepancies between the numerical model and a perfect cloak (including the non zero field in the hole of the cloak).

The rule (1) is applied but a small problem arises in practice: the material properties are defined piecewise on various domains and it is very useful to know explicitly the boundaries of these domains, e.g. to build the finite element mesh. These boundaries are curves in the cross section and are thus contravariant objects. Therefore, their transformation requires the inverse map φ^{-1} from M to N . Fortunately, map (2) is very simple to invert. On Fig. (2) the image by φ^{-1} of the triangle in the left side picture is the curvilinear triangle inside the cloak in the right side picture. In practice, this anamorphosis of the triangle is described by three splines interpolating each 40 points.

REFERENCES

- [1] J.B. Pendry, D. Shurig, D.R. Smith "Controlling electromagnetic fields", *Science* **312**, pp. 1780-1782 (2006).
- [2] J.K. Rowling, *Harry Potter and the Chamber of Secrets*, Bloomsbury Publishing PLC (1998).
- [3] G. W. Milton, M. Briane, J. R. Willis "On cloaking for elasticity and physical equations with a transformation invariant form", *New Journal of Physics* **8**, 248 (2006).
- [4] F. Zolla, G. Renversez, A. Nicolet, B. Kuhlmeier, S. Guenneau, D. Felbacq *Foundations of Photonic Crystal Fibres*, ICP Press (2005).
- [5] A. Nicolet, J. F. Remacle, B. Meys, A. Genon, W. Legros "Transformation methods in computational electromagnetism", *J. Appl. Phys.* **75**, pp. 6036-6038 (1994).
- [6] A. Nicolet, F. Zolla, S. Guenneau "Electromagnetic analysis of cylindrical cloaks of an arbitrary cross section", *Optics Letters* **33**, Issue 14, pp. 1584-1586 (2008).
- [7] F. L. Teixeira "Differential form approach to the analysis of electromagnetic cloaking and masking", *Microwave Opt. Technol. Lett.* **49**, pp. 2051-2053 (2007).
- [8] P. Dular, C. Geuzaine, F. Henrotte, W. Legros "A general environment for the treatment of discrete problems and its application to the finite element method", *IEEE Trans. Mag.* **34**, 5, pp. 3395-3398 (1998). <http://www.geuz.org/getdp/>

Micromagnetic Analysis of a Shielded Write Head Using Symmetric Multiprocessing System

Yasushi Kanai*, Kazuya Koyama*, Manabu Ueki*, Toshio Tsukamoto*,
Kazuetsu Yoshida**, Simon J. Greaves*** and Hiroaki Muraoka***

* IEE, Niigata Institute of Technology, 1719 Fujihashi, Kashiwazaki 945-1195, Japan

** ICE, Kogakuin University, 1-24-2 Nishi-shinjuku, Tokyo 163-8677, Japan

*** RIEC, Tohoku University, Katahira 2-1-1, Aoba-ku, Sendai 980-8577, Japan

kanai@iee.niit.ac.jp

Abstract— Acceleration of micromagnetic calculations on symmetric multiprocessing (SMP) system is investigated. A speed up of more than 20 times has been realized compared with the serial processing software. The SMP system with the optimized software has a speed up of 5.6 times compared to a previous version on an 8-CPU cluster system. Micromagnetic analysis of a write head with trailing and side shields is performed to derive the dynamic recording field and magnetization rotation process. The dynamic recording field is found to be affected by the shields.

I. INTRODUCTION

Micromagnetic simulation is a powerful tool to understand the complicated phenomena in recording write heads [1] that occur in the sub-nanosecond and sub-nanometer regions, where experiments are fairly hard. In micromagnetic analysis the computational load is large; therefore, parallel computing is essential. We have previously reported on a cluster system and parallelized program with full Fast Fourier Transform (FFT) [2]. In that system the communication time is not negligible and amounts to almost half the total computation time if a Gigabit network is used. An *infiniband* network would reduce this time but they are fairly expensive.

The first half of this paper investigates the acceleration of the micromagnetic analysis. We have used the symmetric multiprocessing (SMP) system to avoid problems with communication time between nodes and optimized the software. The major contributions to the speed-up are the use of a three-dimensional FFT in place of the two-dimensional FFT, and the reduced FFT procedure. In the second half, a single-pole-type (SPT) head with trailing shield (TS) and/or side shields (SSs) is analyzed, and the dynamic recording field and the magnetization rotation process are investigated. It is found that the recording field is affected not only by the magnetization rotation process of main pole (MP) but also the presence of trailing and side shields.

II. CALCULATION MODEL

Throughout this paper we use the SPT head model shown in Fig. 1 with material characteristics shown in Table I, where M_s is the saturation magnetization, K_u is the anisotropy energy, A is the exchange constant, and α is the Gilbert damping factor. For both the head and media soft underlayer (SUL), the anisotropy direction is assumed to be the cross-track (+y) direction. The recording layer was assumed to be air. The model dimensions are close those of commercial

heads except that the main pole tip has a large area (160 nm wide \times 260 nm long) with a throat height of TS = 200 nm and a neck height of MP = 200 nm. The model is divided into 20-nm side cubic cells and the total number of cells is 3,672,000. The recording field distributions are observed at 28 nm from the air-bearing surface (ABS), where the distance between ABS and SUL = 66 nm.

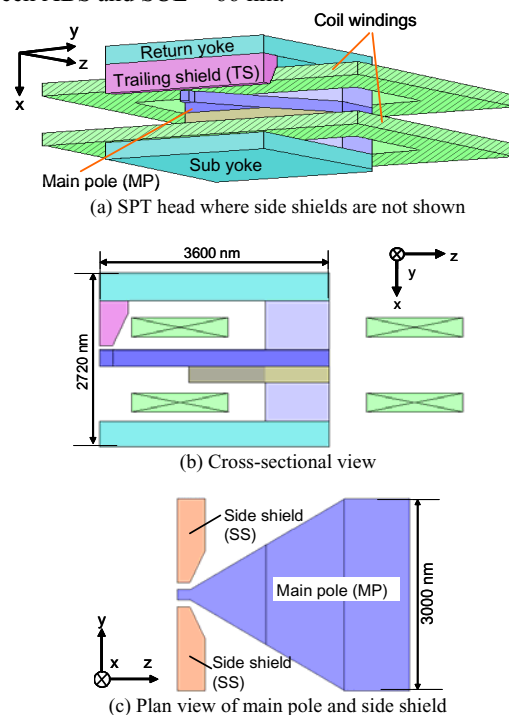


Fig. 1. SPT head model with trailing and side shields. Medium (soft underlayer) is not shown.

TABLE I
MATERIAL CHARACTERISTICS FOR HEAD AND SOFT UNDERLAYER

	SPT head	Soft underlayer
M_s emu/cm ³	1910	955
$(4\pi M_s)$ kG	24	12
K_u erg/cm ³	3×10^4	3×10^4
A erg/cm	1×10^{-6}	1×10^{-6}
α	0.2	0.2

The Landau-Lifshitz-Gilbert (LLG) micromagnetic analysis,

$$(1 + \alpha^2) \dot{\mathbf{M}} = -\gamma |\mathbf{M} \times \mathbf{H} - \frac{\gamma \alpha}{M_s} \mathbf{M} \times (\mathbf{M} \times \mathbf{H}) \quad (1)$$

that treats the whole magnetic material micromagnetically was

solved by using the finite-difference method, where \mathbf{M} is the magnetization vector, \mathbf{H} is the effective field vector and V is the gyro magnetic constant.

III. ACCELERATION OF MICROMAGNETIC CALCULATIONS

In Tables II and III the hardware and software used are shown. We have optimized the software on an Intel Xeon SMP system. The speed-ups are summarized in Fig. 2 for one-thread and eight-threads, where the original program was the parallelized program optimized for the cluster system. Program 1 is a serial processing program where the message passing interface (MPI) feature has been removed from the original program. Program 2 was parallelized using OpenMP and automatic parallelization was performed with a compilation option. Program 3 uses the three-dimensional FFT in place of the two-dimensional FFT. In program 4, the FFT procedure was reduced with the help of the symmetric nature of the FFT. Program 4 has a calculation speed which is more than 20 times faster than program 1. It is also noted that the processing speed of program 4 on the Xeon SMP system is 5.6 times faster than the 8-CPU Pentium4 cluster system. With regard to the memory requirement, the SPT head model can be solved with 8.5 GB. Note that the recording fields obtained by program 1 and program 4 agree with 6 digits of precision.

	Cluster system [2]	SMP system
CPU	Pentium4	Xeon
Clock	3.0 GHZ	2.5 GHz
RAM	4 GB (x 8)	16 GB
Compiler	Intel Fortran 9.1	Intel Fortran 10.1
Library	Intel MKL 8.1	Intel MKL 10.0
Notes	8 nodes	Quad core x 2

Name	Major feature	Parallel/serial
Program 1	Cluster program, MPI removed	Serial
Program 2	OpenMP + automatic parallelization	Parallel
Program 3	3-D FFT	Parallel
Program 4	3-D FFT + reduced FFT procedure	Parallel

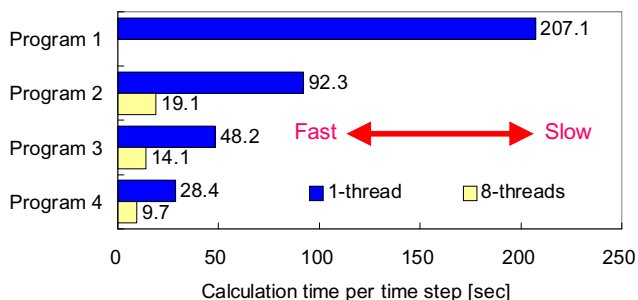


Fig. 2. Comparison of calculation times on Xeon SMP System.

IV. CALCULATED RESULTS FOR VARIOUS SHIELD SPT HEADS

In Fig. 3, head field time variations are shown for various head structures: head 1 has no TS and no SS; head 2 has TS (60 nm from MP) and no SS; head 3 has TS (60 nm from MP) and SSs (60 nm from MP). Shielded head 3 has the smallest

field amplitude and the response is quite different from the other two heads. In Fig. 4, snapshots of the magnetization vectors in MP, in the cells facing ABS, are shown for head 1 and head 3 at $t = 1.5$ ns when current is 0; $t = 1.65$ ns when the driving current reaches positive peak; and $t = 2.05$ ns when the current starts to decrease from the positive peak. It is seen that the magnetization in MP is affected by the trailing and side shields, and directed towards the TS and SSs. It is also seen that, in dynamic response, the magnetization rotation process in MP is affected by the magnetization in the shields, which finally affects the head field response.

The head field time variations and the magnetization process for various head structures and materials will be shown in the full paper. We will also try to propose a SPT head with fast response, large recording field, and small stray field to the adjacent tracks.

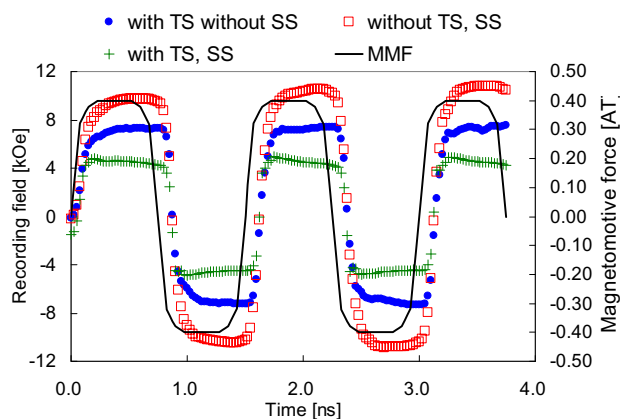


Fig. 3. Head field time variations for head 1 (without TS, SS), head 2 (with TS, without SS) and head 3 (with TS, SS). Driving current frequency is 667 MHz.

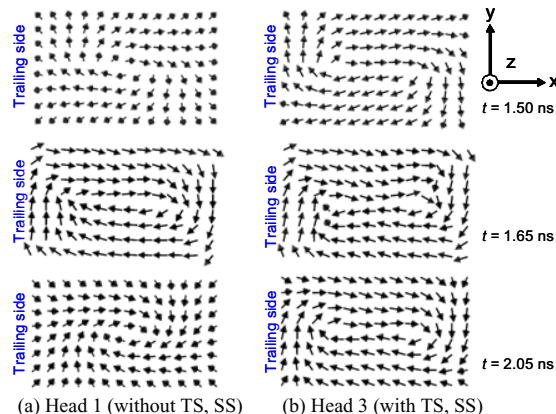


Fig. 4. Magnetization vectors in MP for head 1 and head 3.

V. REFERENCES

- [1] K. Takano, L. Guan, Y. Zhou, J. Smyth, and M. Dovek, "Micromagnetic simulation of various pole-tip design PMR heads," *53rd MMM Conf.*, DT-09, Austin, TX, U.S.A., Nov. 2008.
- [2] Y. Kanai, M. Saiki, K. Hirasawa, T. Tsukamoto, and K. Yoshida, "Landau-Lifshitz-Gilbert micromagnetic analysis of single-pole-type write head for perpendicular magnetic recording using full-FFT program with PC cluster system," *IEEE Trans. on Magn.*, vol. 44, no.4, pp. 1602-1605, June 2008.

Efficient implementation of UPML in the finite integration technique using hexahedral and prismatic elements

R.R.Torrado, L. Bernard, and L. Pichon

Laboratoire de Gnie Electrique de Paris, CNRS UMR 8507; SUPELEC; UPMC; Univ Paris-Sud;
11 rue Joliot-Curie, Plateau de Moulon, F-91192 Gif-sur-Yvette Cedex

Abstract—We show how to use hexahedral and prismatic elements for the efficient development of UPML around an unstructured tetrahedral primal mesh using the finite integration technique (FIT). Taking into account the properties of the UPML medium, we obtain a simple scheme for the time-domain solution of Maxwell's equations. The implementation of the method is presented for the general 3D case, and numerical results are given for a 2D test case.

I. INTRODUCTION

Perfectly matched layers (PML) have been developed for the numerical approximation of electromagnetic radiation and/or scattering problems by the finite element method (FEM) and the finite difference time domain method (FDTD). PML have been introduced by Berenger in 1994 in the context of the FDTD method using a formulation in cartesian coordinates [1]. Berenger derived a split-field formulation of Maxwell's equations where each vector field component is split into two orthogonal components. Subsequently, another formulation has been proposed by Chew and Weedon [2] using the concept of stretching complex coordinates. Both of these approaches yield non-Maxwellian fields within the PML domain.

It has been demonstrated by Sacks et al [4] that Maxwellian PML can be realized as a uniaxial anisotropic medium with suitably defined permittivity and permeability tensor. The introduction of losses into these tensors results in a perfectly matched absorbing medium. This mathematical model (UPML) was first applied within the FDTD method by Gedney [5].

The implementation of the UPML-FDTD method is simple for the termination of regular hexahedral meshes [3]. UPML termination of an unstructured tetrahedral mesh is much more difficult. It can be performed with time-domain finite element method, but this approach has some difficulties in terms of computational and analytic effort, especially because of the convolution term [7]-[8].

In this paper, a new efficient implementation of UPML is proposed for the finite integration technique. Hexahedral and prismatic elements are used to extend the tetrahedral primal mesh. The resulting scheme is very similar to the usual FDTD one but can be applied to the termination of general unstructured meshes.

II. IMPLEMENTATION OF UPML IN THE FIT

We start with the tetrahedral primal mesh of an hexahedral region (PML free region) around which we have to build the PML. The PML mesh is built by extrusion of the primal triangular faces of the boundaries. There are two types of region to study in the PML:

- Regions where the absorption is done in one direction. In these regions, the mesh is obtained by normally extruding the triangular faces of the boundaries: the resulting mesh is prismatic.
- Corner regions, where the absorption is done in two or three directions, are made up of hexahedral elements.

The dual mesh is assumed to be the barycentric one on for all regions.

In corner regions, the FIT formulation is based on the direct application of the FDTD-UPML [3], using appropriate diagonal constitutive matrices. In the other type of region, we consider that x is the absorption direction. Amperes Law in the matched UPML is expressed as

$$rotH = jw\epsilon \begin{pmatrix} \frac{1}{S_x} & 0 & 0 \\ 0 & S_x & 0 \\ 0 & 0 & S_x \end{pmatrix} E \quad (1)$$

where $S_x = \kappa_x + \frac{\sigma_x}{j\omega\epsilon}$ with κ_x and σ_x the PML parameters. Direct transformation into the time domain would lead to a convolution between the tensor coefficients and the E field. This approach has some difficulties because implementing this convolution would be computationally intensive. A much more efficient approach is to define the proper constitutive relationship to decouple the frequency-dependent terms. We chose to define D in order to obtain an isotropic time independent behavior for the UPML in the directions perpendicular to the absorption direction (y,z):

$$D_x = \epsilon \frac{1}{S_x} E_x \quad (a); \quad D_y = \epsilon E_y \quad (b); \quad D_z = \epsilon E_z \quad (c) \quad (2)$$

Then, applying the inverse Fourier transform and using the identity $j\omega \rightarrow (\frac{\partial}{\partial t})$:

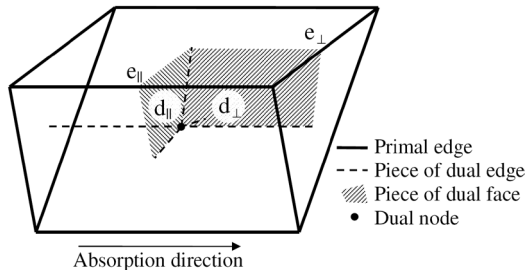


Fig. 1. Notations for primal and dual meshes in the prismatic PML region

$$rotH = \frac{\partial}{\partial t} \begin{pmatrix} 1 & 0 & 0 \\ 0 & \kappa_x & 0 \\ 0 & 0 & \kappa_x \end{pmatrix} D + \frac{1}{\epsilon} \begin{pmatrix} 0 & 0 & 0 \\ 0 & \sigma_x & 0 \\ 0 & 0 & \sigma_x \end{pmatrix} D \quad (3)$$

The FIT formulation is obtained by integrating equation (3) on the faces of the dual mesh (Fig. 1). For the faces associated to a primal edge parallel to the absorption direction, the equation is implemented directly by the following expression:

$$(Rh)_{\parallel} = \frac{\partial d_{\parallel}}{\partial t} \quad (4)$$

where R is the discrete rotational operator, h and d the degrees of freedom. On the dual faces associated with edges perpendicular to the absorption direction, we have:

$$(Rh)_{\perp} = \kappa_x \frac{\partial}{\partial t} d_{\perp} + \frac{\sigma_x}{\epsilon} d_{\perp} \quad (5)$$

Then, it is necessary to formulate the constitutive relations. A special constitutive matrix is built in order to take advantage of the choice made for equations (2). The edges parallel to the absorption direction are assumed to be independent of the edges perpendicular to the absorption direction. In consequence, equation (2a) can be directly expressed by:

$$d_{\parallel} = \epsilon \frac{1}{S_x} \frac{S}{l} e_{\parallel} \quad (6)$$

where l is the length of the primal edge and S the surface of the dual face. By transformation into the time domain, this equation gives an update scheme similar to the one of an FDTD implementation. As equations (2b) and (2c) are both independent of time, the constitutive relation can be treated in a similar way that in the PML free region: for each layer of the PML, the edges perpendicular to the absorption direction form a 2D triangular mesh. The associated entries of the constitutive matrix can be calculated using the 2D Galerkin's method [6], taking into account the thickness of the layer.

A similar formulation can be obtain for the other Maxwell's equation and constitutive law.

III. NUMERICAL RESULTS

For validation, a parallel plate waveguide is considered. A plane TE gaussian pulse is generated at one end of the waveguide, and the UPML medium is used to absorb the pulse

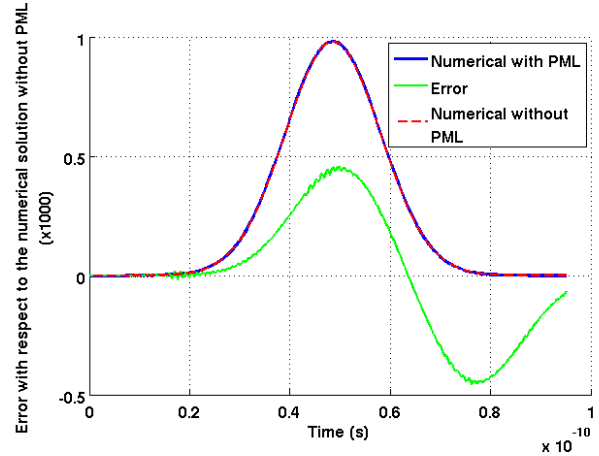


Fig. 2. Error with respect to the numerical solution without PML (x1000 of the maximum value of the pulse) near the UPML medium

at the other end. The mesh consists of triangular elements in the waveguide, and rectangular elements in the UPML. The electric field is computed at a point near the PML boundary. The result is compared to the numerical solution obtained without PML but on a longer waveguide avoiding any reflection during the simulation time. The error is given by the difference between these two numerical solutions (Fig.2). It remains under 5.10^{-4} on the whole simulation time which shows that the UPML is efficient.

IV. CONCLUSIONS

In this paper, we have introduced the use of hexahedral and prismatic elements for the development of UPML. We have shown that the implementation using the FIT is very simple, practical and compatible with unstructured primal tetrahedral meshes. Normally extruded prisms and an appropriate choice of the UPML scheme give the key to an efficient FIT formulation. Numerical results on a 2D problem show the applicability of the method. A complete 3D problem with absorption in all directions will be presented at the conference.

REFERENCES

- [1] J.P.Berenger. A perfectly matched layer for the absorption of electromagnetic waves. *J.comput. Phys.*, 114:185–200, October 1994.
- [2] W. Chew and Weedon. A 3d perfectly matched medium from the modified maxwelles equations with stretched coordinates. *Microw. Opt Technol.*, 7:599–604, 1994.
- [3] A. Taflove. *A Finite Difference Time Domain Method for Electrodynamical Analyses*. NY: Artech House, 1995.
- [4] Z.S Sacks, D. M. Kingsland, R. Lee, and J-F. Lee. A perfectly matched anisotropic absorber for use as an absorbing boundary condition. *IEEE Trans. Antennas Propag.*, 43:1460-1463, December 1995.
- [5] S. D. Gedney. An anisotropic PML Absorbing Medium for the truncation of FDTD lattices. *IEEE Trans. Antennas Propag.*, 44:1630-1639, December 1995.
- [6] A. Bossavit. 'Generalized finite differences' in computational electromagnetics. *PIER*, 32:45-64, 2001.
- [7] J. Jin. *The finite element method in electromagnetics*. Wiley-Interscience, 2002.
- [8] O. Ozgun and M. Kuzuoglu. Non-Maxwellian locally-conformal PML Absorbers for finite element mesh truncation. *IEEE Trans. Antennas Propag.*, 55:931-937, March 2007.

An Electromagnetic Field Computation Using Space-Time Grid and FIT

Graduate School of Engineering, Tetsuji Matsuo
Kyoto University
Kyotodaigaku-katsura Nishi-ku, Kyoto, 615-8510, Japan
tmatsuo@kuee.kyoto-u.ac.jp

Abstract— A finite integration technique (FIT) on a space-time grid is studied for electromagnetic wave computation, where nonuniform time-step distribution is naturally introduced. Orthogonality between dual grids is given by the Lorentz metric to obtain a constitution equation for electromagnetic variables. An analysis of TE-wave scattering by the FIT on a nonuniform space-time grid is presented.

I. INTRODUCTION

The finite difference time domain (FDTD) method [1] is widely used for electromagnetic field computation because of its efficiency and accuracy. However, the conventional Yee grid requires brick-type representation of analyzed objects. The finite integration technique (FIT) [2], [3] can use flexible spatial grids including tetrahedron, prism, and pyramid elements. However, both conventional FDTD method and FIT use a uniform time-step. The FDTD method using sub-grids [4], [5] uses nonuniform time-steps, but it uses only brick-type spatial grids.

On the other hand, space and time are handled in a unified manner by the special theory of relativity [6]. Although usual electromagnetic field computation does not require the relative theory, electromagnetic fields can be analyzed in space-time because Maxwell equations are not affected by the special theory of relativity.

This study examines an electromagnetic field computation on a space-time grid, where nonuniform time-step distribution is naturally introduced.

II. FINITE INTEGRATION METHOD ON A SPACE-TIME GRID

The Euclid metric is used in this article for an analogous explanation to the conventional electromagnetics in two- or three-dimensional (2D or 3D) space.

For simplicity, permittivity ϵ and permeability μ are assumed to be constant. A time-variable w is introduced as

$$w = ct, \quad c = (\epsilon\mu)^{-1/2}. \quad (1)$$

A 2D electromagnetic field is described by (2) and (3), where E_x , E_y and B_z propagate in (x, y, w) space-time.

$$\partial\epsilon_x/\partial x - \partial\epsilon_y/\partial y + \partial B_z/\partial w = 0 \quad (2)$$

$$\partial\mathfrak{C}_z/\partial y - \partial D_x/\partial w = 0, \quad -\partial\mathfrak{C}_z/\partial x - \partial D_y/\partial w = 0 \quad (3)$$

$$\epsilon_x = E_x/c, \quad \epsilon_y = E_y/c, \quad \mathfrak{C}_z = H_z/c \quad (4)$$

Two electromagnetic vectors are formally defined in (x, y, w) space-time as

$$\mathbf{F} = (\epsilon_y, -\epsilon_x, B_z), \quad \mathbf{G} = (-D_y, D_x, \mathfrak{C}_z). \quad (5)$$

Equations (2) and (3) can be rewritten with \mathbf{F} and \mathbf{G} as

$$\nabla_2 \cdot \mathbf{F} = 0, \quad \nabla_2 \times \mathbf{G} = 0 \quad (6)$$

where ∇_2 means $(\partial/\partial x, \partial/\partial y, \partial/\partial w)$.

The integral form of (6) is given as

$$\oint_S \mathbf{F} \cdot \mathbf{n} dS = 0, \quad \oint_C \mathbf{G} \cdot \mathbf{t} ds = 0 \quad (7)$$

where \mathbf{n} and \mathbf{t} are the unit normal and tangential vectors, respectively.

Equation (7) derives an FIT in the space-time using electromagnetic variables defined as

$$e_x = \int \epsilon_x dw dx, \quad e_y = \int \epsilon_y dy dw, \quad b = \int B_z dx dy \quad (8)$$

$$d_x = \int D_x dy, \quad d_y = \int D_y dx, \quad h = \int \mathfrak{C}_z dw \quad (9)$$

The integration of d_x , d_y , and h along the z -direction is implicitly assumed for unit length in (9).

When orthogonal primal and sub grids in (x, y, w) space-time are used, the FIT reduces (7) to (see Fig. 1)

$$-b_{i,j}^{n-1} + e_{x,i,j-1/2}^{n-1/2} - e_{y,i-1/2,j}^{n-1/2} + b_{i,j}^n - e_{x,i,j+1/2}^{n-1/2} + e_{y,i+1/2,j}^{n-1/2} = 0 \quad (10)$$

$$-d_{y,i+1/2,j}^{n-1/2} - h_{i,j}^n + d_{y,i+1/2,j}^{n+1/2} + h_{i+1,j}^n = 0 \quad (11)$$

$$+ d_{x,i,j+1/2}^{n-1/2} - h_{i,j}^n - d_{x,i,j+1/2}^{n+1/2} + h_{i,j+1}^n = 0. \quad (12)$$

Those result in the conventional FDTD scheme.

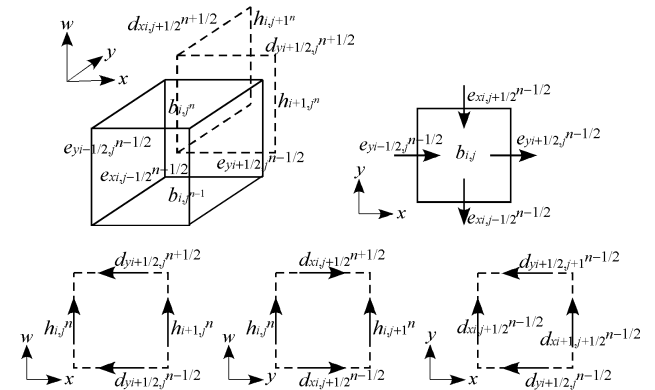


Fig. 1 FIT using orthogonal space-time mesh.

The following electromagnetic variables are defined when a non-orthogonal primal grid and its dual grid are used.

$$f = \int \mathbf{F} \cdot \mathbf{n} dS, \quad g = \int \mathbf{G} \cdot \mathbf{t} ds \quad (13)$$

Variables f and g are defined on the primal and sub grids, respectively. Integration of g along the z -direction is assumed implicitly for unit length in (13).

Let $\mathbf{n}_p = (n_1, n_2, n_3)$ be the normal vector of a face of the primal grid. To relate f to g , the tangential vector of the corresponding edge of the sub grid is given as $\mathbf{t}_s = (-n_1, -n_2, n_3)$, as presented in Fig. 2. Thereby,

$$\begin{aligned} \mathbf{F} \cdot \mathbf{n}_p &= \mathcal{E}_y n_1 - \mathcal{E}_x n_2 + B_z n_3 \\ &= (\mu/\epsilon)^{1/2} (D_y n_1 - D_x n_2 + \mathcal{K}_z n_3) = Z \mathbf{G} \cdot \mathbf{t}_s. \end{aligned} \quad (14)$$

$$Z = (\mu/\epsilon)^{1/2} \quad (15)$$

It is noted that \mathbf{t}_s is orthogonal to the corresponding face of the primal grid by the Lorentz metric.

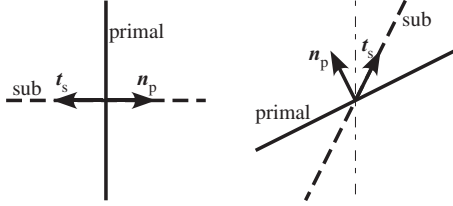


Fig. 2 Relation between face of primal mesh and edge of sub mesh

III. APPLICATION TO TE-WAVE COMPUTATION

Fig. 3 depicts a space-time primal grid with 2D-space. The grid has three domains according to the time-step: (I) the domain with time-step Δw , (II) the domain with $\Delta w/2$, and (III) the domain connecting (I) and (II). The FIT can use prism elements in domain (II) similarly to the usual brick elements. Fig. 3(c) and (d) portray connecting domain (III). An explicit time-marching scheme is developed for the space-time grid.

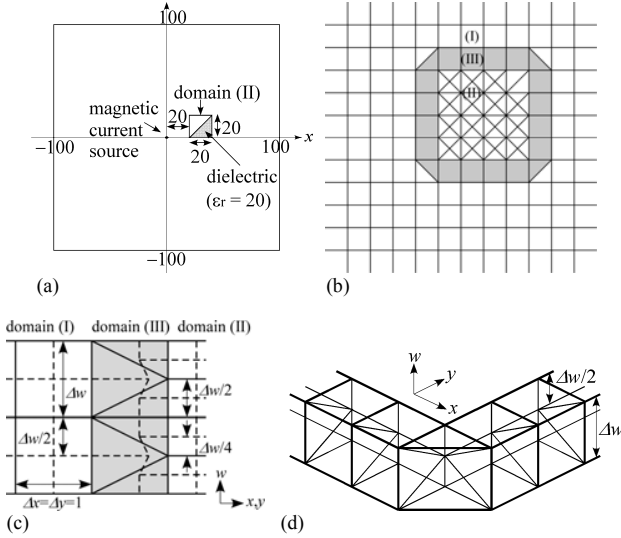


Fig. 3 Geometry of application example and space-time grid: (a) source and domain (II), (b) three domains, (c) connecting part (solid lines: primal grid, dashed lines: sub grid), and (d) domain (III)

The TE-wave induced by a magnetic current source is analyzed, where the TE-wave is scattered by a triangle dielectric. The permittivity and permeability are set to unity by normalization in the domains except the dielectric. The dielectric has $\epsilon = 20$ and $\mu = 1$, which occupies half of domain (II). The spatial cell size is unity and $\Delta w = 0.5$ in domain (I).

Domain (II) and the magnetic current source with normalized frequency of 0.1 are located as depicted in Fig. 3(a).

Fig. 4 depicts distributions of B_z obtained from the FIT on space-time grid and from the conventional FDTD method. The FDTD uses the same cell size and time-step as in domain (I) uniformly. Fig. 8(b) shows that the FDTD method results in insufficient resolution in the dielectric because of the fixed cell size. The FIT on space-time grid can zoom in/out according to the locally required resolution of the electromagnetic wave.

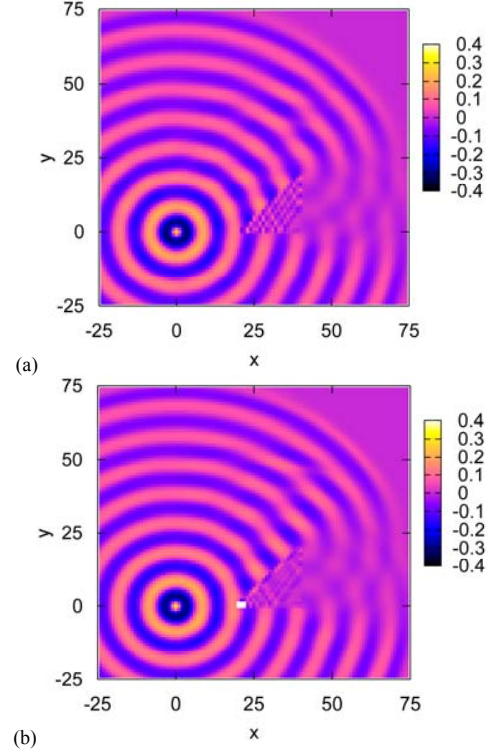


Fig. 4 Distribution of B_z : (a) by FIT on the space-time grid, and (b) by FDTD

IV. ACKNOWLEDGMENT

The author would like to express his gratitude to Mr. A. Kameari, Science Solutions International Laboratory, Inc. for his advice on the orthogonality in space-time.

V. REFERENCES

- [1] K. S. Yee, "Numerical solution of initial boundary value problems involving Maxwell's equations in isotropic media," *IEEE Trans. Antennas Propagat.*, 14: 302-307, May 1966.
- [2] T. Weiland, "Time domain electromagnetic field computation with finite difference methods," *Int. J. Numer. Model.*, 9: 295-319, 1996.
- [3] I. E. Lager, E. Tonti, A.T. de Hoop, G. Mur, and M. Marrone, "Finite formulation and domain-integrated field relations in electromagnetics - a synthesis," *IEEE Trans. Magn.*, 39: 1199-1202, May 2003.
- [4] M. W. Chevalier, R.J. Luebbers, and V.P. Cable, "FDTD local grid with material traverse," *IEEE Trans. Antennas Propagat.*, 45: 411-412, March 1997.
- [5] P. Thoma and T. Weiland, "A consistent subgridding scheme for the finite difference time domain method," *Int. J. Numer. Model.*, 9: 359-374, 1996.
- [6] A. Einstein, "Zur Elektrodynamik bewegter Körper," *Ann. Phys.*, 17: 891-921, 1905.

Solution of the frequency domain Maxwell equations by a high order non-conforming discontinuous Galerkin method

Mohamed El Bouajaji, Victorita Dolean and Stéphane Lanteri
 INRIA Sophia Antipolis-Méditerranée
 06902 Sophia Antipolis Cedex, France
 Mohamed.El_bouajaji@inria.fr
 dolean@unice.fr, Stephane.Lanteri@inria.fr

Ronan Perrussel
 Laboratoire Ampère, CNRS
 69134 Ecully Cedex, France
 Ronan.Perrussel@ec-lyon.fr

Abstract—We report on recent efforts towards the development of a high order, non-conforming, discontinuous Galerkin method for the solution of the system of frequency domain Maxwell's equations in heterogeneous propagation media. This method is an extension of the low order one which was proposed in [1].

I. INTRODUCTION

In the recent years, there has been an increasing interest in discontinuous Galerkin (DG) methods for solving the time-domain Maxwell equations [2]- [3] due to their ability to easily deal with unstructured meshes and heterogeneous media. The development of DG methods for solving the frequency domain Maxwell equations has been less impressive and mostly done in the context of the Maxwell eigenvalue problem [4]. Besides, a hp -adaptive DG method has been proposed in the context of the low-frequency time-harmonic Maxwell equations [5]. In this paper, we report on recent efforts towards the development of a discontinuous Galerkin method for the solution of the system of frequency domain Maxwell's equations in heterogeneous propagation media. This DGFDF (Discontinuous Galerkin Frequency Domain) method is formulated on simplicial meshes (triangle in 2D and tetrahedron in 3D). Within each mesh element, the approximation of the electromagnetic field relies on an arbitrarily high order nodal polynomial interpolation. Moreover, as a first step towards the development of a hp -adaptive method, the approximation order p is allowed to vary across mesh elements resulting in a non-conforming DGFDF method. We present preliminary results for the simulation of two-dimensional propagation problems.

II. DGFDF METHOD

We consider solving the non-dimensioned time-harmonic Maxwell equations in the first order form:

$$i\omega\varepsilon_r\mathbf{E} - \text{curl}\mathbf{H} = 0 \quad , \quad i\omega\mu_r\mathbf{H} + \text{curl}\mathbf{E} = 0, \quad (1)$$

where \mathbf{E} and \mathbf{H} are the unknown electric and magnetic fields. Parameters ε_r and μ_r are respectively the complex-valued relative dielectric permittivity and the relative magnetic permeability; we consider here the case of linear isotropic media. Eq. (1) is solved in a bounded domain Ω . On the

boundary $\partial\Omega = \Gamma_a \cup \Gamma_m$, the following boundary conditions are imposed: a perfect electric conductor condition on Γ_m : $\mathbf{n} \times \mathbf{E} = 0$, and a Silver-Müller (first-order absorbing condition) condition on Γ_a : $\mathbf{n} \times \mathbf{E} + \mathbf{n} \times (\mathbf{n} \times \mathbf{H}) = \mathbf{n} \times \mathbf{E}^{\text{inc}} + \mathbf{n} \times (\mathbf{n} \times \mathbf{H}^{\text{inc}})$. Vectors \mathbf{E}^{inc} and \mathbf{H}^{inc} represent the components of an incident electromagnetic wave and \mathbf{n} denotes the unitary outward normal. Eq. (1) can be further rewritten under the following form:

$$i\omega G_0 \mathbf{W} + G_x \partial_x \mathbf{W} + G_y \partial_y \mathbf{W} + G_z \partial_z \mathbf{W} = 0. \quad (2)$$

Let Ω_h denote a discretization of the domain Ω into a union of conforming tetrahedral elements $\bar{\Omega}_h = \bigcup_{K \in \mathcal{T}_h} K$. We look

for the approximate solution $\mathbf{W}_h = (\mathbf{E}_h, \mathbf{H}_h)^t$ of (2) in $V_h \times V_h$ where the functional space V_h is defined by $V_h = \{\mathbf{U} \in [L^2(\Omega)]^3 / \forall K \in \mathcal{T}_h, \mathbf{U}|_K \in \mathbb{P}_p(K)\}$ where $\mathbb{P}_p(K)$ denotes a space of vectors with polynomial components of degree at most p over the element K . The discontinuous Galerkin discretization of system (2) leads to find \mathbf{W}_h in $V_h \times V_h$ such that:

$$\begin{aligned} & \int_{\Omega_h} (i\omega G_0 \mathbf{W}_h)^t \bar{\mathbf{V}} dv \\ & + \sum_{K \in \mathcal{T}_h} \int_K \left(\sum_{l \in \{x,y,z\}} G_l \partial_l (\mathbf{W}_h) \right)^t \bar{\mathbf{V}} dv \\ & + \sum_{F \in \Gamma^m \cup \Gamma^a} \int_F \left(\frac{1}{2} (M_{F,K} - I_{FK} G_{\mathbf{n}_F}) \mathbf{W}_h \right)^t \bar{\mathbf{V}} ds \\ & - \sum_{F \in \Gamma^0} \int_F (G_{\mathbf{n}_F} \llbracket \mathbf{W}_h \rrbracket)^t \{ \bar{\mathbf{V}} \} ds \\ & + \sum_{F \in \Gamma^0} \int_F (S_F \llbracket \mathbf{W}_h \rrbracket)^t \llbracket \bar{\mathbf{V}} \rrbracket ds \\ & = \sum_{F \in \Gamma^a} \int_F \left(\frac{1}{2} (M_{F,K} - I_{FK} G_{\mathbf{n}_F}) \mathbf{W}^{\text{inc}} \right)^t \bar{\mathbf{V}} ds, \end{aligned} \quad (3)$$

$\llbracket \mathbf{V} \rrbracket \in V_h \times V_h$, where Γ^0 , Γ^a and Γ^m respectively denote the set of interior (triangular) faces, the set of faces on Γ_a

and the set of faces on Γ_m . The unitary normal associated to the oriented face F is \mathbf{n}_F and I_{FK} stands for the incidence matrix between oriented faces and elements whose entries are given by 0 if the face F does not belong to element K , 1 if $F \in K$ and their orientations match, -1 if $F \in K$ and their orientations do not match. We also define respectively the jump and the average of a vector \mathbf{V} of $V_h \times V_h$ on a face F shared by two elements K and \tilde{K} : $[\![\mathbf{V}]\!] = I_{FK}\mathbf{V}|_K + I_{F\tilde{K}}\mathbf{V}|_{\tilde{K}}$ and $\{\mathbf{V}\} = \frac{1}{2}(\mathbf{V}|_K + \mathbf{V}|_{\tilde{K}})$. Finally, the matrix S_F , which is hermitian positive, allows to penalize the jump of a field or of some components of this field on the face F and the matrix $M_{F,K}$ is a numerical flux which can be either a centered flux or all the upwind flux (see [1] for more details).

III. NUMERICAL RESULTS

Numerical results are presented here for the solution of the 2D TMz Maxwell equations. We first illustrate the convergence properties of the conforming (i.e. p is the same for all elements $K \in \mathcal{T}_h$) DGFD- \mathbb{P}_p method by considering the propagation of a plane wave ($F=300$ MHz) in vacuum. The computational domain is the unit square $[0,1] \times [0,1]$ discretized by non-uniform triangular meshes. The numerical convergence of the method is visualized on Fig. 1 and convergence orders are summarized in Tab. I. One can note that an optimal convergence order is obtained in the case of an upwind numerical flux function.

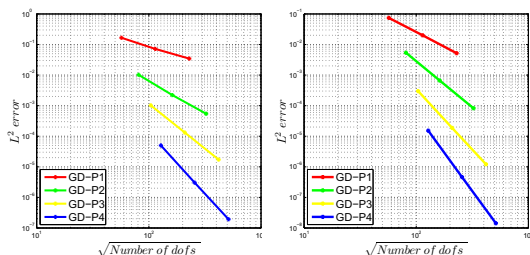


Fig. 1. Propagation of a plane wave in vacuum. Numerical convergence of the DGFD- \mathbb{P}_p method: central flux (left) and upwind flux (right).

TABLE I

PROPAGATION OF A PLANE WAVE IN VACUUM. CONVERGENCE ORDERS OF THE DGFD- \mathbb{P}_p METHOD.

Numerical flux	\mathbb{P}_1	\mathbb{P}_2	\mathbb{P}_3	\mathbb{P}_4
Centered	1.1	2.1	2.9	4.0
Upwind	1.9	3.0	3.9	5.0

The second test problem that we consider is the scattering of a plane wave ($F=300$ MHz) by a dielectric cylinder. For that purpose, we make use of a highly non-uniform triangular mesh which consists of 2078 vertices and 3958 triangles. The relative permittivity of the inner cylinder is set to 2.25 while the vacuum is assumed for the rest of the domain. We compare the solutions obtained using a conforming DGFD- \mathbb{P}_p method for $p = 1, 2, 3, 4$ and a non-conforming DGFD- \mathbb{P}_{pK} method and adopting a centered numerical flux function. In the latter case, the approximation order is defined empirically

at the element level based on the triangle area resulting in a distribution for which the number of elements with $p = 1, 2, 3, 4$ is respectively equal to 1495, 2037, 243 and 183. For each method, the algebraic systems resulting from the discretization of the time-harmonic Maxwell equations is solved using an optimized sparse direct solver. In Tab. II we summarize the performances of the methods in terms of accuracy (L_2 error on the E_z component using the existing analytical solution for the considered problem), the CPU time and the memory overhead (for storing the L and U factors). These results clearly show the benefits resulting from a local definition of the approximation order, especially in terms of memory requirements and overall computational efficiency. The present work is currently proceeding towards the design of a p -adaptive solution strategy in the context of the proposed non-conforming DGFD- \mathbb{P}_{pK} method, and its extension to the 3D case.

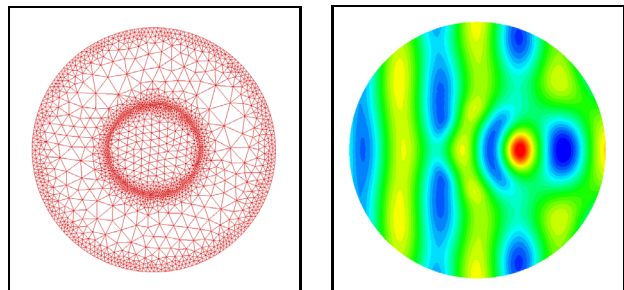


Fig. 2. Scattering of a plane wave by a dielectric cylinder. Non-uniform triangular mesh (top) and contour lines of E_z for the non-conforming DGFD- \mathbb{P}_{pK} method (bottom).

TABLE II

SCATTERING OF A PLANE WAVE BY A DIELECTRIC CYLINDER. PERFORMANCE FIGURES.

Method	L_2 error on E_z	CPU	RAM (LU)
DGFD- \mathbb{P}_1	0.37977	1.3 sec	29 MB
DGFD- \mathbb{P}_2	0.58304	4.1 sec	84 MB
DGFD- \mathbb{P}_3	0.05527	7.9 sec	180 MB
DGFD- \mathbb{P}_4	0.05522	15.7 sec	317 MB
DGFD- $\mathbb{P}_{1,2,3,4}$	0.05586	3.7 sec	83 MB

REFERENCES

- [1] V. Dolean, S. Lanteri, and R. Perrussel, "A domain decomposition method for solving the three-dimensional time-harmonic Maxwell equations discretized by discontinuous Galerkin methods," *J. Comput. Phys.*, vol. 227, no. 3, pp. 2044–2072, 2007.
- [2] J. Hesthaven and T. Warburton, "Nodal high-order methods on unstructured grids. I. Time-domain solution of Maxwell's equations," *J. Comput. Phys.*, vol. 181, no. 1, pp. 186–221, 2002.
- [3] L. Fezoui, S. Lanteri, S. Lohrengel, and S. Piperno, "Convergence and stability of a discontinuous Galerkin time-domain method for the 3D heterogeneous Maxwell equations on unstructured meshes," *ESAIM: Math. Model. Num. Anal.*, vol. 39, no. 6, pp. 1149–1176, 2005.
- [4] J. Hesthaven and T. Warburton, "High-order nodal discontinuous Galerkin methods for the Maxwell's eigenvalue problem," *Royal Soc. London Ser. A*, vol. 362, pp. 493–524, 2004.
- [5] I. Perugia and D. Schotzau, "The hp -local discontinuous Galerkin method for low-frequency time-harmonic Maxwell equations," *Math. Comp.*, vol. 72, pp. 1179–1214, 2003.

Identification of Hidden Ferrous 3D Objects Using a GMR Sensor Array

Alice Köstinger*, Michael Jaendl*, Markus Kienesberger*, Christian Magele*, Werner Renhart* and Gunter Winkler**

*Institute for Fundamentals and Theory in Electrical Engineering

**Institute for Electronics

Graz University of Technology

Kopernikusgasse 24/3, A-8010 Graz, Austria

Email: alice.koestinger@tugraz.at

Abstract—By exploitation of eddy current effects, hidden conductive objects can be detected on principle. A particular challenge is posed by the task of exactly recognizing the position of an object known in shape while hidden by other material with sensor - object distances of several centimeters. This paper will show how positioning parameters of the device under test can be obtained by a sensor array, consisting of commercially available standard-GMRs (giant magnetoresistors), and according algorithms for solving the inverse problem. The array of sensors allows to obtain all measurement data within a single measurement operation.

Index Terms—Identification, ECT, Inverse Problem, GMR

I. INTRODUCTION

Electromagnetic methods enabling the localization of conductive objects hidden by non- or weakly conductive materials are well known and are used for numerous applications (e.g. [1]). However, if the object's position or attitude should be retrieved, sensor arrays offering finer resolutions and appropriate evaluation algorithms need to be applied or developed.

GMRs ([2]) are used for the realization of a cost-efficient sensor array featuring resolutions as high as possible. GMRs are available as ICs and deliver voltages proportional to the magnetic flux density. Apart from small geometric dimensions, GMRs have the advantage to deliver relatively high output voltages. The high sensitivity resulting from this fact clears the way to identify objects in large distances to the sensors.

A copper ring serves as the device under test. Its degrees of freedom and therefore the parameters for the reconstruction algorithms are the azimuthal angle ϑ_{obj} and the y-position y_{obj} (Fig. 1).

The raw measurement data obtained by the GMRs is then fed into algorithms designed for solving inverse problems. The forward problem is simulated using a 3D FEM model.

II. CONFIGURATION OF THE MEASUREMENT SYSTEM

The time harmonic excitation field is produced by two opposed saddle coils. 9 GMRs are positioned on a semi circle shaped circuit board inside the saddle coils. To get a sensor array, three layers of sensors are positioned along the y-axis at a distance of 1 cm from each other (sensor layer 1, 2 and 3). A conductive copper ring with given dimensions but variable

position (ϑ_{obj} and y_{obj}) as well as the excitation coil is shown in Fig. 1.

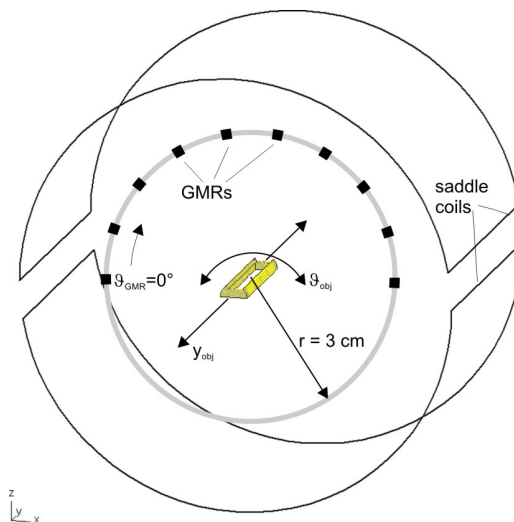


Fig. 1. Scheme of the present measurement configuration.

III. SOLVING THE INVERSE PROBLEM

In order to retrieve both parameters ϑ_{obj} and y_{obj} describing position and attitude of the device under test from the measurement data, an inverse problem has to be solved. Therefore, it is necessary to simulate the forward problem with different sets of $(\vartheta_{obj}, y_{obj})$. The results obtained then have to be compared to the measurement readings.

Since these 3D calculations are very time-consuming, it stands to reason to approximate the simulation results in an adequate way. Using neural networks, this can be achieved very advantageously [3]. A qualified selection of simulation results is used to initially train the network. This training phase requires data sets consisting of the variable parameters ϑ_{obj} and y_{obj} and the respective simulated measurement values (Fig. 2). With these data sets, of which input and output are hence known, the neural network is built. It can then be used as a solver for the forward problem, once the error compared to simulated data is small enough. This work

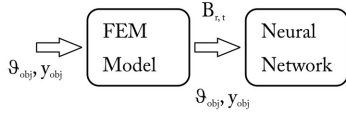


Fig. 2. Training Process: the neural network is trained by using simulated FEM solutions $B_{r,t}$, which is the radial component of the magnetic flux density \mathbf{B} .

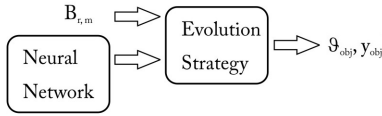


Fig. 3. Identification Process with the measured data $B_{r,m}$ and the already trained neural network.

uses a feed forward network containing an input and a hidden layer, each comprising five tan-sigmoidal neurons.

An (8/2, 20) evolution strategy [4] is employed for identification (Fig. 3). The objective function of given in (1) was set up in a least square sense, taking the difference between the actual data values ($B_{i,act}$), calculated with the forward problem solver (the neural network), and the measured data values ($B_{i,meas}$).

$$of = \sum_i (B_{i,act} - B_{i,meas})^2 \quad (1)$$

IV. RESULTS

Currently only one layer of GMR is available for measuring purposes. A complete array with three layers of GMRs and the necessary electronics will be available soon and presented in the full paper. Fig. 4 shows a comparison of the measured and simulated data, which shows a very good agreement. In a preliminary step, measurement data is obtained using the FEM package EleFAnT3D [5] with some noise added.

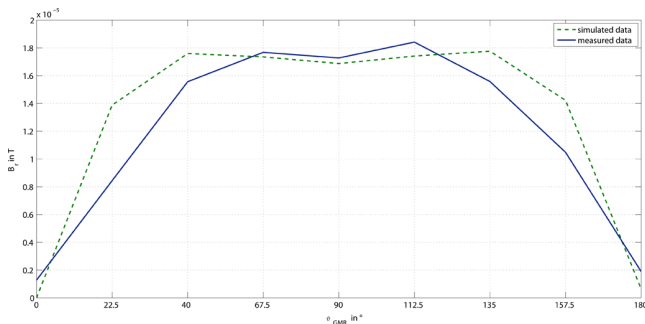


Fig. 4. Comparison of simulated and measured data.

Fig. 5 shows the "simulated measurements" of the GMR located at 90° in each layer for different y -positions of the

TABLE I
COMPARISON OF THE EXACT AND THE RECONSTRUCTED DATA, WHICH HAS BEEN FOUND AFTER 240 FUNCTION CALLS.

	ϑ_{obj}	y_{obj}
exact position	5°	1 cm
reconstructed position	3.2°	0.98 cm

conductive ring. There is a distinguishable difference of the obtained voltages even if the difference of the magnetic flux density is not more than $0.2 \mu T$. Using this data, the position $(\vartheta_{obj}, y_{obj})$ of the conductive ring could be determined very well (see Tab. I).

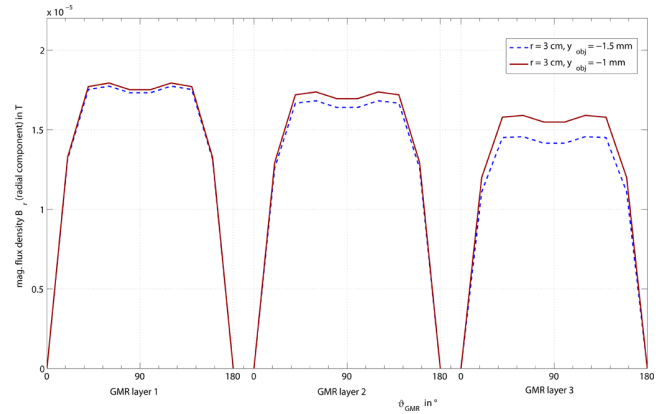


Fig. 5. Simulation results at different object positions y_{obj} .

V. CONCLUSION AND OUTLOOK

A sensor array using GMRs was used to measure the magnetic field distorted by a hidden conductive ring. These measurements can advantageously be used to detect different parameters of the hidden object.

The first results concerning the reconstruction of two parameters seem to be very promising. Further investigations will focus on the following topics:

- Finding the most suitable objective function.
- Design of the sensor array arrangement.
- Increase in parameters respectively degrees of freedom of the measurement object.
- Taking low conductive material into account.

REFERENCES

- [1] C. Magele et al., *Identification of hidden ferrous 3D objects using finite elements*, COMPEL Vol. 20 No. 3, 2001, pp. 689-698
- [2] C.H. Smith et al., *Eddy-Current Testing with GMR Magnetic Sensor Arrays*, Rev. Prog. in QNDE 22, 419, (2003).
- [3] Coccorese, E et al., *A neural network approach for the solution of electric and magnetic inverse problems*, IEEEtrans. Magn., Vol. MAG-30, September, pp. 2829-39
- [4] I. Rechenberg, *Evolutionsstrategie 94*, Frommann-Holzboog, Stuttgart, 1994.
- [5] Computer program package EleFAnT3D, IGTE TU Graz, <http://www.igte.tugraz.at>

Multiobjective Particle Swarm Approach for the Design of a Brushless DC Wheel Motor

Leandro dos Santos Coelho¹, Leandro Zavarez Barbosa² and Luiz Lebensztajn²

¹Automation and Systems Laboratory, LAS/PPGEPS, Pontifical Catholic University of Paraná
Rua Imaculada Conceição, 1155, Zip code 80215-901, Curitiba, Paraná, Brazil

E-mail: leandro.coelho@pucpr.br

²Universidade de São Paulo, LMAG-PEA

Av. Prof. Luciano Gualberto 158, Zip code 0550-900, São Paulo, SP, Brazil

E-mail: leandro.barbosa@poli.usp.br, leb@pea.usp.br

Abstract—In recent years, particle swarm optimization (PSO) approaches has been successfully implemented to different problem domains with multiple objectives. In this paper, a multi-objective PSO approach, based on concepts of Pareto optimality, dominance, archiving external with elite particles and Cauchy distribution, is proposed and applied in the design with the constraints presence of a brushless DC wheel motor. Promising results in terms of convergence and spacing performance metrics indicate that the proposed multi-objective PSO scheme is capable of producing good solutions.

I. INTRODUCTION

In the last decades, many bio-inspired algorithms have been developed for optimization of electromagnetic devices, such as evolutionary algorithms and swarm intelligence paradigms. These methods have attracted a great deal of attention, because of their high potential for optimization problems in environments, which have been resistant to solution by classical mathematical programming techniques. The design of electromagnetic devices provides many optimization problems involving multiple objectives (multi-objective optimization, MOPs), which should be optimized simultaneously. There is a set of compromise solutions in multi-objective optimization problem and none of the corresponding trade-offs can be said to be better than the others in the absence of preference information.

A considerable number of multi-objective algorithms have been proposed for solving MOPs because they can deal simultaneously with a set of possible solutions in a single run instead of a series of separate runs as in the traditional optimization techniques. In this context, particle swarm optimization (PSO) approaches can be useful in MOPs [1].

PSO is a stochastic optimization technique developed by Eberhart and Kennedy [2] that is inspired by the emergent motion of a flock of birds searching for food. Generally, PSO approaches present reduced memory requirement, computationally effective and is easier to implement when compared to typical evolutionary algorithms. PSO is based on the hypothesis that members of a swarm can profit from their past experiences and the experiences of other particles. During the exploration of the search space, each particle has access to two kinds of information: the best potential solution (*gbest*, global best) that it has encountered and the best potential solution encountered by its vicinity (*pbest*, personal best).

The aim of this paper is to propose an enhanced multi-objective PSO (EMOPSO) approach based on Pareto dominance, archiving external and Cauchy distribution to the design with the constraints presence of a brushless DC wheel motor. We compare our results with those generated by another multi-objective PSO (RNMOPSO) proposed by Raquel and Naval [3]. RNMOPSO incorporates the concept of nearest neighbor density estimator for selecting the global best particle, mutation operator and the constraint-handling technique from the NSGA-II [4]. The EMOPSO proposed in this paper is inspired in [3].

II. FUNDAMENTALS OF EMOPSO

The RNMOPSO algorithm had difficulties in striking a balance between exploration and exploitation. Hence, the global search ability of PSO algorithm is restricted. To address this problem, some improvements proposed in EMOPSO are made on RNMOPSO as described.

The EMOPSO uses a truncated Cauchy distribution to update the social and cognitive factors. EMOPSO does not use the mutation operator. The implementation of EMOPSO is based on following steps:

- i) Initialize a swarm (population), NP , with positions and velocities using a generator of random solutions based on uniform distribution. Set the initial value of counter of iterations (generations), $t = 0$;
- ii) Evaluate the particles and store nondominated ones in an archive A with size A_s . Pareto-dominance concept is used to evaluate the fitness of each particle and thus determine which particles should be selected to store in the archive of non-dominated solutions. The archive absorbs superior current non-dominated solutions and eliminates inferior solutions in the archive through interacting with the generational population in every iteration.
- iii) Compute the crowding distance of each member of A ;
- iv) Sort A in descending crowding distance order;
- v) Randomly select the *gbest* for the swarm from a specified top portion (e.g. top 20%) for the sorted A and store its position in *gbest*.
- vi) Update velocities and positions according to:

$$v_i(t+1) = w \cdot v_i(t) + c_1 \cdot cd \cdot [p_i(t) - x_i(t)] + c_2 \cdot Cd \cdot [p_g(t) - x_i(t)] \quad (1)$$

$$x_i(t+1) = x_i(t) + \Delta t \cdot v_i(t+1) \quad (2)$$

where $\Delta t=1$, w is the inertia weight; $v_i=[v_{i1}, v_{i2}, \dots, v_{in}]^T$ stands for the velocity of the i -th particle, $x_i=[x_{i1}, x_{i2}, \dots, x_{in}]^T$ stands for the position of the i -th particle of population, and $p_i=[p_{i1}, p_{i2}, \dots, p_{in}]^T$ represents the best previous position of the i -th particle. Positive constants c_1 and c_2 are the cognitive and social factors, respectively, which are the acceleration constants responsible for varying the particle velocity towards p_{best} and g_{best} , respectively. Index g represents the index of the best particle among all the particles in the swarm. Variables cd and Cd are two random numbers using truncated Cauchy distribution in range $[0, 1]$.

- vii) Evaluate the particles in swarm;
- viii) Insert all new nondominated solution into A if they are not dominated by any of the stored solutions;
- ix) Update the iteration counter, $t = t + 1$;
- x) Return to Step (iii) until a criterion is met. In this work, a maximum number of iterations, t_{max} , is adopted.

III. RESULTS

The optimization problem is the design of a brushless DC wheel motor for a race solar car [5], which has 10 optimization variables and 6 constraints (see Fig.1). The objective functions are the minimization of the mass (f_1) and the maximization of the efficiency (f_2). In this work, we include a penalty function on f_1 and f_2 to punish unfeasible solutions. The penalty function measures how much the solution has violated the constraints. Due to a weight, only feasible solutions could become a nondominated solution.

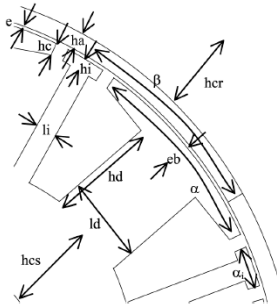


Fig. 1. The geometry of the brushless DC wheel motor.

On [5], the authors propose 3 different benchmarks. In this work, we will analyze a problem, which concerns all the variables except the number of poles (fixed to 6). The variables are: the stator diameter (D_s), the induction in the air gap (B_e), the density current on the windings (δ), the average magnetic induction in the teeth (B_d), the magnetic length of the motor (L_m), the average magnetic induction in the stator back iron (B_{cs}), the ratio of the length rotor-stator (R_{rs}), the airgap (e), the DC bus voltage (U_{DC}) and the average magnetic induction in the rotor back iron (B_{cr}).

The great majority of the optimization variables are associated to the magnetic circuit unless U_{DC} , which is linked to the electronic converter. In this problem, the constraints play a very important role and they have a very different nature. There are typical sizing constraints, like the internal

diameter, thermal constraint, magnetic constraints, like the average magnetic induction in the stator back yoke iron and electrical constraints, like the current rise time. The problem is typically a multidisciplinary optimization one.

We adopted the following control parameters for RNMOPSO [3] and EMOPSO for the motor design: population size $NP = 30$, factors $c1=c2=1.0$, size of archive $A_s = 200$, and $t_{max}=200$ iterations.

In comparative studies, the choice of performance metrics is very important. The optimization goal of multiobjective algorithms is (i) to minimize distance between the generated and Pareto front, (ii) to obtain a good distribution and (iii) to obtain a good spread. Thirty independent simulation runs with different initial conditions were performed to evaluate the performance of RNMOPSO and EMOPSO on the brushless DC wheel motor design. Simulation results were presented in Fig. 2 showed and the non-dominated solutions (30 runs) obtained by EMOPSO dominated the solutions obtained by RNMOPSO.

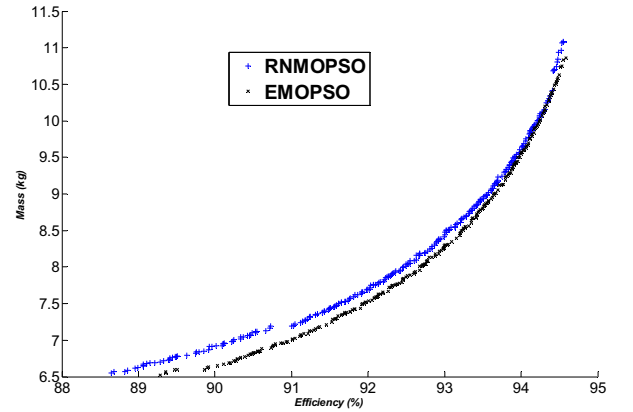


Fig. 2. Pareto set points using RNMOPSO and EMOPSO.

IV. CONCLUSION

In this paper, the RNMOPSO and EMOPSO approaches are compared. Fig. 2 shows the effectiveness of the proposed EMOPSO algorithm, which produces solution sets that are highly competitive in terms of convergence, diversity and distribution with the RNMOPSO.

REFERENCES

- [1] M. R. Sierra and C. A. C. Coello, "Multi-objective particle swarm optimizers: a survey of the state-of-the-art," *International Journal of Computational Intelligence Research*, vol. 2, no. 3, pp. 287-308, 2006.
- [2] J. Kennedy and R. C. Eberhart, "Particle swarm optimization," in: *Proceedings of IEEE International Conference on Neural Networks*, Perth, Australia, pp. 1942-1948, 1995.
- [3] C. R. Raquel and P.C. Naval, Jr., "An effective use of crowding distance in multiobjective particle swarm optimization," in *Proceedings of Genetic and Evolutionary Computation Conference (GECCO 2005)*, Washington DC, USA, 2005.
- [4] K. Deb, A. Pratap, S. Agrawal and T. Meyarivan, "A fast and elitist multiobjective genetic algorithms: NSGA-II," *IEEE Transactions on Evolutionary Computation*, vol. 6, no. 2, pp. 182-197, 2002.
- [5] S. Brisset and P. Brochet, "Analytical model for the optimal design of a brushless DC wheel motor," *The International Journal for Computation and Mathematics in Electrical and Electronic Engineering (COMPEL)*, vol. 20, no. 3, pp. 829-848, 2005.

Coupling Particles Swarm Optimization for Multimodal Function Optimization

Minh-Trien Pham, Baatar Nyambayar, Chang Seop Koh, *Senior Member, IEEE*
 School of Electrical & Computer Engineering, Chungbuk National University,
 San 48, Cheongju, Chungbuk 361-763, Korea
 pmtrien@chungbuk.ac.kr

Abstract — This paper proposes a novel multimodal optimization method, Coupling particles swarm optimization (PSO), to find all optima in design space. This method based on the conventional Particle Swarm Optimization with modifications. The Coupling method is applied to make a couple from main particle and then each couple of particles searches its own optimum by using *non-stop-moving* PSO. We tested out our method and other one, such as Clustering Particle Swarm Optimization and Niche Particle Swarm Optimization, on three analytic functions. The Coupling Particle Swarm Optimization is also applied to solve a significant benchmark problem, the TEAM workshop benchmark problem 22.

I. INTRODUCTION

In many electromagnetic designs, a stationary design which has small design sensitivities is preferred to an optimum design having big design sensitivities. It is because a design with big design sensitivities, when it is related with mass production process, may have a poor performance due to a manufacturing error. Finding all optima of an objective function, in this viewpoint, is necessary so that a designer may select a good robust design taking account of constraints. In recent years, therefore, there have been many attempts to improve particles swarm optimization (PSO) so that it may find not only a global optimum point but also all optima including local optimum point [1]-[2]. The Clustering PSO and Niche PSO, among them, are popular.

The Clustering PSO has its base on clustering algorithm which classifies particles into different groups and allows each group to move toward not a global best point but a group best point [1]. On the other hand, the Niche PSO basically follows the conventional PSO at the beginning of iterations, and divides the whole particles into several groups and, then, follows the idea of Clustering PSO [1]-[2]. This is known more effective than the Clustering PSO, however, it failed to find all optima, or it requires a huge number of objective function calculations when it is applied to engineering optimization problems [3].

In this paper, a robust and efficient PSO algorithm, Coupling PSO, is developed to locate all optima of a multimodal function with less number of objective function calculations. The proposed algorithm is applied to some analytic functions to test its effectiveness and applied to TEAM problem 22 [4].

II. COUPLING PARTICLES SWARM OPTIMIZATION ALGORITHM

In the conventional PSO, the velocity of i -th particle is updated as follows [1]-[3]:

$$\mathbf{v}_i(t) = \omega \cdot \mathbf{v}_i(t-1) + \alpha_1 \cdot r_1 \cdot (\mathbf{p}_i(t-1) - \mathbf{x}_i(t-1)) + \alpha_2 \cdot r_2 \cdot (\mathbf{g}(t-1) - \mathbf{x}_i(t-1)), \quad i = 1, 2, \dots, N \quad (1)$$

where \mathbf{x}_i , \mathbf{v}_i , \mathbf{p}_i are the position, velocity and personal best position of the i -th particle, respectively, and \mathbf{g} is the global best position, ω is the inertia, α_1 , α_2 are cognitive and social coefficients, and r_1 , r_2 are uniform random number within [0,1], and N is the total number of the particles. When the coefficient α_2 is set to zero, equation (1) is called as *cognition only* model.

The overall flow of the proposed Coupling PSO is summarized as follows:

Step 1. Initial particles

Initially N main particles are randomly generated, and allowed to move according to the *cognition only* model. Each main particle is expected to move toward not a global optimum point but its nearest local optimum point.

Step 2. Coupling

When a main particle updates its personal best position, i.e., when $F(\mathbf{x}_i(t)) < F(\mathbf{p}_i(t-1))$ is satisfied, it forms a i -th couple by generating a new particle near by itself as shown in Fig. 1. The position of the new particle is given randomly as follows:

$$\mathbf{c}_i(t) = \mathbf{x}_i(t) + r_i \cdot (\mathbf{x}_i(t) - \mathbf{p}_i(t-1)) \quad (2)$$

where r is a uniform random number within [0,1].

Step 3. Movement of a couple

The movement of a couple is just like that of a group in the Clustering PSO. The two particles in this i -th couple will move according to the following rule:

$$\mathbf{v}_k(t) = \omega \cdot \mathbf{v}_k(t-1) + \alpha_1 \cdot r_1 \cdot (\mathbf{p}_k(t-1) - \mathbf{x}_k(t-1)) + \alpha_2 \cdot r_2 \cdot (\mathbf{c}_i(t-1) - \mathbf{x}_k(t-1)) + \delta \cdot r_3 \cdot \varepsilon, \quad k = 1, 2. \quad (3)$$

where \mathbf{c}_i is the couple best position of i -th couple and r_3 is a uniform random number within [0,1], and ε is a very small number (for example, 10^{-4} % of the design space). The last term is for *non-stop-moving* and δ becomes 1 only when the condition, $\mathbf{c}_i(t) = \mathbf{p}_k(t) = \mathbf{x}_i(t)$, $k = 1, 2$, is satisfied for 3 consecutive iterations.

Step 4. Elimination of a couple and main particle

When a couple or a main particle is very near to another couple, the couple or the main particle is eliminated as shown in Fig. 2. This process will increase the numerical efficiency of the proposed Coupling PSO.

Step 5. Stopping criterion

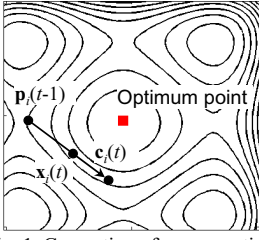


Fig. 1. Generation of a new particle.

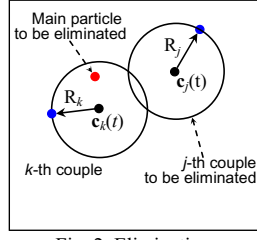


Fig. 2. Elimination.

The i -th couple will stop its moving when its movement is very small (for example, less than 10^{-4} % of the design space) for 10 consecutive iterations and its couple best position will be an optimum. The algorithm will be terminated when all couples stop without regard to main particles.

III. NUMERICAL RESULTS AND DISCUSSION

A. Analytical Problems

In order to check the validity and numerical efficiency of the proposed Coupling PSO, the following three analytic functions with two design variables are considered:

$$F_1(\mathbf{x}) = (x_1^2 + x_2 - 11) + (x_1 + x_2^2 - 7)^2 - 200, \mathbf{x} \in [-5, 5]^2 \quad (4)$$

$$F_2(\mathbf{x}) = \sum_{i=1}^2 \{x_i^2 - 10 \cos(2\pi x_i) + 10\}, \mathbf{x} \in [-1.3, 1.3]^2 \quad (5)$$

$$F_3(\mathbf{x}) = \frac{1}{4000} \sum_{i=1}^2 x_i^2 - \prod_{i=1}^2 \cos\left(\frac{x_i}{\sqrt{i}}\right) + 1, \mathbf{x} \in [-9.5, 9.5]^2 \quad (6)$$

The three functions are tested 100 times. In each test the number of initial particles is set to 50, and the maximal iteration is limited to 800. The performances of three methods are compared in Table I by their percentages of successful trials

TABLE I
EXPERIMENTS RESULTS

Function	Optima	% of all optima found			Average function calls	
		Clustering	Niche	Proposed	Niche	Proposed
$F_1(\mathbf{x})$	4	100	100	100	40,000	20,546
$F_2(\mathbf{x})$	9	83	100	100	40,000	26,144
$F_3(\mathbf{x})$	17	14	100	100	40,000	38,352

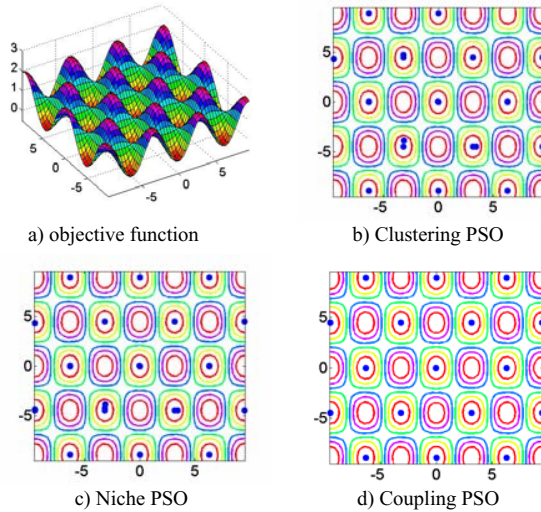


Fig. 3. Positions of particles for function $F_3(\mathbf{x})$ after 800 iterations.

of finding all optima. It is clearly shown that, the Coupling PSO and Niche PSO successfully locate all optima while the Clustering PSO can not, and the Coupling PSO requires less number of function calls than the Niche PSO. It is thought because the Coupling PSO eliminates the couples and main particles which would locate the same local optimum. It is also shown that the number of function calls in the proposed Coupling PSO is proportional to the number of optima found. Fig. 3 shows that the Coupling PSO gives better convergence to optimal points than other PSOs for $F_3(\mathbf{x})$.

B. Optimization in Electromagnetic Device

TEAM problem 22 was chosen to show the application of Coupling PSO in electromagnetic optimization. The aim is to find the maximum stored magnetic energy with minimum stray field B_{stray} . It can be evaluated by (7) with three design variables as shown in Table II:

$$B_{stray}^2 = \frac{1}{22} \sum_{i=1}^{22} B_{stray,i}^2 \quad (7)$$

If the B_{stray} values of these optima are similar, solution with higher stored magnetic energy is preferred. Therefore, in this study, firstly the minima of B_{stray} are located by using Coupling PSO, and then the stored magnetic energy values at these minima are calculated as shown in Table III. Finally, by considering the maximum stored magnetic energy values at these minima of B_{stray} , the minimum 1 is selected as the solution because it has small stray field and high stored magnetic energy.

IV. REFERENCES

- [1] A. Passaro et al., "Clustering particles for multimodal function optimization," *Proceedings of ECAI Workshop on Evolutionary Computation*, published on CD, ISSN 1970-5077, 2006.
- [2] A. P. Engelbrecht, et al., "Enhancing the Niche PSO," *IEEE Congress on Evolutionary Computation (ECE 2007)*, pp. 2297-2302
- [3] J. H. Seo, et al., "An improved PSO algorithm mimicking territorial dispute between groups for multimodal function optimization problems," *IEEE Trans. on Magn.*, Vol. 44, No. 6, pp. 1046-1049, 2008.
- [4] B. Brandstaetter, "SMES optimization benchmark, TEAM Problem 22, 3 parameter problem," http://www.igte.tu-graz.ac.at/archive/team_new/team3.php.

TABLE II
VARIABLE RANGES AND VALUES USED

Variable [Unit]	R_1 [m]	$h_1/2$ [m]	d_1 [m]	R_2 [m]	$h_2/2$ [m]	d_2 [m]	J_1 [MA/m ²]	J_2 [MA/m ²]
Min	-	-	-	2.6	0.204	0.1	-	-
Max	-	-	-	4.5	1.1	0.6	-	-
Value	2.0	0.8	0.27	-	-	-	22.5	-22.5

TABLE III
OPTIMIZATION RESULTS

Minimum	R_2 [m]	$h_2/2$ [m]	d_2 [m]	B_{stray}^2	Energy [MJ]
1	3.758	0.207	0.314	2.68E-06	201.268
2	3.001	0.491	0.236	6.62E-06	178.731
3	3.264	0.288	0.233	8.19E-06	177.425
4	4.115	0.590	0.105	9.04E-06	201.412
5	3.516	0.402	0.126	2.05E-05	180.172
6	4.346	0.237	0.289	4.05E-05	229.293
7	3.430	0.707	0.161	4.82E-05	211.692
8	2.782	0.484	0.112	5.03E-05	150.323

Automatic Differentiation Applied for Optimization of Dynamical Systems

Enciu Petre*, Gerbaud Laurent* and Wurtz Frédéric*

*Grenoble Electrical Engineering lab. (G2ELab), UMR5269, CNRS/UJF/INPG
ENSE3, Domaine Universitaire, BP 46, F-38402 Saint Martin d'Hères Cedex, FRANCE
Email: Petre.ENCIU@g2elab.grenoble-inp.fr

Abstract—Simulation is ubiquitous in many scientific areas. Applied for dynamic systems usually by employing differential equations, it gives the time evolution of system states. In order to solve such problems, numerical integration algorithms are often required. Automatic Differentiation (AD) is introduced as a powerful technique to compute derivatives of functions given in the form of computer programs in a high level programming language such as FORTRAN, C or C++. Such technique fits perfectly in combination with gradient based optimization algorithms, provided that the derivatives are valued with no truncation or cancellation error. This paper intends to use Automatic Differentiation employed for numerical integration schemes of dynamical systems simulating electromechanical actuators. Then, the resulting derivatives are used for sizing such devices by means of gradient based constrained optimization.

I. INTRODUCTION

Sizing by optimization is nowadays of major interest since it provides a fast and reliable way to achieve, with low manufacturing costs, desired performances for products lacking of optimality usually by means of minimizing a cost function. We are particularly interested by constrained gradient based optimization using Sequential Quadratic Programming (SQP) algorithms [1]. Such algorithms require accurately valued derivatives of the objective function. This may be the origin of serious problems provided that often such functions may result from complex numerical algorithms. We are particularly interested in this paper by those objective functions resulting from numerical integration of Initial Value Problems (IVPs) of Ordinary Differential Equations (ODEs) simulating the motion of an active body actuated by the electromagnetic force in the context of electromechanical actuators.

A good compromise in the optimization context is Automatic Differentiation (AD) that is a term applied for a technique able to compute derivatives of functions described by computer programs. That is, this paper only uses AD for sizing dynamical actuators by means of gradient based constrained optimization. In particular, AD will be applied using ADOL-C tool [2].

II. OPTIMIZATION PROBLEM

This paper considers the particular optimal problem of an IVP formulated as in (1) to (5):

$$\text{minimize } J(x_f, P) \quad (1)$$

$$\dot{x} = f(x, u(x, P)) \quad (2)$$

$$\dot{x} = f(x, u(x, t, P)) \quad (3)$$

$$x(0) = x_0 \quad (4)$$

$$x_i(t_f) = \tilde{x}_f, \quad \tilde{x}_f \in P \quad (5)$$

where $x \in \mathbb{R}^n$ denotes the state with its associated initial values x_0 . In the paper, two formulations of the state system are intentionally specified. The formulation in (2) represents an autonomous system, meaning that the time variable does not appear in the differential equation, while the formulation in (3) refers to a non-autonomous system. $P \in \mathbb{R}^p$ is the constraint design parameters set and u denotes the control. The objective function J depends on the reached final states and parameters. Equality (5) represents the simulation end criterion in Fig. 1, meaning that the simulation stops when a state x_i reaches a prescribed final state, $\tilde{x}_f \in \mathbb{R}$. This implies the existence of the final time or response time, t_f , depending implicitly on parameters. Note that \tilde{x}_f makes part of design parameters.

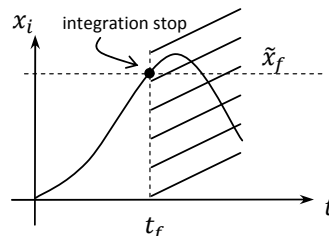


Fig. 1. Integration end criterion

The gradient based optimization algorithms applied for the optimization problem in (1) require the gradients of the objective function. These are evaluated like in (6) provided that the final states depend also on parameters:

$$\nabla J = \left[\frac{\partial J}{\partial x_f} \right] \left[\frac{\partial x_f}{\partial P} \right] + \left[\frac{\partial J}{\partial P} \right] \quad (6)$$

Also, one may calculate the partial derivatives of the response time with respect to parameters set. So, the response time is carried out in optimization as a constrained parameter in addition to formulation in (1).

III. AUTOMATIC DIFFERENTIATION

Automatic Differentiation is introduced as a powerful technique that computes error-free derivatives, up to machine precision, of functions described as computer programs in high-level languages such FORTRAN or C/C++. In [5] a rich list of tools implementing AD is provided. Therefore, an AD

tool could be a library that instruments a user program in order to be differentiated. Such tools require minor modifications on the initial source and they are implemented in packages like ADOL-C that is subject to this paper. In general they are using the operator overloading capabilities of certain programming languages such C++ and FORTRAN95. In order to value the partial derivatives in (1) one may employ ADOL-C over a numerical scheme integrating the ODE system in (2) or (3). The paper is then subject to two numerical integration strategies. First, it applies AD over an adaptive step size Runge-Kutta (RK) scheme as in (7):

$$x_{t_{i+1}}(P) = x_{t_i}(P) + h(P) \cdot \dot{x} \quad (7)$$

where \dot{x} denotes a slope estimation and h is the integration step which depends on design parameters for an adaptive step size scheme.

Recent studies [4] were carried out for differentiating such schemes. The difference in [4] is that the response time is prescribed in advance at a fixed value. Our approach intends to make use of it as a constrained design parameter carried out further in optimization, so, its corresponding derivatives are to be valued as explained before.

Secondly, truncated Taylor Series (TS), as in [5] are applied to advance the solution of the ODE system in (2) or (3) over a time interval as in (8):

$$x_{t_{i+1}}(P) = x_{t_i} + \frac{x_1}{1!} \cdot h + \frac{x_2}{2!} \cdot h^2 + \dots + \frac{x_n}{n!} \cdot h^n \quad (8)$$

where $x_i = (d^i x)/(dt^i)$ denotes the i^{th} order Taylor coefficient. Paper [5] provides numerical solutions for adaptive step size schemes for ODE solvers using Taylor expansion. Interesting here is that AD is used for solving the dynamic system, provided that ADOL-C is capable to value high-order Taylor coefficients of the autonomous system in (2) supposing that f is sufficiently smooth. In the non-autonomous case like in (3) a special version of the ADOL-C routine responsible for Taylor coefficients valuation is applied. The differentiation of such integration schemes is made by using special drivers implemented in ADOL-C.

The differentiation of a RK integration scheme in (7) tends to be slower since the slope usually is represented by a complex algorithm in the case of schemes up to second degree. Contrary, the differentiation of (8) is faster since it represents a sum expansion. However, here a cost of high-order derivatives computation should be paid up to second degree. In the full paper comparisons will be carried out for both schemes in terms of efficiency as also as helpful aspects regarding the AD of such numerical integration algorithms.

IV. OPTIMIZATION GOAL

The benchmark in [6] of the electromechanical actuator modeling a circuit breaker in Fig. 2 is proposed for sizing by gradient constrained optimization. When the switch is turned off, the vacuum force produced by the magnet equilibrate the spring force. The simulation starts when the switch turns on. The electromagnetic force created by the coil cancels

partially the magnet force. Consequently, the plunger will move, starting from initial position, z_0 , toward the upper bound, z_{max} .

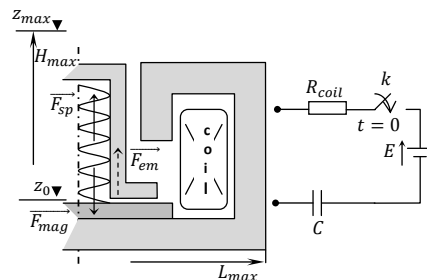


Fig. 2. Electromechanical actuator

The dynamical system of the proposed device combines both the equations of the electrical circuit feeding the coil and the movement equations. The states are:

$$\dot{x} = \begin{pmatrix} i & di/dt & z & v \end{pmatrix} \quad (9)$$

The response time is found from the end criterion in (5), that is satisfied when the mobile plunger is bounded at z_{max} .

A multi objective optimization problem raises from this particular case. These objectives are given in table I.

TABLE I
OPTIMIZATION SPECIFICATIONS

Variable	Constraint	Formula
Percussion energy at z_{max}	[0.12, 10] J	$m \cdot v^2/2$
Response time	[0, 3.5] ms	-
Total force at z_{max}	15 N	-
Shock resistance at z_0	[2000 - 10000] m/s ⁻²	$\frac{F_{sp} - F_{mag}}{m}$
Total mass	minimize	-

The design parameters in (2) are represented by all geometrical parameters of the studied benchmark. The optimization results will be presented in the full paper.

V. CONCLUSION

This paper presents a particular optimization problem on a benchmark dealing with state variables in Ordinary Differential Equations. Runge-Kutta and Taylor expansion integration schemes are used to approximate these states. Both schemes are differentiated by employing Automatic Differentiation in order to value the gradients needed by SQP algorithms.

REFERENCES

- [1] N. I. M. Gloud and D. P. Robinson, "A second derivative SQP method: local convergence", *STFC*, Rutherford Appleton Laboratory, UK, 2009.
- [2] A. Griewank, D. Juedes and J. Utko, "Algorithm 755: ADOL-C: A Package for the Automatic Differentiation of Algorithms Written in C/C++", *ACM Transactions on Mathematical Software*, 22(2):131-167, 1996.
- [3] M. Bücker and P. Hovland, "Automatic Differentiation", available at www.autodiff.org, 2000.
- [4] A. Walter, "Automatic Differentiation of explicit Runge-Kutta methods for optimal control", *Computational Optimization and Applications*, Springer 2007.
- [5] R. Barrio, "Performance of Taylor Series method for ODEs/DAEs", *Applied Mathematics and Computation*, No. 163, pp. 525-545, Elsevier, 2005.
- [6] E. Atienza, M. Parrault, F. Wurtz, V. Mazauric and J. Bignon, "A Methodology for the Sizing and the Optimization of an Electromagnetic Release", *IEEE Transactions on Magnetics*, vol. 36, No.4, July 2000.

Influence of Sensor Variations on the Condition of the Magnetostatic Linear Inverse Problem

Roland Eichardt*[†], Jens Haueisen*

*Institute of Biomedical Engineering and Informatics, Ilmenau University of Technology, Ilmenau, Germany,
Email: Roland.Eichardt@tu-ilmenau.de, Jens.Haueisen@tu-ilmenau.de

[†] Biomagnetic Center, Clinic for Neurology, Friedrich-Schiller-University Jena, Jena, Germany

Abstract—We examine the influence of randomized variations of the sensor direction on the condition of the linear inverse problem in magnetostatics. Setups with varied sensor directions are compared with setups using perfectly in parallel oriented sensors. As evaluation criterion for the condition of the linear inverse problem, the condition number of the leadfield matrix is used. The results indicate that for mono-axial planar sensor setups the condition of the linear inverse problem can be considerably improved, when the sensors are oriented non-uniformly.

I. INTRODUCTION

In geoprosection, magnetic field distributions are measured by moving a SQUID based sensor system over a field of interest [1]. Since the movement of the sensor system is performed by a vehicle and the underground is typically very rough, the orientation of the sensors in the measurement system is altered while moving. This results in slightly different sensor orientations for each measurement position. When analyzing such measured magnetic field distributions with varying sensor orientations it turned out, that the reconstruction was more robust than in some of our simulation runs with perfectly aligned parallel sensor directions. Consequently, the aim of this paper is to analyze the influence of random variations in sensor orientation on the solution robustness of the magnetostatic linear inverse problem. With simulations we evaluate, if the experimentally observed effect holds also on simple generic sensor setups.

II. METHODS

A. Inverse Model

In our study we consider the linearized inverse problem of estimating the activity vector \vec{p} on basis of the measurement vector \vec{m} corresponding to $\vec{m} = L \cdot \vec{p} + \vec{n}$, whereas \vec{n} represents noise and L the leadfield matrix. The leadfield matrix incorporates all relevant information on the sensor setup, source space grid, and the forward model. The source space is formed by regular grids given in Tab. I (positions are given in m). At each grid position, three orthogonal magnetostatic dipoles are located to facilitate arbitrary source directions. Parameters for the sensor setups are shown in Tab. II. Setup B represents a three-axial setup with three orthogonal magnetometers at each sensor position. Default configurations used in this study are represented by the combinations A1, A2, B1, B2, and C3.

TABLE I
PARAMETERS OF THE REGULAR SOURCE SPACE GRIDS.

	X,Y-Directions			Z-Direction			Number of Sources
	Grid	Min(pos)	Max(pos)	#Rows	Min(pos)	Max(pos)	
1	-0.01	0.21	10	-0.11	-0.11	1	100
2	-0.01	0.21	15	-0.11	-0.11	1	225
3	-0.005	0.205	8	-0.15	-0.20	2	128

TABLE II
PARAMETERS FOR THE SIMULATED PLANAR SETUPS IN THE Z=0 PLANE.

Setup	X,Y-Directions		Sensor Directions	Number of Sensors
	Min(pos)	Max(pos)		
A	0	0.2	-Z	144
B	0	0.2	+X, +Y, -Z	3 × 144 = 432
C	0	0.2	-Z	441

These default configurations were each changed with random variations as follows.

B. Random Variations

Sensor directions were changed by Δdir using Gaussian distributed random numbers with standard deviations $SD(\Delta\text{dir})$ between 0.5° and 25° . For setup B, the orthogonality between the three sensors was preserved. To examine the influence of random variations on the sensor directions, 100 repeated runs for each of the configurations A1 - C3 were conducted. In Fig. 1, A1 with randomly varied sensor directions is shown.

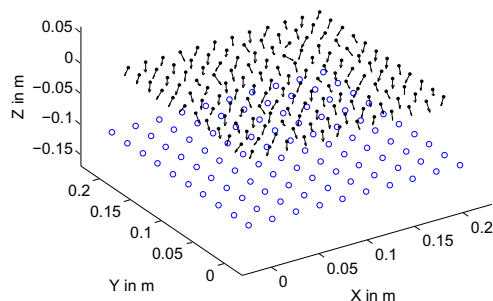


Fig. 1. Example configuration A1 with source positions of grid 1 (○) and sensor positions of setup A (●). The sensors are randomly oriented around the -Z direction with $SD(\Delta\text{dir}) = 10^\circ$.

TABLE III
CN AND DIMENSIONS (DIM) OF THE LEADFIELD MATRICES L^0 FOR THE
DEFAULT CONFIGURATIONS A1 - C3.

Configuration	CN(L^0)	dim(L^0)
A1	2.0184e+08	144 × 300
A2	1.5753e+08	144 × 675
B1	3.5559e+10	432 × 300
B2	5.5170e+13	432 × 675
C3	3.6253e+17	441 × 384

TABLE IV
EVALUATION OF THE CONDITION USING RANDOMLY VARIED SENSOR
DIRECTIONS FOR CONFIGURATIONS A1 - C3.

Config.	SD(Δ dir)	Mean(CN)	SD(CN)	Mean(Δ CN)	SD(Δ CN)
A1	0.5°	1.26e+07	3.116e+06	0.0625	0.01544
	5°	6.23e+06	1.628e+06	0.0308	0.008065
	10°	4.88e+06	1.129e+06	0.0242	0.005592
A2	0.5°	1.28e+07	3.293e+06	0.0809	0.02091
	5°	6.35e+06	1.557e+06	0.0403	0.009883
	10°	5.01e+06	1.17e+06	0.0318	0.007425
B1	0.5°	3.56e+10	2549	1	7.167e-08
	5°	3.56e+10	2999	1	8.434e-08
	10°	3.56e+10	3234	1	9.094e-08
B2	0.5°	5.52e+13	9.646e+09	1	0.0001748
	5°	5.52e+13	1.049e+10	1	0.0001814
	10°	5.52e+13	1.049e+10	1	0.0001902
C3	0.5°	3.28e+17	2.628e+16	0.845	0.06768
	5°	2.93e+17	1.748e+16	0.754	0.04502
	10°	2.88e+17	2.306e+16	0.742	0.05938

C. Criterion for Comparing Sensor Arrays

To evaluate the condition of the linear inverse problem, we use the condition number (CN) of the related leadfield matrix L (see also [2], [3]). Relative changes to the CN when random sensor variations are applied are denoted by $\Delta\text{CN}(L_i) = \text{CN}(L_i)/\text{CN}(L^0)$, where $\text{CN}(L^0)$ is the CN for the leadfield matrix of the default configuration given in section II-A, and $\text{CN}(L_i)$ is the CN for the i -th of 100 leadfield matrices created from the configuration described by L^0 but using randomly varied sensor directions. Mean value and standard deviation (SD) for $\Delta\text{CN}(L_i)$ and $\text{CN}(L_i)$ are computed for $1 \leq i \leq 100$.

III. RESULTS

As indicated in Fig. 2, the CN of leadfield matrices representing mono-axial setups (A,C) can be significantly reduced by small random variations of the sensor directions compared to a perfectly to -Z directed sensor array (Tab. III). Larger variations of the directions lead to higher reductions of the CN (Fig. 3 and Tab. IV). The decay of the average CN is reduced for larger values of Δ dir. The improvements of the CN by variations of the sensor directions of the 12×12 setup A are higher compared to the denser 21×21 sensor setup C. As expected, the CN of leadfield matrices for the three-axial setup B are not influenced by variations of the sensor directions. In the tested two examples, the CN of the mono-axial sensor array A is superior to the three-axial array B, whereas both are using identical sensor positions and source grids.

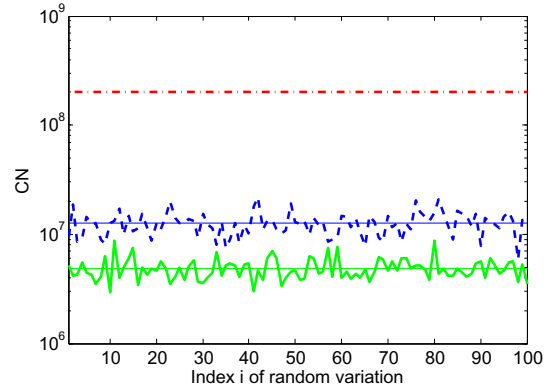


Fig. 2. Effect of 100 random variations of the sensor directions on the CN for configuration A1 using SD(Δ dir) of 0.5° (dashed line in the middle) and 10° (bold line at the bottom). The mean values are indicated by the thin lines, the default CN by the dash-dotted line on the top.

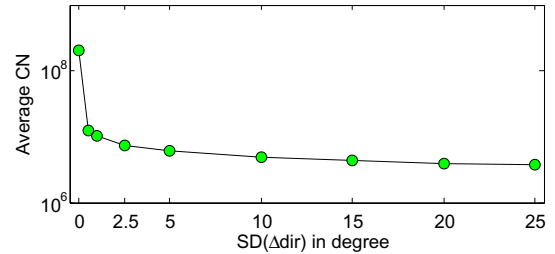


Fig. 3. Average CN (o) for configuration A1 using randomly varied sensor directions with SD(Δ dir) between 0.5° and 25°. The value for Δ dir = 0° represents the default CN for A1.

IV. CONCLUSION

Small variations in the sensor directions compared to sensors that are perfectly oriented to -Z lead for mono-axial setups to clearly smaller CN and consequently to an improved condition of the inverse problem. Therefore, mono-axial sensors should be directed non-uniformly in sensor arrays to support more robust source reconstructions. In future work we will evaluate the influence of random variations of sensor and source positions. Besides the CN, further evaluation criteria will be used.

ACKNOWLEDGMENT

This study was financially supported by the State of Thuringia / Germany (TAB 2008VF0001 / 2008FE9048) under participation of the European Union within the European Funds for Regional Development.

REFERENCES

- [1] R. Eichardt, D. Baumgarten, L. Di Rienzo L, et al., *Localisation of buried ferromagnetic objects based on minimum-norm-estimations a simulation study*, COMPEL, to appear.
- [2] L. Rouve, L. Schmerber, O. Chadebec, et al., *Optimal magnetic sensor location for spherical harmonics identification applied to radiated electrical devices*, IEEE Trans. Magn., 42(4):1167-1170, 2006.
- [3] S. Lau, R. Eichardt, L. Di Rienzo, et al., *Tabu Search Optimization of Magnetic Sensor Systems for Magnetocardiography*, IEEE Trans. Magn., 44(6):1442-1445, 2008.

The Application of Topological Gradients to Defect Identification in Magnetic Flux Leakage-type NDT

Min Li, and David A. Lowther
 McGill University
 3480 University Street, Montreal, H3A 2A7, Canada
 David.lowther@mcgill.ca

Abstract — An inverse problem is formulated to identify the shape and size of the defects in a nonlinear ferromagnetic material using the signal profile from magnetic flux leakage-type NDT. This paper presents an efficient algorithm based on topological shape optimization which exploits the topological gradient to accelerate the process of shape optimization to identify the defect.

I. INTRODUCTION

The magnetic flux leakage (MFL) method is a fast and reliable nondestructive testing (NDT) technique that has been widely used for decades. When a piece of ferromagnetic material is placed in a magnetic field and is magnetized to saturation, small defects or flaws in the material cause a significant flux anomaly due to the permeability variation. The anomalous fields are captured by Hall-effect probes or sensing coils, placed closely above the surface of the test object, which generate signals that can be used to identify the defect.

A key problem in the design and analysis of a MFL sensing system is the ability to determine the shape, size and location of the defect rapidly and precisely in the presence of a large number of uncertainties, expressed as noise in the signal. The use of finite element method (FEM) based simulation of MFL began in the late 1980's [1], [2].

In this paper, an inverse algorithm for defect identification in the MFL-type NDT is presented. The novel approach employs topological sensitivity analysis to first explore the search space and then to predict an appropriate initial structure for the use of efficient shape optimization. The robustness of the solution in the presence of noise will also be investigated, and this may provide useful information for improved sensor design and computer-enhanced signal processing.

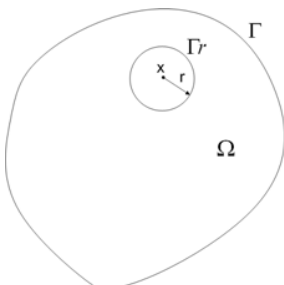


Fig. 1. A design domain with a small hole

II. TOPOLOGICAL GRADIENT BASED TOPOLOGY AND SHAPE OPTIMIZATION

Although shape optimization is being extensively studied in electromagnetic design, it suffers from the limitation that the overall change in a device is usually relatively small and

no topological change is allowed. However, the topological gradient (TG) provides the sensitivity information of a design with respect to topological changes, such as the insertion of a small air hole at any point inside the solid material. Topological sensitivity analysis, which originated from the classical shape gradient information, is derived using a topological asymptotic expansion for PDE systems. Fig.1 illustrates a design domain Ω defined on \mathbb{R}^n ($n=2$ or 3), with boundary Γ . Consider a small hole $B(x, r)$ in Ω , where x is the center and r is the radius of the hole. The topological gradient $G(x)$ is given as :

$$G(x) = \lim_{r \rightarrow 0} \frac{\Psi_{obj}(\Omega \setminus B(x, r)) - \Psi_{obj}(\Omega)}{\delta(\Omega)}. \quad (1)$$

where Ψ is an objective function defined on Ω , $\Omega \setminus B(x, r)$ is the domain excluding the small hole B , and $\delta(\Omega)$ is the volume of B with a negative sign.

Assuming a perturbation of the boundary of the small hole $B(x, r)$, the shape sensitivity of a scalar function $J = \Psi(\Omega \setminus B(x, r))$ can be expressed in terms of the state variable A and adjoint variable λ from the field solution [3]

$$J'(r) = \int_{\Gamma_r} L(A_1, \lambda_2) d\gamma. \quad (2)$$

$$L(A_1, \lambda_2) = (v_1 - v_2)(\nabla \times A_1)(\nabla \times \lambda_2)$$

After some manipulation [4], J' is approximated as:

Fig. 1. A design domain with a small hole

$$J'(r) = -4\pi r L(A_1, \lambda_2) + o(r). \quad (3)$$

Hence, we obtain

$$\begin{aligned} \Psi_{obj}(\Omega \setminus B(x, r)) - \Psi_{obj}(\Omega) &= J(r) - J(0) \\ &= \int_0^r J'(\rho) d\rho = -2\pi r^2 L(A_1, \lambda_2) + o(r^2) \end{aligned} \quad (4)$$

Combining (4) and (1), $G(x)$ is given, in 2D, as:

$$G(x) = 2L(A_1, \lambda_2). \quad (5)$$

(1) can be re-written using a local expansion as:

$$\Psi_{obj}(\Omega \setminus B(x, r)) - \Psi_{obj}(\Omega) = \delta(\Omega)G(x) + o(\delta(\Omega)). \quad (6)$$

In order to minimize the objective function Ψ , i.e. $\Psi(\Omega \setminus B(x, r)) - \Psi(\Omega) < 0$, a hole should be created in the region where $G(x)$ is greater than zero. Thus the following optimality conditions must be satisfied [4]

$$\begin{aligned} G(x) &= 0 & \text{on } \Gamma \\ G(x) &\leq 0 & \text{in } \Omega \end{aligned} \quad (7)$$

III. NUMERICAL EXAMPLE

A. FEM modeling of MFL

A permanent magnet MFL model and a test plate 6mm thick is created using MagNet [5]. The back yoke and the iron arm are made of linear material and test plate is made of cold rolled steel with a nonlinear permeability. A sensing array is placed 4.5 mm above the testing plate. For simplicity, the magnetic fields are solved with 2D finite-element analysis.

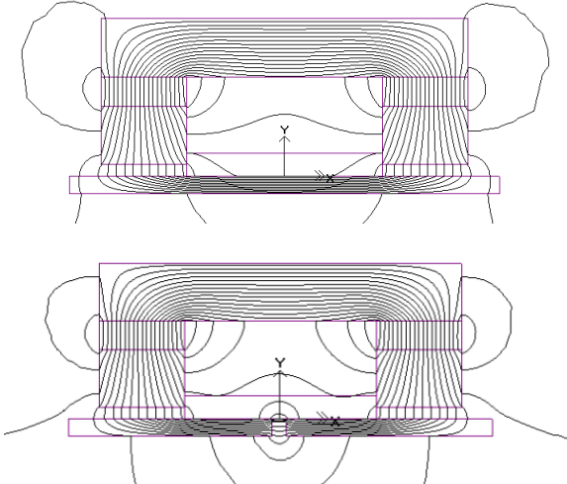


Fig. 2. Magnetic flux plot for model with and /without defect

The upper plot in Fig. 2 shows the magnetic field without the defect, while the lower one shows the effect of a defect, on the far side of the test plate, on the field.

B. Calculation of Topological gradient

In order to identify the size and the shape of the defects in the material, an objective function F is formulated from the field signals B_{io} captured by MFL sensors (obtained from the simulation model with the defect in Fig. 2) and the field values B_i computed from the FEM solution of a model where the shape of the plate is allowed to change at each iteration as the system tries to create the defect shape to minimize F .

$$F = \sum_{i=1}^n (B_i - B_{io})^2 \quad (8)$$

Based on the asymptotic expansion of (6) and the optimality condition (7), we would expect that the defects lie in the regions where the topological gradient has the largest positive value.

The domain of interest is defined as a region from $x = -15$ to 15 in the center of the plate. It is then divided to 6X40 small blocks, and the topological gradient is evaluated at the center of each block.

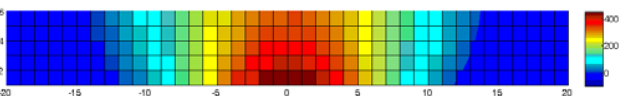


Fig. 3. Topological gradient plot for one defect model

Fig. 3 presents the topological gradient plot for the model with one defect of 5 mm wide and centers at $x = 0$; Fig. 4

illustrates the topological gradient of a model with two defects of 4 mm wide and center at $x = -12$ and $x = 12$ respectively. As can be seen from the above figures, the regions of the highest values of topological gradient coincide with the position of the defects.

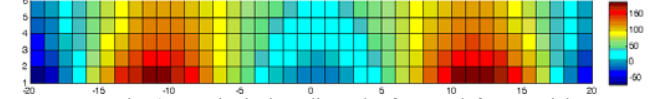


Fig. 4. Topological gradient plot for two defects model

C. Determination of defect size and shape

In order to test the topology prediction, a defect is created on the near side of the steel of 5 mm wide and 80% of the thickness in depth. The topological gradient is computed over the domain of interest. From this, about 5% of the area is removed from the domain. Next, the boundary of this hole is modified through a shape optimizer using continuum design sensitivity analysis [3].

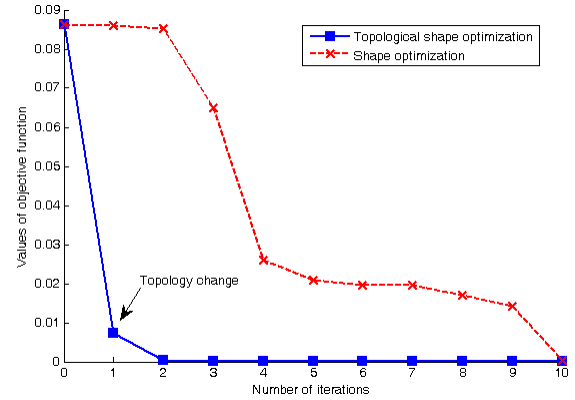


Fig. 5. Objective function values through the optimization

The values of objective function F during the shape optimization are shown in Fig. 5. The initial value of the objective is 0.0865. The topological change reduces it to 10% of this value. The remaining improvement is then obtained through shape optimization. Fig. 5 also shows the convergence of the process if only shape optimization is used.

IV. CONCLUSION

The topological gradient provides information which can be used to reduce the objective function value. It provides a fast, but approximate, exploration of the solution space. Shape optimization can then refine the solution. The full paper will provide results for buried defects in 2-D and 3-D.

V. REFERENCES

- [1] Atherton, D. L. and M. G. Daly, "Finite element calculation of magnetic flux leakage detector signals." *NDT International*, 20(4): 235-238, 1987.
- [2] Al-Naemi, F. I., J. P. Hall, et al., "FEM modelling techniques of magnetic flux leakage-type NDT for ferromagnetic plate inspections." *Journal of Magnetism and Magnetic Materials*, 304(2), 2006.
- [3] Dong-Hun, K., K. S. Ship, et al., "Applying continuum design sensitivity analysis combined with standard EM software to shape optimization in magnetostatic problems." *Magnetics, IEEE Transactions on*, 40(2): 1156-1159, 2004.
- [4] Cea, J., S. Garreau, et al., "The shape and topological optimizations connection." *Computer Methods in Applied Mechanics and Engineering*, 188(4): 713-726, 2000.
- [5] MagNet user's manual, <http://www.infolytica.ca>.

Grid-enabled Tabu Search for Electromagnetic Optimization Problems

S. Carcangiu, A. Fanni, A. Mereu, and A. Montisci

Department of Electrical and Electronic Engineering, University of Cagliari

Piazza d'Armi, 09123, Cagliari, Italy

{s.carcangiu; fanni; anna.mereu; augusto.montisci}@diee.unica.it

Abstract—The use of Grid computing to solve electromagnetic optimization problems using the Tabu Search algorithm is proposed in this paper. In order to significantly reduce the prohibitive computational cost of the numerical analyses required by the majority of iterative algorithms, two different grid-enabled Tabu Search strategies have been ported in the grid. Both strategies belong to the Domain Decomposition family: the decomposition of the search space and the decomposition of the neighborhood. The performances of the different parallel implementations have been evaluated on some electromagnetic benchmarks.

I. INTRODUCTION

In the design of electromagnetic structures, it is often necessary to analyze the electromagnetic field distribution using numerical techniques such as the Finite Element Method (FEM). In order to optimize the design, it is usual to apply iterative techniques to search the potentially optimal configuration in the solutions domain. Moreover, when the number of design parameters to be optimized is considerable, the number of electromagnetic problems to be solved could be of the order of thousands. Since numerical electromagnetic solutions are often computationally intensive, the use of numerical solutions during the iterative optimization process can be unfeasible. One way to overcome this problem is to use approximating techniques, such as neural networks [1]. The main drawback of using approximating models is represented by the approximation errors, which can alter the value of the solution corresponding to the same design parameters.

Another way to avoid the prohibitive computational time of iterative optimization is to use the new Grid Computing technology. Grid computing is a family of technologies for dynamically and opportunistically provisioning computing power from a pool of resources. The Grid is a type of parallel and distributed system that enables the sharing, selection, and aggregation of geographically distributed “autonomous” resources dynamically at runtime depending on their availability, capability, performance, cost and user's quality-of-service requirements [2].

In this paper, a Tabu Search (TS) is proposed as search strategy, and its parallel implementation on a computational grid is presented. TS is a family of meta heuristic procedures, which perform the search for the optimal solution exploring the variable space and storing the features that correspond to bad previous moves. Such features are labeled as tabu and they are avoided during the search for the optimum [3].

In literature, different approaches have been adopted to implement a parallelization of the TS. In [4], a hierarchical

classification of the parallel TS strategies is presented. Two main types of parallelization can be performed: the first is the so-called *Multiple* TS task category, in which multiple TS algorithm are run in parallel that may differ for different parameters such as the initial solution and the tabu list size; the second class is the so-called *Domain Decomposition*. In this work, we will compare the performances of two parallel TS strategies belonging both to the Domain Decomposition family: the decomposition of the search space and the decomposition of the neighborhood. The decomposition of the search space implies that the domain space is decomposed in a number of smaller domains. Each sub-domain has to be solved by separate TS. The decomposition of the neighborhood is performed by assigning to each task a different portion of the neighborhood to evaluate. In this work the performances of the two types of Domain Decomposition strategies will be compared.

II. GRID-ENABLED TABU SEARCH ALGORITHMS

The computing infrastructure we used is based on several computation centers localized in the main research institutions and academies in Sardinia, Italy, and it consists of more than 100 nodes 1U System x3455 (200 CPU AMD Opteron 2218, 400 CPU core). The fiber optics connections allow to dynamically aggregate the distributed resources and to reach a pick aggregated computation power of some TeraFlops.

The optimization problem under investigation consists of finding a set of design parameters that allows the device to produce the desired effect depending on the value of the electric or magnetic field in prefixed points, under feasibility constraints.

In order to formalize the problem, the range of each design variable is subdivided into a finite number of sub-ranges uniformly distributed. A symbol of a discrete alphabet is associated to each sub-range, so that every configuration in the continuous can be identified with an ordered sequence of symbols. According to this choice, the search for the optimal solution is performed by the TS moving from one discrete solution to another by simply modifying the value of one variable at a time. At each iteration, the neighborhood associated to the current configuration is built performing all the possible moves that can be played starting from that configuration.

The simple iterative scheme of the TS is enhanced introducing several rule-of-thumb criteria such as intensification (deeply exploration of a region looking

promising), or diversification (leave a region that does not look promising).

A. Parallel strategy

The idea for a straightforward parallelization scheme is to decompose the search space into a set of disjoint subspaces, each of them explored by an instance of TS on a different CPU. When each process finishes, it writes in a secondary memory the obtained results. Once all the processes finish, a new process reads all the secondary memory files and gathers the results to obtain the optimal solution. The resulting parallel algorithm is simple, because inter-process communication is not necessary, and only a synchronization point is needed.

B. Master-Slave strategy

The previously described parallelization schema does not fully exploit the peculiarity of the TS meta-heuristics to make use of the past history of the search to enhance the solutions domain. An alternative use of the Grid-Computing paradigm is made in this paper, by decomposing the neighborhood. In fact, the most important requirement in using a TS algorithm consists of defining the set of admissible moves, i.e., in defining the neighborhood set of a given configuration. As previously mentioned, our TS implements Cartesian moves, which consists of changing the value of one design parameter at a time. The exploration of a single variable can be carried out by independent jobs, which means that, for each configuration in the neighborhood, a FEM analysis has to be performed in order to evaluate the fitness of that solution. It is important to notice that in the Grid the execution of cyclic jobs is not allowed. This leads us to design the core of our algorithm to run locally in the user interface and to run the parallel exploration of the neighborhood in the Grid. This has been possible by splitting the program in a master-slave architecture. To each slave, a different variable to explore is assigned, and it runs different FEM analyses. When the jobs are done, the master program analyzes the entries written by the slaves and performs the optimal current move.

III. RESULTS

The T.E.A.M Problem 25 “Optimization of Die Press Model” [5] is used here to compare the performance of the two grid-enabled TS codes. The four design parameters of the die mold have to be set up so that the magnetic flux density is radial and equal to 0.35 T in the cavity where the magnetic powder is inserted. The computation of the magnetic field is done using a magneto-static nonlinear FEM. The bi-dimensional model was created in FreeFem++ open source finite element code [6].

The performances of the Grid-enabled TS with the *Master-Slave* strategy are reported in Table I in terms of the speedup and the efficiency parameters usually used to evaluate the performance of parallel algorithms [7]. As the Grid we used is composed by a number of identical CPUs, we can extend the concept of speed up and efficiency, used in parallel systems, in the grid environment. The speedup is the ratio of the

TABLE I
PERFORMANCE OF THE GRID-ENABLED TS VERSUS SEQUENTIAL TS

p	T_p [s]	S_p	E_p
1	1550	1	-
4	773	2	50%
8	593	2.6	32%
16	503	3.1	19%
20	485	3.2	16%
32	458	3.4	10%
40	449	3.5	9%
80	431	3.6	4%

execution time of the algorithm when executed on one processor to that when executed on p processors: $S_p = T_1/T_p$, whereas the efficiency is the ratio of the actual speedup versus the theoretical maximum speedup equal to p. Here T_1 and T_p are the total times required to run one iteration of TS on a single CPU, and on p CPUs respectively. The maximum efficiency is obtained when the speedup is the closest to the theoretical speedup. Note that the algorithm in Grid environment has speedup limits and appears to saturate due mainly to communication overhead, and to some uncertain factors as instability of computing nodes, dynamic change of Grid environment, total load on the Grid, and so on.

IV. CONCLUSIONS

In the full paper, two Grid-enabled TS codes will be tested on standard electromagnetic test problems. The performed experiments showed that the porting of the algorithm on a computational Grid greatly reduces the computation cost, even if a degree of overhead is introduced. This is mostly due to the communication delay between the computing elements. The overhead can be neglected if the parallelized jobs have a high computational load, as it is the case of FEM analyses.

ACKNOWLEDGMENT

This work makes use of results produced by the Cybersar Project managed by the Consorzio COSMOLAB, a project co-funded by the Italian Ministry of University and Research within the PON 2000-2006. More information is available at <http://www.cybersar.it>.

V. REFERENCES

- [1] D. Cherubini, A. Fanni, A. Montisci, and P. Testoni, “Inversion of MLP Neural Networks for Direct Solution of Inverse Problems,” *IEEE Trans. Mag.*, vol. 41, no. 5, pp. 1784–1787, May 2005.
- [2] R. Buyya, Grid Computing: Making the global cyberinfrastructure for eScience a reality, *CSI Communications*, vol. 29, no. 1, July 2005.
- [3] E. Cogotti, A. Fanni, F. Pilo, “A comparison of optimization techniques for Loney’s solenoids design: an alternative Tabu Search approach,” *IEEE Trans. Mag.*, vol.:36, no. 40, pp. 1153–1157, July 2000.
- [4] E.G. Talbi, Z. Hafidi and J.M. Geib, “Parallel Tabu Search for Large Optimization Problems”, in *Meta-heuristics: Advances and Trends in Local Search Paradigms for Optimization.*, Boston, pp. 345-358, 1999.
- [5] N. Takahashi, “Optimization of die press model,” in *Proc. TEAM Workshop, Okayama, Japan, Mar. 20–21*, pp. 61–69, 1996.
- [6] <http://www.freefem.org/ff++/>.
- [7] F. Luna, A. J. Nebro, E. Alba, “Observations in using Grid-enabled technologies for solving multi-objective optimization problems,” *Parallel Computing*, vol. 32, pp. 377–393, 2006.

An Exact Optimization Code Combined with a Hybrid Model for Magnetic Couplings Design

Julien Fontchastagner¹, Frédéric Messine², and Yvan Lefèvre³

¹ Groupe de Recherche en Electrotechnique et Electronique de Nancy (GREEN) - Nancy-Université
INPL-ENSEM, 2 avenue de la Forêt de Haye, 54516 Vandœuvre-lès-Nancy, France

Julien.Fontchastagner@ensem.inpl-nancy.fr

² Institut de Recherche en Informatique de Toulouse (IRIT) - Université de Toulouse - CNRS

³ Laboratoire Plasma et Conversion d'Énergie (LAPLACE) - Université de Toulouse - CNRS

INPT-ENSEEIH, 2 Rue C. Camichel, BP 7122, 31071 Toulouse Cedex 7, France

{Frederic.Messine, Yvan.Lefevre}@enseeiht.fr

Abstract—The purpose of this paper is to show a new methodology for solving inverse problems of design. It is based on the use of a deterministic global optimization algorithm. In front of limitations induced by the use of analytical models, the authors present a way to associate Interval Branch and Bounds techniques and numerical computations based on finite element method. Thank to this methodology, we are able to solve exactly the associated inverse problem of a magnetic coupling design.

I. INTRODUCTION

Magnetic couplings are very useful devices for many applications as seal-less pumps in the chemical and petrochemical industries, or the aeronautical and maritime ones for instance. Their functionalities are to transmit a motion between two separated zones without mechanical contacts. The studied structure is a co-axial synchronous magnetic torque coupling. It consists of two rings of permanent magnets separated by an insulating partition. On each side of it, we find an airgap and a binding band.

A. Previous Methodology

In [1], the authors solve the problem of such devices design by applying a rational methodology. The problem is understood and defined as an *inverse problem*, i.e. from some characteristic values given by the schedule of conditions (for example the torque), get the dimensions as well as the structure and the composition of a co-axial magnetic torque coupling. These inverse problems are formulated as a *mixed constrained global optimization problem*.

In order to solve exactly the so-formulated global optimization problems, a particular algorithm (called IBBA) based on a Branch and Bound technique where the bounds are computed using interval analysis has been developed and extended. See [1], [2] and [3] for details.

The advantages of these kinds of methods are :

- they use mixed variables (real, integer, boolean, ...);
- they do not need a starting point (or a set of ones);
- they guarantee to obtain the global minimum of the problem (they are *deterministic* and *global*).

Their main drawbacks are their computation times and the fact that they need (until nowadays) explicit analytic expressions of criteria and constraints.

The inverse problem of couplings design problem is formulated as a mixed constrained global optimization problem defined as follow :

$$\begin{cases} \min_{\substack{x \in \mathbb{R}^{n_r}, z \in \mathbb{N}^{n_e}, \\ b \in B^{n_b}, \sigma \in \prod_{i=1}^{n_c} K_i}} f(x, z, \sigma, b) \\ g_i(x, z, \sigma, b) \leq 0 \quad \forall i \in \{1, \dots, n_g\} \\ \Gamma(x, z, \sigma, b) = \Gamma_{fixed} \end{cases} \quad (1)$$

where f is a real function (for example the volume), K_i represents an enumerated set of categorical variables (for instance, the kind of magnet), and $B = \{0, 1\}$ is the boolean set (for the fact that there are binding bands or not). g_i are some geometrical constraints. Moreover, an equality constraint upon the maximum electromagnetic torque Γ is added, traducing the fact that it must be equal to a fixed value (Γ_{fixed}).

The torque expression comes from an analytical model based on the resolution of Poisson's equations using the separation of variables by keeping only the term due to the first non-zero harmonic (the fundamental) [1].

Several techniques of constraints propagation, and others adaptations were applied in order to reduce the time convergence. Indeed, it was very difficult to compute efficient bounds with interval arithmetic, because of the complexity of our torque formula. Thanks to these techniques, the authors obtained encouraging results dealing with the minimization of the global volume or with the volume of magnets. In our knowledge, it was the first time that such a problem was solved.

B. Need of a More Accurate Model

If a finite element software is used to compute the electromagnetic torque and the mean value of flux density in yokes (the physical constraints of our problem), we notice a non-negligible difference between the values given by our model and the numerical ones (around 20%). However, the kind of

analytical models used is known to provide results closed to those obtained by a numerical method [4]. Actually, the observed gap is due to the fact that we do not have considered the harmonics greater than the fundamental, and moreover the optimization process is inclined to maximize the error due to these assumptions.

II. NEW APPROACH : USE A HYBRID MODEL

The idea is to associate the advantages of two kind of models : the swiftness of analytics and the accuracy of finite elements based techniques.

The analytic expression of the electromagnetic torque is given by the resolution of Poisson's equations using the separation of variables. Instead of taking into account only the fundamental (Γ_{o1}) as in [1], the used expression (Γ_{o3}) is the sum of the two first non-zero harmonics (1 and 3). The thickness of iron yokes are deduced from the Gauss's law of magnetism and the fact that the mean value of flux density in the yokes B_y must be less or equal to the maximum value $B_M(\sigma_y)$ above which the iron is definitively saturated.

A specially dedicated finite element code has been written in order to automatically draw the geometry, create the mesh, and perform a magneto-static resolution of a magnetic coupling. In output, the torque Γ_{FE} (computed with the Maxwell Stress Tensor) and the mean values of flux density in the inner and outer yokes (B_{yi}^{FE} and B_{yo}^{FE}) are given in less than 1 second. This tool is in the form of a black-box (named NUMTFD) which can be easily called by another program.

III. FORMALIZATION OF THE NEW DESIGN PROBLEM

Now the question is to know how to associate such a model with an Interval Branch and Bound Algorithm.

A. Inverse Problem Formulation

The design problem must be re-formulated. In fact it is not possible to directly include our black-box as a constraint. Indeed, when the optimization process begins, the lengths of the intervals are too large to perform a valid finite element computation [3].

The idea is to defined several zones corresponding to different expressions. If we are far to the wanted value (Γ_{fixed}), we use Γ_{o1} . If we get close, but not close enough to call Γ_{FE} , Γ_{o3} is used. The associate problem is then :

$$\left\{ \begin{array}{l} \min_{\substack{x \in \mathbb{R}^{n_x}, z \in \mathbb{N}^{n_z}, \\ b \in B^b, \sigma \in \prod_{i=1}^{n_c} K_i}} f(x, z, \sigma, b) \\ g_j(x, z, \sigma, b) \leq 0 \quad \forall j \in \{1, \dots, n_g\} \\ \left\{ \begin{array}{l} (1 - \lambda_{ana})\Gamma_{fixed} \leq \Gamma_{o1} \leq (1 + \lambda_{ana})\Gamma_{fixed} \\ (1 - \lambda_{FE})\Gamma_{fixed} \leq \Gamma_{o3} \leq (1 + \lambda_{FE})\Gamma_{fixed} \\ \Gamma_{FE}(x, z, \sigma, b) = \Gamma_{fixed} \\ B_{yi}^{FE}(x, z, \sigma, b) \leq B_M(\sigma_{yi}) \\ B_{yo}^{FE}(x, z, \sigma, b) \leq B_M(\sigma_{yo}) \end{array} \right. \end{array} \right.$$

where λ_{ana} and λ_{FE} are used to define the different zones (for the tests, we have chosen 40% and 20%). Two inequality constraints are added to ensure that the yokes are not saturated.

B. New Interval Branch & Bound Algorithm

The corresponding Interval Branch & Bound Algorithm (IBBA+NUMTFD) has been coded. Its principle is to bisect the initial domain into smaller and smaller boxes and then to eliminate the boxes where the global optimum cannot occurs:

- by proving, using interval bounds, that no point in a box can produce a better solution than the current best one;
- by proving, using interval arithmetic, that at least one constraint cannot be satisfied by any point in such a box.

Some techniques of constraint propagation and limitations have been included to improve the convergence.

IV. RESULTS AND CONCLUSION

The problem corresponding to the minimization of the global volume of a studied magnetic coupling is solved and results are given in Table I (strike-through text represents non-satisfied constraints). We have chosen $\Gamma_{fixed} = 10$ N·m, the real parameters represent geometric quantities, the integer p is the number of poles pairs, and the different σ values are used to choose the kinds of materials. To compare with the previous methodology, the problem is solved using only Γ_{o1} (IBBA), next using Γ_{o3} (IBBAo3), and finally using our hybrid model (IBBA+NUMTFD).

TABLE I
MINIMIZATION OF THE MAGNETIC COUPLING'S GLOBAL VOLUME V_g

Param.	Bounds	Unit	IBBA	IBBAo3	IBBA+ NUMTFD
$\theta_{int}; \theta_{ext}$	[30; 70]	%	48.1; 30.0	55.6; 30.0	52.5; 37.5
$R_1; R_2$	[1; 5]	cm	2.20; 2.50	2.20; 2.50	2.87; 3.17
$R_3; R_4$	[1; 5]	cm	2.70; 3.00	2.70; 3.00	3.39; 3.69
p	[[4; 9]	-	6	6	5
$\sigma_{mi}; \sigma_{me}$	{1, 2}	-	2; 2	2; 2	1; 1
$\sigma_{yi}; \sigma_{ye}$	{1, 2}	-	1; 1	2; 1	2; 1
V_g		cm ³	84.37	84.78	116.27
Γ_{o1}		N·m	9.80	10.96	13.61
Γ_{o3}		N·m	8.02	9.80	11.05
Γ_{FE}		N·m	7.39	8.98	9.92
$B_{yi}^{FE}; B_{yo}^{FE}$		T	1.71; 2.12	1.85; 2.13	1.53; 1.54
CPU Time			0'17"	0'21"	181'37"
Iterations			32124	38991	80514
Numerical Computations			-	-	19951

Only the results corresponding to the new methodology answer perfectly to our *non-homogeneous mixed constrained global optimization problem*.

REFERENCES

- [1] J. Fontchastagner, Y. Lefèvre, and F. Messine, "Some Co-axial Magnetic Couplings Designed Using an Analytical Model and an Exact Global Optimization Code," *IEEE Transactions on Magnetics*, Vol. 45, N. 3, pp. 1458-1461, 2009.
- [2] F. Messine. *Essays and Surveys in Global Optimization*, Chap.10 "A Deterministic Global Optimization Algorithm for Design Problems," pp. 267-292, Ed. P. Hansen and G. Savard, Springer, 2005.
- [3] J. Fontchastagner, F. Messine and Y. Lefèvre, "Design of Electrical Rotating Machines by Associating Deterministic Global Optimization Algorithm With Combinatorial Analytical and Numerical Models", *IEEE Transactions on Magnetics*, Vol. 43, pp. 3411-3419, N. 8, 2007.
- [4] M. Couderc, C. Henaux, and B. Nogarède, "Analytical modelling of high speed electrical machines in view of their optimal design," the IEEE 32nd Ann. Conf. Ind. Electron. (IECON), Paris, France, 2006.

Electromagnetic Device Design Based on New Sequential Optimization Strategies

Gang Lei¹, K. R. Shao¹, Youguang Guo², Jianguo Zhu², *Senior Member, IEEE*, and J. D. Lavers³, *Fellow, IEEE*
¹College of Electrical and Electronic Engineering, Huazhong University of Science and Technology, Wuhan, 430074, China.
 gangleimc@gmail.com; krshao@hust.edu.cn.

²Faculty of Engineering, University of Technology, Sydney, N.S.W. 2007, Australia.

³Department of Electrical and Computer Engineering, University of Toronto, Toronto, ON M5S 3G4, Canada.

Abstract—we present two new strategies to sequential optimization method (SOM) for optimization design problems of electromagnetic devices. One is a new space reduction strategy; the other is selection strategy of sequential optimization models. In the implementation, two kinds of radial basis functions (RBF) approximate models are considered for the response surface reconstruction of design objectives and constraints. Then, by two design examples of TEAM benchmark problems, we show that our methods can significantly speed the design process and obviously reduce the computational cost of finite element analysis.

I. INTRODUCTION

Electromagnetic optimization and design problems are often solved by means of two kinds of methods, direct optimization method and optimization based on approximate models. The former is always implemented with finite element model and stochastic optimization algorithms [1]. However, it is computationally expensive. So the latter has been widely considered as an alternative method [2]-[3]. They are proved fast, but not very accurate.

To improve the optimization efficiency, we have present sequential optimization method (SOM) to the electromagnetic design problems [4]-[5]. SOM can optimize the model and algorithm simultaneously. However, SOM was discussed only for response surface model (RSM) and Kriging model in the former study, and the sampling method is unique. In this paper, we will present a system discussion about the space reduction strategy and model selection strategy for SOM, including two kinds of radial basis functions (RBF) models.

II. RBF APPROXIMATE MODELS

RBF model is one of the most widely used approximate models to solve electromagnetic optimization problems. It uses a linear combination of RBF to interpolate sampled data. Given n sample points $\{x_1, x_2, \dots, x_n | x_i \in \mathbb{R}^D\}$ and responses $\{y_1, y_2, \dots, y_n | y_i \in \mathbb{R}\}$, for an input $x \in D \subseteq \mathbb{R}^D$, the response value of RBF model is given by

$$\hat{y}(x) = \sum_{i=1}^n \beta_i \cdot \varphi(\|x - x_i\|), \quad (1)$$

where β_i s are model parameters, $\varphi(r)$ is the RBF. Gauss and multiquadric (MQ) RBF are considered in this work.

RBF model can rapidly and effectively replace the finite element analysis for optimization tasks and conditions. However, it is generally globally supported and poorly conditioned, especially when the number of sampling points increases significantly.

Compactly supported RBF (CSRBF) model is a promising improvement. When CSRBF model is used, the evaluation of (1) will not run over the whole set of points and the coefficient matrix will be sparse. Several criteria for positive definiteness of CSRBF have been provided and a series of positive definite CSRBF have been produced. The following two CSRBF are studied in this work; they have the form as

$$\varphi_{C1}(r) = (1-r)_+^6 (6 + 36r + 82r^2 + 72r^3 + 30r^4 + 5r^5), \quad (2)$$

$$\varphi_{C2}(r) = (1-r)_+^8 (1 + 8r + 25r^2 + 32r^3), \quad (3)$$

where r is a norm with respect to the radius of the compactly supported domain, $(1-r)_+$ is a truncated function.

III. NEW SEQUENTIAL OPTIMIZATION STRATEGY

SOM has been successfully employed to solve optimization design of electromagnetic devices. It is composed of coarse optimization process and fine optimization process [4]. The main purpose of the former is to reduce the design space and find the most interesting region. Space reduction equation plays an important role in this process. A new reduction strategy is given as follows.

Let $I^{(k)}$, $h^{(k)}$ and $N^{(k)}$ are the interval, step size and number of the k th sampling and optimization process, respectively. $x_o^{(k)}$ is the optimization result of the approximate models. The new reduction strategy is designed with two steps.

Reduction step:

$$\hat{x}_{li}^{(k+1)} = \max \left\{ x_{li}^{(k)}, \text{round} \left[8(x_{oi}^{(k)} - \Delta l) / h_i^{(k)} \right] \cdot h_i^{(k)} / 8 \right\}, \quad (4)$$

$$\hat{x}_{ui}^{(k+1)} = \min \left\{ x_{ui}^{(k)}, \text{round} \left[8(x_{oi}^{(k)} + \Delta l) / h_i^{(k)} \right] \cdot h_i^{(k)} / 8 \right\}, \quad (5)$$

Correction step:

$$x_{li}^{(k+1)} = x_{li}^{(k)} + \text{round} \left[2(\hat{x}_{li}^{(k+1)} - x_{li}^{(k)}) / h_i^{(k)} \right] \cdot h_i^{(k)} / 2, \quad (6)$$

$$x_{ui}^{(k+1)} = x_{ui}^{(k)} + \text{round} \left[2(\hat{x}_{ui}^{(k+1)} - x_{ui}^{(k)}) / h_i^{(k)} \right] \cdot h_i^{(k)} / 2, \quad (7)$$

where $[x_{li}^{(k)}, x_{ui}^{(k)}]$ is the boundary of the i th variable, function $\text{round}(x)$ is round to the nearest integer of x . $\Delta l = l_i^{(k)} / n_l$, in which n_l is the reduction factors. If $n_l = p$, the interval of reduced space is $p/2$ of the last interval; default value is 4. The starting point of new reduction strategy is very different from the former [4]. We focus on the reduction speed in the former SOM, while sampling points of last set can be employed sufficiently in the current modeling process by the new reduction strategy. So the cost of finite element analysis can be saved to a great extent.

IV. EXAMPLES

In the section, we will compare the results with different reduction factors to discuss the limit cases of SOM. Moreover, model selection strategy will be discussed for SOM.

A. TEAM Workshop Problem 22

It is a well known benchmark problem for the optimization of superconducting magnetic energy storage (SMES) [1]-[2], [4]. The three-variable (R_2 , h_2 , d_2) case of SMES is a discrete problem which should be optimized with respect to the following objectives: (1) The stored energy should be 180 MJ; (2) $B_{\max} \leq 4.92$ T (superconductivity constraint); (3) The stray field (B_{stray}) should be as small as possible. Table I shows the optimal results given by SOM with different RBF models.

TABLE I
OPTIMIZATION RESULTS OF SMES

Var. Unit	R_2 m	$h_2/2$ m	d_2 m	B_{stray} mT	E MJ	FESP
DEA	3.18	0.428	0.211	1.03	180.00	2310
G-RBF	3.12	0.309	0.295	0.93	179.94	214
MQ-RBF	3.07	0.295	0.328	0.97	179.64	129
φ_{c1}	3.06	0.302	0.325	1.01	179.45	122
φ_{c2}	3.03	0.316	0.325	1.23	179.24	122
G- $n_l=6$	3.17	0.372	0.238	0.97	180.14	131
G- $n_l=8$	3.12	0.358	0.262	1.00	180.04	120

In Table I, DEA means the results derived from differential evolution algorithm (DEA) with finite element model. G-RBF shows the results given by SOM with Gauss RBF model. G- $n_l=6$ means the results given by Gauss RBF model with reduction factor $n_l = 6$; others cases have similar meanings.

(1) All the methods can deliver satisfied results, especially those based on RBF models.

(2) 2310 finite element sample points (FESP) are needed for DEA to get the optimal results. All FESP of SOM based on RBF and CSRBF models are less than 1/10 compared with that of DEA.

(3) The best results are from the case of Gauss RBF model with $n_l = 4$. If we use $n_l = 6$ and 8 to reduce design space, the FESP can be reduced obviously while the optimal results are only a little worse than that of the former case.

Fig.1 shows the convergence rate of SOM with different models, including RSM, RBF, CSRBF and Kriging models. From the comparison, we can see that RSM, RBF and Kriging are better than CSRBF for the modeling process of SOM.

B. TEAM Workshop Problem 25

This is also a benchmark problem for the optimization of die press model [3]. The three parameters (R_2 , L_2 , L_4) case is considered in this work. It is a continuous problem which should be optimized to maintain the radial magnetic induction equal to 0.35 T at the specified place. The objective function is the square error of the calculated and specified values. Table II shows the results given by our methods. As an abstract, we only present the SOM results based on MQ RBF model with different reduction factors.

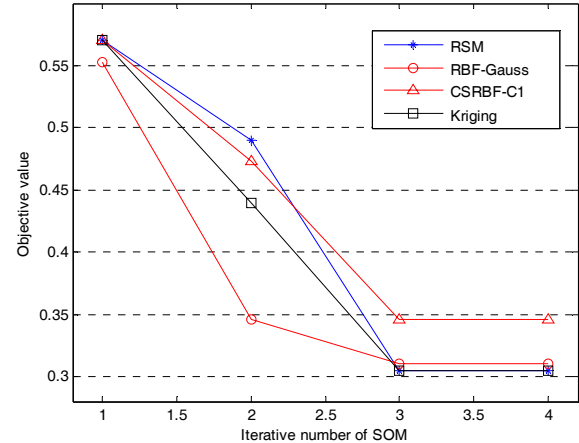


Fig.1. Convergence rate of SOM with different models

From the table, we can see that 2420 FESP are sampled to get the optimization results by DEA. For the case of default SOM, only 331 FESP are needed, which is 13.68% compared with that of DEA. And for the case of $n_l = 6$ and 8, the optimal results can be derived with only 161 FESP, which are 6.65% compared with that of DEA, and less than half of the former case. The results given by SOM only a little worse than that by DEA, but they also satisfy design objectives.

TABLE II
OPTIMIZATION RESULTS OF TEAM WORKSHOP PROBLEM 25

Var. Unit	R_1 mm	L_2 mm	L_4 mm	f	FESP
DEA	7.5554	14.7212	14.8666	4.14×10^{-4}	2420
MQ-RBF	7.6125	14.6250	15.7188	1.49×10^{-3}	331
MQ- $n_l=6$	7.7500	14.6250	16.1875	1.85×10^{-3}	161
MQ- $n_l=8$	7.7500	14.6250	16.1875	1.85×10^{-3}	161

V. CONCLUSION

We present new strategies for SOM to solve design problems of electromagnetic devices, including two kinds of RBF models. From two TEAM benchmark examples, we can see that the computational cost of finite element analysis can be obviously saved by our methods.

VI. REFERENCES

- [1] F. Campelo, F. G. Guimaraes, H. Igarashi, and J. A. Ramirez, "A clonal selection algorithm for optimization in electromagnetics," *IEEE Trans. on Magnetics*, 41(5): 1736-1739, 2005.
- [2] L. D. Wang and D. A. Lowther, "Selection of approximation models for electromagnetic device optimization," *IEEE Trans. on Magnetics*, 42(2): 1227-1230, 2006.
- [3] L. Lebensztajn, C. A. R. Marretto, M. C. Costa, and J. L. Coulomb, "Kriging: a useful tool for electromagnetic device optimization," *IEEE Trans. on Magnetics*, 40(2): 1196-1199, 2004.
- [4] Gang Lei, K. R. Shao, Youguang Guo, Jianguo Zhu, and J. D. Lavers. "Sequential optimization method for the design of electromagnetic device," *IEEE Trans. on Magnetics*, 44(11): 3217-3220, 2008.
- [5] Gang Lei, K. R. Shao, Youguang Guo, et al, "Improved sequential optimization method for high dimensional electromagnetic optimization problems," in *Proc. INTERMAG 2009*, Accepted.

A Metaheuristic Algorithm for Multiobjective Designs of Inverse Problems

S. L. Ho¹, and Shiyou Yang^{1,2}

¹Department of Electrical Engineering, The Hong Kong Polytechnic University, Hong Kong

²College of Electrical Engineering, Zhejiang University, Hangzhou, 310027, China

Abstract—A metaheuristic encapsulating a novel selecting strategy for finding the best solutions of both individual and a group, a desirability function to quantitatively take into account of dominance, the scaling of the objective functions etc., as well as an iterative mechanism of particle swarm optimization is proposed. Two numerical examples are reported to demonstrate the pros and cons of the proposed metaheuristic algorithm.

I. AN MULTIOBJECTIVE METAHEURISTIC

In engineering synthesis, it is not uncommon to ask the designer to satisfy several seemingly conflicting criteria/objectives simultaneously. Such problems therefore require the finding of the best possible designs to satisfy a set of objectives under different tradeoff scenarios. To reach this goal, increasing endeavors have been devoted to develop metaheuristic algorithms such as, to name but a few, genetic, differential evolution, simulated annealing, tabu search, and particle swarm optimization, in finding a near-complete and near-optimal Pareto front. However, most available metaheuristics have difficulties in finding the best tradeoffs to distributing the computational resources uniformly whilst accomplishing the aforementioned ultimate goal. In this regard, a metaheuristic encapsulating some improved approaches and an iteration mechanism of the Particle Swarm Optimization (PSO) method is proposed with the goal to try alleviating the deficiency of available vector algorithms.

The details about particle swarm optimization method are referred to [1],[2]. Hereafter only the approaches and methodologies for extending the PSO in solving a multiobjective design problem are described.

A. Selection of Best Solutions of Individual and Group

The solution of a multiobjective problem is not unique but is a set of tradeoffs of different objectives referred as the Pareto optimals. As a consequence, the best solutions searched by a particle, denoted by p_{best} stored in P_{best} , and those by its neighbors, denoted by g_{best} memorized in G_{best} , are multiple and these numbers will exceed one as the evolution advances. Since the fitness value of different Pareto optimals may be the same, this will give rise to difficulties when selecting the best solutions of both individual and the group. For example, if the best solutions are selected in a completely random way, due to considerable differences in the positions of the two selected best particles in the parameter space, the particle will oscillate within the parameter space in subsequent iterations, resulting in an inefficient iterative procedure; On the other hand, if the best solutions are always selected in a deterministic way, the distributions of the particles may have limited diversity, leading to a less robust vector optimizer for finding a well-

distribution of Pareto optimals. To keep the best balance of efficiency and robustness of the algorithm, the p_{best} and g_{best} of a particle are selected by using the roulette wheel selection mechanism, but for the former with a probability proportional to the distances of the specified particle to those of P_{best} and for the later, with a probability proportional to the fitness values of the components of G_{best} .

B. Taking Amount of Domination into Consideration

To assess the quality of a particle in a Pareto optimal sense, the dominance concept is commonly used to assign the fitness value [3]. However, such approaches can only determine qualitatively the relationships of dominances among different solutions, it cannot measure quantitatively the 'level' of domination [4]. However, a proper usage of such 'level' could guide the search towards the finding of more and better Pareto optimals with enhanced convergence performances. Hence a desirability function is introduced in that for the particle x_i in question, if its closest Pareto optimal searched so far is denoted by x_i^p , its j^{th} desirability function is formulated as

$$d_j(x_i) = \exp(-|Y_j'|^{n_j}) \quad (1)$$

$$Y_j' = (2Y_j - (USL_j + LSL_j)) / |USL_j - LSL_j| \quad (2)$$

where; $Y_j = |f_j(x_i) - f_j(x_i^p)|$; USL_j and LSL_j are, respectively, the upper and lower specification levels characterizing a symmetric desirability around a target value in the middle between two limits of the j^{th} objective or criterion; $n_j > 0$ controls the shape of the two-sided desirability function.

Once the desirability functions for all objectives are determined, the desirability function characterizing the "level" of dominances is defined as

$$d(x_i) = \prod_{j=1}^{N_f} d_j(x_i) \quad (3)$$

This *ad hoc* desirability function will then be used to incorporate the 'level' information into the fitness value of a particle using the following formula,

$$f_{fit}(x_i) = w_1 f_{fit}^{nor}(x_i) + (1 - w_1) [d(x_i) / \sum_{j=1}^{N_p} d(x_j)] \quad (4)$$

where, $f_{fit}^{nor}(x_i)$ is the normally defined fitness of x_i , w_1 is a weighting constant, N_p is the size of the swarm.

C. Scaling of Different Objectives

For an engineering design problem, different criteria or objectives have significant differences in magnitude, which

will result in an unevenly distributed Pareto frontier [5]. To eliminate this problem, the objectives are normalized to

$$\hat{f}_i = (f_i - f_i^{\min}) / (f_i^{\max} - f_i^{\min}) \quad (5)$$

where f_i^{\min} and f_i^{\max} are, respectively, the minimum and maximum values of the i^{th} objective function.

To fully use the information gathered from the so far searched Pareto solutions, a continuous approximation of these solutions at the end of each swarm is constructed using a 'support vector machine based' response surface model. As more promising solutions might be found on this response surface, an intensifying search is then designed to exploit the sampling points generated by means of an interpolation on this surface in order to find more Pareto solutions. Moreover, the multiplicative scheme for implementing the ε -dominance [6] is used to guarantee the diversity of the final solutions on the Pareto front.

II. NUMERICAL EXAMPLES AND CONCLUSIONS

Extensive numerical experiments on different multi-objective design problems are conducted to validate and to demonstrate the pros and cons of the proposed algorithm. However, due to the limitation of space, only the numerical results on two case studies are reported.

A. Example One

As the first application, the proposed algorithm is utilized to study the multiobjective shape optimization of a coreless solenoid with a rectangular cross-section $a \times b$ [7]. If the current is assumed to be uniformly distributed over the cross-section, the inductance L [μH] and the volume V [m^3] can be approximated by F_1 and F_2 , respectively, as follows:

$$F_1 = \frac{31.49 \frac{k_1^2}{4\pi^2 b}}{9 + 6 \frac{a}{b} + 5 \frac{k_1 k_2}{\pi a b^2}} \quad (6)$$

$$F_2 = \frac{\pi a^2 b}{4} + \frac{k_1^2 k_2^2}{4\pi a^2 b} + \frac{k_1 k_2}{2}$$

Under some simplifications [7], this multiobjective design problem can be formally defined as: maximize the inductance $L(a,b)$ and minimize the volume $V(a,b)$ of the solenoid for a given length $k_1 = 10$ m and cross-section $k_2 = 10^{-6}$ m^2 of the current carrying wire, subject to $a > \sqrt{k_1 k_2 / (4\pi b)}$. The searched Pareto front for this case study using the proposed algorithm is depicted in Fig. 1. It can be seen that the proposed algorithm produces a uniformly sampling of the Pareto front.

B. Example Two

The geometrical design of the multi-sectional pole arcs of a large hydrogenerator [8] is selected as another application of the proposed metaheuristic. The goals of the optimal design includes: maximize the amplitude of the fundamental component of the flux density in the air gap, B_{f1} ; minimize both the distortion factor of a sinusoidal voltage of the machine at no-load, e_v , and the Telephone Harmonic Factor,

THF . It is found that, for a typical run, after 2315 iterations, the proposed metaheuristic yields a set of acceptable Pareto solutions in the objective space, as shown in Fig. 2. Based on these experimental results, it can be seen that the viability of applying the proposed algorithm to multiobjective inverse problems is validated.

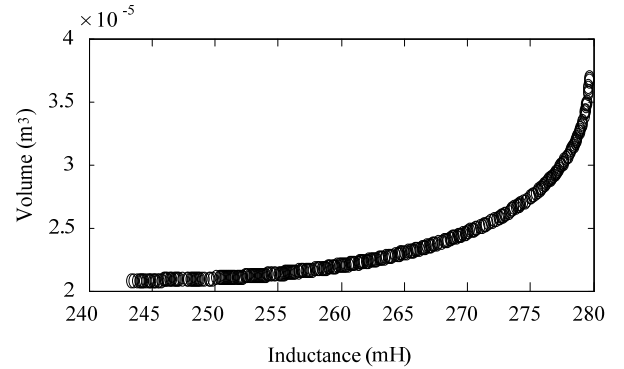


Fig.1. The final solution of the proposed algorithm for example one.

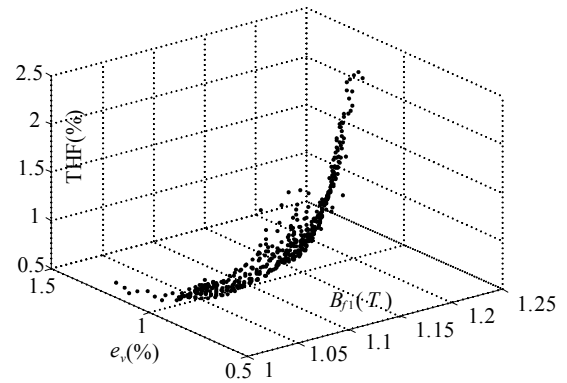


Fig. 2. The searched Pareto optimals by using the proposed method for example two.

III. REFERENCES

- [1] J. Kennedy, and R. Eberhart, "PSO optimization," *Proceedings of IEEE International conference on Neural Networks*, Perth, Australia, vol. IV, IEEE Service Center, Piscataway, 1995, vol. 4, pp. 1941-1948.
- [2] Ho S.L., Shiyong Yang, Guangzheng Ni, Wong H.C., "A particle swarm optimization method with enhanced global search ability for design optimizations of electromagnetic devices," *IEEE Trans. Magn.*, vol. 42, pp.1107-1110, 2006.
- [3] C. A. Coello-Coello, "An updated survey of GA-based multiobjective optimization techniques," *ACM Computing Surveys*, vol. 32, pp. 109-143, 2000.
- [4] Bandyopadhyay S., Saha S., Maulik U., and Deb K., "A simulated annealing-based multiobjective optimization algorithm: AMOSA," *IEEE Transactions on Evolutionary Computation*, vol. 12, pp. 269-283, 2008.
- [5] Messac A., and Mattson C., "Generating well-distributed sets of Pareto points for engineering design using physical programming," *Optimization and Engineering*, vol. 3, pp. 431-450, 2002.
- [6] A. G. Hernández-Díaz, L. V. Santana-Quintero, Carlos A. Coello Coello, and Julián Molina, "Pareto-adaptive ε -dominance," *Evolutionary Computation*, vol. 15, pp. 493-517, 2007.
- [7] P. Di Barba, M. Farina, and A. Savini, "An improved technique for enhancing diversity in Pareto evolutionary optimization of electromagnetic devices," *COMPEL*, vol. 20, pp. 482-496, 2001.
- [8] S. L. Ho, S. Y. Yang, G. Z. Ni, and K. F. Wong, "An efficient multiobjective optimizer based on genetic algorithm and approximation techniques for electromagnetic design," *IEEE Transactions on Magnetics*, vol. 43, pp. 1605-1608, 2007.

The Use of Feature Selection to Create a Compact Prototype for Electromagnetic Device Optimization

Jun Ouyang and David A. Lowther

Department of Electrical and Computer Engineering, McGill University,
3480 University Street, Montreal, H3A 2A7, Canada
jun.ouyang@mail.mcgill.ca, david.lowther@mcgill.ca

Abstract— The design space of an electromagnetic (EM) device is huge and complicate since such devices consist of a large number of interacting sub-components and strong inter-dependencies among elements related to a variety of physical areas such as mechanical, electrical and thermal. However, not all information is necessary when given a design task to build an EM device. In order to eliminate redundant information and speed up the design process, we have developed a compact EM device prototype through feature selection techniques which is described in this paper.

I. INTRODUCTION

Design is an ill-structured problem since its specifications are not always complete and functional goals are often inconsistent; and the corresponding definitions of algorithmic solutions lack clarity. Furthermore, the complexity of the design task increases as the designer addresses the intricacies of a field such as electromagnetic devices [1]. The problem to be considered is that of how to explore the design space with a very large number of dimensions (design features) in order to derive solution candidates which can be quickly improved through an optimizer. Thus it is necessary to develop a compact prototype with reasonable multi-dimensional size and enough information to model an electromagnetic device. One feasible approach to solving this problem is to use feature subset selection techniques. Such a system, as a critical preprocessing step to an intelligent learning system, is an effective way to identify and remove as much irrelevant and redundant information as possible. This reduces the dimensionality of the design space and may allow the design process to perform faster and more effectively. In some cases, accuracy on a future design task can be improved; in others, the derived design prototype is a more compact, easily interpreted representation of the target concept. The intention of this paper is to investigate the feasibility of building a compact prototype for electromagnetic device optimization. To do this, it is imperative to develop a methodology for determining “feature relevance” as a standard to measure the goodness of a selected feature subset in a generic situation. The remainder of this paper is going to illustrate the related concepts, theoretical fundamentals and algorithms. Finally, induction motor case instances are used as a test example to explain the practical significance of developing a compact prototype.

II. FEATURE RELEVANCE MEASURES

Based on the statement from Genari et al., features are relevant if their values vary systematically with category membership [2], the concepts and theoretical background of

how well a particular feature subset can be applied to represent the original design space are formally described with the following definitions and formulae. First, we adopt the definitions of strong relevance, weak relevance and irrelevance in any feature set as described in the paper from John et al.[3]; then introduce how to use correlation between two features as a measure to find the relevant features from the original feature space.

Given an original set of features F , let $F_i \in F$ and $S_i = F - \{F_i\}$.

The following definitions are then made:

Defintion1: (Strong relevance) A feature F_i is strongly relevant iff

$$P(C|F_i, S_i) \neq P(C|S_i)$$

Defintion2: (Weak relevance) A feature F_i is weakly relevant iff

$$P(C|F_i, S_i) = P(C|S_i) \text{ and} \\ \exists S'_i \subset S, \text{ such that } P(C|F_i, S'_i) \neq P(C|S'_i)$$

Defintion3: (Irrelevance) A feature F_i is irrelevant iff

$$\forall S'_i \subseteq S_i, P(C|F_i, S'_i) = P(C|S'_i)$$

Here $P(C|S_i)$ is the probability distribution of different category memberships given the feature values in S_i and $P(C|F)$ is the original distribution given the feature values in F . C is a set of different category memberships.

In order to evaluate the relevance of features for a given classification task, we adopt the correlation between two features as an approximation measure, then it is safe to state a good feature subset is one that contains features highly correlated with the class, yet uncorrelated with each other. So far there are two constant ways to calculate the correlation between feature variables. The first one is based on linear correlation and defined as follows.

For a pair of feature variables (X, Y) , the linear correlation r is defined by the following formula. Here \bar{x}_i is the mean of X , and \bar{y}_i is the mean of Y . The range of r is $[-1, 1]$.

$$r = \frac{\sum_i (x_i - \bar{x}_i)(y_i - \bar{y}_i)}{\sqrt{\sum_i (x_i - \bar{x}_i)^2 (y_i - \bar{y}_i)^2}} \quad (1)$$

The second is based on the information-theoretical concept of entropy, a measure of uncertainty of a random feature variable. It is defined as follows.

$$\text{entropy}(X) = -\sum_i P(x_i) \log_2(P(x_i)) \quad (2)$$

The entropy $(X|Y)$ is defined as the following formula.

$$\text{entropy}(X|Y) = -\sum_j P(y_j) \sum_i P(x_i | y_j) \log_2(P(x_i | y_j)) \quad (3)$$

Another concept, information gain (IG) [4], is given by the following formula.

$$\text{IG}(X|Y) = \text{entropy}(X) - \text{entropy}(X|Y) \quad (4)$$

It is applied to rank the level of correlation of one feature compared with the other two features. In other words, we can say that a feature Y is regarded more correlated to the feature X than to feature Z , if $\text{IG}(X|Y) > \text{IG}(Z|Y)$.

III. A FILTER FEATURE SELECTION ALGORITHM FOR EM DEVICES

The general process of feature subset selection is to iteratively evaluate a candidate subset of features, modify the subset and evaluate if the new subset has a better performance than the old. Since our purpose is to build a compact prototype for electromagnetic device optimization, it is necessary to explore as many design feature subsets as possible. Thus we adopt a filter algorithm [5] that employs correlation-based measures to evaluate the candidate feature subset and different search methods to generate a subset. The framework of a filter algorithm is presented in Fig.1. An induction motor case-base with 11 design features and 22 instances is chosen to test the feasibility of the method for selecting a feature subset from an original design space.

A filter algorithm

```

Input:  $D(F_0, F_1, \dots, F_{n-1})$  // an initial space with N features
       $S_0$  // an initial subset to start the search
       $\delta$  // a stopping criterion
Output:  $S_{\text{best}}$  // an optional subset
1 begin
2 initialize:  $S_{\text{best}} = S_0$ ;
3  $\gamma_{\text{best}} = \text{correlation-sub-eval}(S_0, D)$ ; //correlation-
   based evaluation criterion
4 do begin
5  $S = \text{generate}(D)$ ; // generate a subset for evaluation
6  $\gamma = \text{correlation-sub-eval}(S, D)$ ;
7 if ( $\gamma$  is better than  $\gamma_{\text{best}}$ )
8  $\gamma_{\text{best}} = \gamma$ ;
9  $S_{\text{best}} = S$ ;
10 end until ( $\delta$  is reached);
11 return  $S_{\text{best}}$ ;
12 end.
```

Fig. 1. The framework of a filter algorithm

The purpose of this experiment is to estimate the

dependencies between functional and geometrical design features. Here we choose a critical geometrical feature, stator outer diameter, as the classification feature against other functional features. The experimental result shown in the following table reflects the fact that it is consistent with the domain knowledge in an induction motor.

TABLE I
CRITICAL FUNCTIONAL FEATURES FOR STATOR OUTER DIAMETER

Original features	Selected features
power(KW)	
power(HP)	
poles	
Speed	
rated-current	rated-current
Efficiency	efficiency
power factor	power factor
locked-rotor-current	locked-rotor-current
locked-rotor-torque	locked-rotor-torque
max-torque	max-torque

This case base has been built with the help of MotorSolve provided by Infolytica Corporation [6].

IV. CONCLUSION

A filter feature selection algorithm to reduce the size of the design space for electromagnetic devices has been presented and applied to a database of induction motor designs. Using the information derived, it is possible to create a compact EM device prototype which can be used as the starting point for an optimization process. In effect, the feature subset selection technique provides an efficient and fast approach to exploring the potential design space allowing the optimizer to concentrate on the exploitation phase. The full paper will provide details of the algorithm and more experimental results to demonstrate the feasibility of the methodology presented in this paper.

V. REFERENCES

- [1] Q.V.Vo, "Case-based reasoning approach for the Non-Routine design of Electromagnetic devices", PhD Thesis. Electrical engineering, McGill University, Montreal, QC, Canada, 2000.
- [2] J. H. Gennari, P. Langley, and D. Fisher, "Models of incremental concept formation," *Artificial Intelligence*, (40):11-61, 1989.
- [3] G.John, R.Kohavi, and K.Pfleger, "Irrelevant feature and the subset selection problem," In *Proceeding of the 11th International Conference on Machine Learning*, pages 121-129, 1994.
- [4] J.R. Quinlan, *C4.5 Programs for machine learning*. Morgan Kaufmann, 1993
- [5] H. Liu and L. Yu, "Toward Integrating Feature Selection Algorithms for Classification and Clustering", *IEEE Trans. on Knowledge and Data Engineering*, 17(4):491-502,2005
- [6] *MotorSolve Users Manual*, Infolytica Corporation, Montreal, Canada, 2009.

Optimization of Electromagnetic and Magnetic Shielding using ON/OFF Method

Norio Takahashi, Shunsuke Nakazaki, Daisuke Miyagi

Dept. Electrical and Electronic Eng., Okayama University
3-1-1 Tsushima, Okayama 700-8530, Japan (E-mail: norio@elec.okayama-u.ac.jp)

Abstract — The ON/OFF method which was developed for the static field problem is extended to the dynamic field problem. The method makes them particularly useful in topology optimization, where the parameterization enables all feasible shapes of electromagnetic devices to be explored. We applied the ON/OFF sensitivity method to the steady state linear eddy current problem in order to determine the optimal topology of the electromagnetic and magnetic shield. As a result, the optimal shape of electromagnetic and magnetic shield, which we could not imagine beforehand can be obtained using the ON/OFF method. A criterion of how to choose the sensitivity with respect to the reluctivity or conductivity is discussed. It is shown that the ON/OFF method can be used for the design of electromagnetic or magnetic shielding, even when the material is the magnetic steel sheet which have two kinds of variables, magnetic permeability and conductivity. The best shielding configuration can be obtained for each frequency using a larger design sensitivity.

I. INTRODUCTION

We have already developed the ON/OFF method[1,2] which is attractive for the designer by applying it to the static magnetic field problem. If the ON/OFF method is extended to the optimization of eddy current problem, we may be able to get an optimal electromagnetic or magnetic shielding [3,4] from a comprehensive point of view by distributing conducting materials or magnetic materials in the design domain. As the electrical steel has both large permeability (small reluctivity ν) and conductivity σ , two kinds of design sensitivity $\partial W/\partial \nu$ and $\partial W/\partial \sigma$ (W : objective function) can be considered. However, a criterion for selecting the sensitivity $\partial W/\partial \nu$ or $\partial W/\partial \sigma$ for the optimal design of shielding is not clear.

In this paper, the ON/OFF method is extended to the optimization of the eddy current problem using the step by step method and the adjoint variable method. The shape of electromagnetic shielding (non-magnetic material) and that of magnetic shielding (non-conducting material) are obtained using the ON/OFF method. The possibility of optimizing the shape of shielding having two types of design variables, e.g. ν and σ , like the electrical steel sheet is examined, and the optimization is carried out.

II. OPTIMIZATION OF ELECTROMAGNETIC AND MAGNETIC SHIELDING

The shape of shield is optimized so that the average flux density in a target region is reduced. The analyzed model of the electromagnetic and magnetic shield is shown in Fig. 3. This is a model that the ac magnetic flux produced by the coil is shielded. The shieldings are set between a coil and target region (5mm×40mm×40mm) in which the magnetic flux should be reduced. The design domain (5mm×200mm×200mm) for forming the shielding is divided into cells. The current of the coil is set as 1939AT (60Hz, 1kHz and 10kHz). When the material is a solid (electrical steel), the conductivity σ is 0.7×10^7 (S/m), and the relative permeability μ_r is 1000 in the design region. When the material is a void, the conductivity σ is 0.1×10^3 (S/m), and the relative permeability is unity in the design region. The non-zero conductivity is put to the void, in order to design a current circuit.

The objective function is defined as follows in order to minimize the magnetic flux density at the target region:

$$W = \frac{1}{ne} \sum_{ie} \left\{ |B_x^{(ie)}|^2 + |B_y^{(ie)}|^2 + |B_z^{(ie)}|^2 \right\} \quad (1)$$

where ne is the number of elements in the target region, B_x , B_y , and B_z are the x -, y - and z -components of the magnetic flux density.

When the electrical steel is used in the ac field, it has two kinds of shielding properties, electromagnetic shielding and magnetic shielding. The applicability of the newly developed ON/OFF method which use larger sensitivity between $dW^{(istep)}/d\sigma$ and $dW^{(istep)}/d\nu$ is examined using such a shielding

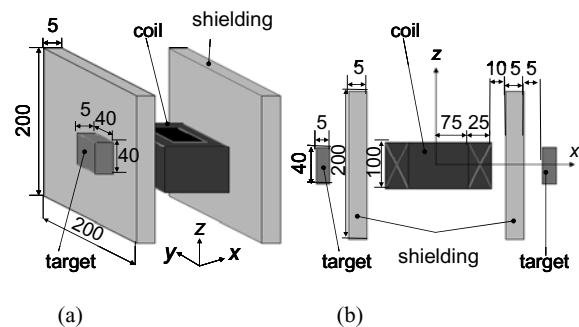


Fig. 1. Analyzed model. (a) overview, (b) x - z plane.

6. Optimization

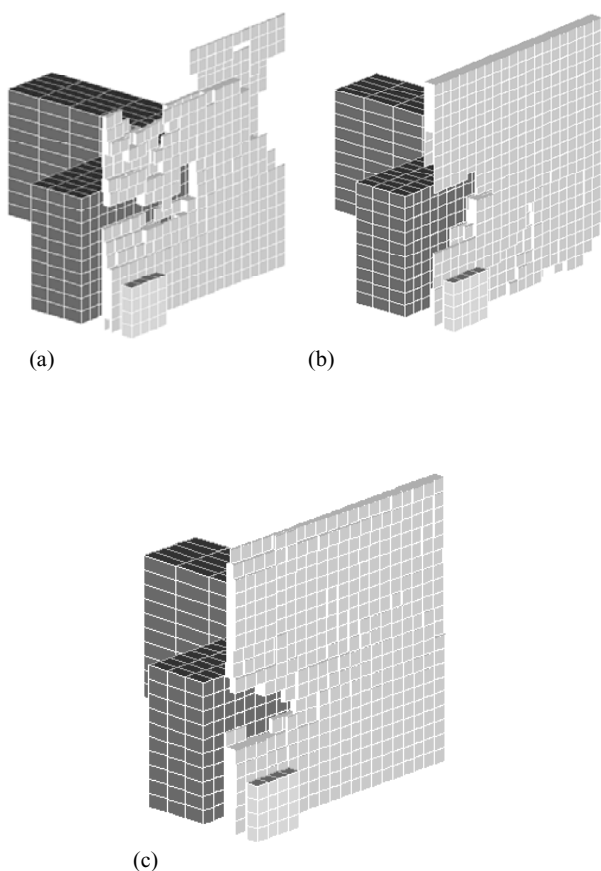


Fig.2. Optimal shapes obtained using various design variables (10kHz). (a) method A, (b) method B, (c) method C.

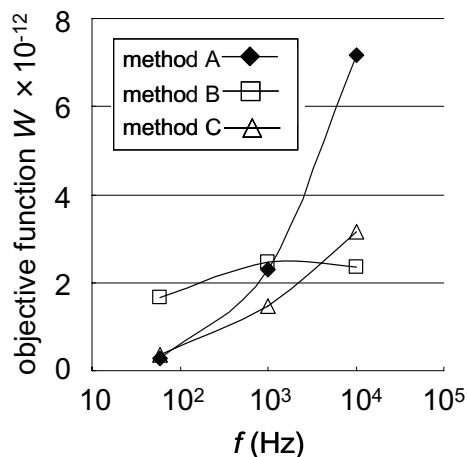


Fig.3. Objective function of optimal topology at each frequency.

composed of electrical steels. The following three kinds of optimization were performed:

(method A)

The design variable is the reluctivity. In this case, the sensitivity $dW/d\nu$ is only calculated.

(method B)

The design variable is the conductivity. In this case, the sensitivity $dW/d\sigma$ is only calculated.

(method C)

The design variables are both reluctivity and conductivity. The sensitivity for each design variable is calculated independently and the sensitivity of which the absolute value is larger is adopted.

Fig.2. Optimal shapes obtained using various design variables (10kHz). (a) method A, (b) method B, (c) method C.

Fig. 2 shows obtained optimal shapes of shielding at 60Hz and 10kHz. Fig. 9 shows the objective function of the optimal shape at each frequency. The flux density in the target region of the initial shape is about 6.6mT, and the value of the objective function is 1.2×10^{-10} . The shielding was most effective in the method A at 60Hz. The flux density in the target region is reduced to about 0.39mT. The shielding was most effective in the case B at 10kHz. This corresponds to the electromagnetic shielding.

The results of methods A and C (50Hz) are similar, and those of method B and C (10kHz) in Fig. 2 are similar. These facts suggests that the optimal topology of electromagnetic shielding or magnetic shielding can be automatically obtained using the technique of method C, which use the larger sensitivity between $dW/d\sigma$ and $dW/d\nu$. In this model, a best configuration of magnetic circuit is obtained by the method C at 1kHz as shown in Fig. 3. The case of 1kHz is the intermediate situation between magnetic shielding and electromagnetic shielding. In such a state, the method C proposed here is very effective.

III. CONCLUSION

The ON/OFF method for the topology optimization is extended to the linear eddy current problem. The technique to optimize the magnetic circuit composed of the material with two kinds of design variables (conductivity and reluctivity) is investigated. It is shown that the electromagnetic shielding and magnetic shielding can be automatically selected, moreover, the best shielding configuration can be obtained for each frequency using a larger design sensitivity with respect to design variable.

REFERENCES

- [1] Y. Okamoto, K. Akiyama, and N. Takahashi, "3-D topology optimization of single-pole-type head by using sensitivity analysis", *IEEE Trans. Magn.*, vol. 42, no.4, pp. 1087-1090, April, 2006.
- [2] K. Akiyama, D. Miyagi, and N. Takahashi, "Design of CF-SPT head having large recording field and small stray field using 3-D ON/OFF method", *IEEE Trans. Magn.*, vol. 42, no.10, pp. 2431-2433, October, 2006.
- [3] M. Blank (Ed.), *Electromagnetic Fields, Biological Interactions and Mechanisms*, American Chemical Society, 1995.
- [4] W. F. Horton & S. Goldberg, *Power Frequency Magnetic Fields and Public Health*, CRC Press, 1995.

Reducing the Design Space of Standard Electromagnetic Devices using Bayesian Response Surfaces

Linda Wang and David A. Lowther

Department of Electrical & Computer Engineering, McGill University, Montreal, Quebec, Canada H3A 2A7

Email: linda.wang@mail.mcgill.ca

Abstract – This work proposes a procedure that reduces the design space of a standard electromagnetic device by using response surface methodology with multivariate Bayesian analysis. Our method seeks to provide a reduced design space that contains the optimal design with a probability of P , where P is specified by the designer and can be arbitrarily close to 1. The reduced design space can then be searched for the optimal device.

I. INTRODUCTION

When designing a standard electromagnetic device, an engineer often has available a library of existing optimal designs for the same type of device made to different specifications. The goal of our work is to make use of this library in order to reduce the search space of new designs. By using response surface methodology and multivariate Bayesian analysis, our method seeks to provide a reduced design space that contains an optimal new design with a probability P , where P is specified by the designer and can be arbitrarily close to 1. The reduced design space can then be searched using standard optimization algorithms.

II. BACKGROUND

The goal of device design is to find values for a set of design variables \mathbf{d} (such as physical dimensions) that satisfy a set of design specifications \mathbf{s} , while minimizing an objective (such as mass). Our work models the relationship between \mathbf{d} and \mathbf{s} by curve-fitting data from existing optimal device designs. This model is then used to predict new designs. The most common type of model used for curve-fitting is *linear regression*. This section explains the multivariate Bayesian version of linear regression that is used in this work.

A. Classic Linear Regression

Linear regression models a *response variable* y as a linear function of the components of a *covariate vector* \mathbf{x} . Note that the components of \mathbf{x} may be transformations of other underlying variables (e.g., $x_1 = s_2 + s_3^2$), so although the model is linear, it can take on many forms including polynomials.

The linear regression model is built by using n pairs of responses and covariates (y_i, \mathbf{x}_i) that already exist. The underlying statistical assumption is that each existing response y_i was generated by a random variable Y_i that has the form

$$Y_i = \beta_1 x_{i1} + \beta_2 x_{i2} + \dots + \beta_p x_{ip} + \varepsilon_i = \mathbf{x}_i^T \boldsymbol{\beta} + \varepsilon_i, \quad (1)$$

where $\boldsymbol{\beta}$ is a vector of p unknown constants called the *model parameters* (the same $\boldsymbol{\beta}$ is used to model all n Y_i 's), and ε_i a zero-mean normally distributed random variable with an unknown variance σ^2 (all n ε_i 's are identically distributed).

The matrix form of (1) is $\mathbf{Y} = \mathbf{X}\boldsymbol{\beta} + \boldsymbol{\varepsilon}$ for $\mathbf{Y} = (Y_1, Y_2, \dots, Y_n)^T$. Given the n pairs of existing responses and their covariates, the elements of $\boldsymbol{\beta}$ are then estimated for this model using least-squares analysis. Using this estimate, a new response at covariates \mathbf{x}_{new} can be predicted as $y_{\text{new}} = \hat{\boldsymbol{\beta}}\mathbf{x}_{\text{new}}$, where $\hat{\boldsymbol{\beta}}$ is the estimate of $\boldsymbol{\beta}$.

In response surface methodology (RSM) [1], this prediction model $y = f(\mathbf{x}) = \hat{\boldsymbol{\beta}}\mathbf{x}$ is called a *response surface*. RSM usually builds response surfaces to model device performance (i.e., the elements in the design specifications \mathbf{s}) as functions of design variables \mathbf{d} . This work, however, models \mathbf{d} as a function of \mathbf{s} instead (this is explained in Section III).

B. Bayesian Multivariate Linear Regression

The classic linear regression model can be modified to be Bayesian [2]. For this work, there are two major advantages of Bayesian analysis: 1) It provides a *distribution*, rather than just a single value, for any predicted response. This distribution takes into account the uncertainties in estimating model parameters. 2) It provides a way of modeling multiple responses that take into account their correlations.

When there are q response variables to be modeled instead of just one, then the single response y becomes a response vector $\mathbf{y} = (y_1, y_2, \dots, y_q)^T$. A *multivariate* model is then built with n pairs of responses and covariates $(\mathbf{y}_i, \mathbf{x}_i)$, where each $\mathbf{y}_i = (y_{1i}, y_{2i}, \dots, y_{qi})^T$. Whereas the univariate model in (1) assumes that each single response y_i was generated by a random variable Y_i , the multivariate model assumes that each response vector \mathbf{y}_i was generated by a random vector \mathbf{Y}_i . The elements of \mathbf{Y}_i are jointly distributed as follows:

$$\mathbf{Y}_i = \mathbf{B}\mathbf{x}_i + \mathbf{u}_i, \quad (2)$$

where \mathbf{B} , a $q \times p$ matrix of unknown constants, is the multivariate version of $\boldsymbol{\beta}$ in (1). \mathbf{u}_i is a zero-mean random vector with an unknown covariance matrix $\boldsymbol{\Sigma}$ (all n \mathbf{u}_i 's are identically distributed).

The matrix version of (2) is $\mathbf{Y} = \mathbf{X}\mathbf{B}^T + \mathbf{U}$, where \mathbf{Y} is an $n \times q$ matrix. For this work, we are interested in studying the *joint distribution* of a predicted response vector \mathbf{Y}_{new} . Given the n pairs of existing response vectors and their covariates, this joint distribution is estimated using Bayesian analysis (we use non-informative prior distributions as in [2]). It is found that the predicted \mathbf{Y}_{new} at \mathbf{x}_{new} has a multivariate student t distribution with mean vector $\hat{\mathbf{B}}\mathbf{x}_{\text{new}}$, and a covariance matrix given by

$$\mathbf{S} = \frac{\nu}{\nu - 2} \left(\frac{\nu((\mathbf{Z} - \mathbf{X}\hat{\mathbf{B}}^T)^T(\mathbf{Z} - \mathbf{X}\hat{\mathbf{B}}^T))^{-1}}{1 + \mathbf{x}_{\text{new}}^T(\mathbf{X}^T\mathbf{X})^{-1}\mathbf{x}_{\text{new}}} \right)^{-1}, \quad (3)$$

where \mathbf{X} is the $n \times q$ matrix formed by stacking the n existing covariates \mathbf{x}_i 's, \mathbf{Z} is the $n \times q$ matrix formed by stacking the n corresponding \mathbf{y}_i 's, $\hat{\mathbf{B}} = \mathbf{Z}^T \mathbf{X} (\mathbf{X}^T \mathbf{X})^{-1}$ is the estimate of \mathbf{B} , and $\nu = n - p - q + 1$ is the degree of freedom of the distribution. This distribution takes into account the errors in $\hat{\mathbf{B}}$ as well as correlations among the elements of \mathbf{Y}_{new} .

C. Confidence Region of Multivariate Normal Distribution

When the degree of freedom of a multivariate t distribution is high, it can be approximated by a multivariate normal distribution. Compared to the multivariate t distribution, much more is known about the properties of the multivariate normal distribution [3]. In particular, standard confidence regions can be constructed for a multivariate normal distribution [4]. If we assume that the distribution of a response vector \mathbf{Y}_{new} predicted at \mathbf{x}_{new} can be approximated by a multivariate normal distribution, then a P confidence region for \mathbf{Y}_{new} is a q -dimensional hyper-ellipse defined by

$$(\mathbf{y} - \hat{\mathbf{B}}\mathbf{x}_{\text{new}})^T \mathbf{S}^{-1} (\mathbf{y} - \hat{\mathbf{B}}\mathbf{x}_{\text{new}}) = \chi_{1-P, q}^2, \quad (4)$$

where $0 < P < 1$, $\hat{\mathbf{B}}$ and \mathbf{S}^{-1} are as defined in the previous section, q is the length of \mathbf{Y}_{new} , and $\chi_{1-P, q}^2$ is the value of the chi-squared distribution with q degrees of freedom evaluated at $1 - P$. This means that the probability that a vector generated by \mathbf{Y}_{new} falls within the given region is P .

III. PROPOSED METHOD

As explained in Section II, the goal of device design is to find a vector of optimal design variable values \mathbf{d}_{opt} that satisfies a specification vector \mathbf{s} while minimizing an objective. Our method seeks to reduce the design space so that the probability of finding \mathbf{d}_{opt} in that space is P . We achieve this by modeling design variables \mathbf{d} as a function of design specifications \mathbf{s} using existing optimal designs. In other words, \mathbf{d} is considered to be a vector of response variables, while a transformation of \mathbf{s} (see Section II-A) is the covariate vector \mathbf{x} . The details of our procedure is described as follows:

- 1) Build a multivariate linear regression model given in (2), where the design variables are the responses to be modeled.
- 2) Given a new set of design specifications, find the covariance matrix given by (3) for the predicted distribution of the design variables at this new specification point.
- 3) Using this covariance matrix, construction a P confidence region given in (4). The probability of finding \mathbf{d}_{opt} in the confidence region is ideally P .

IV. EXPERIMENTAL SETUP

We studied magnetic actuators in this work in order to test the proposed procedure. This required building a library of existing optimal actuator designs first. In order to do this, we optimized 28 actuators (using MagNet [5]) that met specifications found in manufacturers' catalogues [6] [7] while achieving minimum mass. These actuators have five design variables (NI, coil height, coil thickness, plunger diameter, and bushing height) and two design specifications (force and stroke). Fig. 1 shows the design specifications for the actuators.

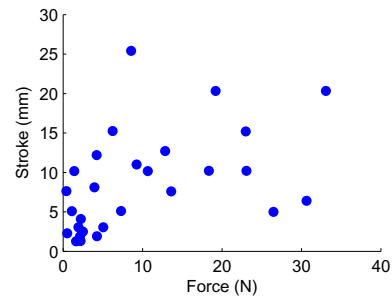


Fig. 1. Specifications of the 28 existing actuator designs

TABLE I
OBSERVED FRACTION OF OPTIMAL DESIGNS IN P CONFIDENCE REGION

	Polynomial order			
	1	2	3	4
$P = 0.99$	0.87	0.86	0.83	0.79
$P = 0.95$	0.81	0.82	0.75	0.71
$P = 0.90$	0.80	0.79	0.69	0.63
$P = 0.75$	0.73	0.73	0.59	0.55
$P = 0.50$	0.55	0.63	0.45	0.37
$P = 0.25$	0.38	0.46	0.31	0.30

After the library was built, the data was fitted to four polynomial models of orders one to four (step 1 in the proposed method). Using steps 2 and 3, the method was tested with 121 new specifications located on an 11×11 grid covering the space shown in Fig. 1. Given a value of P , a confidence region was constructed for each new specification that ideally contains the desired optimal design with probability P . In order to verify whether the optimal design is indeed in the confidence region, we again used MagNet to find the true optimal design at each specification point.

V. PRELIMINARY RESULTS

Table I shows the fraction of optimal designs actually observed in the P confidence regions. For example, the $P = 0.50$ confidence region for the first-order polynomial model contained the optimal design in 66 out of the 121 test cases, hence the observed fraction is $\frac{66}{121} = 0.55$. The observed values show a reasonable correspondence with the ideal P , hence demonstrating that the proposed method is practical. The discrepancies between the observed and ideal values are caused by: 1) the approximation of the multivariate t distributions by multivariate normal distributions (especially for the higher order polynomial models), 2) the small number of samples tested, 3) the limitations in using RSM to model the design space.

REFERENCES

- [1] R. H. Myers and D. C. Montgomery, *Response Surface Methodology*, 2nd ed. Wiley, 2002.
- [2] E. del Castillo, *Process Optimization*. Springer, 2007.
- [3] S. Nadarajah and S. Kotz, "Percentage points of the multivariate t distribution," *International Statistical Review*, vol. 74, no. 1, 2006.
- [4] V. Chew, "Confidence, prediction, and tolerance regions for the multivariate normal distribution," *Journal of the American Statistical Association*, vol. 61, no. 315, 1966.
- [5] *MagNet 6.25*, Infolytica Corp., 2007.
- [6] *Ledex©Tubular Linear Solenoids*, Johnson Electric, 2008.
- [7] *Tubular Solenoids*, Magnetic Sensor Systems, 2008.

Nonlinear Filtering on Mesh Discretization Errors by Neural Networks

D. A. G. Vieira*, A. C. Lisboa*, Vasile Palade† and R. R. Saldanha*

*Department of Electrical Engineering, Federal University of Minas Gerais, Brazil

†Computing Laboratory, Oxford University, UK

{douglas,adriano,rodney}@cpdee.ufmg.br

Abstract—This paper considers the mesh discretization error as a source of noise which entails a non-smooth behaviour in the evaluated electromagnetic fields. This noise is filtered by a neural network (NN), which is constrained to impose a certain level of smoothness, such a way to retain the functions nonlinearities whilst filtering the noise. This is automatically achieved by a multiobjective training algorithm. Results considering a problem with a known analytical solution and a micro motor are presented. They show that this approach can be used to decrease the computational burden in the design of electromagnetic devices.

Index Terms—Mesh density, optimisation, neural networks.

I. INTRODUCTION

For many engineering problems, the objective functions and/or constraints, can only be evaluated by means of numerical techniques, such as the finite element method (FEM), which usually implies a huge computational burden. The FEM requires a mesh generator (a discretization of the domain), and, the evaluation of the real physical properties, are closely related to the mesh quality. Moreover, due mainly to discretization errors, the functions inherit a non-smooth behaviour which renders a more complex optimisation context. This can generate artificial local minima which can trap deterministic techniques and slow down the stochastic ones.

One way to avoid this shortcoming is increasing the mesh density. However, this increases the computational effort required in the optimisation procedure, which can become prohibitive in many cases. This paper treats this discretization error as a source of noise. This noise is then filtered by a NN trained with a multiobjective learning algorithm [1].

Some authors have applied machine learning techniques as an auxiliary tool in the optimisation of electromagnetic devices in the past years. Rashid et al. [2] have applied neuro-fuzzy methods in global optimisation of electromagnetic devices considering an evolutionary step, and, afterwards, a deterministic step using the neuro-fuzzy models. Their approach is based on the approximation of the function and its derivatives by analytically calculating the sensitivity information [3].

A similar approach [4] considers, instead of neuro-fuzzy models, a parallel layer perceptron (PLP) [5] neural network. The main advantage of the latter is a simpler analytical formulation and a faster training and testing algorithm. A slight different approach [6] integrates the NN in the optimisation procedure, where a neural network model is trained to define a deterministic operator inside a genetic optimisation algorithm.

The novelty of this paper relies on the fact that the global approximations are constrained to impose a certain level of smoothness to the objective function. This level of smoothness is automatic defined using the Q -norm complexity measure [7]. This technique is called the minimum gradient method (MGM) and it is applied to the PLP network [5]. The smoothness is defined by an adaptive filtering process. The MGM resembles the weight decay and pruning methods with the advantage of using only convex functions, and, therefore, a closed-form solution, in its formulation. Moreover, it has also some similarities with the Wiener filter [1].

The noise is treated as an uncorrelated residual in the cross-validation procedure. This guarantees to track the main behaviour of the evaluated functions, including nonlinearities. Wanner et al. considered second order model to fit the data and, even though it is capable to filter the noise, it does not model the real nonlinearities of the model [8]. Indeed their aim was to generate a hybrid deterministic/stochastic optimisation tool, which differs from the purpose of this work.

The NN formulation is shortly addressed in the next section. Next, are shown results considering a problem with a known analytical solution and a micro motor design.

II. NEURAL NETWORK FORMULATION

To achieve the desired filtering properties, the NN learning is modelled as a bi-objective optimisation problem which considers simultaneously the minimisation of the empirical error and network output complexity. It is theoretically reasonable to use the norm of the network output gradient as a complexity measure [7], based on output smoothness, high-frequency filtering, the concept of the larger margin, among others. In this way, the gradient norm can be used to compute the complexity for a given machine learning problem and, consequently, the learning problem can be formulated as

$$\min_w \begin{cases} R_{emp}(w) \\ \Omega(w) = \sum_{t=1}^{Tr} \|\nabla_x f(x_t, w)\|^2 \end{cases} \quad (1)$$

where R_{emp} is the empirical error, Ω is smoothness constraint, w are the NN weights, $\nabla_x f(\cdot)$ is the gradient of the NN output, and Tr is the training set size. The aim of this problem is to achieve the equilibrium between the two factors, which are in general conflicting. This equilibrium is responsible for the machine generalization abilities. For the PLP, this problem

can be solved in the linear layer by the closed-form solution,

$$l^* = [\lambda C^T C + (1 - \lambda)Q]^{-1} \lambda C^T d, \quad (2)$$

where l^* is the vector of optimal parameters, C enforces the error minimisation, the matrix Q defines the filtering, λ is defined by the minimum cross-validation error, and d is the desired output vector. See [7] for further details.

III. ELECTROMAGNETIC PROBLEM WITH KNOWN ANALYTICAL SOLUTION

This section considers the results for an electromagnetic problem with analytical solution. The problem is composed by a wire with circular cross-section of radius r carrying a constant current density J . The magnetic flux density B at $a > r$ away from the wire centre is given by $B(r) = \frac{\mu_0 J r^2}{2a}$.

The analytical, the FEM and the FEM smoothed solutions to several radii are shown in Fig. 1. The FEM smoothed solution is closer to the analytical solution than the FEM raw solution. This is due to discretization errors. The Fourier transform of the residual have a white noise characteristic, i.e., it ranges the whole frequency spectrum.

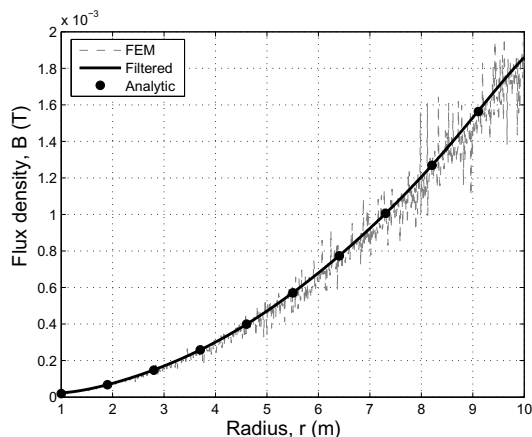


Fig. 1. Analytical, FEM, and FEM smoothed solutions for the wire electromagnetic problem.

IV. MICRO MOTOR

This section considers the average torque $\tau_m(x)$ of a electrostatic micro motor as in [9], parameterized by the rotor and stator teeth width in x . Given an initial design point x_0 , an optimising direction d , and a step α , Fig. 2 shows $\tau_m(x_0 + \alpha d)$ for the FEM result on a coarse mesh, its filtered version using NN, and the FEM result on a fine mesh. The smoothed FEM solution on a coarse mesh captured the main tendency of the problem, which would allow an effective use of derivative based methods.

V. CONCLUSION

This paper treated the mesh discretization error as a source of noise and it was filtered using a nonlinear filter based on NNs. These were trained with a multiobjective algorithm. This

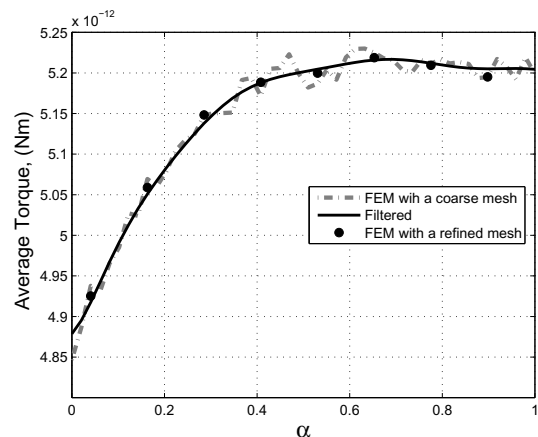


Fig. 2. Results considering the average torque of a micro motor. The filtered version of the FEM solution with coarse is very close to the FEM solution considering a refined one.

assumption was investigated in a problem with known analytic solution and a micro motor, where a correct smoothing was observed. Although this cannot fully replace the FEM solution obtained with a good mesh, the proposed technique can be very useful in some intermediate step in the optimisation and design of electromagnetic devices. Finally, the proposed technique is based on a novel neural network training algorithm which is less dependent on user's defined parameters. This is a very important feature, since automatic design is required in many applications, and the cost to set the parameters can make approximation techniques unfeasible.

ACKNOWLEDGMENT

This work was supported by CNPq and FAPEMIG under grants n^o 305265/2005-9, 13348 and 13180, Brazil.

REFERENCES

- [1] D. A. G. Vieira et al., "Signal denoising in engineering problems through the minimum gradient method," *Neurocomputing*, pp. 1–7, 2009.
- [2] K. Rashid, J. A. Ramirez, and E. M. Freeman, "A general approach for extracting sensitivity analysis from neuro-fuzzy model," *IEEE TMag*, vol. 36, no. 4, pp. 1066–1070, 2000.
- [3] N. Mai-Duy and T. Tran-Cong, "Approximation of function and its derivatives using radial basis function networks," *Applied Mathematical Modelling*, vol. 27, no. 3, pp. 197–220, March 2003.
- [4] D. A. G. Vieira, W. M. Caminhas, and J. A. Vasconcelos, "Extracting sensitivity information of electromagnetic devices models from a modified ANFIS topology," *IEEE TMag*, vol. 40, no. 2, pp. 1180–1183, 2004.
- [5] W. M. Caminhas, D. A. G. Vieira, and J. A. Vasconcelos, "Parallel layer perceptron," *Neurocomputing*, vol. 55, pp. 771–778, 2003.
- [6] D. G. Vieira et al., "A hybrid approach combining genetic algorithm and sensitivity information extracted from a parallel layer perceptron," *IEEE TMag*, vol. 41, no. 5, pp. 1740–1743, May 2005.
- [7] D. A. G. Vieira et al., "The Q -norm complexity measure and the minimum gradient method: a novel approach to the machine learning structural risk minimization problem," *IEEE TNN*, vol. 19, no. 8, pp. 1415–1430, 2008.
- [8] E. F. Wanner et al., "Multiobjective memetic algorithms with quadratic approximation-based local search for expensive optimization in electromagnetics," *IEEE TMag*, no. 6, pp. 1126–1129, June 2008.
- [9] U. Beerschwinger et al., "Coupled electrostatic and mechanical fea of a micromotor," *Microelectromechanical Systems, Journal of*, vol. 3, no. 4, pp. 162–171, Dec 1994.

Particle Swarm Optimization of Coupled Electromagnetic-Electromechanical Systems

N. Al-Aawar¹, T. M. Hijazi¹, A. A. Arkadan^{1,2}, Fellow IEEE

1-Hariri Canadian University, Mechref, Lebanon

2-Marquette University, Milwaukee WI 53203, USA

hijazitm@hcu.edu.lb

Abstract— Design optimization environment utilizing an Electromagnetic-Team Fuzzy Logic, EM-TFL, robust identifier for use with Particle Swarm Optimization, PSO, technique is presented. The developed environment is applied in a case study to optimize various components of a prototype Hybrid Electric Vehicle, HEV, powertrain. This optimization necessitates the characterization of the key electromechanical components of the HEV power train system which includes a generator, an electric motor drive system, and a battery pack in addition to an Internal Combustion Engine, ICE. The basic objective of improving the fuel economy while maintaining the performance of the vehicle is met through the implementation of a PSO algorithm.

I. INTRODUCTION

Growing concerns for clean environment and energy savings increased the demand for more environmentally friendly and fuel-efficient vehicles such as the Hybrid Electric Vehicle, HEV. The HEV makes use of hybrid powertrain which typically consists of an integrated Internal Combustion Engine, ICE, and electric power system. These two systems can be arranged into various configurations. The simplest and the most used configuration is the series configuration shown in Fig. 1 where the ICE is connected to a generator used to charge the batteries and deliver power to an electric motor drive that propels the vehicle [1]. This paper presents an Electromagnetic-Team Fuzzy Logic, EM-FL, module used to setup a robust identifier which is utilized with a Particle Swarm Optimization, PSO, algorithm for the design optimization of a prototype HEV powertrain system. The objective is to improve the efficiency and fuel economy of the HEV while maintaining maximum operating torque.

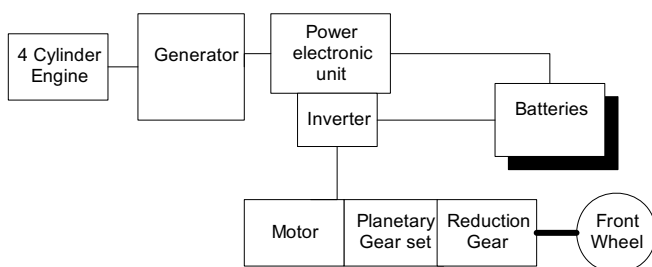


Fig. 1: HEV Series Configuration

II. INTEGRATED OPTIMIZATION ENVIRONMENT

A novel design optimization environment is developed and applied for the design optimization of HEV powertrain systems. The design optimization environment consists mainly of a PSO module and an Electromagnetic-Team Fuzzy Logic,

EM-TFL, module (robust identifier). The major components (functions) of this environment are shown in Fig. 2. It involves setting up several PSO populations to identify each objective and the different output powers used for each component

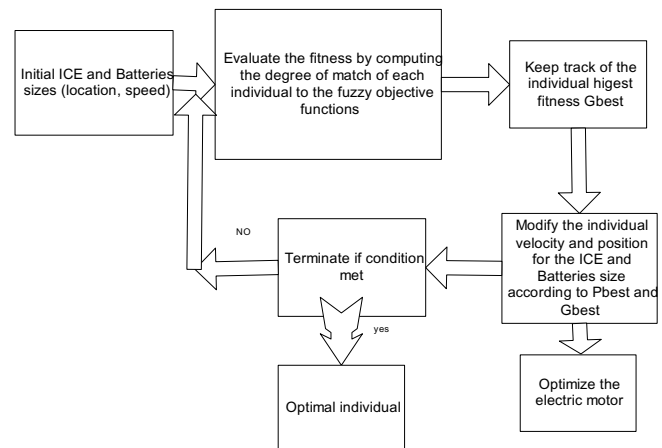


Fig. 2: Block Diagram of the Optimization Process of HEV

A. Particle Swarm Optimization

PSO is a population stochastic optimization technique developed by Eberhart and Kennedy in 1995 [3]. The system is initialized with a population of random solutions and searches for optima by updating generations. In PSO, the potential solutions, called particles, fly through the problem space by following the current optimum particles. Each particle keeps track of its coordinates in the problem space which are associated with the best solution, P_{best} , or fitness it has achieved in the process.

Another "best" value that is tracked by the particle swarm optimizer is the best value obtained during the optimization by any particle in the neighborhood of the particle. This location is called l_{best} . When a particle takes all the population as its topological neighbors, the best value is a global best and is called G_{best} .

B. HEV Powertrain Robust Identifier

The main components of the HEV series configuration under consideration, Fig. 1, are the electrical system which utilizes a Permanent Magnet, PM, generator and a Synchronous Reluctance Motor, SynRM, drive system in addition to an Internal Combustion Engine, ICE [4]. The design methodology of electromechanical systems must

include a robust identifier coupled with a design optimization model that “accurately” and “quickly” predict the performance and optimize the design of the system. The proper modeling of the electric drive under consideration must account for anisotropic effects, saturation effects resulting from the nonlinearity of the material, space harmonic effects resulting from the machine complex geometry and time harmonic effects resulting from the switching of power electronics in the motor drive system. This task is very involving as it requires extensive computations if one to use conventional computational electromagnetics in design optimization cases. In this work, an Electromagnetic-Team Fuzzy Logic, EM-TFL, environment is used for the characterization of the electrical components [5, 6], accordingly, setting up a robust identifier for use in a design optimization process.

This EM-TFL approach consists of two components. The first is the Electromagnetic, EM, module which utilizes a Finite Element-State Space, FE-SS, technique to accurately characterize the electric drive. This EM module is developed to provide the high accuracy needed for the Artificial Intelligence module. It involves iteration between the Finite Element and the State Space models based on the family of curves approach [5] and it is used to generate, mainly offline, a data base necessary to train and setup the second component which is a Team Fuzzy Logic, TFL, Artificial Intelligence, AI, module. This TFL based module is used online to quickly and accurately predict the performance characteristics of the electric drive for a wide range of design parameters and operating conditions [5]. The resulting robust identifier is used next for the design optimization of the HEV series configuration using a PSO technique.

III. APPLICATION AND RESULTS

The developed environment of Fig. 2 was used for the design optimization of a prototype HEV system. The objective is to compute the best size of the ICE, batteries and electric motors to obtain high efficiency and better fuel economy and performance HEV. In order to achieve this goal the ICE has to be sized to operate in the most efficient regions and the developed torque of the electric motor has to be maximized while minimizing its losses.

The HEV power train of Fig.1 includes the following major components: a 1.9-L, 4-cylinder 66 kW output power, 43 % maximum fuel efficiency turbo-charged compression-ignition direct-injection ICE; a 90 kVA PM generator; a 90 kVA SynRM drive; a five-speed transmission; and a battery pack which has a nominal voltage rating of 312 V with an energy content of about 1.56 kWh.

As a result of the optimization process, the ICE and battery bank ratings were determined to be at about 36 kW and 56 kW, respectively. Accordingly, the initial design ICE rated at 1.9-L, 4-cylinder, 66 KW output power was replaced by a smaller engine rated at 1.2-L, 4-cylinder, 36 KW output power. In addition, the electric motor was optimized to reach high torque to weight ratio and to minimize losses. The initial design of the SynRM had a rotor with 4 flux paths and a 4 pole stator with 4 slots per pole per phase, Fig. 3. The required

output torque was selected to be at 90 NM. The optimization process identified a solution with 5 flux paths [6]. A summary of results are shown in Table I where it is shown that both the torque ripple and machine losses were reduced, thus improving the HEV efficiency and fuel economy. In addition, the ICE performance indices are shown in Table II. An increase of 22% in predicted fuel economy and a significant decrease in the concentration of the harmful gas emission are found for the best solution as a result of utilizing smaller engine’s size.

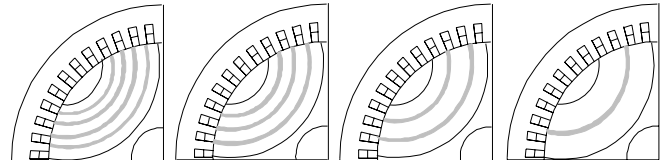


FIG.3. NUMBER OF FLUX PATHS VARIATION

Table I: Electric Motor Initial and Optimal Design

	Initial Design	Optimal Design	Improvement
Losses (W)	6265	2400.9	61.7%
Torque Ripple	52%	29.85%	42.6%
Torque Average	90 N.m.	90 N.m.	N/A

Table II: ICE Output Indices Before and After Optimization

		Before optimization	After optimization
Fuel economy		38.6 mpg	47.1 mpg
Emissions	HC	0.673	.391
	CO	2.641	1.444
	NOx	.462	.322

IV. CONCLUSION

A novel design optimization environment utilizing an Electromagnetic-Team Fuzzy Logic, EM-TFL, robust identifier for use with Particle Swarm Optimization, PSO, technique was developed. The PSO algorithm is capable of optimizing various electromechanical components of HEV powertrain system despite the complexity of the optimization search space. This technique is equally applicable to various coupled electromagnetic – electromechanical systems.

V. REFERENCES

- [1] B. Fahimi, A. Emadi, and R. B. Sepe, Jr., “A Switched Reluctance Machine-Based Starter/Alternator for More Electric Cars,” *IEEE Trans. on Energy Conversion*, VOL. 19, No. 1, pp. 116-124, March 2004.
- [2] M. Cuddy and K. Wipke, “Analysis of the Fuel Economy Benefit of Drivetrain Hybridization,” *SAE Paper 970289*, 1997.
- [3] J. Kennedy, and R. C. Eberhart, “Particle Swarm Optimization”. *Proceedings of IEEE International Conference on Neural Networks*, Piscataway, NJ. pp. 1942-1948, 1995.
- [4] D. Clerk, “The Gas Engine,” Longmans, Green & Co., London, 1886.
- [5] A.A Arkadan, N. Al-Aawar, and T. Ericsen, “EM-TFL Environment for the Design Optimization of Electromagnetic Launchers,” *IEEE Trans. on Magnetics*, VOL. 41, NO. 5, pp.1772 – 1775, May 2005.
- [6] A.A. Arkadan, M. N. ElBsat, and M. A. Mneimneh, “Particle Swarm Design Optimization of ALA Rotor SynRM for Traction Applications,” A Companion Paper Accepted for Presentation at CEFC 2008, Athens Greece, May 11-14, 2008.

Self-Adjoint Material Sensitivity Analysis for Solving Inverse Problems in RF Domain

Jin-Kyu Byun¹, Hyang-Beom Lee¹, Hyeong-Seok Kim², and Dong-Hun Kim³

¹School of Electrical Engineering, Soongsil University, 511 Sangdo-dong, Dongjak-gu, Seoul 156-743, Korea

²School of Electronic Engineering, Chung-Ang University, Seoul 156-756, Korea

³School of Electrical Eng. & Computer Sci., Kyungpook Nat'l. Univ., Daegu 702-701, Korea

E-mail Address: dh29kim@ee.knu.ac.kr

Abstract—This paper presents a new self-adjoint sensitivity formulation for optimal designs and inverse problems in the RF domain. The proposed method is based on continuum approach and material sensitivity analysis. It eliminates the need of solving the adjoint system additionally when the objective function is the function of S -parameter. For verification, the method is applied to the numerical example of dielectric material reconstruction problem in the parallel plate waveguide.

I. INTRODUCTION

Since early '90s, sensitivity analysis has been widely adopted for optimal designs and inverse problems in low frequency domain. In RF domain, these gradient-based methods have also been used over the last several decades, but most of the work has been based on analytic sensitivity calculation with small number of design parameters.

Recently, increasing efforts have been made to introduce adjoint variable method in RF optimization and inverse problems for fast and efficient calculation of sensitivity. Our previous works afford an example, where dielectric waveguide filter [1], and microstrip low-pass filter (LPF) with defected ground structure [2] were optimized utilizing the adjoint variable method.

The heart of the adjoint variable method is to construct the adjoint system and to calculate the adjoint variables. In a normal method, an artificial adjoint source is obtained by differentiating the objective function with respect to the design variables. Then the additional adjoint system with new adjoint source is solved to get the adjoint variables. These adjoint variables are used along with the solutions of the primary (original) system to calculate sensitivity.

In the meantime, there have been some studies to remove this additional step and calculate the adjoint variable directly from the state variable of the primary system. In the low-frequency domain, using self-energy formulation derived from the mutual energy, the sensitivity can be calculated from the solution of the primary system alone if the objective function is defined in terms of the self flux-linkage in the source coil. As for RF systems, Nikolova et al. have presented time-domain formulation for S -parameter sensitivity based on discrete approach that does not require solution of the adjoint system [3]. However, this approach requires field solutions at regular perturbation grid points, making it best suited for the finite-difference time-domain (FDTD) method.

In this paper we propose a new frequency-domain, self-adjoint formula for S -parameter sensitivity calculation with respect to material properties. This method is based on the

recently derived continuum sensitivity analysis for RF systems, and does not require regular meshing of the design region or specific analysis method. The proposed method is applied to the reconstruction of dielectric material distribution inside parallel plate waveguide.

II. SELF-ADJOINT MATERIAL SENSITIVITY FORMULATION

Fig. 1 shows an exemplary 2-port RF system (rectangular waveguide) with dielectric discontinuity inside analysis domain Ω . Port 1 and 2 are defined on boundaries Γ_1 and Γ_2 .

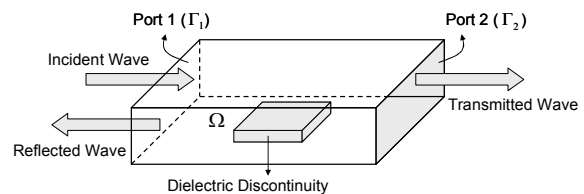


Fig. 1. Rectangular waveguide with dielectric discontinuity.

Let's assume an objective function O is a function of s_{11} . Then O can be defined on boundary Γ_1 as

$$O = \int_{\Gamma_1} g(\mathbf{H}(\mathbf{p})) d\Gamma \quad (1)$$

where g is a scalar function, and the system parameter vector \mathbf{p} consists of permittivity ϵ or permeability μ . On Γ_1 where incident field is imposed, boundary condition of the third kind should be defined, which may be expressed as

$$\epsilon_r^{-1} \hat{\mathbf{n}} \times (\nabla \times \mathbf{H}) + \gamma_h \hat{\mathbf{n}} \times (\hat{\mathbf{n}} \times \mathbf{H}) = \mathbf{V} \quad (2)$$

where γ_h is a known parameter and \mathbf{V} is a known vector that has a magnitude proportional to that of the incident field.

In order to deduce a sensitivity formula, the variational form of the vector wave equation is added to (1) based on the augmented Lagrangian method.

$$\bar{O} = \int_{\Gamma_1} g d\Gamma + \int_{\Omega} \boldsymbol{\lambda} \cdot [-\nabla \times (\epsilon_r^{-1} \nabla \times \mathbf{H}) + k_0^2 \mu_r \mathbf{H}] d\Omega \quad (3)$$

where $\boldsymbol{\lambda}$ is the Lagrange multiplier vector interpreted as the adjoint variable. Applying the first vector Green's theorem to (3), we obtain

$$\bar{O} = \int_{\Gamma_1} g d\Gamma + \int_{\Omega} [-\epsilon_r^{-1} (\nabla \times \boldsymbol{\lambda}) \cdot (\nabla \times \mathbf{H}) + k_0^2 \mu_r \boldsymbol{\lambda} \cdot \mathbf{H}] d\Omega - \int_{\Gamma} \epsilon_r^{-1} \boldsymbol{\lambda} \cdot (\hat{\mathbf{n}} \times \nabla \times \mathbf{H}) d\Gamma \quad (4)$$

The only nonzero contribution of the second surface integral comes from Γ_1 . Substituting (2) into (4), we obtain

$$\begin{aligned} \bar{O} = & \int_{\Gamma_1} g \, d\Gamma + \int_{\Omega} \left[-\varepsilon_r^{-1} (\nabla \times \boldsymbol{\lambda}) \cdot (\nabla \times \mathbf{H}) + k_0^2 \mu_r \boldsymbol{\lambda} \cdot \mathbf{H} \right] d\Omega \\ & - \int_{\Gamma_1} \left[\gamma_h (\hat{n} \times \boldsymbol{\lambda}) \cdot (\hat{n} \times \mathbf{H}) + \boldsymbol{\lambda} \cdot \mathbf{V} \right] d\Gamma \end{aligned} \quad (5)$$

By taking the variation of both sides of (5) with respect to small changes $\delta \mathbf{p}$ of the system parameters, material sensitivity formula in RF system is derived as:

$$\frac{d\bar{O}}{d\mathbf{p}} = \int_{\Omega} \left[-\frac{\partial(\varepsilon_r^{-1})}{\partial \mathbf{p}} (\nabla \times \mathbf{H}) \cdot (\nabla \times \boldsymbol{\lambda}) + k_0^2 \frac{\partial \mu_r}{\partial \mathbf{p}} \mathbf{H} \cdot \boldsymbol{\lambda} \right] d\Omega \quad (6)$$

where $\boldsymbol{\lambda}$ is given by the following adjoint equation, given in a variational form as:

$$\begin{aligned} \int_{\Omega} \left[-\varepsilon_r^{-1} (\nabla \times \bar{\boldsymbol{\lambda}}) \cdot (\nabla \times \boldsymbol{\lambda}) + k_0^2 \mu_r \bar{\boldsymbol{\lambda}} \cdot \boldsymbol{\lambda} \right] d\Omega \\ - \int_{\Gamma_1} \left[\gamma_h (\hat{n} \times \bar{\boldsymbol{\lambda}}) \cdot (\hat{n} \times \boldsymbol{\lambda}) + \bar{\boldsymbol{\lambda}} \cdot \mathbf{g}_H \right] d\Gamma = 0 \end{aligned} \quad (7)$$

where $\bar{\boldsymbol{\lambda}} = (\delta \mathbf{H} + (\partial \mathbf{H} / \partial \mathbf{p}) \delta \mathbf{p})$ can be an arbitrary variable, and $\mathbf{g}_H \equiv \partial g / \partial \mathbf{H}$. Comparing the second and the third term on the right-hand side of (5) with (7), it can be seen that the only difference between the primary system and the adjoint one is the source \mathbf{V} and \mathbf{g}_H on the mixed boundary Γ_1 .

If the objective function is given as

$$O = \int_{\Gamma_1} |S_{11} - S_0|^2 \, d\Gamma \quad (8)$$

where S_0 is the target value of the S -parameter. Then the adjoint source \mathbf{g}_H can be written as

$$\mathbf{g}_H = 2(S_{11} - S_0) \frac{\partial S_{11}}{\partial \mathbf{H}}. \quad (9)$$

Since S_{11} is a linear function of \mathbf{H} on Γ_1 , \mathbf{g}_H can be considered as a constant coefficient. Therefore, by the linearity of the system equation, the adjoint field $\boldsymbol{\lambda}$ can be obtained by dividing the primary solution by the magnitude of \mathbf{V} , and accordingly multiplying the result by the magnitude of \mathbf{g}_H .

III. NUMERICAL EXAMPLE

The proposed method is applied to the reconstruction problem of dielectric material distribution in parallel plate waveguide. For this example, the S -parameter target value S_0 is calculated from dielectric material distribution shown in Fig. 2(a) at 27 frequency points between 300 MHz~3 GHz. The design variable is the normalized material density in each unit cell, which in turn controls the permittivity [1]. The reconstructed dielectric distribution is shown in Fig. 2(b), and the S -parameter plot is shown in Fig. 3. The normalized objective function converged to -48 dB after 728 iterations.

The sensitivity vector $d\bar{O}/d\mathbf{p}$ calculated with the proposed method agrees very well with those calculated by solving an additional adjoint equation. In other words, all components of the sensitivity vectors obtained from the two methods exactly match up to 7 significant figures as shown in Fig. 4.

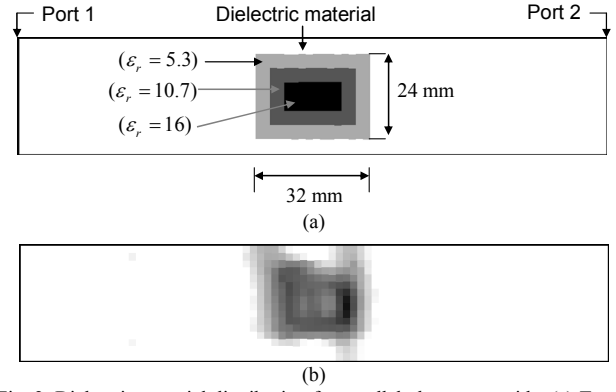


Fig. 2. Dielectric material distribution for parallel plate waveguide. (a) Target model. (b) Reconstructed permittivity distribution.

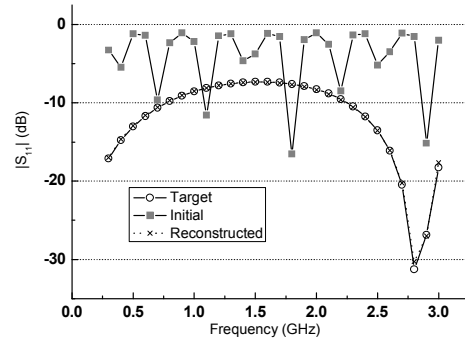


Fig. 3. S_{11} plot of the target model, initial model, and reconstructed model.

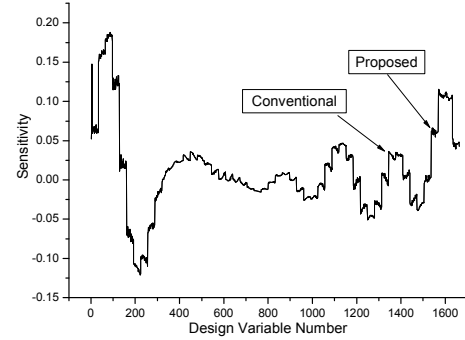


Fig. 4. Comparison of the sensitivity obtained by the proposed and conventional method.

IV. CONCLUSION

This paper proposes a new methodology for optimal design and inverse problems of RF devices, where there is no need to solve the adjoint problem.

V. REFERENCES

- [1] J.-K. Byun and I.-H. Park, "Design of dielectric waveguide filters using topology optimization technique," *IEEE Trans., Magnetics*, vol. 43, no. 4, pp. 1573-1576, 2007.
- [2] J.-K. Byun, J.-H. Ko, H.-B. Lee, J.-S. Park, and H.-S. Kim, "Application of the sensitivity analysis to the optimal design of the microstrip low-pass filter with defected ground structure," *IEEE Trans., Magnetics*, vol. 45, no. 3, pp. 1462-1465, 2009.
- [3] N. K. Nikolova, H.W. Tam, and M. H. Bakr, "Sensitivity analysis with the FDTD method on structured grids," *IEEE Trans., Microw. Theory Techn.*, vol. 52, no. 4, pp. 1207-1216, 2004.

Spatio-temporal reconstruction of magnetic nanoparticle distributions.

Daniel Baumgarten^{1,2} and Jens Haueisen¹

¹Institute of Biomedical Engineering and Informatics, Ilmenau University of Technology, Ilmenau, GERMANY

²Biomagnetic Centre, Department of Neurology, Friedrich Schiller University Jena, Jena, GERMANY

daniel.baumgarten@tu-ilmenau.de

Abstract— The estimation of magnetic nanoparticle distributions is essential for their medical application. In this paper, novel spatio-temporal minimum norm approaches for this inverse problem are presented. These methods are quantitatively evaluated in simulations and compared to the conventional static technique. Our results indicate that the novel spatio-temporal approaches significantly improve the reconstruction quality.

I. INTRODUCTION

Medical applications of magnetic nanoparticles, like magnetic cell labeling, magnetic hyperthermia, magnetic drug targeting and tumor diagnosis, require the quantitative determination of distributions of these particles. Different approaches to this determination have been presented recently [1, 2, 3]. Our approach is based on magnetorelaxometry (MRX) [4]: The particles in the region of interest are magnetized by an externally applied magnetic field. After switching off this excitation field, the magnetic behavior of the particles is read out spatially resolved. From these measurements the distribution of the magnetic nanoparticles can be determined by means of inverse methods. Until now, inverse algorithms like the standard minimum norm estimation (MNE) were applied only to single time steps of the spatio-temporal signals. We propose a way to improve the reconstruction results by integrating the qualitatively known relaxation behavior. In this paper, reconstruction approaches incorporating both spatial and temporal information are investigated and compared to the conventional static inverse computation. In computer simulations, the reconstruction performance of these approaches is examined quantitatively.

II. INVERSE METHODS

A. Forward model

For all reconstruction approaches, the sources are approximated by multiple dipoles positioned on a regular grid below the measurement system. We use the magneto-static dipole to model the sources at the grid points. The magnetic field \vec{B} at position \vec{r} that is produced by a magnetic dipole at position \vec{r}' with moment \vec{m} (μ_0 is the permeability of free space) is computed according to

$$\vec{B}(\vec{r}) = \frac{\mu_0}{4\pi} \left(\frac{3\vec{m} \cdot (\vec{r} - \vec{r}')}{|\vec{r} - \vec{r}'|^5} (\vec{r} - \vec{r}') - \frac{\vec{m}}{|\vec{r} - \vec{r}'|^3} \right). \quad (1)$$

B. Static reconstruction approach

In the conventional static approach, the information on sensor positions and grid sources is merged to the leadfield (sensitivity) matrix L . To find the optimal dipole magnitude

vector \vec{m}_r , the difference between the forward computed field and the measurement vector \vec{b} has to be minimized:

$$\vec{m}_r = \arg \min_{\vec{m}} (L \cdot \vec{m} - \vec{b}) \quad (2)$$

\vec{m}_r can then be determined by a minimum norm estimation [5] using a Truncated Singular Value Decomposition (TSVD) method [6] neglecting singular values of L that are smaller than the regularization parameter σ_r :

$$\vec{m}_r = L_r^+ \cdot \vec{b} = (U \Sigma V^T)_r^+ \cdot \vec{b} = \sum_{i=0}^r \frac{\vec{u}_i^T \vec{b}}{\sigma_i} \vec{v}_i \quad (3)$$

C. Spatio-temporal reconstruction approaches

A simple model to approximate the temporal characteristics of MRX signals is the logarithmic decay [7], with the amplitude a and the relaxation time constant τ :

$$f(t) = a \cdot \ln\left(1 + \frac{\tau}{t}\right) \quad (4)$$

To incorporate this information in the inverse solution, three approaches were implemented:

- 1) Fit of measurement data channels to the model function (4) followed by minimum norm estimation on fitted amplitudes (3)
- 2) Static minimum norm estimation for every sample (3) followed by fit of estimated dipole magnitudes to the model function (4)
- 3) Spatio-temporal minimum norm estimation

For the last approach, the static forward model and therewith the leadfield matrix is expanded following Darvas et al. [8]. The spatio-temporal leadfield matrix L_T is computed as the Kronecker product of $f_T = (f(t_1), f(t_2), \dots, f(t_T))^T$ and L :

$$L_T = f_T \otimes L \quad (5)$$

Replacing L by L_T and \vec{b} by $\vec{b}_T = (\vec{b}(t_1), \vec{b}(t_2), \dots, \vec{b}(t_T))^T$ in (2) and subsequently applying the same TSVD method results in an estimated optimal relaxation amplitude for each dipole.

III. SIMULATIONS

For the evaluation of the performance of the spatio-temporal reconstruction techniques and the comparison to the conventional static approach, we perform simulations varying relevant parameters. We employ the setup of a 16 channel micro SQUID sensor system located at the BIOMAG centre Jena for our simulations, since this system has been involved in spatially resolved MRX experiments. The 16 sensors of the system are arranged in a rectangular area of 32 x 32 mm.

With respect to the low spatial resolution of the sensor setup, the simulated source is formed by a single dipole positioned 10 mm off the centre in both directions and 20 mm

below the sensor plane. The magnitude of the dipole decays following (4) with $\alpha=1 \text{ nAm}^2$ and $\tau=10 \text{ ms}$, which is consistent with measurement values. White Gaussian noise leading to different signal-to-noise ratios (SNR) is added to the simulated data and 50 simulation runs with different noise realizations are conducted. The added noise is realized independently to channels and samples, respectively. The goodness-of-fit (GOF_{nn}), i. e. the root mean square error between the field of the estimated sources and the respective noise-free input data, is selected as the figure of merit in this study.

IV. RESULTS

All spatio-temporal methods yield nearly identical results in the performed simulations with the given setup. Thus, in the following only the results of the third approach and the static approach are compared, respectively. Fig. 1 shows sample results of static and spatio-temporal reconstruction.

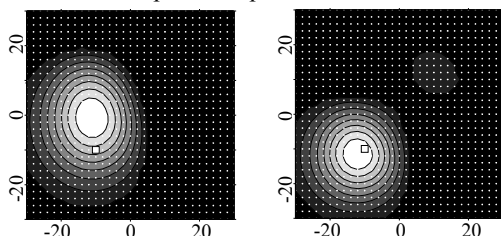


Fig. 1. Sample reconstructions for the static (left) and spatio-temporal (right) approach (SNR of input data: 20 dB; $\sigma_r = 0.05$). The \square identifies the position of the source dipole. All units are mm, step between isolines: $0.25 \cdot 10^{-12} \text{ Am}^2$.

The influence of the regularization parameter σ_r on the reconstruction quality is displayed in Fig. 2. Generally, the values are significantly higher for the spatio-temporal methods. Both spatio-temporal and static approach show the best values for $\sigma_r = 0.05$.

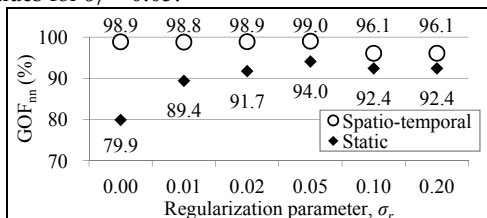


Fig. 2. Mean GOF_{nn} values for different values of the regularization parameter σ_r (SNR of input data: 10 dB; 50 simulation runs, $\text{SD} < 1.5$).

To quantitatively evaluate the sensitivity of the compared approaches towards noise, GOF_{nn} values for different SNRs in the simulated data are investigated (see Fig. 3). For all examined noise levels, the GOF_{nn} of the spatio-temporal approach is above 97 % and significantly larger than the value of the static approach. With increasing SNR, the difference between both methods decreases.

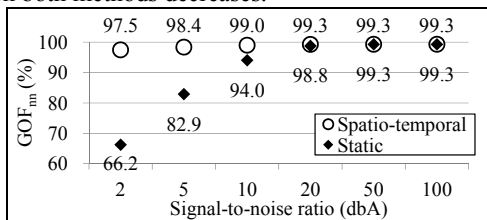


Fig. 3. Influence of noise on the reconstruction quality: Mean GOF_{nn} values for simulated data with different SNRs ($\sigma_r = 0.05$).

We also investigated the influence of the selection of the relaxation time constant in the model function of the spatio-temporal methods. As Fig. 4 shows, the GOF_{nn} decreases with the increasing deviation of the time constants of the inverse model function and the simulated data.

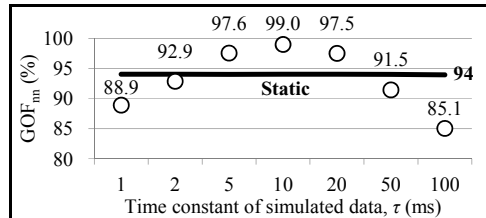


Fig. 4. Mean GOF_{nn} value for different time constants τ in the simulated data spatio-temporally reconstructed with a model function time constant of $\tau = 10 \text{ ms}$; the static approach is invariant to the temporal model function (SNR of input data: 10 dB; $\sigma_r = 0.05$; 50 simulation runs, $\text{SD} < 0.5$).

V. CONCLUSION

Our simulations show that the integration of temporal information in the reconstruction of magnetic nanoparticle distributions from MRX measurements considerably improves the reconstruction quality, regardless of the regularization parameter. The robustness against noise significantly increases. Even with slight deviations between the time constants in the inverse model function and the data, the spatio-temporal approaches still show better results than the conventional static approach.

Planned work comprises intensive studies on the properties of the spatio-temporal reconstruction approaches with respect to more complex model functions accounting for different relaxation processes and the size distribution of the particles.

VI. ACKNOWLEDGEMENTS

This study was supported by the State of Thuringia/Germany (2008VF0001; 2008FE9048) under participation of the European Union within the European Funds for Regional Development (EFRE).

VII. REFERENCES

- [1] E. R. Flynn and H. C. Bryant, "A biomagnetic system for in vivo cancer imaging", *Phys Med Biol*, vol. 50, pp. 1273–1293, 2005.
- [2] B. Gleich and J. Weizenecker, "Tomographic imaging using the nonlinear response of magnetic particles", *Nature*, vol. 435, no. 7046, pp. 1214–1217, 2005.
- [3] F. Wiekhorst, R. Jurgons, D. Eberbeck et al., "Quantification of magnetic nanoparticles by magnetorelaxometry after local cancer therapy with magnetic drug targeting", *J Nanosci Nanotechnol*, vol. 6, no. 9–10, pp. 3222–3225, 2006.
- [4] D. Baumgarten, M. Liehr, F. Wiekhorst, et al., "Magnetic nanoparticle imaging by means of minimum norm estimates from remanence measurements", *Med Biol Eng Comput*, vol. 46, pp. 1177–1185, 2008.
- [5] J. Z. Wang, S. J. Williamson, L. Kaufman, "Magnetic source images determined by a lead-field analysis: The unique minimum-norm least squares estimation", *IEEE Trans Biomed Eng*, vol. 39, no. 7, pp. 665–675, 1992.
- [6] P. C. Hansen, "The truncated SVD as a method for regularization", *BIT*, vol. 27, pp. 534–553, 1987.
- [7] D. Eberbeck, S. Hartwig, U. Steinhoff, et al., "Description of the magnetization decay in ferrofluids with a narrow particle distribution size", *Magneto hydrodynamics*, vol. 39, no. 1, pp. 77–83, 2003.
- [8] F. Darvas, U. Schmitt, A. K. Louis, "Spatio-Temporal Current Density Reconstruction (stCDR) from EEG/MEG-Data", *Brain Topogr*, vol. 13, no. 3, pp. 195–207, 2001.

Non-Iterative Methods for Locating Inclusions in Electrical Impedance Tomography

Flavio CALVANO¹, Guglielmo RUBINACCI¹ and Antonello TAMBURRINO²

¹ Ass. EURATOM/ENEA/CREATE, DIEL, Università degli Studi di Napoli Federico II, Italy

² Ass. EURATOM/ENEA/CREATE, DAEIMI, Università di Cassino, Italy

flavio.calvano@unina.it, rubinacci@unina.it, tamburrino@unina.it

Abstract—Electrical Resistance Tomography (ERT) is a body of methods and techniques aimed to reconstruct the spatial distribution of the conductivity of a material starting from the knowledge of boundary measurements such as, for instance, the Neumann-to-Dirichlet map. This inverse problem is ill-posed and nonlinear and, therefore, its solution require a considerable computational effort. In this paper we discuss three fast non-iterative reconstruction methods for locating inclusions in an otherwise homogeneous material. These methods, potentially, are candidate for near real-time applications.

I. INTRODUCTION

This paper is focused on the Electrical Resistance Tomography (ERT) to detect inclusions in conducting materials by non-iterative methods. Non-iterative methods have attracted a lot of interest because they provide a test for evaluating if a point of the domain (or a subregion) is part or not of the anomaly, regardless other points (or subregions). The test is usually very cheap from the computational viewpoint. On the other hand iterative methods, representing the most common approaches to inverse problems, update iteratively the current estimate of the spatial distribution of the conductivity. At each step of the algorithm at least one forward problem has to be computed thus, the computational cost is an issue and, moreover, the solution can be trapped in false solutions.

In ERT a major role is played by the Neumann-to-Dirichlet map that is the operator Λ mapping the boundary (applied) currents f into the boundary (measured) voltages $u|_{\partial\Omega}$, i.e. $\Lambda: f \rightarrow u|_{\partial\Omega}$ where

$$\begin{cases} \nabla \cdot \sigma \nabla u = 0 & \text{in } \Omega \\ \sigma \partial u / \partial \nu = f & \text{on } \partial\Omega \end{cases} \quad (1)$$

Ω is the conducting domain under investigation and ν is the outward normal on $\partial\Omega$.

It is well known (see [1]–[5]) that the inverse problem of reconstructing the conductivity σ from the knowledge of Λ has an unique solution when the conductivity satisfies some assumptions. In particular, here we face the reconstruction of piecewise smooth conductivities (for the uniqueness see [1]).

Here we assume a constant background conductivity constant conductivities into each inclusion. In addition, each inclusion occupies a simply connected domain with enough smooth boundary. The union of all inclusion is the set $B \subset \Omega$.

In this paper we are going to show three fast and non-iterative algorithms that we have implemented and a comparison of the related performances.

II. NON-ITERATIVE IMAGING METHODS

A. First method

The first algorithm is based on the factorization method proposed by Bruhl and Hanke in [6]. This method requires the knowledge of the background Neumann-to-Dirichlet map Λ_0 (i.e. the map when no anomalies are present in Ω) and the measured map Λ corresponding to the domain with defects.

In [6] and references therein, it is shown that a point $z \in \Omega$ belongs to an inclusion if and only if the boundary value $g_{z,d} = G_{z,d}|_{\partial\Omega}$ is in the range of $(\Lambda - \Lambda_0)^{1/2}$, i.e.:

$$\sum_{k=1}^{+\infty} \langle g_{z,d}, v_k \rangle^2 / \lambda_k < +\infty \quad (2)$$

where the v_k 's and λ_k 's are the eigenfunctions and eigenvalues of $\Lambda - \Lambda_0$, respectively and $G_{z,d}$ is the solution of:

$$\begin{cases} \Delta G_{z,d} = \Delta D_{z,d} & \text{in } \Omega \\ \partial G_{z,d} / \partial \nu = 0 & \text{on } \partial\Omega. \end{cases} \quad (3)$$

In (3) $D_{z,d}$ is the dipole potential:

$$D_{z,d}(x) = \frac{(z-x) \cdot d}{2\pi|x-z|^n}, \quad x \neq z \quad (4)$$

and d is a fixed but otherwise arbitrary unit vector.

B. Second method

The second method is an algorithm based on the Multiple Signal Classification method (MUSIC) that has been shown to be closely related to the Factorization method if small inclusions are considered [7]. The MUSIC algorithm has been developed by Devaney [8] to locate point scatterers from multistatic measurements in wave propagation inverse problems. The same principle can be applied to small cavities that can take the role of the point scatterers. If each inclusion centered in z_k is surrounded by a circle of radius εr_k , it is possible to show [7] that the Neumann-to-Dirichlet map Λ_ε converges to Λ_0 as $\varepsilon \rightarrow 0$ and that the range of the difference $\Lambda_\varepsilon - \Lambda_0$ is finite dimensional. In the limit for small ε , a point z is in the inclusion if and only if the function $g_{z,d}$ of II.B is in the range of $\Lambda_\varepsilon - \Lambda_0$. Therefore, the MUSIC algorithm constructs the spatial map:

$$\cot\theta(z) = \frac{\|Pg_{z,d}\|}{\|(I-P)g_{z,d}\|} \quad (5)$$

where P is the orthoprojector operator in the range of $\Lambda_\varepsilon - \Lambda_0$ and θ represents, geometrically, the angle between $g_{z,d}$ and the range of $\Lambda_\varepsilon - \Lambda_0$. By construction $\cot\theta(z)$ is very large when z is inside an inclusion because $g_{z,d}$ has a vanishing projection in the subspace orthogonal to range of $\Lambda_\varepsilon - \Lambda_0$, i.e. $(I-P)g_{z,d}$ is very small. In the presence of noise having level δ the orthoprojector P is reduced from the range of $\Lambda_\varepsilon - \Lambda_0$ to the linear space spanned by the first Ritz vectors of $\Lambda_\varepsilon - \Lambda_0$ whose Ritz values are greater than δ .

C. Third method

The third method is based on an imaging method developed by the authors in [9]. The method relies on the idea that inclusions with higher electrical resistivity increase the boundary voltages in some sense [10]. In particular, is possible to demonstrate the following monotonicity for the Neumann-to-Dirichlet map:

$$B_1 \subseteq B_2 \Rightarrow \Lambda_2 - \Lambda_1 \geq 0 \quad (6)$$

where \geq means positive semi-definite and Λ_k is the Neumann-to-Dirichlet map corresponding to anomalies occupying region B_k . The inversion algorithm [9] is based on:

$$\Lambda - \Lambda_{\text{test}} \geq 0 \text{ false} \Rightarrow \Omega_{\text{test}} \not\subseteq B \quad (7)$$

that follows directly from (6) where Ω_{test} is a generic test anomaly used to reconstruct the unknown anomaly B .

The imaging method checks (7) for different trial anomalies, for instance those obtained by partitioning the domain Ω in non-overlapped subsets (see figure 1). Then, it is possible to establish if a generic subset of this partition is part or not of the unknown anomaly B . Then, the reconstruction is the union of the subset that, through test (7), result to be included in B .

Test (7) can be performed by evaluating the sign of the eigenvalues of $\Lambda - \Lambda_{\text{test}}$. In order to avoid false negative due to the presence of noise that can alter the eigenvalues closer to zero, we associate to the test anomaly in subdomain k the following quantity (sign index):

$$s_k = \sum_j \lambda_{k,j} / |\lambda_{k,j}| \quad (8)$$

where $\lambda_{k,j}$ are the eigenvalues of $\Lambda - \Lambda_k$ and Λ_k is the Neumann-to-Dirichlet map related to test domain k . Then, the spatial map $1/(1 - s_k)$ reveals the presence of anomalies in the peaks.

III. NUMERICAL EXAMPLE

This preliminary numerical example is related to an almost rectangular inclusion embedded in a circle with a radius of 1cm. The defect has a resistivity that is 100% larger than those of the background. The synthetic data have been obtained by

an in-house FEM code. Random noise has been added to the numerically Neumann-to-Dirichlet map in order to avoid the inverse crime.

In the full paper we will give further details of the methods and we will propose an exhaustive comparison between these methods.

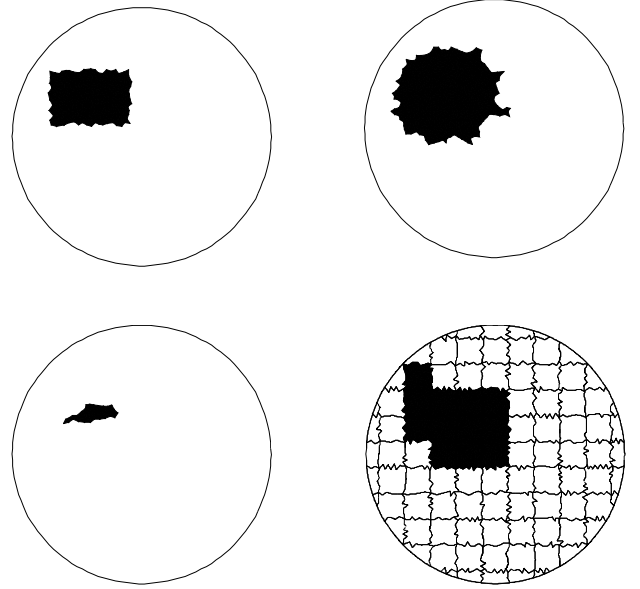


Fig. 1: Top: the real inclusion (left) and the reconstruction obtained by the factorization method (right). Bottom: the reconstruction obtained by MUSIC (left) and by the monotonicity method (right). The grid of the subdivision in test subdomains is also shown (bottom, right).

IV. REFERENCES

- [1] Kohn R and Vogelius M1984 Determining conductivity by boundary measurements *Commun. Pure Appl. Math.* **37** 289–98
- [2] Sylvester J and Uhlmann G 1987 Global uniqueness theorem for an inverse boundary value problem *Ann. Math.* **125** 153–69
- [3] Nachman A I 1988 Reconstruction from boundary measurements *Ann. Math.* **128** 531–76
- [4] Nachman A I 1995 Global uniqueness for a two-dimensional inverse boundary value problem *Ann. Math.* **142** 71–96
- [5] Isakov V 1993 Uniqueness and stability in multi-dimensional inverse problems *Inverse Problems* **9** 579–621
- [6] M. Brühl and M. Hanke, Numerical implementation of two noniterative methods for locating inclusions by impedance tomography, *Inverse Problems*, pp. 1029–1042, 2000.
- [7] M. Hanke and M. Brühl, Recent progress in electrical impedance tomography, *Inverse Problems*, pp. S65–S90, 2003.
- [8] Devaney A J, Super-resolution processing of multi-static data using time and reversal and MUSIC, *J. Acoust. Soc. Am.*, 2004.
- [9] A. Tamburrino and G. Rubinacci, A new non-iterative inversion method for electrical impedance tomography, *Inverse Problems*, pp. 1809–1829, 2002.
- [10] D. G. Gisser, D. Isaacson and J. C. Newell, “Electric current computed tomography and eigenvalues”, *SIAM J. of applied Mathematics*, pp. 1623–1634, 1990.

A Research of PTP MRAM about Shape Optimization for High Gb/Chip

Hyuk Won, Gwan Soo Park, Dong Sok Kim, and Jae Min Kim

School of Electrical Engineering, Pusan National University

Jangjeon-dong, Guemjeong-gu, Busan, 609-735, Korea

raafil98@pusan.ac.kr; gspark@pusan.ac.kr; kdongsok@pusan.ac.kr; jmin@pusan.ac.kr

Abstract— This paper presents a new MRAM using perpendicular magnetic tunnel junction device about shape optimization for high capacity. Conventional MRAM need more increasing current power as smaller size for high capacity. It is critical problem that need more increasing current power. As a solution, we propose a new MRAM that has two additional high permeable poles in this paper. Proposed new MRAM has a strong switching field owing to two poles added on both sides of the free layer, just like perpendicular magnetic recording heads. For high Gb/Chip, by change of shape design, new MRAM can have a strong switching field on the same injected current. We show results that are variation of a switching field owing to two poles added on both sides of the free layer by thickness of the free layer and cell square size, injected current density. So we present an optimization design of new MRAM for high Gb/Chip. This research was done using three dimensional FEM with injected current density of $5 \times 10^6 \text{ A/cm}^2 \sim 6 \times 10^8 \text{ A/cm}^2$.

I. INTRODUCTION

Partly because conventional MRAM has a faulty structure using a simple write current injection system, magnetoresistive random access memory (MRAM) is reducing its expectation as a commercial non-volatile memory. For downsize scalability, the major problem that is the mere write current is required at the smaller bit size should be solved with a new design [1]-[2]. STT MRAM technology has advantages conventional (toggle) MRAM on injected current and cell size. STT writing technology, by directly passing a current through MTJ, overcomes these hurdles with much lower switching current, simpler cell architecture which results in a cell that can be as small as 6F2 (for single-bit cells) and reduced manufacturing cost, and more importantly, excellent scalability to future technology nodes [3].

In this paper, we presents a new technology that has advantages conventional MRAM on injected current and cell size. It is Pole Type Perpendicular MRAM (PTP MRAM). PTP MRAM uses perpendicular magnetic field in order to change the state of the free layer in a perpendicular magnetic tunnel junction (pMTJ) [4]-[5]. PTP MRAM uses two high permeability poles on both sides of the free layer in order to enhance switching field. Switching filed of conventional MRAM generated by injected current is equally distributed on the space but most of the field in PTP MRAM passes through the additional poles with high permeability. PTP MRAM has downsize scalability and is expected to be utilized usefully as a commercial memory with high capacity for having the enhanced switching field. Also PTP MRAM solves thermally assisted self-demagnetizing problem because this system is able to use high coercivity free layer.

We show results that are variation of a switching field owing to two poles added on both sides of the free layer by thickness of the free layer and cell square size, injected current density. So we present an optimization design of new MRAM for high Gb/Chip. This research was done using three dimensional FEM with injected current density of $5 \times 10^6 \text{ A/cm}^2 \sim 6 \times 10^8 \text{ A/cm}^2$.

II. THE PTP MRAM CELL

Fig. 1 shows a schematic drawing of the PTP MRAM element. PTP MRAM element has two poles added on both sides of the free layer. The material of these poles has high permeability and then this system is able to have enhanced switching field. We call bit pole for the one on top of the free layer and word pole for the other beneath the free layer. Both poles have a single current line at the side. PTP MRAM has pMTJ on the bottom of the word pole. Fig. 2 (a) ~ (c) describes the write process of PTP MRAM. Memory status is “0” in fig. 2 (a) because having same direction of magnetization in the free layer and the fixed layer. When bit current and word current are injected. Magnetization of the free layer is changed rapidly by the switching field assisted by the bit pole and word pole as fig. 2 (b). Finally the state of the free layer is changed like fig. 2 (c) and then the cell has the status “1”. Usually the name of pMTJ stands for a set of free layer, fixed layer and junction but in this paper pMTJ shows only junction part like fig. 2 (d).

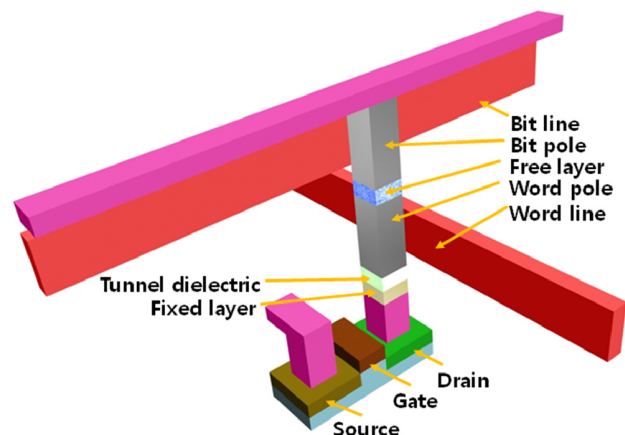


Fig. 1. Schematic drawing of the PTP MRAM cell. PTP MRAM has a two high permeability poles added on both sides of free layer, named bit pole on top of free layer and word pole beneath the free layer. This system has the pMTJ beneath the word pole and fixed layer is poisoned beneath the pMTJ.

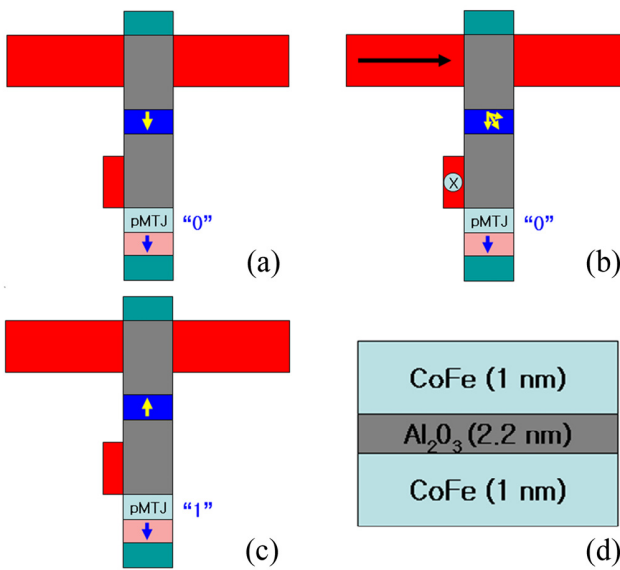


Fig. 2. . Write process of the PTP MRAM and structure of the pMTJ. (a) shows "0" status. When direct current is injected in bit and word line, status of free layer is changed like (b). Finally status of the free layer is stabilized to be "1" status as (c). (d) shows the structure of the pMTJ.

III. RESULT AND DISCUSSION

The PTP MRAM has superior magnetic field efficiency than conventional MRAM because this novel system has additional high permeability poles, which are expected to generate stronger switching field than conventional MRAM system. So this system has downsize scalability and high coercivity magnet can be used in the free layer. Figure 3 shows magnetic field intensity on the center of the free layer in PTP MRAM and conventional MRAM with direct current densities $I = 5 \times 10^6 \text{ A/cm}^2 \sim 6 \times 10^8 \text{ A/cm}^2$. Clearly the stronger switching field is generated in PTP MRAM than in conventional MRAM at the same direct current.

Fig. 4 shows a result that is magnetic field intensity by changing free layer thickness on the center of the free layer of PTP MRAM with a direct current densities factor $I = 5 \times 10^6 \text{ A/cm}^2$. We can know that switching field will be strong for decreasing free layer's thickness of the PTP MRAM. But to

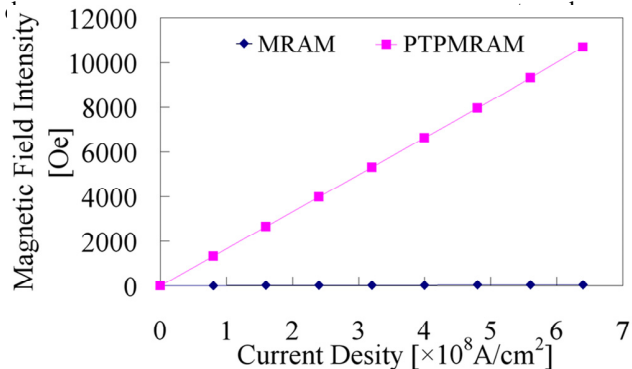


Fig. 3. Comparison of magnetic field intensity on the center of the free layer of PTP MRAM and conventional MRAM with a direct current densities factor $I = 8 \times 10^7 \text{ A/cm}^2 \sim 6 \times 10^8 \text{ A/cm}^2$. Clearly the graph shows PTP MRAM has a stronger field than conventional MRAM on the same current density injected.

TABLE I
MAJOR SPECIFICATIONS USED FOR CALCULATIONS

	Single Current Type
Cell Square Size	50 nm (W) X 50 nm (H)
pMTJ Thickness	2.2nm
Fixed Layer Thickness	30 nm
Free Layer Thickness	10 ~ 30 nm
Metal Contact Thickness	30 nm
Pole Length	400 nm
Cell Gap	50 nm
Current Line Cross-section	50 nm (W) X 400 nm (H)
Current Range	$5 \times 10^6 [\text{A/cm}^2]$

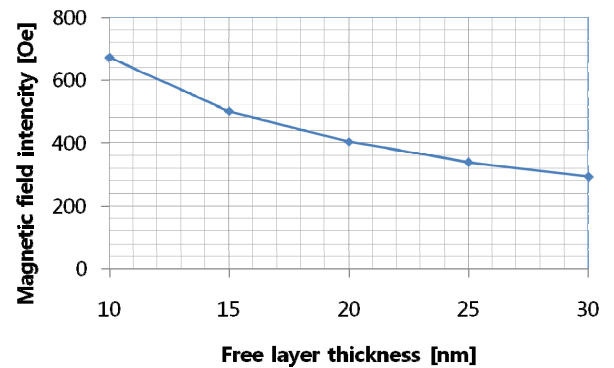


Fig. 4. Results of magnetic field intensity by changing free layer thickness on the center of the free layer of PTP MRAM with a direct current densities factor $I = 5 \times 10^6 \text{ A/cm}^2$.

Free layer's thickness increases the coercivity.

IV. CONCLUSION

We present an optimization design of new MRAM for high Gb/Chip. This research was done using three dimensional FEM with injected current density of $5 \times 10^6 \text{ A/cm}^2 \sim 6 \times 10^8 \text{ A/cm}^2$. Next time, research will more be optimizing the switching field and injection current.

V. REFERENCES

- [1] Mark Durlam, Peter J. Naji, Asim Omair, Mark DeHerrera, John Calder, Jon M. Slaughter, Brad N. Engel, Nicholas D. Rizzo, Greg Crynkewich, Brian Butcher, Clarence Tracy, Ken Smith, Kelly W. Kyler, J. Jack Ren, Jaynal A. Molla, William A. Feil, Rick G. Williams, and Saied Tehrani, "A 1-Mbit MRAM Based on 1T1MTJ Bit Cell Integrated With Copper Interconnects", IEEE J. Sol. Sta. Circ., vol. 38, No. 5, MAY 2003.
- [2] Jianguo Wang and P. P. Freitas, "Low-Current Blocking Temperature Wriing of Double-Barrier MRAM Cells", IEEE Trans. On Mag., vol. 40, No. 4, July 2004. AAPS Bulletin, vol. 18, No. 6, December 2008.
- [3] Yiming Huai, "Spin-Transfer Torque MRAM (STT-MRAM): Challenges and Prospects",
- [4] Naoki Nishimura, Tadahiko Hirai, Akio Koganei, Takashi Ikeda, Kazuhisa Okano, Yoshinobu Sekiguchi, and Yoshiyuki Osada, "Magnetic tunnel junction device with perpendicular magnetization films for high-density magnetic random access memory", J. Appl. Phys., vol.91, Apr. 2002.
- [5] Xiaochun Zhu and Jian-Gang Zhu, "Spin Torque and Field-Driven Perpendicular MRAM Designs Scalable to Multi-Gb/Chip Capacity", IEEE Trans. On Mag, vol. 42, No. 10, October 2006.

Brain source localization: a MILP approach

Fabio Freschi

Department of Electrical Engineering

Politecnico di Torino, Italy

Email: fabio.freschi@polito.it

Abstract—The purpose of this work is to propose and test a mixed integer linear programming formulation for the problem of brain source localization. Such technique allows the localization of the minimum number of currents that are able to reconstruct potentials recorded at the scalp. The algorithm makes use of binary variables in order to be less sensible to noise on input data. Some preliminary simulation results show that the algorithm is effective in source localization and robust with respect to errors on measurement data.

I. INTRODUCTION

The localization problem of brain sources from scalp potential recordings is a key problem in computational bioelectromagnetism, and its solution is an active research field [1]. Primary sources are generally modeled as ideal point current dipoles.

In the up-to-date literature the source location inverse problem from the knowledge of scalp potentials is commonly solved by Nelder-Mead simplex method [2]. The functional to be minimized is a suitable norm of the reconstruction error. The main disadvantages of the simplex method is that it requires multi-start and it can fail when the nodes of the simplex fall inside a single element. It is possible to overcome these drawbacks with a proper formulation of the problem. In fact, there are classes of problems, *e.g.* convex problems, that can be solved with deterministic techniques, that guarantee the reaching of the global solution in a finite number of steps.

This work describes a mixed integer linear programming (MILP) formulation of the brain localization problem and some results on a simulation test case are presented and discussed.

II. IDENTIFICATION ALGORITHM

A. Direct problem

When modeling neural sources, it is widely adopted the static approximation of current conduction equation (displacement currents are usually neglected). Under the hypothesis of stationary field, the problem can be described by the Poisson equation in terms of electric scalar potential φ :

$$\nabla \cdot (\sigma \nabla \varphi) = \nabla \cdot \vec{J}_s \quad (1)$$

where \vec{J}_s are the source current densities. In this work, (1) is discretized by means of the cell method [3]. The algebraic counterpart of stationary current field Poisson equation, is:

$$\tilde{\mathbf{D}}\mathbf{M}_\sigma\mathbf{G}\varphi = \mathbf{A}\varphi = \tilde{\mathbf{D}}\mathbf{i}_s. \quad (2)$$

\mathbf{G} is the discrete gradient operator (edge-to-node incidence matrix), \mathbf{M}_σ is the conductance constitutive matrix (diagonal when hexahedral discretization is adopted), $\tilde{\mathbf{D}} = -\mathbf{G}^T$ is the discrete (dual) divergence operator, \mathbf{i}_s the source current vector. It is worth noting that the number of elements in \mathbf{i}_s equals the number of edges in the mesh.

B. Lead field matrix

The solution of the inverse problem requires the definition of the so called *lead field matrix* \mathbf{L} [4], the linear operator that maps the source vector to the vector of scalp potentials. If \mathbf{A}^{-1} is a suitable factorization of the stiffness matrix (*e.g.* obtained by Cholesky factorization), potentials can be calculated by:

$$\varphi = \mathbf{A}^{-1}\mathbf{G}^T\mathbf{i}_s. \quad (3)$$

Since the reconstruction problem starts from the knowledge of potentials in a subset $\hat{\varphi}$ of surface potentials that belong to electrodes, a projection matrix \mathbf{P} is defined, such that:

$$\hat{\varphi} = \mathbf{P}\varphi. \quad (4)$$

In addition the localization problem can be appropriately guided by some *a-priori* information on the localization of brain sources, *e.g.* coming from functional magnetic resonance imaging [1]. From a mathematical point of view, it is possible to define an interpolation matrix \mathbf{Q} that expands the restricted vector of current sources to the complete vector of sources:

$$\mathbf{i}_s = \mathbf{Q}\mathbf{i}_r. \quad (5)$$

By collecting (3), (4) and (5) the reconstruction problem can be formulated as:

$$\hat{\varphi} = \mathbf{P}\mathbf{A}^{-1}\mathbf{G}^T\mathbf{Q}\mathbf{i}_r = \mathbf{L}\mathbf{i}_r. \quad (6)$$

The system (6) is under-determined, since the number of electrodes is typically smaller than the number of possible current sources.

C. Mixed integer linear programming

In this work the attention is focused on a single current dipole lying parallel to one of the coordinate axes. Under this hypothesis it is possible to formulate the source localization problem as a MILP.

The vector of unknowns is made by a current value i_k (continuous) and a binary value δ_k for each edge k . These variables are linked by the relation:

$$-I_{\max}\delta_k \leq i_k \leq I_{\max}\delta_k. \quad (7)$$

TABLE I
GEOMETRY AND TISSUE PROPERTIES

tissue	outer radius	conductivity
	cm	S/m
scalp	9.2	0.43478
skull	8.74	0.00625
CSF	8.28	1.538
gray matter	7.82	0.3334
white matter	7.37	0.1428

Variable δ_k defines the on/off status of the k th edge current. The novelty of the proposed algorithm is to impose the identification of electrode potentials as constraint and not as objective. To be less prone to measurement uncertainties on scalp potentials, (6) is reformulated as inequality constraint¹:

$$(1 - \alpha) \hat{\varphi}^{\text{meas}} \leq \mathbf{L}\mathbf{i}_r \leq (1 + \alpha) \hat{\varphi}^{\text{meas}} \quad (8)$$

where $\alpha > 0$ is an estimation of measurement uncertainties and $\hat{\varphi}^{\text{meas}}$ are the measured potentials. When noise is present, a common problem in reconstruction algorithms is the raise of spurious sources that compensate the potential fluctuations with respect to the exact values. These undesired effects are mitigated by the definition of the objective function. The linear algorithm should minimize the number of sources, that can be formulated as a linear combination of the binary variables:

$$\min \sum_k \delta_k \quad (9)$$

By the definition of objective (9) and constraints (7), (8), the MILP algorithm searches for the minimum number of currents that matches the recorded potentials with the desired precision.

III. CASE STUDY

The test case is a modified five-layer spherical model (Fig. 1(a)), whose geometrical and material parameters are reported in Table I. The discretization is characterized by 61565 hexahedra and 67368 nodes. 17 electrodes are regularly placed on the upper half of the outer sphere (Fig. 1(b)), while a current dipole of $100 \mu\text{Am}$ is randomly placed on the outer surface of gray matter. This corresponds to have 8068 possible locations for currents. In order to prove the robustness of the algorithm with respect to measurement errors, a random white noise is added to scalp potentials. Noise amplitude is progressively increased from 0% to 25% of the signal values. In all cases the algorithm is capable of detecting a single source and locating the exact position of the current dipole, with a maximum error on current magnitudes lower than 8% (Fig. 2). The average computational times of the different MILP phases for this case are: LP relaxation 27 sec, generation of cuts 16 sec, branch and bound 184 sec. Search is performed by Xpress-IVE software [5] on a Intel Core 2 Duo, 2.4 GHz with 4 GB of RAM.

¹Equation (8) holds when $\hat{\varphi}^{\text{meas}} > 0$, otherwise inequality signs must be reversed.

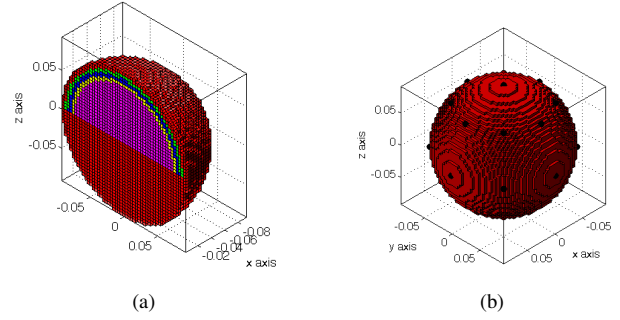


Fig. 1. Geometry: (a) vertical cut showing 5 tissues and (b) position of electrodes.

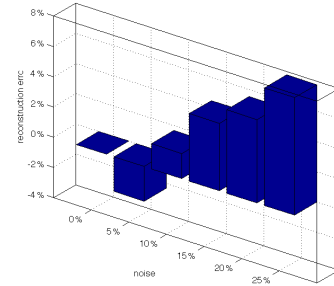


Fig. 2. Error on current magnitude for different random noise on scalp potential measurement.

IV. DISCUSSION AND FUTURE WORK

The proposed method is effective in reconstructing scalp potential due to a single dipole. By suitably using binary variables, the algorithm has proved to be robust with respect to noise on input data. It has been shown the possibility of introducing some knowledge in the search by an appropriate definition of the interpolation matrix \mathbf{Q} .

These promising preliminary results will be extended in the full paper, where a more accurate simulation protocol will be followed. In particular there will be shown how the algorithm can be extended to sources with arbitrary orientation, by the definition of nodal currents. Moreover, the scalability of the algorithm with respect to the number of sources and the model resolution will be analyzed. Finally some simulations will be performed on a realistic head model in order to verify the effects of complex geometries on the algorithm performances.

REFERENCES

- [1] B. He and Z. Liu, "Multimodal functional neuroimaging: integrating functional MRI and EEG/MEG," *IEEE Reviews in Biomedical Engineering*, vol. 1, pp. 23–40, 2008.
- [2] L. Zhukov, D. Weinstein, and C. Johnson, "Independent component analysis for EEG source localization," *IEEE Engineering in Medicine and Biology*, vol. 19, no. 3, pp. 87–96, May/June 2000.
- [3] F. Freschi, L. Giaccone, and M. Repetto, "Educational value of the algebraic numerical methods in electromagnetism," *COMPEL - The International Journal for Computation and Mathematics in Electrical and Electronic Engineering*, vol. 27, no. 6, pp. 1343–1357, 2008.
- [4] D. Weinstein, L. Zhukov, and C. Johnson, "Lead-field bases for electroencephalography source imaging," *Annals of Biomedical Engineering*, vol. 28, pp. 1059–1065, 2000.
- [5] "Dash optimization," www.dashoptimization.com, accessed April 6, 2009.

A Hybrid Design of Distribution Transformers Using 2D-FE and a Conventional Method

M.A. Arjona, *IEEE Senior Member*, C. Hernández, *IEEE Member*

Instituto Tecnológico de la Laguna, División de Estudios de Posgrado e Investigación

Blvd Revolución y Calz. Cuauhtemoc, 27000, México

Email: marjona@ieee.org

Abstract— Integrating Finite Elements into the design procedure of electromagnetic devices has always been a challenge for researchers and design engineering community. This paper presents the application of a hybrid method that involves the application of conventional design methodology and two-dimensional finite elements. The optimization is carried out using a Genetic Algorithm which allows finding the global minimum and then a determinist algorithm is used to find the final solution. The methodology is illustrated in the design of a 1500 kVA distribution transformer.

I. INTRODUCTION

The necessity of being competitive in global marketing has led transformer manufacturers to require computing systems with the capacity to produce rapidly: optimal, reliable and feasible transformer designs. These systems constitute a powerful tool for manufacturers that are willing to have in their design departments in their constant search for: (a) saving experimented engineering-design man-hours, (b) increasing their design capacity, (c) reducing the delivery cycle and (d) optimizing the use of materials. This is particularly true in cases where the reduction of fabrication costs and the payment of specialized engineer salaries may define the survival of a small factory.

Traditional design methods consist of calculating losses, leakage impedance and magnetizing current with approximate formulae which most of the cases are derived from empirical knowledge owned by the experimented designers. With the appearance of numerical methods, as the Finite Elements (FE), the electromagnetic performance of transformers can be predicted with higher accuracy. Using FE models in optimization has always been a challenge for the electromagnetic analysts, being the computation time one of the main obstacles.

This paper uses both approaches, i.e. traditional methodology and FE models, which when properly combined; it can lead to better designs. A Genetic Algorithm (GA) is used firstly with the conventional-design equations; this allows finding an approximate global solution. Afterwards, a deterministic method uses the obtained design model and employs FE models for calculating iron and winding losses, leakage reactance and magnetizing current. The hybrid methodology is tested in the design of a 1500 kVA, 13.2/0.22 kV three-phase distribution transformer.

II. TRADITIONAL DESIGN METHODOLOGY

The general problem of design may be defined as that of determining the most suitable form of the transformer [1],[2].

An optimal design is not obtained simply by the solution of a set of equations; it requires iterations. The sinusoidal induced voltage, V , in any transformer winding is given by:

$$V = 4.44NfB_m A_c \quad (1)$$

where N represents the number turns, f the frequency (Hz), B_m is the amplitude of sinusoidal flux density (Teslas) and A_c denotes the net cross section area (m^2) of the iron carrying the sinusoidal flux.

The transformer has different voltage levels; therefore it is needed to determine the electric clearances of windings, coils, core and yoke to avoid insulation failure due to high electric field stresses. Dimensions of ventilation ducts between groups of coils are also taken into account at this stage, which will be dependant on the type of transformer. The total number of calculated turns must be accommodated in the transformer window area, thus an initial distribution of windings must be computed. A distribution transformer must satisfy a set of design constraints to avoid penalized costs from the customer. These constraints are: a) efficiency, b) percentage of leakage impedance, and c) no-load current. In addition, the designer must guarantee the specified electrical power of the unit. The dc resistance loss of a single winding was calculated with the following equation

$$P_R^w = \frac{J^2 \rho m_{cu} \times 10^9}{\rho_{d,cu}} \quad (2)$$

where J stands for the current density (A/mm^2), ρ denotes the conductor resistivity ($\Omega\text{-mm}$), m_{cu} is the copper weight (kg) and $\rho_{d,cu}$ is the density of cooper (kg/m^3). The copper weight can be computed with

$$m_{cu} = \rho_{d,cu} N l_m s \quad (3)$$

where l_m is the length of mean turn (m) and s is the cross-sectional area of a conductor (m^2). It must be recalled that total joule loss is three times the joule loss of a phase (low and high voltage windings).

The total winding loss is

$$P_{cu} = P_R + P_{eddy} \quad (4)$$

where P_R and P_{eddy} denotes total joule and eddy current winding losses, respectively.

$$\%R = P_{cu} \times 100/S \quad (5)$$

$$\%X = fIN \left(s_0 + \frac{s_1 + s_2}{3} \right) \cdot 8 \times 10^{-5} / (hE/N) \quad (6)$$

$$\%Z = \sqrt{(\%R)^2 + (\%X)^2} \quad (7)$$

$$\eta = \left[1 - \frac{(P_{fe} + P_{cu})}{(S \cdot PF + P_{fe} + P_{cu})} \right] \times 100 \quad (8)$$

where S stands for the rating transformer power (VA), s_{0-2} (mm^2) denote mean turn diameters multiplied by the gap of between windings and thickness of primary and secondary windings respectively. P_{cu} represents the total winding losses, PF denotes the power factor and P_{fe} is the no-load loss (W) obtained from the magnetizing curve and core flux density data. Although a transformer is a simple device, its numerous, highly interrelated and heterogeneous design parameters make a closed-form solution to the design problem impossible.

III. HYBRID DESIGN OPTIMIZATION

The hybrid design consists in using stochastic optimization with conventional design procedures, as briefly explained in the last section, and deterministic optimization with FE models as it is illustrated in Fig. 1. The improved design calculations employing FE models are: leakage reactance, magnetizing current, eddy losses and no-load losses. Leakage reactance and winding eddy current loss are calculated using an asymmetric model of the transformer. No load losses are obtained with a voltage fed cartesian FE model without load, the same model is used for estimating the magnetizing current. The summary of equations needed for making the above calculations are [3]:

$$\frac{\partial}{\partial z} \frac{v}{r} \frac{\partial(rA)}{\partial z} + \frac{\partial}{\partial r} \frac{v}{r} \frac{\partial(rA)}{\partial r} + \frac{j\omega\sigma}{r}(rA) = J_s \quad (9)$$

$$\begin{bmatrix} S + j\omega N & -P \\ j\omega Q & R + j\omega L \end{bmatrix} \begin{bmatrix} A \\ I_w \end{bmatrix} = \begin{bmatrix} 0 \\ V_e \end{bmatrix} \quad (10)$$

where S is the FE stiffness matrix, P and Q are weighting winding matrices, R is the external resistance, L external inductance, I_w a vector of winding currents, V_e denotes the external potential sources, A represents a vector of complex potentials, ω is the angular frequency, v stands for the reluctivity, r is radius, J_s is the source complex current and σ is the electric conductivity.

A GA was used to solve the equation related to the conventional design. A GA is a stochastic method that employs probabilistic and non-local search heuristics that simulate natural evolution, which works on the chromosomes [4]. When the convergence is reached, an optimization with the Gauss-Newton method is launched where FE models are used. The proposed methodology was applied to the design of a 1500 kVA, 13.2/0.22 kV three-phase distribution transformer and the achieved results are shown in Table I.

IV. CONCLUSIONS

This paper has presented a novel approach that combines the conventional design method of transformers with 2D-FE models to improve calculations. Firstly, a Genetic Algorithm is used until a solution is found using the conventional model and then the optimization is switch to the Gauss-Newton. By using this approach, better designs results in a shorter period

of time are achieved because finite element models are employed in the last step of the optimization process.

TABLE I
HYBRID OPTIMIZATION DESIGN RESULTS

Design variable	Optimization	
	GA Conventional	Gauss-Newton FE-Conventional
Efficiency (%)	98.963	98.952
No load loss (%)	0.154	0.154
Load loss (%)	0.68	0.63
Reactance (%)	4.99	4.93
Resistance (%)	0.68	0.69
Impedance (%)	4.99	4.99
Magn. Current (%)	0.40	0.211
Flux density	1.513043	1.513043
LV Current density	2.484883	2.484883
HV Current density	3.438826	3.438826
Core Diameter (mm)	274.943817	274.943833
Height Winding (mm)	549.048645	549.048645
Gap LV-HV	24.520662	24.520662

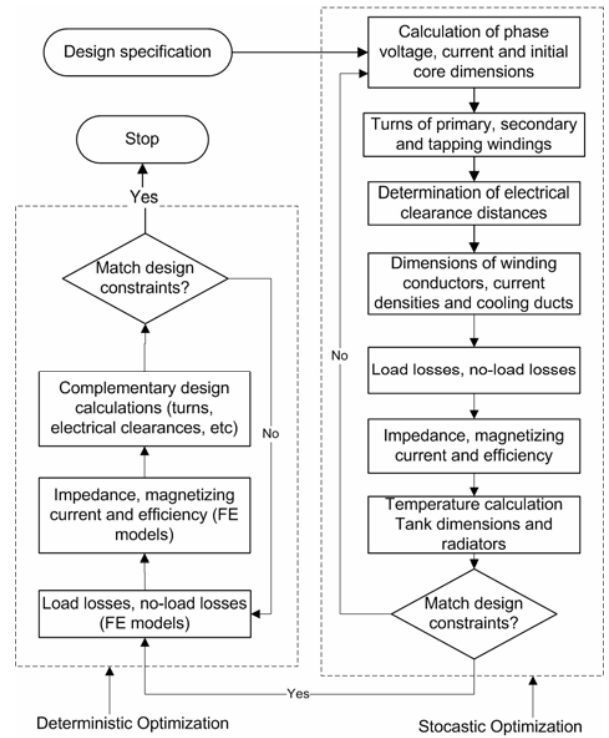


Fig. 1. A Hybrid method used for the design distribution transformers.

V. REFERENCES

- [1] R.M. Del Vecchio, et al, *Transformer Design Principles with applications to core-form power transformers*, Taylor & Francis, New York, 2002. pp. 200-250.
- [2] C. Hernández, M.A. Arjona and S. Dong. "Object-Oriented Knowledge-Based System for Distribution Transformer Design," *IEEE Transactions on Magnetics*, Vol. 44, No. 10, 2008, pp. 2332-2337.
- [3] A. B. J. Reece and T. W. Preston, *Finite Element Methods in Electrical Power Engineering*, Oxford University Press, Oxford, 2000. pp 20-60.
- [4] J.A. Hageman, R. Wehrens, H.A. van Sprang, and L.M.C. Buydens, "Hybrid genetic algorithm-tabu search approach for optimizing multilayer optical coatings," *Analytica Chimica Acta*, vol. 490, pp. , June 2003, 211-222.

Inverse Magnetic Field Calculation For Underground Grid Condition Monitoring

S. Salon, MVK Chari, J. Braunstein, J. Selvaggi
 ECSE Department RPI
 Troy, NY 12180-3590
 salon@rpi.edu

Abstract— This paper illustrates the methods which were developed to diagnose and evaluate the condition of the grounding grid used in electric substations. The grid is made of copper conductors which are buried to a depth of typically up to 2 meters. The safety of the substation depends on the continuity of the grounding grid where direct visual inspection of the grounding grid is not possible. RPI has developed an inverse method which can be used to detect breaks in the underground grid as well as the location of the buried conductors. We have performed forward and inverse calculations and have made field measurements on a simulated grid and at a substation.

I. INTRODUCTION

A schematic of a substation grounding grid is shown below in Figure 1. The substation equipment such as transformers, switchgear, towers, etc is grounded and to ensure a low resistance ground a grid of copper conductors is buried underneath the substation. Each piece of equipment and tower is connected to this grid, which in turn is connected to grounding rods down into the water table. Since the safety and security of the substation depends on the proper operation of this grid, we must insure that it has not degraded over time or the welded connection have broken [1]-[3].

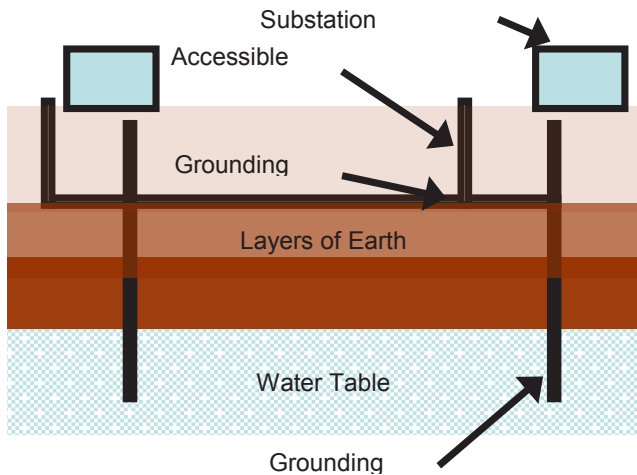


Figure 1: Schematic of Substation

II. ANALYSIS

The grid is usually set out in a rectangular pattern with allowance made for the location of the substation equipment. In the initial phase of the investigation we solved the forward problem [4]. This was to insure that a good signal could be

picked up at the surface. Current was injected into the grid at one corner and removed at the other. The current distribution was found including resistive and inductive effects and the skin effect in each of the conductors. The grid is shown in Figure 2.

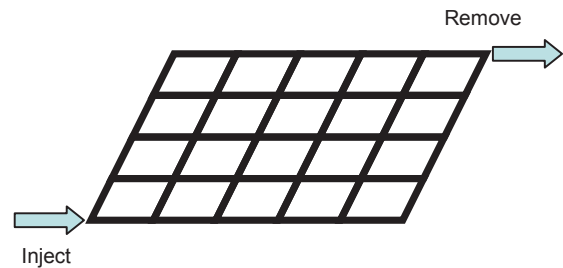


Figure 2: Test Grid

The results (magnitude of the Flux Density) at 200 mm above the grid is shown in Figure 3. We see that the shape and size of the grid are clearly visible and the magnitude of the field was in a range that is easily measured. In the case of a healthy grid, the signature is symmetric.

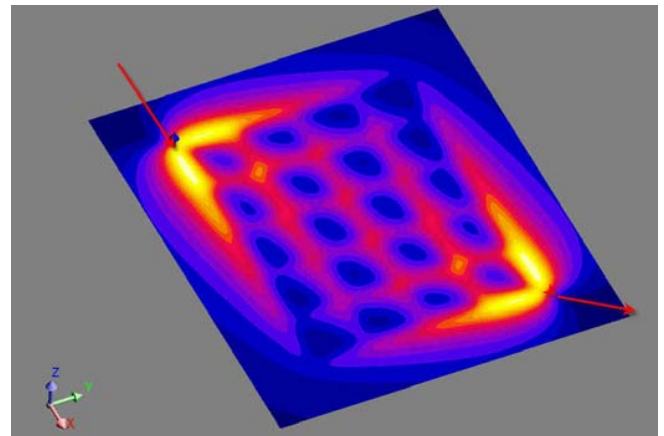


Figure 3: Flux Density for Healthy Grid

We explored various faults and excitation patterns which will be detailed in the full paper. The case of the excitation of Figure 2 with 3 faults is shown in Figure 4.

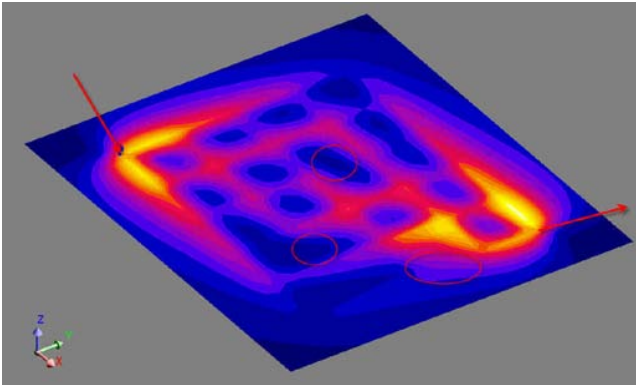


Figure 4: Results with 3 Faults

The indentation for subheadings is 0.1 in.

III. INVERSE PROBLEM

We now turn to the inverse problem. If we assume a set of loop currents in the grid, we can find the influence functions that give the flux density at the field points in terms of the unknown currents. If we have breaks in the grid, the currents in the affected branches will naturally be zero.

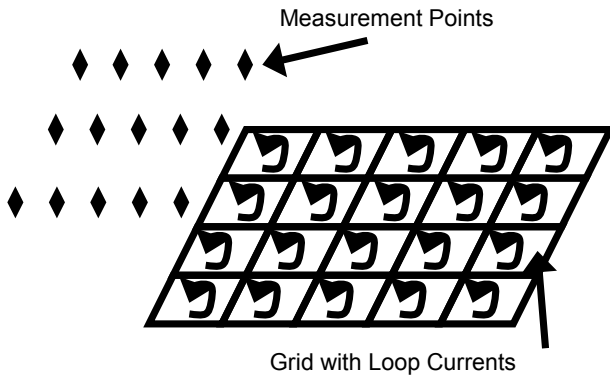


Figure 5: Set-up For Inverse Problem

After much algebra (included in the full paper) we obtain

$$\begin{Bmatrix} B_1 \\ \vdots \\ B_n \end{Bmatrix} = \begin{pmatrix} a_{11} & \dots & \\ \vdots & \ddots & \vdots \\ & \dots & a_{nn} \end{pmatrix} \begin{Bmatrix} i_1 \\ \vdots \\ i_n \end{Bmatrix}$$

We solve this full matrix for the loop currents and then convert this to branch currents. Results from this method confirm that the currents can accurately be found from good measurements.

Another type of inverse problems allows us to take surface measurement and then locate the path of the conductor. Figure 6 shows actual flux density measurements taken at a substation and the final path computed by our algorithm. In this case, the current in the conductor is known and the algorithm finds the path. The development will be given in the full paper.

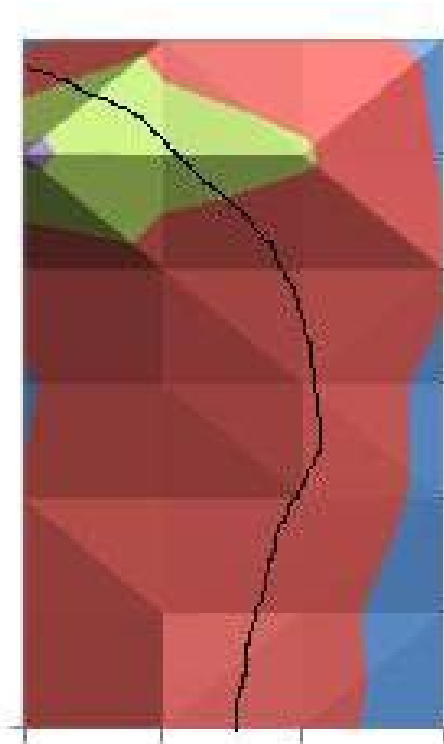


Figure 6: Measured Flux Density and Calculated Conductor Location

IV. CONCLUSIONS

We introduce the idea of using surface field measurements to diagnose the integrity of the grounding grid. The forward problem shows that we can diagnose problems with the grounding grid. We illustrate 2 types of inverse problems. In the first one we take field measurements with an assumed geometry and show that we can find the branch currents. In the second example we take real data and locate the path of the underground current. The indication is that field measurements can be a valuable technique to diagnose problems in the grounding grid.

References

- [1] Zhang B., Zhao Z., Cui X., and Li L. "Diagnosis of Breaks in Substation's Grounding Grid by Using the Electromagnetic Method." *IEEE Trans. Magnetics.*, vol. 38, no. 2, pp. 473-476, March 2002.
- [2] Yuan J., Yang H., L. Zhang, Cui X., and Ma X., "Simulation of substation grounding grids with unequal-potential," *IEEE Trans. Magnetics.*, Vol. 36, pp. 1468-1471, July 2000.
- [3] Dawalibi F. P., "Electromagnetic fields generated by overhead and buried short conductors Part 2—Ground conductor," *IEEE Trans. Power Delivery*, vol. PWRD-1, pp. 112-119, Oct. 1986.
- [4] INCA User Guide, Magsoft Corporation, 2009 conventional nodal analysis technique," *IEEE Trans. Power Delivery*, Vol. 14, pp. 873-878, July 1999.

A Practical Approach to Robust Design of a RFID Triple-Band PIFA Structure

Jae-Hyeong Ko¹, Dong-Hun Kim², Hyang-Beom Lee³ and Hyeong-Seok Kim¹

¹School of Electrical and Electronics Eng., Chung-Ang Univ., Seoul 156-756, Korea, kimcaf2@cau.ac.kr

²School of Electrical Eng. and Computer Sci., Kyungpook Natl.Univ., Daegu 702-701, Korea, dh29kim@ee.knu.ac.kr

³Department of Electrical Eng., Soongsil Univ., Seoul 156-743, Korea, hyang@ssu.ac.kr

Abstract— This paper presents a practical methodology of finding a robust optimal solution for a multi U-slot PIFA(Planar Inverted F-Antenna) structure with triple bands of 433 MHz, 912 MHz and 2.45 GHz. Using evolutionary strategy, a global optimum is first sought out in terms of the lengths and widths of the slots and the shorting strip. Then the optimized values are modified by Taguchi quality method in order to obtain robustness against the change of material constant and feed position. To verify the method, the performance of the antenna is accurately predicted by general-purpose electromagnetic software and optimized results are thoroughly examined compared to the initial design.

I. INTRODUCTION

The success of wireless communication service is heavily dependent on the development of reliable RF components. As a core of RF components, the antenna should satisfy various demands for small size as well as versatile functions. Especially, multi-band function is needed to provide the RF systems with flexibility and mobility in wide use. Up to date, intensive research has been carried out to find an efficient and reliable structure of multi-band RFID antennas, which works well regardless of standard frequencies used. As part of the efforts, U-slots are adopted to get multi-band characteristic, where a parametric study is conducted to seek proper design parameters starting with the approximated formula on resonance frequency [1]. In other works, a U-slot based PIFA structure is used but it usually requires a lot of computing time because of the three-dimensional (3D) structure itself [2].

This paper proposes a practical methodology of finding a robust optimum for a U-slot based PIFA structure with triple bands 433MHz, 912 MHz and 2.45 GHz. To achieve this, Taguchi quality method (TM) is complemented with evolution strategy (ES) algorithm. An initial design starts with two U-slots in the metal patch on the substrate located above the ground. The lengths and widths of the two U-shaped slots and position of the shorting vertical strip are selected for design parameters during ES optimization[3]. The optimized design yields better performance than the initial one alone with 3D electromagnetic simulation. However, it cannot give a guarantee of the optimized design because there are fabrication errors in real world that may deteriorate good performance predicted

Therefore the optimized values from ES should be modified to become insensitive to possible changes in the coaxial feed position (FP) and the permittivity of the substrate (PS), which are uncontrollable factors in reality. Applying TM to the design optimized by ES, robust optimal values are obtained to take into account the noise factors of FP and PS.

From results, it is confirmed that the final design produces satisfactory performances especially in terms of robustness to the noise factors.

II. PRACTICAL APPROACH TO ROBUST DESIGN

This paper proposes a practical approach to achieving a robust optimal solution of triple-band antenna structure, where Taguchi method (TM) is complemented with evolution strategy (ES) algorithm. In general, it is difficult in seeking out an optimal solution in infinite design space only by Taguchi method because of its restriction on the number and level size of design parameters. To overcome the drawback, (1+1) evolution strategy is first utilized in order to find a global optimum for an initial design considered. Then the robust optimization by Taguchi method is executed with the optimal design values previously obtained from the evolution strategy. After all, the proposed method can give a robust design target around the global optimum while keeping the product performance insensitive to the effects of noise factors that may appear in manufacturing process. The procedure of the robust optimization proposed involves four main stages.

- 1) Defining design parameters and objective function and executing evolution strategy algorithm for searching a global optimum.
- 2) Selecting sensitive parameters based on the above as well as noise factors.
- 3) Setting the optimal solution as an initial design and executing numerical experiments according to orthogonal array.
- 4) Using analysis of mean (ANOM) and variance (ANOVA) techniques to obtain optimal setting of parameters for robust design.

Then, the robust optimal solution is investigated in terms of the concepts of signal-to-noise (SN) ratio and loss function

III. RESULTS

A. Analysis model

The geometry of the problem is illustrated in Fig. 1 where a metalized patch lies on top of the substrate located above the ground plane. The metal patch is connected to the ground plane by means of the shorting strip and the coaxial feed. Such the PIFA resonates around certain frequencies suggested by the approximate formula presented in [1] and [2]. Here the initial geometry of the patch is decided for 433 MHz resonance. Then the initial lengths and widths of the U-shaped slots are roughly determined for the radiation at 912 MHz and 2.45 GHz. To accurately predict the performance of the

antenna, the 3D EM simulation technique in the time-domain, FIT are used with the perfect matched layers (PMLs).

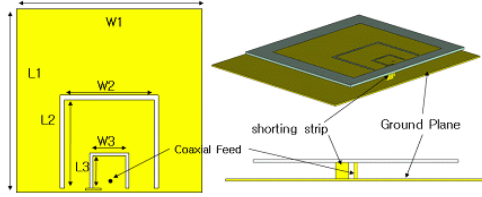


Fig. 1. Configuration of the triple-band PIFA structure

B. Size optimization using evolution strategy

Among 6 design parameters shown in Fig. 1, four crucial parameters, W2, L2, W3 and L3, forming U-shaped slots are selected for size optimization using (1+1) ES. The design goal is to obtain optimal slot dimensions for triple-band PIFA at frequencies of 433, 912 and 2,480 MHz. To achieve this, the multi-objective function with constraints is defined as:

$$\text{Minimize } F = \sum_{i=1}^3 \alpha_i (|f_i - f_{oi}|)^2 \quad (1)$$

subject to $S_{11}(f_i) \leq -15$ dB

where α_i is weighting factor, f_i band frequency computed at each design iteration, f_{oi} target frequency value and S_{11} reflection coefficient. For saving computing time, the design parameters are forced to be selected from finite integer sets.

The initial and optimized design values are presented in Table I and the reflection coefficient values are compared in Fig. 2. From the results, it is observed that the performance of the optimized design coincides well with the design goal even though only the integer values are permitted for design parameters. But, at this stage, we have no idea of how robust the optimum is.

TABLE I. DESIGN PARAMETERS AND PERFORMANCE

Parameter	Unit	Initial values	Optimal values
W2	mm	41	50
L2	mm	41	43
W3	mm	15	13
L3	mm	15	16
Frequency / S_{11}	MHz	439.5/-25.15	430/-40.82
	dB	981.5/-15.90	910.5/-27.22
		2,563/-7.13	2458.5/-16.24

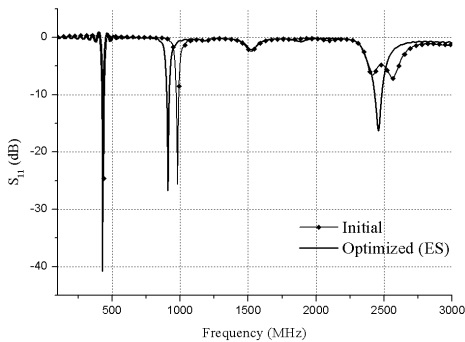


Fig. 2. Comparison of reflection coefficient before and after EV optimization

C. Robust optimization using Taguchi method

Starting with the optimized design by ES, robust optimization is carried out by Taguchi method in order to find a new optimal solution insensitive to noise factors. For the four design parameters, the x and y coordinates of feeding point and substrate permittivity are considered as noise factors.

Based on the number of design and noise parameters and the settings considered in Table II, a standard orthogonal array $L9(3^4 \times 3^4)$ was selected for the matrix numerical experiments, where the parameters are assumed to be mutually independent.

For the “nominal the best characteristic” case, which resembles the minimization of the performance (1), the SN ratio can be calculated by

$$\text{SN ratio} = -10 \log(\bar{y}_i^2 / V_i) \quad (2)$$

where \bar{y} and V denote the mean and variation of performance values, respectively and the subscript i belongs to the i th row of the orthogonal array used. Through the somewhat routine process of Taguchi quality control, an optimal setting of the design parameters can be determined. It is revealed that the performance deviation (i.e. robustness) predicted from the setting improved by more than 70% compared to the optimized design in ES. Fig. 3 compares the reflection coefficient profiles before and after robust design procedure.

TABLE II. DESIGN AND NOISE PARAMETERS FOR THE FIRST SETUP

Type	Parameter	Level		
		1	2	3
Control Factor	W2 (mm)	49.8	50	50.2
	L2 (mm)	12.9	13	13.1
	W3 (mm)	42.8	43	43.2
	L3 (mm)	15.9	16	16.1
Noise Factor	Feeding point x coordinate	-0.1	0	0.1
	Feeding point y coordinate	-0.1	0	0.1
	Substrate permittivity (ϵ_r)	4.36	4.4	4.44

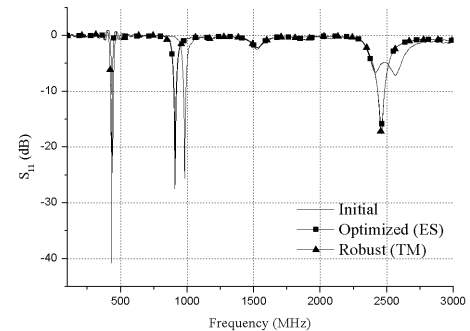


Fig. 3. Comparison of reflection coefficient before and after robust optimization

IV. CONCLUSION

A practical approach to robust optimization of triple-band antenna structure is proposed, where TM is complemented with ES algorithm. From results, it is referred that the final design is insensitive to noise factors and also nearly close to the global optimum. Our extended paper will include comparison of experimental and simulated data.

V. REFERENCES

- [1] Salamat C. D., Haneishi M., Kimura Y., “L-probe Fed Multiband Microstrip Antennas with Slots”, *Microwave Conference, 2006. APMC 2006, Asia-Pacific*, pp. 1515-1518, Dec., 2006.
- [2] H. Park, M. il. Kand, J. H. Choi, “Design of an Internal Antenna with Wide and Multiband Characteristic for mobile handset”, *Microwave and optical Technology Lett.*, vol. 48. no. 5, pp. 947-950, May 2006.
- [3] Muller, S. D., Schraudolph, N. N., Koumoutsakos, P. D., “Step size adaptation in evolution strategies using reinforcement learning”, *Evolutionary Computation, CEC '02. Proceedings of the 2002 Congress on*, vol. 1, pp.151-156, May 2002.

Parameter Extraction and Optimal Design of Spiral Inductor Using Evolution Strategy and Sensitivity

Jae-Hyeong Ko*, Jin-Kyu Byun**, and Hyeong-Seok Kim*

*School of Electrical and Electronics Eng., Chung-Ang University, Seoul 156-756, Korea,
kojh77@gmail.com, kimcaf2@cau.ac.kr

**School of Electrical Engineering, Soongsil University, 511 Sangdo-dong, Dongjak-gu, Seoul 156-743, Korea,
jkbyun@ssu.ac.kr

Abstract — Patterned ground shield of on-chip spiral inductor is designed using deterministic optimization method. Separation between inductor and ground strip is modified during design process, as well as widths of ground strips and slots. For sensitivity analysis, approximate adjoint variable method is used. Significant increase in Q -factor is observed in final design while reduction of inductance is minimal.

I. INTRODUCTION

On-chip spiral inductors are widely used in a variety of radio frequency integrated circuits (RF IC's). For spiral inductors in silicon-based RF IC's, substrate loss at high frequencies can degrade quality factor (Q). Also, noise coupling may appear at gigahertz frequencies. One of the popular design techniques to alleviate this problem is to insert a patterned ground shield (PGS) to block inductor electric field from entering the silicon [1]. Patterned slots on the PGS cut off the path of induced loop current, hence reducing disturbance of inductor magnetic field.

When designing spiral inductor with PGS, many parameters should be considered including widths of ground strips and slots, separation between spiral and ground shield, and number of overlap turns between ground strip and inductor. So far, these design variables were determined by trial and error in most cases, resulting in high design cost and time.

In this paper, deterministic optimization method is applied to the optimal design of PGS of on-chip spiral inductor. Design goal is to maximize Q -factor while keeping inductance reduction minimal. Sensitivity analysis of objective function is performed by approximate adjoint variable method.

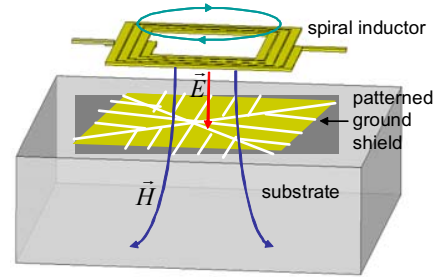
II. DESIGN OF SPIRAL INDUCTOR WITH PGS

Fig. 1 explains improvement of Q -factor of spiral inductor with PGS. Electric field of inductor in substrate direction is blocked by a ground shield and dissipation loss is reduced. Magnetic field disturbance is small because eddy current on ground shield is suppressed by patterned slots.

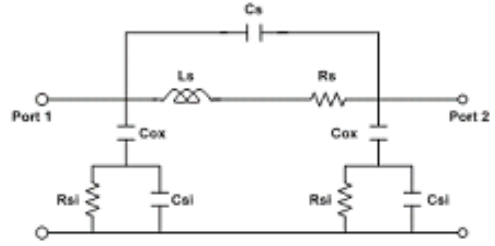
L_s and R_s denote inductance and resistance of the line and coupling capacitance between overlapping lines are written as C_s . Capacitance of oxide layer between silicon board and line is modeled by C_{ox} , and parasitic capacitance and resistance of silicon board are modeled by C_{si} and R_{si} , respectively [2].

Electromagnetic simulation of inductor will significant error compared to the measurement if the material parameters are

entered inaccurately. In order to obtain EM simulation result similar to the TSMC process, accurate electric conductivity of the inductor substrate is determined by evolution strategy (ES).



(a) Picture of Spiral inductor with patterned ground shield



(b) Equivalence circuit of Spiral inductor

Fig. 1. Schematic picture of spiral inductor with patterned ground shield.

The objective function F is expressed by a function of Q -factor and inductance, where Q is given by

$$Q = 2\pi \times \frac{\text{magnetic energy stored}}{\text{energy loss in one cycle}}. \quad (1)$$

Sensitivity of objective function F with respect to design variable p is calculated using approximate adjoint variable method [2] and written as

$$\frac{\partial F}{\partial p_n} \approx \frac{\partial^e F}{\partial p_n} - \int_0^{T_{\max}} \iiint_{\Omega} (\hat{E}_x)_n \cdot \Delta_n R(\bar{E}_x) d\Omega dt \quad (2)$$

where

$$\Delta_n R(\bar{E}_x) = (\Delta_n \mathcal{L}) E_x - (\Delta_n \alpha) D_t E_x - \Delta_n (\beta D_t J_x). \quad (3)$$

\mathcal{L} is a finite-difference operator, α and β are coefficients defined by grid size and time step, and $D_t J_x$ is a difference of current density at $t + \Delta t/2$ and $t - \Delta t/2$ [3]. The design variables are explained in Fig. 2.

6. OPTIMIZATION(B)

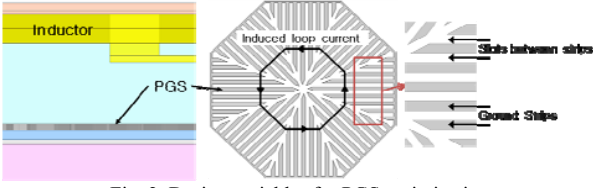


Fig. 2. Design variables for PGS optimization.

III. DESIGN RESULTS

A. Analysis model using evolution strategy

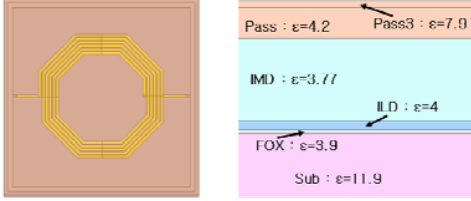


Fig. 3. Spiral inductor of TSMC process

For the inductor structure used in EV simulation with ES, the number of the coil turns is 5.5, width of the top metal $6 \mu\text{m}$, and radius of inner coil $98.04 \mu\text{m}$ as shown in Fig. 3.

The design parameters are set as electric conductivity of each layer of the substrate, named pass2, pass, IMD, ILD, FOX, Sub (Fig. 3). The main characteristics of inductor are inductance and Q-factor, and the objective function is defined as a function of them:

$$\text{Minimize } F = \sum_{i=1}^{12} \alpha_i (|L_i - L_{oi}|)^2 + \sum_{i=1}^{12} \beta_i (|Q_i - Q_{oi}|)^2 \quad (4)$$

where α_i and β_i are weighting factors for inductance L_i and Q-factor Q_i from EM simulation, and L_{oi} , Q_{oi} are target values of inductance and Q-factor obtained from equivalent circuit analysis.

Design result and optimized values are shown in table I and II. Also, inductance and Q-factor results are compared in Fig. 4 and 5.

TABLE I. DESIGN PAMETERS

Parameter	Unit	Initial values	Optimal values
Pass3	S/m	0	0.5
Pass	S/m	0	0.5
IMD	S/m	0	0.002
ILD	S/m	0	0.002
FOX	S/m	0	0.002
Sub	S/m	0	14

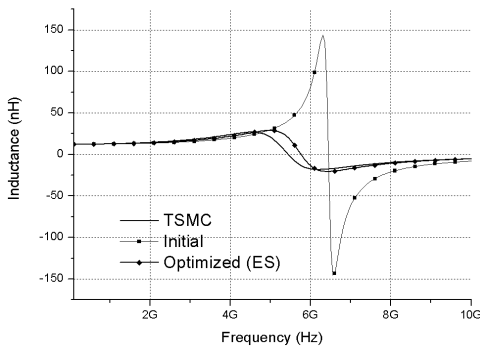


Fig. 4. Comparison of inductance before and after EV optimization

TABLE II. PERFORMANCE

Performance	Unit	1GHz	2GHz	3GHz	4GHz	5GHz
Inductance	nH	12.582/	13.512/	15.483/	19.538/	29.705/
Initial/Optimal		12.568	13.810	16.503	21.797	28.973
Q-factor		7.062/	11.706/	13.083/	11.785/	8.505/
Initial/Optimal		6.037	7.435	5.546	3.116	1.165

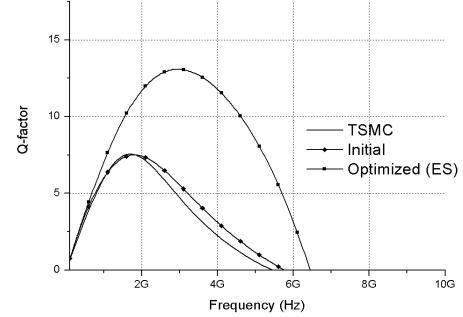


Fig. 5. Comparison of Q-factor before and after EV optimization

B. PGS optimization

Optimization was performed for 2 target frequencies (1 and 2.5 GHz). In Table III and Fig. 6, Q-factor and inductance of spiral inductor with optimized PGS is compared with those with no PGS and with solid ground shield. Significant drop in both inductance and Q-factor is observed for inductor with solid ground shield because of eddy current in ground shield, whereas for optimized PGS, Q-factor is improved by as much as 16.6% while inductance reduction is small.

TABLE III. Q-FACTOR AND INDUCTANCE COMPARISON

Frequency (GHz)	Inductance		Q-factor	
	1	2.5	1	2.5
Non-PGS	12.568	14.927	6.037	6.701
Solid ground shield	3.712	3.895	2.115	4.274
PGS	11.928	14.258	5.967	7.439

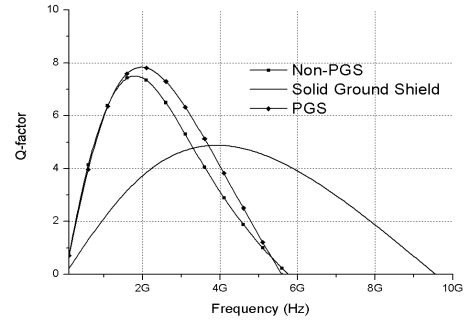


Fig. 6. Comparison of Q-factor Non-PGS and PGS

Detailed optimization procedure which is implemented in our study will be expressed in details on Compumag conference. Also, we will show effectiveness of our approach by comparing with the conventional one.

IV. REFERENCES

- [1] C. P. Yue, and S. S. Wong, "On-chip spiral inductors with patterned ground shields for Si-based RF IC's," *IEEE J. Solid-State Circuits*, vol. 33, no. 5, pp. 743-752, May 1998.
- [2] C. P. Yue, S. S. Wong, "Physical Modeling of Spiral Inductors on Silicon," *IEEE Trans. MTT*, vol.47, no. 3, Mar. 2000.
- [3] N. K. Nikolova, H. W. Tam, and M. H. Bakr, "Sensitivity analysis with the FDTD method on structured grids," *IEEE Trans. Microwave Theory Tech.*, vol. 52. no. 4, pp. 1207-1216, April 2004

Optimization of perfectly matched layer parameters for finite element modeling of grounding systems

Luiz Lebensztajn, Viviane Cristine Silva, Lucas Blattner Martinho

Universidade de São Paulo LMAG/PEA

Av. Prof. Luciano Gualberto, T3 N.158, 05508-900, São Paulo SP Brazil, leb@pea.usp.br, viviane@pea.usp.br

Abstract — An approach to estimate perfectly matched layers parameters for finite-element modeling of grounding systems is proposed. It is based on two optimization techniques, namely Kriging models and Multiobjective Evolutionary algorithm. Results are compared with both theoretical and experimental data.

I. INTRODUCTION

In the finite element analysis (FEA) of grounding systems, a suitable mesh truncation scheme is needed in order to delimit the unbounded three-dimensional domain. Perfectly matched layers (PML) have been efficiently used for this purpose in the numerical solution of 2D problems governed by Laplace equation [3]-[5]. Nevertheless, the parameter estimation of PML has proved to be problem dependent. This is also true in the case of 3D FEA of grounding systems [4].

Here, an attempt is made to develop guidelines for their selection by firstly parameterizing the PML in terms of the relevant dimensions of a grounding system and then to determine these values with the aid of optimization techniques. A previous, similar attempt has been reported in [5] for Electrostatics in 2D.

In this work, a Multiobjective Evolutionary algorithm [7] is used to find a set of PML parameters that provides a highly accurate solution. Kriging models replace the numerical solution to evaluate the relevant quantities and therefore to save computing time [6].

II. PROBLEM DESCRIPTION

The proposed strategy is firstly tested in a canonical example, composed of a single, vertically buried electrode. Although a 2D problem in nature, it is solved in 3D, since both theoretical and experimental data are available for this configuration [1]-[2]. The case of a 32-m bare copper stake [2], buried in a soil with a resistivity of 450 $\Omega\cdot\text{m}$, is used as test case. The quantities to be analyzed are low-frequency ground impedance, R , and surface potential, V , computed at a distance of 1.0 m from the electrode.

The parameters involved in the construction of a PML are (see Fig. 1): a) thickness of the buffer region, d_{buff} ; b) thickness of the absorbing layers, d_{PML} ; c) material coefficient, a . As a first attempt, the thicknesses, d_{buff} and d_{PML} , are parameterized in the geometrical model of the ground system as:

$$d_{\text{buff}} = 2h + \alpha L \quad \text{and} \quad d_{\text{PML}} = n\beta h, \quad (1)$$

where h is a distance taken as 1.0 m, $0 \leq \alpha \leq 5.0$ and $1.0 \leq \beta \leq 10.0$ are dimensionless, real values; n is the number of absorbing layers ($1 \leq n \leq 10$), and L is the electrode length. The material

coefficient, a , was initially restricted to the range [1,50]. Therefore, the actual parameters chosen to be optimized are all dimensionless values: α , β , n and a .

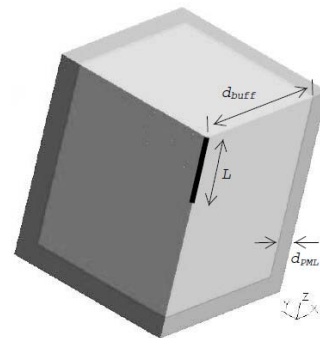


Fig. 1 3D model of a single-wire grounding system showing PML parameters.

III. METHODOLOGY

Quantities R and V , which are relevant in the low-frequency performance of grounding systems, are computed and the corresponding error compared with their theoretical values is to be minimized.

First, let the errors, e_R and e_V (associated, respectively to the grounding resistance and the surface potential) be defined as follows:

$$e_R = (R_{th} - R_{num})/R_{th} \quad \text{and} \quad e_V = (V_{th} - V_{num})/V_{th}, \quad (2)$$

where the subscripts th and num indicate theoretical and numerical values, respectively. The optimization problem can be written as:

$$\min \begin{cases} e_R^2 \\ e_V^2 \end{cases}, \text{ with respect to } \alpha, \beta, n \text{ and } a. \quad (3)$$

The errors are squared in order to enhance absolute low-valued errors. This corresponds to an unconstrained, multiobjective optimization problem, which will provide a set of rules to build an efficient PML for the grounding system problem scenario.

The minimization is performed with a multiobjective genetic algorithm, as proposed in [7]. The algorithm stores both dominated and non-dominated solutions. In order to obtain faster convergence, only the non-dominated solutions, as well as the ones close to the Pareto set, enter the selection process. A clearing technique in the parameter space, associated to a niche approach in the objective space, is performed so as to avoid similarities between solutions. In both cases a specific criterion is used to penalize one of the individuals.

In order to construct inexpensive approximations of computationally expensive engineering analyses and simulations (such as FEA), Kriging models [6] are adopted. The design of the computer experiment was based on Latin hypercubes [8] in order to fill the space of the input data. These procedures are used to derive some relationships between pairs of PML parameters, which are expected to lead to lower errors in both R and V .

IV. RESULTS

Fig. 2 presents the Pareto set, achieved after minimization of both e_R^2 and e_V^2 . Fig. 3 shows histograms of PML parameters associated to that Pareto set, i.e., those parameters which lead to the lowest errors. Fig. 4 illustrates histograms for some ratios between pairs of PML parameters, which are useful as a guidance to choose the more appropriate values for the test case described in II.

With the aid of Figs. 3 and 4, the following parameters might be selected: $d_{buff} = 135$ m, $a = 47$, $n = 10$ and $d_{PML} = 30$ m. By adopting these values, the FEA of the problem depicted in Fig. 1 yielded the results summarized in Table I.

Some results in Figs. 3 are shown in absolute values (m) for clarity, although the optimization schemes were applied in the dimensionless variables of (3).

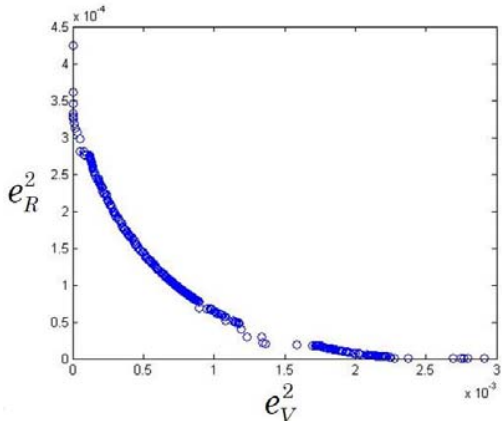


Fig.2 Pareto set after minimization of e_R^2 and e_V^2 .

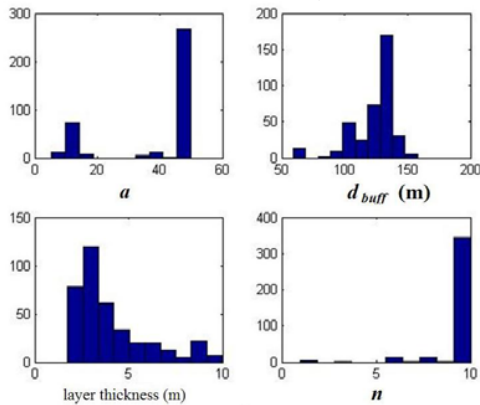


Fig.3 Histograms of PML parameters of problem of Fig. 1.

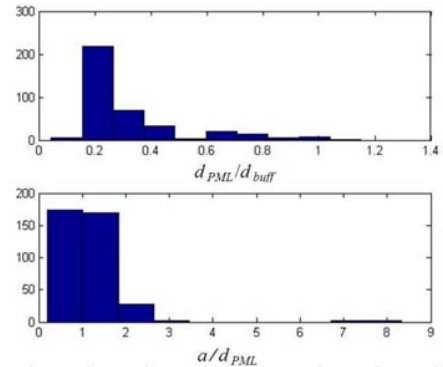


Fig.4 Histograms of some useful ratios between pairs of PML parameters.

TABLE I
NUMERICAL \times THEORETICAL RESULTS

	Theoretical[1]	FEA	$e_{R,V}$ (%)
Ground resistance (Ω)	20.98 (Exp. 21 [2])	21.25	1.2
Surface Potential (V) ¹	9309	9092	2.3
Electric Field (V/m) ¹	2237	2097.4	6.2

¹ at 1.0 m of the stake

V. CONCLUSION

The proposed optimization strategy to determine PML parameters for FE modeling of grounding systems was based only on geometrical parameters in this preliminary approach. A more complete analysis should include other significant variables in (3), such as soil resistivity, discretization refinement, as well as other grounding grid configurations, e.g. horizontal electrodes. These additional issues are intended to be addressed in the paper's extended version

VI. REFERENCES

- [1] E. D. Sunde, *Earth Conduction Effects in Transmission Systems*, Dover Publishing, NY, pp. 75/90, 1967.
- [2] S. Bourg, et al., "Deep earth electrodes in highly resistive ground: frequency behaviour", *IEEE Int. Symposium on EMC*, 584-9, 1995.
- [3] W. Pinello et al., "A new numerical grid truncation scheme for the finite difference/finite element solution of Laplace's equation", *IEEE Trans. on Magnetics*, 32(3), 1397-1400, 1996.
- [4] V.C. Silva, J.R. Cardoso, "Determination of grounding system impedance by FEA with the use of special elements", *Record of the 15th COMPUMAG*, Vol. 3, 246-7, Shenyang, China, June 26-30, 2005.
- [5] L. Dedek et al., "Optimization of Perfectly Matched Layer for Laplace's Equation", *IEEE Trans. on Magnetics*, 38(2), 501-4, 2002.
- [6] L. Lebesztajn et al., "Kriging: a useful tool for electromagnetic device optimization", *IEEE Trans. on Magnetics*, 40(2), 1196-9, 2004.
- [7] S. L. Avila et al., "Sensitivity analysis applied to decision making in multiobjective evolutionary optimization", *IEEE Trans. on Magnetics*, 42(4), 1103-6, 2006.
- [8] M. D. McKay et al. "A comparison of three methods for selecting values of input variables in the analysis of output from a computer code," *Technometrics* 21(2), 239-245, 1979

Corrosion diagnosis of a ship mock-up from near electric field measurements

A. Guibert, J.-L. Coulomb, O. Chadebec, C. Rannou

Grenoble Electrical Engineering Lab – Grenoble-INP / Université Joseph Fourier / CNRS
ENSE³, BP 46, 38402 Grenoble, FRANCE

GESMA – DGA – Groupe d'Etudes Sous-Marines de l'Atlantique – CC42 – 29240 BREST
arnaud.guibert@g2elab.grenoble-inp.fr

Abstract — We present here an original application linking an electrochemical phenomenon and the computational aspect of electromagnetic fields to provide a corrosion diagnosis of a protected underwater steel structure. This is possible with the pairing of a numeric method, the BEM, and the study of inverse problems. After a defined operating time, it is mandatory to check an underwater steel structure. Sadly, current examinations techniques require immobilize the structure for a long time and are less efficient. The purpose of this paper is to replace this checking by a series of close electrical measurements in the electrolyte which provides a corrosion diagnosis of the structure. The new method introduced ensures a great time-saving but also an accuracy never reached before. This paper presents this method and its checking through real measurements on a frigate mock-up.

I. INTRODUCTION

During its operating life, an underwater structure suffers from corrosion. This phenomenon starts when iron paint defects appear on its surface, electrically linked to noble metals (propellers in Bronze and Nickel for example). This reaction, called galvanic coupling, makes the iron an anode and bronze a cathode. To fight against this reaction, two main methods have been developed:

- The Sacrificial Anode Cathodic Protection (SACP): some less noble elements than iron (Zinc, Aluminium, etc...) are placed on the structure to protect it. They are going to be corroded instead of the iron of the structure itself, becoming the new anode of the reaction.
- The Impressed Current Cathodic Protection (ICCP): Platinum anodes are distributed on the structure, injecting currents in the seawater. This places the iron in its passivation zone and protects it.

These two protections lead to a circulation of currents in the seawater, inducing the presence of a varying electromagnetic field. The first step of the study is to predict this electromagnetic field from the electric boundary conditions. Then, the problem will be inversed and a corrosion diagnosis will be deducted, starting from near electric field measurements and leading to the corroded areas localization. This paper, based on electric fields and applied to real measurements on a mock-up, extensively improves a method previously introduced [1].

II. FORWARD MODELING

As said before the forward modeling aims to predict the electric potential and the electromagnetic field from physic

boundary conditions. Trying to achieve to diagnosis tool, the numeric method used must directly link the boundary conditions to the measurement locations, advantage provided by the Boundary Elements Method. Moreover, this method permits a simple modeling of the infinity region [2] [3].

Starting from the Laplace equation, the principle is to use the third Green's identity to write an integral equation on the Γ boundaries of the problem:

$$h(M).\varphi(M) + \oint_{\partial\Gamma} \varphi(P) \cdot \frac{\partial}{\partial n_q} G(M,P) dl - \oint_{\partial\Gamma} G(M,P) \cdot \frac{\partial}{\partial n_q} \varphi(P) dl = 0 \quad (1)$$

where φ is the electric potential and $\partial\varphi/\partial n$ the opposite of the normal current density, within the conductivity σ factor. P is the integration point on the boundary and M the point where the computation is made. $h(M)$ is the solid angle seen by M and G is the Green function $1/r$, where r is the distance [MP].

After the surfaces have been meshed, a point matching approach of (1) at the barycenter of each element can be provided, leading to a matrix system..

$$[A_{Green}] \begin{bmatrix} \varphi \\ \partial\varphi/\partial n \end{bmatrix} = 0 \quad (2)$$

Making such an approximation is known as not very precise, but, as the main goal is the development of an inverse method, it is acceptable for us. Of course, this system has more unknowns than equations. To solve it requires the introduction of boundary conditions. At the last step of this forward modeling, we get a non linear system due to the form of the polarization law ($\partial\varphi/\partial n = f(\varphi)$) introduced by the presence of polarizable steel on the boundaries. This system is then usually solved by an iterative Newton-Raphson process.

The electric field anywhere in the domain is then available thanks to the gradient of (1):

$$\mathbf{E}(M) = \frac{1}{4\pi} \oint_{\partial\Gamma} \varphi(P) \left(-3 \cdot \frac{(\mathbf{r}\cdot\mathbf{n})\mathbf{r}}{r^5} + \frac{\mathbf{n}}{r^3} \right) + \frac{\partial\varphi(P)}{\partial n} \cdot \frac{\mathbf{r}}{r^3} dl \quad (3)$$

If the electric field is expressed in several points, the last equation can be represented by the following system:

$$[A_{Measurement}] \begin{bmatrix} \varphi \\ \partial\varphi/\partial n \end{bmatrix} = E \quad (4)$$

III. INVERSE METHOD AND IMPROVEMENTS

The main goal is, from real electromagnetic measurements contained in the E vector and the construction of the system (4), to find the X vector. This problem is very ill posed, due to a different number of unknowns and equations, numeric approximations and measurements error. It leads to a very bad

condition number for (4) and a direct inversion provides a good mathematical results but with no physic behavior.

An original method to get a better condition number is to add the Green equations from (2) linking all unknowns on the boundaries. This ensures to have a physical result and permits to reduce the number of measurements to make. This first step permits a real facilitation of the inversion [1]:

$$\begin{bmatrix} A_{Measurement} \\ A_{Green} \end{bmatrix} \begin{bmatrix} \varphi \\ \partial\varphi/\partial n \end{bmatrix} = \begin{bmatrix} E \\ 0 \end{bmatrix} \quad (5)$$

In a second time a regularization technique is needed to get the best solution of (5). The one chosen is Tikhonov's method, its principle being to find a solution minimizing [4]:

$$\min(\|A.X - B\| + \lambda\|L.X\|). \quad (6)$$

The L matrix is called the regularization matrix: a 0-order regularization (L is the identity matrix) privileges solutions with minimum norm; a 1-order one favors continuous solutions and a 2-order one accentuates this continuous behavior. In our study, a 2-order method is chosen. The λ choice, image of the importance given to this regularization (symbolizing the compromise between solution precision and regularization effect) is made thanks to the well-known L-curve technique.

IV. METHOD CHECKING WITH REAL MEASUREMENTS

To check the diagnosis method explained before, real measurements are employed: a composite 1/40th mock-up of a frigate has been equipped with an adapted ICCP, electrically linked to iron plates (simulating the paint defects) disposed on the hull. The mock-up is then placed in a salted water with a controlled conductivity (5,16 S/m).



Fig. 1. 1/40th mock-up set in measurement conditions

When the ICCP is running, some electric field measurements are made on lines at different depths.

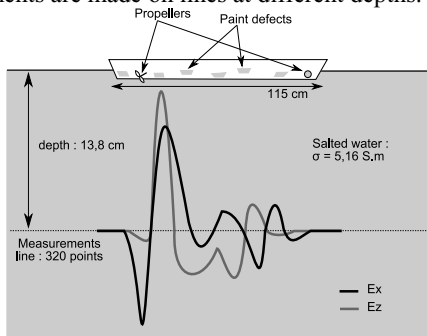


Fig. 2. Real electromagnetic measurements on a 1/40th mock-up

These measurements have been made in the Physical Scale Modeling (PSM) facility of the US Naval Research Laboratory (NRL) located in Key West (Florida). In fact, 640 measurements are made: 320 Ex and 320 Ez, no one made on the y (transverse) axis. The complex meshing of the structure gives 3103 elements, making the system under determined.

By adding the 3103 Green equations through A_{Green} , the new system gets a better condition number. An interpolation is finally made from the electric field measurements, to get a sufficient number of equations and make the problem over determined.

The current density on each anode is known (in the range of the hundred A/m²) as an evaluation of the mean value of the current density on the propellers. The previous improved inverse method gives the following results on the hull:

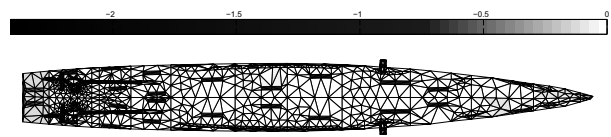


Fig. 3. Current density on the boundaries in A/m²

Current density results are only shown, because of their visibility, but potentials are also obtained. The scale is negative as we want to see the currents going back to the hull, which are the corroded ones. These parts correspond to the less potential areas. The result matches the real location of the iron plates, giving a good diagnosis, with less than 5% of error. The method guarantees good results with a complex geometry and real measurements.

V. CONCLUSION

This diagnosis method succeeds in locating the corroded areas of an immersed part of a hull with real electric field measurements. But some other structures can be studied, as pipelines, offshore platforms, etc... Potential measurements can also be the basis but the use of electric field sensors is more widespread. Moreover, the numerical tools used here can be applied to other scientific domains, such as heat problems for example.

VI. REFERENCES

- [1] A. Guibert, J.-L. Coulomb, O. Chadebec, C. Rannou "Ships hull corrosion diagnosis from close measurements of electric potential in the water", IEEE Trans. Magn., vol.45 in press, 2009.
- [2] J. A. Brebbia, J. C. F. Telles and L. C. Wrobel, *Boundary Elements Techniques, Theory and Applications in Engineering*, Springer-Verlag, Berlin, 1984.
- [3] N. G. Zamani, J. M. Chuang and J. F. Porter, "BEM simulation of cathodic protection systems employed in infinite electrolytes", International Journal For Numerical Methods In Engineering, vol. 24, pp. 605-620, 1987.
- [4] C. Hansen, "Rank-Deficient and Discrete Ill-Posed Problems, Numerical Aspects of Linear Inversion", 1998

Dynamic Multiobjective Clonal Selection Algorithm for Engineering Design

Lucas S. Batista¹, Diogo B. Oliveira¹, Frederico G. Guimarães², Elson J. Silva¹ and Jaime A. Ramírez¹

¹Depto de Engenharia Elétrica, Universidade Federal de Minas Gerais, Belo Horizonte, 31720-901, Brazil.

²Depto de Computação, Universidade Federal de Ouro Preto, Ouro Preto, 35400-000, Brazil.

This paper presents a Multiobjective Clonal Selection Algorithm (MCSA) with dynamic variation of its main parameters. The method performs a somatic hypermutation step using different probability distributions, balancing the search in the algorithm. In order to illustrate the efficiency of the MCSA, we compare its performance with the Nondominated Sorting Genetic Algorithm II (NSGA-II), and illustrate its application in an industrial electromagnetic design.

Index Terms—Multiobjective optimization, clonal selection algorithm.

I. INTRODUCTION

The solution of real-world engineering design problems can be, in some cases, translated into optimization problems that involve multiple, often conflicting, objectives. For these multiobjective optimization problems, there is not a single optimal solution, but a set of trade-off solutions, known as Pareto-optimal solutions, in which each point represents different degrees of importance for the objectives. Multiobjective algorithms try to find an estimate set that best approximates the Pareto-optimal set, allowing the designer to consider alternative solutions for the design problem.

To deal with these multiobjective optimization problems, many evolutionary approaches have been proposed since the 1990's, including algorithms based on artificial immune systems (AIS), which have presented very promising results [1]. See [2] for an overview on multiobjective algorithms based on AIS.

As the AIS-based methods have a special ability in solving multimodal functions, mapping the best local solutions, some further mono-objective works have employed these systems to perform high computational cost optimization problems, see for instance [3] and [4]. In order to investigate the efficiency of these algorithms for multiobjective optimization, we extended the ideas presented in our previous work [4] to the multiobjective clonal selection algorithm (MCSA). Although this approach has presented useful results, it requires the adjustment of many initial parameters. In this paper, we propose an enhanced version of the MCSA, with a dynamic control of its parameters. The algorithm is compared with the nondominated sorting genetic algorithm (NSGA-II). In addition, we illustrate an application of the MCSA to an industrial electromagnetic design.

II. DESCRIPTION OF THE ALGORITHM

The algorithm is essentially defined by four main steps, namely affinity evaluation, cloning, affinity maturation and

replacement. The N_{pop} candidate solutions are evaluated over all objective functions, and each point receives an affinity value according to the fast nondominated sorting with crowding distance assignment.

The n_{sel} best solutions are selected for cloning and each one of these points receives a number of clones given by:

$$N_C^i = \left\lceil nc \times \frac{\xi_i}{\sum_{i \in n_{sel}} \xi_i} \right\rceil \quad (1)$$

in which $\xi_i \in [0, 1]$ is the normalized crowding distance and nc is the total number of clones produced.

The maturation of the immune response is implemented by the somatic hypermutation and receptor editing operators. Given the population of clones, the hypermutation consists of adding different kinds of perturbations to them [4], in which the best n_{dN} copies are perturbed using a Gaussian distribution, and the n_{dC} remaining are perturbed using a Chaotic distribution, such that $n_{dN} + n_{dC} = 1$.

In this paper, the mutation radius $\gamma \in [0, 1]$ and the relation between n_{dN} and n_{dC} are adjusted dynamically. In this way, while the population evolves, the value of γ decreases and the value of n_{dN} increases, intensifying the local refinement in the algorithm towards the end of the optimization process. These parameters are stated next:

$$\begin{aligned} \gamma(n_{eval}) &= (\gamma_o - 0.05) \exp(-\lambda_1 n_{eval}) + 0.05 \\ n_{dN}(n_{eval}) &= 1 - ((\epsilon_o - 0.1) \exp(-\lambda_2 n_{eval}) + 0.1) \end{aligned} \quad (2)$$

in which n_{eval} represents the current number of evaluations, $\gamma_o = 0.40$, $\epsilon_o = 0.50$, $\lambda_1 = 5/n_{eval}^{max}$ and $\lambda_2 = 3/n_{eval}^{max}$.

The receptor editing operator can be viewed as a special kind of mutation employed by a simple differential evolution (DE) algorithm. Here, we adopt a similar procedure to the best n_{sel} antibodies, producing new solutions v_i , $i \in [1, n_{sel}]$, according to (3), with random and different indexes $r1, r2, r3 \in [1, n_{sel}]$ and $\omega = 1$.

$$v_i = x_{r1} + \omega(x_{r2} - x_{r3}) \quad (3)$$

In order to maintain the diversity of the solutions, the replacement operator generates $N_{pop} - n_{sel}$ new random points within the search region.

Manuscript received April 6th, 2009.

Corresponding Author: J.A. Ramírez (jramirez@ufmg.br).

This work was supported by the National Council of Technological and Scientific Development of Brazil under CNPq Grant 306910/2006-3.

Algorithm 1: The Multiobjective Clonal Selection Algorithm

```

1 begin
2    $\mathcal{P}_t \leftarrow$  Generate the initial  $N_{pop}$  solutions;
3    $\Phi_t \leftarrow$  Evaluate the points in  $\mathcal{P}_t$ ;
4   while Not stop criterion do
5      $\mathcal{F}_t \leftarrow$  Classify the solutions ( $\mathcal{P}_t, \Phi_t$ );
6      $\mathcal{S}_t \leftarrow$  Select the best  $n_{sel}$  solutions ( $\mathcal{F}_t$ );
7      $\mathcal{C}_t \leftarrow$  Perform the cloning process ( $\mathcal{S}_t$ );
8      $\mathcal{Q}_t \leftarrow$  Perform the affinity maturation ( $\mathcal{S}_t, \mathcal{C}_t$ );
9      $\mathcal{R}_t \leftarrow$  Replacement and diversity generation;
10     $\mathcal{P}_{t+1}, \Phi_{t+1} \leftarrow (\mathcal{F}_t^1 \cup \mathcal{Q}_t \cup \mathcal{R}_t)$ ;
11     $t \leftarrow t + 1$ ;
12  end
13 end

```

All new solutions produced by the hypermutation, editing and replacement operators are classified into nondominated fronts, and the first one is stored in an archive whose maximum size is \mathcal{L} . The best N_{pop} points, i.e., the less dominated ones with greater crowding distance, are selected for the next iteration. The previous steps are summarized in the Alg. 1.

III. RESULTS

A. Analytical Problems

The MCSA parameters have been chosen as $N_{pop} = 30$, $n_{sel} = 0.90$ and $nc = 70$. The NSGA-II has been set with simulated binary crossover (SBX) and polynomial mutation. A population archive of $\mathcal{L} = 100$ has been adopted for both methods.

We have selected three benchmark problems with three objectives: DTLZ6, DTLZ7 and DTLZ8. These problems allow to investigate the ability of the methods (i) to converge to a degenerated curve (DTLZ6), (ii) to identify disconnected Pareto-optimal regions in the search space (DTLZ7), and (iii) to deal with constraint functions (DTLZ8).

The results presented in the Fig. 1 have been estimated using the S-metric. By considering that the hypervolume calculated should increase as generations evolve, the progress of the median of the S-metric gives a picture of the convergence speed of each algorithm. In this case, the MCSA has outperformed the NSGA-II in all DTLZ problems. The algorithms were executed 30 times with a stop criterion of 50,000 function evaluations.

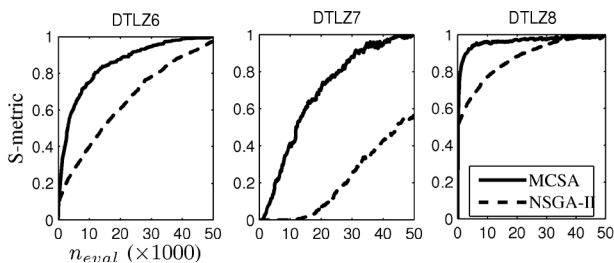


Fig. 1. Statistic values of convergence speed.

B. Microwave Heating Device

The microwave heating device has applications in sterilization processes where it is used to heat a water layer. Its structure consists of six dielectric layers (l_1, \dots, l_6) which receive microwave power from both sides, see Fig. 2.

The design is described by 09 variables, which are the six layers, the power density sources (P_1, P_2), and the position of P_2 (d). As stated next, the optimization problem consists of the maximization of the quantity of water and the minimization of the spent energy, ensuring a water temperature between 100°C and 121°C:

$$\begin{aligned} \min F = & \begin{cases} f_1(\vec{x}) = -l_3 \\ f_2(\vec{x}) = (P_1 + P_2)\Delta t_h \end{cases} \\ \text{subject to } & \begin{cases} g_1(\vec{x}) = -T + 100^\circ\text{C} \leq 0 \\ g_2(\vec{x}) = T - 121^\circ\text{C} \leq 0 \end{cases} \end{aligned} \quad (4)$$

in which Δt_h is the spent heating time.

Regarding the same MCSA parameters, we have attained an estimated Pareto-optimal in a single run of the method, with a stop criterion of 16,000 function evaluations. For the decision-making process, we have selected the point which corresponds to the most efficient device, in which the energy efficiency (eff) is the relation between the coupled and the reflected energy. The solution achieved by the MCSA presents an efficiency gain of 26% when compared with the SPEA-II.

Method	$f_1(\vec{x})$	$f_2(\vec{x})$	eff	CPU Time
MCSA	-0.0558	0.0252	0.68%	830 min ¹
SPEA-II	-0.0400	0.0204	0.54%	990 min ²

¹Intel32 Core 2 Duo CPU T8300, 2.4GHz - 2GB RAM (in a single core).

²AMD Athlon64 Processor 3500+, 2.2GHz - 2GB RAM.

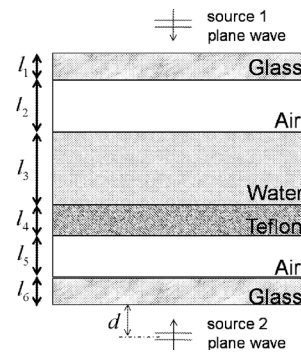


Fig. 2. Microwave Heating Device.

REFERENCES

- [1] L.N. de Castro and F.J. Von Zuben, "The Clonal Selection Algorithm with Engineering Applications", *Proc. of GECCO*, Jul 2000.
- [2] F. Campelo, F.G. Guimarães, H. Igarashi, "Overview of artificial immune systems for multi-objective optimization", 4th International Conference on Evolutionary Multi-criterion Optimization, EMO 2007, *Lecture Notes on Computer Science*, vol. 4403, pp. 937–951, 2007.
- [3] F. Campelo, F.G. Guimarães, H. Igarashi, and J.A. Ramírez, "A Clonal Selection Algorithm for Optimization in Electromagnetics", *IEEE Trans. on Magnetics*, vol. 41, no. 5, pp. 1736–1739, May 2005.
- [4] L.S. Batista, F.G. Guimarães, and J.A. Ramírez, "A Distributed Clonal Selection Algorithm for Optimization in Electromagnetics", *IEEE Trans. on Magnetics*, vol. 45, no. 3, pp. 1598–1601, Mar 2009.

Stochastic uncertainty quantification of the conductivity in EEG source analysis by using polynomial chaos decomposition

R. Gaignaire¹, G. Crevecoeur², L. Dupré², P. Dular^{1,3}, and C. Geuzaine¹

¹Dept. Electrical Engineering and Computer Science (ACE), University of Liège, Sart Tilman B28, B-4000 Liège, Belgium
E-mail: rgaignaire@ulg.ac.be

²Dept. of Electrical Energy, Systems and Automation, Ghent University, Sint-Pietersnieuwstraat 41, B-9000 Ghent, Belgium

³Fonds de la Recherche Scientifique, F.R.S.-FNRS, Belgium

Abstract—The electroencephalogram (EEG) is one of the techniques that is used for the non-invasive diagnosis of patients suffering from epilepsy. EEG source localization identifies the neural activity, starting from measured EEG. This numerical localization procedure has a resolution, which is difficult to determine due to uncertainties in the EEG forward models. More specifically, the conductivity values of brain and skull in the head models are unknown. In this paper, we propose the use of non intrusive probabilistic methods for quantifying the possible errors introduced by the uncertain head conductivity values. This paper illustrates the accuracy and computational advantages of the non intrusive method for EEG source analysis. We validate the presented method with Monte Carlo simulations.

I. INTRODUCTION

Neurological disorders, such as epilepsy, can be diagnosed by the use of the electroencephalogram (EEG). The EEG measures potentials on the scalp of the patient under study by means of electrodes over a period of time. These potentials are the result of electrical activity produced by the brain. The number of electrodes may vary, but typically 20 to 40 electrodes are placed on the scalp of the patient. The malfunctioning region in the brain needs to be identified using the EEG. To this end, EEG measurements can be coupled to a numerical procedure in order to identify the neural sources, in a so-called *EEG source analysis*. For EEG source analysis, two subproblems need to be solved: a forward and an inverse problem.

The EEG forward problem consists in simulating the EEG potentials for a given neural electrical activity. For this, the following needs to be provided: a head model, i.e. a model that incorporates the anatomy of the head with the different brain tissues, and a source model, i.e. a physical and mathematical model for the brain activity. By solving the EEG inverse problem, sources are determined which correspond with the measured EEG potentials. These sources can be identified with good temporal resolution, contrary to other biomedical imaging techniques, but fail to have a high spatial resolution. The need exists for quantifying the errors that are made when recovering the neural sources when using a certain inverse numerical procedure. In the head model, the geometry can

give rise to errors [1] but through the use of accurate Magnetic Resonance Images, these errors can be limited. Large uncertainties however are introduced with model parameters that are difficult to determine: the conductivity values of the brain and the skull. We propose to use so-called *non intrusive probabilistic algorithms* to quantify the uncertainties on the location of the neural sources, which only assume the conductivity to be of finite variance [2], [3].

II. INCORPORATION OF STOCHASTIC UNCERTAINTY IN EEG SOURCE ANALYSIS

A. Definition of the problem

The EEG forward problem starts from the location and orientation of neural sources, where conductivity values of the brain and skull need to be provided, and calculates the EEG electrode potentials. We assume for simplicity of analysis that the neural activity is represented by a single electrical dipole with a given location $\mathbf{r} = [r_x, r_y, r_z]^T$ and orientation. This is a widely used approximation of the neural activity of patients suffering from epilepsy. The brain to skull ratio of the conductivity X is the important model parameter when solving the EEG forward problem. Since we want to propose a method that takes into account the uncertainty on the conductivity and where the error due to geometrical modelling is not considered, we employ a coarse approximation of the head: the spherical head model. This model is a widely-used approximation of the head where the head is represented by three spheres: the inner sphere represents the brain, the intermediate layer represents the skull and the outer layer represents the scalp (cf. Fig. 1a). In this case a semi-analytical expression exists for the computation of the EEG potentials [4]. In our numerical tests we always use a standard configuration of 27 electrodes.

Spreading out the uncertainty from the conductivity to the position of the dipole is an inverse problem. To solve this inverse problem we use the Nelder-Mead simplex method in combination with a non intrusive stochastic approach based upon a chaos polynomial decomposition of both the conductivity and the dipole position [2]. The only assumption on the conductivity is that it is a random variable of finite variance. We do not make any assumption on the shape of the probabilistic distribution of the position of the dipole.

This work was supported by the Belgian Science Policy under grant IAP P6/21 and by NSF under grant DMS-0609824.

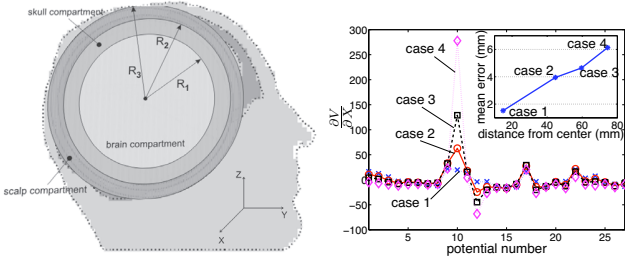


Fig. 1. (a) Three-shell spherical head model and (b) larger mean error for dipoles for which the potential is very sensitive to the conductivity.

B. Non intrusive method for EEG source analysis

Assuming that the conductivity is a random variable of finite variance, we can expand it as a truncated series of order p_{in} of Hermite polynomials of a random gaussian variable $\xi_i(\omega)$, known as *Hermite chaos polynomials* [2]:

$$X(\omega) = \sum_{i=0}^{p_{in}} X_i h_i(\xi(\omega)), \quad (1)$$

where h_i is the polynomial of Hermite of order i and ω is random coordinate.

The inverse deterministic problem allows us to compute the value of the position of the dipole from the value of the conductivity (X). This process can be seen as a “blackbox” such as $\mathbf{r} = \mathbf{r}(X(\xi(\omega)))$. Hence the dipole position along the spatial direction x (resp. y or z) belongs to a space that can be spanned by the polynomials $h_i(\xi(\omega))$, and can thus be written as a truncated series at an order p_{out} :

$$\mathbf{r}_x(\omega) = \sum_{i=0}^{p_{out}} \mathbf{r}_x^m h_i(\xi(\omega)). \quad (2)$$

To compute the value of the unknown real coefficients \mathbf{r}_x^m , we use the orthogonality properties of the Hermite polynomials:

$$\mathbf{r}_x^m = \frac{E(\mathbf{r}_x(\omega) h_m(\xi(\omega)))}{E(h_m(\xi(\omega))^2)}, \quad (3)$$

where $E(\cdot)$ is the mathematical expectation. The denominator can be computed analytically. To compute the numerator (which is an integral) we use a Hermite Gauss integration scheme with d integration points [2]:

$$E(\mathbf{r}_x(\omega) h_m(\xi(\omega))) \approx \sum_{i=1}^d w_i \mathbf{r}_x(X(t_i)) h_m(t_i), \quad (4)$$

where t_i is the i -th Gauss point and w_i the associated weight. This only requires to compute the inverse deterministic problem d times, with the conductivity evaluated through (1) with $\xi(\omega) = t_i$, $i = 1, \dots, d$.

III. RESULTS AND DISCUSSION

We performed computations using the Monte Carlo (MC) and the non intrusive (NI) methods for several test cases corresponding to dipoles located increasingly farther from the center of the head (Case 1 to 4). In all cases the Monte Carlo simulations were performed using a sample size of 2000 and the non intrusive method used $p_{in} = 13$, $p_{out} = 6$ and $d = 10$. The brain to skull conductivity ratio X is chosen as a uniform

TABLE I

MEAN OF THE POSITION OF THE DIPOLE (MM) FROM THE CENTER IN THE x , y AND z -DIRECTION FOR SEVERAL TEST CASES.

Case	Method	\bar{r}_x (mm)	\bar{r}_y (mm)	\bar{r}_z (mm)
Case 1	MC	7.72	7.72	7.73
	NI	7.72	7.72	7.73
Case 2	MC	23.54	23.34	23.65
	NI	23.52	23.32	23.64
Case 3	MC	31.75	31.62	31.73
	NI	31.72	31.60	31.71
Case 4	MC	39.49	40.07	39.33
	NI	39.46	40.03	39.31

TABLE II

STANDARD DEVIATION OF THE POSITION OF THE DIPOLE IN DIFFERENT CASES.

Case	Method	σ_{r_x} (mm)	σ_{r_y} (mm)	σ_{r_z} (mm)
Case 1	MC	0.53	0.53	0.53
	NI	0.54	0.54	0.53
Case 2	MC	1.38	1.50	1.31
	NI	1.40	1.51	1.33
Case 3	MC	1.63	1.70	1.64
	NI	1.65	1.72	1.66
Case 4	MC	2.17	1.91	2.26
	NI	2.19	1.85	2.28

random variable between $1/40$ and $1/9$. A fixed orientation (y -direction) of the dipole is assumed, and its location is measured from the center of the head model.

The results in Table I show the mean obtained by MC and NI for the four different EEG data sets. The results obtained using both methods are in very good agreement. The computational time required by the Monte Carlo method is about 8000 seconds on a $2.26GHz$ personal computer, whereas non intrusive method requires only 40 seconds.

Table II shows that for increasing distances from the center of the head, larger standard deviations are observed. This means that the uncertainty on the spatial position of the source increases when the source approaches the electrodes. This is due to the fact that the sensitivity of the potentials to the conductivity becomes larger when the source is farther from the center (cf. Fig. 1.b). Here again, one can note the good agreement between both numerical methods.

The full paper will provide additional details on the non intrusive probabilistic method and compare this method with classical techniques used in the EEG community, such as the Cramer-Rao boundary method.

REFERENCES

- [1] N. von Ellenrieder, C.H. Muravchik, and A. Nehorai, “Effects of geometric head model perturbations on the EEG forward and inverse problems,” *IEEE Transactions on Biomedical Engineering*, vol. 53, pp. 421-429, 2006.
- [2] R. Gaignaire, O. Moreau, B. Sudret, B. and S. Clnet, “Propagation d’incertitudes en lectromagnétisme statique par chaos polynomial et rsolution non intrusive,” *NUMELEC2006*, Lille, Novembre 2006.
- [3] R. Gaignaire, O. Moreau, B. Sudret, B. and S. Clnet, “Current calculation in electrokinetics using a spectral stochastic finite element method,” *IEEE Transactions on Magnetics*, vol. 4, pp. 754-757, 2008.
- [4] Y. Salu, L. Cohen, D. Rose, S. Sato, C. Kufita, and M. Hallett, “An improved method for localizing electric brain dipoles,” *IEEE Transactions on Biomedical Engineering*, vol. 37, pp. 699-705, 1990.

The EMC Method Applied to the Design of Local and Asymmetric Gradient Coils for MRI

Hector Sanchez Lopez, Michael Poole, Feng Liu, Stuart Crozier
School of Information Technology and Electrical Engineering, University of Queensland, Australia
hsanchez@itee.uq.edu.au

Abstract—The design of local, asymmetric gradient coils is of great importance for magnetic resonance imaging (MRI). Such local coils promise increased gradient strengths and slew rates that have the potential to acquire image data with increased spatial and/or temporal resolution. Conventional coil design techniques are limited to specific geometries (e.g. cylindrical, planar) by their mathematical formulation. In order to more closely surround the sample of interest a symmetry-free, inverse boundary element method (BEM) was employed to design local gradient coils without relying on symmetry to parameterize and simplify the mathematical problem. With several examples we illustrate the versatility of this approach and the superiority of the performance of local gradient coils.

I. INTRODUCTION

High performance gradient coils are critical for the ever increasing demands of new techniques in magnetic resonance imaging (MRI). Many methods for designing gradient coils have been presented [1, 2] with the aim of tailoring the wire pattern of the coil to generate linear axial magnetic field gradients in a region of interest (ROI) with high efficiency (η , field gradient per unit current measured in T/m/A) and low stored magnetic energy (low inductance L , μH). It is known that reducing the coil size and re-designing the wire pattern accordingly increases the coil performance [3], often measured as the ratio η^2/L [1]. However, conventional coil design methods based on the target field approach [1] were developed for specific geometries such as cylinders and are difficult to apply to local gradient coil. Employing a symmetry-free gradient coil design method allows us to tailor the shape of the gradient coil to more closely conform to the ROI. Such a boundary element method (BEM) was first presented for gradient coil design by Pissanetzky [4] and has been extended [5] and applied to more complex design problems [6]. An alternative approach was used in this study that employs the equivalency between a magnetized volume and a surface current density, which we have therefore termed the “equivalent magnetization current” (EMC) method [7]. The versatility of the EMC method is demonstrated by the design of asymmetric, high-performance, local gradient coils. It is illustrated that conforming the coil design surface to the sample shape increases the performance of the resulting gradient coil

II. MATERIALS AND METHODS

The EMC method considers an isotropic, rigid, non-hysteretic, arbitrary volume, V , of thickness h , bounded by the

surface S ($S \in \mathfrak{R}^3$) that possesses a magnetization, $\mathbf{M}(\mathbf{r}')$, normal to S . A volume of “well-behaved” magnetization $\mathbf{M}(\mathbf{r}')$ can be considered as equivalent to a uniform current density on its surface [8]. If h is small and $\mathbf{M}(\mathbf{r}')$ is piecewise-linear throughout the thin volume, V , it can be shown that (See Eqs. (1)-(9) in [7])

$$\mathbf{M}(\mathbf{r}')h = \psi(\mathbf{r}') \cdot \hat{\mathbf{n}}(\mathbf{r}'), \quad \mathbf{r}' \in S, \quad (1)$$

where $\psi(\mathbf{r}')$ is the scalar piecewise-linear stream-function of the current density flowing on S and $\hat{\mathbf{n}}(\mathbf{r}')$ is the normal vector to S at \mathbf{r}' . The arbitrarily-shaped surface is discretized into triangular elements with N nodes defining the corners of each boundary element. $\psi(\mathbf{r}')$, can be expressed as a sum of unknown nodal stream-function values, s_n , and basis-functions, $\Psi_n(\mathbf{r}')$; $\psi(\mathbf{r}') = \sum_{n=1}^N s_n \hat{\psi}_n(\mathbf{r}')$ [7], for which $\hat{\psi}_n(\mathbf{r}')$ is linear in each triangle and can be expressed as:

$$\hat{\psi}_n(\mathbf{r}') = \begin{cases} 1 - \frac{(\mathbf{r}' - \mathbf{r}_n) \cdot \mathbf{d}_{ni}}{|\mathbf{d}_{ni}|^2} \hat{u}(\mathbf{r}'), & \hat{u}(\mathbf{r}') = \begin{cases} 1, & \mathbf{r}' \in \Delta_{ni} \\ 0, & \mathbf{r}' \notin \Delta_{ni} \end{cases} \end{cases} \quad (2)$$

for $i = 1, \dots, O$, where \mathbf{d}_{ni} is the perpendicular distance vector from \mathbf{r}_n to the far side of each triangle Δ_{ni} , associated with the n^{th} node and O is the number of triangles associated with the node n . Equation (2) simply ensures that $\hat{\psi}_n(\mathbf{r}')$ in each triangle has value of one at the node n and falls linearly to zero at the edge opposite to the node n . In the rest the conducting surface ($\mathbf{r}' \notin \Delta_{ni}$) $\hat{\psi}_n(\mathbf{r}')$ is zero. The flux density of the magnetic field, \mathbf{B} , produced by a magnetized thin volume was deduced by applying the curl operator to the magnetic vector potential, \mathbf{A} , Eq. (5.103), pg 197 in [8]. Substituting the product $\psi(\mathbf{r}') \cdot \hat{\mathbf{n}}(\mathbf{r}')$ for the magnetization-thickness function, $\mathbf{M}(\mathbf{r}')h$, the magnetic flux density can be written as:

$$\mathbf{B}(\mathbf{r}) = -\frac{\mu_0}{4\pi} \sum_{n=1}^N s_n \sum_{i=1}^O \nabla_{\mathbf{r}} \int_{A_{ni}} \hat{\mathbf{n}}_{ni}(\mathbf{r}') \cdot \hat{\psi}_n(\mathbf{r}') \cdot \nabla_{\mathbf{r}'} \left(\frac{1}{R} \right) dA_{ni} \quad (3),$$

where A_{ni} is the area of the triangle i associated with node n . The stored magnetic energy, force and torque can be calculated assuming an equivalent surface current density, \mathbf{J} , flowing in the surface of the triangle that belongs to the node n . The axial component of (3) $B_z(\mathbf{r})$ is linear with respect to s_n , as are the net torque and net force generated by the coil in the intense, uniform background magnetic field, $B_0 \mathbf{z}$. The stored magnetic energy is quadratic with respect to s_n . The optimization was therefore stated as a quadratic programming (QP) problem in the present work. The *quadprog* function, provided in MATLAB's[®] optimization toolbox, was employed

9. Numerical Techniques

to solve the QP problem. The solutions, s_n , are the stream-function values corresponding to the gradient coil with minimum inductance that satisfies the constraints placed upon the net torque and net force and the inequality constraints of the linearity of $B_z(\mathbf{r})$. Equally-spaced contours of $\psi(\mathbf{r}')$ were generated to approximate the continuous current density by an arrangement of discrete current-carrying wires [6].

III. RESULTS AND DISCUSSIONS

For comparison, a figure of merit (FoM) given by η^2/L , was used to characterize performance of the coils. The maximal deviation from the target flux density in the ROU was calculated using Eq. (6) in [6].

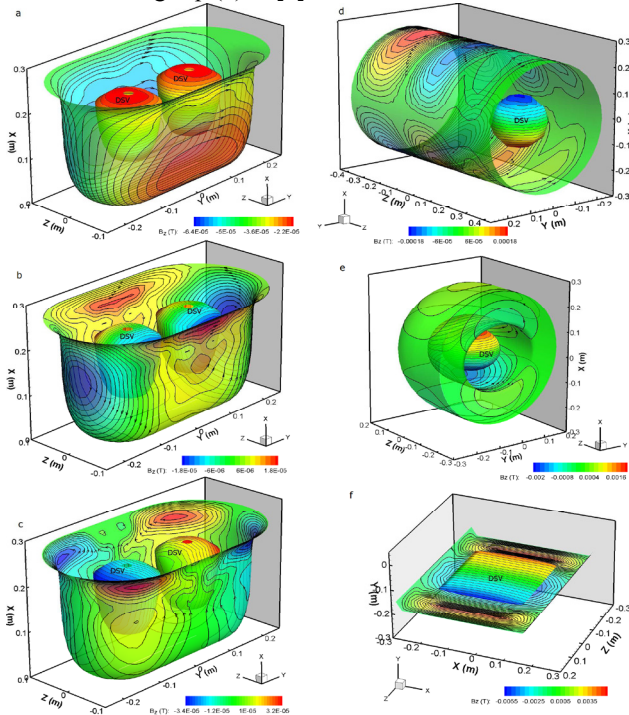


Fig. 1. The three axis local x-,z-,y- gradient coils for breast imaging (a,b,c). Asymmetric torque balanced transverse x-gradient coils for head imaging (d,e). The uniplanar insertable z-gradient coil. The arrow in the coil pattern represents the sense of the current. Contour line at the DSV represents the values of the axial magnetic field component (units in Tesla).

A three-axis (x, y, z) gradient coil for breast imaging was designed using the EMC approach. Figs. 1 (a, b, c) show the wire pattern of each coil and the two ROIs used to specify the target linear magnetic field. The proposed coils would permit imaging of both breasts simultaneously. The FoM of the designs resulted $11.113 \cdot 10^{-4} \text{ T}^2 \cdot \text{m}^{-2} \cdot \text{A}^{-2} \cdot \text{H}^{-1}$, $10.5 \cdot 10^{-4} \text{ T}^2 \cdot \text{m}^{-2} \cdot \text{A}^{-2} \cdot \text{H}^{-1}$ and $9.04 \cdot 10^{-4} \text{ T}^2 \cdot \text{m}^{-2} \cdot \text{A}^{-2} \cdot \text{H}^{-1}$ for the x-, y- and z-gradient coils, respectively. If one large ROI is used instead of two smaller ones, the coil FoM decreases by as much as 0.7 times, the resistance increases dramatically and the gap between wires is reduced from 1 mm to 0.0001 mm producing a complex and an impractical design. The FoM of the local gradient coils can be up to 130 times larger that the same value produced by standard whole body gradient coil. A second

design was two torque-balanced, asymmetric gradient coils for head imaging. Figs. 1. (d, e) shows the wire patterns of the transverse x-gradient coils. The pattern in Fig. 1 (d) shows the ROI shifted towards one end for patient access. However, this feature is obtained with detriment of coil performance; the FoM is reduced 4.6 times from the original value and the resulting torque is minimized 1000 times from an unbalanced coil. Providing shielding for such a coil would make it easier to torque balance as the shield wires flow with opposite sense to the primary wires. Fig. 1 (e), presents an ultra-short head x-gradient coil with a similar target ROI. Due to the shape of this structure the resulting FoM was 120 times larger than the same value produced by the coil Fig. 1 (d). A minimal torque of $0.0001 \text{ N/m} \cdot \text{A} \cdot \text{T}$ along the y-direction would be generated by the coil when immersed in a homogenous magnetic field. A uniplanar, open structure was also studied using the EMC method. This coil could be used for spinal imaging, for example. Due to the closeness to the sample, high gradient strengths could be generated. The efficiency of this design was $\eta = 0.34 \cdot 10^{-3} \text{ T/m}$ (approximately one order higher than the standard local coils), the resistance was expected to be $66 \cdot 10^{-3} \Omega$ using a maximal copper strip width of 1.4 cm and the minimal value was 3.5 mm with a 1 mm of gap between strips.

IV. CONCLUSIONS

Several examples of local gradient coil with increased performance over whole body coils have been presented. This was made possible by employing a symmetry-free coil design to optimally tailor the shape of the coil to more closely conform to that of the imaging region. The use of two ROIs instead of one large one simplifies the coil current pattern and hence superior coil performance is obtained.

V. ACKNOWLEDGMENT

This work was supported by the Australian Research Council.

VI. REFERENCES

- [1] R. Turner, "Gradient coil design: A review of methods," *Mag. Reson. Imag.*, vol. 11, pp. 903-920, 1993.
- [2] M. A. Brideson, L. K. Forbes, and S. Crozier, "Determining complicated winding patterns for shim coils using stream functions and the target-field method," *Concepts Magn Reson*, vol. 14, pp. 9 - 18 2002.
- [3] S. Crozier, S. Dodd, and D. M. Doddrell, "Design of Shielded Quadrupolar Gradient Coils for Magnetic Resonance Microscopy by Simulated Annealing," *IEEE Trans. Magn.*, vol. 30, pp. 1242-1246, 1994.
- [4] S. Pissanetzky, "Minimum energy MRI gradient coils of the general geometry," *Meas. Sci. Technol.*, vol. 3, pp. 667-673, 1992.
- [5] G. N. Peeren, "Stream Function Approach For Determining Optimal Surface Currents," *Journal of Computational Physics*, vol. 191, pp. 305-321, 2003.
- [6] M. Poole and R. Bowtell, "Novel Gradient Coils Designed Using a Boundary Element Method," *Concepts Magn Reson Part B*, vol. 31B, pp. 162-175, 2007.
- [7] Hector Sanchez Lopez, Feng Liu, Michael Poole, and S. Crozier, "The Equivalent Magnetization Current Method Applied to the Design of Gradient Coils for MRI," *IEEE Trans Magn*, vol. 45, pp. 1-9, 2009.
- [8] J. D. Jackson, *Classical Electrodynamics*, 3rd ed. New York: Wiley, 1998.

Two complementary methods to face with convexity issues in topology optimization problems

Thibaut Labbé

F.R.S.-FNRS fellow
Centre for Research in Mechatronics
Université Catholique de Louvain
Louvain-la-Neuve, BELGIUM
thibaut.labbe@uclouvain.be

François Glineur

Center for Operations Research
and Econometrics
Université Catholique de Louvain
Louvain-la-Neuve, BELGIUM
francois.glineur@uclouvain.be

Bruno Dehez

Centre for Research in Mechatronics
Université Catholique de Louvain
Louvain-la-Neuve, BELGIUM
bruno.dehez@uclouvain.be

Abstract—To perform parameter and shape optimization, an initial topology is required which affects the final solution. Topology optimization methods have the advantage to release this constraint. They are based on a splitting of the design space into cells, in which they attempt to distribute optimally some given materials.

Several convexity issues were already highlighted in topology optimization of electromagnetic devices. The optimization algorithm gets trapped in local minimizers and the final solution differs according to the initial conditions. In this paper, two main causes of this lack of convexity are studied. The first one is linked to the handling of intermediate materials, especially those that are a combination of windings and iron. The second one appears when the optimization objective is computed by a difference of magnetic energy between different positions of the rotor.

The methods proposed to manage these convexity issues focus on the shape of the optimization domain of each cell, in terms of materials. They are based on the use of parameterized hyperbolic functions to define the boundaries of the optimization domain and to modify them during the optimization process.

I. INTRODUCTION

Optimization methods differentiate themselves from the design parameters on which they are performed. Parameter optimization is concerned with some dimensions of the drive topology, such as the length of a tooth. However, the range of solutions that may be obtained is limited by the topology fixed initially. Shape optimization experiences the same issue at a lower level.

In topology optimization, the design space is split into cells. The method is then concerned with distributing predefined materials into the cells, such as air, copper or iron [1]–[4]. The design parameters are thus the electric and magnetic properties in each cell, i.e. the current density and the permeability. The main advantage of this approach is that no initial topology is required and that the design parameters enable any topology to be represented. However, this problem often turns out to lack of convexity, which has already been experimented in [5], [6].

In this paper, two complementary methods are suggested to affect the convexity. The first one is related to cells containing a combination of iron and copper, for which the current density and the permeability must be adjusted carefully. The second method concerns problems where the objective function is computed by the difference of magnetic energy between

TABLE I
ELECTRIC AND MAGNETIC PROPERTIES OF THE MATERIALS

Material	Permeability (μ)	Current Density (j)
Air	μ_0	0
Iron	$\mu_0\mu_r$	0
Copper	μ_0	J

different rotor positions. The two methods are explained on the basis of the three materials described in Table I.

II. CONVEXITY ISSUES RELATED TO INTERMEDIATE MATERIALS

The development described in this section is based on Fig.1, which illustrates the optimization domain in a cell. The three black points represent the three possible materials. The horizontal and vertical boundaries are easily delimited, respectively for a material moving between air and iron and air and copper. However, when a cell is moving between copper and iron, we must determine the maximum allowable values for the current density and the permeability.

There are two extreme choices for this boundary. If we allow the electromagnetic properties to move in the whole rectangle (boundary 1 on Fig.1), we can expect a convex shape for the objective function. Indeed, a cell can then be filled with an intermediate material having the maximum permeability and current density at the same time and thus more valuable than copper or iron alone, as illustrated on Fig.1(b). The other extreme is motivated by the fact that eventually, the cells should contain a unique material and not a combination of them. We could thus reduce the domain to the horizontal and the vertical segments (boundary 5). In this case, there is no combination of iron and copper anymore, a cell must be emptied of copper before being filled with iron.

At the beginning of the optimization, we want the problem to be convex in order to avoid the algorithm to be trapped in local minimizers. Since the cells must eventually be filled with a unique material, we have to reduce progressively the optimization domain. In order to modify the domain boundaries, we suggest the use of hyperbolic functions, which is illustrated by the boundaries 2, 3 and 4.

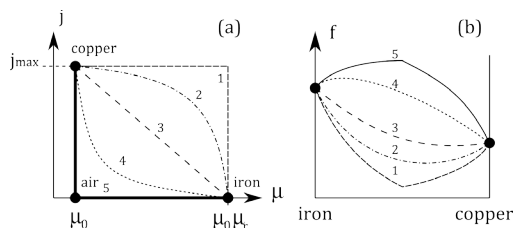


Fig. 1. (a) Optimization domain in a cell for the design variable μ and j (b) Illustration of the convexity evolution

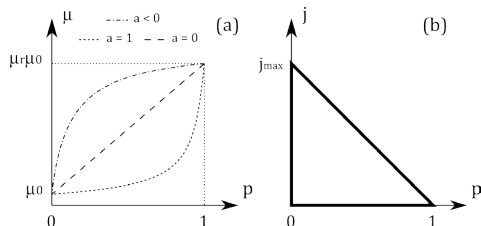


Fig. 2. (a) Mapping between the permeability μ and the design variable p (b) Optimization domain in a cell for the design variable p and j

In the literature, the topology optimization is usually performed on a design variable p linked to the permeability by a given mapping, rather than on the permeability itself. Here, a mapping could also be used to simplify the optimization. Indeed, the shape of the optimization domain is complex because of its hyperbolic boundary. Thanks to the following mapping, the optimization can be performed on the triangular domain represented on Fig.2:

$$\mu = \mu_0 \frac{1 + (\mu_r - 1)(1 - a)p}{1 + (\frac{1}{\mu_r} - 1)ap}, \quad (1)$$

where $a \in [-\infty, \frac{\mu_r}{\mu_r - 1}]$ is a parameter. When p stays in the triangular domain, the set of possible values for the permeability and the current density change according to the parameter a . Increasing progressively its value is similar to a progressive reduction of the optimization domain using a hyperbolic boundary in terms of μ and j .

III. CONVEXITY ISSUES RELATED TO THE DIFFERENCE OF MAGNETIC ENERGY

In a finite element model, the torque of an actuator can be computed in different ways. One of them is to compute the difference of magnetic energy between two rotor positions. However, we observe that using a difference as an objective function creates convexity issues. A solution is then to allow having different rotor shapes for the two positions at the beginning of the optimization.

We define p_1 the permeability of a cell in the rotor position 1 and p_2 the permeability of the corresponding cell in position 2. The idea is to allow these two permeabilities to be different at the beginning of the optimization and to reduce progressively the difference between them. This can be achieved by using the optimization domains shown on Fig.3: the boundaries are defined by hyperbolic functions and the domain is reduced during the optimization to become eventually a straight line.

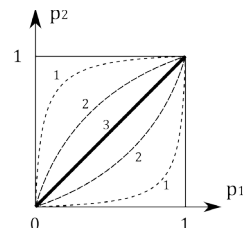


Fig. 3. Optimization domain for the rotor part

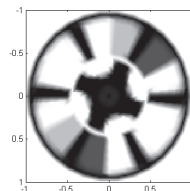


Fig. 4. Optimal topology of a reluctant actuator

IV. APPLICATION

The two methods described in this paper were applied for the optimization of a reluctant actuator. The optimization result is illustrated on Fig.4.

V. CONCLUSION

In conclusion, the two methods presented along this paper are based on the utilization of hyperbolic boundaries for the optimization domain in the cells. They allow reducing significantly the issues linked to convexity for the topology optimization of electromagnetic drives.

REFERENCES

- [1] D. Dyck and D. Lowther, "Automated design of magnetic devices by optimization material distribution," *IEEE Transactions on Magnetics*, vol. 32, no. 4, pp. 1188–1193, May 1996.
- [2] S. Wang, S. Park, and J. Kang, "Multi-domain topology optimization of electromagnetic systems," *COMPEL: The International Journal for Computation and Mathematics in Electrical and Electronic Engineering*, vol. 23, no. 4, pp. 1036–1044, 2004.
- [3] J. Byun, J. Lee, I. Park, and H. Lee, "Inverse problem application of topology optimization method with mutual energy concept and design sensitivity," *IEEE Transactions on Magnetics*, vol. 36, no. 4, pp. 1144–1147, Jul. 2000.
- [4] T. Labbé, F. Glineur, and B. Dehez, "Topology optimization method applied to the design of electromagnetic devices: focus on convexity issues," in *8th International Symposium on Advanced Electromechanical Motion Systems, Electromotion 2009, EPE Chapter Electric Drives*, 2009.
- [5] J. Byun, I. Park, and S. Hahn, "Topology optimization of electrostatic actuator using design sensitivity," *IEEE Transactions on Magnetics*, vol. 38, no. 2, pp. 1053–1056, Mar. 2002.
- [6] J. Yoo, S. Yang, and J. Choi, "Optimal design of an electromagnetic coupler to maximize force to a specific direction," *IEEE Transactions on Magnetics*, vol. 44, no. 7, pp. 1737–1742, Jul. 2008.
- [7] D. Dyck and D. Lowther, "Composite microstructure of permeable material for the optimized material distribution method of automated design," *IEEE Transactions on Magnetics*, vol. 33, no. 2, pp. 1828–1831, Mar. 1997.
- [8] J. Yoo, "Modified method of topology optimization in magnetic fields," *IEEE Transactions on Magnetics*, vol. 40, no. 4, pp. 1796–1800, Jul. 2004.
- [9] J. Yoo, N. Kikuchi, and J. Volakis, "Structural optimization in magnetic devices by the homogenization design method," *IEEE Transactions on Magnetics*, vol. 36, no. 3, pp. 574–580, May 2000.

A Multiobjective Gaussian Particle Swarm Approach Applied to Electromagnetic Optimization

Leandro dos Santos Coelho¹, Helon Vicente Hultmann Ayala¹, and Piergiorgio Alotto²

¹Automation and Systems Laboratory, LAS/PPGEPS, Pontifical Catholic University of Paraná
Rua Imaculada Conceição, 1155, Zip code 80215-901, Curitiba, Paraná, Brazil

E-mail: leandro.coelho@pucpr.br, helon.ayala@pucpr.br

²Dip. Ingegneria Elettrica, Università di Padova

Via Gradenigo 6/A, 35131, Italy

E-mail: alotto@die.unipd.it

Abstract— The development of optimization techniques for multiobjective problems in electromagnetics has been flourishing in the last decade. This paper proposes an improved multiobjective particle swarm optimization (PSO) approach and applies it to the multiobjective version of TEAM workshop problem 22. Simulation results show that improved multiobjective PSO finds a better Pareto-optimal front with respect to more classical PSO methods while maintaining a better spread of nondominated solutions along the front.

Index Terms— TEAM workshop benchmark problem 22, particle swarm optimization, electromagnetic optimization, multiobjective optimization.

I. INTRODUCTION

Recent literatures suggests that multiobjective approaches based on meta-heuristics can serve as a more exploratory and effective tool in solving multiobjective optimization problems than traditional optimizers in electromagnetics optimization. In this context, recent work has presented the effectiveness of multiobjective particle swarm optimization (MOPSO) [1]. Particle swarm optimization (PSO) is a meta-heuristic technique developed by Eberhart and Kennedy in 1995 [2], inspired by social behavior of bird flocking or fish schooling. PSO has been successfully used to solve single-objective optimization because of its high convergence speed and relative simplicity. These features motivated researchers to extend PSO to multiobjective problems. Recently, a considerable number of MOPSO algorithms have been proposed [3].

This paper evaluates a MOPSO, based on [4], which is improved by social and cognitive time-variant factors and an operator of velocity updating based on truncated Gaussian distribution (G-MOPSO). G-MOPSO is tested on the multiobjective version of TEAM benchmark problem 22.

II. FUNDAMENTALS OF PSO, MOPSO AND G-MOPSO

The PSO algorithm uses a number of particles which constitute a swarm. These particles fly with a certain velocity and, at each iteration, adjust their velocity vector, based on their momentum and the influence of their own best position (*pbest*) as well as the best position of their neighbors (*gbest*). In other words, the swarm direction of a particle is defined by

the set of particles neighboring the particle and its history experience.

A. MOPSO

Moore and Chapman proposed the first extension of the PSO strategy for solving multi-objective problems in 1999 [5].

However, the high speed of convergence in MOPSO approaches often implies a rapid loss of diversity during the optimization process. [4] proposes a MOPSO incorporating the concept of nearest neighbor density estimator for selecting the global best particle and also for deleting particles from the external archive A of nondominated solutions. This approach uses the mutation operator proposed in [6] in such a way that it is applied only during a certain number of generations at the beginning of the process. Finally, the authors adopt the constraint-handling technique from the NSGA-II [7].

The implementation of MOPSO given in [4] is based on following fundamental steps (obvious ones are omitted):

- i) Initialize a swarm with random positions and velocities
- ii) Evaluate the particles and store nondominated ones in A ;
- iii) Compute the crowding distance of each member of A ;
- iv) Sort A in descending crowding distance order;
- v) Randomly select the global best for the swarm from a specified top portion (e.g. top 10%) for the sorted A and store its position in *gbest*.
- vi) Update velocities and positions according to:

$$v_i(t+1) = w \cdot v_i(t) + c_1 \cdot ud \cdot [p_i(t) - x_i(t)] + c_2 \cdot Ud \cdot [p_g(t) - x_i(t)] \quad (1)$$

$$x_i(t+1) = x_i(t) + \Delta t \cdot v_i(t+1) \quad (2)$$

where w is the inertia weight; $v_i = [v_{i1}, v_{i2}, \dots, v_{in}]^T$ stands for the velocity of the i -th particle, $x_i = [x_{i1}, x_{i2}, \dots, x_{in}]^T$ stands for the position of the i -th particle of population, and

$p_i = [p_{i1}, p_{i2}, \dots, p_{in}]^T$ represents the best previous position of the i -th particle. Positive constants c_1 and c_2 are the cognitive and social factors, respectively, which are the acceleration constants responsible for varying the particle velocity towards *pbest* and *gbest*, respectively. Index g represents the index of the best particle among all the particles in the swarm. Variables ud and Ud are two random numbers [0,1].

- vii) Perform the mutation operation proposed in [6];
- viii) Evaluate the particles in swarm;
- ix) Insert all new nondominated solution into A if they are not dominated by any of the stored solutions. All dominated solutions in A . If the archive is full, the solution to be replaced is determined by: a) compute the crowding distance values of each nondominated solution in the archive A ; b) sort the nondominated solutions in A in descending crowding distance values, and iii) randomly select a particle from a specified bottom portion (e.g. lower 10%) and replace it with the new solution;
- xi) Return to Step (iii) until a criterion is met, usually a sufficiently good fitness or a maximum number of iterations, t_{\max} . In this work, the t_{\max} value is adopted.

B. The proposed G-MOPSO approach

The proposed G-MOPSO approach uses social and cognitive time-variant factors [8] and a velocity update operator based on truncated Gaussian distribution [9]. In particular the updating of c_2 is given by [8]:

$$c_2 = (c_{2f} - c_{2i}) \frac{t}{t_{\max}} + c_{2i} \quad (3)$$

where c_{2i} and c_{2f} are constants. In this work, the adopted values are suggested by [10] and given by $c_{2i} = 0.4$ and $c_{2f} = 2.05$.

III. OPTIMIZATION RESULTS

TEAM workshop problem 22 consists in determining the optimal design of a superconducting magnetic energy storage (SMES) device in order to store a significant amount of energy in the magnetic field with a fairly simple and economical coil arrangement which can be rather easily scaled up in size.

The multiobjective version of TEAM workshop problem 22 [10] is a continuous, constrained, eight-parameter benchmark with two conflicting objectives: the attainment of a required stored energy and the minimization of the stray field along two given lines. The setup of the MOPSO and G-MOPSO methods involved binary tournament selection, population size $P=30$, and stopping criterion $t=200$ generations. In the MOPSO, a unitary value was adopted in c_1 and c_2 , and w with linear decreasing of 0.9 to 0.4 during the generations, while in G-MOPSO equation (7) is used to update the c_1 and c_2 values.

Simulation results for 30 runs (Figs. 1 refers to the Pareto front obtained by G-MOPSO) show that the non-dominated solutions obtained by G-MOPSO dominate the solutions obtained by MOPSO. Furthermore, it can be observed that in terms of spacing metric [11] the solutions obtained by G-MOPSO are more uniformly spaced than MOPSO approach. The spacing obtained using MOPSO was 133.8798 and in the case of G-MOPSO was 2.1843.

IV. CONCLUSIONS

PSO is becoming very popular due to its simplicity of implementation and ability to quickly converge to a reasonably good solution.

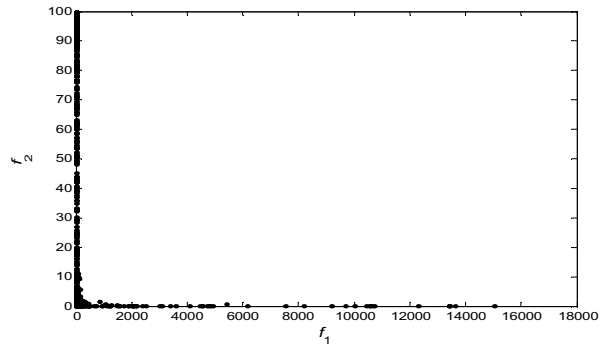


Fig. 1. Pareto front obtained by G-MOPSO.

Furthermore it can be quite easily extended to multiobjective problems. In this paper the performance of a variant of MOPSO is tested on the multiobjective version of TEAM benchmark problem 22 with good results. In the extended version of the paper a thorough comparisons of the fronts obtained by MOPSO and G-MOPSO will presented together with a detailed description of the algorithmic details of G-MOPSO.

Acknowledgments

This work was partially supported by the National Council of Scientific and Technologic Development of Brazil — CNPq — under Grant 309646/2006-5/PQ.

REFERENCES

- [1] U. Baumgartner, C. Magele and W. Renhart, "Pareto optimality and particle swarm optimization," *IEEE Trans. on Magnetics*, vol. 40, no. 2, pp. 1172-1175, 2004.
- [2] J. Kennedy and R. C. Eberhart, "Particle swarm optimization," in: *Proceedings of IEEE Int. Conf. on Neural Networks*, Perth, Australia, pp. 1942-1948, 1995.
- [3] M. R. Sierra and C. A. C. Coello, "Multi-objective particle swarm optimizers: a survey of the state-of-the-art," *International Journal of Computational Intelligence Research*, vol. 2, no. 3, pp. 287-308, 2006.
- [4] C. R. Raquel and P.C. Naval, Jr., "An effective use of crowding distance in multiobjective particle swarm optimization," in *Proc. of Genetic and Evolutionary Computation Conf. 2005*, Washington DC, USA, 2005.
- [5] J. Moore and R. Chapman, "Application of particle swarm to multiobjective optimization," Department of Computer Science and Software Engineering, Auburn University, country, 1999.
- [6] C. A. Coello Coello, G. T. Pulido, and M. S. Lechuga, "Handling multiple objectives with particle swarm optimization," *IEEE Trans. on Evolutionary Computation*, vol. 8, no. 3, pp. 256-279, 2004.
- [7] K. Deb, A. Pratap, S. Agrawal and T. Meyarivan, "A fast and elitist multiobjective genetic algorithms: NSGA-II," *IEEE Transactions on Evolutionary Computation*, vol. 6, no. 2, pp. 182-197, 2002.
- [8] A. Ratnaweera, S. K. Halgamuge and H. C. Watson, "Self-organizing hierarchical particle swarm optimizer with time varying acceleration coefficients," *IEEE Trans. Evol. Comp.*, vol. 8, no. 3, pp. 240-255, 2004.
- [9] L. S. Coelho and R. A. Krohling, "Predictive controller tuning using modified particle swarm optimisation based on Cauchy and Gaussian distributions," in *Soft Computing: Methodologies and Applications*, F. Hoffmann, M. Köppen, and R. Roy (eds.), Springer Engineering Series in Advances in Soft Computing, Springer, London, UK, pp. 287-298, 2005.
- [10] P. Alotto, U. Baumgartner, F. Freschi, M. Jaindl, A. Koestinger, Ch. Magele, W. Renhart, M. Repetto and G. Steiner, "SMES Optimization Benchmark Extended: Introducing Uncertainties and Pareto Optimal Solutions into TEAM22," *IEEE Trans. on Magn.*, 44(6): 106 -109, 2008.
- [11] C. A. Coello Coello, "A comprehensive survey of evolutionary-based multiobjective optimization techniques," *Knowledge Inf. Systems*, vol. 1, no. 3, pp. 269-308, 1999.

Magnetic Field Synthesis in the Design of Inductors for Magnetic Fluid Hyperthermia

P. Di Barba¹, F. Dughiero², E. Sieni²

¹University of Pavia, Department of Electrical Engineering, via Ferrata, 1 - 27100 Pavia, Italy

²University of Padova, Department of Electrical Engineering, via Gradenigo 6/a - 35131 Padova, Italy
paolo.dibarba@unipv.it, {fabrizio.dughiero,elisabetta.sieni}@unipd.it

Abstract — A Magnetic Fluid Hyperthermia (MFH) inductor design using multiobjective evolution strategy techniques has been proposed. Uniformity of the magnetic field and solution sensitivity are the objective functions chosen for the selection of the inductor geometry .

I. INTRODUCTION

MFH provides the heating of cancer lesions until a temperature that can damage tumoral tissues. In this therapy nanoparticles, injected in the human tissues, are heated by means of an AC magnetic field which should be as much as possible uniform in the treatment area [1]. Such a kind of equipment was installed e.g. at the Charité hospital in Berlin [2]. The field source is a coil with a ferrite yoke which is able to guarantee, in a cylinder with diameter of 20 cm a magnetic field strength with a uniformity of 90 % [2]. In the paper, the synthesis of an iron-free magnetic field source, inspired by Loney solenoid system [3], is proposed. The aim is to synthesize a uniform field in the treatment region, insensitive to small variations of coil system parameters.

Actually, in various applications of bioengineering, the generation of uniform magnetic fields is required. For instance, in magnetic resonance imaging (MRI) [3], as well as in magnetic induction tomography (MIT) [7], the field synthesis problem is characterized by a small size of the controlled region and a high degree of uniformity (in the order of ppm). Instead, in MFH the controlled region size is one order bigger than in MRI and MIT systems, because the anthropometric dimensions should be taken into account; this, in turn, has a consequence in terms of the degree of field uniformity achievable in practice.

Scope of the paper is to propose an automated optimal-design procedure of inductors for MFH clinical treatment of cancer lesions, with the final aim of providing a control in the uniformity of magnetic field and hence a uniform therapeutic temperature in wide body regions. In particular, an air-cored solenoid system, which offers a possible advantage in terms of reduced size due to the lack of ferromagnetic material is considered. The design problem is formulated in terms of a multiobjective problem [4].

II. THE DEVICE

In Fig. 1 an half of the longitudinal section of the device, with the controlled region Ω , and design variables, is sketched. L_1 and L_2 are the lengths of main and correcting coils, respectively, x_1 is the radius of main coil, dx the gap between main and correcting coil, z_1 the distance of the main coil from

the z axis, dz is the shift of the correcting coil with respect the main one. The square at the system centre, with side L_x , is the area where the field uniformity is to be controlled. In Table I the variation ranges of design variables and the fixed values of parameters are reported.

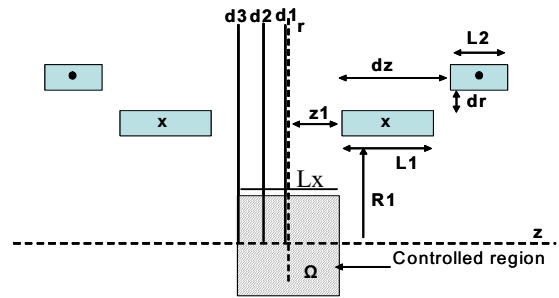


Fig. 1: geometry of the system

TABLE I
VALUES OF THE PARAMETERS

	R1[m]	dr[m]	Z1[m]	dz[m]	L1[m]	L2[m]	I1[A]	I2[A]
Min	0.25	0.05	0.15	-0.05	0.2	0.15	1000	500
Max	0.5	--	0.4	0.45	--	--	--	--

III. DIRECT PROBLEM

The magnetic field has been computed using a semi-analytical model, i.e. superposing the field generated by each turn composing a coil. To this end, a classical formula [5] that involves the evaluation of elliptic integrals has been used. This method has been chosen for its computational speed in repeated field analyses, and in view of an optimization procedure.

A. Field analysis

The inhomogeneity function, f , is defined as follows:

$$f = \frac{H_{\max} - H_{\min}}{H_{\text{mean}}} \quad (1)$$

where H_{\max} , H_{\min} , and H_{mean} are maximum, minimum and average value of the magnetic field in the controlled region Ω , respectively; numerically, inhomogeneity has been computed in a set of $N=231$ points, located in Ω .

B. Sensitivity evaluation

An inexpensive evaluation of sensitivity is possible when a set of $n_p \gg 1$ points discretizing the search space is available. Each point of the set is considered as the centroid of a hypercube ω composed of all the other points which distance

from the given one is less than a threshold [6]. Then, sensitivity s is approximated as :

$$s(\tilde{g}) \equiv [f(\tilde{g})]^{-1} [\sup_g f(g) - \inf_g f(g)], \quad g \in \omega \quad (2)$$

where \sup and \inf are computed within ω , and $f(\tilde{g})$ is the inhomogeneity function value at the hypercube centroid \tilde{g} . In

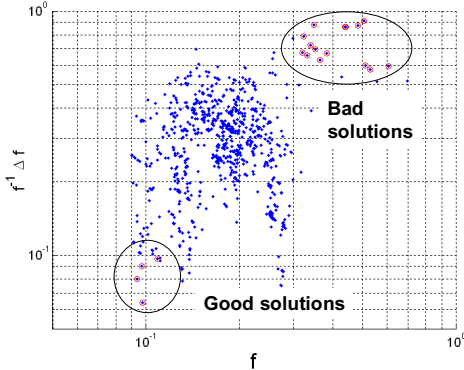


Fig. 2 sensitivity versus inhomogeneity function. Points in the lower left and upper right corner are good and bad solutions, respectively.

Fig. 2, sensitivity s is plotted as a function of inhomogeneity f . The cloud of points has been obtained after sampling the three-dimensional search region formed by variables x_1 , z_1 and dz . In particular, z_1 and dz have a practical significance because they have to be adjusted during the set-up phase of therapy equipment, and their setting depends on the patient size. The sampling is based on a random search governed by a uniform probability density function, and is composed of 1,000 points.

IV. DESIGN PROBLEM

The aim of the magnetic system is to generate a field uniform enough in the controlled region Ω . The shape design of the system has been performed using a multiobjective formulation. Ensuring the maximum homogeneity of the magnetic field in a prescribed volume was the main target of the design. In fact, a uniform magnetic field is a preliminary condition for an uniform power density and then for an almost uniform heating of human body tissues. On the other hand, since the opening of the system has to be adjusted depending on the anthropometric sizes of the patient, the sensitivity of configurations minimizing the field inhomogeneity should be evaluated. This way, among all feasible solutions, the ones exhibiting both low inhomogeneity and sensitivity will be selected. Therefore, the design problem has been cast as a two-objective optimization problem: find the set of feasible solutions x such that both $f(x)$ and $s(x)$ are minimum, according to Pareto optimality [4].

V. RESULTS

In Fig. 3a and 3b two feasible geometries are shown: the former is an example of good solution, the latter of bad solution. The first one represents a optimum case and the second one a not-optimal case. In Fig. 4 the percentage variation of the H field is shown; the maximum of the magnetic field H is close to 15000 A/m. The maximum has been evaluated as the global one along three directions (d_1, d_2, d_3), defined inside the controlled region (Fig. 1). It can

be noted that between 2 and 20 cm from the axis system the field uniformity is higher than 95%.

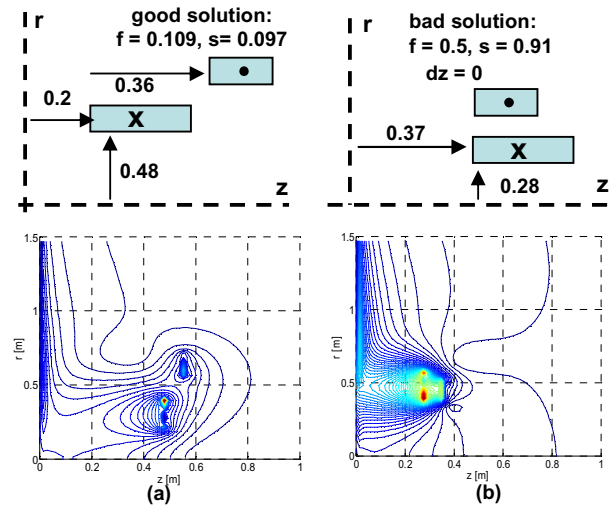


Figure 3: geometry and H field lines for a (a) good and a (b) bad solution.

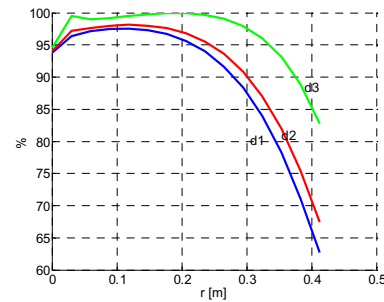


Fig. 4: percentage variation of H field.

In the full-length paper the Pareto front of the problem will be identified by means of an optimization procedure based on evolutionary computing. Eventually, for assessing the optimization results, a finite-element based thermal analysis of a human tissue subject to the synthesized magnetic field will be developed.

VI. REFERENCES

- [1] G. F. Goya, V. Grazú, M. R. Ibarra "Magnetic Nanoparticles for Cancer Therapy", *Curr. Nanosc.*, pag. 1-16, 2008
- [2] U. Gneveckow, A. Jordan, R. Scholz Volker Brüß, N.t Waldöfner, J. Ricke, A. Feussner, B. Hildebrandt, B. Rau, P. Wust, "Description and characterization of the novel hyperthermia and thermoablation-system MFH@300F for clinical magnetic fluid hyperthermia", *Med. Phys.*, pag. 1444-1451, 2004
- [3] P. Di Barba, F. Dughiero, F. Trevisan, "Optimization of the Loney's solenoid through Quasi-analytical strategies: a benchmark problem reconsidered", *IEEE Trans Magn.*, pp. 1864-1867, 1997
- [4] P. Di Barba, "Evolutionary Multiobjective Optimization Methods for the Shape Design of Industrial Electromagnetic Devices", in press on *IEEE Transactions on Magnetics*
- [5] E. Durand, *Magnétostatique*, Masson 1968
- [6] P. Di Barba, and R. Palka "Optimization of the HTSC-PM Interaction in Magnetic Bearings by a Multiobjective Design", *Proc. Int Symp. Electromagnetic Fields in Mechatronics, Electrical and Electronic Eng.*, pp. 94-95, 2007
- [7] P. Di Barba, M.E. Mognaschi, R. Palka, A. Savini, "Optimization of the MIT Field Exciter by a Multiobjective Design", in press on *IEEE Transactions on Magnetics*.

Stochastic Finite Element Analysis for Parasitic Extraction of Interconnects with Material Parameter Variations

Xiaoyu Xu¹, Hui Qu¹, Li Kong¹, and Zhuoxiang Ren²

¹ Institute of Electrical Engineering, Chinese Academy of Sciences, 100190, Beijing, China

² Mentor Graphics Corporation, San Jose, CA 95131, USA

E-mail: xuxiaoyu@live.com

Abstract — The approaches to process the process variations in the parasitic extraction of interconnects are still indigent and how to implement spectral stochastic finite element method (SSFEM) is still a little ambiguous. In this paper, the clear flow of SSFEM is detailed and three important points such as the stochastic field, the post-processing for calculation of capacitance, are emphasized.

I. INTRODUCTION

During this ultra-deep submicron and nanoscale integrated circuit technology era, it's irrefutable that the process variations have become pivotal issues in integrated circuit design and verification, and an ample solver to handle the variability shall be a crucial goal in EDA. Of all types of variations [1], material parameter variations, especially at the interconnect structure level are studied in this paper.

In brief, the stochastic analysis in numerical computation was firstly applied in the structural mechanics and gradually extended to the field of electromagnetic [2]-[3]. Usually, the finite element method (FEM) is used to analyze material variations [4] while the integral equation method (IEM) and the boundary element method (BEM) are utilized to discuss geometric variations [5]-[6]. Ideas of SSFEM and polynomial chaos (PC) are practiced in [2], but some key procedures of SSFEM for electromagnetism computation are not appropriately explained and practices in analyzing interconnects parasitic are not yet made.

In this paper, based on the scheme of stochastic finite element methods and stochastic field theory, we will show clearly the overall flow of SSFEM and introduce the way to analysis the material properties with correlation functions which becomes probable requirements henceforth.

II. STOCHASTIC FINITE ELEMENT METHODS

Neumann expansion stochastic FEM (NSFEM) traced here is usually used to solve randomness problems.

For FEM's matrix system $\mathbf{K}\Phi = \mathbf{b}$, given $\mathbf{K} = \bar{\mathbf{K}} + \Delta\mathbf{K}$, $\mathbf{P} = \bar{\mathbf{K}}^{-1}\Delta\mathbf{K}$, according to Neumann series expansion [2],

$$\mathbf{K}^{-1} = (\bar{\mathbf{K}} + \Delta\mathbf{K})^{-1} = (\mathbf{I} + \bar{\mathbf{K}}^{-1}\Delta\mathbf{K})^{-1} \bar{\mathbf{K}}^{-1} \quad (1)$$

$$= (\mathbf{I} + \mathbf{P})^{-1} \bar{\mathbf{K}}^{-1} = (\mathbf{I} - \mathbf{P} + \mathbf{P}^2 - \mathbf{P}^3 + \dots) \bar{\mathbf{K}}^{-1}$$

$$\Phi_0 = \bar{\Phi} = \bar{\mathbf{K}}^{-1}\mathbf{b}, \quad \Phi_i = -\bar{\mathbf{K}}^{-1}\Delta\mathbf{K}\Phi_{i-1}, \quad i \geq 1, \quad \Phi = \sum_{i=0}^{\infty} \Phi_i \quad (2)$$

III. PROBLEMS

Parasitic extraction of interconnects is readily an electrostatic field problem or a steady electric field problem:

$$\text{div}(\varepsilon \cdot \text{grad } \varphi) + \rho = 0, \quad \text{or} \quad \text{div}(\sigma \cdot \text{grad } \varphi) = 0 \quad (3)$$

Let us consider a small domain spatial D or an element Ω_e with random permittivity. If the permittivity is supposed to be uniform within D , we call it *constant distribution*, while if the distribution obeys some correlation function, we call it *field distribution*. If ε is random, but its variance is finite in real space, it can be expressed as a stochastic field,

$$\varepsilon(\mathbf{x}, \theta) \equiv H(\mathbf{x}, \theta)\varepsilon(\mathbf{x}) \quad (4)$$

A. Stochastic field

Karhunen-Loève expansion (K-L) and orthogonal series expansion (OS) are usually used to discrete stochastic field into expressions in random space. For example, the K-L expansion of stochastic field $H(\mathbf{x}, \theta)$ is shown as

$$H(\mathbf{x}, \theta) = \mu(\mathbf{x}) + \sum_{i=1}^{\infty} \sqrt{\lambda_i} \varphi_i(\mathbf{x}) \xi_i(\theta) \quad (5)$$

In the above, $\mu(\mathbf{x})$ is the mean of the whole domain D , $\xi_i(\theta)$ is a standard normal variable (SNV), λ_i and $\varphi_i(\mathbf{x})$ are value pairs of eigenvalues and eigenfunctions relative to the correlation function of the stochastic field. Under a certain condition, we can get the closed form solution, while under other conditions, we can choose another orthogonal functions set [2]. In constant distribution, $\varphi_i(\mathbf{x}) \equiv 0$, $\lambda_i \equiv 1$ equivalently.

Then the element coefficient matrix and ensemble coefficient matrix can be re-written as,

$$\mathbf{k}^e(\theta) = \mathbf{k}_0^e(\theta) + \sum_{i=1}^{\infty} \mathbf{k}^e(\theta) \xi_i(\theta) = \mathbf{k}_0^e(\theta) + \sum_{i=1}^{\infty} \xi_i(\theta) \sqrt{\lambda_i} (\quad (6)$$

$$\int_{\Omega_e} \varphi_i(\mathbf{x}) \varepsilon_0 \text{grad} w \mathbf{J}^{-T} \cdot \mathbf{J}^{-1} \text{grad} w \det(\mathbf{J}) d\Omega_e)$$

$$\left[\mathbf{K}_0 + \sum_{i=1}^{\infty} \mathbf{K}_i \xi_i(\theta) \right] \cdot \Phi(\theta) = \mathbf{b} \quad (7)$$

B. Governing equation of stochastic response

Expand equation (7) via Neumann method, then

$$\Phi(\theta) = \sum_{k=0}^{\infty} (-1)^k \left[\sum_{i=1}^{\infty} \mathbf{K}_0^{-1} \cdot \mathbf{K}_i \xi_i(\theta) \right]^k \cdot \Phi_0 \quad (8)$$

With the growing of k as well as the amount of constant distribution domains, the product of $\xi_i(\theta)$ -s becomes increasingly complex.

C. Polynomial chaos

The complex items of $\xi_i(\theta)$ -s can be mapped to another normalized orthogonal basis set $\{\Psi_j(\theta)\}_{j=0}^{\infty}$, such as Hermite polynomial, Legendre polynomial and *etc* in space L^2 . Of course $\{\Psi_j(\theta)\}_{j=0}^{\infty}$ is well-defined by $\{\xi_k(\theta)\}_{k=1}^{\infty}$, so each stochastic response quantity $\phi_i(\theta)$ can be expressed as

$$\phi(\theta) = \sum_{j=0}^{\infty} \phi_j \Psi_j(\theta), \quad \text{while } \Psi_{\mathbf{a}}(\theta) = \prod_{i=1}^M h_{\alpha_i}(\xi_i(\theta)) \quad (9)$$

The number of M -dimension and p -order polynomial items is $P = \sum_{k=0}^p C_{M+k-1}^k [2]$ -[3].

D. General stochastic coefficient matrix

Based on equations (7-9), the matrix items are truncated at advisable dimensions and series degree to form a residue,

$$\text{err}_{M,p} = \left[\sum_{i=0}^M \mathbf{K}_i \xi_i(\theta) \right] \cdot \left[\sum_{j=0}^{P-1} \Phi_j \Psi_j(\theta) \right] - \mathbf{b} = \sum_{i=0}^M \sum_{j=0}^{P-1} (\mathbf{K}_i \xi_i(\theta)) \cdot \quad (10)$$

$$\Phi_j \Psi_j(\theta) - \mathbf{b} = \sum_{i=0}^M \sum_{j=0}^{P-1} \mathbf{K}_i \cdot \Phi_j \xi_i(\theta) \Psi_j(\theta) - \mathbf{b}$$

Set $c_{ijk} = E[\xi_i \Psi_j \Psi_k]$, $\mathbf{b}_k = E[\Psi_k \mathbf{b}]$, $\mathbf{K}_{jk} = \sum_{i=0}^M c_{ijk} \mathbf{K}_i$, and

implemented by Galerkin scheme, the general stochastic coefficient matrix is approximately formed as

$$\begin{bmatrix} \mathbf{K}_{00} & \cdots & \mathbf{K}_{0,p-1} \\ \vdots & & \vdots \\ \mathbf{K}_{p-1,0} & \cdots & \mathbf{K}_{p-1,p-1} \end{bmatrix}_{\substack{(N \times P) \\ \times \\ (N \times P)}} \cdot \begin{bmatrix} \Phi_0 \\ \vdots \\ \Phi_{p-1} \end{bmatrix}_{\substack{(N \times P) \\ \times \\ (1)}} = \begin{bmatrix} \mathbf{b}_0 \\ \vdots \\ \mathbf{b}_{p-1} \end{bmatrix}_{\substack{(N \times P) \\ \times \\ (1)}} \quad (11)$$

Then we get the stochastic response,

$$\Phi(\theta) = \sum_{j=0}^{P-1} \Phi_j \Psi_j(\theta) \quad (12)$$

The above method is so called SSFEM, and it's a *real* one in the case of *field distribution*.

E. Post-processing

Using equation (12), we can obtain statistics moments and probability distribution conveniently for Ψ_j is determinate functions of SNV. Calculation of capacitance can be referred to the electric flux surrounding a conductor

$$F = \int_{\Omega_{\Sigma}} \varepsilon(\theta) \mathbf{k} \cdot \text{grad} v d\Omega \quad (13)$$

where Ω_{Σ} is a closed *thick* surrounding surface. Finally the capacitance is also a function of Ψ_j .

Particularly, we use Latin hypercube sampling (LHS) method instead of direct Monte Carlo sampling method to verify the validity and effectiveness of SSFEM; LHS turns out to be more efficient and credible.

IV. EXEMPLIFICATION

A simple example (Fig 1) is drawn to validate the idea of interconnects parasitic extraction with SSFEM.

Homogeneous permittivity and $M=2$ -dimension are assumed, for that the variations is quite small, choose $p=5$, then $P=21$. The FEM matrix is 898×898 while SSFEM matrix is 18858×18858 .

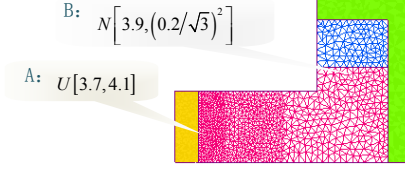


Fig. 1. Sketch of example of multi-domains with probability distribution.

Results are shown in Table I, the unit of capacitance is $fF/\mu\text{m}$, unit of time is s . We can find that if field distribution is under consideration, the time consumption booms sharply and the error is also notably fluctuated.

TABLE I. COMPARING SSFEM AND FEM USING LHS

Type	Value	SSFEM	LHS
Nominal mean		0.014310	
Constant distribution	mean	0.01428	0.01430
	std	0.002721	0.002796
Field distribution	time	326	1,226
	mean	0.01483	0.01526
(correlation function of exponential type)	std	0.003230	0.005045
	time	472	1931

V. CONCLUSION AND OUTLOOK OF SSFEM

Three points during the detailed steps of SSFEM are emphasized: the NSFEM procedure, the stochastic field distribution, and the capacitance formula as the function of PCs. But it's still not known clearly which distribution are the actual one, which perhaps strictly obeys some physical processes; and the orthonormal functions we select as the space basis maybe cannot exactly keep the characteristics of the original field. More efforts to in-depth research in stochastic field are required.

SSFEM explodes the amount of calculation and memory needed, so high efficiency algorithms is another key point. Adverting to the current programs, the techniques of multi-core CPU, GPGPU, *etc* are surely worthy of attention.

VI. REFERENCES

- [1] D.S. Boning, K. Balakrishnan, *et al*, "Variation", *Semiconductor Manufacturing, IEEE Transactions on*, 21(1): 63-71, 2008.
- [2] R.G. Ghanem and P.D. Spanos, *Stochastic Finite Elements : A Spectral Approach*, Springer Verlag, 1991.
- [3] J. Wang, P. Ghanta, S. Vrudhula, "Stochastic analysis of interconnect performance in the presence of process variations", in *Proceedings of ICCAD-2004. IEEE/ACM International Conference on Computer Aided Design*, pp. 880-886, 2004.
- [4] R. Gaignaire, S. Clenet, *et al*. "3D Spectral Stochastic Finite Element Method in Electromagnetism", *IEEE Trans. on Magnetics*, 43(4): 1209-1212, 2007.
- [5] Z.H. Zhu. *Efficient Integral Equation Based Algorithms for Parasitic Extraction of Interconnects with Smooth or Rough Surface*. MIT Ph.D. Thesis. 2004.
- [6] Riki Honda. "Stochastic BEM with spectral approach in elastostatic and elastodynamic problems with geometrical uncertainty". *Engineering Analysis with Boundary Elements*. 29(5): 415-427, 2005.

Kriging assisted design of a synchronous superconducting generator with YBCO windings

B. Lukasik, K. F. Goddard, M. D. Rotaru and J. K. Sykulski
 School of Electronics and Computer Science, University of Southampton
 SO17 1BJ, Southampton, UK

bl05r@ecs.soton.ac.uk, kfg@ecs.soton.ac.uk, mr@ecs.soton.ac.uk, jks@soton.ac.uk

Abstract — This paper describes the applicability of a kriging assisted method to the design of a synchronous generator with a high temperature superconducting (HTS) rotor winding. The derived algorithm provides pareto optimal fronts maximising the air-gap flux density while minimising the length of YBCO tapes.

I. INTRODUCTION

The prospect of reducing the size and weight of a machine through using HTS windings is very appealing, especially for applications such as offshore wind power generation. Until recently the performance of such machines was somewhat hampered by the limited capabilities of the available BiSCCO tapes. Now that the second generation (2G) HTS tapes have become commercially available [1], with improved tolerance to the perpendicular component of the magnetic field, the possibility of building much smaller and lighter electrical machines is becoming a reality. The design of such devices requires substantial simulation effort; structural and thermal as well as electromagnetic requirements may require modelling. The cost is greatly increased if optimisation is required.

II. THE SPECIFIC OPTIMISATION PROBLEM

As an example, we consider a 6-pole arrangement with a 2G HTS rotor winding which may be used to demonstrate the principle of a high torque slow rotating multi-pole machine working in applications such as wind power generation. The objective is to maximise the air-gap flux density using the shortest possible length of the HTS tape

There are a number of possibilities regarding the rotor configuration (Fig.1). Although a coreless rotor is clearly the best choice to achieve the substantial mass reduction required to justify the use of a HTS winding in a full size machine, use of some iron may be warranted in a demonstrator. The choice of rotor configuration is a compromise between obtaining a high air-gap flux density and making the small demonstrator as similar as possible to the full-size machine. Similarity to the full size machine is not easily quantified; each configuration was therefore optimised separately, allowing the final choice to be informed by the results of these optimisations.

Each of the arrangements of Fig. 1 has two possible stator configurations: ‘slotted’ and ‘slotless’. In a conventional machine, the stator teeth are required to help raise the air-gap flux density by providing a low-reluctance flux path through the stator winding. The high current densities available in a HTS field winding may allow a high air-gap flux density to be obtained without the aid of teeth, suggesting that they are not required; hence they could be removed to save weight.

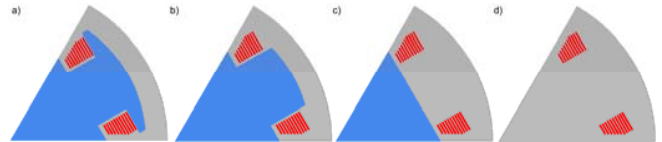


Fig. 1. Rotor configurations chosen for the design study: a) fully cored, b) inner core and coil core, c) inner core, d) fully coreless.

Moreover, the high flux density may saturate the teeth, reducing their effectiveness. It has also been found that modulation of the air-gap field by the stator teeth can induce quite substantial tooth ripple losses in the rotor. While these considerations favour the removal of the teeth, it should be noted that the teeth provide mechanical support for the winding and a radial thermal conduction path to help cool the winding. If they are removed, alternative arrangements must be sought to ensure support and cooling of the winding.

Optimising the design of an electrical machine is a computationally expensive process requiring repetitive use of finite element models. An added complication arises from the use of HTS windings. Since the critical current density of the HTS tape depends on the magnetic field that impinges on it, the critical current is a function of the current in the winding. This implies that for any configuration to be analysed the critical current density needs to be found iteratively, further increasing the computational cost. An efficient algorithm is therefore required, which should minimise the number of evaluations for which finite-element modelling is required. In this work we propose a methodology based on surrogate modelling using kriging [2, 3] to improve the efficiency of the optimization process.

III. SURROGATE MODELLING

The response surface methodology fits an approximation function to data obtained from the computationally expensive objective function at a small number of points. This response surface can then be used to predict the value of the objective function at intermediate positions in the search space. After constructing the response surface from an initial set of data points (off-line learning), it is used to guide the optimiser in selecting a new design vector for evaluation. As each new point is added, the surface fitting is repeated to take advantage of the new data point (on-line learning).

Kriging is a form of response surface modelling based on the principle of maximum likelihood and, in addition to providing a response surface that passes through all the data points, provides a meaningful estimate of the uncertainty of its predictions. Using these two values it is possible to estimate

the expected improvement that may be obtained by adding a new data point to the existing set. Using this measure to determine where the next point should be added greatly reduces the risk of the optimiser getting trapped in a local minimum. However, this technique is not foolproof; the algorithm may still fail to find the global minimum if the kriging function significantly underestimates the uncertainty in this region of the search space.

The goal of this study is to find a design which will give the highest possible air-gap flux density while using the least amount of superconducting tape. Due to the anisotropy of the tape both magnitude and direction of the magnetic flux density need to be considered. The manufacturer's data for the dependence of the critical current of the YBCO tape on the field, in both the perpendicular and parallel directions, has been incorporated into the command script executing in the finite element package. The critical current is taken to be the lower of the value estimated from the maximum normal component of B and that estimated from the maximum parallel component of B . The critical current is found by repeatedly solving the model and changing the assumed current in the superconductor towards the minimum value given by the graphs of $I_c(B)$ until satisfactory convergence is obtained. The fundamental D-axis component of the air-gap flux density predicted by the model is then returned to the optimisation algorithm written in MATLAB.

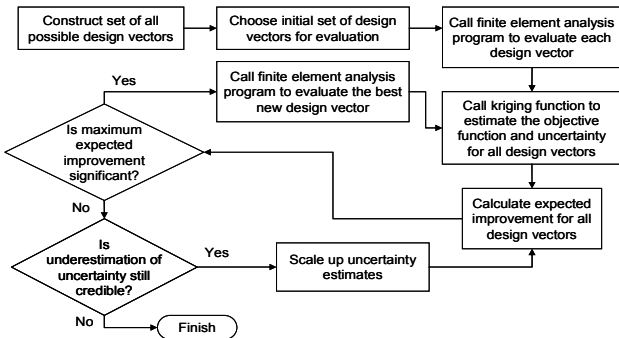


Fig. 2. Optimization algorithm.

A simplified illustration of the algorithm is presented in Fig. 2. The optimizer varies the following parameters: the number of turns in the largest coils, the number of coils and the number of coils that have reduced number of turns to leave space between adjacent poles. A constraint was imposed on the minimum bend radius at the ends of the HTS coils.

A set of 16 points is first chosen using the Latin sampling cube [4]. After evaluating these points and fitting a surface the algorithm finds the maximum of the expected improvement

$$E[I(x)] = (f_{\min} - y)\Phi\left(\frac{f_{\min} - y}{s}\right) + s\phi\left(\frac{f_{\min} - y}{s}\right) \quad (1)$$

and evaluates the objective function at the new point. In (1) f_{\min} is the minimum value of the objective function at the sampled points, y is the predicted value at point x , s is the square root of the expected square error at point x predicted by the surrogate model, ϕ is the standard normal distribution function and Φ is its integral. This equation is easily obtained by integrating the product of the improvement and the estimated (assumed normal) probability density function.

Use of the expected improvement to drive the algorithm seems reasonable, but it has its limitations. First, as noted previously, it is likely that the values of expected square error predicted by the kriging function are under-estimated; hence the algorithm could stop after finding a good local minimum but fail to find the global minimum. Secondly, maximising the expected improvement for each new point is a short-term objective and places no value on the knowledge gained by adding new data points. Scaling up the uncertainty estimates as proposed in Fig. 2 should overcome the first problem, although the method of deciding whether under-estimation of uncertainty is still credible needs further consideration. While the optimiser can be encouraged to explore more widely by deliberately over-estimating the uncertainty, the expected value of the information obtained from a new data point is difficult to estimate. More discussion about exploration versus exploitation and enhanced formulations will be provided in the extended paper. Figure 3 shows the pareto optimal front obtained for a coreless rotor at 40K in a slotless stator.

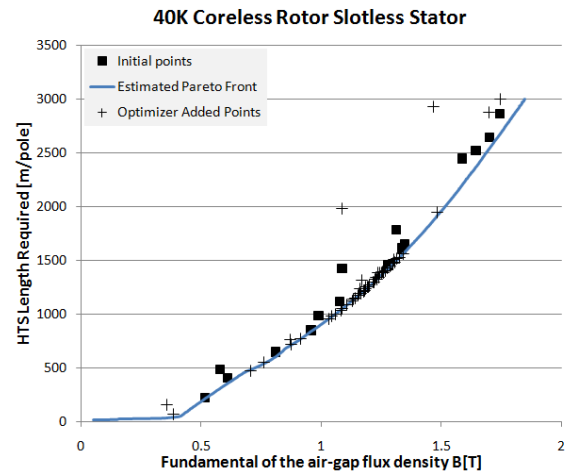


Fig. 3. Pareto optimal front for one of the considered configurations.

IV. CONCLUSIONS

The paper demonstrates the use of surrogate modelling and kriging assisted optimisation in the context of the design of a synchronous generator having a superconducting rotor winding made of YBCO tapes. The necessary repetitive use of finite element models makes the design process computationally expensive but is helped by efficient use of the response surface methodology. The criterion of expected improvement is applied but the balance between exploitation and exploration needs to be carefully controlled.

V. REFERENCES

- [1] <http://www.amsc.com/products/htswire/2GWireTechnology.html>
- [2] D. R. Jones, M. Schonlau, and W. J. Welch, "Efficient Global Optimization of Expensive Black-Box Functions," *J. of Global Optimization*, vol. 13, pp. 455-492, 1998.
- [3] G. Hawe and J. K. Sykulski, "Considerations of accuracy and uncertainty with kriging surrogate models in single-objective electromagnetic design optimisation," *IET Science, Measurement & Techn.*, vol. 1, pp. 37-47, 2007.
- [4] M. D. McKay, W. J. Conover, and R. J. Beckman, "A comparison of three methods for selecting values of input variables in the analysis of output from a computer code," *Technometrics*, vol. 21, pp. 239-245, 1979.

Multiobjective Efficient Global Optimization – A Win-win Approach to Optimal Design and Model Development

A. Berbecea, S. Kreuawan, F. Gillon, and P. Brochet

Laboratoire d'Electrotechnique et d'Electronique de Puissance de Lille (L2EP)
Ecole Centrale de Lille, Cité Scientifique, BP 48, 59651, Villeneuve d'Ascq Cedex, France
E-mail: Alexandru.Berbecea@ec-lille.fr

The advantage of using a surrogate-assisted optimization algorithm is the small number of finite element evaluations. A surrogate-assisted optimization algorithm, called Multiobjective Efficient Global Optimization, suited for grid computing is presented in this paper. The surrogate model used by the algorithm is the Kriging model. An application to the Superconducting Magnetic Energy Storage (SMES) system of Team benchmark problem 22 is presented. The Pareto optimality front, representing the trade-off curve between objectives is obtained at low cost. At the end of the optimization process, the surrogate model and the finite element model are very close to each other in the subspace around the Pareto front.

Index Terms—surrogate-assisted optimization, multiobjective optimization, Kriging surrogate model, grid computing, optimal design, SMES, Team benchmark problem 22.

I. INTRODUCTION

In the design optimization process, analytical models are usually used in order to simulate the behavior of the designed product. The Finite Element Analysis (FEA) is used in the later stages of product development, in order to validate the obtained design.

The recent trend is to integrate the Finite Element Analysis in the early stages of the product development cycle, allowing this way a significant reduction of the product development delay. Even though the computing resources have developed exponentially during the last decade, the FEA still remains time consuming, and its direct integration in the optimization process remains marginal. This is due to the great number of function calls of an optimization algorithm. The surrogate-assisted optimization strategies appear a promising approach [1], allowing the integration of high fidelity models, such as FEA, in the optimization process, and with a reasonable time cost. The application to the optimal design of an electrical machine using multiphysic model including FEA can be found in [2]. Some extensions to the multiobjective optimization case have been developed recently [3].

Real design engineering problems are complex, presenting many conflicting objectives and constraints. The trade-off curve between objectives (called Pareto optimality front) obtained through multiobjective optimization helps engineers in the difficult task of decision making. In this paper a new multiobjective surrogate-assisted optimization algorithm is presented. A new infill criterion, called Pseudo distance, suited for the multiobjective optimization case is presented. The Kriging surrogate models developed by the algorithm through the optimization process present the particularity of being very close to the FEA model in the subspace around the Pareto front. The algorithm was applied to the Team benchmark problem 22, which deals with the optimization of a superconducting magnetic energy storage system (SMES).

II. SURROGATE-ASSISTED OPTIMIZATION

This section describes the Surrogate-Assisted Optimization strategy. The algorithm presented in this paper is based on [2], which was adapted for the multiobjective case, and suited for grid computing. The surrogate models used by the algorithm are Kriging models.

A. Kriging Surrogate Model

In the Kriging model formulation, an unknown function $y(x)$ can be expressed as a sum of two terms: one that gives the global trend of the function, called the regression or polynomial model, and another one that gives the local deviations from the global trend. The correlation function controls the smoothness of the model. The Gaussian correlation function between points i and j is:

$$R(x^{(i)}, x^{(j)}) = \exp \left[- \sum_{k=1}^{n_k} \theta_k |x_k^{(i)} - x_k^{(j)}|^2 \right] \quad (1)$$

where x is the design variable vector, θ_k represents the unknown correlation function parameter vector.

The Kriging model predicts the estimated response value \hat{y} . The Mean Square Error (MSE) is the expected value of difference between the true response and the estimated one. Since Kriging interpolates the data, MSE is zero at the sampled points. At unknown points, MSE should be minimized in order to obtain a good approximation.

Fig. 2 presents a one dimensional example. The Kriging model is constructed using 5 sample design points. At the sample points the standard error is zero and higher in the gaps between sampled points. This tells us that the Kriging model gives the exact value at the sample points (interpolation model) and may have some error at other design vectors. This important information is used by the infill criteria to locate the infill point to be added.

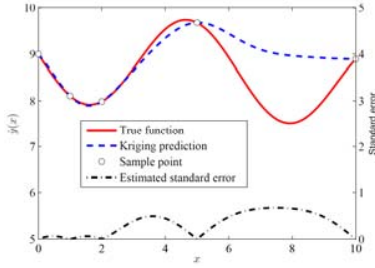


Fig. 2 – One dimensional illustration example showing the true model, Kriging prediction and its standard error.

B. Algorithm

The algorithm starts by sampling the initial points using the Design Of Experiments (DOE) method. The set of initial points is then evaluated using the high fidelity model, such as FEA model. A Kriging surrogate model is fitted for each objective and constraint function individually. A new infill point selection criterion was developed in order to generate a set of infill points instead of a single point. This allows the distribution of the FEA model evaluations over each available CPU. Each of these points is then validated against accept conditions and if these conditions are met, it will be added to the improvement solution set. In both cases, the point is added to the sample data set. If the prescribed stopping criteria are met, the algorithm ends, obtaining the non-dominated solutions forming the Pareto front. Otherwise, it goes back and uses the new obtained infill points to fit new Kriging models.

More details on the algorithm will be given in the full paper.

C. Infill Point Selection Criteria

In this paper a new infill criterion, called *pseudo distance* is proposed for the multiobjective optimization case. It is based on the non-dominate concept. The pseudo distance is composed of two terms: the dominate distance D_d , and the neighboring distance D_n , presented in (2)-(4).

$$D_{pseudo}(x) = D_n(x) + D_d(x) \quad (2)$$

$$D_n(x) = \sum_{i=1}^m \left(\left(\frac{f_i^{(s_i)} - \hat{f}_i(x)}{f_{i,max} - f_{i,min}} \right) \cdot \hat{\delta}_i(x) \right) \quad (3)$$

$$D_d(x) = \sum_{j=1}^{n_{dom}} \sum_{i=1}^m \left(\left(\frac{f_i^{(s_j)} - \hat{f}_i(x)}{f_{i,max} - f_{i,min}} \right) \cdot \frac{1}{\hat{\delta}_i(x)} \right) \quad (4)$$

An example is given in Fig. 3 to explain the concept.

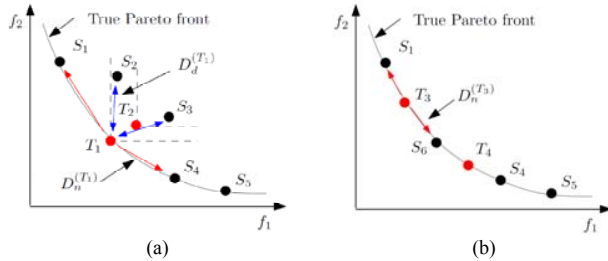


Fig. 3 – (a) Dominate distance, (b) Neighboring distance

D_d gives a design vector with the smallest estimated standard error (small $\hat{\delta}$), i.e. accurate Kriging predictions that will dominate with the greatest distance the existing non-dominated front (NF). Starting from a non-dominated front $NF_1=[S_1, S_2, S_3, S_4, S_5]$, from the previous iteration, the point T_1 will be preferred to another point T_2 , due to its greater dominate distance, as presented in Fig. 3a.

On the contrary, the D_n will focus to the neighborhood of the trial point. It will give a design vector with a high standard error (high $\hat{\delta}$), i.e. the greatest distance between the trial point and its neighboring non-dominated points. It sacrifices prediction accuracy in order to spread the points along the front, filling up the largest gap between two existing non-dominated points, as shown in Fig. 3b. This time, the point T_3 will be preferred to T_4 , because of the greater D_n .

The next design vector is located by maximizing (2), using a mono objective optimization algorithm. This step is repeated until a prescribed number of infill points are obtained, depending on the number of available CPUs.

III. APPLICATION TO TEAM WORKSHOP PROBLEM 22

The algorithm was applied to the eight-parameter multiobjective Team workshop problem 22. The obtained results are presented in Fig. 4. The non-dominated front is obtained through 300 FEA model evaluations (220 infill points and 80 initial points using Latin hypercube sampling). The problem was formulated as follows:

$$\min \begin{cases} f_1 = B_{stray}^2 / B_{norm}^2 \\ f_2 = |E - E_{ref}| / E_{ref} \end{cases} \quad (5)$$

with $E_{ref}=180\text{MJ}$, $B_n=200\mu\text{T}$ and subject to quench condition.

The presented algorithm allows obtaining the Pareto non-dominated front with low number of FEA evaluations.

REFERENCES

- [1] D. R. Jones, "A Taxonomy of global optimization methods based on response surfaces", *Journal of global optimization*, vol. 21, pp. 345-383, 2001.
- [2] S. Kreuzer, F. Gillon, and P. Brochet, "Efficient global optimization: An efficient tool for optimal design", in *Proc. COMPUMAG 2007*, June 2007, Aachen, pp. 803-804.
- [3] G. I. Hawe, and J. K. Sykulski, "An enhanced probability of improvement utility function for locating Pareto optimal solutions", in *Proc. COMPUMAG 2007*, June 2007, Aachen, pp.965-966.

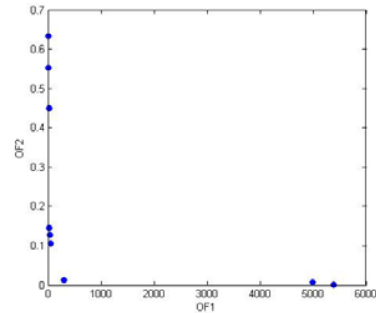


Fig. 4 – TEAM workshop problem 22 optimal design results

Parallel hybrid algorithms based on Artificial Life for Multimodal Optimization

S. Coco¹, A. Laudani¹, F. Riganti Fulginei² and A. Salvini²

¹ DIEES, University of Catania, V.le A. Doria 6, Catania I-95125, Italy

² DEA, University of Roma Tre, Via della Vasca Navale, 84, Roma I-00146, Italy

alaudani@diees.unict.it, asalvini@uniroma3.it

Abstract — A hybrid algorithm based on the combination of the Flock of Starlings Optimization (FSO) and the Bacterial Chemotaxis Algorithm (BCA) is presented for multimodal optimization tasks. In particular the FSO, that is a modification of the well known Particle Swarm Optimization, is a powerful instrument for exploring the whole space of solutions, whereas the BCA, that virtually emulates the motion of a real bacterium looking for food (i.e. fitness function), shows its better performances in local search. The present approach uses the FSO to explore the solution space and the BCA for refining solutions. A parallel strategy is implemented: the FSO is permanently running, and any time it found a possible solution, the BCA is launch, and so on. Test on general optimization benchmark and on the TEAM22 problem are shown.

I. INTRODUCTION

In this paper is presented a hybrid algorithm based on the combination of two heuristics inspired from Artificial life: the Flock of Starlings Optimization (FSO) [1] and the Bacterial Chemotaxis Algorithm (BCA) [2]. The approach is particularly suitable for multimodal optimization tasks. The FSO as described in [1] is a modification of the well known Particle Swarm Optimization (PSO) [3] by adding a topological rule to the metric rules typical of the PSO. In fact, the FSO is inspired to recent naturalistic observation about the real starling flights [4]. As it is shown in [1], the FSO is particularly suitable for exploration and multimodal analysis. On the other hand, the BCA virtually emulates the motion of a real bacterium looking for food (i.e. fitness function). It is a heuristic that shows its better performances in local search [5]. The present approach uses the FSO to explore the solution space and the BCA for refining solutions. Moreover, a parallel strategy is implemented: the FSO is permanently running, and any time it found a possible solution, the BCA is launch, and so on. Test on general optimization benchmark and on the TEAM22 problem are shown.

II. THE APPROACH

A. The FSO

The classical PSO algorithm [3] is based on the control of the velocity shown by particles moving into the solution space. The updating at the (t+1)-th calculation step of the k-th component of the velocity vector, $v_{kPSO}^j(t+1)$, of each j-th particle is ruled by the following expression:

$$v_{kPSO}^j(t+1) = \omega^j v_{kPSO}^j(t) + \lambda^j (p_{bestk}^j - x_k^j(t)) + \gamma^j (g_{bestk} - x_k^j(t)) \quad (1)$$

where $k = 1 \dots \Delta$, and Δ is the dimension of the solution space of the x variables; ω^j , λ^j and γ^j are the so-called *inertial*, *cognize* and *social* coefficients respectively (often governed by the random (0,1) function) [3]; g_{bestk} is the coefficient global best of the whole swarm, while p_{bestk}^j is the personal best of each j-th particle.

The FSO algorithms add to (1) a new term due to the observation [4] that in real flock each generic h-th bird controls and follows the flight of a number, N_{crl_birds} , no matter what are their positions inside the flock: $\delta^j \cdot Mccb_k^j$; where δ^j is the so-called *topological coefficient* [1]. Finally, the updating at the (t+1)-th calculation step of the k-th component of the velocity vector, $v_{kFSO}^j(t+1)$, of each j-th particle is ruled by the following expression:

$$v_{kFSO}^j(t+1) = v_{kPSO}^j(t+1) + \delta^j \cdot Mccb_k^j \quad (2)$$

where: $Mccb_k^j = \frac{1}{N_{crl_birds}} \sum_{h=1}^{N_{crl_birds}} v_{FSO}^{h,j}$ is the mean value of the

k-th velocity components, $v_{kFSO}^j(t+1)$, of each h-th controlled starling of the flock by the j-th birds. The values g_{bestk} and $g_{bestk} \forall j, k$ are evaluated at each step t. These best values are computed by a suitable fitness function that estimates the goodness of the actual solution. As it has been proof in [1] for the case of identification of hysteresis models, the FSO can find a solution even if the dimension of the solution space is very high and moreover it is particularly suitable for multimodal optimization tasks.

B. The BCA

The BCA [5] takes inspiration by the motion characteristics of particular micro-organisms (bacteria) that is due to the different chemical properties encountered in the habitat (bacterial chemotaxis). A real bacterium differently reacts to the gradients of nutritive substance concentration (fitness) or of harmful substances. A mathematical description of the bacterium motion can be developed by the determination of suitable probabilistic distributions referred both to the motion duration and to the velocity vector (speed and direction) of the bacterium. For space reason, we invite to refer to [2] for a detailed description of the algorithm. More details will be given in the extended version of this paper.

C. The Hybridization and Parallelization

The present approach is hybrid since when the FSO finds a possible optimum, the BCA is launched to refining this

solution. But the FSO does not stop his search and goes on looking for other possible solutions. For implementing this approach we use 20 PC dual-cores. One of this is the Master on which the FSO runs; one is used to store the found solutions; whereas the other 18 units manage the BCAs. In this way it is possible to combine the high exploration capability of the FSO with the high fastness of the BCA in local search.

III. VALIDATION ON GENERAL BENCHMARKS

Let us apply the proposed algorithm to a 2D famous benchmark: the *bird function* which is expressed by $f(x, y) = \sin(x)e^{(1-\cos(y))^2} + \cos(y)e^{(1-\sin(x))^2} + (x-y)^2$. Into the range $x, y \in [-2\pi, +2\pi]$, it shows several local minima and two global minima equal to $f_{\min} = -106.7645367$ (approximation by limiting to 7 digits the decimal point precision) for two different pairs of coordinates: $(-1.58214, -3.13024)$ and $(4.70104, 3.15294)$. By comparing PSO, FSO and hybrid FSO+BCA we found the following results: the FSO found each minimum with good accuracy without to be launched more than one time: $(-1.58, -3.14)$ with $f_{\min} \approx -106.72$ and $(4.64, 3.13)$ with $f_{\min} \approx -106.24$; the PSO was entrapped into the closest global minimum encountered (depending on initialization of guess values) but showing the same level of accuracy of FSO; FSO+BCA improve the accuracy of the single FSO: it found both the global minima achieving the same value of $f_{\min} = -106.7645367$ for both minima.

IV. VALIDATION ON TEAM PROBLEM 22

The goal of the Team problem 22 [6-8] is to optimize the performance of the considered superconducting magnetic energy storage device systems consisting of two superconducting solenoid coils of rectangular cross section carrying opposite currents. This system has to be optimized in terms of its geometrical dimensions and currents carried, taking care that the magnetic stray field should be minimized without reducing the stored energy value. Consequently the target energy stored is fixed to 180 MJ, while the stray flux density should be as small as possible; in addition the maximum magnetic field within conductors must not exceed a certain critical value (in the present test, all the used optimization constrains are those reported in [8]). The optimization problem consists of finding all or a subset of the 8 parameters: $R_1, h_1, d_1, J_1, R_2, h_2, d_2, J_2$ (see Fig. 1). In this optimization problem we use as performance indices both the energy target and the stray field, i.e. the magnetic flux density RMS value measured along the two lines shown in Fig. 1 (for this evaluation we have considered 22 equally spaced points):

$$\xi = \frac{1}{22} \left(\frac{\sum_{i=1}^{22} |B_{stray,i}|^2}{B_{norm}^2} \right) + \frac{|Energy - E_{ref}|}{E_{ref}} \quad (3)$$

where E_{ref} is 180 MJ and B_{norm} is 3 mT. The magnetic flux density, B , can be easily obtained by using the Biot-Savart law, whereas the energy can be computed by considering the system in term of mutually coupled inductors. The self and

mutual inductances have been evaluated according to [9][10]. The present test is referred to the 3-parameter optimization. We have fixed $(h_1, R_1, d_1) = (3.0916, 2.8071, 0.1162)$ [m] and the current densities $(J_1, J_2) = (23.3809, -19.5511)$ [MA/m²]. Random guess values have been used for FSO which found a solution in $(h_2, R_2, d_2) = (1.56, 2.34, 0.39)$ [m] returning $\xi = 0.026$ by (3). Then, the FSO values have been used for initializing the BCA that found a refined solution in $(h_2, r_2, d_2) \approx (1.56101, 2.34240, 0.39395)$ [m] (just 5 decimal digits of 16 are here reported) corresponding to $\xi \approx 2.16 \cdot 10^{-4}$ that is a significant result [8].

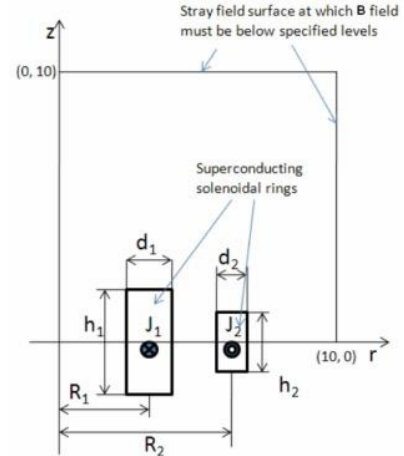


Fig 1. – Team problem 22 geometrical and optimization parameters

V. REFERENCES

- [1] F. R. Fulginei, A. Salvini, "Hysteresis model identification by the Flock-of-Starlings Optimization, Int. Journal of applied Electromagnetics and Mechanics, IOS Press, in press.
- [2] S.D. Muller, J. Marchetto, S. Airaghi, P. Kournoutsakos, "Optimization Based on Bacterial Chemotaxis", IEEE Trans. on Evolutionary Computation, Vol. 6, No. 1, February 2002, pp. 16-29.
- [3] Kennedy, J., & Eberhart, R., (1995). Particle swarm optimization, Proceedings of the IEEE International Conference on Neural Networks, Perth, (vol. IV, pp. 1942-1948) Australia.
- [4] Ballerini, M., Cabibbo, N., Candelier, R., Cavagna, A., Cisbani, E., Giardina, I., Lecomte, V., Orlandi, A., Parisi, G., Procaccini, M., Viale, M., & Zdravkovic, V., (2008). Interaction ruling animal collective behavior depends on topological rather than metric distance: Evidence from a field study, *Proceedings of the National Academy of Science*, (pp. 1232 – 1237)..
- [5] F. Riganti Fulginei, A. Salvini, Comparative Analysis between Modern Heuristics and Hybrid Algorithms, COMPEL, The Int. Journal for Computation and Mathematics in Electrical and Electronics Engineering, March 2007, Vol. 26, No. 2, pp. 259-268.
- [6] P. Alotto, A.V. Kuntsevitch, C. Magele, G. Molinari, C. Paul, K. Preis, M. Repetto, K.R. Richter, "Multiobjective optimization in magnetostatics: a proposal for benchmark problems", IEEE Transactions on Magnetics, Volume 32, Issue 3, Part 1, May 1996, pp. 1238 - 1241
- [7] [Online] http://www.igte.tugraz.at/archive/team_new/description.php
- [8] K.R. Davey, "Latin Hypercube Sampling and Pattern Search in Magnetic Field Optimization Problems", IEEE Transactions on Magnetics, June 2008 Volume: 44, Issue: 6, pp. 974-977
- [9] Ki-Bong Kim, E. Levi, Z. Zabar, L. Birenbaum, "Mutual inductance of noncoaxial circular coils with constant current density", IEEE Transactions on Magnetics, Volume 33, Issue 5, Part 3, Sept. 1997, pp. 4303 - 4309
- [10] Yu Dingan, K. Han, "Self-inductance of air-core circular coils with rectangular cross section", IEEE Transactions on Magnetics, Volume 23, Issue 6, Nov 1987, pp. 3916 – 3921.

Two-level refined direct method for electromagnetic optimization and inverse problems

Guillaume Crevecoeur, Ahmed Abou-Elyazied Abdallah, and Luc Dupré

Dept. of Electrical Energy, Systems & Automation, Ghent University, Sint-Pietersnieuwstraat 41, B-9000 Ghent, Belgium

Abstract—Electromagnetic optimization and inverse problems require a large number of evaluations in numerical forward models. These computer models simulate complex problems through the use of numerical techniques, and hence the evaluations need a large computational time. Two-level methods have been developed that include a second model so to accelerate the inverse procedures. Contrary to existing two-level methods, we propose a scheme that enables acceleration when the second model is based on the initial numerical model with coarse discretizations. This paper describes the proposed refined direct optimization scheme and validates the method onto algebraic test functions. Finally, we apply the method for solving an electromagnetic inverse problem.

I. INTRODUCTION

THE classical equations of Maxwell can be solved when the geometry, material characteristics and sources are specified. Using efficient numerical techniques, electromagnetic computer models can be built, which solve the so-called forward problem. Optimization and inverse problems on the other hand, need to identify a priori unknown parameter values by starting from an objective or electromagnetic measurements. Traditional direct optimization procedures strive towards the minimization of a predefined cost function by the use of one forward model. These methods have an update scheme that is based on the responses and eventual first and second order derivatives of the forward model. However, when dealing with complex problems where a single evaluation of the numerical forward problem is very time demanding, it is possible that solving optimization and inverse problems becomes difficult, time demanding and not practical.

In this perspective, so-called two-level optimization methods, e.g. space mapping [1], manifold mapping [2], etc., were conceived which accelerate the optimization procedure by incorporating an additional coarse model in the procedure. These methods propose an iterative scheme that includes a coarse model (low accuracy, time efficient) and a fine model (high accuracy, very time demanding), but fail to converge in a computationally efficient way when the computational time of the coarse model is not sufficiently smaller than the computational time of the fine model [2]. This is for example the case when the coarse model is based on the initial fine numerical model with coarse discretizations. Indeed, when dealing with complex electromagnetic problems, it is not always possible to build a very fast analytical model that is similar to the fine model. Therefore, we propose an alternative method that enables to solve optimization problems in a more efficient way, when including such a coarse model. This paper describes this so-called refined direct optimization scheme

in detail and implements the scheme with the Nelder-Mead simplex method and non-linear least squares methods. In order to validate the method, we apply the method onto algebraic test functions and an electromagnetic inverse problem.

II. REFINED DIRECT OPTIMIZATION (RDO) SCHEME

The computational effort in existing two-level schemes can become high because the coarse model is sequentially optimized with different objective values. In this paper, we carry out only one optimization of a surrogate-based model, that is iteratively refined during the optimization itself. The basic idea of the RDO scheme is to alter the optimization of the cost \mathcal{Y} , e.g. least-squares difference between measurements and simulations, of the fine model \mathbf{f} :

$$\mathbf{x}_f^* = \arg \min_{\mathbf{x}} \mathcal{Y}(\mathbf{f}(\mathbf{x})) \quad (1)$$

to the optimization of the cost of the surrogate model: $\mathbf{x}_s^* = \arg \min_{\mathbf{x}} \mathcal{Y}(\mathbf{s}(\mathbf{x}))$. Metamodels can be used as surrogate models within optimization schemes. These models are built by interpolating response data, obtained by evaluating the model $\mathbf{f}(\mathbf{x}_i)$ for a certain set of sample points \mathbf{x}_i , $i = 1, \dots, N$ in the design space. N is the number of design points. When dealing with complex problems, N needs to be large in order to obtain a sufficiently accurate metamodel. Here, we use metamodels for interpolating the coarse model response data to the fine model response data. The relation between coarse model response and fine model response is less complex and less difficult to determine. In this way, N can be reduced. The surrogate model, used in the RDO scheme has the following form: $\mathbf{s}(\mathbf{x}) = \mathbf{c}(\mathbf{x}) + \mathbf{e}(\mathbf{x})$ with error function $\mathbf{e}(\mathbf{x})$ that is determined using metamodels. In this paper, we use the Kriging metamodel, see e.g. [3], for making the interpolation. The surrogate model $\mathbf{s}(\mathbf{x})$ is refined during the optimization procedure by performing a limited number of fine model evaluations. The number of updates depends on how accurate the coarse model is, compared to the fine model. The proposed method has the same features as the traditional direct optimization method, i.e. start value, stopping criteria, etc., where the internal parameters of the RDO method are self-tunable. The method uses a trust-region strategy for updating the surrogate model. An outline of the algorithm is given:

Step 1: N design points are generated around start value $\mathbf{x}^{(0)}$ within the trust region radius $\Delta^{(0)}$: $\mathbf{x}_i^{(0)}$. Here, the latin hypercube sampling method is used. Evaluations are then carried out in the coarse and fine model.

Step 2: Construction of surrogate model $\mathbf{s}^{(0)}$ by determining $\mathbf{e}(\mathbf{x})$. We initialize $m = 0$.

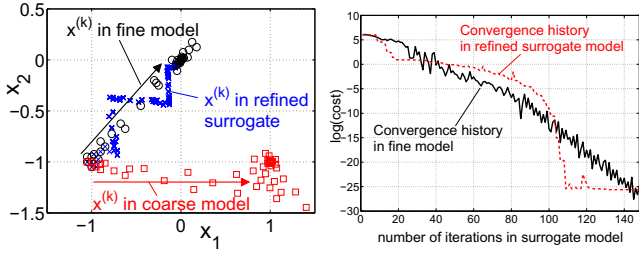


Fig. 1. (a) Minimization of \mathcal{J}_1 , and (b) of \mathcal{J}_2 .

Step 3: Partial run of direct optimization method using surrogate model $\mathbf{s}^{(m)}$. Updates $\mathbf{x}^{(k)}$, $k = 1, \dots, K$ are carried out, depending on the used direct optimization method. The partial run of direct optimization method is stopped when $\mathbf{x}^{(K)}$ is near the trust region boundary. $\mathbf{x}^{(m)}$ becomes $\mathbf{x}^{(K)}$.

Step 4: Update of surrogate model: $\mathbf{s}^{(m+1)}$ in region $\Delta^{(m)}$. A limited number of evaluations are carried out in the fine model, so to refine the surrogate model in the next trust region.

Step 5: Determine the accuracy of the surrogate model so to determine the new trust region $\Delta^{(m+1)}$. The accuracy of the previous surrogate model $\mathbf{s}^{(m-1)}$, depends on the fidelity of the coarse model $\mathbf{c}(\mathbf{x})$ and the accuracy of the error function $\mathbf{e}(\mathbf{x})$. The accuracy is determined as follows:

$$\rho^{(m)} = \frac{\mathcal{Y}(\mathbf{f}(\mathbf{x}^{(m-1)})) - \mathcal{Y}(\mathbf{f}(\mathbf{x}^{(m)}))}{\mathcal{Y}(\mathbf{s}^{(m-1)}(\mathbf{x}^{(m-1)})) - \mathcal{Y}(\mathbf{s}^{(m-1)}(\mathbf{x}^{(m)}))}. \quad (2)$$

On the basis of $\rho^{(m)}$, we determine $\Delta^{(m+1)}$, similar to [4].

Step 6: If the termination criteria of the direct optimization method are not satisfied, then go to step 3, and set $m = m + 1$.

III. RDO APPLIED ONTO ALGEBRAIC TEST FUNCTIONS AND AN ELECTROMAGNETIC INVERSE PROBLEM

We compared the RDO method with the traditional direct optimization scheme. Firstly, we applied the RDO onto the following algebraic function: $\mathcal{J}_1(\mathbf{f}(\mathbf{x})) = -\exp(-(x_1^2 + x_2^2))$ with $\mathbf{x}_f^* = [0, 0]^T$. The implemented coarse model is similar to the fine model but where output and input are altered with optimal value $\mathbf{x}_c^* = [1, -1]^T$. Fig. 1a shows the points $\mathbf{x}^{(k)}$ that are updated in the traditional Nelder-Mead simplex method in order to obtain \mathbf{x}_f^* and \mathbf{x}_c^* . The figure shows the alternative path followed by the RDO algorithm in order to achieve convergence to $\mathbf{x}_s^* = \mathbf{x}_f^*$. The path followed by the iterates differ from the fine model one, but convergence is obtained with a limited number (20) of evaluations in the fine model.

Secondly, we applied the RDO onto the minimization of the two-dimensional Rosenbrock test function, with fine model: $\mathcal{J}_2(\mathbf{f}(\mathbf{x})) = 100(x_2 - x_1^2)^2 + (1 - x_1^2)$. The coarse model is again, seriously altered in input and output space. Fig. 1b compares the convergence history of the traditional method with cost $\log(\mathcal{Y}(\mathbf{f}(\mathbf{x}^{(k)})))$ with the RDO method with cost $\log(\mathcal{Y}(\mathbf{s}(\mathbf{x}^{(k)})))$ in each k -th iteration.

Finally, we applied the RDO method on the identification of the anhysteretic B - H characteristic of a magnetic ring core. The magnetic ring core, shown in Fig. 2a, is partially excited with an excitation angle 230° , where the introduced air gap is approximately 1 mm. This geometry is a simplified

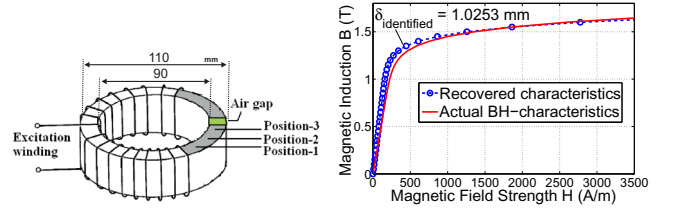


Fig. 2. (a) Configuration of the partially excited magnetic ring core with air gap. (b) Recovered BH-characteristics using RDO and actual B - H characteristics.

magnetic circuit of an electromagnetic device. Due to the lack of extra samples to perform measurements with e.g. the classical single sheet tester, the B - H characteristics remain unknown. Therefore, we identify the material properties on the magnetic circuit itself, using a coupled experimental-numerical inverse approach based on the RDO technique. The results are compared with a traditional least-squares non-linear method.

The fine and coarse models are three-dimensional numerical models based on the finite element method (FEM), with fine and coarse mesh respectively. The FEM model solves the non linear quasi-static Maxwell's equation with non-linear permeability. The single-valued nonlinear constitutive relation of the magnetic material, is modelled by means of three parameters $[H_0, B_0, \nu]$:

$$\frac{H}{H_0} = \left(\frac{B}{B_0}\right) + \left(\frac{B}{B_0}\right)^\nu. \quad (3)$$

The inputs of the forward problem are the excitation currents and the magnetic material parameters for well known ring core dimensions. However, the output is the magnetic induction at specific position, e.g. position 2, as shown in Fig. 2a. On the other hand, the inputs of the inverse problem are the measured excitation currents and the measured local magnetic induction, e.g. at position 2. The output of the inverse problem is the magnetic material parameters. The identified material characteristics are depicted in Fig. 2b, where the recovered material characteristics approximate the actual B - H characteristic. The result is obtained in a computational efficient way with 20 % acceleration compared to the traditional optimization method.

IV. CONCLUSION

This paper proposes a method that decreases the computational time that is needed when optimizing or solving electromagnetic inverse problems. The results show that such problems can be solved with considerably improved acceleration as compared to the traditional inverse solutions.

REFERENCES

- [1] J. Bandler, Q. Cheng, S. Dakroury, A. Mohamed, M. Bakr, K. Madsen, and J. Sondergaard, "Space mapping: state of the art," *IEEE Trans. Microwave Theory Tech.*, vol. 52, pp. 337–361, 2004.
- [2] D. Echeverria, "Multi-level optimization: space mapping and manifold mapping," PhD thesis, Universiteit van Amsterdam, 2007.
- [3] L. Lebensztajn, C.A.R. Maretto, M. Costa, and J.-L. Coulomb, "Kriging: a useful tool for electromagnetic devices optimization" *IEEE Transactions on Magnetics*, vol. 40, pp. 1196–1199, 2004.
- [4] G. Crevecoeur, P. Sergeant, L. Dupré, and R. Van de Walle, "A universal two-level genetic algorithm for electromagnetic optimization," *IEEE Transactions on Magnetics*, in revision.

Application of Response Surface Methodology to Electric Machine Design with Multivariate Adaptive Regression Splines

Kenta Takayasu¹, Asuka Otake¹, Masahiko Miwa¹, Shinji Wakao¹,
Tamio Okutani², Yasuhito Takahashi³, Masahiro Tanai⁴, Kazuhiko Onda⁴

¹Waseda University, 3-4-1 Ohkubo Shinjuku-ku, Tokyo 169-8555, Japan

²Railway engineering Co., Ltd, 1-3-8 Shibadaimon, Minato-ku, Tokyo 105-0012, Japan

³Kyoto University, Yoshida-Honmachi, Sakyo-ku, Kyoto 606-8501, Japan

⁴The Nippon Signal Co.,Ltd, 1836-1 Ezura, Kuki, Saitama 346-8524, Japan
e-mail: wakao@waseda.jp

Abstract— This paper describes the application of multivariate adaptive regression splines (MARS), one of the response surface methodologies, for reducing the calculation cost in electric machine design. Some numerical examples are reported for confirming the validity and effectiveness of MARS. And then, we also apply the proposed optimization method with MARS to a practical optimization problem.

I. INTRODUCTION

Recently, the practical application of design optimization method has been gradually spread. However, increasing calculation cost remains as an essential issue. Then, in this paper, we propose the adoption of multivariate adaptive regression splines (MARS), one of the response surface methodologies (RSM), for reducing the calculation cost in electric machine design. MARS adequately decomposes the search domain into some sections with basis functions so as to hold the abundant expressiveness and versatility. This paper reports some numerical examples, e.g., mathematical and benchmark models, to demonstrate the effectiveness of the proposed optimization approach with MARS.

II. MULTIVARIATE ADAPTIVE REGRESSION SPLINES (MARS)

MARS adopts the nonparametric regression model [1] as follows.

$$y_i = \hat{f}(x_i) + \varepsilon_i \quad (1)$$

where y_i is the objective function value at the i th experimental point. $\hat{f}(x_i)$ and ε_i stand for the approximate function value and the error at the point, respectively. And then, $\hat{f}(x)$ is expressed with plural basis functions B_m and truncation functions as shown in (2) and (3).

$$\hat{f}(x) = \alpha_0 + \sum_{m=1}^M \alpha_m B_m(x) \quad (2)$$

$$B_m(x) = \prod_{l=1}^{L_k} [s_{ml}(x_{v(m,l)} - t_{ml})]_+^q \quad (3)$$

where α is the unknown parameters to be calculated.

III. APPLICATION OF MARS TO MATHEMATICAL MODEL

First, we apply MARS to the mathematical model shown in (4) in order to examine its effectiveness by comparing its numerical results with that of the conventional high-order polynomial approximation in (5).

$$f = -2 \exp \left[15 \left\{ -(x_1 - 0.1)^2 - x_2^2 \right\} \right] - \exp \left[20 \left\{ -(x_1 - 0.6)^2 - (x_2 - 0.6)^2 \right\} \right] + \exp \left[20 \left\{ -(x_1 + 0.6)^2 - (x_2 - 0.6)^2 \right\} \right] + \exp \left[20 \left\{ -(x_1 - 0.6)^2 - (x_2 + 0.6)^2 \right\} \right] + \exp \left[20 \left\{ -(x_1 + 0.6)^2 - (x_2 + 0.6)^2 \right\} \right] \quad (4)$$

$$\hat{f}(l) = \beta_0 + \sum_{i=1}^m \beta_{i+m} l_i + \sum_{i=1}^m \beta_{i+2m} l_i^2 + \sum_{i=1}^m \beta_{i+3m} l_i^3 + \sum_{i=1}^m \beta_{i+4m} l_i^4 + \sum_{i=1}^m \beta_{i+5m} l_i^5 + \sum_{i=1, j < j}^m \beta_{ij} l_i l_j + \sum_{i=1, j < j}^m \beta_{ij} l_i^2 l_j \quad (5)$$

Figure 1 shows the approximation results. The figures clearly demonstrate the difference of the accuracies between MARS and the conventional polynomial approximation, which indicates the effectiveness of MARS.

IV. APPLICATION OF MARS TO BENCHMARK PROBLEM

Next, we apply MARS to the benchmark model, i.e., Die Press Model [2]. In this model, the function W_1 for the angle of the flux density and the function W_2 for the amplitude of the flux density are objective functions, respectively.

The proposed optimization procedure is shown in Fig. 3. In the procedure, to estimate the accuracy of the pareto optimal solutions obtained by the response surface with MARS, we recalculate their objective functions' values by the FE analysis, and compared them. By properly reducing the search domain around the space existing the obtained tentative pareto optimal solutions, it's expected that the conclusive pareto solutions are searched at short times diminishing the influence of the approximation error of the response surface.

6. Optimization

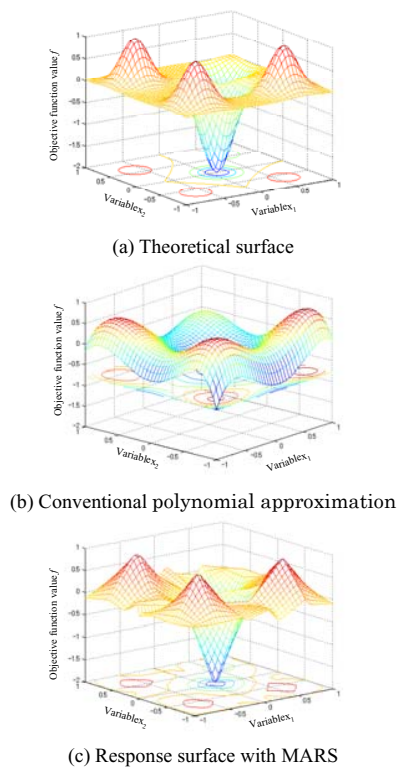


Fig. 1. Response surface configurations

Figure 4 shows the optimization results. The pareto optimal solutions obtained by the proposed method, i.e., RSM with MARS, are superior to ones without RSM. In addition, the total calculation time of the proposed approach is about 44% of the whole compared with that of the conventional method.

Incidentally, most of the calculation time with the proposed approach is spent on computing the response surface with MARS. So, the introduction of the parallelization with OpenMP is attempted with a view to enhancing the effectiveness of the proposed method. Furthermore, it's possible that the parallelization of the FE analysis at the experimental points leads to less calculation time. By actually calculating, the parallelization results in the reduction of the calculation time to almost 16% of the whole compared to that without parallelization and RSM.

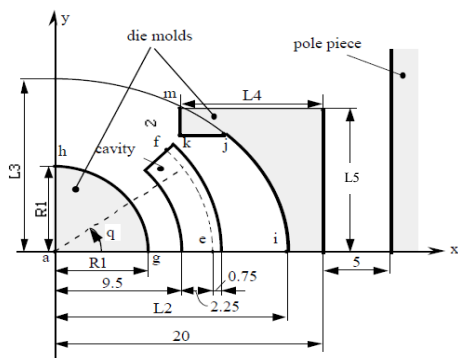


Fig.2. Die Press Model

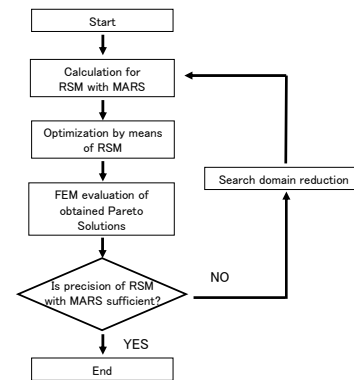


Fig. 3. Iterative optimization procedure

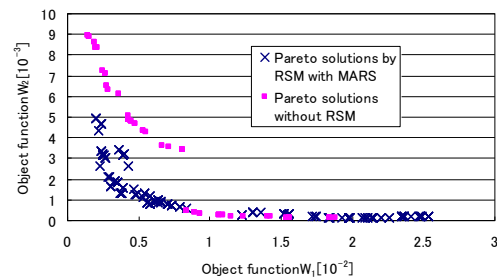


Fig. 4. Distributions of pareto solutions

V. OPTIMIZATION OF SHIELD CONFIGURATION

As the effectiveness of MARS is confirmed in the previous chapters, the application of MARS to the more complicated and practical model will be reported in the full paper.

The details of the optimization problem are as follows. As shown in Fig. 5, the signal receiver for the train operation control is placed under the train floor, where the noise from equipments such as the inverter has a negative influence on the signal reception from the rail currents. For the purpose of reducing the noise influence, we will efficiently carry out the design optimization of shield configuration without lowering the receiving level by using the proposed approach with MARS.

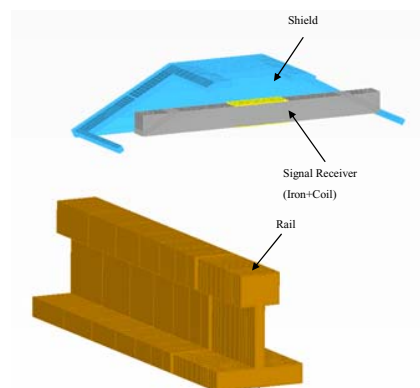


Fig. 5. Analysis model (half model)

VI. REFERENCES

- [1] J. Friedman: Multivariate adaptive regression splines, p.1-141, Ann. Stat., vol. 19, no.1(1991)
- [2] <http://www.compumag.co.uk/problems/problem25.pdf>

A Research on the Optimum Design of Magnet Structure for Improving Measurement Accuracy in the Dual Magnetic Float Type Level Gauge

Dong Sok Kim, Jae Min Kim, and Gwan Soo Park, *Member IEEE*
 Pusan National University, Busan 609-735, South Korea
kdongsok@pusan.ac.kr, jmin@pusan.ac.kr, gspark@pusan.ac.kr

Abstract — For the measurement of liquid level in ship's cargo tank, ballast tank, fuel oil tank and fresh water tank, several types of gauge meter are used such as tubular type, magnetic float type, reflex type, transparent type and welding pad type. Among them, magnetic float type gauge meter is environmental friendly device because it is free of power source and maintenance. The main obstacle of the device is relatively large error bound. In this paper, finite element method is used to design and analysis of the magnetic float type gauge meter. The operation of reed switch according to the magnetic field has been successfully described and agreed well with experimental measurement. The optimum geometry with combination of permanent magnet and reed switches are designed to achieve 95% and 98% accuracy of fluid level.

I. INTRODUCTION

Recently, the increase of a ship accident has a lot of economical and environmental problems. There are many causes but the explosion accident by inaccurate measure of the oil level has the biggest damage and is preventable. So, to detect the position of alert level is very important.^[1] For preventing the accident, the stability and exactitude is requested to a measuring instrument.^[2]

For the measurement of liquid level in ship's cargo tank, ballast tank, fuel oil tank and fresh water tank, several types of gauge meter are used such as tubular type, magnetic float type, reflex type transparent type and welding pad type.^[3] Among them, magnetic float type gauge meter is environmental friendly device because it is free of power source and maintenance. The main obstacle of the device is relatively large error bound. Mutual influence of magnets cause reed switch to malfunction in the dual magnetic float type gauge to detect a specific level.

In this paper, we designed the combination of permanent magnet and suitable distance of dual level gauge that reed switch operate exactly. The optimum geometry with combination of permanent magnet and reed switches are designed to achieve 98% reliability of fluid level.

II. STRUCTURE OF THE MAGNETIC FLOAT TYPE LEVEL GAUGE

The magnetic float type level gauge includes magnetic floats and reed switches. The reed switch is the magnetic field sensor. The magnetic float is comprised of permanent magnets and stainless steels (permeability: 1) like Fig.1. The magnets (Alnico 5) are round stick. And stainless steels set the magnets and move the fixed pipe. The reed switch module (two reed

switch) keep 'On' in a high magnetic density level and change to 'Off' at a low level.

It is distributed into four-magnet and six-magnet model by the number of magnets. The Material of magnets is Alnico 5. The ring type metal plates and metal pipe for fixing the permanent magnet are made stainless steel. The magnetic floats move by a buoyancy. The reed switch being the key element of the sensing part organizes two thin reed switches and a small glass pipe. If we put the magnet near the reed switch, magnetic field is concentrated at a magnetic material. The switch 'On/Off' are decided by the magnetic flux intensity and direction.

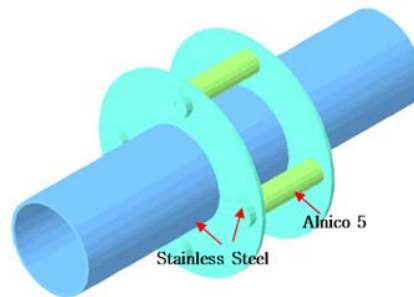


Fig. 1. Structure of Magnetic Float (4-magnet)

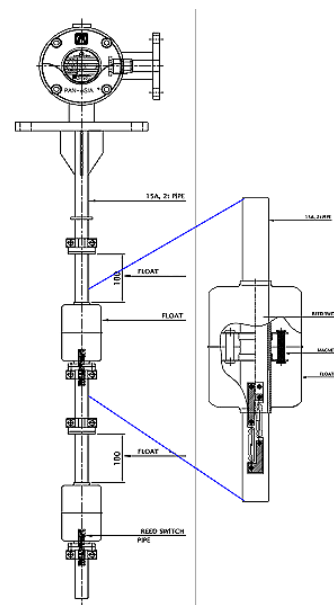


Fig. 2. Structure of Magnetic Float type level gauge

The two magnetic float type level gauge set at the upper position (98% of a whole tank) and the lower position (95% of a whole tank). The Magnetic Float is moved according to the quantity of fluid inside a tank and the sensor module is changed ‘On’ or ‘Off’ according to value of magnetic flux density in pipe. When it is ‘Off’ status, the system ring the alert sounds. However, if higher magnetic flux density than operation point (this system is 25[G]) of the switch, a range of switch operation is widen. Accordingly, a detection of correct position is impossible and we don’t measure the accurate position (95%, 98%). Also, if distance of two Magnetic Floats is close, the reed switch has error by mutual influence. In this paper, we researched on the optimal design for improving measurement accuracy using finite element method.

III. CHARACTERISTIC ACCORDING TO THE NUMBER OF MAGNETS

Fig. 3 is analyzed the magnetic flux density distribution of the magnetic float according to the number of magnets. And fig. 4 is values of magnetic flux density in Magnetic Float’ center. We can see magnetic flux density of type-II is higher than type-I. Accordingly, accuracy of type I is higher than type II.

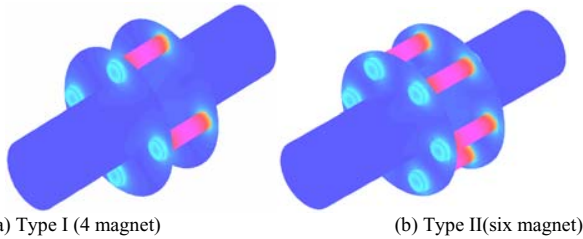


Fig. 3. Magnetic flux density of Magnetic Float

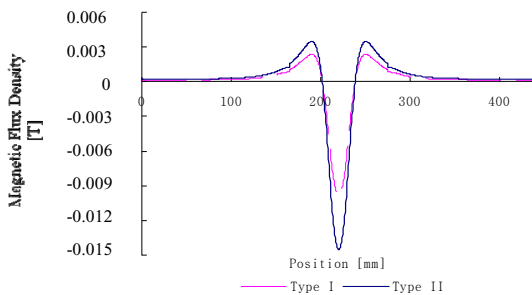


Fig. 4. Magnetic flux density distribution of Magnetic Float’ center

IV. MUTUAL INFLUENCE OF DUAL MAGNETIC FLOAT

Two magnetic float type level gauges are on the position of 95% and 98% of inside the tank. When Dual Magnetic Float are situation 95% position and 98% position, magnetic field at the low position doesn’t have influence on sensor module of the high position. But, if distance is close, the magnetic floats

of a low position and high position have influence on each sensor module.

We analyzed a mutual influence of center’s magnetic flux density according to pole arrangement in dual magnetic float type level gauge. First structure is that magnetizing direction is NS(Magnetic Float of 95%’ position)-NS(Magnetic Float of 98%’ position). Second is structure of SN(Magnetic float of 95% position)- NS(Magnetic Float of 98%’ position).

Where, influence according to the number of magnets is analyzed together. Table I is to compare fore case. As a result, when use four magnets and are SNNS status, we get good result that distance of influencing each other is short and magnetic flux density value in middle point is 0[G].

TABLE I
INFLUENTIAL RANGE BY THE NUMBER OF PERMANENT MAGNET AND DISPOSITION OF POLE

	The number of Magnets	Pole Status of Manget (MF1-MF2)	Rang of non_interference (Reed Switch of 20[G] Range)	Magnetic Flux Density between two Magnetic Float
Type I	4	NS - NS	140[mm]	5[G]
	4	SN - NS	140[mm]	0[G]
Type II	6	NS - NS	86[mm]	6.8[G]
	6	SN - NS	87[mm]	0[G]

V. CONCLUSION

There are many kinds of the level gauge of measuring level of a kind of fluids. Among them, the magnetic float type level gauge needs not extra-power and is semi-permanent sensor system. This system includes reed switches and magnetic float. The reed switch become ‘On’ when it is near the high magnetic flux density. It is ‘Off’ during the low. If the range of ‘On’ is wide, the sensitivity of the level gauge is lower. And if distance between two magnetic float is short, mutual interference is caused and the reed switch is wrongly operated. So, this paper suggests the optimum structure and position of this level gauge by analyzing magnetic characteristic of the system and motion characteristic of reed switch. We analyzed a influence according to the number of permanent magnets and the arrangement of magnetized direction. In the result, when Magnet float has four magnets and arrangement of magnetized direction is SN-NS, it has the highest sensitivity and the lowest interference.

VI. REFERENCES

- [1] Yaogeng Tag, Song Gao, Huibin Ouyang, “Development of the intelligent isotope level gauge”, Proc. Of Fifth World Congress on Intelligent Control and Automation, pp. 3834-3836 Vol.5, 2004.
- [2] Gulden, P., Vossiek, M., Pichler, M., Stelzer, A., “application of state-space frequency estimation to a 24-GHz FMCW tank level gauging system”, Proc. Of IEEE Conference on European Microwave, pp. 995-998, 2003.
- [3] Kaichun Ren, “Te influence by temperature and product density to accuracy of magnetostrictive level gauge”, Proc. Of IEEE conference on Information Acquisition, PP. 410-412, 2004.

Examination of Optimal Design of IPM Motor using ON/OFF Method

Takaya Yamada, Norio Takahashi, Daisuke Miyagi
 Dept. Electrical & Electronic Eng., Okayama University
 3-1-1 Tsushima, Okayama 700-8530, Japan
 norio@elec.okayama-u.ac.jp

Abstract — The topology optimization by distributing the magnetic material in the design domain, which is called as the ON/OFF method, is attractive for designers of magnetic devices, because an initial conceptual design, which we could not imagined beforehand, may be obtained. We examined how to apply the ON/OFF sensitivity method to the IPM motor in order to determine the optimal topology of the rotor. A technique to apply the ON/OFF method to the design of motor considering the nonlinearity and rotation of rotor is shown. The effect of various design requirements on the obtained topology of motor core is discussed.

I. INTRODUCTION

It is required to design an efficient and miniature motor with small cogging torque. If the ON/OFF method [1] is used, there is a possibility that a new magnetic circuit is discovered, because it is not necessary to set design variables in advance. There are few reports of the optimal design of motors [2] using the ON/OFF method.

In this paper, the ON/OFF method is expanded to the optimal design of permanent magnet motor, and techniques how to satisfy constraints, such as the limitation of terminal voltage, are examined. The effect of design requirements, such as the improvement of efficiency, on the optimal shape of motor core is also shown.

II. METHOD OF ANALYSIS

In the ON/OFF method, the sensitivity dW/dp (W : objective function, p : design variable) of an element is calculated by using the adjoint variable method. If the sensitivity is negative, the air is put in the element. If it is positive, the iron is put in the element. The sensitivity of the i -th element is obtained by differentiating the objective function W by the design variable ν .

$$\left(\frac{dW}{d\nu_i} \right)_k = \frac{\partial W}{\partial \nu} + \frac{\partial W}{\partial A} \frac{\partial A}{\partial \nu} \quad (1)$$

where ν_i is the reluctivity of the i -th element. The sensitivity $(dW/d\nu_i)_k$ is calculated at each rotor position k . The sensitivity $dW/d\nu_i$ which is used for judging ON(iron) or OFF(air) of material is the sum of $(dW/d\nu_i)_k$ during one pole pitch for example, 90deg, as follows:

$$\frac{dW}{d\nu_i} = \left(\frac{dW}{d\nu_i} \right)_1 + \dots + \left(\frac{dW}{d\nu_i} \right)_k + \dots + \left(\frac{dW}{d\nu_i} \right)_n \quad (2)$$

where, n is the number of steps during the rotation.

The objective function of the obtained shape by using the ON/OFF method is calculated using FEM and the torque is calculated using the nodal force method. The calculation is terminated when this process is repeated and the objective function does not decrease.

III. OPTIMIZATION OF THE ROTOR OF THE IPM MOTOR

The analyzed model of the rotor of the IPM motor is shown in Fig.1. The thickness in the z -direction is 100mm. The initial material of elements in the design region was set as a magnetic material.

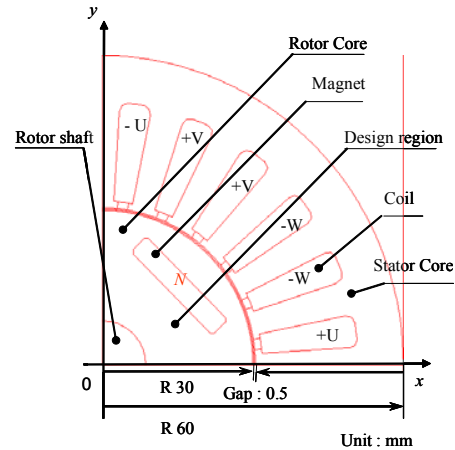


Fig.1. Model of IPM motor.

The current of each phase is given by:

$$\begin{cases} I_U = I_m \sin(\omega t + \beta) \\ I_V = I_m \sin(\omega t - 120^\circ + \beta) \\ I_W = I_m \sin(\omega t + 120^\circ + \beta) \end{cases} \quad (3)$$

β is the current phase, which is set to 45° . The maximum ampere turns of the coil are set 1297AT (50Hz). The specification of analysis is shown in Table I.

TABLE I
SPECIFICATION OF ANALYSIS

Material	Stator core	35H230
	Rotor core (design domain)	35H230
	Magnet	HS-40FH
Direction of magnetization (T)		1.23
Magnetization		Parallel
Speed (min^{-1})		1500
Number of Nodes		14420
Number of Elements		6964

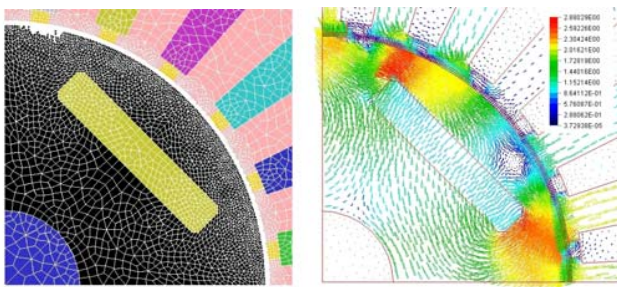
The objective function was defined as follows in order to minimize the torque ripple of the rotor and maximize the torque of the rotor:

$$W_1 = \sum_{i=1}^n [T_i - T_{ave}]^2 \quad (4)$$

$$W_2 = \sum_{i=1}^n \left(\frac{1}{T_i}\right)^2 \quad (5)$$

$$W = k_1 W_1 + k_2 W_2 \quad (6)$$

Both k_1 and k_2 are chosen as unity. T_i is the torque of a rotor at an angle i . T_{ave} is the average torque during a pole pitch angle. The optimal shape is shown in Fig.2 (a). The flux at the 1st step is shown in Fig.2 (b). Fig.3 shows the cogging torque.



(a)optimal shape (b)flux distribution
Fig.2. Result of analysis.

By removing a small part of rotor surface, the cogging torque of optimal shape is reduced. It is thought that the magnetic flux is transmitted to the teeth smoothly from the rotor. The torque ripple and average torque is shown in Table II. The torque ripple r_d is calculated by

$$r_d = \frac{T_{max} - T_{min}}{T_{ave}} \times 100 \quad (7)$$

where T_{max} is the maximum of the torque and T_{min} is the minimum of the torque. T_{ave} is the average of the torque. Compared with initial shape, the average torque of the optimal shape is a little reduced, because the air gap is increased at the removed part of the rotor. But the cogging torque is about 2% improved.

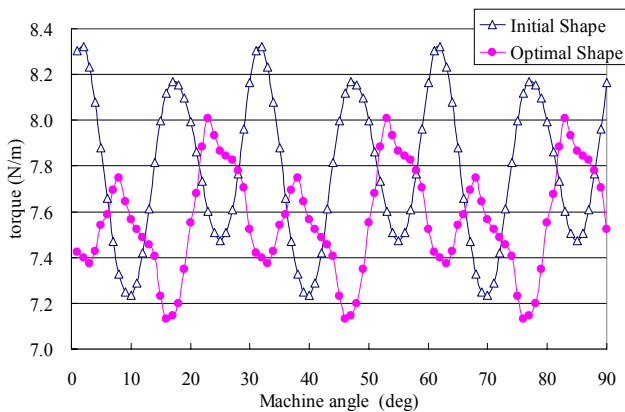


Fig.3 Cogging torque.

TABLE II
TORQUE RIPPLE AND AVERAGE TORQUE

	torque ripple (%)	average torque(N/m)
Initial Shape	13.96	7.79
Optimal Shape	11.56	7.56

Fig.4 shows the objective functions W_1 and W_2 in (3) and (4). It is understood that W depends on mainly W_1 .

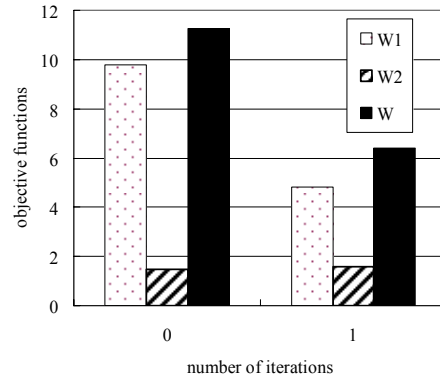


Fig.4 Objective function.

IV. CONCLUSION

It is shown that the ON/OFF method can be applied to the design of rotor shape by using the sum of the sensitivity at each angle of rotor. A technique how to satisfy a constraint of limitation of terminal voltage, and the effect of design requirement of improving the efficiency will be shown in the full paper.

REFERENCES

- [1] N.Takahashi, S.Nakazaki, D.Miyagi: "Examination of optimal design method of electromagnetic shield using ON/OFF method", IEEE Trans. Magn.,vol.45.,2009.
- [2] S.Wang, J.kang, J.Noh: "Topology optimization of a single-phase induction motor for rotary compressor", IEEE Trans. Magn., vol. 40, no.3, pp.1591-1596, 2004.

Optimization of Inductors Using Evolutionary Algorithms and Its Experimental Validation

K. Watanabe¹⁾, F. Campelo¹⁾, Y. Iijima²⁾, K. Kawano²⁾, T. Matsuo³⁾, T. Mifune³⁾ and H. Igarashi¹⁾

1) Hokkaido University, Kita 14, Nishi 9, Kita-ku, Sapporo, 060-0814, JAPAN

2) Taiyo Yuden Co., 3) Kyoto University

watanabe@ssi.ist.hokudai.ac.jp

Abstract— This paper presents parameter optimization of inductor shapes using immune algorithm (IA) and micro genetic algorithm (GA). It is shown that the inductor volume can be almost halved satisfying constraints on values of inductance under different DC current conditions. The best results of the parameter optimization obtained from IA and micro-GA are similar to each other. During the optimization processes, values of inductance are repeatedly computed using finite element method taking the nonlinear BH characteristics into account. The dependence of inductance on the imposed current obtained by the present method is in good agreement with the experimentally measured results.

I. INTRODUCTION

Inductors are important electric parts widely used in electric and electronic devices such as mobile phones and computers. Size reduction, higher operation frequency and larger current tolerance have been strongly required from the industries. While development of new materials having better characteristics is important to meet these requirements, improvements in inductor shapes are also indispensable. For the latter purpose, shape optimization based on computational electromagnetism is thought to be effective.

The goal of this study is to develop reliable optimization methods for inductor shapes on the basis of computational electromagnetism. Evolutionary optimization methods are suitable for this kind of optimization because objective functions often present non-linearities due to the ferromagnetic material, and complicated constraint conditions must be considered. In this paper, we adopt immune algorithm (IA) and micro genetic algorithm (μ -GA) which has good computational efficiency compared with the conventional GA. The values of inductance under a high DC current bias are computed using the finite element method. The parameter and topology optimization are studied, with only the former results shown in this digest due to page limitation. We also test the reliability of the optimal solutions by comparing their performance with experimentally measured results.

II. OPTIMIZATION METHODS

A. Immune algorithm

The IA draws inspiration from the *Clonal Selection Principle*, and combines local and global search characteristics [1]. In the parameter optimization, each candidate solution is referred to as an *antibody* according to our immunological metaphor. The procedure of IA is described below [2].

1. Generate an initial population of N random candidate solutions.
2. Evaluate the objective function and the constraint condition for each *antibody*.
3. Test a stop criterion. If it is satisfied, stop the procedures.
4. Eliminate P (%) low-ranking *antibodies*.
5. Generate *clones* for each surviving *antibodies*. The highest-ranking *antibodies* receive a higher number of clones.
6. A small-amplitude Gaussian noise is applied to the *clones*, which are then evaluated over the objective and constraints. Only the best candidate solution from each subset of (parent *antibody* + *clones*) is allowed to survive to the next generation.
7. Add randomly generated *antibodies* to replace the ones eliminated in Step 4, in order to keep the population size constant.
8. Back to step 2.

Steps 5 and 6 have a role of regulating the local search of the algorithm, while step 7 promotes global search. We can control the balance of local and global search by adjusting the parameters N and P .

B. Micro genetic algorithm

The main difference between μ -GA and the conventional GA is that very small populations are used in the former [3]. To avoid the convergence to local optima, all individuals except the best-ranking one are replaced by randomly generated individuals if the population is converged to a local optimum. The procedures of μ -GA are shown below.

1. Generate a small number N of initial individuals randomly. In this work, N is set to 5.
2. Evaluate the objective function and the constraint condition for each individual, preserving the best one.
3. Test the stop criterion. If it is satisfied, stop the procedures.
4. Make pairs by randomly selecting two individuals, and the higher ranking individual for each pairs is called the parent.
5. Select two pairs randomly, and apply the crossover operation to the parents of selected pairs. This yields the children. Steps 4 and 5 are repeated until the number of children reaches $N-1$.
6. Check the convergence of population. If the population falls into a local optimum, $N-1$ individuals are replaced by randomly generated ones. These individuals and the reserved best individual remain for the next generation.
7. Back to step 2 until the end criterion is satisfied.

III. OPTIMIZATION SETTINGS

The inductor optimized in this study consists of a bobbin-shaped ferrite core and a coil surrounding it. The parameter optimizations with 5 variables (X_1 , X_3 , Y_1 , Y_2 , Y_3) shown in Fig. 1 are performed using IA and μ -GA. Note here that X_2 depends on X_1 and Y_1 because the coil area is fixed to that of the original mass product model whose inductance in specification is $100(\mu\text{H})$. Other settings such as material properties are also fitted to the original model.

The objective of the optimization is to reduce the volume of inductor keeping the inductance to the specification value for small AC currents. Moreover, it is important to reduce the variation in the inductance against DC bias current, because this type of inductors is used for AC signal with high DC bias current. Considering these requirements, we define the objective function to be minimized as,

$$f = |L_{AC1} \times 10^6 - 100| + 10^8 W^2 H + \text{penalty}, \quad (1a)$$

$$\text{penalty} = \begin{cases} 80 - 10^6 L_{AC2} & (L_{AC2} < 80 \times 10^{-6}) \\ 0 & \text{otherwise} \end{cases}, \quad (1b)$$

where L_{AC1} is the inductance at AC current of 0.2 [A] without DC bias, L_{AC2} is that inductance under DC bias current of 1 [A], W [mm] and H [mm] denote the radius and height. The finite element analysis taking the nonlinear BH relations into account is performed for computation of L_{AC1} and L_{AC2} . The constraint condition is $Y_1 \leq Y_2 \leq Y_3$, and the range of parameters is $0 < X_1 < 2$, $0.5 < X_3 < 4$, $1 < Y_1 < 4$, $1 < Y_2 < 5$, $1 < Y_3 < 5$ [mm].

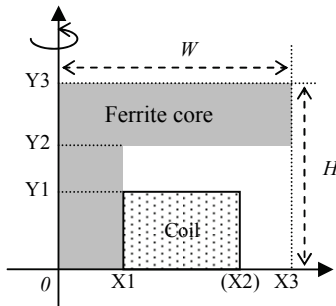


Fig. 1. 1/4 Model for parameter optimization.

IV. OPTIMIZATION RESULTS

Table I and Figure 2 summarize the best solutions obtained by the IA and μ -GA. We can see that the inductor volumes in the optimal solutions are around 55% of the original model. Moreover, these optimal solutions have similar tendencies: low height (Y_3), wide width (X_2), and fat radius of core (X_1).

We manufacture a trial piece shown in Fig. 3(a) based on the solution obtained by IA to test reliability of numerical analysis. Figure 3(b) shows that the numerical results are in good agreement with the experimentally measured results.

We also performed topology optimizations which result in finding a novel shape. It will be discussed in the full version.

TABLE I OPTIMIZATION RESULTS

Method	Value of f	L_{AC1} (μH)	L_{AC2} (μH)	Volume ratio against the original model (%)
IA	2.71	100.03	80.11	55
μ -GA	2.74	99.99	82.54	56

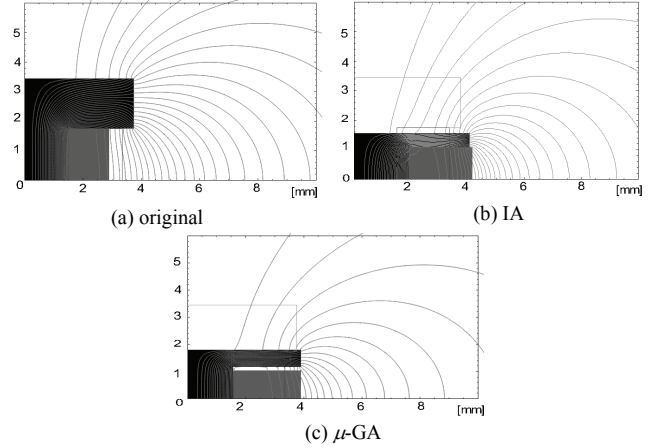


Fig. 2. Optimized shapes and flux distributions.

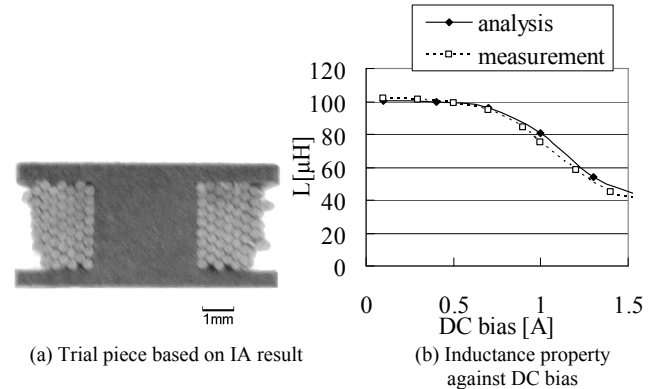


Fig. 3. Numerical and experimentally measured results.

V. ACKNOWLEDGEMENT

This research was supported in part by the Japan Science and Technology Agency (JST); and by the Ministry of Education, Culture, Sports, Science and Technology of Japan (MEXT).

VI. REFERENCES

- [1] L. N. de Castro and J. Timmis, "Artificial immune systems: a new computational intelligence approach", *Springer-Verlag*, 2002.
- [2] F. Campelo, F.G. Guimaraes, H. Igarashi, J.A. Ramirez, "A Clonal Selection Algorithm for Optimization in Electromagnetics", *IEEE Trans. on Magnetics*, vol. 41(5): 1736 – 1739, 2005.
- [3] David E. Goldberg, "Sizing Populations for Serial and Parallel Genetic Algorithms", Proceedings of the Third International Conference on Genetic Algorithms, pp. 70-79, *Morgan Kaufmann Publishers Inc.*, 1989.

Multiobjective Optimization of Electrooptic Modulators with Floating Electrodes

Ademar Muraro Jr.¹, André Côrtes¹, Angelo Passaro¹, Nancy M. Abe¹, Airam J. Preto², Stephan Stephany²

¹Instituto de Estudos Avançados - Comando-Geral de Tecnologia Espacial
Rodovia dos Tamoios, km 5,5, S.J.Campos, 12228-001, Brazil

²Instituto Nacional de Pesquisas Espaciais
Av. dos Astronautas, 1758, S.J.Campos, 12227-010, Brazil
ademarm@ieav.cta.br

Abstract— This work presents results of a multiobjective approach for optimization of design parameters of Mach-Zehnder lithium niobate modulators with additional floating electrodes. This process uses a genetic algorithm to search for geometrical parameters of the modulators and their characterization is performed by the finite-element method. The multiobjective approach is based on the weighted sum method in order to mapping the Pareto frontier, optimizing simultaneously three characteristics of a modulator.

I. INTRODUCTION

Mach-Zehnder modulators made of titanium diffused lithium niobate (Ti:LN) substrate with traveling-wave electrodes present low bias drift and large electrooptic coefficients [1], and technological advances in this kind of devices have produced high-quality LN modulator components for use in many sectors of the society.

A LN modulator can be characterized, in a quasi-static regime, by the analysis of the some electrical characteristics such as: the characteristic impedance (Z_c), the half-wave voltage ($V\pi$), the effective index of the microwave (N_m) and the driving power for the modulator (P_{in}), which depend on a large number of parameters. Stochastic methods are often employed in optimization techniques to analyze the effects of the geometric parameters, which affect the characteristic of these devices. These methods present good trade-off between the quality of the solution and the processing time.

However, to treat multiobjective problems, in which more than one characteristic have to be optimized at once, specific optimization techniques have been developed to reduce time development, analyzing different models and are able to choose the most convenient models.

II. THE MACH-ZEHNDER MODULATOR

The cross-section of a Mach-Zehnder modulator with CPW is presented in Fig. 1. Three extra floating electrodes are included under the main electrodes and deposited on the LN substrate without electrical contacts with any other part of the device. The purpose of these extra electrodes is to apply the available RF voltage directly across the indiffused optical waveguides, increasing the coupling between electric field and optical field. The expected result is to improve modulation, reducing the required RF input [2]. In this figure, T_b is the thickness of the buffer layer, T_e is the electrode thickness, G is the gap between the hot electrode and the ground electrode, W_H is the width of the hot electrode and g is the gap of the

floating electrodes.

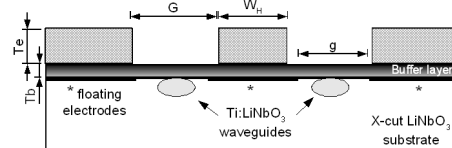


Fig. 1. Cross sectional structure of a X-cut floating electrodes LN modulator.

III. CHARACTERIZATION OF A MODULATOR

The modulation of the LN modulators is produced by a voltage-induced change in the refractive index. To change this index, either large voltages or long electrode lengths are needed to obtain an adequate modulation. A useful figure of merit for modulation is the product of the half-wave voltage ($V\pi$) and the electrode length (L). By using traveling-wave electrodes, in which the electrical signal propagates along the same direction as the optical wave, much higher bandwidths can be obtained, but they are limited by the mismatch between the electrical and optical propagation constants.

Other electrical characteristics of the modulator, which are determined from the microwave propagation (electromagnetic wave) characteristics of its electrodes, are the effective index of the microwave N_m , the characteristic impedance Z_c and the driving power for the modulator (P_{in}). These characteristics can be calculated by using quasi-static analysis. Simple quasi-TEM analysis using scalar potential function can be performed using the Finite-Element Method which is capable of handling transmission lines with rather arbitrary configurations, such as thick metal electrodes, ridge type structures, besides the anisotropic permittivity of the LN [3].

Several parameters, as cited in section II, have to be analyzed in order to obtain a modulator model that satisfies the required performance, using a lossless quasi-static analysis.

IV. DESIGN OPTIMIZATION APPROACH

An optimization problem consists of finding one or more solutions (usually the best ones) from all solutions in a feasible region which correspond to extreme values, minimum or maximum, of one or more objectives. Some basic factors in this type of problem are an objective function, which it is intended to minimize or maximize; a set of variables, or parameters, which affect the value of the objective function and, a set of constraints that allow some values for the variables and exclude others.

A stochastic method, the genetic algorithm – GA, is used in this work for the design optimization process. GA's have been widely applied for optimization and for inverse problems in several areas. GA's mimic the survival of the fittest individual among competing organisms [4].

Multiobjective optimization aims the optimization of more than one characteristic of the problem. In this case, there is one objective function for each characteristic to be optimized. It is desirable to identify a set of solutions known as Pareto-optimal solutions in which each optimal solution corresponds to a particular trade-off of the different objectives [5]. The multiobjective optimization tries to find as many optimal solutions as possible. Many of the solutions obtained by the GA are going to be on the Pareto front, the line formed by the optimal solutions. An approach to find the Pareto-optimal solutions that compose the Pareto-optimal front is the weighted sum method. This method compose a multiobjective function $F(x)$ by performing the weighted sum of the objective functions $f_i(x)$ of each characteristic to be optimized. The multiobjective optimization is converted to a single objective optimization, as follows:

$$\text{Min } F(x) = \sum_{i=1}^n w_i f_i(x) \text{ and } \sum_{i=1}^n w_i = 1, w_i \in [0,1]. \quad (1)$$

where x is the parameters vector that defines the modulator geometry and w_i is the weight of the n -th objective function.

V. RESULTS

In a previous work [3], the weighted sum method was used to performed multiobjective experiments in order to optimize two characteristics at a time of a conventional and a floating electrodes LN modulators.

In this work, three design parameters, the gap (G) and the thickness (Te) of the electrodes and the gap (g) of the floating electrodes were encoded in the individual chromosome, to obtain preliminary results of the optimization for three characteristics at a time for the floating electrodes LN modulator, that are: the $V\pi L$, Z_c and N_m . The optimal value for the first characteristic is 0 Volts, while the optimal value for Z_c is the impedance of commercial microwave sources, namely 50Ω and the optimal value for N_m is N_o (2.142), the effective index of the optical wave. Also, a constraint was defined: a penalty term added to the objective function, if the calculated electric field between the electrodes and the air exceeds a threshold value. For all configurations analyzed in this work, the calculated electric fields were bellow the adopted threshold (1.0E6 V/m).

The minimization of the three respective objective functions yielded the Pareto-optimal solutions presented in Fig. 2. The points of the Pareto frontier, obtained from each set of weight w_i , were plotted on a surface graph. In order to illustrate the differences of the obtained configurations, two regions (A and B) are pointed. The region A includes the matching of the characteristic impedance, Z_c values near 50Ω , but with penalties in the $V\pi$ and N_m . Otherwise, in region B, it is obtained excellent values of $V\pi$ and N_m but mismatching Z_c . Notice that for this region small driving power are obtained,

despite the mismatch of the characteristic and source impedance. Despite possible losses caused by reflection of electromagnetic wave, resulting in a decrease in a bandwidth, this type of configuration of modulator may be of interest for operation in environments with limited energy source and to operate the device at small frequencies. Tables I and II present the values of characteristics and geometric parameters, respectively, for two configurations of modulators, obtained in the regions cited above.

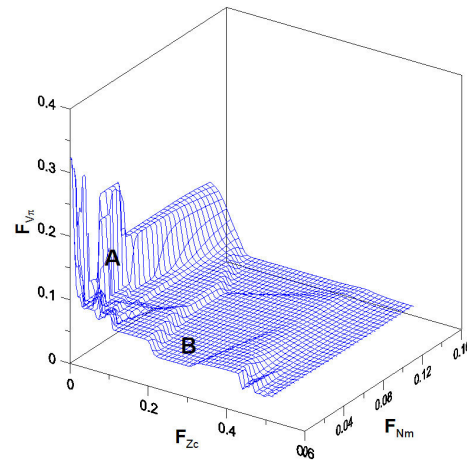


Fig. 2. Surface graph of the solutions for Z_c , $V\pi$ and N_m characteristics for floating electrodes modulators.

TABLE I
CHARACTERISTICS OF THE FLOATING ELECTRODES MODULATORS NAMED A AND B IN FIG. 2

region	Z_c (Ω)	$V\pi.L$ (V.cm)	N_m	P_{in} (W.cm ²)
A	49.75	32.21	2.178	2.59
B	15.10	3.96	2.148	0.055

TABLE II
GEOMETRIC PARAMETERS OF THE FLOATING ELECTRODES MODULATORS NAMED A AND B IN FIG. 2

region	G (μm)	Te (μm)	W_H (μm)	g (μm)
A	35	28	6	35
B	5	17	36	5

VI. REFERENCES

- [1] E. L. Wooten, K. M. Kissa, A. Yi-Yan, E. J. Murphy, D. A. Lafaw, P. F. Hallemeier, D. Maack, D. V. Attanasio, D. J. Fritz, G. J. McBrien, and D. E. Bossi, "A review of lithium niobate modulators for fiber-optic communications systems", *IEEE J. Select. Topics Quantum Electron.*, 6(1): 69-82, 2000.
- [2] S. Hopfer, Y. Shani, and D. Nir, "A novel, wideband, lithium niobate electrooptic modulator", *J. Ligth. Technol.*, 16(1): 73-77, 1998.
- [3] A. Muraro Jr., A. Passaro, N. M. Abe, A. J. Preto, and S. Stephany, "Design of Electrooptic Modulators using a Multiobjective Optimization Approach", *IEEE/OSA Journal of Lightwave Technology*, 26(16): 2969-2976, 2008.
- [4] R. L. Haupt, and S. E. Haupt, *Practical Genetic Algorithms*. USA: John Wiley & Sons, Ltd., 2004.
- [5] K. Deb, *Multi-Objective Optimization using Evolutionary Algorithms*. England: John Wiley & Sons, Ltd., 2002.

A Multi-frequency Strategy for Reconstruction of Deep Stress Corrosion Cracks from ECT Signals of Multiple Liftoffs

Li Wang and Zhenmao Chen

MOE Key Laboratory for Strength and Vibration, School of Aerospace Engineering,
Xi'an Jiaotong University, West Xianning Road 28, Xi'an, 710049, China,
Tel/Fax:86-2982668736, Email:chenzm@mail.xjtu.edu.cn

Abstract — In this paper, a layering analysis scheme for reconstruction of deep Stress Corrosion Cracks (SCC) from ECT signals is proposed based on a strategy of multi-frequency and multiple liftoff in order to improve the sizing accuracy. The shape profiles and conductivity of the crack are reconstructed respectively using a hybrid inversion scheme. The profiles of several cracks are reconstructed from simulated signals of conductive notches and measured signals of artificial SCC. It is demonstrated that the new strategy is promising for improvement of the sizing precision.

I. INTRODUCTION

Sizing of Stress Corrosion Cracks (SCC) is an important task once such kind of defect is detected in key structural components of a nuclear power plant in order to evaluate its propagation behaviors. Ultrasonic Testing (UT) is a major NDE tool for this purpose currently. However, UT is not efficient especially for shallow SCC because of their complicated microstructures [1] and the anisotropic property of welding joint. As a supplement of UT, the Eddy Current Testing (ECT) technique has been applied to the reconstruction of several kinds of natural cracks including some SCC recently [2]-[4]. For a deeper SCC, however, the reconstruction accuracy is still not satisfactory even using the conductive crack model, because the crack conductivity and shape may significantly change at different crack depth.

In this paper, a scheme to improve the ECT inversion accuracy for a deep SCC is proposed, which reconstructs crack profile at different depth with signals of different excitation frequencies and liftoffs. Several cracks are reconstructed to demonstrate the efficiency of the new strategy for sizing of artificial SCC.

II. A LAYERING ANALYSIS SCHEME USING SIGNALS OF MULTIPLE FREQUENCY AND LIFTOFF

The eddy current density exponentially decays with the perpendicular distance from the conductor surface because of skin depth effect. Therefore, higher excitation frequency gives a better possibility to detect surface small defect. On the other hand, the ECT signals of high excitation frequency contain less crack information from deeper position. It is an issue that deserves to be weighed between improving the detection sensitivity and the penetration depth of ECT. Recently, the potential of using multi-frequency eddy current technique for nondestructive testing applications has been explored [5]-[7].

On this background, a layering analysis scheme for reconstruction of a deep SCC is proposed based on multi-frequency excitation and multiple liftoff strategy in order to improve the sizing accuracy of SCC in this paper.

A. Crack Reconstruction using Multi-Frequency Signals

Since the signal of high excitation frequency mainly depends on crack profile at the near surface layers, more information of crack at deeper position will appear in signals of smaller excitation frequency. Therefore, if crack profile at the surface layers has been reconstructed properly by using signals of high frequency, a signal of smaller frequency is more suitable for the reconstruction of the crack profile at deeper layers. In this way, the sizing accuracy is possibly to be improved by using signals of multiple frequencies based on this layering analysis scheme.

B. Reconstruction Using Multiple Liftoff Signals

There is certain error using above-mentioned layering analysis strategy as the crack conductivity reconstructed of upper layers is an equivalent result. In order to reduce the cumulative error further in the layering analysis, a multiple liftoff strategy is also introduced. The strategy is based on the phenomenon that the proportion of crack information from the deep layers is bigger for the signals of large liftoff than that of a small liftoff. Therefore, for the reconstruction of crack segments in the upper layers, signals of smaller liftoff should be applied, while the signals of larger liftoff is more suitable for reconstruction of crack segments at deeper layers. Together with the multi-frequency strategy, further improvement on the accuracy of SCC reconstruction can be expected.

C. Layering Analysis Strategy for SCC Reconstruction

In practice, the layering analysis strategy is realized as follows. The inspection target is divided into a group of layer segments (see Fig. 1), where the crack conductivity and length are supposed as different values in each layer. The depth of each layer is set as a constant value referring to the skin depth of the selected highest excitation frequency. As the crack width and the crack conductivity affect the crack signal together [8], the crack width is supposed as a constant for all crack segments, which will be estimated based on the signal of high frequency, i.e., the reconstructed crack conductivity will become an equivalent parameter. The crack profile of the top layer is predicted by adopting ECT signals of high frequency and small liftoff using the conventional ECT inversion scheme [9]-[10]. By utilizing crack information reconstructed at top layers, the crack profiles

6. Optimization

of deeper layers can be evaluated efficiently by using signals of lower frequency and bigger liftoff. The multiple frequencies and liftoffs inversion strategy is illustrated in Fig. 2. Based on the proposed inversion strategy, profiles of several conductive cracks are reconstructed from the simulated ECT signals. The numerical results show that the proposed strategy can improve the sizing precision of SCC.

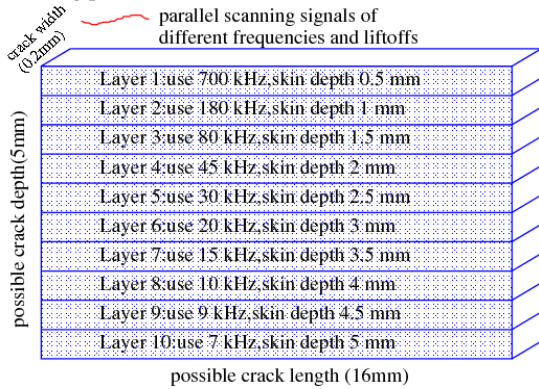


Fig. 1. An example of selected frequency and crack layers

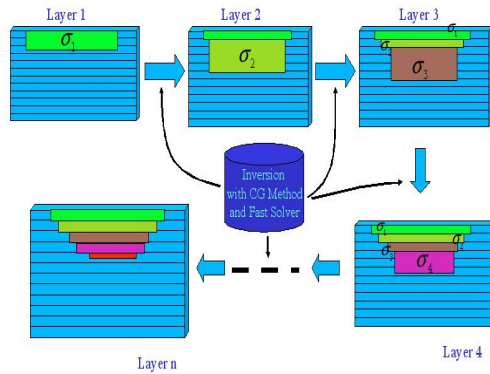


Fig. 2. Layering analysis and multiple frequencies and liftoffs strategy

III. A COMBINATORIAL INVERSION SCHEME FOR CRACK

Concerning the significantly different effects of crack conductivity and shape on the crack signal, it is not efficient to solve them by using the same inversion scheme. Hence a hybrid scheme of the Conjugate Gradient (CG) method and the advance-retreat algorithm [11] is applied.

IV. A NUMERICAL EXAMPLE

To validate the proposed scheme, cracks in a SUS 316 plate of 5 mm thickness (conductivity 1.4 MS/m) is taken as examples to be reconstructed. A small plus-point coil (inner diameter 4.5 mm, outer diameter 5.5 mm and thickness 2.0 mm) and a big plus-point coil (inner diameter 7.5 mm, outer diameter 12.5 mm and thickness 2.5 mm) are applied as the inspection probe, while excitation frequencies are chosen as those shown in Fig. 1 for each layer, i.e. the thickness of each layer is 0.5 mm.

To establish the database for the fast forward solver, the selected possible crack region (search region) is taken as 16 mm in length, 5 mm in depth and 0.2 mm in width, and subdivided into 120 (6×10×2) crack cells.

A rectangle conductive crack of 4.5 mm depth, 14 mm in length is reconstructed from the signals of multiple excitation frequency and multiple liftoff at first. The reconstructed crack depth is 4.48 mm by using the new strategy, while the result is 3.75 mm with the conventional method (see Fig. 3). This result shows that the proposed strategy gives a good possibility to improve the sizing precision for a deeper SCC. Results using experimental signals will be presented in the full paper.

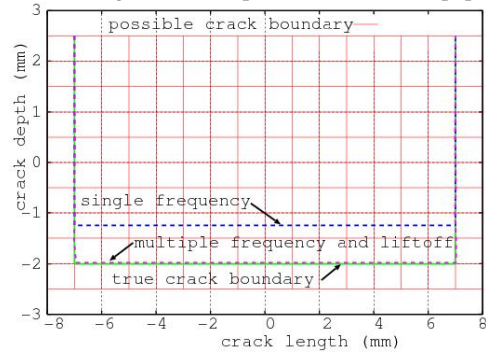


Fig. 3. Comparison of results reconstructed by using multi-frequency and multiple liftoff scheme for a rectangle conductive crack model

ACKNOWLEDGMENT

This work was supported in part by the National Natural Science Foundation of China through Grant No.50677049 and the National Basic Research Program of China through Grant No.2007CB707702, No.2006CB601206, and the MOE Program of New Century Excellent Talents in University.

V. REFERENCES

- [1] W.Cheng and et al., Depth sizing of partial contact SCC from ECT signals, *NDT&E Int.*, Vol.39, 374-383, 2006.
- [2] N.Yusa, Z.Chen and K.Miya, Sizing of stress corrosion cracks in piping of austenitic stainless steel from eddy current NDT signals, *Nondestructive Evaluation*, Vol.20, 103-114, 2005.
- [3] Z.Chen, M.Rebican, N.Yusa and K.Miya, Fast simulation of ECT signal due to a conductive crack of arbitrary width, *IEEE Trans. Mag.*, Vol.42, 683-686, 2006.
- [4] N.Yusa, Z.Chen, K.Miya, Quantitative profile evaluation of natural crack in steam generator tube from eddy current signals, *Int.J. Appl. Electromagn. Mech.*, Vol.12, 139-150, 2000.
- [5] J. Moulder, C.E. Uzal and J.H. Rose, Thickness and conductivity of metallic layers from eddy current measurements, *Rev Sci Instrum*, Vol.63, 3455-3465, 1992.
- [6] W.Yin, A.J.Peyton, Thickness measurement of non-magnetic plates using multi-frequency eddy current sensors, *NDT&E Int.*, Vol.40, 43-48, 2007.
- [7] V. Sundararaghavan, A multi-frequency eddy current inversion method for characterizing conductivity gradients on water jet panned components, *NDT&E Int.*, Vol.38, 541-547, 2005.
- [8] Noritaka Yusa, K.Miya, Discussion on the equivalent conductivity and resistance of stress corrosion cracks in eddy current simulations, *NDT&E Int.*, Vol.42, 9-15, 2009.
- [9] Z.Chen, K.Miya, ECT inversion using a knowledge based forward solver, *Journal of Nondestructive Evaluation*, Vol.17, 157-165, 1998.
- [10] Z.Chen, K.Miya, M.Kurokawa, Rapid prediction of eddy current testing signals using A- θ method and database, *NDT&E international*, Vol.32, 29-36, 1999.
- [11] Li Wang, Zhenmao Chen and et al., Sizing of long stress corrosion crack from 2D ECT signals by using a multisegment inverse analysis strategy, *Int.J. Appl. Electromagn. Mech.*, Vol.28, 155-161, 2008.

Accelerating Evolution Algorithm Using Kriging Metamodel

Dong-Kyun Woo, Jang-Ho Seo, Chany Lee, and Hyun-Kyo Jung

School of Electrical Engineering, Seoul National University, Shillim-dong, Kwanak-gu, Seoul, 151-742, Korea
E-mail underdamp@snu.ac.kr

Abstract — This paper presents and analyzes in detail a evolution strategy (ES) assisted by Kriging metamodeling to pre-select the most promising solution. The role of Kriging metamodeling is to predict objective function value for new candidate solution by exploiting information recorded during previous generations. The use of promising solution for screening the candidate solutions makes it possible to significantly reduce the computational cost of ES. The efficiency and usefulness of proposed method are verified by means of mathematical test cases.

I. INTRODUCTION

Evolution Strategies are excellent optimization tools for solving complex parameter problems where classical deterministic methods are known to have failed [1]. However, like other population based algorithms they require a very high number of fitness function evaluations.

The cost of optimizing expensive problem is dominated by the number of fitness function evaluations in order to reach a global optimum with adequate precision. Therefore, standard ES is not practical for such application.

ES using computationally expensive evaluation may reduce the cost through metamodeling [2]. Metamodel should be understood as surrogate evaluation model that is built by exploiting information of evaluated individuals [3]. This information can be used to adapt the recombination and the mutation operator in order to sample promising offspring. Evaluated individuals are obtained during one or more generations of ES and the algorithm can get back once more to the true fitness function for updating the metamodel with newly evaluated points expected to be closer to the global optimum. Therefore, the prediction quality generally improves with a growing number of evaluated points in the optimization process.

From the various existing modelisation methods, Kriging is chosen since it is more suitable for the design and analysis of computer experiments (DACE).

In this paper, Kriging replaces the objective function during the optimization process and decreases the number of expensive fitness evaluations which results in a better convergence rate of the algorithm.

II. PROPOSED ALGORITHM

As stated briefly in the Introduction, the main feature of proposed algorithm is the reduction of fitness function evaluation by Kriging-metamodel assisted ES (KAES). The proposed method adopts the concept of elite which stores superior solution. The element of the elite is replaced with

much superior or improved solution during the optimization iteration.

Total process of the proposed algorithm is as follows :

A. Step 0 - Initialization

a) Initialize α_{min} , α_{max} , α_{init} for each design variable.

α_{min} The minimum variation of design variable.
This factor controls the convergence rate.

α_{max} The maximum variation of design variable.

α_{init} Initial value for α_i .

α_i Evolution range of the i th design variable.

If the i th individual is p_i , the child generation is generated within $[p_i - \alpha_i, p_i + \alpha_i]$ where $\alpha_{min} < \alpha_i < \alpha_{max}$. This factor is modified during the generation except at the starting time.

b) Create initial population by (1)-(2) and save in a database

$$n = \left(\prod_{i=1}^n (b_i - a_i) \right)^\delta, \quad 0.5 < \delta < 1.5, \quad (1)$$

$$a_i < x_i < b_i, \quad i = 1, \dots, n, \quad (2)$$

n The size of initial population.

x_i x_i means the i th design variable.

δ According to the problem characteristic and the design variable of range, δ can be adjustable.

In the KAES, since the convergence ratio is decisively dependent upon the fitness landscape by initial sample s, an adequate selection of δ is essential.

B. Step 1 - Generation of initial parent set

Among initial population with n individuals, μ solutions are selected as members of the initial parent set. Those are determined by following rules.

a) Put the currently best solution into the parent set and check the position of the best solution.

b) Find another best solution except the checked position and repeat a) until μ elite solutions are found.

C. Step 2 - Generating Children

Make new λ children within evolution range.

D. Step 3 - Annealing

If the current elite solution is improved compared to prior generation, the evolution range is increased by dividing 0.8. If the elite solution is not improved, the evolution range is decreased by multiplying 0.8.

E. Step 4 - Shaking

Random solution is generated in the whole search space. In standard ES, since a high shaking ratio drops the

convergence rate, the ratio is decreased generally according to convergence degree. However, in case of the KAES, since the random solutions improve overall quality of the fitness landscape, the shaking ratio is increase in proportion to optimization iteration.

F. Step 5 - Reshaping

a) Update check

The metamodel is continually updated using the new datas obtained during iteration that does not satisfy the convergence criterion [4]. One drawback of the Kriging Interpolation with a growing number of samples is a computational cost. Then, we adapt the reconstruction algorithm to probable behavior of the evolutionary algorithm. It is assumed that the set of data points obtained in the early stages are weakly correlated with the global optimum and that those obtained in later generations are better and better correlated. Therefore, a reasonable strategy is to use a high value of p reshape probability in the early stages of iteration and to reduce this value near to zero in the later generations. The proposed reconstruction method is hence :

$$p = r \left(1 - \frac{g}{g_{\max}}\right)^{\omega} < 1, \quad (3)$$

$$0 < r < 1, \quad (4)$$

$$0 < \omega < 1, \quad (5)$$

where r is the random number, g_{\max} is the maximum number of generation allowed and ω is the control parameter. Because the reconstruction algorithm depends on ω control parameter, an understand on the influence of this parameter would be necessary.

b) Mean square error check

If the prior model is updated by the reconstruction algorithm, we search the best promising solution in the new fitness landscape and examine local mean square error (MSE) at that position. If a candidate solution has more MSE than specified criterion, the algorithm scatters samples near the candidate solution and repeats until lower than basis.

G. Step 6 - Convergence check

Repeat A - G until the solution is not improved any more.

III. NUMERICAL TEST AND RESULT

The proposed algorithm was applied to the optimization of the mathematical function. Fig. 1 and Fig. 2 show two examples of the test functions and optimized results. From the figures, we can see that the results show very fast convergence speed and the proposed method is very efficient to find the global optimum.

IV. CONCLUSION

In this paper, an algorithm of the ES for the reduction of fitness function evaluation was proposed. The algorithm is based upon combination of the evolution strategy and the Kriging metamodeling. The usefulness of the proposed

method was verified by the application to various test functions.

V. REFERENCES

- [1] T. Bick, U. Hammel and H.-P. Schwefel, "Evolutionary Computation: Comments on the History and Current State", *IEEE Trans. on Evol. Comput.*, 1(1): 3-17, 1997.
- [2] Y. Jin, M. Olhofer and G. Sendhoff, "A framework for evolutionary optimization with approximate fitness functions", *IEEE Trans. on Evol. Comput.*, 6(5): 481-494, 2002.
- [3] A. J. Booker, J. E. Dennis, P. D. Frank, D. B. Serafini, V. Torczon and M. W. Trosset, "A rigorous framework for optimization of expensive functions by surrogates", *Struct. on Optimization*, 17(1): 1-13, 1999.
- [4] L. Lebensztajn, C. A. R. Marretto, M. C. Costa and J. L. Coulomb, "Kriging: a useful tool for electromagnetic device optimization", *IEEE Trans. on Magnetics*, 40(2): 1196-1199, 2004.

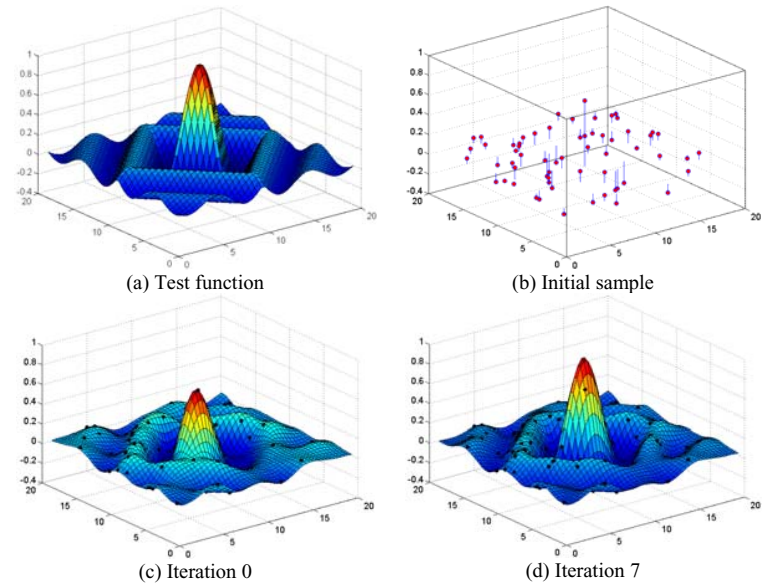


Fig. 1. Optimization result for a test function($n = 41, \mu = 2, \lambda = 2$)

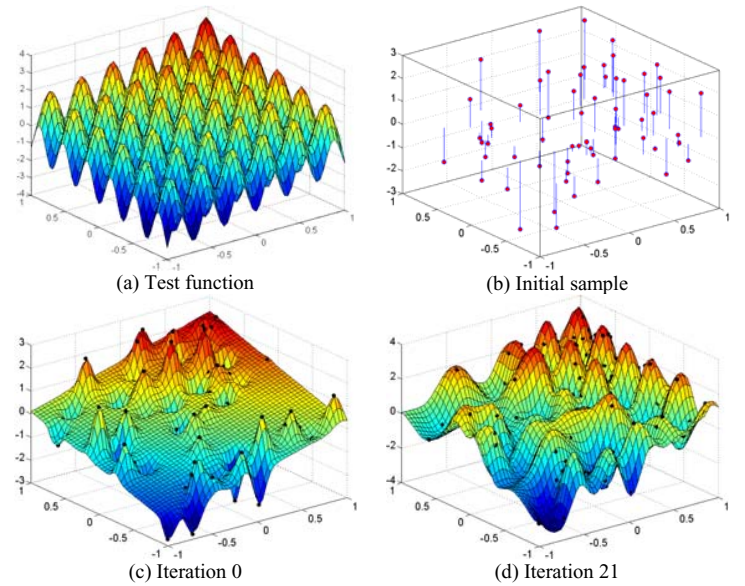


Fig. 2. Optimization result for a test function($n = 64, \mu = 2, \lambda = 2$)

Topology Optimization of Electrostatic Actuator Using Level Set Method and Shape Design Sensitivity

Young Sun Kim, and Il Han Park

School of Information and Communication Engineering, Sungkyunkwan University
300, Cheoncheon-dong, Jangan-gu, Suwon, 440-746, Korea
youngsun@skku.edu, ihpark@skku.ac.kr

Abstract— This paper treats a level set method for topology optimization of electrostatic actuator. The classical shape optimization has meshing problem for shape change. To overcome this difficulty, the level set method is employed because of its efficient representation of evolving geometry. The velocity field is required for solving the level set equation of Hamilton-Jacobi equation and it is obtained by the continuum shape sensitivity in a closed form by the material derivative concept. The optimization problem is modeled as coupled system of Poisson's equation and the level set equation and they are solved using a standard FEM in time domain. The design goal is to obtain a maximum torque for operating actuator. A result of optimal shape and topology of the salient pole actuator is presented.

I. INTRODUCTION

The classical shape optimization has been applied to many design problems for electromagnetic systems. One of its major difficulties is related the meshing problems coming from the shape modifications. In order to circumvent this kind of technical difficulties of the moving mesh problems, a couple of researches have tried to formulate shape optimization with fixed mesh analyses based on fixed grid finite elements. This approach was naturally associated with the Level Set description of the geometry to provide an efficient treatment of such problems involving geometry change and discontinuities. The level set method is a numerical technique first developed to track moving interface. It was first devised by Osher and Sethian [1] and has been recently introduced in the field of structure shape optimization [2],[3]. The level-set method has several advantages. Its main advantage is to enable an accurate description of the boundaries on a fixed mesh. Therefore it provides with fast and efficient numerical algorithms. It can also handle topological changes since it allows the boundary in a natural way to split apart or merge together with no extra technique by controlling the level-set function of a Hamilton–Jacobi equation. Such treatment of topological change can transform the difficult topology optimization problem into a relatively easier shape optimization problem. In this paper, we apply the level set method to a topology optimization of electrostatic actuator using continuum sensitivity [4],[5] for the velocity field that is inserted into the Hamilton–Jacobi equation for the level set function. The goal of actuator design is to generate maximum torque operation. The numerical algorithm is implemented

with a standard finite element procedure.

II. LEVEL SET METHOD

We employ the level set method to define evolving boundaries since it provides a convenient way to describe closed interfaces of curves and surfaces. The level set function is expressed in an implicit form of a high dimensional function, and then the boundary changes are traced by the deformation of this function. In shape optimization, the design boundaries are changed to minimize or maximize an objective function.

Generally, for a given region Ω with arbitrary boundary, we assume the implicit function $\phi(\mathbf{x})$ as

$$\begin{aligned} \phi(\mathbf{x}) > 0 & \quad \mathbf{x} \in \Omega^+ & : \text{free space} \\ \phi(\mathbf{x}) = 0 & \quad \mathbf{x} \in \partial\Omega & : \text{boundary} \\ \phi(\mathbf{x}) < 0 & \quad \mathbf{x} \in \Omega^- & : \text{dielectric} \end{aligned} \quad (1)$$

To compute an evolving domain, one can define the function and determine the evolution of domain Ω^- via

$$\Omega^-(t) = \{ \phi(\mathbf{x}, t) < 0 \}. \quad (2)$$

The boundary $\Gamma(t)$ of $\Omega^-(t)$ is given by the zero level set,

$$\Gamma(t) = \{ \phi(\mathbf{x}, t) = 0 \} \quad (3)$$

The evolution of the shape is determined by a velocity \mathbf{V} .

$$\frac{d\mathbf{x}(t)}{dt} = \mathbf{V}(\mathbf{x}(t), t), \quad (4)$$

Since the zero level set holds at any time t , its total derivative is expressed by using an Eulerian formulation and chain rule as

$$\frac{\partial \phi}{\partial t} + V_n |\nabla \phi| = 0 \quad (5)$$

This is called Hamilton-Jacobi equation and the level set function is determined by solving it. The velocity \mathbf{V} has to be given depending on each objective of design problem.

III. OPERATION OF ELECTROSTATIC ACTUATOR

Fig. 1 shows the initial shape of electrostatic actuator with 16 electrodes around the dielectric materials. The actuator is driven by switching the voltages clockwise. The initial shape of actuator is given 19 dielectric regions that will be topologically modified to generate maximum torque.

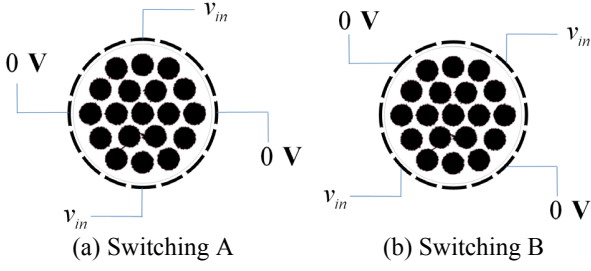


Fig. 1. Initial shape of electrostatic actuator containing 19 dielectric regions. Voltage switching position of (a) maximizing and (b) minimizing an electrostatic energy.

IV. FORMULATION OF OPTIMIZATION PROBLEM

To generate maximum torque, the electrostatic energy of switching A position must be maximized and be minimized at switching B position. In other words, the energy difference between two positions is maximized. Therefore an optimization problem in this case can be defined as

$$\begin{aligned} & \text{Maximize : } F = (W_A - W_B) \\ & \text{Subject to :} \end{aligned} \quad (6)$$

$$\begin{aligned} & \nabla^2 V = -\rho / \varepsilon(\phi) \quad : \text{ electric field equation} \\ & \int_{\Omega} H(\phi) d\Omega = S^* \quad : \text{ constraint of constant area} \end{aligned}$$

where the design domain is represented by Ω . The Poisson equation for electrostatics is used to calculate the electric scalar potential V and the electric permittivity ε is determined by using $\varepsilon(\phi) = \varepsilon_1 H(\phi) + (1 - H(\phi))\varepsilon_0$ where ε_1 is the material permittivity and ε_0 is the permittivity of free space.

Design variables are the movable boundary between dielectric and free space. The design boundary $\partial\Omega$ is represented using the level set function such that

$$\phi(\mathbf{x}, t) = 0 \quad : \text{ zero level set} \quad (7)$$

The velocity field determines shape variation and it results in variation of the objective function through the Poisson's equation. In order to impose a constraint condition of constant volume, the velocity field is modified from V_n to \hat{V}_n using Lagrange multiplier technique as

$$\hat{V}_n = V_n - V_0 \quad \text{where } V_0 = \int_{\gamma} V_n d\Gamma / \int_{\gamma} d\Gamma \quad (8)$$

V. CONTINUUM SENSITIVITY ANALYSIS FOR SHAPE DERIVATIVE

The total derivative of any objective function in electromagnetic systems can be derived in a closed form using the material derivative concept of continuum mechanics and an adjoint variable technique.

Firstly, the continuum sensitivity formula of switching position A is represented as

$$\frac{dF}{dt} = \int_{\gamma} G_A(V, \lambda) V_{nA} d\Gamma \quad (9)$$

where

$$G_A(V, \lambda) = \left(\frac{\varepsilon_1}{\varepsilon_2} - 1 \right) \left[\varepsilon_1 E_n(V^*) E_n(\lambda^*) + \varepsilon_2 E_t(V^*) E_t(\lambda^*) \right] \quad (10)$$

V_{nA} the normal component of the velocity field vector, λ an adjoint variable, γ design boundary.

The sensitivity of switching A position represents the relation between the objective function and the velocity field. If the velocity field is taken as

$$V_{nA} = G_A(V, \lambda) \quad : \text{ switching A position,} \quad (11)$$

the system energy will increase since it is in a gradient direction. Also, if the sensitivity of switching B position is chosen as

$$V_{nB} = -G_B(V, \lambda) \quad : \text{ switching B position,} \quad (12)$$

the system energy will decrease. The velocity field is inserted into the level set equation (5) in order to obtain a maximum torque of electrostatic actuator.

$$\frac{\partial \phi}{\partial t} + [G_A(V, \lambda) - G_B(V, \lambda)] |\nabla \phi| = 0 \quad (13)$$

Here we can see that the iterative optimization procedure is transformed to a first-order PDE in time domain.

VI. NUMERICAL RESULTS

In order to generate a maximum torque, the difference of the electrostatic system energy between two voltage switching positions has to be maximized. Numerical results showed that the proposed algorithm produced the optimal shape and topology of the salient pole actuator without previous information of dielectric layout as in Fig. 2.

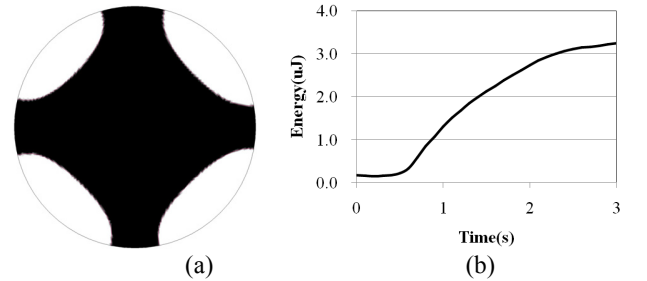


Fig. 2. (a) Final shape of dielectric area and (b) electrostatic energy variation with time.

VII. REFERENCES

- [1] Stanley Osher and Ronald Fedkiw, *Level Set Methods and Fast Dynamic Implicit Surfaces*, Springer, 2003.
- [2] Young Sun Kim, Se Hee Lee, Hong Soon Choi, and Il Han Park, "Application of the Level Set Method to Finite Element Modeling of Moving Objects in Electromagnetic Field," *IEEE Trans. on Magnetics*, Vol. 45, No. 3, pp. 1144-1147, March 2009.
- [3] Young Sun Kim, Se-Hee Lee, Hong Soon Choi and Il Han Park, "Shape formation of ferrofluid under external magnetic fields using level set method," *Journal of Applied Physics*, 105, 07D539, April, 2009.
- [4] J. K. Byun, S. Y. Hahn, and I. H. Park, "Topology optimization of electrical devices using mutual energy and sensitivity," *IEEE Trans. Magn.*, Vol. 35, Sept. 1999, pp. 3718-3720.
- [5] R. J. Yang, "Multidiscipline topology optimization," *Comp. Struct.*, vol. 63, no. 6, 1997, pp. 1205-1212.

Electromagnetic Characterization of Biological Tissues with Particle Swarm Optimization

N. Siauve⁽¹⁾, C. Lormel⁽¹⁾, R. Marion⁽¹⁾, J. Dardenne^(1,2) and F. Sixdenier⁽¹⁾

Université de Lyon, Lyon, F-69622, France^(1,2)

Université Lyon 1, Villeurbanne, F-69622, France⁽¹⁾ – INSA Lyon, Villeurbanne, F-6921, France⁽²⁾

CNRS, UMR 5005, Laboratoire Ampère⁽¹⁾ – CNRS UMR 5220, INSERM U630, CREATIS-LRMN⁽²⁾

nicolas.siauve@univ-lyon1.fr

Abstract— The objective of this research is the electromagnetic characterization of biological tissues in radiofrequency domain. In this aim, a measurement bench including a vector network analyzer and an open-end coaxial probe was introduced. The complex permittivity identification of the middle under testing is performed by solving an inverse problem. A quadratic fitness function that represents the difference between reflection coefficient measurement and reflection coefficient acquired with the normalized aperture admittance is minimized. The optimization is based on a heuristic algorithm: particle swarm. The approach is validated on well known dielectric middle and then tested on biological tissues.

I. INTRODUCTION

Numerical simulations of electric field distribution in the human body exposed to radiofrequencies waves require the knowledge of dielectric tissues properties [1]. In the radiofrequency domain, several experimental techniques can be used for measuring permittivity ($\epsilon^* = \epsilon_r - i\epsilon_i = \epsilon_r + i\sigma/\epsilon_0\omega$): free space, resonant technique, transmission/reflection line and open-ended coaxial [2]. In our study, the open-ended coaxial probe has been selected for its suitability for liquid or soft materials such as biological materials without specific preparation. Temperature can be easily controlled and after the bench calibration several samples can be rapidly treated. This point is crucial since biological samples can be easily altered or desiccated. The bench measurement provides an electric Scattering (S) parameter or reflection. The permittivity is identified on the base of an inverse method that using Particle Swarm Optimization (PSO) procedure for minimizing the quadratic difference between the measured and the calculated reflection from a direct model. In the first part, the global procedure measurement is described and the method to identify the permittivity of the Middle Under Testing (MUT) is exposed. In the second section, the proposed approach is validated on MUT known and then tested on biological tissues.

II. PROCEDURE

The characterization contents two parts, the reflection coefficient measurement from probe aperture/MUT interface and the identification of permittivity from the reflection coefficient measured. A sensitivity analysis has been performing so as to optimize the experiments. Calibration, sensitivity and identification procedure are in C-language.

A. Measurement bench and calibration

The experimental radiofrequency bench is composed of a Vector Network Analyzer (VNA), an open-ended coaxial

probe and an optical fiber thermometer. The probe is a semi-rigid coaxial line (UT85) mounted on a N connector. The probe is 200 mm long, inner and outer radius are respectively $a=0.255\text{mm}$ and $b=0.84\text{mm}$. The reflection coefficient (S_{11} parameter) of the MUT is obtained with VNA in the frequency range fixed (0.5 to 4 GHz) and for each frequency imposed by the linear step.

To determine the correct reflection coefficient of MUT, it is necessary to apply to the measured parameter $S_{11,m}^*$ some correction coefficients [3]. These coefficients are obtained from three additional measurements, on well known middles, respectively j =short circuit ($S_{11,m}^* = -1$), air ($\epsilon_r=1$, $\epsilon_i=0$) and de-ionized water ($\epsilon_s=25$, $\epsilon_o=4.3$, $\tau=170\text{ps}$) (1). The corrected $S_{11,c,MUT}$ is then calculated for each frequency (1).

$$S_{11,m,j}^* = E_D + \frac{E_R S_{11,c,j}^*}{1 - E_S S_{11,c,j}^*} \quad (1)$$

B. Inverse problem

The identification of the MUT permittivity is based on the normalized aperture admittance [4]:

$$Y^* \approx \frac{-i2\omega\epsilon_0\epsilon^*}{\ln b/a} \quad (2)$$

$$\int_a^b \int_a^b \int_0^\pi \frac{\cos \varphi}{r} + ik \cos \varphi - \frac{k^2 r}{2} \cos \varphi - i \frac{k^3 r^2}{6} \cos \varphi \cdot d\varphi \cdot d\rho \cdot d\rho'$$

with $k = \omega \sqrt{\mu_0 \epsilon_0 \epsilon^*}$, the propagation constant for the MUT, $r = \sqrt{\rho^2 + \rho'^2 - 2\rho\rho' \cos \varphi}$, the distance between the source point and the field point, ρ' and ρ are respectively the radial coordinates of these points at the aperture of coaxial probe. The reflection coefficient is related to the normalized probe admittance (3) with $Y_0=1/50$.

$$S_{11,adm}^* = \frac{Y_0 - Y^*}{Y_0 + Y^*} \quad (3)$$

The Fitness Function (FF) to minimize is given by (4).

$$FF = \left(\frac{\text{Re} \{ S_{11,adm}^* - S_{11,c,MUT}^* \}}{\text{Re} \{ S_{11,c,MUT}^* \}} \right)^2 + \left(\frac{\text{Im} \{ S_{11,adm}^* - S_{11,c,MUT}^* \}}{\text{Im} \{ S_{11,c,MUT}^* \}} \right)^2 \quad (4)$$

This minimization problem is solving with PSO technique. PSO involves simulating social behavior among individuals (particles) “flying” through a multidimensional search space, each particle representing a single intersection of all search dimensions [5]. Particles in a swarm move in discrete steps based on their current velocity, memory of where they found

their best fitness value, and a desire to move toward where the best fitness value was found so far by all of particle during a previous iteration (Fig. 1). Each particle has a position and a velocity: their values are randomized initially. The position with highest fitness score in each iteration is set to be the entire swarm's global best (gbest) position, towards which other particles move. In addition, each particle keeps its best position that it has visited, known as the particle's personal best (pbest). Each particle n of the swarm is defined as a potential solution to the problem.

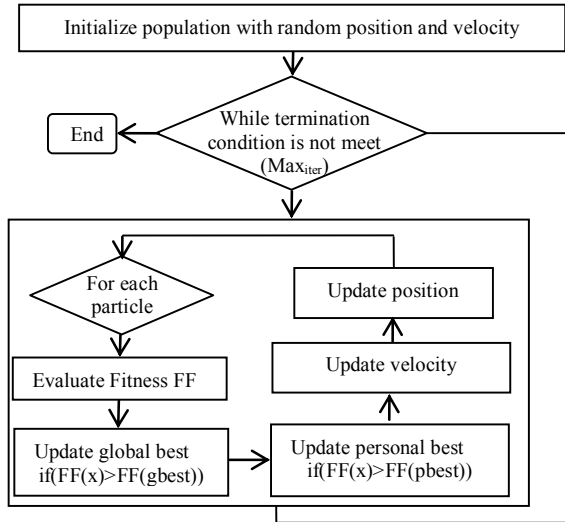


Fig.1. The Particle Swarm Optimization algorithm.

The particle dynamics are governed by the following rules which update particle positions x_n and velocities:

$$v_n = wv_n + c_1 \text{rand} 1 \frac{pbest_n - x_n}{\Delta t} + c_2 \text{rand} 2 \frac{gbest - x_n}{\Delta t} \quad (5)$$

After a new velocity for each particle, the position is calculated according to $x_{n+1} = x_n + v_n \Delta t$. Where x_n is the current position of particle n , Δt the time step equal to 1, x_{pbest} is the best position attained by particle n , x_{gbest} is the swarm's global best position, v_n is the velocity of particle n , w is a random inertia weight, c_1 and c_2 are two positive constants, called the social and cognitive parameter, $\text{rand}1$ and $\text{rand}2$ are random numbers between 0 and 1.

III. VALIDATION AND RESULTS

All the measurements presented in the following are realized on MUTs at 23°C for 1 000 frequencies linearly spaced. The swarm size is fixed to 10 particles. In a purpose of comparison an ethanol MUT has been tested and our proposed approach has been compared to Debye model (6) with these parameters $\epsilon_\infty=4.3$, $\epsilon_s=25$ and $\tau=170\text{ps}$ (Fig. 2).

$$\epsilon(\omega)^* = \epsilon_\infty + \frac{\epsilon_s - \epsilon_\infty}{1 + i\omega\tau} \quad (6)$$

Validation results are presented, a good agreement is found between the Debye model and our model approach results, the impact of calibration is also studied (Fig. 2). Then our approach is used on pork skin tissues (Fig. 3), since a sensibility analysis with reduced sensitivity functions has shown the ability to easily identify both imaginary and real of

the permittivity in the range of frequencies by using the imaginary part or the phase of the reflection coefficient.

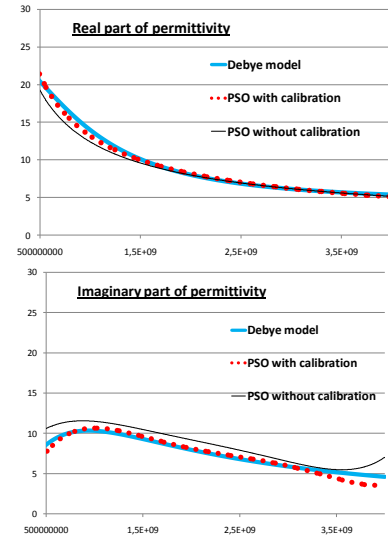


Fig.2. Validation on ethanol sample with and without calibration.

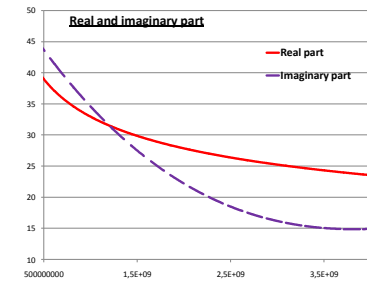


Fig.3. Complex permittivity of pork skin tissues.

IV. CONCLUSIONS AND PERSPECTIVES

Several perspectives of this work are considering. Firstly, a comparison in term of efficiency between the Levenberg Marquardt and the genetic algorithm will be done with application of the sensitivity conclusions. Secondly, the mono-layer approach presented in this paper will be enhanced for applications on bi-layered or multi-layered MUT and thirdly a micro coaxial probe will be developed.

V. ACKNOWLEDGMENT

This work is wholly supported by French National Agency (ANR) through Jeunes Chercheuses Jeunes Chercheurs Program (Project BioRFmod n°ANR-06-JCJC-0124).

VI. REFERENCES

- [1] N. Siauve, L. Nicolas, C. Vollaive, A. Nicolas and J.A. Vasconcelos, "Optimization of 3D SAR distribution in local hyperthermia", *IEEE Trans. on Magnetics*, 40(2): 1264-1267, 2004.
- [2] M.S. Venkatesh and G.S.V. Raghavan, "An overview of dielectric properties measuring techniques", *Can. Biosyst. Eng.*, 47, 2005.
- [3] M. Scheffler and M. Dressel, "Broadband microwave spectroscopy in Corbino geometry for temperatures down to 1.7K", *Rev. Sci. Instrum.* 76, 074702, 2005.
- [4] E. Ritz and M. Dressel, "Analysis of broadband microwave conductivity and permittivity measurements of semiconducting materials", *J. Appl. Phys.* 103, 084902, 2008.
- [5] R. Eberhart and J. Kennedy, "A new optimizer using particle swarm theory", *IEEE Proceedings Sixth International Symposium on Micro Machine and Human Science*, pp. 39-43, 1995.

Analysing the Relevant Features of GPR Scattered Waves in Time- and Frequency-Domain

X. L. Travassos Jr¹, D. A. G. Vieira², Vasile Palade³, and N. Ida⁴

¹SENAI - Centro Integrado de Manufatura e Tecnologia, Bahia, Brazil

²Department of Electrical Engineering, Federal University of Minas Gerais, Brazil

³Computing Laboratory, Oxford University, UK

⁴Department of Electrical and Computer Engineering, The University of Akron, USA

Abstract—his paper studies the relevance of features in time- and frequency-domain given a scattered Ground Penetrating Radar (GPR) wave. This wave is used to identify inclusions, such as reinforcement bars and fissures, in concrete structures. The right choice of features is fundamental to the design of intelligent machines to support the detection, qualification and quantification of fissures. This work analyses the problem of classifying the material inside a concrete structure, which may be conductor, water or air. Both noiseless and features selected given a white Gaussian noise are considered. Many features were extracted and those selected are presented, indicating that the features in the frequency-domain are the most relevant.

Index Terms—Ground Penetrating Radar, Inverse Problems, Noise, Neural Networks, Multiobjective Training Algorithms.

I. INTRODUCTION

As existing concrete structures age, effective inspection has become a greater issue due to environmental, economical and socio-political aspects. Virtually all concrete structures exposed to natural environments experience deterioration over time. Consequently, passive concrete facilities will have to demonstrate that they are capable of continuing to fulfil their intended function with an adequate level of safety when seeking to extend their operating life. Better ways of doing this evaluation can avoid tragedies and decrease maintenance cost. This paper is based on the use of Ground Penetrating Radar (GPR) techniques together with machine learning techniques to support the detection of faults in a non-destructive way. This is known as one of the best options to detect fissures in concrete structures [1]. Even though the reflected wave amplitude is a good feature to detect the presence of inclusions, it is not sufficient to determine properties such as its geometry.

In [2] it was empirically proposed the use of three features to train a Neural Network (NN) classifier. Even though they proved useful in a homogenous problem, they were not successful when non-homogenous host media were considered [3]. The non-homogenous medium is a better representation of a real concrete structure but it brings more variables to the problem. The most important problem when working with many variables and NN is the difficulty to process the vast data set in high-dimensional space. The Parallel Layer Perceptron (PLP) network [4] was applied as the main classifier in [3].

The approach presented here is to use the feature selection algorithms, Simba and Relief [5], to select parameters from a scattered GPR wave. These are based on the concept of margin

to define the relevant features of the data. Both algorithms have selected similar parameters as the most important, and these are presented. The inclusions were considered to be conductor, water or air given both noiseless and noisy situations. The results show that features in the frequency-domain are the most relevant and that they are also more robust in the presence of noise than those in the time-domain. The purpose of this work is to increase the level of information extracted in the non-destructive evaluation of concrete structures by using intelligent systems and electromagnetic field computation.

II. FEATURE SELECTION

Feature selection (also known as subset selection) is a process commonly used in machine learning, wherein a subset of the features available from the data are selected for application of the learning algorithm. The best subset contains the least number of dimensions that most contribute to accuracy; we discard the remaining, unimportant dimensions. This is an important stage of pre-processing and is one of two ways of avoiding the well known curse of dimensionality (the other is feature extraction). Feature selection is, therefore, the task of choosing a small subset of features which is sufficient to predict the target labels. This step is fundamental to build reliable classifiers.

Feature selection aims at choosing for a given data set a sub-set which can capture the relevant information. The choice of features is important to avoid the curse of dimensionality and, therefore, guarantee good convergence of the learning machines. It can also provide some understanding concerning the nature of the problem, as it indicates the main physical properties needed to classify an underground target. This paper will consider feature selection algorithms based on the filter model to feature selection, Relief and Simba [5]. In this case the feature selection is a type of pre-processing, using some pre-defined cost function, suchh as the separation margin of classes.

III. THE GPR PROBLEM

For radar assessment of concrete, the objective is to determine the features needed to characterize inclusions in a dielectric slab by identifying electrical (permittivity and conductivity) and geometrical (depth and radii) properties. The computation of the electric field is done by the FDTD method

as forward solver. A data set obtained with a FDTD model with 1071 samples of the reflected wave from cylindrical inclusions buried in a non-homogeneous concrete model was considered [3]. The depth was defined in the range [0.05:0.010:0.25]m and the radius [0.02:0.005:0.1]m. Water, air and conductor inclusions were considered. From the reflected wave, 14 features were selected. The following were selected in the time-domain:

- delay of the first reflection (Delay) [2],
- maximum amplitude (max(W)) [2],
- reflected wave mean (mean(W)),
- reflected wave standard deviation (std(W)),
- mean of the wave derivative (mean(dW)),
- standard deviation of the wave derivative (std(dW)).

Using the Fourier Transform of the reflected wave the following features were extracted in the frequency-domain:

- maximum amplitude of the Fourier transform (mFFT),
- frequency of maximum amplitude of the Fourier transform (fmFFT),
- energy in six different bands (B_1, B_2, \dots, B_6) of the Fourier transform.

Some features are shown in Fig. 1.

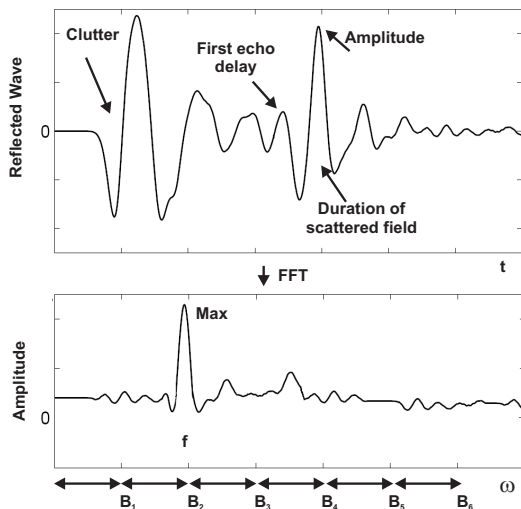


Fig. 1. Parameters considered for Simba and Relief algorithms in both time- and frequency-domain.

IV. RESULTS

The experiments produced the reflected waves from cylindrical inclusions with and without a white Gaussian noise of 6 dB signal-to-noise ratio. Water/Air/Conductor discrimination was evaluated, taken in pairs. The results are outlined in Tables I and II where F_1 indicates the most relevant feature and F_4 the fourth one. The remarkable point is that both algorithms, which are based on different concepts of feature selection, have selected the same set of features but with different ordering. This can help separate the clutter from the target reflections

since each feature is related with a different aspect of the problem. It is also interesting that most of the features are related to the frequency-domain. In the noisy situation they are more robust than, for instance, the amplitude and the first delay, which are hard to calculate given some noise.

TABLE I
SUMMARY OF THE RESULTS WITHOUT NOISE.

Inclusions	Method	F_1	F_2	F_3	F_4
Water/Air	Relief	mFFT	fmFFT	Delay	B_1
Water/Air	Simba	fmFFT	Delay	mFFT	B_1
Water/Cond.	Relief	mFFT	fmFFT	max(W)	Delay
Water/Cond.	Simba	mFFT	fmFFT	B_1	B_2
Air/Cond.	Relief	fmFFT	Delay	mean(dW)	mean(W)
Air/Cond.	Simba	fmFFT	Delay	mFFT	B_1

TABLE II
SUMMARY OF THE RESULTS WITH A 6dB SNR WHITE GAUSSIAN NOISE.

Inclusions	Method	F_1	F_2	F_3	F_4
Water/Air	Relief	mFFT	B_1	fmFFT	std(W)
Water/Air	Simba	mFFT	fmFFT	B_2	B_6
Water/Cond.	Relief	mFFT	fmFFT	B_1	B_3
Water/Cond.	Simba	mFFT	B_1	fmFFT	std(W)
Air/Cond.	Relief	fmFFT	mFFT	max(W)	Delay
Air/Cond.	Simba	fmFFT	mFFT	B_1	max(W)

V. CONCLUSION

This paper introduced the use of feature selection algorithms in the study of the GPR reflected waves. The feature subset selection problem in supervised learning for a non-homogeneous GPR problem was described, which involves identifying the relevant or useful features in a dataset obtained by electromagnetic field computation and providing only that subsets to the learning algorithm. In addition, the relevance and irrelevance of features was investigated, and two degrees of relevance: weak and strong were defined.

Water, air and conductor inclusions were considered as non homogeneous media. The conditions were considered in the presence of Gaussian noise as well as in the absence of noise. Many features were considered in the study. Some features were extracted in the time-domain, others in the frequency-domain. Two different algorithms were applied and showing consistent results. The results indicate that the features in the frequency-domain are more relevant and more robust in the presence of noise. These results support our claim that subset selection can improve accuracy, and that this approach can help separate clutter from buried targets information.

REFERENCES

- [1] D. J. Daniels, *Ground Penetrating Radar*, The Institute of Electrical Engineers, London, 2004.
- [2] S. Caorsi and G. Cevini, *An electromagnetic approach based on neural networks for the GPR investigation of buried cylinders*, IEEE Geoscience and Remote Sensing Letters, v.2, n.1, pp. 3-7, January 2005.
- [3] L. Travassos, D. A. G. Vieira, N. Ida, C. Vollaire and A. Nicolas, *Characterizing inclusions in a non-homogenous GPR problem by Neural Networks*, IEEE Trans. on Magnetics, v. 44, pp 1630-1633, 2008.
- [4] W. M. Caminhas, D. A. G. Vieira and J. A. Vasconcelos, *Parallel layer perceptron*, Neurocomputing, v. 55, n.3-4, pp. 771-778, October 2003.
- [5] K. Kira and L. Rendell, *Feature selection: Evaluation, application and small sample performance*. IEEE PAMI, v. 21, n. 3, pp. 153-158, 1997.

Recent achievements on a DGTD method for time domain electromagnetics

Hassan Fahs, Loula Fezoui and Stéphane Lanteri
 INRIA Sophia Antipolis-Méditerranée
 06902 Sophia Antipolis Cedex, France
 Hassan.Fahs@inria.fr, Loula.Fezoui@inria.fr
 Stephane.Lanteri@inria.fr

Victorita Dolean and Francesca Rapetti
 J.A. Dieudonné Mathematics Laboratory (UMR CNRS 6621)
 University of Nice-Sophia Antipolis
 06108 Nice Cedex 02, France
 dolean@unice.fr, frapetti@unice.fr

Abstract—We report on recent results concerning the development of a discontinuous Galerkin time domain (DGTD) method for the solution of the system of Maxwell equations in general domains and heterogeneous propagation media. This DGTD method is formulated on simplicial meshes (triangles in 2D and tetrahedra in 3D). Within each mesh element, the electromagnetic field components are approximated by an arbitrarily high order nodal polynomial interpolation while time integration is achieved either by an explicit or an hybrid explicit-implicit scheme.

I. INTRODUCTION

Nowadays, a variety of methods exist for the numerical treatment of the time domain Maxwell equations ranging from the well established finite difference time domain (FDTD) methods [1] to finite element time domain (FETD) methods [2] and discontinuous Galerkin time domain (DGTD) methods. In the recent years, there has been an increasing interest in the latter methods due their ability to easily deal with unstructured meshes. Besides, when combined with explicit time stepping schemes, DGTD methods lead to block diagonal mass matrices, a feature which is often recognized as one of the main advantages with regards to classical FETD methods. Such DGTD methods have been developed on quadrangular/hexahedral [3] and triangular/tetrahedral [4] meshes. In this paper, we report on some recent achievements concerning the development of a high order DGTD- \mathbb{P}_p method on simplicial meshes that was originally introduced in [5]. We first present results regarding the design of a hp -like DGTD method that allows for both a non-conforming local refinement of the mesh and a local definition of the approximation order. Then, we discuss issues related to the definition of a time stepping strategy for overcoming grid-induced stiffness in a DGTD method. The works discussed here are continuations of preliminary studies respectively presented in [6] and [7].

II. NON-CONFORMING DGTD METHOD

One of the distinguishing features of a DGTD method is that it can easily accommodate a non-conforming locally refined mesh (*i.e.* h -refinement) as well as a local definition of the approximation order (*i.e.* p -enrichment), or of both of them in the context of hp -adaptive solution strategy. In [6] we have reported on the lessons from a preliminary investigation of a h -refinement non-conforming DGTD method, by mainly

concentrating on stability issues. The non-conforming DGTD method discussed in [6] combines a centered scheme for the evaluation of the integral term defined on the interface between neighboring elements of the mesh, with a second order leap-frog scheme for time integration. The resulting DGTD method is non-dissipative and stable under a CFL-like condition. Thereafter, this initial study has progressed towards the development of a hp -like DGTD method combining h -refinement and p -enrichment, in the context of the solution of the 2D Maxwell equations.

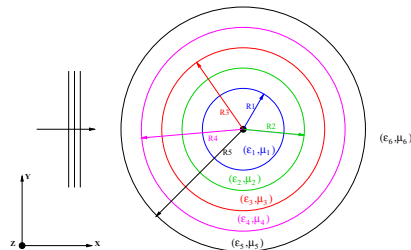


Fig. 1. Scattering of a plane wave by a multi-layered dielectric cylinder. Problem setting and computational domain.

We illustrate the capabilities of the resulting hp -like DGTD method by considering the simulation of the scattering of a plane wave ($F=300$ MHz) by a multi-layered dielectric cylinder (see Fig. 1). Each layer consists of a dielectric non-magnetic material, with $\epsilon_i > 1$ for $2 \leq i \leq 5$ and $\epsilon_1 = \epsilon_6 = 1$ (relative values). We first construct a conforming mesh consisting of 14401 nodes and 28560 triangles and we use different DGTD- \mathbb{P}_p methods, where the interpolation order p is uniform in space. Then, a non-conforming mesh is obtained by locally refining a coarse conforming mesh where the level of refinement depends on the local wavelength in each region. The resulting non-conforming mesh consists of 27640 triangles and 14441 nodes in which 920 are hanging nodes. In that case, the interpolation order is allowed to vary across the layers. Results are shown on Fig. 2 in terms of the x -wise 1D distribution along $y = 0.0$ m of the E_z component. One can observe that the proposed non-conforming DGTD method treats very well the steep variations of the field at the material interfaces.

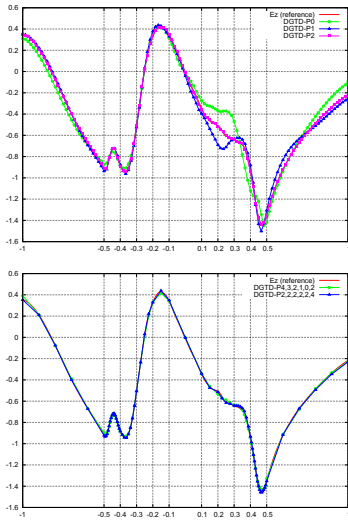


Fig. 2. Scattering of a plane wave by a multi-layered dielectric cylinder. 1D distribution of E_z along $y = 0$. Conforming (top) and non-conforming (bottom) DGTD- \mathbb{P}_i methods.

III. HYBRID EXPLICIT-IMPLICIT DGTD METHOD

Existing DGTD methods generally rely on explicit time integration schemes and are thus constrained by a stability condition that can be very restrictive on highly refined meshes, and when the local approximation relies on high order polynomial interpolation. An implicit time integration scheme is a natural way to obtain a time domain method which is unconditionally stable, but at the expense of the inversion of a global linear system at each time step. A more viable approach consists in applying an implicit time integration scheme locally in the refined regions of the mesh, while preserving an explicit time scheme in the complementary part. Such a hybrid explicit-implicit DGTD method has been proposed by Piperno in [8]. In this method, the elements of the mesh are assumed to be partitioned into two subsets, \mathcal{S}_i and \mathcal{S}_e , on the basis of an appropriate geometrical criterion. Then, the elements of \mathcal{S}_i are handled using a Crank-Nicolson scheme while those of \mathcal{S}_e are time advanced using a variant of the classical leap-frog scheme known as the Verlet method (see [8] for more details). We have recently completed a stability analysis of this method and subsequently implemented it for the solution of the 2D and 3D time domain Maxwell equations discretized in space by a high order conforming DGTD- \mathbb{P}_p method on simplicial meshes.

The effectiveness of the resulting hybrid explicit-implicit DGTD- \mathbb{P}_p method is demonstrated here by considering the simulation of the propagation of an electromagnetic wave emitted by a localized dipole type source in a heterogeneous geometrical model of head tissues (see Fig. 3). The underlying tetrahedral mesh consists of 61358 vertices and 366208 elements. The non-uniformity of this mesh can be assessed by evaluating the ratio between the maximum and minimum values of the local time step which is approximately equal to 135 in the present case. In particular, the smallest elements

of the mesh are in the vicinity of the source (localized near the right ear) and in the skin thickness. For the particular choice of geometric criterion adopted for this simulation, the distribution of mesh tetrahedra is such that $|\mathcal{S}_e| = 5142$ and $|\mathcal{S}_i| = 361066$ and the implicit elements are time advanced with a global time step which is approximately 4.7 times larger than the smallest time step of the mesh. The linear system of equations associated to the implicit elements is solved using an optimized sparse direct solver. The factorization of the implicit matrix is performed once for all before entering the time stepping loop and the resulting L and U factors are used for triangular solves at each time step. The simulations have been carried out on a workstation equipped with an Intel Xeon 2.3 GHz and 16 GB of RAM. The simulation time for the fully explicit DGTD- \mathbb{P}_1 method is 14 h 22 mn for a total of 42940 time steps, while the corresponding time for the hybrid explicit-implicit DGTD- \mathbb{P}_1 method is 1 h 49 mn for a total of 2780 time steps. The memory overhead induced by the use a sparse direct solver is 774 MB and the time for the factorization of the implicit matrix is 98 sec.

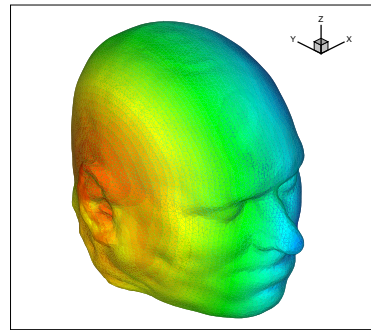


Fig. 3. Head tissues exposure to an electromagnetic wave emitted from a localized source. Contour lines of the normalized SAR in log scale.

REFERENCES

- [1] A. Taflov and S. Hagness, *Computational electrodynamics: the finite-difference time-domain method - 3rd ed.* Artech House Publishers, 2005.
- [2] S. Pernet, X. Ferrières, and G. Cohen, "High spatial order finite element method to solve Maxwell's equations in time-domain," *IEEE Trans. Antennas and Propag.*, vol. 53, no. 9, pp. 2889–2899, 2006.
- [3] G. Cohen, X. Ferrières, and S. Pernet, "A spatial high order hexahedral discontinuous Galerkin method to solve Maxwell's equations in time-domain," *J. Comput. Phys.*, vol. 217, no. 2, pp. 340–363, 2006.
- [4] J. Hesthaven and T. Warburton, "Nodal high-order methods on unstructured grids. I. Time-domain solution of Maxwell's equations," *J. Comput. Phys.*, vol. 181, no. 1, pp. 186–221, 2002.
- [5] L. Fezoui, S. Lanteri, S. Lohrengel, and S. Piperno, "Convergence and stability of a discontinuous Galerkin time-domain method for the 3D heterogeneous Maxwell equations on unstructured meshes," *ESAIM: Math. Model. Numer. Anal.*, vol. 39, no. 6, pp. 1149–1176, 2005.
- [6] H. Fahs, L. Fezoui, S. Lanteri, and F. Rapetti, "Preliminary investigation of a non-conforming discontinuous Galerkin method for solving the time-domain Maxwell equations," *IEEE Trans. Magn.*, vol. 44, no. 6, pp. 1254–1257, 2008.
- [7] A. Catella, V. Dolean, and S. Lanteri, "An unconditionally stable discontinuous Galerkin method for solving the 2D time-domain Maxwell equations on unstructured triangular meshes," *IEEE Trans. Magn.*, vol. 44, no. 6, pp. 1250–1253, 2008.
- [8] S. Piperno, "Symplectic local time stepping in non-dissipative DGTD methods applied to wave propagation problem," *ESAIM: Math. Model. Num. Anal.*, vol. 40, no. 5, pp. 815–841, 2006.

Detection of Defects in Wiring Networks using Time Domain Reflectometry

M. K. Smail¹, L. Pichon¹, M. Olivas², F. Auzanneau², and M. Lambert³

¹Laboratoire de Génie Electrique de Paris, UMR 8507 CNRS, SUPELEC,

Université Paris-Sud, Université Pierre et Marie Curie, 11 rue Joliot-Curie, 91192 Gif-sur Yvette cedex, France

²CEA-LIST, Laboratoire de Fiabilisation des Systèmes Embarqués, 91191 Gif-sur-Yvette cedex, France

³Laboratoire des Signaux et Systèmes, UMR 8506, CNRS, SUPELEC, Université Paris-Sud

3 rue Joliot-Curie, 91192 Gif-sur-Yvette cedex, France

mostafa.smail@lgep.supelec.fr

Abstract — A new technique is proposed to reconstruct faulty wiring networks from the time domain reflectometry response. The developed method is also for characterization of defects in the branches of the network. The direct problem (propagation along the cables) is modelled by RLCG circuit parameters computed by finite elements (FEM) and the Finite Difference Time Domain (FDTD) method. Genetic Algorithms (GAs) are used to solve the inverse problem. The proposed method allows to accurately locating wire faults. Some examples are presented to validate and illustrate the ability of this reconstruction method.

I. INTRODUCTION

Aging wiring in cars, aircraft, trains, and other transportation mean is identified as a critical security area. Fault location in wiring is a major cause for concern in automotive health maintenance. As automotive wires age increases they become brittle and are subject to several electrical, chemical and mechanical stresses. This leads to the occurrence of defects in the wiring. Wiring networks can be affected with two types of faults: “soft ones” are created by the change of the impedance along the line due to simple deformation in the wire, “hard faults” such as open and short circuits. For the first type of faults, the reflectometry response of the faulty network presents a simple deviation or variation versus the impedance of the fault, in the defects location. In the case of hard faults the structure of network as well as the response changes. According to the application domain, the defects of cables may have catastrophic consequence [1].

There are several emerging technologies that may help to locate and characterize the fault on the wires [1]-[3]. The most widely used technique for testing wires is reflectometry. It is based on the same principle that radar. A high frequency electrical signal is sent down the wire, where it reflects from any impedance discontinuity such as open or short circuits. The difference (time delay or phase shift) between the incident and reflected signal is used to locate the fault on the wire. However the reflectometry response itself is not self-sufficient to identify and locate the defects in the wire. There is the need to solve efficiently the inverse problem which is to deduce knowledge about the defects from the response at the input of the line. For such analysis an adequate wave propagation model is required in order to simulate the response of the line.

The novelty of this paper is to propose an efficient method for the detection, characterization and localization of defects in faulty wiring networks using the time domain reflectometry response and genetic algorithms. As a first step a suitable model describes the propagation of the electromagnetic wave along multiconductors transmission lines (MTL) in the time domain: the model is based on the telegrapher’s equations where the per-unit-length electrical parameters matrices of R, L, C and G are computed by a finite element technique. Then the wave propagation equations are solved with the Finite Difference Time Domain (FDTD) method. In order to deal with the inverse problem a genetic algorithm is used to minimize the error between the reflectometry response and the response given by the direct model. Several examples illustrate the ability of the proposed approach.

II. WAVE PROPAGATION MODEL

The propagation in a multiconductor transmission line (including n conductors) can be modelled by a RLCG circuit model [4] and is governed by the telegrapher’s equations (MTL equations):

$$\frac{\partial}{\partial z} V(z, t) = -R \cdot I(z, t) - L \cdot \frac{\partial}{\partial t} I(z, t) \quad (1)$$

$$\frac{\partial}{\partial z} I(z, t) = -G \cdot V(z, t) - C \cdot \frac{\partial}{\partial t} V(z, t) \quad (2)$$

where V and I are $n \times 1$ vectors of the line voltages and line currents, respectively. The position along the line is denoted as z and time is denoted as t . The $n \times n$ matrices R (resistance), L (inductance), C (capacitance) and G (conductance) contain the per-unit-length parameters. The coefficients of these matrices are computed either with a 2D finite element approach for the case of uniform transmission lines or with a full wave approach for more complex configurations [5]. The case of twisted wire cables is treated with the approach developed in [6]. The time-domain analysis of the MTL is determined by the Finite Difference Time Domain (FDTD) method which converts the differential equations into recursive finite difference equations.

III. RESULTS

In the problem, both the reflectometry response (measured or simulated) and the direct model are used to characterize the defects or reconstruct the wiring network.

3. Wave Propagation

From the reflectometry data of the wiring network under test, the methodology leads to solve an inverse problem: GA's are used to minimize the objective function F given by:

$$F(v) = \left\{ \int_0^T \frac{|v^{\text{TDR}}(t) - v^{\text{Mod}}(t)|^2}{|v^{\text{TDR}}(t)|^2} dt \right\}^{1/2} \quad (3)$$

where $v^{\text{TDR}}(t)$ is the given initial impulse response and $v^{\text{Mod}}(t)$ the response given by the direct model.

A. Identification of modified local impedance

The faulty network shown in figure 1 is first considered. The terminations of the branches are open circuits. It is assumed to be affected by a single defect. The reflectometry response used as the input of GA corresponds to a defect located at 2 m from the input. The change of impedance (due to the defect) is respectively of the order 10%, 20% and 60% of the characteristic impedance of the healthy wire. Figure 2 illustrates the time variation of the signals corresponding to the characteristics of the defects deduced from GA.

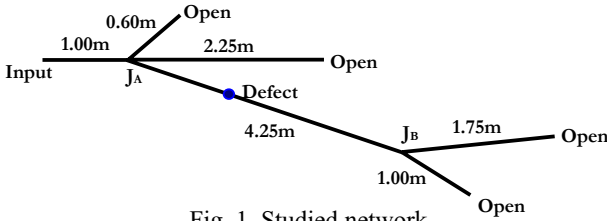


Fig. 1. Studied network

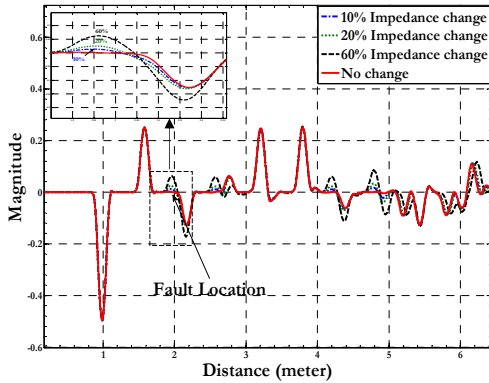


Fig. 2. Time Domain Reflectometry response

B. Reconstruction of a wiring network

This second example illustrates the performances of the approach for the reconstruction of a network (location of hard faults). The healthy wiring network of figure 1 is considered. The reflectometry response used as the input is obtained from measurements provided by a vector network analyzer in frequency domain. The parameters of GA are the lengths of the different branches $L = [L_1, L_2, \dots, L_i]$ with i is the total number of branch. Figure 3 shows the reconstructed network and Figure 4 compares the reflectometry response of the healthy network (measurements data) and the reconstructed one.

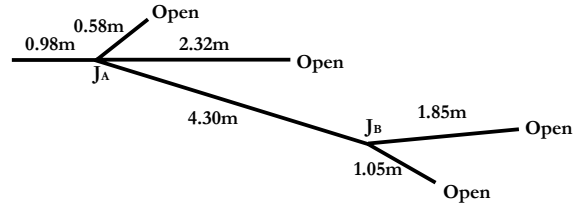


Fig. 3. Reconstructed network.

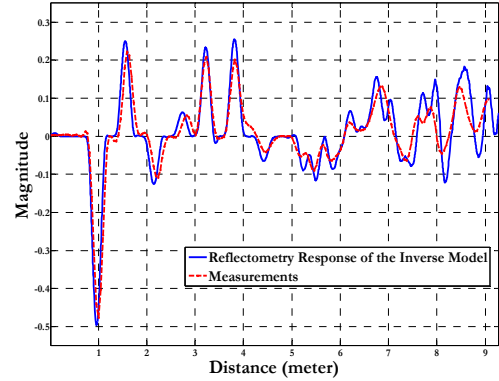


Fig. 4. Comparison between the reflectometry responses of the network reconstructed with GA with the healthy version.

IV. CONCLUSION

This paper describes a numerical model and an inverse procedure dedicated to time domain reflectometry for the location and characterization of defects in wiring networks. The work addresses both the modification of local impedance and the reconstruction of faulty wiring networks affected by hard faults.

ACKNOWLEDGMENT

This work is part of the project SEEDS (Smart Embedded Electronic Diagnosis Systems), in cooperation between Delphi, Serma Ingénierie, MondiTech, Renault Trucks, CEA-LIST, INRIA, LGEP and supported by the RTRA Digiteo and Région Ile de France.

REFERENCES

- [1] C. Furse, Y. C. Chung, C. Lo, and P. Pendaraya, "A Critical Comparison of Reflectometry Methods for Location of Wiring Faults," *Journal of Smart Structures and System*, vol.2, no.1, pp. 25-46, 2006.
- [2] C. Furse, Y. C. Chung, R. Dangol, M. Nielsen, G. Mabey and R. Woodward, "Frequency Domain Reflectometry for On Board Testing of Aging Aircraft Wiring," *IEEE Transactions on Electromagnetic Compatibility*, vol. 45, no. 2, pp. 306-315, May 2003.
- [3] C. Bucella, M. Feliziani and G. Manzi, "Detection and Localization of Defects in Shielded Cables by Time-Domain Measurements With UWB Pulse Injection and Clean Algorithm Postprocessing," *IEEE Transactions on Electromagnetic Compatibility*, vol. 46, no.4, pp. 597-605, 2004.
- [4] C R. Paul, *Analysis of Multiconductor Transmission Lines*, New York: Wiley, 1994.
- [5] C. Bucella, M. Feliziani, G. Manzi, "Three-Dimensional FEM Approach to Model Twisted Wire Pair Cables", *IEEE Transactions on Electromagnetic Compatibility*, vol. 43, no.4, pp. 1373-1376, 2007.
- [6] B. Essakhi, J. Benel, F. Duval, G. Akoun, B. Mazari and L. Pichon, "Interconnect Macromodeling from 3D Field Computation," *IEEE Transactions on Magnetics*, vol.44, no.6, pp. 1454-1457, 2008

Finite Element Multiharmonic Modelling for Nonlinear Optics

Pierre Godard

Aix-Marseille Université
Ecole Centrale de Marseille
CNRS, Institut Fresnel UMR 6133
F-13397 Marseille cedex 20, France

Frédéric Zolla

Aix-Marseille Université
Ecole Centrale de Marseille
CNRS, Institut Fresnel UMR 6133
F-13397 Marseille cedex 20, France

André Nicolet

Aix-Marseille Université
Ecole Centrale de Marseille
CNRS, Institut Fresnel UMR 6133
F-13397 Marseille cedex 20, France
Email: <http://www.fresnel.fr/perso/nicolet/>

Abstract—In this paper, we present a multiharmonic model able to take into account general nonlinear optical media [1]. As a particular example, two- and three-photon processes are considered here. The numerical model is based on the finite element method that allows to take into account the inhomogeneities of the refraction index due to the nonlinearities. It consists of several harmonic equations at various frequencies coupled via some nonlinear terms.

I. MULTIHARMONIC NONLINEAR MODEL

In this paper, we propose a numerical model for nonlinear optics based on a systematic approach of the nonlinearity in the frequency domain together with a very general setting via the finite element method. This model aims at applications in nanophotonics since the size of the scattering objects are of the same order of magnitude as the wavelength of the incident waves that are infrared or visible light. Considering a given incident monochromatic electric field of pulsation ω_I , we would like to solve the nonlinear vector wave equation:

$$\nabla \times (\mu^{-1} \nabla \times \mathbf{E}) + \partial_t^2 \mathbf{D} = 0.$$

for a given geometry and where the material properties are $\mathbf{D} = \varepsilon_0 \mathbf{E} + \mathbf{P}$ and $\mathbf{B} = \mu_0 \mathbf{H}$. We assume here that the polarization \mathbf{P} is of the form:

$$\begin{aligned} \mathbf{P}(\mathbf{s}, t) = & \mathbf{P}^{(0)}(\mathbf{s}) + \\ & \sum_{n \in \mathbb{N}} \varepsilon_0 \int_{-\infty}^{\infty} d\omega_1 \cdots \int_{-\infty}^{\infty} d\omega_n \chi^{(n)}(\mathbf{s}, \omega_1, \dots, \omega_n) \\ & \hat{\mathbf{E}}(\mathbf{s}, \omega_1) \cdots \hat{\mathbf{E}}(\mathbf{s}, \omega_n) e^{-i(\omega_1 + \dots + \omega_n)t}, \end{aligned}$$

where $\hat{\mathbf{E}}(\mathbf{s}, \omega)$ is the Fourier transform of $\hat{\mathbf{E}}$ with respect to time. We set $\mathbf{E}_p := \hat{\mathbf{E}}(\mathbf{s}, p\omega_I)$ and we note that $\mathbf{E}_{-p} = \bar{\mathbf{E}}_p$. The $\chi^{(n)}$ tensors describe the physical behaviour of the media. We now make the simplifying assumption that $\chi^{(n)}(\omega_1, \dots, \omega_n) = 0$ if $\omega_i \neq p\omega_I$, $p \in \mathbb{Z}$ so that the electric field is $\mathbf{E}(\mathbf{s}, t) = \sum_{p \in \mathbb{Z}} \mathbf{E}_p(\mathbf{s}) e^{-ip\omega_I t}$. To further simplify and to obtain tractable problems, we set $\chi^{(n)} = 0$ if $n > 3$. We introduce the following notations for the nonlinear terms involving the $\chi^{(n)}$:

$$[\mathbf{E}_{p_1}, \dots, \mathbf{E}_{p_n}]_{\omega_I} := \chi^{(n)}(p_1\omega_I, \dots, p_n\omega_I) \mathbf{E}_{p_1} \cdots \mathbf{E}_{p_n}$$

and for the linear part \mathcal{M}_p^{lin} of the wave operators:

$$\mathcal{M}_p^{lin}(\mathbf{E}_p) := -c^2 \nabla \times (\nabla \times \mathbf{E}_p) + (p\omega_I)^2 \varepsilon_r^{(1)}(p\omega_I) \mathbf{E}_p$$

where $\varepsilon_r^{(1)} = 1 + \chi^{(1)}$. With the previous assumptions, the time domain problem becomes an infinite set of coupled harmonic equations:

$$\begin{aligned} \mathcal{M}_p^{lin}(\mathbf{E}_p) + (p\omega_I)^2 \left(\sum_{q \in \mathbb{Z}} [\mathbf{E}_q, \mathbf{E}_{p-q}] + \right. \\ \left. \sum_{(q,r) \in \mathbb{Z}^2} [\mathbf{E}_q, \mathbf{E}_r, \mathbf{E}_{p-q-r}] \right) = 0, \quad \text{for } p \in \mathbb{Z}. \end{aligned}$$

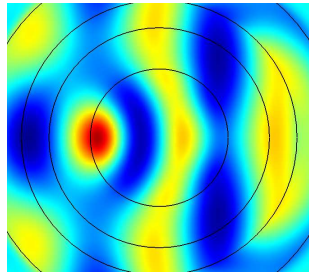
Moreover, we limit our nonlinear phenomena to two- and three-photon processes. The corresponding problems are encountered in numerous nonlinear optics experiments involving second and third harmonic generation. Therefore we have $p \in \{-3, -2, -1, 1, 2, 3\}$, and a system of three coupled nonlinear equations is obtained:

$$\begin{aligned} \mathcal{M}_1^{lin}(\mathbf{E}_1) \\ + \omega_I^2 \left(2[\mathbf{E}_3, \mathbf{E}_{-2}] + 2[\mathbf{E}_2, \mathbf{E}_{-1}] \right. \\ + 6[\mathbf{E}_3, \mathbf{E}_1, \mathbf{E}_{-3}] + 3[\mathbf{E}_3, \mathbf{E}_{-1}, \mathbf{E}_{-1}] + 3[\mathbf{E}_2, \mathbf{E}_2, \mathbf{E}_{-3}] \\ \left. + 6[\mathbf{E}_2, \mathbf{E}_1, \mathbf{E}_{-2}] + 3[\mathbf{E}_1, \mathbf{E}_1, \mathbf{E}_{-1}] \right) = 0, \end{aligned}$$

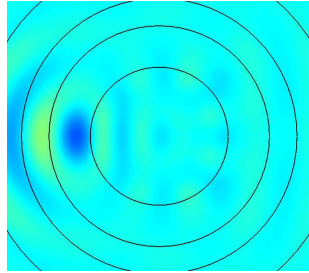
$$\begin{aligned} \mathcal{M}_2^{lin}(\mathbf{E}_2) \\ + (2\omega_I)^2 \left(2[\mathbf{E}_3, \mathbf{E}_{-1}] + [\mathbf{E}_1, \mathbf{E}_1] \right. \\ + 6[\mathbf{E}_3, \mathbf{E}_2, \mathbf{E}_{-3}] + 6[\mathbf{E}_3, \mathbf{E}_1, \mathbf{E}_{-2}] + 3[\mathbf{E}_2, \mathbf{E}_2, \mathbf{E}_{-2}] \\ \left. + 6[\mathbf{E}_2, \mathbf{E}_1, \mathbf{E}_{-1}] \right) = 0, \end{aligned}$$

$$\begin{aligned} \mathcal{M}_3^{lin}(\mathbf{E}_3) \\ + (3\omega_I)^2 \left(2[\mathbf{E}_2, \mathbf{E}_1] \right. \\ + 3[\mathbf{E}_3, \mathbf{E}_3, \mathbf{E}_{-3}] + 6[\mathbf{E}_3, \mathbf{E}_2, \mathbf{E}_{-2}] + 6[\mathbf{E}_3, \mathbf{E}_1, \mathbf{E}_{-1}] \\ \left. + 3[\mathbf{E}_2, \mathbf{E}_2, \mathbf{E}_{-1}] + [\mathbf{E}_1, \mathbf{E}_1, \mathbf{E}_1] \right) = 0. \end{aligned}$$

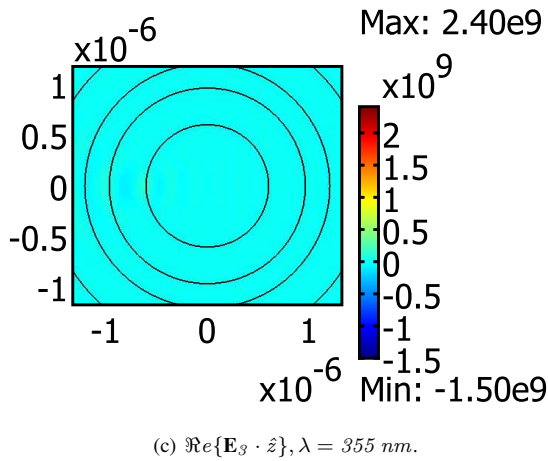
A geometry invariant along the z -axis and an appropriate principal axis for the $\chi^{(n)}$ tensors are considered here together with a polarization of the electric field along this axis in order to reduce the problem to a scalar two-dimensional one. The numerical implementation is performed in COMSOL Multiphysics with triangular finite elements. The incident field is a plane wave imposed via a virtual antenna [2], a special



(a) $\Re\{\mathbf{E}_1 \cdot \hat{z}\}, \lambda = 1064 \text{ nm}.$



(b) $\Re\{\mathbf{E}_2 \cdot \hat{z}\}, \lambda = 532 \text{ nm}.$

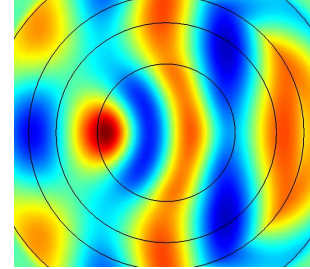


(c) $\Re\{\mathbf{E}_3 \cdot \hat{z}\}, \lambda = 355 \text{ nm}.$

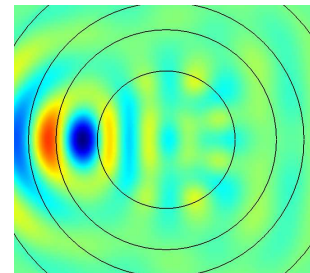
Fig. 1. $A^i = 10^9 \text{ V/m}$: non-linear effects are present in the second harmonic but the retroaction on the fundamental frequency is negligible.

numerical technique specially designed for these nonlinear scattering problems. Fig. 1 shows a circular cylinder (radius= $1\mu\text{m}$) made of BBO (the inner circle). The amplitude of the incident electric field is 10^9 V/m . A second harmonic field appears but the third harmonic field is negligible. On Fig. 2, the amplitude of the incident electric field is 3.10^9 V/m and the second and the third harmonic fields are present with peak values of the same order of magnitude as the one of the fundamental frequency. In this case, a significant amount of energy is transferred from the fundamental frequency to

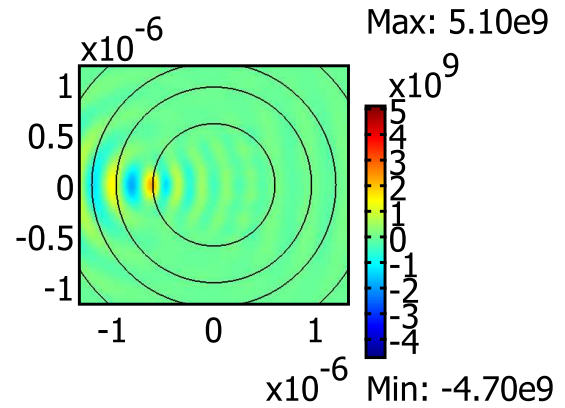
the higher harmonics and the usual assumption of the non depletion of the pump wave is no more valid.



(a) $\Re\{\mathbf{E}_1 \cdot \hat{z}\}, \lambda = 1064 \text{ nm}.$



(b) $\Re\{\mathbf{E}_2 \cdot \hat{z}\}, \lambda = 532 \text{ nm}.$



(c) $\Re\{\mathbf{E}_3 \cdot \hat{z}\}, \lambda = 355 \text{ nm}.$

Fig. 2. $A^i = 3.10^9 \text{ V/m}$: depletion of the pump wave.

REFERENCES

- [1] R.W.Boyd, *Non Linear Optics*, 2nd edition. Academic Press, Amsterdam, 2003.
- [2] P. Godard, F. Zolla, A. Nicolet, *Scattering by a 2-Dimensional Doped Photonic Crystal Presenting an Optical Kerr Effect Photonic Crystal*, COMPEL, to appear.

An Amplitude Finite Element Formulation for Multiple-Scattering by a Collection of Convex Obstacles

C. Geuzaine¹, P. Dular^{1,2}, R. Gaignaire¹ and R. V. Sabariego¹

¹University of Liège, Dept. of Electrical Engineering and Computer Science, B-4000 Liège, Belgium

²Fonds de la Recherche Scientifique, F.R.S.-FNRS, Belgium

E-mail: cgeuzaine@ulg.ac.be

Abstract—We present a multiple-scattering solver for non-convex geometries obtained as the union of a finite number of convex surfaces. The algorithm is a finite element reformulation of the high-frequency integral equation technique proposed in [1]. It is based on an iterative solution of the scattering problem, where each iteration leads to the resolution of a single scattering problem in terms of a slowly oscillatory amplitude.

I. INTRODUCTION

Solving multiple-scattering problems at high frequencies is a challenging problem, especially when the wavelength is significantly smaller than the size of the scattering obstacles.

For non-convex geometries obtained as the union of a finite number of convex surfaces, an efficient algorithm was proposed in [1] based on three main elements: 1) an iteratively computable Neumann series for the currents induced on the scattering surfaces, which accounts rigorously for multiple scattering; 2) a generalized ansatz that allows for *a priori* determination of the highly oscillatory phase of the currents in each term of the series; and 3) use of the single-scattering boundary-integral solver from [2] for the efficient evaluation of each one of the terms in this series.

In this paper we present a reformulation of this algorithm using a finite element approach, which requires a fundamental rethinking of steps 2) and 3) since the fields are to be computed in the volume instead of only on the boundary of the scatterers. This new finite element approach exhibits many interesting features, amongst which possible extensions to non-homogeneous media and more complex geometries. Also, the proposed finite element formulation uses standard basis functions and can thus be easily implemented in existing finite element codes.

II. MULTIPLE-SCATTERING ITERATIONS

We investigate the numerical solution of the time-harmonic acoustic scattering problem of a plane wave $u^{\text{inc}}(\mathbf{x}) = e^{ik\boldsymbol{\alpha}\cdot\mathbf{x}}$, $|\boldsymbol{\alpha}| = 1$, by a collection of impenetrable obstacles $\Omega_p^- \subset \mathbb{R}^2$, $p = 1, \dots, N$, with closed boundaries Γ_p (this is equivalent to solving a TE- or TM-electromagnetic problem in 2D). Setting $\Omega^- = \cup_{p=1}^N \Omega_p^-$, $\Gamma = \cup_{p=1}^N \Gamma_p$ and $\Omega^+ = \mathbb{R}^2 \setminus \overline{\Omega^-}$, the boundary value problem reads:

$$\begin{aligned} \Delta u + k^2 u &= 0 \quad \text{in } \Omega^+, \\ u &= -u^{\text{inc}} \text{ or } \partial_n u = -\partial_n u^{\text{inc}} \quad \text{on } \Gamma, \\ \lim_{|\mathbf{x}| \rightarrow +\infty} |\mathbf{x}|(\nabla u \cdot \frac{\mathbf{x}}{|\mathbf{x}|} - ik u) &= 0. \end{aligned} \quad (1)$$

This work was supported by the Belgian Science Policy under grant IAP P6/21 and by NSF under grant DMS-0609824.

Instead of trying to solve (1) directly, we look for the solution in terms of the series $u = \sum_{m=1}^{\infty} \sum_{p=1}^N u_p^{(m)}$, where $u_p^{(m)}$ is the solution of the problem:

$$\begin{aligned} \Delta u_p^{(m)} + k^2 u_p^{(m)} &= 0 \quad \text{in } \mathbb{R}^2 \setminus \overline{\Omega_p^-}, \\ u_p^{(m)} &= s_p^{(m)} \text{ or } \partial_n u_p^{(m)} = \partial_n s_p^{(m)} \quad \text{on } \Gamma_p, \\ \lim_{|\mathbf{x}| \rightarrow +\infty} |\mathbf{x}|(\nabla u_p^{(m)} \cdot \frac{\mathbf{x}}{|\mathbf{x}|} - ik u_p^{(m)}) &= 0, \end{aligned} \quad (2)$$

with

$$s_p^{(m)} = \begin{cases} -u^{\text{inc}} - \sum_{q=1}^{p-1} u_q^{(m)} & \text{for } m = 1, \\ -\sum_{q=1}^{p-1} u_q^{(m)} - \sum_{q=p+1}^N u_q^{(m-1)} & \text{for } m > 1, \end{cases} \quad (3)$$

In other words, we perform a Gauss-Seidel-type iteration where at each step we solve a scattering problem around the single obstacle Ω_p^- , using the fields scattered from the other obstacles as boundary condition [3]. As each correction $u_p^{(m)}$ can be interpreted as the correction introduced by the m -th wave reflection [1], [3], the iteration can be stopped when the norm of all corrections at step m is smaller than a prescribed tolerance.

Note that instead of performing this Gauss-Seidel iteration, other iterative schemes can be used as well. Indeed, the Dirichlet or Neumann boundary condition in (2) can equivalently be written in vector form as:

$$U^{(m+1)} - AU^{(m)} := F = \begin{cases} -U^{\text{inc}} & m = 1 \\ 0 & m > 1 \end{cases}, \quad (4)$$

where A is the iteration operator acting on the traces of the field, mapping the traces at iteration (m) onto those at iteration $(m+1)$. The desired solution of this problem satisfies

$$(I - A)U^* = F, \quad (5)$$

which can be solved iteratively e.g. with a Krylov subspace method like a preconditioned GMRES. An explicit expression of the iteration operator A in the context of integral equations was given in [1].

III. FINITE ELEMENT SOLUTION

A standard finite element code could be used to solve (2), but the cost of each iteration would be similar to the cost of solving the original problem (1) and this would thus present little practical interest. However, if the obstacles Ω_p^- are convex each step in the iterative process can be accelerated with the phase reduction (PR) procedure proposed in [4],

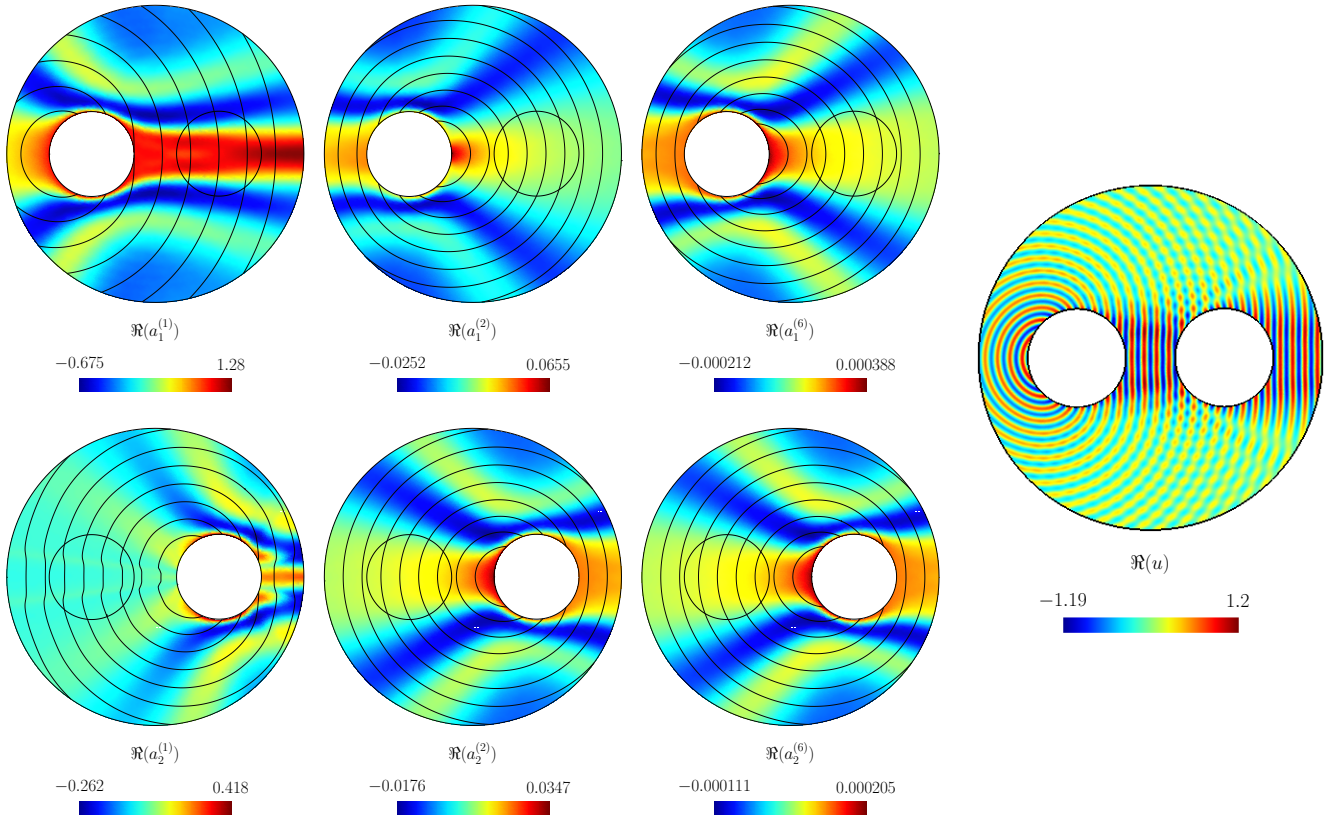


Fig. 1. Iterative solution around two circular cylinders of unit radius R for an incident plane wave arriving from the left, with $kR = 25$. Left: Real part of the amplitudes $a_p^{(m)}$ for $p = 1$ and $p = 2$ (top to bottom) and $m = 1, 2, 6$ (left to right). On each graph iso-curves of the approximate phase $\phi_p^{(m)}$ are superimposed. Right: Real part of the final solution $u = \sum_{m=1}^6 \sum_{p=1}^2 a_p^{(m)} e^{i25\phi_p^{(m)}}$.

[5]. Indeed, if Ω_p^- is convex then (2) amounts to solving a *single scattering* problem in $\mathbb{R}^2 \setminus \Omega_p^-$. The PR procedure approximates the phase $\phi_p^{(m)}$ of the solution of the p -th single scattering problem at iteration m and replaces the original unknown $u_p^{(m)}$ of the single scattering problem with a slowly oscillatory amplitude $a_p^{(m)} = u_p^{(m)} e^{-ik\phi_p^{(m)}}$, which can be represented on a coarse grid.

IV. NUMERICAL TEST

As an example, we consider the scattering of a plane wave e^{ikx} by two circular cylinders of unit radius R , separated by a distance $d = R$. We use a Bayliss-Gunzburger-Turkel-like radiation condition to truncate the infinite domain. Using a prescribed tolerance of 10^{-3} the iterative process converges after 6 iterations. Figure 1 shows, for $kR = 25$, the amplitude $a_p^{(m)}$ and the phase $\phi_p^{(m)}$ for $m = 1, 2, 6$ and $p = 1, 2$, as well as the final solution u .

Of particular notice is how each term in the series is not highly oscillatory and can thus be computed on a coarser grid than the final solution. In this example we used about 2 points per wavelength to compute the approximate phase and the slowly oscillating amplitude, leading to a mesh containing 4300 nodes. The original problem would have required a mesh density of at least 10 points per wavelength, leading to about 25 times more unknowns.

The full paper will provide details on the variational formulation and analyze the results on different geometrical configurations.

REFERENCES

- [1] C. Geuzaine, O. Bruno, and F. Reitich, "On the $\mathcal{O}(1)$ solution of multiple-scattering problems," *IEEE Transactions on Magnetics*, vol. 41, no. 5, pp. 1488–1491, 2005.
- [2] O. Bruno, C. Geuzaine, J. Monro, Jr., and F. Reitich, "Prescribed error tolerances within fixed computational times for scattering problems of arbitrarily high frequency: the convex case," *Philosophical Transactions of the Royal Society (Series A: Mathematical, Physical and Engineering Sciences)*, vol. 362, no. 1816, pp. 629–645, 2004.
- [3] C. T. Tai, "An iterative method of solving a system of linear equations and its physical interpretation from the point of view of scattering theory," *IEEE Transactions on Antennas and Propagation*, pp. 713–714, Sept. 1970.
- [4] C. Geuzaine, J. Bedrossian, and X. Antoine, "An amplitude formulation to reduce the pollution error in the finite element solution of time-harmonic scattering problems," *IEEE Transactions on Magnetics*, vol. 44, no. 6, pp. 782–785, 2008.
- [5] X. Antoine and C. Geuzaine, "Phase reduction models for improving the accuracy of the finite element solution of time-harmonic scattering problems I: General approach and low-order models," *Journal of Computational Physics*, In Press, Available online 21 January 2009.

Finite Element Analysis of Electromagnetic Scattering Using p -Adaption and an Iterative Absorbing Boundary Condition

P. Paul¹, and J. P. Webb²

¹Core CAD Technologies, Intel Corporation

Oregon, USA. Email: prakash.paul@mail.mcgill.ca

²Department of Electrical and Computer Engineering, McGill University

3480 University Street, Montreal, H3A 2A7, Canada. Email: jon.webb@mcgill.ca

Abstract—Solving scattering problems using the finite element method (FEM) introduces two sources of error: from the discretization and from the truncation boundary. Here both errors are addressed in an iterative, balanced way. For the discretization error, p -adaption is used. An *a posteriori* error indicator automatically determines which elements should be increased in order to reduce and equi-distribute the discretization error. For the boundary error, an iterative absorbing boundary condition is applied. The overall scheme starts with low order polynomials and a first order absorbing boundary condition and progressively improves the quality of the solution by a combination of p -adaption and updating the boundary condition, so that both the discretization and the boundary errors are similar at each stage. Results are presented to show the reduction of computation time when p -adaption is used as opposed to an earlier approach of uniformly increasing the element orders.

I. INTRODUCTION

When the finite element method (FEM) is applied to the scattering of electromagnetic waves, the infinite domain has to be reduced to a finite volume by the introduction of a truncation boundary, S_1 . Maxwell's equations are solved in the finite volume, subject to a condition on S_1 that absorbs the scattered field. Of the many ways of doing this, one of the most appealing is the iterative absorbing boundary condition (IABC) [1], [2], because at each iteration it is computationally inexpensive and yet it can converge to a highly accurate absorber. Initially, a first-order ABC is applied to S_1 ; then the fields inside are computed, and the boundary condition on S_1 is updated by making use of the computed fields on an inner surface, S_2 (which may be on the surface of the scatterer itself). The fields inside are computed again, and so on.

At every iteration there is a solution error introduced by the IABC, called the boundary error. This is in addition to the error arising from the finite elements themselves, called the discretization error. The latter can be controlled by adaption, which can be carried out at each iteration of the IABC. In the present work, p -adaption is chosen, making use of the hierarchical properties of the vector tetrahedral elements described in [3]. A control scheme is used to balance the two sources of error, so that the overall error reduces as rapidly as possible with increasing computational cost.

The present contribution builds on earlier work [4] in which the element orders, while varying from one iteration to the next, were kept uniform throughout the mesh, i.e., no p -adaption was involved. The incorporation of p -adaption requires changes to the control scheme, and the development of a suitable error indicator, described next.

II. ERROR INDICATOR

The implicit indicator presented here is related to the goal oriented error indicator described in [5]. In this paper, a similar approach is used to yield a general indicator of the field error. A formulation employing the magnetic field \mathbf{H} is used for the solution of the 3-D electromagnetic scattering problem. The weighted residual formulation is of the form [6]:

$$a(\mathbf{H}, \mathbf{w}) = b(\mathbf{w}) \quad \forall \mathbf{w} \quad (1)$$

where \mathbf{w} is a weight function; a and b are bilinear and linear forms, respectively [2]. Suppose that $\bar{\mathbf{H}}$ is a computed solution of (1). We aim to estimate the error arising from element k by the following expression:

$$\mathbf{e}_k = \mathbf{H}_k - \bar{\mathbf{H}} \quad (2)$$

where \mathbf{H}_k is the computed field when the order of element k is incremented by 1. The error indicator η_k for element k is based on the 'energy norm' of \mathbf{e}_k and is defined by [7]:

$$\eta_k = \|\mathbf{e}_k\|_a = \sqrt{|a(\mathbf{e}_k, \mathbf{e}_k)|} \quad (3)$$

which can also be evaluated as:

$$\eta_k = \sqrt{|b(\mathbf{e}_k) - a(\bar{\mathbf{H}}, \mathbf{e}_k)|} \quad (4)$$

When \mathbf{e}_k is exactly as given by (2), expressions (3) and (4) are identical. However, (4) is less sensitive than (3) to errors in \mathbf{e}_k when \mathbf{e}_k is approximated.

III. APPROXIMATING THE ERROR INDICATOR

Equation (1) can be discretized using the Galerkin method with a set of functions \mathbf{N}_i used as both weight and trial functions. The result will have the form [6], [7]:

$$[K] \{\bar{H}\} = \{b\} \quad (5)$$

where $[K]$ is a symmetric matrix, $\{b\}$ is the source term arising from the incident plane wave, and $\{\bar{H}\}$ is the vector of coefficients to be determined. After evaluating $\{\bar{H}\}$, the field $\bar{\mathbf{H}}$ can be found:

$$\bar{\mathbf{H}} = \{\mathbf{N}\}^T \{\bar{H}\} \quad (6)$$

where superscript \mathbb{T} denotes the transpose. After incrementing the element order of the k^{th} element, (5) becomes:

$$\begin{bmatrix} [K_k^{oo}] & [K_k^{no}] \\ [K_k^{on}] & [K_k^{nn}] \end{bmatrix} \begin{Bmatrix} \{H_k^o\} \\ \{H_k^n\} \end{Bmatrix} = \begin{Bmatrix} \{b_k^o\} \\ \{b_k^n\} \end{Bmatrix} \quad (7)$$

where $\{H_k^o\}$ is the vector of coefficients corresponding to the original (old) DOFs. $\{H_k^n\}$ is the vector of coefficients corresponding to the new DOFs added to element k to raise its order by 1. b_k^o and b_k^n are the corresponding old and new source terms. A reasonable approximation can be made by putting $\{H_k^o\} = \{\bar{H}\}$. Equation (7) then gives the following small matrix equation, which can be solved for each element k , in turn:

$$[K_k^{nn}] \{H_k^n\} \approx \{b_k^n\} - [K_k^{on}] \{\bar{H}\} \quad (8)$$

After substituting $\{H_k^n\}$ in (2), the error of element k is:

$$\mathbf{e}_k \approx \{\mathbf{N}^n\}^T \{H_k^n\} \quad (9)$$

where $\{\mathbf{N}^n\}$ is a column vector of the trial functions associated with the new DOFs. Then $b(\mathbf{e}_k)$ and $a(\bar{\mathbf{H}}, \mathbf{e}_k)$ can be evaluated as:

$$b(\mathbf{e}_k) \approx \{H_k^n\}^T \{b_k^n\} \quad (10)$$

$$a(\bar{\mathbf{H}}, \mathbf{e}_k) \approx \{\bar{H}\}^T [K_k^{on}] \{H_k^n\} \quad (11)$$

Then the error indicator (4) can be calculated.

IV. CONTROL SCHEME

The control scheme used here is similar to the one used in [4]. In this paper, instead of increasing the order of all elements uniformly, only a certain percentage of the elements are adapted. Also in [4], after increasing the element order, a boundary update was always performed as it was found that this was needed following an increment of the order of all elements by one. But, with the p -adaptive scheme, it is not needed. A modified flow chart will be presented in the extended paper.

V. RESULTS

The example consists of two dielectric spheres, as shown in Fig. 1. The incident plane wave propagates in the $-x$ -direction, with y -polarized electric field. The truncation boundary is a rectangular box placed $l = 0.1\lambda$ away from the spheres (Fig. 1). 6,685 elements are used. The problem is first solved at order 3 and the radar cross section (RCS) obtained after 10 iterations is used as the reference solution. Then the same FE problem is solved twice using the p -adaptive control scheme. First, at each p -adaptive step, 75% of elements with the highest error (4) are increased in order; this is the curve "75% adaption". In the second solution, all of the elements are increased in order ("100% adaption"). Fig. 2 also shows

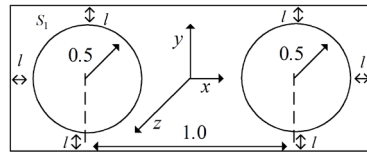


Fig. 1. Two dielectric spheres along with the truncation boundary S_1 . All the dimensions are in wavelengths. The dielectric constant of each sphere is $\epsilon_r = 2$. $l = 0.1$ is the separation between the spheres and truncation boundary.

the error when the order is fixed at 3 throughout. Total time is the summation of the field solution time and the boundary update time for all the solutions up that point. Average error (dB) is the average error in the value of $10 \log_{10}(\text{RCS}/\lambda^2)$ over the range $(\phi = \pi/2, 0 \leq \theta \leq \pi)$. From the graph it is clear that the new p -adaptive scheme is more effective at reducing the error than either the use of an element order that is fixed order throughout the iteration (i.e., just boundary iteration) or the use of an order that changes but is uniform throughout the mesh.

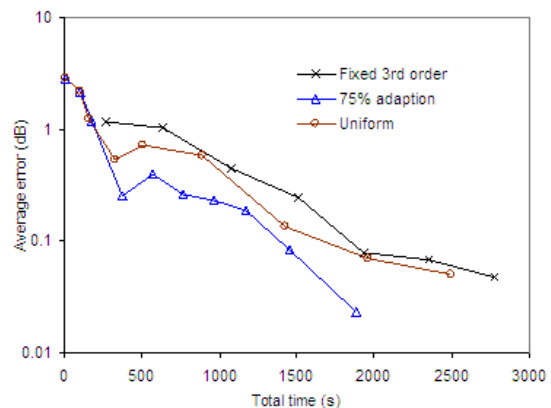


Fig. 2. Average error in the bistatic RCS in the plane $\phi = \pi/2$ (the yz plane) as a function of total time. Triangles represent results using 75% adaption; circles represent the results using uniform order; crosses represent the results obtained using 3rd order elements at every iteration.

REFERENCES

- [1] S. Alfonzetti, G. Borzi, and N. Salerno, "Iteratively-improved robin boundary conditions for the finite element solution of scattering problems in unbounded domains," *International Journal for Numerical Methods in Engineering*, vol. 42, no. 4, pp. 601-629, 1998.
- [2] P. Paul, and J.P. Webb, "An iterative absorbing boundary condition using varying element orders," *IEEE Transactions on Magnetics*, vol. 43, no. 4, pp. 1325-1328, 2007.
- [3] J. P. Webb, "Hierarchical vector basis functions of arbitrary order for triangular and tetrahedral finite elements," *IEEE Transactions on Antennas and Propagation*, vol. 47, no. 8, pp. 1244-1253, 1999.
- [4] P. Paul, and J.P. Webb, "Balancing boundary and discretization errors using an iterative absorbing boundary condition," *IEEE Transactions on Magnetics*, vol. 44, pp. 1362-1365, 2008.
- [5] M. M. Gavrilovic, and J. Webb, "Error indicator for the calculation of global quantities by the p -adaptive finite element method," *IEEE Transactions on Magnetics*, vol. 33, no. 5, pp. 4128-4130, 1997.
- [6] J.-M. Jin, *The finite element method in electromagnetics*, New York: Wiley, 2000.
- [7] O. Zienkiewicz, and R. Taylor, *The finite element method, vol. 1: Basic formulation and linear problems*, New York: McGraw-Hill, Fourth edition, 1989.

Investigation on the shading effect of reinforced concrete construction to lightning radiation field based on TDIE method

Zhibin ZHAO, Mingxia ZHANG, Xiang CUI, Lin LI, and Tiebing LU
 North China Electric Power University
 619 Yonghuabei Street, Baoding City, Hebei Province, 071003, P. R. C
 E-mail: zhibinzhao@yahoo.com

Abstract—By using the method of time domain integral equation (TDIE) and equivalent principle, the shading effect of reinforced concrete construction to lightning radiation field is analyzed. The reinforced concrete surface is assumed to be metallized and modeled based on the equivalent principle. The electromagnetic field inside and out of the reinforced concrete are both calculated by using the time domain electric field integral equation. The proposed technique, which is efficient to analyze the far field, is more applicable to evaluate the shading effect of reinforced concrete construction to lightning radiation magnetic field in time domain.

I. INTRODUCTION

Due to the widespread existence of tall reinforced concrete constructions in city, the lightning radiation electromagnetic field detected by nearby lightning location sensor may be influenced. Accordingly the peak value and derivative of the corresponding lightning current derived from the measured lightning radiation magnetic field may deviate from their real values. In order to obtain lightning current reliable enough, it is necessary to investigate the shading effect of the reinforced concrete construction to the lightning radiation magnetic field and determine the minimum distance from the lightning detection system to nearby tall building further.

Generally the shielding effect of reinforce concrete construction on the radiation electromagnetic field in space is concerned in literature, typically as discussed in [1, 2]. There are two approaches widely used to identify the shielding effect of the reinforced concrete buildings exactly. The first is based on FDTD or TLM method [1], which is complicated for reinforce concrete despite the relatively simple separation of space. Additionally, it is not convenient to determine the electromagnetic field of any point in space. The Second one, using volume cell MoM to investigate the scattering field of concrete block or analogical lump medium [2], is also not applicable for reinforce concrete. In the analysis of the shading performance of reinforced concrete construction to electromagnetic field in space, both the influence of steel grid and that of concrete should be taken into account, thus more efficient calculation is of requirement.

In this paper, a method in time domain to investigate the shading effect of reinforced concrete construction to lightning radiation magnetic field is developed based on the time domain integral equation (TDIE) and equivalent principle. The electromagnetic response caused by the interaction between the inner surface and the outer surface of the concrete, which is usually not easy to be identified, is modeled by

introducing electric currents on the surface. With the concrete surface taken to be metallized, an equivalent surface electric current is introduced on the surface. The field in the concrete is resulted from the equivalent surface electric current on the concrete surface and the line current flowing on the steel grid buried in the concrete. While the field out of the concrete is generated by the equivalent surface electric current and the incidence lightning radiation electromagnetic wave. On the concrete surface, the fields inside and outside the concrete satisfy the continuity of tangential electric field.

Thus the spatial electromagnetic field intensity can be determined to evaluate the shading effect of reinforced concrete construction. Since the inversion of lightning current is mainly dependent on the lightning radiation magnetic field intensity, only the waveform of the radiation magnetic field is displayed. At last, the proposed method is used to analyze the effect of a simplified reinforced concrete building to the lightning radiation magnetic field.

II. DESCRIPTION OF THE APPROACH

A. Basic Model of Reinforce Concrete Block

In order to reasonably simplify the calculation model of reinforced concrete construction, the following two assumptions are necessary. 1) The medium of the concrete is uniform and isotropic; 2) Compared with the thickness of the concrete, the steel conductors buried in the concrete is of radius small enough that can be modeled as thin wire.

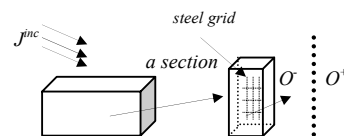


Fig.1 The model of a section of concrete

The geometry of the simple reinforce concrete block model is shown in Fig.1. The steel grid is buried in concrete. The concrete surface separates the whole space into two sections, namely the space in and outside the concrete, with the interior surface O and exterior surface O^+ .

Based on the two assumptions, an equivalent electric current pair \mathcal{J}^c is introduced on the exterior surface O^+ and interior surface O of the reinforced concrete block. The outside field, therefore, is the sum of the field produced by the equivalent current source \mathcal{J}^c and that from outer excitation source \mathcal{J}^{inc} , while the field in the concrete is yielded by \mathcal{J}^c plus the scattering field of current I^v flowing on the steel grid.

According to the equivalent theorem, the scattering field from the metal conductor buried in the concrete can be analyzed as that in the uniform medium.

Since electric field intensity is continuous on the concrete surface and the tangential electric field component on the surface of steel grid is equal to the voltage drop in the conductor, the continuity discussed above on the surface of reinforced concrete yields the following equations.

$$\mathbf{E}_t^o(\mathbf{J}^{inc}) + \mathbf{E}_t^o(\mathbf{J}^c) = \mathbf{E}_t^i(\mathbf{J}^c) + \mathbf{E}_t^i(\mathbf{J}^w) \quad (1)$$

$$\mathbf{E}_t^w(\mathbf{J}^c) + \mathbf{E}_t^w(\mathbf{I}^w) = Z\mathbf{I}^w \quad (2)$$

Equation (1) and (2) are for the concrete surface and the steel surface respectively. Where $\mathbf{E}_t^o(\mathbf{J}^{inc})$ and $\mathbf{E}_t^o(\mathbf{J}^c)$ are the tangential electric field at O^+ due to \mathbf{J}^{inc} and \mathbf{J}^c respectively. $\mathbf{E}_t^i(\mathbf{J}^c)$ and $\mathbf{E}_t^i(\mathbf{I}^w)$ are the tangential electric field given by \mathbf{J}^c and \mathbf{I}^w respectively at O^- . The tangential component $\mathbf{E}_t^w(\mathbf{J}^c)$ and $\mathbf{E}_t^w(\mathbf{I}^w)$ on steel surface is resulted from \mathbf{J}^c and \mathbf{I}^w respectively. And Z is the impedance per unit length of the steel grid.

By using the method of moment equation (1) and (2) can be solved. Since the reinforced concrete construction is supposed to be rectangular volume, the surfaces are discretized into a lot of rectangular patches. The roof-top basic functions are adopted to expand the unknown electric currents on these patches and wire segments.

B. Electromagnetic Field out of the Concrete Block

In order to simplify the calculation, the ground out of the concrete is supposed to be perfect electric conductor.

As illustrated by the engineer model of lightning return stroke, the lightning current flows in the lightning channel as does in transmission line. The following is the most simple relation expression

$$i(z', t) = i(t - z'/v) \quad (3)$$

where z' is the height of return stroke front along the lightning channel, v is velocity of return stroke. The double exponential function is adopted to represent the channel base current in our calculation. Since the lightning channel concerned here is relatively very far from the involved building, the effect of the scattering from the building on lightning current is neglected, namely the original lightning radiation field is considered to be incidence field. The calculation equation for the field out of the concrete can be established based on following formula.

$$\left(\frac{\partial^2}{\partial t^2} - c^2 \nabla \nabla \cdot \right) \mathbf{A} \Big|_{\tan} = \frac{\partial}{\partial t} \mathbf{E}^i \Big|_{\tan} \quad (4)$$

where c is the lightning speed in free space, \mathbf{E}^i is the lightning radiation electric field, and $\mathbf{A}(\mathbf{r}, t)$ is the vector potential generated from the surface electric current in free space.

C. Electromagnetic Field in the Concrete Block

The surface current \mathbf{J} on the inside surface of the concrete and the current \mathbf{I}^w flowing on the steel grid of the concrete produce the electric field in the concrete block. The concrete is modeled as lossy medium with permittivity ϵ , conductivity σ , and permeability μ . There is no inject field existing in the reinforce concrete block, thus the integral equation of time domain electric field is given by

$$\left(\frac{\partial^2}{\partial t^2} + a^2 c^2 \frac{\partial^2}{\partial t^2} - c^2 \nabla \nabla \cdot \right) \mathbf{A} \Big|_{\tan} = 0 \quad (5)$$

where $a = \sqrt{\mu\sigma}$, $c = 1/\sqrt{\mu\epsilon}$. The vector potential $\mathbf{A}(\mathbf{r}, t)$ is expressed as

$$\mathbf{A}(\mathbf{r}, t) = \mu \int_s \mathbf{J}(\mathbf{r}', t) g(|\mathbf{r} - \mathbf{r}'|, t) d\mathbf{r}' \quad (6)$$

where $g(|\mathbf{r} - \mathbf{r}'|, t)$ is the three dimensional scalar Green function for the lossy medium wave equation [3].

III. ANALYSIS OF THE INFLUENCE

In view of the irregular outline and various dimension of constructions, some usually used hypotheses are necessary, they are:

- 1) The construction is rectangular volume;
- 2) The steel grid is in the center of the construction;
- 3) The lightning channel is also vertical to the ground.

Based on these assumptions, the profile of calculation model can be expressed in Fig.2 as

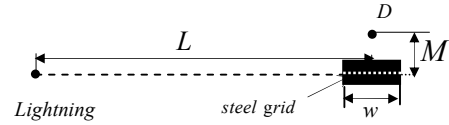


Fig. 2 Calculation model profile

Suppose that lightning channel is 150km far from the building, Fig.3 shows the lightning radiation magnetic field waveform calculated on ground level at 50m from the building for the cases that the width of building is 50m, 100m, 150m, 200m, and 500m, as well as that without the existence of the building. The resistivity and relative permittivity of the building, which is 50m high, are $50\Omega\cdot\text{m}$ and 8 respectively. The steel grid in the concrete is $1 \times 1\text{m}^2$.

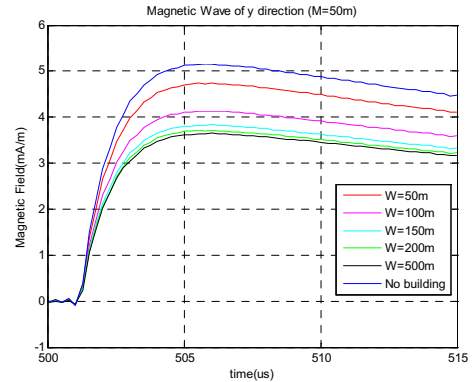


Fig. 3 Lightning radiation magnetic field 50m far from the building

IV. REFERENCES

- [1] C. Buccella; S. Cristina, and A. Orlandi, "Shielding performances of reinforced walls to the field radiated by lightning," 1992. *Eighth International Conference on Electromagnetic Compatibility*, pp. 60-66, September 1992
- [2] K. Yamazaki, K. Kato, K. Ono, and etc., "Analysis of magnetic disturbance due to buildings," *IEEE Transactions on Magnetics*, Vol. 39, No. 5, pp. 3226-3228, September 2003.
- [3] P. L. Jiang, E. Michielssen, "Temporal acceleration of time domain integral equation solvers for electromagnetic scattering from objects residing in lossy media," *Microwave and Optical Technology Letters*, Vol. 44, No.3, pp.223-230, 2005.

2D Scattering Integral Field Equation Solution through a IMLS Meshless-Based Approach

Williams L. Nicomedes¹, Renato C. Mesquita², Fernando J. S. Moreira¹

Federal University of Minas Gerais, Dept. of Electronic Engineering (1) and Dept. of Electrical Engineering (2)

Av. Antonio Carlos 6627, 31270-901, Belo Horizonte, Brazil

wlnicomedes@yahoo.com.br, renato@ufmg.br, fernandomoreira@ufmg.br

Abstract – In this work, we apply a meshless-based method to a set of integral equations arising in electromagnetic wave propagation and scattering. The objective is not only to solve these equations through a meshless-based method, but also to find a way to build shape functions that could work for any cross-sectional geometry. We have found that the Moving Least Squares (MLS) approximation is not able to provide useful shape functions in every situation. This technique relies on matrix inversions and, according to the geometry, singular matrices can occur. In order to avoid this problem, we have taken the Improved Moving Least Squares (IMLS) approximation, that doesn't depend upon matrix inversions and works well in a number of cross-sectional geometries.

I. INTRODUCTION

Meshless methods have successfully been applied in Mechanics as an alternative to the traditional finite element method (FEM). Now they are being brought to the study of electrodynamics and presented as an additional aid in the solution of high-frequency [1] problems. In this work we take a different approach by applying a meshless discretization directly into the classical integral field equations instead of applying it to the weak form. We have already solved the problem for a circular cylinder using the MLS approximation [2], but the solution is not as general as to be applied to every cross-section form. For other geometries (e.g. rectangular) the MLS approximation fails in providing accurate results, because singular local matrices are obtained, leading to an inconsistent outcome. The IMLS approximation thus seemed to be the right one; despite having to build an orthogonal basis first, the associated matrices are diagonal, there is no need for inversions and the shape functions could then be built consistently for any cross-sectional geometry.

II. PROBLEM DESCRIPTION

In the investigated problems, a monochromatic incident plane wave is scattered by perfect electric conductor (PEC) cylinder infinite in the z -direction. For a TM^z polarized incident wave, the electric surface current density \vec{J}_s is directed along the z -direction. One of the equations governing the phenomenon is the electric field integral equation (EFIE):

$$E_z^i(\vec{\rho}) = \frac{\omega\mu}{4} \oint J_s(\vec{\rho}') H_0^{(2)}(kR) dl' \quad (1)$$

$E_z^i(\vec{\rho})$ is the incident electric field at $\vec{\rho}$, $R = \|\vec{R}\| = \|\vec{\rho} - \vec{\rho}'\|$, $\vec{\rho}$ and $\vec{\rho}'$ locate the observation and source points at the perimeter, respectively, $\omega = 2\pi f$, where f is the

wave frequency, and $H_0^{(2)}$ is the zero-order Hankel function of the second type. The other is the magnetic field integral equation (MFIE):

$$[\hat{n} \times \vec{H}_i(\vec{\rho})] \cdot \hat{z} = \frac{1}{2} J_s(\vec{\rho}') + \frac{jk}{4} \oint J_s(\vec{\rho}') H_1^{(2)}(kR) [\hat{n} \cdot \hat{R}] dl' \quad (2)$$

where $\vec{H}_i(\vec{\rho})$ is the incident magnetic field at $\vec{\rho}$, $H_1^{(2)}$ is the first-order Hankel function of the second type and \hat{n} is the unit surface normal. The EFIE and MFIE formulation can be seen in [3]. To avoid spurious resonant solutions one can form the combined field integral equation (CFIE) through a linear combination from the EFIE and MFIE:

$$CFIE = \alpha EFIE + (1 - \alpha) \eta MFIE \quad (3)$$

where α is a parameter ranging from zero to one and η is the intrinsic impedance of the exterior medium [3].

III. THE MESHLESS APPROACH

The meshless approach begins by spreading nodes over the domain of the problem to be solved. In the present study, the domain of interest is the perimeter of the cylinder cross section. To each node a shape function with compact support is associated. The vicinal region in which the shape function is different from zero is called the *influence domain* of the corresponding node [4]. The main difference between meshless methods and mesh-based methods (like the FEM) is that the *element* concept is not present. The influence domains are arbitrary (the only restriction is that the set of influence domains must cover the entire domain) and can overlap. So, the nodes can be distributed arbitrarily without generating an element mesh.

Once the shape functions have been determined, the approximated value of a function u in a point \vec{x} is given by u^h and is expressed as

$$u^h(\vec{x}) = \sum_{I=1}^N \phi_I(\vec{x}) \hat{u}_I \quad (4)$$

where $I = 1 \dots N$ are the nodes whose influence domains include the point \vec{x} and the numbers \hat{u}_I associated to each node are called the *nodal parameters*.

There are several ways to build the shape functions [4]; among them we chose the moving least squares approximation (MLS). The MLS approximation begins by expressing u^h as

$$u^h(\vec{x}) = \sum_{i=1}^m p_i(\vec{x}) a_i(\vec{x}) = p^T(\vec{x}) a(\vec{x}) \quad (5)$$

where $p_i, i = 1 \dots m$ are monomial functions, m is the number of terms in the basis p and a_i are coefficients (e.g., in two dimensions, one could have $p^T = [1, x, y]$). The next step is to force the difference between the approximation u^h and the exact value at the nodal points to reach a minimum through the minimization of a weighted functional; this takes several matrix manipulations whose detailed descriptions can be found in [4]. The results are:

$$[\phi_1(\vec{x}), \phi_2(\vec{x}), \dots, \phi_N(x)] = p^T(\vec{x}) A^{-1}(\vec{x}) B(\vec{x}), \quad (6)$$

$$A(\vec{x}) = P^T W(\vec{x}) P \text{ and } B(\vec{x}) = P^T W(\vec{x}) \quad (7)$$

$$P = \begin{pmatrix} p_1(\vec{x}_1) & \dots & p_m(\vec{x}_1) \\ \vdots & \ddots & \vdots \\ p_1(\vec{x}_N) & \dots & p_m(\vec{x}_N) \end{pmatrix} \quad (8)$$

and W is a diagonal matrix whose elements are

$$[W(\vec{x})]_{ii} = w(\vec{x} - \vec{x}_i) \quad (9)$$

$w(\vec{x} - \vec{x}_i)$ is a weight function with compact support (i.e. a cubic spline [4]).

The MLS approximation doesn't always provide useful shape functions, because sometimes the A -matrices become singular, preventing inversion. This phenomenon occurs for some geometries, like the rectangular one. The reason is that for points lying in regions along the sides, *away from the corners*, the parameter that describes the contour line experiments variation only in one variable (x only or y only). For a given point \vec{x} in the rectangle upper side, for example, the y -variable is a constant $y = c$. So the basis becomes $p^T = [1, x, c]$. One sees that all N nodes whose influence domains act upon \vec{x} have the y -coordinate equal to c . Consequently, P has two constant columns. So, the product $A = P^T W P$ will have two linearly dependent columns. Hence, A is singular.

One way to solve that is to make the nodal influence domains bigger than the side of the rectangle, in order to assure that inside this domain there will be points distributed along two adjacent sides. By doing this, both x and y will vary, P will no longer have two linearly dependent columns and A shall not be singular. But it revealed to be a bad approach: one sees that as the influence domains become larger, the local perspective of the method is destroyed. Besides that, the results are not so much accurate.

To remedy this problem, a different approximation was developed: the improved moving least squares (IMLS) [5]. In the IMLS, it is required that the terms of the basis p be orthogonal to each other. In order to do so, they are viewed as belonging to a Hilbert space in which the following inner product between functions f and g is defined:

$$\langle f, g \rangle = \sum_{l=1}^N w(\vec{x} - \vec{x}_l) f(\vec{x}_l) g(\vec{x}_l) \quad (10)$$

The orthogonality condition is assured through the property ($k, j = 1, 2, \dots, m$):

$$\langle p_k, p_j \rangle = \sum_{l=1}^N w(\vec{x} - \vec{x}_l) p_k(\vec{x}_l) p_j(\vec{x}_l) = \begin{cases} A_k, & k = j \\ 0, & k \neq j \end{cases} \quad (11)$$

After some matrix manipulations [5], one concludes that inversions are no longer necessary. The shape functions are

$$[\phi_1(\vec{x}), \phi_2(\vec{x}), \dots, \phi_N(x)] = p^T(\vec{x}) \bar{A}(\vec{x}) B(\vec{x}) \quad (12)$$

where \bar{A} is a diagonal matrix whose elements are given by

$$[\bar{A}(\vec{x})]_{ii} = \frac{1}{\langle p_i, p_i \rangle} \quad (13)$$

IV. PRELIMINARY RESULTS

For a rectangular cross-section cylinder, we have begun by spreading nodes over the contour and applying the IMLS approximation to build the shape functions. We can express the unknown surface current density at a nodal point $\vec{\rho}_i$ along the contour as in (4), with u^h replaced by J and \vec{x} by $\vec{\rho}_i$. The next step is to insert that expression for J in (3) and get a linear system that can be solved in order to find the nodal parameters. The following results were obtained (scattering by a square cylinder with sides $2a$, where $a = 1/k$ and $k = 2\pi/\lambda$ is the wave number, λ being the wavelength):

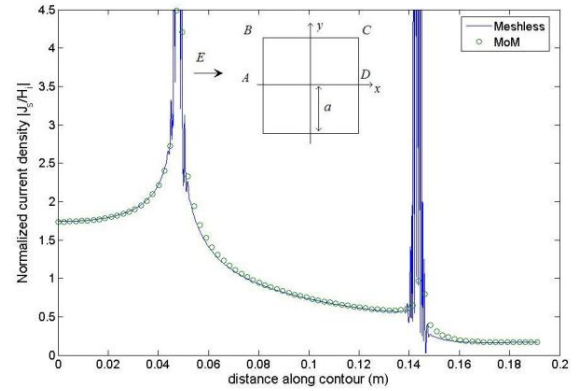


Fig. 1. Normalized current density along cylinder contour

The figure above shows the absolute value of the normalized current density (with respect to the incident magnetic field H_i) along the path ABCD. One sees that the result is accurate when compared to the method of moments (MoM). The peaks in the current density at the vertices B and C are theoretically predicted for a TM incident wave.

Further studies on the precision and the convergence of the method will be presented in the final paper. We have found out that the MLS approximation is not general enough to deal with any cross-sectional geometry. It should be noted that the IMLS approximation runs faster than the MLS, as there is no need for matrix inversion.

VI. REFERENCES

- [1] Manzin, A., Bottauscio, O. "Element-free galerkin method for the analysis of electromagnetic-wave scattering", *IEEE Transactions on Magnetics*, 44 (6), pp. 1366-1369, 2008.
- [2] Nicomedes, W. L.; Mesquita, R.C.; Moreira, F.J.S. "Electromagnetic Scattering Problem Solving by an Integral Meshless-Based Approach", accepted for presentation in the *8th International Symposium on Electric and Magnetic Fields*, to be held in Mondovi, Italy in May 26-29 2009.
- [3] Peterson, Andrew F., Ray, Scott L., Mittra, Raj; *Computational Methods for Electromagnetics*. IEEE Press, 1998.
- [4] Liu, G. R. *Mesh Free Methods: Moving Beyond the Finite Element Method*. CRC Press, chapter 5, section 4.
- [5] Peng M, Cheng Y. "A boundary element-free method (BEFM) for two-dimensional potential problems". *Engineering Analysis with Boundary Elements*, vol. 33, n°1, pp. 77-82, 2009

Numerical Techniques for Multi-Objective Synthesis of an Inverted-S Antenna

Lei Liu¹, Junwei Lu², Shiyu Yang¹, and Guangzheng Ni¹

¹College of Electrical Engineering, Zhejiang University, Hangzhou, 310027, China

²Faculty of Engineering and Information Technology, Griffith University, Australia

Abstract—The synthesis of a dual-frequency band Inverted-S Antenna (ISA) using low profile PCB configuration is studied. To manipulate the multi-objectives and the huge amount of turning work involved in the synthesis of a dual-frequency band Inverted-S Antenna, special numerical techniques such as approaches to integrating different objectives, an improved vector genetic algorithm and a modified radial basis function based response surface model are proposed. Numerical results as reported serve to demonstrate the pros and cons of the proposed techniques.

I. NUMERICAL TECHNIQUES FOR ISA SYNTHESIS

Nowadays, a large amount of commercial PC cards are operating at 2.4 GHz and 5 GHz. Consequently, the compact dual-frequency antenna becomes a topical research subject in both academic researches and engineering applications. In this point of view, the Inverted-S Antenna (ISA) is a promising candidate since it can achieve an adjustable dual frequency with omnidirectional radiation patterns. In contrast to the inverted-F antenna (IFA), which is now widely used in handsets, ISA is a kind of micro-strip antennas with a centrally located parasitic element between a folded and feed element, originally developed in the early 1990's and patented in Australia [1] and USA [2]. In this smart configuration, the folded element connected to the ground line and the feed element connected to the feed produce an adjustable dual frequency and provide omnidirectional radiation patterns at two different frequency bands. Moreover, the element connected to ground determines the lower operating frequency, and the feed element the higher one. In addition, the two operating-frequencies of the antenna are found to have the same polarization plane and broadside radiation patterns. However, as a large number of objectives, decision parameters and considerable parameter tuning work are involved, as well as the field coupling between different elements is required to take into consideration in the synthesis of an ISA, the promising performances of an ISA can only be pursued when some specified robust synthesis methodologies are applied.

A. Mathematical Model

To design an ISA with desirable performances, apart from the minimization of the volume of the antenna, the goals of the optimization are proposed further to include: maximize the bandwidth of S_{11} and minimize the return loss at the two resonant frequencies. Such synthesis problem is a many-objective synthesis, which might result in dramatic deteriorations of the selective pressure when a vector genetic algorithm is employed. Therefore, it would be desirable if the objectives could be reduced without sacrificing the solution quality. In this point of view, the bandwidth and return loss

requirements for each resonant frequency are integrated into a new fitness function of the bandwidth of S_{11} . Mathematically, the proposed fitness functions are formulated as:

$$f_j = \sum_i^N [1 + \delta(f_i - f_{c_j})][S_{11}(f_i) - 10] (j=1,2) \quad (1)$$

where, f_{c_j} is a resonant frequency, i.e. 2.4GHz or 5GHz, $\delta(f - f_{c_j})$ is the Dirac function, N is the number of sweeping frequency points within 5% bandwidth of the resonant frequency.

By using this new defined fitness function, the fitness assignment mechanism will favour trying on different intermediate solutions when these solutions, other things being equal, have the same bandwidths, which will sustain the necessary diversity of the population in the optimization process.

After introducing the two new fitness functions f_j ($j=1,2$), the optimal goals of the synthesis of an ISA read as: minimize f_j ($j=1,2$) and the volume of the antenna.

B. An Improved Vector Optimizer

The Non-dominated Sorting Genetic Algorithm-II (NSGA-II) [3] is extended as the vector optimizer for solving the ISA synthesis in this paper. Since the penalty-parameterless constraint-handling approach of NSGA-II often gives unfeasible geometric parameters for finite element modeling, one introduced and incorporated some geometrical constraints into the optimal model. Moreover, these constraints are transformed into two linear constraints with preconditioned variable bounds, resulting in a simple randomly iterative sampling procedure in the numerical implementation. Finally, thanks to the success in the development of some specific intermediate recombination manipulator as the crossover operator, all the individuals generated are automatically met these linear constraints.

C. Field Computation and the Application of a Response Surface model

To consider the coupling effect of different elements, the finite element method is used to determine the performance parameters of an ISA. However, the heavy computational burdens of a considerable large number of total finite element analysis required by NSGA-II are unaffordable for some engineering applications. In this regard, the multiquadric radial basis function [4] based response surface model is extended and used. It should be pointed out when the number of sampling points employed is within certain limits, a small shape parameter is better in view of constructing the profile of the response surface. However, this will lead to inaccurate numerical results. Moreover, with the increase of sampling points, an ill-conditioned matrix will appear. To alleviate

these deficiencies, some regularization technique, or the introduction of smoothness parameter together with a stabilizing function, are proposed. In this regard, Engl's criterion to optimize the smoothness parameter is introduced, resulting in not only a more smoothed response surface, but also an improvement of the condition number for the interpolation matrix.

II. NUMERICAL EXAMPLE AND CONCLUSION

The proposed numerical techniques are employed to optimize a dual-frequency band inverted-S antenna operating at 2.4 GHz and 5 GHz. In the numerical experiments, the finite element method is used to determine the performance parameter of the antenna.

To start with, 800 sampling points are firstly generated and the performance parameters of these sampling points are determined by means of finite element analysis; and the improved multiquadric radial basis function is then used to reconstruct the optimal problem; finally, the NSGA-II is run on the reconstructed problem to efficiently find the Pareto optimal of the optimal problem. If no proper solutions are searched in the current iterative cycle, some sampling points are added and the aforementioned procedures are repeated until some good solutions are attainable. In the numerical implementation of NSGA-II, the size of population is set to 100, and the number of maximum generations is set to 1000.

The final Pareto solution searched by using the proposed methodology is shown in Fig. 1. To compare performances of the optimized configuration and the original design which is obtained by using a rule of thumb, of the ISA, a solution in the Pareto front as marked in red circle is selected and the details are tabulated in Table I. The corresponding curves for Parameter S_{11} are depicted in Figs.2~3. From these numerical results, it is obvious that the proposed methodology can find a set of best compromising solutions of a many-objective design problem in a single run. Moreover, the performance parameters for the selected specific solution are much better than those of the original design. Therefore, the paper provides not only robust synthesis technique for an ISA design, but also provide more freedoms for a decision maker to select a specific solution from these Pareto solutions according to his/her preferences.

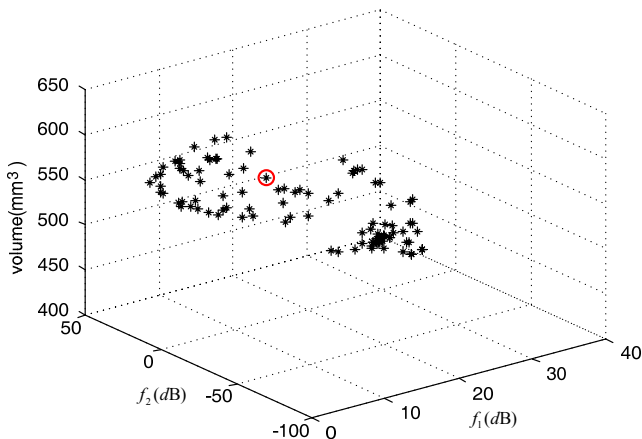


Fig. 1 The searched Pareto solution of the proposed methodology: the red circle is a specified solution highlighted in this paper

TABLE I
COMPARISON BETWEEN THE ORIGINAL AND THE OPTIMAL DESIGN FOR A SPECIFIC SOLUTION SELECTED FROM THE SEARCHED PARETO SOLUTIONS

	Bandwidth (2.4GHz)	Return loss (2.4GHz)	Bandwidth (5GHz)	Return loss (5GHz)
Original	5.3%	-15dB	10.7%	-20dB
Optimal	6.97%	-33.6dB	14.97%	-34dB

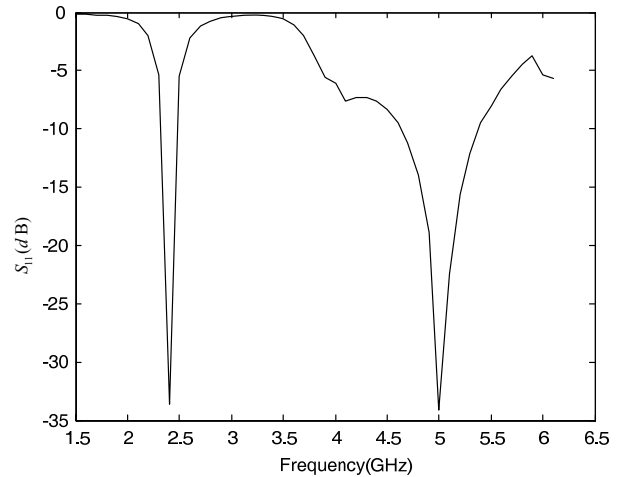


Fig 2. The return loss of the optimized dual frequency ISA.

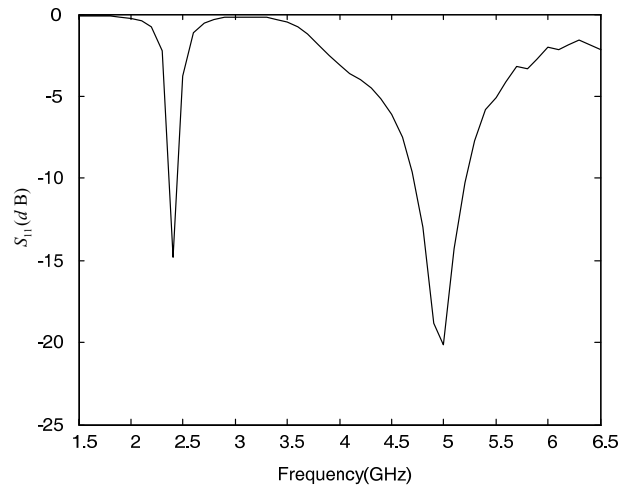


Fig. 3. The return loss of the original dual frequency ISA.

III. ACKNOWLEDGMENT

This work is supported by the National Natural Science Foundation of China (NSFC) under Grant No. 50777054 and the Specialized Research Fund for the Doctoral Program of Higher Education of China under Grant No. 20070335031.

IV. REFERENCES

- [1] D. Thiel, J. Lu and S. O'Keefe: Antennas for Use in Portable Communication Devices, PCT Specification 679992, *Australian Patent*, 1995.
- [2] D. Thiel, S. Okeefe and J. Lu: Directional Antennas, *USA Patent # 62886 B1*, 2001.
- [3] Deb, K., Pratap, A., Agarwal, S., Meyarivan, T., "A fast and elitist multiobjective genetic algorithm: NSGA-II," *IEEE Transactions on Evolutionary Computation*, vol.6, pp. 182 – 197, 2002.
- [4] Hardy R., "Multiquadric Equations of Topography and other Irregular Surfaces," *Journal of Geophysical Research*, vol. 76, pp. 1905-1915, 1971.

Blending PSO and ANN for Optimal Design of FSS Filters with Koch Island Patch Elements

Rossana M. S. Cruz*, Paulo H. da F. Silva**, and Adaildo G. d'Assunção*

*Federal University of Rio Grande do Norte

UFRN – Department of Electrical Engineering

Postal Code 1655, CEP: 59072-970, Natal, RN, Brazil, Phone: +55-84-3215-3700

** Federal Institute of Education, Science and Technology of Paraíba

IFPB – Group of Telecommunications and Applied Electromagnetism

CEP: 58015-430, João Pessoa, PB, Brazil, Phone: +55-83-3208-3055

E-mails: mscrossana@gmail.com, henrique@cefetpb.edu.br, adaildo@ct.ufrn.br

Abstract—This work presents an alternative method of electromagnetic (EM) optimization applied to design frequency selective surfaces (FSSs) with Koch island patch elements and desired stop band filter specifications. The problem is addressed by means of the natural optimization algorithm based on particle swarm optimization (PSO). Multilayer perceptrons (MLP) artificial neural network (ANN) was trained for FSS modeling with the efficient resilient backpropagation (RPROP) algorithm. The resultant MLP model for FSS design was used for fast and accurate evaluation of cost function in PSO iterations. The results for one FSS design example are presented and the advantages of the PSO-ANN algorithm are discussed.

I. INTRODUCTION

The design of frequency selective surfaces using fractals was originally proposed in [1] through the use of space-filling properties of certain fractals, such as the Minkowski loop and the Hilbert curve, in order to reduce the overall size of the FSS elements. The self-similarity property of these fractals enables the design of multiband fractal elements or fractal screens [2]-[4].

This work investigates the use of periodic arrays of Koch island patch elements to design FSS stop band filters. In order to control the FSS resonant frequency and bandwidth we modify the metallic shape of Koch elements adjusting the fractal iteration-factor and iteration-number. A parametric analysis is accomplished through the use of the Ansoft Designer™ commercial software. To verify the simulations some FSS prototypes were fabricated and measured through a network analyzer (model N5230A, Agilent Technologies).

The obtained EM-dataset from full-wave parametric analysis of FSS filters was used for the training of the MLP model. The training dataset comprises 48 examples that correspond to the input parameter values: the substrate dielectric constant ($\epsilon_r = 2.2, 3.0, 4.0, 4.8, 6.15, 7.0$), iteration-factor ($a = 3, 4, 6, 9$) and iteration-number ($k = 1, 2$). The FSS filter resonant frequency (f_r) and bandwidth (BW) were defined as design output parameters.

The Koch FSSs were constructed from a conventional array of rectangular patch elements on a single substrate layer. The Koch island patch elements are illustrated in Fig. 1, where W , W_1 and W_2 are the width and L , L_1 and L_2 are the length of the patch at levels 0, 1 and 2, respectively. For the Koch island fractal initiator, we consider a rectangular patch printed on a FR-4 fiberglass substrate ($\epsilon_r = 4.4$, thickness = 1.5 mm), with

dimensions: $W = 4.93$ mm, $L = 8.22$ mm, $t_x = 8.22$ mm and $t_y = 12.32$ mm, resulting a resonance of 16.57 GHz.

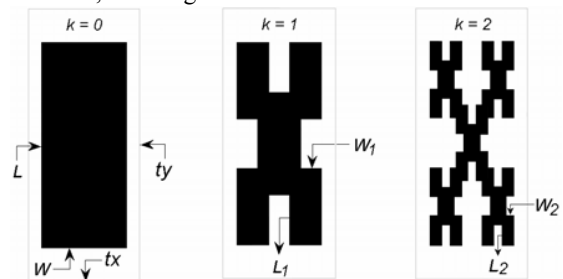


Fig. 1. Periodic array of rectangular patch elements.

II. PARTICLE SWARM OPTIMIZATION

PSO is a natural algorithm inspired by the social behavior of animals, such as bird flocking or fish schooling. Each PSO swarm individual (or particle) moves about the cost surface with an individual velocity. The velocities and positions of the particles are updated based on the local and global best solutions [5]. A flow chart of the proposed PSO algorithm is shown in Fig. 2(a). The innovation is the introduction of the MLP model for PSO cost function evaluation. The used MLP network configuration is shown in Fig. 2(b). Only five hidden neurons were enough to solve the modeling learning-task with the RPROP training algorithm [6]. The outputs of the MLP model are computed by means of (1):

$$\mathbf{y} = \mathbf{V} \cdot \left[-1 \cdot \frac{1}{1 + \exp(-\mathbf{W} \cdot \mathbf{x})} \right] \quad (1)$$

where $\mathbf{x} = [-1, k, a, \epsilon_r]^T$ is the input vector, \mathbf{W} and \mathbf{V} are the MLP weight matrix, and $\mathbf{y} = [f_r, BW]^T$ is the output vector.

Given a Koch FSS filter desired specification ($f_{r,desired}$, $BW_{desired}$), the goal is the minimization of the quadratic cost function as defined in (2) in terms of absolute percent errors:

$$\text{cost}(n, m) = \left(\frac{f_{r,desired} - f_r(\epsilon_{rm}^n, a_m^n)}{f_{r,desired}} + \frac{|BW_{desired} - BW(\epsilon_{rm}^n, a_m^n)|}{BW_{desired}} \right)^2 \quad (2)$$

The integers n and m take into account the n -th particle at the m -th PSO iteration. The PSO algorithm updates the velocities and positions of the particles based on the local and global best solutions according to (3) and (4), respectively.

$$\mathbf{v}_n^{m+1} = C \left[r_0 \mathbf{v}_n^m + \Gamma_1 r_1 (\mathbf{p}_n^{localbest(m)} - \mathbf{p}_n^m) + \Gamma_2 r_2 (\mathbf{p}_n^{globalbest(m)} - \mathbf{p}_n^m) \right] \quad (3)$$

$$\mathbf{p}_n^{m+1} = \mathbf{p}_n^m + \mathbf{v}_n^{m+1} \quad (4)$$

Here, \mathbf{v}_n is the particle velocity, \mathbf{p}_n is the particle position, r_0 , r_1 and r_2 are independent uniform random numbers; Γ_1 is the cognitive parameter and Γ_2 is the social parameter, $\mathbf{p}_n^{localbest(m)}$ and $\mathbf{p}_n^{globalbest(m)}$ is the best local and global solution, respectively and C is the constriction parameter.

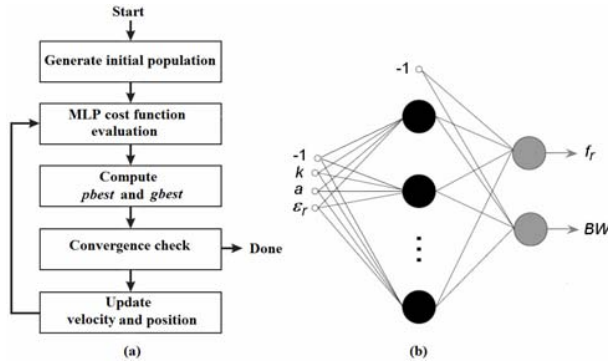


Fig. 2. (a) Flow chart of PSO-ANN algorithm; (b) MLP configuration.

III. RESULTS AND DISCUSSION

In the design example presented in this section we tested PSO-ANN algorithm implementation with the input/output parameters: $\epsilon_r = 4.4$, $k = 2$, $a = 5$, $f_r = 10$ GHz and $BW = 2.1$ GHz. Fig. 3 shows the cost surface contours, the initial, intermediate and final swarms, as well as the best path obtained from the PSO-ANN simulations, which converges for the optimal solution: $\epsilon_r = 4.4$ and $a = 5$. Fig. 4 shows the evolution of the average cost and best global cost for the PSO swarm. It is observed that the best-fit individual of the PSO final swarm converges to the global minimum of the cost function given in (1) and the algorithm is limited in precision to the round off error of the computer. Fig. 5 presents a comparison between the simulated and measured results for the transmission coefficient (in dB) of the Koch fractal FSS used as design example. A good agreement can be verified between simulated and measured data.

IV. CONCLUSION

The PSO-ANN algorithm showed to be faster and easier to implement as a global design tool in synthesizing FSS structures. These technique main advantages are related to its great flexibility of application in structures that do not have an explicit analytical cost function. It also presents a very low time processing, which is a very desired characteristic.

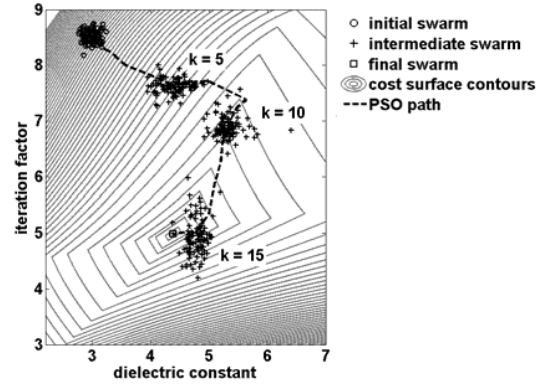


Fig. 3. PSO simulation for the Koch fractal FSS.

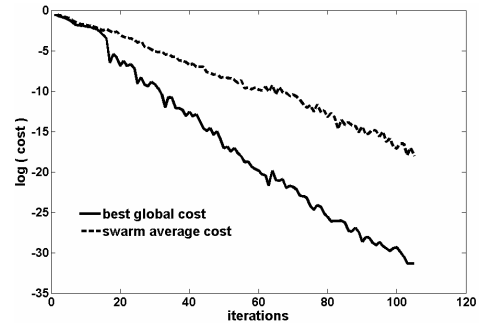


Fig. 4. PSO cost function for the Koch fractal FSS.

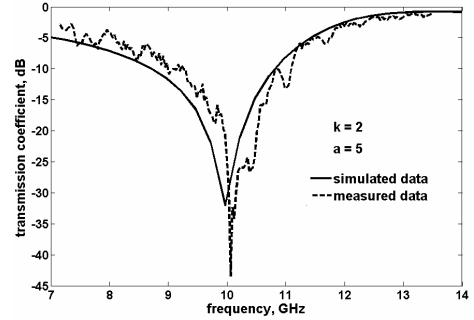


Fig. 5. Simulated and measured transmission coefficient (dB).

V. REFERENCES

- [1] E. A. Parker and A. N. A. El Sheikh, "Convolved array elements and reduced size unit cells for frequency-selective surfaces," *IEE Proceedings-H*, Vol. 138, No. 1 (1991), 19-22.
- [2] B. Hou, G. Xu and W. Wena, "Tunable band gap properties of planar metallic fractals", *Journal of Applied Physics*, Vol. 95, No. 6 (2004), 3231-3233.
- [3] A. R. Chandran et al., "Scattering behaviour of fractal based metallo-dielectric structures", *Progress in Electromagnetics Research, PIER 69*, 2007, 323-339.
- [4] J. P. Gianvittorio, J. Romeu, S. Blanch and Y. Rahmat-Samii, "Self-similar pre-fractal frequency selective surfaces for multiband and dual-polarized applications", *IEEE Transactions on Antennas and Propagation*, Vol. 51, No. 11 (2003), 3088-3096.
- [5] L. Kennedy and R. C. Eberhart, "Particle swarm optimization", *Proc. IEEE Conf. Neural Networks IV*, Piscataway, NJ, 1995.
- [6] M. Ridmiller and H. Braun, "A direct adaptive method for faster backpropagation learning: the RPROP algorithm", *Proceedings of the IEEE International Conference on Neural Networks*, San Francisco, EUA, 1993, 586-591.

Coefficients of Finite Difference Operator for Rectangular Cell NS-FDTD Method

Tadao Ohtani¹, Kenji Taguchi², Tatsuya Kashiwa³, Yasushi Kanai⁴

¹Mitsubishi Heavy Industries, Ltd., Nagoya 455-8515, Japan

²Kumamoto National College of Technology, Kumamoto 861-1102, Japan

³Kitami Institute of Technology, Kitami 090-8507, Japan

⁴Niigata Institute of Technology, Kashiwazaki 945-1195, Japan

E-mail: kanai@iee.niit.ac.jp

Abstract—The accuracy of the NS-FDTD method is dependent on the coefficients of the finite difference (FD) operators, however, they have not been derived analytically for rectangular cells. It is therefore necessary to obtain the coefficients numerically such that the phase velocity error is minimized, as we have previously reported. However, the calculation cost is very expensive. In this paper, we propose a new method to obtain the coefficients with a far lower computational cost. It is shown that the method reduces the computational time to 1/360 or less compared to the previous one.

I. INTRODUCTION

The NS-FDTD method is a time-domain analysis technique for electromagnetic waves with a fixed frequency [1]-[3]. A superior feature of the NS-FDTD method is the high accuracy based on the excellent isotropy. The quality of the isotropy is dependent on the coefficients α_v , where the special FD operators [1] with opposite anisotropic phase velocity errors are combined. Therefore, obtaining proper α_v for the best error cancellation is very important to guarantee the high accuracy of the NS-FDTD method. Analytical expressions for α_v for cubic cells have been given [1], but the α_v for rectangular cells have not yet been presented. Previously, we reported a method to obtain α_v numerically in a rectangular cell [3]. However, the method employs a stable, but an inefficient direct search technique, so the calculation cost may be more expensive than the NS-FDTD calculation itself in three-dimensions.

In this paper, we propose a semi-analytical method to obtain α_v with a low computational cost in three dimensions. Our proposed method can reduce the computation time to 1/360 or less compared with the previous method [3].

II. PRESENT METHOD

We consider the normalized FD Laplacian in the NS-FDTD, $[\sum_{\zeta} d_{\zeta}^{(1)} d_{\zeta}^{(0)} \psi / s_k^2(\Delta_{\zeta})] / (k^2 \psi)$, where $d_{\zeta}^{(0)} = \sum_{v=1,2,3} \alpha_v d_{\zeta}^{(v)}$ is the special FD operators [1], Δ_{ζ} the spatial increments, $s_k(\Delta_{\zeta}) = 2 \sin(k \Delta_{\zeta} / 2) / k$, and $\psi = e^{\pm i k \cdot r}$ with k the physical wavenumber and r the position. If we assume that the 3D normalized FD Laplacians correspond to the 2D normalized FD Laplacians on (Δ_x, Δ_y) , (Δ_x, Δ_z) and (Δ_y, Δ_z) for $\theta = \pi/2$, $\phi = 0$ and $\phi = \pi/2$, respectively, it yields the relations

$$\left(\frac{\sin(k_{\xi} \Delta_{\xi} / 2)}{\sin(k \Delta_{\xi} / 2)} \right)^2 \left[\alpha_1 + \alpha_2 \cos k_{\zeta} \Delta_{\zeta} + \frac{\alpha_3}{2} (\cos k_{\zeta} \Delta_{\zeta} + 1) \right] \Bigg|_{3D} = \left(\frac{\sin(k_{\xi} \Delta_{\xi} / 2)}{\sin(k \Delta_{\xi} / 2)} \right)^2 \left[\alpha_0 + (1 - \alpha_0) \cos k_{\zeta} \Delta_{\zeta} \right] \Bigg|_{2D}, \quad (1)$$

where $\xi, \zeta = x, y, z$ and $\xi \neq \zeta$. From (1), we can obtain the following relations by the definition $\alpha_1 + \alpha_2 + \alpha_3 = 1$ [1]:

$$\alpha_2 = 1 - 2\alpha_0 + \alpha_1, \quad \alpha_3 = 2(\alpha_0 - \alpha_1). \quad (2)$$

Using the relations (2), it is only necessary to determine α_1 in three dimensions, although the two-dimensional coefficient α_0 should be obtained according to [3] prior to the calculation. Next, using (2), we define the error in the normalized FD Laplacian as

$$\varepsilon(\theta, \phi) = 1 - \sum_{\eta, \xi, \zeta} \left(\frac{\sin(k_{\eta} \Delta_{\eta} / 2)}{\sin(k \Delta_{\eta} / 2)} \right)^2 \left[\alpha_1 + (1 - 2\alpha_0 + \alpha_1) \cos k_{\xi} \Delta_{\xi} \cos k_{\zeta} \Delta_{\zeta} + (\alpha_0 - \alpha_1) (\cos k_{\xi} \Delta_{\xi} + \cos k_{\zeta} \Delta_{\zeta}) \right], \quad (3)$$

where $\eta, \xi, \zeta = x, y, z$ and $\eta \neq \xi \neq \zeta$. Using (3), the $\alpha_1(\theta, \phi)$ in the semi-analytical solution that satisfies $\varepsilon(\theta, \phi) = 0$ is given by

$$\alpha_1(\theta, \phi) = \left[1 - \sum_{\eta, \xi, \zeta} \left(\frac{\sin(k_{\eta} \Delta_{\eta} / 2)}{\sin(k \Delta_{\eta} / 2)} \right)^2 \left[(1 - 2\alpha_0) \cos k_{\xi} \Delta_{\xi} \cos k_{\zeta} \Delta_{\zeta} + \alpha_0 (\cos k_{\xi} \Delta_{\xi} + \cos k_{\zeta} \Delta_{\zeta}) \right] / \left[\sum_{\eta, \xi, \zeta} \left(\frac{\sin(k_{\eta} \Delta_{\eta} / 2)}{\sin(k \Delta_{\eta} / 2)} \right)^2 (1 + \cos k_{\xi} \Delta_{\xi} \cos k_{\zeta} \Delta_{\zeta} - \cos k_{\xi} \Delta_{\xi} - \cos k_{\zeta} \Delta_{\zeta}) \right] \right]. \quad (4)$$

Here, we define the average error for $\alpha_1(\theta, \phi)$ by

$$\varepsilon^{Average}(\alpha_1(\theta, \phi)) = \left(\frac{2}{\pi} \right)^2 \int_{\theta'=0}^{\pi/2} \int_{\phi'=0}^{\pi/2} |\varepsilon(\theta', \phi', \alpha_1(\theta, \phi))| d\theta' d\phi', \quad (5)$$

where $\varepsilon(\theta', \phi', \alpha_1(\theta, \phi))$ is given by equation (3) but with $\alpha_1(\theta, \phi)$ instead of α_1 . In our proposed method, we select the $\alpha_1(\theta, \phi)$ which minimizes the average error (5) as the coefficient α_1 . Our proposed algorithm is shown in Fig. 1.

III. NUMERICAL VERIFICATION

Using the algorithm shown in Fig. 1, α_1 coefficients were obtained for various rectangular cells, as shown in Table I.

Here, λ is the wavelength. In the calculations, the angular steps, $\Delta\theta$ and $\Delta\phi$, were set to 1° , so the number of calculation loops was $3 \times 91 \times 91$. The calculation time was 7 seconds on an Intel Core 2 Duo processor (2.4 GHz) and is independent of N , the number of significant digits of α_v . In the previous method, the computational cost is proportional to $10^{2N} \times 91 \times 91$ for $\alpha_{v=1,2}$ and it took 42 minutes to obtain α_v .

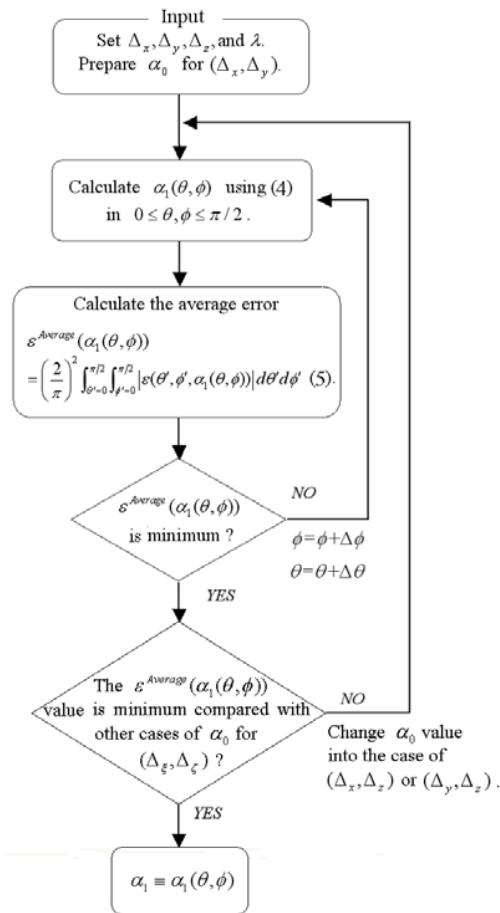


Fig. 1. Search algorithm for α_1 in three dimensions. To obtain the best α_1 , 2D coefficient α_0 that gives minimum value of $\epsilon^{Average}(\alpha_1(\theta, \phi))$ from three cases of (Δ_x, Δ_y) , (Δ_x, Δ_z) , and (Δ_y, Δ_z) is selected at the 2nd decision part.

for $N=4$, i.e. the cost was 360 times. We found that $N=6$ was necessary to maintain the high accuracy of the NS-FDTD, so the computational time becomes 42×10^4 minutes for the previous method. Note that the computing time to derive α_0 is negligible in Fig. 1. Thus our new method can reduce the calculation time dramatically.

Fig. 2 shows the minimum and maximum values of the normalized numerical phase velocity c_n/c_0 obtained from the numerical dispersion equation [3] for propagation angle θ , where the cell size is $(\Delta_x = \lambda/10, \Delta_y = \lambda/20, \Delta_z = \lambda/40)$ as an example. For comparison the results are shown when the coefficients $\alpha_{1,2,3}$ are obtained using the previous method [3]

and $\alpha_{1,2,3}$ for cubic cells [1], [2] are used. It is clear that the NS-FDTD has high accuracy and isotropy when our coefficient α_1 is used, as was also the case with the previous method. Consequently, the validity of our proposed method for α_v has been verified.

TABLE I
 α_1 IN THREE DIMENSIONS

Δ_x	Δ_y	Δ_z	α_1
$\lambda/10$	$\lambda/10$	$\lambda/10$	0.707742 ($\alpha_0 = 0.831119$)
$\lambda/10$	$\lambda/10$	$\lambda/20$	0.686118 ($\alpha_0 = 0.831119$)
$\lambda/10$	$\lambda/20$	$\lambda/30$	0.756030 ($\alpha_0 = 0.830203$)
$\lambda/10$	$\lambda/20$	$\lambda/40$	0.733334 ($\alpha_0 = 0.830203$)

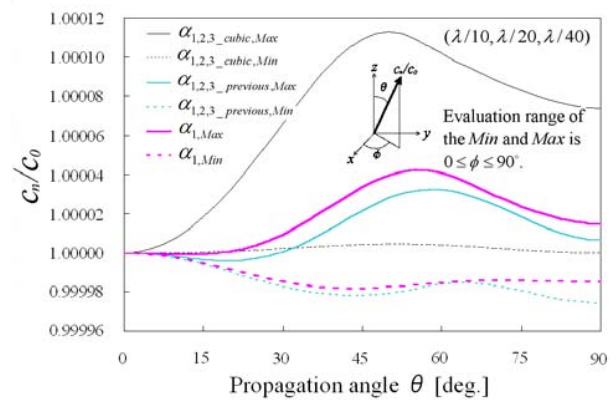


Fig. 2 Minimum and maximum values of the normalized numerical phase velocity c_n/c_0 versus propagation angle θ in $0 \leq \phi \leq 90^\circ$ range. The subscript “cubic” means $\alpha_{1,2,3}$ of cubic cell was used [1], [2], “previous” means $\alpha_{1,2,3}$ of the previous method [3] was used. c_0 is the physical phase velocity.

IV. CONCLUSION

We have proposed an efficient method to obtain the coefficients α_v of the finite difference operators for the rectangular cell NS-FDTD method. As a result, our method reduces the computing time dramatically for obtaining the three-dimensional α_v while maintaining the accuracy of the NS-FDTD.

V. REFERENCES

- [1] J. B. Cole, “High accuracy nonstandard finite-difference time-domain algorithms for computational electromagnetics: Applications to optics and photonics,” in *Advances in the Applications of Nonstandard Finite Difference Schemes*, R. E. Mickens, Ed. Singapore: World Scientific, 2005.
- [2] T. Ohtani, H. Kudo, and T. Kashiwa, “Scattering analysis of large-scale cavities using the nonstandard FDTD Method,” *Electronics and Communications in Japan*, Part 2, vol. 84, no. 12, pp. 8-16, Dec. 2001.
- [3] T. Ohtani, K. Taguchi, and T. Kashiwa, “New optimization parameters for the nonstandard FDTD method,” *Microwave Opt. Technol. Lett.*, vol. 42, no. 2, pp. 161-163, Oct. 2005.

Investigation of UHF Circular Loop Antennas for RFID

K. Preis¹, Member IEEE, O. Bíró¹, T. Bauernfeind¹ and Igor Tičar²

¹Institute for Fundamentals and Theory in Electrical Engineering, Graz University of Technology
Kopernikusgasse 24, 8010 Graz, Austria

kurt.preis@tugraz.at

²Faculty of Electrical Engineering and Computer Science, University of Maribor, Smetanova ul. 17, 2000
Maribor, Slovenia

Abstract — In Radio Frequency Identification (RFID), the design and investigation of UHF circular loop antennas used as reader antennas as well as tag antennas is of growing importance. Since these antennas are electrically short, a 2D FEM analysis using a single-component magnetic vector potential together with PML's at the boundary is proposed in this paper in order to perform very fast and accurate axisymmetric simulations compared with very time consuming 3D calculations. In addition, the capacitances of the tag loops have been calculated using a 3D quasi-static electric approach taking the gap of the loops into account.

I. INTRODUCTION

UHF-RFID systems [1] consisting of a reader and one or more tag antennas are working at frequencies of about 1 GHz. In case of axisymmetric reader loops, tag loops and objects to be identified, a 2D axisymmetric FEM analysis using a one component magnetic vector potential and Perfectly Matched Layers (PML's) at the boundary can be used with advantage (high accuracy combined with minimal computational effort compared with 3D solutions [2]). However, the axisymmetric assumption is only valid, if the loops are small enough compared with the wavelength (electrically short).

In Fig. 1, the half model of a tag loop is shown. It consists of a loop with a gap where the IC is placed. The loop is on the surface of a substrate. Typical parameters of such a tag loop made of copper are a mean radius of 9mm, a cross section of 500 x 35µm and a substrate permittivity of 4. The thickness of the substrate is assumed to be 0.6mm. The gap width is taken to be 400µm and is neglected in case of solving the wave equations but not for calculating the capacitances.

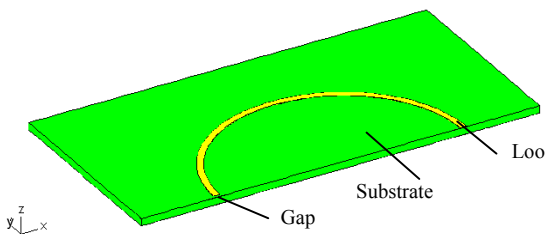


Fig. 1. Half model of a circular tag loop. Gap in the axisymmetric solution neglected

Reader loops are built similarly. Due to their larger radius

(radius = 40 mm in the example), they have several gaps equally spaced along the circumference, whereby appropriate lumped capacitances are connected to the gaps in order to provide a constant current along the loop.

II. FORMULATIONS

Wave propagation phenomena can be described by Maxwell's equations using a magnetic vector potential \mathbf{A} and an electric scalar potential v (\mathbf{A}, v formulation). The field quantities \mathbf{E} and \mathbf{B} and the governing differential equations using a complex conductivity σ_c are then given by:

$$\mathbf{B} = \text{curl} \mathbf{A} \quad \text{and} \quad \mathbf{E} = -j\omega(\mathbf{A} + \text{grad} v) \quad (1)$$

$$\text{curl}(v \text{curl} \mathbf{A}) + j\omega\sigma_c \mathbf{A} + j\omega\sigma_c \text{grad} v = \mathbf{0} \quad (2)$$

$$-\text{div}(j\omega\sigma_c \mathbf{A} + j\omega\sigma_c \text{grad} v) = 0 \quad (3)$$

together with the appropriate boundary conditions.

In the axisymmetric case, (2) and (3) reduce to

$$\frac{\partial}{\partial r} \left(v \frac{\partial r A}{\partial r} \right) + \frac{\partial}{\partial z} \left(v \frac{\partial A}{\partial z} \right) - j\omega\sigma_c A = -\sigma_c \frac{U_e}{2\pi r}, \quad (4)$$

where U_e is the impressed voltage per loop.

Applying the superposition principle yields the admittance matrix \mathbf{Y} of the loop system. To get the matrix, as many calculations as there are loops in the system must be performed. Using a direct solver, only multiple right hand sides have to be taken into account. The loops can be voltage or current driven a fact that can be taken into account with the aid of the expression

$$\mathbf{I} = \mathbf{Y} \mathbf{U}, \quad (5)$$

where \mathbf{I} and \mathbf{U} are the vectors of the loop currents and voltages, respectively.

The capacitances of the tag loops are neglected in the axisymmetric model. They can be taken into account by additional 3D quasi-static electric field calculations. The differential equation for these analyses is

$$\text{div } \sigma_c \text{ grad} V = 0 \quad (6)$$

together with the appropriate boundary conditions. The loops are excited in the gap by a given voltage. The capacitance of the loops can be obtained from the electric energy. The capacitances thus computed can be used to update the admittance matrix \mathbf{Y} . This quasi-static approach is possible, since the dimension of the tag loops (radius = 10mm) is small compared with the wavelength of 300mm at 1GHz.

III. EXAMPLES

To verify the method, a circular loop antenna with a mean radius of 9.625mm with rectangular cross section of 0.25 x 0.25mm (conductivity = $5.7 \cdot 10^7$ S/m) has been analyzed at a frequency of 1GHz. By integration of the Poynting vector over a closed surface, a radiation resistance of 0.3273 Ω results. The analytical result for a circular filament loop with a radius of 9.625mm given by

$$R_r = \frac{2}{3} \pi \eta \left(\frac{2\pi^3 r^2}{\lambda^2} \right)^2 \quad (7)$$

is 0.3257 Ω showing an excellent agreement. In addition, the eddy current losses in the loop result in an AC resistance of 0.6267 Ω which is almost two times higher than the radiation resistance.

In the example shown in Fig. 2, the loop system consists of a reader and a stack of two close coupled tag loops (10mm distance) at a distance of 70mm from the reader. The reader is driven by 1V. The tag loops are terminated by $Z_1 = 50\Omega$ and $Z_2 = 50\Omega$. From the admittance matrix and with $U_1 = Z_1 I_1$ and $U_2 = Z_2 I_2$, the currents in the tag loops and in the reader can be obtained from (5).

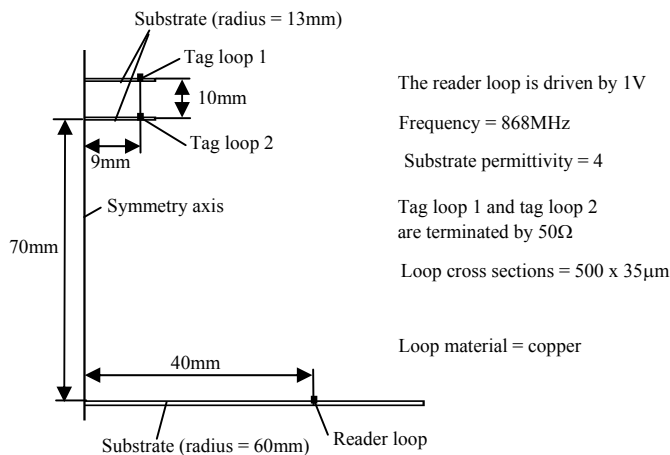


Fig. 2. System of a reader loop and two close coupled tag loops. Up to 100 tag loops can be stacked in special arrangements.

The results are shown in Table 1. The currents and the phases in the tag loops are quite the same. In this example, the

capacitances of the tag loops are not taken into account. They can be considered by updating Z_1 and Z_2 .

TABLE I
CURRENTS IN THE READER AND TAG LOOPS

	Current (μ A)	Phase (deg)
Tag-loop 1	8.316	46.37
Tag-loop 2	10.94	53.41
Reader	692.1	-88.06

The capacitances of the tag loops can be calculated using the quasi-static electric approach solving equation (6). In Fig. 3, the potential distribution is shown at the surface of a single loop and at the surface of the substrate.

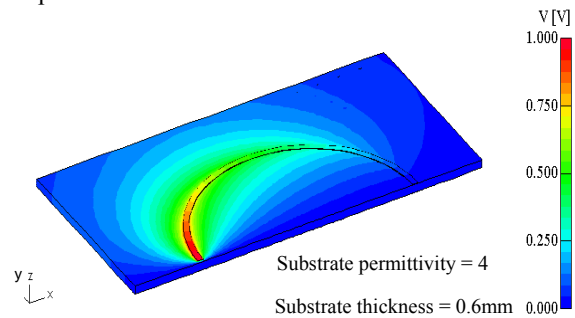


Fig.3. Single tag loop: $C = 0.138$ pF (without substrate: $C = 0.0661$ pF).

The capacitance obtained from the 3D quasi static electric field calculation is 0.138pF and the inductance from the axisymmetric approximation is 47nH.

For comparison, the 3D full wave solution for the single loop at $f = 868$ MHz results in $C = 0.135$ pF and $L = 47.3$ nH.

In the second case (Fig. 4), a close coupled tag loop system (distance = 1.54mm) is shown. In this case the lower loop is driven and the upper loop is at floating potential. The capacitance is more than twice as high as that of the single loop without substrate.

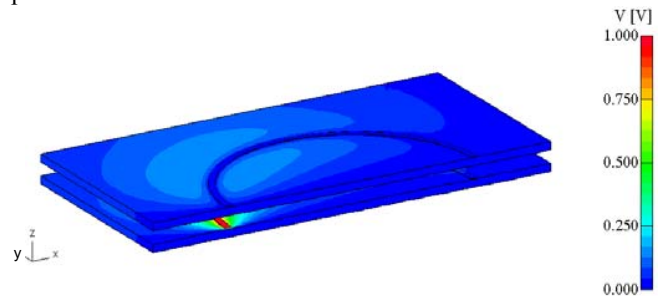


Fig. 4. Stack of two close coupled tag loops. The distance of the loops is 1.54mm. The lower loop is driven. $C = 0.159$ pF

IV. REFERENCES

- [1] P. V. N. Nikitin, K. V. S. Rao, S. Lazar, "An Overview of Near Field UHF RFID," *IEEE International Conference on RFID*, 2007, pp.167-174.
- [2] K. Hollaus, O. Biro, K. Preis, C. Stockreiter, "Edge finite elements coupled with a circuit for wave problems," *Proceedings of 10th ICEAA '07*, Torino, Italy, 2007

Full Wave Analyses of Electromagnetic Fields with an Iterative Domain Decomposition Method

A. Takei¹, S. Sugimoto¹, M. Ogino², S. Yoshimura¹, and H. Kanayama²

¹Department of Systems Innovation, School of Engineering, The University of Tokyo,
7-3-1, Hongo, Bunkyo-ku, Tokyo 113-8656, Japan

²Department of Mechanical Engineering, Faculty of Engineering, Kyushu University,
744, Motoooka, Nishi-ku, Fukuoka 819-0395, Japan
takei@save.sys.t.u-tokyo.ac.jp

Abstract— This paper describes large-scale full wave analyses of electromagnetic fields by the finite element method with an iterative domain decomposition method. A stationary Helmholtz equation for the high-frequency electromagnetic field analyses is solved taking an electric field as unknown functions. Then, to solve subdomains by the direct method, the direct method based on the LDL^T decomposition method is introduced in subdomains. If the direct method is applied for solving subdomain problems, the computation time seems to be reduced by the improved accuracy of subdomain problems, and storing matrices that are results of the decomposition on main memory.

I. INTRODUCTION

The finite element method has been used to solve the Helmholtz equations in high-frequency electromagnetic problems, resulting in solving large-scale systems of simultaneous linear equations. Dealing with such large-scale problems is a crucial issue in solving system of equations derived from finite element discretization of the Helmholtz equations in high-frequency electromagnetic problems[1]. Currently, we are conducting research on large-scale finite element analyses for electromagnetic fields in the range of several MHz to several GHz by using parallelization techniques based on the iterative domain decomposition method (IDDM). The IDDM based on the conjugate orthogonal conjugate gradient (COCG) method is applied to solve the interface problem. Previously, an iterative method was applied to the subdomain problem. However, the convergence property of the interface problem was not good in solving large-scale problems of over 10 million complex DOFs. In this study, the direct method based on the LDL^T decomposition method is applied to the subdomain problem. In this paper, we provide the numerical examples of about 50 million complex DOFs based on the formulation of the E Method[2].

II. FINITE ELEMENT FORMULATION

Let Ω be a domain with the boundary $\partial\Omega$. The Helmholtz equations which describe an electromagnetic field with single angular frequency ω [rad/s] are drawn from Maxwell's equations containing the displacement current. The Helmholtz equations describing an electric field \mathbf{E} [V/m] are given by (1a) and (1b) below, using the current density \mathbf{J} [A/m²] and the electric field \mathbf{E} , and assigning j as an imaginary unit:

$$\text{rot}(\frac{1}{\mu} \text{rot} \mathbf{E}) - \omega^2 \varepsilon \mathbf{E} = j\omega \mathbf{J} \quad \text{in } \Omega \quad (1a)$$

$$\mathbf{E} \times \mathbf{n} = \mathbf{0} \quad \text{on } \partial\Omega \quad (1b)$$

$$\mathbf{J} = \sigma \hat{\mathbf{E}} \quad (1c)$$

Permittivity and permeability are given by ε [F/m] and μ [H/m], respectively. In this formulation, permittivity becomes complex permittivity $\varepsilon = \varepsilon' + \sigma/j$. The electric field \mathbf{E} on known points is substituted into (1a) by equation (1c), where the electrical conductivity is denoted as σ . By solving equation (1a), with imposing the boundary condition of (1b), we calculate the electric field \mathbf{E} . The magnetic field \mathbf{H} is then calculated from the electric field \mathbf{E} by post-processing using equation (2) below, which is one of Maxwell's equations[2].

$$\text{rot} \mathbf{E} - j\omega \mu_0 \mu_r \mathbf{H} = \mathbf{0} \quad (2)$$

Finally, we assume that

$$\text{div} \mathbf{J} = 0 \quad \text{in } \Omega \quad (3)$$

Next, we describe the finite element discretization. The electric field \mathbf{E} is approximated with Nedelec elements (edge elements)[3]. The finite element approximation is performed as follows.

Find \mathbf{E}_h such that

$$(\frac{1}{\mu} \text{rot} \mathbf{E}_h, \text{rot} \mathbf{E}_h^*) - \omega^2 (\varepsilon \mathbf{E}_h, \mathbf{E}_h^*) = j\omega (\mathbf{J}_h, \mathbf{E}_h^*) \quad (4)$$

where (\cdot, \cdot) denotes the complex valued L^2 -inner product. Here, \mathbf{J}_h is a corrected electric current density with consideration of the continuity[4].

III. ITERATIVE DOMAIN DECOMPOSITION METHOD

We introduce the IDDM to high-frequency problems using the E method. Let us put the finite element equations of (4) in matrix form, as follows:

$$Ku = f \quad (5)$$

where K denotes the coefficient matrix, u the unknown vector, and f the known right-hand side vector. The domain Ω is partitioned into non-overlapping subdomains. Then the linear system (5) is rewritten as follows:

$$\begin{bmatrix} K_I^{(1)} & \cdots & 0 & K_{IB}^{(1)} R_B^{(1)T} \\ 0 & \ddots & \vdots & \vdots \\ 0 & \cdots & K_I^{(N)} & K_{IB}^{(N)} R_B^{(N)T} \\ R_B^{(1)} K_{IB}^{(1)T} & \cdots & R_B^{(N)} K_{IB}^{(N)T} & \sum_{i=1}^N R_B^{(i)} K_{BB}^{(i)} R_B^{(i)T} \end{bmatrix} \begin{bmatrix} u_I^{(1)} \\ \vdots \\ u_I^{(N)} \\ u_B \end{bmatrix} = \begin{bmatrix} f_I^{(1)} \\ \vdots \\ f_I^{(N)} \\ f_B \end{bmatrix} \quad (6)$$

where subscripts I, B correspond to nodal points in the interior of the subdomains and on the interface boundary, respectively. Here, $R_B^{(i)T}$ represents the internal DOFs $u_B^{(i)}$ of subdomain $\Omega^{(i)}$ about u_B . It is a 0-1 procession to restrict.

At first, the unknown vector u_B is obtained from the application of the COCG method. After solving u_B , the vector $u_I^{(i)}$ is solved by the direct method with the LDL^T decomposition method, and can also be solved independently in each subdomain. Hence, we can get the unknown in the

whole domain[2][4]. The IDDM is implemented in a parallel computing environment using the hierarchical domain decomposition method (HDDM). In this paper, we use P-mode that is one of the parallel data handling types of HDDM, see [2] and [4].

IV. NUMERICAL EXAMPLES

A reentrant resonator model is used to verify the accuracy and performance of the parallel computation, of our proposed method. It is one of the benchmark problems defined as TEAM (Testing Electromagnetic Analysis Method) Workshop Problem 29[5]. The verification is performed on three kinds of meshes, as described in Table I. Mesh(1)-(4) are divided into first-order tetrahedral Nedelec elements.

TABLE I
MESHES FOR VERIFICATIONS

Mesh	Element	DOF	Num. of Subdomain
(1)	108,787	134,889	60 x 11
(2)	5,043,711	6,792,202	60 x 494
(3)	17,367,244	23,213,252	60 x 1,703
(4)	40,349,688	54,236,667	60 x 3,956

A. Accuracy Verification

Accuracy verification is performed using Mesh (1). To detect the resonant frequency and to compare solutions with actual measurements, the resonance state is investigated. The frequency band of 60 [MHz]-140 [MHz] is calculated for 2 [MHz] steps, and the response for every frequency step is investigated. All calculations are performed on a 15-node (60-core) PC cluster with Core2Quad Q6600 (2.40 GHz / L2 8 MB) and 8 GB RAM. A comparison between the measured resonant frequencies and the solutions obtained by the FDTD method in each mode is shown in Table II. The obtained solutions are in very good agreement. The maximum error rate between the obtained solution and the measurement is 4.96% in the 1st mode. As the mode becomes higher, the error rate decreases. The same tendency is shown in the comparison of the error rate with solution of the FDTD method. Therefore, it is proved that the solution obtained by the proposed method has sufficiently high accuracy.

TABLE II
RESONANT FREQUENCIES IN MHz ((): ERROR RATE BETWEEN MEASURED DATA AND NUMERICAL SOLUTIONS [%])

Mode	Measured ^(s)	FDTD ^(s) 25mm mesh	Result
1 st	68.6	67 (2.33)	65.2 (4.96)
2 nd	110	110	109 (0.91)
3 rd	134	134	134

B. Performance Verification

Performance verification by large-scale computation using Mesh (2)-(4) is described next. In the analyses, the 1st mode (65.2 [MHz]) frequency is analyzed. Other calculation conditions are the same as those for Mesh (1). Average CPU time and average memory requirements are shown in Table III. For Mesh (2) solving with the direct method based on the LDL^T decomposition method to the subdomain problem, the CPU time is reduced by 56% as compared to that of the incomplete Cholesky conjugate orthogonal conjugate gradient (ICCOCG) method to the subdomain problem. For Mesh (3)

and (4), solving with the ICCOCG method to the subdomain problem does not converge, but the direct method successfully converges to compute a result. Although the direct method uses approximately 40% more memory, the total amount used exceeds 65% of the available RAM, even for Mesh (4). Therefore, we do not consider memory usage to be a problem. The residual norm convergence history of COCG iterations in the interface problem is shown in Fig. 1. In the calculations with Mesh (4), we can see the convergence behavior of the ICCOCG method to the subdomain problem. Here the interface problem does not converge even after 40,000 iterations. In contrast, by the direct method, convergence is achieved after 29,235 iterations with a calculation time of 20.7 [h]. Those results confirm the superiority of the direct method to the subdomain problem in large-scale computations. It is also demonstrated that the proposed method using a direct method for subdomain problems is able to solved high-frequency electromagnetic field problems of more than 50 million complex DOFs.

TABLE III
CPU TIME AND MEMORY REQUIREMENTS FOR EACH MESH

	Solver for Subdomains	Iteration counts	CPU time[h]	Memory size [M Byte]
Mesh(2)	LDL^T	5,625	0.8	83
	ICCOCG	6,532	1.8	59
Mesh(3)	LDL^T	8,513	3.0	294
	ICCOCG	—	—	—
Mesh(4)	LDL^T	29,235	20.7	683
	ICCOCG	—	—	—

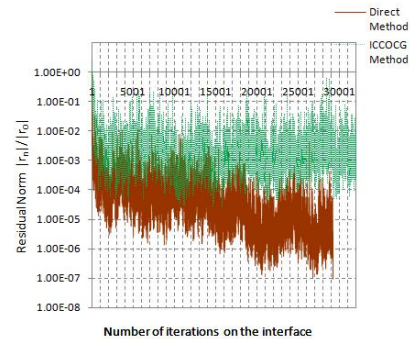


Fig. 1. Residual norm on the interface (Mesh(4))

V. REFERENCES

- [1] P. Liu, Y. Q. Jin, "The Finite-element Method with Domain Decomposition for Electromagnetic Bistatic Scattering from the Comprehensive Model of a Ship on and a Target Above a Large-scale Rough Sea Surface", IEEE Trans. Geos., Vol.42, No.5, pp.950-956(2004)
- [2] A.Takei, S. Yoshimura, H. Kanayama, "Large-Scale Parallel Finite Element Analyses of High Frequency Electromagnetic Field in Commuter Trains", CMES: Computer Modeling in Engineering & Sciences, Vol.31, No.1, pp.13-24 (2008)
- [3] F. Kikuchi, "Numerical Analysis of Electrostatic and Magnetostatic Problems", Sugaku Expositions, Vol.6, No.1, pp.33-51 (1993)
- [4] H. Kanayama, S. Sugimoto, "Effectiveness of A- ϕ Method in a Parallel Computing with an Iterative Domain Decomposition Method", IEEE Trans. Mags., Vol.42, No.4, pp.539-542 (2006)
- [5] Y.Kanai, "Description of TEAM Workshop Problem 29:Whole body cavity resonator", TEAM Workshop in Tucson (1998)

A New Waveguide Design Based in Thin Films of Niobium and Tantalum

Marcílio Nunes Freire and José Patrocínio da Silva
Environmental Science Department, UFERSA, Mossoró/RN, 59624-900, Brazil
patroc@ufersa.edu.br, nunesfreire@ufersa.edu.br

Abstract — Results of a simplified experimental apparatus used to obtain *in situ* optoelectrochemical measurements of the anodizing voltage versus time versus especular reflectance are used to design a new type of waveguide. The application of experiment was used to determine the thickness and refractive index (for wave-length of 0.6329 μm) of the waveguide. The proposed structure exhibits a simple geometry, and has been analyzed through a vectorial finite element BBP, FE-VBPM.

Keywords — Numerical Techniques, Waveguide, Thin Films.

I. INTRODUCTION

It's well known that thin films of niobium and tantalum pentoxides and its mixed oxides $(Nb,Ta)_2O_5$ can be grown anodically on the surface of metals, Nb, Ta and its alloys Nb-Ta, by placing samples in an electrochemical cell containing aqueous solution and three electrodes under a suitable anodic voltage. The anodizing process occurs under direct current until the applied voltage is no more sufficient to produce it. These films exhibit several colors depending upon the thickness [1, 2]. The anodic oxide films grown on the substrate surface of niobium and tantalum and its alloys may be applied as electronic devices just as: store condenser of random access memory [3], gate in transistors [4], electronic holes [5], electroluminescent panels [6], pH and humidity sensors [7], and optical waveguide [8]. The anodic oxide films have accepted attention in last decades due its good dielectric properties. These films constitute the proposed structure that is formed by one fine layer of $(Nb20\%wTa)_2O_5$ on a niobium pentoxide substrate as showed in Fig. 1. The new waveguide proposed has been analyzed by efficient vectorial finite element method [9].

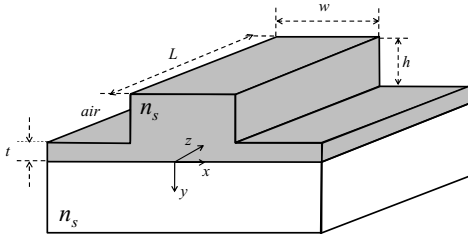


Fig. 1. Rib waveguide

II. FINITE ELEMENT FORMULATION

We start from the second order vectorial Helmholtz equation in two dimensions, including the perfectly matching layers in order to avoid reflections,

$$\nabla \times \left(\bar{\bar{k}} \nabla \times \bar{H} \right) - k_0^2 \bar{H} = 0 \quad (1)$$

where, $\bar{\bar{k}} = 1/\bar{\bar{\epsilon}}$, with $\bar{\bar{\epsilon}}$ being the relative permmissivity tensor. Considering the dielectric media with transverse anisotropy, and defining the \hat{u}_x , \hat{u}_y and \hat{u}_z associated with x, y, and z

directions, respectively, $\bar{\bar{\epsilon}}$ can be written as $\bar{\bar{\epsilon}} = \epsilon_{xx}\hat{u}_x\hat{u}_x + \epsilon_{xy}\hat{u}_x\hat{u}_y + \epsilon_{yx}\hat{u}_y\hat{u}_x + \epsilon_{yy}\hat{u}_y\hat{u}_y + \epsilon_{zz}\hat{u}_z\hat{u}_z$. After some algebraic manipulations and assuming that the media and fields vary very slowly along the propagation coordinate [10]-[11], the equation (1) can be written as:

$$\begin{aligned} \bar{k}_a \frac{\partial^2 \bar{h}_T}{\partial z^2} - 2\gamma \bar{k}_a - \bar{k}_b \nabla_T (\nabla_T \cdot \bar{h}_T) - \nabla_T \times \bar{k}_{zz} \nabla_T \times \bar{h}_T \\ + (\bar{k}_c + \gamma^2 \bar{k}_a) \bar{h}_T = 0 \end{aligned} \quad (2)$$

Consequently the transverse tensors in (1) are defined as,

$$\bar{k}_a = \begin{bmatrix} k_{yy} & -k_{yx} \\ -k_{xy} & k_{xx} \end{bmatrix} \quad (2a)$$

$$\bar{k}_b = \gamma^{-1} \frac{\partial \bar{k}_a}{\partial z} - \bar{k}_a \quad (2b)$$

$$\bar{k}_c = k_0 - \gamma^{-1} \frac{\partial \bar{k}_a}{\partial z} \quad (2c)$$

$$\nabla_T = \hat{u}_x \alpha_x \frac{\partial}{\partial x} + \hat{u}_y \alpha_y \frac{\partial}{\partial y} \quad (2d)$$

where α_x , and α_y are parameters linked to the PML or virtual loss media. Since the waves are assumed to propagate along the z direction, the parameters α_x , and α_y have to be determined in such a way that the wave impedance is continuous across the interfaces formed between the inner computational domain and the PML. This ensures perfect wave matching over such interfaces, allowing the undesired radiation to leave the effective computational domain freely without any reflection. The PML parameters are specified from the parameter S given by $S = 1 - j(3c/2\omega_0 nd)(\rho/d)^2 \ln(1/R)$ [9], where ω_0 is the angular frequency, d is the thickness of the PML, n is the refraction index of the adjacent medium, ρ is the distance from inner PML's interface, R is the reflection coefficient, and c is the free-space speed of light.

Applying the conventional finite element method to the transverse variation of (2), the following differential equation is obtained:

$$[M] \frac{\partial^2 \{\bar{h}_r\}}{\partial z^2} - 2\gamma[M] \frac{\partial \{\bar{h}_r\}}{\partial z} + ([K] + \gamma^2[M]) \{\bar{h}_r\} = \{0\} \quad (3)$$

where $\{\bar{h}_r\}$ represents a column vector containing the unknowns hxj and hyj , $\{0\}$ is the null column vector, and $[M]$ and $[K]$ are the so-called global matrices, defined in [9]. Applying the Padé (1,1) approximation [9], to (4) the matrix equation given below is obtained,

$$[\tilde{M}] \frac{d\{\bar{h}_r\}}{dz} + [K]\{\bar{h}_r\} = \{0\} \quad (4)$$

with, $[\tilde{M}] = [M] - \frac{1}{4\gamma^2}([K] + \gamma^2[M])$.

III. NUMERICAL RESULTS

The results of a simplified experimental apparatus used to obtain in situ optoelectrochemical measurements of the anodizing voltage versus time versus specular reflectance, while the oxide films were growing by galvanostatic anodizing, has been used to design a new waveguide type. The results of the experiment were used to determine the thickness and refractive index (for wave-length of 0.6329 μm) of the films. The Table I shows that characterization of experiment to obtain the refractive indexes.

TABLE I
REFRACTIVE INDEX AND THICKNESS OF ANODIC OXIDE FILMS
GROWN IN *Nb* AND *Nb-Ta* SUBSTRATE

Material	Thickness (\AA)	Wavelength (μm)	Refractive index
<i>Nb₂O₅</i>	2.025 ± 64	0.6329	2.02 ± 0.06
<i>Nb20%wTa</i>	1.652 ± 32	0.6329	2.64 ± 0.05

In order to confirm the application of the FE-VBPM for analysis of the waveguide shown in Fig. 1, we consider $n_s = 2.02$, $n_g = 2.64$, $L = 500 \mu\text{m}$, $t = 0.1 \mu\text{m}$, $w = 1.4 \mu\text{m}$ and $h = 0.85 \mu\text{m}$. The substrate thickness was 3.5 μm and the computational domain considered was 9 μm (x direction) x 9 μm (y direction) surrounded by PML's with thickness $d = 1 \mu\text{m}$ covered by 12,000 linear elements with a propagation step size $\Delta z = 0.1 \mu\text{m}$. The structure was excited with one gaussian beam, given by $h_y = A \exp(-x^2 + y^2)/2\sigma$, where A is the amplitude of the beam and σ is the spot beam. The wavelength considered was $\lambda = 0.6329 \mu\text{m}$. Fig. 2 shows magnetic-field distributions of the y -polarized guide, Fig.2a shows the y -component of magnetic field launched in the structure, Fig. 2b shows the y -component of magnetic field after 500 μm propagated.

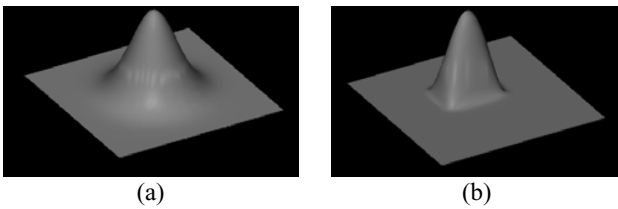


Fig. 2. Magnetic-field distributions of the y -polarized mode rib waveguide for (a) $z = 0 \mu\text{m}$, (b) $500 \mu\text{m}$.

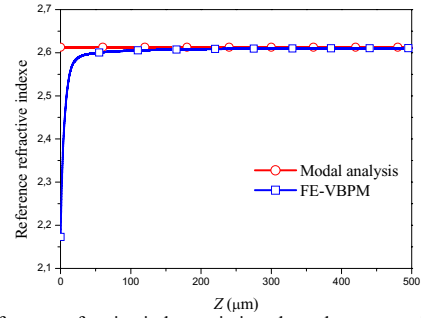


Fig. 2. Reference refractive index variation along the propagation distance

Fig. 3 shows the convergence of the reference refractive index along the propagation direction in comparison with the results obtained using the modal analysis [10]. The loss in the waveguide after 1.0 km of the propagation is around 2.56×10^{-16} dB. This value has been obtained through of the subtraction between the maximum value of the magnetic field after 1.0 km of propagation and the maximum value of the magnetic field obtained through the modal analysis.

IV. CONCLUSIONS

A vectorial finite-element BPM for transverse anisotropic media was applied successfully to the analysis of a rib waveguide constituted by *Nb* and alloy of *Nb-Ta*. The refractive indexes used for constitute the waveguide was obtained thought experiments using anodic oxide films grown on *Nb* and alloy of *Nb-Ta* substrates by *in situ* monitoring. The resulting structure has a simple geometry and its optimization by using genetic algorithms is under consideration for applications in Passive Polarization Converter.

ACKNOWLEDGEMENT

The authors would like acknowledging the FAPERN and CNPq financial support (process number 563271/2008-6).

V. REFERENCES

- [1] M. Nunes Freire, "Estudo e Caracterização de Filmes Óxidos Anódicos Crescidos sobre Ligas Nb-Ta por Monitoração In Situ", *Master Thesis Universidade Federal do Rio Grande do Norte, Brazil*, pp. 01, 2001.
- [2] M. N. Freire, U. U. Gomes and J. F. Julião, "Study on Anodic Oxide Films in Nb-Ta Alloys by In Situ Optoelectrochemical Measurements", *ICCE 8*.
- [3] G. S. Oehrlen, F. M. d'Heurle, A. Reisman, *J. Appl. Phys.*, 55, 3716, 1984.
- [4] K. Nomura, H. Ogawa, A. Abe and T. Nitta. *Proceedings of Japan Display "83"*, 574, 1983.
- [5] R. Cabanel, J. Chaussy, J. Mazuer, G. Delabouglise, C. Jaubert, G. Barral and C. Montella. *J. Electrochem. Soc.*, 137, 1444, 1990.
- [6] J. Kuwata, Y. Fujita, T. Matsuoka, T. Thoda, M. Nishikawa and A. Abe, *Jpn. J. Appl. Phys.*, 24, 413, 1985.
- [7] M. A. Biazon Gomes and L. O. S. Bulhões, *Anais de VI SIBEE*, pp. 346-353, 1988.
- [8] O. D. Vol'pyn, Yu. A. Obod and P. P. Yakovlev, *J. Opt. Technol.*, 67(10), pp. 889-891, 2000.
- [9] J. P. da Silva, H. E. Hernandez-Figueroa and A. M. F. Frasson, "Improved vectorial finite-element BPM analysis for transverse anisotropic media, *IEEE Journal Light. Techn.*, 21 (2003), 567-576.
- [10] H. E. Hernández-Figueroa, F. A. Fernández, Y. Lu and J. B. Davies, *Vectorial finite element modelling of 2D leaky waveguides, IEEE Trans. Magn.* 31, 1710-1712, (1995).

Analysis of Simple FSS Cascading With Dual Band Response

Antonio L. P. S. Campos¹, Robson H. C. Maniçoba², Lincoln M. Araújo², and Adaildo G. d'Assunção²

¹ Instituto Federal de Educação, Ciência e Tecnologia do Rio Grande do Norte, Campus Natal – Zona Norte, Rua Brusque, 2926, Conj. Santa Catarina – Potengi, CEP: 59112-450 Natal, RN, Brazil. Phone/Fax: +55-21-84-4006-9509 E-mail: antonioluiz@cefetrn.br

² Federal University of Rio Grande do Norte, Department of Electrical Engineering Caixa Postal 1655, CEP: 59072-970; Natal, RN, Brazil.

E-mails: robsonhcm@gmail.com, machado.lincoln@gmail.com, adaildo@ct.ufrn.br

Abstract — Numerical and experimental investigations are presented for a dual-band frequency selective surface (FSS) with perfectly conducting rectangular patch elements. The work was developed in two steps. In the first step two single-band FSS screens were designed to obtain resonant frequencies at 9.5 GHz and 10.5 GHz, each one with about 1.5 GHz bandwidth. In the second step these single FSS screens were cascaded and separated by an air gap layer to achieve a dual-band response. The Moment Method is used to analyze the structures single band. After this, a numerical cascading technique is used to analyze the effect of the air gap between the cascading structures.

I. INTRODUCTION

Recently, we can observe an increasing demand on the multifunctional antennas for communication that requires the development of FSS with multi-band characteristics [1]. The use of frequency selective surfaces (FSS) has been successfully proven as a mean to increase the communication capabilities of satellite platforms. In space missions such as Voyager, Galileo, and Cassini, the use of dual-reflector antennas with FSS sub-reflectors has made it possible to share the main reflector among different frequency bands.

Therefore frequency selective surfaces with dual-band and multi-band responses have been studied by several researchers. Hill and Munk in [2] used a perturbation technique in a single-band FSS to obtain a single-layer dual-band FSS, but attenuation lower than -10 dB was obtained.

Wu in [3] designed and measured a four-band FSS with double square loop patch elements. The designed structure was complex with two layers separated by a honey comb. The structure was designed to reflect the Ka-band signal and transmit the S-, X-, and Ku-band signals. In [4], Wu and Lee designed a FSS with with circular concentric non symmetric rings. A very complex structure was developed, with three layers and with cells out of phase.

This paper shows that a dual-band or multi-band FSS response can be obtained by cascading two or more single-band FSS screens with simple elements, such as rectangular conducting patches. Two prototypes were analyzed, fabricated and measured. These prototypes were cascading to obtain a dual band response. A numerical cascading technique was used to analyze the effect of the air gap between the FSSs with single response. A good agreement between numerical and experimental results was obtained.

II. SINGLE BAND STRUCTURE ANALYSIS

The single band analyzed structure is shown in Fig. 1. It is composed by an array of rectangular patch elements on a dielectric isotropic layer. A low cost fenolite dielectric substrate with height (h) equal to 1.5 mm and relative permittivity equal to 3.9 was used. The unit cell can be seen in Fig. 1(b). The cell has periodicity T_x and T_y in x and y directions, respectively. The rectangular conducting patch has width W and length L .

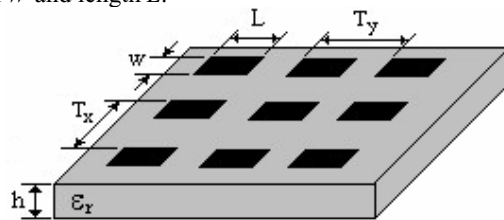


Fig. 1. FSS geometry: (a) Single band structure and (b) Unit cell.

The analysis of scattering from a bi-dimensional FSS involves the solution of the induced surface current on the conducting element of FSS by an incident plane wave. The response of the FSS on the frequency domain is obtained as a sum of the incident field and the scattered field radiated by the induced surface current density. It can be seen in (1) [5]:

$$\vec{E}_t^s + \vec{E}_t^{inc} = 0 \quad (1)$$

We assume that the FSS is infinitesimally thin and the entire domain basis functions are employed to represent the unknown induced surface current density in the patch elements. The scattered field is related to the surface current density using the components of the Green's function as we can see in (2) [5]:

$$\begin{bmatrix} \tilde{E}_x^s \\ \tilde{E}_y^s \end{bmatrix} = \sum_{m,n} \begin{bmatrix} \tilde{Z}_{xxmn} & \tilde{Z}_{xymn} \\ \tilde{Z}_{yxmn} & \tilde{Z}_{yy mn} \end{bmatrix} \begin{bmatrix} \tilde{J}_{xmn} \\ \tilde{J}_{ymn} \end{bmatrix} e^{j(x\alpha_m + y\beta_n)} \quad (2)$$

where \tilde{J}_x and \tilde{J}_y are the x and y components of the Fourier transforms of the current density; and \tilde{Z}_{xx} , \tilde{Z}_{xy} , \tilde{Z}_{yx} , and \tilde{Z}_{yy} are the components of the Green's function. The parameters α_m and β_n in (2) may be expressed as [5]:

$$\alpha_m = (2\pi m / T_x) + k_x^{inc} \quad (3)$$

$$\beta_n = (2\pi n / T_y) + k_y^{inc} \quad (4)$$

where k_x^{inc} and k_y^{inc} are the projections of the incident plane wave vector along the x and y directions, respectively.

III. DUAL BAND STRUCTURE ANALYSIS

The interaction among the N structure can be accounted for by using the scattering matrices. To be exact, the matrices are of infinite order. Here, we use the so-called "one-mode interaction." It means that only the main beam is used in calculating the interaction. Using the one-mode interaction, the final results of reflection and transmission coefficient for the cascading structure in Fig. 2 are [6]

$$T = A - (BC/D) \quad (5)$$

$$R = -(C/D) \quad (6)$$

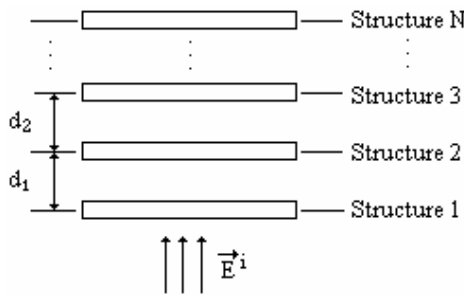


Fig. 2. Cascading FSS Structures.

The coefficients (A , B , C , D) are calculated in the following steps. First, for each sheet, we determine a 2×2 scattering matrix S , here

$$\bar{\bar{S}}_n = \begin{bmatrix} T_n(1 - R_n^2/T_n^2) & (R_n/T_n)e^{j2kl_n} \\ -(R_n/T_n)e^{-j2kl_n} & 1/T_n \end{bmatrix} \quad (7)$$

$$l_n = d_1 + d_2 + \dots + d_{n-1} \quad (8)$$

then

$$\begin{bmatrix} A & B \\ C & D \end{bmatrix} = \bar{\bar{S}}_n \bar{\bar{S}}_{n-1} \dots \bar{\bar{S}}_3 \bar{\bar{S}}_2 \bar{\bar{S}}_1 \quad (9)$$

IV. RESULTS

Fig. 3 shows a comparison between numerical and experimental results and a good agreement is observed. The structure 1 has a resonance that occurs at 9.3 GHz, with -26.96 dB for the results obtained with MoM, and it occurs at 9.55 GHz, with -54.08 dB for the measured results. The structure 1 has a resonance that occurs at 10.40 GHz, with -20.6 dB for the results obtained with MoM, and it occurs at 10.27 GHz, with -26.42 dB for the measured results.

Fig. 4 shows a comparison between numerical and experimental results for a cascading structure. We can observe a little difference between the results. The air gap was 1.5mm.

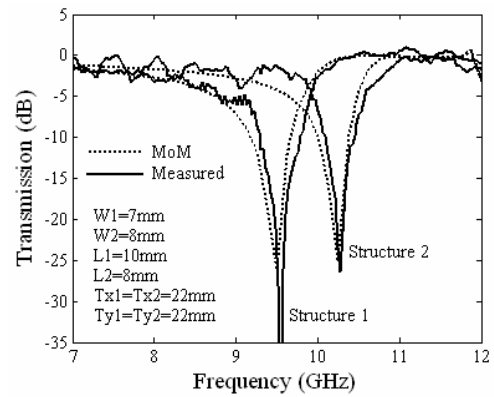


Fig. 3. Single band structure responses.

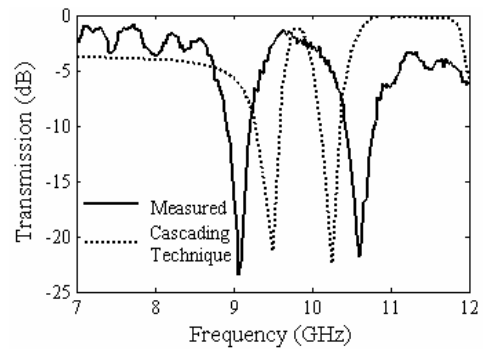


Fig. 4. Dual band structure response.

V. CONCLUSIONS

In this paper, a simple dual-band frequency selective surface was analyzed, fabricated and measured. We can see that the use of simple elements such as rectangular conducting patches can be used to obtain dual-band response. Numerical and experimental results were presented for single and dual-band FSSs. The agreement observed between experimental and numerical results validates the various analysis approaches described in this paper. The air gap can be used to control the separation between the cascaded FSS bands.

VI. REFERENCES

- [1] J. Romeu and Y. R. Samii, Fractal FSS: A novel dual-band frequency selective surface, *IEEE Trans Antennas Propagat* 48 (2000) 1097-1105.
- [2] R. A. Hill and B. A. Munk, The effect of perturbing a frequency selective surface and its relation to the design of a dual-band surface, *IEEE Trans Antennas Propagat* 44 (1996) 368-374.
- [3] T. K. Wu, Four-band frequency selective surface with double square loop patch elements. *IEEE Trans Antennas Propagat* 42 (1994) 1659-1663.
- [4] T. K. Wu and S. W. Lee, MultiBand frequency selective surface with multiring patch elements. *IEEE Trans Antennas Propagat* 42 (1994) 1484-1490.
- [5] A. L. P. S. Campos, A. G. d'Assunção, and L. M. Mendonça, "Scattering by FSS on anisotropic substrate for TE and TM excitation", *IEEE Transactions on Microwaves Theory and Techniques*, vol. 50, no 1, pp. 72-76, 2002.
- [6] S. W. Lee, G. Zarrillo e C. L. Law, "Simple Formulas for Transmission Through Periodic Metal Grids or Plates", *IEEE Transactions on Antennas and Propagation*, vol. 30 (5), 904 - 909, 1982.

A broadband symmetric surface integral equation based on Calderón projector

Annalisa Buffa⁽¹⁾, Guglielmo Rubinacci⁽²⁾ and Antonello Tamburrino⁽³⁾

⁽¹⁾ Istituto di Matematica Applicata e Tecnologie Informatiche, Via Ferrata 1, 27100 Pavia, Italy

⁽²⁾ Dipartimento di Ingegneria Elettrica, Università di Napoli Federico II

Via Claudio 21, Napoli, 80125, Italy

⁽³⁾ DAEIMI, Università di Cassino

Via G. Di Biasio 43, Cassino (FR), 03043, Italy

annalisa@imati.cnr.it, rubinacci@unina.it, tamburrino@unicas.it

Abstract—In this paper we consider the interaction of an electromagnetic wave with an homogeneous dielectric material. The numerical model of the interaction is described by a surface integral equation obtained by using the Calderón projector. This approach allows to improve significantly the condition number of the resulting linear system of equations as well as allows to develop an efficient preconditioner.

I. INTRODUCTION

In the last few decades we have experienced an unprecedented growth in the numerical methods for computing the electromagnetic field. Despite the intense effort made by researchers all around the World, the demands for faster and reliable numerical models is continuously increasing with the complexity of the devices such as electronic circuits, IC etc. Currently, computer aided design is entered in the common practice of electronic and electrical design and, moreover, the computational power of modern computers provides the resources to face problems of unpaired complexity. A current trend is in the development of numerical methods for the simulation of multiscale problems in a broad frequency range.

In this context, surface integral equations are very attracting for solving problems involving impenetrable bodies (usually PEC) or piecewise homogeneous penetrable materials [1]-[3]. Surface integral equations require the discretization of only the surfaces of PEC and/or the interfaces between different penetrable materials and incorporate the radiation condition. Moreover, fast numerical methods such as fast-multipole methods and SVD compression (see [4]-[7] and references therein) can be successfully used to reduce the computational cost when using iterative solvers to solve the related linear algebraic systems characterized by fully populated stiffness matrices.

The present contribution deals with frequency domain surface integral equations (EFIE type) for evaluating the full-wave 3D interaction of an electromagnetic wave with a homogeneous (eventually lossy) dielectric body. Classical EFIE operator present singular values accumulating at zero and

infinity [8]. Therefore, the condition number of the stiffness matrix arising from the discretization grows rapidly with the discretization thereby compromising the accuracy when applied to structures with subwavelength geometric features. In this framework, the role of the preconditioner is crucial. Recently, it has been show that the EFIE equation written by exploiting the Calderón projector operator bring to very effective preconditioners [9], [10]. These techniques exploit that the square of the EFIE operator does not have eigenvalues accumulating at zero or infinity [11]-[14]. In this contribution we want to lay the basis for: (i) a broadband numerical model for treating homogeneous dielectric bodies by using the Calderón projector operator and (ii) the related preconditioner. The integral equation is those proposed in [16] and will be coupled with a proper choice of shape functions to overcome the arise of the low-frequency breakdown problem [15]. Homogeneous dielectric materials have also been treated by means of Calderón projector operator in [17]. Here we are considering the integral model of [16], that is of minimum order, and we are developing the related efficient preconditioner.

II. NUMERICAL MODEL

The reference problem, sketched in figure 1, consists of the evaluation of the interaction of an electromagnetic field with a penetrable scatterer. The scatterer is homogenous, characterized by the material properties ε_1 and μ_1 and hosted in a homogenous infinite space (having material properties characterized by ε_2 and μ_2). The incident field is $(\mathbf{E}_2^{inc}, \mathbf{H}_2^{inc})$, the scattered field is $(\mathbf{E}_2, \mathbf{H}_2)$ and the transmitted field is $(\mathbf{E}_1, \mathbf{H}_1)$.

The integral equation follows from the concept of Calderón projector applied to full wave Maxwell equations as proposed in [16]:

$$\begin{bmatrix} M_1 + M_2 & \alpha_1 C_1 + \alpha_2 C_2 \\ \alpha_1^{-1} C_1 + \alpha_2^{-1} C_2 & M_1 + M_2 \end{bmatrix} \begin{bmatrix} \mathbf{m}_2 \\ \mathbf{j}_2 \end{bmatrix} = \begin{bmatrix} I/2 - M_1 & I/2 - \alpha_1 C_1 \\ I/2 - \alpha_1^{-1} C_1 & I/2 - M_1 \end{bmatrix} \begin{bmatrix} \mathbf{m}_0 \\ \mathbf{j}_0 \end{bmatrix} \quad (1)$$

where $\mathbf{m}_2 = \hat{\mathbf{n}} \times \mathbf{E}_2|_{\Sigma_+}$, $\mathbf{j}_2 = j\omega \hat{\mathbf{n}} \times \mathbf{H}_2|_{\Sigma_+}$, $\mathbf{m}_0 = \hat{\mathbf{n}} \times \mathbf{E}^{inc}|_{\Sigma_+}$, $\mathbf{j}_0 = j\omega \hat{\mathbf{n}} \times \mathbf{H}^{inc}|_{\Sigma_+}$, $\alpha_j \triangleq k_j^{-1} \mu_j$, M_k and

Antonello Tamburrino is also with the department of Electrical and Computer Engineering, Michigan State University, USA.

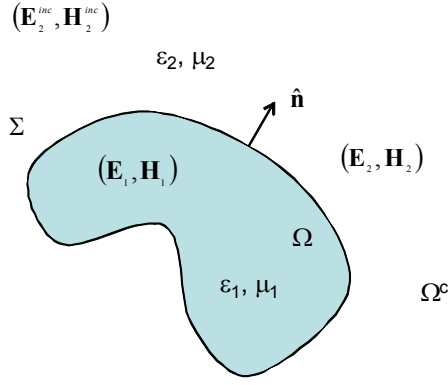


Fig. 1. The reference configuration: an incident electromagnetic field $(\mathbf{E}_2^{inc}, \mathbf{H}_2^{inc})$ produced in the homogeneous region Ω^c impinges on an homogeneous obstacle Ω . $(\mathbf{E}_1, \mathbf{H}_1)$ is the total (transmitted) field in Ω whereas $(\mathbf{E}_2, \mathbf{H}_2)$ is the scattered field in Ω^c . The material properties are (ε_1, μ_1) in Ω and (ε_2, μ_2) in Ω^c . The problem is full-wave and 3D.

C_k are properly defined operators and Σ_+ is the external page of Σ . It is worth noting that the unknowns of (1) are the tangential components of the electric and magnetic field onto Σ . Moreover, all the tangential traces are element of the functional space \mathbf{X} defined as $\mathbf{X} \triangleq \left\{ \boldsymbol{\lambda} \in V'_\pi | \nabla_S \cdot \boldsymbol{\lambda} \in H^{-1/2}(\Sigma) \right\}$, V'_π being the dual space of $V_\pi \triangleq \left(\hat{\mathbf{n}} \times H^{1/2}(\Sigma) \right)^3 \times \hat{\mathbf{n}}$.

The discrete model is obtained by means of the following non-standard Galerkin projection onto the test functions $\tilde{\mathbf{m}}$ and $\tilde{\mathbf{j}} \in \mathbf{X}$:

$$B \left(\begin{bmatrix} (M_1 + M_2) \mathbf{m}_2 + (\alpha_1 C_1 + \alpha_2 C_2) \mathbf{j}_2 \\ (\alpha_1^{-1} C_1 + \alpha_2^{-1} C_2) \mathbf{m}_2 + (M_1 + M_2) \mathbf{j}_2 \end{bmatrix}, \begin{bmatrix} \tilde{\mathbf{m}} \\ \tilde{\mathbf{j}} \end{bmatrix} \right) = B \left(\begin{bmatrix} (I/2 - M_1) \mathbf{m}_0 - \alpha_1 C_1 \mathbf{j}_0 \\ -\alpha_1^{-1} C_1 \mathbf{m}_0 + (I/2 - M_1) \mathbf{j}_0 \end{bmatrix}, \begin{bmatrix} \tilde{\mathbf{m}} \\ \tilde{\mathbf{j}} \end{bmatrix} \right) \quad (2)$$

where

$$B \left(\begin{bmatrix} \mathbf{m} \\ \mathbf{j} \end{bmatrix}, \begin{bmatrix} \tilde{\mathbf{m}} \\ \tilde{\mathbf{j}} \end{bmatrix} \right) = \int_\Sigma \tilde{\mathbf{m}} \cdot (\mathbf{j} \times \hat{\mathbf{n}}) dS - \int_\Sigma \tilde{\mathbf{j}} \cdot (\mathbf{m} \times \hat{\mathbf{n}}) dS. \quad (3)$$

By applying (3) to (2) and after some manipulations we obtain:

$$\int_\Sigma \tilde{\mathbf{m}} \cdot [(\alpha_1^{-1} C_1 + \alpha_2^{-1} C_2) \mathbf{m}_2 + (M_1 + M_2) \mathbf{j}_2] \times \hat{\mathbf{n}} dS + \int_\Sigma \tilde{\mathbf{j}} \cdot [(M_1 + M_2) \mathbf{m}_2 + (\alpha_1 C_1 + \alpha_2 C_2) \mathbf{j}_2] \times \hat{\mathbf{n}} dS = \mathbf{v}_0$$

where \mathbf{v}_0 is known and depends on \mathbf{m}_0 and \mathbf{j}_0 . The elementary contributions are $\int_\Sigma \tilde{\mathbf{a}} \cdot C_j \mathbf{a} \times \hat{\mathbf{n}} dS$ and $\int_\Sigma \tilde{\mathbf{a}} \cdot M_j \mathbf{a} \times \hat{\mathbf{n}} dS$ that, as shown in [16], are symmetric (i.e. $\int_\Sigma \tilde{\mathbf{a}} \cdot C_j \mathbf{a} \times \hat{\mathbf{n}} dS = \int_\Sigma \mathbf{a} \cdot C_j \tilde{\mathbf{a}} \times \hat{\mathbf{n}} dS$ and $\int_\Sigma \tilde{\mathbf{a}} \cdot M_j \mathbf{a} \times \hat{\mathbf{n}} dS = \int_\Sigma \mathbf{a} \cdot M_j \tilde{\mathbf{a}} \times \hat{\mathbf{n}} dS$).

Finally, the numerical models is obtained by a finite dimensional approximation of \mathbf{X} by means of div-conforming Whitney elements defined onto the surface Σ . One advantage for this formulation is that it is possible to adapt the existing preconditioners for the Electric Field Integral Equation (EFIE) as the one proposed in [18] and implemented and tested in [9]. Indeed, in (1), the operators C_i are the ones of the EFIE with coefficients from outside and from inside, whereas the operators M_i can be seen as compact perturbations. This last statement is valid in the case of sufficient regular dielectric interface, as it

is proved, e.g., in the book [8]. If we denote by A_h the matrix associated to the proposed numerical method, the construction given in [18] leads to a uniform multiplicative preconditioner i.e., to the construction of a matrix \mathcal{A}_h such that the spectral radius for $B_h^{*-1} \mathcal{A}_h B_h^{-1} A_h$ is uniformly bounded, where B_h denotes here a stable discretization of the bilinear form $B(\cdot, \cdot)$.

In the full paper we will discuss the details of the numerical formulation, together with its coupling with proper shape functions and the development of the preconditioner.

REFERENCES

- [1] S. M. Rao, D. R. Wilton, and A.W. Glisson, "Electromagnetic scattering by surfaces of arbitrary shape," IEEE Trans. Antennas Propagat., vol. 30, pp. 409–418, May 1982.
- [2] S. M. Rao and D. R. Wilton, "E-field, H-field and combined field solution for arbitrarily shaped three-dimensional dielectric bodies" Electromagnetics, vol. 10, pp. 407–412, 1990.
- [3] E. Arvas, A. Rahhal-Arabi and A. Sadigh, "Scattering from multiple conducting and dielectric bodies of arbitrary shape", IEE Antennas and Propagation Magazine, vol. 33, no. 2, 1991.
- [4] H. Cheng, L. Greengard, and V. Rokhlin, A fast adaptive multipole algorithm in three dimensions," J. Comput. Phys., vol. 155, pp. 468–498, 1999.
- [5] R. J. Burkholder, Jin-Fa Lee, "Fast Dual-MGS Block-Factorization Algorithm for Dense MoM Matrices", IEEE Trans. Antennas Propag., vol. 52, no 7, July 2004.
- [6] A. Maffucci, G. Rubinacci, A. Tamburrino, S. Ventre, F. Villone, "Fast Low-Frequency Impedance Extraction using a Volumetric Three-Dimensional Integral Formulation", 23rd Annual Review of Progress in Applied Computational Electromagnetics (ACES), Verona (Italy), pp. 1652-1657, 2007.
- [7] G. Rubinacci, S. Ventre, F. Villone, Y. Liu, "Fast technique applied to the analysis of Resistive Wall Modes with 3D conducting structures," Journal of Computational Physics, v. 228, no. 5, pp. 1562-1572, March 2009.
- [8] J.C. Nédélec, "Acoustic and Electromagnetic Equations: Integral representation for Harmonic problems", Springer-Verlag, 2001.
- [9] F. P. Andriulli, K. Cools, H. Bağcı, F. Olyslager, A. Buffa, S. Christiansen and E. Michielssen, "A Multiplicative Calderon Preconditioner for the Electric Field Integral Equation", IEEE Trans. on Antennas and Propagation, v. 56, no. 8, August 2008.
- [10] K. Cools, F.P. Andriulli, F. Olyslager, E. Michielssen, "Calderón preconditioned time-domain integral equation solvers," IEEE Antennas and Propagation Society International Symposium, pp.4565-4568, 9-15 June 2007.
- [11] R. J. Adams, "Physical and analytical properties of a stabilized electric field integral equation," IEEE Trans. Antennas Propag., vol. 52, no. 2, pp. 362–372, Feb. 2004.
- [12] H. Contopanagos, B. Dembart, M. Epton, J. Ottusch, V. Rokhlin, J. Visher, and S. M. Wandzura, "Well-conditioned boundary integral equations for three-dimensional electromagnetic scattering," IEEE Trans. Antennas Propag., vol. 50, no. 12, pp. 1824–1930, Dec. 2002.
- [13] S. H. Christiansen and J.-C. Nédélec, "A preconditioner for the electric field integral equation based on Calderon formulas," SIAM J. Numer. Anal., vol. 40, no. 3, pp. 1100–1135, 2003.
- [14] S. Borel, D. P. Levadoux, and F. Alouges, "A new well-conditioned Integral formulation for Maxwell equations in three dimensions," IEEE Trans. Antennas Propag., vol. 53, no. 9, pp. 2995–3004, Sep. 2005.
- [15] M. Burton and S. Kashyap, "A study of a recent moment-method algorithm that is accurate to very low frequencies," ACES J., vol. 10, no. 3, pp. 58–68, 1995.
- [16] A. Buffa, R. Hiptmair, T. von Petersdorff, C. Schaub, "Boundary element methods for Maxwell transmission problems in Lipschitz domains", Numerische Mathematik, v. 95, pp. 459–485, 2003.
- [17] B. Cranganu-Cretu, R. Hiptmair and Z. Andjelic, "Transmission Through Arbitrary Apertures in Metal-Coated Dielectric Bodies", IEEE Trans. on Magnetics, v. 41, no. 5, May 2005.
- [18] A. Buffa and S. H. Christiansen, "A dual finite element complex on the barycentric refinement," Math. Comp., vol. 76, pp. 1743–1769, 2007.
- [19] "Uniformly stable preconditioned mixed boundary element method for low-frequency electromagnetic scattering", Comptes Rendus Mathématique Volume 336, Issue 8, pp 677-680.

Local Timestepping Techniques Using Taylor Expansion for Modeling Electromagnetic Wave Propagation with Discontinuous Galerkin - FEM

S. Schomann¹, N. Gödel¹, *Student Member, IEEE*, T. Warburton,² and M. Clemens¹, *Senior Member, IEEE*,

¹Helmut-Schmidt-University, University of the Federal Armed Forces Hamburg, Faculty of Electrical Engineering, Chair for Theory of Electrical Engineering and Computational Electromagnetics, P.O. Box 700822, D-22008 Hamburg, Germany

²Computational and Applied Mathematics, Rice University, 6100 Main Street MS-134, Houston, TX, USA

Abstract—A time integration scheme based on Taylor expansion using the higher order discontinuous Galerkin finite element method (DG-FEM) is presented. The special properties of the scheme allow for using explicit time integration as well as local timestepping. The algorithm is introduced, its characteristics are analyzed and first benchmarks are presented.

Index Terms—Time Domain, Local Timestepping, Discontinuous Galerkin, FEM.

I. INTRODUCTION

The simulation of radio frequency and microwave engineering problems requires the solution of the Maxwell equation. The semidiscrete formulation of DG-FEM allows for using explicit time integration schemes, which are more efficient compared to implicit implementations. However, explicit time integration is not unconditionally stable. The maximum stable time step can be computed by evaluating the Courant-Friedrichs-Lewy (CFL) condition for every finite element. To guarantee global stability, the smallest time step has to be used for the computation. Since grids of many physical applications have a diversity of element sizes, a local timestepping strategy provides the opportunity of minimizing computation time.

Local timestepping for DG-FEM has been published by Piperno [1], Warburton [2] and Montseny [3]. A 3D local timestepping scheme with the linear multistep method using DG-FEM was presented in [4] based on results in [5], where a third order Adams-Bashforth (AB) time integration method was used. In addition to the fixed AB order, the stability region is smaller than well-established explicit Runge-Kutta (ERK) methods [6], which are based on Taylor expansion.

In this paper a local timestepping algorithm based on a Taylor expansion is presented. Relevant results of using Taylor series have been published in [7]. This approach combines the larger time stability and a flexible scheme with a variable order.

II. DESCRIPTION OF THE MODEL

Starting from Maxwell's two curl equations the conversion in a weak formulation and DG-discretization, as published in [2], can be summarized as:

$$\frac{d}{dt} \varepsilon \mathbf{E} = \mathbf{M}^{-1} \mathbf{S} \mathbf{H} - \mathbf{M}^{-1} \mathbf{F} [\hat{n} \cdot (f_E - f_E^*)], \quad (1)$$

$$\frac{d}{dt} \mu \mathbf{H} = -\mathbf{M}^{-1} \mathbf{S} \mathbf{E} + \mathbf{M}^{-1} \mathbf{F} [\hat{n} \cdot (f_H - f_H^*)]. \quad (2)$$

Here, \mathbf{M} and \mathbf{S} denote mass- and stiffness-matrices. The numerical flux $\mathbf{F} [\hat{n} \cdot (f - f^*)]$ defines the integration over adjacent face values f^* of neighboring finite elements. The fields can be approximated by using local high-order multi-dimensional Lagrange polynomials. To simplify equations (1) and (2), \mathbf{Q} is defined as

$$\mathbf{Q} = \begin{pmatrix} \mathbf{E} \\ \mathbf{H} \end{pmatrix} \quad \text{resulting in} \quad \frac{d}{dt} \mathbf{Q} = \mathcal{L}(\mathbf{Q}). \quad (3)$$

The right-hand-side (RHS) terms of (1), (2) are summarized by the linear operator \mathcal{L} .

III. TAYLOR EXPANSION

A time integration scheme with Taylor expansion [2] has, in addition to the good stability properties, a further advantage: adaption to local timestepping. The temporal evolution of the electromagnetic fields can be approximated using Taylor series of order P

$$\mathbf{Q}(t) = \mathbf{Q}^n + \sum_{p=1}^P \frac{(t - t^n)^p}{p!} \mathcal{L}^p \mathbf{Q}^n : t \in [t^n, t^n + \Delta t]. \quad (4)$$

in the discrete time steps. To find a solution for (3) an explicit timestepping scheme, like

$$\mathbf{Q}^{n+1} - \mathbf{Q}^n = \int_{t^n}^{t^{n+1}} \mathcal{L}(\mathbf{Q}(t)) dt \quad (5)$$

is necessary. This method uses Taylor series with the derivatives $\mathcal{L}^p \mathbf{Q}^n$ of the order $P + 1$ for a time step from t^n to t^{n+1} . The straightforward implementation of the time discrete formulation

$$\mathbf{Q}^{n+1} = \mathbf{Q}^n + \sum_{p=1}^{P+1} \frac{(\Delta t)^p}{p!} \mathcal{L}^p \mathbf{Q}^n \quad (6)$$

is another advantage. The maximum stable time step is defined by the CFL condition as $\Delta t = C \cdot \left\{ \frac{\Delta x_{\min}}{v} \right\}$, with C being the Courant number, x_{\min} the characteristic size of the smallest element and v the wave speed.

IV. LOCAL TIMESTEPPING STRATEGY

Most physical applications have large aspect ratios in element sizes, shown in Fig. (1). The finest element dictates the global time step for the entirety of the mesh, however most numerical costs are contributed by considerably coarser elements. To simplify the investigation a less complicated

strategy is used. Domain decomposition is necessary for the local timestepping approach, splitting the set of all elements into two subsets, Ω_C and Ω_F , referring to the coarse and the fine elements, respectively. First all elements are classified

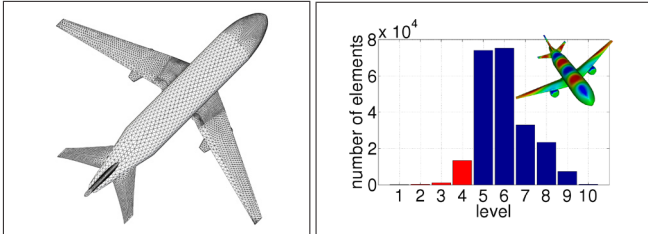


Fig. 1. Grid and histogram of an airplane with 227 960 elements and a aspect ratio of 634.

in levels of element size $2^{(\text{level}-1)} \cdot \Delta x_{\min}$ in Fig. 1. As preprocessing, an algorithm calculates the best position for the fine-to-coarse boundary, in this case between Level 4 and 5, to obtain minimal effort. All elements up to level 4 are summarized in Ω_F and advance in time with the microstep. All coarse elements advance in time every 16th microstep. The majority of the finite elements use a larger time step and a bulk of unnecessary computation is economized. In addition, problems of multi-level local timestepping with complex level coupling [4] are prevented.

$$Q_F^{n+1} - Q_F^n = \int_{t^n}^{t^{n+1}} (\mathcal{L}_{FF}Q_F + \mathcal{L}_{FC}Q_C) dt \quad (7)$$

$$Q_C^{n+1} - Q_C^n = \int_{t^n}^{t^{n+1}} (\mathcal{L}_{CC}Q_C + \mathcal{L}_{CF}Q_F) dt \quad (8)$$

In (7) and (8) a full time step $\Delta t_C = t^{n+1} - t^n$ is presented, whereas the integral in (7) has to be split up in microsteps. The RHS operation on the coarse and on the fine grid is denoted by \mathcal{L}_{CC} and \mathcal{L}_{FF} . The terms \mathcal{L}_{CF} and \mathcal{L}_{FC} adopt the coupling of both grids. The boundary of coarse and fine elements are the focus of further investigation and need a special implementation.

V. FIRST NUMERICAL RESULTS

First numerical results are presented for stability and accuracy of the Taylor time integration with order 4 and polynomial order 4 for a cavity, discretised with 398 tetrahedrons, in Fig. 2. The normalized energy at the top shows minimal dissipative behavior, resulting in a loss of 0.05% per 1000 periods and 1 329 673 micro time steps. The local timestepping scheme with $C = 2.124$, which equates 90% of the maximum stable time step, shows most dissipation. This effect is reducible in combination with an improvement of the maximum local error, if the Courant number C is decreased. The same accuracy of the global and local timestepping scheme with the same factor C is obvious in the diagram, highlighting the maximum E-field error. In Fig. 3 the maximum stable time step for the global and local timestepping algorithm for the cavity is illustrated. With higher Taylor order the stability of the scheme is increasing. The gap between the maximum local and global time step in Fig.3 was also encountered by Montseny et al. [3], who used a leapfrog scheme and proposed a factor of 0.8. For this academic example of a cavity a speedup of 1.3 is encountered, for further physical applications higher speed ups are estimated.

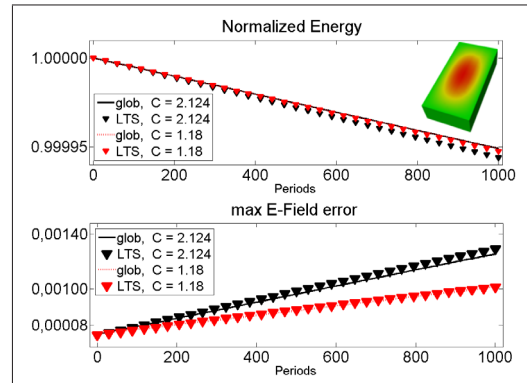


Fig. 2. Energy and accuracy of a cavity with 398 elements, the energy is normalized to the analytic solution. Due to an oscillatory behavior of both graphs, a fitting is used for better visibility.

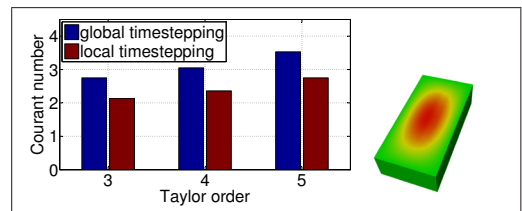


Fig. 3. Maximum Courant number for a stable microstep of Taylor time integration method.

VI. CONCLUSION

In this paper, a local timestepping technique based on Taylor expansion was presented. The one step one stage method is more suitable for local timestepping than ERK methods. Additionally, better stability characteristics than previously used one stage methods like AB schemes have been encountered. First simulation results were shown for a cavity to validate the timestepping scheme. The full paper will provide a more detailed description of the algorithm as well as further simulations of realistic examples.

ACKNOWLEDGMENT

The authors gratefully acknowledge the support of AFOSR under grant number FA9550-05-1-0473. The opinions expressed are the views of the authors. They do not necessarily reflect the official position of the funding agencies.

REFERENCES

- [1] S. Piperno, "DGT methods using modal basis functions and symplectic local time-stepping application to wave propagation problems," *M2AN*, vol. 40, no. 5, pp. 815–841, 2008.
- [2] J. S. Hesthaven and T. Warburton, *Nodal Discontinuous Galerkin Methods: Analysis, Algorithms, and Applications*. Berlin: Springer-Verlag, 2008.
- [3] E. Montseny, S. Pernet, X. Ferrières, and G. Cohen, "Dissipative terms and local time-stepping improvements in a spatial high order discontinuous galerkin scheme for the time-domain maxwell's equations," *J. Comput. Phys.*, vol. 227, no. 14, pp. 6795–6820, 2008.
- [4] N. Gödel, S. Schomann, T. Warburton, and M. Clemens, "Local timestepping discontinuous Galerkin methods for electromagnetic RF field problems," *IEEE APS – Full paper accepted for publication*, 2009.
- [5] C. Gear and D. Wells, "Multirate linear multistep methods," *BIT*, vol. 24, pp. 484–502, 1984.
- [6] E. Hairer and G. Wanner, *Solving Ordinary Differential Equations II*. Berlin: Springer-Verlag, 2002.
- [7] M. Dumbser and C.-D. Munz, "Arbitrary high-order discontinuous galerkin schemes," *Numerical methods for hyperbolic and kinetic problems*, pp. 295–333, 2005.

Safety Assessment of UWB Radio Systems for Body Area Network by the FDTD Method

V. De Santis¹, M. Feliziani¹, and F. Maradei²

¹ Dept. of Electrical and Computer Engineering, University of L'Aquila, L'Aquila, Italy
valerio.desantis@univaq.it, mauro.feliziani@univaq.it

² Dept. of Electrical Engineering – Sapienza University of Rome, Rome, Italy
fr.maradei@ieee.org

Abstract — The paper deals with the numerical prediction of the specific absorption (SA) of ultra wideband (UWB) radio systems for wireless body area network (BAN). The electromagnetic analysis is performed by the frequency-dependent finite difference time domain (FDTD) method in which the first order Debye approximation is used to model the frequency-dependent properties of the human body in the frequency range of the UWB signals. Different models of the human bodies are considered.

I. INTRODUCTION

Body Area Network (BAN), consists of a set of radio sensors, either wearable or implanted into the human body, which monitor body parameters and movements [1]. These devices, communicating through wireless technologies, transmit data from the body to a home base station, from where the data can be forwarded to a remote network.

The safety of radio sensors for BAN applications must be compliant with the IEEE standard C95.1 [2] in the USA and, up to now, with ICNIRP [3] in Europe. The IEEE 1-g specific absorption (SA) peak limit for a 6-min exposure is 576 J/kg, while 2 mJ/kg averaged over 10 g of tissue is settled in the ICNIRP safety guideline. Due to their characteristics, ultra wideband (UWB) radio sensors will be widely used in future BAN applications, and therefore they are analysed in this study to evaluate the critical aspect of safety. Different human head models excited by an UWB antenna are analyzed by the frequency-dependent finite difference time domain (FDTD) formulation ((FD)²TD) in order to predict the SA.

II. MODELS AND METHODS

A. Frequency-Dependent FDTD Method

Electromagnetic field in frequency domain are described by Maxwell's curl equations:

$$\nabla \times \mathbf{E}(\omega) = -j\omega\mu \mathbf{H}(\omega) \quad (1a)$$

$$\nabla \times \mathbf{H}(\omega) = j\omega\varepsilon_0\hat{\varepsilon}_r(\omega)\mathbf{E}(\omega) \quad (1b)$$

where $\mathbf{E}(\omega)$ is the electric field, $\mathbf{H}(\omega)$ the magnetic field, μ the permeability, ε_0 the free space permittivity, $\hat{\varepsilon}_r(\omega)$ the frequency-dependent complex relative permittivity given by:

$$\hat{\varepsilon}_r(\omega) = \varepsilon_r(\omega) - j\frac{\sigma(\omega)}{\omega\varepsilon_0} = \varepsilon_\infty - j\frac{\sigma_0}{\omega\varepsilon_0} + \chi(\omega) \quad (2)$$

with $\varepsilon_r(\omega)$ and $\sigma(\omega)$ the frequency-dependent relative permittivity and conductivity, respectively, ε_∞ the permittivity as $\omega \rightarrow \infty$, σ_0 the conductivity as $\omega \rightarrow 0$, and $\chi(\omega)$ the electric susceptibility. The dielectric properties of biological tissues vary with frequency owing to relaxation process [4]. In the frequency range of interest for UWB applications (i.e., 3.1-10.6 GHz), it is a satisfactory approximation to consider a single relaxation process that can be modelled by the first order Debye dispersion relation. For such a medium the electric susceptibility is given by [5]:

$$\chi(\omega) = \frac{\varepsilon_s - \varepsilon_\infty}{1 + j\omega\tau_0} \quad (3)$$

where ε_s is the static permittivity and τ_0 the relaxation time. Moving (1) to the time-domain, it yields:

$$\nabla \times \mathbf{E}(t) = -\mu \frac{\partial \mathbf{H}(t)}{\partial t} \quad (4a)$$

$$\nabla \times \mathbf{H}(t) = \sigma_0 \mathbf{E}(t) + \varepsilon_0 \varepsilon_\infty \frac{\partial \mathbf{E}(t)}{\partial t} + \varepsilon_0 \frac{\partial [\mathbf{E}(t) * \chi(t)]}{\partial t} \quad (4b)$$

where the symbol * denotes the convolution operator. Time-domain Maxwell's equations (4) can be numerically solved by the (FD)²TD method as described in [5].

B. Human Body Models

The electro-geometrical configuration of the human body is a critical point for the numerical analysis. The body models considered in the proposed investigation are (see Fig. 1):

- Visible Human Project (VHP) model, which is public and therefore has the advantage to be widely used and permits the benchmark of different numerical techniques [6];
- CAD model obtained by the atlas of the human body, which permits to modify in a simple way the electro-geometrical configuration (scaling, anatomical detail modification, ...) [7].
- Specific Anthropomorphic Mannequin (SAM) model, which is obtained by homogenizing the CAD model with a unique tissue of dielectric properties similar to the brain and therefore suitable for comparison with measurements.

C. SA Calculation

The field distribution calculated by the (FD)²TD is used to evaluate the SA by [8]:

$$SA = \int_0^{T_{max}} \frac{\mathbf{E}(t) \cdot \mathbf{J}(t)}{\rho} dt \quad (4)$$

where T_{max} is the maximum calculation time, ρ the mass density and $\mathbf{J}(t)$ the transient current density obtained by the inverse Fourier transform as [8]:

$$\mathbf{J}(t) = F^{-1}[\mathbf{J}(\omega)] \quad (5)$$

where

$$\mathbf{J}(\omega) = \sigma(\omega)\mathbf{E}(\omega). \quad (6)$$

It should be noted that the SA calculated by (4) must be averaged over a portion of tissue to be compared with the standard limits, as described in the Introduction Section.

III. NUMERICAL RESULTS

We consider the configuration of an UWB patch antenna whose characteristics are reported in [9]. It is placed at 2 mm from the ear of the three different human head tri-dimensional models (i.e., CAD, VHP and SAM), as shown in Fig. 1. These configurations are analyzed by the (FD)²TD when exciting the antenna by the UWB doublet signal shown in Fig. 2.

The presence of the human head affects the field radiated by the UWB patch antenna. The return loss $|S_{11}|$ calculated by the (FD)²TD for the three head models is reported in Fig. 3. It should be noted that the different geometries (see the simulations for the VHP and CAD models) influence the solution much more than the different tissue composition (see the simulations for the CAD and SAM models).

Finally, the SA distribution inside the human head is numerically calculated on the different models for a single UWB pulse, as shown in Fig. 4, where the SA maps are reported in dB defined as $SA_{dB} = 10 \log_{10}(SA / 1 \text{ pJ/kg})$. From this figure you can note as the higher values of SA are located in the human tissues characterized by higher water content or in close proximity to the UWB antenna. In the extended version of the paper, further human body-antenna configurations will be examined and several UWB modulation schemes will be considered. The SA calculated for a train of UWB pulses will be also presented under the IEEE and ICNIRP safety limits.

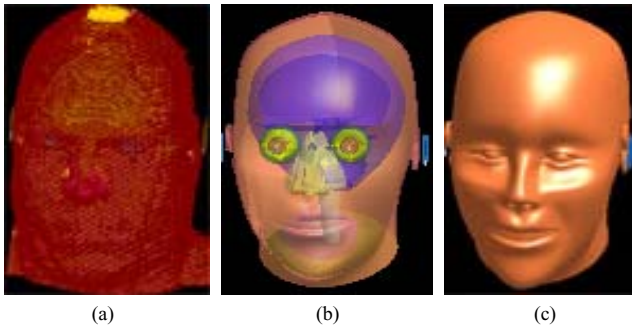


Fig. 1. Human head models: (a) VHP, (b) CAD, (c) SAM.

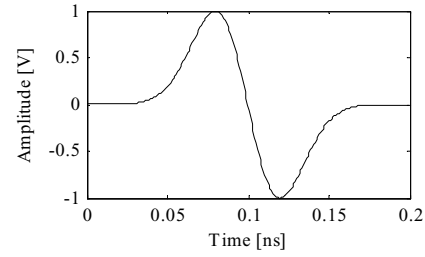


Fig. 2. UWB doublet pulse.

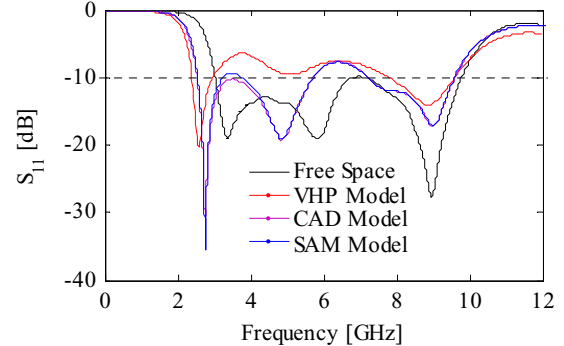


Fig. 3. Return loss $|S_{11}|$ of the UWB patch antenna for the three different head models.

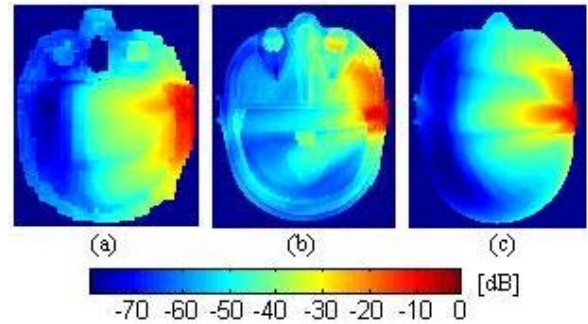


Fig. 4. SA_{dB} maps inside the head models: (a) VHP, (b) CAD, (c) SAM.

REFERENCES

- [1] <http://www.ieee802.org/15/pub/TG6.html>.
- [2] IEEE Std C95.1-1991 - 1999 Edition. Revised 2005. "Safety Levels With Respect to Human Exposure to Radiofrequency Electromagnetic Fields, 3 kHz to 300 GHz".
- [3] International Commission on Non-Ionizing Radiation Protection. ICNIRP Guidelines: Guidelines for Limiting Exposure to Time-Varying Electric, Magnetic, and Electromagnetic Fields (up to 300 GHz). *Health Physics*, Vol. 74, pp. 494-522, 1998.
- [4] C. Polk, and E. Postow, *CRC Handbook of biological effects of electromagnetic fields*, CRC Press, Boca Raton, Florida, 1986.
- [5] R. J. Luebbers, F. Hunsberg, and K. S. Kunz, "A frequency-dependent finite-difference time-domain formulation dispersive materials," *IEEE Trans. Electromag. Compat.*, vol. 32, no. 3, pp. 222-227, Aug. 1990.
- [6] The visible human project (2000). http://www.nlm.nih.gov/research/visible/visible_human.html.
- [7] C. Buccella, V. De Santis, and M. Feliziani, "Prediction of temperature increase in human eyes due to RF sources," *IEEE Trans. Electromag. Compat.*, vol. 49, no. 4, pp. 825-833, Nov. 2007.
- [8] Q. Wang and J. Wang, "SA/SAR Analysis for multiple UWB pulse exposure," 2008 Asia-Pacific Symp. on EMC, 19-22 May 2008, Singapore.
- [9] Z. N. Chen, A. Cai, T. S. P. See, X. Qing, and M. Y. W. Chia, "Small planar UWB antennas in proximity of the human head," *IEEE Trans. Microwave Theory Tech.*, vol. 54, no. 4, pp. 1846-1857, Apr. 2006.

Computation Method for Transients in Underground Cables with Lossy Earth Return Path

Xose M. Lopez-Fernandez⁽¹⁾, Casimiro Alvarez-Mariño⁽¹⁾ and Vitor Malo-Machado⁽²⁾

⁽¹⁾Dept. of Electrical Engineering, Universidade de Vigo, ETSEI, E36310 Vigo, Spain

⁽²⁾Instituto Superior Técnico, Technical University of Lisbon, 1049-001 Lisbon, Portugal

Abstract — In this paper, a detailed method for computing the transient voltage distribution in underground cables is described. The proposed model is based on RLCG lumped frequency-dependent parameters for time-domain analysis. The numerical Laplace transform in s -complex plane is used. The method is appropriate to solve underground cable systems at high frequencies (HFs) with lossy ground-return path included. Numerical results confirm good agreement with reference solutions taken from the literature.

I. INTRODUCTION

Computation of very fast electromagnetic transients (VFETs) plays a crucial role in the determination of overvoltage stresses on electrical equipment. Nowadays, special attention is paid to power transmission underground cables by utilities who are concerned with accurate and efficient computation methods for ensuring the insulation coordination and the mitigation of transients.

A large variety of computing programs for overhead lines based on very well established methodologies is readily available. There is no alternative for underground cables, since their electrical characteristics are significantly different from overhead lines. Their parameters have to be properly calculated from the cable geometry and frequency dependent. Proximity and skin effects, as well dielectric losses have to be taken into account with real lossy earth return path (ERP).

In this paper, modal analysis, numerical Laplace transform technique and lossy earth Machado's solution are applied to compute transient voltage and current oscillations in cable conductors. Numerical solutions at HF are more accurate than classical Pollaczek's approach when the outer cable radius and the influence of earth-air surface cannot be negligible.

II. CALCULATION OF PARAMETERS WITH LOSSY EARTH PATH

Maxwell's equations for power transmission system can be formulated in frequency domain by [1]

$$\frac{d}{dx}V = -ZI, \quad \frac{d}{dx}I = -YI, \quad (1)$$

where Z and Y are the frequency dependent (FD) series impedance and shunt admittance matrices per unit length, respectively, and V and I are the voltages and currents vectors at a distance x along the cable. For the case of underground cables system due to the soil acting as an electrostatic shield between cables, Y only represents the capacitive coupling between elements of each cable itself [2]. However, Z may be expressed according to [3] by

$$Z = Z_{ps} + Z_{soil}, \quad (2)$$

where Z_{ps} is obtained by Schelkunoff's [2] formulas and represents the FD series-impedance matrix under a perfect soil, which means a perfect conducting earth ($\sigma_{ps} = \infty$). Whereas the matrix Z_{soil} accounts for the influence of the lossy ERP due to a finite electric conductivity of the real soil. The form and dimensions of above matrices depend on the number of conducting cable system elements (core, sheath, armour, etc.).

The proposed model is valid for homogenous semi-infinite earth, where Machado's ground-return impedance approach was implemented [3]. Thus, the diagonal submatrix elements of Z_{soil} are the self-impedance of the ERP of each conductor calculated by

$$Z_{soil-self} = \left[-\frac{x_c J_o}{2J_1} - \frac{x_c^2 G_o}{2 C_o} \left(H_o - \frac{J_o H_1}{J_1} \right) \right] R_{dc}. \quad (3)$$

The non-diagonal submatrix elements of Z_{soil} represent the mutual impedance of ERP between conductors which are obtained by

$$Z_{soil-mutual} = \left[-\frac{x_c^2 G_o}{2 C_o} \left(H_o - \frac{J_o H_1}{J_1} \right) \right] R_{dc}, \quad (4)$$

where x_c , J_o , J_1 , G_o , C_o , H_o and R_{dc} are specified in [3]. Classical Pollaczek's approach is a particular solution when the outer cable radius is smaller than skin earth depth penetration.

III. MATHEMATICAL MODEL FOR MODAL APPROACH

From equations (1), a transmission system with N phases is partitioned as

$$\frac{d}{dx}V_i = -\sum_{j=1}^N Z_{ij} I_j, \quad \frac{d}{dx}I_i = -\sum_{j=1}^N Y_{ij} V_j, \quad i = 1, \dots, N. \quad (5)$$

Equations (5) are applied to discretize cables into sections in a equivalent π -circuit given by (6) and (7). The cables are divided into K homogenous sections according to

$$V_i(k) = V_i(K) + \sum_{r=k+1}^K \sum_{j=1}^N Z_{a,ij}(r) I_j(r), \quad k = 0, 1, \dots, K-1, \quad (6)$$

$$I_i(k) = I_i(K+1) + \sum_{r=k}^K \sum_{j=1}^N \left(Y_{b,ij}(r+1) + Y_{c,ij}(r) \right) I_j(r), \quad k = 0, 1, \dots, K, \quad (7)$$

where, $i=1, \dots, N$, $Z_{a,ij}$, $Y_{b,ij}$ and $Y_{c,ij}$ are the overall series impedance and overall shunt admittance of the r th section between i th and j th cables given by [4]. Operating (6) and (7) the following set of matrix equations are defined:

$$\begin{bmatrix} I_B \\ V' \end{bmatrix} = \begin{bmatrix} A & B \\ C & D \end{bmatrix} \begin{bmatrix} V_B \\ V' \end{bmatrix}, \quad (8)$$

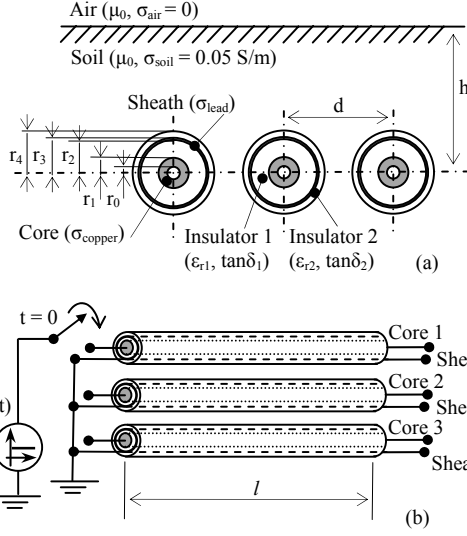


Fig. 1. Underground transmission system. a) Geometric configuration. b) Cable system connection diagram.

TABLE I
PHYSICAL DATA OF TESTED CABLE SYSTEM

Dimensions		Properties	
h	0.762 m	ϵr_1	3.5
d	0.1524 m	$\tan \delta_1$	0.002
r_0	0 m	ϵr_2	3.3
r_1	0.0127 m	$\tan \delta_2$	0.0005
r_2	0.0282 m	σ_{soil}	0.05 S/m
r_3	0.293 m	σ_{copper}	5.81E7 S/m
r_4	0.345 m	σ_{lead}	7.25E6 S/m

where V_B represents the voltage at cable terminals, I_B is the current entering each terminal of cable, and V' is the voltage at the internal nodes. The matrices A , B , C , and D are functions of the impedance $Z_{a,ij}$, and the admittances $Y_{b,ij}$ and $Y_{c,ij}$ as specified in [5].

Manipulating (8), the modal form of the solution is obtained from

$$\begin{aligned} V' &= C_L V_B + Q h P_t V_B, \\ I_B &= Y_{BB} V_B + P \xi h P_t V_B = Y_B V_B, \end{aligned} \quad (9)$$

where the matrices C_L , Q , h , P_t , Y_{BB} , P , ξ , h and Y_B are specified in [5]. The time domain solution is computed applying the numerical Laplace transform [6].

IV. TESTED CASES AND SIMULATION RESULTS

The proposed method is tested with underground cable system of the Fig. 1, applying a unit impulse to the core of phase 1 [7]. The data of the transmission line is given in Table I. Figure 2 shows the transient waveforms obtained for the remote node in core 1 of phase 1 for three different lengths of cable (10, 20 and 40 miles). Figure 3 shows the induced voltage obtained for the remote node in the sheath of each phase, evaluating the influence of the dc resistance of the lead sheath ($R_{dc-lead}$). Those numerical results are compared with the solution computed by Wedepohl & Wilcox [7] and Uribe [8].

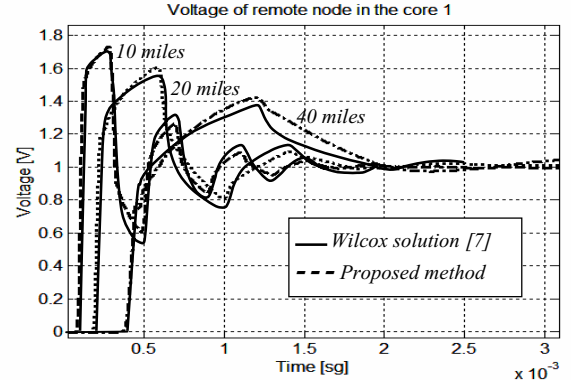


Fig. 2. Voltages for the remote node in the core 1 of the phase 1.

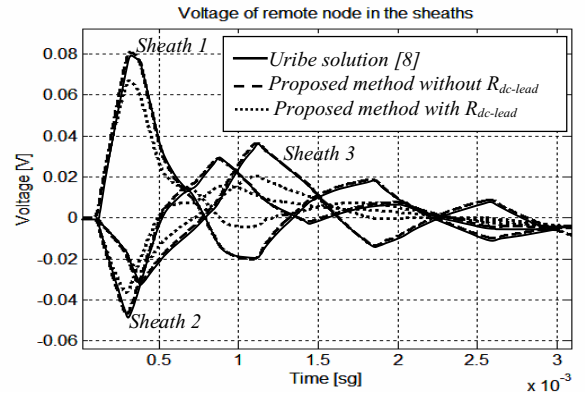


Fig. 3. Voltage of the remote node in the sheaths for 10 miles.

V. CONCLUSION

The proposed method implements the lossy earth Machado's solution for computing VFETs in cable systems with success for firts time. While Ametani approach works up to 10 kHz, and Wedepohl & Wilcox method up to 100 kHz, the Machado's solution does up to 1-10 MHz. The proposed methodology becomes an alternative for solving cable systems with lossy ERP at VFETs.

VI. REFERENCES

- [1] M. Condon, "Time-Domain Simulation of Coupled Interconnects", *COMPEL*, Vol. 21, No. 3, 2002, pp. 438-450.
- [2] A. Ametani "A General Formulation of Impedance and Admittance of Cables" *IEEE Trans. on Power Apparatus and Systems*, Vol. PAS-99, No. 3, May/June 1980.
- [3] V.M. Machado and J.F.B. Silva, "Series-Impedance of Underground Cable Systems" *IEEE Trans. on Power Delivery*, Vol.3, No.4, Oct. 1988.
- [4] D.J. Wilcox, M. Condon, "Time-Domain Model for Multiconductor Power Transmission Lines" *IEE Proc. Gener. Transm. Distrib.*, Vol. 145, No. 4, July 1998.
- [5] D.J. Wilcox, T. P. Mchale "Modified Theory of Modal Analysis for the Modelling of Multiwinding Transformers" *IEE Proc. C*, Vol. 139, No. 6, pp. 505-512, November 1992.
- [6] D. J. Wilcox, "Numerical Laplace Transformation and Inversion", *Int. J. Elect. Eng. Educ.*, Vol. 15, pp. 247-265, 1978.
- [7] F.A. Uribe, "Electromagnetic Transients in Underground Transmission Systems through the Numerical Laplace Transform" *Elsevier Electrical Power and Energy Systems* 24 (2002) 215-221.
- [8] P. Gomez, F.A. Uribe, "The Numerical Laplace Transform: An Accurate Technique for Analyzing Electromagnetic Transients on Power System Devices", *Int. J. Electr. Power Energ. Syst.* (2008), doi: 10.1016/j.ijepes.2008.10.006.

FDTD Analysis of a Metamaterial with Particles Having O_h Point Group Symmetry

Tiago C. Martins and Victor Dmitriev

Department of Electrical Engineering, Federal University of Pará (UFPA)

Av, Augusto Corrêa nº 01, CEP 66075-900, Brazil

Email: tiagocm@ufpa.br, victor@ufpa.br

Abstract— In this work, we analyze a metamaterial with particles of cubic geometry described by O_h point group symmetry. We investigate the case of the negative refraction index, and we demonstrate that the material does not have isotropic behavior, when the dimensions of the particles of the metamaterial are of the order of the operating wavelength. The analysis is performed with FDTD method implemented in FORTRAN 90 code.

I. INTRODUCTION

Metamaterials are artificial media with the properties which are not met in natural substances. One of them intensively studied in the last years is the materials with negative refraction index. The electromagnetic response of such a material is characterized by simultaneously negative permeability and negative permittivity [1,2]. Some consequences of these unusual properties of the medium are the inverse Cherenkov and Doppler effects, negative refraction and a theoretical possibility of construction of a “perfect lens” [3]. However, a realization of such effects depends on the design of isotropic metamaterials. By using theory of groups [1,2], it was demonstrated that isotropic materials can be obtained using elements with cubic symmetries, such as the element with O_h symmetry shown in Fig. 1. This element is a cubic particle that has four-gap single-split-ring on each side.

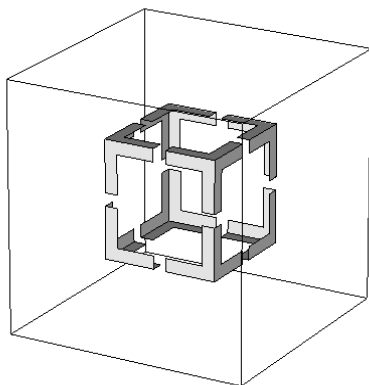


Fig. 1. Particle with O_h symmetry

II. FDTD ANALYSIS OF PERIODIC STRUCTURES

The finite difference time domain (FDTD) method has been frequently used to analyze periodic structures. As a result, a variety of FDTD technique modifications to analyze

electromagnetic scattering for periodic structures in arbitrary incident angles are available in literature [4]. These techniques are divided in two classes: direct field methods (sine-cosine method, multiple unit cell method, and angle update method), and field transformation methods (multispatial grid method, and split-field method). Amongst these methods, split-field method is the most popular technique. Recently, F. Yang et al. [5] developed a new FDTD technique to analyze these structures and it is called as constant wavenumber method. In this work we implemented this technique in FORTRAN 90 code to simulate electromagnetic scattering for metamaterials.

In Fig. 2, it is shown the FDTD computational scheme used in our simulations. Note that the computational domain is truncate with convolutional perfectly matched layers (CPML) and periodic boundary conditions (PBC), respectively, in z and horizontal directions x and y. The periodicity of the structure is a , and the angle between the incident wave vector and the z direction is θ .

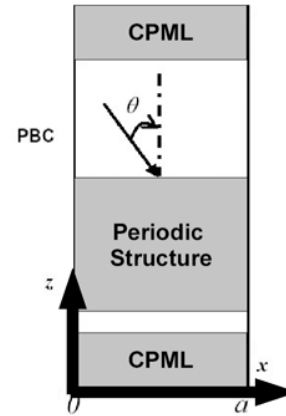


Fig. 2. FDTD computational domain

The periodic boundary condition in frequency domain is given by the expression (1)

$$\begin{aligned} \mathbf{E}(x=0, y, z) &= \mathbf{E}(x=a, y, z) \exp(jk_x a) \\ \mathbf{H}(x=0, y, z) &= \mathbf{H}(x=a, y, z) \exp(jk_x a) \end{aligned} \quad (1)$$

where k_x is the horizontal wavenumber, which is provided by the following equation:

$$k_x = k_0 \cdot \sin \theta = \omega \sin \theta / C \quad (2)$$

In the constant wavenumber method, (1) is not transformed in time domain, but instead both electric and magnetic fields are declared as complex variables, and the value of k_x is taken

as a constant. After the simulation is complete, we can choose a value for θ , and it will be possible to obtain the results in function of ω .

The main advantages of the constant wavenumber method are the simplicity of implementation (no change in the formulation of the conventional FDTD method is necessary) and computational efficiency (same stability condition of conventional FDTD, i.e, time step is independent of incident angle and horizontal wavenumber, which is not the case for other techniques).

III. RESULTS

In [2], the author suggested the use of particles with O_h symmetry, as shown in Fig. 1, to produce isotropic metamaterials with negative refractive index, however, we will demonstrate that the isotropy can not be realized when the dimensions of these particles are of the order of the operating wavelength. One layer of cubic particles was analyzed in this work; the unit cell of this structure is illustrated in Fig. 1. The edge size of cube is 1.8 mm, size gaps are 0.2 mm, and edge size of unit cell is 2.6 mm. The reflection coefficient in 85-95 GHz obtained with FDTD, for some values of k_x , and CST Microwave Studio for normal incidence is showed in Fig. 3. This structure presents negative refractive index in 83.3-92.5 GHz, and the periodicity is about 76% of the wavelength. In order to obtain the refractive index, we used the procedure proposed in [6].

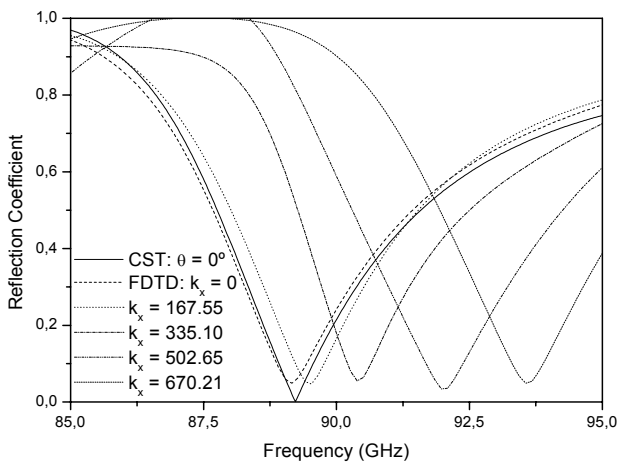


Fig. 3. Reflection coefficient of the analyzed structure

In spite of cubic symmetry of the particles, the material does not have isotropy, it is observed in TABLE I, for angles greater than 10° , we obtained a difference of reflection coefficient above 10%, in relation to reflection coefficient for normal incidence. For the highest analyzed frequency (92.5 GHz), the structure has a less isotropic behavior.

TABLE I
REFLECTION COEFFICIENT FOR SOME VALUES OF k_x

k_x	Frequency (GHz)	θ	Reflection Coefficient	Difference from Normal incidence (%)
0	83.3	0°	0.9908	-
167.55	83.3	5.5°	0.9536	3.75
335.10	83.3	11.1°	0.88611	10.56
502.65	83.3	16.7°	0.75615	23.68
0	92.5	0°	0.61386	-
167.55	92.5	5.0°	0.61832	0.72
335.10	92.5	10.0°	0.49457	19.40
502.65	92.5	15.0°	0.12019	80.42

IV. CONCLUSIONS

When the wavelength is of the order of its dimensions, in spite of cubic symmetry of the particles, these structures does not have isotropy. In the full paper we will analyze isotropic metamaterials for other relations between the wavelength and the dimensions or periodicity of the structure.

V. REFERENCES

- [1] N. Wongkasem, A. Akyurtlu, J. Li, A. Tibolt, Z. Kang, and W. D. Goodhue, "Novel broadband terahertz negative refractive index metamaterials: analysis and experiment," *Progress In Electromagnetic Research, PIER* **64**, 205 (2006).
- [2] W. J. Padilla, Group theoretical description of artificial electromagnetic metamaterials, *Optics Express* **15**, 1639 (2007).
- [3] J. B. Pendry, "Negative refraction makes a perfect lens," *Phys. Rev. Lett.*, vol. 85, no. 18, pp. 3966–3969, Oct. 2000. B. Smith, "An approach to graphs of linear forms," unpublished.
- [4] A. Taflove, S. C. Hagness, *Computational Electrodynamics: The Finite-Difference Time-Domain Method*, third ed., Artech House, Norwood, MA, 2005.
- [5] F. Yang, Y. Rahmat-Samii, *Electromagnetic Band Gap Structure in Antenna Engineering*, Cambridge, New York, NY, 2009.
- [6] X. Chen, T. M. Grzegorzcyk, Bae-Ian Wu, J. Pacheco, Jr. and J. A. Kong, "Robust method to retrieve the constitutive effective parameters of metamaterials," *Phys. Rev. E*, vol. 70, 016608, 2004

Discrete Constitutive Relations for the Discrete Geometric Approach over Hexahedral Grids

Lorenzo Codecasa¹, Ruben Specogna², and Francesco Trevisan²

¹Dip. di Elettronica ed Informazione, Politecnico di Milano, 20133 Milano, Italy

²Dip. di Ingegneria Elettrica, Gestionale e Meccanica, Università di Udine, 33100 Udine, Italy
codecasa@elet.polimi.it, ruben.specogna@uniud.it, trevisan@uniud.it.

Abstract—As a first step, we will investigate the extent of the consistency error for an hexahedral primal grid due to the use mass matrices of Finite Elements within the Discrete Geometric Approach (DGA) as discrete counterparts of the constitutive relations. Such matrices are constructed by resorting to *mixed elements* edge and face vector functions. Then we will propose a novel set of geometric vector basis functions for hexahedra which guarantee consistency and stability of the constitutive matrices for the DGA constructed according to the so called *energetic approach*.

Index Terms—Discrete geometric approaches, constitutive matrices, hexahedral meshes.

I. INTRODUCTION

The Finite Integration Technique (FIT) [1], the Cell Method (CM) [2] and the geometrical reinterpretation of Finite Elements demonstrated by A. Bossavit [3] suggest a Discrete Geometric Approach (DGA) for discretizing an electromagnetic field problem with respect to a pair of interlocked grids in the spatial domain of interest.

A grid is a collection of oriented nodes, edges, faces and volumes [2]. The grids are one dual of the other, since the oriented nodes, edges, faces and volumes of the primal grid one-to-one correspond with the oriented volumes, faces, edges and nodes of the dual grid respectively. Now, integral variables can be univocally associated with the geometric elements of the pair of dual grids [2]. For instance, circulations of electric field are associated with the primal edges, while electric currents are associated with the faces of the dual grid.

The fundamental laws of electromagnetism, formulated as *balance equations*, are discretized into sets of *exact* equations relating circulations and fluxes associated with the geometric elements of each of the grids [2], [4]. For instance, Ampere’s law relates the current through a dual face with the circulations of the magnetic field along the dual edges forming the boundary of that dual face. The discrete counterparts of the constitutive relations are introduced as *approximate* algebraic equations which relate either the circulations along the primal edges with the fluxes through the dual faces or viceversa. For instance, the magnetic constitutive relation is a matrix mapping the fluxes of magnetic induction through primal faces to the circulations of magnetic field along dual edges [2], [5].

As a known result [4], in order to ensure the consistency and the stability of the overall final system of algebraic equations, the discrete constitutive relations have to satisfy

both *stability* and *consistency* requirements. The stability requirement prescribes that the constitutive matrix is symmetric and positive definite. The consistency requirement prescribes that the constitutive matrix *exactly* maps either circulations along primal edges into fluxes through dual faces or viceversa, at least for element-wise *uniform* fields.

Stable and consistent discrete constitutive matrices can be easily obtained for pairs of grids in which the primal grid is composed of tetrahedra and the dual grid is obtained according to the barycentric subdivision of the primal. The recipe is to construct the so called “Galerkin Hodge”, where Whitney’s edge and face basis functions are used to compute the mass matrices [3]; for such a pair of grids, where the primal is simplicial, both Whitney’s basis functions and the Galerkin Hodge admit a simple geometric interpretation, [5], [6]. Alternatively, we proposed in [6] novel constitutive matrices not only for tetrahedra but also for (oblique) prisms with triangular base; this result was achieved with the introduction of a novel set of purely geometric edge and face vector functions combined with an energetic approach.

Therefore, if we limit to tetrahedra, Finite Elements and DGA are akin each other, so that the mass matrices of Finite Elements can be borrowed as constitutive matrices for the DGA.

However difficulties arise when discrete constitutive matrices for hexahedral primal grids need to be considered within the DGA. A simple theoretical counter-example, described in [7], shows that the mass matrices constructed by means of the *mixed elements* edge and face vector functions [8] for hexahedra, do *not* satisfy the consistency property for any choice of the dual grid. Thus, such mass matrices *cannot* be borrowed as constitutive matrices for the DGA. In this paper the consistency error of mass matrices introduced by the mass matrices of Finite Elements will be evaluated by numerical investigations. Moreover, to overcome this difficulty, a novel set of edge and face basis vector functions, suited for hexahedral primal grids, will be presented, capable to exactly represent a uniform field and satisfying a geometric consistency property. In this way, novel stable and consistent constitutive matrices can be easily derived, resorting to the energetic approach.

II. INCONSISTENCY OF MASS MATRICES OVER HEXAHEDRAL GRIDS

We will present a numerical study to evaluate the extent of the consistency error when the standard mass matrices of

Finite Elements are used in DGA as discrete counterparts of the constitutive relations over an hexahedral primal grid.

In a domain D , consisting of a cube of unitary edge, we consider a primal grid made of nodes n_i , edges e_j , faces f_h and hexahedra v_k , Fig. 1. A dual grid is constructed from it according to the barycentric subdivision of the *boundary* of the primal grid: a dual node \tilde{n}_k is chosen¹ within v_k , a dual edge \tilde{e}_h is a broken line joining the pair of dual nodes, within the pair of hexahedra having the primal face f_h in common, and passing through the *barycenter* g_{f_h} of the primal face f_h . A dual face \tilde{f}_j is a non planar surface consisting of the union of four portions; each of the portions is tailored inside an hexahedron and it has the *barycenter* g_{e_j} of edge e_j as common vertex. We will consider a pair of reference

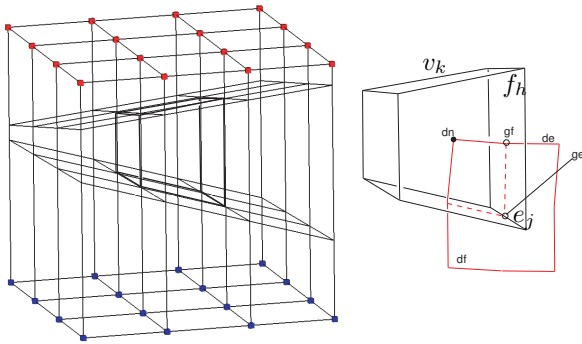


Fig. 1. On the left side: Grid of hexahedra filling the domain of interest D . On the right side: An hexahedron v_k is shown, together with a primal face f_h , a primal edge e_j , a primal node n_i ; a dual face \tilde{f}_j , a dual edge \tilde{e}_h and a dual node \tilde{n}_k . Moreover the barycenters g_{e_j} of edge e_j and g_{f_h} of face f_h are shown.

static problems characterized by a uniform field solution: a magnetostatic (MS) and a current conduction (CC) problems, which can be formulated in a discrete way [9] as

$$\mathbf{C}^T \boldsymbol{\nu} \mathbf{C} \mathbf{A} = \mathbf{0} \quad (\text{MS}), \quad \mathbf{G}^T \boldsymbol{\sigma} \mathbf{G} \mathbf{V} = \mathbf{0} \quad (\text{CC}), \quad (1)$$

where \mathbf{C} , \mathbf{G} are the faces-edges and edges-nodes incidence matrices of the primal complex respectively, \mathbf{A} is the array of the circulations of the magnetic vector potential associated with the primal edges and \mathbf{V} is the array of the electric scalar potentials associated with the primal nodes. The sources are assigned by specifying proper boundary conditions; for this reason the right hand sides in (1) are null. Finally, $\boldsymbol{\nu}$, $\boldsymbol{\sigma}$ are matrices representing discrete counterparts of the constitutive relations, of dimension $\dim(\boldsymbol{\nu}) = \mathcal{F}$ and $\dim(\boldsymbol{\sigma}) = \mathcal{E}$ respectively, where \mathcal{F} , \mathcal{E} are the number of faces or edges of the primal grid. The matrix $\boldsymbol{\nu}$ or $\boldsymbol{\sigma}$ is obtained by assembling local constitutive matrices computed for each hexahedron v_k of the grid. The entry of a local constitutive matrix is now computed by forming the mass matrices with an element-wise uniform reluctivity ν or conductivity σ as

$$\boldsymbol{\nu}_{ij}^{km} = \int_{w_k} w_i^f \cdot \nu w_j^f dv, \quad \boldsymbol{\sigma}_{ij}^{km} = \int_{w_k} w_i^e \cdot \sigma w_j^e dv, \quad (2)$$

¹In the full paper, we will see that \tilde{n}_k can be in an *arbitrary* location inside v_k .

where w_i^f , w_i^e are the *mixed elements* edge and face vector functions [8] for hexahedra. The boundary conditions have been set in order to generate in D a uniform magnetic induction field of amplitude $B=1$ T and a uniform current density field of amplitude $J = 4 \cdot 10^7$ A/m² respectively, both directed as the z axis.

Correspondingly, the consistency error for volume v^k is computed as follows

$$e^{kMS} = \boldsymbol{\nu}^{km} \mathbf{C}^k \mathbf{A}^k - \mathbf{F}^k, \quad e^{kCS} = \boldsymbol{\sigma}^{km} \mathbf{G}^k \mathbf{V}^k - \mathbf{I}^k, \quad (3)$$

where the subscript k attached to an array, represents the local subarray for volume v^k and $(\mathbf{F}^k)_i = \int_{\tilde{e}_i} \mathbf{H} \cdot d\mathbf{l}$, $(\mathbf{I}^k)_i = \int_{\tilde{f}_i} \mathbf{J} \cdot d\mathbf{s}$ are the circulations and fluxes of the actual uniform magnetic field \mathbf{H} or uniform current density \mathbf{J} in v^k respectively. Considering the primal grid presented in Fig. 1, the maximum extent of $|e^{kMS}|$, $|e^{kCS}|$ is about 5.5 %.

III. NEW VECTOR BASE FUNCTIONS

In order to guarantee consistency of the constitutive matrices $\boldsymbol{\nu}$ or $\boldsymbol{\sigma}$ at least for element wise uniform fields, we will propose a novel set of vector base functions v_i^e , v_i^f attached to a primal face or to a primal edge of hexahedron v_k respectively. These vector base functions will be described in detail in the full paper, can be constructed in purely geometric way and comply with the following properties: *i*) they form a base, *ii*) they can represent a uniform field (magnetic induction \mathbf{B} , electric field \mathbf{E}) from the Degrees of Freedom (fluxes or voltages) and *iii*) they comply with the following geometric consistency properties [4]

$$\int_{v_k} v_i^f dv = \tilde{e}_i, \quad \int_{v_k} v_i^e dv = \tilde{f}_i, \quad (4)$$

where \tilde{e}_i , \tilde{f}_i are the edge and face vectors associated with \tilde{e} , \tilde{f} respectively.

REFERENCES

- [1] T. Weiland, "Time domain electromagnetic field computation with finite difference methods," Int. J. Numer. Model. Eng., Vol. 9, 1996, pp. 295–319.
- [2] E. Tonti, "Finite Formulation of the Electromagnetic Field," IEEE Trans. Mag., Vol. 38, No. 2, 2002, pp. 333–336.
- [3] Bossavit, "How weak is the Weak Solution in finite elements methods?," IEEE Trans. Mag., Vol. 34, No. 5, 1998, pp. 2429–2432.
- [4] A. Bossavit, L. Kettunen, "Yee-like Schemes on Staggered Cellular Grids: A synthesis Between FIT and FEM Approaches," IEEE Trans. Mag., Vol. 36, No. 4, 2000, pp. 861–867.
- [5] A. Bossavit, "Computational electromagnetism and geometry. (5): The 'Galerkin hodge'," J. Japan Soc. Appl. Electromagnetism & Mech., Vol. 2, pp. 203–209, 2000.
- [6] L. Codecasa, R. Specogna, F. Trevisan, "Symmetric Positive-Definite Constitutive Matrices for Discrete Eddy-Current Problems", IEEE Trans. Mag., Vol. 43, pp. 510–515, 2007.
- [7] L. Codecasa, R. Specogna, F. Trevisan, "Discrete constitutive equations over hexahedral grids for eddy-current problems", CMES, vol.1, no.1, pp.1–14, 2008.
- [8] P. Dular, J.-Y. Hody, A. Nicolet, A. Genon, W. Legros, "Mixed Finite Elements Associated with a Collection of Tetrahedra, Hexahedra and Prisms," IEEE Trans. Mag. Vol. 30, No. 5, 1994, pp. 2980–2983.
- [9] F. Trevisan, L. Kettunen "Geometric interpretation of finite dimensional eddy current formulations," Int. J. Num. Meth. Eng., Vol. 67, No. 13, 2006, pp. 1888–1908.

Domain Decomposition Methods with Second Order Transmission Conditions for Solving Multiscale Electromagnetic Wave Problems

Zhen Peng, Vineet Rawat, and Jin-Fa Lee
 ElectroScience Laboratory
 1320 Kinnear Road, Columbus, Ohio 43212, USA
 peng.98@osu.edu

Abstract— Non-overlapping domain decomposition (DD) methods with complex first-order Robin-type transmission conditions (TCs) provide an efficient iterative solution for Maxwell's equation. Unfortunately, the first order TCs do not effectively account for some eigenmodes of the system matrix, which limits the scalability of the methods. In this work, we derive a new type of Robin TCs with second order tangential derivatives to improve the performance. We then investigate the use of this new second order TCs for non-conformal and non-overlapping DD methods. Numerical results illustrate their effectiveness of the proposed methods on some model problem and on several large scale problems of practical interest.

I. INTRODUCTION

Finite Element based DD methods have recently garnered considerable attention due to their ability to accurately and efficiently solve large and multiscale electromagnetic radiation and scattering problems [2]-[4]. The methods are attractive because they allow the solution of large problems with only modest computational resources. They are also inherently parallel, an important consideration in keeping with current trends in computer architecture. In general, the DD method derives its efficiency by modifying the original large FEM problem by decomposing it into several smaller, more manageable sub-domains. The sub-domains are solved individually and the interactions between the sub-domains are communicated through a proper transmission condition (TC). TCs not only enforce the continuity of tangential fields on the interfaces, but also play a crucial role in the convergence performance of DD method.

For the vector wave equation, the majority of non-overlapping DD methods employ complex first-order Robin-type transmission conditions (FOTCs). The FOTCs provide a simple, efficient, and parallel preconditioner for the DD matrix equation that yields fast and robust iterative solution. Unfortunately, it is recognized that there are two types of eigenmodes of the DD system matrix, which are propagative and evanescent modes. the FOTCs provide a convergent solution for propagative modes, but do not effectively account for evanescent modes of the system matrix. This limits the scalability of the method and one must turn to higher order TCs to further improve the performance. Similar to the higher absorbing boundary conditions, the complete second order TCs and higher order TCs are hard to implement and the reason of that is the surface divergence terms. Instead of complete second order TCs, this work adds a second order tangential differential operator to the FOTC. We refer this

family of TCs as second order TCs (SOTCs). Here we investigate non-conformal, non-overlapping DD methods with the use of SOTCs at the interfaces of sub-domains. Numerical results demonstrate that by using the SOTCs, the convergence of DDM can be greatly improved.

II. DDM BOUNDARY VALUE PROBLEM

For simplicity, we consider only partitioning the problem domain into two sub domains. The particular DDM that we are interested in this application is the non-overlapping DDM. Thus the problem domain Ω is partitioned into two non-overlapping sub-domains, Ω_1 and Ω_2 . We shall denote the boundary that separates Ω_1 and Ω_2 by Γ_{12} . Thus, the proposed non-overlapping DDM can be formulated through the following iteration process: given \vec{E}_1^0 and \vec{E}_2^0 , for $n \geq 1$ solve

$$\begin{aligned} \nabla \times \frac{1}{\mu_{r_1}} \nabla \times \vec{E}_1^n - k^2 \epsilon_{r_1} \vec{E}_1^n &= 0 && \text{in } \Omega_1 \\ \vec{n}_1 \times \frac{1}{\mu_{r_1}} \nabla \times \vec{E}_1^n + \alpha \vec{n}_1 \times \vec{E}_1^n \times \vec{n}_1 + \gamma \nabla_\tau \times \frac{1}{\mu_{r_1}} \nabla_\tau \times \vec{E}_1^n \\ &= -\vec{n}_2 \times \frac{1}{\mu_{r_2}} \nabla \times \vec{E}_2^{n-1} + \alpha \vec{n}_2 \times \vec{E}_2^{n-1} \times \vec{n}_2 + \gamma \nabla_\tau \times \frac{1}{\mu_{r_2}} \nabla_\tau \times \vec{E}_2^{n-1} && \text{on } \Gamma_{12} \\ \nabla \times \frac{1}{\mu_{r_2}} \nabla \times \vec{E}_2^n - k^2 \epsilon_{r_2} \vec{E}_2^n &= 0 && \text{in } \Omega_2 \\ \vec{n}_2 \times \frac{1}{\mu_{r_2}} \nabla \times \vec{E}_2^n + \alpha \vec{n}_2 \times \vec{E}_2^n \times \vec{n}_2 + \gamma \nabla_\tau \times \frac{1}{\mu_{r_2}} \nabla_\tau \times \vec{E}_2^n \\ &= -\vec{n}_1 \times \frac{1}{\mu_{r_1}} \nabla \times \vec{E}_1^{n-1} + \alpha \vec{n}_1 \times \vec{E}_1^{n-1} \times \vec{n}_1 + \gamma \nabla_\tau \times \frac{1}{\mu_{r_1}} \nabla_\tau \times \vec{E}_1^{n-1} && \text{on } \Gamma_{21} \end{aligned} \quad (1)$$

α and γ are parameter to choose. It is straightforward to show that the two TCs imply the needed field continuities on the interface. Compare to the FOTC in [2], the new interface conditions add two second order tangential differential operators.

III. CONVERGENCE ANALYSIS

By using Fourier analysis [3], we can obtain the following convergence factors for the new SOTCs.

$$|\rho_{TE}| = \left| \frac{j k_z + \alpha + \gamma(k^2 - k_z^2)}{j k_z - \alpha - \gamma(k^2 - k_z^2)} \right|^2 \quad (2)$$

for the TE modes, and

$$|\rho_{TM}| = \left| \frac{\frac{j k_z^2}{k_z} + \alpha}{\frac{j k_z^2}{k_z} - \alpha} \right|^2 \quad (3)$$

for the TM modes, where we have made use of the dispersion relation $k^2 = k_x^2 + k_y^2 + k_z^2$. k_z^2 is the z-directed wave number.

By choosing $\gamma = 0$, we will obtain the first order Robin type TC. Normally we will choose $\alpha = -jk_0$ to guarantee all the TE and TM propagating modes converge. However, for the evanescent modes, $|\rho_{TE}| = |\rho_{TM}| = 1$. This is the reason FOTC has the issue of scalability with respect to mesh density or polynomial order.

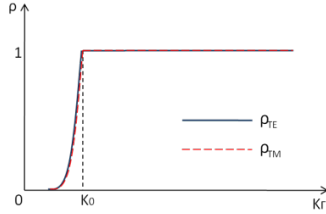


Fig. 1. Convergence factor of first order Robin TC

For the new SOTC, we still choose $\alpha = -jk_0$ to obtain the same convergence rate for all the TE and TM propagating modes. Now we have an additional degree of freedom for the second order tangential differential term. This parameter is chosen to accelerate the convergence for the TE evanescent modes. We refer this type of SOTC as SOTC-TE.

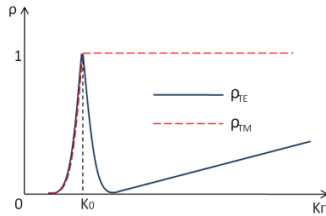


Fig. 2. Convergence factor of second order TC TE

There are other forms of SOTC [5,6] by choosing different value of α and γ . The details are omitted here and will report in the future.

IV. NUMERICAL EXPERIMENT

A. Eigenspectra of DD Matrices

The first numerical experiment involves a small cubical waveguide with size of 0.5λ , which is partitioned into two sub-domains. We use it to examine the eigenspectra produced by the DD methods using the FOTC, SOTC. From Fig. 3(a) we can see that many eigenvalues lie on the shifted unit circle, which are the evanescent modes. The remaining eigenvalues within the unit circle are the propagating modes. As the mesh is refined, the number of evanescent modes increases and the eigenvalues quickly approach zero. These small but non-zero eigenvalues will significantly degrade the performance of iterative Krylov subspace method. It is clearly seen from Fig. 3(b) the eigenspectra of the SOTC shows improvements over FOTC. The evanescent modes which are nearest to zero are brought well within the shifted unit circle and the eigenvalues are clustered in the center. We also note that some eigenvalues remains unchanged and these correspond to the TM modes. However, as SOTC take care of the most troublesome evanescent modes, it is very effective in improving the condition number of the DD matrix.

Next we use an "COBRA" cavity [7] excited by plane wave and operating at 4GHz to examine the accuracy and scalability of the methods with respect to mesh size. The mesh size decreases from $h = \lambda/5$ to $\lambda/12$. Fig. 4 shows the

convergence of the FOTC and SOTC for different mesh size. We see that the performance of FOTC significantly degrade as the mesh is refined. The SOTC however, provides a near constant number of iterations as the mesh is refined.

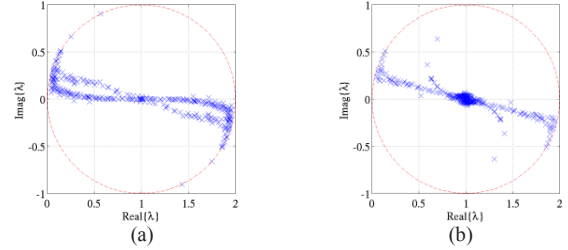


Fig. 3. Eigenspectra for a waveguide (a) FOTC; (b) SOTC

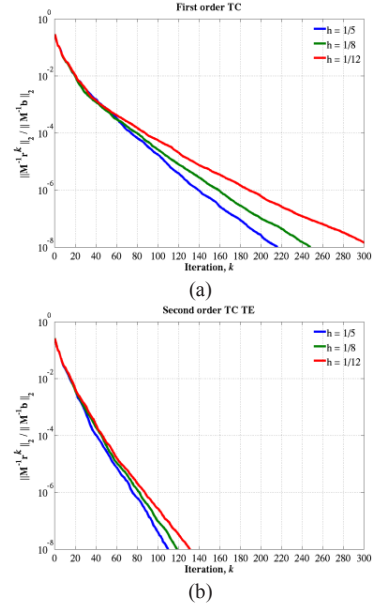


Fig. 4. Iterative solver convergence for "COBRA" Cavity (a) FOTC; (b) SOTC

V. REFERENCES

- [1] J.-D. Benamou, B. Després, "A domain decomposition method for the Helmholtz equation and related optimal control problems," *J. Comput. Phys.* 136(1997) 68-82.
- [2] S.-C. Lee, M. Vouvakis, and J. F. Lee, "A non-overlapping domain decomposition method with non-matching grids for modeling large finite antenna arrays," *J. Comput. Phys.*, vol. 203, no. 1, pp. 1-21, 2005.
- [3] Y.-J. Li and J.-M. Jin, "A new dual-primal domain decomposition approach for finite element simulation of 3-D large-scale electromagnetic problems," *IEEE Trans. Antennas and Propagation*, vol. 55, no. 10, pp. 2803-2810, Oct. 2007.
- [4] K. Zhao, V. Rawat, S.-C. Lee, and J.-F. Lee, "A domain decomposition method with nonconformal meshes for finite periodic and semi-periodic structures," *IEEE Trans. Antennas and Propagation*, vol. 55, no. 9, pp. 2559-2570, Sept. 2007.
- [5] M.-J. Gander, F. Magoulès, and F. Nataf, "Optimized Schwarz methods without overlap for the Helmholtz equations," *SIAM J. Sci. Comput.*, 24 (2002), pp. 38-60.
- [6] Ana Alonso-Rodriguez, Luca Gerardo-Giorda, "New non-overlapping domain decomposition methods for the harmonic Maxwell system," *SIAM J. Sci. Comput.*, vol. 28, no. 1, pp. 102-122, 2006.
- [7] Zhen Peng and Xin-Qing Sheng, "A Flexible and Efficient Higher Order FE-BI-MLFMA for Scattering by a Large Body With Deep Cavities," *IEEE Trans. Antennas and Propagation*, vol. 456, pp. 20321-2042, July, 2008.

Improving the Mixed Formulation for Meshless Local Petrov–Galerkin Method

¹Alexandre R. Fonseca, ²Bruno C. Corrêa, ²Elson J. Silva and ²Renato C. Mesquita

¹Department of Computing – Federal University of Jequitinhonha and Mucuri Valleys
Rua da Glória, 187 – Centro – Diamantina, 39100-000, Brazil

²Department of Electrical Engineering – Federal University of Minas Gerais
Avenida Antônio Carlos, 6627 – B. Pampulha – Belo Horizonte, 31270-010, Brazil
arfonseca@ufvjm.edu.br, billccorrea@gmail.com, elson@cpdee.ufmg.br, renato@ufmg.br

Abstract— The meshless local Petrov–Galerkin method (MLPG) with a mixed formulation to impose Dirichlet boundary conditions is investigated in this paper. We propose the use of Shepard functions for inner nodes combined with the radial point interpolation method with polynomial terms (RPIMp) for nodes close to the Dirichlet boundaries. Whereas the Shepard functions have lower computational costs, the RPIMp imposes in a direct manner the essential boundary conditions. Results show that the technique leads to a good trade-off between computational time and precision.

I. INTRODUCTION

Meshfree methods do not need any connectivity structure among nodes, avoiding the mesh generation problem. It is a very attractive choice, especially when solving problems that involve movement, boundary and shape deformation. However, because of the absence of a mesh, a few drawbacks are introduced such as neighbour search, local matrix inversions and other computations that ultimately increase the computational cost. Consequently, in order to increase the methods efficiency special techniques should be employed. Other problem with meshless methods is the imposition of the essential boundary conditions since some of the meshless shape functions do not satisfy the Kronecker delta condition.

In [1] a mixed formulation to impose boundary conditions is presented. The moving least squares (MLS) is used for inner nodes and the radial point interpolation method with polynomial terms (RPIMp) is used for boundary nodes. However, the MLS functions are more expensive than RPIMp when the number of neighbors is low. To reduce the computational time, in this work we propose a faster shape function instead of MLS, namely Shepard functions.

In 1968 Shepard introduced shape functions in the context of data interpolation that can be interpreted as an inverse distance weighting [2]. Actually, Shepard's method is a subcase of the MLS procedure with 0th order consistency. Using the Shepard method to construct shape functions has the important advantage of low computational cost and simplicity of computation. However, the low order of consistency makes the Shepard shape functions fail for the solution of even second order boundary value problems [2]. Moreover, both MLS and Shepard have low precision when the essential boundary conditional is not well imposed. In this paper we show that when using the penalty method [3] to impose boundary conditions the results present high oscillation over the whole domain. When using the proposed mixed

formulation, the results show that the mixed method is still faster than using only RPIMp and maintains good precision. This is true even in cases where a few nodes are used for the integration of subdomains.

II. MLPG

MLPG uses a procedure named local weak form [3]. In this technique, each node defines its own sub-domain that is independent from the remaining. Those sub-domains are allowed to have any size and shape (Fig. 1) and they eliminate the need of a grid for numerical integration. Furthermore, the Petrov–Galerkin method allows the trial and shape functions to be chosen from different spaces. These two features make this method very flexible and distinguishes MLPG as a truly meshfree method.

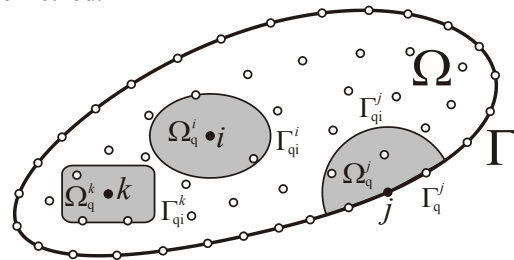


Fig. 1. Domain representation

For electrostatic problems, the local weak form can be written as

$$\int_{\Omega_q} w(\nabla \cdot (\varepsilon \nabla V^h)) d\Omega + \alpha \int_{\Gamma_q} w(V^h - V_u) d\Gamma = 0 \quad (1)$$

where w is the test function chosen to be the Heaviside step functions which leads to a MLPG5 variant of MLPG [4]. The second integral is used to enforce Dirichlet boundary conditions by the penalty method, where α is a constant with high value (10^6).

III. SHAPE FUNCTIONS

In a broad sense, shape functions are interpolation functions [3]. The approximation function V^h is obtained by taking the sum of the known values at some points weighted by their respective shape functions. Therefore, at any point of the domain, the approximated value of the function is given by

$$V^h(\mathbf{x}) = \sum_{i=1}^n \phi_i V_i \quad (2)$$

where V_i is the fictitious nodal value of the unknown function at \mathbf{x}_i , n is the number of known points and ϕ_i is the shape function of node \mathbf{x}_i .

A. Radial point interpolation method with polynomial terms

Amongst the approximation techniques commonly used in meshless methods, the RPIMP is one of the few that will lead to a shape function that possess the Kronecker delta property [1]. However, its computational cost is higher if compared with the other approaches:

$$\phi_i(\mathbf{x}) = \mathbf{R}^t(\mathbf{x})\mathbf{S}\mathbf{a}_i + \mathbf{p}^t(\mathbf{x})\mathbf{S}\mathbf{b}_i \quad (3)$$

$$\mathbf{S}\mathbf{a} = \mathbf{R}_0^{-1}[1 - \mathbf{P}\mathbf{S}\mathbf{b}] = \mathbf{R}_0^{-1} - \mathbf{R}_0^{-1}\mathbf{P}\mathbf{S}\mathbf{b} \quad (4)$$

$$\mathbf{S}\mathbf{b} = [\mathbf{P}'\mathbf{R}_0^{-1}\mathbf{P}]^{-1}\mathbf{P}'\mathbf{R}_0^{-1} \quad (5)$$

$$\mathbf{P} = [\mathbf{p}(\mathbf{x}_1)\mathbf{p}(\mathbf{x}_2)\cdots\mathbf{p}(\mathbf{x}_n)]^t \quad (6)$$

$$\mathbf{R}^t(\mathbf{x}) = [w(\mathbf{x} - \mathbf{x}_1)w(\mathbf{x} - \mathbf{x}_2)\cdots w(\mathbf{x} - \mathbf{x}_n)] \quad (7)$$

$$\mathbf{R}_0^t = [\mathbf{R}(\mathbf{x}_1)\mathbf{R}(\mathbf{x}_2)\cdots\mathbf{R}(\mathbf{x}_n)] \quad (8)$$

where $w(\mathbf{x} - \mathbf{x}_i)$ is some weight function centered at \mathbf{x}_i , usually a Radial Basis Function (RBF), and $\mathbf{p}(\mathbf{x})$ is a vector containing monomials of a complete polynomial basis with m terms. In this work we used $\mathbf{p}^t(\mathbf{x}) = [1 \ x \ y]$.

B. Moving least squares [1]

MLS shape functions are given by:

$$\phi_i(\mathbf{x}) = \mathbf{p}^t(\mathbf{x})\mathbf{A}^{-1}(\mathbf{x})\mathbf{B}_i(\mathbf{x}) \quad (9)$$

$$\mathbf{A}(\mathbf{x}) = \sum_{k=1}^n w(\mathbf{x} - \mathbf{x}_k)\mathbf{p}(\mathbf{x}_k)\mathbf{p}^t(\mathbf{x}_k) \quad (10)$$

$$\mathbf{B}_i(\mathbf{x}) = w(\mathbf{x} - \mathbf{x}_k)\mathbf{p}(\mathbf{x}_k) \quad (11)$$

C. Shepard

The Shepard functions can be interpreted as a MLS simplification with $\mathbf{p}(\mathbf{x}) = [1]$ which leads to

$$\phi_i(\mathbf{x}) = \frac{w(\mathbf{x} - \mathbf{x}_i)}{\sum_{k=1}^n w(\mathbf{x} - \mathbf{x}_k)} \quad (12)$$

IV. MIXED FORMULATION

The mixed formulation [1] uses RPIMP to define the approximation for the nodes along the boundaries (boundary nodes) with Dirichlet boundary conditions and those close to them, and a faster shape function for the remaining nodes (inner nodes). This approach eliminates the need of using the penalty method to enforce essential boundary conditions.

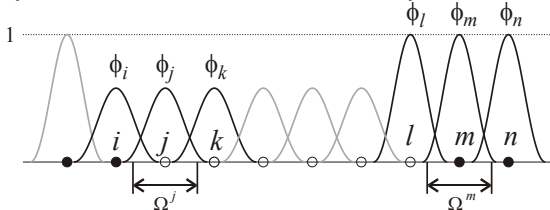


Fig. 2. Mixed Formulation: black nodes are classified as boundary nodes and white nodes are classified as inner nodes. Integration of inner nodes uses a faster shape function and integration of boundary nodes uses a shape function with Kronecker delta property.

V. RESULTS

To test the approach, the problem described by Fig. 3a was simulated with an uniform 100x100 node distribution. Table I shows the relative times for the various shape functions. Using only Shepard functions we obtain the best times but due to the lower consistence order and the penalty method to impose boundary conditions, the result has lots of oscillation (Fig. 3c). The same problem occurs with MLS but in minor scale. When using mixed formulation with RPIMP + Shepard functions, the time consuming is a little higher than using only Shepard but the precision is much better (Fig. 3d).

TABLE I
COMPARISON AMONG METHODS, BASED ON RELATIVE TIMES

n	9	16
RPIMP	1.94	7.54
MLS	2.26	3.25
Shepard	1.00	1.21
RPIMP + MLS	2.20	3.86
RPIMP + Shepard	1.07	2.15

n is the number of neighbour nodes used to build the shape function approximation in a sub-domain.

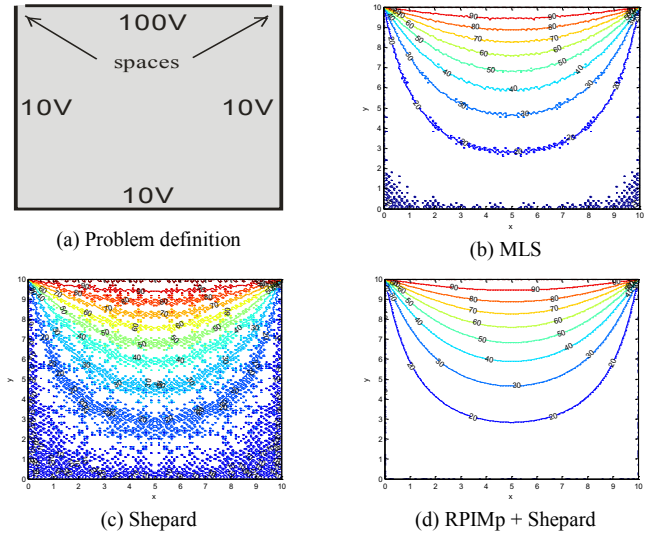


Fig. 3. Sample results. (a) defines de test problem. (b) result using MLS (c) results using Shepard (d) results using mixed formulation with RPIMP and Shepard. An uniform grid of 100x100 nodes over the domain and 9 nodes in the neighborhood of each domain (1st column of Table I) were used for all tests.

VI. REFERENCES

- [1] A. R. Fonseca, S. A. Viana, E. J. Silva, R. C. Mesquita "Imposing boundary conditions in the meshless local Petrov-Galerkin method", *IET Sci. Meas. Technol.*, 6(2): 387-394, 2008.
- [2] T. P. Fries, H. G. Matthies, "Classification and overview of meshfree methods", Technical report, Technical University Braunschweig, Department of Mathematics and Computer Science, 2004.
- [3] G. R.Liu, "Mesh Free Methods: Moving Beyond the Finite Element Method", *CRC Press*, 2002.
- [4] S. N. Atluri, S. A. Shen.: "The meshless local Petrov-Galerkin (MLPG) method - A simple and less-costly alternative to the finite element and boundary element methods", *Comput Model Eng Sci*, 3: 11-51, 2002.

Effectiveness of Higher Order Time Integration in Time Domain Finite Element Analysis

Yoshifumi Okamoto^{1,2}, Koji Fujiwara³, and Yoshiyuki Ishihara³

¹Research Center of Applied Electromagnetic Energy, Doshisha University, Kyoto 610-0321 Japan

²The Oita Prefectural Organization for Industry Creation, Oita 870-0037 Japan

³Department of Electrical Engineering, Doshisha University, Kyoto 610-0321 Japan

E-mail: {re-okamo, koji.fujiwara, yishihar}@mail.doshisha.ac.jp

Abstract— The accuracy of the time domain magnetic field analysis occasionally dropped when the first order backward difference (backward Euler) is adopted as time integration technique. Backward Euler technique is widely applied to the analysis of various electrical machines. In this paper, the effectiveness of higher order time integration is investigated against the time domain analysis using finite element method.

I. INTRODUCTION

The magnetic field analysis in time domain is indispensable to the practical design of electric machines. The first order backward difference technique (Backward Euler method) is widely applied to the magnetic field analysis [1], [2] according to the stable characteristic in the time domain. However, the computation accuracy occasionally gets worse.

In this paper, we applied the GEAR's stiffly stable algorithm [3] to the eddy current analysis of magnetic shielding model with magnetic nonlinearity [4]. The accuracy of the higher order time integration is compared with the one of backward Euler method.

II. FORMULATION

The weighted residual G_e and G_n in the time $t = t_0$ is given as follows:

$$G_{ei}^{(t_0)} = \iiint_V (\nabla \times N_i) \cdot (\nu \nabla \times \mathbf{A}^{(t_0)}) dV - \iiint_V N_i \cdot \mathbf{J}_0^{(t_0)} dV + \iiint_V N_i \cdot \left\{ \sigma \left(\frac{\partial \mathbf{A}}{\partial t} \Big|_{t_0} + \nabla \phi^{(t_0)} \right) \right\} dV = 0, \quad (1)$$

$$G_{ni}^{(t_0)} = \iiint_V \nabla N_i \cdot \left\{ \sigma \left(\frac{\partial \mathbf{A}}{\partial t} \Big|_{t_0} + \nabla \phi^{(t_0)} \right) \right\} dV = 0, \quad (2)$$

where \mathbf{A} is the magnetic vector potential, ϕ is the electric scalar potential, N_i is the edge-based vector shape function, N_i is the nodal scalar shape function, the material constant ν and σ are the magnetic reluctivity and conductivity, \mathbf{J}_0 is the source current density, respectively. The boundary integral term can be omitted here.

The time derivative term using backward Euler method is given as follows:

$$\frac{\partial \mathbf{A}}{\partial t} \Big|_{t_0} = \frac{\mathbf{A}^{(t_0)} - \mathbf{A}^{(t_0 - \Delta t)}}{\Delta t}, \quad (3)$$

where Δt is the time step size. Introducing GEAR's stiffly stable algorithm (2nd or 3rd order) to the implicit time

integration, and then the time derivative term is expressed by multi magnetic vector potentials obtained in past several time steps as follows:

$$\frac{\partial \mathbf{A}}{\partial t} \Big|_{t_0} = \frac{3\mathbf{A}^{(t_0)} - 4\mathbf{A}^{(t_0 - \Delta t)} + \mathbf{A}^{(t_0 - 2\Delta t)}}{2\Delta t}, \quad (4)$$

$$\frac{\partial \mathbf{A}}{\partial t} \Big|_{t_0} = \frac{11\mathbf{A}^{(t_0)} - 18\mathbf{A}^{(t_0 - \Delta t)} + 9\mathbf{A}^{(t_0 - 2\Delta t)} - 2\mathbf{A}^{(t_0 - 3\Delta t)}}{6\Delta t}. \quad (5)$$

The \mathbf{A} - ϕ formulation of Newton-Raphson method in each time step is given as follows:

$$\begin{bmatrix} \mathbf{S}_{AA} & \mathbf{S}_{A\phi} \\ \mathbf{S}_{\phi A} & \mathbf{S}_{\phi\phi} \end{bmatrix} \begin{Bmatrix} \delta \mathbf{A} \\ \delta \phi \end{Bmatrix} = - \begin{Bmatrix} G_{ei} \\ G_{ni} \end{Bmatrix}, \quad (6)$$

where $\delta \mathbf{A}$ and $\delta \phi$ are the increment of \mathbf{A} and ϕ , and $\mathbf{S}_{AA} - \mathbf{S}_{\phi\phi}$ are the components of the Jacobian matrix. In the case of second order, left side matrix of (6) becomes symmetry when (2) is multiplied by $2\Delta t / 3$ in both sides. For example, components of $\mathbf{S}_{\phi A}$, $\mathbf{S}_{\phi\phi}$, and G_{ni} are described as follows:

$$\mathbf{S}_{\phi A} \Big|_{i,j} = \iiint_V \sigma \nabla N_i \cdot \nabla N_j dV, \quad (7)$$

$$\mathbf{S}_{\phi\phi} \Big|_{i,j} = \iiint_V \frac{2}{3} \sigma \Delta t \nabla N_i \cdot \nabla N_j dV, \quad (8)$$

$$G_{ni}^{(t_0)} = \iiint_V \nabla N_i \cdot \sigma \left(\frac{3\mathbf{A}^{(t_0)} - 4\mathbf{A}^{(t_0 - \Delta t)} + \mathbf{A}^{(t_0 - 2\Delta t)}}{3} + \frac{2}{3} \Delta t \nabla \phi^{(t_0)} \right) dV. \quad (9)$$

In the case of third order, left side matrix of (6) becomes symmetry when (2) is multiplied by $6\Delta t / 11$ in both sides. The components $\mathbf{S}_{\phi\phi}$ and G_{ni} are transformed as follows:

$$\mathbf{S}_{\phi\phi} \Big|_{i,j} = \iiint_V \frac{6}{11} \sigma \Delta t \nabla N_i \cdot \nabla N_j dV, \quad (10)$$

$$G_{ni}^{(t_0)} = \iiint_V \nabla N_i \cdot \sigma \left(\frac{11\mathbf{A}^{(t_0)} - 18\mathbf{A}^{(t_0 - \Delta t)} + 9\mathbf{A}^{(t_0 - 2\Delta t)} - 2\mathbf{A}^{(t_0 - 3\Delta t)}}{11} + \frac{6}{11} \Delta t \nabla \phi^{(t_0)} \right) dV. \quad (11)$$

Above formulation is same applied into more higher order time integration.

At the 1st step computation using GEAR's 2nd order, backward Euler method is adopted. Similarly, at the use of

GEAR's 3rd order computation, 1st order and 2nd order time integrations are adopted as the 1st and 2nd step computation.

III. VERIFICATION

A. Analyzed model and condition

The finite element mesh of magnetic shielding model [4] is shown in Fig. 1. The shield thickness is 1 mm, and the magnetic material is SS400. The nonlinear magnetic property of SS400 is considered. The number of elements, nodes, and unknowns of the edge-based first order hexahedral elements are 60,950, 65,753, and 185,276, respectively.

The linear equations in NR steps were solved by ICCG solver under the convergence criterion $\|r_n\|_2 / \|r_0\|_2 < \varepsilon_{cg}$, where $\|r_n\|_2$ is a 2-norm of the residual of linear equation at the n -th iteration, here, ε_{cg} was set up as 10^{-2} . The line search technique (functional NR [0, 1.0]) [5], [6] is introduced to improve the nonlinear convergence characteristics. The Newton-Raphson iteration is terminated under the condition $|\delta B| < 10^{-3}$ T, where δB is the increment of magnetic flux density B on the element center. The waveform of current is sinusoidal with the frequency 50 Hz, and the current is imposed during two cycles.

B. Analyzed results

The numerical error and convergence characteristics in higher order time integration are compared with backward Euler method. The instantaneous eddy current loss ($t = t_0$) is computed by using

$$P_{Je}^{(t_0)} = \iiint_V \sigma \left| \frac{\partial A}{\partial t} \Big|_{t_0} + \nabla \phi^{(t_0)} \right|^2 dV. \quad (10)$$

Time step size Δt is set as 0.5556 ms, and number of time

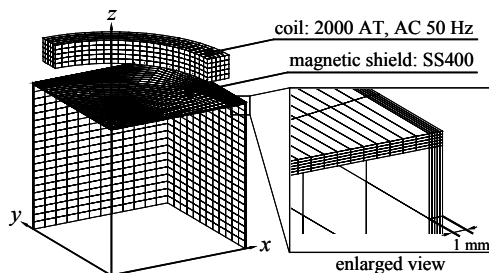


Fig. 1. Finite element mesh (shield thickness: 1 mm).

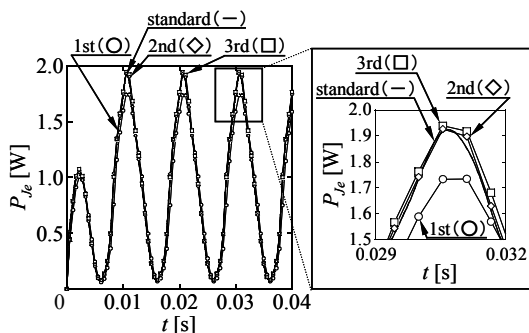


Fig. 2. Behavior of instantaneous eddy current loss ($d = 1.0$ mm).

steps is 72. The temporal behavior of instantaneous eddy current loss is shown in Fig. 2. The standard solution is obtained from the 1,440 steps computation with the backward Euler method. Maximum value obtained from backward Euler method in steady state is improved by the utilization of 2nd or 3rd order time integration as shown in TABLE I. The nonlinear and ICCG convergence characteristics in using the higher order time integration are almost same as conventional 1st order characteristic as shown in TABLE II. It is shown that the accuracy of eddy current loss is improved by higher order time integration on the condition of nearly same CPU time.

	standard	the order of GEAR's algorithm		
		1st	2nd	3rd
P_{Je} [W]	1.915	1.733	1.938	1.926
relative error [%]	—	9.5	1.2	0.6

	the order of GEAR's algorithm		
	1st	2nd	3rd
total ICCG ite. / ave.	51,324 / 712.8	53,635 / 744.9	50,707 / 704.3
total NR ite. / ave.	458 / 6.4	474 / 6.6	457 / 6.3
CPU time [h]	2.1	2.3	2.3

CPU: Intel Core 2 Duo E6850 processor / 3.0 GHz & 2.0 GB RAM

IV. CONCLUSIONS

In this paper, GEAR's stiffly stable algorithm (2nd or 3rd order) is introduced to the time integration in the nonlinear eddy current analysis using finite element method. The accuracy of instantaneous eddy current loss is improved by utilization of higher order time integration, and convergence characteristics of ICCG and Newton-Raphson method is almost same as conventional backward Euler method. The effectiveness of GEAR's algorithm is more investigated in the practical analysis such as motor in the full paper.

V. REFERENCES

- [1] T. Yamaguchi, Y. Kawase, S. Suzuki, K. Hirata, T. Ohta, and Y. Hasegawa, "Dynamic analysis of linear resonant actuator driven by DC motor taking into account contact resistance between brush and commutator", *IEEE Trans. on Magn.*, vol. 44, no. 6, pp. 1510-1513 (2008).
- [2] K. Yamazaki, S. Tada, H. Mogi, Y. Mishima, C. Kaido, S. Kanao, K. Takahashi, K. Ide, K. Hattori, and A. Nakahara, "Eddy current analysis considering lamination for stator ends of turbine generators", *IEEE Trans. on Magn.*, vol. 44, no. 6, pp. 1502-1505 (2008).
- [3] G. William GEAR, *Numerical Initial Value Problems in Ordinary Differential Equations*. Prentice-Hall, Inc. Englewood Cliffs, New Jersey (1971)
- [4] Y. Takahashi, S. Wakao and A. Kameari, "Large scale and highly accurate magnetic field analysis of magnetic shield," *J. Applied Physics*, 99, 08H904, (2006).
- [5] Y. Okamoto, K. Fujiwara, and R. Himeno, "Exact minimization of energy functional for NR method with line-search technique," *IEEE Trans. on Magn.*, vol. 45, no. 3, pp. 1288-1291 (2009).
- [6] K. Fujiwara, Y. Okamoto, A. Kameari, and A. Ahagon, "The Newton-Raphson method accelerated by using a line search - comparison between energy functional and residual minimization -," *IEEE Trans. on Magn.*, vol. 41, no. 5, pp. 1724-1727 (2005).

Extended Meshfree Point Collocation Method for Electromagnetic Problems with Layered Singularity

Young-Cheol Yoon* and Do Wan Kim**

* Department of Civil Engineering, Myongji College
356-1 Hongoeun2-Dong, Seodaemun-Gu, Seoul, 120-776, Republic of Korea
ycyoon@mjc.ac.kr

** Department of Applied Mathematics, Hanyang University, Republic of Korea
1227 Sangnok-gu, Ansan 426-791
dokim@hanyang.ac.kr

Abstract — A novel meshfree point collocation method for the solving of electromagnetic potential problems with layered singularity is presented. The approximation based on the moving least squares technique is extended by introducing jump, scissor and wedge functions. It is able to model discontinuities electromagnetic potential and gradient fields. Discretization of the partial differential equations yields a linear system consisting of residual equations. Solving the system provides the nodal solutions together with jump strengths on the singular layer. Numerical experiments for electrostatic problems with layered singularity show that the developed method is highly efficient and reliable.

I. INTRODUCTION

The meshfree method [1] has been actively applied to singular problems like crack propagation problem because it has strong advantages in changing geometry modeling. It requires no connectivity among nodes in construction of the approximation function so that geometry change involves minimal node operation. However, the drawbacks such as expensive computational cost in derivative calculation, numerical quadrature and essential boundary treatment have been major obstacles to extension of the Galerkin based meshfree method to more various applications. Therefore, despite of the advantageous geometry modeling, application to the interface problems like electrostatic problem with layered singularity rarely appeared.

The meshfree point collocation method overcomes the drawbacks stated above. It was already applied to fluid and solid problems [2]-[3] and proved to be simple and fast in the formulation and computation, respectively. Kim and Kim [4] solved electromagnetic problem with complex geometry by using the meshfree point collocation method. Furthermore, heat conduction problem with interface has been successfully solved using only regular node set [5]; special functions generating derivative discontinuity across the interface was devised and immersed in the approximation so that numerical complexity due to the singularity was effectively eliminated.

This study presents a novel meshfree point collocation method for solving electrostatic problem with layered singularity. This work is an extension of [5]. New meshfree approximation to be proposed here is able to model jumps not only in the potential field but also in the normal and tangential derivative fields. Nodal operation is very easy since it does not require grid structure. The numerical scheme inherits the framework of the conventional meshfree point collocation method. The discretization of partial differential equation is

straightforward. In the next, the brief review and important numerical features of the method are presented.

II. EXTENDED MESHFREE APPROXIMATION

An electrostatic problem with layered singularity is considered. The layered singularity brings about jumps in the potential and the gradient fields. For easy awareness of the approximation, let us take one dimensional case into account. For a given function $u(\mathbf{x}) \in C^m(\bar{\Omega})$, m-th order Taylor polynomial at arbitrary position \mathbf{y} is given by

$$\begin{aligned} u_L(x, y) &= u(y) + \left(\frac{x-y}{\rho}\right) \frac{\rho}{1!} u^{(1)}(y) + \left(\frac{x-y}{\rho}\right)^2 \frac{\rho^2}{2!} u^{(2)}(y) \\ &+ \dots + \left(\frac{x-y}{\rho}\right)^m \frac{\rho^m}{m!} u^{(m)}(y) \\ &= \mathbf{p}_m^T \left(\frac{x-y}{\rho}\right) \mathbf{a}(y) \end{aligned} \quad (1)$$

which yields the local approximation of $u(\mathbf{x})$. The components of $\mathbf{a}(y)$ include the derivative of $u(x)$ at y up to m-th order and $\mathbf{p}_m^T \left(\frac{x-y}{\rho}\right) = \left(1, \left(\frac{x-y}{\rho}\right), \left(\frac{x-y}{\rho}\right)^2, \dots, \left(\frac{x-y}{\rho}\right)^m\right)$. ρ indicates the radius of influence; it turns into the radius of weight function in the Moving Least Squares procedure. The unknown vector $\mathbf{a}(y)$ is obtained from the stationary condition of the weighted residual constructed at each node as is in the conventional meshfree methods.

Let us consider the approximation near singular layer. For the jump modeling in potential field, heavy-side step function $b_\Gamma(\mathbf{x})$ is introduced into the approximation; for the jump modeling in the normal and tangential derivative fields, wedge function $b_n(\mathbf{x})$ and scissor function $b_t(\mathbf{x})$ are employed respectively. The regular approximation in (1) takes the form as following

$$\begin{aligned} u_L(x, y) &= \mathbf{p}_m^T \left(\frac{x-y}{\rho}\right) \mathbf{a}(y) + \frac{1}{2} [u]_\Gamma b_\Gamma(\mathbf{x}) \\ &+ \frac{1}{2} \left[\frac{\partial u}{\partial n} \right]_\Gamma b_n(\mathbf{x}) + \frac{1}{2} \left[\frac{\partial u}{\partial t} \right]_\Gamma b_t(\mathbf{x}) \end{aligned} \quad (2)$$

where $\frac{1}{2} [u]_\Gamma$, $\frac{1}{2} \left[\frac{\partial u}{\partial n} \right]_\Gamma$, and $\frac{1}{2} \left[\frac{\partial u}{\partial t} \right]_\Gamma$ stands for the strengths of the jumps in potential, normal derivative and tangential derivative fields, respectively. The strengths are obtained from the governing equations. \mathbf{n} and \mathbf{t} are the normal and tangential vector to the singular layer Γ . The mathematical background can be referred to [5]. The unknown vector $\mathbf{a}(y)$ can be

calculated by the same manner as in regular approximation. The derivative of the extended meshfree approximation can then be written as

$$\begin{aligned}
 D_x^\alpha u^h(\mathbf{x}) &= \sum_I \Phi_I^\alpha(\mathbf{x}) u_I \\
 &+ \frac{1}{2} [u]_\Gamma \left\{ D_x^\alpha b_\Gamma(\mathbf{x}) - \sum_I \Phi_I^\alpha(\mathbf{x}) b_\Gamma(\mathbf{x}_I) \right\} \\
 &+ \frac{1}{2} \left[\frac{\partial u}{\partial n} \right]_\Gamma \left\{ D_x^\alpha b_n(\mathbf{x}) - \sum_I \Phi_I^\alpha(\mathbf{x}) b_n(\mathbf{x}_I) \right\} \\
 &+ \frac{1}{2} \left[\frac{\partial u}{\partial t} \right]_\Gamma \left\{ D_x^\alpha b_t(\mathbf{x}) - \sum_I \Phi_I^\alpha(\mathbf{x}) b_t(\mathbf{x}_I) \right\}
 \end{aligned} \tag{3}$$

where multi-index notation is used for the sake of convenience.

The differential operator denotes $D_x^\alpha := \partial_{x_1}^{\alpha_1} \partial_{x_2}^{\alpha_2} \dots \partial_{x_n}^{\alpha_n}$; $\Phi_I(\mathbf{x})$ is the regular meshfree shape function; $\Phi_I^\alpha(\mathbf{x})$ is α -th derivative of the shape function.

III. DISCRETIZATION

The Poisson type partial differential equations for the electrostatic problem with layered singularity are given by

$$\nabla \cdot (\beta \nabla u) = f \text{ in } \Omega \setminus \Gamma \tag{4}$$

$$u = \bar{u} \text{ on } \partial\Omega \tag{5}$$

$$[u]_\Gamma = \bar{g} \text{ on } \Gamma \tag{6}$$

$$\left[\beta \frac{\partial u}{\partial n} \right]_\Gamma = \bar{h} \text{ on } \Gamma \tag{7}$$

where f and β denotes electromagnetic source and permeability, respectively. Discontinuous β generates jump across Γ in the potential and the gradient fields and f may be discontinuous. It should be noted that Laplace equation without permeability term can also be solved easier than the PDE given in (4)-(7).

The governing equations are discretized based on nodes. Difference equations (or residual equations) are constructed at each node. The equations involve the derivative approximation of (3) and set up the linear algebraic system. Solving of the system yields nodal solution and jump strengths.

IV. NUMERICAL RESULTS

For numerical validation of the developed method, an electric potential function $u(x, y)$ governed by (4)-(7). Fig. 1(a) depicts the geometry and boundary of the problem. In computing the meshfree shape function, we used second-order basis polynomial, i.e. $m=2$. The singular layer is discretized with sufficient number of points that are irrelative to nodes. Nodal solutions are obtained at the nodes together with the strength of jumps at the layer points. The conjugate gradient solver is used. As shown in fig 1(b), the number of CGM iterations for this problem with 6400 nodes is around 180, which achieve the successive tolerance implying that the stiffness matrix is well conditioned. Fig 2(a) shows the convergence rate of L^∞ relative error for the potential and gradient. The order of accuracy appears to be more than second order. Fig 2(b)-2(d) illustrates surface plots for the

electrostatic potential, x and y components of the gradient, respectively. Note that the jumps are captured sharply without smearing. These computational results reveal that the developed method is efficient, accurate and robust in solving electromagnetic problems with layered singularity.

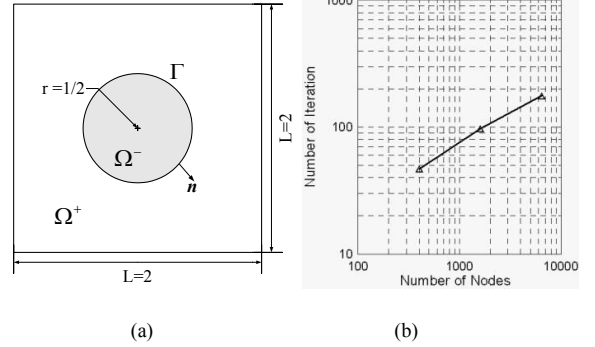


Fig. 1 Electrostatic problem (a) Configuration (b) The number of CGM iterations according to the number of nodes

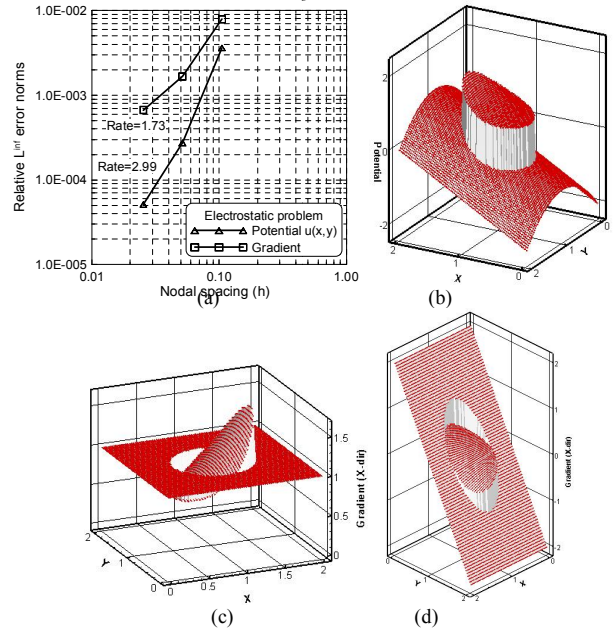


Fig. 2 Numerical results (a) Convergence rates (b) Electric potential (c) Gradient of the potential (x-dir.) (d) Gradient of the potential (y-dir.)

V. REFERENCES

- [1] T. Belytschko, Y. Y. Lu, and L. Gu, "Element-free galerkin methods", *International Journal for Numerical Methods in Engineering*, 37: 229-256, 1994.
- [2] D. W. Kim and Y. Kim, "Point collocation methods using the fast moving least squares reproducing kernel approximation", *International Journal for Numerical Methods in Engineering*, 56: 1445-1464, 2003.
- [3] S.-H. Lee and Y.-C. Yoon, "Meshfree point collocation method for elasticity and crack problems", *International Journal for Numerical Methods in Engineering*, 61(1): 22-48, 2004.
- [4] D. W. Kim and H.-K. Kim, "Point collocation method based on the FMLSrk approximation for electromagnetic field analysis", *IEEE Trans. on Magnetics*, 40(2): 1029-1032, 2004.
- [5] D.W. Kim, Y.-C. Yoon, W. K. Liu, and T. Belytschko, "Extrinsic meshfree approximation using asymptotic expansion for interfacial discontinuity of derivative", *Journal of Computational Physics*, 221: 370-394, 2007.

Strategies for Accelerating Non-linear Convergence for T-Ω Formulation

P. Zhou, D. Lin, B. He, S. S. Kher and Z.J. Cendes
Ansoft Corporation
225 W. Station Square Dr. Pittsburgh 15219 USA
ping@ansoft.com

Abstract — This paper details the derivation of the Jacobian matrix and the residual vector in terms of the T-Ω formulation. Then, a scheme is proposed to efficiently find the optimum relaxation factor for improving global convergence. Further, a local damping factor is introduced to address some local convergence issues by damping the updating of the nonlinear material property during nonlinear iterations.

I. INTRODUCTION

The Newton sequence with an arbitrary initial guess may converge at a very slow rate, or oscillate, or even diverge. It is also known that convergence is more difficult with the magnetic scalar potential than with magnetic vector potential [1]. Hence, under-relaxation is commonly used to improve convergence. If an optimum relaxation factor is used, convergent solution can always be obtained using a linear search algorithm [1]. However, it may take a very long time to find the optimum relaxation factor. [2] uses linearization to reduce the computation cost based on two values of the residual. However, the assumption that the residual changes quadratically with the relaxation factor is far from reality for most practical applications. In addition, the use of the optimum relaxation factor does not guarantee fast convergence because the “optimum” is only in the global sense and thus may not be suitable for some local elements. This may lead to poor local convergence due to large over-shoot correction or possible oscillation. This undesirable local convergence behavior may also have a significant impact on solution accuracy, such as in the case of considering eddy current in the nonlinear region.

In this paper, the Jacobian matrix and the residual vector are first derived in terms of the T-Ω formulation. Then, a method is proposed to efficiently find the optimum relaxation factor for improving global convergence performance. Further, to address the local convergence issue, a local damping scheme is introduced to damp the updating of the nonlinear material property for a small portion of elements that exhibit the largest changes in the equivalent dynamic permeability.

II. NEWTON NONLINEAR T-Ω FORMULATION

To apply Newton’s method, let us define

$$F_1(\Omega, \mathbf{T}) = \nabla \times \frac{1}{\sigma} \nabla \times \mathbf{H} + \frac{d\mathbf{B}}{dt} \quad (1.a)$$

$$F_2(\Omega, \mathbf{T}) = \nabla \cdot \mu \mathbf{H} = \nabla \cdot \mu (\nabla \Omega + \mathbf{T} + \mathbf{H}_p) \quad (1.b)$$

where \mathbf{H}_p is the source field component. The corresponding Newton iteration forms are

$$-F_{1(\partial T)}^k (\mathbf{T}^{k+1} - \mathbf{T}^k) - F_{1(\partial \Omega)}^k (\Omega^{k+1} - \Omega^k) = F_1^k \quad (2.a)$$

$$-F_{2(\partial T)}^k (\mathbf{T}^{k+1} - \mathbf{T}^k) - F_{2(\partial \Omega)}^k (\Omega^{k+1} - \Omega^k) = F_2^k \quad (2.b)$$

Taking the Frechet partial derivative of $F(\Omega, \mathbf{T})$ and performing some manipulations, we arrive at

$$\begin{aligned} F_{1(\partial T)}' &= \nabla \times \frac{1}{\sigma} \nabla \times () + \frac{1}{dt} [\hat{\mu}] () & F_{1(\partial \Omega)}' &= \frac{1}{dt} [\hat{\mu}] \nabla () \\ F_{2(\partial T)}' &= \nabla \cdot [\hat{\mu}] () & F_{2(\partial \Omega)}' &= \nabla \cdot [\hat{\mu}] \nabla () \end{aligned} \quad (3)$$

where tensor $[\hat{\mu}]$ can be considered as an equivalent dynamic permeability and derived by [3]

$$[\hat{\mu}] = \frac{\partial \mathbf{B}}{\partial \mathbf{H}} = \mu + \frac{\mu' - \mu}{H^2} (\underline{\mathbf{H}} \cdot \tilde{\mathbf{H}}) \quad (4)$$

where μ' is the permeability derivative. After discretization of (2), applying the Galerkin method, and integrating over the problem domain V , we have

$$J_{11} (\underline{\mathbf{T}}^{k+1} - \underline{\mathbf{T}}^k) + J_{12} (\underline{\Omega}^{k+1} - \underline{\Omega}^k) = \underline{\mathbf{R}}_1 \quad (5.a)$$

$$J_{21} (\underline{\mathbf{T}}^{k+1} - \underline{\mathbf{T}}^k) + J_{22} (\underline{\Omega}^{k+1} - \underline{\Omega}^k) = \underline{\mathbf{R}}_2 \quad (5.b)$$

where J_{11} , J_{12} , J_{21} and J_{22} are the blocks of the Jacobian matrix

$$J_{11} = \int \underline{\mathbf{t}} F_{1(\partial T)}^k \tilde{\mathbf{t}} dV \quad J_{12} = \int \underline{\mathbf{t}} F_{1(\partial \Omega)}^k \tilde{\alpha} dV \quad (6)$$

$$J_{21} = \int \underline{\alpha} F_{2(\partial T)}^k \tilde{\mathbf{t}} dV \quad J_{22} = \int \underline{\alpha} F_{2(\partial \Omega)}^k \tilde{\alpha} dV$$

and $\underline{\mathbf{R}}_1$ and $\underline{\mathbf{R}}_2$ are the residual vector

$$\underline{\mathbf{R}}_1 = - \int \underline{\mathbf{t}} F_1^k dV \quad \underline{\mathbf{R}}_2 = - \int \underline{\alpha} F_2^k dV \quad (7)$$

The details of derivation will be provided in the full paper. To consider the material property variations within the element, Gauss quadrature numerical integration is used in (6) and (7).

III. OPTIMUM RELAXATION FACTOR SEARCHING ALGORITHM

In order to reduce computation time, the following searching algorithm for the optimal under-relaxation factor is proposed: Let the relaxation factor α (between 1 and zero) be equally sampled with step of 0.2 as shown in Fig. 1. Here, $\alpha=0$ corresponds to the previous Newton iteration solution and $\alpha=1$ to the ordinary nonlinear Newton iteration scheme. The residuals at these two values of α are already available as part of the regular solution process. Thus, the evaluation of the residual can start from $\alpha=0.8$. For each α , after the solution candidate is obtained, we update the permeability and compute the residual. If the current residual is smaller than the previous one, we continue to the next value of α . If the current residual is greater, we use the current and the previous two values of α to construct a quadratic polynomial and find the optimal under-relaxation factor associated with the minimum residual value. If for $\alpha=0.2$, the corresponding residual value still does not increase, the sub-region of α between 0.2 and 0 is further sub-divided with a step of 0.05 and the search is continued.

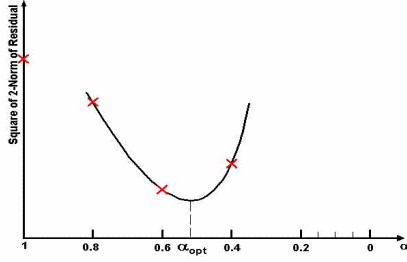


Fig. 1 Search for the optimal under-relaxation factor

In order to improve efficiency, a large step size of 0.2 is used in the above algorithm. This has the added advantage of making the algorithm less sensitive to local minimum. However, the large step size may lead to a large error in the computed optimal under-relaxation factor. To address this, we can insert two additional α points in between the above obtained three points and compute corresponding residuals. This will effectively reduce the step size to 0.1 and the optimal under-relaxation factor will be determined based on the appropriately selected set of three points: the point with the smallest residual and two neighbouring points on each side.

IV. LOCAL MATERIAL UPDATE DAMPING ALGORITHM

A local damping factor β is introduced for updating $[\hat{\mu}]$

$$[\hat{\mu}]^{k+1}_{actual} = [\hat{\mu}]^k + \beta([\hat{\mu}]^{k+1} - [\hat{\mu}]^k) \quad (8)$$

It should be emphasized that this modification should be applied to only a very small percentage of elements with the highest rate of change in the equivalent dynamic permeability tensor. This ensures that the efficiency of Newton-Raphson approach will not be adversely affected. The number of elements to be damped can be determined by

$$n = 3 * \ln\left(\frac{N_e}{n_0}\right) \quad \text{when } N_e > n_0 \quad (9)$$

where N_e is the total number of nonlinear elements in the solved domain and n_0 is the nonlinear element size threshold. The local damping algorithm is only applied if the element size is greater than this threshold.

The first step is to identify the n elements with the highest values of k_e out of entire set of nonlinear elements, where k_e is the change rate of $[\hat{\mu}]$. Next, the smallest k_e in the list is used as the reference damping rate k_{ref} . Thus, the damping factor for each element of the n elements is determined by

$$\beta = 0.35 + 1.5e^{-\frac{k_e}{k_{ref}}} \quad (10)$$

The range of β from (10) is approximately between 0.35 and 0.9. The lower bound is used to avoid over damping; the upper bound is used to prevent altering of the convergence property of the Newton-Raphson method due to a trivial modification.

V. BENCHMARK EXAMPLE

The benchmark problem No. 10 of TEAM Workshop is used here to check the nonlinear convergence and simulation accuracy [4]. The investigation includes three scenarios: constant under-relaxation factor; the adaptive optimal relaxation factor without local damping; and the adaptive optimal relaxation factor with local damping. Table 1 shows the comparison of the computation time for the three cases.

TABLE I. COMPUTATION TIME COMPARISON (37,385 ELEMENTS)

Relaxation algorithm	Time
Constant relaxation factor $\alpha = 0.1$ (greater than 0.1 does not converge)	32 hours 47 minutes
Optimal relaxation factor without local damping	3 hours 2 minutes
Optimal relaxation factor with local damping	2 hours 14 minutes

Fig. 2 shows the comparison of the computed average flux densities over the cross sections S_1 , S_2 , and S_3 [4] between the cases with local damping and without local damping. Fig. 3 compares the induced eddy current densities at the points P_1 , P_2 , and P_3 of the nonlinear conducting steel channels [4] for the cases with and without local damping. Measurement profiles for both average flux densities and the induced eddy current densities can be found in [4]. It is clear that while the local damping algorithm does not show obvious effects on the computed flux densities, it does have a significant impact on the more sensitive induced eddy current densities. The local damping algorithm has effectively eliminated the unphysical noises which also appeared in other researches' results [4]-[5].

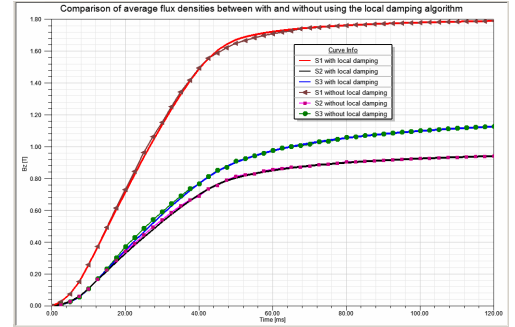


Fig. 2 Comparison of average flux densities over cross sections S_1 , S_2 , and S_3

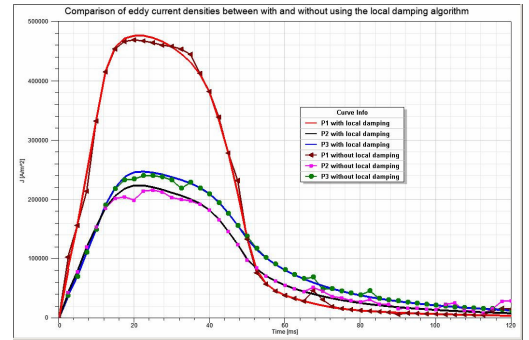


Fig. 3 Comparison of induced eddy current densities in points P_1 , P_2 , and P_3

VI. REFERENCES

- [1] T. Nakata, N. Takahashi, K. Fujiwara, N. Okamoto and K. Muramatsu, "Improvements of convergence characteristics of Newton-Raphson method for nonlinear magnetic field analysis", *IEEE Trans. on Magnetics*, vol. 28, no. 2, pp. 1048-1051, Mar, 1992.
- [2] K. Fujiwara, Y. Okamoto, A. Kameari and A. Ahagon, "The Newton-Raphson method accelerated by using a linear search – comparison between energy functional and residual minimization," *IEEE Trans. on Magnetics*, vol. 41, no. 5, pp. 1724-1727, May, 2005.
- [3] D. Lin, P. Zhou, Z. Badics, W.N. Fu, Q.M. Chen and Z.J. Cendes "A new nonlinear anisotropic model for soft magnetic materials" *IEEE Trans. on Magnetics*, vol. 42, no. 4, pp. 963-966, April 2006.
- [4] T. Nakata, K. Fujiwara, "Results for benchmark problem 10 (Steel plates around a coil)", *COMPEL*, vol. 9, no3, pp. 181-190, 1990.
- [5] O. Biro, K. Preis and K.R. Richter, "Various FEM formulation for the calculation of transient 3d eddy currents in nonlinear media" *IEEE Trans. on Magnetics*, vol. 31, no. 3, pp. 1307-1312, May 1995.

Shape Optimization of Rotating Machines Using Time-Stepping Adaptive Finite-Element Method

Katsumi Yamazaki, and Yuji Kanou

Dept. of Electrical, Electronics, and Computer Engineering, Chiba Institute of Technology
2-17-1, Tsudanuma, Narashino, Chiba, 275-0016, Japan
yamazaki.katsumi@it-chiba.ac.jp

Abstract — A time-stepping adaptive finite-element method is proposed for shape optimization of rotating machines. In the proposed method, different mesh-modification procedures are applied to the core and the other regions, respectively, for the purpose of the fast iron-loss calculation. A method of automatic separation and connection between the stator and rotor meshes are introduced for the rotation. The proposed method is applied to the shape optimization of a permanent magnet motor for the loss reduction. The usefulness of the proposed method is clarified.

I. INTRODUCTION

It is well known that most of the electrical energy is produced by rotating generators and that nearly half of the energy is consumed by the rotating motors in industrialized countries. Owing to environmental problems, the optimization of the rotating machines from viewpoint of the loss minimization has become one of the important subjects.

In these cases, automatic mesh-generation techniques and time-stepping analyses that consider the harmonics in the machines are often required. The adaptive finite element method [1]-[5] must be effective in automatically obtaining the appropriate mesh for each shape. In the method, the finite elements are iteratively generated due to the error estimations of the electromagnetic field.

However, few papers applied the adaptive finite-element meshing to the optimization of the rotating machines using the time-stepping analysis. One reason is the vast computation time by the multiple loops of the time stepping and adaptive finite-element meshing. Reference [4] proposed the mesh modification at each time step. It can reduce the number of the iterative calculation. However, the estimation of the iron loss in the stator and rotor cores requires the fixed mesh during one time-period [6]. In addition, more generalized mesh-modification technique for the rotation of the rotor is desired.

From these viewpoints, we propose a novel procedure of

the time-stepping adaptive finite-element method for the shape optimization of the rotating machines. In the method, different mesh-modification procedures are applied to the core and the other regions, respectively, for the purpose of the fast iron-loss calculation. A method of automatic separation and connection between the stator and rotor meshes are also introduced in order to take the rotation into account. The proposed method is applied to the shape optimization of a permanent magnet motor for the loss reduction. The usefulness is confirmed.

II. MESH GENERATION PROCEDURE

A. Mesh modification due to rotation

Fig. 1 shows the modification method of the adaptive finite-element mesh due to rotation of the rotor. First, the stator and rotor meshes used in the last time-step are separated. After rotating the rotor, the stator and rotor regions are automatically connected. This mesh is used for the initial mesh of the adaptive-mesh iteration in the next time-step. In the separation of the stator and rotor regions, only the elements that cross the center line of the air gap are removed. By using this procedure, most of the elements in the last time-step can be utilized for the next time-step. As a result, the number of the adaptive-mesh iteration can be reduced because the difference in the electromagnetic field during one time-step is slight.

B. Mesh modification due to elemental error estimation

The error estimations of the finite elements [2] are carried out at each time-step. The finite element meshes at each part of the machine is modified due to the estimated errors. In the proposed method, different mesh-modification procedures are applied in the core and the other regions as shown in Table I.

In the core region, a fixed mesh during one time-period is required for the iron-loss calculation [6]. Therefore, following procedure are employed during two time-periods of the

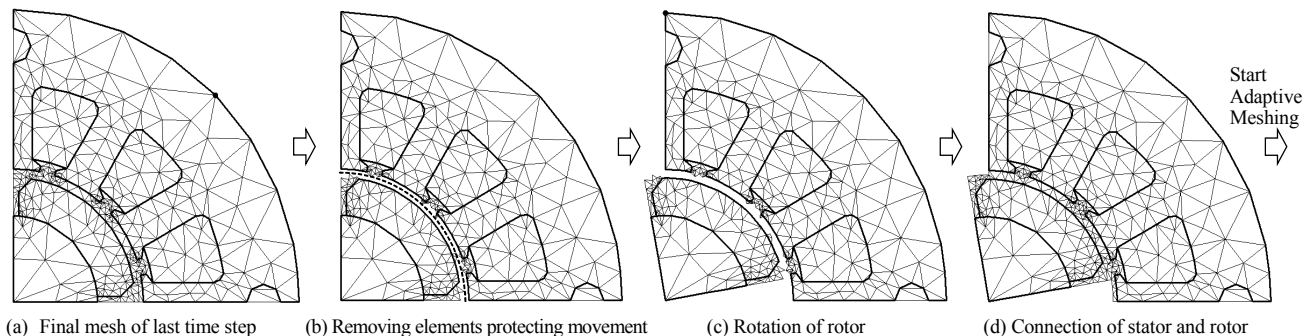


Fig. 1. Mesh modification due to rotation.

TABLE I

METHOD OF MESH MODIFICATION DUE TO ERROR ESTIMATION

	1 st time period	2 nd time period
Core region	Addition of nodes	Fixed
Other regions	Addition and cancellation of nodes	

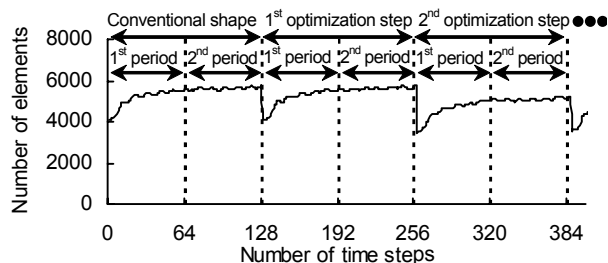


Fig. 2. Number of elements during optimization.

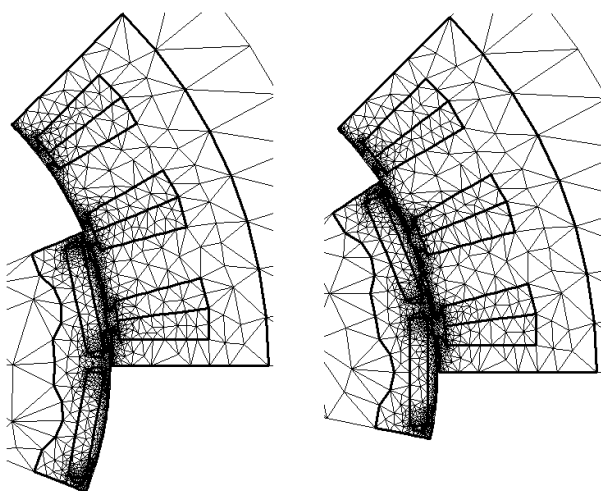


Fig. 3. Fixing mesh in core for iron-loss calculation

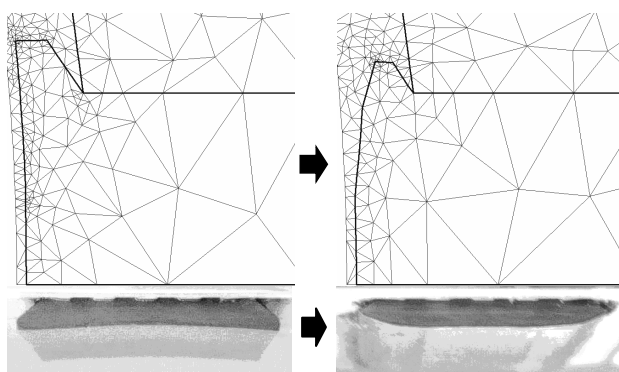
rotation: In the first time-period, nodes are simply added on the elements whose estimated error is larger than the permissive error at each time-step. Consequently, the number of the finite elements in the core increases in this time-period. The final mesh obtained by this procedure can be regarded as satisfying the permissive error at any angle of the rotor. Therefore, in the second time-period, the mesh in the core is fixed to the final mesh of the first time-period. Then, the iron loss is obtained from the solution of the second time-period.

On the other hand, in the other regions including the air gap, the fixed mesh is not required. Therefore, not only the node addition but also the node cancellation [4] is applied to avoid increasing the number of the elements in both the first and the second time-periods.

Although the proposed method requires the analysis during the two time-periods, practical results and computation time are expected because the method can reduce the number of the adaptive-mesh iterations.

III. APPLICATION

The proposed method is applied to the shape optimization of an interior permanent-magnet motor. The Rosenbrock's method is combined with the proposed method. The design variables are the coordinates on the top of the stator teeth. The



(a) Conventional

(b) Optimized (106th optimization step)

Fig. 4. Conventional and optimized stator teeth (Meshes and photographs).

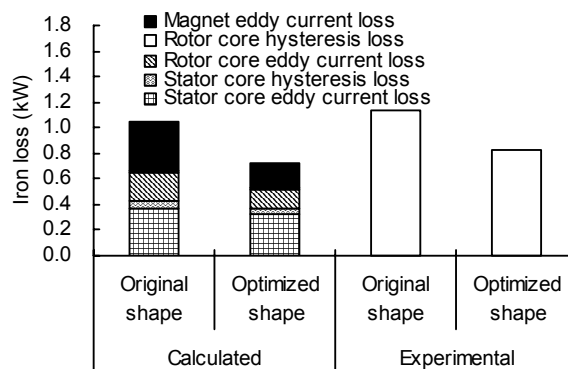


Fig. 5. Experimental and calculated iron losses (Current 300 A, 80deg).

objective function is the efficiency of the motor. The total calculation time is 8h 48m using a Pentium 4, 3.6GHz PC.

Fig. 2 shows the number of the finite elements. It can be observed that the number of the elements increases in the first time-period and becomes constant in the second time-period. Fig. 3 shows the variation in the finite element mesh during the second time-period. It indicates that the meshes in the core are fixed during this period for the iron-loss calculation in the core.

Fig. 4 shows the conventional and optimized stator tooth. Fig. 5 shows the measured and calculated iron losses including the magnet eddy current loss. The loss is reduced to 70% by the optimization, while the torque is nearly the same. The usefulness of the proposed method is confirmed.

IV. REFERENCES

- [1] Z. J. Cendes, D. N. Shenton, "Adaptive mesh refinement in the finite element computation of magnetic field", *IEEE-Trans. Magn.*, vol.21, no.5, pp.1811-1816, 1985.
- [2] O.C.Zienkiewicz and J.Z.Zhu,"A simple error estimator and adaptive procedure for practical engineering analysis," *International Journal for Numerical Methods in Engineerings*, vol.24, pp.337-357, 1987.
- [3] L. Janicke and A. Kost, "Error estimation and adaptive mesh generation in the 2D and 3D finite element method", *IEEE-Trans. Magn.*, vol.32 no.3, pp.1334-1337, 1996.
- [4] S. Dufour, G. Vinsard and B. Laport, "2-D Adaptive Mesh with Movement", *IEEE-Trans. Magn.*, vol.37, No.5, pp. 3482-3485, 2001.
- [5] K. Yamazaki and T. Saeki, "Adaptive mesh generation within nonlinear iterative calculations for analyses of electric machines," *IEEE-Trans. Magn.*, vol.39, no.3, pp.1654-1657, 2003.
- [6] K. Yamazaki, "Torque and efficiency calculation of an interior permanent magnet motor considering harmonic iron losses of both the stator and rotor", *IEEE-Trans. Magn.*, vol.39, no.3, pp.1460-1463, 2003.

Algorithmically Efficient Ray Tracing for the Simulation of Wall Heating in Particle Accelerator Structures

E. M. Scholz^{1,2}, M. Clemens², *Senior Member, IEEE*, M. Dohlus³

¹ Department of Mathematics and Department of Physics, University of Hamburg, Germany

² Helmut-Schmidt-University, University of the Federal Armed Forces Hamburg, Faculty of Electrical Engineering, Chair for Theory of Electrical Engineering and Computational Electromagnetics, P.O. Box 700822, D-22008 Hamburg, Germany

³ Deutsches Elektronen Synchrotron Hamburg, Germany

Abstract—This paper proposes a concurrent ray tracing algorithm for rotationally symmetric problems improving central parts from $O(\log(n))$ to $O(1)$ time complexity. Rotationally symmetric problems arise naturally when computing the heating generated by high frequency wake fields in cryogenic particle accelerator structures.

I. INTRODUCTION

Ray tracing methods are well researched for general three dimensional problems, but relatively little effort has been spend to develop improved ray tracing algorithms for purely rotationally symmetric cases. However, these cases do occur when computing the wall heating generated by high frequency wake fields in particle accelerator structures. For this purpose ray tracing has been used e.g. in [1].

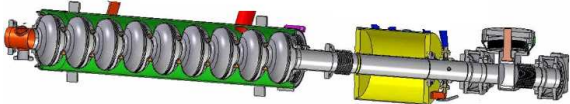


Fig. 1. A modern particle accelerator structure

Modern particle accelerator structures require an elaborate cryogenic infrastructure [5]. To estimate the required cooling capacity, it is necessary to estimate all effects heating the structure. The algorithmic improvements proposed later in this paper are used to estimate the heating energy generated by high frequency wake fields. Wake fields are usually spurious electromagnetic fields generated by the accelerated particles. (For details see [2],[3] or [5]). Wake fields will lower the kinetic energy of the particles that get accelerated, heat the cryogenic structure and lower the efficiency of the accelerator.

II. LINEAR OPTICS

Using the Lorenz gauge, Maxwell's equations can be transformed into a set of wave equations (see e.g. [6][4]). Therefore every solution of Maxwell's equations can be constructed from plane waves. For sufficiently high frequencies the accelerator structures can be assumed being large in comparison to the wavelength. Therefore the approximations done by linear optics are applicable. As usual in linear optics the electromagnetic field is approximated by rays. These rays are interpreted as the trajectories of photons. It is further assumed that the shape of the accelerator structures is smooth and

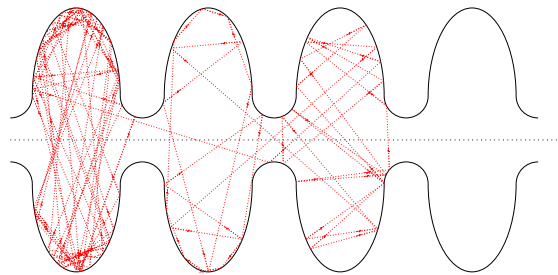


Fig. 2. Example trace generated by the proposed algorithm

that its curvature is small in relation to the wave length. Reflections on the surface of the structure are then sufficiently approximated as reflections on a flat surface tangent to the reflection point. For an incoming ray with energy E_{in} and angle θ_{in} and the outgoing ray with energy E_{out} and angle θ_{out} the central equations are:

$$\begin{aligned}\theta_{in} &= \theta_{out} \\ E_{in} &= t(\omega) E_{out}\end{aligned}$$

where $t(\omega) \in [0, 1]$ is the energy transmission coefficient and $1 - t(\omega)$ is the energy heating the structure.

III. OPTIMIZED CONCURRENT RAY TRACING FOR ROTATIONALLY SYMMETRIC STRUCTURES

The first step in building an efficient algorithm for this problem is the development of an efficient representation of the rotationally symmetric cavity in which the wake field is propagating. Mathematically, the cavity is simply represented as a curve

$$\begin{aligned}\gamma : [0, e] &\rightarrow \mathbb{R}^2 \\ e &\in \mathbb{R}\end{aligned}$$

that will be rotated around the x-axis. For an efficient computational representation a curve should be build from simple predefined curves like lines or elliptical arcs. These curve building blocks are called segments. The curve is then constructed using the following concatenation rule where $\gamma_1 : [0, e_1] \rightarrow \mathbb{R}^2$ and $\gamma_2 : [0, e_2] \rightarrow \mathbb{R}^2$ with $\gamma_1(e_1) = \gamma_2(0)$:

$$\gamma := t \mapsto \begin{cases} \gamma_1(t) & \text{if } t \in [0, e_1] \\ \gamma_2(t - e_1) & \text{if } t \in [e_1, e_1 + e_2] \end{cases}$$

Using this rule is simple if all segment types (e.g. lines or elliptical arcs) are defined relative to a starting point. Building the curve of the structure becomes:

- 1) set current start point to initial start point
- 2) add new segment relative to current start point
- 3) set current start point to end point of new segment
- 4) if not finished repeat with 2.

This sequence resembles the building of a list of segments. Thus the most efficient way to store this list is as a plain array of an algebraic data type called segment. Algebraic data types are types that combine a finite number of parameterized choices. In our implementation a segment is either a line or an elliptical arc. Further details on algebraic data types can be found in [8]. Despite their usefulness algebraic data types are not directly supported by commonly used languages like C. However they can be easily expressed by using a union type:

Listing 1. Algebraic Data Type Mimicry in C

```

union segment_t {
  enum { ELLIPSE_SEG, LINE_SEG } type;
  struct {
    size_t padding; /*enum storage*/
    ... /* ellipse data */
  } ellipse;
  struct {
    size_t padding; /*enum storage*/
    ... /* line data */
  } line;
};

```

The code that generates the example trace in Fig. 2 uses this technique, which is more awkward to use than a natively supported algebraic data type, but works fine. With this type the whole geometry is storable as a compact array. For generic 3D ray tracers the best memory structure representing the scene is a tree structure. In this case we are able to use an array and therefore improve time complexity from $O(\log(n))$ to $O(1)$. Besides of having an $O(1)$ read and write time complexity the array has a higher locality of the data and is therefore more cache efficient as well.

To achieve an efficient concurrent implementation it is important to remember that data written by several threads should not be near each other since otherwise the requirement of cache coherency in concurrent systems will cause a lot of cache reloads. Therefore concurrency is exploited by assigning each thread the task to compute the trace of a given initial ray.

IV. THE TRACE OF A RAY

The trace of a ray is represented as an array of rays with some additional data, where the start point of each ray is the collision point of the previous ray with the structure. There are two additional values that should be recorded in the trace for fast trace analysis. First the index number of the segment a ray collides with, second the arc length from the beginning of the curve to the point of collision. If the collision is at $\gamma(t_{coll})$ it is necessary to compute the integral

$$s_{coll} = \int_0^{t_{coll}} \sqrt{\gamma'_x(t)^2 + \gamma'_y(t)^2} dt$$

where γ_x and γ_y denote the x and y component of the curve describing the whole structure. Even if it is not computationally cheap to integrate this for certain segments like for the elliptical segments of our code, it is straightforward to compute a numerically cheap approximation of this arc length function, when the geometry is build up. Thus, during the ray tracing process evaluation of the integral is computationally efficient.

V. OPTIMIZED TRACE ANALYSIS

Given several traces of rays, the next and final step is to count the rays hitting every surface element summing up the energy transferred onto these elements of the structure. For this part of the algorithm the computed arc length can be used cheaply to store this data in an array (Fig. 2) where again usually a tree structure would be required. This improves the time complexity from $O(\log(n))$ to $O(1)$ for this part of the algorithm.

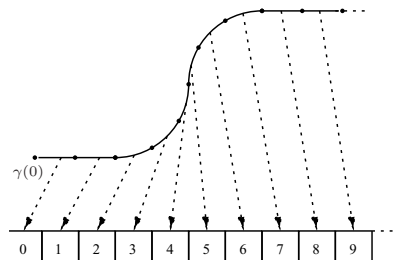


Fig. 3. storage organisation of final result data

VI. CONCLUSION

Rigorously exploiting the benefits a rotationally symmetric problem allows strong simplifications for central parts of the ray tracing algorithm. Commonly required tree data structures can be replaced with arrays, improving time complexity from $O(\log(n))$ to $O(1)$ for operations on these structures. The upcoming full paper will contain more details on the algorithm, simulation results and benchmarks for realistic linear particle accelerator.

VII. ACKNOWLEDGEMENTS

The authors thank Prof. Dr. J. Struckmeier from the mathematics department and Prof. Dr. J. Roßbach from the physics department of the university of Hamburg for their kind cooperation.

REFERENCES

- [1] A. Jöstingmeier, M. Dohlus, C. Cramer, Photon Diffusion Model for TTF-2, TESLA Report 2000-11, July 2000
- [2] T. Weiland, R. Wanzenberg, Wake Fields and Impedances, 1990 Joint US-CERN Accelerator Course Hilton Head, So. Carolina
- [3] L. Palumbo, V. G. Vaccaro, M. Zobov, Wake Fields and Impedance, LNF-94/041 (P) Laboratori Nazionali Di Frascati, 5. September 1994
- [4] J. D. Jackson, Klassische Elektrodynamik, 3. Überarbeitete Auflage, Walter de Gruyter, 2002
- [5] Helmut Wiedeman, Particle Accelerator Physics, Third Edition, Springer, 2007
- [6] W. Nolting, Grundkurs Theoretische Physik 3 Elektrodynamik, 7. Auflage, Springer 2004
- [7] G. H. Spencer, M. V. R. K. Murty, General Ray-Tracing Procedure, Journal of the Optical Society America vol 52 No 6, June 1962
- [8] D. J. Lehmann, M. B. Smyth, Algebraic Definition of Data Types: A Synthetic Approach, Mathematical Systems Theory 14, 1981

Hierarchical Sparsified Models for the Substrate of Integrated Circuits

Daniel Ioan and Gabriela Ciuprina

”Politehnica” University of Bucharest, Electrical Engineering Faculty, Numerical Methods Lab.
Splaiul Independenței 313, 060042, Bucharest, Romania
lmm@lmm.pub.ro

Abstract—The paper proposes a new approach for the efficient modeling of the substrate in integrated circuits. The approach is valid at intermediate frequencies, the electroquasistatic field being used in conjunction with the magnetostatic field. The main idea is to perform a hierarchical sparsification based on an exponential partitioning scheme of the substrate with an impressive impact on the model extraction time. A circuit model of linear complexity is extracted.

I. INTRODUCTION

With the continuous downscaling of CMOS devices analog, RF and digital circuitry are integrated on a single chip. However, due to the conducting nature of the common substrate, noise generated by the digital circuitry can be easily injected into and propagate through the silicon substrate. Accurate and efficient modeling of the electromagnetic effects in the semiconductor substrate is an important still open problem for the EDA community [1], [2].

The IC substrate is a semiconductor body represented by computational domains of rectangular shapes. It is usually structured in homogeneous layers, with constant material parameters. The traces of the circuit devices on the top surface of the substrate are called *connectors* or *contacts*. The bottom surface of the substrate is the *backplane contact*, which is usually a grounded or a floating metallic layer [3]. The top surface of the computational domain and its lateral surfaces have a virtual character, being conventional cuts in the real semiconductor substrate body. The contacts are also conventional surfaces [1], [3]. The number, shapes and sizes of the contacts are very much dependent of the actual circuit layer as well as of the modeling approach. Inhomogeneous high-conductivity layers and structures such as the epi-layer, wells, diffusion gradients, and buried layers are usually included in the substrate models, but a simpler solution we will consider is the one in which the modeled substrate contains only the homogeneous Silicon bulk.

The substrate models are based on electromagnetic (EM) field modeling. The choice of the most appropriate EM field regime for a particular model of the substrate is dependent on the values of the material constants, as well as on the required operating frequency-range. In the low frequency case, the substrate behavior is well described by static regimes, the most appropriate model being obtained by using in conjunction electrostatics (ES), electric conduction (EC) and magnetostatics (MS). Only for inhomogeneous substrate structures the

use of electroquasistatic (EQS) in conjunction with MS can be justified. Numerical studies in [4] show that the EQS assumptions are not valid in the case of high-resistivity substrates at frequencies above 20 GHz. In the case of low-resistivity substrates EQS can be used at least for frequencies up to 100 GHz.

Even in the simplest static regimes, the complexity of the extracted model with n connectors is $O(n^2)$, since the number of lumped circuit elements linking the connectors is given by $n(n+1)/2$. For instance, millions of R, L or C elements are required to model 2000 connectors in EC, MS or ES regimes. RC ”equivalent” circuits are extracted from the EQS field solution. Fortunately, not all these elements have a similar importance in the model, as many of them describe weak interactions. Typical examples are links between far connectors or connectors screened by other connectors. The procedure to approximate a model with another of smaller size (with fewer elements) is called *sparsification*. The name is inspired by the fact that the admittance matrix of the new model is a sparse one, whereas the original matrix is dense. Several hierarchical approaches are described in [1], [5].

II. HIERARCHICAL APPROACH

The substrate modeling approach we propose is valid at frequencies where the EQS regime may be considered valid. In order to model also the magnetic/inductive field effects, we consider in the substrate the EQS field in conjunction with the MS one. Thus two independent models are extracted, to be connected in the global model of the IC. We use for this the domain partitioning (DP) technique as described in [6]. The IC devices and the substrate interact by means of EM *hooks* [6]. The hierarchical sparsification we propose is based on an exponential partitioning scheme of the substrate (Fig. 1).

Virtual contacts (hooks) are buried in the substrate at

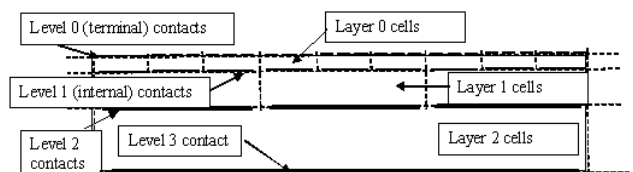


Fig. 1. Partitioning of the substrates in macro-cells.

different depths (according to their levels), thus realizing a domain-partitioning of the substrate in horizontal layers structured in rectangular super-elements (macro-cells). The cell-walls generate thus an adapted *discretization macro-grid*, progressively refined from bottom to top. Unlike the literature, in our approach, the equivalent contacts have a physical meaning, being the terminals of the macro-cells. Thus, sparse hierarchical circuit-models with reduced number of lumped elements are generated. Moreover, since the macro-cells have similar geometries, the field has to be computed (and consequently the circuit model has to be extracted) only in one of them, *the standard cell*. For instance, considering such a cell with 14 terminals, 9 on the top face and one on bottom, the number of levels is $\ln(n)/\ln(9)$ and the total number of cells is $(n-1)/8$, while the complexity of the equivalent circuit is $O(11n)$. A model with six levels can handle about one million top-connectors, using about ten millions lumped elements. The linear order of the extracted model is another great advantage of this approach.

The main reason which makes our hierarchical sparsification approach valid is the exponential decay of the field variation on deeper horizontal planes. For instance, in EC, ES and MS field regimes, the scalar potential satisfies in homogeneous media the Laplace equation. By imposing zero Dirichlet boundary conditions on the bottom surface ($z = 0$), zero Neumann on vertical sides ($x = 0, x = a, y = 0, y = b$) and by using a double Fourier series, it can be proved that the Fourier coefficients of the solution $V(x, y) = \sum_{i=0}^n \sum_{j=0}^n V_{ij} \cos(\lambda_i x) \cos(\mu_j y)$ satisfy $|V_{ij}/V_0| \leq ab/(4\pi^2 ij) \exp\left(-\sqrt{\lambda_i^2 + \mu_j^2}(c-z)\right)$.

The Fourier series may be truncated, but in order to keep a minimal accuracy on the top surface ($z = c$), the number of retained terms (spatial harmonics along each direction) should be at least the total number of contacts in that direction. On deeper planes $z < c$, for same accuracy ε , only a lower number of terms n_z, m_z may be retained:

$$\varepsilon = \frac{ab}{4\pi^2 nm} \geq \frac{ab}{4\pi^2 n_z m_z} \exp\left(-\sqrt{\lambda_i^2 + \mu_j^2}(c-z)\right). \quad (1)$$

Going down in the substrate, the number of degrees of freedom (dofs) necessary to describe the solution decreases exponentially. A lower number of dofs means a lower number of hooks (contacts) on deeper layers. Hence, the grid necessary to describe field may be coarser, deeper in substrate. In any layer, the number of contacts can be decreased from its top to bottom q times:

$$q = \frac{n_c m_c}{n_0 m_0} = \exp\left(\pi \sqrt{(n/a)^2 + (m/b)^2} c\right). \quad (2)$$

For instance if $q = 9$, $a = b$ and $n = m$ it follows that $\Delta z \approx a/n$. Consequently, the standard cell of top layer should be a parallelepiped having its height at least the size of the top contacts. By increasing q , the approximation error of the hierarchical sparsification becomes higher.

III. RESULTS

In order to verify the proposed approach, a simple study case of a micro-strip dual conductor line in SiO₂ over a lossy Si

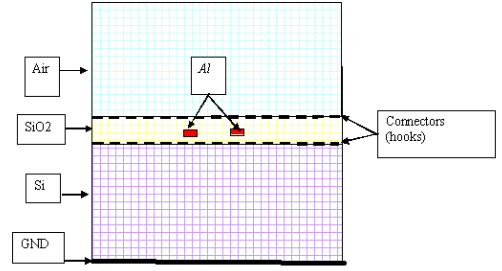


Fig. 2. Computational domain partitioned in three parts. Conform grids are shown.

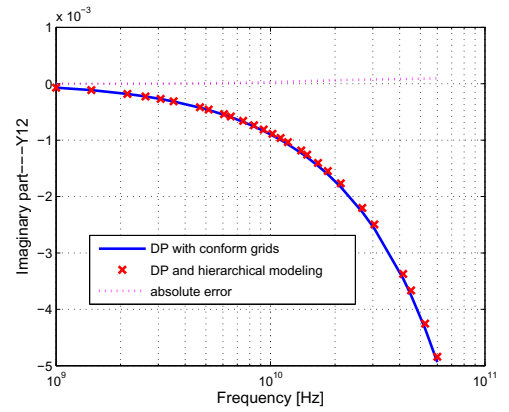


Fig. 3. Hierarchical approach is as accurate as DP with conform grids.

substrate was considered. The line admittance was computed by FIT, using DP with conform grids (Fig. 2) and with the hierarchical modeling for the substrate. The result shown in Fig. 3 validates the latter approach.

The substrate was decomposed into 10 layers having progressive increasing thicknesses with a constant rate. The CPU time needed to extract the admittance matrix by hierarchical sparsification was 0.093 sec, whereas the same time when using DP with conform grids was 42.4 sec. This result illustrates the important reduction of the extraction time.

REFERENCES

- [1] R. Gharpurey, "Modeling and analysis of substrate coupling in integrated circuits," Ph.D. dissertation, Univ. of California, Berkeley, 1995.
- [2] H. Lan, "Synthesized compact models for substrate noise coupling in mixed-signal ICs," Ph.D. dissertation, Stanford University, 2006.
- [3] S. Kristiansson, F. Ingvarson, S. Kagganti, N. Simic, M. Zgrda, and K. Jeppson, "A surface potential model for predicting substrate noise coupling in integrated circuits," *IEEE Journal of Solid-State Circuits*, vol. 40, no. 9, pp. 1797–1803, 2005.
- [4] G. Veronis, Y.-C. Lu, and R. W. Dutton, "Modeling of wave behavior of substrate noise coupling for mixed-signal IC design," in *ISQED '04: Proc. of the IEEE International Symposium on Quality Electronic Design*. San Jose, CA, USA, 2004, pp. 303–308.
- [5] J. R. Phillips and L. M. Silveira, "Simulation approaches for strongly coupled interconnect systems," in *ICCAD '01: Proceedings of the Int. Conf. on Computer-Aided Design*. San Jose, California, 2001, pp. 430–437.
- [6] D. Ioan, G. Ciuprina, and L. Silveira, "Effective domain partitioning with electric and magnetic hooks," *IEEE Trans. on Magnetics*, vol. 45, no. 3, pp. 1328–1331, 2009.

SUPG 3D vector potential formulation for electromagnetic braking simulations

François Henrotte¹, Enno Lange¹, Holger Heumann², Kay Hameyer¹

¹RWTH Aachen University, Institute of Electrical Machines, D-52056 Aachen, Germany

²ETH Zürich, Seminar for Applied Mathematics, CH-8092 Zürich, Switzerland

E-mail: fh@iem.rwth-aachen.de

Abstract—The calculation of motion-induced eddy currents in massive conductors yields a 3D convection-diffusion problem. Up-winding and SUPG formulations are well-established methods to obtain stable discretizations of the scalar convection-diffusion equations in the case of singular perturbation, but there is very little reported experience with the stability of convection in the vector case, i.e. in electromagnetism. Numerical experiments with the up-winding method proposed by Xu et al. [1] has proven its efficiency to be limited, and an alternative approach based on a consistent discretization within the finite element Galerkin context of the material derivative implied by the convection phenomenon is proposed.

I. INTRODUCTION

The problem of electromagnetic braking can be solved by a quasi-stationary approach by discretizing the model in the rest frame. According to e.g. [1], the governing equations are $\mathbf{b} = \nabla \times \mathbf{a}$, $\mathbf{e} = -\partial_t \mathbf{a} - \nabla V$ and $\nabla \times \mathbf{h} = \mathbf{j}$ with the material constitutive relations $\mathbf{b} = \mu \mathbf{h}$ and

$$\mathbf{j} = \sigma(\mathbf{e} + \mathbf{v} \times \mathbf{b}), \quad (1)$$

where the velocity field \mathbf{v} is different from zero in the moving domain. There are several interpretations found in literature for formulae like (1). The interpretations of Xu [1], Bossavit [5], Thorne [6] and Van Bladel [7] will be discussed and compared in the full paper.

On the other hand, it would seem natural, by analogy with mechanics to work with Eulerian coordinates, i.e. to replace the equation

$$\sigma \partial_t \mathbf{a} + \text{curl } \nu \text{curl } \mathbf{a} = \mathbf{j}_s \quad (2)$$

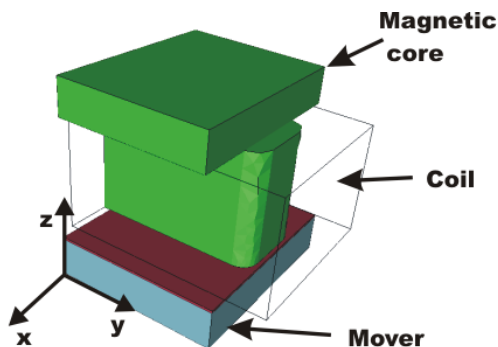


Fig. 1. Geometry of the 3D braking system.

valid when there is no motion, with the equation

$$\sigma D_t \mathbf{a} + \text{curl } \nu \text{curl } \mathbf{a} = \mathbf{j}_s \quad (3)$$

where D_t denotes the convective derivative. This would be a justification for importing stabilization SUPG scheme from Mechanics, in particular computational fluid dynamics [2], [3], into electromagnetic problems. We therefore have first to answer the question: Is electromagnetic braking a convection problem?

Given a placement map $p_t : M \mapsto N$, one can define the co-moving time derivative as the derivative operator that fulfills

$$\partial_t \int_{\Omega} \alpha = \int_{\Omega} \mathcal{L}_{\mathbf{v}} \alpha.$$

The co-moving time derivative of differential forms of various degrees write as follows

$$\mathcal{L}_{\mathbf{v}} f = \partial_t f + \mathbf{v} \cdot (\text{grad } f) \quad (4)$$

$$\mathcal{L}_{\mathbf{v}} \mathbf{a} = \partial_t \mathbf{a} + \text{grad } (\mathbf{a} \cdot \mathbf{v}) - \mathbf{v} \times \text{curl } \mathbf{a} \quad (5)$$

$$\mathcal{L}_{\mathbf{v}} \mathbf{b} = \partial_t \mathbf{b} + \text{curl } (\mathbf{b} \times \mathbf{v}) + \mathbf{v} \text{ div } \mathbf{b} \quad (6)$$

$$\mathcal{L}_{\mathbf{v}} \rho = \partial_t \rho + \text{div } (\rho \mathbf{v}) \quad (7)$$

in terms of classical vector and tensor analysis operators. The co-moving derivative of 0-forms (5) and 3-forms (7) are commonly used in computational fluid dynamics where they are called (amongst many other names) convective derivative, $\mathcal{L}_{\mathbf{v}} \equiv D_t$.

The electric field writes in the absence of motion $\mathbf{e} = -\partial_t \mathbf{a} - \text{grad } u$ becomes in an Eulerian representation,

$$\begin{aligned} \mathbf{e} &= -\mathcal{L}_{\mathbf{v}} \mathbf{a} - \text{grad } u \\ &= -(\partial_t \mathbf{a} + \text{grad } (\mathbf{a} \cdot \mathbf{v}) - \mathbf{v} \times \text{curl } \mathbf{a}) - \text{grad } u \end{aligned}$$

in the presence of motion. One observes the introduction through the co-moving time derivative of the classical $\mathbf{v} \times \mathbf{b}$ (1). But one observes also a motion induced correction to the electric scalar potential, $\text{grad } (\mathbf{a} \cdot \mathbf{v})$, which is not considered in the classical definition of motion induced eddy currents. The electric field can actually be rewritten

$$\mathbf{e}' = -\partial_t \mathbf{a}' - \text{grad } u'$$

with the auxiliary fields: $\mathbf{e}' = \mathbf{e} - \mathbf{v} \times \text{curl } \mathbf{a}$, $\mathbf{a}' = \mathbf{a}$ and $u' = u + \mathbf{a} \cdot \mathbf{v}$. The co-moving time derivative appears thus to be related with the Lorentz invariance of Maxwell's equations, as can be shown in a slightly extended theoretical context.

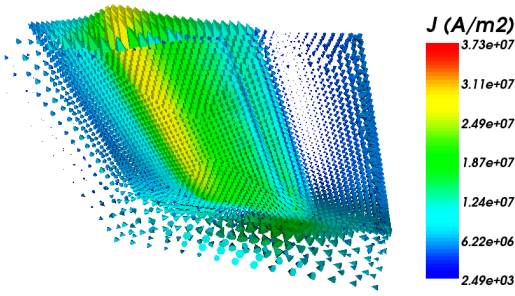


Fig. 2. Current density computed in the mover.

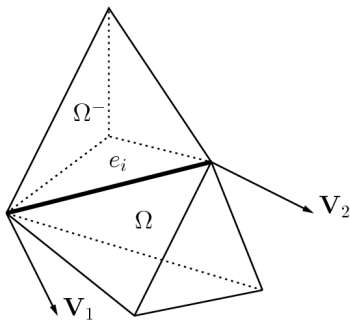


Fig. 3. Arbitrary finite element Ω and its upwind element Ω^- .

II. XU'S SUPG APPROACH

Assuming a stationary process, $\partial_t \mathbf{a} = 0$, the scheme proposed by Xu et al in [1], directly inspired from computational fluid dynamics, is as follows:

$$\int_{\Omega} \mu^{-1} \text{curl} \mathbf{a} \cdot \text{curl} \mathbf{w} \, d\Omega + \int_{\partial\Omega} (\mathbf{w} \times \mu^{-1} \text{curl} \mathbf{a}) \cdot \mathbf{n} \, d\Omega = - \int_{\Omega} \sigma (-\mathbf{v} \times \text{curl} \mathbf{a} + \text{grad} u) \cdot \mathbf{w} \, d\Omega$$

In analogy with the upwind scalar shape functions (with a free parameter τ):

$$w = w_0 + \tau \frac{\mathbf{v} \cdot \text{grad} w_0}{\|\mathbf{v}\|^2}, \quad \tau = \frac{\mathbf{v}h}{2} \left(\coth \frac{Pe}{2} - \frac{2}{Pe} \right)$$

upwind vector shape functions are defined as

$$\mathbf{w} = \mathbf{w}_1 - \tau \sigma \mathbf{v} \times \text{curl} \mathbf{w}_1$$

Numerical 3D simulations done with this approach, Fig. 2, show that a stabilization effect is indeed observed, but leaves still a severe limitation on the convection speed \mathbf{v} .

III. A GEOMETRICAL SCHEME

In their report [4], Heumann and Hiptmair have successfully exploited differential geometry concepts to obtain a geometrical discretization of the convection operator in 2D. Their approach is based on the extrusion operator introduced by

Bossavit [5]. The purpose of this paper is to generalize their 2D scheme to 3D finite element computations.

Consider the situation depicted in Fig. 3. Let Ω be an arbitrary finite element in a 3D mesh. A particular edge of that element e_i is considered, at both ends of which the velocity vector has been represented. This edge e_i represented in the figure is such that its upwind extrusion lays outside Ω , i.e. in a neighbour element $\Omega^- \neq \Omega$. For the FE discretisation, one has to evaluate:

$$\int_{\Omega} \sigma \mathcal{L}_{\mathbf{v}} \mathbf{a} \cdot \omega_i^e \, d\Omega = \sum_i \left\{ \int_{e_i} \mathcal{L}_{\mathbf{v}} \mathbf{a}(\Omega_i^-) \right\} \int_{\Omega} \sigma \omega_i^e \cdot \omega_i^e \, d\Omega, \quad (8)$$

where ω_i^e is an edge-based trial function. But the tangential component of $\mathcal{L}_{\mathbf{v}} \mathbf{a}$ is not continuous. The fact that the derivative $\mathcal{L}_{\mathbf{v}}$ is a limiting process involving the upwind extrusion of e_i , which lays in the upwind element Ω^- relative to the edge e_i under consideration, imposes thus to evaluate the circulation of $\mathcal{L}_{\mathbf{v}} \mathbf{a}$ in that element, i.e. $\int_{e_i} \mathcal{L}_{\mathbf{v}} \mathbf{a}(\Omega_i^-)$. In the evaluation of the residual (8) of the finite element Ω , the adjacent upwind elements Ω_i^- plays thus a role. This is incompatible with the classical element by element assembly of FE elementary matrices, hence an implementation difficulty.

An algorithm to evaluate $\int_{e_i} \mathcal{L}_{\mathbf{v}} \mathbf{a}(\Omega_i^-)$ will be described in the full paper. This expression has 3 terms (5). In particular, it will be shown that

$$\int_{e_i} \mathbf{v} \times \text{curl} \mathbf{a} = \sum_{jl} A_j \frac{V_1^l + V_2^l}{2} T_{ilj}$$

with

$$T_{ilj} = \mathbf{i}_{e_i} \mathbf{i}_{e_l} \text{curl} \omega_j^e(\mathbf{x})$$

a constant matrix with ± 1 and 0 elements that only depends on the topology of the tetrahedron.

IV. CONCLUSION

We have discussed the validity of introducing convection based concepts in context of electromagnetism, and shown that this is done by the co-moving time derivative. The concept of extrusion yields a geometrical upwind scheme without free parameter that can however not be assembled element by element. More numerical results will be given in the full paper.

REFERENCES

- [1] E.X. Xu, J. Simkin and S.C. Taylor, "Streamline Upwinding in 3D Edge-Element method modelling eddy currents in moving conductors", IEEE Trans. on Magnetics, 42(4), 667-670, 2006.
- [2] A.N. Brooks and T.J.R. Hughes, "Streamline-upwind/Petrov-Galerkin formulations for convection dominated flows with particular emphasis on the incompressible Navier-Stokes equations", Comput. Meth. Appl. Mech. Engrg., 32, pp. 199-259, 1982.
- [3] P. Bochev, "A discourse on variational and geometric aspect of stability of discretization", In 33rd Computational Fluid Dynamics Lecture Series, VKI LS 2003-05, edited by H. Deconinck, ISSN0377-8312, 2003.
- [4] H. Heumann and R. Hiptmair, "Discretization of generalized convection diffusion equations", in Proceedings of the Seminar for Applied Mathematics, ETH Zürich, 2008.
- [5] A. Bossavit, "Extrusion, contraction: their discretization via Whitney forms", COMPEL, 22, pp. 470-480, 2003.
- [6] K. Thorne, "Chapter 18, Magnetohydrodynamics", www.pma.caltech.edu/Courses/ph136/yr2004/0418.1.K.pdf.
- [7] J. Van Bladel, *Relativity and Engineering*, Springer Verlag, 1984.

Robust FEM-BEM Coupling for Magnetostatics on multi-connected Domains

D. Pusch and J. Ostrowski

ABB Switzerland Ltd., Corporate Research, CH-5405 Baden 5 Dättwil
e-mail: joerg.ostrowski@ch.abb.com, david.pusch@ch.abb.com

Abstract—This paper presents a method for the computation of magnetostatic problems based on finite element and boundary element coupling. In our method, we are introducing a reduced scalar magnetic potential in the unbounded air region. This enables the treatment of multi-connected domains in contrast to formulations based on total scalar magnetic potentials. Moreover, the computation of materials with high permeability is possible without stability problems, because of the usage of a vector potential in the solid parts.

I. INTRODUCTION

Similar methods have been proposed in the past. In [1] a vector potential is used in the solid parts and a total scalar approach for the unbounded domain, respectively. This approach is restricted to simple connected conductors. Other approaches are based only on total scalar potentials and/or reduced scalar potentials instead, see [2], [3], [4]. These methods suffer from cancellation errors and lack stability in presence of high permeability (e.g. $\mu_r = 500$) if the reduced scalar magnetic potential is used inside the permeable bodies, [6], [2]. Our proposed method circumvents these problems and enables simulations of highly permeable parts of general topology.

Thus, let us consider an inner domain Ω of general topology that consists of magnetic or non-magnetic parts. The unbounded outer air region is $\Omega^+ = \mathbb{R}^3 \setminus \bar{\Omega}$, with $\mu = \mu_0$. The interface boundary is assigned by $\Gamma = \partial\Omega$. We search a magnetic flux density \mathbf{B} that solves the magnetostatic field equations

$$\operatorname{curl} \frac{1}{\mu} \mathbf{B} = \mathbf{j} \quad \text{in } \Omega, \quad (1)$$

$$\operatorname{curl} \frac{1}{\mu_0} \mathbf{B} = \mathbf{j} \quad \text{in } \Omega^+, \quad (2)$$

$$\operatorname{div} \mathbf{B} = 0 \quad \text{in } \Omega \cup \Omega^+. \quad (3)$$

In order to solve the equations we are applying a finite element (FEM) formulation based on the magnetic vector potential for the inner domain. In the outer domain we are introducing a reduced potential, which is treated by a boundary element method (BEM). Taking into account the interface conditions, we are coupling both approaches and obtain an overall system of equations that has to be solved.

II. INNER DOMAIN Ω

In the inner domain Ω we are introducing the mentioned vector potential $\mathbf{B} = \operatorname{curl} \mathbf{A}$, and obtain

$$\operatorname{curl} \frac{1}{\mu} \operatorname{curl} \mathbf{A} = \mathbf{j} \quad \text{in } \Omega. \quad (4)$$

For regularization we apply Coulomb gauge

$$\operatorname{div} \mathbf{A} = 0. \quad (5)$$

In order to derive a variational formulation we multiply (4) and (5) with a testfunction v and q , respectively. After integration by parts and introducing a new variable p we obtain a weak formulation. Taking into account the correct function spaces, we have to find (\mathbf{A}, p) in $H(\operatorname{curl}) \times H^1(\Omega)$

$$\begin{aligned} \int_{\Omega} \frac{1}{\mu} \operatorname{curl} \mathbf{A} \cdot \operatorname{curl} v \, d\Omega - \int_{\Gamma} \left(\frac{1}{\mu} \operatorname{curl} \mathbf{A} \times \mathbf{n} \right) \cdot v \, d\Gamma \\ + \int_{\Omega} \nabla p \cdot v \, d\Omega = \int_{\Omega} \mathbf{j} \cdot v \, d\Omega \end{aligned} \quad (6)$$

$$\int_{\Omega} \mathbf{A} \cdot \nabla q \, d\Omega - \int_{\Omega} p \int_{\Omega} q \, d\Omega = 0. \quad (7)$$

for all (v, q) in $H(\operatorname{curl}) \times H^1(\Omega)$. It can be shown, that this new unknown function p has the property $p = \text{const} = 0$, see [1].

III. OUTER AIR DOMAIN Ω^+

Assuming that there are no magnetic materials, i.e. $\mu = \mu_0$ in the entire \mathbb{R}^3 , then a solution \mathbf{B}_0 of (1), (2) and (3) can be found by Biot-Savart integration. Considering the real configuration, we find the relation

$$\operatorname{curl} \left(\frac{1}{\mu} \mathbf{B} - \frac{1}{\mu_0} \mathbf{B}_0 \right) = 0 \quad \text{in } \mathbb{R}^3. \quad (8)$$

That means, we are now allowed to introduce a reduced scalar magnetic potential φ with

$$\nabla \varphi = \mathbf{B} - \mathbf{B}_0 \quad \text{in } \Omega^+ \quad (9)$$

without topological restrictions on Ω^+ . Considering equation (3) and taking into account that $\operatorname{div} \mathbf{B}_0 = 0$, the so-called reduced scalar potential φ can be found by solving a Laplace equation in the outer domain

$$\Delta \varphi = 0 \quad \text{in } \Omega^+. \quad (10)$$

It is well known that a solution for the Laplace equation can be obtained by an indirect single layer approach

$$\begin{aligned} \varphi = V\rho \quad \text{with} \quad (11) \\ (V\rho)(x) = \int_{\Gamma} \rho(y) G(x, y) ds_y \end{aligned}$$

and the kernel $G(x, y) = \frac{1}{4\pi} \|x - y\|^{-1}$. The normal derivative at the boundary Γ is given by

$$\begin{aligned} \nabla\varphi \cdot \mathbf{n} &= (K' - \frac{1}{2}I)\rho \quad \text{with} \quad (12) \\ (K'\rho)(x) &= \int_{\Gamma} \rho(y) \frac{\partial G}{\partial n_x}(x, y) ds_y \end{aligned}$$

where the appearing boundary integral operator K' is the adjoint double layer potential, I denotes the identity operator and \mathbf{n} is the outward unit normal vector. For mapping properties of the integral operators see e.g. [5].

IV. COUPLING FEM/BEM

At the interface between the solid parts Ω and the outer region Ω^+ we have to fulfill the interface conditions

$$[\mathbf{B}\mathbf{n}] = 0, \quad [\mathbf{H} \times \mathbf{n}] = 0. \quad (13)$$

If we are inserting the vector potential \mathbf{A} and the reduced scalar potential φ we obtain from the continuity of the normal component of the \mathbf{B} -field

$$\mathbf{curl} \mathbf{A} \cdot \mathbf{n} = \nabla\varphi \cdot \mathbf{n} + \mathbf{B}_0 \cdot \mathbf{n}, \quad (14)$$

and from the continuity of the tangential component of the \mathbf{H} -field

$$\frac{1}{\mu} \mathbf{curl} \mathbf{A} \times \mathbf{n} = \frac{1}{\mu_0} (\nabla\varphi + \mathbf{B}_0) \times \mathbf{n}. \quad (15)$$

Now we can replace the boundary integral in formula (6) with our boundary operators (11) and (12). Finally, we have to find a solution $(\mathbf{A}, p, \varphi, \rho)$ in $H(\mathbf{curl}, \Omega) \times H^1(\Omega) \times H^{1/2}(\Gamma) \times H^{-1/2}(\Gamma)$ that fulfills the final summarized system of equations

$$\begin{aligned} \int_{\Omega} \frac{1}{\mu} \mathbf{curl} \mathbf{A} \mathbf{curl} \mathbf{v} d\Omega + \int_{\Omega} \nabla p \mathbf{v} d\Omega - \\ \int_{\Gamma} \frac{1}{\mu_0} \varphi (\mathbf{curl} \mathbf{v} \mathbf{n}) d\Gamma = \int_{\Omega} \mathbf{j} \mathbf{v} d\Omega + \int_{\Gamma} \left(\frac{1}{\mu_0} \mathbf{B}_0 \times \mathbf{n} \right) \mathbf{v} d\Gamma \\ \int_{\Omega} \mathbf{A} \nabla q d\Omega - \int_{\Omega} p \int_{\Omega} q d\Omega = 0 \\ \int_{\Gamma} (\mathbf{curl} \mathbf{A} \mathbf{n}) w d\Gamma - \int_{\Gamma} (K' - \frac{1}{2}I) \rho w d\Gamma = \int_{\Gamma} (\mathbf{B}_0 \mathbf{n}) w d\Gamma \\ - \int_{\Gamma} \varphi \tilde{w} d\Gamma + \int_{\Gamma} (V\rho) \tilde{w} d\Gamma = 0 \end{aligned} \quad (16)$$

for all $(\mathbf{v}, q, w, \tilde{w})$ in $H(\mathbf{curl}, \Omega) \times H^1(\Omega) \times H^{1/2}(\Gamma) \times H^{-1/2}(\Gamma)$.

The corresponding discrete spaces are the standard space of edge elements \mathcal{W}_h , the space of piecewise linear elements \mathcal{V}_h , the space of piecewise linear and constant boundary elements \mathcal{X}_h and \mathcal{Y}_h , respectively. Hence, the resulting system in matrix notation is given as

$$\begin{pmatrix} A & B & C & 0 \\ B^{\top} & -P & 0 & 0 \\ C^{\top} & 0 & 0 & \frac{1}{2}I - K' \\ 0 & 0 & -I & V \end{pmatrix} \begin{pmatrix} \underline{A} \\ \underline{p} \\ \underline{\varphi} \\ \underline{\rho} \end{pmatrix} = \begin{pmatrix} \underline{f} \\ 0 \\ \underline{g} \\ 0 \end{pmatrix}. \quad (17)$$

V. NUMERICAL RESULTS

Our model problem consists of a cylinder made of copper ($\sigma = 5.7 * 10^7 (\Omega m)^{-1}$, $\mu = \mu_0$) with a current excitation of $I = 100A$. The surrounding core is non-conductive with a relative permeability $\mu_r = 500$. Let us remark, that the cylinder is not in the center of the core, but a bit moved towards a corner. In Fig. 1 the solution of the system of equations (16) for the \mathbf{B} -field is shown. The magnetic flux

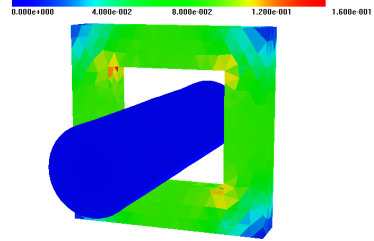


Fig. 1. B-field, FEM-BEM, magnetostatic

density is concentrated in the high permeable core. At the reentrant corners we have singularities, which are difficult to compare with our reference solution, that has been computed by a pure FEM solver for magnetostatics, see Fig. 2. Note,

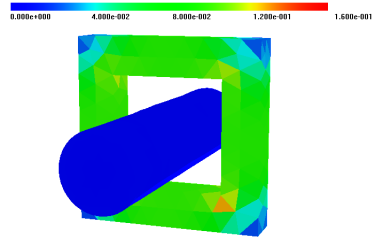


Fig. 2. B-field, FEM, magnetostatics

that the scale was set to the same range as in Fig. 1. The results of both methods match very well, which confirms the validity of our proposed general FEM-BEM approach. In order to compute using finer meshes we have to apply compression methods, which are currently under implementation.

REFERENCES

- [1] M.Kuhn and O.Steinbach, Symmetric coupling of finite and boundary elements for exterior magnetic field problems, *Math.Meth.Appl.Sci.*, 2002, Vol.25, pp.357–371
- [2] A.Frangi, P.Faure-Ragani and L.Ghezzi, Magneto-mechanical simulations by a coupled fast multipole method-finite element method and multigrid solvers, *Computers and Structures*, Vol.83, No. 10-11, 2005, pp.718–726
- [3] W.Hafla, Andre Buchau and W.M.Rucker, Accuracy improvement in nonlinear magnetostatic field computations with integral equation methods and indirect total scalar potential formulations, *COMPEL*, Vol.24, No.3, 2006, pp.565–571
- [4] P.Salgado and V.Selgas, A symmetric BEM-FEM coupling for the three-dimensional magnetostatic problem using scalar potentials, *Engineering Analysis with Boundary Elements*, Vol.32, No.8, 2008, pp.633–644
- [5] M.Costabel, Boundary integral operators on Lipschitz domains: Elementary results, *SIAM J.Math.Anal.* 19, 1988, pp.613–626
- [6] S.Balac and G.Caloz, Magnetostatic field computations based on the coupling of finite element and integral representation methods, *IEEE Trans.Magn.*, Vol.38, No. 2, 2002, pp.393–396

Edge element multigrid solution of time-harmonic 3-D non-linear eddy-current problems

Chao Chen and Oszkár Bíró

Institute for Fundamentals and Theory in Electrical Engineering, Graz University of Technology
Kopernikusgasse 24, 8010-Graz, Austria

Chao.Chen@tugraz.at

Abstract— A geometric multigrid method for the efficient solution of time-harmonic three-dimensional non-linear eddy-current problems is presented. A finite element method with scalar potentials and vector potentials is used to describe the problems. The iteration time of the multigrid solution is compared to a standard conjugate gradient with incomplete Cholesky factorization iteration.

I. INTRODUCTION

In recent years, edge elements have become state of the art for the calculation of linear or non-linear time-harmonic eddy-current problems with finite elements [1]. Particularly in the three-dimensional (3-D) case the finite element method (FEM) formulation results in a large system of equations. Iterative methods like the conjugate gradient method with incomplete Cholesky factorization (ICCG) as preconditioner are normally used for solving these systems of equations. However, the number of iterations increases substantially with the number of unknowns. A very fast method for solving a system of equations is the geometric multigrid (MG) method [2].

In this paper, the eddy-current problem is described by the FEM using the \mathbf{A} , V formulation. To decrease the solution time of non-linear problems we present a nonlinear geometric multigrid algorithm for edge elements which is based on a modified Picard-Banach method [3]-[4].

II. FEM-FORMULATION

An eddy current problem involves two regions: a conducting region Ω_c with an unknown current density distribution and a non conducting region Ω_n with a given source current density \mathbf{J}_0 .

In the non conducting region, the magnetic vector potential \mathbf{A} is defined as usual by $\mathbf{B} = \text{curl}\mathbf{A}$. Neglecting the dielectric displacement leads to the differential equation $\text{curl}(\nu\text{curl}\mathbf{A}) = \mathbf{J}_0$ in Ω_n , where $\nu = \nu(\mathbf{x})$ is the reluctivity of the material, \mathbf{J}_0 can be described as the curl of a vector potential \mathbf{T}_0 .

In the conducting region, an additional modified electric scalar potential V is introduced as $\mathbf{E} = -j\omega\mathbf{A} - j\omega\text{grad}V$ where ω is the angular frequency of the current excitation.

Since there are two unknowns, \mathbf{A} and V , an additional equation has to be used. It is common to use the divergence free property of the total current density, $\text{div}\mathbf{J} = 0$. This leads to the following system of differential equations:

$$\text{curl}(\nu\text{curl}\mathbf{A}) + j\omega\sigma\mathbf{A} + j\omega\sigma\text{grad}V = \text{curl}\mathbf{T}_0 \quad (1)$$

$$-\text{div}(j\omega\sigma\mathbf{A} + j\omega\sigma\text{grad}V) = 0 \quad (2)$$

where σ is the conductivity in the conducting region.

Using n_e edge basis functions N_i for the vector potential and n_n nodal basis functions N_i for the scalar potential, the Galerkin equations can be written as

$$\begin{aligned} (\text{curl}N_i, \nu\text{curl}\mathbf{A}_h) + j\omega(N_i, \sigma\mathbf{A}_h) + j\omega(N_i, \sigma\text{grad}V_h) = \\ (\text{curl}N_i, \mathbf{T}_0) \quad i = 1, 2, \dots, n_e \end{aligned} \quad (3)$$

$$j\omega(\text{grad}N_i, \sigma\mathbf{A}_h) + j\omega(\text{grad}N_i, \sigma\text{grad}V_h) = 0 \quad i = 1, 2, \dots, n_n \quad (4)$$

where $\mathbf{A}_h = \sum_{i=1}^{n_e} a_i N_i$ and $V_h = \sum_{i=1}^{n_n} V_i N_i$ are the approximations of the vector potential and scalar potential respectively. The resulting system of equations is singular, since applying the divergence operator to (1) will result in (2).

III. MULTIGRID

A geometric multigrid algorithm is used for solving this singular system of equations. One iteration step of the classical two-grid algorithm applied to the solution of the equation system $\mathbf{A}_h \mathbf{x}_h = \mathbf{b}_h$ can be described as follow

$$\begin{aligned} \tilde{\mathbf{x}}_h &= S^{n_1}(\mathbf{x}_h, \mathbf{b}_h) - n_1 \text{ pre-smoothing operations} \\ \mathbf{d}_h &= \mathbf{A}_h \tilde{\mathbf{x}}_h - \mathbf{b}_h - \text{calculation of the defect} \\ \mathbf{d}_H &= \mathbf{R}\mathbf{d}_h - \text{restriction of the defect on the coarser grid} \\ \mathbf{e}_H &= \mathbf{A}_H^{-1} \mathbf{d}_H - \text{solution of the coarse grid equation} \\ \mathbf{x}_h &= \tilde{\mathbf{x}}_h - \mathbf{P}\mathbf{e}_H - \text{correction of } \tilde{\mathbf{x}}_h \\ \mathbf{x}_h &= S^{n_2}(\mathbf{x}_h, \mathbf{b}_h) - n_2 \text{ post-smoothing operations} \end{aligned} \quad (5)$$

where S^{n_i} denotes n_i iterations using a smoother S , and the subscripts h and H refer to the fine and coarse grids, respectively. The linear mapping $\mathbf{d}_H = \mathbf{R}\mathbf{d}_h$ is called restriction and the coarse-to-fine interpolation $\mathbf{e}_h = \mathbf{P}\mathbf{e}_H$ prolongation. The multigrid algorithm can be obtained by replacing step 4 in the two-grid algorithm (5) by another two-grid step. This idea can be applied recursively, using coarser and coarser grids, generating a MG V-cycle.

For edge elements, the entry of the $n_h \times n_H$ prolongation matrix \mathbf{P}^e is defined as [4]

$$p_{ij}^e = \int_{\text{global edge}_{h,i}} N_{H,j}(x, y, z) \cdot dl \quad (6)$$

where $1 \leq i \leq n_h^e$ and $1 \leq j \leq n_H^e$.

Using nodal elements, the natural choice for the entries of the prolongation matrix P^n are the values of the coarse grid basis functions N_H at the fine grid nodes \mathbf{x}_{hj} :

$$p_{ij}^n = N_{H,i}(\mathbf{x}_{h,j}) \quad (7)$$

In a formulation using both nodal and edge elements, the prolongation matrix can be written as

$$P = \begin{bmatrix} P^e & 0 \\ 0 & P^n \end{bmatrix} \quad (8)$$

The transpose of P has been used as the restriction matrix R , i.e., $R = P^T$.

For the \mathbf{A} , V -formulation described in section II, a Gauss-Seidel type smoother can be applied to the nodal element and edge element space respectively. This is due to the fact that (4) takes care of the kernel of the curl operator [5].

In ferromagnetic materials the connection between \mathbf{B} and \mathbf{H} is nonlinear. For nonlinear problems, a modified Picard-Banach method has been used. This means a series of linear problems has to be solved

$$A_h(\mathbf{x}_{h,i})\mathbf{x}_{h,i+1} = \mathbf{b}_h \quad (9)$$

In each nonlinear iteration step, the nonlinear reluctivity ν has to be calculated in the Gaussian points of the finite elements, using the previous approximation for \mathbf{x}_h .

Since the matrices A_h depend on the reluctivity ν , they have to be reassembled in every nonlinear iteration step. For the MG method, the only meaningful solution for calculating ν is the solution \mathbf{x}_h on the finest grid, which is used to compute ν on a coarser grid as well. This yields the corresponding reluctivity at each MG level resulting in a proper hierarchy of finite element grids and systems of equations which can be described by the following algorithm [4]. It is assumed that the number of multigrid levels l and starting value ν_0 are given:

- Assemble the matrices $A_q(\nu_i)$, $q = 1, 2, \dots, l$;
- Solve $A_l(\nu_i)\mathbf{x}_{l,i+1} = \mathbf{b}_l$ with MG algorithm;
- Calculate $\nu_{i+1}(\mathbf{x}_{l,i+1})$;
- If $\|\nu_{i+1}/\nu_i\|_{\max} \geq \varepsilon$, $i = i+1$, back to step 2.

IV. NUMERICAL EXAMPLES

To demonstrate the applicability of the proposed scheme, a 3-D numerical example is considered. The geometry of the problem and the discretization of the coarse grid with hexahedral elements of second order can be seen in Fig. 1. The iron plate has conductivity of $\sigma = 4 \times 10^6$ S/m. Its nonlinear magnetization curve is depicted in Fig. 2. The current and frequency of the coil is 1×10^7 A/m² and 50Hz respectively.

In Table I, the solution time for solving the non-linear eddy-current problem, using ICCG and MG, have been compared. Especially for finer finite element mesh the multigrid method is faster than the ICCG.

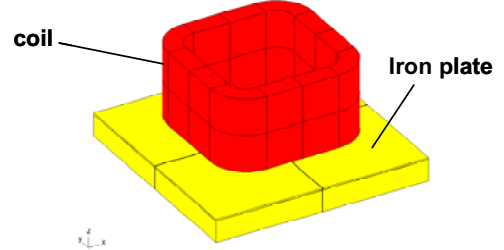


Fig. 1. Geometry and discretization of 3-D problem.

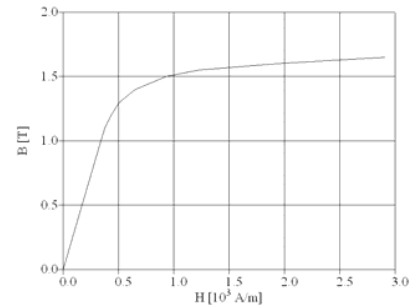


Fig. 2. Non-linear magnetization of the iron plate.

TABLE I
COMPUTATION TIME OF ICCG AND MULTIGRID

Number of equations	Computation time (seconds)	
	ICCG	MG
275797	1318	1266
618657	4310	2374

V. CONCLUSION

In this paper we have presented a solution by an MG method for nonlinear eddy-current problems described by a system of nonlinear equations obtained by an edge finite element. Numerical results have shown the advantage of MG method for non-linear eddy-current problems.

VI. REFERENCES

- [1] O. Biró, "Edge element formulations of eddy current problems," *Comput. Methods Appl. Mech. Engrg.*, vol. 169, pp. 391-405, 1999.
- [2] W. Hackbusch, *Multi-grid Methods and Applications*, Springer Verlag, Berlin.
- [3] O. Biró, K. Preis, K.R. Richter, "Various FEM formulations for the calculation of transient 3d eddy currents in nonlinear media," *IEEE Trans. Mag.*, vol. 31, no. 3, pp. 1307-1312, May 1995.
- [4] B. Weiß, O. Biró, "Edge element multigrid solution of nonlinear magnetostatic problems," 9th International IGTE Symposium on Numerical Field Calculation in Electrical Engineering, Graz, Austria, 11-13 September 2000.
- [5] B. Weiß, O. Biró, "Multigrid for transient 3d eddy current analysis," *COMPEL.*, vol. 22, no. 3, pp. 779-288, 2003.

FE Analysis of Magnetic Particle Dynamics on Fixed Mesh with Level Set Function

Young Sun Kim, Myung Ki Baek, and Il Han Park
 School of Information and Communication Engineering, Sungkyunkwan University
 300, Cheoncheon-dong, Jangan-gu, Suwon, 440-746, Korea
youngsun@skku.edu, myungki79@naver.com, ihpark@skku.ac.kr

Abstract— Magnetic particle is used in various areas from engineering to biomedical field. The particles are controlled by external magnetic field and the magnetized particles interact between themselves to show some interesting behaviors. Various computational analysis works have been recently presented. But, since most of them are based on a point-dipole model, the accurate effects of finite volume and mutual interactions are not calculated. In addition, full field analysis has serious problem in remeshing for moving particles. This paper propose a new approach, where the movement of particles is captured using level set function on a fixed background mesh for magnetic field analysis. The magnetic force on each particle by body force density are inserted into driving forces in dynamic equations.

I. INTRODUCTION

Recently, magnetic particle is attracting much attention because their role is increasing in various areas from engineering to biomedical field. Some typical examples include site-specific drug delivery, separation of tagged DNA, enhanced magnetic resonance imaging, hyperthermic cell treatment, magnetorheological fluids for controllable linear dampers, rotary brakes, and vibration dampers, etc. Therefore, the accurate analysis for their particle dynamics is required for appropriate estimation of the particle behaviors before a real test procedure, which needs a lot of cost and time. Applied magnetic field controls the particles in a fluid domain by exerting magnetic force on the particles. But, the magnetized particles also interact between themselves to produce other complex phenomena.

Various computational works have been presented recently for its characteristics analysis: molecular dynamics simulations, density functional theory, particle dynamics method, Monte Carlo method [1]. However, since they are based on a point-dipole model, the accurate effects of finite volume and mutual interactions are not calculated. So, it turns out that full magnetic field is required for accurate calculation of nonlinear dynamics with many particles. But, the existing finite element method has a serious problem of remeshing for evolving geometrical modeling for many moving particles. Therefore, in this paper we propose a new approach, where the movement of particles is captured using level set function on a fixed background mesh for magnetic field analysis. The magnetic forces on each particle are calculated by body force density and inserted into driving forces in dynamic equations. The proposed method is applied to estimation of chain aggregation of ferromagnetic particles under external magnetic field.

II. BOUNDARY AND MATERIAL SETTING

For arbitrary region Ω with boundary, the implicit function $\phi(\mathbf{x})$ is assumed as follow

$$\begin{aligned} \phi(\mathbf{r}) > 0 & \quad \mathbf{r} \in \Omega^+ & : \text{fluid} \\ \phi(\mathbf{r}) = 0 & \quad \mathbf{r} \in \partial\Omega & : \text{boundary} \\ \phi(\mathbf{r}) < 0 & \quad \mathbf{r} \in \Omega^- & : \text{particle} \end{aligned} \quad (1)$$

Magnetic particle region can be defined the boundaries of domain Ω^- via

$$\Omega^-(t) = \{ \phi(\mathbf{r}, t) < 0 \}. \quad (2)$$

The boundary $\Gamma(t)$ of $\Omega^-(t)$ is then given by the zero level set,

$$\Gamma(t) = \{ \phi(\mathbf{r}, t) = 0 \} \quad (3)$$

The boundaries of particles can be expressed the zero level set using the signed distance function and the boolean union function min. Fig. 1(a) shows the distributions of level set function [2].

$$\begin{aligned} \phi(\mathbf{r}) &= \min(\mathbf{r} - \mathbf{r}_i) \quad \text{for all } \mathbf{r}_i \in \partial\Omega \\ \phi(\mathbf{r}) &= 0 \quad \text{on the boundary where } \mathbf{r} \in \partial\Omega \end{aligned} \quad (4)$$

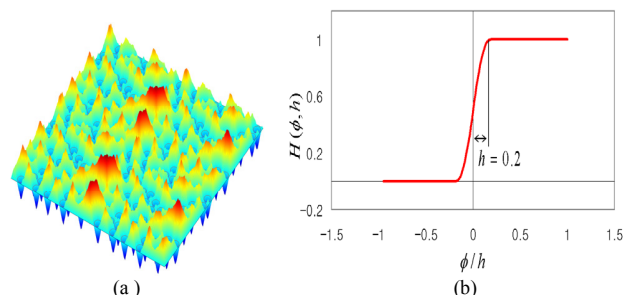


Fig. 1. (a) Level set function and (b) smeared Heaviside function.

Heaviside function is proper to set the material property of magnetic particle. It is not strict but continuously changes on the boundary in numerical processing because the boundaries can intersect an element. So, we used a smeared Heaviside function that gives a continuous permeability distribution near the zero level set. But, the material density near the boundary can be as abrupt as possible by regulating the tunable parameter h .

$$\mu = \mu_0 H(\phi, h) + (1 - H(\phi, h)) \mu_r \mu_0 \quad (5)$$

$$\mu(\phi, h) = \begin{cases} \mu_0 & \phi \leq 0 \\ \mu_r \mu_0 & \phi > 0 \end{cases} \quad (6)$$

where μ , μ_r and μ_0 denote permeability, relative permeability

and permeability of free space(fluid) respectively. Fig. 1(b) represents a smeared form of Heaviside function that is used in the proposed algorithm. By introducing the level set function to material setting process, we don't have to remesh the model geometry that is changed by moving objects.

The integration of surface and boundary integral are expressed using Heaviside function $H(\phi)$ and Dirac-Delta function $\delta(\phi)$.

$$\int_S f(\mathbf{r}) dS = \int_{\Omega} f(\mathbf{r}) H(\phi(\mathbf{r})) d\Omega \quad (7)$$

$$\int_{\Gamma} f(\mathbf{r}) d\Gamma = \int_{\Omega} f(\mathbf{r}) \delta(\phi(\mathbf{r})) |\nabla \phi(\mathbf{r})| d\Omega \quad (8)$$

III. FORCE ON PARTICLE AND DYNAMICS ANALYSIS

To calculate force on moving magnetic particles we employ a body force density that can be easily integrated for a total force using the level set function. The velocities and displacements of magnetic particles are calculated by the motion equation. Collision with other particles is assumed to be elastic and friction between particles is ignored to simplify the problem. The total forces on each particle are an integration of the force density [3].

$$\mathbf{F} = \int_{\Omega} \frac{\sigma_{m2}}{2} \left(\frac{\mathbf{H}_1 + \mathbf{H}_2}{2} + \frac{\sigma_{m2}}{2\mu_0} \mathbf{n}_2 \right) H(\phi) d\Omega \quad (9)$$

where, \mathbf{H} is field intensity of each side, σ_{m2} is magnetic charge of fluid, \mathbf{n}_2 is the normal unit vector on surface and Ω is a region of magnetic particles. The velocities and positions of particles are analyzed by the motion equation

$$m \frac{d^2 \mathbf{s}}{dt^2} + D \mathbf{v} = \mathbf{F} \quad (10)$$

where m is mass of a particle, D is damping coefficient such as viscosity or friction, and \mathbf{s} and \mathbf{v} denote position and velocity of particles.

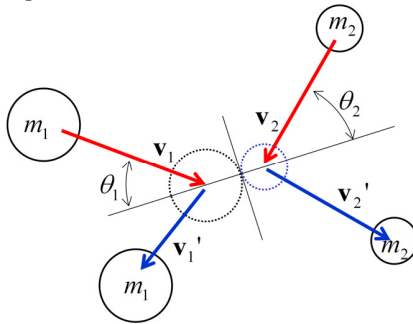


Fig. 2. Collision diagram between particles.

When the particles come into collision with other particle or boundary wall, collision involves forces that are a change in velocity as in (11) and (12). Collision is assumed to be elastic, meaning they conserve energy and momentum. The magnitude of the velocity difference at impact is called the closing speed. The state variables of dynamics are concerned with moving and colliding objects. The above analysis procedure is executed until movement of particle is small enough for convergence.

$$m_1 \mathbf{v}_1 + m_2 \mathbf{v}_2 = m_1 \mathbf{v}_1' + m_2 \mathbf{v}_2' \quad (11)$$

$$\frac{1}{2} m_1 \mathbf{v}_1^2 + \frac{1}{2} m_2 \mathbf{v}_2^2 = \frac{1}{2} m_1 \mathbf{v}_1'^2 + m_2 \mathbf{v}_2'^2 \quad (12)$$

The overall flow chart of this procedure is shown as in Fig. 3. The dynamic equations of particles are numerically solved using Runge-Kutta algorithm for nonlinear ordinary differential equations.

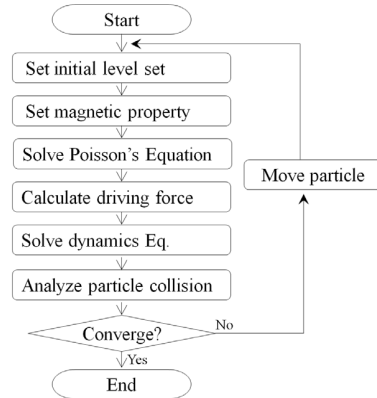


Fig. 3. Flow chart of particle dynamics analysis.

IV. NUMERICAL RESULTS

The proposed modeling method for evolving geometry is numerically tested for a magnetic particle dynamics analysis. The test problem is dynamics of 228 magnetic particles in a box as Fig. 4(a) which shows the initial distributions of particles in absence of external field. After a uniform magnetic field of 1(T) is applied, the particles are redistributed and clustered to form long chains along the applied field direction as in Fig. 4(b). Using this model we can also predict the changed material property of the system in the presence of interactions. These results are consistent with experimental data [4].

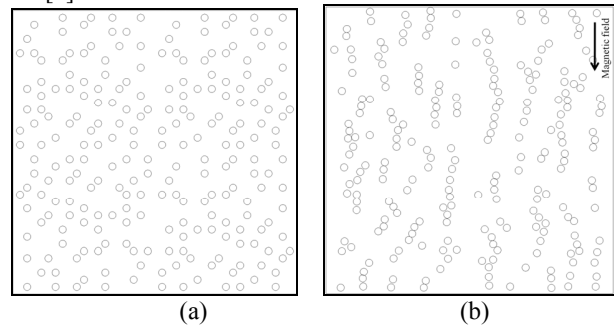


Fig. 4. Magnetic particles in (a) zero field and (b) a uniform field

V. REFERENCES

- [1] R. E. Rosensweig, *Ferrohydrodynamics*, Cambridge University Press, Cambridge, 1985.
- [2] Osher, S. and Fedkiw, R., *Level Set Methods and Dynamic Implicit Surfaces*, Springer, New York, 2003.
- [3] Hong Soon Choi, Il Han Park and Se Hee Lee, "Concept of Virtual Air Gap and Its Applications for Force Calculation," *IEEE Trans Magnetics*, Vol. 42, No 4, April, 2006, pp. 663-666.
- [4] Patrick H. Hess and P. Harold Parker Jr., "Polymers for stabilization of Colloidal Cobalt," *Journal of Applied Polymer Science*, Vol. 10, 1966, pp. 1915-1927.

A Step Forward in Wavelet-Based Algebraic Multigrid Method Using the Lifting Technique

Fabio Henrique Pereira^{1,2}, Silvio Ikuyo Nabeta²

¹Industrial Engineering Post Graduation Program – UNINOVE-SP

²Electrical Machine and Drives Lab – GMACq – USP - SP

Av. Francisco Matarazzo, 612 – Água Branca, 05001.100 – São Paulo, SP - Brazil

fabiohp@uninove.br; nabeta@pea.usp.br

Abstract — This paper presents a progress in the development of a recent and promising wavelet-based Algebraic Multigrid method with the use of the lifting technique. This new approach allows creating an algorithm with smaller memory requirement and a reduced number of floating point operations, if long filters are used, keeping the efficiency of the multigrid technique. The performance of the proposed approach is verified by solving the three-dimensional Poisson equation defined in a uniform grid and also in the TEAM 28 Problem. The standard Incomplete Cholesky Conjugate Gradient solver and the Incomplete LU preconditioner are used for comparison.

I. INTRODUCTION

A combination of the Discrete Wavelet Transform (DWT) and the Algebraic Multigrid method (AMG) was introduced recently in [1] producing a new method called WAMG. In that new approach a modified DWT, using only low-pass filter bank, was applied to the original matrix to produce an approximation of it in each level of the multiresolution process.

The WAMG has revealed to be a very efficient and promising method for several problems related to computation of electromagnetic fields, in both serial and parallel computation [1],[2]. The method can be either used as an iterative solver or as a preconditioning technique, presenting in many cases a better performance than some of the most advanced and current AMG algorithms.

Due to the WAMG efficiency and potentiality further researches have been carried out for its improvement and this paper is part of this effort. In order to accomplish this task this work build a modified discrete wavelet transform using the tool called the lifting scheme [3]. The lifting technique is a method introduced by W. Sweldens [4], which allows some improvements on the properties of existing wavelet transforms. The technique has some numerical advantages as a reduced number of floating point operations which are fundamental in the context of the iterative solvers. Actually, it is known that the lifting algorithm is asymptotically twice as fast as the standard algorithm for long filters [2].

II. THE WAVELET-BASED ALGEBRAIC MULTIGRID

The key point of the WAMG is the application of a modified (incomplete) DWT, as a filter bank with only low-pass filters, to generate the hierarchy of matrices in the AMG method.

This approach is very interesting mainly because it avoids the coarsening process and the heuristic parameters present in

the standard AMG, simplifying the use of the method as well as its parallel implementation in distributed memory computers [1],[2].

III. THE IMPLEMENTATION USING THE LIFTING TECHNIQUE

In [5] Daubechies and Sweldens have shown that every wavelet filter can be decomposed into lifting steps. Therefore, all discrete wavelet transforms used for WAMG can be implemented with the lifting scheme. The main algorithmic advantages of this technique are:

a) Smaller memory requirement – the calculations can be performed in-place;

b) Efficiency: reduced number of floating point operations;

c) Parallelism –inherently parallel feature;

More details about these advantages as well as others important structural advantages of the lifting can be found in [3],[4].

In fact, there are basically three forms for representing a wavelet transform: equation form (lifting), filter form (filter bank) and matrix form. However, only the first two are appropriate in the multigrid implementation.

The representations of the Daubechies 4 wavelet in the lifting form and in the filters form are presented in (1)-(3). These representations were extracted from [3], which shows the details for converting between these two forms (one can also see [4]).

A. Lifting form

$$\begin{aligned} s^{(1)}[n] &= S[2n] + \sqrt{3}S[2n+1], \\ d^{(1)}[n] &= S[2n+1] - \frac{1}{4}\sqrt{3}s^{(1)}[n] - \frac{1}{4}(\sqrt{3}-2)s^{(1)}[n-1], \\ s^{(2)}[n] &= s^{(1)}[n] - d^{(1)}[n+1], \\ \tilde{s}[n] &= \frac{\sqrt{3}-1}{\sqrt{2}}s^{(2)}[n], \quad \tilde{d}[n] = \frac{\sqrt{3}+1}{\sqrt{2}}d^{(1)}[n]. \end{aligned} \quad (1)$$

B. Filter Form

$$h_4 = \frac{1}{4\sqrt{2}}[1 + \sqrt{3}, 3 + \sqrt{3}, 3 - \sqrt{3}, 1 - \sqrt{3}], \quad (2)$$

$$g_4 = \frac{1}{4\sqrt{2}}[1 - \sqrt{3}, -3 + \sqrt{3}, 3 + \sqrt{3}, -1 - \sqrt{3}]. \quad (3)$$

The coefficients $s[n]$ and $d[n]$ in (1) are, respectively, the approximation and the details coefficients of the input signal S . Therefore, for the multigrid implementation in the Lifting

form the last equation in (1) is not necessary. In (2) and (3) h_4 and g_4 are the low-pass and high-pass filter bank, respectively.

IV. THE NUMERICAL TEST PROBLEM

The performance of the proposed approach is verified by solving the three-dimensional Poisson equation defined in a uniform grid on the cube $[-1,1]^3$. The spatial discretization of the Poisson equation uses Lagrange finite-element functions and second order elements, both implemented in the C++ Finite Element Library - LibMesh [6]. The resulting symmetric positive definite matrix has 29791 rows and 1771561 nonzero entries.

The WAMG method with the lifting implementation (LAMG) was used as a stand-alone solver and as a preconditioner for Bi-Conjugate Gradient Stabilized (BiCGStab). The results are shown in Table I. For comparison, the standard Incomplete Cholesky Conjugate Gradient (IC-CG) solver is used.

TABLE I
RESULTS FOR THE TEST PROBLEM

Method	Number of steps	Time in seconds		
		Setup	Solver	Total
LAMG	5	3.65	3.85	7.50
LAMG-BiCGStab	3		4.58	8.23
LAMG-CG	3		4.04	7.69
IC-CG	10	6.78	2.59	9.37
IC-BiCGStab	5		2.08	8.86

V. APPLICATION IN THE TEAM 28 PROBLEM

The performance of the LAMG is also verified in the steady-state analysis of Compumag TEAM 28 Problem. This problem relates to the modeling of an electrodynamic device which consists of two stationary concentric exciting coils interacting with a moveable round conducting plate. The used model, which was created using the Finite Element Method Magnetic (FEMM) [7], applies the Kelvin transformation [8] for investigating the steady-state levitation height of the plate. The resulting complex symmetric matrix has 54723 rows and 380957 nonzero entries.

The LAMG method was used as a preconditioner for BiCGStab. Again, the Incomplete Cholesky and the Incomplete LU preconditioners were used for comparison. The results are shown in Table II.

TABLE II
RESULTS FOR THE TEAM 28 PROBLEM

Method	Number of steps	Time in seconds		
		Setup	Solver	Total
LAMG-BiCGStab	42	1.11	15.92	17.03
ILU-BiCGStab	244	0.36	81.17	81.53
IC-BiCGStab	223	0.58	33.99	34.57

The Magnetic flux density B (module) for this problem is presented in Fig. 1.

VI. CONCLUSION

The proposed approach seems to be very promising. The numerical advantages of the lifting technique allow an efficient computational implementation of the method, as can be seen from the setup time for the test problem in Table I. On the other hand, the LAMG presented a small convergence rate for the TEAM 28 problem, especially when it is used as a preconditioner, when compared with the incomplete Cholesky and incomplete LU preconditioners. The number of steps in Table II illustrates this superiority. This LAMG performance for this problem is especially interesting because the corresponding matrix is complex symmetric and, curiously, there is not much literature available on iterative solvers for complex symmetric problems, given the number of diverse applications in which these problems arise.

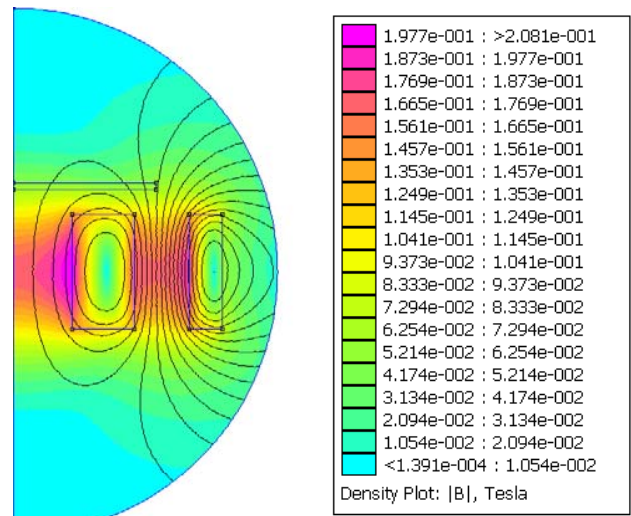


Fig. 1. Magnetic flux density B (module).

VII. ACKNOWLEDGEMENTS

The authors would like to thank FAPESP (2006/59547-5) for the financial support.

VIII. REFERENCES

- [1] F. H. Pereira, S. L. L. Verardi, S. I. Nabeta, "A Wavelet-based Algebraic Multigrid preconditioner for sparse linear systems", *Appl. Math. and Comput.*, **182**, pp. 1098-1107, 2006.
- [2] F. H. Pereira, M. F. Palin, S. L. L. Verardi, S. I. Nabeta. "A Parallel Wavelet-based Algebraic Multigrid black-box Solver and Preconditioner". In: *16th Conference on the Computation of Electromagnetic Fields*, 2007, Aachen.
- [3] A. Jensen, A. la Cour-Harbo, *The Discrete Wavelet Transform*, Ripples in Mathematics, Springer, Berlin 2001.
- [4] W. Sweldens. "The lifting scheme: A custom-design construction of biorthogonal wavelets". *Appl. Comput. Harmon. Analysis.*, **3**(2), pp. 186-200, 1996.
- [5] I. Daubechies and W. Sweldens, "Factoring Wavelet Transforms into Lifting Steps", *J. Fourier Anal. Appl.*, **4**(3), pp. 247-269, 1998.
- [6] B. Kirk, et. al., "LibMesh: A C++ Library for Parallel Adaptive Mesh Refinement/Coarsening Simulations". *Engineering with Computers*, **22**(3-4), pp. 237-254, 2006.
- [7] D. Meeker, *Finite element method magnetic: User's manual*. Massachusetts, USA, FEMM Version 4.2. 2003.
- [8] Q. Chen and A. Konrad, "A review of finite element open boundary techniques for static and quasistatic electromagnetic field problems," *IEEE Trans. on Magnetics*, **33**(1), pp. 663-676, 1997.

Solution of Static Field Problems with Random Domains

D.H.Mac^{1,3}, S. Clénet^{1,2}, J.C.Mipo³, and O. Moreau⁴

¹L2EP/Art et Métiers Paris Tech, Lille, 8 boulevard Louis XIV 59046 Lille cedex-France

²LAMEL/ Art et Métiers Paris Tech, 8 boulevard Louis XIV 59046 Lille cedex-France

³VALEO-Systèmes Electriques, 2 Voie André Boulle 94000 Créteil-France

⁴LAMEL/EdF R&D, 1 avenue du Général de Gaulle 92141 Clamart Cedex-France

Abstract— A method to solve stochastic partial differential equations in random domains consists in using a one to one random mapping function which transforms the random domain into a deterministic domain. The randomness is then supported by the behavior law of the material. This paper addresses an application of this method for an electrokinetic problem with uncertain dimensions. An example is presented to illustrate the method.

I. INTRODUCTION

In several models used to predict the behavior of a physical phenomenon, the available information is known with a finite level of confidence. Since the numerical models are more and more accurate thanks to the availability of new numerical methods (in 3D for example) and also to the increasing of computer performances, some of these uncertainties can not be considered negligible any longer. In several works, random variables were used in order to taking into account of these uncertainties. There are three kinds of uncertainties: Those on the terms sources, those on the material behavior and those on the dimensions. In [2], methods proposed in literature [4] to account for uncertainties on the material behavior were used to solve static field problems. However, the case of uncertainties on the geometry is much less studied. In [1], a method to solve differential equations in random domains based on a one to one random mapping function which transforms the random domains to a deterministic one is proposed.

In this paper, we propose to use such approach to solve a static field problem with random dimensions. In the first part of this paper, we present the approach that consists in transferring the randomness on the dimensions on the material behaviors. Then, known methods can be used to solve the stochastic problem. A numerical example will be presented in the second part.

II. PROBLEM DESCRIPTION

A. Deterministic problem

The electrokinetic problem defined in domain D can be written:

$$\begin{cases} \operatorname{div} \mathbf{J}(x) = 0 \\ \operatorname{curl} \mathbf{E}(x) = 0 \end{cases} \quad (1)$$

with \mathbf{J} the current density and \mathbf{E} the electric field. The constitutive law is given by $\mathbf{J}(x) = \sigma(x) \cdot \mathbf{E}(x)$, where $\sigma(x)$ is

the conductivity of the domain D . If we denote $\varphi(x)$ the scalar potential such that $\mathbf{E} = -\operatorname{grad} \varphi(x)$, equation (1) can be written:

$$\operatorname{Div}(\sigma(x) \cdot \operatorname{grad} \varphi(x)) = 0 \quad (2)$$

We assume that the domain D is bounded by the surface $\Gamma = \Gamma_1 \cup \Gamma_2 \cup \Gamma_3$ where the boundary conditions are given by:

$$\begin{cases} \mathbf{J}(x) \cdot \mathbf{n} = 0 & \text{on } \Gamma_1 \\ \varphi(x) = 0 & \text{on } \Gamma_2 \\ \varphi(x) = V & \text{on } \Gamma_3 \end{cases} \quad (3)$$

where \mathbf{n} is normal unity vector and V the imposed voltage. A weak formulation is used to solve numerically (2):

$$\int_D \operatorname{grad}^T \varphi(x) \cdot \sigma(x) \cdot \operatorname{grad} \lambda(x) \cdot d\Omega = 0 \quad (4)$$

where $\lambda(x)$ is a scalar test function that is equal to zero on Γ_2 and Γ_3 . To approximate the scalar potential and also for the test functions, nodal shape function are used.

III. PROBLEM WITH UNCERTAINTIES ON THE BEHAVIOR LAW

As will be shown later, the solution of a problem with random dimensions can be equivalent to a problem with random behavior laws. In the following, we will recall shortly how this kind of randomness can be taken into account. The uncertainties on behavior law can be modeled by the random fields $\sigma(x, \theta)$, where θ is the outcome. The scalar potential becomes now a random field $\varphi(x, \theta)$. The weak formulation becomes:

$$\int_D \operatorname{grad}^T \varphi(x, \theta) \cdot \sigma(x, \theta) \cdot \operatorname{grad} \lambda(x) \cdot d\Omega = 0 \quad (5)$$

This problem can be studied using Monte Carlo Simulation Method (MCSM) that is a very reliable method but very time consuming. Alternative methods can also be used that were studied in [2-4]: Spectral Stochastic Finite Element Method (SSFEM) and Non-Intrusive Method (NIM). SSFEM and NIM consist in projecting the field $\varphi(x, \theta)$ on space $K(x, \theta) = S(x) \otimes H(\theta)$ where $S(x)$ is spatial space spanned by the set of nodal shape functions $\lambda(x)$ (see section II) and $H(\theta)$ is spanned by a set of orthogonal polynomials $\{H_i(\theta)\}$. The main difference between SSFEM and NIM is that with SSFEM, the projection $\varphi(x, \theta)$ is undertaken simultaneously

on $S(x)$ and $H(\theta)$ while with NIM we project $\varphi(x, \theta)$ firstly on $S(x)$ and secondly on $H(\theta)$.

IV. PROBLEM WITH UNCERTAINTIES ON GEOMETRY

In SSFEM, MCSM and NIM, one difficulty in case of random domains compared to the case with random behavior law is that, a priori, geometric variation leads to the re-meshing of the system. Furthermore, the space S is no longer independent on $H(\theta)$, therefore the random scalar potential $\varphi(x, \theta)$ can not be directly approached by the projection in these spaces. To overcome that difficulty, an idea based on a one to one random mapping function that transforms the random domain to a deterministic domain is proposed in [1]. We will clarify this in following part. We use a one to one random mapping function $X = X(\theta, x)$ which transforms the random domain D to deterministic domain E . Thus, formulation (5) becomes:

$$\int_E \text{grad}^t \varphi(X, \theta) \frac{T^t(X, \theta) \cdot \sigma(X) \cdot T(X, \theta)}{|\det(T(X, \theta))|} \text{grad} \lambda(X) d\Omega = 0 \quad (6)$$

where T is the Jacobian matrix of the transformation. If we denote the conductivity:

$$\sigma'(X, \theta) = \frac{T^t(X, \theta) \cdot \sigma(X) \cdot T(X, \theta)}{|\det(T(X, \theta))|} \quad (7)$$

the problem with geometric uncertainties on the domain D can be considered equivalent to a problem with uncertainties on a modified behavior law with a conductivity $\sigma'(X, \theta)$ on the domain E . Methods have been already proposed to solve such kind of problems. One can note that to use the method, a one to one random mapping function has to be defined that is not necessarily always obvious.

V. NUMERICAL APPLICATION

We focus now on the following electrokinetic problem presented in figure 1. It is a cubic domain D_2 with a conductivity $\sigma_2 = 1 (\Omega.m)^{-1}$ with an edge length ($2a = 4m$). This domain surrounds another cube D_1 with random dimensions (l_1, l_2, l_3) with a conductivity $\sigma_1 = 10 (\Omega.m)^{-1}$. $l_1(\theta), l_2(\theta)$ and $l_3(\theta)$ are independent uniform random variable in the interval $[1; 1.5](m)$. On two opposite sides of the domain D_2 a voltage difference $V = 2$ (Volt) is prescribed. Since the dimensions of D_1 are random so does the energy.

We define a transformation $X = X(\theta, x)$ to transform the domain D into a domain E with $l_1 = l_2 = l_3 = 1m$. On the domain E , the conductivity is then random and given by (7). To determine the Jacobian transformation matrix (6), we divide the domain D into several sub-domains. We apply a linear transformation (dilation) in each sub-domain which leads to a constant Jacobian transformation matrix.

To study the problem, we use both the NIM and the MCSM. In MCSM, we use a sample of length 10000. With NIM we use an expansion of order 4 for the multivariate

Legendre polynomials. The Legendre Gauss quadrature method is used to calculate the coefficients of the polynomial expansions ($4^3 = 64$ points are calculated).

We compared the statistical moments of a global random variable (energy) given by the two methods. The statistical moments are reported in the Table I. We notice that the NIM gives statistical moments that belong to the 95% confidence interval obtained with the MCSM.

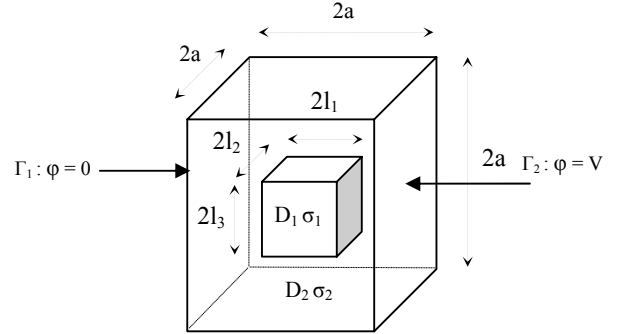


Fig. 1. Electro-kinetic system

TABLE I
MONTECARLO SIMULATION METHOD COMPARED WITH NON-INTRUSIVE METHOD

Information	Monte Carlo method (95% confidence interval)	Non-intrusive method
	Energy (J)	Energy (J)
Mean	[28.86 : 28.99]	28.91
Standard deviation	[3.34 : 3.42]	3.38
Skewness	[0.43 : 0.56]	0.49
Kurtosis	[2.40 : 2.69]	2.55

VI. CONCLUSION

We have presented a method to treat the problem with uncertainties on the geometric dimensions. This method consists in using a geometric transformation that allows transferring the randomness on the behavior law. The choice of the transformation is however a delicate point of this method. Further investigations should be undertaken to find and to specify this transformation in a simpler way.

VII. REFERENCES

- [1] Dongbin Xiu et Daniel M. Tartakovsky. *Numerical methods for differential equations in random domains*. SIAM J.SCI COMPUT. No 3, pp.1167-1185.
- [2] R.Gaignaire, S.Clenet, O.Moreau, and B.Sudret. *3D spectral stochastic finite element method in electromagnetism*. IEEE Trans.Magn. vol.43, no.4, pp. 1209-1212,2007.
- [3] R.Gaignaire, S.Clenet, O.Moreau, B.Sudret. *Current Calculation in Electrokinetics Using a Spectral Stochastic Finite Element Method*. Magnetics, IEEE Transactions Volume 44, Issue 6, June 2008 Page(s):754 - 757.
- [4] R. Ghanem, Spanos P.D, "Stochastic Finite Elements: A spectral approach", Dover, New York, 2003

Quality Evaluation of Automatically Generated Hexahedral Mesh for FEA

Yuichiro Motooka, So Noguchi, and Hajime Igarashi
 Graduate School of Information Science and Technology, Hokkaido University
 Kita 14 Nishi 9 Kita-ku, Sapporo, 060-0814, JAPAN
 noguchi@ssi.ist.hokudai.ac.jp

Abstract— We have previously proposed an automatic hexahedral mesh generator. It is necessary to understand about the quality and characteristic of mesh to perform hexahedral edge finite element analysis in electromagnetic. Therefore, we have compared high-quality mesh with poor-quality mesh, and investigated about the factors that affect the accuracy and the computation time. We will conclusively apply the result to improving the automatic hexahedral mesh generator.

I. INTRODUCTION

In order to perform a finite element analysis (FEA), the analysis domain has to be divided into finite elements. Hexahedral mesh has advantages over others at accuracy and speed. Therefore, we have previously proposed an automatic hexahedral mesh generator [1], [2]. The quality of mesh generated by the proposed mesh generator is affected by the smoother, i.e. the *Laplacian* smoothing in [2].

The quality and density of mesh are the most important factors to perform FEA in electromagnetic. In order to achieve highly accurate analysis and short computation time, a high-quality hexahedral mesh with graded mesh densities should be employed. In common, it is known that the regular hexahedral element is the best. However, the generation of mesh with only regular hexahedron is very difficult under various conditions. Therefore, we have to investigate about the characteristic of generated mesh.

In this paper, some evaluation functions are defined to check the element shape. It was investigated whether those evaluation functions correlate with the accuracy and the computation time. The result of this paper helps to improve the smoothing process in the proposed automatic hexahedral mesh generator [2].

II. EVALUATION METHOD

A. Orthogonality Evaluation

It is empirically known that the regular hexahedron and the rectangular parallelepiped are the high-quality element. Therefore, the orthogonality of element is an important factor. The orthogonality evaluation value ϕ is defined as follows:

$$\phi = \sum_{i=1}^N \phi_i / N, \quad \phi_i = \sum_{j=1}^{24} \phi_{ij} / 24, \quad \phi_{ij} = \cos^{-1}(\mathbf{e}_a \cdot (\mathbf{e}_b \times \mathbf{e}_c)), \quad (1)$$

where N is the number of elements, and \mathbf{e} is the unit vector along the edge, as shown in Fig. 1. When ϕ_i is 0 deg., the element is a rectangular parallelepiped. On the other hand, when ϕ_i is large, the element is distorted with poor quality.

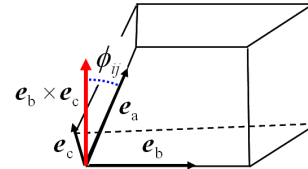


Fig. 1. Conceptual Illustration of Orthogonality Evaluation Method.

B. Planarity Evaluation

In the method proposed in [2], the conclusive position of nodes depends on the smoothing arrangement. Then, 4 nodes of a hexahedral facet might not be on plane. Therefore, the planarity evaluation function δ is defined as follows:

$$\delta = \sum_{i=1}^N \delta_i / N, \quad \delta_i = \sum_{j=1}^6 \delta_{ij} / 6, \quad (2)$$

$$\delta_{ij} = \frac{|(\mathbf{P}_b - \mathbf{P}_a) \cdot [(\mathbf{P}_c - \mathbf{P}_a) \times (\mathbf{P}_d - \mathbf{P}_b)]|}{|(\mathbf{P}_c - \mathbf{P}_a) \times (\mathbf{P}_d - \mathbf{P}_b)|^2}, \quad (3)$$

where \mathbf{P} is the located vector of the node, as shown in Fig. 2. When δ_i is large, the facet of the element is curved.

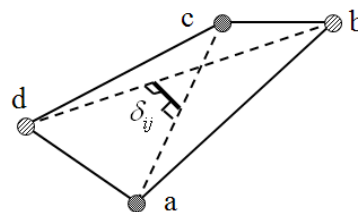


Fig. 2. Conceptual Illustration of Planarity Evaluation Method.

C. Diagonal Length Ratio Evaluation

The diagonal length ratio evaluates the distortion of element. The evaluation function of the ratio between the longest and the shortest diagonal of the element, λ , is defined as follows:

$$\lambda = \sum_{i=1}^N \lambda_i / N, \quad \lambda_i = 1 - \frac{l_{i,\max}}{l_{i,\min}}, \quad (4)$$

where l is the length of the diagonal, as shown in Fig. 3. When λ_i is large, the element is distorted.

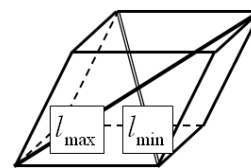


Fig. 3. Conceptual Illustration of Diagonal Length Ratio Evaluation Method.

D. Volume Ratio Evaluation

The ratio between the volume of the element and the cube, whose edge length is that of the longest edge of the element, is defined as the volume ratio evaluation ε . It is calculated as follows:

$$\varepsilon = \sum_{i=1}^N \varepsilon_i / N, \quad \varepsilon_i = 1 - \left(\frac{V_i}{h_i^3} \right)^{\frac{1}{3}}, \quad (5)$$

where h is the length of the longest edge and V is the volume of the element, as shown in Fig. 4. When ε_i is large, the element is flat or slender.

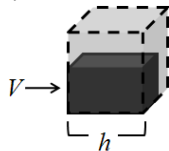


Fig. 4. Conceptual Illustration of Volume Ratio Evaluation Method.

III. EVALUATED MODEL AND MESHES

In this paper, a simple model consisting of a permanent magnet (1.0 T) and an iron is tested, as shown in Fig. 5. The ICCG is used as a solver. The properties of the generated mesh are shown in Table I. The Mesh (A) consists of only regular hexahedron, as shown in Fig. 6(a). For comparison, some distorted meshes are prepared. The Mesh (B) is generated by randomly moving the nodes of Mesh (A), as shown in Fig. 6(b). The Meshes (C) and (D) are generated by zigzag moving the nodes of Mesh (A) into z - and x -direction, respectively, as shown Figs. 6(c) and (d).

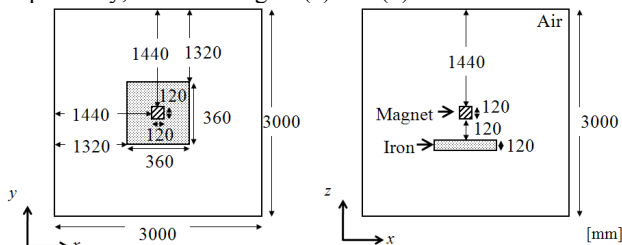


Fig. 5. Test Model consisting of a permanent magnet and an iron.

TABLE I
MESH PROPERTIES

Nodes	Elements	Edges of Unknown
438,976	421,875	1,232,100

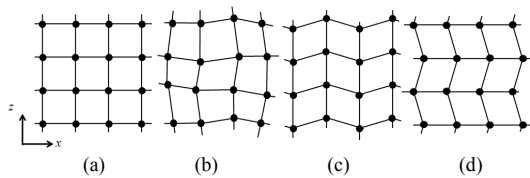


Fig. 6. Conceptual Illustrations of Meshes.

IV. EVALUATION OF MESH QUALITY

First, the convergence properties of ICCG are investigated, as shown in Fig. 7, where “Mesh (B)-5” means that the randomly moving distance of nodes is 5.0 mm at longest in Mesh (B). In Fig. 7(b), the degradation of convergence properties of Mesh (C) is prominence. Secondly, the

correlativity between the evaluation values of mesh quality and the number of ICCG iteration is investigated, as shown in Fig. 8, where the convergence criterion of ICCG is 1.0×10^{-6} . In Fig. 8(c), the diagonal length ratio is strongly correlated. Finally, the error of the solution is compared. The maximum error values are 0.0433 T at Mesh (B), 0.0374 T at Mesh (C) and 0.0215 T at Mesh (D) as compared with Mesh (A). All the solutions are accurate enough.

The mesh quality strongly affects the ICCG convergence. To decrease the diagonal length ratio λ leads to the speed-up. Therefore, in the smoothing process of the proposed mesh generator [2], the nodes should move so as to decrease the diagonal length ratio λ .

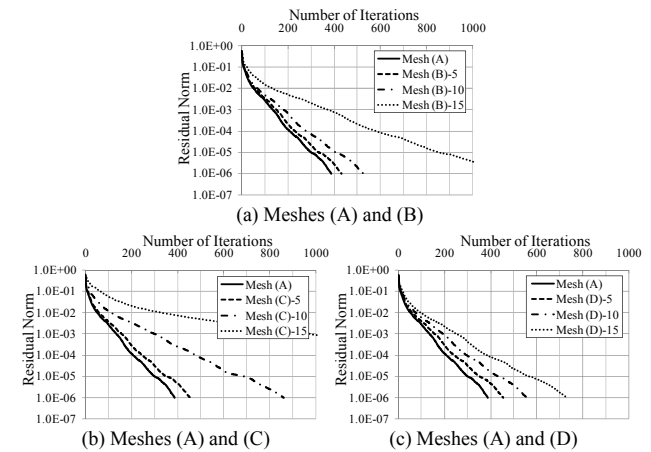


Fig. 7. ICCG Convergence Properties.

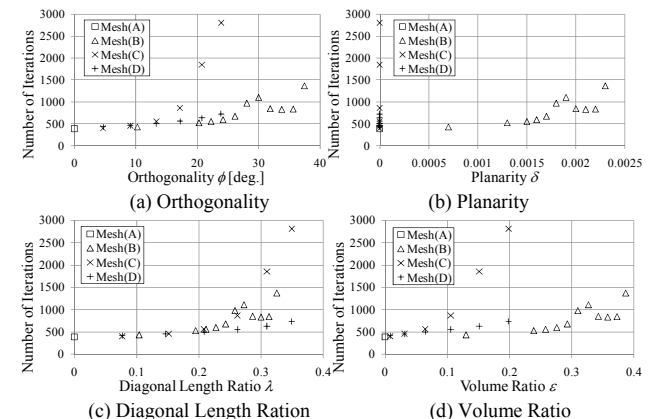


Fig. 8. Evaluation of Mesh Quality.

V. SUMMARY

It was clarified that the diagonal length ratio evaluation correlates with the ICCG convergence. In the future, the smoothing process in the proposed mesh generator [2] has to be developed to decrease the diagonal length ratio.

VI. REFERENCES

[1] S. Nagakura, S. Noguchi and H. Yamashita, “Automatic Hexahedral Mesh Generation for FEA Using Shape Recognition Technique and Tree Method”, *IEEE Trans. on Magnetics*, 38(2): 417-420, 2005.
 [2] H. Fujimori, S. Noguchi, H. Igarashi and H. Yamashita, “An Automatic Hexahedral Mesh Generation to Control Shape of Elements”, *IEEE Trans. on Magnetics*, 43(4): 1505-1508, 2007.

Parallel Sparse Matrix Solver on the GPU Applied to Simulation of Electrical Machines

Wendell O. Rodrigues
LIFL - USTL

Frédéric Guyomarc'h
LIFL - USTL

Jean-Luc Dekeyser
LIFL - USTL

Yvonnick Le Menach
L2EP USTL

INRIA Lille Nord Europe - 59650INRIA Lille Nord Europe - 59650INRIA Lille Nord Europe - 59650 Cité Scientifique Bat.P2 - 59655
Villeneuve d'Ascq - France Villeneuve d'Ascq - France Villeneuve d'Ascq - France Villeneuve d'Ascq - France
wendell.rodrigues@inria.fr frederic.guyomarch@inria.fr jean-luc.dekeyser@lifl.fr yvonnick.le-menach@univ-lille1.fr

Abstract—Nowadays, several industrial applications are being ported to parallel architectures. In fact, these platforms allow acquire more performance for system modelling and simulation. In the electric machines area, there are many problems which need speed-up on their solution. This paper examines the parallelism of sparse matrix solver on the graphics processors. More specifically, we implement the conjugate gradient technique with input matrix stored in CSR, and Symmetric CSR and CSC formats. This method is one of the most efficient iterative methods available for solving the finite-element basis functions of Maxwell's equations. The GPU (Graph Processing Unit), which is used for its implementation, provides mechanisms to parallel the algorithm. Thus, it increases significantly the computation speed in relation to serial code on CPU based systems.

I. INTRODUCTION

An electromagnetic field analysis is one of the most complex problems of physics. And, the modeling and simulation of electrical systems use a very large computational algorithms to solve their problems. One of this algorithms is based on the conjugate gradient (CG) method [2]. The CG method is an effective technique for symmetric positive definite systems. It is suitable for systems of the form $Ax=b$, where A is a known, square, symmetric, positive-definite matrix, x is a unknown solution vector and b is a known vector. Iterative methods like CG are suited for use with sparse matrices.

The solution of large, sparse linear systems of equations is the single most computationally expensive step. Thus, any reduction in the linear system solution time will result in a significant saving in the total process time. This need demands for algorithms and software that can be used on parallel processors.

This paper describes the use of the GPU as platform to implement a CG method to solve a linear system. The sample inputs are matrix stored in Symmetric CSR (compressed sparse row) [2] format obtained from a simulation of electric machines. The algorithms use standard BLAS library and two implemented kernels for matrix-vector product (SpMV). The next section describes the GPU which is the platform used and how to program it with CUDA. Section 3 depicts the matrix used and how to implement the solver. A execution performance is discussed in following section. Finally, some concluding remarks are made about obtained results.

II. GPU

GPU (Graphics Processing Unit) is a manycore processor attached to a graphics card dedicated to calculating floating point operations. Even if GPUs are a manycore processors, their parallelism continues to scale with Moore's law. It is necessary to develop application software that transparently scales its parallelism. CUDA (Compute Unified Device Architecture) [3] is a parallel programming model and software environment designed to overcome this challenge while maintaining a low learning curve for programmers familiar with standard programming languages such as C.

A. Processor Architecture

The GPU devotes more transistors to data processing rather data caching and flow control. This is the reason why the GPU is specialized for compute intensive. NVIDIA GPU, specifically, is composed of array of SM(Streaming Multiprocessors), each one is equipped with 8 scalar cores (the SP or Streaming Processors), 16834 32-bit registers, and 16KB of high-bandwidth low-latency memory shared for up to 1024 co-resident threads. GPUs such as the NVIDIA GeForce GTX 280 contain 30 multiprocessors, so 30K threads can be created for a certain task. Further, each multiprocessor executes groups, called *warps*, of 32 threads simultaneously.

B. Memory Architecture

In the NVIDIA GPU memory model, there are per-thread local, per-block shared, and device memory which comprehends global, constant, and texture memories. Shared Memory can be only accessed by threads in the same block. Because it is on chip, the Shared Memory space is much faster than the local and Global Memory spaces. But only 16KB of shared memory are available on each SM.

C. CUDA Programming Model

CUDA is a C language extension developed by NVIDIA to facilitate writing programs on GPUs. It allows the programmer to define C functions, called *kernels*, that, when called, are executed N times in parallel by N different *CUDA threads*, as opposed to only once like regular C functions. One of the main features of CUDA is the provision of a Linear Algebra library(CuBLAS) and an Fast Fourier Transform library

(CuFFT) [3]. The next section describes the implementation of CG on the GPU and the use of CuBLAS library.

III. IMPLEMENTATION

The Conjugate Gradient was applied to 30880x30880 symmetric sparse matrix A with 449798 nonzero double precision elements. It is stored in full or symmetric CSR format files which include the unknown elements vector x and the result vector b . The CG algorithm used to implement the program is below.

Require: init variables

- 1: **for all** k such that $1 \leq k \leq N$ **do**
- 2: $\alpha \leftarrow \frac{(r^T r)}{(p^T A p)}$
- 3: $x \leftarrow x + \alpha p$
- 4: **break if convergence**
- 5: $r \leftarrow r - \alpha A p$
- 6: $\beta \leftarrow \frac{(r_k^T r_k)}{(r_{k-1}^T r_{k-1})}$
- 7: $p \leftarrow r + \beta p$
- 8: **end for**

All the internal loop operations are executed on GPU. The scalar product and $axpy$ functions on lines 3,5,7 use CuBLAS functions. Since BLAS is only for dense matrix, naturally it is necessary to create a *CUDA kernel* for sparse matrix. For that reason, a SpMV algorithm for matrix-vector multiplication should be implemented to execute the $A p$ product on line 2. Let $A = (L + D + U)$, where D is the main diagonal part of A , L is its strictly lower triangular part and U is its strictly upper triangular part. Since A is symmetric, $U^T = L$. Thus, A can be stored in CSR format of $(L + D)$.

Three algorithms were implemented in this work. The first one is a trivial solution of $y = Ax$ in which each thread executes $y[tid] += A[i-1] * x[jA[i-1] - 1]$, where tid is the thread identify, and $[i,jA]$ are obtained from vectors of the stored matrix. The two other solutions explore the symmetry characteristic. The aim is to cut down the time and memory allocation cost. The figure 1 shows the procedure of algorithm conception. The *kernels* are composed of blocks and each block has certain threads. Only one kernel can execute in same time on same device and there are a few blocks in execution simultaneously in each SM. Sequentially the *kernel 1*(SCSR) and *kernel 2*(SCSC) are executed and they take care of $L + D$ and U respectively. To avoid writing conflicts on y vector in global memory, the *kernel 2* calls *atomic functions* and that allows just one thread write in a memory address at given moment. As the number of elements of a column or a row can be greater than the number of threads in a block, it is necessary that the algorithm calculates the quantity of elements for each thread.

IV. RESULTS

A double precision version of CG was created on a contemporary conventional CPU and this one was used as a reference to calculate the speed-up. Two other versions were developed on the GPU. The first one is a single precision version which was tested on a NVIDIA Tesla C870 card. The second one is

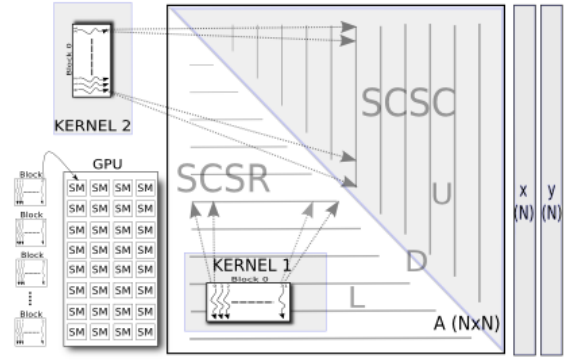


Fig. 1. SpMV on Symmetric CSR and CSC storage format

a double precision version which was executed on a NVIDIA GeForce GTX 280.

The matrix reading from files takes time to be done properly. Approximately 6ms in our tests. Because this operation is basic for all experiments, it is not necessary to evaluate it. It is important to examine the *Scalar Product*, *AXPY*, and *SpMV* execution time because these functions are called repetitively in each loop interaction. Yet, all the time that the interactive CG loop takes. The table I shows the operations and their respective spent time values. The application not use the *sym SpMV*, its times are there just for benchmarking.

TABLE I
SPEED-UP RESULTS

Operation	CPU Time	Single Prec. C870	Double Prec. GTX280
dotProd	0.290ms	0.529ms	0.450ms
AXPY	0.109ms	0.014ms	0.008ms
SpMV	5.966ms	0.013ms	0.005ms
SpMV(sym)	-	0.040ms	0.035ms
CG/ # int	2392ms/328	400ms(5.8x)/324	370ms(6.4x)/323

V. CONCLUSION

This approach issues the viability of using GPU on sparse matrix solvers. The obtained results allow us to evaluate two important impacts in finite-element method of Maxwell's equations using Conjugate Gradient algorithm. The first one is concerned to speed gain. On the GPU, the CG arrives faster than on the CPU due its parallel architecture. The second one is the impact of storing symmetric matrix in memory. Although it can store in memory almost half of the matrix, the performance of algorithm decreases as shown in table of speed-up results. This is due the repetitive way that the *kernel* computes and accumulates the $y = Ax$ result. However, both cases contribute significantly to accelerate the computation of basis functions.

REFERENCES

- [1] A. Bossavit. *Computational Electromagnetism*, Hardcover. Academic Press, 1998
- [2] Y. Saad. *Iterative methods for sparse linear systems*, 3rd ed., 2000.
- [3] NVIDIA CUDA Compute Unified Device Architecture Version 2.0. NVIDIA corporation, 2008

Design of Conventional C-core Magnets Using a Multi-Step Optimization Procedure

Felipe Campelo^{1,2}, Jaime A. Ramírez² and Hajime Igarashi¹

¹Laboratory of Hybrid Systems, Hokkaido University, Sapporo 060-0814, Japan.

²Departamento de Engenharia Elétrica, Universidade Federal de Minas Gerais, Belo Horizonte 31720-901, Brazil.

We consider, in this work, the design of conventional C-core magnets for particle accelerators, focusing primarily on the shape design of the iron core. We propose an integrated technique that uses topology and parameter optimization, which are connected by a model generation module. Specific characteristics of this kind of device are also considered in the definition of the final shape, particularly in the final parameterization of the pole shape.

Index Terms—C-core magnet, multi-step optimization, electromagnetic design.

I. INTRODUCTION

Conventional C-core dipole magnets are important components in the design of some particle accelerators, where this kind of device is employed for changing the trajectories of charged particle beams [1]. Such devices usually consist of one or more excitation coils, or in some cases, permanent magnets, placed around a C-shaped core, hence the name, of ferromagnetic material, shaped in a way such as to provide a highly homogenous magnetic field within a certain region where the charged particles are to pass. Particles moving at high speeds through this region are subject to the magnetic component of the Lorentz force,

$$\mathbf{F} = q(\mathbf{v} \times \mathbf{B}) \quad (1)$$

where \mathbf{F} is the force vector, q and \mathbf{v} are respectively the charge and speed vector of the particle, and \mathbf{B} is the magnetic flux density vector. The trajectories of the particles are bent perpendicularly to their speed and the direction of the field, and a ring arrangement of several magnets is capable of maintaining the particle beam in a stable circular trajectory.

Despite the lower field intensities of conventional electromagnets, when compared to the more impressive superconducting ones, conventional, copper-coil C-core magnets still provide an interesting alternative to the superconducting solution. First, the costs involved in building, maintaining, operating, and replacing conventional magnets are sensibly smaller than those of a superconducting one; also, in cases where multi-Tesla magnetic fields are not required, conventional C-core magnets are capable of providing the intensities and performance needed. One such example is the Large Electron-Positron (LEP) collider from CERN, predecessor to the current Large Hadron collider (LHC) [1], with its 3,280 dipole magnets. Better designs for C-core dipoles can, therefore, lead to cheaper or more efficient particle accelerators, two interesting goals for organizations developing such experiments.

Manuscript received April 6th, 2009.

Corresponding Author: F. Campelo (pinto@em-si.eng.hokudai.ac.jp)

This work was supported by the Ministry of Education, Culture, Sports, Science and Technology of Japan.

II. DESIGN REQUIREMENTS

It is regarded that one of the most important requirement of a C-core dipole in an accelerator is field homogeneity within the target region (see figure 1), which must be within a few parts per million in order to keep the particles in stable trajectories. Matematically, the design problem can be stated as:

$$\begin{aligned} \text{minimize: } f &= \frac{\max(|\mathbf{B}_m - \mathbf{B}_{ref}|)}{10^{-6}} + V_{core} \\ \text{subject to: } \max|\mathbf{B}_m - \mathbf{B}_{ref}| &\leq 10^{-5} \end{aligned} \quad (2)$$

where \mathbf{B}_m and $\mathbf{B}_{ref} = [0.0, 0.13]^T$ are respectively the observed and ideal magnetic flux densities within the target region (in Tesla); and V_{core} is the observed volume (in m^3) of the variable portion of the core, figure 1. While the reduction of the volume is not an essential requirement in this particular problem, a volume term is included in the objective function as a regularization term.

In this particular design case, the core is manufactured as series of laminated low-carbon steel plates embedded in cement mortar, following the LEP design [2]. The excitation of the magnet is provided by two solid copper bars carrying a total current of 4480A. A detailed description of the device, along with the specifications of all materials used, will be provided in the full paper.

III. DESIGN PROCEDURES

In order to obtain an optimal shape for the magnet core a multi-step optimization procedure [3] is performed. These design steps are briefly presented in this section, and will be discussed in depth in the full paper.

A. Topology optimization

The design process starts with the topology optimization (TO) step to find a rough estimate of the size and shape of material required for the fulfillment of the design requirements. An evolutionary TO algorithm [3] is, then, applied on the design model shown in figure 1, in order to obtain a good initial distribution of steel within the L-shaped *design region*.

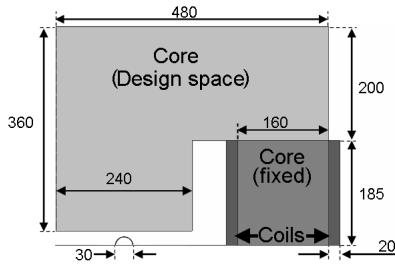


Fig. 1. Design layout (upper half) for the C-core dipole magnet, showing the fixed and variable portions of the core, the coils, and the design region (30mm half circle under the magnet pole). This device presents linear symmetry, with a depth of 3000mm. All units are in millimeters.

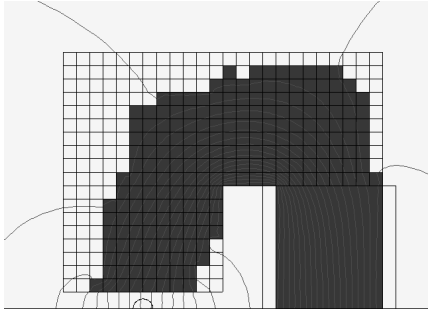


Fig. 2. Rough shape obtained after topology optimization

B. Shape refinement

The result obtained by the topology optimization algorithm is used to generate a parametric model of the device, in order to allow for further refinement of the shape. The parameterization of the TO result is done by means of an automated feature-recognition routine, based on simple edge- and corner-detection techniques [3]. This parameterization routine is able to represent the shape obtained by the TO process by means of a series of connected lines and Bézier splines.

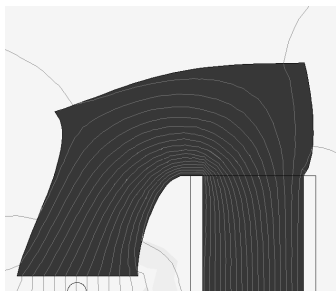


Fig. 3. Core shape after parameterization and parametric shape optimization.

The parametric model is, then, optimized by means of a regular evolutionary algorithm, yielding the shape shown in figure 3.

C. Pole Design

It has been shown that optimal pole shapes for C-core dipoles present shims in order to compensate for the effects of finite pole length. Following the recommendations given by Russenckuck [1], the dimensions of the pole shims were

obtained by means of numerical algorithm, in this case an evolutionary method. The final pole shape obtained is shown in figure 4.

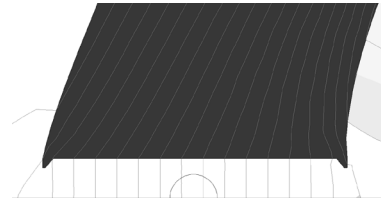


Fig. 4. Detailed view of the pole after shim optimization.

Table I describes the characteristics obtained at the end of each step in the design process for the device of interest.

TABLE I
RESULTS OBTAINED AFTER EACH STEP OF THE DESIGN PROCESS

	$\max \mathbf{B}_m - \mathbf{B}_{ref} $ [T]	V_{core} [m ³]
Topology Optimization	2.11×10^{-5}	0.2532
Shape refinement	1.68×10^{-5}	0.2762
Pole design	1.25×10^{-5}	0.2764

The results in Table I show that the use of a multi-step design methodology was able to yield progressively better characteristics for this particular device, considering the magnetic field characteristics that are the main focus of the current design procedure. While the final result obtained after the optimization of the pole shims is still slightly over the $10\mu T$ threshold, this small constraint violation should be within the tolerance limits for the intended application. The full paper will discuss the results in greater depth.

IV. CONCLUSIONS

In this paper the design of a conventional C-core dipole magnet was considered. A multi-step optimization procedure was employed, including the initial topological design; the parameterization of the topology obtained; the refinement of the parametric model; and the determination of the pole shims. The characteristics obtained at each of the design steps illustrate the potential of this multi-step methodology to generate progressively better designs for the dipole under consideration. A discussion on the manufacturability of the shapes obtained and on the optimization techniques employed are included in the full paper.

REFERENCES

- [1] S. Russenckuck, "Electromagnetic design of accelerator magnets", *CERN Internal report*, 2006. Accessed on Nov. 15th, 2008, from: <http://documents.cern.ch/cgi-bin/setlink?base=yellowarticle&categ=2006-002&id=p411>
- [2] M. Giesch, J. P. Gourber, "The bending magnet system of LEP", *Proceedings of the 11th International Conference on Magnet Technology*, Tsukuba, Japan, August 1989.
- [3] F. Campelo, "Evolutionary design of electromagnetic systems using topology and parameter optimization", Ph.D. Thesis, Graduate School of Information Science and Technology, Hokkaido University, Japan, January 2009.

Self-consistent Optimization of Multi-Quantum Well Structures by a Genetic Algorithm

Angelo Passaro, Roberto Y. Tanaka, Ademar Muraro Jr, Gustavo S. Vieira, Nancy M. Abe
 Instituto de Estudos Avançados - Comando-Geral de Tecnologia Aeroespacial
 Rodovia dos Tamoios, km 5.5, S.J.Campos, 12228-001, Brazil
 angelo@ieav.cta.br

Abstract — This work presents a self-consistent optimization approach of multi-quantum well structures. A Genetic Algorithm meta-heuristic is used for the search mechanism. The computer code, based on the solution of both the Poisson and the Schrödinger equations self-consistently by using the Finite-Element Method, obtains the characteristics of each individual. The results of two tests are presented and discussed.

I. INTRODUCTION

Commercial CAD tools for simulating semiconductor devices usually do not deal with the quantizing effects of nanometric heterostructures. When they deal with heterostructures, they do it in a quite limited way. A number of commercially available or developing devices, such as quantum-well infrared photodetector [1], QWIP, quantum dot infrared photodetector [2], QDIP, and quantum cascade laser [3], QCL, depend on a detailed design of its band structure, in what has become known as band engineering [4]. Many structures of academic interest have also been intensively studied, in the past decades, improving the understanding of fundamental physics involved in such devices [5]-[9]. Since many of the used heterostructures have free charges from doping, a more precise calculation of the quantum levels should include the effect of charge distribution, solving the Poisson and Schrödinger equations self-consistently.

More recently, computational optimization techniques have been used to the design of nanostructured semiconductor devices. A brute force technique was employed to optimize an InGaAsN/GaAs multi-quantum well structure, MQW, in order to obtain a QCL of high operation frequency [3]. The simulated annealing meta-heuristic was used to maximize the optical rectification of an AlGaAs/GaAs MQW, varying the Al concentration of each barrier [10].

In this work, we present the optimization of MQW structures by using the Genetic Algorithm meta-heuristic, GA.

II. OPTIMIZATION APPROACH

The design optimization is an iterative process in which candidate solutions are successively generated by an optimization, or search, algorithm and evaluated by an analysis tool.

In this work, the GA selects tentative solutions, i.e., design parameters of the quantum wells that are responsible for specific characteristics of the structure. Each design parameter is represented by a binary code and the number of bits of this code is associated to the search space of the parameter. The binary codes of each design parameter are appended one after another to form the individual, or chromosome. The individuals of the initial population are

generated randomly. The core of the optimization tool used in this work has been used in the optimization of electrooptic modulators and of electrooptic sensors [11].

When analyzing periodic semiconductor MQW, the calculation of energy levels without taking into account charge redistribution usually gives reasonable results [8],[9], since the changes in the relative energy position of the subbands are not dramatic. Otherwise, if the periodicity is broken with a well of different width, charge separation increases and a self-consistent calculation becomes essential even for a qualitative understanding of electrical dynamics in the structure [12]. In this work, the analysis tool is based on the Finite Element Method, FEM, and solves the Poisson and Schrödinger equations self-consistently. The complete formulation is presented in [13] and the computational tool we developed was already presented in [14]. This tool is already in use for research purposes [12], [15].

III. RESULTS

In this section, results from two cases are presented. The genetic operators used in the test cases are: elitism of one individual, the roulette wheel technique for the reproduction operator with one crossover point chosen randomly, the occurrence probability for the crossover is set to 0.8 and for the mutation is set to 0.05.

The first case is a very simple problem: a symmetric heterostructure of GaAs/Al_xGa_{1-x}As, composed by two wells surrounding a third, larger one. A doped barrier is allowed between the external wells and the substrate. Fig. 1 illustrates the structure. In a periodic MQW, the current at low bias is believed to occur via tunneling between the first subband of adjacent wells [9],[8]. A larger well introduced in the structure should generate a charge accumulation and consequently a potential increase. The final subband alignment between the larger well and neighbor wells is important for understanding the charge transport in the structure.

The exercise is to choose design parameters to obtain a symmetric structure in which the energy of the second subband of the central well, E_{2c} , is equal to the energy of the first subbands of the right and left lateral wells, E_{1r} and E_{1l} . The objective function is given by:

$$F = |E_{2c} - E_{1l}| - \alpha * |E_{1l} - E_{1r}| \quad (1)$$

where α is a constant. Therefore, we try to minimize the difference among the energy of these subbands. As additional constraints, we impose that the structure has to be symmetric in terms of the thickness of the layers with respect to the central one. Also, all barriers must have the same concentration of aluminum. The doping concentration can be

different in each well and barrier. Additional penalty is imposed if there is less than 2 subbands in the central well. The range of variation of each design parameter is:

$$\begin{aligned} 0.2 \leq x \text{ (aluminum concentration)} &\leq 0.5, \\ 1 \text{ nm} \leq \text{thickness of the lateral well} &\leq 10 \text{ nm}, \\ 10 \text{ nm} \leq \text{thickness of the central well} &\leq 50 \text{ nm}, \\ 5 \text{ nm} \leq \text{thickness of the inner barriers} &\leq 10 \text{ nm}, \\ 1 \text{ nm} \leq \text{thickness of the doped external barriers} &\leq 5 \text{ nm}, \\ 10^{15} \text{ cm}^{-3} \leq \text{doping concentration} &\leq 9.0 \times 10^{16} \text{ cm}^{-3} \text{ or zero, and} \\ \text{thickness of the non doped substrate layer} &= 50 \text{ nm}. \end{aligned}$$

Fig. 1 shows the best individual obtained after 100 generations of 26 individuals each. As expected, the best individual presents almost a symmetric doping concentration.

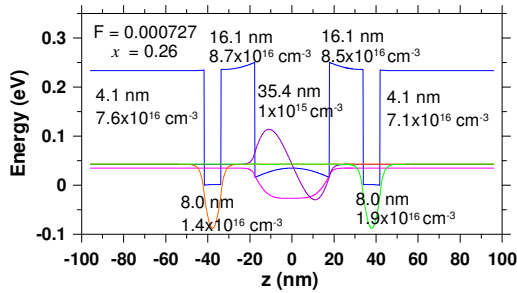


Fig. 1. The best solution is almost symmetric in terms of the doping concentration.

The second case is also a symmetric structure, a MQW composed by ten identical internal wells, surrounded by larger wells. The larger well aims to simulate the effect of the electric contact on MQW structures, which is an acceptable approximation if the number of subbands confined is high enough. In this case, the objective is to obtain a structure in which the energy of the first subband of each internal well, E_i , is as close as possible to the Fermi energy, E_F :

$$F = \sum_{i=1}^n |E_i - E_F| \quad (2)$$

where n is the number of inner quantum wells. In this example, $n = 10$. The alignment is a necessary condition to obtain a device presenting a quasi-ohmic behavior when submitted to low (quasi-zero) voltages.

In this case the aluminum concentration, the thickness of the non doped substrate layer, the thickness of the inner barriers, and the thickness of the inner wells are kept constant. The range of variation of the other design parameters is:

$$21 \text{ nm} \leq \text{thickness of the lateral wells} \leq 50 \text{ nm}, \\ 10^{16} \leq \rho_{in} \leq 9.9 \cdot 10^{18} \text{ cm}^{-3} \text{ or zero, and } \rho_{in} \leq \rho_{la} \leq 9.9 \cdot 10^{18} \text{ cm}^{-3},$$

where ρ_{in} and ρ_{la} are the doping concentration of the inner wells of the lateral wells, respectively.

Fig. 2 shows one of the best solutions found that minimizes the objective function (2). The contact layers (the larger wells) are strongly doped with respect to the MQW inner structure.

The main objective of the test was to verify the convergence of the GA for this problem. The test is very hard, because the self-consistent computation converges rapidly when doping concentrations are lower than $5.0 \cdot 10^{17} \text{ cm}^{-3}$, but the time of convergence increases for higher doping

concentrations and it is very high for concentrations about 10^{18} cm^{-3} .

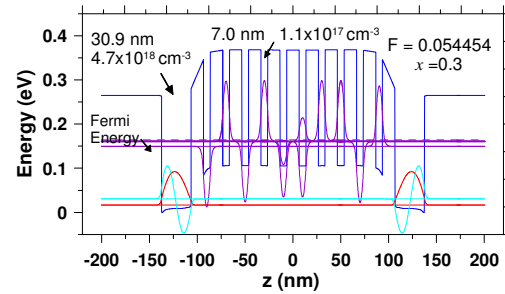


Fig. 2. One of the best solutions obtained.

IV. FINAL COMMENTS

The module of optimization of nanostructured semiconductors based on quantum wells is operational and in the early stage of testing. The optimizations process was executed in a distributed computational environment with up to nine processing units. Nowadays, the main effort is to improve the convergence process of the self-consistent computation for structures with high doping concentrations, characteristic desired for the design of QWIPs. In the next steps, we intend to optimize structures minimizing or maximizing some features of interest for QWIPs.

V. REFERENCES

- [1] B. F. Levine, "Quantum-well infrared photodetectors", *J. Appl. Phys.*, 74 (8):1-81, 1993.
- [2] V. Ryzhii, "The theory of quantum-dot infrared phototransistors", *Semicond. Sci. Technol.*, 11(5): 759-765, 1996.
- [3] J. R. Freeman et al, "Improved wall plug efficiency of a 1.9 THz quantum cascade laser by an automated design approach". *Appl. Phys. Lett.*, 93, 191119, 2008.
- [4] F. Capasso, "Band-gap engineering via graded gap, superlattice, and periodic doping structures: Applications to novel photodetectors and other devices", *J. Vacuum Sci. Technol. B*, 1(2): 457-461, 1983.
- [5] L. L. Chang, L. Esaki, and R. Tsu, "Resonant Tunneling in Semiconductor Double Barriers", *Appl. Phys. Lett.*, 24, 593, 1974.
- [6] L. Esaki and L. L. Chang, "New Transport Phenomenon in a Semiconductor "Superlattice", *Phys. Rev. Lett.*, 33(8), 495-498, 1974.
- [7] Sbmicro 8. F. Capasso, K. Mohammed, and A. Y. Cho, "Sequential resonant tunneling through a multi-quantum well superlattice," *Appl. Phys. Lett.*, 48, 478, 1986.
- [8] K. K. Choi, et al, "Periodic negative conductance by sequential resonant tunneling through an expanding high-field superlattice domain," *Physical Review B* 35: 4172-4175, 1987.
- [9] G. S. Vieira, et al, "Resonantly enhanced photon-assisted tunneling in a multiple-quantum-well superlattice," *Phys. Rev. B* 58: 7136-7140, 1998.
- [10] J. Radovanovic, et al, "Global optimization of semiconductor quantum well profile for maximal optical rectification by variational calculus," *Semiconductor Science and Technology*, 17: 716-720, 2002.
- [11] Muraro Jr., et al., "Design of Electrooptic Modulators using a Multiobjective Optimization Approach," *Journal of Lightwave Technology*, 26(16): 2969-2976, 2008.
- [12] W. H. M. Feu, et al, "Current bi-stability in a weakly coupled multi-quantum well structure: a magnetic field induced "memory effect", *Journal of Physics D*, to be published in 2009
- [13] L. R. Ram-Mohan, K. H. Yoo, and J. Moussa, "The Schrödinger-Poisson Selfconsistency in Layered Quantum Semiconductor Structures", *J. Appl. Phys.* 95: 3081-3092, 2004
- [14] R. Y. Tanaka, et al., "Self-Consistent Analysis of Quantum Well Based Structures." *Proc. 13th Biennial IEEE Conference on Electromagnetic Field Computation, CEFC2008*, pp.550, 2008.
- [15] R. Y. Tanaka, et al., "A self-consistent analysis of subband alignment in a superlattice with one larger well", submitted to ISEM2009.

Impact of Wave Propagation Effects in Electrical Tomography

M. Neumayer and G. Steiner

Institute of Electrical Measurement and Measurement Signal Processing
Graz University of Technology, Kopernikusgasse 24/IV, A-8010 Graz, Austria
Email: neumayer@tugraz.at

Abstract—Algorithms and methods to solve inverse problems in Electric Field Tomography (EFT) often use a quasi-static model assumption. At higher measurement frequencies where wave propagation effects appear these simplifications of the model could lead to corrupted reconstruction results. In this work we investigate the impact of unmodeled physical effects in electrical impedance tomography. We recapitulate physical considerations about the emerge of wave propagation effects and perform simulations to verify these results.

I. INTRODUCTION

The usability of electric fields for industrial and medical tomography applications is commonly known and for a longer period a field of applied and theoretical research. By measurements of electrical impedances these methods aim at the reconstruction of the spatially distributed electrical material parameters and present them as an image. Typically the electric conductivity σ or the relative permittivity ϵ_r are reconstructed. Also methods that evaluate the both quantities together have been implemented [1], [2]. These methods aim at the complex impedance $\sigma + j\omega\epsilon_0\epsilon_r$ which is appropriate if the ohmic current and the displacement current are in the same order of magnitude. For the physical modeling of the problems in most cases an elliptic differential equation for the electric scalar potential is used. However, in the case of high working frequencies also wave propagation effects could appear. If these effects are not negligible in their amplitude the relatively simple models fail and a loss in the quality of the reconstruction results has to be expected. In this paper we investigate the physical effects within the sensor and give a statement about the choice of a model. For this we recapitulate the theoretical background and compare our considerations with previous results. We perform field simulations to compare the electrical quantities of different models and monitor the impact of un-modeled physical effects on reconstruction tasks.

II. SENSOR SETUP

Figure 1 depicts a possible hardware scheme for complex electrical impedance tomography. 16 electrodes are mounted equidistantly on the exterior of a plastic pipe. The sensor is based on current measurements which means that the electrical potential on the electrode is fixed. It is aimed to reconstruct material distributions with relative permittivities up to $\epsilon_r = 80$ and conductivity values of about $\sigma = 0,2 \text{ Sm}^{-1}$ (saline water). The measurement frequency of the sensor is 40 MHz. For this

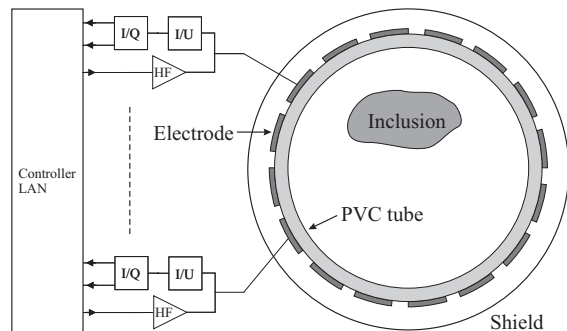


Fig. 1. Schematic of the sensor system.

frequency σ is in the same order of magnitude as $\omega\epsilon_0\epsilon_r$, which is a precondition for complex impedance tomography [3].

III. PHYSICAL CONSIDERATIONS ABOUT WAVE PROPAGATION

A decision rule for the consideration of wave propagation is given by [3]

$$\omega\mu\sigma L_c \left(1 + \frac{\omega\epsilon}{\sigma}\right) \ll 1, \quad (1)$$

where L_c is defined as a characteristic distance over which the electric field \vec{E} varies significantly. If equation (1) is satisfied then a quasi-static formulation can be used. From transmission line theory it is known that a criterion for the occurrence of wave propagation effects is given by the ratio of object size to wavelength λ . Typically at a ratio of one over ten of object size to wavelength it is said, that wave propagation effects can not be neglected. The wavelength λ of an electromagnetic wave can be calculated by the complex propagation constant

$$p = \sqrt{j\omega\mu(\sigma + j\omega\epsilon)} = \alpha + j\beta, \quad (2)$$

which ends up in

$$\lambda = \frac{2\pi}{\beta} = \frac{2\pi c}{\omega} = \frac{2\sqrt{2}\pi}{\sqrt{\omega\mu(\sqrt{\sigma^2 + \omega^2\epsilon^2}) + \omega\epsilon}}. \quad (3)$$

Table I lists the results of the left hand side of equation (1) and (3) for different materials. The parameter L_c has been set to $L_c = 0,01 \text{ m}$. This value was found by the evaluation of field simulations. The results in table I give a hint that already for distilled water wave propagation effects should not be neglected.

TABLE I
WAVELENGTHS AND THE LEFT HAND SIDE OF EQUATION (1) FOR DIFFERENT FILLINGS AT A FREQUENCY OF $f = 40$ MHz ($\mu_r = 1$).

Nr.	Filling	σ Sm ⁻¹	ϵ_r 1	λ m	Equation (1) 1
1	Air	0.0	1	7.49	0.007
2	Distilled water	0.0	80	0.84	0.562
3	Saline water	0.2	80	0.75	1.194
4	Sea water	5	80	0.22	16.354

IV. FIELD SIMULATIONS

To give precise statements about the appearance of wave propagation the sensor has been modeled with a finite element software tool. For a saline water filled sensor ($\sigma = 0,2 \text{ Sm}^{-1}$, $\epsilon_r = 80$) a quasi-static and a full simulation of the Maxwell's equations have been performed for a shielded and a unshielded sensor. Figure 2 depicts the ratio of the induced current density to the potential driven current density in the interior of the sensor. One can see that the induced current density is almost a tenth of the potential driven current density. The impact sounds not to be negligible. Bode diagrams figured a first significant spread between the quasi-static and the full simulations at a frequency of 30 MHz.

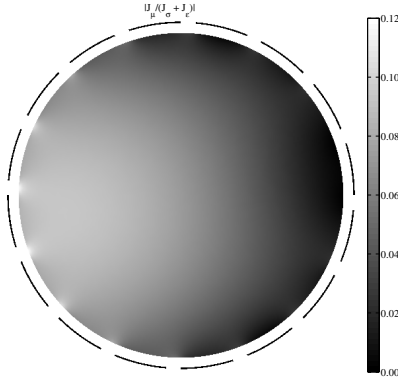


Fig. 2. Ratio of the induced to the potential-driven current for a saline water ($\sigma = 0,2 \text{ Sm}^{-1}$, $\epsilon_r = 80$) filled sensor at $f = 40$ MHz.

V. RECONSTRUCTION ALGORITHM

For the reconstruction a Gauss-Newton formulation is used. The inverse problem is solved by

$$\arg \min_{\sigma, \epsilon_r} \mathbf{r}_c^H \mathbf{r}_c + \alpha_\sigma \|\mathbf{L}\sigma\|_2^2 + \alpha_{\epsilon_r} \|\mathbf{L}\epsilon_r\|_2^2, \quad (4)$$

where \mathbf{r}_c denotes the complex-valued residual vector. The vectors σ and ϵ_r contain the material values of the finite elements which are in the interior of the pipe. The parameters α_σ and α_{ϵ_r} are regularization parameters. A detailed description of the algorithm and the used calibration method can be found in [2].

VI. RECONSTRUCTION RESULTS

Figure 3 depicts the result of a reconstruction task for a material distribution of two oil bubbles ($\sigma = 0 \text{ Sm}^{-1}$, $\epsilon_r = 2$)

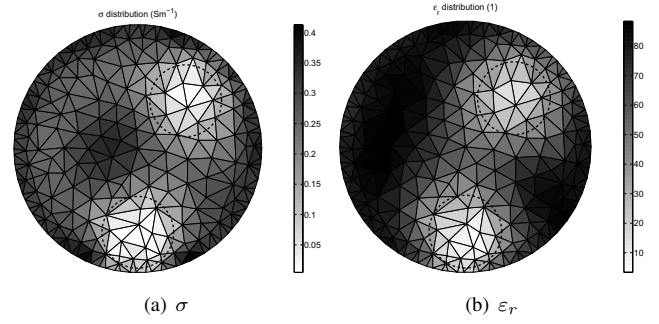


Fig. 3. Reconstruction of the measurement data obtained by a simulation of the full Maxwell's equations.

within saline water ($\sigma = 0,3 \text{ Sm}^{-1}$, $\epsilon_r = 80$). The positions of the two inclusions are marked by dashed circles. The measurement data was obtained by a full simulation of the Maxwell's equations. By defining the error measure

$$\epsilon_x = \frac{\int_{\Gamma} |x_{Wave} - x_{Qstat}| d\Gamma}{\int_{\Gamma} |x_{Qstat}| d\Gamma} \times 100, \quad (5)$$

the impact of wave propagation effects amounts $\epsilon_\sigma = 8,89\%$ and $\epsilon_{\epsilon_r} = 7,87\%$ compared to a reconstruction of measurement data which was obtained by a quasi-static simulation.

VII. CONCLUSION

Although the obtained reconstruction result looks quite accurate an appreciable difference appears. To demonstrate the impact of unmodeled effects a synthetic setting of calibration and measurement data has been used. In the normal case better reconstruction results can be achieved as all measurements imply the same characteristics. The results about the appearance of wave propagation in section III are a hint that wave propagation effects should not be neglected. Especially equation (1) suggests an evidence for wave propagation effects. An explanation for the small impact in the reconstruction results is the geometry of the sensor. Considerations about wave propagation are typically for free space propagation. Due to the large cover angle of the electrodes the sensor is nearly completely screened. The results of the simulations of the unshielded sensor confirm this. The shielding causes a suppression of wave propagation effects. Conventional rules of thumb for a prognosis of the model have therefore be handled carefully. In combination with a suitable calibration an expansion of the frequency range or the dimensions of the sensor should be possible by a retention of a quasi-static model.

REFERENCES

- [1] K. Hollaus, C. Gerstenberger, C. Magele, and H. Hutten. Accurate reconstruction algorithm of the complex conductivity distribution in three dimensions. *Magnetics, IEEE Transactions on*, 40(2):1144–1147, March 2004.
- [2] M. Neumayer and G. Steiner. Industrial process tomography for complex impedance. In *Proceedings of the 13th International IGTE Symposium on Numerical Field Calculation in Electrical Engineering*, Graz, Austria, September 2008.
- [3] Marko Vauhkonen. *Electrical impedance tomography and prior information*. PhD thesis, University of Kuopio, 1997.

Optimal Design of Electromagnetic Valve Actuator using Generic Algorithm

Jinho Kim¹, Junghwan Chang² and Kyuyoung Han³

¹School of mechanical engineering, Yeungnam University, Gyeongsan, Gyeongbuk, Korea

²Department of electrical engineering, Dong-A University, 840 Hadan2-dong, Saha-gu, Busan 604-714, Korea

³Wavebender Reshaping Communications, Milpitas, CA 95035, USA

¹jinho@ynu.ac.kr

Abstract — This paper presents the design optimization of new electromagnetic engine valve in a limited space of the entire by multidisciplinary simulation using MATLAB and MAXWELL. This aims to maximize the frequency of vibration in order to reduce the transition time of engine valve. The results show the enhanced performance of optimized actuator.

I. INTRODUCTION

The variable valve timing is a key technology in combustion engine of automobile to improve fuel efficiency up to 15%, enhance torque output up to 10% and reduce CO2 emission up to 15% because VVT makes possible the optimization of these outputs at different engine operating conditions [1][2]. Kim and Lieu introduced a new design of electromagnetic engine valve actuator using permanent magnet [3] to achieve VVT in combustion engine. It saves a large amount of electric power for operation compared with conventional solenoid-driven actuator two main advantages. First, the residual induction of the permanent magnet can hold the valve at the closed position at the initial stage. In addition, no power is needed between valve events and current is only fed into system at each valve transition period.

Fig. 1 shows the schematic diagram and operating principle of newly suggested actuator. This actuator is composed of two pieces of permanent magnet, electromagnetic coil (solenoid), a laminated steel core and armature, two springs and valve body. The armature and the valve are one continuous body. Accordingly, the engine valve closes and opens as the armature moves up and down. The total travel distance of armature is 8 mm. The solid arrows show the magnetic flux generated by the permanent magnets and the dotted arrows show the flux generated by the electromagnetic coil. At start, the permanent magnets latch the armature at the upper position, i.e. the valve is closed because the magnetic force exceeds the spring force. To open the engine valve, the coil is energized. As the flux of permanent magnets is partially cancelled, the spring force exceeds the magnetic force and the armature is released and accelerated by the stored energy in the springs. Thus, the engine valve starts opening. After the armature passes neutral position of stroke, the electromagnetic coil is reversely energized. Then, the permanent magnets and the electromagnetic coil catch the armature at the lower end position. The motion from the lower end to the upper end is the inverse operation of the steps above.

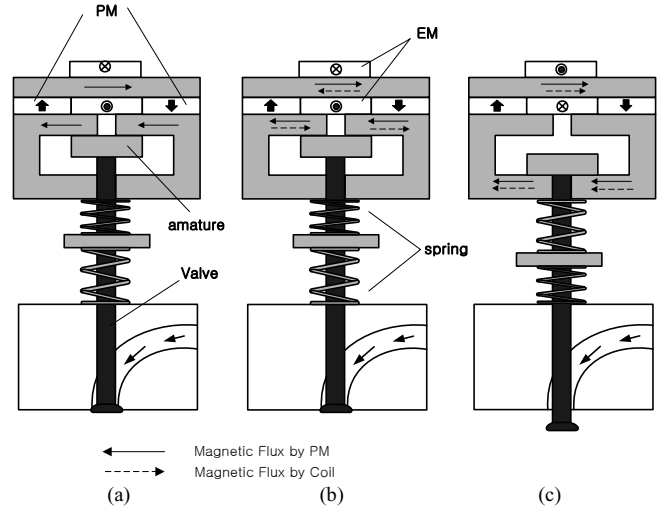


Fig.1. Schematic diagram and operating principle of suggested actuator (a) at the upper end (b) at starting and (c) at the lower end

The transition time is defined as the duration for the valve to move from closed position to opened position or from opened position to closed position and as the transition time is smaller, the engine valve actuator can accomplish higher maximum engine speed. The transition time of valve is shortened by the increment of the frequency of vibration because the actuator is mainly operated by mass-spring oscillation. The frequency of vibration is called by natural frequency (ω_n) that is defined by $\sqrt{k/m}$. Here, k is the equivalent spring stiffness and m is the moving mass.

In this paper, actuator design is optimized to maximize the frequency of vibration, which results in the reduction of the transition time of stroke.

II. DESIGN OPTIMIZATION

Fig. 2 shows design variables for optimization and the goal of this structure is to maximize the frequency of vibration expressed by (1).

$$\omega_n = \sqrt{\frac{k}{m}} = \sqrt{\frac{(F_{Latching} - 100) / x_{max}}{v_a \times \rho_s + m_v}} \quad (1)$$

where,

k : Spring stiffness

m : Moving mass including armature and engine valve

ω_n : Frequency of vibration (natural frequency)

- $F_{Latching}$: Magnetic latching force
- x_{max} : Distance from neutral to lower end of stroke
- v_a : Volume of armature
- ρ_{steel} : Mass density of steel
- m_v : Mass of engine valve

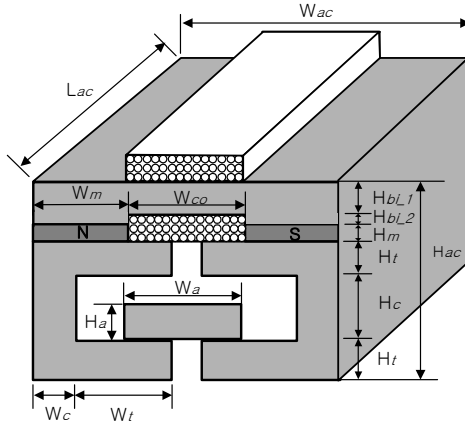


Fig. 2. Design optimization variables for maximizing frequency of vibration at bottom end position of armature

The optimization is achieved by multidisciplinary simulation of MAXWELL and MATLAB based on finite element analysis (FEA) that is widely used in design of electromagnetic devices and the generic algorithm (GA) that is a robust stochastic search methods based on natural selection and mutation which drives biological evolution [4]. First, a population of actuator is randomly generated. Each individual in the population is a series of binary string (chromosome) that representing one complete actuator. Then, each gene in the chromosome is decoded to actual parameters using a binary-decoding method. The decoded parameters are passed to the Maxwell for evaluation. The goodness of each chromosome is determined by MAXWELL. In the simulation platform, MATLAB writes a VBScript to execute MAXWELL for electromagnetic simulation and reads the value of latching force to determine the frequency of vibration. Upon the completion of simulation for a given population, GA acts on the chromosomes to generate a new population through crossover and mutation operation. Several independent runs are performed varying population sizes, ratio of crossover and mutation to assure the convergence to the optimal design. Fig. 3 shows a good convergence to some optimal values.

III. OPTIMIZATION RESULTS

Table I shows the optimized dimension of actuator and Table II shows the comparison of characteristics of existing design and optimal design. The magnetic latching force at end position of stroke falls from 1525 N to 1262 N that reduces the obtainable maximal stiffness of spring by 18.4 % from 358 kN/m to 292 kN/m and at the same time, the moving mass

including armature and engine valve falls by 52.1 % from 284 gram to 136 gram. In results, the natural frequency is improved by 30 %.

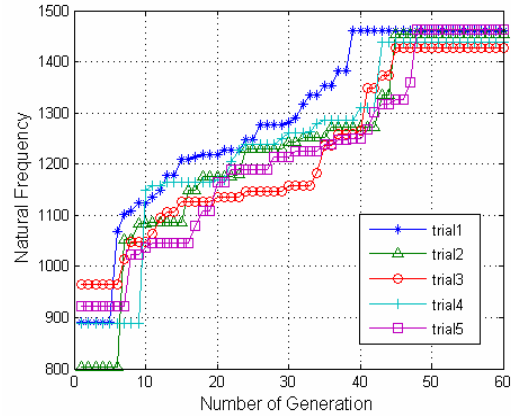


Fig. 3. The best fitness values in each generation

TABLE I
COMPARISON OF EXISTING DESIGN AND OPTIMAL DESIGN

Characteristics	Existing design	Optimal design
Magnetic latching force	1525 (N)	1262 (N)
Available Spring stiffness	358 (kN/m)	292 (kN/m)
Moving mass	0.284 (kg)	0.136 (kg)
Natural frequency	1123	1465

TABLE II
ACTUATOR DIMENSIONS (ALL DIMNENS IN MILLIMETERS)

Symbol	Quantity	Exiting dimensions	New optimized dimensions
L_{ac}	Thickness of actuator	38.1	38.1
W_{ac}	Width of actuator	120.65	120.65
H_{ac}	Height of actuator	93.34	95
W_{co}	Width of coil	31.75	31.75
W_m	Width of magnet	44.45	44.45
H_m	Height of magnet	4.7625	4.7625
W_a	Width of armature	44.45	30.216
H_a	Height of armature	19.03	12
W_t	Width of teeth	34.29	27.325
H_t	Height of teeth	19.05	19
W_c	Width of core	19.05	28
H_c	Height of core	27.05	20
H_{bi1}	Height of back iron 1	19.05	28.75
H_{bi2}	Height of back iron 2	4.7625	3.5

IV. REFERENCES

- [1] P. Barkan, and T. Dresner, "A Review of Variable Valve Timing Benefits and Modes of Operation," SAE Technical Paper Series, Paper 891676, 1989.
- [2] M. Pischinger and W. Salber et al., "Benefits of the Electromechanical Valve Train in Vehicle Operation," SAE Technical Paper Series, Paper 2000-01-1223, 2000
- [3] J. Kim and D. K. Lieu, "Designs for New, Quick-Response, Latching Electromagnetic Valve," *Proceeding of International Electric Machines and Drives Conference 2005*, pp. 1773-1779, 2005
- [4] J. M. Johnson and Y. Rahmat-Samii, "Genetic Algorithms in Engineering Electromagnetics," *IEEE Antennas Propagation. Magazine.*, vol. 39, no. 4, pp. 7-21, Aug. 1997.

Niched Pareto-Archived Evolutionary Programming for Multi-Objective Electromagnetic Optimization

Emanuele Dilettoso, Santi Agatino Rizzo and Nunzio Salerno

Dip. Ing. Elettrica, Elettronica e dei Sistemi, Università di Catania – Viale A. Doria, 6 – I-95125 Catania– Italy
edilettoso@diees.unict.it, sarizzo@diees.unict.it, nsalerno@ieee.org

Abstract — The main targets of a Multi-Objective Evolutionary Algorithm (MOEA) is to find a uniformly distributed and well-spread non-dominated solution set (NDSS) close to the true Pareto optimal front (TPOF). This paper presents a new MOEA called Niched Pareto-Archived Evolutionary Programming (NPAEP). It is able to find a good NDSS with few objective function evaluations. During the selection and reproduction processes it uses information about the uniformity distribution and extension of the NDSS. Comparisons were made with other well-known MOEAs on different test problems.

I. INTRODUCTION

In industrial applications optimized design is often problematic because of the simultaneous occurrence of many conflicting targets. Real-world optimization problems, in fact, often exhibit multiple optima, hence it is suitable to give the decision maker a wide range of solutions to choose from. Some optimization methods solve a single multi-objective function obtained by a weighted sum of targets [1]-[2]. The main difficulty in using this approach is setting a good value for the weights so as to scale the objectives appropriately [1]. Other MOEAs search for a set of multiple equivalent solutions, called a non-dominated solution set [1]-[3]. Unfortunately, they can be extremely expensive. This is especially harmful in the optimization of electromagnetic devices, where each estimation of the objective function calls for a numerical solution by means of the Finite Element Method (FEM) [4].

In this paper we present a new MOEA called Niched Pareto-Archived Evolutionary Programming that is able to obtain the same results as well-known MOEAs with fewer objective function evaluations.

II. THE NPAEP ALGORITHM

The main target of a MOEA is to find an NDSS close to the TPOF, uniformly distributed and maximally extended. During the selection and reproduction processes, NPAEP uses information about the degree of satisfaction of these targets and it maintains an archive of the best solutions found so far.

Fig. 1 shows the pseudo-code of the algorithm, where Q is the set of dominated individuals, P is the archive of the best solutions, n_{pop} is the population size, n_{gen} is the number of generations and n_Q is the number of individuals in Q at generation t .

Fig. 2 shows the pseudo-code for the fitness assignment, where n_P is the number of individuals in P at generation t , $df_{i,j}$ is the normalized [0,1] Euclidean distance between individuals

```

begin
  Create  $n_{pop}$  random solutions
  Move the non-dominated individuals to  $P$  and the others to  $Q$ 
  Set the age of every individual belonging to  $Q$  to zero
  do  $t=1$  to  $n_{gen}$ 
    Increase the age of individuals belonging to  $Q$ 
    Compute the fitness  $F$  of each individual
    Select one parent among them by means of a roulette wheel
    if then (parent belonging to  $Q$ ) then
      Reset the age of the parent to zero
    endif
    Mutate  $x_{offspring} = m(x_{parent})$ 
    if (offspring dominates some individuals of  $P$ ) then
      Move them to  $Q$  and their ages are set to zero
      Move offspring to  $P$ 
    elseif (offspring and  $P$  are non-dominated by each other) then
      Move offspring to  $P$ 
    else
      Move offspring to  $Q$  and set its age to zero
    endif
    if ( $n_Q > n_{pop}$ ) Delete the eldest  $n_Q - n_{pop}$  individuals of  $Q$ 
  enddo
end

```

Fig. 1. Pseudo-code of NPAEP algorithm

i and j in the search space, OP is the subset of P containing the best solutions of every objective function, $rand$ is a random number $\in [0,1]$ and it has a uniform probability density function, $n_{DOM,i}$ is the number of individuals that dominate i . The fitness is assigned to an i -individual of P as follows:

$$F_i = \begin{cases} 1 & \text{if } (dfm = d \min_i) \\ \frac{1}{n_i} \left(\frac{1}{n_i \cdot dfm} \sum_{j=1}^{n_i} df_{i,j} \right) & \text{if } (dfm > d \min_i) \end{cases} \quad (1)$$

where n_i is the number of j -individuals belonging to P for whom $df_{i,j}$ is less than dfm and dfm is $\max(\min(df))$.

The NPAEP algorithm uses a maximum mutation displacement computed as follows:

$$\sigma_{i-k} = \frac{1}{2} \frac{\rho_k}{1 + n_P} \left(1 + n_P \frac{F_{max} - F_i}{F_{max} - F_{min}} \right) \left(1 - \frac{0.75 * t}{n_{gen}} \right) \quad (2)$$

where ρ_k is the range of the k -th design parameter, F_{min} and F_{max} are the minimum and maximum values of F respectively. Hence, the mutation operator is obtained as:

$$x_{offspring-k} = m(x_{parent-k}) = x_{parent-k} + rand * \sigma_{parent-k} \quad (3)$$

where $rand \in [-1, 1]$ and has a uniform probability density.

```

begin
do i=1 to nP (xi∈P)
  dmini = 1
  do j=1 to nP (xj∈P, i≠j)
    if (dmini > dfi,j) dmini = dfi,j
  enddo
enddo
dfm = max(dmini) (xi∈P)
do i=1 to nP (i∈P)
  use (1) to compute Fi
  if (i∈OP) then
    if (Fi==1) then
      Fi = Fi + rand
    else
      Fi = Fi + (1-Fi)* rand
    endif
  endif
enddo
nT = nP + nQ
do i=1 to nQ (xi∈Q)
  Fi = min(Fj)*(nT - nDOM,i) / nT (xj∈P and xj dominates xi)
enddo
end

```

Fig. 2. Pseudo-code of the fitness assignment

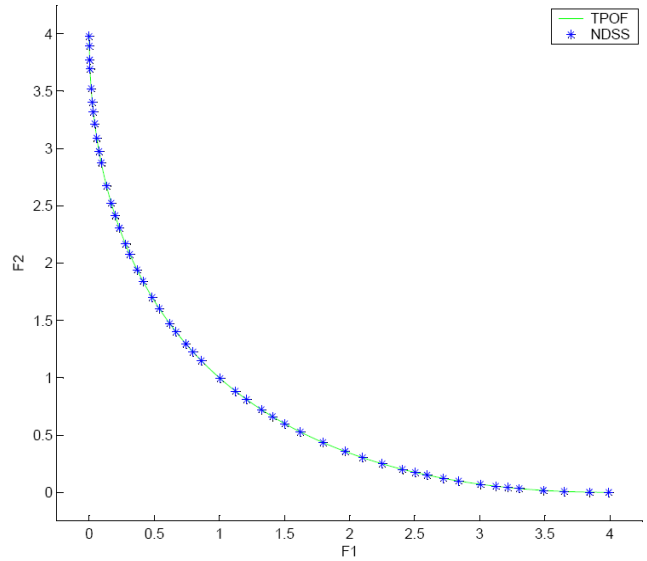


Fig. 3. Non-dominated solution set obtained by means of NPAEP on the SCH function

TABLE I
CONVERGENCE METRIC Υ

	SCH		FON	
	mean	variance	mean	variance
NSGA II real-coded	0.003391	0	0.001931	0
NSGA II binary-coded	0.002833	0.000001	0.002571	0
SPEA	0.003403	0	0.125692	0.000038
PAES	0.001313	0.000003	0.151263	0.000905
NPAEP	0.003266	0	0.002439	0
NPAEP 2500	0.003559	0	0.006126	0

III. MATHEMATICAL RESULTS

In multi-objective optimization there are several performance metrics [5]. We adopt the metrics and objective functions described in [3] to compare NPAEP with the results given in the same paper. The convergence metric Υ measures the degree of convergence to a known TPOF. The diversity metric Δ measures the extent of spread achieved among the NDSSs obtained.

Tables I and II show the mean value and variance of the convergence metric Υ and the diversity metric Δ respectively: a lower value means better performance. Performance was obtained with 25000 function evaluations averaged over 10 runs, as in [3]. Moreover, in the last row we show the NPAEP performance with only 2500 function evaluations.

Fig.3 shows the true Pareto optimal set for the SCH function [3] and the non-dominated solution set obtained by means of NPAEP using 25000 function evaluations.

IV. CONCLUSION

Many MOEAs exist in the literature but they can be extremely expensive. This is especially harmful in electromagnetic problems, where each estimation of the objective function calls for a numerical solution by means of

TABLE II
DIVERSITY METRIC Δ

	SCH		FON	
	mean	variance	mean	variance
NSGA II real-coded	0.477899	0.003471	0.378065	0.000639
NSGA II binary-coded	0.449265	0.002062	0.395131	0.001314
SPEA	1.021110	0.004372	0.792352	0.005546
PAES	1.063288	0.002868	1.162528	0.008945
NPAEP	0.201082	0.000007	0.208932	0.000047
NPAEP 2500	0.464268	0.000051	0.211756	0.000166

the Finite Element Method (FEM). Hence the proposed MOEA is more suitable for solving this class of problems because, using fewer objective function evaluations than well-known MOEAs, it achieves similar or better performance.

More results and electromagnetic examples will be presented in the full paper.

V. REFERENCES

- [1] A. Ghosh, S. Dehuri, "Evolutionary Algorithms for Multi-Criterion Optimization: A Survey", *International Journal of Computing & Information Sciences*, 2004, vol.2, n.1, pp.38-57.
- [2] E. Dilettoso, S. A. Rizzo, N. Salerno, "SALHE-EA: a New Evolutionary Algorithm for Multi-Objective Optimization of Electromagnetic Devices", *Intelligent Computer Techniques in Applied Electromagnetics*, Springer-Verlag, vol. 119, Berlin, 2008, pp. 37-45.
- [3] K. Deb, A. Pratap, S. Agarwal, T. Meyarivan, "A Fast and Elitist Multiobjective Genetic Algorithm: NSGA-II", *IEEE Transactions on Evolutionary Computation*, 6(2): 182-197, 2002.
- [4] P. G. Alotto et al., "Stochastic algorithms in electromagnetic optimization," *IEEE Transactions on Magnetics*, vol. 34, n. 5, pp. 3674-3684, Sep. 1998.
- [5] T. Okabe, Y. Jin, B. Sendhoff, "A Critical Survey of Performance Indices for Multi-Objective Optimization", *Proc. of the IEEE Congress on Evolutionary Computation*, vol.2, 878-885, 2003

Optimization of Vibratory Behavior of Electromagnetic Devices through Material Properties Evaluation

Nassira Ferkha^{1,2}, Mohamed Rachid Mekideche¹, Abdellatif Miraoui², Abdesslem Djerdir²

¹LAMEL Laboratory, Jijel University
BP 98, Ouled Aissa, Jijel, Algeria

²System and Transport Laboratory SET
University of Technology of Belfort UTBM, 90010 Belfort, France
E-mail: nassira.ferkha@gmail.com

Abstract — The aim of this paper is to propose a methodology to optimize the design of cylindrical electromagnetic devices regarding to the vibration phenomena. This approach combines the Artificial Intelligent (AI) and Finite Element (FE) analysis to solve the electromechanical inverse problem for identifying the material proprieties (Young modulo and mass density) in different regions of the studied system. Thus, a multilayer perceptron neural network (MLP) is used as forward model and Genetic Algorithm (GA) is used to solve the Optimization Problem (OP) in the Inverse Problem (IP).

I. INTRODUCTION

IPs in electromagnetic are usually formulated and solved as OPs, so iterative methods are commonly used approaches to solve this kind of problems [1]. The numerical models such as FE model are used to represent the forward process. However, iterative methods using the numerical based forward models are computationally expensive. Neural networks (NNs) are utilized for solving the forward process in the iterative methods [2]. Parameters identification using NNs can be recast as a problem in multidimensional interpolation, which consists of finding the unknown nonlinear relationship between inputs and outputs in a space spanned by the activation functions associated with the NN nodes. The input space corresponds to the material characteristics (Young modulo and mass density) and the output corresponds to the dynamic response of the electromagnetic device [3]. This paper proposes a GA based inverse algorithm for parameters identification of electromagnetic devices, witch induce a minimum level of vibration (noise). In the proposed algorithm, a MLPNN is used as forward model, and GA is used to solve the OP in the IP.

II. NEURAL NETWORK ARCHITECTURE

An ANN is an information processing system that has certain performance characteristics in common with biological neural networks and therefore, each network is a collection of neurons that are arranged in specific formations. The basic elements of neural network comprise neurons and their connection strengths (weights). One of the attractive features of ANNs is their capability to adapt themselves to special environmental conditions by changing their connection

strengths or structure. One of the most influential developments in ANN was the invention of the back-propagation algorithm, which is a systematic method for training multilayer ANNs [4]. The standard back-propagation learning algorithm for feed-forward networks aims to minimize the mean squared error defined over a set of training data. In feed-forward ANNs neurons are arranged in a feed-forward manner, so each neuron may receive an input from the external environment or from the neurons in the former layer, but no feedback is formed. The network always has an input layer, an output layer and at least one hidden layer. In our case, there is only one hidden layer. A neuron's activity is modeled as a function of the sum of its weighted inputs, where the function is called the activation function, which is typically nonlinear, thus giving the network nonlinear decision capability. Each layer is fully connected to the succeeding layer. The arrows indicate flow of information (Fig.1) [5].

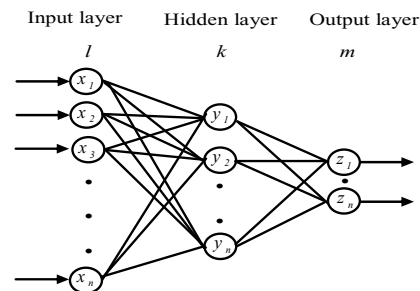


Fig. 1 Feed forward neural network

where n_l is the number of neurons in the input layer, n_H is the number of neurons in the hidden layer, n_O is the number of neurons in the output layer, x_l are the inputs to the input layer where $l=1, \dots, n_l$, y_k is the value of the hidden layer where $k=1, \dots, n_H$, z_m is the value of the output layer where $m=1, \dots, n_O$. $w_{lk}^{[1]}$ is the weight connecting the l th neuron in the input layer to k th neuron in the hidden layer, and $w_{km}^{[2]}$ is the weight connecting the k th neuron in the hidden layer to the m th neuron in the output layer. The nodes of the hidden and output layer are:

$$y_k = f\left(\sum_{l=1}^{n_l} w_{lk} x_l\right) \quad k = 1, \dots, n_H \quad (1)$$

and

$$z_m = f\left(\sum_{k=1}^{n_k} w_{mk} y_k\right) \quad m = 1, \dots, n_O \quad (2)$$

where the activation function f is traditionally the Sigmoid function defined as

$$f(x) = \frac{1}{(1 + e^{-x})} \quad (3)$$

The back-propagation method is based on finding the outputs at the last (output) layer of the network and calculating the errors or differences between the desired outputs and the current outputs. When the outputs are different from the desired outputs, corrections are made in the weights.

III. GENETIC ALGORITHM

GAs are probabilistic parallel search algorithms based on natural selection. GAs are capable of finding a global optimum among multiple local optima. A GA usually begins with a randomly generated set of potential solutions, called the initial population [6]. A fitness function is used as a measure of the closeness of each member in the population to the global optimum solution. Then, members from the population are selected to produce new members, called descendents or children, by applying stochastic operators to the selected members. The most common genetic operators are crossover and mutation. A crossover operator combines the features presented in parents to produce descendents. A mutation operator slightly perturbs a selected member in a random manner. Crossover operations ensure that the new population inherits highly fit features while mutation operations may add previously unexploited features into the population.

IV. STUDIED ELECTROMAGNETIC DEVICES

Two electromagnetic cylindrical devices are studied in this paper. So, the first one consists on the determination of the optimal mechanical parameters of the ferromagnetic cylinder shown in fig. 2, regarding to the vibratory behavior. The second one is an application of the developed model on an electrical machine. The data are generated by means of a 2D FE model, implemented under Matlab software. Fig 3 and 4 show respectively the evolutions of the objective function and the mass density with respect to the identification iterations.

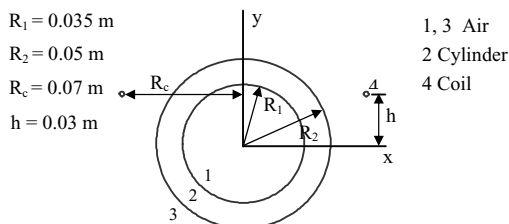


Fig.2 geometry of the studied cylinder

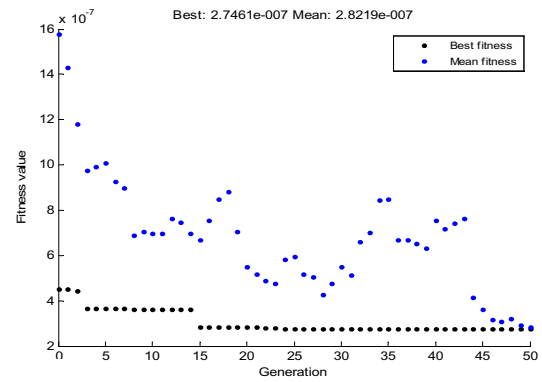


Fig.3 Evolution of the objective function

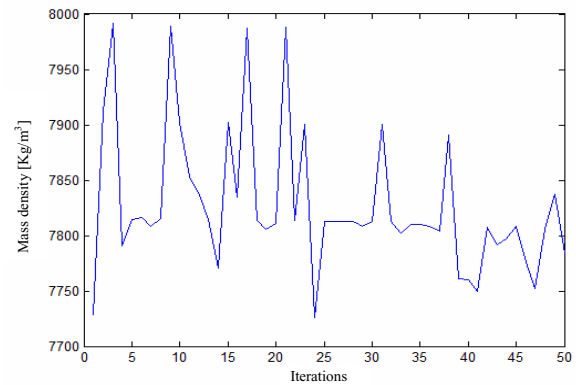


Fig.4 Evolution of the mass density with iterations

The obtained results for the studied electrical machine and their validation will be presented in the full paper.

V. CONCLUSION

Material approach is advantageous because it offers the possibility to optimize mostly a given geometry. In fact, in the case of electrical machines, the geometry is usually determined after an optimization process. The combination finite element-neural network has permitted to reduce the computing time needed to resolve the electromechanical problem. The obtained results are satisfactory and open interesting prospects for the vibratory optimisation in electrical machines. In the full paper, more details will be given on the finite element model, the optimization method and the obtained results.

VI. REFERENCES

- [1] A. Fanni and A. Montisci, A neural inverse problem approach for optimal design, IEEE Trans. Magnetics, vol. 39, no. 3, pp. 1305-1308, 2003.
- [2] S. Haykin, Neural networks: A comprehensive foundation, Englewood Cliffs, NJ: Prentice-Hall, New York, 1999.
- [3] Z. Tang, P. Pillay, A. M. Omekanda, C. Li, C. Cetinkaya, Young's modulus for laminated machine structures with particular reference to switched reluctance motor vibrations, IEEE Transactions on Industry Applications, vol. 40, n° 3, Mai / June 2004.
- [4] N.P. De Alcantara, J. Alexandre, M. De Carvalho, Computational investigation on the use of FEM and ANN in the non-destructive analysis of metallic tubes, Proc. 10th Biennial Conf. Electromagnetic Field Computation, Italy, 2002.
- [5] K. Mehrotra, C. K. Mohan and S. Ranka, Elements of artificial neural networks, MA: MIT Press, Cambridge, 1997.
- [6] M. Srinivas, L.M. Patnaik, Genetic algorithms: a survey, Computer, vol. 27, no. 6, pp.17-26, 1994.

An Improved Continuous Genetic Algorithm for Electromagnetic Optimization

Paulo H. da F. Silva*, Rossana M. S. Cruz**, and Adaildo G. D'Assunção**

* Federal Institute of Education, Science and Technology of Paraíba
IFPB – Group of Telecommunications and Applied Electromagnetism
CEP: 58015-430, João Pessoa, PB, Brazil
Phone: +55-83-3208-3055

**Federal University of Rio Grande do Norte
UFRN – Department of Electrical Engineering
Postal Code 1655, CEP: 59072-970, Natal, RN, Brazil
Phone: +55-84-3215-3700

E-mails: henrique@cefetpb.edu.br, mscrossana@gmail.com, adaildo@ct.ufrn.br

Abstract—This work presents an improved genetic algorithm (GA) applied for electromagnetic optimization. A real-value mutation operator is proposed to improve the algorithm convergence. The well-established theory of capacitive mesh filter is revisited for application of the proposed algorithm. Modeling of mesh filters is accomplished with an equivalent-circuit, a numerical analysis with Ansoft Designer™ method of moments software, and a multi-layer perceptrons neural network. A comparative study between the improved-GA and continuous-GA was done. The obtained results show the superior performance of the proposed genetic algorithm.

I. INTRODUCTION

Natural optimization algorithms, such as, the simulated annealing (SA) and genetic algorithm (GA) are stochastic population-based global search methods inspired in the nature. They are effective for optimization problems with a large number of design variables and inexpensive cost function evaluation. However, the main computational drawback for electromagnetic (EM) optimization relies on the repetitive evaluation of numerically expensive cost functions. Finding a way to shorten the optimization cycle is highly desirable. Several schemes are available to improve the GA performance, such as: the use of fast full-wave methods, micro-genetic algorithm, which aims to reduce the population size, and parallel GA using parallel computation [1]-[2].

In this paper, the authors describe a hybrid EM-optimization method, which blends an improved version of continuous-GA and a multilayer perceptrons (MLP) model. The method is applied to design spatial mesh filters.

II. CONTINUOUS GENETIC ALGORITHMS

Assuming a GA optimization problem with $Nvar$ input variables and $Npop$ individuals, the population at the k -th iteration is a matrix $\mathbf{P}(k)_{Npop \times Nvar}$ of floating-point elements, denoted by $p_{m,n}^k$, with each row corresponding to an individual (or chromosome). In this way GA chromosome is defined by (1) as a vector with $Nvar$ optimization variables.

$$chromosome(k, m) = [p_{m,1}^k, p_{m,2}^k, \dots, p_{m,Nvar}^k] \quad (1)$$

Based on the cost associated to each chromosome, the population evolves through the generations by the application of standard genetic operators: roulette wheel selection, blending crossover method and real-value mutation [1]-[2].

Inspired in simulating annealing cooling schedules [2], we propose a new mutation operator for continuous-GA as given in (2). It is used to improve the GA convergence at the neighborhood of global minimum of a cost function. When the GA global-cost ($gcost$) decreases or the number of GA iterations increases, the quotient function Q given in (3) decreases the standard deviation of mutation operator (2). The parameter $A = 40$ is a constant standard deviation value and $B = 1E-8$ is a cost value neighbor to the global minimum. The continuous-GA using the real-value mutation definition given in (2) and (3) is denominated improved-GA.

$$p_{m,n}^{k+1} = p_{m,n}^k + randn() \cdot \frac{(p_{max} - p_{min})}{Q(k, gcost(k))} \quad (2)$$

$$Q(k, gcost(k)) = \begin{cases} A, & gcost \geq B \\ A + k \cdot [\log(gcost(k))]^4, & gcost < B \end{cases} \quad (3)$$

III. DESIGN EXAMPLE AND CONCLUSION

The GA optimization was done considering for spatial mesh filter design with a plane periodic array of square metallic patches (freestanding or printed on a single substrate layer), as illustrated in Fig 1(a). The side of square patches is $L = g/2$, where g is the cell size. The filter resonant frequency (f_r) and bandwidth (BW) were evaluated through the equivalent-circuit model [3]. A parametric analysis with Ansoft Designer™ method of moments (MoM) software was done for design region of interest defined by the substrate dielectric constant ($\epsilon_r = 1.0, 3.4, 10.2$) and cell size ($g = 3.75, 6, 10, 15, 20, 25, 30, 40, 70, 100$ mm) variations. The substrate thickness $h = 1.5$ mm was assumed for all dielectric layers. The obtained EM-data from parametric analysis of filters was used for the training of a one hidden layer MLP network model (see Fig. 1(b)). For this purpose, it was utilized the efficient resilient backpropagation algorithm [4].

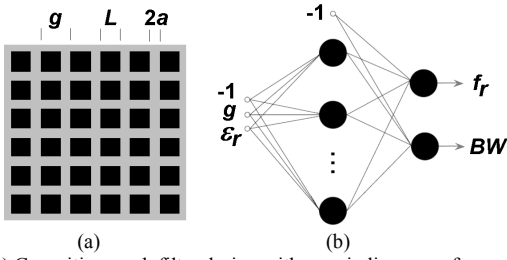


Fig. 1. (a) Capacitive mesh filter design with a periodic array of square patch-elements; (b) MLP model with 10 hidden neurons

Figure 2(a) shows the simulated results for the resonant frequency obtained through the implemented mesh filter models. Equivalent-circuit model [3] is CPU efficient but reasonable accuracy is only obtained for freestanding case. Numerical MoM model is very accurate but its high CPU requirement turns its use prohibitive for EM-optimization. To overcome these problems a fast and accurate one hidden layer MLP model was developed. Figure 2(b) shows the MLP approach results for the mesh filter bandwidth.

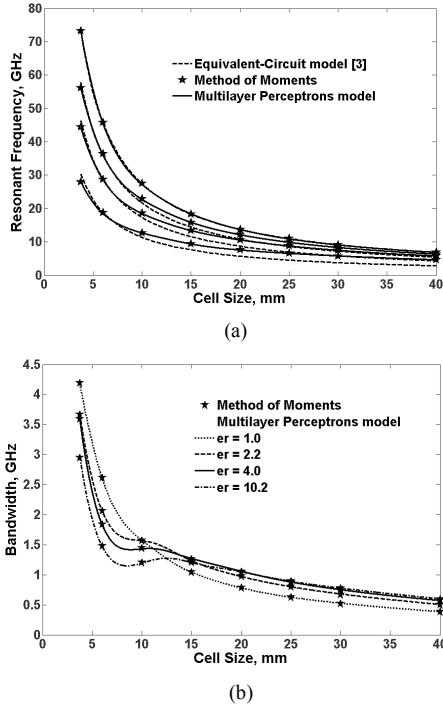


Fig. 2. Capacitive mesh filter modeling: (a) resonant frequency, (b) bandwidth

Given a filter design specification (f , BW), the goal is the minimization of the cost function defined in (4). The functions $f_r(g_m^k, \varepsilon_{r_m}^k)$ and $BW(g_m^k, \varepsilon_{r_m}^k)$ are evaluated using the developed MLP model.

$$\text{cost}(k, m) = \frac{(f - f_r(g_m^k, \varepsilon_{r_m}^k))^2}{f^2} + \frac{(BW - BW(g_m^k, \varepsilon_{r_m}^k))^2}{BW^2} \quad (4)$$

Assuming $f_r = 10$ GHz and $BW = 1.0$ GHz we simulated 500 GA iterations. In Fig. 3(a) is presented the improved-GA path over the contours of cost surface defined in (4) as well the distributions of GA population composed by 100 individuals.

Fig. 3(b) shows the evolving of global-cost for the best individual of GA population. The final global-cost values for improved-GA and continuous-GA were $2.13E-27$ and $1.52E-13$, respectively. The CPU spent-time for GA optimization was ≈ 30 s. The optimized values $g = 20.75$ mm and $\varepsilon_r = 4.404$ were obtained (see final population in Fig. 3(a)). To verify if these results satisfy the filter specifications, the transmission coefficient of optimal mesh filter was simulated with MoM. The obtained results $f_r = 10$ GHz and $BW = 1.03$ GHz are in excellent agreement with desired design values.

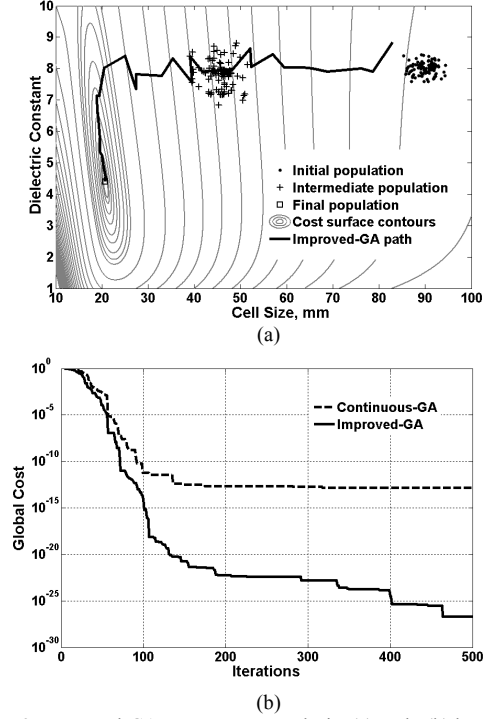


Fig. 3. Improved-GA convergence analysis: (a) path (b) best cost

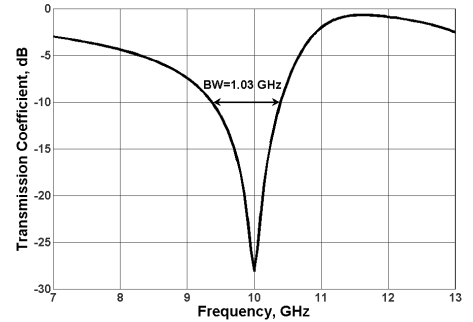


Fig. 4. Transmission coefficient of designed mesh filter for 10 GHz

IV. REFERENCES

- [1] R.L. Haupt and D.H. Werner, Genetic algorithms in electromagnetics. New York: John Wiley & Sons, 2007.
- [2] R.L. Haupt and S.E. Haupt, Practical genetic algorithms. New Jersey: John Wiley & Sons, 2004.
- [3] R.C. Compton and D.B. Rutledge, "Approximation techniques for planar periodic structures," *IEEE Trans. on Microwave Theory and Techniques*, 33(10): 1083-1088, 1985.
- [4] M. Ridmiller and H. Braun, "A direct adaptive method for faster backpropagation learning: the RPROP algorithm," *Proceedings of the IEEE International Conference on Neural Networks*, San Francisco, EUA, 1993, pp. 586-591.

Differential Evolution-based Technique for Thermal Parameters Identification of a Transformer FEM model

A. Glotic¹, J. Pihler¹, N. Sarajlic², M. Kasumovic², M. Tesanovic²

1 - Faculty of Electrical Engineering and Computer Science, University of Maribor, 2000 Maribor, Slovenia

2 - Faculty of Electrical Engineering, University of Tuzla, 75000 Tuzla, Bosnia and Herzegovina
adnan.glotic@uni-mb.si

Abstract— This paper deals with identification of thermal parameters for transformer's FEM model. The identification technique is based on stochastic optimization algorithm called differential evolution (DE). As the accuracy of the model depends on its parameters, the goal of DE is to identify adequate thermal parameters, in order to achieve best possible agreement between measured and model-calculated values of temperature. The inclusion of identified/optimal thermal parameters into the model, results in good model's accuracy.

I. INTRODUCTION

Operational reliability of electric power system strongly depends on transformers, therefore to predict and to determine thermal phenomena in its compounding parts is an important step in machine designing process. Distribution of thermal field in transformer can be determined by using FEM model [1], [2]. Building of a model requires data of device geometry, sources and boundary conditions. Data of material properties are also required. These are usually obtained from different sources and thus contain some amount of uncertainties. However, this data affects model's accuracy. To achieve model behavior as close to real object, the mentioned data needs to be precisely identified. The novelty of this paper is DE-based technique for identification of model thermal parameters. The goal of DE [3], [4] is to minimize the difference between measured and model-calculated temperature.

II. MODEL OF A POWER TRANSFORMER

Fundamental criterion, which limits the transformers degree of loading and its lifetime, is temperature. Consequentially, the correct determination of temperature distribution in machine design process is important and it can be obtained by using an accurate FEM model. Many physical phenomena are described by similar partial differential equations (PDE). Two examples are equations for magnetic

$$\nabla \cdot (\nu \nabla A) - \sigma(T) \frac{\partial A}{\partial t} = -\sigma(T) V \quad (1)$$

and thermal field

$$\nabla \cdot (k \nabla T) - \rho c \frac{\partial T}{\partial t} + q_t = 0 \quad (2)$$

where ν is the magnetic reluctivity tensor, A the magnetic vector potential, σ the electric conductivity, V the source voltage, T the temperature, ρ the mass density, c the specific heat, k the thermal conductivity and q_t the total losses.

FEM is widely used for solving PDE. In this paper the FEM based programme tool FLUX2D [5] is used for this purpose. For modeling of the thermal processes in transformer, the FEM model that describes coupled electromagnetic and thermal field is used [1], [2]. Coupled electromagnetic-thermal field basically presents two FEM problems (electromagnetic and thermal) and two functions of coupling (losses and temperature dependency of materials).

III. IDENTIFICATION OF THERMAL PARAMETERS BY DE

Modeling process in FLUX2D requires precise data of device geometry, boundary conditions and heat sources, which are quite easy to obtain. On the other hand, required data of material thermal properties and coefficients of convection and radiation are not. As some of these thermal parameters are hard or even impossible to measure, they are usually accessible through catalogues and literature [6]. Consequentially, their accuracy is questionable.

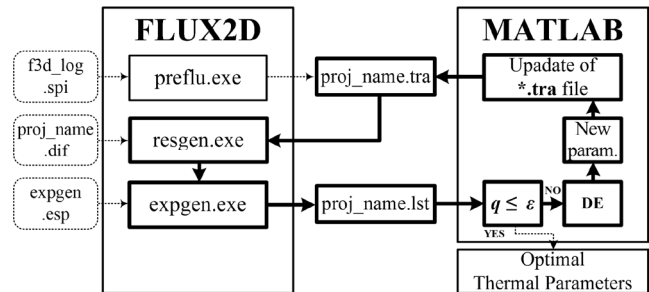


Fig. 1. Schematic presentation of parameters identification process

However, all device data entered in FLUX2D command window is stored in file *f3d_log.spi* (Fig. 1) in command log form. On the basis of this file, the preprocessor *preflu.exe* creates *proj_name.tra* file, which contains all information regarding the model. Calculation parameters such as time step and calculation time are defined in file *proj_name.dif* and used by solver *resgen.exe*. After the calculation completes, the postprocessor *expgen.exe* is employed to display results for various quantities. Desired quantities (in our case temperature) are defined in *expgen.esp* and their calculated values are printed out in file *proj_name.lst*. The important step, after the model simulation completes, is evaluation of the difference between measured and model-calculated values.

Search for optimal thermal parameters is realized by iterative procedure of updating the FEM model with new thermal parameters, calculating the temperature and evaluating

the difference regarding the measured values. New thermal parameters for each update of the *.tra file are generated by DE, which iteratively searches for better solution. Generating the parameters, updating the *.tra file and the automation of the FLUX's calculation process is realized in program tool MATLAB.

Optimal thermal parameters presented in Table I were identified by DE. The goal of the optimization was best possible agreement between measured and calculated temperature. The heating of transformer from cold start-up during 12000 s of operation at nominal load was measured at two locations; one is a specific point of transformer core (point P1) and a second one specific point of winding (point P2). Definition of the objective function q for DE originates from the difference between calculated and measured temperature. Temperature's disagreement can be evaluated by calculating the mean square difference in the given time interval $t \in [t_1, t_2]$

$$q_{P1} = \frac{1}{t_2 - t_1} \int_{t_1}^{t_2} e_{P1}(\tau) d\tau \quad (3)$$

where the difference between measured T_{P1m} and model-calculated temperature T_{P1} in point P1 is defined by $e_{P1}(t) = T_{P1m}(t) - T_{P1}(t)$. The objective function q_{P2} is defined analogically to (3) and it measures the difference between measured and calculated temperature in point P2. Both objective functions are minimized during the optimization procedure and thermal parameters are identified by DE when the objective functions' values become minimal. In order to minimize both objective functions simultaneously, the unified objective function q is introduced by $q = 0.5q_{P1} + 0.5q_{P2}$.

IV. RESULTS

Coupled electromagnetic-thermal field transient calculation results (obtained by using FEM model with identified/optimal parameters) shows good agreement with measured values of temperature, especially in point P1 (Fig. 2). On the other hand, the model containing initial parameters showed obvious disagreement in both points. Such disagreements between measured and model-calculated values have been appearing in early iterations of DE, indicated as higher values of the objective function q as it can be seen in Fig. 3.

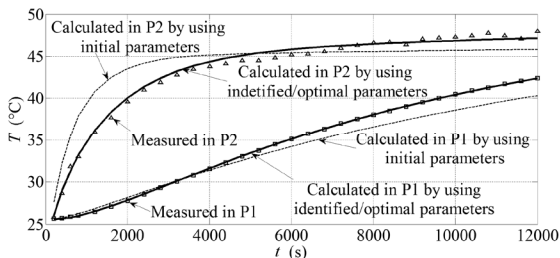


Fig. 2. Measured and model-calculated temperatures

The DE algorithm seeks for better solutions throughout the entire optimization by keeping the current best solution until it finds a better one. This can be seen from convergence course

of the optimization process (Fig. 3). Finally, after approximately 80 iterations, DE has found an optimal solution (identified/optimal thermal parameters) where the disagreement q between calculated and measured temperature has become minimal.

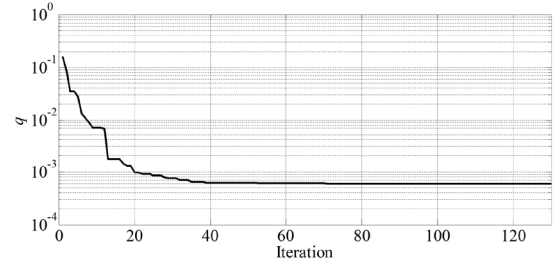


Fig. 3. Convergence course of differential evolution

TABLE I
OPTIMIZATION SET VALUES

Physical Quantity	Parameter	Lower value	Upper value	Initial value	Optimal value
Al. Conductivity slope (1/°C)	p_1	-0.0743	-0.0322	-0.0612	-0.0407
Al. Th. Conductivity (W/m °C)	p_2	76	245	204	245
Al. Sp. Heat Capacity slope (1/°C)	p_3	2388	39800	6960	39749
Al. Spec. Heat Capacity (J/m ³ °C)	p_4	0.79e6	4.46e6	2.32e6	3.91e6
Steel Conductivity slope (1/°C)	p_5	-0.0422	-0.0233	-0.0377	-0.0404
Steel Th. Conductivity (W/m °C)	p_6	12	90	59.1	14.15
Steel Spec. Heat Capacity (J/m ³ °C)	p_7	1.18e6	3.78e6	1.25e6	1.66e6
Air Th. Conductivity (W/m °C)	p_8	0.014	0.05	0.025	0.05
Convection coefficient (W/m ² °C)	p_9	10	100	25	27.86
Radiation Coefficient	p_{10}	0	1	0.28e-7	0.7e-9

V. CONCLUSION

The aim of this work was to identify thermal parameters of the transformer FEM model in order to be able to accurately describe the heating of the transformer and predict the temperature distribution. For this purpose, the optimization method based on DE was employed. The goal of the optimization was best possible agreement between measured and model-calculated temperature values. The results show that a very good agreement is achieved thus proving that the proposed DE-based technique can be used as a tool for thermal parameters identification.

VI. REFERENCES

- [1] J. Driesen, G. Deliege, R. Belmans and K. Hameyer, "Coupled Thermo-Magnetic Simulation of a Foil-Winding Transformer Connected to a Nonlinear Load", *IEEE Transactions on Magnetics*, Vol. 36, No. 4, 2000.
- [2] J. Driesen, R. Belmans and K. Hameyer, "Methodologies for Coupled Transient Electromagnetic-Thermal Finite Element Modeling of Electrical Energy Transducers", *IEEE Transactions on Industry Applications*, Vol. 38, No. 5, 2002.
- [3] R. Storn and K. Price, "Minimizing the real functions of the ICEC'96 contest by differential evolution," in *Proc. IEEE Conf. Evol. Comput.*, Nafoya, Japan, 1996, pp. 842-844.
- [4] K. Price, R. M. Storn, and J. A. Lampinen, *Differential Evolution: A Practical Approach to Global Optimization*, New York: Springer, 2005.
- [5] FLUX2D, Version 7.60: CAD package for electromagnetic and thermal analysis using finite elements, CEDRAT, France, 2001.
- [6] A. F. Mills, *Basic Heat and Mass Transfer*, University of California: Prentice Hall, 1999.

Multi-objective Optimization of an Axial Flux Wind Generator

J. A. Vasconcelos¹, S. R. Silva¹, L. M. Araújo¹, C. L. Sabioni¹, J. A. A. Pereira¹, M. F. V. Lessa and B. M. Lopes²

¹Electrical Engineering Department, Federal University of Minas Gerais

²Companhia Energética de Minas Gerais

Av. Pres. Antônio Carlos, 31270-010, Brazil

jvasconcelos@ufmg.br, selenios@cpdee.ufmg.br

Abstract— This paper presents the multi-objective optimization of an axial flux wind generator of 10kW using NdFeB permanent magnets. The four objectives considered in this work were weight, efficiency, active material cost and volume. The optimization problem was modeled considering seven continuous variables and three discrete ones. The optimization problem was solved using a multi-objective evolutionary algorithm with on-line and off-line populations, with elitism. In each generation, the non-dominated solutions are saved in the off-line population. This generator was designed to match with a three-blade horizontal axis wind turbine characteristics that was planned to operate in the complex terrain wind regime for the countryside of Brazilian land. After founding the non-dominated solutions, the choice of the appropriated one by a decision maker can be made using a decision procedure.

I. INTRODUCTION

The development of renewable energy resources has taken an accelerated pace with the ever increasing concerns on global warming and environmental protection. In the last ten years, the wind power became a reality in terms of its commercial competitiveness, technological maturity and aggressive expanding in power installations all over the world. For wind power systems, the core element is the electrical generator and in this issue several developments has been completed. As in a conventional electric machine design, the efficiency, the weight, the volume and the cost of the electric generator particularly for wind power generation are the major important design figures of merit.

Some works deal with the complicated task of comparison among different topologies of permanent magnet machines, mainly for wind power application. In these studies, the double external rotor and central stator axial flux permanent magnet machines have been appeared as a competitive solution.

The availability of modern high energy density magnet materials, such as sintered NdFeB, has made possible to design special topologies such as toothless stators with air gap windings. They aggregate several unique features such as high efficiency, high power and torque densities, low rotor losses and small magnetic thickness.

The technology of small-sized wind power generators, mainly for isolated applications and grid connected rural systems, represents an adequate challenge, balancing a few number of commercial equipment in the Brazilian market for the expected large latent demand.

Based on the conventional sizing equation and design procedures from former works [1]-[2], this paper presents the multi-objective optimization of a 10kW axial flux Torus generator using NdFeB permanent magnets, considering the variables and bounds shown in Table I. The variables used were the current density on the stator conductor (J_a), linear current density (A_m), peak value of the magnetic flux density on the air gap (B_{mg}), peak value of the magnetic flux density on the stator core (B_{cs}), peak value of the magnetic flux density on the rotor core (B_{cr}), magnetic remanence of the permanent magnet (B_r), inner and outer diameters ratio (K_d), the nominal stator voltage (V), poles number (P) and the number of parallel coils per phase (A_p).

TABLE I

BOUNDS OF THE OPTIMIZATION VARIABLES

Variables	J_a	A_m	B_{mg}	B_{cs}	B_{cr}	B_r	K_d	V	P	A_p
Units	MA/m ²	KA/m	T	Wb	Wb	Wb	--	V	--	--
Lower	3	42	0.3	1.7	1.4	1.1	0.4	100	14	1
Upper	9	98	0.9	1.9	1.6	1.4	0.7	280	20	20

First, different alternatives of generator design were analyzed, since its rotational speed and power accordance with the wind rotor that defines its gearless nature, up to the electrical compatibility with the power electronics converter that rectify its energy and supply the low short-circuit power rural electric power grid.

The chosen design configuration for this axial flux PM generator was as follows:

- 1) axial-gap type with two external rotors and an internal stator;
- 2) NdFeB permanent magnets with maximum thickness equal to 6mm;
- 3) The outer diameter of the nacelle must not exceed 10% of the diameter of the turbine;
- 4) Maximum stator nominal voltage limited to 400V DC bus of the converter.

Fig. 1 shows the design configuration used.

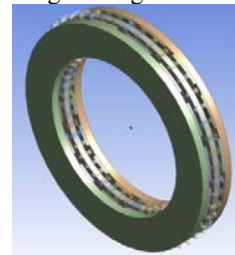


Fig. 1 Double external rotor and central stator axial flux generator.

Considering four objective functions (weight, efficiency, active material cost and volume), this problem was optimized using a multi-objective evolutionary algorithm [3]. In this optimization, 1001 efficient solutions were generated. The Figs. 2 - 4 show the non-dominated solutions plotted in the objectives spaces.

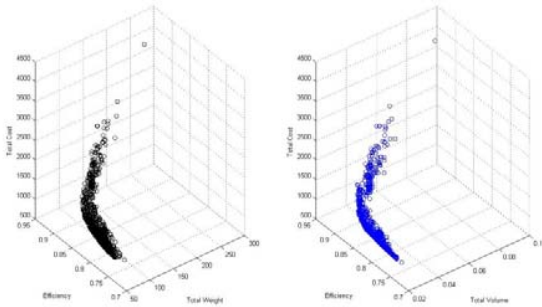


Fig. 2 Efficient solutions in the space of total weight x efficiency x active material cost (left) and total volume x efficiency x active material cost (right).

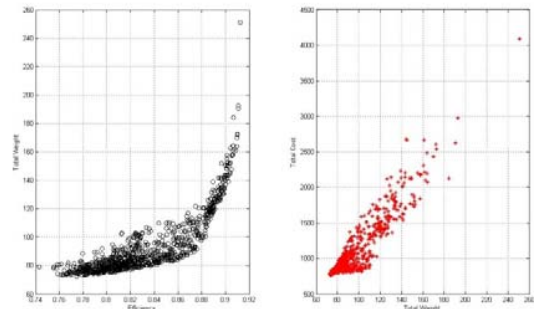


Fig. 3 Efficient solutions in the space of total efficiency x total weight (left) and total weight x active material cost (right).

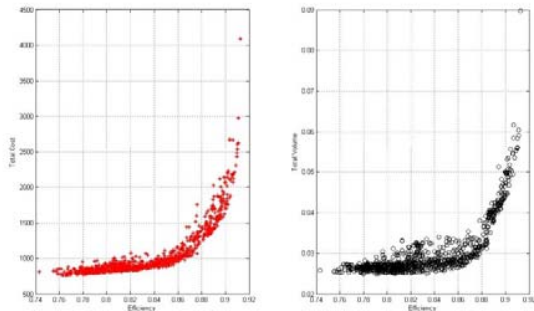


Fig. 4 Efficient solutions in the space of efficiency x active material cost (left) and efficiency x total volume (right).

TABLE II

DECISION MAKING BASED ON EACH OBJECTIVE AS PRIORITY

Weights	Ja	Am	Bmg	Bcs	Bcr	Br	Kd	V	P	Ap
	MA/m ²	KA/m	T	Wb	Wb	Wb	--	V	--	--
1,0,0,0	9,00	92.37	0.366	1.867	1.597	1.399	0.700	151	20	20
0,1,0,0	3,00	48.66	0.863	1.700	1.454	1.249	0.679	272	20	20
0,0,1,0	8.99	97.95	0.304	1.744	1.592	1.394	0.700	251	20	20
0,0,0,1	8.97	73.41	0.347	1.854	1.598	1.330	0.548	272	20	20

TABLE III

OBJECTIVE VALUE FOR THE DECISION MAKING OF TABLE II

Weights	Total Weight	Efficiency	Cost	Volume
	Kg	%	US\$	dm ³
1,0,0,0	72.51	77.48	775.87	26.90
0,1,0,0	250.97	91.28	4000.09	89.70
0,0,1,0	73.21	76.30	765.82	27.30
0,0,0,1	89.51	79.18	973.02	25.00

TABLE IV

DECISION MAKING BASED ON COMBINATION OF OBJECTIVES

Weights	Ja	Am	Bmg	Bcs	Bcr	Br	Kd	V	P	Ap
	MA/m ²	KA/m	T	Wb	Wb	Wb	--	V	--	--
0.25,0.25,0.25,0.25	8.81	54.87	0.698	1.706	1.596	1.399	0.699	272	20	20
0.33,0.34,0.33,0.00	8.81	54.87	0.698	1.706	1.596	1.399	0.699	272	20	20
0.00,0.33,0.34,0.33	6.79	50.88	0.597	1.703	1.582	1.400	0.674	154	20	20
0.00,0.50,0.50,0.00	6.01	51.56	0.519	1.703	1.572	1.378	0.697	110	20	20
0.50,0.50,0.00,0.00	8.89	5.703	0.807	1.867	1.598	1.394	0.700	274	20	20

TABLE V

OBJECTIVE VALUE FOR THE DECISION MAKING OF TABLE III

Weights	Total Weight	Efficiency	Cost	Volume
	Kg	%	US\$	dm ³
0.25,0.25,0.25,0.25	101.13	88.11	1270.09	32.00
0.33,0.34,0.33,0.00	101.13	88.11	1270.09	32.00
0.00,0.33,0.34,0.33	114.13	88.31	1354.30	35.20
0.00,0.50,0.50,0.00	116.51	88.51	1318.60	38.20
0.50,0.50,0.00,0.00	100.21	88.31	1466.70	32.30

To choose the better solution according to the decision maker preferences, a fuzzy algorithm [4] was used. The objectives were weighted in different ways to permit a better comprehension of this problem. Tables II - V show these results.

These results show that 20 poles, 272V, with 20 parallel ways per phase is an interesting solution that aggregated good efficiency, light weight, small volume and an acceptable price. This solution shows that the efficiency is about 88.11 %, the weight is only 101.13 Kg and the active material cost is US\$1.270.09 and the volume is lower as 32 dm³. This solution seems to be a good solution if compared with the results published in the literature [5].

II. REFERENCES

- [1] J. Azzouzi, N.A. Karim, G. Barakat, B. Dakyo, "Axial flux PM synchronous generator design optimization: robustness test of the genetic algorithm approach", EPE 2005 – Dresden, ISBN:90-75815-08-5.
- [2] J. F. Gieras, Rong-Jie Wang, M.J. Kamper, Axial Flux Permanent Magnet Brushless Machines, 2nd edition, Springer, 2008.
- [3] A.H.F. Dias, J.A. Vasconcelos, "Multiobjective genetic algorithms applied to solve optimization problems", IEEE Trans. on Magnetics, 38(2), 1133-1136, 2002.
- [4] R.O. Parreiras, J.H.R.D. Maciel, J.A. Vasconcelos, "The A Posteriori decision in multiobjective optimization problems with Smarts, Promethee II, and a fuzzy algorithm", IEEE Trans. on Magnetics, 42(4): 1139-1142, 2006.
- [5] E. Muljadi, C. P. Butterfield, Yih-huie Wan, "Axial-Flux Modular Permanent-Magnet Generator with a Toroidal Winding for Wind-Turbine Applications", IEEE Trans. on Industry Applications, 35(4), 831-836, 1999.

GA-based Optimized Design of the Novel Compact Transversal-Type UWB Bandpass Filter

¹Sungtek Kahng, ¹Eunchul Shin¹, ²Koon-Tae Kim and ²Hyeong-Seok Kim

¹Dept. of Info. & Telecomm. Eng., University of Incheon, Incheon 402-749, Korea, kahng@incheon.ac.kr

²Dept. of Electrical and Electronics Eng., Chung-Ang University, Seoul 156-756, Korea, kimcaf2@cau.ac.kr

Abstract — A new transversal UWB bandpass filter with a reduced size is realized based upon the use of the Genetic Algorithm(GA) optimization. The proposed design is carried out to have the required performance(Insertion loss, return loss, flat group-delay) over the very wide frequency range. Also we can effectively reduce the entire structure by assigning diverse transmission line segments to each of the two transversal signal paths(increased degree of freedom in design). The design results will be presented theoretically and experimentally.

I. INTRODUCTION

The UWB bandpass filters should have the low insertion and return loss over the ultra-wide band 3.1 GHz - 10.6 GHz and higher selectivity[1]. Particularly, the steep skirt around the band edges is needed, avoiding the increased size of the filter. For this, multi-mode coupling design is adopted in size-constraints[2-5], but is followed by cumbersome extra tuning.

The transversal geometry is brought up to have sharper rejection(steeper skirts) with the size limit[6]. However, the previous works of this structure fail in suggesting the size-reduction technique and forming the ultra-wide band. So we need the minimized structure of the transversal filter and enlarged bandwidth just right for the UWB applications.

We now assign diversified impedance steps in the transversal signal paths, which increases the design degree of freedom for a smaller but higher order filter. Many design unknowns are effectively found by the GA optimization work when the ranges of variables are reasonably given. The design is verified by the comparison with the trustworthy simulation and measurement on the fabricated filter.

II. STANDARD TRANSVERSAL FILTER

The sketch of the basic transversal filter geometry is given in Fig. 1. Elaborating on the geometry of interest, it is composed of the transmission line paths connected in parallel. In [6], they assign only one type of transmission line to each of the two paths which has a very limited number of design variables such as one pair of the length and the characteristic impedance of a transmission line.

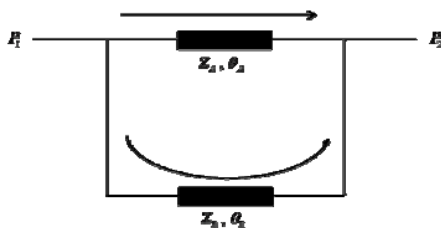


Fig. 1. Basic configuration of the conventional transversal filter

As is shown clearly in Fig. 1, there are just two pairs of design parameters, say, (Z_A, θ_A) and (Z_B, θ_B) . If we adjust the phase difference between the two paths, transmission zeros can be created which determine the band edges and steepness of the skirt. Here comes a set of formulae that describe the scattering parameters and admittance matrix elements.

$$S_{11} = \frac{(Y_0 - Y_{11})(Y_0 + Y_{22}) - Y_{12}Y_{21}}{(Y_0 + Y_{11})(Y_0 + Y_{22}) - Y_{12}Y_{21}}$$

$$S_{21} = \frac{Y_0 Y_{21}}{(Y_0 + Y_{11})(Y_0 + Y_{22}) - Y_{12}Y_{21}} \quad (1)$$

$$Y_{11} = Y_{22} = \frac{1}{jZ_A \tan \theta_A} + \frac{1}{jZ_B \tan \theta_B}$$

$$Y_{12} = Y_{21} = \frac{j}{Z_A \sin \theta_A} + \frac{j}{Z_B \sin \theta_B}$$

where the characteristic admittance of the port(reference) admittance $Y_0 = 1/Z_0$.

The design is to find (Z_A, θ_A) for path A and (Z_B, θ_B) for path B that make the outputs of the two shunt paths out of phase, namely, 180° 's phase difference at the frequency points as the transmission zeros. Due to the lower design degree of freedom(4 design parameters), the path B can't be shorter than 270° , when path A is as long as 90° . So, in order to reduce the size, what comes next is how we will have a sufficient number of the design parameters to improve the frequency response and miniaturization.

III. PROPOSED TRANSVERSAL FILTER AND DESIGN WITH GA.

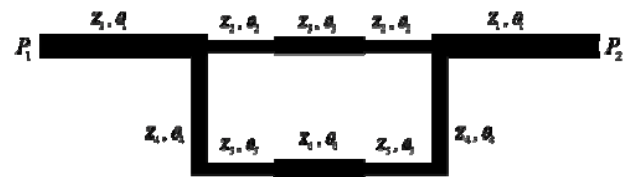
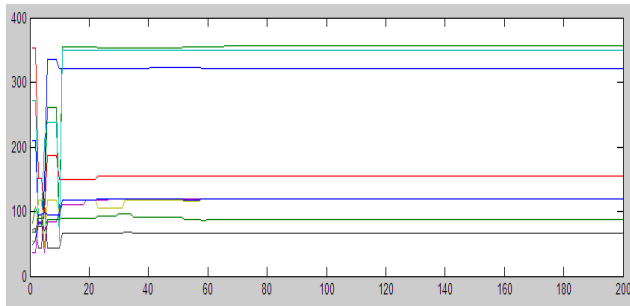


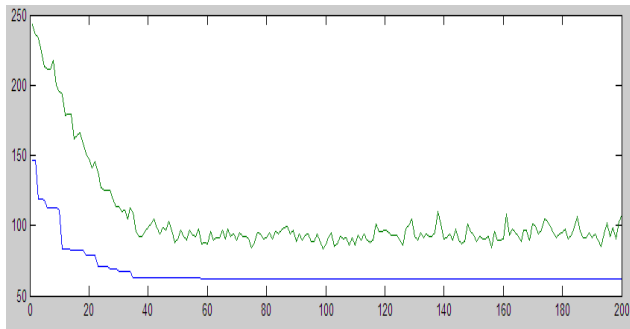
Fig. 2. Basic unit of the proposed transversal Bandpass filter

To get over the shortcomings of the standard transversal-type filter, such as the resultant increment in the overall size to comply with the specifications with 4 design parameters and the narrow stopbands, we come up with the segmentation of each of the two paths and the diversification of the segments' impedance and length. The steps between the neighboring segments result in the impedance differences and this, along with the different lengths of segments, will play the key role in reducing the size of the entire structure and enhance the

problem(Path B of Fig. 2 is roughly 3 times less than that of Fig. 1). Now we can divide a horizontal part of the transmission line loop into 3 segments when a vertical part is assumed to have one segment. Then, the loop transmission line has 8 segments and a total of 16 design parameters as the unknowns. Though the symmetry between the input and output ports is assumed, we have 10 unknowns. Inevitably, the nonlinear equations should be solved numerically. This pushes us to think of the GA optimization to identify the desired values of the 10 or more unknowns. Particularly in the GA optimization process, the number of generations is set as 200 and there are 100 individuals that will be selected by regular GA procedure with crossover, mutation and elitism.



(a) Convergence behavior of the unknowns

(b) Convergence of Cost function(average: upper line , fittest : lower line)
Fig 3. Convergence of the physical/electrical variables and the cost function

For the sake convenience, the cost function is defined to have $|S_{21}| < -20\text{dB}$ at ≤ 3.1 GHz and ≥ 10.9 GHz, and $|S_{11}| < -20\text{dB}$ over 3.2 GHz ~ 10.8 GHz.

Fig. 3 presents that the convergence behaviors of the 10 unknowns and cost function. Both figures tell us that over generation number 20, the unknowns begin to approach the optimal design values for the UWB passband formation. Also, the average cost function is oscillatory, but smooth line is that of the fittest in Fig. 3(b). Each of the individuals and the cost functions are going convergent very fast, since the cost function is defined deterministically with the positions of the target transmission zeros and the levels of transmission and reflection coefficients. Fig. 4 shows the desirable way the unknowns in the design have been identified by the GA and they are converted and trimmed to the right physical dimensions. The results convince us of the validity of the design and proposed filter structure.

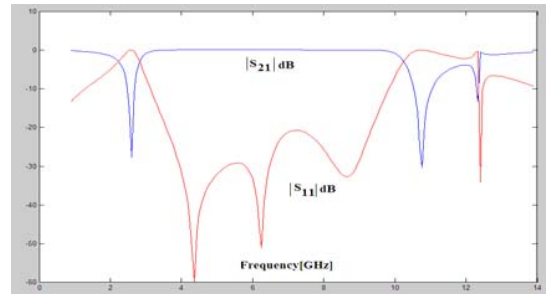
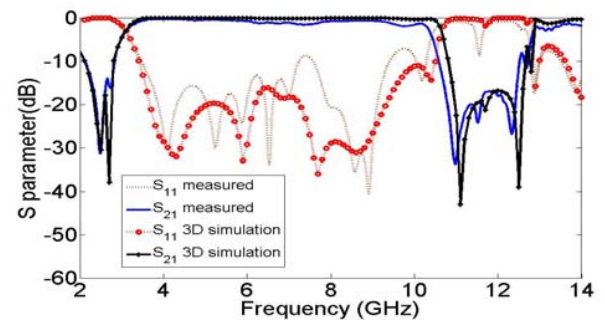
(a) $|S_{21}|$ and $|S_{11}|$ with the trimming from the unknowns found by the GA(b) Measured $|S_{21}|$ and $|S_{11}|$ compared with the simulation

Fig. 4. S-parameters of the measurement and those of the further tuning starting from the initials obtained by the GA approach

IV. CONCLUSION

A novel transversal-type UWB bandpass filter has been designed on the basis of the Genetic Algorithm Optimization. Its frequency response meets the requirements on the UWB bandpass filtering and has the effect of size-reduction owing to the diversified impedance steps in the divided signal paths. Though the geometry is assumed symmetric with respect to the bi-section line in this paper, but it will be meaningful to deal with the asymmetry leading to the more unknowns in the next step. Detailed implementation procedures including fabrication and measured data will be presented in the final version of this paper, which prove the validity of the proposed design along with the more elaborated figures of the Genetic Algorithm

V. REFERENCES

- [1] Sungtek Kahng, and J. Ju, "Minaturized Metamaterial UWB Bandpass filter with Enlarged Stopband", *Patent Issued* 10-2007-0097825, 2008.
- [2] A.C.Kundu and L. Awai, "Control of Attenuation pole Frequency of a Dual-mode Microstrip Ring Resonator Bandpass Filter," *IEEE Trans. Microwave Theory Tech*, MTT-49, June.2001. Page. 1113-1117
- [3] Sungtek Kahng, M. Uhm, S. Lee, "A dual-mode narrow-band channel filter and group-delay equalizer for a Ka-band satellite transponder," *ETRI Journal*, vol. 25, no. 5, pp. 379-386, Oct. 2003.
- [4] Sungtek Kahng, "Efficient Design of Waveguide Filters Reducing Modal Interference through Cross-Shaped Slots", *Journal of The Korea Electromagnetic Engineering Society*, Vol.5 No.1, pp. 21 ~ 25, 2005. 3.
- [5] Sungtek Kahng, "Efficient Design of Waveguide Filters Reducing Modal Interference through Cross-Shaped Slots", *Journal of The Korea Electromagnetic Engineering Society*, Vol.5 No.1, pp. 21 ~ 25, 2005. 3
- [6] Gomez-Garcia, R.; Alonso, J.I.;"Design of sharp rejection and low-loss wide-band planar filters using signal-interference techniques", *Microwave and Wireless Components Letters, IEEE*, Volume 15, Issue 8, Aug. 2005 Page(s):530 – 532

Optimization of Weakly Coupled Multiphysical Problems using Object Oriented Programming

Michael Jaendl*, Alice Köstinger*, Ralph Kutschera*, Christian Magele* and Werner Renhart*

*Institute for Fundamentals and Theory in Electrical Engineering

Graz University of Technology

Kopernikusgasse 24/3, A-8010 Graz, Austria

Email: michael.jaendl@tugraz.at

Abstract—In a demand for continuously shortening engineering cycles and time-to-market windows, precise simulation and problem optimization pose a necessity and a challenge at the same time. Still, accurate problem formulation requires the skills of professionals, for which simulation software serves as a tool in their business, which ought to fit to numerous diverse tasks in a versatile way.

This paper describes the methodology to create such a tool that covers all parts of a multiphysical optimization problem in electrical engineering and its adjoining disciplines as an application of the finite element method.

Making use of modern software engineering principles and well-grounded design, it provides model handling functionality supporting all partitions of prevailing optimization processes.

Index Terms—Object Oriented Programming, Coupled Problems, Optimization.

I. INTRODUCTION

A typical optimization cycle making use of the finite element method (FEM) [1] covers four domains: problem setup, model creation and discretization, solving the equation system, and interpretation of the results to feed the next iteration, if necessary, as shown in Fig. 1.

Well-defined interfaces are mandatory for obtaining best results within such a cycle. Internally, one physic model's calculation relies on the results obtained by another one and vice versa, making accessible data structures mandatory. Externally, interfaces with optimization toolboxes or equation system solvers need to be found. These data structures form the major part of the research reported in this paper.

The central objectives aimed for consist of:

- The facilitation of solving forward problems because of direct - thus fast - data access
- Dynamically adjustable model discretizations in both granularity and geometry
- Option of different models and discretizations for different physics
- Encapsulation of solution data, enabling access control for certain user groups.

As a matter of fact, existing software packages such as EleFAnT [2] impose difficulties on targeting all these objectives equally. In addition, the first and last objective raise a manifest contradiction. To counteract this, methods of object oriented programming (OOP) need to be employed.

II. OBJECT ORIENTED APPROACH

For validating the concept, MATLAB [3] was selected as development environment, while the numerical solutions of the implementation were successfully proven with EleFAnT. The choice came down to MATLAB as it features a number of practical analysis and debugging tools, and starting with version 7.6, native object oriented programming patterns are fully supported.

Compared to procedural programming, the advantage of object orientation for solving FEM optimization problems is obvious. Objects store their own status, so that data can be retrieved any given time. This status can, for example, be the electrical potential of a node object. There is no need to reconstruct the potential from a whole solution matrix, the node of interest is just called for its solution value.

Above that, objects can offer methods to compute some data using sub-objects they instantiate. Thus, the solution value of any given point within a finite element can be calculated using the data provided by the element's nodes.

This leads to consistently defined interfaces. The superclass `FiniteElement`, for example, offers all functionality a finite element has to consist of, regardless of its shape or dimensionality.

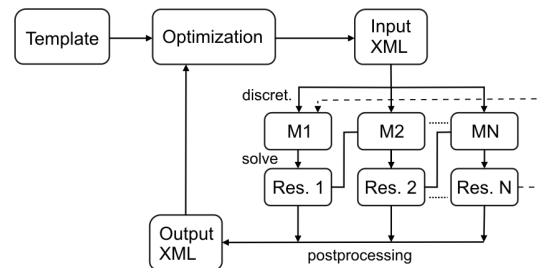


Fig. 1. Optimization Cycle with Data Interfaces

Of course, object oriented programming approaches face their downsides - compared to imperatively coded solutions - when it comes to memory consumption or CPU time usage. Nevertheless, the former fact can be seen to be of minor concern in modern computing surroundings.

Given the respective infrastructure, even the increased CPU usage can be overcome. When, for example, the calculation is

transferred to a clustered computing machine, one can benefit not only from facilitated parallelization of the independent code portions represented by objects, but also from the ability to control the program's flow from independent, relatively cheap machinery.

III. WEAKLY COUPLED OOP FEM EXAMPLE

Hardening of steel components is commonly done using the method of annealing. This often requires controlled heating up of the workpieces to exact temperatures in order to effectuate the desirable material properties.

Therefore, the design of an appropriate heating device would include the determination of the dimensions a heating plate should have, given the fact that the device is supplied with a fixed voltage. The two-dimensional cross-section model of such an appliance is shown in Fig. 2 together with its feed connections shown on either side of the heating plate.

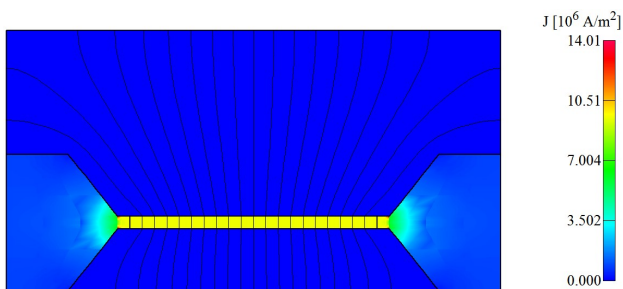


Fig. 2. Current Flow Simulation of Hardening Device

As a result of the current flowing through the heating plate (as depicted in Fig. 2), it will heat up and thus serve as a source for the thermal model simulation. Within this model, the feed connections can be neglected, but as, of course, the workpiece to be hardened has to be taken into account, a problem space discretization entirely different to the current flow model's is the result.

Now, taking advantage of the finite elements being realized as software objects, the input values for source elements of the thermal model can easily be determined for each finite element's integration points. As each FE object of the current flow problem offers its own postprocessing functionality, exact input values - the power dissipation in each integration point as a result of the current density \vec{J} - can be retrieved and fed into the new thermal source elements.

Also, the temperature values in the test points required by the optimization control tool are retrieved in the same manner from the temperature model's FE objects and are then returned to the superordinate control structure for further interpretation.

IV. INTERFACES TO OPTIMIZATION CONTROL STRUCTURES

For interfacing with optimization control structures, XML was chosen as a means of data interchange [4]. XML can easily be created and interpreted, and leaves space for custom extensions. It is therefore widely used for exchanging data in inhomogeneous computing environments.

Leaving further details to the full paper, it is worth being noticed, that the input data specification allows for setting up multiple problem spaces depending on each other to be solved consequently, as shown in the example in III. Different problem spaces can also interdepend on each other, which could further expand the mentioned example by re-feeding the calculated temperature values into the material properties of the current flow problem. In case the change of these properties to be adjusted reaches a percentage lower than a given threshold or stopping condition, the calculation cycle can be halted and the transient state of the whole problem model can be considered stable. The data scheme used for controlling this process is depicted in Fig. 3.

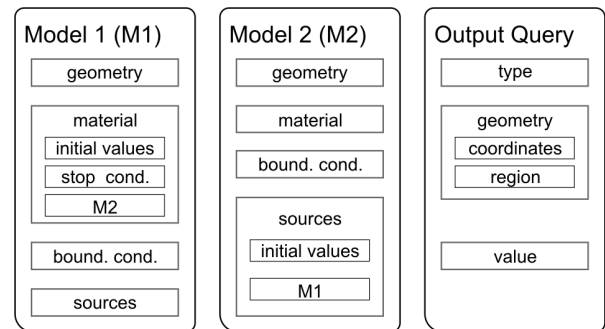


Fig. 3. XML Data Scheme for Controlling Multiple Simulation Models

The results of interest can be queried in a similar manner as well. A part of the input XML string states the properties to be retrieved, i.e. the temperature reached at certain points. The values queried from the finite element objects are then used for populating the appropriate XML entities and passing it back to the control structure.

Also, the program control structure offers tools to users with limited access to perform parameter studies with less degrees of freedom on already created model setups, thus making modelling efforts reusable by others not involved in the optimization process itself but depending on its results.

V. CONCLUSION

It has been shown that object oriented patterns together with careful interface design greatly ease the design process involving optimization in electrical engineering, especially when coupled problems are to be solved.

REFERENCES

- [1] B. Cranganu-Cretu, M. Jaendl, A. Köstinger, C. Magele, W. Renhart and J. Smajic, *Multi-Objective Optimization of Shielding Devices for Eddy-Currents using Niching Evolution Strategies*, Proceedings of the 10th OIPE Workshop, Ilmenau, 2008.
- [2] Computer program package *EleFAnT2D*, IGTE TU Graz, <http://www.igte.tugraz.at>
- [3] Computer program package *MATLAB*, The MathWorks, Inc., <http://www.mathworks.com/>
- [4] T. Bray, J. Paoli, C. M. Sperberg-McQueen, E. Maler and F. Yergeau, *Extensible Markup Language (XML) 1.0 (Fourth Edition)*, W3 Consortium, <http://www.w3.org/TR/2006/REC-xml-20060816/>

Sensitivity based generation of optimized data set for ECT inversion

Sz. Gyimóthy, I. Kiss, J. Pávó, S. Bilicz

Budapest University of Technology and Economics, Egry J. u. 18, H-1521 Budapest, Hungary

E-mail: gyimothy@evt.bme.hu

Abstract: An adaptive sampling method is proposed for creating a forward database that can facilitate the inverse problem solution in NDT. The available sensitivity data are utilized for obtaining an optimal sampling with respect to the piecewise linear interpolation applied for data retrieval. The resulting database provides guaranteed quality of approximation using a relatively few number of samples. The efficiency of the method is demonstrated through a test example.

I. INTRODUCTION

The industrial application of nondestructive testing (NDT) requires sufficiently fast operation in addition to reliability. In a modern computer aided, model based defect reconstruction method a discrete inverse problem has to be solved, in which the most time is spent to the numerical computation of the corresponding forward problem. This is because the latter has to be carried out several times in an optimization loop. In order to reduce the reconstruction time, one should use a fast approximator of the forward problem based on its pre-calculated samples.

In preceding papers the authors proposed the interpolation in a so-called *mesh database* for that purpose [1]. In this method a simplex mesh is spanned over the space of defect model parameters, and the solutions of the forward problem for selected defect prototypes are stored in its nodes. The mesh is generated in an adaptive-incremental manner, so that it results in guaranteed interpolation properties with the fewest possible nodes. In the current paper in turn, it is shown how a much more efficient mesh database can be built by utilizing the sensitivity information on the forward problem. Notably, sensitivity data are easy to get analytically in many electromagnetic problems, this is the case in the problem we are considering now [2].

A. The studied example

Let us introduce the proposed approach through the solution of a simple defect reconstruction problem using eddy current testing (ECT). A relatively large non-magnetic conducting plate is supposed to contain a defect (Fig. 1). The plate is tested with a pancake type coil driven by sinusoidal current. The excited eddy current field is perturbed by the defect, thereby changing the impedance of the probe coil. This impedance change is measured at several probe positions above the plate (in this example they form a rectangular grid of $N = 11 \times 41$ points), and called together the impedance signal, Z_i ($i = 1 \dots N$).

The defect is hypothesized as a single void crack opening onto the backside surface of the plate (OD type), having negligible thickness compared to its other dimensions, and a rectangular shape. Assuming that its position and orientation are known, this crack can be characterized by two parameters, the length l and the depth d . The inverse problem targets the estimation of these model parameters by using the measured impedance signal.

B. The forward problem and the sensitivities

The forward problem aims at determining the measurable impedance change at the i -th probe position, $Z_i(l, d)$, for the given crack parameters l and d . This problem can be formulated as an integral equation derived from the so-called thin crack model [3] and, for instance, can be solved numerically using the method of moments [4].

Sensitivity expresses the variation of the ECT signal with respect to the variation of the crack parameters. For the i -th component of the measured data it can be interpreted as a gradient in the parameter space,

$$\nabla Z_i = \left(\frac{\partial Z_i}{\partial l} \quad \frac{\partial Z_i}{\partial d} \right). \quad (1)$$

The sensitivity values for given l and d can be calculated analytically by solving the specified forward problem and its adjoint problem. The numerical realization can be done using the method described in [2].

II. UTILIZATION OF SENSITIVITY DATA

An approximator of the forward problem is said to be of guaranteed quality if the error of approximation, h , is below the prescribed limit, δ , for all conceivable parameter combinations, l and d , that is

$$h(l, d) \equiv \|\mathbf{Z}(l, d) - \bar{\mathbf{Z}}(l, d)\|_2 < \delta \quad \forall l, d \quad (2)$$

where $\mathbf{Z}(l, d) = [Z_i(l, d)]$ is the impedance signal of the crack, and $\bar{\mathbf{Z}}(l, d)$ its approximate. In our method this latter is a piecewise linear (PL) interpolant based on a simplex mesh. The threshold δ is practically identified with the resolution of the real measurement [1].

In order to meet the requirement (2) with our mesh database, a kind of “distance mapping” is carried out in the background during database generation. Each edge of the mesh is associated with a linear spring. The rest length of such an edge-spring is a function of the impedance data stored in the connected nodes. The whole mesh, as a spring system, is relaxed in a hypothetical *control space*. The size and shape of mesh elements in the control space at equilibrium gives instructions on where the database should be refined. For further details the reader is referred to [5].

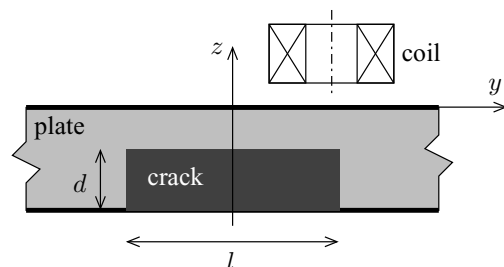


Figure 1: The studied ECT configuration.

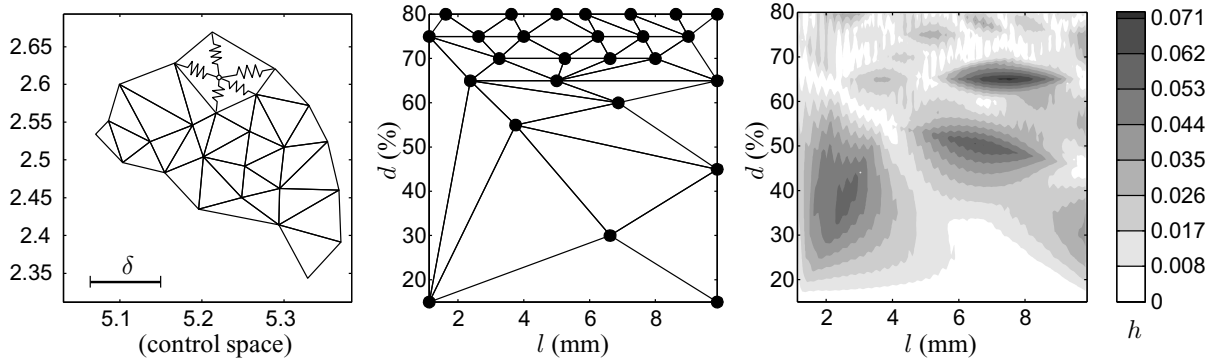


Figure 3. Middle: database structure in the parameter space (d is given in percentage of plate thickness); Left: the structure as seen in the control space (the springs serve for illustration); Right: distribution of the interpolation error $h(l, d)$ over the parameter space (the prescribed limit was 0.08).

Originally, the rest length of spring segments were simply chosen equal to the data distance between the connected nodes [5]. It was demonstrated that with this choice a mesh database showing uniform element density in the control space is optimal with respect to a nearest neighbor (NN) type interpolation. It was also pointed out that this principle can be extended to other interpolation methods, if the rest length is set equal to the interpolation error measured along the given edge.

By using the available sensitivity data we can estimate the average PL interpolation error made along an edge, as illustrated in Fig. 2. First we compute the directional derivatives $\frac{\partial Z_i}{\partial \eta}$ using the gradient in (1), where η is the length parameter along the edge. A higher order approximation, $\hat{Z}_i(\eta)$, of $Z_i(\eta)$ can then be established by using the data $Z_i(0)$, $Z_i(L)$, $\frac{\partial}{\partial \eta} Z_i(0)$ and $\frac{\partial}{\partial \eta} Z_i(L)$, respectively. The average interpolation error for the i -th data component along the k -th edge is defined as

$$h_i^k = \sqrt{\frac{1}{L^k} \int_0^{L^k} |\hat{Z}_i^k(\eta) - \bar{Z}_i^k(\eta)|^2 d\eta^k}. \quad (3)$$

Finally, the rest length of the k -th edge-spring is set equal to the Euclidean norm of the vector $\mathbf{h}^k = (h_1^k, h_2^k, \dots, h_N^k)$.

III. TEST RESULTS

The forward database of the studied problem was generated and optimized for PL interpolation using adaptive mesh generation techniques and spring analogy. The value $\delta = 0.08$ was prescribed as the upper bound of interpolation error (its unit and other details are ignored here). The procedure started with three randomly chosen points. The final database contains 26 nodes. Their distribution in the parameter space is plotted in Fig. 3 (middle).

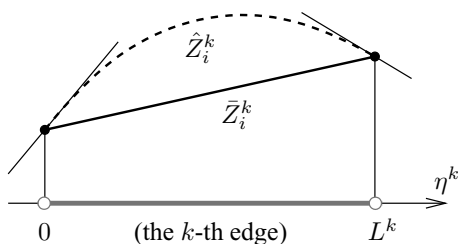


Figure 2: Estimation of the interpolation error.

The picture of the mesh in the control space can be seen in Fig. 3 (left). Some spring segments as well as a “yardstick” of length δ are drawn for illustration. Since the mesh looks quite homogeneous, with its edges slightly shorter than δ , we expect good interpolation characteristics from the corresponding database.

In order to check this latter, the distribution of the error of linear interpolation was computed at several points in the parameter space and is plotted with grayscale shading in Fig. 3 (right). The picture tells that the interpolation error falls below the prescribed δ value everywhere in the studied parameter domain.

IV. CONCLUSIONS

For comparison we generated a database that is optimal with respect to NN interpolation (not shown here) according to [5] using the same error bound δ . It contains 1463 nodes, which clearly shows the difference in favour of the new method.

Certainly, one could use the available sensitivity data to set up a higher order interpolation over simplices, which would even result in higher accuracy. However, the approximation error was not controlled in that case, and in turn this is the main point in the proposed approach.

The developed method requires that the forward problem behaves “smoothly”. Even if this is the case, the mesh resulting in the parameter space is not necessarily valid. The convergence of the method for other types of problems, e.g. allowing more defect parameters, needs further investigations.

REFERENCES

- [1] J. Pávó and S. Gyimóthy, “Adaptive inversion database for electromagnetic nondestructive evaluation,” *NDT&E International*, vol. 40, no. 3, pp. 192–202, 2007.
- [2] J. R. Bowler, S. J. Norton, and D. J. Harrison, “Eddy-current interaction with an ideal crack. II. The inverse problem,” *Journal of Applied Physics*, vol. 75, no. 12, pp. 8138–8144, 1994.
- [3] J. R. Bowler, “Eddy-current interaction with an ideal crack. I. The forward problem,” *Journal of Applied Physics*, vol. 75, no. 12, pp. 8128–8137, 1994.
- [4] J. Pávó and D. Lesselier, “Calculation of eddy current probe signal with global approximation,” *IEEE Transaction on Magnetics*, vol. 42, no. 4, pp. 1419–1422, 2006.
- [5] S. Gyimóthy, I. Kiss, and J. Pávó, “Adaptive sampling technique based on moving meshes for building data-equidistant inversion databases for NDT,” *International Journal of Applied Electromagnetics and Mechanics*, 2009 (to appear).

Dynamic Multilevel Optimization of Machine Design and Control Parameters for PMSM Drive System Based on Correlation Analysis

Shuhong Wang, Xiangjun Meng, Jie Qiu

Faculty of Electrical Engineering, Xi'an Jiaotong University, Xi'an 710049, China;
shwang@mail.xjtu.edu.cn

Jian Guo Zhu, Yi Wang, Youguang Guo, Dikai Liu, Wei Xu

School of Electrical, Mechanical and Mechatronic Systems, University of Technology, Sydney, NSW 2007, Australia

Abstract—In this paper, a multilevel optimization method is proposed for a motor drive system which includes a surface mounted permanent magnet synchronous machine (SPMSM), the converter/inverter, and the control schemes. Firstly, the multilevel optimization is described by using the problem matrix which may be used to allocate the design variables on different levels. The parameters in the problem matrix are deduced by using correlation analysis. Secondly, the architecture and implementation of Multilevel Genetic Algorithm (MLGA) are carried out. As one of the advantages of MLGA, the dynamic adjustment strategy of GA operators is utilized to improve optimal performance. The algorithm is applied to a three-level optimization problem in which the optimization of SPMSM design and the control parameters of drive are considered in different levels. Finally, some results and discussions about the application of the proposed algorithm are presented.

I. INTRODUCTION

Multilevel optimization is an effective method to solve complex optimization problem and it has been reported. Bartheley [1] used problem matrix method to describe the relationship between the objective functions and variables. Q. S. Li, et al. [2] presented Multilevel Genetic Algorithm (MLGA) for the optimization of actively control building under earthquake excitations. Multilevel optimizations are difficult to solve due to the characteristics of nonlinearity, multi-modal functions and mixed discrete variables.

Permanent magnetic synchronous machines (PMSMs) have been an attractive choice for many applications because of its high efficiency and power density. In this paper, MLGA is presented for design optimization of a motor drive system consisting of the drive circuit and an SPMSM controlled by using Field Oriented Control (FOC) to minimize the cost of copper and permanent magnets, and to maximize the efficiency of the motor and the drive system as well as the overshoot and ripples of output torque, speed and d-axis component of current. The finite element analysis (FEA) of the motor is used to calculate the no-load magnetic field, the back-electromagnetic force (back-EMF), the d- and q-axis components of the stator winding inductances.

II. FORMULATION OF MULTILEVEL OPTIMIZATION PROBLEM

In multilevel optimization problems, the relationship between the design variables, constraints and objective functions can be described by a Problem Matrix, as shown in

Fig.1. In Fig. 1, the symbols P_{xx} , i.e. P-values, are the coefficients, which indicate the relative importance between design variables and objective functions, as well as constraints in Correlation Analysis [3]. The larger the P-value is, the less relative importance of the design variable for the objective function is. In this paper, the samples of variables are determined by Design of Experiment (DOE) method. Some commercial statistic software packages, such as Minitab, can provide the module for the relative importance analysis.

Design variables	x_1	x_2	x_3	x_4	\dots	x_m
Objective function	P_{01}	P_{02}	P_{03}	P_{04}	\dots	P_{0m}
Constraint 1	P_{11}	P_{12}	P_{13}	P_{14}	\dots	P_{1m}
Constraint 2	P_{21}	P_{22}	P_{23}	P_{24}	\dots	P_{2m}
\vdots	\vdots	\vdots	\vdots	\vdots	\vdots	\vdots
Constraint n	P_{n1}	P_{n2}	P_{n3}	P_{n4}	\dots	P_{nm}

Fig. 1. Problem matrix

According to P-values in the Problem matrix, the design variables may be arranged on diverse levels. For one objective function, the variables possess similar P-values will be managed on the same level.

III. MULTILEVEL GENETIC ALGORITHM

The architecture of MLGA is shown in Fig. 2. In MLGA the design optimization variables are classified and allocated to different levels according to the relative importance among the variables and objective functions, constraints, as well as the practical engineering weight and optimization sequence. The variables on different levels are encoded independently. Each level may have multiple populations and each of them can adopt different dynamic genetic operators and parameters. Furthermore, the relationship between sub-problems in multilevel problems can be handled by MLGA. The details about Genetic Algorithm (GA) operators, implementation process of MLGA will be presented in the full paper.

IV. APPLICATION OF MULTILEVEL OPTIMIZATION USING MLGA

An SPMSM controlled by FOC, rated at 950W output power, 2000 r/min speed and 128V line-to-line voltage, is used to verify the MLGA for multilevel optimization. The multilevel structure of optimization is shown in Fig. 3.

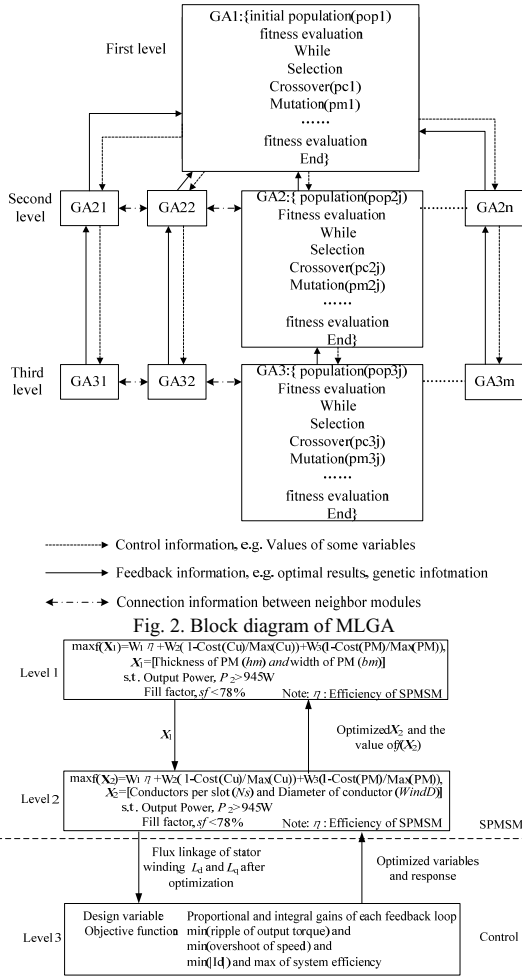


Fig. 3. Three-level structure of optimization

The design variables and objective functions defined on each level based on correlation analysis will be presented in the full paper.

On each level, if the fitness maintains in a defined interval during several consecutive generations, the mutation operator P_{mu} is automatically adjusted according to (1)

$$P_{mu} = \begin{cases} P_m & , n_{unchange} = 0 \\ \frac{n_{unchange}}{\maxgeneration} \omega & , n_{unchange} > 0 \end{cases} \quad (1)$$

where P_{mu} is dynamic mutation value, P_m is initial mutation value, $n_{unchange}$ is the number of unchanged consecutive generations of population fitness, ω is the regulator and \maxgeneration is the terminating iteration.

The design variables, optimal results and comparison of MLGA and traditional GA on Level 1 and 2 are listed in TABLE I.

The proportional and integral gains calculated on the third level are listed in Table. 2. Fig. 4 illustrates the speed of SPMSM before and after PI controller parameters optimization. The transient d-axis component of current,

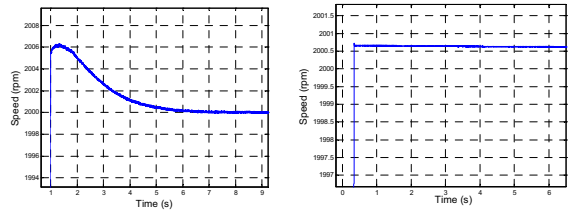
torque and system efficiency will be analyzed and discussed in full paper.

TABLE I
OPTIMAL RESULTS FOR SPMSM IN LEVEL 1 AND 2

Variables and performances	Original design	Multilevel GA	Traditional GA
Thickness of PM, h_m / cm	0.18	0.23	0.21
Width of PM, b_m / cm	3.14	3.03	3.03
Conductors per slot, N_s	72	67	66
Diameter of conductor, $WindD / \text{mm}$	0.5	0.56	0.56
Back-EMF, E_0 / V	66.0	61.9	60.9
q-axis component of current, I_q / A	4.78	5.27	5.37
d-axis component of current, I_d / A	1.60	0.05	0.15
Efficiency, $\eta (\%)$	83.7	86.4	86.1
Cost of winding / RMB	72.6	84.7	83.5
Cost of PM / RMB	41.3	50.9	45.5
Output power, P_2 / W	946	949.5	951
Fill factor, $sf (\%)$	67	77.7	76.5

TABLE II
OPTIMAL RESULTS FOR CONTROL IN LEVEL 3

Variables and performances	Initial values	MLGA
Proportional gain in speed loop	1	18
Integral gain in speed loop	1	0.2
Proportional gain in I_d loop	1	20
Integral gain in I_d loop	1	0.32
Proportional gain in I_q loop	1	29
Integral gain in I_q loop	1	2



(a) Before optimization (b) After optimization
Fig. 4. Transient speed before and after optimization

V. CONCLUSION

According to the features and decision-making sequences, many real-world optimization problems in the engineering systems could be solved in multilevel procedures. This paper proposes an MLGA algorithm for SPMSM drive system to achieve complex multi-objective functions. The Correlation analysis is applied to construct the three-level structure and dynamic mutation operators on each level may dependently improve the convergence of the MLGA. It can be seen that the performances of both SPMSM and its controller can be optimized by using MLGA.

VI. REFERENCES

[1] Barthelemy J-FM. Engineering design application of multilevel optimization methods. In Computer Aided Optimum Design of Structures, Brebbia CA, Hernandez S (eds). Springer: Berlin, 1989; 113–122.
 [2] Q. S. Li, D. K. Liu, A. Y. T. Leung, N. Zhang and Q. Z. Luo. "A multilevel genetic algorithm for the optimum design of structural control systems". *Int. J. Numer. Meth. Engng* 2002; 55:817–834.
 [3] R. Hooke and T.A. Jeeves, "Direct Search", *Journal of ACM*, Vol.8, 1961, pp.212–229.

Variational Level Set Methods in the Roentgen Images Segmentation

Tomasz Rymarczyk¹, Stefan F. Filipowicz^{1,2}, Jan Sikora^{1,3}, Marek Tymburski³,

¹ Electrotechnical Institute, ul. Pozaryskiego 28, 04-703 Warsaw, Poland, e-mail: tomasz@rymarczyk.com

² Institute of Theory of Electrical Engineering, Measurement and Information Systems, Warsaw University of Technology, ul. Koszykowa 75, 00-662 Warsaw, Poland, e-mail: 2xf@nov.iem.pw.edu.pl

³ Lublin University of Technology, Department of Electronics, Nadbystrzycka 38d, 20-618 Lublin

Abstract — The applications of the level set function for images segmentation of the teeth was presented in this paper. There was used the idea of the level set method and variational formulation for geometric active contours. This formulation of the level set method consists of an internal energy term that penalizes the deviation of the level set function and an external energy term that drives the motion of the zero level set toward the desired image features. The proposed algorithm has been applied to real pictures with promising results in the roentgen images segmentation.

I. INTRODUCTION

This paper presents the applications of the level set function for images segmentation of the teeth. The level set idea, devised in Osher and Sethian [4], is known to be a powerful and versatile tool to model evolution of interfaces. Variational formulation for geometric active contours that forces the level set function to be close to a signed distance function [3]. This formulation of the level set method consists of an internal energy term that penalizes the deviation of the level set function and an external energy term that drives the motion of the zero level set toward the desired image features.

II. LEVEL SET METHOD

The level set idea, devised in Osher and Sethian [4], is known to be a powerful and versatile tool to model evolution of interfaces. The original idea behind the level set method was a simple one. Given an interface Γ in \mathbb{R}^n of dimension one, bounding an open region Ω . It was analyzed and computed its subsequent motion under a velocity field \vec{v} . This velocity can depend on position, time, the geometry of the interface (e.g. its normal or its mean curvature) and the external physical conditions. The idea is merely to define a smooth function $\phi(x, t)$, that represents the interface as the set where $\phi(x, t) = 0$. The motion is analyzed by the convection the ϕ values (levels) with the velocity field. The Hamilton-Jacobi equation of the form [2], [5], [6], [7]

$$\frac{\partial \phi}{\partial t} + \vec{v} \cdot \nabla \phi = 0 \quad (1)$$

When flat or steep regions complicate the determination of the contour, reinitialization is necessary. The reinitialization procedure is based by replacing by another function that has

the same zero level set but behaves better. This is based on following partial differential equation:

$$\frac{\partial}{\partial t} \phi + S(\phi)(\nabla \phi - 1) = 0 \quad (2)$$

Figure 1 presents the images segmentation by using the level set method with reinitialization.

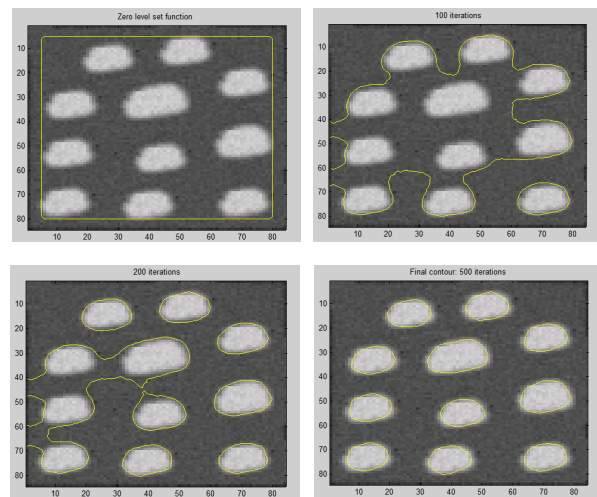


Fig. 1. Image reconstruction – the level set method with reinitialization

III. VARIATIONAL LEVEL SET METHOD

This formulation of the variational level set method consists of an internal energy term that penalizes the deviation of the level set function and an external energy term that drives the motion of the zero level set toward the desired image features. Variational formulation for geometric active contours that forces the level set function to be close to a signed distance function, and therefore completely eliminates the need of the costly reinitialization procedure. The resulting evolution of the level set function is the gradient flow that minimizes the overall energy functional [3]:

$$P(\phi) = \int_{\Omega} \frac{1}{2} (|\nabla \phi| - 1)^2 dx dy \quad (3)$$

An external energy for a function $\phi(x, y)$ is defined as below:

$$E(\phi) = \mu P(\phi) + E_m(\phi) \quad (4)$$

$P(\phi)$ – internal energy,

$E_m(\phi)$ – external energy.

The process for minimization of the functional E is the following:

$$\frac{\partial \phi}{\partial t} = \mu \left[\Delta \phi - \operatorname{div} \left(\frac{\nabla \phi}{|\nabla \phi|} \right) \right] + \lambda \delta(\phi) \operatorname{div} \left(g \frac{\nabla \phi}{|\nabla \phi|} \right) + \omega g \delta(\phi) \quad (5)$$

For more than two phases was introduced the multiple level sets idea by Vese and Chan [1]. The algorithm set formulation and algorithm for the general Mumford-Shah minimization problem in image processing, to compute piecewise-smooth optimal approximations of a given image. The problem can be easily generalized to the case where the domain contains more than two materials.

Then material c is representing following:

$$c = c_1 H(\phi) + c_2 (1 - H(\phi)) \quad (6)$$

where H is the Heaviside function

IV. IMAGE SEGMENTATION

Figure 2 presents the roentgen images segmentation in the following iterative process. The algorithm of the image reconstruction consists variational level set method and the Mumford-Shah function.

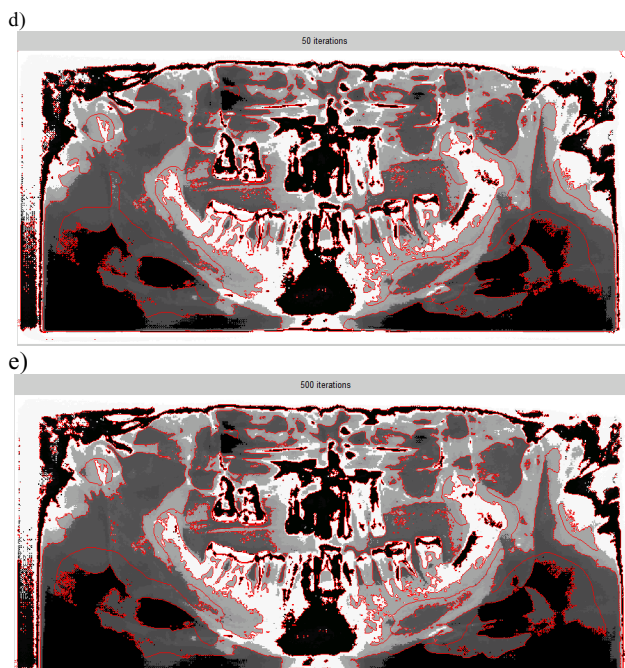
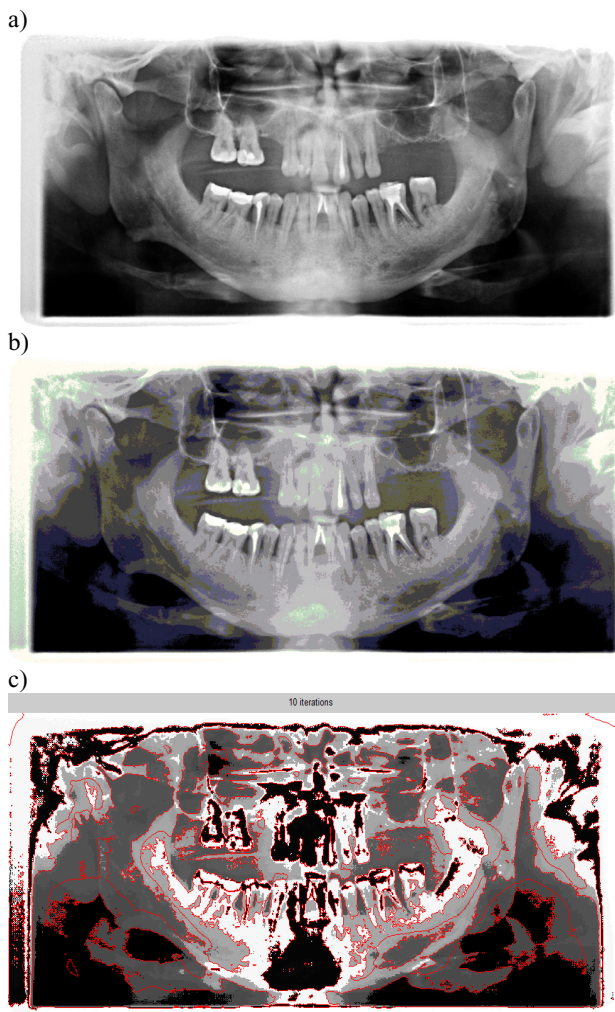


Fig. 2. Image reconstruction: a) the original image , b) the image 256 colors , c) reconstruction after the 10 iterations, d) reconstruction after the 50 iterations, e) reconstruction after the 500 iterations

V. CONCLUSION

The applications of the level set function for images segmentation in the stomatology was presented in this paper. The level set idea is known to be a powerful and versatile tool to model evolution of interfaces. Variational formulation for geometric active contours that forces the level set function to be close to a signed distance function, and therefore completely eliminates the need of the costly reinitialization procedure. The proposed algorithm has been used to real pictures with promising results in the roentgen (teeth) images segmentation.

VI. REFERENCES

- [1] Chan T. and Vese L., "Active contours without edges", *IEEE Trans. Imag. Proc.*, vol. 10, pp. 266-277, 2001.
- [2] Filipowicz S.F., Rymarczyk T., Sikora J., "Level Set Method for inverse problem solution in electrical impedance tomography", *XII ICEBI & V EIT Conference*. Gdańsk 2004.
- [3] Li C., Xu C., Gui C., and M. D. Fox., "Level set evolution without re-initialization: A new variational formulation", *In IEEE Conference on Computer Vision and Pattern Recognition (CVPR)*, volume 1, pages 430-436, 2005.
- [4] Osher S., Sethian J.A., "Fronts Propagating with Curvature Dependent Speed: Algorithms Based on Hamilton-Jacobi Formulations", *Journal of Computational Physics* 79, 12-49, 1988.
- [5] Osher S., Fedkiw R., "Level Set Methods and Dynamic Implicit Surfaces", *Springer*, New York 2003.
- [6] Osher, S., Fedkiw, R., "Level Set Methods: An Overview and Some Recent Results", *Journal of Computational Physics* 169, 463-502, 2001.
- [7] Sethian J.A., "Level Set Methods and Fast Marching Methods", *Cambridge University Press* 1999.

Numerical tool for the design of magnetic sensors based on GMI effect

Léna Abi Rached, Francisco Alves, Yann Le Bihan

LGEP CNRS UMR8507; SUPELEC; Univ Paris Sud-11; UPMC Univ Paris 6, 91192 Gif Sur Yvette, FRANCE/
lena.abirached@lgep.supelec.fr

Abstract — In this paper, we present a numerical procedure for calculating the impedance of a three-layered sandwich, consisting of two metallic ferromagnetic layers separated by a non-magnetic conductive layer, serving to optimize the performances (impedance variation) of these three-layered giant magneto-impedance (GMI) sensors. It consists in the calculation of impedance using finite elements method (FEM). The effective permeability μ_{eff} is obtained from experimental data of the resistive and inductive parts of the impedance. This numerical tool, compared to analytical approaches is more realistic and allows taking into account the leakage flux when the sensor is submitted to high fields.

I. MOTIVATION

Sandwiched GMI sensors are mainly formed of three insulated foils $\text{Fe}_{75}\text{Si}_{15}\text{B}_6\text{Cu}_1\text{Nb}_3/\text{Cu}/\text{Fe}_{75}\text{Si}_{15}\text{B}_6\text{Cu}_1\text{Nb}_3$ [1] or $\text{CoFeSiB}/\text{Cu}/\text{CoFeSiB}$ [2] (Fig.1). In this work, we develop an electromagnetic simulation tool to design sandwiched structures (see Fig.2) in order to optimize geometrical parameters such as width, length and thickness of each layer. Structures, analyzed with different dimensions, are tested to improve the response of the GMI sensor.



Fig. 1 : Sandwiched structure with Finemet® and copper foils (thicknesses 20 μm)

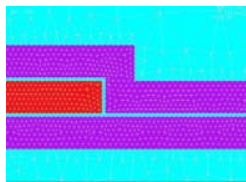


Fig. 2 : GMI 2D model, due to the symmetry of the sensor only half part is meshed

The impedance for the GMI structures is calculated and analyzed as a function of the physical parameters of the device and frequency. This tool should reduce costs and manufacturing time for the micro-sensors fabrication using micro-technology facilities.

From another side, “closed” structure with the magnetic film closing at the edges along the width, and an “open” structure without flux closures are simulated. The “closed” structure is more efficient magnetically and presents a highly inductive response to much higher frequencies than the

“open” structure. The results obtained are practically applicable to the design of GMI magnetic sensors.

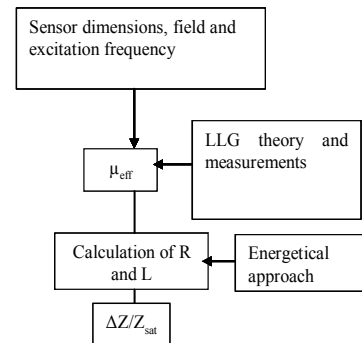


Fig. 3: Flow chart of the design procedure

II. MODEL IMPLEMENTATION

Fig. 3 presents the flow chart of the design procedure. The modeling of GMI sensors allows evaluating and improving of their performances without the need to multiply the realization of costly prototypes. A fine modeling of GMI sensors require the use of numerical modeling methods. Among them, the finite element method (FEM) is particularly adapted since it allows considering structures of arbitrary geometry and taking into account of anisotropic or nonlinear behavioral laws. The FEM is based on a weak variational formulation of the problem. The solution of this formulation is done on a discretized space obtained by meshing the study domain with elements. The fields to be calculated are obtained by a linear combination of simple functions (shape functions) deduced from the size and shape of the elements. These functions are generally defined at the nodes of the elements and are expressed as a linear combination of polynomial functions. The solving of the algebraic system provides an approximate solution of the problem. For the modeling of the GMI sensor, a magneto-dynamic formulation was used taking into account the eddy currents and neglecting the displacement currents. It is based on the calculation of the magnetic vector potential and of the electric scalar potential at the nodes of the meshing with a current as source. Taking into account the high length of a GMI sensor compared to its depth and width, a bidimensional representation of it was adopted. A cross-section of the sensor is then considered and meshed with surfacic elements (triangular in our case since it allows meshing arbitrary shaped areas). After solving of the system, the electric and magnetic fields are deduced from the potentials. These fields allow computing the power losses and

the magnetic energy which provides the sensor impedance real and imaginary parts, respectively.

III. RESULTS

The impedance values of the sandwiched structures with different geometrical dimensions are computed using the finite element method (FEM). The giant magneto-impedance (GMI) is calculated from the difference of the impedance values obtained with high and low permeability (at field saturation) of the magnetic material.

$$\left(\frac{\Delta Z}{Z}\right)_{sat} = 100 \times \frac{|Z_{Hext}| - |Z_{Hsat}|}{|Z_{Hsat}|}$$

Fig.4 shows the experimental results of impedance versus field carried out at 150 kHz. In our samples, the inductive part of the impedance is much higher than the resistive one. The impedance per meter at zero-field is 9Ω/m. For an applicative point of view, we can remark that this sensor requires a bias field if we need to maximize sensitivity of the sensor to AC fields.

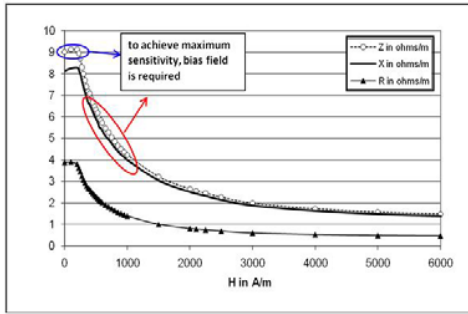


Fig. 4 : Experimental curves Z(H) for an excitation current at 150 kHz

Fig.5 represents simulation (FEM) results by varying the permeability value of the magnetic foil. We observe that the variation of the impedance as function of the permeability fits the experimental curve at 9Ω/m for $\mu_{eff}=4000$. This method only gives values of impedance at zero and saturation fields. In the full paper, we present an implementation of Landau-Lifshitz-Gilbert equation (to estimate μ_{eff}) in the design procedure (Fig.3) in order to determine the MI ratio whatever the magnitude of the external magnetic field is.

We have optimized geometrical dimensions of a sandwiched GMI micro-sensor with the aim to obtain maximum effect at the smallest frequencies. As an example, in Fig.6, a 2D-FEM simulation highlights the frequency behavior of the magnetic/copper width ratio on the MI effect and Fig. 7 presents impedance ratio versus magnetic/Cu width ratios, showing the material width have a determinant effect on the sensor performances at a certain level.

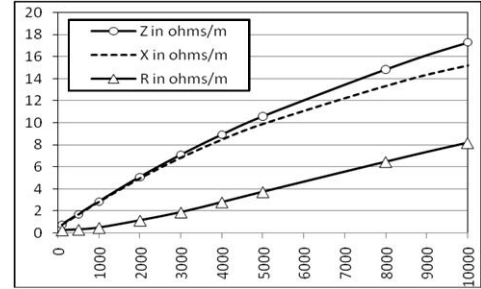


Fig. 5 : Calculated real (Re) and imaginary (Xe) parts of impedance Ze versus relative permeability of the magnetic foils at 150 kHz

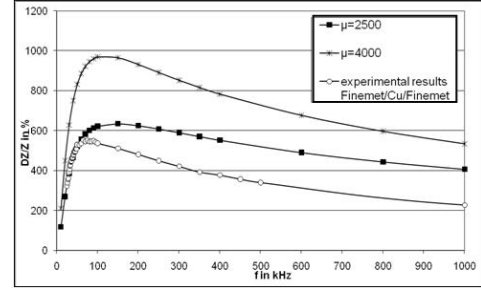


Fig. 6 : Comparison between measurements and FEM simulations on the frequency behavior of MI effect.

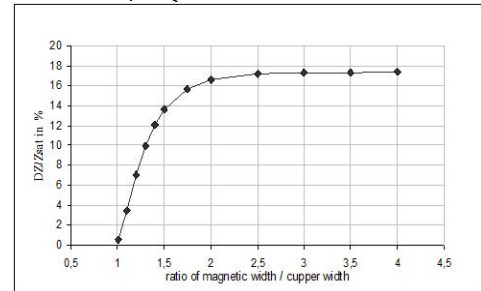


Fig. 7 : Impedance ratio versus magnetic/Cu width ratios. Ferromagnetic and Cu thicknesses are respectively 2μm and 4μm (1:2:1 configuration). Cu width is 100μm. Frequency of excitation current is 150 kHz.

The results depend considerably on shape factors, demonstrating that edge effects are decisive for the GMI performance.

IV. CONCLUSION

The conclusions of this study are of great importance for the successful design of miniaturized GMI devices. The consideration of the influence of the geometry on the GMI helps identify the discrepancies between theory and experiments. Besides we demonstrate that the geometry of the sample must be carefully chosen to improve device performances, especially the length of the sensor had to be taken into account by 3D FEM simulations, in progress.

V. REFERENCES

- [1] F. Alves, J. Moutoussamy, C. Coillot, L. Abi Rached, B. Kaviraj, "Performances of a high sensitive tri-layer F/Cu/F GMI sensor", *Sensors and Actuators A* 145-146 (2008) 241-244
- [2] F. Amalou and M.A.M. Gijs, "Giant magnetoimpedance in trilayer structures of patterned magnetic amorphous ribbons", *Applied Physics Letters* 81, n°9 (2002), 1654-1656.

Harmony Search with Cauchy Operator Applied to the Hysteresis Modeling of a Transformer

Leandro dos Santos Coelho¹ and Viviana Cocco Mariani²

¹Automation and Systems Laboratory, LAS/PPGEPs, Pontifical Catholic University of Paraná
Rua Imaculada Conceição, 1155, Zip code 80215-901, Curitiba, Paraná, Brazil
E-mail: leandro.coelho@pucpr.br

²Department of Mechanical Engineering, PPGEM, Pontifical Catholic University of Paraná
Rua Imaculada Conceição, 1155, Zip code 80215-901, Curitiba, Paraná, Brazil
E-mail: viviana.mariani@pucpr.br

Abstract— The Jiles-Atherton (J-A) model is widely used to the modeling of the nonlinear characteristics of magnetic materials. It can include the effects of stress, temperature and external field frequency and is given in the form of a set of non-linear and first-order ordinary differential equations. This paper presents a harmony search (HS) optimization method based on Cauchy distribution (CHS) to the parameter identification of the J-A model of hysteresis is proposed. The performance of the HS and the proposed CHS optimization approach are evaluated and compared with result of hysteresis modeling, which is included in the dynamic model of a single-phase transformer, of recent literature.

Index Terms— magnetic hysteresis, modeling, Jiles-Atherton model, optimization, harmony search, transformer.

I. INTRODUCTION

Hysteresis are encountered in a wide range of physical systems and devices, such as magnetic materials, piezoelectric and piezoceramic actuators, shape memory alloys, electronic relay circuits, among others. Hysteresis is a complex process. Only complicated models describe this phenomenon with satisfying accuracy.

The description of magnetization processes in soft magnetic materials proposed by Jiles and Atherton [1] still remains one of the most widely used ones and has been the subject of considerable interest in the scientific community due to its physical backgrounds and the possibility to include the effects of stress, temperature and external field frequency. It is given in the form of a set of non-linear and first-order ordinary differential equations. Such model typically contains a set of parameters referred to herein as “model parameters” or “material parameters,” that need to be extracted from experimental data.

The paper presents an attempt to estimate the parameters of Jiles and Atherton (J-A) model description of magnetization process using an improved harmony search (HS) optimization method using Cauchy operator (CHS). The proposed CHS method was validated into dynamical model of a single-phase transformer. In this context, the data of single-phase transformer used in validation was also employed in [2].

II. DYNAMIC MODEL OF A TRANSFORMER AND J-A HYSTERESIS MODEL

By using simplifications presented in [2] and knowing transformer geometry, a single-phase transformer model obtains the following form

$$u_1 = i_1 R_1 + L_{\sigma 1} \frac{di_1}{dt} + N_1 A \frac{dB}{dH} \left(\frac{N_1}{l} \frac{di_1}{dt} + \frac{N_2}{l} \frac{di_2}{dt} \right) \quad (1)$$

$$u_2 = i_2 R_2 + L_{\sigma 2} \frac{di_2}{dt} + N_2 A \frac{dB}{dH} \left(\frac{N_1}{l} \frac{di_1}{dt} + \frac{N_2}{l} \frac{di_2}{dt} \right) \quad (2)$$

where u_1 , u_2 , and i_1 , i_2 are the primary and secondary voltages and currents, respectively; R_1 and R_2 are the primary and secondary resistances, $L_{\sigma 1}$ and $L_{\sigma 2}$ are the primary and secondary leakage inductances, N_1 and N_2 are the primary and secondary number of turns, A is the average area of the transformer iron core, l is the mean path length of the magnetic flux, H is the magnetic field, and B is magnetic flux densities.

In Eqs. (3) and (4), term dB/dH can now be determined using the J-A hysteresis model. The original J-A hysteresis model with magnetic field as an independent variable, delivered from [3], [4] is given by [2]

$$\frac{dM}{dH} = \frac{(1-c) \frac{dM_{irr}}{dH_c} + c \frac{dM_{an}}{dH_e}}{1 - \alpha c \frac{dM_{an}}{dH_e} - \alpha(1-c) \frac{dM_{irr}}{dH_c}} \quad (3)$$

$$\frac{dM_{an}}{dH_e} = \frac{M_s}{a} \left[1 - \coth^2 \left(\frac{H_e}{a} \right) + \left(\frac{a}{H_e} \right)^2 \right] \quad (4)$$

$$\frac{dM_{irr}}{dH_e} = \frac{\gamma(M_{an} - M_{irr})}{k\delta} \quad (5)$$

$$\delta = \begin{cases} +1, & dH/dt \geq 0 \\ -1, & dH/dt < 0 \end{cases} \quad (6)$$

$$\gamma = \begin{cases} 1, & (M_{an} - M_{irr})dH_e \geq 0 \\ 0, & (M_{an} - M_{irr})dH_e < 0 \end{cases} \quad (7)$$

$$\frac{dB}{dH} = \mu_0 \left(1 + \frac{dM}{dH} \right) \quad (8)$$

where M_{an} and M_{irr} are the anhysteretic and irreversible magnetizations, respectively; μ_0 is the permeability of vacuum, and dH_e is denoted as $dH_e = dH + \alpha \cdot dM$. The parameters of the original J-A hysteresis model that must be identified are: the anhysteretic behavior a , the main field parameter α , the saturation magnetization M_s , the parameter which is proportional to the hysteresis loop width and domain flexing constant c , and the pinning parameter k .

III. FUNDAMENTALS OF HARMONY SEARCH

The HS algorithm proposed by [5] is a metaheuristic optimization algorithm based on the musical process of searching for a perfect state of harmony, such as jazz improvisation. In this improvisation process, members of the musical group try to find the best harmony as determined by an aesthetic standard, just as the optimization algorithm tries to find the global optimum as determined by the objective function. The notes and the pitches getting played by the individual instruments determine the aesthetic quality, just as the objective function value is determined by the values assigned to design variables.

The optimization procedure of the HS algorithm consists of steps 1-5, as follows:

1. Define the optimization problem and HS algorithm parameters.
2. Initialize the harmony memory.
3. Improvise a new harmony from the harmony memory.
4. Update the harmony memory.
5. Repeat Steps 3 and 4 until the termination criterion is satisfied.

In the proposed CHS approach, an operator based on Cauchy distribution is introduced in step 3 of classical HS to escape from local optima.

IV. OPTIMIZATION RESULTS

The objective function to be minimized using HS and CHS is given by

$$F = \sqrt{\frac{\sum_{i=1}^N (B_{i\text{meas}} - B_{i\text{model}})^2}{N}} \quad (9)$$

where $B_{i\text{meas}}$ is the measured magnetic flux density, $B_{i\text{model}}$ is the calculated magnetic flux density from the model, and N is the number of points of measured magnetic flux density. For the measurement purpose, the transformer was supplied with sinusoidal voltage whilst the primary voltage and current were being measured. The hysteresis loop with magnetization curve was then determined from known geometry of the iron core and measured data [2].

Parameters identified using HS and CHS for the J-A model are presented in Table I. In terms of mean and minimum F values in 30 runs (adopted 60,000 evaluations of objective function in each run), results shown in Table I indicate that CHS can tackle the J-A modelling more efficiently than the classical HS. Fig. 1 presents a comparison of measured and calculated hysteresis loop using the best results obtained by

CHS. Table II present the best results using CHS and the result using differential evolution (DE) given in [2]. Based on results of Table II, the DE and CHS presented similar performance in terms of F values.

TABLE I
BEST RESULTS OF F (30 RUNS) FOR THE J-A MODEL

Optimization Techniques	Objective Function F in 30 Runs			
	Maximum (Worst)	Mean	Minimum (Best)	Std. Dev.
HS	0.03894	0.03316	0.03155	0.00230
CHS	0.03474	0.03257	0.03154	0.00104

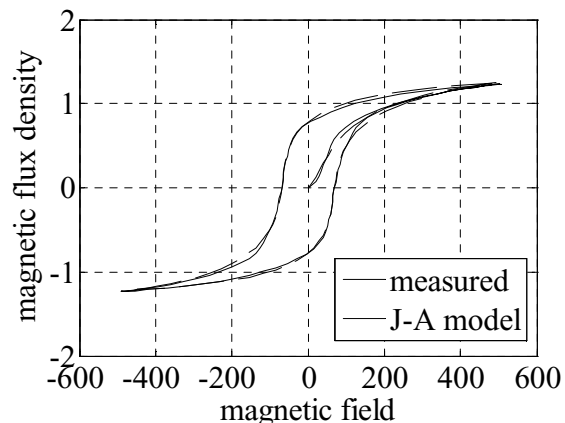


Fig. 1. Comparison of measured and calculated B - H hysteresis loop.

TABLE II
PARAMETERS OBTAINED BY BEST RESULTS

Parameter	DE [2]	CHS
a (A/m)	226.25	223.27
α	$0.502 \cdot 10^{-3}$	$0.497 \cdot 10^{-3}$
M_s (A/m)	$1.335 \cdot 10^6$	$1.331 \cdot 10^6$
c	0.724	0.721
k (A/m)	300.05	295.49
F	0.03154	0.03154

V. CONCLUSION

Hysteresis is a complex phenomenon, which is important both from theoretical and practical points of view. A relevant approach to describe hysteresis can be found in the J-A model. In this paper a novel approach to estimation of J-A model parameters has been presented. The proposed CHS approach was successful to estimate the J-A model parameters.

REFERENCES

- [1] D. C. Jiles and D. L. Atherton, "Theory of ferromagnetic hysteresis," *Journal of Magnetism and Magnetic Materials*, vol. 61, no. 1-2, pp. 48-60, 1986.
- [2] M. Toman, G. Stumberger, and D. Dolinar, "Parameter identification of the Jiles-Atherton hysteresis model using differential evolution," *IEEE Transactions on Magnetics*, vol. 44, no. 6, pp. 1098-1101, 2008.
- [3] J. V. Leite, N. Sadowski, P. Kuo-Peng, N. J. Batistela, J. P. A. Bastos, and A. A. de Espindola, "Inverse Jiles-Atherton vector hysteresis model," *IEEE Trans. Magn.*, vol. 40, no. 4, pp. 1769-1775, Jul. 2004.
- [4] J. P. A. Bastosa and N. Sadowski, *Electromagnetic Modeling by Finite Element Methods*. Boca Raton, FL, USA: CRC Press, pp. 438-455, 2003.
- [5] Z. W. Geem, J. H. Kim, and G. V. Loganathan, "A new heuristic optimization algorithm: harmony search," *Simulation*, vol. 76, no. 2, pp. 60-68, 2001.

Automatic Design of Insulation Structure of Power Transformer Based on Sensitivity Analysis

Liu Yang, Cui Xiang

School of electrical and electronic engineering, North China Electric Power University
Box 10, 619 Yonghua North Street, Baoding city, Hebei province, 071003, P.R. China
E-mail: hdwllly@163.com

Abstract—Based on the finite element method, a new algorithm for evaluating the sensitivity of electric field intensity to geometric parameters is presented in this paper. By means of this algorithm, the sensitivity can be evaluated as like the nodal potential solution. Adopting Hermite polynomial instead of Taylor polynomial greatly decreased the order of the high-order cross sensitivity. Numerical results show that this algorithm is very effective and can be used in the automatic design of the insulation structure in power transformer.

I. INTRODUCTION

In the automatic design of electromagnetic apparatus, the optimization technique based on the derivatives of objective function, i.e. sensitivity, is often selected as a numerical tool. It is key to evaluate the partial derivatives of objective function with respect to the geometric parameters in this technique. Dr. J. L. Coulomb proposed a Taylor polynomial approximation of objective function and an algorithm based on Jacob's matrix [1]. In general Taylor polynomial order is relatively high, and the stability of objective function is low. It takes up too much memory of computer and the allowable variation of the designed parameters is limited.

In this paper, the multi-dimensional Hermite polynomial and a new algorithm of computing the sensitivity which has nothing to do with Jacob's matrix is presented.

II. HERMITE POLYNOMIAL

The 2D Hermit polynomial $f_h(p,q)$ can be expressed as follows:

$$\begin{aligned} f_h(p,q) = & f_{ij}\alpha_{ij} + f_{i+1,j}\alpha_{i+1,j} + f_{i,j+1}\alpha_{i,j+1} \\ & + f_{i+1,j+1}\alpha_{i+1,j+1} + f'_{i,j(p)}\beta_{i,j} + f'_{i+1,j(p)}\beta_{i+1,j} \\ & + f'_{i,j+1(p)}\beta_{i,j+1} + f'_{i+1,j+1(p)}\beta_{i+1,j+1} + f'_{i,j(q)}\gamma_{i,j} \\ & + f'_{i+1,j(q)}\gamma_{i+1,j} + f'_{i,j+1(q)}\gamma_{i,j+1} + f'_{i+1,j+1(q)}\gamma_{i+1,j+1} \\ & + f''_{i,j(pq)}\eta_{i,j} + f''_{i+1,j(pq)}\eta_{i+1,j} + f''_{i,j+1(pq)}\eta_{i,j+1} \\ & + f''_{i+1,j+1(pq)}\eta_{i+1,j+1} \end{aligned} \quad (1)$$

where $f_{i,j}, f_{i+1,j}, f_{i,j+1}, f_{i+1,j+1}$ are the function values of the four corners of each division, $f'_{i,j}, f'_{i+1,j}, f'_{i,j+1}$ and $f'_{i+1,j+1}$ are one order partial derivatives, $f''_{i,j}, f''_{i+1,j}, f''_{i,j+1}$ and $f''_{i+1,j+1}$ are two order cross partial derivatives and $\alpha_{ij}(p,q), \beta_{ij}(p,q), \gamma_{ij}(p,q), \eta_{ij}(p,q)$ are division fundamental functions of the sixth power. The results in [2] show this technique is effective.

III. COMPUTATION OF SENSITIVITY

For electrostatic field problem, the finite element equation is:

$$K \varphi = 0 \quad (2)$$

where φ is nodal potential, K is stiffness matrix. If three-node triangular element is used, K can be calculated by

$$K_{ij}^e = \varepsilon \iint_{\Delta_e} \nabla N_i^e \cdot \nabla N_j^e dx dy \quad (3)$$

$$N_i^e = \frac{1}{2\Delta_e} (a_i + b_i x + c_i y) \quad (4)$$

where N_i^e is the function in the e -th triangular element, where Δ_e, a_i, b_i, c_i are functions depended on the nodal coordinates.

A. One Parameter Problem

Let p be a geometric parameter, then $\partial K_{ij}^e / \partial p$ may be calculated as follows:

$$\begin{aligned} \frac{\partial K_{ij}^e}{\partial p} = & \frac{\partial K_{ij}^e}{\partial \Delta_e} \sum_{k=1}^3 \left(\frac{\partial \Delta_e}{\partial x_k} \frac{\partial x_k}{\partial p} + \frac{\partial \Delta_e}{\partial y_k} \frac{\partial y_k}{\partial p} \right) + \frac{\partial K_{ij}^e}{\partial b_i} \sum_{k=1}^3 \left(\frac{\partial b_i}{\partial y_k} \frac{\partial y_k}{\partial p} \right) \\ & + \frac{\partial K_{ij}^e}{\partial b_j} \sum_{k=1}^3 \left(\frac{\partial b_j}{\partial y_k} \frac{\partial y_k}{\partial p} \right) + \frac{\partial K_{ij}^e}{\partial c_i} \sum_{k=1}^3 \left(\frac{\partial c_i}{\partial x_k} \frac{\partial x_k}{\partial p} \right) + \frac{\partial K_{ij}^e}{\partial c_j} \sum_{k=1}^3 \left(\frac{\partial c_j}{\partial x_k} \frac{\partial x_k}{\partial p} \right) \end{aligned} \quad (5)$$

Suppose E^e is the electric field intensity in the e -th element

$$E^e = \sqrt{(E_x^e)^2 + (E_y^e)^2} \quad (6)$$

$$\text{Then} \quad \frac{\partial E^e}{\partial p} = \frac{1}{E^e} \left(E_x^e \frac{\partial E_x^e}{\partial p} + E_y^e \frac{\partial E_y^e}{\partial p} \right) \quad (7)$$

The terms in (7) can be calculated by following way

$$\frac{\partial E_x^e}{\partial p} = -\frac{E_x^e}{\Delta_e} \frac{\partial \Delta_e}{\partial p} - \frac{1}{2\Delta_e} \sum_{i=1}^3 \left(\varphi_i \frac{\partial b_i}{\partial p} + b_i \frac{\partial \varphi_i}{\partial p} \right) \quad (8)$$

$$\frac{\partial E_y^e}{\partial p} = -\frac{E_y^e}{\Delta_e} \frac{\partial \Delta_e}{\partial p} - \frac{1}{2\Delta_e} \sum_{i=1}^3 \left(\varphi_i \frac{\partial c_i}{\partial p} + c_i \frac{\partial \varphi_i}{\partial p} \right) \quad (9)$$

The column matrix in (8) and (9) may be solved from (2)

$$\frac{\partial \varphi}{\partial p} = -K^{-1} \frac{\partial K}{\partial p} \varphi \quad (10)$$

Optimization

B. Two Parameters Problem

Now suppose that p and q are two geometric parameters. Then we can derive (7) respect to the parameter q , and find the new formula of the derivatives of E^e :

$$\begin{aligned} \frac{\partial^2 E^e}{\partial p \partial q} = & -\frac{1}{E^e} \frac{\partial E^e}{\partial p} \frac{\partial E^e}{\partial q} + \frac{1}{E^e} \frac{\partial E_x^e}{\partial p} \frac{\partial E_x^e}{\partial q} + \frac{E_x^e}{E^e} \frac{\partial^2 E_x^e}{\partial p \partial q} \\ & + \frac{1}{E^e} \frac{\partial E_y^e}{\partial p} \frac{\partial E_y^e}{\partial q} + \frac{E_y^e}{E^e} \frac{\partial^2 E_y^e}{\partial p \partial q} \end{aligned} \quad (11)$$

where $\frac{\partial^2 E_x^e}{\partial p \partial q}$ and $\frac{\partial^2 E_y^e}{\partial p \partial q}$ can be calculated from (8) and (9):

$$\begin{aligned} \frac{\partial^2 E_x^e}{\partial p \partial q} = & -\frac{1}{\Delta_e} \frac{\partial \Delta_e}{\partial p} \frac{\partial E_x^e}{\partial q} + \frac{E_x^e}{\Delta_e} \frac{\partial \Delta_e}{\partial p} \frac{\partial \Delta_e}{\partial q} - \frac{E_x^e}{\Delta_e} \frac{\partial^2 \Delta_e}{\partial p \partial q} \\ & + \frac{1}{2\Delta_e^2} \frac{\partial \Delta_e}{\partial q} \sum_{i=1}^3 (\varphi_i \frac{\partial b_i}{\partial p} + b_i \frac{\partial \varphi_i}{\partial p}) - \frac{1}{2\Delta_e} \\ & \sum_{i=1}^3 (\frac{\partial b_i}{\partial p} \frac{\partial \varphi_i}{\partial q} + \varphi_i \frac{\partial^2 b_i}{\partial p \partial q} + \frac{\partial \varphi_i}{\partial p} \frac{\partial b_i}{\partial q} + b_i \frac{\partial^2 \varphi_i}{\partial p \partial q}) \end{aligned} \quad (12)$$

$$\begin{aligned} \frac{\partial^2 E_y^e}{\partial p \partial q} = & -\frac{1}{\Delta_e} \frac{\partial \Delta_e}{\partial p} \frac{\partial E_y^e}{\partial q} + \frac{E_y^e}{\Delta_e} \frac{\partial \Delta_e}{\partial p} \frac{\partial \Delta_e}{\partial q} - \frac{E_y^e}{\Delta_e} \frac{\partial^2 \Delta_e}{\partial p \partial q} \\ & + \frac{1}{2\Delta_e^2} \frac{\partial \Delta_e}{\partial q} \sum_{i=1}^3 (\varphi_i \frac{\partial c_i}{\partial p} + c_i \frac{\partial \varphi_i}{\partial p}) - \frac{1}{2\Delta_e} \\ & \sum_{i=1}^3 (\frac{\partial c_i}{\partial p} \frac{\partial \varphi_i}{\partial q} + \varphi_i \frac{\partial^2 c_i}{\partial p \partial q} + \frac{\partial \varphi_i}{\partial p} \frac{\partial c_i}{\partial q} + c_i \frac{\partial^2 \varphi_i}{\partial p \partial q}) \end{aligned} \quad (13)$$

The column matrix $\frac{\partial^2 \varphi}{\partial p \partial q}$ in (12) and (13) may be solved from (10) as follows:

$$\frac{\partial^2 \varphi}{\partial p \partial q} = -K^{-1} \left(\frac{\partial K}{\partial p} \frac{\partial \varphi}{\partial q} + \frac{\partial^2 K}{\partial p \partial q} \varphi + \frac{\partial K}{\partial q} \frac{\partial \varphi}{\partial p} \right) \quad (14)$$

IV. NUMERICAL VERIFICATION

For showing the application of above algorithm, we analysis the field a coaxial cable with inner radius $R_1=1\text{cm}$, outer radius $R_2=5\text{cm}$, applying 100V between conductors. The sensitivity of electric field intensity to R_1 and R_2 at five specified points is evaluated. Numerical results and analytic values are shown in Table I. These results show that the new algorithm in this paper is very effective.

TABLE I. COMPUTATIONAL RESULTS OF SENSITIVITIES

Specified points		X=0.86 Y=4.56	X=2.94 Y=0.96	X=1.66 Y=1.69	X=0.85 Y=1.66
E	Values(V/cm)	48.09	32.22	19.77	13.00
	Error(%)	-3.49	2.65	0.29	-1.12
$\frac{\partial E}{\partial R_1}$	Values(V/cm ²)	30.53	19.88	12.20	8.03
	Error(%)	-1.39	1.94	-0.43	-1.82
$\frac{\partial E}{\partial R_2}$	Values(V/cm ²)	-5.98	-4.01	-2.46	-1.59
	Error(%)	-3.47	2.67	0.34	-2.59
$\frac{\partial^2 E}{\partial R_1 \partial R_2}$	Values(V/cm ³)	-7.47	-4.97	-3.03	-1.98
	Error(%)	-2.87	2.55	-0.44	-2.72

Fig. 1 is a simplified model in the lower part of the insulation structure of a 500kV power transformer. Let the maximum of the electric field intensity on the outer surface of the insulation layer of the electrostatic ring be the objective function $f(x)$. Suppose that R_1 and B be two geomrteic parameters.

In this design, the objective function is defined by

$$f(B, R_1) = (E - E_0)^2 \quad (15)$$

where E is the maximum of electric field intensity on the outer surface of the insulation layer of the electrostatic ring and E_0 is the specified design electric field intensity. Now, we hope to obtain a design so that $E_0=5.60\text{kV/mm}$ when $500/\sqrt{3}\text{ kV}$ is applied between the high-voltage winding and the low-voltage winding. Applying above procedure of automatic design based on the genetic algorithm to the design, through computation of 6 generations and 37 seconds *cpu* time, we can obtain a desired design with $E=5.60\text{kV/mm}$ in which $B=83.0\text{mm}$, $R_1=10.7\text{mm}$. In order to check verification of the design, we also use the finite element method to calculate the maximum of electric field intensity that is 5.64kV/mm . The relative error is 0.71% between the electric field intensities calculated by the finite element method and by the sub-region Hermite polynomials. Therefore, above procedure of automatic design is very effective.

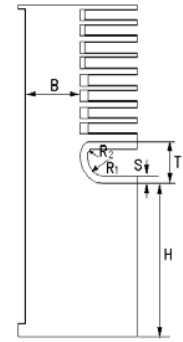


Fig. 2. Insulation structure of a 500kV transformer.

V. CONCLUSION

This optimization method has adopted Hermite polynomials in stead of Tolor polynomial, which has greatly decreased the order of the high cross sensitivity. The computation of sensitivity discussed in this paper is based on the finite element method. Numerical results show that this algorithm is very effective.

VI. REFERENCES

- [1] J.L.Coulomb, *A methodology for the determination of global electromechanical quantities from a finite element analysis and its application to the evaluation of magnetic force, torque and stiffness*, *IEEE Trans. Magn.*, vol. 19, no. 6, pp.2514-2519, November 1983
- [2] Yang Liu, Xiang Cui, *Sensitivity analysis of electric field intensity to geometric parameters in shape optimization*, *Proceedings of the Fourth International Conference on Electromagnetic Field Problems and Applications*, Tianjin, China, September 18-20, 2000, pp. 230-233.

The Use of Case-Based Reasoning in Creating a Prototype for Electromagnetic Device Optimization

Jun Ouyang and David A. Lowther

Department of Electrical and Computer Engineering, McGill University,
3480 University Street, Montreal, H3A 2A7, Canada
jun.ouyang@mail.mcgill.ca, david.lowther@mcgill.ca

Abstract — The effectiveness of a case-based reasoning system for the preliminary design of electromagnetic (EM) devices is heavily dependent on a highly competent case base to allow fast exploration of the design space and make high-quality decisions. However, sufficient good cases are difficult to obtain from industrial examples. In this paper, the construction of a competent case base for EM devices based on a refined combined competence model is described. This case base involves functional, geometrical and material information for EM devices.

I. INTRODUCTION

The optimization of an electromagnetic device or system, such as an electrical machine, needs a starting point in the design space for the search. There are two approaches to this task. The first is known as “sizing” and relies on simple (and often inaccurate) magnetic circuit models. The second is an approach used by experienced designers and is based on previous solutions. While the former approach has been used in computer based systems, the latter paradigm is somewhat more difficult to implement as it requires a significant amount of data mining and classification. The approach which embodies this is known as “Case-Based Reasoning” (CBR) [1]. The problem to be considered is that of a search space with a very large number of dimensions (design parameters) and performance requirements (which may be multi-objective). This results in an extremely complex Response Surface which is difficult, if not impossible, to model. The approach proposed using CBR provides a methodology for exploring the design space based on previous design information, i.e. the performance results of tested designs. While, in the conventional industrial approach, these designs in the database would normally be those which have been built and tested, the existence of advanced analysis tools and a virtual laboratory provides an opportunity to generate a synthetic database which could include both “good” and “bad” designs and can complement those actually constructed. Two previous papers have described the construction of an effective case base library, its role in the design process and the theoretical fundamentals of competence for a case-base[2],[3], and it is the intention of this paper to further explore an approach to classifying the cases in terms of their “competence”, or their usefulness in representing the design space, and thus to refine the original combined competence model given in [3]. To do this, it is necessary to develop a methodology for determining “competence”.

II. A REFINED COMBINED COMPETENCE MODEL

The refined combined competence model presented here is evolved from the previous work to include the calculation of

the the coverage-range of low-quality as well as high-quality cases. The concept of how well a particular example can be generalized to represent the surrounding design space is embodied in a “combined competence” model which is formally described with the following concepts and formulae. First, this model adopts the definitions of coverage, reachability, and the four classes of cases in any case base as described in Smyth and McKenna’s competence model [4]; then it illustrates how to compute the case base competence in two situations. The first relates to a uniform distribution of cases; and the second to a nonuniform distribution. Finally, it calculates the cover-range of competent cases [4].

Given a case-base $C = \{c_1, \dots, c_n\}$, for $c \in C$, $\text{Adaptable}(c, b)$ is an adaptation process which transforms a case retrieved (c) into a solution appropriate for the presented problem (b).

The following definitions are then made:

$\text{Coverage}(c) = \{c_i \in C : \text{Adaptable}(c, c_i)\}$

$\text{Reachable}(c) = \{c_i \in C : \text{Adaptable}(c_i, c)\}$

Note that these are conditions which should hold for any optimization algorithm.

Then we can define the following:

- Pivotal Case: $\text{Reachable}(c) - \{c\} = \emptyset$

- Auxiliary Case: $\exists c_i \in \text{Reachable}(c) - \{c\}$:

$\text{Coverage}(c) \subsetneq \text{Coverage}(c_i)$

- Spanning Case: $\neg \text{Pivotal}(c) \wedge \text{Coverage}(c) \cap \bigcup_{c_i \in \text{Reachable}(c) - \{c\}} \text{Coverage}(c_i) \neq \emptyset$

- Support case: $\exists c_i \in \text{Reachable}(c) - \{c\}$:

$\text{Coverage}(c_i) \subset \text{Coverage}(c)$

- A competence of a group of cases (G): is defined as the group coverage of G in the following (were, $\text{SM}(a, b)$ is a function used to calculate the similarity between two cases):

$$\text{Casedensity}(c, G) = \frac{\sum_{c_i \in G - \{c\}} \text{SM}(c, c_i)}{|G| - 1} \quad (1)$$

$$\text{Groupdensity}(G) = \frac{\sum_{c \in G} \text{Casedensity}(c, G)}{|G|} \quad (2)$$

$$\text{Group coverage}(G) = 1 + |G|(1 - \text{Groupdensity}(G)) \quad (3)$$

- Case Base Competence: is defined as follows:

$$\text{Situation}_1 = \sum_{G_i \in G} \text{GroupCoverage}(G_i) \quad (4)$$

$$\text{Overlap coverage} = \sum_{c_i \in C^*} \text{Coverage}(c_i) \cap \text{Coverage}(CB - C^*) \quad (5)$$

$$\text{Situation}_2 = \text{Situation}_1 - \text{Overlap coverage} \quad (6)$$

- Competence group cover-range (CGCR): is defined as the maximum weighted distance between any pair of cases (c_p, c_q) in a competence group.

$$CGCR(G_i) = \max d^{(w)}(c_p, c_q) \quad (7)$$

- Flag case cover-range (FCCR): is defined as the minimum weighted distance between a pivotal case and a competence group.

$$FCCR(c_p^*) = \min d^{(w)}(c_p^*, c_q) \quad (8)$$

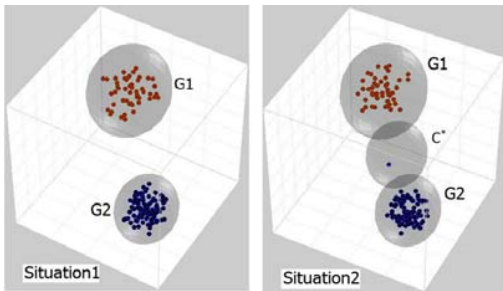


Fig. 1. EM device cases in a multi-dimensional design space

$C^* = \{c_1^*, \dots, c_n^*\}$ is the pivotal case collection of a case-base. Here the case-base is classified into two situations, in situation 1, it consists of disjoint subsets: $\{G_1, \dots, G_n\}$; in situation 2, there exist pivotal cases (Fig. 1).

III. THE USE OF COMPETENCE IN PRODUCING A DESIGN PROTOTYPE

Each of the competence groups found by the process developed above provides a search group for matching a set of design specifications. If the specifications exactly match those of the competence group then a prototype can be developed from the group with a high confidence level that it is a good starting point. However, as the search moves away from the group, the confidence in a prototype developed from the group reduces. At some point, a prototype might be developed by combining features from two different competence groups. For example, a stator from one group might be combined with a rotor from another. In addition, some examples in the database might indicate areas of the search space, for the given specifications, which will not produce satisfactory solutions. These are areas to be avoided and can have negative inputs to the construction of a prototype.

IV. A COMPETENT CASE BASE FOR INDUCTION MOTORS

According to the refined combined competence model above, a competent case base for induction motors is designed as a structured database with entities and relationships tying together building blocks to form designs. This case base presents rich information to describe an induction motor, such as the steady state equivalent circuit, geometry, material, coil windings and performance analysis results, and it also includes the four classes of cases (pivotal, auxiliary, spanning and support). Simulation can be used to complement and extend the cases available from industrial designs with new examples within the design space. However, even then, the number of points in the design space that can be created is

relatively small compared to the size of the space. In addition, since all the devices represent points in the design response surface, both good and bad examples (in terms of design requirements) may be included. Such a database has been constructed and consists of a set of induction motors with varying performance characteristics and a variety of physical structures. These devices form the data set for the competence algorithm. Fig. 2 shows a slice through the multi-dimensional design space for the full load power against the machine outer diameter and efficiency. As can be seen, these cases are clustered into groups which can be identified by the competence algorithm.

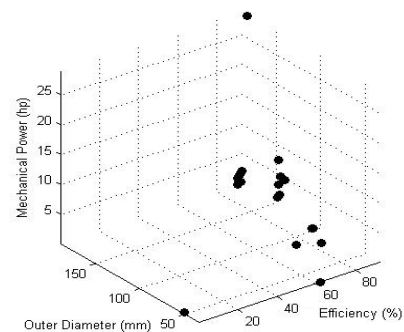


Fig. 2. An illustrating induction motor case base

This case base has been built with the help of MotorSolve provided by Infolytica Corporation [5].

V. CONCLUSION

A refined combined competence model has been developed and applied to a database of induction motor designs. Using the information generated, it is possible to generate a potential candidate for a prototype device which can be used as the starting point for an optimization process. In effect, the case-based system provides an efficient and fast method for exploring the potential design space allowing the optimizer to concentrate on the exploitation phase. The full paper will provide details of the case-base, the algorithms involved in competence determination and an example of their use.

VI. REFERENCES

- [1] J.Kolodner, "Case-based Reasoning," Morgan Kaufmann: San Mateo, CA, 1993.
- [2] J.Ouyang and D.A.Lowther, "A Hybrid Design Model for Electromagnetic Devices," IEEE Transactions on Magnetics, Vol. 45, No. 3, March 2009, pp. 1442-1445.
- [3] J.Ouyang, D.Lowther and L.Han, "A Combined Competence Model: EM Device Cases" Proceedings of the 13th International IGTE Symposium, Graz, Austria, September 2008.
- [4] B.Smyth and E.McKenna, "Remembering To Forget: A Competence-Preserving Case Deletion Policy for Case-Based Reasoning Systems," Proceedings of the Fourteenth International Joint Conference on Artificial Intelligence, IJCAI 95, Montréal, Québec, Canada, pp 377-383, 1995.
- [5] MotorSolve Users Manual, Infolytica Corporation, Montreal, Canada, 2009.

Slot Shape Optimization for Permanent Magnet Synchronous Machines by Evolution Strategy and Time-Stepped Finite Element Analysis

Yang Zhan and Andrew M. Knight

Department of Electrical and Computer Engineering, University of Alberta
Edmonton, Alberta, T6G 2V4, Canada
knight@ece.ualberta.ca

Abstract— This paper presents the application of (1+4) and (1,4) evolution strategies to minimize the losses in a permanent magnet synchronous machine designed for operation in a flywheel energy storage system. The optimization strategies are used to adjust the stator slot shape to reduce the open circuit iron loss and magnet eddy-current loss calculated using time-stepped finite element analysis. At each generation of the optimization, the fitness of each candidate is evaluated in parallel. The performances of the (1+4) and (1,4) algorithm are compared, and an optimal slot shape design is presented.

I. INTRODUCTION

Permanent magnet synchronous machines (PMSM) is an attractive candidate for use with flywheel energy storage systems as they have high power density, high efficiency and are relatively simple to control. Even though PMSM are typically considered to be high efficiency machines, particular attention should be made to losses in a machines designed for use in with a flywheel. Total loss should be as low as possible, in order to maximize round-trip energy efficiency. High frequency eddy current losses in the magnets should be minimized, as the rotor of the system is typically evacuated, eliminating conductive and convective heat transfer from the rotor.

Adjustment of the stator slot shape is an economical approach to contribute towards loss reduction after an initial design using low-loss materials has been carried out. In the process of design optimization, machine losses are evaluated for each design, and an optimization algorithm is required to seek the optimal design according to certain criteria. The slot shape design optimization for loss reduction has been investigated in a number of papers, e.g. [1], [2]. However, losses due to flux density space harmonics contribute significantly to both magnet and iron losses in a high speed machine. The time-stepped finite element analysis (FEA) may fully model the effect of rotor motion on the electromagnetic harmonics, therefore its use with an optimization algorithm is considered in this paper.

Regarding the optimization algorithm, there are a wide variety of options on deterministic or probabilistic search and optimization techniques. As a probabilistic technique based on adaption and evolution, evolution strategy (ES) has been successfully applied to some attempts at machine design optimization [3], [4], [5]. In this paper, within each ES iteration, time-stepped FEA is implemented in parallel to evaluate the machine losses of each candidate.

The flywheel application in flywheel system places a number of requirements on the PMSM design and drive system. As the flywheel may be frequently accelerated or decelerated, the PMSM is required to be operated at a wide range of high speeds, and the field weakening control is required at these high speeds. Initial design of the PMSM is carried out using an analytical lumped-parameter prediction, then verified by magnetostatic FEA. Once these parameters are determined, operation under load is simulated using time-stepped FEA to obtain full evaluations of iron loss, magnet eddy-current loss, efficiency, power factor, etc. The initial design uses a rotor with surface mounted magnets (SPM) and two-layer fractional-slot short-pitched distributed windings. Details about the initial design & operational requirements can be found in [6].

II. SLOT SHAPE VARIABLES AND COST FUNCTION

The stator slot shape is described using 6 objective variables shown in Fig.1. The adjustment of these variables is constrained to ensure that total slot area (A) is above a minimum value determined by the slot current density. Additional constraints include d - and q - axis inductances (L_d , L_q) and permanent magnet flux linkage (λ_m). The optimal slot shape should maintain the design values of inductance and flux linkage to ensure that field weakening control may be applied efficiently. As this PMSM adopts a SPM design with the equal L_d and L_q , their constraints are similar. The constraints on L_d , L_q and λ_m are determined with quantitative analysis based on the d - q axis equations and the field weakening conditions. The constraints on the objective variables and other relevant parameters are shown in Table II.

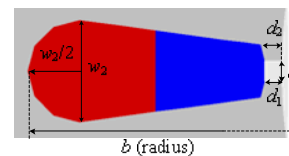


Fig. 1. Slot shape variables

The cost function to be minimized is constructed by superimposing the penalty functions on the total machine loss:

$$C = W + P_1(A) + P_2(L_d) + P_3(\lambda_m) \quad (1)$$

W is the total machine Watts loss. The penalty functions P_1 , P_2 and P_3 may add positive numbers to the cost function when the constrained parameters violate the constraints. To determine the penalty factors in the penalty functions for L_d

and λ_m , one needs to evaluate the effect of L_d and λ_m variations on the machine performances using the d-q axis equations.

TABLE I
VARIABLE AND PARAMETER CONSTRAINTS

	δ (mm)	d_1 (mm)	d_2 (mm)	w_1 (mm)	w_2 (mm)	b (mm)	A (mm ²)	L_d, L_q (mH)	λ_m (Wb)
Lower	1.90	0.30	1.00	2.00	4.00	70.00	206.4	0.275	0.085
Upper	4.00	3.00	5.00	8.00	20.00	105.00	--	0.418	0.108

As the flywheel PMSM would rarely operate at steady speeds, it is impractical to minimize the machine losses under a range of varying load conditions. The variation of machine loss brought by the slot shape adjustment can be evaluated with the simulations on the open circuit operations. The PMSM losses at open circuit comprise the iron loss and the magnet eddy-current loss. The latter can be calculated by time-stepped eddy-current FEA, while the former can be evaluated by substituting the flux densities obtained by time-stepped FEA into the classical equations [7].

III. OPTIMIZATION BY EVOLUTION STRATEGY

ES seeks the optimum by simulating the biological evolution. There are two categories of ES algorithm: (μ, λ) -ES and $(\mu+\lambda)$ -ES. $(\mu+\lambda)$ -ES differs from (μ, λ) -ES in the stage of selection. $(\mu+\lambda)$ -ES selects the best μ as the parents for the next generation from the combination of μ parents and λ children. The (1+1)-ES [3], [5] and the (1,5)-ES [4] algorithms have been applied to PMSM and induction motor design.

In this paper both the (1+4)-ES and the (1,4)-ES are applied to the slot shape design optimization for minimization of the open circuit losses at the speed of 28,000 rpm. Parallelized (1+4)-ES and (1,4)-ES algorithms are efficiently carried out on a quad-core computer. Both strategies start from the same initial slot design, with the progress of the cost function plotted in Fig. 2. It is clear that the (1,4)-ES converges to a smaller cost function value than the (1+4)-ES, which is trapped into a local minimum. This phenomenon can be explained by comparing the manner of selection of the two algorithms. In the (1+4)-ES any child inferior to its parent will not survive for the next generation, therefore this algorithm may escape from a local optimum only if it reproduces by chance a mutant which is out of the close neighborhood of the local optimum and superior to its parent. With the (1,4)-ES a child inferior to its parent still has the opportunity to survive for more than one generation, and may eventually help the algorithm converge to the global optimum.

Tables II and III summarize the initial slot design and the optimal results obtained by the (1,4)-ES. The optimal design reduces the total machine loss by 12.7%. Fig. 3 shows the loss density distribution of the initial and optimal designs. The optimization gives a shorter and narrower slot shape design with a smooth tip-tooth transition. This optimal design reduces the fluctuation of air gap flux density and brings a notable improvement that the magnet eddy-current loss is reduced by 57.6%. This may greatly reduce the risk of overheating and demagnetizing the permanent magnet.

TABLE II INITIAL AND OPTIMAL DIMENSIONS

	δ (mm)	d_1 (mm)	d_2 (mm)	w_1 (mm)	w_2 (mm)	b (mm)	A (mm ²)	L_d, L_q (mH)	λ_m (Wb)
Initial	2.44	2.00	2.49	6.20	12.00	90.58	248.05	0.310	0.102
Optimal	1.94	0.90	3.97	4.88	11.93	87.89	206.40	0.319	0.103

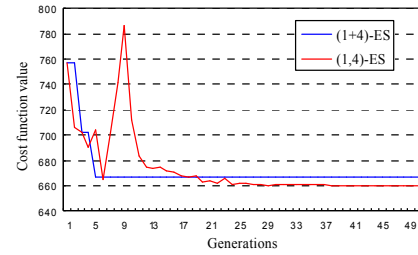


Fig. 2. Cost function values of parents

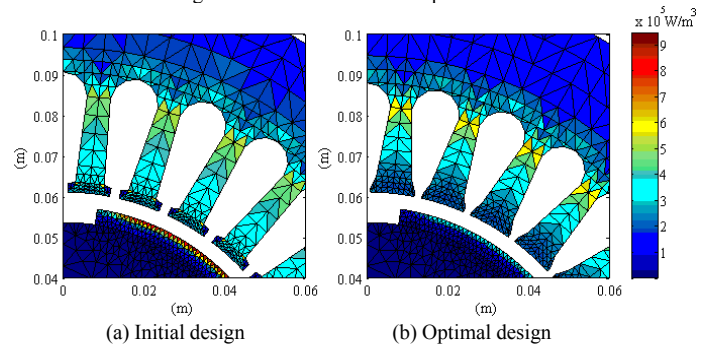


Fig. 3. Loss density distribution

TABLE III INITIAL AND PREDICTED LOSSES

	Total (W)	Iron(W)	Magnet (W)
Initial	756.86	707.49	49.37
Optimal	660.55	639.64	20.91

IV. CONCLUSIONS

Parallelized (1+4)-ES and (1,4)-ES are utilized with Time stepped FEA to improve the stator slot design of a flywheel PMSM to minimize open circuit losses. The parallel approach significantly reduces the time required to evaluate the fitness of the children, and is practical to implement on a quad-core computer. The (1,4)-ES result is superior to the (1+4)-ES and significantly reduces the total machine loss and the magnet eddy-current loss.

V. REFERENCES

- [1] S. Park, H. Lee, S. Hahn and I. Park, "Stator slot shape design of induction motors for iron loss reduction," *IEEE Trans. Magnetics*, vol. 31, no. 3, May 1995, pp. 2004-2007
- [2] S. Lee, S. Kim and J. Hong, "Investigation on core loss according to stator shape in interior permanent magnet synchronous motor," *IEEE International Conference on Electric Machines and Systems*, Oct. 17-20, 2008, pp. 3158-3161
- [3] J. Chun, H. Jung and J. Yoon, "Shape optimization of closed slot type permanent magnet motors for cogging torque reduction using evolution strategy," *IEEE Trans. Magnetics*, vol. 33, no. 2, Mar 1997, pp. 1912-1915
- [4] D. Bochnia, W. Hofmann and H. Hupe, "Design optimization of permanent magnet motors by evolution strategies and finite element analysis," *IEEE International Conference on Electric Machines and Drives*, Sept. 1-3, 1999, pp. 297-301
- [5] M. Kim, C. Lee and H. Jung, "Multiobjective optimal design of three-phase induction motor using improved evolution strategy," *IEEE Trans. Magnetics*, vol. 34, no. 5, Sept. 1998, pp. 2980-2983
- [6] M. Jiang, J. Salmon and A.M. Knight, "Design of a permanent magnet synchronous machine for a flywheel energy storage system within a hybrid electric vehicle," *IEEE International Conference on Electric Machines and Drives*, May 3-6, 2009, to be published.
- [7] K. Atallah, Z.Q. Zhu and D. Howe, "An improved method for predicting iron losses in brushless permanent magnet DC drives," *IEEE Trans. Magnetics*, vol. 28, no. 5, Sept. 1992, pp. 2997-2999

Numerical-analytical coupled optimization of a mechatronic system with particular attention to the embedded linear machine

Alexander Oswald
 Technische Universität München
 Institute of Energy Conversion Technology
 Munich, Germany, Bavaria
 Email: alexander.oswald@mytum.de

Hans-Georg Herzog
 Technische Universität München
 Institute of Energy Conversion Technology
 Munich, Germany, Bavaria
 Email: hg.herzog@tum.de

Abstract—The following digest gives a short overview about the analytical modeling of a electrical linear generator in combination with numerical optimization and modeling methods. The final paper will be more detailed and contains results. The digest gives an overview about the general project steps. The complete mechatronic system is described by basic differential equations. Those are combined with analytical terms which describe the linear machine. Several complexity levels are shown and will be compared with the results of an FE model in the final paper.

I. INTRODUCTION

Engineers developing electrical machines at university normally optimize of such machines for special purposes. Therefore only single aspects like efficiency or room of the machine shall be optimal. The system in which the machine is mounted, is usually neglected in those projects.

In this case however a specific combined heat and power system (see fig. 1) shall be optimized. It exists of a pneumatic pressure excited alternating piston that is stiff coupled to a linear permanent magnetic excited synchronous machine (LPMSM). The complete system should produce about 3-6kW electric power.

Our task is the design of the linear machine under specific limitations like maximum speed, acceleration, minimal weight and low complexity. Other work deals with the design and modeling of linear induction machines[4]. Especially for space use or elevator systems one can find well designed machines [2]. But to achieve high power density a tubular LPMSM shall be applied within the system. The best configuration is a tubular polysolenoid type (e.g.[1]).

In our project we use a new "multidisciplinary" approach to optimize the machine. The system is reduce to it's basic

parameters like pressure, dimensions, weight or forces. Then a numerical simulation with differential equations and optimization algorithms is used to find best parameter sets. The feedback of the linear machine is refined more and more with each phase of the project. The design and optimization process combines analytic methods, finite element methods and numerical optimization what is a new approach in developing electrical machines.

II. OPTIMIZATION AND DESIGN PROCESS

Fig. 2 gives a general overview about the complete process we are using to design a machine which fits the system-requirements. As we know the topology we start directly on the system level. To do a quick an accurate system optimization those parameters have to be detected against which the system behaves sensitive. For those different known optimization methods like genetic algorithms and particle swarm algorithms are used to find the best parameter configuration of the complete system which fits the requirements best in terms of the criteria. Those are minimal weight, small room, best dynamics and best efficiency. The first iterations use simple analytical methods to get feedback of the linear machine. The feedback has been detected to be mainly the movers mass, the linear force and the maximum speed of the system. The methods are refined with each step. After we have a good quality profile we start with a further level within wich we design the principal dimensions of the machine and use analytical methods again for the feedback. On the last level

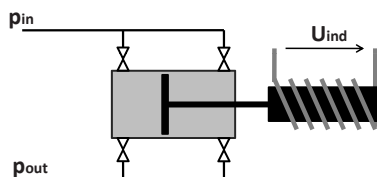


Fig. 1. Principal view of the system

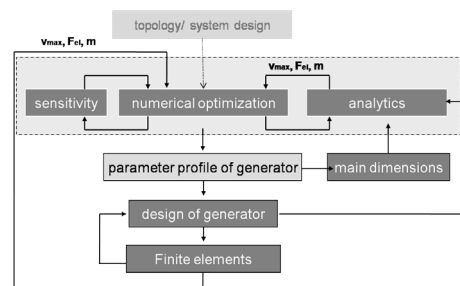


Fig. 2. Optimization and design process.

an exact analytical model is implemented and FE methods are added. On this level we do several iterations to find a complete machine design which interacts with the complete mechatronic system in such a way, that the configuration is optimal to fit the requirements.

III. ANALYTICAL SIMULATION MODEL

The coupled analytical simulation and optimization of the mechatronic system is done with Simulink. For this purpose we describe the whole system with differential equations based on equilibrium of forces (see eq. (1)).

$$F_{piston} - F_r - F_{el} - m \cdot \ddot{s} = 0 \quad (1)$$

To find out sensitivities of the system a continuous analytical description would be necessary. But the electromagnetic force of the generator and the pneumatic force of the piston are both nonlinear, not discrete and depend on different variables (see fig. 3). Especially the speed, which is a result of the system simulation, provides problems. Therefore the system is analyzed in discrete intervals, where such variables don't have a knick or a saltus. For particular sensitive parameters like those which influence the force of the piston and those which influence the force of the generator the optimization is done several times while the feedback of the generator is considered. This feedback is a big challenge of this work. As it is not reasonable to do a complete design process of the machine each step we have to use approximations based on the desired force-speed characteristics. Therefore the mass of the generator is calculated based on the load factor, a maximum air gap flux density and a maximum current distribution. The speed, acceleration and the maximum pressure of the system are used as boundaries.

$$P_{el} \rightarrow C_{load} \rightarrow \hat{B}_{delta} \approx 0,8 T, \hat{a} \approx 230 \frac{kA}{m} \quad (2)$$

$$\tau = \hat{B}_{delta} \cdot \hat{a} \rightarrow A_{Gen,surf} \rightarrow m_{Gen}(l_{ax}, r_{tube}) \quad (3)$$

After completing this phase a profile of the system is available which contains the optimal parameters and main dimensions to fit the requirements.

IV. EXACT ANALYTICAL MACHINE MODEL

In the next step the analytical model of the generator is refined and a detailed design process is set up. We run through this phase several times and add features to the analytics each time. The aim is to find out, which level of detail has to be modeled to achieve high quality results for the system profile. For the machine a classical approach is chosen. The force-generating terms are described by a fourier transformation

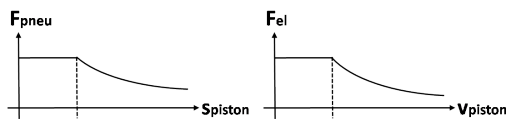


Fig. 3. Pneumatic force on piston depending on the axial position and force of linear machine depending on the speed.

of the exciting stator currents and a replacement flux of the permanent magnets. Then the force is calculated and the inductances of the machine. The complete design process is aided by a Matlab script what helps to find valid configurations of the geometry and the windings fast.

The results of this phase are more detailed information of the coupling between generator and system. This information is gained by an overlaid optimization process which tries to find best configurations. In the final paper there will be room for more detailed information about limitations and reductions which have to be made to make the optimization converge within reasonable time.

V. FE FEEDBACK

The last step is an overlay with Finite Elements. This is more or less a verification of the results from above. With the parameters we get from the FE we want to do further work to refine the analytical modeling and gain best quality results within shortest time. It exists an easy 2D model which directly gets it's information from the optimizer and is used to verify the dynamic behavior. A second 3D model is only used to detect losses. Especially losses within the machine are a big challenge and will be added in later work to the analytics.

VI. CONCLUSION

Within this short digest, we are not able to show results. This digest gives an overview over the complete project and it's several steps which have to be done. All in all we can say, that with modern optimization algorithms it is possible to gain fast and reliable parameters profiles of complete mechatronic systems. The best way is to be reduce systems to minimal models first and add complexity in several steps. Then in early states now configurations can be checked under consideration of main design rules. When the system is fixed, the design process it self for the single components can start. The time-costly FE process is placed at the end as verification. This is a now approach for time effective development of electrical drives.

REFERENCES

- [1] A.W. van Zyl, C.G. Jeans, R.J. Cruise and C.F. Landy, *Comparison of force to weight ratios between a single-sided linear synchronous motor and a tubular linear synchronous motor*, Electric Machines and Drives, 1999. International Conference IEMD '99 , vol., no., pp.571-573, May 1999
- [2] C.C. Tsai; S.M. Hu; C.K. Chang, *Vertical linear motion system driven by a tubular linear induction motor*, Mechatronics, 2005. ICM '05. IEEE International Conference on , vol., no., pp. 162-167, 10-12 July 2005
- [3] K. Baoquan, L. Liyi and Z. Chengming, *Analysis and Optimization of Thrust Characteristics of Tubular Linear Electromagnetic Launcher for Space-Use*, Magnetics, IEEE Transactions on, 2009.
- [4] R. Haghmaram, A. Shoulaie, *Transient modeling of multiparallel tubular linear induction motors*, Magnetics, IEEE Transactions on , vol.42, no.6, pp.1687-1693, June 2006
- [5] B. Tomczuk, G. Schroeder, A. Waindok, *Finite-Element Analysis of the Magnetic Field and Electromechanical Parameters Calculation for a Slotted Permanent-Magnet Tubular Linear Motor*, Magnetics, IEEE Transactions on , vol.43, no.7, pp.3229-3236, July 2007
- [6] G. Mueller, K. Vogt and B. Ponick, *Elektrische Maschinen: Berechnung elektrischer Maschinen*, 6th. Ed., WILEY-VHC, 2008.
- [7] G. Mueller and B. Ponick, *Elektrische Maschinen: Grundlagen elektrischer Maschinen*, 9th. Ed., WILEY-VHC, 2006.

3-D Optimal Design of Laminated Yoke of Billet Heater for Rolling Wire Rod using ON/OFF

Norio Takahashi¹, Shunsuke Nakazaki¹, Daisuke Miyagi¹,
Naoki Uchida², Keiji Kawanaka², and Hideyuki Namba²

¹Dept. Electrical and Electronic Eng., Okayama University, Okayama 700-8530, Japan
(E-mail: norio@elec.okayama-u.ac.jp)

²Mitsui Engineering & Ship building Co. Ltd., Tamano, Okayama 706-0014, Japan

Abstract — The optimization method using the ON/OFF sensitivity analysis has an advantage that an epoch-making construction of magnetic circuit may be obtained. Therefore, it is attractive for designers of magnetic devices. We have already developed the ON/OFF method for the optimization of a static magnetic field problem, and the effectiveness is verified by applying it to the optimization of magnetic recording heads. In this paper, the ON/OFF sensitivity method is extended to the optimization of the eddy current problem using the adjoint variable. The newly developed ON/OFF method is applied to the determination of the optimal topology of the yoke of the billet heater for rolling wire rod. As a result, the optimal shape of yoke, which we could not imagine beforehand can be obtained. It is shown that the local heating of the yoke was reduced without decreasing the heating efficiency.

I. INTRODUCTION

If a topology optimization method which can determine the optimal topology by distributing materials in a design domain is used, there is a possibility that a new magnetic circuit can be discovered, because it is not necessary to set design variables in advance[1-4]. The application of the ON/OFF method to the 3-D static magnetic field problem, such as magnetic recording head[1] has already been reported. The topology optimization of a simple linear eddy current problem is reported[1,2]. But, the topology optimization method which is applicable to the 3-D eddy current problem of actual magnetic device is not yet developed. Although a technique for calculating the design sensitivity by representing it by a finite difference equation is proposed[8], a long CPU time is necessary because an adjoint variable method[2] was not utilized.

In this paper, the ON/OFF method is extended to the optimization of the 3-D eddy current problem by combining the ON/OFF method with the step-by-step method and the adjoint variable method. The ON/OFF method is applied to the optimization of the laminated yoke of a billet heater for rolling wire rod. The laminated yoke is installed in the outside of the coil as the return path of flux which flows in the billet. There is a problem that the heating efficiency of the billet decreases by the eddy current loss generated in the laminated yoke. Then, a 3-D optimal topology of the laminated yoke of the model of an actual billet heater which avoids this problem is obtained using the newly developed ON/OFF optimization

method.

II. ON/OFF METHOD FOR EDDY CURRENT PROBLEM USING ADJOINT VARIABLE

The region (design domain) of which the shape (topology) is determined is subdivided into many design cells (finite elements). The material distribution is updated so that the desired result can be obtained, which allows each design cell to have only one state, that of a void (this state is called as “OFF”) or a solid (“ON”). We call this algorithm as an “ON/OFF method”. To determine the material distribution by judging ON or OFF, the sensitivity dW/dp (p : design variable (conductivity or reluctivity), W : objective function) of each cell is evaluated.

The adjoint variable method[2] is applied for calculating the sensitivity analysis method. If the objective function W is the function of A' (time differential of vector potential $\partial A'/\partial t$) and design variable p , the derivative of W with respect to p is given as:

$$\frac{dW}{dp} = \left. \frac{\partial W}{\partial p} \right|_{A'=const} + \left. \frac{\partial W}{\partial A'} \right|_{p=const} \frac{\partial A'}{\partial p} \quad (1)$$

III. OPTIMIZATION OF LAMINATED YOKE OF BILLET HEATER

Fig. 1 shows the analyzed model of the billet heater. This is a 1/8 model. Although the original billet heater has four yokes around the coil, it is assumed that there are only two yokes in order to reduce the number of elements. Material constants are shown in Table I. Since the yoke is laminated, the conductivity in the x direction of the yoke is set to zero. The relative magnetic permeability was set as 1000, and the linear analysis is carried out. The current of the coil is set as 50000AT (700Hz). The conductivity of the billet at 1200 °C is used. The copper shield was installed on both sides of yoke in order to reduce the perpendicular flux which invades into a side surface of the yoke.

The objective function is defined as follows in order to maximize the eddy current loss in the billet (this is equal to minimize W_1), and minimize the eddy current loss W_2 in the laminated yoke:

6. Optimization

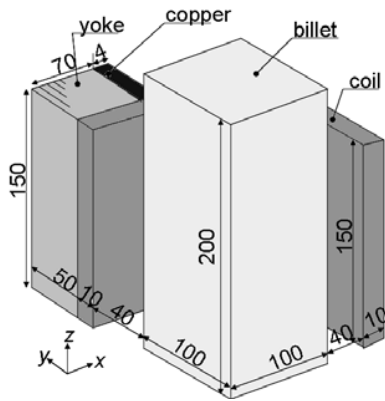


Fig. 1. Model of billet heater.

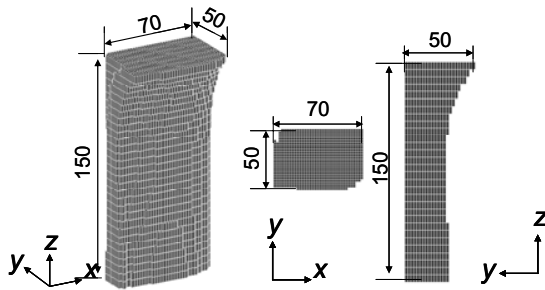


Fig. 2. Optimal shape of laminated yoke.

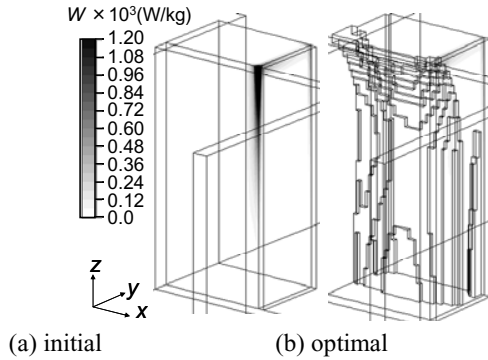


Fig. 3. Eddy current loss in yoke.

$$W = k_1 \cdot W_1 + k_2 \cdot W_2 \quad (17)$$

$$W_1 = \sum_{ie} V^{(ie)} \left\{ \frac{(J_{ex}^{(ie)})^2}{\sigma_x} + \frac{(J_{ey}^{(ie)})^2}{\sigma_y} + \frac{(J_{ez}^{(ie)})^2}{\sigma_z} \right\}^{-1} \quad (18)$$

$$W_2 = \sum_{ie} V^{(ie)} \left\{ \frac{(J_{ey}^{(ie)})^2}{\sigma_y} + \frac{(J_{ez}^{(ie)})^2}{\sigma_z} \right\} \quad (19)$$

$$k_1 = 1, \quad k_2 = \frac{W_1}{W_2} \quad (20)$$

where, ie is the element number in the target region. The target region is the billet in the case of W_1 , and is the yoke in

the case of W_2 . J_{ex} , J_{ey} and J_{ez} are the x -, y - and z -components of the eddy current vector, σ_x , σ_y and σ_z are the conductivities, V is the volume of the element. k_1 and k_2 are the weighting factors. They were calculated using the previous values of W_1 and W_2 in order to arrange the amplitudes of first and second terms of Eq. (5) as nearly the same values. In the optimal design, the conductivity σ is chosen as the design variable p .

The optimized shape using the ON/OFF method is shown in Fig. 2. The yoke became thin toward the center. The flux flows into the wide entrance of yoke. Fig. shows the eddy current loss distribution in the yoke. The concentration of the eddy current loss in the yoke edge is reduced by optimizing the yoke. Since the volume of a yoke is decreased compared with the initial shape, the eddy current loss in the yoke is also decreased. Table I shows the eddy current losses at each part. W_{eyoke} , $W_{eshield}$ and $W_{ebillet}$ are the eddy current loss in the yoke, shield and billet in the 1/8 region. W_{eyoke} and $W_{eshield}$ are reduced (-52% and -15%) by the optimization, but $W_{ebillet}$ is almost the same (-2.5%).

TABLE I
EDDY CURRENT LOSSES (1/8 REGION)

	initial	optimal
W_{eyoke} (W)	11.9	5.7
$W_{eshield}$ (W)	165.7	141.1
$W_{ebillet}$ (W)	25797	25146

IV. CONCLUSION

The ON/OFF method for topology optimization is extended to the linear eddy current problem by combining the ON/OFF method with the step-by-step method. The newly developed ON/OFF method is applied to the optimization of the model of actual billet heater. As a result of optimization of the laminated yoke of billet heater, the local overheating of the yoke was decreased without reducing the heating efficiency. The speed up of calculation, the nonlinear analysis etc. are the future subjects.

REFERENCES

- [1] Y. Okamoto, K. Akiyama, and N. Takahashi, "3-D topology optimization of single-pole-type head by using sensitivity analysis", *IEEE Trans. Magn.*, vol. 42, no.4, pp. 1087-1090, April, 2006.
- [2] H. I. Park, I. G. Kwak, H. B. Lee, S. Y. Hahn, and K. I. Lee, "Design sensitivity analysis for transient eddy current problems using finite element discretization and adjoint variable method", *IEEE Trans. Magn.*, vol. 32, no.3, pp. 1242-1245, 1996.
- [3] N. Takahashi, S. Nakazaki, and D. Miyagi: "Examination of optimal design method of electromagnetic shield using ON/OFF method", *IEEE Trans. Magn.*, vol.45, 2009.

Multiobjective Differential Evolution Approach for the TEAM Workshop Problem 25

Luiz Lebensztajn¹ and Leandro dos Santos Coelho²

¹Universidade de São Paulo, LMAG-PEA

Av. Prof. Luciano Gualberto 158, Zip code 0550-900, São Paulo, SP, Brazil E-mail: leb@pea.usp.br

²Automation and Systems Laboratory, LAS/PPGEPS, Pontifical Catholic University of Paraná

Rua Imaculada Conceição, 1155, Zip code 80215-901, Curitiba, Paraná, Brazil

E-mail: leandro.coelho@pucpr.br

Abstract—Recently, there are several attempts to extend the Differential Evolution (DE) to solve multiobjective problems. In this paper, an enhanced multiobjective version with external archive to store nondominated solutions of the DE method (EMODE) is proposed. The validity of the given algorithm is tested to solve the TEAM workshop benchmark problem 25. Optimization results on TEAM problem 25 indicate that EMODE outperforms the classical multiobjective differential evolution algorithm in the global search ability.

Index Terms—multiobjective optimization, differential evolution, electromagnetic optimization.

I. INTRODUCTION

Many electromagnetic devices optimization problems can be treated as optimizations with multiple objectives and sometimes more than one decision-maker is involved in selecting an appropriate solution.

Among various evolutionary algorithms, such as evolutionary programming, evolution strategy, and genetic algorithms, differential evolution (DE), which characterized by the different mutation operator and competition strategy from the other classical evolutionary algorithms, has shown great promise in many numerical benchmark problems [1]-[2].

To improve the global optimization property of DE, a novel enhanced multiobjective DE (EMODE) algorithm, which uses an updating strategy, is proposed in this paper. In this work, EMODE was evaluated for the TEAM workshop benchmark problem 25. The proposed EMODE is compared to the classical MODE proposed in [2] and outperform it, thus demonstrating its potential.

II. MULTIOBJECTIVE DIFFERENTIAL EVOLUTION

DE is a stochastic population-based optimization approach [1-2] for global optimization over continuous search spaces. It initializes the population randomly by uniform distribution over search space and maintains a population with NP individuals in each generation. A new vector is generated, by adding a weighted difference between two random vectors, to a third vector. This operation is called mutation. The mutated vector is then mixed with the components of another predetermined vector and this operation is called crossover. If the generated vector by crossover (the offspring) has a lower objective function value than the predetermined vector, than it replaces the vector, and this operation is called selection. The above evolution process is repeated until some termination conditions are met.

Recent studies have shown that in general, the most effective DE strategies are DE/rand/1/bin and DE/best/2/bin. The variant implemented in this paper was the DE/rand/1/bin. The following is the outline of the MODE inspired in the algorithm proposed on [1].

- i) Initialize a population of individuals (solution vectors) $x(t)$, $i=1, \dots, n$, with random values generated according to a uniform probability distribution in the n dimensional problem space. Set the generation counter, $t=0$;
- ii) Evaluate the population of individuals (potential solutions of optimization problem) using an objective function, F .
- iii) Generate a new population using mutation operation where each new vector (child) is created, according to

$$z_i(t+1) = x_{i,r_1}(t) + f_m \cdot [x_{i,r_2}(t) - x_{i,r_3}(t)] \quad (1)$$

- iv) Following the mutation operation, crossover is applied in the population. For each mutant vector, $z_i(t+1)$, an index $rnbr(i) \in \{1, 2, \dots, NP\}$, where NP is the population size, is randomly chosen using uniform distribution, and a trial vector, $u_i(t+1) = [u_{i_1}(t+1), u_{i_2}(t+1), \dots, u_{i_n}(t+1)]^T$, is created:

$$u_{i_j}(t+1) = \begin{cases} z_{i_j}(t+1), & \text{if } (randb(j) \leq CR) \text{ or } (j = rnbr(i)), \\ x_{i_j}(t), & \text{if } (randb(j) > CR) \text{ or } (j \neq rnbr(i)) \end{cases} \quad (2)$$

To decide whether or not the vector $u_i(t+1)$ should be a member of the population comprising the next generation, it is compared to the corresponding vector $x_i(t)$. In this context, if F is the objective function under minimization, then

$$x_i(t+1) = \begin{cases} u_i(t+1), & \text{if } F(x_i(t+1)) < F(x_i(t)), \\ x_i(t), & \text{otherwise} \end{cases} \quad (3)$$

- v) Select a new parent solution between parent and child vectors based on nondominated solution criterion. More details are presented in [1];
- vi) Update the external archive. If the archive size A_s exceeds the maximum size, it selected the less crowded solutions based on crowding distance to keep the archive size at N_{max} .
- vii) Increment the generation count, $t = t + 1$;
- viii) Loop to step (iii) until a stopping criterion is met, usually a maximum number of iterations (generations), t_{max} .

In the above equations, $i=1, 2, \dots, NP$ is the individual's index of population; $j=1, 2, \dots, n$ is the parameter index; t is the time (generation); $x_i(t) = [x_{i_1}(t), x_{i_2}(t), \dots, x_{i_n}(t)]^T$ stands for the position of the i -th individual of population of NP real-

A Populational Particle Collision Algorithm Applied to Electromagnetic Optimization

Leandro dos Santos Coelho¹ and Piergiorgio Alotto²

¹Automation and Systems Laboratory, LAS/PPGEPS, Pontifical Catholic University of Paraná
Rua Imaculada Conceição, 1155, Zip code 80215-901, Curitiba, Paraná, Brazil

E-mail: leandro.coelho@pucpr.br

²Dip. Ingegneria Elettrica, Università di Padova

Via Gradenigo 6/A, 35131, Italy

E-mail: alotto@die.unipd.it

Abstract— Recently, a new class of stochastic optimization algorithms called Particle Collision Algorithm (PCA) has been proposed. PCA is loosely inspired by the physics of particle interactions in a nuclear reactor, particularly scattering and absorption. This paper introduces the basics of PCA, proposes a modified version of the PCA approach and tests its efficiency on Loney’s solenoid benchmark problem.

Index Terms— Loney’s solenoid design, electromagnetic optimization, particle collision algorithm.

I. INTRODUCTION

Electromagnetic optimization problems often exhibit multiple optima in the feasible domain and therefore stochastic optimization methods are commonly used, mainly due to their ability to avoid being trapped in local optima of the objective function. A typical example of the rough objective function surface typical of many electromagnetic problems is shown by Loney’s solenoid problem [1]-[6].

This paper proposes a modified version of a recently proposed stochastic optimization algorithm called Particle Collision Algorithm (PCA) [7]-[11] to solve Loney’s solenoid problem.

PCA is loosely inspired by the physics of the interaction of nuclear particles inside nuclear reactors, mainly scattering, in which an incident particle is scattered by a target nucleus, and absorption, in which the incident particle absorbed by the target nucleus.

II. FUNDAMENTALS OF PCA

PCA is a Metropolis-based algorithm that was introduced as an alternative to the classical Simulated Annealing (SA) algorithm. In PCA a “particle” that reaches a promising area of the search space is “absorbed”, while one that hits a low-fitness region is “scattered”. Like SA, also PCA is a Metropolis algorithm, i.e. a solution worse than the current best one may be accepted with a certain probability (Metropolis criterion) which decreases during iteration.

The starting point of the algorithm to be presented in this paper is called populational PCA or PPCA [10]-[11], and its pseudo code is shown in Figure 1. In contrast with the basic PCA in which only one solution evolves in time, in PPCA a population of candidate solutions evolve in parallel.

```

For  $i = 1$  to  $Pop\_Size$ 
  - Generate an initial solution  $Old\_Config[i]$ 

For  $n = 0$  to  $N_{iter}$ 
  For  $i = 1$  to  $Pop\_Size$ 
    - Call the Perturbation function
    - If  $F(New\_Config[i]) < F(Old\_Config[i])$ 
       $Old\_Config[i] := New\_Config[i]$ 
      Call the Exploration function
    Else
      Call the Scattering function
  End For
  - Call  $New\_Pop$  function
End For

Perturbation function
- For  $i = 0$  to (Dimension-1)
   $Upper := Superior\ Limit\ [i]$ 
   $Lower := Inferior\ Limit\ [i]$ 
   $Rnd = Random(0,1)$ 
   $New\_Conf[i] := Old\_Conf[i] + ((Upper - Old\_Conf[i])*Rnd) - ((Old\_Conf[i] - Lower)*(1-Rnd))$  (1)
  If  $(New\_Config[i] > Upper\ or\ New\_Config[i] < Lower)$ 
     $New\_Config[i] := Upper\ or\ Lower$ 

Exploration function
For  $n = 0$  to # of iterations
  - Generate a small stochastic perturbation of the solution
  - If  $F(New\_Config[i]) < F(Old\_Config[i])$ 
     $Old\_Config := New\_Config$ 

Scattering function
-  $p_{scattering} = F(New\_Config[i]) / best\ F$ 
- If  $p_{scattering} < random(0, 1)$ 
   $Old\_Config[i] := random\ solution$ 
Else
  Call Exploration function

New_Pop function
- Cross two random individuals from population
- Rank parents and siblings in descending fitness order
- Pick the first  $Pop\_Size$  ranked individuals
  
```

Figure 1. Pseudo-code of the classical populational PCA algorithm.

cm and $l=1.0871$ cm with $F(s,l)=2.03920 \cdot 10^{-8}$.

A. Modified populational PCA (MPPCA) approach

In PPCA the mechanism through which new population members are generated is embodied in the Perturbation function. Here we propose a Modified PPCA (MPPCA) in which the uniform distribution in range $[0,1]$ is substituted by a truncated Cauchy distribution. Furthermore, the Perturbation function is modified by substituting Eq. 1 of Fig. 1 by:

$$\begin{aligned} \text{New_Config}[i] := & \text{Old_Config}[i] + ((\text{Upper} - \\ & \text{Old_Config}[i]) * \text{Rand} * U) - \\ & ((\text{Old_Config}[i] - \text{Lower}) * (1 - \text{Rand}) * P), \end{aligned} \quad (2)$$

where U and P are variables with value 0 or 1 with 50% of probability for each.

III. LONEY'S SOLENOID DESIGN

Appropriately stated, Loney's solenoid design problem consists in determining the position and size of two correcting coils in order to generate a uniform magnetic flux density B within a given interval on the axis of a main solenoid.

The upper half plane of the axial cross-section of the system is presented in Figure 1. The interval of the axis, where the magnetic flux density B_0 must be as uniform as possible is $(-z_0, z_0)$. The current density J_0 in the coils is assumed to be constant [6]. The separation s and the length l of the correcting coils are to be determined while all other dimensions are given. Both s and l are bounded in $[0,0.2]$ according to the problem definition and optimized by MPPCA.

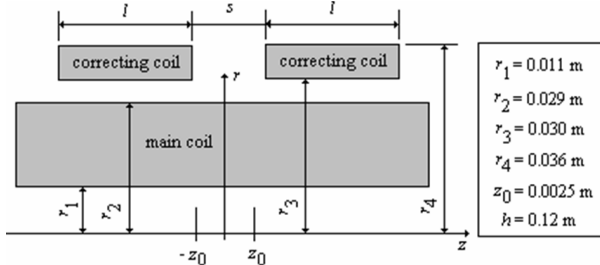


Figure 1. Axial cross-section of Loney's solenoid (upper half-plane).

In particular, three different basins of attraction of local minima can be recognized in the domain of F with values of $F > 4 \cdot 10^{-8}$ (high level region), $3 \cdot 10^{-8} < F < 4 \cdot 10^{-8}$ (low level region), and $F < 3 \cdot 10^{-8}$ (very low level region - global minimum region) [4].

In this work, the parameters of PPCA and MPPCA are set as follows: the population size is 30 and the stopping criterion was 200 iterations, in other words, both PCA approaches performed 6,000 objective function evaluations in each run.

In order to eliminate stochastic discrepancy, in each case study 30 independent runs were made for each of the optimization methods.

The classical PPCA found the best design with $s=13.5994$ cm and $l=4.0420$ cm with $F(s,l)=2.4338 \cdot 10^{-8}$, and the proposed MPPCA obtained the best design in 30 runs with $s=10.7332$

TABLE I

SIMULATION RESULTS OF F IN 30 RUNS

Optimization Method	$F(s, l) \cdot 10^{-8}$			
	Maximum (Worst)	Mean	Minimum (Best)	Std. Dev.
Populational PCA	21.5249	8.1522	3.4251	5.1175
MPPCA	13.4685	5.8887	2.3920	2.5359

IV. CONCLUSIONS

The effectiveness of MCCPA with respect to PCA has been shown on Loney's solenoid design problem. In the extended paper the algorithm will be commented in greater depth, further modifications to it will be analyzed and the algorithm will be compared with other stochastic optimization methods.

ACKNOWLEDGMENTS

This work was supported by the National Council of Scientific and Technologic Development of Brazil — CNPq — under Grant 309646/2006-5/PQ.

REFERENCES

- [1] P. Di Barba and A. Savini, "Global optimization of Loney's solenoid by means of a deterministic approach," *International Journal of Applied Electromagnetics and Mechanics*, vol. 6, no. 4, pp. 247-254, 1995.
- [2] L. S. Coelho, "Novel Gaussian quantum-behaved particle swarm optimiser applied to electromagnetics design," *IET Science, Measurement & Technology*, vol. 1, no. 5, pp. 290-294, 2007.
- [3] P. Di Barba, F. Dughiero and F. Trevisan, "Optimization of the Loney's solenoid through quasi-analytical strategies: a benchmark problem reconsidered," *IEEE Transactions on Magnetics*, vol. 33, no. 2, pp. 1864-1867, 1997.
- [4] L. S. Coelho and P. Alotto, "Loney's solenoid design using artificial immune network with local search based on Nelder-Mead simplex method," *COMPUMAG*, Aachen, Germany, 2007.
- [5] E. Cogotti, A. Fanni and F. Pilo, "A comparison of optimization techniques for Loney's solenoids design: an alternative tabu search algorithm," *IEEE Transactions on Magnetics*, vol. 36, no. 4, pp. 1153-1157, 2000.
- [6] G. Ciuprina, D. Ioan and I. Munteanu, "Use of intelligent-particle swarm optimization in electromagnetics," *IEEE Transactions on Magnetics*, vol. 38, no. 2, pp. 1037-1040, 2002.
- [7] W. F. Sacco and C. R. E. de Oliveira, "A new stochastic optimization based on particle collision metaheuristic," *Proceedings of 6th World Congresses of Structural and Multidisciplinary Optimization*, Rio de Janeiro, RJ, Brazil.
- [8] W. F. Sacco, H. A. Filho, N. Henderson and C. R. E. de Oliveira, "A Metropolis algorithm combined with Nelder-Mead simplex applied to nuclear reactor core design," *Annals of Nuclear Energy*, doi:10.1016/j.anucene.2007.09.006
- [9] W. F. Sacco and C. R. E. de Oliveira, "A new stochastic optimization algorithm based on particle collisions," *Transactions of the American Nuclear Society*, vol. 92, 2005 ANS Annual Meeting, San Diego, CA, USA.
- [10] W. F. Sacco, H. A. Filho and C. R. E. de Oliveira, "A population particle collision algorithm applied to a nuclear reactor core design optimization," *Proc. of Joint Int. Topical Meeting on Mathematics & Computation and Supercomputing in Nuclear Applications (M&C + SNA 2007)*, Monterey, California, CA, USA, 2007.
- [11] W. F. Sacco, C. R. E. de Oliveira and C. M. N. Pereira, "Two stochastic optimization algorithms applied to nuclear reactor core design," *Progress in Nuclear Energy*, vol. 48, pp. 525-539, 2006.

Microstrip Ring Antennas on Double-Layered Ferrimagnetic Substrates

C.F.L. Vasconcelos¹, S.G. Silva¹, M.R.M.L. Albuquerque¹, J.R.S. Oliveira², and A.G.d'Assunção¹

¹Universidade Federal do Rio Grande do Norte (UFRN)

59072-970 Natal, RN, Brazil

²Centro Federal de Educação Tecnológica do Rio Grande do Norte (CEFET-RN)

59015-000 Natal, RN, Brazil

cflinvas@yahoo.com.br; sandro@ct.ufrn.br; mrmla@yahoo.com.br; ramabir@cefetrn.br; adaildo@ct.ufrn.br

Abstract— The propagation characteristics of the fundamental mode of annular ring microstrip antennas (ARMSA) on double-layered ferrite substrates are discussed. A full-wave analysis is formulated based on the spectral domain technique in conjunction with Galerkin approach. It takes into account the effects of the applied dc magnetic bias field in the behavior of these structures. Numerical results of resonant frequencies and radiation patterns are found as functions of some geometrical and ferrite parameters.

I. INTRODUCTION

The ever increasing demand on wireless communication systems requires the development of lightweight, low-profile, low-cost and flush-mounted antennas. Microstrip patch antennas offer these useful features and are ideally suited for applications requiring compactness and integration with monolithic microwave integrated circuits (MMICs) [1]-[4].

One of the advantages of using ARMSA is that it offers smaller size and larger bandwidth when compared to other conventional microstrip antennas, for a given frequency. The small size is an important requirement for portable communication equipment, such as global positioning satellite (GPS) receivers and several mobile communication applications. If a magnetized ferrite is used as a substrate instead of an isotropic dielectric, an additional degree of freedom to the design of the antenna is provided due to the permeability characteristic of the ferrite. Also, the high permittivity of the ferrimagnetic material leads to a reduction in the antenna dimensions allowing miniaturization.

In most cases, the analysis of the ARMSA on ferrite has been performed using approximate methods [1]. However, accurate results can be obtained adopting a full-wave approach in conjunction with the method of moments [4].

This paper presents an analysis of ARMSA printed on a double-layered substrate that is constituted by an isotropic and a ferrite layers. Suspended antennas and antennas on a single isotropic layer can be analyzed as particular cases. The analysis uses the full-wave formulation by means of the Hertz vector potentials method in the Hankel transform domain. The dyadic Green function and Galerkin's method are used to determine the resonant frequencies and radiation patterns.

II. THEORY

A cross section view of the ARMSA is shown in Fig. 1. Region 3 has thickness d_3 and is filled up with a dielectric, whose permittivity is ϵ_3 . The ferrite layer (region 2) has thickness d_2 , scalar permittivity ϵ_2 , and tensor permeability $\vec{\mu}$. For a ferrite magnetized in the z direction, $\vec{\mu}$ is given by [2]:

$$\vec{\mu} = \begin{bmatrix} \mu & 0 & j\kappa \\ 0 & \mu & 0 \\ -j\kappa & 0 & \mu_0 \end{bmatrix} \quad (1)$$

where the components μ and k are dependent on the operating frequency ω , the saturation magnetization of the ferrite $4\pi M_s$, and the applied dc magnetic-field H_0 . The region 1 has permittivity ϵ_0 and permeability μ_0 denoting the free-space.

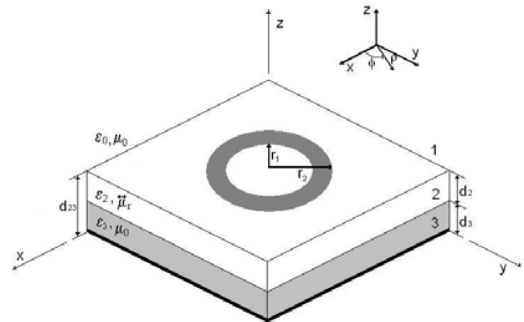


Fig. 1. Annular ring microstrip patch antenna on ferrite substrate.

The electric and magnetic Hertz potential vectors, $(\vec{\pi}_e)$ and $(\vec{\pi}_h)$, respectively, are defined along the z -direction, according to the orientation of the applied magnetic bias field, and can be written in terms of cylindrical functions [3].

In the spectral domain, the electric and magnetic fields are expressed in terms of the $E_{\pm} = E_{\rho} \pm jE_{\phi}$, as follows:

$$E_{\pm i} = e^{jn\phi} \int_0^{\infty} \alpha \left[\omega \mu_0 \mu_{ri} \tilde{\pi}_{hi} \mp \frac{1}{\mu_{ri}} \frac{\partial^2 \tilde{\pi}_{ei}}{\partial z^2} \right] J_{n\pm 1}(\alpha \rho) \alpha d\alpha \quad (4)$$

Similarly, for the magnetic field, we can write that:

$$H_{\pm i} = e^{jn\phi} \int_0^{\infty} -\alpha \left[\omega \epsilon_0 \epsilon_{ri} \frac{1}{\mu_{ri}} \tilde{\pi}_{ei} \pm \omega \epsilon_0 \epsilon_{ri} \frac{k_{ri}}{\mu_{ri}^2} \tilde{\pi}_{hi} \pm \frac{\partial^2 \tilde{\pi}_{hi}}{\partial z^2} \right] J_{n\pm 1}(\alpha \rho) \alpha d\alpha \quad (5)$$

On the conducting patch plane, $z = d_{23}$ (Fig. 1), by imposing the boundary conditions, the transformed electric field components are written as functions of the transformed

current density components allowing the determination of the impedance matrix, in the Hankel domain, as follows [3]-[4]:

$$\begin{bmatrix} \tilde{E}_x \\ \tilde{E}_z \end{bmatrix} = \begin{bmatrix} \tilde{Z}_{11} & \tilde{Z}_{12} \\ \tilde{Z}_{21} & \tilde{Z}_{22} \end{bmatrix} \begin{bmatrix} \tilde{J}_x \\ \tilde{J}_z \end{bmatrix}, \quad (6)$$

Parseval's theorem and Galerkin's method are used to obtain the determinantal equation that enables the numerical calculation of the resonant frequencies.

III. RESULTS AND DISCUSSIONS

Numerical results are presented for the ARMSA depicted in Fig. 1. The ring patch has inner radius r_1 and outer radius r_2 . The dc magnetic bias field H_0 is applied along z direction.

The curves obtained for ARMSA printed on a double-layered substrate are shown in Fig. 2 and Fig. 3. It is observed in Fig. 2 that the resonant frequency increases with the dielectric thickness (d_3). The influence of the magnetic-bias field H_0 is also verified. Radiation pattern for E_θ field is shown in Fig. 3. The patch is supported by a double layered substrate. The dc magnetic bias field is $H_0 = 1500$ Oe. The isotropic layer has permittivity $\epsilon_{r3} = 2.32$. It is considered three different values for d_3 thickness. It is observed that the directivity increases with the isotropic layer thickness.

Fig. 4 depicts the influence of the air gap thickness on the resonant frequency of ARMSA, against H_0 . The air gap is varied from 0.7 mm to 2 mm. It is found that the resonant frequency of the suspended ARMSA can be tuned by adjusting the air gap width. Observe also the effect of a varying dc bias field on the resonant frequency and a magnetic tuning possibility.

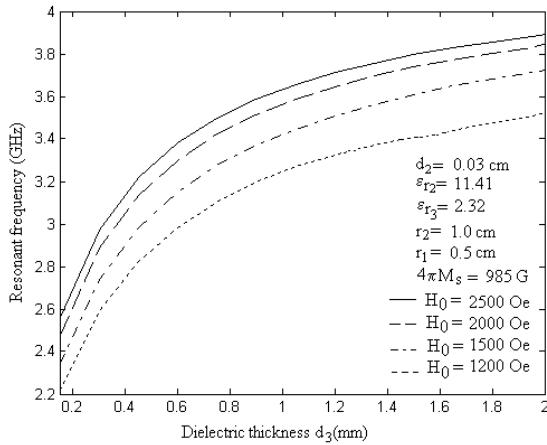


Fig. 2. Resonant frequency as a function of the dielectric thickness.

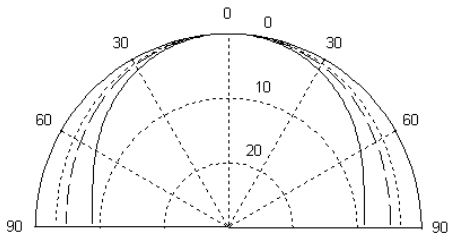


Fig. 3. Radiation pattern (E_θ) as a function of three different values of the dielectric ($\epsilon_{r3} = 2.32$) thickness: --- $d_3 = 0.20$ mm, -- $d_3 = 0.45$ mm, and — $d_3 = 3$ mm. Ferrite substrate: $H_0 = 1500$ Oe.

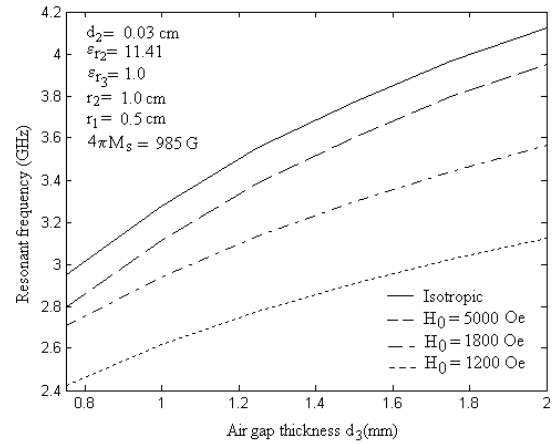


Fig. 4. Resonant frequency as a function of the air gap thickness.

Fig. 5 shows the behavior of the resonant frequency as a function of the ratio r_2/r_1 ($r_1 = 0.35$ cm), for different values of H_0 . Note that the resonant frequency of the antenna shifts to a higher frequency and the results approach those for the isotropic case as the dc magnetic field strength increases. For a particular value of H_0 , the resonant frequency increases when the annular ring dimensions are decreased.

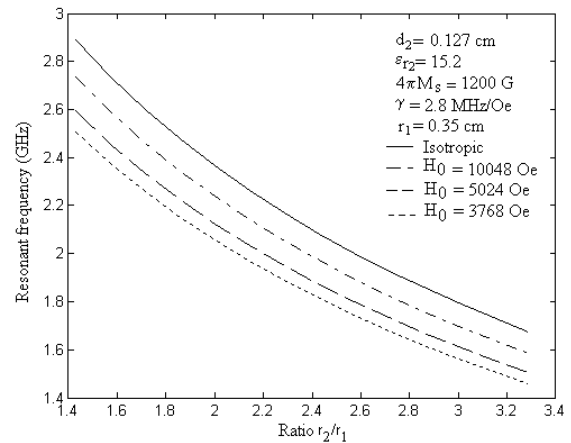


Fig. 5. Resonant frequency as a function of the ratio r_2/r_1 .

IV. CONCLUSION

This paper has described an analysis of the behavior of the ARMSA supported by ferrite material. Ferrite-resonator antennas exhibit greater agility in controlling their radiation characteristics by the application of a dc magnetic bias field.

V. REFERENCES

- [1] J. R. James and P. S. Hall, Eds., Handbook of Microstrip Antennas, Peter Peregrinus, London, England, 1989.
- [2] B. Lax and J. Button, Microwave Ferrites and Ferrimagnetics, McGraw-Hill, New York, 1962.
- [3] C. F. L. Vasconcelos, S. G. Silva, M. R. M. L. Albuquerque, J. R. S. Oliveira, and A.G. d'Assunção, "Annular ring microstrip antennas for millimeter wave applications", Int. Journal of Infrared Millimeter Waves, vol. 28, pp. 821–829, 2007.
- [4] J-S. Row, "Design of aperture-coupled annular-ring microstrip antennas for circular polarization", IEEE Trans. Antennas Propagat., vol. AP-53, pp. 1779–1784, 2005.

CFL Conditions for Finite Integration Methods Using Parallelogram and Parallelepiped Grids

Tetsuji Matsuo

Graduate School of Engineering, Kyoto University
Kyotodaigaku-katsura Nishi-ku, Kyoto, 615-8510, Japan
tmatsuo@kuee.kyoto-u.ac.jp

Abstract — The CFL conditions for finite integration methods using parallelogram and parallelepiped elements are derived. Piecewise uniform elements allow time-step that is $\sqrt{3}$ times as large as that for linearly interpolated elements.

I. INTRODUCTION

Finite integration (FI) methods [1]-[4] enable the use of nonorthogonal grids in electromagnetic-wave analysis. Several methods to construct permittivity and reluctivity matrices have been proposed [3]-[5] because they greatly affect the efficiency and accuracy of FI methods. The efficiency depends on the computational cost of permittivity matrix inversion and on the Courant-Friedrichs-Lewy (CFL) condition, which gives the maximum time-step for stable computation. Previous works have derived the CFL conditions for nonorthogonal grids [6]-[9]. However, the CFL criterions are not explicitly deduced from the permittivity and reluctivity matrices. This article derives CFL conditions for FI methods using parallelogram and parallelepiped grids.

II. CFL CONDITION

The time-stepping of the FI method is written as

$$\mathbf{e}^{k+1} = \mathbf{e}^k + \Delta t \boldsymbol{\varepsilon}^{-1} \mathbf{C}^T \mathbf{v} \mathbf{b}^{k+1/2}, \quad \mathbf{b}^{k+3/2} = \mathbf{b}^{k+1/2} - \Delta t \mathbf{C} \mathbf{e}^{k+1} \quad (1)$$

where \mathbf{e} denotes the vector of line integrals of the electric field along the edges of primal grid, \mathbf{b} is the vector of magnetic fluxes across the faces of primal grid, \mathbf{C} is the curl matrix for primal grid, $\boldsymbol{\varepsilon}$ is the (global) permittivity matrix, and \mathbf{v} is the (global) reluctivity matrix.

The CFL condition is given as [8]

$$\Delta t \leq 2 / \gamma_{\max}^{1/2} \quad (2)$$

where γ_{\max} is the maximum eigenvalue of $\boldsymbol{\Gamma}$ given by

$$\boldsymbol{\Gamma} = \mathbf{C} \boldsymbol{\varepsilon}^{-1} \mathbf{C}^T \mathbf{v}. \quad (3)$$

III. CFL CONDITIONS FOR PARALLELOGRAM ELEMENTS

Fig. 1(a) shows a parallelogram element used for FI analysis of TE wave, where \mathbf{l}_1 and \mathbf{l}_2 are two edges of primal grid. (Whitney-like) Linearly interpolated basis functions for parallelogram edge element are given as

$$\begin{aligned} \mathbf{w}_1(\mathbf{r}) &= (1-t)\mathbf{f}_1/S, & \mathbf{w}_2(\mathbf{r}) &= (1-s)\mathbf{f}_2/S, \\ \mathbf{w}_3(\mathbf{r}) &= t\mathbf{f}_1/S, & \mathbf{w}_4(\mathbf{r}) &= s\mathbf{f}_2/S \end{aligned} \quad (4)$$

where $\mathbf{r} = s\mathbf{l}_1 + t\mathbf{l}_2$, $\mathbf{f}_1 = \mathbf{l}_2 \times \mathbf{e}_z$, $\mathbf{f}_2 = \mathbf{e}_z \times \mathbf{l}_1$, $S = |\mathbf{l}_1 \times \mathbf{l}_2|$, and \mathbf{e}_z is the unit vector along the z -direction. Piecewise uniform basis functions [4] are given as

$$\begin{aligned} \mathbf{w}_1(\mathbf{r}) &= U(1/2-t)\mathbf{f}_1/S, & \mathbf{w}_2(\mathbf{r}) &= U(1/2-s)\mathbf{f}_2/S, \\ \mathbf{w}_3(\mathbf{r}) &= U(t-1/2)\mathbf{f}_1/S, & \mathbf{w}_4(\mathbf{r}) &= U(s-1/2)\mathbf{f}_2/S \end{aligned} \quad (5)$$

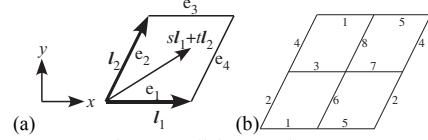


Fig. 1. Parallelogram element

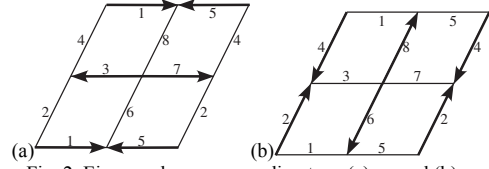


Fig. 2. Eigenmodes corresponding to $\boldsymbol{\varepsilon}$: (a) \mathbf{e}_1 , and (b) \mathbf{e}_2

where $U(x) = 0$ ($x < 0$), $1/2$ ($x = 0$), and 1 ($x > 0$).

Local permittivity matrix $\boldsymbol{\varepsilon}_L = \{\varepsilon_{Lij}\}$, $\varepsilon_{Lij} = \varepsilon \int \mathbf{w}_i \cdot \mathbf{w}_j dS$ for the linearly interpolated basis functions is written as

$$\boldsymbol{\varepsilon}_L = \frac{\varepsilon S}{12} \begin{pmatrix} 4\mathbf{w}_1 \cdot \mathbf{w}_1 & 3\mathbf{w}_1 \cdot \mathbf{w}_2 & 2\mathbf{w}_1 \cdot \mathbf{w}_1 & 3\mathbf{w}_1 \cdot \mathbf{w}_2 \\ 3\mathbf{w}_1 \cdot \mathbf{w}_2 & 4\mathbf{w}_2 \cdot \mathbf{w}_2 & 3\mathbf{w}_1 \cdot \mathbf{w}_2 & 2\mathbf{w}_2 \cdot \mathbf{w}_2 \\ 2\mathbf{w}_1 \cdot \mathbf{w}_1 & 3\mathbf{w}_1 \cdot \mathbf{w}_2 & 4\mathbf{w}_1 \cdot \mathbf{w}_1 & 3\mathbf{w}_1 \cdot \mathbf{w}_2 \\ 3\mathbf{w}_1 \cdot \mathbf{w}_2 & 2\mathbf{w}_2 \cdot \mathbf{w}_2 & 3\mathbf{w}_1 \cdot \mathbf{w}_2 & 4\mathbf{w}_2 \cdot \mathbf{w}_2 \end{pmatrix}. \quad (6)$$

It has eigenvalues $\lambda_1 = \varepsilon S \mathbf{w}_1 \cdot \mathbf{w}_1 / 6 = \varepsilon l_2^2 / 6S$ and $\lambda_2 = \varepsilon S \mathbf{w}_2 \cdot \mathbf{w}_2 / 6 = \varepsilon l_1^2 / 6S$ for eigenvectors $\mathbf{e}_{L1} = (1, 0, -1, 0)$ and $\mathbf{e}_{L2} = (0, 1, 0, -1)$, respectively. The piecewise uniform basis functions give $\boldsymbol{\varepsilon}_L$ eigenvalues $3\lambda_1$ and $3\lambda_2$ for eigenvectors \mathbf{e}_{L1} and \mathbf{e}_{L2} .

The global permittivity matrix $\boldsymbol{\varepsilon}$ is constructed by assembling $\boldsymbol{\varepsilon}_L$. For simplicity, a regular parallelogram grid as depicted in Fig. 1(b) is used with periodic boundary conditions for eigenvalue analysis. The permittivity ε and permeability μ are assumed to be uniform. The linearly interpolated basis functions give $\boldsymbol{\varepsilon}$ eigenvalues $2\lambda_1$ and $2\lambda_2$ for eigenvectors $\mathbf{e}_1 = (1, 0, -1, 0, \dots)^T$ and $\mathbf{e}_2 = (0, 1, 0, -1, \dots)^T$, respectively (see Fig. 2) whereas the piecewise uniform basis functions give $\boldsymbol{\varepsilon}$ eigenvalues $6\lambda_1$ and $6\lambda_2$.

On the other hand, the reluctivity matrix \mathbf{v} is given as

$$\mathbf{v} = 1/\mu S \mathbf{1} \quad (7)$$

where $\mathbf{1}$ is the unit matrix.

According to the eigenvalues and eigenvectors above, matrix $\boldsymbol{\Gamma}$ has the maximum eigenvalue $\gamma_{\max} = 12c^2 (1/l_1^2 + 1/l_2^2)$ or $4c^2 (1/l_1^2 + 1/l_2^2)$ for the linearly interpolated basis functions or the piecewise uniform basis functions, respectively, which has an eigenvector $(1, -1, \dots)^T$. Consequently the CFL conditions is written as

$$\Delta t \leq \alpha / c (1/l_1^2 + 1/l_2^2)^{1/2} \quad (8)$$

where α is $1/\sqrt{3}$ for the linearly interpolated functions and is 1 for the piecewise uniform functions.

IV. CFL CONDITIONS FOR PARALLELEPIPED ELEMENTS

Fig. 3(a) shows a parallelepiped element used for FI analysis, where \mathbf{l}_1 , \mathbf{l}_2 , and \mathbf{l}_3 are three edges of primal grid. Linearly interpolated basis functions for parallelepiped edge element are given at position $\mathbf{r} = s\mathbf{l}_1 + t\mathbf{l}_2 + u\mathbf{l}_3$ as

$$\begin{aligned} \mathbf{w}_1 &= (1-t)(1-u)\mathbf{f}_1/V, & \mathbf{w}_2 &= (1-u)(1-s)\mathbf{f}_2/V, & \mathbf{w}_3 &= (1-s)(1-t)\mathbf{f}_3/V, \\ \mathbf{w}_4 &= t(1-u)\mathbf{f}_1/V, & \mathbf{w}_5 &= u(1-s)\mathbf{f}_2/V, & \mathbf{w}_6 &= s(1-t)\mathbf{f}_3/V, \\ \mathbf{w}_7 &= (1-t)u\mathbf{f}_1/V, & \mathbf{w}_8 &= (1-u)s\mathbf{f}_2/V, & \mathbf{w}_9 &= (1-s)t\mathbf{f}_3/V, \\ \mathbf{w}_{10} &= tu\mathbf{f}_1/V, & \mathbf{w}_{11} &= us\mathbf{f}_2/V, & \mathbf{w}_{12} &= st\mathbf{f}_3/V \end{aligned} \quad (9)$$

where $\mathbf{f}_1 = \mathbf{l}_2 \times \mathbf{l}_3$, $\mathbf{f}_2 = \mathbf{l}_3 \times \mathbf{l}_1$, $\mathbf{f}_3 = \mathbf{l}_1 \times \mathbf{l}_2$, and $V = (\mathbf{l}_1 \times \mathbf{l}_2) \cdot \mathbf{l}_3$. Piecewise uniform basis functions [4] are similarly defined.

The local permittivity matrix $\boldsymbol{\varepsilon}_L$ is given by $\varepsilon_{L,ij} = \int \mathbf{w}_i \cdot \mathbf{w}_j dV$. It has eigenvalues $\lambda_1 = \varepsilon S_{23}^2/36V$, $\lambda_2 = \varepsilon S_{31}^2/36V$, and $\lambda_3 = \varepsilon S_{12}^2/36V$ corresponding to eigenvectors $(1, 0, 0, -1, 0, 0, -1, 0, 0, 1, 0, 0)^T$, $(0, 1, 0, 0, -1, 0, 0, -1, 0, 0, 1, 0)^T$, and $(0, 0, 1, 0, 0, -1, 0, 0, -1, 0, 0, 1)^T$, respectively, for the linearly interpolated basis functions, where $S_{ij} = |\mathbf{l}_i \times \mathbf{l}_j|$. The piecewise uniform basis functions give $\boldsymbol{\varepsilon}_L$ eigenvalues $9\lambda_1$, $9\lambda_2$, and $9\lambda_3$.

The global permittivity matrix $\boldsymbol{\varepsilon}$ is constructed on regular parallelepiped grid with periodic boundary conditions as in Fig. 3(b). Corresponding to $\boldsymbol{\varepsilon}_L$, the matrix $\boldsymbol{\varepsilon}$ has eigenvalues $4\lambda_1$, $4\lambda_2$, and $4\lambda_3$ with eigenvectors $(1, 0, 0, -1, 0, 0, \dots)^T$, $(0, 1, 0, 0, -1, 0, \dots)^T$, and $(0, 0, 1, 0, 0, -1, \dots)^T$, respectively, for the linearly interpolated basis functions. The piecewise uniform basis functions give $\boldsymbol{\varepsilon}$ eigenvalues, $36\lambda_1$, $36\lambda_2$, and $36\lambda_3$.

Linearly interpolated basis functions for parallelepiped face element are given as

$$\begin{aligned} \mathbf{w}_1^f &= (1-s)\mathbf{g}_1/V^2, & \mathbf{w}_2^f &= (1-t)\mathbf{g}_2/V^2, & \mathbf{w}_3^f &= (1-u)\mathbf{g}_3/V^2, \\ \mathbf{w}_4^f &= s\mathbf{g}_1/V^2, & \mathbf{w}_5^f &= t\mathbf{g}_2/V^2, & \mathbf{w}_6^f &= u\mathbf{g}_3/V^2 \end{aligned} \quad (10)$$

where $\mathbf{g}_1 = \mathbf{f}_2 \times \mathbf{f}_3$, $\mathbf{g}_2 = \mathbf{f}_3 \times \mathbf{f}_1$, $\mathbf{g}_3 = \mathbf{f}_1 \times \mathbf{f}_2$. The corresponding local reluctivity matrix \mathbf{v}_L is given by $v_{L,ij} = 1/\mu \int \mathbf{w}_i^f \cdot \mathbf{w}_j^f dV$ as

$$\mathbf{v}_L = \frac{V}{12\mu} \begin{pmatrix} 4\mathbf{w}_1^f \cdot \mathbf{w}_1^f & 3\mathbf{w}_1^f \cdot \mathbf{w}_2^f & 3\mathbf{w}_1^f \cdot \mathbf{w}_3^f & 2\mathbf{w}_1^f \cdot \mathbf{w}_4^f & 3\mathbf{w}_1^f \cdot \mathbf{w}_5^f & 3\mathbf{w}_1^f \cdot \mathbf{w}_6^f \\ 3\mathbf{w}_1^f \cdot \mathbf{w}_2^f & 4\mathbf{w}_2^f \cdot \mathbf{w}_2^f & 3\mathbf{w}_2^f \cdot \mathbf{w}_3^f & 3\mathbf{w}_2^f \cdot \mathbf{w}_4^f & 2\mathbf{w}_2^f \cdot \mathbf{w}_5^f & 3\mathbf{w}_2^f \cdot \mathbf{w}_6^f \\ 3\mathbf{w}_1^f \cdot \mathbf{w}_3^f & 3\mathbf{w}_2^f \cdot \mathbf{w}_3^f & 4\mathbf{w}_3^f \cdot \mathbf{w}_3^f & 3\mathbf{w}_3^f \cdot \mathbf{w}_4^f & 3\mathbf{w}_3^f \cdot \mathbf{w}_5^f & 2\mathbf{w}_3^f \cdot \mathbf{w}_6^f \\ 2\mathbf{w}_1^f \cdot \mathbf{w}_4^f & 3\mathbf{w}_2^f \cdot \mathbf{w}_4^f & 3\mathbf{w}_3^f \cdot \mathbf{w}_4^f & 4\mathbf{w}_4^f \cdot \mathbf{w}_4^f & 3\mathbf{w}_4^f \cdot \mathbf{w}_5^f & 3\mathbf{w}_4^f \cdot \mathbf{w}_6^f \\ 3\mathbf{w}_1^f \cdot \mathbf{w}_5^f & 2\mathbf{w}_2^f \cdot \mathbf{w}_5^f & 3\mathbf{w}_3^f \cdot \mathbf{w}_5^f & 3\mathbf{w}_4^f \cdot \mathbf{w}_5^f & 4\mathbf{w}_5^f \cdot \mathbf{w}_5^f & 3\mathbf{w}_5^f \cdot \mathbf{w}_6^f \\ 3\mathbf{w}_1^f \cdot \mathbf{w}_6^f & 3\mathbf{w}_2^f \cdot \mathbf{w}_6^f & 2\mathbf{w}_3^f \cdot \mathbf{w}_6^f & 3\mathbf{w}_4^f \cdot \mathbf{w}_6^f & 3\mathbf{w}_5^f \cdot \mathbf{w}_6^f & 4\mathbf{w}_6^f \cdot \mathbf{w}_6^f \end{pmatrix} \quad (11)$$

It has eigenvalues $\kappa_1 = l_1^2/6\mu V$, $\kappa_2 = l_2^2/6\mu V$, and $\kappa_3 = l_3^2/6\mu V$ with eigenvectors $(1, 0, 0, -1, 0, 0)^T$, $(0, 1, 0, 0, -1, 0)^T$, and $(0, 0, 1, 0, 0, -1)^T$, respectively, for the linearly interpolated basis functions (see Fig. 4). The piecewise uniform basis functions give \mathbf{v}_L eigenvalues $3\kappa_1$, $3\kappa_2$, and $3\kappa_3$.

Corresponding to \mathbf{v}_L , the global permittivity matrix \mathbf{v} has eigenvalues $2\kappa_1$, $2\kappa_2$, and $2\kappa_3$ with eigenvectors $\mathbf{e}_1^f = (1, 0, 0, -1, 0, 0, \dots)^T$, $\mathbf{e}_2^f = (0, 1, 0, 0, -1, 0, \dots)^T$, and $\mathbf{e}_3^f = (0, 0, 1, 0, 0, -1, \dots)^T$, respectively, for the linearly interpolated basis functions. The piecewise uniform basis functions give \mathbf{v} eigenvalues $6\kappa_1$, $6\kappa_2$, and $6\kappa_3$.

According to the eigenvalues and eigenvectors above, the maximum eigenvalue γ_{\max} of $\boldsymbol{\Gamma}$ is given by.

$$\gamma_{\max} = p_1 + (p_1^2 - 4p_0)^{1/2} \quad (12)$$

$$\begin{aligned} p_1 &= \{ (\kappa_2 + \kappa_3)/\lambda_1 + (\kappa_3 + \kappa_1)/\lambda_2 + (\kappa_1 + \kappa_2)/\lambda_3 \} / 3\alpha^2, \\ p_0 &= (1/\lambda_1\lambda_2 + 1/\lambda_2\lambda_3 + 1/\lambda_3\lambda_1)(\kappa_2\kappa_3 + \kappa_3\kappa_1 + \kappa_1\kappa_2) / 9\alpha^4 \end{aligned} \quad (13)$$

The coefficient α is $1/\sqrt{3}$ for the linearly interpolated basis functions and is 1 for the piecewise uniform basis functions. The corresponding eigenvector is a linear combination of \mathbf{e}_1^f , \mathbf{e}_2^f , and \mathbf{e}_3^f .

When $S_{23} = l_2 l_3$ and $S_{31} = l_3 l_1$, the CFL condition becomes

$$\Delta t \leq \alpha / c \{ (1/l_1^2 + 1/l_2^2) / \sin^2 \theta_{12} + 1/l_3^2 \}^{1/2} \quad (14)$$

where θ_{12} is the angle between \mathbf{l}_1 and \mathbf{l}_2 . Eq. (14) for the piecewise uniform functions ($\alpha=1$) agrees with the CFL condition for the conventional FDTD method ($\sin \theta_{12} = 1$).

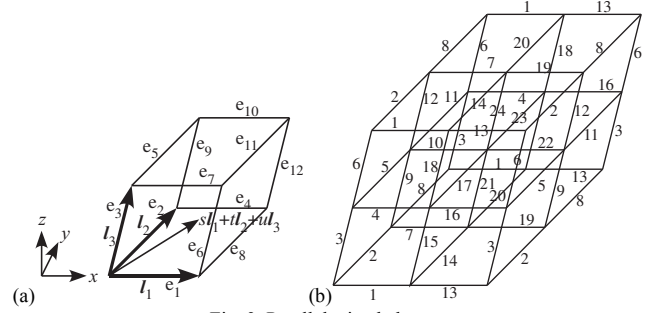
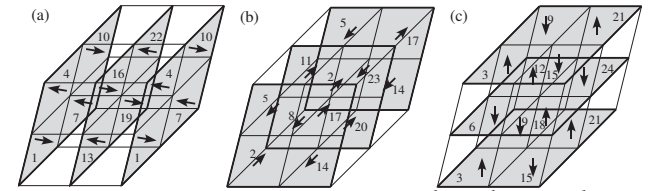


Fig. 3. Parallelepiped element

Fig. 4. Eigenmodes corresponding to \mathbf{v} : (a) \mathbf{e}_1^f , (b) \mathbf{e}_2^f , and (c) \mathbf{e}_3^f

V. CONCLUDING REMARKS

A piecewise uniform parallelogram or parallelepiped element allows a time-step that is $\sqrt{3}$ times as large as that for a linearly interpolated element. Detailed discussions and numerical verification will be presented in the extended paper.

VI. REFERENCES

- [1] T. Weiland, "Time Domain electromagnetic field computation with finite difference methods," *Int. J. Numer. Model.*, 9: 295-319, 1996.
- [2] I.E. Lager, E. Tonti, A.T. de Hoop, G. Mur and M. Marrone, "Finite formulation and domain-integrated field relations in electromagnetics - a synthesis," *IEEE Trans. Magn.*, 39(3): 1199-1202, 2003.
- [3] A. Bossavit and L. Kettunen, "Yee-like schemes on a tetrahedral mesh with diagonal lumping," *Int. J. Num. Model.*, 12: 129-142, 1999.
- [4] L. Codecasa, V. Minerva, and M. Politi, "Use of barycentric dual grids for the solution of frequency domain problems by FIT," *IEEE Trans. Magn.*, 40(2): 1414-1419, 2004.
- [5] M. Cinali and A. Schiavoni, "A stable and consistent generalization of the FDTD technique to nonorthogonal unstructured grids," *IEEE Trans. Antennas Propagat.*, 54(5): 1503-1512, 2006.
- [6] J.F. Lee, R. Palandech, and R. Mittra, "Modeling three-dimensional discontinuities in waveguides using nonorthogonal FDTD algorithm," *IEEE Trans. Microwave Theory Tech.*, 40(2):346-352, 1992.
- [7] R. Schuhmann and T. Weiland, "FDTD on nonorthogonal grids with triangular fillings," *IEEE Trans. Magn.*, 35(3): 1470-1473, 1999.
- [8] S.D. Gedney and J.A. Roden, "Numerical stability of nonorthogonal FDTD methods," *IEEE Trans. Antennas Propagat.*, 48(2): 231-239, 2000.
- [9] T. Matsuo and T. Mifune, "CFL conditions for finite integration methods on triangular meshes," *IEEE Trans. Magn.*, 45(3): 1348-1351, 2009.

A hybrid model for path loss calculation in urban environment

Leandro Carísio Fernandes, Antonio José Martins Soares
 Universidade de Brasília (UnB), Departamento de Engenharia Elétrica
 Campus Universitário Darcy Ribeiro, 70.910-900, Brasília, DF, Brasil
 carisio@gmail.com, martins@ene.unb.br

Abstract — In this paper a genetic algorithm is used to obtain an equation for path loss in an urban environment. The model was developed from measurements at 947 MHz, in Munich, Germany, and validated with data from measurements in Ottawa, Canada, at 910 MHz.

I. INTRODUCTION

The calculation of the transmitted power attenuation as it propagates through space (path loss) is a fundamental component in the design of wireless communication systems. The electromagnetic wave between the transmitter and receiver propagates through different paths, from direct line of sight (LOS) to a situation where the environment is obstructed by buildings, trees etc [1].

Several propagation models are available to calculate the fluctuations in the signal intensity in urban environment. Due to the nonlinear and complex characteristics of propagation in these environments, some researchers suggest the use of artificial intelligence techniques to predict the path loss [2]-[3]. In this work, a new hybrid model is presented, which combines measures with genetic algorithm to obtain an equation that considers various characteristics of the propagation environment.

II. THE PROPOSED MODEL

The log-distance path loss model, used for the mean path loss is given by the equation:

$$L_B(\text{dB}) = L_B(d_0) + 10n \log_{10} \left(\frac{d}{d_0} \right) \quad (1)$$

where n is the path loss exponent which indicates the rate at which the path loss increases with the distance d ; and d_0 is the reference distance, normally 1 km when large coverage cellular systems are used or 1 m to 100 m in microcellular systems. In (1), $L_B(d_0)$ is the mean path loss at reference distance d_0 , calculated using some model or through field measurements [1]. In this model, n is defined in a subjective manner, being dependent on the propagation environment. For example, $n = 2$ for free space; $2.7 \leq n \leq 3.5$ for urban area cellular radio; and $4 \leq n \leq 6$ when the path is obstructed by buildings. Even for a particular kind of environment, there is a range of values to be chosen. In order to quantify the different characteristics of the propagation environment, the following equation is proposed to calculate the mean path loss, which has the advantage of quantifying the environment, removing the subjective nature in the choice of n in (1):

$$L_B(\text{dB}) = A - 20 \log_{10}(h_T) - 20 \log_{10}(h_R) \\ + B f(C + D m_a) + E g(F + G b_n) \\ + [H + I h(J + K m_a) + L i(M + N b_n)] \log_{10} \left(\frac{d}{d_0} \right) \quad (2)$$

where h_T and h_R are the height of transmitter and receiver antennas, respectively; m_a and b_n varies with the receiver position and the propagation environment between the transmitter and receiver.

The parameter m_a is defined in the $[0, 1]$ interval and quantifies the building occupation in an area within a sector of 30° from the transmitter towards the receiver. Its value is obtained by simple average of the percentage of area covered by buildings for distances equal to $d/3$, $2d/3$ and d . Thus, a higher correlation between m_a and the path loss is obtained. The value of b_n is the number of buildings that block the direct line of sight between transmitter and receiver.

The constants A, B, C, D, \dots, N and the functions $f()$, $g()$, $h()$ and $i()$ were determined by a genetic algorithm, a tool that provides a simple way to test various functions and constants without using brute force technique. For the genetic algorithm input, measurements provided by Mannesmann Mobilfunk covering an area of $2.4 \text{ km} \times 3.4 \text{ km}$ in Munich, Germany were used [4]. The database contains building data in vector format, the height of each building, and measures of path loss to around 2300 points on 3 different routes. The measurements were performed at 947 MHz and the heights of transmitting and receiving antennas were 13 m and 1.5 m respectively. Measured values are available for distance between approximately 100 m and 2 km. This database was separated into two sets of measures: one for training and another for testing. The set used for training was formed from 44 measurements selected to represent different values for the triple (m_a, b_n, d) .

In this genetic algorithm, each chromosome represents the constants A to N and the functions $f()$, $g()$, $h()$ and $i()$ shown in (2). Each constant was coded with a 15-bit binary string: 1 bit for the signal, 7 for the fractional part, and 7 for the integer part. The functions were coded in a 3-bit binary string.

For each of the 44 samples of the test database, the path loss is determined using (2) and the constants and functions given by the chromosome decoding. The mean square error between the measurements and the predicted path loss

determines the chromosome fitness. The higher the error, the lower the fitness and vice versa.

Using this methodology, the following equation was obtained for the path loss:

$$L_B(\text{dB}) = 107.3 - 20\log_{10}(h_T) - 20\log_{10}(h_R) + 60m_a + 12.17\log_{10}(0.21 + 0.05b_n) + (53.46 - 50.24m_a + 0.37b_n)\log_{10}\left(\frac{d}{100}\right) \quad (3)$$

III. RESULTS AND CONCLUSION

Figure 1 shows the comparison between measured path loss and the predicted one by the proposed model and the COST 231-Walfish-Ikegame (COST-WI [5]) through the three routes considered. The first order statistics for this cases is presented in Table I. Figure 2 shows the path loss measured, predicted using the proposed model and the COST-WI to data available in [6]. Table II summarizes the first order statistics for this case. As can be seen, the proposed model describes with good accuracy the measured path loss.

The proposed model was developed and tested near 900 MHz for distances between 100 m and 2 km. The results show that the method has remained consistent when the propagation environment is changed. Equivalent models can be built for different frequencies bands, from measurements and (2).

The great advantage of the proposed model is the possibility of obtaining the parameters directly related to the propagation environment using the genetic algorithm. To do this, it is necessary to have measurements in some part of the area of interest. This allows the model to become flexible and easily adaptable to the region of under analysis.

TABLE I
FIRST ORDER STATISTIC FOR MUNICH DATABASE

Model		Route 0	Route 1	Route 2
COST-WI	Mean error (dB)	10.9	14.5	15.5
	Standard deviation (dB)	7.6	6.9	8.7
Proposed	Mean error (dB)	-1.7	-2.6	0.4
	Standard deviation (dB)	5.5	4.6	6.2

TABLE II
FIRST ORDER STATISTIC FOR OTTAWA DATABASE

Model		
COST-WI	Mean error (dB)	5.7
	Standard deviation (dB)	6.2
Proposed	Mean error (dB)	-1.8
	Standard deviation (dB)	4.2

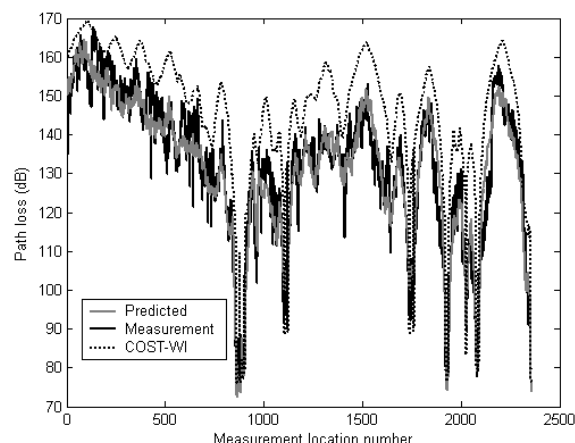


Fig. 1. Comparison between measured and predicted path loss in Munich

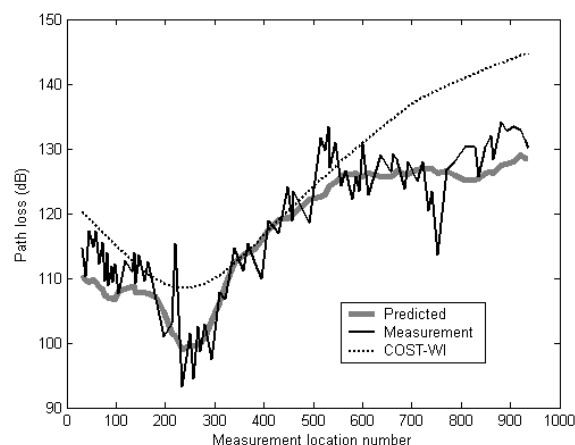


Fig. 2. Comparison between measured and predicted path loss in Ottawa

REFERENCES

- [1] T. S. Rappaport, "Wireless Communications: Principles and Practice", 2nd ed., Hardcover, 2002.
- [2] I. Popescu, I. Nafornita and P. Constantinou, "Comparison of Neural Network Models for Path Loss Prediction", *IEEE International Conference on Wireless and Mobile Computing, Networking and Communications*, 2005, Vol. 1, 22-24 August 2005, pp. 44-49.
- [3] S. Phaiboon, P. Phokharutkul and S. Somkurnpanich, "Multi-Layer Fuzzy Logic Sets for Mobile Path Loss in Forests", *TENCON 2006 IEEE Region 10 Conference*, 14-17 November 2006, pp. 1-4.
- [4] Mannesmann Mobilfunk GmbH, Germany, [Online] Available: <http://www2.ihe.uni-karlsruhe.de/forschung/cost231/cost231.en.html>
- [5] D. J. Cichon and Thomas Kurner, "Propagation Prediction Models", COST 231 Final Report [Online]. Available: <http://www.lx.it.pt/cost231>
- [6] J. H. Wittkeker, "Measurements of Path Loss at 910 MHz for Proposed Microcell Urban Mobile Systems", *IEEE Transactions on Vehicular Technology*, Vol. 37, Issue 3, August, 1988, pp. 125-129.

Temperature Dependence of Optical Fiber Directional Couplers

J. Patrocínio da Silva, V. F. Rodríguez-Esquerre, D. Souza Bezerra

Department of Environmental Science, Federal University of the Semiárid, UFERSA, Mossoró-RN, Brazil
 Department of Electronical and Electrical Technology, DTEE, Federal Institute of Bahia, IFET-BA, Brazil
 Graduate Program in Computer Science, Federal University of the Semiárid, UFERSA, Mossoró-RN, Brazil

H. E. Hernández-Figueroa

Department of Microwave and Optics, State University of Campinas, DMO-FEEC, UNICAMP, Campinas, Brazil

Abstract — It is well known that refractive indexes of materials used for fabricating optical fibers are affected by variations of temperature. In this way, it can be expected a dependence on the temperature for several parameters related with optical fibers and devices based on them. The understanding of this dependence can lead to the design of temperature sensors or athermal devices through the maximization or the compensation of these effects, respectively. In this work we proposed and analyzed the coupling characteristics for a directional coupler based on two ultralow dispersion fibers separated by a small distance for power monitoring purposes. An efficient vectorial finite element method has been used for this purpose.

Keywords — Numerical Techniques, Directional Coupler, Temperature.

I. INTRODUCTION

Optical fibers have several characteristics which permit their use as an excellent transmission medium for short and large distances. The chromatic dispersion is one of the most important parameters and should be carefully analyzed during their design. There are several profiles, including some based on photonic crystals with very low chromatic dispersion for several wavelengths [1-3]. On the other hand, they are also used to design devices to split the power in two or more ports by using directional couplers. In this work, a novel optical fiber [1], See Fig. 1a, where an air hole has been introduced at the core center, has been used to design a directional coupler and their coupling characteristics as well as its temperature dependence has been analyzed by using the beam propagation method based on the frequency domain finite element [4]. The directional coupler is composed by two of these fibers disposed in parallel, See Fig. 1b.

The Sellmeier equation used for the refractive index of fused silica (SiO_2), including the temperature, is:

$$n^2 = A + B / (1 - C / \lambda^2) + D / (1 - E / \lambda^2) \quad (1)$$

where A , B , C and D are the first order temperature Sellmeier coefficients and E is a constant, the values used were taken

J. P. da Silva, patroc@ufersa.edu.br, Tel +55-84-3315-1799, Fax +55-84-3315-1778, V. F. Rodrigues-Esquerre, vitaly@cefetba.br, Tel +55-71-2102-9456, Fax +55-71-2102-9456; D. S. Bezerra, Tel +55-84-3315-1799, amenophis@gmail.com. H. E. Hernández-Figueroa, hugo@dmo.fee.unicamp.br, Tel. +55-21-3527-1001, Fax +55-21-3527-1002

This work has been supported by FAPERJ, FAPESB and CNPq.

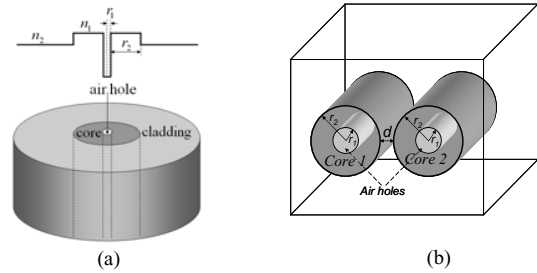


Fig. 1. (a) Refractive index profile of the step index holey fiber and (b) proposed directional coupler.

from [5]: $A = 1,31552 + 6,90754 \times 10^{-6} T$; $B = 78,8404 + 2,35835 \times 10^{-5} T$; $C = 110,199 + 5,84758 \times 10^{-7} T$; $D = 0,91316 + 5,48368 \times 10^{-7} T$ and $E = 100$. Here, T represents the temperature in $^{\circ}\text{C}$ and λ is the wavelength. These coefficients can be used for $26^{\circ}\text{C} < T < 100^{\circ}\text{C}$ and $\lambda > 1.1 \mu\text{m}$.

The refractive index of an optical fiber $n(r, \lambda)$ can be written as $n(r, \lambda) = \eta(r) n_s(\lambda)$, where $n_s(\lambda)$ is the refractive index of fused silica and $\eta(r)$ is the normalized refractive index which only depends on the radial coordinate [3].

II. FINITE ELEMENT FORMULATION

The FEM is widely used for the analysis of photonic devices [1-4], [6-7]. Their accuracy for wave propagation is shown in [4] and [7].

The chromatic dispersion (CD) is a key parameter related to the widening of optical pulses and signal degradation with the propagated distance. In this way, the directional coupler used here was implemented by placing two ultralow dispersion fibers in parallel. The main application of this directional coupler is the power monitoring by tapping a fraction of the transmitted power.

To analyze the coupling characteristics, we start from the vectorial Helmholtz equations in 2D, with perfectly matched layers (PMLs) to avoid reflections from the computational domain,

$$\nabla \times \left(\bar{\bar{k}} \nabla \times \bar{\bar{H}} \right) - k_0^2 \bar{\bar{H}} = 0 \quad (2)$$

where $\bar{\bar{k}} = 1/\bar{\bar{\epsilon}}$ and $\bar{\bar{\epsilon}}$ represent the relative permittivity tensor, respectively. Considering a dielectric material with transversal anisotropy and defining \hat{u}_x , \hat{u}_y e \hat{u}_z associated with the directions x , y e z respectively, $\bar{\bar{\epsilon}}$ can be written as

$\bar{\varepsilon} = \varepsilon_{xx}\hat{u}_x\hat{u}_x + \varepsilon_{xy}\hat{u}_x\hat{u}_y + \varepsilon_{yx}\hat{u}_y\hat{u}_x + \varepsilon_{yy}\hat{u}_y\hat{u}_y + \varepsilon_{zz}\hat{u}_z\hat{u}_z$. After some manipulating algebra and considering an slow variation for the fields and the medium in the propagation direction, z , [4], equation (2) can be rewritten as:

$$\bar{k}_a \frac{\partial^2 \bar{h}_T}{\partial z^2} - 2\gamma \bar{k}_a - \bar{k}_b \nabla_T (\nabla_T \cdot \bar{h}_T) - \nabla_T \times k_{zz} \nabla_T \times \bar{h}_T + (\bar{k}_c + \gamma^2 \bar{k}_a) \bar{h}_T = 0 \quad (3)$$

where \bar{k}_a , \bar{k}_b and \bar{k}_c represent transversal tensors given in [4]. Applying the finite element method for the transversal direction, we obtain,

$$[M] \frac{\partial^2 \{\bar{h}_T\}}{\partial z^2} - 2\gamma [M] \frac{\partial \{\bar{h}_T\}}{\partial z} + ([K] + \gamma^2 [M]) \{\bar{h}_T\} = \{0\} \quad (4)$$

where $\{\bar{h}_T\}$ represents a vector with the unknown fields hxj and hyj , $\{0\}$ is a null vector and $[M]$ e $[K]$ are the global matrices defined in [4]. Using the Padé approximation (1,1) [4], in (3), results in:

$$[\tilde{M}] \frac{d \{\bar{h}_T\}}{dz} + [K] \{\bar{h}_T\} = \{0\} \quad (5)$$

where, $[\tilde{M}] = [M] - \frac{1}{4\gamma^2} ([K] + \gamma^2 [M])$. Finally the finite difference

method is applied in the propagation direction, obtaining a matrix equation,

$$([\tilde{M}(z)] + \theta \Delta z [K(z)]) \{\bar{h}_T(z + \Delta z)\} = ([\tilde{M}(z)] - (1 - \theta) \Delta z [K(z)]) \{\bar{h}_T(z)\} \quad (6)$$

where Δz is the step size along z and θ ($0 \leq \theta \leq 1$) is used to control the stability ($0.5 \leq \theta \leq 1$). For $\theta = 0.5$ we obtain the Crank Nicholson scheme.

The effective index is updated during each propagation step to maintain the accuracy according to [4],

$$n_{eff}^2(z) = \text{Re} \left[\frac{\{\bar{h}_T(z)\}^\dagger [K(z)] \{\bar{h}_T(z)\}}{k_0^2 \{\bar{h}_T(z)\}^\dagger [M(z)] \{\bar{h}_T(z)\}} \right] \quad (7)$$

where \dagger represents the transpose conjugated complex.

III. NUMERICAL RESULTS

We considered two identical optical fibers with parameters: $\eta_1 = 1.05214$, $\eta_2 = 1.0$, $r_1 = 0.2 \mu\text{m}$ and $r_2 = 1.8 \mu\text{m}$ and separated by a distance $d = 0.5 \mu\text{m}$. See Fig. 1b. The coupling characteristics at several operating wavelengths and temperatures were thoroughly analyzed. The ratio of transferred power can be controlled by changing the core separation and the length of the coupler.

The computational domain was $9 \mu\text{m}$ (x direction) and $9 \mu\text{m}$ (y direction) discretized by 12,000 quadratic elements with a propagation step size $\Delta z = 0.1 \mu\text{m}$. The left fiber was

excited with the E_{11}^x mode, which (n_{eff}) is obtained from the relation β/K_0 , through the modal analysis [6]. The Fraction of power as a function of the distance is shown in Fig. 2, for $\lambda = 1.53 \mu\text{m}$. The coupling length obtained by the Vectorial Beam Propagation Method (VBPM) is in good agreement whit the one obtained by the modal analysis by using the beating length definition [7]. The maximum transfer of energy for $T = 28^\circ\text{C}$ happens at $z = 444.5 \mu\text{m}$, and for $T = 300^\circ\text{C}$ it happens at $z = 446 \mu\text{m}$. We have then a small variation of $1.5 \mu\text{m}$ for the coupling length at the above mentioned temperatures. The explanation for small coupling length variations can be explained by the fact that the coupling length of this directional coupler is very short.

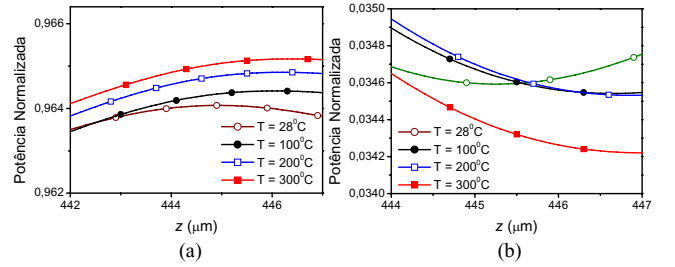


Fig. 2. Fraction of normalized power as a function of the distance in (a) core 2 of Fig 1b (maximum) and (b) core 1 of Fig 1b (minimum).

IV. CONCLUSIONS

In this work, the vectorial frequency domain finite element method has been used to analyze efficiently the temperature dependence of the coupling length of directional couplers. We can observe a small dependence of the coupling length on the temperature. Several other geometries are under analysis and will be presented at the time of the conference.

REFERENCES

- [1] J. P. da Silva ; V. F. Rodríguez-Esquerre ; H. E. Hernández-Figueroa, "Step Index Hole Fiber for Ultra-flattened Chromatic Dispersion," In: Proceedings of Integrated Photonics Research and Applications IPRA2006, Connecticut, CDROM, (2006).
- [2] K. Saitoh, N. Florous, and M. Koshiba, "Ultra-flattened chromatic dispersion controllability using a defected-core photonic crystal fiber with low confinement losses," Opt. Express 13, 8365-8371 (2005).
- [3] D. Correia, V. F. Rodríguez-Esquerre and H. E. Hernández-Figueroa, "Genetic-algorithm and finite-element approach to the synthesis of dispersion-flattened fiber", Microwave and Opt. Technol. Lett, 31, 245-248, (2001).
- [4] J. P. da Silva, H. E. Hernández-Figueroa and A. M. F. Frasson, Vectorial finite-element BPM analysis for transverse anisotropic media, J. Lightwave Technol., 21, 567-576, (2003).
- [5] G. Ghosh, M. Endo, and T. Iwasalu, "Temperature-Dependent Sellmeier Coefficients and Chromatic Dispersions for Some Optical Fiber Glasses", J. Lightwave Technol, 12, 1338-1342, (1994).
- [6] H. E. Hernández-Figueroa, F. A. Fernández, Y. Lu and J. B. Davies, Vectorial finite element modelling of 2D leaky waveguides, IEEE Trans. Magn. 31, 1710-1712, (1995).
- [7] D. Correia, J. P. da Silva and H. E. Hernández-Figueroa, "Genetic Algorithm and Finite-Element Design of Short Single-Section Passive Polarization Converter", IEEE Photonics Technol. Lett., 15, 915-917, (2003).

Analysis of the Effects of Irregular Terrain on Radio Wave Propagation Based on a Three-dimensional Parabolic Equation

Marco Aurélio Nunes da Silva¹, Emanuel Costa², Markus Liniger³

^{1,2}Centro de Estudos de Telecomunicações, Pontifícia Universidade Católica do Rio de Janeiro
Rua Marquês de São Vicente 225, 22451-900 Rio de Janeiro RJ Brasil

¹marcoans@cetuc.puc-rio.br

²epoc@cetuc.puc-rio.br

³LiniKomm GmbH, CH-3012 Bern, Switzerland

³markus_liniger@bluewin.ch

Abstract - The two-dimensional parabolic equation is extensively used to make predictions for the radio wave propagation in the troposphere. However, the effects associated with the lateral variations of a realistic ground are completely ignored by two-dimensional models. In this paper, these effects are considered, extending the two-dimensional parabolic equation for three dimensions. The vector fields are represented in terms of two Hertz potentials. So, depolarization of the fields is automatically included in the formulation. The impedance boundary condition of the ground is applied after a transformation of variables. The problem solution through the finite difference method leads to a sparse system of linear equations more general, which will be solved by an interactive method.

I. INTRODUCTION

Radio signals propagating in the VHF and UHF bands can be strongly attenuated by the effects of irregular terrain. Attenuation in excess to that due to free space is normally estimated using one of many classical (Bullington, Epstein-Peterson and Deygout) or ITU-R models (Recommendations ITU-R P.526 and ITU-R P.1812) [1]. These models are semi-empirical extensions of the basic theoretical model of diffraction by a knife-edge obstacle and have been continually improved by work performed over decades. Computationally-intensive models based on parabolic differential equations, integral equations or ray tracing have also been developed with prediction purposes [1]. In the process, attempts have been made to approximate available experimental data as closely as possible. Although the agreement between predictions and measurements are steadily improving, errors are still high.

All the above are two-dimensional models that assume lateral uniformity of the terrain. This approximation neglects energy propagating outside the vertical plane containing the transmitting and receiving antennas, which may be a reasonable assumption for some environments. However, in the presence of steep terrain, lateral diffraction and scattering may have a significant impact on propagation.

To include the effects of the lateral terrain variations and to investigate the possibility of obtaining better agreement between predictions and measurements, a three-dimensional formulation of the parabolic approximation to the Helmholtz equation will be presented. There are relatively few similar formulations available in the literature [2]-[5], which will

not be discussed here. However, it should be mentioned that they incorporate one or more features which may limit their usefulness for the present application.

The present formulation assumes a two-dimensional irregular terrain on top of the spherical Earth. It is developed with basis on spherical coordinates, which easily accommodates the spreading of the transmitting antenna beam with azimuth. Atmospheric effects are represented by a height-dependent index of refraction. The vector electromagnetic field is expressed in terms of the vertically-oriented electric and magnetic Hertz potentials, each satisfying the scalar Helmholtz equation. This representation automatically guarantees divergent-free electric and magnetic fields at all points of space. The two Hertz potentials, and consequently also the electromagnetic field components, are coupled by the surface of the irregular terrain through the vector impedance boundary condition. So, depolarization is included in the present formulation.

A simple mapping is applied to the region of interest to transform the irregular terrain into a spherical surface. As a consequence of this mapping, the resulting Helmholtz equation and its parabolic approximation include additional variable coefficients, and the components of transformed impedance boundary condition assume more complex forms. On the other hand, the components of the new boundary condition are enforced on a simple spherical surface. The computational domain is truncated by forcing absorbing conditions at the upper and the two lateral boundaries of the region of interest. The absorbing boundary conditions are designed to smoothly weaken the field outside the propagation domain and to avoid spurious reflections originating from the artificial limits imposed to the computational domain.

The parabolic equation and the appropriate boundary conditions define an initial value problem that can be solved using a numerical scheme that progresses along the axial direction. That is, the known field values on a surface transverse to the axial direction are used to determine those on a surface one step further away from the source. For the initial condition, an aperture source distribution is specified to create a Gaussian beam in the far field region.

Model predictions are compared with height-function measurements of field strength performed using an OFCOM (Swiss Federal Office of Communications) vehicle,

equipped with a height-adjustable telescopic mast (up to 11 m in height) that support a Yagi antenna, being able to automatically measure the field strength versus height or azimuth. The measurement data were processed and the final results were calculated, plotted and made available for further studies such as the present one.

II. FORMULATION

Assuming the harmonic dependence with time $e^{-i\omega t}$, source-free media, and assuming that the index of refraction of the atmosphere varies only in the radial direction, the Maxwell equations are manipulated to express the vector electric and magnetic fields in terms of scalar vertically-oriented electric and magnetic Hertz potentials

$$\vec{E} = \frac{1}{n^2} \nabla \times \nabla \times (\Pi^e \hat{r}) + \frac{1}{n^2} i\omega \mu_0 \nabla \times (\Pi^m \hat{r}) \quad (1)$$

$$\vec{H} = \frac{k^2}{i\omega \mu_0} \nabla \times (\Pi^e \hat{r}) + \nabla \times \left[\frac{1}{n^2} \nabla \times (\Pi^m \hat{r}) \right] \quad (2)$$

In the above equations, k is wave number, μ_0 is the permeability of vacuum, n is index of refraction, \hat{r} is the radial unit vector, and the Hertz potentials $\Pi^{e,m}$ satisfy the scalar Helmholtz equation

$$\nabla^2 \Pi^{e,m} + k^2 n^2 \Pi^{e,m} = 0 \quad (3)$$

Next, the complex amplitude $u(r, \theta, \varphi)$ is defined in spherical coordinates by

$$\Pi^{e,m}(r, \theta, \varphi) = \frac{e^{ika\theta}}{r\sqrt{\sin\theta}} u^{e,m}(r, \theta, \varphi) \quad (4)$$

where a is Earth's radius, and the terrain height function $h(\theta, \varphi)$ is taken into account through the mapping

$$\Theta = \theta \quad (5a)$$

$$\Phi = \varphi \quad (5b)$$

$$z = r - a - h(\theta, \varphi) \Rightarrow r = z + a + h(\Theta, \Phi) \quad (5c)$$

$$u^{e,m}(r, \theta, \varphi) = v^{e,m}(z, \Theta, \Phi) \quad (5d)$$

Substituting equations (4) and (5) into equation (3) and introducing the parabolic approximation

$$\left| \frac{\partial^2 v^{e,m}}{\partial \Theta^2} \right| \ll 2ka \left| \frac{\partial v^{e,m}}{\partial \Theta} \right| \quad (6)$$

the modified Helmholtz equation is reduced to

$$\begin{aligned} \frac{\partial v^{e,m}}{\partial \Theta} = & -\frac{r^2}{2ika} \left\{ \left[1 + \left(\frac{1}{r} \frac{\partial h}{\partial \Theta} \right)^2 + \left(\frac{1}{r \sin \Theta} \frac{\partial h}{\partial \Phi} \right)^2 \right] \frac{\partial^2 v^{e,m}}{\partial z^2} - \right. \\ & - \frac{2}{r^2} \left(\frac{\partial h}{\partial \Theta} \frac{\partial^2 v^{e,m}}{\partial z \partial \Theta} + \frac{1}{\sin^2 \Theta} \frac{\partial h}{\partial \Phi} \frac{\partial^2 v^{e,m}}{\partial z \partial \Phi} - \frac{1}{2 \sin^2 \Theta} \frac{\partial^2 v^{e,m}}{\partial \Phi^2} \right) - \\ & - \left(\frac{2ika}{r^2} \frac{\partial h}{\partial \Theta} + \frac{1}{r^2} \frac{\partial^2 h}{\partial \Theta^2} + \frac{1}{r^2 \sin^2 \Theta} \frac{\partial^2 h}{\partial \Phi^2} \right) \frac{\partial v^{e,m}}{\partial z} + \\ & \left. + \left[k^2 \left(n^2 - \frac{a^2}{r^2} \right) + \frac{1}{4r^2} + \frac{1}{4r^2 \sin^2 \Theta} \right] v^{e,m} \right\} \quad (7) \end{aligned}$$

Coupling between the complex amplitude functions v^e and v^m is introduced by the impedance boundary condition [6]

$$\hat{n}_t \times \vec{E} = Z_1 \hat{n}_t \times (\hat{n}_t \times \vec{H}) \quad (8)$$

In equation (8), \hat{n}_t is the unit vector normal to the irregular terrain. Substituting expressions (1), (2), and (3) to (5) into equation (8), each of the three components of the transformed impedance boundary condition is expressed in the general form

$$\begin{aligned} & a_{zz}^e \frac{\partial^2 v^e}{\partial z^2} + a_{z\Theta}^e \frac{\partial^2 v^e}{\partial z \partial \Theta} + a_{z\Phi}^e \frac{\partial^2 v^e}{\partial z \partial \Phi} + a_z^e \frac{\partial v^e}{\partial z} + \\ & + a_{\Theta}^e \frac{\partial v^e}{\partial \Theta} + a_{\Phi}^e \frac{\partial v^e}{\partial \Phi} + a_0^e v^e = \\ = & a_{zz}^m \frac{\partial^2 v^m}{\partial z^2} + a_{z\Theta}^m \frac{\partial^2 v^m}{\partial z \partial \Theta} + a_{z\Phi}^m \frac{\partial^2 v^m}{\partial z \partial \Phi} + a_z^m \frac{\partial v^m}{\partial z} + \\ & + a_{\Theta}^m \frac{\partial v^m}{\partial \Theta} + a_{\Phi}^m \frac{\partial v^m}{\partial \Phi} + a_0^m v^m \quad (9) \end{aligned}$$

The coefficients $a_{ij}^{e,m}$ are specific for each component and depend on partial derivatives of the terrain function $h(\theta, \varphi)$. It is usual to approximate the derivatives with respect to Θ by the expression resulting from the parabolic equation (7). The above three components of the impedance boundary condition are linearly dependent and only two of them are applied at the smoothed boundary $z = 0$ resulting from transformation (5).

The finite difference version of the above equations resulting from the Crank-Nicolson scheme is arranged in the form of a diagonal system of equations. The equations corresponding to points entirely located in the atmosphere display nine coefficients symmetrically arranged around the main diagonal. On the other hand, equations corresponding to points located on the ground display fourteen coefficients asymmetrically arranged around the main diagonal. In each step of the progress along the axial direction defined by the transmitter and receiver, the coefficients are recalculated and the sparse system of linear equations is solved with the help of the PARDISO parallel direct sparse solver, available through the Intel Math Kernel Library. This easy-to-use software solves large sparse symmetric and asymmetric linear systems of equations on shared memory multiprocessors, supporting a wide range of sparse matrix types.

III. REFERENCES

- [1] M. A. N. Silva, E. Costa, and M. Liniger, "Application of Computationally-Intensive Propagation Models to the Prediction of Path Losses Due to Mountainous Terrain in the VHF Frequency Band". *Annals of Commission F Meeting on Climatic Parameters and Diffraction Effects on Radiowave Propagation Prediction (ClimDiff 2005) [paper Diff.23, CD-ROM of ClimDiff 2005]*, Cleveland, OH, EUA, September, 2005.
- [2] R. Janaswamy, "Path Loss Predictions in the Presence of Buildings on Flat Terrain: a 3-D Vector Parabolic Equation Approach". *IEEE Trans. Antennas Propagat.*, 51(8), pp. 1716–1728, August, 2003.
- [3] C.A. Zelle e C.C. Constantinou, "A Three-dimensional Parabolic Equation Applied to VHF/UHF Propagation over Irregular Terrain". *IEEE Trans. Antennas Propagat.*, 47(10), pp. 1586–1596, October, 1999.
- [4] A. A. Zaporozhets and M. F. Levy, "Bistatic RCS calculations with the vector parabolic equation method". *IEEE Trans. Antennas Propagat.*, vol. 47, no. 11, pp. 1688–1696, November, 1999.
- [5] R. S. Awadallah, J. Z. Gehman, J. R. Kuttler, and M. H. Newkirk, "Effects of Lateral Terrain Variations on Tropospheric Radar Propagation". *IEEE Trans. Antennas Propagat.*, vol. 53, pp. 420-434, January 2005.
- [6] T. B. A. Senior and J. L. Volakis, "Approximate Boundary Conditions in Electromagnetics", Piscataway, NJ: The Institution of Electrical Engineers, March, 1995.

Determination of Electromagnetic Sources Through Field Measurements

Ibrahim Akduman⁺, Hülya Şahintürk* and Ali Yapar⁺

⁺ Istanbul Technical University, Electrical and Electronics Eng. Faculty
34469 Maslak Istanbul Turkey

* Yıldız Technical University, Mathematical Engineering Department
34210 Davutpaşa Istanbul Turkey
akduman@itu.edu.tr, hsahin@yildiz.edu.tr, yapara@itu.edu.tr

Abstract — A new, fast and effective method for the determination of locations and current intensities of electromagnetic sources located in an infinite medium is presented. The method is based on the analytical continuation of the total electric field vector measured on a line of finite length. The problem is then reduced to the solution of a non-linear equation which is solved iteratively through linearization in the Newton sense. Numerical evaluations show that the method yields quite accurate results for both the source locations and intensities.

I. INTRODUCTION

Inverse source problems whose aim is to determine the locations and current intensities of electromagnetic sources are of interest due to their potential applications in the areas of non-destructive testing, mobile communications, security, fault diagnosis of electrical machines etc. During the last decade several research activities have been carried out in this direction. Most of methods are developed for sources located inside a spherical domain and spherical harmonic expansions are widely used in the solution process [1-3]. On the other hand, in the real applications such as mobile communications, it is very difficult to perform the measurements on a spherical surface. Instead planar or linear measurement configurations would be preferable. For that reason, methods based on such measurements possibilities should be developed.

The aim of this paper is to give a new, fast and effective algorithm for the determination of both locations and current intensities of current filaments from the electric field vector values obtained through the measurements which are performed on a certain line segment. The method is based on the analytical continuation of the measured total field to the region where the sources are located. The analytical continuation is achieved in terms of the plane wave spectral representation of the total electric field vector. The problem is then reduced to the solution of an operator equation which is linear with respect to intensities and non-linear with respect to locations. The operator equation is solved iteratively via linearization in the Newton sense [4]. The initial estimates for the locations are obtained by plotting the reconstructed total field in the whole space. The method is tested by considering some illustrative examples and it has been shown that it yields quite accurate reconstructions for both intensities and locations.

II. GENERAL FORMULATION OF THE INVERSE SOURCE PROBLEM

We consider the configuration in Fig.1 where n filamentary sources with current intensities (I_1, I_2, \dots, I_n) and locations (r_1, r_2, \dots, r_n) are located in a non-magnetic medium of infinite extend having wavenumber k . The inverse source problem considered here is to reconstruct the current intensities (I_1, I_2, \dots, I_n) and source points (r_1, r_2, \dots, r_n) from the measurement of the total electric field vector on the line $x_2 = \gamma$, say Γ . Note that the measurements can be performed by a receiving antenna R_x moving on the line Γ (See Fig. 1).

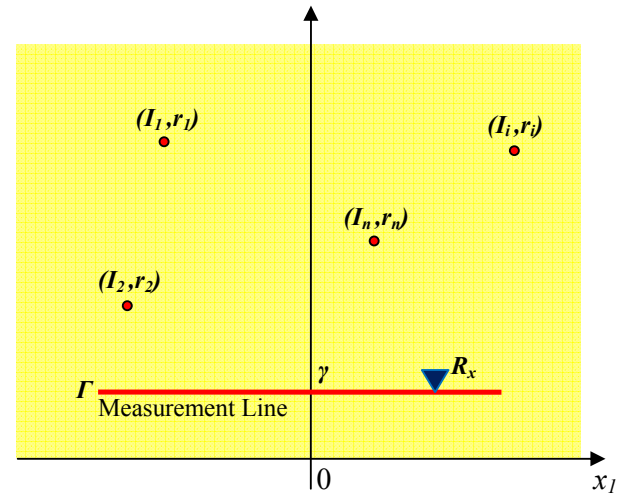


Fig. 1. n filamentary line sources located in a non-magnetic lossless medium and the measurement configuration

In the following, for the sake of simplicity, the analysis will be given by considering $2D$ case where the problem can be formulated as a scalar one in terms of total electric field function $u(x)$. Here $x = (x_1, x_2)$ denotes the position vector in R^2 . Through the measured total field, say $u_m(x)$, the total field in the region above the measurement line can be expressed as a combination of plane waves in the spectral domain, namely;

$$u(x) = \frac{1}{2\pi} \int_{-k}^{+k} \check{u}_m(\alpha) e^{-i\sqrt{k^2 - \alpha^2}(x_2 - \gamma) + i\alpha x_1} d\alpha \quad (1)$$

where $\check{u}_m(\alpha)$ denotes the Fourier transform of the measured total field with respect to x_1 . Note that the plane wave spectral representation in (1) contains only the propagating modes. Equation (1) is nothing but the analytical continuation of the measured data to the region $x_2 > \gamma$ where the sources are located. $u(x)$ is a regular function of x except the source points (r_1, r_2, \dots, r_n) . Thus, basically, one can get the source locations by simply plotting the field $u(x)$ and observing the points where the field is discontinuous. Such an approach gives an approximate source locations which can be used as an initial estimate for the iterative procedure described below.

By considering the explicit expressions of the fields created by individual sources, the problem is then reduced to solution of a functional equation of the form

$$\mathbf{F}(I_1, I_2, \dots, I_n; r_1, r_2, \dots, r_n; \alpha) = \check{u}_m(\alpha) e^{i\sqrt{k^2 - \alpha^2} \gamma}. \quad (2)$$

\mathbf{F} is a known operator which is linear with respect to intensities (I_1, I_2, \dots, I_n) and non-linear with respect to source locations (r_1, r_2, \dots, r_n) . Equation (2) is solved iteratively by linearizing simultaneously with respect to the intensities and the locations. More precisely, given (c_1, c_2, \dots, c_n) for the intensities and (s_1, s_2, \dots, s_n) for the locations, we determine the updates $(c_1 + \mu_1, c_2 + \mu_2, \dots, c_n + \mu_n)$ and $(s_1 + \sigma_1, s_2 + \sigma_2, \dots, s_n + \sigma_n)$ from the linearized equation

$$\begin{aligned} & \mathbf{F}(c_1 + \mu_1^j, \dots, c_n + \mu_n^j; s_1 + \sigma_1^j, \dots, s_n + \sigma_n^j; \alpha) + \\ & \mathbf{F}'(c_1 + \mu_1^j, \dots, c_n + \mu_n^j; s_1 + \sigma_1^j, \dots, s_n + \sigma_n^j; \alpha) \cdot \delta\sigma \\ & = \check{u}_m(\alpha) e^{i\sqrt{k^2 - \alpha^2} \gamma}. \end{aligned} \quad (3)$$

Here \mathbf{F}' denotes the gradient of \mathbf{F} with respect to source locations, j is the iteration number while $\delta\sigma = (\sigma_1, \dots, \sigma_n)$. The equation (3) needs to be solved in a least square sense after collocating it at a sufficient number of collocation points $\alpha_j \in (-k, k)$, $j = 1, \dots, M$. For stability, a penalty term on the unknown locations and intensities has to be added, that is, Tikhonov regularization has to be employed to the solution of (3).

III. NUMERICAL RESULTS

The method described above is tested by considering some illustrative examples. Here we present the results of one of them. Three line sources with current intensities $I_1=1$, $I_2=3$, $I_3=7$ and source locations $r_1=(0,-1.5)$, $r_2=(-1,0)$ and $r_3=(0.5,1.5)$, respectively, are considered. The operating frequency of the sources are 3GHz. The measurements are

performed on the line $x_1 \in (-1.5, 1.5)$, $x_2 = -3$, at 40 points. Note that all the distances are given in meters.

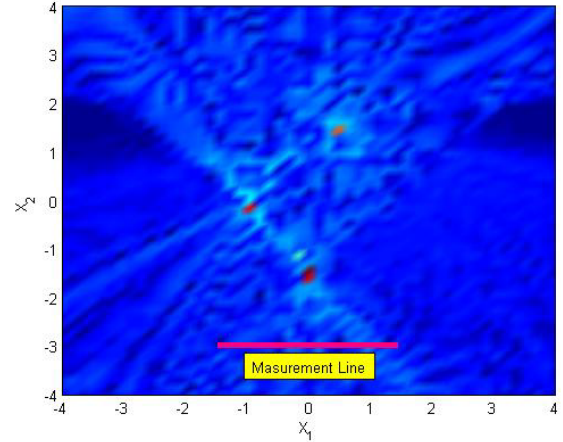


Fig. 1. Two dimensional plot of the reconstructed total field

Fig 2. shows the two dimensional variation of the reconstructed total in the domain $x_1 \in (-4, 4)$, $x_2 \in (-4, 4)$. Obviously, the total field has discontinuities at the source locations. By choosing the points where the field has maximum values as the initial estimate for the source locations and solving the equation (3) iteratively, we get the values of the intensities and source location as given in Table 1. The results are obtained for 11 iterations. The reconstructed intensities and the locations are quite accurate.

TABLE I
Reconstructed current intensities and source locations

Source Number	Intensity (Ampere)	Location (Meters)
I	0.99978	(0.00021, -1.49993)
II	3.01003	(-1.00171, 0.00211)
III	6.92560	(0.49997, 1.50139)

IV. REFERENCES

- [1] J. C.E. Sten and E. A. Marengo, "Inverse source problem in an oblate spheroidal geometry", *IEEE Trans. on Antennas and Propagat.*, 54(11): 3418-3428, 2006.
- [2] A. J.Devaney, G. Kaiser, E. A. Marengo, R. Albenese and G. Erdmann, "The inverse source problem for wavelet fields", *IEEE Trans. on Antennas and Propagat.*, 56(10): 3179-3187, 2008.
- [3] S. Nordebo and M. Gustafsson, "Statistical signal analysis for the inverse source problem in electromagnetic", *IEEE Trans. on Signal Processing*, 54(6): 2357-2361, 2006.
- [4] A. Yapar, O. Ozdemir, H. Sahinturk and I. Akduman, "A Newton method for the reconstruction of perfectly conducting slightly rough surface profiles", *IEEE Trans. on Antennas and Propagat.*, 54(1): 275-279, 2006.

Improved FE-mesh truncation by surface operator implementation to speed up antenna design

W. Renhart, C. Magele, C. Tuerk
 Institute for Fundamentals and Theory in Electrical Engineering
 Graz University of Technology
 Kopernikugasse 24/3, 8010 Graz, Austria
 werner.renhart@tugraz.at

Abstract—Several possibilities to truncate the domain of an unbounded electromagnetic wave problem exist. The ambition of this contribution lies in the improvement of the conditions to be specified along the truncation boundaries in case no scatterer being present. Thereby, the more common case of the outgoing wave to propagate no longer perpendicular to the truncation boundary will be treated. Tracking this idea, an additional surface operator to the widely used surface impedance boundary condition (SIBC) will be built into a finite element formulation. Speed up benefit and accuracy will be evaluated on an asymmetric RFID tag antenna.

I. INTRODUCTION

The variant kinds of mesh truncation when using finite elements always represent a compromise between sufficient accuracy and smallest possible computation effort. The use of absorbing boundaries (ABC) has been improved seriously by some iterative procedures, as reported eg. in [1] and [2]. Multiple calculations of the same problem boost the effort and extend the computation time. The application of perfectly matched layers (PMLs), as suggested eg. in [3], suffers from a condition number degraded set of equations system to be solved. Hence the convergence while applying a solving procedure becomes worse.

The design of antenna geometries belongs to a type of electromagnetic wave problems where scatterer have not to be considered (Fig. 1). Along the truncation bound-

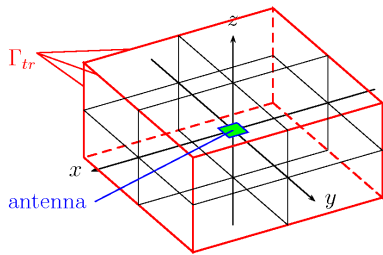


Fig. 1. Basic arrangement, antenna in point of origin, domain truncated by boundary Γ_{tr} .

aries (Γ_{tr}) the propagation direction then is determined by the location of radiating antenna and the truncation surface, only. The knowledge of the incident angle of the outgoing wave all-over Γ_{tr} enables the design of more pre-

cise conditions between the tangential field vectors \vec{E}_t and \vec{H}_t on it.

II. BOUNDARY CONDITIONS FOR THE MESH TRUNCATION

In finding improved boundary conditions for the truncation surface Γ_{tr} we begin with the Maxwell equations

$$\nabla \times \vec{E} = -j\omega\mu\vec{H}, \quad \nabla \times \vec{H} = j\omega\epsilon\vec{E}. \quad (1)$$

Therein, the field vectors \vec{E} and \vec{H} as well as the ∇ operator can be split into a normal and two orthogonal tangential components. The normal component will be described by n and the tangential vector by t . It follows:

$$\vec{E} = \vec{E}_t + \vec{n} E_n, \quad \vec{H} = \vec{H}_t + \vec{n} H_n, \quad \nabla = \nabla_t + \frac{\partial}{\partial n} \vec{n}. \quad (2)$$

With this relations the normal components of the fields, E_n and H_n can be eliminated in (1) to attain

$$\frac{\partial(\vec{n} \times \vec{E}_t)}{\partial n} = -j\omega\mu\vec{H}_t - \frac{1}{j\omega\epsilon}\nabla_t \times (\nabla_t \times \vec{H}_t) \quad (3)$$

$$\frac{\partial(\vec{n} \times \vec{H}_t)}{\partial n} = j\omega\epsilon\vec{E}_t + \frac{1}{j\omega\mu}\nabla_t \times (\nabla_t \times \vec{E}_t). \quad (4)$$

These equations are commonly valid, consequently on the truncation surface, too. On Γ_{tr} we have the situation as

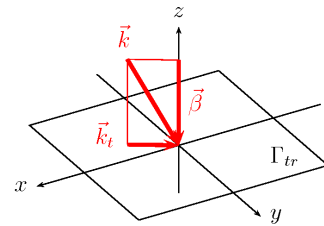


Fig. 2. Incident wave at a point on Γ_{tr} .

shown in Fig. 2. The incident wave is represented by the wave vector \vec{k} , which has been decomposed by the normal vector $\vec{\beta}$ and the tangential vector \vec{k}_t . It follows:

$$\vec{k} = \vec{k}_t + \vec{\beta}, \quad \beta = \pm\sqrt{k^2 - k_t^2}, \quad k = \omega\sqrt{\mu\epsilon}. \quad (5)$$

To get rid of the derivatives $\frac{\partial}{\partial n}$ in (3) and (4), the integration along z for the negative z -half space must be performed. To do so, we can evaluate the field decay in negative z -direction, perpendicular to Γ_{tr} easily by

$$\int_{-\infty}^0 \vec{H}_{t_0} e^{j\beta z} dz = \frac{1}{j\beta} \vec{H}_{t_0}, \quad \int_{-\infty}^0 \vec{E}_{t_0} e^{j\beta z} dz = \frac{1}{j\beta} \vec{E}_{t_0}. \quad (6)$$

\vec{H}_{t_0} and \vec{E}_{t_0} represent the field vectors at $z = 0$. Together with (5) the relations (3) and (4) change to

$$\vec{n} \times \vec{E}_{t_0} = \frac{-\omega\mu\vec{H}_{t_0}}{\sqrt{k^2 - k_t^2}} + \frac{\nabla_t \times (\nabla_t \times \vec{H}_{t_0})}{\omega\epsilon\sqrt{k^2 - k_t^2}} \quad (7)$$

$$\vec{n} \times \vec{H}_{t_0} = \frac{\omega\epsilon\vec{E}_{t_0}}{\sqrt{k^2 - k_t^2}} - \frac{\nabla_t \times (\nabla_t \times \vec{E}_{t_0})}{\omega\mu\sqrt{k^2 - k_t^2}}. \quad (8)$$

These relations between the tangential components of \vec{E}_{t_0} and \vec{H}_{t_0} now can be used to model the higher order boundary conditions on Γ_{tr} .

Transverse components of the outgoing wave may be transformed into the Fourier domain ($e^{-j\vec{k}_t \cdot \vec{r}}$ -terms), only to see, that its tangential derivation can be expressed as $\nabla_t = -j\vec{k}_t$.

An increased incident angle results always in a larger wave vector \vec{k}_t and obviously the curl curl-terms in (7) and (8) become more and more relevance to achieve accurate boundary conditions. If the wave propagates perpendicularly to Γ_{tr} , \vec{k}_t vanishes and the curl curl-terms become zero. The first order SIBCs remain, only.

When applying the Galerkin method to the well known \vec{A} , v or \vec{T} , Φ -formulations [4], the $\vec{n} \times \vec{H}_t$ or the $\vec{n} \times \vec{E}_t$ terms occur, hence (7) or (8) directly can be implemented.

In order to show the performance, we implemented (8) into the \vec{A} , v -formulation. For the weak form of the vectorial equation follows

$$\begin{aligned} & - \int_{\Omega} \nabla \times \vec{N}_i \cdot \frac{1}{\mu} \nabla \times \vec{A} d\Omega + \int_{\Gamma_H} \vec{N}_i \cdot \underbrace{\left(\vec{n} \times \left(\frac{1}{\mu} \nabla \times \vec{A} \right) \right)}_{\vec{n} \times \vec{H}} d\Gamma \\ & + \int_{\Omega} \vec{N}_i \cdot (\sigma + j\omega\epsilon) j\omega (\vec{A} + \nabla v) d\Omega = 0. \end{aligned} \quad (9)$$

In (9) the underbraced term directly may be substituted by (8) and the field \vec{E}_t has to be expressed by the potentials to $\vec{E}_t = -j\omega(\vec{A}_t + \nabla_t v)$.

III. NUMERICAL INVESTIGATION

A symmetric T-folded RFID tag antenna has been evaluated. Its geometry has been chosen from [5] and is shown in Fig. 3. Therein L_1 , L_2 and L_3 indicate the design parameters, either to match the antenna impedance with the transponder chip or to tune the resonant frequency. Consecutively the computational effort for the

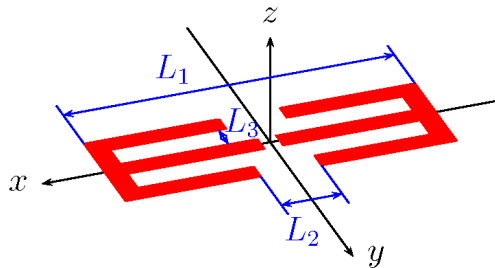


Fig. 3. Symmetric T-folded dipole antenna.

use of standard PMLs and for the proposed boundary conditions has been compared. For our first computations the costs are summarized in Table I. When applying the

TABLE I. COMPUTATIONAL EFFORT

method	DOF	iterations	time [s]
PMLs	64120	10340	1275
proposed BCs	38377	2170	432

proposed boundary conditions no PML-region has to be modeled, so that the DOF changes. Hence the comparison of the values given above limps a bit. Nevertheless, the time score points to get the results faster. No investigations in the influence of the subdivision along Γ_{tr} to the accuracy of the solutions obtained have been done up to now. They are matter of the running activities.

IV. CONCLUSION

For the type of wave propagation problems without containing scattering objects improved mesh truncation conditions have been proposed. Advantage has been taken from the fact, that along the truncation boundaries the incident angle of the outgoing wave is known. Thus improved absorbing conditions containing surface operators can be implemented in an integral term over the truncation boundary. Compared to the PML mesh truncation a smaller domain has to be computed and a well better conditioned equations system must be solved.

REFERENCES

- [1] P. Paul, J.P. Webb, "Balancing Boundary and Discretization Errors Using an Iterative Absorbing Boundary Condition", *IEEE Trans on Magn.*, Vol. 44, No. 6, June 2008, pp. 1362-1365.
- [2] S. Alfonzetti, G. Borzi, "Accuracy of the robin boundary condition iteration method for the finite element solution of scattering problems", *Int. J. Numer. Model.*, Vol. 13, No. 2/3, March-June 2000, pp. 217-213.
- [3] I. Bardi et.al., "Parameter Estimation for PMLs Used with 3D Finite Element Codes", *EEE Trans. Magn.*, Vol. 34, 1998, pp. 2755-2758.
- [4] O. Biro, "Edge element formulations of eddy current problems", *Computer methods in applied mechanics and engineering*, vol. 169, pp. 391-405, 1999.
- [5] B. Yang, Q. Feng, "A Folded Dipole Antenna for RFID Tag", *ICMMT Proceedings*, 2008, DOI 978-1-4244-1880-0/08.

Application of Method of Moments for Near Field Optics with Metal Nanoparticles

Karlo Q. da Costa, and Victor A. Dmitriev
 Electrical Engineering Department, Federal University of Para
 Av. Augusto Corrêa nº 01, CEP 66075-900, Belém-PA, Brazil
 karlo@ufpa.br, victor@ufpa.br

Abstract — This paper presents a near field analysis by method of moments for optical scattering by metal nanoparticles with complex shape illuminated by a plane wave. For testing the developed algorithm, we compare our numerical calculations with the exact Mie scattering theory. The Lorentz-Drude model with one interband term is used to describe complex permittivity of the gold sphere in optical frequencies. The obtained numerical results are the spectral response, resonances, and the regions where the near field is enhanced.

I. INTRODUCTION

The electromagnetic scattering of the metals in optical frequencies possess special characteristics. In these frequencies, there are electron oscillations on the metal, called plasmons with distinct resonant frequencies, which produce strongly enhanced near fields at the surface's metal. The analysis of this effect can be realized with the Lorentz-Drude model of the complex dielectric constant. This study of the electromagnetic optical response of metals nanostructures is known as *plasmonics* or *nanoplasmonics* [1]-[2].

An application of the plasmonics is the design of nanoantennas [3]-[11], which are metal nanostructures used to confine and enhance optical electromagnetic fields. An optical monopole antenna is presented in [4]. In [5]-[7], Bowtie optical antennas are analyzed. Dipoles nanoantennas are presented in [8]-[9], and sphere nanoantennas are discussed in [10]-[11]. Examples of applications of these antennas are ultra-high-density data storage, super-resolution microscopy, integrated nano-optical devices and surface-enhanced Raman scattering [2]-[3].

In this paper, we apply the method of moments (MoM) to the problem of the electromagnetic scattering from complex shape nanoparticles in optical frequencies. To test our algorithm, we compare our numerical results with the exact Mie theory for a gold metal sphere. The Lorentz-Drude theory with one interband term is used to model the complex permittivity of the gold sphere. We present the spectral response, resonances and the localizations with the maximum of the near field.

II. DESCRIPTION OF THE PROBLEM

Fig. 1 shows the geometry of the problem, where a gold sphere of radius a is centered in the origin of the coordinate system. The surrounded medium is the free space. This sphere is illuminated by an E_x -polarized, z -directed plane wave:

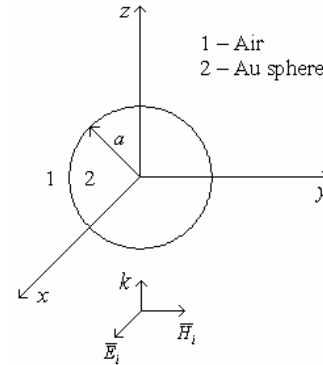


Fig. 1. Incident EM plane wave on a gold sphere

$$\vec{E}_i = E_{i0} e^{j(\alpha x - kz)} \vec{a}_x \quad (1)$$

$$\vec{H}_i = \frac{E_{i0}}{\eta} e^{j(\alpha x - kz)} \vec{a}_y \quad (2)$$

where E_{i0} is the amplitude of the incident electric field, ω the angular frequency, $k = \omega(\mu_0 \epsilon_0)^{1/2} = 2\pi c/\lambda$ the wave number, λ is the wavelength of operation, c is speed of the light, μ_0 the free space permeability, ϵ_0 the free space permittivity, $\eta = 120\pi$ the impedance of the free space. The complex permittivity of the gold sphere is $\epsilon_2 = \epsilon_0 \epsilon_r$, where [2]

$$\epsilon_r = 1 - \frac{\omega_p^2}{\omega^2 - j\Gamma\omega} + \frac{\tilde{\omega}_p^2}{\omega_0^2 - \omega^2 + j\gamma\omega} + 6 \quad (3)$$

being the parameters of this equation: $\omega_p = 13.8 \times 10^{15} \text{ s}^{-1}$, $\Gamma = 1.075 \times 10^{14} \text{ s}^{-1}$, $\omega_0 = 2\pi c/\lambda_0$, $\lambda_0 = 450 \text{ nm}$, $\tilde{\omega}_p = 45 \times 10^{14} \text{ s}^{-1}$, and $\gamma = 9 \times 10^{14} \text{ s}^{-1}$.

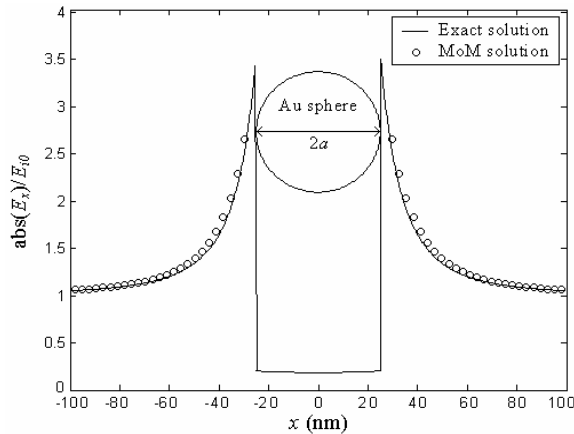
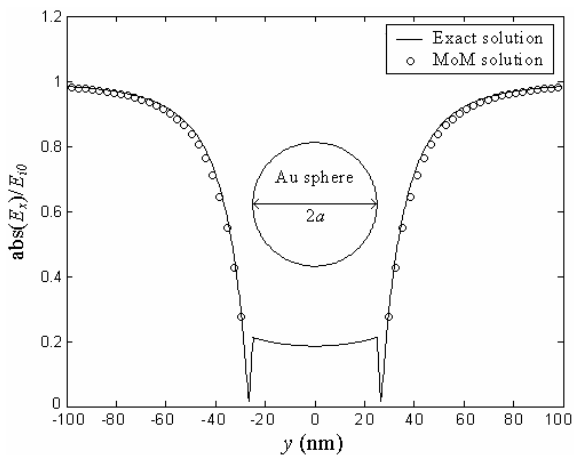
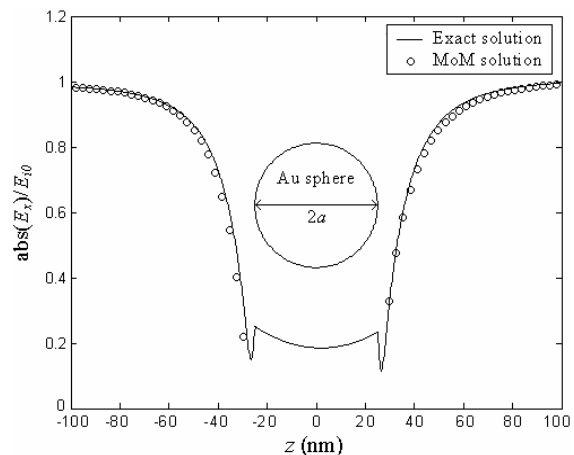
III. THEORETICAL ANALYSIS

The numerical analysis of this scattering problem was done with the exact Mie model [12], and the MoM proposed in [13], which takes account the tensor integral equation of the electric field. In the present analysis, the relative permittivity used for the gold sphere is give by (3).

With these mathematical models, it is possible to calculate the total electric field in all space of the problem (i.e. inside and outside the sphere).

IV. NUMERICAL RESULTS

Two computational programs were developed to analyze the scattering problem. Figs. 2-4 show the calculated electric field along the coordinate axes near the sphere. The radius of the sphere and the wavelength used in the simulations are $a=25\text{nm}$ and $\lambda=700\text{nm}$.

Fig. 2. Normalized E_x field along the x -axisFig. 3. Normalized E_x field along the y -axisFig. 4. Normalized E_x field along the z -axis

From the above Figures, we can observe that the electric field is more enhanced near the sphere (Fig. 2), where the field is normal to the sphere. The field is approximately 3.4 times more than the incident electric field. This result was obtained for $\lambda=700\text{nm}$, but in other wavelengths this enhancement is different. In the full paper version, the complete analysis in the region $500\text{nm} < \lambda < 1200\text{nm}$ will be presented, with the resonance frequencies of this sphere and the correspondent enhancement of the near fields. We shall present also some results for nanoparticles of some others geometries.

V. CONCLUSIONS

In this paper, we presented an algorithm based on the method of moments for the near field analysis for nanoparticles of complex shapes. As an example, we calculated the scattered fields from a gold sphere and compared them with those obtained by Mie's theory. The numerical results achieved by the MoM code are in good agreement with the exact solution. In the full paper variant, we shall give some results for the particles with more complex geometry.

VI. REFERENCES

- [1] M. L. Brongersma, and P. G. Kik, *Surface Plasmon Nanophotonics*, Netherlands: Springer, 2007.
- [2] L. Novotny, and B. Hecht, *Principles of Nano-Optics*, New York: Cambridge, 2006.
- [3] D. W. Pohl, "Near Field Optics as an Antenna Problem", *Near Field: Principles and Applications, The second Asia-Pacific Workshop on Near Field Optics*, Beijing, China October 20-23, pp. 9-21, 1999.
- [4] T. H. Taminiau, et. al., "Near-Fields Driving of a Optical Monopole Antenna", *J. Opt. A: Pure Appl. Opt.*, 9: pp. S315-S321, 2007.
- [5] A. Sundaramurthy, et.al., "Toward Nanometer-Scale Optical Photolithography: Utilizing the Near-Field of Bowtie Optical Nanoantennas", *Nano Letters*, 6(3): pp. 355-360, 2006.
- [6] P. Mühlischlegel, et. al., "Resonant Optical Antennas", *Science*, 308(5728): pp. 1607-1609, 2005.
- [7] B. Hecht, et. al., "Prospects of Resonant Optical Antennas for Nano-Analysis", *Chimia*, 60(11): pp 765-769, 2006.
- [8] O. L. Nuskens, V. Giannini, J. A. Sánchez-Gil, J. G. Rivas, "Optical Scattering Resonances of Single and Coupled Dimer Plasmonic Nanoantennas", *Optic Express*, 15(26): pp.17736-17746, 2007.
- [9] E. Cubukcu, et. al., "Plasmonic Laser Antenna", *Applied Physics Letters*, 89, 2006.
- [10] R. Kappeler, et. al., "Field Computation of Optical Antennas", *J. Comput. Theor. Nanosci.*, 4(3): 686-691, 2007.
- [11] W. Rechberger, et. al., "Optical Properties of Two Interacting Nanoparticles", *Optics Communications*, 220: pp.137-141, 2003.
- [12] J. A. Stratton, *Electromagnetic Theory*, New York: McGraw-Hill, 1941.
- [13] D. E. Livesay, and K. M. Chen, "Electromagnetic Fields induced inside Arbitrary Shaped Biological Bodies", *IEEE Trans. Micro. Theo. Thec.*, 22(12): pp. 1273-1280, 1974.

Eigenvalue analysis of lossy waveguide structures using hybrid $H(\text{curl})$ second order finite elements

Christian Scheiber and Oszkár Bíró

Institute for Fundamentals and Theory in Electrical Engineering

Graz University of Technology, Austria

Email: christian.scheiber@tugraz.at

Abstract—Using a hybrid finite element method, a full wave description for lossy dielectric waveguides is presented. $H(\text{curl})$ -elements span the transversal field components, whereas a scalar potential is described by nodal elements. Second order elements are used on a rectangular mesh. The losses are taken into account by rewriting Maxwell's equations with a complex permittivity term. Using an $A - V$ -formulation the resulting generalized eigenvalue problem has been solved for fully complex eigenvalues.

Index Terms—Lossy waveguides, eigenvalue problems, $H(\text{curl})$ -elements

I. INTRODUCTION

Various numerical methods and different formulations have been presented in the past for solving dielectric waveguide problems. Typical methods are the method of moments [1], spectral-domain methods [2], finite difference methods [3], and finite element methods [4]. Among them, the latter has proved to be a very general and efficient tool. A serious problem for the description of electromagnetic field quantities involving finite elements is the occurrence of spurious modes. In order to overcome these difficulties mainly two approaches have been taken. One is to impose the divergence-free condition, mostly in the case of nodal finite elements approaches. The other is to use $H(\text{curl})$ -tangential elements that are capable of correctly representing the properties of the curl-curl operator [5].

In [6] a waveguiding structure, showing lossy material properties, is considered using triangular hybrid elements. A study covering the anisotropic case is presented in [7]. The work [8] suggests a method to overcome unreliabilities for low frequencies by presenting an algorithm for employing a tree-cotree splitting in order to accomplish an inexact Helmholtz decomposition. There, hierarchical elements are presented.

In this paper we are following the approach of [8] using an $A - V$ -formulation with hybrid finite elements approximating potential functions. In contrast to [6], rectangular elements of second order are used. Imposing an axial gauge, i.e. setting the z -component of the vector potential to zero, the fully complex propagation constant is determined for given operating frequencies by solving a generalized eigenvalue problem.

II. FORMULATION

We consider an $A - V$ -formulation for a source free region and isotropic, lossy material properties. Using ϵ_c as a complex

quantity describing both permittivity (ϵ) and conductivity (σ),

$$\epsilon_c = \epsilon - j\frac{\sigma}{\omega}, \quad (1)$$

and sinusoidal time dependencies the Maxwell equations in the frequency domain can be written as

$$\begin{aligned} \nabla \times \mathbf{E} &= -j\omega\mu\mathbf{H} & \nabla \times \mathbf{H} &= j\omega\epsilon_c\mathbf{E} \\ \nabla \cdot \mathbf{D} &= 0 & \nabla \cdot \mathbf{B} &= 0 \end{aligned} \quad (2)$$

The material properties for a waveguiding structure being uniform in the z -direction, the fields can be described as

$$\begin{aligned} \mathbf{E}(\mathbf{r}, t) &= \mathbf{E}(x, y)e^{-\gamma z}e^{j\omega t} \\ \mathbf{H}(\mathbf{r}, t) &= \mathbf{H}(x, y)e^{-\gamma z}e^{j\omega t} \end{aligned} \quad (3)$$

with \mathbf{r} being a point vector in the waveguide with a cross-section lying in the x, y -plane. γ is the propagation constant built up by the attenuation constant α and the phase constant β :

$$\gamma = \alpha + j\beta. \quad (4)$$

The electromagnetic fields can be rewritten in terms of a vector potential \mathbf{A} and a scalar potential ϕ

$$\begin{aligned} \mathbf{B} &= \nabla \times \mathbf{A} \\ \mathbf{E} &= -j\omega\mathbf{A} - c\nabla\phi \end{aligned} \quad (5)$$

where c is the velocity of light.

In order to arrive at a linear eigenvalue problem, an axial gauge is imposed by choosing $A_z = 0$. With the splitting of the nabla operator to $\nabla \rightarrow \nabla_\tau - \gamma\hat{\mathbf{e}}_z$, Maxwell's equations (2) can be rewritten as

$$\begin{aligned} 0 &= \nabla_\tau \times \frac{1}{\mu_r} \nabla_\tau \times \mathbf{A}_\tau - \gamma^2 \frac{1}{\mu_r} \mathbf{A}_\tau - k_0^2 \epsilon_r \mathbf{A}_\tau + jk_0 \epsilon_r \nabla_\tau \phi \\ 0 &= -\gamma \nabla_\tau \cdot \frac{1}{\mu_r} \mathbf{A}_\tau - jk_0 \gamma \epsilon_r \phi \\ 0 &= -jk_0 \nabla_\tau \cdot \epsilon_r \mathbf{A}_\tau - \nabla_\tau \cdot \epsilon_r \nabla_\tau \phi - \gamma^2 \epsilon_r \phi \end{aligned} \quad (6)$$

In order to ensure a unique solution, the boundary conditions $\mathbf{A}_\tau \times \mathbf{n} = 0$ and $\phi = 0$ are imposed for the simplest case of a perfect electric conductor (PEC).

III. FINITE ELEMENT REPRESENTATION

We represent \mathbf{A}_τ by $H(\text{curl})$ basis functions (\mathbf{N}_i) and ϕ by H^1 basis functions (N_i). The trial functions \mathbf{a}_τ and a_z can be expressed as

$$\mathbf{a}_\tau = \sum_{i=0}^{n_\tau} c_{\tau i} \mathbf{N}_i \quad a_z = \sum_{i=0}^{n_z} c_{zi} N_i \quad (7)$$

Applying Galerkin's method to (6) and considering the boundary conditions, the following generalized eigenvalue equation is obtained:

$$\left[\begin{pmatrix} [A] & [B] \\ [B]^T & [C] \end{pmatrix} - \gamma^2 \begin{pmatrix} [D] & 0 \\ 0 & [E] \end{pmatrix} \right] \begin{bmatrix} \mathbf{c}_\tau \\ \mathbf{c}_z \end{bmatrix} = 0, \quad (8)$$

where \mathbf{c}_τ and \mathbf{c}_z are the coefficient vector for the edge and nodal basis functions. The matrices are given by

$$\begin{aligned} [A] &= \int_{\Omega} \left\{ \frac{1}{\mu_r} (\nabla \times \mathbf{N}_i) \cdot (\nabla \times \mathbf{N}_j) - k_0^2 \epsilon_r \mathbf{N}_i \cdot \mathbf{N}_j \right\} d\Omega \\ [B] &= jk_0 \int_{\Omega} \{ \epsilon_r \mathbf{N}_i \cdot \nabla N_j \} d\Omega \\ [C] &= \int_{\Omega} \{ \nabla N_i \cdot \nabla N_j \} d\Omega \\ [D] &= \int_{\Omega} \left\{ \frac{1}{\mu_r} \mathbf{N}_i \cdot \mathbf{N}_j \right\} d\Omega \\ [E] &= \int_{\Omega} \{ \epsilon_r N_i \cdot N_j \} d\Omega \end{aligned} \quad (9)$$

IV. BASIS FUNCTIONS

The H^1 -nodal basis functions are built from a linear combination of quadratic polynomials in the x- and y-directions. The $H(\text{curl})$ -edge basis functions can be expressed as a linear combination of the nodal basis functions ($f_i(\xi, \eta)$) times the gradient of the respective local coordinate. For the reference element they are obtained through

$$\begin{aligned} \mathbf{N}_i(\xi, \eta) &= f_i(\xi, \eta) \cdot \nabla \xi \quad \text{for } i = 1, 5 \\ \mathbf{N}_i(\xi, \eta) &= f_i(\xi, \eta) \cdot \nabla \eta \quad \text{for } i = 6, 10 \end{aligned} \quad (10)$$

where ξ and η are the coordinates of the reference cell ranging from -1 to 1 .

V. NUMERICAL APPLICATION

As numerical example we consider the case of a microstrip in a dielectric medium. The geometry and the material properties of the substrate are chosen as described in [6]. We are interested in the determination of the dominant propagation mode and therefore are only considering one half of the geometry due to symmetry, as done in [6] too. The variation of the phase and attenuation constant with the frequency is depicted in Fig. 1 and 2.

ACKNOWLEDGMENT

This work has been undertaken as a part of the project DK "Numerical Solution in Technical Sciences", jointly funded by the Graz University of Technology, the Karl Franzens University Graz and the Austrian Science Fund (FWF).

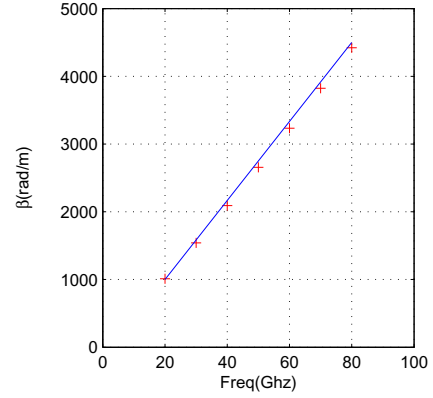


Fig. 1. The dispersion of the phase constant of the microstrip line. The crosses represent our numerical solution compared to the results of [6].

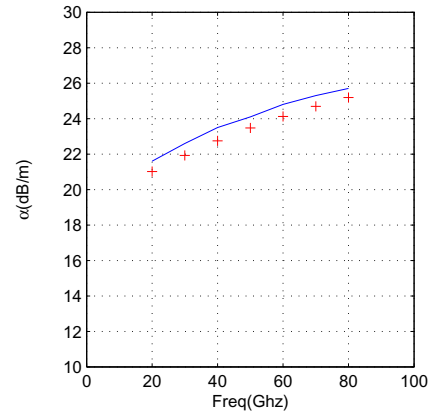


Fig. 2. The dispersion of the attenuation constant of the microstrip line. The crosses represent our numerical solution compared to the results of [6].

REFERENCES

- [1] C. G. Williams and G.K. Cambrell "Numerical Solution of surface waveguide modes using transverse field components," *IEEE Trans. Microwave Theory*, vol. MTT-22, pp. 329-330, Mar. 1974.
- [2] T. Itoh "Spectral domain inimitance approach for dispersion characteristics of generalized printed transmission lines," *IEEE Trans. Microwave Theory*, vol. MTT-28, pp. 733-736, July 1980.
- [3] E. Schwig and W.B. Bridges "Computer analysis of dielectric waveguides: A finite-difference method," *IEEE Trans. Microwave Theory*, vol. MTT-32, pp. 531-541, May 1984.
- [4] S. Bardi, O. Bír6, K. Preis, G. Vrisk and K.R. Richter "Nodal and Edge Element Analysis of Inhomogeneously Loaded 3D Cavities," *IEEE Trans. Magn.*, vol. 29, pp. 1466-1469, 1993.
- [5] D. Sun and Z. Cendes "New vector finite elements for the three-dimensional magnetic fields computations," *J. Appl. Phys.*, vol. 61, no. 8, pp. 3919-3921, Apr. 1987.
- [6] J.-F. Lee "Finite Element Analysis of Lossy Dielectric Waveguides," *IEEE Trans. Microwave Theory*, vol. 42, pp. 1025-1031, June 1994.
- [7] S.-V. Polstyanko and J.-F. Lee, " $H_1(\text{curl})$ Tangential Vector Finite Element Method for Modelling Anisotropic Optical Fibers", *Journ. of lightwave technology*, vol. 13, no. 11, pp. 2290-2295, Nov. 1995.
- [8] S.-C. Lee, J.-F. Lee, "Hierarchical Vector Finite Elements for Analyzing Waveguiding Structures", *IEEE Transactions on Microwave Theory and techniques*, vol. 51, pp. 1897-1905, August 2003.

Efficient Interface Conditions for Finite Difference Time Domain Methods

Dirk Schulz
High Frequency Institute
Friedrich Wöhler Weg 4, 44227 Dortmund, Germany
schulz@hft.e-technik.uni-dortmund.de

Abstract — Finite Difference Time Domain Methods are important for the design of microwave devices. The ordinary Yee scheme commonly used is extended to describe interface conditions between different media adequately in general, when isotropic media are investigated.

I. INTRODUCTION

Finite Difference Time Domain (FDTD) Methods have been extensively used in microwave techniques and have been proposed first by Yee [1]. FDTD methods offer several advantages in contrast to traditional frequency domain approaches. The electromagnetic field is calculated fully vectorial in the time domain while reflection and fringing effects are selfconsistently included. The method exhibits second-order accuracy and does not yield unphysical solutions (spurious modes). A single simulation run allows the extraction of scattering characteristics within a large frequency range. FDTD is easily applicable to a wide range of different structures. Furthermore, the approach allows both exact modelling of field discontinuities at material boundaries and the inclusion of nonlinear effects. Furthermore different material models, i. e. gyromagnetic media, can be included.

In the following we show, that the ordinary discretization scheme does not allow an independent inclusion of interface conditions at interfaces between different media with different permittivities. Therefore, modifications are necessary, which will be introduced. The modifications are simple, but to my knowledge have not been proven and published before.

Yee proposed a discretization scheme according to Fig. 1. The algorithm described is formulated by discretization of Maxwell's curl equations over a finite volume approximating the derivatives with centered difference approximations. Due to the natural choice of the grids and the allocation of the unknown components in space, $\nabla \cdot \vec{D} = 0$ and $\nabla \cdot \vec{B} = 0$ hold. Field vectors are determined at different time steps.

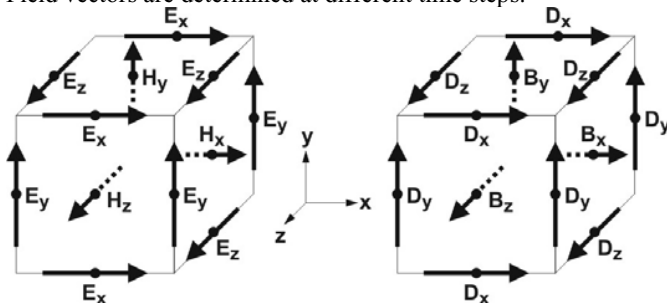


Fig. 1. Yee cell indicating the electric field E, the magnetic field H, the electric flux density D and the magnetic flux density B

II. INCLUSION OF INTERFACE CONDITIONS

All steps of the standard algorithm will be investigated. According to Yee a homogenous medium will be assumed in each discretization cell. Consequently the magnetic field and the electric flux are not absolutely defined at the interfaces. As the electric flux density D is a tangential field component and the magnetic field H is a normal component at the interface, they have to be handled as they are discontinuous [Fig. 2]. The arising difficulties will be discussed. For this purpose all steps needed for the simulation are described.

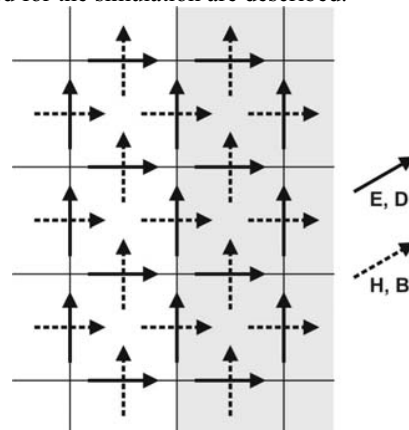


Fig. 2. Field components at an interface

Maxwell's curl equations in integral form have to be applied

$$\oint \vec{H} \cdot d\vec{s} = \iint \frac{\partial \vec{D}}{\partial t} \cdot d\vec{A}, \quad (1a)$$

$$\oint \vec{E} \cdot d\vec{s} = - \iint \frac{\partial \vec{B}}{\partial t} \cdot d\vec{A}, \quad (1b)$$

as well as arbitrary material equations

$$\vec{E} = f_E \{ \vec{D} \}, \quad (1c)$$

$$\vec{H} = f_H \{ \vec{B} \}. \quad (1d)$$

In the following the equations are evaluated in the x-z-plane to simplify the investigation without restriction to the general case.

A. 1st step

According to Yee's scheme the discretization of (1b) leads

to the relation

$$E_1 \Delta x - E_2 \Delta z - E_3 \Delta x + E_4 \Delta z = -\frac{B_{new} - B_{old}}{\Delta t} \Delta x \Delta z \quad (2a)$$

$$\Leftrightarrow B_{new} = B_{old} - \Delta t \left(\frac{E_1 - E_3}{\Delta z} - \frac{E_2 - E_4}{\Delta x} \right). \quad (2b)$$

B_{new} and B_{old} describe the magnetic flux density at time steps $(n+1/2)\Delta t$ and $(n-1/2)\Delta t$. Δx , Δy and Δz are the discretization widths in space. The electric field components E represent the values at time $n\Delta t$. All field components are well defined, so (2b) can be applied at interfaces and included in the algorithm.

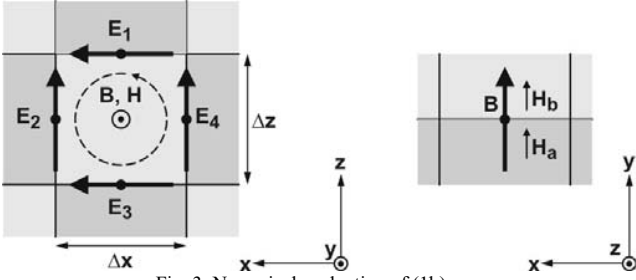


Fig. 3. Numerical evaluation of (1b)

B. 2nd step

The corresponding magnetic material equation (1d) is not uniquely applicable, because the magnetic field components H_a and H_b result from the magnetic flux density B [Fig. 3]. Indeed the values H_a and H_b are of no relevance for the discretization of (1a). According to Fig. 4 the evaluation leads to the following result:

$$\oint \vec{H} \, d\vec{s} \rightarrow H_1 \Delta x - H_2 \Delta z - H_3 \Delta x + H_4 \Delta z \quad (3a)$$

$$\text{with } H_n = \frac{H_{n,a} + H_{n,b}}{2}. \quad (3b)$$

Of course the magnetic material equation has to be solved separately and the calculation of the mean value has to be carried out then increasing the calculation time.

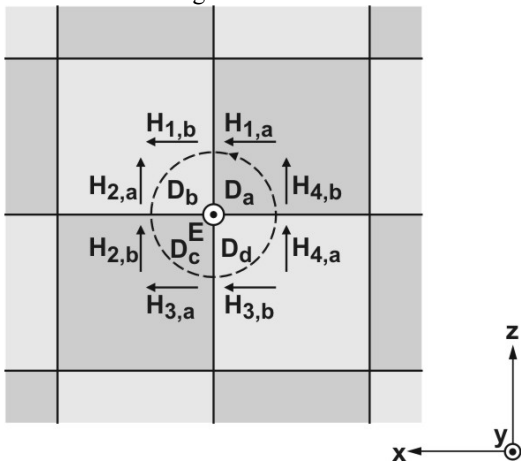


Fig. 4. Numerical evaluation of (1a)

C. 3rd step

Furthermore the discretization of (1b) leads to

$$\oint \vec{H} \, d\vec{s} \rightarrow \frac{D_{a,new} - D_{a,old}}{\Delta t} \cdot \frac{\Delta x}{2} \cdot \frac{\Delta z}{2} + \frac{D_{b,new} - D_{b,old}}{\Delta t} \cdot \frac{\Delta x}{2} \cdot \frac{\Delta z}{2} + \frac{D_{c,new} - D_{c,old}}{\Delta t} \cdot \frac{\Delta x}{2} \cdot \frac{\Delta z}{2} + \frac{D_{d,new} - D_{d,old}}{\Delta t} \cdot \frac{\Delta x}{2} \cdot \frac{\Delta z}{2}. \quad (4)$$

D_{new} and D_{old} describe the magnetic flux density at time steps $(n+1/2)\Delta t$ and $(n-1/2)\Delta t$. Because of the discontinuous electric flux density D (4) includes four separate discretization values for D_a and D_b . According to the chosen discretization for the magnetic field H , the discretized values cannot be calculated separately. This is the mentioned restriction.

D. 4th step

Applying (1c) the electric field components E_a and E_b can be calculated using D_a and D_b . The tangential electric field component must be continuous. Therefore, all discretized electric field values are equivalent.

III. EFFECTIVE PERMITTIVITIES

For isotropic media we can rewrite (3b)

$$H = \frac{H_a + H_b}{2} = \frac{1}{2} \left(\frac{B}{\mu_a} + \frac{B}{\mu_b} \right) = \frac{B}{\mu^*}. \quad (5)$$

The magnetic field component H can be directly evaluated from the magnetic flux by using the effective permittivity

$$\mu^* = \left[\frac{1}{2} \left(\frac{1}{\mu_a} + \frac{1}{\mu_b} \right) \right]^{-1} = \frac{2\mu_a\mu_b}{\mu_a + \mu_b}, \quad (6)$$

so the separate calculation of H_a and H_b is no longer needed. With (6) both steps A and B are carried out simultaneously, leading to

$$H_{new} = H_{old} - \frac{\Delta t}{\mu^*} \left(\frac{E_1 - E_3}{\Delta z} - \frac{E_2 - E_4}{\Delta x} \right). \quad (7)$$

Furthermore the electrical flux density can be calculated according to

$$D^* = \frac{1}{4} (\varepsilon_a + \varepsilon_b + \varepsilon_c + \varepsilon_d) = \varepsilon^* \cdot E \quad (8b)$$

introducing an effective permittivity ε^* . Analogously we will arrive at

$$E_{new} = E_{old} - \frac{\Delta t}{\varepsilon^*} \left(\frac{H_1 - H_3}{\Delta z} - \frac{H_2 - H_4}{\Delta x} \right). \quad (10)$$

By introducing effective permittivities the indicated difficulty is resolved by rearranging (7) and (10).

IV. REFERENCES

- [1] K. S. Yee, "Numerical solution of initial boundary value problems involving Maxwell's equations in isotropic media," *IEEE Trans. on Antenna Propagation*, 14: 302-207, 1966.

FDTD Analysis of UHF-band RFID for Metallic Objects

Yuta Watanabe, Kota Watanabe, and Hajime Igarashi
 Graduate School of Information Science and Technology Hokkaido University
 Kita 14 Nishi 9 Kita-ku Sapporo, 060-0814, JAPAN
 ywata@em-si.eng.hokudai.ac.jp

Abstract— This paper presents an FDTD analysis of communication properties of UHF-band RFID system where IC tags are placed near metallic objects. When the distance between the tag antenna and a metallic plate is increased from zero, the tag antenna impedance also increases; its magnitude is first smaller than those in free space, then the former becomes greater than the latter when the distance is longer than a threshold. Moreover, it is found that the power feeding into the IC chip becomes the maximum at an optimum distance.

I. INTRODUCTION

Radio Frequency Identification (RFID) has widely been used for various industrial and social applications. In particular, RFID based on magnetic induction has been applied to various areas such as rechargeable contactless smart card system, security cards system and retail item management [1]. However, since the magnetic fields reduce in proportion to $1/r^2$ in the quasi-static case, the communication range cannot be longer than several cms. For this reason, the UHF-band RFID using the electromagnetic waves that reduce in proportion to $1/r$ has been studied in order to increase communication range [2]-[4]. The passive UHF-band RFID, where electromagnetic energy is transmitted from the RFID reader to an IC tag, has advantages in its maintenance over active RFID that requires batteries. One of the potential applications of the passive UHF-band RFID is remote sensing of physical and chemical data such as temperature, humidity and material concentration. The remote sensing based on the RFID can be used in, e.g., non-destructive testing, automatic control and environmental monitoring. In these applications, IC tags must often be mounted on metallic surfaces. Hence, the radiation from such metallic surfaces must be carefully considered in the design of the RFID systems. For this reason, special designs of IC tag considering radiation from metallic plates have been studied [5], [6].

This paper presents an FDTD analysis of communication properties of the passive UHF-band RFID system where IC tags are placed near metallic objects. In the followings, the FDTD analysis of tag antenna impedance with near metallic objects will be presented. Then, dependence of the input power of the IC tag on the distance between the tag and metallic plate will be discussed.

II. ANTENNA IMPEDANCE WITH METALLIC OBJECTS

Since impedance matching between the IC tag antenna and the tag chip influences communication range, a proper

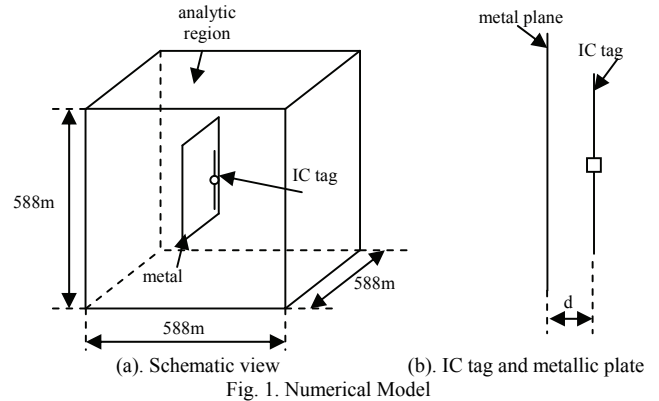


Fig. 1. Numerical Model

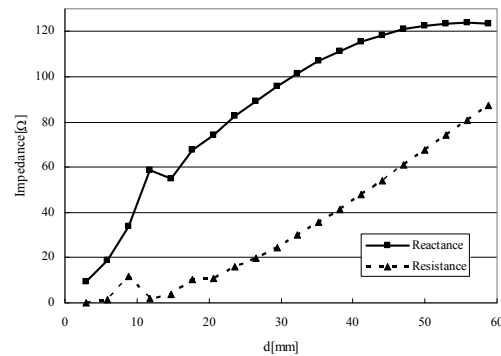


Fig. 2. Antenna Impedance versus distance d

impedance matching between them is very important. For this reason, the impedance of the tag antenna set near the metallic objects is analyzed using FDTD method.

The analysis model is shown in Fig.1. The tag antenna is the half-wave dipole antenna that operates at 1 [GHz], thus the dipole length is set to 150 [mm]. The square metal plane of 180×180 [mm²] is set behind the RFID tag at distance d . The tag antenna and metal plane are divided into 51 and 61 FDTD cells, respectively. The boundary condition for free space environment is the perfect matched layer. The tag antenna impedance $Z_a = R_a + jX_a$ is computed from

$$Z_a = \frac{V(\omega)}{I(\omega)}, \quad (1)$$

where $V(\omega)$ and $I(\omega)$ are the feeding voltage and current which is determined from closed path integral with Ampere's law. The dependence of tag impedance on the distance d is shown Fig. 2. The dipole antenna impedance in free space obtained by FDTD is $Z_a^f = 94.29 + j64.9$. When the distance between the tag antenna and the metal plane is very short, the magnitude of

tag antenna impedance is smaller than Z_a^f . On the other hand, the distance becomes longer, the impedance increases and both real and imaginary part become greater than those of Z_a^f .

III. RECEIVED POWER NEAR METALLIC OBJECTS

The input power received by the tag antenna depends on the antenna gain, the antenna impedance as well as the matching condition between the antenna and IC chip. For this reason, when the IC tag is placed near the metallic objects, the input power changes depending on the distance from the metal.

The numerical model to analyze the influence on the input power from metal objects is shown in Fig.3. The setting and computational conditions are the same as those of the prior analysis. The RFID reader is assumed to be sufficiently away from the IC tag so that the plane wave is illuminated to the IC tag. The power P feeding to the IC chip is computed from

$$P = |I(\omega)|^2 R_c, \tag{2}$$

where $I(\omega)$ is the current induced by the input wave and R_c is the IC chip resistance. The power P normalized by P^f which denotes the received power in free space is plotted against the distance d for two different conditions in Fig.3; in the first condition the chip impedance Z_c is matched to Z_a , that is, $Z_c = Z_a^*$, and in the second they are not matched where $Z_c = R_a - j1.5X_a$. It can be seen in Fig.3 that when the tag antenna is sufficiently close to the metal plane, the feeding power P is smaller than P^f . On the other hand, when the distance between the tag antenna and the metal plane increases, P becomes greater than P^f .

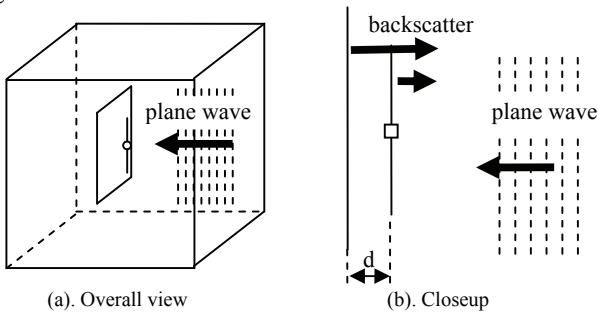


Fig. 3. Input wave and backscatters

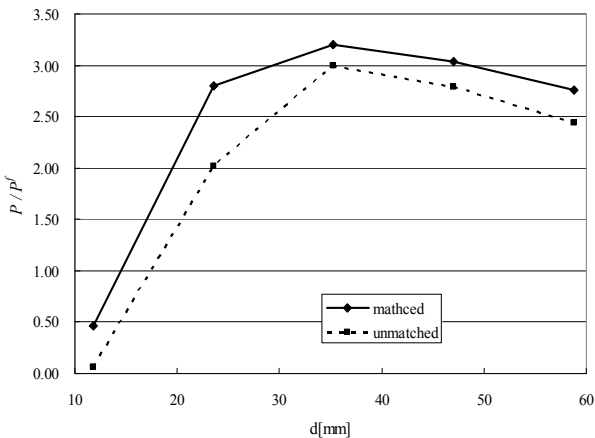


Fig. 4. Normalized feeding powers for matched and unmatched conditions

This would come from that fact that the tag antenna receives the backscatter wave from the metal plane in addition to the input wave. Moreover, there is the optimal distance at which P becomes the maximum that is about three times greater than P^f . These facts suggest that the IC tag for metallic objects could be designed by placing an adequate gap between the IC tag and the metallic surface.

The feeding power P under the matched condition is larger than that under unmatched condition, as expected. It can be found from a further analysis that differences in the real parts of the impedance give little changes in P whereas the differences in imaginary part lead to significant changes. For example, when the relative differences in the imaginary parts are increased from 20% to 70%, the maximum power becomes 87.9 to 51.2 % of the matched case.

IV. CONCLUSION

This paper has presented FDTD analysis of IC-tag antenna impedance and received power when the IC tag is placed in the vicinity of metallic objects. It has been shown that when the distance between the tag antenna and metallic plate is increased from zero, the tag antenna impedance almost monotonously increases and its magnitude becomes greater than that in free space. Moreover, the power feeding to the IC chip placed near a metallic plate can be greater than that in free space. There is an optimal distance between them at which the power becomes the maximum.

The power feeding to the IC chip could be improved by inserting dielectric medium between the IC tag and the metallic plate. This model will be discussed in the long version. Moreover, different antennas such as meander line antenna and loop antenna will be considered to test if the conclusions obtained here is general.

V. REFERENCES

- [1] R. Bansal, "Coming soon to a Wal-Mart near you", *IEEE Antennas Propag. Mag.*, vol.45, pp.105-106, 2003.
- [2] K. V. Seshagiri Rao, "Antenna Design for UHF RFID Tags: A review and Practical Application", *IEEE Transactions on Antennas and Propagation*, vol.53, no.12 pp.3870-3876, 2005.
- [3] Pavel V. Nikitin and K. V. S. Rao, "Theory and Measurement of Backscattering from RFID Tags", *IEEE Antennas and Propagation Magazine*, vol. 48, no. 6, pp. 212-218, 2006.
- [4] Giuseppe De Vita and Gisepe Iannaccone, "Design Criteria for the RF Section of UHF and Microwave Passive RFID Transponders," *IEEE Transactions on Microwave Theory and Techniques.*, vol. 53, no. 9, pp. 2979-2990, 2005.
- [5] Y. Takase, O. Hashimoto and t. Yokota, "Improvement of Radiation Gain of Dipole Antenna Closed to Metal Plate by Using Dielectric and Magnetic Lossy Sheet," *IEICE Technical Report MW(Japan)*, pp.5-9, 2008.
- [6] W. Choi, H. W. Son, J. Bae, G. Y. Ghoi, G. S. Pyo and J. Chae, "An RFID Tag Using a Planar Inverted-F Antenna Capable of Being Stuck to Metallic Objects", *ETRI Journal*, Vol.28 No.2, pp.216-218, 2006.

The Auxiliary Problem For Transient Lossy Transmission Lines With Non-Matched Loads

Karaguler T

Beykent University, Department of Mathematics and Computing,
Sisli-Ayazaga Campus, 34396 Istanbul, Turkey
turhankaraguler@yahoo.com

Abstract—Solving transmission line problem when both transient and lossy states exist is not an easy task. One way of reducing the complexity of the problem is to introduce an auxiliary problem which has previously been applied to the problems of gas dynamics. This approach replaces the actual problem of telegrapher's equations with the equations of auxiliary problem such that non-oscillatory classical finite difference model can be built.

I. INTRODUCTION

A typical lossy transmission line requires all four parameters R, G, L and C to be considered in the model for finding voltage and current distribution along the line. The following equations (1) and (2) named as the telegrapher's equations are in fact the governing equations, or called as the main equations, of the transmission line problem.

$$L \frac{\partial i(x,t)}{\partial t} + \frac{\partial v(x,t)}{\partial x} + Ri(x,t) = 0 \quad (1)$$

$$C \frac{\partial v(x,t)}{\partial t} + \frac{\partial i(x,t)}{\partial x} + Gv(x,t) = 0 \quad (2)$$

These parameters are all taken in per unit length convention as the distance between source and load may be quite large. This further implies that the wave property also exists in the problem as a time delay from source to load can not be ignored. The wave characteristics of the problem can be also noticed from the equation which is obtained by eliminating either voltage or current from the governing equations. The problem will be complete if the boundary conditions of the line are set. These conditions are specified as the input voltage and current profiles applied at the beginning of the line and the Ohm's law at the load end.

Usual way of solving these equations is the direct approximation of the main problem in the time domain [1]. However there is a high possibility that the solution can cause oscillations due to strong dependence of the equations upon the line parameters. Therefore some care should be taken while choosing and applying the numerical method. Here the auxiliary problem is formed and used for the solution.

II. AUXILIARY PROBLEM

The auxiliary problem approach detailed in reference [2] has been applied to some engineering problems such as hydrodynamics and gas dynamics. The simplest case of lossy transmission line problem which is the matched line at the load end is also tested [3]. The method simply replaces the

line functions $i(x,t)$ and $v(x,t)$ with the $I(x,t)$ and $V(x,t)$ auxiliary functions which aim to avoid the space derivatives in the main equations. The following integral equations provide the basis for the main-to-auxiliary problem conversion.

$$L \int_0^x \frac{\partial i(\xi,t)}{\partial t} d\xi + \int_0^x \frac{\partial v(\xi,t)}{\partial \xi} d\xi + R \int_0^x i(\xi,t) d\xi = 0 \quad (3)$$

$$C \int_0^x \frac{\partial v(\xi,t)}{\partial t} d\xi + \int_0^x \frac{\partial i(\xi,t)}{\partial \xi} d\xi + G \int_0^x v(\xi,t) d\xi = 0 \quad (4)$$

The auxiliary and main current and voltage functions are related as below.

$$i(x,t) = \frac{\partial I(x,t)}{\partial x} \quad (5)$$

$$v(x,t) = \frac{\partial V(x,t)}{\partial x} \quad (6)$$

The equations (3-6) will lead to the final form of the auxiliary problem equations which are solved first.

$$L \frac{\partial I(x,t)}{\partial t} + v(x,t) - v(0,t) + RI(x,t) = 0 \quad (7)$$

$$C \frac{\partial V(x,t)}{\partial t} + i(x,t) - i(0,t) + GV(x,t) = 0 \quad (8)$$

III. DISCRETIZATION OF AUXILIARY METHOD AND RESULTS

The conventional finite difference method is applied to the auxiliary problem to obtain the solution. The line is divided into a grid with time and space steps specified beforehand. The integrals are calculated by using common quadrature formula. Then at a grid point, the finite difference equation for the auxiliary voltage is obtained as

$$V_{i,k+1} = V_{i,k} - \frac{\tau}{hC} I_{i,k+1} - \frac{G\tau}{C} \sum_{j=1}^i V_{j,k} - \sum_{j=1}^{i-1} (V_{j,k+1} - V_{j,k}) + \frac{\tau}{hC} i_0(t_k)$$

The current formula can also be obtained in the same way.

In the initial test, the line is assumed to be linear, homogeneous and matched. The line parameter values are given as $R=7.5$ Ohm/m, $L=10$ mh/m, $C=0.4$ F/m and

$G=0.003$ S/m. The length is 1 m and input pulse is 2 Volt with 0.004 ms width. As seen from figure 1 that the output voltage obtained from the method is close enough with the analytical result. The more detailed problem specifications and results can be found in reference [3]. In this paper, the work will be extended to more complex lines with different type of inputs and loads.

- [2] M.A. Rasulov, T. Karaguler and B. Sinsoysal, "A Finite Difference Scheme for solving System Equations of Gas Dynamic in a Class of Discontinuous Functions, ", *Applied Mathematics and Computations*, V. 143: 145-164, 2004.
- [3] T. Karaguler, "A New Method for Solving Transient Lossy Transmission Line Problem," *Lecture Notes in Computer Science, Numeric Analysis and Its Application* Springer, February 2009 pp.338-344

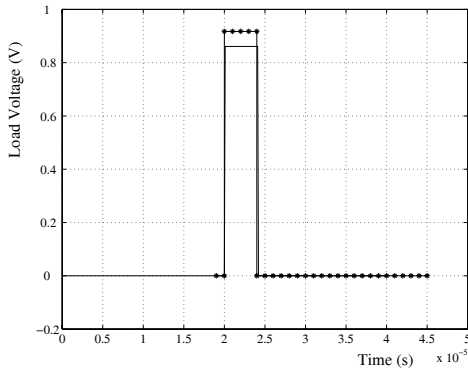


Fig 1. Comparison of load voltages from Auxiliary Problem and Analytical Solution

IV. REFERENCES

- [1] F.H. Branin, "Transient Analysis of Lossless Transmission Lines," *Proc. IEEE*, Vol. 55 1967, pp. 2012-2013.

A low cost parallel and distributed architecture for full micromagnetic numerical codes

C. Ragusa, B. Montrucchio, M. Repetto, V. Giovara, F. Freschi, and B. Xie
 Politecnico di Torino
 Corso Duca degli Abruzzi 24, Torino, 10129, Italy
 E-mail: carlo.ragusa@polito.it

Abstract—A full micromagnetic code has been implemented on a low cost and low latency parallel and distributed architecture based on OpenMP and MPI over Infiniband. Extensive profiling of the original sequential micromagnetic code has been done in order to obtain better parallelization results. Since the most time consuming part of the code resulted in the magnetostatic field calculation algorithm, OpenMP and MPI directives allowed a significant improvement of the performance.

I. PROBLEM FORMULATION

Magnetization dynamics in a nanomagnet is described by the following Landau-Lifshitz-Gilbert (LLG) equation:

$$\frac{\partial \mathbf{m}}{\partial t} = -\mathbf{m} \times \left(\mathbf{h}_{\text{eff}}[\mathbf{m}] - \alpha \frac{\partial \mathbf{m}}{\partial t} \right), \quad (1)$$

where $\mathbf{m} = \mathbf{m}(\mathbf{r}, t)$ is the magnetization vector field normalized to the saturation magnetization M_s , time is measured in unit of $(\gamma M_s)^{-1}$ (γ is the absolute value of the gyromagnetic ratio), α is the dimensionless damping parameter, $\mathbf{h}_{\text{eff}}[\mathbf{m}(\mathbf{r}, t)]$ is the effective field operator which can be obtained by the variational derivative of the free energy functional [1]:

$$\mathbf{h}_{\text{eff}}[\mathbf{m}] = -\frac{\delta g_L[\mathbf{m}]}{\delta \mathbf{m}}, \quad (2)$$

where

$$g_L[\mathbf{m}] = \frac{1}{V_\Omega} \int_\Omega \left[\frac{l_{\text{ex}}^2}{2} |\nabla \mathbf{m}|^2 - \frac{1}{2} \mathbf{h}_m \cdot \mathbf{m} + \varphi(\mathbf{m}) - \mathbf{h}_a \cdot \mathbf{m} \right] dV, \quad (3)$$

$\varphi(\mathbf{m})$ is the anisotropy energy density and $l_{\text{ex}} = \sqrt{(2A)/\mu_0 M_s^2}$ is the exchange length (A is the exchange constant and μ_0 the vacuum permeability), \mathbf{h}_m and \mathbf{h}_a are the demagnetizing and applied fields, respectively, and V_Ω is the body volume. In addition, the homogeneous Neumann boundary condition $\partial \mathbf{m} / \partial \mathbf{n} = 0$ is imposed at the body surface. In order to obtain a spatially discretized version of eq. (1) we consider a partition of the region Ω in N cells Ω_k , with volume V_k and assume that the cells are small enough that the vector fields $\mathbf{m}(\mathbf{r}, t)$ and $\mathbf{h}_{\text{eff}}[\mathbf{m}(\mathbf{r}, t)]$ can be considered spatially uniform within each cell. We denote with $\mathbf{m}_k(t)$ and $\mathbf{h}_{\text{eff}k}$ the vectors associated with the generic k -th cell. Beside the cell vectors, we will consider also the mesh vectors $\mathbf{m} = (\mathbf{m}_1, \dots, \mathbf{m}_N)^T \in \mathbb{R}^{3N}$ containing the whole collection of cell vectors.

If the cells are small enough that $\mathbf{m}(\mathbf{r}, t)$ is spatially uniform in each cell, we can reasonably assume that the magnetization

amplitude is

$$|\mathbf{m}_k| = 1. \quad (4)$$

Now we can write down the discretized LLG equation in the following form that consist of a system of ordinary differential equations:

$$\frac{d\mathbf{m}_k}{dt} = -\mathbf{m}_k \times \mathbf{h}_{\text{eff}k}[\mathbf{m}] + \alpha \mathbf{m}_k \times \frac{d\mathbf{m}_k}{dt}, \quad (5)$$

where \mathbf{m}_k is the average magnetization of the k -th cell. It is worth noting that the effective field in the k -th cell depends on the magnetization of the whole cell collection due to the magnetostatic interaction, namely $\mathbf{h}_{\text{eff}k} = \mathbf{h}_{\text{eff}k}[\mathbf{m}]$.

For the numerical solution of eq. (5), we use the implicit mid-point rule scheme [2]. The midpoint discretized version of eq. (5) is

$$\begin{aligned} \mathbf{m}_k^{n+1} - \mathbf{m}_k^n &= \\ &= -\mathbf{m}_k^{n+\frac{1}{2}} \times (c_\alpha \mathbf{h}_{\text{eff}k}^{n+\frac{1}{2}} + \alpha' \mathbf{m}_k^{n+\frac{1}{2}} \times \mathbf{h}_{\text{eff}k}^{n+\frac{1}{2}}) \Delta t \end{aligned} \quad (6)$$

where the index n refers to time instants, and the following midpoint formulas have been used:

$$\mathbf{m}_k^{n+\frac{1}{2}} = \frac{\mathbf{m}_k^n + \mathbf{m}_k^{n+1}}{2}, \quad (7)$$

$$\mathbf{h}_{\text{eff}k}^{n+\frac{1}{2}} = \mathbf{h}_{\text{eff}k} \left[\frac{\mathbf{m}^n + \mathbf{m}^{n+1}}{2} \right]. \quad (8)$$

The solution of the time-stepping equation (6) requires solving a system of $3N$ nonlinear algebraic equations and provides, at each time step, the $3N$ unknowns \mathbf{m}_k^{n+1} at each mesh element Ω_k . To solve this nonlinear system we use a quasi-Newton technique similar to one described in ref. [2].

The discretized effective field in Eq. (5) is the gradient of a discretized free energy $g_L(\mathbf{m}) = g_L(\mathbf{m}_1, \dots, \mathbf{m}_N)$ which approximates the free energy functional $g_L[\mathbf{m}]$:

$$\mathbf{h}_{\text{eff}k} = -\frac{\partial}{\partial \mathbf{m}_k} g_L(\mathbf{m}_1, \dots, \mathbf{m}_N). \quad (9)$$

The effective field $\mathbf{h}_{\text{eff}k}$ can be represented as

$$\mathbf{h}_{\text{eff}k} = \mathbf{h}_{\text{ex}k} + \mathbf{h}_{\text{an}k} + \mathbf{h}_{\text{m}k} + \mathbf{h}_{\text{a}k} \quad (10)$$

where $\mathbf{h}_{\text{ex}k}$ is the exchange field, $\mathbf{h}_{\text{an}k}$ is the anisotropy field, $\mathbf{h}_{\text{m}k}$ is the magnetostatic field, and $\mathbf{h}_{\text{a}k}$ is the applied field. In our formulation we subdivide the magnetized domain Ω into N tetrahedral elements. The magnetostatic field contribution to the effective field is computed by means of an hybrid

procedure: inside the region Ω occupied by the magnetic body, the magnetostatic problem is formulated by using the Finite Formulation scheme [3] where the magnetic vector potential is assumed as unknown. Conversely, in the exterior region extending to infinity, the magnetic scalar potential at the boundary of the magnetized domain Ω is analytically computed through an integral formulation [4]. Using this method, the resulting stiffness matrix is sparse and all coupling terms between the two formulations are on the right-end-side (RHS) [5]. Starting from a known magnetization distribution, the RHS is computed by a matrix-vector product and the resulting linear system is solved by using a direct method in which the stiffness matrix is LU factorized once and for all at the beginning of the procedure. The computational cost of the LU factorization of the stiffness matrix is $O(N^3)$ and the cost of each subsequent magnetostatic computation is $O(N^2)$. Regarding the calculation of exchange field, as vector \mathbf{m} is approximated by a piecewise constant vector field (at each element Ω_k), there is not a direct way of evaluating the term $|\nabla\mathbf{m}|$ in eq. (3). The exchange field is then computed following a procedure similar to that described by Fredkin in [6].

II. IMPLEMENTATION

A. Hardware and software architecture

Since the most time consuming part of the code is the magnetostatic field algorithm, many existing parallel implementations, such as [7], use Ethernet-based clusters. In our approach we will use a low latency Infiniband network coupled with a low cost multi processor, multi core cluster. The hardware architecture includes a low cost 16 cores cluster composed by two double processor computers each based on the Intel Server Board S5000PSLSATAR motherboard, two quad-core Intel Xeon E5420 2.5GHz, and 32GB RAM. The two computers are connected by means of an Infiniband network [8], composed by two Mellanox ConnectX IB MHGH28-XTC DDR HCA PCI-e 2.0 x8 Memory Free. The Infiniband cards are directly connected together, without using a switch and are put on one PCI Express slot x16 version 1.1. The Operating system is Gentoo Linux. The programming language is FORTRAN. Several tests have been done comparing Intel *ifort* and *gcc* compilers. We have chosen *gcc* for the greater possibilities of the open source approach. With optimal choice of compiler optimization switches, the two Fortran compilers appear very similar from the performance point of view, at least with our code. On each machine, OpenMP [9] has been used for parallel computations, in particular the version included in *gcc*. The Infiniband link is a network channel selected for the MPI communication system [10]. The OpenMPI implementation has been chosen after extensive tests and comparisons with MVAPICH2. Infiniband latency has been experimentally verified as compatible with the Mellanox board specifications.

B. Profiling

Profiling by means of *gprof* [11] has been extensively used in order to better understand the internal structure of the micromagnetic code. Analyzing the profiling results, the most

time consuming part of the code resulted in the magnetostatic field calculation algorithm. It is important to note that, even if Amdahl's law significantly reduces the maximum improvement of performance, in particular in distributed computers, it appears very interesting, given profiling results, the possibility to speedup the micromagnetic code, in particular given the high complexity of some simulation scenarios.

C. Parallelization

At first any standard sequential loop is parallelized to fully exploit all the eight cores each single machine can offer; this has required setting up proper shared/private variables lists. Afterwards, the loop is split in two (n in the general case) data sets, before executing OpenMP. Eventually data is exchanged by means of MPI and merged back. This work has been done repeatedly, until the most computational-expensive functions have been correctly parallelized, always verifying results through the profiler and taking in consideration the optimization flags inserted.

III. RESULTS

A dynamic micromagnetic test case was developed in order to test different implementations of the code. In Table I is reported timing information given OpenMP and/or MPI insertion. Moreover, it is possible to see simulation times for the magnetostatic related functions before parallelization and with OpenMP and/or MPI. The overall speedup for the considered section is consistent with the initial statement. Results show that the optimized part of the micromagnetic code scales accordingly to the number of processors.

TABLE I
SIMULATION RESULTS

	Magnetostatic code [s]	Overall simulation [s]
Normal	71.2	249
MPI	42.1	174
OpenMP	14.1	129
OpenMP+MPI	7.9	59

REFERENCES

- [1] W.F. Brown, Micromagnetics, Wiley (1963).
- [2] M. d'Aquino, C. Serpico, G. Miano, J. Comp. Phys. 209 (2005), 730-753
- [3] E. Tonti, IEEE Transaction Magnetics 38 (2002), 333-336
- [4] C. Giuffrida, G. Gruosso, and M. Repetto, IEEE Transactions on Magnetics 42 (2006) 1503-1511
- [5] C. Giuffrida, C.S. Ragusa, M. Repetto, Physica B Condensed Matter 372, 299 (2006).
- [6] D. R. Fredkin, T. R. Koehler, J. Appl. Phys. 67 (1990), 5544-5548.
- [7] Y. Kanai, M. Saiki, K. Hirasawa, T. Tsukamoto, and K. Yoshida, IEEE Transactions on Magnetics, Vol. 44, 2008, pp. 1602-1605.
- [8] G. M. Shipman, T. S. Woodall, R. L. Graham, A. B. Maccabe, P. G. Bridges, "Infiniband scalability in Open MPI", Parallel and Distributed Processing Symposium, 2006.
- [9] R. Chandra, L. Dagum, D. Kohr, D. Maydan, J. McDonald, R. Menon, "Parallel programming in OpenMP" Morgan Kaufmann Publishers, 2001.
- [10] W. Gropp, E. Lusk, A. Skjellum, "Using MPI - Portable parallel programming with the Message-Passing Interfac", Scientific and Engineering computation series, The MIT Press, 1999.
- [11] S. L. Graham, P. B. Kessler and M. K. McKusick, "gprof: a Call Graph Execution Profiler". SIGPLAN '82 Symposium on Compiler Construction, Boston, June 1982, pp. 120-126.

A Research of Various MRAM Design for High Gb/Chip on Perpendicular Pole System

Hyuk Won, Gwan Soo Park, Kang Seo, and Il Hwan Park

School of Electrical Engineering, Pusan National University

Jangjeon-dong, Guemjeong-gu, Busan, 609-735, Korea

Raafil98@pusan.ac.kr; gspark@pusan.ac.kr; kalam@pusan.ac.kr; honeypark@pusan.ac.kr

Abstract — Conventional MRAM and STT MRAM have same the critical problem that decreases an injection current for high Gb/Chip. In this paper, we present the various MRAM design for solving the problem. As a solution, we proposed new MRAM design that has two additional high permeable poles. Proposed new MRAM design has a strong switching field owing to two poles added on both sides of the free layer, just like perpendicular magnetic recording heads. This structure is usefully more conventional MRAM for simple design and decreasing injection current. We show results that are variation of a switching field owing to two poles added on both sides of the free layer by thickness of the free layer and cell square size, injected current density with injected current density of $5 \times 10^6 \text{ A/cm}^2 \sim 6 \times 10^8 \text{ A/cm}^2$.

I. INTRODUCTION

By portable computers and communication products, the nonvolatile memory is demanded with unlimited read/write endurance. Flash technology is expected by the value and memory capacity but has limited ($10^5 \sim 10^6$) write cycles and low write speed. Conventional MRAM has unlimited read/write endurance but has a low capacity than flash technology. Partly because conventional MRAM has a faulty structure using a simple write current injection system. For downsize scalability, the major problem that is the mere write current is required at the smaller bit size should be solved with a new design [1]-[2].

STT MRAM technology has advantages conventional (toggle) MRAM on injected current and cell size. STT writing technology, by directly passing a current through MTJ, overcomes these hurdles with much lower switching current, simpler cell architecture which results in a cell that can be as small as 6F2 (for single-bit cells) and reduced manufacturing cost, and more importantly, excellent scalability to future technology nodes [3].

We present a various MRAM design that has advantages conventional MRAM on injected current and cell size in this paper. This system is using the added high permeable pole. By the added pole, conventional MRAM or STT MRAM can have a more than simple design, increasing strong switching field and decreasing injection current.

II. DESIGN AND DRIVE OF VARIOUS MRAM

Fig. 1 shows a schematic drawing of the various MRAM elements. Fig. 1 (a) is conventional MRAM. For downsize scalability, the major problem that is the mere write current is required at the smaller bit size should be solved with a new design. We proposed a new design MRAM for a this critical

problem. The system is PTP MRAM and shows Fig. 1 (b). PTP MRAM element has two poles added on both sides of the free layer. The material of these poles has high permeability and then this system is able to have enhanced switching field. We call bit pole for the one on top of the free layer and word pole for the other beneath the free layer. Both poles have a single current line at the side. PTP MRAM has pMTJ on the bottom of the word pole. Fig. 2 (a) ~ (c) describes the write process of PTP MRAM. Memory status is “0” in fig. 2 (a) because having same direction of magnetization in the free layer and the fixed layer. When bit current and word current are injected. Magnetization of the free layer is changed rapidly by the switching field assisted by the bit pole and word pole as fig. 2 (b). Finally the state of the free layer is changed like fig. 2 (c) and then the cell has the status “1”. Usually the name of pMTJ stands for a set of free layer, fixed layer and junction but in this paper pMTJ shows only junction part like fig. 2 (d).

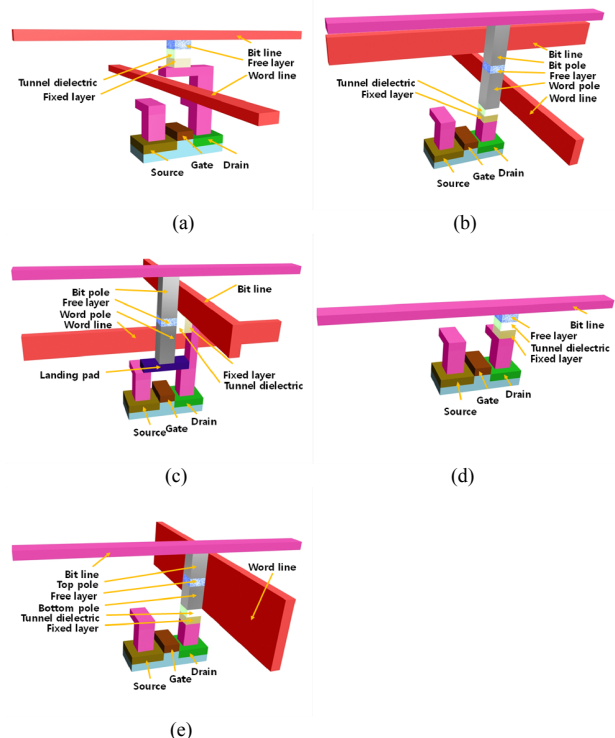


Fig. 1. Schematic drawing of the various MRAM elements. (a) conventional MRAM (b) PTP MRAM has a two high permeability poles added on both sides of free layer, named bit pole on top of free layer and word pole beneath the free layer. (c) SJP MRAM has a two high permeability poles as like PTP MRAM but this system uses a common MTJ. (d) STT MRAM. (e) PTSTT MRAM has a two high permeability poles as like PTP MRAM but this system have a additional current word line.

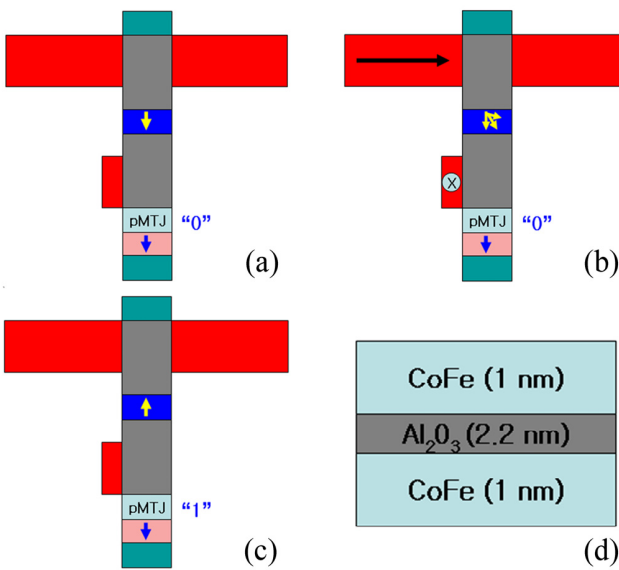


Fig. 2. . Write process of the PTP MRAM and structure of the pMTJ. (a) shows “0” status. When direct current is injected in bit and word line, status of free layer is changed like (b). Finally status of the free layer is stabilized to be ‘1’ status as (c). (d) shows the structure of the pMTJ.

The PTP MRAM has superior magnetic field efficiency than conventional MRAM because this novel system has additional high permeability poles, which are expected to generate stronger switching field than conventional MRAM system. So this system has downsize scalability and high coercivity magnet can be used in the free layer. Figure 3 shows magnetic field intensity on the center of the free layer in PTP MRAM and conventional MRAM with direct current densities $I = 5 \times 10^6 \text{ A/cm}^2 \sim 6 \times 10^8 \text{ A/cm}^2$. Clearly the stronger switching field is generated in PTP MRAM than in conventional MRAM at the same direct current.

Fig. 4 shows write process of the side junction perpendicular MRAM (SJP MRAM). This system uses a common MTJ and added two poles. SJP MRAM system has same results on the switching field but for different MTJ solution, SJP MRAM has a complex structure than PTP MRAM and SJP MRAM have a troublesome problem on the fabrication for perpendicular fabricated MTJ

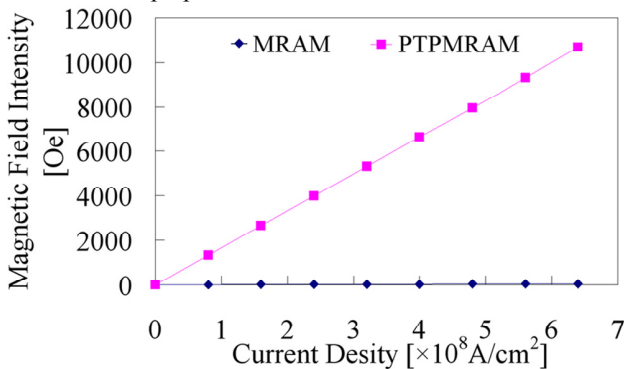


Fig. 3. Comparison of magnetic field intensity on the center of the free layer of PTP MRAM and conventional MRAM with a direct current densities factor $I = 8 \times 10^7 \text{ A/cm}^2 \sim 6 \times 10^8 \text{ A/cm}^2$. Clearly the graph shows PTP MRAM has a stronger field than conventional MRAM on the same current density injected.

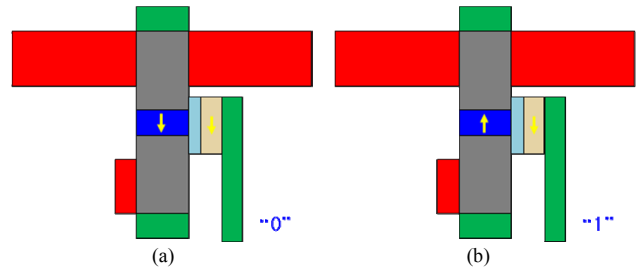


Fig. 4. . Write process of the SJP MRAM (a) shows “0” status. When direct current is injected in bit and word line, status of free layer is changed like (b). Finally status of the free layer is stabilized to be ‘1’

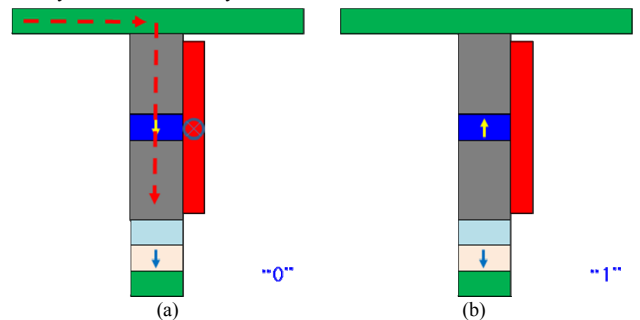


Fig. 5. . Write process of the PTSTT MRAM (a) shows “0” status. When direct current is injected in bit and word line, status of free layer is changed like (b). Finally status of the free layer is stabilized to be ‘1’

SST MRAM technology has advantages conventional (toggle) MRAM on injected current and cell size. Fig. 1 (d) shows SST MRAM element. SST writing technology, by directly passing a current through MTJ, overcomes these hurdles with much lower switching current, simpler cell architecture which results in a cell that can be as small as 6F2 (for single-bit cells) and reduced manufacturing cost, and more importantly, excellent scalability to future technology nodes.

For decreasing the current density, we added pole system on the SST MRAM. It is Pole Type SST MRAM (PTSTT MRAM). Fig. 1 (e) shows a schematic drawing of the PTSTT MRAM element. PTSTT MRAM has a added strong switching field for spin torque reversal as like fig. 5 then this system can decrease current density.

III. CONCLUSION

This paper presents various the MRAM design for breakthrough the critical problem. Next time we will optimizing system for high Gb/Chip.

IV. REFERENCES

- [1] Mark Durlam, Peter J. Naji, Asim Omair, Mark DeHerrera, John Calder, Jon M. Slaughter, Brad N. Engel, Nicholas D. Rizzo, Greg Crynkewich, Brian Butcher, Clarence Tracy, Ken Smith, Kelly W. Kyler, J. Jack Ren, Jaynal A. Molla, William A. Feil, Rick G. Williams, and Saied Tehrani, “A 1-Mbit MRAM Based on 1T1MTJ Bit Cell Integrated With Copper Interconnects”, IEEE J. Sol. Sta. Circ., vol. 38, No. 5, MAY 2003.
- [2] Jianguo Wang and P. P. Freitas, “Low-Current Blocking Temperature Writing of Double-Barrier MRAM Cells”, IEEE Trans. On Mag., vol. 40, No. 4, July 2004. AAPS Bulletin, vol. 18, No. 6, December 2008.
- [3] Yiming Huai, “Spin-Transfer Torque MRAM (STT-MRAM): Challenges and Prospects”,

Theoretical Analysis of Field Distribution and Attenuation in a Ag/GaN Periodic Plasmon Waveguide

Anderson O. Silva¹, Victor Dmitriev²

Faculty of Electrical Engineering – Federal University of Para

P.O. 8619, CEP 66075-900, Belem – Para – Brazil

¹aosilva@ufpa.br, ²victor@ufpa.br

Abstract — The use of surface-plasmons-polaritons (SPPs) is one of the promising ways to develop optical components below the diffraction limit. It was recently demonstrated that gallium nitride (GaN) can play an important role in the improvement of subwavelength optical media, in particular, to serve as a material for plasmon waveguides. We report here a theoretical investigation concerning manipulation of SPPs in a waveguide made of cylindrical nanorods with silver core and GaN cladding. A hexagonal lattice of these rods forms a 2D waveguiding structure. An algorithm based on FDTD method was developed to calculate distribution of optical power of the light beam propagating in the waveguide. Attenuation of the optical signal is also calculated and compared to the results obtained for the analogous device without GaN cladding. Our results show that Ag/GaN waveguiding structure can have lower attenuation.

I. INTRODUCTION

Surface plasmons-polaritons (SPPs) are electromagnetic waves that propagate along a metal-dielectric interface by a resonant interaction between photons and free electrons at the conductor surface [1]. In information technology, SPPs are a suitable choice to implement photonic circuits with subwavelength dimensions. In other words, it can concentrate and guide optical signals through structures much smaller than the wavelength of light, yielding mechanisms for manipulation of photons at nanoscale with unprecedented transmission, processing and storage capacities. In the last five years, it was a high increase in researches in the field of nanoplasmonics.

The main challenge for construction of nanoplasmonic devices is to provide reduction of the large losses encountered by SPP waves along the direction of propagation. Such losses are due to scattering and absorption of SPPs by the involved materials. In order to overcome this problem, different types of conductor-dielectric configurations were already proposed. For instance, thin metal stripes and metallic trenches were considered in [2] and [3], respectively. A photonic crystal composed by silver nanorods is proposed in [4] where SPP propagation over a micrometric length was obtained.

This presentation reports the theoretical investigation of a waveguide composed by nanorods arranged in a hexagonal lattice. Using a developed algorithm based on FDTD (Finite Difference Time Domain) method for dispersive media [5], we show that light propagation is due to coupling between SPPs at the boundary between metallic core and dielectric cladding of the rods. The core is formed by silver and the cladding corresponds to a thin layer of gallium nitride (GaN). As it was experimentally demonstrated in [6], 2D periodic arrays of this

semiconductor can reduce optical losses in subwavelength regime when compared with bulk-GaN applications.

The aim of our work is to employ combination of GaN and silver in the design of the periodic plasmon waveguide in order to achieve lower losses in comparison with the analogous device made only by silver rods.

II. SPP PROPAGATION THROUGH HEXAGONAL LATTICE WAVEGUIDE MADE OF AG/GaN NANORODS

The structure under investigation is made of silver nanorods with diameter of 80 nm, each one surrounded by a thin layer of GaN such that the obtained cylinder has a radius of 50 nm. The rods are periodically organized in hexagonal unitary cells with lattice constant $a=200$ nm. The geometry of this structure is depicted in Fig. 1.

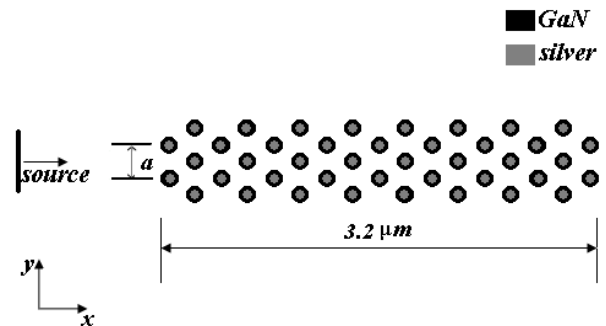


Fig. 1. Geometry of the plasmon waveguide based on nanorods arranged in a hexagonal lattice. Each rod is composed by a silver core and a thin GaN cladding.

The refractive index of GaN is assumed 2.5 and the dielectric function of silver is described by the Drude dispersive model (1).

$$\varepsilon(\omega) = \varepsilon_{\infty} - \omega_p^2 [\omega(\omega - i\Gamma)]^{-1}. \quad (1)$$

The constants that appear in (1) were experimentally determined [7] and they are listed in table I.

TABLE I
CONSTANT VALUES OF DRUDE MODEL

Constants of Drude model	Values
ϵ_∞	3.70
ω_p	13673 THz
Γ	27.35 THz

The simulations were carried out employing our numerical algorithm based on FDTD method for dispersive media [5]. The peculiarity of this approach is the presence of the polarization current density \bar{J}_P (2) in the update equation for electric field \bar{E} by virtue of dependence on frequency of the dielectric constant.

$$\bar{J}_P^{n+1/2} = \left(\frac{2}{2+\Gamma\Delta t} \right) \bar{J}_P^n + \frac{\epsilon_0 \omega_p^2 \Delta t}{4+2\Gamma\Delta t} (\bar{E}^{n+1} + \bar{E}^n), \quad (2)$$

where ϵ_0 is permittivity of vacuum, Δt is the time increment and n is the time step.

To perform numerical calculation we used a Gaussian beam as source with waist of 200 nm. The boundaries of the computational domain where modelled by PML (Perfectly Matched Layer) technique [5]. The light incident into the waveguide is a TE (E_z , H_x , H_y) polarized wave. Intensity distribution in a single Ag/GaN nanorod and in the plasmon waveguide for a Gaussian beam at wavelength of 600 nm is depicted in Fig. 2(a,b).

The mechanism of optical power flow along the waveguide is coupling between surface plasmons excited from one set of Ag/GaN nanorods to the subsequent one.

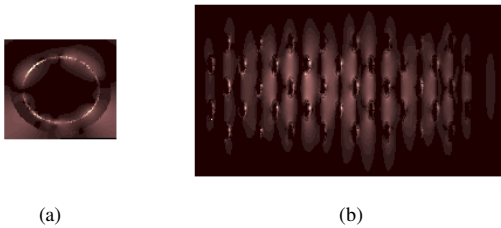


Fig 2: Optical intensity distribution in the waveguide based on Ag/GaN nanorods in hexagonal lattice. A Gaussian beam at wavelength of 600 nm is used as source. (a) Intensity distribution in a single nanorod. (b) Intensity distribution along the waveguide.

The attenuation of light in the waveguide is showed in Fig. 3. Comparison to the attenuation related to simple silver nanorods in hexagonal lattice is also presented. For both cases, the guided wave has lower attenuation for wavelengths longer than 550 nm. Notice that application of GaN layer around the metallic rods leads to a reduction of losses for wavelengths lower than 600 nm and greater than 700 nm. A possible explanation for such decrease is the stronger confinement and coupling of SPPs waves provided by the periodic array of GaN claddings.

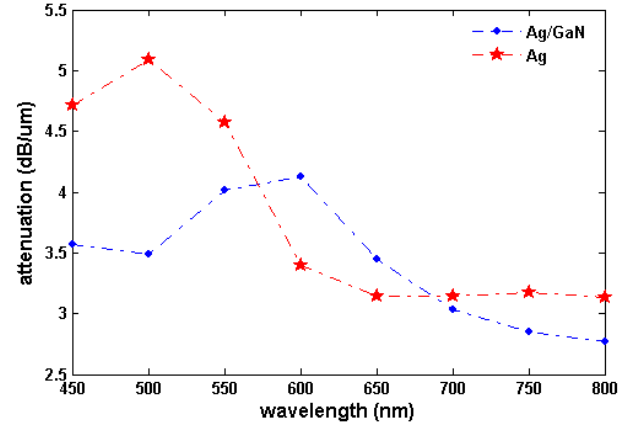


Fig. 3: Attenuation in the periodic plasmon waveguide calculated for incident Gaussian beam at wavelengths in the range 450-800 nm.

Our numerical analysis shows that the used thickness of the GaN cladding can be regarded as the optimum value. Lower thicknesses only slightly decrease the attenuation peak approximately by 1%, having no appreciable impact for other wavelengths in the range. On the other hand, a greater value of thickness cladding diminishes the coupling of SPPs between adjacent rows of nanorods and this leads to increasing of attenuation factor.

III. CONCLUSION

A theoretical investigation of a plasmon periodic waveguide composed by nanorods with silver core and GaN cladding in hexagonal lattice is presented in this work. The numerical simulations show that light can be guided through such structure by coupling of SPPs excited at the Ag/GaN boundaries. A comparison with the analogous waveguide made only by silver rods shows that, for the spectrum under analysis, there are wavelength ranges where light undergoes lower attenuation if GaN is used as cladding material. Thus, our results show that such metal-dielectric composition can potentially be useful for projects including optical waveguides and other photonic components in subwavelength regime.

IV. REFERENCES

- [1] W. L. Barnes, A. Dreux and T. W. Ebbesen, "Surface plasmon subwavelength optics", *Nature*, vol. 424, pp. 824-830, 2003.
- [2] B. Steinberger, A. Honeau, A. Dittbacher, A. L. Stepanov, A. Drezet, F. R. Ausseneg, A. Leitner and J. R. Krenn, "Dielectric stripes on gold as surface plasmon waveguides", *Applied Physics Letters*, vol. 8, pp. 1-3, 2006.
- [3] Y. Satuby and M. Oreinstein, "Surface-plasmon-polariton modes in deep metallic trenches-measurement and analysis", *Optics Express*, vol. 15, pp. 4247-4252, 2007.
- [4] C. L. Zhan, X. F. Ren, Y. F. Huang, K. M. Duan and G. C. Guo, "FDTD studies of metallic cylinder arrays: plasmon waveguide and Y splitter," *Chinese Physical Letters*, vol. 25, pp. 559-562, 2008.
- [5] A. Taflove and S. Hagness, *Computational Electrodynamics: The Finite-Difference Time-Domain Method*, Artech House, Boston, 2005.
- [6] S. Gwo and H. Y. Chen, "Gallium-nitride nanorods serves as subwavelength optical media," *Spie Newsroom*, 2009.
- [7] P. Johnson and R. Christy, "Optical constants of noble metals", *Physics Review B*, vol. 6, pp. 4370-4379, 1972.

Model for Antenna Positioning in Indoor Environments Using 2-D Ray-Tracing Technique Associated to a Particle Swarm Optimizer

S. Grubisic, E. Cabral, and W. P. Carpes Jr.

GRUCAD/EEL/UFSC

C. P. 476, 88040-970, Florianópolis, SC, Brazil

stevan@grucad.ufsc.br, emanela@grucad.ufsc.br, carpes@grucad.ufsc.br

Abstract — This paper presents a model applied to find the best antenna base station (BS) positioning of indoor wireless systems. The model uses a mono-objective Particle Swarm Optimization (PSO) code, associated to a 2D ray-tracing (RT) algorithm. The PSO optimizes the antenna location by maximizing fitness. For a given BS location, the fitness is obtained by calling a RT algorithm that returns the lower electric field value in the regions of interest. The proposed model was applied in a practical indoor environment. The use of PSO in this application was compared with a validated Genetic Algorithm (GA) applied in the same problem. From several simulations, we observed that PSO presented more satisfactory results than GA for this electromagnetic problem.

I. INTRODUCTION

Nowadays, wireless communications systems are present in several applications. The diffusion of these this kind of systems (e. g, IEEE 802.11 standards), caused by the technological progress and the decreasing prices of wireless devices, suggests a more accurate design of these systems in order to have the same quality of wired communication networks, but maintaining the wireless network advantages.

One of the requirements to achieve this quality is through appropriate positioning of the base station (BS). The ideal BS location is that providing good communication between the BS and all users of the cell. Almost all quality parameters of a wireless system are related to the signal level provided by the BS to the network users. Nevertheless, the excessive power from BS can cause interference in near cells sharing the same frequencies, which requires appropriate design.

This paper considers the problem of maintaining, as best as possible, good signal level for all users in the cell covered by BS. The way used to apply this idea was done by maximizing the lower electric field in the regions of interest.

Thus, this paper proposes a new model that uses a optimization code based on the concept of a Particle Swarm Optimization (PSO) algorithm associated with a 2D Ray-Tracing (RT) method for determining the electric fields in all interest regions of the cell by using Geometric Optics (GO) and Uniform Theory of Diffraction (UTD).

In order to validate the proposed model and evaluate the PSO in this type of application, we analyzed a practical indoor scenario where the optimal BS antenna position must to be found for providing proper signal to all network users. We simulated both the present PSO/RT model and the model proposed in [1], which uses Genetic Algorithm (GA) associated to a RT code. As will be shown, the proposed model gives better results for the analyzed example.

II. PROPOSED MODEL

Although the techniques used to develop the model proposed here are well known, the association of these techniques for antenna positioning problems in indoor scenarios is an original work.

The Particle Swarm Optimization (PSO) is a population-based stochastic technique developed by Kennedy and Eberhart [2]. As PSO is effective for electromagnetic optimization problems, it was chosen to be used in the model proposed in the present paper.

The PSO is based on social behavior taken from nature observation, but excluding eventual cognitive factors. Similar to GA, the PSO initiates with a population (composed of many particles) of random solutions [3]. To each potential particle (x_{id}) is assigned a randomized velocity (v_{id}). After the first evaluation of the fitness associated to each particle, it keeps track of the coordinates (p_{id}) in the problem space associated with the best solution ($pbest$) [3]. The overall best value ($gbest$) and its location (p_{gd}) are also stored during the procedure.

With a simple procedure, these stored data are iteratively updated using random parameters and fixed constants (w , c_1 , c_2), changing the particles velocities in order to intelligently explore the search area at each iteration.

$$v_{id} = w * v_{id} + c_1 * rand(\cdot) * (p_{id} - x_{id}) + c_2 * rand(\cdot) * (p_{gd} - x_{id}) \quad (1)$$

$$x_{id} = x_{id} + v_{id} \quad (2)$$

The PSO used in the present model adopts the acceleration constants (c_1 and c_2) both equal to 2.0 [3] and a zero inertia weight ($w = 0$).

In the application example consider here, corresponding to the BS antenna positioning, it is necessary to evaluate the fields in the regions of interest, where users can be connected to the wireless network. Here, the fitness for each BS position corresponds to the lower value of electric field in these regions. The reason behind this choice is that, if the lower field is maximized in the regions of interest, all the users will receive a good signal level. This fitness evaluation is done using a code based on Ray Tracing (RT) technique. RT is an asymptotic method widely used in the prediction of high frequencies coverage problems, with good results. The RT code used in the proposed model is based on image theory (IT) and includes an accurate approach to take into account the shift of the rays transmitted through obstacles [1].

The formulation used in the RT code (based on IT) considers the more relevant paths that leave the BS antenna and reach the reception points. The IT permits field

computation only in the regions of interest. After path definition, the sum of all fields is done. Fields corresponding to each path are computed using a GO/UTD formulation.

The proposed model is intended to be used for indoor environments, where the main mechanisms involved are reflection and transmission through the obstacles. Hence, we neglect the effects of edge diffractions for this application, which allows a significant computation time reduction, given that the code is called many times for the optimization program.

Thus, as said, for a given reception point, the total electric field is given by the sum of the fields due to all considered paths, where the field due to each path is given by:

$$E_R = A_s E_0 e^{-j\beta s} \left\{ \prod_i \Gamma_i \right\} \left\{ \prod_k T_k \right\} \quad (3)$$

where A_s is the spreading factor, s is the total distance (in the air) of the path from a reference point to the receiver; ρ is the distance between the transmitter and the reference point; E_0 is the electric field calculated at this reference point considering a free space propagation in the far-field region; β is the phase constant; Γ_i is the reflection coefficient due to i -th reflection and T_k is the transmission coefficient due to k -th transmission of the ray (taking into account the propagation through lossy obstacles [1]).

III RESULTS

The proposed model was applied in a practical scenario, located at GRUCAD / UFSC laboratory, aiming to optimize the *access point* (i.e., BS) location of the 2.4 GHz WLAN (Wireless Local Area Network – IEEE 802.11g) used in this *indoor* environment.

The reception points do not correspond to the whole scenario, but only in certain regions of interest. The obstacles considered in the environment are the walls, doors and windows, with different types of lossy materials.

To validate the proposed PSO/RT model, the same problem was also simulated with the GA/RT model presented in [1]. In both cases, we used more restrict interest regions compared with [1], in order to decrease the simulation time and permit a more adequate number of iterations/generations. As said, the PSO/RT parameters were $c_1 = c_2 = 2$ and $w = 0$. For the GA/RT case, the crossover probability was 0.95 and the mutation probability was set to 0.05.

In order to compare the models, we used the same number of individuals (equal to 20) and the same number of iterations/generations (equal to 70) for each algorithm. Thus, the whole optimization process requires 1400 RT runs for both models. For the analyzed problem, the large majority of the computation time is spent in computing the field values by the RT tool. Thus, an equal number of RT runs indicates approximately the same computation time for both algorithms.

Fig. 1 shows the fitness of the best individual (g_{best} , for PSO) as a function of the number of RT runs. The curves have been obtained by averaging the results of six simulations

carried out with different initial populations (randomly chosen) for each model.

From the curves, we observed that the PSO/RT converged faster than the AG/PSO model.

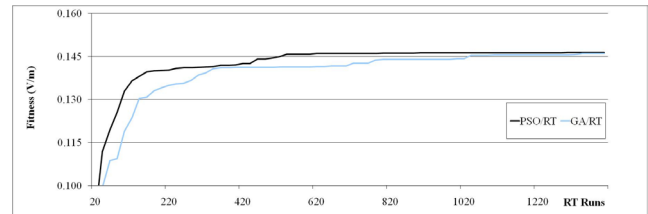


Fig. 1. Comparison between PSO and GA simulations.

Fig. 2 presents the electric field mapping in the environment with the access point antenna placed at the optimal location corresponding to Fig. 1, namely, $X = [6.2311 ; 6.4517]$ (m). The computation for each simulation is about 3h 30min using a 1.6 GHz Intel Dual-Core processor, with a 1 GB RAM memory and an 80 GB HD.

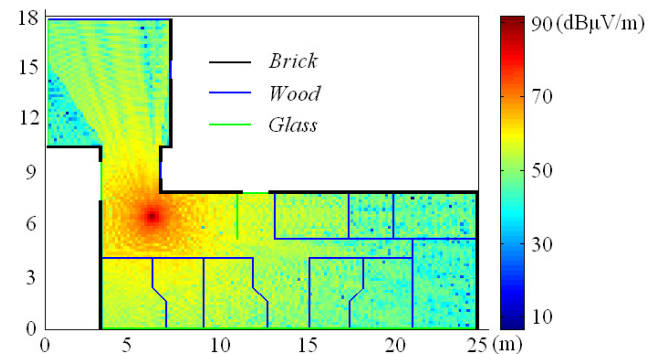


Fig. 2. Field mapping corresponding to the optimal antenna location.

IV CONCLUSION

The PSO/RT presented in this paper was shown to be effective in indoor wireless design applications. The comparison with the GA/RT model in the same problem shown that the PSO/RT presented better results in terms of convergence, which allows obtaining a reduction in the computation time for a given stop criterion.

The extended version of the paper gives more details on the model formulations. Also, we present the results for another application example and a discussion concerning the convergence criterion to be used.

V REFERENCES

- [1] S. Grubisic, W. P. Carpes Jr. and J. P. A. Bastos, "Optimization Model for Antenna Positioning in Indoor Environment Using 2D Ray-Tracing Technique Associated to a Real-Coded Genetic Algorithm", *IEEE Trans. on Magnetics*, vol. 45(6): pp 1626-1629, Mar. 2009.
- [2] J. Kennedy and R. Eberhart, "Particle swarm optimization", *IEEE International Conference on Neural Networks*, vol. 4, pp. 1942-1948, 27 Nov – 1 Dec, 1995.
- [3] R. C. Eberhart and Y. Shi, "Particle Swarm Optimization: Developments, Applications and Resources", *Congress on Evolutionary Computation, 2001*, vol. 1, pp. 81-86, 27-30 May, 2001.

Accurate Transmission-Path Ray-Tracing Computation for Indoor EM Field Prediction

S. Coco, A. Laudani and G. Pollicino
DIEES, University of Catania
V.le A. Doria 6, Catania, I-95125, Italy
alaudani@diees.unict.it

Abstract— In this paper a ray tracing procedure for the prediction of indoor EM fields based on a new accurate formula for the transmission path is presented. The novel formula is derived by using the Snell law and analytically relates the incidence angle and the transmission angle to the wall thickness; this new expression leads to very accurate results in the predictions.

I. INTRODUCTION

The increasing number of wireless communications systems, including WLAN and micro-cell networks, requires a more detailed planning in order to assure adequate covering within the interesting region keeping field levels within the bounds allowed by regulations. The prediction of the EM field strength in indoor environments is generally obtained by using a ray optical method (ray tracing) able to take into account the presence of multipaths, reflections, and diffractions[1]. The ray tracing technique is based on optical geometry (GO) and on its generalization, the geometric theory of diffraction (GTD). The main assumption of GTD is that all the obstacles must have a size larger than the signal wavelength. In Ray Tracing propagation models for indoor and outdoor environments the EM field computing is carried out through separate evaluations of all the field components, due for example to reflection, refraction, diffraction and scattering coming out from the interaction with various obstacles. The field strength is computed by a coherent sum of all those field components [1]. A complicate field distribution arise because of these interactions, so an high accuracy in the evaluation of each single component is required. Two different approaches can be pursued for the determination of propagation loss: the Shooting and Bouncing Rays (SBR) or brute force ray tracing and the Image Theory (IT). The former launches from transmitter a set of rays equally angularly spaced and it computes the field at receiving points by adding all the contributions due to rays arrived or passing in proximity of them. The latter uses image sources in order to compute relevant paths and leads to more accurate results and to a reduction of the computational cost [2]. The main inconvenient of this approach is the need of a more accurate computation of the geometrical characteristic of the various paths, above all regarding the angle of incidence for the transmitted components [3-4].

In this paper a new approach is presented for the evaluation of the transmitted component of the field by using an innovative formula for the accurate computation of the

transmission path in order to enhance electromagnetic field prediction precision in indoor environments. The new deterministic expression uses an iterative procedure to compute the transmission path contribution leading to extremely accurate value of the incident angle after a few iterations. An example of application to a simple indoor environment is also presented in order to show the accuracy of the approach.

II. RAY TRACING TECHNIQUE AND NEW EXPRESSION FOR THE TRANSMISSION PATH COMPUTATION

The construction of EM field strength maps by means of the ray-tracing algorithm consists of two main phases: in the first the visibility between elements of the environment is represented by a visibility tree; in the second phase all the propagation multipaths between a transmitter T and a receiver R (measurement point) are determined and the contributions of these multipaths to the total field strength are computed. The multipaths and the propagation environment is modelled by means of a set of objects O_k , belonging to the various obstacles, which act as virtual sources with respect to the various phenomena of diffraction, scattering and reflection. They contribute to the total field by adding a specific component computed according to appropriate formulas. In order to reduce the time needed for the construction of all the possible paths between T and R (considering also that usually we have to deal with many measurement points), we use “the visibility tree”, which contains a propagation path in each branch. In this way the complete search of all the admissible paths can be easily obtained by visiting the visibility tree. The number of levels of the visibility tree corresponds to the maximum number of interactions between the objects considered in the ray optical propagation model. At the first level there is only the root represented by the transmitting source T. The branches originated from this root T constitute the second level, to which all the objects O_k directly visible from T belong. In this second level each object O_k represents the root for the successive level of the tree constituted by all the objects O_j directly visible from O_k . In this way in the branches of each level it is possible to find all the objects directly visible from the objects belonging to the preceding level, and the connections are in such a way to specify all the admissible paths from T to each object. The construction of the tree can be made recursively and the only condition to check in the extraction of the admissible paths from the visibility tree is that each O_k be present only once for each propagation path. The determination of direct visibility is

performed by using simple geometrical concepts such as intersection of a line with a face and a plane, which represent obstacles. Even in this case a pre-processing of the environment, excluding some obstacles according to their position, allows a reduction of the computational effort. For the computation of the various field contribution (reflected/transmitted/diffracted/scattered from obstacles, etc) apposite expression are used, considering the characteristic parameters of the material constituting each obstacle [1]. The EM field strength is obtained by coherently adding all the field components as follows:

$$E_{tot} = E_{los} + \sum E_r + \sum E_t + \sum E_d + \sum E_s$$

where E_{los} indicates the direct line of sight components and E_r , E_t , E_d and E_s indicate the reflected, transmitted diffracted and scattered components.

When considering a transmission path the accuracy of the ray-tracing field computation is strictly dependent on the evaluation of the transmission coefficient T. For this reason a new closed form expression for obtaining T has been derived based on a geometrical analytical approach, relating the incidence angle and the transmission angle to the wall thickness. The expression is based on relative positions of the source, the wall and the receiver. Starting from geometrical considerations it is possible to obtain:

$$\tan \vartheta_m = \frac{(l_1 + l_2)}{l_1 + l_2 + d} \tan \vartheta_i + \frac{d}{l_1 + l_2 + d} \tan \vartheta_r$$

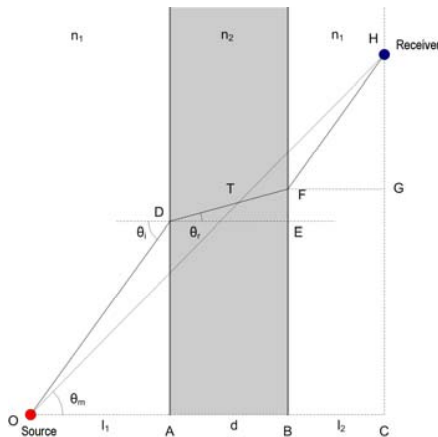


Fig. 1 – Schematization of the transmission path computation

Then, by using the Snell Law, for the relation between the angles, it is possible to obtain the following expression:

$$\begin{aligned} \tan \vartheta_m (l_1 + l_2 + d) - d \frac{n_1}{n_2} \left(\sqrt{\frac{n_2^2 - n_1^2}{n_2^2} + \frac{1}{\tan^2 \vartheta_i}} \right)^{-1} \\ = \frac{(l_1 + l_2)}{l_1 + l_2 + d} \tan \vartheta_i \end{aligned}$$

where n_1 and n_2 are the refractive indexes of the regions; l_1 , l_2 and d are, respectively, the distance between the source and the wall, the thickness of wall and the distance between the wall and the receiver.

$$\vartheta_i = \arctan \left(\frac{2n_2}{\sqrt{n_2^2 - n_1^2}} \frac{\sigma}{1 - \sigma^2} \right)$$

in which σ is the only solution of the following equation:

$$\sigma^4 + 2 \frac{B-1}{A} \sigma^3 + 2 \frac{B+1}{A} \sigma - 1 = 0,$$

where

$$A = \tan \vartheta_m \frac{l_1 + l_2 + d}{d} \sqrt{\left(\frac{n_2}{n_1} \right)^2 - 1} \quad B = \frac{l_1 + l_2}{d} \frac{n_2}{n_1}$$

By using this new expression very accurate results have been obtained in the predictions. More details including comparison with other approach will be given in the full paper.

III. EXAMPLE OF APPLICATION

The following numerical experiment regards the application of the prediction procedure to the determination of intensity of a known EM sources in a real indoor environment (Fig. 2).



Fig. 2 – indoor environment used for numerical experiment and color map of field strength

The region contains obstacles having different dimensions and different electrical features. The source (whose position is shown in the same figure) produces a complicate field distribution because of reflection, refraction, diffraction and scattering due to the interaction with obstacles. In the colour map shown in Fig.2 the distribution of the transmission field component intensity is reported.

IV. REFERENCES

- [1] R.P. Torres, L. Valle, M. Domingo, M.C. Diez,, "CINDOOR: an engineering tool for planning and design of wireless systems in enclosed spaces", *IEEE Antennas and Propagation Magazine*, Sep 1999, Volume: 41, Issue: 4, pp. 11-22
- [2] George Liang and Henry L. Bertoni, "A New Approach to 3-D Ray Tracing for Propagation Prediction in Cities", *IEEE Transactions On Antennas And Propagation*, VOL. 46, NO. 6, June 1998
- [3] Michael C. Lawton and J. P. McGeehan, "The Application of a Deterministic Ray Launching Algorithm for the Prediction of Radio Channel Characteristics in Small- Cell Environments", *IEEE Transactions On Vehicular Technology*, VOL. 43, NO. 4, NOVEMBER 1994
- [4] S. Grubisic, W.P. Carpes, C.B. Lima, P. Kuo-Peng,, "Ray-tracing propagation model using image theory with a new accurate approximation for transmitted rays through walls", *IEEE Transactions on Magnetics*, Volume 42, Issue 4, April 2006, pp. 835 – 838

Study of the Parasitic Effect Caused by Vias in High-Frequency Circuit

A. G. D'Assunção Jr¹, G. Fontgalland², and H. Baudrand³

^{1,2}UFCG/DEE-LEMA, Campina Grande-PB, 58109-970, Brazil

³INPT-ENSEEIH, 31071, Toulouse, France,

¹adaildojr@ee.ufcg.edu.br, ²fontgalland@dee.ufcg.edu.br, ³baudranh@n7.fr

Abstract— This kind of interference may be caused by couplings between the terminals and the circuit lines. This work allows to study the effect of the metal post in the middle, and the radiated energy and the coupling between post. Through the WCIP (wave concept interactive procedure), which uses concepts of incident waves, can be estimated the effect of the fields of posts in metal laminate as the radiation and coupling between the post.

I. INTRODUCTION

Once the circuit conception companies dominate a relatively established technology competence, nowadays the researches attention has focused on the demand for more integration and reduction size of these devices. This integration can be done with the use of the multilayer laminate (and bridges accesses), increasing the packing densities of device or also with the introduction of antennas in chip [1]-[3]. The need for a large flow of data has grown the clock frequency resulting in the increase devices electrical length. Therefore, it inevitable increases the parasitic electromagnetic (EM) coupling between the elements.

In the multilayer configuration the interconnection between layers are made using via of access. In some cases these structures can be characterized as cylindrical metal post. This via high frequency current generates an electric field distribution in the region around it. This field can cause coupling in others via and/or printed circuit nearby.

Can be used the post also isolating a region of electromagnetic interference [4]. This can be used to isolate devices who generate or cannot get much electromagnetic interference.

The representation of electromagnetic fields by waves is used since many years [5]. The WCIP (wave concept interactive procedure) method is based on full wave transverse formulation. The incident wave concept the multiple reflection on the region. The incident wave and scattered wave in the spatial domain and in the spectral domain.

This work studied the effects of via. Will be observed the electric field generated by a source near and one way to minimize this effect.

II. WAVE CONCEPT INTERACTIVE PROCEDURE

The formulation of the iterative method has been described in [6-8]. This method allows representing the electromagnetic (electric and magnetic field) as a function of incident waves (a) and reflected (b), the waves are defined from a surface, see Fig.1.

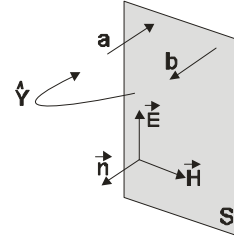


Fig.1. Emitted and reflected waves on surface.

$$\begin{cases} \vec{A} = \frac{1}{2\sqrt{Z_0}} (\vec{E}_T - Z_0 \vec{H} \times \vec{n}) \\ \vec{B} = \frac{1}{2\sqrt{Z_0}} (\vec{E}_T + Z_0 \vec{H} \times \vec{n}) \end{cases} \quad (1)$$

$$\vec{J} = \vec{H} \times \vec{n}$$

With Z_0 is the wave impedance, E and H , the electric and magnetic fields tangential to the surface and n the vector normal to the surface.

Two operators are successively applied to these waves. The scattering operator \hat{S} [6], which takes into account the boundary conditions in the spatial domain ($E_{t1} = E_{t2}$) and $J_1 + J_2 = 0$ on the dielectric, $E_{t1} = E_{t2} = 0$ on the metal. This means when metal $S = -1$ and dielectric on $S = 1$.

The reflection operator $\hat{\Gamma}$, which takes into account the environment's reaction in the spectral domain, is defined as:

$$\hat{\Gamma} = \frac{Y_0 - \hat{Y}}{Y_0 + \hat{Y}} = -1 + \frac{2Y_0}{Y_0 - \hat{Y}} \quad (2)$$

Where \hat{Y} is the admittance the region, and using de induction law of Faraday and the auxiliary potential, can be find de relation of E and J .

$$\hat{Y} = \frac{E}{J} = \frac{(\nabla^2 + k_0^2)}{j\omega\mu_0} \quad (3)$$

Replace (3) in (2), and rewriting the reflection operator

$$\hat{\Gamma} = -1 + \frac{2jY_0\omega\mu_0}{(\nabla^2 + k_0^2 + jY_0\omega\mu_0)} \quad (4)$$

Can approximated the second term of (5) by Hankel function second kind and zero order.

$$\hat{r} = -1 + 2jk_0^2 \int_{r'} H_0^{(2)}(k|\vec{r} - \vec{r}'|) d^2 r' \quad (5)$$

k_0 is the wave number in the free space.

III. SIMULATION

Simulations were made for situations with an operating frequency of 10GHz. Initially is not considered the height of the post, is only the distance d . Considers the post is the cylindrical shape of radius equal to 0.5 mm. Now is considered the case of 1D, but the formulation of the study 3D case was in progress.

The simulations initially are compared when there is only one post in the free-space and three post, with the central is the source and observing the coupling between the central and the two sides.

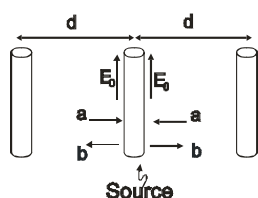


Fig.2. Distribution of post in space

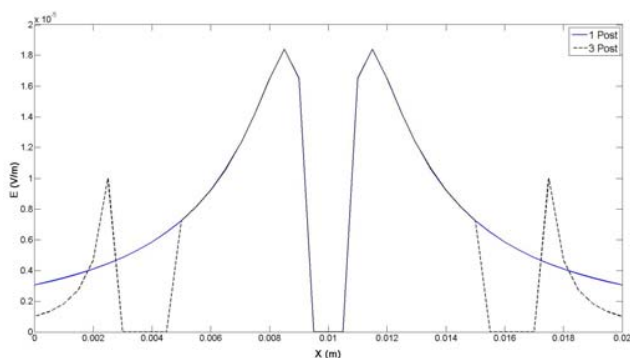


Fig.3. Compared electrical field one post and three post in the free-space.

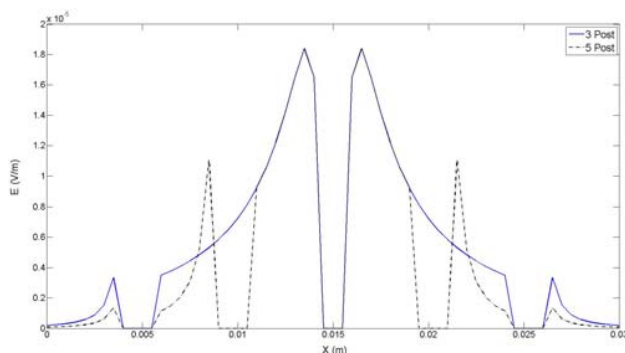


Fig.4. Compared electrical field three post and five post in the free-space.

In Fig.3, is seen the field generated by a source close. Can be seen the effect of coupling between the post. The electric field at the surface of the side post generates a current density, and causing interference.

In Fig.4, note the reduction in the electric field in the lateral post. With the introduction of two new posts may be to reduce interference between the side posts.

With the introduction of side post can notes that there is a decrease in electric field in the region. Notes that the region is the side posts is a reduction of the intensity of field. This effect allows use these post to cause an effect of shielding the region.

IV. CONCLUSION

The use of vias can cause effects of electromagnetic interference in integrated circuit, when using high frequency, as shown in Fig.3 and Fig.4. But the vias or metal post can also be used to reduce the effect of electromagnetic interference in integrated circuits, as can be observed in the simulations. The WCIP method, which uses the concept of incident wave, can characterize the metal post in the central region of the laminate. And thus determining values of distances between post but, also the introduction of post to minimize the effect of electromagnetic interference.

V. REFERENCES

- [1] S. Wane, D. Bajon., H. Baudrand, "Influence of Interrupting Buried Layers and Ring-Loops on Electromagnetic Coupling in RFICs", Antennas and Propagation Society International Symposium 2006, IEEE
- [2] D. McPhee, M.C.E. Yagoub, "New Technique for Efficient Computation of Electromagnetic Coupling", Microwave Symposium Digest, 2006. IEEE MTT-S International.
- [3] Y. Kayano, H. Inoue, "A study on electromagnetic coupling between transmission line on model chip" EMC 2008, IEEE International Symposium on 2008.
- [4] M. Kishihara, K. Yamane, I. Ohta, "Analysis of Post-Wall Waveguide by H-Plane Planar Circuit Approach", Microwave Symposium, 2007. IEEE/MTT-S International.
- [5] K. Kurokawa, "Power Wave and Scattering Matrix" IEEE Trans. on Microwave Theory and Techniques" vol. 13 pp. 194-202, 1965.
- [6] Gharsallah, A., Gharbi, A., Desclos, L., and Baudrand, H.: 'Analysis of interdigital capacitor and quasi-lumped miniaturized filters using iterative method', Int. J. Numer. Model., 2002, 15, pp. 169-179
- [7] Azizi, M., Boussouis, M., Aubert, H., and Baudrand, H.: 'Three dimensional analysis of planar discontinuities by an iterative method', Microw. Opt. Tech. Lett., 1996, 13, (6), pp. 372-376
- [8] Mami, A., Zairi, H., Gharsallah, A., and Baudrand, H.: 'Analysis of micro-strip spiral inductor by using iterative method', Microw. Opt. Technol. Lett., 2002, 35, (4), pp. 302-306

A 3D PEEC Method for the prediction of radiated fields from automotive cables

Wissem Yahyaoui^{1,2}, Lionel Pichon², Fabrice Duval¹

¹IRSEEM, Technopôle du Madrillet, Avenue Galilée BP 10024
76801 Saint Etienne du Rouvray Cedex, France

Wissem.Yahyaoui@esigelec.fr, Fabrice.Duval@esigelec.fr

²LGEP, UMRS 8507 CNRS, SUPELEC, UPS, UPMC

Plateau du Moulon, 91192 Gif-sur-Yvette, France

Lionel.Pichon@supelec.fr

Abstract — The Partial Element Equivalent Circuit method (PEEC) is well suited to extract the conducted electromagnetic disturbances parameters from wiring systems. It provides an efficient tool for the EMC study relevant to automotive cables. However the complete EMC analysis of embedded systems requires also reliable models for the radiated emissions especially at high frequencies. In this paper a new approach based on the PEEC method and involving 3D field calculation is developed to evaluate emissions from radiating cables.

I. INTRODUCTION

In automotive industry the functional safety of electronic systems is a crucial challenge. Actually, the integrated circuits (ICs) and transistors used to construct these electronic systems become more vulnerable to interferences and damages from Electromagnetic (EM) disturbances. The main reasons are : the feature size decrease, the operational speed increase, and the operating voltages fall. Such developments make electronic equipments more easily corrupted by a given electromagnetic disturbance which can be induced inside the car due to the fact that power systems and control systems stand together in the same closed environment. In fact, the majority of these disturbances are propagated between sub-systems through cables in a conducted and/or radiation form, resulting in inaccuracy, malfunction, or failure of these systems. For these reasons, adequate EMC studies are necessary and the prediction of EM behavior is of vital importance to ensure reliable and EM compatible systems.

Therefore, several numerical methods of electromagnetic modeling are available and can be used for electromagnetic analysis. Among these methods, the Partial Element Equivalent Circuit method (PEEC) [1][2] is particularly well suited. In comparison to Finite Element Method or Finite Difference Method, PEEC only needs the discretization of conducting regions or dielectric materials avoiding the mesh of surrounding air environment. Usually the PEEC approach is an efficient way to deal with circuit simulation of distributed structures. In [3] a 3D model based on the PEEC method was proposed in order to take into account the size of automotive wiring systems. It includes resistive, inductive and capacitive effects. Such 3D approach was shown to accurately predict the conducted disturbances by cables above large ground planes. In automotive applications electronic systems are used with increasingly higher frequencies and the radiation of cables cannot be neglected.

In this paper a new approach is developed to evaluate the radiated fields with the PEEC method. The originality of this work is considering both radiated and conducted disturbances in the framework of a PEEC method for large size structures. In a first step the current carried by the conductors are determined from the circuit model deduced with the 3D PEEC method. Then in a second step the field radiated by the wiring systems is evaluated using an analytical calculation deduced from the distribution of currents. The advantage of this approach is a lower processing time for the same desired accuracy as a full wave numerical method.

II. 3D RADIATED FIELD

The PEEC method is based on three main steps. In a first stage, the structure is discretized into a series of cells. An equivalent circuit is deduced in a second step. The third step is to implement this equivalent circuit in a SPICE simulator [4] : the output data are the current and voltage values in each point of the structure. The analytic calculation of the magnetic near-field is based on the equation (1) which uses the previously determined current:

$$\vec{A}_\gamma = \frac{\mu}{4\pi} \vec{J}_\gamma \iiint_{V'} \frac{e^{-jkR}}{R} dv' \quad (1)$$

where $\gamma = x, y, z$ and k is the wave number, \vec{J}_γ is the current density crossing the volume V' , \vec{r} and \vec{r}' defines respectively a point M from where the vector potential has to be determined and a point P in the volume (Fig. 1.).

The distance R between P and M is given by:

$$R = |\vec{r} - \vec{r}'| = \sqrt{(x - x')^2 + (y - y')^2 + (z - z')^2}$$

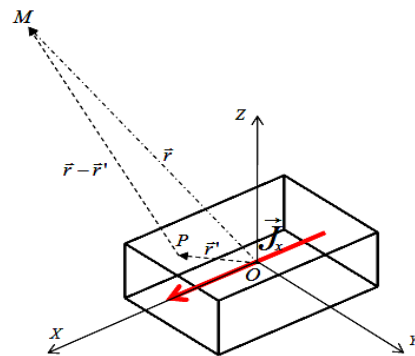


Fig. 1. Cell crossed by \vec{J}_x current

The vector potential can be calculated analytically if each cell is considered as an equivalent 1D dipole [5][6]. But this approach is not realistic because only one dimension of the cell is taken into account: it may lead to inaccurate results near to the conductor. In order to improve the computation, an analytical method extended to 3-D is proposed in the next section to calculate the magnetic near field. Once the magnetic vector potential is computed, the magnetic field can be deduced from the equation (2):

$$\vec{H} = \frac{1}{\mu} \nabla \times \vec{A} \quad (2)$$

III. 3D-CALCULATION OF THE MAGNETIC FIELD WITH A MACLAURIN SERIES

In the proposed approach, the three dimensions of the cells are considered. To insure a high accuracy, no approximation is performed on the current cross section: a 3D series MacLaurin method is used. It is assumed that the dimensions of the discretization cells are very small compared to the wavelength. Therefore, a multivariable function f can be written in a form of a MacLaurin series expansion:

$$f(X) = \frac{e^{-jkR}}{R} = f(0) + \sum_{i=1}^3 \frac{\partial f(0)}{\partial x_i} x_i + \frac{1}{2} \sum_{i=1}^3 \sum_{j=1}^3 \frac{\partial^2 f(0)}{\partial x_i \partial x_j} x_i x_j + \dots \quad (3)$$

where the origin corresponds to the center of the cell.

In the work the expansion is limited to the third order. From the 3D integration of this function an analytic expression of the vector potential can be deduced and then the magnetic near field in the whole area can be determined. The technique has been first validated in different canonical configurations. In the next section a realistic test case is considered.

IV. APPLICATION TO THE RADIATION OF A CABLE: SIMULATION AND MEASUREMENT

The method is tested in the case of a conducting cable (Fig 2.) made up by a wire located 5mm above a ground plane. Such configuration was chosen in order to illustrate the ability of the approach to handle large size systems. The length of the wire is 2 m. It is connected to a 50Ω resistance at an extremity of the ground plane.

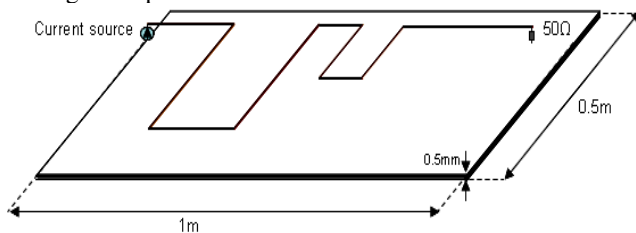


Fig. 2. Description of the studied system

A Vector Network Analyzer (VNA) is used to measure the S11 parameter of the system from which the input impedance is deduced. The comparison of the simulated and measured input impedance is shown on fig. 3. The magnitude and position of the resonance peaks are well recovered.

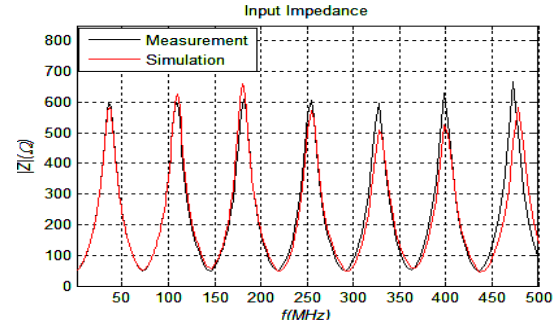


Fig. 3. Measurement and simulation of input impedance

A source current excitation is prescribed at the other extremity. The frequency is 30 MHz. The magnetic field cartography determined by the PEEC method combined with the analytic calculation is compared to measurement results (Fig. 4.a and Fig. 4.b). The values are located on a plane at 2cm above the ground plane. The measurements are obtained with a near-field test bench [7]. A good agreement is shown between the two plots. In the conference different configurations will be analyzed and the influence of the frequency will be studied.

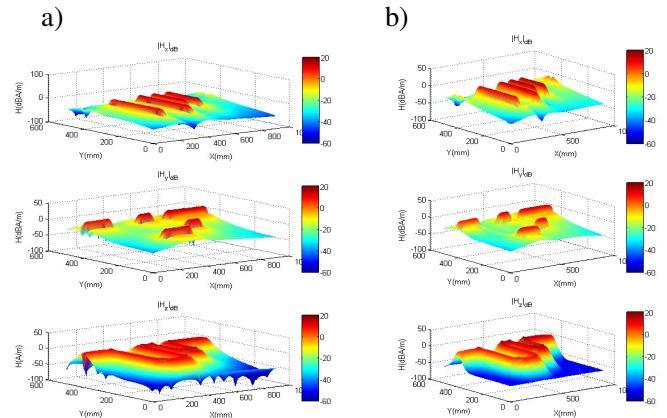


Fig. 4. Magnetic field radiation at 2cm above the ground plane at 30MHz:
a) Simulation b) Measurement

V. REFERENCES

- [1] A. Ruehli, "Equivalent circuit models for three dimensional multiconductor systems", IEEE Transactions. on Microwave Theory and Techniques., vol. 22, no. 3, pp. 216-221, march 1974.
- [2] A. Ruehli and h. Heeb, "circuit models for three-dimensional geometries including dielectrics", IEEE Transactions on Microwave Theory and Techniques., vol. 40, no. 7, pp. 1507-1516, july 1992.
- [3] Islem Yahi , Fabrice Duval, Anne Louis, "A New Capacitive Coupling Consideration in PEEC Method" 2emc IEEE Symposium on embedded EMC, Rouen, October 2007
- [4] Wollenberg C., Gurisch A., "Analysis of 3-D interconnect structures with PEEC using SPICE", IEEE Transactions on Electromagnetic Compatibility" Volume 41, Issue 4, Nov 1999 Page(s):412 - 417
- [5] Yu Zhu "Multigrid Finite Element Methods for Electromagnetic Field Modelling" March 2006, Wiley-IEEE Press
- [6] Constantine A. Balanis "Antenna Theory: Analysis and Design", 2nd edition, May 1996
- [7] Baudry D, Arcambal C, Louis A, Mazari B., Eudeline P., "Applications of the Near-Field Techniques in EMC investigations, IEEE Transactions on Electromagnetic Compatibility" Volume 49, Issue 3, Aug. 2007 Page(s):485 – 493.

Simulation of a Real Overvoltage Transient in a TLM-Modeled Grounding Mesh

Luiz H. A. de Medeiros, Marcos T. de Melo, Fabio R. L. Silva, Andre A. Almeida, Fabio N. Fraga
 Universidade Federal de Pernambuco
 Av. Academico Helio Ramos, S/N, DEESP – CTG, Recife, 50740-530, Brazil
 lhamedeiros@gmail.com

Abstract — This paper presents the behavior of a grounding mesh in presence of a high-frequency overvoltage transient caused by switch closing in electrical substation. The simulation of the mesh is based on Transmission Line Method (TLM). The output of the simulation is the sum of induced and conducted currents caused by such high-frequency overvoltage input in some spot of the mesh. The conductors of the mesh are modeled by thin wires developed by Naylor and Christopoulos. This way, the simulation runs much faster than those with short-circuit nodes. Details on the soil properties such as resistivity and dielectric constant are provided.

I. INTRODUCTION

Electronic devices are widely used in power substations for measurement and control of electrical quantities. It is known that, frequently, these devices are seriously damaged by high frequency outbreaks provoked by operational maneuvers and atmospheric discharges [1], [2]. Therefore, it becomes necessary to implement a simulation method to predict the distribution of electric and magnetic fields through a mesh and develop methods to avoid the problems that such outbreaks might cause to the equipments.

Transmission line modeling (TLM) has been applied as a method for the solution of electromagnetic field, diffusion and network problems [3]. Due to the fact that TLM is a time-domain simulation method, it is possible to verify transient effects in a wide range of frequencies. In that manner, the TLM will be used as the simulation method. Formerly, the conductive nodes in TLM were represented by a node called short-circuit node, which represents the property of the tangential electrical field at the conductor surface. Because of the small radius of most conductors in grounding systems, such node becomes very time-consuming when large volumes are required to be simulated. To overcome this problem, Naylor and Christopoulos proposed a large node that represents a small radius conductor in one direction [4]. This way, larger volumes can be simulated with less time requirements. Previous simulations performed by the authors have shown that the use of the node proposed by Naylor and Christopoulos requires only 5% of the time for the short-circuit node simulation. Moreover, the memory requirements are far lower because of the reduction on the number of nodes.

The authors propose the use of TLM to the simulation of grounding meshes to optimize system protection. A small grounding system is presented in order to show that the effectiveness of the simulation can be extended to big systems such as electrical substations.

The reduction of the simulation time makes possible testing several configurations in order to determine which one is the most efficient with respect to voltages and currents

distributions throughout the grounding mesh. And so, the damages to the electronic devices tend to be reduced.

II. TRANSIENT EXCITATION OF THE MESH

The waveform used as input of the simulation is a real transient overvoltage caused by a switch closing in a 500 kV substation in Itaparica, Northeast Brazil. The measurements were performed using the methodology used in [5]. The measured transient in that occasion is shown in Fig. 1.

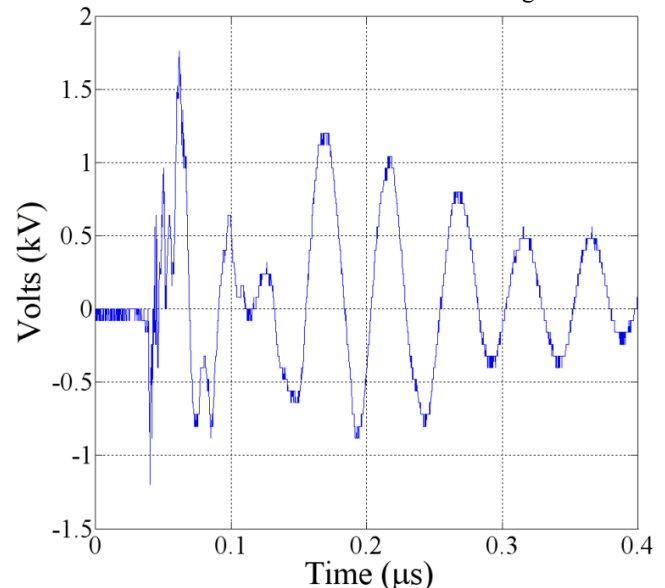


Fig. 1. Measured overvoltage transient in Itaparica electrical substation.

The waveform in Fig. 1 was acquired at the grounding connection of the switch. In other words, that voltage waveform is the one injected in the grounding mesh of the substation during the transient event.

Still in Fig. 1, one sees that peak of more than 1.5 kV is achieved (more than 2.5 kV peak-to-peak). Performing the Fourier Transform in that waveform, frequency components in the order of hundreds of kHz may have considerable levels. Analysis of the frequency components of the measured transient voltages injected in the mesh will be presented.

III. SIMULATION SETUP

The simulated mesh is shown in Fig. 2. The conductors' radii are set to 1 cm; the TLM discretization is $\Delta l = 0.1$ m, and so, the relationship $r \ll \Delta l$ holds [4]. The total dimensions of the simulated volume are $2 \times 4.5 \times 3$ m.

Capacitive nodes were inserted in order to model the soil properties such as variation of dielectric constant and losses [6]. The conductive nodes were modeled based on an admittance model developed by [3], as follows:

$$Y_{cm} = \frac{\sqrt{\epsilon_r}}{60 \ln(0.54 \Delta l / r)}, \quad (1)$$

where Y_{cm} is referred to as common-line admittance, Δl is the length discretization of the TLM model, r is the conductor wire diameter and ϵ_r is the dielectric constant of the medium where the conductor is inserted in. Because the lack of symmetry of the thin wire model node, 3 matrixes were implemented in the simulation routines, one for each of the coordinate axis.

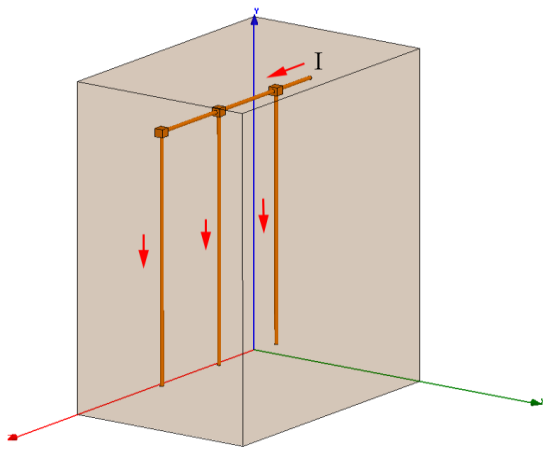


Fig. 2. Simulated grounding system.

The model of the soil regards one layer, whose dielectric constant and resistivity are $\epsilon_r = 3$ and $450 \Omega \cdot m$, respectively. The dielectric constant value was obtained according to the technique outlined in [7]. On the other hand, the resistivity value was measured according to the Wenner method [8].

Absorbing boundary conditions were imposed to the simulated volume so that no reflections are observed at the boundaries of the model.

IV. RESULTS AND DISCUSSIONS

The behavior of the propagating fields, currents and voltages in this mesh indicates whether the grounding system has to be optimized or not. Fig. 3 shows the current in the middle vertical conductor as a result of the incident voltage from Fig. 1. As well as the current, the results can be easily extended to the voltage along the conductors to verify whether electronics devices can be connected to each other (data cables connections, for instance) if they are submitted to different ground potentials during a transient event.

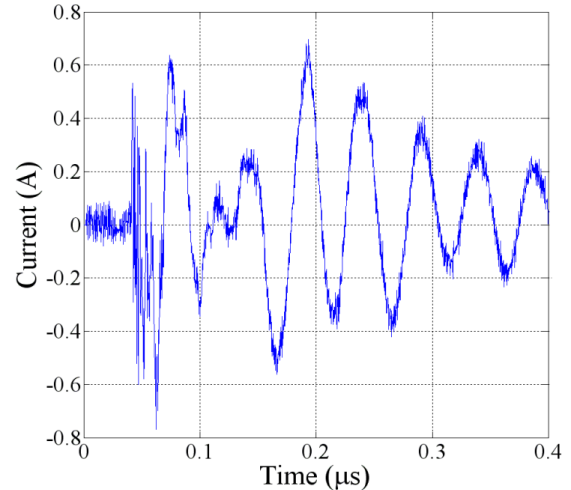


Fig. 3. Simulated current through the middle vertical conductor.

Currently, voltage simulations are being carried out as well as a real grounding mesh prototype is being constructed. Measurements will be performed in the prototype mesh in order to validate the simulated results. Results concerning the distribution of transient voltages in the mesh will be presented.

V. CONCLUSIONS

Effects of a transient in a small grounding system are simulated. Because of the time-saving benefit of thin wire models in TLM, these simulations can be extended to bigger grounding systems such as in electrical substations. The simulation outputs might be current, voltages and electromagnetic fields in one or several spots in the mesh. Thus, grounding systems can be optimized to mitigate high frequency transient effects in electrical substations.

VI. REFERENCES

- [1] C. A. Silveira, G. M. Fonseca, C. A. da Costa, R. R. B. de Aquino, Luiz Henrique A. de Medeiros, "Analyzing low frequency couplings in substations under steady-state conditions - Part I." *IEEE/PES, Transmission and Distribution Conference and Exposition*, São Paulo – Brasil, Vol. 1, pp. 737–742, 2004.
- [2] C. A. Silveira, G. M. Fonseca, R. R. B. de Aquino, Luiz Henrique A. de Medeiros. "Analyzing low frequency couplings in substations under steady-state conditions - Part II." *IEEE/PES Transmission and Distribution Conference and Exposition*, São Paulo – Brasil, Vol. 1, pp. 731–736, 2004.
- [3] P. B. Johns, "A Symmetrical condensed node for the TLM method", *IEEE Trans. on Microwave Theory and Techniques*, Vol. MIT-35, No. 4, pp 370-377, April 1987.
- [4] P. Naylor and C. Christopoulos, "A new wire node for modeling thin wires in electromagnetic field problems solved by transmission line modeling," *IEEE Trans. on Microwave Theory and Techniques*, Vol. 38, No. 3, pp 328-330, March 1990.
- [5] P. A. C. Rosas, Z. D. Lins, J. M. S. Melo, N. G. Santos, H. L. Ferreira, L. H. A. de Medeiros, "High frequency transients and electromagnetic interferences in 69kV substations", *IEEE Transactions on Power Delivery*, submitted for publication.
- [6] C. Christopoulos, *The transmission-line modeling method TLM*, 1st ed., IEEE Press, 1995, pp. 128-138.
- [7] M. T. de Melo, A. Belfort, S. R. O. de Souza and B. G. M. de Oliveira, "Medida da permissividade complexa do gesso tipo piso-cola com baixas perdas em frequências de microondas," *Simpósio Brasileiro de Microondas e Optoeletrônica*, 2002.
- [8] A. P. Sakis Meliopoulos, *Power System Grounding and Transients – An Introduction*, 1st edition, CRC Press, 1988.

Conservativeness of the Head Tissue Equivalent Liquid for Body-Worn SAR Assessments

Vikass Monebhurrin

Department of Electromagnetics, DRE-L2S, SUPELEC
3 rue Joliot-Curie, 91192, Gif-sur-Yvette Cedex France
E-mail: vikass.monebhurrin@supelec.fr

Abstract — The conservativeness of the homogeneous flat phantom filled with head tissue equivalent liquid for the Specific Absorption Rate (SAR) conformity assessment of body-worn wireless communication devices is investigated. Numerical simulations are performed using three flat phantom models – homogeneous, two-layer and three layer structures– and a previously validated commercially available mobile phone model. The SAR is calculated for several distances of the mobile phone with respect to the three phantoms at 900 MHz and 1725 MHz. Results show that the homogeneous phantom is not conservative for some distances at 1725 MHz.

I. INTRODUCTION

The SAR (Specific Absorption Rate) conformity assessment of wireless communication devices operated in close proximity to the ear is currently based on standardized measurement procedures such as IEEE1528 [1] and IEC62209-1 [2]. The SAR measurements are performed using the SAM (Specific Anthropomorphic Mannequin) head-phantom filled with an appropriate tissue equivalent liquid for several intended use positions of the handset. The morphology of the SAM phantom is chosen to be representative of the adult population. The conservativeness of the dielectric properties of the tissue equivalent liquid with respect to the inhomogeneous head counterpart was previously demonstrated [3].

Following the advent of hands-free kits, the intended use position of mobile phones shifted from the ear position to other parts of the body. For example, mobile phones can be worn at the belt or placed in the shirt's or trouser's pocket. An appropriate phantom and corresponding tissue equivalent liquid have therefore to be defined for such novel use positions. Current standardization bodies recommend a flat phantom for measuring the SAR of body-worn wireless communication devices [4]. For practical reasons, it is desirable to use the same tissue equivalent liquid as the one employed for the head SAR conformity assessment. However the characteristics of the biological tissues present in the head are different from those found in other parts of the human body.

A few studies have investigated the conservativeness of the homogeneous flat phantom for the body-worn SAR assessment. For example, numerical simulations based on the FDTD (Finite Difference Time Domain) method were performed using a dipole antenna placed at a number of distances from a homogeneous flat phantom and several multi-layered planar phantoms which were derived from the visible human model [5]. The application of a correction factor – dependent upon the frequency, the considered multi-layered

structure and the distance of the dipole with respect to the phantoms – appeared necessary in order to preserve the conservativeness of the homogeneous flat phantom.

Herein a commercially available dual-band – 900 MHz / 1800 MHz – mobile phone representative of an actual wireless communication device is considered for a similar analysis. The numerical model of the mobile phone consisting of the different components – PIFA (Planar Inverted-F Antenna), PCB (Printed Circuit Board), display, battery, etc.– was previously validated using experimental data [6]. Two multi-layered structures are selected for this study: (a) a two-layer structure consisting of skin and fat tissues representing the abdomen and (b) a three-layer structure consisting of skin, fat and muscle tissues representing the thorax. The calculations are performed for several distances of the mobile phone with respect to the homogeneous phantom and the two multi-layered structures. The relative distance of the antenna and the phantom is expected to influence the return loss and consequently the SAR value. Therefore the mobile phone is considered with either the front side or the back side positioned against the phantoms. The impact of the antenna mismatch on the SAR values can thus be examined.

II. NUMERICAL MODELING

Electromagnetic solvers based on time domain methods such as FDTD are nowadays commonly adopted for SAR calculations. Herein a commercial package of the Transmission Line Matrix (TLM) method is chosen [7]. Fig. 1 shows the main components present in the commercial mobile phone used for the study. These components are embedded in a dielectric support (not shown). The dielectric casing of the mobile phone (also not shown) is drawn to have planar faces. The exact dielectric properties of some components are unknown: approximate values are therefore used. The PCB is modeled as a thin conducting plate i.e. the dielectric substrate and electronic circuits are not considered. All numerical simulations are performed at the two resonance frequencies of the mobile phone: 900 MHz and 1725 MHz.

Fig. 2 shows the three flat phantoms considered for the numerical simulations: (a) homogeneous, (b) two-layer structure and (c) three-layer structure. The thickness of the different layers for the two-layer and three-layer models is provided in Table I. The dielectric properties and mass densities of the tissues are provided in Table II. The homogeneous phantom has the same overall dimensions as the other two phantoms. The dielectric properties and mass density are those of the tissue equivalent liquid recommended

by the standards for the head SAR assessment at a given frequency.

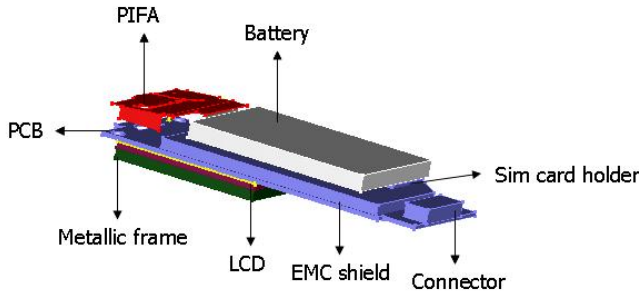


Fig. 1. Numerical model of the PIFA-based commercial mobile phone (the dielectric support and casing are not shown).

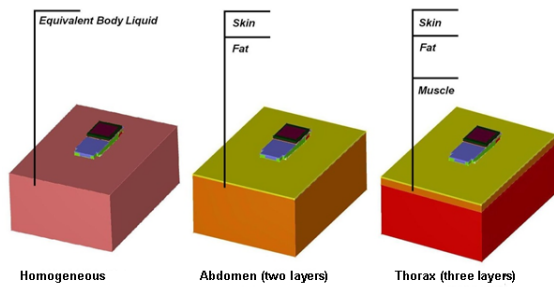


Fig. 2. Flat phantoms considered in this study: (left) homogenous, (middle) two-layer structure (abdomen), and (right) three-layer structure (thorax).

TABLE I
THICKNESS OF THE BIOLOGICAL TISSUES

Tissue	Tissue thickness for the two-layer model [mm]	Tissue thickness for the three-layer model [mm]
Skin	2	2
Fat	98	12
Muscle	NA	86

TABLE II
PROPERTIES OF THE BIOLOGICAL TISSUES

Parameters at given frequency		Skin	Fat	Muscle
900 MHz	Relative permittivity	41.41	5.46	55.03
	Conductivity [S/m]	0.87	0.05	0.94
	Mass density [kg / m ³]	1010	920	1040
1725 MHz	Relative permittivity	39.00	5.36	53.65
	Conductivity [S/m]	1.27	0.08	1.45
	Mass density [kg / m ³]	1010	920	1040

III. RESULTS

Fig. 3 and 4 show the results obtained at 900 MHz and 1725 MHz, respectively, for the configuration of the front side of the mobile phone facing the phantoms. At 900 MHz, the homogeneous phantom provides conservative SAR values for all the considered distances. At 1725 MHz, the three-layer model provides higher SAR value than the homogeneous model for distances greater than 10 mm. The same phenomenon is observed for the configuration of the back side of the mobile phone facing the phantoms. At 1725 MHz, a correction factor is therefore needed in order to obtain conservative SAR values when using the homogeneous phantom.

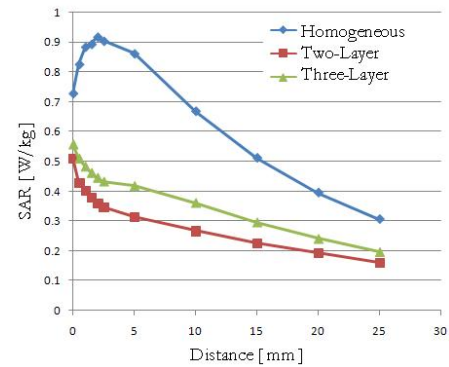


Fig. 3. SAR calculated for several distances of the mobile phone with respect to the phantoms at 900 MHz.

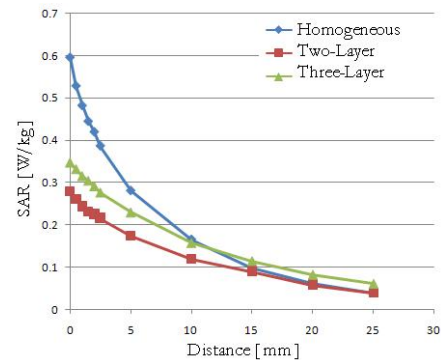


Fig. 4. SAR calculated for several distances of the mobile phone with respect to the phantoms at 1725 MHz.

IV. REFERENCES

- [1] IEEE, "Recommended practice for determining the peak spatial-average Specific Absorption Rate (SAR) in the human head from wireless communications devices: measurement techniques," IEEE Standard 1528, 2003.
- [2] IEC, "Human exposure to radio frequency fields from hand-held and body-mounted wireless communication devices - Human models, instrumentation, and procedures - Part1: Procedure to determine the specific absorption rate (SAR) for hand-held devices used in close proximity to the ear (frequency range of 300 MHz to 3 GHz)," IEC Standard 62209-1, 2005.
- [3] V. Monebhurrun, C. Dale, J-Ch. Bolomey and J. Wiart, "A numerical approach for the determination of the tissue equivalent liquid used during SAR assessments," *IEEE Trans. on Magn.*, 38(2):745-748, 2002.
- [4] IEC, "Human exposure to radio frequency fields from hand-held and body-mounted wireless communication devices - Human models, instrumentation, and procedures - Part2: Procedure to determine the specific absorption rate (SAR) for mobile wireless communication devices used in close proximity to the human body (frequency range of 30 MHz to 6 GHz)," IEC Standard 62209-2, draft.
- [5] A. Pradier, A. Hadjem, D. Lautru, A. Gati, M.-F. Wong, V. Fouad Hanna and J. Wiart, "Evaluation of the SAR induced in a multilayer biological structure and comparison with SAR in homogeneous tissues," *Ann. Telecommun.*, Jan. 2008, pp. 79-86.
- [6] V. Monebhurrun, M.-F. Wong and J. Wiart, "Numerical and experimental investigations of a commercial mobile handset for SAR calculations," in *Proc. 2nd International Conference on Bioinformatics and Biomedical Engineering*, Shanghai, May 2008, pp. 784-787.
- [7] M D. P. Johns, R. Scaramuzza and A. J. Wlodarczyk, "Microstripes - microwave design tool based on 3D-TLM," in *Proc. 1st International Workshop on Transmission Line Matrix (TLM) Modeling - Theory and Applications*, Victoria, BC, Canada, Aug. 1995, pp. 169-177.

Investigation of Electronic Stirring Chamber Phase-shifting Excitation and Load Effects

M.A. Santos Jr.^{1,4}, D. Voyer², C. A. F. Sartori¹, D. Weinzierl³,
R. Perrussel², C. Vollaïre², L Krähenbühl², J.R. Cardoso¹

¹ Laboratório de Eletromagnetismo Aplicado LMAG/PEA/EPUSP. 05508-900. São Paulo-SP, Brazil

² Ampère (CNRS UMR5005), Université de Lyon, Ecole Centrale de Lyon, 69134, Ecully Cedex - France

³ Centro Universitário de Jaraguá do Sul – Rua dos Imigrantes 500, 89254-430, - Jaraguá do Sul/SC - Brazil

⁴ Centro Tecnológico da Marinha em São Paulo – 05508-000 - São Paulo/SP – Brazil

mario_alves@pea.usp.br, Damien.Voyer@ec-lyon.fr, sartori@pea.usp.br, Laurent.Krahenbuhl@ec-lyon.fr

Abstract — This paper presents a theoretical evaluation of the phase-shifting excitation and load effects in a Transmission Line Excitation Chamber. It is suggested as an alternative for immunity tests because of the restrictions related to canonical chambers. Here, two methods are used to calculate the E-field: a semi-analytic approach and a numerical one. The semi-analytic method is based on the well-known modal expansion while a commercial software is used for numerical simulations. The results regarding the field profile and the related statistical indexes of merit are presented and used to evaluate the chamber performance.

I. INTRODUCTION

Canonical chambers - that is Reverberation Chambers (RC) and TEM Chambers - are generally used for electromagnetic immunity testing despite their particular operational restrictions. RCs using mechanical paddles or frequency stirring provide a statistical E-field uniformity in all the directions inside the work volume [1]-[2]. Nevertheless, the frequency operation of RCs is inversely proportional to the chamber dimensions and it is a constraint for low frequencies tests. The International standards recommend the RC configuration for immunity tests over 80 MHz frequencies [2]. TEM Chambers present for low frequencies a deterministic E-field uniform over a work area parallel to the septum, but not in all directions in the chamber volume [3]. Recently, a concept called Transmission Line Excitation Chamber (TLEC) has been proposed, based on a phase-shifting excitation of several transmission lines (TL). For a sake of illustration, a configuration constituted of three-conductor phase-shifting excitation has been investigated in [4].

In this work, we present semi-analytical and numerical approaches for evaluating the performance of a TLEC. Basically, a chamber excited by several TL presents several TEM modes inside the closed metallic cavity. The resulting standing waves depend on the position of the TL as well as the phase-shifting excitation and the loading. Those parameters are important in the search for a suitable chamber working volume; they can be modified electronically, resulting in a random standing wave profile. Based on this, a set of parameters combination can be chosen to improve and satisfy the pre-defined uniformity criteria within a wide frequency range, even at frequencies lower than 80 MHz.

II. SEMI-ANALYTIC AND NUMERICAL APPROACHES

A. Analytic expression of a single TL

Considering the TL geometry given by Fig.1, the E-field of a TEM mode inside the chamber can be evaluated by the following analytical expressions:

$$E_{TEMX}(x, y) = \eta_0 \sqrt{\frac{2}{a}} \sum_{m=1}^{+\infty} \cos\left(\frac{m\pi}{a}x\right) \times \begin{cases} \alpha_{1m} \operatorname{sh}\left(\frac{m\pi}{a}(y-l_1)\right) & y > 0 \\ \alpha_{2m} \operatorname{sh}\left(\frac{m\pi}{a}(y+l_2)\right) & y < 0 \end{cases} \quad (1)$$

$$E_{TEMY}(x, y) = \eta_0 \sqrt{\frac{2}{a}} \sum_{m=1}^{+\infty} \sin\left(\frac{m\pi}{a}x\right) \times \begin{cases} \alpha_{1m} \operatorname{ch}\left(\frac{m\pi}{a}(y-l_1)\right) & y > 0 \\ \alpha_{2m} \operatorname{ch}\left(\frac{m\pi}{a}(y+l_2)\right) & y < 0 \end{cases} \quad (2)$$

with

$$\alpha_{1m} = \frac{J_m \operatorname{th}\left(\frac{m\pi}{a}l_2\right) / \operatorname{ch}\left(\frac{m\pi}{a}l_1\right)}{\operatorname{th}\left(\frac{m\pi}{a}l_1\right) + \operatorname{th}\left(\frac{m\pi}{a}l_2\right)}; \quad \alpha_{2m} = -\frac{J_m \operatorname{th}\left(\frac{m\pi}{a}l_1\right) / \operatorname{ch}\left(\frac{m\pi}{a}l_2\right)}{\operatorname{th}\left(\frac{m\pi}{a}l_1\right) + \operatorname{th}\left(\frac{m\pi}{a}l_2\right)} \quad (3)$$

where η_0 is the vacuum wave impedance and J_m the harmonic coefficients related to the current density on the central conductor. Assuming the conductor as an infinitely thin wire along z axis, one finds:

$$J_m = I_0 \sqrt{\frac{2}{a}} \sin\left(\frac{m\pi}{a}x_0\right) \quad (4)$$

The dependence with z direction is decoupled and equal to e^{-jk_0z} , when an incident wave is considered.

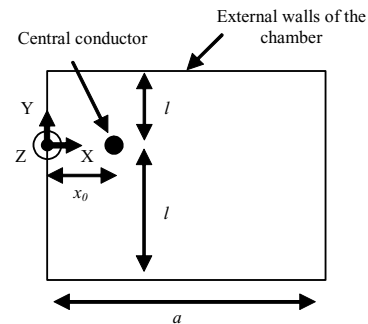


Fig. 1: geometry of a TL in the transverse plane

4. Electromagnetic Compatibility.

B. Phase Shifting and Load Effects Modeling

Several TL can be treated by superposition. When the TLs are ended with the same load, the E-field can be written using the separation of variables in the transverse plane and in the longitudinal direction. The phase shifting between the TLs has then an effect on the repartition of the fields in the transverse plane:

$$\vec{E}_{TOT}(x, y) = \sum_i \vec{E}_{i\text{TEM}}(x, y) e^{j\phi_i} \quad (5)$$

where $E_{i\text{TEM}}$ is the E-field due to the i^{th} TL and ϕ_i represents the applied excitation phase.

The load introduces a reflection coefficient Γ that affects the longitudinal repartition of the field:

$$\vec{E}_{TOT}(x, y, z) = \vec{E}_{TOT}(x, y) \times (e^{-jk_0 z} + \Gamma e^{+jk_0 z}) \quad (6)$$

If we consider when $|\Gamma| = 1$, a stationary wave is expected but the maximum of E-field can be moved changing the phase of Γ . Thus, it is possible to homogenize the field in z direction even if the TL is unmatched.

C. Numerical Approach

Numerical evaluation was performed using FIT [5]. The loads are imposed by boundary conditions while the phase-shifting excitation is implemented by a post-processing approach.

D. Indexes of Merit calculation

Standard deviation for the distribution of E-field in the chamber can be calculated from the definitions in [1] [4] and [6]. Due to the phase and load shifting, the E-field considered at any point of the chamber is the average field.

III. APPLICATION AND RESULTS

A TLEC with dimensions of $0.6m \times 0.6m \times 1.2m$ has been considered. The semi-analytical approach has been applied in the transverse plane $\{x, y\}$ since the variation of E-field in z direction can be canceled using a suitable load-shifting. The area under evaluation is a rectangular $0.3m \times 0.3m$ centered at the middle of the chamber. The study concerns the influence of the phase-shifting when several TL are considered. Results are reported in Table I. It appears that the number of TL is important: the standard deviation decreases of 3 dB when 4 TL are introduced instead of 2 TL. Moreover, the phase-shifting improves of 0.5 dB the performance. A TEM stripline like the one used in TEM Chambers has also been simulated and the E-field uniformity is presented.

TABLE I
STANDARD DEVIATIONS FOR SEMI-ANALYTICAL APPROACH

Chamber Configuration		Standard Deviation (dB)		
Number of TL	Phase-shifting	$\hat{\sigma}_x$	$\hat{\sigma}_y$	$\hat{\sigma}_{x,y}$
1	-----	5.7	6.0	5.9
2	No	6.5	3.3	5.3
2	Yes	6.4	2.0	5.0
4	No	3.2	3.2	3.3
4	Yes, random	2.8	2.6	2.8
TEM Chamber	-----	5.1	3.1	4.6

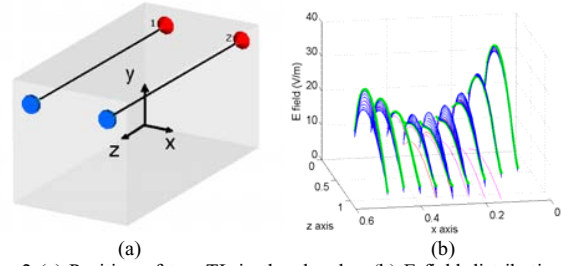


Fig. 2 (a) Position of two TL in the chamber (b) E-field distribution in the horizontal plane at the middle of the chamber (load 50Ω).

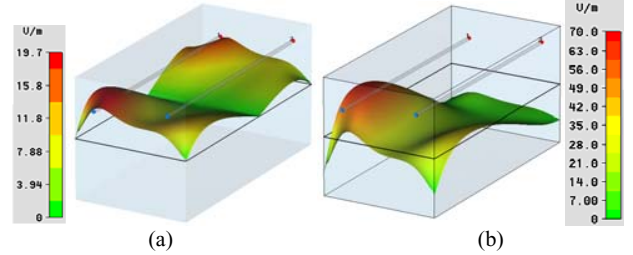


Fig. 3 E-field distribution with different loads (a) $-j500\Omega$ (b) $j500 \Omega$.

3D simulations using commercial software have also been carried out. The interest is that this approach is more realistic since it takes into account the connection of the TLs outside the chamber, which introduces a discontinuity. Table II presents the statistical E-field indexes calculated when the TLs are terminated by a 50Ω load. The volume is defined with the same cross section as previously, and a $0.6m$ length in the z direction. The influence of the phase-shifting on E-Field profile is also given at Fig. 2 in a 2 TL configuration.

TABLE II
STANDARD DEVIATIONS FOR NUMERICAL APPROACH (LOAD 50Ω)

Configuration		Standard Deviation (dB)		
Number of TL	Phase-shifting	$\hat{\sigma}_x$	$\hat{\sigma}_y$	$\hat{\sigma}_{x,y}$
1	-----	7.7	6.6	7.3
2	No	9.0	4.4	6.4
2	Yes, random	7.0	5.1	6.2
4	No	7.1	7.1	7.1
4	Yes, random	5.0	6.3	5.6

The effect of the load is presented in Fig. 3: the maximum of E-field moves between a $-j500\Omega$ and $j500 \Omega$ load.

ACKNOWLEDGMENT

This work was partially supported by Capes-Cofecub (07/0568), and FAPESP (2007/51192-6).

IV. REFERENCES

- [1] IEC61.000-4-21, Electromagnetic Compatibility (EMC), Part 4, Testing and Measurement Techniques – Section 21: Reverberation Chamber Test Methods.
- [2] M. Klingler, S. Egot, J. GHYS, J. Rioult, “On the use of 3D TEM Cells for Total Radiated Power Measurements”, *IEEE Transactions on EMC*, 44 (3): 364-372, 2002.
- [3] J. Perini and L. S. Cohen, “Extending the frequency of mode stir chambers to low frequencies”, IEEE International Symposium on Electromagnetic Compatibility, v. 2, 2000, pp. 633-637.
- [4] D. Hill, “Electronic mode stirring for reverberation chambers”, *IEEE Transactions on Electromagnetic Compatibility*, 36 (4): 294-299, 1994.
- [5] [Online]. Available: <http://www.cst.com/>
- [6] D. Weinzler, C. A. F. Sartori, M. B. Perotoni, J. R. Cardoso, A. Kost, E. F. Heleno, “Numerical evaluation of non-canonical reverberation chamber configurations”, *IEEE Transactions on Magnetics*, v. 44, n. 6, p. 1458-1461, JUN2008.

3D Near-field Reconstruction from PCBs by Equivalent Sources Using Legendre Functions

L. Beghou¹, L. Pichon¹, A. Raizer², and F. Costa³

¹Laboratoire de Génie Électrique de Paris
11, Rue Joliot Curie, Plateau de Moulon, 91192, Gif sur Yvette, France

²Laboratório de Eletromagnetismo e Compatibilidade Eletromagnética
Universidade Federal de Santa Catarina 5024, Florianópolis, Brasil

³Laboratoire des Systèmes et Application des Technologies pour l'Information et l'Energie
61 avenue du Président Wilson, Ecole Normale Supérieure de Cachan, 94235, Cachan, France
Lotfi.beghou@lgep.supelec.fr

Abstract — In this paper a 3D Near field characterization method is presented for the EMC analysis of power printed circuit boards. From a measured magnetic field cartography an equivalent set of magnetic dipoles is deduced solving an inverse problem. The use of Legendre functions in the field expressions allows to address the general case where the distance between the cartography and the circuit is small. This model is devoted to DC-DC complex real case. In this version some theoretical aspects and results on a simple case are presented.

I. INTRODUCTION

Switched mode power supplies (SMPS) are widely used, they provide good power-volume and power- weight ratios. However, they are source of electromagnetic pollution generated by switching mechanisms. In presence of such phenomena malfunction risk is not negligible and sometimes important, depending on the surrounding structures. To avoid such consequences, manufacturers have to make sure their products are electromagnetically compatible. To obtain such a guarantee it becomes necessary to know with a good accuracy the electromagnetic behavior of the switching devices. Near field characterization recently became an efficient way for the analysis of radiated emissions from electronic circuits and components [1]. The cartography of the radiated fields gives meaningful insights of the electromagnetic disturbances and adequate models can be directly build from the cartography. In [2] the radius of a circular loop equivalent to the switching cell is deduced from the maximum of the magnetic field. In [3] an array of equivalent dipoles lying on the printed circuit board and having predefined position is determined by a root mean square procedure. The model presented in [4] addresses a more general case where the position and orientation of equivalent dipoles are unknown : these dipoles are determined from the near field cartography by solving an inverse problem using genetic algorithms. Interesting results have been obtained for a simple case. However, the mathematical approximations used in this model assume that the radius of each magnetic dipole is very small compared to distance between each elementary part of the dipole and the observation point. These approximations allow an easy way to express the model and a reduced computing time. Nevertheless the solution quality tightly depends on the complexity of the studied case and realistic configurations of

power circuits including several radiation sources are difficult to be analyzed.

In this paper a new model without approximations is presented. In this approach the 3D dipoles are generated from the measured values of the magnetic field whatever the distance between the measured cartography and the circuit. The expressions of the radiated field use the Legendre functions which govern the general case relevant to the magnetic dipoles. Preliminary results are presented on a simple case. More complex configurations will be presented in the conference.

II. CHARACTERIZATION METHOD

The characterization method is an inverse-problem based resolution. It aims at finding a set of elemental electric and magnetic dipoles which radiate the same near-field values as the original device by minimizing the following function:

$$J(\vec{X}) = \left\| \vec{H}_{mes} - \vec{H}_{mod} \right\| \quad (1)$$

Where \vec{X} is the vector of the dipoles parameters.

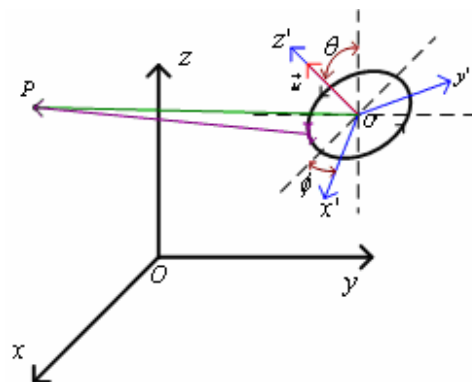


Fig. 1. Magnetic field radiated by a magnetic dipole

The magnetic field in the observation point P is the sum of the contribution of each elementary length along the magnetic dipole (Fig. 1). The magnetic field, radiated by a magnetic

4. Electromagnetic Compatibility

dipole using the Legendre functions (L1, L2), expression for one observation point is:

$$\vec{H} = B \cdot \vec{H}_{cyl} \quad (2)$$

Where \vec{H}_{cyl} is the magnetic field in the cylindrical local coordinates (o', x', y', z') has the following expression [5]:

$$\vec{H}_{cyl} = \begin{cases} \frac{\mu_0 I k}{4\pi\sqrt{a\rho}} \left(-L_1(k) + \frac{a^2 + \rho^2 + z^2}{(a-\rho)^2 + z^2} L_2(k) \right) \\ 0 \\ \frac{\mu_0 I k}{4\pi\sqrt{a\rho}} \left(L_1(k) + \frac{a^2 - \rho^2 - z^2}{(a-\rho)^2 + z^2} L_2(k) \right) \end{cases} \quad (3)$$

B is the coordinates transformation matrix from the cylindrical local coordinates to the global Cartesian coordinates (o, x, y, z). For one magnetic dipole, the parameters vector $\vec{X} = (\phi, \theta, x_0, y_0, I_d, a)$ has dimension (1,6).

For N magnetic dipoles the vector \vec{X} dimension is (1,6*N). The fitness function in (1) becomes highly non linear with a lot of local minima. To optimize this function a genetic algorithm is used. In the conference more details will be given about the theoretical aspects of the inverse problem and the improvement provided by this model when compared to [4].

III. RESULTS

In this part results obtained using the proposed approach for a simple DC-DC converter, are presented.

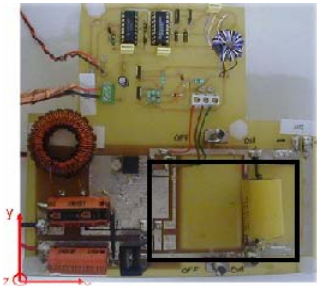


Fig. 2. Simple DC-DC converter (Black area: switching cell)

Field distributions obtained using the new model are presented in figures 3, 4.

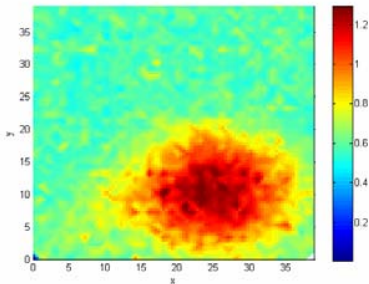


Fig. 3. Measured magnetic field

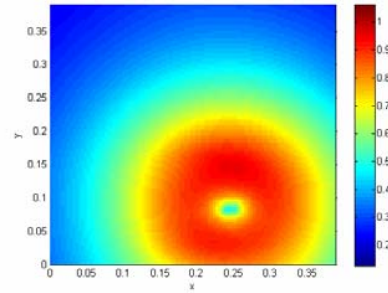


Fig. 4. Calculated magnetic field

In the conference the efficiency of the new model will be illustrated by studying a complex DC-DC case (figure. 5) and will be also compared with the results obtained using the former model.

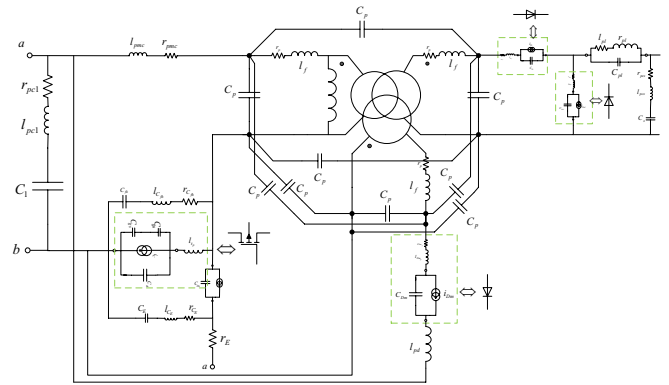


Fig. 5. Forward schema

IV. REFERENCES

- [1] D. Baudry, C. Arcambal, A. Louis, B. Mazari, P. Eudeline., "Applications of the Near-Field Techniques in EMC investigations, *IEEE Transactions on Electromagnetic Compatibility*, Vol. 49, n°3, pp 485 – 493, 2007.
- [2] O. Aouine, C. Labarre, F. Costa, Measurement and Modeling of the Magnetic Near Field Radiated by a Buck Chopper, *IEEE Transactions on Electromagnetic Compatibility* Vol. 49, n°2, pp 485 – 493, 2008.
- [3] Y. Vives-Gilabert, C. Arcambal, A. Louis, F. de Daran, P. Eudeline, B. Mazari, B. "Modeling Magnetic Radiations of Electronic Circuits Using Near-Field Scanning Method", *IEEE Transactions on Electromagnetic Compatibility*, Vol., n° 2, pp 391 – 400, 2007.
- [4] L. Beghou, B. Liu, L. Pichon and F. Costa "Synthesis of Equivalent 3-D Models from Near Field Measurements— Application to the EMC of Power Printed Circuit Boards ", *IEEE Trans. on Magnetics*, 45(3): 1650-1653, 2009.
- [5] E. Durand, *Magnétostatique*. Ed. Masson, 1953, pp. 491-493.

Evaluation of Shielding Effectiveness within Operating Room Using TLM Method

Wilson Valente Junior, Luciana Firmino, and Adroaldo Raizer
 Universidade Federal de Santa Catarina – UFSC
 Grupo de Engenharia em Compatibilidade Eletromagnética – GEMCO
 89840-040 – Florianópolis – Brazil
valente@eel.ufsc.br, luciana.firmino@eel.ufsc.br, raizer@eel.ufsc.br

Abstract—This paper reports a study-case concerning the assessment of shielding effectiveness within a typical operating room in order to evaluate and manage electromagnetic compatibility in health care facilities. Measurement techniques and numerical simulation (using TLM Method) are employed to identify and evaluate critical sources and frequencies, providing a reliable appraisal of the electromagnetic environment.

I. INTRODUCTION

Nowadays, it is possible to observe that Health Care Facilities (HCF) have been endeavoring to incorporate the use of new technologies to provide a number of different medical solutions and improve the quality of clinical procedures. This situation increases the challenge to promote the electromagnetic compatibility (EMC) in clinical environments in order to grant the proper performance of a growing number of equipment operating simultaneously within the same area.

The electromagnetic profile presented in a clinical environment is characterized by a set of complex conditions, which comprises several different sources, wide frequency range, and substantial amplitude variation. This situation complicates the establishment of an associated electromagnetic interference (EMI) potential for electromedical equipment (EME). Hence, it is well known that the awareness of electromagnetic behavior shown by these environments can represent an important tool in order to promote EMC management and avoid the appearance of undesirable phenomena such as EMI [1-2]. As a result of this assessment, a better understanding about the real situation concerning the electromagnetic environment in HCF can be achieved, allowing clinical engineers to define better directives to implement a management program which is adequate to the real need of these hospitals.

During the current research, a number of hospitals have been evaluated by measurement techniques in order to identify important electromagnetic features (critical sources and frequencies) presented in these environments. Some of them were already evaluated by computational means according to specific issues concerning wave propagation, as previously published in [1]. In this paper we deal with another study-case whose main characteristic is related to high electric field levels due to the influence of external sources, such as TV and FM radio broadcasting. In this scenario, clinical engineering staff was designing an RF shielding with the use of appropriated metallic layers in order to coat operating room (OR) walls. Although this approach seems to be a good preliminary option to solve the problem at hand, a detailed evaluation concerning other EMC aspects is needed. So, this

is the main topic of this paper, whose main purpose is to evaluate other important issues regarding EMC management, and to assess the effectiveness of a wall shielding implementation within operating room areas.

II. METHODOLOGY

In order to accomplish the desired results, the methodology used in this research was developed in two main steps, combining measurement techniques and numerical simulation. The idea of the first step is to perform a number of *in situ* electric field measurements within the clinical environment under test. The main energy sources and critical frequencies are then identified with spectral analysis (from 30 MHz to 3 GHz) and classified according to EMI risk stated by IEC 60601-1-2 (EMC collateral standard for EME). During the second step, a numerical model is developed using the *Transmission Line Modeling* (TLM) method. Preliminary measurement results are used as inputs for the numerical simulation and the electric field distribution is estimated to evaluate the influence of significant sources of energy, such as electrosurgical unit (ESU), TV and FM radio broadcasting.

A. TLM Method

The TLM is a differential numerical technique which has been successfully applied to modeling electromagnetic fields for decades [3]. It was developed to take advantage of the analogy between representative equations of transmission-lines and electromagnetic fields. The scattering process is based on light propagation principle stated by Huygens. In this method, the propagation medium is modeled by a network of interconnected transmission-lines (TLM mesh), and material properties are represented by the equivalent lumped circuit components [3]. Figure 1 shows a single network circuit unit named shunt node.

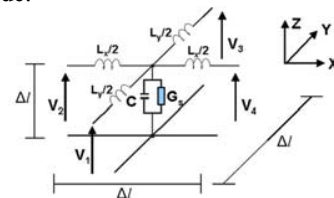


Fig. 1. TLM-2D Shunt Node.

The analogy between Kirchhoff laws for shunt node circuit and wave Maxwell's equations in time domain can define the relation between voltage/current and electrical/magnetic field:

$$E_z = \frac{V_z}{\Delta l} \quad H_x = \frac{I_y}{\Delta l} \quad H_y = \frac{-I_x}{\Delta l} \quad (1)$$

Likewise, it is also possible to establish the relations between TLM cells and medium parameters:

$$\mu = L_d \quad \varepsilon = \left(2C_d + \frac{C_s}{2} \right) \quad \sigma = G_s \quad (2)$$

III. THE ENVIRONMENT UNDER TEST

In this analysis the environment under test is a typical OR of approximately 25 m². The disposal of EME and objects within the room follows clinical staff directives to configure a usual setup for the HCF standard procedure (fig. 2).

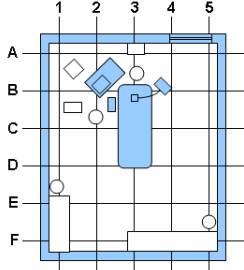


Fig. 2. Typical Environment Under Test.

Concerning computational prediction, the environment under test was modeled by a 600x700 TLM nodes. Each node has an area of 1 cm², and it is characterized by the medium electric parameters: concrete ($\varepsilon = 5.0$, $\sigma = 0.0133$ S/m); wood ($\varepsilon = 4.0$, $\sigma = 0$ S/m); equipment ($\varepsilon = 1.0$, $\sigma = 10^3$ S/m); metal ($\varepsilon = 1.0$, $\sigma = 3e^7$ S/m); plastic ($\varepsilon = 4.0$, $\sigma = 1.0$ S/m); foam ($\varepsilon = 1.3$, $\sigma = 0$ S/m); air ($\varepsilon = 1.0$, $\sigma = 0$ S/m); human body (ε_r and σ values depends on the frequency). All mesh borders are modeled as open boundaries, simulated by a TLM “matched” (absorbing) boundary condition, as described in [3].

IV. PRELIMINARY RESULTS

A. Field Measurements

Figure 3 shows the result of electric field strength measurement. It illustrates two different spectrum situations, both in operation case (with EME turned on) and in rest case (with EME turned off).

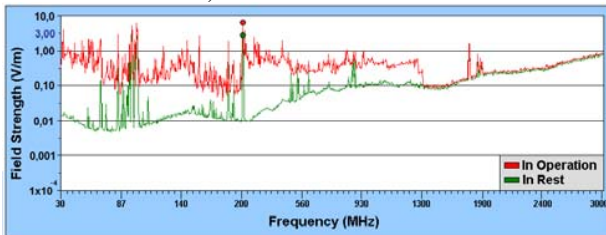


Fig. 3. Electric Field Strengths Measurements (30 MHz to 3 GHz)

Most important sources observed within the room were TV and radio broadcasting. However, ESU electromagnetic content can not be ignored since it was the main responsible for the spectrum rises when EME were turned on. Due to the limited space, in this digest the simulation will be focused only at the 204 MHz contributions of the main sources.

B. Field Prediction

Figure 4 shows the electric fields distribution for individual sources oscillating at 204 MHz. Figure 4a is related to an

incident TV broadcasting wave-front reaching the OR external wall. Figure 4b shows ESU contribution when it is operating in close proximity to the B3 point.

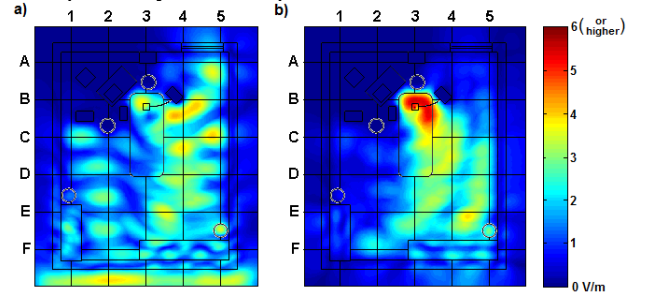


Fig. 4. Field Distribution at 204 MHz: a) TV broadcasting; b) ESU.

On a second simulation scenario, metal conductor layers were included, modeling the designed shielding to the OR walls. Figure 5 compares field distribution profiles for both scenarios: original OR (fig. 5a) and OR with RF shielding (fig. 5b), when both sources from fig. 4 are operating simultaneously.

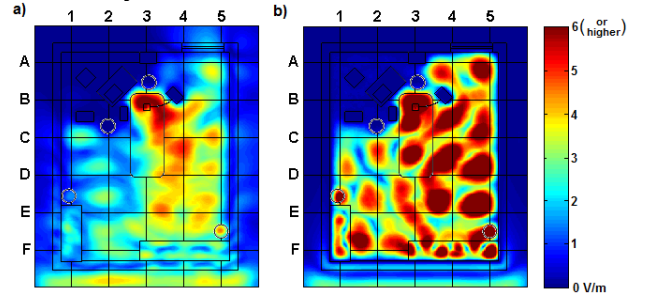


Fig. 5. Field distribution for: a) original OR; b) OR with RF shielding.

It is possible to observe that shielding effectiveness concerning EMC aspects is not only related to the capability of isolating undesired signals individually, but also evaluates the system as a whole. As can be seen on fig. 5, the use of OR wall complete shielding may not be the best alternative, since it confines significant signal sources inside the room raising the average environmental energy level. Although it is an efficient solution to avoid the analyzed external signals (TV and FM broadcasting), it can lead to a worse EMC condition.

V. FINAL CONSIDERATIONS

In the full paper, a better detailing is given to the treatment of this problem, allowing more discussion about the subject. Other important sources and frequencies should be also evaluated by numerical means providing a thorough analysis of EMI situations. Finally, an optimization process will be employed in order to verify different shielding configurations and evaluate its efficiency regarding EMC management.

VI. REFERENCES

- [1] Valente Jr., W.; Dalla'Rosa, A.; Raizer, A.; Pichon, L.; “The use of tlm and kriging methods for electromagnetic compatibility management in health care facilities,” *IEEE Trans. on Magn.*, 44(6): 1478-1481, 2008.
- [2] Schäfer, T. M.; Kayser, T.; Knorz, S.; Wiesbeck, W.; “Wave propagation in hospitals with composite wall structures,” *IEEE Int. Symp. Wireless Communication Systems*, p. 512 – 516, 2006
- [3] C. Christopoulos, *The Transmission-Line Modeling Method - TLM*, New York, IEE Press and Oxford University Press, pp. 69-105, 1995.

Full Wave Solution for Intel CPU with a Heat Sink for EMC Investigations

Junwei Lu, Boyuan Zhu, and David Thiel
 Centre of Wireless Monitoring and Applications, Griffith School of Engineering
 Griffith University, Nathan, Qld, 4111, Australia
 j.lu@griffith.edu.au

Abstract — A CPU with a heat sink (e.g. Intel Pentium 4 and Intel Pentium dual core) is one of the challenging problems for IEEE EMC. A Very Large Scale Integrated (VLSI) device was modelled using the Finite Element Method (FEM) frequency domain as this provides a 3D full wave solution. The electromagnetic (EM) radiation emitted from these high power microelectronic circuits connected to a heat sink was found to have resonant frequencies around 2.4 GHz and 5 GHz with a reflection coefficient less than 19 dBi and 8 dBi. Those resonant frequencies are very close to the operating frequency of both IEEE and Bluetooth wireless communication systems. This paper proposes a new benchmark model based on a dual core CPU.

I. INTRODUCTION

Modern silicon wafer fabrication facilities easily produce component densities that exceed 1 million transistors per die. The power generated from processor currents can exceed 100W with increasing high clock speeds. This combination of switching frequency and power level, in conjunction with the layout of the common mode current paths through the heat sinks, results in a significant level of radiated Electromagnetic Interference (EMI). As a result, circuit designers require an understanding of the radiated emissions from the CPU and its heat sinks. Designers also need to find ways to reduce these emissions. Components such as the Intel Pentium 4, Intel Pentium dual core CPU, and AMD Athlon dual core CPU require separate cooling procedures provided by a fan built into their heat sink or by a fan or cooling device located adjacent to the processor. Since these high-power and high-speed processors are common in recent designs, special techniques are required for EMI suppression and heat removal at the component level. In addition, 3D EM full wave based numerical analysis tools are required to model the radiated emissions. This paper focuses mainly on RF radiated emission problems that consider the EMC source modelling for the CPU and heat sink as a RF radiator [1].

II. EMC SOURCE MODELLING AND MODEL ATTRIBUTES

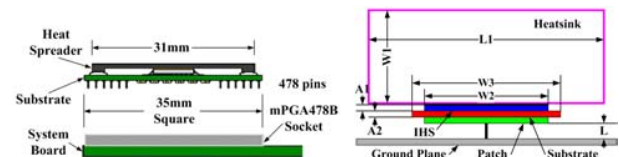
A. CPU Source Model Consideration

EMC/EMI models are commonly represented as three distinct parts: the source of RF energy, the geometry of the model components, and the remaining problem space [2]. To model the CPU with a heat sink structure, it is useful to further divide the structure into three regions; the ground plane, source region and heat sink. A realistic representation of a VLSI circuit must consider the electromagnetic source characteristics and an actual physical representation such as a

conducting patch [3]. Although real heat sinks have fins to increase the thermal convection loss, Brench [4] found that the heat sink could be modelled as a solid block. Das and Roy [5] modelled the source as a monopole that passes through the circuit. This EMC source model was used to address the previous problem confronting the IEEE EMC (486 CPU). The Intel P4 and Intel dual core CPU with a heat sink have completely different structural configurations, therefore a new EMC source model is required for modelling and simulation.

B. Intel P4 CPU Heat Sink and Source Model

The Intel P4 processor with the 478-Pin has different packaging and a different structural configuration (see Figure 1a). In the Intel P4 configuration, a heat spreader is located on top of the VLSI. This heat spreader is electrically isolated from the VLSI packaging. A new EMC source model consists of a multi layered structure forming a microstrip patch antenna structure, which is resonant at frequencies of around 2.4 GHz and 5 GHz respectively. This is shown in Figure 1(b). Several clock frequencies in the band from 1.40 GHz through 2GHz are considered for demonstration purposes, where A1 is 2.378mm, A2 is 1.080mm, L is 2.030mm, L1 is 88.9mm, W1 is 38.1mm, W2 is 31.75mm and W3 is 35mm.

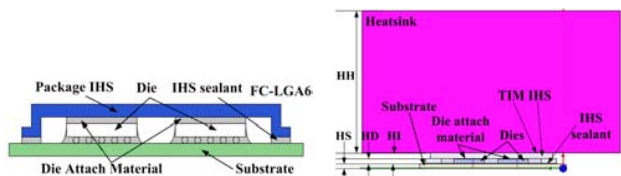


(a) Intel P4 CPU and packaging (b) EMC source model with a heat sink
 Figure 1. Intel P4 CPU heat sink configuration and simulation model.

C. Intel Dual Core CPU Heat Sink Model

A transverse cross-section of the Intel dual die processor with a heat sink is illustrated in Figure 2. The package is a Flip-Chip Land Grid Array (FC-LGA6) and the die is located upon the substrate with the help of die attach material. The sealing is also the integrated heat spreader (IHS) covering the dies in order to protect them. Adhered by the thermal interface material (TIM), the heat sink is in full contact with the top of IHS. Like the Intel P4 CPU model, this dual core CPU model can be simplified to a dual feed microstrip patch antenna structure. The location of feed points is a critical factor that affects the accuracy and validation of the simulation results. Based on the heat distribution on an existing Intel dual die CPU [7], the hottest point is predicted to be the area of highest current distribution where the electromagnetic interference

generated is very significant. Thus the feed points of the equivalent patch were allocated to these regions for the EMC source model assuming a 50 ohm source. Note that the highest current density for a driven patch antenna is immediately adjacent to these probe feeds. The size of the equivalent patch antenna model is simply the resonant size at 2.45 GHz and the second frequency at 5 GHz.



(a) Intel Dual Die packaging (b) EMC source model with a heat sink
Figure 2. Intel dual core CPU heat sink configuration and EMC source model.

III. FULL WAVE SOLUTION

A. Frequency Domain Modelling in EMC/EMI

The most accurate modelling of EMC requires a 3D full-wave solution in which Maxwell's equations are solved. With numerous fast numerical algorithms now available, the FEM in the frequency domain is relatively efficient. The technique finds approximate solutions of partial differential equations and integral equations. The frequency domain vector wave equation for the \mathbf{E} field is:

$$\nabla \times \frac{1}{\mu} \nabla \times \mathbf{E} + \sigma_e \omega \mathbf{E} + \omega^2 \epsilon \mathbf{E} = -j\omega \mathbf{J} \quad (1)$$

where ω is angular frequency, \mathbf{J} is the source current, σ_e is the effective conductivity, and μ and ϵ are the permeability and permittivity of the problem space respectively.

B. Full Wave Solutions for CPU Heat Sink Models

The computation model for the Intel P4 and Intel dual core CPU heat sink fits within the source models developed in this work. These are shown in Figures 1 and 2, where the absorbing boundary condition, PML, is used to surround the computation model to obtain accurate results. The excitation is a vertical probe extending from the ground plane to the base of the conducting patch.

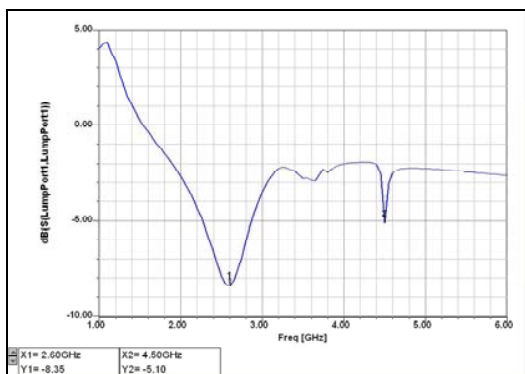


Figure 3. S_{11} impedance matching for the Intel P4 CPU heat sink model.

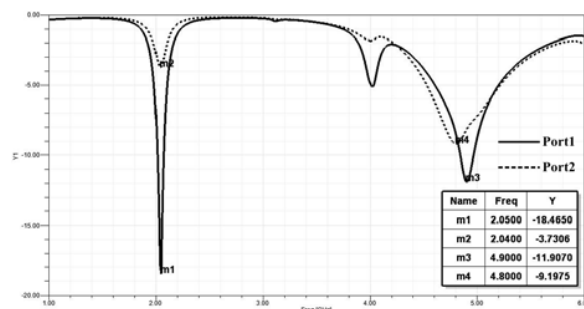


Figure 4. S_{11} impedance matching for the Intel dual core CPU heat sink, where — line indicates the excitation at port 1, and ... line indicates the excitation at port 2. The mark position is indicated by m1, m2, m3 and m4.

This is electromagnetically coupled to the heat sink through the substrate. Figures 3 and 4 show the scattering parameter S_{11} (with a 50 ohm source) across the frequency band. Both models have two resonant frequencies. The S_{11} results indicate that there is maximum radiation from the structure at these two frequencies. The CPU heat sinks cause significant radiated emissions at these frequencies, assuming it is possible that currents in the VLSI circuit have Fourier components at these frequencies.

IV. CONCLUSION

This paper presents a FEM based computation technique for radiated emissions from CPU heat sink models. The CPU heat sink model is significantly different to the conventional CPU heat sink model of IEEE EMC challenge problems. The Intel P4 and Intel dual core CPU heat sink models with insulated configurations were found to radiate at 2.4 GHz and 5 GHz respectively. These two frequencies lie very close to the wireless communication range in computing systems. The source model selection is critical for the CPU heat sink model as it affects the resonant frequencies associated with the CPU clock speed, the CPU core and heat sink structures. The far field radiation patterns from those CPU heat sink models and validation of the CPU dual core benchmark model will be discussed in the full paper.

V. REFERENCES

- [1] J. Lu and X. Duan, EMC computer modelling techniques for CPU heat sink simulation, *Proc. ICCEA* pp. 272-275, Nov. 2004.
- [2] B. Archambeault, C. Brench and O. M. Ramahi: *EMI/EMC Computational Modelling Hand Book*, Second Edition, Kluwer Academic Publishers, 2001.
- [3] K. Li et al: Application of FD-TD Method to Analysis of EM Radiation from VLSI Configurations, *IEEE Trans. EMC*, vol. 35, No. 2, pp 204-213, May 1993.
- [4] C. E. Brench: Heatsink Radiation as a Function of Geometry, *IEEE Symposium on EMC*, pp. 105-109, 1994.
- [5] S. K. Das and T. Roy: An Investigation of Radiated Emissions from Heatsinks, *IEEE Symposium on EMC*, vol. 2, pp. 784-789, 1998.
- [6] J. Lu and F. Dawson, "EMC Computer Modelling Techniques for CPU Heat Sink," *IEEE Trans. Magnetics*, Vol. 42, No. 10, Oct. 2006, pp. 3186-3188.
- [7] Intel® Core™2 Extreme Quad-Core Processor QX6000 Sequence and Intel® Core™2 Quad Processor Q6000 Sequence Datasheet, Intel Corporation, pp. 31-34, Aug.2007

Conductor Positions Optimization of a Transmission Line Excitation Chamber

M. Santos Jr.^{1,4}, S. Avila¹, C. A. F. Sartori¹, D. Weinzierl^{3,1}, L. Krähenbühl², L. Lebensztajn¹, J. R. Cardoso¹

¹ Laboratório de Eletromagnetismo Aplicado LMAG/PEA/EPUSP. 05508-900 - São Paulo/SP – Brazil

² Ampère (CNRS UMR5005), Université de Lyon, Ecole Centrale de Lyon, 69134, Ecully Cedex - France

³ Centro Universitário Jaraguá do Sul – Rua dos Imigrantes 500, 89254-430 - Jaraguá do Sul/SC - Brazil

⁴ Centro Tecnológico da Marinha em São Paulo – 05508-000 - São Paulo/SP – Brazil

mario_alves@pea.usp.br, leb@pea.usp.br

Abstract— This paper presents a multi-objective optimization approach based on numerical, statistical and fitness evaluation concerning the conductor positions in a Transmission Line Excitation Chamber (TLEC). The field profile and the related indexes of merit, like the statistical ones, regarding the working volumes are used to evaluate the chamber configuration performance. The compromise between working volume and E-field standard deviation are show through the Pareto's Front.

I. INTRODUCTION

In previous works the Transmission Line Excitation Chamber (TLEC) performance evaluations have been carried out using different approaches. These were presented in [1] and [2] in which FIT and TLM, and also an optimization tool were used to evaluate the field uniformity within the working volume on a predefined TLEC configuration. The TLEC configuration here presented is based on three-conductor phase-shifting excitation configuration and proposed as an alternative when low frequencies are taken into consideration [3]. Fig.1 shows a sketch of a three-wire reverberation chamber configuration. Thus, the optimization problem aims to maximize the working volume and the E-field, which is restricted to uniformity constraints.

In this work, the main focus is to find the better transmission lines configurations, i.e., wire positions, which present the best TLEC performance related to the aforementioned indexes. A good TLEC performance is associated to a high working volume and E-fields average values. To obtain the wire configuration and the corresponding TLEC performance, a numerical approach has been implemented by applying multi-objective optimization. Deterministic and statistical approaches are applied in the analysis.

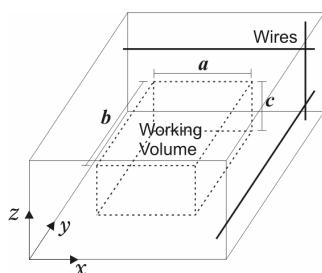


Fig. 1. Sketch of the three-wire reverberation chamber configuration

II. OPTIMIZATION PROCEDURE

A working volume is assumed to be a region inside the reverberation chamber (Fig. 1) where the homogeneity of the electric field attains a prescribed level. EMC tests could be performed only with this minimum homogeneity level, and the mean value within the working volume should be as high as possible considering low input power.

In this work, the main interest is to understand how the reverberation chamber works when associated to a set of transmission lines positions and its related working volumes. It should be mentioned that when the working volume increases the mean electric field decreases. This means that a multi-objective optimization algorithm should be employed (two or more antagonistic goals).

Here, the optimization problem has twelve optimization variables: three pairs coordinates (TL positions), two equatorial radii, polar radius and three parameters associated to the ellipsoid translation (shift) from the chamber's centre (these six last variables define the working volume). In this set, inside some working volume the electric field is high, whereas the volume is low.

There are other working volumes, which belong to this set, but have low electric field and high volume. Inside the working volumes the field homogeneity is constrained by pre-defined values. When the chamber characterization is performed, the engineer could make a choice to obtain the most suitable set of TL to design the TLEC.

In order to solve it, the optimization problem is assumed as an unconstrained optimization problem, where inequality constraint was treated as a penalty function.

A. Modeling the chamber

The mean E-field (\bar{E}_x), the Standard Deviation (σ_x) and Standard Deviation in dB ($\hat{\sigma}_x$) are calculated by (1), (2) and (3)

$$\bar{E}_x = \frac{1}{N} \sum_{k=1}^N E_{xk} \quad (1)$$

$$\sigma_x = \sqrt{\frac{1}{N-1} \sum_{k=1}^N (E_{xk} - \bar{E}_x)^2} \quad (2)$$

$$\hat{\sigma}_x = 20 \log_{10} \left(\frac{\bar{E}_x + \sigma_x}{\bar{E}_x} \right) \quad (3)$$

4. Electromagnetic Compatibility.

Similar equations could be obtained to the y-axis, z-axis and to the combined E-field [1], [2] and it is assumed a value equal to 4 dB as the standard deviation for defining the working volume at frequencies lower than 80 MHz.

B. The Optimization Problem

The conductor position problem could be written as an optimization problem as follows:

$$\begin{cases} \text{Max Working Volume} \\ \text{Max } \bar{E}_{x,y,z} \end{cases} \quad (4)$$

S. t: $\text{Max } (\hat{\sigma}_x, \hat{\sigma}_y, \hat{\sigma}_z, \hat{\sigma}_{x,y,z}) \leq 4\text{dB}$

In order to bounder the optimization parameters, Fig 2 illustrates and shows a cross-section of the chamber to be analyzed. First of all, it is assumed that each wire is parallel to one of the three axis of the chamber as Fig 1 shows. So, each wire could only be placed in the grey region, because it could not be close to the wall, due to the standards. On the other hand, if we put it on the center of the chamber (the forbidden area) the associated working volume will be small. Thus the TLs can only be moved inside a space "close" to the walls in order to avoid solutions that are impossible for practical utilization.

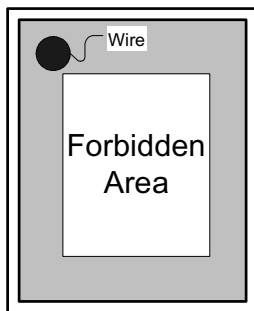


Fig.2 Chamber Cross Section: the position wire

Multi-objective optimization (4) seeks to optimize the components of a vector-valued cost function. Unlike single objective optimization, the solution to this problem is not a single point, but a family of efficient points called Pareto-front. Each point on this surface is optimal in the sense that no improvement can be achieved in a cost vector component that does not lead to degradation in at least one of the remaining components. Each element in the efficient set constitutes a non-dominated (non-inferior or non-superior) solution to the multi-objective problem. With this set of solutions it is possible to understand the dependence between each objective.

The Pareto-set of this multi-objective problem was obtained by using the Multi-objective Genetic Algorithm (MGA)[4]. The MGA is derived from the Genetic Algorithm, which is a stochastic procedure based on the concepts of natural selection in genetics.

C. Coupling the Field Computation Software and the Optimization Environment

The adopted procedure has six fundamental steps:

- i) Random positions for TL are generated, as well the working volumes and ellipsoid radius;

- ii) TL positions are charged to the field computation software, that uses FIT [5];
- iii) The field computation inside the reverberation chamber is performed with FIT [5];
- iv) The values of the E-field are exported considering a regular grid;
- v) The working volume is calculated. For the determination of a particular working volume, Eq. (1) should be solved, and
- vi) The indexes of merit are applied to decide which one are the better TL configurations.

The third and fourth steps are computed by applying the FIT [5] At the end of step iv a file is exported to our optimization environment.

The EMC standards adopt a parallelepiped as a working volume[7]. In this work we have adopted another solid to characterize the volume: an ellipsoid[2].

III. RESULTS

Fig. 2 shows some results which allow us to know the compromise among the searched objectives (max E-field and max working volume), the constraints and the conductor positions.

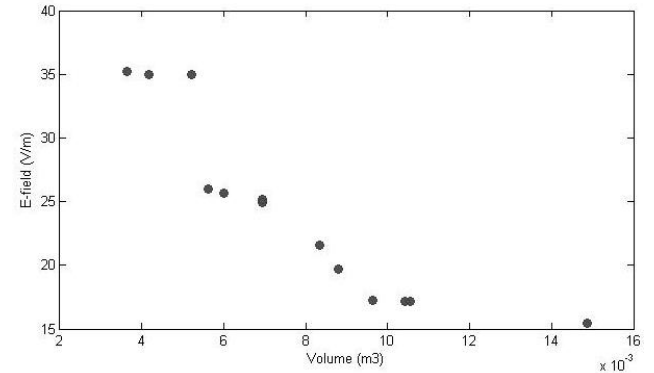


Fig. 2. Compromise between working volume and E-field.

By inspection of Fig. 2 the maximal working volume, taking into account a defined E-field level, can be chosen. For instance, it yields approximately $15 \times 10^{-3} \text{m}^3$ for an E-field level of 15V/m considering the total chamber volume equal to $0,432 \text{m}^3$.

IV. REFERENCES

- [1] D. Weinzierl et al., "Numerical evaluation of non-canonical reverberation chamber configurations", *IEEE Transactions on Magnetics*, v. 44, n. 6, p. 1458-1461, 2008.
- [2] M. A. Santos Jr. et al., "Maximum working volume evaluation in a non-canonical reverberation chamber", *IEEE Transactions on Magnetics*, 45 (3): 1646-1649, 2009.
- [3] J. Perini and L. S. Cohen, "Extending the frequency of mode stir chambers to low frequencies", *IEEE International Symposium on Electromagnetic Compatibility*, v. 2, 2000, pp. 633-637.
- [4] S. L. Avila et. al., Sensitivity Analysis in the Parameters Space Applied to Decision Making in Multi-objective Evolutionary Optimization, *IEEE Transactions on Magnetics*, 42 (4): 1103-1106, 2006.
- [5] CST MICROWAVE STUDIO®, Advanced Topics (www.cst.com).
- [6] T. Weiland, "Time domain electromagnetic field computation with finite difference methods," *Int. J. Num. Mod.: ENDF*, vol. 9, pp. 259-319, 1996.
- [7] IEC61.000-4-21, Electromagnetic Compatibility (EMC), Part 4, Testing and Measurement Techniques – Section 21: Reverberation Chamber Test Methods.

Magnetic Shielding of Apertures Loaded by Resistive Coating

M. D'Amore¹, V. De Santis², and M. Feliziani²

¹ Dept. of Electrical Engineering – Sapienza University of Rome, Italy
marcello.damore@uniroma1.it

² Dept. of Electrical and Computer Engineering, University of L'Aquila, L'Aquila, Italy
valerio.desantis@univaq.it, mauro.feliziani@univaq.it

Abstract— In this paper the numerical prediction of the magnetic shielding of a coated aperture in a perfectly conductive planar shield is investigated. The single layer or multilayer thin film resistive coating is characterized and homogenized by using the transmission line approach. The electromagnetic analysis is performed by the finite element method (FEM). The results obtained in some test configurations are validated by other numerical and analytical methods.

I. INTRODUCTION

Evaluation of the shielding effectiveness (SE) is an important topic in electromagnetic compatibility (EMC) studies and is regulated by several standards (MIL-Std 285, IEEE 299, ASTM D4935,...). The experimental layout for the magnetic shielding measurement consists essentially in locating two oriented loop antennas in two positions: ahead and behind the shield under test. One loop (i.e., transmitting antenna) is used to generate the incident magnetic field H^i , while the other loop (i.e., receiving antenna) is used to measure the transmitted magnetic field H^t through the shield.

The parameter used to quantify the shielding performances is the magnetic shielding effectiveness SE_H defined as the ratio, in decibel, between the incident field, H^i , and the transmitted one, H^t , in a fixed point behind the shield: $SE_H = 20 \log_{10}(|H^i| / |H^t|)$. It should be noted that the incident field H^i is the field at the considered point in absence of the shield. The different standards require that the antennas must be oriented in two positions: coplanar and parallel arrangements, as shown in Fig. 1.

The SE_H of apertures has been studied by many authors using analytical, experimental and numerical techniques [1]-[6]. The new interest for this topic is in the extensive installation of new transparent coating materials to cover windows and apertures, mainly for thermal reasons, of apparatus and transportation systems (trains, cars, aircraft,...). These coatings are generally composed by several layers of conductive thin films of silver, indium tin oxide (ITO),..., combining characteristics of electrical conductivity and optical transparency. These thin films have shielding properties against incident magnetic fields that have to be analyzed.

In this study we consider a coated aperture in a plane conductive sheet or on the wall of an enclosure that is so large that the reflections from the other walls are insignificant compared to the fields that penetrate the aperture [5]. The magnetic shielding analysis is performed by a numerical method that is validated by comparison with other techniques based on approximate analytical and circuital methods [1], [6].

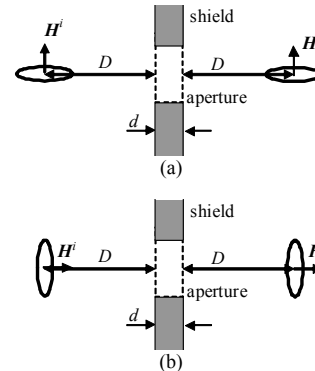


Fig. 1. Arrangements of coplanar (a) and parallel (b) loops.

II. CHARACTERIZATION OF THIN FILM COATING

Assuming the field propagating as a plane wave inside a thin shield as shown in Fig. 2, the electric and magnetic field components tangential the two faces (Γ_0, Γ_d) of a solid planar shield of thickness d are coupled by the lossy transmission line equations [4]-[6]:

$$\begin{bmatrix} E_{\tau 0} \\ H_{\tau 0} \end{bmatrix} = \begin{bmatrix} \Phi_{11} & \Phi_{12} \\ \Phi_{21} & \Phi_{22} \end{bmatrix} \begin{bmatrix} E_{\tau d} \\ H_{\tau d} \end{bmatrix} \quad (1)$$

where $E_{\tau 0}$, $E_{\tau d}$, $H_{\tau 0}$, $H_{\tau d}$ are the field tangential components, and the shield chain matrix $[\Phi]$ is given by

$$[\Phi] = \begin{bmatrix} \cosh(\gamma_s d) & \eta_s \sinh(\gamma_s d) \\ \sinh(\gamma_s d)/\eta_s & \cosh(\gamma_s d) \end{bmatrix} \quad (2)$$

being η_s the intrinsic impedance, γ_s the propagation constant of the solid shield with characteristics $\epsilon_s, \mu_s, \sigma_s$.

For very small values of d in conductive layer, (2) can be approximated by:

$$[\Phi] \approx \begin{bmatrix} 1 & 0 \\ \sigma_s d & 1 \end{bmatrix} \quad (3)$$

For a configuration of a n -layer shield, the total chain matrix $[\Phi]$ can be obtained by:

$$[\Phi] = [\Phi_1][\Phi_2][\Phi_3] \dots [\Phi_n] \quad (4)$$

where $[\Phi_i]$ is the chain matrix of the i th layer whose expression is given in (2) and is valid also for dielectric layers. The chain matrix $[\Phi]$ can be used to model any multilayer shield in frequency domain.

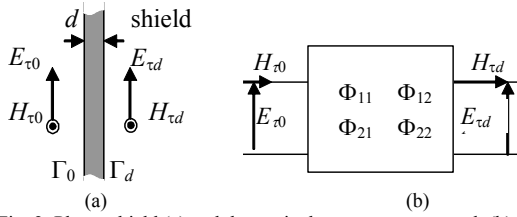


Fig. 2. Planar shield (a) and the equivalent two-port network (b).

III. FEM MODELING OF THIN FILM COATING

Simulation of conductive thin layers embedded in a FEM domain can lead to an excessive number of degrees of freedom (DoF) since the thickness of the thin film coating is very small, about tens of nanometers, and requires a lot of finite elements to discretize adequately the region under examination. To overcome this problem, a reduction of the DoF is necessary. We propose two different methods.

The first approach is based on the Impedance Network Boundary Conditions (INBCs) [3]-[4]. The basic idea of the INBC method is to eliminate from the computational domain the conductive shield by introducing new boundaries where the electric and magnetic tangential fields are coupled by the chain matrix $[\Phi]$ (or by equivalent admittance matrix $[Y]$ or impedance matrices $[Z]$) in order to model the penetration of the electric and magnetic fields inside the thin conductive wall. By considering conductive thin film, the transmitted fields must be constrained imposing on the boundary Γ_d :

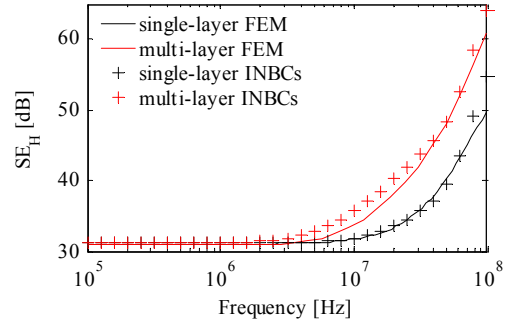
$$E_{\tau d} = E_{\tau 0} \quad (5a)$$

$$H_{\tau d} = H_{\tau 0} - E_{\tau 0} \sigma_s d \quad (5b)$$

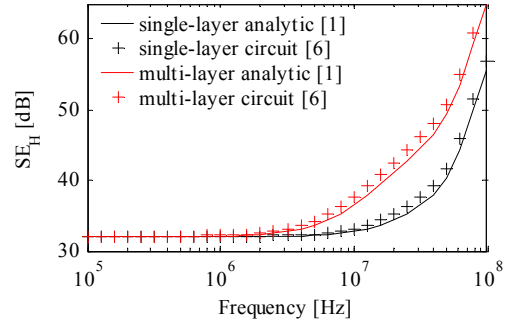
The second approach consists in synthesising a new shield whose chain matrix $[\Phi]$ is identical to that of the thin film shield, but with a much larger thickness. For simply resistive shields of very small thickness, the chain matrix is practically frequency constant, and therefore it can be simply modelled by a resistive layer of equivalent conductivity σ_e and thickness d_e obtained by $\sigma_e d_e = \sigma_s d$ when assuming $d_e \gg d$ and $d_e \ll \delta$, being δ the penetration depth.

IV. APPLICATIONS

The magnetic shielding performances of two different coatings applied to a circular aperture of 0.1 m radius have been analysed for both the parallel and coplanar loop configurations. Fig. 3(a) shows the calculated SE_H by the two proposed FEM methods for the coplanar loop configuration assuming $D = 0.4$ m. The aperture is loaded by a single layer silver coating with $d = 18$ nm and a multilayer sandwich coating (3 Ag layers separated by 2 dielectric layers) assuming $d = 18$ nm for each layer of Ag or dielectric, respectively. The FEM results can be compared with those obtained by approximate analytical [1], and circuit [6] techniques shown in Fig. 3(b), highlighting good accuracy. Finally, the calculated SE_H for the parallel loop configuration is also reported in Fig. 4.



(a)



(b)

Fig. 3. SE_H for a circular aperture of 0.1 m radius and coplanar loop configuration. (a) FEM calculations. (b) Analytical and circuit methods.

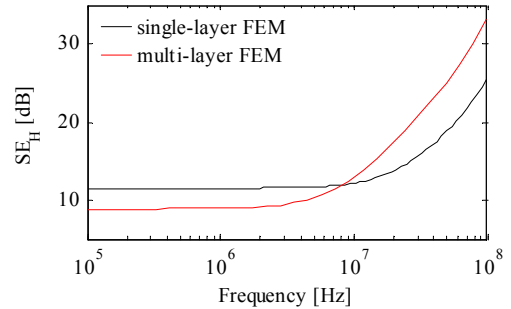


Fig. 4. SE_H for a circular aperture of 0.1 m radius and parallel loop configuration.

REFERENCES

- [1] K. F. Casey, "Low-frequency electromagnetic penetration of loaded apertures," *IEEE Trans. Electromag. Compat.*, vol. 23, no. 4, pp. 367-37, Nov. 1981.
- [2] M. D'Amore, S.Greco, M. S. Sarto, "Transparent electromagnetic shielding of enclosures against EMP penetration," EUROEM 2008, July 21-25, 2008, Lausanne.
- [3] M. Feliziani, F. Maradei and G. L. Tribellini, "Analysis of penetrable conductive shields by the Finite-Difference Time-Domain Method with Impedance Network Boundary Conditions (INBCs)," *IEEE Trans. Electromag. Compat.*, vol. 41, no. 4, pp. 307-319, Nov. 1999.
- [4] M. Feliziani and F. Maradei, "Edge element analysis of complex configurations in presence of thin shields," *IEEE Trans. Magnetics*, vol. 33, no.2, pp. 1548-51, March 1997.
- [5] L.O. Hoefft, T.M. Salas, J.S. Hofstra, W.D.Prather, "Predicted shielding effectiveness of apertures in large enclosures as measured by MIL-STD-285 and other methods," IEEE 1989 National Symp. Electromag. Compat., 23-25 May 1989, pp. 377 - 379.
- [6] M. D'Amore, V. De Santis and M. Feliziani, "Circuit-based modeling for the shielding effectiveness of apertures coated with conductive thin films," EMC Europe Workshop - Materials in EMC Applications, Athens, June 11-12, 2009.

Numerical FEM models for the evaluation of EM fields exposure near welding machines

F. Dughiero¹, M. Forzan¹, E. Sieni²

¹University of Padova, Dept. of Electrical Engineering, via Gradenigo 6/a, 35131 Padova, Italy

²INOVA LAB srl, via Torino, 213 10040 Leini (To), Italy

E-mail: {fabrizio.dughiero,michele.forzan}@unipd.it, e.sieni@inovasrl.it

Abstract— In this paper a numerical FEM analysis for the evaluation of the EM field exposure due to welding equipments has been proposed. The human body model has been reconstructed by means of a segmentation procedure using CT data. A comparison among models with different complexity in terms of organs and tissues has been proposed and discussed.

I. INTRODUCTION

European community has recently issued a directive about the risks deriving by the exposure to electromagnetic fields and has suggested that in working environments the employer must verify the electromagnetic field levels to assure the safety of employees.

In order to protect people from electromagnetic emissions ICNIRP (International Committee Non Ionizing Radiation Protection) [1] has suggested some limits in order to avoid acute effects which are an established consequence of the field exposure. For low frequency exposure between the most important magnetic field sources, welding equipments generate high intensity fields because of the high intensity of the welding current.

Actually for welding equipment few practical directives have been issued. Moreover the measurement of the “action values” in the surroundings of welding machine are very difficult to perform and analyze because of the very short pulsed currents. In this work some investigations about the use of numerical techniques and a modeling of the human body for the estimation of the magnetic field exposure have been presented. For welding equipments the analyzed quantities for the evaluation of the field exposure are the magnetic flux density and the induced current density because the frequency of the current source is under 100 kHz [1]. A three dimensional human model has been tested for the evaluation of worker exposure to the magnetic field produced by an arc welding equipment.

II. COMPUTATION MODELS

The human model has been built from real CT data. Each slice of the CT has been segmented using Amira software (Mercury) in order to generate a 3D mesh. The meshed volumes have been imported in a Finite Element software, and inserted in a volume which represents a simplified human body.

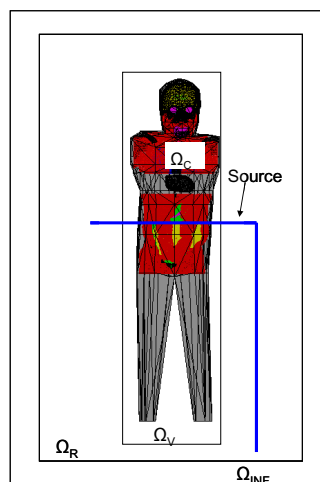
The magnetic flux density and the induced current density have been computed solving the electromagnetic (EM) problem in quasi-static condition [3] [4].

The simulated domain (Fig. 1) includes a conductive region (Ω_C) and two vacuum regions (Ω_V and Ω_R) one of them containing the magnetic field source (Ω_R). In the Ω_C region

the induced current density is computed and the EM problem has been solved using a time-harmonic A,V formulation:

$$\vec{E} = -j\omega\vec{A} - \nabla\dot{V} \quad (1)$$

where \vec{E} is the phasor of the electric field, \vec{A} the phasor of vector potential, \dot{V} the phasor of the scalar electric potentials and ω the angular frequency. From (1) the induced current



density can be derived.

Fig. 1. human body model

The source of the magnetic field is a wire supplied by an electrical current. The evaluation of the magnetic field in the vacuum volume Ω_R , the one that contains the source, is solved in the phasor of the reduced scalar potential, $\dot{\phi}_{RED}$:

$$\vec{H} = \vec{H}_j - \nabla\dot{\phi}_{RED} \quad (2)$$

where \vec{H}_j is the term due to the current source computed by means of Biot-Savart formula. Between Ω_C and Ω_R a region Ω_V has been interposed. In this region the EM problem is solved in terms of the only phasor \vec{A} . This part of the domain has been modeled to surround the conductive region where the EM problem is solved in terms of \vec{A} and \dot{V} potentials in order to properly describe interface condition between conducting and not-conducting regions. At the boundary between Ω_V and Ω_R proper interface conditions have been posed. In Ω_V region the Helmholtz equation has been solved:

$$\nabla^2\vec{A} + k^2\vec{A} = 0, \quad k^2 = j\omega\mu\sigma \quad (3)$$

where μ and σ are respectively the magnetic permeability and the conductivity of the medium and the Lorentz gauge has been imposed. At the boundary of the simulation domain, Ω_{INF} ,

infinite boundary conditions have been posed in order to let the magnetic field vanishing at infinite distance.

A. Data models

The simplified model considers a restricted set of organs in the abdomen and thorax regions listed in Table I, while the complete model contains also the head tissues, muscle and a more extensive set of thorax and abdomen organs. In addition, an homogeneous model describe the human body with constant resistivity value has been considered.

The human body tissues are described with the value of their resistivity, ρ , derived by the Gabriel model [5]. The values at 200 Hz frequency are presented in Table I. The magnetic field source is a cable with a current amplitude of 53.7 Arms.

TABLE I

TISSUES ELECTRICAL CHARACTERISTICS TISSUES ELECTRICAL

tissue	ρ [Ωm]	tissue	ρ [Ωm]	tissue	ρ [Ωm]
Midollus	35.4	Spleen	10.1	Body M_1	5
Kidney	9.3	Stomach	1.9	Body M_2	5
Liver	25.6	Colon	5.3	Body M_3	46.9
Pancreas	1.9	Intestine	1.9	Body M_4	46.9

B. Evaluation rules

In order to limit induced current density in human body tissues, ICNIRP guidelines provide basic restrictions that have been extrapolated from direct effects on human body. The induced current density is related to the electro-stimulation of nerves and muscles. From basic restrictions reference values have been derived by means of suitable models, in order to provide quantities easily measurable using simple instrumentation (e.g. magnetic flux density). Biological effects depends by the magnetic field frequency [1]. Consequently, the reference limits have been expressed as a function of the field frequency. In the present case the limit for the magnetic flux density is 125 μT and for induced current density is 10 mA/m^2 .

III. RESULTS

Four different human models have been developed using the set up shown in Fig. 1. The current density in organs evaluated in the homogeneous model (M_1) has been compared with the ones computed with more detailed models where the resistivity of tissues has been set with reference to the values of Table I. Models M_2 and M_3 contain only organs in abdomen without considering muscle tissue. In model M_1 the resistivity of the volume around organs has been set to the weight average value of all tissues (5 Ωm , as recommended by standards for numerical homogeneous models [6]) whereas the one in model M_3 has been set to the fat resistivity (46.9 Ωm). The model M_4 contains also thorax and head organs and muscle regions. In this case the volume around organs has been described with the fat resistivity.

Some results are shown in Table II. In this table the maximum values of the induced currents and magnetic flux density have been reported in each organ for the four models. The last row of Table II reports the induced current density evaluated in a homogeneous cylinder. Comparing M_1 and M_2 results it should be pointed out that organs that have a resistivity higher than the average value have a lower induced current density than

the one computed in the homogeneous case (M_1). The regions with a lower resistivity have higher induced currents. It should be underlined that the resistivity of the tissue that surrounds the organs affects the value of the computed induced current density. Sometimes, the induced current density considering the correct tissue resistivity is higher than the one computed with an homogeneous model. Models M_3 and M_4 have been built taking into account small differences in organ dimensions and their relative positions in the phantom to verify the reliability of the results.

TABLE II
INDUCED CURRENT DENSITY IN HUMAN BODY TISSUE AND
CORRESPONDING MAGNETIC FLUX DENSITY

tissue	B [μT]	M_1 [mA/m^2]		M_2 [mA/m^2]		M_3 [mA/m^2]		M_4 [mA/m^2]		
		R_L	J	R_L	J	R_L	J	R_L	J	
body	50	0.4	1.88	0.19	1.9	0.19	0.55	0.06	0.67	0.07
colon	44	0.4	0.95	0.10	0.91	0.09	0.76	0.08	1.23	0.12
liver	39	0.3	0.73	0.07	0.19	0.02	0.44	0.04	0.32	0.03
intestin	45	0.4	0.8	0.08	1.87	0.19	2.25	0.23	3.00	0.30
pancre	37	0.3	0.36	0.04	0.92	0.09	0.80	0.08	0.84	0.08
kidney	35	0.3	0.58	0.06	0.35	0.03	0.23	0.02	0.22	0.02
stomac	42	0.3	0.71	0.07	1.46	0.15	1.30	0.13	1.44	0.14
Spleen	42	0.3	0.75	0.08	0.4	0.04	0.31	0.03	0.33	0.03
midolla	29	0.2	0.43	0.04	0.09	0.01	0.08	0.01	0.09	0.01
Cylind.	67	0.5	1.06	0.11						

In the present case ICNIRP limits are satisfied both for magnetic flux density and induced current values. Nevertheless, it can be pointed out that the ratio R_L between the evaluated quantity and the induced current limit is roughly ten times lower than the correspondent ratio computed for magnetic flux density.

IV. CONCLUSION

Numerical models of human body have been investigated for the evaluation of the exposure to low frequency magnetic field in order to compute quantities comparable with basic restrictions. Finally, homogeneous cylindrical models can be useful applied for a preliminary evaluation of the exposure.

V. ACKNOWLEDGMENTS

This project has been developed in the frame of a research contract with Telwin SpA.

VI. REFERENCES

- [1] ICNIRP, "Guidelines for limiting exposure to time-varying electric, magnetic, and electromagnetic fields (up to 300 GHz)," *Health Phys.*, pp.494-522, 1998.
- [2] <http://www.cedrat.com>
- [3] K. J. Binns, P. J. Lawrenson and C. W. Trowbridge "The Analytical and Numerical Solution of Electric and Magnetic Fields", 1992.
- [4] O. Biro, K. Preis, G. Vrisk, K.R. Richter, I. Ticar, "Computation of 3-D magnetostatic fields using a reduced scalar potential", *IEEE Trans. Magn.*, pp. 1329-1332, 1993
- [5] S. Gabriel, R.W. Laul, and C. Gabriel, "The dielectric properties of biological tissues: II. measurements in the frequency range 10 Hz to 20 GHz," *Phys. Med. Biol.*, pp. 2251--2269, 1996.
- [6] EN 50444, Basic standard for the evaluation of human exposure to electromagnetic fields from equipment for arc welding and allied processes, 2008.

Identification of equivalent multipolar electromagnetic sources by space filtering

B. Vincent¹, O. Chadebec¹, J.-L. Schanen¹, K. Berger², R. Perrussel², L. Krähenbühl²

¹ Grenoble Electrical Engineering Lab (CNRS UMR5269), Université de Grenoble, ENSE³, BP 46, 38000 Grenoble, France

{benjamin.vincent, olivier.chadebec, jean-luc.schanen}@g2elab.inpg.fr

² Ampère (CNRS UMR5005), Université de Lyon, École Centrale de Lyon, F-69134 Ecully Cedex, France

{kevin.berger, ronan.perrussel, Laurent.krahenbuhl}@ec-lyon.fr

Abstract— New sensors of magnetic induction in near field, dedicated to studies of electromagnetic compatibility, are proposed according to the principle of the Standard CISPR16-1 coils. The new coil shape allows the sensors to be sensitive to only some specific components of the multipolar expansion, which is similar to a spatial filtering. Our proposition follows previous works. By means of rotations of the spherical harmonics functions, our aim is to simplify the geometry of the sensor coils introduced before. After a description of the tools required, the design method is described. Comparative robustness studies end the article.

I. INTRODUCTION

For electromagnetic compatibility studies, a compact model of the stray magnetic field generated by power electronic systems enables to reduce the design cost. To determine this model, our works focus on experimental approach. In this case, the use of large loop antenna offers advantages, especially by reducing the effect positioning inaccuracies. For instance, to identify the first order of a multipolar expansion (dipole) [1], Standard CISPR 16-1 [2], proposes to use three orthogonal loops (Fig. 1, on the right hand side). This standard applies for the medium frequency range: 9 kHz to 30 MHz.

The problem is that no source is composed of pure dipoles. Therefore, even the standard method can lead to errors. In previous works, we have proposed to take into account higher order terms in the expansion leading to a new and original coils sensors design and improving the accuracy [3]. Here, we introduce a simplification of the sensor design. The principle of this design and some improvements are reminded and a comparative robustness studies are proposed.

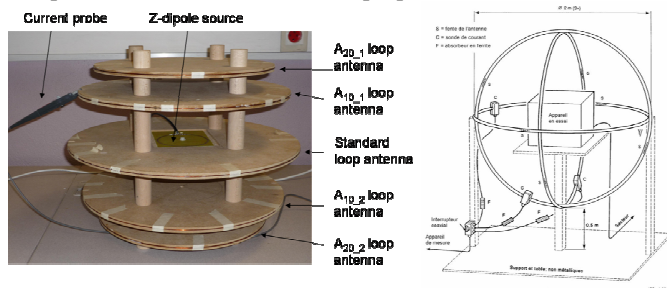


Fig. 1. On the left hand side, the whole system of loop antennas ('A₁₀', 'A₂₀' and 'Standard'). On the right hand side, the loop-antenna system from Standard CISPR 16-1 consisting of three orthogonal loop-antennas

II. MULTIPOLAR EXPANSION

For near field studies and the standard frequency range, the quasi-static approximation is suitable. Outside a sphere including all radiation sources, the magnetic field can be fully described by its magnetic scalar potential Ψ solution of the Laplace equation. For each frequency and in a given spherical coordinate system, the unique multipolar expansion solution is:

$$\mathbf{B} = -\nabla\Psi \quad \text{with:} \quad \Psi(r, \theta, \varphi) = \sum_{n=1}^{+\infty} \sum_{m=-n}^{+n} A_{nm} \cdot \frac{1}{r^{n+1}} \cdot Y_{nm}(\theta, \varphi) \quad (1)$$

where Y_{nm} is real harmonic spherical function of order n and degree m , (r, θ, φ) are the spherical coordinates whose origin is the centre of expansion and A_{nm} the unknown coefficients. This development is hierarchical: for elements of order n the field decreases as $1/r^{n+2}$. A decomposition limited to the order 2 gives a precision considered as sufficient beyond the distance of measurement. There are 8 coefficients to measure (3 for order 1, 5 for order 2).

III. SENSOR DESIGN

The measurement principle is similar to a spatial filtering: according to the coil shape, each sensor is just sensitive to its specific component of the multipolar expansion. Thanks to a rigorous approach, we proposed a system of coils, allowing the identification of the two first orders ($n = 1$ and 2) and not sensitive to the two followings (3 and 4). It leads to the realisation of 8 flux coils sensors topology located on a measurement sphere (radius r_{mes}). The method is detailed in [3]. The 8 sensors are presented on Fig. 2. These first shapes are linked to spherical coordinates: outlines within θ or φ constant. But this solution is too complex in order to make a practical realisation.

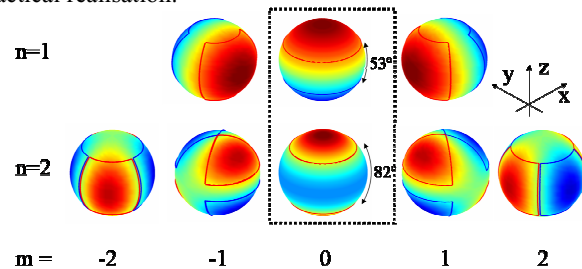


Fig. 2. 8 coils sensors for the identification of 1 and 2 orders. The flux is counted as positive for the red coils and negative for the blue ones

A. Rotation properties of Y_{nm}

We want to simplify this solution in order to build a practical sensor. The basis idea comes from properties of spherical harmonic functions. Indeed, thanks to rotations, it is possible to produce all components of the same n order with only one. Examples are given on Fig. 3. The first order rotation dependency is evident. This is more complex for the second order case. The idea is that it is possible to generalise this property to design sensors. Thus, to reach the simplification, we must start from simpler sensor coils. The A_{10} and A_{20} loop antennas are just constituted of coplanar coils (black frame on Fig. 2).

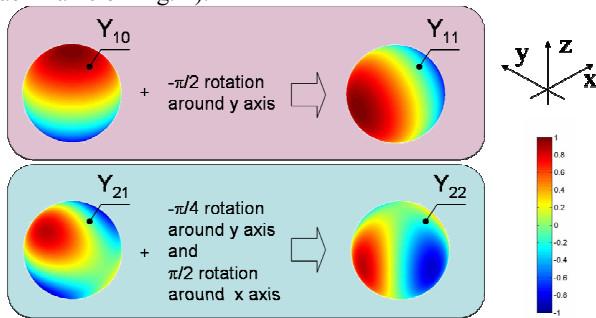


Fig. 3. By n order, same shape.

B. Sensor design

The full set and method are presented on Fig. 4. For the first order, the A_{10} loop antenna direction is just lined with targeted component. The second order case needs A_{20} sensor rotations and composition of the measured fluxes. We demonstrate that the totality of filtering capability is conserved with this new solution. Thus, 2 only different and simple shapes allow identifying the 8 first components of the multipolar expansion.

The complete validation is reached thanks to numerical (by Finite Elements Method) and experimental experiences. Our prototype is presented on Fig 1, on the left hand side. It concerns just the identification of A_{10} and A_{20} components. To these 4 coils, a loop-antenna ($r_{mes} = 0.225$ m) located on the middle plan is added to demonstrate the robustness of our new approach. It corresponds to the initial z -dipole sensor proposed in [2].

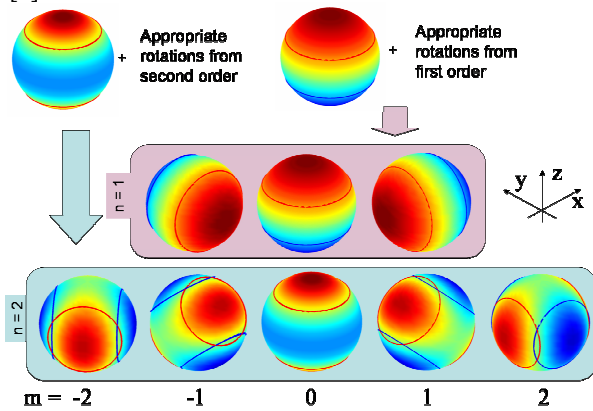


Fig. 4. Sensor set and the design process

C. Comparative robustness

Several cases have been studied. First, numerical experiences enable to demonstrate the efficiency of our solution toward punctual measurements. This integral processing method is more accurate. Furthermore, complete measurement process is faster than 3D mapping solutions with one punctual sensor.

Secondly, we check the robustness of the sensor in comparison with the solution proposed by the standard. This is achieved thanks to the shifting of the source loop versus the center of sensors itself. Only the dipole identification is concerned in this experiment. The measurement results on Fig. 5 show that an error on the dipole determination occurs. In our sensor cases, despite the source shifting, identification error keeps stationary and reasonable (less than 2% of error). With Standard sensor, the error raises to 11%. A decentered dipole implies a more complex field (i.e. higher orders in the decomposition). The error is mainly attributed to the contribution of order 3 multipolar induction term in Standard sensor. In contrary, our sensors are designed to filter this third order term.

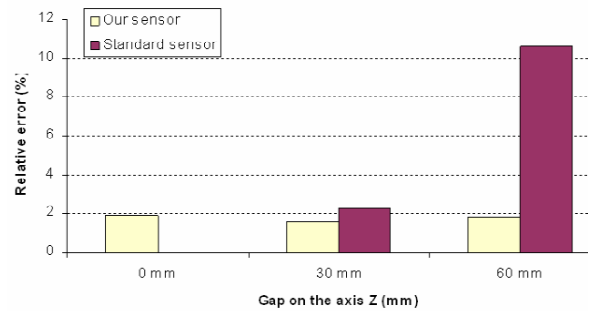


Fig. 5. Comparison between Standard and our sensor identifications: relative error compared to the actual and theoretical z -dipole with different gaps

IV. CONCLUSION

We have shown that it is possible to improve the dipole components measurement of the Standard device. It is also possible to create simple systems of coils which measure di- and quadri-polar components by filtering exactly both high orders.

Furthermore, our identification method is validated by experimental and numerical results. Comparative robustness studies show the interest of using dedicated multipolar component sensors, which are more robust than punctual measurement solution. So, in future work, we can focus on the realization of the full coils system including rotation.

V. REFERENCES

- [1] J.R. Bergervoet and al., "A large-loop antenna for magnetic field measurements," Zurich International Symposium on EMC Proceedings, pp.:29-34, 1989.
- [2] Standard CISPR 16-1, annexe P, pp. 230-237 and 396-409, 2002.
- [3] Vincent B., Chadebec O., Schanen J.-L., Sartori C.A.F., Krähenbühl L., Perrussel R., Berger K., "New robust coil sensors for near field characterization," to be published in Journal of Microwaves, Optoelectronics and Electromagnetic Applications, No 1, June 2009.

Pre-evaluating a SAR Measurement System Performance by Numerical Simulations

M. Perotoni¹, A. M. de Almeida², C.A F Sartori³, J. K. C. Pinto³, J. R. Cardoso³,
S. Mühlen⁴, A. L. Dantas², and M. L. P. Filho⁵

¹ Universidade Federal do ABC – UFABC.

² Fundação CPqD – Campinas, S.P. Brasil.

³ Escola Politécnica da Universidade de São Paulo – EPUSP. São Paulo, Brasil.

⁴ Universidade Estadual de Campinas. UNICAMP.

⁵ Instituto de Pesquisas Tecnológicas – IPT. São Paulo, Brasil.

Marcelo.perotoni@ufabc.edu.br, amarini@cpqd.com.br, sartori@pea.usp.br, jkcunhap@lme.usp.br,
jose.cardoso@poli.usp.br, smuhlen@ceb.unicamp.br, adantas@cpqd.com.br, m.leite@ipt.br

Abstract—SAR validation measurements are already an industry standard, necessary to enable the distribution of commercial mobile phones. Here it is discussed the full wave simulation of a SAR measurement system, used to certify mobile phones in the international market. The electric field measured in a phantom by a mechanical system is modeled and compared with simulations, so that a validation is achieved and further sensitivity analyses can be carried out.

I. INTRODUCTION

The present study covers the simulations of an experiment related to SAR (Spatial-Average Specific Absorption Rate) measurement. In order to get a better understanding of the dynamics of SAR measurements, a thorough analysis of the different parameters and their impact on the final results is carried out. As an example of the importance of this kind of analysis, it should be mention the fact that the liquid which emulates the brain tissue is subjected to variation in its electrical characteristics, due to temperature changes, and the estimation of how it will influence the measured electric field can assume a helpful role during the measurement process.

II. MODELED EXPERIMENT

The modeled experiment is depicted in Fig.1. The measurement setup is completely described in [1]. A plastic phantom is partially filled with a liquid, whose electrical characteristics (real and imaginary permittivity) emulate the human brain tissue. An electric field probe is moved by a robotic system inside the liquid, so that the electronic readout system gives the electric field in its 3 components. This field is generated by a resonant dipole located below the phantom.

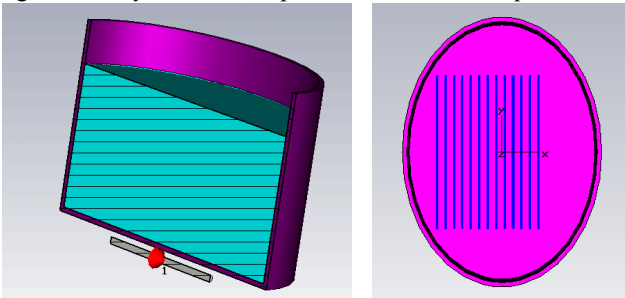


Fig. 1. Picture of the measurement system. The electric field is measured along these 13 different lines, 10mm from the bottom.

The liquid and the dipole have their electromagnetic characteristics determined by [1]: namely, the liquid permittivity ϵ (real and imaginary), and the dipole length that are set for each frequency. Typical frequencies can be as low as 300MHz up to 3GHz. Here, we focus in the mobile phone service frequency, 900MHz. For this frequency, Table I lists the most important parameters for this specific measurement setup.

TABLE I
MAIN PARAMETERS FOR THE 900MHz EXPERIMENT SETUP

Parameter	Value	Meaning
ϵ_r	41.5	Real part of the liquid permittivity
σ	0.98S/m	Liquid Loss (conductivity)
h	15mm	Liquid height in the container
d	1mm	Distance center dipole to the bottom of the container
L	14.9mm	Dipole length

The container is made of plastic 0.5mm thick ($\epsilon_r=3.7$; $\sigma=0.0051\text{S/m}$), and it is an ellipsoid with axes 220mm and 300mm. Its height is 19.5mm, partially filled with liquid as Fig.1 suggests. The actual antenna is fed by a complex balloon system, which is a proprietary design. It was simulated only the dipole, fed by a balanced port. The electronic system assures that the input power at the antenna terminal is 16dBm (approximately 40mW), so all the computed field results are scaled to this power.

III. MEASURED RESULTS

The robotic probe sampled the electric field along the 13 lines, as Fig. 1 shows. The measurement plane is placed 10mm far away from the bottom of the phantom. Therefore the probe is immersed in the liquid.

IV. RESULTS

The simulation was carried out using the Finite Integration Technique (FIT) [2], [3]. The model was built inside the software interface, completely parameterized, so that scenarios for other frequencies can be easily changed, without necessity of starting from the scratch. The FIT method admits solutions both at frequency and time domains. Since we are dealing with a SAR environment (although, at this moment, we are not working directly with SAR values, but electric fields), the

transient (time domain) solver was used. It applies a pulse in the time domain to the structure, and the Maxwell equations are solved in a leap-frog scheme. The results are then displayed in both time and frequency domain, i.e., S-parameters, fields at different frequencies, signals in time domain, etc. Here we are interested in the electric field sampled along the lines displayed in Fig.1.

The results are depicted in Fig.2 and Fig.3, for two different sampled lines.

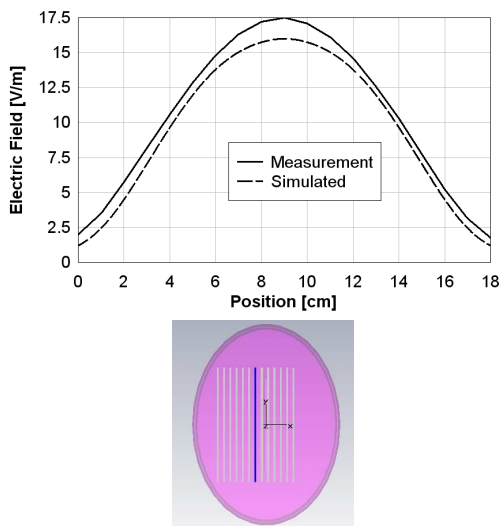


Fig. 2 Measured and simulated electric field for a line placed in the middle of the container (shown in dark color in the picture at the bottom).

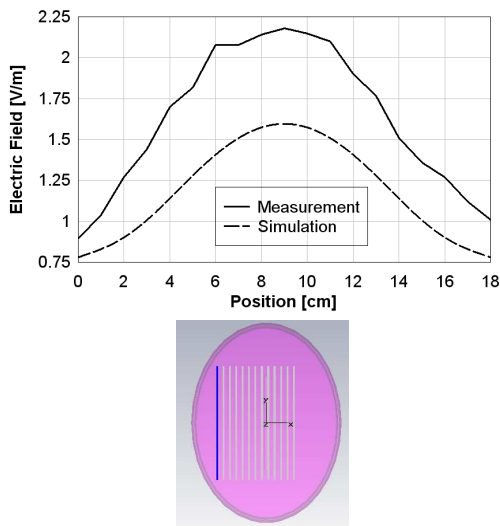


Fig. 3 Measured and simulated electric field for a line placed in the extreme of the container (shown in dark color in the picture at the bottom).

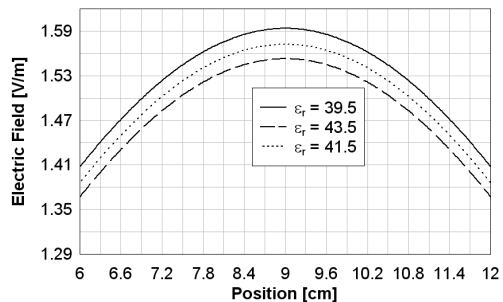


Fig. 4 Computed Electric field for the line displayed in fig.4 bottom, for different relative permittivities.

The discrepancy between the measurement and computed results can be ascribed to the influence of the balloon and other circuitry in the antenna current. The simulated dipole is fed by a perfectly balanced source, so eventual differences in the mechanical system will generate another current pattern in the dipole, therefore generating a different shape in the electric field. The sensitivity of the electric field to accidental variations (with factors like temperature, aging, bacteria, etc) in the liquid characteristics is also analyzed. The result for a variation of ± 1 in the relative permittivity ϵ_r is displayed in Fig.4. From the results presented in Fig.5, it was possible to see that the electric field, in absolute value, is not very sensible to the relative permittivity. Further studies will determine how much this variation can happen with the liquid.

V. CONCLUSION

A numerical evaluation of a real SAR measurement system is presented. The computed numerical results proved to provide a helpful and fast insight into the pre-studies regarding the SAR measurements and the role of the electrical parameters in this process.

ACKNOWLEDGMENT

This work was supported in part by Brazilian National Fund for Telecommunication Development (Fundo Nacional para o Desenvolvimento das Telecomunicações – FUNTTEL).

VI. REFERENCES

- [1] IEEE Standards Coordination Committee, "IEEE Recommendation Practice for determining the peak Spatial-Average Specific Absorption Rate (SAR) in the human head from Wireless Communication Devices: Measurement Techniques", *IEEE Std 1528™ 2003*.
- [2] CST MICROWAVE STUDIO™ V.2009, www.cst.com
- [3] Weiland T., "A discretization method for the solution of the Maxwell's equation for six components fields", *Electron. Communications (AEU)*,31, 3, pp. 116-120.

Computer Analysis of Electromagnetic Transients in Grounding Systems

Rafael S. Alípio, Marco A. O. Schroeder, and Márcio M. Afonso
Federal Center of Technological Education of Minas Gerais (CEFET-MG) - Brazil
Avenue Amazonas, 7675, 30510-000, Brazil

rafael@dppg.cefetmg.br, schroeder@des.cefetmg.br and marciomatias@des.cefetmg.br

Abstract— This paper presents an accurate mathematical model for high frequency transient analysis in grounding systems based on electromagnetic field theory in frequency domain and Method of Moments. The only input data of resultant computational tool is grounding dimensions, soil electromagnetic properties and excitation. Results in both time and frequency domain are provided.

I. INTRODUCTION

Grounding systems are an important element for lightning protection and electromagnetic compatibility (EMC) related problems. Their basic function is to disperse the lightning current to earth without causing any potential differences or induced voltages that might endanger people or damage equipments. Grounding behavior at low frequencies is well understood using simplified analysis based on static approximation [1]. However, when energized by lightning currents, they present a very particular behavior and their analysis cannot be carried out with traditional methodologies employed in low frequency occurrences [1].

The transient analysis of grounding electrodes is usually developed based on three main different approaches [1]: i) electromagnetic field theory, ii) transmission line theory and iii) circuit theory. The first one is considered as the most accurate since it is based on least neglects in comparison to the methods based on transmission line and circuit theory [1]. Also the methodologies may be differentiated by the domain where the transient is solved: i) time domain or ii) frequency domain.

In this work a methodology based on the electromagnetic field theory is applied to investigate the impulsive behavior of grounding. The transient problem is solved in frequency domain taking the great advantage of robustness and easiness to computed electromagnetic fields in this domain. A computational tool is developed and few results of its application in response evaluation of a long horizontal ground electrode to an impulsive current is included.

II. ELECTROMAGNETIC GROUNDING MODEL

The proposed grounding model is based on the Hybrid Electromagnetic Model (HEM), with some suitable modifications [2]. Simulations are performed in frequency domain and the time domain response is obtained by application of an inverse Fourier transform.

The grounding system is represented by a set of cylindrical electrodes. Each electrode is source of a transversal current I_T and longitudinal current I_L , as illustrated in Fig. 1(a) [3]. The current I_T generates a divergent electric field at a generic point. Considering each pair of electrodes, this current promotes

capacitive and conductive couplings (self and mutual ones). The current I_L generates a nonconservative electric field and magnetic field at a generic point. Considering each pair of electrodes, this current promotes inductive and resistive couplings (self and mutual ones). The electromagnetic coupling between the electrodes can be computed by electromagnetic fields integration along each one (see Fig. 1(b)), and leads to the following equations [3]:

$$V_{ij} = \frac{1}{4\pi(\sigma + j\omega\epsilon)L_jL_i} \int_{L_i} \int_{L_j} \frac{e^{-\gamma r}}{r} dl_j dl_i, \quad (1)$$

$$\Delta V_{ij} = -j\omega \frac{\mu}{4\pi} \int_{L_i} \int_{L_j} \frac{e^{-\gamma r}}{r} d\vec{l}_j \cdot d\vec{l}_i, \quad (2)$$

where V_{ij} refers to average potential of electrode i due to the transversal current dispersed by electrode j ; ΔV_{ij} is the voltage drop along electrode i due the longitudinal current flowing along electrode j ; σ , ϵ and μ are, respectively, the medium electric conductivity, electric permittivity and magnetic permeability; γ is the propagation constant and ω is the angular frequency.

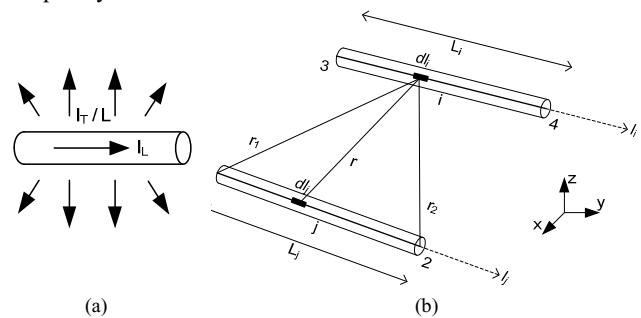


Fig. 1. (a) Current sources in each electrode and (b) Electrodes interaction

The problem formulation and its final solution are obtained by the application of Moments Method (MoM) [4]. The electrode is divided into N elements. The value of N is determined in a way that the thin-wire approximation is valid for the longitudinal current along the element [3], [4]. Also, the length of each one is sufficiently small, so that longitudinal and transversal currents may be considered constant in each element. Naturally each current can change from an element to other. Based on these assumptions, the piecewise-constant current approximation is used [3]. From the above considerations and by applying (1) and (2) to the N elements, two systems of linear equations can be obtained [3]: $V = Z_T I_T$ and $\Delta V = Z_L I_L$. The terms of V and I_T corresponds, respectively,

to the average potential and transversal current in each element and the terms of Z_T corresponds to the transversal impedance between the elements i and j [3]. The terms of ΔV and I_L corresponds, respectively, to the voltage drop and longitudinal current in each element and the terms of Z_L corresponds to the longitudinal impedance between the elements i and j [3]. In Z_T and Z_L computation, the influence of air-soil interface is taken into account approximately by the modified image theory and the reciprocity theorem is valid, what permits a substantially reduction of computational time [3]. The two systems of linear equations relations may be reduced to a unique system by means of two fundamental considerations [2], [3]: i) the average potential in each element is equal to the arithmetic media of nodal potentials and the voltage drop in each element is equal to the difference of nodal potentials; ii) the Kirchhoff's current law is explicitly enforced on all element's junction points. Considering these two assumptions, an only system of linear equations of kind $Ax=b$ is composed and its solution leads to final results.

III. RESULTS

In this section is simulated a 60-m long horizontal electrode with 1-cm radius imbedded in earth with 1.000- Ωm resistivity and relative permittivity of 15. The electrode excitation is made by the injection of two different double exponential current waves: i) a fast one of 1 kA and 1.2/50- μs and ii) a slow one of 1 kA and 12/50- μs .

Fig. 2 illustrates the magnitude of the harmonic grounding impedance $Z(\omega)$, independent of excitation, along typical spectrum of a lightning discharge. As can be observed, at low-frequency range the harmonic impedance is frequency independent and corresponds to the low-frequency resistance concept R . As frequency increases, the impedance value diverges from the resistance value and, after about 100 kHz, it exhibits inductive behavior and its value becomes larger than R . In the analyzed case, the electrode does not present significant capacitive behavior, mainly due to its large length.

Fig. 3(a) illustrates the response of the horizontal electrode to the slow wave: $v(t)$, which is the transient voltage at injection point and $z(t)$, which is the transient impedance, ratio between $v(t)$ and $i(t)$. The slow wave does not have high frequency components of sufficient intensity to excite the inductive behavior of $Z(\omega)$. The response is essentially determined by the frequency independent parcel of $Z(\omega)$. As a result, $v(t)$ is not significantly modified in comparison to current waveform $i(t)$ and their peaks occurs at the same time. The transient impedance $z(t)$ has high values in the first instants of transient, but quickly reduces to lower values and tends, around 8- μs , to the low frequency resistance value ($R=32.75\text{-}\Omega$). Fig. 3(b) illustrates the response of the same electrode to the fast wave. The fast wave has sufficient high frequency content to excite the inductive parcel of $Z(\omega)$ and, as can be observed, $v(t)$ is advanced in time in relation to $i(t)$. This inductive behavior causes larger value of transient voltage peak. The transient impedance $z(t)$ presents similar behavior of the previous case and tends, around 2.5- μs , to the resistance value. The results illustrate the significant influence of wave front time in grounding impulsive behavior.

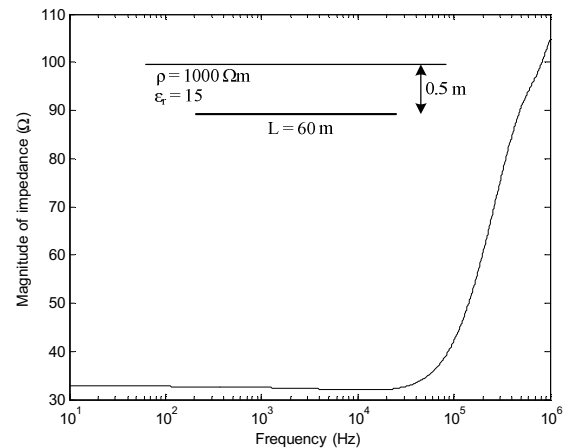


Fig. 2. Magnitude of impedance of a 60-m long horizontal electrode

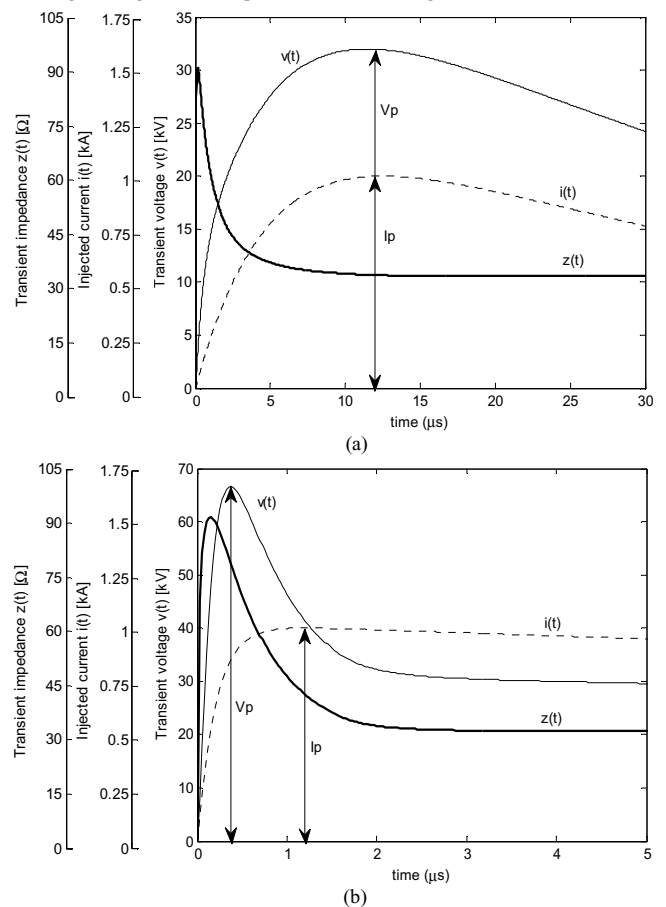


Fig. 3. Electrode response to (a) slow wave and (b) fast wave

IV. REFERENCES

- [1] L. Greev and V. Armutovski-Toseva, "Grounding systems modeling for high frequencies and transients: some fundamental considerations", *Proc. IEEE Bologna Power Tech Conf.*, 2003, vol.3, pp. 1-7.
- [2] S. Visacro and A. Soares, "HEM: A model for simulation of lightning-related engineering problems", *IEEE Trans. Power Del.*, vol. 20, n° 2, pp. 1206-1208, Apr., 2005.
- [3] R. S. Alipio, M. A. O. Schroeder, M. M. Afonso, and T. A. S. Oliveira, "Electromagnetic fields of buried conductors", *Proc. 2006 Int. Conf. Grounding Earthing (GROUND 2008)*, pp. 399-402.
- [4] R. F. Harrington, *Field computation by moment methods*, IEEE Press, New York, 1993.

Proposal of Computational Model Validation for EMC Automotive Tests in Vehicles

L. L. Alvarenga¹, R. L. S. Adriano², J. O. S. Paulino³, J. A. Vascelos³, C. Santos¹, A. Colin¹

¹ Fiat S.A. Betim MG, 32530-000, Brazil.

² Federal University of São João Del-Rei, Ouro Branco MG 36420-000, Brazil

³ Federal University of Minas Gerais, Belo Horizonte MG 31270-009, Brazil

{leonardo.alvarenga, rluiz, josvaldo, joao}@cpdee.ufmg.br, {claudio.santos, arnaud.colin}@fiat.com.br

Abstract — This paper presents an immunity measurement process that can be used to evaluate the performance of numerical methods. This simplified setup possesses the most important characteristics that a numerical model must include when dealing with EMC engineering problems. The results are compared with two numerical methods: one is based on FEM and the other on FDTD.

I. INTRODUCTION

Although the tests of components separately reduce the compatibility problems probability, they can't guarantee the correct functioning of these ones when installed in a vehicle [1]. The reason is that the diverse interactions between components inside a vehicle differ considerably from a model to another. Moreover, the tests performed on each component are not able to predict these phenomena.

To avoid this drawback, numerical methods appears as a solution to predict the radiated emission and to simulate immunity tests before the construction of prototypes, reducing the probability of failing in real EMC tests. The main problem is that the computing domain is very large, due to the fact that a vehicle volume is approximately $7,5\text{m}^3$ and radiated immunity tests use frequencies beyond 1GHz.

This work presents a critical analysis of computing models application for simulating a controlled experiment of radiated immunity in a vehicle. Two software of electromagnetic fields calculation have been used to handle a radiated immunity problem, being one based on the Finite Elements method (FEM) and the other on the Finite Differences method (FDTD). Even simplified, this problem includes the main challenges that are involved in this kind of issues. The results obtained are compared with experimental measures, and questions about accuracy and computational effort are treated.

II. THE IMMUNITY TEST

Figure 1 presents the geometry of the problem. The immunity test consists basically in evaluating the behavior of the device under test (DUT) in presence of an intense electromagnetic field. For this reason, the device is placed close to an antenna which irradiates a strong electromagnetic field. During the test, the device's position and the antenna's polarization must change to better evaluate the electromagnetic wave effects [2].

The antenna geometry and the mainly metallic structure of a vehicle require the use of integrals techniques, such as the

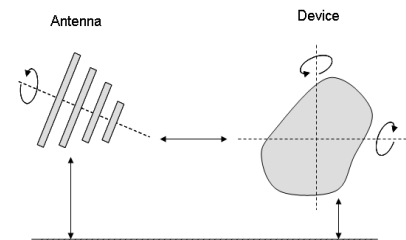


Fig. 1. The immunity test setup

Boundary Integral Equations Method (BEM) or the Moment Method (MM). However, the devices or regions of interest inside the vehicle are filled with different materials that have different electromagnetic and, for this reason, volumetric domain methods like FEM or FDTD are used instead of integration methods.

Due to these characteristics and the changes of the relative position between the antenna and the vehicle during the test, it is impossible to define a better computational technique to handle this problem and a solution that combine different methods must be applied to reduce the computational effort as presented in [3],[4].

In this context, a measurement setup is presented as a reference to evaluate the behavior of numerical methods to handle electromagnetic immunity tests. Although the proposed problem consists in a simplified geometry, this setup preserves the most important challenges for a numerical method which is to deal with immunity test in a vehicle.

III. MEASUREMENT BENCH SETUP

The geometry of the problem is presented in Fig. 2. It is made of a wideband horn antenna (200 to 2000 MHz) placed 1 meter distant from the vehicle. The vehicle height and width are similar to those of a typical vehicle, 1,70m x 1,45m. However, the vehicle length has been reduced to 1,62m considering only the region of the panel and the motor bay where the highest number of electro-electronic devices are placed.

The setup and the excitation system follow the recommendations proposed in the ISO11451-4 standard [2], except for the relative distances between the vehicle and the absorbing walls that have been decreased of 1 m in order to reduce the computing domain and insert dielectric and nonlinear objects, characteristic in the immunity test.

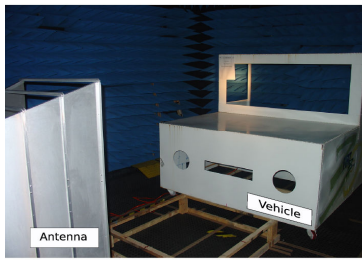


Fig. 2. The measurement setup

Characterizing the different materials inside a vehicle is not an easy task. The solution to introduce an inhomogeneous ambient in the test bench was to place the vehicle near the semi-anechoic chamber’s absorbing wall in order to consider the absorbing surface as non-ideal. Its effects have been introduced in the numerical methods as shown in Fig. 3. The main advantage of using the own absorbing wall consists in the precision of the electromagnetic parameters provided by the manufactory for the test frequency range.

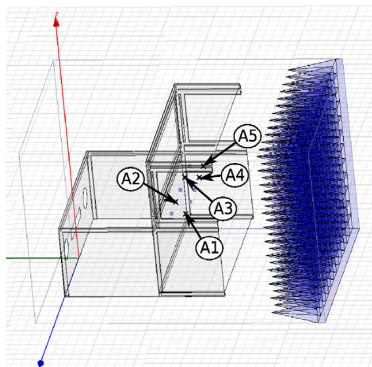


Fig. 3. Magnetization as a function of applied field

IV. RESULTS

The vehicle has been submitted to a constant electromagnetic field, 100 V/m, in frequencies from 200 MHz to 1000 MHz. The simulations results that will be presented are those corresponding to the panel points. Indeed, they are these points that most witnessed the interaction with the semi-anechoic chamber’s wall. See Fig 3. Table I resumes the electric field at the measurement points inside the simplified vehicle (A1 to A4 in fig. 3) in comparison with the results obtained from the reference methods. The results at A5 are shown in Fig. 4. A good similarity has been observed, especially in the 200-600MHz frequency band. Even in the 700-1000 MHz, where the radiation lobe of the antenna used in the experimentation is very narrow, consequently, the nominal variation of the electromagnetic field sensor’s position is more sensitive the results still acceptable. We have to take into account that the measurement errors adopted in the radiated immunity tests are about 1,5 to 2,0 dB.

However, a high computational cost is observed, even with simplified vehicular structures been the main constraint in real applications.

TABLE I
COMPARISON OF ELECTRIC FIELD RESULTS FOR FREQUENCY SWEEP FROM 200 TO 1000 MHz

		200	300	400	500	600	700	800	900	1000
A1	Meas.	28	65	85	54	37	40	56	16	23
	FEM	55	75	76	78	55	28	47	17	31
	FDTD	54	50	72	101	47	19	62	25	31
A2	Meas.	20	68	65	55	52	39	61	18	28
	FEM	46	78	69	95	66	29	48	18	31
	FDTD	48	48	70	75	57	12	61	22	29
A3	Meas.	25	48	50	40	37	75	55	41	38
	FEM	26	38	60	34	33	60	40	40	46
	FDTD	27	35	60	61	30	54	56	29	60
A4	Meas.	22	69	60	65	41	67	34	42	29
	FEM	48	57	72	72	53	20	54	34	28
	FDTD	51	42	81	90	41	30	46	45	30
Computing Effort		FEM 72: 48' 37"				FDTD 29: 06' 04"				

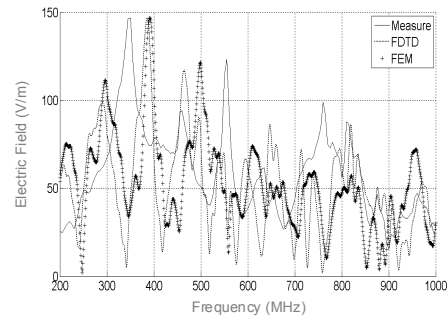


Fig. 4. Simulated and measured electric field at A5.

V. CONCLUSION

In this paper the capacity of two numerical methods are analyzed to solve an EMC immunity test. Although simplified, this test retains the major characteristics that a numerical model must represent. The results point out that computational modeling can be considered as a useful tool for the prediction of electromagnetic fields in the radiated immunity test.

The previous knowledge of field strength in the areas in which the electronic devices and equipments will be located can effectively reduce the reprobation probability in the EMC tests, especially in design of vehicles where the physical tests are very posterior to the development of the components separately. However the computational effort still prohibits practical applications.

VI. REFERENCES

- [1] L. Alvarenga, J. O. Paulino, “Radiated Immunity in Vehicle: Analyzes of Evaluation of the Reduction of Test Setup, SAE, 2007-01-2598.
- [2] ISO. 11451 “Road Vehicles – Vehicle Test Method for Electrical Disturbance from Narrowband Radiated Electromagnetic Energy. Technical report, ISO, Switzerland, 2005.
- [3] Adriano, R. L. S. ; Vasconcelos, J. A. ; Rego, C. G. do ; Silva, E. J. . A generalized iterative multiregion technique to solve the nonhomogeneous electromagnetic wave equation. Microwave and Optical Technology Letters, v. 49, p. 1921-1926, 2007.
- [4] M. Carr and J. L. Volakis. “A Generalized Framework for Hybrid Simulation of Multi-Component Structures Using Iterative Field Refinement” IEEE trans. on Antennas and Propagation, 48(1):22-32, Feb. 2006.

Effect of grounding system on Electromagnetic Fields around Building Struck by Lightning

Bo Zhang, Jinliang He, Rong Zeng, and Shuiming Chen

State Key Lab of Power Systems, Department of Electrical Engineering, Tsinghua University
Beijing, 100084, China
shizbcn@tsinghua.edu.cn

Abstract — In this paper, an approach is proposed to analyze the current distribution and the electromagnetic field of a building struck by lightning. This approach is based on the moment method and can consider the metallic grids under the ground and on the ground all together. Both the potential differences among the grounding parts and the electromagnetic interactions among the grids are taken into account.

I. INTRODUCTION

When lightning strikes building, high current will flow through the metallic grid and will dissipate into the soil from the grounding system. This accident will generate strong transient electromagnetic fields, which may affect the safety of the electrical and electronic units contained inside the building. Thus, the computation of the current distribution and of the electromagnetic fields is an interesting and important engineering problem [1-4].

To calculate the current distribution, the soil conductivity is usually considered to be infinite, which means that the grounding system can be neglected [1-4]. In fact, because the soil conductivity is finite, potential differences always exist among the grounding points. When lightning occurs, the inductance along the grounding electrode will also take effect and the ground potential will be distributed more unevenly. Then, the current distribution and the electromagnetic fields may be different from those with infinite soil conductivity. In this paper, an approach considering soil conductivity effect is proposed to analyze the current distribution and the electromagnetic field of a building struck by lightning. Moment method (MoM) is used to consider the metallic grids under the ground and on the ground all together.

II. NUMERICAL APPROACH

To calculate the electromagnetic field around the building struck by lightning, current distribution on the structure should be obtained first. MoM is used to calculate the current distribution and the multi-line structures should be divided into short segments [5]. Because the size of the building is much less than the wavelength associated with the maximum significant frequency of the lightning current waveform, near field theory can ensure a satisfactory numerical accuracy. By introducing the concept of complex resistivity, which is the combination of both the permittivity and the resistivity, all segments under the ground and on the ground can be taken into account. Then, the concept of leakage currents can be introduced. Meanwhile, some assumptions are used which are also shown in Fig. 1.

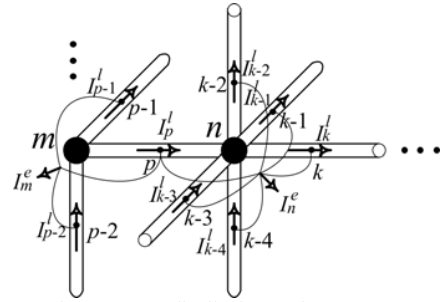


Fig. 1. Current distribution on the segments.

- 1) The longitudinal current in the same segment is constant and is centralized on the axis.
- 2) The leakage currents are distributed evenly around the nodes (the points of intersections between the segments), i.e. each current is leaked evenly from all the half segments connected to corresponding node.
- 3) Each segment can be considered as a filament.

On the surface of each segment, the boundary condition must be satisfied:

$$\mathbf{E}^i + \mathbf{E}^s = 0 \quad (1)$$

where \mathbf{E}^i is the longitudinal component of the external electric field caused by other segments, \mathbf{E}^s is the longitudinal component of the internal electric field. For all segments, by integrating (1) along the longitudinal direction between their two ends, following equation will be obtained [6]:

$$j\omega\mathbf{M}\mathbf{I}^l + \mathbf{A}\mathbf{V}^n + \mathbf{Z}\mathbf{I}^l = 0, \quad (2)$$

where \mathbf{M} is a matrix of the inductances between segments, \mathbf{V}^n is a column vector of the potentials at the nodes, \mathbf{I}^l is a column vector of the longitudinal currents in the segments, \mathbf{Z} is a diagonal matrix of the segments' internal self-resistances [7], \mathbf{A} is a matrix reflecting the connection relationship between segments and nodes. If node j is connected to the end point of segment i , A_{ij} is 1, if node j is connected to the start point of segment i , A_{ij} is -1, or else A_{ij} is zero. The entry M_{ij} in \mathbf{M} can be obtained by [6]

$$M_{ij} = \frac{\mu}{4\pi} \int_{l_i} \int_{l_j} \frac{1}{r} dl_j dl_i, \quad (3)$$

where l_i and l_j are the paths of segment i and segment j , and r is the distance between the source point and the field point. If i is equal to j , l_i is at the axis and l_j is at the surface of segment i . \mathbf{V}^n in (2) can be obtained by

$$\mathbf{V}^n = \mathbf{R}\mathbf{I}^e, \quad (4)$$

where \mathbf{I}^e is a column vector of leakage currents around nodes as shown in Fig. 1, and \mathbf{R} is a matrix of mutual resistances between nodes and leakage currents. From Fig. 1, it should be

noted that the leakage current around a node is distributed evenly from all the half segments connected to the node.

According to the longitudinal current and leakage current distribution in Fig. 1, I^l and I^e have following relationship:

$$I^e = A^T I^l. \quad (5)$$

where A^T is the transpose of A . By substituting (5) into (4) and then into (2), a group of equations is obtained as

$$j\omega MI^l + ARA^T I^l + ZI^l = 0. \quad (6)$$

If segment k has an injected current I_k^s , the corresponding equation can be substituted by $I_k^l = I_k^s$. The suspended segment can be considered as a segment having an injected current with 0 A. Thus, a group of equations with longitudinal currents as unknown variables is obtained from which the longitudinal currents can be solved.

Because the near field is like a quasistatic field, all the parameters are calculated in quasistatic field. The transient electromagnetic fields around the multi-line structures by near-field lightning strokes can be analyzed with the help of fast Fourier transform.

III. COMPLEX RESISTIVITY

In order to take account of the metallic grids under the ground and on the ground all together, concept of complex resistivity is used to calculate R in (4), which is the combination of both the permittivity and the resistivity of the medium:

$$\rho' = \frac{\rho}{1 + j\omega\varepsilon\rho}. \quad (7)$$

where ρ and ε are the resistivity and the permittivity of the medium. Both the air and the soil have their own complex resistivity. Based on the near field theory, by using the image theory, the effect of both the permittivity and resistivity of the medium can be counted for in the Green's function to calculate R in (4) and to calculate the electric field.

IV. VALIDATION AND APPLICATION

We have test the approach in this paper with published results of a simulated lightning current (1/40 μ s, 20 kA) fed into the upper corner of a Faraday's cage shown in Fig. 2 [2]. The cage is constituted by aluminum barrels having 5 \times 30 mm cross section and has a regular 8 \times 8 \times 8 m mesh. The lightning current has a vertical channel length of 400 m. In Fig. 3 and 4 the attenuation along the line CD produced by the cage is shown, where the ratios between the EM field produced by the lightning with or without the presence of the cage are reported. In the case of the lightning without the cage, the lightning channel has been prosecuted until the ground. The variables used in the figures are $\eta = E_{\max}$ with the cage / E_{\max} without the cage and $\zeta = B_{\max}$ with the cage / B_{\max} without the cage. In paper [2], the soil is considered as perfect conductor. In this paper both the results with perfect soil and those with 1 m depth grounding system in 100 Ω m soil are presented.

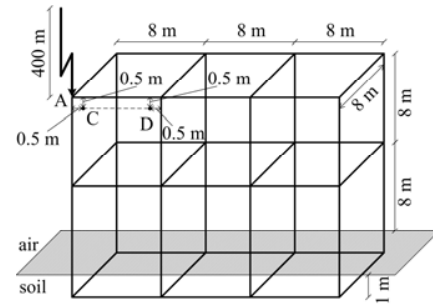


Fig. 2. Calculated model.

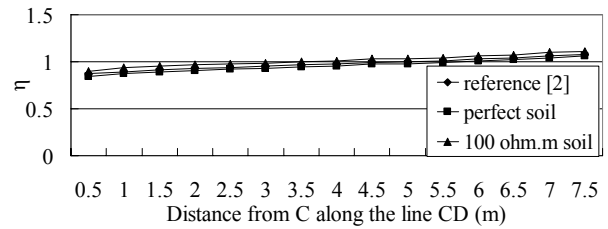


Fig. 3. Profiles of the electric field attenuation along the line CD.

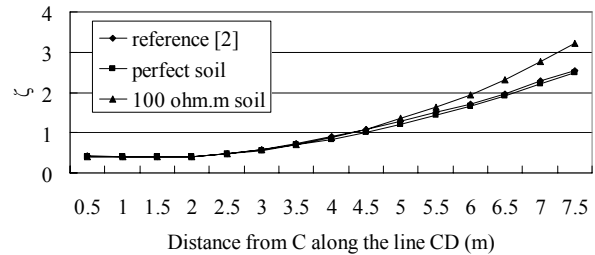


Fig. 4. Profiles of the magnetic field attenuation along the line CD.

It can be seen that when the soil is considered as perfect conductor, the results in this paper are in agreement with those in [2]. For the electric field, its attenuation along the line CD almost does not vary with the resistivity of soil. However, for the magnetic field, its attenuation near D varies greatly with the resistivity of soil. This may be because the current likes flowing to far place through conductor when the resistivity of soil is great. More details will be presented in the formal paper.

V. REFERENCES

- [1] Y. Baba, V.A. Rakov, "Electromagnetic fields at the top of a tall building associated with nearby lightning return strokes," IEEE Transactions on Electromagnetic Compatibility, 49(3): 632 - 643, 2007.
- [2] Marco Angeli, Ermanno Cardelli, "An approach to the analysis of the electromagnetic interferences radiated by metallic grids struck by lightning," IEEE Trans. on Magnetics, 33(2): 1804-1807, 1997.
- [3] S. Cristina, A. Orlandi, "Calculation of the induced effects due to a lightning stroke", IEE proceedings-B, 139(4): 374-380, 1992.
- [4] D. Vecchio, A. Geri, M. Veca, "Calculation of lightning's EM effects on surrounding structure," IEEE Trans. on Magnetics, 24(6): 2697-2699, 1988.
- [5] Roger F. Harrington, Field Computation by Moment Methods, Macmillan, New York 1968
- [6] J. Van Bladel, Electromagnetic Field, Hemisphere Publishing Co. Washington, New York, London, 1985.
- [7] R. L. Stoll, The Analysis of Eddy Currents, Oxford University Press, Oxford, 1974.

Conservativeness of the SAM Phantom for the SAR Evaluation in the Child's Head

Vikass Monebhurrin

Department of Electromagnetics, DRE-L2S, SUPELEC
3 rue Joliot-Curie, 91192, Gif-sur-Yvette Cedex France
E-mail: vikass.monebhurrin@supelec.fr

Abstract — The conservativeness of the SAM (Specific Anthropomorphic Mannequin) for the SAR (Specific Absorption Rate) evaluation in the child's head is investigated. The child's head model is derived from the visible human head model using a morphing technique. Numerical simulations are performed with the SAM phantom and the child head model for the four intended use positions using three excitations – dipole antenna, monopole antenna and PIFA (Planar Inverted-F Antenna)-based mobile phone – at three frequencies corresponding to the currently used mobile communications systems. Overall the SAR calculations show that the SAM phantom is conservative.

I. INTRODUCTION

The ever increasing use of mobile phones by the general public – from adults in the very beginning to children nowadays – has constantly raised questions about the level of electromagnetic exposure and the possible adverse health effects for the user. The basic restriction level was set by ICNIRP (International Commission on Non-Ionizing Radiation Protection) to a maximum 10 g averaged Specific Absorption Rate (SAR) value of 2 W/kg for the head exposure [1]. The SAR compliance test is a pre-requisite prior to the commercialization of a mobile phone. Currently the SAR conformity assessment of mobile phones can only be performed by measurements. The detailed procedures to assess the SAR compliance of mobile phones are provided by international standards such as IEEE1528 [2] and IEC62209-1 [3]. A standard head phantom – the Specific Anthropomorphic Mannequin (SAM) – filled with an appropriate tissue equivalent liquid is recommended for the measurements of the mobile phone according to four basic intended use positions: left cheek, right cheek, left tilt and right tilt. The morphology of the SAM phantom is chosen to be representative of the adult head. Numerical simulations confirm that the values recommended for the dielectric properties of the tissue equivalent liquid are conservative [4].

Since mobile phones are being increasingly adopted by children, the question has been raised about the electromagnetic power absorption in the child's head. It is recognized that the morphology of a child's head is different from an adult's head, especially at the early stages of growth. Little data is available on the dielectric properties of biological tissues of children. Furthermore, numerical models of children's heads are scarce. A simple size reduction of an adult's head model does not provide a good morphological shape of the child's head. A better approach is to perform a morphological transformation of the adult's head: each part of the head is reconstructed with its specific growth rate and the

different parts are recombined with appropriate transition areas to avoid discontinuities [5].

The conservativeness of the SAM phantom with regard to the morphological aspect of the child's head is herein investigated. The morphing technique is applied to derive the child head model from the commonly used visible human head model. Three different excitation sources – dipole, monopole and PIFA (Planar Inverted-F Antenna)-based mobile phone – are considered for the SAR calculations using this child head model and the SAM phantom.

II. NUMERICAL MODELING

Figure 1 shows the two head models used for the study: (a) the SAM phantom and (b) the child head model derived from the visible human head model. A commercial package of the Finite Integration Technique (FIT) is chosen for the numerical simulations. Because of its relatively small size, the full child head model must be considered for the calculations. However the numerical simulations are optimized by considering only the half-head SAM phantom since it can be shown that the other half can be safely neglected.

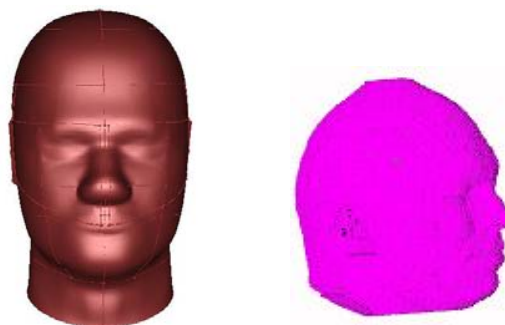


Fig. 1. (left) SAM phantom and (right) child head model (not to scale).

Figure 2 shows the three different sources considered for the SAR calculations: (a) half-wavelength dipole antenna, (b) quarter-wavelength monopole antenna mounted over a metallic box, and (c) PIFA-based mobile phone. All numerical simulations are performed for the three commonly used mobile communications systems: GSM (Global System for Mobile communication) at 900 MHz, DCS (Digital Communication System) at 1750 MHz and UMTS (Universal Mobile Telecommunication System) at 1950 MHz. The dielectric properties of the tissue equivalent liquids employed for the numerical simulations are provided in Table I for the three frequencies.

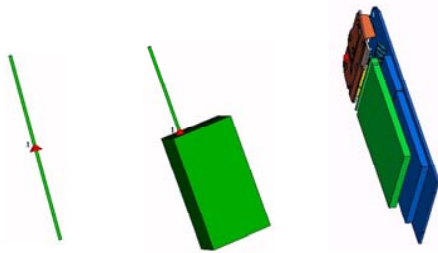


Fig. 2. Excitations used for the numerical simulations: (left) half-wavelength dipole antenna, (middle) quarter-wavelength monopole antenna mounted over a metallic box and (right) PIFA-based mobile phone.

TABLE I

DIELECTRIC PROPERTIES OF THE TISSUE EQUIVALENT LIQUID

Frequency [MHz]	Relative permittivity	Conductivity [S/m]
900 (GSM)	41.5	0.97
1750 (DCS)	40.0	1.40
1950 (UMTS)	40.0	1.40

III. RESULTS

Figures 3, 4 and 5 show the maximum 10 g averaged SAR results obtained for the different configurations using the dipole antenna, the monopole antenna mounted over the metallic box and the PIFA-based mobile phone, respectively. All SAR values are normalized with respect to the highest value obtained among the different configurations. Furthermore, for each configuration, the SAR value is normalized with respect to the accepted power i.e. the antenna mismatch is not taken into account. The highest SAR values are observed with the SAM phantom and the GSM system i.e. at 900 MHz. The PIFA-based mobile phone provides the highest SAR values for the cheek position. For a given antenna configuration, the SAR calculated with the child head model is at least two times lower than the maximum SAR value obtained with the SAM phantom. Overall the SAM phantom is found to be conservative.

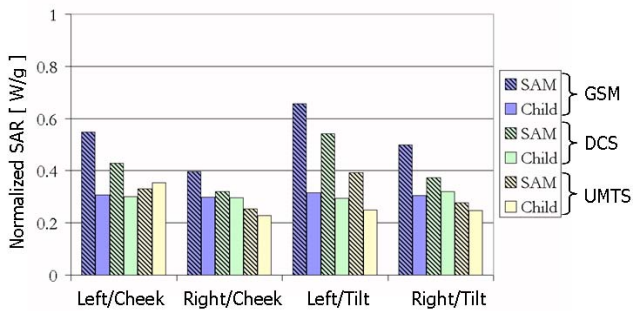


Fig. 3. Normalized SAR values calculated using the half-wavelength dipole antenna.

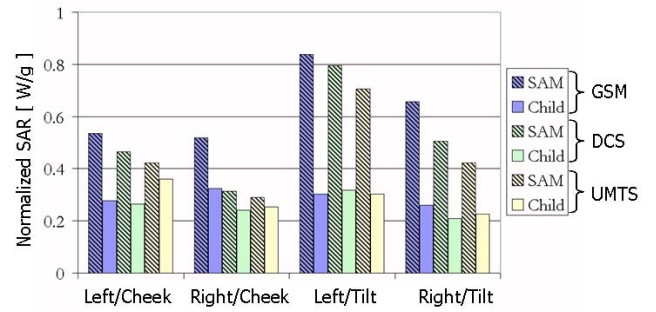


Fig. 4. Normalized SAR values calculated using the quarter-wavelength monopole antenna over the metallic box.

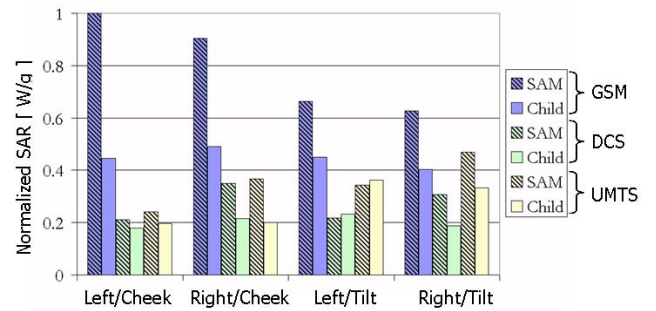


Fig. 5. Normalized SAR values calculated using the PIFA-based mobile phone.

IV. ACKNOWLEDGEMENT

The present work was undertaken in the frame of the ADONIS project sponsored by the RNRT (Réseau National de recherches en Télécommunications), France.

V. REFERENCES

- [1] ICNIRP, "Guidelines for limiting exposure to time-varying electric, magnetic and electromagnetic fields," Health Physics, April 1998, Vol. 74, No. 4, pp. 494-522.
- [2] IEEE, "Recommended practice for determining the peak spatial-average Specific Absorption Rate (SAR) in the human head from wireless communications devices: measurement techniques," IEEE Standard 1528, 2003.
- [3] IEC, "Human exposure to radio frequency fields from hand-held and body-mounted wireless communication devices - Human models, instrumentation, and procedures - Part1: Procedure to determine the specific absorption rate (SAR) for hand-held devices used in close proximity to the ear (frequency range of 300 MHz to 3 GHz)," IEC Standard 62209-1, 2005.
- [4] V. Monebhurrun, C. Dale, J-Ch. Bolomey and J. Wiart, "A numerical approach for the determination of the tissue equivalent liquid used during SAR assessments," *IEEE Trans. on Magnetics*, 38(2):745-748, 2002.
- [5] A. Hadjem, D. Lautru, C. Dale, M. F. Wong, V. F. Hanna and J. Wiart, "Study of specic absorption rate (SAR) induced in two child head models and in adult heads using mobile phones," *IEEE Trans. Microwave Theor. Tech.*, 53(1):4-11, 2005.

3D-Modelling of an Aperture Illuminated by HF Electromagnetic Source for EMC Application

M. DJENNAH*, F. Rioux-D**

* Laboratory Signal and Image - Polytechnic School of Algiers - Algeria

ZAKIMOZA@yahoo.com

** U2R2M, Université Paris XI, UMR CNRS 8081, BAT 220, 91405 Orsay France

F.Rioux-Damidaou@u-psud.fr

Abstract – In this paper, we present numerical method for determining the penetration of electromagnetic fields through a small aperture on enclosure having inside it a conducting component. To solve the problem of coupling between the radiated electromagnetic field and the metallic enclosure we developed a variational formulation in the interior region and an integral formulation in the exterior region by using the equivalent electric on exterior surface of the enclosure. Using a coupling between two methods: finite elements-boundary integral, we compute the electromagnetic field inside the enclosure and in particular on conducting wire. The numerical result obtained with this method show the influence of characteristic parameter (σ, ϵ, μ) and the thickness of enclosure on penetration of electromagnetic field inside the enclosure.

I. INTRODUCTION

Nowadays, more and more of electronics is embarked on board any type of terrestrial or air vehicles with electronic components functioning at frequencies increasingly higher. The multiplication of the possible sources of electromagnetic aggression and their increasing power thus generate new types of dysfunction of the electrical appliance and problems of incompatibility inter-equipment, which can go until their destruction. Electromagnetic compatibility, according to its "fundamental principles" is thus analyzed in terms of emission (not to disturb the environment) and of immunity (not to be disturbed). The two aspects occur at the same time in conduction and in radiation. Consequently, in the scenario of a problem of EMC, one will find three actors: a source of disturbance, a connection, and a victim of the disturbances thus coupled.

II. PHYSICAL MODEL

In our study we are interested in the radiated electromagnetic field. On figure 1 we present a configuration of a problem models related to the EMC.

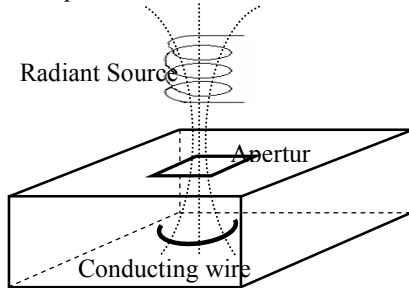


Fig.1.Physical model

The metal enclosure with a small rectangular opening lit by an electromagnetic radiation of a source located in the exterior region. The source is considered harmonic in time.

This problem was the subject of certain work by using various numerical models [1][2][3]. In our study we apply, on the one hand, the finite element method inside and on enclosure and, on the other hand, we express the external field by an integral representation. This one is function of the equivalent electrical currents K carried by external surface of the enclosure. These surface current represent the jump of the tangential component of the magnetic field: $[n \times H]_{\Gamma} = K$

The physical system is defined by the following equations:

- In the enclosure without the conducting wire:

$$i\omega\mu_0 h + \text{Curl}(e) = 0 \quad (1)$$

$$-i\omega\epsilon_0 e + \text{Curl}(h) = 0 \quad (2)$$

- In conducting wire:

$$i\omega\mu_c h + \text{Curl}(e) = 0 \quad (3)$$

$$-(\sigma_c + i\omega\epsilon) e + \text{Curl}(h) = 0 \quad (4)$$

- In the exterior region without source:

$$i\omega\mu_0 h + \text{Curl}(e) = 0 \quad (5)$$

$$-i\omega\epsilon_0 e + \text{Curl}(h) = 0 \quad (6)$$

And we take in all system:

$$\text{div}\mu h = 0 ; \text{div}\epsilon e = 0 \quad (7)$$

III. FORMULATION

The wave equation in terms of the electric field can be obtained:

$$\nabla \times \frac{1}{\mu} \nabla \times E + i\omega(\sigma + i\omega\epsilon)E = 0 \quad (8)$$

Multiplying us the equation (8) by a function test E' :

$$\int_{\Omega} \nabla \times E \cdot \nabla \times E' d\Omega + \int_{\Gamma} (n \wedge \nabla \times E) \cdot E' d\Gamma + i\omega\mu(i\omega\epsilon + \sigma) \int_{\Omega} E \cdot E' d\Omega = 0 \quad (9)$$

Where Γ is the surface enclosing the domain Ω , n is the unit outward normal to Γ . We can write the wire term in the variational formulation as:

$$T_{Wire} = \int_{\Gamma} (n \times \nabla \times E) d\Gamma \cdot E' = \frac{-\partial}{\partial t} \int_S (n \times H) \cdot E' dS \quad (10)$$

$$n \times E = \rho (n \times H) \times n \quad (11)$$

Where S is the Surface enclosing the wire, and ρ is the surface impedance of the wire.

IV. NUMERICAL RESULTS

A. Representation a grid mesh

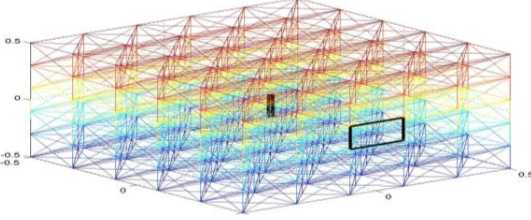


Fig.2. Tetrahedral grid of the enclosure

Number of internal nodes	489
Number of frontier nodes	302
Number of internal edges	3190
Number_of frontier edges	900
Number_of faces	600

It is supposed that the ray of the wire is very small compared with the dimensions of enclosure and we can take it as one or two stop attached, as a sequence of mesh edges. In HF domain, the equation (10) becomes:

$$T_{Wire} = \frac{\partial}{\partial t} \int_w \frac{1}{Z_w} \cdot E_{ij} \cdot E'_{kl} dl ; Z_w = \frac{1+j}{2\pi a} \cdot \sqrt{\frac{\omega \mu}{2\sigma}}$$

Where (a) is the wire radius, Z is the wire impedance per unit length in (Ω/m)

B. Representation of the Magnetic field H

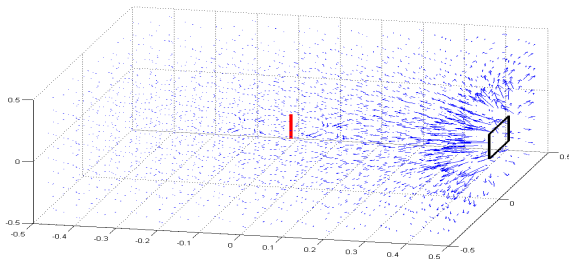


Fig.3. Magnetic field H, $f=1$ MHz

C. Representation of the Electrical field H

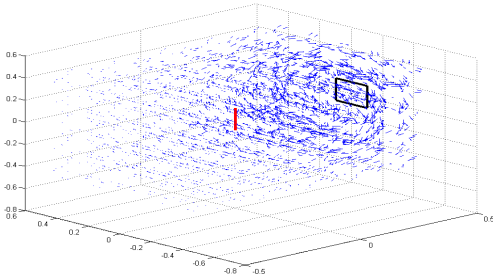


Fig.4. Electric field E, $f=1$ MHz

D. Representation of the iso-value of the electromagnetic field according to plan (YOZ) $X=-0.3$

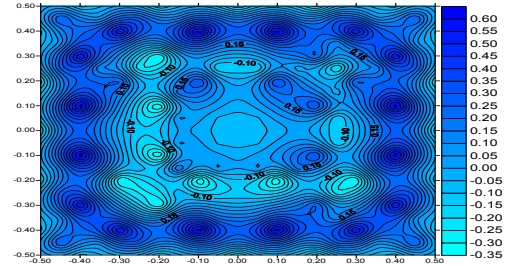


Fig.5. $f=50$ MHz, DD=0.7, RHO= $1.6672 \cdot 10^{-8}$, $J_s = 100$, R=0.2

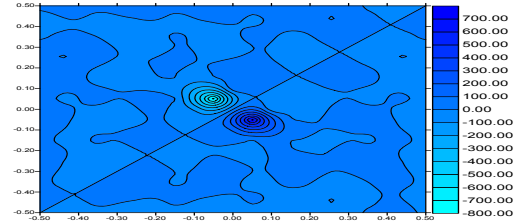


Fig.6 $f=1$ GHz, DD=0.7, RHO= $1.6672 \cdot 10^{-8}$, $J_s = 100$, R=0.2

V. CONCLUSION

In this article we have some numerical results to evaluate the penetration of the electromagnetic field in a metal enclosure. We considered a radiant electromagnetic source in front of an aperture of the enclosure at a limited distance d. We realize a coupling between the boundary integral method outside and the finite element method inside the enclosure to solve our problem. The numerical results show the contribution of each parameter of the problem in the evaluation of the electromagnetic energy penetrated in the enclosure. On the one hand, according to the electromagnetic parameters: electric conductivity and permittivity (σ, ϵ) and magnetic permeability (μ) of the enclosure; in addition, according to the density of the current source, the geometrical position and the frequency of the radiant source, the numerical results show the variation in the values and the form of electromagnetic energy in each point inside the enclosure while varying each time only one parameter. Considering the number of parameters we cannot expose all the results in this paper.

VI. REFERENCES

- [1] W.P.Carpes, L. Pichon, Razek "Analysis of the Coupling of an Incident Wave with a Wire inside a Cavity using an FEM in Frequency and Times Domains" IEEE Transaction on Electromagnetic Compatibility. Vol 44, N°3 August 2002.
- [2] F.Paladian, P.Bonnet, M.Klingler "A frequency-domain prediction model using measured scattering parameters of electrically short lines to determine the per unit length parameters matrices of multiconductor transmission lines" 14th International Zurich Symposium & Technical Exhibition on Electromagnetic Compatibility, Zürich (Suisse), February 2001, Actes du Colloque, pp.293-298.
- [3] M. Djennah, F. D. Rioux, B. Bandelier "Computation of electric charges and eddy currents with an e formulation" J. IEEE Transaction Magnetic 1997, Vol 32, pp1322-25

The Dynamic Circuit Model of the Spark Plug for EMI Prediction

Zheng Ya-li, Yu Ji-hui, Wang Quan-di, Jia Jin
The College of Electrical Engineering, Chongqing University
Shapingba, Chongqing, 400044, People's Republic of China
E-mail: yaya9304@163.com

Abstract— In order to predicate the EMI of the ignition system, the accurate model of the spark plug is needed. This paper extracts the parasitic parameter of the spark plug using FEM approach and analyzes the discharge characteristics and mechanism of the spark plug. Then the dynamic circuit model of the spark plug in the ignition system is established. This model is verified by measurement and simulation results.

I. INTRODUCTION

The spark plug discharge is the main source of EMI in the ignition system of an automobile. For the EMI prediction of the ignition system, the accurate spark plug model is needed.

This article analyzes the internal discharge channel and the discharge characteristics of the spark plug at first, and then establishes the dynamic circuit model of the spark plug which includes the static parasitic capacitance and the non-linear resistance. The simulation and measurement results illustrate the dynamic circuit model is correct.

II. THE PARAMETER EXTRACTION OF THE SPARK PLUG IN THE DYNMAIC CIRCUIT MODEL

Supposed the frequency of the EMI is lower than 300MHz, the electric field of the spark plug can be regarded as electrostatic field and internal discharge channel can be equaled to the circuit model shown in Fig. 1.

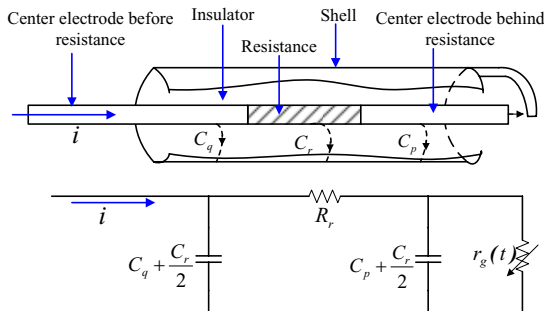


Fig. 1. The discharge channel and dynamic circuit model of the spark plug

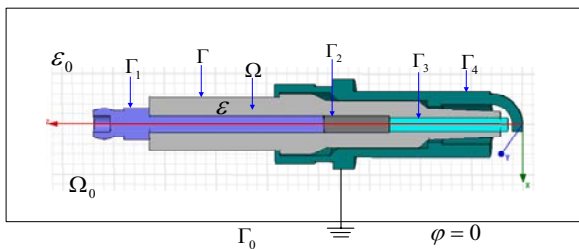


Fig. 2. Solution region of the spark plug

The parasitic capacitance can be extracted using FEM analysis^[1]. Fig. 2 is the solution region of the spark plug.

The spark plug internal electrostatic field satisfies the Laplace equation:

$$\frac{\partial^2 \varphi(x, y, z)}{\partial x^2} + \frac{\partial^2 \varphi(x, y, z)}{\partial y^2} + \frac{\partial^2 \varphi(x, y, z)}{\partial z^2} = 0 \quad (1)$$

To calculate the capacitance matrix, one can solve the problem with a Dirichlet boundary as follows:

$$\begin{cases} \varphi|_{\Gamma_1} = 1 \\ \varphi|_{\Gamma_2, \Gamma_3, \Gamma_4} = 0 \end{cases} \quad (2)$$

$$\varphi|_{\Gamma_0} = 0 \quad (3)$$

In the solution region, there are different mediums. So the medium interface condition is written as:

$$\varepsilon_0 \frac{\partial \varphi_0}{\partial n} = \varepsilon \frac{\partial \varphi}{\partial n} \quad (4)$$

The different medium interface condition (4) is satisfied automatically when functional obtains the minimal value. Therefore the variational problem equaled to (1) is as follows:

$$\begin{aligned} F(\varphi) &= \frac{1}{2} \int_{\Omega_0} \varepsilon_0 \left[\left(\frac{\partial \varphi}{\partial x} \right)^2 + \left(\frac{\partial \varphi}{\partial y} \right)^2 + \left(\frac{\partial \varphi}{\partial z} \right)^2 \right] dx dy dz \\ &+ \frac{1}{2} \int_{\Omega} \varepsilon \left[\left(\frac{\partial \varphi}{\partial x} \right)^2 + \left(\frac{\partial \varphi}{\partial y} \right)^2 + \left(\frac{\partial \varphi}{\partial z} \right)^2 \right] dx dy dz \\ &= \min \end{aligned} \quad (5)$$

Based on the principle of the finite element method, the integrated matrix can be written as:

$$[k][\varphi] = 0 \quad (6)$$

Where: $[K]$ represents contributions from all tetrahedral elements.

Solving (2), (3) and (6), we can obtain the potential function $\varphi(x, y, z)$. The electric field can be written as:

$$\mathbf{E}(x, y, z) = -\nabla \varphi(x, y, z) \quad (7)$$

The electric charge of the conductor is computed from (7):

$$Q_i = \varepsilon \oint_{\Gamma_i} \mathbf{E}(x, y, z) d\Gamma_i \quad (8)$$

Therefore the mutual capacitance is written as:

$$C_{ij} = \frac{Q_i}{\varphi_j} \Big|_{(\varphi_1, \dots, \varphi_{j-1}, \varphi_{j+1}, \dots, \varphi_m) = 0, \varphi_j = 1} \quad (i \neq j) \quad (9)$$

Using the physical structure data of the spark plug, the finite element model can be established. From computation, the parasitic capacitance can be obtained which written as follows: $C_q = 5.3986 \text{ pF}$, $C_r = 5.8701 \text{ pF}$, $C_p = 4.9849 \text{ pF}$.

III. THE AIR-GAP RESISTANCE MODEL OF THE SPARK PLUG IN THE DYNAMIC CIRCUIT MODEL

The spark plug experiences the off stage, the discharge stage and the self-excited discharge stage when it works. The air-gap resistance presents the non-linear nature. The dynamic circuit model of the spark plug in the ignition system is shown in Fig. 3^[2].

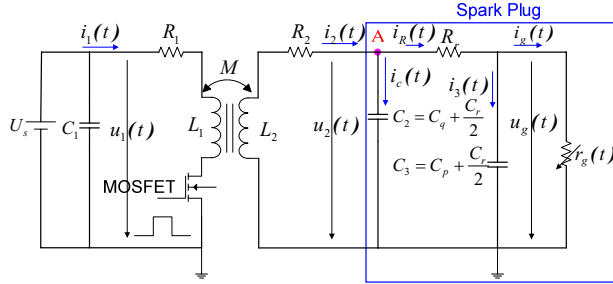


Fig. 3. The dynamic circuit model of the spark plug in the ignition system

A. The air-gap resistance model of the spark plug at the discharge stage

When primary circuit separates instantaneous, the current in primary coil $i_1(t)$ reduces to zero rapidly. The capacitance C_3 is charged rapidly by the induced electromotive force $u_2(t)$. When it increases to the breakdown voltage of the spark plug, the corona can be established between the two electrodes and the ionization starts. The spark plug discharges.

For $i_1(t)=0$ and $di_1(t)/dt \neq 0$, we can obtain the secondary circuit equations as follows:

$$\begin{cases} u_2(t) = -R_2 i_2(t) - L_2 \frac{di_2(t)}{dt} + M \frac{di_1(t)}{dt} \\ i_g(t) = i_R(t) + C_3 \frac{du_g(t)}{dt} \\ u_2(t) = R_3 i_R(t) + u_g(t) \\ u_g(t) = i_g(t) r_g(t) \end{cases} \quad (10)$$

The spark plug resistor can be computed as:

$$r_g(t) = l_g \left\{ \left(2\alpha/p \int_{t_1}^{t_2} i_g^2(t) dt \right) \right\}^{-0.5} \quad (11)$$

Combined (10) and (11), the simplified equations are written as:

$$\begin{cases} u_g'(t) = \frac{1}{C_3} i_g(t) \\ i_g'(t) = \frac{\alpha}{l_g^2 p} u_g^2(t) i_g(t) + \frac{1}{C_3} \frac{i_g^2(t)}{u_g(t)} \\ u_g(t_1) \cong V_{br} \\ i_g(t_1) \cong 0 \end{cases} \quad (12)$$

Where: V_{br} is the breakdown voltage of the spark plug.

B. The air-gap resistance model of the spark plug at the self-excited discharge stage

The plasma presents as soon as the spark plug discharges. The spark plug enters to the self-excited discharge stage. The voltage of the spark plug maintains at a constant value^[3]. In this stage the secondary circuit equations can be written as:

$$\begin{cases} u_2(t) = -R_2 i_2(t) - L_2 \frac{di_2(t)}{dt} \\ C_2 \frac{du_2(t)}{dt} = i_2(t) - i_R(t) \\ i_g(t) = i_R(t) = \frac{u_2(t) - u_g(t)}{R_3} \\ u_g(t) = U_0 \end{cases} \quad (13)$$

When the plasma fades away, the spark plug returns to the off stage.

IV. RESULTS

The dynamic circuit model of the spark plug in the ignition system is established in the circuit simulation software. The voltage of the spark plug is measured at the A point in Fig. 3 mentioned above. The measurement and simulation results are shown in Fig. 4. The results match well and illustrate that the dynamic circuit model can reflect the discharge characteristics of the spark plug accurately.

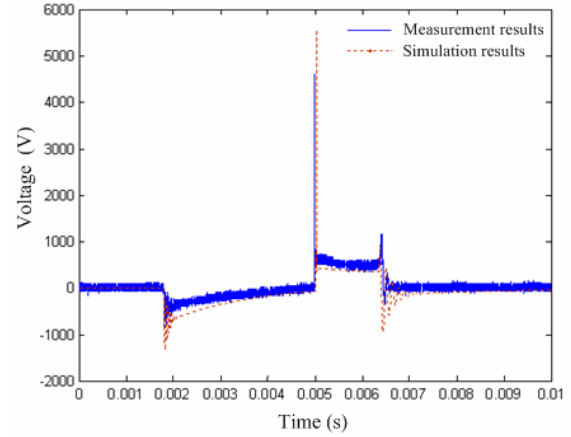


Fig. 4. Measurement and simulation results of the voltage of the spark plug

V. CONCLUSION

In this paper, the dynamic circuit model of the spark plug is established. According to the geometric structure of the spark plug, the parasitic capacitance of the spark plug is extracted by FEM approach. Analyzing the different stages of the spark plug discharge process and mechanism, the non-linear resistance circuit model of the spark plug air-gap is founded. Simulation and measurement results show the model of the spark plug is correct. The model proposed in this paper can be used for EMI predication in the ignition system.

VI. REFERENCES

- [1] R. Laroussi and G. I. Costache, "Finite-Element Method Applied to EMC Problems," *IEEE Trans. on Electromagnetic Compatibility*, 35(2): 178-184, 1993.
- [2] Wu Yuan-jie, Xu Bo-hou and Xu Hang, "Nonlinear modeling of spark plug ignition process and parameter identification," *Transactions of CSIEC*, 17(3): 281-284, 1999.
- [3] Geraldo C. R. Sincero and Jerome Cros, "Arc models for simulation of brush motor commutations," *IEEE Trans. on Magnetics*, 44(6): 1518-1521, 2008.

Steady-state Inductive Coupling to the Underground Pipeline Parallel to Overhead Transmission Line above Two-layer Soil

Lei Qi, Yan Wu, and Xiang Cui

Beijing Key Laboratory of High Voltage & EMC, North China Electric Power University
No.2 Beinong Road, Changping District, Beijing 102206, China
Qilei@ncepu.edu.cn

Abstract— As China's economy continued to grow, the electromagnetic influence on oil/gas pipeline near alternating current transmission line becomes increasingly prominent. Based on the transmission line model of pipeline-earth circuit, the analytic expressions of induced voltage generated by the normally operating ac transmission line are obtained for different terminal loads of the underground pipeline in this paper. The conception of critical length is put forward when the pipeline is terminated by the matched loads at both ends. The two-layer soil model is used for the simulation and the quasi-Monte Carlo integration method is applied to the computation of the Pollaczek integrals in the expressions of the self ground return impedance of the underground pipeline and mutual impedance between the overhead transmission line and underground pipeline.

I. INTRODUCTION

As China's economy continued to grow, the power transmission lines and oil/gas pipelines are in the construction of rapid development for more and more energy demand. Ultra High Voltage (UHV) and West-East gas projects are the national key projects in recent years. Because of the similarity of transmission path selectivity of the power industry and oil/gas industry, the situation of parallelism, oblique approach and crossing between the transmission lines and pipelines has frequently happened. Therefore, the electromagnetic influence on oil/gas pipelines near alternating current (ac) transmission lines becomes increasingly prominent.

The pipelines are subject to interference arising from three parts, i.e. capacitive, resistive and inductive coupling. Capacitive coupling only affects the aboveground pipeline since it has both a capacitance to the transmission line and to earth. And the pipeline buried below ground is shielded by the ground and cannot be affected by capacitive coupling. Resistive coupling between the transmission line and pipeline is only relevant during the grounding fault and lightning strike when significant level of current flows into the earth. And this will result in the potential rise of the tower base and of the neighboring soil with regard to the remote earth. In this situation, the inductive coupling will also take place and put the pipeline at severe risk. Inductive coupling is caused by the time-varying magnetic field produced by the transmission line currents. The induced voltage at the pipeline ends will vary as a function of length of parallelism, soil resistivity, distance between the pipeline and transmission line, and so on. Aerial and underground pipelines are both affected by inductive coupling. When the transmission line is running in a normal condition, the electromagnetic fields dependent on the three

overhead line phases generally balance each other and significantly reduce the net field seen by the pipeline. However, the induced voltage on underground pipeline parallel to normally operating overhead transmission line is very important for being concerned with personal safety, ac corrosion of pipeline and normally operating of pipeline cathodic protection system.

Some research has been carried out and the limits of electromagnetic influence are released in [1]-[4]. These studies mainly focus on the inductive and resistive coupling modeling during the ground fault, switching and lightning surge in power system. The earth is assumed to be semi-infinite and homogeneous in all of these literatures.

In this paper, based on the transmission line model of pipeline-earth circuit, the analytic expressions of induced voltage generated by the normally operating ac transmission line are obtained for different terminal loads of the underground pipeline. The conception of critical length is put forward when the pipeline is terminated by the matched loads at both ends. The two-layer soil model [5] is used for the simulation and the quasi-Monte Carlo integration method is applied to the computation of the Pollaczek integral [6].

II. TRANSMISSION LINE MODEL OF PIPELINE-EARTH CIRCUIT

Considering the location at infinity below the earth as the zero-voltage reference point, the equivalent circuit of the pipeline-earth circuit is shown in Fig.1. The telegrapher's equations are given in frequency domain

$$\frac{dV(x)}{dx} + ZI(x) - E(x) = 0 \quad (1)$$

$$\frac{dI(x)}{dx} + YV(x) = 0 \quad (2)$$

where $V(x)$ and $I(x)$ are respectively the voltage and current along the pipeline; Z and Y are respectively the per-unit-length (PUL) series impedance and shunt admittance; $E(x)$ is the induced electromotive force (EMF) on the PUL pipeline produced by the transmission line. Assuming $E(x)$ along the pipeline to be a constant E , the general solutions to (1) and (2) are as follows

$$V(x) = Ae^{\gamma x} + Be^{-\gamma x} \quad (3)$$

$$I(x) = \frac{E}{Z} - \frac{1}{Z_c} (Ae^{\gamma x} - Be^{-\gamma x}) \quad (4)$$

here

$$\gamma = \sqrt{ZY} = |\gamma| \angle \theta = \alpha + j\beta \quad (5)$$

$$Z_c = \sqrt{\frac{Z}{Y}} \quad (6)$$

where Z_c , γ , α and β are the characteristic impedance, propagation constant, attenuation constant and phase constant of the pipeline-earth transmission line model, respectively. The undetermined constants A and B in (3) and (4) depend on the terminal constraints

$$V(0) = -Z_1 I(0) \quad (7)$$

$$V(L) = Z_2 I(L) \quad (8)$$

Substituting (7) and (8) into (3) and (4) gives

$$A = \frac{E[(1 + \rho_1)\rho_2 - (1 + \rho_2)e^{\gamma L}]}{2\gamma(\rho_1\rho_2 - e^{2\gamma L})} \quad (9)$$

$$B = \frac{E[(1 + \rho_1)e^{2\gamma L} - \rho_1(1 + \rho_2)e^{\gamma L}]}{2\gamma(\rho_1\rho_2 - e^{2\gamma L})} \quad (10)$$

here

$$\rho_1 = \frac{Z_1 - Z_c}{Z_1 + Z_c} \quad (11)$$

$$\rho_2 = \frac{Z_2 - Z_c}{Z_2 + Z_c} \quad (12)$$

where Z_1 and Z_2 are the terminal loads of the pipeline illustrated in Fig.1; ρ_1 and ρ_2 are respectively the reflection coefficients at the beginning and end of the pipeline. Typical values of Z_1 and Z_2 are listed in Table I and corresponding voltage and current solutions to (3) and (4) can be achieved by the above formulas.

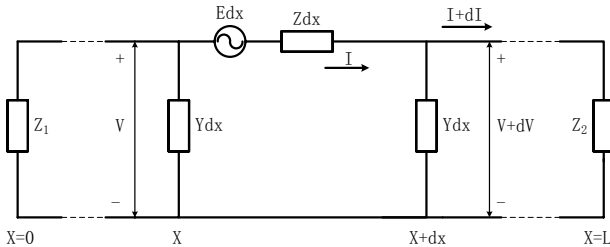


Fig. 1. Equivalent circuit of the pipeline-earth circuit

When the pipeline extends for a few kilometres beyond the parallel routing without earthing, the corresponding reflection coefficients ρ_1 and ρ_2 are zero. The investigation shows that the maximum coating stress voltage appears at the ends of the parallel routing and can be evaluated by

$$V_{\max} = \left| \frac{E(1 - e^{-\gamma L})Y_2}{2\gamma(Y_1 + Y_2)} \right| \quad (13)$$

where V_{\max} is the maximum coating stress voltage, which equals to the difference between the metal pipeline potential and coating potential with regard to the remote earth. Y_1 is the PUL shunt admittance including two parts, the leakage conductance and capacitive reactance of the coating. Y_2 is the PUL ground return admittance.

It can be proved that V_{\max} in (13) firstly increases, then slightly decreases, finally tends to some constant with the increase of parallelism length of the pipeline. In other words, V_{\max} in (13) can achieve some maximum V_m when the parallelism length of the pipeline equals to some critical length L_m . L_m and V_m can be solved by the following equations

$$\begin{cases} \cos(\beta L_m - \theta) = \cos \theta e^{-\alpha L_m} \\ V_m = \left| \frac{E}{2\gamma} \right| \sqrt{1 + e^{-2\alpha L_m} - 2e^{-\alpha L_m} \cos(\beta L_m)} \end{cases} \quad (14)$$

TABLE I
TYPICAL VALUES OF Z_1 AND Z_2

Item	Z_1	Z_2	ρ_1	ρ_2
1	Z_c	Z_c	0	0
2	Z_c	∞	0	1
3	0	Z_c	-1	0
4	∞	∞	1	1
5	0	0	-1	-1
6	0	∞	-1	1

III. COMPUTATION OF POLLACZEK INTEGRAL

Apparently, it is necessary to determine the self ground return impedance of the underground pipeline and mutual impedance between the overhead transmission line and underground pipeline in order to evaluate V_{\max} in (13). The two-layer soil model is used for the simulation and the quasi-Monte Carlo integration method is applied to the computation of the Pollaczek integral in this section.

IV. VALIDATION AND APPLICATION

In this section, the proposed method is validated and applied to the evaluation of power frequency induced voltage on the West-East gas pipeline in parallel with 1000kV UHVAC transmission line.

ACKNOWLEDGEMENT

This work was supported by the National Natural Science Foundation of China (no. 50707008).

V. REFERENCES

- [1] CIGRE, *Guide on the influence of high voltage ac power systems on metallic pipelines*, France: CIGRE, 1995.
- [2] EPRI, *Power line fault current coupling to nearby natural gas pipelines*, Canada: EPRI, 1987.
- [3] F.P. Dawalibi, R.D. Southey, "Analysis of electrical interference from power lines to gas pipelines Part I: computation methods", *IEEE Trans. on Power Delivery*, 4(3): 1840-1846, 1989.
- [4] I. Cotton, K. Kopsidas, Y. Zhang, "Comparison of transient and power frequency-induced voltages on a pipeline parallel to an overhead transmission line", *IEEE Trans. on Power Delivery*, 22(3): 1706-1714, 2007.
- [5] D.A. Tsiamitros, G.K. Papagiannis, D.P. Labridis, P.S. Dokopoulos, "Earth return path impedances of underground cables for the two-layer earth case", *IEEE Trans. on Power Delivery*, 20(3): 2174-2181, 2005.
- [6] X. Legrand, A. Xemard, G. Fleury, P. Auriol, C.A. Nucci, "A quasi-Monte Carlo integration method applied to the computation of the Pollaczek integral", *IEEE Trans. on Power Delivery*, 23(3): 1527-1534, 2008.

A New Stochastic LPP Model for studying ELF Bioelectromagnetic Interaction

E. Calà, S. Coco, and A. Laudani
DIEES University of Catania
Viale A. Doria 6, 95125, Catania, Italy
coco@diees.unict.it

Abstract—In this paper we present a stochastic 3D Langevin-Lorentz-Poisson (LLP) coupled model in order to investigate the ion transport across ionic channels situated on the cell membrane in the presence of external ELF magnetic fields. An iterative scheme is adopted, which alternates the solution of a Poisson problem with the time domain integration of a modified kind of Langevin-Lorentz equations. A Fokker-Planck analysis of the latter equations is performed to compute the statistical parameters of ion motion. An example of application to the analysis of a Ca⁺⁺ membrane ionic channel is also given.

I. INTRODUCTION

In the last years the study of Extremely Low Frequency (ELF) magnetic fields effects on living cells has been a growing interest. Since the activation of signaling among cells depends on ion concentrations, the most plausible mechanism by which ELF magnetic fields are thought to interact with a biological system is an alteration of the signal transduction within the biological system, involving the gating of ionic channels and changes of intracellular ionic concentrations, affecting various critical cellular functions (differentiation, apoptosis, etc) [1][2].

In this paper we present a stochastic 3D Langevin-Lorentz-Poisson (LLP) coupled model in order to investigate the ion transport across ionic channels situated on the cell membrane in the presence of external ELF magnetic fields. In particular a correction function, which takes into account in a probabilistic way the effect of external ELF magnetic fields, has been used in the model following an analogous approach adopted for modeling the gating of voltage-dependent channels. The numerical solution of the coupled problem is performed by integrating the dynamical equations of ions subject to electromagnetic forces inside the ionic channels, assuming a stationary flux of ions. In this case we make use of an iterative scheme, which alternates the solution of a Poisson problem with the time domain integration of Langevin-Lorentz equations which govern the ion motion. A Fokker-Planck analysis of the latter equation is performed to compute the statistical parameters of ion motion. The solution of the coupled problem is achieved by exploiting an appropriate stationary representation of the 3D ion spatial distribution. The developed model also uses a stochastic mechanism of ion injection in membrane channels (describing the fluctuation in time of the total number of particles inside the simulation region), allowing us to carry out more realistic simulations. In order to remarkably reduce the simulation time needed for launching several simulations and managing a huge quantity of data, we used a distributed computing based approach in a

grid infrastructure, in the framework of the PI2S2 project [3].

II. THE STOCHASTICAL LPP MODEL OF ION MOTION

The behaviour of ions inside cellular membrane ionic channels is governed by a system of coupled equations consisting of a Langevin-Lorentz equation for the motion of ions and a Poisson problem for the electrical scalar potential ϕ

$$m \frac{d\mathbf{v}}{dt} = -h\mathbf{v} + q(\mathbf{E}_T + \mathbf{v} \times \mathbf{B}_T) + \mathbf{N}(t) \quad (1)$$

$$\nabla^2 \phi + q \iiint_{\Omega} f(P) d\Omega = 0$$

where m is the generic ion mass, v is its velocity, h is a viscous friction coefficient, modeling the ion interactions with water molecules, q is the ion charge, \mathbf{E}_T and \mathbf{B}_T (if any) are the total electric and magnetic field respectively, $\mathbf{N}(t)$ is a force taking into account the thermal noise; in the Poisson equation (1) Ω indicates the domain of analysis for the ionic channel and $f(P)$ is the space charge distribution function. The total electric field \mathbf{E}_T consists of two terms: the first is due to the scalar potential $-\nabla\phi$, the second, \mathbf{E}_{ESO} , takes into account exogenous electric forces, if any, influencing the ion in the cell environment and summarizing the contributions of the environment to the total electric field. The numerical solution of this coupled electromechanical problem is iteratively carried out by using a self-consistent scheme, which at each step alternates the solution of a Poisson problem with the time-domain integration of the Langevin equation. In particular for each time step the solution of a Poisson problem is calculated by using a point to point method, that is the electric field is computed by adding the contributions due to each ion, assuming a stationary ion flow.

The ion displacements are computed by adding to the deterministic ion displacement component obtained by a time-integration of the Langevin-Lorentz equation in the absence of thermal noise; a stochastic component computed by a Fokker-Planck analysis of the dynamical equation. Assuming that the typical transit time of an ion is of the order of 1 ns, the simulation time interval was chosen greater than this typical transit time. In order to make the analysis compatible with the hypothesized stationary conditions the integration time step was chosen of the order of 1 fs.

This model in this form is not suitable to describe the ELF magnetic field effects for two main reasons: first the simulation time should be about 0.1 s and consequently about 1E+14 steps should be executed (this is beyond currently available computing resources); secondly the model is not

able to take into account the influence of ELF magnetic fields on ionic channel gating. Thus in order to overcome these problems a modified version of the model has been set up, including explicitly ELF magnetic fields effects on channel gating. For this purpose we changed the first equation of (1) with the following equation, taking into account experimental results, which indicate that in the presence of external ELF magnetic fields, for some frequency and intensity windows, the flux of ions in ionic channel increases:

$$m \frac{dv}{dt} = -h\nu + \mathbf{N}(t) + Z(B)(q\mathbf{E}_T)$$

where $Z(B)$ is an expression giving the probability of opening/closing of a single membrane channel as a function of the external ELF magnetic field intensity. This expression is analogous to that describing the probability of opening/closing of the channel as a function of the transmembrane applied voltage

$$Z(B) = \{1 + \exp(-(B - B_0)/\Delta B)\}^{-1}$$

$$B = B_{\max} \sin \omega t$$

Where ΔB , B_0 are parameters derived from experimental measurements [4]. In our simulations we use $B_{\max} = 0.1$ T and $\omega = 2\pi 50$ rad/s. According to this new approach the gating is ruled by the ELF sinusoidal magnetic field. In this way we translate the external ELF magnetic fields effect on the amount of channels which open at the same time.

III. ANALYSIS OF A Ca^{++} CHANNEL

The analysis of a typical ionic flow across a Ca^{++} channel is performed hereafter in order to show the application of the proposed model to a realistic case. For the description of the Ca^{++} channel, we assume a commonly used schematization, in which only the channel region is considered; it consists of a cylinder, with a height of 10 Å and a radius of 5 Å and the cylinder axis coincident with the z axis. A schematic representation of the Ca^{++} channel is shown in figure 1. The aim is to investigate the influence of an external ELF magnetic field on the relation between applied membrane voltage and the number of the ion escapes from the Ca^{++} channel, for an assigned value of the viscous coefficient $\beta = h/m$.

Under these assumptions, thanks to the GRID infrastructure, several hundreds of runs with the original and the modified models have been performed in a very short time. In figure 1 the number of the Ca^{++} ions crossing the channel versus the transmembrane voltage coming out from the original model are shown, for a value of the viscous coefficient equal to $2E+12$; for this configuration it is worth noticing, the quasi-linear increase of the average number of ions crossing the channel as the membrane voltage increases. This result is in good agreement with results coming from other models and with experimental data [5], for analogous configurations. In fig. 2 the number of the Ca^{++} ions crossing the channel versus the transmembrane voltage coming out from modified model are shown. It is worth noticing that the differences between the two models are negligible, and apparently the introduction of probability function $Z(B)$ does not seem to affect the motion

of ions across membrane channels. But if we repeat the same simulation by using a longer simulation time (10 or 100 times) an interesting result is obtained: in the longer time analysis case the modified model gives as result a current crossing the channel of 10% higher than original model. This is clearly due to the influence of the external magnetic field on gating as expected. Further details about results will be given in the full version of the paper.

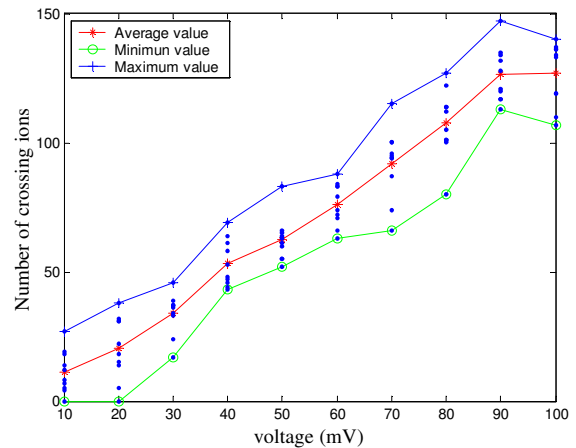


Fig. 1 - Number of ions exiting the channel versus transmembrane voltage ($\beta=2E+12$) by using original model.

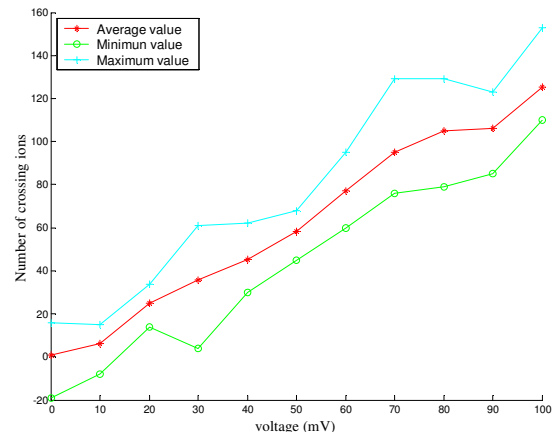


Fig. 2 - Number of ions exiting the channel versus transmembrane voltage ($\beta=2E+12$) by using new model.

IV. REFERENCES

- [1] B. Hille, *Ionic Channels of Excitable Mem-branes*, Sunderland, MA: Sinauer, 1992.
- [2] M. E. Oliveri and , S. Coco, D. S. M. Gazzo, A. Laudani and G. Pollicino, "3-D FE particle based model of ion transport across ionic channels", *Mathematics in Industry (Scientific Computing in Electrical Engineering)*, pp. 57-61, 2006, Springer-Verlag.
- [3] PS2I2 - <http://www.pi2s2.it> and <http://www.consortio-cometa.it>. (30 March 2008)
- [4] Zhang Yuhong; Zhan Yong; Zhao Tongjun; Han Yingrong; Liu Hui;, "Monte Carlo Simulation of the Permeability of Calcium Channels Exposure to Electromagnetic Fields", *ICBBE 2007*, 6-8 July 2007, pp. 767 - 769.
- [5] W. Nonner and B. Eisenberg, "Ion permeation and glutamate residues linked by poisson-nernst-planck theory in l-type calcium channels," *Biophysical Journal*, vol. 75, pp. 1287-1305, September 1998.

An Enhanced Ellipsoid Method for Electromagnetic Devices Optimisation and Design

D. A. G. Vieira, A. C. Lisboa and R. R. Saldanha

Department of Electrical Engineering, Federal University of Minas Gerais, Brazil
 {douglas,adriano,rodney}@cpdee.ufmg.br

Abstract—This paper proposes a novel ellipsoid method for the optimisation of sub-differentiable electromagnetic constrained problems. Unlike the classical method, which can apply only one cut per iteration, this novel algorithm can employ multiple cuts simultaneously. This improves the convergence rate while preserving all the method original theoretical guarantees. The design of a modelled reflector antenna is presented and it asserts the efficiency of the introduced technique.

Index Terms—Optimisation, sub-differentiability, ellipsoid method, reflector antenna.

I. INTRODUCTION

Optimising electromagnetic devices is known as a hard task, since it relies on the evaluation of numerical methods, which implies a huge computational effort. Additionally to improving accuracy and decreasing computational burden of numerical methods, it is also important to develop the optimisation procedures themselves.

Nowadays there are several classes of optimisation algorithms, each of them having their own advantages and disadvantages. Stochastic methods, such as genetic algorithm (GA), immune system (IS) and particle swarm optimisation (PSO), are very popular, as they require little knowledge about the function properties [1], [2]. They are very suitable in situations where continuity and differentiability cannot be assured. Furthermore, they can also be applied to generate an initial design point to deterministic methods. However, they are known to be slow, since they require a considerable amount of function evaluations [3].

Deterministic methods, usually divided into search direction and cutting-plane methods, typically require some kind of function differentiability. Search direction methods typically requires function differentiability, but can make an efficient local search, even in very sensitive problems, as does an extended gradient method when optimising antennas [3], [4]. When sub-differentiability is considered, cutting-plane methods are more suitable than deterministic methods. The ellipsoid algorithm [5] is one of the most popular cutting-plane methods. It can handle constraints directly, without any kind of transformation into unconstrained problems by penalty functions or barrier functions. Deterministic techniques can also be coupled with stochastic methods in a hybrid configuration [6], [7]. Therefore, improving these techniques are useful in many aspects.

Notwithstanding its robustness, the ellipsoid method lacks good performance in practice, specially as dimension in-

creases. To overcome this drawback, this work proposes to apply multiple cuts, instead of the single cut considered in the classical method, inside an inner loop. In the classical method, only one sub-gradient is considered per iteration. There are also closed-form solutions when two cuts (one-sided, parallel and wedge-shaped cuts) are considered, see [8] and references therein.

In the new multiple cuts ellipsoid method (MCEM), several cuts defined in the current evaluation point can be considered at once (e.g. when there are more than one active/violated constraint), as well as cuts memorised from previous iterations. The MCEM relies in a theoretically correct deep cut, instead of heuristic deep cuts [9].

The MCEM will be briefly described and then applied to design a reflector antenna for satellite communication. This problem has 38 control variables and was formulated considering 13 constraints. Hence, the results must test the claim that using multiple cuts improves the convergence rate, and decreases the computational effort entailed by the optimisation process of electromagnetic devices.

II. MULTIPLE CUTS ELLIPSOID METHOD

Consider the single objective optimisation problem

$$\begin{aligned} \min \quad & f(x) \\ \text{s.t.} \quad & g_j(x) \leq 0, \quad j = 1, \dots, n_g \end{aligned} \quad (1)$$

where $f(x)$ and $g_j(x)$ are real valued quasi-convex continuous sub-differentiable functions and $x \in \mathbb{R}^n$ is the vector of parameters. The set of n_i violated constraints is defined as $\mathbb{I} = \{j : g_j(x) > 0\}$. Given an ellipsoid $\mathbb{E}_k = \{x \in \mathbb{R}^n : (x - x_k)^T Q_k (x - x_k) < 1\}$ and an open half space $\mathbb{H}_k(x_k, d_k) = \{x \in \mathbb{R}^n : d_k^T x < d_k^T x_k\}$ the Shor's algorithm makes $\mathbb{E}_{k+1} \supseteq \mathbb{E}_k \cap \mathbb{H}_k$. His main achievement was to find a closed-form solution such that \mathbb{E}_{k+1} has minimal content. The direction d_k is $-\nabla f(x_k)$ if x_k is feasible, or $-\nabla g_j(x_k)$, for some $j \in \mathbb{I}$, otherwise. For quasi-convex functions, an optimal solution $x^* \in \mathbb{E}_k$ implies $x^* \in \mathbb{E}_{k+1}$.

Shor's algorithm only uses of one of the violated constraints. If more than one constraint are violated, it is better to calculate the intersection between the ellipsoid \mathbb{E}_k and the cone $\mathbb{C}_k = \bigcap_j \mathbb{H}_k^-(x_k, \nabla g_j(x_k))$, $\forall j \in \mathbb{I}$, composed by the intersection of cutting halfspaces, instead of a single halfspace.

The existence of a closed-form solution for the minimal content ellipsoid containing $\mathbb{E}_k \cap \mathbb{C}_k$ is unlikely. This paper proposes solving $\mathbb{E}_{k+1} \supseteq \mathbb{E}_k \cap \mathbb{C}_k$ iteratively. Let $\mathbb{E}_{k0} = \mathbb{E}_k$,

$\mathbb{E}_{k(i+1)} \supseteq \mathbb{E}_{ki} \cap \mathbb{H}_i$ for $i = 0, \dots, m-1$, and $\mathbb{E}_{k+1} = \mathbb{E}_{km}$. The MCEM relies on the cut depth

$$\alpha_{ki} = \frac{(x_{k0} - x_{ki})^T d_i}{\sqrt{d_i^T Q_{ki}^{-1} d_i}}, \quad (2)$$

where x_{ki} is the centre of \mathbb{E}_{ki} , $d_i = -\nabla g_j$ for some $j \in \mathbb{I}$. The convergence rate of the classical method improves by using (2) iteratively until α_{ki} becomes enough close to $-1/n$ for any $j \in \mathbb{I}$.

III. THE REFLECTOR ANTENNA PROBLEM

The proposed algorithm was applied in a satellite broadcast communication problem, which is described by Lisboa et al. [4]. In this problem, a reflector antenna in geosynchronous orbit must illuminate a target - the Brazilian territory for instance - on the earth surface. The optimisation problem is to maximise the average gain at n_s sample points \mathbb{P} , constrained to lower bounds of gain at certain sample points $\mathbb{S} \subseteq \mathbb{P}$. Hence, there is one constraint for each sample point in \mathbb{S} . The sample points \mathbb{P} are spread out all over the target. Specifying the minimum of 35dB in 13 points on the southeast region, the most populated in the country, the problem can be written as

$$\begin{aligned} \min_x \quad & f(x) = -\frac{1}{n_s} \sum_{i=1}^{n_s} G(x, p_i), \quad p_i \in \mathbb{P} \\ \text{s.t.} \quad & g_j(x) = 35 - G(x, p_j) \leq 0, \quad p_j \in \mathbb{S}, \quad j = 1, \dots, 13 \end{aligned} \quad (3)$$

In the original formulation these constraints were not considered [4]. The calculation of the gain at each sample point uses numerical techniques that are computationally expensive. The reflector surface was parameterised with 38 control variables. Therefore, it is a complex black box problem.

IV. RESULTS

The initial configuration x_0 was a reference classical paraboloid reflector. The respective radiation pattern is shown in Fig. 1 together with the optimal solution achieved after 19,500 function evaluations using the MCEM.

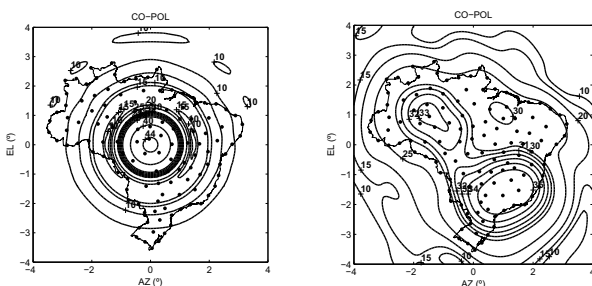


Fig. 1. Initial (left) and optimal (right) radiation pattern.

The convergence of the MCEM is contrasted with Shor's classical algorithm in Fig. 2. The convergence of the MCEM was faster and smoother. The MCEM converged to 30.97dB while the classical method converged to 30.69dB. The classical

method found 62% of infeasible points during the convergence, while the MCEM found 46%, as it discards infeasible points more efficiently by using more than one constraint at each iteration.

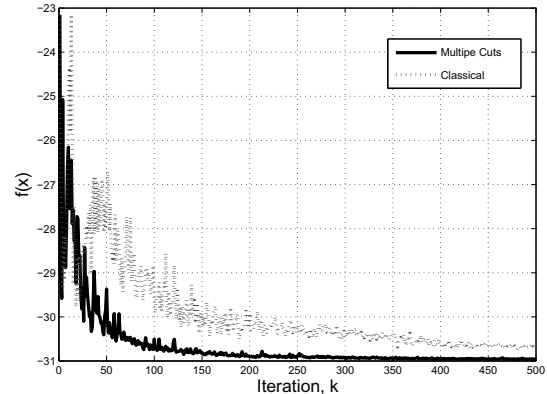


Fig. 2. Convergence curves of the MCEM and Shor's classical algorithm.

V. CONCLUSION

This paper has introduced a novel ellipsoid optimisation method that considers simultaneous multiple cuts. Its formulation takes advantage of the constraint structure to shrink the ellipsoid and, hence, to increase the convergence rate. The results of the application of MCEM to a optimisation problem with 38 variables support this claim. The proposed technique is a robust tool with a simple formulation to handle constraints.

ACKNOWLEDGMENT

This work was supported by CNPq and FAPEMIG under grants n^o 305265/2005-9, 13348 and 13180, Brazil.

REFERENCES

- [1] D. A. G. Vieira et al., "Treating constraints as objectives in multiobjective optimization problems using niched pareto genetic algorithm," *IEEE Transactions on Magnetics*, vol. 40, no. 2, pp. 1188–1191, March 2004.
- [2] S. Goudos et al., "Pareto optimal design of dual-band base station antenna arrays using multi-objective particle swarm optimization with fitness sharing," *IEEE TMag*, vol. 45, no. 3, pp. 1522–1525, March 2009.
- [3] D. A. G. Vieira et al., "Monotonically improving yagi-uda conflicting specifications using the dominating cone line search method," *IEEE Transactions on Magnetics*, vol. 45, no. 3, pp. 1494–1497, 2009.
- [4] A. C. Lisboa et al., "Multi-objective shape optimization of broad-band reflector antennas using the cone of efficient directions algorithm," *IEEE Transactions on Magnetics*, vol. 42, pp. 1223–1226, 2006.
- [5] N. Shor, "Cut-off method with space extension in convex programming problems," *Cybernetics*, vol. 12, pp. 94–96, 1977.
- [6] D. G. Vieira et al., "A hybrid approach combining genetic algorithm and sensitivity information extracted from a parallel layer perceptron," *IEEE Transactions on Magnetics*, vol. 41, no. 5, pp. 1740–1743, May 2005.
- [7] D. Zhou, C. Rajanathan, A. Sapeluk, and C. Ozveren, "Finite-element-aided design optimization of a shaded-pole induction motor for maximum starting torque," *IEEE Transactions on Magnetics*, vol. 36, no. 5, pp. 3551–3554, 2000.
- [8] S. Kim, D. Kim, and K. Chang, "Using two successive subgradients in the ellipsoid method for nonlinear programming," *Journal of Optimization Theory and Applications*, vol. 82, no. 3, pp. 543–554, September 1994.
- [9] R. R. Saldanha et al., "Adaptive deep-cut method in ellipsoidal optimization for electromagnetic design," *IEEE Transactions on Magnetics*, vol. 35, no. 3, pp. 1746 – 1749, 1999.

Robust Optimization Utilizing the Second-order Design Sensitivity Information

Dong-Hun Kim¹, Giwoo Jeung¹, Dong-Wook Kim¹, Heung-Geun Kim¹, David A. Lowther², Jan K. Sykulski³

¹School of Electrical Eng. and Computer Sci., Kyungpook National University, Daegu 702-701, Korea
dh29kim@ee.knu.ac.kr

²ECE Department, McGill University, Montreal, Quebec, H3A 2A7, Canada

³School of ECS, University of Southampton, Southampton, SO17 1BJ, UK

Abstract — This paper presents an effective methodology for robust optimization of electromagnetic devices. To achieve the goal, the method improves the robustness of the objective function by minimizing the second-order sensitivity information, called a gradient index and defined by a function of gradients of performance functions with respect to uncertain variables. The constraint feasibility is also enhanced by adding a gradient index corresponding to the constraint value. The validity of the proposed method is tested with the TEAM Workshop Problem 22.

I. INTRODUCTION

Due to a growing demand for high-performance and high-reliability electromagnetic devices or equipment, attention has recently been focused on the robust optimization of products with the aim of minimizing the variation of the performance as a result of uncontrollable factors such as manufacturing errors, operating conditions, material properties, etc. Until now, most of the attempts which have been made used the Taguchi's robust design concept or Monte Carlo simulation based on the assumption that design parameters are random variables with a probability distribution [1]. However, implementation difficulties usually arise because it is not easy to acquire probability data of uncertain variables and also information about which parameter is dominant may not be available.

To overcome the aforementioned drawbacks, this paper proposes an effective methodology utilizing the second-order sensitivity information, defined as a 'gradient index' (GI), for the robust optimization of electromagnetic systems [2]. The basic concept of the method is to obtain robustness of the objective function by minimizing a GI value calculated from the gradients of performance functions with respect to uncertain variables. Simultaneously, the constraint feasibility is also considered by adding a term determined with a constraint value and a gradient index corresponding to the constraint. Consequently, the method needs neither statistical information on design variations nor calculation of the performance reliability while it is searching for a robust optimal solution.

II. ROBUST OPTIMAL DESIGN USING A GRADIENT INDEX

The TEAM benchmark problem 22 is concerned with the design optimization of a superconducting magnetic energy storage system (SMES) as depicted in Fig. 1. In order to simplify the design problem, a constraint of the current quench condition on the superconductivity magnet is not considered here. A typical optimization problem for minimizing an objective function subject to a set of constraints is expressed as

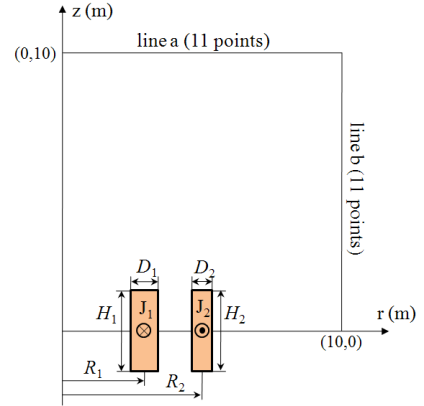


Fig. 1. Configuration of the SMES device with 8 design variables

$$\begin{aligned} \text{Minimize} \quad & f(\mathbf{x}) = \sum_{i=1}^{21} |B_{stray,i}(\mathbf{x})|^2 \\ \text{subject to} \quad & g_1(\mathbf{x}) = \left(\frac{E(\mathbf{x}) - E_o}{0.05 \times E_o} \right)^2 - 1 \leq 0 \\ & g_2 = (R_1 - R_2) + \frac{1}{2}(D_1 + D_2) \leq 0 \\ & \mathbf{x}_L \leq \mathbf{x} \leq \mathbf{x}_U \end{aligned} \quad (1)$$

where \mathbf{x} is a design variable vector, $B_{stray,i}$ the stray field values calculated at the i th design iteration, E the stored magnetic energy and E_o the energy target value of 180 MJ. The values \mathbf{x}_L and \mathbf{x}_U denote the lower and upper bounds of the design variables, respectively.

To complement the above expressions, the proposed robust optimization for improving the robustness of the objective and the constraint functions is formulated as follows:

$$\begin{aligned} \text{Minimize} \quad & GI_f = \max_i |df(\mathbf{x})/du_i| \quad i = 1, 2, \dots, 8 \\ \text{subject to} \quad & g_j(\mathbf{x}) + \Psi_j(g_j(\mathbf{x})) \leq 0 \quad j = 1, 2 \\ & f(\mathbf{x}) \cong M \end{aligned} \quad (2)$$

where GI_f is a gradient function of the objective function with respect to the uncertain variables u_i and M denotes the target value of the objective function. In order to enhance the robustness of the constraint feasibility, the term $\Psi_j(g_j)$ in (2) is added to each constraint

$$\Psi_j(g_j) = \begin{cases} 0 & g_j < CT \\ \frac{\kappa_j GI_{g_j}}{CTMIN - CT} & CT < g_j < CTMIN \\ \frac{\kappa_j GI_{g_j}}{CTMIN - CT} & g_j > CTMIN \end{cases} \quad (3)$$

$$GI_{g_j} = \max_i |dg_j(\mathbf{x})/du_i| \quad i = 1, 2, \dots, 8$$

where GI_{g_j} is a gradient function of the j th constraint function with respect to the uncertain variables. If the constraint is numerically critical ($CT \leq g_j \leq CTMIN$) or violated ($g_j > CTMIN$), a term proportional to GI_{g_j} multiplied by a proper constant κ is added according to the value of the robustness of the constraint feasibility.

III. NUMERICAL IMPLEMENTATION

The proposed method has been implemented by combining the commercial finite element code MagNet [3] with a DOT optimizer [4] as shown in Fig. 2, where a modified feasible direction algorithm with the second-order sensitivity information by finite differencing is used. To obtain the GI values, the first-order sensitivity values are computed by the continuum design sensitivity analysis (CDSA).

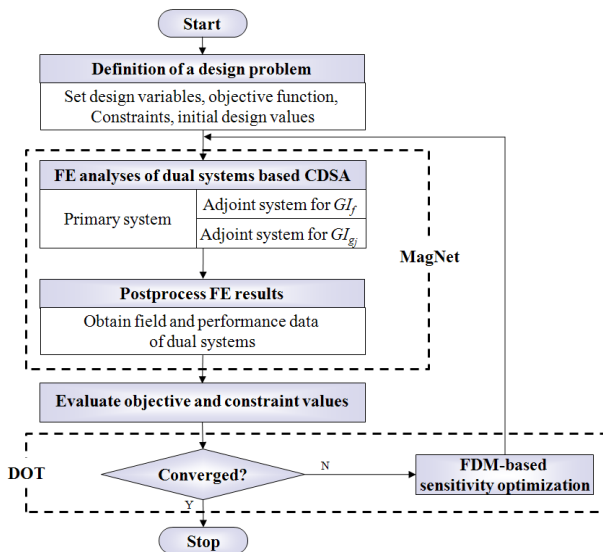


Fig. 2. Flow chart of the proposed robust optimization method

IV. RESULTS

The optimization problem for minimizing the stray fields of the SMES device of Fig. 1 is solved using two methods. The first is a deterministic method based on CDSA that does not take into account the effects of uncertain parameters; the second approach is the proposed robust optimization method. In this paper, all of the 8 design variables used in the deterministic method are selected to be the uncertain variables for the purpose of comparison between the two methods.

Starting with an initial design, the deterministic and the robust optima are presented in Table I. The stored energy values obtained from the two methods almost reach the target value of 180 MJ, but the robust optimum produces a better mean value of the stray fields than the deterministic algorithm. It is inferred that the deterministic optimal solution is trapped in one of the local minima near the constraint boundaries, while a better optimal solution is found by the robust optimization as the feasibility robustness of the constraints is improved. In Figs 3 and 4, the variations of the sensitivity values and the stray fields are compared between the deterministic and the robust optima, respectively.

TABLE I
DESIGN VARIABLES AND PERFORMANCE INDICATORS
AT THE DETERMINISTIC AND ROBUST OPTIMA

Design variables	Unit	Lower bound	Initial values	CDSA optimum	Robust optimum	Upper bound
R1	mm	1000	2000	2108	1977	4000
D1	mm	100	500	412	404	800
H1	mm	200	1500	1504	1507	3600
R2	mm	1800	2500	2462	2348	5000
D2	mm	100	400	294	233	800
H2	mm	200	2000	1756	1871	3600
J1	A/mm ²	10	17	16.39	16.30	30
J2	A/mm ²	10	17	14.49	16.19	30
B _{stray,mean}	μT		23,055	153	34	
Energy	MJ		521	183	181	

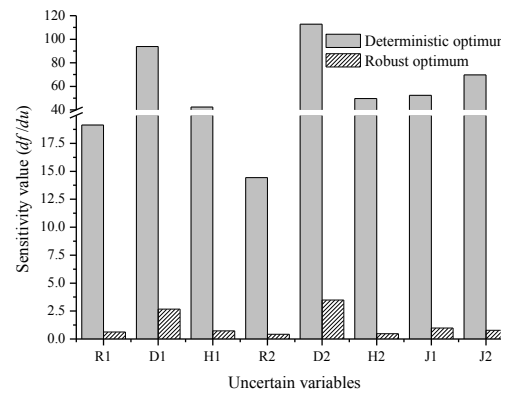


Fig. 3. Comparison of sensitivity values of uncertain variables

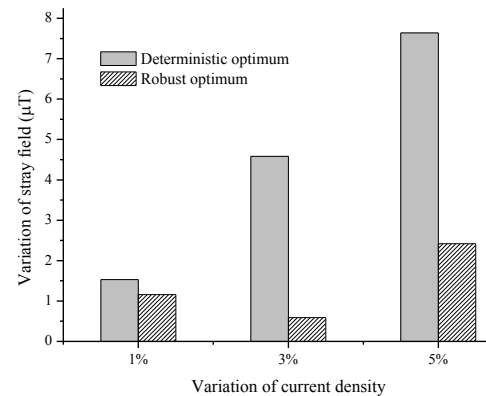


Fig. 4. Comparison of stray field variations when the current density changes

V. CONCLUSION

A robust optimization approach adopting the concept of a gradient index has been introduced in this paper. The results reveal that the proposed method offers high performance as well as robustness of the objective and the constraint functions.

VI. REFERENCES

- [1] G. Steiner, A. Weber and C. Magele, "Managing uncertainties in electromagnetic design problems with robust optimization," *IEEE Transactions on Magnetics*, vol. 40, no. 2, pp. 1094-1099, 2004.
- [2] J. S. Han and B. M. Kwak, "Robust optimization using a gradient index: MEMS applications," *Structural and Multidisciplinary Optimization*, vol. 27, no. 6, pp. 469-478, 2004.
- [3] MagNet User's Manual, Infolytica Corporation, Quebec, Canada, 2008.
- [4] DOT User Manual, Vanderplaats Research & Development, Inc., 2001.

Adapted Output Space-Mapping Technique for a Bi-Objective Optimization

T. V. Tran, F. Moussouni, S. Brisset, and P. Brochet

L2EP, Ecole Centrale de Lille, Cité Scientifique, BP 48, 59651, Villeneuve d'Ascq Cedex, France

Abstract—Multi-objective optimizations by means of 3D finite element models result in very high computation burden. To have an affordable computation cost, the output space-mapping technique is applied with a new method where the scalar correction of the model outputs is replaced by a set of corrective functions. This method is used for the bi-objective optimization of a transformer and allows finding the complete Pareto optimal set in less than two days on a laptop.

Index Terms—Space-mapping, Multi-objective optimization, 3D finite element model, Transformer.

I. INTRODUCTION

THE OPTIMAL design of electromagnetic devices is a complex and complicated task. A way to formulate the problem is to find the trade-off between conflicting goals. Solving this problem requires building the Pareto optimal set with accuracy. With two objectives, the Pareto optimal set can be easily drawn and helps the designer to find a good solution. Many methods are able to find the solutions of a bi-objective optimization: scalar methods such as the well-known weighted sum (WS), ϵ -constraint methods, etc. [1]; and stochastic methods such as non-dominated sorting genetic algorithm II (NSGA II), niched Pareto genetic algorithm (NPGA), etc. [2]. Unfortunately, those methods require a very high number of model evaluations. This is not compatible with the use of a 3D FE magneto-thermal model that requires 2 hours [3].

The purpose of space-mapping (SM) [4]-[7] is to align a coarse model and a fine model to reduce the computation time. In electromagnetic, the fine model is a 2D or 3D FEM and the coarse model is often a lumped mass or analytical model. The Manifold-Mapping [6] and Output Space-Mapping (OSM) [7] techniques are the most recent and effective methods. Unfortunately, no SM algorithm has been developed or adapted to multi-objective optimization problem. The aim of this paper is to adapt the OSM to bi-objective optimization problems.

First, the bi-objective optimization of a safety transformer [3] is presented and the designer's dilemma is raised. Section III proposes a new method to solve this problem that is applied in section IV to the bi-objective optimization of the safety transformer. Finally, some concluding remarks are given.

II. OPTIMIZATION PROBLEM

The safety isolating transformer is a one-phase step-down transformer. It uses grain-oriented E-I laminations. The primary and secondary windings are both wound around the

frame surrounding the central core.

The bi-objective optimization problem of a safety isolating transformer contains 7 design variables. There are three parameters a , b , c for the shape of the lamination, one for the frame d , two for the section of conductors S_1 , S_2 , and one for the number of primary turns n_1 . There are 6 non-linear inequality constraints in this problem. The copper and iron temperatures T_{co} , T_{ir} should be less than 120°C and 100°C, respectively. The magnetizing current I_μ/I_1 and drop voltage $\Delta V_2/V_2$ should both be less than 10%. Finally, the filling factors of both coils f_1 and f_2 should both be lower than 0.5. The objective functions are to maximize the efficiency η and to minimize the total mass M_{tot} of iron and copper materials.

A. Coarse and fine models

The multi-physical phenomena within the transformer are electric, magnetic and thermal. They are modeled by a lumped-mass (coarse) model (LM) and a 3D finite element (fine) model (3D FE) [3].

The LM model is built with the assumption that the voltage drop due to the magnetizing current is neglected. Therefore the maximal induction depends on the primary voltage. The computational time of the coarse model is very short (50 ms on an Intel Pentium M 2.13 GHz machine).

The 3D FE magneto-thermal model is built with the assumption that all magnetic and electric quantities are sinusoidal. The iron loss is computed with Steinmetz formula described in [3] and the leakage inductances are calculated with the magnetic energy. Full-load and no-load simulations are used to compute all characteristics of the safety isolating transformer. The 3D FE model with magneto-thermal coupling requires a very expensive computational time (about 2 hours on an Intel Pentium M 2.13 GHz laptop).

B. Designer's dilemma

Generating 100 optimal solutions of the Pareto optimal set by means of the 3D FE model requires 10 000 hours while 5 minutes only are needed with the LM model. In fact, as solving 3D FE model is very expensive only six points are computed and considered as a reference set (Fig. 1). The points are found by using the classical OSM technique. The LM model is used to build an extended Pareto optimal set in a short time. It is obvious that this last optimal set is far from the reference set.

A first solution to this dilemma is to interpolate the reference set. Unfortunately, no information on the design parameters can be obtained because the interpolation can only be made in the objective space.

Therefore, the authors propose to adapt OSM technique for bi-objective optimization problems in order to generate an extended and accurate Pareto optimal set in less than 100 hours.

III. ADAPTED SPACE-MAPPING TECHNIQUE

A. Bi-objective optimization algorithm

According to the state of the art, the ε -constraint method is a useful approach to build a Pareto optimal set [1]. Moreover, this method may reach Pareto optimal solutions in the non-convex region. The ε -constraint method consists to transform the multi-objective problem in a single-objective problem. Among the objectives, one is kept and the others are transformed in inequality constraints.

B. Space-mapping techniques

Space mapping techniques aim to use both coarse and fine models to reduce the computational time and increase the accuracy of the obtained solution [4]-[7].

One approach of SM techniques, called Output Space-Mapping (OSM) [7] consists to modify the coarse model by adding some corrective coefficients computed with the fine model, in order to align the results of both models.

C. Corrective spline functions

In the case of a mono-objective optimization only a set of scalar coefficients is searched. In the case of a multi-objective optimization, the corrective coefficients' values must be changed for each solution from the Pareto set. So that these coefficients are replaced by corrective functions.

IV. APPLICATION CASE

The bi-objective optimization problem of the safety isolating transformer presented in section II is solved with the proposed algorithm. Fig. 2 shows the Pareto optimal set obtained by using the corrective functions. 30 points are given at each iteration. At the end of the optimization, a Pareto optimal set very close to the reference set is found.

Finally, only 17 3D FE simulations are needed to obtain an accurate Pareto optimal set. The computational time of the

proposed algorithm is approximately 34 hours (1.4 day) on an Intel Pentium M 2.13 GHz laptop. The reference Pareto optimal set requires 60 hours (2.5 days) on the same machine. To have an accurate Pareto optimal set by using the 3D FE model only, approximately 10,000 hours (14 months) are required.

V. CONCLUSION

The output space-mapping technique is adapted to provide a practical way to build an accurate Pareto optimal set in bi-objective optimization using full 3D coupled finite element model and keeping the computational time in an acceptable limit. Cubic spline interpolation functions are used to predict the values of the corrective coefficients. By using these corrective functions, the ε -constraints bi-objective optimization algorithm gives an extended and accurate Pareto optimal set in less than 2 days.

REFERENCES

- [1] A. Murano, A. Passaro, N. M. Abe, A. J. Preto, S. Stephany, "Multiobjective Optimization of Electro-optic Modulators by Using the ε -constraint Method", *proceedings of CEFC 2008*, May, 2008, Athens, Greece.
- [2] A. H. F. Dias, and J. A. de Vasconcelos, "Multiobjective Genetic Algorithms Applied to Solve Optimization Problems", *IEEE Transactions on Magnetics*, vol. 38, no. 2, pp. 1133-1136, 2002.
- [3] T. V. Tran, S. Brisset and P. Brochet, "A Benchmark for Multi-Objective, Multi-Level and Combinatorial Optimizations of a Safety Isolating Transformer", *proceedings of COMPUMAG 2007*, June 2007, Aachen, Germany, all materials can be downloaded at <http://l2ep.univ-lille1.fr/come/benchmark-transformer.htm>.
- [4] H. Choi, D. Kim, I. Park, and S. Hahn, "A New Design Technique of Magnetic Systems using Space Mapping Algorithm", *IEEE Trans. on Magn.*, vol. 37, no 5, pp. 3627-3630, 2001.
- [5] J.W. Bandler, Q.S. Cheng, S.A. Dakroury, A.S. Mohamed, M.H. Bakr, K. Madsen, and J. Sondergaard, "Space Mapping: The State of the Art", *IEEE Trans. Microwave Theory Tech.*, vol. 52, no. 1, pp. 337-361, 2004.
- [6] D. Echeverria, D. Lahaye, L. Encica, E. A. Lomonova, P. W. Hemker, and A. J. A. Vandenput, "Manifold-Mapping Optimization Applied to Linear Actuator Design", *IEEE Trans. on Magn.*, vol. 42, no. 4, pp. 1183-1186, 2006.
- [7] L. Encica, J. J. H. Paulides, E. A. Lomonova, A. J. A. Vandenput, "Aggressive Output Space-Mapping Optimization for Electromagnetic Actuators", *IEEE Transactions on Magnetics*, vol. 44, no. 6, pp. 1106-1109, 2008.

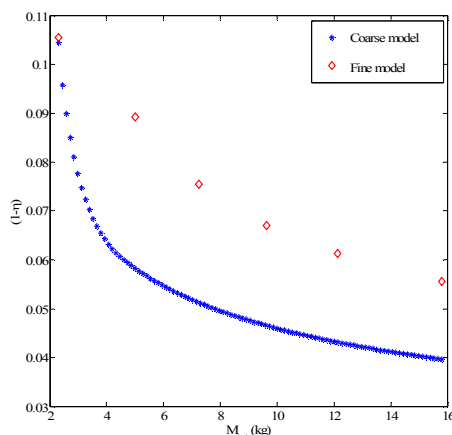


Fig.1. Pareto optimal set using the coarse and fine models.

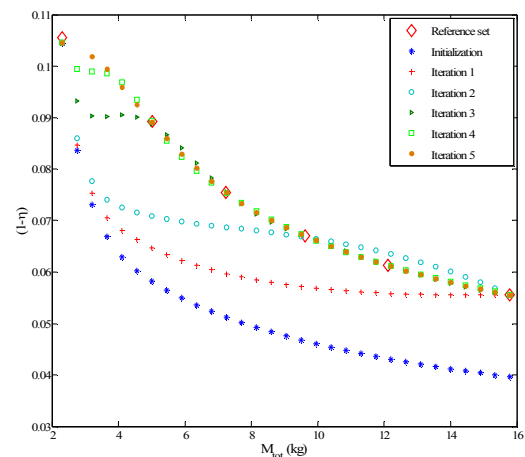


Fig.2. Pareto optimal set obtained at each iteration.

Niching Evolution Strategies for Simultaneously Finding Global and Pareto Optimal Solutions

Christian Magele*, Alice Köstinger*, Michael Jandl*, Werner Renhart*, Bogdan Cranganu-Cretu** and Jasmin Smajic**

*Institute for Fundamentals and Theory in Electrical Engineering, Graz University of Technology

Kopernikusgasse 24/3, A-8010 Graz, Austria

** ABB Switzerland Ltd. Corporate Research

Segelhofstrasse 1, CH-5405 Baden-Dättwil, Switzerland

Email: Christian.Magele@TUGraz.at

Abstract—Many real world optimization problems turn out to be multi-objective optimization problems revealing a remarkable number of locally optimal solutions corresponding to the chosen objective function. Therefore, it seems desirable to detect as many of those solutions with as few objective function calls as possible. A Niching Higher Order Evolution Strategy (NES) can successfully be applied to locate a remarkable number of local solutions during a single optimization run. Additionally, it turns out that all of these solutions can be found next to the front of non-dominated solutions. Therefore, evaluating more than one objective function (in parallel or in series) yields a good approximation of the Pareto-optimal front. The proposed method will be tested against several test functions and then applied to the solution of a magnetic shunting/shielding problem.

Index Terms—Stochastic Optimization, Niching Evolution Strategies, Multi-Objective Problems.

I. INTRODUCTION

Applying optimization algorithms to technical design problems has become a standard procedure within the last decades. Stochastic methods like Evolution Strategies among many others have become frequently used tools for this task. Besides their major advantages like high convergence stability, these methods still suffer from an inherent high number of function calls. Even if CPU power has risen incredibly since the introduction of these methods for optimizing electromagnetic fields, in dealing with complex real world applications one must still economize computational effort. This calls for an optimization strategy which supplies the user with as much information as possible from as few runs as necessary. Niching Higher Order Evolution Strategies (NES) take advantage of a modified recombination operator. In contrast to the classical version [1], NES group the population into clusters and perform recombination within a cluster with a higher probability than among different clusters [2]. It turns out that over the course of the optimization process several sub-populations start to flock together temporarily in the vicinity of different local solutions and give them up again on their way to the final solution. The entity of these local solutions corresponding to a single objective function form a part of the front of the non-dominated solutions [3]. Taking multiple objective functions into account in parallel or in series, more than one part of the front of the non-dominated solutions can be found. Moreover,

in a predominant number of optimization runs, NES finally converges to the global solutions among the detected local ones. The optimization strategy must be able to report on all solutions to the user. It is obvious that the population size has to be related to the number of local solutions. To keep the numerical effort still reasonable, it is very important to estimate the number of these solutions reasonably well and to adapt it continuously during the optimization run. The proposed strategy is applied to several test functions for comparison of the number of function calls or global behaviour and finally to a 2D real world shape optimization problem, namely a magnetic shielding and shunting problem for industrial devices.

II. THE MAGNETIC SHUNT/SHIELDING PROBLEM

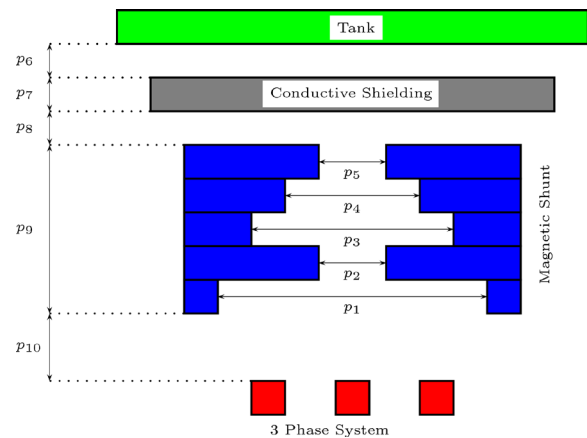


Fig. 1. Topology of the Shunt Problem with Trial Variables p_1 to p_{10}

Figure 1 shows the magnetic shunt/shield problem [4]. Eddy currents can flow in the tank (made of steel) only. The magnetic shunt is made up from a certain number of slices. They all have the same thickness but different widths. A layer of copper acting as a magnetic shield can additionally be inserted between the shunt and the tank. The magnetic field is produced by a three phase system. The goal is to minimize the power losses in the tank while keeping the volume of the magnetic shunts (and later also of the conductive shielding) as low as possible.

III. OPTIMIZATION STRATEGY: NICHING HIGHER ORDER $[\kappa(\mu/\rho, \lambda)]$ EVOLUTION STRATEGY

A higher order $[\kappa(\mu/\rho, \lambda)]$ Evolution Strategy (NES) [1] relies on the application of features of biological evolution, like population, mating and environmental selection, recombination, reproduction and mutation [5]. Recombination is usually done by arithmetic crossover, taking the fitness of all parents under consideration into account. Prior to this step the whole generation is clustered using a complete linkage clustering method [2]. Then, recombination within a cluster is performed with a higher probability than recombination between different clusters. This leads, even after a few generations, to a certain number of sub-populations gathering around local solutions. The best solution of each cluster is stored in order to remember all individual local solutions. Since the population is adjusted depending on the number of clusters under investigation, it is very important to estimate this number as accurately as possible in order to spend CPU resources economically. This can be done by monitoring the cluster radii, both in a static way (comparing the radii of the individual clusters of one generation) and dynamically (tracing the behaviour of the radius of the largest clusters). Then, over the course of the optimization process, one local solution after another is given up, which leads to a continuously decreasing population. At last, all individuals can be found next to the final solution only, which more often than not turns out to be the global of all distinguished solutions.

IV. FRONT OF NON DOMINATED SOLUTIONS

To detect a major part of the front of non-dominated solutions [3], more than only the main objective function is taken into account. Using a fuzzy scheme [6] to supply the NES with a scalar value characterizing the quality of the current configuration, this can be done by selecting appropriate sets of weighting factors as indicated in (1).

$$\mu(\mathbf{p}) = (w_1 + w_2) - w_1\mu_{losses}(\mathbf{p}) - w_2\mu_{volume}(\mathbf{p}). \quad (1)$$

Putting more emphasis on one or the other objective (in parallel or in series), a large part of the pareto front can be detected.

V. RESULTS

A $[\kappa(\mu/\rho, \lambda)]$ NES with $\kappa = 10$ clusters, $\mu = 4$ parents with $\rho = 2$ of them performing recombination leading to $\lambda = 10$ children is used to solve the above magnetic shunt/shielding problem. The electromagnetic field problems are solved using the 2D Finite Element code ELEFANT2D [7]. In the first stage only magnetic shunts are taken into account. Ten trial variables (Fig. 1) can be adjusted to minimize both the losses and the volume of the shunts. In a sequential way, four different objective functions (1) with different weights are used (Fig. 2). Each problem was run once, leading to a single optimal solution for each objective function, respectively. The best result - obtained with $w_1=1$ and $w_2=1$ - was able to decrease the volume by 53% and the eddy current losses by

40% compared with a massive shunt of the same dimensions. Additionally, the best solutions of each of the ten clusters were stored and evaluated. The non dominated ones of each problem were selected and are plotted in Fig. 2 together with a vast number of solutions obtained in the different optimization runs and the respective front of non-dominated solutions. It can be seen that the cluster solutions are quite close to the front of pareto optimal solutions.

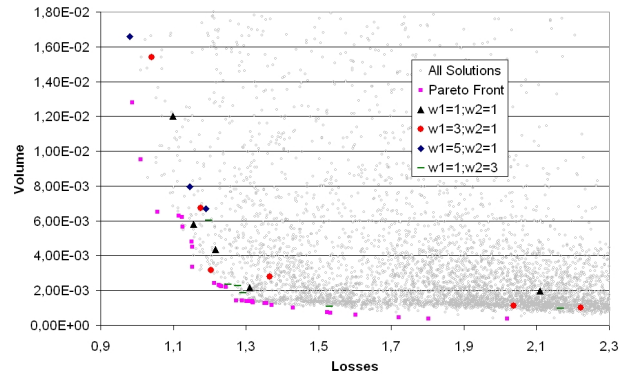


Fig. 2. Front of Non-Dominated Solutions.

VI. CONCLUSION

A Niching Higher Order Evolution Strategy was applied to determine the optimal design and location of five layers of magnetic material in order to shield as much magnetic field from the tank wall of a transformer as possible. Estimating the number of clusters (and hence the number of local solutions) fairly well, the population size can be kept to a minimum, saving CPU time. Running this strategy several times sequentially with different objective functions (stressing one or another objective), it turned out that additionally to the respective optimal designs, several solutions along or close to the pareto front can be detected.

REFERENCES

- [1] I. Rechenberg, "Evolutionsstrategie 94", Frommann-Holzboog, Stuttgart, 1994.
- [2] Aichholzer, O., Aurenhammer, F., Brandstätter, B., Ebner, T., Krasser, H., Magele, C., Mühlmann, M., "Evolution strategy and hierarchical clustering" IEEE Trans. Magn., vol. 38 No. 2, S. 1041 - 1044, 2002.
- [3] Barba P. Di, Farina M., Savini A.: "An improved technique for enhancing diversity in Pareto evolutionary optimization of electromagnetic devices" A COMPEL: Int J for Computation and Maths. in Electrical and Electronic Eng.; Volume 20 No. 2; 2001
- [4] B. Cranganu-Cretu, J. Smajic, W. Renhart, Ch. Magele, "Targeted Optimization Supported Design of Industrial Devices", Accepted for Publication in IEEE Transactions on Magnetics, April, 2008.
- [5] Fogel, D.B., (1995): Evolutionary Computation. *IEEE Press*, 1995.
- [6] Ch. Magele, G. Fürntratt, B. Brandstätter, K.R.Richter: "Self Adaptive Fuzzy Sets in Multi Objective Optimization using Genetic Algorithm" ACES Journal, vol 12, No. 2, pp 26 - 31 1997.
- [7] Computer program package EleFAnT2D, IGTE TUGraz, <http://www.igte.tugraz.at>

Design Optimization of Waveguide Filters Using Continuum Design Sensitivity Analysis

Dong-Hun Kim¹, Nak-Sun Choi¹, Giwoo Jeung¹, Joon-Goo Park¹, and Jin-Kyu Byun²

¹School of Electrical Eng. and Computer Sci., Kyungpook National University, Daegu 702-701, Korea
dh29kim@ee.knu.ac.kr

²School of Electrical Engineering, Soongsil University, 511 Sangdo-dong, Dongjak-gu, Seoul 156-743, Korea

Abstract — This paper presents a new methodology for design optimization of dielectric waveguide filters based on continuum design sensitivity analysis in conjunction with standard electromagnetic software. To achieve this, an analytical sensitivity formula and unified program architecture applicable to optimal design of high-frequency devices are proposed. A three-dimensional dielectric resonator used in waveguide filters has been tested to illustrate the validity of the method.

I. INTRODUCTION

In recent years, a few attempts at optimizing waveguide filters based on the design sensitivity analysis (DAS) have been made. Depending on the technique used to compute the derivative of an objective function, DAS can be categorized as the discrete DSA (DDSA) [1] or the continuum DSA (CDSA) [2]. However, from the practical viewpoint of combing with general-purpose electromagnetic (EM) software packages, DDSA has a critical drawback as it requires some amendments to the software code to perform sensitivity calculation. In the meantime, Yang *et al* [2] proposed the analytical sensitivity formulas by using the bilinear mapping obtained from the weak form of wave equations. Even though CDSA could overcome the aforementioned problem of DDSA, no in-depth work on CDSA concerning high-frequency device design has been carried out to date. It is believed that the complication of the sensitivity derivation based on the bilinear mapping may lead researchers to the ambiguity of the adjoint system.

In this paper, an analytical sensitivity formula for shape optimization in frequency domain is newly derived from a fairly routine procedure, where the augmented Lagrangian method (ALM), the material derivative concept and the adjoint variable method (AVM) are exploited [3]. During the mathematical expansions, the adjoint system equation is systematically deduced and compared to the wave equation referred to as the primary system equation. It is well known that the analytical formula facilitates calculating the first-order gradient information of an objective function with respect to shape design variables and saves a lot of computing time in finding an optimal solution especially as the number of design variables increases. To utilize the advantages of CDSA, a unified program architecture, where engineering software packages are integrated into a design tool, is proposed.

II. SHAPE DESIGN SENSITIVITY FORMULA

In order to deduce the design sensitivity and the adjoint system equation systematically, the variational form of source-free wave equation in time-harmonic case, referred to as the

primary system, is added to objective function g based on the augmented Lagrangian method:

$$\begin{aligned} \bar{F} = & \int_{\Gamma} g(\mathbf{E}(\mathbf{p})) d\Gamma \\ & + \int_{\Omega} [-\mu_r^{-1} \nabla \times \mathbf{E} \cdot \nabla \times \boldsymbol{\lambda} + k_o^2 \epsilon_r \mathbf{E} \cdot \boldsymbol{\lambda}] d\Omega \\ & - \int_{\gamma} [\gamma_e (\mathbf{n} \times \mathbf{E}) \cdot (\mathbf{n} \times \boldsymbol{\lambda}) + \mathbf{V} \cdot \boldsymbol{\lambda}] d\Gamma \end{aligned} \quad (1)$$

where g is scalar functions differentiable with respect to the electric field \mathbf{E} , which is itself an implicit function of design variable vector \mathbf{p} , Γ the boundary of analysis region Ω , $k_o = \omega(\epsilon_o \mu_o)^{1/2}$, $\boldsymbol{\lambda}$ the Lagrange multiplier vector interpreted as the adjoint variable, γ_e a known parameter and \mathbf{V} a known vector. To obtain an explicit expression for the deformation of the interface boundary γ between different materials, Ω_1 and Ω_2 , the second integral on the right-hand side of (1) is split into the two regions. After taking the material derivative on both sides of (1), the adjoint system equation is defined as:

$$\begin{aligned} & \int_{\Omega} [-\mu_r^{-1} \nabla \times \boldsymbol{\lambda} \cdot \nabla \times \mathbf{E}' + k_o^2 \epsilon_r \boldsymbol{\lambda} \cdot \mathbf{E}'] d\Omega \\ & - \int_{\gamma} [\gamma_e (\mathbf{n} \times \boldsymbol{\lambda}) \cdot (\mathbf{n} \times \mathbf{E}') - \mathbf{g}_E \cdot \mathbf{E}'] d\Gamma = 0 \end{aligned} \quad (2)$$

where \mathbf{E}' denotes an arbitrary variable vector and the pseudo-source, $\mathbf{g}_E = \partial g / \partial \mathbf{E}$, plays the role of incident field imposing on the boundary Γ . It is noted that only the boundary value used is different in the dual system consisting of the primary and the adjoint systems.

Finally, the design sensitivity formula applicable to design optimization of high-frequency devices is given by

$$\begin{aligned} \dot{\bar{F}} = & \int_{\gamma} [\omega^2 \mu_o (\mu_2 - \mu_1) (\mathbf{H}_{1n} \cdot \mathbf{H}_{2n}(\boldsymbol{\lambda}) - \mathbf{H}_{1t} \cdot \mathbf{H}_{2t}(\boldsymbol{\lambda})) \\ & - k_o^2 (\epsilon_{r2} - \epsilon_{r1}) (\mathbf{E}_{1n} \cdot \boldsymbol{\lambda}_{2n} - \mathbf{E}_{1t} \cdot \boldsymbol{\lambda}_{2t})] V_n d\gamma \end{aligned} \quad (3)$$

where the subscripts, n and t , are the normal and tangential vectors to the interface boundary, respectively.

III. NUMERICAL IMPLEMENTATION

Using the analytical formula (3), the first-order gradient information of an objective function with respect to the design variables can be easily calculated from the field values obtained in the dual system. To implement this, a unified program architecture applicable to high-frequency device design is presented in Fig. 1. The program consists of three independent modules that are distinguished by the dotted boxes shown in Fig. 1. The optimization module outside the two boxes controls the overall design procedure and evaluates crucial quantities such as the objective functions, adjoint source terms, and design sensitivity. On the other hand, the analysis module inside the upper box estimates the performance of the dual system whenever the design variables

change. The optimization toolbox module provides efficient searching techniques for seeking out an optimal solution in infinite design space and returns optimal displacement values to design variables. The proposed method has been executed by combining the commercial EM code HFSS with the general optimizer DOT, where a modified feasible direction algorithm with the first-order sensitivity information is used.

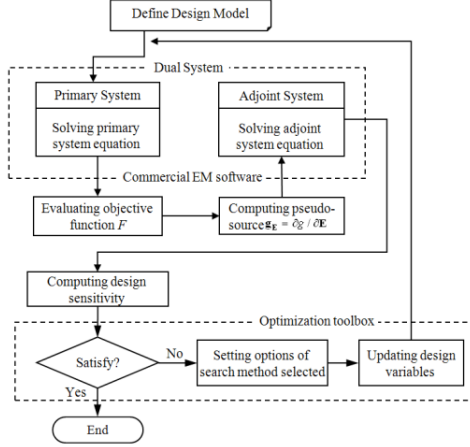


Fig. 1. Flowchart of the proposed method

IV. RESULTS

The proposed program architecture has been successfully applied to optimization of a dielectric waveguide filter in conjunction with the two different commercial software packages without the need to modify the source code. For analyzing the 3-D design model depicted in Fig. 2, the frequency domain solver with the second-order tetrahedral elements is used. The objective function is defined as (4) to achieve a second-order Chebyshev Type I lowpass transfer function from 1.4 GHz to 3.4 GHz, where the cutoff frequency is 2.4 GHz with passband ripple of 0.5 dB.

$$\text{Minimize } F = \sum_{i=1}^n \frac{1}{n} (|T_{ri}| - |T_{ro}|)^2 \quad (4)$$

$$\text{subject to } g_j(\mathbf{p}) = (\mathbf{p}_j - \mathbf{p}_{j+1}) + \varepsilon_j \leq 0 \quad j = 1, \dots, 5$$

where n is total frequency points of 21 selected at 0.1 GHz intervals, T_{ri} the transmission coefficient calculated at the i th frequency, T_{ro} the desired value at the same frequency, g_j the j th constraint function imposed on the design variables. The optimization problem is solved using two different searching techniques. The first adopts finite differencing method (FDM) for calculating the sensitivity information; the second approach is based on CDSA. In this paper, 6 design variables as shown in Fig. 2 are selected for the purpose of comparison between the two methods.

Starting with an initial design, the CDSA-based and the FDM-based optima are presented in Table I. The objective function values obtained from the two methods almost reach the same value of -38.40 dB but total iteration number and computing time required by the CDSA-based method is smaller by nearly 60% compared to the FDM-based method. In Fig. 3, the amplitude of the transfer functions is compared with each other before and after optimization. Even though some discrepancy in the target and optimized values is

observed, it is inferred that the current optimum is the best optimal solution provided by the real 3-D structure.

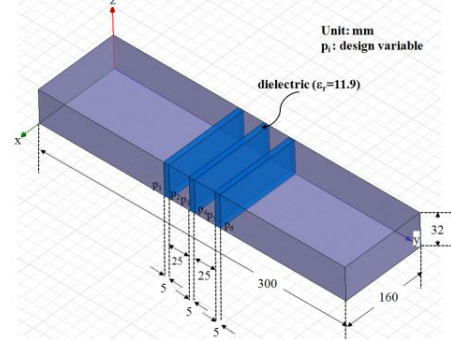


Fig. 2. Configuration of the design model with 6 design variables

TABLE I
DESIGN VARIABLES AND PERFORMANCE INDICATORS
AT THE CDSA AND FDM OPTIMA

Design variables	Unit	Initial values	CDSA optimum	FDM optimum
$\mathbf{p}_1(\mathbf{y})$	mm	117.50	118.56	118.56
$\mathbf{p}_2(\mathbf{y})$	mm	122.50	121.10	121.11
$\mathbf{p}_3(\mathbf{y})$	mm	147.50	147.61	147.62
$\mathbf{p}_4(\mathbf{y})$	mm	152.50	151.63	151.63
$\mathbf{p}_5(\mathbf{y})$	mm	177.50	178.45	178.45
$\mathbf{p}_6(\mathbf{y})$	mm	182.50	180.91	180.92
Objective function F	dB	-20.76	-38.39	-38.40
Computing time	min.		244 (17 iterations)	684 (57 iterations)

A desktop computer equipped with a 2.67 GHz, Intel Xeon processor was used.

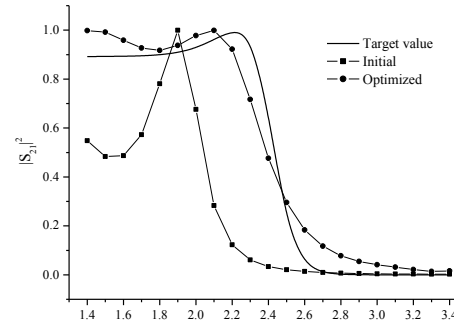


Fig. 3. Transfer functions before and after optimization

V. CONCLUSION

An analytical sensitivity formula and a unified program architecture applicable to high-frequency device design have been introduced in this paper. The results reveal that the proposed method offers high performance compared to FDM-based optimization method.

VI. REFERENCES

- [1] Jin-Kyu Byun and Il-Han Park "Design of dielectric waveguide filters using topology optimization technique," *IEEE Transactions on Magnetics*, vol. 43, no. 4, pp. 1573-1576, 2007.
- [2] Y. Yang, *et al.*, "Gradient optimization of microwave devices using continuum design sensitivities from the adjoint problem," *IEEE Transactions on Magnetics*, vol. 41, no. 5, pp. 1780-1783, 2005.
- [3] D-H Kim, J. K. Sykulski and D. A. Lowther, "Design optimisation of electromagnetic devices using continuum design sensitivity analysis combined with commercial EM," *IET Sci. Meas. Technol.*, vol. 1, no. 1, pp. 30-36, 2007.

Evaluation of Electromagnetic Inspection of Hardened Depth of Spheroidal Graphite Cast Iron using 3-D Nonlinear FEM

Yuji Gotoh¹, Nobuya Sasaguri², and Norio Takahashi³, *Fellow, IEEE*

¹Department of Mechanical and Energy Systems Engineering, Faculty of Engineering, Oita University, 700 Dannoharu, Oita 870-1192, Japan, goto-yuuji@cc.oita-u.ac.jp

²Department of Materials Science and Engineering, Kurume National College of Technology, 1-1-1 Komorino Kurume, Fukuoka 830-8555, Japan, sasaguri@kurume-nct.ac.jp

³Department of Electrical and Electronic Engineering, Graduate School of Natural Science & Technology, Okayama University, 3-1-1 Tsushima, Okayama 700-8530, Japan, norio@elec.okayama-u.ac.jp

Abstract — The inspection of the hardened depth of surface hardening spheroidal graphite cast iron is important in maintenance of various mechanical parts etc. There is a difference of the electromagnetic property in the layer with and without hardening. Therefore, the evaluation of the hardened depth is possible by detecting the difference of the electromagnetic characteristic.

In this paper, the electromagnetic method for measuring the depth of a hardened layer using an alternating magnetic field is proposed. The flux density in the surface hardening spheroidal graphite cast iron is estimated by 3-D nonlinear FEM taking into account of interpolation of the electromagnetic property of the layer with and without hardening. In addition, the experimental verification is also carried out.

I. INTRODUCTION

The surface hardening spheroidal graphite cast iron is used for various mechanical parts etc. It is necessary to inspect the depth of hardened layer in keeping the quality of machine parts etc. The ultrasonic wave testing, or the four-point probe method [1] using the change of resistivity in hardened material are generally used. However, the non-contacting inspection is difficult in these techniques.

The permeability and conductivities of hardened layer is decreased rather than the layer without hardening. Therefore, the evaluation of the hardened depth is possible by detecting the difference of the electromagnetic characteristics [2].

In this paper, the non-contacting inspection method of the hardened depth of surface hardening spheroidal graphite cast iron by applying the alternating magnetic field is investigated. The B-H curves and conductivities of the layer with and without hardening are measured. Then, the evaluation of the flux density between the layer with and without hardening inside the surface hardening spheroidal graphite cast iron is estimated by the 3-D nonlinear FEM taken into consideration of alignment interpolation of these electromagnetic property. In addition, the experimental verification of this method is carried out.

II. INSPECTION METHOD AND MODELING OF MAGNETIC PROPERTY OF SURFACE HARDENING SPHEROIDAL GRAPHITE CAST IRON

Fig.1 shows the 1/2 domain of the proposed non-contacting inspection model for evaluating hardened depth in

the surface hardening spheroidal cast iron. The lift-off between the spheroidal graphite cast iron and the ferrite yoke was set to 0.1mm. Fig.2 shows the initial magnetization curves of the layer with and without hardening of the spheroidal graphite cast iron. Table I shows the conductivities, respectively. The permeability and conductivity are decreased with the increase of the hardness.

Fig. 3 shows the example of a measurement result of the hardness using the Vickers hardness meter when the effective hardening depth is 2.5mm. The figure denotes that the

TABLE I
CONDUCTIVITIES OF LAYER WITH AND WITHOUT HARDENING OF THE SPHEROIDAL GRAPHITE CAST IRON

	Conductivity (S/m)
without hardening (275HV)	6.59×10^5
with hardening (775HV)	4.62×10^5

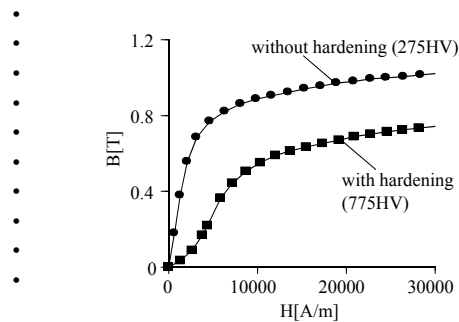


Fig. 1. Initial magnetization curves of the spheroidal graphite cast irons with and without hardening.

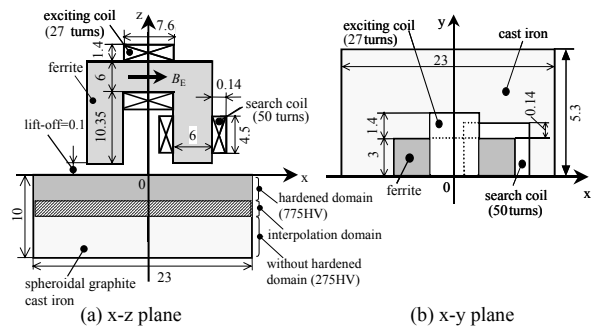


Fig.2 Inspection model of surface hardening spheroidal graphite cast iron (1/2 domain).

hardness in 2.5mm depth from the surface is about 775HV,

7. Material Modeling

the hardness of 2.5mm to 3.5mm depth is decreased rapidly, and that of more than 3.5mm depth becomes about 275HV. The B-H curve of the domain of the depth of 2.5mm to 3.5mm is obtained by the linear interpolation using the B-H curves of the layer with (0mm-2.5mm depth) and without hardening (more than 3.5mm depth). Fig.4 shows the method of linear interpolation of B-H curve using the B-H curves of the layer with (μ_H) and without hardening (μ_A). The angles θ_A and θ_H of the interpolated permeability μ_I at the point of which the depth is equal to D_x shown in Fig.3 is obtained so that the following relationship is satisfied:

$$\frac{\theta_A}{\theta_H} = \frac{D_A - D_x}{D_x - D_H} \quad (1)$$

The conductivity σ is also interpolated similarly.

III. INVESTIGATION OF INSPECTION OF HARDENED DEPTH

Fig.5 shows the effect of the hardened depth on the change of flux density $|Bz|$ of a search coil. Several specimens with 0mm-10mm hardened depth are prepared, and $|Bz|$ is measured and calculated. The frequency and the flux density B_E inside the exciting coil are 100Hz and 0.166T, respectively. The figure denotes that $|Bz|$ is decreased when the hardened depth is increased. Fig.6 shows the distribution of flux density inside the surface of hardening spheroidal graphite cast iron when the hardened depth D_1 is 2.5mm. The figure illustrates that the flux is more distributed in the layer without hardening, since the permeability of hardened domain is lower than that of the layer without hardening.

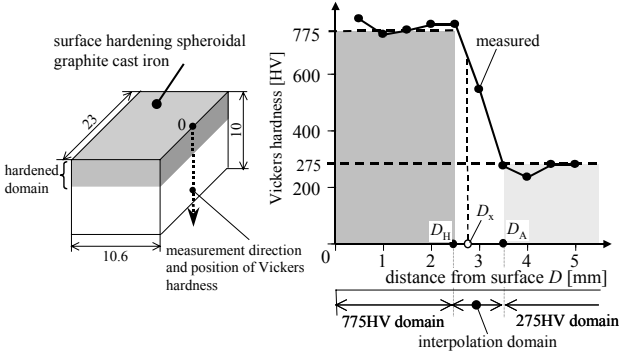


Fig.3. Example of a measurement result of the hardness using the Vickers hardness meter when the effective hardening depth is 2.5mm.

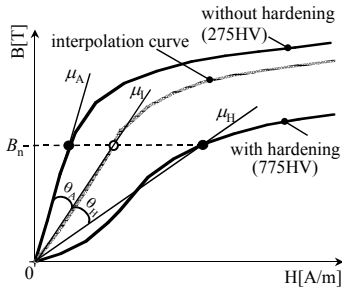


Fig.4. Interpolation of B-H curves.

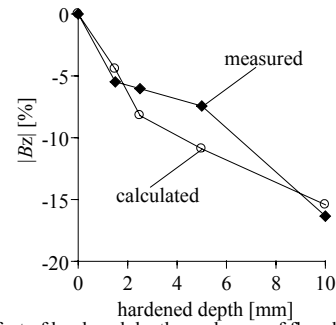


Fig.5. Effect of hardened depth on change of flux density $|Bz|$ in a search coil (100Hz, $B_E = 0.166T$).

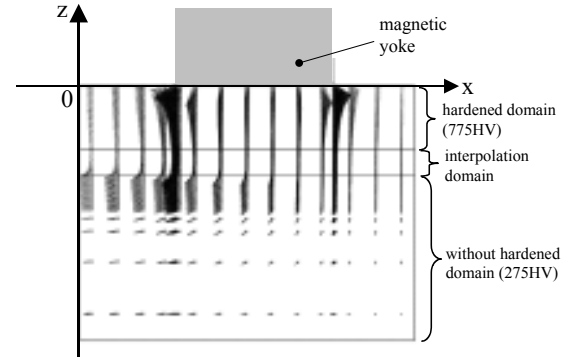


Fig.6. Distribution of flux density in the surface hardening spheroidal graphite cast iron (100Hz, $B_E = 0.166T$, 1/4 domain).

In the full paper, the optimal magnetization condition for the inspection is examined using the 3-D edge-based hexahedral FEM. In addition, the experimental verification is also carried out.

IV. CONCLUSIONS

The results obtained are summarized as follows:

- (1) The permeability and conductivity of the layer with hardening in the surface hardened spheroidal graphite cast iron are lower than that of the layer without hardening.
- (2) The flux density in a search coil of the proposed inspection method is decreased when the hardened depth is increased, because the permeability and conductivity are decreased in the hardened layer. Therefore, the non-contacting inspection of the hardened depth is possible by detecting the change of flux density of search coil.

V. REFERENCES

- [1] F. Takeo, K. Nakajima, T. Baba, Y. Aonahata, and M. Saka, "Arrangement of probes for measuring case depth by means of four-point probes", *Key Engineering Materials*, vols. 270-273, pp.82-88, 2004.
- [2] Y.Gotoh, A.Matsuoka, and N.Takahashi, "Measurement of thickness of nickel-layer on steel using electromagnetic method", *IEEE Transactions on Magnetics*, vol.43, no.6, pp.2752-2754, 2007.

Modelling of Vector Hysteresis in Si-Fe Magnetic Steels and Experimental Verification

E. Cardelli¹, E. Della Torre², A. Faba¹

¹University of Perugia, Dept. of Industrial Engineering, Perugia, Italy

²George Washington University, Electrical and Computer Engineering Dept., Washington, DC 20052, USA

e-mail: ecar@unipg.it

Abstract—The magnetic modeling of Si-Fe magnetic steels is presented in this paper. The modeling is based on a class of vector Hysteresis operators recently introduced. The vector approach works without the additional manipulations and corrections of the scalar case. Some preliminary experimental verifications are also reported.

I. INTRODUCTION

This paper discusses the modelling of vector Hysteresis in Si-Fe magnetic steels. The modelling applied has been recently introduced, and it is based on a vector hysteresis operators, hysterons, defined in the applied field space. The model is rate independent, so that the applied field variation when comparing with experiment must be sufficiently slow so that no dynamic effects are excited. The vector hysterons each of which obey certain behavior rules that depend upon its critical surface, defined in the applied field plane for that hysteron. This critical surface is a closed convex surface so that the model is consistent with the laws of thermodynamics. The magnitude of the magnetization of the hysteron is constant for all fields. Thus, we can normalize it, and we will refer to the magnetization of the hysteron as unit magnitude hysteron. The rules for computing the magnetization of the unit magnitude hysteron are:

- When the applied field lies outside the critical surface, the unit magnitude hysteron magnetization is a conservative function of the applied field.
- When the applied field lies inside the critical surface, the unit magnitude hysteron magnetization is constant.
- When the applied field enters the critical surface, the unit magnitude hysteron magnetization is frozen to the value that it had just before entering the critical surface.
- When the applied field exits the critical surface the unit magnitude hysteron magnetization experiences a Barkhausen Jump to a direction that it is normal to the critical surface.

It is under this last rule that there is a dissipation of energy in the material. Further explanation about the modelling above mentioned can be found in [1], [2], [3]. The resulting model is the extension in 2-d and 3-d of the classical Preisach model in that it obeys the vector generalizations of the congruency and the deletion properties [4]. To obtain realistic behavior for magnetic materials, such as Si-Fe magnetic steels, the classical scalar Preisach model has to be modified introducing

correction and additional terms [5], [6], [7]. The model here presented has intrinsically a reversible component of the magnetization, and the distribution function is intrinsically magnetization dependent, as will be discussed in the full paper. Therefore it can be implemented to the numerical analysis of hysteresis in magnetic materials without the additional manipulations and corrections of the scalar case. This fact is discussed in the paper, where we show the implementation of the model for the case of Si-Fe magnetic steels, and the experimental verification of the material behaviour predicted by the model.

II. NUMERICAL IMPLEMENTATION OF THE MODEL TO THE CASE OF 2-D SI-FE STEELS

The numerical approximation of the model for the Si-Fe Steels has been made following these points:

- 1) It is defined a suitable memory allocations grid defined on the space (H_x, H_y, u) . This structure contains $n_x \times n_y \times n_u$ allocations, where $n_x \times n_y$ is the number of the hysterons for a given value of u , and n_u is the number of the u values taken into account. On each allocation there are stored two parameters: the probability density $P_{i,j,k}$ and the magnetization state $Q_{i,j,k}$ of the corresponding hysteron.
- 2) It is defined the zero magnetization state (virgin state) when the applied field is zero, and the previous history has been deleted. The virgin state is obtained imposing all the $Q_{i,j,k}$ unitary vector to be aligned in the direction that links the center of the hysteron (i, j, k) to the H-plane origin for each location of the memory grid.
- 3) The magnetization state $Q_{i,j,k}$ for a given hysteron is computed through the value v of the orientation of the magnetization calculated by

$$\frac{H_x - H_{lx}}{\cos(v)} - \frac{H_y - H_{ly}}{\sin(v)} = 1 \quad (1)$$

- 4) The probability density values $P_{i,j,k}$ in the memory allocations grid are defined a priori using a suitable identification procedure of the model. These values are constant for the entire magnetization process. When the magnetic field changes, the memory allocations grid also changes in term of hysteron magnetization state. We used her a “Least-Squares” approach with a “Tikhonov regularization” scheme. Defining the following error functional

$$\varepsilon(\mathbf{p}) = \|\mathbf{M}^* - \mathbf{m} \cdot \mathbf{p}\|^2 + \alpha^2 \cdot \|\mathbf{R} \cdot \mathbf{p}\|^2 \quad (2)$$

we find the estimated solution \mathbf{p}_{est} that minimizes ε

$$\mathbf{p}_{est} = (\mathbf{m}^T \cdot \mathbf{m} + \alpha^2 \cdot \mathbf{R}^T \cdot \mathbf{R})^{-1} \cdot \mathbf{m}^T \cdot \mathbf{M}^* \quad (3)$$

The term $\|\mathbf{M}^* - \mathbf{m} \cdot \mathbf{p}\|^2$ represents the quadratic error on the data space (“discrepancy”), whereas α and \mathbf{R} are the regularization parameter and matrix respectively. The probability of the k -th hysteron must be in the range $(0, 1)$. So it has been introduced a projection operator “ \mathbf{F} ” defined as

$$(\mathbf{F}\mathbf{p})_k = \begin{cases} 0 & \text{if } p_k < 0 \\ p_k & \text{if } 0 \leq p_k \leq 1 \\ 1 & \text{if } p_k > 1 \end{cases} \quad (4)$$

The value of α it is chosen in order to have a local minimum of the functional ε . The total magnetization components M_x and M_y are computed for each step using the data stored in the memory allocations grid. For a given index k the products $P_{i,j} \cdot Q_{x,i,j}$ and $P_{i,j} \cdot Q_{y,i,j}$ define two piece-wise values of the surfaces on the $n_x \times n_y$ grid. The volumes defined by these surfaces are calculated and represent a part of the magnetization M_x and M_y . In particular they are the magnetization created by the family of the hysteron with the value of u corresponding to the index k . The sum of these partial magnetizations for k from 1 to n_u gives the total magnetization.

III. NUMERICAL CALCULATION AND EXPERIMENTAL VERIFICATION

In this section we report some preliminary calculations made and the experimental verification of the computational accuracy attained. We used a “single disk tester” [8] to characterize the magnetic behaviour of disks of 3.2% wg Si-Fe steel. The experimental system is driven by a programmable board which generates and records arbitrary waveforms. The signals generated are amplified by a set of linear amplifiers operating in four quadrants in the frequency range DC - 5 kHz. The amplifiers feed the stator of an induction motor with two poles, which generates on the sample of magnetic material a magnetic field driven in modulus and direction. The probes for the detection of the magnetic field and the magnetization components x and y are placed on the sample and connected to the driver board. The applied field frequency is less than 5 Hz, so we can neglect the effect of eddy currents.

In Figure 1 we show the magnetization path predicted and measured when an increasing rotating field is applied starting from the virgin state. In figure 2 rotational and scalar static losses, either computed and measured are shown, for different values of the magnetization.

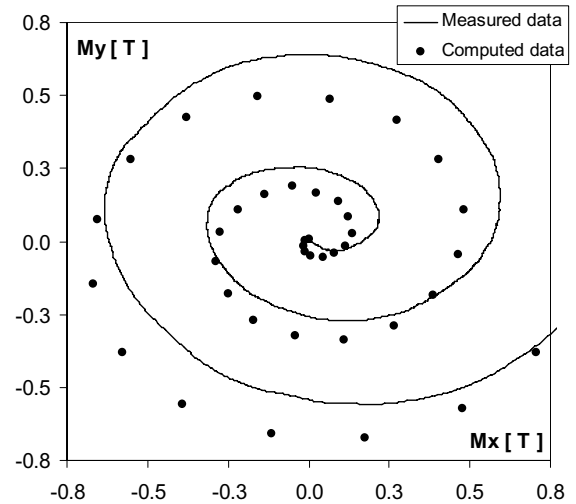


Fig. 1. Comparison between measured and computed rotational magnetization.

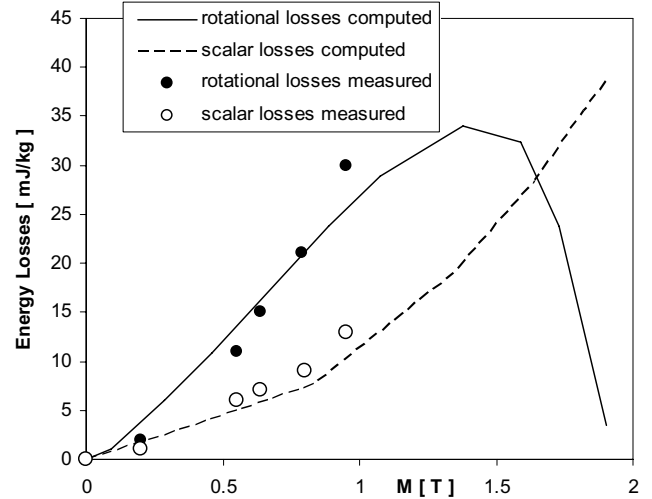


Fig. 2 – Rotational and scalar static losses vs the amplitude of applied magnetic field.

IV. REFERENCES

- [1] E. Della Torre, E. Pinzaglia, E. Cardelli, *Physica B*, Vol. 372, pp. 111-114, 2006.
- [2] E. Cardelli, E. Della Torre, and A. Faba, *IEEE Transaction on Magnetics*, VOL. 45, NO. 3, March 2009.
- [3] P. Burrascano, E. Cardelli, E. Della Torre, G. Drisaldi, A. Faba, M. Ricci, A. Pirani, *IEEE Transaction on Magnetics*, VOL. 45, NO. 3, March 2009.
- [4] E. Cardelli, E. Della Torre, A. Faba, *Journal of Applied Physics* 103, 07D927, 2008.
- [5] I.D. Mayergoyz, *Mathematical Models of Hysteresis*, Springer Verlag, New York (1991).
- [6] E. Della Torre, *Magnetic Hysteresis*. New York, NY: IEEE Press, 2000.
- [7] E. Cardelli, E. Della Torre, B. Tellini, *IEEE Transaction on Magnetics*, VOL. 36, NO. 4, July 2000.
- [8] E. Cardelli, A. Faba, *Physica B* 372 (2006) 143-146.

Size Is in the Eye of the Beholder: Technique for Non-destructive Detection of Parameterized Defects

Flavio Calvano, Pasi Raunonen*, Saku Suuriniemi*, Lauri Kettunen*, and Guglielmo Rubinacci
Ass. EURATOM/ENEA/CREATE, DIEL Università degli Studi di Napoli 'Federico II', I-80125 Napoli, Italy

*Tampere University of Technology, Electromagnetics, P.O. Box 692, FI-33101, Finland
flavio.calvano@unina.it

Abstract—The paper presents a technique to compute magneto-quasi-static non-destructive testing problems with parameterized defect geometry. A single mesh is used for computations within a range of parameters, and the metric variations due to parameter variations are compensated for in the numerical values of the material parameters.

I. INTRODUCTION

A typical problem in non-destructive testing (NDT) is to specify the defect that generates a certain signal into a probe. This is an indirect problem –the geometry of the defect that causes the signal is not known– and consequently, a number of computations is required to sketch the defect. Moreover, finite element-type NDT computations are known to be rather sensitive to numerical errors and all this makes NDT problems burdensome. This paper suggests exploitation of metric properties of space in solving NDT problems. The dimensions of a defect *depend on the metric chosen for a space*. At first this may sound preposterous, as obviously the defect is what it is and cannot be changed by some modeling choice. This is indeed the case, but the issue is *how we as the modelers observe the defect*.

The change of metric is like viewing the defect through eyeglasses that magnify locally the view, making the defect appear large. This alleviates the FE-mesh generation problems caused by narrow defects. Moreover, *the magnification can be made adjustable, and a family of defect widths can then be modeled with a single (topological) mesh*. This reduces the errors sensitive to the mesh. [1]

Practically, the change of eyeglasses in this sense is done by a transformation between different systems that reflect the choices of metric one makes. Pre-processors use hardwired Euclidean metric to measure distances of coordinates. *Standard parameterizations* [1] assign coordinates to points such that their distance equals the measured distance of the points. Reparameterization changes the points' coordinate distances (as we cannot redefine the hardwired coordinate metric) and this induces a new metric into the space. The change of metric affects the constitutive laws' material parameters, whose numerical values depend on the particular metric. Another view to the matter: Each finite element stiffness matrix corresponds to some field problem. If one changes locally the metric, altering the numeric values of distances, one can counterbalance

this by adjusting the material parameters such that the entries of the stiffness matrix remain the same.

II. TRANSFORMATIONS

In most NDT applications, the probe must be placed into the immediate vicinity of the defect in order to detect it reliably, and because the geometry of the probe is independent of the defect width, it is not practical to extend the transformation into the probe. We shall consequently restrict the transformations into the immediate vicinity V of the defect. V may be tessellated into subdomains if practical. The feasible transformations

- must not displace any points at the boundary of V , and
- be continuous and piecewise differentiable with piecewise differentiable inverse.

It is usually practical to tessellate the vicinity into polyhedra [1]. Despite the high number of different transformation types required, the model can be created and the transformations derived with moderate effort. The Jacobians of the transformations must be reasonably well-behaved: Their condition numbers must not be excessive, and their determinants must not be extreme. A rectangular defect example and its boundary regions are shown in figure 1.

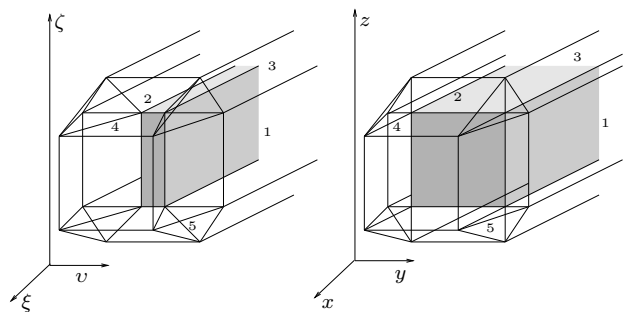


Fig. 1. Defect (shaded) and its vicinity regions

The defect model is drawn to be w wide. The original width of the defect is αw , and the transformation is produced by displacement of points of V in y -direction only. α is a parameter for the computation of a family of defects with different widths. We denote the coordinates as seen in the pre-processor by x, y, z , and the coordinates related to the original metric by ξ, v, ζ . We derive a piece-wise transformation that maps from x -positions to ξ -positions, and denote it by $h = \xi \circ x^{-1}$. The Jacobian J of the transformation h is

Work supported by the Academy of Finland, project 5211066, and ERASMUS exchange program.

needed when the material parameters –readily available in the original metric– are adjusted to the modified metric. The new parameters are [1]:

$$\sigma_x = J^{-1} \sigma_\xi J^{-T} \det(J), \quad \nu_x = \frac{1}{\mu_x} = \frac{J^T \nu_\xi J}{\det(J)}. \quad (1)$$

These expressions are convenient, because the Jacobian is expressed in terms of x -coordinates, and σ_ξ and μ_ξ expressed in ξ -coordinates are constant for the media. The transformations from x to ξ and z to ζ are identities, and the only interesting component of each transformation is y to v , expressed in figures 2 and 3, and equations (2)–(6).

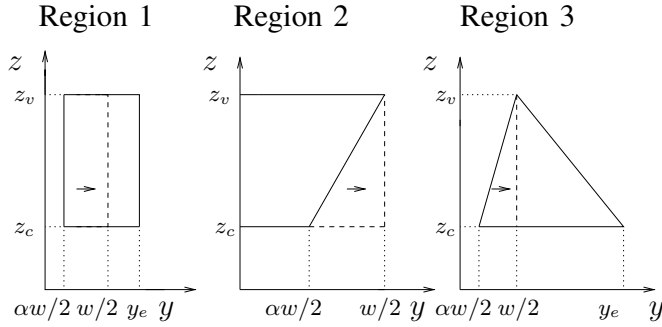


Fig. 2. Regions 1 to 3

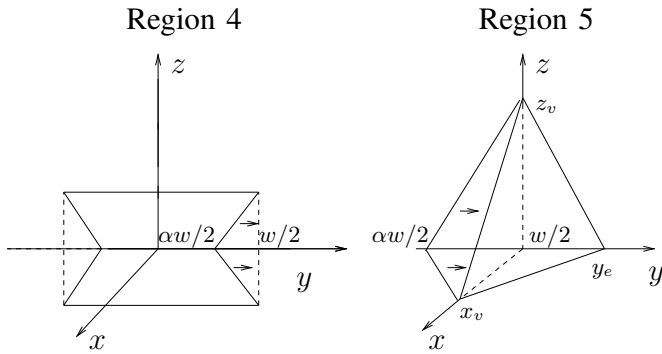


Fig. 3. Regions 4 and 5

$$v_1 = \alpha y, \quad v_1 = y + (1 - \alpha)(w/2) \frac{y - y_e}{y_e - w/2}. \quad (2)$$

$$v_2 = y - y(1 - \alpha) \left(1 - \frac{z - z_c}{z_v - z_c}\right) \quad (3)$$

$$v_3 = y - (1 - \alpha)(w/2) \left(1 - \frac{x - x_c}{x_v - x_c} - \frac{y - w/2}{y_e - w/2}\right) \quad (4)$$

$$v_4 = y - y(1 - \alpha) \left(1 - \frac{x - x_c}{x_v - x_c} - \frac{z - z_c}{z_v - z_c}\right) \quad (5)$$

$$v_5 = y - (1 - \alpha)(w/2) \left(1 - \frac{x - x_c}{x_v - x_c} - \frac{y - w/2}{y_e - w/2} - \frac{z - z_c}{z_v - z_c}\right) \quad (6)$$

III. COMPUTATIONAL EXAMPLE

TEAM test problem number 8 [2] is used as the computational example. The problem features a $40 \times 10 \times 0.5$ mm

rectangular defect at the surface of an austenitic 18-10MO steel plate with relative permeability $\mu_r = 1$ and conductivity $\sigma = 0.14 \times 10^7$ S/m. We used 1A current with 100 turns in the active coil, and calculate the average differential flux in the receptive coils.

This problem demonstrates two strengths of the proposed technique: The high aspect ratio of the defect can be reduced somewhat to ease the meshing, and defects of different width can be computed with a single mesh. Compared to different meshes generated from scratch, the use of a single mesh provides a better idea of the development of the flux estimate when the defect width is altered.

We used the symmetrized version of $A, V - A$ formulation [3] with the tree-co-tree gauge [4]. The models were constructed with gmsh [5], and the computations were carried out with GetDP [6].

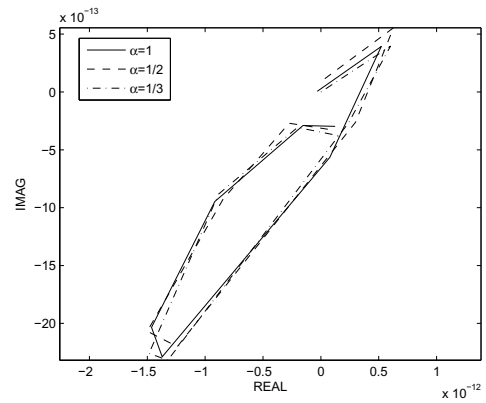


Fig. 4. Real and imaginary part of the magnetic flux in the receptive coils

Figure 4 shows the real and imaginary part of the computed magnetic flux in the receptive coils, for a parallel scan of the active probe [2], with values 1, 1/2, 1/3 for α . The results with different values of α show reasonable mutual agreement. It is to be noted that generation of high quality mesh was easiest when the defect scale-up was greatest.

REFERENCES

- [1] P. Raunonen, S. Suuriniemi, and L. Kettunen, "Parametric models in quasi-static electromagnetics," *IEEE Trans. Magn.*, vol. 45, no. 3, pp. 944–947, 2009.
- [2] J.-C. V erit e, "Application of a 3-d eddy current code (TRIFOU) to nondestructive testing," *COMPEL*, vol. 3, pp. 167–178, 1984.
- [3] O. B ir o and K. Preis, "On the use of the magnetic vector potential in the finite element analysis of three-dimensional eddy currents," *IEEE Transactions on Magnetics*, vol. 25, no. 4, pp. 3145–3159, 1989.
- [4] R. Albanese and G. Rubinacci, "Integral formulation for 3D eddy-current computation using edge elements," *IEE Proc.*, vol. 135, Pt. A, no. 7, pp. 457–462, 1988.
- [5] C. Geuzaine and J.-F. Remacle, "Gmsh: a three-dimensional finite element mesh generator with built-in pre- and post-processing facilities." home page <http://www.geuz.org/gmsh/>.
- [6] P. Dular and C. Geuzaine, "GetDP reference manual: the documentation for GetDP, a general environment for the treatment of discrete problems." <http://www.geuz.org/getdp/>.

An Improved Jacobi-Davidson Method for the Computation of Selected Eigenmodes in Waveguides

Bastian Bandlow, Denis Sievers, and Rolf Schuhmann
 FG Theoretische Elektrotechnik, EIM-E, University of Paderborn
 Warburger Str. 100, D-33098 Paderborn, Germany
 bandlow@tet.upb.de

Abstract — The numerical simulation of open structures requires the truncation of the computational domain and the definition of appropriate boundary conditions. However, this artificial boundary at finite distance causes additional non-physical modes in the eigenanalysis of waveguides which must be excluded from the computed spectrum. We propose an extension of the Jacobi-Davidson method by introducing a special weighting function that enables a reliable suppression of undesired eigenmodes already during the solution process. Moreover, the number of iteration steps as well as the computation time can be drastically reduced by this process. We show the improvement of efficiency by means of an eigenmode computation in a photonic crystal fiber discretized by the finite integration technique.

I. INTRODUCTION

The computation of eigenvalues in two- and three-dimensional electromagnetic structures is a challenging task in engineering. Since dielectric waveguides for optical applications (fibers) can be highly multi-modal, the corresponding 2D-eigenvalue problem may include a high number of guided modes, with only little differences in their propagation constants. For such modes, the power is confined within the core of the fiber, and the field strength in the cross section decays exponentially with increasing radius. With this a-priori knowledge, one may wish to apply an adequate transversal boundary condition, which allows truncating the mesh close to the core of the fiber. Such an 'open boundary' can be modeled, for example, by a perfectly matched layer (PML), which absorbs the evanescent wave parts by real-coordinate stretching [1]. However, the application of any boundary condition changes the discrete eigenvalue problem, and an ideal boundary condition as well as the staggered material layers of the PML themselves can act as a waveguiding structure. This leads to a spoiled spectrum, which consists not only of the desired guided modes within the core, but we observe a lot of additional, non-physical modes, which are guided inside the PML. In order to get rid of these spurious modes, we propose a new variant of the Jacobi-Davidson eigenvalue solver [2, 3] which allows to distinguish between the two classes of eigenvectors *within the solution process* and to produce only the desired core-modes in an efficient way.

II. WEIGHTED JACOBI-DAVIDSON ALGORITHM

The Jacobi-Davidson (JD) algorithm [2, 3] is feasible for the computation of a few interior or exterior eigenvalues of the spectrum. Within the algorithm, the original eigenvalue problem is projected onto (and solved in) a low-dimensional

subspace, which is gradually refined by solving a correction equation. We use a Matlab implementation of the JD-algorithm from its original authors which is available from [3]. As so-called target value, an end of the spectrum or an arbitrary value within the spectrum can be specified. According to this target value, the approximated eigenvalues are sorted in different sophisticated ways during the solution process. The solution of the low-dimensional, projected eigenvalue problem, however, does not only yield approximations of the eigenvalues, but of course we also obtain approximations of the corresponding eigenvectors. If we map them back in the original space, we can interpret these vectors as approximations of field solutions of the discrete formulation. To establish a new criterion for the choice of the desired modes, we test these field distributions against a weighting vector \mathbf{f} , which describes a scalar spatial distribution for each field component with its maximum at the core and an evanescent decay towards the boundaries. We choose a Gaussian profile as components of these vectors, since it is easy to define and it fulfills the requirements of a strong decay toward the boundaries. Now, we can measure the quality of our approximate eigenvectors \mathbf{u}_i within the JD-algorithm very easily. The standard scalar product

$$\Psi = \langle \mathbf{f}, |\mathbf{u}_i| \rangle \quad \text{with } \|\mathbf{u}_i\|_2 = 1, \|\mathbf{f}\|_\infty = 1 \quad (1)$$

can be used to decide, whether the field strength is concentrated around the core ($\Psi > 1$) or whether it is concentrated inside the boundary ($\Psi \ll 1$).

III. NUMERICAL RESULTS

A. Photonic Crystal Fiber

We choose a hollow-core photonic crystal fiber (PCF) [4] as an example, which is operated at $2\mu\text{m}$ wavelength (Fig. 1). It consists of a glass core ($n_G = 1.45$) with a surrounding hexagonal lattice of air holes. Each hole has a radius of $2.9\mu\text{m}$ and the lattice constant is $9.4\mu\text{m}$. The discrete model is truncated by a PML boundary condition and has the dimensions $74\mu\text{m} \times 84\mu\text{m}$. The cross section of the fiber is discretized by the finite integration technique (FIT, [5]), using CST Microwave Studio [6] for all preprocessing steps. The resulting two-dimensional model has 155×193 grid points, and we add 4 grid lines in each transversal direction for the PML boundary condition. The eigenvalue problem [7] for the squared propagation constants β^2 is linear, of the type

$$\mathbf{A}\mathbf{u}_i + \beta_i^2\mathbf{u}_i = 0, \quad (2)$$

and has 64438 degrees of freedom. We are interested in the first two guided modes of the PCF. Fig. 2 shows the part of the spectrum with the smallest real part of the propagation constants β_i . The first 36 modes are guided within the PML region. Modes 37 and 38 are the ones we are looking for and which fulfill our weighting criterion in (1).

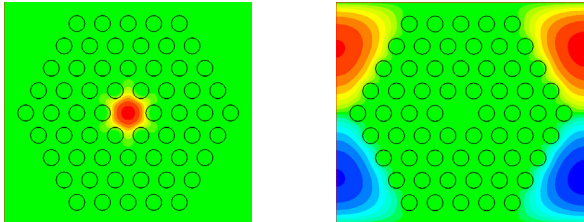


Fig. 1. Electric field strength of a core mode (left) and a spurious mode (right) caused by a transversal truncation of the computational domain.

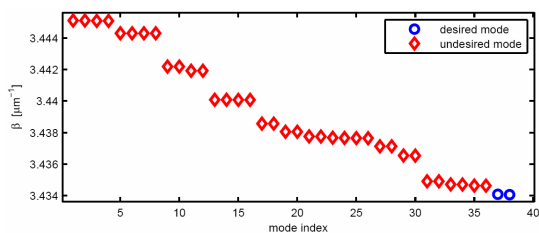


Fig. 2. Propagation modes of the PCF.

B. Performance Comparison

We used the unmodified Jacobi-Davidson solver as well as the weighted JD solver to compute the first two guided modes of the PCF from the previous subsection. For all eigenmodes computations, the system matrix is shifted and scaled before the solver starts, which significantly improves the condition number of the problem. The target is chosen to be the smallest real part. The initial subspace is generated randomly and is fed in each of both solvers in order to have equal starting conditions. The correction equation within the JD algorithm is solved exactly in both solvers. This is time-consuming, but we can expect at least a second order convergence. The results are given in Table 1. We look for two core guided modes, which are found by both solvers. The weighted JD outperforms the standard JD by a factor of 15 in time. The number of iterations, which are needed to gradually refine the subspace, is reduced by a factor larger than two. The reason for the disagreement of these two factors can be seen in the convergence history in Fig. 3. A lot of iterations are needed at the beginning of both algorithms, in order to improve the quality of the subspace. Once refined, the subspace allows the quick computation of the consecutive eigenvalues.

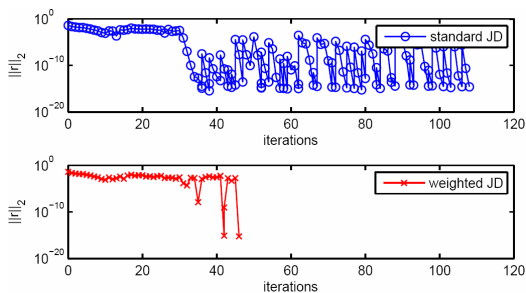


Fig. 3. Convergence history of the standard and the weighted JD method.

TABLE I

RESULTS OF THE STANDARD AND THE WEIGHTED JD METHOD

JD	Core Modes	Total Modes	CPU Time	Iterations
Standard	2	38	2687 s	108
Weighted	2	2	165 s	46

IV. CONCLUSION AND OUTLOOK

We have shown that a simple extension of the selection process of the approximate eigenpairs within a Jacobi-Davidson algorithm leads to a superior convergence behavior for waveguide models which are surrounded by a PML boundary condition. The number of eigenvalues which have to be computed until we arrive at the desired ones is drastically reduced.

The final paper will discuss a couple of improvements concerning the performance, the computationally efficiency, and the range of application of the modified eigensolver: At first, other weighting functions can be used, e.g. it should be possible to find only modes with a specific polarization, modes with an energy transport in specific regions of the cross section, etc. In the current implementation only the values of the electrical grid voltage are taken into account by the weighting function. However, it may also be applied to Poynting's vector or other secondary quantities. Secondly, the performance of the modified Jacobi-Davidson algorithm itself can be significantly improved. An important issue is the solution of the correction equation: An only approximate solution here typically deteriorates the convergence rate in terms of the number of iterations, but increases the overall computationally efficiency. Besides, the number of iterations can be further reduced by re-using the weighting function as start solution of the eigensolver.

Finally, the weighting could also be implemented into other eigensolvers such as the implicitly restarted Arnoldi algorithm, where it should also be possible to eliminate the undesired eigenvectors from the approximate subspace. Of course, this kind of solver can also be applied to other types of waveguides such as microstrip lines with PML boundary conditions.

V. REFERENCES

- [1] J.-P. Berenger, "Application of the CFS PML to the absorption of evanescent waves in waveguides", *Microwave and Wireless Components Letters, IEEE*, vol. 12, no. 6, pp. 218-220, June 2002.
- [2] G. L. G. Sleijpen and H. A. Van der Vorst, "A Jacobi-Davidson iteration method for linear eigenvalue problems", *SIAM J. Matrix Anal. Appl.*, vol. 17, no. 2, pp. 401-425, 1996.
- [3] M. Hochstenbach, "Jacobi-Davidson Gateway", <http://www.win.tue.nl/casa/research/topics/jd/>.
- [4] P. S. Russell, "Photonic-crystal fibers", *J. Lightwave Technol.*, vol. 24, no. 12, pp. 4729-4749, 2006.
- [5] T. Weiland, "Eine Methode zur Loesung der Maxwellschen Gleichungen fuer sechskomponentige Felder auf diskreter Basis", *Archiv fuer Elektronik und Uebertragungstechnik*, vol. 31, pp. 116-120, 1977.
- [6] Computer Simulation Technology AG (CST), "CST Studio Suite 2008", <http://www.cst.com>.
- [7] R. Schuhmann and T. Weiland, "Conservation of discrete energy and related laws in the finite integration technique", in *Geometric Methods for Computational Electromagnetics*, ser. *Electromagnetic Waves: Progress in Electromagnetics Research (PIER)*, F. L. Teixeira, Ed. Cambridge, MA: EMW Publishing, 2001, vol. 32, pp. 301-316.

GPU Accelerated Adams-Bashforth Multirate Discontinuous Galerkin FEM Simulation of High Frequency Electromagnetic Fields

N. Gödel¹, *Student Member, IEEE*, S. Schomann¹, T. Warburton² and M. Clemens¹, *Senior Member, IEEE*

¹Helmut-Schmidt-University, University of the Federal Armed Forces Hamburg, Faculty of Electrical Engineering, Chair for Theory of Electrical Engineering and Computational Electromagnetics, P.O. Box 700822, D-22008 Hamburg, Germany

²Computational and Applied Mathematics, Rice University, 6100 Main Street MS-134, Houston, TX, USA

Abstract—A multirate Adams-Bashforth (AB) scheme for simulation of electromagnetic wave propagation using the discontinuous Galerkin finite element method (DG-FEM) is presented. The algorithm is adapted such that Single Instruction Multiple Thread (SIMT) characteristic for the implementation on a Graphics Processing Unit (GPU) is preserved. Accuracy and performance is analyzed with help of suitable benchmarks.

Index Terms—GPU-computing, Multirate, GPGPU, CUDA, Discontinuous Galerkin, FEM, High Order, Multiscale.

I. INTRODUCTION

Increasing complexity of modern electromagnetic devices is challenging current simulation tools. When large structures should be considered, small parts within these structures are leading to large aspect ratios of the mesh size. These aspect ratios have severe performance effects on explicit time integration schemes in use, since the smallest element is determining the maximum stable timestep for the entire mesh in a global scheme.

One way of coping with these restrictions is the use of multirate timestepping schemes, which integrate elements of different sizes with different timesteps. In this work, a multirate scheme using AB time integration is adapted such that it can be implemented on a GPU. This combines the performance gain of the multirate algorithm with the highly parallel computing power of GPUs. Multirate schemes using AB methods have been presented first in [1]. Relevant results in local timestepping for solving Maxwell's equations with DG-FEM was published by Piperno [2], Hesthaven & Warburton [3] for 2D domains and Montseny et. al. [4] in 3D on hexahedral meshes.

II. DG-FEM DISCRETIZATION

Electromagnetic wave propagation in lossless medium can be described with help of Maxwell's curl equations. A nodal variational form of Maxwell's equations is derived in [3], where the unknown fields are approximated using local high-order multi-dimensional Lagrange polynomials. This leads to a system of ordinary differential equations, reading

$$\frac{d}{dt} \varepsilon \mathbf{E} = \mathbf{M}^{-1} \mathbf{S} \mathbf{H} + \mathbf{M}^{-1} \mathbf{F} (\hat{\mathbf{n}} \times (\mathbf{H}^* - \mathbf{H}^-)), \quad (1)$$

$$\frac{d}{dt} \mu \mathbf{H} = -\mathbf{M}^{-1} \mathbf{S} \mathbf{E} - \mathbf{M}^{-1} \mathbf{F} (\hat{\mathbf{n}} \times (\mathbf{E}^* - \mathbf{E}^-)). \quad (2)$$

Here, \mathbf{E} and \mathbf{H} denote the electric and magnetic field strength, respectively. Regarding elementwise computations, the index $-$ refers to the value in the element, the index $*$ to a combination of field values of neighboring elements. A special characteristic of DG-FEM is that the DG-operators \mathbf{M} , \mathbf{S} and \mathbf{F} yield mass-, stiffness and flux-matrices that have compact support only within each element's boundary. As a consequence, \mathbf{M} is locally defined on the reference element and can be inverted without much numerical effort providing the opportunity of using explicit time integration schemes. Furthermore, this formulation includes good parallelization characteristics [5].

III. MULTIRATE GPU IMPLEMENTATION

A. Timestep Selection

Explicit time integration is not unconditionally stable since the timestep has to comply with the Courant-Friedrichs-Lewy criterion

$$\Delta t_{\min} = \min \left\{ \frac{\Delta x}{v} C \right\}. \quad (3)$$

Here, Δx denotes the characteristic size of the element, v the wave speed and C the Courant number which depends on the time integration scheme and on the spatial approximation order. Regarding multirate timestepping, the use of arbitrary numbers of levels as presented in [6] results in complex code design when all inter-level dependencies are considered. Consequently, a direct transition of the multirate CPU code is not appropriate. Multiple inter-level dependencies would introduce a complexity breaking with the NVIDIA SIMT approach associated to high performance GPU computing.

B. Level Classification

In order to respect the parallelization design aspects, a 2-level multirate scheme with selectable temporal separation is proposed. In this case, temporal separation describes the way fine and coarse elements are classified and also how the fine-coarse boundary is defined. Starting with the timestep Δt_{\min} of the smallest element, all elements with a stable timestep $\Delta t < 2^s \cdot \Delta t_{\min}$ with s being a positive integer greater than zero belong to the fine level. The timestep ratio 2^s is computed adaptively with respect to the mesh, minimizing computational costs. Eqn. (4) highlights the splitting configuration for the

discretized Ampère’s law.

$$\frac{d}{dt} \begin{pmatrix} E_F \\ E_C \end{pmatrix} = \begin{pmatrix} \mathcal{L}_{FF} & \mathcal{L}_{FC} \\ \mathcal{L}_{CF} & \mathcal{L}_{CC} \end{pmatrix} \begin{pmatrix} H_F \\ H_C \end{pmatrix} \quad (4)$$

The linear operator \mathcal{L} represents the right hand side computation in (1). The indices C and F denote coarse and fine elements, CF and FC coarse-fine interactions, respectively.

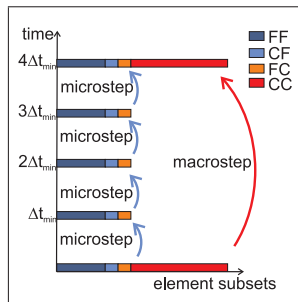


Fig. 1. Multirate scheme for a timestep ratio 4.

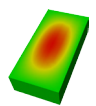

This behaviour has already been reported in [7] and will be investigated in the full paper in detail.

IV. FIRST NUMERICAL RESULTS

As a first numerical benchmark, a cavity discretized with 398 tetrahedra was excited with its fundamental mode. Regarding the different element sizes of the mesh, a level separation with a timestep ratio 4 was chosen. This corresponds to 182 fine elements having an individual stable timestep lower than $4 \cdot \Delta t_{\min}$ and 216 coarse elements having a larger stable timestep. Computations were carried out on a AMD Opteron 8356 CPU at 2.3 GHz and on one of the four NVIDIA TESLA S 1070 GPUs. Table I is listing computation time and speedup

TABLE I

COMPARISON OF GLOBAL CPU, GLOBAL GPU AND MULTIRATE GPU

Example	Implementation	Computation time	Speedup compared to CPU global
	CPU global	4 h 56 min 54 s	1.0
	GPU global	10 min 51 s	27.4
	GPU multirate	8 min 6 s	36.7
	CPU global	29 h 6 min 46 s	1.0
	GPU global	39 min 1 s	44.8
	GPU multirate	11 min 50 s	147.6

for CPU-GPU acceleration and in a second step with enabled multirate. Although this academic example is not providing large aspect ratios, the efficiency can benefit from the multirate scheme. Regarding accuracy, Fig. 2 highlights the maximum error of the electric field during several computations, each evaluating 200 periods of the cavity mode with a maximum of 1 577 781 micro-timesteps. The error of the computation with DG-FEM of order 4 is below 10^{-3} for all computations. In detail, there is almost no difference in accuracy between the GPU multirate and the GPU global scheme.

Regarding efficiency of the multirate scheme, a scattering object as presented in Fig. 3 is discretized with 130 413 tetrahedra, as shown in Fig. 4. The adapted timestep ratio

The benefit of this multirate approach is that all evaluations of the \mathcal{L}_{CC} operator have to be executed only every 2st timestep, as highlighted in Fig.1 for $s = 2$. Regarding stability, the intermediate zones are of special interest. With this configuration, the Courant number has to be chosen slightly smaller than in the global scheme.

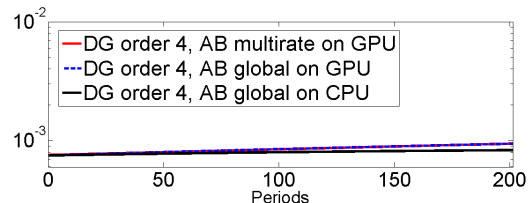


Fig. 2. Maximum relative error of the electric field computed in a 3D cavity with multirate and global schemes on GPU and CPU.

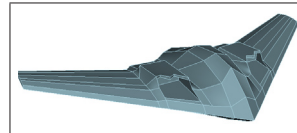


Fig. 3. Scattering object - CAD model.

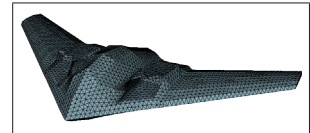


Fig. 4. Scattering object - mesh with 130 413 tetrahedra.

is 4, separating the mesh into 127 676 coarse and 2737 fine elements. The global GPU computation was accelerated by a factor of 44.8 compared to the CPU implementation and could be further accelerated by a factor of 3.3 using the multirate scheme as presented in Table I. The electric field at the surface of the scattering object (y-component) is presented in Fig. 5.

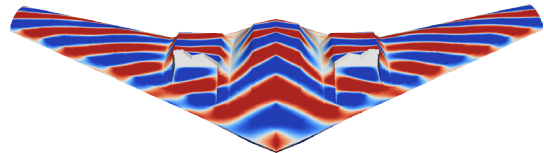


Fig. 5. Electric field of a scatterer hit by a TEM wave, computed with $15.6 \cdot 10^6$ unknowns at 52 043 microsteps.

V. CONCLUSION

A multirate GPU accelerated DG-FEM algorithm was presented. The multirate timestepping scheme can further accelerate GPU computations, especially when high aspect ratios of multiscale problems are of concern. The full paper will provide more detailed information about the theory as well as the stability and accuracy of the timestepping scheme.

ACKNOWLEDGMENT

The authors gratefully acknowledge the support of AFOSR under grant number FA9550-05-1-0473. The opinions expressed are the views of the authors. They do not necessarily reflect the official position of the funding agencies.

REFERENCES

- [1] C. Gear and D. Wells, “Multirate linear multistep methods,” *BIT*, vol. 24, pp. 484–502, 1984.
- [2] S. Piperno, “DGTD methods using modal basis functions and symplectic local time-stepping application to wave propagation problems,” *M2AN*, vol. 40, no. 5, pp. 815–841, 2008.
- [3] J. S. Hesthaven and T. Warburton, *Nodal Discontinuous Galerkin Methods*. Springer, 2008.
- [4] E. Montseny, S. Pernet, X. Ferreres, M. Zweers, G. Cohen, and B. Pecqueur, “A discontinuous Galerkin method to solve maxwell equations in time domain,” *ACES-Conference*, 2007.
- [5] N. Gödel, T. Warburton, and M. Clemens, “GPU accelerated discontinuous Galerkin FEM for electromagnetic radio frequency problems,” *IEEE APS – Full paper accepted for publication*, 2009.
- [6] N. Gödel, S. Schomann, T. Warburton, and M. Clemens, “Local timestepping discontinuous Galerkin methods for electromagnetic RF field problems,” *EUCAP 2009 – Full paper accepted for publication*, 2009.
- [7] E. Montseny, S. Pernet, X. Ferreres, and G. Cohen, “Dissipative terms and local time-stepping improvements in a spatial high order discontinuous galerkin scheme for the time-domain maxwell’s equations,” *J. Comput. Phys.*, vol. 227, no. 14, pp. 6795–6820, 2008.

Determination of Induction Motor End-Winding Leakage Inductances Using 3-D Non-Conforming FE Meshes

Andrej Stermecki^{1,3}, Oszkár Bíró¹, Kurt Preis¹, Siegfried Rainer¹, Klaus Krischan², Georg Ofner⁴

1- Institute for Fundamentals and Theory in Electrical Engineering, Graz University of Technology

2- Institute for Electrical Drives and Machines, Graz University of Technology

3-Christian Doppler Laboratory for Multiphysical Simulation, Analysis and Design of Electrical Machines
Kopernikusgasse 24, 8010 Graz, Austria

andrej.stermecki@tugraz.at

4- ELIN EBG Motoren GmbH, 8160 Preding/Weiz, Austria

Abstract— In this paper, two methods for calculating induction motor (IM) end-winding leakage inductances are presented. The 3-D geometry of the winding ends, the motor cross-section and the motor housing is very complex and difficult to model using a conforming finite element (FE) mesh. Both presented methods propose an alternative to this standard procedure. The first method is based on the numerical calculation of the Biot-Savart field using a non-conforming FE mesh. The Biot-Savart field is used to obtain an edge element representation of the rotational part of the magnetic field. In the second method, the source current distribution of the winding ends is described by spline functions and the rotational part of the magnetic field is defined by identifying the loops generated by co-tree edges within a simple graph associated with only one single finite element at a time. All elements are treated in defined succession using just one sweep. Applying either method, the eddy current analysis is carried out, thus the induced currents in the housing and in the front-end steel plate of the machine are calculated and their influence on the field distribution and on the leakage inductances is taken into account.

I. INTRODUCTION

The end-winding leakage inductance is a very important parameter whose influence is most significant during the starting behavior of the IM. In [1], a strong dependence between the end-winding leakage inductance and the acceleration time of the IM motor has been proven. In order to enable the accurate dynamic simulation of the IM starting procedure, the end-winding leakage inductance should be precisely defined and incorporated in the 2-D FE model as an additional lumped parameter [1]. In order to extract IM equivalent circuit parameters, like stator and rotor leakage inductances, a magnetizing inductance and a rotor resistance, the 2-D finite element method (FEM) is usually used. 3-D leakage fields present in the end region of the machine are, therefore, neglected. These inductances are usually estimated using design formulas that combine approximate analytical results with measurement statistics. In [2], different semi-empirical equations first presented by Alger and Gray are compared with measurement results. The improved analytical approach based on multiple solutions of the Neumann integral and on the method of images is presented in [3]. Owing to the complex geometry of the end-winding and due to the complicated boundary conditions of the problem, these analytical expressions are able to give only a rough

estimation of the leakage inductances. On the other hand, numerical methods can contribute to the accuracy of these calculations. In order to calculate the leakage reactance of the end-winding, a static 3-D FEM simulation has been applied in [4] and [5]. A problem associated with the FEM simulations of the motor end-regions is the modeling process of the end-winding itself. To obtain a conforming FE mesh of the two layered windings and the surrounding air, an enormous number of FE is required which results in a huge computation time. Therefore, the production units only rarely use 3-D FEM computations for defining the leakage inductance. Furthermore, the static FEM analysis of end-region effects is not sufficient. Namely, the induced eddy currents in the front-end steel plate of the machine and in the machine housing have significant influence on the magnetic field distribution and, therefore, on the inductance values. The aim of this paper is to present methods to overcome these problems, hence to propose a numerical procedure that would simplify the modeling of the end-winding, the machine and the surrounding end-region. The influence of the eddy currents on the magnetic field distribution and, consequently, on the leakage inductance is also taken into consideration by performing the FEM analysis in the frequency domain.

II. NUMERICAL ANALYSIS

A. Method 1 – Non-conforming FE mesh

Nowadays, companies commonly use the support of CAD modeling in the manufacturing process, thus drawings of the end-winding are often already available. It is relatively simple to mesh the winding ends without the surrounding air. In the present method, such a FE mesh has been used in order to perform a static current flow analysis and to obtain the current distribution in the winding. Knowing the current distribution, the Biot-Savart field has been calculated in the integration points of another FE mesh representing the motor, its housing and the surrounding air. The two meshes are non-conforming (Fig. 1). The eddy current problem is solved in the frequency domain using the \mathbf{T}, Φ - Φ formulation [6]. Thus, the given current density \mathbf{J}_0 is represented by an arbitrary function \mathbf{T}_0 , which satisfies the following condition:

$$\text{curl}(\mathbf{T}_0) = \mathbf{J}_0 . \quad (1)$$

Knowing the numerically calculated Biot-Savart field \mathbf{H}_s , the rotational part \mathbf{T}_0 of the magnetic field is represented with the aid of the edge element shape functions in order to avoid cancellation errors:

$$t_i = \int_{\text{Edge } i} \mathbf{H}_s dl; \quad \mathbf{T}_0 = \sum_{\text{Edge } i} t_i N_i, \quad (2)$$

where N_i stands for the vectorial edge element shape functions associated with the i -th edge and n_e for number of FE edges.

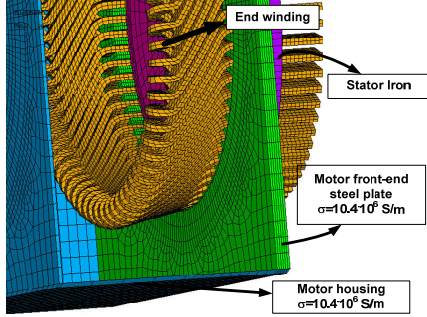


Fig. 1. 3-D FE model of the induction motor, its end-winding and housing

B. Method 2 – Generating \mathbf{T}_0 by a procedure based on element graphs

Since only an edge-element representation of \mathbf{T}_0 is required, it is sufficient to compute the coefficient t_i in (2) in a way that the integral form of (1),

$$\oint_{C_i} \mathbf{T}_0 dl = \int_{\Gamma_i} \mathbf{J}_0 d\mathbf{S} \quad (3)$$

holds for any closed path C_i in a fundamental set of loops in the graph with Γ_i being a surface bounded by the curve C_i . Following the idea first presented in [6], a general algorithm for the generation of \mathbf{T}_0 has been developed. The coefficients t_i in (2) are computed by evaluating the surface integrals of the current density \mathbf{J}_0 over a surface bounded by the loop defined by the co-tree edge in a simple element graph (Fig. 2). The advantage of this method is that the surface integrals are defined equally for each finite element by one fixed co-tree (Fig. 2a), hence it is not necessary to define global loops in the FE mesh.

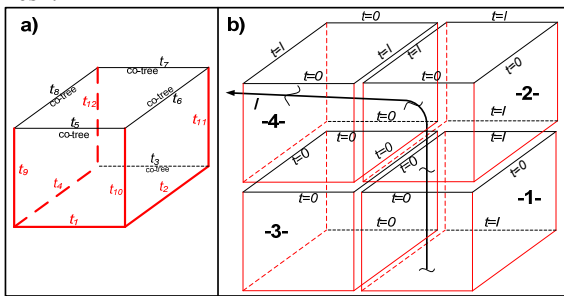


Fig. 2. a) Tree and co-tree definition within FE, b) A simple 3-D mesh

All elements are treated in defined succession which ensures that no element is arrived at after all its neighbors have been treated. The coefficients t_i on tree branches of the treated element are set to zero if no value has been assigned to these edges in previous steps, and the t_i values of the co-tree edges are calculated by numerical surface integration of the current density over the surface generated by the co-tree edge.

A simple example of four elements and one current filament is shown in Fig. 2b. Using this approach, the FE mesh of the end-winding is not required. Additional details of this method with emphasis on the numerical description of the end-winding geometry and the numerical integration procedure will be presented in the full paper.

III. PRELIMINARY RESULTS AND CONCLUSION

Using the first presented method, the magnetic field in a 3-D model of a 2.2 MW IM (Fig. 1) has been calculated. As presented in the Fig. 3 also the eddy currents in the surrounding metal parts were taken into consideration. By calculating the magnetic energy in the motor end-region the leakage inductance of 74 μH has been determined (the leakage inductance of 44.5 μH has been calculated using semi-empirical formulas). A very important influence of the eddy currents on the inductance values has been established, showing that static FEM analyses are not sufficient to calculate the leakage inductance. In the final paper results of both methods are going to be presented, mutually compared and, additionally, advantages and disadvantages of the two procedures are going to be discussed in detail.

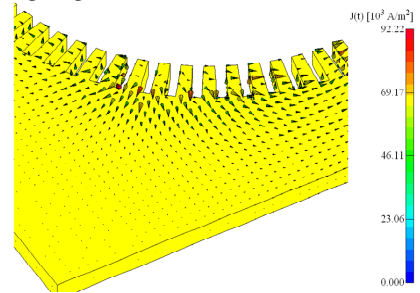


Fig. 3. Induced eddy currents in the surrounding metal parts of the IM.

ACKNOWLEDGMENT

This work has been supported by the Christian Doppler Research Association (CDG) and by the ELIN EBG Motoren GmbH.

IV. REFERENCES

- [1] A. Stermecki, O. Biro, K. Preis, S. Rainer and G. Ofner, "Determination of the Starting and Operational Characteristics of a Large Squirrel Cage Induction Motor Using Harmonic and Transient FEM," presented at 18th International Conference on Electrical Machines, Vilamoura, Portugal, Sep. 2008.
- [2] V. B. Honsinger, "Measurement of End-Winding Leakage Reactance," Power Apparatus and Systems, Part III, Transactions of the American Institute of Electrical Engineers, 78(3): 426-431, 1959.
- [3] D. Ban, D. Zarko and I. Mandic, "Turbogenerator End-Winding Leakage Inductance Calculation Using a 3-D Analytical Approach based on the Solution of Neuman Integrals," IEEE Transactions of energy Conversion, 20(1): 98-105, 2005..
- [4] W. M. Arshad, H. Lendenmann, Y. Liu, J.-O. Lamell and H. Persson, "Finding end winding inductances of MVA machines," in Industry Applications Conference, 40th IAS Annual Meeting, Vol. 4, 2005, pp. 2309-2314.
- [5] A. Tounzi, T. Henneron, Y. Le Menach, R. Askour, E. Dumetz and F. Piriou, "3-D Approaches to Determine the End Winding Inductances of a Permanent-Magnet Linear Synchronous Motor," IEEE Transactions on magnetics, 40(2): 758-761, 2004.
- [6] O. Biro, K. Preis, G. Vrisk, K. R. Richter and I. Tigar, "Computation of 3-D Magnetostatic Fields Using a Reduced Scalar Potential," IEEE Transaction on Magnetics, 29(2): 1329-1332, 1993.

Neural FEM for Hysteretic Materials Unbounded Magnetic Field Analysis

S. Coco¹, A. Laudani¹, F. Riganti Fulginei² and A. Salvini²

¹ DIEES, University of Catania, V.le A. Doria 6, Catania I-95125, Italy

² DEA, University of Roma Tre, Via della Vasca Navale, 84, Roma I-00146, Italy
alaudani@diees.unict.it, asalvini@uniroma3.it

Abstract — A combination of computational techniques for analyzing unbounded magnetic field problems involving ferromagnetic materials is presented. The proposed approach is mainly based on a synergy between a Neural Network (NN) and the Finite Element Method. In particular, the unbounded problem is solved by using an iterative scheme based on a fictitious boundary that encloses all the hysteretic regions. The boundary conditions on the fictitious boundary are initially guessed and successively updated according to the solution obtained in the previous iteration step. The hysteretic nature of the material is taken into account by an original NN able to perform the modelling of any kind of quasi-static loop (saturated and non-saturated, symmetric or asymmetric). An application to a simple 2.5-D geometry is presented in order to illustrate the whole procedure.

I. INTRODUCTION

In this paper the authors present a Finite Element code for the analysis of magnetic problems in unbounded domains combined with a Neural Network (NN) approach for the characterization of magnetic hysteresis. By starting from a small set of measured loops, the NN manages the values of the magnetic field, H , and the flux density, B , as inputs while the differential permeability is the output. In particular, the proposed NN is capable to perform the modelling of saturated and non-saturated, symmetric or asymmetric hysteresis loops. In order to treat boundlessness in the system of coupled equations that must be used for solving the magnetic problem, we adopt an iterative scheme based on a fictitious boundary that encloses all the field sources and the material hysteretic regions with the aim to define a bounded domain. In this way the unbounded coupled problem solution is converted into the iterative solution of a sequence of bounded Dirichlet magnetic hysteresis problems. The boundary conditions on the fictitious boundary are initially guessed and successively updated according to the solution obtained in the previous iteration step. This treatment of boundlessness closely follows an analogous approach, successfully used for the solution of uncoupled electromagnetic problems in unbounded domains [1]. An application to a 2.5-D geometry is presented in order to illustrate the whole procedure.

II. FE SOLUTION OF THE MAGNETIC PROBLEM IN UNBOUNDED DOMAINS

Starting from Maxwell's equation for the stationary magnetic field and considering the constitutive law for magnetic hysteretic materials

$$\mathbf{B} = \mu_0(\mathbf{H} + \mathbf{M}) \quad (1)$$

where \mathbf{M} is the nonlinear magnetization function and μ_0 is the vacuum permeability, it is possible to obtain the following equation in terms of the magnetic potential vector \mathbf{A} :

$$\nabla \times \left(\frac{1}{\mu_0} \nabla \times \mathbf{A} \right) = \mathbf{J} + \nabla \times \mathbf{M} \quad (2)$$

By introducing a fictitious boundary $\partial\Omega$ this equation is considered in a bounded domain Ω_M enclosing all the density current sources \mathbf{J} and all the magnetic materials. In this way the unbounded problem solution is converted into the iterative solution of a sequence of bounded Dirichlet magnetic problems. The boundary conditions on the fictitious boundary are initially guessed and successively updated according to the magnetic vector potential and current density distributions obtained in the preceding iteration step. In particular, the boundary values of magnetic potential vector can be derived by exploiting its Laplacian behaviour in a region which does not contain sources by means of the Green's function. In fact, for a generic harmonic function, Φ , in the external homogeneous unbounded source free region one has:

$$\Phi(\mathbf{r}_F) = - \int_{\Gamma} \left[\frac{\partial \Phi(\mathbf{r})}{\partial \mathbf{n}} G(\mathbf{r}, \mathbf{r}_F) - \frac{\partial G(\mathbf{r}, \mathbf{r}_F)}{\partial \mathbf{n}} \Phi(\mathbf{r}) \right] ds \quad (3)$$

where: Γ is an arbitrary surface contained in Ω_M enclosing all the sources and magnetic materials; \mathbf{n} is the unit vector normal to Γ , oriented toward Ω_M ; \mathbf{r} and \mathbf{r}_F are point vectors relative to Γ and $\partial\Omega_M$, respectively and G is the Green's function for free space. Since in the FEM approximation, the surface curve Γ is conveniently selected as constituted by finite element sides, the (3) can be rewritten for each boundary "unknown" \mathbf{A}_F in the form: $\mathbf{A}_F = \mathbf{R}_M \mathbf{A}$ where \mathbf{R}_M is a rectangular matrix of purely geometrical coefficients. The solution of the coupled problem from equations (2) and (3) are well suited to be solved iteratively, arbitrarily guessing at the beginning the magnetic vector potential on boundary $\partial\Omega_M$. On the other hand even the solution of the discretized equation (2) requires an iterative scheme. Consequently several choices for the hierarchical relationships between the two kinds of iterations are possible; in the full paper the performance of the different schemes will be discussed in details.

III. THE NEURAL NETWORK HYSTERESIS MODEL

The possibility of using Neural Networks to model magnetic hysteresis has been largely verified in literature [2]; and it is a valid alternative to classical models such as the Preisach or Jiles-Atherton ones. In fact, any hysteresis model requires the experimental characterization of the material by

using measured loops. Moreover, as shown in [2], the characterization performed by using the saturated major loop is often not suitable for accurately simulating minor loops. Then the identification of hysteresis models is an open problem as it is testified by the huge production available in literature about this task. Thus, the aim of the presented NN approach is to provide a computational tool able to predict the quasi-static magnetic hysteretic behaviour of a ferromagnetic material by the direct exploitation of few simple measurements. They consist of the generation of an asymmetric loop obtained by following a path involving a portion of the major-saturated-loop branch and an ascending non-symmetric branch as in Fig. 1.

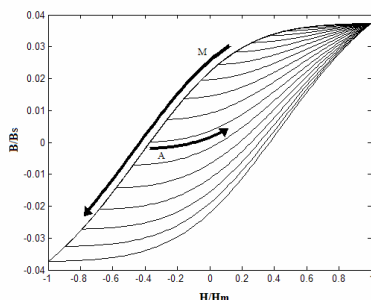


Fig. 1. Example of the Saturated loop used for NN training (M indicates the Major Loop Branch while A indicates the Asymmetric Branch).

In this way the NN is able to simulate any possible kind of loop (symmetrical or asymmetrical, saturated or non-saturated) by exploiting the transplantation technique [4]. In particular, the implemented NN is a simple feedforward net trained by using the Levenberg-Marquardt backpropagation algorithm. The NN consists of two input neurons, representing the magnetic field, H , and the flux density, B , one hidden layer with 9 neurons and one output neuron that gives as a result the value of the differential permeability, $\mu_d(H, B) = dB/dH$. The training set exploits 100 H - B sampled points for each asymmetric saturated hysteresis loop (see Fig.1) obtained by measurements. Altogether, 20 measured loops are used. Moreover, the NN is able to reproduce symmetric loops even if it is trained on asymmetric ones because a symmetric loop can be obtained by the superposition of mirror asymmetric branches (see Fig. 2). Finally, the reconstructions of minor loops are performed in two subsequent steps: while the NN predict the first ascending (or descending) branch of the minor loop, the second descending (or ascending) branch is obtained by the transplantation technique proposed in [4]. Thus, the present approach can be easily and usefully embedded into a set of field equations since it does not require a preliminary knowledge of the H (or B) waveform. More in detail, let us consider the NN input $[H(k), B(k)]$ and the returned NN output $\mu_d(H(k), B(k)) = dB(k)/dH(k)$ at the k -th step of an iterative procedure. Let us assume dH (or dB) the imposed increment of the magnetic field (or flux density). Thus, at the $k+1$ -th step we can input the NN with $[H(k+1) = H(k) + dH(k+1), B(k+1) = \mu_d(H(k), B(k))dH]$ (similarly for an imposed dB). In Fig. 3, an example of validation is shown.

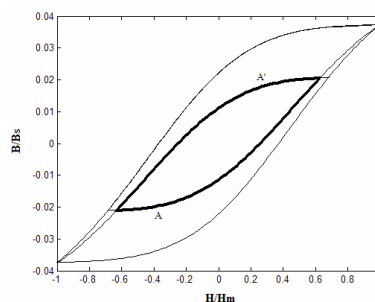


Fig. 2. Symmetric loop obtained by the superposition of mirror asymmetric branches.

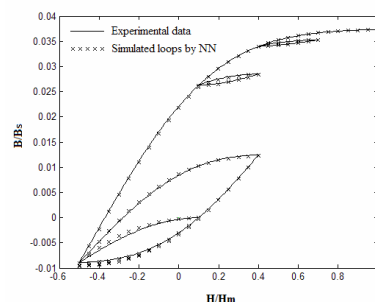


Fig. 3. Example of NN approach validation

IV. EXAMPLE OF APPLICATION

Hereafter a test of the proposed method is applied to a magnetic problem involving a simple geometry: a ferromagnetic cylinder is considered having a length of 8 cm and a radius 1 cm, surrounded by a coil solenoid of inner radius 2 cm, outer radius 2.5 cm and length 10 cm, carrying a uniform current of 1 A. Since the problem is axisymmetric it is possible to analyze only $1/4$ of the whole geometry, as shown in fig. 4, where the domain considered for the problem is represented together with the results expressed in terms of magnetic potential vector intensity.

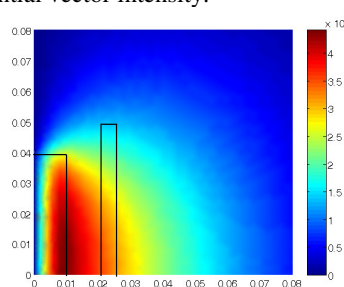


Fig. 4. Magnetic potential vector intensity for the considered example.

V. REFERENCES

- [1] S. Coco and A. Laudani, "Iterative FE Solution of Unbounded Magneto-Thermal Problems", *10th IGTE Symposium on Numerical Field Calculation in Electrical Engineering*, Sept 16-18, 2002 Graz, Austria.
- [2] C. Serpico and C. Visone, "Magnetic Hysteresis via Feed-Forward Neural Networks", *IEEE Trans. On Magnetics*, vol. 34, no. 3: 623-628, May 1998.
- [3] F.R. Fulginei and A. Salvini, "Softcomputing for the Identification of the Jiles-Atherton Model Parameters", *IEEE Trans. On Magnetics*, vol. 41, n. 3: 1100-1108, March 2005.
- [4] E. Zirka and Y. I. Moroz, "Hysteresis modeling based on transplantation," *IEEE Trans. on Mag.*, vol. 31, no. 6, pp. 3509-3511, Nov. 1995.

Homogenization of anisotropic laminated stacks taking into account eddy currents

E. Napieralska*, K.Komez****, N. Hihat*, J.Ph.Leco****, S. Wiak**** and P. Napieralski****

*LSEE - Universite d'Artois, FSA, Technoparc Futura, 62400 Bethune, France

ewa.napieralskajuszczak@univ-artois.fr

** Institute of Mechatronics and Information Systems Technical University of Lodz

Stefanowskiego 18/2, Lodz, Poland wiakslaw@p.lodz.pl

*** Institute of Computer Science Technical University of Lodz, ul. Wólczńska 215, Lodz, Poland

Abstract—The paper presents an innovative computational methodology dedicated to establishing equivalent characteristics of anisotropic laminated structures. The method is based on the homogenization technique. The influence of eddy currents on the equivalent characteristic is also counted.

Key words—anisotropic laminations, equivalent magnetic characteristics, homogenization, eddy currents, lamination stack

I. INTRODUCTION

Iron cores in electrical machines and transformers are usually made of lamination stacks in order to reduce eddy current losses. It is impossible to model with finite element software the eddy currents in each lamination. Indeed, full 3D numerical modeling of such structures is time consuming and it requires large memory. That is why the main idea is to replace the complex three-dimensional structure by a homogenized 'equivalent' material. This material, magnetically equivalent, allows the real 3D structure made of thin sheets to be treated computationally as a 2D problem. It requires to establish a family of equivalent characteristics. For instance, joints in power transformers are made of internal air gaps and thin anisotropic laminations (0.17-0.5mm) of varied rolling directions. Such a structure may be replaced by an equivalent homogenized material [1]. In the first stage, it has been assumed that the normal flux density component B_z is negligible compared to the components B_x and B_y in the lamination surface. As a consequence, the effects of eddy currents have been neglected too and such an approximation inevitably causes some inaccuracies. Although the component perpendicular to the sheets is typically only a few percent of the tangential components, it is distributed on large areas. This paper describes the second stage of the investigation: objective is to replace the 3D region by an equivalent 2D structure taking into account the eddy currents induced by the longitudinal flux. The complete influence of the flux normal to the lamination plane [2-4] will be introduced in a further paper.

II. ANALYSIS OF THE 3-D SIMULATION RESULTS

In order to set out in detail the possible simplifications, several 3D simulations have been made. The influence of the eddy currents created by longitudinal and normal fields are analyzed for the following structures:

1. Several superposed sheets with different lamination directions
2. Corner of Epstein frame
3. Step-lap joint with internal air-gaps.

The main purpose of these 3D simulations is to estimate the effect of the eddy currents induced by the normal flux on the field distribution. For each structure, two simulations were made: with and without the eddy currents.

Conclusions from the 3-D simulation are the following:

- 1) The perpendicular flux is non negligible only in the air gaps and in the non conducting regions because of the continuity of \vec{B}_z between the non conducting and conducting layer, but also because B_z is very low comparing with the longitudinal component).
- 2) The longitudinal flux density component in the air is negligible (the eddy current flowing on the sheet surface are too low to disturb H_x and H_y , so due to the field continuity on the lamination surface, the field and the flux density in the air are very low)
- 3) The surface eddy current in the lamination generated by the normal field causes the adequately losses, but it does not intervene on the flux penetration from one lamination to another.
- 4) It is only necessary only to take into account in the mathematical model the dependence between the longitudinal flux in the lamination and the normal flux penetrating from non conducting layers.

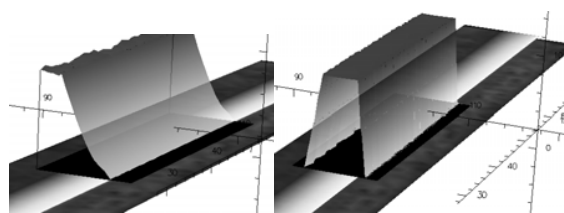


Fig.1 Flux density components for the penetration of flux from one to another lamination by non conducting layer.

a) Longitudinal component in the lamination (max. 1.22T)

b) Normal component in the air-gap between laminations (max. 0.076T)

III. DESCRIPTION OF THE METHOD

The macrostructure in the homogenization technique is a complete stack, while the microstructure is a repeatable set of several layers. It is customary, when describing a family of $B(H)$ curves for different angles, to assume that 0° is in the rolling direction for one lamination and x the direction for the equivalent structure. For every layer i , of the

thickness d_i it has been assumed that the flux density \vec{B}_i and the time derivative of flux density $\frac{\partial \vec{B}}{\partial t}$ is spatial average

$$\left\langle \frac{\partial \vec{B}_i}{\partial t} \right\rangle = \frac{1}{d_i} \int_{-d_i/2}^{d_i/2} \frac{\partial \vec{B}(z, t)}{\partial t} dz \quad (1)$$

The flux density components in a sample of dimensions $\delta x \times \delta y \times \delta z$ may be found as:

$$B_{ix} = \frac{1}{2} \frac{\phi'_{ix} + \phi''_{ix}}{\delta y \delta z}; \quad B_{iy} = \frac{1}{2} \frac{\phi'_{iy} + \phi''_{iy}}{\delta x \delta z}; \quad B_{iz} = \frac{1}{2} \frac{\phi'_{iz} + \phi''_{iz}}{\delta y \delta x}; \quad (2)$$

where $i=1, 2, \dots, n$ denotes the structure's layer, ϕ'_{ix} is the flux 'in' through the surface yz , ϕ''_{ix} is the flux 'out', ϕ'_{iy} , ϕ''_{iy} , ϕ'_{iz} and ϕ''_{iz} are similar fluxes respectively through the surface xz and xy . The field distribution results of the system's tendency to achieve a minimum of magnetic energy. Unknowns in the minimization task are the flux density components in every layer. The starting values for B_{1x} , B_{1y} , B_{2x} , B_{2y} , B_{1z} and B_{2z} follow an initial assumption that magnetic flux goes entirely through the laminations avoiding the gaps. The model is established with the following simplifications:

a) For the non-conducting layers, the three components of the flux density exist. The total energy of the layer is the magnetic field energy $W_{\mu 0} = \frac{(B_{ix}^2 + B_{iy}^2 + B_{iz}^2)}{2} \delta x \delta y \delta z \nu_0$

where ν_0 is the vacuum reluctivity.

b) For each lamination of thickness d_i and electric conductivity σ the analytical solution is established. As they are in every sheet two main magnetic fluxes (one parallel to the lamination surface and the second perpendicular to the lamination surface), two eddy currents densities are considered. The total current density results from the vector superposition of eddy current densities.

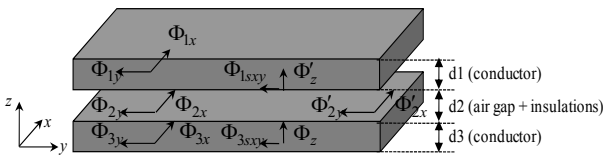


Fig.2 Fluxes in three consecutive layers

When reaching the boundary between non-conducting and conducting layers, the normal component of the flux density turns and became tangential (fig.2). The magnetic flux is harmonic function of time. Compliance of these phenomena is established by the boundary conditions on the surface of the lamination.

The energy W_{μ} per time unit into the i^{th} lamination equals the integral of Poynting's vector along the lamination surface. The current density in the isolating layer is function of all flux density components in the layer and of the normal component in the neighboring isolating layer.

The steady-state eddy current loss density P (W/m³), averaged over a time period and over the lamination thickness, for the

flux parallel to the lamination surface is given by the following expression:

$$P_J = \frac{1}{T} \int_0^T \vec{H}_i \frac{\partial \vec{B}_i}{\partial t} dt = f(\sigma_i, d_i^2, f^2, \langle B_{xi} \rangle^2, \langle B_{yi} \rangle^2, B_{s(i-1)}, B_{s(i+1)}) \quad (3)$$

where $B_{s(i-1)}, B_{s(i+1)}$ are the flux density on the boundaries of the i -th lamination.

For the whole structure, the following argument exploits the system natural tendency to achieve the minimum of the field energy which may be expressed as:

$$W_{\mu \min} = \sum_{i=1}^n W_{\mu i}(\mu_i, \vec{B}_i) \quad (4)$$

where μ_i is the permeability, and \vec{B}_i the induction in individual laminations, n is number of laminations in the microstructure. The equivalent permeability at any point of the core is a function of the resultant flux density and the minimal field energy $\mu(\vec{B}_{eq}, W_{\mu \min})$. A standard Hooke and Jeeves Direct Search Method has been used as it is known to be robust and insensitive to the starting point. The equivalent reluctivity ν_{eq} of the homogenized replacement material may be found by equaling the energies of the real and equivalent structures. In the following, a numerical procedure and the eddy currents generated by the perpendicular flux will be described in detail. The material modeling and its implementation inside the procedure will be discussed. The equivalent characteristics for different anisotropy directions have been computed by varying the equivalent flux density from 0.01T up to saturation for 3D structures presented in advance.

IV. CONCLUSIONS

In order to provide independent verification of the proposed approximations and gain more insight into the behavior of the magnetic field in the laminated structures, and in particular to study the effects of the eddy currents induced by the transverse flux, an attempt was made to model the systems studied using full 3D and homogenized 2D finite element code. The results will be presented in the full paper.

ACKNOWLEDGMENT

This joint research work with ThyssenKrupp Electrical Steel, is sponsored by the region Nord Pas-de-Calais (France), the French ministry and the European funds (FEDER).

REFERENCES

- [1] M.Pietruszka, E.Napieralska, Lamination of T-joints in the transformer core, *IEEE Trans on Magn.*, 32(3), 1996, pp1180– 1183
- [2] L.Krahenbuhl, P.Dular, T.Zeidan, F.Buret. "Homogenization of Lamination Stacks in Linear Magnetodynamics." *IEEE Trans. on Magn.*, 40(2), pp 912-915 (2004)
- [3] Gyselinc J., Dular P. 'A time-domain homogenization technique for laminated iron cores in 3D finite element models', *IEEE Trans. on Magn.*, 2004, 40, (3), pp 1424-1427
- [4] Gyselinc J, L.Vandervelde, J.Melkebeek, P.Dular, F.Henrotte, W.Legros "Calculation of Eddy Currents and Associated Losses in Electrical Steel Laminations." *IEEE Trans. on Magn.*, 35(3), 1999, pp 1191-1194

An Anisotropic Vector Hysteresis Model Using Isotropic Vector Play Model

Tetsuji Matsuo

Graduate School of Engineering, Kyoto University
Kyotodaigaku-katsura Nishi-ku, Kyoto, 615-8510, Japan
tmatsuo@kuee.kyoto-u.ac.jp

Abstract— A simple anisotropic vector hysteresis model is developed for representation of 2D weakly anisotropic vector hysteretic property. An isotropic vector play model is identified from azimuthally averaged vector property of anisotropic material. An anisotropic matrix is multiplied to the isotropic vector play model to represent anisotropy. Vector properties of a non-oriented steel sheet are represented by the proposed model.

I. INTRODUCTION

The play model is an efficient and precise hysteresis model, which has several vector versions [1]-[3]. However, the representation of anisotropic vector hysteretic properties of silicon steel sheets is still an open problem for the play model and other hysteresis models. This article proposes a simple generalization of vector play model for representation of two-dimensional (2D) weakly anisotropic vector hysteretic property, which is observed in non-oriented steel sheets.

II. ISOTROPIC VECTOR PLAY MODEL

An isotropic vector play model is given as

$$\mathbf{H} = \mathbf{P}(\mathbf{B}) = \int_0^{B_s} f(\zeta, \mathbf{p}_\zeta(\mathbf{B})) d\zeta \quad (1)$$

$$f(\zeta, \mathbf{p}) = f(\zeta, |\mathbf{p}|) \frac{\mathbf{p}}{|\mathbf{p}|} \quad (2)$$

where $f(\zeta, \mathbf{p})$ is a shape function, B_s is the saturation magnetic flux density, and \mathbf{p}_ζ is a vector play hysteron having a radius ζ . The hysteron \mathbf{p}_ζ [4] is given as

$$\mathbf{p}_\zeta(\mathbf{B}) = \mathbf{B} - \frac{\zeta(\mathbf{B} - \mathbf{p}_\zeta^0)}{\max(\zeta, |\mathbf{B} - \mathbf{p}_\zeta^0|)} \quad (3)$$

$$\mathbf{p}_\zeta^{0*} = \frac{(B_s - \zeta)\mathbf{p}_\zeta^0}{\max(B_s - \zeta, |\mathbf{p}_\zeta^0|)} \quad (4)$$

where \mathbf{p}_ζ^0 is the vector \mathbf{p}_ζ at the previous time-point.

The play model (1) is a 3D vector model. However, this article discusses its 2D property for the representation of rotational and alternating hysteretic properties of silicon steel sheets.

Anisotropic properties of non-oriented silicon steel sheet (JIS: 50A1300) are averaged along the azimuthal direction to obtain isotropic properties for simulations. An averaged alternating property is used to identify the shape function f . The dashed line in Fig. 1 shows the simulated rotational hysteresis loss of the steel sheet, which is larger than the measured one.

To adjust the rotational hysteresis loss, the vector play model is modified similarly to a vector stop model [5] as

$$\mathbf{P}^*(\mathbf{B}) = (\mathbf{P}(\mathbf{B}) \cdot \mathbf{e}_\parallel) \mathbf{e}_\parallel + r(|\mathbf{B}|) (\mathbf{P}(\mathbf{B}) \cdot \mathbf{e}_\perp) \mathbf{e}_\perp \quad (5)$$

where \mathbf{e}_\parallel and \mathbf{e}_\perp are parallel and perpendicular unit vectors to \mathbf{B} , respectively, and $r(|\mathbf{B}|)$ is the ratio of the measured rotational hysteresis loss to the simulated loss given by \mathbf{P} . The solid line in Fig. 1 shows the rotational hysteresis loss given by \mathbf{P}^* , which agrees with the measured one.

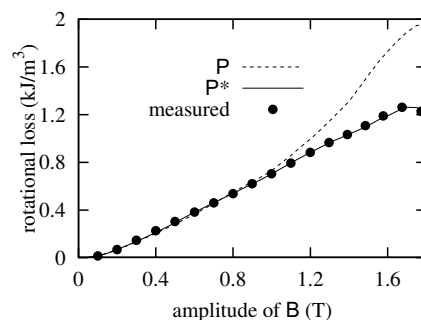


Fig. 1. Rotational hysteresis losses given by isotropic vector play models

III. ANISOTROPIC VECTOR HYSTERESIS MODEL

A simple 2D anisotropic version of the vector play model is given as

$$\mathbf{P}_B(\mathbf{B}) = \mathbf{W}_B(\mathbf{B}) \mathbf{P}^*(\mathbf{B}) \quad (6)$$

where $\mathbf{W}_B(\mathbf{B})$ is a matrix of which components are single-valued function of \mathbf{B} . For example, \mathbf{W}_B is determined so as to reconstruct anisotropic alternating property from averaged alternating property as

$$\mathbf{W}_B(\mathbf{B}) = \begin{pmatrix} w_{B_x}(B, \varphi_B) & 0 \\ 0 & w_{B_y}(B, \varphi_B) \end{pmatrix} \quad (7)$$

$$w_{B_x}(B, \varphi_B) = \frac{H_x(B, \varphi_B)}{H_{\text{ave}}(B) \cos \varphi_B},$$

$$w_{B_y}(B, \varphi_B) = \frac{H_y(B, \varphi_B)}{H_{\text{ave}}(B) \sin \varphi_B} \quad (8)$$

where $\mathbf{B} = |\mathbf{B}|$ and $\varphi_B = \tan^{-1}(B_y/B_x)$; $(H_x(B, \varphi_B), H_y(B, \varphi_B))$ is the measured initial magnetization property for unidirectional input of \mathbf{B} along the φ_B -direction; $H_{\text{ave}}(B)$ is the azimuthally averaged initial magnetization property for unidirectional input, which is accurately represented by the isotropic vector play model \mathbf{P}^* .

Another anisotropic vector play model is given as

$$\mathbf{P}_H(\mathbf{B}) = \mathbf{W}_H(\mathbf{P}^*) \mathbf{P}^*(\mathbf{B}) \quad (9)$$

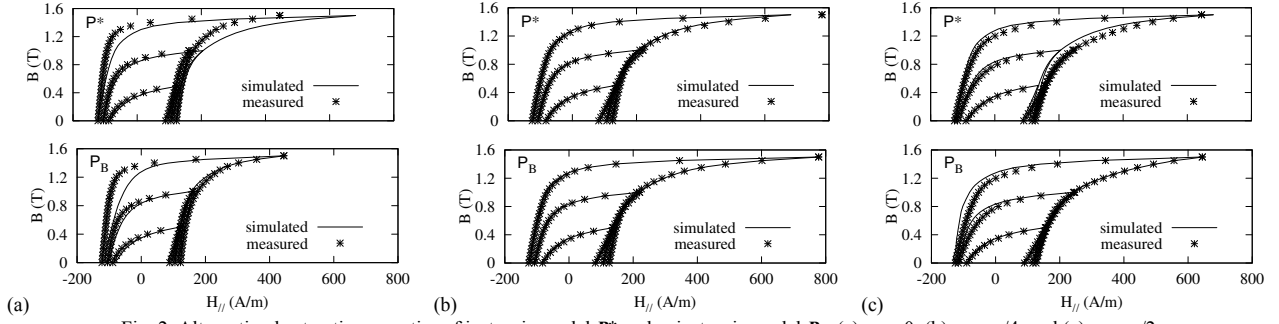


Fig. 2. Alternating hysteretic properties of isotropic model P^* and anisotropic model P_B : (a) $\varphi_B = 0$, (b) $\varphi_B = \pi/4$, and (c) $\varphi_B = \pi/2$.

where W_H is a matrix of which components are single-valued function of P^* . W_H is determined similarly to W_B as

$$W_H(P^*) = \begin{pmatrix} w_{Hx}(P^*, \varphi_H) & 0 \\ 0 & w_{Hy}(P^*, \varphi_H) \end{pmatrix} \quad (10)$$

where $P^* = |P^*|$ and $\varphi_H = \tan^{-1}(P^*_y/P^*_x)$. Functions w_{Hx} and w_{Hy} are given as

$$\begin{aligned} w_{Hx}(H_{ave}(B), \varphi_B) &= \frac{H_x(B, \varphi_B)}{H_{ave}(B) \cos \varphi_B}, \\ w_{Hy}(H_{ave}(B), \varphi_B) &= \frac{H_y(B, \varphi_B)}{H_{ave}(B) \sin \varphi_B} \end{aligned} \quad (11)$$

because $\varphi_H = \varphi_B$ for alternating input.

IV. SIMULATION RESULTS

Vector hysteretic properties of non-oriented silicon steel sheet, JIS: 50A1300, are simulated.

Fig. 2 depicts alternating hysteretic properties of isotropic model P^* and anisotropic model P_B for $\varphi_B = 0, \pi/4, \pi/2$, where $H_{ij} = \mathbf{H} \cdot \mathbf{e}_{ij}$. The anisotropic model gives accurate amplitudes of H_{ij} . The alternating hysteretic property of P_H is not shown because it is similar to P_B .

Figs. 3(a), (b) and (c) portray the loci of \mathbf{H} for counterclockwise rotational inputs of \mathbf{B} with $|\mathbf{B}| = 0.5, 1.0, 1.5$ T, which are simulated by P^* , P_B and P_H , respectively. The isotropic model P^* yields circular loci of \mathbf{H} . The loci obtained by P_B are directly affected by the phase lag of \mathbf{B} to P^* because of $W_B(\mathbf{B})$. The loci obtained by P_H are not affected by the rotational direction because $W_H(P^*)$ does not depend on the phase lag of \mathbf{B} to P^* . Fig. 3(d) shows the loci of \mathbf{H} given by $(P_B + P_H)/2$, which approximately agree with the measured loci.

V. ACKNOWLEDGEMENT

This work was supported in part by the Japan Society for the Promotion of Science, Grant-in-Aid for Scientific Research (C), 19560288.

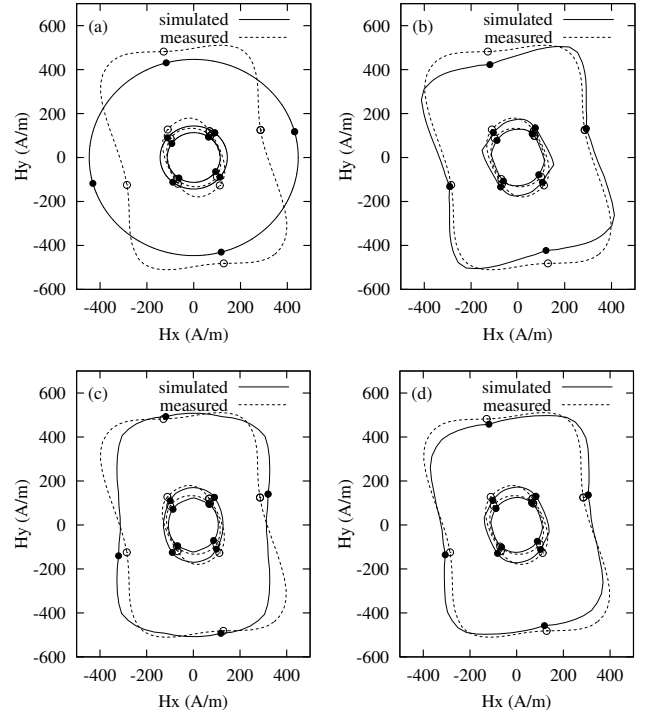


Fig. 3. Simulated loci of \mathbf{H} for rotational inputs of \mathbf{B} , where $B_x = 0$ or $B_y = 0$ at “•” (simulated) and “o” (measured): (a) $\mathbf{H} = P^*$, (b) $\mathbf{H} = P_B$, (c) $\mathbf{H} = P_H$, and (d) $\mathbf{H} = (P_B + P_H)/2$

VI. REFERENCES

- [1] A. Bergqvist, “Magnetic vector hysteresis model with dry friction-like pinning,” *Physica B*, 233: 342-347, 1997.
- [2] C. Serpico, M. d’Aquino, C. Visone, D. Davino, “A new class of Preisach-type isotropic vector model of hysteresis,” *Physica B*, 343: 117-120, 2004.
- [3] T. Matsuo, M. Shimasaki, “Two types of isotropic vector play models and their rotational hysteresis losses,” *IEEE Trans. Magn.*, 44(6): 898-901, 2008.
- [4] T. Matsuo, “Rotational saturation properties of isotropic vector hysteresis models using vectorized stop and play hysterons,” *IEEE Trans. Magn.*, 44(11): 3185-3188, 2008.
- [5] T. Matsuo, “Comparison of rotational hysteretic properties of isotropic vector stop models,” *IEEE Trans. Magn.*, 45(3): 1194-1197, 2009.

Influence of Material Dynamic Hysteresis Modelling in Losses Computation

T.P. DO^{1,2,3}, F. SIXDENIER¹, L. MOREL¹, E. MORIN², L. GERBAUD³, F. WURTZ³,

¹ Université Lyon 1, CNRS UMR5005 Ampère, Villeurbanne F-69622, France

² Schneider Electric Industries SAS, France

³ Grenoble Electrical Engineering Laboratory G2ELab, Grenoble, France

dothai@g2elab.grenoble-inp.fr

Abstract— In electromagnetic applications, hysteresis phenomena in magnetic materials are responsible of considerable causes of losses especially in transformer modelling cases. In specific case, such as current sensor, the output signal can be modified because of this loss. The paper presents the implementation proceeding used for some hysteresis material models and how they are applied in a sensor study case. A priori loss computation, simultaneously carried out with the simulation is one of the main advantages of this implementation. A transformer application is performed with the dynamic hysteresis characteristic taken into account and compared with experimental measurements.

I. INTRODUCTION

Nowadays, electrical engineering is concerned with energy efficiency. In addition, in the case of electromagnetic devices, such as current sensors, the energy losses change the output signals; so, to approach an ideal sensor, losses have to be minimized. Thus, to improve electrical device design, loss computation has to be carried out with a maximal accuracy. Many works allow a posteriori loss estimation [1], however, "Real time" approach, meaning a priori computation is furthermore interesting as it allows more accuracy in simulation.

Generally, in such devices, the total losses come from different sources as resistances and magnetic cores. The first one, copper losses are practically calculable by resistance and current measurements. However, the last one, magnetic losses or iron losses is more complicate to identify. In soft magnetic materials, experimental results show that they can be evaluated in two terms: hysteresis static losses, and dynamic losses. By adding these two terms, we obtain the so called iron losses. The static part corresponds to the $B(H)$ loop area in quasi-static mode, i.e. at low frequency. The dynamic one depends on the variation speed of the excitation source which is more important at high frequency.

II. MATERIAL MODEL WITH HYSTERESIS

A. Hysteresis model

Studies have shown that the mechanism that causes magnetization phenomena depend on many factors [2]: the material, the excitation field, the external environment, etc.

From an experimental point of view, two operating conditions can be distinguished: the quasi-static and the dynamic one. In quasi-static condition, the $B(H)$ loop representing the material behavior does not depend on the excitation frequency. Following the predefined criteria such as induction response and losses computation, some compatible models are identified. Among them, the chemical model [3] provides a good accuracy for soft magnetic materials by a description of two main microscopic mechanisms of the static magnetization: Bloch wall displacement and domain rotation. Furthermore, based on the balance of chemical equation analogies, this model has the advantage of a fast implementation and a quick computation. Another model, with a different approach, is called Derivative Static Hysteresis Model (DSHM). It focuses in the knowledge of memorization effect in the material during the magnetization. DSHM uses a matrix representation. Its accuracy depends only on the matrix size.

In dynamic operating conditions, the loop $B(H)$ expands according to the increasing frequencies (Fig.1).

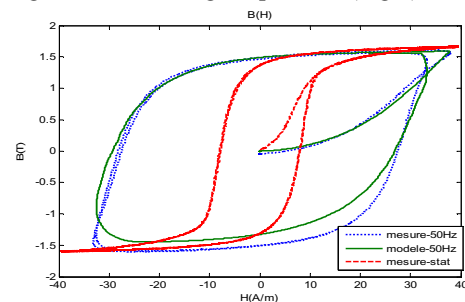


Fig. 1. $B(H)$ loop in static mode measurement (narrow cycle) and dynamic mode by measurements (large cycle in continuous line) and by simulation (large cycle in dotted line)

The area of this loop represents the energy of the material losses during a period. This energy loss is higher in dynamic state (the area is bigger). The flux tube model using a single dynamic parameter has been studied [4] to represent the additional dynamic losses:

$$H_{exc} = H_{stat}(B) + \gamma \frac{dB}{dt} \quad (1)$$

with H_{exc} the excitation field, H_{stat} virtual static excitation field for a given flux density and γ a coefficient depending of the electrical and magnetic properties (resistivity, permeability, etc.) of the material.

B. Model identification on soft magnetic material

A test bench able to automate material characterization proceedings was carried out in Ampère laboratory (Lyon). The output is given in the form of $B(H)$ loops.

For each sample/material, a numerous of measurements corresponding to a variation of excitation field and of frequency are realized. Optimization algorithms allow an automatic identification of models parameters.

III. ELECTROMAGNETIC DEVICE SIMULATION

Once the magnetic material model parameters have been identified, the relation between the excitation current and the flux in the magnetic circuit is established. Magnetic equation system is so obtained. By a coupling with electrical equation system, all the system is completely described.

For the coupling equation solving, some numerical techniques as Newton-Raphson are applied at each time step. A numerical ODE solver is used to give the system behavior in transient mode.

All these algorithms are implemented inside a new tool called RelucTool [5], dedicated for the modelling of low voltage electromagnetic devices.

IV. APPLICATION AND RESULTS

A. Simulation of a current sensor

To illustrate that hysteresis causes considerable losses in electromagnetic devices, a simple current sensor is simulated. The primary coil is supplied by a pseudo-sinusoidal current source, 50Hz with a variable primary current I_p ; the secondary coil is connected to a load, flowed by a current I_s . The magnetic core is made of a grain oriented silicon iron (SiFe) used in industrial production that provides a good characteristic in saturation induction and magnetic losses. In the ideal case, without loss, the I_s/I_p ratio is equivalent to N_p/N_s , the ratio of the number of wire turns respectively in the primary and secondary. Here the ideal ratio I_s/I_p is 0.1.

B. Result

Simulations with a chemical model have been carried out. The comparison with experimental results is taken via the secondary currents and the core losses found out, in two cases, according to the introduced primary current value (fig.2). A very good match between our model and the measures is observed. The non-ideal characteristic of the transformer that is represented by the variation of the quotient I_s/I_p is correctly modeled. The iron losses in the magnetic core, obtained by modelling, are very close to the experimental value.

These losses contribute to the system total losses so the energy balance that is established during the simulation process, not a posteriori.

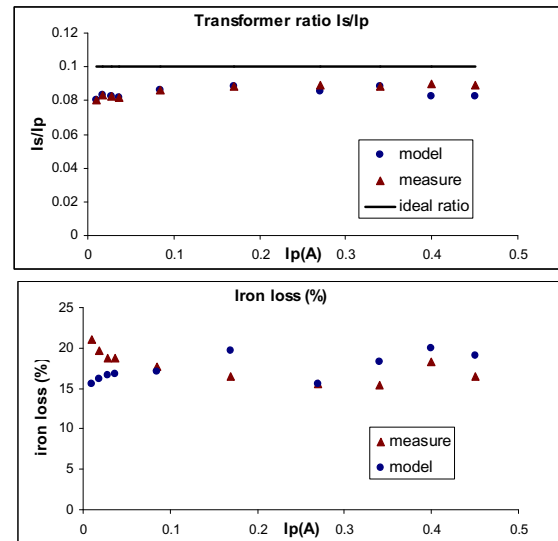


Fig. 2. Comparison of simulation and measurements results. On the top: losses make the ratio I_s/I_p lower than the ideal one. On the bottom: iron losses in percentage of input coil energy.

V. CONCLUSIONS AND INCOMING WORK

Simulations with variable frequency have been carried out. They allow confirming the model performance in dynamic mode.

From these results, the same proceedings can be applied to other hysteresis models. A comparison between different models can be thus performed to aid in the choice of an adapted model according to the application needs. The authors are carrying out a material model library of soft magnetic materials, useful for designers. Additional results will be presented in the full paper.

For sensor applications, further interesting studies can be developed such as amplitude and frequency range limits research thanks to the simulation with dynamic hysteresis models. In the future, a complete electronic component library will allow simulating more complex systems.

VI. REFERENCES

- [1] G. Bertotti, "General properties of power losses in soft ferromagnetic materials," IEEE Transaction on Magnetics, vol. 24, pp. 621–630, 1988.
- [2] Buschow, K.H.J. et De Boer, F.R. 2003. Physics of Magnetism and Magnetic Materials. s.l : Springer, 2003.
- [3] A. Nourdine, G.Meunier, A. Lebouc, "A New Hysteresis Model Generation—Application to the Transverse Axis of GO SiFe Sheet », IEEE Transactions on Magnetis, vol.37, No.5, September 2001
- [4] Rault MA, Sixdenier F, Guinand B, et al., "Limits and rules of use of a dynamic flux tube model", COMPEL, Vol. 27 Issue: 1, p. 256-265, 2008
- [5] B. du Peloux, L.Gerbaud, F.Wurtz, V. Leconte, F. Dorschner, "Automatic generation of sizing static models based on reluctance networks for the optimization of electromagnetic devices", IEEE Transactions on Magnetics, Vol.42, Issue 4, April 2006, pp. 715-718

Interlamination Shorts in Transformer Cores: Estimation of Local Power Dissipation

C. A. Schulz^{1,2}, D. Roger^{1,2}, S. Duchesne^{1,2}, J-N. Vincent³

¹ Univ. Lille Nord de France, F-59000 Lille, France

² UA, LSEE, F-62400 Béthune, France, daniel.roger@univ-artois.fr

³ ThyssenKrupp Electrical Steel, F-62330 Isbergues, France, jean-noel.vincent@thyssenkrupp.com

Abstract—In large transformer cores, burr-induced short circuits can cause hot spots which may locally damage the core. This paper presents a Finite Element (FE) analysis of this problem for Grain Oriented (GO) sheets; results are confirmed by measurements. The equivalent circuit derived from both measurements and FE simulation allows the power dissipated in a hot spot to be determined for the worst case.

I. INTRODUCTION

GO magnetic sheets in transformer cores are insulated on both sides with a thin inorganic coating on the glass film layer that forms during annealing. Before core assembly, the sheets are cut by mechanical shears; although great care is bestowed on this process, burrs may remain which can cause interlaminar shorts on edges of columns and yokes. Such shorts are known to increase eddy current loss [1]. In some cases, the currents circulating in the contact points cause small hot spots which may spread and locally damage the core through melting.

Considering the stochastic nature of a cutting burr, the contact is assumed to have an unknown resistance. The power dissipated in the contact point depends thus on this unknown value, but also on the characteristics of the equivalent electrical circuit in which the current flows. The purpose is to model this equivalent circuit and derive the power dissipation in the contact point in the worst case. A first model is based on experimental results. It is then extended to more general cases using a 3D FE simulation taking into account the strong anisotropy and the non-linearity of GO sheets.

II. MODEL BASED ON EXPERIMENTAL RESULTS

A current may flow in a cutting burr only if a closed path embracing a magnetic flux exists, so at least two contact points are needed. Considering the simplest case, it is possible to model an interlamination short by an equivalent circuit defined through two quantities: the electromotive force (e. m. f.) and the internal impedance. This kind of model is typically linear, therefore, it is important to identify the limits of validity using an experimental test bench built with GO sheets. The e. m. f. is the voltage measured in open circuit condition and the internal impedance is deduced from the short circuit current.

In order to determine these elements experimentally, the random aspect of burr-induced contacts is eliminated. Two low-resistance contacts are created by depositing solder on locally skinned GO sheets. Four thin wires are included in order to measure e. m. f. and voltage drop over the contacts. Fig. 1 shows the two instrumented sheets before stacking. The

short-circuit current is measured by means of a miniaturised Rogowski coil having 350 turns at a thickness of 600 μm and an internal diameter of 5 mm. Since its output voltage is in the range of microvolts, a low-noise differential amplification system and filtering circuitry is used. The phase shift of the filters and the transversal flux density gradient in the Rogowski coil are compensated [2].

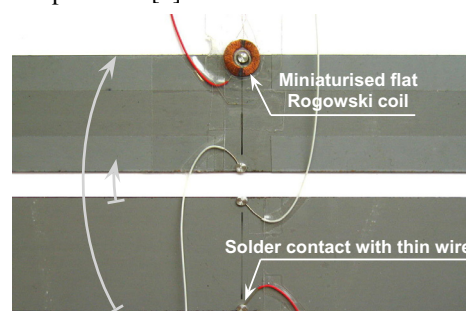


Fig. 1. Instrumented magnetic sheets.

After stacking, the instrumented sheets are placed in a square magnetic circuit with excitation coils, so as to form one of its legs. The main flux is measured with a 10-turn coil directly wound around the instrumented sheets.

The quantities e. m. f. and short circuit current have been recorded for various flux density levels. Fig. 2 presents data for 1,8 T; the plotted curves are normalized with respect to their peak values in order to allow an easy comparison of the waveforms.

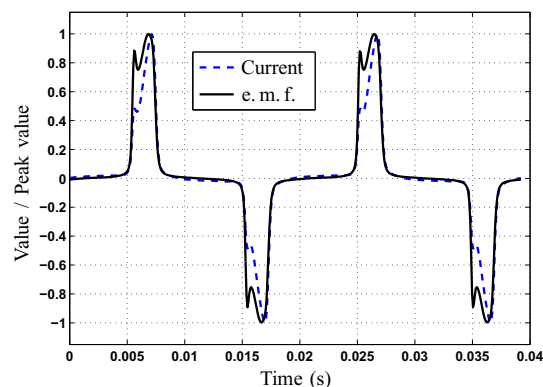


Fig. 2. Short circuit current and e. m. f. under saturation.

Measurement results show that the short circuit current has almost the same waveform as the e. m. f. and that there is no

phase lag. The congruence of the two curves is even better for lower flux densities. A detailed analysis of experimental results has been performed for different flux density levels and sheet widths. The equivalent circuit impedance is determined dividing the e. m. f. by the short circuit current and taking into account the small voltage drop over the artificial contacts. Analysis shows that, admitting an accuracy of 10%, the impedance of the equivalent circuit can be seen as a pure resistance which depends on sheet width and thickness for constant frequency. The e. m. f. is proportional to the cross section of the sheets and can be calculated analytically [3].

III. NUMERICAL MODEL

The FE model is designed to determine the parameters of the equivalent circuit for interlaminar shorts with more complex geometries. Numeric modelling of the short circuit in 3D is challenging since both anisotropy and nonlinearity of the GO material have to be taken into account. Furthermore, the very thin sheets have to yet be meshed with a number of layers to allow eddy currents to be represented correctly. The magnetisation curves $B(H)$ used in simulation were previously measured with Epstein strips cut in rolling direction and in transverse direction. These measurements were done at 1Hz and up to strong saturation; an extrapolation formula yielding points up to 2T and $\mu = \mu_0$ was applied in order to achieve computation convergence with Opera 3D. Fig. 3 presents an example of the simulation results, showing a detail of the mesh and the convergence of the current lines towards a contact point.

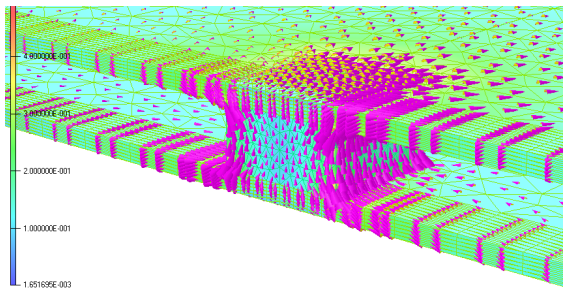


Fig. 3. Mesh and convergence of current lines towards a short-circuit

Short circuit current and e. m. f. are determined in post processing. Calculated quantities are compared to the experimental results for several flux densities and sheet widths. The differences found between simulation results and measurement were 5% for the e. m. f. and 4% for the short circuit current, respectively.

The FE simulation is used to determine e. m. f. and internal resistance of the equivalent circuit for the case when the contacts are not located exactly opposite to each other, as well as for configurations such as non-punctual contacts due to long burrs. Fig. 4 presents results for two shifted punctual contacts.

As predicted by the analytical analysis, the e. m. f. does not depend on the shift s . It can be seen that the short circuit current decreases more slowly than the inverse of the distance between the contacts. Analysis reveals that this phenomenon is due to the spreading of the current in the sheet plane and

amplified by the anisotropy of the material. Fig. 4 also shows that for large shifts of the burr-induced contacts ($s \gg b$), the short circuit current can be neglected.

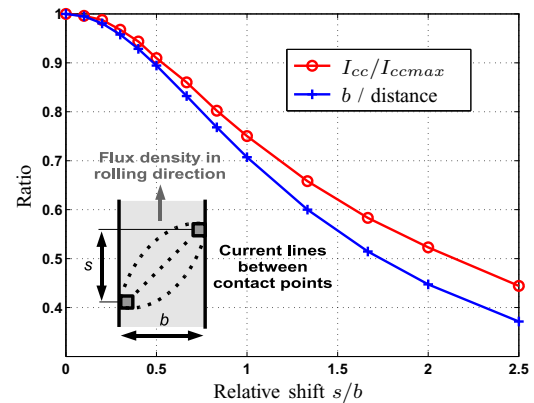


Fig. 4. Influence of a shift between the contacts on the current

For a given transformer core width, it is possible to define the equivalent circuit but not the current, because the burr resistance remains unknown. However, assuming a local contact, the worst case can be defined: it is obtained when the burr resistance is equal to the resistance of the internal circuit. Therefore, the power dissipation in the hot spot can be estimated. For example, assuming a large core ($b = 500$ mm) made of 0,3 mm GO sheets, magnetized at 1,7T, 50 Hz and containing a burr-induced short with zero shift, the equivalent circuit resistance estimation is 10 m Ω and the e. m. f. 85 mV peak. For a perfect contact, the short circuit current is 8,6 A peak. For the worst case, the estimation of the peak power in the hot spot is 0,10 W. This small power can correspond to a very high power density when it is concentrated in a burr of small section.

IV. CONCLUSION

FE simulation of short circuits between GO magnetic sheets has been performed and verified by experimental measurements. Power dissipation in a microscopic short circuit can be estimated for the worst case. Associated with a capacitive test method [4], this model can be used to estimate the extra core loss due to a multitude of microscopic burrs.

ACKNOWLEDGMENTS

The authors gratefully acknowledge support from the European Union (European Regional Development Fund), the Nord-Pas de Calais region, and the French Ministry (FRT).

REFERENCES

- [1] A. J. Moses and M. Aimoniotis, "Effects of artificial edge burrs on the properties of a model transformer core", *Physica Scripta*, 1989, 39, pp. 391-393
- [2] C. A. Schulz, et al., "Short circuit current measurements between transformer sheets", to be published at SMM 19, Sept. 2009, Torino.
- [3] Helmut Pfützner and Georg Krismanić, "The needle method for induction tests: Sources of error", *IEEE Transactions on Magnetics*, vol. 40, No. 3, May 2004, pp. 1610-1616.
- [4] C. A. Schulz, et al., "Capacitive short circuit detection in transformer core laminations", *Journal of Magnetism and Magnetic Materials (JMMM)*, vol. 320, 2008, pp. e911-e914.

Modeling of Magnetoelectric Effect: A Comparison between Homogenization and Finite Element Techniques

Romain Corcolle, Laurent Daniel, and Frédéric Bouillault

Laboratoire de Génie Electrique de Paris

CNRS UMR8507; SUPELEC; UPMC Univ Paris 06; Univ Paris-Sud;

11 rue Joliot-Curie, Plateau de Moulon, F-91192 Gif-sur-Yvette Cedex, FRANCE

Email: romain.corcolle@lgep.supelec.fr

Abstract—Homogenization techniques are efficient tools to determine macroscopic properties of heterogeneous materials. These techniques, mainly developed in the framework of uncoupled behavior, have been recently applied to coupled behavior. Finite Element Method is a classical approach for such heterogeneous problems. We propose to compare these two approaches in the case of magnetoelectric composite materials made of the assembly of piezomagnetic and piezoelectric constituents. The two approaches are shown to be in good agreement in the case of matrix-inclusions microstructures, with a much lower computational cost for homogenization technique.

Index Terms—Magnetoelectric effect, homogenization, finite element method.

I. INTRODUCTION

The study of coupling effects is a long-standing domain of interest in physics. The possibility of applications such as sensors or actuators have made materials with strong coupled properties receive more and more attention in the past years. In the case of magnetoelectric (ME) materials, composite materials made of the assembly of piezomagnetic and piezoelectric constituents have shown to exhibit a much stronger (extrinsic) ME effect than homogeneous materials [1].

In order to design properly corresponding applications, the material microstructure (essential in the definition of the macroscopic properties) has to be accounted for. This is the reason why advanced modeling tools are needed. Finite Element modeling is a classical approach and can provide a full description of the fields in the composite [2]. But its main disadvantage is the computational cost. Another approach is the use of homogenization techniques, that can be adapted to coupled behavior [3], with a very low computational cost (especially in the case of linear behavior for which analytical solutions can be provided).

The purpose of homogenization is the deduction of the effective properties of heterogeneous materials [4], meaning the properties of a (fictive) homogeneous material with the same macroscopic properties than the heterogeneous material. Homogenization techniques only use a few pieces of information about the microstructure and can provide bounds or estimates on the effective properties.

In this paper Finite Element and homogenization approaches are compared in the case of a magneto-electric composite with

matrix-inclusion type microstructure.

II. PIEZOMAGNETIC/PIEZOELECTRIC COMPOSITE

For the composites studied in this paper, the magnetoelectric effect is extrinsic: none of the phases exhibits such an effect. The coupling effect appears through mechanics (see Fig. 1): the piezomagnetic phase deforms when a magnetic field is applied to the composite, then the strain spreads to the piezoelectric phase, leading to an electric polarization (the converse phenomenon also appears: an applied electric field leads to a magnetic polarization).

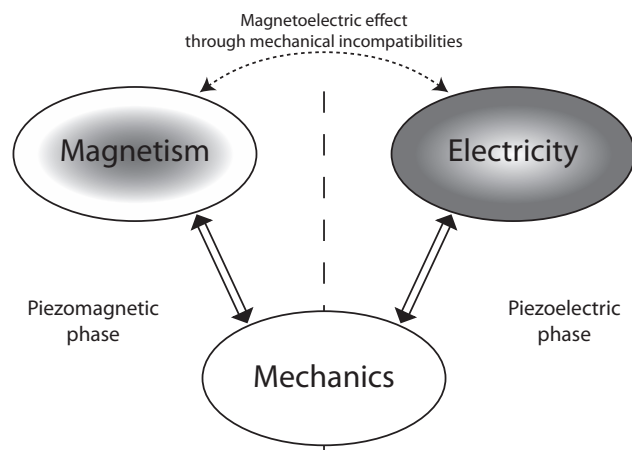


Fig. 1. ME effect in piezomagnetic/piezoelectric composites.

The constitutive laws for the phases are (the subscript m stands for the piezomagnetic phase, e for the piezoelectric phase):

$$\begin{pmatrix} \mathbb{T}_m \\ \mathbb{B}_m \\ \mathbb{D}_m \end{pmatrix} = \begin{pmatrix} \mathbf{C}_m & -{}^t\mathbf{q} & \mathbf{0} \\ \mathbf{q} & \boldsymbol{\mu}_m & \mathbf{0} \\ \mathbf{0} & \mathbf{0} & \boldsymbol{\epsilon}_m \end{pmatrix} \cdot \begin{pmatrix} \mathbb{S}_m \\ \mathbb{H}_m \\ \mathbb{E}_m \end{pmatrix} \quad (1)$$

$$\begin{pmatrix} \mathbb{T}_e \\ \mathbb{B}_e \\ \mathbb{D}_e \end{pmatrix} = \begin{pmatrix} \mathbf{C}_e & \mathbf{0} & -{}^t\mathbf{e} \\ \mathbf{0} & \boldsymbol{\mu}_e & \mathbf{0} \\ \mathbf{e} & \mathbf{0} & \boldsymbol{\epsilon}_e \end{pmatrix} \cdot \begin{pmatrix} \mathbb{S}_e \\ \mathbb{H}_e \\ \mathbb{E}_e \end{pmatrix} \quad (2)$$

where \mathbb{T} and \mathbb{S} are the stress and strain tensors, \mathbb{B} and \mathbb{H} are the magnetic induction and the magnetic field, \mathbb{D} and \mathbb{E} are

the electric induction and the electric field. \mathbf{C} , $\boldsymbol{\mu}$ and $\boldsymbol{\epsilon}$ are respectively the stiffness tensor, the permeability tensor and the permittivity tensor. The tensors \mathbf{q} and \mathbf{e} are respectively the piezomagnetic and piezoelectric coupling tensors.

III. HOMOGENIZATION

The homogenization technique used to model these composites is based on inclusion problems [5]. The method developed in the framework of uncoupled behavior has been extended to coupled behavior thanks to an appropriate decomposition of the fields [3]. The classical homogenization tools still apply and the uncoupled constitutive laws can be extracted. The coupling effects appear through additional relations. The obtained effective properties of the composite are written:

$$\begin{pmatrix} \overline{\mathbb{T}} \\ \overline{\mathbb{B}} \\ \overline{\mathbb{D}} \end{pmatrix} = \begin{pmatrix} \tilde{\mathbb{C}} & -\tilde{\mathbf{q}} & -\tilde{\mathbf{e}} \\ \tilde{\mathbf{q}} & \tilde{\boldsymbol{\mu}} & \tilde{\boldsymbol{\alpha}} \\ \tilde{\mathbf{e}} & \tilde{\boldsymbol{\alpha}} & \tilde{\boldsymbol{\epsilon}} \end{pmatrix} \cdot \begin{pmatrix} \overline{\mathbb{S}} \\ \overline{\mathbb{H}} \\ \overline{\mathbb{E}} \end{pmatrix} \quad (3)$$

where the notation $\overline{\mathbb{X}}$ stands for the average value of \mathbb{X} over the volume. It has to be noticed that the macroscopic constitutive law exhibits a magnetoelectric coupling tensor $\tilde{\boldsymbol{\alpha}}$ whereas none of the phases exhibits such an effect. This coupling tensor links the macroscopic magnetic induction $\overline{\mathbb{B}}$ to the macroscopic electric field $\overline{\mathbb{E}}$ ($\overline{\mathbb{B}} = \tilde{\boldsymbol{\alpha}} \cdot \overline{\mathbb{E}}$) when the macroscopic strain $\overline{\mathbb{S}}$ and the macroscopic magnetic field $\overline{\mathbb{H}}$ are null. It can also be defined as the link between the macroscopic electric induction $\overline{\mathbb{D}}$ and the macroscopic magnetic field $\overline{\mathbb{H}}$ ($\overline{\mathbb{D}} = \tilde{\boldsymbol{\alpha}} \cdot \overline{\mathbb{H}}$) when the macroscopic strain $\overline{\mathbb{S}}$ and the macroscopic electric field $\overline{\mathbb{E}}$ are null.

IV. RESULTS

The example of application is the study of the magneto-electric effect in composites made of $BaTiO_3$ (piezoelectric) and $CoFe_2O_4$ (piezomagnetic). The material properties can be found in [6]. The studied microstructures are random distributions of $CoFe_2O_4$ cylinders in a $BaTiO_3$ matrix (see Fig. 2). Both phases have their poling directions along the y -axis.

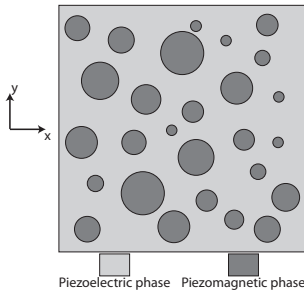


Fig. 2. Matrix-inclusions microstructure (in 2-D).

For this kind of microstructure, a satisfying estimate of the effective properties in homogenization can be obtained with the Hashin & Shtrikman estimate [3]. In this application, the 2-D coupling tensor $\tilde{\boldsymbol{\alpha}}$ has the following shape:

$$\tilde{\boldsymbol{\alpha}} = \begin{pmatrix} \alpha_{11} & 0 \\ 0 & \alpha_{22} \end{pmatrix} \quad (4)$$

The homogenization results (presented in Fig. IV) are compared to the corresponding results obtained from a Finite Element computation using COMSOL software for random 2-D microstructures.

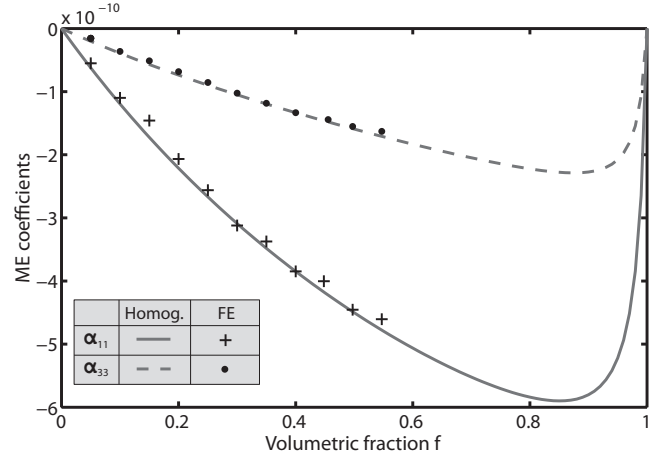


Fig. 3. ME coupling coefficients as a function of the volumetric fraction f of the piezomagnetic phase (homogenization and FE results).

The ME coefficients are shown to depend on the volumetric fraction f of the piezomagnetic phase. The results obtained from homogenization and Finite Element method are very similar. The corresponding computational time is more than a thousand times lower when using the homogenization technique.

V. CONCLUSION

Homogenization approach is able to catch structure effects such as the ME effect exhibited in piezomagnetic/piezoelectric composites. The interest of this modeling approach is its very light computational cost compared to the Finite Element method. The comparison with the results obtained from a Finite Element model shows a very satisfying agreement in the case of matrix-inclusion microstructures. More comparisons with Finite Element computations will be proposed in the full paper.

REFERENCES

- [1] M. Avallaneda and G. Harshe, "Magnetolectric effect in piezoelectric/magnetostrictive multilayer composites", *J. Intell. Mater. Syst. Struct.*, 5, 501, 1994.
- [2] N. Galopin, X. Minging, F. Bouillault and L. Daniel, "Finite element modelling of magneto-electric sensors", *IEEE Trans. Magn.*, 44(6): 834-837, 2008.
- [3] R. Corcolle, L. Daniel and F. Bouillault, "Generic formalism for homogenization of coupled behavior: Application to magneto-electroelastic behavior", *Phys. Rev. B*, 78, 214110, 2008.
- [4] G.W. Milton, *The theory of composites*, Cambridge University Press: New-York, 2001.
- [5] L. Daniel and R. Corcolle, "A Note on the Effective Magnetic Permeability of Polycrystals", *IEEE Trans. Magn.*, 43(7): 3153-3158, 2007.
- [6] J. Lee, J.G. Boyd IV and D.C. Lagoudas, "Effective properties of three-phase electro-magneto-elastic composites", *Int. J. Eng. Sci.*, 43, 790-825, 2005.

Simple Numeric Modelling of Anomalous Eddy Current Taking Account of Domain Wall Motion in Steel Plate

Yanhui Gao¹, Kazuhiro Muramatsu¹, Koji Fujiwara²

¹Dept. of Electrical and Electronic Engineering, Saga Univ., Saga, Saga 840-8502, Japan

²Dept. of Electrical Engineering, Doshisha Univ., Kyotanabe, Kyoto 610-0321, Japan

07643001@edu.cc.saga-u.ac.jp

Abstract — To reduce the loss of reactor driven by inverter power supply using magnetic field analysis, the eddy currents generated in laminated steel plates should be taken into account. To calculate the eddy currents in steel plates accurately, the anomalous eddy current induced by domain wall motion should be considered. In this paper, a simple numeric modelling of anomalous eddy current taking account of domain wall motion is proposed. The proposed method is compared with the ordinary modelling of modifying the conductivity of steel plate in the loss calculation of one sheet of steel plate. It is shown that the eddy current losses obtained from the proposed method can agree with the measured data in lower frequencies, however, error occurs in high frequencies as skin effect is neglected at present.

I. INTRODUCTION

We have developed the method of magnetic field analysis which models a laminated core as a solid one taking account of eddy currents in the steel plate by using the finite element method [1]. In this method, the 1D eddy current sub-analysis of steel plate is carried out for each element in main-analysis of the solid core model and the classical eddy current loss can be obtained directly. However, in the iron loss calculation of reactor under inverter power supply, the calculated iron loss are much smaller than the measured one [2] because the anomalous eddy current loss [3] generated by domain wall motion was neglected. In order to taking account of the anomalous eddy current loss, the numeric modelling of modifying the conductivity of steel plate has already been proposed [3] but the physical phenomena of domain wall motion can not be expressed by this method [4].

In this paper, a simple numeric modelling of anomalous eddy current taking account of domain wall motion, which should be simple for introducing it into the sub-analysis, is proposed. The proposed method is applied to the loss calculation of one sheet of steel plate and compared with the measured data and the ordinary numeric modelling mentioned above.

II. METHODS OF MODELLING

First, the ordinary numeric modelling for considering the loss increase by modifying the conductivity σ of steel plate is described. In this modelling, the classical eddy current in the steel plate with the modified conductivity σ^* is calculated. The

modified conductivity σ^* of steel plate is determined by fitting the calculated eddy current loss of one sheet of steel plate with the measured data. The eddy current is calculated by using the 1D nonlinear eddy current finite element analysis (FEA).

Next, a simple modelling of anomalous eddy current loss taking account of domain wall motion using a 1D domain model shown in Fig. 1 is described. In this model, the steel plate is assumed to be infinity in x and y directions and composed of domains with uniform magnetization M which have y component only and are 180 deg different in turns periodically lining in x direction as shown in Fig. 1. The position of domain wall can be determined by making the average value of magnetization M equal to the applied average flux density B . In this modelling, not only the classical eddy current but also the anomalous eddy current due to domain wall motion can be taken account of as shown in Fig. 1. The eddy currents due to the domain wall motion is calculated by using the 2D linear eddy current FEA in x - z plane only in the region R shown in Fig. 1 due to periodic and symmetric phenomena of the domain model. The length L_x of region R is determined by fitting the calculated eddy current loss with the measured data.

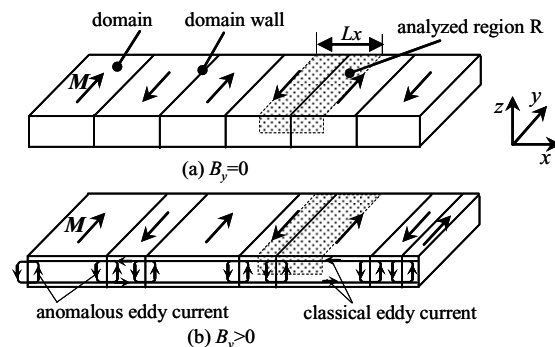


Fig. 1. A simple 1D magnetic domain model (proposed method).

III. VERIFICATION MODEL

Both methods are applied to the eddy current loss calculation of one sheet of steel plate. The magnetic material used for the steel plate is AISI: M-36 (thickness 0.35 mm, $\sigma = 1.852 \times 10^6$ S/m) and the steel plate is assumed to be infinity in x and y directions. In this case, the ordinary and proposed methods become 1D and 2D eddy current analyses, respectively. The saturated magnetization M for the proposed modelling is set to be 2.1T. The applied average flux density B is the sinusoidal waveform with amplitude B_{max} . By fitting the

7. Material Modelling

eddy current loss calculated when the maximum average flux density B_{max} is 0.5 T and the frequency f is 100 Hz with the measured data in catalogue, the modified conductivity σ^* in the ordinary modelling and L_x in the proposed modelling are determined to be 3.0×10^6 S/m and 0.3 mm, respectively.

IV. RESULTS AND DISCUSSION

Fig. 2 shows the flux and eddy current distributions of half region of the steel plate obtained by using the classical 1D eddy current analysis with the real and modified conductivities at the instant when the average flux density in the steel plate is the maximum. It is seen that the eddy current obtained from the modified conductivity is greater than that obtained from the real conductivity, so the eddy current loss increase due to the anomalous eddy current loss can be considered by the modification of the conductivity of steel plate. However, the skin effect is greater when the modified larger conductivity is used than that when the real conductivity is used. This is not the same with the real phenomenon resulted from the domain wall motion and it seems to cause error in the hysteresis loss calculation.

Fig. 3 shows the flux and eddy current distributions of half region of the steel plate obtained by using the proposed modelling at the same instant. It can be seen that the classical eddy current loop and the anomalous eddy current loop due to domain wall motion are represented. However, the skin effect cannot be observed in the flux distribution because the magnetization \mathbf{M} is assumed to be uniform in z direction at present.

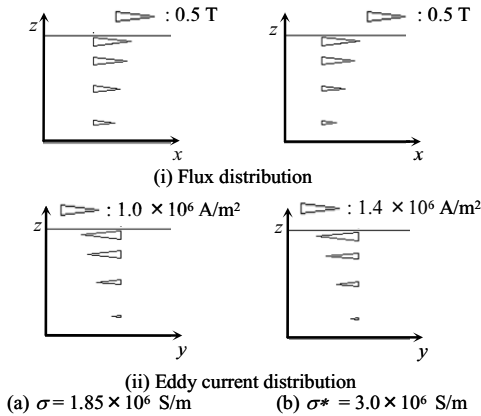


Fig. 2. Flux and eddy current distributions obtained from the ordinary modelling ($B_{max} = 0.5$ T and $f = 1$ kHz).

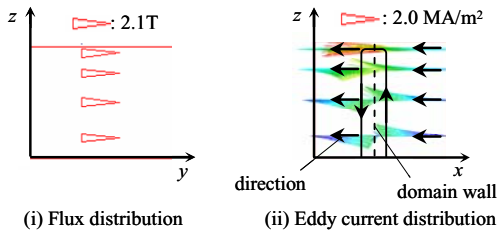


Fig. 3. Flux and eddy current distributions obtained from the proposed modelling ($B_{max} = 0.5$ T and $f = 1$ kHz).

Fig. 4 shows the eddy current losses at different maximum

average flux densities B_{max} s and frequencies f s obtained from the ordinary modelling with the modified conductivity $\sigma^* = 3.0 \times 10^6$ S/m and the measured data. To show the anomalous eddy current loss, the eddy current loss with original conductivity σ at $B_{max} = 0.5$ T is also shown in Fig. 4. The measured eddy current losses are obtained from the iron loss curves at different frequencies f s in catalogue. The eddy current losses of one sheet of steel plate obtained from the ordinary modelling are in good agreement with the measured data in a wide range of frequencies. However, it is not physical modelling.

Fig. 5 shows the eddy current losses obtained from the proposed modelling with $L_x = 0.3$ mm and the measured data. In lower frequencies, the eddy current losses obtained from the proposed modelling are in good agreement with the measured data, however, error occurs in high frequencies due to neglect of the skin effect. The method of considering the skin effect in the proposed modelling will be discussed in the full paper.

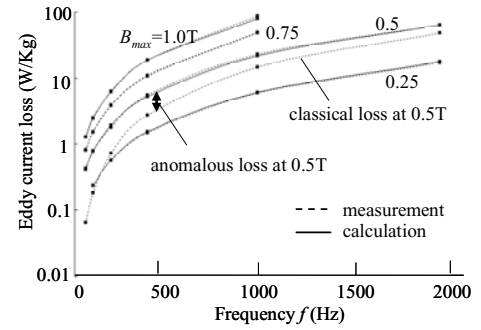


Fig. 4. Comparison of eddy current losses between the ordinary modelling and measured data.

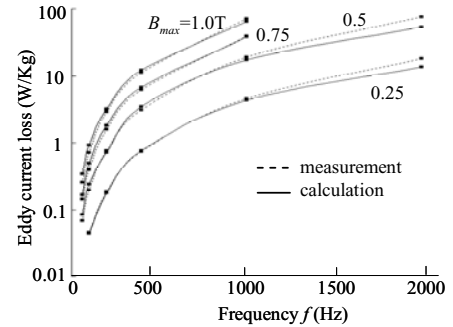


Fig. 5. Comparison of eddy current losses between the proposed modelling and measured data.

V. REFERENCES

- [1] K. Muramatsu, et al., "Method of nonlinear magnetic field analysis taking into account eddy current in laminated core," *IEEE Trans. Magn.*, vol. 40, no. 2, pp. 896-899, 2004.
- [2] Y. Gao, et al., "Loss analysis of reactor under power supply taking into account of anomalous eddy current in steel plate of laminated core," *ibid.*, vol. 45, no. 3, pp. 1044-1047, 2009.
- [3] K. Yamazaki, et al., "Investigation of carrier loss of induction motors considering skin effect in electrical steel plates," *ibid.*, vol. 36, no. 5, pp. 3469-3651, 2000.
- [4] Y. Gao, et al., "Loss analysis of reactor under power supply taking into account of anomalous eddy current in steel plate of laminated core," *J. Magn. Soc. Jpn.*, vol. 33, pp. 54-59, 2009.

Inclusion of Eddy Currents in Laminations in Two-Dimensional Finite Element Analysis

J. Pippuri, A. Belahcen, E. Dlala, and A. Arkkio

Department of Electrical Engineering, Helsinki University of Technology

P.O. Box 3000, FI-02015 TKK, Finland

jenni.pippuri@tkk.fi

Abstract — The inclusion of eddy currents in electrical steel sheets in a two-dimensional (2D) finite-element analysis is studied. For the eddy-current modeling a so-called one-dimensional (1D) approach is applied. Two different techniques for the eddy currents within the 2D field equations are investigated and shown. According to the computation results a suggestion for a proper coupling method is made.

I. INTRODUCTION

A two-dimensional (2D) field analysis is commonly applied to analyze electromechanical applications. Although such an approach is sufficient in many cases, from it certain phenomena such as eddy currents flowing in electrical steel sheets are by definition excluded. For modeling the eddy currents within the 2D analysis, for instance a so-called one-dimensional (1D) approach has been proposed [1], [2]. In this work, this approach is adopted. The novelty of this work lies in the careful analysis of the coupling, i.e. how the eddy-current solution can reliably be included in the 2D equations. The results show the scale of errors to which an improper coupling might lead thus emphasizing the importance of the topic.

II. COMBINED 2D-1D METHOD

In this work, a simple geometry consisting of a stack of electrical steel sheets and a voltage source i.e. a coil is applied. The volume of the stack is 1 m^3 and the volume of the coil side is 0.2 m^3 .

In the 2D scheme the magnetic vector potential and current density are given as

$$\mathbf{A} = A(x, y, t) \mathbf{e}_z \quad (1)$$

$$\mathbf{J} = J(x, y, t) \mathbf{e}_z. \quad (2)$$

in which x and y denote Cartesian spatial coordinates, t denotes time, and \mathbf{e}_z denotes the unit vector of the z -axis.

The magnetic flux density in the studied geometry fulfills

$$\nabla \times (\nu \nabla \times \mathbf{A} + \mathbf{H}_{\text{ec}}) = \frac{N\mathbf{i}}{S}. \quad (3)$$

ν is the reluctivity given as a spline function of the second power of the magnetic flux density, \mathbf{B}^2 , \mathbf{H}_{ec} is the component due to the eddy currents, N is the number of turns in series, \mathbf{i} is the current in the coil, and S is the cross sectional area of the coil.

The voltage in the coil satisfies

$$\mathbf{u} = \frac{IN}{S} \int_S \frac{\partial \mathbf{A}}{\partial t} \cdot d\mathbf{S} \mathbf{e}_z + R\mathbf{i}. \quad (4)$$

in which l denotes the length of the coil and R the DC resistance of the coil.

The 1D eddy-current model of the electrical steel sheets is developed in the lamination depth. The magnetic vector potential and current density are defined as

$$\mathbf{a} = a_x(z, t) \mathbf{e}_x + a_y(z, t) \mathbf{e}_y, \quad (5)$$

$$\mathbf{j} = j_x(z, t) \mathbf{e}_x + j_y(z, t) \mathbf{e}_y. \quad (6)$$

in which z denotes a Cartesian spatial coordinate and \mathbf{e}_x and \mathbf{e}_y are the unit vectors of x - and y -axis, respectively.

The magnetic vector potential in the laminations satisfies

$$\nabla \times (\nu \nabla \times \mathbf{a}) = -\sigma \frac{\partial \mathbf{a}}{\partial t} \quad (7)$$

$$a_x(-d, t) = dB_y \quad a_x(0, t) = 0 \quad (8)$$

$$a_y(-d, t) = -dB_x \quad a_y(0, t) = 0. \quad (9)$$

ν is the reluctivity given as a spline function of the second power of the magnetic flux density, \mathbf{b}^2 , σ and d are the electrical conductivity and half of the thickness of the laminations, respectively, and B_x and B_y are the x - and y -components of the 2D magnetic flux density, respectively.

For the discretization of the coupled problem, the Crank-Nicolson and finite-element method are applied. The nonlinearities of iron are handled by the Newton-Raphson technique. In the 2D scheme, the Newton-Raphson is applied in an incomplete manner. Incomplete, as the terms originating from the \mathbf{H}_{ec} are omitted from the Jacobian matrix. Resulting from this, over-relaxation is required for convergence. For the 1D scheme, a complete Newton-Raphson is applied in a novel manner as discussed in [3].

In the derivations, the eddy-current component, \mathbf{H}_{ec} , is defined as a difference of the 1D magnetic field strength, \mathbf{h} , at the boundary of the sheets ($z = -d$) and the magnetic field strength obtained from the 2D analysis, \mathbf{H}

$$\mathbf{H}_{\text{ec}}(x, y, t) = \mathbf{h}(-d, t) - \mathbf{H}(x, y, t). \quad (10)$$

It will be shown that the accuracy of the coupled method greatly depends on how well the estimation of the magnetic field strength at the boundary of the sheets succeeds. For the estimation, two approaches are proposed. Firstly, one can calculate \mathbf{h} exactly at the boundary (in the point $z = -d$) by the shape functions as a product of magnetic flux density and reluctivity. This option is later referred to as *conventional*. The second option is to use the relation

$$\nabla \times \mathbf{h} = \mathbf{j}. \quad (11)$$

from which following formulae are derivable

$$h_x(-d, t) = \int_{-d}^{z_i} j_y(z, t) \partial z + h_x(z_i, t) \quad (12)$$

$$h_y(-d, t) = -\int_{-d}^{z_i} j_x(z, t) \partial z + h_y(z_i, t). \quad (13)$$

in which z_i is upper value of the integration interval. Term *integration* is used to refer to this approach.

III. RESULTS AND DISCUSSION

The computations were carried out utilizing the example geometry described above. The 1 m² 2D geometry was discretized with eight second-order elements. The thickness and conductivity of the sheets in the stack were 0.65 mm and 2.5 MS/m. For the space discretization of the 1D solution sector (half of the thickness of the sheets, 0.325 mm) three equally sized elements were applied. The input voltage waveform utilized in all the computations is shown in Fig. 1. The time-discretization was done with 400 time steps per period. Altogether 2000 time steps were computed.

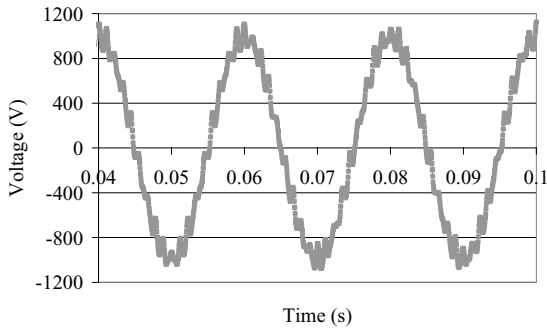


Fig. 1. Input voltage used in the computations.

The successiveness of the coupling of the 2D and 1D field solutions was studied in the frame of two criteria: the power balance and computational efficiency. With both the approaches proposed for the evaluation of h at the boundary, three computations were performed varying the number of integration points in the 1D elements.

The BH-loops obtained with the *conventional* method are depicted in Fig. 2. Furthermore, the input powers, losses, and power balances from the computations are shown in Table I. The eddy-current losses presented in Table I were computed from the eddy-current density and the power balance is defined as the difference of the total losses and the input power divided by the input power. Clearly, with the *conventional* method combined with the first-order elements, the eddy-current phenomenon in the sheets is not properly included in the 2D field analysis. The eddy-current losses integrated from the BH-loop are about half of the ones computed from the eddy-current density. A significant improvement in the accuracy is gained by using higher order elements. With the third-order elements the total losses in the example geometry are almost the same as the input power.

In terms of power balance, the *integration* technique performs very well with the first-order and third-order elements. When utilizing the second-order elements the solution of the coupled problem starts to oscillate as depicted in Fig. 3. This results in a rather significant error in the power balance.

— 1. order elements — 2. order elements * 3. order elements

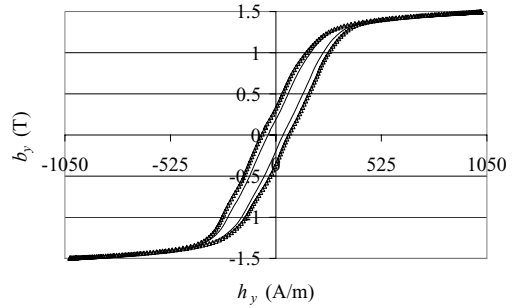


Fig. 2. BH-loops when applying the *conventional* approach.

— 1. order elements — 2. order elements * 3. order elements

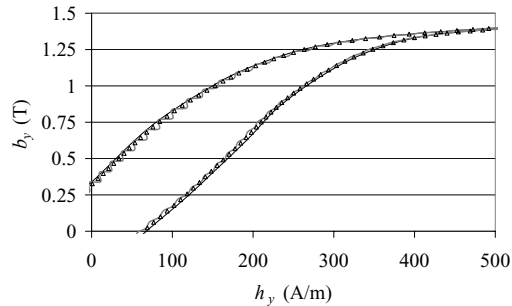


Fig. 3. Close-up of the BH-loops when applying the *integration* approach.

TABLE I
COMPARISON OF THE POWERS AND POWER BALANCE

h at the boundary	Order of 1D elements	Eddy-current loss (W)	Resistive loss of the coil (W)	Input power (W)	Power balance (%)
<i>Conventional</i>	1	16593	247	9004	87.04
	2	15643	248	15613	1.78
	3	15663	248	15946	0.22
<i>Integration</i>	1	16502	248	16705	0.27
	2	16196	248	15376	6.94
	3	15637	248	15872	0.08

The computational times of the two approaches were nearly the same with a certain number and degree of elements. The greatest difference was obtained with the first-order elements; computing one period of line voltage took about 3.4 percent more time with the *conventional* approach than with the *integration* one.

Based on the results the *integration* method seems to be the most promising technique for defining the eddy currents in the 2D analysis. With it, a power balance is achieved with the first-order elements that leads to significant savings in computation time.

IV. REFERENCES

- [1] R. Del Vecchio, "The calculation of eddy current losses associated with rotating magnetic fields in thin laminations", IEEE Trans. Magn., (18)6: 1707–1709, 1982.
- [2] O. Bottauscio and M. Chiampi, "Laminated core modeling under rotational excitations including eddy currents and hysteresis", J. Appl. Phys., (89)11: 6728–6730, 2001.
- [3] A. Belahcen, E. Dlala, and J. Pippuri, "Implementation of an Advanced Eddy-Current Model for Non-Linear Laminated Media", unpublished.

Electromagnetic Multi-scale Homogenization of Carbon Fiber Composite Materials

G. Wasselynck, D. Trichet, and J. Fouladgar

Institut de Recherche en Electrotechnique et Electronique de Nantes Atlantique
CRTT 37 Bd de l'université BP406, 44602 Saint Nazaire cedex, France
guillaume.wasselynck@univ-nantes.fr

Abstract—A new multi-scale homogenization method is introduced to calculate the field and current distribution inside carbon fiber reinforced polymer composites submitted to an external electromagnetic field. In the microscopic scale, the real structure of the material is taken into account and electromagnetic and electrical equivalent properties are calculated using finite elements method. In macroscopic scale, these properties are introduced in an impedance network or in a shell elements-finite elements method according to the working frequency. The results obtained are in accordance with experimental results.

I. INTRODUCTION

Carbon Fiber Reinforced Polymer (CFRP) composites are used in various industrial applications and more especially in aeronautics. This is due to the fact that CFRP has better mechanical characteristics than aluminum for a lighter weight.

In different periods of their life cycle, the CFRP may interact with electromagnetic fields. This is the case for example, of induction welding of the composite structures or the lightning attacks on flying airplanes. The telecommunication or radar transmission between the plane and the earth station is another example of electromagnetic field interaction with the CFRP. According to the application, the field frequency may vary between several kHz and some GHz.

A perfect comprehension of field propagation inside the CFRP needs a through analysis of the conducting and displacement currents distribution in the carbon fibers and in the resin polymer. In fact, in CFRP composites, the conducting carbon fibers are separated from each other by non conductive resin as shown in Fig. 1. The current circulation in the fibers and in the whole material presents a difficult problem which should be solved. In addition, the composite materials are highly anisotropic and non homogeneous. They present also an important scale factor between the fiber diameter which is around $7\ \mu\text{m}$ and the size of the composite sheet which may be up to several meters. In this paper, we study the case of a unidirectional CFRP where the carbon fibers, parallel to each other, are distributed randomly inside the resin as in Fig. 1. The scale factor is too important to simulate the real structure of CFRP. Homogenization method is then used to overcome this problem. A two scales model is introduced to calculate the eddy current distribution. For this purpose, the CFRP sheet is divided into elementary bricks which are representative of the whole material as shown in Fig. 2.

In microscopic scale, the finite elements method (FEM) is used to calculate the equivalent impedance of the bricks. In macroscopic scale, these properties are incorporated in an

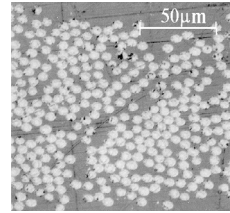


Fig. 1. Section of UD composite

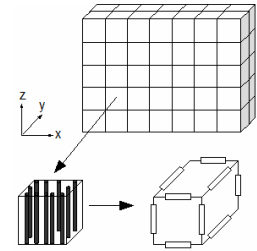


Fig. 2. Elementary brick and Impedance network

impedances network to obtain the current distribution in the whole material.

II. MICROSCOPIC SCALE

The size of the bricks is an important parameter in the homogenization technique. They should contain a reasonable number of fibers to represent statistically the whole material without complicating the local or global solution of the problem. In the full paper we will give more details about the elementary brick size calculation.

To determine the equivalent impedance of each element, it is necessary to find the eddy current circulation in an elementary brick. When an electromagnetic field orthogonal to fibers direction is applied to the material, the current has two possible paths to circulate in the composite as shown in Fig. 3. In the first path (dotted line), the current loop ends in the fiber itself. In the second path (dashed line), the current loop is shared by several fibers passing through the capacities between them. For the two paths, the current has to go through two different impedances. The favorite path is obviously the one with lower impedance. To determine the local impedances of the bricks, one should solve the electromagnetic and electrostatic equations.

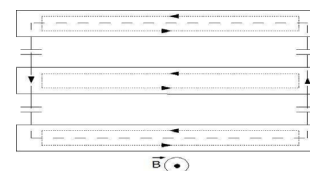


Fig. 3. Circulations of currents

A. Electromagnetic formulation

The resistances, the self inductances and the mutual inductances of the fibers are calculated using the following potential vector formulation of the Maxwell equations [1]:

$$\text{curl}\left(\frac{1}{\mu} \text{curl}\mathbf{A}\right) + j\omega[\boldsymbol{\sigma}]\mathbf{A} = \mathbf{J}_0 = \text{curl}(\mathbf{H}_0). \quad (1)$$

Where μ is the permeability, $[\boldsymbol{\sigma}]$ is the conductivity tensor, ω is the field pulsation and \mathbf{H}_0 is the source magnetic field. Figure 4 presents the geometry of a brick with a random distribution of the fibers. Equation (1) is solved by FEM using Whitney's elements to obtain the vector potential \mathbf{A} , the induction \mathbf{B} , the magnetic field \mathbf{H} and the self and mutual inductances.

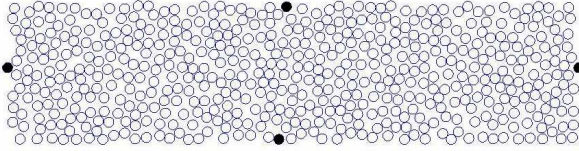


Fig.4. Random distribution of fibers in elementary brick

If the current loop ends in the fiber itself, it has to flow through an inductance L which is calculated as follows:

$$E = \frac{1}{2} \iiint \mathbf{B} \cdot \mathbf{H} \, dV = \frac{1}{2} L \left(\iint \mathbf{J} \cdot d\mathbf{S} \right)^2. \quad (2)$$

Where E is the electromagnetic energy, \mathbf{J} is the current density, V is the volume and S is the section of the fiber.

B. Electrostatic formulation

The capacities are calculated using the Poisson's equation:

$$\Delta V = -\rho / \varepsilon. \quad (3)$$

Where ρ is the electrical charge density, ε is the permittivity of the matrix and V is the electrical potential. This equation is solved using the floating potential concept to obtain the matrix of capacities between the fibers [2].

$$\mathbf{Q} = [\mathbf{C}]\mathbf{V}. \quad (4)$$

In our case, it is not necessary to calculate the whole matrix \mathbf{C} but only the lines corresponding to the fibers, in black in Fig. 4, at the left, right, top and bottom of the cell. The details of the floating potential calculation will be presented in the final paper.

C. Results and discussion

The impedance calculated from (2) is about $1.15 \times 10^{21} \, \Omega/\text{m}$ for a welding frequency of 150 kHz. This impedance is too high compared to the impedance due to the inter fiber capacities which is about $4.44 \times 10^7 \, \Omega$. The possibility that the current loops ends inside the fiber is practically negligible. For this frequency, the impedances due to self and mutual inductances are less than 1% of the fiber resistances. In this case, the equivalent impedance along the fibers is directly related to the filling rate and the carbon conductivity and each cell is linked only to its neighbors. For high frequencies, however, the self and mutual inductances can not be neglected and each cell is coupled inductively to all other cells.

III. MACROSCOPIC SCALE

For the applications such as welding, the field frequency is relatively low. The impedances obtained from microscopic

calculations can be then incorporated in a 3D impedances network [3]. On each node, the electrical potential is calculated by Kirschhoff's law using the finites differences method. The current along each edge is then calculated by:

$$I = ((V_p - V) - j\omega \int \mathbf{A} \cdot d\mathbf{l}) / Z. \quad (5)$$

Where V_p and V are the end electrical potentials of the segment, Z is its impedance and \mathbf{A} is the source potential vector along the segment.

For high frequencies such as radar transmissions, the self and mutual impedance have to be taken into account. In this case, the impedance network method leads to a full matrix which limits the size of material to be studied. To overcome this difficulty, the microscopic phase is used to obtain a complex equivalent conductivity. This property is then introduced in an anisotropic shell elements - finite elements to calculate the field and current distribution inside the material [4]-[5]. This method will be developed in the full paper.

IV. APPLICATION ON HEATING PROBLEM

To validate the model, a rectangular CFRP plate (120mm x80mm x1.5mm) is heated by a rectangular inductor (40mm x20mm) with a RMS current of 1000A at a frequency of 150 kHz. The fibers are in the direction of the length (120mm) and the filling rate of fibers is equal to 70%.

For this frequency, the equivalent impedances are resistive along fiber axis and capacitive along others axes. The calculated heating power is equal to 814 W which is close to experimental results.

V. CONCLUSION

In this paper, a two scales homogenization method of CFRP composites is introduced. In the microscopic scale, the equivalent impedance of an optimized size elementary brick is calculated using FEM to solve both electromagnetic and electrostatic equations. For low frequencies, the macroscopic scale problem is solved by an impedance network approach. For high frequencies, an anisotropic shell elements-finite elements method is applied. In the full paper we will give the details on the brick size calculations and the different methods to obtain the local impedance, the field and the current distribution inside the composite sheets.

VI. REFERENCES

- [1] O. Biro, "Edge element formulations of eddy current problems", *Comput. Methods Appl. Mech. Engrg.*, vol. 169, pp. 391-405, 1999.
- [2] A. Konrad, and M. Graovac, "The floating potential approach to the characterization of capacitive effects in high-speed interconnects", *IEEE Trans. on Magnetics*, 33(2): 1185-1188, 1997.
- [3] N. Orcutt and OM. Gandhi, "A 3-D impedance method to compute current induced in human body exposure to power lines", *IEEE International Symposium on Microwave, Antenna, Propagation and EMC Technologies for wireless Communications Proceeding*, 2005
- [4] S. Bensaid, D. Trichet and J. Fouladgar, "Electromagnetic and thermal behaviors of multilayer anisotropic composite materials", *IEEE Trans. on Magnetics*, 42(4): 995-998, 2006.
- [5] Z. Ren, "Degenerated whitney prism elements - general nodal and edge shell elements for field computation in thin structures", *IEEE Trans. on Magnetics*, 34(5): 2547-2550, 1998.

The Effects of Steel Lamination Core Losses on 3D Transient Magnetic Fields

D. Lin, P. Zhou, Q. M. Chen, and Z. J. Cendes
Ansoft LLC, 225 W. Station Square Dr, Pittsburgh 15219 USA
dlin@ansoft.com

Abstract — A 3-dimensional (3D) transient finite element analysis (FEA) approach taking into account the effects of steel lamination core loss is proposed. When using the T-Ω method, the effects of lamination core loss are considered by introducing an additional field component in lamination regions which is derived from the instantaneous core loss in the time domain. The proposed approach is validated by two applications in terms of the power-balance testing, that is, the input power increase due to the core-loss effects must be equal to the total core loss.

I. INTRODUCTION

The steel lamination core loss with sinusoidal excitation is commonly computed based on loss separation, which breaks the total core loss into static hysteresis loss, classical eddy current loss, and excess loss in the frequency domain [1]. In order to apply the method to the time domain, an equivalent elliptical loop (EEL) method was presented to model the hysteresis loop [2], and therefore, the instantaneous core loss at each time step can be predicted in the transient FEA. However, the instantaneous core loss presented in [2] is computed as “post process”, that is, the effects of the core loss on the transient magnetic field are not taken into account.

In this paper, the effects of the lamination core loss on the 3D transient magnetic field are considered by introducing an additional field component in lamination regions when using the T-Ω method. This additional field component is derived from the total instantaneous core loss including the static hysteresis loss, classical eddy current loss and excess loss. The proposed approach is validated by two applications in terms of the power-balance testing, that is, the input power increase due to the core-loss effects must be equal to the total core loss in the device.

II. EFFECTS OF LAMINATION CORE LOSS

A. Basic field equations

The field equation using T-Ω method [3] is

$$\begin{aligned} \nabla \times ([\sigma_a]^{-1} \nabla \times \mathbf{T}) + \frac{\partial}{\partial t} [\mu] (\mathbf{T} + \nabla \Omega) \\ = -\frac{\partial}{\partial t} [\mu] (\mathbf{H}_s + \mathbf{H}_p) \end{aligned} \quad (1)$$

where \mathbf{T} is the vector electric potential in conducting regions, Ω is the scalar magnetic potential, $[\mu]$, the permeability tensor, is anisotropic in lamination regions [4], $[\sigma_a]$ is the anisotropic conductivity tensor to be discussed below, \mathbf{H}_s corresponds to all exciting current sources, and

$$\mathbf{H}_p = \mathbf{H}_{pc} + \mathbf{H}_{ph} + \mathbf{H}_{pe} \quad (2)$$

is an additional field component due to core loss effects.

In (2), \mathbf{H}_{pc} , \mathbf{H}_{ph} and \mathbf{H}_{pe} correspond to the classical eddy current core loss, static hysteresis core loss and excess core loss, respectively.

B. Effects of eddy current loss caused by the normal component of flux density

When a flux density component in z direction B_z changes, an eddy current field distributed in the xy plane will be produced, as shown in Fig. 1.

The equivalent conductivity in lamination regions is anisotropic, and can be expressed by a conductivity tensor

$$[\sigma_a] = \begin{bmatrix} k_{lam} \sigma & 0 & 0 \\ 0 & k_{lam} \sigma & 0 \\ 0 & 0 & \sigma_{min} \end{bmatrix} \quad (3)$$

where k_{lam} is the lamination factor, σ is the conductivity of the laminated steel, and σ_{min} , the minimum conductivity limit, is used to ensure that the system equation is non-singular.

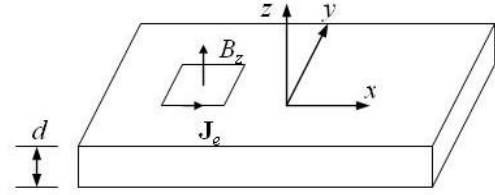


Fig. 1 Eddy current produced by the normal component of flux density

C. Effects of eddy current loss caused by the tangential components of flux density

When the flux density components B_x and/or B_y , tangential to the lamination plane, alternate, the produced eddy current field is bounded in each lamination, as shown in Fig. 2.

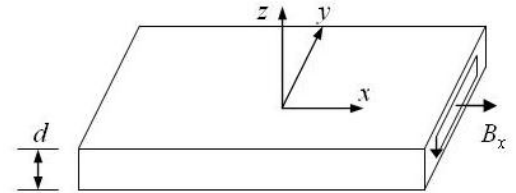


Fig. 2 Eddy current produced by the tangential components of flux density

The effects of eddy current produced by the tangential flux components is considered by means of an equivalent magnetic field component \mathbf{H}_{pc} , which can be computed by eddy current core loss. The eddy current core loss per unit volume is normally given in the frequency domain as shown below

$$p_c = k_c (f B_m)^2 \quad (4)$$

where f is the frequency, B_m is the flux density amplitude, and

k_c is the eddy current loss coefficient. In the time domain, the eddy current core loss is computed from

$$p_c(t) = \mathbf{H}_{pc} \cdot \frac{\partial \mathbf{B}}{\partial t} \quad (5)$$

where

$$\mathbf{H}_{pc} = [k] \frac{\partial \mathbf{B}}{\partial t} \quad (6)$$

with

$$[k] = \begin{bmatrix} k_c / (2\pi^2) & 0 & 0 \\ 0 & k_c / (2\pi^2) & 0 \\ 0 & 0 & 0 \end{bmatrix}. \quad (7)$$

D. Effects of hysteresis loss

The hysteresis core loss per unit volume computed in the frequency domain is given below

$$p_h = k_h f (B_m)^2 \quad (8)$$

where k_h is the hysteresis loss coefficient. In the time domain, the hysteresis core loss can be calculated based on the equivalent magnetic field component \mathbf{H}_{ph} , as expressed below

$$p_h(t) = \mathbf{H}_{ph} \cdot \frac{\partial \mathbf{B}}{\partial t}. \quad (9)$$

The equivalent field component \mathbf{H}_{ph} is determined by the equivalent elliptical loop (EEL) method [2]. Each component in the x , y or z direction is computed independently from

$$\begin{cases} B = B_m \sin(\theta) \\ H_{ph} = H_m \cos(\theta) \end{cases} \quad (10)$$

where B is the current flux density, B_m is obtained from a historical record of the maximum and minimum flux densities, and H_m is

$$H_m = \frac{k_h}{\pi} B_m. \quad (11)$$

E. Effects of excess loss

The excess core loss per unit volume is given in the frequency domain as

$$p_e = k_e (f B_m)^{1.5} \quad (12)$$

where k_e is the excess loss coefficient. In the time domain, the excess core loss can be calculated based on the equivalent magnetic field component \mathbf{H}_{pe} , as expressed below

$$p_e(t) = \mathbf{H}_{pe} \cdot \frac{\partial \mathbf{B}}{\partial t}. \quad (13)$$

The equivalent field component \mathbf{H}_{pe} is determined by requiring that the average excess core loss calculated in the time domain must be the same as that obtained in the frequency domain under the same sinusoidal excitation, and it is derived as

$$\mathbf{H}_{pe} = \frac{k_e}{C_e} \left[\left(\frac{\partial B}{\partial t} \right)_m \right]^{-0.5} \frac{\partial \mathbf{B}}{\partial t} \quad (14)$$

where

$$\left(\frac{\partial B}{\partial t} \right)_m = \sqrt{\left(\frac{\partial B_x}{\partial t} \right)^2 + \left(\frac{\partial B_y}{\partial t} \right)^2 + \left(\frac{\partial B_z}{\partial t} \right)^2} \quad (15)$$

and $C_e = 8.763363$.

III. APPLICATIONS

The first application is for the computation of core loss of 250 kVA three-phase amorphous metal power transformer with five legs. The delta-connected three-phase primary windings are energized by three-phase voltage sources, and the secondary windings are open-circuit.

The input power increase due to core loss effects is shown in Fig. 3, compared with the computed core loss. The average input power increase and the computed core loss in the last period (80ms ~ 100ms) are compared with the measured data in Table I.

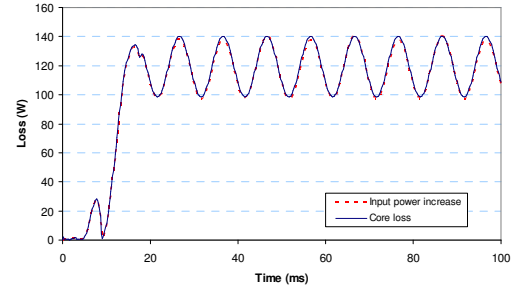


Fig. 3 The input electrical power increase due to the core loss effects compared with the computed core loss ($k_h=21.08$, $k_e=0$, $k_c=0$)

TABLE I. COMPUTED AND MEASURED CORE LOSS OF THE 250 KVA THREE-PHASE AMORPHOUS METAL POWER TRANSFORMER

	Value	Unit
Input power increase	118	W
Computed core loss	119	W
Measured core loss	126	W

The second application is for the no-load core loss computation of a 165W, 4-pole interior permanent magnet (IPM) brushless DC (BLDC) motor. The mechanical input power increase due to core loss effects is compared with the computed core loss in Fig. 4.

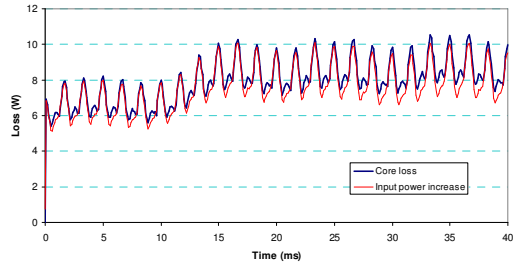


Fig. 4 The input mechanical power increase due to the core loss effects compared with the computed core loss ($k_h=260.4$, $k_e=0.822$, $k_c=40.54$)

IV. REFERENCES

- [1] G. Bertotti, "General properties of power losses in soft ferromagnetic materials," *IEEE Trans. Magn.*, vol. 24, no. 1, pp. 621-630, 1988.
- [2] D. Lin, P. Zhou, W. N. Fu, Z. Badics, and Z. J. Cendes, "A dynamic core loss model for soft ferromagnetic and power ferrite materials in transient finite element analysis," *IEEE Trans. Magn.*, vol. 40, no. 2, pp. 1318-1321, March 2004.
- [3] P. Zhou, W. N. Fu, D. Lin, S. Stanton, and Z. J. Cendes, "Numerical modeling of magnetic devices," *IEEE Trans. Magn.*, vol. 40, no. 4, pp. 1803 - 1809, July 2004.
- [4] D. Lin, P. Zhou, Z. Badics, W. N. Fu, Q. M. Chen, and Z. J. Cendes, "A new nonlinear anisotropic model for soft magnetic materials," *IEEE Trans. Magn.*, vol. 42, no. 4, pp. 963-966, April 2006.

Analytical Calculation of the Interactions between two Cylinder-shaped Magnets

Hicham ALLAG, Jean-Paul YONNET and Benoit DELINCHANT

Laboratoire de Génie Electrique de Grenoble, G2E Lab (UMR 5269 CNRS/INPG-UJF),
Institut Polytechnique de Grenoble, ENSIEG, BP46, 38402 St Martin d'Hères cedex, France

Tel : 33 (0) 476 82 62 97 – Fax : 33 (0) 476 82 63 00

E-mail : <Jean-Paul.Yonnet@g2elab.grenoble-inp.fr>

Abstract — Analytical calculation of interaction forces between two cylindrical magnets is a difficult problem. Solutions can be obtained by elliptic integrals or by numerical computation. Thanks to the development of the analytical calculation for parallelepiped magnets (interaction energy, force and torque), the calculation of the force component between two cylinders can be obtained in analytical form by decomposition in a finite number of elements.

This type of calculation allows the calculation of many systems that uses the forces of interaction between cylinder magnets. For example it can be used to directly calculate the force exerted in permanent magnet bearings in non-centred position.

I. INTRODUCTION

Recent works on the analytical calculation of forces between permanent magnets allow calculating the interactions between magnets of parallelepiped shapes. The forces, interaction energy and couples can be expressed as analytical expressions, parameterized by the geometrical dimensions and magnetization of the magnets [1 to 4].

However, the problem of rod-shaped magnets has never been analytically solved. The simpler problem of the 3D calculation of the magnetic field is made with elliptic integrals. This field calculation needs two integrations. For the calculation of interaction energy and forces, four successive integrations are necessary.

We will present an innovative analytical method, to calculate the interaction forces between two magnets of cylindrical shapes. The final analytical expression is a series with a limited term number. The accuracy depends on the number of elements.

This method allows calculating the interaction forces in three directions, as well as energy interaction, through a relatively simple analytical expression.

II. CALCULATION PRINCIPLE

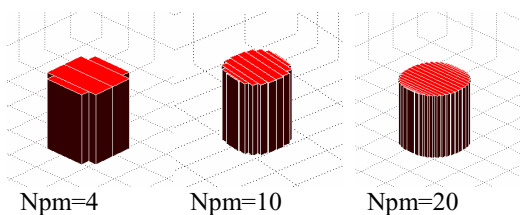


Figure 1: Principle of cutting of the cylindrical magnet in parallelepiped elements.

Figure 1 shows the principle of the cutting of the cylinder in parallelepiped elements. The first case corresponds to a cut in 4 parts, the second 10 and third 20. The number of elements is given by the parameter N_{pm} (Number of elementary permanent magnets).

III. INTERACTION ENERGY

We give in the page 2 of this summary only the expression of the energy of interaction. The forces are then obtained by derivation of this energy.

IV. EXAMPLE OF CALCULATION

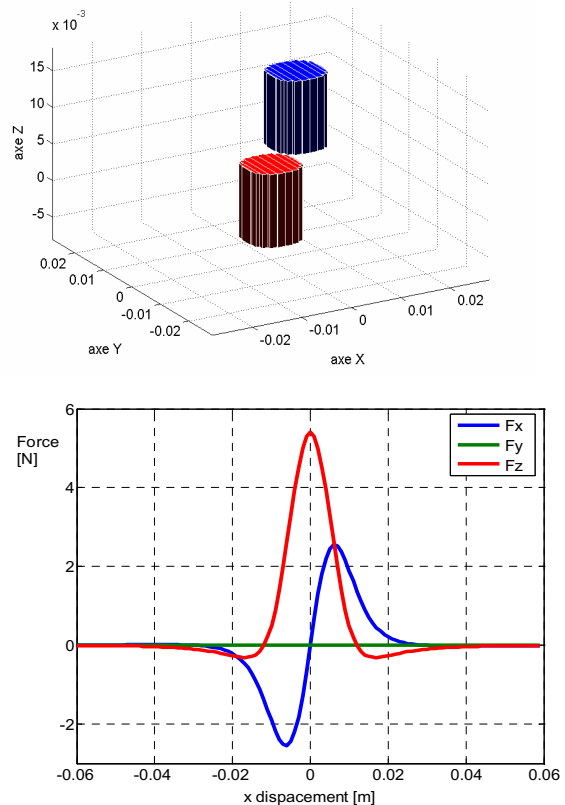


Figure 2: Calculation of the forces components for a magnet moving above a fixed one.

Figure 2 shows a direct example of use of these analytical results. It is the calculation of forces between two cylindrical magnets. The two magnets have a diameter of 10 mm and a height of 10 mm. The second moves horizontally above the first and the distance between the magnets is 5 mm. Polarization J is

Analytical expression of the interaction energy :

$$E = \frac{J \cdot J'}{4\pi\mu_0} \sum_{n=2=1}^{N_{pm} 2} \sum_{n1=1}^{N_{pm} 1} \sum_{i=0}^1 \sum_{j=0}^1 \sum_{k=0}^1 \sum_{l=0}^1 \sum_{p=0}^1 \sum_{q=0}^1 (-1)^{i+j+k+l+p+q} \cdot \psi(U_{ij}, V_{kl}, W_{pq}, r)$$

with:

$$\psi(U, V, W, r) = \frac{U(V^2 - W^2)}{2} \ln(r - U) + \frac{V(U^2 - W^2)}{2} \ln(r - V) + UVW \cdot \operatorname{tg}^{-1}\left(\frac{UV}{rW}\right) + \frac{r}{6}(U^2 + V^2 - 2W^2)$$

The parameters are given by:

$$U_{ij} = (\alpha - \alpha 1(n1) + \alpha 2(n2)) + (-1)^j A(n2) - (-1)^i a(n1)$$

$$V_{kl} = \beta + (-1)^l B - (-1)^k b$$

$$W_{pq} = \gamma + (-1)^q C - (-1)^p c$$

$$r = \sqrt{U_i^2 + V_j^2 + W^2}$$

With:

$$\phi 1(n) = n \cdot pi / N_{pm} 1 \quad xs1(n) = \sqrt{Kc} \cdot \sqrt{R^2 / (1 + \operatorname{tg}^2(\phi 1(n)))} \quad a1(n) = \frac{xs1(n) + xs1(n+1)}{2}$$

$$a1(n) = \frac{|xs1(n) - xs1(n+1)|}{2} \quad b1(n) = |\operatorname{tg}(\phi 1(n)) \cdot xs1(n)| \quad Kc = \frac{\pi \cdot R^2}{4 \sum_{n=1}^{N_{pm}} A(n) \cdot B(n)}$$

normalized to 1 tesla. The results show the values of the three force components, Fx, Fy and Fz.

The accuracy of analytical results is directly related to the number of elementary parallelepiped components used for each of the magnets. The complete study of the accuracy shows that one can easily obtain a relative error less than 1/1000, when the number of elements is sufficient. For this example of two cylindrical magnets, the precision of 1/1000 is achieved when the number of elements is about 20, even for a gap down to 2 mm.

V. APPLICATION TO MAGNETIC BEARING CALCULATION

For example, the calculation of the force exerted in a radial magnetic bearing is a relatively complicated. The permanent magnet magnetic bearings are composed of two rings in magnetic repulsion. Each magnet may be likened to two nested cylinders, representing the external volume, the other representing the internal volume. The problem of calculating the interaction forces between the two rings can be treated as one of four cylinders in interactions. The radial force can be expressed as an analytical expression involving a limited set of sums

. SUMMARY AND CONCLUSION

The calculation of interaction forces between two cylindrical magnets had never been resolved so far as analytical. Following the development of the analytical calculation of parallelepiped magnets, the calculation of these forces between two cylinders can be obtained in analytical form by decomposition to a finite number of elements.

This type of calculation allows the calculation of many systems that uses the forces of interaction between the cylinder magnets. For example it can be used to directly calculate permanent magnet magnetic bearings.

REFERENCES

- [1] G. Akoun, J-P. Yonnet, IEEE Trans. Mag., MAG 20, n° 5 (Sept. 1984) 1962
- [2] J-P. Yonnet, Chap. 9 of "Rare Earth Iron Permanent Magnet" J.M.D. COEY Ed. (Oxford Univ. Press, Sept. 1996)
- [3] J-P. Yonnet, H. Allag and M.E.H. Latreche, Conference MmdE, Bucarest (15-16 june 2008)
- [4] H. Allag and J-P. Yonnet, Conference EMSA, Caen (France) (29 june - 2 july 2008)

Numerical Modelling of Superconducting Filaments for Coupled Problem

T. Satiramatekul¹ and F. Bouillault²

¹Faculty of Engineering, Kasetsart University, Kamphaengsaen Campus, Nakhon Pathom, 73140, Thailand

²LGEP, UMR 8507 CNRS, SUPELEC, Gif sur Yvette Cedex, 91192, France
thitipong.s@ku.ac.th

Abstract — This paper deals with two-dimensional modelling of a multifilamentary wire composed of two superconducting filaments in a conducting matrix. In order to avoid the three-dimensional problem solving, a novel technique is proposed to solve the coupled problem in two-dimensions. For that, it is enough to divide the filaments in several sections in the direction of the length of the wire. The difference of the currents in the superconducting filaments between two successive sections is equal to the current which losses in the copper matrix. The relation between the currents crossing the matrix and the electric fields in the filaments obtained by the analytical method is implemented in the finite element program. For a given geometry, the critical length of the wire where the filaments are coupled can be found. The numerical simulation results present the distributions of the current density in the modelled domain. The influence of the wire length on the total magnetization is also considered.

I. INTRODUCTION

A better understanding of the electromagnetic coupling phenomena in the superconducting filaments can be done by numerical simulation. For that, a finite element program has been developed at the LGEP in France for modelling the superconducting materials.

In [1], we proposed new methods for solving the problem of partially coupled superconducting filaments in two-dimensions. In order to approach the three-dimensional problem with better behaviour, we propose in this paper a new technique by dividing the superconducting filaments into several sections and searching the relation between the currents crossing the copper matrix and the electric fields in the filaments.

II. PROBLEM ANALYSIS

In order to solve the problem, it is well to take the problem of several partially coupled filaments in [1], but by treating the problem with the minimum hypothesis. For that, we have considered a multifilamentary wire constituted of two superconducting filaments embedded in a copper matrix. The current density is supposed parallel to the wire axis in each section and invariant along this axis. It only depends on x , y and t . The magnetic induction is thus parallel to the x - y plane and also depends on x , y and t .

To avoid the large number of elements required by three-dimensional modelling, we have then divided the wire into elementary sections of L/n length, where L and n are the wire length and the number of sections respectively. In a simple case, we have taken $n = 8$. The two-dimensional presentation of the currents and voltages of two filaments along a wire length L shows in Fig. 1. Because of the symmetry of the

problem, only the half of length has been studied in order to reduce the number of sections. Due to the low conductivity of the matrix compared to that of the superconductor, some small currents can circulate between the filaments. The difference of the currents in the filaments for two successive sections is equal to the current circulating in a section of matrix [2]. By using Kirchhoff's current law, we have obtained the relation between the currents inside the superconducting filaments (i) and the currents crossing the copper matrix (i_m) for the section k as follows:

$$i_k = \begin{cases} i_{k+1} + i_{mk} & ; k = 1, 2, \dots, (n/2 - 1) \\ i_{mk} & ; k = n/2 \end{cases} \quad (1)$$

where $i_{m0} = 0$ A.

And by using Ohm's law, we have obtained the relation between the currents and the voltages for the section k as follows:

$$i_{mk} = \begin{cases} 2v_k/R & ; k = 1, 2, \dots, (n/2 - 1) \\ v_k/R & ; k = n/2 \end{cases} \quad (2)$$

where $v_0 = 0$ V and R is representative of the resistance of a section of L/n length, its value could be determined by an electrokinetic formulation. It is interesting to note that, the resistance of the last section is twice because its length is two times smaller.

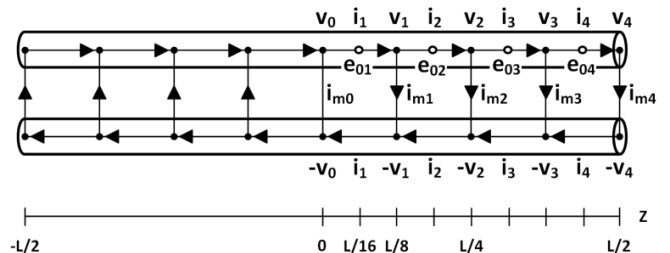


Fig. 1. 2D presentation of two filaments over a wire length L .

The equation of the electric fields (e_0) defined in Fig. 1 could be obtained as in [2].

$$e_{0k} = \frac{(v_{k-1} - v_k)}{(L/n)} \quad \text{at } z = \frac{(2k-1)L}{2n} \quad ; k = 1, 2, \dots, n/2 \quad (3)$$

Equation (3) can be rewritten as follows:

$$v_k = -\frac{L}{n} \sum_{i=1}^k e_{0i} \quad ; k = 1, 2, \dots, n/2 \quad (4)$$

By substituting (2) and (4) in (1), we have obtained the relation between the currents and the electric fields.

$$i_k = \begin{cases} i_{k+1} - \frac{2L}{nR} \sum_{i=1}^k e_{0i} & ; k = 1, 2, \dots, (n/2 - 1) \\ -\frac{L}{nR} \sum_{i=1}^k e_{0i} & ; k = n/2 \end{cases} \quad (5)$$

Equation (5) can be rewritten in the following matrix form:

$$I = [C]E_0 \quad (6)$$

where $I = [i_1 \ i_2 \ \dots \ i_{(n/2)}]^t$, $E_0 = [e_{01} \ e_{02} \ \dots \ e_{0(n/2)}]^t$ and $[C]$ is a matrix of constant value whose dimension is $(n/2) \times (n/2)$. For $n = 8$, we have found that:

$$[C] = \begin{bmatrix} 8c & 6c & 4c & 2c \\ 6c & 6c & 4c & 2c \\ 4c & 4c & 4c & 2c \\ c & c & c & c \end{bmatrix} \quad (7)$$

where $c = -L/8R$.

III. NUMERICAL MODELLING

The domain of the problem shows in Fig. 2 (in 2D). To reduce the computing time, by looking at the symmetries of the problem, we have only modelled a quarter of the domain. A technique proposed for this modelling is to execute $n/2$ computations of finite element in parallel. For that, we have just created a mesh and then regenerated a super mesh with $n/2$ times more elements and $n/2$ times more nodes. The coupling between the calculations of finite element would be done via (6).

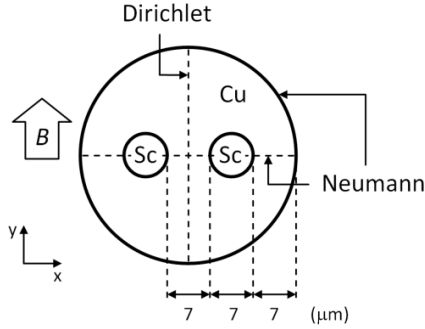


Fig. 2. Domain of the problem in 2D with given boundary conditions.

Bean's critical state model [3], which is replaced by a nonlinear function defined in [4], have been selected to characterize the electrical behaviour law of superconducting materials. As in [1], [5], in this case we have found that the matrix systems obtained by using the finite element method are as follows:

$$[M]\partial_t j_k + [A_e]e_k + [A_{ev}]e_{0k} = F \quad ; \quad k = 1, 2, \dots, n/2 \quad (8)$$

$$[A_{ev}]^t e_k + [A_v]e_{0k} = \partial_t i_k \quad ; \quad k = 1, 2, \dots, n/2 \quad (9)$$

where j is the current density. $[M]$ is the matrix of dimension $m \times m$. $[A_e]$, $[A_{ev}]$ and $[A_v]$ are the matrices of dimension $m \times m$, $m \times (n/2)$ and $(n/2) \times (n/2)$ respectively (m , n are the number of unknowns and the number of sections). F is the source vector.

IV. SIMULATION RESULTS

The simulation results have been obtained by using a code based on the finite element method and Bean's model. A series of numerical simulations has been realized for the superconducting filaments immersed in an external magnetic induction varying sinusoidally in time. Figure 3 shows the results of the current density distributions in the modelled domain at $t = T/8$ where T is the period of the applied

magnetic induction. The four subfigures from left to right indicate respectively the current density distributions at $z = L/16, 3L/16, 5L/16, 7L/16$. In the case that the wire length (L) is equal to the critical length (L_c), we have obtained the results in the case of partially coupled (Fig. 3(a)). We have observed that the total current in the middle of the wire is equal to $J_c \pi r^2$, where r is the radius of the filament and J_c is the critical current density (3×10^9 A/m²). These results show clearly the electromagnetic coupling phenomena in the superconducting filaments and are in agreement with those in [6]. For $L \gg L_c$ and $L \ll L_c$, the obtained results show the case of perfectly coupled (Fig. 3(b)) and perfectly decoupled (Fig. 3(c)) respectively. We could observe that the total current in the filament in Fig. 3(b) is the maximum value and the same in all sections. But in Fig. 3(c), this total current is zero and the same in all sections too. These results are in agreement with those shown in [1], [5]. In addition, the total magnetization of the wire could be computed by using the obtained value of the current density.

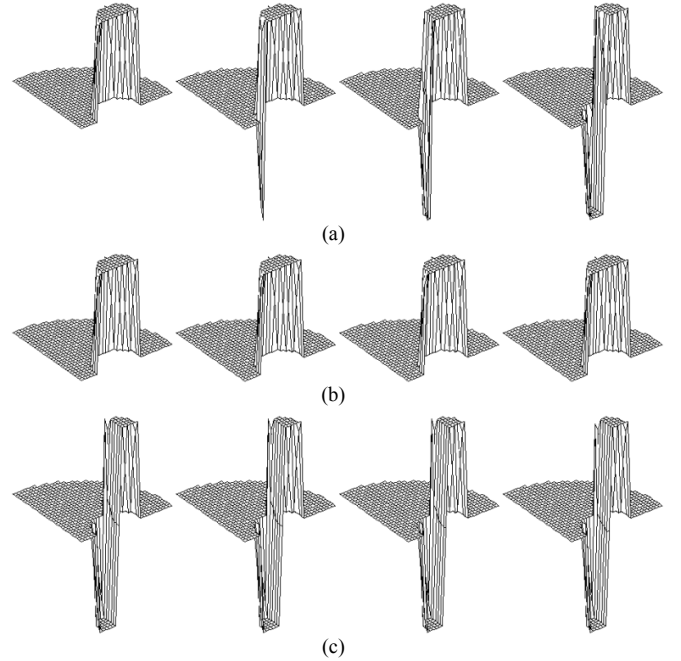


Fig. 3. Current density distributions in the modelled domain: (a) partially coupled case, (b) perfectly coupled case, and (c) perfectly decoupled case.

V. REFERENCES

- [1] T. Satiramatekul, F. Bouillault and L. Santandrea, "Modeling of magnetization curves of partially coupled superconducting filaments with dependence of current density according to applied magnetic field," *IEEE Trans. Magn.*, 42(4): 887-890, 2006.
- [2] T. Satiramatekul, F. Bouillault, A. Devred and D. Leroy, "Magnetization modeling of twisted superconducting filaments," *IEEE Trans. Appl. Supercond.*, 17(2): 3737-3740, 2007.
- [3] C. P. Bean, "Magnetization of hard superconductors," *Phys. Rev. Lett.*, 8(6): 250-253, 1962.
- [4] M. Maslouh, F. Bouillault, A. Bossavit and J. C. Verite, "From Bean's model to the H-M characteristic of a superconductor: some numerical experiments," *IEEE Trans. Appl. Supercond.*, 7(3): 3797-3800, 1997.
- [5] T. Satiramatekul and F. Bouillault, "Magnetization of coupled and noncoupled superconducting filaments with dependence of current density on applied field," *IEEE Trans. Magn.*, 41(10): 3751-3753, 2005.
- [6] M. N. Wilson, *Superconducting magnets*, Oxford: Clarendon, 1983, pp. 174-176.

Improved Accuracy of the Classical Eddy-Current Loss-Computation Technique

A. Belahcen, E. Dlala, and J. Pippuri
Helsinki University of Technology, Dept. of Electrical Engineering
P.O.Box 3000, FIN-02015-TKK, Finland
anouar.belahcen@tkk.fi

Abstract — This paper presents thorough investigations of the accuracy of the classical technique used to compute the eddy-current losses in nonlinear laminated electrical steel. The investigations show the weakness of the classical technique and point out how it should be improved. Based on the investigations and findings, an improvement is proposed and its accuracy is quantified. The accuracy of the classical and the improved technique is assessed by comparing the results of these techniques with results from a previously validated advanced method.

I. INTRODUCTION

The computation of power losses is a key feature in the design stage of electrical machines. The losses are conventionally separated into copper losses and core or iron losses. The latter ones are themselves separated into eddy-current, hysteresis, and excess losses. The adequate modeling of iron losses within the FE simulation of electrical machines requires advanced magnetodynamic vector hysteresis models of the underlying magnetic materials [1]. However, the computation time of these models when used in the design or within an optimization procedure presents a sever drawback.

Simplified techniques based on statistical or analytical methods are used in every day design. The most controversial techniques are related to the computation of eddy-current losses in the lamination of the machines. Two different variations of the classical technique [2] are widely used for this purpose. One is a direct application that does not put any condition on the waveform of the flux density, and the second one uses the Fourier decomposition of the flux density and applies the classical method to each harmonic separately.

In this paper we investigate the accuracy of the classical technique by comparing its results to these obtained from an advanced model [3], which is based on the numerical solution of the magnetic field in the depth of the steel sheet. Investigations on the accuracy of the second technique as well as its comparison with the classical one will be presented in the extended paper.

The advanced model itself has been previously demonstrated to give accurate results when compared with measured ones [4]. We also propose an improvement of the classical technique to make it more accurate without considerably increasing its computational burden.

II. DESCRIPTION OF THE MODELS

The advanced model is based on solving two coupled 1D magnetodynamic equations in the lamination depth. These equations are coupled through the material reluctivity and require iterative solution as the reluctivity is non linear

$$\begin{aligned}\frac{\partial^2 h_x(z,t)}{\partial z^2} &= \sigma \frac{\partial b_x(z,t)}{\partial t} \\ \frac{\partial^2 h_y(z,t)}{\partial z^2} &= \sigma \frac{\partial b_y(z,t)}{\partial t}\end{aligned}\quad (1)$$

where h_x and h_y are the components of the magnetic field strength and b_x and b_y these of the magnetic flux density in the lamination depth z . The instantaneous eddy-current losses are then computed from the current density $\mathbf{J}(z,t)$, the lamination thickness d , and the conductivity of the material σ as

$$p(t) = \frac{1}{d} \int_{-d/2}^{d/2} \frac{\mathbf{J}^2(z,t)}{\sigma} dz \quad (2)$$

The classical model has been derived from the analytical solution of (1), assuming uniform flux density in the depth of the material [2]. In both models the end effects of the eddy currents loops are ignored due to the small size of the lamination thickness.

In the classical model the instantaneous losses are given by

$$p(t) = \frac{\sigma d^2}{12} \frac{\partial \mathbf{B}}{\partial t} \cdot \frac{\partial \mathbf{B}}{\partial t} \quad (3)$$

The classical model does not take into account the nonlinearity of the magnetic material in the depth of the lamination and thus ignores the skin-effect related to this phenomenon. An improvement of the classical model consists of introducing in (3) terms that describe in a way or another, the effect of nonlinearity. In stead of (3), we propose that the instantaneous losses be calculated as follows

$$p(t) = \frac{\sigma d^2}{12} \left(\delta_x \left| \frac{\partial B_x}{\partial t} \right|^{\gamma_x} \frac{\partial B_x}{\partial t} + \delta_y \left| \frac{\partial B_y}{\partial t} \right|^{\gamma_y} \frac{\partial B_y}{\partial t} \right) \quad (4)$$

where $\delta_x = \text{signum}(B_x)$, $\delta_y = \text{signum}(B_y)$, and γ_x and γ_y are functions of B_x and B_y respectively.

In this version, the functions γ are quadratic functions of the magnetic flux density components. Different options for the choice of γ will be presented in the extended paper.

The instantaneous power loss in all the above cases is then integrated to obtain the power per unit volume P over one time period of the fundamental frequency.

III. COMPUTATION RESULTS

The three models described above have been implemented using 1D finite element method for the advanced one and related routines for the classical and improved ones. In all

computations the advanced model is fed from a predefined flux density, which is used to set its boundary values. The waveforms, frequencies, and amplitudes of the source flux density are varied and the relative difference between the power loss per unit volume over one time period of the fundamental frequency from the advanced model and the two other techniques are calculated as

$$\text{relative_error} = \frac{P_{\text{advanced}} - P}{P_{\text{advanced}}} \quad (5)$$

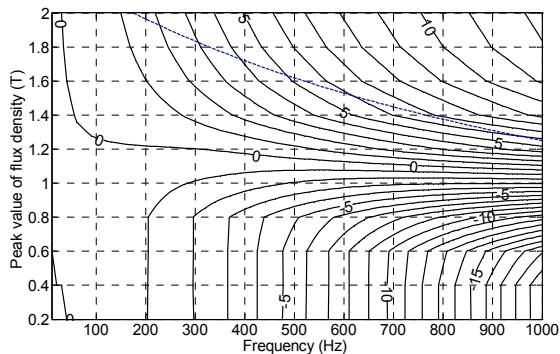


Fig. 1. Relative error in the computed losses from the advanced model and the classical one in the case of alternating flux density with different frequencies and amplitudes. The classical model works fine for most practical flux (under the dashed line) though it overestimates the losses in some cases.

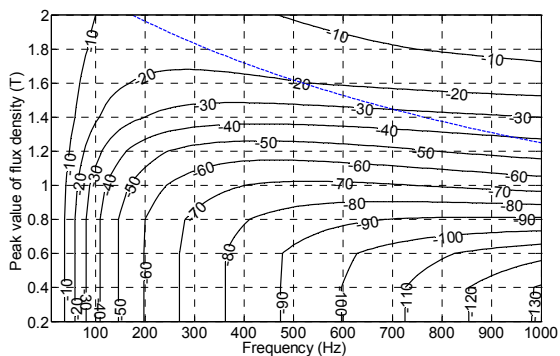


Fig. 2. Relative error in the computed losses from the advanced model and the classical one in the case of alternating fundamental increased with the 25th harmonic with amplitude $B_{25} = 0.05B_1$. The frequencies and amplitudes are these of the fundamental one. The classical model does not give adequate results; it overestimates the losses in all practical cases (under the dashed line).

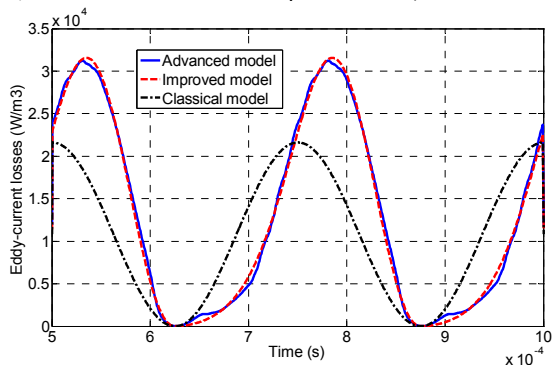


Fig. 3. Time dependence of the losses from the different models. When the flux density is alternating at 2000 Hz with an amplitude of 1.5 T. The classical technique gives losses that are lagging behind these of the advanced one while the improved technique models well the lag.

Fig. 1. shows the contour plot of this relative error (5) for the classical technique, when the source field was alternating with only the fundamental harmonic. Fig. 2. shows similar results when the field was alternating with the fundamental harmonic but contained also the 25th harmonic with an amplitude $B_{25} = 0.05B_1$. Fig. 3 presents the time dependency of the losses computed by the advanced model and these computed by the classical technique and the proposed improved one. It is clear that the classical technique can not model the lag of the losses behind the flux density caused by the time constant of the flux penetration phenomenon. The improved technique on the other hand can deal with this phenomenon thanks to terms that depend on the sign of the time derivative of the flux.

IV. DISCUSSION AND ANALYSIS

The classical eddy-current loss computation technique although gives acceptable average power losses in the case of a single harmonic (see Fig. 1.), does not model correctly these losses in time (see Fig. 3.) and thus introduces large errors as soon as the flux density contains higher harmonics (Fig. 2). The proposed improved method, though is not yet fully studied seems to be able to model the instantaneous power losses adequately (see Fig. 3).

In electrical machines, the situation is so that there is no localization where the variation of the flux density is purely sinusoidal, even if the supply voltage of the machine is sinusoidal. When the machine is used with frequency converters, the situation is even worse as the voltage harmonics of the supply will produce additional harmonics in the flux density resulting in low accuracy of the loss computation if the classical technique is used.

V. CONCLUSIONS

We presented investigations of the accuracy of different techniques for the eddy-current loss computation in nonlinear laminated electrical steel. The investigations showed the weakness of the classical technique and pointed out that there is a need for improved and time efficient techniques as well as the kind of improvements needed (lag of the instantaneous power loss). In the extended paper we will present different improvements and more comparisons of the losses computed with different techniques.

VI. REFERENCES

- [1] E. Dlala, "Comparison of models for estimating magnetic core losses in electrical machines using the finite-element method", *IEEE Trans. on Magnetics*, 45(2): 716-725, 2009.
- [2] G. Bertotti, *Hysteresis in Magnetism for Physicists, Material Scientists, and Engineers*, New York, academic press, 1998:399-400
- [3] O. Bottauscio, M. Chiampi, and D. Chiarabaglio, "Advanced model of laminated magnetic cores for two-dimensional field analysis", *IEEE Trans. on Magnetics*, 36(3): 561-573, 2000.
- [4] E. Dlala, A. Belahcen, A. Arkkio, "Efficient magnetodynamic lamination model for two-dimensional field simulation of rotating electrical machines", *J. of Magnetism and Magnetic Materials*, 320(20):e1006-e1010, 2008.

A New 2D Magnetic Reluctivity Model for Rotating Magnetic Fields and Its Application to FEM

Hee Sung Yoon, Sun-ki Hong*, and Chang Seop Koh, *Senior Member, IEEE*
 School of ECE, Chungbuk National University *Dept. of EE, Hoseo University
 San 48, Gaesin-dong, Cheongju, Chungbuk 361-763, KOREA
 kohcs@chungbuk.ac.kr

Abstract — This paper presents an efficient reluctivity model for taking account of two-dimensional (2-D) magnetic properties of grain-oriented electrical steel sheets. The measured hysteretic H -waveform is approximated to alternating one which the direction of H -waveform can be taken by a constant under a specific B -waveform, and the approximated H -waveform is expressed by using Fourier series expansion. The magnetic reluctivity model is proposed to apply the approximated 2-D magnetic properties to finite element analysis, and the effectiveness of the proposed method is investigated.

I. INTRODUCTION

Recently, an efficient magnetic reluctivity model considering two-dimensional (2-D) magnetic properties of silicon steel sheet has become an important issue for precise performance analysis of electrical machines. There have been researches, therefore, to effectively describe the 2-D magnetic properties of silicon steel including Grain-oriented materials as well as Non-oriented materials [1]-[6]. Under alternating field condition, in order to express the 2-D behavior of the magnetic field intensity (H), some magnetic reluctivity models have been developed [1]-[3]. In these models the hysteretic H -waveforms measured by using 2-D single sheet tester are approximated to alternating waveforms, and their magnitudes and phase angles are modeled as functions of magnitude and direction of the corresponding magnetic flux density (B). Although these models are quite effective and can be expressed as relatively simple form, they can hardly describe the 2-D magnetic properties under rotating magnetic field condition [1]. On the other hand, under rotating field condition, a few reluctivity models are developed based on Chua-type model by means of Fourier series expansion of B - and H -waveforms [4]-[6]. It is proven that the accuracy of these models can be enhanced by taking more harmonic components of the measured H -waveform into account [6]. However, as considering more harmonic components, these models become more complicated and require more data in terms of few hundred megabytes, and accordingly computing time becomes very huge when they are applied to non-linear FEM.

In this paper, a numerically efficient reluctivity model is proposed to describe the 2-D magnetic properties of silicon steel sheet under both the alternating and rotating field conditions, and applied to non-linear FEA.

II. APPROXIMATION OF H -WAVEFORM

For a specimen of silicon steel sheet, the H -waveform corresponding to an arbitrary B -waveform can be measured by using 2-D single sheet tester, shown in Fig. 1, where the

waveform of exciting voltage is controlled using waveform control technique so that a desired B -waveform is obtained. An elliptically rotating B -waveform is expressed, as shown in Fig. 2(a), for given parameters; maximum magnitude B_{max} , axis ratio $\alpha (=B_{min}/B_{max})$ and inclination angle φ , as follows:

$$B_k(\tau) = B_{mk}(\tau) \sin(\tau - \phi_k) \\ = R_{B_k} \cos \tau + I_{B_k} \sin \tau, \quad k = x, y \quad (1)$$

Fig. 2(b) shows the measured hysteretic H -waveform under 50Hz for a specimen of Grain-oriented silicon steel sheet 30PG158 when a rotating B -waveform of which parameters B_{max} , α , and φ are 1.0, 0.5 and 45° , respectively.

In this paper, the measured H -waveform is approximated, as shown in Fig. 2(b), to an alternating one of which maximum magnitude and phase angle are \hat{H} and θ_H , respectively. In this approximation, a magnetic field intensity (H) on the measured H -waveform correspond to its projection (H') on the approximated waveform as shown in Fig. 2(b). The approximated H -waveform for a rotating B -waveform with $(B_{max}, \varphi, \alpha)$ is defined as follows:

$$H'_m(\tau) = H_m(\tau) \cos(\theta_H(\tau) - \theta'_H), \quad 0 \leq \tau \leq 2\pi \quad (2-a)$$

$$\theta'_H(\tau) = \angle H_{max}, \quad 0 \leq \tau \leq 2\pi \quad (2-b)$$

where $H_m(\tau)$ and $\theta_H(\tau)$ are the magnitude and phase angle of H , respectively. In this approximation, H -waveform is expressed

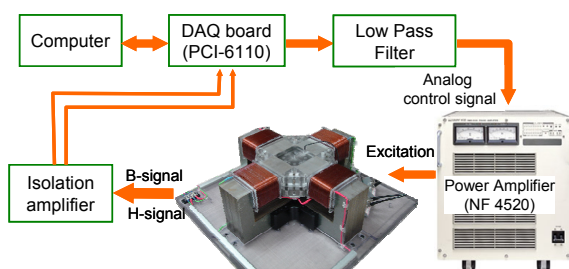


Fig. 1. A two-axes excitation two dimensional single sheet tester.

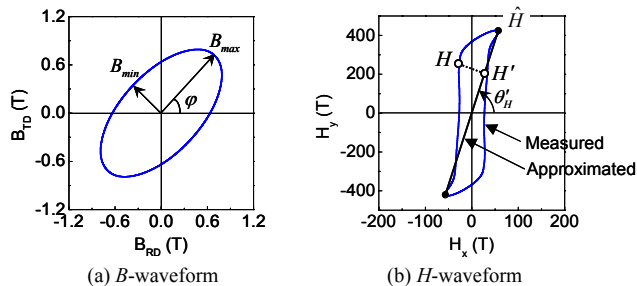


Fig. 2. Approximation of H -waveform ($B_{max}=1.0$, $\alpha=0.5$, $\varphi=45^\circ$)

as a function of direction of B , θ_B , when $(B_{max}, \alpha, \varphi)$ is defined.

III. MAGNETIC RELUCTIVITY MODEL AND FEA APPLICATION

The magnetic reluctivity model considering 2-D magnetic properties of anisotropic materials is defined as follows:

$$\begin{pmatrix} H_x \\ H_y \end{pmatrix} = \begin{bmatrix} v_{xx} & v_{xy} \\ v_{yx} & v_{yy} \end{bmatrix} \begin{pmatrix} B_x \\ B_y \end{pmatrix} \quad (3)$$

The approximated H -waveform is expressed, by using Fourier series expansion considering up to 5-th order harmonics, as follows:

$$\begin{aligned} H_x(\tau) &= \sum_{n=1}^3 H'_{(2n-1)m} \sin[(2n-1)\tau + \phi'_{(2n-1)H_m}] \cdot \cos \theta'_H \\ H_y(\tau) &= \sum_{n=1}^3 H'_{(2n-1)m} \sin[(2n-1)\tau + \phi'_{(2n-1)H_m}] \cdot \sin \theta'_H \end{aligned} \quad (4)$$

Substituting (1) to (3), and comparing (3) with (4), after some algebraic manipulations, the reluctivity tensor in (3) is derived, for fixed parameters $(B_{max}, \alpha, \varphi)$, as follows:

$$\begin{bmatrix} v_{xx} & v_{xy} \\ v_{yx} & v_{yy} \end{bmatrix} = \begin{bmatrix} \cos \theta_H & 0 \\ 0 & \sin \theta_H \end{bmatrix} \begin{bmatrix} k_1 & k_2 \\ k_1 & k_2 \end{bmatrix} \quad (5-a)$$

$$\begin{aligned} k_1 &= P(c_1 + c_2 \cos^2 \tau + c_3 \cos^4 \tau) - Q(c_4 - c_5 \sin^2 \tau + c_6 \sin^4 \tau) \\ k_2 &= R(c_1 + c_2 \cos^2 \tau + c_3 \cos^4 \tau) - S(c_4 - c_5 \sin^2 \tau + c_6 \sin^4 \tau) \end{aligned} \quad (5-b)$$

The coefficients in (5) are obtained, for a specific $(B_{max}, \alpha, \varphi)$, as follows:

$$\begin{aligned} c_1 &= R_{1H} - 3R_{3H} + 5R_{5H}, & c_2 &= 4R_{3H} - 20R_{5H}, \\ c_3 &= 16R_{5H}, & c_4 &= I_{1H} + 3I_{3H} + 5I_{5H}, \\ c_4 &= 4I_{3H} + 20I_{5H}, & c_6 &= 16I_{5H} \end{aligned} \quad (6-a)$$

$$\begin{aligned} P &= I_{B_y} / (R_{B_x} I_{B_y} - R_{B_y} I_{B_x}), & Q &= I_{B_y} / (R_{B_x} I_{B_y} - R_{B_y} I_{B_x}) \\ R &= I_{B_x} / (R_{B_y} I_{B_x} - R_{B_x} I_{B_y}), & S &= R_{B_x} / (R_{B_y} I_{B_x} - R_{B_x} I_{B_y}) \end{aligned} \quad (6-b)$$

where R_{nH} and I_{nH} ($n=1, 3, 5$) are real and imaginary parts of Fourier expansion of the magnitude of H -waveform approximated by the proposed method. The coefficients c in (6-a) are smoothed by using Bezier spline to be applied to the FEM. From (5), it is found that the number of the coefficients in the proposed method is a lot reduced compared with those in [4]-[6]. It is, therefore, expected to give better convergence characteristics when it is applied to FEM.

Fig. 3 shows the magnetic reluctivities calculated from (5) for Grain-oriented silicon steel sheet 30PG158 when the rotating flux condition is $\alpha=0.75$ and $\varphi=45^\circ$. It is observed that the curves are smooth enough to give a good convergence.

Fig. 4 compares the computed magnitudes and phase angles of H -vector using the proposed reluctivity for the case of $B_{max}=1.0$ (T), $\alpha=0.75$ and $\varphi=45^\circ$, shown in Fig. 3, with the measured ones. It can be seen that the computed H -waveform using the proposed magnetic reluctivity model has a good agreement with the measured one although the rotating field is approximated to an alternating field.

The overall flow of the FEM using the proposed reluctivity is as follows:

Step 1. Using conventional B - H curve method, analyze for one period,

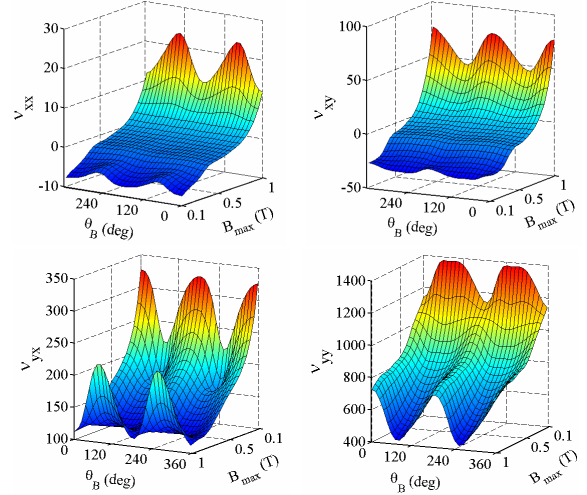


Fig. 3. Magnetic reluctivities when $\alpha=0.75$, $\varphi=45^\circ$

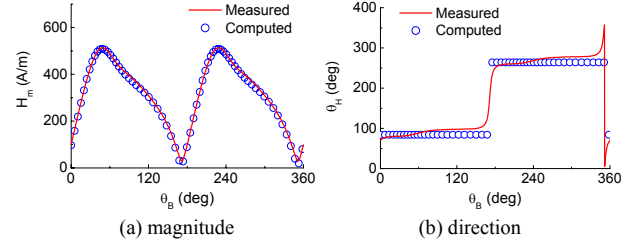


Fig. 4. Computed and measured H -waveforms for $B_{max}=1.0$ (T), $\alpha=0.75$ and $\varphi=45^\circ$.

Step 2. Set the parameters $(B_{max}, \alpha, \varphi)$ for all elements using the analyzed results, and analyze again for one period using the proposed reluctivity. In this analysis, the derivatives, $\partial v_{ij} / \partial A_k = \partial v_{ij} / \partial \theta_B \cdot \partial \theta_B / \partial A_k$, for Newton-Raphson iteration is calculated, from Fig. 3, by using Bezier spline [6].

Step 3. Repeat the *Step 2* until converged parameters are obtained for all elements.

In the version of full paper, the proposed algorithm will be applied to the analysis of the single phase transformer core model in [6], and its results will be compared with experimental ones.

IV. REFERENCES

- [1] H. S. Yoon, et al., "Comparison of magnetic reluctivity models for FEA considering 2D magnetic properties," *IEEE Trans. on Magn.*, vol. 45, no. 3, pp. 1202-1205, March 2009
- [2] T. Nakata, et al., "An improved numerical analysis of flux distributions in anisotropic materials," *IEEE Trans. on Magn.*, vol. 30, no. 5, pp. 3395-3398, Sep. 1994.
- [3] K. Fujiwara, et al., "A proposal of finite-element analysis considering 2D magnetic properties," *IEEE Trans. on Magn.*, vol. 38, no. 2, pp. 889-892, Mar. 2002.
- [4] N. Soda, et al., "Improvement of T-joint part constructions in three-phase transformer cores by using direct loss analysis with E&S model," *IEEE Trans. on Magn.*, vol. 36, no. 4, pp. 1285-1288, Jul. 2000.
- [5] H. Shimoji, et al., "A new modeling of the vector magnetic property," *IEEE Trans. on Magn.*, vol. 38, no. 2, pp. 861-864, Mar. 2002.
- [6] Y. Zhang, et al., "An improved engineering model of vector magnetic properties of grain-oriented electrical steels," *IEEE Trans. on Magn.*, vol. 44, no. 11, pp. 3181-3184, Nov. 2008.

Measurement and Analysis of Magnetic Properties of Soft Magnetic Composite Material Considering 3-D Reluctivity Tensor

Yongjian Li, Qingxin Yang, Youhua Wang, Jingfeng Sun

Province-Ministry Joint Key Laboratory of Electromagnetic Field and Electrical Apparatus Reliability,
Hebei University of Technology, Tianjin, 300130, China

Yongjian.Li@eng.uts.edu.au

Jianguo Zhu, Youguang Guo, Zhiwei Lin, Wei Xu, Yi Wang

School of Electrical, Mechanical and Mechatronic Systems, University of Technology, Sydney, NSW 2007, Australia

Abstract — Soft magnetic composite (SMC) material is widely applied in three-dimensional (3-D) magnetic flux machines. Conventional methods for detecting the magnetic properties of SMC material are not accurate due to the rotational magnetic domains. Taking the 3-D properties into account can help complete the understanding and modeling of the magnetization process. In order to precisely measure magnetic field distribution of the rotating flux machine, 3-D reluctivity tensor should be considered in the electromagnetic field analysis. By using a 3-D magnetic property tester, this paper presents the measurement of 3-D vector magnetic properties considering the 3-D magnetic reluctivity tensor. Moreover, finite element analysis is used in electromagnetic field calculation by means of Femap software package.

I. INTRODUCTION

One and two dimensional (2-D) measurements are widely employed for characterization of soft magnetic materials. However, they are still far from describing the actual properties of the materials, where the vector properties with 3-D magnetic fluxes should be considered [1]. By using a novel 3-D magnetic property tester developed at University of Technology, Sydney (UTS), a kind of SMC material, SOMALOY™500 developed by Höganäs AB, Sweden, is measured and analyzed [2]. A cubic SMC sample with the side length of 22 mm is cut from the cylindrical perform. Some experimental results under time-varying magnetic flux density vector \mathbf{B} loci and magnetic field strength vector \mathbf{H} loci, and the power losses when the \mathbf{B} loci are controlled to be circles with increasing amplitudes and ellipses evolving from a straight line into a circle in three orthogonal planes, respectively [3].

A 3-D reluctivity tensor which is a second-order three-dimensional full rank matrix can be constructed by means of the experimental data of \mathbf{H} vectors and \mathbf{B} vectors. Therefore, taking the off-diagonal elements into account can precisely express the relationship between \mathbf{B} and \mathbf{H} under rotational excitation conditions. The reluctivity tensor is a key factor for accurate numerical analysis of magnetic field in 3-D flux SMC electrical machines [4].

In this paper, the 3-D magnetic properties are expressed through tensor magnetic reluctivity under rotating flux conditions, which is used in the magnetic field analysis with the finite element method (FEM). A model of current-carrying

solenoid is built in Femap, and the FEM results are presented. Some key codes in the program are also presented.

II. IMPROVEMENT OF 3-D TESTING SYSTEM

A. Original Structure

The UTS 3-D magnetic property testing system consists of a tester, a digital control system, a data acquisition and three power amplifiers [2]. Fig. 1 shows the structure of the cubic sample with \mathbf{B} coils and surface \mathbf{H} sensing coils. The components of the sample surface field intensity \mathbf{H} are measured by 12 search coils and the flux density \mathbf{B} components are measured by three search coils wrapped around the cubic sample. The components of \mathbf{H} and \mathbf{B} on each coordinate axis can be calculated from the induced *emf* of the search coils by

$$H_i = \frac{1}{\mu_0 K_{H_i}} \int V_{H_i} dt \quad (i = x, y, z) \quad (1)$$

$$B_i = \frac{1}{K_{B_i}} \int V_{B_i} dt \quad (i = x, y, z) \quad (2)$$

where V_{B_i} and V_{H_i} are the terminal instantaneous voltages of the B_i and H_i search coils, K_{H_i} is the H_i search coil coefficient obtained by calibration, $K_{B_i} = N_{B_i} A_{sp}$ the coefficient of the B_i search coil, N_{B_i} the number of turns of the B_i coil, and A_{sp} the cross-sectional area of the sample.

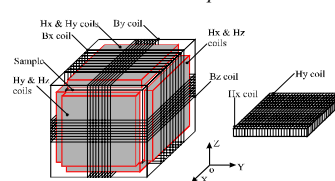


Fig. 1. Cubic sample and \mathbf{B} , \mathbf{H} coils

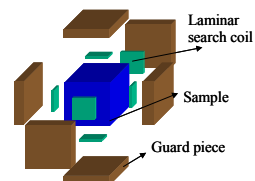


Fig. 2. Improved structure

B. Improved Structure

The original tester structure can be improved considering that the surface area of the \mathbf{H} coil equals that of a side of the cubic sample and the magnetic field in the sensing area may not be uniform. An improved structure is proposed so that the \mathbf{H} coil size is minimized and it can be attached to the central area of each side of the cubic sample, as shown in Fig. 2. It has been found the field near the central area is quite uniform.

The tangential component of \mathbf{H} is continuous if no applied current flows on the sample surface. The sensing area is now centralized and the gap between sample and \mathbf{H} coil is contracted. The adoption of the guard piece which is the same material as the sample, can significantly improve the accuracy of measurement of the sample surface field since this structure can significantly decrease the equivalent reluctance of the magnetic circuit and the excitation current required to magnetize the sample can be reduced. The cubic sample, six \mathbf{H} search coils, and six guard pieces are integrated into the sample house. Furthermore, the method of wire wrapping is adopted, which can shrink the area of the circle and optimize the magnetic circuit.

C. Calibration of Sensing Coils

The \mathbf{H} coils must be calibrated for accurately measuring the magnetic field strength components. The calibration is performed in a long solenoid, which can generate a uniform magnetic field. The surface of the coil is set to be parallel to the generated field. The \mathbf{H} coil coefficient is calculated by

$$K_H = \frac{V_H}{\sqrt{2\pi f} \mu_0 H_m} \quad (3)$$

where f is the excitation frequency, V_H the *rms* value of the induced *emf*, and $\mu_0 H_m$ the peak value of the air flux density in the middle of the solenoid.

In experiment, when the magnetic field to be measured, $H = (H_x, H_y, H_z)$, is not parallel to any axis of \mathbf{H} box, the measured *emfs* in the \mathbf{H} coils can be expressed as

$$\begin{cases} E_x = -\mu_0 \left(K_x^x \frac{dH_x}{dt} + K_x^y \frac{dH_y}{dt} + K_x^z \frac{dH_z}{dt} \right) \\ E_y = -\mu_0 \left(K_y^x \frac{dH_x}{dt} + K_y^y \frac{dH_y}{dt} + K_y^z \frac{dH_z}{dt} \right) \\ E_z = -\mu_0 \left(K_z^x \frac{dH_x}{dt} + K_z^y \frac{dH_y}{dt} + K_z^z \frac{dH_z}{dt} \right) \end{cases} \quad (4)$$

Then the magnetic field components can be worked out.

III. MEASUREMENT RESULTS

By using the 3-D magnetic tester, the magnetic properties of an SMC sample have been systematically measured when the \mathbf{B} vectors with alternating, circular and elliptical loci are controlled to lie in the three orthogonal planes and the corresponding \mathbf{H} vectors have been investigated.

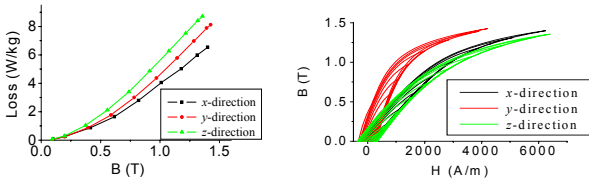


Fig. 3. Hysteresis loops and losses for alternating magnetizations on the x-, y-, and z-axes.

Fig. 3 plots the hysteresis loops and core losses when the \mathbf{B} is controlled to be sinusoidally alternating at 50 Hz along the x, y and z-axis, respectively. It is noticed that the loops for

the x and z axes are similar, while the y axis seems to be the easy axis, though the sample is expected to be isotropic. These measurements will provide the necessary data for modeling the reluctivity tensor and core loss.

IV. 3-D RELUCTIVITY TENSOR

In 3-D condition, \mathbf{H} and \mathbf{B} vectors are not parallel, so the x, y and z-axis components of \mathbf{H} and \mathbf{B} should be expressed as

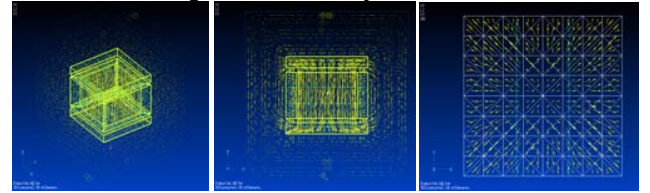
$$\begin{cases} H_x = v_{xx} B_x + v_{xy} B_y + v_{xz} B_z \\ H_y = v_{yx} B_x + v_{yy} B_y + v_{yz} B_z \\ H_z = v_{zx} B_x + v_{zy} B_y + v_{zz} B_z \end{cases} \quad (5)$$

The reluctivity tensor which symbols to the relationship between \mathbf{B} and \mathbf{H} can be written to a second-order three-dimensional full rank matrix as

$$v = \begin{bmatrix} v_{xx} & v_{xy} & v_{xz} \\ v_{yx} & v_{yy} & v_{yz} \\ v_{zx} & v_{zy} & v_{zz} \end{bmatrix} \quad (6)$$

V. NUMERICAL ANALYSIS OF 3-D RELUCTIVITY TENSOR

Fig. 4 shows the finite element analysis of the 3-D model of a square current-carrying solenoid by using Femap software package in several directions. Based on laboratory test results, several types of experimental data at different locations by setting the parameter of the reluctivity tensor, the tendency distribution of magnetic flux density can be obtained.



(a) Diametric view (b) Front view (c) Top view of Solid
Fig. 4. FEM simulation of 3-D magnetic property model

VI. DISCUSSION AND CONCLUSION

This paper presents an improvement method of 3-D magnetic properties testing and simulation. Magnetic anisotropy is found in the 3-D measurement of SMC material. Under 3-D vector excitations, experimental data generates a magnetic reluctivity tensor which is a full matrix with off-diagonal elements due to the rotating magnetic flux. The results are verified by FEM analysis. More detailed analysis and results will be reported in the full paper.

VII. REFERENCES

- [1] Y.G. Guo, J.G. Zhu, P.A. Watterson and W. Wu, "Comparative study of 3D flux electrical machines with soft magnetic composite core," *IEEE Trans. on Industry Application*, 39(6):1696-1703, 2003.
- [2] J.G. Zhu, J.J. Zhong, Z.W. Lin, J.D. Sievert, "Measurement of magnetic properties under 3-D magnetic excitations," *IEEE Trans. on Magnetics*, 39(5):3429-3431, 2003.
- [3] Z.W. Lin, J.G. Zhu, and Y.G. Guo, "Three-dimensional hysteresis of soft magnetic composite," *J. Appl. Phys.* 99:08D909, 2006.
- [4] Y.G. Guo, J.G. Zhu, Z.W. Lin, J.J. Zhong, H.Y. Lu, and S.H. Wang, "Determination of 3-D magnetic reluctivity tensor of soft magnetic composite materials," *J. Magn. Magn. Mater.*, 312:458-463, 2007.

A Model for Specific Losses in Grain-Oriented Steel

Oszkár Bíró¹, Ulrike Baumgartner², Yu Chen¹ and Gerald Leber²

¹Institute for Fundamentals and Theory in Electrical Engineering, Graz University of Technology
Kopernikusgasse 24, 8010 Graz, Austria

biro@tugraz.at

²SIEMENS Transformers Austria GmbH & Co. KG
Elingasse 3, 8160 Weiz, Austria

Abstract— A new model is presented capable of taking account of the dependence of the specific loss curves (giving loss per weight versus flux density) of grain-oriented steel on the angle between the direction of the flux density and the rolling direction. It uses the loss curves in the rolling and transverse (i.e. the principal) directions only. It is assumed that, for constant loss per weight, the flux density vector traces a modified elliptic curve. The curves for flux densities not oriented in one of the principal directions are reconstructed and compared to measurements, illustrating the feasibility of the model.

I. INTRODUCTION

Grain oriented steel is routinely used in transformer cores and various shielding parts. These are invariably made of laminated steel and are designed so that the expected direction of the flux density in them should be parallel to the laminates and coincide with the rolling direction. Deviations from this ideal situation lead to additional losses. On the one hand, flux density components normal to the sheets cause large eddy currents flowing in the laminates. They can be taken into account by bulk models with an anisotropic conductivity [1], [2]. On the other hand, measurements indicate that the specific losses in the sheets (i.e. the sum of eddy current losses, hysteresis losses and excess losses, see e.g. [3]) are higher if the flux density is not parallel to the rolling direction (see Fig. 1).

The specific loss curves are obtained by measurements carried out in an Epstein frame [4] and are usually provided by steel manufacturers for the principal directions, i.e. the rolling direction of easy magnetization and the transverse direction perpendicular to the rolling direction. In some rare cases curves for intermediate directions are also measured (see Fig. 1) indicating that at angles around 60° to the rolling direction, the specific losses can be higher than at the transverse direction.

The aim of this paper is to present a model using the measured specific loss curves for the principal directions which predicts the specific loss curves in intermediate directions, too and takes account of the above behavior.

II. THE MODEL

The starting point is the well-known elliptic model often used for representing the magnetic anisotropy of nonlinear soft magnetic materials [6]. The model assumes that the loci of the magnetic flux density trace an ellipsis if the modulus of the magnetic field intensity is kept constant. This cannot

reproduce the typical property of grain-oriented steel having the worst direction of magnetization not in the transverse direction, but also at angles around 60° with respect to the rolling direction. Following an idea of [7] using modified elliptic curves to describe the loci of the magnetic field intensity for constant values of the co-energy density, a modified elliptical model capable of mimicking this behavior has been proposed recently [8].

Turning to the question of specific losses in anisotropic materials, let p denote the specific loss per unit weight of a grain-oriented steel sheet and B the modulus of the magnetic flux density. Typical measured $p(B)$ (or $B(p)$) curves obtained in an Epstein-frame [4] are shown in Fig. 1 [5]. The curve marked by 0° has been obtained on a cut wherein the magnetic flux density vector \mathbf{B} is parallel to the rolling direction whereas the curve denoted by 90° shows the p -values if \mathbf{B} is perpendicular to the rolling direction, i.e. it points in the transverse direction. For most commercial sheets, these two curves which will be denoted by $B_1(p)$ and $B_2(p)$, respectively, are routinely provided by the manufacturer. It is remarkable that the losses in $B_2(p)$ for flux densities in the transverse direction, are higher than in $B_1(p)$ with \mathbf{B} pointing in the rolling direction.

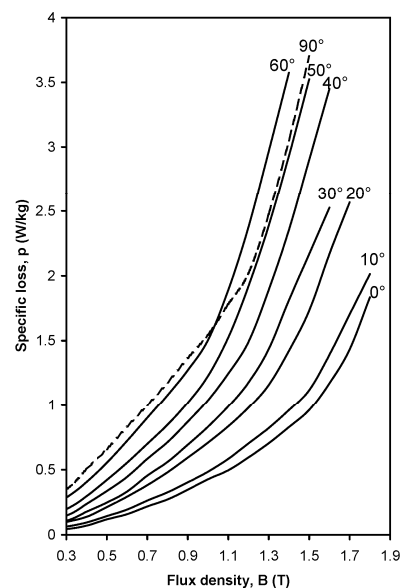


Fig. 1. Measured loss curves of grain-oriented steel in various directions

Let the unit vector \mathbf{e}_1 point in the rolling direction and the unit vector \mathbf{e}_2 in the transverse direction. Our proposed model predicts the losses for an arbitrary vector \mathbf{B} by assuming that, for constant p , \mathbf{B} traces a modified elliptical curve:

$$\left(\frac{\mathbf{B} \cdot \mathbf{e}_1}{B_1(p)}\right)^n + \left(\frac{\mathbf{B} \cdot \mathbf{e}_2}{B_2(p)}\right)^n = 1. \quad (1)$$

The exponent n defines the curve: a value of $n=2$ describes an ellipsis, $n=1$ corresponds to a straight line and for $n \rightarrow \infty$ the curve becomes a rectangle. Fig 2 shows the curve for $n=1.5$ at $p=1.8$ W/kg.

If the model is used to predict the specific losses from the magnetic field distribution obtained by a finite element analysis (as described in e.g. [2]), p has to be determined from (1) if \mathbf{B} is given. Since both $B_1(p)$ and $B_2(p)$ are monotonous functions, the nonlinear equation (1) can be easily solved by a simple regula falsi iterative method.

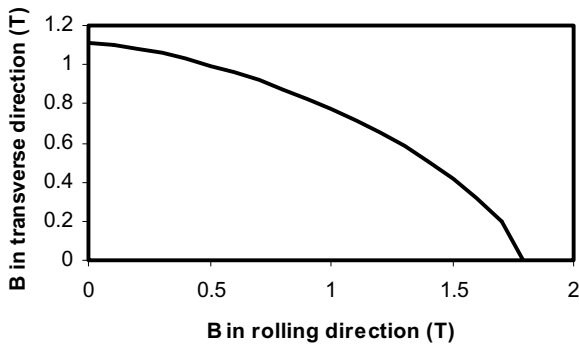


Fig. 2. The loci of \mathbf{B} described by (1) with $n=1.5$ for $p=1.8$ W/kg

III. MODEL TUNING

The key question of the model is the choice of the parameter n . For the particular steel represented in Fig. 1, the measured loss curves for some intermediate angles are also shown in the figure [5]. Using these curves, least-square techniques can be employed to determine the parameter n . It can be made to depend on p to improve the fit. This will be shown in the full paper.

On the other hand, in most practical cases, the measurements for the intermediate angles are not provided. It is, therefore, a relevant question, whether it is possible to obtain a model with a fixed value of n which reproduces the typical behavior seen in Fig. 1, i.e. that the losses for angles around 60° are higher for larger values of B than in the transverse direction. The answer is affirmative: the loss curves for various directions of \mathbf{B} with the choice $n=1.5$ are shown in Fig. 3. Comparison with Fig 1 indicates a good qualitative

agreement. It is, therefore, reasonable to use a value around 1.5 for n if no information on intermediate angles is available.

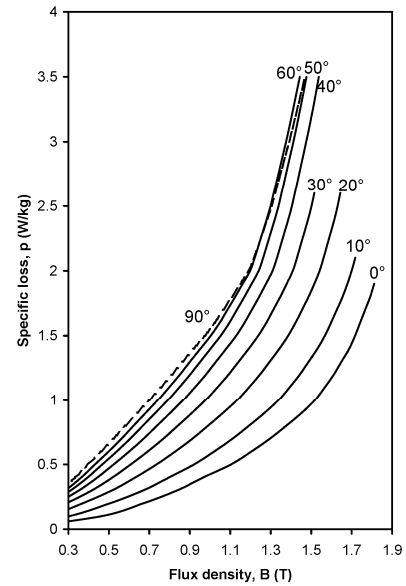


Fig. 3. Loss curves of grain-oriented steel in various directions reconstructed from the curves in the principal directions using (1) with $n=1.5$

IV. ACKNOWLEDGMENT

This work was supported by the Austrian Research Promotion Agency Ltd under project 816113 and by the Styrian Business Promotion Agency under project 1000018145.

V. REFERENCES

- [1] V.C. Silva, G. Meunier and A. Foggia, "A 3-D finite element computation of eddy currents and losses in laminated iron cores allowing for electric and magnetic anisotropy", *IEEE Trans. on Magnetics*, 31(3): 2139-2141, 1995.
- [2] K. Preis, O. Bíró and I. Tičar, "FEM analysis of eddy current losses in nonlinear laminated iron cores", *IEEE Trans. on Magnetics*, 41(5): 1412-1415, 2005.
- [3] G. Bertotti, F. Fiorillo and G. P. Soardo, "The prediction of power losses in soft magnetic materials", *Journal de Physique*, 49(12): 1915-1919, 1988.
- [4] International Standard, Magnetic materials – Part 2: Methods of measurement of the magnetic properties of electrical steel strip and sheet by means of an Epstein frame, IEC 60404-2, ISBN 2-8318-9835-8, 1996.
- [5] Grain-oriented electrical sheet, ORSI, Thyssen Grillo Funke GmbH, 1980 (provided by Siemens Transformers Austria GmbH).
- [6] J. M. Dedulle, G. Meunier, A. Foggia, J.C. Sabonnadiere and D. Shen, "Magnetic fields in nonlinear anisotropic grain-oriented iron sheet", *IEEE Trans. Magn.*, 26(2): 524–527, 1990.
- [7] T. Péra, F. Ossart and T. Waeckerle, "Field computation in non linear anisotropic sheets using the coenergy model", *IEEE Trans. on Magn.*, 29(6): 2425–2427, 1993.
- [8] O. Bíró and S. Außerhofer, "A modified elliptic model of anisotropy in nonlinear magnetic materials", to be presented at *EMF 2009*, May 26-29, 2009, Mondovi (Italy)

Transient Performance of an Induction Motor with the Smith Connection

T. F. Chan¹, L. L. Lai², and L. T. Yan¹

¹Department of EE, the Hong Kong Polytechnic University, Hung Hom, Hong Kong, China

²Energy Systems Group, School of Mathematics and Engineering Sciences, City University London, UK
eetfchan@polyu.edu.hk

Abstract — This paper investigates the starting and braking performance of a three-phase induction motor with the Smith connection. A time-stepping, coupled circuit, two-dimensional finite element method is used for the study. It is found that for certain rotor positions, short periods of speed reversal could happen during starting. Severe torque oscillations at low speeds could be excited when the single-phase voltage is applied at a positive zero-crossing instant. Optimum initial rotor position for starting has been identified. Two methods of electric braking, namely capacitor braking and regenerative braking, are also investigated.

I. INTRODUCTION

The Smith connection (Fig. 1) enables a three-phase induction motor to be started and run on a single-phase supply [1] and is useful for drive applications where only a single-phase supply is available. Transient performance of this asymmetrical motor system, however, has seldom been reported, in particular the dynamic motor response at very low speeds. The analysis is complicated due to the general phase imbalance, heavy saturation, existence of space and time harmonics, deep-bar effect in the rotor conductors, and mechanical motion. A rigorous and comprehensive analysis therefore requires an approach based on the finite element method (FEM). In this paper, a time-stepping, coupled circuit, two-dimensional (2-D) FEM [2] is used for studying the speed and torque responses during motor run up, with special emphasis on the low-speed region. Two important factors that may affect the run-up performance of the Smith motor system, namely, the initial time phase of the supply voltage and the initial rotor position, will be investigated. Typical motor transient run up characteristics of the induction motor will be presented. Besides, the transient performance for two braking modes will also be studied.

II. ANALYSIS METHOD

The time-stepping, coupled-circuit, two-dimensional finite element method (2-D FEM) developed in [3] will be the basis for the present study. Fig. 2 shows the schematic diagram of the FEA which consists of the following steps:

- Establish the state model for the stator circuit connection based on the circuit equations. For the Smith motor circuit, ten state variables, and hence ten state equations, are needed.
- Establish the rotor circuit model: the model will take into account the effect of uneven current distribution in the rotor bars and end rings.
- Coupled circuit and field analysis: the stator and rotor

circuit equations are coupled to the 2-D FEM equations with magnetic vector potentials as variables. The field and circuit equations are solved simultaneously for each rotor time step.

- Time-stepping: the Maxwell's stress method [4] is used to compute the electromagnetic torque and hence the rotor dynamics for rotor time-stepping.

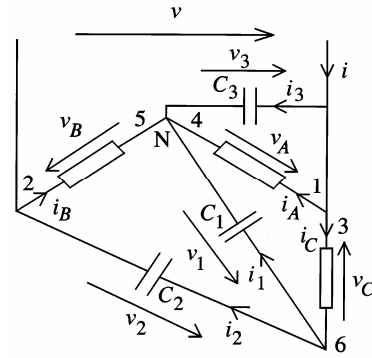


Fig. 1 Smith connection for single-phase operation of a three-phase induction motor.

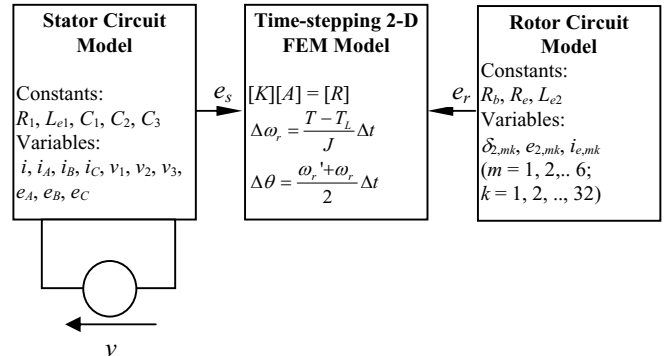


Fig. 2 Time-stepping 2-D FEM model for analysis of induction motor with the Smith connection.

III. RESULTS

A. Starting Performance

The subsequent computations refer to a 2.2-kW, 380-V, 50-Hz, four-pole, three-phase induction motor with the Smith connection (Fig. 2). The motor is started on no load with the starting capacitances ($C_1 = 147 \mu\text{F}$, $C_2 = 35 \mu\text{F}$ and $C_3 = 70 \mu\text{F}$) initially in the circuit. At a rotor speed of 1200 r/min, the starting capacitances are replaced by the running capacitances ($C_1 = 6 \mu\text{F}$, $C_2 = 30 \mu\text{F}$ and $C_3 = 60 \mu\text{F}$) in order to reduce the steady-state torque pulsations.

Two motor parameters that affect the rotor run-up performance are identified. They are the initial phase angle θ_u of the applied voltage and the initial rotor position θ_r . The angle $\theta_u = 0$ means that the motor is started at a voltage zero, while $\theta_u = 90^\circ$ means that the motor is started with maximum instantaneous voltage. The angle $\theta_r = 0$ refers to the rotor position such that the centre line of a rotor slot coincides with the centre line of the first slot of stator phase-A winding. The effect of θ_u on motor torque response, when $\theta_r = 0$, is illustrated in Table I. The initial motor torque is negative in general, implying that a brief period of rotor speed reversal would precede motor run up. It is also found that severe torque pulsations will be produced at low speeds when the the motor is started with $\theta_u = 90^\circ$ and $\theta_r = 0^\circ$, as shown in Fig. 3.

The effect of initial rotor position θ_r on the motor response at starting is shown in Table II. We may conclude that the experimental motor should be started with θ_r between 4° and 9° in order to avoid initial rotor speed reversal, and the best initial speed response is obtained when $\theta_r = 6.75^\circ$.

TABLE I
EFFECT OF INITIAL VOLTAGE PHASE ANGLE ON MOTOR RESPONSE AT LOW SPEEDS ($\theta_r = 0$)

Initial voltage phase angle θ_u ($^\circ$ e)	Initial value of motor torque (N.m)	Maximum value of torque during rotor speed reversal (N.m)	Duration of rotor speed reversal (ms)
90	-1.45	-12.9	6.1
60	-1.08	-15	6.7
30	-0.36	-14.4	7.9
0	0	-14.0	9.5

TABLE II
EFFECT OF INITIAL ROTOR POSITION ON NO-LOAD MOTOR RUN-UP PERFORMANCE

Initial rotor position θ_r ($^\circ$ e)	Initial value of motor torque (N.m)	Maximum value of negative torque (N.m)	Duration of rotor speed reversal (ms)
0	-1.45	-9.74	6.3
2.25	-0.62	-2.36	2.7
4.5	+0.95	nil	nil
6.75	+1.98	nil	nil
9	+0.42	-0.55	1.5

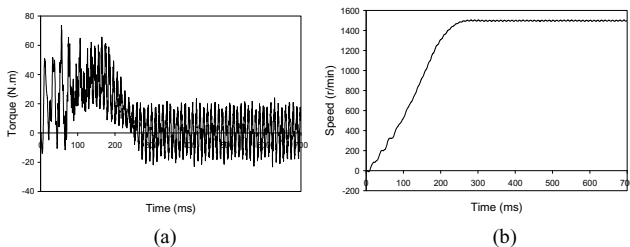


Fig. 3 Computed transient motor run-up performance at no load with starting capacitances ($\theta_u = 0$, $\theta_r = 0$): (a) Torque-time characteristic; (b) Speed-time characteristic.

B. Capacitor Braking

When the single-phase supply is cut out with the induction motor running at normal speed, the capacitances in the motor

circuit is sufficient to cause self-excitation and the machine runs temporarily in the generation mode. An electrical braking torque is produced and the rotor kinetic energy is converted to losses in the motor windings. Fig. 4 shows the speed and torque curves of the motor which is started on no load with the running capacitances and at $t = 600$ ms the supply is cut off. It is observed that an average negative torque is produced and the speed drops from about 1500 r/min to 1000 r/min within 1.2 s.

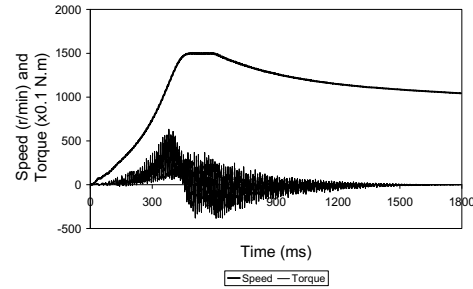


Fig. 4 Transient performance of motor started on no load with running capacitances, followed by capacitor braking.

C. Regenerative Braking

When the load is overhauling in nature, such as in crane hoists or winders, the motor may be driven by the load in the reverse direction. The motor enters the regenerating braking mode and at steady state the motor speed is maintained at a value slightly above synchronous speed. Electric energy is then returned to the single-phase supply. Fig. 5 shows the transient motor performance when a negative torque of 18.6 N.m is applied to the motor at standstill and with $C_1 = 16 \mu\text{F}$, $C_2 = 24 \mu\text{F}$ and $C_3 = 48 \mu\text{F}$.

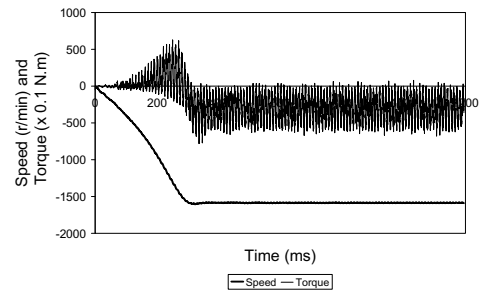


Fig. 5 Transient performance of motor when driven in the reverse direction.

IV. ACKNOWLEDGMENT

This work was supported in part by the Hong Kong Polytechnic University under Research Grant A-PE43.

V. REFERENCES

- [1] O. J. M. Smith, "High-efficiency single-phase motor," *IEEE Trans. Energy Convers.*, 7(3), 1992, pp. 560-569, 1992.
- [2] T. F. Chan and L. L. Lai, "Steady-state analysis of a three-phase induction motor with the Smith connection," *IEEE Power Engineering Review*, 20(10), pp. 45-46, 2000.
- [3] T. F. Chan, L. L. Lai and Lie-Tong Yan, "A coupled circuit and field analysis of a three-phase induction motor with the Smith connection," *IEEE Trans. Magnetics*, 42(4), pp. 1315 - 1318, 2006.

Multi-objective Shape Optimal Design of PMLSM Utilizing Response Surface Method and Grid Computing

Hee Sung Yoon, Nyambayar Baatar, Hong-soon Choi*, and Chang Seop Koh
 Chungbuk National University, *Kyungbuk National University
 San48, Cheongju, Chungbuk 361-763, KOREA
 kohcs@chungbuk.ac.kr

Abstract — A 9 pole 10 slot permanent magnet linear synchronous motor (PMLSM) is optimized in Pareto sense to reduce the detent force and to maximize the thrust force per mass of armature core. In the optimization, the objective functions are approximated by using response surface method with radial basis function to reduce the computing time related with finite element analysis. Additionally, the objective function values at sampling points are computed by using grid computing with 60 personal computers.

I. INTRODUCTION

Conventionally permanent magnet linear synchronous motors (PMLSM) with the structure of ($2\tau_p=3\tau_s$) or ($4\tau_p=3\tau_s$), where τ_p and τ_s are PM pole and winding slot pitches, respectively, have been exclusively used for general purpose applications in factory automation. However, the PMLSMs employing these conventional structures such as PMLSM with 8 poles and 12 slots or PMLSM with 12 poles and 9 slots, generate very big detent force composed of cogging and end force, and impede precise position and speed control purpose applications [1].

Very recently a new structure of ($9\tau_p=10\tau_s$) with two extra end-teeth without armature winding, as shown in Fig. 1, is developed based on that of ($8\tau_p=9\tau_s$) in rotating PM motor, and is proven to give almost no-cogging force [2]. In the new structure, each winding slot locates at $\pi/10$ shifted position from its previous slot, and only generates very small $10n$ order harmonic components of cogging force. This structure, although having very small cogging force, still has quite big detent force due to the end forces acting on the left and right end sides.

In this paper, in order to reduce the detent force and maximize the thrust force per mass of a PMLSM at the same time, the new structure of ($9\tau_p=10\tau_s$) is adopted and the shape of the exterior teeth are optimized in Pareto-optimal sense.

II. DESIGN PARAMETERS AND OPTIMIZATION ALGORITHM

A. Design Objectives and Parameters

The model PMLSM is initially designed as shown in Fig. 1 and Table I. The optimization targets are defined as follows:

$$\begin{aligned} \text{Minimize} \quad & \text{Cogging force} & (1-a) \\ \text{Maximize} \quad & \text{Back-emf/Armature mass} & (1-b) \end{aligned}$$

where the cogging force is computed by using nodal force method and back-emf by calculating the flux linkage of arma-

ture winding from the finite element analysis (FEA) results obtained at 34 moving positions of the primary during a pole pitch without applying armature current. The back-emf per mass is approximated as its maximum value.

In order to achieve the design objectives, the three design parameters are defined as shown in Fig. 2, where the parameter R determines the chamfering while X_1 and X_2 total length and mass of the armature core.

B. Optimization Algorithm

The two design objectives *Minimizing cogging force* and *Maximizing Back-emf/Armature mass* are in conflict with each other. For example, the exterior teeth might have enough thickness for minimizing the cogging force but it will decrease the Back-emf/armature mass via increasing armature mass.

In this paper, hence, Pareto-optimization technique is adopted. The fitness value for a design parameter vector, \mathbf{x}_i , is assigned as its corresponding Pareto strength [3].

As an optimization algorithm, $(1+\lambda)$ evolution strategy is employed. At the same time, in order to reduce the computing time required in non-linear FEA for objective function calculation, the two objective functions defined in (1-a) and (1-b) are approximated in design space by using response surface method with radial basis function. In the response surface construction, sampling points are generated by using random Latin hypercube design, and corresponding objective function values are computed through FEA.

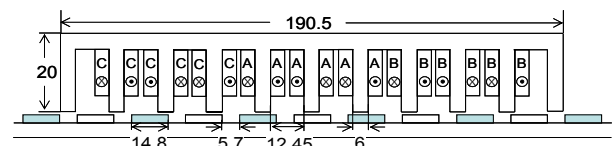
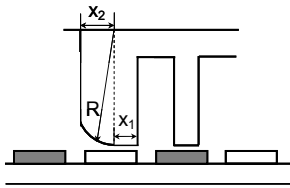


Fig. 1. PMLSM with 9 pole and 10 slot structures.

TABLE I
 SPECIFICATIONS OF 9 POLE 10 SLOT PMLSM

Item	Specification
Thrust force(N)/Detent force(%)	500/± 1.5
Maximum speed (m/s)	3
Speed command error	± 1.5 %
Air-gap(mm)	1.0
Primary	
Ampere-turn/phase	709.4
Lamination(mm)	50
Secondary	
Height(mm)	4.0
Residual magnetic flux density (T)	1.23



Parameter	Specification	
	lower	upper
X_1	0.0	14.0
X_2	4.0	21.0
R	20.0	40.0

Fig. 2. Design parameters.

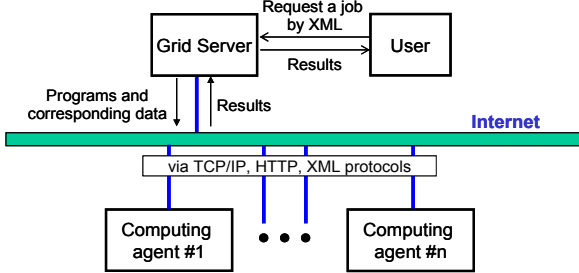


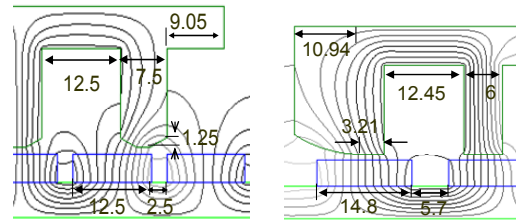
Fig. 3. Architecture of Internet based *sky@home* grid computing framework.

III. GRID COMPUTING BASED ON INTERNET

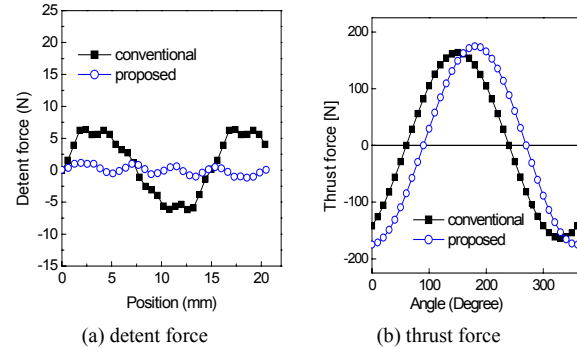
Among the whole process of optimization, most of the computing time is related with non-linear FEA for calculating objective function values. Even when the objective functions are approximated in design space by using response surface method, a lot of computing time should be given to the preparation of the sampling data, i.e. calculation of the objective function values at sampling points. Since the objective function values at sampling points are independent on each other and can be obtained through off-line FEA, the computing time can be dramatically reduced by utilizing grid computing system based on internet.

A grid computing system is generally composed of standardized Internet protocols such as TCP/IP, HTTP based web services, XML, etc. Such protocols have many advantages such as access to a number of computers in Internet, ease of communication, reliability, and firewall friendly. In this paper, the *sky@home* grid framework, which is developed by MEC Korea, Co. Ltd., based on *Korea@home* project [4]-[5], is adopted for the construction of a temporary and dedicated system. In this system, there are, as shown in Fig. 3, three major elements; users which request scheduled job, a server which distributes the job to computing agents according to job scheduling, and computing agents which actually perform assigned job. The user registers a job by sending specific programs and required data to the server. Then the server distributes the job to computing agents, and gathers the calculated results. The overall flow of the grid computing suggested in this paper is summarized as follows:

- Step 1 - Generate sampling points for predefined objective function in design space.
- Step 2 - Request a job by sending FEA, mesh generation programs and all sampling point data to server,
 - Repeat for all sampling points
 - ~ [Server]: to a computing agent, assign a part of job using dynamic load balancing, and send programs and assigned sampling point data



(a) conventional structure (b) proposed structure
Fig. 4. Comparison of the optimized shapes.



(a) detent force (b) thrust force
Fig. 5. Comparison of the performances.

- ~ [Agent]: generate finite element meshes for the sampling points, and calculate the objective function values and return the results to server,
- ~ [Server]: return all computed results to User,

IV. OPTIMIZATION RESULTS AND DISCUSSION

The suggested optimization algorithm is applied to an optimal design of the PMLSM shown in Fig. 1 and Table I. In the optimization, 180 sampling points are generated by using random Latin hypercube design, and 60 personal computers (PC) are employed as computing agent. Each computing agent performs the calculation of objective function values for 3 sampling points i.e., 102 times of non-linear FEA.

Fig. 4 shows a comparison of the optimized shape of the proposed PMLSM with a conventional one having 12 pole and 9 slots. It can be seen that the proposed PMLSM has 11.15(mm) longer armature than the conventional one. Fig. 5 shows the detent and thrust forces of the proposed PMLSM together with those of conventional one. It is shown that the proposed PMLSM gives both smaller detent force and higher thrust force.

V. REFERENCES

- [1] N. Bianchi, S. Bolognani, D. Corte and F. Tonel, "Tubular linear permanent magnet motors: an overall comparison," *IEEE Trans. on Industry Applications*, vol. 39, no. 2, pp. 466-475, March 2003
- [2] S. W.Youn, J.J.Lee, H.S.Yoon, and C.S.Koh, "A new cogging-free permanent-magnet linear motor," *IEEE Trans. on Magn.*, vol. 44, No. 7, pp.1785-1790, July 2008
- [3] K. Deb, *Multi-objective optimization using evolutionary algorithms*, JOHN WILEY & SONS, INC., pp. 261-269, 2004
- [4] MEC Korea, <http://www.meckorea.com>.
- [5] Korea at Home project by Korea Institute of Science and Technology Information, <http://www.koreaathome.org>

End-Effect Equivalent Method for back-EMF of High Speed SPMSM

Ki-Yong Nam¹, Soon-O Kwon², Jeong-Jong Lee², Jung-Pyo Hong²

¹ Department of Power System R&D Center, Samsung Techwin Co., Ltd., Gyeongsangnam-do 641-717, Korea

² Department of Automotive Engineering, Hanyang University, Seoul 133-791, Korea

Soon-o@hanyang.ac.kr, hongjp@hanyang.ac.kr

Abstract — This paper presents the equivalent 2D FEA method for back-EMF of high speed permanent magnet synchronous motor in order to consider a leakage flux in the end region of stator and air-gap. The presented method can be also applied to low speed SPMSM that has a small air-gap length. For the general PMSM having small air-gap provides precise 2D FEA result of back-EMF. However, for the high speed PMSM, due to large air-gap length flux density in the air-gap is not uniform along axis direction. Therefore, 2D FEA does not provide precise analysis results for design. Presented analysis method is applied to the high speed SPMSM using a can, and verified by 3D FEA and experimental results.

I. INTRODUCTION

In maximum torque control of SPMSM, d-axis current will be zero ($i_d=0$) and at that time the electric torque equation is represented by (1). In equation (1), we can know the back-EMF is very important parameter that governs a performance of motor. Therefore, it is important to estimate accurate back-EMF.

$$T_e = \frac{3P}{2} (i_q \times \Lambda_{mf}) \quad (1)$$

where, T_e is electric torque, i_q is q-axis current, P is number of pole, and Λ_{mf} is back-EMF constant for peak of phase voltage per mechanical angular velocity. Generally, SPMSM has small air-gap length, therefore, leakage flux in the end of stator is small, and therefore, there is no problem with back-EMF analysis result. However, a can should be used for the high speed SPMSM, and this leads to the increase magnetic air-gap length and increased leakage flux in the rotor and stator end region [1]-[2]. In addition, for the margin of rotor dynamic, high speed motor generally has short axial length. Therefore, the effect in the stator end region becomes significant. And, the back-EMF analysis results by 2D FEA have significant difference with experiments from 10% to 3%. It is obvious that the 3D FEA provides more precise result. However, modeling and computation are expensive. Therefore, this paper presents the 2D equivalent analysis methods.

II. MODEL AND ANALYSIS METHOD

A. Limitations of 2D FEA Model with Large Air-gap

Fig. 1 shows the 2D FEA model of high speed SPMSM having relatively large air-gap comparing to low speed SPMSM. For the analysis of 2D FEA, it is assumed that the analysis model has symmetric along axial direction with



Fig. 1. 2D FEA model of high-speed motor with can

symmetric flux distribution. However, due to axial leakage flux, 2D FEA results shows higher back-EMF comparing to experiments.

B. Equivalent 2D FEA Model and Assumption

Fig. 2(a) shows a equivalent 2D FEA model corresponding to 2D FEA model, and derating coefficient of back-EMF is calculated by equivalent 2D FEA. In the Fig. 2(a), L is the stack length of stator and R is outer radius of rotor.

For the equivalent 2D FEA, following assumptions are made.

Firstly, the flux in tooth and yoke is not saturated. In general motor design, flux in tooth and yoke is designed to be not saturated. Therefore, the first assumption is reasonable. Secondly, there is linear relation between flux density on a surface of teeth in 2D FEA model and equivalent 2D FEA model. The second assumption is reasonable by the first assumption. In equivalent 2D FEA model, to block flux saturation on teeth and yoke, and to prevent leakage flux that can go to yoke directly, length of teeth, width of yoke and length to yoke from end of permanent magnet is modeled by $3R$, L and $2L$ for each other.

Fig. 2(b) shows definition for line regions of $(slot\ length)/2$ and $(surface\ of\ teeth)$. Line regions have the length that is equal to stack length of stator and y-axis position that is equal to length from zero point to half of slot length by radial direction and length from zero point to teeth for each other.

$$EMF_{derating} = \frac{B_{avg}|_{(slot_length)/2}}{B_{peak}|_{(surface_of_teeth)}} \quad (2)$$

$$EMF_{final} = EMF_{derating} \times EMF_{2d-FEM} \quad (3)$$

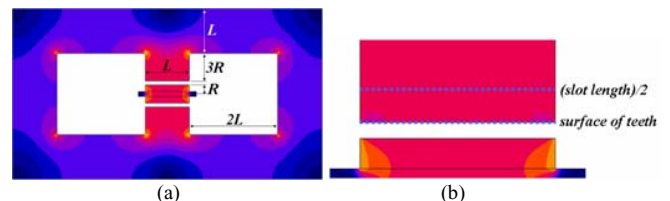


Fig. 2. (a) Equivalent 2D-FEM Model, (b) Definition of line region for $(surface\ of\ teeth)$ and $(slot\ length)/2$

The derating coefficient of back-EMF by equivalent 2D FEA is represented by (2), and final estimated back-EMF is represented by (3). $EMF_{derating}$ is derating coefficient of back-EMF, $B_{avg}|_{(slot\ length)/2}$ is the average flux density at $(slot\ length)/2$ line region, $B_{peak}|_{(surface\ of\ teeth)}$ is the peak flux density at $(surface\ of\ teeth)$ line region, and EMF_{final} is final estimated back-EMF by 2D FEA and equivalent 2D FEA.

Fig. 3 shows flux density distribution at $(surface\ of\ teeth)$ line region. When $B_{peak}|_{(surface\ of\ teeth)}$ is selected, flux density at $(surface\ of\ teeth)$ should be saturated and has constant value at center of teeth by axis direction. If flux density is not saturated around center of teeth, stack length of stator(L) of equivalent 2D FEA model could be modified to be longer more than actual stack length of stator to get more precise result.

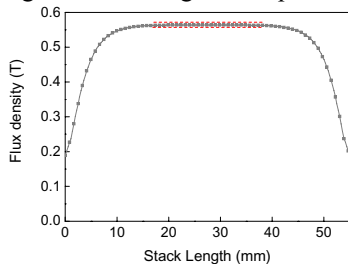


Fig. 3. Definition of saturation flux density on surface of teeth (red line)

C. Analysis Model

Fig. 4 and Table I show the cross-section and brief specifications of the analysis model-1.

Fig. 5 and Table II show the cross-section and brief specifications of the analysis model-2. Especially, permanent magnet of model-2 is buried in magnetic shaft so that flux leakage and drop of back-EMF is larger.

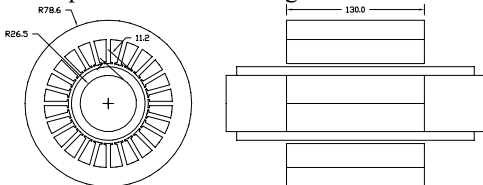


Fig. 4. Cross-section view of analysis model-1

TABLE I
BRIEF SPECIFICATIONS OF ANALYSIS MODEL-1

Item	Value	Item	Value
Pole number	2	Magnet Br (T)	1.084 @ 20 °C
Slot number	24	Recoil Perm.	1.077
Stator outer rad. (mm)	78.6	PM direction	Parallel
Magnetic Air-gap (mm)	11.2	Stack length (mm)	130

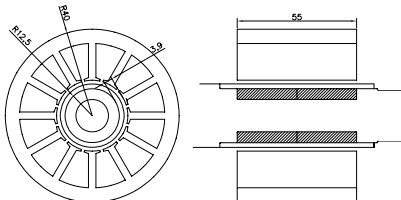


Fig. 5. Cross-section view of analysis model-2

TABLE II
BRIEF SPECIFICATIONS OF ANALYSIS MODEL-2

Item	Value	Item	Value
Pole number	2	Magnet Br (T)	1.100 @ 20 °C
Slot number	12	Recoil Perm.	1.077
Stator outer rad. (mm)	40	PM direction	Parallel
Magnetic Air-gap (mm)	3.9	Stack length (mm)	55

III. RESULT AND DISCUSSIONS

Fig. 6(a) and Fig. 7(a) show the comparison of back-EMF of model-1 calculated by 2D FEA, corrected by equivalent 2D FEA, and measured or 3D FEA back-EMF waveform for each analysis model-1 and model-2. And Fig. 6(b) and Fig. 7(b) show the flux density distribution of equivalent 2D FEA at the position of $(slot\ length)/2$ and $(surface\ of\ teeth)$ along axis for each analysis model-1 and model-2.

Table III shows result of back-EMF peak by 2D FEA, corrected by equivalent 2D FEA, and measured or 3D FEA back-EMF waveform, and error of corrected back-EMF by experimentally measured or 3D FEA.

TABLE III
BRIEF SPECIFICATIONS OF ANALYSIS MODEL-2

Analysis Model	2D FEA	Equivalent 2D FEA	Experimental	3D FEA	Error
Model-1	242.77V	234.52V	233.29V	-	0.5%
Model-2	192.67V	175.52V	-	176.43V	0.5%

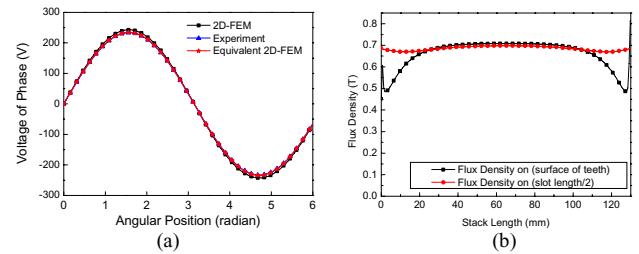


Fig. 6. (a) back-EMF, (b) flux density each line region

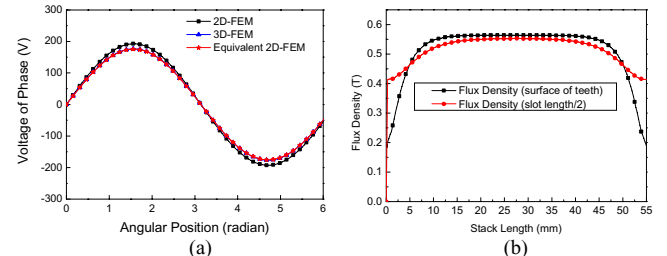


Fig. 7. (a) back-EMF, (b) flux density each line region

IV. CONCLUSION

High speed SPMSM with large magnetic air-gap has flux leakage more than low speed SPMSM in air-gap and stator because of can and larger mechanical air-gap for reducing eddy current loss in can and core loss of stator.

In this paper, correction method of back-EMF is suggested by equivalent 2D FEA, and that is verified by experimental measurement or 3D FEA. And the result of suggested method is very precise with 0.5% error comparing to experimental measurement or 3D FEA.

V. REFERENCES

- [1] Iroshi Murakami, Yukio Honda, Hiroyuki Kiriyama, Shigeo Morimoto, Yoji Takeda, "The Performance Comparison of SPMSM, IPMSM and SynRM in Use as Air-conditioning Compressor", *Industry Applications Conference*, vol. 2, Oct. 1999, pp. 3-7
- [2] J. F. Eastham, M. J. Balchin, P. C. Coles "Full-Scale Testing of a High Speed Linear Synchronous Motor and Calculation of End-Effect.", *IEEE Trans. on magnetics*, vol. 24, no. 6, November, 1988.

A performance model of an induction motor for transient simulation with a PWM drive

Derek N. Dyck, Geoff Gilbert, and David A. Lowther
 Infolytica Corporation
 300 Leo Pariseau, Suite 2222, H2X 4B3, Canada
 derek@infolytica.com

Abstract—The goal of this paper is the simulation of an induction motor driven with a PWM three phase bridge. The approach taken here decouples the circuit simulation from the electromagnetic field simulation by first constructing a performance model of the machine using 2d finite element analysis. The model consists of the complete matrix of the self- and mutual inductances of the stator windings and each of the rotor bars. Skew is taken into account by a correction applied to the winding-bar inductance entries in the matrix.

I. INTRODUCTION

Induction motor design has more than a century of history, but recently a new approach has become necessary. The advent of inexpensive power electronics allows complete control over the synchronous frequency and phase voltage, which gives better performance for variable speed drives but also gives rise to new design challenges. Understanding the design trade-offs requires a multiphysics approach with cosimulation of the electromagnetic and circuit physics. However, the time scale is different for these two domains: the motor rotates at speeds on the order of 10-100 Hz, whereas the PWM bridge usually switches at frequencies on the order of 10-100 kHz. A time-stepping finite element analysis coupled to the circuit equations [1,2] has a prohibitive computational cost if the time step is small enough to capture the switching waveform, since it requires on the order of 10000 time steps to simulate even one revolution of the rotor. This cost is exacerbated if skew is present in the stator or rotor since this requires either the simultaneous solution of several 2d slices [3] or a 3d approach [4] which would be intractable. A 2d unskewed time-stepping approach with coupled circuit equations to a PWM three-phase bridge is presented in [5] and [6], but in both cases the authors do not give the switching frequency or the computational cost of the method.

The alternative is to decouple the electromagnetic and circuit equations. This necessitates a two step process, where the first step is to use finite element analysis (either 2d or 3d) to create a performance model of the motor, after which a time-stepping simulation of the circuit coupled to the performance model is performed in a second step. The conventional equivalent circuit model is not suitable for the performance model, since it treats each phase independently, whereas in reality there is significant coupling between the phases. One successful approach [7-9] uses a D-Q model for the rotor. A similar approach [10] uses an impedance matrix model for the stator coupled with a harmonic decomposition of the rotor currents. A more detailed comparison of these methods is given in [11].

II. METHOD

The approach introduced here uses finite element analysis to create a full impedance matrix model of the motor including the mutual inductances between rotor bars and also between stator windings and rotor bars. This is in contrast to [10] which uses the impedance matrix only for the stator windings.

A. Motor performance model

The full motor impedance matrix can be decomposed into three inductance matrices and two resistance matrices. In the following, a subscript capital ‘‘A’’ refers to the stator windings, while a lowercase ‘‘a’’ refers to the rotor bars. The three inductance matrices are: L_{AA} , a 3×3 matrix of the mutual inductances between stator windings, L_{aa} , a $N_{\text{bar}} \times N_{\text{bar}}$ matrix of mutual inductances between rotor bars, and L_{aA} , a $3 \times N_{\text{bar}}$ matrix of mutual inductances between stator windings and rotor bars. The two resistance matrices are: R_A , a 3×3 diagonal matrix of the resistances of each stator winding, and R_a , an $N_{\text{bar}} \times N_{\text{bar}}$ matrix of rotor resistances. We also use $L_{aA} = L_{AA}^T$, and note that this matrix is actually a function of the rotor position. Also note that the skin-effects due to the PWM will not be taken into account in this model, since it assumes that the current distribution in the rotor bars is fixed.

B. State equations

Given the inductance and resistance matrices, the state equations for the stator and rotor are:

$$V_A = R_A \cdot I_A + L_{AA} \cdot dI_A/dt + L_{aA} \cdot dI_a/dt + dL_{aA}/dt \cdot I_a \quad (1)$$

$$0 = R_a \cdot I_a + L_{aa} \cdot dI_a/dt + L_{aA} \cdot dI_A/dt + dL_{aA}/dt \cdot I_A \quad (2)$$

where I_A is the vector of stator winding currents, I_a is the vector of rotor bar currents, and V_A is the vector of stator winding voltages. Solving the second equation for dI_a/dt gives:

$$dI_a/dt = -L_{aa}^{-1} (R_a \cdot I_a + L_{aA} \cdot dI_A/dt + dL_{aA}/dt \cdot I_A) \quad (3)$$

Substituting this into the first equation and collecting factors of the current terms gives:

$$V_A = (R_A - L_{aA} \cdot L_{aa}^{-1} \cdot dL_{aA}/dt) \cdot I_A + (dL_{aA}/dt - L_{aA} \cdot L_{aa}^{-1} \cdot R_a) \cdot I_a + (L_{AA} - L_{aA} \cdot L_{aa}^{-1} \cdot L_{aA}) \cdot dI_A/dt \quad (4)$$

Equation (4) can be solved for dI_A/dt in conjunction with the circuit equations of the three-phase PWM bridge.

C. Matrix Structure

The physics of the induction motor imply that there are far fewer unknowns in the model than the number of matrix entries. This section gives the detailed structure of each

matrix, which allows it to be represented more economically and, more importantly, determined more accurately.

A. Stator matrices

Assuming a balanced symmetric three-phase winding, the stator inductance matrix L_{AA} has only two independent values, the self-inductance and the mutual inductance between any two stator phases. The stator resistance matrix R_{AA} is diagonal with only one independent value.

B. Rotor matrices

By symmetry, and ignoring the effect of stator slots, the rotor bar-bar inductance matrix L_{aa} is a symmetric Toeplitz matrix, which means it has only $N_{bars}/2+1$ independent values. Solving the state equations requires the inverse of L_{aa} , which is also Toeplitz and symmetric, and can be precomputed before the circuit simulation. The rotor resistance matrix is tridiagonal (the off-diagonal terms are due to end-ring resistance).

C. Stator-rotor matrix

The mutual inductance matrix between stator winding and rotor bars is position dependent, but the entire matrix can be represented by a function of the angle between the stator winding and the rotor bar. Since this function is even and periodic, a Fourier cosine series can be used to represent it.

III. DETERMINATION OF MATRIX VALUES

The matrix values are determined using a least squares fit to three time-harmonic finite element solutions. The first solution is at the rated voltage and slip, and is quasi-nonlinear in that permeabilities are taken from the material B-H curve at the RMS field values. The permeabilities are frozen for the other two solutions, the first of which excites one stator winding, the second excites one rotor bar.

IV. RESULTS AND CONCLUSION

This model was validated by comparison to a time-stepping transient simulation of a 12 slot, 13 bar, 4 pole induction motor at 1000 rpm and driven with sinusoidal voltages. Comparison of the rotor bar currents (Fig. 1) shows that the model agrees well with the time-stepping simulation and also shows that it captures effects which are not present in the simpler D-Q models (the ripple on the bar currents). It should be noted that each time step of the circuit simulation requires several matrix multiplies, however the entire simulation including the FE solves for parameter estimation is more than 100 times faster than the time-stepping transient FE simulation. Finally, Fig. 2 shows the waveforms from a simulation with a PWM three-phase bridge. In conclusion it can be said that this model has been demonstrated to be accurate and compatible with a circuit simulator.

REFERENCES

- [1] Preston, T.W., Reece, A.B.J. & Sangha, P.S., "Induction motor analysis by time-stepping techniques", *IEEE Transactions on Magnetics*, vol. 24, no. 1, January 1988, pp. 471 - 474.

- [2] Arkko, A., Time-stepping finite element analysis of induction motors, *Proceedings of International Conference on Electrical Machines (ICEM 88)*, Pisa, Italy, September 12-14, 1988, pp. 275 - 280.
- [3] Ho, S.L., Fu, W.N., Wong, H.C., "Direct modeling of starting process of skewed induction motors using a multi-slice technique," *IEEE Trans. on Energy Conversion*, vol. 14, no. 4, Dec 1999 pp. 1253 - 1258.
- [4] D. N. Dyck, B. Forghani, C. S. Brett, J. P. Webb, D. A. Lowther, "A T-Omega Finite Element Method for Arbitrary Motion in 3D," *Proceedings of COMPUMAG 2005*, Shenyang, China, June 26-30, 2005.
- [5] Ho, S.L. Shiyong Yang Rahman, M. Wong, H.C., "Transient analysis of PWM inverter-fed AC motor drives using finite element method coupling with external circuit model," *Proceedings of the IEEE International Conference on Power Electronics and Drive Systems 1999 (PEDS '99)*, vol. 2, pp. 591-596.
- [6] Jeong-Jong Lee, Hyuk Nam, Young-Kyon Kim, Jung-Pyo Hong, Don-Ha Hwang, "Finite element analysis of 3-phase induction motor with PWM inverter," *Sixth International Conference on Electrical Machines and Systems, 2003 (ICEMS 2003)*, vol. 2, pp. 744- 746.
- [7] Dolinar, D., De Weerd, R., Belmans, R., Freeman, E.M., "Calculation of two-axis induction motor model parameters using finite elements," *IEEE Transactions on Energy Conversion*, vol. 12, no. 2, pp. 133 - 142.
- [8] Do-Wan Kim, Hyun-Kyo Jung, Song-Yop Hahn, "Equivalent circuit modeling for transient analysis of induction nmotors with three dimensional finite element analysis," *Intl. Conference on Electric Machines and Drives, 1999. (IEMD '99)*, May 1999, pp. 201-203.
- [9] Alberti, L., Bianchi, N., Bolognani, S., "Finite element modeling of induction motor for variable speed drives," *18th International Conference on Electrical Machines, 2008 (ICEM 2008)*, 6-9 Sept. 2008, pp. 1-5.
- [10] Williamson, S., Begg, M., "Analysis of cage induction motors - A combined fields and circuits approach," *IEEE Transactions on Magnetics*, vol. 21, no. 6, pp. 2396 - 2399
- [11] Knight, A.M., "A comparison of time stepped finite element modelling methods for induction motor analysis," *International Conference on Power Electronics, Machines and Drives, 4-7 June 2002* pp. 375 - 380.

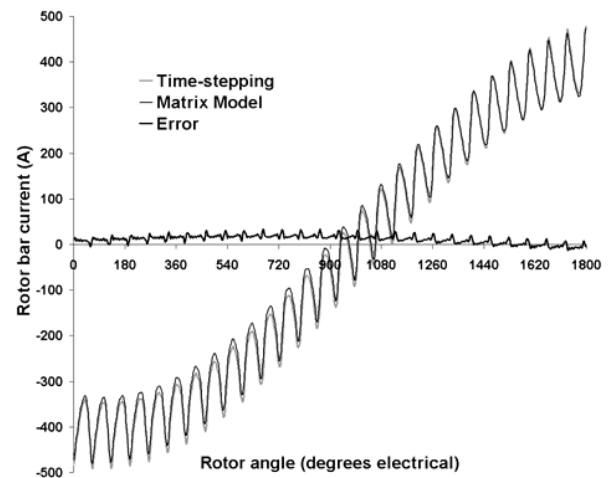


Figure 1 – Comparison with conventional method showing the current in one rotor bar over 5 periods under sinusoidal excitation.

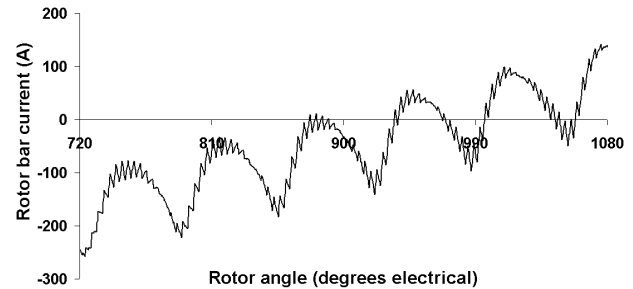


Figure 2 - Current in same bar over 3 periods under PWM excitation

Design of a Dual-Rotor Dual-Output Radial-Flux Motor for Variable Speed Air Conditioners

Min-Fu Hsieh¹, Yu-Han Yeh¹, D. G. Dorrell², and Samsul Ekram¹

¹Department of Systems and Naval Mechatronic Engineering, National Cheng Kung University, Tainan, Taiwan

²Faculty of Engineering, University of Technology, Sydney, Australia

Abstract—This paper presents the design, analysis and test of a dual-rotor, dual-output-shaft, radial-flux, PM BLDC motor. In conventional air conditioners, two motors are usually used to drive the condenser and evaporator. This paper develops a motor with two rotors and two shaft outputs as an alternative. The motor has an inner and outer rotor with a stator in between which is toroidally-wound (such that the two rotors are synchronous). The power sharing on the two rotors is designed to meet the requirement of the condenser and evaporator. Finite element analysis (FEA) is employed to verify the design. A prototype is made and tested for performance evaluation. Surface (radial) windings for individual rotors to achieve asynchronous rotation between the rotors are also investigated using FEA.

I. INTRODUCTION

Some applications, such as the condenser and evaporator drives in an air conditioner, require two electric motors of different speeds and power ratings in the same unit for high efficiency operation. The power rating of the evaporator motor is less than that of the condenser motor. Usually, two independent motors of appropriate ratings are used. Alternatively, one motor with two side shaft outputs can be utilized although it may not meet the requirement for the different power ratings and cause low system efficiency.

This paper aims to develop a radial-flux PM brushless DC motor with dual rotors, dual air-gaps and two output shafts to fit the demand of air conditioners, as illustrated in Fig. 1(a). Dual rotor induction machines were first reported by Kelly [1]. Qu and Lipo [2-3] discussed dual-rotor, radial-flux, toroidally-wound PM machines. However, the machine combined the two rotors to form a joint shaft output. The characteristics of the individual rotors were not discussed and it is not suitable for the application here. Some comparative analyses for dual-air-gap radial-flux machines and axial-flux machines were described in [4-6]. Both types of machines were designed to produce a joint shaft output.

In this paper, the individual specifications of the inner and outer rotors are first determined from the load requirement of the condenser and evaporator in an air conditioner. With a toroidally-wound stator [2], the two rotors are designed to satisfy the two output power ratings. Hence, this configuration has a different design principle from that presented in [2-3]. It only has one control and allows the two rotors to run only at the same synchronous speed. To explore the feasibility of operating the two rotors asynchronously, the stator can be radially-wound in slots with two independent winding sets, as shown in Fig. 1 (b). In this paper, FEA is conducted to verify the design and a prototype machine is fabricated. Experiments are carried out to evaluate the machine performance.

II. MACHINE SPECIFICATIONS AND DESIGN

The dual-shaft (dual-rotor), radial-flux, permanent-magnet (DSRFPM) machine has a power sharing ratio for the rotors of 62.5 % and 37.5 %. This is obtained from a total power rating of 80 W, as indicated in Table I. This specification was derived from the test data of an air conditioner manufacturer. At a speed of 1150 rpm, the two rotors should be able to separately offer 50 W and 30 W at 35 V. The outer rotor, with a larger diameter, is more suitable as the larger condenser drive while the inner one is used as the evaporator drive. When designing the DSRFPM motor, the output characteristics of both rotors can be regulated by other parameters such as magnet length, etc., to meet the specification (Table I).

Some air conditioners may require the evaporator to operate with variable speed. For the present study, the evaporator is set to run at 1150 rpm, 950 rpm and 850 rpm while the condenser remains at 1150 rpm.

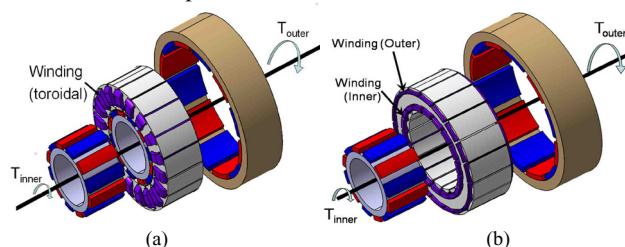


Fig. 1. DSRFPM motor with (a) toroidal and (b) radial windings.

TABLE I
DSRFPM MOTOR SPECIFICATIONS

Parameter	Value	Parameter	Value
Rated voltage [V]	35	Overall rated power [W]	80
Outer rotor power [W]	50	Inner rotor power [W]	30
Rated speed [rpm] (cond.)	1150	Rated torque [N-m] (cond.)	0.415
Rated speed [rpm] (evap.)	1150 (regulable to 950, 850)	Rated torque [N-m] (evap.)	0.249
Magnet (NdFeB)	Br = 1.243 T; Hcb = 943kA/m; Hcj = 1469kA/m		

The stator has 18 slots while each rotor has 12 poles. The effective length for both rotors is the same but the diameters are different. The torque of a motor can be expressed as:

$$T = kD^2L \quad (1)$$

where k is a constant for the electric and magnetic loadings, D is the diameter of the rotor/air-gap, and L is the motor stack length. The ratio of the inner diameter to the outer diameter (D_i/D_o ratio) can roughly determine the load sharing characteristics for the two rotors. An appropriate selection of the length-to-diameter ratio (L/D ratio) allows the motor to be compact, hence increasing power density. The main dimensions of the design results are shown in Table II.

TABLE II
DESIGN RESULTS FOR DSRFPM MOTOR

Parameter	Value	Parameter	Value
Outer rotor diameter [mm]	79.9	Air-gap length [mm]	0.67
Inner rotor diameter [mm]	46.7	Magnetic length [mm]	3
Stack length [mm]	25.6	Air-gap Flux density [T]	0.92

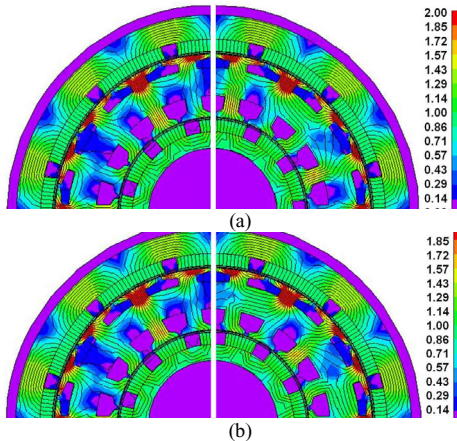


Fig. 2. Asynchronous flux distributions for two different relative rotor positions at: (a) 1150 rpm/950 rpm and (b) 1150 rpm/850 rpm

III. FINITE ELEMENT ANALYSIS

FEA is used to verify the design. The toroidally-wound arrangement (which has synchronous-speed rotors) was studied but is omitted in this digest. For the radially-wound stator (Fig. 1), the speeds of the inner and outer rotors can be asynchronous. Example flux distributions are given in Figs. 2(a) and (b) (1150 rpm outer - 950 rpm inner; 1150 rpm outer - 850 rpm inner); they show some flux interaction which varies with the relative position of the two rotors and their position with respect to the stator. Nevertheless, the flux linkage from the other side of the stator will still contribute to torque production with a noticeable but minor effect. In Fig. 3, the air-gap flux density for individual rotors at the three speed ratios is not significantly affected by the asynchronous speeds between the two rotors. Another simulation (result not presented here) also reveals that the peak flux linkage in any phase of the inner stator for the 1150 rpm - 850 rpm case drops by only about 10 % compared to the synchronous case. The performance drop seems acceptable when compared to the advantages gained from the machine configuration. This indicates that it is feasible to utilize radial windings in the DSRFPM machine for asynchronous operation. The complete simulation results will be presented in the final manuscript.

The DSRFPM design was fabricated (Fig. 4) and tested to verify the design and FEA analysis. The verification proved successful. Detailed findings are omitted here; however, the synchronous operation of the rotors over a speed range is shown in Fig. 5, where the test power sharing matches that of the design. Also, the efficiency for both rotors is around 85 %.

IV. CONCLUSION

A dual rotor, dual output shaft, radial flux, permanent magnet brushless DC motor has been developed for a variable-speed air conditioner. The two rotors have been designed to meet the requirement for the condenser and evaporator under

the machine configuration. FEA and experiments were carried out to verify the design. The design successfully achieved the requirement. Also, from the simulation, the performance drop due to flux interaction between the two rotors during asynchronous operation was found to be acceptable. From the results presented in this paper, a cost-competitive high-power-density motor design, suitable for use in an air conditioner application, has been achieved.

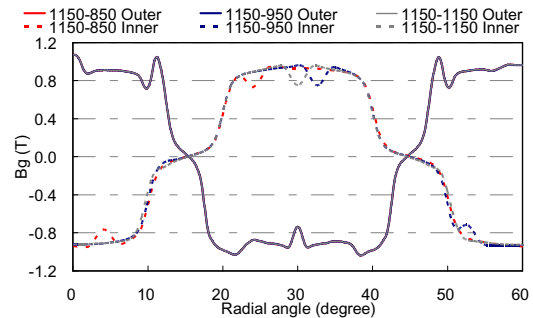


Fig. 3. Air-gap flux density for the two rotors at different speed ratios

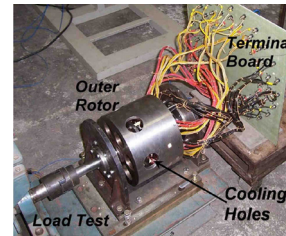


Fig. 4. Motor prototype

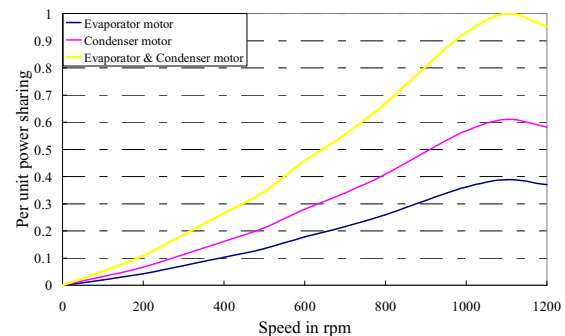


Fig. 5. Measured load sharing of inner and outer rotor at different speed (based on the measured overall output power 76.7 W)

REFERENCES

- [1] D. H. Kelly, "Double-rotor induction motor," *IEEE Trans. Power Apparatus and Systems*, vol. PAS-88, no.7, pp. 1086-1092, July 1969.
- [2] R. Qu and T. A. Lipo, "Dual-rotor, radial-flux, Toroidally wound, permanent-magnet machines", *IEEE Trans. IA*, Vol. 39, No.6, 2003.
- [3] R. Qu, and T. A. Lipo, "Design and parameter effect analysis of dual-rotor, radial-flux, toroidally wound, permanent-magnet machines," *IEEE Trans. Indus. Appl.*, vol. 40, no.3, pp.771-779, 2004.
- [4] Qu, R., M. Aydin and T.A.Lipo, "Performance comparison of dual-rotor radial-flux and axial-flux permanent-magnet BLDC machines" *IEEE IEMDC Conference*, Madison, WI, pp. 1948-1954, June 1-4, 2003.
- [5] K. Sitapati and R. Krishnan, "Performance comparisons of radial and axial field, permanent-magnet, brushless machines", *IEEE Trans. Indus. Appl.*, vol. 37, no. 5, pp. 1219-1226, 2001.
- [6] N. B. Simsie and H. B. Ertan, "A comparison of torque capabilities of axial flux and radial flux type of brushless DC (BLDC) drives for wide speed range applications", *IEEE International Conference on Power Electronics and Drive Systems*, PEDS'99, Hong Kong, July 1999.

Vibration Synthesis for Electrical Machines based on Force Response Superposition

Matthias Boesing, Timo Schoenen, Knut A. Kasper and Rik W. De Doncker
Institute for Power Electronics and Electrical Drives of RWTH Aachen University
Jaegerstr. 17/19, 52066 Aachen, Germany bs@isea.rwth-aachen.de

Abstract—An approach for synthesizing electromagnetically excited vibrations in electrical machines is presented. The structural vibration responses for a machine’s generic set of force excitation shapes are calculated. They are scaled by the operating point dependent force excitation amplitudes and superposed. This leads to a computationally efficient process. It allows to use complex structural 3D models and to synthesize the vibrations in the entire operating range of the machine. Furthermore, the influence of different control strategies on the vibration characteristics can be investigated. As a first result, measured and synthesized vibration spectrograms of a run-up test on a traction motor are presented.

I. INTRODUCTION

For electric or hybrid electric vehicles low acoustic emissions of the electric traction motor are required. The acoustic characterization of the machine needs to be efficiently integrated into the design process. This addresses machine designer (machine configuration, force shapes), control engineer (operating point dependent currents) and mechanical design engineer (housing, mounting).

The approach presented here can be summarized as follows: In a first step, the force excitation for the entire operating range of a machine is calculated using 2D electromagnetic FEM. The vibration responses for the machine’s generic force excitation shapes are calculated in a second step by 3D structural FEM for the entire frequency range. Operating point dependent machine vibrations are subsequently found by superposing the vibration responses scaled by the operating dependent force excitation. The high computational costs that typically limit 3D models to selected frequencies as pointed out in [1] can be overcome with the presented approach. Simulated and measured run-up spectrograms are a first result and underline the validity of this approach. The electromagnetic noise components inherent to the machine design [2] are considered. Switching frequency harmonics are currently not included. The force decomposition and vibration synthesis is performed using MATLAB. ANSYS is used for solving the electromagnetic and structural FE models. SolidWorks is used for CAD data handling.

II. ELECTROMAGNETIC FORCE EXCITATION

The investigation is based on a 15 kW interior permanent magnet synchronous machine (IPMSM) for a hybrid electric vehicle. The outer diameter is 30 cm and the stack length 7.5 cm. It is a 3 phase machine with 10 pole pairs, 24 stator slots and $q = 0.4$ slots per pole per phase.

IPMSM for traction applications are typically current controlled in terms of d- and q-axis currents (i_d, i_q) [3]. The force excitation has been calculated for the entire i_d/i_q range. It is mapped to the torque T and speed n range as defined a control strategy. The effect of different control strategies will be investigated.

The electromagnetic simulations here are performed statically using non-linear 2D FE models of a symmetry section of the machine. The force distribution $f_{d,M}(\alpha)$ in N/m along the airgap is described by the superposition of excitation modes m up to the M^{th} spatial component as

$$f_{d,M}(\alpha) = \sum_{m=0}^M (a_{d,m}(t) \cdot \cos(m\alpha) + b_{d,m}(t) \sin(m\alpha)), \quad (1)$$

where α is the angle of a location in the airgap. Index d denotes the direction, i.e. radial ('r') or tangential ('t'). Skewed machines are going to be investigated in a next step.

The time dependent amplitude factors $a_{d,m}(t)$ and $b_{d,m}(t)$ are decomposed into their complex frequency components [4].

$$a_{d,m}(t) \circ \bullet A_{d,m}(f) \quad \text{and} \quad b_{d,m}(t) \circ \bullet B_{d,m}(f) \quad (2)$$

Displaying $A_{d,m}$ and $B_{d,m}$ over the i_d/i_q or T/n range allows to judge and compare the force excitation characteristics of a machine as will be shown in the full paper.

Due to the magnetic configuration of the machine in this study, the frequency components of all modes are multiples of $20f_{\text{mech}}$. The circumferential orders of the two dominant excitation modes are 0 and 4. Mode 0 has frequency components at $60, 120, \dots f_{\text{mech}}$ while those for mode 4 are at $20, 40, 80, 100, \dots f_{\text{mech}}$ with f_{mech} being the shaft speed in Hz.

III. STRUCTURAL VIBRATION RESPONSE

The 3D structural model is built directly from the machine assembly’s CAD drawing. Non-critical structural details are eliminated to decrease the model size. In this study, the model consists of the machine stator in a test bench housing which is flange mounted to a test bench.

Harmonic analyses based on the modal superposition method using force excitations $\mathbf{F}_{\text{unit},k}$ are performed. $\mathbf{F}_{\text{unit},k}$ represents a force excitation with a unit amplitude of 1 N and a spatial distribution associated with one particular $A_{d,m}$ or $B_{d,m}$.

$$\mathbf{v}_{\text{unit},k}(f) = \mathbf{H}(f) \cdot \mathbf{F}_{\text{unit},k} \quad (3)$$

where $\mathbf{H}(f)$ is the general structural transfer function and $\mathbf{v}_{\text{unit},k}(f)$ the resulting surface vibration for one spatial force excitation shape with unit amplitude.

IV. VIBRATION SYNTHESIS

For synthesizing the machine vibration $\mathbf{v}(f)$ at a frequency f for a particular operating point, the K unit force velocity responses $\mathbf{v}_{\text{unit},k}(f)$ from (3) are superposed with the complex amplitudes $F_k(f)$ of force excitation modes k as weighting factors for this particular operation point,

$$\mathbf{v}(f) = \sum_{k=1}^K \mathbf{v}_{\text{unit},k}(f) \cdot F_k(f). \quad (4)$$

$F_k(f)$ represents an $A_{d,m}(f)$ or $B_{d,m}(f)$ from (2).

Superposing the force contributions leads to low computational costs for the full frequency range 3D structural simulations (6 h in total on a 2 GHz Intel Core 2 PC with 3 GB of RAM for a 44405 element model and 345 frequency points). The superposition can be performed within seconds.

The interface between electromagnetic force excitation and structural dynamic response on the basis of force excitation shapes is very flexible. Any type of model (FE, analytical, etc.) and simulation (2D or 3D, static or transient, etc.) can be used. For example, an analytical force calculation may be used as in [5] for an induction machine.

V. RESULTS

Using the above presented process of force excitation calculation, structural dynamic response calculation and vibration synthesis, a run-up spectrogram is synthesized as shown in Fig. 1. The force excitation uses mode 0 at 60 and $120f_{\text{mech}}$ and mode 4 at 20, 40, 80 and $100f_{\text{mech}}$ with radial and tangential components. The simulated spectrogram is compared to a measured spectrogram of this run-up in Fig. 2. For the sake of comparability, higher electromagnetic frequency components, low frequency mechanical noise components and switching frequency harmonics are filtered from the measurement. Both figures use the same dB-scale on the color-axis. The vibration was measured at 4 sensor positions along the circumference of the housing, evaluated as the power sum of these signals and synthesized accordingly.

The simulated and measured spectrograms match well, in particular in terms of the amplitudes of the simulated vibration. The simulated eigenfrequencies tend to be higher than the measured ones which is attributed to a too high stiffness for the stator and the neglected winding mass in the simulation. Structural tests (i.e. an experimental modal analysis [6]) or a detailed analysis of material parameters (e.g. for laminations [7] and windings; damping ratios) have not been performed on the model. This data would further improve the results.

VI. CONCLUSION

A modular and universal approach for simulating electrical machine vibrations is presented and validated. The given results show that the vibration characteristics of a machine can be synthesized without any measurement input, only based

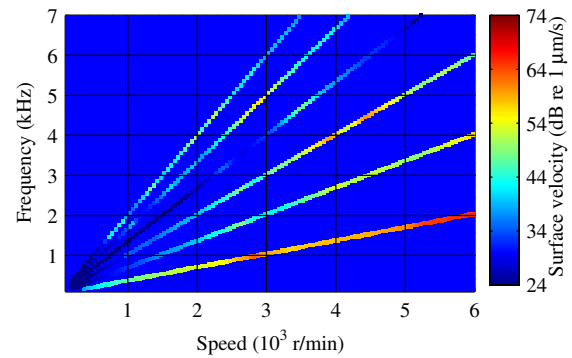


Fig. 1. Spectrogram of synthesized surface vibration for run-up from 0 to 6000 r/min

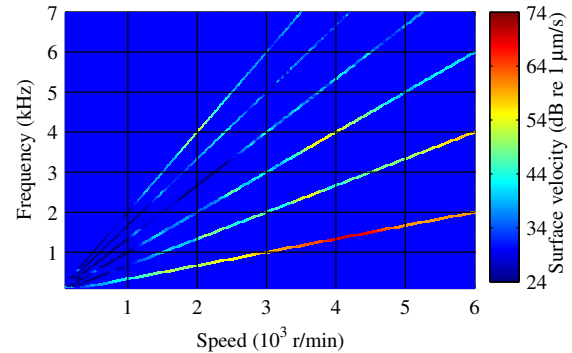


Fig. 2. Spectrogram of measured surface vibration for run-up from 0 to 6000 r/min

on machine configuration, control strategy and engineering drawings. The approach presented here can easily be applied to other electrical machines or vibrating structures in general. Skew or eccentricity effects as well as mechanical vibrations and switching harmonics can be included. Further details and results will be given in the full paper.

REFERENCES

- [1] M. van der Giet, C. Schlensok, B. Schmulling, and K. Hameyer, "Comparison of 2-D and 3-D coupled electromagnetic and structure-dynamic simulation of electrical machines," *IEEE Transactions on Magnetics*, vol. 44, no. 6, pp. 1594–1597, Jun. 2008.
- [2] J. F. Gieras, C. Wang, and J. C. Lai, *Noise of Polyphase Electric Motors*. Taylor and Francis Group, 2006.
- [3] B.-H. Bae, N. Patel, S. Schulz, and S.-K. Sul, "New field weakening technique for high saliency interior permanent magnet motor," in *Conference Record of the Industry Applications Conference, 38th IAS Annual Meeting*, vol. 2, October 2003, pp. 898–905.
- [4] M. Boesing, K. Kasper, and R. De Doncker, "Vibration excitation in an electric traction motor for a hybrid electric vehicle," in *INTER-NOISE 2008, the 37th International Congress and Exposition on Noise Control Engineering*, Shanghai, China, November 2008.
- [5] J. Le Besnerais, V. Lanfranchi, M. Hecquet, G. Lemaire, E. Augis, and P. Brochet, "Characterization and reduction of magnetic noise due to saturation in induction machines," *IEEE Transactions on Magnetics*, vol. 45, no. 4, pp. 2003–2008, Apr. 2009.
- [6] D. J. Ewins, *Basic and state-of-the-art modal testing*. Sādhanā - Academy Proceedings in Engineering and Sciences, Indian Academy of Science, 2000, vol. 25, no. 3.
- [7] Z. Tang, P. Pillay, A. M. Omekanda, C. Li, and C. Cetinkaya, "Young's modulus for laminated machine structures with particular reference to switched reluctance motor vibrations," *IEEE Transactions on Industry Applications*, vol. 40, no. 3, pp. 748–754, May/Jun. 2004.

Torque Ripple Analysis Method for Permanent Magnet Synchronous Reluctance Motor

Ki-Chan Kim, and Ju Lee, *senior member, IEEE*
 Dept. of Electrical Engineering, Hanbat National University
 Dukmyung-dong, Yuseong-gu, Daejeon, 305-719, South Korea
 Email : kckim@hanbat.ac.kr

Abstract— This paper presents the efficient calculation method for torque ripple of permanent magnet assisted synchronous reluctance motor (PMA-SynRM) by FEM analysis for load angle curve. On an assumption that the sinusoidal current of stator is controlled by inverter, torque ripple characteristic according to load angle is calculated by superposing load angle curves from each instantaneous three phase current. Therefore, the load angle range having minimum torque ripple as well as the average torque according to the load angle can be induced easily by the proposed method. Finally, torque ripple characteristics of PMA-SynRM with different rotor are analyzed.

I. INTRODUCTION

Although PMA-SynRM is similar to interior permanent magnet (IPM) motor from an aspect of utilizing reluctance torque as well as magnetic torque, demerit of IPM motor compared with PMA-SynRM is the generation of large d-axis current at a high speed region which corresponds to field weakening control [1]. On the contrary PMA-SynRM has larger torque ripple due to its complex barrier structure. So, several papers for decreasing method of torque ripple have been presented [2]. The target of this paper is not the study on the reduction of torque ripple, but the study on the analytical calculation method for torque ripple. In this paper, we present an efficient calculation method for torque ripple of PMA-SynRM without steady state analysis by FEM including motion equation. The magnitude of torque ripple as well as average torque according to load angle is changed.

The paper presents torque ripple calculation method from an analysis of load angle curves with each instantaneous three phase current. We also perform the experiment for the verification of proposed method. We can find the load angle for minimum torque ripple with ease by proposed method. Moreover, we analyzed the torque ripple characteristics according to rotor types.

TABLE I
 SPECIFICATIONS OF ANALYSIS MODEL

	Item	Unit	Specification
Rated	Voltage / Current	V / A	12 / 10.5
	Speed	rpm	1000
	Power	W	130
Stator	Stack width / Outer diameter	mm	40 / 86
	Parallel Circuit		4
	Series turns / phase		44
Rotor	Number of poles		4
	Outer diameter	mm	46.2
	Rib Thickness	mm	0.3
	Remanence of Magnet	T	1.2 @ 20°C
	Mechanical air gap	mm	0.4

II. ANALYSIS MODEL

For the best use of reluctance torque with PMA-SynRM, barriers in the rotor and stator slots are designed to have the maximum saliency ratio and maximum gap of d-axis and q-axis inductance [3]. Three pieces of permanent magnets per pole are inserted in the middle of each barrier. Fig. 1 shows the picture of analysis model, and Table I shows the specification of size and rated operation point of the motor.

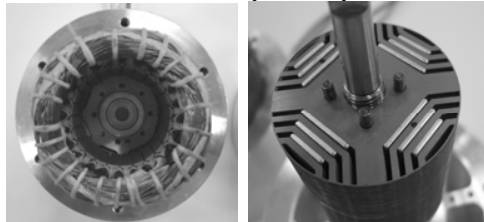


Fig. 1. Stator and permanent magnet rotor structure of PMA-SynRM.

III. TORQUE RIPPLE ANALYSIS BY LOAD ANGLE CURVES

The general method for calculating load angle curve by FEM is as follows. We input $\sqrt{2}$ times of rated current into the region of coil A, and then we input the half times of rated current with minus sign into the regions of coil B and C. Secondly, we calculate the output torque according to rotating angle while rotating the rotor. This is somewhat adequate analytical method for load angle curve with small reluctance torque or no reluctance torque such as interior PMSM and surface PMSM.

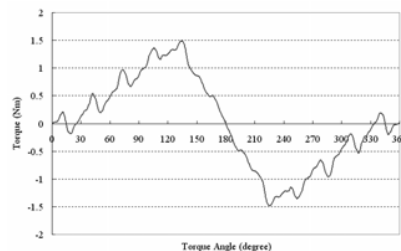


Fig. 2. The analysis results of load angle curve by using static FEM.

Fig. 2 shows the load angle curve of PMA-SynRM. There is so much fluctuation in it. In this figure, we cannot calculate the average torque owing to load angle. This paper presents the effective calculation for torque ripple as well as average torque without dynamic FEM simulation of time domain. Fig. 3 shows the balanced sinusoidal current waveform of three phase winding. The load angle curve in Fig. 2 is analyzed under the condition of dc current set at 1st state in Fig. 3. In

case the motor is operated with sinusoidal current controller, we can calculate another load angle curve with the dc current set at 2nd state. The remaining dc current set from 3rd to 7th state also can calculate load angle curves in the same way. The dc current conditions are repeated again with interval of 30°. We can make synthetic load angle curve by superposition of seven kinds of load angle curves as shown in Fig. 4.

In Fig. 4, average torque curve is calculated by averaging seven torque values at each load angle, and torque ripple curve is calculated by subtracting minimum torque from maximum torque at each load angle. We can find that torque ripple in the vicinity of 90° load angle is smaller than that of 130° load angle. That is, the PMA-SynRM is usually expected to be controlled with 130° load angle for the maximum torque production. However, torque ripple is also increased at this load angle.

In order to verify the proposed method, we perform the dynamic analysis by FEM with sinusoidal rated current 10.5A and load angles of 90° and 130°, respectively. Fig. 5 shows the results of torque ripple waveform and it gives good agreement with torque ripples by the proposed method.

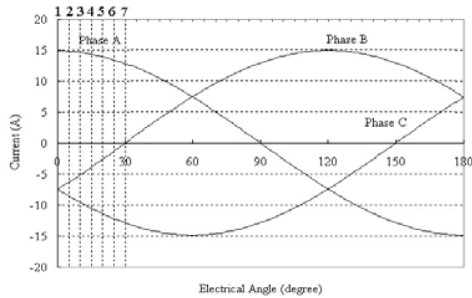


Fig. 3. Condition of input currents for load angle curve analysis

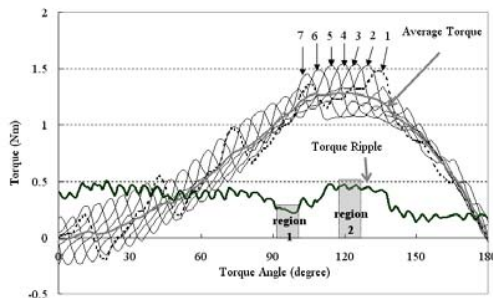


Fig. 4. Torque ripple and average torque owing to load angle

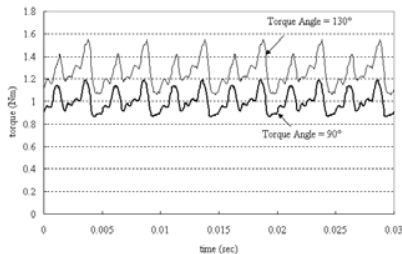


Fig. 5 Torque waveform according to load angles by dynamic FEM simulation

IV. EXPERIMENT AND DISCUSSION

Fig. 6 shows the experimental set for load angle test of PMA-SynRM. The test result of load angle curve is shown in

Fig. 7(a) when dc current set of 1st state is inputted in each winding and the rotor is rotated by dynamometer, we can see the fluctuation of torque according to the load angle is similar to Fig. 4. Fig. 7(b) shows the experimental results of torque at two kinds of load angle 90° and 130°. Vector inverter is used and the rated current is distributed to d-axis and q-axis current relevantly according to the load angle. The comparison results between analysis and experimental result of load angle curve is shown in Fig. 8 for the verification of validity of the proposed method.

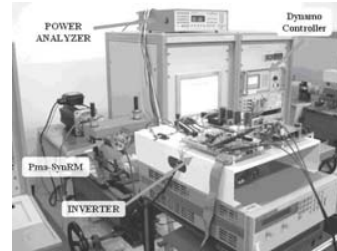
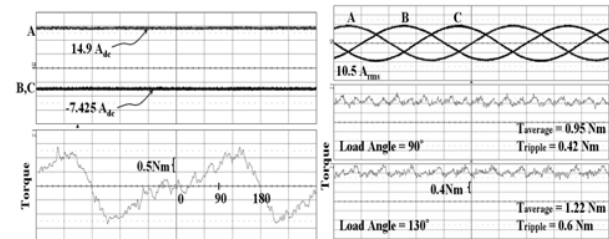


Fig. 6. Experimental set for load angle test



(a) Load angle curve test by dc current source
(b) Test results on the average torque and torque ripple at 90° and 130° load angle by vector inverter

Fig. 7. Experimental results.

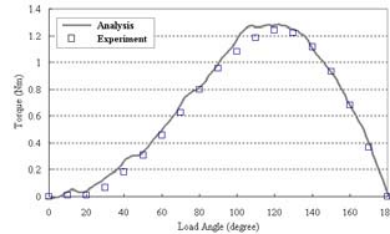


Fig. 8. Load angle curve by analysis and experiment. (average torque)

V. CONCLUSION

In this paper, we proposed a calculation method for torque ripple of PMA-SynRM by superposing load angle curves calculated by FEM. Moreover, we calculate an exact load angle curve which represents the average torque at each load angle in case of a motor with large torque ripples.

VI. REFERENCES

- [1] Niazi, P. and Toliyat, H.A., "Design of a low-cost concentric winding permanent magnet assisted synchronous reluctance motor drive", Industry Applications Conference, Fortieth IAS Annual Meeting. Vol. 3, pp. 1744-1748, 2-6 Oct. 2005.
- [2] Ohnishi, T. and Takahashi, N., "Optimal design of efficient IPM motor using finite element method", IEEE Transactions on Magnetics, Vol. 36, Issue 5, Part 1, pp. 3537-3539, Sep. 2000.
- [3] I. Boldea, T. Fukao, T.A. Lipo, L. Malesani, T.J.E. Miller and A. Vagati, Synchronous Reluctance Motors and Drives A New Alternative, IEEE IAS 29th Annual Meeting, Oct. 1994.

On the Importance of Incorporating Iron Losses in the Magnetic Field Solution of Electrical Machines

Emad Dlala, Anouar Belahcen, and Antero Arkkio
Helsinki University of Technology, P.O. Box 3000 FI-02015 TKK, Finland
Email: emad.dlala@tkk.fi

Abstract—This paper is aimed at studying the effects of iron losses on the magnetic field solution and evaluating their impacts on the overall performance of electrical machines. Because of the complications associated with the inclusion of iron losses into the magnetic field solution, the losses are usually computed as a posteriori and hence omitted in the finite-element (FE) analysis, leading to an inaccurate solution of the magnetic field and other relevant quantities. We propose a comparative FE analysis to assess the role of iron losses in defining the behavior and operation of electrical machines.

I. INTRODUCTION

Recent developments in material modeling have helped estimate iron losses using macroscopic models that can imitate the magnetization behavior quite accurately. From an engineering point of views, modeling of the magnetization curves (or the B - H loops) can be considered as the most “accurate and simple” way to predict iron losses, including the static hysteresis and dynamic eddy-current losses. Such an iron-loss model based on modeling the loop shapes usually entails the development of a hysteresis model incorporated into Maxwell equations. The resulting magnetodynamic problem is three-dimensional (3-D) in nature, but it can be reduced to the solution of two 1-D penetration equations when the edge effects are neglected. If the geometry of the device at hand can be expressed by a 2-D instead of 3-D approach, as is the common practice adopted for modeling an electrical machine, then coupling the 2-D model of the machine with the 1-D model can represent a somewhat complete analysis of iron losses. In practical situations, even the latter simplification cannot be sufficient to avoid a highly augmented computation time and convergence problems resulting from solving the two coupled nonlinear problems of the 1-D and 2-D models. Another occurrence that complicates the numerical analysis of an electrical machine and requires the employment of vector hysteresis models is the rotation of flux density in significant parts of the machine.

For all these reasons and perhaps more, researchers and developers of finite-element (FE) software packages have frequently given up the inclusion of iron losses in the field solution. Their alternative to predict iron losses is the employment of much more simplified techniques as a posteriori (usually based on the statistical loss theory), leading to the avoidance of the hysteresis and eddy-current models while using a lossless single-valued magnetization curve for the field solution. In addition to their recognized inaccuracy, the

simplified techniques have no means to include the iron losses into the field solution.

The third possibility that could be best suited for many applications is to predict the iron losses by employing the 1-D model as a *posteriori*. This would alleviate the computation time and convergence problems, but will, on the other hand, affect the accuracy to some extent that has not been well figured out. It is therefore highly desirable to assess the significance of incorporating the iron losses into the field solution of electrical machines. To do so, we propose to conduct a comparative analysis on two electrical machines using a simplified version of the 1-D model, called the hybrid model, which also, like the 1-D model, predicts the magnetization curves and loop shapes but it is more stable and efficient. The hybrid model will first be incorporated into a 2-D time-stepping FE code and, second, be also implemented as a posteriori in the same code while using a lossless single-valued magnetization curve for the magnetic field computation.

The machines chosen for the analysis are an induction machine and a machine-like device that has no air-gap (see Fig. 1). In rotating electrical machines, the air-gap plays a vital role in characterizing the behavior and operation of the machine and could therefore depreciate the impacts of iron losses.

II. MODEL FOR ANALYSIS

The constitutive nonlinear relation can be expressed by the fixed-point method as follows:

$$\mathbf{H} = \nu_f \mathbf{B} + \mathbf{M} \quad (1)$$

where \mathbf{H} is the magnetic field strength, \mathbf{B} is the magnetic flux density, \mathbf{M} is a magnetization-like quantity, and ν_f is a constant, which is optimally calculated at each time-step.

If a 2-D approach is performed, applying the magnetic vector potential ($\mathbf{B} = \nabla \times \mathbf{A}$) with the fixed-point formulation (1) results in the following

$$-\nabla \cdot (\nu_f \nabla A) + \sigma \frac{\partial A}{\partial t} - J = (-\nabla \times \mathbf{M})_z \quad (2)$$

where A and J are the z -components of the magnetic vector potential and the electric current density, respectively. The resulting 2-D FE equations are coupled with the voltage equations of the stator windings and rotor cage. The overall system of equations of the FE equations is solved iteratively and discretized in time using the Crank-Nicolson time-stepping scheme [1].

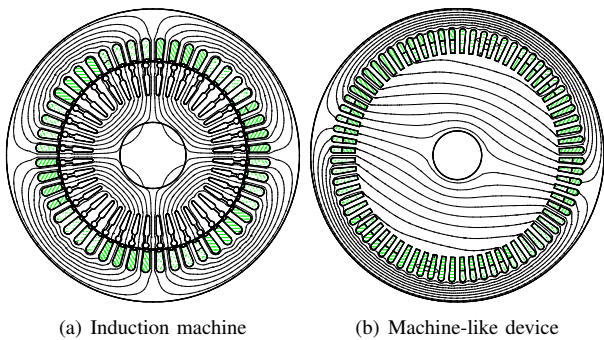


Fig. 1. Flux distributions and geometries of the simulated machines.

The Mayergoyz model of vector hysteresis is applied in its inverted version [1] as the magnetic flux density \mathbf{B} is projected over several directions e_{φ} specified by an angle φ to calculate the magnetic field strength

$$\mathbf{H}(\mathbf{B}) = \frac{1}{Q} \sum_{i=1}^N e_{\varphi_i} H_{\varphi_i}(B_{\varphi_i}) \quad (3)$$

where N is the number of directions, Q is a parameter to be identified, B_{φ_i} are the projections of \mathbf{B} along e_{φ_i} .

Now depending on whether the iron losses are included into the field solution or are only computed as a posteriori by the hybrid model, the scalar function $H_{\varphi_i}(B_{\varphi_i})$ will be served by

$$H_{\varphi}(B_{\varphi}) = H_h(B_{\varphi}) + H_{ed}(B_{\varphi}) + H_{ex}(B_{\varphi}) \quad (4)$$

or

$$H_{\varphi}(B_{\varphi}) = H_{sv}(B_{\varphi}) \quad (5)$$

where in (4), the hybrid model is used to predict three magnetic field strength components, H_h , H_{ed} , and H_{ex} , which are respectively responsible for generating the iron hysteresis, eddy-current, and excess losses. In (5), the function H_{sv} is a single-valued curve and must be prepared by averaging the major loop used by H_h in (4) to ensure that the same magnetic properties are used (most importantly the saturation property).

The procedure is carried out as follows:

- When the iron losses are *included* into the field solution, (4) is employed and subsequently used with (3), (1), and (2) in the iterative, time-stepping solution.
- When the iron losses are *not included* into the field solution and only computed *posteriorly*, (5) is employed and subsequently used with (3), (1), and (2) in the iterative, time-stepping solution. After the field solution is obtained at each time-step, (4) and (3) are employed to compute, posteriorly, \mathbf{H} , and hence, the iron losses.

In the two cases, the iron losses are determined using the Poynting vector theorem. It should be noted that even in the case when the iron losses are not included into the field solution, (3) was used to calculate \mathbf{H} with the single-valued function (5) in order to make sure again that the saturation properties for the two cases of (4) and (5) are identical, even though one would not normally need to use (3) in the case of (5).

III. NUMERICAL RESULTS

The influence of iron losses on the field solution will be evaluated here through the simulations of two electrical machines: a conventional squirrel-cage induction machine and a machine-like device, which has a conventional stator topology but no air-gap in it, as the rotor has not been punched out from the stator sheets (see Fig. 1 and [2]).

Numerical results carried out at the synchronous speed are shown in Table I. The results were obtained by feeding the machines from a 50-Hz, 380-V sinusoidal voltage supply. The time-stepping, 2-D FE simulations of the models introduced in Section II were run until the steady-state was reached.

TABLE I
SIMULATIONS CARRIED OUT WHEN THE IRON LOSSES WERE INCLUDED IN FIELD SOLUTION AND WHEN THEY WERE NOT

(a) Induction machine			
Computed Quantity	Iron loss included	Iron loss not included	Relative error %
Terminal current [A]	22.76	22.56	-0.87
Shaft power [W]	-146.12	-26.58	-81.80
Stator winding losses [W]	107.48	105.54	-1.80
Rotor-cage losses [W]	8.43	6.22	-26.21
Iron losses [W]	483.13	497.05	+2.90
Air-gap flux density [T]	0.845	0.845	+0.00
Power factor	0.0289	0.0056	-80.62
(b) Machine-like device			
Computed Quantity	Iron loss included	Iron loss not included	Relative error %
Terminal current [A]	0.75	0.26	-65.33
Stator winding losses [W]	1.60	0.20	-87.50
Iron losses [W]	365.76	391.69	+7.12
Air-gap flux density [T]	0.260	0.264	+1.54
Power factor	0.7125	0.0011	-99.84

The simulated results show that the inclusion of iron losses into the field solution has influenced the physical quantities of the two machines, especially, the machine-like device. The air-gap has a dominant role in rotating electrical machines as manifested in the current drawn by the induction motor, which is mainly resulting in reactive power. The loss inclusion has obviously increased the power factor in the two machines, particularly in the machine-like device. The effect of the iron-loss incorporation on the iron losses themselves is not that significant in the two machines, it could be also because the machines were fed from a voltage source.

The induction machine was deliberately run at the synchronous speed in order to provide a basis for comparison with the machine-like device. It is therefore interesting to study the effects of iron losses on a loaded machine. The type of supply, whether sinusoidal or non-sinusoidal, voltage or current source, is of interest too. These issues will be dealt with in the extended paper in which experimental results will be provided to support the simulations.

REFERENCES

- [1] E. Dlala, "Comparison of models for estimating magnetic core losses in electrical machines using the finite-element method," *IEEE Trans. Magn.*, 45(2), 716-725, 2009.
- [2] A. Belahcen, "Vibrations of rotating electrical machines due to magneto-mechanical coupling and magnetostriction," *IEEE Trans. Magn.*, 42(4), 971-974, 2006.

Efficiency Evaluation of PMASynRM Vs. SynRM Using Coupling FEM & Preisach Modeling

Jung Ho Lee, *Member, IEEE*, Tae Won Yun, Yong Hyun Kim
Dept. of Electrical Engineering, Hanbat National University
Dukmyung-Dong Yuseong-Gu, Daejeon, 305-719, KOREA
E-mail: komosin@nate.com

Abstract—This paper deal with the efficiency evaluations in a Synchronous reluctance motor(SynRM) Vs. PMASynRM using a coupled transient finite element method(FEM) and preisach modeling, which is presented to analyze the characteristics under the effect of saturation and hysteresis loss.

The focus of this paper is the efficiency evaluation relative to hysteresis loss, copper loss, etc. on the basis of load condition in a SynRM and PMASynRM. Computer simulation and experimental result for the efficiency using dynamometer shoe the propriety of the proposed method.

I. INTRODUCTION

In high-speed applications of a SynRM, hysteresis loss can become the major cause of power dissipation. Therefore, whereas in other kinds of machines a rough estimation of hysteresis loss can be accepted, their importance in a SynRM justifies a greater effort in calculating them more precisely.

The preisach model is now generally accepted to be a powerful hysteresis model, and is therefore intensively studied [1]-[3].

By adding a proper quantity of permanent magnets the torque density and power factor of SynRM can be greatly increased. It is called Permanent Magnet Assisted Synchronous Reluctance Motor (PMASynRM).

But, it must be that PMASynRM is more saturated than SynRM, due to the additional magnet flux density.

In this paper, a coupled finite element analysis and Preisach modeling for a PMASynRM and SynRM are presented and characteristics analysis and efficiency evaluations are performed under the effect of saturation and hysteresis loss.

The focus of this paper is the efficiency evaluation relative to hysteresis loss, copper loss, etc. on the basis of load condition in a SynRM and PMASynRM.

Also, TMS320C31 DSP installed experimental device and dynamometer are equipped and experiments are performed.

Computer simulation and experimental results for efficiency show the propriety of the proposed a coupled a coupled finite element analysis and Preisach model.

II. ANALYSIS METHOD

A. Governing Equation of PMASynRM and SynRM

Maxwell's equations can be written as

$$\nabla \times \vec{H} = \vec{J}_0 \quad (1)$$

$$\nabla \cdot \vec{B} = 0 \quad (2)$$

$$\vec{B} = \frac{1}{\nu_0} \vec{H} + \vec{M} \quad \vec{B} = \frac{1}{\nu_0} \vec{H} + \vec{M}_{PM} \quad (3)$$

where, \vec{M} , \vec{M}_{PM} are the magnetization of magnetic material and permanent magnet with respect to the magnetic intensity \vec{H} . \vec{M}_{PM} is removed in a SynRM. The magnetic vector potential \vec{A} and the equivalent magnetizing current \vec{J}_m , \vec{J}_{PMm} are expressed as follows

$$\vec{B} = \nabla \times \vec{A} \quad (4)$$

$$\vec{J}_m = \nu_0 (\nabla \times \vec{M}), \quad \vec{J}_{PMm} = \nu_0 (\nabla \times \vec{M}_{PM}) \quad (5)$$

The governing equation derived from (1)-(5), is given by

$$\nu_0 (\nabla \times \nabla \times \vec{A}) = \vec{J}_0 + \vec{J}_m + \vec{J}_{PMm} \quad (6)$$

B. System Matrix

The system matrix can be written as

$$[K^{(e)}] \{A^{(e)}\} + \{F^{(e)}\} + \{M^{(e)}\} + \{M_{PM}^{(e)}\} = 0 \quad (7)$$

The overall model is therefore described by the matrix as follows

$$[K] \{A\} + \{F\} + \{M\} + \{M_{PM}\} = 0 \quad (8)$$

C. Application of Preisach's Model

The magnetization M can be expressed as a scalar model, because the rotor rotates according to the input current angle synchronously. Therefore, it can be supposed that the domain in stator is an alternating field with reference to x axis and y axis. B and H of the domain in rotor is constant and is a rotating field, but it is an alternating field with reference to x axis and y axis, also [4]-[6]. It is natural that M, H which is calculated on the same axis has a same vector direction.

$$M(t) = \iint_{\alpha \geq \beta} \mu(\alpha, \beta) \gamma_{\alpha\beta}(H(t)) d\alpha d\beta \quad (9)$$

$$= \iint_{S^+(t)} \mu(\alpha, \beta) d\alpha d\beta - \iint_{S^-(t)} \mu(\alpha, \beta) d\alpha d\beta$$

A more convenient treatment of this model is also to substitute the Everett plane for Preisach's one as shown in (10).

$$E(\alpha, \beta) = \iint_{\alpha \geq \beta} \mu(\alpha, \beta) \gamma_{\alpha\beta}(H(t)) d\alpha d\beta \quad (10)$$

In the Everett plane, the distributions of M, which is accepted from experimental data of material S40 and ferrite magnet, are Gaussian ones.

D. Computing Algorithm

The simple iteration method is applied to the iteration loop for the rapid convergence and magnetization M is modified.

$$M_{i+1}^{(\theta)} = M_i^{(\theta)} + r(M_{i+1}^{(\theta)} + M_i^{(\theta)}) \quad (11)$$

Where r is the relaxation factor and 0.5 is used in this paper.

Flux density and magnetic field intensity, which are composed of x-axis and y-axis components, are calculated from FEM. Each component of magnetization is calculated independently from x-axis and y-axis magnetic field intensity with Everett density distribution.

III. RESULT AND DISCUSSION

In this case of PMASynRM and SynRM, the hysteresis responses of a teeth part's element are shown in Fig. 3, 4 when P.M. is 0.4[T] and current i_d is 5[A], 25Hz.

It can be found that PMASynRM is more saturated than SynRM, but have similar hysteresis characteristics in spite of inserting a permanent magnet.

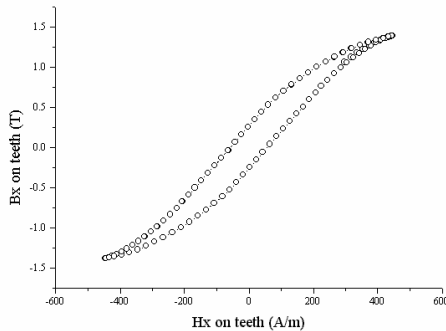


Fig. 1 B-H Curve in a teeth of SynRM

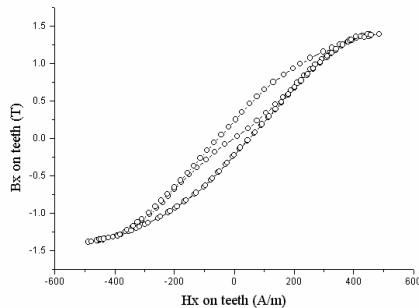


Fig. 2 B-H Curve in a teeth of PMSynRM

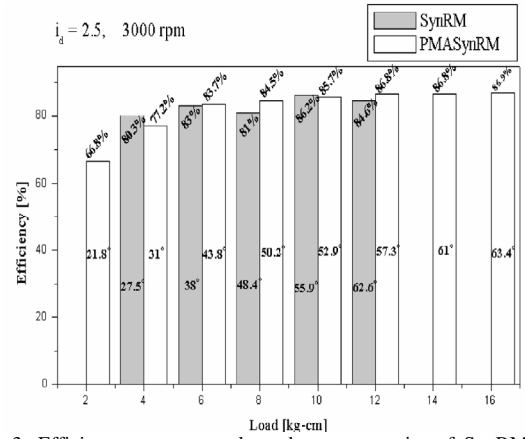


Fig. 3. Efficiency, current angle and runaway point of SynRM and PMASynRM according to load in experimental test

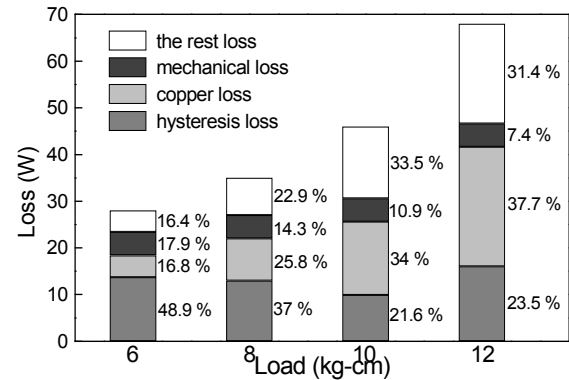


Fig. 4 loss analysis in each load condition of SynRM

Experimental Comparisons are given with output power and currents characteristics of normal Synchronous reluctance motor (SynRM) and those of PMASynRM according to load as shown in Fig. 3, respectively. And It is confirmed that the PMASynRM result in high output power performance than SynRM. Fig. 4 shows the each loss ratio to the total loss in each load condition of SynRM.

Through the more detailed analysis, the various loss and efficiency evaluations of PMASynRM and SynRM will be represented in next extended version.

IV. REFERENCES

- [1] A. Ivanyi, Hysteresis Models in Electromagnetic Computation, AKADEMIAI KIADO, BUDAPEST
- [2] I. D. Mayeroz, "Mathematical Models of Hysteresis." *IEEE Trans. In Magnetics*, Vol. MAG-22, No.5, pp.603-608 Sept. 1986
- [3] A. Visintin, Differential models of hysteresis, Applied Mathematical Sciences, Springer, 1994.
- [4] J. H. Lee, D. S. Hyun, "Hysteresis Analysis for permanent Magnet Assisted Synchronous Reluctance Motor by Coupled FEM & Preisach Modelling", *IEEE Transaction on Magnetics*, Vol. 35, No. 5, pp. 1203-1206. May 1999.
- [5] J. H. Lee, J. C. Kim, D. S. Hyun, "Effect of Magnet on Ld and Lq Inductance of Permanent Magnet Assisted Synchronous Reluctance Motor", *IEEE Tran.on Magn* Vol.35, No. 5, pp. 1199-1202, May 1999.
- [6] J. H. Lee, J. C. Kim, D. S. Hyun, "Dynamic Characteristic Analysis of Synchronous Reluctance Motor Considering Saturation and Iron Loss by FEM", *IEEE Transaction on Magnetics*, Vol. 34, No. 5, pp. 2629-2632, Sep. 1998.

Optimization of Magnetic Bearing applied to a Ventricular Assist Device

Everton Shigueaki Yoshida, Luiz Lebensztajn

Departamento de Engenharia de Energia e Automação Elétricas da EPUSP
Av. Prof. Luciano Gualberto, tr. 3 n°380, 05508-970, São Paulo-SP - Brazil
everton.yoshida@gmail.com, leb@pea.usp.br

Abstract — This work proposes the optimization of a Magnetic Bearing applied to a Ventricular Assist Device using the Pareto Archived Evolution Strategy. The optimization problem is to minimize the power consumption and rotor oscillation. The optimization of the control system was also taken into account. The magnetic force was computed by the Finite Element Method to allow a dynamic simulation of the magnetic bearing.

I. INTRODUCTION

The Ventricular Assist Device (VAD) and similar equipments that provide assistance to patients with cardiological diseases plays an important role in Health. Based on information from Brazilian Health Ministry, heart diseases represent about 27% of all deaths caused by pathological reasons in 2002. Previous studies about one degree of freedom magnetic bearing [1] shows that high consumption of energy makes unviable the implantation of a VAD for long periods. The magnetic bearing control system should be highly reliable.

The objective of this work is to elaborate a methodology to perform the optimization of magnetic bearing in order to work in an efficient and stable condition. Therefore, a process that uses the Finite Elements Method (FEM), a bearing dynamic model to evaluate the mechanical solution and an algorithm to perform the optimization, using the Pareto Archived Evolution Strategy (PAES), have been developed. The obtained solutions were used to improve the performance of an existing prototype.

II. PROBLEM DESCRIPTION

The magnetic bearing suspension provides to the rotor the elimination of the attrition by magnetic forces. The active magnetic bearing, as shown in Fig.1 [2], has a control circuit with a sensor on the base of the rotor. Thus, the circuit increases or decreases the current of the coils connected on series to control the force and the position of the rotor. Only the rotor will have contact with the blood.

A. Bearing dynamic model

A simulation using FEM software has been done, and the resultant forces on the rotor were computed as a function of several parameters as position, number of turns and current. Theses forces values allow calculating the position of the rotor as a function of time, when an external mechanical perturbation is present on the bearing.

A control circuit is then necessary, as presented on prototype and a proportional-derivative control was adopted in our simulations. In this model, a reference current (I_{ref}) is

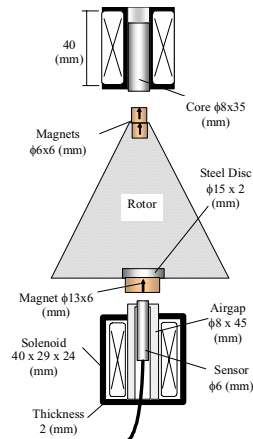


Fig.1. Magnetic Bearing and Rotor Structure

adopted to make the resultant forces null. The current is adjusted 300 times per second to keep the rotor stable even with external forces actuating over it.

For each pair of numbers of turns N_1 and N_2 for the electromagnets, a different reference current (I_{ref}) value is necessary to sustain the rotor. Hence, in order to not calculate the reference current at the beginning of each simulation, a database, which determinate these current as a function of N_1 and N_2 has been done and the current is calculated by interpolation of these points.

The Proportional-Derivative control circuit parameters K_p and K_d should be also evaluated. After some computer experiments we have observed that for a given ratio N_1/N_2 , is possible to determine K_p and K_d , which provide a minimum overshoot and settling time.

B. The Optimization Problem

The standard PAES, as proposed in [3] were adopted with some adaptations to include the constraints existing on magnet bearing design. The objective functions are to minimize the average power consumption during the simulation and to minimize the rotor oscillation. In order to measure this oscillation, we sum up the squares of the differences between the actual rotor position and the nominal rotor position. In this work, we will call it $\Sigma(\text{Displacement})^2$. The problem has the following constraints: the coil region for the upper and for the lower electromagnet was fixed; the ratio between coil volume and copper volume was defined as 0.80, the wire section varies from 1 to 39 AWG, the wire section was defined to occupy all available volume and the position (x) is constrained to a maximum value and a minimum value. The integration of

11. ELECTRIC MACHINES AND DRIVES C) ACTUATORS

the electromechanical problem with the optimization problem could be understood on Fig.2

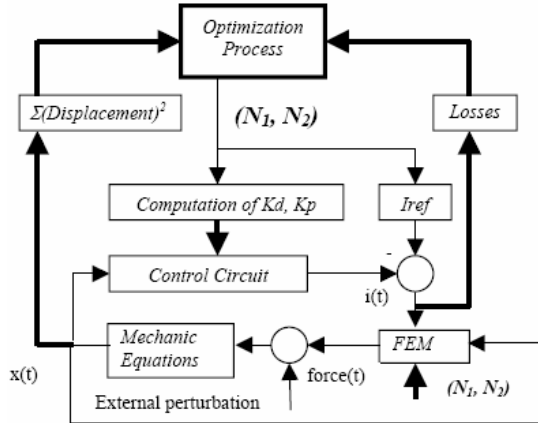


Fig.2 . The Optimization Process

III. RESULTS

The first step to solve this problem is to correlate the reference current and the parameters of the PD control system with respect to N_1 and N_2 . Fig 3 and.4 show the used data.

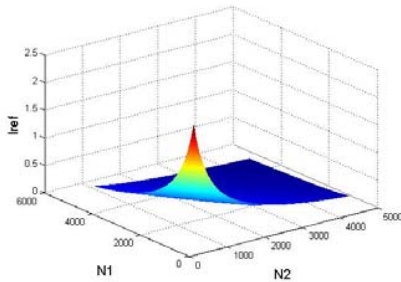


Fig 3 Reference Current as a function of N_1 and N_2

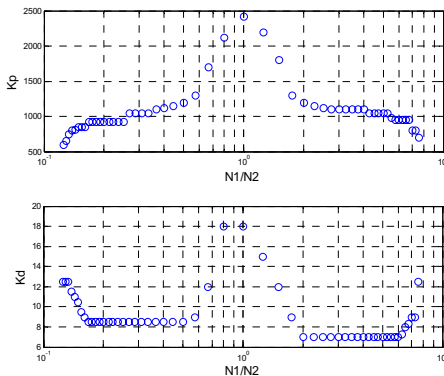


Fig 4 Parameters of the PD Control System as a function of the ratio N_1/N_2

Due to the complexity of the dynamic model, the computation of the power consumption and rotor movement in function of time spend about five seconds for each pair (N_1 , N_2). The final result was obtained after 36000 iterations or five hours of processing. Fig. 5 is a zoom of the Pareto-set generated by PAES with some points generated by an exhaustive search. The nondominated solutions have a trend toward results between 3.7 W and 3.9 W and $\Sigma(\text{Displacement})^2$ about 50mm^2 .

Fig. 6 represents the position and the current for one of the non-dominated solution. It is possible to observe the reaction of the bearing for the 4 external perturbations, except for the initial condition, they are respectively, 20N upward, 20N downward, 0 to 30N upward and 0 to 10N downward. These same perturbations were applied in all generated solutions and the Average Power Consumption and the $\Sigma(\text{displacement})^2$ were computed.

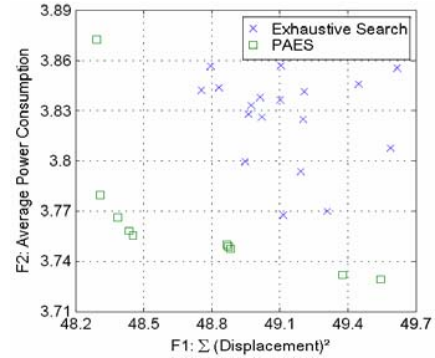


Fig.5 Pareto Set – PAES and Exhaustive Search

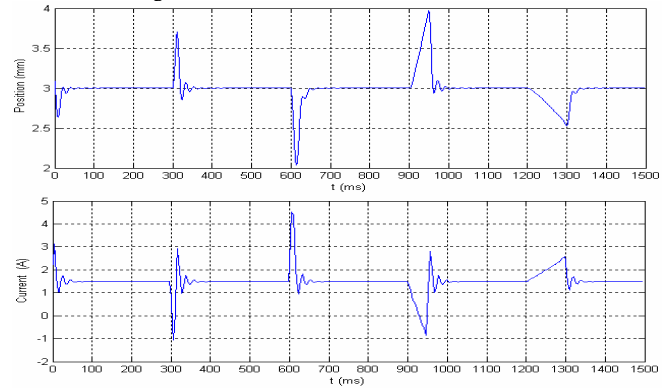


Fig 6. Position and current as a function of time for a non-dominated solution

IV. CONCLUSIONS

In this work, a multi-objective optimization of a magnetic bearing was performed. Besides the improvement suggested to the device, it has also changed some process on PAES algorithm, adapting it to handle with a constraint problem. Using the dynamic model of the bearing, the FEM simulation was only necessary in the beginning to obtain the Force x Position curve, while varying the number of turns and the current. Therefore, it was possible to apply the methodology to the magnetic bearing problem, obtaining the optimal values for its construction. This methodology has proved to be potentially appropriate and applicable to the optimization of an electric device.

V. REFERENCES

- [1] I. da Silva, O. Horikawa, Experimental Development of a One-Degree-of-freedom Controlled Magnetic Linear Bearing, EPUSP *IEEE Transactions on Magnetics* Vol. 41(11) 4257-4260, 2005.
- [2] A. E. M. Lee, C. A. F. Fernandes, *Aplicação de Mancal Magnético no Dispositivo de Auxílio Ventricular do Instituto Dante Pazzanese de Cardiologia*, Technical Report, EPUSP,2006 (in portuguese).
- [3] J. D. Knowles, D. W. Corne, The Pareto Archived Evolution Strategy: A New Baseline Algorithm for Pareto Multiobjective Optimization, *Proceedings of CEC*, 99-105, 1999.

Design of High Performance Line Start Permanent Magnet Synchronous Motor with High Inertia Load

Jian Li, Byongkuk Kim, Yunhyun Cho
 Dept. of Electrical Engineering
 Hadan 2 Dong, #840, Saha-gu, 604714, South Korea
 lijian613@gmail.com

Abstract—This paper describes the design process of a high performance 3-phase 3.7kW 4-pole line start permanent magnet synchronous motor. The starting torque characteristics of line-start with high inertia load were optimized by studying the width and height of permanent magnet. Time-step two-dimensional finite element analysis was utilized to perform electromagnet simulation. The dynamic characteristics are described and compared with those of the squirrel cage induction motor.

I. INTRODUCTION

The induction motors have been widely used in industry application. But in recent years, the high efficiency motors are demanded in a large variety of industrial products for energy save. The line start permanent magnet synchronous motor (LSPMSM) has a high efficiency and an advantage in constant speed operation regardless of the effect of load variation, presenting an interesting alternative for induction motors. It has permanent magnets (PMs) buried bellow the squirrel cage in rotor, thus operates in steady state as conventional interior permanent magnet synchronous motor (PMSM); the squirrel cage is used for line starting on a conventional AC power source and damping of dynamic oscillations at fast load changes. Thus it combines the advantages of induction motor (robust construction and line-starting capability) and PMSM (high efficiency, power factor and torque density). So, characteristics of LSPM have very complex characteristics until the synchronization and if the design is not suitable, the LSPM cannot be synchronized [1]-[2].

II. DESIGN PROCESS

Through a combination of optimization methods and standard design techniques, the efficiency of an induction motor is increased by 3.8%. This motor is then used as basis for the design of a line start permanent magnet synchronous motor. Fig.1 shows the configuration of V-shape magnet LSPMSM and rotor of prototype. The performance of the 3-Phase 3.7kW 4-poles LSPM was simulated by dynamic finite element analysis and was compared with the squirrel-cage induction motor in Table 1. At full load, the rms phase current decreased from 7.6A to 6.4A, and the efficiency increases by 10%.

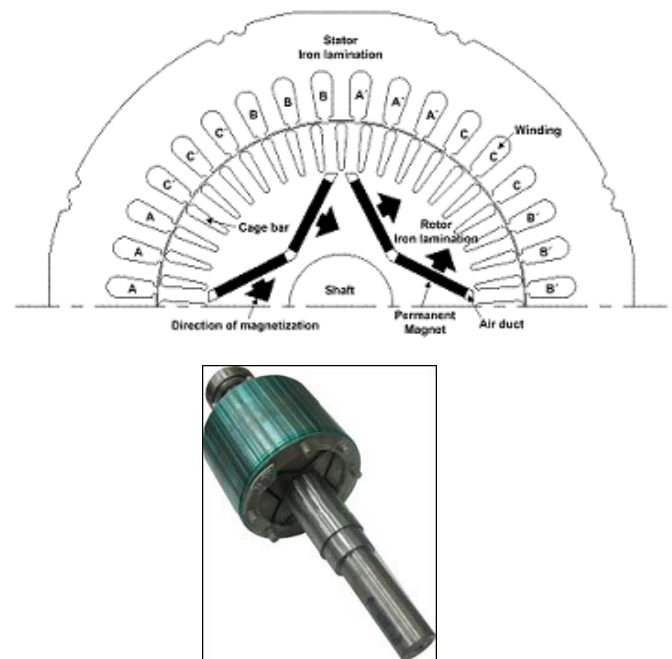


Fig. 1. Configuration of V-shape magnet LSPMSM and rotor of prototype.

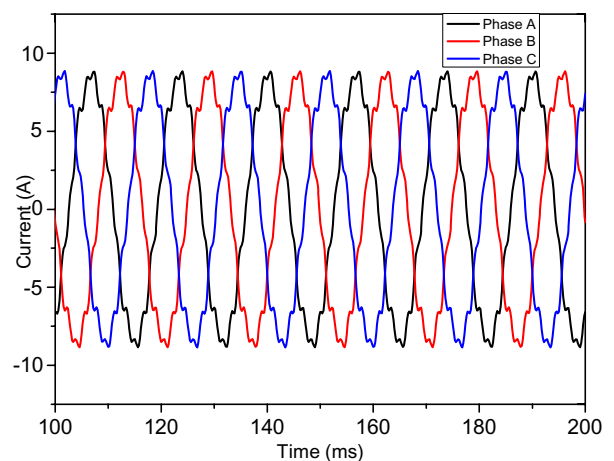


Fig. 2. Phase currents of LSPMSM.

Items	Induction motor		LSPM	
	Simulation	Experiment	Simulation	Experiment
Input voltage [V]	380	380	380	380
Input current [A]	8.2	7.6	6.5	6.4
Rated speed [rpm]	1,730	1,760	1,800	1,800
Rated torque [Nm]	20.4	20.0	19.6	20.0
Efficiency [%]	84.4	86.3	94.3	94.1
Power factor	0.81	0.80	0.91	0.90
Output [W]	3,700	3,686	3,700	3,768

A LSPM, which presents good steady state performances, may have problems to start and synchronize, especially with high inertia load [3]. The start can fail because of a too high braking torque in comparison to the asynchronous torque. The braking torques (due to permanent magnets and flux barriers) in the asynchronous operation region, which mainly depends on the placement and dimensions and the value of energy product of PMs, has principle effect on the synchronization capability. The design of high performance motor should make compromise between an adequate starting characteristic in the asynchronous operating region and power rating and efficiency in the motor's synchronous operating region.

Fig.3 shows the simulation results of the characteristics of LSPMSM braking torque with different height and width of permanent magnet. The nonlinear relationship between leakage flux and the permanent magnet thickness is shown in Fig.3 (a). Torque characteristics changes a lot with different saturation degree between air duct and squirrel cage bar. The linear relationship of braking torque with difference permanent magnet width is shown in Fig.3 (b).

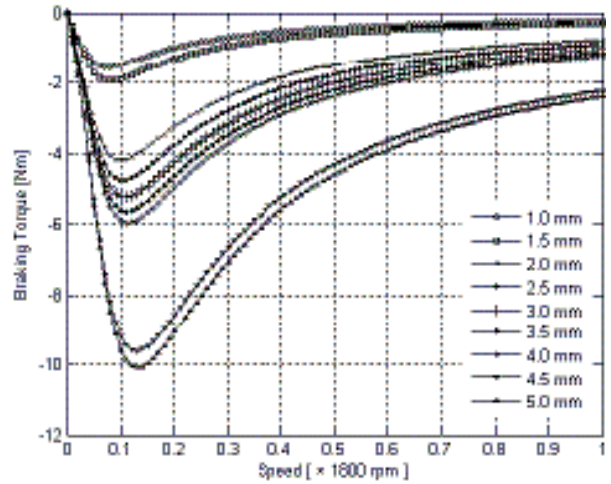
Table1 shows the result of simulation and experimental comparison between induction motor and LSPM. The efficiency of LSPM is 10% higher than induction motor according to experimental test. Performance experimental results and FEM result are matched, which verifies the validity of this analysis.

III. CONCLUSIONS

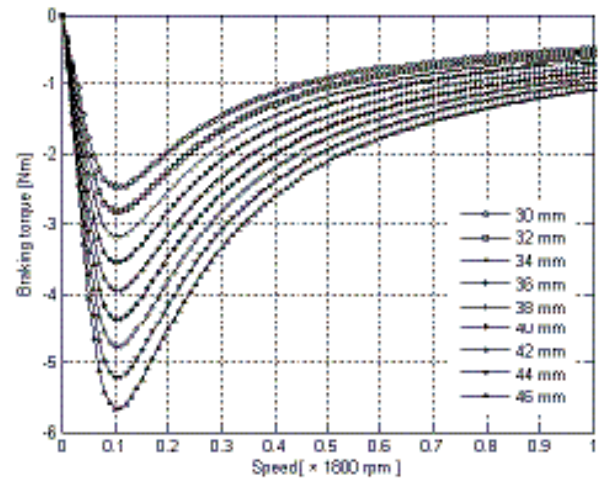
The design process of a high performance 3-phase 3.7kW 4-pole line start permanent magnet synchronous motor was describes in this paper. Based on a high efficiency induction motor, the prototype was designed and analyzed by using time-step finite element method. The efficiency of LSPM is 10% higher than induction motor according to experimental test. In order to improve the starting capability, models with permanent magnet of different widths and heights were simulated. It could found that the shape of permanent magnet embedded under rotor bar has a large influence on braking torque.

IV. ACKNOWLEDGEMENT

This work is the outcome of a Manpower Development Program for Energy & Resources supported by the Ministry of Knowledge an Economy (MKE).



(a)



(b)

Fig. 3. Comparison of braking torque characteristics according to the change of the magnet shape: (a) braking torque curves according to thickness. (b) Braking torque curve according to width.

V. REFERENCES

- [1] Li Gies, Guo Zhongbao, Wang Chunyuan, Giu Hong, Guo Daling, "High Starting Torque and High Efficiency REPM Synchronous Motor", Proceeding of the Seventh International Workshop on Rare Earth-Cobalt Permanent Magnets and Their Applications, Beijing, China, Sept. 1983, China Academic Publishers, pp.13-20
- [2] M.A Rahman and T.M. Osheiba, "Performance of a large line-start permanent magnet synchronous motor", IEEE Trans. Energy Conversion, vol. 5, pp.211-217, Mar.1990.
- [3] T.J.E. Miller, "Synchronization of line-start permanent magnet AC motor", IEEE Trans., vol.PAS-103, Juillet 1984, pp 1822-1828.

Slit Effect on Laminated Stator Core in Transverse Flux Rotary Machine

Ji-Young Lee¹, Seung-Ryul Moon¹, Do-Hyun Kang¹, and Jung-Pyo Hong²

¹Korea Electrotechnology Research Institute, Changwon, Gyeongnam, 641-120, Korea

²Department of Automotive Engineering, Hanyang University, Seoul, 133-791, Korea
jylee@keri.re.kr, srmoon@keri.re.kr, dhkang@keri.re.kr, and hongjp@hanyang.ac.kr

Abstract — This paper shows a transverse flux rotary machine (TFRM) with laminated stator cores, which consists of two part laminated silicon steel cores in which the direction are perpendicular to each other. Although the TFRM is laminated to reduce eddy current losses, it exhibits rapidly increasing core losses as frequency increases. To solve the problem, slits are introduced on the stator core. The effect of the slits is confirmed experimentally first, then the effect is explained by 3-dimensional finite element analysis of eddy current losses in nonlinear laminated cores.

I. INTRODUCTION

Transverse Flux Machines (TFM) have a 3-dimensional magnetic flux path, and due to this characteristic, fabrication with silicon steel cores can be difficult. [1] and [2] present stators with silicon steels, in which the silicon steel pieces are laminated circumferentially. Since TFMs have 3-dimensional flux path, either the stator or rotor has to be skewed; however, for manufacturing the stators, it is difficult to bend the laminated stator core pieces.

In the prototype transverse flux rotary machine (TFRM) of this paper, in order to ease the manufacturing process with laminated stator core and to eliminate bending, the TFRM is manufactured with two part laminated stator cores in different directions. Although the lamination is incorporated to reduce eddy current losses, it exhibits increasing core losses as frequency increases. To solve the problem, slits are introduced on the stator core.

This paper presents the slit effect with both experimental and analysis results. First, the configuration of the prototype TFRM is introduced in section II. And to show the slit effect, the experimental condition and the results are presented in section III. Then, the effect is explained by 3-dimensional finite element analysis (FEA) of eddy current losses with nonlinear laminated cores in section IV.

Usually, lamination is not modelled in order to reduce computation time in the FEA process. In this paper, however, the lamination is expressed in the analysis to show the high eddy current loss even on the laminated core. To reduce the number of elements and save the computation time, the lamination is expressed with a few layers and with boundary condition instead of air-gap between layers, and electromotive force (EMF) is calculated by source variation without motion instead of rotor movement.

II. A TFRM WITH LAMINATION STATOR CORE

Fig. 1 shows the configuration of a permanent magnet (PM) type, direct drive TFRM. A brief specification including

magnetic material information is listed in Table 1. The PMs on rotor are arranged in circumferential direction and magnetized as shown in Fig. 1 (b) to concentrate the magnetic flux to the rotor core. Although such a construction is good for producing high power density, skewing the rotor to allow for the 3-dimensional flux path can be difficult. Therefore, the stator is divided into two sections that are laminated in different directions. The inner and outer sections are a yoke and teeth, respectively, and the laminations of two sections are perpendicular to each other as shown in Fig. 1 (b). Additionally, the outer teeth core is divided into upper and lower parts, and the lower teeth are shifted by a half pole-pitch with respected to upper teeth to create skewing effect.

Fig. 2 shows flux path on cross section of L-L' in Fig. 1 (b) when current flows in counter-clockwise. From the Fig. 2, it is clear to see that both inner and outer laminations accommodate the flux flow and do not interfere. The lamination also intends to reduce core losses.

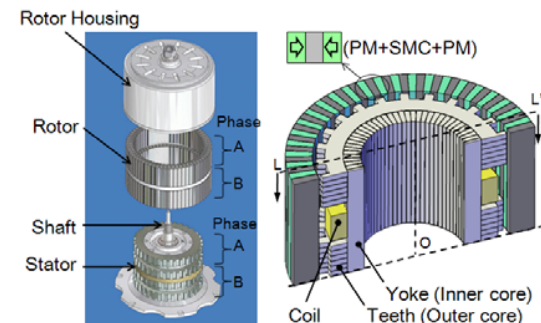


Fig.1. Conceptual drawing of a prototypal TFRM

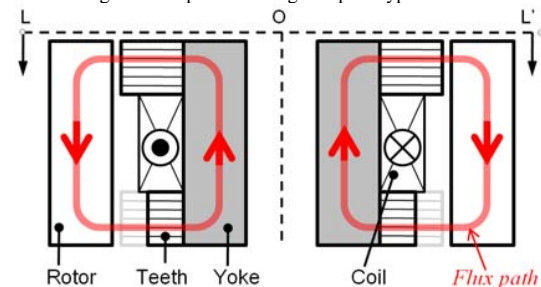


Fig.2. Flux path on the cross section area along L-L'

Table 1. Specifications of a Prototyp TFRM

Stator	Material	S23 (Silicon steel, Lamination core)
	No. of Phase	2 phases (phase A and phae B)
Mover	Material	Somaloy 550 (Soft magnetic composite (SMC) core) + Ferrite PM

III. EXPERIMENTAL RESULTS

Fig. 3 shows the original stator configuration without slits and modified stator configurations with different numbers of slits. Slits are only on the outer teeth core. Fig. 4 shows the experimental results of EMF of different configurations as a function of electric frequency under no load condition. The EMF value is normalized with the base value being the EMF at 50 Hz.

When the stator has no slit ($N_s=0$), as shown in Fig. 3 (a), the EMF is highly non-linear as shown in Fig. 4. This result indicates that the core loss of the prototype TFRM is increasing rapidly as frequency increases.

While experimenting to reduce core losses, slits are inserted as shown in Fig. 3 (b), (c), and (d), and the experimental results show that the slits on teeth core improve the problem. As shown in Fig. 4, as the number of the slits increases the EMF characteristic become more linear. This experimental result indicates that the core losses are reducing with increasing the number of slits.

IV. 3-DIMENSIONAL FEA OF EDDY CURRENT LOSSES

The prototype TFRM exhibits high core losses in spite of laminated core construction. The experiment indicates that the slits reduce the core losses, and to confirm and understand the slit effect from experimental results, the original and modified conditions are analyzed.

Three models are considered for analysis. First is modeled without lamination as shown in Fig. 5 (a). Second and third is modeled with lamination as shown in Fig. 5 (b); however, the second does not include slits, while the third model includes slits.

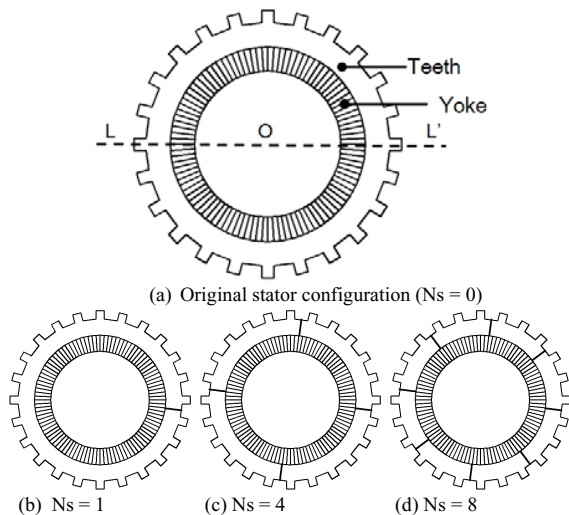


Fig.3. Stator configuration depending on number of slits (N_s)

To explain the slit effect, eddy current losses in nonlinear laminated cores of the three models are computed by 3-dimensional FEA. For effective computation, transformer EMF is calculated instead of motional EMF by time varying current. Furthermore, the lamination is modeled by boundary condition instead of air-gap modeling between layers [3].

From the FEA, the eddy current state on the stator cores and the quantity of core losses and magnetic flux are compared among the three models. The analysis results will be presented in extended paper.

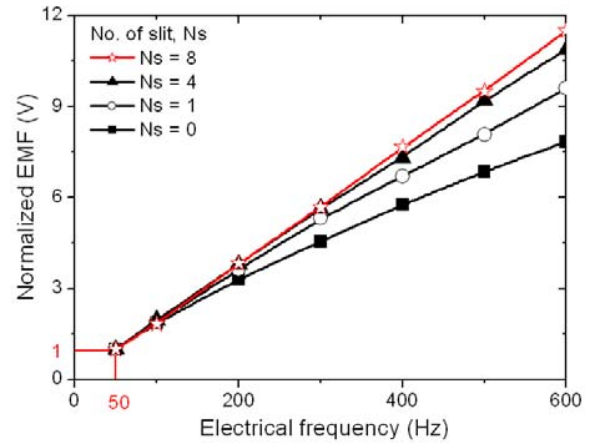


Fig.4. Normalized EMF from experimental results for electrical frequency variation

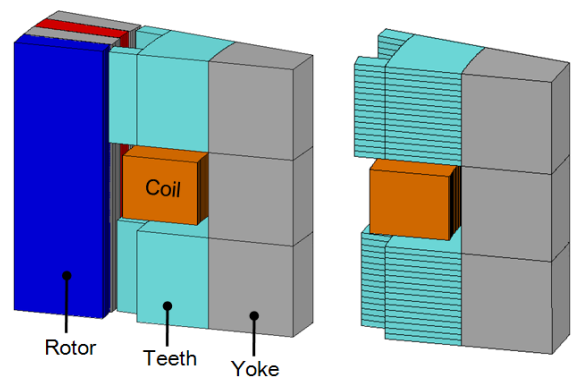


Fig.5. Analysis model for 3D FEA

V. REFERENCES

- [1] A. Babazadeh, N.Parspour, and A.Hanifi, "Transverse Flux Machine for Direct Drive Robots: Modeling and Analysis," *Proceedings of the 2004 IEEE Conference on Robotics, Automation and Mechatronics*, pp.376-380, December, 2004
- [2] Wilhelm Hackmann, *Comparison of Different Gear Hub Drive for Rail Transport: Asynchronous Machine, Permanent Magnet Synchronous Machine, Transverse Flux Machine*, Technical University of Darmstadt, PhD dissertation, 2003, pp. 113
- [3] Kurt Preis, Oszkar Biro, and Igor Ticar, "FEM Analysis of Eddy Current Losses in Nonlinear Laminated Iron Cores," *IEEE Trans. on Magnetics*, Vol. 41, No. 5, pp. 1412-1415, May 2005

Design and Analysis of a Written-pole Motor Using a Symmetric Field and FE Methods

Byung-Taek Kim¹, *IEEE, member*, Dae-kyong Kim², *IEEE, member* and Byung-il Kwon³, *IEEE, member*

¹Department of Electrical Engineering, Kunsan National University, Kunsan 573-701, Korea

²Korean Electronics Technology Institute, Gwangju 420-140,

³Department of Mechatronics Engineering, Hanyang University, Ansan 426-791, Korea

btkim@kunsan.ac.kr

Abstract— In this paper a design and analysis method for a single-phase written-pole (WPM) is proposed. The magnet properties for a WPM are determined by using FEM. With the determined magnet, a steady state analysis is carried out with an equivalent circuit based on a symmetric field method. Experimental tests are also performed and compared with simulation results.

I. INTRODUCTION

A written-pole motor (WPM) is a very special synchronous motor because it has an exciter in stator which is a magnetization fixture [1]-[3]. A WPM also has self-starting ability owing to conducting bars and end-ring on a rotor, like an induction motor. The interesting feature of a WPM is such that the magnet on a rotor loses its magnetism by field of stator during start-up and it regains the magnetism through action of the exciter just before synchronization, which brings an advantage of no braking torque and high efficiency simultaneously.

Authors previously published a study on design of exciter pole [3]. In this paper, for a next procedure, methods for design and characteristic analysis of a single-phase WPM are suggested. At first, the design procedure for magnet using FEM is proposed, and then the analysis method for a steady state is given by using a symmetric field method.

II. DESIGN AND ANALYSIS METHOD OF A SINGLE-PHASE WPM

Fig. 1 shows the structure and circuit of a WPM which consists of a stator and a rotor. As shown in Fig. 1, the stator has an exciter pole which is driven by a common voltage source just before the rotor gets into synchronization.

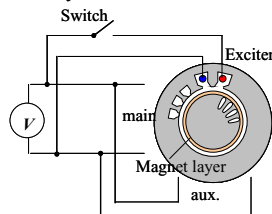


Fig. 1. A single-phase WPM

A. Design of Magnet Layer

For a WPM to normally operate, the magnet should be demagnetized as much as possible during start-up. Conversely it should not be demagnetized up to the maximum load after re-magnetization by exciter operation. Thus the coercive force of magnet is a very important factor for design of a WPM. In

this study, a coercive force is searched through FE-analysis for an Nd-bonded magnet which has a flux density of 0.7T and a thickness of 1.5mm. In order to determine it, first, the field intensity in the magnet is calculated for the maximum load condition in synchronous operation without considering irreversible demagnetization. In other words, the linear B-H curve is used in the analysis, and a point *a* is found in Fig. 2. In turn, by analyzing field intensity during start-up, the point *b* is also found.

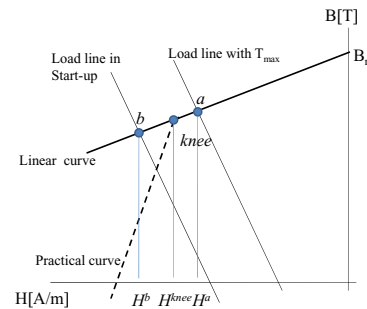


Fig. 2. Properties for magnet for a WPM

Two simulations above are respectively performed, and both the maximum fields in the magnet obtained by simulations are depicted according to angular positions in Fig. 3. From the results, we can see that the point *a* is near -400kA/m and the point *b* is near -500kA/m. So we determine -450kA/m for the knee point and -500kA/m for coercive force.

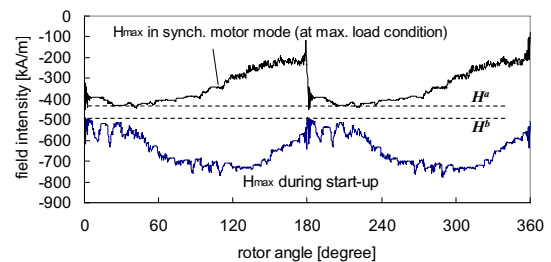


Fig. 3. Magnetic field intensities on magnet (without consideration of irreversible demagnetization)

To calculate how much demagnetization occurs in start-up, the no-load starting characteristics are simulated with FEM considering the irreversible demagnetization. Assuming that the initial magnet has been fully magnetized with 0.7T, the residual induction after start-up is calculated as shown in Fig. 4. It shows that most part of magnet is demagnetized above

50% of the initial state.

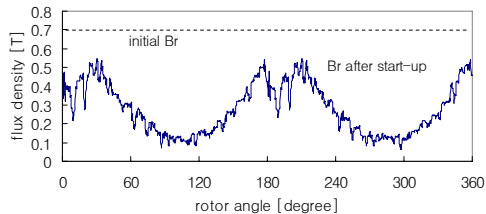


Fig. 4. Residual induction of magnet after start-up

B. Steady State Analysis

As stated above, the exciter in Fig. 1 operates and magnetizes the magnet just before synchronization. The design of an exciter pole and winding was presented in previous study [3]. The magnetization waveform is plotted in Fig. 5 and the back EMF can also be expected as 160V (RMS).

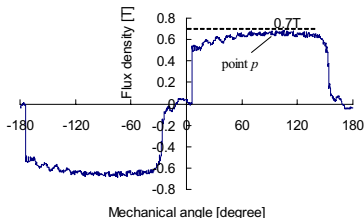


Fig. 5. Residual flux density in magnet (Simulation)

In operation in synchronous speed, steady state characteristics can be obtained by using time-step FEM but it requires very huge computation times. Therefore, in this study, the symmetric field method is introduced to analysis of a WPM in steady state. With the symmetric field method, the stator circuit is depicted in Fig. 6 where the subscript p and n mean positive and negative components respectively. Using superposition theory, the circuit including a rotor part is represented in Fig. 6 where $E(d)$ means a back EMF in the load angle d . The calculated torque, power distributions and efficiency in steady state characteristics are shown in Fig. 8.

Designed WPM is actually fabricated and back EMF is measured after exciter operation as shown in Fig. 9. The measured voltage (153V) coincides with the simulated value (160V). Other measured characteristics such as efficiency and maximum torque will be reported in the full paper.

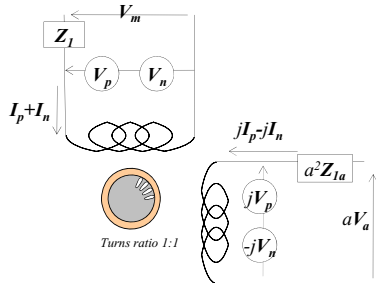


Fig. 6. Symmetric fields in a WPM

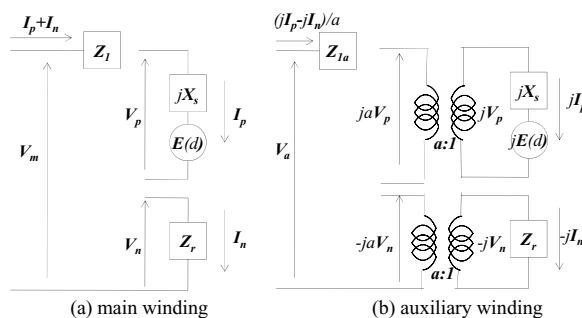


Fig. 7. Equivalent circuit of WPM based on symmetric field theory

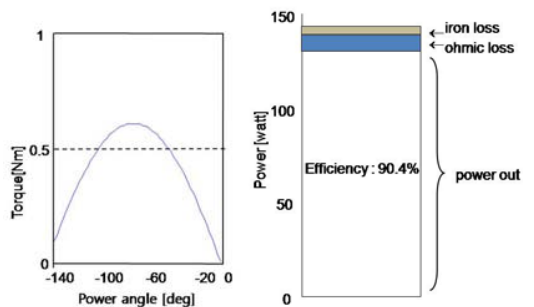


Fig. 8. Characteristics (simulation)

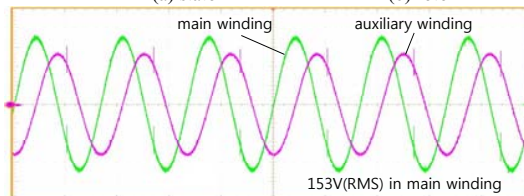
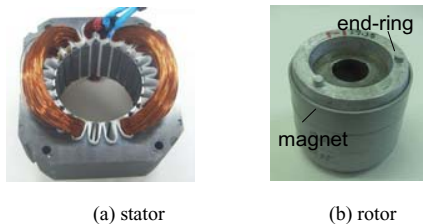


Fig. 9. Fabricated WPM and back-EMF

ACKNOWLEDGMENT

This work is the outcome of a Manpower Development Program for Energy & Resources supported by the Ministry of Knowledge and Economy (MKE) and a second stage BK21 project of Korean Research Foundation.

III. REFERENCES

- [1] S. Hoffman, B. Banerjee and M. Samotyj, "Written-pole Revolution", *IEEE Power Engineering Review*, pp. 6-9, 1997
- [2] Alan Hannah, "Electrical Field Measurements on an EPRI Two-pole, 20-HP Written Pole Motor", *IEEE Transactions on Industry Applications*, 33(2): 408-414, 1997.
- [3] B. T. Kim, et al, "Exciter design and characteristic analysis of a written-pole motor, *IEEE trans. on Magnetics*, 45(3): 1768-1771, 2009.

Inductance Calculation and Measurement of Interior Permanent Magnet Synchronous Motor

Tao Sun, Soon-O Kwon, Jeong-Jong Lee, Geun-Ho Lee, and Jung-Pyo Hong
 Department of Automotive Engineering, Hanyang University
 Haengdang-dong, Seongdong-gu, Seoul, 133-971, Korea
 laplace_sun@hotmail.com, hongjp@hanyang.ac.kr

Abstract — A calculation method and an experiment method for the d- and q-axis inductances of interior PM synchronous motor are introduced in this paper. The calculation method is based on the torque and energy relationship, which are calculated by the magneto-static field finite element analysis. And the experiment is a standstill method. The motor is excited by 3-phase AC voltage source. The measured 3-phase voltage and current will be used to calculate the inductances. Both the calculation and experiment methods consider the saturation and couple-magnetization effects, i.e. the inductances are described with the current magnitude and vector angle. Finally the calculated and experiment results will be verified by the results of conventional method.

I. INTRODUCTION

The dominant influences in the correct prediction of the steady-state characteristics and precise vector control for the interior PM synchronous motor (IPMSM) are the d- and q-axis armature inductances [1]. However, due to the nonlinear electromagnetic characteristics including the saturation and cross-magnetization effect in the rotor of IPMSM [2], the d- and q-axis armature inductances of IPMSM become much difficult to be calculated accurately.

So far, the most arguments on the inductance calculation methods of IPMSM concentrate on three finite element methods (FEM). They are frozen permeabilities method, flux linkage vector method, and flux-linkage perturbation method.[3] Unfortunately, however, there is no special d- and q-axis calculation module in the most commercial FEM software. And making an associated program is not easy for usual users. A general method which is suit for all FEM software becomes more meaningful. Based on this issue, a novel d- and q-axis inductances calculation method is proposed in this paper. It uses the magnetic energy and average torque which can be easily calculated by any commercial FEM software to calculate the inductances. This method not only can consider the saturation and cross-magnetization effect like the previous numerical methods, but also can easily eliminate the influence of space harmonics.

Considering the practical requirements, this paper proposes a relative low cost, simple and tradeoff inductance measurement method. It measures the inductances in standstill condition, in order to avoid utilization of dynamometer. It uses a 3-phase low voltage AC source so that the vector controller and inverter are not required. Hence, it is very suitable for normal laboratory experiment. The most meaningful point is that this method still can consider the saturation and cross-magnetizing effect. In this paper, the principle of this method

will be introduced. And then, based on the deduced equations, the experiment scheme and the processing methods of measured data will be proposed. After briefly introduce a conventional inductance calculation method which has been verified by previous literatures, the results from the proposed calculation and measurement methods will be compared with those of the conventional method. These two inductance evaluation methods will be suitable for most software and hardware environments.

II. PRINCIPLE OF INDUCTANCE CALCULATION METHOD

A. Magneto-static field FEA

The 2D magneto-static field FEM is used to calculate the magnetic field distribution and energy with the known current waveforms. Its governing equation, i.e. the nonlinear Poisson equation, is described in (1).

$$\nabla \times v(\nabla \times A) = J + \nabla \times (v\mu_0 M) \quad (1)$$

where A : magnetic potential vector,

J : current density vector,

M : magnetization vector,

v : reluctivity,

B. Flux linkage vector method

Flux linkage vector method has been verified by the previous literatures. Its principle is shown in Fig. 1, the IPMSM phasor diagram in steady state in the dq frame of reference. As the relationship between the no-load flux linkage vector and load flux linkage vector, (2) and (3), the formula of the d- and q-axis inductances calculation can be obtained.[1]

$$L_d = \frac{\psi_0 \cos \alpha - \psi_a}{i_d} \quad (2)$$

$$L_q = \frac{\psi_0 \sin \alpha}{i_q} \quad (3)$$

C. Energy-torque method

A novel calculation method which makes use of the magnetic energy and torque are proposed in this paper. The principle is,

Step 1: Calculating magnetic energy in no-load condition W_m and flux linkage of PM with FEM;

Step 2: Calculating magnetic energy in load condition W_l with certain current magnitudes and vector angles, meanwhile, get the generated torque.

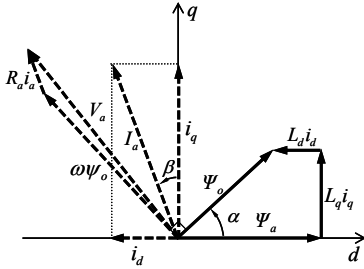


Fig. 1. Phasor diagram of IPMSM in dq frame of reference

Step 3: Calculating the mean value of obtained torques.

Step 4: Depending on the simultaneous equations (4), (5), and (6), the d- and q-axis inductances can be calculated.

$$W_l = W_t - W_m \quad (4)$$

$$W_l = \frac{1}{2} (L_d i_d^2 + L_q i_q^2) \quad (5)$$

$$T_{mean} = P [\psi_a i_q + (L_d - L_q) i_d i_q] \quad (6)$$

where W_m : magnetic energy in no-load condition,

W_t : total energy in load condition,

W_l : magnetic energy in armature windings,

Due to the using of magnetic energy and mean torque, this method is named energy-torque method. The advantages and shortages of this method will be analyzed in the extended paper.

III. PRINCIPLE OF INDUCTANCE MEASUREMENT METHOD

The voltage equation of the IPMSM in the stationary reference frame is described in (1) [4].

$$\begin{bmatrix} v_q^s \\ v_d^s \end{bmatrix} = \begin{bmatrix} r_s & 0 \\ 0 & r_s \end{bmatrix} \begin{bmatrix} i_q^s \\ i_d^s \end{bmatrix} + \begin{bmatrix} p & 0 \\ 0 & p \end{bmatrix} \begin{bmatrix} \psi_q^s \\ \psi_d^s \end{bmatrix} \quad (7)$$

$$\begin{bmatrix} \psi_q^s \\ \psi_d^s \end{bmatrix} = \begin{bmatrix} L_q & -L_{qd}^s \\ -L_{qd}^s & L_d \end{bmatrix} \begin{bmatrix} i_q^s \\ i_d^s \end{bmatrix} + \begin{bmatrix} \psi_m \sin \theta_{er}^s \\ \psi_m \cos \theta_{er}^s \end{bmatrix}$$

$$L_q^s = L + \Delta L \cos(2\theta_{er}^s)$$

$$L_d^s = L - \Delta L \cos(2\theta_{er}^s)$$

$$L_{qd}^s = \Delta L \sin(2\theta_{er}^s)$$

where the subscript e : the unit in electrical angle,

θ_{er}^s is the rotor position in stationary reference frame,

and

$$L = \frac{L_q^r + L_d^r}{2} \quad (8)$$

$$\Delta L = \frac{L_q^r - L_d^r}{2} \quad (9)$$

i.e.,

$$L_q^r = L + \Delta L \quad (10)$$

$$L_d^r = L - \Delta L \quad (11)$$

where L_q^r and L_d^r are the desired q- and d-axis inductances in the rotation reference frame.

It is obvious that the terms with ω_{er}^s can be eliminated in the standstill condition. And in order to eliminate the sine and

cosine terms, the rotor position θ_{er}^s is set to 0° (or 90°). Thus (7) are simplified as (12).

$$v_q^s = r_s i_q^s + L_q^r \frac{d}{dt} i_q^s$$

$$v_d^s = r_s i_d^s + L_d^r \frac{d}{dt} i_d^s \quad (12)$$

According to the dq transformation in the stationary reference frame, the d- and q-axis inductances can be represented by 3-phase voltages and currents that are directly measurable variables. The experiment configuration is shown in Fig 2. More explanation will be extended in the full paper.

IV. RESULTS AND DISCUSSION

Fig. 3 shows the calculated d- and q-axis inductance results by the flux linkage vector method. And Fig. 4 shows the experiment results by the proposed inductance measurement method. The large difference can be seen in d-axis inductances. The measured is greater. This is because the d-axis aligns to the stator tooth at standstill condition. The motor parameters and more discussion will be presented in the full paper.

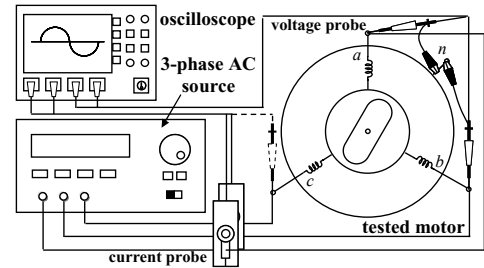


Fig. 2. Experiment configuration of proposed measurement method

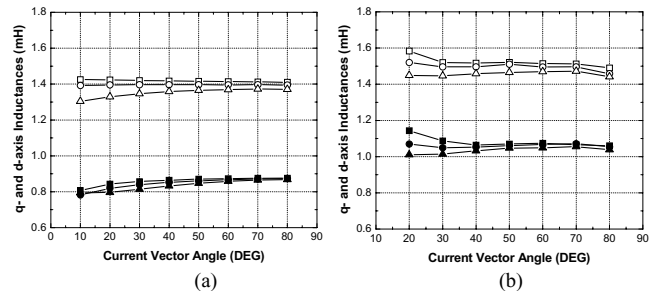


Fig. 3. Inductances: (a) calculated inductances, (b) measured inductances

V. REFERENCES

- [1] G. H. Kang, J. P. Hong, etc., "Improved parameter modeling of interior permanent magnet synchronous motor based on finite element analysis," *IEEE Trans. Magn.*, Vol. 36, No. 4, Jul. 2000.
- [2] B. Stumberger, G. Stumberger, etc., "Evaluation of saturation and cross-magnetization effects in interior permanent-magnet synchronous motor," *IEEE Trans. Ind. Appl.*, Vol. 39, No. 5, Sept./Oct. 2003.
- [3] T. Sun, S. O. Kwon, S. K. Lee and J. P. Hong, "Investigation and comparison of inductance calculation methods in interior permanent magnet synchronous motors," *Electrical Machines and Systems International Conference, 2008. ICEMS 2008*, pp. 3131-3136, Oct. 2008.
- [4] G. D. Andreescu, etc., "Combined Flux Observer With Signal Injection Enhancement for Wide Speed Range Sensorless Direct Torque Control of IPMSM Drives," *IEEE Trans. Energy Conv.*, vol.23, no. 2, pp.393-402, June. 2008.

Shape Optimization of a Thomson-coil Actuator for Fast Response Using Topology Modification

Wei Li, Jiang Lu, Young-woo Jeong*, and Chang Seop Koh, *Senior Member, IEEE*
 Chungbuk National University *LSIS Co. Ltd.
 Chungbuk National University, Cheongju, Chungbuk, 361- 763, Korea
 liwei@chungbuk.ac.kr

Abstract — The shape optimization of a Thomson-coil actuator used in an arc eliminator is done for fast response by adopting topology modification method. The performance of the actuator is analyzed by using an equivalent circuit method. Both shape optimization and performance analysis are accomplished based on the segmentation of plate. The effectiveness of the proposed method is proved by the comparison of results before and after the shape optimization.

I. INTRODUCTION

An arc eliminator (AE) is a fault throwing device, as shown in Fig. 1, to protect electric systems and human lives from an arc fault by bypassing the power current to a ground with high speed in terms of just a few milliseconds at the moment of an arc fault ignition. Owing to the fast function, the AE can provide arc extinction and mitigate the after-effects by the prolonged arc with poisonous and contaminating gas flow. For this reason, Thomson-coil actuator is being more and more employed as the driving unit of the arc eliminator for its remarkable high speed compared with a conventional electromagnetic actuator utilizing electromagnetic attractive force [1].

The Thomson-coil actuator is mainly composed of, as shown in Fig. 1, an exciting coil and a moving plate having ground connection. In order to get a quick ground connection when the switch S is on, the parameters, such as capacitance and its initial charging voltage, exciting coil configuration, might be optimally decided. When selection of the parameters is limited for economic reason (the peak current is very often limited for a cheap switching device), however, the shape optimization of the conducting plate is a good alternative for quick response.

In this paper, the conducting plate of a Thomson-coil actuator for an arc eliminator is shape optimized using ON/OFF method based on the contribution of each segment to objective function [2].

II. PERFORMANCE ANALYSIS

The electromagnetic force of the Thomson-coil actuator is generated by the interaction between the magnetic field by the exciting coil and eddy current induced on the conducting plate. The precise approximation of the eddy currents on the plate, therefore, is essential for accurate performance analysis. In this paper, the conducting plate is divided into a series of segments, as shown in Fig. 2(a), and the eddy current, in each segment, is assumed to be uniform. Each segment, then, physically corresponds to a conductive ring with its circuit parameters of resistance and inductance as shown in Fig. 2(a).

In this way the whole system is transformed into equivalent circuits as shown in Fig. 2(b). The circuit equations, magnetic flux equations and motional equation are obtained, if the plate is divided into N segments, as follows [3]:

$$q/c + I_s R_s + d\lambda_s/dt = 0, \quad (1)$$

$$I_i R_i + d\lambda_i/dt = 0 \quad i = 1, 2, \dots, N \quad (2)$$

$$\frac{d\lambda_s}{dt} = L_{ss} \frac{dI_s}{dt} + \sum_{j=1}^N L_{sj} \frac{dI_j}{dt} + \sum_{j=1}^N I_j \frac{\partial L_{sj}}{\partial z} \frac{dz}{dt}. \quad (3-a)$$

$$\frac{d\lambda_i}{dt} = L_{is} \frac{dI_s}{dt} + I_s \frac{\partial L_{is}}{\partial z} \frac{dz}{dt} + \sum_{j=1}^N L_{ij} \frac{dI_j}{dt}, \quad i = 1, 2, \dots, N \quad (3-b)$$

$$(M + M_a) \frac{d^2 z}{dt^2} = (F_e - F_g - F_f) \quad (4)$$

where the subscripts s and i stand for the exciting coil and i -th segment of the plate, respectively, λ is the linkage flux, F_e , F_g , and F_f are the electromagnetic, gravitational and friction forces, M and M_a are masses of the plate and mechanical appendage, respectively, and other symbols have their usual meaning. The electromagnetic force, F_e , acting on the conducting plate is computed as follows:

$$F_e = \sum_{i=1}^N f_i = - \sum_{i=1}^N I_s I_i \frac{\partial L_{si}}{\partial z} \quad [N] \quad (5)$$

III. SHAPE OPTIMIZATION USING ON/OFF METHOD

The optimization target, in this paper, is the displacement of the conducting plate after 3.5 milliseconds from switching-on. When the conducting plate is divided into N small segments, each segment will contribute to acceleration of the plate by developing electromagnetic force on its eddy current

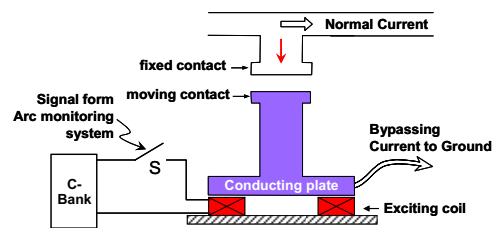


Fig. 1. The simplified mechanism of the Thomson coil type actuator.

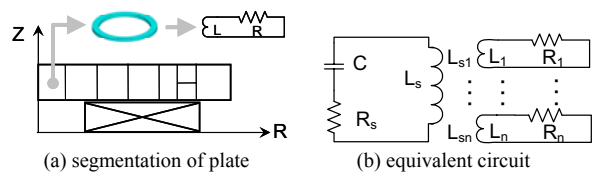


Fig. 2. Equivalent circuit model of the system.

and, at the same time, to deceleration by its own gravitational force.

The acceleration of the plate is calculated from (4), and can be rewritten as follows:

$$a = [F_e - (M + M_a)g - F_f] / (M + M_a) \quad (6)$$

where g is the acceleration of gravity. When the i -th segment is removed from the plate, the acceleration of the plate will be expressed as follows:

$$(a)_i = \{ (F_e)_i - ((M)_i + M_a)g - F_f \} / ((M)_i + M_a) \quad (7)$$

where $(\cdot)_i$ is the quantity obtained without i -th segment. It is assumed, here, that elimination of the i -th segment does not change the friction force and eddy currents in other segments. The contribution factor of i -th segment to the acceleration of plate is finally estimated as follows:

$$c_i = \int_{t_i}^{t_f} (a - (a)_i) dt = m_i / (M + M_a - m_i) \int_{t_i}^{t_f} (a_i - a) dt \quad (8)$$

$$a_i = (f_i - m_i g) / m_i \quad (9)$$

where m_i is the mass of the i -th segment. The final displacement of the plate, finally, can be increased by removing the segments which have small contribution factor from the plate after computing the contribution factors for all segments.

The overall procedure of the shape optimization of the proposed algorithm is summarized as follows:

Step 1. Decision of the initial segmentation

The number of segments should be enough to guarantee an accurate performance analysis.

Step 2. Performance analysis and calculation of contribution factors

The final displacement of the conducting plate, contribution factors of all segments are computed through performance analysis by using the equivalent circuit method.

Step 3. Modification of topology

According to the contribution factors the segments having small contribution factor are removed from the plate. At this stage some segments can not be removed due to a structural constraint.

Step 4. Accept or not the modified topology

With the modified topology, the performance will be analyzed again. If the modified topology gives a better performance (i.e. more displacement), the new topology is accepted as a new topology and go to Step 3 for next iteration.

Step 5. Refinement of the segments

If the modified topology gives worse performance than the previous topology in Step 4, it means the optimum shape exists between the previous and current topologies. If the sizes of all the segments to be removed are small enough, the previous topology is considered as an optimal shape. If some of the segments to be removed are not small enough, they will be divided into smaller segments, and go to Step 2 for more precise topology modification.

IV. RESULTS AND DISCUSSION

Fig. 3 shows the initial structure of the plate with the moving contact and structural constraints for enough me-

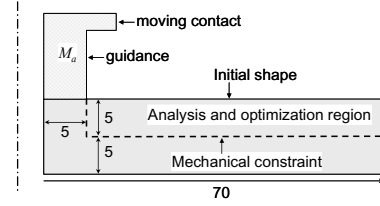
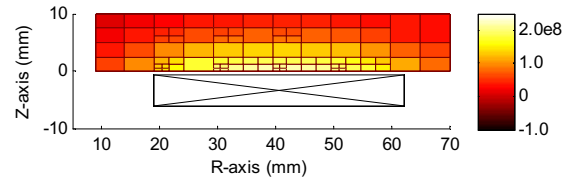


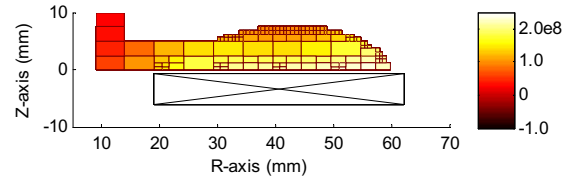
Fig. 3. Initial structure of plate and moving contact.

TABLE I
CIRCUIT PARAMETERS

voltage (V)	capacitor (μ F)	layers	Turns/layer	diameter (mm)
250	25000	19	2	2.6



(a) initial shape.



(b) final shape.

Fig. 4. Plate shape and eddy current density distribution.

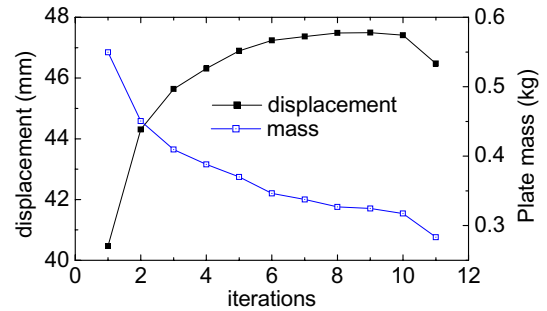


Fig. 5. Final displacement and mass at each iteration.

chanical strength. In the performance analysis the moving contact is ignored, and its mass is taken into account as the additional mass. The exciting circuit parameters are shown in Table.1. The optimized shape of plate with eddy current density distribution is compared with the initial one as shown in Fig. 4. Fig. 5 shows the variation of the final displacement and mass of the plate with respect to iterations. After 10 iterations, an optimum shape which gives 47.5mm displacement with 0.325kg mass is obtained.

V. REFERENCES

- [1] T. Takeuchi, et al., "Electromagnetic analysis coupled with motion for high-speed circuit breakers of eddy current repulsion using the tableau approach," *Electrical Engineering in Japan*, 152(4), pp. 8-16, 2005.
- [2] N. Takahashi, S. Nakazaki, and D. Miyagi, "Examination of Optimal Design Method of Electromagnetic Shield Using ON/OFF Method", *IEEE Trans. on Magnetics*, 45(3): 1546-1549, 2009.
- [3] S.M. Lee, et al., "Reduced modeling of eddy current-driven electromechanical system using conductor segmentation and circuit parameters extracted by FEA", *IEEE Trans. on Magnetics*, 41(5):1448-1451, 2005.

Optimized Axially Magnetized Permanent Magnet Tubular Actuator: Pole-Piece Shaping

Laurentiu Encica, Johan J.H. Paulides, Koen J. Meessen, Bart L.G. Gysen, Jorge L. Duarte, and Elena A. Lomonova

Electromechanics and Power Electronics Group, Eindhoven University of Technology
Den Dolech 2, P.O. Box 513, 5600MB Eindhoven, The Netherlands
E-mail: l.encica@tue.nl

Abstract—Axially magnetized tubular permanent magnet actuators can be designed to obtain a sinusoidal back-electromotive force waveform and almost zero cogging force. The shape optimization of the translator iron pole-pieces is proposed to further enhance the actuator design. This is particularly beneficial for actuators with an external translator where a significant permanent magnet leakage flux is apparent. A space-mapping type of optimization algorithm is implemented to solve the corresponding design problem. A modified approach that considers a semi-analytical coarse model employing Fourier analysis and a simplified magnetic equivalent circuit is proposed and verified in this paper.

I. INTRODUCTION

TUBULAR permanent magnet (PM) actuators provide high efficiency, high power/force density and excellent servo characteristics [1]. In this respect, it has been shown that the particular topology of the tubular PM actuators using axially magnetized patterns have a number of attractive characteristics such as a sinusoidal back-electromotive force (back-EMF) waveform, which coincides with a very low electromagnetic force ripple, and the possibility of being optimized to achieve almost zero cogging force [2]. A particularly attractive advantage is the ease of manufacture of the axially magnetized translator. For an inner translator configuration without back-iron, this magnetization pattern provides virtually "self-shielding", hence most of the magnetic loading is concentrated in the airgap. However, when an external translator configuration is considered, a large amount of leakage magnetic flux is apparent. The shape optimization of the iron pole-piece is proposed in this paper to reduce the leakage flux. This approach provides both an increased airgap flux density and a lower translator mass. The resulting core geometry is also rather easy to manufacture.

To enable a fast optimization procedure, a space-mapping (SM) based technique is considered [3]. Automated electromagnetic actuator design can be achieved by means of several approaches. For example, one might consider fast, however, accuracy deficient coarse models or, in contrast, the design could be achieved exclusively by employing accurate, time expensive, fine models. The SM-based optimization, with its input, output or implicit mapping implementations, merges the advantages of the two extremes. Generally, finite element (FE) models are the predominant choice for fine models, while magnetic equivalent circuits (MEC) are considered as

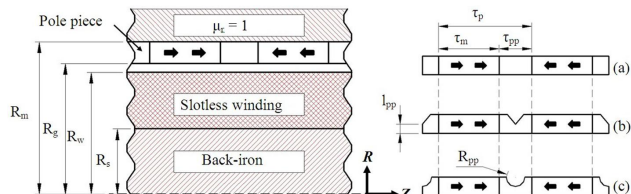


Fig. 1. Cross-section of the external translator tubular PM actuator with axially magnetization pattern illustrating (a) rectangular magnets (b, c) shape optimized pole-pieces (b) triangular, (c) circular.

coarse models for actuators due to the presence of the iron core [4]. However, MEC models provide only a restricted validity because of the designer pre-defined flux paths, which makes these models rather unsuited for optimization problems that can lead to significant modifications of the geometrical configuration of the actuator. Therefore, this paper proposes a modified approach where a semi-analytical model, considering Fourier analysis and a simplified MEC, is employed as a coarse model.

II. SEMI-ANALYTICAL COARSE MODEL

The tubular structure of the actuator presents an axial symmetry and hence a 2D-cylindrical coordinate system, (r, z) , can be considered. This semi-analytical model calculates the airgap field due to the PMs, where a linear PM demagnetization characteristic, infinite iron permeability and infinite motor length are assumed. As shown in Fig. 1, four regions are considered: the slotless winding region (R_s to R_w), the airgap (R_w to R_g), the PM region (R_g to R_m) and the air region outside the actuator. The PM region is separated to include the pole-pieces. Appropriate boundary conditions are defined at the interfaces between the defined regions and on the outside boundary of the design domain. Essentially, at this stage the back-iron and the pole-pieces are excluded from the problem. The resulting boundary value problem is solved by considering the magnetostatic Maxwell equations, reduced to a Poisson equation written in terms of the magnetic vector potential \vec{A} as $\vec{B} = \nabla \times \vec{A}$,

$$\nabla^2 \vec{A} = -\mu_0 \nabla \times \vec{M}, \quad (1)$$

where $\vec{M} = 0$ for the winding the airgap regions. Fourier analysis is employed to describe the magnetization vectors in

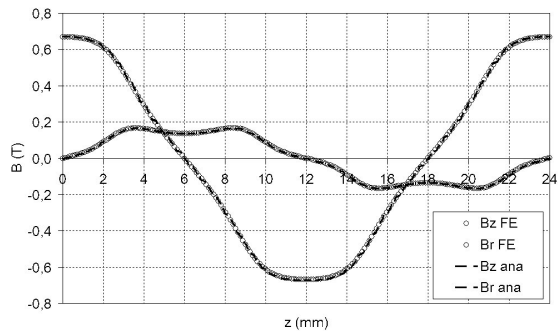


Fig. 2. Flux density in the middle of the source free region by semi-analytical means compared to FE analysis.

the PM region and consequently, the solution for the radial and axial flux density distribution is obtained as a Fourier series [5]. The Poisson equation (1) is solved with the method of separation of variables. This approach provides for a very good agreement with the FE analysis if highly permeable, linear iron is considered or saturation is not reached for non-linear core material. Such a situation is illustrated in Fig. 2. Once the distribution and amplitude of the magnetic flux in the airgap and PM regions are obtained, a simplified MEC model is used to approximate the magnetic flux amplitude in the back-iron and pole-pieces. As such the geometry of the pole-piece is included in the problem by approximation. It is understood that this does not represent the real non-linear material or flux distribution and hence an FE model is introduced as a fine model to accurately determine the influence of varying the shape of the pole-pieces. The SM optimization routine compensates the misalignment between the coarse and fine models by exploiting a reduced number of fine model evaluations and effectively directs the optimization effort onto the coarse model.

III. OPTIMIZATION APPROACH

The main idea of SM optimization is to replace a computationally expensive fine model, $\mathbf{f} : \mathbf{X} \subseteq \mathbb{R}^n \rightarrow \mathbb{R}^m$, with a surrogate based on an iteratively updated coarse model, $\mathbf{c} : \mathbf{Z} \subseteq \mathbb{R}^n \rightarrow \mathbb{R}^m$, which is significantly less time demanding at the expense of accuracy. As a principle, the aggressive output space-mapping (AOSM) algorithm, which is considered in this paper, replaces the original optimization problem $\mathbf{x}^* = \operatorname{argmin}_{\mathbf{x} \in \mathbf{X}} \|\mathbf{f}(\mathbf{x}) - \mathbf{y}\|$, where \mathbf{y} is a set of design specifications, with the surrogate problem given by $\mathbf{x}^* = \operatorname{argmin}_{\mathbf{x} \in \mathbf{X}} \|\mathbf{o}(\mathbf{c}(\mathbf{x})) - \mathbf{y}\|$, where \mathbf{o} is a so-called output mapping. However, from an algorithmic point of view, the following inverse formulation to obtain a new iteration point is preferred:

$$\mathbf{x}_{k+1} = \operatorname{argmin}_{\mathbf{x} \in \mathbf{X}} \|\mathbf{c}(\mathbf{x}) - \mathbf{t}_k(\mathbf{y})\|, \quad (2)$$

i.e., the unmodified coarse model is re-optimized with respect to an updated set of specifications. The updated coarse model specifications, \mathbf{y}_k , account for the misalignment between the coarse and fine models and are determined from quasi-Newton steps considering a Broyden-type Jacobian update [4].

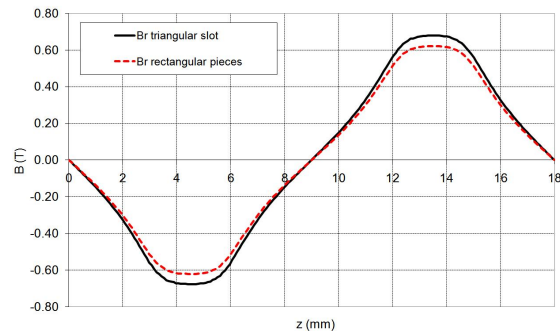


Fig. 3. Airgap flux density for the rectangular and triangular pole-pieces (Fig. 1b).

IV. RESULTS

The proposed analysis and optimization approach is used to determine the optimal magnet to pole-piece ratio (τ_m/τ_{pp}) and the depth of the triangular slot of the external translator tubular PM actuator for a given set of design specifications regarding the actuator force, a maximum limit on the iron flux density and a minimized translator mass. The influence of a modified pole-piece on the airgap flux density is shown in Fig. 3. This figure shows that the peak and RMS values of the airgap flux density are increased when the pole-piece shape is considered in the design procedure. Consequently, the pole-piece shape directly influences the force and acceleration of the external translator tubular PM actuator.

V. CONCLUSIONS

The shape optimization of the translator iron pole-pieces of a tubular PM actuator with external translator is proposed in this paper. As such, an increase in airgap flux density and a reduction of the translator mass can be obtained. A computationally efficient SM-based optimization algorithm is employed to obtain the corresponding design solutions. In this paper, a modified approach is proposed that exploits a semi-analytical coarse model, considering Fourier analysis and a simplified MEC, and an FE fine model. This combined approach for the coarse model provides a significantly higher accuracy of the airgap field calculation compared to a traditional MEC model.

REFERENCES

- [1] J.F. Eastham, "Novel synchronous linear machines: linear and disc," in *Inst. Elect. Eng.*, vol. B-137, 1990, pp. 49 – 58.
- [2] H. Muamer, L. Chen, and S. Liu, "Design and simulation of a moving coil linear actuator for automotive applications," in *IEEE Int. Conf. on Ind. Technology (ICIT)*, 2004, pp. 1023–1027.
- [3] J.W. Bandler, R.M. Biernacki, S.H. Chen, P.A. Grobelny, and R.H. Hemmers, "Space mapping technique for electromagnetic optimization," *IEEE Trans. on Microwave Theory Tech.*, vol. 42, no. 12, pp. 2536–2544, December 1994.
- [4] L. Encica, J.J.H. Paulides, and E.A. Lomonova, "Space-mapping optimization in electromechanics: an overview of algorithms and applications," *International Journal for Computation and Mathematics in Electrical and Electronic Engineering (COMPEL)*, to be published.
- [5] J. Wang, D. Howe, and G.W. Jewell, "Fringing in tubular permanent magnet machines: Part I - magnetic field distribution, flux-linkage, and thrust force," *IEEE Trans. Magn.*, vol. 39, no. 6, pp. 3507–3516, November 2003.

Permanent Magnet Wheel Motor for Electric Vehicle Applications

Konstantinos I. Laskaris, Anastasios G. Vichos, and Antonios G. Kladas *Member IEEE*

Faculty of Electrical and Computer Engineering, National Technical University of Athens,
Electric Power Division

Tel: (+30)-210-7723765, e-mail: laskaris@central.ntua.gr

Abstract— Permanent magnet motors due to their increased efficiency are favored for electric vehicle applications. The geometry optimization of the motor enables to achieve an adequate compromise between the two important parameters of performance and efficiency. The paper presents a methodology based on 2D FEM and sensitivity analysis techniques providing such optimization for the cases of surface and internal permanent magnet motors. The obtained results are validated by measurements on respective prototypes.

I. INTRODUCTION

Wheel motor is a promising traction solution that minimizes transmission loss. Meanwhile the cost of energy storage is considerably higher than the motor production cost and thus affects importantly the design and construction procedures of Electric Vehicle (EV) motors [1], [6].

Torque optimization is a very important issue when selecting a direct coupling of the motor into the wheel, as it is no more possible to increase power by increasing speed. The mean Magnetic Flux Density (MFD) in the air gap, per pole part, determines importantly the output torque capability of a motor. However, over sizing the magnetic loading of a motor can create disadvantages, due to the associated core loss [2].

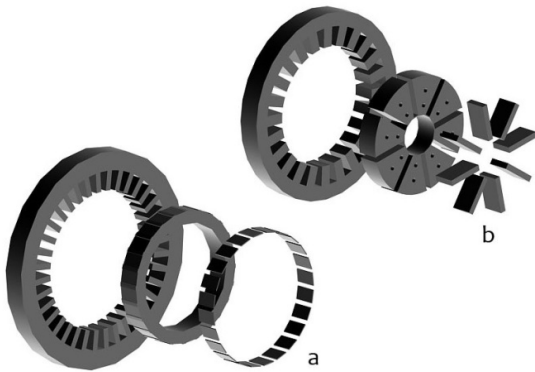


Fig. 1. Wheel Motor Magnetic components geometry
a. SPMM configuration, low magnetic loading 0.6 Tesla
b. IPMM configuration, high magnetic loading 1.2 Tesla

Two motor topologies and the respective prototype implementations, with different MFD values in the air gap, are being studied. A low power compaction 24 pole, 10 kW, Surface Permanent Magnet Motor (SPMM) shown in fig. 1a and a high power compaction 8 pole, 12 kW, Internal Permanent Magnet Motor (IPMM) shown in fig. 1b.

II. METHODOLOGY

A. Sensitivity analysis based on 2D FEM

A two dimensional finite element model (2D FEM) has been employed to analyze the alternative motor topologies. Geometry optimization has been performed by using sensitivity analysis techniques, in order to obtain an appropriate compromise involving all geometrical criteria of the motor configuration [1].

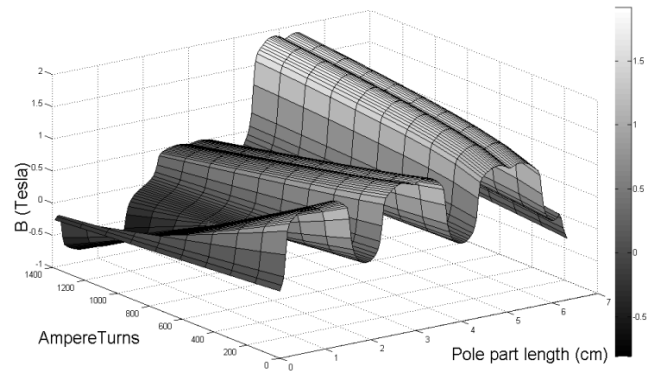


Fig. 2. IPMM flux density distribution for different values of loading current

As shown in Fig. 2 the important flux on the right side of the pole part brings the iron core into saturation area. The MFD accumulation, limits down the capacity of the motor to produce torque [3], [5].

B. Iron loss evaluation technique

This section introduces our method of computing iron core loss for a given motor geometry.

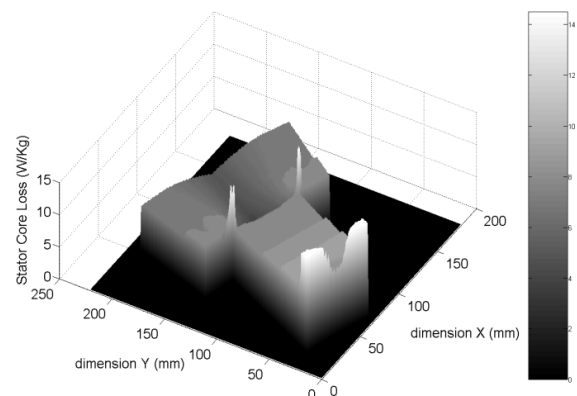


Fig. 3. IPMM Loss Matrix graphical representation at 50 Hz under no load

The motor area is quantized into small subregions, each of which is assigned the value of losses that derives from the material core loss curve, accordingly. The method makes use of the formula (1), in order to determine the total stator core loss:

$$P_{core} = th \cdot P \cdot l_a \cdot \Delta S \cdot \sum_i w(B_{max,i} | f) \quad (1)$$

where th is the number of stator teeth per pole, P is the number of poles, l_a is the axial length of the motor, ΔS is the cross section area of the elementary surface used and w is the volume specific loss, as a function of the maximum flux density during rotation of one pole pitch and the supply frequency. i regards every square element that composes one stator tooth.

C. Global optimization procedure

The optimization procedure is based on a composite cost function that takes into account the total cost of construction and defines the relationship between performance, efficiency and cost. The adopted composite optimizing function F to be minimized is defined in (2), and consists of two parts, denoted by C_K and C_A , defined in (3) and (4) respectively, which are expressed in cost units.

$$F(p_1, p_2, \dots, p_n) = C_K(p_1, p_2, \dots, p_n) + C_A(p_1, p_2, \dots, p_n) \quad (2)$$

where p_1, p_2, \dots, p_n are the parameters that affect construction or operation cost.

$$C_K = c_{mV} \cdot V_m + c_{IL} \cdot L_l + c_{IS} \cdot S_l + c_{FeV} \cdot V_{Fe} + c_{wL} \cdot L_w \quad (3)$$

$$C_A = c_e \cdot E_{tot} \quad (4)$$

where C_K : total construction cost
 C_A : total operation cost
 c_{mV} : specific magnet cost (€/cm³)
 c_{IL} : specific lamination cost (€/m)
 c_{IS} : specific laminated iron core cost (€/m²)
 c_{FeV} : specific solid iron core cost (€/m³)
 c_{wL} : specific winding cost (€/m)
 c_e : specific energy cost (€/kWh)
 $V_x/S_x/L_x$: Volume/Surface/Length x respectively
 E_{tot} : total energy consumed in motor lifetime.

The parts assembly of the optimizing function is made according to the needs and design specifications. The convergence obtained by using different numerical methods such as Golden Section Search, Simulated Annealing and Enumeration is investigated [7].

III. RESULTS AND DISCUSSION

The proposed methodology has been implemented in the design of a surface and an internal permanent magnet motor, shown in Fig. 1. In order to validate the simulation results, two respective prototypes have been constructed.

As an example, Fig. 4 compares the simulated values of the losses compared to the measured ones in the case of IPM motor configuration. The phase voltage ripple observed is mainly caused by the stator tooth harmonic distortion. Loading current increase accumulates field in one side of the pole, which is translated from space to time by distorting the

voltage waveform, as shown in Fig. 5. Core saturation not only increases iron loss but also makes stator current less capable of producing torque [4], [5]. Saturation effects during high load can equally be observed in Fig. 5.

The good agreement between simulated and measured results illustrates the proposed method suitability for this class of problems.

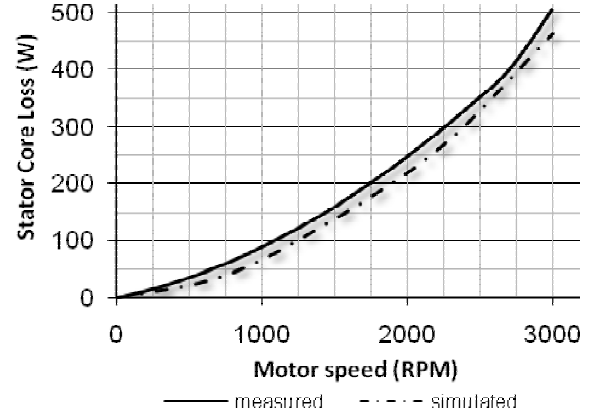


Fig. 4. IPMM Stator Core loss at 50 Hz under no load

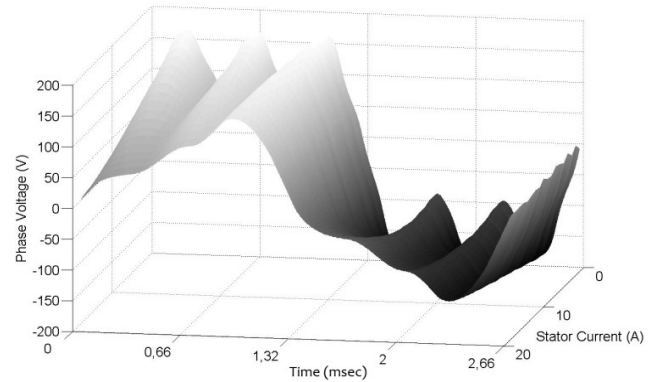


Fig. 5. IPMM Measured phase voltage for different values of loading current

IV. REFERENCES

- [1] K. Laskaris and A. Kladas, "High Torque Internal Permanent Magnet Wheel Motor for Electric Traction Applications", *International Conference on Electrical Machines*, Villamoura-Portugal, 2008.
- [2] K. J. Tseng, S. B. Wee, "Analysis of Flux Distribution and Core Losses in Interior Permanent Magnet Motor", *IEEE Trans. on Energy Conversion*, Vol. 14, No 4, Dec. 1999.
- [3] K. Nakamura, K. Saito, and O. Ichinokura, "Dynamic Analysis of Interior Permanent Magnet Motor Based on a Magnetic Circuit Model", *IEEE Trans. on Magnetics*, Vol. 39, No. 5, Sept. 2003.
- [4] Yee-Pien Yang and Down Su Chuang, "Optimal Design and Control of a Wheel Motor for Electric Passenger Cars", *IEEE Trans. on Magnetics*, Vol. 43, No. 1, Jan. 2007.
- [5] T. Ohnishi and N. Takahashi, "Optimal design of efficient IPM motor using finite element method", *IEEE Trans. on Magnetics*, vol. 36, no. 5, pp. 3537-3539, 2000.
- [6] K. Yamazaki, "Torque and Efficiency Calculation of an Interior Permanent Magnet Motor Considering Harmonic Iron Losses of both the Stator and Rotor", *IEEE Trans. on Magnetics*, Vol. 39, No 3, May 2003.
- [7] P. Venkataraman, "Applied optimization with MATLAB® Programming", *John Wiley & Sons*, New York, 2002.

11. Electric Machines and Drives

Optimized geometrical parameters of a SRM by numerical-analytical approach

A. Bentounsi, R. Rebbah, F. Rebahi, H. Djeghloud, H. Benalla, S. Belakehal and B. Batoun
 Laboratoire d'Electrotechnique de Constantine (LEC), Université Mentouri de Constantine, Algérie.
 E-mail : amar_bentounsi@yahoo.fr

Abstract – The multiple advantages of the switched reluctance machines (SRM) allow them to have various applications. Hence, this led to a growing interest for the design of new structures more successful and better adapted to the new requirements. This paper describes the influence of the geometrical parameters, especially the shape of the teeth, on the performance of SRM based on a coupled finite elements method and equivalent magnetic circuit approach FEM-EMC for an optimal design.

Keywords – SRM, FEM, equivalent magnetic circuit, geometrical parameters, optimization.

I. INTRODUCTION

The robustness, simplicity, reduced cost and high mass torque ratio of the SRM allow them to have various applications at high speed or low speed and high torque [1], [2]. The drawback of these machines is the presence of a pulsatory torque that the researchers try to minimize by optimizing the geometric and control parameters [3-9].

The prediction of the behavior of an electromagnetic system from the knowledge of its non-linear parameters, also connected to external sources, has always been a difficult problem to solve. The numerical solution is *a priori* appealing for solving complex problems with better accuracy but the computing time is penalizing [10]. While easy to implement, the analytical models are relatively inaccurate due to the simplifying assumptions [11].

Consequently, we choose a numerical-analytical method by FEM-EMC modeling to properly design a prototype of a doubly salient 6/4 SRM. The initial results are validated and are encouraging for an optimization procedure of geometric parameters which we develop in this paper [12]. The originality of this work is mainly the study of the influence of the teeth shape, particularly their tilting.

II. PRELIMINARY DESIGN PROCESS

A. The choice of a structure for study

The choice of the number of stator N_s and rotor N_r teeth is important since they have significant implications on the torque. Usually, N_s is selected to be greater than N_r with some conditions [13]. Since the speed is related to the frequency of the supply ($f = N_r * \Omega$), to minimize the iron losses without using material of high quality, we try to reduce the number of rotor poles. Among the most frequently used structures, we finally chose to study a three phase 6/4 SRM represented Fig.1.

The parameters of the 110 Nm, 3000 rpm, 6/4 SRM studied machine are given in Table I.

B. Choosing angles teeth

The choice of the stator and rotor angles teeth ($\beta_s ; \beta_r$) has significant effects on the torque ripple, duration of output torque, winding space and is an important factor in motor design optimization. Initially, they can be selected in the middle of the lower half of the feasible triangle where $\beta_s \leq \beta_r$ and with the three following conditions [7], [8], [13]

$$(2\pi / 3Nr) = 30^\circ \leq \beta_s \leq 45^\circ = (\pi / Nr) \quad (1)$$

$$(2\pi / 3Nr) = 30^\circ \leq \beta_r \leq 60^\circ = (4\pi / 3Nr) \quad (2)$$

$$(\beta_s + \beta_r) < 90^\circ = (2\pi / Nr) \quad (3)$$

III. FEM-EMC MODELING

A. Results by FEM simulation

By combining all of the electromagnetic equations, the vector potential equation governing the problem is

$$\nabla \times \left(\frac{1}{\mu} \nabla \times A \right) = J \quad (4)$$

where A is the vector potential, J is the current density and μ is the permeability.

We solve equation (4) by finite element method which is implemented in FEMM software [14].

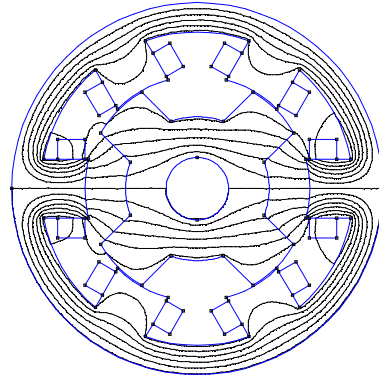


Fig. 1. Flux plot at fully unaligned position of the studied 6/4 SRM

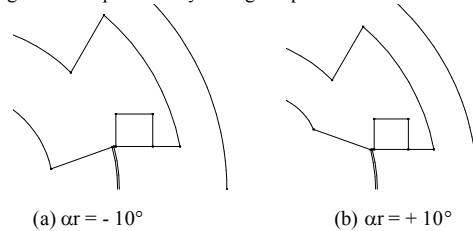


Fig. 2. Tilting of the rotor teeth

11. Electric Machines and Drives

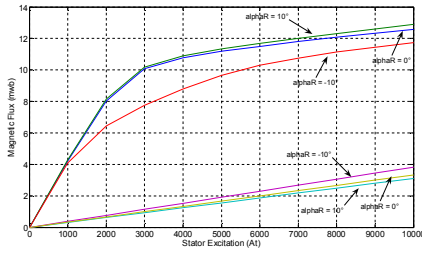


Fig. 3. Effect of rotor teeth tilting on magnetic flux curves

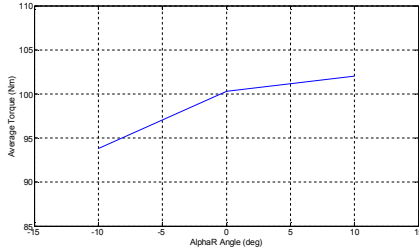


Fig. 4. Effect of rotor teeth tilting on average torque

Among the various results obtained by FEM approach and validated [3-8], we will present in this paper only the influence of the slope of rotor teeth (Fig.2) which is not studied in any paper. In the case of the slope inclined towards the outside ($\alpha_s > 0$), Fig. 3 shows an increase in the area included between the magnetic characteristics of aligned and unaligned positions which induces an increase in the average torque (Fig. 4). We obtained the same results for the stator teeth.

B. Results by EMC simulation

This is a classic analytical method based on the calculation of reluctance portions of the equivalent magnetic. For the two extreme positions of the rotor, we had to work with seven equal flux tubes quite representative of the field lines [15]. We have exploited the previous results of the FEM to make our calculations under *MATLAB* environment with very user-friendly software. The process of optimization is based on the constancy of the following expression of the copper losses

$$P_{cu} = K\rho Lm(NtI)J \quad (5)$$

where K represents the current waveform coefficient, ρ the copper resistivity, Lm the mean length of turn, Nt the number of turns per phase, I the current level and J the current density. Since the excitation NtI is a constant for a design, copper losses are thus proportional to current density.

Among the various results obtained by EMC approach, we show here the optimal values: $\beta r \approx 40^\circ$ for the rotor tooth (Fig. 5) and $kcs \approx 1$ for the stator yoke thickness ratio (Fig. 6).

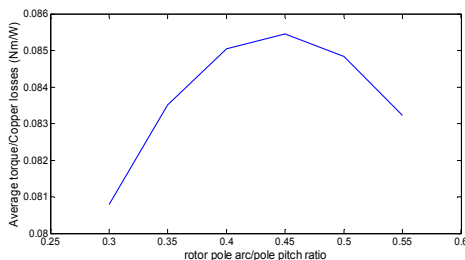


Fig. 5. Effect of rotor pole arc on average torque/copper losses ratio at $\beta_s = 30^\circ$

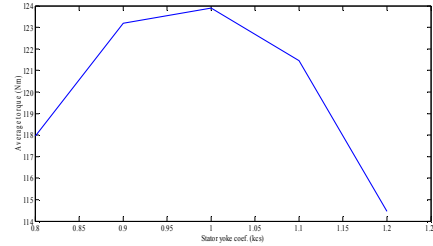


Fig. 6. Average torque vs. kcs ratio at $P_{cu} = 1513$ W and $\beta_s = \beta_r = 30^\circ$

TABLE I
PARAMETERS OF THE STUDIED 6/4 SRM

Quantity	Value
Stack length	150 mm
Outer diameter	250 mm
Rotor diameter	150 mm
Shaft diameter	42 mm
Air-gap length	0.8 mm
Height of stator teeth	26.2 mm
Height of rotor teeth	28 mm
Stator yoke thickness	24.8 mm
Number of turns per phase	23

IV. CONCLUSION

In this paper, we presented a sufficiently simple numerical-analytical procedure by *FEMM* to *MATLAB* software to design and optimize the geometrical parameters of a 6/4 SRM. The obtained results are very interesting.

V. REFERENCES

- [1] H. Kuß et al., "Design of a high SRM for spindle drive", 5th Int. Conf. – Workshop - *CPE*, 2007.
- [2] T. L. Angle et al., "A New Unique HP Pump System", *Proc. 22nd Int. pump users symposium*, 2005.
- [3] M. Geoffroy, "Etude de l'influence des paramètres géométriques du circuit magnétique sur les formes d'onde de perméances et de couple des machines cylindriques à reluctance variable à double saillance", *Thèse Doctorat*, 27 Janvier 1993, Univ. Paris-Sud, France.
- [4] T. Wichert, H. Kuß, "Influence of modified rotor geometry on torque ripple and average torque of a 6/4 SRM", *Proc. of XLII SME'2006*, 3-6 July, Cracow, Poland.
- [5] A. Deihimi and S. Farhangi, "A conceptual optimal design of switched reluctance motors under similar asynchronous motors constraints", *Proc. of EPE'99*, Lausanne, Switzerland.
- [6] E. Hoang et al., "Influence of stator yoke thickness and stator teeth shape upon ripple and average torque of SRM", *SPEEDAM*, 8-10 June 1994, Taormina, Italy, pp. 145-149.
- [7] J.Y. Le Chenadec et al., "Torque ripple minimisation in SRM by optimization of current wave-forms and of tooth shape with copper losses and "V.A. silicon" constraints", *ICEM'94*, Paris, 5-7 Sept. 1994, Vol. 2, pp. 559-564.
- [8] B. Multon et al., "Pole Arcs Optimization of Vernier Reluctance Motors Supplied with Square Wave Current", *Electric Machines and Power Systems*, vol.21, No 6, 1993.
- [9] E. Bizkevelci, H.B. Ertan and K. Leblebicioglu, "Effects of control parameters on SRM", *Proc. of ICEM'2007*, 10-12 Sept. 2007, Turkey.
- [10] B. Parreira, S.Rafael, A.J.Pires and P.J.Costa Branco, "Obtaining the magnetic characteristics of an 8/6 SRM: from FEM analysis to the experimental tests", *IEEE Trans. On Ind. Electronics*, vol. 52, No 6, December 2005, pp. 1635-1643.
- [11] H.C. Lovatt, "Analytical model of a classical SRM", *IEE Proc. Electr. Power Appl.*, 2004.
- [12] A. Bentounsi et al., "Design and modeling of a doubly salient variable reluctance machine", *ICEM'2008*, 6-9 Sept. 2008, Vilamoura, Portugal.
- [13] P.J. Lawrenson et al., "Variable-Speed SRM", *Proc. IEE*, vol.127, Pt.B, No 4, July 1980, pp. 253-265.
- [14] *FEMM*, finite elements software by D. Meeker free downloaded on Web.
- [15] R. Krishnan, "SRM Drives : Modeling, Simulation, Analysis, Design & Applications", Industrial Electronics Series.

Methods for efficient computation and visualization of magnetic flux lines in 3D

Martin Hafner¹, Marc Schöning¹, Marcin Antczak², Andrzej Demenko² and Kay Hameyer¹

1 - Institute of Electrical Machines – RWTH Aachen University

2 - Institute of Electrical Engineering and Electronics – Poznan University of Technology

E-mail: Martin.Hafner@IEM.RWTH-Aachen.de, Marcin.Antczak@doctorate.put.poznan.pl

Abstract—Flow visualization is essential to provide an insight into complex flow patterns of electromagnetic devices. In this paper, a method for the detection and evenly-spaced seeding of closed flux lines in 3D quasi-static electromagnetic fields is presented. The seeding is performed by weighting the magnetic flux on a specified cutting surface. Due to discretization of a finite element simulation, which is also applied for the flux density solution, the force lines are usually not closed. Therefore, an algorithm is introduced, monitoring the force line computation, to provide the generation of closed force lines.

I. INTRODUCTION

An intuitive method for the visualization of vector fields are flux lines, which provide a straightforward visual impression of the field characteristic and the magnetic circuit. Applying this technique to an electromagnetic field solution, one directly encounters the problem of closed flux line computation arising from its solenoidal field characteristics. In this paper, a method is introduced that monitors the stream computation to detect closed curves and minimize the computational effort. Afterwards, the flux line algorithm is combined with a seeding strategy that places starting points in correlation with the flux on a specified cutting surface to support quick flow pattern recognition. The proposed method is generally applicable to the electromagnetic field and comparable flow fields such as eddy current distributions.

II. CLOSED FLUX LINE COMPUTATION

A. Flux Line Computation

A flux line is an oriented curve ρ in a vector field ν on a domain Ω , which is everywhere tangential to the vector flow, with the properties

$$\frac{\partial \rho}{\partial \tau}(\tau) = \nu(\rho(\tau)) \quad (1)$$

$$\rho(\tau = 0) = a \quad (2)$$

where $\rho(\tau)$ is a certain point on the flux line, $\nu(\rho(\tau))$ the corresponding field vector and a an arbitrary start point in Ω . Each point in Ω is strictly mapped to exact one curve ρ .

According to Maxwell equations, the evoked electromagnetic vector field has an solenoidal field characteristic, so that each flux line ρ has a characteristic, but unknown length L , where

$$\rho(\tau + n \cdot L) = \rho(\tau), \forall n \in \mathbb{N} . \quad (3)$$

For a given start point $\rho(\tau = 0)$, the flux line ρ is obtained by integrating (2) iteratively over a discrete length $\Delta\tau$ (integration

step length), yielding

$$\rho(\tau + \Delta\tau) = \rho(\tau) + \int_{\tau}^{\tau + \Delta\tau} \nu(\rho(\tau)) \partial\tau \quad (4)$$

For a rapid and accurate flux line computation, (4) is solved by using a fourth-order Runge-Kutta integrator with adaptive step size and error control [1].

B. Closed Loop Detection

In general, the numeric solution of (4) leads to a continuous summation of the integration error, so that a computed curve does not comply to (3), a typical example is given in fig. 1. To detect such closed flux lines, without any knowledge of

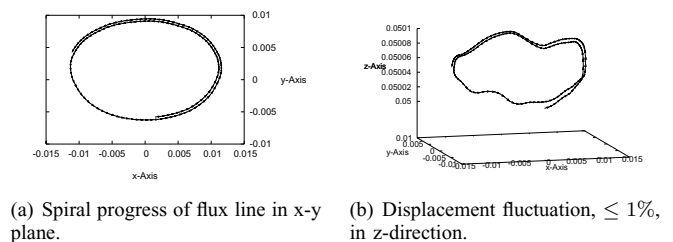


Fig. 1. Typically integration error of eq. (4) in 3D Space. Top and lateral view of a flux line around a current excited rectangular wire in z direction.

the location and shape within the magnetic field, stop criteria are necessary that evaluate the integration process step-by-step and detect the characteristic length L . Basically, an end point $\rho(\tau_i)$ is located in a sphere around $\rho(\tau_0)$ with an error radius ϵ , e.g.

$$\|\rho(\tau_i) - \rho(\tau_0)\| \leq \epsilon . \quad (5)$$

Since the mesh size of Ω typically varies, e.g. in the comparison of an air gap to a back yoke, a more accurate end point detection is required.

Therefore the basic idea of the algorithm is to monitor the integration process and evaluate a modification of (5) by only verifying a possible closing of the curve in 3D space. Counting the number of sign reversal in:

$$\delta(\tau_{i+1}) = \|\rho(\tau_{i+1}) - \rho(\tau_i)\| \cdot \|\rho(\tau_1) - \rho(\tau_0)\| \quad (6)$$

A closed curve, independent from the simulated geometry, requires at least $2k + 1, k \in \mathbb{N}^0$ sign alternations. For point candidates that meet the latter precondition, the point distance perpendicular to the stream direction, given by

$$\|(\rho(\tau_i) - \rho(\tau_0)) \times (\rho(\tau_1) - \rho(\tau_0))\| \leq \epsilon \quad (7)$$

is computed and compared to ϵ . The error control by (7) is, in contrast to (5), independent from the displacement in curve direction, caused by the variable step size $\Delta\tau$.

III. SEEDING STRATEGY

Magnetic flux lines provide a visual impression of the vectorial field direction, and if colored an additional information of the intensity of magnetic field density. To support a quick recognition of the flow pattern by a set of flux lines, their seeding points have to be correlated with the magnitude of the vector field. By this requirement, the better part of seed points is located in an area with high field values and vice versa. Therefore, in this paper a seed point computation on a user defined cutting surface, $C \subseteq \Omega$, is presented. The proposed algorithm is as follows:

- Initially, the flux on all cutting elements in C is evaluated by

$$\Phi = \vec{B}_C \cdot \vec{a}_C \quad (8)$$

where \vec{B}_C is the vectorial flux per element and \vec{a}_C the corresponding oriented surface vector.

- According to a used specified flux range $[\Phi_{min}, \Phi_{max}]$, the plane C is sub-divided into a given number N_{plane} of sub-planes

$$C = \{C_1, C_2, \dots, C_{N_{plane}}\} \quad (9)$$

so that each sub-domain contains all elements with the corresponding flux interval.

- To weight the flux in each sub-domain C_i , the average flux $\Phi_i^{average}$ over all elements N_{C_i} on C_i , given by

$$\Phi_i^{average} = \sum_i^{N_{C_i}} \Phi_i^{elem} \quad (10)$$

is computed, [2], [3].

- For a given number of starting point N_{tot} , the ratio of

$$N_i = \frac{\Phi_i^{average}}{\sum_i^{N_{plane}} \Phi_i^{average}} N_{tot} \quad (11)$$

defines the number of seeding point per sub-domain N_i .

In the final step of the seeding algorithm, the points N_i are placed in the sub-domains C_i . At present state, the starting points are moved to those elements within C_i which have the largest magnitude of the magnetic flux. This leads, as exemplified in fig. 3, to a rough evenly-spaced seeding. An alternative placing strategy is to place N_i on the inner boundary of C_i equidistantly. The latter method is in preparation and will be discussed and compared to the flux-value-based seeding strategy in the full paper.

IV. APPLICATION

A rectangular wire surrounded by air is used as a test model for the seeding strategy in combination with the presented closed flux line algorithm presented in section II-B and III. The source current density J_s is injected into the cross section area of the wire. Fig 2, visualized by [4], shows the applied test scenario together with its vectorial representation of the

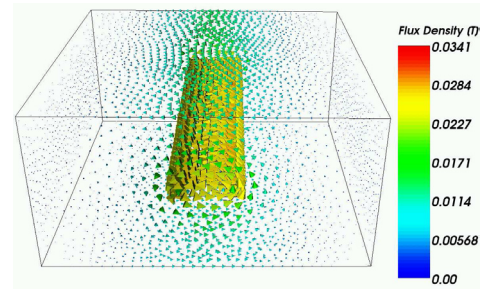


Fig. 2. Current excited rectangular wire in z direction together with its flux density distribution.

flux density distribution, obtained by [5]. Fig. 3 shows the seed point distribution of 100 start point, by a chosen flux interval from 50 to 100 and a decomposition into 10 subdomains. It can be noticed, that the starting point population density

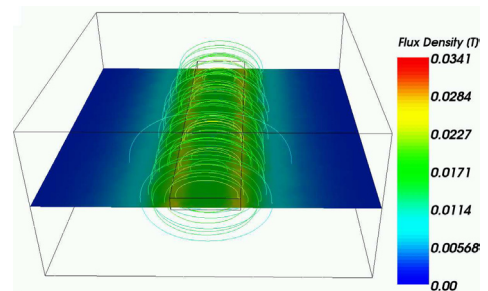


Fig. 3. Closed flux lines seeded around the current excited rectangular wire.

increases by a distance reduction from the wire. The latter provides a visual impression of the flux density distribution. The flux lines are rough evenly-space which helps to recognize the corresponding flow pattern.

V. CONCLUSION

In this paper, an algorithm which detects closed flux lines by extending the integration process by a monitoring routine is presented. The method relies on the assumption of a solenoidal vector field characteristic. To give a visual impression of the vector field solution, a seeding strategy is presented which places seeding points in correlation with the magnetic flux on a cutting surface. As a first test case, the proposed method is exemplified on a 3D air surrounded wire model yielding a flux line distribution which corresponds to the expected flow field pattern.

REFERENCES

- [1] J. D. Lambert, *Numerical Methods for Ordinary Differential Systems: The Initial Value Problem*. Wiley, Sep. 1991.
- [2] V. Cingoski, T. Kuribayashi, K. Kaneda, and H. Yamashita, "Improved interactive visualization of magnetic flux lines in 3-D space using edge finite elements," *Magnetics, IEEE Transactions on*, vol. 32, no. 3, pp. 1477–1480, 1996.
- [3] X. Ye, D. Kao, and A. Pang, "Strategy for seeding 3D streamlines," in *Visualization, 2005. VIS 05. IEEE*, 2005, pp. 471–478.
- [4] I. Kitware, *VTK User's Guide Version 5*, 5th ed. Kitware, Inc., Sep. 2006.
- [5] D. van Riesen, C. Monzel, C. Kaehler, C. Schlensock, and G. Henneberger, "iMOOSE-an open-source environment for finite-element calculations," *Magnetics, IEEE Transactions on*, vol. 40, no. 2, pp. 1390–1393, 2004.

Calculation of Copper Losses in Intercell Transformers by 2D FEM simulation

Bernardo Cougo*, Thierry Meynard*, François Forest**, and Eric Labouré***

*LAPLACE (Laboratoire Plasma et Conversion d’Energie)
2, rue Charles Camichel, 31071, Toulouse. FRANCE.
cougo@laplace.univ-tlse.fr

Abstract— This paper presents an accurate method to calculate high frequency copper losses in InterCell Transformers (ICTs) made with low permeability cores. Since this type of transformer cannot be well represented by 1D model, analytical calculation of the high frequency resistance is not accurate. The method presented here is based on 2D FEM simulations of the ICT. By the nature of this type of transformers, some 2D FEM simulations must be made in order to take into account non-sinusoidal differential and common-mode currents.

I. INTRODUCTION

Interleaved converters are used when high power density is needed. This type of converter has some advantages when comparing to standard converters, such as the increase of the apparent frequency of the voltage applied across the output filters and the improvement in the dynamic behavior of the converter.

Usually an interleaved converter is composed by some identical commutation cells with the outputs interconnected through separate inductors. The association of these inductors may result in large ripple in the current flowing in each cell [1]. This leads to high conduction losses in the switches and high copper losses in the inductors. If we magnetically couple the inductors, we may obtain the same relative current ripple in the commutation cells and at the output. This is obtained by the use of InterCell Transformers (ICTs) [2].

II. SIMPLE INTERCELL TRANSFORMERS

Let’s analyze the operation of ICTs by taking as an example the transformer on Fig. 1. In this transformer, each winding is connected to a commutation cell in such a way that the fluxes from both legs (Φ_1 and Φ_2) are summed up and are obliged to pass by the air (leakage flux). If we use the transformer of Fig. 1 in an interleaved converter composed of 2 commutation cells, and supposing that output voltage is filtered (which is usually the case), we can note that the voltage across each winding is rectangular. Consequently, a triangular flux is imposed in each leg of the transformer.

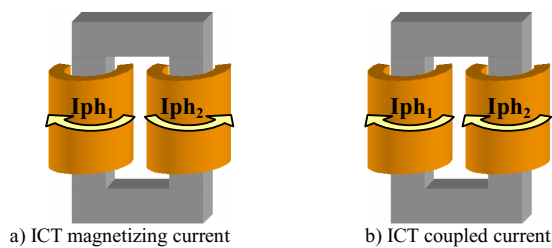


Fig. 1. Simple intercell transformer and current directions

A. Low Permeability Cores Used in Intercell Transformers

Usually high permeability cores are used in the construction of ICTs in order to minimize magnetizing current. However, in certain applications it is preferable to use low permeability cores if we regard globally the magnetic flux density saturation, cost, size and loss density when designing the transformer.

In an ICT, if a low permeability core is used, the core reluctance is comparable to the leakage reluctance. In this case, the current in each cell will be the sum of the magnetizing current (which the fundamental frequency is equal to the switching frequency) and the coupled current (which the fundamental frequency is equal to the double of the switching frequency), as shown in Fig. 2.

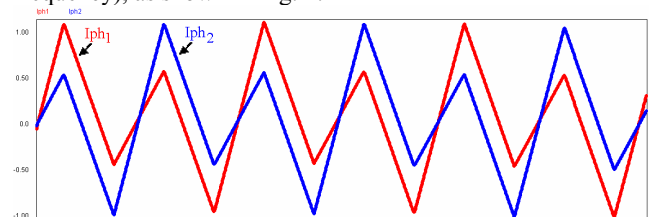


Fig. 2. Phase currents of a 2-phase ICT

III. FEM SIMULATION TO COPPER LOSSES

Analytical calculation of AC resistance of conductors in a transformer was explained by Dowell, in his famous paper from 1966 [3]. He explains the proximity effect mathematically, solving Maxwell’s equations for a 1-D model of transformers. Since Dowell’s 1-D analytical approach models a 3-D phenomenon, several authors make use of FEM simulation to obtain more precise results [4,5]. In our case, 2D and/or 3D simulation is necessary since a great part of the windings is not contained inside the core window.

The use of 3D FEM simulation may result on accurate calculation of the copper losses, but it is very time consuming. 2D FEM simulation can be considered if the procedure used in the simulation takes into account 3D effects.

As we can see in Fig. 2, the component of the current due to the magnetizing current in cell 1 has 180° of phase difference when comparing to the same one in cell 2. Additionally, the components of the current due to the coupled current are in phase in both cells. These facts confirm the need of FEM simulations. In this case, two different 2D simulations are needed: one for the magnetizing current and another one for the coupled current.

The drawing of the transformer in the FEM software is the same for both simulations. When simulating the magnetizing current, the current imposed in each winding must have the same direction inside the core window, as in Fig. 1a. However, when simulating the coupled current, the current imposed in each winding must have opposite directions inside the core window, as in Fig. 1b.

Since most of FEM softwares only allow sinusoidal current simulation, Fourier analysis may be applied to non-sinusoidal currents [6]. Both magnetizing and coupled currents must be decomposed into Fourier series, and a simulation for each important harmonic must be carried out. The easiest way to calculate total AC copper losses is to simulate for each frequency separately and then sum up all results to post calculate 4 equivalent AC resistances, which are:

$R_{ACeqintmag}$ (AC equivalent resistance of the conductors inside the core window, due to the magnetizing current), $R_{ACeqextmag}$ (AC equivalent resistance of the conductors outside the core window, due to the magnetizing current), $R_{ACeqintcou}$ (AC equivalent resistance of the conductors inside the core window, due to the coupled current) and $R_{ACeqoutcou}$ (AC equivalent resistance of the conductors outside the core window, due to the coupled current). The equation of the ratio between the equivalent AC resistance and the DC resistance has the following form:

$$Fr_{eq} = \frac{R_{ACeq}}{R_{DC}} = \sum_{n=1}^{\infty} Fr_n a_n^2 \quad (1)$$

where Fr_n is the ratio between the equivalent AC resistance and the DC resistance of the n^{th} harmonic and a_n is the normalized amplitude of the n^{th} harmonic of the triangular current. a_1 is always equal to 1 to facilitate the calculation.

The DC resistances (R_{DCint} and R_{DCext}) are different for the conductors inside and outside the core window since their lengths may be different. For example, in the transformer in Fig. 1, the length of the conductors inside the core window is equal to the core window depth, while the mean length of the conductors outside the core window is equal to the mean turn length subtracted by the core window depth.

IV. SIMULATION RESULTS

An example will be used to illustrate the method. The ICT of Fig. 1, draw with 6 turns in each winding, was simulated using FEMM software, version 4.2. An example of the simulation output graphs, for one specific frequency, is shown in Fig. 3. We can see the difference between the magnetizing and coupled current density distributions. We also observe a difference in the current density distribution when comparing the current passing inside and outside the core window.

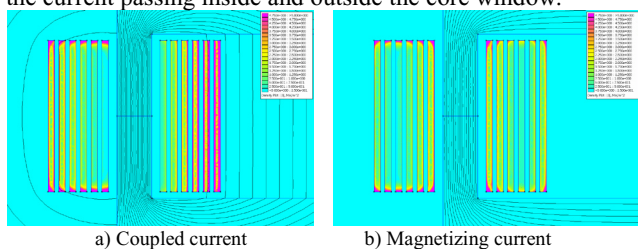


Fig. 3. FEMM simulation of a simple ICT (Current density plot)

The ratios between AC and DC resistances simulated in FEMM are shown in Table I along with the first 5 terms of the Fourier series of the magnetizing and coupled currents when the duty cycle is equal to 0.25 (as the one shown in Fig. 2). Simulations were made at fundamental frequency equal to 15kHz.

TABLE I
AC/DC RESISTANCE RATIO SIMULATION RESULTS

Harm nic	a_n Imag	Fr_n ext-mag	Fr_n int-mag	a_n Icou	Fr_n ext-cou	Fr_n int-cou
1	1	1,64	1,43	1	3,12	2,28
2	0,3536	2,12	1,81	0	4,78	5,86
3	0,1111	2,58	2,26	0,1111	6,58	11,29
4	0	3,07	2,78	0	8,55	17,97
5	0,04	3,58	3,38	0,04	10,60	25,30
		Fr_{eq} ext-mag	Fr_{eq} ext-mag		Fr_{eq} ext-cou	Fr_{eq} int-cou
TOTAL		1,95	1,69		3,21	2,46

Note that the equivalent AC/DC resistance ratios for the conductors outside the core window are different from the ones related to the conductors inside. Also, these ratios are usually higher for coupled current since its fundamental frequency is the double of that for magnetizing current.

Having the four Fr_{eq} , we can calculate the four equivalent AC resistances. The total copper losses are calculated by using these resistances and the phase current.

V. CONCLUSION

Intercell transformers are used in interleaved converters in order to reduce current ripple in each commutation cell. Low permeability cores may be used in intercell transformers but its utilization results in the increase of the magnetizing current, which is superposed to the existing coupled current. We have proposed a simple procedure, based on 2D FEM simulations, which allows the precise calculation of AC resistances associated to the magnetizing and coupled currents, inside and outside the core window. Accurate prediction of these resistances is crucial in an ICT design. An example was given to illustrate the method.

VI. REFERENCES

- [1] Pit-Leong Wong, Peng Xu, P. Yang, and F.C. Lee, "Performance improvement of interleaving VRMs with coupling inductors," *IEEE Trans. on Power Electronics*, vol.16, pp 499-507, 2001
- [2] In Gyu Park, Seon Ik Kim, "Modeling and analysis of multi-interphase transformers for connecting power converters in parallel," *IEEE* 1997, pp 1164-1170.
- [3] P. L. Dowell, "Effect of eddy currents in transformer windings," *Proceedings IEE (UK)*, vol. 113, No. 8, pp. 1387-1394, 1966.
- [4] H. Rossmannith, and M. Albach, "Fast and precise calculation of winding losses in P-, RM- and ETD-ferrite core inductors," *2nd Int. Conf. on Auto. Power Elect, Sept. 2007*.
- [5] C. F. Foo, and X. H. Gong, "Determination of winding losses of high frequency planar-type transformer using finite-element method," *IEEE 6th Power Elect. And Varia. Speed Drives*, pp. 477-482, Sept. 1996.
- [6] W. G. Hurley, E. Gath, and J. G. Breslin, "Optimizing the AC resistance of multilayer transformer windings with arbitrary current waveform," *IEEE Trans. on Power Elect.*, vol. 15, No. 2, pp. 369-376, Mar. 2000.

Loss Analysis and Efficiency Evaluations of Synchronous Reluctance Motor Using Coupled FEM & Preisach Modelling

Jung Ho Lee, *Member, IEEE*, Il Kyo Lee, Yung Hyun Kim
 Dept. of Electrical Engineering, Hanbat National University
 Dukmyung-Dong Yuseong-Gu, Daejeon, 305-719, KOREA
 E-mail: 82donin@naver.com

Abstract — This paper deals with the loss analysis and efficiency evaluations in a synchronous reluctance motor (SynRM) using a coupled transient finite element method (FEM) and Preisach modeling, which is presented to analyze the characteristics under the effect of saturation and hysteresis loss. The focus of this paper is the efficiency evaluation relative to hysteresis loss, copper loss, etc. on the basis of speed, load condition in a SynRM. Computer simulation and experimental result for the efficiency using dynamometer show the propriety of the proposed method.

I. INTRODUCTION

In high-speed applications, hysteresis loss can become the major cause of power dissipation. Therefore, whereas in other kinds of machines a rough estimation of hysteresis loss can be accepted, their importance in a SynRM justifies a greater effort in calculating them more precisely. The Preisach model is now generally accepted to be a powerful hysteresis model, and is therefore intensively studied [1]-[3].

Some papers which discussed the influence of hysteresis loss on a machine have been presented.

Reference [4], [5] have been investigated the steady state characteristics of inductances etc. using coupled FEM & Preisach modeling in a PMA SynRM. Reference [6], [7] have been developed the transient analysis method coupled with vector control algorithm in a LIM and a SynRM respectively.

Reference [8], [9] have been discussed the hysteresis loss influence on the transient behavior of a SynRM and which have the coupled control algorithm & the analysis method.

Reference [10] have been proposed the control algorithm, which selects appropriate stator d, q-axis current component combination that the influence of iron core loss on the developed torque can be minimized in torque control, by the coupled finite element analysis and Preisach modeling in a SynRM.

In this paper, a coupled finite element analysis and Preisach modeling for a SynRM are presented and dynamic characteristic analyses are performed under the effect of saturation and hysteresis loss. The focus of this paper is the efficiency evaluation relative to hysteresis loss, copper loss, etc. on the basis of speed, load condition in a SynRM.

Also, TMS320C31 DSP installed experimental device and dynamometer are equipped and experiments are performed.

Computer simulation and experimental results for efficiency show the propriety of the proposed a coupled finite element analysis and Preisach modeling method.

II. Coupled Fem And Preisach'S Modeling

Coupling governing equation and circuit equation, the system matrix is given as follows:

$$\left[\begin{array}{cc} \mathbf{v}_0[S] & -[N] \\ [0] & [R] \end{array} \right] + \frac{1}{\Delta t} \left[\begin{array}{cc} [0] & [0] \\ [LG]^T & [L_0] \end{array} \right] \left\{ \begin{array}{c} \{A\} \\ \{I\} \end{array} \right\} = \quad (1)$$

$$\frac{1}{\Delta t} \left[\begin{array}{cc} [0] & [0] \\ [LG]^T & [L_0] \end{array} \right] \left\{ \begin{array}{c} \{A\} \\ \{I\} \end{array} \right\}_{t-\Delta t} + \left\{ \begin{array}{c} \{M\} \\ \{V\} \end{array} \right\}_t$$

Where, $\{E\}$: emf. vector in the winding, $\{V\}$: Supplying voltage vector, $\{I\}$: Phase current vector, $[L_0]$: Leakage inductance, $[LG]$: Coefficient matrix related to emf, $\{M\}$: Magnetization calculated by Preisach modeling

Fig. 1 shows the simulation scheme for the proposed analysis method. The torque acting on SynRM at each time is calculated by the line integral of the Maxwell stress tensor.

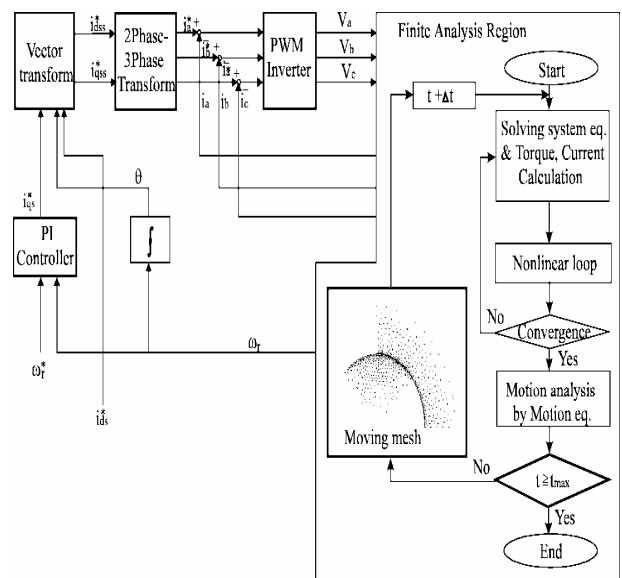


Fig. 1 Block diagram of analysis system

III. Result & Discussion

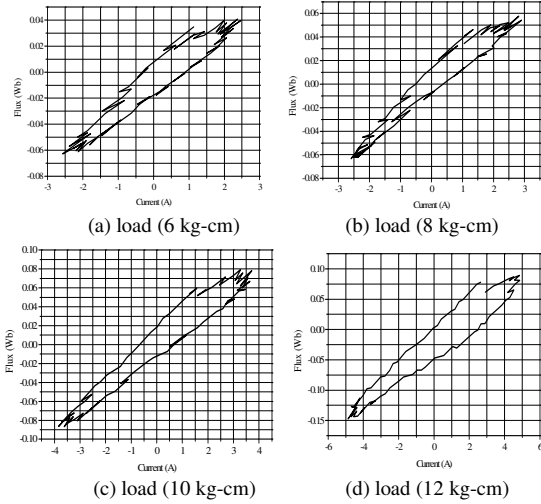


Fig. 2 i-λ loci in each load condition at 2000 rpm

TABLE I
LOSS EVALUATION IN SIMULATION AT 2000 RPM

load (kg-cm)	output (W)	Hysteresis loss (W)	Copper Loss (W)	mechanical loss (W)	the rest loss (W)	phase current (A)
6	122	13.70	4.7	5	4.6	2.2
8	163	12.96	9.03	5	8.01	2.7
10	204	9.92	15.65	5	15.4	3.68
12	244	16.02	25.61	5	21.3	4.7

TABLE II
EFFICIENCY EVALUATION IN EXPERIMENTAL TEST AT 2000 RPM

Load (kg-cm)	input (W)	output (W)	Efficiency (%)	q-axis current (A)	phase current (A)	current angle (deg.)
6	150	122	80	2.35	2	39.2
8	198	163	82	2.8	2.77	47.9
10	250	204	83	3.3	3.65	55.2
12	312	244	78	3.9	4.7	61.5

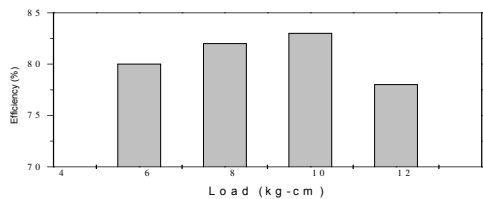


Fig. 3 Efficiency in each load condition

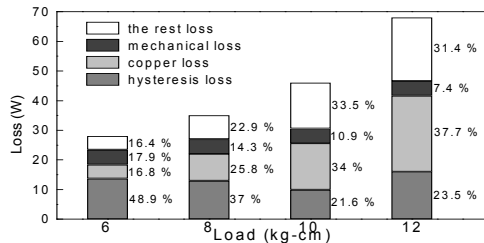


Fig. 4 loss analysis in each load condition

Fig.2 shows the i-λ loci per 1 cycle in each load condition at 2000 rpm.

The hysteresis loss can be calculated by the area of the i-λ loci times the frequency (66.7 Hz), and the copper loss can be calculated by the resistance times rms value square of phase current.

The mechanical loss is about 5 (W) in each load condition, which is experimental data.

The rest losses are the eddy current loss and the stray load loss, etc. These losses are denoted in TABLE I.

Output powers in simulation are the same with that developed in experimental test. Therefore, phase currents are similar to the experimental phase current as shown in TABLE II.

Fig.3 shows the efficiency of each load condition.

It is confirmed that the maximum efficiency current angle (55.2°) is deviated from 45°, as shown in Fig. 3.

Fig. 4 shows the each loss ratio to the total loss in each load condition. Whereas in copper loss increasing current due to the increasing load should be enlarged, their rate in a hysteresis loss should be minimized in maximum efficiency condition precisely.

Through the more detailed analysis and experiment for the another speed (rpms), the variable comparisons for performance of the SynRM will be represented in next extended version

IV. REFERENCES

- [1] A. Ivanyi, Hysteresis Models in Electromagnetic Computation, AKADEMAI KIADO, BUDAPEST
- [2] I. D. Mayeroyz, "Mathematical Models of Hysteresis," *IEEE Trans. In Magnetics*, Vol. MAG-22, No.5, pp.603-608 Sept. 1986
- [3] A. Visintin, Differential models of hysteresis, Applied Mathematical Sciences, Springer, 1994.
- [4] J. H. Lee, D. S. Hyun, "Hysteresis Characteristics Computation on PWM Fed Synchronous Reluctance Motor Using Coupled FEM & Preisach Modeling", *IEEE Transaction on Magnetics*, Vol. 36, No. 7, pp 1209-1212, July 2000.
- [5] J. H. Lee, S. C. Ahn, D. S. Hyun, "Dynamic Characteristic Analysis of LIM Using Coupled FEM & Control algorithm", *IEEE Transaction on Magnetics*, Vol. 36, No. 7, pp 1876-1879, July 2000.
- [6] J. H. Lee, J. C. Kim, D. S. Hyun, "Hysteresis Modelling of Synchronous Reluctance Motor Considering PWM input Voltage", *Journal of Physica B*, Vol. 275, pp 238-247, Jan. 2000.
- [7] J. H. Lee, D. S. Hyun, "Hysteresis Analysis for Permanent Magnet Assisted Synchronous Reluctance Motor by Coupled FEM & Preisach Modelling", *IEEE Transaction on Magnetics*, Vol. 35, No. 5, pp. 1203-1206, May 1999.
- [8] J. H. Lee, J. C. Kim, D. S. Hyun, "Effect of Magnet on Ld and Lq Inductance of Permanent Magnet Assisted Synchronous Reluctance Motor", *IEEE Transaction on Magnetics*, Vol. 35, No. 5, pp. 1199-1202, May 1999.
- [9] J. C. Kim, J. H. Lee, I. S. Jung, D. S. Hyun, "Vector Control Scheme of Synchronous Reluctance Motor Considering Iron Core Loss", *IEEE Transaction on Magnetics*, Vol. 34, No. 5, pp. 2522-2525, Sep. 1998.
- [10] J. H. Lee, J. C. Kim, D. S. Hyun, "Dynamic Characteristic Analysis of Synchronous Reluctance Motor Considering Saturation and Iron Loss by FEM", *IEEE Transaction on Magnetics*, Vol. 34, No. 5, pp. 2629-2632, Sep. 1998.
- [11] D. H. Everett, A general approach hysteresis, Part III., "A formal treatment of the independent domain model of hysteresis", *Trans. on Faraday Soc.*, Vol. 50, pp1077-1096, 1954.

A Novel Calculation Method of Distributed Parameters in Transformer Winding

Zhao Chun¹, Du Zhiye¹, Ruan Jiangjun¹, Peng Ying², and Chen Liang¹

¹School of Electrical Engineering, Wuhan University, Wuhan, Hubei, 430072, China

²Hubei Electric Power Company, No. 341 Xudong Ave, Wuhan, Hubei, 430077, China
chunzi207@126.com

Abstract — In order to investigate the propagation of partial discharge pulses in transformer winding, the simulation models of a 40 turn and a 180 turn continuous transformer winding based on multi-conductor transmission line (MTL) theory are constructed. A novel method is proposed to calculate the K matrix that decreases distinctly calculation cost without loss of accuracy. This new method also has been extended to inductance and resistance calculation, and obtained very good effect. To verify this method further, we solve PD propagation along winding, and compare with the experimental result. And in consequence, the simulation result can meet the experimental result very well. Therefore, this novel method is very reliable.

I. INTRODUCTION

In order to study the partial discharge (PD) propagation characteristics along transformer winding, we have built a distributed line model based on multi-conductor transmission line (MTL) theory [1]. Apparently, the calculation of distributed parameters is quite important for MTL model because it greatly determines the accuracy and efficiency of numerical model. However, although the analytical method is most commonly used, it is very limited because the formulas are from experience and just suitable for special winding with a simple geometry. According to the complexity of transformer winding, the field method has been proved to be more applicable. But for a large n -conductor system, it is considerably time consuming. Therefore, this paper proposes a novel method to calculate distributed parameters which decreases distinctly calculation cost without loss of accuracy.

II. THE ESTABLISHMENT OF WINDING MODEL

This paper chooses to establish two winding model: 40 turn winding model and 180 turn winding model. The structural diagram for winding model is shown as Fig. 1. The 40 turn winding is a single layer continuous hollow winding model. The 180 turn winding consists of 18 coils sections.

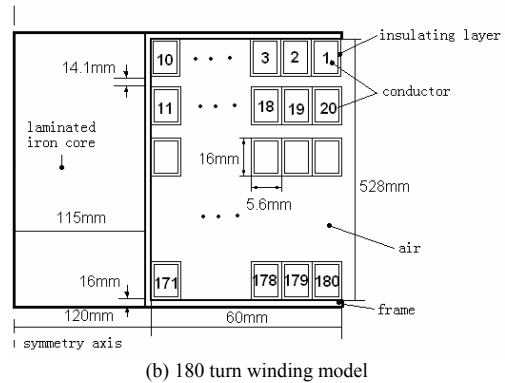
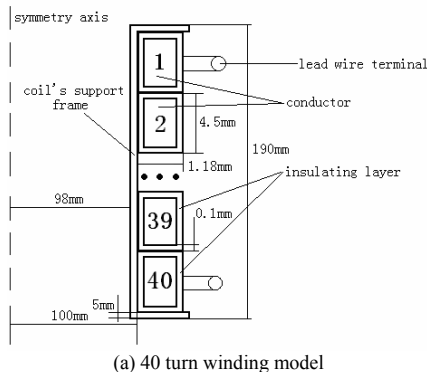


Fig. 1. Structural diagram for winding model

III. THE PROPOSAL OF NOVEL CALCULATION METHOD

In order to simplify the verification for this novel method, we choose 40 turn winding model as analysis model firstly. If this method proves to be reliable, it can be extended to 180 turn winding model. Because induction coefficient is scarcely affected by frequency, the distributed law is easier to analyze than inductance and resistance. Therefore, we try to propose a novel method by analyzing the induction coefficient calculation result firstly. Then, we can apply to inductance and resistance calculation to verify this novel method.

Usually, we can calculate induction coefficient based on electromagnetic theory, total static electric energy W of an n -conductor system in region V can be written as follows [2]:

$$W = \frac{1}{2} \sum_{i=1}^n \left(K_{ii} U_i^2 + \sum_{\substack{j=1 \\ j \neq i}}^n K_{ij} U_i U_j \right) \quad (1)$$

As the winding's special structure, analytical formulas are hard to list. So a normal procedure to evaluate K by field method is as follows.

K_{ii} —First, apply a unit potential on the i th conductor, while the others are set to zero potential. Due to an approximate axisymmetrical structure of the model, a 2-D static electric field FE analysis can calculate W . Then by (1), the diagonal elements of K are obtained.

K_{ij} —Apply unit potentials on the i th and j th conductor, while the other $n-2$ conductors are set to zero potential. As in step 1, after the FE analysis, other elements of K are obtained as well by (1). ($i \neq j$, i is from 1 to $n-1$, j is from $i+1$ to n)

Following the procedures above requires $n(n+1)/2$ FE solution steps to get K , which is almost impossible for large-scale transformer winding ($n > 100$) [3]. Some alternative methods should be carried out. By analyzing K of 40 turn

winding model, we can find some interesting characteristics that will help us overcome this difficulty. It is known that the K_{ij} decrease rapidly with the distance between i th and j th conductor increasing due to the shielding effect of their interval turns. This feature enables that we need fill a few elements in \mathbf{K} only, which greatly reduce \mathbf{K} 's half bandwidth and changes it to a banded matrix. Because $K_{i,i+3}$ is little enough to be ignored, we only consider the interaction between each coil with adjacent two turns. Considering that the winding model is symmetric with respect to the 20th turn, we can calculate the first 21 turns, and then obtain $\mathbf{K}[40 \times 40]$ by matrix transformation. According to the novel method, we only require $3(n/2+1)$ FE solution steps to get \mathbf{K} . As shown in Fig. 2, this novel method decreases distinctly calculation cost without loss of accuracy. Thus, the novel method can be applied to inductance and resistance calculation.

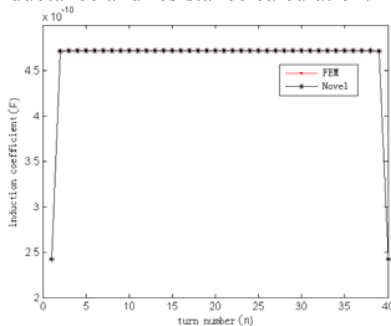


Fig. 2. Distributed law of K_{ij} ($i=1,2,\dots,40$)

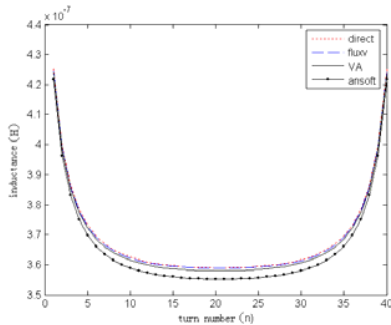


Fig. 3. Distributed law of L_{ii} ($i=1,2,\dots,40$) at 1 MHz

Due to the frequency effect, AC inductance and resistance should be calculated. However, if completely adopting FEM to calculate \mathbf{L} and \mathbf{R} , it would occupy great system resources and cost maximal computing time. Even if in static magnetic field, DC inductance calculation of 40 turn winding should cost 40GB hard disk space. So we must do some simplifications in calculation process. In this paper, we propose calculation of AC inductance and resistance based on the relation between apparent power and complex impedance [4]. In this method, inductance and resistance can be calculated together. Because of winding's symmetry, we also only need calculate the first 21 turns just as the induction coefficient calculation. It takes $n/2+1$ FE solution steps and $(n/2+1)(n/2+n)/2$ postprocessing steps to get \mathbf{L} or \mathbf{R} . Owing to considerable reduction of FE solution steps, the efficiency of this novel method can be improved greatly. To our excited, the novel method can replace completely FEM very well as shown in Fig. 3. In Fig. 3, both "direct" and "fluxv" are based

on magnetic induction intensity integration. "VA" represents this novel method, and "ansoft" is inner macro instruction based on energy principle in ANSOFT environment. The efficiency and accuracy of this novel method are shown as TABLE I.

TABLE I
COMPARISON OF DIFFERENT CALCULATION METHODS

Parameter	Calculation method	FE solution steps	Maximum error	Computing time(min)
\mathbf{K}	FEM	$n(n+1)/2$	0	138
	Novel method	$3(n/2+1)$	0.5%	25
\mathbf{L}	FEM	$n(n+1)/2$	0	255
	Novel method	$n/2+1$	1%	53
\mathbf{R}	FEM	$n(n+1)/2$	0	255
	Novel method	$n/2+1$	1%	53

Because the novel method has been verified by calculation result of 40 turn winding model, it can be extended to 180 turn winding model. According to theory of novel method, except K_{ii} , we need only evaluate the K_{ij} ($i=1,2,\dots,n$, $i+1 \leq j \leq i+2$) in the same section and next to the section. As shown in Fig. 1(b), for example, in order to calculate the induction coefficient of 18th conductor, it is necessary to consider 11 conductors in all coils: the 16th,17th,18th,19th,20th conductor in second section, the 2nd,3rd,4th conductor in first section, and 22nd,23rd,24th in third section. Furthermore, only half of conductors (1~10 section) are necessary to be calculated due to the plane symmetry of transformer winding model.

IV. SOLUTION OF PD IMPULSE ALONG WINDING

In order to verify the parameter calculation result further, we can solve PD propagation characteristics along winding. If the simulation result can meet the experimental result very well, the distributed parameters can be verified once more. Therefore, this novel method can be extended to the parameter calculation of real transformer winding model.

V. CONCLUSION

Because of the shielding effect of interval turns, the turn's K_{ij} decreases rapidly with the distance. \mathbf{K} can be simplified as a banded matrix, and most of its elements need not to be evaluated. A novel method is proposed to calculate the \mathbf{K} matrix that decreases distinctly calculation cost without loss of accuracy. This novel method also can be extended to inductance and resistance calculation. It is very important for us to research on PD propagation characteristics in winding.

VI. REFERENCES

- [1] C. Paul, *Analysis of multi-conductor transmission lines*, New York: John Wiley & Sons, 1994.
- [2] Peng Ying, and Ruan Jiangjun. "Investigation of very fast transient overvoltage distribution in taper winding of tesla transformer," *IEEE Trans. on Magnetics*, 42(3): 434-441, March, 2006.
- [3] Wang Zanji. "Modeling for simulating very fast transient in transformer windings," *Proceeding of the CSEE*, 16(5): 299-355, September, 1996.
- [4] Du Zhiye, Ruan Ling, and Zhao Chun, et al. "Calculation of electrical parameters for studies on propagation characteristic of PD along transformer winding," *Int. Conf. on Computer and Electrical Engineering*, Phuket, Thailand, December, 2008.

Optimal Regularization for MEG Source Reconstruction by Inverse Methods

Feng Luan, Chany Lee, Jong-Ho Choi, Hyun-Kyo Jung

School of Electrical Engineering and Computer Science, Seoul National University, Seoul 151-742, Korea
luanfeng1979@hotmail.com

Abstract — The accuracy of reconstruction of the MEG source is crucially dependent on the conditioning of the leadfield matrix to be inverted. However, the problem of reconstructing MEG source distributions from leadfield is very often ill-posed. In such cases, Tikhonov regularisation is widely employed in order to produce reasonable solutions. However, determination of the amount of regularisation is not straightforward in practical applications without prior knowledge of either the MEG sources or the contaminating measurement noise. Thus, two methods have been introduced, GCV and the L-curve method, which do not require prior information in order to determine the optimal regularisation parameter. In the present work, the abilities of the two methods are illustrated when these kinds of inverse problems are dealt with using Tikhonov regularisation. Finally, through simulations, some guidelines are proposed for determining the optimal degree of regularization for MEG inverse problems.

I. INTRODUCTION

Magnetoencephalography (MEG) is a typical non-invasive human brain mapping technique to estimate neuronal electrical activities on the human cerebral cortex. The main object of MEG inverse problems is to accurately estimate neural current sources from external electromagnetic measurements [1, 2]. For the inverse problem, the field is sampled at different sensor locations and the underlying activity pattern must be determined [3, 4]. The accuracy of reconstruction of the MEG source is crucially dependent on the conditioning of the leadfield matrix to be inverted. However, the problem of reconstructing MEG source distributions from leadfield is very often ill-posed. In such cases, by using only the simple least-squares method, one cannot ensure a successful reconstruction of the MEG source distribution. Therefore, Tikhonov regularisation is widely employed in order to produce reasonable solutions. However, determination of the amount of regularisation is not straightforward in practical applications without prior knowledge of either the MEG sources or the contaminating measurement noise. Thus, two methods have been introduced, GCV and the L-curve method, which do not require prior information in order to determine the optimal regularisation parameter [5-7]. In the present work, the abilities of the two methods are illustrated when these kinds of inverse problems are dealt with using Tikhonov regularisation. Finally, through simulations, some guidelines are proposed for determining the optimal degree of regularization.

II. SIMULATIONS AND RESULTS

We use simulations for the advantage that the correct answer is known a priori, allowing more detailed illustrations of the performance of the methods. A three-shell BEM model

is made as the physical model. The outer shell models the skin, and the middle shell represents the skull surrounding the centrally located brain tissue. Fig.1 shows the cortical source patches to construct artificial MEG data which is contaminated by different levels of noise.

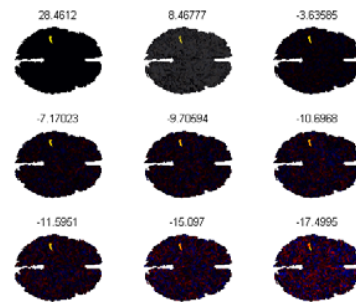


Fig. 1. True sources with contaminating noise

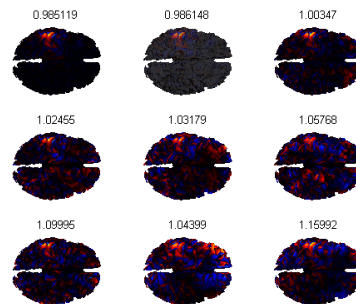


Fig. 2. Reconstruction results produced by Tikhonov regularization using L_curve (contaminated sources)

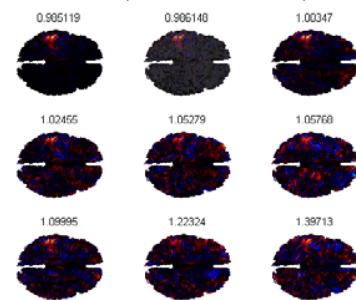


Fig. 3. Reconstruction results produced by Tikhonov regularization using GCV (contaminated sources)

As illustrated in Fig.2, Fig.3 and TABLE I, the relative errors of L_curve and GCV is almost same, however as the signal noise ratio (SNR) of active sources decreases the L_curve method produces more successful reconstruction results than the GCV method.

In order to compare directly the abilities of the two regularization parameter-determination methods in the different measurement noise environment, Fig.4 shows the sensor data with different SNR.

TABLE I
RELATIVE ERRORS IN THE L_CURVE AND GCV
RECONSTRUCTIONS OF CONTAMINATED SOURCES

One Activity			Two Activities		
SNR(dB)	L_curve	GCV	SNR(dB)	L_curve	GCV
28.4612	0.985119	0.985119	30.744	0.977975	0.977975
8.4677	0.986148	0.986148	10.737	0.97877	0.97877
-3.63585	1.00347	1.00347	-1.23164	0.986418	0.986263
-7.17023	1.02455	1.02455	-4.83143	0.999696	0.999696
-9.70594	1.03179	1.05279	-7.28637	1.02531	1.02531
-10.6968	1.05768	1.05768	-8.27992	1.03035	1.03035
-11.5951	1.09995	1.09995	-9.18213	1.03204	1.03204
-15.097	1.04399	1.22324	-12.7257	1.11327	1.12574
-17.4995	1.15992	1.89713	-15.2689	1.17833	1.19953

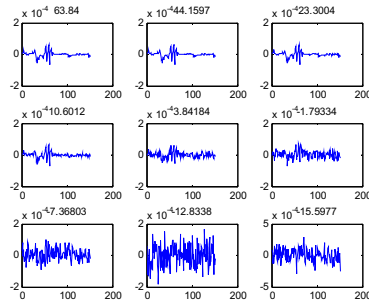


Fig. 4. Sensor data with contaminating noise

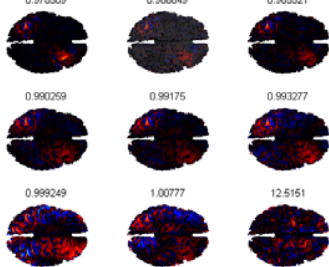


Fig. 5. Reconstruction results produced by Tikhonov regularization using L_curve (contaminated sensor measurement data)

It is clearly evident from Fig.5, Fig.6 and TABLE II that GCV seems to be more robust than the L_curve in the region with relatively high level noise contaminating the sensor measurement data. In other word, GCV method works well particularly in the regions completely dominated by measurement errors compared with L_curve. Therefore, based on the results presented, there seems to be no best method for determining proper regularization parameters in all situations. However, in the cases investigated, L_curve can be more reasonable when the sources with contaminating noise, whilst the GCV method may provide an effective method when the MEG sources reconstructed results are mainly dominated by measurement noise.

III. CONCLUSIONS

The abilities of two different methods, GCV and the L_curve method, for the determination of the proper degree of

regularisation have been simulated for a range of MEG reconstruction conditions in conjunction with sensor and source error. Based on the results of the numerical simulations, it appears that GCV is a better choice for estimating optimal regularisation parameters when the sensor noise levels are relatively high. However, the L_curve method seems to be a more effective method when the active sources are mainly dominated by errors such as contaminating noise. The results presented here may become useful guidelines for the right choice of regularisation parameter-determination method in real-world MEG source reconstruction.

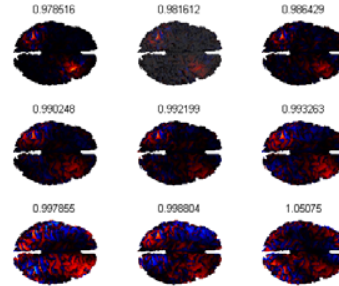


Fig. 6. Reconstruction results produced by Tikhonov regularization using GCV (contaminated sensor data)

TABLE II
RELATIVE ERRORS IN THE L_CURVE AND GCV
RECONSTRUCTIONS OF CONTAMINATED SENSOR DATA

One Activity			Two Activities		
SNR(dB)	L_curve	GCV	SNR(dB)	L_curve	GCV
63.84	0.985377	0.985596	65.7671	0.978509	0.978516
44.1597	0.987616	0.985836	45.6149	0.986649	0.981612
23.3004	0.988211	0.989551	24.3205	0.985521	0.986429
10.6012	0.992303	0.992243	10.3191	0.990259	0.990248
3.84184	0.9944	0.995172	5.02998	0.99175	0.992199
-1.79334	0.993747	0.993935	-0.792998	0.99327	0.993263
-7.36803	8.58595	0.996125	-7.54336	0.999249	0.997855
-12.8338	418.819	0.99963	-12.2077	1.00777	0.998804
-15.5977	689.006	0.999796	-15.3296	12.5151	1.05075

IV. REFERENCES

- [1] C. M. Michel, M. M. Murray, G. Lantz et al., "EEG source imaging," *Clinical Neurophysiology*, vol. 115, no. 10, pp. 2195-2222, Oct, 2004.
- [2] I. Chang-Hwan, L. Chany, A. Kwang-Ok et al., "Precise Estimation of Brain Electrical Sources Using Anatomically Constrained Area Source (ACAS) Localization," *Magnetics, IEEE Transactions on*, vol. 43, no. 4, pp. 1713-1716, 2007.
- [3] B. D. VanVeen, W. vanDrongelen, M. Yuchtman et al., "Localization of brain electrical activity via linearly constrained minimum variance spatial filtering," *Ieee Transactions on Biomedical Engineering*, vol. 44, no. 9, pp. 867-880, Sep, 1997.
- [4] S. Baillet, J. C. Mosher, and R. M. Leahy, "Electromagnetic brain mapping," *Ieee Signal Processing Magazine*, vol. 18, no. 6, pp. 14-30, Nov, 2001.
- [5] R. Bortel, and P. Sovka, "Regularization techniques in realistic Laplacian computation," *Ieee Transactions on Biomedical Engineering*, vol. 54, no. 11, pp. 1993-1999, Nov, 2007.
- [6] J. Schreiber, J. Haueisen, and J. Nenonen, "A new method for choosing the regularization parameter in time-dependent inverse problems and its application to magnetocardiography," *Ieee Transactions on Magnetics*, vol. 40, no. 2, pp. 1104-1107, Mar, 2004.
- [7] Y. Kim, and P. A. Nelson, "Optimal regularisation for acoustic source reconstruction by inverse methods," *Journal of Sound and Vibration*, vol. 275, no. 3-5, pp. 463-487, Aug 23, 2004.

Dynamic Force Analysis of Saturated Core HTS FCL under Short-Circuit Operation

Xu Fang, Jie Qiu, Shuhong Wang, Hongli Xiao

Faculty of Electrical Engineering, Xi'an Jiaotong University, 28 West Xian Ning Road, Xi'an, 710049, China

shwang@mail.xjtu.edu.cn

Weizhi Gong, Ying Xin

Innower Superconductor Cable Co., Ltd, Beijing, 100176, China

Jian Guo Zhu, Youguang Guo, Yi Wang, Wei Xu

Faculty of Engineering, University of Technology, Sydney, P.O. Box 123, Broadway, NSW2007, Australia

Xiaoyang Zhang

Shaanxi Electric Power Company, Xi'an 710048, China

Abstract—In this paper, the transient short circuit current of a three-phase saturated core high temperature superconducting (HTS) fault current limiter (FCL) is investigated by using a method combining 3-dimensional (3D) finite element analysis (FEA) and equivalent dynamic nonlinear model. The numerical computations are verified by the experiment results on a 380V prototype. Based on the short circuit current of the FCL, the three phase transient magnetic field is simulated and analyzed by 3D FEA. According to the simulated results, the short circuit electromagnetic forces of a 220kV and a 35kV saturated core HTS FCLs are calculated. Combined with numerical calculation method, the relationship between prestress and peak dynamic force and displacement of each pancake coil are analyzed and the influence of prestress on axial kinetic characteristics of winding is revealed. Elliptical and circular windings are applied on the 35kV and 220kV FCLs respectively, and the dynamic force and displacements of each pancake coil of the two types of windings are compared and analyzed.

I. INTRODUCTION

Short circuit is one of the major problems facing the power system, which immensely affects the system safety and reliability. All the devices in the power system, such as circuit breakers and transformers, have to be designed to withstand high mechanical and thermal stresses caused by the short-circuit current. The superconducting fault current limiter (FCL) has been expected as a possible type of power apparatus to reduce the fault current in power transmission lines, and various types of FCLs have been proposed and tested [1-2]. The saturated core high temperature superconducting (HTS) FCL offers a fast and effective current limitation with automatic recovery [3].

When the short-circuit fault occurs, an enormous short-circuit electromagnetic force is induced and the windings may be distorted and damaged resulting in limiting-current failure of FCL. Therefore, it is very important to calculate the short-circuit electromagnetic force on the windings of saturated core HTS FCL and to analyze the displacements of each pancake coil and the influence of prestress on axial kinetic characteristics of the windings.

II. CALCULATION OF SHORT-CIRCUIT CURRENT AND ELECTROMAGNETIC FORCE

This paper carries out the numerical simulation for the performance of a designed three phase HTS FCL using a method combining 3-dimensional (3D) FEA and equivalent mathematic modal, which can achieve high accuracy for transient performance calculation. Because of the nonlinearity of the ferromagnetic core, the inductance of the HTS FCL is associated with the currents flowing through the AC windings and DC windings. The nonlinear inductance of the FCL is calculated using the energy perturbation method [4] based on FEA. The transient short current could be acquired from the solution of equivalent dynamic nonlinear model, using the characteristics of inductance versus current (L-I curve).

The computed transient current of FCL in both normal and three phase fault conditions are conformed through the measurement on the 380V prototype. Fig. 1 illustrates the measured and simulated currents, respectively. The transient currents of 35kV and 220kV FCLs are also calculated by using the same method. Fig. 2 shows the simulated current of 35kV FCL when three phase short circuit fault (the worst situation) occurs. Fig. 3 shows the simulated current of phase A of 220kV FCL. The figures of other two phases will be presented in the final paper.

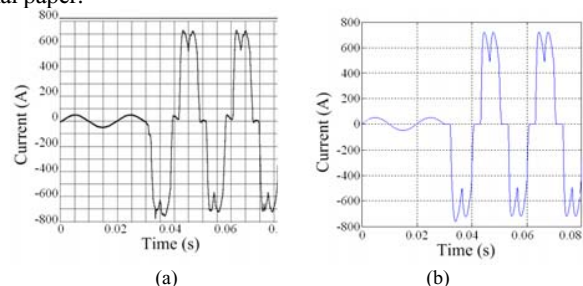


Fig. 1. Comparison between the measured and simulated current of a 380V FCL: (a) Measured, (b) Simulated.

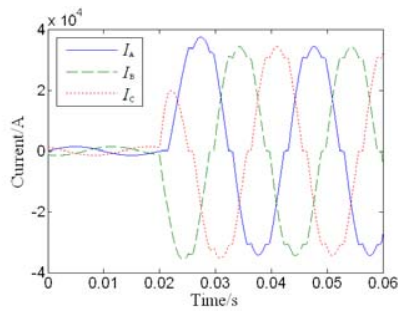


Fig. 2. Simulated current of a 35kV FCL

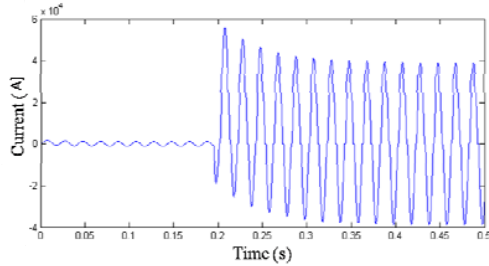


Fig. 3. Simulated current of a 220kV FCL

Numerical calculation is carried out based on the theory of finite element method, considering the saturation of the silicon sheet and the non-sine variations of the current. 3D transient electromagnetic field in the saturated core FCL under short-circuit condition is calculated, and then the distribution of electromagnetic field is obtained. Radial and axial electromagnetic forces are calculated by using the Lorentz formula. Based on the results, circumferential stress of each disk unit is calculated to check the strength of windings under short-circuit condition.

Figs. 4 to 7 show the electromagnetic force of 220kV FCL. More results and analyses about the electromagnetic force will be presented in the final paper.

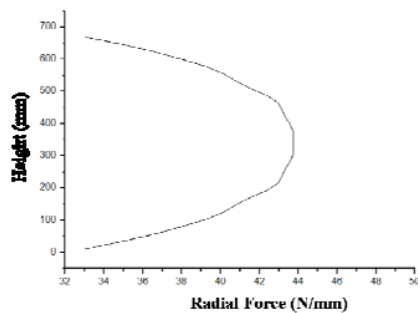


Fig. 4. Distribution of radial force

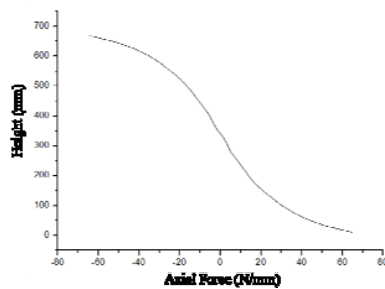


Fig. 5. Distribution of axial force

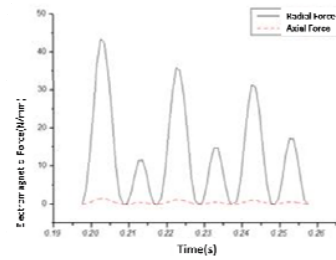


Fig. 6. Transient electromagnetic force of the middle pancake coil

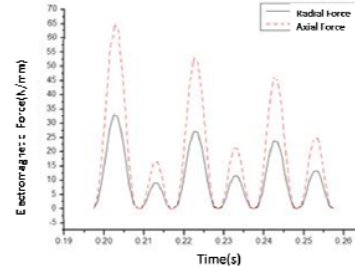


Fig. 7. Transient electromagnetic force of the bottom pancake coil

During the transient process of short-circuit, both short-circuit current and leakage magnetic field change continuously. Therefore, the short-circuit force, which is generated by the interaction between short-circuit current and leakage magnetic field, are a dynamic force actually. The calculation of dynamic force should consider these factors: the mechanical property of various insulation materials, inertia force, elastic force, and friction force which acts on the displacement of the structures. Combined with numerical calculation method, the relationship between prestress and peak dynamic force and displacement of each pancake coil are analyzed and the influence of prestress on axial kinetic characteristics of winding is revealed. The dynamic force and displacements of each pancake coil of elliptical and circular windings are compared and analyzed. The two types of modals are shown in Fig. 8. The calculated results of dynamic force and displacement of each pancake coil and their analysis will be presented in the final paper.

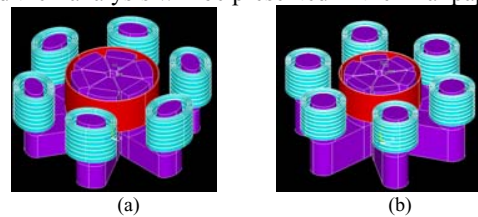


Fig. 8. Half modal of saturated core HTS FCLs with (a) elliptical windings, (b) circular windings

III. REFERENCES

- [1] T. Kataoka and H. Yamaguchi, "Comparative study of transformer type superconducting fault current limiters considering magnetic saturation of iron core," *IEEE Trans. on Magnetics*, 42(10):3386-3388, 2006.
- [2] Ying Xin, Weizhi Gong, Xiaoye Niu, *et al.*, "Development of saturated iron core HTS fault current limiters," *IEEE Trans. on Applied Superconductivity*, 17(2):1760-1763, 2007.
- [3] Fan Kai, Jie Qiu, Shuhong Wang, *et al.*, "Transient simulation and analysis for three-phase saturated core high temperature superconducting fault current limiter," in digest book of CEFC 2008, Athens, Greece, 2008.
- [4] Chen Zhen-mao and Xu Jia-xuan, "The nonlinear vibration of large transformer windings," *Chinese Journal of Applied Mechanics*, 7:21-30, 1993

Adaptive Ablation Treatment Based on Impedance Imaging

I.M.V. Caminiti¹, F. Ferraioli², A. Formisano¹, R. Martone¹

¹Dipartimento di Ingegneria dell'Informazione, Seconda Università di Napoli

Via Roma 29, I-81031 Aversa CE, Italy

E-mail: idamariavincenza.caminiti@unina2.it

²Ansaldo Ricerche S.p.A. Naples Branch Office

Via Nuova Delle Brece 260, I-80147 Naples, Italy

Abstract — In the international scientific community there is an increasing interest in the application of minimally invasive techniques to the treatment of primary and metastatic tumours. Among the possible techniques, RadioFrequency Ablation (RFA) is considered potentially successful. For the monitoring of ablative treatment, Electrical Impedance Tomography (EIT) arises particular interest for its low cost and good sensitivity to tissue electrical properties changes. In this paper, an adaptive ablation treatment based on EIT measurements is presented. Remarks for configuring the ablation electrodes system are proposed in order to optimize the distribution of power deposition, in particular minimizing the power delivered to the more sensible healthy tissues.

I. INTRODUCTION

RFA is a technique used in the field of medical oncology, for the treatment of primary and metastatic tumours, in particular when patients are not candidates for surgical resection [1]-[3]. RFA destroys pathological tissue by raising their temperature. To this purpose, a radio frequency alternating current (450–550 kHz) is injected into the tissue through needles inserted percutaneously, laparoscopically, or during surgery [1]-[3]. The system is completed with an adhesive return electrode to close the circuit and to allow the current flow through the patient. A current field is, therefore, created between the probe and a return electrode usually placed on the back of the patient. When the temperature of cells exceeds 45–50 °C, the denaturation of intracellular proteins and destruction of cell membranes occurs; furthermore if the temperature is higher than 90°C the carbonization of tissues is achieved. The success of the treatment, therefore, relies on the accurate prediction of the thermal field distribution in pathological tissues as well as in adjacent healthy tissue. The selectivity in the treatment is most important indeed, because of healthy tissues have not to be affected, and consequently their temperature must be kept below 42 °C [5].

The EIT is a non invasive imaging technique based on the identification of the complex admittivity profile inside a domain from measurements of electrical currents and voltages made on its boundary [6]-[10]. It has potential application in several fields such as geophysics, clinical diagnostics on human body, environmental sciences and non-destructive testing on materials. In particular, its clinical applications are intensively investigated because it exhibits some important advantages such as the absence of ionizing radiations,

portability and relatively low cost of the instrumentation [9], and a good time resolution, which makes it particularly suitable for continuous monitoring of patients [10]. In addition the suitability of the EIT for real time monitoring of the temperature rise in ablation treatments have been assessed [6]-[8]. In particular, it has been shown how a further improvement in EIT sensitivity could be achieved if using the RFA needle as a further electrode [6].

In this paper, the possibility of optimizing the distribution of Ohmic power deposited by the RFA treatments, minimizing the power delivered to sensible healthy tissues, is investigated. This is achieved by using a multiple return electrodes system, and designing an “optimal” current map starting from internal admittivity profiles, obtained using EIT measurements. In the following of this digest, an example of optimized ablation procedure will be presented, and some preliminary results will be briefly outlined.

II. PROBLEM FORMULATION

The temperature map actually achieved in internal tissues during a RFA treatment can be analysed using a coupled electrical and biothermal model [5]. Note that to be effective, RFA treatments require on one hand a localized temperature rise in cancerous tissue, but on the other hand safety issues must be taken into account in order to avoid unwanted damage of healthy tissues, causing eventually internal bleeding. For this reason any tool allowing to estimate and eventually drive the current density pattern in the patient’s body would be of great benefit, allowing to improve even state of the art RFA procedures.

In this paper a formulation of the problem based on the estimation of the tissues properties during the treatment based on the EIT is presented. Such a piece of information can be used to optimise the current path driven by the RFA equipment.

In order to include the therapeutical needs in the mathematical model of the RFA, a *target* distribution of power density P_T [W/m³] is defined, considering the physiopathological conditions of the subject to be treated. The target map P_T is such that the power delivered to the tumour region allows sufficient temperature rise for treatment, while keeping sensible tissues “protected” by preventing excessive temperature rises. As a matter of fact, the power density portraying the instantaneous situation in the coupled biothermal-electromagnetic model is $\sigma_m J^2$, J being the module

of the current density field, while σ_m is the electrical conductivity, eventually estimated in real time by the EIT. The most general scenario envisages the use of FEM/BEM discretization of the subject's body based on MRI pictures.

The treatment efficiency can be optimized by minimizing the weighted discrepancy $D(J, \sigma_m)$ between target and actual Ohmic power delivered to the internal of patient's body (which is described as a regular non homogeneous domain Ω):

$$D(J; \sigma_m) = \iint_{\Omega} \lambda(\mathbf{r}) \left\| \sigma_m(\mathbf{r}) J^2(\mathbf{r}) - P_T(\mathbf{r}) \right\|_{L^2}^2 d\Omega \quad (1)$$

where \mathbf{r} is the field point in Ω and λ is a weighting function accounting for different relevance of the tissues and for their sensitivity to temperature rises.

In the minimization of D , the control parameter is represented by the current density amplitude J , while σ_m represents a parameter which cannot be modified but, nevertheless, impacts on D , and must be consequently kept under control (e.g. using EIT measurement for its estimation).

The current density map is in turn "shaped" by adopting multiple return electrodes on the patients skin, connecting each to a different voltage or current source in the power supply system, and selecting the voltage/current sources amplitude able to minimize D .

In the full paper, the adaptive strategy for power distribution design will be illustrated in detail, while a simple example of application is presented here.

III. PRELIMINARY RESULTS

For the sake of simplicity, a 2-D domain Ω , representing the section of a patient's torso, has been considered in this study. A subdomain Ω_T representing the tumoral tissue and a subdomain Ω_p to be protected from temperature rise are defined, and a two return electrodes system has been considered in alternative to the standard single electrode one (see Fig.1). The total area of the two electrodes in the configuration (b) is equal to the area of the single return electrode of the configuration (a).

Comparisons between the total delivered power density, the power delivered in Ω_p and in Ω_T for the two different return electrodes configurations have been computed using a FEM model, and are reported in Table I. In addition, in Fig. 2 the Ohmic power density maps for case (a) and (b) are reported, limitedly to the region Ω_p . Note the different scale of delivered power density.

The simple example highlights how a careful design of the return path of the current can be importantly influence the selectivity of the treatment without affecting its effectiveness.

IV. REFERENCES

[1] R. Lencioni, et al., "Percutaneous Ablation of Hepatocellular Carcinoma: State-of-the-Art", *Liver Transplantation*, 10(2): S91-S97, 2004.

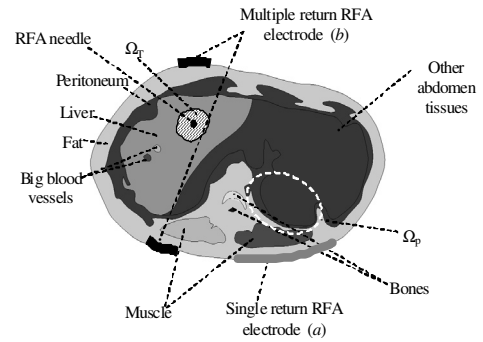


Fig. 1. Return electrodes configurations examined to optimize an RFA treatment: standard one (grey, a) and multiple electrodes one (black, b)

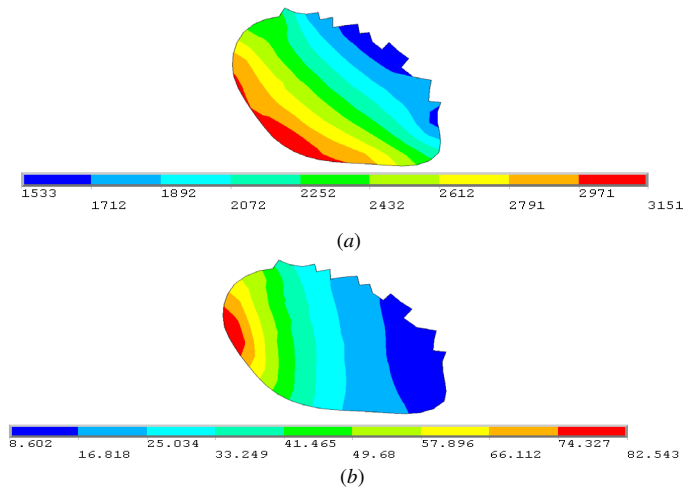


Fig. 2. Ohmic power density in Ω_p for different electrodes configuration.

[2] H. Rhim et al., "Radiofrequency Thermal Ablation of Abdominal Tumors: Lessons Learned from Complications", *Radiographics*, 24(1): 41-53, 2004.

[3] S. Tungjitkusolmun et al., "Three dimensional finite-element analyses for radio-frequency hepatic tumor ablation," *IEEE Trans. Biomed. Eng.*, 49(1): 3-9, 2002.

[4] I. A. Chang and U. D. Nguyen, "Thermal modeling of lesion growth with radiofrequency ablation devices," *BioMed. Eng. OnLine*, 3(27): 1-19, 2004.

[5] F. Ferraioli, A. Formisano and R. Martone, "Effective exploitation of prior information in electrical impedance tomography for thermal monitoring of hyperthermia treatments", *IEEE Trans. on Magnetics*, 45(3): 1554-1557, 2009.

[6] K. D. Paulsen, M. J. Moskowitz, and T. P. Ryan, "A combined invasivenoninvasive conductivity profile reconstruction approach for thermal imaging in hyperthermia," in *Proc. Ann. Conf. IEEE Eng. Med. Biol. Soc.*, 13 (1): 323-324. 1991

[7] H. Griffiths and A. Ahmed, "Applied potential tomography for non-invasive temperature mapping in hyperthermia," *Clinical Phys. Physiol. Meas.*, 8: 147-153, 1987.

[8] J. Conway, "Electrical impedance tomography for thermal monitoring of hyperthermia treatment: An assessment using in vitro and in vivo measurements," *Clinical Phys. Physiol. Meas.*, 8: 141-146, 1987.

[9] M. Cheney, D. Isaacson, and J. C. Newell, "Electrical impedance tomography," *SIAM Rev.*, 41: 85-101, 1999.

[10] R. H. Bayford, "Bioimpedance tomography (electrical impedance tomography)," *Ann. Rev. Biomed. Eng.*, 8: 63-91, 2006.

A contactless dielectrophoretic handling of diamagnetic levitating water droplets in air

P. Kauffmann^{1,2}, P. Pham², A. Masse¹, T. Honegger³, D. Peyrade³, V. Haguet² and G. Reyne¹

¹G2Elab, UMR 5269 INPG-UJF-CNRS, Grenoble

²Commissariat à l’Energie Atomique (CEA), Grenoble

³LTM CNRS CEA, Grenoble

G2Elab, Bât. ENSE3, BP 46, 38402 St Martin d’Hères CEDEX, FRANCE

paul.kauffmann@g2elab.grenoble-inp.fr

Abstract— In previous works, microfabricated permanent magnets were designed and fabricated for levitating picoliter water droplets in air. Manipulating levitating water droplets is a contamination-free alternative to digital-microfluidic systems on surface used in biotechnologies. Here, the possibility of adding dielectrophoretic (DEP) forces to control the position of levitating droplets along a magnetic groove is numerically evaluated. The diamagnetic forces are computed using CADES framework while the DEP forces are computed with Comsol Multiphysics™ (Finite Element Method). Errors made using the point dipole model and the 2D approximation are evaluated by comparison with the full 3D problem. Based on these results, an electric sequence for polarizing planar interdigitated ITO electrodes is proposed in order to provide a stable and accurate control of the droplets micropositioning along the gap.

I. INTRODUCTION

For the last twenty years, microfluidic and lab-on-a-chip devices have been widely investigated for biomedical or chemical applications. Miniaturization provides better sensitivity for molecular detection and reduces the volume of solvents and reactants handled. However, contamination phenomena raise significant issues for such small samples. Diamagnetic levitation above bulk magnets [1]-[2]-[3] or integrated micromagnets [3] have been investigated for providing a contactless handling of picoliter droplets. A “MEMS compatible” method to convey contactless some levitating droplets along a magnetic groove perpendicularly to the diamagnetic forces is presented. It combines diamagnetic levitation and dielectrophoresis (DEP). Corresponding computations are developed in this paper.

II. DIAMAGNETIC LEVITATION AND DIELECTROPHORESIS

A. Diamagnetic levitation

Water is a diamagnetic element which corresponds to a so weak negative susceptibility ($\chi_{\text{water}} = -9 \cdot 10^{-6}$ SI) that the demagnetization field can be neglected. Hence, under a non uniform magnetic induction \vec{B} , water droplets experiment a small repulsive force [1]-[2]:

$$\vec{F}_m = \iint_S \frac{\chi_{\text{water}}}{2\mu_0} B^2 d\vec{S} \quad (1)$$

Due to the favorable reduction scale laws in magnetism [4], water picoliter droplets can levitate above micrometric magnetic grooves. The grooves can be micromachined from bulk magnets (Fig. 1A) or fabricated by NdFeB sputtering

onto patterned silicon wafers [5]-[6] (Fig. 1B). The devices are then magnetized vertically ($1.2\text{T} < B_r < 1.4\text{T}$).

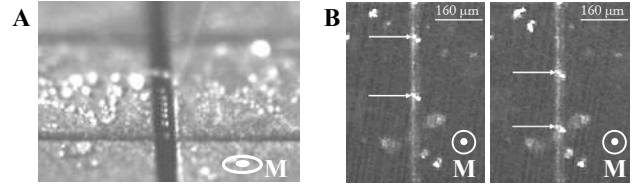


Fig. 1. Levitating droplets (30µm in diameter) within magnetic grooves above (A) bulk or (B) integrated NdFeB micromagnets [2],[3].

B. Dielectrophoresis

DEP is an electrical phenomenon which attracts (positive DEP) or repels (negative DEP) polarizable particles by applying a non uniform AC electrical field [7]. For the particular case of water droplets in air, only the positive (attractive) DEP is possible [8]. The electric field is obtained from Indium Tin Oxide (ITO) planar interdigitated transparent electrodes (10 µm wide, gap of 10 µm) deposited on a glass lid perpendicularly to the magnetic groove (Fig.2).

III. MICROSYSTEM MODELLING

A. Description of the microsystem

The DEP actuation of a 40µm diameter levitating droplet above a 50µm-deep and 50 µm-wide groove is presented (Fig. 2). The system is inspired from Honegger’s works [9] where a 45 µm thick microfluidic photopatternable silicone channel is bonded between two glass wafers where electrodes are deposited. Here, a 50 µm-thick magnetic layer sputtered on a patterned Si wafer replaces the bottom electrodes. The magnetic layer can be modeled by 55 µm-large rectangular parallelepiped magnets.

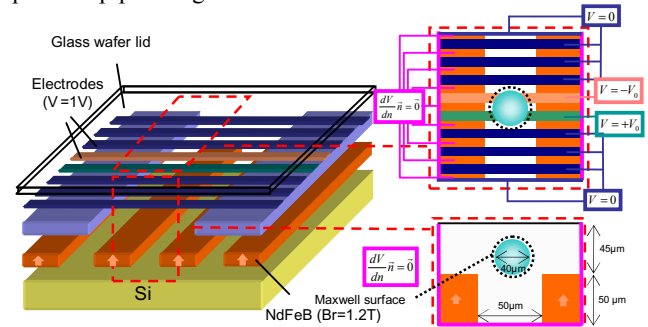


Fig. 2. Magnetic-DEP microdevice for the levitation and the translational transport of water droplets.

B. Forces Computation

The magnetic field created by the magnets is analytically computed in the CADES framework [10]. The diamagnetic forces are computed by integrating the magnetic energy over the droplet boundary (1).

The electric potential created by the interdigitated electrodes is determined by solving Laplace's equation, using the Finite Element Method with Comsol Multiphysics™. As for the DEP force, the dipolar approach commonly used is compared to the 2D and 3D Maxwell stress tensor methods applied on the computed electric field. Results show when droplet size (40 μm) is not negligible compared to the electrode dimensions (width = gap = 10 μm), the usual point dipole approximation and the 2D Maxwell stress tensor method reach errors around 100 % compared to the full 3D computation. The 3D Maxwell stress tensor method was thus selected for this study.

IV. NUMERICAL RESULTS

A. Force balance

According to the superposition principle, the vertical resultant force (\vec{F}_z) applying on a droplet is:

$$\vec{F}_z = \vec{P} + \vec{F}_{MAG} + \vec{F}_{DEP} \quad (2)$$

where \vec{P} is the droplet's weight, \vec{F}_{MAG} and \vec{F}_{DEP} are the vertical components of the magnetic force and of the DEP force, respectively.

The electrode voltage is tuned so the droplet remains in stable diamagnetic levitation while having the strongest horizontal actuation. Curves of Fig. 3 show that a droplet has a stable levitation height between 16 and 18 μm above the micromagnets for a voltage magnitude below 2.5 V.

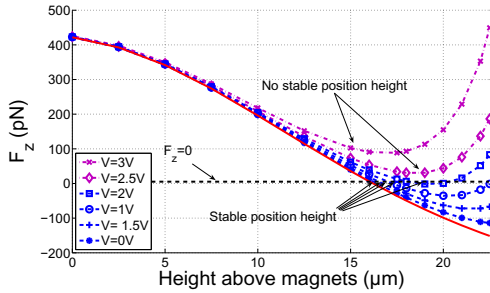


Fig. 3. Vertical resultant force (F_z) vs. the height of the droplet: stable levitation ($F_z=0$ and $dF_z/dz < 0$) applies for a voltage inferior or equal to 2.5 V.

B. Voltage pulse sequence

To actuate droplets along the magnetic groove using DEP, two adjacent electrodes are polarized with a 180° phase shift (Figures 2 & 4). The magnetic force component parallel to the channel direction is negligible [8]. Therefore, in the horizontal direction, the droplet motion is governed by the DEP force. Conversely, the vertical DEP force magnitude (~1 pN, Fig. 4) is far weaker than the diamagnetic one (~100 pN range). The diamagnetic levitation height is thus not disturbed by DEP, and the droplet reaches a stable position just under the electrode pair. For a DEP force of 0.5 pN (1 V, 10 kHz), the droplet can move at ~70 μm.s⁻¹ due to the weak viscosity of

air. Finally, joule heating is negligible: evaluation of heating and power consumption will be discussed in the full paper.

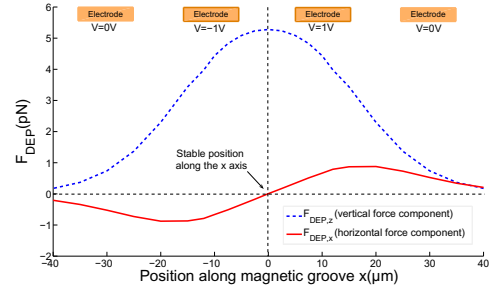


Fig. 4. Horizontal and vertical DEP forces along the magnetic groove for a 40 μm droplet levitating at a 16 μm height.

V. CONCLUSION AND PERSPECTIVES

Computations show that a contactless DEP actuation of levitating micrometric water droplets in air in magnetic grooves is possible. This study raises some interesting questions about the models to use. Although the 3D Maxwell stress tensor is CPU consuming, the point dipole method appears to provide imprecise data. A multipolar approach may provide a satisfying compromise. Conversely, our semi-analytical diamagnetic force computations presently need an integration over the droplet boundary. Considering diamagnetic susceptibilities, a similar comparison with the point dipole and the multipole approaches could avoid using surface integration.

VI. REFERENCES

- [1] F. Lyuksyutov, D. G. Naugle, and K. D. D. Rathnayaka, "On-chip manipulation of levitated femtodroplets", *Appl. Phys. Lett.*, 85:1817, 2004.
- [2] H. Chetouani, C. Jeandey, V. Haguet, H. Rostaing, C. Dieppedale, and G. Reyne, "Diamagnetic levitation with permanent magnets for contactless guiding and trapping of microdroplets and particles in air and liquids", *IEEE Trans. Magn.*, 42(10):3557, 2006.
- [3] C. Jeandey, H. Chetouani, V. Haguet, F. Chatelain, and G. Reyne, "Diamagnetic levitation based digital microfluidics", *Proc. MicroTAS*, vol. 2, pp. 922-924, Paris, France, Oct. 7-11, 2007.
- [4] O. Cugat, J. Delamare, and G. Reyne, "Magnetic micro-actuators and systems (MAGMAS)", *IEEE Trans. Magn.*, 39:3607, 2003.
- [5] N. Dempsey, A. Walther, F. May, D. Givord, K. Khlopkov, and O. Gutfleisch, "High performance hard magnetic NdFeB thick films for integration into micro-electro-mechanical systems" *Appl. Phys. Lett.*, 90:092509-3, 2007.
- [6] H. Chetouani, V. Haguet, C. Jeandey, C. Pigot, A. Walther, N. M. Dempsey, F. Chatelain, B. Delinchant, and G. Reyne, "Diamagnetic levitation of beads and cells above permanent magnets", *Proc. Transducers & Eurosensors*, vol. 1, pp. 715-718, Lyon, France, June 10-14, 2007.
- [7] T. B. Jones, *Electromechanics of Particles*, Cambridge University Press, Cambridge (UK), 1995.
- [8] P. Kauffmann, H. Chetouani, P. Pham, V. Haguet, and G. Reyne, "Magnetophoretic and dielectrophoretic actuations coupled with diamagnetic trapping in air and liquids", *Sens. Lett.*, to be published.
- [9] T. Honegger, K. Berton, T. Pinedo-Rivera, and D. Peyrade, "Design and realization of a microfluidic system for dielectrophoretic colloidal handling", *Microelectron. Eng.*, to be published.
- [10] H. Chetouani, B. Delinchant, and G. Reyne, "Efficient modeling approach for optimization of a system based on passive diamagnetic levitation as a platform for bio-medical applications", *COMPEL*, 26(2):345, 2007.

Compact Electromagnetic Bandgap Structures for Notch Band in Ultra-Wideband Applications

Mihai D. Rotaru and Jan K. Sykulski
 School of ECS, University of Southampton
 Highfield, Southampton, SO17 1BJ, UK
 mr@ecs.soton.ac.uk, jks@soton.ac.uk

Abstract — This paper introduces a novel approach to create notch band filters in the front-end of ultra-wideband (UWB) communication systems based on electromagnetic bandgap (EBG) structures. The design presented here can be implemented in any structure that has a microstrip in its configuration. The EBG structure is first analyzed using a full wave electromagnetic solver and then optimized to work at WLAN band (5.15-5.825GHz). Two UWB passband filters are used to demonstrate the applicability and effectiveness of the novel EBG notch band feature. Simulation results are provided for two cases studied.

I. INTRODUCTION

In recent years there has been a lot of interest in investigating electromagnetic bandgap (EBG) structures for various kinds of applications at microwave frequencies. EBG structures proposed over the past few years have been used primarily to enhance the functionality of antennas [1], but other applications – such as filters and baluns at microwave frequencies – have also been explored [2]. Moreover, the EBG structures have inherent features that can be used to reduce or suppress completely electromagnetic interferences (EMI) that can occur in electronic systems leading to electromagnetic compatibility (EMC) issues [3]. The EBG structures suppress the propagation of surface waves over specific frequency bands that directly depend on the dimensions and types of materials used to fabricate the EBGs. However, in this work we focus on a slightly different application of these structures. Consider the design of a notch band structure that can be used in ultra wideband (UWB) radio systems and can be easily integrated with microstrip circuitry fabricated with printed circuit board (PCB) technology. Since February 2002, when the Federal Communication Commission (FCC) released the 3.1-10.6GHz band for commercial communication usage, UWB has been receiving a lot of attention from both academia and industry. Unlike other existing wireless communication standards, which are narrowband, UWB has a very wide bandwidth, 7.5GHz wide to be precise. However, the UWB emission power is limited to a maximum of -41.3dBm/MHz therefore it can co-exist with other narrow band services that occupy the same spectrum. One such service is the 802.11a WLAN that is located at 5.15-5.45GHz and 5.725-5.825GHz. Recent work has shown that the effect of the 802.11a interference on UWB can be harmful and, depending on the probability of signal overlap and the relative distance between the two transceivers, the 802.11a interference can cause significant signal degradation of the attainable throughput of the UWB system [4]. Therefore it is very important to incorporate means that

can mitigate the effects of 802.11a in an UWB front end. Different types of structures for the physical layers and techniques for the MAC layers have been suggested recently. The previously proposed notch filter solutions are very specific to certain types of filters or antennas, therefore they cannot be easily integrated in a different design [5, 6, 7]. In this paper we propose a more general approach that can be implemented in any physical design that has at least a microstrip structure in its front end.

II. THE EBG STRUCTURE

As mentioned in the Introduction, EBG structures have been used for different types of applications in the past few years. The most popular mushroom like EBG structure was first introduced by Sievenpiper in 1999 [1]. The physical mechanism of the mushroom like EBGs can be explained by a simple equivalent LC parallel resonant circuit. However, more recently the EBG structures have been used to suppress the noise propagating in parallel plate waveguide structures, such as the power planes of high speed electronic systems. In this environment the equivalent circuit that can be used to explain the EBG behavior is somewhat different to the initial LC parallel resonant circuit used by Sievenpiper to explain the behavior of the EBGs in an open environment. Due to the EBG's proximity to the two metal planes in this set-up, the capacitances to the plane above and below the mushroom are much higher than the capacitance between the edge of the adjacent mushrooms. Therefore these capacitances will now dominate the response of the EBG structure.

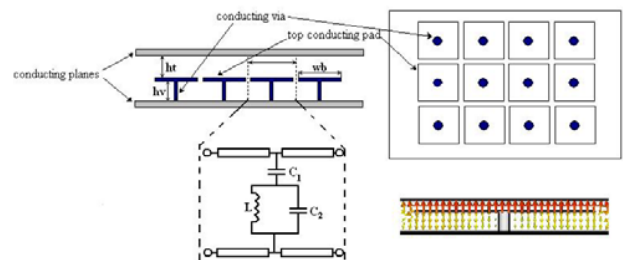


Fig. 1. EBG embedded between two metal planes and its equivalent circuit

In this configuration the EBG behaves like a stop band filter for the electromagnetic wave propagating in the parallel plate waveguide. The center of the stop band frequency and the bandwidth of the stop band are determined by C_1 , C_2 and L , where C_1 is the capacitance between the top conducting pad and the above metal structure, C_2 is the capacitance between the pad and the bottom metal plane and L is the inductance of the via connecting the bottom metal plane to the pad. The

capacitances of the structure C_1 and C_2 are determined by the size of the pad, the distance from the top and bottom planes and the dielectric material between the two planes. The inductance of the structure L is determined by the size of the via (length, diameter) but also by its position with respect to the center of the patch. As the distance between the two parallel plates is much smaller than the size in the xy direction, it can be assumed that the only mode travelling in this waveguide is a TEM mode. Therefore it is expected that, if the EBG structure is embedded within another wave guiding structure supporting a TEM mode, a similar response will be obtained. This has been confirmed through simulation of a microstrip line run above the EBG. As previously, the observed behavior can be explained by the circuit in Fig.1. The return loss of the microstrip routed above one mushroom has a zero at frequency f_1 and a pole at f_2 , where f_1 and f_2 are:

$$f_1 = \frac{1}{2\pi\sqrt{L(C_1 + C_2)}} \quad \text{and} \quad f_2 = \frac{1}{2\pi\sqrt{LC_2}} \quad (1)$$

Hence the stop band appears at the frequency f_1 . Another interesting behavior of this circuit is that the relative bandwidth of the circuit is proportional to $\sqrt{(C_1 + C_2)/L}$; therefore by controlling the size and the design of the EBG element one can tune frequency of the stop band as well as its bandwidth. This behavior has also been confirmed through numerical simulation.

The size of the EBG structure is critical when it has to be integrated into a practical design. Unfortunately the size of a mushroom EBG to be integrated into a practical substrate such as FR4 is quite large (4.4x4.4mm) if for example the 5.5GHz is chosen as the resonant frequency. Another drawback of the mushroom structure is the fact that its inductance is very small while C_1 and C_2 are much bigger; therefore the bandwidth of the stop band is relatively large and may not be useful for a notch filter application. A compact and novel EBG element based on small planar inductor is introduced to solve the above problem. The design and optimization of the size and shape of the inductor based EBG is done using a full wave simulation software. The numerical tool (CST-Microwave Studio) used for this work is based on Finite Integration Technique (FIT) [8]. Through this approach a much smaller EBG structure is obtained, only 2x2mm for a FR4 substrate. Moreover, the corresponding inductance is much higher while the two capacitances are much smaller. However, the design of such structure is not as straightforward as the design of a simpler mushroom structure as its total inductance and capacitances have to be computed through a rigorous three dimensional numerical model. The appropriate ratio between total capacitance and inductance of the structure has to be calculated carefully and an iterative process is necessary to obtain the optimum design.

III. UWB FILTERS WITH EMBEDDED EBG ELEMENT

Using the features described above one can design small structures with notch band characteristics that can be incorporated into existing designs without large and costly modifications. In this section two band pass filters that can be

used in UWB applications were modified to incorporate the notch band feature for the WLAN. All the following results were obtained through full wave simulation using CST Microwave Studio.

The first UWB filter studied here is based on the broadside coupling between a microstrip and a coplanar waveguide (CPW). The CPW is on the ground of the microstrip, while the two microstrip lines on the top surface are separated by a small gap. The second UWB filter has two coupled L-shaped microstrips on the top layer and a stepped impedance resonator (SIR) on a defected-ground structure (DSG) on the bottom layer. The UWB filters described above are considered to be built on different types of a substrate. The first design uses a dielectric substrate with a dielectric constant of 2.17 whereas the second filter has a substrate with a constant of 4.4 (FR4).

The simulations results in terms of the magnitude of the insertion loss ($|S_{21}|$) obtained from the full wave numerical solution are presented in Fig. 2. It can be observed that both designs have a sharp stop band feature in the WLAN band without serious degrading of the passband for the designs with the novel inductor based EBG implemented.

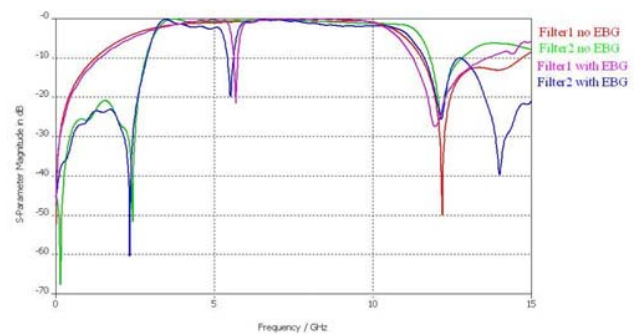


Fig. 2. Magnitude of the return loss for the four cases studied

IV. REFERENCES

- [1] D. Sievenpiper, L. Zhang, R. F. J. Broas, N. G. Alexopolous, and E. Yablonovitch, "High-impedance electromagnetic surfaces with a forbidden frequency band," *IEEE Trans. Microw. Theory Tech.*, vol. 47, no. 11, pp. 2059–2073, Nov. 1999.
- [2] H. Hsu, M. J. Hill, J. Papapolymerou, and R. W. Ziolkowski, "A planar X-band electromagnetic band-gap (EBG) 3-pole filter," *IEEE Microwave Wireless Components Lett.*, vol. 12, pp. 255–257, July 2002.
- [3] T. Kamgaing and O. M. Ramahi, "Design and modeling of high-impedance electromagnetic surfaces for switching noise suppression in power planes," *IEEE Trans. Electromagn. Compat.*, vol. 47, no. 3, pp. 479–489, Aug. 2005.
- [4] B. Firoozbakhsh, T. G. Pratt, and N. Jayant, "Analysis of IEEE 802.11a Interference on UWB Systems," *IEEE Conference on Ultra Wideband Systems and Technologies*, Nov 2003, pp 473-477
- [5] K. Li, "Ultra-wide (UWB) Bandpass Filters: Full Passband and with Notch," *IEEE Conference on Microwave and Millimeter Wave Technology*, April 2007.
- [6] Pai-Yi Hsiao and Ro-Min Weng, "A Compact Ultra-Wideband Bandpass Filter with WLAN Notch Band," *Wiley Periodicals Microwave and Optical Technology Letters.*, vol. 51, no. 2, February 2009 pp. 503-506.
- [7] K.H. Kim, Y.J. Cho, S.H. Hwang and S.O. Park, "A band-rejected UWB planar monopole antenna with a ring-shaped parasitic patch," *IEEE Microwave Conference Proceedings, 2005 AMPC.*, December 2005
- [8] Microwave Studio – www.cst.com

Microwave Characterization using Least-Square Support Vector Machines

T. Hacib, H. Acikgoz, Y. Le Bihan, O. Meyer, and L. Pichon

Laboratoire de Génie Electrique de Paris, Supélec, UMR 8507 CNRS, UPMC Univ. Paris 06, Univ. Paris-Sud.
11 Rue Joliot-Curie, Plateau de Moulon 91192 Gif-sur-Yvette Cedex, France
tarik.hacib@lgep.supelec.fr

Abstract— This paper presents the use of the least-square support vector machines (LS-SVM) technique, combined with the finite element method (FEM), to evaluate the microwave properties of dielectric materials. The LS-SVM is a statistical learning method that has good generalization capability and learning performance. The FEM is used to create the data set required to train the LS-SVM. Numerical simulations demonstrate that the LS-SVM method can determine the permittivity of materials with a high accuracy.

I. INTRODUCTION

The problems of the determination of dielectric constant ϵ' and loss factor ϵ'' of dielectric materials are usually formulated and solved as optimization problems; so iterative methods are commonly used to solve this kind of problems. These methods involve solving a well-behaved forward problem in a feedback loop. Numerical methods such as finite element method (FEM) can be used to represent the forward process. However, iterative methods using a numerically based forward model are computationally expensive. In this situation the neural network (NN) and other machine learning tools such as support vector machines (SVM) are a good alternative to iterative methods [1].

SVM are a recent powerful machine learning method. They are developed on the basis of statistical learning theory. A lot of successful applications in nonlinear classification and function estimation have shown that SVM can handle high dimensional data with relatively few training samples and that they exhibit good generalization capability [2]. The SVM adjustment is obtained using complicated quadratic programming methods, which are often time consuming and difficult to implement. Least-squares support vector machines (LS-SVM) are reformulations of the standard SVM which lead to solve linear equations instead of a quadratic programming problem [3].

In this paper, we propose a new method for the evaluation of the microwave properties of dielectric materials (complex permittivity) from the admittance measured at the discontinuity plane of a coaxial open-ended probe. The method is based on the FEM and a LS-SVM scheme.

The FEM provides the data set required for the training of LS-SVM. A data set is constituted of input (complex admittance, frequency) and output (ϵ' , ϵ'') pairs.

II. LS-SVM FOR FUNCTION ESTIMATION

Given a training set $(x_k, y_k)_{k=1}^N$ with input data $x_k \in R^n$ and output data $y_k \in R$, the LS-SVM model for function

approximation has the following representation in feature space,

$$y(\mathbf{x}) = \mathbf{w}^T \boldsymbol{\varphi}(\mathbf{x}) + b \quad (1)$$

Here the nonlinear function $\boldsymbol{\varphi}(\cdot): R^n \rightarrow R^{n_k}$ maps the input space to a higher dimension feature space. b is a bias term and $\mathbf{w} \in R^n$ is the weight vector. The optimization problem is defined as:

$$\min \mathbf{J}(\mathbf{w}, \mathbf{e}) = \frac{1}{2} \mathbf{w}^T \mathbf{w} + \gamma \frac{1}{2} \sum_{i=1}^N \mathbf{e}_i^2 \quad (2)$$

Subject to the equality constraints:

$$y_i = \mathbf{w}^T \boldsymbol{\varphi}(x_i) + b + \mathbf{e}_i \quad i = 1, \dots, N \quad (3)$$

where the fitting error is denoted by \mathbf{e}_i . The hyper-parameter γ controls the trade-off between the smoothness of the function y and the accuracy of the fitting. This optimization problem leads to a solution,

$$y(\mathbf{x}) = \sum_{i=1}^N \alpha_i K(\mathbf{x}, x_i) + b \quad (4)$$

where α_i, b comprise the solution to the linear system obtained after constructing the Lagrangian and $K(\mathbf{x}, x_i) = \boldsymbol{\varphi}^T(\mathbf{x}) \boldsymbol{\varphi}(x_i)$ is the so-called kernel function. The most usual kernel functions are polynomial, Gaussian or sigmoid.

III. MEASUREMENT SETUP AND NUMERICAL METHOD

The characterization cell, called SuperMit, consists in a junction between a coaxial waveguide and a circular waveguide which is filled by the dielectric material. In order to study liquids, a coaxial window is inserted between the two guides (Fig. 1). The whole device is connected to an impedance analyzer.

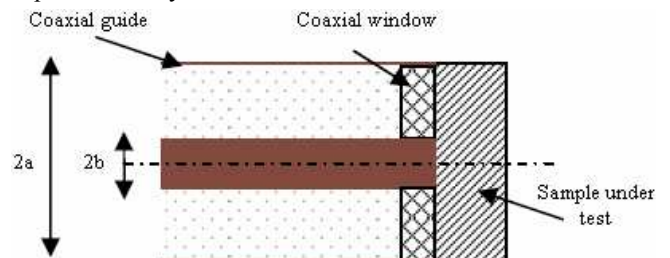


Fig. 1. SuperMit measuring cell

The electromagnetic problem is solved by using the FEM. The problem is expressed in terms of the electric field \mathbf{E} which satisfies the following harmonic wave equation:

$$\text{curl} \left[-\frac{1}{i\omega\mu} \text{curl} \mathbf{E} \right] - i\omega\epsilon \mathbf{E} = 0 \quad (5)$$

ω is the pulsation, ϵ ($\epsilon = \epsilon_0(\epsilon' - i\epsilon'')$) and μ are the permittivity and the permeability, respectively. ϵ_0 is the permittivity of the free space. The meshing of the axially symmetric characterization cell is shown in Fig. 2.

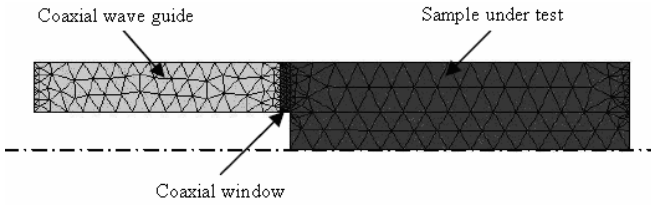


Fig. 2. View of the meshed measurement cell

IV. IMPLEMENTATION OF THE LS-SVM

Two single-output LS-SVM corresponding to the two estimated quantities ϵ' and ϵ'' are used. The inputs of a LS-SVM are the values of the complex admittance (real part G , imaginary part B) and the measurement frequency (f).

The dataset is divided into three different sets training, validation and test set. The LS-SVMs were trained with 4500 learning examples.

In this study, radial basis function (RBF) kernels are used with LS-SVM,

$$K(\mathbf{x}, \mathbf{x}_i) = \exp \left(-\frac{\|\mathbf{x} - \mathbf{x}_i\|^2}{\sigma^2} \right) \quad (6)$$

where $\sigma > 0$ is a constant defining the kernel width.

It should be noted that predetermined parameters in LS-SVM algorithms with RBF kernel are γ and σ^2 , which are less numerous than those in standard SVM. A split-sample procedure [4] was used to train and test the LS-SVM under various hyper-parameter settings. To tune γ and σ^2 , a range of their values is scanned and optimal values of these hyper-parameters is the one corresponding to the minimum of the generalization error estimation obtained on the validation set.

V. EXPERIMENTAL RESULTS

Measurements have been carried out by using an impedance analyzer Agilent 4291A on an ethanol sample whose dielectric characteristics are known. The window coaxial is made of Plexiglas with a thickness of 0.82 mm and a dielectric constant of 2.7. The thickness of the sample under test is 13.8 mm. The coaxial guide is a standard APC7 ($a = 3.5$ mm, $b = 1.52$ mm). The measurement frequency band is from 1 MHz to 1.8 GHz. Hyper-parameters in LS-SVM for ϵ' , ϵ'' and root mean squared relative error (RMSRE) are given in Table I. In this case, the obtained results on the test set are quite good for both LS-SVM as shown in Fig. 3 and Fig. 4.

TABLE I
PARAMETERS IN LS-SVM WITH RBF KERNEL

Outputs	γ	σ^2	RMSRE (%)
ϵ'	$8.1113 \cdot 10^2$	1.5380	$3.6055 \cdot 10^{-1}$
ϵ''	$5.3367 \cdot 10^3$	0.3921	$5.8539 \cdot 10^{-2}$

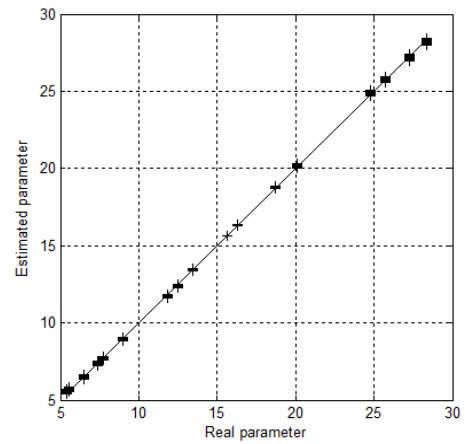


Fig. 3. Comparison between LS-SVM output and real value of ϵ'

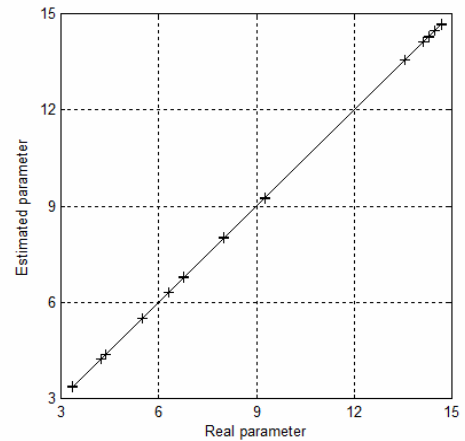


Fig. 4. Comparison between LS-SVM output and real value of ϵ''

The results obtained show clearly that the LS-SVM inversion agrees very well with the real ones.

VI. CONCLUSION

LS-SVM were presented and applied to inversion of microwave measurement data. The results indicate that LS-SVM could be used to microwave dielectric characterization. The applied data set at the testing stage of the LS-SVM demonstrates their abilities to perform identification with good accuracy. The validity of the proposed LS-SVM based inversion method is being assessed by comparing the results obtained using the proposed method with those obtained from a multilayer perceptron NN (MLP) and experiment.

VII. REFERENCES

- [1] H. Acikgoz, Y. Le Bihan, O. Meyer, L. Pichon, "Microwave characterization of dielectric materials using Bayesian neural networks," *Progress In Electromagnetics Research*, 03: 169-182, 2008.
- [2] V. Vapnik, *Statistical learning theory*. John Wiley and Sons. New York, 1998.
- [3] J.A.K. Suykens, "Nonlinear modelling and support vector machines," *IEEE Instruments and Measurement Technology Conference*. Budapest, Hungary, 2001.
- [4] C.M. Bishop, *Neural networks for pattern recognition*. Oxford University Press, 1995.

Electromagnetic disruption loads on ITER blanket modules

R. Albanese¹, M. Furno Palumbo², R. Palmaccio², G. Rubinacci¹, P. Testoni³, F. Villone²

¹Ass. EURATOM/ENEA/CREATE, DIEL, Università di Napoli Federico II, Via Claudio 21, Napoli, Italy

²Ass. EURATOM/ENEA/CREATE, DAEIMI, Università di Cassino, Via Di Biasio 43, Cassino (FR), Italy

³Fusion For Energy, C/ J. Pla 2, Barcelona, Spain

Abstract— In this paper we compute the electromagnetic loads (forces, torques, Joule losses) on passive conductors of the ITER (International Thermonuclear Experimental Reactor) fusion device, currently under construction, following a disruption event, i.e. the sudden loss of magnetic confinement. An original integral formulation is used, able to automatically deal with complex topologies like the ones to be studied. Non-isotropic homogenized resistivities are used to take into account fine geometrical details. A suitable inverse problem is solved in order to compute the forcing terms.

I. INTRODUCTION

In devices for the controlled thermonuclear fusion, the plasma disruptions are associated to a sudden loss of magnetic confinement, which causes the magnetic and thermal energy stored in the plasma to be released to surrounding structures. The consequent electromagnetic forces and heat load have an impact on the operational lifetime of several components and in extreme cases seriously damage the integrity of the devices themselves. For this reason, the problem of the disruptions is of the major concerns for both existing and future fusion devices [1], and plays a fundamental role in the design of new experimental devices like ITER (International Thermonuclear Experimental Reactor), currently in the construction phase in Cadarache, France, which will be the biggest tokamak ever built.

To study this problem, we use an integral formulation of the eddy-currents equations [2], which is very advantageous in the description of fusion devices, since it is required to give a discretization only of the conducting structures, which are typically a small fraction of the overall solution domain in such devices. Moreover, it is possible to give separate discretizations of non-connected conductors, hence allowing easily a zooming approach. This integral formulation is able to deal automatically with complex geometries and topologies [3], like the ones arising for the present study.

II. NUMERICAL FORMULATION

We assume that no magnetic materials are present and that the conducting materials are linear, although possibly anisotropic. Integral methods are therefore well suited for this analysis. They are characterized by full matrices, but the number of unknowns needed to get a required accuracy is relatively small, as only the conducting region has to be meshed, and the regularity conditions at infinity are automatically taken into account. The results have been obtained using the CARIDDI code, based on an integral formulation in terms of two-component current density vector

potential [2]. The current density is expanded in terms of solenoidal shape functions with normal component zero on the boundary as $\mathbf{J}=\sum_k \nabla \times \mathbf{T}_k$, whose coefficients are determined applying Galerkin procedure in the time domain:

$$\{L\} d[I]/dt + \{R\} [I] = d[U]/dt \quad (1)$$

and:

$$L_{ij} = \frac{\mu_0}{4\pi} \int_{V_c} \int_{V_c} \frac{\nabla \times \mathbf{T}_i \cdot \nabla \times \mathbf{T}_j}{|\mathbf{x} - \mathbf{x}'|} dV dV' \quad (2)$$

$$R_{ij} = \int_{V_c} \nabla \times \mathbf{T}_i \cdot \eta \nabla \times \mathbf{T}_j dV \quad (3)$$

$$U_i = - \int_{V_c} \nabla \times \mathbf{T}_i \cdot \mathbf{A}_0 dV \quad (4)$$

where t is the time, η is the resistivity tensor, V_c is the conducting domain, and \mathbf{A}_0 is the magnetic vector potential due to the external sources (plasma and current driven coils).

III. PRELIMINARY RESULTS

The geometry of interest includes the following items:

- the blanket modules (BM), with the aim of shielding neutrons originating from nuclear reactions;
- the vacuum vessel (VV), made by two nested shells with port extensions and port plugs;
- the divertor, which must carry the heat load and particle flux.

The disruptive event to be represented is a so-called VDE (Vertical Displacement Event), in which the plasma experiences an unstable vertical axisymmetric evolution. This is originally represented by a variable number of moving toroidal filaments, each carrying a time-varying current, whose values have been computed by the DINA MHD code [4]. Several different VDEs will be considered, both upwards and downwards.

A. Equivalent filaments

We have given an equivalent representation of the VDE in terms of a given number of fixed filaments, located inside the plasma region. The waveforms of the current in each filament are obtained by imposing that:

- a) the multipolar expansion of the original plasma current density and of this set of filamentary currents is the same up to the sixth order;
- b) the flux and the flux time derivative at a given set of points of the two current distributions are the same.

The resulting algebraic system of linear equations (suitably normalized) is solved using the Tikhonov regularization. A typical result is reported in Fig. 1, showing a good agreement.

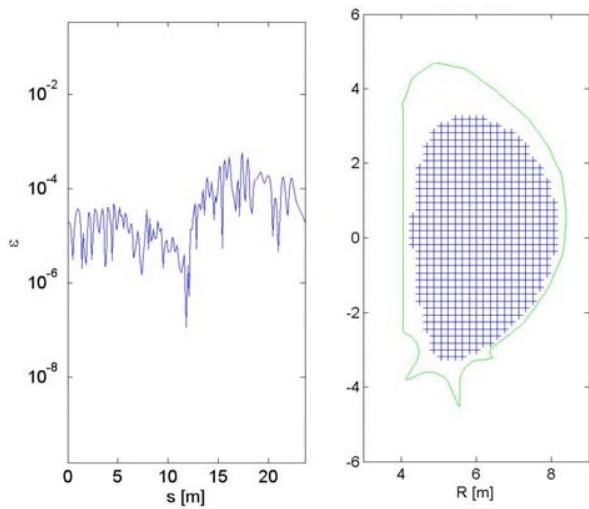


Fig. 1. Original current filaments (right) and relative error on magnetic flux over the green line using a set of fixed filaments

B. Equivalent anisotropic resistivity

The BM have a rather complex geometry: the front panel (FP) facing the plasma is made by a beryllium layer, followed by a copper layer and a stainless steel (SS) layer, each having a number of void channels inside. Further from the plasma, the shielding block (SB) is present, which is a volumetric SS structure with void channels, slits, pockets etc.

Figure 2 shows one typical example – around 20 different typologies of BM are present. While slits and pockets have been fully represented in the discretized model, the presence of channels has been taken into account via an an-isotropic equivalent resistivity. In particular, for each direction the void fraction α has been computed, and the resistivity has been enhanced of a factor $1/(1-\alpha)$. Whenever possible/applicable, we estimated the resistivity enhancement factor using the Clausius-Mossotti formula, or resorting to 2D simplified computations, as proposed in [5].

Meshes with three different levels of discretization have been produced for each BM. We have compared the power losses, forces and torques following a VDE, finding a good agreement (within around 10%). Moreover, in one single case also a mesh accounting for all geometrical details (including channels) has been considered, obviously with the reference bulk isotropic values of resistivity for each material. The agreement on the aforementioned parameters, as computed using the equivalent anisotropic resistivity, is around 15%.

C. Overall model

The overall discretized model has been successfully produced, including all the aforementioned geometrical features. The mesh is reported in Fig. 3, and is currently being used for quantitative computations of the overall electromagnetic loads due to disruptive events in ITER. As anticipated, the complex topology of the conductors is automatically treated.

This work has been supported by Fusion for Energy contract F4E-2008-OPE-08 (ES-AC). The views expressed in this publication are the sole responsibility of the author and do not necessarily reflect the views of Fusion for Energy. Neither

Fusion for Energy nor any person acting on behalf of Fusion for Energy is responsible for the use which might be made of the information in this publication.

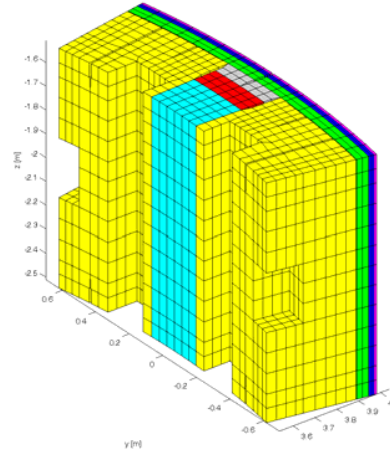


Fig. 2. Typical geometry of one BM. The colors denote materials with different anisotropic resistivities.

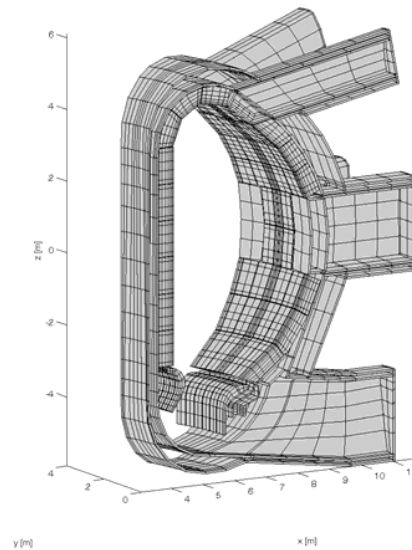


Fig. 3. Overall ITER geometry

IV. REFERENCES

- [1] V. Riccardo, "Disruptions and disruption mitigation", *Plasma Phys. Contr. Fus.* 45: A269-A284 (2003)
- [2] R. Albanese, G. Rubinacci, "Integral formulation for 3D eddy current computation using edge-elements", *IEE Proc.* 135A (5): 457-462, 1988
- [3] G. Rubinacci, A. Tamburrino, F. Villone, "Circuits/fields coupling and multiply connected domains in integral formulations", *IEEE Trans. on Magnetics* 38 (2): 581-584, 2002
- [4] M. Sugihara et al., "Disruption scenarios, their mitigation and operation window in ITER", *Nucl. Fusion* 47 (2007) 337-352.
- [5] R. Albanese, R. Fresa, "Electromagnetic analysis with equivalent models of complex conducting structures", *IEEE Trans. on Magnetics*, 34 (5): 3256-3259, 1998

Fast Computation Technique of Forces Acting on Moving Permanent Magnet

Marek Ziolkowski^{1,2} and Hartmut Brauer¹

¹ Ilmenau University of Technology, Helmholtzplatz 2, D-98684, Ilmenau, Germany

² West Pomeranian University of Technology, Sikorskiego 37, PL-70313, Poland

Email: marek.ziolkowski@tu-ilmenau.de, hartmut.brauer@tu-ilmenau.de

Abstract — Relative movements of permanent magnets and conductors cause forces which can be used to study the material characteristics of the conducting object. The paper describes a fast technique to compute the forces acting on a permanent magnet using the finite element method. The proposed approach allows studying the possibilities of defect identifications in conductors if e.g., the Lorentz force eddy current testing technique is applied.

I. INTRODUCTION

Moving a permanent magnet above a conducting object or moving a conducting object in the vicinity of a permanent magnet causes induction of eddy currents in the object (Fig. 1). The interaction between the magnetic field of the permanent magnet and induced eddy currents leads to two types of Lorentz forces acting on the magnet, the first one which tries to stop the magnet (*drag* force) and the second one which lifts the magnet (*lift* force). In the paper, we consider the force calculations which are important in Lorentz force velocimetry [1] or a non-destructive material testing.

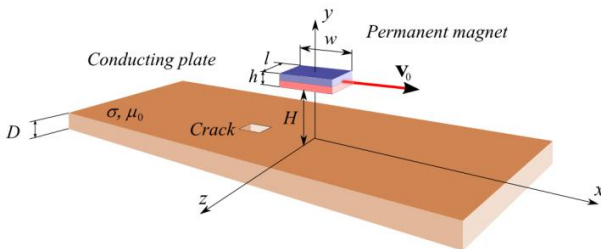


Fig. 1. Permanent magnet moving above conducting plate

II. DESCRIPTION OF METHODS

To solve above problem we have applied three approaches: (a) *transient* approach (TR), in which the global coordinate system is associated with the conducting plate and the permanent magnet is moving with a constant velocity \mathbf{v}_0 along x -axis, (b) *quasi-static* approach (QS), where the global coordinate system is associated with the permanent magnet and the conducting plate with a crack is moving with a constant velocity $-\mathbf{v}_0$ along x -axis, and (c) *fast quasi-static* approach (FAST), in which the global coordinate system is associated with the permanent magnet and the moving conducting plate contains no crack. In all analyzed cases, to avoid influence of edges effects, we have assumed that the moving magnet and the crack region are far away from the walls of the plate. Forces acting on the permanent magnet are

calculated indirectly, by calculating Lorentz forces acting on the plate (Newton's third law).

A. Transient approach (TR)

Assuming that the external current density \mathbf{J}^e equals 0, we have to solve the following equation [2]:

$$\sigma \frac{\partial \mathbf{A}}{\partial t} + \nabla \times \left(\frac{1}{\mu_0} \nabla \times \mathbf{A} - \mathbf{M} \right) = 0 \quad (1)$$

where \mathbf{A} is a magnetic vector potential and \mathbf{M} a magnetization vector defined as $\mathbf{B} = \mu_0(\mathbf{H} + \mathbf{M})$. To realize this approach, we define above the plate a rectangular region where the permanent magnet is moving (Fig. 2). In the movement region, the magnetization vector is defined as:

$$\mathbf{M} = M_0 f(x, z, t) \mathbf{1}_y, \quad (2)$$

$$f(x, z, t) = \mathcal{H}(x - x_0 - vt) - \mathcal{H}(x - x_0 - w - vt), \quad |z| \leq \frac{l}{2}$$

where $\mathcal{H}(\cdot)$ is the Heaviside step function, x_0 is the start position of the magnet, w is the width of the magnet, and v_0 is the velocity of the movement.

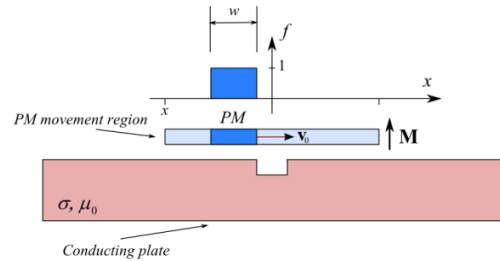


Fig. 2. Definition of material regions in a transient approach

In the numerical implementation, we have to take into consideration two facts: first, the finite element mesh in the movement region should be regular to fit the shape of the magnet (Fig. 3), and second, the time step used in a solution

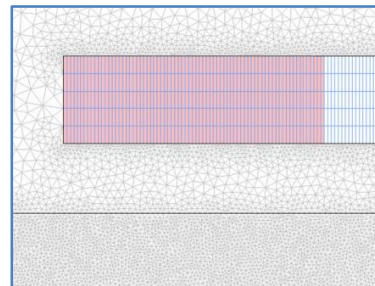


Fig. 3. Sample finite element mesh with marked magnet position (2D, $t = 0$)

procedure should be chosen in such a manner that the position of the magnet coincides with the finite element mesh in the particular time.

B. Quasi-static approach (QS)

In the quasi-static approach, we have to solve the following equations:

$$\nabla \times \left(\frac{1}{\mu_0} \nabla \times \mathbf{A} - \mathbf{M} \right) - \sigma \mathbf{v} \times (\nabla \times \mathbf{A}) + \sigma \nabla V = 0 \quad (3)$$

$$\nabla \cdot [\sigma \mathbf{v} \times (\nabla \times \mathbf{A}) - \sigma \nabla V] = 0$$

Although, the quasi-static formulation is fully correct for problems without spatial material changes in the movement direction, i.e. for the plate without crack, we have applied it to find the limits of its application when the plate contains a crack (Fig. 4) [3].

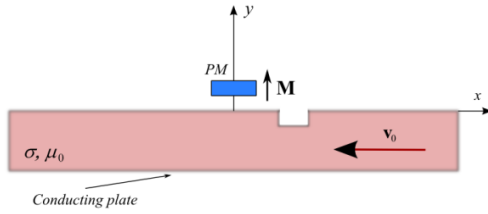


Fig. 4. Configuration of the problem used in the quasi-static approach

The implementation of the quasi-static approach is much easier and gives the results faster as in the transient one. The only problem which we have to take into consideration is a proper finite elements size in the conducting region determined with the help of Peclet number ($Pe = v_0 \sigma \mu_0 \Delta x$) in order to avoid spurious solutions [4].

C. Fast quasi-static approach (FAST)

In the fast quasi-static approach, we solve (3) for the plate without crack. The presence of the crack is taken into account only in the force calculations where the region with the crack is simply eliminated from the integration loop (Fig. 5).

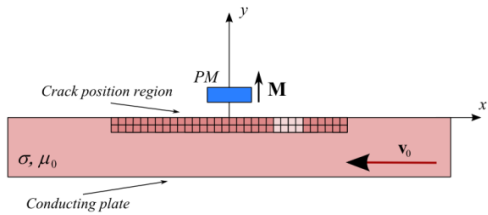


Fig. 5. Configuration used in the fast quasi-static approach

This kind of analysis is the fastest one because we have to solve the field problem only once and due to a suitable definition of the region with the possible crack position (e.g. by definition of several regions with different material codes) we receive the possibility to analyze various positions and shapes of the crack.

III. RESULTS AND DISCUSSION

We have realized all methods as Matlab® procedures using Comsol® as the FEM solver. In the digest, we present only sample 2D calculations of the drag force in the vicinity of the crack (Fig. 6). We can observe that the FAST approach gives results which are qualitatively closer to the transient approach than the QS approach even for high velocities. In the full paper we will present the results of 3D simulations as well as a detailed analysis of errors of the applied methods.

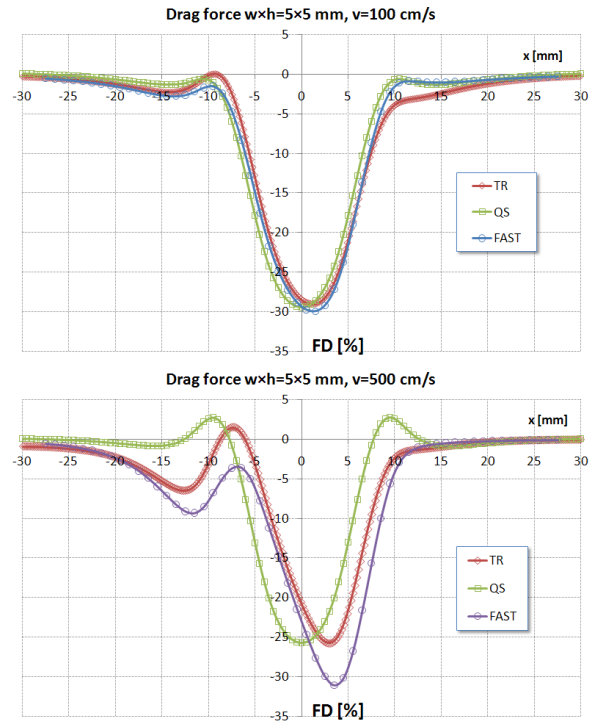


Fig. 6. Drag force distribution in the vicinity of crack ($w \times h = 5 \times 5$ mm) for different velocities

IV. CONCLUSIONS

The paper describes a fast technique to compute the forces acting on a permanent magnet that is moving relatively to a conductor. The proposed technique allows studying the velocity range in which the quasi-static approach can be used and thus, extensive transient FEM calculations can be avoided. The approach is very useful if the Lorentz force eddy current testing technique is applied to defect identifications in conductors.

V. REFERENCES

- [1] A. Thess, E. Votyakov, B. Knaepen, and O. Zikanov, "Theory of the Lorentz force flowmeter," *New Journal of Physics*, vol. 9, pp. 299-326, 2007 (<http://www.njpp.org>).
- [2] D. Rodger and H.C. Lai, "A Comparison of Formulations for 3D Finite Element Modeling of Electromagnetic Launchers," *IEEE Trans. on Magnetics*, 37(1): 135-138, 2001.
- [3] M. Ziolkowski and H. Brauer, "Validation of Force Calculations in Lorentz Force Eddy Current Testing," *Proceedings of 13th IGTE Symposium*, Graz, 21-24.09.2008, pp. 364-368.
- [4] E.K.C Chan and S. Williamson, "Factors Influencing the Need for Upwinding in Two-Dimensional Field Calculation," *IEEE Trans. on Magnetics*, 28(2): 1611-1614, 1992.

A model to relate SAR to surface field measurements in human phantoms

Oriano Bottauscio ([°]), Mario Chiampi (^{*}), and Luca Zilberti (^{°*})

([°]) Istituto Nazionale di Ricerca Metrologica
Strada delle Cacce 91, 10135 Torino, Italy
o.bottauscio@inrim.it, luca.zilberti@polito.it

(^{*}) Dip. Ing. Industriale, Politecnico di Torino
Corso Duca degli Abruzzi 24, 10129 Torino, Italy
mario.chiampi@polito.it

Abstract — This paper presents a numerical approach, based on the Boundary Element Method, able to reconstruct the induced current and SAR distribution inside a human phantom from the knowledge of field quantities on the body surface. Some examples of application are reported and the parameters affecting the accuracy of the reconstruction are analyzed and discussed.

I. INTRODUCTION

Guidelines limiting human exposure to electromagnetic fields are set by the International Commission on Non-Ionising Radiation Protection (ICNIRP) [1]. Basic restrictions are established in terms of induced currents (up to 10 MHz), specific absorption rate (SAR) (between 100 kHz and 10 GHz), and incident power density (from 10 GHz to 300 GHz). In Europe, the directive EC 2004/40/EC “Physical Agents Directive” [2] will make the provisions of ICNIRP a legal requirement with respect to the exposure of workers to electromagnetic fields.

Artefact standards for SAR exist only within the frequency range 380 MHz to 6 GHz, while difficulties arise in the lower and higher frequency ranges. As a consequence, limitations to future use of high power radio-frequency in industrial and medical applications (e.g. plastic welding, induction furnaces, and Magnetic Resonance Imaging) may arise, particularly for frequencies below 380 MHz. Within this context, the EURAMET-iMERA project [3] aims at providing traceable metrology for SAR in the whole ICNIRP frequency range. In this work, we describe and discuss some results obtained in the aforementioned project, with specific attention to the development of models able to relate surface field measurements to SAR in human phantoms. This approach will provide a valuable tool for more accurately assessing work place exposures in the low frequency range.

The numerical simulations are based on an integral formulation (IE) of the electromagnetic field equations. In particular, the Boundary Element Method (BEM), which deduces the fields within a homogenous body from the surface values, seems to be tailored for the specific requirements. The results of simulations performed by BEM on a simplified version of the standard SAM phantom [4] are first compared with those provided by a commercial code based on Finite Integration Technique (FIT) [5]. The parameters affecting the reconstruction of induced currents and SAR starting from a limited set of surface field measurements are finally discussed.

II. MODELING APPROACH

In order to relate field quantities induced within the body to the fields measured on its surface, we derive an integral formulation of the complete Maxwell’s equations, assuming sinusoidal supply conditions with angular frequency ω :

$$\nabla \times \nabla \times \mathbf{E} = k^2 \mathbf{E} - i\omega\mu \mathbf{J}_s \quad (1)$$

$$\nabla \times \nabla \times \mathbf{H} = k^2 \mathbf{H} + \nabla \times \mathbf{J}_s$$

The field source is a known current density \mathbf{J}_s , distributed in a domain Ω_s . Considering the source and phantom sizes and the wavelengths at the considered frequency range, the near field assumption can be assumed and we refer to a magnetic field source. \mathbf{E} and \mathbf{H} are the phasors of the electric and magnetic fields. The complex propagation constant $k = \omega\sqrt{\mu\tilde{\epsilon}}$ depends on the magnetic permeability μ and the complex electric permittivity of the media $\tilde{\epsilon} = \epsilon' - i\epsilon''$. Here ϵ' is the dielectric constant and $\epsilon'' = \sigma/\omega$, where the equivalent electrical conductivity σ includes all material losses. The values of $\tilde{\epsilon}$ are given as a function of frequency. The medium is isotropic, so that vector \mathbf{E} and \mathbf{J} are always collinear.

By applying the Green vector identity over the phantom body (domain Ω), the integral form of (1) for the electric field (EFIE) within the considered body becomes [6]:

$$T(\mathbf{r})\mathbf{E}^{(1)} = -\sum_e \int_{\partial\Omega_e} (\mathbf{n}^{(1)} \times \mathbf{E}^{(1)}) \times \nabla\psi^{(1)} ds - \sum_e \int_{\partial\Omega_e} (\mathbf{n}^{(1)} \cdot \mathbf{E}^{(1)}) \nabla\psi^{(1)} ds + i\omega\mu^{(1)} \sum_e \int_{\partial\Omega_e} (\mathbf{n}^{(1)} \times \mathbf{H}^{(1)}) \psi^{(1)} ds \quad (2)$$

The body surface $\partial\Omega$, separating the external region in air (volume 0) from the internal one filled by a weakly conductive medium (volume 1), is discretized into N triangles. In (2) the field quantities \mathbf{E} and \mathbf{H} are assumed to be constant on each triangle e ($e = 1, \dots, N$), $T(\mathbf{r})$ represents the singularity factor, the normal unit vector $\mathbf{n}^{(1)}$ points outward (toward volume 0) and ψ is the Green’s function satisfying Helmholtz equation. The electric and magnetic field values in the right-hand side are deduced from the external measured quantities (in volume 0) through the interface conditions. Relation (2) enables the computation of the value of $\mathbf{E}^{(1)}$ and $\mathbf{J}^{(1)} = i\omega\tilde{\epsilon}^{(1)}\mathbf{E}^{(1)}$ in any point inside Ω ; the local values of SAR are then deduced as $\Re(EJ^*)/\delta$, being δ the mass density of the media.

III. DISCUSSION OF RESULTS

The numerical model has been applied to the analysis of the homogeneous SAM phantom (see pictures in Fig. 2). In the results here reported, the phantom is exposed to the magnetic field generated by a small loop located laterally to the head, at a distance of ~ 4 cm. Assuming a working frequency of 100 MHz, the electric conductivity, relative permittivity and mass density of the SAM phantom are 0.33 S/m, 76 and 1000 kg/m^3 , according to average properties of muscle tissues [7].

In order to validate the proposed approach and verify its accuracy, the electromagnetic fields on the body surface are determined by a numerical solution of problem (1). For such a purpose, we add to the discretized relation (2) the magnetic field integral equation (MFIE) for the external volume:

$$T(\mathbf{r})\mathbf{H}^{(0)} = -\sum_e \int_{\partial\Omega_e} (\mathbf{n}^{(0)} \times \mathbf{H}^{(0)}) \times \nabla \psi^{(0)} ds - \sum_e \int_{\partial\Omega_e} (\mathbf{n}^{(0)} \cdot \mathbf{H}^{(0)}) \nabla \psi^{(0)} ds + i\omega \tilde{\epsilon}^{(0)} \sum_e \int_{\partial\Omega_e} (\mathbf{n}^{(0)} \times \mathbf{E}^{(0)}) \psi^{(0)} ds + \int_{\Omega_s} \mathbf{J}_s \times \nabla \psi^{(0)} dv$$

Following the BEM approach, a set of algebraic equations is then obtained by projecting Eqns. (2) and (3) along local coordinate systems, defined on each triangle by the normal and tangential unit vectors, and introducing interface conditions on the field quantities [6]. The system solution provides the electric and magnetic field on each surface triangle, effectively substituting the set of experimental values. The use of the numerical field solution allows us an easy investigation about the factors that affect the reconstruction of induced quantities and SAR within the body. Thus, we can verify the influence of the number of measuring points, of their distance from the investigation point and of the contributions of the single terms in (2) containing the electric and magnetic field components.

The induced currents flowing in the SAM phantom, together with the distribution of SAR are depicted in Fig. 1, making reference to a unitary supply current in the loop.

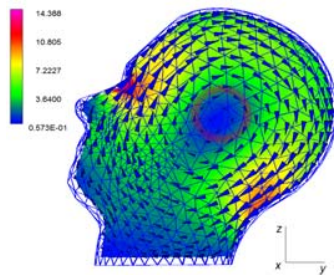


Fig. 1. Map of SAR distribution (values in mW/kg) over the central plane.

The corresponding induced electric field, along the investigation line A shown in Fig. 2, obtained by BEM approach are compared with those provided by a commercial code, based on Finite Integration Technique [5]. The same figure presents two additional curves obtained including for each evaluation point only the contribution within a given sphere of influence (having radius R). The results prove that

this simplifying assumption does not give rise to a satisfactory reconstruction of the induced field. More encouraging results are obtained neglecting the contributions of the normal component of the electric field on the body surface. The effect of the tangential components of \mathbf{E} and \mathbf{H} cannot be disregarded (see Fig. 3).

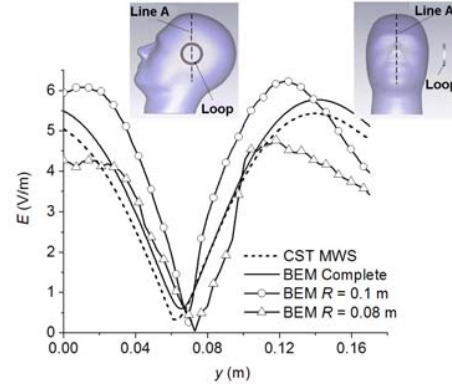


Fig. 2. Model of the SAM phantom, with field source and computed values of the induced electric field along the investigation line A.

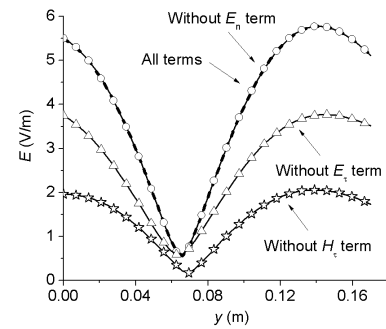


Fig. 3. Influence of the surface \mathbf{E} and \mathbf{H} components on the reconstruction of the induced electric field along the investigation line A.

IV. ACKNOWLEDGMENT

Research supported by iMERA-Plus Project, TP4-JRP07, "Traceable measurements of field strength and SAR for the Physical Agents Directive", 2008-2010.

V. REFERENCES

- [1] ICNIRP, Guidelines for limiting exposure to time-varying electric, magnetic, and electromagnetic fields (up to 300 GHz), ICNIRP Guidelines 1998.
- [2] Directive 2004/40/EC of the European Parliament and of the Council of 29 April 2004 on the minimum health and safety requirements regarding the exposure of workers to the risks arising from physical agents (electromagnetic fields).
- [3] iMERA-Plus Project, TP4-JRP07, "Traceable measurements of field strength and SAR for the Physical Agents Directive", 2008-2010.
- [4] EN 62209-1:2006-07. Std., "Human exposure to radio frequency fields from hand-held and body-mounted wireless communication devices - Human models, instrumentation, and procedures", 2006.
- [5] CST, Microwave Studio Suite, <http://www.cst.com>.
- [6] C.J. Huber, W. Rieger, M. Haas and W.M. Rucker, "Application of Curvilinear Higher Order Edge Elements to Scattering Problems Using the Boundary Element Method", IEEE Trans. Magn., Vol. 35. No. 3. 1999, pp. 1510-1513.
- [7] C.H. Durney, D.A. Christensen, "Basic Introduction to Bioelectromagnetics", CRC Press, London, 2000.

Design of Railway Wheel Detector Insusceptible to Electromagnetic Noise

Asuka Otake¹, Kenta Takayasu¹, Shinji Wakao¹, Tamio Okutani²,
Yasuhito Takahashi³, Masahiko Saito⁴, Akihisa Toyoda⁴

¹Waseda University, 3-4-1 Ohkubo Shinjuku-ku, Tokyo 169-8555, Japan

²Railway engineering Co., Ltd, 1-3-8 Shibadaimon, Minato-ku, Tokyo 105-0012, Japan

³Kyoto University, Yoshida-Honmachi, Sakyo-ku, Kyoto 606-8501, Japan

⁴The Nippon Signal Co.,Ltd, 1836-1 Ezura, Kuki, Saitama 346-8524, Japan
e-mail: wakao@waseda.jp

Abstract — This paper investigates a mutually reverse (MR) unit coil as a wheel detector which is more insusceptible to electromagnetic noise than conventional wheel detectors. We carry out the design optimization of the coil for the improvement of reception sensitivity by means of magnetic field computations.

I. INTRODUCTION

Recently, with the advancement of semiconductor devices, the wide spreading of railcars equipped with VVVF has become an issue due to the electromagnetic noises it creates. Therefore, the environment of the railway signaling system is deteriorating [1]. When developing new railway signaling devices, we need to consider the protection against noise. Especially, the noise reduction is indispensable in the case of wheel detectors, which are one of the railway signaling devices.

Thus, this paper deals with mutually reverse (MR) unit coil as a wheel detector, which is more insusceptible to electromagnetic noise than conventional wheel detectors. Unlike the conventional detector with only single receiving coil, in the MR wheel detector, two receiving coils are arranged one above the other. As the output, the difference of voltage which is induced in the two receiving coils is utilized. Therefore, the noise, i.e., magnetic field generated by the traction power converter of the railcar, is canceled by using two receiving coils, which results in the high accuracy of the wheel detector.

For the further improvement of reception sensitivity, we evaluate the performance and carry out the design optimization of MR wheel detector by using electromagnetic field computations.

II. INVESTIGATED MODEL

MR wheel detector is made up of a transmitting coil and two receiving coils, and a magnetic field from a transmitting coil which induces the voltage in receiving coils. When the wheel comes beside the detector, induced voltage of receiving coils is decreased by electromagnetic shielding effect due to eddy current generated in the wheel. The wheel detector judges the wheel presence based on the variation of signaling receive level.

In this paper, we analyze the MR wheel detector shown in Fig. 1. The current in transmitting coil is 500 mA, 33 kHz.

III. METHOD OF ANALYSIS

We adopt finite element method (FEM) using the magnetic vector potential A and electric scalar potential ϕ in analysis. We adequately utilize two kinds of mesh, i.e., the hexahedral and tetrahedral meshes [2]. Coils, wheel, and rail are independently divided with hexahedral elements. On the other hand, the tetrahedral mesh is applied to the air regions around both the coils and the wheel, which enables us to easily connect the meshes of each region mentioned above. This also makes it possible to easily displace the coils and wheel in the optimization procedure.

IV. ANALYSIS RESULTS

We compare the computational results with the measured value of signaling receive level. As a sampling rate, MR wheel detector judges signaling receive level at the points when the wheel comes right beside the receiving coils (0 mm), and when the wheel is in front or behind the receiving coils by 125 mm. And if signaling receive level is less than the threshold, the wheel is detected (Fig. 2). The wheel detector is more insusceptible as the attenuation of induced voltage in receiving coil becomes larger, which results in the prevention of false detection. First, we calculate signaling receive level in the following three cases, and compare the calculated values with the measured ones (TABLE I).

1. Static state (in case of no wheel)
2. When the wheel is located 125 mm away from the coils
3. When the wheel is located right beside the coils (0 mm)

The flux density distributions around the receiving coils in each case are shown in Fig. 3. In the case of no wheel, interlinkage flux of the lower receiving coil is decreasing more than that of the upper receiving coil due to the effect of eddy currents generated in the mounting hardware. Accordingly, we can obtain the obvious difference of signaling receive level between two receiving coils. On the other hand, flux density becomes parallel to the receiving coils when the position of the wheel is at 125 mm, resulting in the variation of signaling receive level. Additionally flux magnitude rapidly decreases when the wheel comes to the point of 0 mm due to the shield effect of the wheel. TABLE I shows that the calculated values of signaling receive level are well coincident with the measured ones.

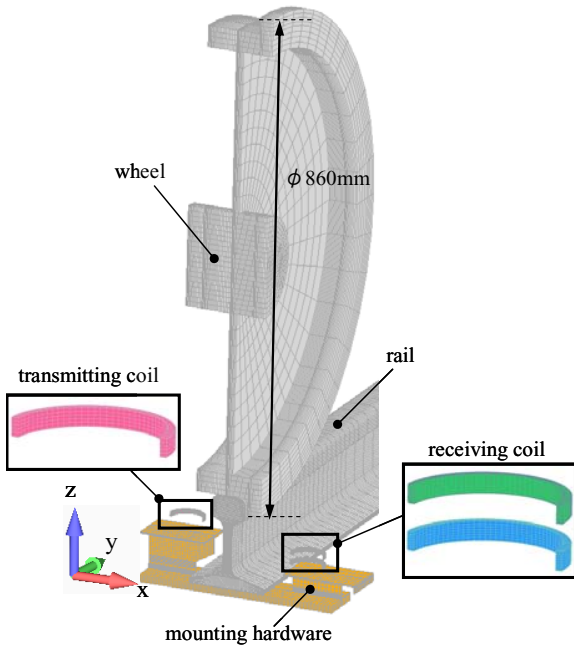


Fig. 1. MR wheel detector (half model).

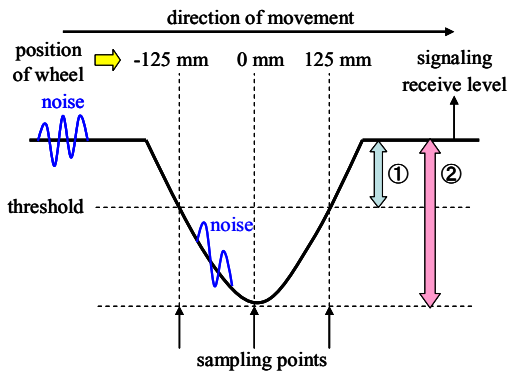


Fig. 2. Conceptual figure of wheel detector principle.

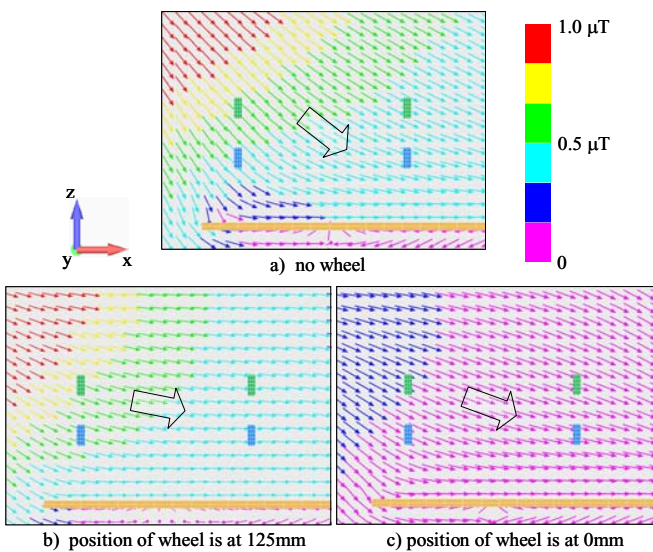


Fig. 3. Distributions of magnetic flux density.

TABLE I
COMPARISON BETWEEN MEASURED AND CALCULATED SIGNALING RECEIVE LEVEL

	Signaling receive level (dBV)		
	No wheel	Position of wheel	
		125 mm	0 mm
calculated	-43.26	-53.43	-63.01
measured	-44.89	-52.59	-63.09

V. IMPROVEMENT OF RECEPTION SENSITIVITY

In this chapter, as a design example, we carry out the layout optimization of receiving coils in the simulated wheel model so as to maximize the variation of signaling receive level. Considering the sizes of the coil case and mounting hardware, we assume the following constraint conditions for the receiving coils' position.

1. Distance between center of upper and lower receiving coils : 15-35 mm
2. Position of upper receiving coil : 80-105 mm
3. Position of lower receiving coil : 95-120 mm

Here, the coil position is defined as the distance between the top of the rail and the center of the coil.

The result of design optimization is shown in TABLE II. The layout optimization, taking account of the flux distributions effected by the wheel and mounting hardware, indicates the possible improvement of the reception sensitivity.

In the full paper, we will model the electromagnetic noise from the traction power converter, and investigate the design optimization of the receiving coils in detail.

TABLE II
IMPROVEMENT OF RECEPTION SENSITIVITY

	No wheel (dBV)	With wheel (dBV)	Variaton (dB)
Initial layout	-43.26	-62.25	18.99
Optimized layout	-41.07	-61.61	20.54

VI. REFERENCES

- [1] Tomoyuki Ogawa, Shinji Wakao, Keiichiro Kondo, and Nobuo Terauchi, "Theoretical analysis of return current harmonics in the inverter-controlled DC electric railcar," *35th Annual IEEE Power Electronics Specialists Conference (PESC04)*, pp. 711-716, Aachen, Germany, 2004.
- [2] Akihisa Kameari, "Magnetic Field Analysis Using Hybrid Mesh of Linear Hexahedral and Tetrahedral Edge Elements," *IEEE Trans. on Magnetics*, 44(6): 1182-1185, 2008.

Simulation of Internal Myocardium Defibrillation using Macroscopic Anisotropy Models and Finite Element Analysis

Maryam Golshayan and Steve McFee

Department of Electrical and Computer Engineering, McGill University
3480 University Street, Montreal, Quebec, H3A 2A7, Canada
steve.mcfee@mcgill.ca

Abstract — The purpose of this contribution is to evaluate the feasibility, potential benefits and associated costs, of generalizing and improving finite element formulations used to model, analyze and simulate, the theoretical and practical operation and efficacy of internal myocardium defibrillation systems. The primary focus of this study addresses the issue of generalizing the finite element models to better represent the biological tissue anisotropies of the myocardium, for the purpose of simulating the bioelectromagnetic response to conventional internal defibrillation stimuli. From the electrical viewpoint, the dominant impact of the tissue anisotropy affects conductivity modeling. The critical goal of this research is to establish the importance of modeling myocardium conductivity anisotropy for predicting internal defibrillation performance, and to determine the quality and detail of the models required to yield operationally correct results. Full tensor anisotropy formulations suitable for representing individual myocardial fibre bundles and sheets are considered and evaluated against simpler models. It is shown that isotropic tissue models can overestimate defibrillation efficacy, while macroscopic anisotropy formulations are sufficient to predict accurate and reliable bioelectromagnetic responses, for a range of practical internal defibrillation case study applications.

I. INTRODUCTION

Ventricular fibrillation (VF) is a dangerous, unstable state of the heart in which the cardiac muscles of the ventricles tend to twitch or quiver in an unsynchronized and chaotic manner. VF is commonly linked to malfunctioning electrical activity of the heart, and usually yields abnormal contractions which prevent efficient distribution of blood and oxygen to the tissues. VF is responsible for about 300,000 deaths in the USA annually [1].

The most effective approach to resolve VF is using internal defibrillation, i.e. by applying electrical shocks directly to the heart via an implantable cardioverter-defibrillator (ICD). The performance and operational lifespan of an ICD is tied to both the placement of the electrodes surrounding the heart muscle, and the energy storage capacity of the batteries which power it. Optimizing ICD electrode design, configuration and discharge characteristics can play a vital role in increasing the reliability and safety of defibrillation, as well as in reducing the electric shock energies required, and increasing the ICD lifespan [1].

Until relatively recently, these issues were addressed largely based on practical clinical trial results, until the introduction of detailed thoracic and cardiac models facilitated computational simulations of heart defibrillation. These models are now used to optimize both electrode design and placement, and electrical stimulation strength and waveform, to improve the efficacy of

the defibrillation process [2], [3]. However, due to the lack of concrete conductivity data for the myocardium, finite element studies seldom attempt to represent the anisotropies associated with the highly fibrous and multilayered structure of the tissue, and the potential ramifications and impact of these aspects for practical internal defibrillation systems remain unclear [4], [5].

The defibrillation threshold (DFT) is conventionally defined as the minimum electrical stimulation required for a successful defibrillation result. While this specification is not unanimous, a widely held interpretation is the critical mass hypothesis [4]. This DFT stipulates that 75-90% of the myocardium should be raised to an average electric voltage gradient of 300-800 V/m, or more directly, exposed to an average electric current density of 70-200 A/m², for the duration of the stimulation, in order to achieve defibrillation [6]. It should be noted that higher tissue stimulation levels are also used in some applications, but they need higher capacity ICD energy storage sources, and render a greater risk of localized cardiac electrode-tissue damage. The critical mass hypothesis DFT is considered in this study.

The primary purpose of this contribution is to determine the potential advantages and related costs of generalizing the finite element formulations used to model, analyze and simulate the practical operation and efficacy of ICD systems, to account for the inherent electrical anisotropies of the myocardium tissues. At the cellular level, the myocardium consists of muscle fibres composed of co-aligned myocytes (muscle cells), organized in complex three-dimensional laminar structures (muscle sheets), which are oriented transversally to the heart walls [7], [8]. At the macroscopic level, sets of adjoining and similarly directed muscle sheets can be interpreted to represent averaged laminar muscle layers, which specify undulating and twisting preferred electrical conduction paths that transect the myocardium walls. In terms of macroscopic material conductivity modeling, these layers may be described using anisotropic conductivity tensors, with preferred conductivity directions aligned along the “flow” of the layers, which circulate azimuthally around the heart, and non-preferred conductivity directions oriented perpendicular to the muscle fibres. Other conductivity anisotropies also arise at sub-macroscopic levels, but they are operationally secondary.

An application-specific, recursive-refinement, second-order, isoparametric, tetrahedral, finite element formulation, with full tensor continuum conductivity modeling, for both macroscopic and sub-macroscopic analyses, is used in this study. The intent of this research is to establish the merits of using macroscopic anisotropy models for analyzing practical ICD performance.

II. ILLUSTRATIVE EXAMPLE AND RESULTS

A straightforward example that demonstrates the importance of modeling the anisotropic nature of myocardial conductivity for predicting ICD performance and efficacy is presented. The physical system geometry and finite element model for a basic, low-frequency ICD stimulation study are described by Fig. 1. In this case, two small rectangular patch electrodes are used to externally stimulate the lower mass of the left ventricle (LV) of the myocardium. Fig. 1 illustrates an exploded cut-away view of the LV tissue mass and the ICD electrode configuration.

Three sets of results are reported, for three mean equivalent LV tissue conductivity models: (i) isotropic $\sigma = 0.240\text{S/m}$; (ii) anisotropic with $\sigma = 0.48\text{S/m}$ along the fibres and $\sigma = 0.12\text{S/m}$ perpendicular to the fibres; (iii) anisotropic with $\sigma = 0.412\text{S/m}$ along the fibres, $\sigma = 0.206\text{S/m}$ perpendicular to the fibres and tangential to sheets, and $\sigma = 0.103\text{S/m}$ normal to fibre sheets. Sample LV wall field penetration plots are presented in Fig. 2.

In opposition with the conclusion of [9], the results in Fig. 3 indicate that using isotropic myocardium conductivity models in ICD DFT analyses can yield significantly different threshold predictions, compared to using anisotropic models. In fact, the isotropic model results over-estimate the anisotropic minimum DFT stimulation levels by 50-85%, in the 70-90% range of the LV tissue volume. This difference may be due to modeling the anisotropy of myocardial sheets – which was not done in [9]. In addition, Fig. 3 also indicates that it may not be necessary to model all the detail of the myocardial sheets to estimate useful DFT results; macroscopic anisotropy models may be adequate.

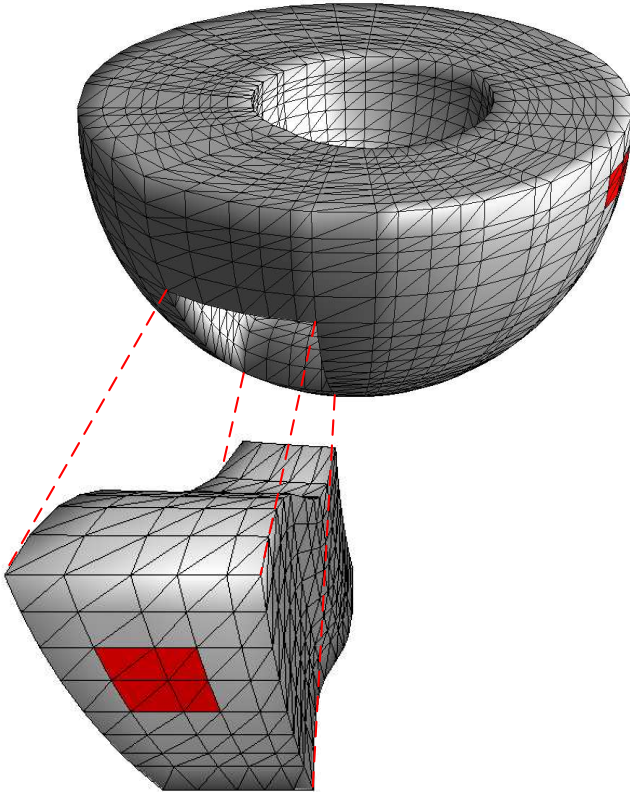


Fig. 1. Exploded cut-away view of the second-order, curvilinear, tetrahedral mesh for the lower portion of the LV (39,690 elements and 57,009 DOF). The cutout section illustrates the laminar structure of the myocardial wall; the ICD patch electrodes are shown in red (one on the cutout; one at the upper right).

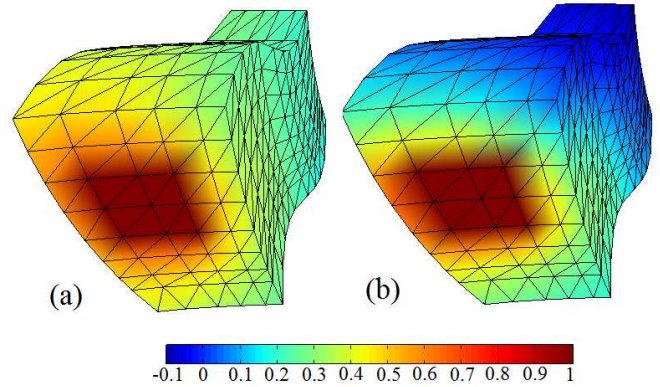


Fig. 2. Normalized scalar electric potential solution plots for steady-current flow analysis over cutout section: (a) represents the homogeneous isotropic conductivity result [case (i)]; (b) represents the layers included anisotropic tissue response [case (iii)]. Both correspond to $\pm 1\text{V}$ electrode excitations. Note the sizable difference in potential field penetration into the LV free-wall.

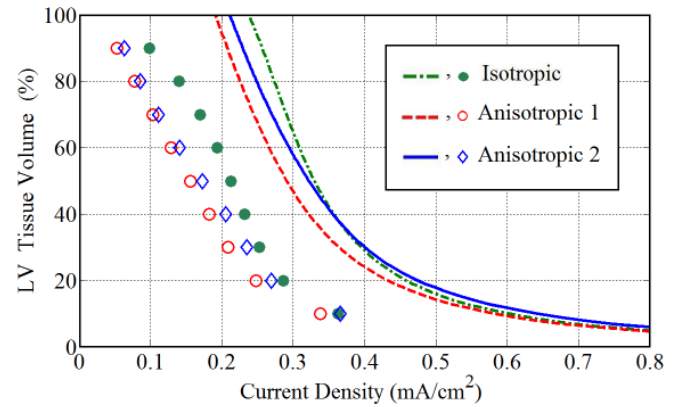


Fig. 3. DFT results for the isotropic and anisotropic conductivity simulations: the curves describe the maximum average current density magnitude achieved per fractional volume of the LV myocardium; the knots indicate the minimum current density stimulation levels delivered to these partial LV tissue masses.

III. REFERENCES

- [1] W.A. Tacker, *Defibrillation of the heart: ICDs, AEDs and manual*, Mosby-Year Book Inc., Elsevier, 1994.
- [2] M.A. Camacho, L. Lehr and S.R. Eisenberg, "A three-dimensional finite element model of human transthoracic defibrillation: paddle placement and size", *IEEE Trans. Biomed. Eng.*, 42(6): 572-578, 1995.
- [3] W.J. Karlou, S.R. Eisenberg and J.L. Lehr, "Effects of paddle placement and size on defibrillation current distribution: A three-dimensional finite element model", *IEEE Trans. Biomed. Eng.*, 40(3): 246-255, 1993.
- [4] Y. Wang, P.H. Schimpf, D.R. Haynor, G.H. Bardy and Y. Kim, "Analysis of defibrillation efficacy from myocardial voltage gradient with finite element modeling", 46(9): 1025-1036, 1999.
- [5] N. Trayanova, "Defibrillation of the heart: insights into mechanisms from modeling studies", *Ex. Physiol.*, 91(2): 323-337, 2006.
- [6] R.E. Ideker, P.D. Wolf, C. Alfemess, W. Krassoska and W.M. Smith, "Current concept for selecting the location, size, and shape of defibrillation electrodes", *Pacing Clin Electrophysiol.*, 14(2 Pt 1): 227-40, 1991.
- [7] J. Legrice, P.J. Hunter and H. Smaill, "Laminar structure of the heart: a mathematical model", *Am. J. Physiol.*, 272(5): H2466-2476, 1997.
- [8] D. Rohmer, A. Sitek, and G.T. Gullberg, "Reconstruction and visualization of fiber and sheet structure with regularized tensor diffusion MRI in the human heart", E.O. Lawrence National Laboratory, Life Science Division, Berkeley, California, U.S.A., 2006.
- [9] Y. Wang, D.R. Haynor and Y. Kim, "An investigation of the importance of myocardial anisotropy in finite-element modeling of the heart: methodology and application to the estimation of defibrillation efficacy", *IEEE Trans. Biomed. Eng.*, 48(12): 1377-1389, 2001.

Novel Applications of Inductive Method for Measuring Critical Current Density

Atsushi Kamitani¹, Teruou Takayama², and Soichiro Ikuno³

¹ Yamagata University, Yonezawa, Yamagata 992-8510, JAPAN, E-mail: kamitani@yz.yamagata-u.ac.jp

² Yamagata University, Yonezawa, Yamagata 992-8510, JAPAN, E-mail: takayama@yz.yamagata-u.ac.jp

³ Tokyo University of Technology, Hachioji, Tokyo 192-0982, JAPAN, E-mail: ikuno@cc.teu.ac.jp

Abstract— The inductive method for measuring the critical current density in a high-temperature superconductor (HTS) has been investigated numerically. In the method, a HTS sample is exposed to the magnetic field which is generated by a small coil placed just above the sample. While applying an ac current $I(t)=I_0 \sin 2\pi ft$ in the coil, the 3rd-harmonic voltage V_3 induced in the coil is measured. In order to simulate the inductive method, I_0 - V_3 curves are numerically determined and the critical current density is estimated from their characteristics. The results of computations show that, for a HTS bulk, the accuracy of the inductive method is significantly influenced by the coil radius. In addition, for double-sided HTS films on an MgO substrate, the accuracy is strongly affected by the substrate thickness.

I. INTRODUCTION

The inductive method [1]-[3] has been widely used for measuring the critical current density j_c of a high-temperature superconductor (HTS) thin film since it was developed by Claassen *et al.* [1] Recently, Mawatari *et al.* [3] have improved the inductive method so that it can be applicable to the measurement of j_c in a HTS bulk. In the method, a HTS sample is exposed to an inhomogeneous ac magnetic field that is generated by an N_c -turn coil placed just above the HTS sample. While applying an ac current $I(t) = I_0 \sin 2\pi ft$ in the coil, the third-harmonic voltage $V_3 \sin(6\pi ft + \theta_3)$ is measured. On the basis of the measured values, $I_0 - V_3$ curves are obtained. In the inductive method, the value of j_c is estimated from the characteristics of the curves. However, their shapes differ remarkably depending on what type of a HTS sample is used: a bulk or a thin film. Hence, the j_c -estimation method for a bulk is widely different from that for a film.

By using the critical state model, Mawatari *et al.* analyzed the mechanisms of the V_3 generation to get the following formulas [2], [3]:

$$j_c^S = 2\pi f G_3 I_0^2 / V_3, \quad (1)$$

$$j_c^A = 2F_m I_\tau / b. \quad (2)$$

Here, j_c^S and j_c^A denote the value of j_c for a bulk and that for a film, respectively, and b is the thickness of a HTS film. Furthermore, G_3 and F_m are both constants determined only by the configuration of a coil and a HTS sample. In the inductive method, the value of j_c for a HTS bulk and that for a HTS film are estimated by using (1) and (2), respectively.

The purpose of the present study is to numerically investigate the applicability of the inductive method to a HTS bulk or to double-sided HTS films on a substrate. In particular, we elucidate the following two problems:

- 1) How is the inductive method for a HTS bulk affected by the experimental conditions?
- 2) Can the inductive method be applied to the j_c -measurement for double-sided HTS films on a substrate?

II. GOVERNING EQUATIONS

We assume that a HTS-sample shape is a disk of radius R and thickness b , and that a coil has a rectangular cross section of width W and height H . In addition, the coil is placed so that its symmetry axis may correspond to that of the HTS sample. Since these assumptions lead to the axisymmetric problem, we can use the cylindrical coordinate (r, θ, z) . In terms of the coordinate, the cross section of the coil is expressed as $D = \{(z, r) : |z - z_c| < H/2, |r - r_c| < W/2\}$.

Under the multiple-thin-layer approximation, the state of the shielding current density can be represented in terms of a vector-valued function $\vec{S}(r, t) \equiv [S_1(r, t), \dots, S_M(r, t)]^T$, where $S_p(r, t)$ is z -component of the current vector potential in the p th layer. In addition, the time evolution of $\vec{S}(r, t)$ is governed by the following integral-differential equations [4]:

$$\mu_0 \frac{\partial}{\partial t} \left(\hat{Q} + \frac{1}{\varepsilon} \hat{I} \right) \vec{S} + \frac{\partial}{\partial t} \vec{B} + \vec{E}_R = \vec{0}. \quad (3)$$

Here, \vec{B} and \vec{E}_R originate from the applied magnetic flux density and the electric field, respectively, and 2ε denotes the thickness of each layer. Moreover, \hat{I} is an identity operator, whereas \hat{Q} is the operator defined in [4]. For the J - E constitutive relation, the following power law is assumed:

$$\vec{E}_p = E(j_p) \hat{j}_p / |j_p|, \quad E(j) = E_C (j/j_c)^N, \quad (4)$$

where E_C denotes the critical electric field and N is a constant.

For the initial and the boundary conditions to (3), we assume $\vec{S}(r, 0) = \vec{S}(R, t) = \vec{0}$. The time evolution of the shielding current density can be determined by solving the initial-boundary-value problem of (3). By using the high-performance integration method [5], the authors recently developed an accurate numerical code for solving the problem.

III. NUMERICAL SIMULATION FOR HTS BULK

In the present section, we investigate the accuracy of the inductive method for a HTS bulk. To this end, two dimensionless quantities are defined as follows:

$$I_0^* \equiv I_0 / (j_c R b),$$

$$V_3^* \equiv V_3 / \left[2\pi f G_3 j_c (R b)^2 \right].$$

12. DEVICES AND APPLICATIONS

In terms of the above quantities, the relative error between j_C^S and j_C can be written as

$$\varepsilon_r = |1 - (1/k_0^*)^2|, \quad (5)$$

where k_0^* denotes a slope of a $I_0^* - (V_3^*)^{1/2}$ curve at the origin. As is apparent from (5), it is k_0^* that determines the value of ε_r . Hence, k_0^* can be used as a measure of the accuracy of the inductive method. Throughout the present section, the physical and the geometrical parameters are fixed as follows: $N_c = 400$, $f = 1$ kHz, $W = 1.2$ mm, $H = 1$ mm, $z_c = 0.75$ mm, $R = 10$ mm, $b = 0.4$ mm, $M = 10$, $N = 16$, $E_C = 1$ mV/m, and $j_C = 10$ MA/m².

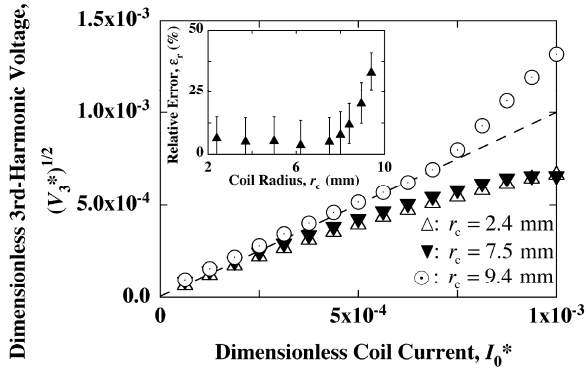


Fig. 1. The dimensionless third-harmonic voltage V_3^* as functions of the dimensionless coil current I_0^* . The inset shows the dependence of the relative error ε_r on a coil radius r_c .

The $I_0^* - (V_3^*)^{1/2}$ curves are numerically determined for various values of r_c and are depicted in Fig. 1. We see from this figure that $k_0^* \cong 1.00$ for $r_c \leq 7.5$ mm and $k_0^* \cong 1.20$ for $r_c = 9.4$ mm. In other words, the relatively good accuracy is achieved for $r_c \leq 7.5$ mm, whereas the accuracy is drastically degraded for $r_c = 9.4$ mm. For the purpose of investigating these tendencies quantitatively, k_0^* is determined by applying the least-squares fitting to the $I_0^* - (V_3^*)^{1/2}$ curves and, subsequently, the relative error ε_r is evaluated by using (5). The results of computations are shown in the inset of Fig. 1. This inset indicates that, for $r_c \leq 7.5$ mm, the relative error slightly decreases with an increasing coil radius. On the other hand, for $r_c \geq 7.5$ mm, it drastically increases with r_c . This result suggests that there exists an optimum value of the coil radius.

IV. NUMERICAL SIMULATION FOR DOUBLE-SIDED HTS FILMS

As is well known, double-sided HTS films are generally grown on an MgO substrate and are frequently used for RF filter designs. In the present section, we numerically investigate whether the inductive method is applicable to the j_C -measurement of double-sided HTS films on an MgO substrate. Throughout the present section, the geometrical and the physical parameters are fixed as follows: $N_c = 300$, $f = 1$

kHz, $W = 1.25$ mm, $H = 3$ mm, $(z_c, r_c) = (1.56$ mm, 1.625 mm), $R = 10$ mm, $b = 500$ nm, $M = 1$, $N = 16$, $E_C = 1$ mV/m, and $j_C = 3.3 \times 10^3$ MA/m². Note that b does not denote the total thickness of a sample but the thickness of each film. In the following, the thickness of an MgO substrate is denoted by d .

The $I_0 - V_3$ curves are numerically determined for various values of d and are depicted in Fig. 2. Especially, for the case with $d = 5 \times 10^{-1}$ mm, the behavior peculiar to double-sided HTS films is observed. Just after I_0 exceeds the threshold current I_{T1} , V_3 abruptly develops. A further increase in I_0 will cause a monotonous increase in V_3 until V_3 reaches a plateau at $I_0 = I_{T2}$. Moreover, for the case with $I_0 > I_{T2}$, it increases again with I_0 . In other words, just after $I_0 = I_{T1}$ or just after $I_0 = I_{T2}$, the third-harmonic voltage rapidly develops with an increase in I_0 . Such a rapid increase in V_3 is attributable to the breakdown of the magnetic shielding behind either an upper film or a lower one. These tendencies are also observed in Saito's experiment [6]. In the following, the value of V_3 at $I_0 = I_{T2}$ is called an upper third-harmonic voltage. Fig. 2 also indicates that an upper third-harmonic voltage monotonously decreases with a decrease in d until it almost vanishes for the case with $d = 2 \times 10^{-2}$ mm. Hence, the equality $I_{T1} = I_{T2}$ is approximately satisfied for this case. This result suggests that, for $d \leq 2 \times 10^{-2}$ mm, the accuracy of (2) is deteriorated remarkably.

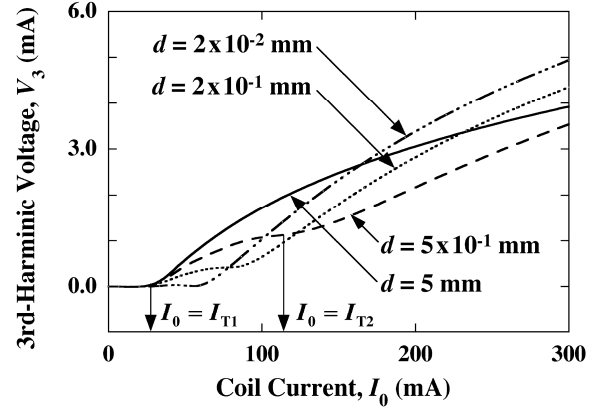


Fig. 2. The third-harmonic voltage V_3 as functions of the coil current I_0 .

V. REFERENCES

- [1] J. H. Claassen, M. E. Reeves, and R. J. Soulen, Jr., "A contactless method for measurement of the critical current density and critical temperature of superconducting films," *Rev. Sci. Instrum.*, 62(4): 996-1004, 1991.
- [2] Y. Mawatari, H. Yamasaki, and Y. Nakagawa, "Critical current density and third-harmonic voltage in superconducting films," *Appl. Phys. Lett.*, 81(13): 2424-2426, 2002.
- [3] Y. Mawatari, H. Yamasaki, and Y. Nakagawa, "Inductive measurements of third-harmonic voltage and critical current density in bulk superconductors," *Appl. Phys. Lett.*, 83(19): 3972-3974, 2003.
- [4] A. Kamitani and S. Ohshima, "Magnetic shielding analysis of axisymmetric HTS plates in mixed state," *IEICE Trans. Electron.*, E82-C(5): 766-773, 1999.
- [5] A. Kamitani, T. Takayama, and S. Ikuno, "Numerical simulation of inductive method and permanent-magnet method for measuring critical current density," *IEEE Trans. Magn.*, 44(6): 926-929, 2008.
- [6] A. Saito and S. Ohshima, Yamagata Univ., Yamagata, Japan, private communication, 2009.

Hybrid generation of subject specific head models

Jacek Starzyński, Robert Szmurło, Bartosz Sawicki, Stanisław Wincenciak
 Warsaw University of Technology, Electrical Engineering
 Koszykowa 75, 00-662, Warsaw, Poland
 jstar@iem.pw.edu.pl

Abstract— In this paper an effective approach to generate specimen-specific finite element head models for bioelectromagnetic simulations is presented. The goal of the research is to develop a fast and automatic methodology for generation of such models.

The method uses a hybrid mixture of spatial transformation and image registration. The spatial transformation is used to transform the standard reference model, which was created with an elaborate manual segmentation, into individually fit model. The goal of this step is to morph the reference model to obtain the same external shape as the individual model. The image registration algorithm is then used to segment brain tissues, which are later put inside the skull. The final model is constructed of skull and skin obtained from morphing, and internal structure from image registration algorithm used for the brain.

I. INTRODUCTION

Numerical models in bioelectromagnetism created for the finite element method, need dividing the volume of the head into huge number of small elements, reflecting the size of the anatomical details.

The classical approach to the construction of such a model starts with obtaining a series of two-dimensional MRI scans. Each scan is then processed in order to improve the sharpness and the contrast between interesting tissues. Next step is a segmentation of images to extract boundaries between the different tissues. Next the voxelization follows in which the segmented cross-sections are combined into the 3D model. The 3D volume mesh is then generated by dividing each voxel into the relevant elements. In the final stage the reduction procedure decreases the number of elements and smoothes the model (see Fig. 1a).

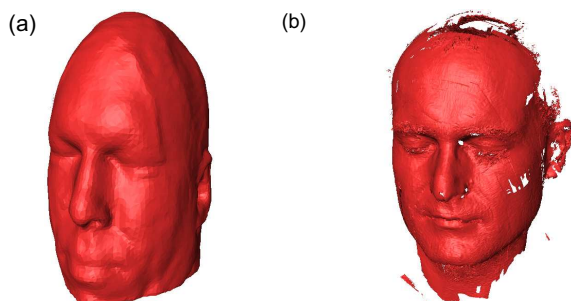


Fig.1. (a) Head model generated from VH images [5] (b) External scan of the head made with Faro Laser ScanArm.

Some phases described above cannot be fully automated. The classical, semi-automatic approach becomes more painful with demand for even more realistic, patient-specific models of the human body. Individually tuned simulations could help to

design effective and possibly non-invasive configuration of medical devices for electromagnetic stimulation. However they need fast and robust procedure to create models based on individual features for certain patient [1]-[4].

The automatic segmentation of particular region depends on the medical imaging technique used to obtain data. It is quite easy to segment the brain tissues from MRI images. The skull can be more effectively segmented using CT data. There have been attempts to combine those techniques to improve the quality of models. Those algorithms however require additional effort like scaling and alignment of the models.

II. MORPHING APPROACHES

The new approach which is aimed to solve the presented problems emerged from methodology used in computer animation. It has already been used for relatively simple organs like bones and fingers, but we have adapted it to speed up creation of patient specific realistic head models.

The investigated morphing approach is based on works presented in [1]-[2] proposing two different methodologies but based on the same kind of idea. They start with fine discretized standard model and geometrical data of a target patient. These data can be based on some external measurements (see Fig.1b) or, preferably, on some medical imaging of the internal structure. Then the base model is morphed according to some criteria grounded in differences between the standard model and the target patient. The morphing can in principle be made on several levels—starting from the raw measurements (or images) up to the 3D discrete mesh. It is obvious, that morphing the mesh is the most difficult but as well the most wanted approach.

Several algorithms of the morphing were proposed. The most interesting from our point of view seems to be a combination of two methods: Automated Wrapping [1] and Volume Registration (VR) [2]. Automated wrapping was successfully applied to create individual model of bones. It needs relatively small amount of input data, but is not able to map the internal structure of the model. The VR method allows to obtain more accurate structured models, but it needs very fine input data. Authors of [2] have used tomography scans of the base patient and the target patient to obtain input data for the morphing criteria. Both scans were made in exactly the same device and same configuration. The morphing algorithm compared, pixel by pixel, scans of the base and target to calculate the morphing transformation. Obtaining similar input data for the head models seems to be extremely difficult if at all possible.

III. MORPHING IMPLEMENTATION

The basic technique assumes that we have a detailed model of sub-domains of a head. In this technique operator with help of a specialized software applies a stretch-shrink vectors set (see Fig.2). The set is then used by the algorithm to perform the morphing. This procedure can of course be automated.

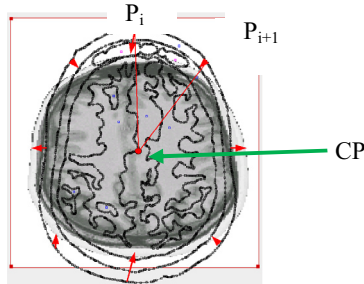


Fig.2. Central point (CP) and Vectors (v_i) defining the stretch-shrink parameters for the algorithm.

In the proposed algorithm the domain is divided into the slices which are defined by a single central point (CP) and a set of vectors V_i . Each vector besides the direction and length has a location P_i . The slices are defined by the central point CP and two adjacent stretch-shrink vector locations P_i and P_{i+1} . Displacement of each vertex is defined by the two adjacent base vectors.

$$v_i = a_n r_n V_n + a_{n+1} r_{n+1} V_{n+1} \quad (1)$$

where

$$a_n = \frac{\langle x_i, P_{n+1} \rangle}{\langle P_n, P_{n+1} \rangle}, \quad a_{n+1} = \frac{\langle x_i, P_n \rangle}{\langle P_n, P_{n+1} \rangle} \quad (2)$$

$$r_n = \frac{|x_i|}{|P_n - CP|}, \quad r_{n+1} = \frac{|x_i|}{|P_{n+1} - CP|}$$

We can say that with the transformation defined by (1) and (2) the vertex is translated by the weighted sum of the adjacent base vectors V_n, V_{n+1} .

The presented transformation preserves the sub-domains from the base model in the morphed model. Proper definition of base vectors allows to adjust the external shape of the reference model to the current MRI image. In Fig.3 the reference and morphed models are presented. We can see that the external shape of the morphed model fits the shape of the subject, however the internal structure of the head differs.

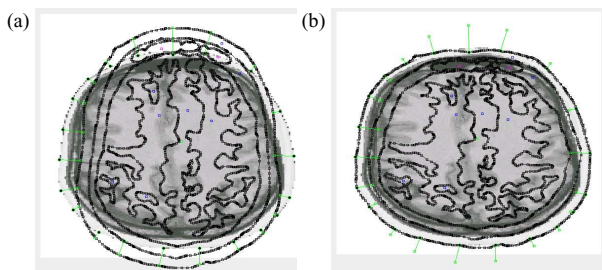


Fig.3. Domains of the head before stretching-shrinking (a) and after execution of the algorithm (b).

To obtain the proper structure of the internal region we have removed the white matter obtained from the morphing (see Fig.4b) and added the white matter from image

registration algorithm. The image registration was performed with simple hence robust histogram-based method.

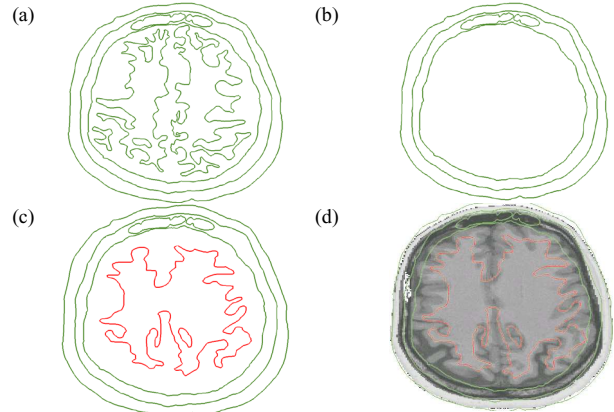


Fig.4. Domains of the head after stretching-shrinking (a) and with replaced white matter subdomain from image registration (b).

IV. CONCLUSIONS

The most crucial is the development of indicators, which will assess the quality (fidelity) of the derived model. This is due to the fact that the target model is unknown. These indicators should be based on measurements of the patient's head. The simplest indicators can be based solely on simple anthropometric measurements, but it can prove to be insufficient because of the complexity of a large numerical model. The morphing transformation which must be properly defined and needs large number of data can be automated what makes the method highly advantageous. Simple morphing is of course insufficient, because the shape of the outer surface of the head does not determine its internal structure. To obtain specific internal structure of the head the MRI scans can be used. The authors have used them as input data for image registration to get the internal structure. It was later put together with external domains (skin and skull) from morphing to obtain the complete subject specific model. In the authors opinion the proposed method can be fully automated. This will significantly reduce the time from data acquisition to patient specific model.

V. REFERENCES

- [1] M. Tada, H. Yoshida, M. Mochimaru, Geometric Modeling of Living Tissue for Subject-Specific Finite Element Analysis, Engineering in Medicine and Biology Society, 28th Annual International Conference of the IEEE, 2006, pp. 6639-6642
- [2] Sigal IA, Hardisty MR, Whyne CM, Mesh-morphing algorithms for specimen-specific finite element modeling, J Biomech. 2008, pp. 1381-1389
- [3] Inou N., Koseki M., Jonishi M., Maki K., Patient-Specific Finite Element Modeling of Human Skull Based on X-ray CRT Images, Proceedings of 1st AOTULE Studens Workshop and 5th KAIST-Tokyo Mechanical Engineering Workshop, Daejeon, Korea, 2007, p. 17.
- [4] R. Szmurło, J.Starzyński, Specimen-specific finite element models of human head obtained with mesh-morphing, Przegląd Elektrotechniczny (Electrical Review), R. 85 NR 4/2009, pp. 47-49
- [5] Visible Human Project, <http://www.nlm.nih.gov/research/visible/>

Modeling a “flying carpet” stable in both the positive and negative z-directions

Mikhail Kustov, Orphée Cugat, and Gilbert Reyne
G2Elab - Grenoble Electrical Engineering Lab
ENSE3 - BP 46 - 38402 St Martin d'Hères Cedex, France
mikhail.kustov@g2elab.grenoble-inp.fr

Abstract — An original levitation device, stable in both the positive and negative z-directions is modelled and simulated. The device may be used either in the Earth gravity field or under weightless conditions. The semi-analytical modelling and optimization suite MacMEMS / CADES [1, 2] was used.

I. INTRODUCTION: DIAMAGNETIC LEVITATION DEVICES

Diamagnetic levitation of diamagnetic materials above permanent magnets is now being widely published [3-5]. Diamagnetic forces, in a variety of devices, can be used against gravity. However the vertical stability of such structures depends on the compensation between gravity and diamagnetic repulsion, which makes them usable in one orientation only and in the Earth's gravity field.

Fig. 1. describes a proposed +/-Z stable levitation device. The "flying carpet" is a 30 μm thick plate of highly oriented pyrolytic graphite (HOPG), coated with 20 nm of iron. The "base" element is a 50 μm thick permanent magnet film, magnetically patterned into stripes [6, 7].

The device is designed to be microfabricated. MEMS and microtechnologies are perfectly suited to the diamagnetic levitation [8], because diamagnetic effects improve with miniaturization: they become comparable to gravity around the sub-mm scale.

In the "traditional" diamagnetic levitating devices [9, 10], the permanent magnet base has two functions: on Earth, its main function is to provide lift against gravity, along the vertical (Oz) axis. Additionally, possible configurations in the Ox and Oy axes are very variable, allowing translations along Ox or Oy or both, or rotation around Oz, or even no freedom at all. Here in our example, the chosen stripe-like magnetization pattern allows one degree of freedom: Ox translation along the stripes.

II. NOVELTY: BI-DIRECTIONAL STABILITY ALONG OZ

However, these devices do not work upside-down nor in zero-gravity because the forces along Oz are purely repulsive. Our innovation is the addition of a 20 nm thin film of soft ferromagnetic material which is deposited onto the HOPG plate, on the far side from the magnets. This ferromagnetic layer generates an attraction force towards the base, which can stabilize the carpet along Oz if properly calculated: this is the topic of our paper.

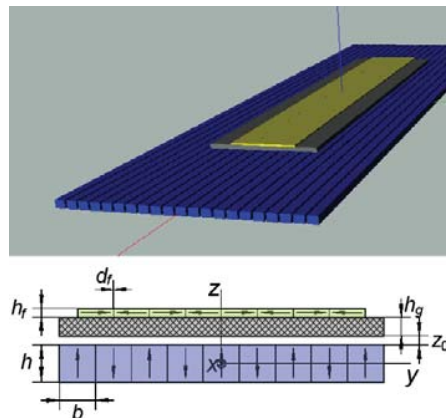


Fig. 1: The array at the bottom is the permanent magnet film integrated on Si, magnetised in an up/down array (remanence B_r). The middle layer is the micro-layer of HOPG (susceptibility χ_{dia}). The stripe on top is the nano-layer of soft magnetic material (saturation magnetization M_s). All dimensions along

Ox-axis are much larger than those along Oy-axis.

Magnets: $b = h = 50 \mu\text{m}$, $B_r = 1.4 \text{ T}$, Graphite: $h_g = 30 \mu\text{m}$, $\chi_{\text{dia}} = -450.10^{-6}$; Soft film: $h_f = 20 \text{ nm}$, $d_f = 1 \mu\text{m}$, $\mu_0 M_s = 1 \text{ T}$

III. MODELING AND OPTIMIZATION OF THE DEVICE

The force acting between the array of magnets which generate magnetic fields and gradients, and the diamagnetic element of the carpet, is repulsive:

$$dF_z \approx \frac{1}{\mu_0} \left(\chi_x B_x \frac{\partial B_x}{\partial z} + \chi_y B_y \frac{\partial B_y}{\partial z} + \chi_z B_z \frac{\partial B_z}{\partial z} \right) dV = \frac{1}{2\mu_0} \left(\chi_x \frac{\partial B_x^2}{\partial z} + \chi_y \frac{\partial B_y^2}{\partial z} + \chi_z \frac{\partial B_z^2}{\partial z} \right) dV \quad (1)$$

with flux density $\mathbf{B} = (B_x, B_y, B_z)$, and susceptibility $\chi_{\text{dia}} < 0$.

On the other hand, the force acting on the ferromagnetic nano-layer attracts the carpet towards the array of magnets; equation (2) shows the approximate expression for the force acting on a volumetric unit of an isotropic magnetic element, in its saturated state with the saturation magnetization $\mathbf{M}_s = (M_{s_x}, M_{s_y}, M_{s_z})$:

$$dF_z \approx \left(M_{s_x} \frac{\partial B_x}{\partial z} + M_{s_y} \frac{\partial B_y}{\partial z} + M_{s_z} \frac{\partial B_z}{\partial z} \right) dV \quad (2)$$

Here we make the assumption that the nano-layer is fully saturated in the fashion shown on Fig. 1. Within the vertical displacement range of the carpet, the magnetic field produced by the permanent magnet array is enough to saturate this very thin soft magnetic film (permalloy, for example) in-plane almost everywhere except very small wall regions d_f where the Y-component of the external magnetic field is near zero (for

the worst case d_f is assumed to be $1\ \mu\text{m}$, when the flying distance is $9\ \mu\text{m}$). The possible interaction between these regions and the permanent magnet base is not taken into consideration because their volume is much smaller compared to the total volume of the ferromagnetic film. These assumptions allow us to use the semi-analytical modelling and optimization tools MacMMEMS / CADES.

As can be seen from (1) and (2) and illustrated on Fig. 2, the repulsive and attractive forces are functions of the partial derivatives of the different powers of magnetic field, therefore they decrease differently with the distance: this difference allows a compensation to happen at a fixed distance z_0 , which is extremely dependent on geometrical parameters and on the magnetic multipolar configuration of the base. Here, the flying carpet would levitate at a stable position $z_0 = 2.3\ \mu\text{m}$ above the base; this distance would decrease to $2.1\ \mu\text{m}$ if gravity is taken into account, and $2.5\ \mu\text{m}$ when upside-down (Fig. 3).

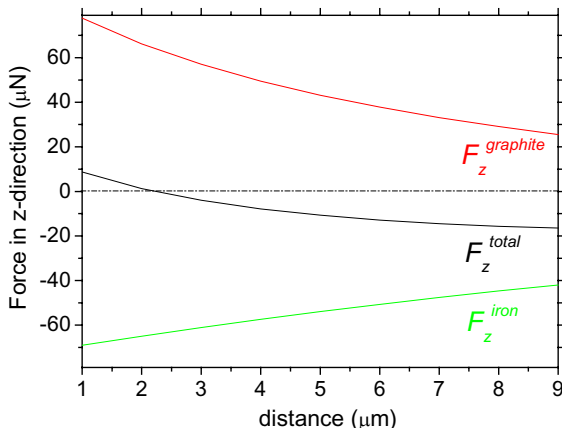


Fig. 2. Forces acting on the graphite layer, on the iron layer, and total force, versus the distance (airgap) between the levitating part and the magnet array (base).

Fig. 3 shows that the total magnetic force (both positive and negative) acting on the flying carpet is much higher than the gravity force ($1\ \mu\text{N}$ on Earth) within a $10\ \mu\text{m}$ distance range: this allows the system to withstand moderate accelerations of about $+5\ \text{G}$ before contact or about $-7\ \text{G}$ before separation.

The optimization aims at improving the allowed displacement range of the levitating body, with respect to the given specifications. Once the material is chosen, the physical and magnetic constants are fixed, thus only the geometrical dimensions of the system need to be optimized.

Optimizations were done in the CADES framework where sensitivities of constrained specifications to the geometric parameters were automatically computed from algebraic equations of the model. A sequential quadratic programming (SQP) algorithm was used in order to find the best solution for each of the three applications. One optimization with a standard PC takes about 10 iterations and less than 1 minute per iteration.

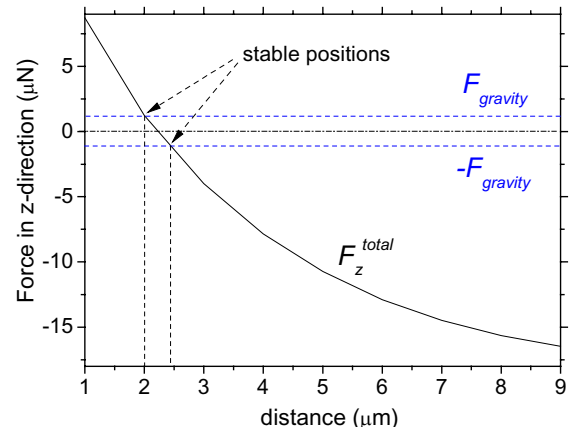


Fig. 3. Total magnetic force vs. airgap, compared with the gravity force.

This kind of devices could be used in micro-robotics, both on Earth and in space under low-gravity conditions, for transporting micro-objets and nano-particles, as well as for friction-less 3D micro-sensors (acceleration, rotation...) for example.

The experimental work on the flying carpet is presently in progress within the MINATEC facilities.

This work is financed by *Fondation Nanosciences* RTRA.

IV. REFERENCES

- [1] H.L. Rakotoarison, B. Delinchant, and O. Cugat, "Methodology and Tool for generating Semianalytical Models, used to Pre-design Electromagnetic MEMS (Mag-MEMS)", *12th IEEE COMPUMAG 2006*, p. 444.
- [2] H. Chetouani, B. Delinchant, and G. Reyne, "Efficient modeling approach for optimization of a system based on passive diamagnetic levitation as a platform for bio-medical applications", *COMPEL*, 26(2), 2007
- [3] I.F. Lyuksyutov, D.G. Naugle, and K.D.D. Rathnayaka, "On-chip manipulation of levitated femtodroplets", *Appl. Phys. Lett.*, 85, 2004, pp. 1817–1819.
- [4] H. Chetouani, V. Haguët, C. Jeandey, C. Pigot, A. Walther, N.M. Dempsey, F. Chatelain, B. Delinchant, and G. Reyne, "Diamagnetic Levitation of Beads and Cells Above Permanent Magnets", *IEEE Transducers*, 2007, pp. 715–718.
- [5] P.A. Dunne, J. Hilton, and J.M.D. Coey, "Levitation in paramagnetic liquids" *J. Mag. Mag. Mat.*, 2007, 316, pp. 273–276.
- [6] N. Dempsey, A. Walther, F. May, D. Givord, K. Khlopov, and O. Gutfleisich, "High performance hard magnetic NdFeB thick films for integration into Micro-Electro-Mechanical-Systems", *Appl. Phys. Lett.*, 90, 2007, 092509.
- [7] S. Chigirinsky, M. Kustov, N. Dempsey, C. Ndao, and R. Grechishkin, "Calculations and measurements of the magnetic field of patterned permanent magnetic films for lab-on-chip applications", *Rev. Adv. Mater. Sci.*, 19, 2009, pp. 14–34.
- [8] C. Pigot, H. Chetouani, G. Poulin, and G. Reyne, "Diamagnetic Levitation of Solids at Microscale", *IEEE Trans. on Magnetism*, 44(11), 2008, pp. 4521–5524.
- [9] R. Moser, J. Sandtner, and H. Bleuler, "Diamagnetic Suspension Assisted by Active Electrostatic Actuators" *6th International Symposium on Magnetic Suspension Technology*, Torino, Italy, 2001.
- [10] H. Chetouani, L. H. Rakotoarison, B. Delinchant, G. Gruosso, A. Canova and M. Repetto, "Graphite Levitation over four magnets: Benchmarking Micrometer Diamagnetic Modeling", *COMPUMAG 2007*, pp. 602–603.

3D Voltage Driven Finite Element Analyses of Eccentric Rotor Positions of a Novel Hybrid Radial Active Magnetic Bearing

Erich Schmidt, Matthias Hofer

Institute of Electrical Drives and Machines, Vienna University of Technology, Vienna, Austria
erich.schmidt@tuwien.ac.at, matthias.hofer@tuwien.ac.at

Abstract – The paper discusses electromagnetic parameters of a novel arrangement of a permanent magnet biased radial active magnetic bearing with three poles. The control currents of the three poles produce a heteropolar distribution of the magnetic field whereas the permanent magnets cause a homopolar configuration of the magnetic field. Thus, 3D finite element analyses have to be used to accurately obtain the parameters such as inductances and electromagnetic forces. In order to finally using a position-sensorless control algorithm for the hybrid magnetic bearing, the dependence of the electromagnetic parameters on the rotor position is of great interest. Consequently, special attention will be given to the modelling of various eccentric rotor positions yielding a fast computation environment suitable for the prototype design.

I. DESIGN OF THE RADIAL MAGNETIC BEARING

Fig. 1 shows the cross section of the prototype of the hybrid active magnetic bearing with three poles. The three coils on the poles produce a heteropolar configuration of the magnetic field while the permanent magnets additionally inserted in the stator generate a homopolar distribution of the magnetic field [1]–[3]. The permanent magnets will act as the source of the bias magnetic field. Thus, the coil currents are used only as control currents reducing the overall size and therefore leading to a more compact design. Further, the number of the permanent magnets can be adopted in order to obtain a hybrid magnetic bearing with characteristics according to various applications.

II. FINITE ELEMENT MODELLING

The electromagnetic parameters of an active magnetic bearing can be calculated by means of analytical methods based on an assumption of designated paths of the magnetic field [4], [5]. With centered rotor positions, these results are quite accurate to predict the behaviour of the bearing. On the other hand, for non-centered rotor positions only numerical analyses will yield accurate results due to the more significant cross-coupling of the various magnetic paths [6], [7].

Fig. 2 shows the active parts of the stator including permanent magnets and stator coils of the finite element model. In order to obtain a fast modelling and solution environment for taking into account eccentric rotor positions, a sliding surface approach and a domain decomposition algorithm can successfully be applied [8]. For each concerned radial eccentric rotor

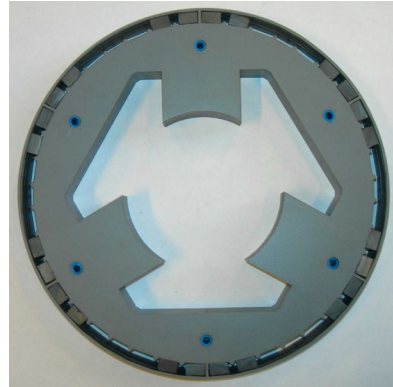


Fig. 1: Cross section of the stator of the permanent magnet biased radial active magnetic bearing with three poles, arrangement with four magnets

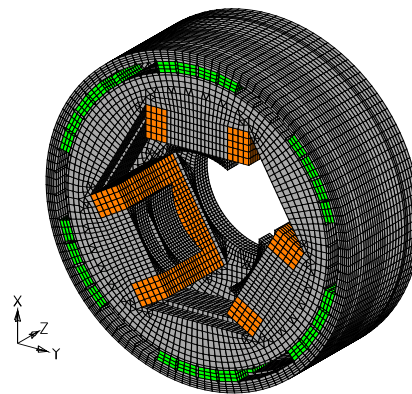


Fig. 2: Finite element model of the stator of the permanent magnet biased radial active magnetic bearing with three poles, arrangement with four magnets

position, only the air-gap region between the sliding surface and the rotor boundary has to be remeshed. Consequently, different numerical errors with respect to the angular rotor position are avoided.

III. SAMPLE ANALYSIS RESULTS – INDUCTANCES

The three control windings in the stator are star-connected, $I_1 + I_2 + I_3 = 0$. Therefore, the two axes approximation

$$\begin{pmatrix} I_x \\ I_y \end{pmatrix} = \begin{bmatrix} 2/3 & -1/3 & -1/3 \\ 0 & 1/\sqrt{3} & -1/\sqrt{3} \end{bmatrix} \begin{pmatrix} I_1 \\ I_2 \\ I_3 \end{pmatrix} \quad (1)$$

yields the flux linkages according to

$$\begin{pmatrix} \Psi_x \\ \Psi_y \end{pmatrix} = \begin{bmatrix} L_{xx} & L_{xy} \\ L_{yx} & L_{yy} \end{bmatrix} \begin{pmatrix} I_x \\ I_y \end{pmatrix} \quad (2)$$

Due to the symmetric arrangement of the three coil windings, the cross-coupling inductances $L_{xy} = L_{yx}$

are vanishing in the centered rotor position. But with an eccentric rotor position, in particular in the y -direction, the cross-coupling inductances are significant as shown with the full paper.

Fig. 3 and Fig. 4 show the inductances L_{xx} and L_{yy} in dependence on radial and angular position of the rotor eccentricity for the arrangement with four magnets. As these inductances directly depend on the eccentric rotor position, the presented novel radial active magnetic bearing shows a high suitability for a position sensorless control.

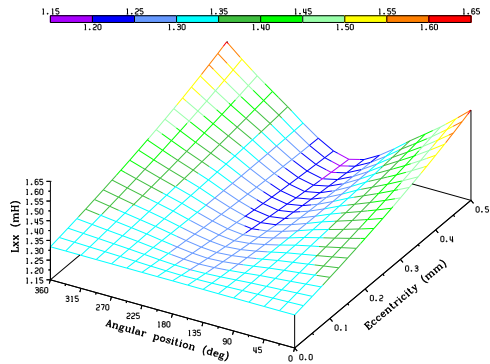


Fig. 3: Inductance L_{xx} versus radial and angular position of the eccentricity, arrangement with four magnets

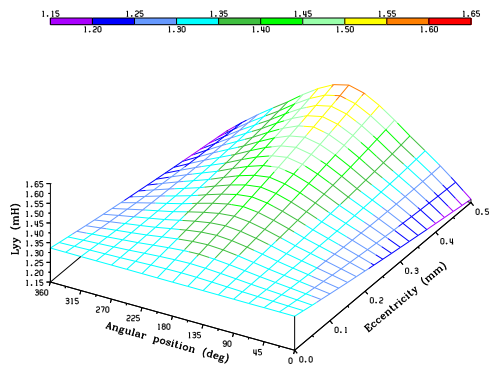


Fig. 4: Inductance L_{yy} versus radial and angular position of the eccentricity, arrangement with four magnets

Accordingly, Fig. 5 and Fig. 6 show the transient current response obtained from the voltage driven analysis and from measurements resulting from applied voltage pulses suitable for the subsequent evaluation of the eccentric rotor position which is presented in detail with the full paper.

IV. CONCLUDING REMARKS

The paper discusses 3D finite element analyses of a prototype design of a permanent magnet biased radial active magnetic bearing with three poles. To obtain a fast analysis environment suitable for the initial design, the sliding surface method and a domain decomposition algorithm are used for analyzing in particular various eccentric rotor positions. In the full paper, the presented results are focussed on the inductances of the coil windings carrying the control currents, the electromagnetic forces acting on the rotor and the current gain provided by the bearing as the most impor-

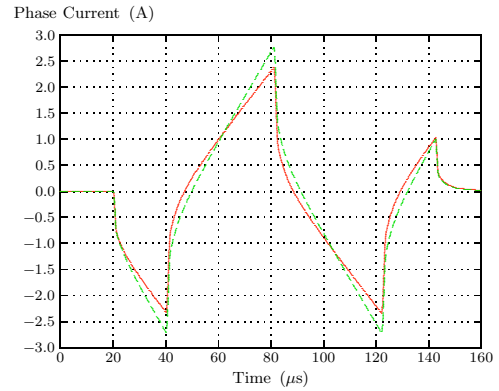


Fig. 5: Transient current response with eccentric rotor positions $\Delta x = +0.4$ mm (solid line) and $\Delta x = -0.4$ mm (dashed line), finite element results

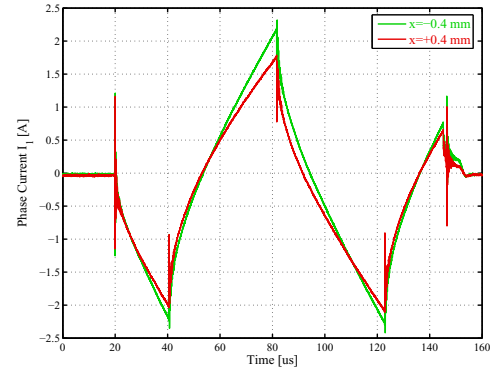


Fig. 6: Transient current response with eccentric rotor positions $\Delta x = +0.4$ mm and $\Delta x = -0.4$ mm, measurement results

tant parameter for controlling the hybrid radial active magnetic bearing.

REFERENCES

- [1] Schweitzer G., Traxler A., Bleuler H.: *Magnetlager, Grundlagen, Eigenschaften und Anwendungen berührungsfreier, elektromagnetischer Lager*. Springer, Berlin, 1993.
- [2] Allaire P.E., Maslen E.H., Humphris R.R., Knospe C.R., Lewis D.E.: "Magnetic Bearings". *CRC Handbook of Lubrication and Tribology*, Vol. 3, 1994.
- [3] Shyh-Leh C., Chan-Tang H.: "Optimal Design of a Three-Pole Active Magnetic Bearing". *IEEE Transactions on Magnetics*, Vol. 38, No. 5, September 2002.
- [4] Zong M., Liu Y., Shen J., Wang F.: "Force Analysis for Hybrid Radial Magnetic Bearing Biased by Permanent Magnet". *Proceedings of the International Conference on Electrical Machines and Systems, ICEMS*, Nagasaki (Japan), 2005.
- [5] Lei H., Guangzhou Z., Heng N., Yikang H.: "Modeling and Design of Permanent Magnet Biased Radial-Axial Magnetic Bearing by Extended Circuit Theory". *Proceedings of the International Conference on Electrical Machines and Systems, ICEMS*, Seoul (Korea), 2007.
- [6] Schmidt E., Platter T., Springer H.: "Force and Stiffness Calculations in Magnetic Bearings – Comparison between Finite Element Method and Network Theory". *Proceedings of the 5th International Symposium on Magnetic Bearings, ISMB*, Kanazawa (Japan), 1996.
- [7] Xu Y., Dun Y., Wang X., Kong Y.: "Analysis of Hybrid Magnetic Bearing with a Permanent Magnet in the Rotor by FEM". *IEEE Transactions on Magnetics*, Vol. 42, No. 4, April 2006.
- [8] Schmidt E., De Gerssem H., Weiland T.: "Application of a Computationally Efficient Air-Gap Element within the Finite Element Analysis of Magnetic Bearings". *IEEE Transactions on Magnetics*, Vol. 42, No. 4, April 2006.

Contact Parameter Computation and Analysis of Air Circuit Breaker with Permanent Magnet Actuator

Shuhua Fang¹, Heyun Lin¹, Siu-lau Ho², Xianbing Wang¹, Ping Jin¹

¹ School of Electrical Engineering, Southeast University, Nanjing 210096, P. R. China

² Department of Electrical Engineering, Hong Kong Polytechnic University, Kowloon, Hong Kong

Abstract— Contact of air circuit breaker (ACB) switches on or off the power supply. In this paper, a new type of contact is presented with double breakers for the ACB with permanent magnet actuator (PMA). 3-D finite element method (FEM) is employed to compute electro-dynamic repulsion force including Holms force and Lorenz force acted on static and movable contacts. The repulsion force is obtained for different number of contact, which value increases step by step from the outer contact to inner one. The contact of double breaker is manufactured according to our analysis results.

I. INTRODUCTION

Circuit breaker plays an important role in power system. In order to improve the circuit breaker reliability, new concept circuit breaker is developed with permanent magnet actuator (PMA) [1]-[4]. The proposed PMA offers many advantages such as low component counts and high reliability when compared with spring operated circuit breaker (SOCB) both vacuum circuit breaker (VCB) and air circuit breaker (ACB).

Compared with the conventional spring circuit breaker, the permanent magnet circuit breaker has much more key problem to be solved. Contactor parameter computation is indeed important to determine the ACB structure parameter. The author has proposed a method to compute the temperature of the ACB with spring actuator [5]. In this paper, a new type of contact is proposed with double breakers for the ACB with permanent magnet actuator (PMA). 3-D finite element method (FEM) is employed to compute electro-dynamic force between static and movable contacts. The computed results show that the repulsion force increases step by step from the outer contact to inner contact. In addition, the repulsion force is also computed for the contact arranged with permanent magnet and will be discussed in full paper. The contact of double breaker is manufactured according to our analysis results.

II. MATHEMATICS MODEL AND CONTACTOR ASSEMBLY

The static magnetic field method is used to compute electro-dynamic repulsion force. Since the eddy current has little effect on the electro-dynamic repulsion force, the static magnet field equation can be employed to solve current density and flux density distribution. Vector potential \mathbf{T} is served to calculate the current density

$$\mathbf{J} = \nabla \times \mathbf{T} \quad (1)$$

\mathbf{T} satisfies the governing equation

$$\nabla \times \left(\frac{1}{\sigma} \nabla \times \mathbf{T} \right) = 0 \quad (2)$$

The current constrain condition is

$$\oint_s \mathbf{T} \cdot d\mathbf{l} = I \quad (3)$$

If the current density \mathbf{J} is obtained, vector magnetic potential \mathbf{A} is employed to depict the flux density \mathbf{B}

$$\mathbf{B} = \nabla \times \mathbf{A} \quad (4)$$

The whole area vector magnetic potential satisfies the following governing equation

$$\nabla \times \left(\frac{1}{\mu} \nabla \times \mathbf{A} \right) = \mathbf{J} \quad (5)$$

The contact force density f is calculated based on the relationship of current, magnetic field and electromagnetic force

$$\mathbf{F} = \int_V f dV = \int_V \mathbf{J} \times \mathbf{B} dV \quad (6)$$

where V is the contact volume. Electro-dynamic repulsion force of contacts uses the electrical bridge model, the Holms force and Lorenz force acting on the contactor can be computed in finite element method (FEM).

Fig. 1 shows the proposed contact for the ACB with PMA. The mechanical system mainly consists of the PMA, a rotating shaft, a cam and a movable contact.

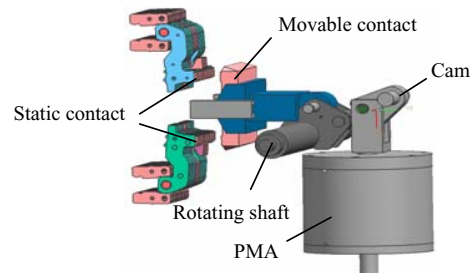


Fig. 1. Assembly of the contact located on the ACB

III. FINITE ELEMENT ANALYSIS

Fig. 2 shows the parallel contact of the quarter model. The contact uses double breaker structure, mainly including static contact and movable contact. 3-D FEM is employed in analyzing the contacts. Fig. 2 shows the meshes of quarter model. The element number is 46539 and nodes are 53925, respectively. Fig. 3 shows the current density distribution including parallel and single contacts. It is noted that the maximum current density distribution is located on the contacts point.

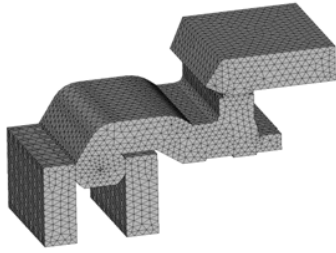
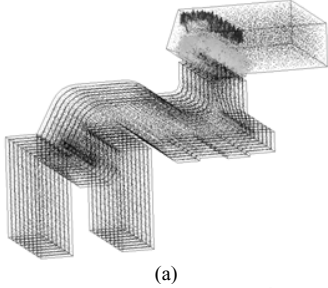
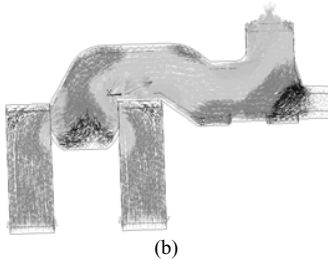


Fig. 2. Meshes of 1/4 model



(a)



(b)

Fig. 3. Current density distribution (a) parallel contacts (b) single contact

Fig.4 shows the magnetic field distribution. It can be found that the maximum magnetic field distribution is also located on the contact point.

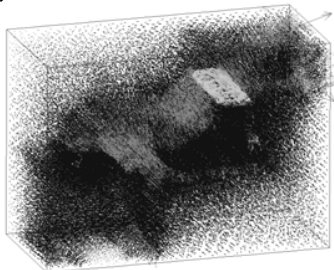


Fig. 4. Magnetic field distribution

IV. ANALYSIS AND DISCUSSION

Fig.5 shows the computed results of electro-dynamic repulsion force. It can be observed that the repulsion force increase with the static contact number increasing from outer to inner. The maximum absolute increasing value reaches to 23.3%. Such result shows that the inner repulsion force is higher than that of the outer repulsion force and can be referenced as our ACB design. Fig.6 presents the contact matched with the ACB. In addition, the repulsion force is also computed for the contact arranged with permanent magnet and will be discussed in full paper.

V. CONCLUSION

3-D FEM is successfully to compute electro-dynamic force of double breakers contact for the ACB with PMA. The repulsion force is obtained for different number of contact.

Computed results show that the repulsion force increases step by step from the outer contactor to inner one. The maximum absolute increasing value reaches to 23.3%. The contact with the double breaker is manufactured according to our analysis results.

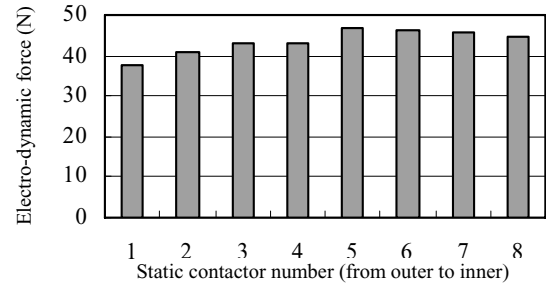


Fig. 5. Comparison of electro-dynamic repulsion force with different number of static contactor

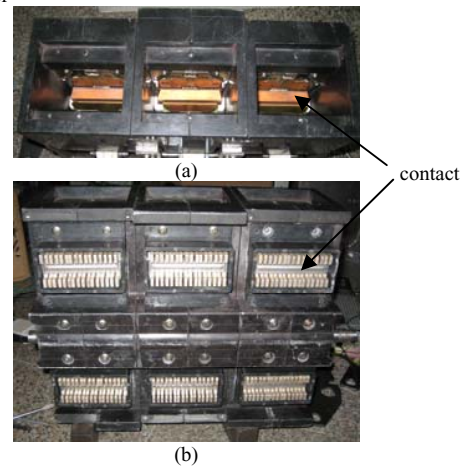


Fig. 6. Prototype and contactors (a) Top overview (b) Back overview

ACKNOWLEDGMENT

This work was jointly supported by the National High Research and Development of China under Project 2006AA05Z224 and the "Qing Lan Project" Program of Jiangsu Province, China.

VI. REFERENCES

- [1] E. Dullni, "A vacuum circuit-breaker with permanent magnetic actuator for frequent operations," in *Proc. XVIIIth Int. Symp. Discharges and Electrical Insulation in Vacuum*, Aug. 1998, vol.2, pp. 688-691.
- [2] K. I. Woo and B. I. Kwon, "Characteristic analysis and modification of PM-type magnetic circuit breaker," *IEEE Trans. Magn.*, vol. 40, no. 2, pp. 691-694, Mar. 2004.
- [3] F. G. Liu, H. Y. Guo, Q. X. Yang, L. Zhang and W. L. Yan, "An Improved Approach to Calculate the Dynamic Characteristics of Permanent Magnetic Actuator of Vacuum Circuit Break," *IEEE Trans. on Applied Superconductivity*, vol. 14, no. 2, pp. 1918-1921, 2004.
- [4] S. H. Fang, H. Y. Lin and S. L. Ho, "Transient Co-simulation of Low Voltage Circuit Breaker with Permanent Magnet Actuator," *IEEE Trans. Magn.*, vol. 45, no. 3, 2009.
- [5] H. G. Xiang, D. G. Chen, X. W. Li, L. Ji; W. X. Tong, "Calculation of the Short-time Withstand Current for Air Circuit Breaker," *Electrical contacts - 2007, the 53rd IEEE Holm Conference on*, pp.251-255, 2007.

Reduction of Repulsion Forces on Current-Carrying Contact using 3-D FEM

Tomohiro Ota¹, Satoshi Suzuki¹ and Katsuhiko Hirata²

¹PCB Analysis Division, Panasonic Electric Works Analysis Center Co., Ltd., Japan

²Department of Adaptive Machine Systems, Graduate School of Engineering, Osaka University, Japan

E-mail: t_oota@panasonic-denko.co.jp

Abstract— This paper describes the 3-D finite element analysis of repulsion forces on current-carrying contacts of a relay for a hybrid electric vehicle. The mechanism of repulsion force generation is clarified in the analysis. Furthermore the model reduced repulsion forces is proposed.

I. INTRODUCTION

Efforts are under way worldwide to develop electric vehicles and hybrid electric vehicles in response to energy conservation and atmospheric pollution concerns. The vehicles are equipped with a high voltage battery over 100 V to drive some motors, and must be equipped with relays which can interrupt a large dc-current. Since the battery is moreover considered to be of a higher voltage as one way of improving energy efficiency, the relays are required and must improve a contact capacity. Under the circumstances, it becomes quite important to decrease the repulsion forces on current-carrying contact.

Recently, computer simulations are widely used in various engineering fields because of the significant improvement of computer performance, and can be applied to complex phenomena.

In the previous papers of repulsion forces on contact have been reported. Holm has computed the repulsion forces by the magnetic field analysis using simplified model of current-carrying contact [1]. In the model, two cylindrical terminals contact with its center, and it is assumed that the current flows radially through the spherical micro-contact. Therefore the influence of complex current distribution caused by the change of contact position on the repulsion forces has not been considered. Kawase and Ito have reported the repulsion force calculation by analyzing the current distribution using the 3-D finite element model, in which the contact part between two cylindrical terminals is modeled as the cylindrical micro-contact [2]. This report has clarified the influence of contact position and contact separation on repulsion forces, however, the reduction of repulsion forces has not been computed.

In this paper, we clarify the mechanism of repulsion force generation of relays for hybrid electric vehicles using 3-D finite element method (FEM), and propose the model improved repulsion forces.

II. ANALYSIS METHOD

A. Current Distribution Analysis

Since the distributions of current density vectors flowing in the contact are complicated, and analyzed by 3-D FEM using the current vector potential T as follows:

$$\operatorname{rot}\left(\frac{1}{\sigma}\operatorname{rot}T\right)=0, \quad J_0=\operatorname{rot}T, \quad \oint T \cdot ds=I \quad (1)$$

Where σ is the conductivity, J_0 is the current density, and I is the current.

B. Magnetic Field Analysis

The fundamental equations of the magnetic field can be written using the magnetic vector potential A and the current density J_0 as follows:

$$\operatorname{rot}(v\operatorname{rot}A)=J_0 \quad (2)$$

Where v is the reluctivity.

C. Calculation of Repulsion Forces

The magnetic force F on the current-carrying contact is computed as follows:

$$F=\int_V(J_0 \times B)dv=\int_V f dv \quad (3)$$

Where V is the volume of current-carrying part, B is the magnetic flux density, and f is the magnetic force density.

The repulsion forces between terminals can be calculated by the sum of z direction component of magnetic force density in each element.

III. ANALYZED MODEL AND CONDITION

Fig.1 shows the 3-D finite element mesh of relays for hybrid electric vehicles. This model consists of cylindrical stationary terminals, flat movable terminal, and cylindrical micro-contacts. The dc current flows through stationary terminals, contacts, and movable terminal while the coil is excited. The movable terminal is released from stationary terminals to interrupt the current by the restoring spring when the coil is not excited. The repulsion forces on contact are analyzed except the coil because of little influences. The diameter, height and conductivity of cylindrical micro-contact, which is thought to be the plastic deformation by the contact between micro-convexities of movable and stationary terminal, are 0.05 mm, 0.1 mm, and 6.0×10^7 S/m, respectively.

IV. ANALYZED RESULTS

Fig.2 shows the distribution of current density vectors and magnetic force density vectors, respectively. From the figure, the concentrations of current and magnetic force density are confirmed around contacts between movable and stationary terminals. It is considered that repulsion forces are decided by the flux density and the horizontal component of current near the contacts. Fig.3 shows the comparison of the computed repulsion force characteristics on current. The calculated results by Holm's equation are different from those by this analysis, showing the effectiveness of the 3-D FEM in the complex terminal shape model. The measured result of repulsion forces is about 4.5 N when the current of 2000 A is applied, then agrees well with computed ones. As a result, the validity of this method is confirmed.

Fig.4 shows the influence of contact position on repulsion forces. From this figure, the repulsion force at the center position is the lowest of y-direction change of contact position. This reason is thought that the horizontal component of current is increased as the contact position moves from the center position. The repulsion forces in x-direction change of contact position are decreased, as the contact is located at the inner side of relays. It is found that the influences of x- and y-

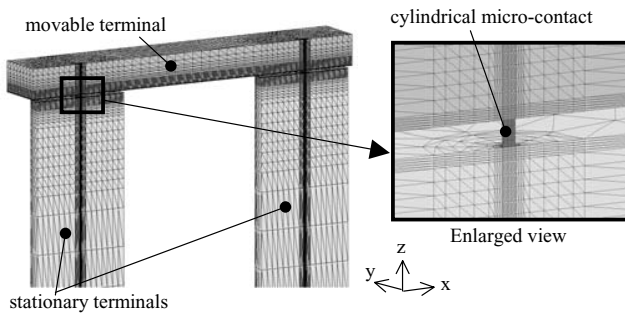


Fig.1 3-D finite element mesh of relays (1/2 region).

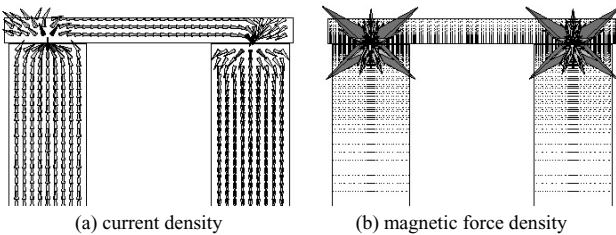


Fig.2 Distributions of current density vectors and magnetic density vectors.

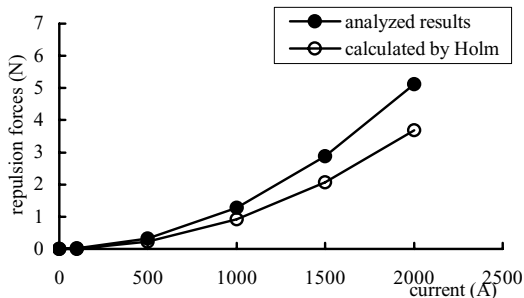


Fig.3 Repulsion forces characteristics on current.

direction change of contact position on the repulsion forces are different.

Fig. 5 shows the distributions of magnetic force density vectors near the contact point. From this figure, the distributions of magnetic force density near the contact point seem to be almost the same. In addition, the repulsion forces are analyzed in detail. The movable terminal is separated in steps of 0.5 mm to clarify the influence of the contact position. Fig. 6 shows the distributions of repulsion forces on the movable terminal. It is found that the repulsion forces are generated not only near the contact but also on the center of movable terminal. From these results, as the contact is located at the inner side of relays, the reduced effect of repulsion forces is effective because the repulsion forces generated on the movable terminal are decreased. Furthermore the improved model of repulsion forces will be opened in the full paper.

V. REFERENCES

- [1] R.Holm : "Electric Contacts", 4th Ed., Springer-Verlag (1967).
- [2] Y.Kawase, H.Mori, and S.Ito, "3-D Finite Element Analysis of Electrodynamic Repulsion Forces in Stationary Electric Contacts Taking into Account Asymmetric Shape (Invited)", *IEEE Trans. on Magnetics*, Vol.33, No.2, 1994 (1997).

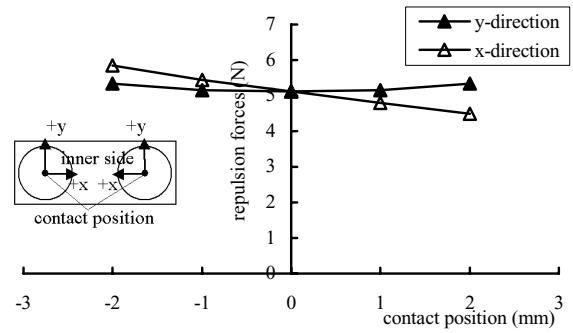


Fig.4 Influence of contact position on repulsion forces.

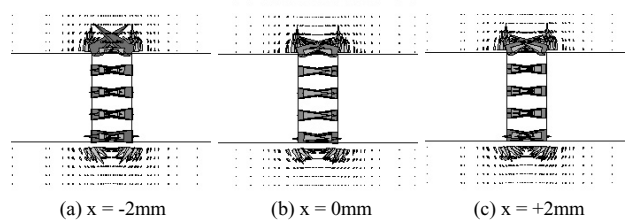


Fig.5 Distributions of magnetic density vectors in near contact point.

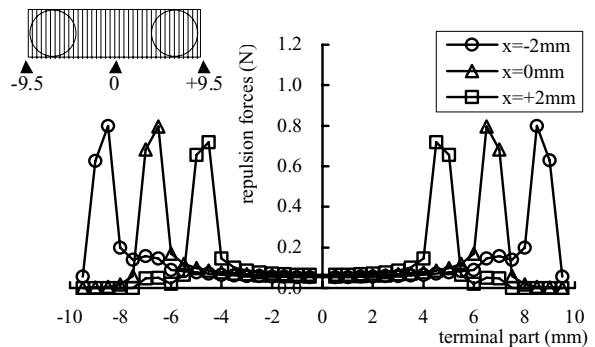


Fig.6 Distributions of repulsion forces on movable terminal.

Dynamic Analysis Method for Electromagnetic Artificial Muscle Actuator under PID Control

Yoshihiro Nakata, Hiroshi Ishiguro and Katsuhiko Hirata

Department of Adaptive Machine Systems, Graduate School of Engineering, Osaka University
2-1 Yamada-oka, Suita Osaka, 565-0871, Japan
yoshihiro.nakata@ams.eng.osaka-u.ac.jp

Abstract— We have been studying an interior permanent magnet linear actuator for an artificial muscle. This actuator mainly consists of mover composed of permanent magnets, magnetic cores and a non-magnetic shaft, and a stator composed of 3-phase coils and a back yoke. In this paper, the dynamic analysis method under PID control is proposed employing the 3-D finite element method (3-D FEM) to compute the dynamic response and current response when the positioning control is active. As the results, computed results show good agreement with measured ones of a prototype.

I. INTRODUCTION

Generally, servo motors and air servo actuators have been used as driving sources of various parts of robots. Our humanlike robot (android) is composed of air servo actuators. These actuators have no backlash, but low response because of the pneumatic control. The authors therefore have been studying the direct drive electromagnetic linear actuator to solve the above problem. This actuator is expected to have long stroke, high response and large thrust using interior permanent magnets effectively, and shows higher dynamic performance as compared with the actuator using Halbach array of magnets [1], [2].

In this paper, we propose the dynamic analysis method for the actuator under PID control employing the 3-D FEM. This method is applied to compute the dynamic response and current response when the positioning control is active. The validity of the analysis is verified through the comparison with the measurement of a prototype. In addition, it is found that this actuator shows high response characteristics.

II. ANALYZED MODEL AND OPERATING PRINCIPLE

The cross-section of our linear actuator is shown in Fig. 1. The diameter and the length of this actuator are 20mm and 180mm respectively. The mover is mainly composed of permanent magnets, magnetic cores and a non-magnetic shaft. The magnetization of a magnet (NdFeB, Br=1.4T) is shown in Fig. 1. The structure of the mover can generate the high magnetic flux, especially effective radial component of flux along the outside of the magnetic core periodically. The stator is composed of 3-phase coils and a back yoke.

When these coils are excited, they are forced to move by Lorentz force. The mover is driven by the thrust as this reaction force while the stator is fixed. The mover is freely controlled by switching the 3-phase coil currents.

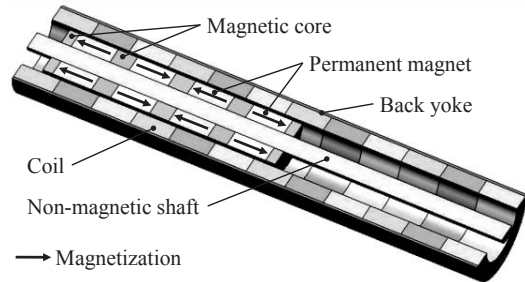


Fig. 1. Basic structure of an electromagnetic linear actuator

III. ANALYZED METHOD

A. Magnetic Field Analysis Coupled with Motion Equation

In this method, the equations of the magnetic field and the electric circuit are coupled, which are given by the magnetic vector potential \mathbf{A} and the exciting current I_0 as follows [3]:

$$\text{rot}(\nu \text{rot } \mathbf{A}) = \mathbf{J}_0 + \nu_0 \text{rot } \mathbf{M} \quad (1)$$

$$E = V_0 - RI_0 - \frac{d\Psi}{dt} = 0 \quad (2)$$

$$\mathbf{J}_0 = \frac{n_c}{S_c} I_0 \mathbf{n}_s \quad (3)$$

where ν is the reluctivity, \mathbf{J}_0 is the exciting current density, ν_0 is the reluctivity of the vacuum, \mathbf{M} is the magnetization of permanent magnet, V_0 is the applied voltage, R is the effective resistance, Ψ is the interlinkage flux of exciting the coil. n_c and S_c are the number of turns and the cross-sectional area of the coil respectively. And \mathbf{n}_s is the unit vector along with the direction of exciting current.

The motion of the mover is described as follows.

$$M \frac{d^2 z}{dt^2} + D \frac{dz}{dt} \pm F_s = F_z \quad (4)$$

where M is the mass of the mover, z is the displacement of the mover and D is the viscous damping coefficient. F_z and F_s is the z -axial component of the electromagnetic force and the dynamic friction force.

B. Consideration of Servo Controller

Fig. 2 shows the system configuration on the servo system. In target trajectory generator, the trajectory from start point to goal point is computed from position of goal point, maximum velocity and acceleration according to trapezoidal velocity role. The PID controller computed target torque (i_q^*) from the

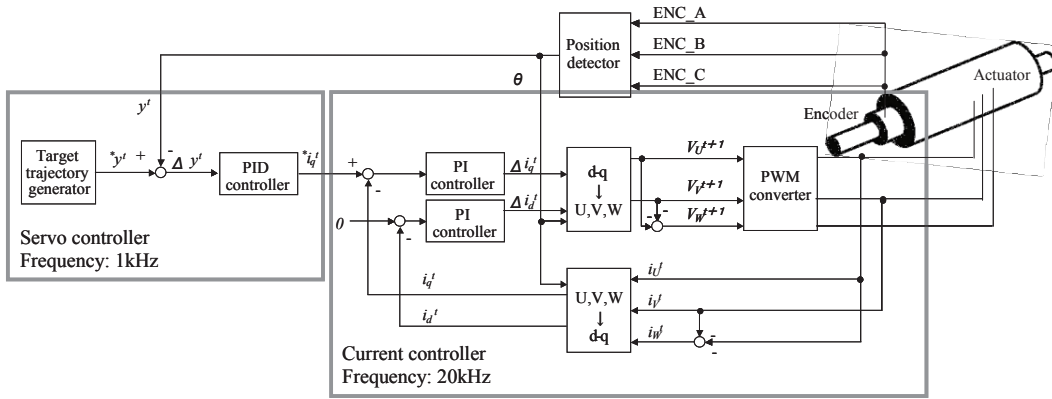


Fig. 2. System configuration of the servo system

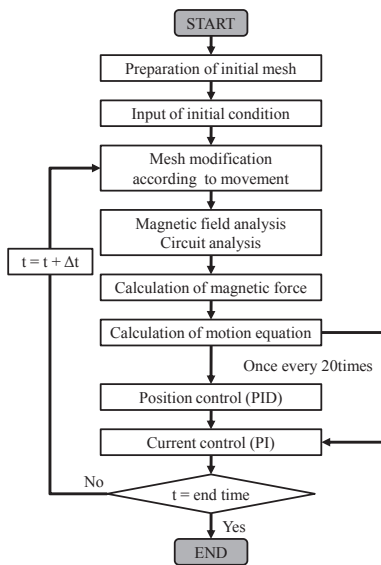


Fig. 3. Flowchart for dynamic analysis under PID control

difference ($\Delta y'$) between target position (y^*) and current position (y') from encoder (frequency: 1 kHz).

C. Consideration of Current Controller

Measured 3-phase currents (i_U^l, i_V^l, i_W^l) are transformed to field current (i_d^l) and torque current (i_q^l). PI control is adopted in the difference of field current and torque current (frequency: 20 kHz). These results are transformed inversely to next step voltage values ($V_U^{l+1}, V_V^{l+1}, V_W^{l+1}$).

Fig. 3 shows the flowchart for dynamic analysis under the PID control. The position control is adapted once every 20 times.

IV. RESULTS AND DISCUSSION

The dynamic performances of the actuator under PID control are computed while the mover moves from 0 to 3.2mm. Fig. 4 shows the computed time variations of position and U-, V-, W-phase currents. Fig. 5 shows the measured results of a prototype. As can be seen, both results of the time variations of position are in good agreement and this actuator shows high response characteristics. And, both results of the time

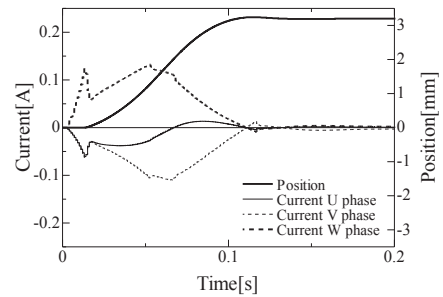


Fig. 4. Computed results

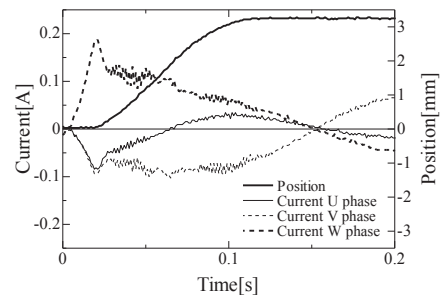


Fig. 5. Measured results

variations of U-, V-, W-phase currents are in good agreement qualitatively, however, the peak value of currents during rest and the current waveforms at the goal point are different. This is because the prototype has relatively large friction. In the final paper, the analyzed accuracy will be improved by taking into account of the dynamic friction in the computation.

V. REFERENCES

- [1] K. Halbach, "Application of permanent magnets in accelerators and electron storage rings", *Journal of Applied Physics*, vol.57, 1985, pp. 3605-3608.
- [2] Masayuki MISHIMA, Hiroshi ISHIGURO and Katsuhiro HIRATA, "Development of a new linear actuator for androids", 2008 IEEE International Conference on Robotics and Automation, 2008, pp. 3594-3599.
- [3] K. Hirata, T. Yamamoto, T. Yamaguchi, Y. Kawase and Y. Hasegawa, "Dynamic Analysis Method of Two-Dimensional Linear Oscillatory Actuator Employing Finite Element Method", *IEEE Transaction on Magnetics*, vol.43, No.4, 2007, pp. 1441-1444.

Controllable Reactor Simulation using Integral Equation Method

Z. Andjelic¹, D. Pusch², Xiaobo Yang³

¹ABB Corporate Research, 5405 Baden-Daettwil, Switzerland (zoran.andjelic@ch.abb.com)

²ABB Corporate Research, 5405 Baden-Daettwil, Switzerland (david.pusch@ch.abb.com)

³ABB Corporate Research, Beijing, China, China (xiaobo.yang@cn.abb.com)

Abstract – The shunt reactors are important components in the EHV/UHV (Eltra/Ultra High Voltage) power systems used for the voltage regulation issues. One of their important roles is to compensate the reactive power. Typically for such compensation the *fixed* shunt reactors are used. Alternative concepts introduced recently are the *controllable* reactors. Among various controllable reactors schemes, the orthogonal flux type controllable reactor is remarked for its low harmonics and fast response time. The *controlling* effect of orthogonal flux type controllable reactor is achieved by controlling the saturation level of the parts of the magnetic core (saturable reactor). In this paper we present an efficient approach for the simulation of such controllable reactors using Integral Equation Method (IEM). The key information when analyzing this kind of devices are the controllable reluctances. The paper demonstrates usage of IEM for the computation of the inductances as a function of the DC current changes depending on the saturation levels of the magnetic material. The results are compared with the calculation results based on equivalent magnetic circuit calculation model.

I. CONTROLLABLE REACTORS

Voltage regulation using shunt reactors is one of the key issues in the long power transmission lines. They are especially important when building the long distance power transmission lines for the EHV/UHV application, in which the line voltage is higher than 500kV. When the line is energized but not loaded or only loaded with a small current, there is a voltage rise along the line (the Ferranti-effect^[1]), Fig. 1. The overvoltage increases the stress of insulation level on the primary components or restriction of transfer capacity of the transmission lines, especially at the terminals.

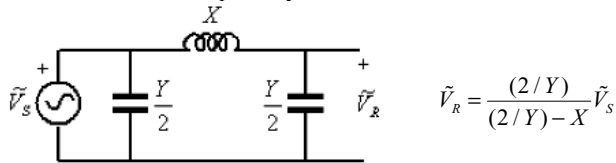


Fig. 1: Illustration of the voltage dependency at the end of the line caused by the line capacitances

One solution for these problems is to employ the controllable reactor, which can regulate the bus voltage level and transmission capacity according to line's load level.

Till now, the references dealing with the reactor simulations are quite restricted and mostly limited to the FEM-based simulation of the *fixed* value shunt reactors, [2-4]. The basic principles and the design of the controllable reactor are discussed in [5].

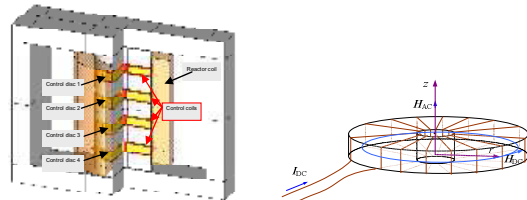
In this paper we present a procedure for 3D IEM-based simulation of the orthogonal flux type controllable reactor. The simulation method provides accuracy analysis results to

accelerate the development procedure. The simulation results can also be used for calibration of the mathematic model. We discuss the main features and advantages of presented methodic for this type of simulations. The simulation results are compared with the calculation method on a simple geometry model.

II. MODELING OF THE CONTROLLABLE REACTOR

A. The magnetizing curve and its ideal model

The key problems when simulating this kind of devices are efficient treatment of the controllable *magnetic reluctances*. The “control” of the reluctances is achieved by the control of the saturation level of the “control discs” in the reactor's central limb. Fig. 2(a) shows the structure of controllable reactor with air-gaps between the control discs and uncontrolled discs. By adding air-gaps, the control range can be adjusted and thus decrease the total cost of the controllable reactor.



(a) The structure of controllable reactor (b) the control disc
Fig. 2: Structure of the controllable reactor with air-gaps between the discs

The main reactor coil is excited by the AC voltage. The control discs are excited by the auxiliary DC coils wound around each of them. The structure of the control disc is shown in Fig 2(b).

B. The magnetizing curve and its ideal model

The ideal magnetizing curve of the magnetic material can be expressed as:

$$B = B_m + \mu_0 H \quad (1.1)$$

Where $B_m = 1.91T$.

C. The Inductance calculation

The inductance of the controllable reactor can be estimated by the magnetic circuit theory and using (1.1).

III. SIMULATION OF THE CONTROLLABLE REACTORS

The simulation of the above phenomena is performed using IEM. As mentioned before, the major task is to calculate the changes of the inductance due to changes of the DC excitations around controlled discs.

A. IEM Formulation

The analysis of the non-linear problems in magnetostatic by IEM is performed using the improved procedure described initially in [6]. The magnetic field in any space point can be found as:

$$\mathbf{H} = \mathbf{H}^J + \mathbf{H}^M \quad (2.1)$$

where \mathbf{H}^J is a field component produced by the excitation current in free space and \mathbf{H}^M is a field produced by the magnetic charges. The first field component can be easily calculated by Bio-Savart law. For the calculation of the second one we use the formula:

$$\mathbf{H}^M = \frac{1}{4\pi} \oint_{S_J} \sigma_J \mathbf{K}_1 dS_J + \frac{1}{4\pi} \oint_{V_N} \rho_N \mathbf{K}_2 dV_N \quad (2.2)$$

where σ_J and ρ_N are the fictitious surface and volume magnetic charges, and \mathbf{K}_1 and \mathbf{K}_2 are the kernels of the type \mathbf{r}/r^3 . The surface charges are obtained by solving second Fredholm integral equation:

$$\sigma_I - \frac{\lambda_I}{2\pi} \oint_S \sigma_J G_1 dS_J = 2\lambda_I \mathbf{H}_I' \cdot \mathbf{n}_I + \frac{\lambda_I}{2\pi} \oint_{V_N} \rho_N G_2 dV_N \quad (2.3)$$

where G_1 and G_2 are the kernels of the type $\mathbf{r} \cdot \mathbf{n}/r^3$.

Here it important to stress the main features of IEM when solving the non-linear magnetostatic problem. In spite of the fact that it is necessary to mesh the volume of the non-linear magnetic parts, the number of unknowns for the non-linear problem is same as the number of unknowns for the linear one. This is due to the fact that the non-linear contribution (second term on the right-hand side of (2.3) appears just as the correction term and is calculated throughout the iteration procedure from the previous iteration. More detailed description will be given in the full paper.

B. Inductance calculation

The inductance calculation is based on the calculation of the flux density. For example, the self-inductance of the reactor coil can be calculated as:

$$L = \frac{1}{I_R} \int_{S_c} \mathbf{B} ds \quad (2.4)$$

where \mathbf{B} is a vector of magnetic flux density through the cross-section plane S_c positioned within the reactor coil.

IV. EXAMPLE

The above model of the reactor shown in Fig. 2 is used for the simulation.

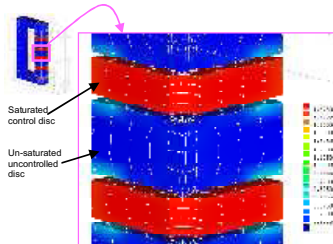


Fig. 3: Flux distribution through the central limb; model a) with air-gaps. The flux through the control discs is at the saturation level and is circulating orthogonally to the direction of the AC flux.

The simulation is performed using BEM-based software package POLOPT for single- and multi-physics problems analysis. Fig. 3 shows the flux distribution through the central limb build of sequences of controlled and uncontrolled discs.

A. The magnetizing behavior of control disc

The AC side magnetizing curves under different DC magnetizing strength is obtained by POLOPT, as shown in Fig. 4, in which the red curves are calculation results by using Equation(1.1), and the blue markers are simulation results obtained by using POLOPT. The results imply that the ideal model can provide enough accuracy for engineering application.

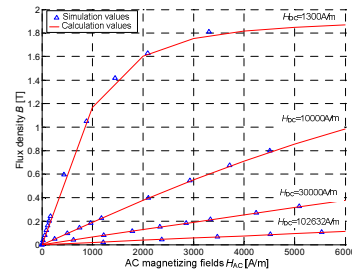


Fig. 4 AC magnetic curves under different DC magnetic fields

B. The inductance of the controllable reactor

Fig. 5 shows the simulation results of the inductance of the controllable reactor, which is compared with calculation results.

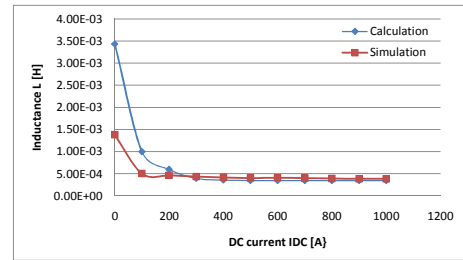


Fig. 5 The inductance of controllable reactor: calculation and simulation results

More detailed analysis such as of inductance vs. different airgaps and the impact of the distribution of DC winding on the inductance value will be presented in the full paper.

V. REFERENCES

- [1] Sungook Hong: *Forging Scientific Electrical Engineering: Joh Ambrose Fleming and the Ferranti Effect*, Isis, 1995, 86, 30-51
- [2] Xiang Cui, Huiqi Li, Lin Li, Jianxin Lui: *Finite element analysis of shunt reactors with auxiliary windings*, Int. Journal of Applied Electromagnetics and Mechanics 20(2004), 133-140.
- [3] Liu Jlanxin, Cui Xiang, Fei Zengyao, Shao Hanguang: *3D non-linear anisotropic magnetostatic field computation in reactor*, COMPEL, Vol. 17, No 1/2/3, 1998, p.239-243
- [4] Y. Ishihara, T. Morino, T. Taodaka: *Analysis of Magnetic Field of a Delta Type Shunt Reactor*, IEEE Tran. on Mag., vol. 25, No.4, July 1989
- [5] Torbjörn Wass, Sven Hörnfeldt, Stefan Caldemarsson: *Magnetic Circuit for a Controllable Reactor*, IEEE Tran. on Mag, Vol. 42, No.9, Sep. 2006
- [6] B. Krstajic, Z. Andjelic, S. Milojkovic, S. Babic, S. Salon: *Nonlinear 3D Magnetostatic Field Calculation by the Integral Equation Method with Surface and Volume Magnetic Charges*, IEEE Tran. on Mag., vol.28, No.2, March 1999

SAR Calculations Using Realistic Phone Models: Uncertainty Due to Positioning

Vikass Monebhurrin¹, A. Gati², M.-F. Wong², and J. Wiart²

¹Department of Electromagnetics, DRE-L2S, SUPELEC
3 rue Joliot-Curie, 91192, Gif-sur-Yvette Cedex France

E-mail: vikass.monebhurrin@supelec.fr

²Orange Labs R&D, RESA/SAFE

38-40 rue du Général Leclerc, 92794, Issy-Les-Moulineaux Cedex 9 France

E-mail: azeddine.gati@orange-ftgroup.com, manfai.wong@orange-ftgroup.com, joe.wiart@orange-ftgroup.com

Abstract — Inter-laboratory comparisons of Specific Absorption Rate (SAR) calculations sometimes show discrepancies between the results even for the case of simplified phone models. A possible cause could be an incorrect positioning of the device against the head. Two commercially available mobile phones with different antenna configurations are selected to evaluate the error induced by incorrect positioning. The SAM (Specific Anthropomorphic Mannequin) head phantom for which the positioning of the device is clearly defined by the standards is employed for the numerical simulations. Results show that deviations with respect to the reference positions may induce a few percent differences in the maximum 10°g averaged SAR values.

I. INTRODUCTION

The SAR (Specific Absorption Rate) conformity assessment of mobile phones is currently based on standardized measurement procedures such as IEEE1528 [1] and IEC62209-1 [2]. The SAM (Specific Anthropomorphic Mannequin) head-phantom filled with tissue equivalent liquid is employed for the SAR measurements of four intended use positions of the mobile phone: left/cheek, left/tilt, right/cheek and right/tilt. A rigorous measurement procedure is enforced – liquid verification, system validation, accurate positioning of the device, etc. – to ensure that the maximum averaged 10 g SAR value fits within less than 30 % uncertainty. The overall SAR compliance test of a mobile phone is time-consuming and costly. For instance, the compliance test of a dual-band mobile phone requires a full day using standard dosimetric test facilities.

Until recently, numerical dosimetry was approached to investigate power absorption in realistic head models using rather simplified phone models such as a quarter-wavelength monopole antenna mounted over a metallic box or a PIFA (Planar Inverted-F Antenna) over a PCB (Printed Circuit Board). The availability of fast computers at low cost and user-friendly electromagnetic software has paved the way for numerical simulations using more realistic phone models which account for the different components present in commercially available mobile phones: battery, camera, casing, display, support, etc. Obviously, the presence of such components – especially those having metallic elements – has a non-negligible impact on the SAR result. For example, the metallic frame usually present around the LCD (liquid crystal display) may modify the SAR distribution in the phantom.

Although the actual CAD (Computer-Aided Design) of the mobile phone may be sometimes available, the electromagnetic simulation is not straightforward. Indeed, such CAD models are initially developed for mechanical engineering purposes and most electromagnetic solvers cannot easily handle the complexity of the models. Furthermore, the presence of tiny elements or curvatures produces relatively high mesh densities which slow down the computational times. In fact, when using the Finite Difference Time Domain (FDTD) technique – which is nowadays commonly employed for SAR calculations – the mesh density of the mobile phone actually dictates the overall mesh with the SAM phantom i.e. the cell size may become much smaller than the typical recommended value of a tenth of the wavelength in the tissue equivalent liquid. To overcome this problem, it may sometimes be desirable to numerically reconstruct the phone model. By taking into account the relative electromagnetic importance of the different components of the mobile phone, simplifications of the model can be achieved. This methodology was applied to reconstruct the numerical model of a commercially available PIFA-based mobile phone which was validated using experimental data [3].

Even when the numerical simulations are feasible, the evaluation of the uncertainty associated to a given SAR calculation remains a critical issue. Usually the suitability of the mesh density employed for the numerical modeling is tested through a convergence analysis of the results. The initial high mesh density may then be relaxed to provide fast run times for efficient SAR calculations with the SAM phantom. A recent international comparison on SAR calculations found that one of the possible causes of discrepancy observed between the different participating laboratories could be due to the incorrect positioning of the handset with respect to the phantom [4]. When performing SAR calculations using inhomogeneous head models, the positioning error is expected to be amplified because of (i) the presence of irregularities along the surface of the head model and (ii) undefined standard reference points which help position the handset. To evaluate the uncertainty due to the positioning of the handset with respect to the head, two commercially available mobile phones are herein selected for SAR calculations. The SAM phantom for which the positioning of the handset is clearly defined by the standards is chosen for the numerical simulations.

II. NUMERICAL MODELING

Electromagnetic solvers based on time domain methods such as FDTD are usually employed for SAR calculations. Herein a commercial package of the TLM (Transmission Line Matrix) method is adopted [5]. The numerical models of the two reconstructed commercial mobile phones placed against the SAM phantom for the left/cheek position are shown in Figure 1 and 2, respectively. The first numerical phone model is a PIFA-based commercial mobile phone. A previous numerical study of this mobile phone showed that the results – return loss, total radiated power and SAR – obtained with the reconstructed model agree well with measurements [4]. The return loss data showed that some specific components of the mobile phone – for example, the speaker – can induce undesired resonances which cannot be easily accounted for by the numerical modeling. The total radiated power data showed that the losses of the mobile phone were consistent with the dielectric properties employed for the different components. The maximum averaged 10 g SAR values at 900 MHz and 1725 MHz were within the 30 % uncertainty level of the dosimetric test facility.

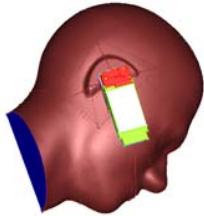


Fig. 1. PIFA-based commercial mobile phone (casing not shown) positioned against the SAM phantom.

The second model is another commercially available mobile phone with an external helicoidal antenna. For both numerical models, the PCB is modeled as a thin conducting plate i.e. the dielectric substrate and electronic circuits are not considered. The dielectric casing of the mobile phones (not shown in the figures) is drawn to have planar faces which enable a more accurate positioning of the device against the phantom (the actual casing of the devices are non-planar).

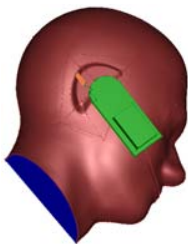


Fig. 2. Commercial mobile phone with external helicoidal antenna (casing not shown) positioned against the SAM phantom.

Both mobile phones are dual-bands and they can be operated at 900 MHz and 1725 MHz. The dielectric properties of the tissue equivalent liquid used at these two frequencies are provided in Table I. A first set of numerical simulations are performed for the four intended use positions which constitute the reference positions. Further simulations are undertaken for small deviations of the position of the mobile phones with respect to these four reference positions. For comparable results, the same mesh is applied for all the numerical simulations with a given mobile phone model.

TABLE I
DIELECTRIC PROPERTIES OF THE TISSUE EQUIVALENT LIQUID

Frequency [MHz]	Relative permittivity	Conductivity [S/m]
900	41.5	0.97
1725	40.0	1.40

III. RESULTS

Results show that for deviations of the position of the two mobile phones such that the distance between the antenna element and the tissue equivalent liquid is practically the same (e.g. 1 degree rotations in a plane parallel to the sagittal plane), the error in the SAR value is about 1 %. For other deviations of the position (e.g. 1 degree rotations perpendicular to the sagittal plane), the error in the SAR value is about 5 % for the PIFA-based mobile phone and 8 % for the mobile phone with the helicoidal antenna.

IV. REFERENCES

- [1] IEEE, "Recommended practice for determining the peak spatial-average Specific Absorption Rate (SAR) in the human head from wireless communications devices: measurement techniques," IEEE Standard 1528, 2003.
- [2] IEC, "Human exposure to radio frequency fields from hand-held and body-mounted wireless communication devices - Human models, instrumentation, and procedures - Part1: Procedure to determine the specific absorption rate (SAR) for hand-held devices used in close proximity to the ear (frequency range of 300 MHz to 3 GHz)," IEC Standard 62209-1, 2005.
- [3] V. Monebhurrn, M.-F. Wong and J. Wiart, "Numerical and experimental investigations of a commercial mobile handset for SAR calculations," in Proc. 2nd International Conference on Bioinformatics and Biomedical Engineering, Shanghai, May 2008, pp. 784-787.
- [4] B. Beard *et al.*, "Comparisons of computed mobile phone induced SAR in the SAM phantom to that in anatomically correct models of the human head," *IEEE Trans. Electromagn. Compat.*, 48(2):397-407, 2006.
- [5] M D. P. Johns, R. Scaramuzza and A. J. Włodarczyk, "Microstripes - microwave design tool based on 3D-TLM," in Proc. 1st International Workshop on Transmission Line Matrix (TLM) Modeling - Theory and Applications, Victoria, BC, Canada, Aug. 1995, pp. 169-177.

Antenna Modeling for Inductive RFID Applications Using the PEEC Method

Peter Scholz, Wolfgang Ackermann, and Thomas Weiland
 Technische Universität Darmstadt
 Institut für Theorie Elektromagnetischer Felder
 Darmstadt, Germany
 E-mail: {scholz,ackermann,weiland}@temf.tu-darmstadt.de

Christian Reinhold
 University of Paderborn
 Sensor Technology Group
 Paderborn, Germany
 E-mail: christian.reinhold@enas-pb.fraunhofer.de

Abstract—In this paper equivalent circuits of inductive coupled radio frequency identification (RFID) antenna systems are extracted by means of the partial element equivalent circuit (PEEC) method. Each antenna impedance is analyzed separately regarding frequency dependent behavior including skin- and proximity effects as well as parasitic capacitances. In contrast to that, the inductive coupling between any two coils is computed for an arbitrary 3D spatial arrangement by a filamentary mutual inductance computation technique, allowing for fast spatial sweeps. Both models are combined to a single equivalent circuit that maintains the topology of mutually coupled inductances. The described approach is tested with a conventional reader transponder arrangement and compared with the full PEEC models.

I. INTRODUCTION

Inductive coupled RFID systems which are typically operating at the center frequency of 13.56 MHz are well described by equivalent circuits based on the transformer concept because of the dominance of inductive near field coupling [1]. In order to quantify the port impedances of the coil system for varying spatial arrangements different approaches can be applied. The most obvious but not necessarily most efficient approach would be to repeatedly simulate the complete system for each variation of the geometric parameters with a 3D full wave solver. A more flexible approach is to separate the calculation of the mutual antenna coupling from the location independent self impedances of the antennas. The combination of the separated models is recovered in the circuit representation. Therefore, it is necessary to ensure an equivalent circuit topology that inhibits the mutually coupled inductances as shown in Fig. 1.

A numerical method that is well suited for this task is the PEEC method [2]. The conducting regions are discretized leading to an equivalent RLC network representation with partial resistive, inductive and capacitive elements. These circuit elements are connected according to the Kirchhoff's laws and can then be analyzed via circuit solvers like SPICE.

II. PEEC MODELS

In order to compute the self impedances of spiral printed coils including skin- and proximity effects with the standard PEEC method, the conductor's volumes have to be subdivided in cross section. A common starting point is to choose the width of the outermost volume cell to be less or equal to the skin depth at the highest frequency of interest. Increasing the width of the volume cells towards the interior of the conductors reduces the discretization effort and reflects the decaying current distribution. The conductors of the tag antenna of the

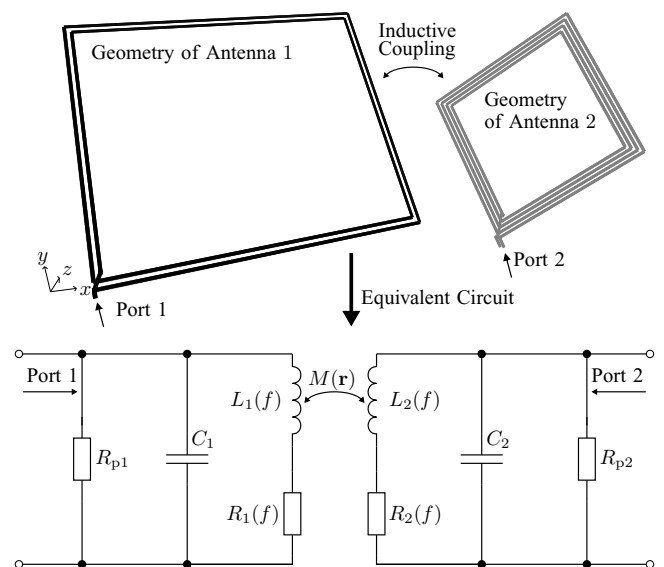


Fig. 1. Equivalent circuit representation of two inductive coupled antennas.

model setup in Fig. 2 are subdivided into 9 segments in width and 3 segments in thickness leading to 756 unknown currents (Reader antenna: 132 unknown currents).

The consideration of capacitive effects requires an additional discretization of the conducting surfaces because the free charges are limited to the surfaces. It is sufficient to represent the thin conductors by a 2D approach [3]. Hereby, the simulation time is reduced and dielectrics can be easily included by adapting the Green's function [4]. For the model setup, the surface is discretized with 9 panels in width for the tag (11 for the reader) resulting in 504 (88) unknown surface charges. Using a mesh based circuit formulation [5] the port impedances can be calculated as presented for the tag antenna in Fig. 3.

For the calculation of the mutual coupling between multiple coils, the discretization level is reduced to a minimum taking only inductive effects into account. In detail, each straight conductor is modeled by a single filament (abbr. Fils) leading to $4N$ (N = number of turns) unknowns for each antenna. The mutual inductance can then be expressed as [1]

$$M = \sum_{\text{Fils coil } i} \sum_{\text{Fils coil } j} L_{ij}. \quad (1)$$

The partial inductances L_{ij} are computed analytically [6].

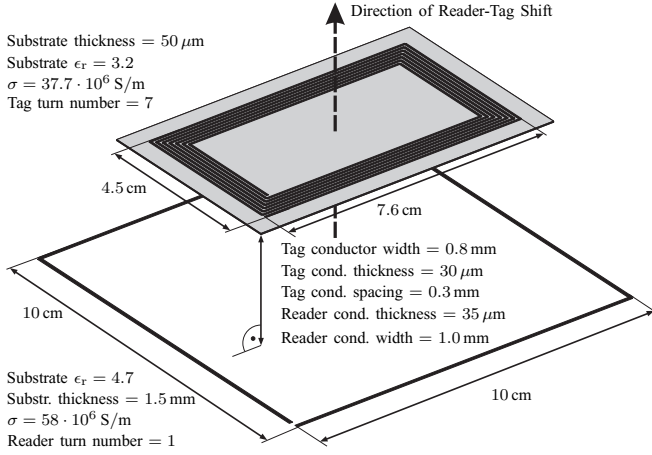


Fig. 2. Illustration of the test setup. A square reader antenna (substrate not visualized) is coupled to a multi turn tag antenna.

TABLE I
PARAMETERS OF FIG. 1 AND (2) FOR THE TEST SETUP IN FIG. 2.

	Reader	Tag
R	$R_{DC}=194 \text{ m}\Omega$ $f_R=939 \text{ kHz}$, $A_R=0.233$	$R_{DC}=1.64 \Omega$ $f_R=750 \text{ kHz}$, $A_R=0.185$
L	$L_{ext}=406 \text{ nH}$, $L_{int}=10.8 \text{ nH}$, $f_L=617 \text{ kHz}$, $A_L=-0.56$	$L_{ext}=5.38 \mu\text{H}$, $L_{int}=74.4 \text{ nH}$, $f_L=918 \text{ kHz}$, $A_L=-0.677$
C	$C_1=0.78 \text{ pF}$	$C_2=1.55 \text{ pF}$
R_p	$R_{p1} \rightarrow \infty$	$R_{p2} \rightarrow \infty$

III. EQUIVALENT CIRCUIT MODELS

The circuit element parameters of Fig. 1 are obtained by analyzing the frequency behavior of the coil impedances. While curve fitting techniques like vector fitting [7] are available without any a priori knowledge of the structures, a more physical approach for determining the equivalent network of spiral inductors is achieved by the following strategy: First, the partial matrix elements are calculated once. The parasitic capacitance is extracted by solving the system with and without capacitive effects at the frequency of interest. The difference in admittance reveals the capacitance C and eventually a parallel resistance R_p that is typically in the range of several $M\Omega$. The frequency dependent inductance and resistance are obtained by magnetic quasistatic evaluation without the capacitive cells. From the DC limit, the resistance R_{DC} and the total inductance $L_{ext} + L_{int}$ are obtained, the frequency dependent behavior is extracted by a curve fitting technique requiring the evaluation of a few frequency points only. Here, the frequency behavior of the resistance and inductance is chosen as follows

$$R(f) = R_{DC} \sqrt{1 + \frac{f^2}{f_R^2}}^{A_R}, \quad L(f) = L_{ext} + L_{int} \sqrt{1 + \frac{f^2}{f_L^2}}^{A_L}, \quad (2)$$

which allows to approximate the curves with a few design parameters (f_R , f_L , A_R , A_L , L_{int}). More details about the fitting technique will be presented in the final version of this paper. The computed parameters for the arrangement of Fig. 2 are given in Table I, the impedance curve for the tag antenna is shown in Fig. 3.

In the following, the mutual coupling is computed for both antennas for a varying spatial separation from 0 to 10 cm as presented in Fig. 2. For this setup the mutual port coupling is

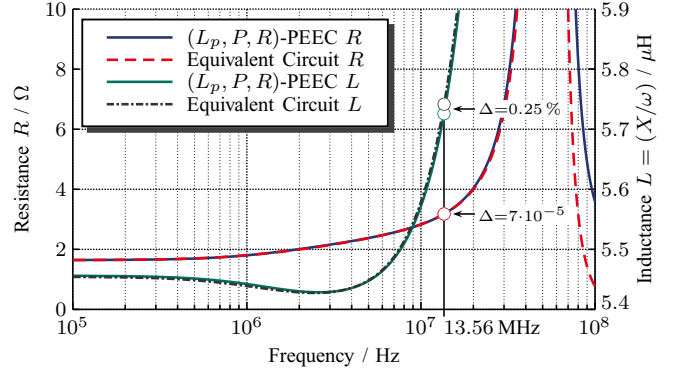


Fig. 3. Tag antenna impedance. The error of the equivalent circuit with the parameters of Table I is well below 1% for the frequencies smaller than the resonance.

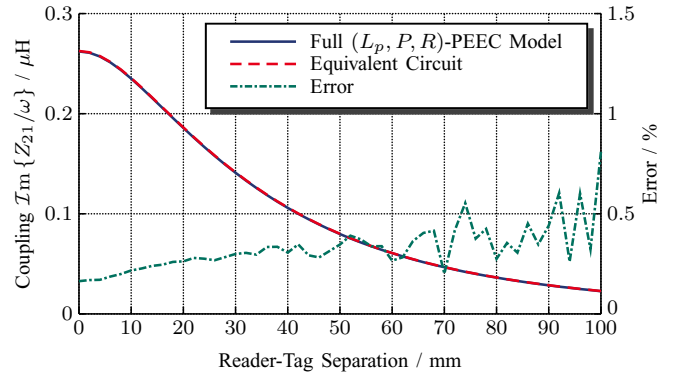


Fig. 4. Simulation results and error of the mutual impedance computed by the full PEEC model and the reduced circuit at 13.56 MHz. The error is again below 1% for all presented separations.

calculated in two different ways: The full PEEC models with a total unknowns of 1480 and the reduced circuit model with 6 fixed self impedance elements and 32 varying filaments for calculating the mutual inductance. Both techniques are best compared when visualizing the transmission behavior by the imaginary part of the mutual impedance Z_{21} which is shown in Fig. 4.

REFERENCES

- [1] C. Reinhold, P. Scholz, W. John, and U. Hilleringmann, "Efficient antenna design of inductive coupled RFID-systems with high power demand," *Journal of Communications*, vol. 2, no. 6, pp. 14–23, Nov. 2007. [Online]. Available: <http://www.academypublisher.com/jcm/vol02/no06/jcm02061423.pdf>
- [2] A. E. Ruehli, "Equivalent circuit models for three-dimensional multiconductor systems," *IEEE Trans. Microw. Theory Tech.*, vol. MTT-22, no. 3, pp. 216–221, Mar. 1974.
- [3] P. Scholz, W. Ackermann, and T. Weiland, "PEEC antenna modeling of rectangular spiral inductors for RFID systems," to be published at the Symposium on Electric and Magnetic Fields, EMF, May 2009.
- [4] P. D. Patel, "Calculation of capacitance coefficients for a system of irregular finite conductors on a dielectric sheet," *IEEE Trans. Microw. Theory Tech.*, vol. 19, no. 11, pp. 862–869, Nov. 1971.
- [5] M. Kamon, N. A. Marques, L. M. Silveira, and J. White, "Automatic generation of accurate circuit models of 3-d interconnect," *IEEE Trans. Compon., Packag. Manuf. Technol. B*, vol. 21, no. 3, pp. 225–240, Aug. 1998.
- [6] F. W. Grover, *Inductance Calculations*. D. Van Nostrand Co., New York, 1946; reprinted by Dover Publications, New York, 2004.
- [7] G. Antonini, D. Deschrijver, and T. Dhaene, "Broadband macromodels for retarded partial element equivalent circuit (rPEEC) method," *IEEE Trans. Electromagn. Compat.*, vol. 49, no. 1, pp. 35–48, Feb. 2007.

Design and Implementation of a High Frequency Flyback Converter Using New-developed Polymer-bonded Magnetic Cores

K. DING, K. W. E. CHENG, *Senior Member, IEEE*

Abstract—A novel polymer-bonded magnetic materials has been developed. The new magnetic material is composed of polymer matrices and special magnetic powder. By using the new materials, light weight, low cost and non-brittle magnetic cores of flexible shapes and different sizes can be made. To fully investigate the magnetic performance of the EI transformer, finite element analysis (FEA) has been applied. Based on the new-developed magnetic cores, 100Watt flyback power converter has been developed. The design guideline of how to use the new materials for power conversion has been given. PCB prototype and experimental results are provided to validate the feasibility of the application of the proposed novel materials for power conversion.

Index Terms—Polymer-bonded, Power conversion, finite element analysis, Flyback, Magnetic core.

I. INTRODUCTION

THE technology and engineering domains constantly set demanding requirements of magnetic materials. Materials such as Ferrites and Molybdenum Permalloy Powder (MPP) are famous for their low loss characteristics and high frequency operation, leading to wide applications in various fields. In particular, they are very popular for power conversion. One of the applications is the power converter which uses magnetic materials to construct inductors and transformers. The design of the magnetic device also depends on the permeability, loss factor and size and shape of the materials. Recently, polymer bonded magnetic materials have attracted a great deal of attention in the fields of magneto-electrics and magneto-optics. These materials are composed of polymer matrices and magnetic powders, which may be produced using traditional polymer processing methods[1-7]. Polymer bonded magnetic materials offer significant advantages over conventional materials[8, 9]. For example, polymer bonded magnetic materials can be molded more easily, lowering the cost of manufacturing and of quality control. Nonetheless, the polymer-bonded magnetic materials have not typically been applicable in power conversion. The outstanding work needed in the optimization and the permeability study has prevented developing the materials into a product.

K. DING, K.W.E.CHENG are with the Department of Electrical Engineering, Hong Kong Polytechnic University, Hong Kong, China (852-27666162 e-mail:eeecheng@polyu.edu.hk).

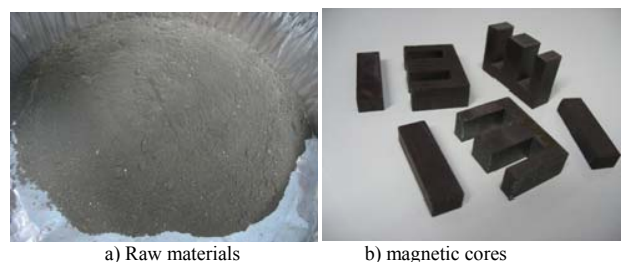


Figure 1: Photos of polymer-bonded magnetic materials and EI40 cores

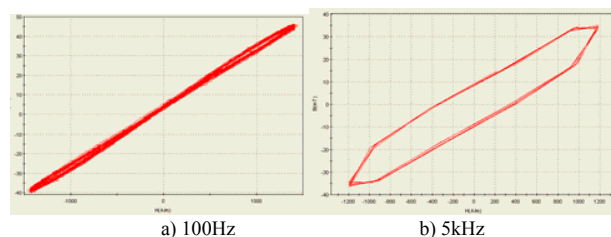


Figure 2: B-H Curve of the new-developed polymer-bonded magnetic materials

II. POLYMER-BONDED MAGNETIC MATERIALS FOR POWER CONVERSION

A. Development of Polymer-bonded Magnetic Material

A new polymer-bonded magnetic material has been developed in Hong Kong Polytechnic University. The new-developed material is produced by compounding from 10 weight percent of polyethylene resins (PE), 90% weight percent of a magnetic powder taken from NiZn Ferrite, and 15 weight percent (against magnetic powder) of Titanium (IV) Isopropoxide (C₁₂H₂₈O₄Ti) as a coupling agent. The developed materials and EI40 cores are shown in Figure 1

B-H Loop was measured by using EI40 shape cores. The Measured B-H loop of the material is shown in Figure 2.

B. Finite Element Analysis

To fully investigate the magnetic performance of the EI transformer, finite element analysis (FEA) has been applied. The purpose of FEA is to explore the magnetic flux distribution along the polymer and flux leakage can be calculated according to flux value from each finite element. Three dimensional model has been constructed to fully explore the magnetic characteristics. With current excitation of 1A from the primary coil, flux has been built up along the magnetic path as shown in Figure 3.

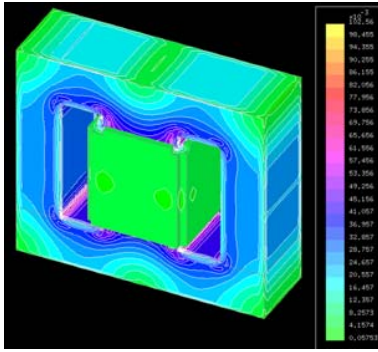
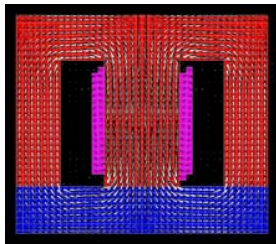
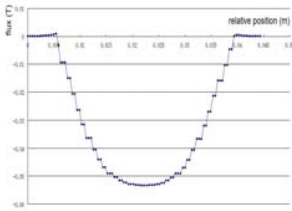


Figure 3: 3D flux distribution

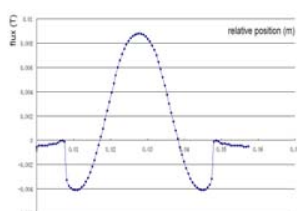
A “3D cut” vertical to the arms of the transformer is performed along the finite element model. As can be seen from Figure 4 (a), most flux distributes along the E and I core respectively since the air region has a relatively large reluctance. For a precise numerical analysis, the flux from each element along the horizontal edge of one arm is selected according to its relative position to verify a negligible leakage flux. It can be seen from Figure 4 (b) that flux dominates along the polymer and diminishes rapidly along the air region. Similarly the flux plot along the vertical edge of one arm can be found in Figure 4 (c)



(a)



(b)



(c)

Figure 4: (a) 2D flux distribution and flux plot according to relative positions (b) horizontal and (c) vertical

III. DESIGN AND IMPLEMENTATION OF A 100W FLYBACK CONVERTER

A. Flyback Converter

The flyback converter is one of the simplest topology isolated converter. Its basic circuit is shown in Figure 5. It only consists of coupled inductors, a transistor T, a rectifier diode D and filter capacitor C. The primary and secondary sides are isolated by a coupled inductor (some time is referred as a transformer). When transistor T is conducting, V_{in} is developed across the primary winding causing a linear increase in current as energy is stored in the coupled inductor increases[10].

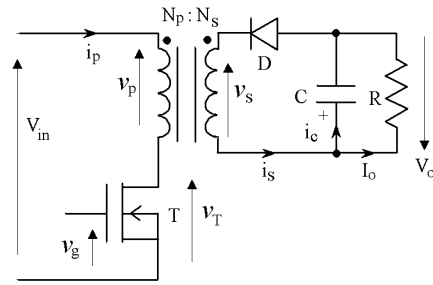


Figure 5: Flyback converter

Table 1: Electrical specification of the polymer-bonded flyback converter

Description	Symbol	Min	Typ	Max	Units
Input					
Voltage	V_{in}	85	110	130	VAC
Frequency	f_{line}	47	50/60	64	Hz
Output					
Output Voltage	V_{out}		30		V
Output Ripple Voltage	V_{ripple}			200	mV
Output Current	I_{out}	0.1		3	A
Output Power	P_{out}			100	W
Switching Frequency	f_s		400		kHz
Efficiency	η		70		%
Ambient Temperature	T_{AMB}	0		85	$^{\circ}C$

Table 2: Effective Core parameters of an EI 40core

Symbol	Parameter	Value	Unit
V_e	effective volume	11100	mm^3
l_e	effective length	77.5	mm
A_e	effective area	143	mm^2

B. Design Guideline of 100Watt Flyback Converter by Using New-developed Magnetic cores

Table 1 shows the electrical specification of the 100Watt Flyback converter. EI40 core is selected for the development of the power converter, the parameter of the EI40 core is shown in Table 2. The maximum switching on time for the primary power transistor T will occur at minimum input voltage (85VAC) and maximum load (100Watt). For this development, it will be assumed that the maximum switching on time is 45% (Duty Ratio, D) of a total period of operation. The switching frequency is selected to be 400 kHz. So the period of the switching cycle is

$$T_s = \frac{1}{f_s} = \frac{1}{400 * 10^6} = 2.5 * 10^{-6} \quad (1)$$

The switching “on” time is:

$$t_{on} = DT_s = 1.125 * 10^{-6} \quad (2)$$

The absolute calculation of this voltage in practical application is difficult[11], as it depends on a number of factors which are not well defined. For this application, a fair approximation of the working value of V_s at full load will be given by using a factor of 1.3 times the RMS input voltage. So, at a line input of 85V RMS, the DC voltage V_s will be approximately

$$V_s = 85 * 1.3 = 110.5V \quad (3)$$

The effective area of the center leg of EI40 is $143mm^2$. The saturation flux density is 36mT shown in Figure 2(b), with operating frequency of 400 kHz, the maximum peak-to-peak ac

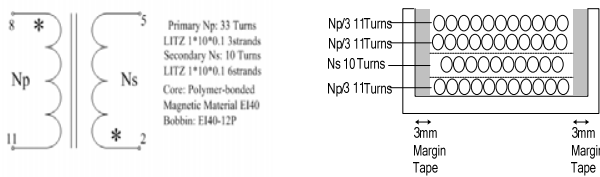
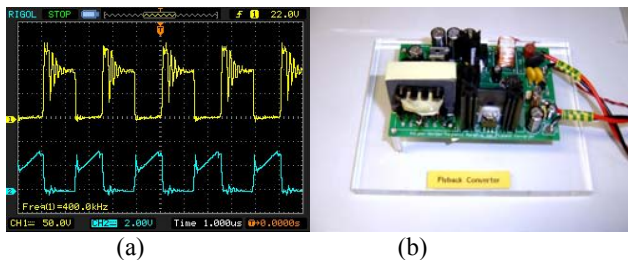


Figure 6: Transformer specification of the polymer flyback converter



(a) AC input: 85VAC, Upper: VDRain, 100V/div, 1us/div; Lower: IDrain, 1A/div, Operating Frequency 400 kHz, Power at 100W
(b) PCB prototype
Figure 7: Measured waveforms and PCB prototype of Polymer-bonded flyback converter

flux density B_{ac} is chosen at 26mT to provide a good working margin.

$$\Delta B_{ac} = 26mT \quad (4)$$

The primary turns can be calculated by:

$$N_p = \frac{V_s t_{on}}{\Delta B_{ac} * A_e} = 33.43 \quad (5)$$

The required output voltage for the main controlled line is 30V. Allowing for a voltage drop of 0.7V in the rectifier diode and 0.6V in interconnecting tracks and the transformer secondary, The voltage at the secondary of the transformer should be, say, 31.3V. Hence, the secondary turns would be

$$N_s = \frac{V_{out} N_p}{V_s} = \frac{(30+0.7+0.6) * 33}{110} = 9.39 \quad (6)$$

In this application, the turns of primary side is 33 and the secondary turns is 10. The transformer specification is shown in Figure 6. The measured experimental waveform and the PCB prototype are shown in Figure 7.

IV. CONCLUSION

Polymer-bonded magnetic materials are composed of polymer processing methods. Hence, it offers significant advantages over the conventional Ferrite. It is bonded with polymer and hence, there is an evenly distributed air-gap that is what we needed for high frequency power electronics. To fully investigate the magnetic performance of the EI transformer, finite element analysis (FEA) is applied. The purpose of FEA is to explore the magnetic flux distribution along the polymer and flux leakage can be calculated according to flux value from each finite element. Three dimensional model is constructed to fully explore the magnetic characteristics. With current excitation of 1 A from the primary coil, flux is built up along the magnetic path. By using the new-developed materials based magnetic core, a real application of 100Watt Flyback converter has been fully implemented. The design guideline of the

development for the flyback converter using the proposed materials has been illustrated. Experimental results show that the polymer-bonded magnetic cores can substitute the traditional ferrite in the applications for power conversion.

REFERENCES

- [1] K. W. E. Cheng, C. Y. Tang, D. K. W. Cheng, H. Wu, Y. L. Ho, and Y. Lu, "Investigation of polymer bonded magnetic materials for power conversion," presented at IEEE Annual Power Electronics Specialists Conference, Cairns, Australia, 2002.
- [2] L. Wang, L. X. Feng, T. Xie, and X. F. Qing, "New route for preparing magnetic polyolefins with well dispersed nanometer magnetic particles in polymer matrix using supported Fe₃O₄/AlR₃/TiCl₄ nanometer magnetic Ziegler-Natta catalyst," *Journal of Materials Science Letters*, vol. 18, pp. 1489-1491, 1999.
- [3] X. F. Wang, D. Lee, and Z. L. Jiang, "Magnetic properties of hybrid polymer bonded Nd-Fe-B/ferrite magnets," *Journal of Applied Physics*, vol. 99, pp. 08-513, 2006.
- [4] J. Xiao and J. Otaigbe, "Polymer-bonded magnets III. Effect of surface modification and particle size on the improved oxidation and corrosion resistance of magnetic rare earth fillers," *Journal of Alloys and Compounds*, vol. 309, pp. 100-106, 2000.
- [5] J. Xiao and J. U. Otaigbe, "Polymer-bonded magnets: Part I. Analytic thermogravimetry to determine the effect of surface modification on dispersion of Nd-Fe-B fillers," *Journal of Materials Research*, vol. 14, pp. 2893-2896, 1999.
- [6] J. Xiao and J. U. Otaigbe, "Polymer bonded magnets. II. Effect of liquid crystal polymer and surface modification on magneto-mechanical properties," *Polymer Composites*, vol. 21, pp. 332-342, 2000.
- [7] J. Xiao, J. U. Otaigbe, and D. C. Jiles, "Modeling of magnetic properties of polymer bonded Nd-Fe-B magnets with surface modifications," *Journal of Magnetism and Magnetic Materials*, vol. 218, pp. 60-66, 2000.
- [8] K. Ding, K.W.E.Cheng, W.T.Wu, and D. H. Wang, "Research on Polymer-Bonded Magnetic Materials for a buck converter," presented at 2nd International Conference on Power Electronics Systems and Applications Proceedings, Hong Kong, Nov 13-14, 2006.
- [9] W. T. Wu, Y.W.Wong, and K.W.E.Cheng, "Temperature Dependence of Magnetic Properties of a Polymer bonded Magnetic Material," presented at 2nd International Conference on Power Electronics Systems and Applications Proceedings, Nov 13-14, 2006.
- [10] K. W. E. Cheng, *Classical Switched Mode and Resonant Power Converters*. Hong Kong: The Hong Kong Polytechnic University, 2002.
- [11] K. Billings, *Switching Mode Power Supply Handbook*, 2nd ed: McGraw Hill, 1999.

Evaluation of Discharge Current by Generalized Energy Method and Integral Ohm's Law

Se-Hee Lee,¹ Il-Han Park,² Francis O'Sullivan,³ Markus Zahn,³

Leif Pettersson,⁴ Rongsheng Liu,⁴ Olof Hjortstam,⁴ Albert Jaksts,⁴ Tommaso Auletta,⁴ and Uno Gafvert⁴

¹School of Electrical Eng. and Computer Science, Kyungpook National University, Daegu 702-701, Korea

²School of Information and Communication Eng., Sungkyunkwan University, Suwon 440-746, Korea

³Department of Electrical Eng. and Computer Science, Massachusetts Institute of Technology, Cambridge, MA 02139, USA

⁴ABB Corporate Research, Sweden

shlees@knu.ac.kr

Abstract — The terminal current in voltage driven systems is an essential role for characterizing the pattern of electric discharge such as corona, breakdown, etc. Until now, to evaluate this terminal current, the Sato's equation has been widely used in the areas of high voltage and plasma discharge. Basically this Sato's equation was derived by using the energy balance equation and its final form described some physical meanings explicitly. To give more general abilities in Sato's equation, we, here, present a generalized approach by directly using the Poynting's theorem incorporating the Finite Element Method (FEM). When the magnetic field effect or the time-dependent voltage source should be considered, this generalized energy method can be easily applicable to those problems with any dielectric media such as gas, fluid, and solid. As an alternative approach, the integral Ohm's law resulting in small numerical distortions has an ability to be applied to multi-port systems. To test the generalized energy method and the integral Ohm's law, the results from two proposed methods were compared to those from the Sato's approach and an analytic solution.

I. INTRODUCTION

Calculation of the current flowing between any two electrodes during discharge simulation is important because the terminal current is often one of the only parameters that can be measured during actual breakdown testing. In high voltage discharge and plasma analysis, the Sato's equation has been widely used for calculating a terminal current [1]. The original Sato's equation was derived with an assumption that the applied voltage is constant in a gap. For many applications, however, it is necessary to calculate the terminal current considering time-varying applied voltages such as lightning impulse, rf, or pulsed input sources. To overcome this weakness, the original equation was expanded into a new version with including a time-dependent applied voltage [2]. This final form can be successfully applied to most of discharge problems. As in the arc simulation, however, when the magnetic field effect is significant, the calculating method for terminal current should be modified and generalized.

With the energy balance equation, here, we present a generalized method to calculate a terminal current by directly adopting the Poynting's theorem incorporating the Finite Element Method (FEM) which has been successfully applied to discharge analysis. In this approach, the global quantities such as energy and Ohmic dissipation were directly employed in the expression of Poynting's theorem with terminal quantities, current and voltage. This generalized energy method naturally covers the time-varying voltage sources,

magnetic field effect, and any dielectric media. In addition to this, the FEM gives more accurate global quantities such as energy and total power dissipation because the procedure of FEM follows the global energy minimization condition. This generalized energy method, therefore, is harmony well with the FEM.

As an alternative method, we also tested the integral Ohm's law, which can be applied to multi-port systems. The Sato's equation and the generalized energy method, however, can be applied to only a two-terminal electromagnetic system because it is difficult to separate the energy contributions for each port. Even though the integral Ohm's law has an ability to calculate a terminal current at each port, the result has some numerical distortions when we took a conductor surface as an integrating surface. To test two proposed methods, the results were compared to those from the Sato's equation and an analytic solution [3].

II. GOVERNING EQUATIONS AND FINAL SATO'S EQUATION

The general expression of governing equations for space charge propagation can be analyzed by using the hydrodynamic diffusion-drift model for the electron (N_e), positive ions (N_p), and negative ions (N_n) as [2]

$$\frac{\partial N_e}{\partial t} + \nabla \cdot (N_e \mathbf{V}_e - D_e \nabla N_e) = S + N_e \alpha |\mathbf{V}_e| - N_e \eta |\mathbf{V}_e| - N_e N_p \beta_{ep} \quad (1)$$

$$\frac{\partial N_p}{\partial t} + \nabla \cdot (N_p \mathbf{V}_p - D_p \nabla N_p) = S + N_e \alpha |\mathbf{V}_e| - N_e N_p \beta_1 - N_n N_p \beta_2 \quad (2)$$

$$\frac{\partial N_n}{\partial t} + \nabla \cdot (N_n \mathbf{V}_n - D_n \nabla N_n) = N_e \eta |\mathbf{V}_e| - N_n N_p \beta_2 \quad (3)$$

where t denotes the time, \mathbf{V}_e , \mathbf{V}_p , and \mathbf{V}_n the electron, positive and negative ion drift velocities, D_e , D_p , and D_n the electron, positive and negative ion diffusion coefficients, and α , η , and β the ionization, attachment, and recombination coefficients, respectively. S denotes the source term due to photoionization, and here its effect was neglected. To take the electric field effect, those continuity equations should be solved with the Poisson's equation simultaneously as

$$\nabla \cdot (-\epsilon \nabla V) = e(N_p - N_e - N_n) \quad (4)$$

where ϵ is the dielectric permittivity, e the electron charge, and V the electric scalar potential.

The expanded Sato's equation considering three carriers and a time-dependent applied voltage was expressed as [2]

$$I = \frac{1}{V_a} \int_{\Omega} \mathbf{J}_c \cdot \mathbf{E}_L dv + \frac{\varepsilon_0}{V_a} \int_{\Omega} \frac{\partial \mathbf{E}_L}{\partial t} \cdot \mathbf{E}_L dv \quad (5)$$

with

$$\mathbf{J}_c = e(N_p \mathbf{V}_p - N_e \mathbf{V}_e - N_n \mathbf{V}_n - D_p \nabla N_p + D_e \nabla N_e + D_n \nabla N_n)$$

where I is the external circuit current, V_a the applied voltage, \mathbf{J}_c the conduction current, \mathbf{E}_L the solution of Laplace's equation, ε_0 the dielectric permittivity in air, and $\int_{\Omega} dv$ a volume integral over the discharge space.

III. INTEGRAL OHM'S LAW AND GENERALIZED ENERGY METHOD FOR CALCULATING A DISCHARGE CURRENT

In general the terminal current is due to conduction current in a dielectric medium as well as displacement current due to the time rate of change of the surface charge on the electrodes as

$$I = \int_S \left(\mathbf{J}_c + \varepsilon \frac{\partial \mathbf{E}}{\partial t} \right) \cdot d\mathbf{a} \quad (6)$$

where \mathbf{E} is the total electric field intensity due to the applied voltage and space charge distributions, and (6) is known as the integral's Ohm's law.

By considering any general field within a volume, one realizes that the energy contained by that field must be distributed throughout space with a local energy density W at every point in the volume. Similarly, power dissipation can occur at every point within the volume at a rate P_d . The power flows with a density \mathbf{S} , the Poynting vector, so that the power crossing a surface S_a is given by $\int_{S_a} \mathbf{S} \cdot d\mathbf{a}$. With these field generalizations and quasi-static approximations, the power flowing into a volume Ω , enclosed by the surface S_a , can be expressed as

$$\sum_{i=1}^n V_i I_i = \frac{d}{dt} \int_{\Omega} W dv + \int_{\Omega} P_d dv \quad (7)$$

with $W = (1/2)\varepsilon \mathbf{E} \cdot \mathbf{E} + (1/2)\mu \mathbf{H} \cdot \mathbf{H}$ and $P_d = \mathbf{E} \cdot \mathbf{J}_c$

where V_i is an applied voltage at a terminal, I_i the corresponding current at that terminal, μ the magnetic permeability, and \mathbf{H} the magnetic field intensity.

It is important point out that it is only possible to use (5) and (7) to establish the current flowing into a volume when $n=1$, i.e., when the volume only has two terminals. On the contrary, the integral Ohm's law can be applied to a multi-port system when $n>1$.

IV. TERMINAL CURRENT IN PARALLEL PLANE ELECTRODES

To verify our numerical setup and compare with each other, first, we simplified our governing equations to one carrier

system in plane-plane 2-D XY geometry as shown in Fig. 1. The governing equations are the Poisson's equation and the charge conservation equations as

$$\frac{\partial N}{\partial t} + \nabla \cdot (N\mathbf{V}) = 0 \quad (8)$$

$$\nabla \cdot (-\varepsilon \nabla V) = eN \quad (9)$$

As we can see the Fig. 2, the energy approaches, the Sato's equation and generalized energy method, produced almost the same results as analytic solutions [3]. Even though the integral Ohm's law has an ability of measuring the terminal current on each electrode, it contained some numerical distortions where the value of space charge was high. In extended paper, tip-plane electrodes with the field emission condition, Fowler-Nordheim charge injection condition, will be presented and discussed in detail.

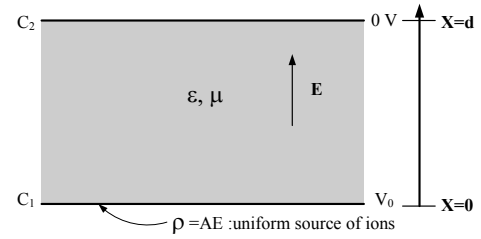


Fig. 1. The lower electrode at $x=0$ is a source of injected positive charge with mobility μ in the medium of permittivity ε . Here, ρ denotes charge density and A the linear injection coefficient.

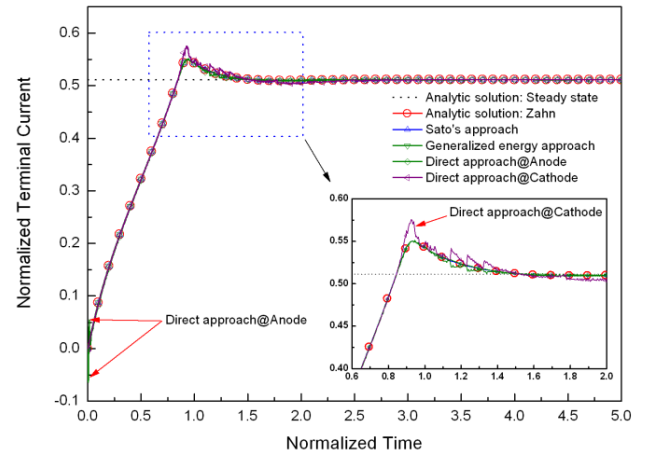


Fig. 2. Terminal current profiles from the various methods. The analytic solution was evaluated by Zahn's approach in [3]. Here, the direct approach represents the integral Ohm's law.

V. REFERENCES

- [1] N. Sato, "Discharge current induced by the motion of charged particles," *J. Phys. D: Appl. Phys.*, No. 13, pp. L3-6, 1980.
- [2] R. Morrow and N. Sato, "The discharge current induced by the motion of charged particles in time-dependent electric fields; Sato's equation extended," *J. Phys. D: Appl. Phys.*, No. 32, pp. L20-L22, 1999.
- [3] Markus Zahn, Cheung Fung Tsang, and Shing-Chong Pao, "Transient electric field and space-charge behavior for unipolar ion conduction," *Journal of Applied Physics*, Vol. 45, No. 6, pp. 2432-2440, June 1974.

On the equivalence of Finite Element and Finite Integration formulations

A. Demenko*, J.K. Sykulski**, R. Wojciechowski*

*Poznań University of Technology, ** University of Southampton

*ul Piotrowo 3A, 60-965 Poznań, Poland, ** Southampton SO17 1BJ, UK

*andrzej.demenko@put.poznan.pl, ** J.K.Sykulski@soton.ac.uk

Abstract—The paper offers a comparative study of numerical methods of analysis of electromagnetic fields. The focus is on the Finite Element Method (FEM) and Finite Integration Technique (FIT), but with the cell and equivalent network approaches also considered. It is shown how the approximate integrals describing coefficients of the FEM need to be derived for a mesh with parallelepiped elements to achieve consistency with FIT equations. The equivalence of FEM and FIT formulations for a triangular mesh in 2D is highlighted. The TEAM Workshops Problem No. 7 is used as an example for numerical comparisons. Edge values of magnetic vector potential A and nodal values of electric scalar potential V are used throughout.

I. INTRODUCTION

The finite element method (FEM) has established itself as the prime numerical technique for electromagnetic field computations, but some researchers prefer and promote the use of the finite integration technique (FIT) [1], the cell method (CM) [2] or the equivalent electric and magnetic networks (ENM) [3]. The similarities between CM, FIT and FEM were observed in [4, 5] and explored thoroughly in [6]. The main differences between the different approaches are related to the way in which space is discretised and equation coefficients set up, in particular the so-called ‘mass matrices’ of the FEM theory. [4]. The CM, FIT and ENM formulations rely on a discretisation which is equivalent to hexahedral FEM elements of 8 nodes and 12 edges (or curved rectangular parallelepipeds under cylindrical symmetry). The FEM mass matrices are non-diagonal, unlike the ones arising in CM, FIT and ENM. The purpose of this paper is to extend and enhance the previous comparative analysis of the methods. It is demonstrated that the CM, FIT and ENM equations may be considered a special case of the FEM formulation. The derived approximate integration formulae yield the equations equivalent (identical).

II. EQUATIONS OF FEM AND FIT

Both nodal elements using scalar potentials Ω , V and edge elements in terms of vector potentials A , T are considered. The FEM equations for scalar potentials correspond to the nodal equations of the edge network with branches coinciding with element edges (Fig. 1a) [6]. The permeances, conductances and capacitances forming the mass matrix may be found from

$$\Lambda_{i,j}^{(p,q)} = \int_{V_e} \mathbf{w}_{ei,j} \mu \mathbf{w}_{ep,q} dv, G_{i,j}^{(p,q)} + pC_{i,j}^{(p,q)} = \int_{V_e} \mathbf{w}_{ei,j} (\sigma + p\epsilon) \mathbf{w}_{ep,q} dv, \quad (1a,b)$$

where $\mathbf{w}_{ei,j}$, $\mathbf{w}_{ep,q}$ are interpolation functions of an edge element for the edges $P_i P_j$ and $P_p P_q$ respectively, $p=d/dt$, and V_e is the volume of the element. The FEM equations for vector potentials, on the other hand, represent loop equations of the

facet network, the branches of which cross the element facets. A portion of a network of a parallelepiped element is shown in Fig. 1b. The reluctances and impedances of the element model relate to the mass matrix elements and are described by

$$R_{\mu i,q} = \int_{V_e} \mathbf{w}_{fi} \mu^{-1} \mathbf{w}_{fq} dv, Z_{i,q} = \int_{V_e} \mathbf{w}_{fi} (\sigma + p\epsilon)^{-1} \mathbf{w}_{fq} dv, \quad (2a,b)$$

where \mathbf{w}_{fi} , \mathbf{w}_{fq} are interpolation functions of a facet element for the facets S_i , S_q [6].

The FEM mass matrices are non-diagonal; consequently so are the matrices of the equivalent network models. In the models of Fig. 1, the branches which are not perpendicular to each other will have a mutual coupling. Such couplings will also occur within the triangular 2D elements of Fig. 2. A model with mutual reluctances may be established using a facet model of a five sided prism [7].

Equations arising from the CM, FIT and ENM formulations may appear to be similar to those obtained from the FEM, but there is an important difference that they do not contain mutual couplings and thus the mass matrices are diagonal, for example

$$R_{\mu 5,5} = R_{\mu 6,6} = h_z / (2\mu h_x h_y), \Lambda_{i,i+4}^{(i,i+4)} = \mu h_x h_y / (4h_z) \quad (i=1,2,3,4), \quad (3a,b)$$

where h_y , h_x , h_z are dimensions as in Fig. 1b. In the reluctance model of a triangle $R_{\mu i,i} = h_i / (\mu s_i)$, with h_i and s_i shown in Fig. 2.

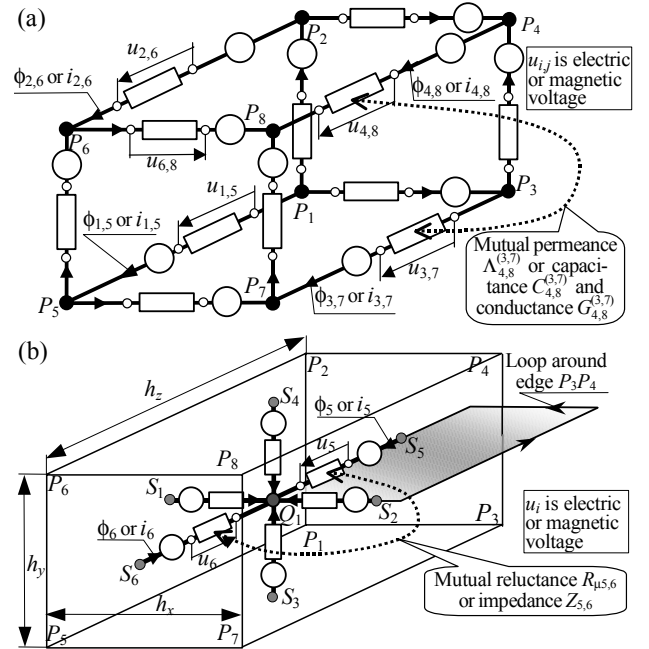


Fig. 1. Edge (a) and facet (b) model of element

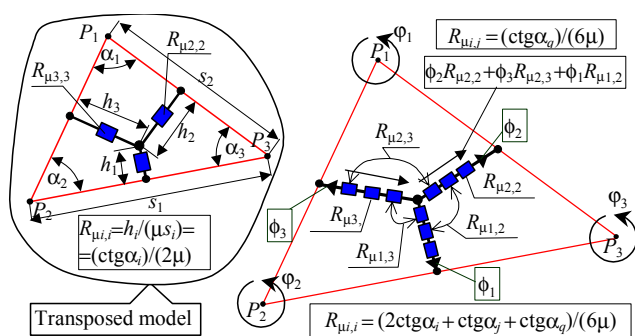


Fig. 2 Reluctance (facet) model of triangle

III. DERIVING FEM EQUIVALENT TO FIT

From circuit theory it is well known that a three branch star with mutual couplings may be converted into an equivalent one without any couplings, as demonstrated by Fig. 2. This may be achieved by exploiting the condition $\sum \phi_i = 0$. It is therefore possible to start with different mass matrices for FEM and FIT and yet achieve identical matrix coefficients for both formulations. The above transposition, regrettably, does not apply to 3D systems. Notwithstanding, it is still possible to derive a FEM formulation which is equivalent to FIT by calculating the integrals (1) and (2) – required for setting up the mass matrix – using a simplified formula

$$\int_{V_e} f dv = V_e / 8 \sum_{i=1}^8 f(P_i), \quad (4)$$

which results in models free of mutual couplings, thus with coefficients the same as if obtained from FIT. Unfortunately, the procedure described by (4) is only successful – in terms of making the matrix diagonal – in the case of parallelepiped elements (it also works for curved rectangular parallelepipeds). The mass matrices of tetrahedral and five sided prism elements may be made diagonal only if complemented by additional assumptions regarding fluxes or currents; for example by imposing (or assuming) one of the facet flux or current densities in a tetrahedra to be negligibly small.

IV. EXAMPLE

The TEAM Workshops Problem No. 7 (Fig. 3) has been selected to illustrate the theoretical investigations [8]. The magnetic field and eddy current distributions have been calculated for a conducting plate with a hole, with the excitation provided by a multi-turn coil. An A - V formulation has been adopted with edge elements for the vector potential A and nodal elements for the scalar potential V . The bounded space has been subdivided into about 150 thousand elements, some 16 thousand of which were placed in the conducting region. The resultant system of equations corresponds to a reluctance-conductance network consisting of about half a million loop equations related to the magnetic network and 20 thousand nodal equations of the electric network. The relevant parameters for the FEM model were derived using (1) and (2), thus creating mutual conductances and reluctances. A block relaxation method, combined with incomplete Cholesky decomposition, has been used to solve the final system of equations. Table I shows example values of the flux and current densities at selected points P_1 and P_2 as marked in Fig. 3.

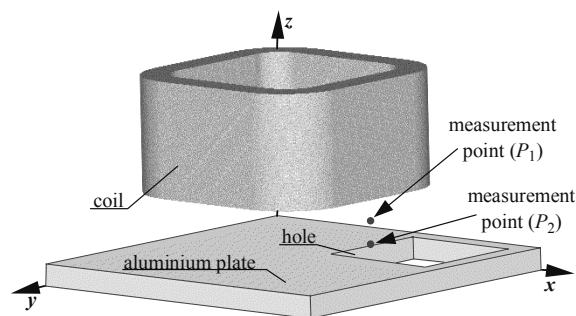


Fig. 3 TEAM Workshops Problem No.7

TABLE I
COMPARISON BETWEEN FIT AND FEM RESULTS

Method Quantity	FIT	FEM
Flux density in point P_1		
B_x [T]	-0.010689	-0.010747
B_y [T]	0.003581	0.003583
B_z [T]	0.008145	0.008165
Current density in point P_2		
J_x [A/m ²]	83275.85	83196.15
J_y [A/m ²]	1713894.52	1710454.18
J_z [A/m ²]	-39703.18	-39469.81

The values are given for an instant of time when the coil current was at its maximum (a 50Hz supply has been assumed).

For all points considered, the differences between the FIT and FEM results do not exceed 0.6% for flux density and 0.7% for current density, respectively. It appears therefore reasonable to conclude that the proposed approximation (4) – which leads to equations equivalent to the FIT method with a diagonal mass matrix – is perfectly acceptable without noticeable loss of accuracy. Moreover, the diagonal matrix is easy to invert, thus seeking edge values of A , representing loop fluxes in the model of Fig. 1b, may be conveniently replaced by an easier task of finding nodal potentials associated with element centres (nodes Q_i). In the case of diffusion problems the additional advantage of making the mass matrix diagonal is a possibility of applying explicit numerical schemes [4].

V. REFERENCES

- [1] T. Weiland, "A discretization method for the solution of Maxwell's equations for six-component fields," *Electron. Commun. AEU*, 31(3), pp. 116-120, 1977.
- [2] E. Tonti, "A direct formulation of field laws: The cell method," *CMES*, 2(2), pp. 237-258, 2001.
- [3] J. Sykulski et al, *Computational Magnetics*, Chapman & Hall, 1995.
- [4] A. Bossavit and L. Kettunen, "Yee-like schemes on staggered cellular grids: A synthesis between FIT and FEM approaches," *IEEE Trans. on Magnetics*, 36(4), pp. 861-867, 2000.
- [5] M. Clemens, Stefan Feigh, T. Weiland "Construction principles of multigrid smoothers for curl-curl equations," *IEEE Trans. on Magnetics*, 41(5), pp.1680-83, 2005.
- [6] A. Demenko and J. K. Sykulski, "Network equivalents of nodal and edge elements in electromagnetics," *IEEE Trans. on Magnetics*, 38 (2), pp. 1305-08, 2002.
- [7] A. Demenko, L. Nowak, W. Szelag, "Reluctance network formed by means of edge element method," *IEEE Trans. on Magnetics*, 34(5), pp. 2485-88, 1998.
- [8] O. Biro, K. Preis, W. Renhart, K.R. Richter, G. Vrisk, "Performance of different vector potential formulations in solving multiply connected 3D eddy current problems," *IEEE Trans. Magnetics*, 26 (2), pp. 438-41, 1990.

A Fast Numerical Analysis of Electromagnetic Fields in Large Grounding Systems

Hongxia Huang, Lin Li

School of Electrical and Electronic Engineering, North China Electric Power University, P.O. Box 10
Baoding 071003, Hebei, China
h hx_1982@163.com

Abstract—A fast algorithm for transient analysis of grounding grids or above ground conductors is presented. The algorithm is based on the modified image theory and the Fast Multipole Method (FMM). Validation of the algorithm is achieved by comparison with other algorithm. The results show the flexibility, efficiency and accuracy of this algorithm.

I. INTRODUCTION

It is important to study the transient performance of grounding systems of substation for lightning surges in order to ensure the safety of personnel and prevent damage of installations. Three different analytical approaches have been used, which are based on circuit theory [1], transmission line theory [2] and electromagnetic field theory [3], respectively. Though the last approach is rigorist in theory, the presence of the lossy ground implies the computation of the slowly converging Sommerfeld integrals. The FMM [4] reduces the computational complexity from $O(N^2)$ to $O(N^{1.5})$, but it can't be used to evaluate electromagnetic fields if the Sommerfeld integrals are evaluated directly. The developed algorithm used the modified images to establish the EFIE and FMM to solve it. The remarkable efficiency and flexibility makes it possible to evaluate the lightning electromagnetic fields for grounding grid or overhead transmission lines.

II. FORMULATION

A. Modified Image Theory

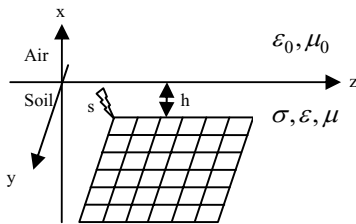


Fig. 1. A grounding grid of substation

In Fig.1, a transient current is assumed to flow through the grounding grid, and every small segment of the grid can be expressed as a line current source. The influence of the interface is taken into account approximately by the modified images [5]. The electric field can be evaluated by means of the current sources and their images:

$$I' = \frac{j\omega\epsilon + \sigma - j\omega\epsilon_0}{j\omega\epsilon + \sigma + j\omega\epsilon_0} I = \Delta I \quad (1)$$

B. Electric Field Integral Equation

The EFIE for a lossless conductor is:

$$\mathbf{t} \cdot (\mathbf{E}^i + \mathbf{E}_1^s + \mathbf{E}_2^s) = 0 \quad (2)$$

where \mathbf{E}^i is the incident electric field, \mathbf{E}_1^s and \mathbf{E}_2^s are the scattered electric fields related with the current source and its

image, respectively. The subscript 1 indicates the variable or the parameter relative to the current sources and subscript 2 indicates that relative to the images. The scattered electric field can be evaluated by means of the Green function:

$$\mathbf{t} \cdot \mathbf{E}_j^s = \frac{1}{4\pi(\sigma + j\omega\epsilon)} \int_l I_l(\mathbf{r}_j') G(\mathbf{r}, \mathbf{r}_j') dl \quad j = 1, 2 \quad (3)$$

$$G(\mathbf{r}, \mathbf{r}_j') = [\nabla^2 - \gamma^2] \frac{e^{-\gamma|\mathbf{r}-\mathbf{r}_j'|}}{|\mathbf{r}-\mathbf{r}_j'|} \quad (3a)$$

$$\gamma = \sqrt{j\omega\mu(\sigma + j\omega\epsilon)} \quad (3b)$$

C. Method of Moment

The Galerkin method is employed to solve the EFIE (2) in the frequency domain. The longitudinal current is expanded as:

$$I_l = \sum_{n=0}^N I_n F_n \quad (4)$$

where I_n denotes the unknown coefficients to be determined, F_n is an expansion function which is expressed as:

$$F_n = \frac{\sinh \gamma(\Delta l - |l - l_n|)}{\sinh \gamma\Delta l}, \quad |l - l_n| < \Delta l \quad (5)$$

where $\Delta l = l_n - l_{n-1} = l_{n+1} - l_n$. The rigorous expression for the electric field of a sinusoidal dipole with unit amplitude is in a local cylindrical coordinate system illustrated in Fig.2:

$$E_{jzn} = \frac{1}{4\pi(\sigma + j\omega\epsilon)} \frac{\gamma}{\sinh \gamma\Delta z} \left(\frac{e^{-\gamma R_{j1n}}}{R_{j1n}} + \frac{e^{-\gamma R_{j3n}}}{R_{j3n}} - 2 \cosh \gamma\Delta z \frac{e^{-\gamma R_{j2n}}}{R_{j2n}} \right) \quad (6)$$

$$E_{j\phi n} = \frac{1}{4\pi(\sigma + j\omega\epsilon)\rho} \frac{\gamma}{\sinh \gamma\Delta z} \left(e^{-\gamma R_{j1n}} \cos \theta_1 + e^{-\gamma R_{j3n}} \cos \theta_3 - 2 \cosh \gamma\Delta z e^{-\gamma R_{j2n}} \cos \theta_2 \right) \quad (7)$$

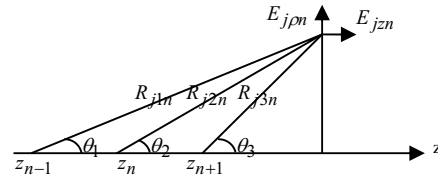


Fig.2. Local coordinate system

The linear algebraic equations can be attained as follows:

$$Z_{N \times N} I_{N \times 1} = U_{N \times 1} \quad (8)$$

where the elements in $U_{N \times 1}$ are the mutual impedances between the dipoles and the incident monopoles, the element z_{mn} in $Z_{N \times N}$ is the mutual impedance between the dipoles m and n :

$$z_{mn} = \int_{l_n} F_m \mathbf{t} \cdot (\mathbf{E}_{1n} + \Delta \mathbf{E}_{2n}) dl \quad (8a)$$

D. Fast Multiple Method

Dividing the wire segments into M homogeneous groups, \mathbf{o}_j and \mathbf{o}_j' are the centers of groups \mathbf{m}_j and \mathbf{n}_j , respectively. Applying FMM, (8) can be rewritten as follows:

$$(Z^{near} + Z^{far})_{N \times N} I_{N \times 1} = U_{N \times 1} \quad (9)$$

The matrix element Z^{near} represents the interaction from nearby regions, evaluated by MoM, used the expression (8a), and Z^{far} represents the interactions from non-nearby regions. For the non-nearby regions, by applying the addition theory, the Green's function is rewritten as:

$$\frac{e^{-\gamma|r-r_j'|}}{|r-r_j'|} = \frac{e^{-jk|X_j+d_j|}}{|X_j+d_j|} \approx -\frac{ik}{4\pi} \int d^2\hat{k} e^{-ik \cdot d_j} T_j(\hat{k} \cdot \hat{X}_j) \quad (10)$$

where

$$\mathbf{r} - \mathbf{r}_j' = \mathbf{r}_{m_j n_j} = \mathbf{X}_j + \mathbf{d}_j = \mathbf{r}_{o_j o_j'} + (\mathbf{r}_{m_j o_j} - \mathbf{r}_{n_j o_j'}) \quad (10a)$$

$$\hat{\mathbf{k}} = (\sin \theta \cos \phi + \sin \theta \sin \phi + \cos \theta) \quad (10b)$$

$$\mathbf{k} = k\hat{\mathbf{k}} = \frac{\gamma}{i} \hat{\mathbf{k}} \quad (10c)$$

$$T_j(\hat{\mathbf{k}} \cdot \hat{X}_j) = \sum_{l=0}^L (-i)^l (2l+1) h_l^{(2)}(kX_j) P_l(\hat{\mathbf{k}} \cdot \hat{X}_j) \quad (10d)$$

$$L = kD + 2 \log(kD + \pi) \quad (10e)$$

where $\int d^2\hat{k}$ is the integral over the unit sphere, and $d_j < X_j$.

D is the maximum group size.

$$G(\mathbf{r}, \mathbf{r}_j') \approx -\frac{ik}{4\pi} \int d^2\hat{k} (\nabla^2 - \gamma^2) e^{-ik \cdot d_j} T_j(\hat{\mathbf{k}} \cdot \hat{\mathbf{r}}_j) \quad (11)$$

$$z_{mn}^{far} = \frac{-\gamma^3}{16\pi^2 (\sigma + j\omega\epsilon)} \int d^2\hat{k} V_m [T_1(\hat{\mathbf{k}} \cdot \hat{\mathbf{r}}_1) + AT_2(\hat{\mathbf{k}} \cdot \hat{\mathbf{r}}_2)] V_n \quad (12)$$

$$V_m = \int_{l_m} F_{m_1} (\nabla^2 - \gamma^2) e^{-ik \cdot \mathbf{r}_{m_1 o_1}} dl = \int_{l_m} F_{m_2} (\nabla^2 - \gamma^2) e^{-ik \cdot \mathbf{r}_{m_2 o_2}} dl \quad (12a)$$

$$V_n = \int_{l_n} F_{n_1} (\nabla^2 - \gamma^2) e^{ik \cdot \mathbf{r}_{n_1 o_1}} dl' = \int_{l_n} F_{n_2} (\nabla^2 - \gamma^2) e^{ik \cdot \mathbf{r}_{n_2 o_2}} dl' \quad (12b)$$

where V_m, T_j, V_n represents the matrix of aggregation, translation, disaggregation respectively. Because the conductors are divided symmetrically, T_j has a translational invariance and for the elements in different groups, when $\mathbf{r}_{m_j o_j}$ and V_m are the same, V_n also has the same nature. Furthermore, V_m, V_n are unchanged for the current sources and their images, and these properties reduce the computational complexity and the computer memory significantly.

In the case of lossy conductors, the boundary condition (2) needs to be modified as follows:

$$\mathbf{t} \cdot (\mathbf{E}^i + \mathbf{E}_1^s + \mathbf{E}_2^s) = Z_s I_1(r') \quad (14)$$

$$Z_s = \frac{\lambda_s}{2\pi a (\sigma_s + j\omega\epsilon_s)} \frac{J_0(\lambda_s a)}{J_1(\lambda_s a)} \quad (15)$$

where Z_s is the surface internal impedance, $\sigma_s, \epsilon_s, \mu_s$ are the conductivity, permittivity and permeability of the conductor, respectively, $\lambda_s \approx \omega^2 [\mu_s (\epsilon_s + \frac{\sigma_s}{j\omega}) - \mu (\epsilon + \frac{\sigma}{j\omega})]$, a is the radius of the conductor segment, J_0, J_1 are the first kind of zero and one order Bessel functions, respectively.

Once the current distribution along the conductors has been evaluated, the electric field can be calculated at any point by summing the contributions due to the currents in each segment.

III. NUMERICAL RESULTS

In order to examine the validity of the developed algorithm, we computed the longitudinal current along a wire placed horizontally in a lossy ground. It is assumed that the wire is excited by a sinusoidal current with unit amplitude of frequency $f=6.741\text{MHz}$. Fig.3 shows the current distribution along the wire calculated by the developed algorithm and by MOM directly, and the operation time for a different number of unknowns is given in Fig.4. It can be found the flexibility, efficiency and accuracy of this algorithm. The detailed results (including those calculated and measured) and analysis about grounding grids of the substation will be described in the extended paper.

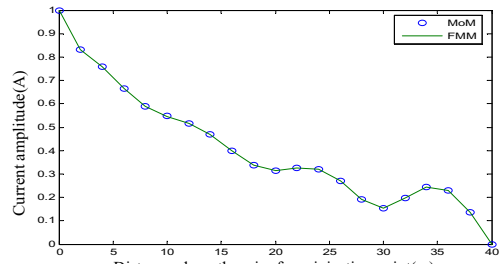


Fig.3. Current distribution along the wire.

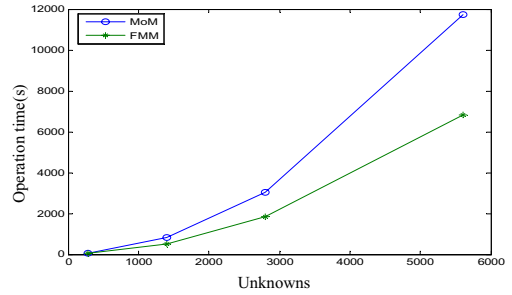


Fig.4. Operation time

IV. CONCLUSIONS

A fast algorithm is presented to compute electromagnetic field of a grounding grid. The method used the modified images to replace the ground effect, and utilized the FMM for solving the EFIE. The method can be used in analyzing lightning electromagnetic field problems of substation grounding systems or overhead transmission lines.

V. REFERENCES

- [1] M. Ramamoorthy, M.M.B. Narayanan, S. Parameswaran, and D. Mukhedkar, "Transient Performance of Grounding Grids", *IEEE Trans. on Power Delivery*, 4(4): 2053-2059, 1989.
- [2] Yaqing Liu, Nelson Theethayi, and Rajeev Thottappillil, "An Engineering Model for Transient Analysis of Grounding System Under Lightning Strikes: Nonuniform Transmission-Line Approach", *IEEE Trans. on Power Delivery*, 20(2): 722-730, 2005.
- [3] V.Cooray, "On the validity of several approximate theories used in quantifying the propagation effects on lightning generated electromagnetic fields," presented at the 8th Int. Symp. Lightn. Prot. SIPDA, Sao Paulo, Brazil, Nov.2005
- [4] Ronald Coifman, Vladimir, and Stephen Wandzura, "The fast multipole method for the wave equation: a pedestrian prescription", *IEEE Antennas and Propagation Magazine*, 35(3): 7-12, 1993.
- [5] Leonid D. Grcev, "Computer analysis of transient voltages in large grounding systems", *IEEE Transactions on Power Delivery*, 11(2): 815-823Apr. 1996.

Overlapping Finite Elements for Arbitrary Surfaces in 3D

Guillaume Krebs¹, Stéphane Clénet^{1,2} and Igor Tsukerman²

¹L2EP/AMPT Lille, 8, Bd Louis XIV, 59046 Lille Cedex, France - stephane.clenet@ensam.eu

²Department of Electrical and Computer Engineering, The University of Akron, Akron, OH 44325-3904, United States - tsukerman@uakron.edu

Abstract— The overlapping method is usually employed to connect two surfaces or subdomains meshed separately. This method has been developed in 2D and in 3D for plane surfaces. The paper extends the overlapping method to arbitrary non-planar surfaces; this is accomplished by introducing new shape functions. The proposed method is compared with the classical overlapping method.

I. INTRODUCTION

The finite element method is a useful and reliable tool to study electromagnetic devices. 2D problems can be solved in seconds on today's personal computers. However, accounting for real 3D geometries involves complex mesh generators and solvers and can be very time consuming. Mesh generation can be simplified by relaxing the constraints on the mesh and connecting non-conforming surface meshes. This approach has many advantages. First, mesh propagation of a dense mesh into adjacent areas can be avoided. Second, for moving surfaces no re-meshing is required and the motion step is completely free. Finally, the decoupling of different subdomains can be taken advantage to parallelize the calculations.

Various methods have been proposed to connect two meshed surfaces. If the surfaces are in contact, interpolation, Lagrange Multipliers or the Mortar methods [1] are used. If the surfaces are separated by a constant gap, the overlapping method [2] can be applied and is very attractive because it leads to a sparse linear system of equations. However, if the surfaces to be connected are irregular (e.g. have ripples or bulges), the overlapping elements developed previously cannot be directly used. To overcome this problem, an extension of the overlapping method is proposed in this paper. First, the approach developed earlier is presented. The problems encountered for irregular surfaces are discussed. Modified shape functions are proposed in the overlapping element area. Finally, a test example for the new overlapping method is presented.

II. THE OVERLAPPING ELEMENTS DEVELOPED PREVIOUSLY

The overlapping method was originally introduced in [2] and afterwards independently in [3] for taking into account rotation of electrical machines in 2D. Then, it has been adapted in 3D for hexahedral meshes [4] and extended to tetrahedral elements and prisms [5]. We first review the construction of overlapping elements using the scalar potential formulation in magnetostatics as an example. If we denote the source field with \mathbf{H}_s , and the scalar potential with Ω , the magnetic field \mathbf{H} can be expressed by (1).

$$\mathbf{H} = \mathbf{H}_s - \text{grad}\Omega \quad (1)$$

On the computational domain D , the equation to solve is:

$$\text{div}(\mu(\mathbf{H}_s - \text{grad}\Omega)) = 0 \quad (2)$$

Where μ is the magnetic permeability. To solve (2), the scalar potential is approximated using nodal shape functions w_i ($i \in \mathcal{N}$ with \mathcal{N} the set of nodes) and \mathbf{H}_s using edge shape functions \mathbf{w}_i ($i \in \mathcal{E}$ with \mathcal{E} the set of edges). Applying the Galerkin method leads to a linear system $\mathbf{M}\boldsymbol{\Omega} = \mathbf{N}\mathbf{H}_s$ with \mathbf{M} an $\mathcal{N} \times \mathcal{N}$ matrix and \mathbf{N} is a $\mathcal{N} \times \mathcal{E}$ matrix with the following coefficients:

$$M_{i,j} = \int_D \mu \text{grad}w_i \cdot \text{grad}w_j d\tau \quad \forall i, j \in \mathcal{N} \quad (3)$$

$$N_{k,j} = \int_D \mu \mathbf{w}_k \cdot \text{grad}w_j d\tau \quad \forall k \in \mathcal{E} \text{ and } j \in \mathcal{N} \quad (4)$$

Here $\boldsymbol{\Omega}$ and \mathbf{H}_s the vectors of nodal values of Ω and of circulations of \mathbf{H}_s along the edges, respectively. In the overlapping method, one considers an area D_0 between the two surfaces S_1 that bounds a region D_1 , and S_2 that bounds D_2 , as shown in Fig. 1.a. D_1 and D_2 are two meshed subdomains of the domain D ($D=D_0 \cup D_1 \cup D_2$). Next, the nodes of each surface are projected on the other one. The projections create virtual nodes represented by asterisks in Fig 1.b and also virtual elements in the area D_0 . Two meshes M_1 and M_2 that overlap and are made of prisms are thus defined.

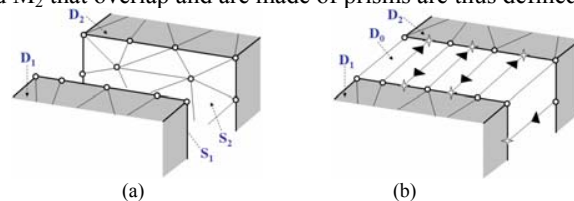


Fig. 1. Projection of the nodes in the non-meshed area .

The virtual nodes do not introduce new degrees of freedom; they are only used to define the shape functions associated with the nodal unknowns (see Fig 2.a). The problem is then to calculate the terms (3) on “overlapping elements” in D_0 . In [5], a methodology based on a common submesh of both meshes M_1 and M_2 is developed to retrieve the integration areas where numerical quadratures are applied to approximate the integral (3).

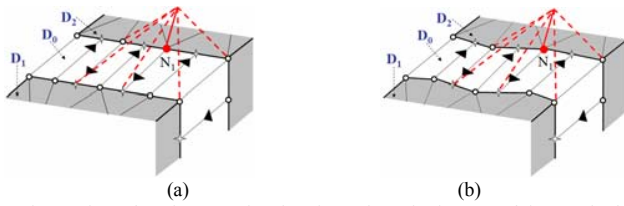


Fig. 2. Shape function associated to the node N_1 in the case of the standard overlapping method (a) and with the extended overlapping method (b).

III. NEW OF APPROXIMATION FUNCTIONS

When the meshed surfaces being connected are not planes (Fig.2.b), the elements are not prisms anymore. Consequently, the shape functions have to be modified. These functions must remain piecewise-differentiable and capable of approximating the solution of the problem accurately in D_0 .

To define a shape function associated with a node N_1 located on the surface S_1 (see Fig.3.a), let us consider the prism P obtained by extrusion of the facet f with vertices N_1, N_2 and N_3 . Let p be a point $p(x,y,z)$ in P . Let the projections of the nodes on the other surface S_2 be N_{11}, N_{22} and N_{33} . A volume V is then defined by the nodes $N_1, N_2, N_3, N_{11}, N_{22}$ and N_{33} . To calculate the nodal shape function at the point p , two projections of this point are required (e_0 on the surface S_1 and e_{00} on the surface S_2). Thus two distances, x_0 and x_{00} between p and e_0 and e_{00} can be defined respectively.

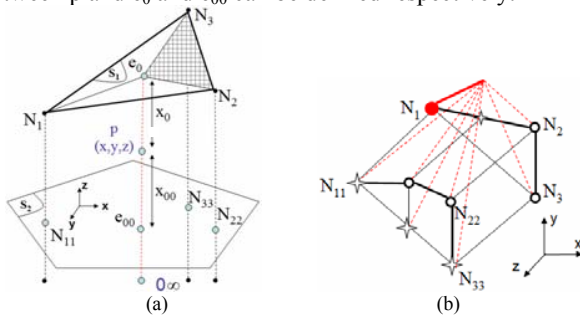


Fig. 3. Definitions of the nodes N_{11}, N_{22}, N_{33} and the distances x_0 and x_{00} (a) and one example of integration area in D_0 for the case of Fig.2 (b)

The value of the nodal shape function associated with node N_1 at the point p is then given by the expression (5).

$$w_{N_1} = \frac{x_{00}}{x_{00} + x_0} \frac{A}{S_{N_1N_2N_3}} \quad (5)$$

The variable A and $S_{N_1N_2N_3}$ are the areas of the triangles ($e_0; N_2; N_3$) and ($N_1; N_2; N_3$). If p is located on S_1 , x_0 is equal to zero, w_{N_1} is equal to the ratio of A and $S_{N_1N_2N_3}$. The function w_{N_1} is so continuous through the surface S_1 . Now, if p is located on the surface S_2 , one can easily check that the value of the shape function is equal to zero. The prolongation of the nodal shape function w_{N_1} in D_0 insures the continuity of the function at the interfaces between D_0 and D_1 and D_0 and D_2 and so on the whole domain D . Once all the shape functions are defined, the calculation of the integral in (3) is carried out in the same way as in [5].

IV. APPLICATION

The case studied involves a coil inside a mobile air box, see Fig.4. The coil is placed above a metal plate with a corrugated surface (sinusoidal shape). We aim at calculating the variation of the flux linkage through the coil as a function of position. In order to implement the standard and the extended overlapping methods, the gap between the mover and the metal is divided into two regions. Region 1 is between two plane surfaces. The remaining part defines region 2. If region 1 is not meshed, the standard overlapping method can be used. The new extended version is employed with the two areas 1 and 2 unmeshed. In fig. 5, we show the field distribution in the overlapping area. The flux linkages calculated with the classical and extended overlapping methods are close and equal to $1.4 \mu\text{Wb}$ and $1.44 \mu\text{Wb}$, respectively. Details of the simulation will be provided in the extended paper at the conference.

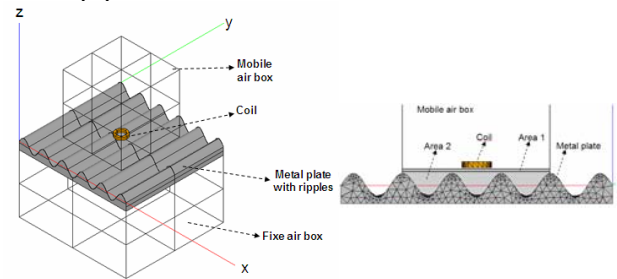


Fig. 4. Case study, moving coil above a non plane metal plate.

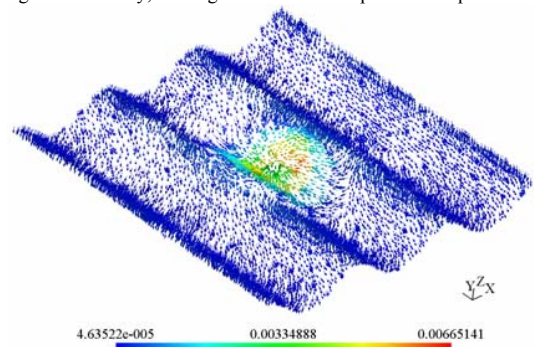


Fig. 5. Field distribution in the overlapping area

REFERENCES

- [1] F. Rapetti, "The mortar edge element method on non-matching grids for eddy current calculations in moving structures", *Num. Meth. In Engng.* 14(6): 457-477.
- [2] I.A. Tsukerman, "Overlapping finite element for problems with movement", *IEEE Trans. On Mag.*, 28(5): 2247-2249, September 1992.
- [3] S. Lepaul, J.K. Sykulski, "Coupling of motion and circuits with electromagnetics analysis", *IEEE Trans. On Mag.*, 35(3): 1602-1605, May 1999.
- [4] N. Boukari, Y. Lefèvre, and P. Spitéri, "Modeling the Movement of Electrostatic Motors in a 3D Finite Element Code", *IEEE Trans. On Mag.*, 36(4): 722-727, July 2000.
- [5] G. Krebs, S.Clénet, A. Abakar, F. Locment, F. Piriou, "Method to connect non-conforming mesh in 3D", *IEEE Trans. on Magnetics*, 45(3): 1420-1423, March 2009.

Basis functions for divergence constraints in the finite element method

C. M. Pinciuc, A. Konrad, and J. D. Lavers
 Department of Electrical and Computer Engineering
 University of Toronto
 Toronto, Ontario, Canada, M5S 1A4
 Email: chris.pinciuc@utoronto.ca

Abstract—A method for implementing divergence constraints in the finite element method is given. This method yields a linearly independent, sparse set of constraints for a mesh of brick elements. The solutions for the resonant frequencies of a cubic cavity are in good agreement with the exact values, and there are no spurious modes.

I. INTRODUCTION

A vector field, such as the electric or magnetic field, can be uniquely determined from its curl, divergence and appropriate boundary conditions [1]. In light of this, several methods have been developed for implementing divergence constraints in the finite element method [2]–[5]. Konrad [2] specifies divergence constraints for a single curvilinear brick, while Kobelansky and Webb [3] provide a method for deriving global basis functions that are divergence free. Both of these methods reduce the size of the curl matrices and preclude the existence of spurious modes, but neither method can, in general, preserve the sparsity of the curl matrices that is necessary for solving large problems. Cendes and Wong [4], [5] construct a mesh that allows for smooth interpolation of random data. This mesh enables the divergence constraints to be implemented inside of the mesh elements and across their boundaries.

The earliest paper on edge elements is due to Nedelec [6]. This method does not constrain the divergence of the field, but rather ensures that the null space of the curl operator is modeled accurately. Tangential continuity conditions at tetrahedra boundaries are explicitly enforced but normal continuity conditions are not. This method does not eliminate spurious modes, but instead guarantees that they are static and thus can be characterized by their frequency. Advantages and disadvantages of edge elements are discussed further by other authors [7]–[9].

The method introduced in the present paper enables divergence constraints to be imposed within brick elements and across their interfaces. This is accomplished using a mixture of cubic Hermite splines and second order Lagrange interpolation polynomials. This method models the divergence of the field with second order accuracy on the interior of the brick elements and enables the divergence to be a continuous function across element boundaries. Spurious modes in eigenvalue problems are eliminated when the divergence constraints are imposed.

II. BASIS FUNCTIONS

In many cases the divergence of the field is a continuous function, including the specific case where the divergence is zero everywhere. One way to guarantee that the finite element approximation of the divergence will be a continuous function is to require that $\partial E_x/\partial x$, $\partial E_y/\partial y$ and $\partial E_z/\partial z$ are each continuous functions. For a mesh comprised of brick elements, this can be accomplished by using a mixture of cubic Hermite splines, H_i , and second order Lagrange interpolation polynomials, L_i , within each brick.

$$E_x(x, y, z) = \sum_{i=0}^3 \sum_{j=0}^2 \sum_{k=0}^2 \alpha_{ijk} H_i(x) L_j(y) L_k(z) \quad (1)$$

$$E_y(x, y, z) = \sum_{i=0}^3 \sum_{j=0}^2 \sum_{k=0}^2 \beta_{ijk} H_i(y) L_j(x) L_k(z) \quad (2)$$

$$E_z(x, y, z) = \sum_{i=0}^3 \sum_{j=0}^2 \sum_{k=0}^2 \gamma_{ijk} H_i(z) L_j(x) L_k(y) \quad (3)$$

In the expansion above, x , y , and z are local coordinates for a given brick, which means that they are translated and scaled so that they are each between 0 and 1. In what follows, the single index of the Lagrange polynomials corresponds to the nodes $L_0(0) = 1$, $L_1(\frac{1}{2}) = 1$, and $L_2(1) = 1$ and the single index of the Hermite splines correspond to nodal values $H_0(0) = 1$, $H'_1(0) = 1$, $H_2(1) = 1$, and $H'_3(1) = 1$, where primes denote derivatives. Different field components have nodes that are located in different positions, as shown in fig 1. Each node in the figure corresponds to a value of the field component and a value of its derivative.

To illustrate that $\partial E_x/\partial x$ is continuous using these basis functions, consider its continuity across each face of a brick. For points that are on the surfaces $x = 0$ and $x = 1$,

$$\frac{\partial E_x}{\partial x}(0, y, z) = \sum_{j=0}^2 \sum_{k=0}^2 \alpha_{1jk} L_j(y) L_k(z) \quad (4)$$

and

$$\frac{\partial E_x}{\partial x}(1, y, z) = \sum_{j=0}^2 \sum_{k=0}^2 \alpha_{3jk} L_j(y) L_k(z), \quad (5)$$

respectively. Thus, continuity of $\partial E_x/\partial x$ can be enforced explicitly by equating α_{1jk} and α_{3jk} from adjacent bricks.

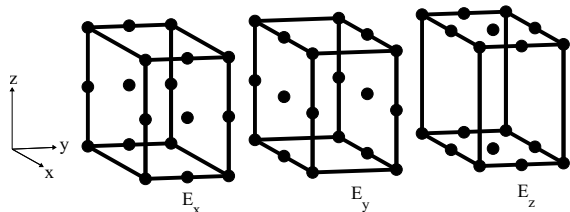


Fig. 1. Field component nodes

On each of the other four faces, $\partial/\partial x$ is a derivative that is tangential to each face and so continuity of $\partial E_x/\partial x$ is automatically satisfied if E_x is continuous everywhere on each face. This does not depend on using Hermite splines and it is also true using the standard nodal basis functions for tetrahedra [10]. Similar arguments hold for establishing the continuity of $\partial E_y/\partial y$ and $\partial E_z/\partial z$. Note that using the basis functions above, $\partial E_x/\partial y$, for example, is not guaranteed to be continuous across the face $y = 0$.

III. DIVERGENCE CONSTRAINTS

The derivatives of cubic Hermite splines can be expressed as a linear combination of second order Lagrange polynomials. Thus it is possible to expand the divergence of the field within a given brick using only polynomials of the latter type.

$$\nabla \cdot \mathbf{E}(x, y, z) = \sum_{i=0}^2 \sum_{j=0}^2 \sum_{k=0}^2 d_{ijk} L_i(x) L_j(y) L_k(z) \quad (6)$$

The divergence equation yields 27 linearly independent constraints per brick. A relatively simple set of equations is obtained if (6) is evaluated at the nodes of the Lagrange polynomials. In this case, the constraint at a given corner, for example, involves only coefficients corresponding to nodes at that corner. Furthermore, the constraints at a given corner due to different bricks are identical. These results would not be obtained if third order Lagrange polynomials were used in place of cubic Hermite splines. Similar results hold for the constraints at the midpoint of each edge and at the center of each face. Consequently, a linearly independent set of constraints over the entire mesh may be obtained using constraints from each corner, edge and face in the mesh, as well as constraints from the center of each brick. These constraints are implemented by eliminating coefficients in the curl matrices, resulting in modified curl matrices of reduced dimension. As a result of using the set of constraints described above, the number of non-zero elements in the modified curl matrices is less than the number of non-zero elements in the original curl matrices. A detailed explanation is omitted due to lack of space.

IV. CAVITY PROBLEM

Consider an empty cubic cavity with sides of unit length. The cavity modes are obtained by minimizing the functional

$$\mathcal{F}(\mathbf{E}) = \iiint_V \left[\frac{1}{\mu} (\nabla \times \mathbf{E})^2 - \omega^2 \epsilon \mathbf{E}^2 \right] dx dy dz \quad (7)$$

TABLE I
EIGENVALUES, ω^2 , OF CUBIC CAVITY. MULTIPLICITY IN PARENTHESES.

Exact	FEM
19.7392(3)	19.7399(3)
29.6088(1)	29.6095, 29.6099
49.3480(6)	49.3686(6)
59.2176(3)	59.2318(2), 59.2342, 59.2382, 59.2385(2)
78.9568(3)	78.9973(3)
88.8264(3)	88.8473, 88.8509, 88.8510, 88.8652(3)
98.6960(6)	98.9183(6)

subject to the constraint $\nabla \cdot \mathbf{E} = 0$ and the boundary condition $\hat{n} \times \mathbf{E} = 0$. The eigenvalues obtained with an $8 \times 8 \times 8$ mesh are shown in table I along with the exact values obtained analytically. There are no spurious modes.

V. CONCLUSION

A method for implementing divergence constraints in the finite element method has been discussed. The divergence constraints are linearly independent and sparse. In the description given above, a uniform mesh, similar to that used in the finite difference time domain method [11], is required. This work has already been extended for refined meshes with non-uniform brick size and for inhomogeneous objects. The divergence is modeled to second order accuracy and does not necessarily have to be zero or continuous. The divergence constraints can be implemented in a wide variety of problems, not just eigenvalue problems. The method is being extended to include non-brick elements.

REFERENCES

- [1] P. M. Morse and H. Feshbach, *Methods of Theoretical Physics*, vol. 2. New York: McGraw-Hill, 1953, pp. 1767-1773.
- [2] A. Konrad, A Direct Three-Dimensional Finite Element Method for the Solution of Electromagnetic Field Problems in Cavities, *IEEE Trans. Magn.*, vol. MAG-21, pp. 2276-2279, Nov. 1985.
- [3] A. J. Kobelansky and J. P. Webb, Eliminating spurious modes in finite-element waveguide problems by using divergence-free fields, *Electronics Letters*, vol. 22, pp. 569-570, May 1986.
- [4] Z. J. Cendes and S. H. Wong, C^1 Quadratic Interpolation Over Arbitrary Point Sets, *IEEE Computer Graphics and Applications*, Nov. 1987, pp. 8-15.
- [5] S. H. Wong and Z. J. Cendes, Combined finite element-modal solution of three-dimensional eddy current problems, *IEEE Trans. Magn.*, vol. 24, pp. 2685-2687, Nov. 1988.
- [6] J. C. Nedelec, Mixed Elements in R3, *Numer. Math.*, vol. 35, pp. 315-341, 1980.
- [7] G. Mur, Edge Elements, their Advantages and their Disadvantages, *IEEE Trans. Magn.*, vol. 30, pp. 3552-3557, Sept. 1994.
- [8] G. Mur, The fallacy of edge elements, *IEEE Trans. Magn.*, vol. 34, pp. 3244-3247, Sept. 1998.
- [9] G. Mur and I. E. Lager, On the causes of spurious solutions in electromagnetics, *Electromagnetics*, vol. 22, pp. 357-367, May 2002.
- [10] P. Silvester, Tetrahedral polynomial finite elements for the Helmholtz equation, *Int. J. Num. Meth. Engng*, vol. 4, pp. 405-413, May 1972.
- [11] K. S. Yee, Numerical solution of initial boundary value problems involving Maxwell's equations in isotropic media, *IEEE Trans. Antennas Propagat.*, vol. AP-14, pp. 302-307, May 1966.

Agglomeration-based algebraic multigrid for linear systems coming from edge-element discretizations

François Musy¹, Laurent Nicolas² and Ronan Perrussel²

¹ Institut Camille Jordan, CNRS UMR5208; ² Laboratoire Ampère, CNRS UMR5005
 Université de Lyon, École Centrale de Lyon, 69134 Écully cedex, France
 e-mails: firstname.name@ec-lyon.fr

Abstract—An algebraic multigrid algorithm based on element agglomeration is proposed for linear systems coming from edge-element discretizations. The edge prolongation operator satisfies commutativity and energy-minimization properties. Robustness is illustrated on 2D numerical examples.

Multigrid methods are beyond the most performing linear system solvers and these solvers are a key point in finite element method libraries. Here, we focus on the discretization on a triangular mesh with the lowest order edge element of

$$\operatorname{curl} \delta \operatorname{curl} \mathbf{U} + \gamma \mathbf{U} = \mathbf{f} \text{ on } \Omega \subset \mathbb{R}^2, \quad (1)$$

which gives rise to a linear system $Ax = f$. As solver we propose an Algebraic MultiGrid (AMG) algorithm which keeps a good efficiency with non-smooth functions δ and γ and with unstructured triangulations. The coarsening process is based on *element agglomeration*. A *low-energy* edge prolongator satisfying a *commutativity property* [1] is obtained from the solution of local linear systems. Numerical examples demonstrate the robustness of our method.

I. COMPONENTS OF THE ALGORITHM

A. Levels

Starting from an initial fine grid partitioned into triangles, we build a hierarchy of generalized meshes $\tau^h = (\mathcal{D}^h, \mathcal{A}^h, \mathcal{S}^h)$. $\mathcal{D}^h = \{D_i^h\}_{i \in I_{\mathcal{D}^h}}$ is a family of open polygons we call elements. On the finest mesh they are the original triangles. $\mathcal{A}^h = \{A_i^h\}_{i \in I_{\mathcal{A}^h}}$ is a family of open one-dimensional manifolds we call edges. $\mathcal{S}^h = \{S_i^h\}_{i \in I_{\mathcal{S}^h}}$ is a family of single points we call vertices. The coarsening procedure which builds a generalized mesh $\tau^H = (\mathcal{D}^H, \mathcal{A}^H, \mathcal{S}^H)$ from a generalized mesh $\tau^h = (\mathcal{D}^h, \mathcal{A}^h, \mathcal{S}^h)$ must satisfy constraints defined in [2], [3]. Moreover, any edge in family \mathcal{A}^H is a connected path of edges belonging to \mathcal{A}^h and has two different endpoints which are vertices in \mathcal{S}^H (Fig. 1). From the family

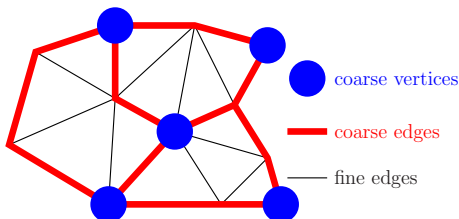


Fig. 1. Example of a coarse mesh τ^H builds from the finest mesh τ^h .

of generalized mesh $\tau^h = (\mathcal{D}^h, \mathcal{A}^h, \mathcal{S}^h)$, we define a family of oriented simple graphs. For each vertex S_p^h of \mathcal{A}^h a node p is created and 2 separate nodes p, q are connected by an arc each time an edge of \mathcal{A}^h has S_p^h and S_q^h as endpoints. An arc starts from a node p to a node q if $p < q$. The arc-node incidence matrices denoted G^h can be viewed as discrete gradient operators on the meshes.

B. Prolongation operator properties

For each couple of generalized meshes (τ^h, τ^H) , τ^H being obtained from τ^h by a coarsening procedure, we give us a nodal prolongator P^{nod} with a prescribed non-zero pattern and with all row sums equal to 1. We build then an edge prolongator P^{edg} with a prescribed non-zero pattern and with low-energy columns $(P^{\text{edg}})^e$, $e \in I_{\mathcal{A}^h}$. It must also satisfy a node-edge commutativity property [1]: $P^{\text{edg}}G^H = G^hP^{\text{nod}}$. The energy function on a mesh τ^h is defined by

$$g(x^e, e \in I_{\mathcal{A}^h}) = \sum_{e \in I_{\mathcal{A}^h}} \|x^e\|_{K^h}^2 = \sum_{e \in I_{\mathcal{A}^h}} (x^e)^t K^h x^e \quad (2)$$

where K^h is a sparse symmetric definite positive matrix. For its non-zero pattern we require that $K_{i,i'}^h = 0$ if both edges A_i^h and $A_{i'}^h$ do not belong to the interior of the closure of the same element. Such a property is satisfied on the finest mesh by the finite element matrix A .

To define the non-zero pattern of the nodal prolongator P^{nod} and the edge prolongator P^{edg} we mimic the situation in geometric multigrid on nested meshes:

- If S_p^h belongs to the interior of the closure of an element of \mathcal{D}^H , $P_{p,n}^{\text{nod}} = 0$ if S_n^H does not belong to its boundary.
- If S_p^h is an endpoint of an edge of \mathcal{A}^h included in edge A_e^H of \mathcal{A}^H with endpoints $S_{n_k}^H$, $k = 1, 2$; if $S_p^h = S_{n_k}^H$, $P_{p,n}^{\text{nod}} = 0, \forall n \neq n_k$, else $P_{p,n}^{\text{nod}} = 0, \forall n \neq n_1, n_2$.
- If edge A_i^h of \mathcal{A}^h is included in edge A_e^H of \mathcal{A}^H , $P_{ee'}^{\text{edg}} = 0, \forall e' \neq e$ (Fig. 2(a)).
- If edge A_i^h of \mathcal{A}^h is included in the interior of the closure of an element of \mathcal{A}^H , $P_{i,e}^{\text{edg}} = 0$ if A_e^H is not included in its boundary (Fig. 2(b)).

C. Solution of the constrained minimization problem

An element D_a^H of \mathcal{D}^H being fixed, we denote by $\{A_i^h\}_{i \in I_{\text{int}}}$ (resp. $\{A_i^h\}_{i \in I_{\text{bound}}}$) the family of edges of \mathcal{A}^h included in the interior of its closure $\overline{D_a^H}$ (resp. included in

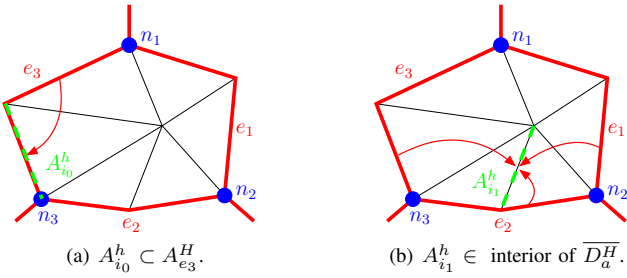


Fig. 2. A coarse element D_a^H . Coarse edges are in wide lines ($m = 3$). Coarse vertices are large bullets. Arrows indicate prolongation.

its boundary), $A_{e_1}^H, A_{e_2}^H, \dots, A_{e_m}^H$ the path of the edges of \mathcal{A}^H included in its boundary. This path defines on the coarse graph an elementary cycle of nodes denoted $n_1, n_2, \dots, n_m, n_1$.

Let A_i^h of \mathcal{A}^h with starting point p and ending point q . Two different cases have to be considered :

- 1) If $i \in I_{\text{bound}}$, then A_i^h is included in an edge A_e^H of \mathcal{A}^H (Fig. 2(a)). The non-zero entries of row i of P^{edg} are settled by the commutativity property since it writes

$$P_{i,e}^{\text{edg}} = P_{i,e}^* \text{ with } P_{i,e}^* = P_{p,n}^{\text{nod}} - P_{q,n}^{\text{nod}} \quad (3)$$

and S_n^H the starting endpoint of A_e^H .

- 2) If $i \in I_{\text{int}}$ (Fig. 2(b)) the commutativity property writes

$$\begin{aligned} \epsilon_{n_k}(e_{k-1})P_{i,e_{k-1}}^{\text{edg}} + \epsilon_{n_k}(e_k)P_{i,e_k}^{\text{edg}} \\ = P_{p,n_k}^{\text{nod}} - P_{q,n_k}^{\text{nod}}, \quad \forall k \in \llbracket 2; m \rrbracket, \end{aligned} \quad (4)$$

where $\epsilon_{n_k}(e)$ denotes 1 (resp. -1) if n_k is the starting point (resp. ending point) of the arc e .

We deduce that the non-zero entries of row i of P^{edg} are defined up to a real constant θ_i as follows :

$$\begin{aligned} P_{i,e_k}^{\text{edg}} = \epsilon_{n_k}(e_k)P_{i,e_k}^* + \theta_i \epsilon_{n_k}(e_k) \\ \text{with } P_{i,e_k}^* = \left[\sum_{l=2}^k P_{p,n_l}^{\text{nod}} - \sum_{l=2}^k P_{q,n_l}^{\text{nod}} \right]. \end{aligned} \quad (5)$$

It can be proved that the prolongator with the lowest energy is obtained with the values θ_i , $i \in I_{\text{int}}$ solution to a local linear system :

$$K^{D_a^H} \theta = K^{\overline{D_a^H}} b,$$

where $K^{D_a^H}$ (resp. $K^{\overline{D_a^H}}$) is the matrix obtained from the matrix K^h by keeping the entries $K_{i,j}^h$, $i, j \in I_{\text{int}}$ (resp. $K_{i,j}^h$, $i \in I_{\text{int}}, j \in I_{\text{int}} \cup I_{\text{bound}}$). b is given by:

$$b_i = -\frac{1}{m} \sum_{k=1}^m \epsilon_{n_k}(e_k)P_{i,e_k}^*, \quad i \in I_{\text{int}} \cup I_{\text{bound}}.$$

II. NUMERICAL RESULTS

The robustness of the method with parameters δ and γ is illustrated using examples of [4]. The domain is simply a unit square and Dirichlet boundary conditions are enforced.

In our strategy (Aggl. in the tables), coarse elements are obtained by double-pairwise agglomeration of elements. The results obtained by our method are compared with the Reitzinger and Schöberl (RS in the tables) strategy [1]. The

comparison is based on the convergence rate σ_{est} in energy norm: $\sigma_{\text{est}} = (\text{er}_k^t \text{Aer}_k / \text{er}_0^t \text{Aer}_0)^{1/(2k_f)}$ with er_k the error at the k -th iteration and k_f the iteration where the stopping criterion is reached. The smoother is a symmetric version of this proposed in [5] in a geometric multigrid context ((pre-, post-) smoothing steps in the tables).

For the homogeneous case in Table I, the two-grid convergence rate is quasi-independent of the size of the problem for both methods but the convergence rate of our method is better than for RS method and should lead to an optimal multigrid strategy. Moreover, increasing the number of pre- and post-smoothing steps significantly improves the convergence rate for the agglomeration. This behavior is confirmed in Table II and Table III for oscillating and discontinuous δ coefficients and two-grid and multigrid solver respectively. For this example, $f = C(2 + \sin(40\pi x))^2(2 + \cos(40\pi y))^2$ with $C = 10$ in $]0, 0.5[\times]0, 0.5[$, 10^4 in $]0.5, 1[\times]0, 0.5[$, 10^{-1} in $]0, 0.5[\times]0.5, 1[$ and 10^2 in $]0.5, 1[\times]0.5, 1[$.

TABLE I
RESULTS OBTAINED WITH A TWO-GRID SOLVER AND $\delta = \gamma = 1$.

	d.o.f. fine grid	736	3008	12160	48896
Aggl.	d.o.f. coarse grid	232	976	4000	16192
	(1, 1), σ_{est}	0.22	0.22	0.22	0.22
	(2, 2), σ_{est}	0.08	0.07	0.07	0.12
	(3, 3), σ_{est}	0.04	0.04	0.04	0.04
RS	d.o.f. coarse grid	184	751	3040	12224
	(1, 1), σ_{est}	0.62	0.68	0.70	0.71
	(3, 3), σ_{est}	0.52	0.64	0.69	0.70

TABLE II
RESULTS OBTAINED WITH A TWO-GRID SOLVER AND $\delta = f(x, y)$ AND $\gamma = f(y, x)$.

	d.o.f. fine grid	736	3008	12160	48896
Aggl.	d.o.f. coarsest grid	232	976	4000	16192
	(1, 1), σ_{est}	0.39	0.41	0.32	0.21
RS	d.o.f. coarsest grid	187	788	3087	12404
	(1, 1), σ_{est}	0.61	0.72	0.87	0.68

TABLE III
RESULTS OBTAINED WITH A W-CYCLE SOLVER AND $\delta = f(x, y)$ AND $f(y, x)$ ON THE GRID WITH 48896 DOFS.

	# grids	3	4	5	6	7
Aggl.	d.o.f. coarsest grid	4000	976	232	52	10
	(1, 1), σ_{est}	0.37	0.37	0.37	0.37	0.37
RS	d.o.f. coarsest grid	3279	844	216	55	11
	(1, 1), σ_{est}	0.83	0.89	0.93	0.95	0.97

The method is robust in 2D. The main difficulty for 3D problems is to find a fast and reliable agglomeration algorithm.

REFERENCES

- [1] S. Reitzinger and J. Schöberl, "An algebraic multigrid method for finite element discretizations with edge elements," *Numerical Linear Algebra with Applications*, vol. 9, no. 3, pp. 223–238, 2002.
- [2] J. K. Kraus and J. Synka, "An agglomeration-based multilevel-topology concept with application to 3D-FE meshes," Tech. Rep., RICAM, 2004.
- [3] J. E. Pasciak and P. S. Vassilevski, "Exact de Rham sequences of spaces defined on Macro-Elements in two and three spatial dimensions," *SIAM Journal on Scientific Computing*, vol. 30, no. 5, pp. 2427–2446, 2008.
- [4] J. Jones and B. Lee, "A multigrid method for variable coefficient Maxwell's equations," *SIAM Journal on Scientific Computing*, vol. 27, no. 5, pp. 1689–1708, 2006.
- [5] R. Hiptmair, "Multigrid method for Maxwell's equations," *SIAM Journal on Numerical Analysis*, vol. 36, no. 1, pp. 204–225 (electronic), 1999.

A 2D robust FE-FV mixed method to handle strong nonlinearities in superconductors

A. Kameni¹, S. Mezani¹, F. Sirois², D. Netter¹, J. L ev eque¹, B. Douine¹

¹ GREEN-UHP, Facult e des Sciences, BP. 239, 54506, Vandoeuvre-l es-Nancy, France

² Ecole Polytechnique de Montr al, Montr al, QC H3C 3A7, Canada

Email: smail.mezani@green.uhp-nancy.fr

Abstract — A robust numerical method based on 2-D mixed finite elements - finite volumes (FE-FV) allows the solution of diffusion problems in superconducting (SC) materials. The proposed approach handles the strong nonlinearity of the E(J) constitutive power law of high temperature superconductors (HTS). The method is tested in the case of a SC cylinder under a sinusoidal transport current. The current density distributions as well as the AC losses are computed. Comparisons to a FE analysis that uses the magnetic field as state variable show the validity of the proposed approach. It can be seen that the proposed method is very stable even for large n-values for which the FE method doesn't converge.

I. INTRODUCTION

The constitutive power law is widely used to characterize high temperature superconductors. It is written as:

$$J = J_c (E / E_c)^{1/n} \quad (1)$$

where J is the current density, E the electric field, E_c the critical electric field, J_c the critical current density and n the power law exponent. $n=1$ corresponds to a normal conductor and $n=\infty$ represents the critical state model suggested by Bean.

Finite element methods are widely used to compute the magnetic field distribution in superconductors using different formulations [1, 2]. Unfortunately, the use of (1) leads to numerical oscillations and convergence problems for high n-values (typically for $n>50$).

We propose a mixed FE-FV discretization of the electric field diffusion in HTS materials. This approach is shown to be robust for n values up to 200. It has been successfully used in solving nonlinear diffusion-convection-reaction equations in porous media [3].

II. PRINCIPLE OF THE METHOD

We set $u=E/E_c$, $\beta(u)=J/J_c$, and $c=\mu_0 J_c E_c$.

The superconductor has a vacuum magnetic permeability μ_0 . In 2D Cartesian problems, J and E are scalar quantities having only one component in the z direction. The SC domain is noted Ω and its boundary Γ .

Using Maxwell equations and the constitutive law (1), the problem to solve is:

$$\begin{cases} c \frac{\partial \beta(u)}{\partial t} - \Delta u = 0 & \text{in } \Omega \\ \vec{\nabla} u \cdot \vec{\nu} = C_b(t) & \text{on } \Gamma \end{cases} \quad (2)$$

The boundary condition on Γ results from the variation of the magnetic field according to Faraday's law:

$$C_b(t) = E_c^{-1} (\partial B_y / \partial t, -\partial B_x / \partial t) \cdot \vec{\nu} \quad (3)$$

B_x, B_y are respectively the x, y components of the flux density and $\vec{\nu}$ is the outward normal vector on Γ .

The method exposed here exploits the duality of the FE and FV meshes as well as the footbridge operators. It is applied to the weak formulation of (2) in the time interval $[t_p, t_{p+1}]$:

$$\begin{aligned} \int_{\Omega} c \frac{\beta(u^{p+1}) - \beta(u^p)}{\Delta t_p} \varphi d\Omega - \int_{\Omega} \vec{\nabla} u^{p+1} \cdot \vec{\nabla} \varphi d\Omega \\ - \int_{\Gamma} \vec{\nabla} u^{p+1} \cdot \vec{\nu} \varphi d\Gamma = 0 \end{aligned} \quad (4)$$

Where φ are a set of FE base functions and u^p is the solution at instant t_p and Δt_p the time step.

A. FV mesh construction

From a triangulation of Ω , the FV partition is obtained as shown in Fig.1.

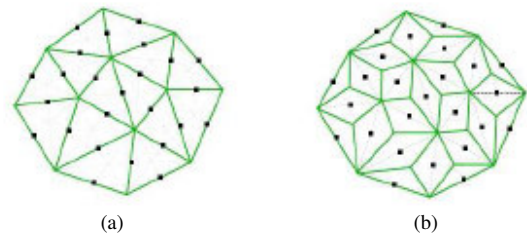


Fig. 1. Association of each node of the FE mesh to the cells of the FV mesh: we link the centers of gravity of two contiguous triangles through the vertex of their common edge.

(a) The nodes N_i correspond to the middle of the edges

(b) The nodes N_i correspond to the center of the cells D_i

B. Footbridge operators

Let u^{FE} and u^{FV} be the respective solutions of the FE and FV approaches. The footbridges operators $\pi_{EV} (\pi_{EV}(u^{FV}) = u^{FE})$ and $\pi_{VE} (\pi_{VE}(u^{FE}) = u^{FV})$ between the FE and the FV approximation spaces are well described in [4]. They are defined as:

9. Numerical techniques

$$\int_{\Omega} |\pi_{EV}(u) - u|^2 d\Omega = \min_{w \in FE} \int_{\Omega} |w - u|^2 d\Omega \quad (5)$$

$$\int_{\Omega} \pi_{VE}(u) \varphi d\Omega = \int_{\Omega} u \varphi d\Omega \quad (6)$$

The basis functions of the FV approximation space are obtained from the indicatrix functions of each cell of the FV mesh.

The first order FE base functions φ_i are constructed on the nodes N_i of the FE triangulation. Each of them can be prolonged to the corresponding FV cell. In so doing, we obtain another FE space approximation. Using the footbridge operators (5) and (6), we prove that $u^{FE} = u^{FV}$ [4].

C. Numerical scheme

The numerical discretization of the Laplacian operator is well established using the FE method whereas it is not adapted to the strong nonlinearity of the β term. Instead, we use the FV method to deal with this nonlinear term:

$$\int_D \frac{\beta(u^{p+1}) - \beta(u^p)}{\Delta t_p} dD = \frac{\beta^{p+1} - \beta^p}{\Delta t_p} D \quad (7)$$

Where D is the surface of a FV cell and β^p is the mean value of $\beta(u^p)$.

Hence, using the footbridge operators, we combine FE-FV methods to take advantage of both of them in the same numerical scheme.

In the FV method, the flux $\Phi_{i,j}$ between two adjacent cells i and j must be continuous. The mixed numerical scheme is justified if the diffusion on a FE node is equal to the convection in the FV cell. This leads to:

$$\underbrace{\int_{D_i} \text{div}(\vec{v}u) dD_i}_{FV} = \underbrace{\int_{\Omega} \vec{v}u \cdot \vec{\nabla} \varphi_i d\Omega}_{FE} \quad (8)$$

To ensure the equality in (8), the $\Phi_{i,j}$ are constructed from the mass matrix coefficient $S_{i,j}$ of the FE discretization as follows:

$$\sum_{j \neq i} |D_i \cap D_j| \Phi_{i,j} = - \sum_j S_{i,j} u_j \quad (9)$$

If we define $S_{i,i} = - \sum_{j \neq i} S_{i,j}$, the local conservation property of the FV formulation is ensured.

For the internal FV cells, the discrete problem is written as:

$$c \frac{\beta_i^{p+1} - \beta_i^p}{\Delta t_p} D_i = \sum_j S_{i,j} u_j^{p+1} \quad (10)$$

and for the boundary cells, we write:

$$c \frac{\beta_i^{p+1} - \beta_i^p}{\Delta t_p} D_i = \sum_j S_{i,j} u_j^{p+1} + |\Gamma_i| C_b^{p+1} \quad (11)$$

The obtained nonlinear system of algebraic equations is solved using a Newton-Raphson method.

III. APPLICATION EXAMPLE

We consider a SC cylinder having a radius of 1.5 mm. The SC material is characterized by $n=25$, $J_c=14.15$ A/mm² and $E_c=10^{-4}$ V/m.

The cylinder is submitted to a sinusoidal transport current $i(t)=I_{max} \cdot \sin(2\pi ft)$ ($f = 0.5$ Hz and $I_{max} = 40.8$ A). B_x, B_y used in the boundary condition (3) are obtained by Ampere's theorem.

We have compared in Fig.2, the instantaneous self field losses obtained by the FE-FV method and these issued from a pure FE method based on H-formulation [2]. The agreement is good.

However, for $n=200$ the FE method didn't converge. In this case, the average AC losses obtained by our method are 0.024W/mm. The Bean formula gave 0.028 W/mm which seems to validate the FE-FV method in the case of strong nonlinearity.

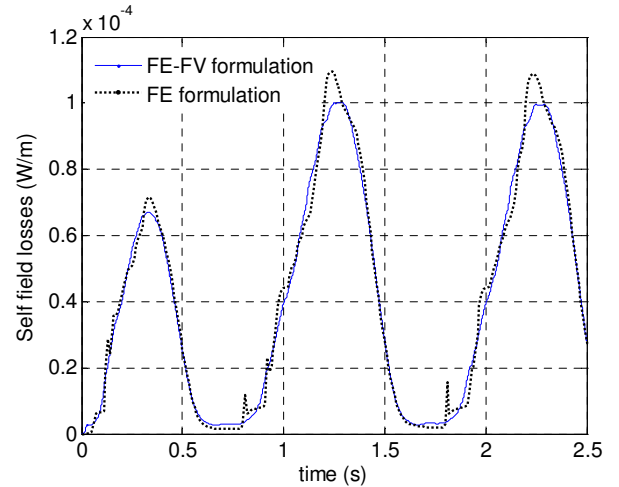


Fig. 2. Comparison of self field losses

IV. REFERENCES

- [1] E. Vinot, G. Meunier and P. Tixador, "Different formulations to model superconductors," *IEEE Trans. Magn.*, 36(4), 1226-1229, 2000.
- [2] R. Brambilla, F. Grilli and L. Martini, "Development of an edge-element model for AC losses computation of high-temperature superconductors," *Supercond. Sci. Technol.*, vol. 19, 1-9, 2006.
- [3] R. Eymard, D. Hilhorst and M. Vohralik, "A combine finite volume-nonconforming/Mixed-hybrid finite element scheme for degenerate parabolic problems," *Numer Math*, 105, 73-131, 2006.
- [4] F. Pascal and J.M. Ghidaglia, "Footbridge between finite volumes and finite elements with applications to CFD," *Internat. J. Numer Methods Fluids*, 37(8), 951-986, 2001.

A Posteriori Error Estimation and Adaptive Mesh Refinement Controlling in Finite Element Analysis of 3D Steady State Eddy Current Fields

Jinbiao Li^{1,2}, Dexin Xie¹ and Xiaoming Liu¹

¹School of Electrical Engineering, Shenyang University of Technology, ²CHINT Electric CO. Ltd
111, Shenhao West Road, Shenyang Economic & Technical Development Area, Shenyang, Liaoning 110178, China
xiebaiy@mail.sy.ln.cn

Abstract — Several methods of a posteriori error estimation and adaptive refinement controlling in finite element analysis of 3D steady state eddy current field is researched in this paper. An improved Z-Z method is proposed. The numerical models of TEAM Problem 7 and 21A are used to verify the validity of the method presented.

I. INTRODUCTION

The finite element (FE) analysis of 3D steady state eddy current fields plays an important role in performance evaluation of electrical devices and non-destructive testing with eddy current detection. The complicated configuration and very small skin depth of the metal parts in the calculated region make the effective FE analysis rather difficult. The a posteriori error estimation and adaptive mesh generation provide an efficient approach for dealing with the problem. Some researches have been done regarding these subjects. A comparison between complementary algorithm and energy method applied to eddy current detection was presented in [1]. The residual method used in a posteriori error estimation of eddy current field analysis [2] was described by [3] and [4]. Ref. [5] employed Z-Z method [6] in the eddy current analysis of moving conductors. In this paper, a posteriori error estimation and adaptive mesh refinement using the Z-Z method are described and improved for the 3D eddy current field analysis using the pair of magnetic vector potential A and electric scalar potential ϕ .

II. GOVERNING EQUATIONS IN COMPLEX DOMAIN

According to [7], a 3D steady state eddy current field boundary value problem can be expressed as

$$\text{in } \Omega_1 : \begin{cases} \nabla \times \nu \nabla \times A - \nabla \nu \nabla \cdot A + j\omega\sigma A + \sigma \nabla \phi = \mathbf{0} \\ \nabla \cdot (-j\omega\sigma A - \sigma \nabla \phi) = 0 \end{cases} \quad (1)$$

$$\text{in } \Omega_2 : \nabla \times \nu \nabla \times A - \nabla \nu \nabla \cdot A = \mathbf{J}_s \quad (2)$$

with certain boundary conditions under the sinusoidal excitation, where Ω_1 and Ω_2 denote the eddy current region and non-eddy current region respectively. Based on the theory of electromagnetic field the magnetic flux density and electric field intensity are given by

$$\mathbf{B} = \nabla \times \mathbf{A} \quad (3)$$

and

$$\mathbf{E} = -j\omega \mathbf{A} - \nabla \phi \quad (4)$$

III. A POSTERIORI ERROR ESTIMATION FOR NODE-FINITE ELEMENT ANALYSIS OF EDDY CURRENT FIELD WITH POTENTIAL PAIR OF A - ϕ

The Z-Z method was proposed aiming at the second order elliptic equations, and it is proved that the method is also efficient for the a posteriori error estimation of FE Analysis for non-elliptic problems. However, there are not many papers applying this method to the eddy current field analysis. Considering the principle of Z-Z [6] and the property of eddy current field boundary value problems, the a posteriori error estimation is given by

$$\eta_e = c_1 \|\mathbf{B}^* - \mathbf{B}_h\| + c_2 \|\mathbf{E}^* - \mathbf{E}_h\| \quad (5)$$

where \mathbf{B}_h and \mathbf{E}_h express the calculated value, \mathbf{B}^* and \mathbf{E}^* for the recovery value of the flux density and electric field in an element respectively, c_1 and c_2 denote the constants related to the size of the element, and $\|\bullet\|$ expresses the energy norm. In some paper only the first term in (5) is used when carrying out the a posteriori error estimation using the Z-Z method. It is not complete for analyzing of the eddy current case. Based on the numerical experiments by the authors, if the second term of (5), which is closely related to the electric current density, is neglected in the eddy current region, the computational precision of eddy current losses can not be ensured easily, especially for the case of skin depth less than 1 mm.

Furthermore, equation (5) provides the a posteriori estimation of the discretization error in the whole solved region, but does not directly give the evaluation of the computational precision for the eddy current losses, in which the engineers are interested. Therefore, when determining the criterion for the end of adaptive iterations, the eddy current losses should be used directly.

\mathbf{B}^* and \mathbf{E}^* are obtained through the Least Square Fitting (LST) in the patch of elements based on the Z-Z method [6]. In our case, the LST is used only at the boundary and the interface of different materials, with the Inverse Distance Weighting (IDW) method applied to the recovery calculation of \mathbf{B}^* and \mathbf{E}^* in the patch of elements. This method proposed is called Combined IDW with Least square fitting (CIL) in the following text. It is obvious that the computation effort of the CIL method is much less than the original Z-Z method.

IV. COMPUTATION RESULTS AND ANALYSIS

To verify the method presented in this paper, the TEAM Workshop problem 7 and Problem 21A are used as the examples. Fig. 1 shows the comparison of the error estimation versus the node number using the Z-Z method, CIL approach and uniformed refinement for the adaptive FE analysis of Problem 7. The x - and y -axis are both in logarithmic scale. Fig. 2 and Fig. 3 are the initial mesh and the mesh of fifth adaptive refinement respectively. It can be seen from Fig. 1 that the Z-Z method and CIL approach have the similar convergent property. Compared with the uniformed refinement, Z-Z and CIL methods are of higher computational efficiency. Taking the mesh refinement of Fig. 2 and Fig. 3 into account, it is concluded that the Z-Z and CIL methods can be used as the error indicator for the adaptive FE analysis of 3D eddy current fields.

The eddy current losses versus the node number of the TEAM Workshop Problem 21A with the adaptive mesh refinement controlling of Z-Z, CIL and CIL* method respectively are shown in Fig. 4, where CIL* expresses the method of CIL including only the first term of (5). In view of the complex governing equations, the relative permeability of the steel plate in Problem 21A is assigned approximately as a constant of 1000. According to the measured value of 9.28W [8] and comparing the loss curves with the three methods in Fig. 4, it is seen that for the problem with small skin depth, like Problem 21A, using (5) to fulfill error estimation is appropriate, while the computation without the second term of (5) will result in relatively large computational deviation of the eddy current loss.

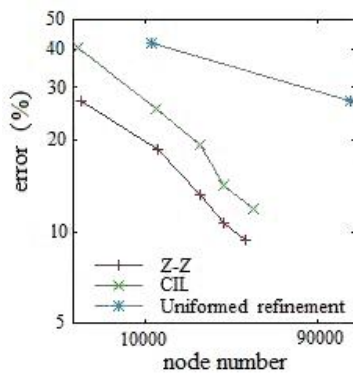


Fig. 1 A posteriori error versus the node number of TEAM Problem 7

V. CONCLUSIONS

The Z-Z method used in the FE analysis of 3D steady state eddy current field is described, and a more efficient method of CIL is proposed in this paper. The issues how to apply the Z-Z and CIL method to conduct the mesh refinement are researched. The numerical models verify the validity of the method proposed.

VI. REFERENCES

[1] G. Krebs, A. Abakar, S. Clenet, Comparison of Error Estimators in Eddy

Current Testing. *IEEE Trans. on Magn.*, 45(3): 968-971, 2009

[2] Mark Ainsworth, J. Tinsley Oden, A Posteriori Error Estimation in Finite Element Analysis. New York: A Wiley-Interscience Publication, 2000
 [3] W. Zhang, F. Zhang, Adaptive finite element frequency domain method for eddy current problems. *Compu. Methods Appl. Mech. Engrg.*, 197: 1233-1241, 2008
 [4] R. Beck, R. Hiptmair, R. Hoppe, et al, Residual based a posteriori error estimators for eddy current computation. *M²AN*, 34(1): 159-182, 2000
 [5] K. Yamazaki, Adaptive Finite Element Meshing for Eddy Current Analysis of Moving Conductor. *IEEE Trans. on Magn.*, 2004, 40(2): 993-996
 [6] O.C.Zienkiewicz, R.L.Taylor. The finite element method, volume 1: the basis, 5th edition. New York: Butterworth-Heinemann, 2005, 365-398
 [7] Oszkar Biro, Kurt Preis, On the Use of the Magnetic Vector Potential in the Finite Element Analysis of Three-Dimensional Eddy Currents. *IEEE Trans. on Magn.*, 1989, 25(4): 3145-3159
 [8] Zhiguang Cheng, Norio Takahashi, TEAM-based Benchmark Family: Problem 21/21^a/21^b/21^c. <http://www.compumag.co.uk/team.html>

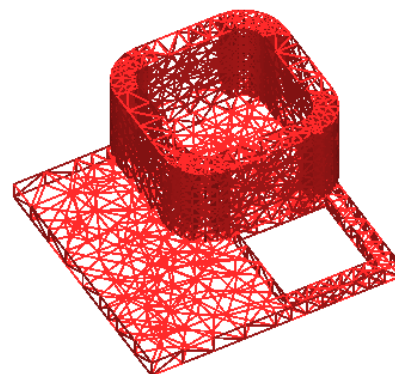


Fig. 2 Initial meshes on the surface of coil and plate of Problem 7

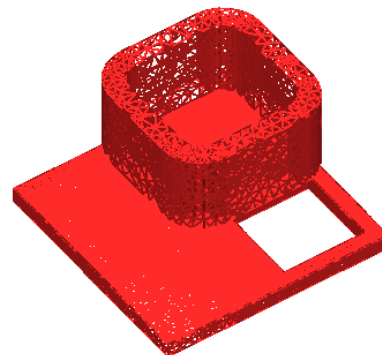


Fig. 3 The fifth meshes on the surface of coil and plate of Problem 7

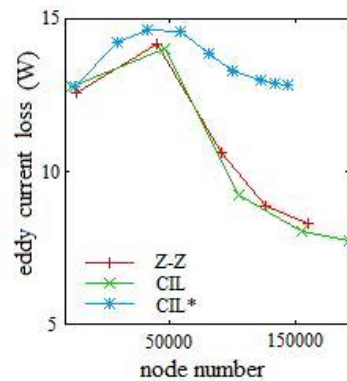


Fig. 4 Eddy current loss versus the node number of TEAM Problem 21A

Auto adaptive interface treatment for the EFGM in electromagnetic problems

Carlos A. S. J. Gulo*, José Márcio Machado[§], Gleber Nelson Marques*

Abstract—The interpolating Element Free Galerkin Method (EFGM) combined with the domain truncation technique has been shown to be an easy and efficient technique for treating physical discontinuities in the Poisson’s equation. A good accuracy for this approach is achieved when the material interfaces lines are properly refined. This work describes an auto adaptive algorithm for handling the refinement process of such interfaces.

Index Terms—Galerkin method, interface treatment, auto adaptive algorithm.

I. INTRODUCTION

THE EFGM [1] is an attractive meshfree method for solving partial differential equations (pde) whose applications have been reported in the specialized literature of many fields of science and engineering, e.g. computational mechanics [1] and electromagnetism [2], magnetohydrodynamic (mhd) [3], quantum physics [4] and recently plasma simulations [5].

The EFGM theoretical foundations rely on the idea of constructing a functional basis composed by the so called (EFGM) shape functions. These shape functions are constructed from a local Moving Least Square (MLS) approximation performed on the discretization points, and provide the required functional basis for the well-known Galerkin discretization procedure for solving pde’s. Different from the Finite Element Method (FEM), the standard approach of the EFGM [1] does not provide interpolating EFGM approximations. In this case, additional techniques must be used for enforcing the prescribed boundary conditions as well as the material interface conditions for a correct physical description of the phenomenon and for avoiding spurious oscillations.[6]

Naturally the requirement of such techniques is undesirable due to: 1) the increasing of the total number of unknowns caused by most used techniques, e.g. Lagrange Multipliers and Penalty methods, and 2) the loss of the positive definite character of the stiffness matrix in the final linear system [7], [6]. The interpolating EFGM-domain truncation approach proposed in [8] completely avoids the use of these additional techniques at the cost of carefully take care about the boundary lines, specially the material interface ones. Depending on the complexity of the device geometry, an iterative procedure of inspecting approximations near the material interfaces of the domain may take place and become a boring and time-consuming task.

[§] José Márcio Machado is with São Paulo State University, São José do Rio Preto, São Paulo (email: jmarcio@ibilce.unesp.br). * Carlos A. S. J. Gulo and Gleber Nelson Marques are with Mato Grosso State University, Alto Araguaia, Mato Grosso (email: sander@unemat.br and gleber.nmarques@gmail.com).

[†]The authors thank FAPEMAT for the project financial support (Grant n. 002.229/2007).

This paper describes an auto adaptive algorithm for treating material interface conditions by using the interpolating EFGM together the modified domain truncation technique [6].

A. The interpolating EFGM approach

Suppose we are interested in solving the Poisson’s equation for the unknown function $u(x)$ in a domain containing material interfaces. Consider a set of discretization points at which the approximation $u^h(x)$ will be performed. To each node is associated a weight function $w_l(x)$ whose support defines the nodal influence domains. Starting from a local MLS approximation whose coefficients are determined by the minimization of a weighted L_2 norm of the error between the local MLS approximation and the nodal variables u_l , one can obtain the EFGM shape functions $\phi_l(x)$:

$$\phi_l(x) = \sum_j^m p_j(x) \left(A^{-1}(x) B(x) \right)_{jl}, \quad (1)$$

often found in the following expansion:

$$u^h(x) = \sum_l \phi_l(x) \cdot u_l. \quad (2)$$

The matrices \mathbf{A} and \mathbf{B} are defined as usual [1], [6], [2]. Our code implements the consistency approach for avoiding the inversion of matrix \mathbf{A} . [9]

The interpolating character of the EFGM approximation can be obtained by defining singular weight functions $\tilde{w}_i(x)$:

$$\tilde{w}_i(x) = w_i(x) / (1 - w_i(x) + \varepsilon), \quad (3)$$

where the parameter ε is a prescribed precision for the singularity, and the truncated Schwarz function was chosen as $w_i(x)$ [6]. Since the interpolating condition is satisfied only punctually at the nodes, a more refined discretization along the boundaries and interfaces can provide a correct global and local description of the phenomenon.[6]

B. Treatment of the interface conditions

The presence of material interfaces in electromagnetic problems leads to field discontinuities. Since the proposed approximation inherits the continuity of the Schwarz function, the state variable approximation and its derivatives will be continuous and differentiable functions. Thus, additional techniques must be used for obtaining a correct description of the physical field discontinuity.

We use the modified domain truncation technique for interpolating EFGM formulation [6], where the influence domains

of the nodes localized at a specified material are truncated across material interfaces. This means that nodes localized in a specified material sub-domain S_1 will only participate in the approximation of evaluation points belonging the same material, S_1 . The discontinuous approximations of each material sub-domain are connected by the nodes distributed along the material interfaces which participate in the approximation of points belonging to both materials. No Lagrange multipliers are required due to the interpolating character of the approximation. It can be mentioned that the error for computing the field near the interface is an increasing function of the magnitude of the physical discontinuity and decrease for more refined discretizations. [6]

C. Auto adaptive algorithm for treating interface conditions

We take as a reference problem the computation of a stationary electric field involving different conductor materials, however, the procedures here developed can be applied for computing stationary fields associated to the Poisson's equation in inhomogeneous media. From theory the physical discontinuity of the normal component of the electric field crossing the material interface of two conductors, is given by

$$\sigma_1 E_{1n} = \sigma_2 E_{2n}, \quad (4)$$

from which we can estimate a mean local error near the interface for a set of arbitrary test points distributed parallel and very close, δ , the interface line as show in Fig.1

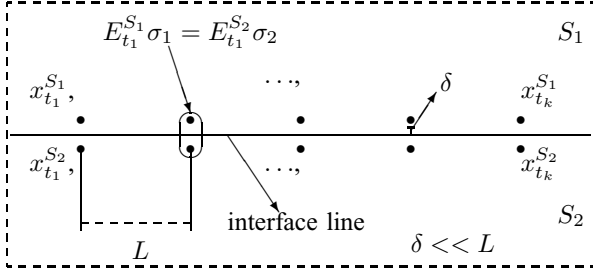


Fig. 1. Distribution pattern of interface test-points

Lets $x_{t1}^{S1}, \dots, x_{tk}^{S1}$ be the interface test-points belonging material S_1 and, correspondingly $x_{t1}^{S2}, \dots, x_{tk}^{S2}$ be the ones belonging to material S_2 . Similarly, let $E_{t1}^{S1}, \dots, E_{tk}^{S1}$ and $E_{t1}^{S2}, \dots, E_{tk}^{S2}$ be the computed normal field component at the interface test-points. If $\hat{E}_{t1}^{S2}, \dots, \hat{E}_{tk}^{S2}$ are the theoretically expected values at the test points $x_{t1}^{S2}, \dots, x_{tk}^{S2}$ algebraically obtained from (4), then the mean relative local error in the approximation of the normal field component at the specified interface test-points can be defined as:

$$E_I = \sum_{t_i=t_1}^{t_k} \left| \frac{E_{t_i}^{S2} - \hat{E}_{t_i}^{S2}}{k \cdot \hat{E}_{t_i}^{S2}} \right| = \sum_{t_i=t_1}^{t_k} \left| \frac{E_{t_i}^{S2} - \left(\frac{\sigma_{S1}}{\sigma_{S2}} E_{t_i}^{S1} \right)}{k \cdot \hat{E}_{t_i}^{S2}} \right|. \quad (5)$$

By using the above defined interface error we propose an auto adaptive algorithm as follows:

1) After the preprocessing stage of the simulation, e.g., the device design and physical specifications, generate the sets of test-points for each material interface of interest;

- 2) Compute the approximation at the given discretization nodes;
- 3) Compute the component of the electric field normal to the material interface line for all the interface test-points;
- 4) Compute the mean relative errors E_I (5) for each set of interface test-points;
- 5) For each interface, compare its E_I (5) with a prescribed interface precision ε_I , and, if ($E_I \leq \varepsilon_I$) :
 - a) then, the prescribed precision has been achieved for this interface, consider next interface;
 - b) else ($E_I > \varepsilon_I$), refine the discretization nodes along this interface and consider next interface;
- 6) If the number of discretization nodes has changed (this means that step 5.b was executed) then return to step 2.

The fast h -convergence of the EFGM has already been demonstrated in previous works for stationary electric [6], magnetic fields [8] as well as in scattering problems [2], which have encouraged a software engineering for including new object-oriented classes of such auto adaptive algorithms in our EFGM code.

II. FINAL DISCUSSION AND FURTHER DEVELOPMENTS

The auto adaptive algorithm proposed in this work is based on the error estimative obtained from the physical interface conditions theoretically expected. It automates an iterative process of inspecting the approximation errors near physical discontinuities. This work has being developed in the context of the LExVE (Laboratory for Virtual Experiences in Engineering) research project associated with the LEVSOFT system [10]. A rigorous analysis of the performance and robustness of the proposed algorithm, is being carried out and will be further reported.

REFERENCES

- [1] T. Belytschko, Y. Y. Lu, and L. Gu, "Element free galerkin methods," *Int. J. for Num. Meth. in Eng.*, vol. 37, pp. 229–256, 1994.
- [2] A. Manzini and O. Bottauscio, "Element-free galerkin method for the analysis of electromagnetic-wave scattering," *IEEE Trans. Magn.*, vol. 44, no. 6, pp. 1366–1369, June 2008.
- [3] S. L. L. Verardi, J. M. Machado, and Y. Shiyou, "The application of interpolating mls approximations to the analysis of mhd flows," *Finite Elements in Anal. and Design*, vol. 39, pp. 1173–1187, 2003.
- [4] M. Sugawara, "Adaptive basis set for quantum-mechanical calculation based on element-free galerkin method," *Chem. Phys. Lett.*, vol. 314, pp. 522–528, 1999.
- [5] G. N. Marques, A. J. Preto, S. Stephany, A. Passaro, A. C. J. Paes, and N. M. Abe, "Uma abordagem meshfree para simulao de plasmas no colisionais," in *Proc. of the XXVIII Iberian Latin Amer. Congr. on Comput. Methods in Eng.*, Porto Portugal, June 2007.
- [6] G. N. Marques, J. M. Machado, S. L. L. Verardi, S. Stephany, and A. J. Preto, "Interpolating efgm for computing continuous and discontinuous electromagnetic fields," *COMPEL*, vol. 26, no. 5, pp. 1411–1438, June 2007.
- [7] G. R. Liu, *Meshfree Methods, Moving Beyond the Finite Element Method*. CRC Press, 2002.
- [8] G. N. Marques, J. M. Machado, S. L. L. Verardi, and Y. Shiyou, "An application of the element free galerkin method with interpolating shape functions to the analysis of electromagnetic fields in inhomogeneous media," in *COMPUMAG*, vol. 2, 2005, pp. 68–69.
- [9] P. Breitkopf, A. Rassineux, G. Touzot, and P. Villon, "Explicit form and efficient computation of mls shape functions and their derivatives," *Int. J. for Num. Meth. in Eng.*, vol. 48, pp. 451–466, 2000.
- [10] A. Passaro, N. M. Abe, M. Franco, J. M. Machado, and Y. Shiyou, "Simulation of needle-type corona electrodes by the finite element method," in *Plasma Sci. & Tech.*, vol. 9, 2007, pp. 698–701.

Automatic treatment of multiply connected regions in Integral Formulations

Guglielmo Rubinacci¹ and Antonello Tamburrino²

¹Ass. Euratom-ENEA-CREATE, DIEL, Università di Napoli Federico II, Via Claudio 21, 80125 Napoli, Italy

²Ass. Euratom-ENEA-CREATE, DAEIMI, Università di Cassino, Via Di Biasio 43, 03043 Cassino, Italy
rubinacci@unina.it, tamburrino@unicas.it

Abstract— This paper deals with the volume integral formulation of the eddy current problem in terms of the electric vector potential. Its aim is to present a simple topological algorithm for finding the additional degrees of freedom required in the discretization of a multiply connected region when using edge elements. The algorithm is completely automated and it is based, as other previous approaches, on the application of the spanning tree technique on the edge element based topological graph defined on the boundary surface of the conducting domain.

I. INTRODUCTION

In several numerical formulation of the eddy current problem, the field in the vacuum region is conveniently expressed in terms of the magnetic scalar potential. However this potential may become multi-valued when the source region is multiply connected. For this case, it is necessary to introduce suitable cuts for making the domain simply connected or, more rigorously, loop-free. This topic has draw considerable attention [1-4] and several automatic algorithms for finding cuts have been already proposed.

In this respect, our problem is different because it involves the topological treatment on the surface corresponding to the boundary of the eddy current region. The integral formulation we deal with is written in terms of the eddy current density vector whose solenoidality is assured by expressing it as the curl of the electric vector potential \mathbf{T} . The uniqueness of \mathbf{T} is imposed on the discrete by adopting edge elements shape functions and by imposing the tree-cotree gauge condition [5-6]. When the conducting region is multiply connected, a set of boundary edges may not be the boundary of a simply connected patch lying on the boundary of the conductor. For this reason the boundary condition assuring that the current density does not flow outside the domain cannot be imposed by zeroing the tangential component of \mathbf{T} on the boundary. As a matter of fact the circulation of \mathbf{T} on a closed line lying on the boundary may be related to current loops inside the domain. The main ideas behind the proposed approach have been already discussed in previous papers [6-8]. In these cases the *nonlocal* additional degrees of freedom were automatically obtained in an algebraic way as the columns spanning the null space of the incidence matrix relating fluxes across elementary boundary faces and edges lying on the boundary. In this paper, we present a much simpler approach that exploits the spanning tree technique applied to the topological graph made of boundary facets (nodes) and edges for automatically finding these *nonlocal* DOFs. The underlying idea of *nonlocal* basis functions was also discussed by Kettunen in [9]. In that frame, he pointed out that “these nonlocal functions can be rather

easily found once the representative Σ and γ of the equivalence classes are known. (In many cases – although not always – it is easy to say what the Σ and γ cuts are. The difficulty is to detect them automatically)”.

II. THE INTEGRAL FORMULATION

The reference geometry which we deal with is made by a multiply connected domain, with several feeding electrodes on its boundary. We solve the eddy current problem using the integral formulation described in [5-6]. Expressing the electric field as

$$\mathbf{E} = -\frac{\partial \mathbf{A}}{\partial t} - \nabla \phi \quad (1)$$

and using the Biot-Savart law for calculating the magnetic vector potential \mathbf{A} , the Ohm’s law, imposed in the weak form gives:

$$\begin{aligned} & \text{find } \mathbf{J} \in Q \text{ such that} \\ & \int_{\Omega} \mathbf{w} \cdot \eta \mathbf{J} dV + \int_{\Omega} \mathbf{w}(\mathbf{r}) \cdot \frac{\partial}{\partial t} \int_{\Omega} \frac{\mathbf{J}(\mathbf{r}')}{|\mathbf{r} - \mathbf{r}'|} dV' dV + \int_{S_e} \phi \mathbf{w} \cdot \hat{\mathbf{n}} dS = \\ & - \int_{\Omega} \mathbf{w} \cdot \frac{\partial}{\partial t} \mathbf{A}_0 dV, \quad \mathbf{w} \in Q \end{aligned} \quad (2)$$

where $Q = \{ \mathbf{q} | \nabla \cdot \mathbf{q} = 0, \mathbf{q} \cdot \hat{\mathbf{n}} = 0 \text{ on } \partial\Omega \setminus S_e \}$ and S_e is the surface of all the electrodes. In order to guarantee that $\mathbf{J} \in Q$, we impose $\mathbf{J} = \nabla \times \mathbf{T}$ in Ω , where the uniqueness of \mathbf{T} is assured by a two component gauge condition [5]

III. THE NUMERICAL FORMULATION

The conducting domain is discretized in a number of finite elements, such that each electrode is approximated by a set of boundary mesh facets. The vector potential \mathbf{T} is expressed in terms of edge element shape functions \mathbf{N}_k as $\mathbf{T} = \sum_k I_k \mathbf{N}_k$, so that $\mathbf{J} = \sum_k I_k \nabla \times \mathbf{N}_k$. The gauge condition is directly imposed on the shape functions by giving a tree-cotree decomposition of the mesh and retaining only the degrees of freedom associated with the edges of the cotree. The internal edges of the co-tree are retained with no additional manipulation. On the other hand, a special treatment is required for the n_c active edges belonging to the boundary $\partial\Omega$ of the conducting domain Ω , in order to force $\mathbf{J} \cdot \hat{\mathbf{n}} = 0$ over $\partial\Omega$ [6-8].

In a simply connected region without electrodes, boundary condition $\mathbf{J} \cdot \hat{\mathbf{n}} = 0$ can be easily imposed, by forming the tree firstly connecting boundary nodes with boundary edges and then zeroing the cotree edges belonging to the boundary. As a

matter of fact in this case any line integral on a closed line made by edges lying on the boundary represents a current flux crossing a surface which lies on the boundary.

IV. MULTIPLY CONNECTED REGIONS

With reference to a multiply connected region, we firstly discuss the case in the simpler hypothesis that the boundary of the conducting domain is without electrode facets. We propose the following procedure to find the nonlocal additional DoFs required. The procedure is repeated for each separate piece.

We firstly supply few definitions:

- Dual vertex: facet
- Dual edge: edge
- Dual graph: the graph made by considering the facets as vertices and the edges as edges. Notice that, by definition, any edge connects two vertices (facets in this case)
- Degree: the degree of a vertex is the number of edges connected to that vertex
- Leaf: a leaf is a vertex of degree 1

Procedure

1. Form a tree by firstly connecting boundary nodes with boundary edges;
2. Select the cotree edges on the boundary $\partial\Omega$;
3. Form the facets-edges dual graph for all the edges of cotree on $\partial\Omega$;
4. recursively remove all the leaves. In this way, the closed loops left are made by sets of edges that are candidates to represent the nonlocal additional DoFs;
5. form the tree-cotree decomposition of the dual graph obtained at points 3-4;
6. any cotree edge of this dual cotree close a loop that represents an additional DoF.

As a matter of fact, the edges of any additional DoF produce zero flux across the boundary facets (on the primary graph) and assure the possibility of having a flux different from zero, associated to proper closed paths on the boundary having one edge of this DoF as the only active edge.

In the presence of the electrodes the procedure should be modified as follows:

1. Form the tree by connecting first boundary nodes with boundary edges for every electrode surface; then continue as in the step 1 of the previous procedure;
2. by construction any contour of any surface of the electrodes presents a unique edge belonging to the cotree; identify the facet of the electrode associated to this edge;
3. when building the dual graph (point 3 of the previous procedure), connect all the facets previously identified (point 2) to a common fictitious dual vertex.
4. execute points 3-6 of the previous procedure.

However, as already remarked in previous papers, only a part of these nonlocal basis functions are related to net current fluxes circulating inside the conducting region, whereas others would be related to current fluxes across surfaces external to

the conductor. The last ones are redundant because inside the conducting region they are linear combinations of the other degrees of freedom. On this basis, their selection can be obtained with the same algorithm already described in [8].

V. AN EXAMPLE

The procedure is here illustrated with reference to the torus shown in fig. 1a. The cotree edges are drawn as red arrows in the same figure. In fig. 1b the dual graph is shown with the leaves sequentially removed marked in green. The remaining facet marked in blue are also shown in fig. 1.c. Finally in fig. 1.d, the two nonlocal DoFs are drawn in blue and red, respectively. Only the DoF marked in red is associated to a current flux circulating inside the conducting region.

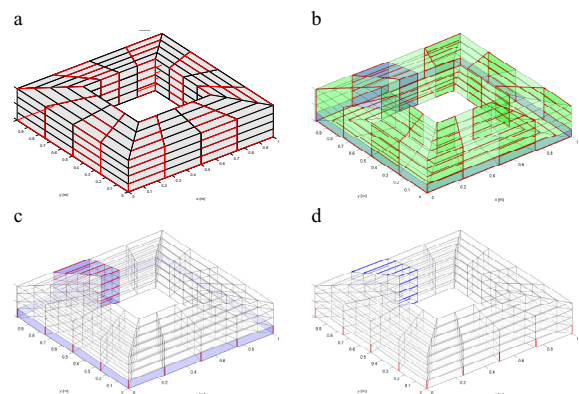


Fig. 1. a: the conducting domain and the co-tree edges on $\partial\Omega$; b: the dual graph with in green the removed leaves; c: the dual graph after removing the leaves. d: the non local additional DoF s; Only the DoF marked in red is associated to a current flux circulating inside the conducting region.

VI. REFERENCES

- [1] P.R. Kotiuga, Toward an algorithm to make cuts for magnetic scalar potentials in finite element meshes, *J. Appl. Phys.* 63(8): 3357-3359, 1988; erratum 64(8): 4257, 1988.
- [2] Z. Ren, T- Ω formulation for eddy-current problems in multiply connected regions, *IEEE Trans. on Magnetics*, 38(2): 557-560, 2002.
- [3] L. Kettunen, K. Forsman, A. Bossavit, Formulation of the eddy current problem in multiply connected regions in terms of h, *Int. J. Num. Meth. Eng.*, 41: 935-954, 1998
- [4] P. Dlotko, R. Specogna, F. Trevisan, A homological algorithm for the automatic generation of cuts suitable for the T- Ω eddy-current geometric formulation, 5th Workshop on Advanced Computational Electromagnetics (ACE'09) Rome, on January 12-14, 2009.
- [5] R. Albanese, G. Rubinacci, "Integral Formulation for 3D Eddy Current Computation using Edge-Elements" *IEE Proc. Pt A*, 135(5): 457-462, 1988
- [6] R. Albanese and G. Rubinacci, "Finite Element Methods for the Solution of 3D Eddy Current Problems", *Advances in Imaging and Electron Physics*, Peter W. Hawkes ed., Vol. 102, pp. 1-86, Academic Press, 1998.
- [7] R. Albanese, G. Rubinacci, "Treatment of multiply connected regions in two component electric vector potential formulations", *IEEE Trans. Magnetics*, 26(2): 650-653, 1990
- [8] G. Rubinacci, A. Tamburrino, F. Villone, "Circuits/Fields Coupling and Multiply Connected Domains in Integral Formulations" *IEEE Trans. Magnetics*, 38(2): 581-584, 2002
- [9] L. Kettunen, Fields and Circuits in Computational Electromagnetism, *IEEE Trans. on Magnetics*, 37(5): 3393-3396, 2001

Complex Adjoint Variable Method for Finite Element Analysis of Eddy Current Problems

Hajime Igarashi, Member IEEE, Kota Watanabe, Member IEEE
 Graduate School of Information Science and Technology, Hokkaido University,
 Kita 14, Nishi 9, Kita-ku, 060-0814 Sapporo, Japan
 igarashi@ssi.ist.hokudai.ac.jp

Abstract—This paper presents finite element analysis of time-harmonic eddy current problems using the complex adjoint variable method (C-AVM). In the sensitivity analysis as well as optimization based on FE analysis of time-harmonic eddy current fields, response and objective functions are often real-valued functions, while unknown variables for the FE analysis are complex. When the AVM is applied to such problems, the real-valued functions must be differentiated in terms of the complex variables. However, such differentiation cannot be defined because the Cauchy-Riemann equation does not hold. In this paper, the C-AVM is introduced to overcome this difficulty, and is applied to sensitivity analysis and optimization.

I. INTRODUCTION

The adjoint variable method (AVM) has widely been applied to various problems in computational electromagnetism to compute sensitivity of response functions, and derivative of objective functions in optimization problems and inverse problems. It is the advantage of AVM that computational cost for computation of derivatives of the response (or objective) function in terms of parameters little grows as the number of the parameters increases.

In AVM, the adjoint equation must be solved before the computation of the derivative. The right-hand-side vector in the adjoint equation is the derivative of the response function in terms of the unknown variable of the field analysis. When time-harmonic eddy current fields are analyzed using finite element method (FEM), the unknown variables are complex. On the other hand, the response functions are often chosen as real valued functions which represent, e.g., energy, loss and magnitude of magnetic induction. In such cases, the derivative cannot be defined because the Cauchy-Riemann equation cannot hold in general. The similar situation can also be found in other cases such as microwave problems including complex permittivity or permeability, magnetic field analysis based on the effective permeability, and so on.

In this paper, the complex AVM, referred here C-AVM, will be introduced by adequate modification of the conventional AVM and be applied to sensitivity analysis of time-harmonic eddy current fields.

II. COMPLEX ADJOINT VARIABLE METHOD

Let us consider a quasi-static electromagnetic field governed by

$$\text{rot}(\nu \text{rot} \mathbf{A}) + j\omega\sigma\mathbf{A} = \mathbf{J}, \quad (1)$$

where \mathbf{A} and \mathbf{J} are vector potential and current density, ν , ω and σ are the reciprocal of magnetic permeability, angular frequency and conductivity. The edge-based finite element method applied to (1) yields a system of linear equations

$$[K]\mathbf{a} = \mathbf{b}, \quad (2)$$

where $[K] \in \mathbb{C}^{E \times E}$, $\mathbf{a} \in \mathbb{C}^E$, $\mathbf{b} \in \mathbb{R}^E$ and E denotes the number of edges in the finite element mesh. The entities of $[K]$ and \mathbf{b} are given by

$$\begin{aligned} K_{ij} &= \int_v (\nu \text{rot} \mathbf{N}_i \cdot \text{rot} \mathbf{N}_j + j\omega\sigma \mathbf{N}_i \cdot \mathbf{N}_j) dv, \\ \mathbf{b}_i &= \int_v \mathbf{N}_i \cdot \mathbf{J} dv, \end{aligned} \quad (3)$$

where \mathbf{N}_i denotes the vector basis function for the edge-based element.

Now let assume that the electromagnetic field depends on design parameters $\mathbf{p} = [p_1, p_2, \dots, p_n]^t$, which are, for example, shape and material parameters. In this situation, we can write $\mathbf{a} = \mathbf{a}(\mathbf{p})$. Moreover, let us consider the numerical evaluation of sensitivity $\partial W / \partial p_k$, $k = 1, 2, \dots, n$ for a real valued function $W(\mathbf{a}(\mathbf{p}))$ against parameter changes. In real situations, the function W would express quantities such as electromagnetic energy, loss, and magnitude of magnetic induction. In order to evaluate the sensitivity, we employ the AVM where the adjoint equation to (2),

$$[K]\bar{\mathbf{a}} = \frac{\partial W}{\partial \mathbf{a}} \quad (4)$$

must be solved to obtain the adjoint variable $\bar{\mathbf{a}}$. However, the right-hand-side of (2), which is the differentiation of the real-valued function in terms of the complex variable, cannot be defined because it is not guaranteed the function W satisfies the Cauchy-Riemann differential equation

$$\begin{aligned} \frac{\partial W^{\text{re}}}{\partial a_m^{\text{re}}} &= \frac{\partial W^{\text{im}}}{\partial a_m^{\text{im}}}, \\ \frac{\partial W^{\text{re}}}{\partial a_m^{\text{im}}} &= -\frac{\partial W^{\text{im}}}{\partial a_m^{\text{re}}}, \end{aligned} \quad (5)$$

which is equivalent to

$$\frac{\partial W}{\partial a_m^*} = 0, \quad (6)$$

where $m = 1, 2, \dots, E$ and the suffixes re and im denote real and imaginary parts.

To overcome this difficulty, we consider the modified adjoint equation

$$[K]\bar{\mathbf{a}} = \frac{\partial W}{\partial \mathbf{a}^{\text{re}}} - j \frac{\partial W}{\partial \mathbf{a}^{\text{im}}} \quad (7)$$

in stead of (4). Note here that the right-hand-side of (7) only contains the differentiation of W in terms of real variables. The equation (7) is further modified to

$$\begin{bmatrix} K^{\text{re}} & -K^{\text{im}} \\ K^{\text{im}} & K^{\text{re}} \end{bmatrix} \begin{bmatrix} \bar{\mathbf{a}}^{\text{re}} \\ \bar{\mathbf{a}}^{\text{im}} \end{bmatrix} = \begin{bmatrix} \partial W / \partial \mathbf{a}^{\text{re}} \\ -\partial W / \partial \mathbf{a}^{\text{im}} \end{bmatrix}, \quad (8)$$

where the first and second equations of (8) correspond to the real and imaginary parts of (7). For simplicity, we define the variables

$$\begin{aligned} \boldsymbol{\alpha} &= [\mathbf{a}^{\text{re}}, -\mathbf{a}^{\text{im}}]^t, \\ \bar{\boldsymbol{\alpha}} &= [\bar{\mathbf{a}}^{\text{re}}, -\bar{\mathbf{a}}^{\text{im}}]^t, \end{aligned} \quad (9)$$

then (8) becomes

$$\begin{bmatrix} K^{\text{re}} & K^{\text{im}} \\ K^{\text{im}} & -K^{\text{re}} \end{bmatrix} \bar{\boldsymbol{\alpha}} = \frac{\partial W}{\partial \boldsymbol{\alpha}}. \quad (10)$$

We write the matrix in the left-hand-side of (10) as $[\tilde{K}]$, which is symmetric.

Moreover, we divide (2) into real and imaginary parts to obtain

$$\begin{bmatrix} K^{\text{re}} & K^{\text{im}} \\ K^{\text{im}} & -K^{\text{re}} \end{bmatrix} \begin{bmatrix} \mathbf{a}^{\text{re}} \\ -\mathbf{a}^{\text{im}} \end{bmatrix} = \begin{bmatrix} \mathbf{b} \\ \mathbf{0} \end{bmatrix}. \quad (11)$$

Rewriting (11) using $\boldsymbol{\alpha}$ and $[\tilde{K}]$, we have

$$[\tilde{K}]\boldsymbol{\alpha} = \tilde{\mathbf{b}}, \quad (12)$$

where $\tilde{\mathbf{b}} = [\mathbf{b}, \mathbf{0}]^t$. By differentiating (12) in terms of the parameter p_k , we have

$$[\tilde{K}] \frac{\partial \boldsymbol{\alpha}}{\partial p_k} = -\frac{\partial [\tilde{K}]}{\partial p_k} \boldsymbol{\alpha}. \quad (13)$$

Multiplying $\bar{\boldsymbol{\alpha}}^t$ to both sides of (13) and taking its transpose, we obtain

$$\left(\frac{\partial \boldsymbol{\alpha}}{\partial p_k} \right)^t [\tilde{K}] \bar{\boldsymbol{\alpha}} = -\boldsymbol{\alpha}^t \frac{\partial [\tilde{K}]}{\partial p_k} \bar{\boldsymbol{\alpha}}. \quad (14)$$

Substitution of (12) into (14) yields

$$\frac{\partial W}{\partial p_k} = -\boldsymbol{\alpha}^t \frac{\partial [\tilde{K}]}{\partial p_k} \bar{\boldsymbol{\alpha}}, \quad (15)$$

which gives the sensitivity. Moreover it can be shown that

$$\boldsymbol{\alpha}^t \frac{\partial [\tilde{K}]}{\partial p_k} \bar{\boldsymbol{\alpha}} = \text{Re} \left(\mathbf{a}^t \frac{\partial [K]}{\partial p_k} \bar{\mathbf{a}} \right). \quad (16)$$

Hence, it is concluded that (15) can be expressed as

$$\frac{\partial W}{\partial p_k} = -\text{Re} \left(\mathbf{a}^t \frac{\partial [K]}{\partial p_k} \bar{\mathbf{a}} \right). \quad (17)$$

which will be used in our sensitivity analysis. The similar sensitivity expression as (17) has been obtained for the microwave circuit problem [1].

III. NUMERICAL RESULTS

The present method is applied to the sensitivity analysis of a system of non-destructive testing, shown in Fig.1. In this model, the alternative current of 100 [AT] flows along the coil at 10 [kHz]. The aluminum plate, whose conductivity is set to 36×10^6 [S/m], contains a rectangular flaw. The sensitivity dB/dh in the magnetic induction B measured at point p against the thickness h of the flaw is computed using the present C-AVM and numerical differentiation $\Delta B/\Delta h$. The thickness h is set to 1 [mm]. The whole system including the air region is subdivided into 102,580 tetrahedral elements with 123,555 unknowns. The derivative $\partial[K]/\partial p_k$ in (17) is computed using finite difference. The numerical results are summarized in TABLE I. It is clear that the finite difference $\Delta B/\Delta h$ approaches dB/dh computed by C-AVM as Δh decreases.

TABLE I
COMPARISON OF RESULTANT SENSITIVITY

method	C-AVM	finite difference		
Δh [mm]	-	0.02	0.01	0.005
dB/dh	0.01297	0.01209	0.01214	0.01279

IV. CONCLUSIONS

In this paper, C-AVM has been presented and applied to sensitivity analysis. The sensitivity obtained by C-AVM is shown to be accurate. In the long version, sensitivity analysis containing more parameters will be presented. Moreover, identification of flaws based on C-AVM will be discussed.

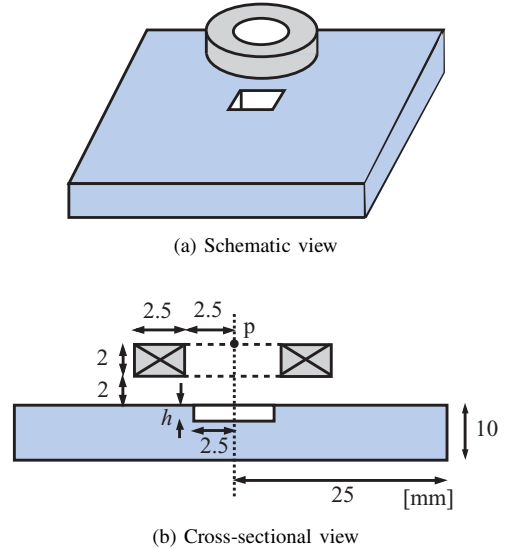


Fig.1 Coil and aluminum plate containing a flaw

REFERENCES

- [1] N.K. Nikolova J.W. Bandler, M.H. Bakr, "Adjoint Techniques for sensitivity analysis in high-frequency structure CAD," *IEEE Transactions on Microwave Theory and Tech.*, vol. 52, no. 1, pp. 403-419, 2004.

New Method Analysis of Non-rotating Magnetoacoustic Tomography with Magnetic Induction

Yang Zhang¹, Guoqiang Liu¹, Baodong Bai², Dexin Xie²

¹ Research Department of Frontiers, Electrical Engineering Institute of Chinese Academy of Sciences, China

² School of Electrical Engineering, Shenyang University of Technology, China

Abstract—A new image reconstruction method of magnetoacoustic tomography with magnetic induction (MAT-MI) is described. It breaks through some illogical supposes that the existing methods applied and can improve the spatial resolution of the image available. Besides it can avoid rotating the static magnetic field which is very difficult to come true in application, therefore the development of MAT-MI technique can be promoted greatly. To test the validity of the new method, a test model is analyzed, and the availability of the method is demonstrated.

I. INTRODUCTION

Magnetoacoustic tomography with magnetic induction (MAT-MI) is bring forward by B He etc. in 2003. It is the combination of Electromagnetic tomography (EMT) and ultrasonic tomography, so it combines the good contrast of EMT with the good spatial resolution of ultrasonic tomography^[1]. Compared with other electromagnetic tomography techniques, MAT-MI has several unique features. Firstly, it has no shielding effect, that is it will not be affected by the low-conductivity layer of the tissue at/near the surface of the human body. Secondly, for the eddy current which produces the Lorentz force distributes throughout the imaging body, so the ultrasonic waves which take valid information of magnetic parameter character are abundant accordingly, and this is the main reason why the spatial resolution of MAT-MI is good^[2].

Image reconstruction algorithm is the key problem of MAT-MI, but the existing algorithms are not perfect. They either need to adopt some illogical approximate hypothesis which will decrease the quality of the reconstructed image greatly, such as looking the time varying impulse as a step one and supposing the distribution of object is piecewise, or need to rotate the static magnetic field which is very difficult to come true in application, and these baffle the improvement of MAT-MI greatly. Therefore new image reconstruction algorithms of MAT-MI technique are needed especially.

Refer to the reconstruction method of magnetic resonance electrical impedance tomography (MREIT) which apply the single component of magnetic induction intensity to reconstruct the distribution of electromagnetic parameters^[3], the author bring forwards a new image reconstruction method of MAT-MI technique. Through substituting the single component of the divergence of Lorentz force density, the new method can not only break through the illogical supposes, but also can avoid rotating the static magnetic field and solve the choke point of MAT-MI. Besides, the method applies the transient field analysis method to take into account the electromagnetic effect produced by the time-varying excitation. Therefore, it can

improve the trueness of the image, and can also promote the development of MAT-MI effectively.

II. FORMULATIONS

For MAT-MI, the object is in a static magnetic field and a time-varying magnetic field. The time-varying magnetic field induces an eddy current in the object. Consequently, the object will emit ultrasonic waves through the Lorentz force produced by the combination of the eddy current and the static magnetic field. The ultrasonic waves are then collected by the detectors located around the object. Then, through the image reconstruction the image which can reflect the tissue's electromagnetic parameters can be reconstructed.

The process of image reconstruction is very important, and this process can be divided into two steps. In the first step, the divergence of Lorentz force's density distribution will be reconstructed from sound pressure through the analysis of sound field reverse problem. In the second step, the distribution of electromagnetic parameters will be reconstructed from the divergence of Lorentz force density through the analysis of electromagnetic field reverse problems. The first step can be accomplished with the back-projection algorithm, and it is mature comparatively. The second step is more challenging. To avoid rotating the static magnetic field, in the new method we apply the method of substituting the single component of the divergence of Lorentz force density. Beside, to improve the trueness of the image reconstruction, we apply the transient field analysis method to take into account the effect of the time-varying excitation.

Because the reverse problem of electromagnetic field is based on the forward one, so at first the formulations of forward problem will be introduced.

A. Forward problem of electromagnetic field

The field equation system with $A-\phi, A$ formulations with the Coulomb gauge can be given as:

$$\begin{cases} \nabla \times \frac{1}{\mu} \nabla \times A = -\sigma \left(\frac{\partial A}{\partial t} + \nabla \phi \right) \\ \nabla \cdot \left[\sigma \left(\frac{\partial A}{\partial t} + \nabla \phi \right) \right] = 0 \end{cases} \quad (1)$$

Where, A is the magnetic vector potential with or without ϕ , the electric scalar potential, μ and σ are the magnetic reluctivity and conductivity respectively.

In the forward problem of electromagnetic field, the known quality is the distribution of σ , and the calculating target is the divergence of Lorentz force density $\nabla \cdot (\vec{J} \times \vec{B})$.

To ensure the symmetrical characteristics of equation coefficient matrix, φ is introduced, where $\phi = \frac{\partial \varphi}{\partial t}$, and the matrix form of the transient field equation can be given as

$$[K]\{A\} + [D]\frac{\partial}{\partial t}\{A\} = \{F\} \quad (2)$$

Where, K, D are coefficient matrices of the field equation, and F is the known quantity matrices of source.

Formulation (2) can be solved by Runge-Kutta methods, and according to the corresponding relation, B and J can be calculated, and then the divergence of Lorentz force density $\nabla \cdot (\vec{J} \times \vec{B})$ at each time step can be obtained accordingly.

B. Inverse problem of electromagnetic field

In the inverse problem of electromagnetic field, the known quality is the divergence of Lorentz force density $\nabla \cdot (\vec{J} \times \vec{B})$, and the calculating target is the distribution of σ .

Through calculating we find that comparing with the static magnetic field the time-varying magnetic field and the magnetic field produced by the eddy current is small enough to be neglected, so the divergence of Lorentz force density can be regarded as $\nabla \cdot (\vec{J} \times \vec{B}_0)$.

$$\nabla \cdot (\vec{J} \times \vec{B}_0) = \vec{B}_0 \cdot (\nabla \times \vec{J}) = \vec{B}_0 \nabla \times \vec{J} \Big|_z \quad (3)$$

For B_0 is a constant we known, so $\nabla \times \vec{J} \Big|_z$ can be obtained.

Besides formulation (1), σ and A also satisfy the following equation,

$$\left(\nabla \sigma \times \frac{\partial \vec{A}}{\partial t} \right) \Big|_z + (\nabla \sigma \times \nabla \phi) \Big|_z + \sigma \nabla \times \frac{\partial \vec{A}}{\partial t} \Big|_z = -\nabla \times \vec{J} \Big|_z \quad (4)$$

Through iterative calculating between formulation (1) and (4), the distribution of σ can be reconstructed.

III. APPLICATION

To verify the availability of the new method, a test model is analyzed. There are two coils and a conductive object which composed by 16 blocks with different conductivity in the model. The subdivision of the model is shown in Fig.1. When an impulse current which the max value is 98.71A and the actuation duration is 5.2us is added to the coils, a transient changed magnetic field will be induced accordingly, and in the conductive object area the magnetic field is homogeneous spatially. Magnetic induction intensity B together with the eddy current J and Lorentz force density $J \times B$ are calculated. The curves of the calculated results of 3 sample points are shown in Fig.2-4, and the image of σ distribution is shown in Fig.5.

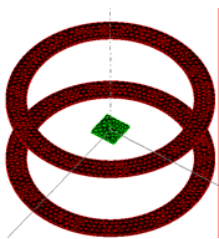


Fig.1 Subdivision of the model

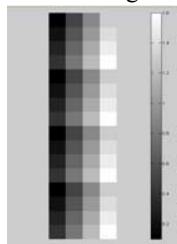


Fig.5 Distribution of σ

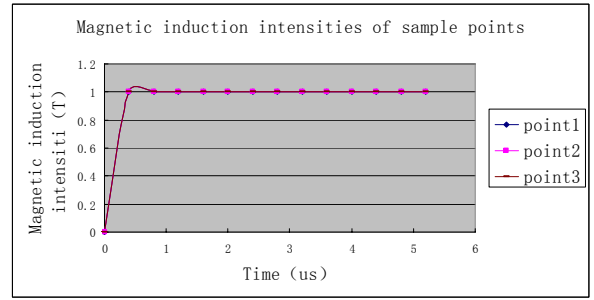


Fig.2 Curve of magnetic induction intensity results

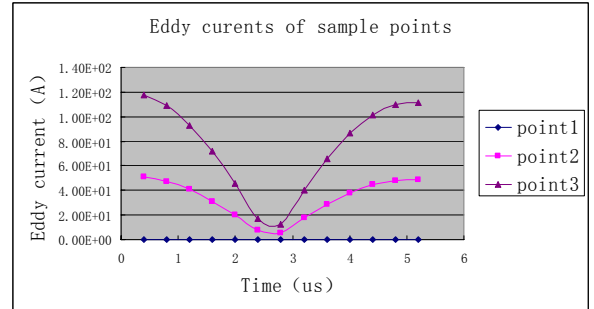


Fig.3 Curve of eddy current results

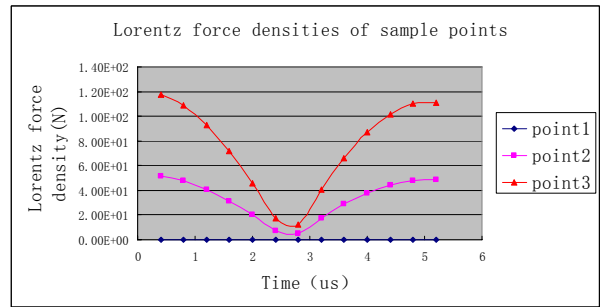


Fig.4 Curve of Lorentz force density results

IV. CONCLUSION

A new image reconstruction algorithm of MAT-MI is presented in this paper. Through substituting the single component of the divergence of Lorentz force density, the problem of rotating static magnetic field can be solved availably, therefore the application of MAT-MI technique will be promoted. Besides, the transient magnetic field analysis is used to take into account the effect of the time-varying excitation, and accordingly the quality of image can be improved effectively. A test model is analyzed to test the availability of the new method. The detailed comparison of the numerical results with the measured ones will be described in the full paper.

V. REFERENCES

[1] X.Yuan, B. He. Magnetoacoustic Tomography with Magnetic Induction(MAT-MI) [J]. Phys. Med. Biol. 2005. Vol.50, pp.5175-5187

[2] Wang Hao, Liu Guoqiang. et.al. Inverse Problem of Magnetoacoustic Tomography with Magnetic Induction. Proceedings of NFSI & ICFBI 2007.290~292

[3] Birgul O, Eyuboglu BM, Ider YZ. 2003. Experimental results for 2D magnetic resonance electrical impedance tomography (MR-EIT) using magnetic flux density in one direction, Phys. Med. Biol. 48:3485-3504

Combined Spectral-Element, Finite-Element Discretization for Magnetic-Brake Simulation

Herbert De Gersem

Katholieke Universiteit Leuven, Wave Propagation and Signal Processing Research Group

Etienne Sabbelaan 53, 8500 Kortrijk, Belgium

herbert.degersem@kuleuven-kortrijk.be

Abstract—The performance of a magnetic brake is calculated by a cross-sectional model where stator and air-gap are discretized by finite elements whereas the nonlinear ferromagnetic rotor is discretized by spectral elements in order to guarantee a sufficient resolution of the thin eddy-current layers.

I. INTRODUCTION

Magnetic brakes and solid-rotor induction machines generate eddy currents in their rotors, which on their turn cause an accelerating or braking torque. Many devices have a rotor which is uniform in the direction of motion. Then, an Eulerian formulation may be more convenient than a Lagrangian formulation [1]. Eulerian formulations, however, suffer from spurious oscillations of numerical nature when high velocities are applied. These can be suppressed by upwinding, possibly in combination with adaptive mesh refinement. Nevertheless, FEs are cumbersome for resolving the thin eddy-current layers arising at high speeds, especially when a higher accuracy is required, e.g., when high saturation levels are attained in the eddy-current layer. In this paper, the rotating rotor is discretized by spectral elements (SEs), which is embedded in an overall FE model.

II. EULERIAN FORMULATION AND FE DISCRETIZATION

Here, the motional eddy currents are simulation by a time-harmonic, Eulerian magnetoquasistatic formulation in terms of the magnetic vector potential \mathbf{A} :

$$\nabla \times (\nu \nabla \times \mathbf{A}) - \sigma \mathbf{v} \times \nabla \times \mathbf{A} + j\omega \sigma \mathbf{A} = \mathbf{J}_s \quad (1)$$

with ν the reluctivity, σ the conductivity, ω the angular frequency, \mathbf{v} the velocity and \mathbf{J}_s the applied current density. In the standard 2D FE discretization

$$\underbrace{(\mathbf{K}_{fe} + \mathbf{L}_{fe} + j\omega \mathbf{M}_{fe})}_{\mathbf{A}_{fe}} \mathbf{u}_{fe} = \mathbf{f}_{fe}, \quad (2)$$

\mathbf{K}_{fe} , \mathbf{L}_{fe} and \mathbf{M}_{fe} are the discrete counterparts of the operators in (1), \mathbf{f}_{fe} are the discretized applied currents and \mathbf{u}_{fe} is a vector of the degrees of freedom (DOFs) for the z -component A_z of \mathbf{A} . The solution of (2) may turn out to be inaccurate when the FE mesh does not resolve the *motional skin depth* $\delta_m = \nu/(\sigma|\mathbf{v}|)$ [1]. Then, the solution may exhibit spurious oscillations which, on their turn, hamper the error-estimation and adaptive-mesh-refinement procedure [2]. Typically, an upwinding technique is applied to overcome this problem [3]. The simplest scheme consists of adding *artificial diffusion*, i.e., increasing ν such that locally the expected motional skin depth exceeds the mesh size. The slightly better *streamline diffusion*

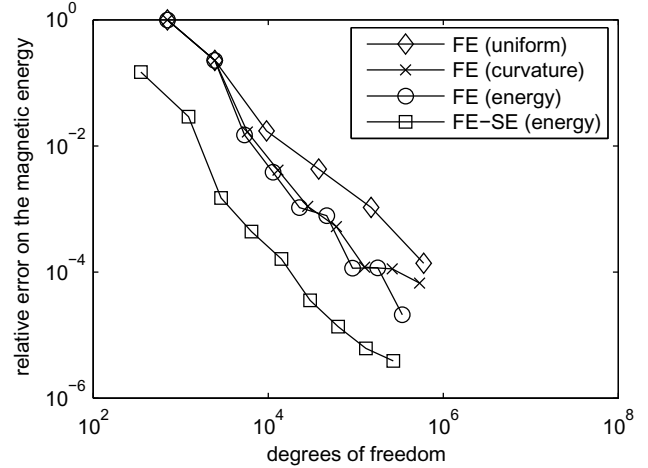


Fig. 1. Convergence of a FE model with uniform mesh refinement, a FE model with error-controlled adaptive mesh refinement and a combined FE-SE model with uniform mesh refinement.

technique adds an anisotropic diffusion term only along the direction of motion. The *streamline-upwind Petrov-Galerkin* (SUPG) technique does not change the model but applies modified test functions for discretization [4]. The convergence of discretization error for a FE-SUPG model with several error-controlled refinement strategies is shown in Fig. 1.

III. SE DISCRETIZATION

The moving part of the model is a hollow cylinder with inner radius r_1 and outer radius r_2 . For such a regular domain, a superior convergence of the discretization error is expected when orthogonal functions are used for discretizing A_z [5]–[7]. The (r, θ) -domain $[r_1, r_2] \times [0, 2\pi[$ is mapped onto the (s, θ) -domain $[-1, 1] \times [0, 2\pi[$ by $s = \frac{1}{e_m} \ln \frac{r}{r_m}$ with $r_m = \sqrt{r_1 r_2}$ the mean radius and $e_m = \ln \sqrt{r_2/r_1}$ a form factor. The corresponding mapping of (1) reads

$$\frac{1}{e_m^2} \frac{\partial}{\partial s} \left(\nu \frac{\partial A_z}{\partial s} \right) + \frac{\partial}{\partial \theta} \left(\nu \frac{\partial A_z}{\partial \theta} \right) - \sigma \omega_m r^2 \frac{\partial A_z}{\partial \theta} = 0 \quad (3)$$

with ω_m the angular velocity. The z -component of the magnetic vector potential is discretized by Chebyshev polynomials $T_q(s)$ in s -direction and harmonic functions $e^{-j\lambda\theta}$ in θ -direction, i.e.,

$$A_z(s, \theta) = \sum_{q \in \mathcal{Q}} \sum_{\lambda \in \Lambda} \alpha_{q,\lambda} T_q(s) e^{-j\lambda\theta} \quad (4)$$

where $\alpha_{q,\lambda}$ are the DOFs and \mathcal{Q} and Λ denote the set of orders of the Chebyshev polynomials and the harmonic functions,

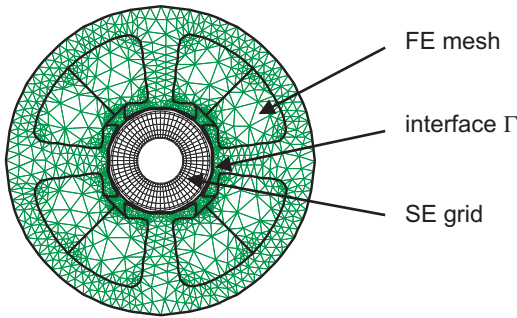


Fig. 2. FE mesh (stator and air gap) and SE grid (rotor) discretizing a four-pole magnetic brake.

respectively. In practice, a tensor-product grid combining the Chebyshev-point distribution along s with an equidistant distribution along θ is constructed (Fig. 2). The values for A_z at the grid points serve as DOFs \mathbf{u}_{se} in the formulation. The collocation of the residual of (3) at the grid points leads to the matrix formulation

$$\underbrace{(\mathbf{L}_s \mathbf{M}_\nu \mathbf{L}_s + \mathbf{L}_\theta \mathbf{M}_\nu \mathbf{L}_\theta - \sigma \omega_m \mathbf{R}^2 \mathbf{L}_\theta)}_{\mathbf{A}_{se}} \mathbf{u}_{se} = 0; \quad (5)$$

$$\mathbf{L}_r = \frac{1}{\epsilon_m} \mathbf{D}_s \otimes \mathbf{I}_{|\Lambda|}; \quad \mathbf{L}_\theta = \mathbf{I}_{|\Omega|} \otimes \mathbf{D}_\theta, \quad (6)$$

The matrix factors in (5) and (6) mimic the operators in (3). The Kronecker products in (6) resemble the tensor-product grid structure. \mathbf{D}_s and \mathbf{D}_θ are fully populated first-order differentiation matrices along the s - and θ -direction respectively [8]. \mathbf{R} and \mathbf{M}_ν are diagonal matrices with the radii and reluctivities at the collocation points. The exponential convergence behavior of this SE formulation has been shown in [7]. The Newton linearization of (5) will be documented in the full paper.

IV. COUPLING

Both formulations are coupled at the circular rotor-air-gap interface Γ (Fig. 2). A partial FE model is built by omitting the rotor part and imposing homogeneous Neumann boundary conditions at Γ . The DOFs allocated at nodes of Γ are selected by the operators \mathbf{Q}_{fe} and \mathbf{Q}_{se} respectively. The coupled system of equations reads

$$\begin{bmatrix} \mathbf{A}_{fe} & \mathbf{0} & \mathbf{Q}_{fe}^T \\ \mathbf{0} & \mathbf{A}_{se} & -\mathbf{Q}_{se}^T \\ \mathbf{Q}_{fe} & -\mathbf{Q}_{se} & \mathbf{0} \end{bmatrix} \begin{bmatrix} \mathbf{u}_{fe} \\ \mathbf{u}_{se} \\ \mathbf{v}_{lg} \end{bmatrix} = \begin{bmatrix} \mathbf{f}_{fe} \\ \mathbf{0} \\ \mathbf{0} \end{bmatrix} \quad (7)$$

where \mathbf{v}_{lg} contains n_Γ Lagrange multipliers corresponding to the n_Γ nodes at Γ . The third row of (7) imposes the continuity of A_z , which is equivalent to the normal continuity of the magnetic flux density. The terms $\mathbf{Q}_{fe}^T \mathbf{v}_{lg}$ and $-\mathbf{Q}_{se}^T \mathbf{v}_{lg}$ can be interpreted as surface currents at Γ , which cancel out each other and, hence, ensure the tangential continuity of the magnetic field strength. It would be possible to eliminate the DOFs at one side of Γ at the expense of a fill-in in \mathbf{A}_{fe} or \mathbf{A}_{se} . Here, however, the saddle-point system (7) is kept in order to preserve the different structure of both matrices. The coupled system of equations is solved by the Bi-Conjugate

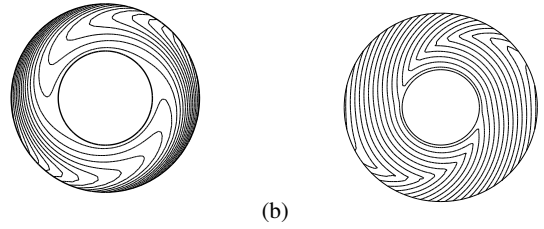


Fig. 3. Magnetic flux lines for the results of (a) the linear comparative simulation and (b) the nonlinear simulation at a velocity of 100 rad/s.

Gradient Stabilized (BiCGStab) method [9] and preconditioned by incomplete LU-factorization. The convergence of the discretization error for the coupled method is demonstrated in Fig. 1. The convergence order is determined by the FE discretization of the stator and rotor domains and is, therefore, the same as for the full FE case. The convergence factor is substantially lower because of the better resolution of the SE discretization.

V. EXAMPLE

The coupled method is applied to a magnetic brake (Fig. 2). This model is used to illustrate the convergence of the different discretizations for a velocity of 100 rad/s in Fig. 1. The magnetic flux lines are shown in Fig. 3. The linear calculation is technically irrelevant and serves only for comparison. The ferromagnetic saturation prohibits high magnetic fluxes at the surface of the cylinder. Hence, the flux is distributed more to the inside of the cylinder, causing a larger effective motional skin depth. This fact motivates the use of a SE scheme offering a high resolution.

VI. CONCLUSIONS

A SE model for a ferromagnetic rotor at high speed circumvents upwinding and alleviates the poor accuracy which is typical for a FE discretization of an Eulerian formulation. The SE model part is embedded in an overall FE model dealing with the remaining parts of a magnetic brake.

REFERENCES

- [1] H. De Gersem, H. Vande Sande, and K. Hameyer, "Motional magnetic finite element method applied to high speed rotating devices," *COMPEL*, vol. 19, no. 2, pp. 446–451, 2000.
- [2] H. De Gersem and K. Hameyer, "Simulation of motional eddy current phenomena in soft magnetic material," *Journal of Magnetism and Magnetic Materials*, vol. 226, no. 2, pp. 1237–1238, May 2001.
- [3] H. Vande Sande, H. De Gersem, and K. Hameyer, "Finite element stabilization techniques for convection-diffusion problems," *7th International Journal of Theoretical Electrotechnics*, pp. 56–59, Mar. 1999.
- [4] K. Morton, *Numerical Solution of Convection-Diffusion Problems*. London: Chapman and Hall, 1996.
- [5] B. Fornberg, *A Practical Guide to Pseudospectral Methods*. Cambridge: Cambridge University Press, 1996.
- [6] C. Canuto, M. Hussaini, A. Quarteroni, and T. Zang, *Spectral Methods: Fundamentals in Single Domains*. Berlin: Springer, 2006.
- [7] H. De Gersem, "Spectral-element method for high-speed rotating cylinders," in *Proc. EPNC*, Lille, France, Jul. 2008, pp. 47–48.
- [8] L. Trefethen, *Spectral Methods in Matlab*. Philadelphia: SIAM, 2000.
- [9] H. van der Vorst, "Bi-CGSTAB: a fast and smoothly converging variant of Bi-CG for the solution of nonsymmetric linear systems," *SIAM J. Sci. Stat. Comput.*, vol. 13, p. 631644, 1992.

Weight Function Control of Moving Least-Squares Interpolants: Application to Axisymmetric Shielding Current Analysis in HTS

Soichiro Ikuno¹, Teruou Takayama², and Atsushi Kamitani²

¹Tokyo University of Technology, 1404-1 Katakura, Hachioji, Tokyo 192-0982, Japan

²Yamagata University, Johnan 4-3-16, Yonezawa, Yamagata 992-8510, Japan

E-mail ikuno@nal.ikulab.org

Abstract—The modified base functions of element-free Galerkin method generated by weight function control of Moving Least-Squares interpolants are investigated. Moreover, the modified base functions are applied to the numerical code for analyzing shielding current density in high temperature superconductor. The results of computations show that the proposed base functions leads essential phenomena.

I. INTRODUCTION

The critical current density of high temperature superconductor (HTS) is one of the most important parameters of HTSs, and it is necessary to take hold on the critical current density in order to understand the characteristics of the HTS. Therefore, methods for measuring the critical current density of HTS have been desired.

Ohshima *et al.* have proposed the permanent magnet (PM) method for measuring critical current densities [1]. Bringing a permanent magnet closer to an HTS thin film caused the electromagnetic repulsive force acting on the film and the maximum force was approximately proportional to the critical current density. They observed that the critical current density can be determined by measuring the electromagnetic interaction between the magnet and the HTS film. However, the position of point whose current density was measured is uncertain because the permanent magnets have a width. Moreover, critical current densities were measured at only center of HTSs by the system of permanent magnet method.

The shielding current density in axisymmetric HTS can be determined by solving a system of time-dependent integro-differential equation. The system is discretized by using element-free Galerkin (EFG) method [2] and completely implicit method in (r, θ, z) plane by taking the symmetry axis as z -direction and a nonlinear system is obtained. However, the values of the shielding current density on $r = 0$ are non zero though it should be zero essentially. The reason for the non zero values of the shielding current density will be attributable to the selected functional space of the base functions of EFG [2].

The purpose of the present study is to develop the numerical code for analyzing shielding current density in axisymmetric HTSs and to propose the modified base functions of EFG generated by weight function control of Moving Least-Squares

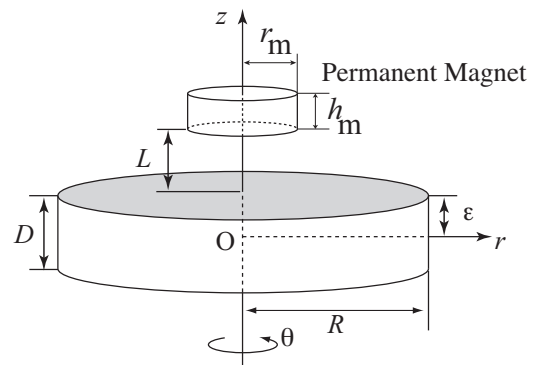


Fig. 1. The schematic view of the Permanent Magnet method for measuring the critical current density in HTS thin film.

(MLS) interpolants. By using the numerical code, the permanent magnet method is also simulated numerically.

II. AXISYMMETRIC SHIELDING CURRENT ANALYSIS

In this study, the target HTS to measure its critical current density is disk-shaped film; its radius is R and its thickness is $D = 2\varepsilon$, and the area of its circular cross-section is constant along the thickness direction. The schematic view of PM method is shown in Fig. 1. The cylindrical permanent magnet is located above the film whose radius is r_m and whose height is h_m . The film is exposed to the magnetic flux density \mathbf{B} generated by the magnet. The PM method is carried out as follows. The permanent magnet is brought closer to the film at a constant speed then it is raised at the same speed. That is to say, the distance L between the permanent magnet and the surface of the film changed from L_{\max} to L_{\min} and then L_{\min} to L_{\max} . Let τ_0 denote the moving time of the magnet from L_{\max} to L_{\min} .

The problem can be treated as axisymmetric. We assume that the shielding current density does not flow along c -axis because thickness is very thin compared with the radius of HTS (i.e., $R \gg \varepsilon$). Throughout this paper, let us use the cylindrical coordinate (r, θ, z) by taking the symmetry axis of HTS as z -direction.

Under these assumptions, there exists a scalar function $S(r, t)$ such that the shielding current density \mathbf{j} satisfies following equation.

$$\mathbf{j} = \frac{1}{\varepsilon} \nabla S \times \mathbf{e}_z. \quad (1)$$

Here \mathbf{e}_z denotes the unit vector in the z -direction. Using the scalar function $S(r, t)$, the behavior of the shielding current density in HTS can be expressed by the following time-dependent integro-differential equation.

$$\begin{aligned} \mu_0 \frac{\partial}{\partial t} \left(\int_0^R Q(r, r') S(r', t) r' dr' + \frac{S}{\varepsilon} \right) \\ = - \frac{\partial(\mathbf{B}_0 \cdot \mathbf{e}_z)}{\partial t} - (\nabla \times \mathbf{E}) \cdot \mathbf{e}_z, \end{aligned} \quad (2)$$

where μ_0 denotes the magnetic permeability of vacuum. The function $Q(r, r')$ uses the same function as the Ref. [3].

Let us scatter N nodes $0 = r_1 < r_2 < \dots < r_N = R$ on the analytic domain and the boundary for a discretization. As is well known that the base functions of meshless approaches are obtained on an each node by MLS interpolants. In addition, shapes of the base functions are different depending on the selecting weight function of MLS interpolants.

In the present study, we especially select the weight functions that contain r_1 and r_2 in the support R of the functions as following equation so that the delta function property might satisfies at $r = 0$.

$$\begin{aligned} w_1(r) &= \begin{cases} 1; & r \leq r_2, \\ 0; & r > r_2, \end{cases} \\ w_2(r) &= \begin{cases} 1; & r \leq r_2, \\ f(r, R); & r > r_2, \end{cases} \\ w_i(r) &= \begin{cases} f(r, |r_i - r_2|); & r \leq r_i, |r_i - r_2| \leq R, \\ f(r, R); & r > r_i, |r_i - r_2| \leq R. \end{cases} \end{aligned}$$

Here, function $f(r, \tilde{r})$ is denoted by following equation.

$$f(r, \tilde{r}) = \begin{cases} \frac{e^{-r^2} - e^{-\tilde{r}^2}}{1 - e^{-\tilde{r}^2}}; & r_i \leq \tilde{r}, \\ 0; & r_i > \tilde{r}. \end{cases} \quad (3)$$

In order to vanish the value of the derivative of the base functions at $r = 0$, the components of which constitute base functions of polynomial are defined as follows.

$$\mathbf{p} = \begin{cases} [1, r^2]^T; & r < r_2, \\ [1, r]^T; & \text{other wise.} \end{cases} \quad (4)$$

Following the standard manner of MLS interpolants, we can obtain modified base functions of EFG method. In Fig.2, we show the base functions of EFG. The inset indicate the weight functions for these base functions. This figure indicates that gradients of the base functions become zero at $r = 0$. That is to say, the derivative of the base functions at $r = 0$ satisfies $d\phi/dr = 0$.

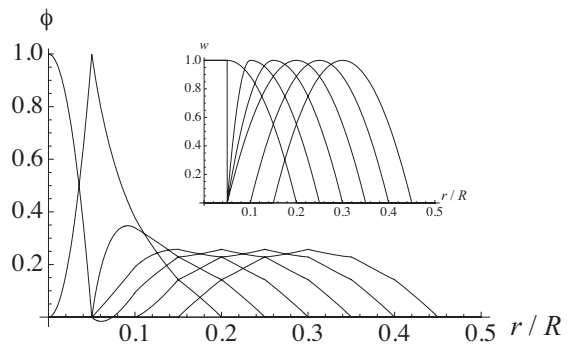


Fig. 2. The base functions of EFG. The inset denotes the modified weight functions of MLS interpolants.

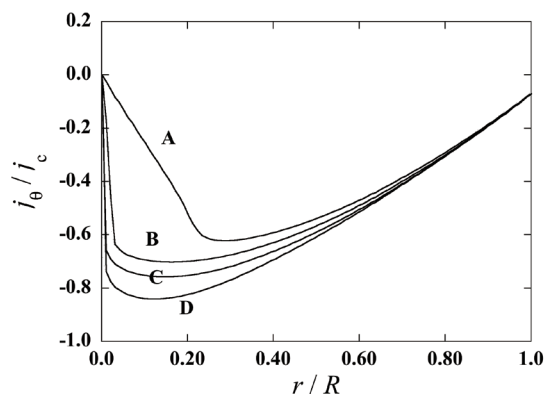


Fig. 3. The spatial distributions of the shielding current density of θ component in case of $j_c = 1.0$ MA/cm², $r_m = 2.5$ mm. Here j_c denotes the critical current density. A: $t/\tau_0 = 1/5$, B: $t/\tau_0 = 2/5$, C: $t/\tau_0 = 3/5$, D: $t/\tau_0 = 4/5$.

III. SHIELDING CURRENT ANALYSIS

The governing equation (2) and its associated conditions can be discretized by using EFG with modified base functions and the numerical code has been developed. The shielding current density in HTS thin film can be determined at any time step by the numerical code.

The spatial distributions of the shielding current density of θ component j_θ in the HTS are also obtained by the code and are shown in Fig. 3. We can see from this figure that the shielding current density rapidly flows to the vicinity of the center of HTS as the magnet approaches HTS. Note that the shielding current density at $r = 0$ becomes zero in both cases because of proposed base functions.

REFERENCES

- [1] S. Ohshima, K. Takeishi, A. Saito, M. Mukaida, Y. Takano, T. Nakamura, I. Suzuki, and M. Yokoo, "A simple measurement technique for critical current density by using a permanent magnet," *IEEE Trans. Appl. Supercond.*, vol. 15, no. 2, pp. 2911-2914, 2005.
- [2] T. Belytschko, Y. Y. Lu and L. Gu, "Element-free Galerkin methods," *Int. J. Numer. Methods Eng.*, vol. 37, pp. 229-256, 1994.
- [3] S. Ikuno, T. Takayama, and A. Kamitani, "Evaluation of AC Losses in High T_c Superconductor Thin Film by Element-Free Galerkin Method and Double Exponential Formula," *IEEE Trans. Magn.*, vol. 18, no. 2, pp. 1349-1352, 2008.

Interior Penalty Discontinuous Galerkin Method for the Time-Domain Maxwell's Equations

Stylianos Dosopoulos and Jin-Fa Lee
dosopoulos.1@osu.edu

Abstract— Discontinuous Galerkin(DG) methods support elements of various types, non-matching grid and varying polynomial order in each element. In DG methods continuity at element interfaces is weakly enforced with the addition of proper penalty terms on the variational formulation commonly referred to as numerical fluxes. An interior penalty DG method for solving the two first order Maxwell's equations in the time domain is presented. The proposed method is explicit and conditionally stable. In addition, a local time-stepping strategy is applied to increase efficiency and reduce the computational time.

I. INTRODUCTION

Discontinuous Galerkin(DG) finite element methods offer an alternative to FDTD for time-domain simulations and were recently applied for the solution of Maxwell's equations[1]. Moreover, they provide great flexibility since they allow for various shapes of elements, non-conformal meshes, non-uniform degrees of approximation. Furthermore, the resulting mass matrix is a block diagonal matrix with the block size equal to the degrees of freedom in the element. Therefore, the method can lead into a fully explicit and conditionally stable time-marching scheme. In addition, information exchange is required only between neighboring elements which is suitable for parallelization. In addition, a local time-stepping strategy [3] is necessary to reduce the computational time in multi-scale problems. Moreover, in this work we present a memory efficient implementation. Finally, validation of the method is presented through numerical examples.

II. FORMULATION

A. Original Boundary Value Problem(BVP)

We consider the time-dependent Maxwell's equations in three dimensions.

$$\begin{aligned}\nabla \times \mathbf{E} &= -\mu \frac{\partial \mathbf{H}}{\partial t} & \text{in } \Omega \\ \nabla \times \mathbf{H} &= \frac{\partial \mathbf{E}}{\partial t} & \text{in } \Omega\end{aligned}\quad (1)$$

On the boundary $\partial\Omega$ of the domain Ω we apply metallic or absorbing boundary conditions.

B. DGTD Formulation-Spatial Discretization

Let Ω be the computational domain of interest and T_h the discretization of Ω into tetrahedra K . Denote by F_h the set of all faces. Assuming that the material properties are constant within each element we can then proceed to define the following finite-dimensional discrete trial space

$V_h^k = \left\{ \mathbf{v}, \nabla \times \mathbf{v} \in [L^2(\Omega)]^3 : \mathbf{v}|_K \in [P^k(K)]^3 \right\}$. The interior

penalty discontinuous Galerkin method can be written as:

Find $(\mathbf{w}, \mathbf{v}) \in V_h^k \times V_h^k$ such that

$$\begin{aligned}\int_{\Omega} \mathbf{w} \cdot \left(\nabla \times \mathbf{v} + \frac{\mu \partial \mathbf{w}}{\partial t} \right) d\Omega - \int_{\Omega} \mathbf{v} \cdot \left(\nabla \times \mathbf{w} - \frac{\varepsilon \partial \mathbf{v}}{\partial t} \right) d\Omega \\ + \int_{F_h} \{ \{ \mathbf{v} \} \} \cdot [\mathbf{w}] dS - \int_{F_h} \{ \{ \mathbf{w} \} \} \cdot [\mathbf{v}] dS \\ - e \int_{F_h} [\mathbf{v}] \cdot [\mathbf{v}] dS - f \int_{F_h} [\mathbf{w}] \cdot [\mathbf{w}] dS = 0.\end{aligned}\quad (2)$$

where $\gamma_\tau(\mathbf{u}_i) = \mathbf{n}_i \times \mathbf{u}_i$, $\pi_\tau(\mathbf{u}_i) = \mathbf{n}_i \times \mathbf{u}_i \times \mathbf{n}_i$ and $\{ \{ \mathbf{u}_i \} \} = (\pi_\tau(\mathbf{u}_i) + \pi_\tau(\mathbf{u}_j)) / 2$, $[\mathbf{u}_i] = \gamma_\tau(\mathbf{u}_i) + \gamma_\tau(\mathbf{u}_j)$.

Finally, $e = \frac{1}{2Z_\Gamma}$ and $f = \frac{1}{2Z_\Gamma}$ with $Z_\Gamma = \frac{1}{2} \left(\sqrt{\frac{\mu_i}{\varepsilon_i}} + \sqrt{\frac{\mu_j}{\varepsilon_j}} \right)$ and

$$Y_\Gamma = \frac{1}{2} \left(\sqrt{\frac{\varepsilon_i}{\mu_i}} + \sqrt{\frac{\varepsilon_j}{\mu_j}} \right).$$

C. DGTD Formulation-Time Discretization

Within each element the electric and magnetic fields are expanded in terms of trial functions in V_h^k . Thus, the following semi-discrete system of coupled differential equations is obtained:

$$\begin{aligned}\mathbf{M}_\varepsilon \frac{\partial \mathbf{e}}{\partial t} &= \mathbf{S}_\varepsilon \mathbf{h} - \mathbf{F}_\varepsilon \mathbf{h} - e \mathbf{P}_\varepsilon \mathbf{e} \\ \mathbf{M}_\mu \frac{\partial \mathbf{h}}{\partial t} &= -\mathbf{S}_\mu \mathbf{e} + \mathbf{F}_\mu \mathbf{e} + f \mathbf{P}_\mu \mathbf{h}\end{aligned}\quad (3)$$

where \mathbf{e} and \mathbf{h} are the time dependent coefficient vectors for the electric and magnetic field respectively. The above system is discretized in time with a leap-frog scheme. The electric field unknowns are evaluated at $t_n = n\delta t$ and the magnetic field unknowns are evaluated at $t_{n+1/2} = (n+1/2)\delta t$. The first derivatives are approximated using central differences. The fully discretized update equation then becomes

$$\begin{aligned}\mathbf{e}^{n+1} &= \tilde{\mathbf{B}}\mathbf{e}^n + \tilde{\mathbf{C}}\mathbf{h}^{n+1/2} \\ \mathbf{h}^{n+3/2} &= \tilde{\mathbf{E}}\mathbf{h}^{n+1/2} + \tilde{\mathbf{F}}\mathbf{e}^{n+1}\end{aligned}\quad (4)$$

III. LOCAL TIME STEPPING

The resulting update scheme a mentioned above is explicit and conditionally stable. The stability condition is [2]:

$c_i \delta t \left[2\alpha_i + \beta_{ik} \max \left(\sqrt{\frac{\mu_i}{\mu_k}} + \sqrt{\frac{\varepsilon_i}{\varepsilon_k}} \right) \right] < \frac{4V_i}{P_i}$ where V_i is the volume of element K_i , $P_i = \sum_j S_j$, (S_i is surface of face i),

$c_i = 1/\sqrt{\varepsilon_i \mu_i}$ and α_i, β_{ik} are dimensionless constants that depend on the order of the basis functions. Note that for higher order basis or locally refined meshes the stability condition provides a very small δt and thus greater CPU time. To reduce the computational time a local time-stepping strategy is applied [3]. The set of elements is partitioned into N classes before the time-marching simulation. The partition is based on the stability condition. For the i^{th} class $\delta t_i = (2m+1)^i \delta t_{min}$. We choose $m=1$ so that each class has a time step three times larger than the previous class. To illustrate the method assume two classes (class 0 class 1) with $\delta t_0 = \delta t_{min}$ and $\delta t_1 = 3\delta t_{min}$. The update scheme is summarized below:

<i>E-Update</i>	<i>H-Update</i>
$\mathbf{e}^{n+1} = \tilde{\mathbf{B}}_1 \mathbf{e}^n + \tilde{\mathbf{C}}_1 \mathbf{h}^{n+1/2}$	$\mathbf{h}^{n+3/2} = \tilde{\mathbf{E}}_1 \mathbf{h}^{n+5/6} + \tilde{\mathbf{F}}_1 \mathbf{e}^{n+1}$
$\mathbf{e}^{n+4/6} = \tilde{\mathbf{B}}_0 \mathbf{e}^{n+2/6} + \tilde{\mathbf{C}}_0 \mathbf{h}^{n+3/6}$	$\mathbf{h}^{n+7/6} = \tilde{\mathbf{E}}_0 \mathbf{h}^{n+5/6} + \tilde{\mathbf{F}}_0 \mathbf{e}^{n+1}$
$\mathbf{h}^{n+5/6} = \tilde{\mathbf{E}}_0 \mathbf{h}^{n+3/6} + \tilde{\mathbf{F}}_0 \mathbf{e}^{n+4/6}$	$\mathbf{e}^{n+8/6} = \tilde{\mathbf{B}}_0 \mathbf{e}^{n+1} + \tilde{\mathbf{C}}_0 \mathbf{h}^{n+7/6}$
$\mathbf{e}^{n+1} = \tilde{\mathbf{B}}_0 \mathbf{e}^{n+4/6} + \tilde{\mathbf{C}}_0 \mathbf{h}^{n+5/6}$	$\mathbf{h}^{n+3/2} = \tilde{\mathbf{E}}_0 \mathbf{h}^{n+7/6} + \tilde{\mathbf{F}}_0 \mathbf{e}^{n+8/6}$

IV. NUMERICAL EXAMPLES

A. Coated Sphere

In this example we calculate the RCS of a coated sphere. The inner radius of the sphere is $a = 1$ m, the outer radius is $b = 1.2$ m and the coating has $\varepsilon_r = 4.0$. The absorbing boundary condition is set one λ at 300 MHz from the coating. The coated sphere is illuminated by a Gaussian pulse $\mathbf{E}^{inc} = \mathbf{E}_0 e^{-[t-t_0 - \mathbf{k} \cdot (\mathbf{r}-\mathbf{r}_0)/c]^2 / \tau^2}$ with $\mathbf{E}_0 = E_x$, $\mathbf{k} = k_z$, $t_0 = 5$ ns and $\tau = 0.6$ ns. From the Fourier transform of the time-dependent electric and magnetic currents on the sphere's surface we can evaluate the RCS at multiple frequencies. Fig.1 illustrates the computed RCS at the frequency of 300 MHz. A good agreement is observed between the numerical solution and the analytical solution.

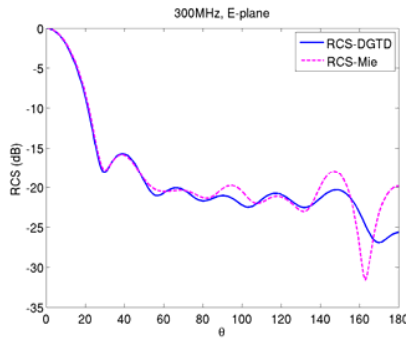


Figure 1. E- and H-plane RCS(dB) at 300 MHz (blue-DGTD, pink-Mie series).

B. Scattering from a F-16 aircraft

In this example we calculate the RCS of a F-16 aircraft illuminated by a Gaussian pulse with $\mathbf{E}_0 = E_x$, $\mathbf{k} = k_z$, $t_0 = 5$ ns and $\tau = 0.6$ ns. The generated mesh in this case is an unstructured locally refined mesh with strong element-size disparities. In this case $\delta t_{min} = 4.35e-13$ and $\delta t_{max} = 7.98e-11$ which leads into 5 classes and the local time stepping provides a CPU gain of approximately 5 compared to the standard leap-frog scheme. Finally a matrix free implementation was applied to provide better memory efficiency. In this approach there is no assembly and storage of global matrices. The matrix-vector multiplications that are necessary for the update equation are performed in element level using the BLAS library for better performance.

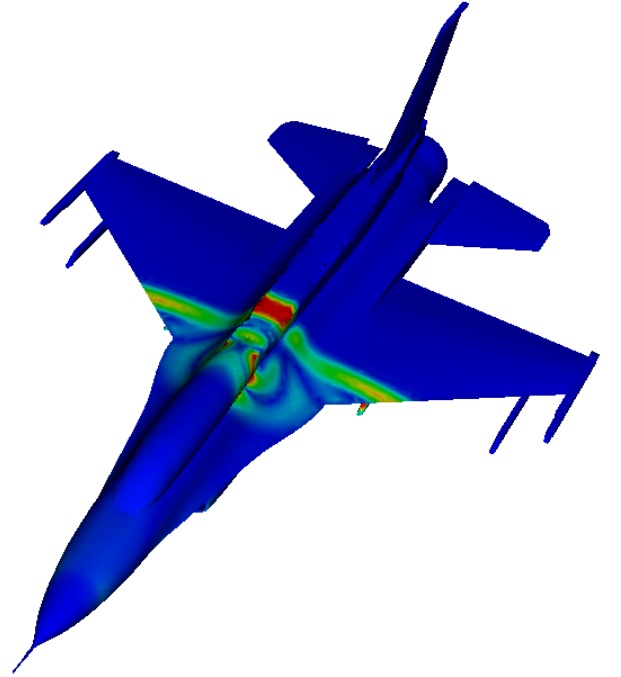


Figure 2. Snapshot of the magnitude of the E field distribution of the Gaussian pulse propagating on the F-16 surface.

TABLE I
CLASS PARTIONING

Class	2	3	4	5
1				
36	2552	129318	240890	81400

V. REFERENCES

- [1] J. S. Hesthaven and T. Warburton, "Nodal high-order methods on unstructured grids", *J. Comput. Phys.*, vol. 181, 2002.
- [2] L. Fezoui and S. Lanteri and S. Lohrengel and S. Piperno, "Convergence and stability of a discontinuous galerkin time-domain method for the 3D heterogeneous maxwell equations on unstructured meshes", *ESAIM: M2AN*, 2005, pp. 1149-1176.
- [3] E. Montseny and S. Pernet and X. Ferrieres and G. Cohen, "Dissipative terms and local time-stepping improvements in a spatial high order Discontinuous Galerkin scheme for the time-domain Maxwell's equations," *J. Comput. Phys.*, vol. 227, 2008.

A FEM Approach for Analyzing the Corona Ionized Field of Bipolar Bundled Conductors

Haiyan Yuan¹, Zhengcai Fu¹ and Junwei Lu²

1. Department of Electrical Engineering, Shanghai Jiao Tong University, Shanghai 200240, China
(e-mail: haiyan_yuan@sjtu.edu.cn)

1. Department of Electrical Engineering, Shanghai Jiao Tong University, Shanghai 200240, China
(e-mail: zcfu@sjtu.edu.cn)

2. Centre of Wireless Monitoring and Applications, Griffith University, Brisbane, QLD 4111, Australia
(e-mail: j.lu@griffith.edu.au)

Abstract— A finite element method is proposed for an investigation of the bipolar bundled conductor ionized field. A computation program for the corona ionized field analysis was developed in which Deutsch's assumption was waived. The subconductors were considered as separate parts where the mutual impact was included. Each electric field line was initiated from the subconductor surface. The electric field was calculated by adopting the third order interpolating method. Furthermore, a method of estimating the initial space charge density of flux-tubes was introduced and then calculated by using the fourth order Runge-Kutta method. Finally, the computation program was verified and the corona current and related field properties of a $\pm 800\text{kV}$ HVDC transmission line were investigated.

I. INTRODUCTION

Many numerical attempts have been made to evaluate the ionized field associated with single and bundled conductors for monopolar transmission lines [1]-[3].

Some attempts have also been made to solve the bipolar ionized field equations. Sarma developed a method of calculating the electric field for bipolar lines based on Deutsch's assumption first [4]. Later, though Deutsch's assumption is waived, the bipolar ionized field equations were only solved in single conductor-to-plane configurations [5]-[6]. In [7] an integral form of the current continuity equation was used (instead of Poisson's equation) to compute the space potential with a bipolar bundled conductor line in a double circuit.

Al-Hamouz has done much more on the ionized field analysis. The main idea was solving Poisson's equation by using the FEM and calculating the charge density along the flux-tubes divided by field lines in the ionized field. His investigating range varied from monopolar to bipolar, from single conductor to bundled conductor, and to extending the limited boundary to infinity [1, 3, 6, 8]. However, the bipolar and bundled configuration aspects have not been taken into account simultaneously.

In this paper, an iterative FEM based numerical method is developed to solve Poisson's equation for the bipolar bundled conductor. Firstly, the computation process is explained in detail and then it is verified. Finally, the program is used to analyze the corona ionized field of a $\pm 800\text{kV}$ transmission line.

II. DESCRIPTION OF THE BIPOLAR IONIZED FIELD

The bipolar ionized field can be described by a group of equations:

$$\nabla \cdot \vec{E} = (\rho_+ - \rho_-) / \epsilon_0 \quad (1)$$

$$\vec{J}_{\pm} = k_{\pm} \rho_{\pm} \vec{E} \quad (2)$$

$$\nabla \cdot \vec{J}_{\pm} = \mp R_i \rho_{\pm} \rho_{\pm} / e \quad (3)$$

$$\vec{J} = \vec{J}_+ + \vec{J}_- \quad (4)$$

$$\nabla \cdot \vec{J} = 0 \quad (5)$$

where (1) is Poisson's equation; (2) is the equation of the positive and negative current density vectors \vec{J}_{\pm} ; (3) is the equation for \vec{J}_{\pm} continuity; (4) is the equation of the total current density vector \vec{J} ; and (5) is the equation for \vec{J} continuity. \vec{E} is the electric field, k_+ and k_- are the mobilities of positive and negative ions, ρ_+ and ρ_- are the modulus of the positive and negative space charge density values, R_i is the ion recombination coefficient in air, and e is the electron charge.

Using the FEM based numerical approach, with associated boundary and constraint conditions, the above partial differential equations can be solved.

III. PROPOSED ANALYSIS METHOD OF A BIPOLAR BUNDLED CONDUCTOR IONIZED FIELD

A general configuration of a bipolar HVDC transmission line is illustrated in Figure 1. A $\pm 800\text{kV}$ HVDC transmission line is used as an example. The triangular finite element grid is generated from quadrangles produced by the intersection of field lines with equipotential contours. In either the bipolar or monopolar component, the FEM is applied to obtain an evaluation of the nodal potential. The third order interpolating method is then adopted to calculate the electric field.

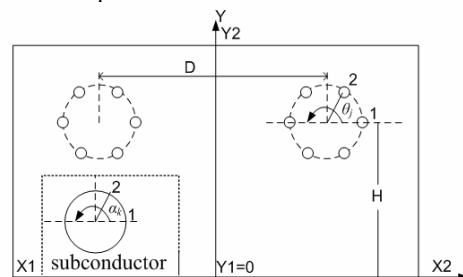


Fig. 1. Configuration of a $\pm 800\text{kV}$ HVDC transmission line

For the monopolar component, the initial estimation of the space charge density of each field line is:

$$\rho d_{j,k} = \rho_{ej} \cos((\pi - \alpha_k)/2), k = 1, 2, \dots, nd_{sub} \quad (6)$$

$$\rho_{ej} = \rho_e \cos((\pi - \theta_j)/2), j = 1, 2, \dots, n$$

where $\rho d_{j,k}$ is the space charge density in the monopolar component, nd_{sub} is the number of electric field lines in the monopolar component, ρ_{ej} is the value of $\rho d_{j,k}$ at $\alpha_k = \pm\pi$, n is the number of conductor bundles, ρ_e is the value of ρ_{ej} at $\theta_j = \pm\pi$ and can be calculated from an existing formula, and α_k and θ_j are shown in Figure 1.

In addition, the initial space charge density values in the bipolar component are assumed as [8]

$$\rho s_{j,k} = 0.02(\rho d_{j,k}), k = 1, 2, \dots, ns_{sub} \quad (7)$$

where $\rho s_{j,k}$ is the space charge density in the bipolar component, and ns_{sub} is the number of electric field lines in the bipolar component.

The fourth order Runge-Kutta method is then used to evaluate the space charge density of all nodes. The process is repeated until the errors of potential and space charge density calculated in two successive iterations are satisfied with the required accuracy. The errors of potential and space charge density are δ_1 and δ_2 respectively.

Figure 2 shows a block diagram of the solution procedure, where the corona current can be obtained.

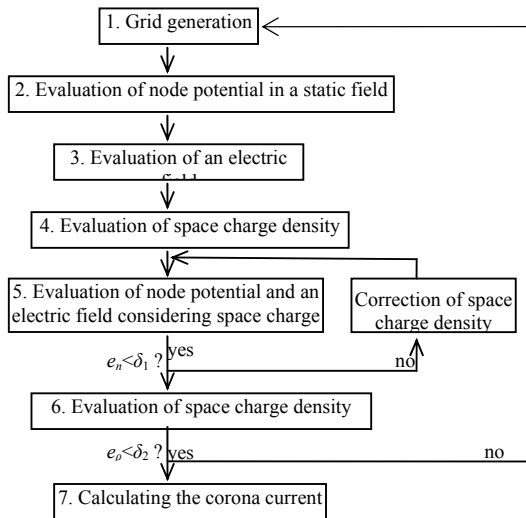


Fig. 2. The solution procedure

IV. VERIFICATION OF REAL ± 500 kV BIPOLAR LINES

In order to verify the proposed numerical program, a ± 500 kV transmission line model with experimental results was used to evaluate the corona ionized field as shown in Figure 3. The computation result (the solid line) was consistent with the experiment result (the star line). Thus, the computation program can be used to validate the ionized field of a bipolar bundled conductor.

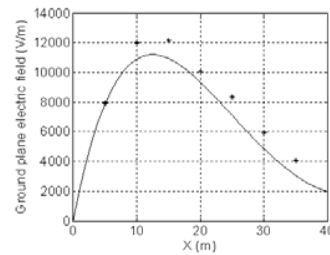


Fig. 3. ± 500 kV line ground-plane electric field, the solid line is the calculated result and the star line is the experimental result.

V. RESULTS AND DISCUSSION ON ± 800 kV HVDC TRANSMISSION LINE IONIZED FIELDS

The proposed program is adopted to analyze the corona ionized field of a ± 800 kV HVDC transmission line. The configuration is shown in Figure 1. The algorithm converges in three mesh generations, each with 13 iterations for the HVDC models. The errors of δ_1 and δ_2 are less than 0.5%. The corona current, ground electric field and ground current density are calculated for a ± 800 kV HVDC transmission line.

VI. CONCLUSION

(1) The proposed FEM based numerical method is effective for calculating the ionized field of a bipolar bundled conductor.

(2) An increase in the number of bundles decreases corona current, while an increase in bundle spacing increases corona current. If the monopolar component is not included, the corona current will be overestimated. The ground electric field and ground current density of the present ± 800 kV HVDC transmission line is less than 30kV/m and 100nA/m² respectively.

(3) The computation program can be used as an effective numerical tool for evaluating the electromagnetic environment around the HVDC transmission line.

VII. REFERENCES

- [1] Z. Al-Hamouz, "Finite element solution of monopolar corona as influenced by ion lifetime", *Proc. IEEE-IAS Annual Meeting on Industry Applications*, Vol. 4, pp. 1919-1924, 1996.
- [2] M. Abdel-Salam, M. Farghally, S. Abdel-Sattar, "Monopolar corona on bundle conductors", *IEEE Trans. Power Apparatus and Systems*, PAS-101(10): 4079-4089, 1982.
- [3] Z. M. Al-Hamouz, "Finite-Element Solution of Monopolar Corona on Bundle Conductors", *IEEE Trans. Industry Applications*, 35(2): 380-385, 1999.
- [4] M. P. Sarma, "Analysis of corona losses on dc transmission lines: II-Bipolar lines", *IEEE Trans. Power Apparatus and Systems*, PAS-88(10): 1476-1491, 1969.
- [5] B. L. Qin, J. N. Sheng, Z. Yan, G. Gela, "Accurate calculation of ion flow field under HVDC bipolar transmission lines", *IEEE Trans. Power Delivery*, 3(1): 368-376, 1988.
- [6] Z. M. Al-Hamouz, M. Abdel-Salam, "Improved Calculation of Finite-Element Analysis of Bipolar Corona Including Ion Diffusion", *IEEE Trans. Industry Applications*, 34(2): 301-309, 1998.
- [7] T. Taknma, T. Kawamoto, "A very stable calculation method for ion flow field of HVDC transmission lines", *IEEE Trans. Power Delivery*, 2(1): 189-198, 1987.
- [8] Z. M. Al-Hamouz, "Adaptive finite-element ballooning analysis of bipolar ionized fields", *IEEE Trans. Industry Applications*, 32(6), 1266-1277, 1996.

The Solution of Electromagnetic Field Problems using a Sliding Window Gauss-Seidel Algorithm on a Multi-Core Processor

Hussein Moghnieh and David Lowther

Department of Electrical and Computer Engineering, McGill University
3480 University Street, Montreal, Quebec, H3A 2A7, Canada
hussein.moghnieh@mail.mcgill.ca,david.lowther@mcgill.ca

Abstract—Chip based multi-core processors (CMP) raise the possibility of significant improvement in the performance of electromagnetic simulation tools. They can impact the mesh generation, solution and result evaluation phases. This paper investigates the parallelization and scalability of Gauss-Seidel on CMP by using a new cache blocking technique to overcome the small cache problem while using a thread synchronization technique for better cache sharing and to maximize thread cycle utilization.

I. INTRODUCTION

The computer-based simulation of an electromagnetic field problem using a differential technique such as finite differences or elements consists of several phases which are computationally intensive and have complexities which can be beyond linear. These include mesh generation, equation solution and result evaluation. The introduction of chip-based multi-core processors (CMP), both within the main CPU and as part of high performance graphics systems, provides the possibility of significant speedups over the existing single core systems. Each phase of the simulation system presents its own challenges to parallelization. This paper is targeted at the equation solution phase.

In a differential method, the equation sets produced are both large and sparse and their solution has been the subject of considerable research over the last four decades and, for many problems, the algorithm of choice at present is the Incomplete Choleski-Congugate Gradient approach which has a complexity of approximately $O(N^{1.5})$. This is, however, a predominantly sequential algorithm optimized for a single processor machine. It is not obvious that this is an ideal algorithm for the new generation of processors and thus it is worth revisiting a range of solver algorithms and to re-examine their performance on the new architectures.

II. PROCESSOR ARCHITECTURE AND SOLVERS

One of the key issues in considering an algorithm for a multi-core system is the architecture of the processor. This must be considered as the given environment and the goal is to find an efficient algorithm for this architecture, not develop an effective architecture for a particular parallel algorithm. Most multi-core machines have been designed to handle several relatively small tasks in parallel – not to divide one large task amongst the processors which is the case for multiprocessor based computers. Although CMP has the advantage of low inter-thread communication and synchronization due to cache sharing, the cache memory is small relative to the

computational power of the cores and the amount of cache available for each core is limited. In addition, the memory bandwidth between the cores and the main system memory is relatively small. Consequently, the ideal algorithm for this architecture is one which can allow for the equation set to be broken up between the cores and to maximize the utilization of the equation set present in the cache.

In recent years, the high performance computing community has been revisiting both currently and long abandoned numerical methods to gain performance in solving large system of linear equations. In this paper, we investigate the speedup of a parallel Gauss-Seidel algorithm on a CMP. As a preliminary test of the algorithm, it is applied to the structured linear system of equations resulting from the finite difference solution of a parallel plate capacitor.

Iterative methods, such as Jacobi and Gauss-Seidel, have been investigated on parallel systems. The main concern was to reduce the synchronization points between processors leading to schemes known as chaotic or relaxation schemes [1] which are not suitable for implementation on a CMP.

The performance of parallel Gauss-Seidel as a multi-grid smoother on CMP has also been investigated in [2], where cache blocking [3], a technique to reuse data in cache, was used to decrease cache misses, hence increasing performance. It was used in conjunction with red-black and natural reordering techniques of the problem - techniques used on parallel systems where synchronization is expensive. However, a strong order of execution was imposed on threads, leading to lower thread execution time relative to thread waiting time.

It appears that, for larger problems, the gap between the slow data access due to a small cache relative to the high number of flops available is higher on CMP than other hardware architectures. For this reason, we used a more execution time hungry threading approach together with a cache blocking technique to solve the system of linear equations. Synchronized pipelined threading techniques, i.e. a producer-consumer model, [4], are used to provide better communication and synchronization between threads and to provide fair cache sharing and partitions between cores of the CMP.

III. METHODOLOGY

Gauss-Seidel is an iterative method used to solve a large sparse linear system of equations $AX = b$. The method is expressed in (1) for $A_{n \times n}$ matrix.

$$X_i^{(\Gamma+1)} = \frac{1}{a_{ii}} \left(b_i - \sum_{j<i} a_{ij} X_j^{(\Gamma+1)} - \sum_{j>i} a_{ij} X_j^{(\Gamma)} \right) \quad (1)$$

$i = 1, 2, 3, \dots, n$ and $j = 1, 2, 3, \dots, n$

Let S_{ss*n} be a sub block of matrix A_{n*n} , where ts is the total number of sub blocks and p is a sub-block index indicator

$$A_{n*n} = \bigcup_{p=1}^{ts=n/ss} S_{ss*n}^p \quad (2)$$

Let W_{w*n} be a block that is constructed from 1, 2, 3, ..., or N contiguous sub blocks S_{ss*n} and q is a block index indicator

$$W_{w*n}^q = \bigcup_{p=q}^{q+N} S_{ss*n}^p \quad (3)$$

Let T = the number of blocks to apply Gauss-Seidel on simultaneously or the number of threads

Let $\mathfrak{B}_r = \{W_{w*n}^q\}$ be a set of contiguous T blocks from A_{n*n} , where

$$\bigcap_{q=r}^{r+T} W_{w*n}^q = \emptyset \quad (4)$$

The matrix A_{n*n} is divided into ts blocks that are queued into Q as shown in Fig.1. At every new iteration Γ , a sub block S_{ss*n} is passed from Q to the first thread and subsequently each thread passes its last sub block S_{ss*n} to the next thread or back to Q . Threads communicate through buffers to avoid resource locking and contention. Each thread applies Gauss-Seidel on its correspondent element in \mathfrak{B}_r , updates its local solution x_w and has a read only access to the global solution X_n . Since threads have the same data size at each iteration, they will reach the synchronization point almost simultaneously before proceeding to the next iteration leading to a minimal thread waiting time.

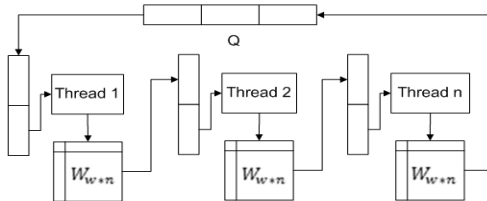


Fig. 1. Synchronized Producer-Consumer model

IV. SIMULATIONS AND RESULTS

We ran our algorithm on a 10000x10000 sparse system of equations, using different combinations of block, W , and sub-block, S , sizes. We calculated thread cycle utilization as the ratio of thread execution time to thread waiting time. The results were compared to a single thread execution of the algorithm ($W=10000$ and $S=10000$). As can be seen in Fig.2, the speedup when using smaller W and S was super linear for 4 threads and less on a Quad-Core CMP machine with 2*2MB cache. Another observation is that there was a relatively high speedup, slightly sub linear, even when the number of threads exceeded the number of cores of the CMP. To further illustrate those results, Fig.3 shows the effect of increasing thread

numbers on speedup, thread utilization, and convergence rate when $W=500$, $S=100$. We notice that convergence rate is essential to speedup and thread utilization greatly impacts the speedup (between 6 and 8 threads) for this particular problem.

V. CONCLUSION AND EXTENDED WORK

We conclude that speedup can be achieved even when using more threads than the number of cores. Cache blocking affects convergence; however, maximizing thread utilization is important. In the full paper, the performance of the algorithm on an unstructured mesh produced by an FEM code will be examined. In addition, the use of a GPU(Graphics Processing Unit) to accelerate the calculation at each iteration on each block will be investigated.

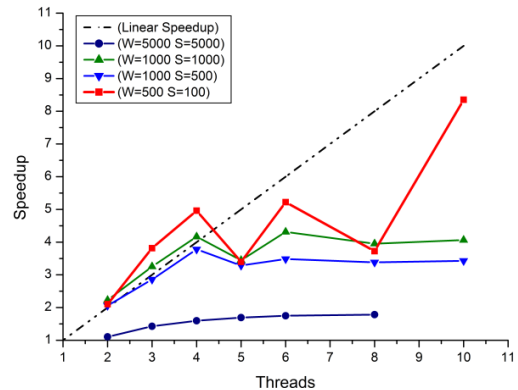


Fig.2 Speedup for different block W and sub-block S sizes

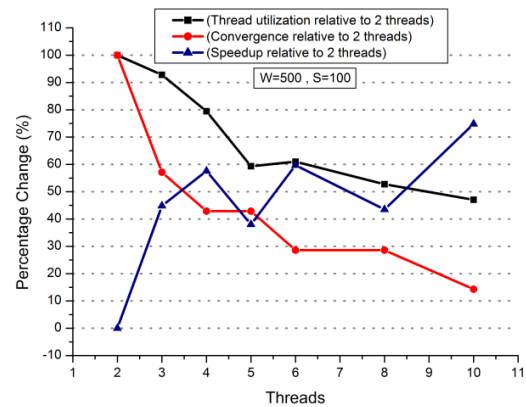


Fig.3 Comparing the effect of increasing thread numbers from 2 on speedup, thread utilization and convergence rate when $W=500$, $S=100$

VI. REFERENCES

- [1] G. M. Baudet, "Asynchronous Iterative Methods for Multiprocessors", *Journal of the Association for Computing Machinery*, 25(2): 226-244, April 1978.
- [2] D.Wallin,H.Lof,E.Hagersten and S.Holmgren, "Multigrid and GaussSeidel Smoothers Revisited:Parallelization on Chip Multiprocessors," in *Proceedings of the 20th annual international conference on Supercomputing*,2006,pp.145-155.
- [3] C.Weib,W.Karl,M.Kowarschik and U.Rude, "Memory Characteristics of Iterative Methods," in *Proceedings of the 1999 ACM/IEEE conference on Supercomputing*, 1999.
- [4] S.N. Vadlamani and S.F. Jenks,"The synchronized pipelined parallelism model," in *Proceedings of the IASTED International Conference on Parallel and Distributed Computing and Systems*,2004 .pp.163-168

Speeding Up the Process of Building High-Quality Finite-Element Meshes

Cássia R. S. Nunes, Renato C. Mesquita*, David A. Lowther†

Universidade Federal de São João del-Rei, Campus Alto Paraopeba, Ouro Branco, Minas Gerais, Brazil

* Universidade Federal de Minas Gerais, Departamento de Engenharia Elétrica, Belo Horizonte, Minas Gerais, Brazil

† McGill University, Department of Electrical and Computer Engineering, Montreal, Quebec, Canada

e-mail: cassia.nunes@ufsj.edu.br, renato@ufmg.br* and david.lowther@mcgill.ca†

Abstract—In finite-element analysis, high-quality meshes are necessary to provide good conditioning of the system. It minimizes errors and avoid singularities that might arise. However, most triangle meshes can hardly be called satisfactory without any kind of post-processing to improve their intrinsic qualities. This work presents an effective and efficient algorithm to improve the quality of surface meshes representing models generated by the application of the Boolean and assembly operations to predefined primitives, like spheres and blocks; and also models obtained from surface reconstruction.

I. INTRODUCTION

Many researchers are investigating ways to automate the finite-element method (FEM), thus allowing improved productivity, more accurate solutions, and use by less trained personnel. Often the most time consuming and experience requiring task faced by an analyst is the discretization of the general geometric definition of a problem into a valid and well conditioned finite-element mesh. For complex geometries, the time spent on geometry description and mesh generation are the pacing items in the computational simulation cycle.

Automatic generation of consistent, reproducible, high quality meshes without user intervention makes the power of the finite element analysis accessible to those not experts in the mesh generation area. Therefore, tools for an automated and efficient mesh generation are important prerequisites for the complete integration of the FEM with design processes in CAD, CAE, and CAM systems.

Most of the research on development of fully automatic unstructured mesh generators has been concentrated on various triangulation schemes. The advantage of them lies in the fact that simplicial elements (triangles and tetrahedra) are most suitable to discretize domains of arbitrary complexity, particularly when locally graded meshes are needed. While the meshing schemes for the discretization of 2D problems matured into very robust and efficient algorithms, there are still many open issues in 3D, including not only theoretical guarantee of convergence, quality bounds but also implementation aspects as robustness and versatility.

The long-term goal for developers of meshing tools is the generation of high quality meshes directly from CAD models, without user intervention.

The main contribution of this paper is to speed up the generation process of high quality finite-element mesh from poor quality initial surface mesh, which can be obtained using a solid modeler [1]; or a surface reconstruction algorithm [2]. Here, the remeshing process driven by a smooth approximation of the mesh vertices is modified to take advantage of the multicore platforms.

II. MODEL GENERATION

Usually, automatic mesh generators can produce surface meshes with a specified quality degree for simple predefined primitives, like spheres, cylinders or prisms. However, to generate models with high complexity two options frequently can be chosen: the application of the Boolean (union, intersection or subtraction) and assembly operations over predefined primitives [1]; or the reconstruction of surfaces by an acquisition process, such as medical imagery, laser range scanners, contact probe digitizers, radar and seismic surveys [2]. Unfortunately, both methods produce surface meshes with a large number of badly shaped elements. For the Boolean and assembly operations, the elements in the intersection areas are usually split into degenerate ones, decreasing drastically the elements quality, as Figure 1 illustrates. The surface meshes with this level of quality cannot be used as input for finite element volumetric mesh generators.

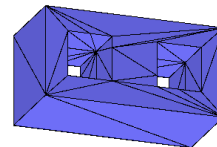


Figure 1. Surface mesh generated by the application of Boolean operations over predefined primitives

Badly shaped triangles also raises in meshes generated by an acquisition process. During the reconstruction process, the algorithm guarantees good approximation for the geometry and topology, but it does not guarantee the triangle shape quality. In many cases, the generated mesh possess a large amount of triangles and many of them are badly shaped, which sometimes makes impracticable the volumetric mesh generation. Figure 2 shows an example of reconstructed mesh.

As consequence, the surface meshes of models generated by: the application of the Boolean and assembly

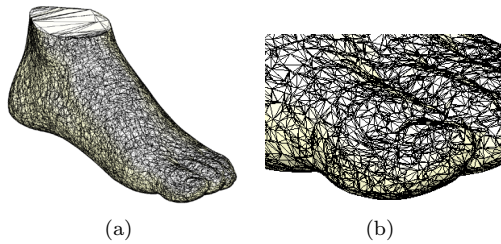


Figure 2. a) Reconstructed surface from a points cloud, b) Zoom In

applications over simple models; or from an acquisition process, should be improved, before being used as input to electromagnetic simulation by FEM.

III. STRATEGY TO IMPROVE THE SURFACE MESH QUALITY

Generally, tetrahedral mesh generators can add new vertices and edges to a surface mesh, when necessary, to try to generate a volumetric mesh with good quality. Nevertheless, vertices, edges, faces, slits and holes from the input geometric description are constraints that cannot be removed by them. Remeshing is very important to reduce the number of sharp angles, as well as improving the node distribution and their interconnections. Applying a series of local mesh modification operators that can enrich, simplify or locally improve the mesh is a good approach for improving the quality. This approach is known as a mesh adaptation process and works directly on the surface mesh. To avoid losing model geometric characteristics during the process, it is necessary to know the model surface geometry.

Unfortunately, after the surface is reconstructed, only the vertices and their interconnections are known. To overcome the lack of geometric information, an approximation of the model surface geometry is necessary. The surface approximation can control the movements of the vertices and ensure that they stay located on the original model surface during the application of the local mesh modifications. Since our set of points P was sampled from a smooth surface S , approximating them by a smooth surface is straightforward. B-Spline surfaces can give good approximations for a large variety of models, as has been proposed by Nunes et al. in [1]. Each mesh face is approximated by a B-Spline surface patch using the least squares formulation. To evaluate a patch, the vertices of the face we want to approximate and the vertices that surround it are used. The problem then consists of looking for an approximating B-Spline surface patch s , which minimizes:

$$F = \sum_{\tau=0}^{\mu} \|s(u_{\tau}, v_{\tau}) - p_{\tau}\|^2 = \sum_{\tau=0}^{\mu} \left[\sum_{\omega=0}^{\nu} \mathbf{M}_{\omega}(u_{\tau}, v_{\tau})c_{\omega} - p_{\tau} \right]^2 \quad (1)$$

where, c_{ω} are the control points, \mathbf{M}_{ω} are the blending functions and p_{τ} are the vertices around a given face. The model surface approximation is then a collection of overlapping B-Spline patches. Differently of Eck and Hoppe

work [3], this approach avoids the global parametrization. The overlapping set of patches gives a good approximation of the model and provides the necessary geometric information to the local mesh modification operators. The surface mesh is modified iteratively by the operators (edge-swapping, edge-collapsing, edge-splitting and vertex relocation) in order to improve the quality of the mesh elements.

The remeshing algorithm proposed in Nunes et al. in [1] is effective to produce high-quality finite-element meshes, but it is inefficient in time. Its computational cost is proportional to the number of mesh vertices.

We propose two main modifications on the Nunes et al. remeshing process. First, optimize the choice of the next element for the application of a local mesh modification operator, instead of scanning, in sequence, all edges of the model. This is done by having a priority queue, where the first element has the worst quality factor.

Second, applying parallel computational techniques to the remeshing algorithm. With the development of multi-core machines, parallelization of processes becomes very attractive to reduce the processing time of high computational cost tasks. The step of generating the B-Spline patches that represents the smooth approximation of the model geometry can easily be converted. The necessary information to produce each patch does not change during this step, then it is only necessary to coordinate the patches generation, sending to each core what they need to know. The adaptation process can also be parallelized. The mesh elements should be divided by sectors and each sector can be evaluated by different cores, but it is very important to evaluate carefully the intersection areas to guarantee consistency.

IV. CONCLUSION

An important goal of mesh generation is that the finite-element mesh should be formed by relatively well shaped elements. Elements with small angles may degrade the quality of the numerical solution, because they can make the system of algebraic equations ill-conditioned and this compromises the solution accuracy.

The modified remeshing algorithm obtain significant improvements in the surface mesh quality, without losing the models original features, in a fair amount of time. Optimization and parallel computational techniques are applied to speed up the generation of high-quality finite-element meshes.

REFERENCES

- [1] C. R. S. Nunes, R. C. Mesquita, and D. A. Lowther, "Remeshing driven by smooth surface approximation of mesh nodes," *IEEE Transactions on Magnetics*, vol. 43, pp. 1541–1544, April 2007.
- [2] N. Amenta, S. Choi, and R. Kolluri, "The power crust, unions of balls, and the medial axis transform," *Computational Geometry: Theory and Applications*, vol. 19, no. 2-3, pp. 127–153, 2001, <http://www.cs.utexas.edu/users/amenta/powercrust/>.
- [3] M. Eck and H. Hoppe, "Automatic reconstruction of b-spline surfaces of arbitrary topological type," *Computer Graphics*, vol. 30, pp. 325–334, 1996.

Extended Boundary-Node Method: Application to Potential Problem

Ayumu Saitoh¹⁾, Taku Itoh²⁾ and Atsushi Kamitani³⁾

1) University of Hyogo, 2167, Shosha, Himeji, Hyogo 671-2280, Japan, E-mail: saito@eng.u-hyogo.ac.jp

2) Seikei University, 3-3-1, Kichijoji-Kitamachi, Musashino, Tokyo 180-8633, Japan, E-mail: taku@st.seikei.ac.jp

3) Yamagata University, 4-3-16, Jōnan, Yonezawa, Yamagata 992-8510, Japan, E-mail: kamitani@yz.yamagata-u.ac.jp

Abstract— The dual-reciprocal boundary-node method has been reformulated without using integration cells. In the proposed method, boundary integrals are directly calculated by use of the vector equation of the boundary. The performance of the proposed method has been compared with the dual-reciprocal boundary-element method (DRM). The results of computations show that the accuracy of the proposed method is superior to that of the DRM. In addition, when the number of boundary nodes exceeds a certain limit, the speed of the proposed method becomes almost equal to that of the DRM.

I. INTRODUCTION

Since the boundary-node method (BNM) [1] is one of the meshless methods, the preparation of data is considerably simplified. However, a boundary must be divided into a set of cells to evaluate boundary integrals. In other words, a concept of elements partly remains in the BNM.

On the other hand, the method has been proposed for depicting a three-dimensional object by use of an implicit function [2], [3]. In the method, an implicit-function surface $g(\mathbf{x}) = 0$ is determined from nodes and unit normals on an object surface. Subsequently, the object surface is reconstructed by drawing the surface $g(\mathbf{x}) = 0$. If boundary integrals are evaluated by use of $g(\mathbf{x})$, the demerit of the BNM can be eliminated completely.

The purpose of the present study is to formulate the boundary-node method by using the implicit function $g(\mathbf{x})$ and to compare the performance of the resulting method with that of the dual-reciprocal boundary-element method (DRM).

II. DUAL-RECIPROCAL BOUNDARY-NODE METHOD

As a potential problem, we consider a two-dimensional Poisson problem:

$$-\Delta u = \rho \quad \text{in } \Omega, \quad (1)$$

$$u = \bar{u} \quad \text{on } \partial\Omega, \quad (2)$$

where Ω denotes a region bounded by a simple closed curve $\partial\Omega$. In addition, ρ and \bar{u} are known functions in Ω and on $\partial\Omega$, respectively.

Although (1) can be transformed to an equivalent boundary integral equation, the equation contains not only boundary integrals but also a domain integral. In order to approximate the domain integral as the sum of boundary integrals, we employ the idea of the DRM. In other words, we assume that $\rho(\mathbf{x})$ is written as

$$\rho(\mathbf{x}) = \sum_{l=1}^{N+K} \alpha_l f(|\mathbf{x} - \mathbf{z}_l|/R). \quad (3)$$

Here, $\mathbf{z}_1, \mathbf{z}_2, \dots, \mathbf{z}_N$ are boundary nodes on $\partial\Omega$ whereas $\mathbf{z}_{N+1}, \mathbf{z}_{N+2}, \dots, \mathbf{z}_{N+K}$ are nodes in Ω . Moreover, R and α_l 's are all constants. For the function $f(r)$, we adopt a compactly supported radial basis function $f(r) = H(1-r)(1-r)^3(3r+1)$, where $H(x)$ denotes Heaviside's step function.

Substituting (3) into the boundary integral equation, we get

$$\begin{aligned} & \oint_{\partial\Omega} \frac{\partial w^*(\mathbf{x}(s), \mathbf{y})}{\partial n} [u(\mathbf{x}(s)) - u(\mathbf{y})] ds - \oint_{\partial\Omega} w^*(\mathbf{x}(s), \mathbf{y}) q(\mathbf{x}(s)) ds \\ &= \sum_{l=1}^{N+K} \alpha_l \left\{ \oint_{\partial\Omega} \frac{\partial w^*(\mathbf{x}(s), \mathbf{y})}{\partial n} [\hat{u}_l(\mathbf{x}(s)) - \hat{u}_l(\mathbf{y})] ds \right. \\ & \quad \left. - \oint_{\partial\Omega} w^*(\mathbf{x}(s), \mathbf{y}) \hat{q}_l(\mathbf{x}(s)) ds \right\}, \end{aligned} \quad (4)$$

where $w^*(\mathbf{x}, \mathbf{y}) = -\log|\mathbf{x} - \mathbf{y}|/2\pi$. In addition, \hat{u}_l is a particular solution of $-\Delta \hat{u}_l = f(|\mathbf{x} - \mathbf{z}_l|/R)$ and \hat{q}_l denotes its normal derivative. Furthermore, s indicates an arclength along $\partial\Omega$.

From the standard manner of the BNM, (4) and its associated boundary condition can be discretized to a linear system. By solving the system, we can determine the distributions of u and q on $\partial\Omega$.

III. EXTENDED BOUNDARY-NODE METHOD

A. Vector Equation of Boundary

In the conventional BNM, the boundary $\partial\Omega$ must be divided into a set of cells to evaluate boundary integrals. In this sense, a concept of elements has not been completely removed from the BNM. In the present study, the integrals are directly calculated by use of the vector equation of $\partial\Omega$. In III.A, let us briefly explain the method for determining the vector equation.

First, the implicit-function representation $g(\mathbf{x}) = 0$ is determined for the curve that passes through all boundary nodes, $\mathbf{z}_1, \mathbf{z}_2, \dots, \mathbf{z}_N$, on $\partial\Omega$. Subsequently, we numerically solve the following ordinary differential equation:

$$\frac{d\mathbf{x}}{ds} = \mathbf{R} \left(\frac{\pi}{2} \right) \cdot \frac{\nabla g}{|\nabla g|}, \quad (5)$$

where $\mathbf{R}(\theta)$ denotes a tensor representing a rotation through an angle θ . Apparently, the analytic solution of (5) gives the vector equation $\mathbf{x} = \mathbf{x}(s)$ of the curve $g(\mathbf{x}) = 0$. However, even if the higher-order Runge-Kutta method is applied to (5), the numerical solution $\mathbf{x}^{(n)}$ does not always satisfy $g(\mathbf{x}^{(n)}) = 0$. This

is mainly due to the discretization error. In order to diminish the error, we use the novel algorithm in which $\mathbf{x}^{(n+1)}$ is calculated from $\mathbf{x}^{(n)}$ by use of the following three steps.

- (i) An approximate solution of \mathbf{x}^* at the $(n+1)$ th step is determined by means of the forward Euler scheme:

$$\mathbf{x}^* = \mathbf{x}^{(n)} + \mathbf{R} \left(\frac{\pi}{2} \right) \cdot \left[\frac{\nabla g}{|\nabla g|} \right]_{\mathbf{x}^{(n)}} \delta s.$$

- (ii) For the purpose of determining an intersection of the straight line $\mathbf{x} = \mathbf{x}^* + \lambda (\nabla g)_{\mathbf{x}^*}$ and the curve $g(\mathbf{x}) = 0$, the nonlinear equation $g(\mathbf{x}^* + \lambda (\nabla g)_{\mathbf{x}^*}) = 0$ is solved for λ by using the Newton method.

- (iii) The numerical solution $\mathbf{x}^{(n+1)}$ is calculated as $\mathbf{x}^{(n+1)} = \mathbf{x}^* + \lambda (\nabla g)_{\mathbf{x}^*}$.

Finally, P data points, $\mathbf{x}^{(1)}, \mathbf{x}^{(2)}, \dots, \mathbf{x}^{(P)}$, are interpolated by using the cubic spline and, as a result, the vector equation $\mathbf{x} = \mathbf{x}(s)$ can be numerically determined. By means of the vector equation, boundary integrals can be easily evaluated without any integration cells.

B. Periodic shape functions

If the circumference of $\partial\Omega$ is denoted by L , $\mathbf{x}(s)$ is a periodic function with a period L . Thus, the integrands of boundary integrals become periodic only when the shape functions $\Phi_i(s)$'s have the same periodicity.

By means of the MLS approximation, the periodic shape functions $\Phi_i(s)$'s are easily determined as

$$\Phi_i(s) = \mathbf{p}(s)^T \mathbf{A}^{-1}(s) \mathbf{c}_i(s), \quad (6)$$

where $\mathbf{A}(s)$ and $\mathbf{c}_i(s)$ are given by

$$\mathbf{A}(s) = \sum_{i=1}^N w(d(s, s_i)) \mathbf{p}(s_i) \mathbf{p}(s_i)^T, \quad (7)$$

$$\mathbf{c}_i(s) = w(d(s, s_i)) \mathbf{p}(s_i). \quad (8)$$

Moreover, $d(s, s^*)$ is the distance between $\mathbf{x}(s)$ and $\mathbf{x}(s^*)$ along $\partial\Omega$, and $w(r)$ denotes a weight function. For the m -dimensional vector $\mathbf{p}(s)$, we assume the following type:

$$\mathbf{p}(s)^T = \begin{cases} 1 & ; m = 1, \\ (\cos(2\pi s/L), \sin(2\pi s/L)) & ; m = 2. \end{cases} \quad (9)$$

The above two techniques are incorporated into the method explained in II. Throughout the present study, the resulting method is called the eXtended Boundary-Node Method (X-BNM).

IV. PERFORMANCE OF X-BNM

In this section, we compare the performance of the X-BNM with that of the DRM. To this end, both two methods are applied to a simple Poisson problem. The boundary $\partial\Omega$ is assumed as

$$\partial\Omega = \left\{ \mathbf{x} \in \mathbf{R}^2 \mid g(\mathbf{x}) \equiv x^2 + (y/2)^2 - 1 = 0 \right\}. \quad (10)$$

In addition, ρ and \bar{u} are chosen so that the analytic solution of (1) and (2) may be given by

$$u = 3e^{-(x^2+y^2)} - \cosh x \sin y + \cos x \sinh y. \quad (11)$$

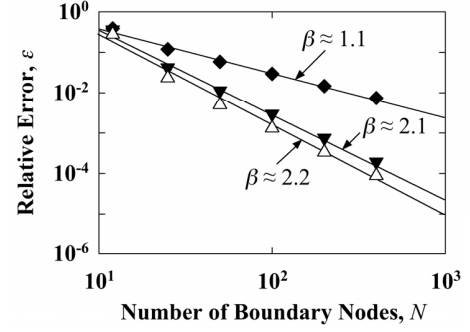


Fig. 1. Dependence of the relative error ε on the number N of the boundary nodes. Here, the symbols, \blacklozenge , \triangle and \blacktriangledown , indicate the values for the linear DRM, the X-BNM ($m = 1$) and the X-BNM ($m = 2$), respectively.

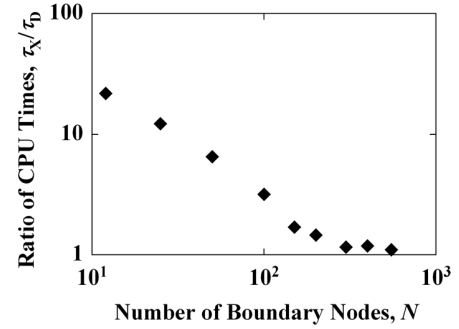


Fig. 2. Dependence of the ratio τ_X/τ_D on the number N of the boundary nodes.

Throughout the present study, the value of R is fixed as $R = 1$ and K is determined so as to satisfy $K \propto N^2$.

Let us first investigate the accuracy of the X-BNM and the DRM. The relative errors are calculated as a function of N and are depicted in Fig. 1. We see from this figure that, for both methods, the relative errors are almost proportional to $N^{-\beta}$ and that the power indices β 's satisfy $\beta \approx 1.1$, $\beta \approx 2.2$ and $\beta \approx 2.1$ for the linear DRM, the X-BNM ($m = 1$) and the X-BNM ($m = 2$), respectively. The above results indicate that the accuracy of the X-BNM is much higher than that of the DRM.

Next, we compare the speed of the X-BNM with that of the DRM. The ratio τ_X/τ_D of CPU times is calculated as a function of N and is depicted in Fig. 2. Here, τ_X and τ_D denote the CPU times for the X-BNM ($m = 1$) and that for the DRM, respectively. This figure indicates that τ_X/τ_D decreases monotonously with an increase in N until $\tau_X/\tau_D \approx 1$ is satisfied for $N \gtrsim 10^2$. This tendency shows that, for $N \gtrsim 10^2$, the speed of the X-BNM is almost equal to that of the DRM.

From the above results, we might conclude that the X-BNM can be a powerful method for solving a potential problem.

V. REFERENCES

- [1] Y.X. Mukherjee and S. Mukherjee, "The boundary node method for potential problems," *Int. J. Numer. Methods Eng.*, 44: 797-815, 1997.
- [2] G. Turk and J.F. O'Brien, "Shape transformation using variation implicit function," *Proc. ACM SIGGRAPH 99*, 335-342, 1999.
- [3] Y. Ohtake, A. Belyaev, M. Alexa, G. Turk and H.P. Seidel, "Multi-level partition of unity implicits," *ACM Trans. Graphics*, 463-470, 2003.

Reduction of Eddy Current Losses by several Cuts in Conductors

A.Kost¹, M.Ehrich²

¹Technische Universität Berlin, Einsteinufer 11, 10587 Berlin, Germany

kost@iee.tu-berlin.de

²Helmut-Schmidt-Universität Hamburg, Holstenhofweg 85, 22043 Hamburg, Germany

larsole@UniBw-Hamburg.DE

Abstract-- It is known, that the eddy current losses of conductors of circular or rectangular cross section can be reduced by cutting them into sectors. This paper presents an analytical-numerical mixed solution of this problem as reference for numerical methods like FEM.

I. INTRODUCTION

Due to the necessary energy saving multiple efforts are made to reduce losses in electric circuits, networks etc. Recently shape and distance of bar conductors for high current systems have been optimised and hereby demonstrating reduction of power losses [1]. Another thesis [2] minimised the losses by optimising the conductors' shape, applying the Evolution Strategy and Finite Element Method (FEM). In [3] it was shown how the eddy current losses in circular and rectangular conductors can be reduced by dividing them into semi- and quarter-circular or -rectangular ones (Fig.1). Although in principle known and applied for high frequency twisted conductors since long time this effect should be exploited also in electrical energy saving.

This paper deals particularly with the semi- and quarter-circular conductors, approaching each other (Fig.2) perfectly. For these cases an analytical-numerical method will be derived.

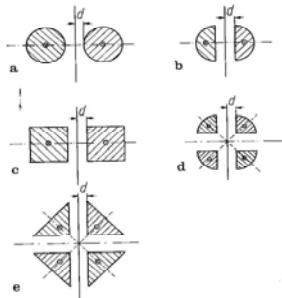


Fig.1. Cross-sections of different conductors with cuts

II. ANALYTICAL-NUMERICAL MODELING

The time harmonic field problem to be solved for the cut conductors, see fig.2, is governed by the complex inhomogeneous Helmholtz equation inside ($r \leq a$) and the Laplace equation outside ($r \geq a$) the conductors:

$$\Delta A - j\omega\kappa\mu A = -\kappa\mu C \quad r \leq a \quad (1)$$

$$\Delta A = 0 \quad r \geq a \quad (2)$$

A is the complex vector potential, ω, κ, μ angular frequency,

conductivity, permeability, a the conductor radius and C a so far undetermined constant, also known as impressed electric force.

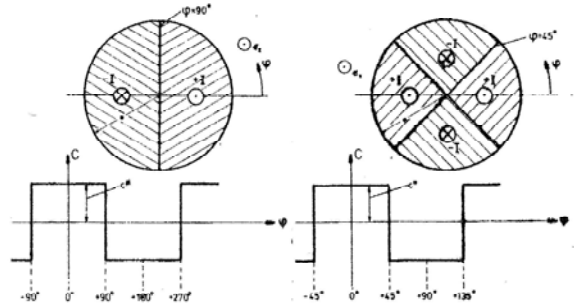


Fig.2. Semicircular (left) and quartercircular (right) conductor with related constants C . I : given current.

$C(\varphi)$ as shown in fig.2 is expanded in a Fourier series, and the homogeneous solution $A_h(r, \varphi)$ and particular solution $A_p(r, \varphi)$ of (1), composing the total solution

$$A^i(r, \varphi) = A_h(r, \varphi) + A_p(r, \varphi) \quad (3)$$

have to be found.

A. The semicircular conductor

A_h is found by separation of variables and its radial dependence is typically given by Bessel functions J_{2k+1} . Instead of these for the particular solution a sum of power series is chosen, which after applying several recurrence relations leads to the following total solution:

$$A^i(r, \varphi) = \sum_{k=0}^{\infty} \cos(2k+1)\varphi [a_k J_{2k+1}(pr) - c_k M_{2k+1}(pr)] \quad (4)$$

containing the particular solution

$$M_{2k+1}(pr) = \sum_{n=1}^{\infty} \frac{(pr)^{2n}}{\prod_{\mu=1}^n [(2k+1)^2 - 4\mu^2]} \quad (5)$$

the graph of which will be shown in the full paper. So far unknown coefficients are a_k , and c_k are the coefficients of the Fourier series expansion of the piecewise constant C , and $p^2 = -j\omega\kappa\mu$. Interestingly the derived functions $M_{2k+1}(z)$ are, apart from the sign, identical with a subclass of

Lommel functions $s_{\mu,\nu}(z)$ for $\mu=1$ and $\nu=2k+1$, as we found in the literature [4].

B. The quartercircular conductor

Unfortunately in this case and also in higher divided conductors (e.g. circle divided by 6,8,...) the setup of a sum of power series as particular solution was leading to contradictions in the recurrence relations. Finally the following way was successful: the angle of 90 degrees of the conductors was replaced by $90/1+\epsilon$ with $\epsilon \ll 1$, power series applied and then taking the limit $\epsilon \rightarrow 0$ let us discover a new term

$$\ln(pr) \cdot J_{2(2k+1)}(pr) \tag{6}$$

the behaviour of which was so far missing in the particular solution. The whole solution will be shown in the full paper, and it cannot be expressed by known closed form functions like those of Lommel or Struve.

III. CURRENT DENSITY, LOSSES AND INDUCTIVITY

Finally the boundary conditions at $r=a$ enable to define the coefficients a_k . The current density is related to the vector potential by

$$G(r, \varphi) = -j\omega\kappa A(r, \varphi) + C \tag{7}$$

and the integration of the current density over the conductors' cross section, equalling the given total current I, delivers the constant C. Losses and inductivity are related to this constant by a simple formula [5].

IV. NUMERICAL RESULTS

Fig.3 shows, that the current density distribution in the case of the quartercircular conductor is more uniform than with the semicircular one, indicating already higher eddy current losses in the latter one. This is quantitatively proven and shown together with the inductivity in fig.4.

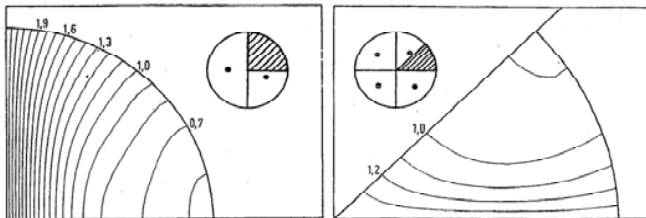


Fig.3. Lines of constant current density (amount) for the normalized frequency $\lambda = \sqrt{F\omega\kappa\mu} = 5$, F : cross section area of go and return conductor.
Left: semicircular conductor. Right: quartercircular conductor

The results, documented in fig.3 and fig.4, were calculated by the analytical-numerical method. The curves fit the results calculated by FEM.

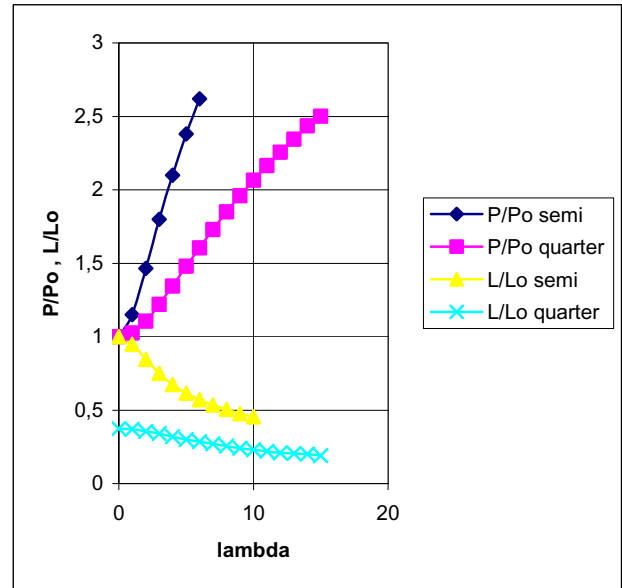


Fig.4. Power losses P and inductivity L in dependence on normalized frequency λ . P_o, L_o are reference values for DC ($\lambda = 0$) and semicircular conductor

V. CONCLUSIONS

The contribution shows quantitatively, how conductors, cut into sectors, can reduce power losses in the example of semi- and quarter-circular conductors. The latter example turned out to be much more difficult to find an analytical-numerical solution of the inhomogeneous Helmholtz equation than the first one, where the solution is related to Lommel functions. The two solutions found by this contribution can now serve as reference for numerical methods like FEM.

VI. REFERENCES

- [1] J.P.Gonnet, "Optimisation des canalisations électriques et des armoires de distribution", Dr. Thesis, Université Joseph Fourier, Grenoble, France, 2005
- [2] M.Kasper, "Die Optimierung elektromagnetischer Felder mit Hilfe der Finiten Elemente Methode und deren Anwendung auf ein Wirbelstromproblem", Dr.-Ing. thesis, TU Berlin, Germany, 1989
- [3] M.Kasper, A.Kost, "Skin - and proximity- effect in transmission lines of different cross sections", Archiv für Elektrotechnik 70, pp.333-339, 1987
- [4] I.S.Gradshcheyn, I.M.Ryzhik, "Table of Integrals, Series and Products", Academic Press, N.Y., London, Toronto, Sidney, San Francisco, 1980
- [5] M.Ehrlich, "A simplified method to calculate power dissipation and inductance of plane eddy current problems", Archiv für Elektrotechnik 60, pp.129-135, 1978

Fields and Current BEM Formulation for Radiofrequency Antennas

Nabil El Alami, Bernard Bandelier and Françoise Rioux-Damidau
 U2R2M, Université Paris XI, UMR CNRS 8081
 Bat 220, 91405 Orsay, France
 bernard.bandelier@u-psud.fr

Abstract—A new boundary formulation for the computation of the current and electromagnetic fields on a printed circuit antenna is presented. The state variables are the surface current density j on the metal, the tangential electrical field on the dielectric boundary and the tangential magnetic field on the whole boundary. We obtain good results. We give comparisons between numerical results and experimental measurements.

I. INTRODUCTION

We are interested by modelling printed circuit antennas made of thin metallic layers on a dielectric substrate. It is then necessary to use an integral fields representation but, as the metal is not a perfect conductor, we have to satisfy Ohm law. This one imposes that the current and the electric field are expanded with the same basis functions. This implies a real problem as e and h being naturally expanded with edges elements, the surface current density j has to be expanded with edge elements rotated by $\frac{\pi}{2}$. A few years ago, in [1], we proposed a formulation where the unknowns were the surface currents on the metallic layer and the electrical and magnetic fields on the whole boundary of the system. But the Ohm law was only weakly satisfied. This formulation permitted to treat the case of a substrate widely covered by a thin metallic layer but the simulation of a printed-circuit antenna was not efficient enough for all frequencies and geometries. We here propose a different method where the unknown quantities are j on the metal, $n \times e$ on the dielectric boundary and $n \times h$ on the total boundary. The current j and the field e never appear together at the same place and the Ohm law is strongly verified.

II. PHYSICAL PROBLEM

Let Ω be a dielectric substrate of permittivity ϵ_d ; its boundary is Γ . A part of Γ is covered by a metallic layer (with slit) of small thickness d and conductivity σ ; it is called Γ_m and the other part of Γ is called Γ_d ; the boundary line between Γ_m and Γ_d is called γ_0 . \vec{n} is the outward normal to Ω on Γ and \vec{N} is the outward normal to γ_0 tangent to Γ . A source field (h^s, e^s) is applied at angular pulsation ω ; skin-depth δ in the metal is such that $\delta \gg d$. On Γ_m , Ohm law gives:

$$j = \sigma de$$

where j is a surface current density.

Across Γ_m :

- $n \times e$ is constant upon d as $\delta \gg d$,

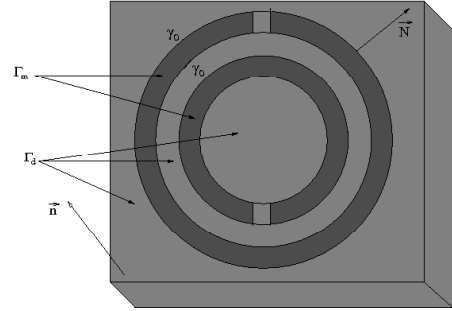


Fig. 1. The system

- $n \times (h_a - h_d) = j$, h_a being the magnetic field on the external face of Γ in the air and h_d on the internal face in the dielectric.

Across Γ_d :

- $n \times e$ and $n \times h$ are continuous.

III. INTEGRAL REPRESENTATIONS OF THE FIELDS

By using Stratton-Chu formulae [2], we obtain an integral representation of the tangential electric field on the external face of Γ :

$$\begin{aligned} \frac{n \times e}{2}(x) &= n(x) \times e^s(x) \\ &+ i\omega\mu_0 n(x) \times \int_{\Gamma} G_a(x, y)(n \times h_a)_y \\ &- \frac{1}{i\omega\epsilon_0} n(x) \times \text{grad} \int_{\Gamma} G_a(x, y) \text{div}_{\Gamma}(n \times h_a)_y \\ &+ n(x) \times \int_{\Gamma} \text{grad}_x G_a(x, y) \times (n \times e)_y. \end{aligned} \quad (1)$$

where G_a and G_d are the Green functions in the air and in the dielectric for the Helmholtz equation.

By noting that Stratton-Chu formulae inside Ω do not contain the source field, we have on the inside face of Γ :

$$\begin{aligned} -\frac{n \times e}{2}(x) &= i\omega\mu_0 n(x) \times \int_{\Gamma} G_d(x, y)(n \times h_d)_y \\ &- \frac{1}{i\omega\epsilon_d} n(x) \times \text{grad} \int_{\Gamma} G_d(x, y) \text{div}_{\Gamma}(n \times h_d)_y \\ &+ n(x) \times \int_{\Gamma} \text{grad}_x G_d(x, y) \times (n \times e)_y. \end{aligned} \quad (2)$$

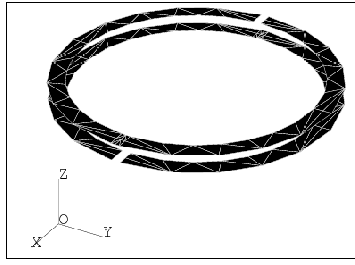


Fig. 2. The antenna (metallic layers only)

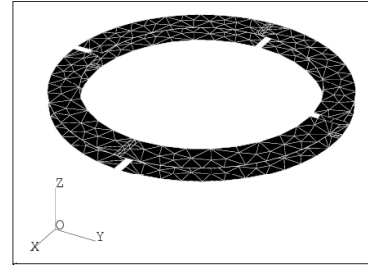


Fig. 4. Second antenna

We shall take as variable for the magnetic field:

$$h = h_d, \text{ and we have : } n \times h_a = n \times h + j \quad (3)$$

As j is the jump of the tangential magnetic field across Γ , it has to be defined in the same functional space than $n \times h$ and $n \times e$. But as $j = \sigma de$, j must be defined in the same functional space than e and would be discretized with the same basis functions. Clearly, there is an incompatibility, because it would necessitate to have the same discretization for j and $n \times j$. The only way to avoid this problem is to never have both the unknowns j and e in the same place. So, we adopt j as state variable on Γ_m and e on Γ_d .

By making the difference between equations (1) and (2), replacing e by $j/\sigma d$, multiplying by a test current j' and integrating on Γ_m we obtain a first variational equation. By multiplying by a test field e' and integrating on Γ_d , we obtain a second one. Finally, by taking the sum between equations (1) and (2), multiplying by h' and integrating on Γ we obtain the third variational equation.

IV. RESULTS

We take a dielectric disc with radius equal to 8 cm and height equal to 1.6 mm; it is covered with two metallic layers, one on the upper face and the second one on the lower face. We see the layers and their meshing on fig. 2.

We computed the numerical resonance frequency ($f_0= 44$ Mhz) and numerical quality factor Q ($Q_0= 44$) from numerical (NF) curve of resonance (fig. 3). The error percentage is 8 % in comparison with experimental measurement ($f_{exp} = 48, Q_{exp} = 48$).

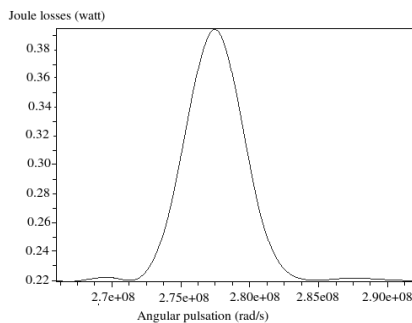


Fig. 3. The resonance curve

We next take a dielectric disc with radius equal to 10 cm and height equal to 0.788 mm; it is covered with two metallic layers, one on the upper face and the second one on the lower face, 2 slits in each layers like in fig. 4.

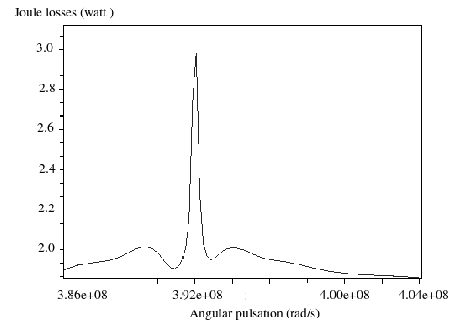


Fig. 5. The resonance curve

We computed the numerical resonance frequency $f_0= 62.3$ Mhz and numerical quality factor $Q_0= 432$ from numerical (NF) curve of resonance of the second antenna (fig. 5). The error percentage is 8 % in comparison with experimental measurement ($f_{exp} = 67.9, Q_{exp} = 400$).

V. CONCLUSION

This method uses an integral representation formula of the tangential fields on the boundary, such that the Ohm law is strongly verified. The comparison with experimental measurements was interesting and we can use this method for several types of antennas.

VI. REFERENCES

- [1] B. Kebaili, B. Bandelier, and F. Rioux-Damidaou, "Modelling a thin shell system submitted to an electromagnetic wave", *IEEE Trans. Magn.*, vol 37, 2001, pp. 3277-3280.
- [2] J. A. Stratton, *Electromagnetic theory*, Mac Graw Hill, New York, 1941.
- [3] J. C. Nédélec, "Mixed Finite Elements in \mathbb{R}^3 ," *Numer. Math.*, vol.35, 1980, pp. 315-341.

A New Method to Solve 3D Magnetodynamic Problems without Assembling an $Ax = b$ system

J.P.A. Bastos and N. Sadowski
GRUCAD/EEL/CTC, Universidade Federal de Santa Catarina
CP. 476, Florianópolis, SC, 88040-900, Brazil
jpab@grucad.ufsc.br and nelson@grucad.ufsc.br

Abstract — In this paper we present a technique to solve magnetodynamic FEM cases where the assembling, storing and solving the matrix system $Ax = b$ is performed in a different way compared with the classical techniques. The application of this technique for static cases was already presented. Using the T- Ω formulation, we consider here eddy currents in the conductive parts of the domain using time stepping discretization. As main result, the implementation is much simpler than traditional techniques widely used in virtually all the FEM codes. The final results match the ones obtained by the classical methods with very good accuracy.

I. INTRODUCTION

In a previous work we presented this method for static cases [1]. Here, we consider the time stepping dynamic cases, where eddy currents exist in the conductive parts of the domain. The T- Ω formulation is here employed. It means that the unknown variables are the scalar potential Ω on the nodes and the circulation T of vector electrical potential \mathbf{T} on the edges of the conductive elements [2][3].

The FEM requires the calculation of the elemental contribution matrices, whose evaluation is normally performed element by element and assembled in the global matrix system commonly designated $Ax = b$. Boundary conditions are inserted and the system is solved by a direct method (as Gauss Elimination) or by an iterative one (as ICCG). With the proposed technique, we operate mainly by nodes (it was called *N Scheme* in the previous paper). Now we must consider also the \mathbf{T} potentials on the edges of the 3D, first order tetrahedron elements and time discretization.

The resulting implementation is much simpler compared to the regular way of classical FEM codes because it is not necessary to assemble, store and solve an $Ax = b$ system as normally done. These steps are performed in only a single procedure. The only drawback is the computation time which is somewhat higher than traditional implementations. In spite of this drawback, the new scheme is effective and provides reliable results.

II. THE PROPOSED TECHNIQUE – *N SCHEME*

For didactical purposes, we replicate here the description of the method, already presented in [1]. For the same reason, a very simple 2D mesh is here considered, even though the T- Ω formulation is applied in 3D cases. The *N scheme* requires working node by node using element “cells” around the nodes.

In Fig. 1, the nodes are indicated by numbers while the elements by letters. Suppose that the nodes 3, 5, 7 and 11 are

unknowns and the others (1, 2, 4, 6, 8, 9, 10, 12, 13 and 14) have imposed boundary condition values.

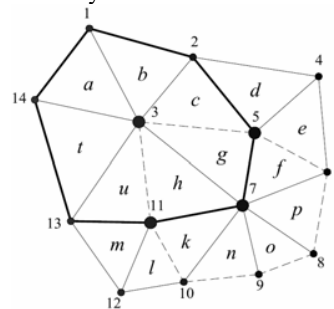


Fig. 1 – 2D mesh

Firstly, let us consider the node 3. The corresponding elements are: a, b, c, g, h, t and u and this cell is indicated in thick lines (the cell of the node 7 is indicated with dashed lines). When calculating the elemental matrix for this element (a typical rigidity matrix for a linear 2D triangular element), we obtain an $a(3,3)$ matrix; for the source we have a $s(3)$ vector. Suppose that the potential unknown is called v and that the element a is the only one acting for the node 3. If the nodes numbering created by the mesher has the sequence 14, 3 and 1, the elemental matrix system given by this sole element is:

$$\begin{bmatrix} a_{1,1} & a_{1,2} & a_{1,3} \\ a_{2,1} & a_{2,2} & a_{2,3} \\ a_{3,1} & a_{3,2} & a_{3,3} \end{bmatrix} \begin{bmatrix} v_{14} \\ v_3 \\ v_1 \end{bmatrix} = \begin{bmatrix} s_1 \\ s_2 \\ s_3 \end{bmatrix} \quad (1)$$

Supposing that the values of v_1 and v_{14} are known (as Dirichlet boundary conditions, for instance) we can write, for the potential v_3 :

$$a_{2,2}v_3 = s_2 - a_{2,1}v_{14} - a_{2,3}v_1 \quad (2)$$

The above expression must interact with other elements surrounding the node 3. Similar equations are calculated for all the elements of this cell. Using the notations of [1], we proceed with the sum of all the diagonal terms related to the node $n=3$ as:

$$diag_sum = a_{nn}^a + a_{nn}^b + a_{nn}^c + a_{nn}^g + a_{nn}^h + a_{nn}^t + a_{nn}^u$$

The sum of the right hand side of (2) is also calculated for all the elements as

$$right_sum = r_{jl}^a + r_{jl}^b + r_{jl}^c + r_{jl}^g + r_{jl}^h + r_{jl}^t + r_{jl}^u$$

The node 3 has interaction with the unknown nodes 5, 7 and 11 through the common elements c, g, h and u . Since the procedure is iterative, the potential of these nodes will be placed on the right hand side with their current values (exactly

as the boundary condition nodes). Once $diag_sum$ and $right_sum$ are calculated, the value of v_3 is given by:

$$v_3 = (right_sum)/(diag_sum) \quad (3)$$

Similar operations are performed for the v_5, v_7, v_{11} unknowns. Once it is done, we have a first approximation for these unknowns. Then the second iteration starts, with unknown values somewhat closer to the solution. As the iterative procedure progresses, the convergence is reached. This procedure is strictly equivalent to the application of the Gauss-Seidel iterative method with a relaxation technique [4][5].

In this work we must take into account the potential circulation T on the edges of the conductive elements. For doing so, we apply a similar procedure: for each edge having an unknown T , it is necessary to consider the elements "surrounding" the edge and the same technique is applied. However, there is a coupling between the potentials Ω and T , but it does not imply in any particular difficulty. In fact, the resulting matrix system can be written, as:

$$\begin{bmatrix} P & Q \\ Q^T & A \end{bmatrix} \begin{bmatrix} T^i \\ \Omega^i \end{bmatrix} = \begin{bmatrix} R & Q \\ 0 & 0 \end{bmatrix} \begin{bmatrix} T^{i-1} \\ \Omega^{i-1} \end{bmatrix} + \begin{bmatrix} 0 \\ U \end{bmatrix} \quad (4)$$

whose values are indicated in [2][3]. T^{i-1} and Ω^{i-1} are known from the previous time step. Therefore, applying the same principle as for the static case above, for generic T^i and Ω^i unknown we have their values given by:

$$T^i = (-P^*T^i - Q\Omega^i + RT^{i-1} + Q\Omega^{i-1})/sum_diagT^i \quad (5)$$

$$\Omega^i = (-Q^T T^i - A^* \Omega^i + U)/sum_diag\Omega^i \quad (6)$$

In the matrices P^* and A^* the diagonal terms are not considered. They are present on the diagonal sums.

III. IMPLEMENTATION

As similar to [1], it is necessary to set an array furnishing the elements "around" the unknown nodes and here another one with the elements "around" the edges T . Then the N scheme for this formulation is:

Loop of iterations:

Loop for the N unknowns Ω_n^i

- Calculate the diagonal sum;
- Calculate the right hand side sum;
- Calculate the new value of Ω_n^i by (6);

End of the Nodes loop;

Loop for the M unknowns T_m^i

- Calculate the diagonal sum;
- Calculate the right hand side sum;
- Calculate the new value of T_m^i by (5);

End of the T edges loop;

End of the iterations loop (until convergence).

IV. EXAMPLE

As example, we have the magnetic circuit of the Fig. 2a. The conductive part is at the right of the U-type magnetic piece which is surrounding a coil. A pulse of current is imposed on the coil, generating the eddy currents on the massive part. In Fig. 2a the magnetic induction is indicated by the arrows. The larger ones in the figure are located in the conductive part since its cross section is relatively thin. In Fig. 2b the induced current density distribution is shown.

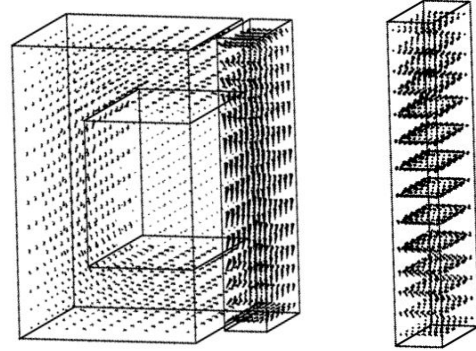


Fig. 2a – Flux distribution

Fig. 2b – Eddy currents

The number of elements is 16410. There are 3400 (unknown) nodes and 4000 T unknown edges (only in the conductive piece). The computation time with the traditional technique is 33 seconds and, with the proposed method, 61 seconds. As in [1], the calculation is longer with this method. The relative errors are 1.1%, 0.2% and 1.4% on the maximal B values, magnetic energy and eddy current losses, respectively. It is an accurate result for two different methods.

V. FINAL CONSIDERATIONS

The main focus of this work is to show that the N scheme proposed in [1] could be used on time stepping, eddy currents cases as well. We can also inform that, in a parallel work, it has been successfully employed on vector potential edge elements cases [6]. Our goal from now is to concentrate efforts on the convergence procedure in order to diminish the computational time. If this investigation yields good results, it will be possible to propose a technique as fast as the traditional one providing implementation advantages.

VI. REFERENCES

- [1] J.P.A. Bastos, "Is it possible to solve a FEM static case without assembling and storing an $Ax=b$ matrix system?", *ICS Newsletter*, Vol. 16 (1), ISSN: 1026-0854, March 2009.
- [2] Le Menach, Y., Clénet, S., Piriou, F., "Determination and utilization of the source-field in 3D magnetostatic problems", *IEEE Trans. on Magnetics*, 1998, Vol. 34 (5)
- [3] Dular, P., Robert, F., Remacle, J.F., Umé, M., Legros, W., "Computation of the source current density in inductors of any shape using a mixed formulation", *3rd International Workshop on Electrical and Magnetic Fields*, 1996, pp 107-112
- [4] Southwell, "Relaxation methods in theoretical Physics", *Oxford U.P.*, 1946, Vol I and II
- [5] Varga, R.S., "Matrix iterative analysis", Prentice-Hall (E. Cliffs, N.J.), 1962
- [6] J.P.A. Bastos, N. Sadowski, "A method to solve FEM statics cases without assembling a matrix system: application to 3D edge elements", to be presented in *EMF conference*, Mondovi, Italy, 26 to 29 May 2009.

Multiphysics problems via the Cell Method: the role of Tonti diagrams

P. Alotto⁽¹⁾, F. Freschi⁽²⁾, M. Repetto⁽²⁾

⁽¹⁾ Università di Padova, Dip. Ingegneria Elettrica, Padova, Italy

⁽²⁾ Politecnico di Torino, Dip. Ingegneria Elettrica, Torino, Italy
fabio.freschi@polito.it

Abstract—A common structure of several physical laws emerges naturally from the Tonti diagrams of different physical theories so that topological operators can be built only once and used to assemble resolving matrices of the various problems. This process is known in algebraic topology as coboundary process and is briefly presented as the theoretical background for solving multiphysics problems.

I. INTRODUCTION

One of the most important ideas in the work of Tonti and his algebraic formulation of physical theories [1], is the rigorous classification of physical variables and their link to geometrical entities. This classification is not specifically related to one particular physical phenomenon but, as a fundamental issue, highlights the common space-time structure underlying many physical theories. For this reason Tonti's work is a natural environment for developing a multiphysics analysis based on a numerical technique, which will be hereinafter called Cell Method (CM). Many aspects of the CM are common with the Finite Integration Theory [2] and similar ideas have been explored extensively by many researchers, e.g. [3].

II. PRIMAL AND DUAL CELL COMPLEX

In the algebraic formulation of physical theories, variables are associated with oriented space-time geometrical entities. Two discretizations are defined over the problem domain: the usual discretization adopted by many numerical methods forms a complex of space elements called *primal complex* but another cell complex is also defined, which is intertwined with the primal one by duality relations. Thus dual volumes are one-to-one associated to primal nodes, dual faces are dual geometrical entities of primal lines, dual lines of primal faces and dual points of primal volumes. Depending on their nature, global variables are associated to the primal or dual complex [1]. Equations that link a quantity defined on the primal complex and another on the dual complex are called constitutive equations and can be represented by square matrices due to the duality of the complexes. When global variables are used, physical equations can be written in a discrete form. The discrete operators that are representative of gradient, curl and divergence operators are the incidence matrices \mathbf{G} (edge-to-node), \mathbf{C} (face-to-edge), \mathbf{D} (volume-to-face). Since the same spatial entities are present in the dual complex, similar incidence matrices can be defined for the dual complex. They are represented by a tilde sign: $\tilde{\mathbf{G}}$, $\tilde{\mathbf{C}}$, $\tilde{\mathbf{D}}$. At least for topologically trivial complexes of cells, duality

relations impose that:

$$\tilde{\mathbf{D}} = -\mathbf{G}^T; \quad \tilde{\mathbf{C}} = \mathbf{C}^T; \quad \tilde{\mathbf{G}} = \mathbf{D}^T. \quad (1)$$

Topological laws link variables defined on the same cell complex by making use of these discrete operators. Topological equations are of three possible kinds:

- 1) *balance equations*, in particular conservation laws: in a differential setting they are expressed by the *div* operator; in algebraic methods they make use of $\tilde{\mathbf{D}}$;
- 2) *circulation equations*: in a differential setting they are expressed by the *curl* operator, while in a discrete setting by a $\tilde{\mathbf{C}}$ matrix
- 3) *difference equations*: in a differential setting they are expressed by the *grad* operator or by \mathbf{G} in discrete formulation.

Different phenomena sharing the same topological equation on the same space discretization (for instance thermal flow and electric flow balance) keep the same matrix equation structure and differ only by their constitutive matrices.

III. COBOUNDARY PROCESS

In order to define the *coboundary process* it is necessary to introduce some algebraic topology concepts. The reader can refer to [4] for a thorough introduction to this subject. Given a global physical quantity associated with a generic p -cell of a cell complex (where p is the spatial dimension), the knowledge of the amount of a physical variable associated with a set of p -cells is called *p -cochain*. As an example, in heat conduction problems, the assignment of the temperature to every node (0-cell) gives rise to a 0-cochain. In current flow problems, the assignment of voltage to every edge (1-cell) gives rise to a 1-cochain. The $(p+1)$ -cells that share a generic common p -cell are called *cofaces*.

The *coboundary process* is a procedure that starting from a p -cochain gives rise to a $(p+1)$ -cochain by a two-step process:

- 1) for every p -cell the value of the physical variable associated with it is transferred to all cofaces of the p -cell, with the correct incidence number;
- 2) for every $(p+1)$ -cell all these values are added together. In this way we obtain a new physical variable, with the same physical dimensions, associated with every $(p+1)$ -cell. In this way a new $(p+1)$ -cochain is obtained.

The coboundary process is the theoretical background of all topological laws based on discrete gradient, curl and divergence. Since these operators are built as a coboundary process,

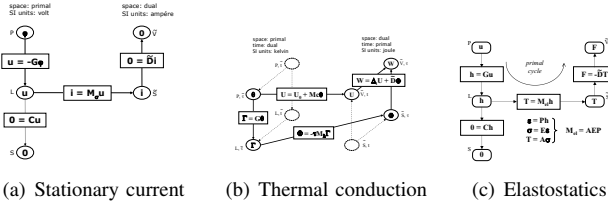


Fig. 1. Tonti diagrams.

it is easy to understand that they are incidence matrices. The most important consequence is that the coboundary process is a purely topological operation, it is not related to a specific physical theory but it is common to different problems. When studying a multiphysics problem, if the different fields share the same discretization, discrete operators that are representative of gradient, curl and divergence still remain the same for all problems.

IV. ELECTRO-THERMO-MECHANICAL PROBLEM

In this section the aforementioned coboundary process is applied to the multiphysics study of a microresistor beam involving electrical, thermal and mechanical effects. The example is taken from a library of test cases provided by the COMSOL Multiphysics finite element program [5] which is used as reference. In this particular application electric current generates heat, and the temperature increase leads to displacement through thermal expansion.

A. Stationary current field

The global variables used in stationary current problems are electric scalar potential φ , voltage u and electric current i . Their placement in Tonti diagram is reported in Fig. 1(a). Ohm's discrete constitutive matrix \mathbf{M}_σ for tetrahedra can be built by making use of Whitney edge-elements [6]. By following the primal cycle, i.e. starting from the electric scalar potential on the primal complex in order to obtain given sources on the dual complex, it is easy to obtain the equation:

$$\mathbf{G}^T \mathbf{M}_\sigma \mathbf{G} \varphi = 0. \quad (2)$$

B. Transient thermal conduction field

In Fig. 1(b) the Tonti diagram for transient thermal conduction is shown: by assembling the topological and constitutive equations presented, following equation is obtained

$$\left(\mathbf{M}c + \frac{\tau}{2} \mathbf{G}^T \mathbf{M}_\lambda \mathbf{G} \right) \theta_k = \left(\mathbf{M}c - \frac{\tau}{2} \mathbf{G}^T \mathbf{M}_\lambda \mathbf{G} \right) \theta_{k-1} + \frac{1}{2} (\mathbf{W}_k + \mathbf{W}_{k-1}) \quad (3)$$

where: \mathbf{M} is the mass matrix of dual volumes, c is the thermal capacity, τ the amplitude of primal time interval, \mathbf{M}_λ the discrete matrix of thermal conductivity. Since \mathbf{M}_λ links temperature difference and heat flux, which are defined on primal edges and dual faces, respectively, this constitutive matrix is built in the same way as the discrete electrical conductivity matrix. The coupling terms with the stationary current field are the thermal dependence of electrical conductivity and joule losses as thermal sources. Equation (3) proposes the Crank-Nicholson time integration scheme, but it is possible to derive other integration schemes by a suitable definition of duality in time discretization [7].

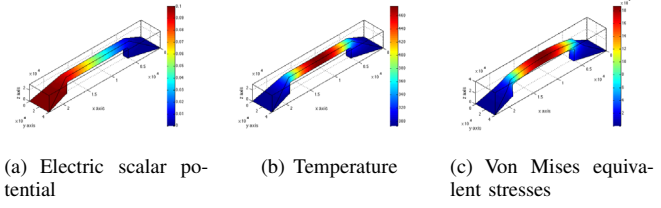


Fig. 2. Results of coupled electro-thermo-mechanical analysis (steady state).

TABLE I
COMPARISON BETWEEN COMSOL AND DUALLAB

	Total current, A	max T, K	max Δz , m
COMSOL	0.773	1017.4	8.18E-8
DualLab	0.775	1017.1	8.28E-8

C. Elastostatics

Tonti diagram for elastostatics is depicted in Fig. 1(c). By following the same rationale of other physical theories, with the only difference in the constitutive equation \mathbf{M}_E and neglecting details for the sake of conciseness, the equation of elastostatics is:

$$\mathbf{G}_3^T \mathbf{M}_E \mathbf{G}_3 \mathbf{u} = \mathbf{F}_v \quad (4)$$

\mathbf{G}_3 is a tri-block diagonal matrix, where each block is made by the \mathbf{G} matrix that appears in (2) and (3).

D. Results

The aforementioned formulation, implemented in the DualLab code, has been applied to the described benchmark problem, and maps of electric scalar potential, temperature and Von Mises stresses are shown in Fig. 2. A comparison with results obtained with COMSOL is shown in Table I (note that high temperature values are due to a voltage of 1 V applied between the electrodes).

V. CONCLUSIONS

The described approach, based on Tonti diagrams, has been shown to deliver an elegant approach for the efficient implementation of multiphysics problem formulations. More complicated multiphysics applications will be presented in the full paper together with CPU time and memory usage comparisons with leading finite element codes.

REFERENCES

- [1] E. Tonti. Finite Formulation of Electromagnetic Field. *IEEE Transactions on Magnetics*, 38:333–336, 2002.
- [2] M. Clemens and T. Weiland. Discrete electromagnetism with the finite integration technique. *Progress in Electromagnetic Research, PIER*, 32:65–87, 2001. 65–87.
- [3] A. Bossavit and L. Kettunen. Yee-like schemes on staggered cellular grids: A synthesis between FIT and FEM approaches. *IEEE Transactions on Magnetics*, 36(4):861–867, 2000.
- [4] P.W. Gross and Kotiuga P.R. *Electromagnetic Theory and Computation: A Topological Approach*. Cambridge University Press, 2004.
- [5] COMSOL Multiphysics. www.comsol.com.
- [6] R. Specogna and F. Trevisan. Discrete constitutive equations in a $\alpha - \chi$ geometric eddy-current formulation. *IEEE Transactions on Magnetics*, 41(4):1259–1263, Apr 2005.
- [7] P. Alotto, R. Specogna, and F. Trevisan. A θ -method for eddy currents in time-domain with a discrete geometric approach. *IEEE Transaction on Magnetics*, 42(4):779–782, Apr. 2006.

Time-domain geometric eddy-current A formulation for hexahedral grids

Lorenzo Codecasa¹, Patrick Dular², Ruben Specogna³, and Francesco Trevisan³

¹Dipartimento di Elettronica e Informazione, Politecnico di Milano, I-20133 Milano, Italy,

²Département d'électricité, électronique et informatique, Université de Liège, B-4000 Liège, Belgium,

³Dipartimento di Ingegneria Elettrica, Gestionale e Meccanica, Università di Udine, I-33100 Udine, Italy, ruben.specogna@uniud.it.

Abstract—The aim of the paper is to present a three-dimensional geometric time-domain eddy-current A formulation for hexahedral grids. The resulting singular differential algebraic linear system of equations (DAE) is solved by means of a *Singly-Diagonally Implicit Runge-Kutta* (SDIRK) variable step-size solver. The formulation is validated by comparing the results from a benchmark problem with respect to a Finite Elements commercial software.

Index Terms—Cell Method (CM), Finite Integration Technique (FIT), Discrete Geometric Approach (DGA), eddy-currents, time-domain.

I. INTRODUCTION

The so-called “Discrete Geometric Approach” (DGA) [1], similarly to the Finite Integration Technique (FIT) [2] or the Cell Method [3], allows to solve directly Maxwell’s equations in an alternative way with respect to the classical Galerkin method in Finite Elements.

In this paper, a three-dimensional geometric time-domain eddy-current formulation suitable for hexahedral grids based on the circulation A of a magnetic vector potential \mathbf{A} is described.

The domain of interest D of the eddy-current problem has been partitioned into a passive conductive region D_c , a source region D_s and a non-conductive region D_a . The domain D is covered by a finite element mesh of hexahedra; The corresponding cell complex [3] is denoted as \mathcal{K} . From \mathcal{K} , the barycentric dual complex \mathcal{B} is also introduced [3]. The incidence matrix between edges e and nodes n is denoted by \mathbf{G} , the incidence matrix between faces f and edges e is denoted by \mathbf{C} and the incidence matrix between hexahedra v and faces f is denoted by \mathbf{D} . The matrices $\tilde{\mathbf{G}} = \mathbf{D}^T$, $\tilde{\mathbf{C}} = \mathbf{C}^T$ and $\tilde{\mathbf{D}} = -\mathbf{G}^T$ describe the mutual interconnections of the dual barycentric complex [3].

Next, we consider the integrals of the field quantities with respect to the oriented geometric elements of the mesh, yielding the Degrees of Freedom (DoF) arrays:

- Φ is the array of magnetic fluxes associated with faces $f \in D$; \mathbf{F} is the array of m.m.f.s associated with dual edges $\tilde{e} \in D$; \mathbf{I} is the array of currents associated with dual faces $\tilde{f} \in D_c$. In D_s we introduce the array \mathbf{I}_s of impressed currents; \mathbf{U} is the array of e.m.f.s on primal edges $e \in D_c$.

- \mathbf{A} is the array of circulations of the magnetic vector potential A along the primal edges $e \in D$.

Maxwell’s laws can be written *exactly* as topological balance equations between DoFs arrays, as

$$\begin{aligned} (\mathbf{C}^T \mathbf{F})_e &= 0, & e \in D_a \\ (\mathbf{C}^T \mathbf{F})_e &= (\mathbf{I}_s)_e, & e \in D_s \\ (\mathbf{C}^T \mathbf{F})_e - (\mathbf{I})_e &= 0, & e \in D_c \end{aligned} \quad (1)$$

$$(\Phi)_f = (\mathbf{C}\mathbf{A})_f, \quad f \in D \quad (2)$$

where (1) is the Ampère’s Law, (2) involves the array \mathbf{A} in such a way that Gauss’ Law $\mathbf{D}\Phi = 0$ is satisfied identically (since $\mathbf{D}\mathbf{C} = 0$). The discrete counterpart of the constitutive laws can be written as

$$\mathbf{F} = \boldsymbol{\nu} \Phi, \text{ in } D \quad (\text{a}) \quad \mathbf{I} = \boldsymbol{\sigma} \mathbf{U}, \text{ in } D_c \quad (\text{b}) \quad (3)$$

where the matrices $\boldsymbol{\nu}$ and $\boldsymbol{\sigma}$ are square symmetric positive-definite and consistent matrices which can be efficiently constructed in a pure geometric way for an hexahedral primal grid, as described in [4].

Combining the discrete Faraday’s law $(\mathbf{C}\mathbf{U})_f = -\frac{d}{dt}(\Phi)_f$, $f \in D_c$, with (2) yields

$$(\mathbf{U})_e = \left(-\frac{d\mathbf{A}}{dt} \right)_e, \quad e \in D_c. \quad (4)$$

II. TIME-DOMAIN EDDY-CURRENT A FORMULATION

The symmetric algebraic system of equations, having $\mathbf{A}(t)$ as unknown, can be obtained by combining (3a), (3b), (2) and (4) into (1)

$$\begin{aligned} (\mathbf{C}^T \boldsymbol{\nu} \mathbf{C} \mathbf{A}(t))_e &= 0, & e \in D_a \\ (\mathbf{C}^T \boldsymbol{\nu} \mathbf{C} \mathbf{A}(t))_e &= (\mathbf{I}_s(t))_e, & e \in D_s \\ (\mathbf{C}^T \boldsymbol{\nu} \mathbf{C} \mathbf{A}(t))_e + (\boldsymbol{\sigma} \frac{d}{dt} \mathbf{A}_c(t))_e &= 0, & e \in D_c \end{aligned} \quad (5)$$

where \mathbf{A}_c contains the entries of \mathbf{A} relative to the edges of D_c . The source currents vector $\mathbf{I}_s(t)$ can be expressed as $\mathbf{I}_s \cdot s(t)$, where \mathbf{I}_s can be computed as described in [5] for a unit current and $s(t)$ is a function of time that describes the time evolution of the source current.

III. INTEGRAL SOURCES

When modeling stranded coils, it is useful to introduce integral sources, which do not require the coils to be meshed. With this aim, we express the array \mathbf{A} as $\mathbf{A} = \mathbf{A}_s + \mathbf{A}_r$, where \mathbf{A}_s contains the contribution produced by the source currents in D_s and \mathbf{A}_r due to the eddy-currents in D_c . Equation (5) can be rewritten as

$$\begin{aligned} (\mathbf{C}^T \boldsymbol{\nu} \mathbf{C} \mathbf{A}_r(t))_e &= 0, & e \in D_a \\ (\mathbf{C}^T \boldsymbol{\nu} \mathbf{C} \mathbf{A}_r(t))_e + (\boldsymbol{\sigma} \frac{d\mathbf{s}(t)}{dt} \mathbf{A}_r(t))_e &= -(\mathbf{v}(t))_e, & e \in D_c \end{aligned} \quad (6)$$

where $(\mathbf{v}(t))_e = \left(\boldsymbol{\sigma} \mathbf{A}_s \frac{ds(t)}{dt} \right)_e$. Each entry $(\mathbf{A}_s)_e$ of the array \mathbf{A}_s can be pre-computed as $(\mathbf{A}_s)_e = \int_e \mathbf{A}_s \cdot d\mathbf{l}$, where e is a primal edge in D_c and \mathbf{A}_s is the magnetic vector potential due to a unit source current in D_s .

IV. NUMERICAL RESULTS

The time-domain A geometric eddy-current formulation, with both meshed and integral sources, is implemented in the GAME code [6].

It should be noted that the matrices in (5) and (6) are singular and to solve (5) or (6) we rely on a in-house developed Singly-Diagonally Implicit Runge-Kutta (SDIRK) DAE solver with a variable step-size [7].

A fully three-dimensional geometry consisting of a circular coil placed above a conducting plate ($\sigma_c = 4 \cdot 10^7$ S/m) is considered as a benchmark problem, see Fig. 1. The source is

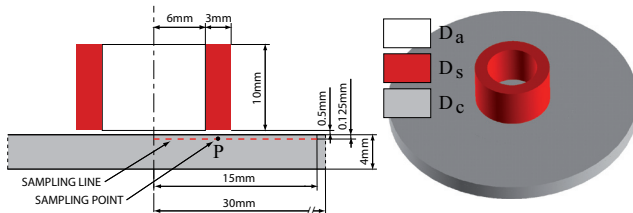


Fig. 1. The geometry of the benchmark problem is shown.

enforced by a stranded circular coil D_s with $s(t) = 400 \cdot (1 - e^{-t/\tau})$, where $\tau = 1$ ms.

To compare the results obtained with the A geometric formulation, the ANSYS commercial Finite Elements software is used. Since the problem is axisymmetric, a first solution is computed with ANSYS using a two-dimensional quadrilateral mesh consisting of about 50,000 elements of second order (time step of 0.01 ms). Then, the full three-dimensional simulations, using the same mesh consisting of 19,136 hexahedra (59,330 DoFs), are run with ANSYS and the GAME code (fixed time-step of 0.05 ms for both ANSYS and GAME).

The amplitude of the current density along a number of points evenly distributed along a sampling line shown in Fig. 1 for $t = 1$ ms is represented in Fig. 2. In Fig. 3, the time behavior of the module of the current density in the point P (situated on the sampling line, at a distance of 7.5 mm from the axis) is shown. The results obtained by the DGF are in very good agreement with ANSYS. The CPU time will be described in detail in the full paper.

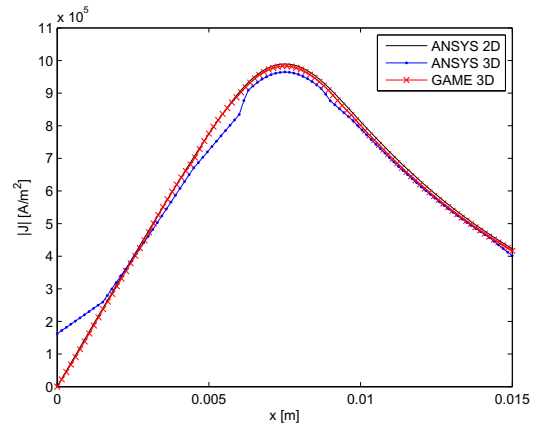


Fig. 2. Amplitude of the current densities along a sampling line.

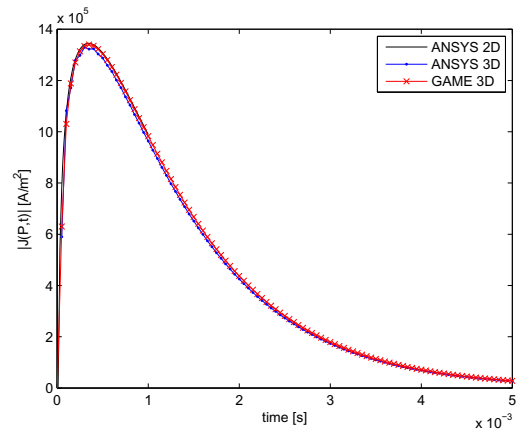


Fig. 3. Time behavior of the module of the current density in the point P .

V. CONCLUSIONS

A three-dimensional geometric time-domain eddy-current A formulation suitable with hexahedral meshes has been presented. The formulation has been successfully validated using a Finite Elements commercial software.

REFERENCES

- [1] A. Bossavit, "How weak is the Weak Solution in finite elements methods?", IEEE Trans. Magn., Vol 34, No. 5, 1998, pp. 2429-2432.
- [2] T. Weiland, "A discretization method for the solution of Maxwell's equations for six-component fields", Electron. Commun. (AEÜ), Vol. 31, No. 3, 1977, p. 116.
- [3] E. Tonti, "Algebraic topology and computational electromagnetism", 4-th International Workshop on Electric and Magnetic Fields, Marseille (Fr), 12-15 May 1988, pp. 284-294.
- [4] L. Codecasa, R. Specogna, F. Trevisan, "Discrete constitutive equations over hexahedral grids for eddy-current problems", CMES: Computer Modeling in Engineering & Sciences, Vol.31, No.3, 2008, pp. 129-144.
- [5] R. Specogna, F. Trevisan, "Discrete constitutive equations in $A - \chi$ geometric eddy-currents formulation", IEEE Trans. Magn., Vol. 41, No. 4, 2005, pp. 1259-1263.
- [6] R. Specogna, F. Trevisan, "The GAME (Geometric Approach to Maxwell's Equations) code", <http://www.quickgame.org>, copyright 2003-2009.
- [7] F. Cameron, R. Piché, and K. Forsman, "Variable step size time integration methods for transient eddy current problems", IEEE Trans. Magn., Vol. 34, No. 5, 1998, pp. 3319-3322.

A finite element method for structures defined by a regular 3D grid of material properties

Huanhuan Gu¹, J. Gotman² and J. P. Webb¹

¹Department of Electrical and Computer Engineering, McGill University, Montreal, QC, H3A 2A7, Canada

²Montreal Neurological Institute, McGill University, Montreal, QC, H3A 2B4, Canada
jon.webb@mcgill.ca

Abstract—In bioelectromagnetics and other domains, the structures in which the electromagnetic field is to be computed are sometimes defined by a fine Cartesian grid of voxels (3D cells), in each of which the material properties are specified. A novel finite element method is proposed for such cases. A simple, regular mesh of cube elements is constructed, each containing the same, integer number of voxels. There may be several different materials present within an element, but this is accommodated by computing element basis functions that approximately respect the interface conditions between different materials. Results are presented for a test model consisting of nested conducting cubes, driven by a current dipole, which is a crude version of the electroencephalography forward problem. The static potential computed with the new method agrees well with that of a conventional finite element code.

I. INTRODUCTION

Tomographic techniques such as magnetic resonance imaging (MRI) provide information on the size, shape and material properties of a slice through a complex 3D structure, and an assembly of such slices allows us to construct the geometry of the entire structure as a Cartesian grid of voxels. This can be used as the starting point for a finite element (FE) analysis of the electromagnetic fields. The conventional approach is to construct a solid model from the voxel data and to subdivide that into finite elements [1]. The process is time-consuming and prone to error. An alternative strategy was proposed in 2D in [2] and is here extended to 3D. A simple, regular mesh of cube elements is superimposed directly on the voxel grid. In general, each cube will contain several different materials, possibly with large differences in their electromagnetic properties. This is not possible with conventional finite elements, but the usual basis functions of the cube element are replaced by computed basis functions that take into account the different materials.

II. THE METHOD OF COMPUTED BASIS FUNCTIONS IN 3D

The computational domain Ω consists of $n \times n \times n$ voxels. Each voxel has a known electromagnetic material property, e.g. conductivity σ . There may be material discontinuities in this model, represented by neighboring voxels of different materials. This type of voxelization is used to approximate smooth geometric objects with abrupt boundaries in tomographic techniques.

Consider the following partial differential equation in Ω :

$$Lu = g \quad (1)$$

where u is an unknown scalar function, L is a partial differential operator depending on the material property, and g is a known excitation applied in Ω . We subdivide domain Ω into a set of cube elements, and each element consists of $p \times p \times p$ voxels. Each element may contain several different materials. One such element is shown in Fig. 1. Color shading indicates different materials.

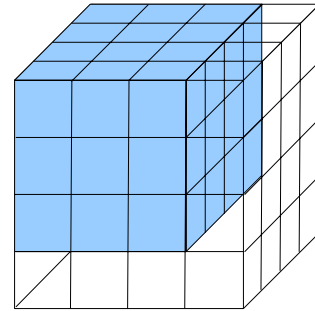


Fig 1. A $p \times p \times p$ cube finite element containing two different materials. Here $p = 4$.

The conventional FE method does not allow different materials within one element. The element basis function therefore does not depend on materials but only on the geometry. In our method, we use computed basis functions to allow for this material difference within one element. The computed basis function satisfies the following equation

$$Lu = 0 \quad (2)$$

approximately within each element. In this way, the computed basis function tends to respect the internal discontinuities and therefore serves as a reasonable local approximation even with non-uniform filling material.

The computed basis function also needs to satisfy the continuity condition between adjacent elements. This continuity is obtained by imposing the same computed functions for all the edges and faces shared by neighboring elements. First we compute the functions for edges. Take the edge from $(0, ph)$ to (ph, ph) in Fig. 2 as an example. This edge is shared by four neighboring cube elements. The edge function $e(x)$ for node (ph, ph) is the solution to:

$$\begin{aligned} Le(x) &= 0 \\ \text{s.t. } e(0) &= 0 \quad e(ph) = 1 \end{aligned} \quad (3)$$

The equation is solved by the finite difference method. The material property for each point on this edge is obtained by taking the average material property of the four voxels sharing the point.

These edge functions are next used as boundary conditions in solving for the face functions, $f(x, y)$. Suppose we are solving for the face function for node (ph, ph) in Fig. 2. The boundary conditions are as follows:

$$\begin{aligned} f(x, ph) &= e(x) & f(ph, y) &= e(y) \\ f(x, 0) &= 0 & f(0, y) &= 0 \end{aligned} \quad (4)$$

where $e(x)$ and $e(y)$ are edge functions for node (ph, ph) .

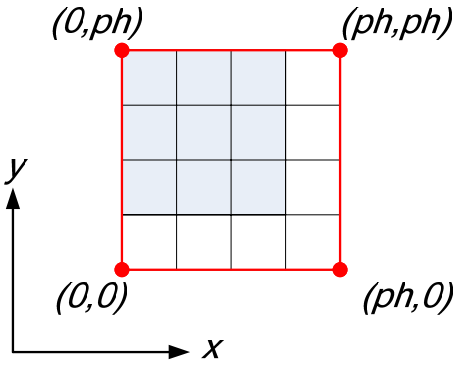


Fig 2. An element face, which is shared by two elements. $p=4$.

After we obtain all the face functions, we use them to compute the element basis function. This is done by solving the differential equation (2) throughout the volume of the cube element. The boundary condition on each face of the cube is defined by a face function.

When all the element basis functions are obtained, they are used in a conventional FE variational formulation to find the scalar u throughout Ω .

III. TEST CASE

In electroencephalography (EEG), the forward problem can be defined as: given the position and moment of current dipoles in the brain, find the electric potential distribution over the scalp. The head model obtained by MRI consists of voxels representing anatomical tissue of the head and this can be used in the forward problem computation.

A case similar to the EEG forward problem is analyzed by the new method and the results compared with those from a conventional FE method. A rectilinear geometry is chosen, so that the voxelized version matches exactly the geometric model treated by the conventional FE method; this would not be the case if, for example, a spherical geometry were used, because of the staircase approximation to the spherical surfaces that is unavoidable in voxelized data such as that obtained by tomography. In this way, the intrinsic accuracy of the new method can be established, without the added geometric uncertainty caused by the voxelization. We apply our method to a four layer cube model consisting of

128x128x128 voxels. The sides of the concentric “scalp”, “skull” and “brain” cubes have lengths 104, 96 and 88 voxels respectively. The conductivities are 1 Sm^{-1} , 0.0125 Sm^{-1} , and 1 Sm^{-1} for brain, skull and scalp, respectively. A current dipole is placed symmetrically. Fig. 3 is the middle slice of the model on a coronal plane.

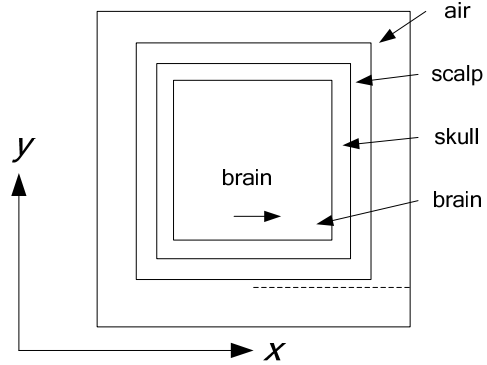


Fig 3. A cube model consisting of 128x128x128 voxels

An element size of 4x4x4 voxels is used and the potential is sampled along a line one voxel away from the scalp. The sample line is shown as dashed in Fig. 3. The result is compared with those obtained by ElecNet [3] which uses a fine mesh of conventional, 3rd-order, tetrahedral elements. Then we perturb the problem by increasing the size of each nested cube (except the outermost one) by 2 voxels. Comparisons for both cases are plotted in Fig.4. Both results show good agreement, which indicates the competence of the new method in dealing with elements containing strong material discontinuities.

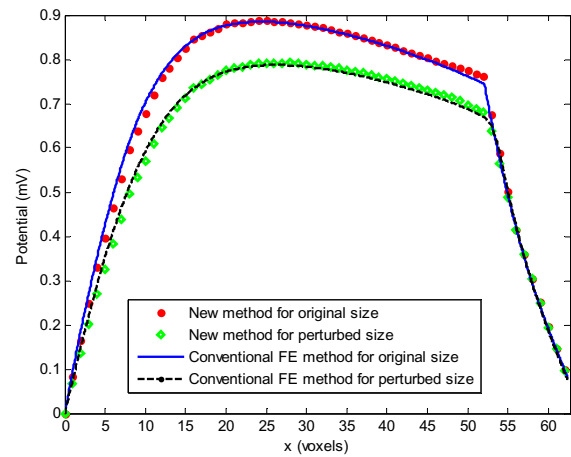


Fig 4. Comparison of the new method with conventional FE method

IV. REFERENCES

- [1] Y C Zhang, S A Zhu and Bin He, “A second-order finite element algorithm for solving the three-dimensional EEG forward problem,” *Phys. Med. Biol.* 49, pp. 2975-2987, 2004.
- [2] H. Gu, J. Gotman, and J. P. Webb, “Finite-element simulation in bioelectromagnetics without the need for modeling and meshing,” *Magnetics, IEEE Transactions on*, vol. 45, pp. 1678-1681, 2009.
- [3] ElecNet 6.17, 2007, Infolytica Corporation, Montreal, Canada, <http://www.infolytica.com/>

Hysteresis Losses' Calculation of Magnetostrictive Ultrasonic Transducer with Jiles-Atherton Hysteresis Model

Jianbin. Zeng, Baodong. Bai, Haiquan. Zeng, Dexin. Xie
Shenyang University of Technology

No.111, Shenliao West Road, Economic & Technological Development Zone, Shenyang, 110178, China
E-mail: Jianbin.Zeng@Gmail.com

Abstract— The giant magnetostrictive material Terfenol-D show superior properties that combine both a broad bandwidth, high force and small or moderate displacements. As a kind of active material, it can be used in ultrasonic power transducer. Hysteresis losses are the main source for heating the Terfenol-D ultrasonic power transducer. A new method of calculation for hysteresis losses, which based on Jiles-Atherton hysteresis model and electro-magnetic field finite element analysis, is proposed in this paper. The hysteresis losses obtained by this method can be used as thermal sources in electro-thermal finite element analysis.

I. INTRODUCTION

The giant magnetostrictive material Terfenol-D show superior properties that combine both a broad bandwidth, high force and small or moderate displacements. Furthermore, the advent of magnetostrictive equipment including new magnetic materials and design concepts have made it possible to manufacture high-frequency, high-power transducers for ultrasonic applications³. Transducers capable of delivering up to 6 kW mechanical power have recently been commercially available and a 25 kW is under development³. This transducer will continuously operate at its rated maximum power, which should be about one order of magnitude higher than competing technologies such as PZT transducers. One of the big disadvantages with PZT in ultrasonic transducers is the very low heat conductivity. This limits the power rating to about 4.5 kW. A high frequency, high-power transducer would significantly increase the commercial use of ultrasonic transducers in sono-chemistry, e.g. applied to petroleum production and processing, accelerated chemical reaction studies and in the dairy industry.

The eddy current losses and hysteresis losses are the main source for heating the magnetostrictive material in Terfenol-D ultrasonic magnetostrictive transducer. The eddy current losses can be reduced significantly by laminating the magnetostrictive material. However, the hysteresis losses are the main source for heating the ultrasonic magnetostrictive power transducer. The hysteresis losses can be used as thermal sources in electro-thermal finite element analysis. The calculation of hysteresis losses is very important for designation of Terfenol-D ultrasonic magnetostrictive transducer.

In this paper, a method combined of Jiles-Atherton hysteresis model [1][2] and time-step electromagnetic field finite element analysis for hysteresis losses' calculation of magnetostrictive ultrasonic power transducer is used. By this

method, the hysteresis losses of Terfenol-D transducer are calculated accurately.

II. INVERSE JILES-ATHERTON HYSTERESIS MODEL

A. Original Jiles-Atherton Hysteresis Model

In original Jiles-Atherton hysteresis model, the magnetization M can be defined as addition of the reversible component M_{rev} and irreversible component M_{irr} .

$$M = M_{irr} + M_{rev} \quad (1)$$

Considered the magnetization process of the material, the relationship of the M_{rev} , M_{irr} and M_{an} is given by follow equation.

$$M_{rev} = c(M_{an} - M_{irr}) \quad (2)$$

The remained equations of the Jiles-Atherton hysteresis model is given as equation (3-6).

$$\frac{dM_{irr}}{dH_e} = \frac{M_{an} - M_{irr}}{k\delta} \quad (3)$$

$$M_{an} = Ms \left[\coth\left(\frac{He}{a}\right) - \frac{a}{He} \right] \quad (4)$$

$$He = H + \alpha M \quad (5)$$

$$B = \mu_0(H + M) \quad (6)$$

In above equations, Ms is the saturate magnetization of the material which can be obtained from manufacture. c , k , α and a are the parameters can be extracted from experimental data [3]. δ is a directional parameter and takes the value 1 for $dH/dt > 0$ and -1 for $dH/dt < 0$. M_{an} is the anhysteretic magnetization.

B. Inverse Jiles-Atherton Hysteresis Model

With the proposed inverse Jiles-Atherton model [4], H will be calculated from the magnetic induction B , integrating a differential equation in terms of dM/dB .

$$\frac{dM}{dB} = \frac{(1-c) \frac{dM_{irr}}{dB_e} + \frac{c}{\mu_0} \frac{dM_{an}}{dH_e}}{1 + \mu_0(1-c)(1-\alpha) \frac{dM_{irr}}{dB_e} + c(1-\alpha) \frac{dM_{an}}{dH_e}} \quad (6)$$

$$\frac{dM_{irr}}{dB_e} = \frac{M - cM_{an}}{1 - c} \quad (7)$$

$$\frac{dM_{an}}{dH_e} = \frac{M_s}{a} \left[1 - \coth^2 \frac{H_e}{a} + \left(\frac{a}{H_e} \right)^2 \right] \quad (8)$$

III. FILED EQUATION OF TIME-STEP FINITE ELEMENT ANALYSIS

This way to include hysteresis in field calculation is to introduce a differential reluctivity ν_d defined as

$$\nu_d = \frac{dH}{dB} \equiv \frac{\Delta H}{\Delta B} = \frac{H(t+\Delta t) - H(t)}{B(t+\Delta t) - H(t)} \quad (9)$$

From (4), the magnetic field $H(t + \Delta t)$ at time $(t + \Delta t)$ is

$$H(t + \Delta t) = \nu_d \Delta B + H(t) \quad (10)$$

Applying (5) in Ampère's law and using the magnetic vector A potential gives the final equation for this formulation

$$\text{rot } \nu_d \text{rot } A(t + \Delta t) = J(t + \Delta t) + \text{rot } \nu_d \text{rot } A(t) - \text{rot } H(t) \quad (11)$$

In equation (6), ν_d is calculated in each time step $t + \Delta t$. $A(t)$ and $H(t)$ is known in previous time step.

The hysteresis is included in magnetic field analysis by (11). The hysteresis losses are obtained by integral B with H [5].

$$P_t = \frac{1}{\rho T} \int_0^T \left(H_x \frac{dB_x}{dt} + H_y \frac{dB_y}{dt} \right) dt \quad [\text{W / kg}] \quad (12)$$

IV. RESULT

In this paper, A magnetostrictive ultrasonic power transducer with a moderate driving current of 10A and the frequency of 21kHz is used to analysis the hysteresis loss. Its magnetic field distribution in the time of 1/4 current period is shown as Fig.1. In the Fig.1, the area with green color is the air, the grey area is the silicon sheet, the pink area is the Terfenol-D and the yellow area is the copper and the dark red area is the steel.

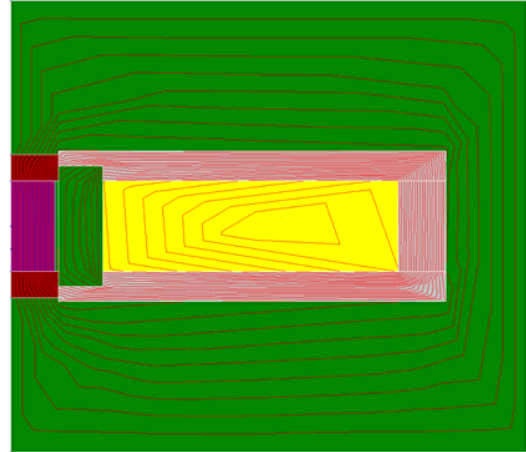


Fig. 1. Magnetic field in the time of 1/4 current period

V. CONCLUSION

Hysteresis losses are the main source for heating the Terfenol-D ultrasonic power transducer. A new method combined of Jiles-Atherton hysteresis model and time-step electromagnetic field finite element analysis for hysteresis losses calculation is proposed in this paper. By this method, the hysteresis losses of Terfenol-D transducer are calculated accurately. In the near future, the calculation of eddy current and anomalous losses will be undertaken.

VI. ACKNOWLEDGEMENT

This work was supported by National Natural Science Foundation of China (50875177).

VII. REFERENCES.

- [1] D. C. Jiles and D. L. Atherton, "Theory of ferromagnetic hysteresis," *Magn. Magn. Mater.*, vol. 61, pp. 48–60, 1986.
- [2] D. C. Jiles and J. B. Thoeke, "Theory of ferromagnetic hysteresis: Determination of model parameters from experimental hysteresis loops," *IEEE Trans. Magn.*, vol. 25, pp. 3928–3930, Sept. 1989.
- [3] D. C. Jiles, J. B. Thoeke, and M. K. Devine, "Numerical determination of hysteresis parameters for the modeling of magnetic property using the theory of ferromagnetic hysteresis," *IEEE Trans. Magn.*, vol. 28, pp. 27–35, Jan. 1992.
- [4] N. Sadowski, N. J. Batistela, J. P. A. Bastos, and M. Lajoie-Mazenc, "An Inverse Jiles-Atherton Model to Take into Account Hysteresis in Time-Stepping Finite-Element Calculations," *IEEE. Transaction on Magnetics*, Vol. 38, NO.2, March 2002
- [5] L. A. Righi, N. Sadowski, R. Carlson, J. P. A. Bastos, and N. J. Batistela, "A new approach for iron losses calculation in voltage fed time stepping finite elements," in *Proc. CEFC'2000, Milwaukee, WI*

Implementation of an Advanced Eddy-Current Model for Non-Linear Laminated Media

A. Belahcen, E. Dlala, and J. Pippuri

Helsinki University of Technology, Dept. of Electrical Engineering

P.O.Box 3000, FIN-02015-TKK, Finland

Anouar.belahcen@tkk.fi

Abstract— This paper presents an efficient method to implement an advanced eddy-current model with bidirectional flux feeding and investigates the techniques required for its incorporation in the 2D FE analysis of electrical machines. The results show that the implementation and the incorporation of the advanced model in FE analysis are feasible. Furthermore the proposed implementation produces results close to the ones observed in measurements.

I. INTRODUCTION

Accurate power loss computation is needed for the design of electrical machines. In addition to the losses in the windings, the losses in the iron core are of great interest. The core losses are usually separated into hysteresis, eddy currents, and excess losses, the accurate computation of which requires advanced vector-hysteresis models [1]. When the iron core is modeled with a single-valued non-linear BH-curve, the only part of the core losses that can be accurately modeled is the eddy currents part. In this work, the so-called 1D eddy-current model [2] is used for this purpose.

This paper presents an efficient method to implement the advanced model and investigates the techniques required for its incorporation in the 2D FE analysis of electrical machines. The latter task is carried out using a 2D-like procedure. Results of application in FE simulation are presented in [3].

II. THE ADVANCED MODEL AND ITS IMPLEMENTATION

The adequate modeling of eddy currents is intrinsically a 3D problem. However if the behavior of the eddy currents at their loop edges is ignored, the problem reduces to two coupled 1D equations [2]. This assumption is reasonable since the dimensions of the lamination in the x - y direction are larger than its thickness. If σ is the material conductivity, \mathbf{h} the magnetic field strength, \mathbf{b} the magnetic flux density and z the coordinate in the depth of the lamination, the equations are

$$\begin{aligned} \frac{\partial^2 h_x(z,t)}{\partial z^2} &= \sigma \frac{\partial b_x(z,t)}{\partial t} \\ \frac{\partial^2 h_y(z,t)}{\partial z^2} &= \sigma \frac{\partial b_y(z,t)}{\partial t} \end{aligned} \quad (1)$$

Eq. (1) can be solved in terms of \mathbf{h} and \mathbf{b} but it requires boundary values of \mathbf{h} , which are not known a priori. We propose the use of a two-component vector potential to reformulate (1) as in (2) and solve it with FEM.

With $\mathbf{a} = a_x(z,t)\mathbf{e}_x + a_y(z,t)\mathbf{e}_y$ and $\mathbf{j} = j_x(z,t)\mathbf{e}_x + j_y(z,t)\mathbf{e}_y$,

$$\begin{aligned} \frac{\partial}{\partial z} \left(\nu \frac{\partial a_x}{\partial z} \right) + \sigma \frac{\partial a_x}{\partial t} &= 0 \\ \frac{\partial}{\partial z} \left(\nu \frac{\partial a_y}{\partial z} \right) + \sigma \frac{\partial a_y}{\partial t} &= 0 \end{aligned} \quad (2)$$

where ν is the reluctivity, which is given as a spline function of \mathbf{b}^2 . After discretization in the lamination depth, one obtains

$$\begin{bmatrix} \mathbf{S} & \mathbf{0} \\ \mathbf{0} & \mathbf{S} \end{bmatrix} \begin{bmatrix} \mathbf{a}_x \\ \mathbf{a}_y \end{bmatrix} + \frac{2}{\Delta t} \begin{bmatrix} \mathbf{T} & \mathbf{0} \\ \mathbf{0} & \mathbf{T} \end{bmatrix} \begin{bmatrix} \mathbf{a}_x \\ \mathbf{a}_y \end{bmatrix} = \begin{bmatrix} \mathbf{0} \\ \mathbf{0} \end{bmatrix}$$

$$\text{where } S_{ij} = \int_{\Omega} \nu(a_x, a_y) \nabla N_i \cdot \nabla N_j d\Omega \quad (3)$$

$$T_{ij} = \int_{\Omega} \sigma N_i N_j d\Omega$$

$$\text{and the boundary values } \begin{aligned} a_x(d,t) &= d \cdot b_y(t); & a_x(0,t) &= 0 \\ a_y(d,t) &= -d \cdot b_x(t); & a_y(0,t) &= 0 \end{aligned} \quad (4)$$

with d half of the depth and the origin of the z -axis is at the middle of the lamination. The solution of (3) presents difficulties originating from the non-linearity of the reluctivity and its dependency on both components of the magnetic vector potential or magnetic flux density. This step requires some attention, as we only know how ν depends on \mathbf{b}^2 . We suggest the use of the same value of ν in both directions to keep the material isotropic i.e. $\nu(a_x, a_y) = \nu(\mathbf{b}^2(a_x, a_y))$.

Applying the Newton-Raphson method, one obtains

$$\begin{bmatrix} \mathbf{P}_x & \mathbf{P}_{xy} \\ \mathbf{P}_{xy} & \mathbf{P}_y \end{bmatrix} \begin{bmatrix} \Delta \mathbf{a}_x \\ \Delta \mathbf{a}_y \end{bmatrix} = \begin{bmatrix} \mathbf{R}_x \\ \mathbf{R}_y \end{bmatrix} \quad (5)$$

$$\begin{aligned} P_{xij} &= S_{ij} + \frac{2}{\Delta t} T_{ij} + \\ & 2 \sum_{m=1}^n \sum_{l=1}^n \int_{\Omega} \frac{\partial \nu}{\partial \mathbf{b}^2} a_{xl} a_{xm} (\nabla N_i \cdot \nabla N_l) (\nabla N_j \cdot \nabla N_m) d\Omega \\ P_{yij} &= S_{ij} + \frac{2}{\Delta t} T_{ij} \\ & 2 \sum_{m=1}^n \sum_{l=1}^n \int_{\Omega} \frac{\partial \nu}{\partial \mathbf{b}^2} a_{yl} a_{ym} (\nabla N_i \cdot \nabla N_l) (\nabla N_j \cdot \nabla N_m) d\Omega \\ P_{xyij} &= 2 \sum_{m=1}^n \sum_{l=1}^n \int_{\Omega} \frac{\partial \nu}{\partial \mathbf{b}^2} a_{xl} a_{ym} (\nabla N_i \cdot \nabla N_l) (\nabla N_j \cdot \nabla N_m) d\Omega \end{aligned} \quad (6)$$

The residuals ($\mathbf{R}_x, \mathbf{R}_y$) are computed in a conventional FE manner. The inclusion of P_{xy} in the jacobian matrix allows for a fastest convergence (quadratic convergence is achieved).

Fig. 1 shows the computed flux density distribution in the z -axis at a given time for the case of alternating flux in a direction $\theta = 45^\circ$. Fig 2. shows the same result for the case of rotating flux (circular). Both results are at 500 Hz and 1.5 T.

III. INCORPORATION OF THE ADVANCED MODEL IN 2D FE

The implemented advanced eddy-current model can be coupled with the FE simulation of the electrical machines. An intrinsic coupling quantity is the reluctivity. This approach has been used in the time-harmonic simulation of electrical machines [4].

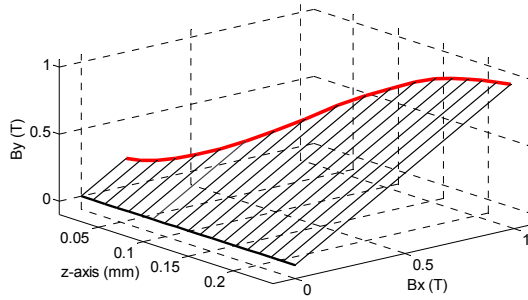


Fig. 1. Computed flux density distribution in the depth of the sheet when the model is fed by alternating flux at 500 Hz, 1.5 T at 45°. The dark line at $x=0$, $y=0$ represents the 1D model and the other straight lines the magnetic flux density vector at the center of each 1D element (only half the depth is shown).

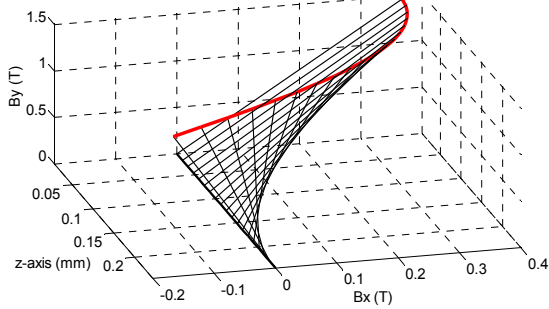


Fig. 2. Computed flux density distribution in the depth of the sheet when the model is fed by circular flux at 500 Hz, 1.5 T.

However, the same approach is not possible in time stepping; the reluctivity is negative at certain times. We propose the use of the magnetic field strength to incorporate the advanced model in the 2D FE simulation. The magnetic field strength H_{1D} seen by the 2D model is calculated as the product of the magnetic flux density at the surface of sheet and the reluctivity at that point. The BH-curves obtained with this approach are shown in Fig. 3 for the case of an elliptic flux and Fig. 4 for the case of alternating flux (non coupled case).

H_{1D} is assumed to be the sum of the magnetic field strength in the 2D simulation H_{2D} and a component H_{ec} due to the eddy currents. The governing equation of the 2D problem $\nabla \times \mathbf{H}_{1D} = \mathbf{J}$ is reformulated as $\nabla \times \mathbf{H}_{2D} = \mathbf{J} - \nabla \times \mathbf{H}_{ec}$. The 2D FE equations are then derived in a conventional manner except that $-\nabla \times \mathbf{H}_{ec}$ is added to the right-hand side.

To test the coupling methodology, we use a 2D-like model, which is fed by a predefined magnetic field strength \mathbf{H} . The iterations are carried out in a sequential manner with an over-relaxation for the 2D-like model until convergence.

The results of the 2D-like model are affected when it is coupled with the advanced model. This is seen from Fig. 4, where the BH-loops from coupled computations and non coupled are shown for an alternating magnetic field strength at 200 Hz, 1000 A/m increased by the 5th harmonic at 200 A/m.

IV. DISCUSSION AND ANALYSIS

The advanced model implemented in this work has been previously used in conjunction with hysteresis models [2], [5]. The merits of this paper reside in the extension of the model to be used in conjunction with the single-valued bidirectional problems. The statement that the same reluctivity is to be used in both directions guarantees isotropy and the use of the derived coupling terms in the jacobian matrix of the advanced model achieves fast convergence.

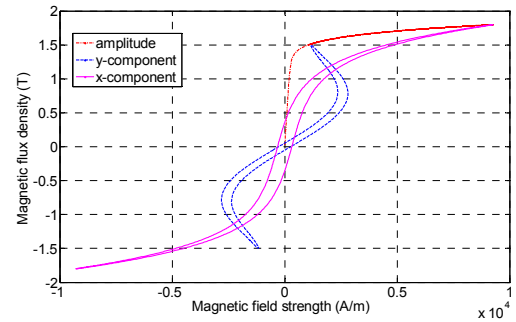


Fig. 3. Computed dynamic BH-loop when the model is fed by elliptic flux at 500 Hz with $b_x=1.8$ T and $b_y=1.5$ T. The single-valued BH-curve is also shown.

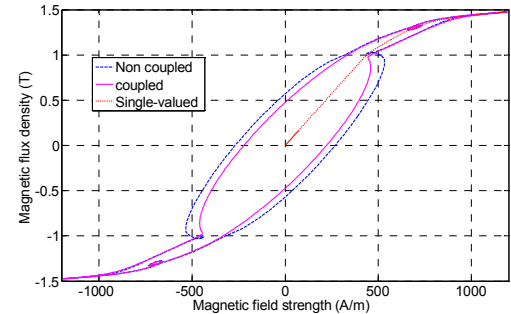


Fig. 4. Computed BH-loops when the advanced model is incorporated in the simple H-fed model (coupled) and without (non coupled). The simple model is fed from an alternating magnetic field strength with a fundamental at 200 Hz, 1000 A/m with the 5th harmonic at 1000 Hz, 200 A/m.

The purpose of the test runs is two-folds. The feasibility of the incorporation is demonstrated and some phenomena caused by the eddy currents in the lamination are raised. The eddy currents damp the flux, resulting in narrow BH-loop and lower computed losses (loop areas in Fig. 4). The eddy currents also distorted the components of the BH-loops in the case of elliptic field as can be seen from Fig. 3.

V. CONCLUSIONS

The investigations carried out in this work show that the advanced eddy-current model can be efficiently implemented when it is fed from a bidirectional flux too. It is also shown that the incorporation of the advanced model in a 2D FE program is possible and that this incorporation results in better computation of the eddy-current losses in the lamination. A better accuracy is expected in the computation of other quantities such as line currents and torque since they depend directly on the field solution.

VI. REFERENCES

- [1] E. Dlala, "Comparison of models for estimating magnetic core losses in electrical machines using the finite-element method", *IEEE Trans. on Magnetics*, 45(2): 716-725, 2009.
- [2] O. Bottauscio, M. Chiampi, and D. Chiarabaglio, "Advanced model of laminated magnetic cores for two-dimensional field analysis", *IEEE Trans. on Magnetics*, 36(3): 561-573, 2000.
- [3] J. Pippuri, A. Belahcen, E. Dlala, and A. Arkkio, "Inclusion of eddy currents in laminations in two-dimensional finite element analysis", *Compumag*, unpublished, 2009.
- [4] J. Pippuri, A. Arkkio, "Time-harmonic induction-machine model including hysteresis and eddy currents in steel laminations", *IEEE Trans. on Magnetics*, to be published, 2009.
- [5] E. Dlala, A. Belahcen, A. Arkkio, "Efficient magnetodynamic lamination model for two-dimensional finite element simulation of rotating electrical machines", *J. of Mag. and Mag. Mat.*, 320(20):e1006-e1010, 2008.

Vector Magnetic Hysteresis Modeling of Soft Magnetic Composite Material

Youguang Guo¹, Haiyan Lu², Jianguo Zhu¹, Zhiwei Lin¹, Jinjiang Zhong¹, and Shuhong Wang³

¹School of Electrical, Mechanical and Mechatronic Systems, University of Technology Sydney, 2007, Australia

²School of Software, University of Technology Sydney, NSW 2007, Australia

³Faculty of Electrical Engineering, Xi'an Jiaotong University, Xi'an, Shaanxi 710049, China.
youguang@eng.uts.edu.au, helenlu@it.uts.edu.au, joe@eng.uts.edu.au, jacklin@eng.uts.edu.au

Abstract—Thanks to the unique magnetic properties, soft magnetic composite (SMC) materials and their application in electromagnetic devices have achieved significant development. The typical example of SMC application is the electrical machine with complex structure, in which the magnetic flux is basically rotating. To design and analyze such devices, vector magnetic properties of the core material should be properly determined, modeled and applied. This paper presents the modeling of vector magnetic hysteresis of SMC based on a Stoner-Wohlfarth (S-W) elemental operator. A phenomenological mean-field approximation is used to consider the interaction between particles. With the presented model, the magnetization processes of SMC under both alternating and rotating fluxes are numerically simulated. The simulations have been verified by experimental measurements.

I. INTRODUCTION

Thanks to their many unique properties such as 3-D magnetic isotropy, very low eddy current loss, design flexibility and low production process for electromagnetic devices, SMC (soft magnetic composite) materials and SMC electrical machines have undergone significant development in the past decade [1]. Typical applications include claw pole and transverse flux machines in which the flux flows substantially in 3-D space [2]. The conventional laminated electrical steel is not suitable for constructing the core of such machines because the flux component perpendicular to the steel plane may cause excessive eddy current loss. The SMC material seems to be an ideal substitute.

The relationship between the magnetic flux density (\mathbf{B}) and the magnetic field strength (\mathbf{H}) is among the basic properties of magnetic materials. When \mathbf{B} and \mathbf{H} are restrained in the same direction, their relation is reduced to the well-known scalar B-H loop. However, in the 3-D flux machines, \mathbf{B} and \mathbf{H} are not aligned. Furthermore, both \mathbf{B} and \mathbf{H} are rotating and \mathbf{B} lags \mathbf{H} by an angle. In other word, both the magnitudes and directions of the \mathbf{B} and \mathbf{H} may vary, as well as the directional angle difference between the two vectors [2]. Therefore, the vector magnetic properties, such as the vector \mathbf{B} - \mathbf{H} relation and core loss, under different vector magnetizations, should also be investigated. Owing to the very complex mechanism of the magnetic hysteresis, particularly the vector hysteresis, which is not yet fully understood so far, the development of mathematical models of magnetization process has not been successful, in particular for the engineering practice.

A huge amount of work has been conducted by various researchers for modeling the vector magnetic hysteresis.

Among the noticeable work are: (a) the Stoner and Wohlfarth (S-W) model that was postulated based on the rotation of magnetic moments of single domain particles with respect to their easy axes [3]; (b) the vector Preisach model constructed by the superposition of scalar Preisach models [4]; and (c) the combined model that incorporates the vector elemental operator of the S-W model into the Preisach diagram such that the new model has the vector nature of the S-W model while retaining the efficiency of the Preisach model [5]. However, the phenomenological modeling of vector hysteresis has long been centered on the classical S-W model [6]-[7] because of the vector nature of the model.

This paper presents the modeling of vector magnetic hysteresis of SMC based on a Stoner-Wohlfarth (S-W) elemental operator [6]. A phenomenological mean-field approximation is used to consider the interaction between particles [7]. With the presented model, the magnetization processes of SMC under both alternating and rotating fluxes are numerically simulated. The simulations have been verified by experimental measurements.

II. MODELING OF VECTOR HYSTERESIS

Under a magnetic field \mathbf{H} , the magnetic moment \mathbf{m}_s of an S-W particle rotates to the orientation which results in a minimum energy. The position of \mathbf{m}_s changes with respect to \mathbf{H} , and the domain rotation can be reversible or irreversible. The equilibrium orientation of \mathbf{m}_s can be evaluated by the asteroidal rule in the plane containing \mathbf{H} and the easy axis as shown in Fig. 1, where \mathbf{H}_e and \mathbf{H}_p are the \mathbf{H} components along the easy axis and the perpendicular direction respectively, $H_k=2K/(\mu_0 m_s)$, and K is the domain crystal anisotropy constant.

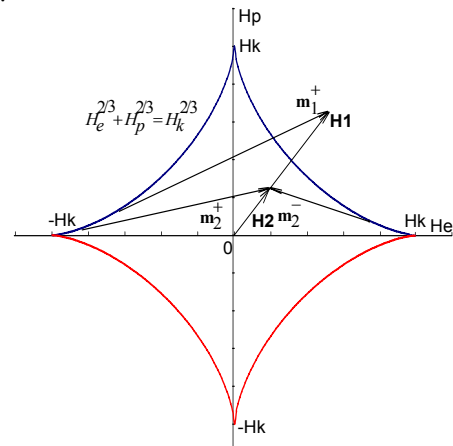


Fig. 1. Asteroid vector elemental hysteresis operator

A mean field term is added to account for the macroscopic effect of interaction between S-W particles [7], $\mathbf{H}_{\text{eff}} = \mathbf{H} + k\mathbf{M}$, where k is a constant feedback coefficient and can be theoretically determined from experimental data [8]. The contribution of an S-W particle can be expressed by $\mathbf{M} = \mathbf{S}(\mathbf{H}_{\text{eff}})$, where $\mathbf{S}()$ stands for the S-W model. The bulk material can be considered as a collection of many S-W single domain particles and the total magnetization is the vector sum of contributions of all these constitute domains. In numerical implementation, the magnetization is computed by the vector sum of \mathbf{m}_i of a group of magnetic particles.

III. NUMERICAL IMPLEMENTATION

The magnetization processes of SMC with isotropic magnetic properties under both alternating and rotating magnetic fields have been simulated numerically. The results (Fig. 2 and Fig. 3) show that in an isotropic magnetic material \mathbf{M} and \mathbf{H} vector are collinear for an alternating magnetic field excitation, while for a rotating magnetic field excitation of constant magnitude M vector lags the \mathbf{H} vector for a certain angle.

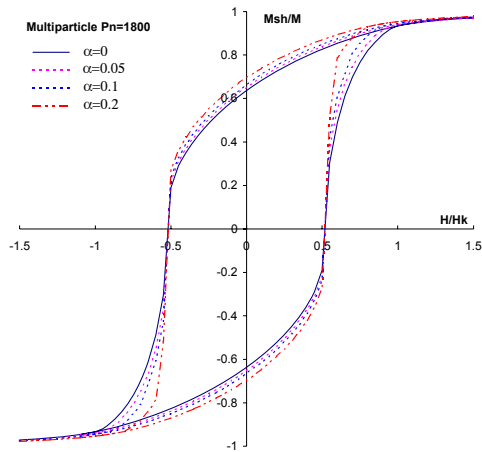
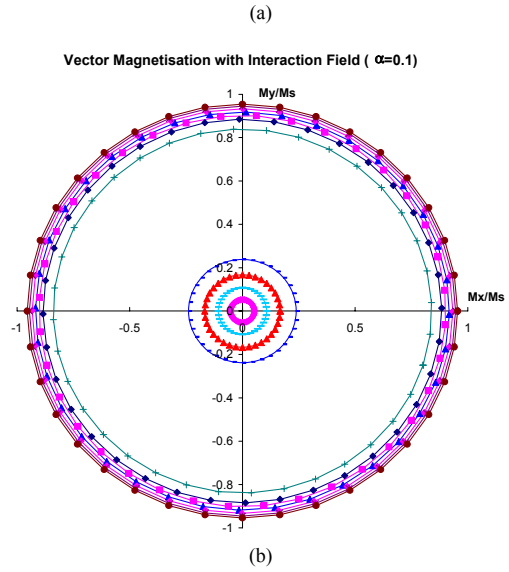
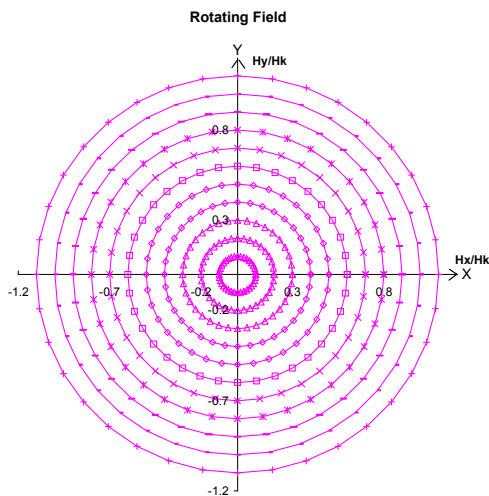


Fig. 2. Hysteresis loops under alternating magnetic field excitation

Fig. 3. Loci of (a) rotating magnetic field \mathbf{H} , and (b) magnetization \mathbf{M}

IV. EXPERIMENTAL RESULTS

The B-H relationships of SMC samples under various alternating and 2-D and 3-D rotating magnetic excitations have been measured by the authors [9], validating the numerical simulations by using the presented model.

The detailed implementation process and more simulation results will be presented in the full paper. The simulation and experimental results will be compared and analyzed in detail.

V. REFERENCES

- [1] The latest development in soft magnetic composite technology, 1997-2009, Höganäs AB, Sweden, available at <http://www.hoganas.com/>.
- [2] Y. G. Guo, J. G. Zhu, Z. W. Lin, and J. J. Zhong, "Measurement and modeling of core losses of soft magnetic composites under 3D magnetic excitations in rotating motors," *IEEE Trans. on Magnetics*, 41(10):3925-3927, 2005.
- [3] E. C. Stoner and E. P. Wohlfarth, "A mechanism of magnetic hysteresis in heterogeneous alloys," *Phil. Trans. Roy. Soc.*, 240A:599-642, 1948.
- [4] I. D. Mayergoyz, *Mathematical Models of Hysteresis*, Springer-Verlag, 1991.
- [5] J. Oti and E. D. Torre, "A vector moving model of both reversible and irreversible magnetizing processes," *J. Appl. Phys.*, 67(9):5364-5366, 1990.
- [6] J. J. Zhong, J. G. Zhu, Y. G. Guo, and Z. W. Lin, "A 3D vector magnetization model with interaction field," *IEEE Trans. on Magnetics*, 41(5):1496-1499, 2005.
- [7] D. L. Atherton and J. R. Beattie, "A mean field Stoner-Wohlfarth hysteresis model," *IEEE Trans. on Magnetics*, 26(6):3059-3063, 1990.
- [8] D.C. Jiles and D.L. Atherton, "Theory of ferromagnetic hysteresis," *J. Magnetism and Magnetic Materials*, 61:48-60, 1986.
- [9] J. G. Zhu, Z. W. Lin, Y. G. Guo, and Y. K. Huang, "3D measurement and modelling of magnetic properties of soft magnetic composite", *Przegląd Elektrotechniczny (Electrical Review)*, Poland, 2009(1):11-15, 2009. Special Topic on 1 & 2 Dimensional Magnetic Measurements.

On the Use of Multi-Direction Si-Fe Sheet Sample Magnetic Properties Measured by Epstein Frame in Finite Element Analysis

Dexin Xie¹, Qilin Liu¹, Zhiqiang Ren¹, Xiaoyan Wang¹, Yanli Zhang¹ and Zhiguang Cheng²

¹School of Electrical Engineering, Shenyang University of Technology; ²R&D Center, Baoding Tianwei Group
111, Shenhao West Road, Shenyang Economic & Technical Development Area, Shenyang, Liaoning 110178, China
xiebaiy@mail.sy.ln.cn

Abstract — A method using multi-direction Si-Fe sheet sample magnetic properties measured by the Epstein frame for finite element analysis is presented in this paper to consider the 2D magnetic anisotropy of the sheet. The validity of the method is verified by the comparison between the computational results and measured ones of a model of three phase transformer.

I. INTRODUCTION

Although the method of measuring magnetic characteristics of Si-Fe sheet by 1D single sheet tester has been included in the IEC standard for years, and an advanced 2D measuring method to consider the vector magnetic properties was proposed [1], the method of Epstein frame are still used by many electrical sheet manufacturers and industrial users according to the international standard [2]. The deficiencies of the measurement with the Epstein frame were indicated by authors of [3]-[4], etc. However, in view of its widely use, if we can do something with the Epstein test, and try to improve its traditional measuring method, this work is also of significance. A method using multi-direction Si-Fe sheet sample magnetic properties measured by the Epstein frame for finite element analysis is presented in this paper to involve the 2D magnetic anisotropy of the sheet.

II. METHOD DESCRIPTION

There are many researches have been done with the measuring and modeling of 2D magnetic properties of the silicon steel sheet. K. Fujiwara et al proposed an anisotropic reluctivity tensor, given as [5]

$$\nu = \begin{bmatrix} \nu_x & 0 \\ 0 & \nu_y \end{bmatrix} = \begin{bmatrix} \frac{H \cos \theta_H}{B \cos \theta_B} & 0 \\ 0 & \frac{H \sin \theta_H}{B \sin \theta_B} \end{bmatrix} \quad (1)$$

where θ_H and θ_B denote for the angle to x -axis of \mathbf{H} and \mathbf{B} respectively. With a 2D Single Sheet Tester (SST) [1], a rotational magnetic field is excited and \mathbf{H} and \mathbf{B} with different direction in a Si-Fe sheet can be measured while the sheet sample is fixed in space. Taking the hint of 2D SST, we can set the magnetic field fixed in space and let the sheet samples which consist of the Epstein frame have different angles to the rolling direction, as if the sheets “rotate”. However, the difference between the Epstein frame and 2D SST is that the measurement with the former is one dimensional. Therefore, the following method is used to deal with the problem.

A. B - H curves of multi-direction Si-Fe sheet samples measured by Epstein frame

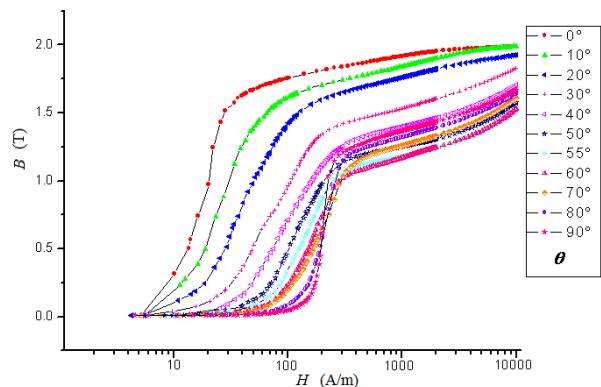


Fig.1. B - H curves of multi-directions (30ZH120 Si-Fe sheet)

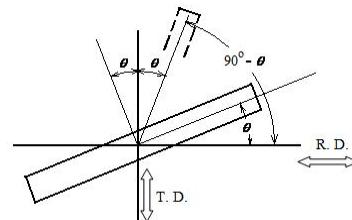


Fig. 2 Angle from the rolling direction to the measurement direction: θ and $90^\circ - \theta$

In multi-direction sampling, the angle from the rolling direction to the measurement direction is set in advance, such as 0° , 10° , 20° , 30° , 40° , 50° , 55° , 60° , 70° , 80° and 90° . For this kind of multi-direction samples, according to the report of [6] we know that when using narrow sample (25mm×300mm) \mathbf{B} and \mathbf{H} remained in a direction parallel to the length of the sample for both low and high level of magnetization. This is the case close to the Epstein test. After the Epstein testing at different measurement directions, the every corresponding B - H curve is yielded as shown in Fig.1. One can find the relationships of those curves measured at different specified measurement directions. For example, the curves at 20° and 70° represent the magnetic properties from two orthogonal measurement directions, see Fig.2. This is easy to understand as long as we notice that here $20^\circ + 90^\circ = 110^\circ$, and along this direction the magnetic property is the same as 70° according to the symmetry of the sample. By using these curves, the 2-D magnetic properties can be obtained.

B. Formulation in finite element analysis of magnetic fields

The governing equation under a global coordinates including 2D magnetic properties is given by

$$\frac{\partial}{\partial x} \left(v_{yx} \frac{\partial A}{\partial y} - v_{yy} \frac{\partial A}{\partial x} \right) - \frac{\partial}{\partial y} \left(v_{xx} \frac{\partial A}{\partial y} - v_{xy} \frac{\partial A}{\partial x} \right) = J \quad (2)$$

Eq. (2) is solved with FE analysis and the Newton-Raphson iteration.

To use the multi-direction B - H curves, a local coordinate system x' - y' is set in each element, and another iterative process of local reluctivities is needed. The corresponding reluctivity of an element is given by

$$v^k = \begin{bmatrix} v_{x'}^k & 0 \\ 0 & v_{y'}^k \end{bmatrix} \quad (3)$$

where the superscripts denote the iteration number, and

$$v_{x'}^k = f_1(B_x^{k-1}, \theta^{k-1}), \quad v_{y'}^k = f_2(B_y^{k-1}, 90^\circ - \theta^{k-1}) \quad (4)$$

in (4) θ^{k-1} is the angle from the direction of B^{k-1} to the rolling direction. Based on a coordinate transformation, the relation of the global and local reluctivities can be deduced, which is given as

$$\begin{cases} v_{xx} = v_{x'} \cos^2 \alpha + v_{y'} \sin^2 \alpha \\ v_{xy} = v_{x'} \cos \alpha \sin \alpha - v_{y'} \sin \alpha \cos \alpha \\ v_{xy} = v_{yx} \\ v_{yy} = v_{x'} \sin^2 \alpha + v_{y'} \cos^2 \alpha \end{cases} \quad (5)$$

where α is the angle between the local and global coordinates.

C. Numerical Model

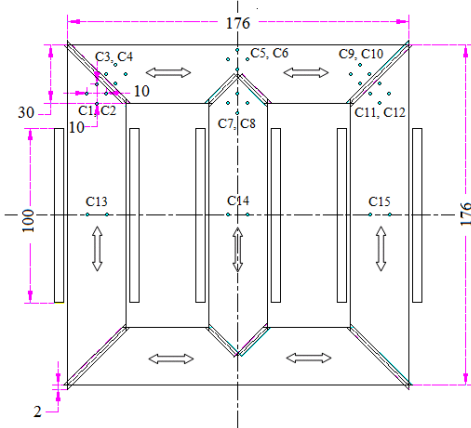


Fig. 3 A model of transformer without secondary coils

A model of three-phase transformer without the secondary coils is taken as a numerical example. Three windings of 106 turns are placed on each limb of the iron core which is made of laminated grain-oriented silicon steel sheets of 30ZH120, shown in Fig. 3. The computation steps are as follows.

Step 1: Set the iteration number $k = 0$, input the initial reluctivities $v_{x'}^0$ and $v_{y'}^0$ for each element.

Step 2: Solve (2) with FEM, then calculate B_x^0 , B_y^0 , and

$$\theta^0 = \begin{cases} \arctan(|B_y^0|/|B_x^0|) & \text{in the area of the limbs} \\ \arctan(|B_x^0|/|B_y^0|) & \text{in the area of the yoke} \end{cases} \quad \text{for each element.}$$

Step 3: $k = k+1$, determine the B - H curves of element according to (4) with an interpolation, calculate $v_{x'}^k$ and $v_{y'}^k$, then solve (2) with Newton-Raphson iteration, and calculate B_x^k, B_y^k .

Step 4: $\Delta B_x^k = |B_x^k - B_x^{k-1}|$, $\Delta B_y^k = |B_y^k - B_y^{k-1}|$. If the total iterative error $\sum \sqrt{\Delta B_x^2 + \Delta B_y^2} \leq \varepsilon_1$, then stop; or else continue, where ε_1 is a tolerance specified in advance.

Step 5: modify θ^k according to a relaxation rule, then go to Step 3.

III. RESULTS

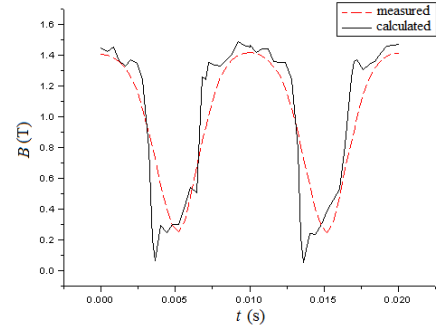


Fig. 4 Comparison of measured and calculated $|B|$

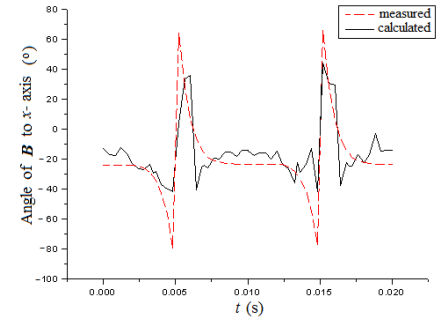


Fig. 5 Comparison of measured and calculated angle of B to x -axis

Fig. 4 and Fig. 5 show the comparisons of measured and calculated flux density B at the position of test coil C3 and C4 for the maximum electric current of 2.6A. More results and discussions will be proposed in the extended paper.

IV. REFERENCES

- [1] M. Enokizono et al, "Rotational power loss of silicon steel sheet," *IEEE Trans. on Magnetics*, 26(5): 2562-2564, 1990.
- [2] IEC Standard 60404-2-2008: Magnetic materials - Part 2: Methods of measurement of the magnetic properties of electrical steel strip and sheet by means of an Epstein frame.
- [3] T. Nakata, K. Fujiwara, N. Takahashi et al, "An Improved Numerical Analysis of Flux Distributions in Anisotropic Materials," *IEEE Trans. on Magnetics*, Vol. 30, No. 5, 1994, pp.3395-3398
- [4] E. Antonelli, et al, "Epstein Frame: How and When It Can Be Really Representative About the Magnetic Behavior of Laminated Magnetic Steels," *IEEE Trans. on Magnetics*, 41(5): 1516-1519, 2005
- [5] K. Fujiwara, et al, "A proposal of finite-element analysis considering two-dimensional magnetic properties," *IEEE Trans. on Magnetics*, 38(2): 889-892, 2002
- [6] N. J. Layland, A. J. Moses, N. Takahashi and T. Nakata, "Effects of shape on samples of silicon-iron on the directions of magnetic field and flux density," *Nonlinear Electromagnetic Systems*, 800-803, 1996, A. J. Moses and A. Basak (Eds.) IOS Press

A Study for Harmonic Iron Loss for Electrical Steel under Alternating Magnetic Field

Sun-Ki Hong¹, and Chang Seop Koh², Member IEEE

¹Dept. of System & Information Eng., Hoseo Univ., Asan, ChungNam, 336-795, KOREA. skhong@hoseo.edu

²School of ECE, Chungbuk National University, Cheongju, Chungbuk 361-763, KOREA kohcs@chungbuk.ac.kr

Abstract — In this paper, the nature of iron losses in electrical steel during alternating field excitation is investigated more closely. A more exact definition of the ac iron losses is proposed by accurately measuring the losses for conditions of both sinusoidal H and sinusoidal B . In addition, inverse hysteresis model considering eddy current loss is developed to analyze the iron loss when the input is voltage source. With this model, inrush current in inductor or transformer as well as the iron loss can be calculated. The results of this new approach to iron loss calculations in electrical steel are compared to experimentally-measured losses.

I. INTRODUCTION

For a precise design and analysis of electric machine, iron loss analysis becomes very important and essential part [1]. For measuring hysteresis loss, the input can be sinusoidal magnetic field intensity or the sinusoidal flux density. The iron losses in these two cases are not same, but this fact has received almost no attention to date. If harmonics are present in the excitation, the iron loss calculation becomes even more complex. One approach [2] for including harmonics in the iron loss analysis uses Discrete Fourier Transform to decompose the flux density into its harmonic components. The iron losses at each element are then calculated using iron loss data sheet and the total loss is obtained by summation of the iron losses at all of the elements. However, the results of this approach can be too large in comparison to the actual iron losses. The purpose of this research is to investigate more closely the nature of iron losses in electrical steel during alternating field excitation. In this work, a more exact definition of the ac iron losses is proposed by accurately measuring the losses for conditions of both sinusoidal H and sinusoidal B . In addition, inverse magnetization-dependent hysteresis model considering eddy current loss is developed to analyze the iron loss when the input is voltage source. With this model, inrush current in inductor or transformer as well as the iron loss can be calculated. The results of this new approach to iron loss calculations in electrical steel are compared to experimentally-measured losses.

II. IRON LOSS FOR ALTERNATING MAGNETIC FIELD

A) Hysteresis loss

Hysteresis loss is the B-H loop area not including the eddy current loss by applying the lowest frequency. Fig. 1 shows the two kinds of B-H loops of the bulk ring, whose areas represent iron losses for the input of 0.2[Hz]. The dotted line shows the loop whose input is magnetic field intensity and the output becomes magnetic flux density.

Let's call this as sinH condition loop and it means the input H is sinusoidal. The solid line is sinB loop and the sinusoidal flux density B becomes input. To accomplish these experiments, a apparatus shown in Fig. 2 is developed and the shapes of H or B can be controlled. As can be seen in Fig. 1, the loop areas under sinH and sinB are different. Under sinH condition, the flux density waveform is no more sinusoidal and it becomes to have harmonics which cause harmonic eddy current losses. As a result, the hysteresis loss needs to be measured under the sinusoidal flux density condition.

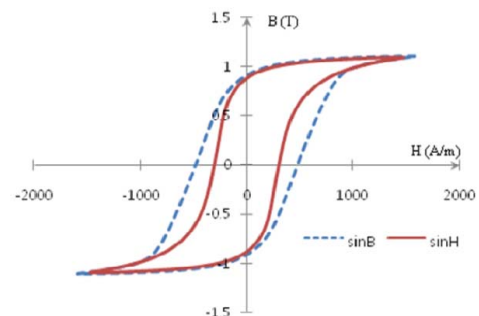


Fig. 1. Measured B-H loops for sinB and sinH conditions

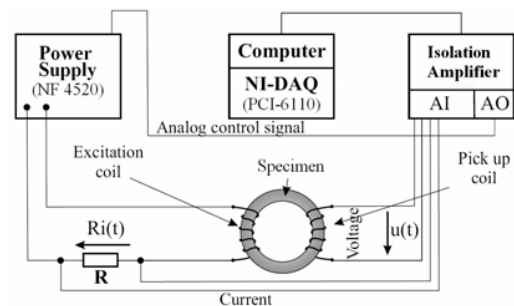


Fig. 2. Measurement system.

B) Iron Losses including harmonics

The current of exciting coil and flux density can be measured with the measurement system in Fig. 2. Fig. 3 shows the measured B-H loop (solid line) under sinH condition and separated loops according to their frequencies by FFT. As can be seen, the fundamental frequency loop (dotted line, 1st B) is larger than the original loop (all B). This means the iron loss cannot be calculated by the summation of the each frequency component and it must be calculated by measuring the loop area. If the B-H data are known or measured, the loss can be calculated by integrating the magnetic field intensity for the flux density [3]. Table 1 shows the measured and FFT results for Fig. 3.

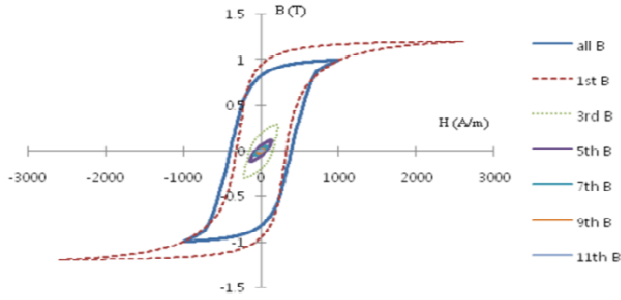


Fig. 3. Original and harmonic loops

Table 1. Measured and FFT loops results for Fig. 4.

	Freq.	Phase (degree)	Bm[T]	Loss/ Iperoid	Total Loss
Original B	1Hz		0.993149	0.186105	0.186105
FFT 1st	1Hz	0	1.196438	0.232240	0.494115
3rd	3Hz	11.60586	0.289885	0.049908	
5th	5Hz	8.67891	0.114318	0.014979	
7th	7Hz	-3.53840	0.049945	0.004099	
9th	9Hz	5.09336	0.020309	0.000801	
11th	11Hz	-18.28070	0.006875	0.000123	

Fig. 4 shows the waveforms measured by the developed system in Fig. 2. In the figure, the magnetic field intensity, magnetic flux density, minor loops and initial magnetization curves are shown. These experiments are under sinB condition. As can be seen in the figures, the measured results are different according to the input conditions. When the input is sinH, the flux density becomes like square waves, so they include lots of harmonics and increase iron loss because the eddy current loss increases.

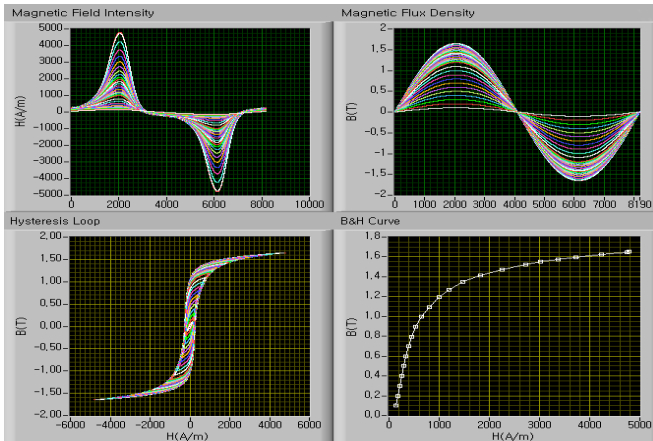


Fig. 4. Experiment results under sinB.

III. INVERSE HYSTERESIS ALGORITHM

In many cases, the input becomes not current but voltage, and then the input element for iron loss calculation needs to be also not magnetic field intensity but magnetic flux density. Therefore the inverse algorithm $H = f^{-1}(B)$ is required. If the flux density $B(H)$ changes, by changing the magnetic field intensity with ΔH , $B(H)$ can be determined using Preisach algorithm. To reduce the calculation efforts and error,

interpolation method is used. For example, if $B(t_p) > B(t_{p-1})$ and exact value $B(t_p)$ is between the two calculated flux densities where p is a time step, $H(t_p)$ can be calculated by (1) and any iteration process is not needed.

$$H(t_p) = H_2 \frac{B(t_p) - B_1}{B_2 - B_1} + H_1 \frac{B(t_p) - B_2}{B_1 - B_2} \quad (1)$$

When the load is R-L circuits, the voltage equation can be transformed to discrete equation as (2). By solving this equation for flux ϕ , flux density, iron loss, inrush current etc. can be calculated.

$$\phi(k+1) = \phi(k) + \frac{\Delta t}{n} [E_m \sin(\omega \cdot t_k + \theta) - r \cdot i] \quad (2)$$

Where k is time step, n is number of turn or ring core and θ is the phase angle of voltage. The eddy current loss can be considered with (3) where δ is the thickness of the steel, w is the width, and ρ is the electrical resistivity. Eddy current i_e can be calculated because P_e can be calculated with (3) and the applied voltage is known. The total current is calculated by adding i_e to i in (2).

$$P_e = \frac{1}{\delta w} \int_V \rho J^2 dV = \frac{1}{\delta w} \int_{-\frac{\delta}{2}}^{\frac{\delta}{2}} \rho \left(\frac{x}{\rho} \frac{dB}{dt} \right)^2 w dx \quad (3)$$

$$= \frac{\delta^2}{12\rho} \left(\frac{dB}{dt} \right)^2$$

IV. CONCLUSION

In this paper, exact definition of hysteresis loss is proposed. That is, it needs to be measured under the sinusoidal flux density condition. In addition, the iron loss including harmonics is defined by the experimental results. The iron loss cannot be calculated by the summation of the each frequency component and it must be calculated by the real loop area through integrating the magnetic field intensity for the flux density. To simulate this phenomenon, inverse algorithm is proposed and inrush current in an inductor is experimented and simulated. They are compared and it shows good agreement.

Acknowledgment

This work was supported by KESRI(R-2007-2-068), which is funded by MKE.

REFERENCES

- [1] K. Yamazaki, "Torque and Efficiency Calculation of an Interior Permanent Magnet Motor Considering Harmonic Iron Losses of Both the Stator and Rotor", IEEE Trans. On Magn, vol. 39, No.3, pp.1460-1463, May, 2003.
- [2] H. Nam, K.H. Ha, J.J. Lee, J.P. Hong and G.H. Kang, "A Study on Iron Loss Analysis Method Considering the Harmonics of the Flux Density Waveform Using Iron Loss Curves Tested on Epstein Samples", IEEE Trans. on Magn., vol. 39, No.3, pp.1472-1475, May, 2003.
- [3] K. Atallah and D. Howe, "Calculate of the rotational power loss in electrical steel laminations from measured and," IEEE Trans. on Magn., vol. 29, no. 6, pp. 3547-3549, Nov. 1993.
- [4] Hong-Kyu Kim, Sun-Ki Hong and Hyun-Kyo Jung, "Analysis of hysteresis motor using finite element method and magnetization-dependent model", IEEE Trans. on Magn., vol. 36, No. 4 part1, pp.685-688, July 2000.

An Improved Reluctivity Model for Vector Magnetic Properties of Silicon Steels under Distorted Magnetic Flux Density

Yanli Zhang, Jingguo Yuan, Dexin Xie, and Chang Seop Koh*, *Senior Member, IEEE*

School of Electrical Engineering, Shenyang University of Technology, Shenyang, Liaoning 110023, China

*College of Electrical & Computer Engineering, Chungbuk National University, Cheongju, Chungbuk 361-763, Korea

E-mail: zhangyanli_sy@hotmail.com

Abstract — This paper presents an improved magnetic reluctivity model for vector magnetic properties of anisotropic electrical steel sheet under distorted magnetic flux density condition. In the modeling, the non-sinusoidal magnetic flux density (B) waveform is expanded into fundamental and higher harmonic components using Fourier series expansion. For the fundamental component, the relationship between B and H (magnetic field intensity) is expressed by an improved reluctivity model with higher accuracy. For the higher harmonic components, their eddy current effects are estimated into the vector relationship based on a lot of experimental tests. The accuracy of the proposed model is verified by comparing its results with experimentally measured B - and H -waveforms with 30PG110 silicon steel sheet.

I. INTRODUCTION

An effective expression of two-dimensional (2-D) magnetic properties of electrical steel sheet is necessary to analyze field performance and loss characteristics of electromagnetic devices accurately. There have been foregoing researches, therefore, to develop some permeability (or reluctivity) models to express the 2-D magnetic properties under sinusoidal magnetic flux density (B) condition, that is under pure alternating or rotating magnetic flux conditions [1]–[3]. In the researches, the magnetic reluctivity parameters are obtained by using Fourier series expansion of the waveforms of magnetic field intensity (H) using direct description of the relationship between B and H . However, the accuracy of the permeability model is greatly affected by the order of harmonic components considered in the Fourier series expansion. For example, the reluctivity model considering only the first and third harmonic components is proven not accurate enough to describe the vector magnetic properties as soon as the material is saturated [4].

On the other hand, the B -waveform in electric machines and transformers is often distorted from sinusoidal one. For a precise field analysis, hence, a magnetic permeability model under distorted B -waveform is also necessary. However, experimental measurements under distorted B -waveform condition are very difficult because of the nonlinearity of the material properties and lack of the criterion for measurement. Very recently, Enokizono proposed a reluctivity model by estimating the H -waveforms generated by the eddy currents induced by the higher harmonic components of the magnetic flux density [5]. But, the modeling of 2-D properties of silicon steels under distorted B -waveform is still in its infancy, and requires more experimental verifications.

In this paper, an improved 2-D magnetic reluctivity model under distorted B -waveform is developed taking account of both the modeling accuracy and computational cost when combined with finite element analysis (FEA). The magnetic field intensity affected by the eddy currents induced by the higher harmonic components of B -waveform is numerically modeled based on measured data.

II. MAGNETIC RELUCTIVITY MODEL FOR SINUSOIDAL MAGNETIC FLUX DENSITY

The distorted B -waveform can be expressed using the Fourier series expansion as follows:

$$B_x(\tau) = B_{1mx} \sin(\tau + \varphi_{1B_x}) + \sum_{n=2}^N \{B_{nm_x} \sin[(2n-1)\tau + \varphi_{nB_x}]\} \\ = B_{1x}(\tau) + \sum_{n=2}^N B_{nx}(\tau) \quad (1)$$

where only x -directional equations are shown and the y -directional ones can be obtained by substituting ‘ y ’ instead of ‘ x ’. The first term in (1) is the fundamental component of which frequency is 50Hz or 60Hz, and others are higher harmonic terms, as shown in Fig.1.

Under a purely rotational magnetic flux condition, a magnetic reluctivity model for 2-D magnetic property of grain-oriented silicon steel is proposed in [1], and can be defined as follows:

$$H_{1x} = v^{xr} B_{1x} + v^{xi} \frac{\partial B_{1x}}{\partial \tau} \quad (2)$$

where H_{1x} is the magnetic field intensity obtained when the specimen is excited by 50Hz sinusoidal B -waveform. The magnetic reluctivity coefficients v^{xr} and v^{xi} can be expressed as in (3) considering only the first and third harmonic components of the measured H -waveforms using the 2-D single sheet tester under sinusoidal B -waveform condition.

$$v^{xr} = \kappa^{-xr} + \kappa^{-xi} \cdot B_{1x}^2 + \kappa^{-xi} \cdot B_{1x} \cdot \frac{\partial B_{1x}}{\partial \tau} + \kappa^{-xi} \cdot \left(\frac{\partial B_{1x}}{\partial \tau}\right)^2 \quad (3)$$

In this paper, it is revealed that the hysteresis model in (3) considering only the first and third harmonic components of H -waveform is not accurate enough to describe the vector magnetic property especially when the material is magnetically saturated, as shown in Fig.2. Thus, improved reluctivity models for v^{xr} and v^{xi} considering both the higher harmonic components up to 7 and computational cost are proposed in this paper as follows:

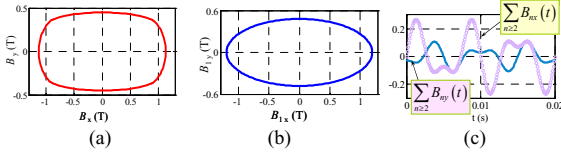


Fig. 1 Distorted magnetic flux density. (a) B -waveform; (b) fundamental component; (c) higher harmonic components.

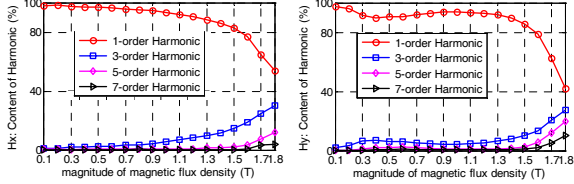


Fig. 2 Harmonic components of H_x and H_y .

$$\nu^{xr,xi} = \kappa_0^{xr,xi} + \kappa_1^{xr,xi} \cos^2 \tau + \kappa_2^{xr,xi} \sin^2 \tau + \kappa_3^{xr,xi} \cos^4 \tau + \kappa_4^{xr,xi} \sin^4 \tau + \kappa_5^{xr,xi} \cos^6 \tau + \kappa_6^{xr,xi} \sin^6 \tau \quad (4-a)$$

$$\begin{aligned} \kappa_0^{xr} &= (R_{1H_{1x}} - 3R_{3H_{1x}} + 5R_{5H_{1x}} - 7R_{7H_{1x}}) P_x \\ &\quad + (I_{1H_{1x}} + 3I_{3H_{1x}} + 5I_{5H_{1x}} + 7I_{7H_{1x}}) Q_x \\ \kappa_2^{xr} &= (-4I_{3H_{1x}} - 20I_{5H_{1x}} - 56I_{7H_{1x}}) Q_x \\ \kappa_4^{xr} &= (16I_{5H_{1x}} + 112I_{7H_{1x}}) Q_x; \quad \kappa_6^{xr} = -64I_{7H_{1x}} Q_x \end{aligned} \quad (4-b)$$

Fig. 3 shows a comparison of H -waveforms computed from (4) and (3) and experimentally measured for 30PG110 Grain-oriented silicon steel. It can be seen that the improved reluctivity models in (4) give better agreement with the measured ones. In the version of full paper, detailed derivations and more discussions will be given.

III. IMPROVED RELUCTIVITY MODEL CONSIDERING HIGHER HARMONIC COMPONENTS OF B -WAVEFORM

For the higher harmonic components of B , it is hard to give an effective vector relationship between B and H directly because measurements under distorted B -waveform are difficult due to nonlinearity of the material properties and lack of criterion for the measurement. In order to consider the effects of eddy current induced from the higher harmonic components of B , the reluctivity model proposed in [4] was based on the skin depth of the eddy current and effective thickness d_{eff} was employed instead of the thickness d of the steel sheet. With the assumption that eddy current decreases linearly instead of exponentially toward the center from the surface, the following relation can be obtained

$$J_{ey} = \sigma \frac{d}{2d_{eff}} \frac{\partial B_x}{\partial t} z \quad (5)$$

where z denotes the position in thickness-direction. The eddy current loss W_e generated by J_{ey} is given by

$$W_e = \frac{f}{\rho} \int_T \left(\frac{\sigma d_{eff} d}{6} \frac{\partial B_x}{\partial t} \right) \frac{\partial B_x}{\partial t} dt \quad (6)$$

where ρ is the material density. On the other hand, the power loss due to the eddy current is defined by the following equation

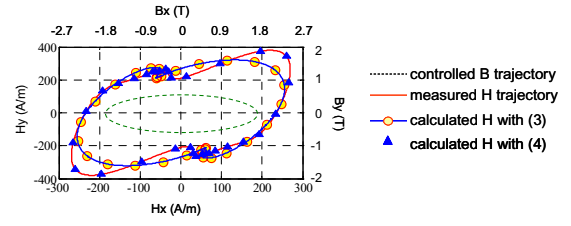


Fig. 3 Comparison of the measured and calculated H -waveforms.

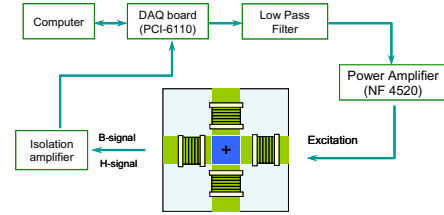


Fig. 4 2-D single sheet tester.

$$W_e = \frac{f}{\rho} \int_T H_{ex} \frac{\partial B_x}{\partial t} dt \quad (7)$$

The magnetic field intensity due to higher harmonic components of B -waveform, thus, can be written as follows

$$H_e = \frac{\sigma d_{eff} d}{6} \frac{\partial B}{\partial t} \quad (8)$$

By considering the (1), (2) and (8), the magnetic field intensity corresponding to a distorted B -waveform can be written as follows

$$H_x = \nu^{xr} B_{1x} + \nu^{xi} \frac{\partial B_{1x}}{\partial \tau} + \frac{\sigma d_{eff} d}{6} \frac{\partial}{\partial t} \sum_{n=2}^N B_{nx}(t) \quad (9)$$

In this paper, to make clear the behavior of distorted flux density and the magnetic field intensity, we have verified the estimation modeling method expressed in (9) based on sufficient measurement data under distorted flux conditions using a 2-D single sheet tester shown in Fig. 4.

The experimental verification and more discussions including FEA application will be given in the version of full paper.

IV. REFERENCES

- [1] S. Kanaoi and M. Enokizono, "Improvement of t-joint part constructions in three-phase transformer cores by using direct loss analysis with E&S model," IEEE Trans. Magn., vol. 36, no. 4, pp. 1285–1288, Jul. 2000.
- [2] M. Enokizono, H. Shimoji, and T. Horibe, "Loss evaluation of induction motor by using magnetic hysteresis E&S model," IEEE Trans. Magn., vol. 38, no. 9, pp. 2379–2381, Sep. 2002.
- [3] S. Urata, M. Enokizono, T. Todaka, and H. Shimoji, "Magnetic characteristic analysis of the motor considering 2-D vector magnetic property," IEEE Trans. Magn., vol. 42, no. 4, pp. 615–618, Apr. 2006.
- [4] Yanli Zhang, Young Hwan Eum, Wei Li, Dexin Xie, and Chang Seop Koh, "An improved modeling of vector magnetic properties of electrical steel sheet for FEM application and its experimental verification," IEEE Trans. on Magnetics, vol. 45, no. 3, pp. 1162–1165, March 2009
- [5] M. Enokizono, "Magnetic characteristics analysis of electrical machines by dynamic vector magneto-hysteretic E&S modeling", Proceeding of ICEMS'07, Oct. 8~11, Seoul, Korea, pp. 1332-1339.

Inrush Currents in a Three-Phase Transformer Taking Into Account Vector Hysteresis

J. V. Leite¹, A. Benabou² and N. Sadowski¹, *Member IEEE*

¹GRUCAD/EEL/UFSC, Po. Box 476, 88040-970, Florianópolis, Santa Catarina, Brazil

²Université Lille1, L2EP, Bat P2, 59655 Villeneuve d'Ascq Cedex, France

jean@grucad.ufsc.br

Abstract — The presented work investigates the modeling of inrush currents in a three phase transformer under sinusoidal operating conditions. The transformer core is modeled taking into account the magnetic hysteresis. A Jiles-Atherton vectorized model is used for the nonlinear core modeling. The key advantage of this vector model is its reluctivity tensor which is appropriated for the Finite Element Analysis implementation. A time-domain simulation was carried out and the results are compared with experimental data for the procedure validation.

I. INTRODUCTION

Inrush currents are high magnitude currents generated during energization of a transformer. In fact, these are the consequence of a residual magnetic flux that is added to the magnetizing flux when the device is turned on. This phenomenon leads to a highly saturated transitory state of the magnetic core of the transformer. The magnitude of inrush current can reach initially several times the rated load current but slowly decreases by the effect of oscillation damping due to winding and magnetizing resistances of the transformer as well as the impedance of the system where it is connected. Finally it reaches the rated current value. This process typically can take several electrical periods [1].

These currents have undesirable effects as potential damage, reduction of the life of the transformer, protective relay miss operation and reduced power quality on the system. Furthermore, nowadays, power transformers usually operate at higher magnetic flux density values as high performance grain oriented steels are used more and more. It results that modern transformers will have higher inrush currents. This affects the transformer design and size.

In the present work, the Jiles-Atherton (J-A) inverse vector model was chosen to model the iron core behaviour. This model is able to represent a possible anisotropic steel behaviour as well as the rotational flux in the transformer T-joints. If the flux does not change its space direction, the model reduces itself to the scalar model.

The J-A vector hysteresis model is incorporated in a 2D Finite Element (FE) code, with vector potential formulation, using the magnetic differential reluctivity tensor. The mathematical model is used for the calculation of the inrush currents in a three-phase transformer. The magnitude of the inrush current being also strongly dependent on the voltages switching instant, we focus in this work on the switching instant of the three phase voltage source. The presented model must be able to perform an analysis of inrush amplitudes by simulating arbitrary voltages switching instants.

Comparison between the calculated and measured curves is also performed.

II. NONLINEAR CORE MODEL

The non linear behaviour of a transformer core can be modelled by different methods. The use of a vector model allows us to take into account the fields in the principal lamination directions avoiding the approximation of an average permeability in each finite element, performing a more realistic calculation. To this purpose, a vector model is the more appropriate choice to take into account magnetic hysteresis.

Bergqvist proposed a vector generalisation of the Jiles-Atherton scalar hysteresis model [2][3]. In its inverse version, i.e., giving the magnetization with the induction as input variable, the main equation is [4]:

$$d\mathbf{M} = \frac{1}{\mu_0} [\mathbf{1} + f_\chi(\mathbf{1} - \bar{\alpha}) + \bar{c}\bar{\xi}(\mathbf{1} - \bar{\alpha})]^{-1} \cdot [f_\chi + \bar{c}\bar{\xi}] d\mathbf{B} \quad (1)$$

with $f_\chi = \bar{\chi}_f |\bar{\chi}_f|^{-1} \bar{\chi}_f$ and where the auxiliary vector variable $\bar{\chi}_f$ is given by $\bar{\chi}_f = \bar{k}^{-1}(\mathbf{M}_{an} - \mathbf{M})$. \mathbf{M}_{an} and \mathbf{M} are, respectively, the anhysteretic magnetization and the total magnetization. \bar{k} , $\bar{\alpha}$ and \bar{c} are second rank tensors which terms must be obtained experimentally. $\mathbf{1}$ is the diagonal unity matrix and $\bar{\xi}$ is the diagonal matrix of the anhysteretic functions derivatives with respect to the effective field components.

Using $d\mathbf{M}$ obtained from equation (1), one can write $d\mathbf{H} = \|\partial v\| d\mathbf{B}$, where $\|\partial v\|$ is the differential reluctivity tensor.

III. VOLTAGE FED AND MAGNETIC VECTOR POTENTIAL FORMULATION

The formulation, with a magnetic vector potential \mathbf{A} and an electric scalar potential φ , is obtained from the weak form of the Ampere's law [5][6]:

$$\begin{aligned} & (\|\partial v\| \operatorname{curl} \mathbf{A}(t + \Delta t), \operatorname{curl} \mathbf{A}')_{\Omega} - (\|\partial v\| \operatorname{curl} \mathbf{A}(t), \operatorname{curl} \mathbf{A}')_{\Omega} + \\ & + (\mathbf{H}(t), \operatorname{curl} \mathbf{A}')_{\Omega} + (\sigma \partial_t \mathbf{A}, \mathbf{A}')_{\Omega_c} + (\sigma \operatorname{grad} \varphi, \mathbf{A}')_{\Omega_c} + \\ & - (\mathbf{J}_s, \mathbf{A}')_{\Omega_s} = 0, \quad \forall \mathbf{A}' \in F_a(\Omega), \end{aligned} \quad (2)$$

where $F_a(\Omega)$ denotes the space function defined on Ω which contains the basis and test functions for both vector potentials $\mathbf{A}(t+\Delta t)$, $\mathbf{A}(t)$ and \mathbf{A}' . The function $\|\partial v\|$ represents the magnetic behavior law, which comes from the 2D vector hysteresis model. The block $(\cdot, \cdot)_{\Omega}$ denotes a volume integral in Ω of scalar or vector fields products. The electric field \mathbf{E} and the magnetic flux density \mathbf{B} , as well as the magnetic field \mathbf{H} and the current density \mathbf{J} , are expressed in terms of the potentials \mathbf{A} and φ by

$$\mathbf{E} = \sigma^{-1} \mathbf{J} = -\partial_t \mathbf{A} - \text{grad} \varphi \quad \text{in } \Omega_c, \quad (3)$$

$$\mathbf{B} = \|\mu\| \mathbf{H} = \text{curl} \mathbf{A} \quad \text{in } \Omega. \quad (4)$$

The circuit relation associated with a stranded inductor $j \in \Omega_s$, relating its current I_j to its voltage φ_j , has been established for the \mathbf{A} -formulation as follows

$$\partial_t (\mathbf{A}, \mathbf{w})_{\Omega_s} + R I_j = -\varphi_j, \quad (5)$$

where R is the resistance of the inductor and \mathbf{w} is called the wire density vector [7].

IV. RESULTS

The numerical simulation of the inrush currents was performed at no load and the three-phase voltage source was at 230V-50Hz. The switching instant of the transformer corresponds to the first phase passing through zero. To have the same initial magnetic conditions in the numerical simulation and in the experimental measurements, the transformer was initially demagnetized before switching on for the inrush currents measurement. The identification of the hysteresis model parameters was achieved using experimental measurement on a sample of the same FeSi steel used in the construction of the transformer.

The measured and calculated transitory inrush currents behavior for the transformer no-load operation are shown, respectively, in Figs. 1 and 2.

Figures 1 and 2 show that the FE model results are in a very good agreement with the measured inrush current. This indicates that the developed FE model is able to represent with accuracy the nonlinear magnetization of the studied transformer.

From a numerical aspect, a better convergence of the nonlinear system has been observed when using the vector model. One can note that an average of five numerical iterations was sufficient for each time-step calculation. This robustness can be explained by the natural match between the reluctivity tensor and the field equations.

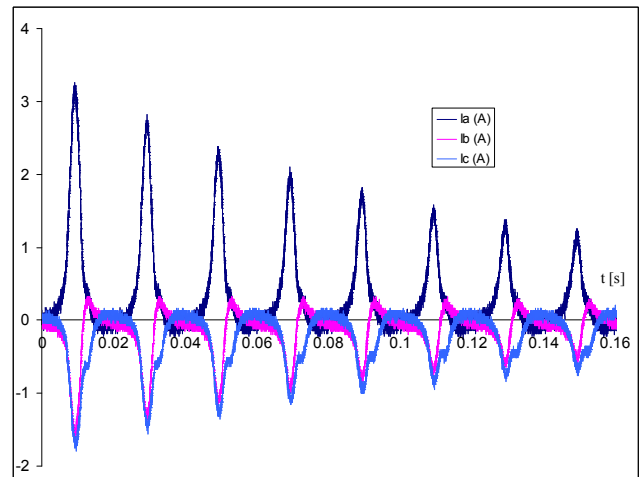


Fig. 1. Measured inrush currents.

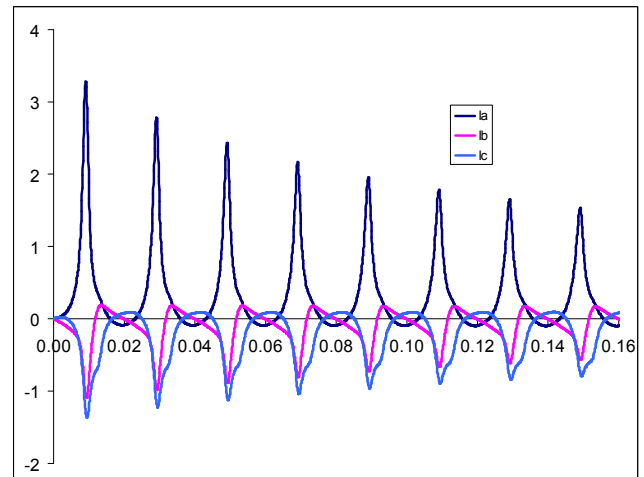


Fig 2. Calculated inrush currents.

V. REFERENCES

- [1] R. S. Girgis and Ed G. teNyenhuis, "Characteristics of Inrush Current of Present Designs of Power Transformers", *Power Engineering Society General Meeting, 2007, IEEE*, 1-6, 24-28 June 2007.
- [2] D. C. Jiles and D. L. Atherton, "Theory of Ferromagnetic Hysteresis", *Journal of Magn. and Magn. Mat.*, vol 61, 48-60, 1986.
- [3] A. J. Bergqvist, A simple vector generalization of the Jiles-Atherton model of hysteresis, *IEEE Trans. on Magn.*, 32(5): 4213-4215, 1996.
- [4] J. V. Leite, N. Sadowski, P. Kuo-Peng, N. J. Batistela, J.P.A. Bastos, "Inverse Jiles-Atherton vector hysteresis model", *IEEE Trans. on Magn.*, 40(4): 1769-1775, 2004.
- [5] J.P.A. Bastos, N. Sadowski, "Electromagnetic Modeling by Finite Element Methods", Marcel Dekker Inc., ISBN: 0-8247-4269-9, New York, 2003, USA.
- [6] P. Dular, P. Kuo-Peng, C. Geuzaine, N. Sadowski, and J.P.A. Bastos, "Dual magnetodynamic formulations and their source fields associated with massive and stranded inductors", *IEEE Trans. Magn.*, 36(4): 1293-1299, 2000.
- [7] J. V. Leite, A. Benabou, N. Sadowski and M. V. F. da Luz, "Finite Element Three-Phase Transformer Modeling Taking Into Account a Vector Hysteresis Model", *IEEE Trans. on Magn.*, 45(3): 1716-1719, 2009.

Study of Different FEM Models to Analyze Homogenized Iron Lamination with Electrical Fault

J. L. Müller¹, A. Benabou², T. Henneron², F. Piriou², J. P. A. Bastos³, J-Y. Roger¹
 EDF R&D¹, L2EP – LAMEL², GRUCAD³
 EDF, 1 avenue du Général de Gaulle - 92141 Clamart, France
 L2EP, Université Lille1 – Nord de France - 59655 Villeneuve d'Ascq, France
 GRUCAD, CTC – UFSC, CP. 476 - 88040-970 - Florianópolis - SC - Brasil
 juliana-luisa.muller@ed.univ-lille1.fr

Abstract — In this paper we compare different approaches for the lamination stack homogenization with a short-circuit due to an electrical fault between several sheets. The presented techniques are based on the determination of a complex equivalent magnetic permeability for the homogenized domain. The eddy current losses are calculated in the homogenized lamination stack and in the fault. These losses are compared with those obtained from a reference system where the lamination is modeled with its real geometry.

I. INTRODUCTION

Stator laminations of large generators are coated with insulating varnishes to avoid electrical contact that leads to additional Joule losses. In some situations due, for example to manufacturing faults or local overheating, the insulation can be damaged and electrical contacts appears between the laminations. It may generate electrical currents, which can be significant during electrical faults. Such a situation may be very dangerous for the machine integrity [1].

To investigate the effect of eddy currents on the global behaviour of the system, it is necessary to use a technique that takes into account the magneto-dynamic effects in the lamination stack without modelling the real geometry of the laminations. Homogenization techniques can be very useful in such a case. Nevertheless, adding a fault between several sheets in the laminations modifies the assumptions made for the homogenizing model.

The purpose of this work is to evaluate the accuracy of a homogenized lamination stack considering an electrical fault. The Joule losses are calculated in both parts of the system, i.e. the homogenized and the fault parts. Several approaches [2, 3], based on the low and high frequency assumptions, are investigated for the lamination stack homogenization, and their behaviour when a fault is inserted in the homogenized region. A comparison is made with a reference system which models the real sheet geometry of the lamination.

II. MATHEMATICAL MODEL

We consider a domain Ω whose boundary is denoted Γ . Two sub-domains are introduced in Ω : an electrically conducting domain Ω_c with boundary Γ_c and a homogenized domain Ω_h that simulates the equivalent magnetic behaviour of a lamination stack (Fig. 1).

In time harmonic magnetodynamics, the Maxwell's equations can be written as,

$$\text{curl } \underline{\mathbf{E}} = -j\omega \underline{\mathbf{B}} \quad \text{and} \quad \text{div } \underline{\mathbf{B}} = 0 \quad (1)$$

$$\text{curl } \underline{\mathbf{H}} = \underline{\mathbf{J}}_s + \underline{\mathbf{J}}_{\text{ind}} \quad \text{and} \quad \text{div } (\underline{\mathbf{J}}_s + \underline{\mathbf{J}}_{\text{ind}}) = 0 \quad (2)$$

with $\underline{\mathbf{H}}$ the magnetic field, $\underline{\mathbf{B}}$ the magnetic flux density, $\underline{\mathbf{E}}$ the electric field, $\underline{\mathbf{J}}_s$ the current density supposed to be known in stranded inductors, $\underline{\mathbf{J}}_{\text{ind}}$ the eddy current density and ω the pulsation. To ensure the uniqueness of the solution, homogeneous boundary conditions are applied on the fields ($\Gamma = \Gamma_B \cup \Gamma_H$ and $\Gamma_c = \Gamma_E \cup \Gamma_{\text{Jind}}$). The electric and magnetic behaviour laws are given by,

$$\underline{\mathbf{H}} = \nu \underline{\mathbf{B}} \quad \text{in } \Omega - \Omega_h, \quad \underline{\mathbf{J}}_{\text{ind}} = \sigma \underline{\mathbf{E}} \quad \text{in } \Omega_c \quad (3)$$

$$\underline{\mathbf{H}} = \|\tilde{\nu}\| \underline{\mathbf{B}} \quad \text{in } \Omega_h \quad (4)$$

with ν the magnetic reluctivity, σ the electric conductivity and $\|\tilde{\nu}\|$ a complex reluctivity tensor. Each component of $\|\tilde{\nu}\|$ can be expressed such as $\tilde{\nu}_{ij} = \tilde{\nu}'_{ij} + j\omega \tilde{\nu}''_{ij}$. To solve this problem, the electric formulation can be used. From (1.a) and (1.b), two potentials are introduced: the magnetic vector potential $\underline{\mathbf{A}}$ in the whole domain Ω and the electric scalar potential ϕ in Ω_c . Then, the magnetic flux density and the electric field can be rewritten such that,

$$\underline{\mathbf{B}} = \text{curl } \underline{\mathbf{A}} \quad \text{and} \quad \underline{\mathbf{E}} = -j\omega \underline{\mathbf{A}} - \text{grad } \phi \quad (5)$$

By using (2), (3) and (4), the weak formulation to solve can be obtained such that,

$$\begin{aligned} & (\nu \text{curl } \underline{\mathbf{A}}, \text{curl } \underline{\mathbf{A}}')_{\Omega - \Omega_h} + (\|\tilde{\nu}\| \text{curl } \underline{\mathbf{A}}, \text{curl } \underline{\mathbf{A}}')_{\Omega_h} \\ & + (\sigma j\omega \underline{\mathbf{A}}, \underline{\mathbf{A}}')_{\Omega_c} + (\sigma \text{grad } \phi, \underline{\mathbf{A}}')_{\Omega_c} - (\underline{\mathbf{J}}_s, \underline{\mathbf{A}}')_{\Omega_s} = 0 \end{aligned} \quad (6)$$

with $\underline{\mathbf{A}}'$ a test function defined in the same space as $\underline{\mathbf{A}}$. To discretize the fields and the potentials, Whitney's elements are used.

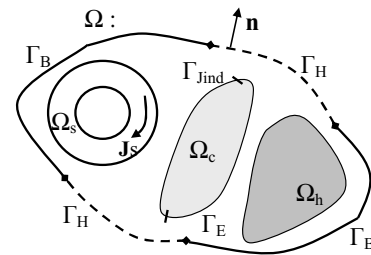


Fig. 1. Studied domain

For the homogenization of the lamination stack magnetic behaviour, different approaches have been considered. The

7. Material Modelling

first one [2], based on a static approach (S-Model), represents the anisotropy of the stack by using the components \tilde{v}'_{ij} (\tilde{v}''_{ij} are fixed to zero). If the steel sheets are on the xy plane, \tilde{v}'_{11} and \tilde{v}'_{22} are the tangential components and \tilde{v}'_{33} is the normal component. A wide-frequency-band model (W-F Model) is proposed [3], considering $\delta = (\pi f \sigma \mu)^{-1/2}$ the skin depth and d the lamination thickness. Thus, we have,

$$\tilde{v}_{ij} = \tilde{v}'_{ij} + j\omega \tilde{v}''_{ij} = \frac{\sigma_{ij} d \delta_{ij} \omega (1+j)}{8} \frac{\sinh((1+j)d/\delta_{ij})}{\sinh^2((1+j)d/(2\delta_{ij}))}. \quad (7)$$

Here both components \tilde{v}' and \tilde{v}'' are complex. For lower frequencies, a simplified model (L-F model) can be obtained from equation (7),

$$\tilde{v}_{ij} = \tilde{v}'_{ij} + j\omega \tilde{v}''_{ij} = 1/\mu_{ij} + j\omega(\sigma_{ij} d^2/12). \quad (8)$$

With these techniques eddy currents can be considered. Moreover, combining the static approach for the lamination stack anisotropy and eddy currents effects (model [2] + [3]), it is possible to introduce the permeability tensor in (7). The skin depth δ is calculated according to this tensor.

III. APPLICATION

A simple geometry representing a lamination stack was chosen, considering only the linear case. For the reference system, the lamination stack dimensions are 30 mm x 30 mm with 6 sheets whose thickness is 500 μm . Two successive sheets are separated by a 10 μm insulating layer.

The mesh has about 60000 prismatic elements. The magnetic flux is imposed on the way that the average magnetic induction is 1.5 Tesla. To have good accuracy for the eddy currents in the reference system, each lamination is meshed with four elements in its thickness dimension. In case of homogenization, the same mesh is used but without the lamination and insulation separation.

To test the robustness of the homogenization techniques in case of a fault between several sheets, a short circuit represented by a cylindrical volume is placed in the middle of the lamination stack. This volume remains with the same physical properties in the reference and homogenized models.

The iron parts have been considered with an isotropic conductivity $\sigma=2 \times 10^6$ S/m and a magnetic permeability $\mu=1000\mu_0$, where $\mu_0=4\pi \times 10^{-7}$ H/m. The insulation has $\sigma=0$ and $\mu=\mu_0$. The electrical cylinder fault, when considered, has the same characteristics as the iron. The eddy current losses (P_{EC}) are calculated as follows,

$$P_{EC} = \int_V \underline{E} \underline{J}^*_{ind} dv. \quad (9)$$

The magnetic energy of the system is calculated as,

$$W_{mag} = \int_V \frac{1}{2} \underline{B} \underline{H}^* dv \quad (10)$$

Solving the system with the $\mathbf{A}\text{-}\phi$ formulation considering the electrical fault, the magnetic energy of the entire system is given in Tab.1 and the eddy current losses in the electrical fault are given in Tab. 2.

Frequency	Magnetic energy in the entire system (J)	
	50 Hz	1000 Hz
Reference	0.121	0.126
S-Model	0.120	0.124
L-F Model	0.118	0.121
W-F Model	0.118	0.123
S-Model + W-F	0.129	0.133

Tab.1 Magnetic energy in the entire system, $\mathbf{A}\text{-}\phi$ formulation

Frequency	Eddy current losses in the fault (W/kg)		
	25 Hz	50 Hz	100 Hz
Reference	9.00	23.17	39.29
S-Model	9.63	28.44	58.06
L-F Model	9.42	27.59	55.66
W-F Model	9.41	27.59	55.66
S-Model + W-F	9.61	28.38	57.41

Tab.2 Eddy current losses in the electrical fault, $\mathbf{A}\text{-}\phi$ formulation

From results in Tab.1, we can see that the global magnetic energy obtained with the different homogenization approaches remains close with the one of the reference system, even for the frequency 1 kHz. Nevertheless, if we focus on the eddy current losses in the electrical fault given in Tab.2, the homogenization approaches give satisfactory results up to 50 Hz in the case of the studied system. At the frequency 100 Hz, the error becomes much larger. Such results are predictable as the electrical fault introduces a non-homogeneity in the supposed homogenized lamination stack.

IV. CONCLUSION

Different homogenization methods for lamination stacks were presented and compared. The results show that all the models are valid including the case when an electrical fault is inserted in the homogenized volume, especially for lower frequencies.

In the extended version we intend to explore more in detail the obtained results, showing also the results using the $\mathbf{T}\text{-}\Omega$ formulation. We will also present a study in which the number of short-circuited sheets varies, and we will evaluate its influence on the results. All these calculations will be performed in the industrial frequency range.

V. REFERENCES

- [1] J.-Y. Roger, E. Vrignaud, T. Henneron, A. Benabou, J.-P. Ducreux, « Electromagnetic Modelling of Short Circuited Coreplates », *COMPEL*, to be published, 2009.
- [2] J.P.A. Bastos, G.Quichaud, "3D Modelling of a Non-Linear Anisotropic Lamination", *IEEE Trans. on Magnetics*, 21(6): 68 – 73, 1985.
- [3] P. Dular, J. Gyselinck, C. Geuzaine, N. Sadowski, J. P. A. Bastos, « A 3-D Magnetic Vector Potential Formulation Taking Eddy Currents in Lamination Stacks Into Account », *IEEE Trans. on Magnetics*, 39(3): 1424 – 1427, 2003.

Three-Phase Transformer Modelling Using the Vector Hysteresis Model and Including the Eddy Current and the Anomalous Losses

Mauricio V. Ferreira da Luz¹, Jean V. Leite¹, Abdelkader Benabou² and Nelson Sadowski¹

¹GRUCAD/EEL/CTC, C.P. 476, 88040-900, Florianópolis, SC, Brazil.

²L2EP, Bat P2, USTL, 59655, Villeneuve d'Ascq Cedex, France.

E-mail: mauricio@grucad.ufsc.br

Abstract — This paper presents a 2D finite element model to analyze the iron losses in a three-phase transformer. In this model, the effects of non-linear core behavior is taken into account by means of a vector hysteresis model incorporated in the finite element formulation by using a magnetic differential reluctivity tensor. The reluctivity tensor emerges naturally from the vectorized Jiles-Atherton model. The complete model includes eddy current losses and the anomalous losses. The magnetization currents are calculated and compared with the measured ones. Calculations of hysteresis loops at spotted points of the transformer are also performed. The comparisons between the iron losses measured and calculated with vectorial hysteresis are performed.

I. INTRODUCTION

The core of magnetic devices can experiment two different types of magnetic fluxes. The alternating flux occurs when the flux changes its magnitude but not its spatial direction. The rotational flux is present when the magnetic flux rotates in the plane of the lamination. The losses due to the rotational flux are higher than the one due to the alternating flux.

In a three-phase transformer, rotational flux is observed in the corner joints (T-joints). In T-joints the magnetic behaviour is very complex, differently from the central limb. That is the reason why, under rotational flux conditions, the vector relationship between magnetic field and induction must be considered. The rotational losses, which can be more important than alternating ones, contribute to a significant part of the global losses [1].

In this paper, a vector hysteresis model is incorporated in a 2D finite element (FE) code, with magnetic vector potential formulation, using the magnetic differential reluctivity tensor. This model emerges naturally from the vectorized Jiles-Atherton model. The complete model includes eddy current losses and the anomalous losses.

The FE model is used for the analysis of a non loaded three-phase transformer. The magnetization currents are calculated and compared with the measured ones. Calculations of hysteresis loops at spotted points of the transformer are also performed. The comparisons between the iron losses measured and calculated with vectorial hysteresis will be performed and the results will be presented on the extended paper.

II. MAGNETODYNAMIC FORMULATION

A bounded domain Ω of the two or three-dimensional Euclidean space is considered. Its boundary is denoted Γ . The equations characterising the magnetodynamic problem in Ω are [2]:

$$\text{curl } \mathbf{H} = \mathbf{J}, \quad \text{curl } \mathbf{E} = -\partial_t \mathbf{B}, \quad \text{div } \mathbf{B} = 0, \quad (1a-b-c)$$

$$\mathbf{B} = \mu \mathbf{H}, \quad \mathbf{J} = \sigma \mathbf{E}, \quad (2a-b)$$

where \mathbf{H} is the magnetic field, \mathbf{B} is the magnetic flux density, \mathbf{E} is the electric field, \mathbf{J} is the electric current density, including source currents \mathbf{J}_s in Ω_s and eddy currents in Ω_c (both Ω_s and Ω_c are included in Ω), μ is the magnetic permeability and σ is the electric conductivity.

The boundary conditions are defined on complementary parts Γ_h and Γ_e , which can be non-connected, of Γ ,

$$\mathbf{n} \times \mathbf{H}|_{\Gamma_h} = 0, \quad \mathbf{n} \cdot \mathbf{B}|_{\Gamma_e} = 0, \quad \mathbf{n} \times \mathbf{E}|_{\Gamma_e} = 0, \quad (3a-b-c)$$

where \mathbf{n} is the unit normal vector exterior to Ω . Furthermore, global conditions on voltages or currents in inductors can be considered [2].

A. Inclusion of the differential reluctivity tensor

The relationship between $d\mathbf{H}$ and $d\mathbf{B}$ is given by [1]

$$d\mathbf{H} = \|\mathbf{v}_d\| d\mathbf{B}, \quad (4)$$

where $\|\mathbf{v}_d\|$ is called as magnetic reluctivity tensor.

Using Euler's scheme to represent the derivatives, (4) becomes

$$\Delta\mathbf{H} = \|\mathbf{v}_d\| \Delta\mathbf{B}, \quad (5)$$

where $\Delta\mathbf{H} = \mathbf{H}(t+\Delta t) - \mathbf{H}(t)$, $\Delta\mathbf{B} = \mathbf{B}(t+\Delta t) - \mathbf{B}(t)$, and (5) can be written as

$$\mathbf{H}(t+\Delta t) = \|\mathbf{v}_d\| \Delta\mathbf{B} + \mathbf{H}(t), \quad (6)$$

with (6) one can write Ampere's law (1a) for time $(t+\Delta t)$, as

$$\text{curl} [\|\mathbf{v}_d\| \Delta\mathbf{B} + \mathbf{H}(t)] = \mathbf{J}(t+\Delta t), \quad (7)$$

using $\mathbf{B}(t+\Delta t) = \text{curl } \mathbf{A}(t+\Delta t)$ and $\mathbf{B}(t) = \text{curl } \mathbf{A}$, where \mathbf{A} is the magnetic vector potential, (7) becomes [1]

$$\text{curl} [\|\mathbf{v}_d\| \text{curl } \mathbf{A}(t+\Delta t)] = \mathbf{J}(t+\Delta t) + \text{curl} [\|\mathbf{v}_d\| \text{curl } \mathbf{A}(t)] - \text{curl } \mathbf{H}(t). \quad (8)$$

B. Voltage fed and magnetic vector potential A-formulation

The \mathbf{A} -formulation, with a magnetic vector potential \mathbf{A} and an electric scalar potential V , is obtained from the weak form of the Ampère equation (1a) and (2a-b) [2], i.e.

$$\begin{aligned} & \langle \|\mathbf{v}_d\| \text{curl } \mathbf{A}(t+\Delta t), \text{curl } \mathbf{A}' \rangle_{\Omega} - \langle \|\mathbf{v}_d\| \text{curl } \mathbf{A}(t), \text{curl } \mathbf{A}' \rangle_{\Omega} + \\ & \langle \mathbf{H}(t), \text{curl } \mathbf{A}' \rangle_{\Omega} + (\sigma \partial_t \mathbf{A}, \mathbf{A}')_{\Omega_c} + (\sigma \text{grad } V, \mathbf{A}')_{\Omega_c} + \\ & - (\mathbf{J}_s, \mathbf{A}')_{\Omega_s} = 0, \quad \forall \mathbf{A}' \in F_d(\Omega), \end{aligned} \quad (9)$$

where $F_d(\Omega)$ denotes the function space defined on Ω which contains the basis and test functions for both vector potentials $\mathbf{A}(t+\Delta t)$, $\mathbf{A}(t)$ and \mathbf{A}' . The block $(\cdot, \cdot)_{\Omega}$ denotes a volume integral in Ω of scalar or vector fields products.

The circuit relation associated with a stranded inductor $j \in \Omega_s$, relating its current I_j to its voltage V_j , has been established for the \mathbf{A} -formulation as follows [2].

$$\partial_t(\mathbf{A}, \mathbf{w})_{\Omega_s} + R I_j = -V_j, \quad (10)$$

where R is the resistance of the inductor and \mathbf{w} is called the wire density vector.

C. Inclusion of the eddy current losses and the anomalous losses in the finite element modelling

The \mathbf{A} -formulation considering the inclusion of the eddy current losses and the anomalous losses in the FE modelling is given by [3]

$$\begin{aligned} (\kappa \operatorname{curl} \mathbf{A}(t+\Delta t), \operatorname{curl} \mathbf{A}')_{\Omega} - (\kappa \operatorname{curl} \mathbf{A}(t), \operatorname{curl} \mathbf{A}')_{\Omega} + \\ (\mathbf{H}(t), \operatorname{curl} \mathbf{A}')_{\Omega} + (\sigma \partial_t \mathbf{A}, \mathbf{A}')_{\Omega_c} + (\sigma \operatorname{grad} V, \mathbf{A}')_{\Omega_c} + \\ - (\mathbf{J}_s, \mathbf{A}')_{\Omega_s} = 0, \quad \forall \mathbf{A}' \in F_d(\Omega). \end{aligned} \quad (11)$$

The term κ is given by [3]

$$\kappa = \left(\|\mathbf{v}_d\| + \frac{\sigma d^2}{12 \Delta t} + \sqrt{\sigma G V_o S} \frac{1}{\Delta t^{0.5} |\Delta \mathbf{B}|^{0.5}} \right), \quad (12)$$

where d is the magnetic sheet thickness, S is the cross section of the magnetic sheet, G is the magnetic object (MO) friction coefficient, V_o is the relation between the number of MO taking place in the magnetization process and the excess magnetic field [3].

III. APPLICATION

The experimental device used for the validation of the proposed approach is a three phase transformer of 2 kVA. The magnetic core is made of FeSi electrical steel laminations which thickness is 0.5 mm. Fig. 1 shows the studied domain (left) and the 2D mesh (the air regions are not shown) of the calculation domain (right).

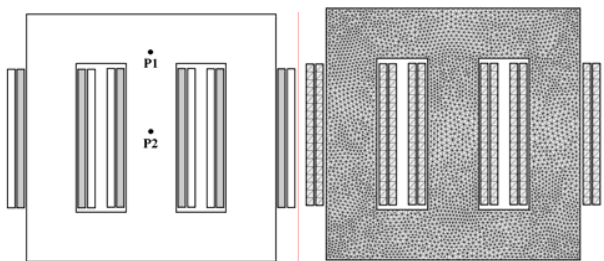


Fig. 1. The studied domain (left) and the 2D mesh (the air regions are not shown) of the calculation domain (right).

The magnetic flux distribution and the magnetic flux density in the calculation domain are shown in Fig. 2 (left) and Fig. 2 (right), respectively.

The BH loops in the points P1 and P2 (see Fig. 1(left)) are shown in Fig. 3.

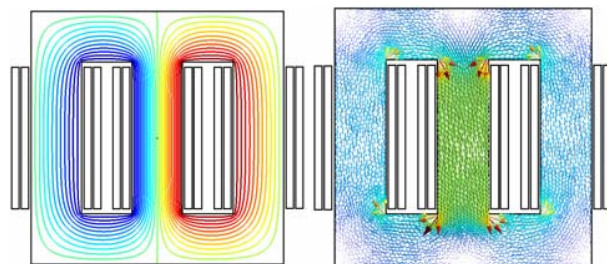


Fig. 2. The magnetic flux distribution (left) and the magnetic flux density (right) in the calculation domain.

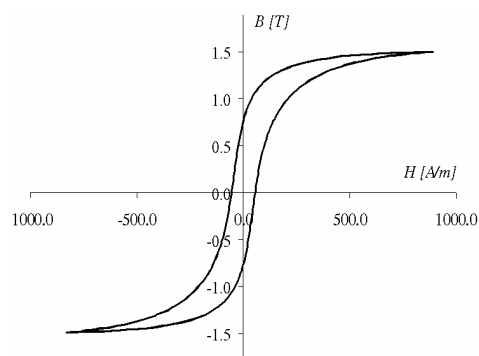


Fig. 3a. The BH loop in the point P2 (central limb).

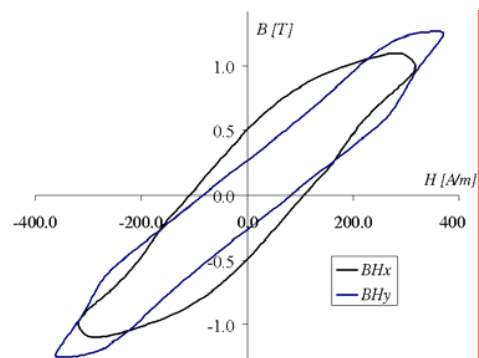


Fig. 3b. The BH loops in the point P1. The rotational flux in the T-joint increases the magnetic losses.

From the figures above, one can observe that the vector hysteresis model naturally reduces itself to a scalar model if in presence of an alternating flux (central limb) and it is able to represent the vector relationship in the transformer T-joint.

The results on the iron losses measured and calculated with vectorial hysteresis will be compared and presented on the extended paper.

IV. REFERENCES

- [1] J. V. Leite, A. Benabou, N. Sadowski and M. V. Ferreira da Luz, "Finite element three-phase transformer modeling taking into account a vector hysteresis model", *IEEE Transactions on Magnetics*, Vol. 45, No. 3, pp. 1716-1719, 2009.
- [2] M. V. Ferreira da Luz, P. Dular, N. Sadowski, C. Geuzaine, J. P. A. Bastos, "Analysis of a permanent magnet generator with dual formulations using periodicity conditions and moving band", *IEEE Transactions on Magnetics*, Vol. 38, No. 2, pp. 961-964, 2002.
- [3] J. P. A. Bastos and N. Sadowski, *Electromagnetic Modeling by Finite Elements*. Marcel Dekker, Inc, New York, USA, 2003.

Iron-Loss Modeling for Rotating Machines: Comparison between Bertotti's Three-Term Expression and 3-D Eddy-Current Analysis

Katsumi Yamazaki, and Noriaki Fukushima

Dept. of Electrical, Electronics, and Computer Engineering, Chiba Institute of Technology
2-17-1, Tsudanuma, Narashino, Chiba, 275-0016, Japan
yamazaki.katsumi@it-chiba.ac.jp

Abstract — Two calculation methods for iron-loss estimation of rotating machines are investigated. One is based on the conventional three-term expression. In this case, the losses are calculated from the time variation in the flux density obtained by the finite element analysis, which approximates the stator and the rotor cores as the solid magnetic material without the conductivity. The other is based on the 3-D eddy current analysis in the electrical steel sheet. In this case, the excess loss is calculated with a simple approximation. It is clarified that both methods can estimate the no-load iron loss in the similar accuracy and that the method based on the eddy current analysis is suitable for the estimation of high-order harmonic iron losses.

I. INTRODUCTION

Owing to environmental problems, the estimation of iron loss in rotating machines became more important subject in recent years. Many papers reported the iron-loss estimation using the 2-D or 3-D finite element methods.

The iron loss can be classified into three components, which are the hysteresis loss, eddy-current loss and excess loss [1]. In this case, appropriate coefficients of each loss are determined by experiments of the electrical steel sheets. The losses are usually calculated from the time variation in the flux density obtained by the finite element analysis, which approximates the stator and the rotor cores as the solid magnetic material without the conductivity. This method is widely applied and developed by many researchers [2]-[4].

On the other hand, when the frequency of the magnetic field is high, the flux and eddy currents must concentrate at the surface of the electrical steel sheets due to the skin effect [5] because the sizes of the domains in non-oriented steels employed for the rotating machines are usually much smaller than the thickness of the sheets [6]. This phenomenon cannot be taken into account by the conventional modeling. Therefore, we proposed an iron-loss model based on the 3-D eddy current analysis in the electrical steel sheet [7]. In this case, the excess loss is estimated with a simple approximation.

It can be stated that the above-mentioned methods are based on the different approximations. As a consequence, they must have the strong and weak points, respectively. In this paper, both methods are applied to several kinds of rotating machines and the results are compared. The experimental validations are also carried out. It is clarified that both methods can estimate the no-load iron loss of machines in the similar accuracy and that the proposed method is suitable for the estimation of the high-order harmonic iron losses.

II. IRON LOSS MODELING

The conventional three-term iron-loss model [1]-[4] is:

$$\begin{aligned} W_i &= W_e + W_h + W_{ex} \\ &= \frac{\sigma h^2}{12} \frac{1}{T} \int_0^T \int_{iron} \left(\frac{dB}{dt} \right)^2 dv dt \\ &\quad + \frac{K_h D}{T} \int_{iron} B_m^\alpha \left(1 + \sum_{i=1}^n \frac{\beta}{B_m} (\Delta B_i) \right) dv \\ &\quad + \frac{K_{ex} D}{T} \int_0^T \int_{iron} \left| \frac{dB}{dt} \right|^{1.5} dv dt \end{aligned} \quad (1)$$

where W_e , W_h , W_{ex} are the eddy-current loss, hysteresis loss, and excess loss in the core, σ is the conductivity, h is the thickness of the electrical steel sheets, D is the density, T is the time period, K_h , α , and β is the hysteresis coefficients, f is the fundamental frequency, B_m is the maximum flux density during the time period, ΔB_i is the local amplitude of the flux density that cause minor hysteresis loss, K_{ex} is the excess loss coefficient. The flux density B is estimated by the finite-element method that neglects the eddy currents in the steel sheets.

On the other hand, in the proposed model, the iron loss is expressed by two terms as follows:

$$\begin{aligned} W_i &= W_e' + W_h' = \frac{1}{T} \int_0^T \int_{iron} \kappa \sigma |E|^2 dv dt \\ &\quad + \frac{K_h D}{T} \int_{iron} B_m^\alpha \left(1 + \sum_{i=1}^n \left(\frac{\beta}{B_m} \Delta B_i \right) \right) dv \end{aligned} \quad (2)$$

where W_e' is the eddy-current loss including excess loss, W_h' is the hysteresis loss, κ is the modified coefficient of the excess loss, and E is the electric field. The electric and magnetic fields are calculated by the 3-D nonlinear time-stepping eddy-current analysis in the electrical steel sheet. By using this model, both the eddy-current loss and the hysteresis loss are calculated by taking into account the concentration of the electric and magnetic fields near the surface of the steel sheets.

By applying several assumptions, the coefficients in (1) and (2) can be determined from the iron-loss characteristics of the electrical steel sheets obtained by the Epstein-frame test.

III. APPLICATIONS

First, the methods are applied to the calculation of no-load iron loss in a permanent magnet motor. Fig. 1 shows the 3-D finite element mesh in half the thickness of the electrical steel sheet. The applied steel sheet is 20RMHF1200, whose thickness is 0.2 mm. the skin effect can be considered as small. On the other hand, the excess loss is relatively large [8]. Fig. 2 shows the calculated eddy current distribution.

Fig. 3 shows the experimental and calculated no-load iron losses. The difference in the total losses obtained by the conventional and proposed method is slight.

Next, the methods are applied to the calculation of harmonic iron losses in an induction motor driven by a PWM inverter. Fig. 4 shows the 3-D finite element mesh. The applied steel sheet is 50A1300, whose thickness is 0.5mm. The excess loss is negligible [8]. On the other hand, the skin effect is large. Fig. 4 shows the flux density waveform at a tooth. It can be observed that the harmonic ripples concentrate at the surface of the sheet.

To confirm the accuracy in the high-order harmonic iron losses, the loss caused by the inverter-carrier harmonics $W_{carrier}$ is separated not only by the calculation but also by the experiment as follows:

$$W_{carrier} = W_{inv} - W_{sin} \quad (3)$$

where W_{inv} and W_{sin} are the total losses when the motor is driven by the inverter and a sinusoidal power supply,

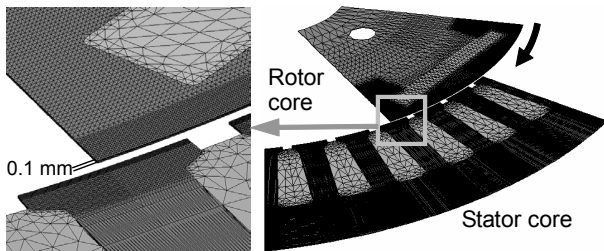


Fig. 1. 3-D finite element mesh for PM (1,186,127 tetrahedron elements).

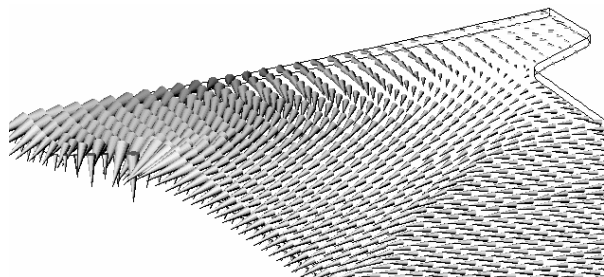


Fig.2. Eddy current distribution near top of stator tooth.

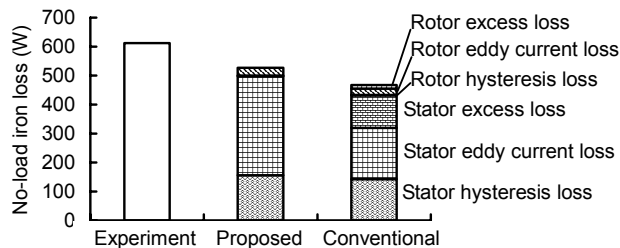


Fig. 3. Experimental and calculated no-load iron loss (1000min⁻¹).

respectively. $W_{carrier}$ mainly consists of the losses in the cores.

Fig. 6 shows the experimental and calculated $W_{carrier}$. The accuracy is much improved by the proposed method. It is clarified that the proposed method is especially suitable for the estimation of the high-order harmonic iron losses.

IV. REFERENCES

- [1] G. Bertotti, "General Properties of Power Losses in Soft Ferromagnetic Materials", *IEEE Trans. Magn.*, vol. 24, no.1, pp.621-630, 1988.
- [2] K.Atallah, Z. Q. Zhu and D. Howe, "An improved method for predicting iron losses in brushless permanent magnet motor", *IEEE Trans. Magn.* vol. 28, no. 5, pp. 2997-2999, 1992.
- [3] C. I. McClay and S. Williamson, "The Variation of Cage Motor Losses with Skew", *IEEE Trans. Ind. Applicat.*, vol. 36, no. 6, pp.1563-1570, 2000.
- [4] N. Sadowski, J. P. A. Bastos, M. V. Ferreira Da Luz, P. Kuo-Peng and M. Lajoie-Mazenc, "The rain-flow method for evaluation of iron losses in electrical machines," *IEEE Trans. Magn.*, vol.36, no.4, 1923, 2000.
- [5] C. Kaido and T. Wakisaka, "Modeling of the high-frequency magnetic properties of electrical steel sheet", *Trans. on the applied magnetics society of Japan*, vol. 23, pp.1565-1568, 1999 (in Japanese).
- [6] A. Hubert and R. Schafer, "Magnetic domains", Springer, 3rd printing, 2009.
- [7] K. Yamazaki and M. Tanida, "Iron loss modeling for high-speed synchronous permanent magnet motors considering skin effect and excess loss in electrical steel sheets," *COMPUMAG- Shenyang*, PB3-1, 2005.
- [8] K. Yamazaki, M. Tanida, and H. Satomi, "Calculation method for iron loss in rotating machines by direct consideration of eddy currents in electrical steel sheets", *IEEJ Trans. on IA*, vol. 128, no. 11, pp. 1298-1307, 2008 (in Japanese).

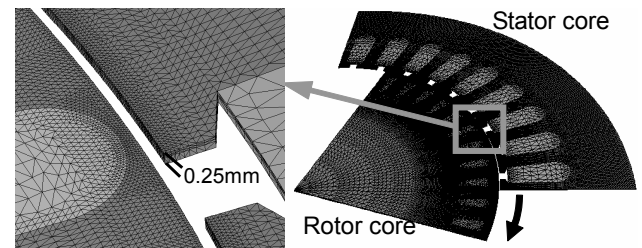


Fig. 4. 3-D finite element mesh for IM (798,858 tetrahedron elements).

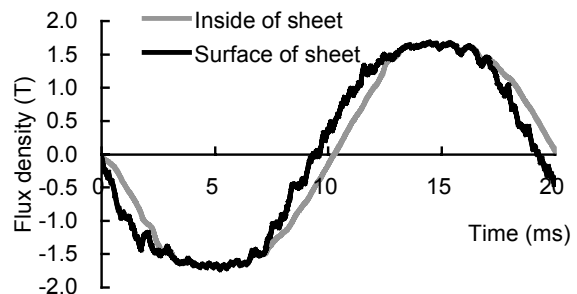


Fig. 5. Calculated flux density waveform at tooth ($f_i=50\text{Hz}$, 180V).

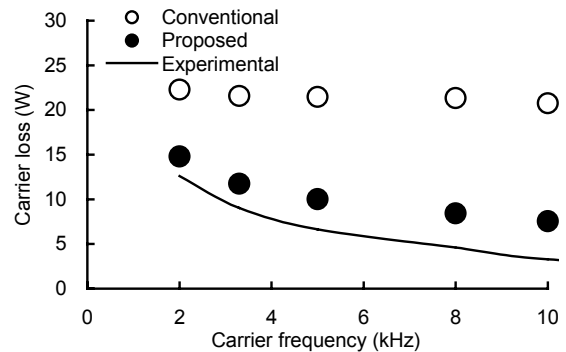


Fig. 6. Experimental and calculated carrier loss of motor ($f_i=50\text{Hz}$, 180V).

Effect of Temperature Dependence of Magnetic Properties on Heating Characteristics of Induction Heater

Norio Takahashi¹, Hiroyuki Kagimoto¹, Hiroaki Kurose¹, Daisuke Miyagi¹, Naoki Uchida² and Keiji Kawanaka²

¹Dept. Electrical and Electronic Eng., Okayama Univ., Okayama 700-8530, Japan
(E-mail: norio@elec.okayama-u.ac.jp)

²Mitsui Engineering & Shipbuilding Co., Ltd., Tamano, Okayama 706-0014, Japan

Abstract — In order to improve the induction heating system for an object of magnetic material, it is necessary to clarify the heating property due to eddy current loss by using a magneto-thermal coupled analysis taking account of the temperature dependence of magnetic properties of magnetic material to be heated. In this paper, the effect of temperature dependence of magnetic properties on heating characteristics of a billet heater is analyzed considering the heat emission, heat conduction and temperature dependence of magnetic characteristics of the billet. It is shown that the consideration of temperature dependence of magnetic properties is indispensable for the accurate analysis of the phenomena. The heat emission should also be taken into account for the precise analysis. The skin depth is increased because the resistivity of the billet is increased and the permeability is decreased at high temperature. As a result, the flux in the billet is reduced, and then the power (eddy current loss) in the billet is decreased.

I. INTRODUCTION

In order to control the billet heater accurately so that the input and output of heat is well controlled, and to avoid billets which were not heated at a desired temperature, it is necessary to clarify the heating properties of billets by the magneto-thermal coupled analysis [1]. Although the heating characteristics of the billet made of magnetic material is affected by the temperature dependence of magnetic properties, the report of precise discussion is few.

In this paper, the detailed behavior of the eddy current loss and the temperature distribution in billets are analyzed by the magneto-thermal coupled method considering the heat emission, the heat conduction and the temperature dependence of magnetic characteristics of the billet. The effect of the temperature dependence of magnetic properties on heating characteristics is discussed in detail.

II. MODEL AND METHOD OF ANALYSIS

Fig. 1 shows the examined billet heater. The material of the billet is S45C (carbon steel). The insulating material is rolled out of the fire-resistant material. The Curie temperature of the billet is 760°C. We assumed that the model is isotropic.

3-D FEM using edge elements is used for the magnetic field analysis, and 3-D FEM using nodal elements is used for the thermal field analysis. Although coils are divided into parts in an actual billet heater, it is assumed that they are not divided

into parts in the analysis in order to make the analysis simple. Fig. 1 shows the cross section of the examined model. We considered the division of coils by feeding the current at the instant when the analyzed region corresponds to the cross section with the coil or by feeding no current at the instant when it corresponds to that without the coil. The boundaries of analyzed region in Fig. 1 are assumed as the adiabatic boundaries.

The B-H curves are changed with the temperature. Fig.3 shows B-H curves as a reference.

III. EFFECT OF TEMPERATURE DEPENDENCE OF MAGNETIC PROPERTIES

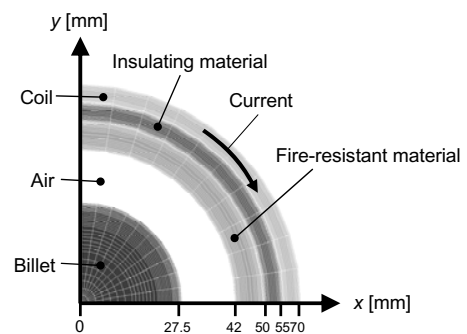


Fig.1. Analyzed model (1/4 model).

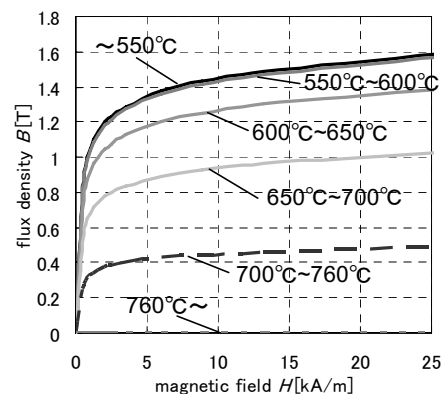


Fig.2. Temperature dependence of B-H curve of billet (reference).

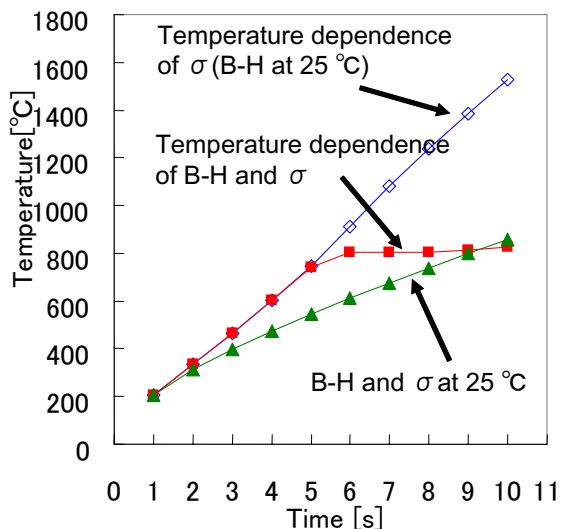


Fig.3. Effect of temperature dependence of B-H curve and conductivity σ .

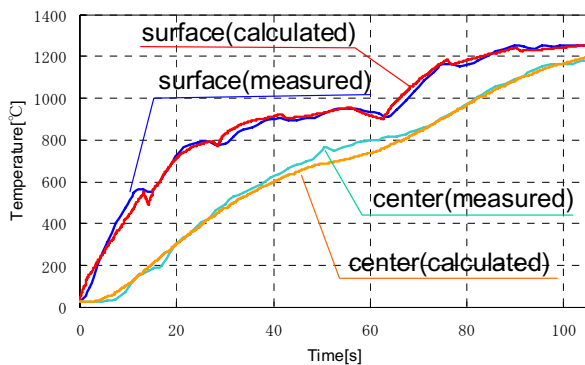


Fig.4 Comparison of calculated and measured temperature at the center and on the surface of billet.

Fig.3 shows an example of the calculated result of the change of temperature. The figure denotes that the behavior of temperature is completely different, if the temperature dependence of conductivity and B-H curve is neglected. Fig. 4 shows the comparison of calculated temperature with the measured one. The temperature is measured using thermocouples. As the measured B-H curves are used in the analysis, the calculated results are considerably in good agreement with the measured ones.

Fig. 5 shows the temperature distribution at $t=105$ sec. The figure denotes that the heat emission should be taken into account, because the temperature distribution is considerably affected by the heat emission at high temperature.

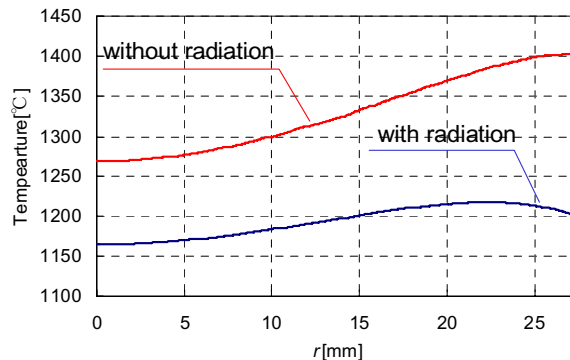


Fig.5. Effect of heat emission.

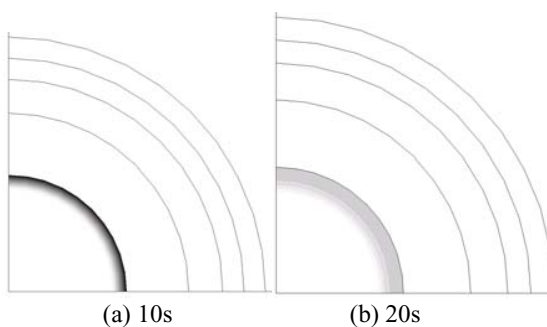


Fig.6. Distribution of eddy current loss.

Fig. 6 shows the distribution of power (eddy current loss) and temperature in the billet. The power invades inside the billet with the increase of temperature, and its value is reduced. The reason is as follows: The skin depth is increased due to the decreased of the conductivity and permeability, and the flux is also decreased due to the decrease of the permeability at such high temperature. As a result, the generated eddy current loss (power) is decreased.

IV. CONCLUSION

The effect of the temperature dependence of magnetic properties on heating characteristics is discussed in detail. The effect of the temperature dependence of magnetic properties on the distortion of the voltage waveform of the coil, etc. will be discussed in the full paper.

REFERENCE

[1] H.Kurose, D.Miyagi, N.Takahashi, N.Uchida, and K.Kawanaka, "3-D eddy current analysis of induction heat apparatus considering heat emission, heat conduction and temperature dependence of magnetic characteristics", *IEEE Trans. Magn.*, vol.45, no.3, pp.1847-1850, 2009.

Evaluation of Electromagnetic Inspection of Retained Austenite in High Chromium Cast Iron using 3-D Nonlinear FEM Considering Non-Uniform Permeability

Yuji Gotoh¹, Akira Nishishita¹, Nobuya Sasaguri², and Norio Takahashi³, *Fellow, IEEE*

¹Department of Mechanical and Energy Systems Engineering, Faculty of Engineering, Oita University, 700 Dannoharu, Oita 870-1192, Japan, goto-yuuji@cc.oita-u.ac.jp

²Department of Materials Science and Engineering, Kurume National College of Technology, 1-1-1 Komorino Kurume, Fukuoka 830-8555, Japan, sasaguri@kurume-nct.ac.jp

³Department of Electrical and Electronic Engineering, Graduate School of Natural Science & Technology, Okayama University, 3-1-1 Tsushima, Okayama 700-8530, Japan, norio@elec.okayama-u.ac.jp

Abstract — The inspection of volume fraction of retained austenite in the high chromium cast iron is important in keeping the quality of hot-rolling etc. The permeability and the conductivity of the cast iron are decreased when the volume fraction of retained austenite is increased. Therefore, the inspection of volume fraction of retained austenite is possible by detecting the difference of the electromagnetic characteristic. However, the inspection is not easy, because the permeability of the cast iron is usually non-uniform. As a result, the signal of the electromagnetic inspection has a magnetic noise.

In this paper, the inspection technique for reducing the effect of the non-uniformity of the permeability on the large magnetic noise, and that for measuring the retained austenite is examined using 3-D edge-based hexahedral nonlinear FEM. In addition, the experimental verification is also carried out.

I. INTRODUCTION

High chromium cast iron is used as abrasion proof components of such as, a steel of hot-rolling, a ball and a liner of mill for mineral pulverization. The hardness is reduced by the appearance of the retained austenite in the cast iron [1,2]. Therefore, the evaluation of volume fraction of retained austenite (γ) in the cast iron is important in keeping the quality of steel of hot-rolling etc. The permeability of the cast iron decreases when γ is increased, because the austenite is a nonmagnetic material. Therefore, the evaluation of the amount of γ in the cast iron is possible by detecting the change of the magnetic characteristic using the electromagnetic inspection. However, the inspection is not easy, because the permeability of the cast iron is usually non-uniform. As a result, the signal of the electromagnetic inspection has a magnetic noise [3].

In this paper, the inspection technique for reducing the effect of the non-uniformity of the permeability on the large magnetic noise, and that for measuring γ is examined using 3-D edge-based hexahedral FEM, and the experimental verification is also shown.

II. MEASUREMENT OF INITIAL MAGNETIZATION CURVE, NON-UNIFORMITY OF PERMEABILITY AND CONDUCTIVITY

Fig.1 shows the initial magnetization curves for various γ in

the cast iron. In addition, Fig. 2 shows the conductivities for various γ . These figures denote that the permeability and conductivity of the cast iron are decreased with the increase of the retained austenite. Fig.3 shows the maximum dispersion rate ε_u of non-uniformity of permeability with different amount of γ in the high chromium cast iron. The figure denotes that the non-uniformity (ε_u) of permeability is increased when γ is increased. When the magnetic field is increased in the high chromium cast iron, ε_u is decreased, because the direction of each magnetic moment becomes nearly the same.

III. ELECTROMAGNETIC INSPECTION OF RETAINED AUSTENITE IN HIGH CHROMIUM CAST IRON

A. Effect of Non-uniformity of Permeability in High Chromium Cast Iron

Fig.4 shows the 1/2 domain of the proposed inspection model for evaluation of γ in the high chromium cast iron. The

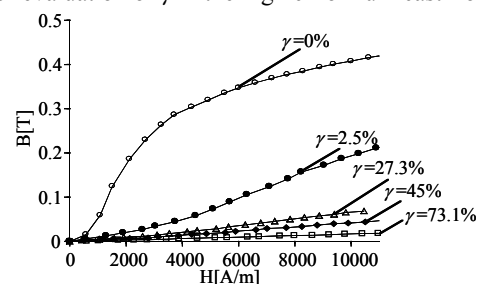


Fig.1. Initial magnetization curves of the high chromium cast iron with different γ (Cr=17%).

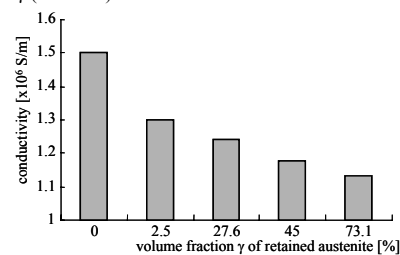


Fig.2. Conductivity of high chromium cast iron with different γ (Cr=17%).

7. Material Modeling

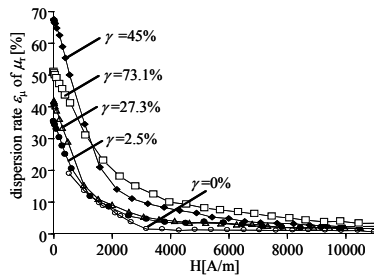


Fig.3. Dispersion rate ε_{μ} of permeability of high chromium cast iron ($Cr=17\%$).

non-uniformity of flux density in a search coil is estimated by calculation. Many kinds of B-H curves with the dispersion within ε_{μ} are generated for various average flux density B_{ave} in the specified region in the cast iron, and they are distributed in random in each element in the cast iron. The movement of magnetic yoke is simulated by shifting the permeability and conductivity inside the high chromium cast iron region in the x-direction by 1mm step. The B-H curves of the high chromium cast iron ($\gamma=45\%$) with the largest non-uniformity of initial permeability are used for investigation. The exciting frequency is 500Hz. Fig.5 shows the calculated results of flux density in a search coil when the magnetic yoke is moved. The figure denotes that ε_B is reduced when the flux density B_E inside the exciting coil is increased. In this magnetic yoke, the heat generation of the exciting coil is large when the exciting flux density B_E is more than 0.08T. But, ε_B is remained about $\bullet 0.07\%$, even if B_E is larger than 0.08T. Therefore, the exciting flux density B_E in this model was set as 0.08T.

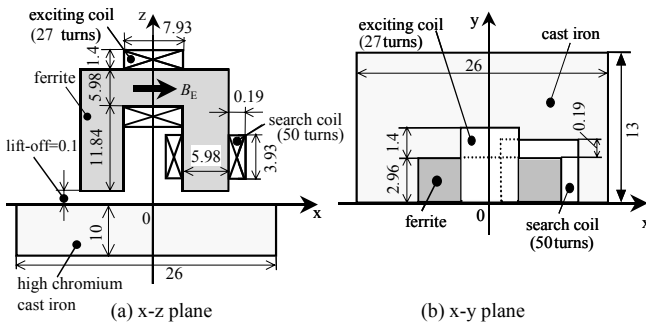


Fig.4. Electromagnetic inspection model for high chromium cast iron with different γ (1/2 domain).

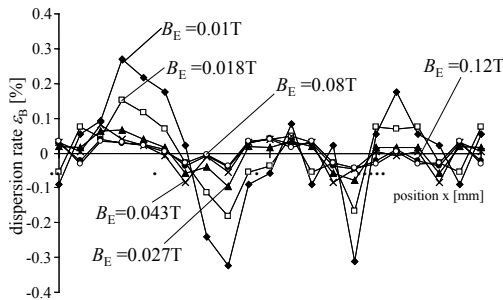


Fig.5. Effect of non-uniformity of permeability in high chromium cast iron (calculated, 500Hz, $\gamma = 45\%$, $Cr=17\%$).

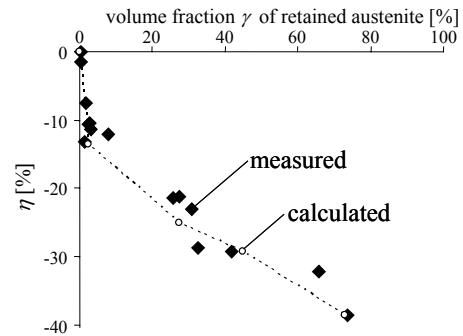


Fig.6. Effect of γ in high chromium cast iron on change of flux density in a search coil (500Hz, $B_E = 0.08T$, $Cr=17\%$).

B. Inspection of Retained Austenite

Fig.6 shows the effect of γ on the change η of flux density $|B|$ of a search coil. 14 pieces of the high chromium cast irons with various volume fractions γ of retained austenite were measured. The frequency and exciting flux density B_E are 500Hz and 0.08T, respectively. The measured values are in agreement with the calculated ones. In the full paper, the optimal magnetization condition for the inspection is examined using the 3-D edge-based hexahedral FEM. In addition, the experimental verification is also carried out.

IV. CONCLUSIONS

The results obtained are summarized as follows:

- (1) When the volume fraction of retained austenite in high chromium cast iron is increased, the permeability and conductivity are decreased and the non-uniformity of permeability is increased. However, when the magnetic field is increased, the non-uniformity of permeability is decreased, because the direction of each magnetic moment becomes nearly the same.
- (2) The flux density in a search coil of the proposed electromagnetic inspection method is decreased when the volume fraction of retained austenite in high chromium cast iron is increased, because the permeability and the conductivity are decreased. Therefore, if the exciting flux density that reduces the non-uniformity of the permeability in high chromium cast iron is applied, the non-destructive inspection of the volume fraction in the cast iron of retained austenite is possible by the proposed inspection method.

V. REFERENCES

- [1] S.Inthidech, P.Sricharoenchai, N.Sasaguri and Y.Matsubara, "Behavior of hardness and retained austenite in heat treatment of high chromium cast iron for abrasion wear resistance", *Transactions of American Foundry Society*, vol.112, pp.899-910, 2004.
- [2] K.Mumtaz, S.Takahashi, J.Echigoya, Y.Kamada, L.F.Zhang, H.Kikuchi, K.Ara and M.Sato, "Magnetic measurements of the reverse martensite to austenite transformation in a rolled austenitic stainless steel", *Journal of Materials Science*, vol.39, pp.1997-2010, 2004.
- [3] Y.Gotoh and N.Takahashi, "3D FEM analysis of electromagnetic inspection of outer side defects on steel tube using inner coil", *IEEE Transactions on Magnetism*, vol.43, no.4, pp.1733-1736, 2007.

3-Dimensional Modelling of Magnetostriction in Iron Core with Equivalent Nodal Forces

Yanhui Gao¹, Kazuhiro Muramatsu¹, Koji Fujiwara², Yoshiyuki Ishihara², Shigemasa Fukuchi³, and Tetsumi Takahata³

¹Dept. of Electrical and Electronic Engineering, Saga Univ., Saga, Saga 840-8502, Japan

²Dept. of Electrical Engineering, Doshisha Univ., Kyotanabe, Kyoto 610-0321, Japan

³Sao Electric Mfg. Co. Ltd., Yukuhashi, Fukuoka 824-0032, Japan

07643001@edu.cc.saga-u.ac.jp

Abstract — In order to investigate the noise reduction of a reactor under inverter power supply, coupled magnetic and mechanical analyses should be carried out taking account of magnetostriction or electromagnetic force in the iron core. In this paper, a method of modeling the magnetostriction 3-dimensionally with equivalent nodal forces is proposed to enable the mechanical analysis taking account of the magnetostriction. Then, the spatial distributions of displacements in the core of a single phase of reactor due to magnetostriction and electromagnetic force are calculated to determine the dominant cause of noise. It is shown that both causes should be taken into account for a reactor.

I. INTRODUCTION

Recently, inverter power supplies have been widely used for electrical machines. However, because of the harmonics, noises from electrical machines are loud. Generally, the major cause of noise for non-rotating machines such as transformers is considered to be magnetostriction [1]. And for rotating machines it is considered to be electromagnetic force in the gaps between the rotor and stator [2]. Moreover, for reactors, both mechanisms are considered to be responsible for the noise because it is non-rotating machines with large gaps in the core. To investigate the noise reduction for such various machines, 3-dimensional (3D) coupled magnetic and mechanical analyses should be carried out. In the mechanical analysis, the local force distribution in the iron core is required. The 3D local forces due to electromagnetism can be calculated by the nodal force method [3]. However, for magnetostriction, only 2D modelling has been reported [1],[2].

In this paper, the method of modeling the magnetostriction 3-dimensionally with equivalent nodal forces is proposed to enable the 3D mechanical analysis taking account of the magnetostriction. In this modeling, the nodal forces in the core due to magnetostriction are calculated by using the flux distribution obtained from the magnetic field analysis. In order to show the effectiveness of the proposed method, the spatial 3D distributions of displacements in the iron cores of a single phase of reactor due to magnetostriction and electromagnetic force are calculated by the static structure analysis using the nodal forces obtained from the proposed method and the nodal force method, respectively, and are compared with each other.

II. 3D MODELLING OF MAGNETOSTRICTION

The magnetostriction in the iron core is modeled with equivalent nodal forces. The material of the core is assumed to be isotropic in this paper. The nodal forces $f_{ms}^{(ip)}$ due to

magnetostriction at each node ip of each element ie when subject to flux density $B^{(ie)}$ are obtained by using the following method. First, when the magnetic material is subject to flux density B , the magnetostriction ε_p and ε_v in the directions parallel and vertical to B respectively are assumed to be

$$\varepsilon_p = \alpha B^2 \quad (1)$$

$$\varepsilon_v = -\nu \varepsilon_p, \quad (2)$$

where α and ν are constants obtained from experiment. ν corresponds to the Poisson's ratio. The shape change of a cylinder with length L and radius R due to magnetostriction subject to flux density in the parallel direction to the axis of the cylinder is illustrated in Fig. 1. In the element ie with center of gravity O on the cylinder axis as shown in Fig. 1, the displacement $u^{(ip)}$ on node ip can be represented by

$$u^{(ip)} = \varepsilon_p l i_p + \varepsilon_v r i_v, \quad (3)$$

where l and r are the lengths of the axial and radial components of the line $O-ip$ respectively, as shown in Fig. 2. i_p and i_v are unit vectors in the axial and radial directions respectively. The equivalent nodal force f_{ms} on each node of element ie are obtained by using the displacement u at each node and the stiffness matrix K [4] defined by the finite element method as following

$$f_{ms} = K u. \quad (4)$$

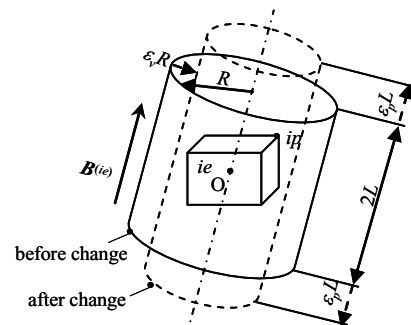


Fig. 1. Change in the shape of a cylinder due to magnetostriction.

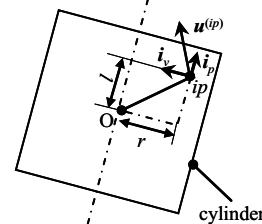


Fig. 2. Displacement on node ip (cross section of Fig.1).

7. Material Modelling

In order to investigate the validity of the proposed method, the nodal forces f_{ms} for a cubic element with edges of 2 m, Young's modulus E of 200 GPa, ν of 0.3, and α of 7.8×10^{-6} subject to flux densities (0, 0, 1 T) and (0.577 T, 0.577 T, 0.577 T) are calculated. The distributions of the flux densities B , displacements u , and nodal forces f_{ms} are shown in Fig. 3. This figure shows the validity of the proposed method because the element extends in the direction parallel to the flux density and contracts in the direction vertical to the flux density.

The nodal forces in the core can be obtained by adding up the nodal forces f_{ms} in each element.

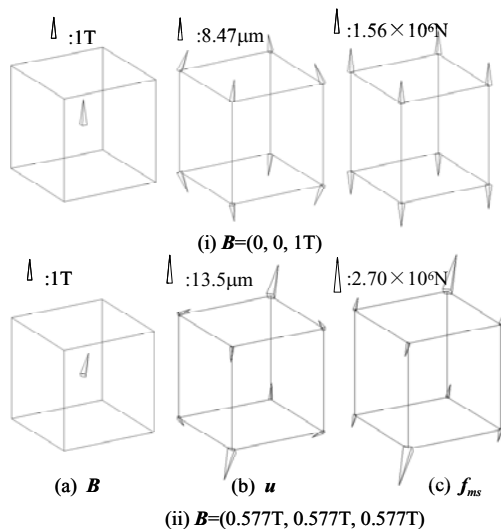


Fig. 3. Distributions of (a) Flux densities B , (b) displacements u , and (c) nodal forces f_{ms} when subject to flux densities (i) $B=(0, 0, 1T)$, (ii) $B=(0.577T, 0.577T, 0.577T)$.

III. APPLICATION

To investigate the effectiveness of the proposed method, the spatial distributions of displacements in the iron core of a single phase of reactor, described in Ref. [5], due to magnetostriction and electromagnetic force are calculated and compared with each other.

For calculating the magnetic field distribution, 3D nonlinear eddy current finite element analysis using the $A-\phi$ method (where A and ϕ are the magnetic vector and electric scalar potentials, respectively) is carried out. The laminated core of reactor is modeled as an anisotropic solid core considering the gaps between the steel plates and eddy currents in the steel plates [5].

The flux distribution and the nodal force distributions for magnetostriction and electromagnetism in the middle plane of the core and at the instant when the flux is the maximum are shown in Fig. 4. The nodal forces due to magnetostriction are larger near the gaps and holes where the flux densities change suddenly. The nodal forces due to magnetostriction are about six times as those due to electromagnetism. The nodal forces due to electromagnetism are attractive forces generated between cores. The nodal forces due to electromagnetism are obtained by using the nodal force method and the Maxwell stress tensor of the Chu model [3].

The spatial distributions of displacements obtained from the static structure analysis using the nodal forces due to the magnetostriction and electromagnetism in the same plane at the same instant are shown in Fig. 5. The displacements due to magnetostriction in the yoke are larger than those in the leg. This is because the yoke is longer than the leg. The displacements due to electromagnetism in the yoke are large whereas those in the leg are very small. This is because the yoke is only acted upon by forces pulling from the leg, whereas the leg is acted upon by nodal forces in opposite directions which can cancel with each other. Both displacements are of the same order. Therefore, both causes should be taken into account in the noise reduction.

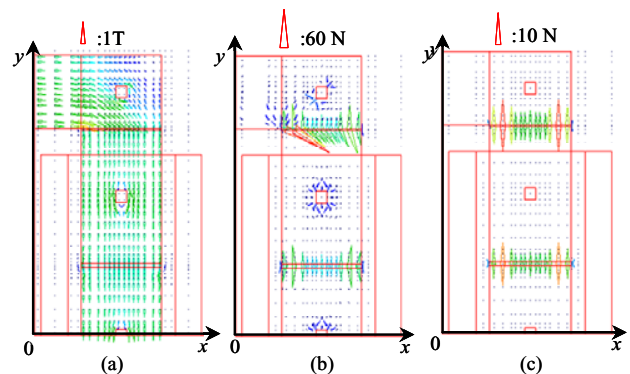


Fig. 4. Distributions of (a) flux densities, (b) nodal forces due to magnetostriction, and (c) nodal forces due to electromagnetism.

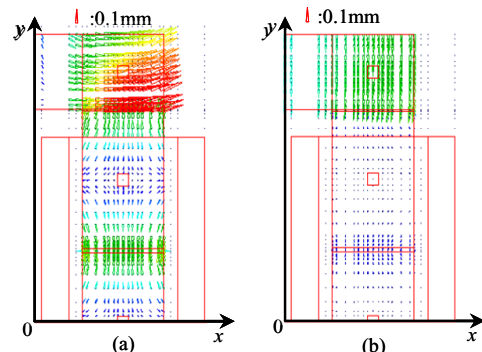


Fig. 5. Distributions of displacements due to (a) magnetostriction, and (b) electromagnetism.

IV. REFERENCES

- [1] W. Kitagawa, et al., "Analysis of structural deformation and vibration of a transformer core by using magnetic property of magnetostriction", *IEEJ Trans. Power and Energy B*, vol. 128, no. 4, pp.654-660, 2008.
- [2] K. Delaere, et al., "Comparison of induction machine stator vibration spectra induced by reluctance forces and magnetostriction," *IEEE Trans. on Magn.*, vol. 38, no. 2, pp. 969-972, 2002.
- [3] A. Kameari, "Local force calculation in 3D FEM with edge elements," *International Journal of Applied Electromagnetics in Material*, vol. 3, pp. 231-240, 1993.
- [4] O. C. Zienkiewicz, *The Finite Element Method*, Fourth Edition, McGraw-Hill, 1994.
- [5] Y. Gao, et al., "Loss calculation of reactor connected to inverter power supply taking account of eddy currents in laminated steel core," *IEEE Trans. on Magn.*, vol. 45, no. 3, pp. 1044-1047, 2009.

Tolerance Analysis of NMR Magnets

Alessandro Formisano and Raffaele Martone

Dipartimento di Ingegneria dell'Informazione, Seconda Università di Napoli

Via Roma 29, Aversa (CE), I-81031, Italy

Alessandro.Formisano@unina2.it

Abstract — Due to manufacturing and assembly variations, there are tolerances associated with the nominal dimensions of complex electromagnetic devices. A possible approach to take into account such tolerances in the early design phases is the “worst case tolerance analysis”, whose goal is to determine the effect of the smallest and largest assembly dimensions on the product performance. On the other hand, when many tolerances must be considered, locating the worst case with combinatorial effects could get very time consuming, since performance assessment of such devices may require numerical field analysis. In the paper, a fast approach based on the performance sensitivity with respect to design parameters is presented, and applied to the tolerance analysis of nuclear magnetic resonance magnets.

I. INTRODUCTION

The main requirement in the design of superconducting (SC) magnets for Nuclear Magnetic Resonance (NMR) is the high uniformity of the magnetic field that must be guaranteed within a very tight limit inside a suitable Volume Of Interest (VOI). The uniformity is usually evaluated as the maximum discrepancy of the magnetic field amplitude with respect to the nominal value on the boundary of the VOI. In order to guarantee the right resolution, such uniformity must be within few parts per million (ppm). Unfortunately, in practical realisations, due to construction and assembling tolerances, the actual magnets differ from the nominal ones [1, 2]. Then, suitable sets of shimming coils are included able to counteract the error field. However, before starting construction, especially for such expensive devices, an assessment of the impact of tolerances is required, to verify if design performance are guaranteed also for real magnets, and, in addition, to evaluate the actual requirements of shimming systems.

On the other hand, the treatment of the tolerances in the design phase implies a relevant impact on the computational cost, since the relationship among design parameters and device performance indexes is usually a complex non-linear function, possibly involving numerical magnetic field computations. In the paper, a fast approach to tolerance analysis, based on the worst case approach and on the use of performance index sensitivity, will be presented, and applied to the performance assessment of NMR magnets.

II. TOLERANCE ANALYSIS

Tolerancing plays a key role in design and manufacturing of industrial products. In the following, according to [3], *tolerances* are defined as the maximum deviations from a nominal specification within which the part is acceptable for

its intended purpose. Tolerances are usually expressed as lower and upper deviations from the nominal value.

Basically, tolerancing implies two different aspects:

- Tolerance *analysis*, involving identification of related tolerances in a design, and calculation of the stackup of these related tolerances. If design requirements are not met, tolerance values are adjusted and the stackup recalculated.
- Tolerance *synthesis*, the process of distributing tolerance values among dimensions in order to guarantee functionality or assemblability.

In general, tolerance analysis involves building linear or nonlinear models of the problem at hand, depending upon the design complexity.

A tolerancing problem can be solved either using a worst-case approach or a statistical approach. In the first case, the extreme values of tolerances are considered, while in the second case, tolerance calculation are performed based on the fact that actual dimensions are randomly distributed around their nominal values.

Statistical tolerancing, as it allows to reduce the average cost by accepting to include in the overall production also a (possibly small) number of unacceptable elements, is well-suited for mass production. Some of the popular methods for statistical tolerance analysis are search-space smoothing using Monte Carlo yield estimation, statistical model-based methods, and six-sigma tolerance analysis tools [3, 4].

The worst-case approach is better suited for single piece or small-lot productions for critical applications; of course the design of high field magnets falls in the second class. The typical approach uses nominal values for all variables except for one, which is once simulated with the upper and once with the lower boundary. Then, the next variable is chosen. It is missing the effect of the combination of several tolerances that might together cross the performance acceptance threshold. In principle also the cross effects of the tolerances could be considered. However this implies to calculate each possible combination of tolerance term boundaries, leading to a strong growth of computing time which is exponential in the number of tolerance sources. The interval arithmetic approach also suffers from the curse of dimensionality described above.

The topic of tolerance analysis has received a great deal of attention from researchers in the field of mechanics [3-6], and also relevant contributions are available in the field of electronic circuits design (a few, non exhaustive examples are [7], [8]). On the other hand, the complexity of electromagnetic devices performance assessment limited the

investigation in the field until sufficient computational power was made available.

Aim of the paper is to propose an approach to reduce the computational cost for worst case localization, based on the availability of the sensitivity of device performance index with respect to the design and constructive parameters. As a matter of fact, the array of sensitivities can be related to the gradient of the performance index in the parameters space, and the worst case is likely to be identified by following the gradient direction.

On the other hand, constraints are usually present among different parameters, limiting the actual values that each parameter can take inside the tolerance range. In addition, in some cases the gradient could become very small, and higher order derivatives must be considered in the search for the worst case.

In the full paper, an approach able to systematically take into account the above cited issues will be proposed. For exemplification purposes, in the following section the tolerance assessment of field homogeneity for a MRI magnet will tackled, either using worst case analysis taking advantage of sensitivities, and using Monte Carlo method, to compare drawbacks and advantages of both approaches.

III. ASSESSMENT OF MRI DESIGN

The possibility of locating worst case using performance index sensitivity in the design of demanding electromagnetic devices has been evaluated with reference to a SC magnet for NMR spectroscopy, described in Fig. 1 and Table I.

TABLE I
PARAMETERS OF NMR MAGNET

Parameter	Value
Number of Coils	6 NbTi coils
Central Field	2.5 T
Field Uniformity	3.2 ppm on 5 cm sphere
Minimum inner radius	210 mm
Overall length	640 mm
Tolerances	+/- 1 μ m for all dimensions, except radial and longitudinal coord. of barycentre for Coil 1, for which a tolerance of +/- 1 mm is assumed

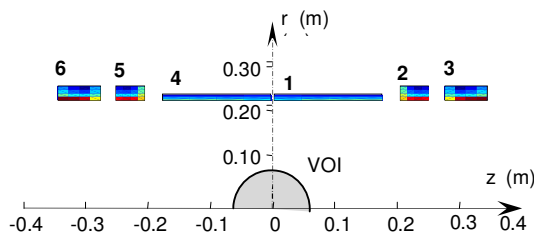


Fig. 1 – Sketch of the magnet for NMR spectroscopy considered in the paper.

In order to get meaningful results from stochastic analysis within a reasonable computation time, the tolerances on all geometrical dimensions have been assumed very small (1 μ m) except for radial and longitudinal coordinates of coil 1 baricentre, for which tolerances of +/-1 mm have been

assumed. No constrains among design variables are considered. In this way convergence of statistical analysis was achieved after 20000 cases for Monte Carlo method, and provided a worst case uniformity of 316 ppm. Worst case analysis using sensitivities (in this case, simply multiplying the sensitivity with respect to each parameter times the related tolerance, and summing absolute values for all dimensions) provided a worst case uniformity of 319 ppm. Cumulative distribution function (CFD) of performance, average performance and worst case are reported in Fig. 2.

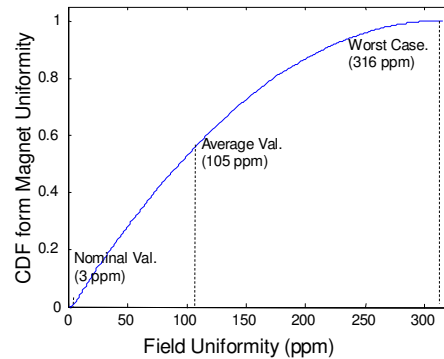


Fig. 2 – CDF, average and worst performance for NMR magnet.

IV. OUTLOOK

A possible fast approach for worst case tolerance analysis, based on the use of sensitivity information, has been introduced and its effectiveness has been checked in the case of tolerancing of NMR magnets. The comparison with usual statistical analysis showed that worst case performance is practically the same, yet requiring in the latter case a much higher computational effort. In the full paper, a complete description of the method will be presented, including the treatment of constraints and of possible vanishing gradient components.

V. REFERENCES

- [1] M. Cioffi, A. Formisano, R. Martone, "Statistical Analysis in Robust Design of Superconducting Magnets", *Compel*, 24 (3): 427-435, 2005.
- [2] M. Cioffi, A. Formisano, R. Martone, "Stochastic Handling of Tolerances in Magnet Design", *IEEE Transactions on Magnetics*, 40 (2): 1252-1255, 2004.
- [3] R. C. Dorf, A. Kusiak, *Handbook of Design, Manufacturing, and Automation*, New York: J. Wiley, 1994, pp. 155-169.
- [4] Z. Shen, G. Ameta et al., "A Comparative Study of Tolerance Analysis Methods", *Journ. Of Computing and Information Science in Engineering*, 5: 247-256, 2005.
- [5] H. Yang, and P.I. Chen, "Robust Design: Tolerance Design Method", *Proc. of ASME Symposium on Conceptual and Innovative Design for Manufacturing*, 3: 101-116, 1999.
- [6] W. H. Greenwood and K. W. Chase, *Worst-Case Tolerance Analysis with Nonlinear Problems*, New York: John Wiley, 1992.
- [7] K. J. Antreich, H. E. Gräb and C. U. Wieser, "Practical Methods for Worst-Case and Yield Analysis of Analog Integrated Circuits", *Int. Journal of High Speed Electronics and Systems*, 4 (3): 261-282, 1993.
- [8] Y. Lin and S. W. Foo, "Fast Search Algorithm for Tolerance Design", *IEE Proceedings of Circuits Devices and Systems*, 145: 19-23, 1998.

homogenization in electromagnetism: a thermodynamic insight

Vincent G. Mazauric

Schneider Electric, Innovation Department, 38050, Grenoble Cedex 9, France

vincent.mazauric@schneider-electric.com

Abstract—Homogenization procedure is investigated from spatial averaging techniques and variational principles. The mean-field approximation requested by the procedure is clearly given and dispersive behavior laws are derived at the macroscopic scale. The technique is used to discuss the problem of dynamic hysteresis and extra-losses in soft magnetic materials. A validation is proposed by assessing losses on a 2D-Pry and Bean iron sheet. Discussion also includes a confrontation with Bertotti's experiments.

Index Terms—homogenization, multi-scale approach, magnetic materials, eddy currents, transient formulations, anomalous losses.

I. INTRODUCTION

Homogenization techniques consist in replacing an original problem described from deep within material by an equivalent one where the rapidly space-varying lengths at the design scale are discarded. From that viewpoint, macroscopic electromagnetism is already an homogenized theory, but further homogenizations could be carried out to take advantage of the spatial regularity occurring in various media. The benefits of homogenization are obvious: While taking into account the fine structure would be a huge or impossible task, the equivalent problem may be solved more cheaply, with a reasonable mesh size and a better conditioning. However a challenging task of any homogenization procedure consists in deriving unconventional behavior laws from a basic resolution at a “unit cell” scale in order to restore properly the dissipative phenomena occurring therein.

Some previous works paid attention to the conservation of local averages involved in the Maxwell equation set, *e.g.* [1]. Conversely, we adopt here a thermodynamic viewpoint where the conservation of global energy quantities, such as Gibbs' free energy or electrical power, comes first; whereas the structure of Maxwell equations is automatically kept as far as the variational principles are enforced. Hence, the mean field approximation requested to successfully achieve the homogenization is rigorously highlighted thanks to a spectral analysis.

A validation of the procedure is proposed by assessing anomalous losses on a 2D-Pry and Bean iron sheet [2]. Whereas numerical results are successfully faced with experiments, the domain of validity of the prior models is also emphasized.

II. VARIATIONAL PRINCIPLES IN ELECTROMAGNETISM

The magnetodynamic behavior of any electrical system may be derived from the variational principle [3]:

$$P_{\text{mech}}(\Omega) - \frac{dG}{dt}(\Omega) + P_{\text{elec}}(\Omega) = \min_{\mathbf{h}, \mathbf{e}} \left(\int_C \sigma^{-1} (\mathbf{curl} \mathbf{h})^2 d^3x + \frac{d}{dt} \int_{\Omega} (\mathbf{b}(\mathbf{h}) \cdot \mathbf{h} + \mathbf{d}(\mathbf{e}) \cdot \mathbf{e}) d^3x \right) \quad (1)$$

where the functional in the RHS exhibits:

- the magnetic field \mathbf{h} related to free and displacement currents according to the Maxwell-Ampere equation. The quasi-static approximation enforces $\mathbf{d} \equiv 0$ in conductors;
- the Joule losses P_{Joule} monitored in conductors $C \subset \Omega$. This term is even to respect invariance of losses with inversion of current $\mathbf{j} = \mathbf{curl} \mathbf{h}$ (σ^{-1} is the resistivity);

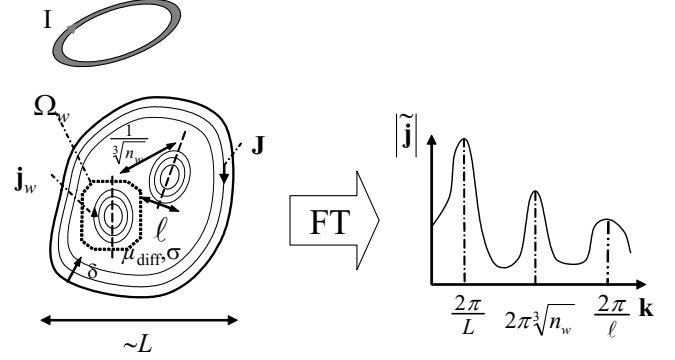


Fig. 1. Spectral decomposition of the current density: While the low-frequency peak involves scales given by the classical skin effect, the medium-frequency peak (resp. high-frequency) is associated to “unit cell” periodicity (resp. eddy currents pattern occurring in one unit cell). The splitting of this results from diluted enough unit cells to allow a mean field approximation.

- the variation with time of the electromagnetic energy coupling the field with the generator I and the mass V_0 ;
- the magnetic $\mathbf{b}(\mathbf{h})$ and electrostatic $\mathbf{d}(\mathbf{e})$ behavior laws derived from thermostatic equilibrium of the contribution of Ω to the Gibbs' potential:

$$G(T, I, V_0, \Omega) = \int_{\Omega} \left(\int_0^{\mathbf{h}} (-\mathbf{b}(\mathbf{h})) \cdot \delta \mathbf{h} + \int_0^{\mathbf{e}} (-\mathbf{d}(\mathbf{e})) \cdot \delta \mathbf{e} \right) d^3x \quad (2)$$

Extending the electric field in the conductor according to Ohm's law $\mathbf{e} = \sigma^{-1} \mathbf{j} - \mathbf{v} \times \mathbf{b}$, Faraday's law $\mathbf{curl} \mathbf{e} = -\partial_t \mathbf{b}$ may be viewed as acting *locally* to check *globally* a tendency towards reversibility. This striking property provides a thermodynamic-oriented insight of the variational theory of electromagnetism [4]. Hence, the minimum in (1) matches the LHS including the variations with time of the co-energy $-G(\Omega)$, the mechanical power $P_{\text{mech}}(\Omega)$ acting on Ω , and the electrical power $P_{\text{elec}}(\Omega) = -\oint_{\partial\Omega} (\mathbf{e} \times \mathbf{h}) \cdot d^2x$ supplied to Ω .

Taking advantage of their quadratic properties, thermodynamic functionals (1) and (2) support spatial filtering operations to provide a fully multi-scale framework: It is the key to derive robust homogenized models.

III. MACROSCOPIC FORMULATION

As matter of fact, the basis of the free current density \mathbf{j} in regular conducting structures involves a superposition of compact distributions of microscopic currents \mathbf{j}_w located within each “unit cell” Ω_w at position \mathbf{x}_w , with a density $n_w(\mathbf{x})$; and a possible macroscopic free current density \mathbf{J} . This description leads to the spectral decomposition given at the figure 1 where the splitting in several peaks means diluted unit cells and allows a *mean-field* hypothesis [5] which consists in performing independant minimizations for $k \geq k_{lp}$. Whereas the low-pass filtering process ($k < k_{lp}$) is equivalent to a smoothing procedure on the various fields [6], the high frequencies restore the

deepest magnetodynamic mechanisms. Hence, the restriction to C of the minimization in the RHS of (1) becomes:

$$\min_{\langle \mathbf{h} \rangle(t)} \int_C (\sigma^{-1} (\mathbf{curl} \langle \mathbf{h} \rangle)^2 + \partial_t (\langle \mathbf{b} \rangle \cdot \langle \mathbf{h} \rangle)) d^3x \quad (3a)$$

$$+ \sum_{w \in C} \min_{\mathbf{h}_\mu(t)} \int_{\Omega_w} (\sigma^{-1} (\mathbf{curl} \mathbf{h}_\mu)^2 + \partial_t (\mathbf{b}_\mu \cdot \mathbf{h}_\mu)) d^3x \quad (3b)$$

where $\langle \mathbf{h} \rangle$ (resp. $\langle \mathbf{b} \rangle$) denotes the averaged magnetic field (resp. averaged flux density) and is obtained through a convolution by the low-pass filter $\rho_{lp} \langle \mathbf{h} \rangle(\mathbf{x}) = \int \mathbf{h}(\mathbf{x}') \rho_{lp}(\mathbf{x} - \mathbf{x}') d^3x'$. Similarly, \mathbf{h}_μ (resp. \mathbf{b}_μ) stands for the rapidly space-varying part of the magnetic field (resp. flux density) and is obtained thanks to a convolution by a high-pass filter. Hence, the consistency between low- and high-spatial frequencies is enforced by:

- the conservation of the magnetic flux density after the smoothing procedure, *i.e.* $\mathbf{B} = \langle \mathbf{b} \rangle$;
- the modification of the Maxwell-Ampere equation according to the dynamic behavior of independent unit cells given by the minimization (3b). After the smoothing procedure on the microscopic eddy currents at the first order, the averaged magnetic field $\langle \mathbf{h} \rangle$ is shifted by the microscopic dynamic eddy currents to check a modified Maxwell-Ampere equation:

$$\mathbf{curl} (\langle \mathbf{h} \rangle + \sigma \Lambda^2 \partial_t \mathbf{B}) = \mathbf{J} \quad (4)$$

where Λ denotes a length parameter lumping *locally* all the complexity due to spatial dependence of \mathbf{j}_w [7].

Some additional assumptions on the magnetization mechanisms occurring in the media are necessary to resume the homogenization.

1) *Local media*: The knowledge of the local field \mathbf{h} in \mathbf{x} prescribes entirely the local flux density \mathbf{b} herein. Each unit cell may be viewed as large enough to achieve a thermodynamic equilibrium described by the Gibbs' free energy density. Its hessian provides locally the differential permeability as a positive tensor and the macroscopic behavior law is nothing but the average of the local behavior law. Introducing the macroscopic magnetic field $\mathbf{H} = \langle \mathbf{h} \rangle + \sigma \Lambda^2 \partial_t \mathbf{B}$ according to (4), the homogenization results in the delayed diffusion model [8]:

$$\delta \mathbf{B} = \mu_{\text{diff}}(\mathbf{H}) \cdot \delta (\mathbf{H} - \sigma \Lambda^2 \partial_t \mathbf{B}) \quad (5)$$

and Ohm's law is possibly kept at the macroscopic scale.

2) *Non-local media*: The thermodynamic equilibrium depends on a large neighborhood of \mathbf{x} . It is obviously the case for ferromagnetic materials because the domain pattern depends of the shape of the material. However, quasi-static approximation assumes that each time step checks a magnetostatic equilibrium described by the Gibbs' free energy G . Its density, at the *macroscopic scale*, is a function of the macroscopic magnetic field $\mathbf{H} = \langle \mathbf{h} \rangle + \sigma \Lambda^2 \partial_t \mathbf{B}$ and its hessian provides the differential permeability μ_{diff} as a positive tensor. Thus, small variations of the flux density follow the magnetic law:

$$\delta \mathbf{B} = \mu_{\text{diff}}(\mathbf{H}) \cdot \delta \mathbf{H} \quad (6)$$

Hence, stationary variations of (3a) with respect of $\langle \mathbf{h} \rangle$, yields, at the first order time-derivative, the macroscopic Maxwell-Faraday equation $\mathbf{curl} (\sigma^{-1} \mathbf{curl} \langle \mathbf{h} \rangle) = -\partial_t \mathbf{B}$ so that the macroscopic electric field \mathbf{E} appears, in the rest frame of the conductor, through a *deviated* Ohm's law:

$$\mathbf{E} = \sigma^{-1} \mathbf{J} - \mathbf{curl} (\Lambda^2 \partial_t \mathbf{B}) \quad (7)$$

In the following, the delayed diffusion model (5) and the deviated Ohm's law model (6)-(7) are adapted to the Pry and Bean geometry of domains occurring in an iron sheet [2].

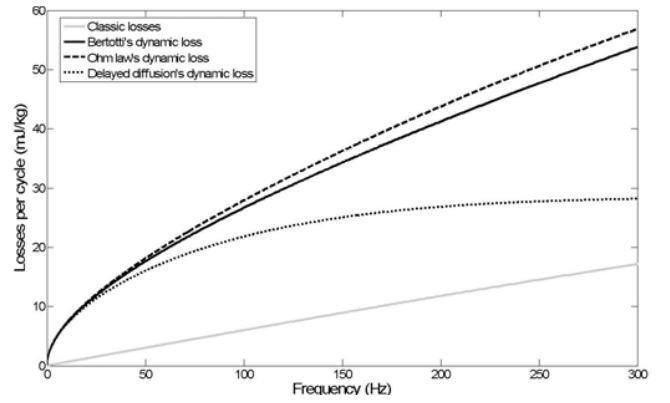


Fig. 2. Loss assessment provided for an iron sheet (thickness $d = 0.21$ mm; $\mu_{\text{diff}} = 10,000\mu_0$; $\Lambda = 125 \mu\text{m}$). While solid line denotes the Bertotti's model derived from experimental data, the dashed lines (resp. dotted) are provided from the deviated Ohm's law (resp. delayed diffusion) model.

IV. RESULTS AND CONCLUSION

Both models provide domain wall motion-induced extra losses. But the latter follows Bertotti's experimental results [9] whereas the former does not restore the frequency dependence of excess losses on a large enough band, and actually underestimate them (Fig.2). These preliminary results argue for a diluted pattern of domain walls, the equilibrium of which being obtained at the macroscopic scale. Conversely, the delayed diffusion model seems more suitable to homogenize a stack of laminations from the behavior of one sheet.

In our knowledge, it is the first report of calculations able to reproduce the loss sketch observed in an iron lamination sheet by exhibiting the experimental dependence of anomalous losses on the frequency. Hence, implementing homogenized behavior laws suitable for Finite Element Analysis is very critical to achieve energy efficiency or reliability of power electrical devices [10]. Such developments are currently under progress in order to take into account transient regime, non-linear media involving several magnetic states, and massive magnetic cores.

REFERENCES

- [1] M. E. Feddi, Z. Ren, A. Razek, and A. Bossavit, "Homogenization technique for maxwell equations in periodic structures," *IEEE Transactions on Magnetics*, vol. 33, no. 2, pp. 1382–1385, 1997.
- [2] R. Pry and C. Bean, "Calculation of the energy loss in magnetic sheet materials using a domain model," *Journal of Applied Physics*, vol. 29, no. 3, pp. 532–533, 1958.
- [3] V. Mazauric, "From thermostatics to maxwell's equations: A variational approach of electromagnetism," *IEEE Transactions on Magnetics*, vol. 40, no. 2, pp. 945–948, 2004.
- [4] P. Hammond, *Energy methods in electromagnetism*. Monographs in electrical and electronic engineering, New York, USA: Clarendon, Oxford University Press, 1981.
- [5] J. Yeomans, *Statistical mechanics of phase transitions*. Oxford, UK: Oxford University Press, 1992.
- [6] G. Russakoff, "A derivation of the macroscopic maxwell equations," *American Journal of Physics*, vol. 38, no. 10, pp. 1188–1195, 1970.
- [7] H. Williams, W. Shockley, and C. Kittel, "Studies of the propagation velocity of a ferromagnetic domain boundary," *Physical Review*, vol. 80, no. 6, pp. 1090–1094, 1950.
- [8] M.-A. Raulet, B. Ducharme, J.-P. Masson, and G. Bayada, "The magnetic field diffusion equation including dynamic hysteresis," *IEEE Transactions on Magnetics*, vol. 42, no. 2, pp. 872–875, 2004.
- [9] G. Bertotti, "General properties of power losses in soft ferromagnetic materials," *IEEE Transactions on Magnetics*, vol. 24, no. 1, pp. 621–630, 1988.
- [10] M. Drouineau, V. Mazauric, J.-N. Vincent, and A. Anglade, "Eco-design stakes of electrical steel: Dynamic losses sensitivity," *Journal of Magnetism and Magnetic Materials*, vol. 320, pp. e1070–e1073, 2008.

FE Analysis of Plasma Discharge and Sheath Characterization in Dry Etching Reactor

Gwang-Jun Yu¹, Young Sun Kim¹, Se-Hee Lee², and Il Han Park¹

¹School of Information and Communication Engineering, Sungkyunkwan University, Suwon, 440-746, Korea

²School of Electrical Engineering and Computer Science, Kyungpook National University, Daegu 702-701 Korea

joonynet@naver.com, youngsun@skku.edu, shlees@knu.ac.kr, ihpark@skku.ac.kr

Abstract—This paper presents a full finite element analysis for plasma discharge in etching process of semiconductor circuit. The charge transport equations of hydrodynamic diffusion-drift models and the electric field equation are numerically solved in a fully coupled system by using a standard finite element procedure for transient analysis. The proposed method is applied to a real plasma reactor in order to characterize the plasma sheath that is closely related to the yield of the etching process. The base electrode of the reactor is modified to improve the edge effect for the uniformity. The experiment and numerical results are examined along with SEM data of etching quality. The feasibility and usefulness of the proposed method is shown by both numerical and experimental results.

I. INTRODUCTION

Plasma etching and deposition is currently in widespread use in the manufacturing process of semiconductor circuit. However, despite of the importance of plasma processing, gas glow discharge is not well understood. This comes from the non-equilibrium nature of the plasma, and the complex interaction among potential field, transport phenomena, plasma chemistry, and surface reaction kinetics. So design of plasma reactor is still based largely on empirical approaches. Main requirements of plasma etching include high etching rate, uniformity, anisotropy, and selectivity. However, it is very difficult to satisfy all of the above requirements simultaneously. In addition, as the wafer size continues to increase, it becomes more difficult to satisfy uniformity and anisotropy.

Recently, there has been increasing interest in developing mathematical models and numerical analysis of the plasma process in an effort to better understand the process and to improve the design of plasma reactors. The most frequently used algorithms are method of characteristics, flux-corrected-transport(FCT) method and particle-in-cell(PIC) method. The above algorithms are so complex for numerical implementation that extra delicate techniques are required. In addition, they cost long computation time and sometimes cause numerical instability [1]-[4].

In this paper, we propose a full finite element approach where the charge transport equations of hydrodynamic diffusion-drift models and the electric field equation are numerically solved in a fully coupled system by using a standard finite element procedure for transient analysis. The proposed method is applied to a real plasma reactor in order to characterize the plasma sheath just above a targeted silicon wafer. The plasma sheath is closely related to the yield of the

etching process since it accelerates the bombing ions, whose motional properties determine the etching quality such as uniformity and anisotropy. Also, in this work the base electrode of the initial reactor is modified to improve the edge effect deteriorating the uniformity, and its experiment results of etching quality are compared with ones of the initial one by examining data of SEM(scanning electron microscope). That is, the feasibility and usefulness of the proposed method is shown by both numerical and experimental results.

II. ANALYSIS MODEL OF DRY ETCHING CHAMBER

Fig. 1 shows a cross-sectional diagram of the chamber for dry etching process. A wafer is placed between two electrodes. The upper electrode is connected to a voltage source and the lower one is set as ground. The electrodes supply external energy into the chamber for generating and sustaining the plasma. The electric field between the electrodes is downward and drives charge carries. The plasma sheath is formed just above the wafer and it accelerates heavy ions that bomb the wafer surface for etching. But the electric field above the wafer is not uniform in intensity and direction because of the fringing effect on the edge side. In this work, the uniformity of electric field is improved by substituting an existing quartz ring, which is located below the wafer, with an aluminum ring.

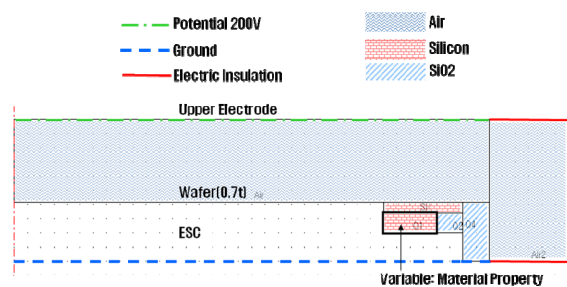


Fig. 1. Axis-symmetric geometry of dry etching chamber and design variables.

III. HYDRODYNAMIC DIFFUSION-DRIFT MODELS OF DISCHARGE

To analyze the phenomena of plasma discharge, hydrodynamic diffusion-drift models are employed. Three governing equations coupled with Poisson's equation are solved simultaneously for the concentration of the electron(N_e), positive(N_p) and neutral (N_n) with respect to time [5], [6]. The equations are as follow,

$$\begin{aligned} \frac{\partial N_e}{\partial t} + \nabla(N_e V_e) &= S + N_n \alpha |V_e| - N_e N_p \beta_{ep} \\ \frac{\partial N_p}{\partial t} + \nabla(N_p V_p) &= S + N_n \alpha |V_e| - N_e N_p \beta_{ep} \quad (1) \\ \frac{\partial N_n}{\partial t} + \nabla(N_n V_n) &= S - N_n \alpha |V_e| + \gamma \end{aligned}$$

where, V_e , V_p and V_n denotes the electron, positive and neutral ion drift velocities and α and β denotes the ionization and recombination coefficients, γ denotes the concentration of new supplied gas. S denotes the source term.

The electric field is calculated using Poisson's equation with the net charge of electron and ion.

$$\nabla(-\epsilon \nabla V) = e(N_p - N_e) \quad (2)$$

where, ϵ is electric permittivity, e is the quantity of electric charge and V is the electric scalar potential.

IV. NUMERICAL AND EXPERIMENTAL RESULTS

The discharge phenomena in chamber are modeled with the three transport equations coupled with Poisson's equation and they are calculated using the axisymmetric 3D finite element analysis. In Fig. 2(a) the electric potential along a z-direction is almost constant in the middle of two electrodes, meaning that plasma is neutral. A sheath region above the wafer is shown in Fig. 2(b).

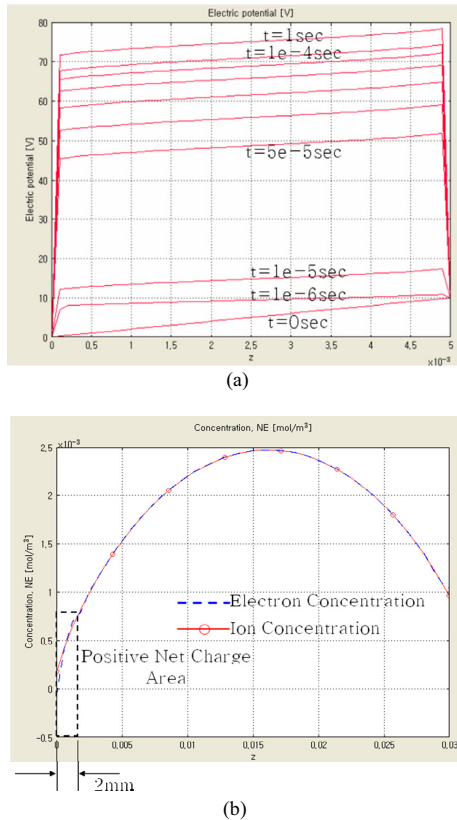


Fig. 2. Variation of (a) electric potential and (b) electron/ion density along the z-direction

From the field analysis of plasma chamber, the uniformity of electric field near wafer edge is improved as shown Fig. 3(b). It means that an incidence angle of ion to the wafer etching target is more perpendicular compared with Fig. 3(a).

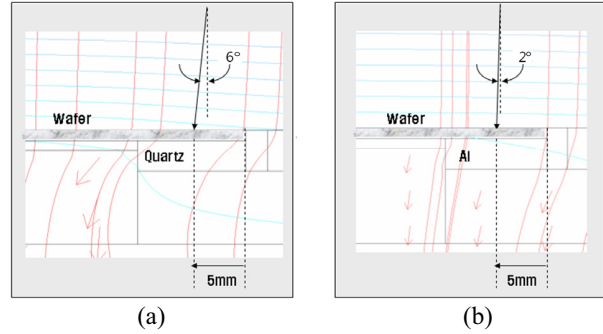


Fig. 3. Comparison of electric field distributions when the Q1 block is (a) quartz and (b) aluminum ring

Fig. 4(a) shows the SEM image of the cross section near the wafer edge after dry etching is performed. The trench near the edge is not perpendicular to wafer surface because of the fringing effect of electric field near the wafer edge. By substituting the quartz block with a aluminum one, the tilt angle of trench is improved as shown in Fig. 4(b).

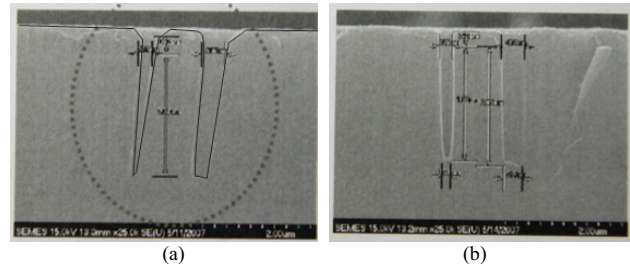


Fig. 4. SEM images of wafer trench in (a) the existing quartz block and (b) the improved aluminum block.

V. REFERENCES

- [1] R. Morrow, "Theory of negative corona in oxygen," *Phys. Rev. A*, vol. 32, no. 3, 1985, pp. 1799–1809.
- [2] G. Steinle, D. Neundorf, W. Hiller, and M. Pietralla, "Two-dimensional simulation of filaments in barrier discharges," *J. Phys. D: Appl. Phys.*, vol. 32, 1999, pp. 1350–1356.
- [3] J. Paillol, P. Espel, T. Reess, A. Bibert, and P. Domens, "Negative corona in air at atmospheric pressure due to a voltage impulse," *J. Appl. Phys.*, vol. 91, no. 9, 2002, pp. 5614–5621.
- [4] G. E. Georghiou, A. P. Papadakis, R. Morrow, and A. C. Metaxas, "Numerical modelling of atmospheric pressure gas discharges leading to plasma production," *J. Phys. D: Phys.*, vol. 38, pp. R308–R328, 2005.
- [5] F. H. Harlow, "A Machine Calculation Method for Hydrodynamic Problems," *Los Alamos Scientific Laboratory report LAMS-1956*, 1955.
- [6] Se-Hee Lee, Se-Yeon Lee, and Il-Han Park, "Finite Element Analysis of Corona Discharge Onset in Air with Artificial Diffusion Scheme and under Fowler-Nordheim Electron Emission Condition," *IEEE Trans. on Magnetics*, vol. 43, no. 4, April, 2007, pp. 1453–1456.

Permanent-Magnet Synchronous Generator Supplying an Isolated Load

T. F. Chan¹, Weimin Wang¹ and L. L. Lai²

¹Department of EE, the Hong Kong Polytechnic University, Hung Hom, Hong Kong, China

²Energy Systems Group, School of Mathematics and Engineering Sciences, City University London, UK
eetfchan@polyu.edu.hk

Abstract — The steady-state and transient performance of a surface-inset permanent-magnet synchronous generator (PMSG) feeding an isolated load is studied using a couple-circuit, time-stepping, two-dimensional finite-element analysis. Nonlinearities in the field and electric circuit are taken into consideration and both passive ac load bridge rectifier dc load are analyzed. The computed results have been verified by experiments on a 2.5 kVA generator.

I. INTRODUCTION

Permanent magnet synchronous generators (PMSGs) are increasingly used for distributed generation and many stand-alone applications. For these applications the PMSG may supply a passive R-L load or a dc load via a diode bridge rectifier connected across the armature terminals [1]. The nonlinear electric and field systems pose considerable difficulties in analysis. In this paper, a time-stepping, coupled field-circuit finite element method [2], [3] is used for performance analysis of a surface-inset PMSG feeding an isolated load. Besides the field characteristics, the coupled field-circuit solution also yields other useful generator information, taking in consideration the armature current effect, magnetic saturation, and circuit nonlinearities. The analysis result helps in improving the generator design aspects. The computed results have been verified by experiments on a 2.5 kVA generator.

II. ANALYSIS

The electric circuit of a star-connected PMSG that supplies a three-wire R-L load comprises has six circuit variables, namely the resultant generated phase EMFs e_A , e_B , and e_C and the phase currents i_A , i_B and i_C . The external circuit comprises the armature resistance R , armature end-winding leakage inductance L_e , and the load impedance. In the case of a bridge rectifier load, additional circuit components include the six diodes D_1 to D_6 , the load resistance R_L , and the load inductance L_L . In the present FEA study the field circuit coupling is accomplished via the phase EMFs e_A , e_B , and e_C .

Maxwell's equations, applied to PMSG domains, will give rise to the diffusion equations

$$\begin{aligned} \nabla \times (\nu \nabla \times A) &= 0, & \text{in iron and air gap} \\ \nabla \times (\nu \nabla \times A) &= \frac{i_s}{s}, & \text{in armature windings (1)} \\ \nabla \times (\nu_{PM} \nabla \times A) &= \nabla \times (\nu_{PM} B_r), & \text{in permanent magnets} \end{aligned}$$

where A , ν , i_s , S , B_r and ν_{PM} are magnetic vector potential, reluctivity, armature phase current, total cross-sectional area

of one turn, remanent flux density of the PM and equivalent reluctivity, respectively.

The time-stepping, coupled field-circuit, 2-D FEA was performed in order to study the steady-state and transient performance the experimental PMSG with surface-inset rotor [3]. Constant speed operation is assumed and the PMSG supplies an isolated load. Fig. 1 shows the cross-section of the machine and the field plot obtained.

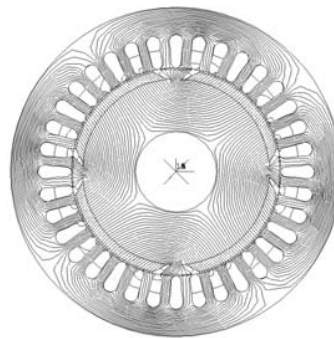


Fig. 1 Cross-section of PMSG with surface-inset rotor and the flux plot obtained from FEA.

III. GENERATOR PERFORMANCE

A. PMSG Supplying Isolated Load

Fig. 2 shows the computed and experimental waveforms of the PMSG on no load and Fig. 3 shows the computed and experimental waveforms of phase voltage and phase current when the PMSG is supplying a load resistance of 9.1Ω per phase. The increased harmonic distortion in phase voltage is due to increase in the triplen harmonics. Since a three-wire load is being supplied, the current waveform is practically sinusoidal since triplen harmonics are suppressed across the lines.

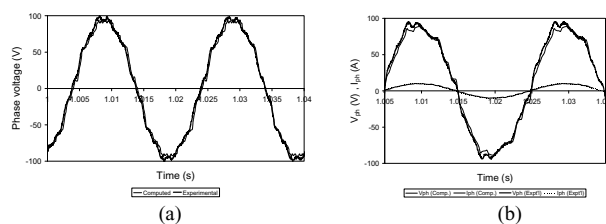


Fig. 2 Smith connection for single-phase operation of a three-phase induction motor.

B. Load Switching Transients

The time-stepping coupled field-circuit method was next used to study the transient performance of the PMSG. The PMSG was operating on no-load at rated speed when a balanced resistive load of 12.45 Ω per phase was connected across the generator terminals. As shown in Fig. 3, a brief transient period follows the application of load at time $t = 1.018$ s, and a notch is produced in the voltage waveform. Agreement between the computed and experimental waveforms is good in general, but the deviation in frequency becomes more pronounced due to the speed drop in the experimental machine set, a fact which was not accounted for in the FEA.

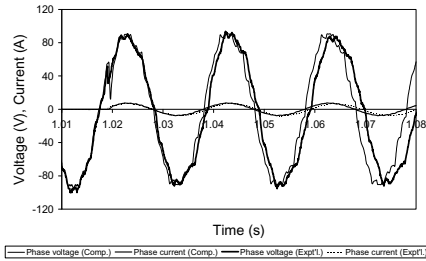


Fig. 3 Waveforms of phase voltage and phase current when a load resistance of 12.45 Ω per phase is switched across the generator terminals.

C. Short-Circuit Transients

The time-stepping coupled field-circuit method was also used for studying the short-circuit performance of the PMSG and the computed results are shown in Fig. 4. The PMSG is assumed to be running on open circuit when a three-phase short circuit occurs at the terminals. Since triplen harmonic currents cannot flow, the triplen harmonic voltage components remain in each phase during the short circuit (Fig. 4a). The steady-state short-circuit current, however, is quite sinusoidal as observed from Fig. 4b. The peak short-circuit current reaches 131 A, while the steady-state short-circuit current is 107 A (peak), or 76 A (rms), which is almost six times the rated current.

Fig. 5 shows the distribution of the normal flux density at the mean air gap of the PMSG computed at the instant when maximum short-circuit current (131 A) is flowing. Due to the inset rotor construction, the flux density is large in the interpolar regions (I) where the soft iron rotor pole pieces are located. Over the surfaces of magnets (II), however, the flux density is smaller due to the demagnetizing effect of the armature currents. There are also places with flux reversal, implying that partial demagnetization in the adjacent magnet regions is likely to occur in the event of a terminal short circuit.

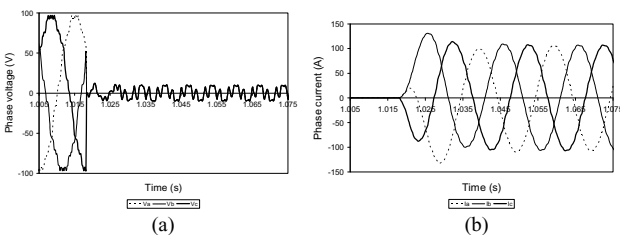


Fig. 4 Three-phase short-circuit transients of PMSG: (a) Phase voltage waveforms; (b) phase current waveforms.

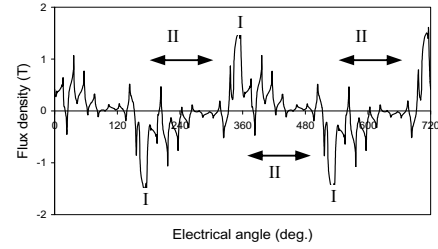


Fig. 5 Computed air gap flux density distribution of PMSG when Phase A is carrying maximum instantaneous short-circuit current (I: interpolar regions; II: surfaces of magnets).

D. Rectifier Load

Figs. 6a and 6b show the computed and experimental waveforms of the PMSG-rectifier-load system when $R_{dc} = 9.2$ Ω. Compared with the waveforms for passive loads (Fig. 2), the harmonic distortion the phase voltages and phase currents is more severe due to the nonlinear load. During commutation overlap, the phase voltage is approximately constant at 50 V while the phase current increases (or decreases) approximately linearly, giving rise to quasi-trapezoidal current pulses in the positive and negative half cycles (Fig. 6-a+b).

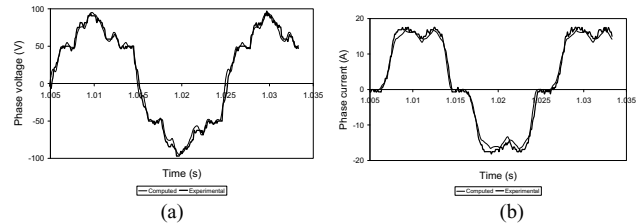


Fig. 6. Computed and experimental waveforms of phase current when the PMSG is supplying a rectifier load ($R_{dc} = 9.2$ Ω).

IV. ACKNOWLEDGMENT

The work described in this paper was fully supported by a grant from the Research Grants Council of the Hong Kong Special Administrative Region, China (Project No. PolyU 5121/06E).

V. REFERENCES

- [1] O. Ojo and J. Cox, "Investigation into the performance characteristics of an interior permanent magnet generator including saturation effects," in *Conf. Rec. 1996 IAS Annual Meeting*, vol. 1, pp. 533-540.
- [2] S. Williamson and A. F. Volshen, "Time-stepping finite-element analysis for a synchronous generator feeding a rectifier load," *IEE Proc.—Elect. Power Appl.*, vol. 142, no. 1, pp. 50–56, 1995.
- [3] T. F. Chan, L. L. Lai and L. T. Yan, "Analysis of a stand-alone permanent-magnet synchronous generator using a time-stepping coupled field-circuit method," *IEE Proc.—Elect. Power Appl.* 152(6), pp. 1459-1467, 2005.

Development of Flux Reversal Linear Synchronous Motor with Multiple Auxiliary Salient Poles

Shi-Uk Chung^{1,2}, Hong-Joo Lee³, Byung-Chul Woo¹, Ji-Won Kim¹, Seung-Ryul Moon¹
and Sang-Moon Hwang²

¹Electric Motor Research Center, Korea Electrotechnology Research Institute, Changwon, 641-120, KOREA

²School of Mechanical Engineering, Pusan National University, Busan 609-735 KOREA

³CRINO Co., Ltd., Annex 3rd floor, #257-11, An-Dong, Gimhae-Si, 621-914, KOREA

suchung@keri.re.kr

Abstract — This paper introduces design and analysis of two different flux reversal linear synchronous motor(FRLSM) by 2D finite element method(FEM). The analysis models are optimized by response surface methodology(RSM) for a realistic comparison. Analysis results show that the proposed FRLSM with multiple auxiliary salient poles effectively increases thrust. A prototype of the proposed configuration is made and experimental results validate the design and analysis.

I. INTRODUCTION

Conventional flux reversal machine (FRM) consists of a passive rotor and multiple pole PMs of alternating polarity on each stator salient tooth. FRM can exhibit servo quality characteristics when driven by 3-phase sinusoidal vector control [1]. Most of previous research works related to FRM concentrated mainly on rotary machine except flux reversal linear oscillomachine for short stroke application [2]. Recent research works on FRLSM showed feasibility for long stroke linear motion systems [3], [4].

The proposed model in this paper introduces auxiliary salient poles between adjacent PMs. This unique magnetic circuit reduces flux leakage and also increases reluctance force, and thus thrust. This paper also analyzes a pole-PM type FRLSM which is linearized based on the conventional FRM for force comparison. For a realistic comparison between the analysis models, this paper performs optimization to maximize average thrust at rated MMF(magneto-motive force) using RSM which has been considered as an effective approach for electric machine optimization [6]. However, RSM optimization requires a large number of computations. Therefore, to reduce the number of computations, this paper adopts co-energy variation method to evaluate the average thrust by one phase since resultant thrust is a sum of thrust generated by each phase. Maxwell stress method is also applied for the performance comparison of the optimized models. The analysis reveals that the proposed configuration generates higher thrust than the conventional one. The proposed configuration is finally made based on the optimization results to validate the design and analysis.

II. ANALYSIS MODELS

Fig. 1 shows half model of each configuration and both models have the same external dimensions. Fig. 1(a) is a 5-PM FRLSM, which is linearized and modified based on a pole-PM FRM with odd number of PMs on a stator tooth [1], [3]. Fig. 1 (b) is the proposed FRLSM with multiple auxiliary salient poles. Major specifications of the models are listed in Table I.

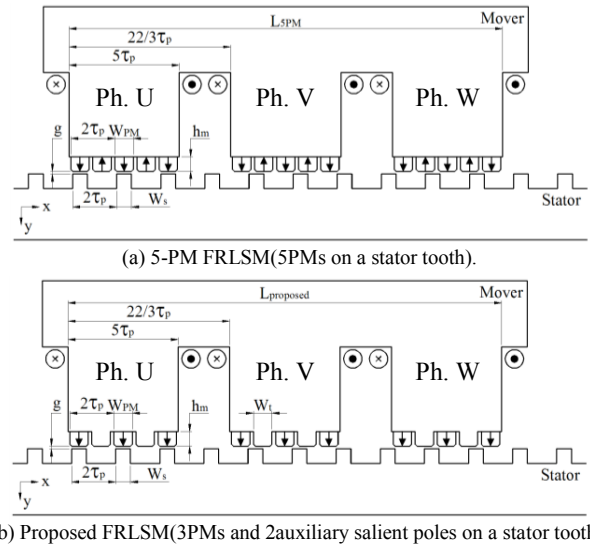


Fig. 1. Configurations of analysis models.

III. COMPUTATION METHODS

For magneto-static analysis, 2D FEM is performed using the commercial software ANSYS/Emag. To calculate average thrust, this paper adopts two different methods, maxwell stress method(MST) and co-energy variation method(CEV). It is computationally more efficient to apply CEV(2) than MST(1) since CEV needs only two computations(at 0 and τ_p) for the average thrust. Therefore, CEV is used for the optimization and MST is also used for steady-state comparison of the optimized models since MST provides thrust, normal force, and force ripple characteristics altogether.

TABLE I
SPECIFICATIONS OF ANALYSIS MODELS

Symbol	Item	Value	Unit
τ_p	Pole-pitch	6.0	mm
W_{PM}	PM width	To be optimized	mm
h_m	PM thickness	To be optimized	mm
g	Mechanical airgap	0.7	mm
h_s	Stack length	100.0	mm
W_s	Tooth width	To be optimized	mm
W_t	Salient pole width	$=W_{PM}$	mm
N	Number of turns/coil	50	-
L_{SPM}	Mover effective length	118	mm
$L_{proposed}$	Mover effective length	118	mm
MMF_{rated}	Rated MMF	400	AT
PM	$B_r = 1.3T, \mu_r = 1.05$	-	-
-	Mover/stator core material	S23	-

$$F_x = \frac{1}{\mu_0} \oint B_x B_y dl, \quad F_y = \frac{1}{2\mu_0} \oint (B_y^2 - B_x^2) dl \quad (1)$$

$$F_{x_avg.} = \frac{\Delta W_c}{\Delta x} \quad (2)$$

where F_x , F_y , μ_0 , B_x , B_y , $F_{x_avg.}$, W_c and J denote thrust, normal force, air permeability, x and y component of airgap flux density, average thrust, co-energy, and current density, respectively.

IV. OPTIMIZATION BY RSM

This paper adopts central composite design(CCD) for appropriate response models [5], [6]. Three important design parameters, W_{PM} , h_m and W_s , which are closely related to average thrust, are chosen in optimization. After statistical evaluations, the polynomial models of the responses are given as (3) and (4). The results obtained by each response model at optimal values and rated MMF are compared with those by MST and CEV in Table II. The average thrust values obtained by the three different methods show good agreement with each other with about 3% difference.

For steady-state operation of the optimized models, three-phase sinusoidal current is assumed to be applied in phase with each no load phase back-EMF. More detailed comparison by MST is numerically summarized in Table III. On average, the proposed FRLSM generates 22% higher thrust density than the 5-PM FRLSM. For the comparison of thrust ripples, this paper applies a multi-slices 2D model to consider skewing effects on the thrust ripples [7]. It can be seen in Table III that all models show extremely low force ripples after $2/3\tau_p$ skewing [3],[4].

$$F_{x_5PM} = -22.4 + 15.41W_{PM} - 11h_m + 5.27W_s - 1.24W_{PM}^2 - 0.68h_m^2 - 1.02W_s^2 \quad (3)$$

$$F_{x_proposed} = -87.16 + 38.67W_{PM} + 13.28h_m + 16.61W_s - 3.21W_{PM}^2 - 1.83h_m^2 - 2.4W_s^2 \quad (4)$$

V. PROTOTYPE EXPERIMENTS

A prototype of the proposed configuration is made after slight modifications from the optimized model. Fig. 2 and 3 show the prototype FRSLM unit and the mover core with PMs, respectively.

To validate the analysis, static thrust is measured by a force sensor at different positions and MMFs under DC current excitation between Ph. U and Ph. V since the motor is WYE connected and neutral point is not connectable. Fig. 3 compares analyses and experiments and shows quite good agreement.

TABLE II
RESULTS COMPARISON AT OPTIMAL VALUES AND RATED MMF

Design Parameters [mm]	5-PM FRLSM			Proposed FRLMS				
	Optimal value	MST [N]	CEV [N]	RSM [N]	Optimal value	MST [N]	CEV [N]	RSM [N]
W_{PM}	6.0				6.0			
h_m	2.0	55.4	56.0	57.6	3.6	79.6	80.6	82.1
W_s	3.0				3.5			

TABLE III
DETAILED COMPARISON BETWEEN 5-PM FRLSM AND PROPOSED FRLSM

MMF	Thrust density [kN/m ²]			Thrust Ripple [%]	
	5-PM	Proposed	Proposed/5-PM	5-PM	Proposed
200	7.9	10.3	131%	1.0	1.1
400	15.8	20.0	127%	0.6	0.7
600	23.7	28.3	120%	0.5	0.6
800	31.3	34.9	111%	0.5	0.6
Avg.			122%	0.7	0.7

- Force generating area=Mover effective length×stack length

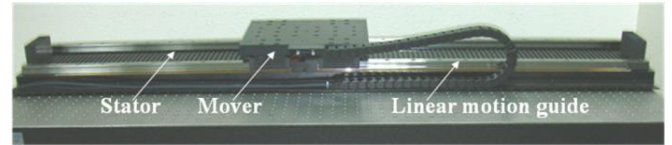


Fig. 2 Prototype FRLSM

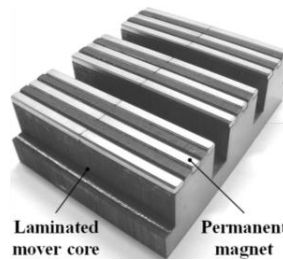


Fig. 3 Mover core with PMs.

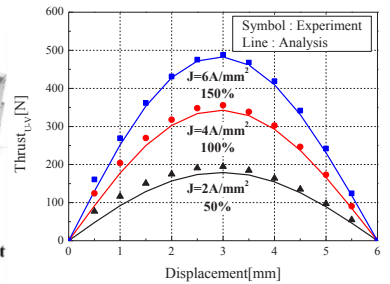


Fig. 4 Analyses and experiments.

VI. CONCLUSION

This paper proposes and analyzes FRLSM with multiple auxiliary salient poles. The comparison results of the optimized models by RSM verify that the proposed configuration effectively increases thrust. The experiments also confirms validity of the design and analysis. Dynamic characteristics will be extensively investigated in the future.

VII. REFERENCES

- [1] I. Boldea, J. Zhang and S. A. Nasar, "Theoretical characterization of flux reversal machine in low-speed servo-The pole-PM configuration," *IEEE Trans. Ind. Appl.*, vol. 38, pp. 1549-1557, Nov.-Dec. 2002.
- [2] I. Boldea, I. Congxiao Wang, Bin Yang and S.A. Nasar, "Analysis and design of flux-reversal linear permanent magnet oscillating machine," *33rd IAS Annual Meeting*. vol.1, pp.136 – 143, Oct. 1998.
- [3] S.U. Chung, H. J. Lee and S. M. Hwang, "A Novel Design of Linear Synchronous Motor Using FRM Topology," in *Proc. Compomag '2007*, Aachen, Germany, June 2007, pp. 365-366.
- [4] S.U. Chung, Do-Hyun Kang, Jung-Hwan Chang, Ji-Won Kim and Ji-Young Lee, "New Configuration of Flux Reversal Linear Synchronous Motor," in *Proc. ICEMS '2007*, Seoul, Korea, Oct. 2007, pp. 864-867.
- [5] D. C. Montgomery, *Design and Analysis of Experiments*. New York: Wiley, 2001.
- [6] Sung-Il Kim, Jung-Pyo Hong, Young-Kyoum Kim, Hyuk Nam and H and Han-Ilk Cho, "Optimal Design of Slotless-Type PMLSM Considering Multiple Response by Response Surface Methodology," *IEEE Trans. Mag.*, vol. 42, pp. 1219-1222, April. 2006.
- [7] S. Williamson, T. J. Flack, and F. Volschenk, "Representation of skew in time-stepped two-dimensional finite element models of electrical machines," *IEEE Trans. Ind. Appl.*, vol. 31, no. 5, pp. 1009-1015, 1995.

Reduction of Cogging Torque for Axial Flux Generator Applied to Small Wind Turbine

Min-Fu Hsieh¹, Yu-Han Yeh¹, D. G. Dorrell², and Samsul Ekram¹

¹Department of Systems and Naval Mechatronic Engineering, National Cheng Kung University, Tainan, Taiwan

²Faculty of Engineering, University of Technology, Sydney, Australia

Abstract—This paper presents a cogging torque reduction technique in axial-flux PM generators for small wind turbines. The compactness, large diameter and high power density make them suitable for wind turbines. The inherent cogging torque can cause problems during turbine cut-in. Here, a turbine is characterized via wind tunnel measurements to determine generator design specification. A “hybrid skew” method is proposed for cogging torque reduction. 3-D FEA is applied to evaluate the method and an 88 % reduction of peak cogging torque is obtained. This significantly improves the turbine performance by achieving low start-up speed. This method avoids confusion in N/S pole placement for manufacturing cost reduction.

I. INTRODUCTION

Axial-flux slotted PM machines have high power/torque density and simple construction; hence, they are suitable for wind turbine applications (particularly the two-sided configuration which balances the axial forces) [1]. Studies have been carried out to reduce cogging torque in axial flux machines (AFM) [2-4]. Some of these techniques require complex magnet shapes that increase manufacture cost or reduce magnet area that may reduce flux linkage and overall torque. There has been research on AFMs applied to wind turbines [5-6]; very few discuss reduction of cogging torque, which may cause potential start-up problems, noise and vibration. Past studies often used coreless designs [5-6] to avoid cogging torque; this may result in low power density [1].

In this paper, a double-rotor slotted AFM is investigated (for high flux linkage, low copper loss) for use in a direct-coupled wind turbine, with a solution put forward for cogging torque reduction. The proposed “hybrid skew” technique combines stator slot displacement to reduce cogging torque. In this technique, which is different from common methods, the North Poles have different shapes from the South Poles (Fig. 1(a)), where a complex shape is not required. The advantages are: (a) simple magnet shape to reduce manufacturing cost, (b) clarity of N/S pole orientation and placement, (c) little loss in magnet volume to maintain performance. For verification, 3-D FEA is applied. A performance comparison is made between the proposed hybrid skew approach and a machine which has no skew and exhibits cogging torque.

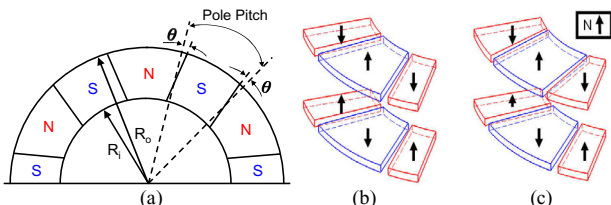


Fig. 1. (a) Hybrid skew in magnet, (b) symmetric arrangement and (c) asymmetric arrangement for the investigated axial flux machine

II. TURBINE CHARACTERIZATION AND GENERATOR DESIGN

The generator specifications can be determined by characterizing the turbine. This is critical since the turbine and generator should match each other on speed, torque and power for high efficiency energy conversion. The turbine (1.36 m in diameter) was installed in a wind tunnel with a dynamometer to measure the output torque and speed. The turbine output power measured under various wind speeds (V_a) is normalized to determine the power conversion coefficient (C_p) curve (Fig. 2(a)), where the peak conversion rate was found to be 32 % at a tip speed ratio (TSR) of 4.6. The TSR and C_p can be defined:

$$TSR = R_t \omega / V_a \quad (1)$$

$$C_p = T \omega / 0.5 \rho A V_a^3 \quad (2)$$

where R_t is the turbine radius, ω the turbine angular speed in rad/s, ρ the air density, A the turbine area facing the wind, and T the turbine shaft torque. In actual application, the rated wind speed is set at 11 m/s, where the turbine shaft output to the generator is 400 W (Fig. 2(b), which is expanded from Fig. 2(a)). At the rated point, the turbine speed and torque are 660 rpm and 5.79 N-m, which are used to determine the specifications of the generator, as shown in Table I.

TABLE I
GENERATOR SPECIFICATIONS

Rated voltage (V)	48	Rated speed (RPM)	660
Rated power (W)	580	Rated torque (N-m)	5.79
Number of pole	12	Number of slots	18
Magnet (NdFeB)	Br=1.24 T, H _{cb} =943kA/m kOe, H _{cj} =1585 kA/m		

The designed generator has a rated output voltage of 48 V at 11 m/s wind; this matches the input of a battery charger. The machine has double outer rotors with NdFeB magnets and a center inner stator (Fig. 3(a), with major dimensions). The detailed design process is not shown but it follows the procedure described in [7]. The air-gap is 0.67 mm and the magnet length is 3 mm. It should be noted that the 12-pole 18-slot configuration has a very high cogging torque and is used to emphasize the effectiveness of the proposed technique.

III. COGGING TORQUE ANALYSIS

The cogging torque can be expressed as [3]:

$$T_{cog} = -\frac{1}{2} \phi^2 \frac{dR}{d\theta} \quad (3)$$

where ϕ is the air-gap flux, R is the air-gap reluctance and θ is the angular position in electrical degrees.

For the dual-rotor generator, two parameters are defined for cogging torque analysis: one is the known stator slot displacement factor (K_d - stator slot displacement divided by slot pitch) [3] and the other is the “hybrid skew” angle θ (Fig.

1) proposed here. The proposed hybrid skew method when combined with an appropriate selection of K_d will give a significant reduction in cogging torque. This will be investigated using FEA.

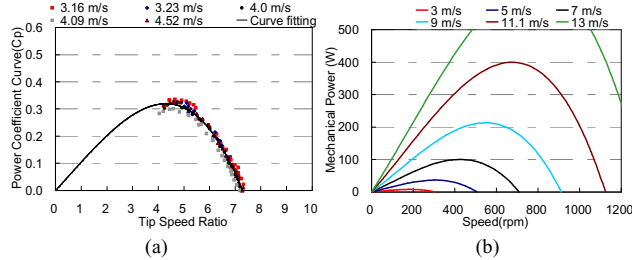


Fig. 2. Turbine characteristics: (a) measured C_p , (b) power-speed curves

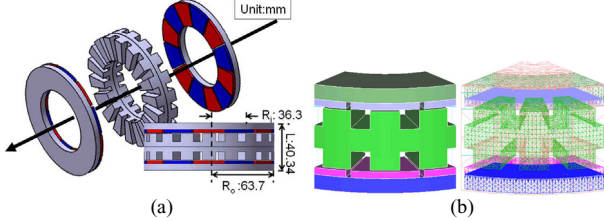


Fig. 3. (a) The designed generator with main dimensions, (b) FE model

Two rotor arrangements are considered: symmetry and asymmetry, as shown in Figs. 1(b) and (c). For asymmetry, the skew in the magnet of one rotor is opposite to that in the other while it is the same for the symmetrical case. From a manufacturing point of view, the symmetrical case is preferable since all N Pole magnets have a different shape from all S Pole magnets. Although magnet skew is a popular method [3-4], it may result in torque ripple or overall torque reduction. The proposed method aims to avoid this problem.

IV. SIMULATION RESULTS

The 3-D FE model is shown in Fig. 3(b). The individual action of slot displacement [3] and hybrid skew is first investigated, and the results are shown in Figs. 4(a) and (b). At $K_d = 0.1875$, the generator has the least cogging torque. The peak cogging torque for varying skew angles at $K_d = 0$ is the smallest at $\theta = 2.5$ deg. for the asymmetric case, as shown in Fig. 4(b) and Fig. 5. It is found that the proposed hybrid skew on its own reduces the cogging torque by 57 %.

The simulation results for the proposed technique combined with slot displacement [3] are presented in Fig. 6(a) (symmetric case). The best reduction in peak cogging torque is 88 % compared to the non-skewed magnet case, which verifies the effectiveness of the developed method. Another comparison is shown in Fig. 6(b), where the average air-gap flux density for the hybrid-skew machine is similar to the original arrangement without skew. The torque comparison and complete results will be shown in the final paper. This confirms that the proposed method does not affect the machine performance. The comparisons with other pole-slot combinations will also be provided in the final manuscript.

The target turbine has a start-up speed of 3.16 m/s with an output torque of 0.6 N-m. The peak cogging torque obtained using the proposed technique is very small and should not affect turbine power output and overall performance. In contrast, a non-skewed machine will have difficulty in starting when matched with the turbine.

V. CONCLUSION

A “hybrid skew” technique has been developed to reduce cogging torque in an axial-flux PM generator for a small wind turbine. A challenging 12-pole 18-slot axial flux machine with high cogging torque has been investigated. 3-D finite element analysis was used to carry out the simulation. It was found that the proposed method can achieve an excellent 88 % reduction in peak cogging torque when combined with the slot displacement method. Consequently, start-up problem of the wind turbine will be solved and the overall performance will not be affected. There will also be a reduction in manufacturing complexity and cost.

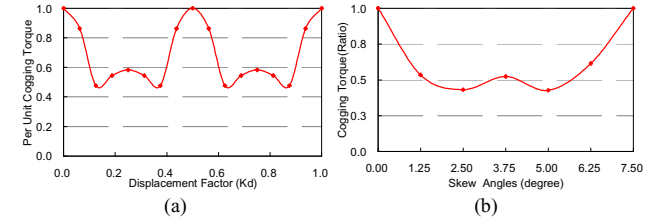


Fig. 4. (a) Peak cogging torque (per unit) with respect to K_d , (b) peak cogging torque for various skew angles (symmetrical, based on non-skewed)

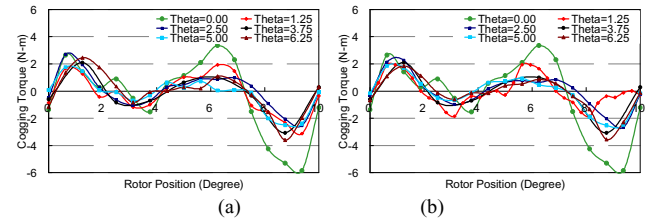


Fig. 5. Cogging torque for varying θ ($K_d=0$): (a) symmetry, (b) asymmetry

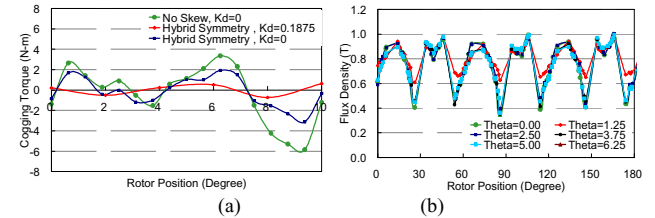


Fig. 6. (a) Cogging torque comparison, (b) air-gap flux density for non-skewed and hybrid symmetrical skew ($\theta = 0$ means non-skewed)

REFERENCES

- [1] Y. Chen, P. Pillay and A. Khan, “PM wind generator topologies,” *IEEE Trans. Indus. Appl.*, vol. 41, no. 6, pp. 1619 – 1626, 2005.
- [2] M. Aydin, Q. Ronghai and T. A. Lipo, “Cogging torque minimization technique for multiple-rotor, axial-flux, surface-mounted-PM motors: alternating magnet pole-arcs in facing rotors,” *IEEE Industry Applications Society Annual Meeting*, vol. 1, pp.555-561, Oct. 2003.
- [3] A. Letelier, J. A. Tapia, R. Wallace and A. Valenzuela, “Cogging torque reduction in an axial flux PM machine via stator slot displacement and skewing,” *IEEE Trans. Indus. Appl.*, vol. 43, no. 3, 2007.
- [4] D. A. Gonzalez, J. A. Tapia and A. L. Bettancourt, “Design consideration to reduce cogging torque in axial flux permanent-magnet machines,” *IEEE Trans. on Magn.*, vol. 43, no. 8, pp.3435-3440, 2007.
- [5] T. F. Chan and L. L. Lai, “An axial-flux permanent-magnet synchronous generator for a direct-coupled wind-turbine system,” *IEEE Trans. Energy Conv.*, vol. 22, no. 1, 2007.
- [6] E. Muljadi, C. P. Butterfield, and Y.-H. Wan, “Axial-flux modular permanent-magnet generator with a toroidal winding for wind-turbine applications,” *IEEE Trans. Indus. Appl.*, vol. 35, no. 4, 1999.
- [7] Jack F Gieras, Rong-Jie Wang and Maarten J. Kamper, *Axial Flux Permanent Magnet Brushless Machines*, Kluwer Academic Publishers, London, 2004.

Comparison of Magnetic Characteristics according to Stator Core Composition in Transverse Flux Rotary Machine

Ji-Young Lee¹, Ji-Won Kim¹, Byung-Chul Woo¹, Sang-Ho Lee², and Jung-Pyo Hong²

¹Korea Electrotechnology Research Institute, Changwon, Gyeongnam, 641-120, Korea

²Department of Automotive Engineering, Hanyang University, Seoul, 133-791, Korea

jylee@keri.re.kr, jwkim@keri.re.kr, bcwoo@keri.re.kr, sh80@hanyang.ac.kr, and hongjp@hanyang.ac.kr

Abstract— This paper presents a comparison of magnetic characteristics according to stator core composition in transverse flux rotary machine (TFRM) in order to have high power density and reduce core losses. For one rotor, three types of stators are constructed depending on composition of soft magnetic composite core and silicon steel lamination core. The flux linkage, electromotive force, torque, and core losses of the three analysis models for the three stators, are calculated by 3- dimensional finite element analysis.

I. INTRODUCTION

Soft magnetic composite (SMC) has recently been developed as an alternative magnetic material, which can be utilized to reduce the iron losses in electric machine. Moreover SMC give a lot of degree of freedom for design of electric machines where the magnetic flux has to flow in the 3- dimension in the magnetic parts. However, SMC has less attractive magnetic properties than silicon steels. Because SMC is made from a mixture of ferromagnetic material and electrically insulating material, they have low saturation flux densities and permeability due to fact that there are air gaps between the iron particles. Moreover the shaping process for SMC's induces strain and stress in the particles. These can only be partially removed by a stress annealing process, since the electrically insulating material cannot withstand the temperatures needed for complete annealing. That limitation increase hysteresis losses considerably [1]-[2].

With silicon steel, magnetic circuits are established by stacking magnetic sheet. In these magnetic circuits, the magnetic flux has to flow in directions parallel to sheet steel's surface. This kind of material has very good magnetic properties but the anisotropy of laminated electrical steel and constraints due to their manufacturing impose limits on the geometries of the magnetic circuits possible [2].

This paper attempts to find a good composition with these two representative materials, SMC and silicon steel, in order to have high power density and reduce core losses in the design process of transverse flux rotary machine (TFRM) with 3- dimensional magnetic flux paths. Three analysis models are considered depending on the composition. In the analysis models, rotor is identical and stator has three types which are made by only SMC, by only silicon steel, and by both SMC and silicon steel. The conditions of the three analysis models are the same except of stator core materials, and the electromagnetic parameters for each model are computed by 3-dimensional finite element analysis (FEA).

Flux linkage, electromotive force (EMF), and torque are obtained by computation results of the time-domain magnetic fields in 3-dimension. And the core losses are calculated with both the magnetic computation results and core loss sample data instead of experimental equations [3]. In the case of the silicon steel, if the material class is fixed core thickness is the only variable of core samples' configuration. In the case of SMC core, however, the three dimensions, which are width (thickness), height, and area of the cross section, can be the variables of core samples' configuration. Therefore core losses of lots of samples are measured, which are made depending on variation of dimensions of cross section area.

The theoretical results are compared with experiments on a prototype machine with SMC stator core. This comparison gives reliance of analysis results and a comparison of magnetic characteristics in the three analysis models.

II. ANALYSIS MODELS

Fig. 1 shows a conceptual configuration of one phase in prototype permanent magnet (PM) excited TFRM and the magnetic flux path by current excitation. A brief specification of the prototype including magnetic material information is listed in Table 1.

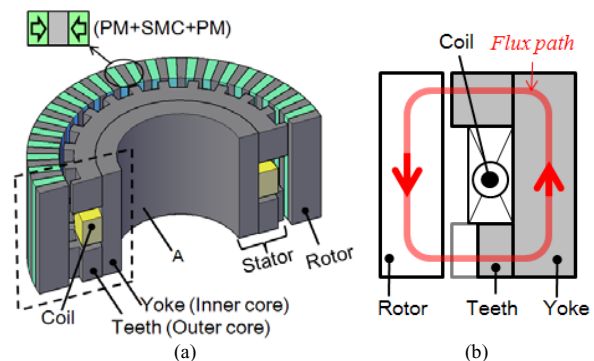


Fig.1. Conceptual drawing of one phase in a TFRM; (a) configuration of a TFRM, and (b) flux path on the cross section of A

Table 1. Specifications of a prototype TFRM

Stator	Material	Somaloy 550 (SMC core)
	No. of Phase	2 phases
	No. of turns	135 turn /phase
	Rated current	4.6 Arms/phase
Rotor	Material	Somaloy 550 + Ferrite PM (Br=0.4T)
	No. of pole	PM=64, SMC core=64 (per phase)

The rotor consists of PMs and SMC cores, which are arranged in circumferential direction and the PMs are magnetized as shown in Fig. 1 (a) to concentrate the magnetic flux to the rotor core. The one phase stator consists of a coil and three pieces of cores which are a pair of outer core and one inner core - the inner and outer sections are a yoke and teeth, respectively. The outer teeth core is divided into upper and lower parts, and the lower teeth are shifted by a half pole-pitch with respect to upper teeth to reduce torque ripple and make high power density.

According to make the inner and outer cores with what kind of materials, the number of analysis models become three as shown in Fig. 2. The models are named as SM and LM as shown in Fig. 2 (a) and (b) if the materials of stator cores are SMC and silicon steel, respectively. If the material of inner and outer cores are SMC and silicon steel respectively, the model are named as SLM as shown in Fig. 2 (c).

For construction, model SM does not need to consider the 3-dimensional flux path as shown in Fig. 1 (b); however the model LM and SLM should be considered the stacking direction. In the analysis model, the lamination direction is considered.

III. MAGNETIC CHARACTERISTICS

3-dimensional magnetic field FEA is conducted to calculate the electromagnetic parameters and core losses of the three models.

The b-h curves of core materials and core loss sample data are shown in Fig. 3. Fig. 3 (b) is SMC core losses according to variation of frequency and peak magnetic flux density by the Epstein test method, and these data are an example among measured data of 13 kinds of samples depending on cross section area dimensions.

Flux linkage, EMF, torque, and core losses of the three analysis models are obtained by computation results of the time-domain magnetic fields at rated current. The experiments are performed for prototype, SM model. Analytical and experimental EMF and torque are compared as shown in Fig. 4 to show reliability of analysis results and a comparison of magnetic characteristics in the three analysis models.

The analysis results and comparisons of magnetic characteristics between three models will be presented in extended paper.

IV. REFERENCES

- [1] Gene Shane Liew, Nesimi.Etrugrul, Wen Liang Soong, and John Gayler, "An Investigation of Advanced Magnetic Materials for Axial Field Brushless Permanent Magnet Motor Drives for Automotive Applications," *IEEE Power Electronics Specialists Conference*, pp.1-7, June, 2006
- [2] Patrick Lemieux, O.Jude Delma, Maxime R.Dubois, and Roderick Guthrie, "Soft Magnetic Composite with Lamellar Particles Application to the Clawpole Transverse Flux Machine with Hybrid Stator," *Proceeding of the 2008 International Conference on Electrical Machines*, Paper ID 909, 2008
- [3] Ji-Young Lee, Ji-Won Kim, Seung-Ryul Moon, Jung-Hwan Chang, Shi-Uk Chung, Do-Hyun Kang, and Jung-Pyo Hong, "Dynamic Characteristic Analysis Considering Core Losses in Transverse Flux Linear Machine with Solid Cores," *IEEE Trans. on Magnetics*, Vol. 45, No. 3, pp. 1776-1779, March 2009

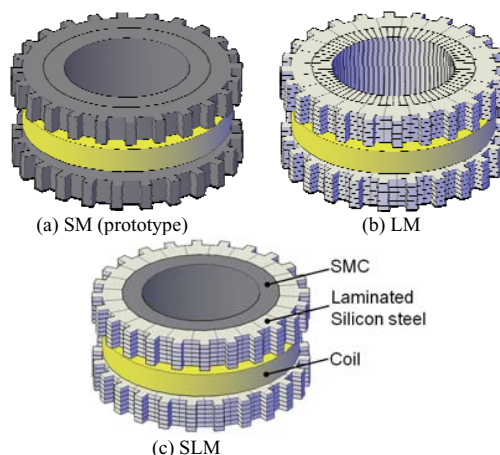
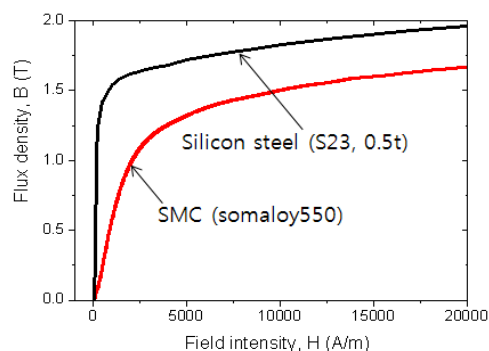
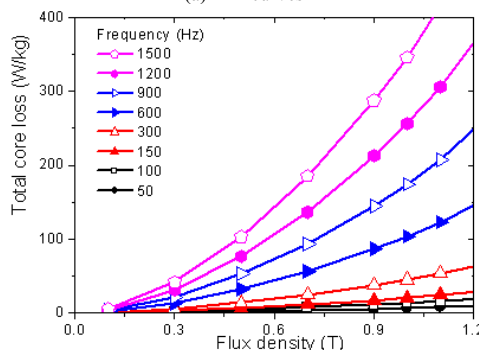


Fig.2. Conceptual drawing for one phase stator of three analysis models



(a) B-H curves



(b) core losses of SMC core sample (6.7X6.7mm²)

Fig.3. Magnetic characteristics of core materials

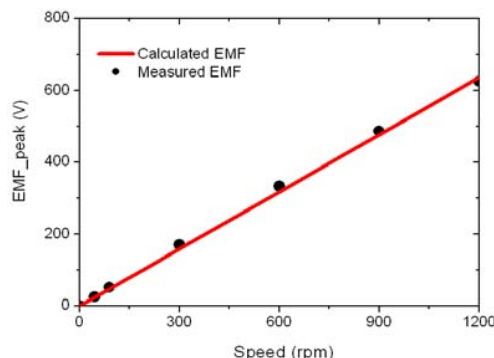


Fig.4. Comparison of calculated and measured EMF in model

Design of the Cage-bars for Single Phase LSPMSM considering the Starting Torque and Magnetic Saturation

Seung Joo Kim, Won Ho Kim, Kwang Soo Kim, Jong Bin Im, and Ju Lee, *Senior Member, IEEE*
 Dept. of Electrical Engineering, Hanyang University
 17 Haengdang-dong, Seongdong-gu, Seoul, 133-791, South Korea
 w3ksj@hanmail.net

Abstract— This paper presents the optimal design method of cage-bars in a single-phase line-start permanent magnet synchronous motor (LSPMSM) considering the starting torque and magnetic saturation. This method consists of two procedures. First, the basic design of cage-bars is made by analytic method of an induction motor. In this case, the equivalent magnetic circuit method is used but this method cannot consider nonlinear characteristic as magnetic saturation and leakage flux. Second, for considering the nonlinear characteristics, the optimal design of cage-bars is performed by the FEM and the response surface method (RSM). To validate the proposed method, the prototype motor is manufactured and the simulation results are verified by experiment.

I. INTRODUCTION

The line-start permanent-magnet synchronous motor (LSPMSM) is a hybrid PM/re reluctance motor that has high-efficiency alternative to the induction motor [1].

In general, the stator with winding and air-gap volume (D^2L) in LSPMSM is the same as conventional single-phase induction motor for a wide use. Therefore, the design parameters of the LSPMSM are restricted to the rotor such as magnets, barriers and cage-bars. Among the design parameters, the shape of cage-bars is very important parameter because it related to the torque in stator state and the magnetic flux path in steady state. But conventional researches of LSPMSM deal with only design of magnets and barriers in rotor.

In this paper, the optimal design method of cage-bars is proposed in the LSPMSM. This method consists of the two procedures. First, the basic design of cage-bars is made by analytic method of an induction motor [2]. In this case, the equivalent magnetic circuit method is used but this method cannot consider nonlinear characteristic as magnetic saturation and leakage flux. Second, for considering the nonlinear characteristics, the optimal design of cage-bars is performed by the finite element method (FEM) and the response surface method (RSM). To validate the proposed method, the prototype motor is manufactured and the simulation results are compared with the experimental results.

II. PROCEDURE FOR OPTIMAL DESIGN OF LSPMSM

The rotor design process of LSPMSM is shown in Fig. 1. First, using the widely accepted D^2L of single-phase induction motor, the outside diameter of rotor can be determined. Next, the basic cage-bars design to maximize the starting torque is performed. It gives a full explanation in chapter III. After the basic cage-bars design is determined, the shape and position of permanent magnet are determined. The position of

permanent magnet is determined as close as possible to the cage-bar to maximize magnetic flux density of air-gap. The size of permanent magnet is determined by considering the demagnetization and the magnetic flux density of air-gap at rated torque. And the barrier is designed to minimize leakage of magnetic flux. The previous design process is very rough, but the design of cage-bars doesn't have big problems. Because the optimal designed cage-bars can be performed by controlling flux of permanent magnet at steady state, the basis design can be compensated by blocking the leakage flux. Finally, the cage-bar optimal design is explained in chapter IV in detail.

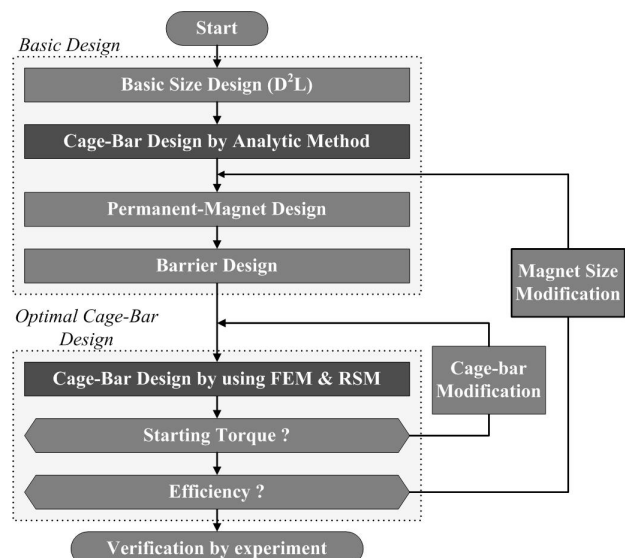


Fig. 1. Flowchart of proposed design procedure of LSPMSM

III. BASIC DESIGN OF CAGE-BARS BY ANALYTIC METHOD

Based on past experience, slot combination between the stator and rotor numbers of slots is chose to reduce parasitic torque, additional losses, radial forces, noise, and vibration.

Single phase LSPMSM has same starting performance of single phase induction motor due to using rotor cage at starting. So, through improving starting torque of single phase induction motor, we try to improve starting torque of LSPMSM. The starting torque of single phase induction motor can be calculated as follows:

$$T_s = \frac{2p_1}{\omega_1} I_s R_{rm} \quad (1)$$

$$Z_s = \sqrt{(R_{sm} + R_{rm})^2 + (X_{sm} + X_{rm})^2} \quad (2)$$

The method that starting current is increased is undesirable for high starting torque. Therefore, rotor cage resistance is very important factor for high starting torque.

Rotor cage resistance is to subdivide it into two part, rotor bar resistance and end ring resistance. We can write the following resistance equations.

The equation of equivalent cage resistance is:

$$R_{be} = R_b K_R + \frac{R_{ring}}{2 \sin^2(\pi p_1 / N_r)} \quad (3)$$

Where K_R is skin effect resistance coefficient for bar, N_r is number of rotor slot. The skin effects increase with the slot height for slip frequency.

Notice that equivalent cage resistance has to be reduced to the stator. Therefore rotor cage resistance can be calculated as follows:

$$R_{rm} = R_{be} \frac{12 K_{wm}^2 W_m^2}{N_r} \quad (4)$$

In this study, we design only rotor of LSPMSM using stator of single phase induction motor. Therefore we consider only equivalent cage resistance, we can write the following equivalent cage resistance equations again.

$$R_{be} = \left[\rho_{Al} \frac{l_b h_r}{\left(\frac{d_1 + d_2}{2}\right) h_r + \frac{\pi d_1^2}{4}} \sqrt{\omega_l \mu_0} + \frac{\rho_{Al} l_{ring}}{2 \sin\left(\frac{\pi p_1}{N_r}\right) A_{ring}} \right] \quad (5)$$

In this equation, assume the change of end ring is little, so the adjustable variables are slot upper width, slot lower width and slot height. These variables are adjusted for high starting torque motor.

IV. OPTIMAL DESIGN OF CAGE-BARS BY NUMERICAL METHOD AND RSM

The basic design of rotor is only considered to the starting torque at starting state. Because the magnetic flux path is adjusted by the barrier as well as the cage bar, we cannot consider the magnetic saturation and leakage flux using analytic method. So, the optimal design is necessary. Fig. 2 shows flux density by using FEM analysis. We choose the points which can be doubted the saturation region or the leakage flux region by using FEM analysis. And the parameter design of the cage-bars is tried not to exceed the limited value of flux density at this region. Finally, the optimal value is obtained by optimal design using FEM analysis and RSM.

Fig. 3 shows the starting characteristic of the conventional induction motor and the proposed LSPMSM. Although the LSPMSM has the breaking torque due to permanent magnet, the induction motor and the LSPMSM have similar starting time due to the designed cage-bars.

V. EXPERIMENT

The LSPMSM with the proposed design method is manufactured as shown in Fig. 4(a). In order to verify the validity of the optimal design method, the experiment results of the rating torque are compared with the results of the simulation as shown in Fig. 4(b). From the results, it is evident

that the FEM analysis gives good agreement with the experimental one.

VI. CONCLUSION

In this paper, the optimal design method of cage-bars considering starting torque and magnetic saturation by using FEM and RSM is proposed in LSPMSM. To verify the validation of proposed design method, the results of simulation are compared with characteristics of proto type.

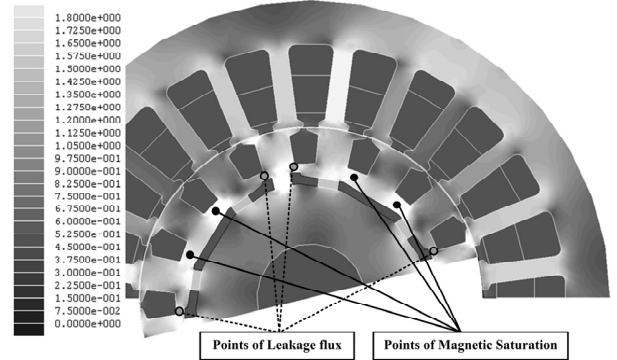


Fig. 2. Flux density plot with points of leakage flux and the magnetic saturation

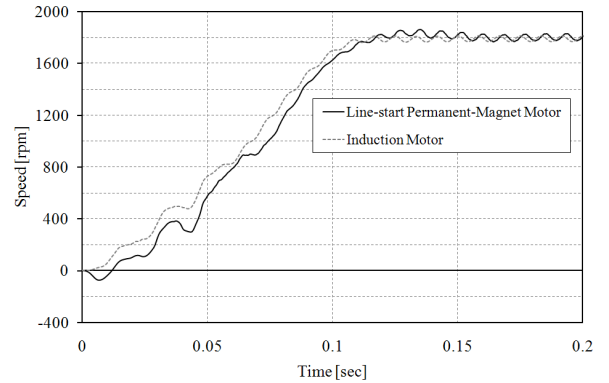
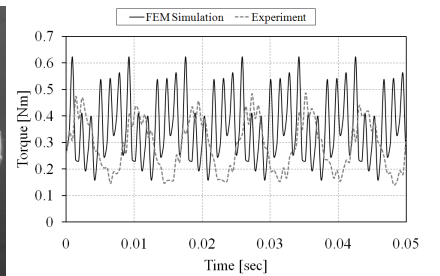


Fig. 3. Starting characteristics comparison of LSPMSM with Induction Motor



(a) Prototype of LSPMSM (b) Torque comparison of Experiment with FEM
Fig. 4. Experiment results

VII. REFERENCES

- [1] Andrew M. Knight and Catherine I. McClay, "The Design of High-Efficiency Line-Start Motors," *IEEE Trans. Ind. Applicat.*, vol. 36, no. 6, pp.1555-1562, November/December 2000.
- [2] Kazumi Kurihara and M.Azizur Rahman, "High Efficiency Line-Start Interior Permanent Magnet Synchronous Motors," *IEEE Trans. Ind. Applicat.*, vol. 40, no.3, pp.789-796, May/June, 2004.

Analysis of Very Fast Transient Overvoltages and Electric Field Stresses in Conventional Tesla Transformers Using FDTD Method

E. Agheb, E. Hashemi, K. Niayesh, A. Mousavi and M. Faridi
School of Electrical and Computer Engineering, University of Tehran
Azad University of Khodabandeh
e.agheb@gmail.com

Abstract — Very fast transient overvoltages (VFTOs) in the secondary winding of air-cored Tesla transformers have been surveyed using a comprehensive model based on Multi-conductor Transmission Lines (MTLs) theory. The governing equations have been solved by Finite Difference Time Domain (FDTD) method. Voltage distribution in two different structures of Tesla transformers, tapered single layer and multi-layer secondary windings has been investigated. The experimentally validated simulation results show considerable fluctuations and overvoltages in some sections of the transformer winding that should be considered in insulation coordination.

I. INTRODUCTION

In pulsed power generators, the amplitude of output pulse of a Tesla transformer is even higher than several hundred kilovolts. The induced traveling waves in the secondary windings of such transformers include high-order harmonics that can bring about internal resonance and cause exceedingly uneven turn to ground and inter-turn voltage distributions. Since this unevenness can cause inter-turn insulation failure or partial discharge, it is essential to investigate the voltage distribution in the secondary winding of Tesla transformers. Mainly there are three models to study the VFTOs in the windings of transformers: Lumped circuit model [1], Multi-conductor Transmission-Lines theory [2] and full-wave solution [3].

An appropriate simulation model is the most fundamental condition for the research of the voltage distribution in transformer windings. Since the frequency of VFTO is very high, the lumped parameter model could not satisfy the computation request and also the full-wave solution is hard to obtain due to the complexity of model and lots of degrees of freedom. Considering the fact that the MTL theory is very accurate in case of pulses with short rise/fall times and where the coils are long compared to the wavelength, in the current study, this model is utilized for very fast transient simulations.

To study the voltage distribution in transformer windings under VFTO, a model for transformer windings has been developed based on MTLs theory. A common way of determining the time-domain response of a MTL is the use of finite difference-time-domain method.

In this paper, based on FDTD method, distribution of voltage in the secondary winding of two conventional types of Tesla transformers, tapered single layer and multi-layer, is studied and turn to ground, inter-turn and inter-layer overvoltages are evaluated. Furthermore, numerical results are

compared with measurements. Simulation and measuring results obviously demonstrate the fluctuation and oscillation of the voltage in different turns which would result in insulation failure.

II. THE WINDING MODEL

To have a proper evaluation of time domain response, the electrical parameters should be assessed precisely. For this purpose, these parameters are evaluated via Finite Element Method (FEM). Moreover, the frequency dependency of the parameters is considered in this method. The recursion relations of voltage and current are as follows:

$$V_k^{n+1} = V_k^n - \frac{\Delta t}{\Delta z} C^{-1} (I_k^{n+\frac{1}{2}} - I_{k-1}^{n+\frac{1}{2}}). \quad (1)$$

$$\begin{aligned} I_k^{n+\frac{1}{2}} = & F^{-1} \left(I \frac{\Delta z}{\Delta t} - A \frac{\Delta z}{2} + B \frac{\Delta z}{\sqrt{\pi \Delta t}} Z_0(0) \right) I_k^{n+\frac{1}{2}} \\ & - F^{-1} B \frac{\Delta z}{\sqrt{\pi \Delta t}} \sum_{m=1}^n (I_k^{n+\frac{1}{2}-m} - I_{k-1}^{n+\frac{1}{2}-m}) Z_0(m) \\ & - F^{-1} \left[(V_{k+1}^{n+1} - V_k^{n+1}) + \frac{\Delta z}{2} (V_{Fk}^{n+\frac{1}{2}} - V_{Fk}^{n+\frac{1}{2}}) \right] \end{aligned} \quad (2)$$

Two different structures of Tesla transformers are being studied, tapered single layer and multi-layer which are illustrated in Fig. 1.

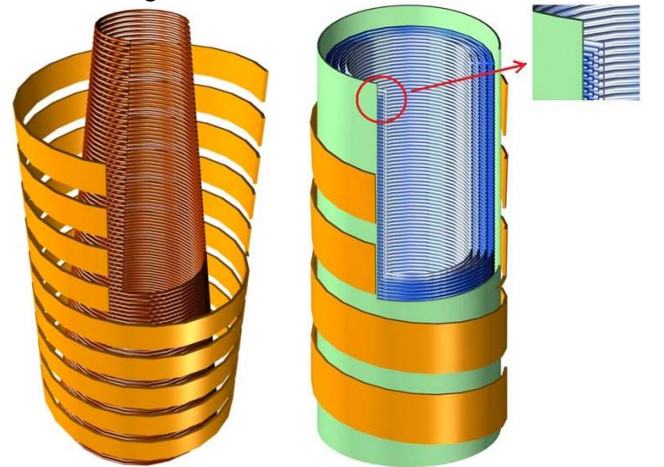


Fig. 1. Two conventional structures, single layer (left) and multi-layer (right)

III. RESULTS

Voltage at different turns of the high voltage winding is shown in fig. 2 for a transformer with single layer winding structure. As shown in this figure there is high magnitude transient over voltages across the terminal turns (see fig. 2f). Similar pattern has been achieved for two layer structure and is depicted in Fig. 3.

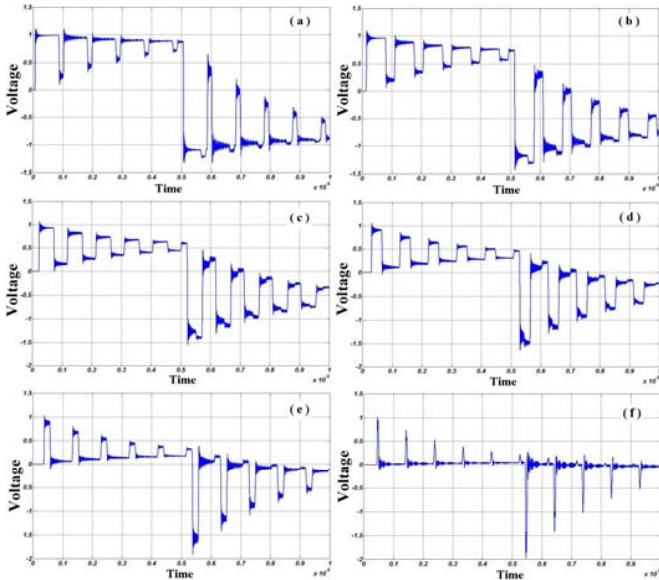


Fig. 2. Voltage at different conductors in a single layer winding if input is a 100 kHz pulse at conductors: a) 15th, b) 30th, c) 45th, d) 60th, e) 75th and f) 95th

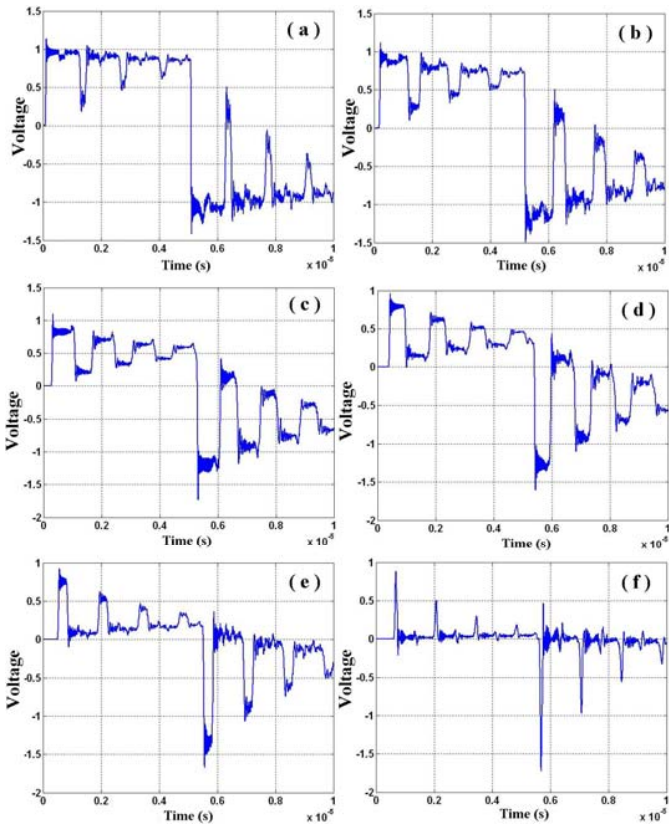


Fig. 3. Voltage at different conductors in a two layer winding if input is a 100 kHz pulse at conductors: a) 15th, b) 30th, c) 45th, d) 60th, e) 75th and f) 95th

Maximum inter-turn overvoltage plays an important role in insulation design of transformer windings. As depicted in Fig. 4 maximum overvoltage happens in middle part of the winding where winding direction inverses (red circle in fig. 1). It must be noted that this voltage difference should be zero under steady state condition, but in transient condition the insulation material is subjected to very high stresses.

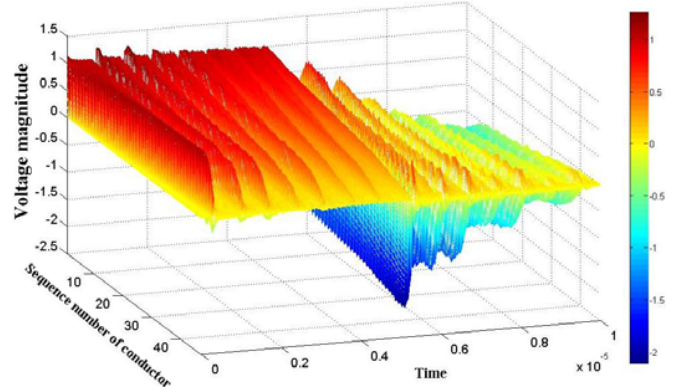


Fig. 4. Voltage difference between two layers

According to calculated overvoltages, electric field stresses have been analyzed by FEM method in discussed structures. These transient overvoltages have been investigated by using a test setup including windings similar to the simulation ones. Measurements are in good agreement with the simulation results. The measured values clearly show that the highest overvoltages occur at head end of winding in case of single layer and at the middle of the winding in the case of two layer winding structure, as predicted by simulations.

IV. CONCLUSION

The study of VFTO in an air-cored Tesla transformer’s winding is important for insulation co-ordination. It is especially important to determine the position of maximum inter-turn overvoltage, which depends on the configuration of the winding and wave style. In this paper, studying voltage distribution in the secondary windings of conventional Tesla transformers based on FDTD method, the maximum overvoltages in these windings have been simulated. Calculation of the electric field stresses demonstrates the risk of insulation failures in different parts of the high voltage winding depending on its structure.

V. REFERENCES

- [1] W. Zanji, “Modeling for simulating very fast transient in transformer windings,” in *Proc. CSEE*, vol. 16, China, Sep. 1996, pp. 299–305.
- [2] M. Popov, L. van der Sluis, G. C. Paap, and H. De Herdt, “Computation of very fast transient overvoltages in transformer windings,” *IEEE Trans. Power Del.*, vol. 18, no. 4, pp. 1268–1274, Oct. 2003.
- [3] H. Yamashita, V. Cingoski, E. Nakamae, A. Namera, and H. Kitamura, “Design improvements on graded insulation of power transformers using transient electric field analysis and visualization technique,” *IEEE Trans. Energy Convers.*, vol. 14, no. 4, pp. 1379–1384, Dec. 1999.
- [4] E. Agheb, A. A. Shayegani Akmal, A. Hayati, J. Jadidian and E. Hashemi, “Estimation of Very Fast Transient Voltage Distribution in Air-Cored Pulsed Transformer Winding Based on FDTD Method”, *Journal of Plasma and Fusion Research Series*, to be published.
- [5] C. R. Paul, *Analysis of Multiconductor Transmission Lines*, 2nd ed., Wiley, 1994, pp. 295-329.

Computational Analysis of Fringing Fields and Forces in the Cylindrical Coordinate System

B. L. J. Gysen, K. J. Meessen, J. J. H. Paulides and E. A. Lomonova

Electromechanics and Power Electronics Group, Department of Electrical Engineering,
Eindhoven University of Technology
P.O. Box 513, 5600MB, Eindhoven, The Netherlands
Email: b.l.j.gysen@tue.nl

Abstract—This paper discusses the calculation of fringing fields and forces which exist in slotted tubular permanent magnet actuators. The magnetic field distribution will be calculated in a semi-analytical manner and with two-dimensional finite element analysis in the cylindrical coordinate system. The semi-analytical model is based on Fourier analysis to describe various magnetization profiles and the resulting magnetic field distribution. A periodic model with a single semi-closed slot geometry will be considered for both models which reduces the computational time. These modeling techniques allow for accurate calculation of the fringing fields and the resulting cogging force.

Index Terms—Actuator, cylindrical, permanent magnet, slotting effect.

I. INTRODUCTION

When tubular permanent actuators with a high force density are required, a slotted armature is more preferred since the effective airgap is reduced. However, the introduction of the slots results in a distortion of the magnetic field due to the magnets, giving fringing fields at the tooth tips. This field distortion leads to a force ripple which is generally referred to as a cogging force. It is beneficial to predict the resulting force ripples for various slot-pole combination in a fast way in order to choose the optimal slot-pole combination regarding the application. The effect of slotting on the magnetic field distribution is extensively investigated in the literature, providing analytical and numerical tools for predicting the resulting cogging forces. Recently, Liu [1], presented an exact semi-analytical solution of the airgap flux density for slotted linear machines with an extension to rotary machines. Based upon his work, this paper provides the exact semi-analytical solution for the cylindrical coordinate system including the more complicated semi-closed slot geometry as shown in Fig. 2. The slotting effect will be described for a single slot traveling across one pole-pair. The cogging force due to a single slot can be calculated and the total solution can be obtained by synthesis of the single slot solution, [2]. From the semi-analytical field solution, the cogging force can be calculated by means of the Maxwell-Stress method. Next to that, a 2D finite element model will be considered for calculation of the slotting effect and the related cogging force. This force component will be calculated by means of the virtual work method. Comparisons between the two models will be made in terms of accuracy and computational time.

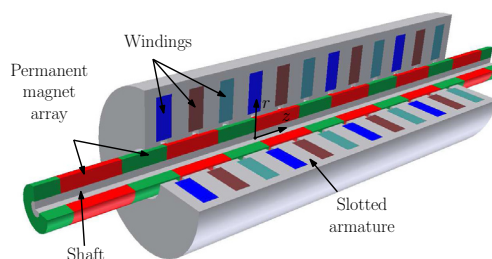


Fig. 1. A three phase slotted tubular permanent magnet actuator.

II. THE SEMI-ANALYTICAL MODEL

The tubular structure inhibits angular symmetry and hence a 2D-cylindrical coordinate system, (r, z) , can be considered. The iron is assumed infinitely permeable, hence saturation is not included. The magnets are modeled having a linear second quadrant characteristic. Although only a single slot is considered, it should be noted that it is possible to consider the total solution, including all slots in once, however the complexity increases drastically and numerical instability becomes dominant, these influences will be shown in the final paper. Furthermore, three different magnetization profiles (radial, quasi Halbach and axial) will be considered since the boundary value problem is different for each of them. For example, when axial magnetization is considered, five different regions, need to be distinguished, the shaft (I), the permanent magnet (II), the airgap (III), the slot opening (IV) and the slot (V) region, respectively, see Fig. 2. This boundary value problem is solved by considering the magneto static Maxwell equations, which can be reduced to a Poisson equation written in terms of the magnetic vector potential \vec{A} as $\vec{B} = \nabla \times \vec{A}$,

$$\nabla^2 \vec{A} = -\mu_0 \nabla \times \vec{M}, \quad (1)$$

where, $\vec{M} = 0$ for regions I, III, IV and V. Fourier analysis will be used to describe the magnetization vectors and consequently, the solution for the radial and axial flux density distribution will be written as a Fourier series which will be given in the final paper. Note that this semi-analytical model is an exact solution for the magneto static Maxwell equations with the limitation that only a finite number of harmonics can be included in the numerical implementation. This gives inaccuracies of the magnetic field solution at discontinuous

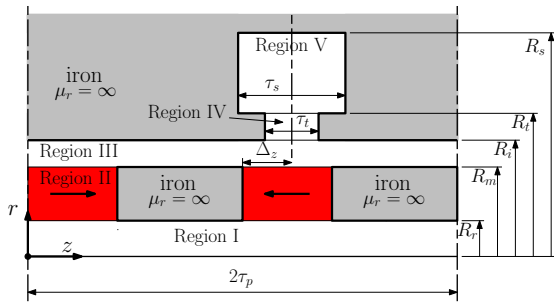


Fig. 2. The boundary value problem with division in regions for the axial magnetized topology.

points in the structure, for example at the boundary of the magnets or at the corner points of the slotted armature. However, for calculation of the cogging force, the Maxwell Stress method is used at the center of the airgap where a more accurate field solution can be obtained since the harmonic content is lower here.

III. THE FINITE ELEMENT MODEL

In order to be able to minimize the slotting effect by means of finite element analysis, a model is preferred which only considers the slotting effect without the effect due to the finite stator length (end effect). In [3], this is obtained by converting the tubular actuator to a rotary actuator which allows for periodic modeling in finite element packages. An alternative way is to consider only the cogging force due to a single slot and obtaining the total solution by means of synthesis of the single slot solution for the proper pole-slot combination, [2]. This allows one to focus on the single slot cogging force calculation which significantly reduces the model and allowing for implementation of the finite element model for only one period as done for the semi-analytical model. Periodic boundary conditions are applied to the axis symmetric model at 0 and $z = 2\tau_p$ and triangular mesh elements are used where the airgap consists of two layers of mesh elements in the airgap. In order to make a fair comparison with the semi-analytical model, the tangential component of the magnetic field strength is set to zero at the soft-magnetic boundary of the slotted stator.

IV. COMPARISON

The radial and axial component of the flux density in the center of the airgap are shown in Fig. 3 for the semi-analytical and finite element model. A close up of the slotting effect is shown next to the figure. It can be observed that excellent agreement is obtained which is as expected since the linear 2D FE model has the same assumptions as the semi-analytical model. For the finite element modeling, the virtual work method is applied to calculate the cogging force which is compared with the semi-analytical solution in Fig. 4 for radial, quasi Halbach and axial magnetization where excellent agreement is obtained. The final paper will give a more detailed discussion about numerical accuracy and stability of the analytical solution. The semi-analytical calculation is around 40 times faster than a finite element calculation.

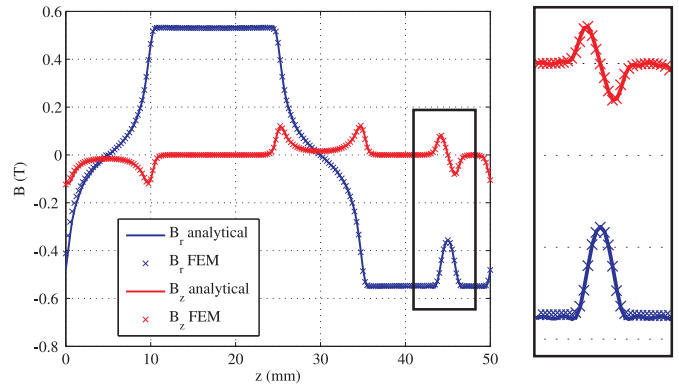


Fig. 3. Magnetic field solution of the axial magnetized topology in the center of the airgap, $\Delta z = 20$ mm.

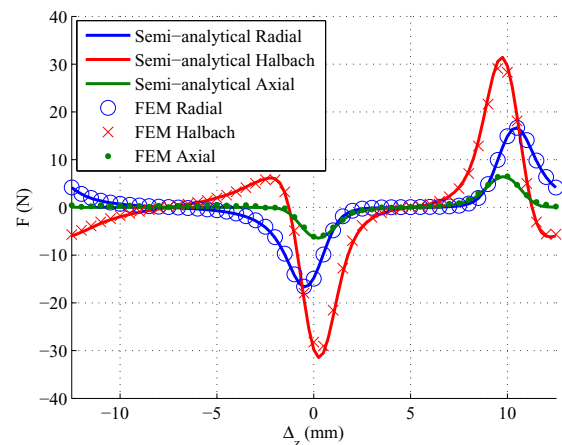


Fig. 4. Cogging force calculation with the semi-analytical and finite element model.

V. CONCLUSION

This paper compares computational methods for calculation of the fringing fields and resulting cogging forces due to the slotted armature in tubular permanent magnet actuators. The semi-analytical and the finite element method are compared in terms of accuracy and computational time. The solution is given for a single slot traveling across one pole-pair where besides quasi Halbach magnetization, radial and axial magnetization will be considered in the final paper. Excellent agreement between the semi-analytical and finite element model is obtained for the magnetic field distribution and cogging force calculation.

REFERENCES

- [1] Z. J. Liu and J. T. Li, "Analytical solution of air-gap field in permanent-magnet motors taking into account the effect of pole transition over slots," *IEEE Transactions on Magnetics*, vol. 43, no. 10, pp. 3872–3883, October 2007.
- [2] Z. Q. Zhu, S. Ruangsinchaiwanich, and D. Howe, "Synthesis of cogging torque in permanent magnet machines by superposition," *Second International Conference on Power Electronics, Machines and Drives*, vol. 2, no. 3, pp. 828–833, March/April 2004.
- [3] J. L. G. Janssen, J. J. H. Paulides, E. A. Lomonova, and A. J. A. Vandenput, "Cogging force reduction in tubular permanent magnet actuators," *IEEE Int. Electric Machines and Drives Conference (IEMDC'07)*, vol. 1, pp. 266–271, May 2007.

Field Calculation in the Innovative Transformers with Amorphous Modular Cores

B. Tomczuk*, K. Zakrzewski** and D. Koterak*

**Tech. Univ. of Lodz, Inst. of Mechatronics and Information Systems, 90-924 Lodz, Poland,

*Opole Univ. of Technology, Dept. of Industrial Electr. Eng., ul. Luboszycka 7, 45-036, Opole, Poland

b.tomczuk@po.opole.pl, d.koterak@po.opole.pl

Abstract — The magnetic fields in 1-phase and 3-phase transformers with amorphous modular cores have been analyzed. Scalar magnetic potentials have been implemented for 3D Finite Element (FE) field calculation. Due to inability to simulate each thin amorphous layer, we introduced supplementary permeabilities of the core along the main directions of magnetization. Calculated fluxes in the cores were tested on the prototype.

I. INTRODUCTION

Usually to build the transformer core thin sheets cold rolled, grain-oriented silicon steel are used [8]. The amorphous ferromagnetic alloys were manufactured at the end of the fifties [5]. The right way to manufacture them limits the ribbon thickness from 30 to 50 μm [3]. Due to this, and the material structure, their core losses are several times lower than those in silicon steel [1], [4], and [6].

II. DESCRIPTION OF THE ANALYSED OBJECT

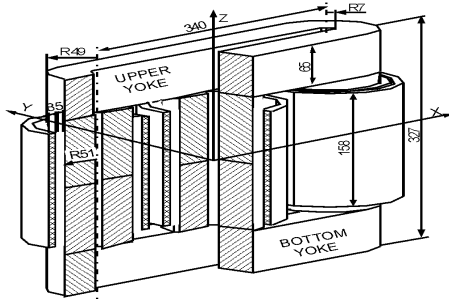


Fig. 1. Transformer with modular amorphous core

The outline of the 3-phase transformer with amorphous modular core is given in Fig. 1, where coordinate system and main dimensions are depicted. Each column consists of two hollow cylinders (toroids). In both prototypes the primary and secondary windings are cylindrical. The primary (internal) ones, which are close to the columns, are divided into two sections: with $N_{11}=116$ and $N_{12}=75$ turns. The turn number of the secondary windings is $N_2=116$. Rated power of the 3-phase transformer prototype is $S=10$ kVA. The nominal currents are $I_{1N}=15.2$ A and $I_{2N}=26$ A.

III. CALCULATION MODEL

The analysed object has XZ plane of symmetry (Fig. 1). After halving the field region, only one part has been chosen for the Finite Element (FE) analysis. For the 3D calculations

we used two scalar potentials: the first one, (called total potential) ψ , and the second one (called reduced potential) ϕ [2]. Total potential is obligatory in the current free regions and satisfies the Laplace's equation

$$\nabla \cdot (\mu \nabla \psi) = 0. \quad (1)$$

In the current carrying regions, the reduced potential ϕ satisfies the elliptic equation

$$\nabla \cdot (\mu \nabla \phi) - \nabla \cdot (\mu \vec{H}_S) = 0. \quad (2)$$

The field intensity \vec{H}_S , arisen from the excited coils, can be calculated independently before the FEM solver runs.

The magnetic flux is parallel to the rolling up direction of the yokes. In each column, it is perpendicular to the direction of the magnetic strip winding. As we were not able to discretize each thin amorphous layer, we introduced supplementary permeabilities of the core along the two directions of magnetization. Thus, in the mathematical model we introduced two different $\mu(H)$ curves for legs and yokes, respectively. For the lamination layers the core losses were neglected in the field modeling.

Using the FE method, after discretization of the equations above, we obtained the difference equations set, which can be written in matrix form

$$[K] [\Phi] = [S] \quad (3)$$

Due to the $\mu(H)$ curves, the equation (3) with the matrix $[K]$, is non-linear. The known right hand side, n-dimensional vector $[S]$, is calculated including the given current excitations and boundary conditions. The vector $[\Phi]$ of the unknown nodal potentials is calculated with Newton-Raphson method [2].

Including the previous solution $[\Phi]^{(k)}$, a the new one, $[\Phi]^{(k+1)}$ is found in the iteration process [1], [2] by solving the linearized system

$$[\Phi]^{(k+1)} = [\Phi]^{(k)} - \{[J]^{(k)}\}^{-1} [R]^{(k)} \quad (4)$$

The residual vector $[R]^{(k)}$ and the Jacobean matrix $[J]^{(k)}$ in the (k) iteration are expressed below

$$[R]^{(k)} = [K]^{(k)} [\Phi]^{(k)} - [S]^{(k)} \quad (5)$$

$$[J]^{(k)} = \frac{\partial}{\partial [\Phi]^{(k)}} ([K]^{(k)} [\Phi]^{(k)} - [S]^{(k)}) \quad (6)$$

IV. CALCULATION RESULTS

We studied two configurations of the modular core transformer system at no load state. The magnetic fields, for several values of the magnetizing current were analysed in the

1-phase configuration. In Fig 2 we presented the flux density B distributions at the plane shifted by $y=1$ cm from the plane XZ (Fig. 1). The B values were excited by the magnetizing current amplitude of $I=1.41$ A. The maximal values are around the yokes and columns connections. The B values at edge points of the core are much lower. Inside the yokes, they are slightly higher than those inside the columns.

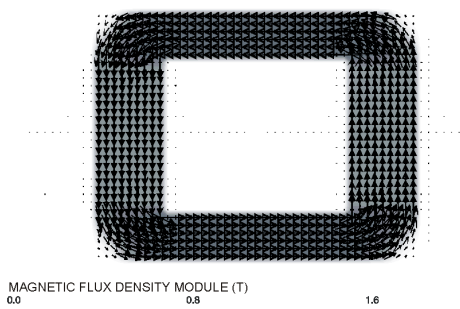


Fig. 2. B_{mod} distribution for $I=1.41$ A

Distribution of flux density modulus and the vectors \vec{B} are also presented for the 3-phase transformer with amorphous modular core (Fig 3). It concerns the current arrangement, with rms values equal to $I_B=1,27A$ and $I_A= I_C=0,705A$. Depicted map is drawn for the surface $y=1$ cm (Fig. 1). Due to the currents, the B values are relatively high in whole region of the middle column. The flux density is lower in the yokes.

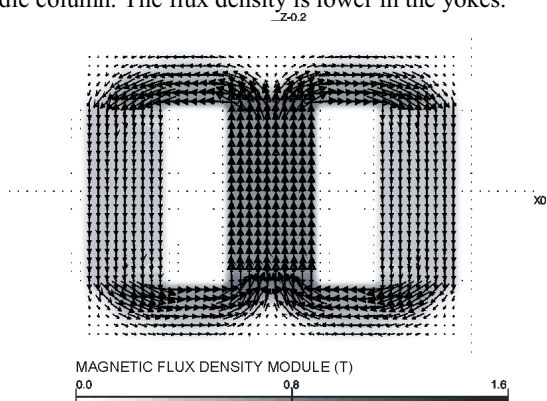


Fig. 3. B_{mod} distribution for $I_B=1.27$ A.

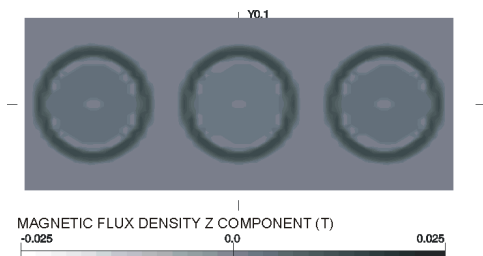


Fig. 4. B_z distribution for 3-phase transformer.

Fields in the described transformers were analyzed under short circuit state, as well. We assumed current values $I_{1N}= I_{2N}=15A$ in

the primary and secondary coils with $N=116$ turns. In Fig. 4 we presented the B_z component distribution at the XY plane.

V. MEASURED VERIFICATION OF THE CALCULATION

Magnetic flux values under the under short circuit state of the 3-phase transformer were compared with the measured ones. They were tested at the middle of each column toroids. The mean values from the three columns were compared in Fig. 5.

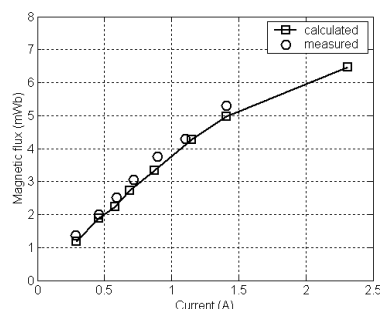


Fig. 5. The mean values of the flux in 3 transformer columns.

VI. CONCLUSIONS

The new constructions of the 1-phase and 3-phase modular transformers with amorphous cores have been studied with FEM. In 3D field calculations, magnetic anisotropy of the amorphous (Fe based) alloy was included. The different magnetization characteristics for the yokes and columns were assumed. The calculated fluxes values were confirmed experimentally. Thanks to modular technique, the described structure is convenient for assembling and repairing.

VII. REFERENCES

- [1] Kincaid D. and W. Cheney, "Numerical analysis. Mathematics of scientific computing", Third edition, Wadsworth Group, a division of Thomson Learning, 2002, pp. 63-121.
- [2] OPERA 3-D User Guide, *Vector Fields Limited*, Oxford, England, 1999, pp. 271-350.
- [3] R. B.Schwarz, T. D. Shen, U.Harms and T. Lillo "Soft ferromagnetism in amorphous and nanocrystalline alloys, *Journal of Magnetism and Magnetic Materials*, 283: 223-230, 2004
- [4] M. Schwartz Ed. " *Encyclopedia of materials, parts, and finishes*" CRC Press LLC, Boca Raton London New York Washington, D.C., 2002, pp. 4-62..
- [5] B. Tomczuk and D. Koterak, "3D field analysis of amorphous modular transformer under short circuit state", *Electrical Review*, 4: 105-108, 2007.
- [6] B. Tomczuk, K. Zakrzewski and D. Koterak "Magnetic field and short-circuit reactance calculation of the 3-phase transformer with symmetrical amorphous core" *Computer Engineering in Applied Electromagnetism*, S. Wiak, A. Krawczyk and M. Trelp (Eds),Springer, Great Britain, 2005, pp. 227-230.
- [7] K. Zakrzewski, B. Tomczuk and D. Koterak, "Simulation of forces and 3D field arising during power autotransformer fault due to electric arc in HV winding", *IEEE Trans. on Magnetics*, 38(2): 1153-1156, 2002.
- [8] K. Zakrzewski, B. Tomczuk and D. Koterak, "Amorphous modular transformers and their 3d magnetic fields calculation with FEM, *Compel The International Journal for Computation And Mathematics in Electrical and Electronic Engineering*, 28(3): 583-592, 2009.

Automated Optimization in the Design Process of a Pending Workbench

J. Albert¹, R. Banucu¹, A. Hafla², A. Huf², V. Reinauer¹, C. Scheiblich¹, and W. M. Rucker¹

¹Institute for Theory of Electrical Engineering, Universitaet Stuttgart
Pfaffenwaldring 47, 70569 Stuttgart, Germany

²Institute for Control Engineering of Machine Tools and Manufacturing Units, Universitaet Stuttgart
Seidenstraße 36, 70174 Stuttgart, Germany

jan.albert@ite.uni-stuttgart.de

Abstract— A pending workbench shall be designed, that is able to perform linear and rotational movements in four axes with high accuracy, so that different operations can be run on the work piece. The design of this workbench is supported by numerical simulations. Since the workbench's movement is free in a certain range, simulations have to be run for the high number of possible positions. When optimizing the device's layout by varying different parameters, simulations are needed for all positions in which the device shows an extreme behavior. The numerousness of simulations leads to very high efforts concerning pre- and post-processing. To reduce these efforts, a CAD software and a mesh software have been automated.

I. INTRODUCTION

Linear induction motors and servo motors can be used for accurate positioning systems. A combination of both principles can realize several degrees of freedom of motion, if the moving part is pending or mounted in a way that allows these movements. The pending part is called flotor. A similar principle was realized for a haptic device in 1999 [1]. Six degrees of freedom of motion have been realized but only with strongly limited translational movements and rotational angles.

This paper deals with the development of a workbench for the machining of small pieces.

II. THE PENDING WORKBENCH

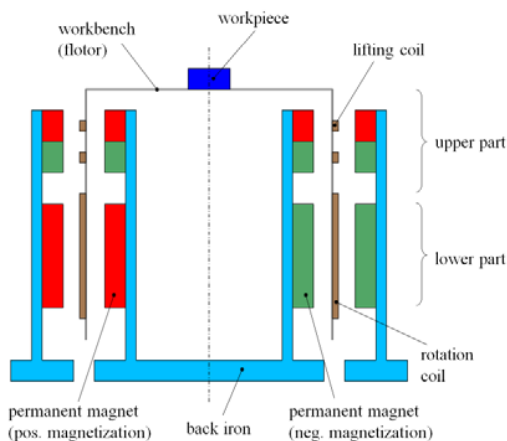


Fig. 1. Cross section through the yz-plane of the workbench device

A pending *flotor* shall carry a small workpiece and perform translational movements in three axes and rotational

movements around the z-axis. The translational movement is limited on the workpiece size. The rotation should cover a range of 360 degrees.

Fig. 1 shows a schematic view on the device. The upper part performs movements in horizontal direction and compensates torques around the x- and y-axis. The lower part performs translations in x- and y-direction and rotations around the z-axis.

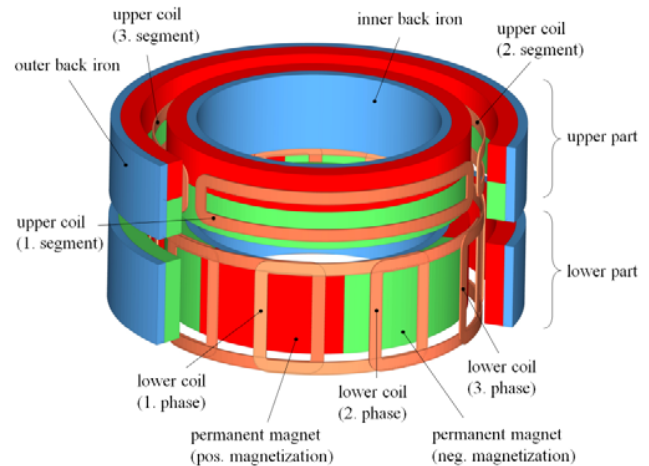


Fig. 2. Isometric view on the flotor's coils and the stator's permanent magnets

Fig. 2 shows an isometric view on the device. A design approach to realize six degrees of freedom of motion is presented in [2]. It also contains a more detailed description of how the different types of motion are realized.

III. THE NUMERICAL SIMULATION

A multitude of simulations has to be run for every design approach. Forces and torques between stator and flotor are obtained by magnetostatic computations and the application of Maxwell's stress tensor. These simulations show, if it is possible to generate forces that can compensate the process forces and carry or accelerate the flotor.

The non-linearity of the magnetic material requires an iterative algorithm, the optimization process requires a large number of computations. These efforts are reduced by the application of a volume integral equation method (VIEM) in combination with the fast multipole method (FMM). Since the air-gaps between coils and permanent magnets are large, only a small number of degrees of freedom occurs compared to a similar FEM simulation.

11. Electric Machines and Drives

A bigger problem from an economical point of view is the manpower invested in preprocessing. This paper deals with how to automate the simulation steps in the design process of the pending workbench.

A. The Optimization Process

A first design approach is developed considering mechanical requirements by means of approximation formulas. The resulting values are chosen as first step parameters of the numerical optimization process.

B. The CAD Tool

The first step in a numerical simulation is to create the geometrical data. The commercial software Rhinoceros® has been chosen, because it is easy to handle and it can be controlled by a Visual Basic Script (VBS) [3].

Many parameters can be varied, as there are geometrical properties such as diameters, or heights, the number of coils and magnetic poles as well as the flotor's position to the stator. Due to the modular design of the implemented script, further parameters can be appended.

The script delivers a CAD-file in IGES-format that can be imported by the meshing tool and a text file with geometrical data that has to be pasted into the input file of the numerical software. Some variables are returned to control the meshing software. Fig. 2 has been created with this script.

C. The Meshing Tool

As a second step, the geometrical bodies have to be divided into finite elements of an appropriate size. The IGES-file is imported by the program Hypermesh®, which creates volume meshes of the coils, magnets, and back irons and puts out a text file with the volume elements' and their respective collectors' data. Hypermesh can be automated by Tool command language (TCL) [4]. Some global parameters like the maximum element lengths are defined in the control program.

D. The Numerical Software FAMU

Our numerical software FAMU is based on the VIEM, the system matrix is reduced by the FMM. The magnetostatic problem is solved by an iterative $\mathbf{M}(\mathbf{H})$ algorithm. The required input parameters are the text file with the mesh data and a text file with control parameters containing information about the coil's and magnet's positions and geometrical shapes and a lot of other control parameters that remain the same in the majority of cases. The changing parameters are set by the control program considering the output of the CAD-tool. The software delivers a text file which contains the needed results.

E. The Control Software

The control software starts the mentioned programs according to a user-set sequence. New design approaches are evaluated by running simulations in critical positions between stator and flotor. To describe the behavior of the chosen design approach, the control software shall be extended in a way that makes it possible to create matrices \mathbf{A} for every

displacement \mathbf{r} and rotation φ which describe the relation between impressed coil currents I and the resulting forces \mathbf{F} and torques \mathbf{M} :

$$\mathbf{A}(\mathbf{r}, \varphi) \begin{pmatrix} I_1 \\ \vdots \\ I_n \end{pmatrix} = \begin{pmatrix} \mathbf{F} \\ \mathbf{M} \end{pmatrix} \quad (1)$$

The x- and y-component of \mathbf{M} are used to compensate unsymmetric process forces and unwanted torques excited by stray fields. The predictions about the device's behavior received from the matrices are computed with a superposition principle which leads to a small error. To reduce computational costs, these errors are neglected, if it can be assured that they are limited to a certain barrier.

IV. NUMERICAL RESULTS

Some preliminary numerical results are presented here. Similar to the synchronous motor, the coils of the lower part have to excite a rotating field to realize rotations. To create the mentioned matrices, it is necessary to know the forces and torques generated by a single coil at every interesting position.

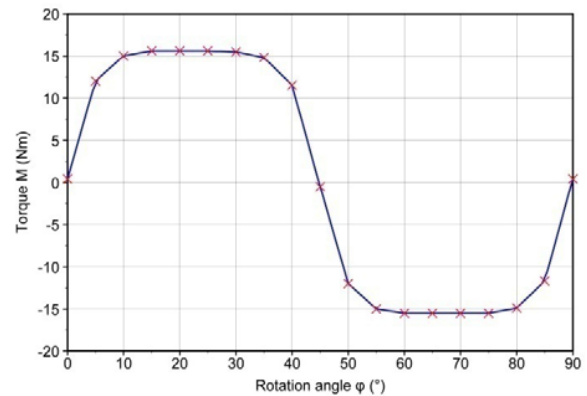


Fig. 3. Torque of a single rotation coil over the rotation angle

Fig. 3 shows the torque generated by applying a constant current to a single rotation coil. The translational deviations are zero and the number of magnetic poles is eight, therefore the rotation angle is varied from 0 to 90 degrees. Hence, the coil passes two different magnetic poles. In the middle of the air-gap the intersection between the magnetic fields of the two different poles is very long. Therefore, the device has to be realized with a small number of poles.

V. REFERENCES

- [1] P. J. Berkelman, "Tool-Based Haptic Interaction with Dynamic Physical Simulations using Lorentz Magnetic Levitation," Dissertation, Carnegie Mellon University, 1999.
- [2] J. Albert, R. Banucu, V. Reinauer, C. Scheiblich and W. Rucker, "Development of a Motor Device Performing Linear and Rotational Movements," Proceedings of the 13th IGTE Symposium, Graz, 2008.
- [3] R. McNeel et al., "RhinoScript for Rhinoceros 4.0," 2007.
- [4] C. Flynt, "Tcl/Tk - A Developer's Guide," Elsevier Science, 2003.

Effects of Load Variation on Eccentricity Fault Diagnosis in Round Rotor Synchronous Motors

Mohammad Etemad Rezaie, Bashir Mahdi Ebrahimi and Jawad Faiz
University of Tehran

Faculty of Engineering, Campus #2, University of Tehran, Kargar Shomali, Tehran, Iran, P.O. Box 14395-515
ebrahimibm@ut.ac.ir

Abstract— So far, effects of load variation have not been investigated for eccentricity fault diagnosis in synchronous motors. In this paper, a synchronous motor under static and dynamic eccentricity with different loads is modeled using winding function method. Self inductances of the stator and rotor, mutual inductances between stator and rotor, stator current, torque and speed motor are evaluated and analyzed. Spectrum of the stator current is utilized for detection of eccentricity occurrence, recognition of its type and determination of its percentage. Variation of eccentricity degrees and loads on the selected index is scrutinized separately and simultaneously. The accuracy of obtained simulation results is verified using experimental results.

I. INTRODUCTION

Fault conditions disturb machines performance and declare their life spans. Also, persistent faults damage the machines and consequently outage time for repairing is extremely costly. Therefore, faults diagnosis and condition monitoring of the synchronous motors as efficient machines in different industries are necessary. In [1]-[2], a salient-pole synchronous generator under dynamic eccentricity has been modeled using winding function method (WFM). Revision of the assumptions and basic equations of the WFM show that the theory differs for non-uniform air gap [3]. In addition, the stator and rotor windings distribution and air-gap permeance have been taken into account in [3] while this has not been considered in [1]-[2]. Amplitude of harmonic components at frequencies 17th and 19th has been employed for dynamic eccentricity in [1]-[3]. So far, round rotor synchronous motors under static and mixed eccentricity have not been investigated. Meanwhile, effects of the load variation on the eccentricity fault diagnosis in synchronous motors have not been studied.

II. SYNCHRONOUS MOTORS MODELING USING WFM

Precise modeling of the faulty machines is the most important stage of any reliable fault diagnosis procedure. Modeling methods which are developed based on magnetic field components of the machines can be utilized to calculate required parameters and signals incisively. Albeit WFM ignores non-linear characteristics of the stator and rotor cores, considers many effective parameters of the machines [1]-[3]. The principal equation of this theory which presents the mutual inductance of two arbitrary windings x and y in respect to the winding distribution is as follows:

$$L_{yx} = 2\pi \langle n_x n_y \rangle - 2\pi \frac{\langle P n_x \rangle \langle P n_y \rangle}{\langle P \rangle} \quad (1)$$

where operator $\langle f \rangle$ is defined as the mean of function f over $[0, 2\pi]$ and P is the permeance distribution of the air-gap.

Since, it is an arbitrary angle in the stator reference frame, it follows that:

$$\langle f \rangle = \frac{1}{2\pi} \int_0^{2\pi} f(\alpha) d\alpha \quad (2)$$

Equations (1) and (2) have been developed by taking into account a more precise distribution of stator phases and rotor excitation windings and also a more precise computation of the air-gap permeance. Air-gap permeance is proportional to the inverse of the air-gap length. Therefore, the air-gap permeance distribution, between the rotor and stator, is as follows:

$$P(\alpha) = \mu_0 \frac{r_{av}(\alpha)}{g(\alpha)} \quad (3)$$

where $r_{av}(\alpha)$ and $g(\alpha)$ are the mean radius of air-gap and air-gap distribution, respectively. These two quantities are constant for all the points between the rotor and stator, in the symmetrical case.

III. PERFORMANCE ANALYSIS OF THE FAULTY MOTOR

A. Stator Inductances

Fig. 1 depicts the per phase self-inductance of the stator winding of a synchronous motor in healthy and 50% static eccentricity. Fig. 1 exposes that the static eccentricity increases the inductance and distorts distribution of the inductance. The reason is that in the static eccentricity case, the air gap permeance depends on the rotor angular position. Since this angle varies continuously the distribution of the inductance is asymmetrical.

B. Rotor Inductances

Fig. 2 illustrates the self-inductance of the excitation winding of a synchronous motor in healthy and 50% static eccentricity. Comparison of Fig. 1 and Fig. 2 shows that the variation rate of the mutual inductance in static eccentricity is higher than that of the self-inductance.

C. Stator current

Stator current of the healthy and faulty synchronous motor and their spectrum have been presented in Fig. 3 and Fig. 4. Referring to these figures presents the considerable increases of amplitude of 17th and 19th harmonic components due to static eccentricity which can be utilized as a proper index for eccentricity fault detection in synchronous motors. This is because of distortion of magnetic flux density which strains motor inductances. Therefore, stator currents are unbalanced and the amplitude of harmonic components is increased.

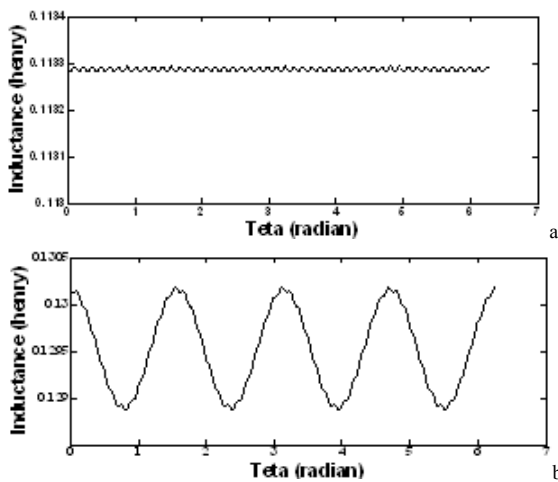


Fig. 1. Per phase self-inductance of the stator winding in (a) healthy and (b) 50%, static eccentricity

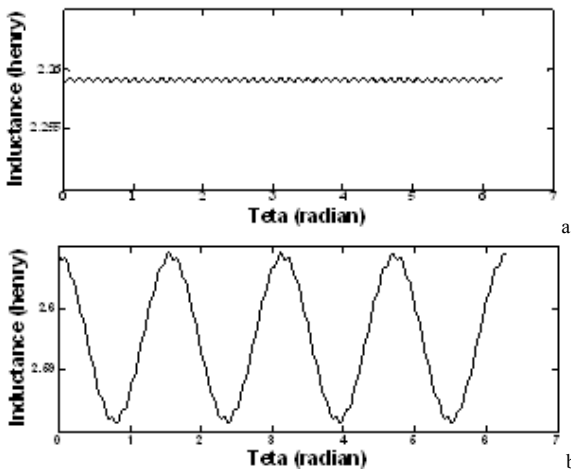


Fig. 2. Per phase self-inductance of the rotor winding in (a) healthy and (b) 50%, static eccentricity

IV. EFFECTS OF LOAD VARIATION

Fig. 4 shows the amplitude of the 17th harmonic component for different loads and different static eccentricity degrees (DED). The peak of harmonic amplitude is seen at the highest DED and the maximum load. On the other hand, the minimum harmonic amplitude is seen at the lowest DED and no-load. As shown in Fig. 4, an increase in the eccentricity degree and load, consequently increases the amplitude of the 17th harmonic component. According to Fig. 6, it is noticeable that the effects of increase of DED are much considerable on the amplitude of 17th harmonic component in which, effects of load variation can be ignored. Indeed, amplitude of the 17th harmonic component is fairly constant against load variation.

V. CONCLUSION

In this paper static and dynamic eccentricities were modeled and analyzed using WFEM. This modeling method provided us with exact calculation and analysis of air gap permeance and so the machine inductances were calculated precisely. It was shown that, static and static eccentricities increase the magnitude, distort the distribution and these both affect on machine inductances.

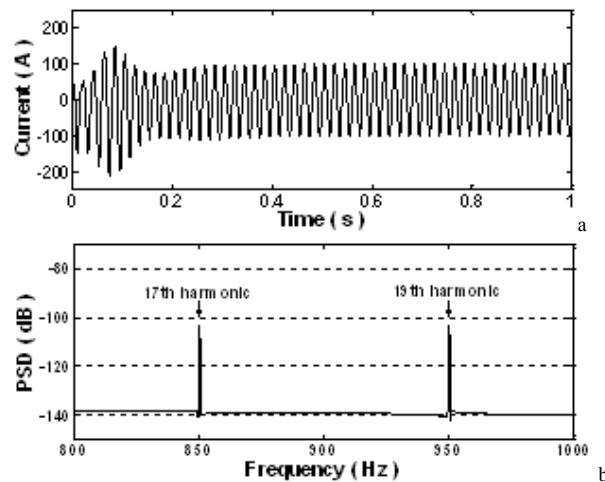


Fig. 3. (a) Stator current waveform of healthy motor and (b) it's spectrum

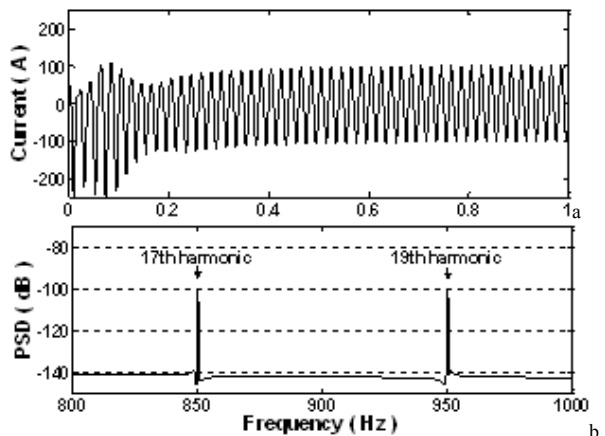


Fig. 3. (a) Stator current waveform of faulty motor under 30% static eccentricity and (b) it's spectrum

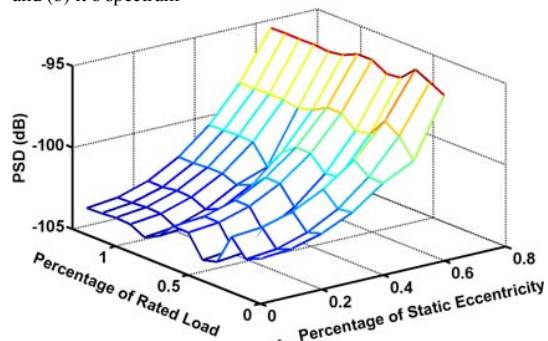


Fig. 4. Amplitude variation of 17th harmonic component versus static eccentricity degree and different loads

VI. REFERENCES

- [1] N.A.Al-Nuaim, H.A. Toliyat, "A Novel Method for Modeling Dynamic Air-Gap eccentricity in synchronous machines based on modified winding Function theory", IEEE Transaction on Energy Conversion, Vol.13, No.2, June 1998, pp.156-162.
- [2] H. A. Toliyat and N. A. Al-Nuaim, "Simulation and detection of dynamic air-gap eccentricity in salient-pole synchronous machines," IEEE Trans. Ind. Applicat., vol. 35, pp. 86–93, Feb. 1999.
- [3] I. Tabatabaei, J. Faiz, H.Lesani and M.Nabavi, "Modeling and Simulation of Salient Synchronous Generators with Dynamic Eccentricity Using Modified Winding fnction Theory", IEEE Transaction on Magnetics, Vol.40, No.3, May 2004, pp.1550-1555.

Dynamic Characteristics Analysis of Spherical Resonant Actuator Using 3-D FEM

Satoshi Suzuki¹, Yoshihiro Kawase¹, Tadashi Yamaguchi¹, Shuhei Kakami¹,
Katsuhiro Hirata² and Tomohiro Ota³

¹Department of Information Science, Gifu University, Japan
e-mail: sato@fem.info.gifu-u.ac.jp

²Department of Adaptive Machine Systems, Graduate School of Engineering, Osaka University, Japan
e-mail: k-hirata@ams.eng.osaka-u.ac.jp

³Advanced Technologies Development Laboratory, Panasonic Electric Works, Ltd., Japan
e-mail: t_oota@panasonic-denko.co.jp

Abstract— This paper describes the dynamic analysis method for a spherical resonant actuator using the three-dimensional finite element method (3-D FEM). In this computation, the magnetic field equation is coupled with the electric circuit equation and the motion equation. And the mesh modification method using the Laplace equation is applied for the rotation of a spherical actuator. The dynamic characteristics of this actuator are quantitatively clarified using this method.

I. INTRODUCTION

Recently, it is desired to develop a magnetic actuator that can move in arbitrary direction without auxiliary mechanism. We have been developing some novel spherical resonant actuators [1]. This paper describes a dynamic analysis method for a spherical resonant actuator using the 3-D FEM [2]. It is difficult to modify the FEM meshes of a complicated spherical actuator in accordance with rotation of an armature. Therefore, the mesh modification method using the Laplace equation is employed. The dynamic characteristics of this actuator are clarified using this method.

II. ANALYSIS METHOD

A. Magnetic Field Analysis

The equations of the magnetic field and the electric circuit are coupled using the 3-D FEM, which are given by the magnetic vector potential \mathbf{A} and the exciting current I_0 as follows:

$$\text{rot}(\nu \text{rot } \mathbf{A}) = \mathbf{J}_0 + \nu_0 \text{rot } \mathbf{M} \quad (1)$$

$$E = V_0 - RI_0 - \frac{d\Psi}{dt} = 0 \quad (2)$$

$$\mathbf{J}_0 = \frac{n_c}{S_c} I_0 \mathbf{n}_s \quad (3)$$

where ν is the reluctivity, \mathbf{J}_0 is the exciting current density, ν_0 is the reluctivity of the vacuum, \mathbf{M} is the magnetization of permanent magnet, V_0 is the applied voltage, R is the effective resistance, Ψ is the interlinkage flux of exciting coil, n_c and S_c are the number of turns and the cross-sectional area of the coil respectively, and \mathbf{n}_s is the unit vector along with the direction of exciting current.

The motion of the armature is described as follows:

$$I \frac{d^2\theta}{dt^2} + D \frac{d\theta}{dt} + k\theta = T_m \quad (4)$$

where I is the moment of inertia, θ is the rotation angle, D is the viscous damping coefficient, k is the spring constant, and T_m is the torque acting on the armature.

B. Mesh Modification by solving the Laplace equation

The procedure of mesh modification for next time step is executed by solving the Laplace equation, which is given as follows [3]:

$$\frac{\partial^2\theta}{\partial x^2} + \frac{\partial^2\theta}{\partial y^2} + \frac{\partial^2\theta}{\partial z^2} = 0 \quad (5)$$

where θ is the potential, which can be regarded as the rotation angle of the armature.

(i) The potential θ_{rotation} , which is the rotation angle of the armature, is given to nodes in the armature region, and the potential zero is given to nodes in the stator region.

(ii) The distribution of potential θ of the armature region is calculated by solving (5).

(iii) The coordinates of nodes in the mesh are modified according to each potential θ .

The meshes of the gap between the armature and the stator are smoothly modified by using this mesh modification method. Fig. 1 shows the flowchart of the dynamic analysis method.

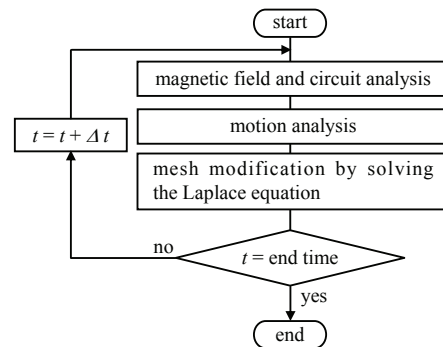


Fig. 1. Flowchart of dynamic analysis.

III. ANALYZED MODEL AND ANALYSIS CONDITIONS

Fig. 2 shows the analyzed model. The stator has four poles and a couple of coils in this study to consider the rotation only in y-axis. The armature is composed of the spherical-shaped core with the ring-shaped permanent magnet, which is connected to the resonance spring. The rotation angle θ is defined as shown in Fig. 3. θ is 0 in the initial position. The magnetic flux caused by the permanent magnet flows as shown in Fig. 4. The armature is stable at the center because of balanced magnetic flux in the gap between the armature and the stator. The torque is generated on the armature when the current is excited to the coil, and the armature rotates in y-axis. Table I shows the analysis conditions. In this computation, the rectangular voltage is applied to the coil. The discretization data and CPU time is shown in Table II.

IV. RESULTS AND DISCUSSION

Fig. 5 shows the waveforms of current and rotation angle of the armature in resonance. From this figure, the effective value of current and the maximum rotation angle are 0.94A and 7.5°, respectively. Fig. 6 shows the characteristics of rotation angle versus operating frequency. From this figure, it is found that this actuator has a resonance frequency of 127Hz. The effectiveness of the calculated results will be confirmed through the comparison with the measured ones in the full paper.

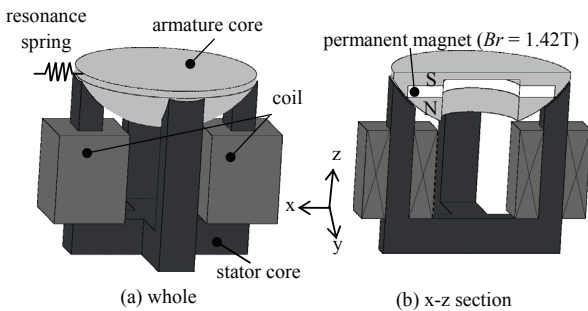


Fig. 2. Analyzed model.

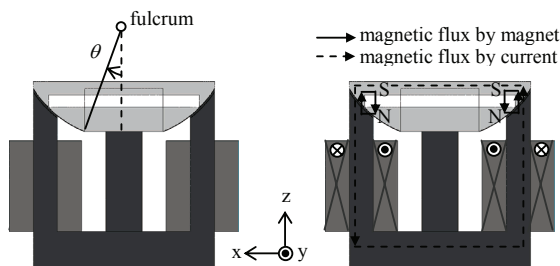


Fig. 3. Rotation of armature.

Fig. 4. Principle of operation.

TABLE I
ANALYSIS CONDITIONS

Coil	Voltage (V)	1.2
	Resistance (Ω)	0.42
	Number of turns (turn)	100
Inertia of armature ($N \cdot m \cdot s^2 / rad.$)		8.05×10^{-6}
Spring constant ($N \cdot m / rad.$)		3.75
Viscous damping coefficient ($N \cdot m \cdot s / rad.$)		1.80×10^{-4}

TABLE II
DISCRETIZATION DATA AND CPU TIME

Number of elements	2,028,744
Number of nodes	344,578
Number of edges	2,386,097
Number of unknown variables	2,347,770
CPU time (hours/step)	1.2

Computer used: Core2 Duo (3.16GHz) PC

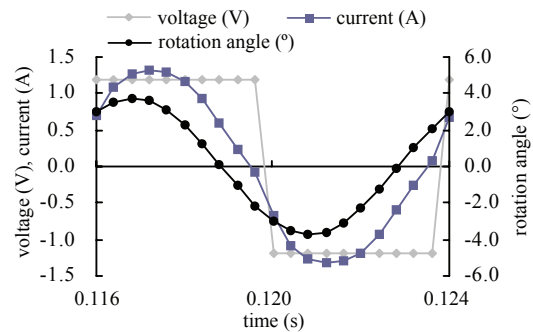


Fig. 5. Waveforms of current and rotation of armature.

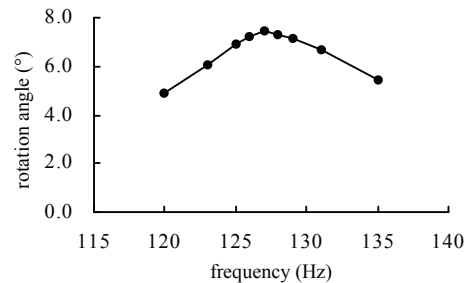


Fig. 6. Characteristics of rotation angle versus operating frequency.

REFERENCES

- [1] Y. Hasegawa, T. Yamamoto, K. Hirata, Y. Mitsutake and T. Ota: "Study of Dynamic Analysis for Spherical Resonant Actuator", The Papers of Technical Meeting on Linear Drives, IEE Japan, LD-07-41, 2007. (in Japanese)
- [2] S. Suzuki, T. Yamaguchi, Y. Kawase, K. Sato, S. Kakami, K. Hirata and T. Ota: "Dynamic Analysis Method of Spherical Resonant Actuator Using 3-D Finite Element Method", Proceedings of the 18th International Conference on Electrical Machines, Paper ID 1400, September 2008.
- [3] Y. Kawase, T. Yamaguchi, M. Watanabe and H. Shiota: "Novel Mesh Modification Method Using Laplace Equation for 3-D Dynamic Finite Element Method", Proceedings of the 16th Conference on the Computation of Electromagnetic Fields, Vol.2, pp.631-632, June 2007.

Finite Element Processing Methods to Peripheral Flux Leakage in Axial Field Flux-Switching PM Machines

Mingyao Lin, Lei Zhang, Xin Li and Haitao Yu

School of Electrical Engineering, Southeast University, Nanjing, 210096, P.R. China
mylin@seu.edu.cn

Abstract—In this paper, a finite element(FE) analysis of the peripheral flux leakage in a novel axial field flux-switching permanent magnet (AFFSPM) machine was presented by using energy method. The size of peripheral air cylinders in FE analysis model of AFFSPM machine was determined by the suggested method. Thus, it was possible to optimize between the computational precision and time. The calculation results are coincide with that by permanent magnet (PM) flux method. In addition, the presented method was also used in 2D FE simulation. The investigation shows that this method is useful in the application of machines with PM in stator.

Index Terms—peripheral flux leakage; air cylinder; energy method; AFFSPM machine.

I. INTRODUCTION

The peak-to-peak values of the PM flux and the induced electromotive force (EMF) computed by FE method are larger than their actual values due to the peripheral flux leakage in a AFSFPM machine with PM in the stator. In order to decrease the computation error, it is necessary to add peripheral air cylinders to the periphery of FE analysis model of machines. However, this increases the workload for meshing, computing and post-processing. Therefore, it's very practical to determine the sizes of air cylinders and to optimize the computation precision and time.

FE simulations of PM machines, including the design, the optimization of machines, the calculation of parameters, have been studied in the literatures. However, how to decide the sizes of peripheral air cylinders in the FE analysis model have rarely been investigated. In this paper, an energy method is suggested to determine the sizes of the air cylinders for a novel AFFSPM machine. The calculated results is compared with that gotten by the PM flux method.

The energy method is discussed in section II. In section III, PM flux method is introduced and the results are compared. In order to illuminate that the energy method is applicable to 2D FE simulation, a 2D FE example is presented in section IV.

II. THE ENERGY METHOD

A. The simulation model of AFFSPM machine

The magnetic energy is a sum of the magnetic co-energy in each element. For each one, the magnetic co-energy is calculated as follows:

$$W_c = \int_{-H_c}^H \{B\} \cdot \{dH\} \quad (1)$$

where W_c is the stored magnetic co-energy, H_c is the coercive force, B is the flux density vector, and H is the magnetic field

intensity vector. For the static magnetic field in the zero-current condition, the interrelated parameters are governed by the following three equations:

$$\begin{cases} \nabla \times H = 0 \\ \nabla \cdot B = 0 \\ B = \mu H \end{cases} \quad (2)$$

where μ is the magnetic permeability. To solve these equations, a magnetic scalar potential is introduced to describe H :

$$H = -\nabla \psi \quad (3)$$

where ψ is the magnetic scalar potential, which could deduce the requisite parameters.

Fig. 1 shows a typical AFFSPM machine of the type to be investigated in this paper. The machine consists of two outer stators and one inner rotor.

There are three peripheral air covers in the FE analysis models of the AFFSPM machine, that is, a radial outer peripheral air cylinder, a radial inner air cylinder and a terminal air cylinder. The three peripheral air cylinders are added in the FE analysis model in turn and their sizes should be determined. Fig.2 shows the 3D FE analysis model of a AFFSPM machine.

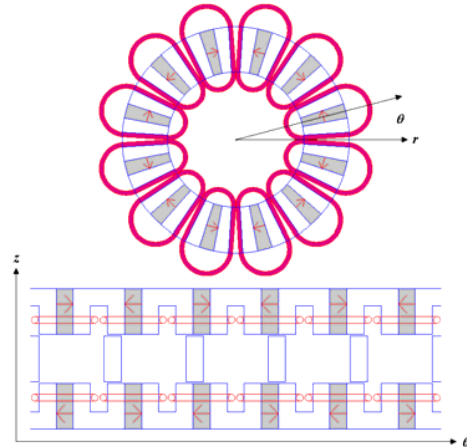


Fig.1. configuration of a AFFSPM machine

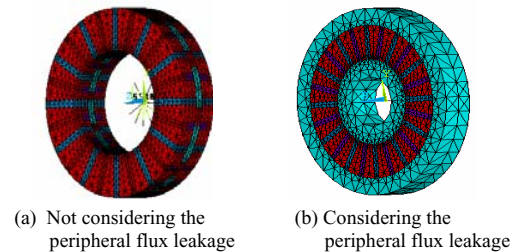


Fig. 2. 3D FE analysis model of AFFSPM machine

11. Electric Machines and Drives

B. Determination of radial peripheral air cylinder size

The outer diameter of the radial peripheral air cylinder was calculated. If k_{oair} is defined as a changeable coefficient for the undetermined parameter, and it is

$$k_{oair} = D_{oair} / D_o \quad (4)$$

Where D_{oair} is the outer diameter of the radial peripheral air cylinder, and D_o is the outer diameter of AFFSPM machine. Fig.3 shows the magnetic energy varied with k_{oair} at initial rotor position angle, and the change of magnetic energy in one cycle at different k_{oair} is shown in Fig.4.

The magnetic energy is constant when k_{oair} is larger than 1.5(Fig.3), which is also demonstrated by the results in Fig.4. Therefore, $1.5D_{oair}$ is determined as the outer diameter of the radial periphery air cylinder.

The sizes of radial inner air cylinder and terminal air cylinder are also determined according to the above analysis. $0.5D_i$ is selected as the inner diameter of radial inner air cylinder, and $1.1h_s$ is the axial depth of the terminal air cylinder, where D_i is the inner diameter of AFFSPM machine, and h_s is the axial length of the stator.

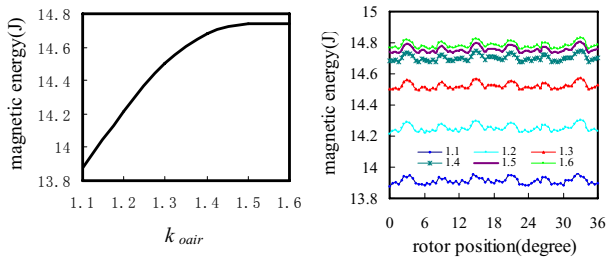


Fig.3. Magnetic energy at the initial position angle Fig.4. Magnetic energy in one cycle

III. THE PM FLUX METHOD

The PM flux is one of most important parameters in the design and optimization of PM machines. The relationship between the peak-to-peak value of the PM flux and the k_{oair} in one phase is shown in the Fig.5. The peak-to-peak value of the PM flux is constant when the k_{oair} value is larger than 1.5, and this is coincide with that obtained from the energy method.

The relations of PM flux peak-to-peak with the sizes of the radial inner air cylinder in one phase and the terminal cylinder are also obtained by the same method. The inner diameter of the radial inner air cylinder is determined as $0.5D_i$, and the axial length of the terminal air cylinder is $1.1h_s$. These are coincide with those obtained by the energy method.

IV. 2D FE ANALYSIS

In the 2D FE analysis model of a radial field flux-switching PM machine, a circle was added to the periphery of the stator to simulate the air condition. Fig.6 shows the FE analysis model of the machine. The outer diameter of the peripheral air circle is determined. The calculated results based on the energy method are shown in Fig.7 and Fig.8, where k_{airso} is the proportion of the outer diameter of the air circle to the outer diameter of the stator. According to the

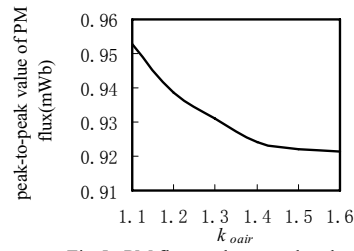


Fig.5. PM flux peak- to-peak value

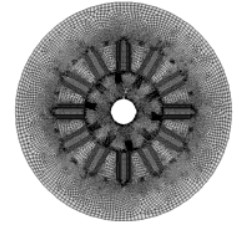


Fig.6. 2D FE analysis model of a radial field flux-switching PM machine

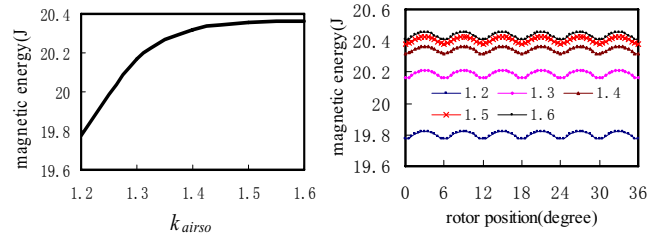


Fig.7. Magnetic energy at the initial rotor position.

Fig.8. Magnetic energy in one cycle

calculation of the magnetic energy, $1.5D_{so}$ is determined as the outer diameter of air circle, where D_{so} is the outer diameter of the stator. This result can also be obtained by using the PM flux method.

V. CONCLUSIONS

In this paper, an energy method is presented and used to determine the sizes of peripheral air cylinders in the FE analysis models of the flux-switching machines. The simulation results are confirmed by the PM flux method in the 3D and the 2D FE simulation. In additional, the peak-to-peak values of the PM flux and the induced EMF computed by the FE method are larger than their actual values, which is caused by the difference of the PM flux at different air cylinder sizes. The determination of the sizes of peripheral air cylinders on the FE analysis models of flux-switching machines is important to obtain the balance between the computation precision and the time. Therefore, it's useful to determine the air cylinder sizes by the energy method in the FE simulation of machines with PM in the stator.

VI. REFERENCES

- [1] M Cheng, Chau K T, Chan C C, "New split-winding doubly salient permanent magnet motor drive", *IEEE Trans. On Aerospace and Electronic Systems*, 2003, 39(1):202-210.
- [2] M.Chen. Design, "Analysis and Control of Doubly Salient Permanent Magnet Motor Drives", *Ph.D thesis. Hong Kong: Hong Kong University*, 2001.
- [3] Wei Hua, M.Chen, Xiaoyong Zhu, etc, "Investigation of End-effect in Novel Doubly-salient Machines With PM in Stator", *Proceeding of the CSEE*, 2007, 27(24):63-67.
- [4] Hoang E, Ben-Ahmed A H, Lucidarme J, "Switching flux permanent magnet polyphased machines", *Proc. European Conf. Power Electronic and Applications*, Trondheim, Norway, 1997, 3:903-908
- [5] Y.liao, F.Liang, T.A.Lipo, "A novel permanent magnet machine with doubly salient structure", *IEEE Transactions on Industry Applications*, 1992, 31(5):1069-1078.

Slotted and Torus PM Generators for Low Speed Direct Drive Applications using an Analytical/Static 2D FEA Design Technique

David G. Dorrell

School University of Technology Sydney, Broadway, Sydney, Australia
ddorrell@eng.uts.edu.au

Abstract — Direct-drive permanent-magnet generators for use in low speed applications are described and compared. A target specification is set and a design procedure is carried out for a radial-flux slotted machine and a Torus machine. The design for the fractional-slot high-pole number brushless permanent-magnet generator is developed using an analytical design package and verified using a finite element analysis. The design is compared with a preliminary Torus machine design.

I. INTRODUCTION

With the development of new generation systems which are both low-speed and variable power there is an increasing need for direct-drive generators. Unfortunately many PM generators suffer from low power factor [1] and will require controlled rectification. It is an advantage to have high p.f. so that a diode bridge load can be utilized for simple and robust operation [2].

The topology of these machines can vary considerably – they can be of conventional radial-flux [2] with slotted stator and surface/internal magnets, axial flux machines with air-gap windings [3], torus arrangements [4] or Vernier hybrid [5].

In the paper a comparison between direct-drive PM generators is made. The basic target specification is outlined and the design carried out and verified using finite element analysis. This paper represents an interesting electromagnetic design challenge and sets out a simple procedure for machine designers using modern design and analysis tools.

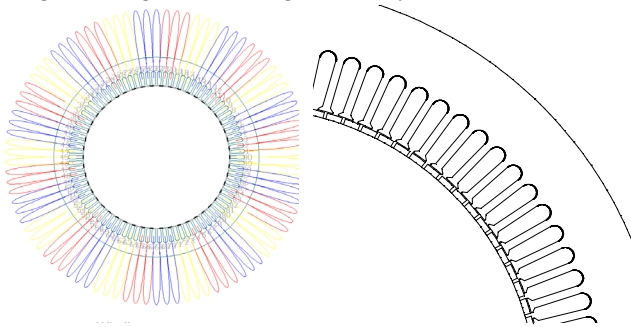


Fig. 1. (a) Winding arrangement and (b) stator cross section.

II. SPECIFICATION AND OUTLINING OF SLOTTED MACHINE

The application here is low speed. If the target speed is 15 rpm and 200 Nm, and allowing a frequency of 12.5 Hz at this speed, then a pole number of 100 is obtained; this was used for the slotted design. The frequency is low because the generator may be required to operate at higher speed (above 60 rpm) and also the pole number would be prohibitively high. This generator is aimed at being used in a Bristol Cylinder [6]. For the slotted design, surface magnets are used to prevent saliency

and minimize X_q . The slot number should be a multiple of 3. A convenient number for 100 poles is 90 slots with two coil-sides per slot. The machine uses rare earth magnets. Fig. 1 shows the machine and winding layout (for 3 phases). The periodicity of this arrangement is 9 slots (10 poles). The use of fractional slot stator topology is necessary to reduce cogging torque.

III. DETAILED SLOTTED MACHINE DESIGN AND ANALYSIS

A. Sizing

If the target speed is 15 rpm, and the frequency of 12.5 Hz at this speed, then the pole number is 100. [7] suggests that the torque per rotor volume (TRV) for a high-performance servo machine should be between 20 and 45 kNm/m³; the low end of the range is taken for a prototype. The total axial length for the machine is 270 mm so the core length of the machine is about half. Using this length gives a rotor diameter of

$$D = 2 \sqrt{\frac{T}{TRV \times \pi L_{stk}}} = 2 \sqrt{\frac{200}{20 \times 10^3} \times \frac{1}{\pi \times 0.135}} = 0.307 \text{ m} \quad (1)$$

Hence, the radius of the rotor is 150 mm and the axial length is 135 mm. The sizing is calculated to fill the generator voids in the cylinder. Fig. 1(a) shows the coil arrangement. The slots and stator are scaled to give appropriate slot area (211 mm²), tooth width (4 mm) and yoke depth (30 mm). This is shown in Fig. 1(b). The outer radius is 420 mm which is much less than the maximum allowed. The slot opening was set to 3 mm and the coils consist of 60 series turns. The gross slot fill is 0.5.

B. Phasor Diagram

The phase winding back-EMF has a good sinusoidal waveform with 3rd harmonic (which does not affect the operation). The torque has little ripple (a mean of 228 Nm). The machine is current fed and the current phasor is on the $-q$ axis. The phasor diagram is also shown in Fig. 2(a). When the machine is attached to a diode bridge rectifier the performance will be degraded, this is because the current will not be in phase with the back-EMF and not sinusoidal. Low $I_q X_q$ will help the diode bridge performance.

C. Finite Element Analysis and I-Psi Diagram

The model was fed through to an FEA package. The model spanned 10 poles. The derived current/flux-linkage loop is shown in Fig. 2(b). This is similar to the loops used in switched-reluctance machines. The current and rotor rotation are cycled round together and the flux linkage measured at each step. The area enclosed is the work done and therefore torque can be calculated in a straightforward manner. If the

11. Electric Machines and Drives

loop is long and thin then the machine is operating poorly however this example shows good conversion. These loops are calculated both analytically (solid line – torque = 222 Nm) and in FEA (dotted line – torque = 254 Nm).

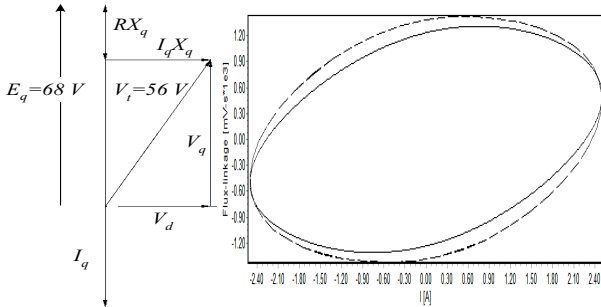


Fig. 2. (a) Phasor diagram and (b) I-Psi loop for one phase

D. Cogging Torque

Cogging torque requires fine detail of the machine magnetic circuit to calculate an accurate model. Cogging torque is very susceptible to numerical error. The air-gap had four regular layers and the distance between the nodes round the central air-gap boundary is equal to the step angle between steps. The cogging torque was found to be about 2.8 Nm peak-to-peak.

IV. TORUS DESIGN

In this section a short comparison is done with an alternative design – the Torus machine. There is little in the literature that gives direct comparison between the two machines.

A. Torus design

The Torus arrangement has the advantage of low armature reactance and can be either radial flux or axial flux [11]. This machine has air-gap windings and the disadvantage to this arrangement is that the coupling with the winding is reduced and available winding area is limited. In addition there can be additional eddy current losses in the air-gap copper so that many parallel strands of thin wire may be required. Therefore to design this machine then maximum diameter should be used in the initial design. Here it was decided to use a 760 mm diameter for the outer diameter of the machine and the same magnet material. The pole number was increased to 120 poles and since there is no cogging torque then an integral number of coils per pole can be utilized (120 coils per phase).

The rotor diameter is 735 mm so that the machine is more of a ring in structure which requires careful mounting within a frame and bearing mountings. The thickness of the winding layer was limited to 1.4 mm with a low 0.7 mm air-gap. This is to attempt to maintain good flux linkage with the rotor. Because the Torus arrangement has limited end-winding (since the coils are wound around the toroidal laminated stator core) it is possible to increase the axial length (up to 170 mm here). This is necessary because of the limited number of turns that can be used so every effort should be made to improve the flux linkage per turn. Since it is easier to wind this machine then the slot fill was increased to 0.7 – this will be difficult to achieve and rectangular conductors would probably have to be used. Fig. 8 shows the finite element analysis of this machine

while Table 1 shows a comparison of the designs.

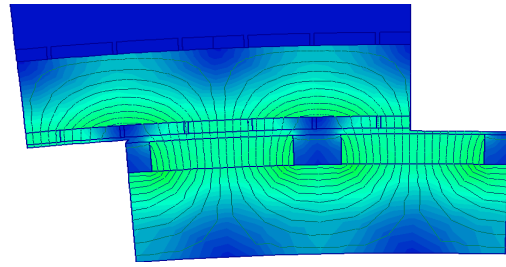


Fig. 3. Radial-flux Torus design showing one pole pair (stator at top showing three coils per pole around stator core).

TABLE I COMPARISON OF MACHINE DESIGNS (AT LOAD AND 15 RPM)

Parameter	Slotted	Torus	Parameter	Slotted	Torus
Outer Diameter [mm]	420	760	Core length [mm]	135	170
Copper [Kg]	12.4	6.5	Magnet [Kg]	2.3	7.6
Load current (set) [A]	1.77	1.77	Torque [Nm]	228	231
Back-EMF [V]	68.3	68.9	Power Factor	0.87	1
Copper losses [W]	99	162.9	Efficiency [%]	69.9	55.5

B. Comparison with slotted machine

Table I shows that the issue with the limited area for the winding leads to the requirement for more magnet material while there is additional copper losses in the winding because it runs with a higher current density in the copper. Even with the increase in poles it is still difficult to get sufficient flux linkage and hence back-EMF. With further design it would probably be possible to obtain better performance by optimizing the magnet thickness and winding window to obtain the optimum back-EMF and copper losses which gives best efficiency. However this does illustrate that the slotted machine is much easier to design for a given specification because of the flexibility of the winding area available.

V. CONCLUSIONS

In this paper a comparison has been made between a slotted machine and a Torus machine using standard design techniques and 2D FEA validation of design calculations. It was found that Torus machine required a larger diameter to meet the specification. A direct comparison highlighted the advantages and disadvantages of both. Neither is of high efficiency; further refinement is needed to improve this.

VI. REFERENCES

- [1] M. R. Harris, G. H. Pajooman and S. M. Abu Sharkh, "The problem of power factor in VRPM (transverse-flux) machine, 8th EMD conference, Cambridge, UK 1997
- [2] D. G. Dorrell. Design Requirements for Brushless Permanent Magnet Generators for Use in Small Renewable Energy Systems. Proceedings of IEEE Industrial Electronics society Annual Meeting (IECON), Taipei, Taiwan, (on CD), 2007
- [3] M. A. Mueller, "Electrical generators for direct drive wave energy converters", IEE Proc Gen, Trans and Dist, Vol 149, 2002
- [4] E. Spooner and B. J. Chalmers, "TORUS: a slotless, toroidal-stator, permanent-magnet generator", IEE Proc EL. Pow. Appl., Vol 139, 1992
- [5] M. A. Mueller and N. J. Baker, "Modelling the performance of the vernier hybrid machine", IEE Proc Elec Pow Appl, Vol 150, 2003.
- [6] D. G. Dorrell, "Permanent Magnet Generators for Renewable Energy Devices with Wide Speed Range and Pulsating Power Delivery", Int. Forum on Systems and Mechatronics, Tainan, Taiwan, Dec 2007.
- [7] J. R. Hendershot and TJE Miller. Design of Brushless permanent Magnet Motors. Clarendon Press, Oxford, 1994.

A General Cuboidal Element for Three-Dimensional Thermal Modeling

R. Wrobel and P. H. Mellor

Department of Electrical and Electronic Engineering,
University of Bristol, Merchant Venturers Building,
Woodland Road, Bristol, BS8 1UB, UK
R.Wrobel@bristol.ac.uk

Abstract — This paper presents a lumped parameter thermal modeling approach for three-dimensional (3D) thermal modeling based upon the use of general 3D elements which are formulated to accurately cater for internal heat generation. Commonly used thermal networks do not account for an internal heat generation that is essential for accurate temperature predictions. In contrast, the general element proposed in this paper includes the internal heat generation as well as a material thermal anisotropy. To validate the technique, a thermal model of an inductor using the equivalent circuit method with the cuboidal element and 3D finite element method (FEM) was constructed and analysed. The calculated results from the cuboidal element method show good agreement with the FEM predictions.

I. INTRODUCTION

One of the main factors limiting the design of an electrical device such as motor or transformer is its thermal performance. Accurate prediction of the temperature within a device is therefore very desirable. There are a number of methods allowing for theoretical predictions of temperature. These include analytical, lumped-parameter thermal network and numerical, finite element method (FEM) and computational fluid dynamics [1]. As the numerical techniques suffer from long model setup and computation times, the analytical lumped-parameter network is still a valuable method.

The resistive element commonly used in the thermal equivalent network can be derived from one-dimensional steady-state heat diffusion equation for zero internal heat generation [2]. This solution however, does not include internal heat generation essential for accurate temperature predictions. To include the internal heat generation a combination of solutions for two heat diffusion equations with zero internal heat generation and zero surface temperatures is required [3]. This approach has proven its usefulness resulting in development of a general cylindrical element that was used in thermal analysis of electrical machines [4]. This paper extends the application of the technique from a cylindrical to a Cartesian coordinate system using a general cuboidal element. The cuboidal element allows for three-dimensional thermal analysis using the equivalent circuit method. This includes internal heat generation as well as a material thermal anisotropy. Initial information about the thermal flux circulation is not required to construct the thermal network when using the cuboidal element. To validate this new approach, a thermal model of an inductor using the equivalent circuit method with the cuboidal element and 3D finite element method (FEM) was constructed and analysed.

II. MATHEMATICAL DESCRIPTION

To define the general cuboidal element an assumption of independent heat transfer within axes of the Cartesian coordinate system has been made. That simplifies the cuboidal element derivation to one-dimensional problem as the all axes of the coordinate system can be analysed individually.

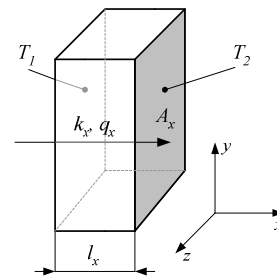


Fig. 1. Outline of a general cuboidal element

Fig. 1 shows a geometrical representation of the general cuboidal element, where T_1 and T_2 are the surface temperatures, k_x is the thermal conductivity in x -axis, q_x is the conduction heat rate in x -axis, A_x is the surface area normal to q_x and l_x is dimension of the cuboid in the x -axis.

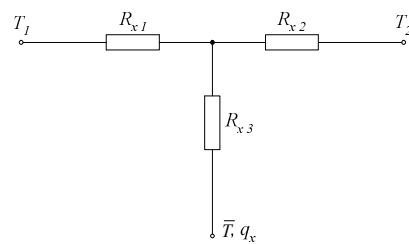


Fig. 2. Equivalent thermal network for a general cuboidal element

The equivalent thermal network in the x -axis for the cuboid is shown in Fig. 2. The mean temperature and the total heat generation within the cuboid are given by \bar{T} and q_x respectively, where

$$q_x = \dot{q}V = \dot{q}A_x l_x \quad (1)$$

To determine the thermal resistances ($R_{1,x}$, $R_{2,x}$ and $R_{3,x}$), the two cases of the one-dimensional, steady-state heat diffusion

equation need to be analysed, *A.* zero internal heat generation and *B.* zero surface temperatures and then applying superposition.

A. Zero internal heat generation

The heat equation for one-dimensional steady-state example with zero internal heat generation and constant thermal conductivity k_x is given in the following form

$$\frac{d}{dx}\left(k_x \frac{dT}{dx}\right) = 0 \quad (2)$$

By solving (2), both of the thermal resistances R_{1x} and R_{2x} can be found

$$R_{1x} = R_{2x} = \frac{l_x}{2k_x A_x} \quad (3)$$

B. Zero surface temperatures

The heat equation for one-dimensional steady-state example with internal heat generation is given in the following form

$$\frac{d^2 T}{dx^2} + \frac{\dot{q}}{k_x} = 0 \quad (4)$$

An average temperature \bar{T} within the cuboid is derived by solving (4) and then the thermal resistance R_{3x} can be found

$$R_{3x} = -\frac{l_x}{6k_x A_x} \quad (5)$$

A complete 3D description of the cuboid has been derived by replicating (2) and (5) for the remaining axes of the Cartesian coordinate system. The equivalent circuits for all the axes are then linked together in the node of the average temperature. A power source and the thermal capacitance of the cuboidal element is also connected to this node.

III. MODEL VALIDATION

To validate the cuboidal element a thermal analysis of an inductor has been carried out. The inductor includes a laminated core pack and Litz wire wound coil. Fig. 3 presents an outline of the inductor together with region labels assumed in the equivalent network model. Due to symmetry only a quarter of the inductor is modeled. The equivalent network model includes only 13 cuboidal elements in contrast to 70,629 elements for the FEA. It has been assumed that the inductor is mounted on a cold-plate at 60°C. Surfaces that are not in contact with the cold-plate are adiabatically insulated. The Litz wire wound coil is represented as a lumped region with anisotropic properties that were obtained experimentally. Calculations were carried out for a constant power loss of 40W within the inductor's winding. Table I includes temperature predictions from both FEM and equivalent network method with cuboidal element showing good agreement.

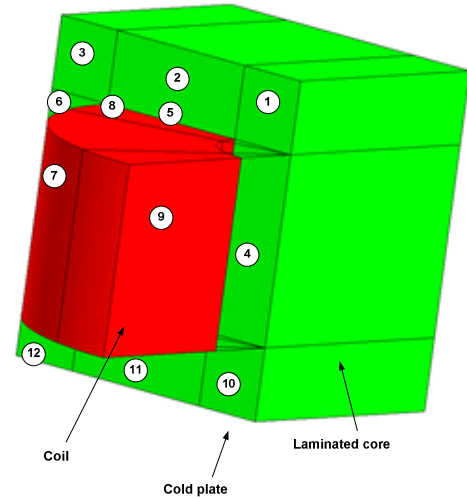


Fig 3. Outline of the inductor's model with region labels.

TABLE I TEMPERATURE PREDICTIONS

Region number	FEM [°C]	Equivalent network method [°C]
1 (core)	67.2	68.7
2 (core)	68.1	69.4
3 (core)	67.9	69.6
4 (core)	64.9	65.2
5 (coil)	70.3	69.5
6 (core)	65.9	68.6
7 (coil)	71.6	69.2
8 (coil)	71.1	69.4
9 (coil)	72.2	69.3
10 (core)	61.0	61.0
11 (core)	60.8	60.7
12 (core)	61.3	61.6

IV. CONCLUSION

The cuboidal element technique presented allows for fast three-dimensional temperature prediction using the equivalent circuit method. This is essential when a transient thermal analysis is required. The element includes the internal heat generation as well as a material thermal anisotropy, in contrast to the commonly used resistive element. Model construction using the cuboidal element does not require initial information about heat flux and only geometrical and material data is used. This new technique has been validated with a 3D FEM model showing good agreement.

V. REFERENCES

- [1] A. Boglietti, A. Cavagnino, D. A. Staton, "TEFC Induction Motors Thermal Models: A Parametric Sensitivity Analysis", *IEEE Transactions on Industry Applications*, 41(3): 756-763, 2005.
- [2] F. P. Incropera, D. P. DeWitt, *Introduction to Heat Transfer*, John Wiley & Sons, 1996.
- [3] P. H. Mellor, *Improvement in the Efficiency and Thermal Ageing of Single and Parallel Machine drives*, PhD Dissertation, University of Liverpool, 1983.
- [4] P. H. Mellor, D. Roberts, D. R. Turner, "Lumped parameter thermal model for electrical machines of TEFC design", *IEE Proceedings-B*, 138(5): 205-218, 1991.

Time-Stepping Finite Element Analysis of a Salient-pole and Round-Rotor Synchronous Generators under Dynamic Eccentricity Fault

Jawad Faiz, Mojtaba Babaie, Bashir Mahdi Ebrahimi and Jalal Nazarzadeh

University of Tehran, Tehran, Iran

Abstract— This paper compares the effects of dynamic eccentricity (DE) on the performance of a salient-pole and round-rotor synchronous generators. Time stepping finite element (TSFE) method has been used for calculating the self and mutual inductances of the stator phases and rotor windings. It also used to determine the influence of the eccentricities on the flux distribution and no-load voltage characteristics in aforementioned generators. Then, new index is introduced for dynamic eccentricity fault detection in the two types of synchronous generators. This index which is extracted from the spectrum analysis of the stator current can be utilized to determine the dynamic eccentricity degree accurately.

I. INTRODUCTION

Operation of generators under faults condition can disturb their performances and declare their life spans. Also, persistent faults can damage the generators and consequence outage time for repairing is extremely costly. Therefore, faults detection and condition monitoring of the generators allow more flexibility in operation by knowing the performance and extend generator life by adjusting the operation to avoid known operating regimes or ranges and cost effectiveness.

Mechanical faults such as eccentricity are one of the major faults in electrical machines caused by mechanical parts such as bearing, shaft and coupling [1]-[2]. In the case of dynamic eccentricity, the center of rotation and the center of stator are the same. Therefore, the air gap length is both time and space dependent [3].

Many researches have been devoted to the eccentricity fault in induction machine [4], but it is considerably poor in the field of the synchronous generator. Hence, study of the generator performance under this fault seems to be necessary.

In this paper, from the basic geometry, nonlinear properties of the magnetic materials and winding layout of the two generators, the FE approach is implemented using Flux2D 10.2 software package. All signal and the characteristics of the two generators have been calculated by TSFE method with a very high accuracy. The standard Galerkin formulation is applied to the field and current equations, moving-band technique is taken into account the movement and Newton-Raphson method has been used to consider the nonlinearity of the magnetic materials.

II. IMPACTS OF THE ECCENTRICITY FAULT UPON THE FLUX DISTRIBUTION IN THE SYNCHRONOUS GENERATORS

The synchronous generators field winding is subject to the dc saturated current equal to 12A at no load condition. The magnetic field equations solved in the given structure via the FE approach. The eccentricity degree, δ , is definite as follows:

$$\delta = \frac{e}{l_g} \times 100 \quad (1)$$

Where e is the displacement of the rotor in the horizontal direction in respect to the stator symmetry center and l_g is the air gap length in healthy condition [3]. In the case of 40% eccentricity degree to the right at no load, it is observed in Fig. 1 that the eccentricity clearly affects the flux distribution in generators and the magnetic flux distributions are not identical on both sides of the generators.

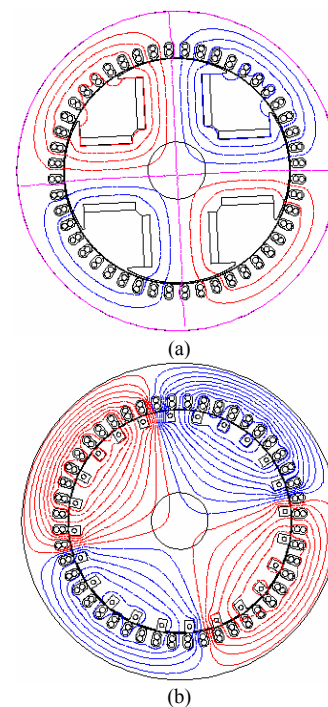


Fig. 2. Flux distribution in the generator at no load in case of the 40% eccentric air gap, (a) salient-pole, (b) round-rotor.

III. SPECTRUM ANALYSIS OF THE STATOR CURRENT FOR DE FAULT DIAGNOSIS IN THE SYNCHRONOUS GENERATORS

In the presence of eccentricity faults, some harmonics related to the faults appear in the air gap field of the synchronous generator. These harmonics will increase as eccentricity degree rises. They should induce corresponding current harmonics in the stationary stator windings. Consequently, the stator current signatures of synchronous generator can be utilized for diagnosis eccentricity fault.

The synchronous generators under dynamic eccentricity (DE) faults are simulated very accurately in full-load condition using TSFE method and current signal are extracted for the analysis and extracting efficient index related to the faults. Fig. 2 shows the frequency spectrum of the stator current of the round-rotor synchronous generator for the healthy and 40% DE faults. It is observe that the 19th harmonic increase from the -88.38 dB to -83.95 dB with increase in 40% DE. Also, amplitudes (in dB) variation of harmonics for healthy, 10%, 20%, 30%, and 40% DE are shown in Fig. 3. It is clear that the 19th harmonic of stator current of the synchronous generator can be utilized for diagnosis the DE fault. Fig. 4 presents the corresponding curve for the salient-pole synchronous generator under above mentioned degrees of DE fault. It indicates that the 29th harmonic is a suitable index which can be used for DE fault diagnosis in salient-pole synchronous generator. Because of the approximately linear rise of 29th harmonic amplitude due to increasing DE fault, it can be used for identify the degree of the DE fault.

IV. CONCLUSIONS

In this paper, comparison between the performance of the round-rotor and salient-pole synchronous generator under DE fault was carried out using 2-D TSFE method. For this, the flux distribution within the generator, self- and mutual-inductances of rotor and stator windings and stator current signature analysis were studied. Stator current signal spectrum analysis was employed for DE fault diagnosis in the synchronous generators. It was shown that the harmonic frequency components of 19th and 29th are suitable indices which can be used for diagnosis of the DE fault and determination of its degree in round-rotor and salient-pole generator, respectively. The completed results for DE fault will be presented in the full paper.

V. REFERENCES

- [1] H. A. Toliyat, and N. A. Al-Nuaim, "Simulation and detection of dynamic air-gap eccentricity in salient-pole synchronous machines," *IEEE Trans. Industry Application*, vol. 35, no. 1, pp. 86-93, 1999.
- [2] I. Tabatabaei, J. Faiz, H. Lesani and M. T. Nabavi-Razavi, "Modeling and simulation of a salient-pole synchronous generator with dynamic eccentricity using modified winding function theory," *IEEE Trans. Magnetics*, vol. 40, no.3, pp. 1550-1555, 2004.
- [3] Faiz, J., B. M. Ebrahimi, and M. B. B. Sharifian, "Different faults and their diagnosis techniques in three-phase squirrel-cage induction motors-a review," *Electromagnetics Journal*, no. 26, pp. 543-569, 2006.

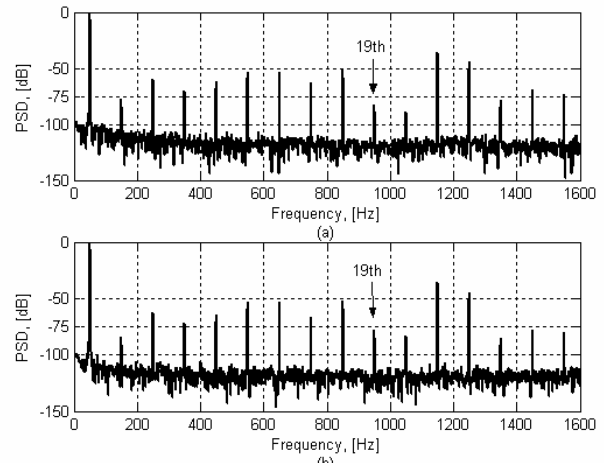


Fig. 2. Normalized spectrum of line current of round-rotor synchronous generator for: (a) healthy, (b) 40% DE.

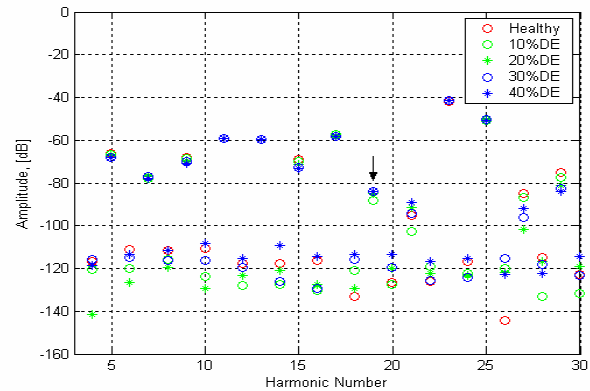


Fig. 3. Variation of harmonic amplitude of the line current in healthy round-rotor generator and the generator with 10%, 20%, 30%, and 40% DE.

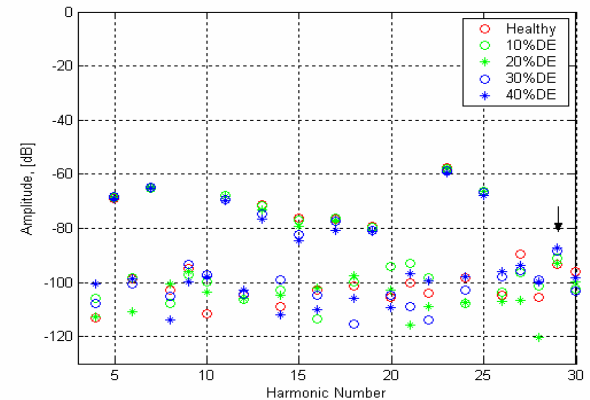


Fig. 4. Variation of harmonic amplitude of the line current in healthy salient-pole generator with 10%, 20%, 30%, and 40% DE.

- [4] S. Nandi, H. A. Toliyat, and X. Li, "Condition monitoring and fault diagnosis of electrical motors-A review," *IEEE Trans. Energy Conversion*, vol. 20, no. 4, pp. 719-729, Dec. 2005.

Magnetic Forces and Displacements Analysis of Large Scale BLDC Motor by Magneto-Mechanical Formulation

¹Pan Seok Shin, ¹Hee Jun Cheong, ¹Sung Hyun Woo, and ²Chang Seop Koh
¹Department of Electrical Eng., Hongik University, Jochiwon, Chungnam 339-701, Korea
²School of ECE, Chungbuk National University, Cheongju, Chungbuk 361-763, Korea
 E-mail Address : psshin@hongik.ac.kr

Abstract— This paper proposes a method to calculate vibration modes and forces of a large scale BLDC motor by using a magneto-mechanically coupling formulation. The mechanical vibrations are the results of the magnetic forces acting on the surfaces of the stator. The procedure of the vibration force calculation is three steps: FEM calculation of the magnetic field, local force density calculation, and calculation of the dynamic displacement and vibration modes of the stator. To verify the algorithm 3 MW BLDC motor is simulated, and the vibration modes, forces and displacement are calculated.

I. INTRODUCTION

A Vibration analysis of the large scale BLDC motor is very important for design of the mechanical structure of the motor as well as for diagnostics of the motor system. For the magnetically forced vibration analysis of the BLDC motor, the calculated magnetic forces from FE analysis are put into the equations of the mechanical motion of the stator.

Additionally, magnetoelastic phenomena is to be taken into account in the magnetic force calculation of the motor. So, it is considered not only electromagnetic exciting force but also magnetostrictive forces which effect on electrical sheets of the large stator core. The permeability and the saturated magnetization of electrical sheets are distorted by the magnetostrictive force.

To verify the proposed algorithm 3 MW BLDC motor is simulated, and the vibration modes, forces and displacement are calculated. As the results of the simulation, the displacement and the 6 major modes are found, and the results are also compared with those of the existence of the magnetostrictive force.

The magnetic field distribution and the mechanical vibrations are calculated by the finite element method. The one pole pitch model(1/32 model) is used for the magnetic field and the surface force density calculation. The whole model of the stator with frame is used for the calculation of the mechanical vibrations.

The calculation of the magnetically forced vibration is divided into three steps: to calculate the transient behavior of the magnet field vectors, to evaluate the force density on the stator surface and to transform it into the mechanical equations, and to calculate the displacement by using the components of force as forward signals.

II. MAGNETIC FIELD, FORCE AND DISPLACEMENT CALCULATION

The electromagnetic force generated by the interaction of load current with the magnet flux is calculated by the Maxwell stress method based on the finite element analysis of the equation:

$$\nabla \times (1/\mu)\nabla \times A = J - j\omega_e\sigma A + \omega_e^2 A, \quad (1)$$

where A is magnetic vector potential, σ electrical conductivity, ω_e power frequency, μ permeability, respectively. The magnetic flux density, B , and the magnetic field intensity, H , are estimated by using A .

The simulation model of the 3 MW BLDC motor has 32 poles, 192 slots with 12-phase winding in the stator. Fig.1 shows the FE model of the motor. To analyze the field in one pole-pitch(1/32 model), a magnetic field computation at 30 stator-rotor positions is carried out.

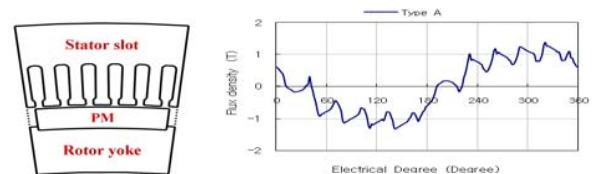


Fig.1. 1/32 Model of 5 MW BLDC motor and airgap flux density in the normal direction

For a linear approximation of the ferromagnetic material, an expression of the local surface force density, κ , is given by the Maxwell's stress tensor:

$$\kappa = \frac{1}{2}n_{12}[B_n(H_{1n} - H_{2n}) - H_t(B_{1t} - B_{2t})] \quad (2)$$

The values B and H represent the magnetic flux density and magnetic field intensity, and the subscript n , 1, and 2 describe the normal direction, region 1 and region 2 respectively(see Fig.2). Equation (2) has some assumptions of the definition of the stress tensor and the electrodynamic field-conditions on the boundary(Div $B=0$ and Rot $H=0$). Because the force is a periodic function in one pole, the surface force density function has to be approximated by a number of models, each with another rotor position. The magnetic force, F , acting on the stator surface, can be calculated by integrating κ over a closed surface.

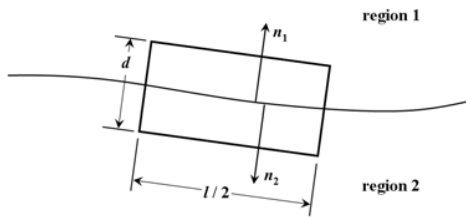


Fig.2 Boundary condition of the surface force density

The FE calculation of the dynamic displacements is based upon the principle of Hamilton, which prescribes to find the minimum of the difference from the kinetic energy and the elastic potential of the whole structure[1]. Using this principle the following system of equations is obtained.

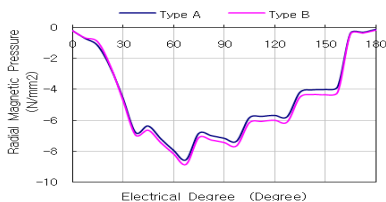
$$M \cdot D'' + K \cdot D = F \text{ or } (K - \omega_{mech}^2 \cdot M) \cdot D = F \quad (3)$$

D'' is the global vector of node displacements, M is the global mass matrix including the information of inertia and K is the global stiffness matrix, describing the elastic features of the structure[2]. The vector F includes the amplitudes of the exciting force densities which is calculated by Eq.(2). For a transient characteristics, a dynamic response analysis is performed at a point by using mode superposition method[3].

The simulation model is shown in Fig. 3(a) for mechanic calculation. The model has about 280 thousands nodes and about 185 thousands tetrahedral meshes. Fig.3(b) shows the surface force density on the stator boundary. Fig.4 shows vibration modes of 3 MW BLDC motor stator with frame: the first mode is 60.55hz, the third mode 127.63Hz, the fifth mode 199.2 hz. Fig.5 shows a time response of displacement on a point of the stator to the radial direction. Fig. 6 shows an effect of the magnetostrictive force on the displacements in the axis direction: type A is the conventional, type B is considered the magnetostrictive force.

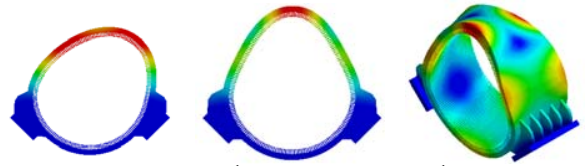


(a) FE model of BLDC motor stator



(b) Force density along stator surface(one pole)

Fig.3 Simulation model of the stator(inner radius : 1450mm) and force density



(a) 1st mode(60.55hz) (b) 3rd mode(127.63Hz) (c) 5th mode(199.2 hz)
Fig.4. Vibration modes of 3 MW BLDC motor stator with frame

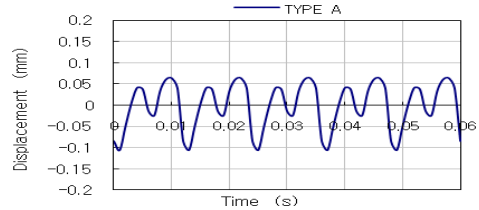


Fig. 5. A time response of displacement on a point of the stator (radial direction)

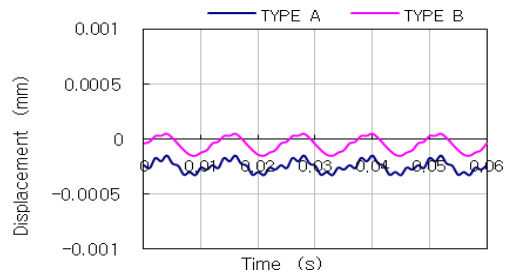


Fig. 6. A comparison of time response of displacements in the axis direction with type A and B.

III. SUMMARY

This paper proposes a method to calculate the vibration modes and forces of a large scale BLDC motor by using an electromechanically coupled formulation. The mechanical vibrations are the results of the magnetic forces acting on the surfaces of the stator. The procedure of the vibration force calculation is three steps: FEM calculation of the magnetic field, local force density calculation, and calculation of the dynamic displacement of the stator. To verify the algorithm 3 MW BLDC motor is simulated, and the vibration modes, forces and displacement are calculated.

ACKNOWLEDGMENT

This work has been supported by ETEP(2006-0273) which is funded by MOCIE (Ministry of Commerce, Industry and Energy, ROK)

IV. REFERENCES

- [1] G. Henneberger, and et.al., IEEE Trans on Magnetics, vol.28, no.2, pp.1351-1354, March 1992
- [2] I. Ramesohl, and et.al., IEEE Trans on Magnetics, vol.32, no.3, pp.1685-1688, March 1992
- [3] Hee Jun Cheong, Master thesis, Hongik University, Korea, August 2008.

Optimized Coil Position for Improvement of Holding Torque of the PM - Spherical Motor

Sung-Hong Won¹, Dong-Woo Kang², Won-Ho Kim², Sung-Chul Go², Cheol-Jick Ree³,
and Ju Lee², *Senior Member, IEEE*
Dongyang Technical college¹
Electric Engineering, Hanyang university²
Electrical Engineering, Daelim college³
Gocheok – dong, 152-080, Seoul, South Korea
sagewide@dongyang.ac.kr

Abstract— A permanent magnet spherical motor is novel concept an electric machine which has two performance features as rotation mode and position one [1]. In this paper the authors propose the modified coil position on the stator of the permanent magnet spherical motor for improving characteristic of position mode. A characteristic of the holding torque depends on the position between stator coils and rotor magnets, because the rotation of the stator and rotor has to be considered on 3-dimensional. A characteristic of the holding torque is important factor to decide the stable tilt angle of the rotor. Therefore the authors researched into the feature of the holding torque as using the finite element method and another numerical one. As following results from the comparison two methods, the improved performance of the spherical motor is verified by experimental results.

I. INTRODUCTION

The manipulator, 3D-measuring instruments, and robot system have a characteristic of multi-degree of freedom performance. These machines have several motors which can rotate as multi-degree of freedom operation.

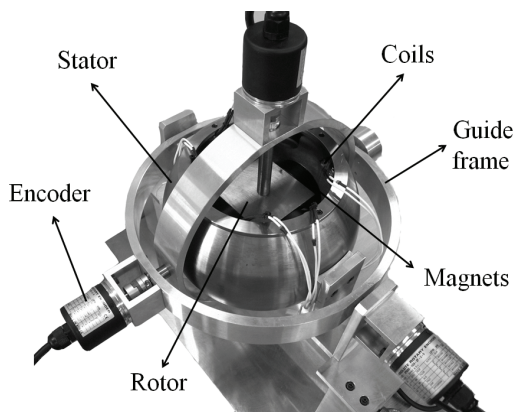


Fig. 1. Permanent-magnet spherical motor

The permanent-magnet spherical motor can perform the multi-degree of freedom as only one motor like Fig. 1. The remarkable feature of the permanent magnet spherical motor is that the shaft can be tilted while the rotor is rotating continuously [2]-[3]. However the characteristic of tilt operation depends on mechanical structure of the machine and position between coils and magnets of the motor. Especially, the coils position has to be optimized for improving the motor

performance first. Besides the coil position relates with torque stabilization and operating range of the rotor tilt degree. Therefore the authors researched into the characteristic of the holding torque by using numerical methods as a function of coil position.

II. TORQUE CHARACTERISTIC

A. Proposed Model

The permanent-magnet spherical motor consists of 4 Nd-permanent magnets on the rotor and 12 coils on the stator. The summed holding torque, which is generated between coils and magnets, decides a rotor position. The structure is shown in fig. 2.

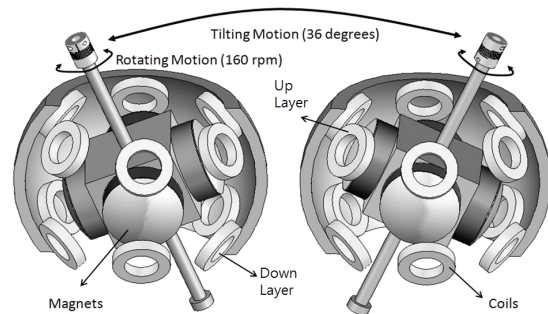


Fig. 2. Structure of permanent magnet spherical motor

B. System Modeling

The components position of rotor and stator is identified as using spherical coordinates system : r , θ , and φ as well as their torque like (1) [4]-[5].

$$\vec{T}_{jk} = f(\varphi_{jk}) \frac{\vec{S}_j \times \vec{R}_k}{|\vec{S}_j \times \vec{R}_k|} n_c i_j \quad (1)$$

n_c : the number of turns per coil
 i_j : the current value of i_{jk}
 S_j : the position vector of j_{th} coil
 R_k : the position vector of k_{th} magnet
 φ_{jk} : the angle between S_j and R_k

The holding torque is summed vector calculated from position as coils and magnets. Therefore the torque is computed by using the torque profile function as $f(\varphi_{jk})$ and unit direction vector of each component as coils and magnets. The torque profile function is calculated by using Finite Element Method. Even though the Finite Element Method is useful computation method for electromagnetic field calculation, the long computation time is a serious

disadvantage. Therefore it has many advantages that the holding torque is computed by the torque profile function.

III. IMPROVEMENT TORQUE CHARACTERISTIC

The torque is generated between coils on the stator and magnets on the rotor. Fig. 3 shows the torque characteristic as function of the position between coil and magnet.

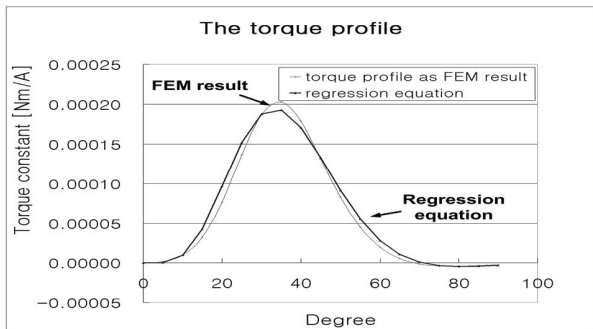


Fig. 3. The torque profile function as using FEM and Regression Method

Fig. 4 shows simulation models for studying the torque characteristic. Each simulation model shows different stability characteristic of the holding torque. In this paper, optimized structure of stator improving coil position is researched.

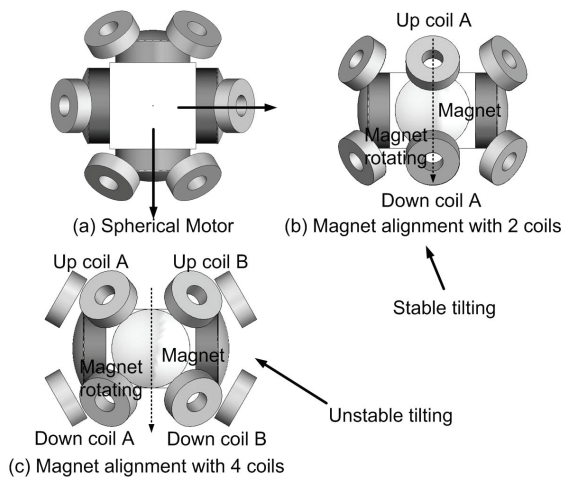


Fig. 4. Simulation model for optimization of the holding torque

Fig. 5 shows simulation results of holding torque profile. The holding torque shows different stability depending on situation of magnet position with coils. Therefore, in this paper, factor of instability holding torque is analyzed and the coil position on the stator is optimized by using numerical method for computation electromagnetic field. Finally the results are verified by experiment.

IV. CONCLUSION

The permanent magnet spherical wheel motor is able to tilt and rotate at 3 axes as the Yaw, Pitch, and Roll. Because the holding torque depends on structure of coils and magnets, however, the torque which is generated from them has to be

simulated by numerical method as 3D FEM. Even though the FEM method is used to analysis for the electromagnetic field, it is a problem to have a long computation time. For improving the disadvantage of calculation time, the authors use novel numerical method as using the torque profile function for calculating electromagnetic field. When the magnet is controlled by 4 coils, the holding torque shows instability phenomenon. Based on this torque feature, the model of 60 degrees coil position which is prototype motor is modified to 36 degrees coil position. Finally the torque is generated for holding the rotor stably.

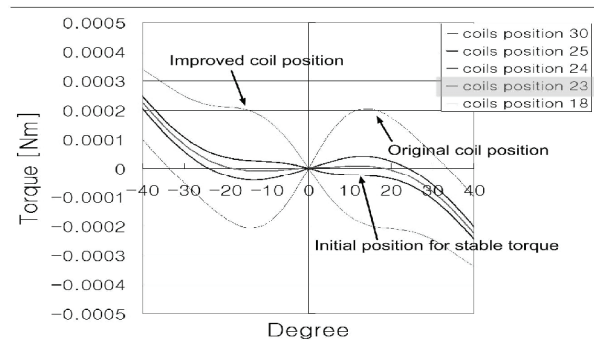


Fig. 5. Comparison data of stability holding torque

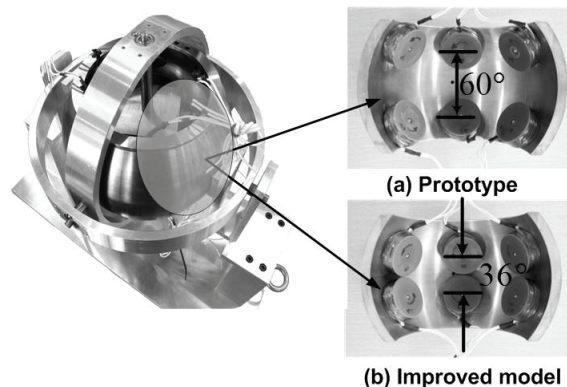


Fig. 6. Optimized structure of stator

V. REFERENCES

- [1] J. Wang, K. Mitchell, G. W. Jewell and D. Howe, "Multi-Degree-of-Freedom Spherical Permanent Magnet Motors", International Conference on Robotics & Automation, pp. 1798-1805, 2001, proceedings of 2001 IEEE.
- [2] Kok-Meng Lee and Hungsun Son, "Torque Model for Design and Control of a Spherical Wheel Motor", International Conference on Advanced Intelligent Mechatronics, pp. 336-340, 2005, proceeding of the 2005 IEEE/ASME.
- [3] Chee Kian Lim, Liang Yan, I-Ming Chen, Guilin Yang and Wei Lin, "A Novel Approach In Generating 3-DOF Motions", International Conference on Mechatronics & Automation, pp. 1485-1490, 2005, proceedings of the IEEE.
- [4] D. SPALEK, "Analytical electromagnetic field and forces calculation for linear, cylindrical and spherical electromechanical converters", BULLETIN OF THE POLISH ACADEMY OF SCIENCES TECHNICAL SCIENCES, pp. 239-250, 2004.
- [5] Kok-Meng Lee, Hungsun Son and Jeffrey Joni, "Concept Development and Design of a Spherical Wheel Motor(SWM)", International Conference on Robotics and Automation, pp. 3652-3657, 2005, proceedings of the 2005 IEEE.

Comparative study of the inductances of an induction motor with rotor eccentricities

E. F. R. Velandia¹, J. A. Santisteban², A. C. Ferreira³.

^{1,2} Universidade Federal Fluminense
Rua Passo da Pátria, 156 – Bloco E Sala 107
São Domingos – Niterói – RJ – Brazil
CEP 240210-240

³ Universidade Federal do Rio de Janeiro
COPPE – Programa de Engenharia Elétrica,
P.O. Box 68.504 21.945-970 – Rio de Janeiro – RJ –
Brazil

elkinrodvel@msn.com, jasantisteban@vm.uff.br and ferreira@coep.ufrj.br

Abstract — In this work the inductances of an induction motor, which rotor may be misaligned, are evaluated. This motor is intended to be used as a self bearing motor with split windings. Two types of analysis are performed: Analytical method (AM) and Finite Element Method (FEM). Results suggest the best reliability of FEM as with AM it is not possible to take into account effects like leakage flux.

I. INTRODUCTION

Induction motors with split windings operating as self bearing motors are being studied since 1989 [1]-[2]. With this configuration it is possible to generate torque and radial positioning forces. With this approach some works were reported in the literature focusing on starting and constant speed operation [3], [4]. Strategies of speed control with good responses were also reported in [5] and [6]. Nevertheless, the effects of possible misalignment between rotor and stator were not considered.

With this in mind, the interaction between magnetic fluxes from induction motor when submitted to misalignment is being studied [7]-[8]. One interesting analytical method (AM) is presented in [9]. This is characterized by considering cylindrical the surfaces of stator and rotor. In this work, this method is compared with simulations using the Finite Elements Method (FEM) which has been consolidated as an useful tool in the study of non-linear phenomena and of great complexity.

The aim of this work is to study the behavior of self and mutual inductances of an induction motor when submitted to radial misalignment. These results will allow for the prediction of possible interferences between the magnetic effects inside the motor: torque and radial forces. These concerns are present in the so called self bearing motor with split windings.

II. ANALYTICAL DETERMINATION OF MOTOR INDUCTANCES WITH NON UNIFORM AIRGAP

The machine analyzed in this work is a four poles, two phase induction motor. Each phase is composed of four windings that are connected in series in normal operation. When operating as a self bearing motor, each of the windings of one phase is supplied separately in order to get radial positioning. The other windings are connected in series and supplied simultaneously allowing starting torque.

A. Analytical Method

Assuming that the eccentricity of the rotor is limited to the airgap, it is possible to approximate the inverse to airgap as the following function [7]:

$$P(\kappa) = \frac{1}{g(\kappa)} = \frac{1}{g_0} \sum_{i=0}^{\infty} P_i \cos(i\kappa - i\alpha). \quad (1)$$

Where κ is the reference angle of stator windings, α is the mechanical angle of displacement of the rotor, g_0 is the uniform airgap, and:

$$P_0 = \frac{1}{\sqrt{1-\varepsilon^2}}$$

$$P_i = 2P_0 \left(\frac{1-\sqrt{1-\varepsilon^2}}{\varepsilon} \right)^i. \quad (2)$$

Where ε is the eccentricity between of the centers of rotor and stator, as shown in Fig. 1.

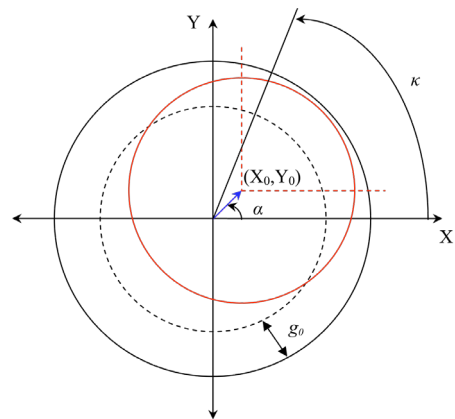


Fig. 1. Eccentricity of airgap.

Due to the variation of magnetic field caused by the eccentricities of airgap along any portion of winding v , it is possible to find:

$$\int_{air-gap} \vec{H}_v(\kappa) \cdot d\vec{l} = n_v(\kappa) i_v. \quad (3)$$

Where H_v is the magnetic field intensity, n_v , the turn function (number of coils), which depends of κ and i_v is the winding current.

Manipulating (3) and (1), using the Gauss law for magnetic fields in closed surfaces, assuming that the magnetic permeability of the core is infinite, that magnetic field is homogenous along the axial direction, that the dispersion of the magnetic field on both extremities of the rotor is neglected and considering that the airgap is very short when compared with the rotor radius, self and mutual inductances can be evaluated as in (4) and (5) respectively.

$$L_{vv} = \frac{\lambda_{vv}}{i_v} = \mu_o r l \int_0^{2\pi} n_v(\kappa) N_v(\kappa) P(\kappa) d\kappa \quad (4)$$

$$L_{vw} = \frac{\lambda_{vw}}{i_w} = \mu_o r l \int_0^{2\pi} n_v(\kappa) N_w(\kappa) P(\kappa) d\kappa \quad (5)$$

Where N_v and N_w are the winding functions.

B. Finite Elements Method (FEM)

The complexity of the machine demands great care in its modeling through FEM. A three dimensional simulation would be more appropriate but it demands a high computational effort. For this reason it was chosen a two dimensional simulation using an appropriated refinement on the mesh.

From electromagnetism the inductance can be expressed as:

$$L = \frac{N}{I} \Psi. \quad (6)$$

Where L is the inductance, I is the current, N is the number of coils and Ψ is the magnetic flux which can be obtained from (7).

$$\Psi = \int (\nabla \times \mathbf{A}) \cdot d\mathbf{s}. \quad (7)$$

According to *Stoke* theorem and calculating the vector potential from its nodal values, it is possible to determine one relationship to calculate the inductance in a general form:

$$L = \frac{N}{I} \frac{l}{S} \sum_{i=1}^m \left(\frac{S_i}{n} \sum_{j=1}^n A_{ij} \right). \quad (8)$$

Where l is the length, A_{ij} the nodal potential vector, S is the total area in study, S_i the element area, m is the number of element and n is the number of nodes by element (first-order triangle elements).

III. COMPARATIVE RESULTS

As an example, the self inductances of horizontal windings of phase-A were evaluated using the two methods. In Fig. 2 were considered horizontal disalignments. As observed, the average error between analytical results and FEM results was around 7% which can be explained by the strong approximations used with the analytical method.

Additionally, with FEM it was possible to evaluate inductance variations when angular changes of the rotor were simulated. The analytical simulation would be extremely complex. As one example, the behavior of self inductance of the second winding of phase-A, when submitted to radial and angular displacements, is shown in Fig. 3.

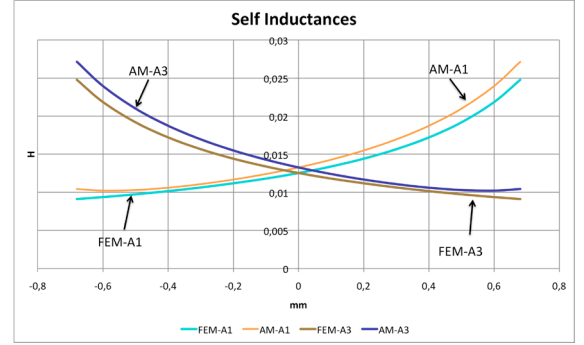


Fig. 2. Self inductances of horizontal windings of phase A submitted to horizontal displacements.

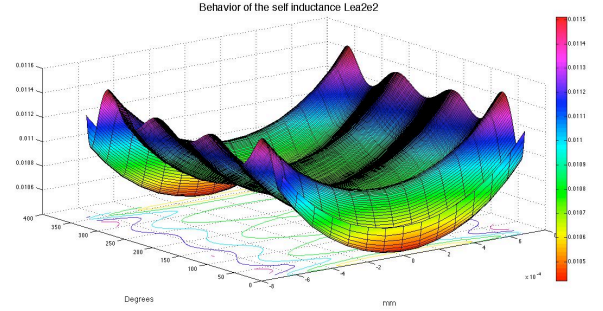


Fig. 3. Behavior of the self inductance of the winding 2 from phase A submitted to linear and angular displacements.

A. Conclusion

The results suggest the reliability on finite elements method in order to calculate inductance variations when there are linear and angular displacements inside an induction motor. The importance of these results is related to the use of them to evaluate the performance of a self bearing motor, where there are simultaneous torque and radial force effects.

IV. REFERENCES

- [1] Salazar, A. O., "Mancais Magnéticos para Motores de Indução Utilizando os Enrolamentos do Estator", Master dissertation, COPPE, UFRJ, Rio de Janeiro, 1989.
- [2] Salazar, A. O., Stephan, R. M., Watanabe, E. H. e Dunford W., "Mancal Magnético para motores CA utilizando enrolamentos do estator", Sep. 1991, Patente INPI No. 910367.
- [3] Gomes, R. R., "Motor Mancal com Controle implementado em um DSP", Master dissertation, COPPE-UFRJ, Rio de Janeiro, 2007.
- [4] Ferreira, J. M. S., "Proposta de Maquinas de Indução Trifásica sem Mancais com Bobinado Dividido", Master dissertation, PGEE-UFRN, Natal, 2002.
- [5] Ferreira, J. M. S., "Modelagem de Máquinas de Indução Trifásica sem Mancais com Bobinados Dividido", Doctoral dissertation, PGEE-UFRN, Natal, 2006.
- [6] Paiva, J. A., "Controle Vetorial de Velocidade de uma Máquina de Indução sem Mancais Trifásica com Bobinado Dividido Utilizando Estimação Neural de Fluxo", Doctoral dissertation, PGEE-UFRN, Natal, December 2007.
- [7] Tera, T., Yamauch Y., Chiba A., "Performances of Bearingless and Sensorless Induction Motor Drive Based on Mutual Inductances and Rotor Displacements Estimation", *IEEE Transactions on Industrial Electronics*, 53 (1), 2006.
- [8] Joksimovic, G. M., "Dynamic Simulation of Cage Induction Maxhine with air gap eccentricity", *IEE Proceedings online*, 152 (4), 2005.
- [9] Faiz, J., Tabatabaei, I., "Extension of Winding Function Theory for Nonuniform Air Gap in Electric Machinery", *IEEE Transactions on Magnetics*, 38 (6): 3654-3657, 2007.

Development of a Flexible Phase Variable Model for Two-Phase Hybrid Stepping Motor Using Virtual Magnetic Gateway based FEA

Jiixin Chen¹, Youguang Guo², Jianguo Zhu², and Weinong Fu³

¹College of Electromechanical Engineering, Donghua University, Shanghai 201620, China

²School of Electrical, Mechanical and Mechatronic Systems, Faculty of Engineering and Information Technology, University of Technology Sydney, P.O. Box 123, Broadway, NSW 2007, Australia

³Department of Electrical Engineering, Hong Kong Polytechnic University, Hong Kong, China
chjiixin@dhu.edu.cn, youguang@eng.uts.edu.au, joe@eng.uts.edu.au, eewnfu@polyu.edu.hk

Abstract— This paper presents the development of a flexible phase variable model for the performance prediction of two phase hybrid stepping motor (HSM) by employing advanced design and analysis techniques. In the parameter calculation of the motor, a virtual magnetic gateway based 2-D magnetic field finite element analysis with multi-levels are conducted to calculate the air gap flux, back electromotive force (*emf*), and self and mutual inductances of the stator windings. To predict the dynamic performance, a Simulink-based phase variable model is built, taking into account the real waveforms of applied phase voltage, back *emf* and current. To increase the flexibility and accuracy of the model, both the mixed digital-analog based technique for different digital-analog mixed systems and the controllable voltage source based technique for the nonlinearity of HSM are introduced. The model has been implemented in the development of a HSM drive system for driving embroidery machine. The predictions are in good agreement with experimental results.

I. INTRODUCTION

Hybrid stepping motors (HSMs) have been popular in low speed applications thanks to their many advantages such as high torque density and high resolution [1]. Considering the wide use of the HSM drives which are often highly nonlinear, it is desired to develop a numerical model with high practical merit for predicting the drive performance. To achieve the practical merit, including the accuracy, efficiency, flexibility and easiness, the following issues should be resolved first: calculation of the parameters in the equivalent electric circuit of HSM, flexible structure of numerical model, and appropriate expression of electrical parts in the circuit [2]-[4].

HSM drives belong to the field-circuit coupled system with high nonlinearity. The HSM features 3-D flux pattern and very tiny air gap which causes high magnetic saturation in the teeth, so 3-D numerical magnetic field analysis is a very challenging task and little satisfactory work has been completed so far. In this paper, a virtual magnetic gateway based 2-D finite element analyses (FEA) with multi-levels are applied to calculate the air gap flux. Based on the field solutions, all the parameters in the equivalent electric circuit of HSM such as back electromotive force (*emf*) and self and mutual winding inductances can be obtained efficiently.

A modern HSM drive system is often composed of both digital subsystem and analogue subsystem. A digital system can be modified by designing the corresponding program in a

block. However, as an analog system has fixed characteristic and a model cannot satisfy the requirement of different systems, it is required that the function of analog system in the simulation tool can be easily modified. In this paper, Simulink is used to build the simulation model, which can provide the functions of digital system and analog system simultaneously.

The self and mutual inductances and back *emf* in the HSM model are generally processed as the function of applied magneto-motive force (*mmf*) and rotor position, but there no such direct corresponding parts in the power electronics block of Simulink. In this paper, the technique of controllable voltage source obtained by combining power electronics block and general simulation block in Simulink is proposed.

II. PHYSICAL PHASE VARIABLE MODEL

The phase variable model of two-phase HSM is given as

$$\begin{bmatrix} U_a \\ U_b \end{bmatrix} = r \begin{bmatrix} i_a \\ i_b \end{bmatrix} + \frac{d}{dt} \begin{bmatrix} \psi_{sa} \\ \psi_{sb} \end{bmatrix} + \begin{bmatrix} e_a \\ e_b \end{bmatrix} \quad (1)$$

$$\begin{bmatrix} \psi_{sa} \\ \psi_{sb} \end{bmatrix} = \begin{bmatrix} L_{aa} & L_{ab} \\ L_{ba} & L_{bb} \end{bmatrix} \begin{bmatrix} i_a \\ i_b \end{bmatrix} \quad (2)$$

$$\begin{bmatrix} \frac{d\psi_a}{dt} \\ \frac{d\psi_b}{dt} \end{bmatrix} = \begin{bmatrix} \frac{\partial \psi_a}{\partial i_a} & \frac{\partial \psi_a}{\partial i_b} \\ \frac{\partial \psi_b}{\partial i_a} & \frac{\partial \psi_b}{\partial i_b} \end{bmatrix} \begin{bmatrix} \frac{di_a}{dt} \\ \frac{di_b}{dt} \end{bmatrix} + \begin{bmatrix} \frac{\partial \psi_a}{\partial \theta} \\ \frac{\partial \psi_b}{\partial \theta} \end{bmatrix} \frac{d\theta}{dt} \\ = \begin{bmatrix} L'_{aa} & L'_{ab} \\ L'_{ba} & L'_{bb} \end{bmatrix} \begin{bmatrix} \frac{di_a}{dt} \\ \frac{di_b}{dt} \end{bmatrix} + \begin{bmatrix} \frac{dL_{aa}}{d\theta} & \frac{dL_{ab}}{d\theta} \\ \frac{dL_{ba}}{d\theta} & \frac{dL_{bb}}{d\theta} \end{bmatrix} \begin{bmatrix} i_a \\ i_b \end{bmatrix} \Omega \quad (3)$$

$$T_e = \frac{e_a i_a + e_b i_b}{\Omega} + T_{cog} \quad (4)$$

$$J \frac{d\Omega}{dt} = T_e - B\Omega - T_L \quad (5)$$

$$d\theta_m / dt = \Omega, \theta = Z_r \theta_m \quad (6)$$

where e_a and e_b are the back *emfs*, the ψ_{sa} and ψ_{sb} are the flux linkages contributed by the stator currents, θ is the electrical

angle, θ_m is the mechanical angle, Z_r is the number of gears on the rotor, L is the apparent inductance and L' is the incremental inductance. The rest variables are used as their conventional meaning.

III. ANALYSIS AND RESULTS

According to (1)-(6), the physical phase variable model of HSM is illustrated in Fig. 1, which consists of two parts: the power electronics circuit block and the digital control system; both of them correspond to the practical HSM drive system.

As an example, the circuit diagram of the phase “a” winding of the HSM is shown in Fig. 2, in which the controlled voltage source (CVS) or the controlled current source (CCS) is used, and all the parameters such as apparent inductance, increment inductance and back *emf* are calculated in advance by FEA and stored in look-up tables.

For parameters calculation, a virtual magnetic gateway based 2-D magnetic FEA with multi-levels are applied to calculate the air gap flux. It is known that the distribution of magnetic flux density in the air gap varies sharply [1]-[2], but the distribution of magnetic flux density varies smoothly in the teeth. According to the FEA results, the magnetic force lines in the tooth root are approximately parallel, showing that the magnetic potential level of each point on the circle with the same radius is similar, then the radial permeance between the stator tooth root and the rotor tooth root can be processed as a function of applied *mmf* and rotor position. Fig. 3 shows the FEA result using the virtual magnet gateway. Based on field solutions, all the parameters in the equivalent electric circuit of HSM such as back *emf*, self and mutual inductances of the stator windings are obtained efficiently. Detailed field analysis will be presented in full paper.

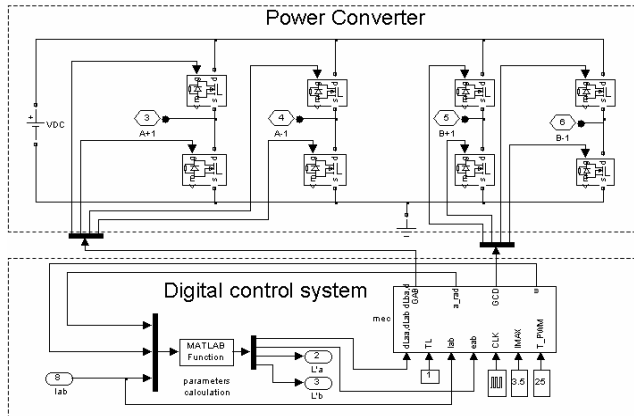


Fig. 1. Developed physical phase variable model

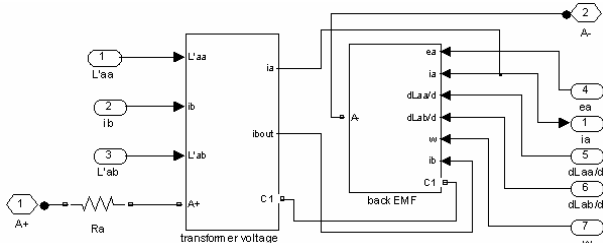


Fig. 2. Circuit diagram of the HSM stator phase winding

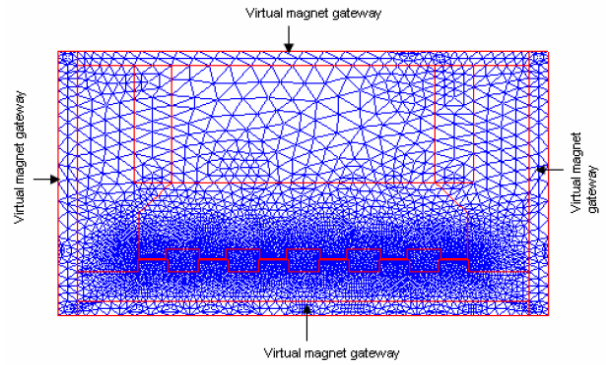


Fig. 3. FEA of a two-phase HSM using virtual magnetic gateway

Running the Simulink based model with the calculated parameters, various drive performance can be obtained and some results are shown in Fig. 4. Experiments have been conducted on the two phase HSM, validating the simulations.

More theoretical analysis and experimental results will be presented in the full paper.

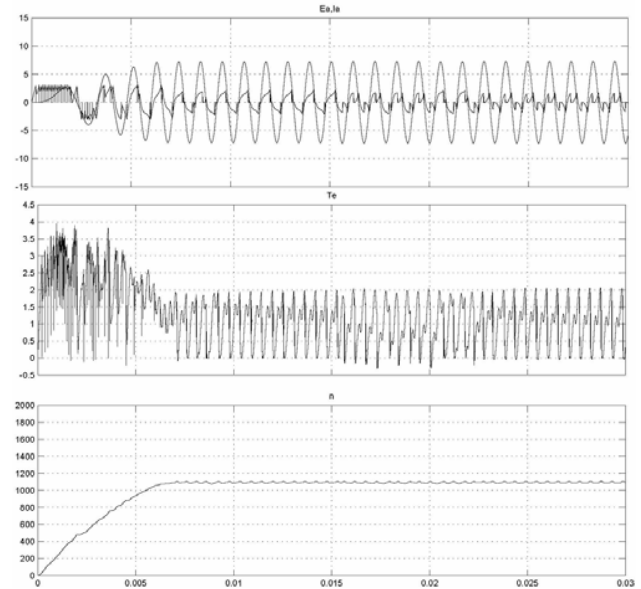


Fig. 4. Simulated results by using the flexible phase variable model

IV. REFERENCES

- [1] K.B. Jang, S.Y. Lim, T.B. Lim, C.S. Jin, Y.H. Cho, Y.T. Kim, and J. Lee, “2-D FE analysis of hybrid stepping motor using virtual magnetic barrier,” *IEEE Trans. on Magnetics*, 39(5): 3268-3270, 2003.
- [2] N. Matsui, M. Nakamura, and T. Kosaka, “Instantaneous torque analysis of hybrid stepping motor,” *IEEE Trans. on Industry Applications*, 32(5): 1176-1182, 1996.
- [3] O.A. Mohammed, S. Liu, and Z. Liu “A phase variable model of brushless dc motors based on finite element analysis and its coupling with external circuits,” *IEEE Trans. on Magnetics*, 41(5): 1576-1579, 2005.
- [4] J.X. Chen, Y.G. Guo, and J.G. Zhu, “Development of a high-speed permanent-magnet brushless dc motor for driving embroidery machines,” *IEEE Trans. on Magnetics*, 43(11) pp. 4004-4009, 2007.

Novel Modeling of Flux-barriers in Interior-type PM Synchronous Motor For Pulsation Torque Reduction: Part I. Various Flux-barrier Design

Liang Fang, Jeong-Jong Lee, Jung-Pyo Hong
 Department of Automotive Engineering, Hanyang University
 Haengdang-dong, Seongdong-gu, Seoul 133-791, Korea
 fangliang@hanyang.ac.kr, hongjp@hanyang.ac.kr

Abstract—This paper examines the flexibility of flux-barrier design for pulsation torque reduction in an interior permanent magnet synchronous motor(IPMSM). As well known, the torque characteristics are significantly related to the magnet pole-arc variation, which can be flexibly determined by the unique flux-barrier design in the IPM rotor. In this study, a prototype conventional single-layer IPMSM model, a popular double-layer IPMSM model and a proposed novel double-barrier IPMSM model are built and optimized for reducing the pulsation torque, consisting torque ripple and cogging torque. The novel IPMSM model has beneficial attributes of economic single-layer IPM for manufacture and flexible double pair of flux-barriers for IPM rotor design. The geometries of buried flux-barriers in analysis models are optimized by using the response surface methodology (RSM). Finite element analysis(FEA) and test results confirmed the validity of presented pulsation torque computation. In final, the proposed novel double-barrier IPMSM model is well proved to be quite effective for pulsation torque reduction.

I. INTRODUCTION

The interior permanent magnet synchronous motors (IPMSM) have wide applications in household goods, industrial use, and electric and hybrid vehicle propulsion[1]. The IPMSMs offer some superior advantages, such as high efficiency, high torque density and wide speed range[1].

However, from the torque characteristic point of view, the significant pulsation torque is an inherent drawback of IPMSM. For most practical applications, the reduction of torque ripple and cogging torque is always an essential requirement, for avoiding mechanical resonance, vibration, acoustic noise and damage to drive component, realizing motor runs smoothly[1]. There are many papers focused on torque ripple or cogging torque reduction in IPMSM, and proposed some effective approaches, such as the magnet pole-arc design method.

As known, the conventional single-layer IPMSM has only one pair of flux-barriers with each single PM piece buried in rotor iron, that propitious to manufacture. And the popular double-layer IPMSMs are attractive since their double pair of flux-barriers can be utilized for reducing torque pulsation[2]. In addition, this paper proposes a novel IPMSM model features double flux-barrier created with each single-layer IPM.

By using response surface methodology(RSM), the shape of flux-barriers in analysis models are optimized. Then, finite element analysis(FEA) and test results confirm the validity of the proposed design is effective for reducing torque pulsation.

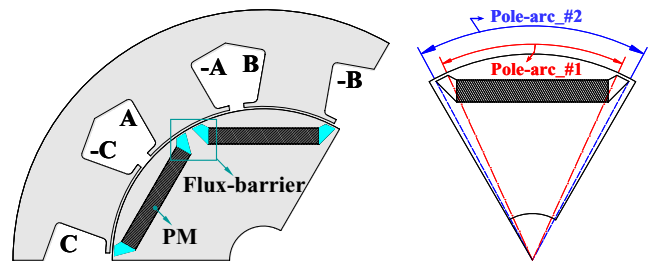


Fig. 1. Configuration of conventional single-layer IPMSM model.

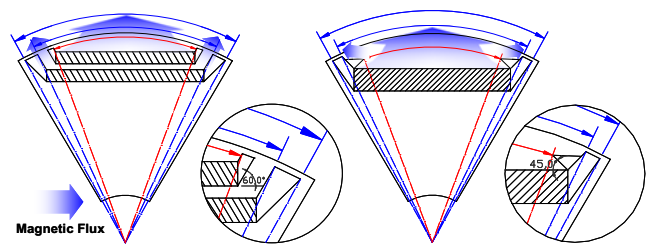
II. ANALYSIS MODELS

As Fig.1 shows, a prototype 6-pole/9-slot IPMSM model is given as a driving compressor of a hybrid electric vehicle. The stator has 3-phase concentrated windings, and the rotor adopts conventional single-layer IPM design, in which the PM pole-arc is described by flux-barrier with pole-arc_#1 and #2.

III. FLUX-BARRIERS DESIGNS IN IPMSM

The effect of various flux-barrier designs on the reduction of pulsation torque in IPMSM is analyzed in this study. Base on the prototype single-layer IPMSM model, a double-layer IPMSM model is built by splitting the same amount of PM into thin pieces. It correspondingly creates two pairs of separated flux-barrier to be utilized for effectively distributing the magnetic flux crossing into air-gap field, as Fig. 2(a) gives. It should be noticed that double-layer IPM design will unavoidably increase the manufacture cost, and may cause PM irreversible demagnetization since thin PMs are employed.

A novel double-barrier IPM rotor model is proposed, as Fig. 2(b) illustrates. The single-layer buried PM has two pairs of connected flux-barrier, which is similar to the effectivity of double-layer IPM design for redistributing magnetic flux.



(a) Double-layer IPM design

(b) Double-barrier IPM design

Fig. 2 Double pairs of flux-barrier designs based on prototype IPM rotor

IV. IPM ROTOR DESIGN OPTIMIZATION

The multiple flux-barriers design is very complex owing to many design factors. Therefore, RSM, as a validated economic optimization technique[3], is applied to flux-barriers optimal design. The torque ripple and cogging torque are chosen as the design objectives in RSM, which are calculated by using the equivalent circuit method coupled with FEA.

In each flux-barrier optimal design, the magnet pole-arcs determined by the flux-barriers variation are used as the only design variables for simple consideration. TABLE 1 lists the experiment ranges of each design variables in RSM.

TABLE 1
RANGES OF DESIGN VARIABLES FOR OPTIMIZATION IN RSM

Analysis IPMSM Model	Pole-arc #0 [Outer layer]	Pole-arc #1 [Inner layer]	Pole-arc #2 [Inner layer]
Single-layer design		41° ~ 48°	54.2° ~ 59.2°
Double-layer design	35.4° ~ 41°	46° ~ 52°	54.2° ~ 59.2°
Double-barrier design	35.4° ~ 41°	46° ~ 52°	54.2° ~ 59.2°

* Outer layer: the upper PM layer closing to rotor surface.
* Pole-arc #0 is defined for the pole-arc of "Outer-layer" PM with red lines.

V. RESULTS AND DISCUSS

The optimal flux-barriers designs of each IPMSM models are determined with desired design objective results in RSM, as Fig. 3 illustrates. And their torque ripple and cogging torque characteristics are confirmed by FEA. Compare with single-layer IPM design, the double-layer IPM design and proposed novel double-barrier IPM design are both effective for reducing the pulsation torque, by which the torque ripple reduced from 16.5% to 10.0% and 7.0% separately, and cogging torque relatively decreased 46.7% and 66.7%, as Fig.4 results show. In addition, the optimized double-layer IPMSM is fabricated and tested as Fig. 5 shows. The tested cogging torque has a good agreement with FEA result, as Fig. 6 gives, and the measured torque ripple [7.8%] is smaller than the FEA result [10.0%]. The error is thought caused by the influence of reduction gear inertial.

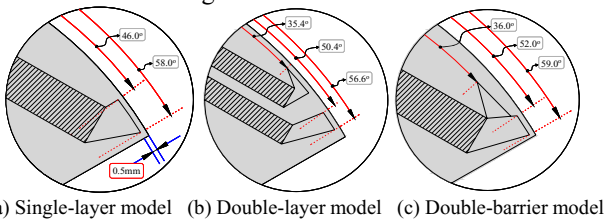


Fig. 3. Optimized flux-barriers designs in IPMSM analysis model

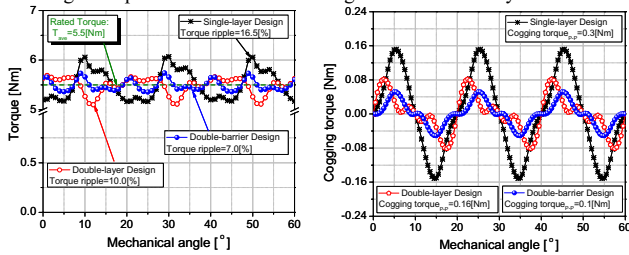
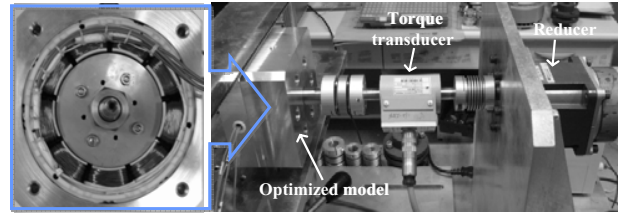


Fig. 4. Torque ripple at rated operation and cogging torque results



(a) Motor appearance. (b) Test apparatus for torque ripple measurement

Fig. 5. Torque performance test of fabricated optimized double-layer IPMSM

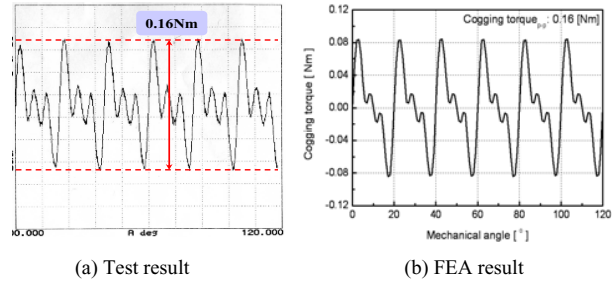


Fig. 6. Cogging torque results of optimized double-layer IPMSM

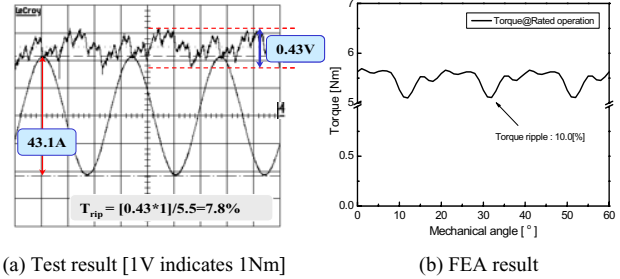


Fig. 7. Torque ripple results @Rated Tave=5.5Nm, and I= 15.3A, $\beta=32.5^\circ$

VI. CONCLUSION

Torque ripple and cogging torque reduction in IPMSMs by flexibly designing the buried flux-barriers is presented in this paper. The proposed novel double-barrier IPMSM design has unique features as each single-layer IPM coupled with double pairs of connected flux-barriers, which shows similar attribute of the popular double-layer IPMSM design, but realizing the simplicity and low-costing for manufacture. The novel double-barrier design is proved to be an effective approach for reducing pulsation torque in IPMSM by comparing with the other two design models. The FEA and test results well confirmed the validity of presented pulsation torque analysis. Generally, the proposed novel IPM design has cost advantage to the double-layer IPM design for effectively reducing pulsation torque.

VII. REFERENCES

- [1] John M. Miller, Propulsion systems for hybrid vehicles, The Institution of Electrical Engineers, 2004.
- [2] Liang Fang; Jae-woo Jung; Jung-Pyo Hong; Jung-Ho Lee, "Study on High-Efficiency Performance in Interior Permanent-Magnet Synchronous Motor With Double-Layer PM Design," *IEEE Trans. Magn.*, vol. 44, Issue 11, Part 2, Nov. 2008.
- [3] Sung-Il Kim; Ji-Young Lee; Young-Kyoun Kim; Jung-Pyo Hong; Hur, Y.; Yeon-Hwan Jung, "Optimization for reduction of torque ripple in interior permanent magnet motor by using the Taguchi method," *IEEE Trans. Magn.*, vol. 41, Issue 5, May 2005.

Parametric Finite Element Analyses of a Permanent Magnet Synchronous Machine with an External Rotor

Erich Schmidt, Marko Sušić

Institute of Electrical Drives and Machines, Vienna University of Technology, Vienna, Austria
erich.schmidt@ieam.tuwien.ac.at, marko.susic@ieam.tuwien.ac.at

Abstract – Permanent magnet synchronous machines with an external rotor nowadays gain in significance for high performance electrical drive systems such as with hybrid electric vehicles. With these applications, the machine will operate in a wide speed range and on the other hand with very fast changing loads in both motor and generator operational modes. In order to achieve a robust machine design, a position-sensorless control scheme using the dependence of the stator inductances on the rotor position is of great interest. With this intent, the paper discusses finite element analyses for the optimization of such permanent magnet machines with external rotors. Regarding the geometry parameters, a magnetic saliency necessary for the sensorless control scheme has to be preserved in the whole range of the operational modes.

I. FINITE ELEMENT MODELLING

Fig. 1 depicts the basic geometry with 24 poles of the investigated permanent magnet synchronous machine with an external rotor. In order to study the torque ripples, both unskewed and skewed stator slots as well as integer and fractional slot windings with concentrated coils are concerned with the analyses.

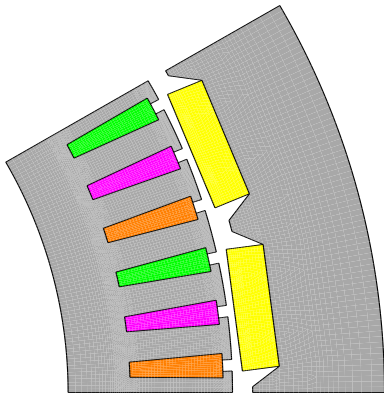


Fig. 1: Cross section of the permanent magnet synchronous machine with an external rotor, angular rotor position 0°

One set of calculation uses current driven analyses to obtain the related parameters such as torque and inductances in dependence on the stator currents and the angular rotor position. As proposed in [1], transient voltage driven analysis with high frequency voltage pulses are additionally used for an evaluation of the position dependent inductances of the permanent magnet synchronous machine.

All analyses utilize separated 2D models of rotor and stator which are coupled by floating boundary

conditions in dependence on the angular rotor position along the sliding surface interface within the air-gap [2], [3]. In case of the skewed stator slots, a multi-slice approach with a Gauss distribution of the slices will be used [4], [5].

II. SPACE VECTOR CALCULUS

In the dq rotor fixed reference frame [6], the normalized stator current and stator flux space vectors are given by

$$\underline{i}_{S,dq} = i_S e^{j\beta} = i_{S,d} + j i_{S,q} , \quad (1)$$

$$\underline{\psi}_{S,dq} = \psi_S e^{j\vartheta} = \psi_{S,d} + j \psi_{S,q} , \quad (2)$$

where β, ϑ are the stator current angle and the stator flux angle, respectively. The components of the stator flux linkage are defined by

$$\psi_{S,d} = l_d i_{S,d} + \psi_M , \quad (3a)$$

$$\psi_{S,q} = l_q i_{S,q} , \quad (3b)$$

where l_d, l_q are the direct and quadrature axis inductances and ψ_M denotes the flux linkage of the permanent magnets.

In order to inject the stator currents in the finite element model, the stator current and stator flux space vectors are transformed as given by

$$\underline{i}_{S,\alpha\beta} = \underline{i}_{S,dq} e^{j\gamma} , \quad (4)$$

$$\underline{\psi}_{S,\alpha\beta} = \underline{\psi}_{S,dq} e^{j\gamma} , \quad (5)$$

where γ denotes the angular rotor position. As the stator winding is Y-connected, any zero sequence stator currents are impossible.

III. SAMPLE ANALYSIS RESULTS

The sample results presented herein are focussed on the magnetic saliency obtained from stator currents only in direct and quadrature axes. Since the machine is highly nonlinear, there are several methods to evaluate a stator inductance in dependence of the stator currents [7]. As the high frequency voltage pulses slightly shift the actual operating point, differential inductances as evaluated underneath will describe the transient behaviour of the machine in an appropriate way.

With the linear dependency $i = i_0 + \Delta i$, the magnetic energy

$$W_m = \int_{\Omega} \mathbf{H} \cdot \mathbf{B} d\Omega \quad (6)$$

allows for an approximation of the normalized magnetic energy

$$w_m(i_0, \Delta i) = w_{m0}(i_0) + w_{m1}(i_0) \Delta i + w_{m2}(i_0) \Delta i^2 \quad (7)$$

yielding the nonlinear inductance as

$$l_{w_m}(i_0) = w_{m2}(i_0) = \frac{w_m(i_0, +\Delta i) - 2w_m(i_0, 0) + w_m(i_0, -\Delta i)}{2\Delta i^2} \quad (8)$$

On the other hand, the flux linkage

$$\Psi = \frac{\int_{\Omega} \mathbf{A} \cdot \mathbf{J} d\Omega}{\int_{\Gamma} \mathbf{J} \cdot \mathbf{n} d\Gamma} \quad (9)$$

allows for an approximation of the normalized flux linkage

$$\psi(i_0, \Delta i) = \psi_0(i_0) + \psi_1(i_0) \Delta i \quad (10)$$

yielding the nonlinear inductance as

$$l_{\psi}(i_0) = \psi_1(i_0) = \frac{\psi(i_0, +\Delta i) - \psi(i_0, -\Delta i)}{2\Delta i} \quad (11)$$

Finally, the fundamental distribution of the radial component of the magnetic flux density along the air-gap obtained from a Fourier series expansion defines the normalized fundamental component of the flux linkage ψ_1 within the air-gap which yields the nonlinear inductance

$$l_{\psi_1}(i_0) = \frac{\psi_1(i_0, +\Delta i) - \psi_1(i_0, -\Delta i)}{2\Delta i} \quad (12)$$

Fig. 2 and Fig. 3 depict the ratio $l_d(i_d)/l_q(i_q)$ of the three inductances (8),(11),(12) for an assumption of linear materials and for the actual nonlinear behaviour of the permanent magnet synchronous machine. Obviously, all three ratios are equal with linear materials and there is no significant magnetic saliency of the machine. On the other hand with nonlinear materials, only the flux linkage inductances (11) and the fundamental inductances (12) are further useable while the inductance values obtained from the magnetic energy (8) are not applicable.

IV. CONCLUDING REMARKS

The full paper will discuss in detail the design variations to obtain the desired magnetic saliency in the whole range of the operational modes. As these position dependent inductances of the permanent magnet synchronous machine are the most important criterion for an application with a high performance drive system and a position-sensorless control scheme, an optimization of the machine design can be carried out in the design stage without any prototype of the machine.

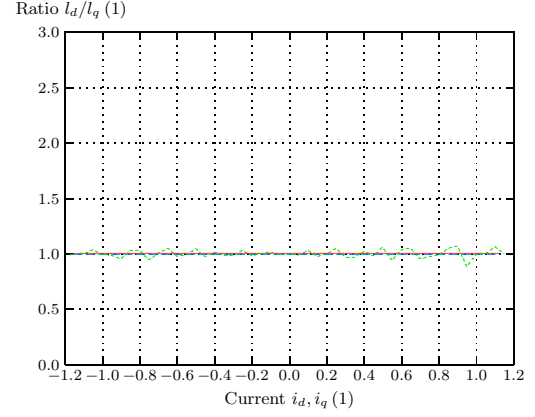


Fig. 2: Ratio $l_d(i_d)/l_q(i_q)$, flux linkage inductances (11) (solid line), fundamental inductances (12) (dashed line), magnetic energy inductances (8) (dotted line), linear analyses

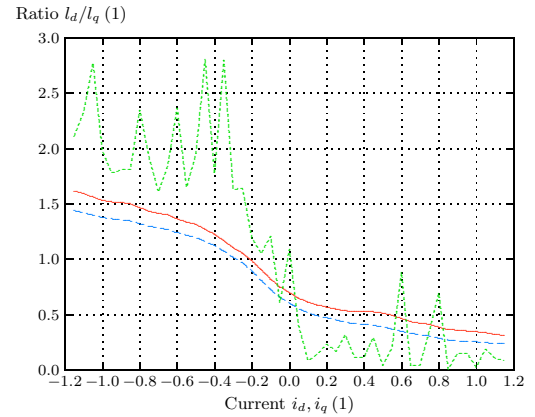


Fig. 3: Ratio $l_d(i_d)/l_q(i_q)$, flux linkage inductances (11) (solid line), fundamental inductances (12) (dashed line), magnetic energy inductances (8) (dotted line), nonlinear analyses

REFERENCES

- [1] Schmidt E., Eilenberger A.: "Calculation of Position Dependent Inductances of a Permanent Magnet Synchronous Machine with an External Rotor by using Voltage Driven Finite Element Analyses". *IEEE Transactions on Magnetics*, Vol. 45, No. 3, March 2009.
- [2] De Gersem H., Mertens R., Lahaye D., Vandewalle S., Hameyer K.: "Solution Strategies for Transient, Field-Circuit Coupled Systems". *IEEE Transactions on Magnetics*, Vol. 36, No. 4, July 2000.
- [3] De Gersem H., Weiland T.: "Harmonic Weighting Functions at the Sliding Surface Interface of a Finite Element Machine Model Incorporating Angular Displacement". *IEEE Transactions on Magnetics*, Vol. 40, No. 2, March 2004.
- [4] Piriou F., Razek A.: "A Model for Coupled Magnetic-Electric Circuits in Electric Machines with Skewed Slots". *IEEE Transactions on Magnetics*, Vol. 26, No. 2, March 1990.
- [5] Gyselinck J., Vandeveld L., Melkebeek J.: "Multi-Slice Finite Element Modeling of Electrical Machines with Skewed Slots - The Skew Discretization Error". *IEEE Transactions on Magnetics*, Vol. 37, No. 5, September 2001.
- [6] Kovacs P.K.: *Transient Phenomena in Electrical Machines*. Elsevier, Amsterdam, 1984.
- [7] Schmidt E.: "Comparison of Different Designs of Normal and Permanent Magnet Excited Reluctance Machines". *Proceedings of the 9th International Conference on Modeling and Simulation of Electrical Machines, Converters and Systems, ELECTRIMACS*, Quebec City (QC, Canada), 2008.

2D Exact Analytical Solution of Open Circuit Magnetic Field in Slotted Surface Mounted PM Radial Flux Synchronous Machines

Y. Amara, J. Raharijaona and G. Barakat

Groupe de Recherche en Electrotechnique et Automatique du Havre - EA 3220, Department of Electronic and Electrical Engineering, University of Le Havre
25 rue Philippe Lebon - B.P. 1123 - 76063 Le Havre cedex, France

Abstract — This paper presents an analytical technique for prediction of open circuit magnetic field distribution in slotted surface mounted permanent magnet radial flux synchronous machines. This technique can either be used in the case of internal or external rotor radial-field machines topologies. It involves solution of Maxwell's equations in slots, airgap and the PM's region. The obtained analytical model is used to estimate the cogging torque and induced back electromotive force. Results from this analytical model are compared to corresponding finite element analyses.

I. INTRODUCTION

This paper attempts to provide analytical tools to facilitate the analysis and design of a class of radial flux PM synchronous machines (fig. 1). The developed model gives exact field distribution due to permanent magnet source in the slots region (radial slots), the airgap region and the PM's region. The developed model embraces both internal and external rotor topologies (figure 1). Most of developed models do not take into account slotting in an explicit manner [1], [2]. In [3], authors presented an exact analytical description of magnetic field in idealized surface mounted permanent magnet structures which does take into account stator slotting. However, the developed model was limited to machines with integer number of slots per pole per phase. The proposed model, in this paper, is more general and can be used for machines with fractional numbers of slots per pole per phase. In [4], authors presented a model which does take into account stator slotting for an axial flux synchronous machine.

II. MAGNETIC FIELD CREATED BY PERMANENT MAGNETS

Figure 2 shows different regions (slots (I), airgap (II), permanent magnets (III), region under magnets (IV)) where the exact analytical solution is established. Region IV is only considered in case of a non-magnetic permanent magnets supporting armature. Permeability of all ferromagnetic parts is assumed to be infinite. The permeability of permanent magnets is assumed to be equal to that of air.

The governing field equations, in terms of the Coulomb gauge, $\nabla \times \mathbf{A} = 0$, are:

$$\begin{cases} \nabla^2 \mathbf{A} = 0, & \text{in regions I, II and IV} \\ \nabla^2 \mathbf{A} = -\mu_0 \nabla \times \mathbf{M}, & \text{in region III} \end{cases} \quad (1)$$

\mathbf{A} only has A_z component which is independent of z (infinitely long machine in axial direction). \mathbf{M} is the magnetization.

Combining equations (1) with boundary conditions, and using separation of variables method, help establish a set of linear equations ($N_H \times N_H$) (where N_H is the number of considered harmonics), where coefficients of magnetic vector potential solution in region III are the unknown. Solving these linear equations and using interface conditions give coefficients of magnetic vector potential in other regions.

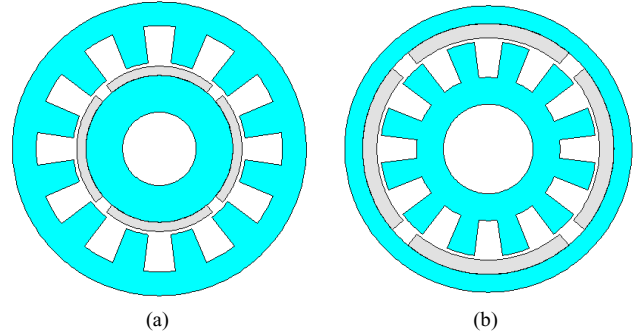


Fig. 1. Radial-field PM machines topologies: internal rotor (a) and external rotor (b).

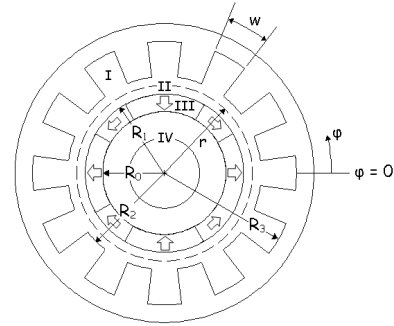


Fig. 2. Polar coordinates system (quasi-Halbach magnets distribution).

Obtained linear equations are solved using Gaussian elimination method. The developed model takes into account rotor movement helping the authors to calculate global quantities such as electromotive force and cogging torque.

III. COMPARISON WITH FINITE ELEMENT ANALYSIS

Figure 3 shows comparisons of flux density components space distribution in the different regions. Table I gives some characteristics of the machine to which both methods (analytical technique and finite element) have been applied. Finite element method has been applied to real geometry of the machine with a relative permeability of $1e6$ for stator core. As seen, the predictions from analytical model are in good agreement with finite element calculations.

Oscillations in the analytical prediction in figure 3.c (radial component B_r) are due to the finite number of terms in the Fourier series ($N_H = 40$). Numerical problems occur in estimation of analytical solution for a number of harmonics $N_H > 40$.

TABLE I – MACHINE'S PARAMETERS

Pole number	6
Slot number	18
Magnets distribution	Quasi-Halbach
R_0, R_1, R_2 and R_3 (mm)	50, 58, 60 and 84
w (rad)	$\pi / 18$

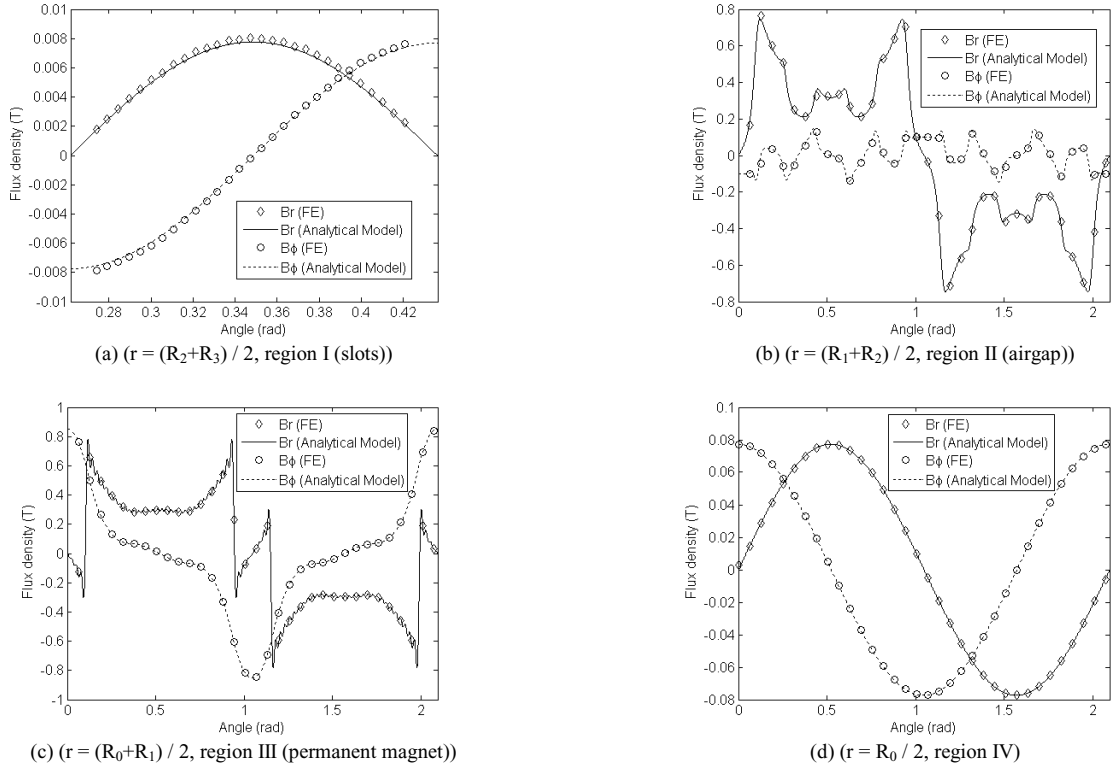


Fig. 3. Comparison of field distribution by both finite element and analytical model (machine with quasi-Halbach magnets distribution and a non-magnetic PM supporting armature).

Indeed, analytical solutions agree extremely well with the finite element results. The analytical model can then be used to estimate and analyze open circuit performance (cogging torque, induced back electromotive force, airgap radial forces distribution) of surface mounted permanent magnet synchronous machines. Cogging torque is estimated using Maxwell stress tensor and E.M.F. is calculated by differentiating magnetic flux passing through a given phase. Induced back electromotive force can be estimated for numerous types of windings distributions (integer or fractional slot number per pole per phase, overlapping or non overlapping windings distributions). Figure 4 compares cogging torque waveforms obtained by both finite elements and analytical model. Cogging torque is computed using Maxwell stress tensor on the PM's surface.

In the full paper, analytical solutions for other machine topologies (magnetic rotor yoke, external rotor topologies) will be compared to corresponding finite element calculations.

IV. CONCLUSION

This paper presents a general analytical model for the analysis and design of a class of surface mounted permanent magnet synchronous machines. The model is developed in the slots, the airgap and the PM's region and its accuracy has been validated by finite element analyses.

In the full paper, the mathematical approach leading to the exact solutions of Maxwell's equations in the different regions will be detailed. Results from other machine topologies will be compared to corresponding finite element calculations.

The developed model will be used to estimate and analyze open circuit performance (cogging torque, induced

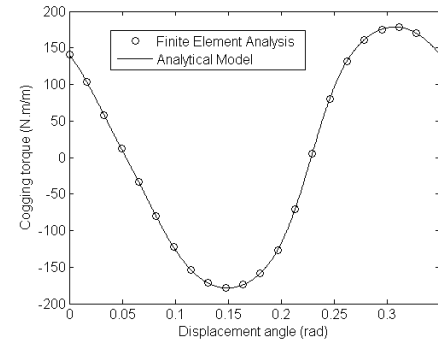


Fig. 4. Cogging torque waveforms obtained by both finite elements and analytical method (machine with quasi-Halbach magnets distribution and a non-magnetic PM supporting armature).

back electromotive force, airgap radial forces distribution) of surface mounted permanent magnet synchronous machines.

V. REFERENCES

- [1] Z. Q. Zhu and D. Howe, "Instantaneous magnetic field distribution in brushless permanent magnet DC motors: Part III: Effect of Stator Slotting," *IEEE Trans. Magn.*, vol. 29, no. 1, pp. 143–151, Jan. 1993.
- [2] K. Ng, Z. Q. Zhu and D. Howe, "Open-circuit field distribution in a brushless motor with diametrically magnetised PM rotor, accounting for slotting and eddy current effects," *IEEE Trans. Magn.*, vol. 32, no. 1, pp. 5070–5072, Sept. 1996.
- [3] B. Ackermann and R. Sottek, "Analytical modeling of the cogging torque in permanent magnet motors," *Electr. Eng.*, vol. 78, no. 2, pp. 117–125, Mar. 1995.
- [4] J. Azzouzi, G. Barakat and B. Dakyo, "Quasi-3-D analytical modeling of the magnetic field of an axial flux permanent-magnet synchronous machine," *IEEE Trans. Energy Convers.*, vol. 20, no. 4, pp. 746–752, December 2005.

Quasistatic Electromagnetic Field Computation by Conformal Mapping in Permanent Magnet Synchronous Machines

Martin Hafner, David Franck and Kay Hameyer
Institute of Electrical Machines – RWTH Aachen University
Schinkelstraße 4, D-52062 Aachen, Germany

E-mail: Martin.Hafner@IEM.RWTH-Aachen.de, David.Franck@IEM.RWTH-Aachen.de

Abstract—In the design of modern servo drives or electrical drives for positioning, torque pulsation, tangential forces and ripple torque are highly undesirable effects. These quantities are directly linked with the occurring harmonic air gap flux density waves. This paper presents a time-effective method to compute the radial and tangential field components in load and no-load condition by conformal mapping in frequency domain. The proposed method is applied to a surface permanent magnet synchronous machine, and compared to numeric results obtained by nonlinear FEA. The analytical results are in good agreement to the finite element simulations.

I. INTRODUCTION

Nowadays the design of electric machines is accomplished by virtual prototyping to short time-to-market. Since finite element analysis (FEA) is time consuming and requires a high computational effort, analytic models are applied that are focused on an estimation of the fundamental air gap flux density. Consequently, the effect of air gap field harmonics on the main machine characteristics, like EMF, cogging-torque and load-torque, as well as the impact of geometry variations on those quantities are neglected. In this paper, an analytic conformal mapping method in frequency domain for permanent magnet synchronous machines (PMSM) is applied to consider the occurring air gap field harmonics for torque and EMF computation. Even if that approach attributes infinite permeability characteristics, a comparison with standard nonlinear FEA shows that it nevertheless gives a good approximation of the air gap flux density spectrum and all derived quantities.

II. COMPUTATIONAL FRAMEWORK

A. Rotor Field Distribution in the Slotless Stator

The analytical technique for computing the 2D magnetic no-load field distribution in the air gap of radial-magnetized permanent magnet rotors has been published by [1]. The derived parametric field solution is applicable for internal and external rotors. In further researches the approach has been generalized to radial and parallel magnetizations, [2]. Recently, [3] published a further extension to radial sine and sinusoidal direction magnetizations. In case of a slotless stator, the radial flux density $B_r(\Theta)$ and the tangential flux density $B_\varphi(\Theta)$ are given by

$$B_r(\Theta) + jB_\varphi(\Theta) = \sum_{n=0}^{\infty} (B_{r,n} + jB_{\varphi,n}) e^{jnp\Theta} \quad (1)$$

where n is the frequency order, p the number of pole pairs, Θ the mechanical angle. The Fourier coefficients $B_{r,n}$ and $B_{\varphi,n}$ represent the solution of the linear Laplace problem with magnets and a slotless stator.

B. Rotor Field Distribution in the Slotted Stator

Stator slotting significantly influences the magnetic field distribution:

- 1) Different radial magnetic permeances of teeth and slot affects the local distribution of the flux in the air gap, so that a flux concentration beneath the stator teeth can be observed.
- 2) In case of slotting, a characteristic peak of the flux density can be observed over the PM vertices in the air gap.
- 3) Slotting mixes up radial and tangential components, as shown by $B_\varphi\lambda_\varphi$ and $B_r\lambda_\varphi$ in (2).

A common method for modeling these effects on the magnetic field distribution are known as "permeance functions" in literature. In a former research, [4] models the impact of effect 1) on the radial flux density component only. The recent publication [5] derives by four complex conformal mappings, including a Schwarz-Christoffel transformation, a permeance function which takes the effects 1) - 3) into account. Assuming a infinite permeable stator core, this ansatz has shown to yield identical flux density results in comparison to FE simulation applying Neumann boundary conditions.

For that approach, the conformal transformations are used to transform slotted stator geometry into a slottless stator, where the Laplace equation for the air gap field can be solved analytically. By this, the impact of slotting on the field distribution keeps considered. Correlating the field distribution with slotting sB to the field without slotting (1) yields the complex permeance $\underline{\lambda}$,

$${}^sB(\Theta) = (B_r + jB_\varphi)\underline{\lambda}^* \quad (2)$$

which describes the individual characteristic of the slotting on the field.

Even if the Laplace equation can be solved analytically, the combined governing equations can not be solved directly. Therefore the local-dependent complex permeance number is evaluated numerically in a nonlinear iterative solution. At each point of an equidistant sampled arc in the air gap with the length of one slot pitch, the complex permeance number, that fulfills (2), is evaluated

$$\underline{\lambda} = \lambda_r + j\lambda_\varphi \quad (3)$$

where λ_r and λ_φ represent the permeance variations in radial and tangential direction. The sampling points of the slot pitch can be expressed by a Fourier-Series and extended to the whole

air gap, yielding,

$$\underline{\lambda}(\Theta) = \sum_0^{N_\lambda} \lambda_{r,n} \cos(nN_s\Theta) + j \sum_1^{N_\lambda} \lambda_{\varphi,n} \sin(nN_s\Theta) \quad (4)$$

where N_s is the number of stator teeth and N_λ the sampling rate depending maximal occurring frequency.

C. Armature winding field

The magnetic field distribution of a current in a single slot, assuming a infinite slot depth and a infinite permeability in a slotless stator, can be obtained by three conformal mappings [6]. Since coils occupy two slots with opposite directed currents, a flux density distribution ${}^c B$ for the whole air gap per coil can be assembled in functions of the coil current I_c and the number coil turns N by

$${}^c B(\Theta, N, I_c) = NI_c \sum_1^{N_a} ({}^c B_{r,n} + j {}^c B_{\varphi,n}) e^{jn\Theta} \quad (5)$$

where N_a denotes the maximal frequency order and the radial and tangential quantities ${}^c B_{r,n}$ and ${}^c B_{\varphi,n}$ the Fourier coefficients of the coil computed for one ampere. According to the winding schema of the PMSM a flux distribution ${}^p B$ for all phases can be found by adding shifted terms of (5). In case of a symmetric current load (UVW) I , the allover armature field ${}^a B$ is given by

$${}^a B(\Theta, I) = ({}^p B_U, {}^p B_V, {}^p B_W) \cdot \left(e^{j\phi_q}, e^{j(\phi_q+120^\circ)}, e^{j(\phi_q+240^\circ)} \right)^T \quad (6)$$

where the angle ϕ_q defines the relative phase orientation to the quadrature axis of the machine.

D. Field Distribution in the Slotted Air Gap

The magnetic air gap field in case of stator slotting can be assumed as a superposition of the field component fields due to permanent magnet and stator excitation.

Introducing a time-discretization Δ_{FE} and a corresponding time-stepping n_{FE} , the rotor flux distribution gives,

$${}^s B^t(f) = {}^s \underline{B}(\Theta) e^{j\omega \cdot \frac{n \cdot n_{FE}}{N_{el} \cdot p}} \quad (7)$$

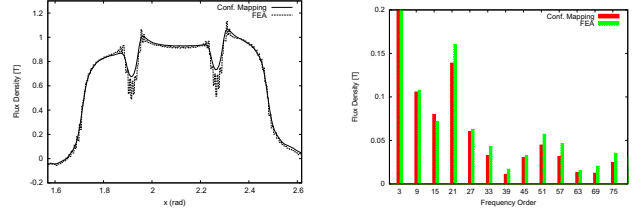
where n is the rotor speed and N_{el} the number of computation steps per electric period. The corresponding time-depend armature field is frequency-shifted by the stator frequency f_1 , yielding

$${}^a B^t(f, I) = {}^a \underline{B}(\Theta, I) e^{j2\pi f_1 t} e^{j\omega n_{FE} \cdot \frac{n \cdot n_{FE}}{N_{el} \cdot p}} \quad (8)$$

For a given time step t (7) and (8) represent the allover load and no-load flux density distribution in the slotted air gap.

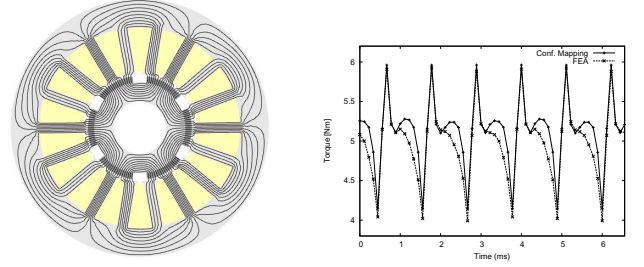
III. APPLICATION

To demonstrate the proposed method, a PMSM, designed by in-house sizing software is investigated. Its cross-section together with the field distribution in rated operation is given in fig. 2(a). The FEA flux density is sampled in the air gap for each time step individually. The spectrum for a certain time instance obtained numerically and by (7), (8) is shown in Fig. 1(b); the corresponding local flux distribution for a pole pitch is given in 1(a). The resulting torque according to Maxwell stress tensor for both magnetic fields are given in fig. 2(b).



(a) Local field distribution of PMSM (b) Flux density amplitude for different order.

Fig. 1. Flux density distribution in time and frequency domain by FEA and conf. mapping in rated operation.



(a) Six pole PMSM with field lines in rated operation. (b) Torque characteristic over electric period.

Fig. 2. PMSM cross section and torque characteristic over an electric period by FEA and conf. mapping in rated operation.

IV. CONCLUSION

Electromagnetic field computations are ubiquitous in the design of electrical machines. Even if established finite-element methods yield very accurate result, their high computational effort inhibits an application in early design stages or multi-object optimizations of electrical drives. In that case, it is worth to seek for approximative and time-saving representations. In this paper, the air gap field of a PMSM under load and no-load is computed by conformal mapping in frequency domain. A first demonstration on a PMSM shows, that the obtained occurring harmonic air gap flux waves under load condition are in good agreement to nonlinear FEA results. A detailed comparison in different load conditions between the proposed method and standard simulation will be presented in the full paper submission.

REFERENCES

- [1] Z. Zhu, D. Howe, E. Bolte, and B. Ackermann, "Instantaneous magnetic field distribution in brushless permanent magnet DC motors. i. open-circuit field," *Magnetics, IEEE Transactions on*, vol. 29, no. 1, pp. 124–135, 1993.
- [2] Z. Zhu, D. Howe, and C. Chan, "Improved analytical model for predicting the magnetic field distribution in brushless permanent-magnet machines," *Magnetics, IEEE Transactions on*, vol. 38, no. 1, pp. 229–238, 2002.
- [3] D. C. Hanselman, *Brushless Permanent Magnet Motor Design*, 2nd ed. The Writers' Collective, Mar. 2003.
- [4] Z. Zhu and D. Howe, "Instantaneous magnetic field distribution in brushless permanent magnet DC motors. III. effect of stator slotting," *Magnetics, IEEE Transactions on*, vol. 29, no. 1, pp. 143–151, 1993.
- [5] D. Zarko, D. Ban, and T. Lipo, "Analytical calculation of magnetic field distribution in the slotted air gap of a surface permanent-magnet motor using complex relative air-gap permeance," *Magnetics, IEEE Transactions on*, vol. 42, no. 7, pp. 1828–1837, 2006.
- [6] K. J. Binns, *Analysis and computation of electric and magnetic field problems*. Pergamon Press; [distributed in the Western Hemisphere by Macmillan, New York], 1963.

Calculation of Inductances in Intercell Transformers by 2D FEM simulation

Bernardo Cougo*, Thierry Meynard*, François Forest**, and Eric Labouré***

*LAPLACE (Laboratoire Plasma et Conversion d'Énergie)

2, rue Charles Camichel, 31071, Toulouse. FRANCE.

cougo@laplace.univ-tlse.fr

Abstract— This paper presents an accurate method to calculate the main inductances associated to InterCell Transformers (ICTs) in order to facilitate the transformer design. In this application the leakage inductance is a key parameter which theoretically requires 3D Finite Element simulation. We show in this paper that a very good estimation can be found using only two 2D FEM simulations: one related to the field contained inside the core window and the other related to the field outside. In the final paper, results obtained for various sizes and shapes of ICTs will be compared to the values measured on actual devices.

I. INTRODUCTION

One of the main goals in power electronics is the increase of power density in converters. The use of interleaved converters is especially interesting since they increase the apparent frequency of the voltage applied across the filters. They also improve the dynamic behavior of the converter. A traditional interleaved converter consists of several identical commutation cells with the outputs interconnected through separate inductors as shown in Fig. 1.

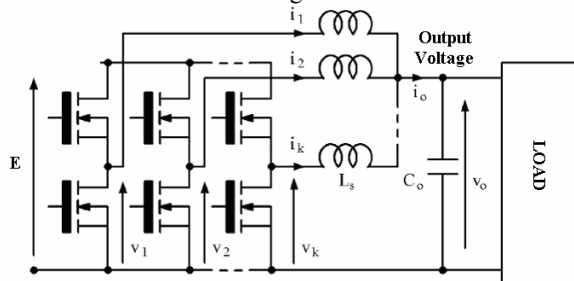


Fig. 1. Traditional interleaved converter

The association of these inductors may result in large ripple in the current flowing in each cell [1]. This leads to high conduction losses in the switches and high copper losses in the inductors. In order to reduce these problems, coupling the inductors allows obtaining the same relative current ripple in the commutation cells and at the output. This is obtained by the use of intercell transformers [2-4]. In such devices, the ripple of the output current i_o is a function of the leakage inductance. For this reason, predicting the current ripple, the AC losses, the voltage ripple, the saturation current and many other crucial parameters requires an accurate prediction of the leakage inductance. An analytic formulation of the field distribution inside the window is easily obtained under the assumption that the window is rectangular and its depth is infinite. However, practical components are far from this assumption, and the field outside the window (which cannot be easily modeled) has a very significant contribution to the overall leakage inductance.

II. MAGNETIC MODEL OF SIMPLE INTERCELL TRANSFORMERS

Let's analyze the operation of intercell transformers by taking as an example the transformer on Fig. 2. In this transformer, each winding is connected to a commutation cell in such a way that the fluxes from both legs (Φ_1 and Φ_2) are obliged to pass by the air (leakage flux).

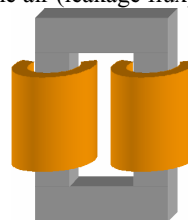


Fig. 2. Physical aspect of a simple intercell transformer

If we use the transformer of Fig. 2 in an interleaved converter composed of 2 commutation cells, and supposing that output voltage is filtered (which is usually the case), we can note that the voltage across each winding is rectangular. Consequently, a triangular flux is imposed in each leg of the transformer. We may calculate the reluctance of the core (R_{mag}) of this simple transformer by using the average magnetic path length of the core, its cross-section and the average permeability of the magnetic path (calculated for gapped and ungapped cores).

A. Low Permeability Cores Used in Intercell Transformers

Usually high permeability cores are used in the construction of intercell transformers in order to minimize magnetizing current. However, in certain applications it is preferable to use low permeability cores if we take into account cost, size and loss density when designing the transformer.

In an intercell transformer, if a low permeability core is used, the core reluctance is comparable to the leakage reluctance. In this case, the current in each cell will be the sum of the magnetizing current (of which fundamental frequency is equal to the switching frequency) and the "coupled" ripple (of which fundamental frequency is equal to the double of the switching frequency).

III. FEM SIMULATION TO FIND LEAKAGE RELUCTANCE

In order to determine the current in each cell, the leakage reluctances must be found. It may be done analytically [5-7] or by the use of finite-elements methods. Although analytical methods allow speeding up the optimization process of transformer design, they are restricted to particular geometries.

The use of 3D FEM simulation may result in accurate calculation of the leakage inductance, but it is very time

consuming. 2D FEM simulation can be considered [8] if the procedure used in the simulation takes into account 3D effects.

This work presents a simple procedure that allows the calculation of the leakage inductance and reluctance of intercell transformers, based on 2D FEM simulations.

This procedure relies on the calculation of 2 linear inductances (inductance per unit of length): one related to the part of the winding inside the core window and the other one to the outside. For a better understanding of this model, let's consider the transformer of Fig. 2. First, we simulate a frontal cut of this transformer only with the conductors inside the core window, as shown in Fig. 3a. Like this, we can calculate the linear inductance (L_{leakin} , H/m) related to the volume inside the core window. Then, a second simulation is needed. We simulate a frontal cut of this transformer only with the conductors outside the core window, as shown in Fig. 3b. Thus we can calculate the linear inductance ($L_{leakout}$, H/m) related to the volume outside the core window.

To calculate the total leakage inductance, we use the following equation:

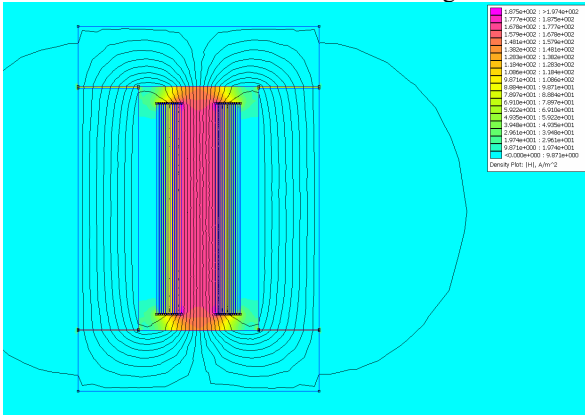
$$L_{leak} = L_{leakin}d_{in} + L_{leakout}d_{out} \quad (2)$$

where d_{in} is the average turn length inside the core window and d_{out} is the average turn length outside the core window.

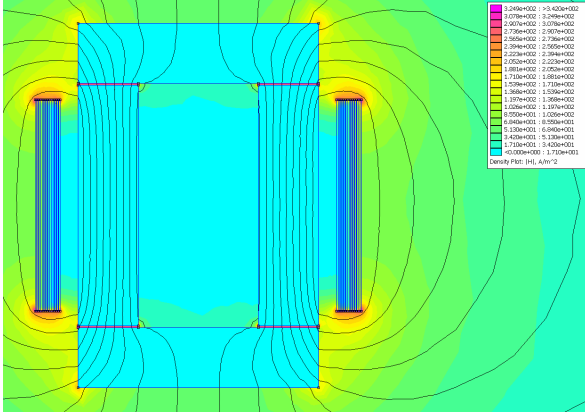
The calculation of the leakage reluctance is simply:

$$R_{leak} = N^2 / L_{leak} \quad (3)$$

where N is the number of turns in each winding.



a) intercell transformer with the conductors inside the core window



b) intercell transformer with the conductors outside the core window

Fig. 2. FEMM simulation of intercell transformer (magnetic field intensity)

IV. EXPERIMENTAL RESULTS

A middle power inductor was used to verify the accuracy of the simulation. This inductor has 14 turns in each leg and it is suitable to be used as an intercell transformer. It is made using a Mega Flux magnetic alloy powder core with a relative permeability equal to 40.

Simulations were made using FEMM software, version 4.2. Simulation output graphs are shown in Fig. 3. Results found are shown in Table I. Measurements were made at 15kHz and low flux density.

TABLE I
SIMULATION AND EXPERIMENTAL RESULTS

	Simulation	Measure
$L_{leakout} * d_{out}$ (μH)	55	
$L_{leakin} * d_{in}$ (μH)	3.5	
L_{leak} (μH)	58.5	61.1
L_{mag} (μH)	69	62

Note that there is only 2.6% of difference between the leakage inductance simulated and measured. The magnetizing inductance was also analytically calculated and its value was the same as that found in the simulation.

The procedure shown in section III was also verified in other transformers tested in the laboratory.

V. CONCLUSION

Intercell transformers are used in interleaved converters in order to reduce current ripple in each commutation cell. Low permeability cores may be used in intercell transformers but magnetizing and leakage inductances must be found with the purpose of estimating current ripple. A simple procedure, based on only two 2D FEM simulations, allows the calculation of the leakage inductance and the accuracy in the design of intercell transformers. Experimental results confirm the accuracy of this method for calculating the leakage inductance.

VI. REFERENCES

- [1] Pit-Leong Wong, Peng Xu, P. Yang, and F.C. Lee, "Performance improvement of interleaving VRMs with coupling inductors," *IEEE Trans. on Power Electronics*, vol.16, pp 499-507. 2001
- [2] In Gyu Park, Seon Ik Kim, "Modeling and analysis of multi-interphase transformers for connecting power converters in parallel," *IEEE 1997*, pp 1164-1170.
- [3] P. Zumel, O. Garcia, J. A. Cobos and J. Uceda, "magnetic integration for interleaved converters," *IEEE 2003*, pp 1143-1149.
- [4] Jieli Li, A. Stratagos, A. Schultz, C.R. Sullivan, "Using coupled inductors to enhance transient performance of multi-phase buck converters," *IEEE 2004*, pp 1289-1293.
- [5] A. Dauhajre, R. D. Middlebrook, "Modelling and estimation of leakage phenomena in magnetic circuits," *17th Annual IEEE Power Electronics Specialists Conference*, pp 213-226, 1986.
- [6] J. P. Ferrieux, F. Forest, *Alimentations à découpage, convertisseurs à résonance*, Second Edition, Masson Editor, 1985, Paris.
- [7] K. J. Binns, P. J. Lawrenson, C.W. Trowbridge, *The analytical and numerical solution of electric and magnetic fields*, John Wiley and sons Editor
- [8] R. Prieto, J. Cobos, V. Bataller, O. Garcia and J. Uceda, "Study of toroidal transformers by means of 2D approaches," *IEEE Power Electronics Specialist Conference (PESC) 1997*.

Study on Analysis Method for Ferrofluid

Yu Okaue, Gaku Yoshikawa, Fumikazu Miyasaka, and Katuhiro Hirata
 Dept. of Adaptive Machine Systems, Graduate School of Engineering, Osaka University
 2-1, Yamadaoka, Suita, Osaka, 565-0871, Japan
 k-hirata@ams.eng.osaka-u.ac.jp

Abstract — We are studying a new analysis method to calculate the shape of ferrofluid spikes. The shape of a ferrofluid is influenced by the magnetic force, surface force, and gravity. Therefore, the electromagnetic field equation is coupled with Navier-Stokes equation employing the MPS and FEM. This paper describes the analysis algorithm of coupled method, and the way to convert particles data for MPS method to elements data for FEM.

I. INTRODUCTION

Recently, a ferrofluid [1] which consist of nano-size magnetic particles and organic solvents is a topic of great interest because of its characteristics [2]. The shape of a ferrofluid is intricately influenced by the magnetic force, surface force, and gravity, and the effective analysis methods to calculate a shape of a ferrofluid have not been proposed.

Under the circumstances, we are studying a new analysis method to calculate the deformation of ferrofluid spikes. In this method, Navier-Stokes equation is solved by the MPS method and magnetic field equation is solved by FEM. Because of the difference between the MPS method data (a group of particles) and FEM data (a group of elements), data conversion is required to couple the MPS method and FEM.

This paper describes the analysis algorithm of coupled method, and the way to convert particles data for MPS method to elements data for FEM.

II. ANALYSIS METHOD

The shape of a ferrofluid is influenced by the magnetic force, surface force, and gravity. Therefore, to analyze the phenomenon, the electromagnetic field Equations (1) is coupled with Navier-Stokes equation (3) as follows. The magnetic force is calculated by Maxwell's stress tensor (2).

$$\text{rot } H = J \quad (1)$$

$$\text{div } B = 0$$

$$T = T_{ij} = \frac{1}{\mu_0} B_i B_j - \frac{1}{2} \delta_{ij} (\mu_0 B^2) \quad (2)$$

H is the magnetic field, J is the current, B is the magnetic flux density, T is Maxwell's stress tensor, μ_0 is the permeability of vacuum.

$$\frac{\partial \psi}{\partial t} = -\frac{1}{\rho} \nabla P + \nu \nabla^2 \psi + f \quad (3)$$

ψ is the flow velocity, ρ is the density, P is the pressure, ν is the kinematic viscosity, f is the external force (gravity, surface tension and magnetic force).

Fig. 1 shows the flowchart of analysis method. Deformation of a ferrofluid is difficult to analyze by conventional fluid

analysis methods such as CDF, FEM and so on. In this method, Navier-Stokes equation is solved by the MPS [3] method

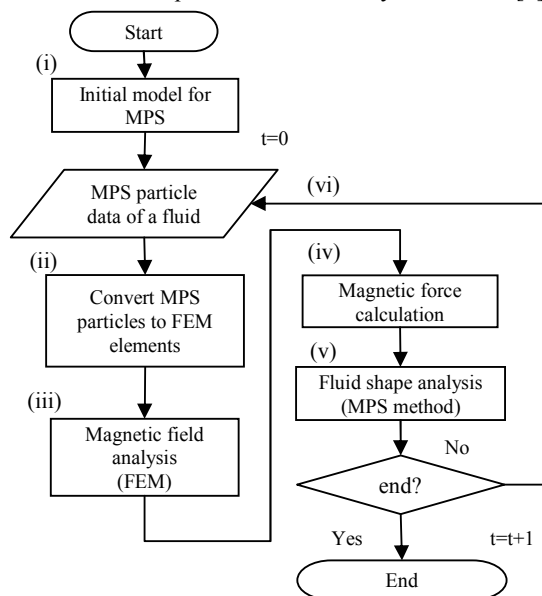


Fig. 1. Flowchart of coupled method

because it is useful to apply large deformed fluid model. On the other hand, magnetic field equation is solved by FEM [4] because it can save CPU time as compared with MPS method. Because of the difference between the MPS method data (a group of particles) and FEM data (a group of elements), data conversion is required to couple the MPS method and FEM.

- (i) Make initial MPS particle data (position, velocity, and pressure of each particle) from shape of a fluid.
- (ii) Convert MPS particles to FEM elements to calculate magnetic field around a fluid (Fig. 2).
- (iii) Calculate magnetic field by FEM.
- (iv) Calculate magnetic force on a particle.
- (v) Calculate shape of a fluid by MPS method.
- (vi) Renew MPS particle data.

The data conversion (Fig. 1 (ii)) is carried out in each analysis step. To calculate motion of a ferrofluid, the data conversion has to be done automatically. This data conversion method adopts the Delaunay partition [5] and Marching Cubes [6].

Fig. 2 shows the flowchart of detail data conversion.

- (i) Create of point data for MPS method.
- (ii) Make boundary faces between a fluid and air region using Marching Cubes.
- (iii) Execute Delaunay partition.
- (iv) Add material conditions.
- (v) Add boundary conditions
- (vi) Produce element data for FEM.

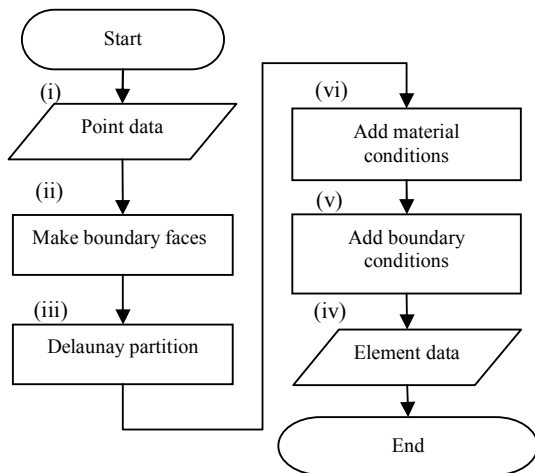


Fig. 2. Flowchart for data conversion of MPS to FEM.

III. ANALYZED MODEL AND DATA CONVERSION RESULTS

Fig. 3 shows the analyzed model of a ferrofluid. It mainly consists of a ferrofluid in a dish and a magnet. A ferrofluid is deformed by magnetic field.

Fig. 4 shows the initial MPS model before deformation. A ferrofluid in a dish is converted into a group of particle. A magnet is omitted to save CPU time. Fig. 5 shows the FEM model converted from MPS model. Table 1 shows the calculated conditions of particle-element conversion.

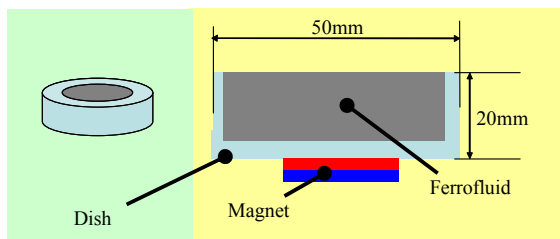


Fig. 3. Analyzed model

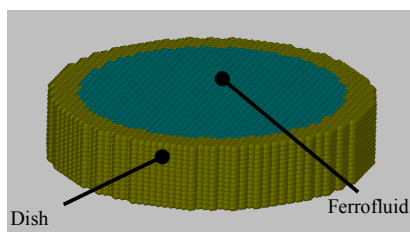


Fig. 4. MPS model

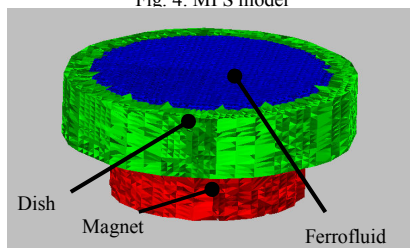
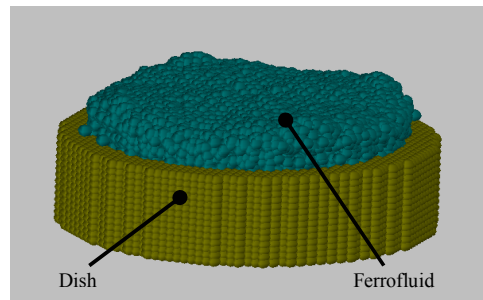


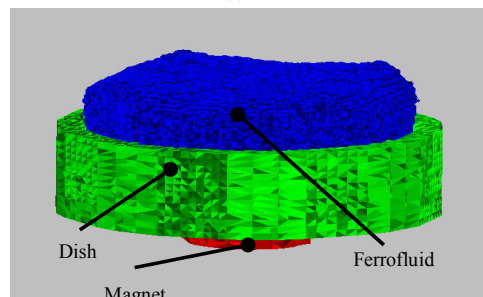
Fig. 5. Converted FEM model

TABLE I
TYPES SIZES FOR CAMERA-READY PAPERS

Number of particle	25256	Number of points	54941
CPU time(s)	80	Number of added points	29685
	Core2	Number of	



(a)



(b)

Fig. 6. An example of conversion

Fig. 6 shows the conversion model after deformation. Fig. 6 (a) shows the calculated shape of a fluid by MPS method. Fig. 6 (b) shows the converted model for FEM. It can be seen from this figure, the calculated deformation of a fluid is well converted to FEM model automatically.

IV. CONCLUSION

In this paper, the numerical method to calculate the shape of a ferrofluid was proposed by coupling the MPS method with FEM. In the final paper, the effectiveness of this method will be shown through the comparison with the measurement.

V. REFERENCES

- [1] Kamiyama Shinich, "Entrance of ferro fluid", Inc. Sangyo tosyo, 1989.
- [2] Furuya Yasubumi, Higuch Toshiro and Imasato Nobuo, "Next-generation Actuator Materials and Devices", CMC Publishing, 2006.
- [3] Seich Koshizuka, "Particle method", Maruzen, 2005.
- [4] Yoshihiro Kawase and Syokich Ito, "New practical Analysis of Electrical and Electric Apparatus by 3-D Finite Element Method", Morikita Publishing, 1997.
- [5] Taniguch Nobuo and Moriwaki Kiyooki, "Auto element divide method for 3D FEM", Morikita Publishing, 2006.
- [6] Takahashi Tomokazu, Yonekura Tatsuhiro and Kishi Yoshiki "A Method of Equi-Valued Surface Construction from Volume Data on Face Centered Cubic Lattice", The Transactions of the Institute of Electronics, Information and Communication Engineers. A, Vol.85, No.11, p1313-1323, 2002.

Isogeometric analysis for electromagnetic problems

Annalisa Buffa, and Rafael Vázquez

Istituto di Matematica Applicata e

Tecnologie Informatiche del CNR

Via Ferrata 1, 27100 Pavia, Italy

Email: annalisa@imati.cnr.it, vazquez@imati.cnr.it

Abstract—Isogeometric Analysis (IGA) is a novel discretization method, introduced in [1], which is based on non-uniform rational B-splines (NURBS). Among other features, IGA uses directly the geometry description coming from computer aided desing (CAD) software without approximation, and the analysis is performed using shape functions of variable (possibly high) regularity. In this work we propose a new discretization scheme based on continuous B-splines, adapting the ideas of [1] to the solution of Maxwell's equations. We present extensive numerical results to show that our scheme is free of spurious modes, and that it approximates singular solutions in non-convex domains.

I. INTRODUCTION

In this work we focus on Maxwell's eigenvalue problem: Find $\omega \in \mathbb{R}$ and $\mathbf{u} \in \mathbf{H}_0(\mathbf{curl})$, $\mathbf{u} \neq \mathbf{0}$, satisfying

$$(\mathbf{curl}\mathbf{u}, \mathbf{curl}\mathbf{v}) = \omega^2(\mathbf{u}, \mathbf{v}) \quad \forall \mathbf{v} \in \mathbf{H}_0(\mathbf{curl}), \quad (1)$$

where $\mathbf{H}_0(\mathbf{curl})$ is the space of square integrable functions such that their curl is also square integrable, and their tangential component is zero on the boundary.

It is known that the solution of (1) with nodal finite elements produces an approximation with spurious modes in non-convex geometries. Instead, edge elements provide a solution which is free of spurious modes and that approximates singular solutions in non-convex geometries. However, the electromagnetic fields computed with edge elements are discontinuous, and in recent years some methods have been introduced in order to discretize the equations with continuous finite elements (see, e.g. [2]-[4]).

In [1] the concept of Isogeometric Analysis (IGA) was introduced with the aim of bridging the gap between computer aided design (CAD) and the finite element method. Loosely speaking, in IGA the space of non-uniform rational B-Splines (NURBS) describing the geometry is also used as the space of trial and test functions in the discrete variational formulation: i.e., an isoparametric concept is adopted. The main advantage of this approach is that *the geometry is exactly described at the coarsest level*, and mesh refinement is done without affecting the geometry. Moreover, NURBS basis functions have higher continuity than usual finite elements. Following the ideas of [1], in this work we present a new numerical technique, based on (non-rational) B-splines, for the numerical solution of problem (1) with continuous functions.

II. B-SPLINES SPACES

In one dimension, B-splines basis functions of order m are constructed from an open knot vector

$$\Xi = \{0 = \xi_1 \leq \xi_2 \leq \dots \leq \xi_{n+m} = 1\}, \quad (2)$$

where the *open* nomenclature means that the first and last knots are repeated m times. Using the iterative procedure described in [1], from the knot vector we can construct n B-splines of degree $p = m - 1$. These B-splines are positive piecewise polynomials which form a partition of unity. If a knot appears only once, the B-splines have $p - 1$ continuous derivatives in that knot. The number of continuous derivatives is reduced by one each time we repeat the knot.

In two dimensions the definition of B-splines is easily generalized by tensor products. We consider two knot vectors Ξ_1 and Ξ_2 , that define a mesh in the parametric domain $\Omega_0 = [0, 1] \times [0, 1]$. The B-splines basis functions are then defined as $B_{ij}(x, y) := B_i(x)B_j(y)$, where B_i is constructed from the knot vector Ξ_1 and B_j from Ξ_2 . These B-splines essentially satisfy the same properties we have seen in one dimension. Associating to each of the B-spline basis functions a positive weight we define the NURBS basis functions N_{ij} as in [1]. Then, requiring a control point $\mathbf{C}_{ij} \in \mathbb{R}^2$ for each function we describe our physical domain Ω by a parametrization of the form

$$\begin{aligned} \mathbf{F} : \Omega_0 &\longrightarrow \Omega \\ \mathbf{x} &\longmapsto \mathbf{F}(\mathbf{x}) := \sum_{i,j} N_{ij}(\mathbf{x})\mathbf{C}_{ij}. \end{aligned} \quad (3)$$

This parametrization also maps the mesh in the patch Ω_0 to a mesh in the physical domain Ω . The refinement of the mesh is done as in [1]: new knots are inserted in the knot vectors, but the parametrization (3) remains unchanged. Moreover, our technique can also be extended to the cases where the geometry is more complicated and described by several patches, analogously as it is explained in [1].

III. DISCRETIZATION TECHNIQUE BASED ON B-SPLINES

We now introduce a discretization scheme for problem (1) such that it satisfies de De Rham diagram. Denoting by $S^{p,q}$ the space of B-splines of degree p in the x -direction, and degree q in the y -direction, we will seek our solutions in the space $S^{p-1,p} \times S^{p,p-1}$. We can prove that with this choice the diagram

$$S^{p,p} \xrightarrow{\mathbf{grad}} S^{p-1,p} \times S^{p,p-1} \xrightarrow{\mathbf{curl}} S^{p-1,p-1} \quad (4)$$

9. Numerical Techniques

is satisfied: i.e., $\ker(\text{curl}) = \text{grad}(S^{p,p})$.

In fact, our discretization technique can be understood as a generalization of edge finite elements. As it is well known, edge elements, combined with an adequate choice of nodal finite elements, satisfy a diagram analogous to (4). Moreover, if the knots of the knot vector (2) are repeated exactly p times, our discretization technique in the parametric domain Ω_0 coincides exactly with an approximation by edge elements. The main advantage of our technique respect to edge elements is that it provides smoother solutions, and in particular the electromagnetic fields can be approximated with continuous functions.

IV. NUMERICAL RESULTS

The error analysis of the numerical technique we presented is still being developed. So far, the convergence of the method has been only proved for regular solutions. However, the method has been used to solve several numerical tests and it performed well in all the cases.

A. Test 1: Maxwell eigenvalues in the square

As the first test case we have solved problem (1) in the square. The problem has been solved considering different degrees and continuities for the space of solutions. In every case our solution is free of spurious modes. Note that degree elevation provides better and better convergence rate (see Fig.1) at the price of very few additional degrees of freedom. For instance, passing from $p = 2$ to $p = 3$ we add only $4(N + 2)$ shape functions, where N is the number of subdivisions of the interval $[0, 1]$, while for standard edge elements the increase would be equal to $8N^2 + 4N$. Moreover, our method provides a solution for which the divergence is well defined, and in this test case it tends to zero with good convergence rates.

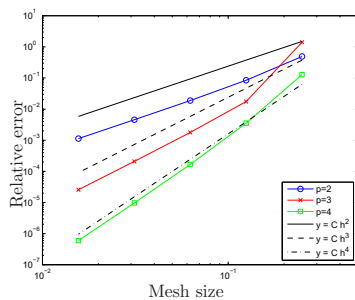


Figure 1. Convergence rates in the square domain, where h is the mesh size.

B. Test 2: Maxwell eigenvalues in an L-shaped domain

The second test we present concerns the computation of Maxwell eigenvalues in a non-convex geometry, in particular an L-shaped domain. The geometry is described with a single C^1 mapping \mathbf{F} from the square Ω_0 (see Fig. 2). It is known that the first eigenfunction is singular (see [5]), and nodal finite elements fail to approximate it. Instead, our method approximates this eigenfunction correctly, as it is seen in Fig. 3.

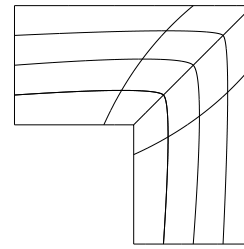


Figure 2. L-shaped domain. Coarsest mesh for computations.

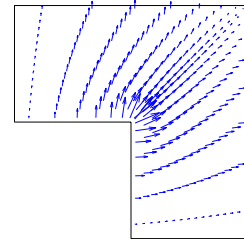


Figure 3. L-shaped domain. Approximation of the first eigenfunction.

V. CONCLUSION

We have presented the first numerical results for the isogeometric generalization of edge elements. In particular, our technique: *i*) is adequate for the optimal treatment of complex geometries, *ii*) produces regular fields preserving the optimal convergence rates also towards singular solutions. Finally, the main drawback of this technique is the patchwise tensor product structure. We emphasize that local refinement and non structured meshes can be obtained by adapting the theory of T-splines [6] to IGA. This goes beyond electromagnetic applications and it is object of intense studies.

REFERENCES

- [1] T.J.R. Hughes, J.A. Cottrell, Y. Bazilevs, "Isogeometric analysis: CAD, finite elements, NURBS, exact geometry and mesh refinement", *Comput. Methods Appl. Mech. Engrg.*, 194(39-41): 4135–4195, 2005.
- [2] R.D. Graglia, G. Lombardi, "Singular higher order complete vector bases for finite methods", *IEEE Trans. Antennas Propagat.*, 52(7): 1672–1685, 2004.
- [3] M. Costabel, M. Dauge, "Weighted regularization of Maxwell equations in polyhedral domains. A rehabilitation of nodal finite elements", *Numer. Math.*, 93(2): 239–277, 2002.
- [4] F. Assous, P. Ciarlet, Jr., J. Segré, "Numerical solution to the time-dependent Maxwell equations in two-dimensional singular domains: the singular complement method", *J. Comput. Phys.*, 161(1): 218–249, 2000.
- [5] M. Costabel, M. Dauge, "Computation of resonance frequencies for Maxwell equations in non-smooth domains", *Topics in computational wave propagation*, vol. 31 of Lect. Notes Comput. Sci. Eng., Springer, Berlin, 2003, pp. 125–161.
- [6] Y. Bazilevs, V.M. Calo, J.A. Cottrell, J.A. Evans, T.J.R. Hughes, S. Lipton, M.A. Scott, T.W. Sederberg, "Isogeometric Analysis using T-splines", submitted for publication.
- [7] A. Buffa, G. Sangalli, R. Vázquez, "Isogeometric analysis for electromagnetic problems", Tech. Rep. IMATI CNR, 2009.

Nonoverlapping and overlapping decomposition methods in 3D BEM multilayered model for Optical Tomography

Tomasz Grzywacz*, Jan Sikora†

*Institute of Theory of Electrical Engineering, Measurement and Information Systems,
Warsaw University of Technology, 75 Koszykowa, 00-662 Warsaw, Poland

†Faculty of Electrical Engineering and Computer Science, 38a Nadbystrzycka, 20-618 Lublin, Poland

Abstract—Diffuse Optical Tomography (DOT) has been intensively developed over recent years. It is an imaging technique which aims to recover the optical properties of biological tissue. The image reconstruction problem in DOT is a non-linear ill-posed problem which requires feasible forward model that describe light propagation within the medium accurately. The forward problem in DOT can be modelled in a frequency domain as a diffusion equation with Robin boundary conditions. In case of multilayered geometries the forward problem can be treated as a set of coupled equations. In this paper we present the solution for diffuse light propagation in a four layer concentric spherical model using overlapping or nonoverlapping domain decomposition methods and the Boundary Element Method.

Index Terms—Diffuse Optical Tomography, Domain Decomposition Methods, Boundary Element Method.

I. INTRODUCTION

Diffuse Optical Tomography in medicine aims to recover the optical properties of biological tissue from measurement of the transmitted light made at multiple points on the surface of the body. This boundary data measurements can be used to recover a spatial distribution of internal absorption and scattering coefficients.

The main topic within this field is the development of an efficient and accurate method for calculating the intensity of light transmitted or reflected from the object under experimental investigation. In case of sufficiently high scattering the diffusion equation with Robin boundary conditions [3] is an acceptable model of light propagation. A method we use to solve this problem includes analytical expression based on Green functions [2], and numerical methods based on Finite Difference Method (FDM) or Finite Element Methods (FEM).

In this paper it is assumed that the object being studied is considered as a set of disjoint simply connected regions with constant optical coefficients within each region, but that may differ between regions. In this case the diffusion equation can be replaced by a set of Helmholtz equations for each domain, together with interface conditions. For this problem, analytical solution isn't easily available. Although volume based PDE solvers such as FDM or FEM can be applied to this problem, there are often practical difficulties in constructing meshes for general geometries that respect the interfaces accurately. In contrast, the use of boundary integral methods (e.g. BEM) involve only representation of the surface meshes and can be much easier to implement.

II. FORMULATION OF THE PROBLEM

The problem of Optical Tomography in a highly diffusive body Ω with boundary Γ can be modelled by the use of the diffusion equation in the frequency domain form:

$$-\nabla \cdot \kappa(\mathbf{r}) \nabla \Phi(\mathbf{r}; \omega) + \mu_a(\mathbf{r}) \Phi(\mathbf{r}; \omega) + \frac{(i\omega)}{c} \Phi(\mathbf{r}, \omega) = q(\mathbf{r}; \omega) \quad (1)$$

with Robin boundary conditions:

$$\Phi(\mathbf{m}; \omega) + 2\alpha\kappa(\mathbf{m}) \frac{\partial \Phi(\mathbf{m}; \omega)}{\partial \nu} = h^-(\mathbf{m}; \omega), \quad \mathbf{m} \text{ on } \Gamma \quad (2)$$

where $\omega \in \mathbf{R}^+$ is the frequency modulation, Φ is the radiance c is the velocity of light, q is an internal source of light in medium, h^- is an incoming flux, α is a boundary term which incorporates the refractive index mismatch at the tissue-air boundary, ν is the outward normal at the boundary Γ , κ and μ_a are the diffusion and absorption coefficients, respectively. We define, $\kappa = \frac{1}{3(\mu_a + \mu'_s)}$, where μ'_s is the reduced scattering coefficient [1], [2]. We use the notation \mathbf{r} for a position vector in Ω and \mathbf{m} for a position vector restricted to a surface.

III. INTEGRAL FORMULATION AND NUMERICAL IMPLEMENTATION

The boundary integral formulation makes use of Green's function of the Helmholtz equation, which in the absence of boundary conditions is also referred to as the fundamental solution. We define a Green's function of Eq. (1) in each sub-domain Ω_l as solution of the equations

$$\nabla^2 G_l(\mathbf{r}, \mathbf{r}'; \omega) - \omega_l^2 G_l(\mathbf{r}, \mathbf{r}'; \omega) = -\delta(\mathbf{r} - \mathbf{r}') \quad (3)$$

with the asymptotic $G_l(\mathbf{r}, \mathbf{r}'; \omega)|_{r \rightarrow \infty} = 0$ where $G_l(\mathbf{r}, \mathbf{r}'; \omega)$ is the response of the infinite media to a single source $q_l = \delta$ at position $\mathbf{r} = \mathbf{r}'$. From equations (3) and (1), by multiplying (3) with $\Phi_l(\mathbf{r}; \omega)$ and (1) with $G_l(\mathbf{r}, \mathbf{r}'; \omega)$, and subtracting we get:

$$\begin{aligned} &\Phi_l(\mathbf{r}; \omega) \nabla^2 G_l(\mathbf{r}, \mathbf{r}'; \omega) - G_l(\mathbf{r}, \mathbf{r}'; \omega) \nabla^2 \Phi_l(\mathbf{r}; \omega) = \\ &-\delta(\mathbf{r} - \mathbf{r}') \Phi_l(\mathbf{r}; \omega) + \frac{q_l(\mathbf{r}; \omega)}{\kappa_l} G_l(\mathbf{r}, \mathbf{r}'; \omega) \end{aligned} \quad (4)$$

As far as numerical implementation is considered the surface interfaces Γ_l are discretised in P_l surface elements $\tau_{l,k}; k = 1, \dots, P_l$ with N_l vertices $N_{l,k}; k = 1, \dots, N_l$

after which we can approximate the functions U_l and V_l by the use of nodal basis functions ϕ_k , restricted to Γ_l .

$$\begin{aligned} U_l(\mathbf{m}; \omega) &\simeq \sum_{k'=1}^{N_l} U_{l,k'}(\omega) \phi_{l,k'}(\mathbf{m}), \\ V_l(\mathbf{m}; \omega) &\simeq \sum_{k'=1}^{N_l} V_{l,k'}(\omega) \phi_{l,k'}(\mathbf{m}) \end{aligned} \quad (5)$$

Representation above expresses both U_l and V_l in terms of the complex coefficients $U_{l,k'}$, $V_{l,k'}$ interpolated by the nodal basis functions and thus enforces V_l to be at least C^0 continuous.

The integrals occurring in the Boundary Integral equations take the form:

$$u_l(\mathbf{m}; \omega) = \sum_{k'=1}^{N_l} U_{l,k'}(\omega) \int_{\Gamma_l} \partial_l G_l(\mathbf{m}, \mathbf{m}'; \omega) \phi_{l,k'}(\mathbf{m}') dS(\mathbf{m}') \quad (6)$$

$$v_l(\mathbf{m}; \omega) = \sum_{k'=1}^{N_l} V_{l,k'}(\omega) \int_{\Gamma_l} \partial_l G_l(\mathbf{m}, \mathbf{m}'; \omega) \phi_{l,k'}(\mathbf{m}') dS(\mathbf{m}') \quad (7)$$

Function $v_l(\mathbf{m}; \omega)$, which is obtained by convolution with a Green's function, is known as a *single layer potential*, and function $u_l(\mathbf{m}; \omega)$, which is obtained by convolution with the normal derivative of a Green's function, is known as a *double layer potential*.

IV. THE FOUR LAYER SPHERICAL MODEL

In our research we have taken into consideration a four layer concentric spherical model. The Generalised Minimum Residuals Method (GMRES) was used to solve the linear matrix equation $\mathbf{K}\mathbf{f} = \mathbf{b}$ obtained from BEM. Here, \mathbf{f} is the discrete version of $\{f\}$ and contains approximations in (5), \mathbf{K} is the system matrix, and \mathbf{b} the vector of known coefficients calculated from the light sources in the problem. \mathbf{K} is a block-bounded asymmetric matrix. In order to solve equation of 20000 unknowns it takes up to 50 hours to a 64-bit Athlon processor. Taking advantage of domain decomposition methods [4] as well as BEM we are able to decrease computation time to minutes. BEM is preferable to other methods because it provides in each node not only the value of the state function but its normal derivative as well. In the Fig. 1 we can see the solution of the state function in concentric spherical model.

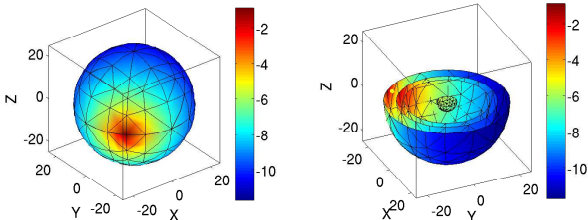


Fig. 1. The logarithm of amplitude of photon density. The outer surface of the object (left) and its cross-section (right).

Generally, there are two kinds of approaches depending on whether the subdomains overlap (Schwarz methods) or are separated (Schur Complement methods)[5]. The latter are

called substructuring methods and are based on nonoverlapping decompositions of the region into a set of subdomains. The number of equations needed to solve this smaller problem is minor, compared to the whole system. Thus the amount of memory required for allocating the equations is smaller too. In the Fig. 2 a scheme of the Dirichlet-Neumann substructuring algorithm is presented.

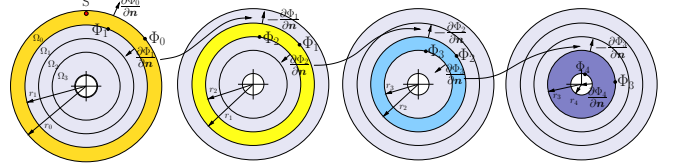


Fig. 2. Boundary condition transmission in the Dirichlet-Neumann algorithm.

The results presented in the Fig. 3 are taken from the nodes located on the circumference of adjacent spheres (cross-section with the largest radius). The chart on the bottom right corner shows results with a relative error less than two percent when compared to the solution without use of any decomposition method.

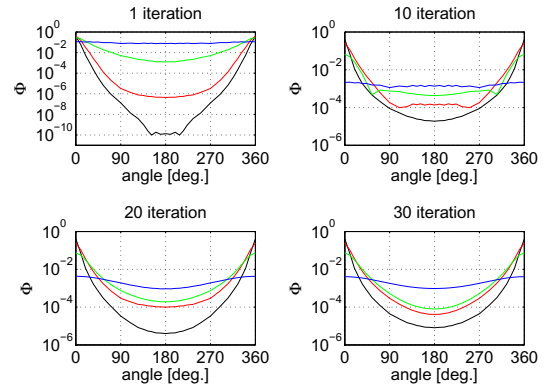


Fig. 3. Results from the Dirichlet-Neumann substructuring algorithm.

In case of overlapping subdomains the decomposition algorithm reduces the number of sequential steps in contrast to the previous one. It is an advantage from standpoint of ill-posed problems which may converge very slow. The main drawback of this approach is the use of greater memory resources as one iteration refers to two regions simultaneously.

REFERENCES

- [1] J. Heino, S.R. Arridge, J. Sikora, E. Somersalo, "Anisotropic effects in highly scattering media", *Physical Review*, E68, 2003.
- [2] J. Sikora, A. Zacharopoulos, A. Douiri, M. Schweiger, L. Horesh, S.R. Arridge and J. Ripoll, "Diffuse photon propagation in multilayered geometries", *Physics in Medicine and Biology*, vol. 51, pp. 497-516, 2006.
- [3] A.D. Zacharopoulos, S.R. Arridge, O. Dorn, V. Kolehmainen, J. Sikora, "Three-dimensional reconstruction of shape and piecewise constant region values for optical tomography using spherical harmonic parametrization and a boundary element method", *Inverse Problems*, vol. 22, pp. 1509-1532, 2006.
- [4] A. Toselli, O. Widlund, *Domain Decomposition Methods - Algorithms and Theory*, Springer, 2005.
- [5] B.F. Smith, P.E. Björstad, W.D. Gropp, *Domain Decomposition: parallel multilevel methods for elliptic partial differential equations*, Cambridge University Press, 1996.

Galerkin Projection Method for Sliding Interfaces in Finite Element Analysis of Electrical Machines

Enno Lange, François Henrotte and Kay Hameyer
 Institute of Electrical Machines – RWTH Aachen University
 Schinkelstraße 4, D-52056 Aachen, Germany
 E-mail: Enno.Lange@IEM.RWTH-Aachen.de

Abstract— This paper proposes the application of the Galerkin projection method to implement the relative motion of stator and rotor in the FE simulations of electrical machines. The non-conforming representation of stator and rotor regions impose no restriction on time or space discretization. The symmetry and sparsity of the system of FE equations are preserved. The method is applied to the 2D simulation of the cogging torque of a synchronous machine and the results are compared with a conforming moving band approach with remeshing of the air gap at each time step.

I. INTRODUCTION

SEVERAL approaches to simulate the movement within a Finite Element analysis (FEA) of electrical machines have been developed. Static and transient analysis of the machines require a flexible variation of the rotor position. An obvious and early adopted approach is the moving band (MB) technique [4] whose principle is to re-generate at each time step a single layer of conforming finite elements in a thin annulus-shaped region of the air gap. However, in practical the automatic remeshing of the air gap is only tractable for 2D rotating machines. For linear motion in 2D and motion in 3D models, air gap remeshing would imply invoking a full-fledged automatic mesh generator at each time step, which is impractical. The mortar element method (MEM) was proposed in [8] and applied to a 2D machine problem in [1]. The Lagrange multiplier (LM) method has been extensively investigated in [2]. Both MEM and LM can be extended to 3D problems, but the MEM requires an additional integration mesh [9], and for the LM the conditioning worsens significantly [6].

The non-conforming approach proposed in this paper is based on a mesh-to-mesh Galerkin projection method (GPM) which has been introduced in [5]. While applications described in [7] project a known field from a source to a target mesh, in this paper the GPM is implemented in a standard FE assembly process.

II. PROJECTION METHOD AND FORMULATION

Let $L^2(\Omega)$ be the space of square integrable functions on $\Omega \subset \mathbb{R}^n$, $n = 1, 2, 3$. The scalar product relative to the L^2 -norm of F and G is defined as

$$(F, G)_\Omega = \int_\Omega F(x) \cdot G(x) dx. \quad (1)$$

A field $F^\Omega \in L^2(\Omega)$ can be interpolated in a discrete domain as:

$$F^\Omega = \sum_{i=1}^n f_i \alpha_i^\Omega \quad (2)$$

where α_i^Ω is the shape function associated to the node or edge i and f_i is the corresponding coefficient.

The sliding boundaries of the rotor (master) and the stator (slave) domain are denoted Γ_N and Γ_M respectively. Note that the choice of the master boundary is based on the discretization: The boundary with the largest number of unknowns is chosen as the master boundary. Let $p : \Gamma_N \mapsto \Gamma_M$ be a bijective mapping. Consider the two magnetic vector potential fields $F^N \in L^2(\Gamma_N)$ and $G^M \in L^2(\Gamma_M)$. One wishes to have $\gamma(F^N \circ p^{-1}) = G^M$ on Γ_M and $F^N = \gamma(G^M \circ p)$ on Γ_N with $\gamma = \pm 1$ according to whether the identification between Γ_N and Γ_M is a symmetry (or an identity) or an antisymmetry. This writes in weak form:

$$\int_{\Gamma_M} (\gamma(F^N \circ p^{-1}) - G^M) \alpha_k^M d\Gamma_M = 0, \quad \forall k = 1 \dots m \quad (3)$$

$$\int_{\Gamma_N} (F^N - \gamma(G^M \circ p)) \alpha_k^N d\Gamma_N = 0, \quad \forall k = 1 \dots n \quad (4)$$

It can be shown that (3) and (4) loose their symmetry on the discrete level. Thus, the idea is to use only the projection p and avoid its inverse p^{-1} by applying p to (3) which leads to the following formulation:

$$\int_{\Gamma_N} (\gamma F^N - (G^M \circ p)) (\alpha_k^M \circ p) d\Gamma_N = 0, \quad (5)$$

$$\int_{\Gamma_N} (F^N - \gamma(G^M \circ p)) \alpha_k^N d\Gamma_N = 0. \quad (6)$$

If, after discretization, F^N and G^M are expressed by (2), (5) and (6) can be written in matrix form

$$\begin{bmatrix} \mathbf{A} & -\gamma\mathbf{B} \\ -\gamma\mathbf{C} & \mathbf{D} \end{bmatrix} \begin{bmatrix} \mathbf{g} \\ \mathbf{f} \end{bmatrix} = 0 \quad (7)$$

with the components of \mathbf{A} and \mathbf{D} being:

$$A_{mj} = \int_{\Gamma_N} (\alpha_m^M \circ p) (\alpha_j^M \circ p) d\Gamma_N, \quad (8)$$

$$D_{ni} = \int_{\Gamma_N} \alpha_n^N \alpha_i^N d\Gamma_N. \quad (9)$$

And the components of \mathbf{B} and \mathbf{C} expand to:

$$B_{mi} = \int_{\Gamma_N} \alpha_m^N (\alpha_i^M \circ p) \, d\Gamma_N, \quad (10)$$

$$C_{nj} = \int_{\Gamma_N} (\alpha_n^M \circ p) \alpha_j^N \, d\Gamma_N. \quad (11)$$

Obviously $B_{mi} = C_{jn}$ and the resulting system (7) is symmetric. The GPM can be incorporated into the equation system of any standard Galerkin FE formulation. Furthermore, no restriction regarding the degree or the type of the degrees of freedom are imposed.

III. APPLICATION: COGGING TORQUE

The GPM has been implemented in the *iMOOSE*-package [10]. The cogging torque of a permanent magnet synchronous machine with surface mounted magnets has been studied. The torque is calculated according to Arkkio's method [3]. The numeric field solution is obtained by means of a standard magnetic vector potential FE formulation combined with either the GPM or the MB technique. Despite its non-conformity, the mesh density for GPM, as shown in Fig. 1, is identical to the one for MB. The mapping $p = f(\varphi)$ is the rotation about the center of the rotor by the angle φ . The simulated cogging torques, normalized to the nominal torque T_0 , are compared in Fig 2. Additionally, the relative difference between the GPM and the MB is shown. The GPM has as well been applied to meshes with slightly differing numbers of unknowns n in Γ_N and m in Γ_M ($0.75 < n/m < 1.25$). The results are similar to the ones shown in Fig. 2.

IV. DISCUSSION

Numerical results show a good agreement between the non-conforming GPM and the conforming MB. In general it can be stated, that the torque calculated by the GPM follows a smoother waveform compared to the one of the MB. The higher harmonics in the MB waveform are suspected to stem from the remeshing process. The differences between the GPM and the MB do not follow a certain pattern. Larger differences occur around the maximum as well as around the zero crossing of the torque waveform.

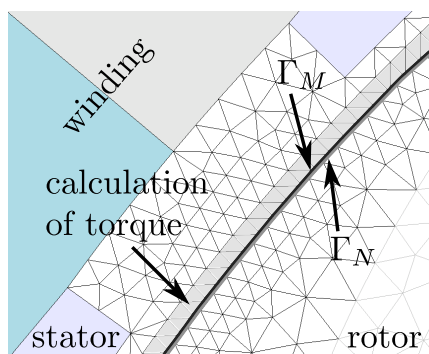


Fig. 1. Nonconforming elements at Γ_N and Γ_M of rotor and stator

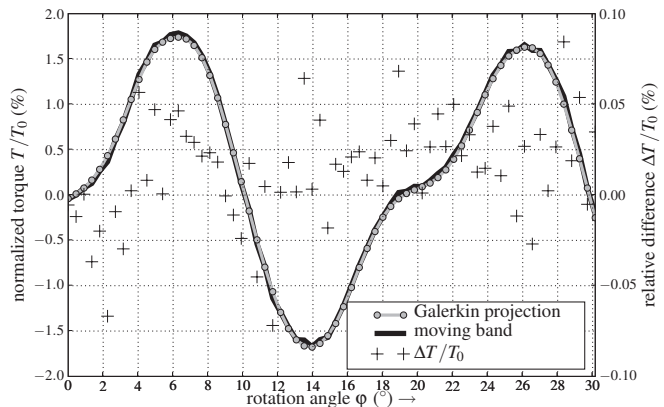


Fig. 2. Cogging torque vs. rotation angle by means of GPM and MB

V. CONCLUSION

This abstract presents a non-conforming method to model the sliding interfaces in electrical machines for FEA. The method is applied to the simulation of the cogging torque of a permanent magnet machine and the results are compared to a classical MB technique. The first results and the straightforward implementation of the GPM compared to MEM or LM approaches for 3D problems promise a flexible and versatile approach to deal with sliding conditions in electrical machines. The application to 3D problems as well as further investigations regarding energy conservation, error estimations, numerical integration and a comparison to measurements will be presented in the full paper.

REFERENCES

- [1] O. Antunes, J. Bastos, N. Sadowski, A. Razek, L. Santandrea, F. Bouillault, and F. Rapetti. Using hierarchic interpolation with mortar element method for electrical machines analysis. *Magnetics, IEEE Transactions on*, 41(5):1472–1475, May 2005.
- [2] O. Antunes, J. Bastos, N. Sadowski, A. Razek, L. Santandrea, F. Bouillault, and F. Rapetti. Torque calculation with conforming and non-conforming movement interface. *Magnetics, IEEE Transactions on*, 42(4):983–986, April 2006.
- [3] A. Arkkio. *Analysis of induction motors based on the numerical solution of the magnetic field and circuit equations*. Electrical Engineering Series. Acta Polytechnica Scandinavica, 59 edition, 1987.
- [4] B. Davat, Z. Ren, and M. Lajoie-Mazenc. The movement in field modeling. *Magnetics, IEEE Transactions on*, 21(6):2296–2298, Nov 1985.
- [5] C. Geuzaine, B. Meys, F. Henrotte, P. Dular, and W. Legros. A galerkin projection method for mixed finite elements. *Magnetics, IEEE Transactions on*, 35(3):1438–1441, May 1999.
- [6] C. Golovanov, J.-L. Coulomb, Y. Marechal, and G. Meunier. 3d mesh connection techniques applied to movement simulation. *Magnetics, IEEE Transactions on*, 34(5):3359–3362, Sep 1998.
- [7] G. Parent, P. Dular, J.-P. Ducreux, and F. Piriou. Using a galerkin projection method for coupled problems. *Magnetics, IEEE Transactions on*, 44(6):830–833, June 2008.
- [8] F. Rapetti, E. Bouillault, L. Santandrea, A. Buffa, Y. Maday, and A. Razek. Calculation of eddy currents with edge elements on non-matching grids in moving structures. *Magnetics, IEEE Transactions on*, 36(4):1351–1355, Jul 2000.
- [9] F. Rapetti, Y. Maday, F. Bouillault, and A. Razek. Eddy-current calculations in three-dimensional moving structures. *Magnetics, IEEE Transactions on*, 38(2):613–616, Mar 2002.
- [10] D. van Riesen, C. Monzel, C. Kaehler, C. Schlensok, and G. Henneberger. imoose-an open-source environment for finite-element calculations. *Magnetics, IEEE Transactions on*, 40(2):1390–1393, March 2004.

Convergence Acceleration of Time-Periodic Electromagnetic Field Analysis by Singularity Decomposition-Explicit Error Correction Method

Y. Takahashi¹, T. Tokumasu², A. Kameari³, H. Kaimori³, M. Fujita², T. Iwashita¹, and S. Wakao⁴

¹Kyoto University, Yoshida-Honmachi, Sakyo-ku, Kyoto 606-8501 JAPAN

²Toshiba Corporation Power Systems Company, 2-4 Suehiro-cho, Tsurumi-ku, Yokohama 230-0045

³Science Solutions International Laboratory, Inc., 2-21-7 Naka-cho, Meguro-ku, Tokyo 153-0065

⁴Waseda University, 3-4-1 Ohkubo, Shinjuku-ku, Tokyo 169-8555

E-mail ytakahashi@i.kyoto-u.ac.jp

Abstract— This paper proposes a novel method for the improvement of the convergence to a steady state in time-periodic transient eddy-current analyses with nonlinear magnetic materials. The proposed method, which is based on the time-periodic finite-element method and the singularity decomposition-explicit error correction method, can extract poorly converged error components corresponding to large time constants of an analyzed system. The correction of the extracted error components accelerates the convergence to a steady state efficiently. Some numerical results verify the effectiveness of the proposed method.

I. INTRODUCTION

For the further speed-up of the electromagnetic field computations by the finite-element method (FEM), a fast iterative linear solver for large-scale sparse system of equations such as a multigrid method [1] and a method to stably accelerate the convergence of the Newton-Raphson (NR) method such as a line search technique [2] have been investigated intensively.

On the other hand, to carry out transient eddy-current analyses taking account of nonlinear magnetic properties, a step-by-step calculation is necessary by using time integration methods such as the backward Euler method. As is the often case with finite-element analyses coupled to electric circuit, an extremely large number of time steps are required to attain steady state solutions in the case that the time constant of the analyzed problem is large. The time-periodic FEM (TPFEM) [3] has an advantage that the steady state solution can be obtained directly without transient calculation. However, we have to treat a large-scale nonsymmetric coefficient matrix, which results in the huge computational costs. Therefore, it is indispensable to improve the convergence characteristic of transient calculation as well as that of linear iterative solvers and the NR method for the further reduction of computational costs required for the analysis of practical problems.

As a solution to the above difficulty, we propose a novel method for the improvement of the convergence characteristic of step-by-step time integrations in nonlinear transient eddy-current analyses. The proposed method, which is based on the TPFEM and the singularity decomposition-explicit error correction (SD-EEC) method [4]-[6], can extract poorly converged error components which correspond to large time constants of an analyzed system. The correction of the

extracted error components accelerates the convergence of transient calculation efficiently. The formulations based on the ordinary or half time-periodic boundary condition are presented. Finally, the effectiveness of the proposed method is examined in the finite-element analysis coupled to electric circuit.

II. METHOD OF ANALYSIS

A. Time-periodic finite-element method

A nonlinear system of equations, for example, derived from the $A\text{-}\phi$ formulation in quasi-static field coupled to electric circuit equations, is expressed as follows:

$$S(\mathbf{x}) + C \frac{\partial}{\partial t} \mathbf{x} = \mathbf{f} \quad (1)$$

where \mathbf{x} is the unknown vector, and \mathbf{f} is the right-hand-side vector. The number of unknowns is m . The matrix S is generally nonlinear because of magnetic properties of magnetic materials and the coefficient matrix C is constant.

When one or half period is divided into n time steps and the θ method is adopted for the time integration scheme, the linearized equations of the TPFEM under the ordinary or half time-periodic boundary condition are given by

$$\begin{bmatrix} \tilde{C}_0 + \tilde{S}_1 & O & \cdots & O & \mp \tilde{C}_n \\ -\tilde{C}_1 & \tilde{C}_1 + \tilde{S}_2 & \cdots & O & O \\ O & -\tilde{C}_2 & \ddots & \ddots & \vdots \\ \vdots & \vdots & \ddots & \ddots & O \\ O & O & \cdots & -\tilde{C}_{n-1} & \tilde{C}_{n-1} + \tilde{S}_n \end{bmatrix} \begin{Bmatrix} \Delta \mathbf{x}_1 \\ \vdots \\ \Delta \mathbf{x}_n \end{Bmatrix} = \begin{Bmatrix} -\mathbf{G}_1 \\ \vdots \\ -\mathbf{G}_n \end{Bmatrix}$$

$$\tilde{C}_i = \frac{C}{\Delta t} - (1-\theta)S_i, \tilde{S}_i = (1-\theta)S_{i-1} + \theta S_i, S_i = \frac{\partial S}{\partial \mathbf{x}}(\mathbf{x}_i). \quad (2)$$

Here, the subscripts indicate the time step, $\Delta \mathbf{x}_i$ is the increment of \mathbf{x}_i , \mathbf{G}_i is the residual, the signs $-$ and $+$ of \tilde{C}_n correspond to the ordinary and half time-periodic boundary conditions $\mathbf{x}(t+T) = \pm \mathbf{x}(t)$, respectively, and T is the period.

The solutions obtained from step-by-step calculations of (1) starting with \mathbf{x}_0 as initial value are equivalent to those obtained from (2) by using forward block Gauss-Seidel (GS) method [3]. It's noted that low frequency error components converge slowly in the GS method. Therefore, in the case that the time constant of (1) is significantly large, a large number of time steps are necessary to obtain steady state solutions.

B. Improvement of convergence characteristic of transient calculation based on the SD-EEC method

The following nonlinear system of equations is considered

$$A(\mathbf{x}) = \mathbf{b}, \quad (3)$$

where $A(\mathbf{x})$ is a nonlinear matrix with respect to \mathbf{x} and \mathbf{b} is the right-hand-side vector. The procedure of the SD-EEC method taking into account the nonlinearity of A is as follows:

- (i) Update the approximate solution $\tilde{\mathbf{x}}$ by iterative methods.
- (ii) Compute $\mathbf{r} = B^T(\mathbf{b} - A(\tilde{\mathbf{x}}))$ by using auxiliary matrix B .

Obtain correction vector \mathbf{p} by solving $B^T \frac{\partial A(\tilde{\mathbf{x}})}{\partial \mathbf{x}} B \mathbf{p} = \mathbf{r}$.

- (iii) Update the approximate solution by $\tilde{\mathbf{x}} \leftarrow \tilde{\mathbf{x}} + B\mathbf{p}$

where the superscript T means transpose.

In order to accelerate the convergence of transient calculation, we apply the SD-EEC procedure to (2). The auxiliary matrix B is constructed so as to approximate the dc error component, which corresponds to large time constants and is poorly converged, in a transient calculation as follows:

$$B = [I \quad \dots \quad I \quad \dots \quad I]^T \quad (4)$$

where I is a $m \times m$ identity matrix and B is a $nm \times m$ matrix. The correction vector \mathbf{p} can be obtained by solving the following equation

$$\left(\sum_{i=1}^n \tilde{S}_i + \tilde{C}_0 \mp \tilde{C}_n \right) \mathbf{p} = -\tilde{C}_0(\mathbf{x}_0) \pm \tilde{C}_n(\mathbf{x}_n). \quad (5)$$

The step-by-step calculation is restarted by adopting the corrected solution $\mathbf{x}_n + \mathbf{p}$ as the initial value \mathbf{x}_0 for the next one or half period. Although the procedure of solving (5) is added to the ordinary transient calculation once per one or half period, the additional computational costs are fairly small compared with the total computational costs required for normal step-by-step calculation.

III. NUMERICAL EXAMPLES

The effectiveness of the proposed method is investigated in a nonlinear eddy-current analysis of the iron core model shown in Fig. 1. The exciting coil is wound around the core and excited by a sinusoidal voltage of 100 Hz. The coil turns is 3000, the resistance of the coil is 45.79 Ω , the conductivity of the core is 7.505×10^6 S/m, and the nonlinear magnetic property is the same as mentioned in [7]. Because of the symmetry, one-eighth part of the whole model is analyzed. The number of elements and unknowns are 29250 and 88081, respectively. One period is divided into 20 time steps.

Fig. 2(a) shows the time variation of the coil current in the case that the applied voltage is $1000 \sin(2\pi f t)$ V. In this problem, we can use the correction method based on the half time-periodic boundary condition. Whereas the steady state solution cannot be obtained from the step-by-step calculation in 5 periods, the proposed method accomplishes the convergence of the transient calculation after only two corrections, which results in the drastic reduction of the computational time. Fig. 2(b) shows the time variation of the coil current in the case that the applied voltage is $1000(1 - \cos(2\pi f t))$ V. The correction method based on the ordinary time-periodic boundary condition is applied to this problem. The steady state solution is attained in two periods.

From the above results, the effectiveness of the proposed method can be confirmed. The detailed discussion about the formulation of the proposed method and more numerical results will be included in the full paper.

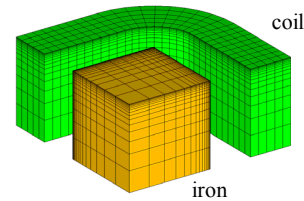


Fig. 1. Analyzed model.

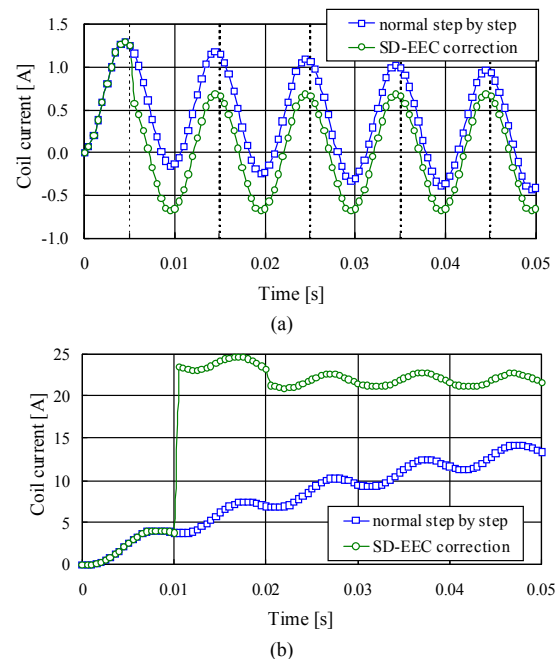


Fig. 2. Time variation of coil current. (a) Correction based on half time-periodicity. (b) Correction based on ordinary time-periodicity.

IV. REFERENCES

- [1] R. Hiptmair, "Multigrid method for Maxwell's equations," *SIAM J. Numer. Anal.*, vol. 36, pp. 204–225, 1998.
- [2] K. Fujiwara, Y. Okamoto, A. Kameari, and A. Ahagon, "The Newton-Raphson method accelerated by using a line search – Comparison between energy functional and residual minimization –," *IEEE Trans. Magn.*, vol. 41, no. 5, pp. 1724–1727 2005.
- [3] T. Hara, T. Naito, and J. Umoto, "Time-periodic finite element method for nonlinear diffusion equations," *IEEE Trans. Magn.*, vol. 21, no. 6, pp. 2261–2264 (1985)
- [4] T. Iwashita, T. Mifune, and M. Shimasaki, "Similarities Between Implicit Correction Multigrid Method and A-phi Formulation in Electromagnetic Field Analysis," *IEEE Trans. Magn.*, vol. 44, no. 6, pp. 946–949 (2008).
- [5] A. Kameari, "Improvement of ICCG Convergence for Thin Elements in Magnetic Field Analysis," *IEEE Trans. Magn.*, vol. 44, no. 6, pp. 1178–1181 (2008).
- [6] T. Mifune, S. Moriguchi, T. Iwashita, and M. Shimasaki, "Convergence Acceleration of Iterative Solvers for the Finite Element Analysis Using the Implicit and Explicit Error Correction Methods," *IEEE Trans. Magn.*, vol. 45, no. 3, pp. 1104–1107 (2009).
- [7] N. Takahashi, T. Nakata, and H. Morishige, "Summary of Results for Problem 20 (3-D Static Force Problem)," *COMPEL*, vol. 14, no. 2&3, pp. 57–75 (1995).

Efficient Block Gauss-Seidel Preconditioner for 3D Full-Wave Finite Element Analysis

Toshio Murayama¹ and Shinobu Yoshimura²

¹Sony Corporation Production Group, Tokyo 141-0031, Japan
Toshio.Murayama@jp.sony.com

²Department of System Innovation, The University of Tokyo, Tokyo 113-8654, Japan
yoshi@sys.t.u-tokyo.ac.jp

Abstract — A novel precondition method for edge-based full-wave electromagnetic finite element method is presented. The method utilizes the symmetric block Gauss-Seidel iteration based on an extension of the node patch edges. Numerical results demonstrate an excellent performance for our proposed preconditioner.

I. INTRODUCTION

Edge-based finite element approach to the simulation of arbitrarily shaped 3D complex structures is an efficient and versatile technique for passive electromagnetic analysis. In edge-element analyses, however, the large null space of the coefficient matrices causes difficulties in convergence when iterative solution techniques are applied. Several approaches have been reported to improve this slow convergence performance by preconditioning the original finite element matrix[1][2]. One of the effective approaches exploits the block Jacobi or block Gauss-Seidel iterations as preconditioning with the blocks composed of the edges around every node[3][4]. Our approach extends this ‘node patch’ to a long stencil whose corresponding block becomes a narrow band matrix. The stencil which consists of the long strip of node patches not only contributes to preserve a divergence free nature of the Maxwell’s equations but also improves global convergence, resulting in an excellent convergence property. Numerical experiments support the effectiveness of our approach.

II. FORMULATION

A. Edge-Based Finite Element Formulation

A time harmonic boundary value problem for the vector wave equation is expressed by the electric field vector as follows:

$$\nabla \times \frac{1}{\mu_r} \nabla \times \mathbf{E} + j\omega\mu_0\sigma\mathbf{E} - \omega^2\mu_0\varepsilon_0\varepsilon_r\mathbf{E} = -j\omega\mu_0\mathbf{J}_v \text{ in } \Omega \quad (1)$$

$$\mathbf{E} \times \mathbf{n} = 0 \text{ on } \Gamma_D \quad (2)$$

where Ω is a finite three dimensional domain with a Dirichlet-type boundary Γ_D and outward normal vector \mathbf{n} . $\mu_0, \mu_r, \varepsilon_0, \varepsilon_r, \sigma, \omega$ and \mathbf{J}_v are the magnetic permeability of free space, the relative magnetic permeability, the electric permittivity of free space, the relative electric permittivity, the conductivity, the angle frequency and the impressed volume electric current density, respectively. Using a Galerkin’s testing procedure leads to the following finite element system:

$$\mathbf{M}_{ee} \mathbf{x}_e = -j\omega \mathbf{f}_e \quad (3)$$

where \mathbf{M}_{ee} is the finite element matrix, \mathbf{x}_e denotes the vector of the unknown expansion coefficients of \mathbf{E} and \mathbf{f}_e is the approximation of the source term associated with the impressed current \mathbf{J}_v [5].

B. Symmetric Block Gauss-Seidel Preconditioning

Preconditioning is a means of transforming the original linear system into well-conditioned one with the same solution, but that is likely to be easier to solve with an iterative algorithm. The popular incomplete Cholesky preconditioner, however, normally results in low-order convergence due to the large null space of an edge-based coefficient matrix. High-order convergence may be achieved by a ‘node patch’ defined by edges around a node shown in Fig.1. A symmetric block Gauss-Seidel preconditioning is used in units of the node patch edges defined at every node.

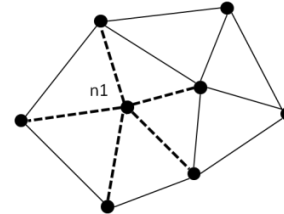


Fig.1 Node-Patch Edges for n1(Dashed Lines)

Symmetric Gauss-Seidel Iteration is given by

```

Input: r; Output: z = M-1r
z=0
for i=1,2,...,p,p-1,...,2,1
  z = z + RiTAi-1Ri(r-Az)
end for
  
```

where \mathbf{M} stands for a precondition matrix and \mathbf{A}_i is a sub-matrix whose elements are chosen according to the edges in the i -th node patch.

III. BLOCK GAUSS-SEIDEL PRECONDITIONER BASED ON A LONG STENCIL OF NODE PATCHES

A. Extended Node Patch for Unstructured Mesh

We extend the definition of the node patch to a long strip stencil depicted in Fig.2, where the extended node patch consists of edges around the nodes $n1, n2, n3$ and $n4$.

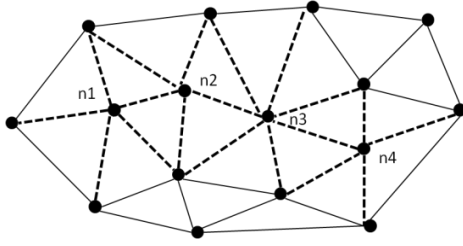


Fig.2 Extended Node Patch Edges for n1, n2, n3 and n4 (Dashed Lines)

B. Extended Node Patch for Structured Mesh

As for a structured mesh, the extended node patch can be easily defined similarly. In an analytical space with hexahedral blocks, for example, one of the practical extended node patch definitions is obtained as the set of edges like:

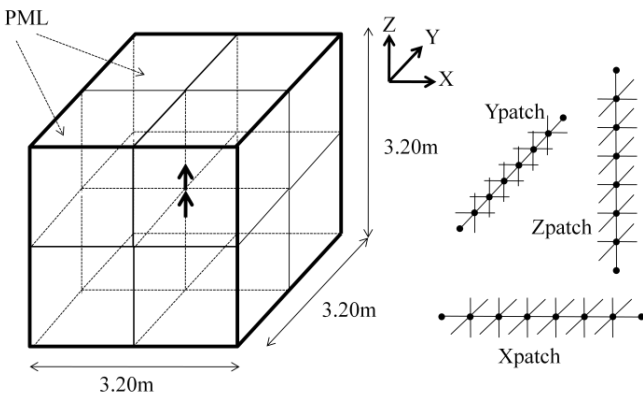
$$\begin{aligned} Xpatch_{ijk} &= \{e \mid e \text{ is originating from } n_{ijk}, i=0, \dots, n_x\}, \\ Ypatch_{ijk} &= \{e \mid e \text{ is originating from } n_{ijk}, j=0, \dots, n_y\} \text{ and} \\ Zpatch_{ijk} &= \{e \mid e \text{ is originating from } n_{ijk}, k=0, \dots, n_z\}, \end{aligned}$$

where e is an edge, n_{ijk} is a node at (i,j,k) , n_x , n_y and n_z are the number of nodes in X, Y and Z direction, respectively. With this definition, the resultant block matrix becomes a narrow block band matrix, which can be quickly factored and solved numerically.

IV. NUMERICAL RESULTS

A. Convergence Behaviors

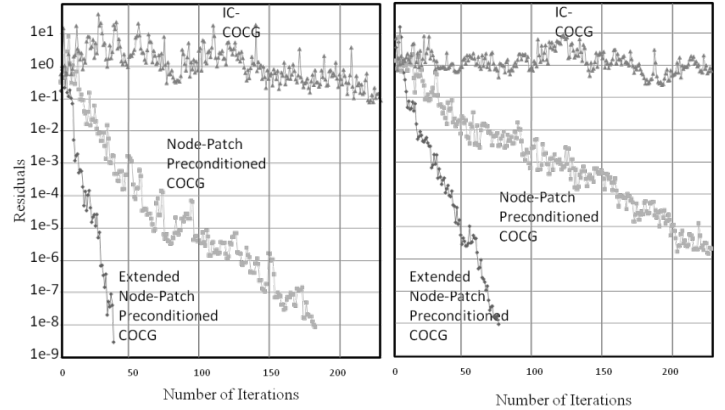
We applied the proposed preconditioning method to the large electromagnetic scattering field depicted in Fig.3. The analysis space is divided into $24 \times 24 \times 24$ cubic elements enclosed by 4-layer perfectly matched layers. Total 92256 unknowns are to be solved in a large, sparse matrix equation preconditioned by the X, Y and Z patches in Fig.3 (b). Current sources as an excitation are located in the center of the space. The convergence profiles in 74MHz and in 148MHz cases are shown in Fig.4. Comparison with the conventional IC-COCC method shows that the excellent convergence property of a normal and an extended node-patch stencil preconditionings.



(a) Analysis Model (b) Extended Node Patches
Fig.3 Overview of the Analysis Model and Stencils

The numerical convergence is measured by the relative

residual defined by $\|\text{current residual}\|/\|\text{initial residual}\|$, in which $\|\bullet\|$ denotes the L2-norm. The iteration process is terminated when it becomes below $10e-8$.



(a) 74MHz (b) 148MHz
Fig.4 Comparisons of the Convergence Behaviors

B. Memory Requirements

The preconditioning method using a normal or extended node patch block iterations requires many number of small size matrix calculations including factorizations and backward and forward substitutions. A normal node patch, for example, requires a 6×6 matrix for each node. The extended node-patches based on our stencil require a long but narrow band matrix, which can be easily factored and solved with the small number of fill-ins. With hexahedral element modeling, the bandwidth is less than that of the original matrix, that means that the method is a very memory-effective preconditioner.

V. CONCLUSION

An efficient and reliable preconditioning method for the edge-based finite element method has been derived, and numerically evaluated. The new preconditioner is based on an extended node-patch symmetric block Gauss-Seidel iteration. The effectiveness in performance and required memory resource has been demonstrated as a preconditioner for the COCC method for a large space electromagnetic scattering problem. The test results serve to validate the method and illustrate the valuable advantages associated with using the newly proposed extended node patch preconditioning procedure for practical 3D electromagnetic scattering analyses.

VI. REFERENCES

- [1] Y. Saad, *Iterative Methods for Sparse Linear Systems*, 2nd ed, Philadelphia, PA: SIAM, 2003.
- [2] H. Igarashi and T. Homma, "On Convergence of ICCG applied to finite element equation for quasi-static fields," *IEEE Trans. Magn.*, vol. 38, no. 2, pp. 565-568, Mar. 2002.
- [3] D. Arnold, R. Falk and R. Winther, "Multigrid in $H(\text{div})$ and $H(\text{curl})$," *Numer. Math.* 85, pp.197-217, 2000.
- [4] M. Mori, K. Yosui, T. Iwashita, E. Kobayashi and S. Abe, "Preconditioned Iterative Methods for High Frequency Edge Finite Element Electromagnetic Field Analyses," (In Japanese) *IEICE VOL. J89-C No. 8*, pp.521-528, Aug. 2006.
- [5] Y. Zhu and A. Cangellaris, *Multigrid Finite Element Methods for Electromagnetic Field Modeling*, The IEEE Press Series on Electromagnetic Wave Theory, 2006.

Numerical Convergence of Method of Moments in the Analysis of Bodies of Revolution

Úrsula C. Resende and Fernando J. S. Moreira*

Dept. Electrical Engineering, Federal Center for Technological Education of Minas Gerais, Brazil

Av. Amazonas 7675, Belo Horizonte, MG, CEP 30480-000

*Dept. Electronics Engineering, Federal University of Minas Gerais

Av. Pres. Antonio Carlos 6627, Belo Horizonte, MG, CEP 31270-901, Brazil

resendeursula@des.cefetmg.br, fernandomoreira@ufmg.br

Abstract — The scattering analysis by method of moments may lead to integral equations with severe singularities in their kernels. In this work we demonstrate that when these singularities are removed by the extraction technique and enough basis functions are used to describe surface current behavior, the numerical solution converges with Z-matrix integrals numerically evaluated using 2-point Gaussian quadrature. The numerical convergence is investigated in the analysis of the electromagnetic scattering by conducting and dielectric spheres.

I. INTRODUCTION

In the analysis of electromagnetic scattering by homogeneous bodies, the numerical evaluation of surface integral equations by the method of moments (MoM) has proved its efficiency to treat surfaces with arbitrary shape. The choice of suitable basis functions to represent the surface currents, the numerical evaluation of singular integrals, and efficient algorithms for the matrix inversion are fundamental to obtain accuracy and convergence from the MoM analysis. However, the numerical evaluation of singularities arising in the integral kernels is not a simple task. In [1] a robust numerical technique (extraction technique) is presented to remove singularities arising in the scattering by conducting bodies of revolution (BOR's). In [2] the method is extended to handle triangular basis functions in a Galerkin scheme.

For homogeneous dielectric BOR's the accuracy of the MoM analysis deteriorates as the dielectric constant increases [3]. In [4] different integral equation formulations are used to overcome this problem, but still with relatively small accuracy. This drawback may be partially overcome by increasing the number of segments used to represent the BOR generatrix, which should be made proportional to the dielectric constant and, consequently, increases the Z-matrix size. In [5] triangular functions for both basis and testing functions were used, simply represented by a series of pulses. It was observed that, to attain certain accuracy, more pulses had to be used to represent the triangular functions as the dielectric constant of the BOR increased. In some sense this leads to the perception that accuracy increases with the number of quadrature points used to evaluate the integrals.

In this work we analyze the plane-wave scattering by conducting and dielectric spheres. We observe that when the extraction technique [2] is applied and a sufficient number of triangular basis functions (TBF's) is used to represent the surface geometry, numerical convergence is attained when 2-point Gaussian quadratures are applied to evaluate the

integrals of the MoM Z-matrix. The accuracy increases if more TBF's are used but does not change with the number of quadrature points.

II. INTEGRAL EQUATION EVALUATION

The MoM solution involving surface electric (EFIE) and magnetic (MFIE) field integral equations leads to many different formulations [3], [6]. The EFIE formulation is the choice for open conducting shells. For closed conducting surfaces the combined field integral equation (CFIE) avoids spurious resonances [6]. The CFIE is a linear combination of EFIE and MFIE. For dielectric bodies, EFIE and MFIE can be linearly combined in several forms [3]. One of the most adopted combination is the Müller formulation [3]. All these formulation, when applied to the analysis of the scattering by BOR's, lead to integrals of the form [2]:

$$I = \int_{\phi=0}^{2\pi} \int_{\alpha=-1}^1 \int_{\alpha'=-1}^1 \left(\frac{ab}{c} \right) F(\phi) \frac{e^{-jkR}}{R^d} d\alpha' d\alpha d\phi, \quad (1)$$

where $R=|\mathbf{r} - \mathbf{r}'|$ is the distance between source and observation points, a may be equal to 1, α' or α'^2 , b may be equal to 1, α or α^2 , c may be equal to 1, ρ , ρ' or $\rho\rho'$, and the exponent $d = 1$ or 3. The integral (1) has removable singularities whenever the observation point \mathbf{r} is very close to the source point \mathbf{r}' . The concept adopted in [2] to treat these singularities is to split the corresponding integrands into two: one that is regular and can be numerically evaluated by a Gaussian quadrature and another that contains a removable singularity and can be integrated analytically.

III. NUMERICAL RESULTS

To evaluate the numerical convergence we consider the CFIE and Müller formulation to the plane-wave scattering by perfect electric conductor (PEC) and dielectric spheres, respectively. The accuracy of the numerical results was verified against analytical solutions based on Mie series using the RMS error:

$$E_{\text{RMS}}(\%) = (E_{J_r} + E_{J_\phi} + E_{M_r} + E_{M_\phi})/4, \quad (2)$$

with E_x representing a RMS defined by

$$E_x(\%) = \sqrt{\frac{1}{N} \sum_{m=1}^N \left(|X_m^{\text{MoM}} - X_m^{\text{Mie}}| / |X_m^{\text{Mie}}| \right)^2}, \quad (3)$$

where X is any one of the electric (J_t or J_ϕ) or magnetic (M_t or M_ϕ) surface current components while X^{MoM} and X^{Mic} represent the corresponding numerical and analytical solutions, respectively.

The first case study is a PEC sphere, as illustrated in Fig. 1. The sphere radius is $1\lambda_0$ (the wavelength in vacuum). Different numbers of segments per λ_0 were used to represent the sphere generatrix. The TBF is defined over two consecutive segments [1]. Over each segment the regular integrals in α and α' of (1) were both evaluated using a NIP-point Gaussian quadrature, with NIP varied from 1 to 10. Singularities were removed by extraction technique [2]. Figure 2 shows the RMS error as function of NIP. Convergence is attained using NIP = 2, independently from the number of segments per λ_0 , which is determinant for the RMS error. When singularities are not removed the RMS error increases, as expected.

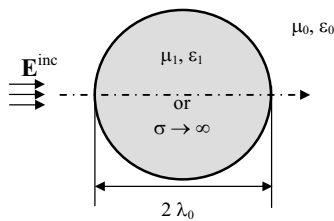


Fig. 1. Plane-wave scattering by homogeneous sphere

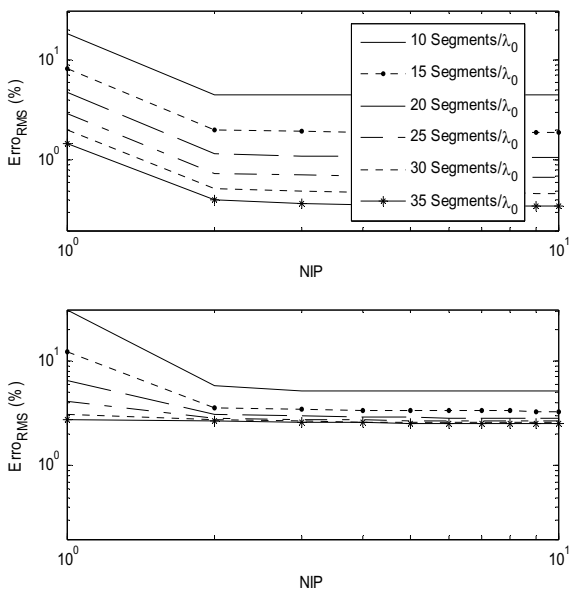


Fig. 2. Error for PEC sphere a) with singularities removal b) without singularities removal

The RMS error for dielectric spheres are illustrated in Fig. 4 for relative permittivity $\epsilon_r = 2$ and 20. Once more, when singularities are removed numerical convergence is attained for NIP = 2. The number of segments/ λ_0 influences the RMS error, which diminishes as more segments are used. When singularities are not removed, convergence is attained only for larger NIP values, especially for large values of ϵ_r .

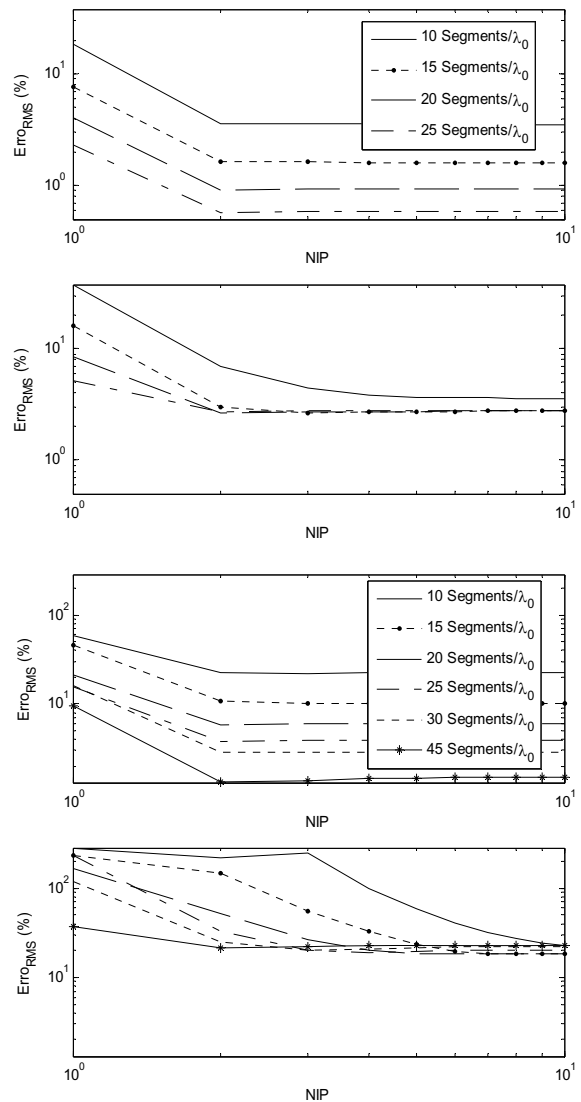


Fig. 3. Error for dielectric sphere a) $\epsilon_r=2$ with singularities removal b) $\epsilon_r=2$ without singularities removal c) $\epsilon_r=20$ with singularities removal d) $\epsilon_r=20$ without singularities removal

IV. REFERENCES

- [1] J. Mautz and R. Harrington, "An improved E-Field solution for a conducting body of revolution," Tech. Report TR-80-1, Dept. Electrical and Computer Engineering, Syracuse University, 1980.
- [2] U. Resende, F. Moreira, and O. Pereira Filho, "Efficient evaluation of singular integral equations in moment method analysis of bodies of revolution," *Journal of Microwaves and Optoelectronics*, vol. 6, no. 2, pp. 373-391, Dec. 2007.
- [3] J. Mautz and R. Harrington, "Electromagnetic scattering from a homogeneous material body of revolution," *AEÜ – Int. Journal of Electronics and Communication*, vol. 33, pp. 71-80, 1979.
- [4] A. Kishk and L. Shafai, "On the accuracy limits of different integral equation formulations for numerical solution of dielectric bodies of revolution," *Can. J. Phys.*, vol. 63, pp. 1532-1539, 1985.
- [5] A. Kishk, and L. Shafai, "Improvement of the numerical solution of dielectric bodies with high permittivity," *IEEE Trans. Antennas Propagat.*, vol. 37, pp. 1486-1490, Nov. 1989.
- [6] J. Mautz and R. Harrington, "H-field, E-field and combined field solutions for bodies of revolution," *IEEE Trans. Antennas Propagat.*, vol. 27, no. 4, pp. 157-164, July 1979.

A 3-D FE Particle-in-Cell Parallel code with adaptive load balancing

S. Coco, A. Laudani, G. Pollicino, P. Tirrò
 University of Catania, DIEES
 V.le A. Doria 6, Catania, I-95125, Italy
 alaudani@diees.unict.it

Abstract — In this paper the authors present a Finite Element PIC Parallel approach, based on an appositely developed parallelization algorithm for the balancing of load among several processors. In particular the master processor establishes the number of slave processors, where the particle tracing procedures must be launched, according to the number of particles and to the simulation time resulting during the previous time step. The tests performed have shown a reduction of about 10-20% of the simulation time in comparison with analysis performed using a fixed processors loading scheme.

I. INTRODUCTION

Particle-in-Cell (PIC) codes are used for the electromagnetic analysis of electron devices in terms of particle trajectories. In fact, the interaction between the electromagnetic fields and the charged particles is described by the classical Maxwell's electrodynamics equations, coupled with the Newton-Lorentz's equations for the motion of particles. However in the evolution of the charged particles beam, the particles themselves are source of electromagnetic fields. Unluckily the analytic solution of the coupled equations system can be obtained only for domains of simple geometry. For realistic devices the domain has complicated boundaries (for example shadow and control grid in electron guns) and the numerical solution is a not trivial task, since it is necessary to manage and process an huge amount of data coming out from the required domain discretization and from the representation of particle distribution. Although the PIC methods are often and successfully used in device simulation for electron trajectories tracing, but these approaches have also a high computational cost.

In this paper the authors present a Finite Element Parallel PIC approach which uses appositely developed parallelization algorithms for the balancing of load among several processors, whose number is not previously fixed, but is modified during the simulation according to the amount of particles to manage. The tests performed have shown a reduction of about 10-20% of the simulation time in comparison with analysis performed using a fixed processors loading scheme.

II. 3-D FE PARTICLE IN CELL APPROACH

The dynamics of a set of charged particles subject to an electromagnetic field in collisionless conditions can be described by means of the Vlasov equation for the particle distribution function $f(t, \mathbf{x}, \mathbf{p})$, defined in the phase space $(\mathbf{x}, \mathbf{p}) \in \mathfrak{R}_x \times \mathfrak{R}_p$ and time t ,

$$\frac{\partial f}{\partial t} + \frac{\mathbf{p}}{m} \cdot \nabla_x f + q(\mathbf{E} + \frac{\mathbf{p}}{m} \times \mathbf{B}) \cdot \nabla_p f = 0 \quad (1)$$

where \mathbf{p} is the particle momentum, m and q are the particle mass and charge respectively. The electric field \mathbf{E} and magnetic field \mathbf{B} satisfy the Maxwell equations, for which the charge and current density

$$\rho(t, \mathbf{x}) = q \int_{R_p} f(t, \mathbf{x}, \mathbf{p}) d\mathbf{p} \quad (2)$$

$$\mathbf{J}(t, \mathbf{x}) = q \int_{R_p} \frac{\mathbf{p}}{m} f(t, \mathbf{x}, \mathbf{p}) d\mathbf{p} \quad (3)$$

are the source terms.

The Vlasov equation together with the Maxwell equations constitutes a system of coupled equations called Vlasov-Maxwell system [1]. An attractive computational tool for numerically solving this nonlinear Vlasov-Maxwell problem is the particle-in-cell (PIC) method, in which the particles' beam is represented by a reasonable number of dot-like macro-particles sources of electromagnetic field, subject to the dynamic equations. Each macro-particle represents an appropriate number of elementary particles of a specific type. A type of particles is characterized by its specific ratio between charge and mass. Since the movement of elementary particles is to be simulated, each macro-particle moves like an elementary particle of the proper type. However, when determining the fields it must be taken into account that each macro-particle consists of many elementary particles. In the solution process the interaction with the 'self-consistent fields' (those generated by the charge particles) and the applied external fields is obtained through an appropriate computational scheme, which schedules at each integration step of the trajectories:

- 1- the distribution of space charge and current density
- 2- the solution of the fields' equations.

To solve the evolution equation we used an FE approach, which is adequate to describe the complex three-dimensional geometries of electron devices by using irregular discretizations. Moreover, the finite element method gives the possibility of using a more accurate modeling of the most critical device regions (such as in proximity of the electrodes, where the gradient of the unknown function is higher), using an adaptive meshing without affecting the number of degrees of freedom.

Although solving the evolution equations of the fields is one of main components of a PIC code; however its execution time accounts for less than 10%–20% of the simulation's total

time. The remaining time is spent on tracing particles' trajectories and calculating the particle-field interactions, expressed computationally as local interpolation operations (in the case of FEM a very time consuming procedure is the individuation of the element containing the moving particle in the case of unstructured mesh). These operations are the major performance bottleneck of PIC codes. Strategies to optimize PIC performance have been studied and implemented extensively for codes running on large scale distributed memory architectures and grid computing environment [1].

III. PARALLELIZATION OF THE PIC ALGORITHM

When parallelizing an algorithm one problem concerns the assignment of the computational tasks to the various processes. In order to have a good load balancing for the trajectories tracing, it is possible to split the macro-particles integration task over processors, but even in this case an optimal parallel code is obtained only by following a dynamic load balancing. To fulfill the dynamic load balancing we define a master processor that at each time-step counts the particles and assigns the various tracing tasks to the slave processors; each slave processor integrates the dynamic equation of macro-particles assigned to it and computes the space charge distribution and current density using a copy of the FE mesh. Then it sends its results together with the copy of the charge and current density vectors ($[\rho]$ and $[J]$ respectively) to the master processor (see figg. 1 and 2 for flow charts of master and slave processors). This "reduces" the vectors $[\rho]$ and $[J]$ by adding the outputs of all the slave processor and solves the fields' equation. Thus, the main time consuming procedure, that is the particles tracing, is "equally" distributed among the processes. In literature [2-3] in order to evaluate the parallelization speedup the total simulation time is compared for simulations with and without load distribution among processors, respectively, and for a different number of particles. It is worth noticing that the speedup curve is very close to the ideal case only if few processes and a huge amount of particles are employed. In addition, it is very far from the optimal case, when the number of processes increases above a certain value. Consequently the number of parallel processes to get optimum speedup depends on the number of particles used in the simulation. In order to overcome this problem a heuristic adaptive algorithm has been developed to avoid excessive inter-process communication. In particular the master processor establishes the optimal number of slave processors, where the particle tracing procedures are launched according to the number of particles and to the simulation time resulting in the previous time step. It is worth noticing to emphasize that in the case of PIC time-dependent solution the total number of particles can vary during the simulation since the pushing of the particles inside the domain and the extraction procedure do not necessarily follow a deterministic law.

So during a run the processors used in the parallelization scheme are not fixed but can increase or decrease, from a time step-iteration to another. The FE PIC parallel code is written in C/MPI and has been developed in the LINUX OS environment. In order to carry out the dynamics load balancing

using a variable number of processors the processors are configured like master-slave structure. At each time step, the master processor establishes the number of the active slave processors, and takes care of the dynamic load balancing, while the slave processors trace the particles trajectories. The minimum number of particles above which the first split is performed is 500k and the maximum number of slave processors used was 8. The tests performed have shown that by using this adaptive load balancing the overall speedup is of about 10-20% with respect to a fixed number of processors. A more detailed description will be given in the full paper, together with application examples.

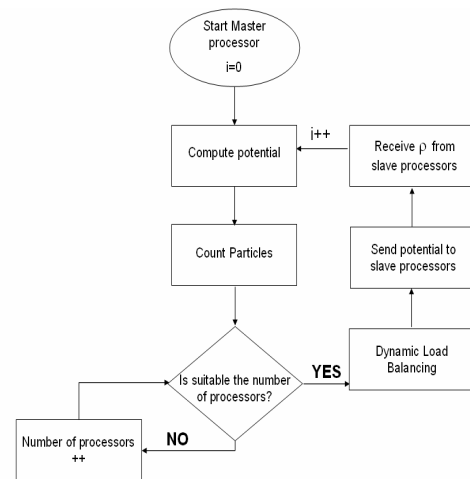


Fig. 1. Flowchart of the parallel PIC code for the master processor

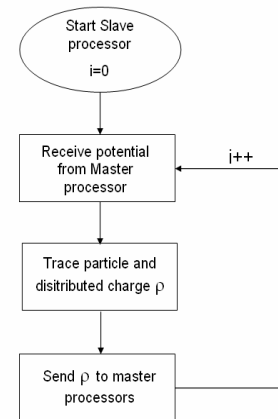


Fig. 2. Flowchart of the parallel PIC code for the slave processor

IV. REFERENCES

- [1] S. Coco, A. Laudani, G. Pollicino, "Distributed computing finite element electromagnetic analysis of traveling wave tubes". *COMPEL*, vol. 27, pp. 1326-1334, 2008.
- [2] A. Candel et al., "Parallel finite element particle-in-cell code for simulations of space-charge dominated beam-cavity interactions", *Proceedings of PAC07*, Albuquerque, New Mexico, USA.
- [3] F. Wolfheimer, E. Gjonaj, T. Weiland, "A Parallel 3D Particle In Cell (PIC) with Dynamic Load Balancing" *Nuclear Instruments and Methods in Physics Research (NIM)*, Vol. 558, 01.02.2006, pp. 202-204.

Parallel Computing of Magnetic Field for Rotating Machines on the Earth Simulator

Tomohito Nakano¹, Yoshihiro Kawase¹, Tadashi Yamaguchi¹,
Masanori Nakamura², Noriaki Nishikawa³ and Hitoshi Uehara³

¹Department of Information Science, Gifu University, Gifu 501-1193, Japan, E-mail: nakan@fem.info.gifu-u.ac.jp

²TOYO DENKI SEIZO K.K., Kanagawa 236-0004, Japan, E-mail: nakamuramas@toyodenki.co.jp

³Japan Agency for Marine-Earth Science and Technology, Kanagawa 236-0001, Japan, E-mail: nnishikawa@jamstec.go.jp

Abstract— In this paper, the outline of the parallel computing method of the magnetic field for rotating machines by using the 3-D finite element method with edge elements is developed. The performance of the method running on the Earth Simulator is quantitatively clarified.

I. INTRODUCTION

In fields such as structural mechanics and fluid dynamics, the large-scale parallel computing on a supercomputer has been already researched. However, for the practical numerical analysis of the magnetic field for rotating machines, the large-scale parallel computing is still in an early stage of investigation.

We have developed the parallel computing method of the magnetic field by using the three-dimensional Finite-Element Method (3-D FEM) with edge elements for rotating machines.

In this paper, we describe the outline of the developed method and an optimization of the method for the Earth Simulator, which is a vector type parallel supercomputer in Japan. Moreover, the performance of the proposed method running on the Earth Simulator is quantitatively clarified.

II. OUTLINE OF PARALLEL COMPUTING METHOD

A. Domain Decomposition Method

The Domain Decomposition Method (DDM) is adopted for the parallel computing [1]. Using the DDM, the analyzed domain is divided into multiple subdomains, and the subdomains are calculated in parallel while doing appropriate data communications between those subdomains.

Fig. 1 illustrates the DDM for FEM with edge elements. This figure shows that one domain is divided in two subdomains.

The number of edges in each subdomain is almost the same to split the CPU power into subdomains evenly. The divided domain has the overlap elements. By using the overlap elements, the data communication between subdomains becomes unnecessary when the element coefficient matrix is made.

B. Data Communication

The overlap element has two kinds of edges, one is called ‘boundary edges’ and another is called ‘external edges’. In Fig. 1 (b), the boundary edges are drawn as the bold line (edge 7 in *Subdomain I*, and edges 8 and 9 in *Subdomain II*), and the external edges are drawn as the dotted lines (edges 8 and 9 in *Subdomain I*, and edge 7 in *Subdomain II*). The boundary

edge in one subdomain is the external edge in another subdomain. By using this relationship, the data communication in the process of matrix solving is achieved properly. Fig. 2 shows the calculation of matrix-vector product divided into two subdomains. In order to calculate the *Subdomain I*, the values of potential of external edges 8 and 9 are obtained from those of the corresponding boundary edges 8 and 9 in *Subdomain II*. Similarly, in order to calculate the *Subdomain II*, the value of potential of external edge 7 is obtained from *Subdomain I*. This procedure is repeated in solving the matrix equation.

The code for the parallel computing is written using the Message Passing Interface (MPI) that allows many computers to communicate with one another.

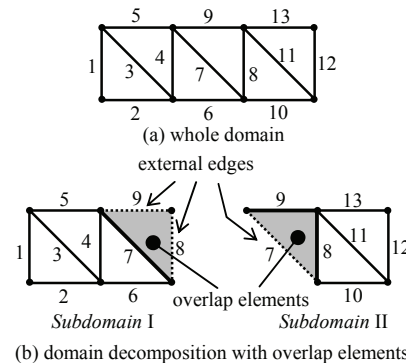


Fig. 1. Domain decomposition method for finite-element method with edge elements

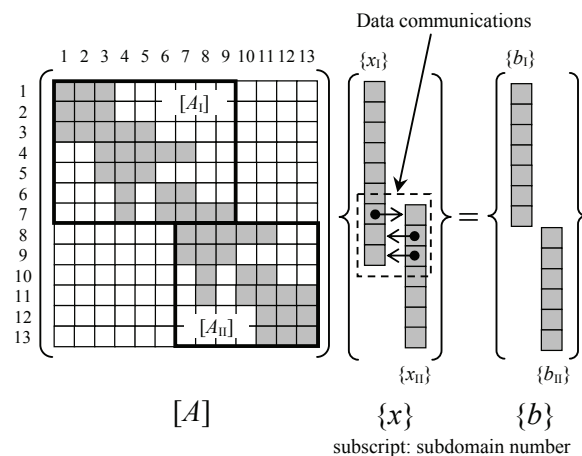


Fig. 2. Calculation of matrix-vector product divided into two subdomains

III. OPTIMIZATION FOR EARTH SIMULATOR

The Earth Simulator is a distributed-memory type parallel computer system, which consists of 640 processor nodes connected by the crossbar network. Each processor node has 8 vector processors. The whole system has 5120 processors with 10 TB of main memory and the peak performance of 40 Tflops.

In our parallel computing method, the Scaled Conjugate Gradient (SCG) method is used as the matrix-solving method because of its simplicity and efficiency.

On the vector processor, the vector efficiency affects computing speed. Therefore, the Descending-order Jagged Diagonal Storage (DJDS) [2] format in Fig. 3 (a) is adopted as the storage of sparse matrix format because it can attain longer vector length and thus lead to higher vector efficiency than the Compressed Row Storage (CRS) format in Fig. 3 (b). The DJDS format involves permuting rows in decreasing order of the number of non-zero elements in each row.

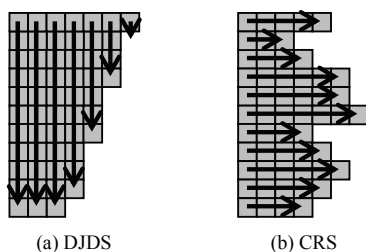


Fig. 3. Storage format of matrix

IV. NUMERICAL RESULTS AND DISCUSSION

A. Fundamental Equation of Magnetic Field

The fundamental equation of magnetic field is given by the magnetic vector potential A as follows:

$$\text{rot}(\nu \text{rot} A) = \nu_0 \text{rot} M + J_0 + J_e \quad (1)$$

where ν is the reluctivity, ν_0 is the reluctivity of the vacuum, M is the magnetization of permanent magnet, J_0 is the exciting current density, J_e is the eddy current density.

B. Analyzed Model

Fig. 4 shows the analyzed model of the IPM motor. In order to evaluate the parallel computing efficiency, we calculate the model using three kinds of meshes: coarse mesh, middle mesh, and fine mesh. The number of unknown variables of the coarse, middle and fine meshes is 328,298, 969,298 and 4,007,888, respectively. Fig. 5 shows the middle mesh that is divided into four subdomains.

C. Performance of Proposed Method

Fig. 6 shows the distribution of flux density vectors calculated in each subdomain.

Fig. 7 shows the speed-up obtained for three kinds of meshes. The speed-up is evaluated in one time step. The saturation of the speed-up for the larger number of CPUs is due to an increase in the ratio of communication cost to computing cost. For any given number of CPUs, the speed-up becomes larger as the number of unknown variables increase. This is because the ratio of the communication cost to the

computing cost decreases, and the average vector length becomes longer. In the fine mesh, the proposed method achieved over 60-fold speed-up by 128 CPUs.

V. CONCLUSION

We have developed a parallel computing method of the 3-D finite element method for rotating machines by the domain decomposition method. In this method, speed-up becomes larger as the number of unknown variables increases. Specifically, in the fine mesh that has 4,007,888 unknown variables, the proposed method achieved over 60-fold speed-up by 128 CPUs. Better speed-up is expected in a larger scale analysis.

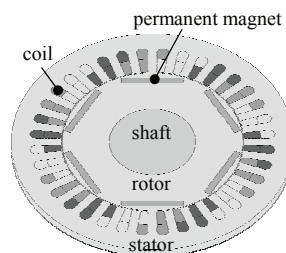


Fig. 4. Analyzed model of IPM motor

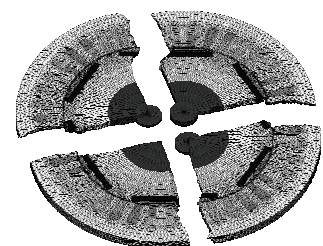


Fig. 5. Divided mesh

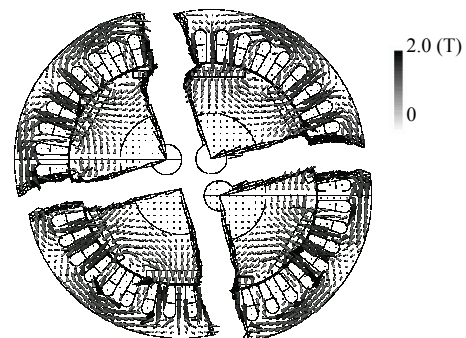


Fig. 6. Distribution of flux density vectors

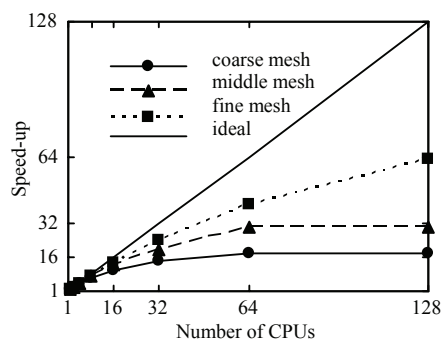


Fig. 7. Speed-up ratio

VI. REFERENCES

- [1] T. Nakano, Y. Kawase, T. Yamaguchi, S. Ukai, M. Nakamura, N. Nishikawa and H. Uehara, "Magnetic field analysis of rotational machine with Earth Simulator", The Papers of Technical Meeting on Static Apparatus and Rotating Machinery, IEE Japan, SA-09-26/RM-09-26, 2009 (in Japanese).
- [2] K. Nakajima and H. Okuda, "Parallel iterative solvers for unstructured grids using an OpenMP/MPI hybrid programming model for the GeoFEM platform on SMP cluster architectures", Experiences and Implementations Lecture Notes in Computer Science, vol.2327: 437-448, 2002.

An efficient algorithm for planar circuits design

A. Serres, G. Fontgalland, J. E. P. de Farias

L.E.M.A.-I.E.C.O.M.-UFCG, Av. Aprígio Veloso, 882, 58.109-979, Campina Grande-PB, Brasil
alex@ee.ufcg.edu.br, g.fontgalland@ieee.org, ewerton@ieee.org

H. Baudrand

LAPLACE-GRE, 2 rue Camichel 31071, Toulouse CEDEX, France
henri.baudrand@laplace.univ-tlse.fr

Abstract — An iterative process based on the wave concept (WCIP) is formulated and applied. A recursive relationship between a wave source and reflected waves from a discontinuity plane is computed. In order to simplify calculations and accelerate the convergence with reduced central processing unit time, a two dimensional Fast Modal Transformation (FMT) algorithm using periodic walls is used with the 2D-FFT algorithm.

I. INTRODUCTION

Several analytical and numerical techniques are reported in the literature for the analysis of monolithic microwave integrated circuits (MMICs), among them: the method of moments [1], the finite elements method and the finite difference time domain method [2]. For the reduction of development times and costs of MMICs, it is of primary importance the use of fast and efficient software tools, which can accurately predict the electrical behavior of a device. The computational time of these numerical techniques is the limiting factor in the practical design of microwaves circuits. In this paper a tool that reduces the required computational effort is proposed. It employs the Wave Concept Iterative Procedure (WCIP), an integral based on generalized wave definitions. This method is not conditioned by the complexity of the circuit design and was proved to be particularly interesting for planar multi-layers circuits [3]-[4]. The WCIP approach consists in separating the structure under study into interfaces with upper and lower homogeneous media. The boundary conditions on the interface are represented by the diffraction operator, S , and in the homogeneous media by the reflection operator, Γ . They are respectively defined in spatial and modal domains. In this case, a formulation based on the periodic walls is applied.

In the work reported herein, the analysis and simulation of a rectangular waveguide including a microstrip open line and a microstrip patch antenna with periodic walls using a WCIP were carried out. Section 2 provides the theoretical formulation used in the development of the WCIP. Simulation results are presented in section 3. Finally, conclusions are included in section 4.

II. FORMULATION OF THE WCIP

The spatial and modal waves are directly deduced from each other with a Fast Modal Transformation (FMT) and its inverse transform (FMT^{-1}). As illustrated in Fig. 1, the FMT is comprised of the 2D-FFT algorithm and transformation from the spectral to the modal domain.

A Fast Modal Transform (FMT) and its inverse ensure conversions between the two domains.

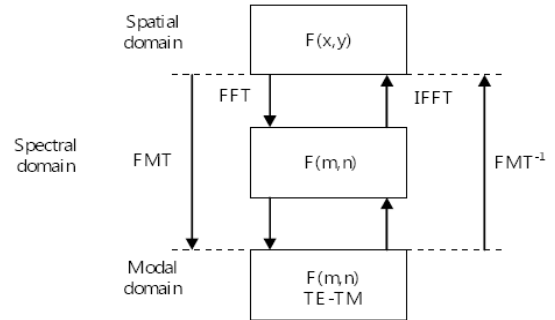


Fig. 1. Block diagram for the Fast Modal Transformation (FMT) algorithm

Let us consider a single, but general, interface problem with its waveguide transversal cut shown on Fig. 2. The Γ operator is described in the modal domain. The S operator expressed in the spatial domain assigns boundary conditions at the interface plan. The air-dielectric interface is divided into cells and includes three sub domains: dielectric, metal, source. The source generates two waves, one in each side of the interface.

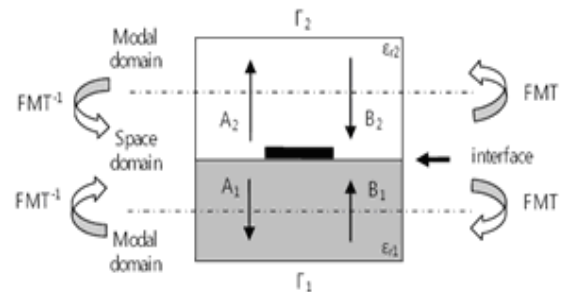


Fig. 2. Iterative Process illustration for a microstrip line

The representation of electromagnetic fields using the Wave Concept is a well-established procedure [5]. This formulation concept is also used in the Transverse Line Matrix method (T.L.M.).

The incident (A) and reflected (B) waves and the electric field (E) and current density (J) can be related by:

$$A_i = \frac{1}{2\sqrt{Z_{0i}}} (E_i + Z_{0i} J_i) \quad (1)$$

$$B_i = \frac{1}{2\sqrt{Z_{0i}}} (E_i - Z_{0i} J_i) \quad (2)$$

Where, Z_{0i} is the characteristic impedance of medium i .

9. Numerical Techniques

The usually used WCIP scheme is very simple. It can be represented through two equations:

$$A = SB + A_0 \quad (3)$$

$$B = \Gamma A \quad (4)$$

Where, A_0 is the local source of the circuit.

Finally, it is possible to express the boundary conditions in terms of waves on each cell.

$$E_i = \sqrt{Z_{oi}} (A_i + B_i) \quad (5)$$

$$J_i = \frac{1}{\sqrt{Z_{oi}}} (A_i - B_i) \quad (6)$$

III. SIMULATIONS RESULTS

In order to present the performance of the proposed tool two case studies were conducted. The simulation results for two different structures are given in sections A and B.

A. Microstrip open line

A microstrip open line in a waveguide of dimension 32mm x 8mm with periodic walls was simulated with the Matlab software. The microstrip line lies on a substrate with $\epsilon_r = 2.2$ and height of 1mm.

The simulated source has dimensions of 2mm x 2mm, while the simulated microstrip line is 2mm wide, and 25 mm long.

Figure 3 shows the computed input impedance, Z_{in} ,

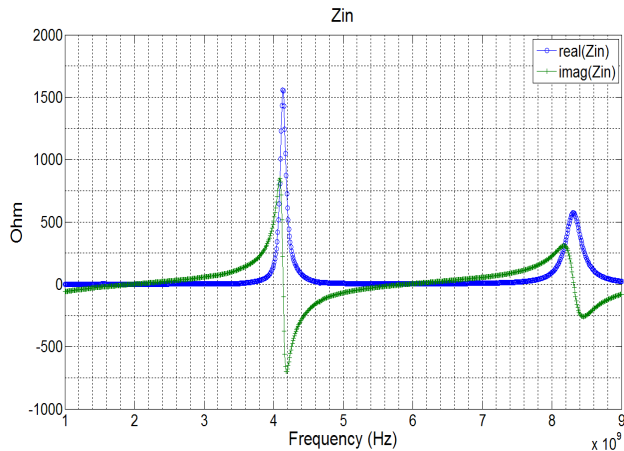


Fig. 3. Input impedance in Ohms as a function of frequency in Hz

The Z_{in} is in conformity with the theory [6]. The Z_{in} imaginary part is calculated by $-\cot(\beta l)$. As expected, the real part reaches a positive peak value at the line resonance frequency.

B. Microstrip patch antenna

A patch antenna with resonance frequency of 1.32 GHz as analyzed in [6], is now considered. Its physical construction guarantees a characteristic impedance of 50 Ohms.

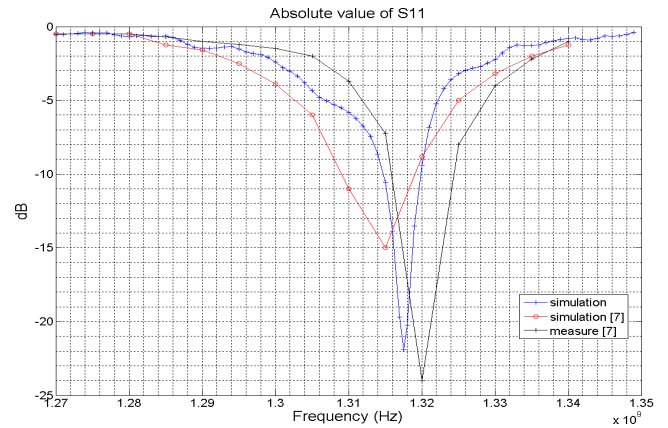


Fig. 4. Absolute value of the input reflection coefficient, $|S_{11}|$ in dB as a function of frequency in Hz

As can be seen in Fig. 4 (blue curve), the resonance frequency simulated result is very close to the measured frequency (about 1.38 GHz). Also, this is in good agreement with the measured frequency presented in [7]. Therefore, it can be used to confirm that the method proposed herein gives rather satisfactory results, as they are closer to the measured ones than those of the simulations in [7], with a comparatively small computational effort.

IV. CONCLUSION

In this paper, an implementation of the WCIP using periodic walls is presented. A microstrip open line and a microstrip antenna patch have been analyzed and simulated. The obtained results show that the method herein formulated and implemented in software, is suitable to electromagnetic analysis of planar circuits. Very good agreement among simulated results, available theory, and physical implementation has been achieved.

Acknowledgement

The authors wish to thank the received financial support of the National Program of Academic Cooperation – CAPES and CNPq, and COPELE/CEEI/UFCG post-graduate program during the development of this project.

V. REFERENCES

- [1] R. F. Harrington, Field computation by moment methods, Macmillan, New York, 1968.
- [2] O. Axelsson, and V. A. Barker, "Finite element solution of boundary value problems: theory and computation" (Academic Press, New York, 1984).
- [3] S. Wane and H. Baudrand, "A new full-wave hybrid differential integral approach for the investigation of multilayer structures including nonuniformly doped diffusions", IEEE MTT., Vol.53. n°1, pp 200-213, January 2005.
- [4] H. Zairi, A. Gharsallah, A. Gharbi and H. Baudrand, "Analysis of Planar Circuits Using a Multigrid Iterative Method", IEE Proc. Ant. & Prop., vol.153, n°3, pp231-236, June 2006.
- [5] K. Kurokawa, "Power Waves and the Scattering Matrix", IEEE Trans, Microwaves Theory and Techniques, vol. 13, pp. 194-202, 1965.
- [6] R. E. Collin, Foundations for Microwave Engineering, 2000.
- [7] Ludovic Cohen, "Contribution à l'Etude et à la Modélisation de Circuits Coplanaires Multicouches par une Méthode Itérative.", Thèse de doctorat Année 2002.

MPI Parallelization for Large Electromagnetic Simulations using Curvilinear Finite Elements

W. Ackermann¹, G. Benderskaya², and T. Weiland¹

¹ Institut für Theorie Elektromagnetischer Felder, TU Darmstadt,
Schlossgartenstraße 8, D-64289, Darmstadt, Germany
{ackermann/weiland}@temf.tu-darmstadt.de

² CST AG – Computer Simulation Technology,
Bad Nauheimer Straße 19, D-64289, Darmstadt, Germany
galina.benderskaya@cst.com

Abstract — This work is devoted to the combined numerical technique which makes possible the effective simulation of very large electromagnetic models. The two principle constituents of the proposed combined approach are the curved finite elements and their realization on the basis of Message Passing Interface (MPI). The usage of the curved finite elements allows to minimize the error introduced by the indispensable spatial discretization, while employing the MPI programming technique makes it possible to significantly speed up the calculation process. In the paper it is demonstrated how the proposed numerical technique can be used to tackle large electromagnetic problems.

I. INTRODUCTION

Electromagnetic problems are formulated on the basis of Maxwell's equations and are completed by the corresponding material relations. The obtained vector valued equations can be solved exactly only for a limited number of problems with reasonable complexity. Problems of practical importance are usually solved only approximately on a discretized level. From the above reasoning it is of crucial importance to make the process of numerical solution robust and effective with respect to the calculation time and memory consumption.

II. FINITE ELEMENT METHOD

During the last decades various discretization techniques have been developed with individual advantages depending on the aspired application. In the current work the focus is put on the classical finite element method for the spatial discretization with vector valued basis functions on tetrahedral elements in a hierarchical setup [1]-[3]. In order to improve the accuracy of the spatial approximation in those cases where non-flat material interfaces are involved, the linear mapping of a unit tetrahedron to any element of the mesh is replaced by a nonlinear variant. For this purpose, the set of scalar basis functions of lowest order employed to set up a transformation that includes merely the corner points of the element is extended by higher order scalar basis functions. On the one hand, increasing the desired order for the interpolation leads to the more geometrically flexible transformation; on the other, it simultaneously increases the numerical efforts since more control points have to be involved into the calculation process.

Quadratic interpolation as the simplest complete nonlinear representative requires the knowledge of ten control points per tetrahedron, where four of them are typically allocated on the

corners of the element and the remaining six are usually placed in the center of the corresponding edges. Thus, each face of such an element can be represented by a function of second order behavior and can therefore smoothly conform to curvilinear interfaces. In case of hierarchical scalar basis functions, the control vectors are represented by difference vectors from the edge centers to the surface points instead of the surface vectors itself. In Fig. 1, two different approaches are visualized.

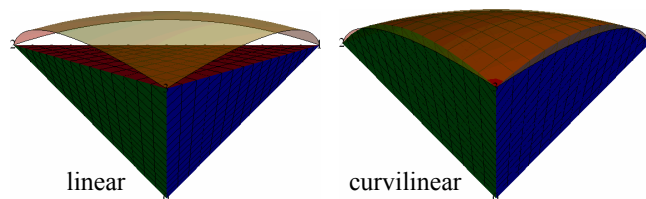


Fig. 1. Linear versus curvilinear transformation of a unit tetrahedron conforming to a sphere of radius 2 touching the element in three corner points

Assuming the notation $A = \{a_{ij}\}$ for the stiffness matrix and $B = \{b_{ij}\}$ for the mass matrix the following definitions

$$a_{ij} = \iiint_{\Omega} \text{curl } \vec{w}_i \cdot \text{curl } \vec{w}_j / \mu \, d\Omega$$

$$b_{ij} = \iiint_{\Omega} \vec{w}_i \cdot \vec{w}_j \, \varepsilon \, d\Omega$$
(1)

are employed. Here, vectors $\vec{w}_i, i = 1, \dots, N_{\text{DoFs}}$ refer to the vector valued basis functions and Ω denotes the entire computational domain. Material properties are given in term of the permeability μ and the permittivity ε .

Due to the compact support of the applied basis functions, the population of the matrices is very sparse. The integration in (1) is typically performed independently for each individual element and a subsequent summation of each contribution allows then to assemble the entire sparse matrix in an efficient parallel strategy. The individual contributions can be summarized to

$$\begin{aligned}
a_{ij}^e &= \iiint_{\Omega_0} \text{curl } \vec{w}'_i \cdot \text{curl } \vec{w}'_j / (\mu |J|) d\Omega \\
b_{ij}^e &= \iiint_{\Omega_0} \vec{w}'_i \cdot \vec{w}'_j \varepsilon |J| d\Omega
\end{aligned} \tag{2}$$

where $\vec{w}'_i = J^{-1} \vec{w}_i$, $\text{curl } \vec{w}'_i = J^T \text{curl } \vec{w}_i$ and matrix J denotes the Jacobian of the involved geometrical transformations. In (2), the integration is performed only on a unit tetrahedron Ω_0 and can be carried out analytically for linear geometry transformations. In contrast to this, in case of higher order spatial transformations with curvilinear elements, a numerical integration technique with sufficient accuracy to capture the variation of the integrand is employed. As soon as an element matrix is calculated, the assembling of the entire system of equations is proceeded step by step by means of inserting those local values into the global system.

III. IMPLEMENTATION

The geometric modeling of the structure is performed within the CST Studio Suite which is also used for the tetrahedral meshing [4]. The necessary information is passed to the FEM program by means of ASCII or binary file transfer. The entire FEM algorithm is implemented in C++ thus enabling high performance and clear arrangement of the whole program [5]. The external mesh information is used in a first step to set up a graph representing the population pattern of the sparse stiffness and mass matrices in a way that only the degrees of freedom (DoF) are considered. Constraints placed due to boundary conditions are incorporated in the matrix setup. The entire graph is initially arbitrarily distributed among all the contributing processes but has to be partitioned in proper clusters of contiguous elements to keep the communication overhead during the computations low. The final distribution of the various DoFs among the processors is determined with the help of the graph partitioning library ParMeTiS [6]. This knowledge is necessary to allocate the memory used to manage the matrices in an advantageous way. An efficient implementation can be found for example within the software package PETSc [7] which also provides proper linear solvers and various preconditioners.

Once the mesh and material information are properly distributed among all the processors, an efficient assembly of the global matrices can be performed. During this step, a distinction is made between elements based on linear geometric mapping and their nonlinear counterparts.

IV. CONVERGENCE ANALYSIS

In the following we refer to the solution of Maxwell's equations within closed perfect conductive structures. The continuous formulation is thus turned into the discrete generalized eigenvalue problem

$$A\vec{c} = \lambda B\vec{c} \tag{3}$$

with the eigenvector \vec{c} collecting all the individual weighting coefficients for the expansion $\vec{E} = \sum_i c_i \vec{w}_i$ of the electric

field intensity. In this setup, the eigenvalue $\lambda = \omega^2$ represents the squared value of the corresponding angular frequency.

For the problem of finding the resonant frequency of the fundamental mode within a hollow perfect conductive sphere, an analytical solution can be derived. Comparing the numerical solutions f obtained on different discretization levels with the analytical one denoted by f_0 enables to carry out a convergence analysis which is illustrated in Fig. 2 for a number of selected approximation schemes.

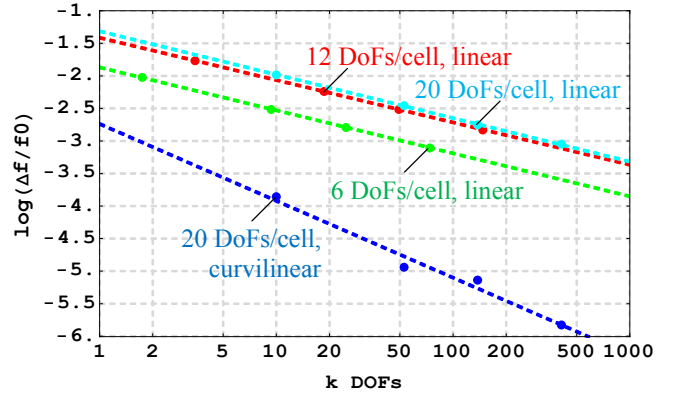


Fig. 2. Convergence analysis for the resonant frequency of the fundamental mode in a unit sphere with perfect conducting boundary conditions

From this graph one can clearly see that all methods enabling linear geometric modeling suffer from an inexact boundary geometry representation whereas the curvilinear geometric modeling overcomes this difficulty.

V. CONCLUSION

In this digest we report on the successive implementation of a parallel FEM kernel featuring curvilinear tetrahedra elements. In contrast to the results reported in the literature, the superior convergence of higher order approximations versus lower order variants can be preserved even on non-flat material interfaces with a usage of a moderate geometrical transformation order. In the full paper we extend the calculations to practically relevant structures.

VI. REFERENCES

- [1] J.P. Webb, B. Forghani, "Hierarchical Scalar and Vector Tetrahedra", *IEEE Trans. on Magnetics*, 29(2): 1495-1498, 1993.
- [2] P. Ingelström, "A New Set of H(curl)-Conforming Hierarchical Basis Functions for Tetrahedral Meshes", *IEEE Trans. on Microwave Theory and Techniques*, 54(1): 106-114, 2006.
- [3] J.P. Swartz, D.B. Davidson, "Curvilinear Vector Finite Elements Using a Set of Hierarchical Basis Functions", *IEEE Trans. on Antennas and Propagation*, 55(2): 440-446, 2007.
- [4] CST AG – Computer Simulation Technology, CST Studio Suite 2009, www.cst.com
- [5] M.J. Quinn, *Parallel Programming in C with MPI and OpenMP*, 1st ed., McGraw-Hill Companies, Inc., Singapore, 2003.
- [6] G. Karypis, K. Schloegel, V. Kumar, ParMeTiS - Parallel Graph Partitioning and Sparse Matrix Ordering Library, Version 3.1, University of Minnesota, 2003
- [7] S. Balay, W.D. Gropp, L.C. McInnes, B.F. Smith, PETSc Users Manual, ANL-95/11 - Revision 3.0, Argonne National Laboratory, 2008

Multicore Acceleration of CG Algorithms using Blocked-Pipeline-Matching Techniques

David M. Fernández, Dennis Giannacopoulos and Warren J. Gross
 Department of Electrical and Computer Engineering, McGill University
 3480 University Street, Montreal (QC), H3A 2A7, Canada

Email: david.fernandezbecerra@mail.mcgill.ca, dennis.giannacopoulos@mcgill.ca, warren.gross@mcgill.ca

Abstract—To realize the acceleration potential of multicore computing environments computational electromagnetics researchers must address parallel programming paradigms early in application development. We present a new blocked-pipeline-matched sparse representation and show speedup results for the conjugate gradient method by parallelizing the sparse matrix-vector multiplication kernel on multicore systems for a set of finite element matrices to demonstrate the potential of this approach.

I. INTRODUCTION

Multicore processors represent one of the newest mainstream computing trends for enhancing the performance of scientific kernels, bringing about new opportunities and challenges to electromagnetic (EM) practitioners. Parallel programming challenges must now be confronted earlier in application development in order to exploit this new trend. Some EM computations are highly parallelizable, offering different opportunities for multicore acceleration (e.g. parallel mesh builders, parallel iterative solvers, etc). Of particular interest to this work is the solution of the large-sparse linear systems that arise when solving EM problems.

This work focuses on accelerating the *conjugate gradient* (CG) solver by parallelizing its dominant computing kernel, the sparse matrix-vector multiplication (SMVM) where a sparse matrix A multiplies a dense vector x . A new block-partitioned sparse format is presented to accelerate the SMVM kernel using both high-level parallelism, e.g., scheduling tasks across cores in multicore or clustered processors, and low-level parallelism within processor cores, such as vectorization, loop transformations and time skewing. First, we identify the key challenges confronted in parallelizing general sparse kernels and then describe the new sparse format and the algorithmic approach, showing performance results to validate it.

II. PREVIOUS WORK

Parallelizing and optimizing dense linear algebra kernels is a well understood task that has given rise to a variety of Basic Linear Algebra Subprograms (BLAS) libraries (e.g. LAPACK, ScaLAPAC) [1], [2]. Sparse kernels on the other hand represent a greater challenge. They enable larger problems, using less memory resources and computing on non-zero matrix entries only; however, drawbacks such as increased instructions overhead and irregular and indirect access to data significantly limit the use of hardware optimization techniques and BLAS operations. Support for parallel sparse kernels

on clustered systems is available in some newer packages (e.g. SPARSEKIT, NIST's Sparse BLAS, and PETSc) which operate on general sparse formats (e.g. compressed sparse row-CSR [3]), but are generally only optimized for dense kernels. Efficient multicore implementations and low-level parallelism on sparse kernels have yet to be thoroughly addressed.

Specialized formats have been used as means to regularize the computations and data layout of general sparse formats at the expense of processing some extra zeros, unveiling better opportunities for high and low-level parallelism. The Block-CSR (BCSR), Ellpack-ITpack and Jagged-diagonals formats are the three classic formats used for this purpose, however they each demand certain matrix properties to be efficient [3]. Recent work on specialized sparse matrix formats [4]–[6] has shown that further performance improvements are possible without such restrictions. In [6] we report up to 14 times speedup (SU) compared to a single core CSR SMVM implementation obtained by designing a specialized sparse format (called pipeline-matched sparse format-PMS).

III. NEW SPARSE FORMAT FOR PARALLEL PROCESSING

Based on the experience gained in [6] we introduce a blocked adaptation of PMS, that exploits both locality and vector units in modern processors, as opposed to other blocked formats that only aim at exploiting locality.

A. Blocked Pipeline-Matched Sparse Representation

The new format called *blocked pipeline-matched sparse* (BPMS) representation defines clear data boundaries for partitions (as PMS [6]), nonetheless it also offers better opportunities to exploit fine grained parallelism. In BPMS the matrix is stored in small dense matrix-blocks, which are enforced to be a multiple of the vector-registers size on the target architecture as in PMS; thus allowing to easily exploit vector or single-instruction multiple-data (SIMD) parallelism in multicore processors. Furthermore, when the size is a multiple greater than one, loop transformations can be implemented to enhance performance (not possible on PMS). BPMS stores the matrix data in four linear arrays as follows: (i) the nonzero elements of the matrix stored in dense square/rectangular blocks by rows (elements in blocks are stored row-wise), with zero padding to match the pipeline width of the target processor (as in PMS); (ii) the column indices of the first element in each block (as in BCSR); (iii) the row index of the first element

in a block that starts a new row (as in BCSR); and (iv) the number of dense blocks preceding the block pointed to by each of the row indices. The row indices can be used to determine high-level boundaries for data-partitions to spread across processing cores. The newly introduced fourth vector aids in load balancing by providing information on the amount of data to compute on for each coarse data-partition defined.

The main advantage of BPMS over other blocked formats such as BCSR, is that it takes advantage of vector units in modern processors. The pipeline-matching in BPMS blocks creates vector-data sets aligned to natural vector boundaries, that ease implementing vector operations. Traditional blocked formats only exploit data-locality by creating small blocks (also achieved by BPMS), but do not align data to vector boundaries nor do they assure data sizes to fit within vector-registers. In addition to this, BPMS includes a fourth vector that provides important information to load balance the matrix data when partitioning it across processors and provides useful information for low level loop optimizations. To further enhance locality and efficiently support building dense blocks minimizing padded-zeros, we apply a reordering technique (reverse Cuthill-McKee [7]) that reduces the matrix bandwidth before creating the BPMS representation. The insight provided by the reordering process can also be used to define coarse data-partition boundaries within the matrix (full details in long version). The two level partitioning used for the PMS format [6] is still used here to stream data across the cores of a multicore processor with user-managed cache (e.g. Cell BE processor) or FPGA based systems.

IV. RESULTS

The new BPMS representation was implemented in an Intel Core2 Quad 2.40GHz CPU, 4GB of global DRAM and 64-bit Linux system. Compilation was done using GCC 4.1.2 with different optimization flags (e.g. -O2, -O3), reporting the best results only. The matrix-blocks were configured as 2-by-2 elements to match the 4-element single-precision floating-points (SPFP) vectors in the Intel processor (common in other multicore chips). Time SU results for the SMVM kernel using CSR versus the new BPMS and PMS formats are shown in Fig. 1 for increasing matrix sizes on one CPU-core. CSR provides the base computing time since it contains no zero padding, whereas PMS and BPMS have extra computational overhead. The SU curve increases as the matrices grow and stabilizes around 1.5x SU, which shows that BPMS performs better than CSR as the cache misses in the CSR kernel become regular. BPMS also demonstrates good scaling for increasing matrix sizes, requiring less padded-zeros. This is true in general, but non-zero padding may slightly increase for very irregularly-structured matrices, e.g., the two matrices in the valley of Fig. 1. The BPMS-SMVM kernel was not vectorized for this test, so a maximum increase of 4X the reported SU can be expected when vectorizing for SPFP on modern processors.

A high-level parallelized version of the SMVM kernel was implemented across different numbers of cores using standard Pthreads and the new BPMS format (configured as before). We

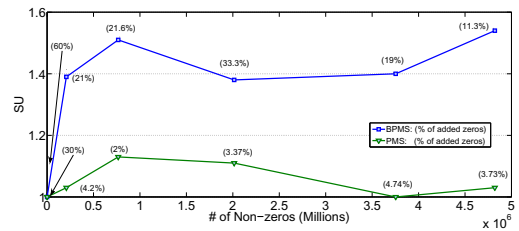


Fig. 1. SU of SMVM with BPMS and PMS versus CSR for one core.

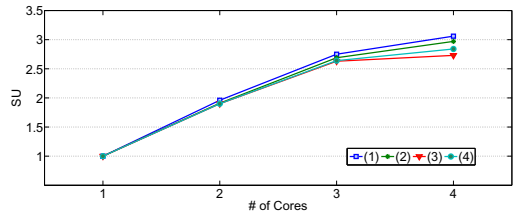


Fig. 2. SU scaling for CG-BPMS using 1-4 cores.

TABLE I
BPMS-CG GFLOPS RESULTS FOR 1 AND 4 CORES.

Matrix Name(#)	fidapm37(1)	bcsstk32(2)	s3dkt3m2(3)	s3dkq4m2(4)
Non-zeros	765944	2014701	3753461	4820891
% added zeros	(21.63%)	(30.36%)	(19.02%)	(11.32%)
BPMS-CG 1-core	0.94	0.90	0.96	1.02
BPMS-CG 4-core	2.86	2.67	2.63	2.89

then used this parallel BPMS-SMVM kernel to accelerate the CG solver (BPMS-CG). The performance scaling with respect to 1-core BPMS-CG is shown in Fig. 2 for the 4 biggest test matrices. Near 3-times increase in performance (measured in GFLOPS) was obtained when running the accelerated BPMS-CG from 1 to 4-cores (see Table I). Table I also shows, that in general, as the non-zero entries of the matrix grow the added zeros due to padding drop, demonstrating the good scalability behavior of the new format. This work demonstrates that by using special sparse formats one can regularize these kernels and significantly increase their performance even when considerable zeros are padded. As an added benefit, the regularization process provides insight into the coarse partition boundaries that can be used for distributing data among processing cores. Full performance results for vectorized BPMS-CG will be presented at the conference and in the long version paper.

REFERENCES

- [1] C. L. Lawson, et al., "Basic linear algebra subprograms for fortran usage," *ACM Trans. Math. Softw.*, vol. 5, no. 3, pp. 308–323, 1979.
- [2] J. J. Dongarra, et al., "A set of level 3 basic linear algebra subprograms," *ACM Trans. Math. Softw.*, vol. 16, no. 1, pp. 1–17, 1990.
- [3] R. Barrett, et al., *Templates for the Solution of Linear Systems: Building Blocks for Iterative Methods*, 2nd ed. Philadelphia, PA: SIAM, 1994.
- [4] Y. El-Kurdi, et al., "Hardware acceleration for finite element electromagnetics: Efficient sparse matrix floating-point computations with FPGAs," *IEEE Trans. Magn.*, vol. 43, no. 4, pp. 1525–1528, April 2007.
- [5] P. T. Stathis, "Sparse matrix vector processing formats," Ph.D. dissertation, Delft University of Technology, Delft, Netherlands, November 2004.
- [6] D. M. Fernandez, D. Giannopoulos, and W. J. Gross, "Efficient Multicore Sparse Matrix-Vector Multiplication for FE Electromagnetics," *IEEE Trans. Magn.*, vol. 45, no. 3, pp. 1392–1395, March 2009.
- [7] E. Cuthill and J. McKee, "Reducing the bandwidth of sparse symmetric matrices," in *Proc. of the 1969 24th nat. conf. ACM*, 1969, pp. 157–172.

A New Approach to the Impedance Method

Airton Ramos, Daniela O. H. Suzuki

Universidade do Estado de Santa Catarina

Campus Universitário Prof. Avelino Marcante, Joinville, Santa Catarina, 89.223-100, Brazil

airton_ramos@joinville.udesc.br

Abstract — This paper presents a new approach based on the use of interpolation for the electric potential which provides a significant increase in the accuracy of field calculation using the impedance method. In a rectangular three-dimensional grid we use a first order interpolation function to describe the distribution of electric potential within each voxel of the mesh. The electric field obtained analytically from this function is used as a solution of the continuity equation applied to each node of the mesh. The system of node equations is then solved and the resulting potential distribution obtained allows us to make the calculation of the electric field and current in each voxel.

I. INTRODUCTION

The impedance method and similar methods use lumped parameters of electric circuit to model the electric properties of the related materials [1,2]. Such methods have been applied in several important situations of electromagnetic modeling in linear materials, especially those involving excitation with sinusoidal sources, where the technique of phasor analysis can be applied [3,4]. These methods are simple to implement, because they basically involve a three-dimensional mesh of rectangular voxels. Naturally, as the method of finite differences, their biggest limitation is the representation of curvilinear surfaces.

The Impedance Method provides accurate results when the size of the medium is small compared with the wavelength of the electric field in the frequency of the source. This method is based on quasi-static approximations of Maxwell's equations, so the potential distribution can be obtained from the equations of the electric circuit theory. Thus, the conductivity and permittivity of the medium are modeled by lumped circuit elements as conductance and capacitance that connect the voxels of the discretization mesh. The impedance and admittance of connection between two neighboring voxels are defined by the following expressions (see Figure 1):

$$Z_{nm} = (V_n - V_m) / I_{nm} = L_{nm} / (\sigma_{nm} + i\omega\epsilon_{nm}) A_{nm} \quad (1)$$

$$Y_{nm} = I_{nm} / (V_n - V_m) = (\sigma_{nm} + i\omega\epsilon_{nm}) A_{nm} / L_{nm} \quad (2)$$

Where σ_{nm} and ϵ_{nm} are the conductivity and permittivity, respectively, in the region around nodes n and m and ω is the angular frequency. A_{nm} is the area of the face and L_{nm} is the distance between the geometrical centers of the neighbor voxels. With this approach one can easily model anisotropic and heterogeneous medium, such as biological materials which have significant differences in electrical conductivity and permittivity between different tissues and organs and in different directions of the applied field.

An important limitation of the impedance method lies in the fact that it allows the calculation of potential or current only in discrete positions of the mesh, which tends to intensify the discretization error. This problem can be minimized with

the use of interpolation to represent the distribution of potential within each voxel.

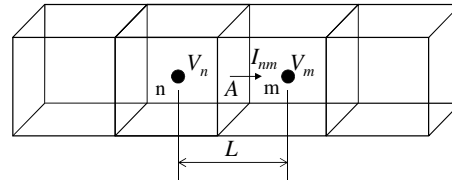


Fig. 1. Connection between two voxels in the Impedance Method.

The aim of this paper is to present a new strategy for numerical modeling with the impedance method that uses interpolation to describe the electric potential within the voxels of the discretization mesh. In this approach, in order to obtain a system of equations for the node potentials, we apply the equation of continuity for the total flow of current around each node.

II. METHOD

Based on the impedance or admittance model of the medium one can calculate the node potentials or the mesh currents in the equivalent circuit through the usual techniques of circuit analysis. Figure 3 shows a voxel with a local numbering of nodes in its vertices. This numbering is identical for all voxels of the mesh. Furthermore, each node is identified by a set of three indexes allocated in accordance with its position in relation to the origin of the reference system. The electric potential inside the voxel is described by the following function:

$$V = k_0 + k_1x' + k_2y' + k_3z' + k_4x'y' + k_5x'z' + k_6y'z' + k_7x'y'z' \quad (3)$$

in the intervals $0 \leq x' \leq \Delta x$, $0 \leq y' \leq \Delta y$, $0 \leq z' \leq \Delta z$.

The coefficients of equation (3) are determined by substituting this expression in each node of the voxel and solving the resulting system composed of eight equations. From equation (3) we obtain the electric field and calculate the current in each direction of the reference system in each voxel by integrating the current density under the assumption that conductivity and permittivity are uniform inside the voxel.

In order to obtain a relationship between the potential of nodes that meets the principle of continuity we establish that the sum of all components of current entering (negative) or leaving (positive) any node of the grid is zero. The resulting equation contains all the potential of nodes of the eight voxels that contains the common node (i, j, k) . That is, this equation relates potential of 27 nodes. It can be written in the following general form:

$$\sum_{n=-1}^1 \sum_{m=-1}^1 \sum_{r=-1}^1 a(n,m,r) V(i+n, j+m, k+r) = I_s(i, j, k) \quad (4)$$

where n, m and r are integers that can take the values 1, 0 or -1 and I_s is the current injected in the node (i, j, k) by the external source. The coefficients $a(n, m, r)$ relates the admittance of the eight voxels involved in each node equation.

The proposed method is to solve the system of equations described by (4) (one equation for each node of the mesh) aiming to obtain the potential of nodes according to the boundary conditions specified for the problem.

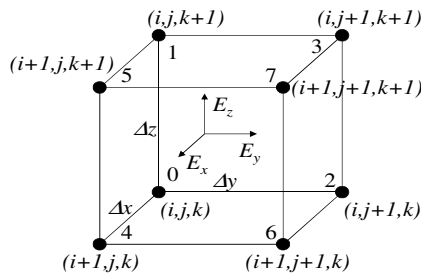


Fig. 2. Representation of a voxel with the numbering of its nodes.

III. RESULTS

As an example of application and adequacy of the proposed method, we analyze a case of simulation in a medium with high dielectric constant and low conductivity. These characteristics are similar to biological tissues. The example has simple geometry to allow obtaining an analytical solution that serves as a reference for the validation of the numerical method. It refers to a spherical region with admittivity four times greater than the external medium in a uniform electric field (see Figure 3). We used a regular grid with $140 \times 50 \times 50$ voxels with a mesh parameter of $100\mu\text{m}$. The electric field is applied through the imposition of fixed potentials of -1V and +1V on the boundary plans in x direction. On the other boundary surfaces we applied the homogeneous Neumann boundary condition. The analytical model for this system is easily obtained from the general solution of Laplace's equation in spherical coordinates with azimuthal symmetry. The potential inside and outside the sphere is given respectively by the following two equations:

$$V_i = -\frac{3\gamma_o}{\gamma_i + 2\gamma_o} E_o r \cos \theta \quad (5)$$

$$V_o = \left[\frac{a^3 (\gamma_i - \gamma_o)}{r^2 (\gamma_i + 2\gamma_o)} - r \right] E_o \cos \theta \quad (6)$$

Where $\gamma = \sigma + j\omega\epsilon$ and the indices i and o indicate internal and external media, respectively.

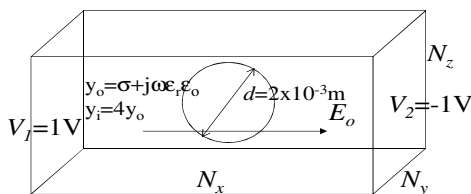


Fig. 3. Model used in the example.

Figure 4 shows the angular distribution of electric potential for four values of the radial distance from the centre of the sphere. The points refer to the simulation and continuous line refers to the analytical model. There is good agreement between these results. It is also presented the root mean square of the deviations of the numerical results in relation to the analytical model, including the results obtained using the traditional Impedance Method [1,2].

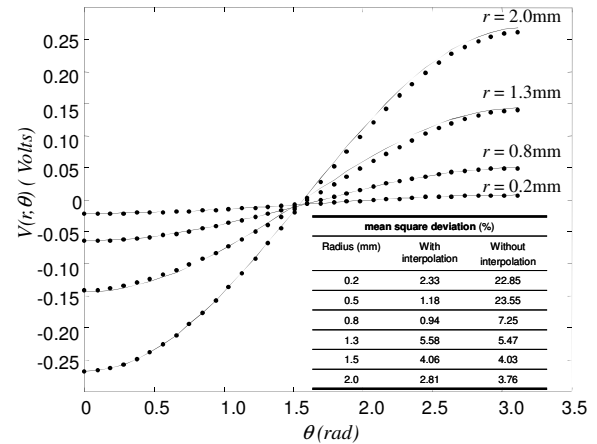


Fig. 4. Angular distribution of electric potential and mean square deviation in relation to the analytical model.

It is observed that for the three smaller radial distances the mean deviation from the analytical model in the simulation with interpolation is much smaller than in the conventional method simulation. The fact that the error is greater for smaller distances indicates great influence of spatial resolution of the mesh, ie there is a predominance of the discretization error in the conventional method. We concluded then that the use of interpolation in obtaining the equations of nodes in the proposed method significantly reduces the error of discretization. Finally, we note that the deviation increases in the vicinity of the radius of the sphere, and this is more an effect of discretization, because in the discrete space the form of the boundary between the two medium is considerably distorted in relation to the spherical shape in the continuum space.

IV. REFERENCES

- [1] N. Orcutt, O.P. Gandhi, A 3-D impedance method to calculate power deposition in biological bodies subjected to time varying magnetic fields, IEEE Trans. Biom. Eng., 35 (1988) 577-583
- [2] A. Ramos, A. Raizer, J.L.B. Marques, A new computational approach for electrical analysis of biological tissues, Bioelectrochemistry, 59 (2003) 73-84.
- [3] N. Orcutt, O.P. Gandhi, Use of the impedance method to calculate 3-D power deposition patterns for hyperthermia with capacitive plate electrodes, IEEE Trans. Biom. Eng., 37 (1990) 36-43
- [4] M. Nadeem, T. Thorleif, O.P. Gandhi, Computation of electric and magnetic stimulation in human head using the 3-D impedance method, IEEE Trans. Biom. Eng., 50 (2003) 900-907

A simplified T - φ formulation for eddy current computation in thin CFRP plates

H. Menana and M. Féliachi

Institut de Recherche en Electrotechnique et Electronique de Nantes Atlantique (IREENA)
CRTT, 37 Boulevard de l'Université, BP 406, 44602, Saint Nazaire Cedex, France
hocine.menana@univ-nantes.fr , mouloud.feliachi@univ-nantes.fr

Abstract — We present a simplified model for eddy current modeling in anisotropic thin multilayered plates. Under certain assumptions, the T - φ formulation is reduced to a simplified formulation involving only the normal component of the electric vector potential. As a validation, the two formulations are compared in a numerical example which consists in the evaluation of the impedance variation of an air cored coil above a thin composite multilayered plate.

I. INTRODUCTION

New synthetic materials such as carbon fiber reinforced polymer composites (CFRPs) are generally made of several anisotropic thin layers. The electromagnetic field modeling in these materials is a challenging problem because of their high anisotropy and scale effects. Dyadic Green's functions are often used when their geometries are simple [1]-[2]; however, these functions do not converge rapidly when the layers are very thin, and difficulties are encountered to derive them when a great number of layers are involved.

In a recent work [3], we developed a numerical model for eddy currents computation in carbon fiber reinforced polymer composites (CFRPs) based on the T - φ formulation. In this work, under certain assumptions, this formulation is simplified so as only the normal component (T_z) of the electric vector potential is retained. This makes the calculation faster and reduces considerably the memory space required for data storage. On the other hand, only the active parts are discretized which permits to overcome the problems related to the scale effects and offers an ease to handle the motion of the moving parts of the system. As a validation, the T - φ and T_z formulations are compared in a numerical example which consists in the evaluation of the impedance variation of an air cored coil above a thin composite multilayered plate. The reciprocity and energy conservation principles are used to evaluate the impedance variation of the coil.

II. FORMULATION

Consider the system presented in figure 1. A nonmagnetic thin multilayered CRFP plate is subjected to the influence of a magnetic field \vec{H}^s produced by an inductor where a current density \vec{J}^s variable in time is imposed. The electromagnetic field behaviour in the plate is described by the equations (1), (2) and (3) [3], involving the electric vector potential T the magnetic scalar potential φ , the resistivity tensor $\vec{\rho}$ of the composite plate, the free space permeability μ_0 and the angular frequency ω .

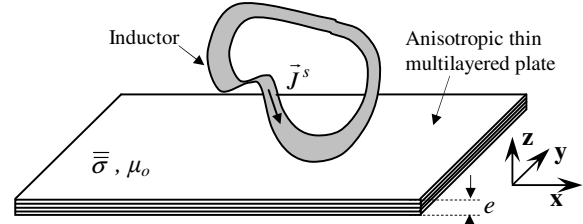


Fig.1. An inductor above a thin multilayered CFRP plate

$$\vec{\nabla} \times \vec{\rho} \vec{\nabla} \times \vec{T} + j\omega\mu_0(\vec{T} - \vec{\nabla}\varphi) = -j\omega\mu_0\vec{H}^s \quad (1)$$

$$\vec{\nabla} \cdot (\vec{H}^s + \vec{T} - \vec{\nabla}\varphi) = 0 \quad (2)$$

$$\vec{n} \times \vec{T} = \vec{0} /_{\Gamma} \quad (3)$$

We assume that the adjacent layers (plies) of the plate are electrically isolated and the eddy currents flow in plans parallel to the surface of the plate (i.e. $J_z = 0$), which is often the case in laminated composite materials such as CFRPs. On the other hand, if the used frequencies are such that the thickness of the plate is considered to be small compared to the skin depth, the derivatives of the electric and magnetic fields with respect to the thickness can be neglected. Also, as the plate is nonmagnetic, the magnetic scalar potential can be removed. With these assumptions, (1) is reduced to (4) involving only the normal component of the electric vector potential. The eddy currents are calculated by means of (6).

$$[\partial_x(\rho_{yx}\partial_y - \rho_{yy}\partial_x) - \partial_y(\rho_{xx}\partial_y - \rho_{xy}\partial_x) + j\omega\mu_0]T_z = -j\omega\mu_0 H_z^s \quad (4)$$

$$\vec{J} = [J_x \quad J_y]^T = [\partial_y T_z \quad -\partial_x T]^T \quad (6)$$

Each ply of the composite plate is constituted of carbon fibers embedded in a polymer matrix. The resistivity tensor of the plate is given by (7) [3], involving the conductivities parallel and transverse to the fibers ($\sigma_{//}$, σ_{\perp}), and the orientation θ of each ply with respect to a reference axis.

$$\vec{\rho} = \begin{pmatrix} \sigma_{//} \cos^2(\theta) + \sigma_{\perp} \sin^2(\theta) & \frac{\sigma_{//} - \sigma_{\perp}}{2} \sin(2\theta) \\ \frac{\sigma_{//} - \sigma_{\perp}}{2} \sin(2\theta) & \sigma_{//} \sin^2(\theta) + \sigma_{\perp} \cos^2(\theta) \end{pmatrix}^{-1} \quad (7)$$

Using the principle of the energy conservation [4], the impedance variation (ΔZ) of the inductor due to the eddy currents flowing in the plate can be calculated by (8), where

the magnetic term is reduced to T_z for the simplified formulation. In (8), Ω_p denote the plate volume and I_s the source current.

$$\Delta Z = \frac{1}{I_s^2} \int_{\Omega_p} \bar{J}^* \bar{\rho} \bar{J} + j\omega\mu_0 \|\bar{T} - \bar{\nabla}\phi\|^2 d\Omega_p \quad (8)$$

III. NUMERICAL EXAMPLE

The two formulations are compared in this numerical example which consists in the evaluation of the impedance variation of an air cored coil above a thin CRFP plate. The geometry of the modelled system is described in figure 2; the numerical values of the different parameters are given in Table I. Only the coil and the plate are discretized. The source field is calculated by the Biot and Savart formulae; (1), (2) and (4) are solved using the finite difference method in the plate [3].

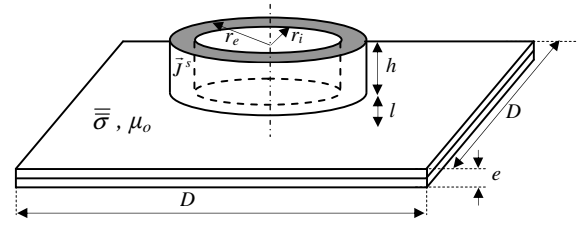


Fig.2. The modeled system

TABLE I
THE NUMERICAL VALUES OF THE SYSTEM PARAMETERS

Regions	Parameters	Numerical values
Plate	Thickness (e) / Side (D)	0.25mm / 50mm
	Conductivities ($\sigma_{//}, \sigma_{\perp}$)	($10^4, 10^2$)S/m
	Number of plies / Orientations	2 / [0°, 90°]
Coil	Number of turns	500
	Inner radius (r_i) / Outer radius (r_e)	5mm / 10mm
	Height (h) / Lift off (l)	1mm / variable

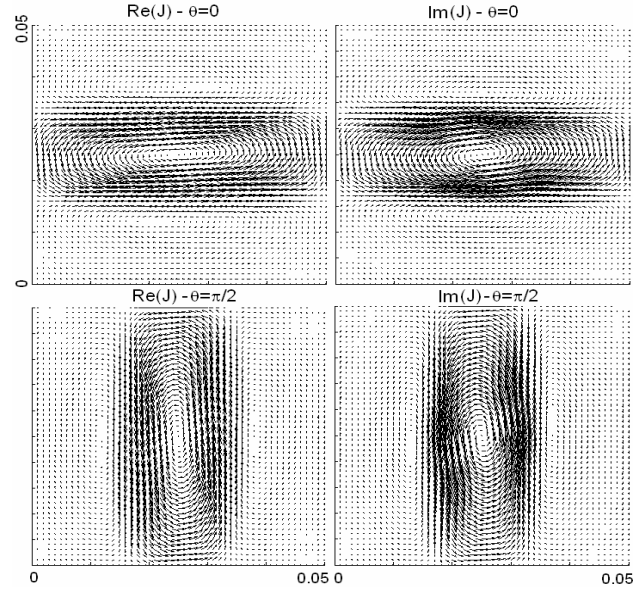


Fig. 3. Repartitions of the real and imaginary parts of the eddy current density in the two plies obtained by the simplified formulation ($l=1mm$)

Figure 3 represents the repartitions of the real and imaginary parts of the eddy current density in the two plies obtained by the T_z formulation. We notice that the imaginary part is concentrated near the coil position whereas the real part is more stretched along the axis of the high conductivity.

For a fixed lift off ($l=1mm$), figure 4 shows the real and imaginary parts of ΔZ for different values of the frequency, obtained by the two formulations. Similarly, for a fixed frequency ($f=1MHz$), figure 5 shows the variations of the real and imaginary parts of ΔZ according to the lift off. As the lift-off decreases, the normal component of the source field becomes predominant and its tangential components decrease until cancellation at the limit when the lift off becomes nil. In this case, we notice a difference between the values of ΔZ obtained by the two formulations. This difference may be due to numerical errors in the $T-\phi$ model engendered by the fact of calculating quantities which are in reality nil.

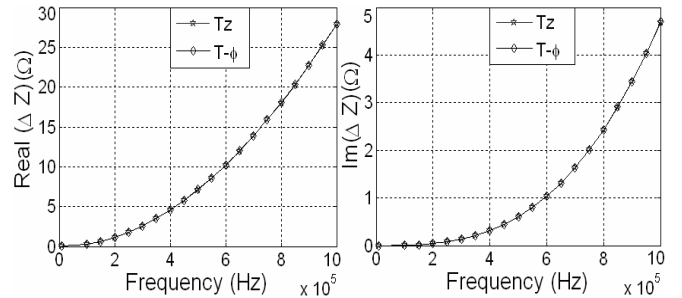


Fig. 4. The variations of the real and imaginary parts of ΔZ according to frequency ($l=1mm$)

IV. REFERENCES

[1] Thomas M. Roberts, Harold A. Sabbagh, L. David Sabbagh, "Electromagnetic Interactions with an Anisotropic Slab," *IEEE Trans. on Magnetics*, 24 (6): 3193-3200, 1988

[2] John R. Bowler, L. David Sabbagh, Harold A. Sabbagh, "A theoretical and computational model of eddy-current probes incorporating volume integral and conjugate gradient methods," *IEEE Trans. on Magnetics*, 24(6): 3193-3200, 1988

[3] Hocine Menana, Mouloud Féliachi, "3-D Eddy Current Computation in Carbon-Fiber Reinforced Composites," *IEEE Trans. On Magnetics*, 45(3): 1008-1011, 2009

[4] N. IDA and W. LORD, "A Finite Element Model for Three-Dimensional Eddy Current NDT Phenomena," *IEEE Trans. on Magnetics*, MAG-21(6): 2635-2643, 1985

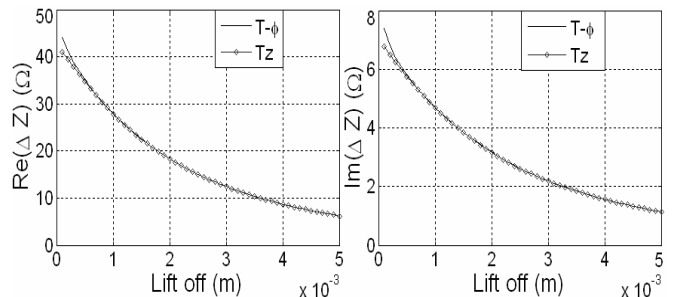


Fig. 5. The variations of the real and imaginary parts of ΔZ according to the lift off ($f=1MHz$)

Preconditioned BICGSTAB Algorithm and its Application to a Moving Linear Electric Motor

Faxi Zhu¹, Haitao Yu¹, S.L. Ho² and Minqiang Hu¹

¹School of Electrical Engineering, Southeast University, Nanjing, 210096, P.R. China

²Department of Electrical Engineering, Hong Kong Polytechnic University, Hong Kong
htyu@seu.edu.cn

Abstract—The finite element method (FEM) is developed to solve the diffusion equation containing the moving term. For the solution of the large sparse non-symmetrical, the preconditioned biconjugate gradient stabilized (PBICGSTAB) method is presented, combining the ILU[p] preconditioner and BICGSTAB method. The magnetic field distribution of Permanent Magnet Linear Motor (PMLM) problems is calculated by the FEM electromagnetic package including the proposed PBICGSTAB algorithm. Then the results are compared to those from the commercial software ANSYS, showing the validation of this analysis technique. Comparisons between PBICGSTAB method and other widely used algorithms show that PBICGSTAB is speedy, applicable to solve system of large-scale non-symmetrical linear equations.

Index Terms—BICGSTAB Algorithm, Precondition technique, Permanent Magnet Linear Motor

I. INTRODUCTION

The study of moving PMLM through analytical methods requires many simplifications, leading to huge errors. Numerical methods have become progressively more important than analytical methods in the solution of nonlinearity, anisotropy and motion problems. Among various numerical methods, FEM is the most powerful one.

A non-symmetrical system with sparse matrix is obtained after Galerkin technique is applied to the convective-diffusion equation which involves the moving effect. In the previous papers, the linear equations were solved using the direct algorithm of Gaussian elimination. However, the cost in terms of computer operations and storage is unbearable when the number of equations is large enough. Iterative methods have become major methods for solving linear systems, especially for the large, sparse one. There are many iterative methods used for non-symmetrical linear systems, such as CGS, BICG, QMR and GMRES methods. However, CGS and BICG methods have irregular convergence behavior[1]. QMR method applies a least squares method to solve and update the BICG residuals, thereby smoothing out the irregular convergence behavior. Also, QMR avoids the breakdown that can occur in BICG, but transpose matrix is required[2]. GMRES method has monotonic convergence and only involves one matrix-vector product with the coefficient matrix, but the amount of storage and operation count increase as the iteration progresses[3]. Therefore, these methods have considerable limitations in the practical application.

The paper is arranged as follows. In section II, a new simulation model for magnetic field of a moving Permanent Magnet linear motor is developed and BICGSTAB algorithm

is expatiated in detail. In order to verify the proposed method, a single-sided PMLM problem is presented as an example in section III.

II. NUMERICAL SIMULATIONS

A. Simulation model

The electromagnetic fields in PMLM can be expressed with the Maxwell equations with the vector magnetic potential \vec{A} as the variable,

$$\nabla \times (\gamma \nabla \times \vec{A}) - \sigma \nabla \times \vec{A} = \vec{J}_s \quad (1)$$

Where; ∇ is the velocity of PMLM; σ and γ is the conductivity and reluctivity, respectively; \vec{J}_s is the equivalent current density for permanent-magnet.

If the PMLM is computed in two-dimensions and it moves along the x-axis, the formulation can be simplified as,

$$\frac{\partial}{\partial x} (\gamma \frac{\partial A}{\partial x}) + \frac{\partial}{\partial y} (\gamma \frac{\partial A}{\partial y}) = V \sigma \frac{\partial A}{\partial x} - J_s \quad (2)$$

By using the Galerkin method, (2) becomes an integral equation,

$$\int_s \nabla W_i \cdot \nabla A ds + V \sigma \int_s \frac{\partial A}{\partial x} W_i ds - \gamma \int_{\Gamma} W_i \nabla A ds = \int_s J_s W_i ds \quad (3)$$

where the weighting function W_i is set to be equal to an interpolation function. The last term on the left hand side is the integral on the boundary Γ enclosing the whole computation region. One can obtain the large sparse linear equations after discretizing (3) and imposing the boundary conditions,

$$[K][A] = [f] \quad (4)$$

where $[K]$ is a coefficient matrix of order n ; $[A]$ is unknown vector to be solved; $[f]$ is the source on the right hand side.

B. BICGSTAB algorithm

BICGSTAB algorithm is a variant of the BICG method. The algorithm can be considered as a product of the BICG method and the GMRES method. The residual vector is

minimized locally by GMRES method local step. BICGSTAB algorithm does not use the transpose of the matrix K in the calculation of the recurrences. This is advantageous for cases where the transpose of the matrix K is not readily available. However, when the GMRES step stagnates, the residual vector is not minimized and the algorithm breaks down.

The iterative formula of BICGSTAB method can be written as follow:

$$(1) \quad r_0 = f - K \cdot x_0, \quad \bar{r}_0 = r_0, \quad p_0 = r_0$$

$$(2) \quad MY_j = p_j, \quad \alpha_j = \frac{(r_j, r_j)}{(r_j, KY_j)}, \quad s_j = r_j - \alpha_j KY_j$$

$$MZ_j = s_j, \quad \omega_j = \frac{(KZ_j, s_j)}{(KZ_j, KZ_j)}$$

$$x_{j+1} = x_j + \alpha_j Y_j + \omega_j Z_j, \quad r_{j+1} = s_j - \omega_j KZ_j$$

$$\beta_{j+1} = \frac{\alpha_j \cdot (r_{j+1}, r_{j+1})}{\omega_j \cdot (r_j, r_j)}, \quad p_{j+1} = r_{j+1} + \beta_j (p_j - \omega_j KZ_j)$$

$$(3) \quad \|r_{j+1}\|_2 / \|r_0\|_2 < \varepsilon,$$

where matrix M is called a preconditioner obtained by ILU[0] method, that is incomplete LU factorization without fill-ins[4];

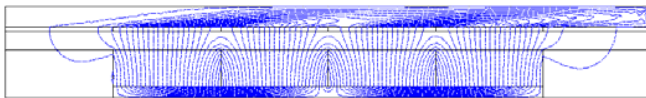
If (3) holds, final result x_{j+1} is got, and the computation is over. Otherwise, set $j = j + 1$, and go back to (2) until (3) is satisfied.

III. ANALYSIS OF A PMLM

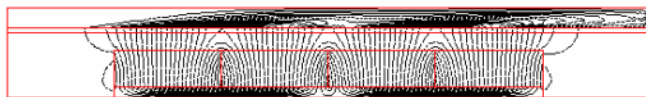
In order to prove the validation of the proposed method, a single-sided PMLM moving at low speed is simulated. Then the results are compared to those from the commercial software ANSYS.

Fig.1 shows us the magnetic field distribution of PMLM when secondary moving relative to primary at a speed of 10cm/s. From Fig.1, one can see that secondary's velocity affects magnetic field distribution, called dynamic longitudinal end effect. It makes the magnetic field increase at entry end and decrease at exit end. The magnitude of effect depends on moving velocity.

Fig.2 shows the flux densities along the centerline of gap. X-axis component and Y-axis component of flux density is provided respectively. As a result of end effect, flux density unequal to zero in the air gap at the end of primary.



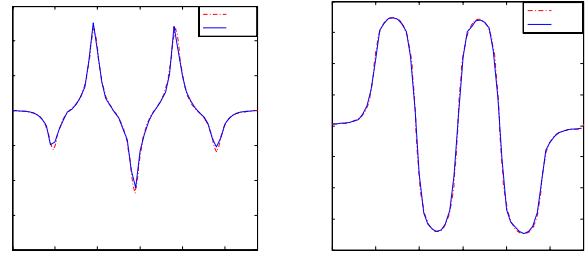
(a) Magnetic field distribution by proposed method



(b) Magnetic field distribution by ANSYS.

Fig. 1 The magnetic field distribution of PMLM

In order to compare the rate of convergence and the convergence characteristic, convergence curves of various



(a) Flux density along X-axis (b) Flux density along Y-axis
Fig. 2 The flux density along air gap

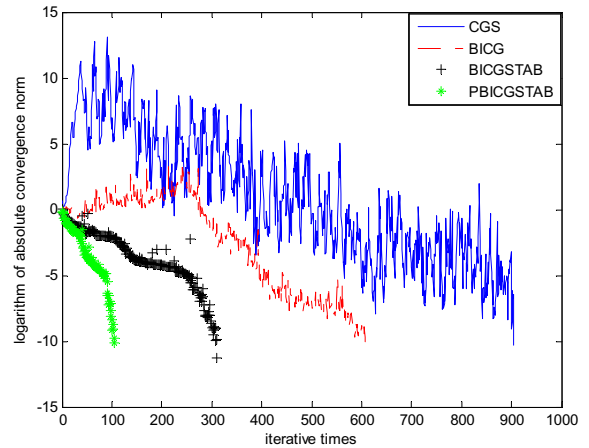


Fig. 3 Convergence curves of iterative methods

iterative methods is provided in the Fig. 3. As we can see in the figure above, the best method is PBICGSTAB method which converges rapidly to the precise results without oscillation. Also, through the contrast between BICGSTAB method and PBICGSTAB method, precondition techniques have been proved to be of great importance in the solution of large, sparse systems.

IV. CONCLUSIONS

In this paper, the mathematical model for magnetic field of moving Permanent Magnet linear induction motors has been developed. A new favorable iterative algorithm has been presented for solving large sparse non-symmetrical systems formed from discretization by finite element methods. A single-sided PMLM has been simulated with the proposed algorithm. The computed results are found to be in good agreement with those obtained from ANSYS shown in Fig. 1 and Fig. 2.

V. REFERENCE

- [1] Madeline K., Steady-State methods for simulation of RF and microwave circuits. Medford: Tufts University, 2002. 48-51.
- [2] Topsakal E, Kindt R, Sertel K, et al. Evaluation of the BICGSTAB(1) algorithm for the finite-element/boundary-integral method. *Antennas and propagation magazine*, 2001, 43(6):124-131.
- [3] Saad Y., Iterative methods for sparse linear systems. New York: PWS, 1996. 265-319.
- [4] Ke C., Matrix preconditioning techniques and applications. London Cambridge University, 2005.

An Efficient Two-Level Preconditioner for FEM-BEM Equations based on Lifting

Fabio H. Pereira^{1,3}, Marcio M. Afonso², and Silvio I. Nabeta³

¹Industrial Engineering Post Graduation Program – UNINOVE-SP

²Electrical Engineering Department - CEFET-MG

³Electrical Machine and Drives Lab – GMACq – USP - SP

Av. Francisco Matarazzo, 612 – Água Branca, 05001.100 – São Paulo, SP - Brazil

fabiohp@uninove.br; marciomatias@des.cefetmg.br; nabeta@pea.usp.br

Abstract — The system resulting from FEM–BEM formulations inherits all characteristics of both finite element and boundary element equation system, i. e., the system is partially sparse and symmetric and partially full and nonsymmetric. Consequently, to solve the resulting coupled equation system is not a trivial task. This paper proposes a new efficient lifting-based two level preconditioner for the FEM-BEM global system. The proposed approach is applied to solve the coupled systems resulting from the electromagnetic scattering problem and its performance is evaluated based on the number of iterations and the computational time. Traditional methods based on incomplete and complete LU decompositions are used for comparison.

I. INTRODUCTION

The Finite Element and the Boundary Element Methods can be considered complementary to each other in many cases. It is particularly true to problems where the domain considered is formed by two (or more) regions where one of them is characterized by non-homogeneous material while the other is free space. This kind of problem is difficult to be solved by any individually method described above. Therefore, a combination of two the previous techniques comes up as a powerful way to solve it [1].

The system resulting from FEM–BEM formulations inherits all characteristics of both finite element and boundary element equation system, i. e., the system is partially sparse and symmetric and partially full and nonsymmetric [1],[2]. Consequently, the efficient solution of the FEM-BEM system has been object of many researches [3],[4]. In fact, most of the proposed approaches are based on some adaptations. In the algebraic multigrid context, for example, one should consider a fast matrix-by-vector multiplication for dense matrices and to use some matrix approximation technique for the BEM dense matrix. In particular, common smoother types do not work properly in the case of the single layer potential [5]. In face of that, this work proposes a new efficient two level preconditioner for the global FEM-BEM system based on the lifting technique. This proposed approach is applied to some real-life FEM-BEM coupled systems and its performance is evaluated based on the number of iterations and the computational time. Traditional methods based on incomplete and complete LU decompositions are used for comparison.

II. PROBLEM FORMULATION

The scattering problem was chosen to show the performance of the proposed approach. This kind of problem

occurs when an object is struck by an electromagnetic wave. To solve this problem by hybrid technique an artificial surface must be chosen, which allows divide scattering problems in two regions. The first, Ω_∞ , is the free space with permeability μ_0 and permittivity ε_0 . The second region Ω may consist in general of non-homogeneous material with permeability $\mu(x,y)$ and permittivity $\varepsilon(x,y)$. Once the two regions are known, the electromagnetic fields in each one can be formulated.

A. Finite element formulation

The Helmholtz differential equation describes the field behavior in region Ω . In general form, the Helmholtz equation could be written as [2]

$$\nabla \cdot (\alpha_1 \nabla u) + k_0^2 \alpha_2 u = 0, \quad (1)$$

where, $k_0^2 = w \sqrt{\mu_0 \varepsilon_0}$ represent the wave number. Also, for electric field polarization $\alpha_1 = 1/\mu_r$, $\alpha_2 = \varepsilon_r$ and $u = E_z$ while for magnetic field polarization $\alpha_1 = 1/\varepsilon_r$, $\alpha_2 = \mu_r$ and $u = H_z$.

The *weak formulation* given by (2) is well known and its derivation will be omitted here [2].

$$\int_{\Omega} \nabla w \cdot (\alpha_1 \nabla u^*) d\Omega - \int_{\Omega} k_0^2 \alpha_2 w \cdot u^* d\Omega - \int_{\Gamma} w \alpha_1 \frac{\partial u^*}{\partial n} d\Gamma = 0 \quad (2)$$

in which u^* is an approximation for u and w is the weight function.

Applying Galerkin's procedure in (2) the following general set of equations is determined [2],

$$[K]\{d\} + [C]\{k\} = 0 \quad (3)$$

where $[K]$ is a $n \times n$ square matrix and $[C]$ is a $n \times m$ rectangular matrix, with m and n representing the total number of the nodes on the boundary and the interior domain, respectively. Also, $\{d\}$ is a column vector for field arguments and $\{k\}$ is a column vector for the normal derivative field arguments.

B. Boundary element formulation

In free space, Ω_∞ , the field also are formulated by Helmholtz equation. The general formulation for both electric and magnetic fields is:

$$\nabla^2 u(\vec{r}) + k_0^2 u(\vec{r}) = f(\vec{r}) \quad \forall \vec{r} \in \Omega_\infty \quad (4)$$

in which, for electric polarization $u = E_z$, $f(\vec{r}) = jk_0 Z_0 J_z - \nabla \times M_i$ and for magnetic polarization $u = H_z$, $f(\vec{r}) = j(k_0/Z_0)M_i - \nabla \times J_z$. Where, Z_0 is the intrinsic impedance of the free space, J_z represents all currents that flow along z-axis and M_i is the impressed magnetic source.

Then, introducing the free space Green's function, the Sommerfeld radiation condition and applying the second scalar Green's theorem and Dirac properties for all nodes on the boundary, it produces [1],[2]

$$\{u\} = \{b\} + [H]\{d\} + [Q]\{k\}, \quad (5)$$

where, $[H]$ and $[Q]$ are $m \times m$ matrices obtained from the discretization and $\{b\}$ is a $m \times 1$ incident field column vector.

The system resulting from FEM-BEM formulations can be expressed in the in following form:

$$\begin{bmatrix} K & C \\ -H & -Q \end{bmatrix} \begin{Bmatrix} d \\ k \end{Bmatrix} = \begin{Bmatrix} 0 \\ b \end{Bmatrix} \quad (6)$$

which is partially sparse and symmetric and partially full and nonsymmetric [1],[2].

III. LIFTING BASED TWO-LEVEL PRECONDITIONER

The approach proposed here is based on a projection method. In this process an approximation for the solution of a linear system is extracted from a subspace \mathcal{K} of \mathbb{R}^n which is the search subspace. If m is the dimension of \mathcal{K} , then the residual vector $b - Ax$ is constrained to be orthogonal to the same subspace \mathcal{K} . Mathematically, denoting by V a $n \times m$ matrix whose column-vectors form a basis of \mathcal{K} , the approximate solution is written as

$$x = x_0 + Vy, \quad (7)$$

in which y is obtained solving the following system of equations from the orthogonality condition [6]

$$V^T AVy = V^T r_0 \quad (8)$$

Then, if the $m \times m$ matrix $V^T AV$ is nonsingular, the expression for the approximate solution \tilde{x} becomes,

$$\tilde{x} = x_0 + V(V^T AV)^{-1}V^T r_0 \quad (9)$$

In the lifting based approach, the matrix $V^T AV$ is obtained by the decomposition of the linear system A induced by the discrete lifting wavelet transform, with the Haar lowpass filter matrix V^T [7]. Therefore, this approach can be viewed as a two-level multigrid algorithm in which the $V^T AV$ matrix is formed by the detail coefficients obtained from the discrete lifting wavelet transform.

IV. NUMERICAL RESULTS

The Lifting based two-level method (LTL) was applied as a preconditioner for the Stabilized Bi-Conjugate Gradient

Method (BiCGStab) in the solution of two global coupled FEM-BEM systems. Both were obtained for a circular cylinder with 0.3λ diameter, $\epsilon_r = 3$ and wave length $\lambda = 1$. The cylinder is struck by a TM_z plane wave with incident angle of $\theta^i = 180^\circ$.

The results related to the number of iterations and setup and solver time are presented in tables I and II. The number of iterations corresponds to the number of BiCGStab steps necessary to reduce the Euclidean norm of the residual vector to the order of 10^{-6} . In the tests, the system with the $V^T AV$ matrix in LTL was solved by incomplete LU solver (LTL-1) and with a direct method (LTL-2). The Incomplete LU (ILU) preconditioner and the direct solver based on the complete LU decomposition were used for comparison.

TABLE I
RESULTS FOR A SMALL GLOBAL FEM-BEM MATRIX ($N=147, NZ=3867$)

Method	Setup time (seconds)	Number of iterations	Solver time (seconds)
LTL-2 and BiCGStab	0,03	24	0,28
LTL-1 and BiCGStab	0,08	28	0,33
ILU and BiCGStab	0,22	17	0,28
Complete LU	--	--	0,13

TABLE II
RESULTS FOR A MEDIUM GLOBAL FEM-BEM MATRIX ($N=2119, NZ=87133$)

Method	Setup time (seconds)	Number of iterations	Solver time (seconds)
LTL-2 and BiCGStab	37,83	93	37,47
LTL-1 and BiCGStab	7,11	118	49,03
ILU BiCGStab	42,81	101	46,42
Complete LU	--	--	306,45

V. CONCLUSIONS

The approach proposed in this work revealed to be very efficient and promising to solve the global systems of coupled FEM-BEM equations, mainly for the medium and large problems. The usual complete LU decomposition method is a good choice for small problems, but is very expensive for larger problems, as can be viewed in table II. For large problems, where an efficient preconditioner is required, the Lifting based two-level method give us the best results.

VI. REFERENCES

- [1] M. M. Afonso, J. A. Vasconcelos, "Two dimensional scattering problems solved by finite element - boundary element method", In: *22th CILAMCE - Iberian Latin-American Congress on Computational Methods in Engineering*, 2001.
- [2] Jin, J., *The finite element method in electromagnetics*, Wiley, New York, 1993.
- [3] G. Aiello, et. al., "An Iterative Solution to FEM-BEM Algebraic Systems for Open-Boundary Electrostatic Problems", *IEEE Trans. on Magnetics*, 43(4): 1249 - 1252, 2007.
- [4] P. Mund, E. P. Stephan, "Adaptive Coupling and Fast Solution of FEM-BEM Equations for Parabolic-Elliptic Interface Problems", *Math. Methods in the Appl. Scienc.*, 20(5): 403-423, 1998.
- [5] D. Pusch, "Efficient Algebraic Multigrid Preconditioners for Boundary Element Matrices", Phd thesis. Johannes Kepler University Linz, Austria, 1997.
- [6] Y. Saad, *Iterative Methods for Sparse Linear Systems*, 2nd ed, SIAM, Philadelphia, 2003.
- [7] T. K. Sarkar, S. P. Magdalena, C.W. Michael, *Wavelet Applications in Engineering Electromagnetics*, Artech House, Boston, 2002.

A Comparison of Parallel Finite Element Analysis Using Domain Decomposition

K. Watanabe, K. Yoneta and H. Igarashi

Hokkaido University

Kita 14, Nishi 9, Kita-ku, Sapporo, 060-0814, JAPAN

watanabe@ssi.ist.hokudai.ac.jp

Abstract — This paper discusses parallel computation of finite element (FE) analyses using domain decomposition. The overlapping domain decomposition method is an effective method for distributed memory computers. A preconditioner based on the Incomplete Cholesky decomposition is introduced for this method so as to improve the convergence of iteration. On the other hand, the hierarchical domain decomposition method is also known as a parallel computation method with high parallel efficiency. We compare a performance between the overlapping and hierarchical domain decomposition method. The numerical results show that the overlapping domain deposition method using stabilized conjugate gradient method has less computational cost than the hierarchical domain decomposition method.

I. INTRODUCTION

It is important to make fast computation of large scale finite element analyses in the development of electromagnetic machines. Although these analyses can be performed using expensive super computers, it is unacceptable in view of reducing the cost of development. Hence, the large scale analyses should be performed fast on popular computation environment such as PC clusters.

The parallel computation methods for electromagnetic field analysis have been investigated so far. The domain decomposition method is one of effective method so as to distribute the large system matrix to the PEs (Processor Elements) [1]. The incomplete Cholesky (IC) decomposition is a useful and stable pre-conditioner for preconditioned conjugate gradient (PCG) method. However, it is not suitable for domain decomposition method due to the cross components between divided sub domains. The simple solution of this difficulty is that the cross components are neglected. However, the convergence of PCG method with this preconditioner is considerably poor. The overlapping domain decomposition method has introduced in order to overcome this difficulty. The disadvantage of the overlapping method is increase of communication cost in the distributed memory environment.

The hierarchical domain decomposition method is another domain decomposition method for distributed memory computers [2-3]. In this method, a solution of governing equation is obtained to solve the unknowns about interface of sub domains (interface problem) and the unknowns about inner sub domains. This method has a significant high parallel efficiency. However, it is difficult to apply the strong preconditioner such as IC decomposition to the interface

problem, because the system matrix for interface problem is given implicitly. Therefore, this method has high computational cost.

In this paper, we compare performance between the overlapping domain decomposition and the hierarchical domain decomposition method on popular computational environment such as a PC cluster.

II. METHODS

A. Overlapping Domain Decomposition

Let us consider the electromagnetic field analysis using the finite element method with edge elements. In order to distribute the whole system matrix K to the PEs, the set of all edges G is divided into non-overlapping subset G_k ($k=1, 2, \dots, n_p$) where n_p is the number of sub domains, and $G_i \cap G_j = \emptyset$, $i \neq j$, i.e., there are no overlapped edges in G_k .

We define set of elements \tilde{E}_k which includes at least one edge in G_k . We also define the set of edges \tilde{G}_k as a set of edges contained in \tilde{E}_k . It is noted that G_k is a subset of \tilde{G}_k . We introduce the restriction operator R_k mapping from the space G spanned by all edges to the space spanned by G_k . The restriction operator \tilde{R}_k mapping from G to \tilde{G}_k is also defined. The preconditioned matrix M can be obtained as,

$$M = \sum_{k=1,2,\dots,n_p} \tilde{R}_k^T \tilde{M}_k \tilde{R}_k^T, \quad (1)$$

where \tilde{M}_k is the IC decomposition matrix corresponding to the overlapping restricted system matrix \tilde{K}_k . The preconditioner defined by (1) is a kind of Additive Schwarz Preconditioner. The convergence of PCG with this preconditioner is better than that of PCG using the simple IC decomposition of the non-overlapping system matrix $K_k \equiv R_k K R_k^T$.

Instead of (1), we introduce a following preconditioned matrix

$$M = \sum_{k=1,2,\dots,n_p} R_k R_k^T \tilde{R}_k^T \tilde{M}_k \tilde{R}_k^T. \quad (2)$$

It is known that the term $R_k R_k^T$ in (2) results in decrease the maximum eigenvalue and the condition number of M , hence, the convergence of PCG can be improved. Moreover,

9. Numerical Techniques

the cost of communication in (2) is less than that in (1). In compensation for these advantages, the matrix M in (2) is non-symmetric. As a result, linear solvers for non-symmetry should be used.

B. Hierarchical domain decomposition

The hierarchical domain decomposition method is an iterative domain decomposition method for improving parallel efficiency. The system equation can be separated as,

$$\begin{bmatrix} K^{II} & K^{IF} & K^{IB} \\ K^{FI} & K^{FF} & K^{FB} \\ K^{BI} & K^{BF} & K^{BB} \end{bmatrix} \begin{Bmatrix} x^I \\ x^F \\ x^B \end{Bmatrix} = \begin{Bmatrix} b^I \\ b^F \\ b^B \end{Bmatrix}, \quad (3)$$

where subscript I denotes inner regions, F denotes interfaces of sub domains, B is the boundary of whole domain [4]. Equation (3) is rewrite the following equations,

$$K^{II} x^I = (b^I - K^{IF} x^F - K^{IB} x^B), \quad (4a)$$

$$\begin{aligned} (K^{FF} - K^{FI} K^{II-1} K^{IF}) x^F &= b^F - K^{FI} K^{II-1} b^I \\ &- (K^{FB} - K^{FI} K^{II-1} K^{IB}) x^B, \end{aligned} \quad (4b)$$

Equation (4a) can be solved easily, however, the interface problem (4b) is hard to solve because the system matrix of (4b) is given implicitly. Therefore it is difficult to construct the preconditioner for (5b). As a result, the computational cost of this method is higher than that of the overlapping domain decomposition method.

III. NUMERICAL RESULTS

To compare the performance of the above described methods for domain decomposition, we analyze a perpendicular magnetic recording head model shown in Fig. 1. The IC decomposition with shift parameter ($=1.12$) is used as preconditioner. The numerical results described below are performed on a PC cluster consisting of 4 PEs (Pentium4 3.4GHz, 2GB RAM for each PE, two gigabit Ethernet are used for communication among PEs). The program code is written in C++ with MPI (Message Passing Interface).

Figure 2 shows an acceleration ratio normalized by the computation time in PE=1. The notation "ICCG" in the Figure is the CG method with the conventional preconditioner defined by (1), "GPBiCR" is a Generalized Product-type Bi-Conjugate Residual method combined with the preconditioner defined by (2). This ratio of these methods linearly increases with the number of PEs. Moreover, GPBiCR method shows good efficiency compared with the ICCG method.

Table I shows a computational time in PEs = 4. The computational time of the hierarchical domain decomposition method is significantly slower than that of other methods, because it takes much iteration to solve (4b). For this reason,

the overlapping domain decomposition method is suited on small size parallel computation environment.

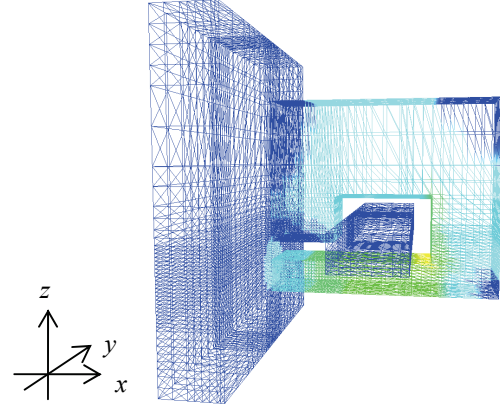


Fig. 1. Analysis model of perpendicular magnetic recording head, (Number of elements = 266112).

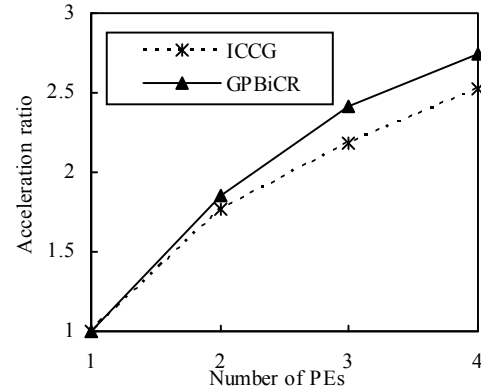


Fig. 2. Parallel efficiency on PC cluster.

TABLE I COMPUTATIONAL TIME IN PE=4

Method	ICCG	GPBiCR	Hierarchical
Elapsed time [s]	19	23	106

IV. REFERENCES

- [1] Y. Saad, "Iterative Methods for Sparse linear Systems Second Edition," SIAM, 2003.
- [2] A. Quarteroni and A. Vali, "Domain Decomposition Methods for Partial Differential Equations," Oxford, U.K.: Clarendon, 1999.
- [3] R. Shioya and G. Yagawa, "Iterative domain decomposition FEM with preconditioning technique for large scale problem," *Proc. ECM' Progress Experimental Comput. Mech. Eng. Mater. Behavior*, pp.255-260, 1999.
- [4] H. Kanayama and S. Sugimoto, "Effectiveness of A-phi method in a parallel computing with an iterative domain decomposition method," *IEEE Trans. Magn.* Vol. 42, No. 4, pp. 539-542, 2006.

Kernel Regularization for Volume Integral Equations

Michael V. Davidovich
Saratov State University
Astrakhanskaya street, 83, Saratov, 410012, Russia
DavidovichMV@info.sgu.ru

Abstract— The methods of reducing of kernel singularity order for volume integral equations have been considered and some new kind of volume integral and integrodifferential equations with surface terms have been proposed.

I. INTRODUCTION

The regularization in the theory of singular integral equation (IE) [1-2] usually means the detachment of singular part of kernel with the posterior full or partial inversion of integral (integrodifferential) operator [1-2]. At that the first kind Fredholm singular IE is transformed into the second kind one. This approach is widely used for one-dimensional IE with Cauchy and logarithmical singularities. The term “regularization” is also used for the solutions of incorrect problems. In the works [3-6] the term “regularization” has been applied as the main kernel singularity detachment and reducing for two-dimensional immittance (impedance or admittance) IE, i.e. it aims only to kernels. The introducing of auxiliary potentials, the application of vector integral theorems, the integration over the observation point, and some other methods have been applied to realize this [3-6]. The reducing of kernel singularity allows one to use the more simple piece-constant or piece-linear base functions which is not applicable for initial IE owing to divergence of matrix elements.

There are volume IEs and integrodifferential equation (IDEs) in applied electrodynamics which may be obtained by several ways [7-10] and have strong nonintegrable singularities. In this work the method of tensor Green’s functions (GFs) has been used to realize this purpose. After the regularization the vector piecewise constant and linear volume finite elements may be applicable to solve the volume IE.

II. THE REDUCTION IE TO IDE

Let consider a dielectric body with volume V confined by regular surface S in the free space which is excited by incident harmonic in time field $\vec{E}_{inc}(\vec{r})$. Let the field sources are located outside the body i.e. the field $\vec{E}_{inc}(\vec{r})$ inside and near the body is solenoidal. Let also the permittivity $\varepsilon(\vec{r})$ is the continuously differentiable function inside the V and may have the jump discontinuity on the S . In the case of jump the normal component of permittivity also has the jump, therefore let denote its values on the inner and outer part of surface S as “-” and “+” correspondingly. The scattered field is determined by GF as

$$\vec{E}(\vec{r}) = \vec{E}_{inc}(\vec{r}) + j\omega\varepsilon_0 \int_V \Gamma^{ee}(\vec{r} - \vec{r}') (\varepsilon(\vec{r}') - 1) \vec{E}(\vec{r}') d\vec{r}', \quad (1)$$

where the electrical tensor (dyadic) GF of electrical kind is introduced [10]:

$$\Gamma^{ee}(\vec{r} - \vec{r}') = \frac{\nabla \otimes \nabla + k_0^2 \hat{I}}{j\omega\varepsilon_0} G(\vec{r} - \vec{r}') = \frac{\nabla' \otimes \nabla' + k_0^2 \hat{I}}{j\omega\varepsilon_0} G(\vec{r} - \vec{r}'). \quad (2)$$

This GF is determined through the scalar GF of free space

$$G(\vec{r}) = (4\pi|\vec{r}|)^{-1} e^{-jk_0|\vec{r}|}. \quad (3)$$

Here the operation \otimes denotes the dyadic or tensor (direct) multiplying (thus $(\vec{a} \otimes \vec{b})_{kl} = a_k b_l$, $k, l = x, y, z$), \hat{I} is the unit tensor, $r \equiv |\vec{r}|$, $\vec{r}_0 = \vec{r}/r$ is the unit vector directed along the radius-vector, $d\vec{r} \equiv dV$ is the volume element, the operator ∇ acts on the observation point coordinates (without stroke), and ∇' - correspondingly on source ones. GF (2) may be presentable in the form

$$\Gamma^{ee}(\vec{r}) = \frac{-e^{-jk_0 r}}{4\pi j\omega\varepsilon_0 r} \left\{ \left(\frac{1}{r^2} + \frac{jk_0}{r} \right) (\hat{I} - 3\vec{r}_0 \otimes \vec{r}_0) + k_0^2 (\vec{r}_0 \otimes \vec{r}_0 - \hat{I}) \right\}, \quad (4)$$

and the volume IE (1) may be written as

$$\vec{E}(\vec{r}) = \vec{E}_{inc}(\vec{r}) + (\nabla \nabla \cdot + k_0^2) \int_V G(\vec{r} - \vec{r}') (\varepsilon(\vec{r}') - 1) \vec{E}(\vec{r}') d\vec{r}'. \quad (5)$$

Here the operator $\nabla \nabla \cdot \equiv grad \cdot div$ is introduced. It acts on arbitrary vector \vec{a} as dyadic multiplication: $\vec{b} = (\nabla \otimes \nabla) \vec{a} = \nabla \nabla \cdot \vec{a} = \nabla \nabla \cdot \vec{a} = grad(div \vec{a}) = (grad \cdot div) \vec{a}$. The relation (1) is the consequence of equivalence the polarization currents to influence of body [7-9]. The strong singularity arises owing to double differentiation of weak singularity $|\vec{r} - \vec{r}'|^{-1}$. Our goal is to transfer the differentiation from not stroked coordinates to stroked ones, i.e. on integrand function. Therefore we want to transform the IE into IDE. Such transformation may lead to surface integrals. We will use the following identities:

$$\nabla G(\vec{r} - \vec{r}') = -\frac{(\vec{r} - \vec{r}') e^{-jk_0|\vec{r} - \vec{r}'|}}{4\pi|\vec{r} - \vec{r}'|^2} \left\{ \frac{1}{|\vec{r} - \vec{r}'|^2} - \frac{jk_0}{|\vec{r} - \vec{r}'|} \right\} = -\nabla' G(\vec{r} - \vec{r}'), \quad (6)$$

$$\nabla \cdot (G(\vec{r} - \vec{r}') \vec{a}(\vec{r}')) = -\nabla' \cdot (G(\vec{r} - \vec{r}') \vec{a}(\vec{r}')) + G(\vec{r} - \vec{r}') \nabla' \cdot \vec{a}(\vec{r}'). \quad (7)$$

Therefore

$$\vec{F}(\vec{r}) = \vec{F}_V(\vec{r}) + \vec{F}_S(\vec{r}) = \vec{E}(\vec{r}) - \vec{E}_{inc}(\vec{r}) - k_0^2 \int_V G(\vec{r} - \vec{r}') (\varepsilon(\vec{r}') - 1) \vec{E}(\vec{r}') d\vec{r}' = \quad (9)$$

$$= \nabla \int_V \left[G(\vec{r} - \vec{r}') \nabla' \cdot \left[(\varepsilon(\vec{r}') - 1) \vec{E}(\vec{r}') \right] - \nabla' \cdot \left[G(\vec{r} - \vec{r}') (\varepsilon(\vec{r}') - 1) \vec{E}(\vec{r}') \right] \right] d\vec{r}',$$

$$\vec{F}_V(\vec{r}) = -\int_V \nabla' \cdot \left[(\varepsilon(\vec{r}') - 1) \vec{E}(\vec{r}') \right] \nabla G(\vec{r} - \vec{r}') d\vec{r}'. \quad (9)$$

$$\begin{aligned} \vec{F}_S(\vec{r}) &= -\nabla \oint_S G(\vec{r} - \vec{r}') (\varepsilon^-(\vec{r}') - 1) \vec{r}' \cdot \vec{E}^-(\vec{r}') dS' = \\ &= \oint_S (\varepsilon^-(\vec{r}') - 1) \vec{r}' \cdot \vec{E}^-(\vec{r}') \nabla G(\vec{r} - \vec{r}') dS'. \end{aligned} \quad (10)$$

Here we list the several kind of IDE with integrable kernels. For sharp body boundary

$$\begin{aligned} \vec{F}(\vec{r}) = & - \int_V \frac{(\vec{E}(\vec{r}') \nabla' \cdot \varepsilon(\vec{r}')) \nabla' G(\vec{r} - \vec{r}')}{\varepsilon(\vec{r}')} d\vec{r}' + \\ & + \oint_S (\varepsilon^-(\vec{r}') - 1) (\vec{\nu}(\vec{r}') \vec{E}^-(\vec{r}')) \nabla' G(\vec{r} - \vec{r}') dS'. \end{aligned} \quad (11)$$

After the transferring the second derivative to source point

$$\begin{aligned} -\vec{F}_V(\vec{r}) = & \int_V \left\{ G(\vec{r} - \vec{r}') \nabla' \cdot [(\varepsilon(\vec{r}') - 1) \vec{E}(\vec{r}')] \right\} - G(\vec{r} - \vec{r}') \nabla' \cdot [(\varepsilon(\vec{r}') - 1) \vec{E}(\vec{r}')] d\vec{r}'. \end{aligned} \quad (12)$$

Using the theorem about gradient it may be transformed to

$$\begin{aligned} \vec{F}_V(\vec{r}) = & \int_V G(\vec{r} - \vec{r}') \nabla' \nabla' \cdot [(\varepsilon(\vec{r}') - 1) \vec{E}(\vec{r}')] d\vec{r}' - \oint_S G(\vec{r} - \vec{r}') \vec{\nu}(\vec{r}') \nabla' \cdot [(\varepsilon(\vec{r}') - 1) \vec{E}(\vec{r}')] dS'. \end{aligned} \quad (13)$$

Let the observation point is inside the S . Surrounding it by infinitely small sphere of radius ρ and using the relation (13) for S and sphere one can get in spherical coordinates coincided with center of sphere

$$\vec{I} = - \oint_{S_\rho} |\vec{r}|^{-1} \vec{\nu}(\vec{r}) f(\vec{r}) dS = - \rho \int_0^\pi \sin \theta d\theta \int_0^{2\pi} f(\rho, \theta, \varphi) \vec{r}_0 d\varphi$$

where $f(\vec{r}) = \text{div} [(\varepsilon(\vec{r}) - 1) \vec{E}(\vec{r}) e^{-jk_0|\vec{r}|}]$. To calculate the projection on the axis z it is necessary to change \vec{r}_0 on $\vec{r}_0 \vec{z}_0 = \cos \varphi$. Since $f(\rho, \theta, \varphi)$ is continuous and finite at $\rho \rightarrow 0$, then the angle integral is finite and the projection tends to zero. We consider that divergence is continuous up to inner side of S , so in the presence of permittivity jump the surface integral must be calculated on the inner side (it is zero on the outer side). Thus,

$$\begin{aligned} \vec{F}(\vec{r}) = & \int_V G(\vec{r} - \vec{r}') \nabla' \nabla' \cdot [(\varepsilon(\vec{r}') - 1) \vec{E}(\vec{r}')] d\vec{r}' + \\ & + \oint_S [(\varepsilon^-(\vec{r}') - 1) (\vec{\nu}(\vec{r}') \vec{E}^-(\vec{r}')) \nabla' G(\vec{r} - \vec{r}') - \vec{\nu}(\vec{r}') G(\vec{r} - \vec{r}') \nabla' \cdot [(\varepsilon(\vec{r}') - 1) \vec{E}(\vec{r}')]] dS'. \end{aligned} \quad (14)$$

Using the foregoing smoothing and calculating the integral over the slab with usage of formula for gradient from the inner product in the value

$$\vec{s}(\vec{r}) = \nabla \nabla \cdot [(\varepsilon(\vec{r}) - 1) \vec{E}(\vec{r})] = -\nabla \nabla \cdot \vec{E}(\vec{r}) = \nabla \frac{\vec{E}(\vec{r}) \nabla \cdot \varepsilon(\vec{r})}{\varepsilon(\vec{r})}$$

one can exactly get the surface integral in (14). Let's consider one more variant of initial equation transformation. Let there are the arbitrary differentiable vector functions $\vec{a}(\vec{r}')$ and $\vec{b}(\vec{r} - \vec{r}')$. Then $\nabla(\vec{a} \cdot \vec{b}) = \nabla'(\vec{a} \cdot \vec{b}) + (\vec{b} \nabla') \vec{a} + \vec{b} \times (\nabla' \times \vec{a})$. Let

$$\vec{F}(\vec{r}) = -\nabla \int_V (\varepsilon(\vec{r}) - 1) \vec{E}(\vec{r}') \nabla' G(\vec{r} - \vec{r}') d\vec{r}'$$

Applying the above relation and using the theorem about gradient, one can get

$$\begin{aligned} \vec{F}(\vec{r}) = & \oint_S \vec{\nu}(\vec{r}') [(\varepsilon(\vec{r}') - 1) \vec{E}(\vec{r}') \nabla' G(\vec{r} - \vec{r}')] dS' - \\ & - \int_V \left\{ \nabla' G(\vec{r} - \vec{r}') \cdot \nabla' [(\varepsilon(\vec{r}') - 1) \vec{E}(\vec{r}')] + \nabla' G(\vec{r} - \vec{r}') \times \nabla' \times [(\varepsilon(\vec{r}') - 1) \vec{E}(\vec{r}')] \right\} d\vec{r}'. \end{aligned} \quad (15)$$

III. THE DIRECT INTEGRATION METHOD

According to Helmholtz's theorem the arbitrary vector may be presented by its solenoidal and potential parts. Let's divide the electrical field into solenoidal and potential parts:

$$\vec{E} = \vec{E}_s + \vec{E}_p, \text{ or}$$

$$\vec{E}(\vec{r}) = \nabla \times \vec{C} - \nabla \Phi. \quad (16)$$

Our goal is to reformulate the equation (9) for \vec{C} and Φ . As \vec{E} is the polar vector that Φ is the scalar, and \vec{C} is the pseudovector (axial vector). The choice of this values is not single-valued as \vec{C} may be added by gradient of arbitrary pseudoscalar ψ , and the potential Φ may be defined accurate within arbitrary constant c_0 . In order to exclude the ambiguity in \vec{C} , let subjugate it by the conditions $\text{div} \vec{C} = 0$, i.e. consider it solenoidal. Thus, the introduced values satisfy relations

$$\nabla \cdot \vec{E}(\vec{r}) = -\nabla^2 \Phi, \quad (17)$$

$$\nabla \times \vec{E}(\vec{r}) = \nabla \times \nabla \times \vec{C} = (\text{grad} \cdot \text{div} - \nabla^2) \vec{C} = -\nabla^2 \vec{C}, \quad (18)$$

$$\vec{E}_{inc}(\vec{r}) = \nabla \times \vec{C}_0(\vec{r}). \quad (19)$$

The equations (17)-(19) have been integrated and, as the result, the new coupled IEs have been obtained for Φ and \vec{C} . The coupling is realizing by virtue of that the field normal component on S is defined by both parts of vector \vec{E} . The function Φ at $k_0 \rightarrow 0$ defines the own potential for charge density under the body polarization by incident field which must tend to zero at infinity. The Poisson equation arises as the result of transformations

IV. NUMERICAL RESULTS AND CONCLUSIONS

The proposed IEs and IDEs have been numerically investigated and used for numerous diffraction and eigenvalue problems. They demonstrate very high effectiveness.

V. REFERENCES

- [1] F.D. Gakhov *The boundary problems*. Moscow: Fizmatgiz, 1963. 640 p.
- [2] V.P. Shestopalov. *Method of Riemann-Hilbert problem in theory of diffraction and electromagnetic wave propagation*. Kharkov: Kharkov Univ. Ed., 1971.
- [3] M.V. Davidovich. "New kind of electrodynamic integral equation based on the kernel regularization", *Transmission lines, functional devices, microwave technological installation units*. Saratov: Saratov Tech. Univ. Ed., 1997. P. 18-28.
- [4] M.V. Davidovich. "Operator-function method for regularization of immittance integral equations of electrodynamics", *Radiophysics and Quantum Electronics*. 42(2): 95-103, 1999.
- [5] M.V. Davidovich. "New kinds of immittance integral equations with integrable kernels", *1998 IEEE Antennas and Propagation International Symposium Digest*. Atlanta, GA. pp. 436-439, 1998.
- [6] M.V. Davidovich. "New technique for kernel regularization of surface integral equations in electromagnetics", *Mathematical Methods in Electromagnetic Theory*, *Proceedings of the 1998 International Conference*. Kharkov, vol. 2, pp. 757-759. 1998.
- [7] N.A. Khizhnyak. "Green's functions of Maxwell equations for inhomogeneous media", *Journal of Technical Physics*, 28(7):1592-1609, 1958.
- [8] M.V. Davidovich. "Photonic crystals: Green's functions, integrodifferential equations, and simulation results", *Radiophysics and Quantum Electronics*, 49(2): 134-146, 2006.
- [9] M.V. Davidovich. "Volume integral equations for dielectric inclusions in coaxial line", *Proceedings of Institutes of Higher Education of Russia. Radio electronics*. S. Petersburg: LETI, 1(1): 20-28, 1998.
- [10] M.V. Davidovich, V.P. Meschanov, N.F. Popova. "Electrodynamic model of coaxial load", *Journal of Communication Technology and Electronics*, 43(12): 1447-1453, 1998.

Error Estimators based on Kriging Interpolation

Vanessa Gomes Cruz, Luiz Lebensztajn

Laboratório de Eletromagnetismo Aplicado da Escola Politécnica da Universidade de São Paulo

Av. Professor Luciano Gualberto, Trav. 3, nº 158 05508-900 São Paulo, SP, Brazil

vanessa.cruz@poli.usp.br, leb@pea.usp.br

Abstract — The calculation of electromagnetic fields, based on the finite element method, involves a judicious division of the domain under study. This division strongly affects the accuracy of numerical results. This work proposes three different error estimators, all based on Kriging interpolation. These estimators have a high ability to identify regions where the solution has high error in the numerical solution. Thus, it is possible to obtain, through a structure based on the computational paradigm of adaptive meshes, a strong improvement in the quality of the mesh and therefore increase the precision of the response of the problem under analysis.

I. INTRODUCTION

The solution of partial differential equations by the Finite Element Method (FEM) has become extremely popular and this can be observed on different branches of engineering. Most of this popularity is associated to the increase computer processing capacity, but the techniques which provide the automatic generation of finite elements also. The objective of this work is to examine a particular form of automatic generation: the adaptive approach. It is an iterative process, which is divided in the following steps [1]:

Step1) Build a finite element mesh

Step2) Solve the FEM problem.

Step3) Error evaluation of the FEM solution.

Step4) Treatment of errors.

Step5) Stopping criterion. If it is satisfied, the process ends.

Step6) A finite element mesh is refined, where high errors were detected to build a new finite element mesh. Go to Step 2

The fundamental problem is to define a robust estimator of errors, a reliable strategy for deal with the errors, an appropriate refinement technique and a good stop criterion. There are several attributes associated to an adaptive finite element mesh process. The definition of a robust error estimator is, probably, the most critical. Error estimation has a strong relationship with the physical phenomenon under study, i.e., there are some guidelines to obtain high precision in the MEF context, and this can be explained in several ways:

1- places where the variation of field is high, are more sensitive to error

2- places where the variation of the stored energy is more intense should be associated with a fine mesh and vice-versa. This is strongly correlated with the previous one.

3- the solution accuracy depends on the size of the element and its shape. Elements with small angles will be avoided [2].

II. THE ADOPTED ERROR ESTIMATORS

In this work, error estimators will be computed based on Kriging interpolation [3], a statistical tool, which has become

very popular in the electromagnetic field community, particularly on works, which deals with optimization.

The error estimators were developed from three different concepts: the error associated to the flux of the magnetic induction vector, the gradient of the magnetic energy with respect to the position and the difference between the two ways of calculating the field. In all three cases, Kriging functions were adopted to perform the error on the FEM solution. With the Kriging interpolation of the magnetic potential vector, it is easy to find the values of the magnetic induction vector.

A. The error associated to the flux of the magnetic induction vector

This adopted error estimator is highly connected to the physical phenomenon. If the solution found by the FEM has high reliability, then a Kriging approximation performed on this solution must also to be a good candidate to solve the differential equation, which governs the phenomenon. Thus, applying the equations of Maxwell on the Kriging approximation is a criterion to measure the FEM solution accuracy. One way to measure this accurately is to observe, for example, the value of the flux of the vector magnetic induction in a closed line, as proposed in [4]. By the nature of the adopted formulation (magnetic vector potential and first order finite element), the FEM will always furnish a null flux for the magnetic induction vector in a closed surface. Nevertheless, the Kriging approximation tends detect any small error on the potential, i.e., when calculating the flux of the magnetic induction vector in a closed area a non-zero value is obtained. This value could be associated with the error in the FEM solution. The choice of the closed surface is quite natural: the triangular element. So the error in each element could be written as:

$$e = \int_{\Delta} \vec{B} \cdot d\vec{s} \quad (1)$$

Where \vec{B} is the induction calculated based on Kriging interpolation of the magnetic vector potential.

B. The error estimator based on the gradient of energy

This error estimator can be obtained by analyzing the regions where changes in stored energy on the field more intense. In these regions, it is desirable that the size of the finite element is small. Thus, the norm of the gradient of the stored magnetic energy could detect regions, where the refinement of the mesh of finite elements should be high. This estimator is consistent with that proposed in [5] to calculate the sensitivity of energy in relation to the nodal position. Here, the proposed estimator has a change in the conceptual point of view with respect to [5]: the Kriging interpolation provides a

direct estimate of the value gradient of magnetic energy stored in any position without any need for approaches to calculate the derivative of magnetic induction as presented in [3], [10].

$$e = \|\nabla W_{mag}\|. \quad (2)$$

C. The error estimator based on the difference between fields

Another way to estimate the error is based on the difference between the field calculated by FEM and calculated by the Kriging approximation. It could be calculated through the following expression, valid for each element:

$$e = \int_{\Omega^e} \langle \vec{B}_{calc} - \vec{B}_{est}, \vec{B}_{calc} - \vec{B}_{est} \rangle d\Omega, \quad (3)$$

where \vec{B}_{calc} is the magnetic induction vector, calculated by FEM and \vec{B}_{est} is the magnetic induction vector, calculated by the calculation of spatial derivatives of the Kriging estimation on the values of field element and $\langle x, y \rangle$ is the scalar product between the vectors x, y.

III. RESULTS

The L-shaped region is an interesting problem for finite element mesh generation. It is a magnetostatic problem and the magnetic vector potential was used. The boundary conditions are shown in Fig.1.

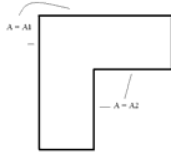


Fig 1 The L-Shaped region

The adaptive mesh will always begin with a coarse mesh, just enough to describe the basic geometry of the problem. With the error estimator based on the flux of the magnetic induction vector, it was necessary 7 iterations to achieve a high correlation between the values of field calculated by FEM and Kriging. Fig. 2 shows the distribution of elements at the end of the process and the evolution of the stored magnetic energy with respect to the iterations.

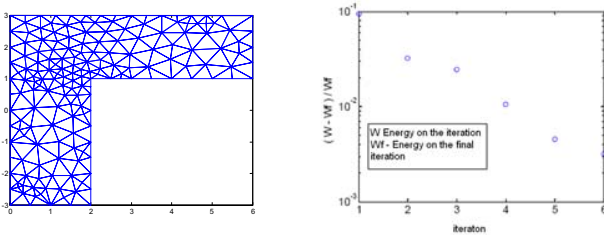


Fig 2 Final Mesh and energy convergence: first estimator

The same problem was analyzed with an estimator that uses the concept of gradient of magnetic energy on the position. The mesh generation starts with the same initial mesh of the previous item. Fig. 3 shows the final mesh (after 5 iterations) and the evolution of the stored magnetic energy with respect to the iterations.

The error estimator, based on the difference the fields, was also used to improve the mesh of the L-shape problem. Kriging interpolation of the magnetic vector potential was

used to compute an approximation of the magnetic induction for each triangle. For this estimator, the behavior of stored magnetic energy is shown in Fig. 4, which is very similar to Fig.2 and Fig.3

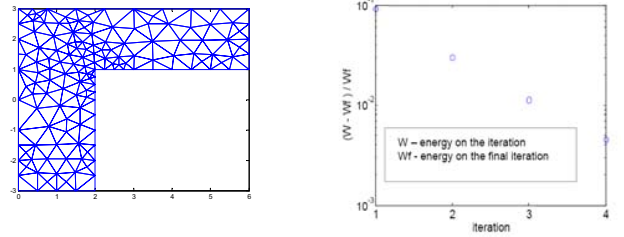


Fig3 Final Mesh and the energy convergence: second estimator

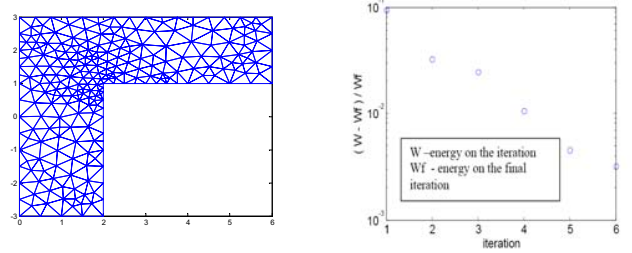


Fig. 4 Final Mesh and the energy convergence: third estimator

The benchmark proposed in [6] to force evaluation is a problem of simple geometry, as shown in Fig. 5. The current on the coil is equal to 1 A, so there is a small force on the iron part. This problem is highly dependent on the mesh due to the different permeability values and the corners. Table I shows the obtained values, for five approaches. Three of the results use the proposed adaptive scheme based on a Kriging interpolation.

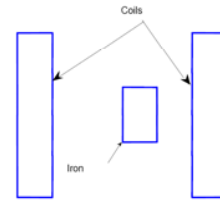


Fig 5 The problem geometry for force evaluation

TABLE I FORCE VALUE FOR SEVERAL METHODOLOGIES

	Reference		Fstimator		
	[6]	[7]	Flux	Gradient	Difference
Force (N) x10 ⁻⁷	2,5567	2,551	2,562	2,543	2,559

IV. REFERENCES

[1] P. Fernandes, P. Girdinio, P. Molfino, M. Repetto, Local error estimates for adaptive mesh refinement. *IEEE Transactions on Magnetics*, 24(1): 299-302, 1988

[2] J. R. Shewchuk, Delaunay Refinement Algorithms for Triangular Mesh Generation, *Computational Geometry: Theory and Applications* v. 22, p.21-74, 2002.

[3] L. Lebensztajn, C.A.R. Marretto, M.C. Costa, J.L. Coulomb, Kriging: a useful tool for electromagnetic device optimization - *IEEE Transactions on Magnetics*, V 40(2) 2004.

[4] M.G. Vanti; A. Raizer, J.P.A. Bastos, A magnetostatic 2D comparison of local error estimators in FEM *IEEE Transactions on Magnetics*, v.29(2): 902-1905, 1993

[5] G. Henneberger, G. Meunier, J.C. Sabonnadiere, P.K. Sattler, D. Shen, Sensitivity analysis of the nodal position in the adaptive refinement of finite element meshes *IEEE Transactions on Magnetics*, v.26(2) 787-790, 1990.

[6] J.Simkin, Recent Developments in Field and Force Computation, *Journal de Physique, Colloque Cl*, v. 45 851- 860. 1984.

[7] D. A. Lowther, R.Rong, B. Forghani, Field smoothing and adaptive mesh generation *IEEE Transactions on Magnetics*,v.29(2), 1890 - 1893, 1993

Investigations on the Accuracy of Maxwell Stress Tensor based Force Calculations

G. Remy¹, G. Krebs¹, and F. Henrotte²

¹ Laboratoire de Génie Electrique de Paris (LGEPE) / SPEE-Labs, CNRS UMR 8507, Supelec, Universités Paris VI et Paris XI. Plateau de Moulon 91192 Gif sur Yvette cedex.

Ghislain.Remy@LGEPE.supelec.fr; Guillaume.Krebs@LGEPE.supelec.fr

² Institute of Electrical Machines - RWTH Aachen University
Schinkelstrasse 4, D-52056 Aachen, Germany
Francois.Henrotte@IEM.RWTH-Aachen.de

Abstract— In micro-positioning devices with ironcore permanent magnet linear synchronous motors (PMLSM), the detent force needs compensation and, therefore, needs to be identified accurately. Different approaches have been proposed to account for the detent force in such devices using 2D finite element methods. In this paper, an analysis of the impact of the thickness of an eggshell layer used in the force calculations is presented. Precisely, the Maxwell Stress Tensor (MST), the Virtual Work Method (VWM) and the Weighed Stress Tensor (WST), also called Eggshell Method, are compared using several mesh sizes, and a special attention is given to the eggshell layer around the PMLSM mover. The accuracies of these force calculation technique are compared and analyzed with regard to the meshes.

I. INTRODUCTION

Permanent Magnet Linear Synchronous Motors (PMLSM) are widely used in many applications, such as micro-positioning devices [1]. In position controlled drive systems, they offer very reliable performances in terms of accuracy and speed. However, at low speeds, they suffer from the existence of detent forces (due to the interactions between the magnets and the mover part), which causes positioning errors at the end of the strokes. Even with optimized actuator designs, a residual force remains. To balance it, the detent force has to be taken into account in the control strategy. Unfortunately, this force is difficult to obtain experimentally and Finite Element simulations are required. In a previous paper [2], a 2D finite element software has been used to calculate the detent force in the magnetostatic case. An approach has been proposed to reduce the discretization errors in the force calculation by using an eggshell layer surrounding the mover.

The purpose of this paper is to present an analysis of the impact of the eggshell layer thickness on the force calculations. First, the studied PMLSM is presented and its main features are given. Then, different force calculation methods are explained. Thirdly, the benefit of the eggshell layer is justified. Finally, numerical results obtained with the force calculation methods are given and compared.

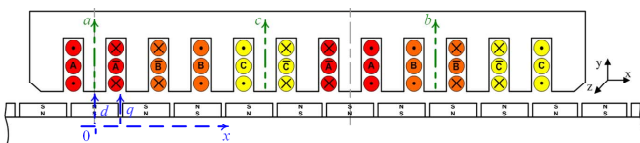


Fig. 1. 2D cutting view of the studied PMLSM [3]

II. DESCRIPTION OF THE STUDIED PMLSM

The studied system is a LMD10-050 linear motor from the ETEL Company, used in many high-precision, high-speed positioning applications, such as Pick-and-Place systems in the semiconductor industry. Figure 1 gives a 2D cutting view of the structure and Table 1 summarizes its main features.

This actuator consists of two parts: the primary part, above, is the mobile one. It is toothed and includes the three-phase concentrated windings. The secondary part, below, is fixed and composed of a set of alternating NdFeB magnets mounted on the surface of a massive ferromagnetic yoke.

TABLE I
Specifications of the LMD10-050 [4]

Parameters Name	Value	Parameters Name	Value
Rated Current	2 Arms	Maximal Current	7.9 Arms
Rated Force	130 N	Maximal Force	554 N
Peak Detent Force	5 N	Attraction Force	177 0N

III. FORCE CALCULATION METHODS

Resultant electromagnetic forces and torques acting on rigid bodies in electrical systems can be calculated using different methods [5]. The most widespread methods in FEM codes are the Maxwell Stress Tensor (MST) [6], the Virtual Work Method (VWM) [2], and the Weighted Stress Tensor [7].

A. The Maxwell Stress Tensor

In the case of the Maxwell Stress Tensor (MST) method, the following tensor is calculated:

$$T_{ij} = \mu_0 (H_i H_j - \frac{1}{2} \delta_{ij} H^2) \quad \text{with } i, j = x, y, z, \quad (1)$$

$H(H_x, H_y, H_z)$ the magnetic field given by its values in the Cartesian frame (x, y, z) , δ_{ij} the Kronecker symbol ($\delta_{ij} = 1$ if $i = j$ otherwise $\delta_{ij} = 0$).

The force is obtained by means of a surface integration over an arbitrary surface Γ in the air region enclosing the moving body:

$$F = \oint_{\Gamma} \mu_0 ((\mathbf{H} \cdot \mathbf{n}) \mathbf{H} - \frac{1}{2} |\mathbf{H}|^2 \mathbf{n}) ds \quad (2)$$

The vector \mathbf{n} is the normal vector to the Γ surface.

B. The Virtual Work Method

This approach is based on the transformation of magnetic energy into mechanical energy. It can be shown that the total force F_s in a direction s is obtained from the magnetic energy variation W of the system after a displacement in this direction. The motion is performed at constant flux [5], [8], [9]. A similar expression can be deduced from the variations of the co-energy W' at a constant current i , with the co-energy W' calculated using an integration over a volume v inside a domain D of the induction b and the magnetic field h .

$$F_s = \frac{\partial W'}{\partial s} \quad | \quad i = cst, \quad \text{with} \quad W' = \int_D \int_0^h b \, dh \, dv \quad (3)$$

C. The Weighted Stress Tensor in the software FEMM

The method implanted in the FEMM software [7] is inspired from the approaches developed in [6] and [10]. The WST method automatically selects a set of elements of the air region forming a thick boundary, or an eggshell, around the moving part. On that set of elements, weighting functions are obtained with an additional Laplace equation and a modified volume integral of the Maxwell Stress Tensor is performed. This method is generally more accurate than one using the Maxwell Stress Tensor [7].

IV. MESHING CONSIDERATIONS

A. Mesh design

The aim is to obtain accurate results on the force calculations. So, particular care is taken with the mesh size of each component. Figure 2 shows a zoom on the mesh designed for the actuator (LMD10-050).

To reduce the number of elements, it seems better to finely mesh only the zones with high gradients of the flux density. Zone 4 is the eggshell and is composed of a thin meshed layer, which is particularly efficient for the force calculation [2]. Indeed, this eggshell allows a more accurate representation of the bending of the flux lines in the magnets' vicinity (Figure 3b). The other zones are defined with a larger mesh size than the air-gap, with an auto-adaptation of the mesh to connect with the finer meshed Zone 4 of the eggshell.

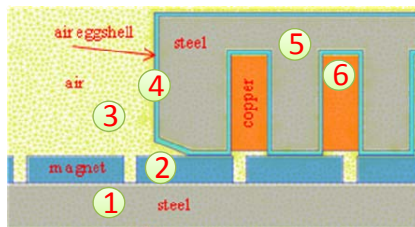


Fig. 2. Geometry with mesh size of 0.3 mm [2].

B. Calculation principle

To validate the mesh quality, force calculations are performed at no-load at a position where the detent force should be zero. As previously described, in the classical case, the mesh in the airgap is usually very fine and the windings are supposed to fill the slots entirely (Figure 3a).

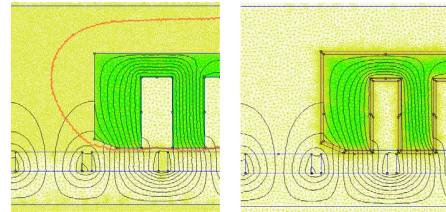


Fig. 3. Contour plot of the WST calculation for the PMLSM a) in the classical case b) with eggshell case.

TABLE II
FEM Results of the detent force calculation

Parameters Name	Classical	Eggshell
Nodes number	130158	132230
Elements number	259692	263994
x-axis Force Error	0.3909 N	0.0221 N
Zone 3 mesh size	0.3 mm	0.8 mm
Zone 4 mesh size	-	0.1mm

V. CONCLUSION

The presented FEM results confirm that the eggshell layer helps to improve the detent force calculation of a PMLSM at no-load using 2D FEM Software. Indeed, with approximately the same number of elements, the accuracy on the detent force calculation is greatly improved (Table 2).

The full paper will present more results on the force calculation using the MST, the VWM and the WST methods. A comparison of the accuracy of these methods regarding the mesh size of the eggshell layer around the PMLSM mover will be added.

VI. ACKNOWLEDGEMENT

This work has been supported by Ralph Coleman of ETEL's Motion Control Research Team.

VII. REFERENCES

- [1] N. Corsi, R. Coleman and D. Piaget, "Status and new development of linear drives and subsystems", LDIA2007, Proc. of the 6th Int. Symposium on Linear Drives for Industrial Applications, France, 2007.
- [2] G. Remy, G. Krebs, A. Tounzi and P.J. Barre, "Detent Force Calculations of a PMLSM using the Finite Element Method", *IEEE Trans. on Industry Applications*, Japan, Vol.129-D, No.5, 2009.
- [3] A. Cassat, N. Corsi, N. Wavre and R. Moser, "Direct Linear Drives: Market and Performance Status", *LDIA2003*, 4th Int. Symposium on Linear Drives for Industry Applications, 2003.
- [4] ETEL, LMD10-050 Datasheet, <http://www.etel.ch/documentation>, viewed on April 2009, 2007.
- [5] A. Bossavit, "Force-related Nuts and Bolts in the Discretization Toolkit for Electromagnetics", *COMPUMAG 2007*, 16th Int. Conference on the Computation of Electromagnetic Fields, pp.885-886, 2007.
- [6] F. Henrotte, G. Delière and K. Hameyer, "The eggshell method for the computation of electromagnetic forces on rigid bodies in 2D and 3D", *CEFC2002*, 10th IEEE Conf. on Electromagnetic Field Computation, 2002.
- [7] D. Mikker, FEMM user manual, <http://femm.foster-miller.net/Archives/doc/manual42.pdf>, viewed on April 2009, 2008.
- [8] W.N. Fu, P. Zhou, D. Lin, S. Stanton, and Z.J. Cendes, "Magnetic Force Computation in Permanent Magnets Using a Local Energy Coordinate Derivative Method", *IEEE Trans. on Magnetics*, 40(2), 2004.
- [9] I. Boldea and S. A. Nasar, *Linear Motion Electromagnetic Systems*, Wiley, New-York, 1985.
- [10] S. McFee, J.P. Webb and D.A. Lowther, "A tunable volume integration formulation for force calculation in finite-element based computational magnetostatics", *IEEE Trans. on Magnetics*, 24(1):439-442, January 1988.

Determination of Uniform Magnetizing Current Density With Stable ICCG Convergence Using Simple Technique and Regularization

Yoshifumi Okamoto^{1,2}, Koji Fujiwara³, Yoshiyuki Ishihara³, and Tetsuji Matsuo⁴

¹Research Center of Applied Electromagnetic Energy, Doshisha University, Kyoto 610-0321 Japan

²The Oita Prefectural Organization for Industry Creation, Oita 870-0037 Japan

³Department of Electrical Engineering, Doshisha University, Kyoto 610-0321 Japan

⁴Department of Electrical Engineering, Kyoto University, Kyoto 615-8510 Japan

E-mail: {re-okamo, koji.fujiwara, yishihar}@mail.doshisha.ac.jp, tmatsuo@kuee.kyoto-u.ac.jp

Abstract—There are some determination techniques of magnetizing current density such as the method using the current vector potential with tree co-tree decomposition, the electric scalar potential obtained from boundary value problem, and so on. However high current density is estimated in inner curve for the cause of solving homogeneous boundary value problem. In this paper, we present the effective method for the computation of magnetizing current density which is uniformly distributed and assured stable ICCG convergence by means of regularization.

I. INTRODUCTION

The data of magnetizing current density in finite element analysis has to be prepared in advance. The distribution of current density should be uniformly modeled to describe the stranded winding. However, inner curved current density is highly estimated when conventional technique such as the solution of homogeneous boundary problem is applied. Some effective methods [1] - [3] for realizing the uniform current density were developed.

In this paper, we propose a new uniform distribution technique for magnetizing current density. The uniform current density is temporary evaluated by using the conventional electric scalar potential method [4] at first. Next, regularization is applied to temporary current density in order to realize the stable ICCG convergence characteristic. The effectiveness of proposed method is investigated by using the inductance value in the IEEJ coil model.

II. DETERMINATION METHOD OF UNIFORM CURRENT DENSITY

A. Determination of current density direction

Firstly temporary vector of current density is determined by using conventional electric scalar potential method [4] in the step 1 as shown in Fig. 1. The weighted residual G_i of the equation of current density continuity using nodal shape function N_i is given as follows:

$$G_i = -\iiint_V \nabla N_i \cdot \mathbf{J}_0 dV + \iint_S N_i \mathbf{J}_0 \cdot \mathbf{n} dS = 0 \quad (1)$$

where \mathbf{J}_0 is the current density vector, and \mathbf{n} is the external unit normal vector. Here, \mathbf{J}_0 is composed of electric scalar potential ϕ as follows:

$$\mathbf{J}_0 = -\sigma \nabla \phi \quad (2)$$

where σ is conductivity, which is considered as homogeneity in the coil region. At the step 2, intensity of \mathbf{J}_0 is normalized as I/S in the center point of all elements as follows:

$$\mathbf{J}_{0_init} = (I/S) \mathbf{t} \quad (\because \mathbf{t} = \mathbf{J}_0 / |\mathbf{J}_0|) \quad (3)$$

where S is the cross-sectional area of current input surface, and the direction of \mathbf{J}_{0_init} is the same of \mathbf{J}_0 . Here the intensity of \mathbf{J}_{0_init} is completely uniform, however \mathbf{J}_{0_init} doesn't satisfy the weak form of equation of continuity.

B. Regularization

The characteristic of ICCG method in edge-based FEM will diverge when the equation of continuity ($\nabla \cdot \mathbf{J}_0 = 0$) is not weakly satisfied [5]. Therefore, the discontinuous vector \mathbf{J}_{0_init} should be corrected by using correction vector \mathbf{J}_{0c} to improve poor ICCG convergence of magnetic field analysis as follows:

$$\mathbf{J}_{0r} = \mathbf{J}_{0_init} + \mathbf{J}_{0c} \quad (\because \mathbf{J}_{0c} \equiv -\nabla \delta \phi) \quad (3)$$

where \mathbf{J}_{0r} is the corrected vector, and $\delta \phi$ is the correction potential. Substituting \mathbf{J}_{0r} for the equation of current density continuity, the weak form is obtained as follows:

$$G_i = \iiint_V \nabla N_i \cdot \nabla \delta \phi - \nabla N_i \cdot \mathbf{J}_{0_init} dV + \iint_S N_i (\mathbf{J}_{0_init} + \mathbf{J}_{0c}) \cdot \mathbf{n} dS = 0 \quad (4)$$

where the second term about the boundary integration is equal to the input current I when the equi-unknown boundary condition is imposed on the correction potential $\delta \phi$ on the input surface. (4) is solved about $\delta \phi$ at the step 3. Next $\delta \phi$ is substituted for (3) at the step 4, and then continuous \mathbf{J}_{0r} can be utilized in magnetic field analysis.

Fig. 2 shows the effectiveness of regularization for the flat motor coil in the case of substituting \mathbf{J}_0 obtained from the two-scalar potential method [1] for \mathbf{J}_{0_init} in (4). The ICCG

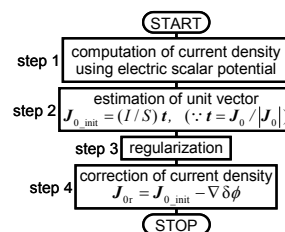


Fig. 1. Flow chart of uniform distributed current density.

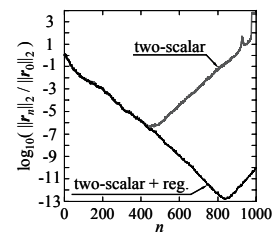


Fig. 2. ICCG convergence using two-scalar potentials.

convergence characteristic of magnetic field analysis is improved by the additional process of regularization.

III. VERIFICATION

A. Analyzed results

Fig. 3 shows the finite element mesh of IEEJ coil model. The number of elements, nodes, and unknowns of the first order hexahedral edge elements are 268,202, 278,832, and 791,101, respectively. The target value of uniform current density is 400×10^3 kA/m² in this model.

The correction vector is mostly distributed for imposing the \mathbf{J}_{0_init} continuity in the connection area of the straight and curved region as shown in Fig. 4. The maximum intensity of correction vector is 25.2 kA/m². The uniformity of current distribution is improved by using proposed method as shown

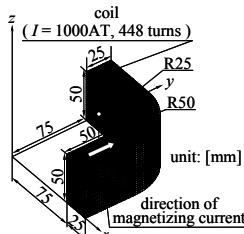


Fig. 3. Finite element mesh.

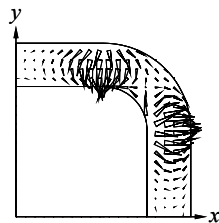
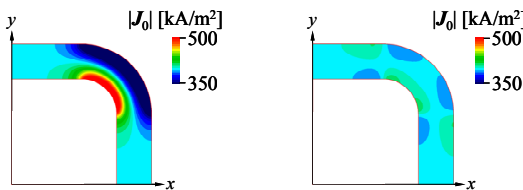


Fig. 4. Correction vector \mathbf{J}_{0c} .



(a) electric scalar potential method (b) proposed method
Fig. 5. Intensities of magnetizing current density.

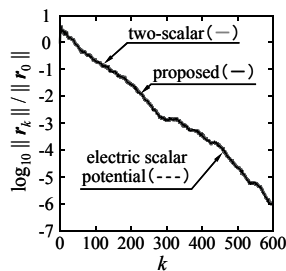


Fig. 6. ICCG convergence characteristics in magnetic field analysis.

TABEL I
COMPUTATION RESULTS OF IEEJ MODEL

method	electric scalar potential	two-scalar	proposed	Biot-Savart	measured
uniformity	1.89	1.00	1.07	—	—
L [mH]	33.77	34.10	34.10	34.18	34.65
inductance error [%]	2.54	1.59	1.59	1.36	—
ICCG ite.	594	595	594	—	—
CPU time [s]	255.8	253.1	259.1	—	—

CPU Intel Xeon X5482 processor / 3.2 GHz & 3.25 GB RAM

ICCG convergence criterion $\|\mathbf{r}_n\| / \|\mathbf{r}_0\| < \epsilon_{cg}$

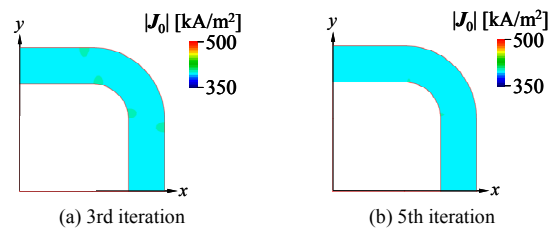
$\epsilon_{cg} = 10^{-15}$ (current density computation), 10^{-6} (magnetic field analysis)

in Fig. 5. The ICCG convergence characteristics in three methods are similar distributions as shown in Fig. 6.

TABLE I shows the computation results obtained from various techniques. The inductance value is close to measured one by using the two-scalar or proposed method. While two-scalar method is applicable to only the coil with rectangular surface of current inflow, proposed method is effective to arbitrary input surface. And the CPU time of proposed method is a little longer than that of the electric scalar potential method for the cause of double computation of same size equation.

B. Iterative process

Iterative process of proposed method is investigated in order to make the current distribution more uniform in IEEJ coil model. Iterative process is composed of the step 2 – step 4 and the process of substitution of \mathbf{J}_{0r} for \mathbf{J}_0 in Fig. 1. Fig. 7 shows the changes of current density intensity. Fig. 8 shows the changes of uniformity and inductance value in five iterations. Inductance value is gradually changed according to the improvement of uniformity. The sufficient solution is obtained at the first step, and then the single computation will be needed in the practical use.



(a) 3rd iteration (b) 5th iteration
Fig. 7. Changes of current density intensity in iterative process.

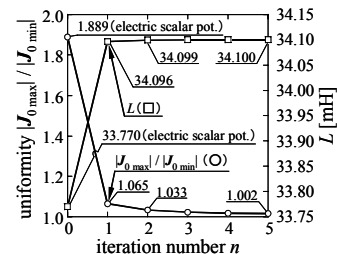


Fig. 8. Changes of inductance and uniformity using iterative process.

IV. REFERENCES

- [1] A. Kameari and K. Koganezawa, "Convergence of ICCG method in FEM using edge elements without gauge condition", *IEEE Trans. on Magn.*, vol. 33, no. 2, pp. 1223-1226 (1997).
- [2] Z. Badić and Z. J. Cendes, "Source field modeling by mesh incidence matrices", *IEEE Trans. on Magn.*, vol. 43, no. 4, pp. 1241-1244 (2007).
- [3] Y. Takahashi and S. Wakao, "Novel approach to current distribution analysis in winding by using current vector potential method", *proceedings of the COMPUMAG 2007*, vol. 4, PD 2-11, pp. 1103-1104 (2008).
- [4] K. Iwata and H. Hirano, "Magnetic field analysis by edge elements of magnetic components considering inhomogeneous", *IEEE Trans. on Magn.*, vol. 45, no. 3, pp. 1288-1291 (2009).
- [5] K. Fujiwara, T. Nakata, N. Takahashi, and H. Ohashi, "On the continuity of the magnetizing current density in 3-D magnetic field analysis with edge element", *IEEE Trans. on Magn.*, vol. 31, no. 3, pp. 1364-1367 (1995).

Parallel Direct Solver For the Finite Integration Technique in Electrokinetic Problems

A. Tinzefté¹, Y. Le Menach¹, J. Korecki¹, F. Guyomarch², F. Piriou¹

¹L2EP-LAMEL, ²LIFL-INRIA, Université de Lille

Cité scientifique 59655 Villeneuve d'Ascq, France

tinzefté@yahoo.fr

Abstract — The Finite Integration Technique (F.I.T) is used to compute the electromagnetic phenomena. This technique is efficient if the mesh is generated by a regular hexahedron. Moreover the matrix system, obtained from a regular mesh can be exploited to use the parallel direct solver. In fact, in reordering the unknowns by the nested dissection method, it is possible to construct directly the lower triangular matrix with many processors without assembling the matrix system. In this paper, the parallel direct solver is described and the efficiency is shown as a function to the number of processors.

I. INTRODUCTION

To compute the electromagnetic phenomena many methods can be used, such as the finite element method (F.E.M), the finite integration technique (F.I.T) [1]-[2]. These methods provide a large system which is usually solved by iterative methods (Krylov) associated to a preconditioner. If the system is very sparse, the Krylov method is very interesting because the utilization of memory is low and consequently the method is fast. Recently, the memory capacity has been increased and can accommodate a larger full system. Moreover, as the CPU clock frequency stagnates, the number of processors increases to keep a constant acceleration of computing power. Nowadays, large systems can be solved by parallel direct methods. In this paper, the F.I.T is used to compute the electromagnetic phenomena for which it's necessary to use a regular mesh. The system obtained has some priorities of regularity which will be used for the parallel computing. In order not to use a large memory, the reordering technique (Nested Dissection [3]) is implemented to minimize the fill-ins during the factorization elimination process. This technique keeps the regular structure of the matrix whose it is easy to extract efficient parallel computing without latency. Due to these conditions, we propose in this paper to compute an academic problem with the F.I.T using a parallel direct solver.

II. THE FINITE INTEGRATION TECHNIQUE

This method is based on the same theory as the F.E.M. But in case of F.I.T, there are no shape function cause a diagonal mass matrix. Also, to construct the model it is necessary to define a dual mesh. It appears that if the primal mesh is regular then the dual mesh should also be regular. Therefore, it is easy to build. In this paper, both potential (scalar end vector) formulations of the electrokinetic problem are treated. In the case of scalar potential formulations the matrix system obtained is :

$$G^T M_{je} G \varphi = -G^T M_{je} G \alpha \quad (1)$$

Where G is the incidence matrix node-edge, M_{je} the mass matrix, φ the electrical scalar potential and α the scalar potential source. With the help of a scalar potential source, a voltage between two electrodes can be imposed.

For the vector potential formulation the matrix system obtained is :

$$R^T M_{ef} R T = -R^T M_{ef} R T_s \quad (2)$$

Where, R is the incidence matrix edge-facet, M_{ef} the mass matrix, T the electrical vector potential and T_s the vector source. With this formulation a current density is imposed through the conductor.

For both formulations a gauge must be defined to solve the numerical system with a direct solver. For the φ -formulation just one unknown is fixed to zero. However a T -formulation is classically gauged with a tree technique. In these conditions both matrix systems (1) and (2) are symmetric positive definite (S.P.D). The matrix given by the φ -formulation (1) have at most 7 non-zero elements in each line and column. On the other side, the T -formulation gives a matrix with a possible 13 non-zero elements in each line and column.

In this paper, for solving both systems, it is proposed that the matrices should be assembled and factorized at the same time. For minimizing the fill-ins in the factorization, the reordering technique Nested Dissection of the nodes is done.

III. NESTED DISSECTION METHOD

The goal of the reordering techniques is to decrease the amount of fill-in and reduce the number of operations in the factorization and resolution of linear systems. The two most classically used reordering methods are the Minimum Degree [5] and the Nested Dissection [3]. The minimum degree algorithm is a local heuristic that performs its pivot selection by selecting from the graph a node of minimum degree. Nested Dissection is a method of finding an elimination ordering. The algorithm uses a divide and conquer strategy on the graph of the matrix. The basic idea of Nested Dissection is to bisect the graph by finding and removing a node separator and labeling the nodes of the two resulting sub-graphs by applying the same technique recursively. Labeling the nodes of the separator after the nodes of the sub-graphs have been labeled (i.e., the separator nodes receive a higher label than any of the nodes of the sub-graph). The recursion terminates when the sub-graphs become too small. The minimum degree algorithm is known to be a very fast and general purpose algorithm, however, the algorithm is intrinsically sequential. On the other hand, the nested dissection is easily parallelizable. In practice, nested dissection produces

orderings which, in terms of fill-in and operation count, give the same results as the ones obtained with minimum degree. Moreover, the elimination trees induced by nested dissection are broader, shorter, and better balanced, and therefore exhibit much more concurrency in the context of the parallel Cholesky factorization.

With a single node separator, a matrix system is split into the following form

$$\begin{bmatrix} A_{11} & 0 & A_{31}^T \\ 0 & A_{22} & A_{32}^T \\ A_{31} & A_{32} & A_{33} \end{bmatrix}$$

A_{33} is the matrix corresponding to the nodes in the node separator, A_{11} corresponds to the first sub-graph, and A_{22} corresponds to the second sub-graph. Since these two sub-graphs are not joined by any edges, A_{21} is zero. Otherwise, A_{11} and A_{22} can be assembled in parallel. With this new reordering, a block matrix system should be obtained, it is shown in figure1.

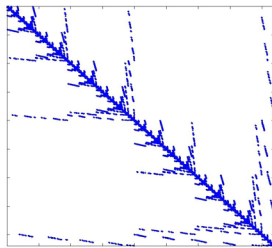


Figure 1. The Matrix to solve with reordering

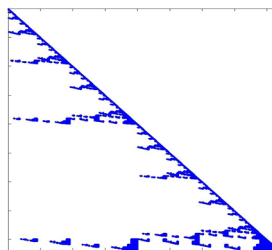


Figure 2. Lower Matrix with reordering

IV. PARALLEL DIRECT SOLVER

A typical direct solver for systems with SPD matrix is Cholesky factorization [4]. Here, the problem is to compute the solution of the linear equation system $Ax = b$, where A is a sparse and S.P.D matrix. The Cholesky factorization consists to decompose A as $A = LL^T$, where L is a lower triangular with positive diagonal elements. We propose here to generate directly the matrix L (figure 2) in parallel because its block structure allows it. Finally, the solution is computed by solving two triangular systems. $Ly = b$ is solved by forward elimination followed by solving $L^T x = y$ with backward substitution. These two substitutions are parallelized because some set of unknowns are independents.

V. APPLICATION

As example, a sample electrokinetic problem is treated. It is an electrical conductor cube. Inside this cube, a rectangular part is placed with smaller electrical conductivity. To increase the efficiency of the method, a regular mesh is used with 64000 hexahedrons. For the ϕ -formulation a voltage of 1V is imposed in the conductor and the system contains 65559 unknowns. In the case of the T -formulation, a current of 1A is imposed through the conductor. As the T is computed on the edge, the system is larger (188759 unknowns). For both formulations, the value of the resistance is computed. We obtained for ϕ -formulation 1.282 m Ω and 1.258 m Ω for the T -formulation. To illustrate the problem, the current density inside the conductor is shown on the figure 3.

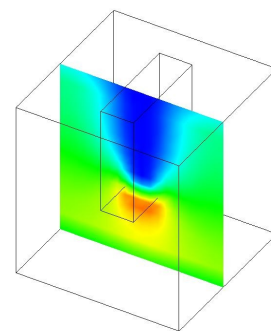


Figure 3 : Distribution current density inside the conductor

In the following table, the acceleration in accordance with the number of processors is shown for the assembling of the matrix L .

Number of processors	1	2	4	8
Speed-up ϕ - formulation	1	1.59	1.97	2.26
Speed-up T - formulation	1	1.69	2.86	4.06

VI. CONCLUSION

In this paper, it is shown that it's possible to generate directly and in parallel the lower triangular matrix L , which guarantees the acceleration of the resolution method. In the final paper, the method will be more developed and many examples will be treated and the results discussed.

VII. REFERENCES

- [1] T. Weiland, "A Discretization Method for the Solution of Maxwell's Equations for Six-Component Fields", *Electronics and Communication (AEÜ)*, Vol. 31(3), pp. 116-120, 1977
- [2] J. Korecki, Y. Le Menach, J.P. Ducreux, F. Piriou, "Numerical solutions in primal and dual mesh of magnetostatic problem solved with the Finite Integration Technique", *COMPEL*, Vol. 27, n° 1, pp. 47-55, 2008
- [3] A. George, "Nested dissection of a regular finite element mesh", *SIAM Journal on Numerical Analysis*, Vol. 10, pp. 345-363, 1973
- [4] J. H. Wilkinson, "The Algebraic Eigenvalue Problem", Oxford University Press, Oxford, UK, 1965.
- [5] P. Amestoy, T. Davis, I. Duff. "An approximate minimum degree ordering algorithm", *SIAM Journal of Matrix Analysis and applications* 17.pp. 886-905, 1996.

Computation of forces using mean and difference potentials

A. F. Licarião Nogueira

Universidade do Estado de Santa Catarina

Campus Universitário Prof. Avelino Marcante, Joinville, Santa Catarina, 89223-100, Brazil

antonioflavio@ieee.org

Abstract — The paper addresses an alternative method for the calculation of global forces. The mean and difference potentials technique is physically related to the virtual work principle, but relies on a reformulation of the computation sequence. The technique is the result of exploiting superposition in magnetically linear systems, and can be applied to any sequence of boundary-value problems which differ only in the placement of their excitations. The method has been successfully applied to solve interior problems with translational symmetry. The present work investigates its performance when used to solve an unbounded axisymmetric problem. Computed forces by the method under investigation are compared to results obtained by two reliable methods: weighted Maxwell stress tensor and Lorentz force.

I. INTRODUCTION

Calculation of forces and torques from numerical field solutions is subject to large numerical errors because their computations are usually based on magnetic flux densities, not to the scalar or vector potential values. The potential distribution produced by conventional finite element analysis represents only a numerical approximation to the true potential distribution, i.e. there is an inherent error in the values of potentials, commonly referred to as error in the approximation function. The evaluation of forces and torques invariably involves some kind of numerical differentiation, and all familiar sources of errors are present in numerical differentiation. Errors in the approximation function are the most critical, even when small, because they are magnified by differentiation algorithms.

In numerical problems involving both differentiation and integration, errors will be minimized if the order of the operations can be so rearranged that all integrations are done numerically, all differentiations analytically [1]. Since numerical integration is a robust process and analytic differentiation is error-free, the results can be expected to be numerically stable. The method of mean and difference potentials is physically related to the virtual work principle and relies on this reformulation of the computation sequence. The method is detailed in [2]-[3] and has been applied to solve interior problems with translational symmetry. The present work investigates the performance of the method when used to solve the unbounded axisymmetric problem proposed by Meeker [4]. The problem concerns the computation of the force acting on an iron ball at various positions relative to an excited wound, air-cored coil. An outline of the problem geometry is shown in Fig. 1. In this drawing, it is shown the configuration where the iron ball is located 1.5" from the center of the coil.

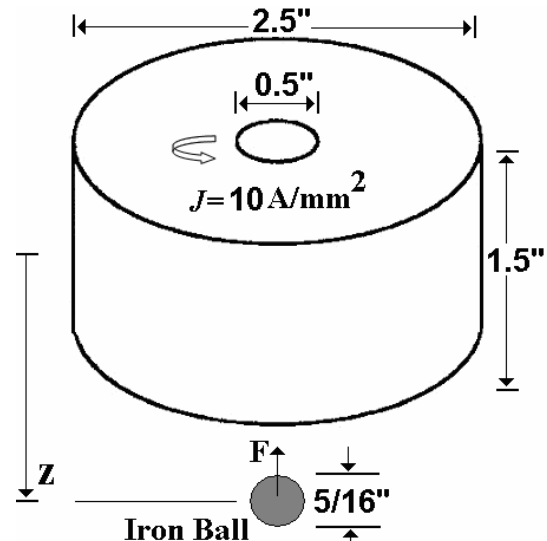


Fig. 1. An excited coil attracts the iron ball; dimensions in inches.

II. METHOD OF ANALYSIS

A sequence of magnetic vector potential solutions is used to simulate the movement of the coil relative to the iron ball. The reaction force acting on the coil is computed by three different methods: (i) mean and difference potentials; (ii) weighted Maxwell stress tensor; (iii) Lorentz force $\mathbf{J} \times \mathbf{B}$.

Were the virtual work approach to be used, there would be two boundary-value problems in A_1 and A_2 corresponding to positions 1 and 2 of the coil. Both problems differ only in the placement of the current distributions J_1 and J_2 , and are subject to the same boundary conditions. The subtraction of the system's total energy at the two coil positions gives the energy difference

$$\delta W = \frac{1}{2} \int_{\Omega} A_1 J_1 d\Omega - \frac{1}{2} \int_{\Omega} A_2 J_2 d\Omega, \quad (1)$$

where Ω denotes the problem region.

If the problem is magnetically linear, superposition can be exploited and, instead of working with the two boundary-value problems in A_1 and A_2 , two other boundary-value problems may be defined. The difference problem, expressed in terms of potentials A_d and current densities J_d , is obtained as half the difference of the two problems above, and is subject to homogeneous boundary conditions as a result of the subtraction. The mean problem, expressed in terms of potentials A_m and current densities J_m , is obtained as half the summation of the two problems, and is subject to the same

boundary conditions of the problems which represent the two consecutive positions. Rewriting the energy difference expressed in (1) in terms of the other two problems yields

$$\delta W = \int_{\Omega} A_d J_m d\Omega + \int_{\Omega} A_m J_d d\Omega. \quad (2)$$

III. TESTS AND RESULTS

To test the method set out above, a magnetic field analysis program [5] has been used to solve the field problems. An outline of the axisymmetric structure is shown in Fig. 2.

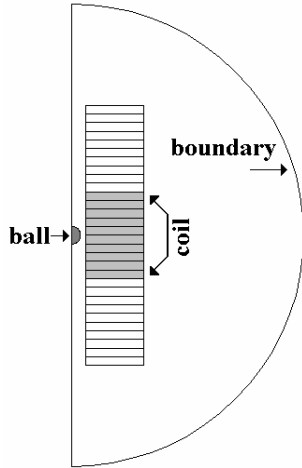


Fig. 2. Regions of the numerical model

To model the unbounded field problem, asymptotic boundary conditions have been used for the field solutions representing the mean problems, as well as for the solutions by the other two methods. For the difference problems the potentials are equal to zero at the semicircular boundary. The numerical model includes several rectangular regions that allow flexibility for simulating the coil movement. In this drawing, it is shown the field problem that represents the iron ball situated at the center of the wound coil; this position represents the stable equilibrium point for the iron ball and the system’s stored energy is maximum. According to the reference frame used, at this position, $z=0$. As the coil moves upwards from the centered position, the force on the iron ball increases up to its maximum value, and this occurs when ball starts to leave the coil region. Further increases in the distance imply a reduction in the force and this starts to vanish when the ball is approaching 1.5” from the centre of the coil.

The coil movement in steps of 0.15” (10% of the total excursion) is simulated by redefining material properties. Different current distributions are the basic feature distinguishing the eleven geometrically distinct problems solved by the other two methods. For these methods, there are force estimates at two consecutive coil positions, as illustrated in Fig. 3(a)-(b). In the mean and difference potentials technique, there are force estimates for the intermediate positions. Here, two distinct field problems are solved to obtain the energy difference δW given by (2), so there are altogether 20 program runs for the new technique. The current distributions of the problems representing half the difference and half the summation of two consecutive coil positions is

illustrated in Fig. 3(c)-(d). Since a single finite-element mesh is used for all computations, the pre-processing script is basically a series of commands to edit the material identification labels attached to the different regions.

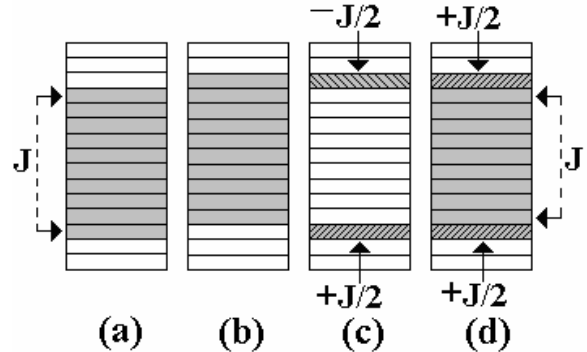


Fig. 3. Current distributions: (a)-(b) Excitations at two consecutive coil positions; (c) Half their difference; (d) Half their summation

Preliminary test results are presented in Fig. 4. Computed forces by mean and difference potentials are marked with “o” whilst results from the weighted tensor method are marked with “*”. These characteristics clearly reproduce the analysis results previously published in [4]. A closer observation of the graph shows that both characteristics trace similar courses, especially along the first half of the simulated path. Given the reliability of the weighted tensor method, the results from the new method are completely satisfactory.

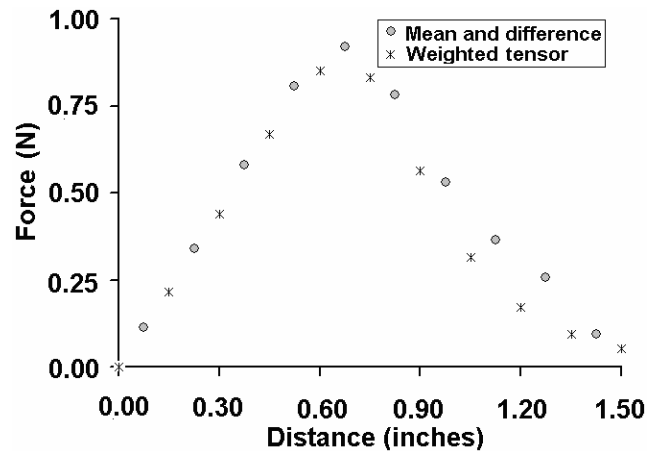


Fig. 4. Computed forces

IV. REFERENCES

- [1] P.P. Silvester, “Differentiation of finite element approximations to harmonic functions”, *IEEE Trans. on Magnetics*, 27(5): 3774-3779, 1991.
- [2] A.F. Licario-Nogueira, “Computation of cogging torques in permanent-magnet machines using the finite element method”, PhD dissertation, University of Wales, Cardiff, 1992.
- [3] E.S. Hamdi, A.F. Licario-Nogueira and P.P. Silvester, “Torque computation by mean and difference potentials”, *IEE Proceedings-A*, 140(2): 151-154, 1993.
- [4] D. Meeker, “Lua Scripting Example: Coil Gun”. Available: <http://femm.foster-miller.net/examples/coilgun/coilgun.htm>
- [5] D. Meeker, “Finite element method magnetics, user’s manual”, 2009. Available: <http://femm.foster-miller.net/wiki/HomePage>

Numerical algorithms for the image reconstruction in electrical impedance tomography

Tomasz Rymarczyk¹, Stefan F. Filipowicz^{1,2}, Jan Sikora^{1,3}

¹ Electrotechnical Institute, ul. Pozaryskiego 28, 04-703 Warsaw, Poland, e-mail: tomasz@rymarczyk.com

² Institute of Theory of Electrical Engineering, Measurement and Information Systems, Warsaw University of Technology, ul. Koszykowa 75, 00-662 Warsaw, Poland, e-mail: 2xf@nov.iem.pw.edu.pl

³ Lublin University of Technology, Department of Electronics, Nadbystrzycka 38d, 20-618 Lublin, Poland

Abstract— The problem of the image reconstruction in Electrical Impedance Tomography (EIT) is a highly ill-posed inverse problem. There are mainly two categories of image reconstruction algorithms, the direct algorithm and the iterative algorithm which was used in this publication. The forward problem can be solved by the finite element method, immersed interface method or boundary element method. The iterative algorithm is based a combination of the level set methods with one of numerical methods. The representation of the shape of the boundary and its evolution during an iterative reconstruction process is achieved by the level set method.

I. INTRODUCTION

In this paper was proposed a method based on the combination level set idea and a few numerical methods to solve the inverse problem arising from electrical impedance tomography. The representation of the boundary shape and its evolution during an iterative reconstruction process is achieved by the level set method [6]-[8]. The shape derivatives of this problem involve the normal derivative of the potential along the unknown boundary.

II. ELECTRICAL IMPEDANCE TOMOGRAPHY

Electrical impedance tomography is a widely investigated problem with many applications in physical and biological sciences [2]-[4]. It is well known that the inverse problem is nonlinear and highly ill-posed. The forward problem in EIT is solving by Laplace's equation:

$$\operatorname{div}(\gamma \operatorname{grad} \varphi) = 0 \quad (1)$$

where φ - electric potential, γ - conductivity.

The following functional is minimized:

$$F = 0.5 \sum_{j=1}^p (\Phi - \mathbf{V}_0)^T (\Phi - \mathbf{V}_0) \quad (2)$$

where p is the number of the projection angles.

III. NUMERICAL ALGORITHMS

A. Level set method

The level set method is known to be a powerful and versatile tool to model evolution of interfaces. The idea is

merely to define a smooth function ϕ , that represents the interface and has the following properties (fig.1):

$$\begin{aligned} \phi(x, t) &> 0 \text{ for } x \in \Omega \\ \phi(x, t) &< 0 \text{ for } x \notin \Omega \\ \phi(x, t) &= 0 \text{ for } x \in \partial\Omega = \Gamma(t) \end{aligned} \quad (3)$$

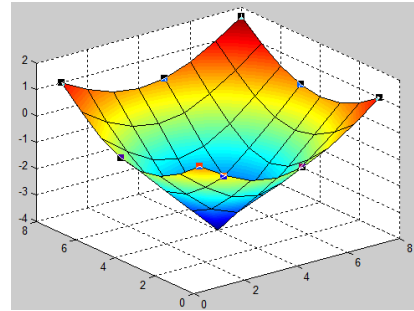


Fig. 1. Level set function.

B. Mumford-Shah model

The Mumford-Shah algorithm set formulation and minimization problem in image processing, to compute piecewise-smooth optimal approximations of a given image. The proposed model follows and fully generalizes work [1], where there was proposed an active contour model without edges based on a 2-phase segmentation and level sets γ_1 and γ_2 . Conductivity γ is represented as:

$$\gamma = \gamma_1 H(\phi) + \gamma_2 (1 - H(\phi)) \quad (4)$$

where H is the Heaviside function.

The derivative of F with respect to γ is given by

$$\frac{\partial F}{\partial \gamma} = - \sum_{j=1}^p \nabla \varphi_j \nabla \bar{\varphi}_j \quad (5)$$

Level set function is updated the following iterative scheme:

$$\phi^{k+1} = \phi^k - \mu \frac{\partial F}{\partial \phi} \quad (6)$$

where coefficient $\mu > 0$ and

$$\frac{\partial F}{\partial \phi} = \frac{\partial F}{\partial \gamma} \frac{\partial \gamma}{\partial \phi} = \frac{\partial F}{\partial \gamma} (\gamma_1 - \gamma_2) \delta(\phi) \quad (7)$$

where δ is the Dirac delta function.

Conductivities are calculated as:

$$\gamma_1^{k+1} = \gamma_1^k - \beta \frac{\partial F}{\partial \gamma_1} \quad (8)$$

$$\gamma_2^{k+1} = \gamma_2^k - \beta \frac{\partial F}{\partial \gamma_2} \quad (9)$$

where coefficient $\beta > 0$.

The delta function $\delta(\phi)$ and Heaviside function $H(\phi)$ are calculated as:

$$\delta_\varepsilon(\phi) = \frac{\varepsilon}{\pi(\phi^2 + \varepsilon^2)} \quad (10)$$

$$H_\varepsilon(\phi) = \frac{1}{\pi} \tan^{-1} \left(\frac{\phi}{\varepsilon} \right) + \frac{1}{2} \quad (11)$$

where $\varepsilon > 0$.

IV. IMAGE RECONSTRUCTION

Figures 2,3,4 presents model of computer simulation an image reconstruction. The numerical model was inserted in the inside of the examined object. The grid was used by 16x16 elements solution.

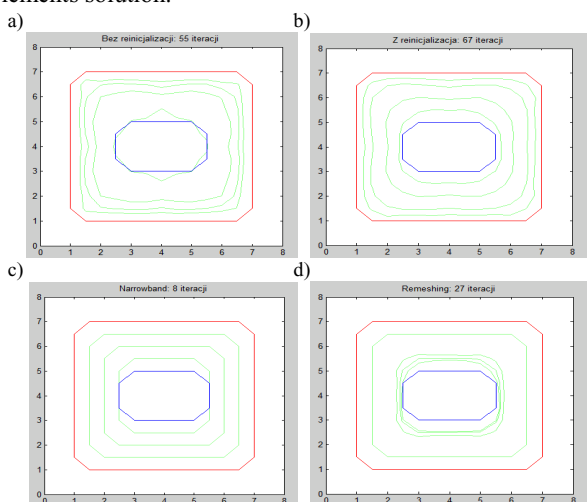


Fig. 2. The image reconstruction by level set method:
a) without reinitialization, b) with reinitialization,
c) with narrowband method, d) with remeshing level set function.

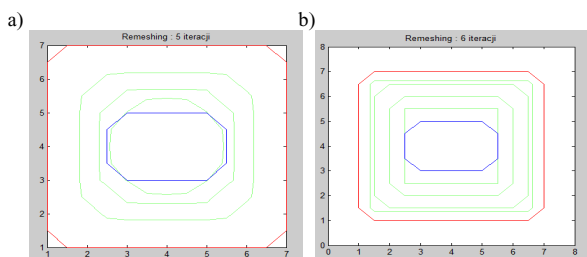


Fig. 3. Images reconstruction with the Mumford-Shah algorithm:
a) $\mu=0.0005$, $\text{eps}=0.001$ with reinitialization,
b) $\mu=0.001$, $\text{eps}=0$ without reinitialization.

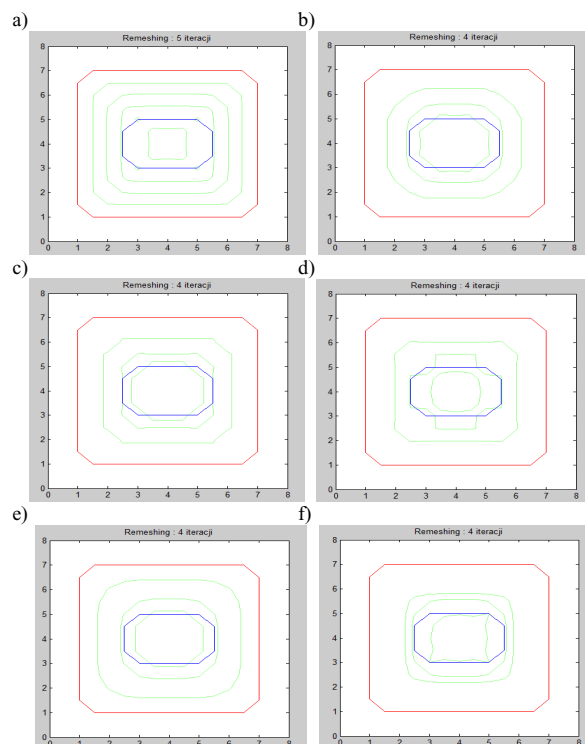


Fig. 4. Images reconstruction with the Mumford-Shah algorithm ($\mu=0.0005$, $\text{eps}=0.0001$ with reinitialization), coefficients for step of time dt:
a) 0.5, b) 0.75, c) 0.9, d) 1.2, e) 1.2, f) 2.

V. CONCLUSION

Application was presented in this paper of the level set function for identifying the unknown shape of an interface in a problem motivated by electrical impedance tomography. Level set methods with Mumford-Shah model give good results. The error of the image reconstruction is caused the rare discretisation.

VI. REFERENCES

- [1] Chan T. and Vese L., "Active contours without edges", *IEEE Trans. Imag. Proc.*, vol. 10, pp. 266-277, 2001.
- [2] Filipowicz S.F., Rymarczyk T., "Tomografia Impedancyjna, pomiary, konstrukcje i metody tworzenia obrazu", *BelStudio*, Warsaw 2003 (in Polish).
- [3] Filipowicz S.F., Rymarczyk T., Sikora J., "Level Set Method for Inverse Problem Solution In Electrical Impedance Tomography", *Proceedings of the XII International Conference on Electrical Bioimpedance & V Electrical Impedance Tomography*, p.519-522, Gdańsk 2004.
- [4] Ito K., Kunish K., Li Z., "The Level-Set Function Approach to an Inverse Interface Problem", *Inverse Problems*, Vol. 17, No. 5, October, 2001, pp. 1225-1242.
- [5] LeVeque R. J., Li Z., "The immersed interface method for elliptic equations with discontinuous coefficients and singular sources", *SIAM Journal Numerical Analysis* 31:1019--1044, 1994.
- [6] Osher S., Fedkiw R., "Level Set Methods and Dynamic Implicit Surfaces", *Springer*, New York 2003.
- [7] Osher S., Sethian J.A., "Fronts Propagating with Curvature Dependent Speed: Algorithms Based on Hamilton-Jacobi Formulations", *Journal of Computational Physics*, 79, 12-49, 1988.
- [8] Sethian J.A., "Level Set Methods and Fast Marching Methods", *Cambridge University Press* 1999.

The Application of System Dynamics in Learning Electromagnetic Contactor Operation

Paulo I. Koltermann⁽¹⁾, Jéferson M. Ortega⁽¹⁾, Valmir M. Pereira⁽¹⁾, Éder R. Martins⁽¹⁾, Luiz A. Righi⁽²⁾
 Federal University of Mato Grosso do Sul – UFMS – DEL/CCET, 79070-900, Campo Grande - MS – Brazil⁽¹⁾
 Federal University of Santa Maria – UFSM – DESP/CT, 97105-900 – Santa Maria – RS – Brazil⁽²⁾
koltermann@del.ufms.br⁽¹⁾, righi@fatec.ufsm.br⁽²⁾

Abstract— The methodology of Systems Dynamics is presented as an alternative to visualizing and learning the operation of physical systems. The objective of this article is to show the applicability of this technology in computer simulation involving an Electromagnetic Contactor. A simulation model based on causal loops and flow diagrams was developed with Powersim® Studio Enterprise 2003, taking the device parameters into consideration. The timely graphical output display becomes a tool in aiding the teaching-learning process, highlighting the importance of the simulation so that students can rethink their models of certain dynamic processes.

I. INTRODUCTION

According to Vygotsky [1], learning is the cornerstone of human development and it includes the interdependence of the individuals involved in the process. With this approach in mind, a more profound modeling reference is anchored, because as proposed by Vygotsky, “language shapes thought”. The issue of modeling in teaching can be approached in, at least, three different perspectives: (a) construction of knowledge, (b) explication and refinement of mental representations of knowledge, and (c) perception of the world through the eyes of dynamic systems. The dynamic systems theory can be interpreted as a “new” way to understand our day-to-day dynamic phenomena, taking into account not only the causal relations between sets of variables, but also system behavior as a whole [2]. From the educational standpoint, the understanding and application of these concepts enable students to comprehend complex dynamic systems and to focus on the models of any given system, as well as the reason why these systems change through time. Human thought is completely dependent on models. Mental concepts are abstractions in our experience and this experience is filtered and modified by our individual perception. Mathematical simulation models belong to the ample class of abstract models that resort to mental images. The dynamic behavior is one of the most important characteristics of a linear electromagnetic device, such as an electromagnetic contactor [3]. In this work, the Powersim® Studio Enterprise software was applied in the construction and exploration of an Electromagnetic Contactor model.

II. SYSTEMS AND MODELS

A system is comprised of a collection of interacting elements (or components) to fulfill a purpose. The Electromagnetic Contactor is a device that is commonly used for switch-controlling induction motors in industrial

processes. Thus, the parts of a Contactor make up a system, albeit each isolated component not even resembles the system of which it constitutes. However, if any of these components were missing, the system would be impaired and unable to execute the functions for which it was originally designed, as a whole. Therefore, when the word Electromagnetic Contactor is mentioned, the student will most certainly be interested in a simplified system capable of simulating some significant characteristics of an actual Contactor.

III. DYNAMIC MODELING OF THE AC CONTACTOR

According to the Maxwell Tensor [4], the instantaneous electromagnetic force that produces the contactor’s closing action movement can be expressed in Newton/Pole by:

$$F_1 = \frac{\phi_1^2 \sin^2 \omega t}{2\mu_0 S_1} \quad (1)$$

$$F_2 = \frac{\phi_{21}^2 \sin^2 \omega t}{2\mu_0 S_{21}} + \frac{\phi_{m1}^2 \sin^2(\omega t - \alpha)}{2\mu_0 S_{22}} \quad (2)$$

Where “ S_1 ” represent the area of the magnetic pole-face 1, “ S_{21} ” and “ S_{22} ” represents the external and internal section fluxes of the ring, respectively; “ ϕ_1 ”, “ ϕ_{21} ” and “ ϕ_{m1} ” represent Magnetic Fluxes in the respectively Air Gaps; “ μ_0 ” represents the magnetic permeability of the air; “ α ” is the angle between two fluxes (coil and short-circuit ring).

The total instantaneous electromagnetic force (half part of the nucleus) is given by $F_e = F_1 + F_2$.

Differential equations are formulated for calculation and behavior analysis of the AC Contactor. The description of the equations system includes mechanical movement (position, velocity and acceleration), circuit current and magnetic flux, simultaneously solved by numerical integration method. Fig. 1 shows the equivalent electric circuit referent to the main coil.

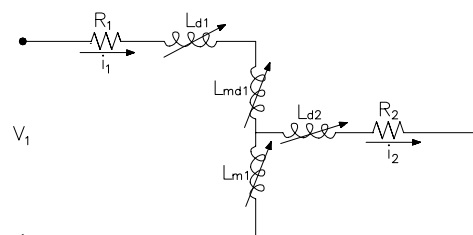


Fig. 1. Equivalent Electric Circuit

In these circuits, “ R_1 and R_2 ” represent the resistance of the coil and of the short-circuit ring, “ Ld_1 , Lmd_1 and Ld_2 ” represent the inductances of coil dispersion and of the short-circuit ring, and Lm_1 represents mutual inductance [5].

All the inductances in this model are detected by software of finite elements methods (FEM), reproducing nonlinear flux behavior (inductance). The equations for current states i_1 e i_2 (x_1 and x_2), are respectively, [5]

$$\begin{bmatrix} Lm_1+Ld_1 & -Lm_1 \\ -Lm_1 & Lm_1+Ld_2 \end{bmatrix} \cdot \begin{bmatrix} \dot{x}_1 \\ \dot{x}_2 \end{bmatrix} = \begin{bmatrix} -R_1 & 0 \\ 0 & -R_2 \end{bmatrix} \begin{bmatrix} x_1 \\ x_2 \end{bmatrix} + \begin{bmatrix} V_1 \\ 0 \end{bmatrix} \quad (3)$$

where $Ld = Ld_1 + Lmd_1$. At each time step, a new inductance matrix is calculated.

Based on Newton’s Second Law, the motion equation is obtained:

$$M \frac{d^2 x}{dt^2} = Fel - Fm - B \frac{dx}{dt} \quad (4)$$

Where “ Fel ” and “ Fm ” represent the resulting electromagnetic and mechanical forces (coil and springs), respectively; “ B ” is the buffering coefficient (shock absorbing); “ M ” is the mass of the moving part and “ x ” is the displacement.

The equations for motion and velocity states are determined from (4). The system of equations (5) is resolved by step-by-step time integration (Runge-Kutta 4th Order Method).

$$\begin{cases} \dot{x}_3 = x_4 \\ \dot{x}_4 = \frac{1}{M}(Fel - Fm - Bx_4) \end{cases} \quad (5)$$

The mechanical force is obtained from the resulting sum of all forces pertaining to Normally Open Springs, Normally Closed Springs and the principal springs.

IV. RESULTS

The analyzed contactor has springs assumed to behave in accordance to Hooke’s Law, with the condition that the strength of the spring varies in relation to the movement “ x ”.

It can be observed in the model on Fig. 2 that: the variables “ x ” for position and “ vx ” for velocity are established in the system dynamics representation; the model’s stock or level, where dx_dt and dvx_dt are rates.

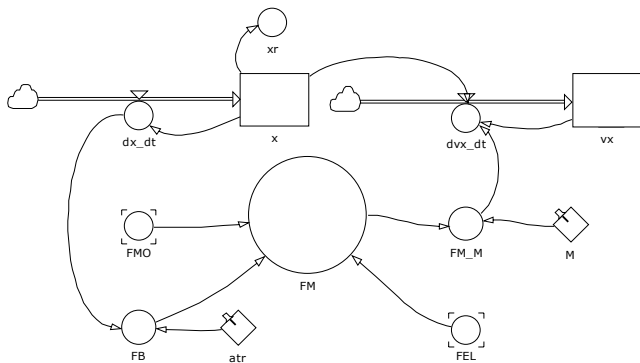


Fig. 2. Stock and flow diagram – Interaction of the contactor forces

The results contemplate, qualitatively and quantitatively, the expected behavior of variables, configuring good modeling performance, as will be explained in full paper.

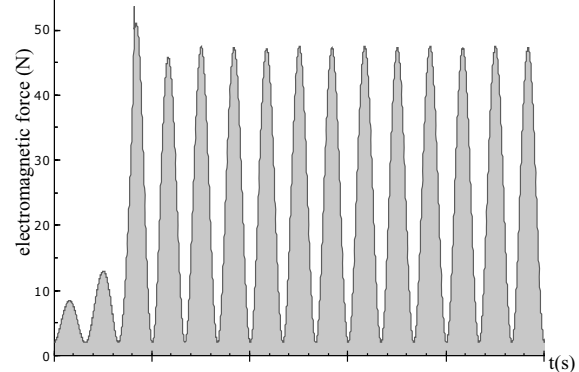


Fig. 3. Behavior of total electromagnetic force

Fig. 3 illustrates the behavior of total electromagnetic force, obtained by the simultaneous effect of currents in the main coil and short-circuit ring. It is perceptible that the force is always positive and greater than zero, allowing the contactor to always remain in the closed position, when of the passage of current or flux by zero.

Therefore, the systems dynamics tool is attributed to be a strong instrument in the study of complex physical systems, in the presence of transitory phenomena, formulated through differential equations. The qualitative vision of the behavior of a physical system is very important in the teaching-learning process, by the mental representation necessary for the compliance of causal loops and by equations system assembly and the respective resolution by numeric methods.

V. CONCLUSION

Simulating a model can be cognitively demanding. The interpretation of movement dynamics requires from the students, besides a mental representation of the physical, a profound mathematical knowledge, mastery of circuit analysis and of numerical methods. System dynamics, through software applications, allow students to interact with these concepts and to establish the possibility of a user-friendly interface for simulation and display of graphical output. The utilization of computer modeling is extremely pedagogical, for it enables students to structure certain concepts or collection of concepts and, within the phenomenon, to establish an alternative pattern of organized learning, thus allowing students to apply knowledge with much greater ease.

VI. REFERENCES

- [1] L. S. Vygotsky, *Pensamento e Linguagem*, Martins Fontes, São Paulo, Brazil, 1993.
- [2] J. W. Forrester, *World Dynamics*, Cambridge, MA, Wright-Allen Press, USA, 1973
- [3] J. Riba Ruiz and A. Garcia Espinosa, "A Novel Parametric Model for AC Contactors," *IEEE Trans. on Mag.*, vol. 44, No. 9, pp. 2215-2218, September 2008.
- [4] J. P. A. Bastos, *Eletromagnetismo para Engenharia: Estática e Quase-Estática*, UFSC Publishing, 2004, Florianópolis, Brazil.
- [5] P. I. Koltermann, J. P. Assumpção Bastos and S. R. Arruda, "A Model for Dynamic Analysis of AC Contactor," *IEEE Trans. on Mag.*, vol. 28, No. 2, pp. 1348-1350, March. 1992.

Educational Software for the Numerical Correction of the Experimental Magnetization Curves

Valentin Ionita and Emil Cazacu

Electrical Engineering Dept., University "Politehnica" of Bucharest
Spl. Independentei 313, RO-060042, Bucharest, ROMANIA
vali@mag.pub.ro, cazacu_emil@yahoo.com

Abstract — The proposed software allows students to perceive the importance of the experimental data accuracy in magnetism. A common error source for the magnetization curves (including hysteresis cycles) is the demagnetization effect and the influence of the magnetic sensor position. Our software helps the user to understand the principle and the effect of each correction method. The graphical user interface (GUI) is designed as a wizard, assisting the student to decide which the best correction procedure is and to obtain the intrinsic magnetic material characteristic to be used in electromagnetic field computation.

I. INTRODUCTION

A modern Electrical Engineering education includes more practical activities during the undergraduate, Master or Ph.D. studies. Consequently, many students learn to work with complex equipment for the experimental characterization of magnetic materials [1], and then use these material data in electromagnetic CAD. However, any measurement is influenced by many factors and the student must know how he/she could correct the experimental data. Therefore, it is useful to have a well-structured educational tool, which helps the user to compare the effect of different correction methods and to choose the best one. The proposed software is based on the correction procedure presented in [2] and has a GUI developed in MATLAB[®].

II. BACKGROUND THEORY

The measured magnetic material curve could be corrected taking into account the sample geometry, its magnetic behavior, the equipment configuration and the measurement probe position. The main influence, especially in open sample measurements, is due to the demagnetization effect: for a non-ellipsoidal sample, the internal magnetic field and the magnetization cannot be simultaneously uniform and an average correction must be performed. The computation of this demagnetizing factor was proposed for rectangular prisms [3] [4], cylinders [5] [6], or ring cores [7].

Another approach is the computation of more accurate factors using the finite element method (FEM) for the experimental device simulation. This procedure allows computing both the demagnetizing factor and the field correction factor, which depends on the position of the magnetic field probe [2]. These correction factors are computed and stored in dedicated files, which can then be visualized by the user. Three measurement types are considered: closed circuit with sample between poles (e.g. hysteresisgraph), closed circuit with surrounding coil (e.g.

single sheet tester) and open circuit (e.g. vibrating sample magnetometer). The sample could be an ellipsoid, a cylinder, a rectangular prism or it could have an arbitrary shape.

III. SOFTWARE DESIGN

The workflow that may be followed by a student for performing several corrections and for selecting the best one is represented in Fig. 1 as an activity diagram, using the modeling language UML (Unified Modeling Language) [8]. The graphical interface is designed in Matlab[®] like a wizard, with successive windows, which guides the student to the final goal: selecting the best correction of the experimental curve, as seen in the window presented in Fig. 2.

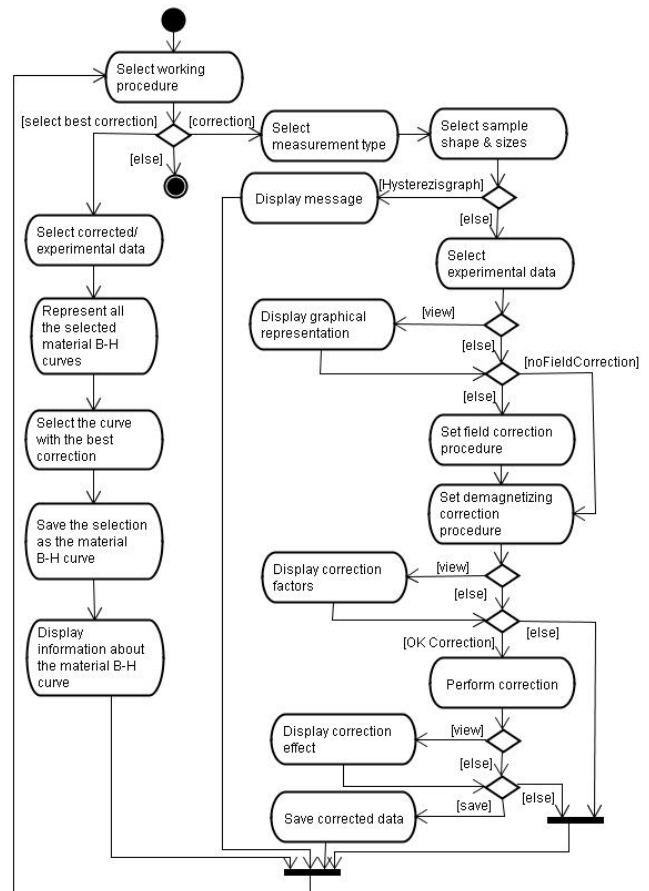


Fig. 1. Activity diagram, using UML

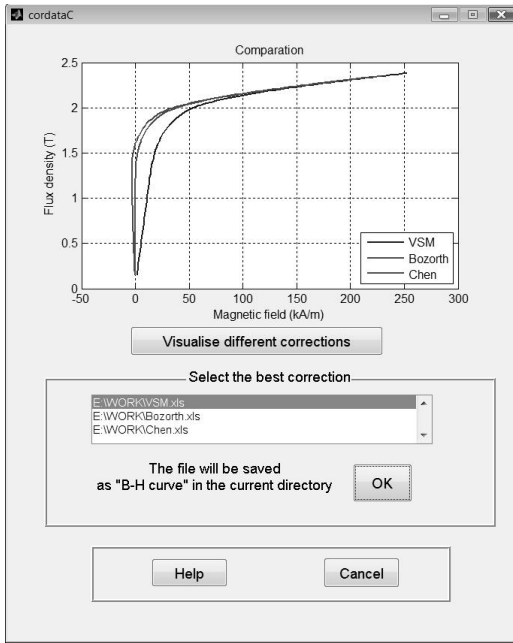


Fig. 2. Visualization of the correction effect for different methods

Each step is assisted by a link to the help file, where the student can find information both about the software commands and about the correction theory. The correction setup includes the choice of the measurement type, sample shape and sizes (Fig. 3). The user can choose between several field correction procedures (considering 2D or 3D simulation of the simplified or of the entire geometry of the experimental device) and between different demagnetizing correction methods: computation of a constant factor; extraction of a constant factor or of a susceptibility-dependent factor from a database. The corresponding files are loaded (using the window presented in Fig. 4) and the user can also visualize the correction factors.

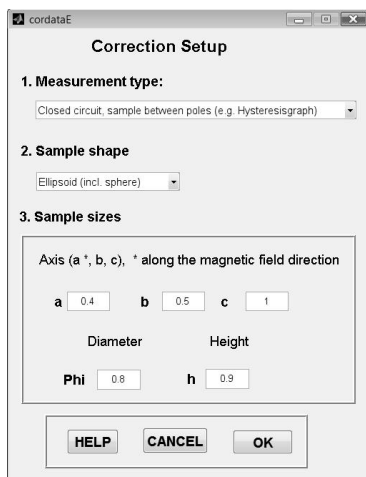


Fig. 3. Setting the correction parameters

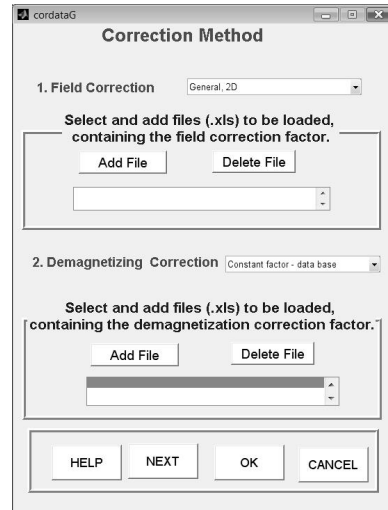


Fig. 4. Setting the correction method

The selected parameters of the correction method are parsed by the corresponding computation subroutine, which saves the corrected data in a dedicated file, the correction effect being analyzed in the graphical window presented in Fig. 2.

For the robustness of the design, the user has the possibility to return to the previous decision at any moment.

IV. CONCLUSIONS

This educational software is useful for understanding the way from the experimental measurement to the final material characteristic. The extensible software architecture allows the development of correction procedures for any other equipment, using new numerical techniques. This integrated correction technique is used in our Laboratory of Technical Magnetism for Master courses. The next step of the software development will be its integration with the dedicated software of each experimental device, in order to have a real-time correction during the measurement.

V. REFERENCES

- [1] F. Fiorillo, *Measurement and Characterization of Magnetic Materials*, Amsterdam: Elsevier, 2004.
- [2] V. Ionita, E. Cazacu, "Correction of measured magnetization curves using finite element method", *IEEE Trans. on Magnetics*, 45 (3): 1174-1177, 2009.
- [3] A. Aharoni, "Demagnetizing factors for rectangular ferromagnetic prisms", *J. Appl. Phys.*, 83 (3): 3432-3434, 1998.
- [4] D.-X. Chen, E. Pardo, and A. Sanchez, "Demagnetizing factors for rectangular prisms", *IEEE Trans. on Magnetics*, 41 (6): 2077-2088, 2005.
- [5] D.-X. Chen, J. Brug, and R. Goldfarb, "Demagnetizing factors for cylinders", *IEEE Trans. on Magnetics*, 27 (6): 3601-3619, 1991.
- [6] D.-X. Chen, E. Pardo, and A. Sanchez, "Radial magnetometric demagnetizing factor of thin disks", *IEEE Trans. on Magnetics*, 37 (11): 3877-3880, 2001.
- [7] D.B. Clarke, "Demagnetization factors of ring cores", *IEEE Trans. on Magnetics*, 35 (11): 4440-4444, 1999.
- [8] A. Dennis, B.H. Wixom, and D. Tegarden, *System Analysis and Design with UML Version 2.0. An Object-Oriented Approach*, New York: John Wiley&Sons, 2005.

Application of the Method of Residues in Comparison to TLM Method in a Practical Case

Sérgio H. L. Cabral and Sávio L. Bertoli
 FURB – Fundação Universidade Regional de Blumenau
 Rua São Paulo, 3250 CEP 89030-000 Blumenau - SC
 scabral@furb.br savio@furb.br

Abstract—Computer programs have become indispensable for solving complex problems of Electromagnetism. Thus, analytical studies of correlated problems have become even more important for establishing bases for the understanding of computational analyses. Thus, the aim of this work is to reinforce the applicability of a very simple analytical method that is the Method of the Residues. This method has already been presented by the authors in previous article through a theoretical example. Now, its applicability is presented through a very practical problem. Comparison to the numerical method TLM is also done. Concordance with TLM and experimental data confirms the proposal of the method of residues as applicable to a wide range of problems of Electromagnetism.

I. INTRODUCTION

Since every power transformer is inherently vulnerable to incidence of lightning voltage surges, several studies regarding effects like these have been published ever since transformer has been put in use [1]. In consequence, several numerical tools and software have been developed for better studying this theme in different degrees of complexity [2]. For its turn, no matter how complex are the design of any transformer and the computational tool, the analysis of the behaviour of any of its winding is often based upon a classical study. This classical study consists in the analytical solution in time-domain of the differential equation that governs the voltage distribution along a continuous and homogeneous winding submitted to a step voltage [1]. Since MR-Method of Residues has been successfully applied to classical study[3], this work presents its applicability to a practical case that is an air-core winding submitted to a practical step voltage. The result is that MR demonstrates to be a very interesting and practical tool for obtaining analytical solution in studies that serves as the fundamental basis for more complex problems that require computational tools. For the sake of a better comparison TLM results are also presented.

II. A PRACTICAL STUDY AND ITS NUMERICAL AND ANALYTICAL SOLUTIONS

In accordance with [1], when a voltage surge hits a continuous winding of a transformer, it is likely to cause an insulation failure. This is due to a sudden voltage distribution that is established along it and that invariably implies into high values of electric field along its former turns. This sudden voltage distribution is ruled by parasitic capacitances. Then, if no failure happens, the voltage distribution along this winding will oscillate, due to changes of energies among charged capacitances and the inductances of the winding. Thus, voltage

oscillations will also cause voltage stresses due to overvoltage along several points of the winding, until steady state is reached. This well-known case has been experimentally investigated in [2], in which test apparatus for applying step voltage was made. Schematic diagram of that apparatus is shown in Fig. 1.

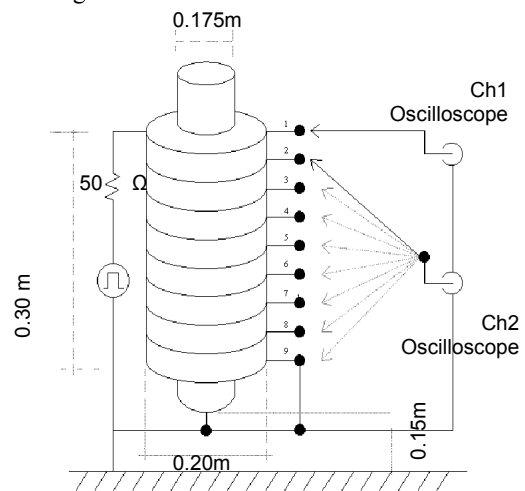


Fig.1. Schematic diagram of the test apparatus

Still in accordance with [2], TLM modelling and simulation of this problem consists in dividing equivalent circuit of the winding into several segments with related capacitances and inductances. In this way it is somehow possible to represent partially those unavoidable non-homogeneities of any winding by setting slightly different values of capacitances and inductances within different segments. Fig. 2 shows the aspect of a well-known circuit for TLM modelling and simulation of a winding like presented in Fig. 1.

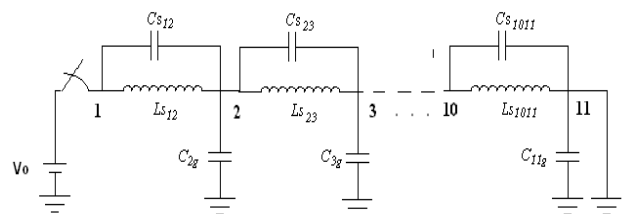


Fig.2. Equivalent circuit for practical winding

For its turn, analytical solution of this problem consists in considering winding as homogeneous and thus solving the following classical equation[1,3]:

$$\frac{\partial^2 V(x,t)}{\partial x^2} = R_s \left(C_g \frac{\partial V(x,t)}{\partial t} + \frac{C_s \ell}{N} \frac{\partial^3 V(x,t)}{\partial t \partial x^2} \right) + L_s \left(C_g \frac{\partial^2 V(x,t)}{\partial t^2} + \frac{C_s \ell}{N} \frac{\partial^4 V(x,t)}{\partial t^2 \partial x^2} \right) \quad (1)$$

In which $V(x,t)$ is voltage to ground along time and length of the winding, R_s is its longitudinal resistance, L_s its effective series inductance, C_g its distributed capacitance to ground, C_s its capacitance between two adjacent turns, N its number of turns and ℓ its length. This winding lies along the x -axis, it is grounded at its end, $x = \ell$, and a step voltage V_o is applied at $x = 0$. The analytical solution by the MR proposed is[3] :

$$V(x,t) = V_o \left(\frac{\ell-x}{\ell} \right) - \frac{2V_o}{\pi\beta_2} \sum_{n=1}^{\infty} \left[\frac{\sin\left(\frac{n\pi x}{\ell}\right)}{n} \left(\left(\frac{\beta_1 A_{n_1} + \beta_2}{\beta_1 A_{n_1} + s_1} \right) s_1 \beta_1 A_{n_1} e^{s_1 t} + \left(\frac{\beta_1 A_{n_2} + \beta_2}{\beta_1 A_{n_2} + s_2} \right) s_2 \beta_1 A_{n_2} e^{s_2 t} \right) \right] \quad (2)$$

For which

$$\beta_o \equiv \frac{NC_g}{\ell C_s}; \quad \beta_1 \equiv \frac{R_s}{L_s}; \quad \beta_2 \equiv \frac{N}{L_s C_s \ell}; \quad A_{n_1} \beta_1 \equiv 1 + s_1; \quad A_{n_2} \equiv 1 + \frac{s_2}{\beta_2} \quad (3)$$

And s_1 and s_2 are obtained from

$$s_{1,2} = \frac{-\beta_1}{2} \pm \sqrt{\left(\frac{\beta_1}{2} \right)^2 - \frac{\beta_2 \left(\frac{n\pi}{\ell} \right)^2}{\beta_o + \left(\frac{n\pi}{\ell} \right)^2}} \quad (4)$$

Thus, since homogeneity is inherent, effects like those due to the existence of tangential components of magnetic or electric fields cannot be taken into account.

III. COMPARISON BETWEEN EXPERIMENTAL DATA AND MR METHOD

For the sake of evaluation of the performance of the MR method a practical air-core winding was experimented. This winding has $C_g = 4\text{nF/m}$; $\ell = 0.4\text{ m}$; $C_s / N = 6.37\text{ pF.m /turn}$; $L_s = 0.4\text{ mH/m}$; $R_s = 0\ \Omega/\text{m}$ and $n = 21$, for (2). Fig. 3 presents the behaviour of voltage to ground at first quarter of the winding that corresponds to tap 3, in Fig. 1. TLM simulation is also presented for the sake of a better comparison. It is important to mention that although effects of non-homogeneity could be considered for the TLM modelling of this winding, they were not made since the aim is to compare to MR under same conditions, as done in [3] and in [4]. Thus, in accordance with Fig.3 it can be seen that results between TLM and MR are very close, while experimental results present a small but natural difference in comparison to

both. This difference is principally due to inherent non-homogeneity of the real winding and to the fact that real voltage source is not a step voltage. In consequence, stray capacitances and inner resistances contribute for a time delay for the practical response. Nevertheless, besides time-delay results from all three simulations have a significantly coherence.

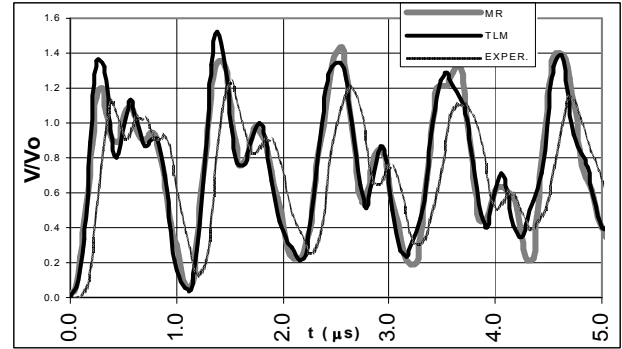


Fig. 3 Voltage to ground along time for the first quarter of the winding.

Also, comparison shows that MR results presents higher peak values of voltage for former oscillations, while lower peak values for following oscillations, in such a way that they compensate themselves under an average point of view. Some reasons for these differences are probably due to chosen number of segments for representing winding, in accordance with Fig. 2, as well as due to value set for n in the series presented in (2).

IV. CONCLUSION

Presented results from a practical simulation of transformer winding show how effective the proposed method of the residues can be for solving analytically classical problems of Electromagnetism. Although real concerns are not taken into account, MR still presents coherent results. In thus way, obtained results encourage future studies for evaluating the influence of terms of series as in (2) as well as studies in which air core winding is substituted by a really practical one, with ferromagnetic core. These presented results also encourage application of the method in other areas of Electromagnetism in view of consolidating this important and simple method.

V. REFERENCES

- [1] Greenwood, A.N. *Electrical Transients In Power Systems*. 2. Ed. New York : John Wiley & Sons, 1991, pp. 327-346.
- [2] Cabral, S.H.L., Raizer, A. "TLM method applied to the study of practical transformer windings submitted to voltage surges". In : 5th Brazilian Congress on Electromagnetism. *Proceedings*. Gramado, 2002. Paper No. 105.
- [3] Cabral, S.H.L., Bertoli, S.L. "Analytical evaluation of voltage distribution along continuous winding of transformer by the method of residues". In: 7th Brazilian Congress on Electromagnetism, *Proceedings*. Belo Horizonte. 2006. Paper No. 075.
- [4] Cabral, S.H.L., Raizer, A. "Resposta ao degrau de tensão para enrolamentos contínuos de transformadores - Comparação entre o método Analítico e o TLM". In: 4th Brazilian Congress on Electromagnetism. *Proceedings*. Natal, 2000. p.179-182. In Portuguese.

Semi-Analytical Solution of 2-D Rotor Eddy-Current Losses due to the Slotting Effect in SMPMM

F. DUBAS and C. ESPANET

ENISYS Department, FEMTO-ST Institute, CNRS UMR 6174, F90010 Belfort, France

E-mail: FDubas@gmail.com

Abstract — In this abstract, the authors present the determination of two-dimensional (2-D) rotor eddy-current losses due to the stator slot-openings in surface mounted permanent-magnet (PM) motors (SMPMM). These parasitic losses are resistance-limited and only determined in the PMs from a new 2-D semi-analytical solution of the magnetic field taking into account the slotting effect. The 2-D rotor eddy-current losses due to the slotting effect have been compared with the finite element analysis (FEA) and calculated both for radial and parallel magnetization. The analytical results are in quite satisfying agreement with those obtained by the FEA.

I. INTRODUCTION

In the SMPMM, the rotor (i.e., the conducting retaining sleeve, the PMs, and the rotor yoke back-iron) is exposed to high order flux density harmonics which are not synchronous with the rotor. The 2-D rotor eddy-current losses computation, caused by these non-synchronous magnetic fields, is a well known problem in conventional synchronous machines design. These parasitic losses have two origins which can coexist. At no-load (at $I = 0$ A with I the RMS value of stator current), they are caused by the reluctance variation due to the slotting effect, while on load these losses in the turning parts result from both stator slotting permeance harmonics [1] and magnetomotive force (MMF) harmonics which are of two types [2]: i) MMF harmonics caused by the discrete positions of stator winding conductors; ii) MMF harmonics caused by time harmonics in the stator current, which result from six-step commutation and Pulse-Width-Modulation (PWM).

The main scientific contribution of this paper deals with by the 2-D rotor eddy-current losses due to the slot-openings, which are little discussed in the literature. These parasitic losses are usually assumed to be resistance-limited (i.e., the influence of the eddy-current reaction field is neglected) and are determined in the PMs from a new 2-D semi-analytical solution [3], which determines the no-load magnetic field distribution in the air-gap taking account into the slotting effect. This new calculation of 2-D eddy-current losses in the PMs due to the slotting effect requires less hypotheses than the method proposed by [1] which uses the 2-D permeance functions, in the sense that the solutions takes into account the real waveform of the teeth and do not use an approximate permeance function. However, the price to pay is the resolution of the Cramer's systems described in [3].

The 2-D eddy-current losses in the PMs evaluation predicted by this new approach of the slotting effect (and calculated for both radial and parallel magnetization) have been compared with the FEA. The semi-analytical results are in quite satisfying agreement with those obtained by the FEA.

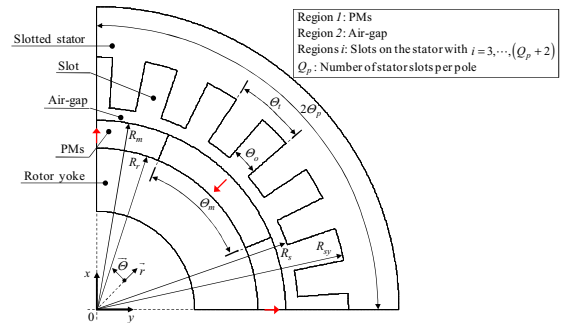


Fig. 1. Cross section of one pole pitch of the multi-pole SMPMM.

TABLE I
PARAMETERS OF SURFACE MOUNTED PM MOTOR

Parameters	Values	Unit
Number of pole pairs, p	1	—
Total number of slots, Q_s	12	—
Magnet pole-arc to pole-pitch ratio, $\alpha_p = \theta_m / \theta_p$	100	%
Stator slot opening to tooth-pitch ratio, $\zeta_o = \theta_o / \theta_t$	33.33	%
Radius of the stator yoke surface, R_{sy}	37	mm
Radius of the stator surface, R_s	20	mm
Radius of the PMs surface, R_m	19	mm
Radius of the rotor yoke surface, R_r	14	mm
Axial length, L	45	mm
Remanent flux density of the PMs, B_{rm}	1.13	T
Relative magnetic permeability of the PMs, μ_{rm}	1.029	—
Electrical conductivity of the PMs, σ_m	0.694×10^6	S
Volumetric mass density of the PMs, ρ_{vm}	7500	kg/m ³

II. A 2-D NEW SEMI-ANALYTICAL SOLUTION [3]

A. Problem Description and Assumptions

Fig. 1 shows the geometric representation of the multi-pole SMPMM for the new 2-D semi-analytical solution used to study the effect of the stator slotting. The main parameters of this geometry are given in the Table I.

The usual assumptions of all models in the literature are: i) End-effects are neglected; ii) The stator and rotor back-iron is infinitely permeable (i.e., the magnetic saturation is neglected); iii) The electrical conductivity of the PMs is assumed to be null to calculate the no-load magnetic vector potential (i.e., no resolution of Diffusion's equations); iv) The PMs are assumed to be nonoriented (with no particular direction of magnetization), isotropic, and having a linear demagnetization characteristic (rare earth magnets); v) Radial slot faces on the stator.

B. No-load Vector Potential Determination

The new semi-analytical solution is based on 2-D analysis in polar coordinates, and involves the solution of Laplace's equations in the air-gap (i.e., concentric region: Region 2) and in the slots on the stator (i.e., non-concentric regions: Regions i) and the solution of Poisson's equations in the PMs (i.e., concentric region: Region 1) [see Fig. 1] with constant magnetic permeabilities. The no-load magnetic field solutions with the slotting effect are obtained by using the Fourier's series and the method of separating variables. However, it now caters for i) internal rotor motor topology; ii) radial and parallel magnetization; iii) curvature effect; iv) depth of the slots.

The no-load magnetic flux density, in each region, has been compared to the FEA calculations, and the agreement was very good considering both amplitude and waveform. The no-load vector potential in Region 1 can be expressed by

$$A_{z1} = B_{rm} \cdot R_m \cdot f_{z1n}(E_{1n}, G_{1n}, r, \Theta_s), \quad (1)$$

where r and Θ_s are respectively the radial position and the mechanical angular position of the stator; n is the spatial harmonic orders, and f_{z1n} is the function in Fourier's series which depend on the integration constants E_{1n} & G_{1n} .

The integration constants of no-load local quantities (i.e., the magnetic flux density and vector potential), in each region, are determined by numerically solving the linear equations (i.e., the Cramer's system) for each Θ_{rs} (with Θ_{rs} the mechanical angular position between the rotor and the stator). The Cramer's system, detailed in [3], for each Θ_{rs} is based on $6 \cdot (n_{max} + 1) + Q_p \cdot (v_{max} + 1)$ equations and unknowns with n_{max} and v_{max} terms in the Fourier's series for the computation of the no-load local quantities.

III. 2-D EDDY-CURRENT LOSSES IN THE PMs CALCULATION

According to Maxwell's equation (i.e., the Faraday's law, the Coulomb's gage and the Ohm's law) and by using (1), the 2-D eddy-current losses in the PMs at the resistance-limited due to the stator slot-openings are given by

$$P_m^{slot} = k_{nsfd} \cdot k_e \cdot N_0^2 \cdot B_{rm}^2 \cdot M_m, \quad (2)$$

where N_0 is the speed of rotation, $M_m = \rho_{vm} \cdot V_m$ is the PMs mass with $V_m = \pi \cdot \alpha_p \cdot L \cdot (R_m^2 - R_r^2)$ is the volume of the PMs, k_e is the eddy-current losses coefficient in the PMs

$$k_e = \frac{\pi^2 \cdot \sigma_m \cdot L^2}{6 \cdot \rho_{vm}}, \quad (3)$$

and k_{nsfd} is the harmonic coefficient of the non-sinusoidal magnetic flux density produced by the PMs due to the slotting effect. This harmonic factor, given in the extended paper, depend principally on E_{1n} , G_{1n} , E'_{1n} & G'_{1n} . The integration constants E'_{1n} & G'_{1n} are determined by numerically solving the derivative of Cramer's system detailed in [3].

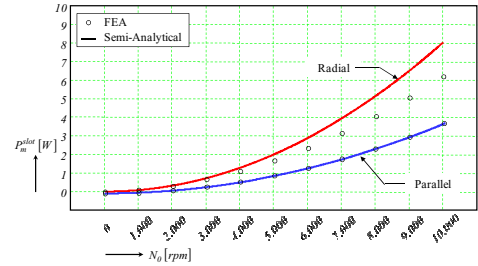


Fig. 2. Variation of 2-D eddy-current losses in the PMs due to the slotting effect versus the speed of rotation.

It can be noted that the harmonic coefficient k_{nsfd} is equal to zero for the slotless motors equipped with PMs.

IV. COMPARISON WITH FINITE ELEMENT SIMULATIONS

The evaluation of P_m^{slot} has been applied to a SMPMM, whose main characteristics are given in the Table I. Fig. 2 shows the influence of the rotor speed on P_m^{slot} , with radial and parallel magnetized PMs, calculated numerically by FEA and semi-analytically by the 2-D new approach with the slotting effect. It can be seen that, although the semi-analytical solution assumes to be resistance-limited, good agreement is obtained. It can be noted that P_m^{slot} calculated semi-analytically, at high fundamental frequencies, are significantly over-estimated in relation to those calculated numerically. These differences are due to eddy-currents effect on the no-load magnetic field which is not taken into account in the new 2-D semi-analytical model developed in [3].

V. CONCLUSION

A new 2-D semi-analytical solution of the magnetic field with the slotting effect has been used to determine the 2-D eddy-current losses in the PMs at the resistance-limited in SMPMM. This new calculation of these parasitic losses is mathematically more rigorous and requires less hypotheses than the method proposed by [1]. The new semi-analytical solution takes significantly less computing time than the FEA. In this comparison, the Cramer's system in [3] has of 486 elements (i.e., with $n_{max} = 49$ and $v_{max} = 30$) which is much smaller than the FEA having 6,000 surfaces elements for the studied SMPMM. Moreover, the semi-analytical solution can be a useful tool for design and optimization of multi-pole SMPMM, e.g., to minimize the 2-D rotor eddy-current losses due to the slotting effect.

VI. REFERENCES

- [1] M. Markovic, and Y. Perriard, "A Simplified Determination of the Permanent Magnet (PM) Eddy Current Losses due to Slotting in a PM Rotating Motor," in *Proc. IEEE ICEMS*, Oct. 17-20, 2008, Wuhan, China.
- [2] Z.Q. Zhu, K. Ng, N. Schofield, and D. Howe, "Improved Analytical Modelling of Rotor Eddy Current Loss in Brushless Machines Equipped with Surface Mounted Permanent Magnets," in *Proc. IEE Electr. Power Appl.*, vol. 151, no. 6, pp. 641-650, Nov. 2004.
- [3] F. Dubas, and C. Espanet, "Analytical Solution of the Magnetic Field in Permanent-Magnet Motors Taking Into Account Slotting Effect: No-Load Vector Potential and Flux Density Calculation," *IEEE Trans. on Magn.*, Accepted paper (Vol. 45, No. 5, Part. 1, June 2009).

14.Benchmarking(Team)

Effect of Source Replacement on both Iron Loss and Flux in Solid and Laminated Steel Configurations

Z.Cheng¹, N.Takahashi², *Fellow, IEEE*, B.Forghani³, *Member, IEEE*
G. Gilbert³, Y.Du¹, Y.Fan¹, L.Liu¹, Z.Zhai¹, W.Wu¹, and J.Zhang¹

1 Baoding Tianwei Group Co., LTD, Tianwei West Road 2399, Baoding 071056, China, E-mail: emlab@btw.cn

2 Dept. of E.E., Okayama University, Okayama 700-8530, Japan

3 Infolytica Corp., 300 Leo Pariseau, Suite 2222, Montreal, Quebec, H2X 4B3, Canada

Abstract- This paper investigates the effect of source replacement on both the iron loss and flux inside solid magnetic steel plates and laminated silicon steel sheets. The working conditions of the proposed models described in the paper are very different from the conditions usually found when modeling the material properties. Therefore, a zoned (3-D and 2-D eddy current sub-regions) approach is employed in the 3-D FEM analysis.

I. INTRODUCTION

Material modeling is usually carried out under certain standard conditions. The material and/or the device, however, work in various complex and non-standard environments. Therefore, the usual material property data cannot be used everywhere in the solved region and special zoned treatment is suggested, in particular, for the lamination configuration which is excited by a perpendicularly applied field.

In this paper, the verification models are proposed in which the magnetic steel component is excited by different sources. The effect of the source replacement on both the iron loss and the flux inside the solid and the laminated magnetic steel configurations is examined in detail.

II. VERIFICATION MODEL

Two verification models, namely P21-B and P21-M1, are established. P21-M1 is a simplified model based on the original benchmark model of P21^c-M1, in which the solid steel plate is removed and the laminated sheets (30RGH120, total 20 sheets) are driven by the exciting source of twin coils (coil 1 and coil 2). Four search coils (20 turns each) are inserted at the specified positions around the laminated sheets of interest. The number of sheets included in each search coil (e.g., no.1 to no.4) is different, as shown in Fig.1. P21-B (coil and solid magnetic steel plate) is a member-model of the Problem 21 Family.

There are three test cases based on the exciting current in coils 1 and 2. Table I lists the current configuration for each test case where the exciting current in the coil ranges from 0A to 25A (rms, 50Hz).

III. MODEL SIMPLIFICATION

The advance experiments to measure the magnetic flux and the loss inside the solid plate or the laminations of the verification model under different excitation conditions have been designed in order to simplify the models. For example, the test results based on P21-M1 show that the average magnetic flux density in the laminations closest to the exciting

source is considerably higher than those far away from the exciting source. The average magnetic flux density quickly drops with the increase in the number of the laminated sheets. The strong eddy currents within a thin layer closest to the source must be considered in the FEM analysis.

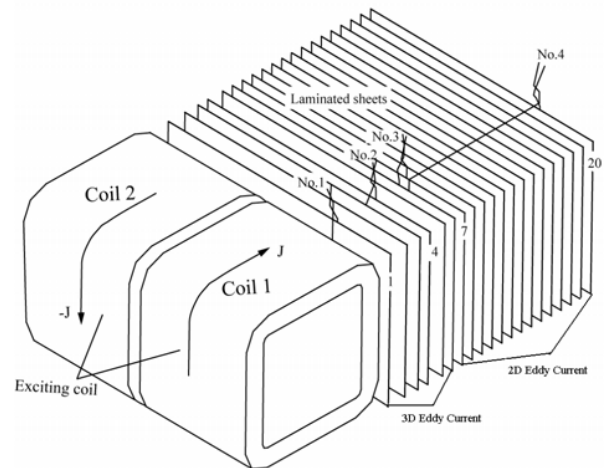


Fig.1. Verification model and search coils (sketch).

TABLE I
DIFFERENT EXCITATION CONDITIONS

Cases	Exciting currents (A, rms, 50Hz)		Main property of flux
	in Coil 1	in Coil 2	
I	J	-J	Perpendicular to steel
II	J	J	Parallel to steel
III	J	0	Partly perpendicular, partly parallel

According to the obtained results, it is found that the entire analyzed region of P21-M1 can be divided into two zones, i.e., the 3-D eddy current region of a thin layer including a few of the silicon sheets with a fine mesh, e.g. 0.15mm thick mesh layer as an initial calculation, and a 2-D eddy current region, treated as a bulk of laminated sheets, in which the eddy currents flow along the planar sheets without the normal component. The nonlinearity and electric and magnetic anisotropy of the laminations are taken into account.

In this zoned modeling the total iron loss W can be expressed as (1)

$$W = \sum_{i=1}^{NE_{2d}} [W_h^{(e)}(B_{mi}^{(e)}) + W_e^{(e)}V_i^{(e)}] + \sum_{i=1}^{NE_{3d}} W_t^{(e)}(B_{mi}^{(e)})V_i^{(e)} \quad (1)$$

Where $W_h^{(e)}$ and $W_e^{(e)}$ denote the specific hysteresis and eddy current loss per element respectively for the 3-D eddy current region; while $W_t^{(e)}$ represents the specific total iron loss per element for the 2-D eddy current region. The W_h - B_m and W_e - B_m curves used in (1) can be measured in advance. $B_m^{(e)}$ and $V^{(e)}$ are the peak value of the flux density and the volume per element respectively; NE_{2d} and NE_{3d} are the numbers of elements of the 2-D and 3-D eddy current regions.

The measured and calculated total iron loss results of P21-M1 (20 sheets) and P21-B are shown in Table II and Table III respectively, and they are in practically good agreement.

TABLE II
TOTAL IRON LOSS UNDER DIFFERENT EXCITING SOURCE (P21-M1)

Current (A, ms, 50Hz)	Case I (W)		Case II (W)		Case III (W)	
	Measured	Calculated	Measured	Calculated	Measured	Calculated
10.0	2.2	2.14	0.66	0.62	0.59	0.57
15.0	5.3	5.15	1.43	1.33	1.39	1.26
20.0	10.2	9.58	2.71	2.45	2.99	2.76
25.0	16.8	15.47	4.72	4.49	5.19	4.91

TABLE III
TOTAL IRON LOSS UNDER DIFFERENT EXCITING SOURCE (P21-B)

Currents (A, ms, 50Hz)	Case I (W)		Case II (W)		Case III (W)	
	Measured	Calculated	Measured	Calculated	Measured	Calculated
10.0	11.97	12.04	11.61	12.83	6.15	6.57
15.0	26.89	27.12	26.52	26.98	13.70	14.43
20.0	49.59	50.92	47.16	47.52	24.73	25.49
25.0	82.39	84.78	74.40	76.30	39.92	40.12

From Table II and Table III the essential difference between P21-M1 and P21-B in iron loss under different excitations can be summarized as follows:

- 1) For the lamination-based model, P21-M1, one can see that

$$\begin{cases} Loss(Case I) \cong 3.5 \times Loss(Case II \text{ or } Case III) \\ Loss(Case II) \cong Loss(Case III) \end{cases} \quad (2)$$

- 2) For the solid plate-based model, P21-B, the results are quite different from that of P21-M1,

$$\begin{cases} Loss(Case I) \cong Loss(Case II) \\ Loss(Case I \text{ or } Case II) \cong 2 \times Loss(Case III) \end{cases} \quad (3)$$

The iron loss results suggest that the eddy current loss induced within a thin layer is strongly dependent on the exciting pattern, such as the cases described in Table I, and on whether the magnetic steel is solid or laminated. There is a complicated relationship between the loss and the exciting sources.

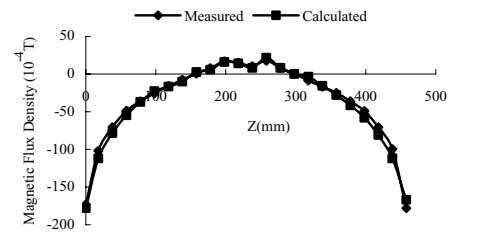
The measured and calculated results of the magnetic flux inside the magnetic steel plate of P21-B are shown in Table IV. To validate the analysis method further, the measured and calculated results of the magnetic flux density at the specified positions in air ($y=0.0\text{mm}$, $x=3.76\text{mm}$, see the coordinate in [2]

or in the definition of Problem 21 at www.compumag.co.uk) under different exciting conditions have been obtained for P21-M1. Fig.2 shows the distributions of B_x of the Case II and Case III. The measured and calculated results are in good agreement.

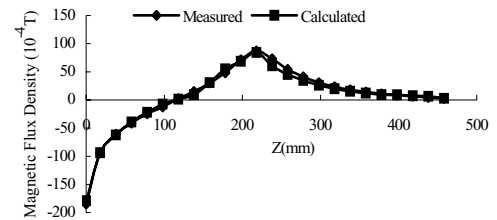
TABLE IV
FLUX UNDER DIFFERENT EXCITING SOURCE (P21-B)

Current (A, ms, 50Hz)	Case I (mWb)		Case II (mWb)		Case III (mWb)	
	Measured	Calculated	Measured	Calculated	Measured	Calculated
10.0	0.158	0.151	0.341	0.386	0.326	0.318
15.0	0.318	0.306	0.513	0.538	0.492	0.481
20.0	0.478	0.458	0.679	0.687	0.652	0.637
25.0	0.618	0.605	0.834	0.841	0.808	0.780

Note: The search coil is located at $z=130\text{mm}$ [1,2].



(a) Case II



(b) Case III

Fig.2. Magnetic flux density B_x at specified positions (P21-M1, current: 10A, rms, 50Hz).

IV. CONCLUSION

The effect of the source replacement on both the iron loss and flux inside the solid magnetic steel plates and the laminated silicon steel sheets is examined in detail based on the proposed models, taking account of both the electric and magnetic anisotropy of the material.

The zoned approach (involving with 3-D and 2-D eddy current sub-regions) is efficient in dealing with the lamination configuration, which is validated by comparing the calculated and measured results.

The different electromagnetic behavior of the magnetic steel components with either laminated or solid geometries is shown.

V. REFERENCES

- [1] Z.Cheng, N.Takahashi, B.Forghani, et al, "Analysis and measurements of iron loss and flux inside silicon steel laminations," *IEEE Trans. on Magn.*, vol.45, 2009.
- [2] Z.Cheng, N.Takahashi, et al, "Loss spectrum and electromagnetic behavior of Problem 21 family," *IEEE Trans. on Magn.*, vol.42, no.4, pp.1467-1470, 2006.

An Adaptive Equivalent Circuit Method for TEAM Problem 28: An Electrodynamic Levitation Device

Wei Li, Jiang Lu, and Chang Seop Koh, *Senior Member, IEEE*
 Chungbuk National University
 Chungbuk National University, Cheongju, Chungbuk, 361- 763, Korea
 liwei@chungbuk.ac.kr

Abstract — An adaptive equivalent circuit method is developed for analyzing the TEAM Problem 28. The problem is solved by transferring the system to an equivalent circuit model which is set up by adaptively divided the plate into a series of segments based on the field continuity condition at the interface of segments. The performance is obtained by solving the circuit equations combined with motional equations with Runge-Kutta-Fehlberg method. The accuracy and efficiency of the proposed method are verified by comparing with FEM calculation and experimental results.

I. INTRODUCTION

TEAM problem 28 is an electrodynamic levitation system utilizing the eddy current induced in conducting plate. This is a complex system involves electric circuits, magnetic fields and mechanical movements. This kind of repulsion system is being involved in many engineering applications due to its very fast response via small inductance. Typical examples are electromagnetic launcher, electromagnetic brake, actuator of circuit breaker and arc eliminator. In order to analyze this kind of system, finite element method (FEM) coupled with circuit and motional equations have been used widely. The FEM, however, require huge computing time related with transient time-stepping analysis. Especially if it is related with parameter optimization of the system, it can be hardly adopted.

For reducing the computing time, hence, paying attention to the fact that the system does not contain any magnetic material, equivalent circuit methods have been developed [1]-[2]. These methods, however, still depend on FEM for parameter calculation with a lot of computing time, and do not explain how to divide the conducting plate for accurate analysis.

In this paper, an adaptive equivalent circuit method is developed, where the conducting plate is adaptively divided into a series of segments considering the field continuity condition at the interface of segments. The accuracy and efficiency of the proposed method are investigated through comparison with FEM and experimental results for TEAM problem 28.

II. ADAPTIVE EQUIVALENT CIRCUIT METHOD

Fig. 1 shows the configuration of the TEAM problem 28 where a cylindrical aluminum plate, of which mass is 0.107(kg), is located above two cylindrical coils. When a sinusoidal current source is supplied to the inner and outer coils, the conducting plate will experience a repulsive force along z direction due to the eddy current induced in the conducting plate.

A. Equivalent Circuit Method

In order to approximate the distribution of eddy currents in the conducting plate, the plate is divided into a series of segments as shown in Fig. 2(a), and the eddy current, in each segment, is assumed to have uniform distribution. Each segment, then, physically corresponds to a conductive ring, as shown in Fig. 2(b), with its circuit parameters of resistance and inductance as shown in Fig.2(c). In this approximation, the whole system can be transformed into equivalent circuits as shown in Fig. 2(d).

The circuit equations of the equivalent circuits are as follows:

$$I_i R_i + d\lambda_i / dt = 0, \quad i = 1, 2, 3, \dots, N. \quad (1)$$

$$\frac{d\lambda_i}{dt} = \sum_{s=1}^2 L_{is} \dot{I}_s + \sum_{j=1}^N L_{ij} \dot{I}_j + \sum_{s=1}^2 I_s \frac{\partial L_{is}}{\partial z} \frac{dz}{dt}, \quad i = 1, 2, \dots, N. \quad (2)$$

where the subscript s denotes the exciting coil, N is the number of segments, R_i , I_i , λ_i are the resistance, eddy current and flux linkage of the i -th segment, respectively, L_{is} is the mutual inductances between i -th segment and exciting coil. The derivative of inductance L_{ij} between segments is zero. Since the inductances depend only on the geometric configuration, they can be computed analytically using Bartky's transformation [3].

The dynamic state equations are obtained by combining (1)-(2) and motional equations as follows:

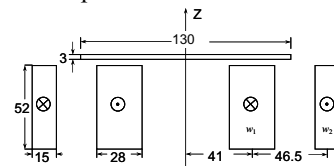


Fig. 1. The dimension of the TEAM Workshop 28 Problem

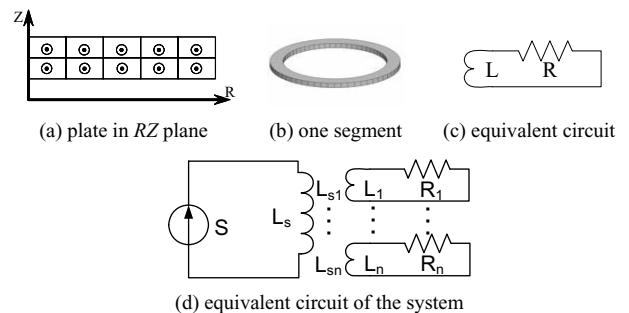


Fig. 2. Equivalent circuits of the TEAM problem 28.

$$\sum_{j=1}^N L_{ij} \dot{I}_j = -I_i R_i - \sum_{s=1}^2 L_{is} \dot{I}_s - \sum_{s=1}^2 I_{N+2} I_s \frac{\partial L_{is}}{\partial z}, \quad i=1, \dots, N \quad (3-a)$$

$$\dot{I}_{N+1} = I_{N+2} \quad (3-b)$$

$$\dot{I}_{N+2} = (F_{em} - F_G)/M \quad (3-c)$$

where I_{N+1} , I_{N+2} and M are the position, speed and mass of the plate, respectively, F_{em} and F_G are the electromagnetic and gravitational forces acting on the plate, respectively. In the solution of (3), I_i ($i=1,2,\dots,N$) and F_{em} are found from the previous time-step, and Runge-Kutta-Fehlberg method is introduced to control the step-size automatically.

After finding the eddy currents in each segment, the electromagnetic repulsive force is computed as follows:

$$F_{em} = -\sum_{s=1}^2 \sum_{i=1}^N I_s I_i \frac{\partial L_{si}}{\partial z} [N] \quad (4)$$

B. Adaptive Segmentation of the Conducting Plate

The efficiency and accuracy of the proposed algorithm strongly depend on the segmentation of the conducting plate since the distribution of the eddy currents in conducting plate is a lot affected by the segmentation just like mesh refinement in FEM. According to the electromagnetic field theory, the tangential component of electric field intensity should be continuous at the interface of two segments. From this, together with Ohm's law, we get, at the interface of segments, the condition of $J_{1t} = J_{2t}$. In this paper, local field continuity error for a segment (e), shown in Fig. 3(a), is defined as follows:

$$e^{(e)} = \int_{t_1}^{t_2} \left(\sum_{k=1}^{N_e} |J^{(e)} - J_k| \cdot l_k / \sum_{k=1}^{N_e} l_k \right) dt \quad (5)$$

where N_e is the number of the neighboring segments of e -th segment, $J^{(e)}$ and J_k are the eddy current densities of the e -th segment and the k -th neighboring segment, respectively, l_k is the length of the overlapped interface between e -th segment and the k -th neighboring segment as shown in Fig. 3 (a). After computing the local error for all segments, the segments with local error of $1.1\bar{e} \leq e^{(e)} \leq 1.5\bar{e}$ is refined into two, and those with $e^{(e)} \geq 1.5\bar{e}$ into four segments, respectively, as shown in Fig. 3(b) and Fig. 3(c).

C. Solving Procedure

The overall solving procedure of the proposed method is summarized as follow:

- Step 1. Divide the conducting plate into several uniform segments.
- Step 2. Calculate all circuit parameters, and set up the state equations.
- Step 3. Solve the state equations in time domain, and calculate the local field continuity error for all segments.
- Step 4. Stop if the final displacement is converged. Otherwise

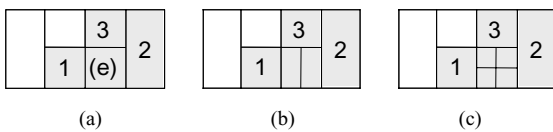


Fig. 3. Segment refinement. (a) before refinement, (b) into two segments, (c) into 4 segments.

refine the segments and go to Step 2.

III. NUMERICAL RESULTS

Fig. 4 shows the distribution of the segments with eddy current density in each segment at different iterations, and Fig. 5 compares the distribution of the eddy current density at the plane of $z=4.6\text{mm}$ as the plate is refined. It is observed that the proposed algorithm gives very smooth eddy current distribution compared with uniform segments. The numerical efficiency and accuracy of the proposed method are shown in Fig. 6 and Table I by comparison with FEM and experimental results. As it is seen from the comparison, the proposed method is much more efficient than FEM and uniform refinement, and also has a good accuracy.

In the version of full paper, the proposed algorithm will be applied to the performance analysis of a Thomson-coil actuator for a high-speed circuit breaker, and the results will be discussed.

IV. REFERENCES

- [1] T. Takeuchi, et al., "Electromagnetic analysis coupled with motion for high-speed circuit breakers of eddy current repulsion using the tableau approach," *Electrical Engineering in Japan*, 152(4), pp. 8-16, 2005.
- [2] S.M. Lee, et al., "Reduced modeling of eddy current-driven electromechanical system using conductor segmentation and circuit parameters extracted by FEA," *IEEE Trans. on Magn.*, 41(5): 1448-1451, 2005.
- [3] Fawzi TH, et al., "The accurate computation of self and mutual inductances of circular coils," *IEEE Trans Power Apparatus Syst.*, 97(2): 464-468, 1978.

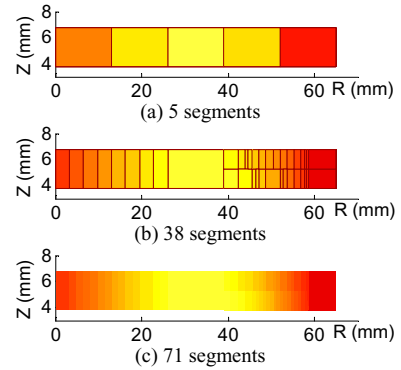


Fig. 4. Segmentation and eddy current density distribution.

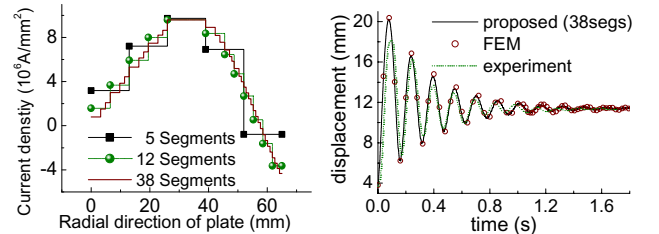


Fig. 5. Distribution of current density

Fig. 6. Comparison of results

TABLE I
COMPARISON OF ACCURACY AND EFFICIENCY

	Measured	FEM	Proposed method (Number of segments)				
			5	11	20	38	71
Final position	11.3	11.39	11.05	11.29	11.37	11.38	11.40
Computing time	-	5340	1	3	19	124	1018

* Position and time are in (mm) and (minutes), respectively.

Proposal of a Benchmark for Multi-Level Optimization with 3D Finite Element Model

T. V. Tran, S. Brisset, and P. Brochet, *Members, IEEE*

L2EP, Ecole Centrale de Lille, Cité Scientifique, BP 48, 59651, Villeneuve d'Ascq Cedex, France

Abstract—A benchmark is proposed in order to compare algorithms for multi-level optimization. The device is a safety transformer. The discrete design variables are belonging to standard values for lamination, frame, and wire leading to 246,078,000 feasible solutions. Two models are available to compute the objectives and constraints: a 3D FE fine model and a lumped model. Their computation times are 2 hours and 50 ms, respectively. Combining their properties during the optimization greatly reduce the computation time.

Index Terms—Multi-level optimization, discrete optimization, space mapping technique, benchmark, 3D FEA

I. INTRODUCTION

Nowadays, the finite element (FE) method is often used to model electromagnetic devices with a high accuracy. The FE models in two or three dimensions (2D, 3D) are considered as virtual prototypes. However, the multi-physical coupling and the great number of unknowns in 3D FE models are very time consuming.

In the design of electrical devices, discrete design variables occur naturally in the optimization problem formulation. For instance, the numbers of slots and magnets are integers, and the type of materials and structure are discrete. However, discrete optimization requires different concept than the conventional continuous problems. Derivatives do not directly apply to the combinatorial optimization problem. So the amount of model evaluations during the discrete optimization is much higher than the continuous one.

Applying directly the optimization methods to 3D FE models may lead to an excessive computation time going from several days to few months. So replacing the 3D FE model by a surrogate model that is less time consuming is an interesting way to reduce the computation time of optimization. However, the quality of the solution should be as good as the one found with the FE model.

According to the state of the art, the global optimization with a FE model and its surrogate version can be done in two steps. The first step consists in the progressive building of a response surface. New points are added in the areas where the surrogate model is not accurate enough. The global optimum is found in the second step with any algorithm requiring a high number of evaluations such as genetic algorithms (GA). Several methods are used to build the surrogate model: diffuse element method [1], Kriging methods [2], artificial neural networks [3]-[5], and radial basis functions [6]. The surrogate model has the advantages to be fast to compute, smooth, and to have explicit derivatives at low cost. Other approaches use an inaccurate surrogate model that is progressively refined where temporary

optimums lie [7]. In the EGO method [8], the surrogate model is also refined with points belonging to areas where the accuracy is low. Unfortunately, all those methods require a high the number of evaluations of the FE model to build the surrogate model. This is cancelling the benefits of the optimization with the surrogate model because the total time of identification and optimization is often similar to the time of a direct optimization with the FE model.

To reduce significantly the number of FE model evaluations, the surrogate model has to contain initially some knowledge. It can be analytical equations describing the physical phenomena within the device or a lumped model. This model is called coarse model and can be improved locally thank to the FE model that is called fine model. Combining both models is called multi-level optimization and the space-mapping techniques are very effective to solve them [9]-[11].

The COMPUMAG TEAM workshops propose two benchmarks for optimization with FE models [12]-[13]. The models are 2D static magnetic and require few minutes for each evaluation. Thanks to them, continuous, discrete, and multi-objective optimization algorithms have been proposed and compared. Unfortunately, no coarse model is available for the superconducting magnetic energy storage system and the die press.

In many electromagnetic devices such as motors, transformers, electromagnets, etc. it is possible to build a lumped model and a FE model. Therefore, this paper proposes a benchmark for multi-level optimization with both models. The device is a transformer and a 3D FE model with a fine mesh is required to have accurate results on the leakage inductance, for instance. The computation time of the fine and coarse models are 2 hours and 50 ms, respectively.

In the next sections, the optimization problem, the fine model and the coarse model are described. A first result is shown in section IV. Finally, some conclusions are given.

II. OPTIMIZATION PROBLEMS

The safety isolating transformer uses grain-oriented E-I laminations. The primary and secondary windings are both wound around the frame surrounding the central core (Fig. 1).

The optimization problem contains 7 discrete design variables: three parameters $\{a, b, c\}$ for the shape of the lamination; one for the frame $\{d\}$; two for the section of conductors $\{S_1, S_2\}$ and one for the number of primary turns $\{n_1\}$ (Fig. 1). There are 24 types of lamination E-I, 62 types of frame F and 63 types of enameled wire W given in standard catalogues. The number of primary turns n_1 is integer but only 1,000 values are allowed, leading to 246,078,000 possible combinations.

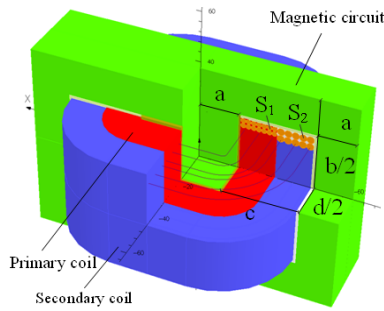


Fig. 1. Geometry of the transformer problem in 3-D.

There are 7 non-linear inequality constraints. The copper and iron temperatures T_{co} , T_{ir} respectively should be less than 120°C and 100°C . The efficiency η should be greater than 80%. The magnetizing current I_μ/I_1 and drop voltage $\Delta V_2/V_2$ should be less than 10%. Finally, the filling factors of both coils f_1, f_2 should be lower than 0.5 for round wire.

The objective function aims to minimize the mass of iron and copper materials. So the problem can be expressed as:

$$\begin{aligned}
 \min \text{ mass}(X) & \quad \text{s.t.} & \quad \eta \geq 0.8 \\
 X = \{a, b, c, d, S_1, S_2, n_1\} & \quad T_{co} \leq 120^\circ\text{C} & \quad I_\mu/I_1 \leq 0.1 \\
 \{a, b, c\} \in \text{E-I} \quad d \in \text{F} & \quad T_{ir} \leq 100^\circ\text{C} & \quad \Delta V_2/V_2 \leq 0.1 \\
 S_1, S_2 \in \text{W} \quad n_1 \in \text{N} & \quad f_1 \leq 0.5 & \quad f_2 \leq 0.5
 \end{aligned} \quad (1)$$

One of the constraints, e.g. the efficiency, may be changed to an objective in order to set up a multi-objective optimization problem: minimize *mass* and maximize η .

III. MODELS

A. 3D finite element "fine" model

Thermal and magnetic phenomena are both modeled by using 3D FEA on one eighth of the transformer due to the symmetries. For the electromagnetic modeling, all magnetic and electric quantities are assumed sinusoidal. Full load and no-load simulations are used to compute all the characteristics. The iron loss is computed with Steinmetz formula and the leakage inductances are calculated with the magnetic co-energy. The magneto-thermal coupling requires about 2 hours.

B. Lumped "coarse" model

The modeling hypotheses are uniform distribution of induction in the iron core and no voltage drop due to the magnetizing current. The thermal assumptions are the same than the 3D FE model except that the temperatures are uniform within the coils and the lamination. The lumped model contains five elements and the computation time about 50 ms.

IV. FIRST RESULT

One algorithm combining Branch-and-Bound method with Output Space-Mapping obtain a solution by using 4 evaluations

of FE model and 127,852 evaluations of lumped model [14]. The total time for optimization is then less than 10 hours.

V. CONCLUSION

A benchmark is proposed in order to compare algorithms for multi-level optimization. The device is a safety transformer. The discrete design variables are belonging to standard values for lamination, frame, and wire leading to 246,078,000 feasible solutions. Two models are available to compute the objectives and constraints: a 3D FE model and a lumped model. Their computation times are 2 hours and 50 ms, respectively.

This benchmark meets the requirements of engineers and scientists working on the design of electromagnetic devices by using 3D FE models. It is dedicated to highlight the most effective multi-level optimization methods.

REFERENCES

- [1] M.C. Costa, J.L. Coulomb, Y. Maréchal, A.B. Dietrich, and S.I. Nabeta, "Diffuse-Element Method and Quadrees: Two Ingredients for an Adaptive Response Surface", *IEEE Transactions on Magnetics*, 38(2): 1085-1088, 2002.
- [2] L. Lebensztajn, Marretto C.A.R., M.C. Costa, and J.L. Coulomb, "Kriging: A Useful Tool for Electromagnetic Device Optimization", *IEEE Transactions on Magnetics*, 40(2): 1196-1199, 2004.
- [3] K. Rashid, J.A. Ramirez, and E.M. Freeman, "Optimization of Electromagnetic Devices using Sensitivity Information from Clustered Neuro-Fuzzy Models", *IEEE Transactions on Magnetics*, 37(5): 3575-3578, 2001.
- [4] A. Fanni, and A. Montisci, "A Neural Inverse Problem Approach for Optimal Design", *IEEE Transactions on Magnetics*, 39(3): 1305-1308, 2003.
- [5] D.G. Vieira, D.A.G. Vieira, W.M. Caminhas, , and J.A. Vasconcelos, "A Hybrid Approach Combining Genetic Algorithm and Sensitivity Information Extracted from a Parallel Layer Perceptron", *IEEE Transactions on Magnetics*, 41(5): 1740-1743, 2005.
- [6] A. Kobetski, J.L. Coulomb, M.C. Costa, Y. Maréchal, and U. Jönsson, « Comparison of Radial Basis Function Approximation Techniques », *COMPEL*, 22(3): 616-629, 2003.
- [7] U. Pahner, and K. Hameyer, « Adaptive Coupling of Differential Evolution and Multiquadratics Approximation for the Tuning of the Optimization Process », *IEEE Transactions on Magnetics*, 36(4): 1047-1051, 2000
- [8] D.R. Jones, M. Schonlau, and W. Welch, "Efficient Global Optimization of Expensive Black-Box Functions", *Journal of Global Optimization*, 13(4): 455-492, 1998.
- [9] H. Choi, D. Kim, I. Park, and S. Hahn, "A New Design Technique of Magnetic Systems using Space Mapping Algorithm", *IEEE Trans. on Magn.*, 37(5): 3627-3630, 2001.
- [10] J.W. Bandler, Q.S. Cheng, S.A. Dakroury, A.S. Mohamed, M.H. Bakr, K. Madsen, and J. Sondergaard, "Space Mapping: The State of the Art", *IEEE Trans. Microwave Theory Tech.*, 52(1): 337 - 361, 2004.
- [11] D. Echeverria, D. Lahaye, L. Encia, E. A. Lomonova, P. W. Hemker, and A. J. A. Vandenput, "Manifold-Mapping Optimization Applied to Linear Actuator Design", *IEEE Transactions on Magnetics*, 42(4): 1183-1186, 2006.
- [12] Alotto P., Kuntsevitch A.V., Magele C., Molinari G., Paul C., Preis K., Repetto M., and Richter K.R., « Multiobjective optimization in magnetostatics: a proposal for benchmark problems », *IEEE Transactions on Magnetics*, Vol. 32, No. 3, Part 1, May 1996, pp. 1238-1241, http://www.igte.tugraz.at/archive/team_new/description.php
- [13] N.Takahashi, K.Ebihara, K.Yoshida, T.Nakata, K.Ohashi and K.Miyata: "Investigation of simulated annealing method and its application to optimal design of die mold for orientation of magnetic powder", *IEEE Trans. on Magnetics*, 32, 3, pp.1210-1213, 1996 <http://www.compumag.co.uk/problems/problem25.pdf>
- [14] T. V. Tran, S. Brisset, and P. Brochet, "A New Efficient Method for Global Discrete Multi-Level Optimization combining Branch-and-Bound and Space-Mapping", *IEEE Transactions on Magnetics*, vol. 45, no. 3, 2009.

Visualization Method of Magnetic Flux Lines with Accurate Allocation Applying Tube System

So Noguchi, Hajime Igarashi and Hideo Yamashita*
Hokkaido University, N14 W9 Kita-ku, Sapporo 060-0814, Japan
E-mail: noguchi@ssi.ist.hokudai.ac.jp

*Hiroshima Institute and Technology, 2-1-1 Miyake, Saeki-ku, Hiroshima 731-5193, Japan

Abstract— This paper presents a visualization method of magnetic flux lines applying Tube System. Incomplete visualization of magnetic flux lines leads to misunderstanding about the magnetic field and the phenomenon to an observer. We have already proposed a method to compute the magnetic flux lines analytically from edge finite element results. In this paper, a method to appropriately allocate the magnetic flux lines in 3-D space applying the Tube System is discussed. In the proposed method, the tube's radius depends on the strength of the magnetic field, which regulates the density of the lines. The proposed method can generate the appropriate visualization of the magnetic flux lines, thus allowing the observer to correctly interpret the magnetic field and the phenomenon.

I. INTRODUCTION

A huge amount of numerical data results from electromagnetic field analysis, with improvement of computer performances and development of analysis methods in recent years. From the huge data, it is difficult to interpret the physical phenomenon and to mine the valuable information. Some ways of electromagnetic field visualization are, therefore, used, such as contour, distribution and vector maps, as a tool of magnetic field analysis software. These ways are effective to quantitatively visualize the field on an arbitrary 2-D plane, but unsuitable for 3-D field visualization. The magnetic flux line visualization is the most effective way to grasp the magnetic field in 3-D space, so it offers the observer the qualitative understanding about the characteristics.

A few methods to visualize the magnetic flux line have been proposed [1], [2]. In [1] and [2], the magnetic flux lines are computed analytically from the tetrahedral and hexahedral edge finite element results. These works, however, do not deal with the problem to appropriately allocate the magnetic flux lines, in proportion to the magnetic flux density. The demands for the visualization of the magnetic flux lines are:

- (i) the density of magnetic flux lines is proportional to the strength of the magnetic flux density, $|\mathbf{B}|$ [T],
- (ii) the tangential direction of magnetic flux line is the same as the direction of the magnetic field at each point.

It is necessary to draw the magnetic flux lines according to the demands mentioned above. The demand (i) reveals that the magnetic flux lines must be allocated in proportion to the magnetic flux density.

In this paper, a method to appropriately allocate the magnetic flux lines applying the Tube system is proposed on demands of magnetic flux line visualization. The Tube System is newly developed for 3-D magnetic flux line visualization based on the Dynamic Bubble System, [3], [4], which is used

for mesh generation. It deals with a sphere, called the *bubble*. However, a magnetic flux line cannot be represented by the sphere. In the newly developed Tube System, a tube surrounding a magnetic flux line is employed. The tube diameter and the attractive force between tubes, called the *tube force*, depend on the magnetic flux density. The tubes move until the distribution reaches a closely-packed configuration.

II. ALLOCATION OF MAGNETIC FLUX LINES

The allocation of magnetic flux lines must obey the demands given in Section I, so that the observer can qualitatively grasp the magnetic field direct from the lines. Before, the method to allocate the magnetic flux lines was proposed in [5]. It has a difficulty to specify a plane intersecting with all the magnetic flux lines by hand. On the intersecting plane, the Dynamic Bubble System [3], [4] is applied to allocate the magnetic flux lines, as shown in Fig. 1. It requires a difficult labor for user and it has the problem that the allocation of magnetic flux lines cannot be obtained when the plane intersecting with all the magnetic flux lines does not exist in the analysis domain.

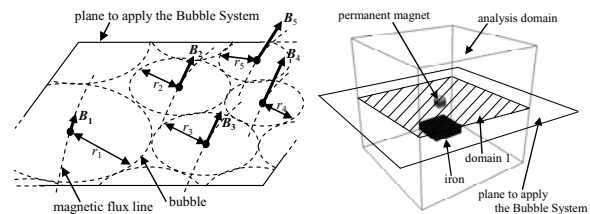


Fig. 1. The previously proposed method has a problem for user to specify a plane which intersects with all the magnetic flux lines.

In order to address the problem, we have developed the method applying the Tube System, which is unnecessary to specify the plane intersecting with all the magnetic flux lines.

In the Tube System, a virtual tube is supposed to surround a magnetic flux line, as shown in Fig. 2. According the demands (i), the radius of tube, R , is in proportion to the strength of magnetic field;

$$R \propto \frac{1}{\sqrt{|\mathbf{B}|}}, \quad (1)$$

where $|\mathbf{B}|$ is the magnitude of magnetic flux density on the center of tube. Thus, the radius of tube changes with the location. In order to effectively visualize the magnetic field,

the tube radius R is controlled by multiplying an arbitrary constant value c ;

$$R = \frac{1}{\sqrt{|B|}} \times c \quad (2)$$

When c is too large, the number of the magnetic flux lines drawn is too small for the user to grasp the phenomenon. In order for the user to effectively grasp the magnetic field, the value of the constant c must be suitably controlled.

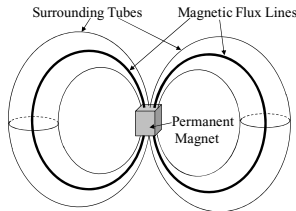


Fig. 2. An example of surrounding tubes and magnetic flux lines generated from a permanent magnet.

In order to closely-packedly allocate the magnetic flux lines, the tubes must move by the tube force, which depends on the tubes' radius and their distance. The tube force is categorized as follows:

- (i) attractive force when $l > r_A + r_B$,
- (ii) zero force when $l = r_A + r_B$,
- (iii) repulsive force when $l < r_A + r_B$,

where l is the distance of tubes, r_A and r_B are the radius of the magnetic flux lines A and B , respectively, as shown in Fig. 3. The function of the tube force [3], [4] is given as

$$F(l) = \alpha l^3 + \beta l^2 + \gamma l + \delta, \quad (3)$$

where $F(l)$ is shown in Fig. 6. The coefficients α , β , γ and δ are obtained from $F(l_0) = 0$, $F'(l_0) = 0$, $F(0) = M$ and $F'(0) = 0$, $l_0 = r_A + r_B$, u_{l_0} and M are the effective range of tube force and the maximum force, respectively.

III. MAGNETIC FLUX LINE VISUALIZATION

A. Permanent Magnet and Iron Model

An example is shown in Fig. 5, where the magnetic flux lines are analytically computed from the FEA result of the

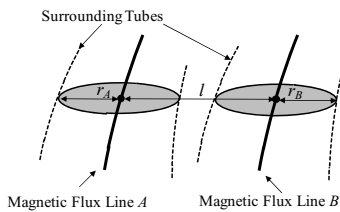


Fig. 3. The tube force acting between magnetic flux lines A and B depends on the radii r_A , r_B and the distance l .

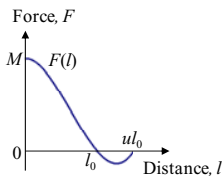
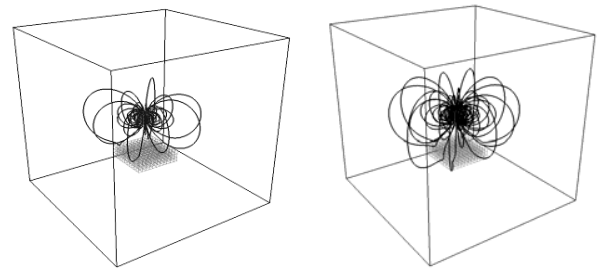


Fig. 4. The tube force is calculated from $l_0 = r_A + r_B$, the maximum force M , and the effective range of the force u_{l_0} .

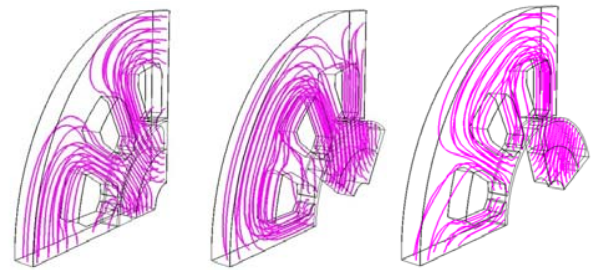
model consisting of a permanent magnet and an iron plate in Fig. 1. Fig. 5(a) shows the result with $c = 50$ in (2), the number of the drawn magnetic flux lines is 32. In Fig. 5(b), 79 magnetic flux lines are drawn with $c = 100$. It is easy to control the number of the drawn magnetic flux lines. In both results, the rational allocations of the magnetic flux lines are achieved.

B. Permanent Magnet Motor Model

The proposed method is applied to a surface permanent magnet motor. It is difficult to visualize the magnetic flux lines since the rotor rotates. Fig. 6 shows the magnetic flux lines of the rotating motor. As the result, it is possible to represent the smoothly changing magnetic flux lines while the rotor is rotating.



(a) 32 lines with $c = 50$ (b) 79 lines with $c = 100$
Fig. 5. The magnetic flux lines are visualized.



(a) 0 deg. (b) 33.3 deg. (c) 66.7 deg.
Fig. 6. The magnetic flux lines of the rotating motor.

IV. CONCLUSION

We have proposed the method to rationally allocate the magnetic flux lines utilizing the Tube System. The proposed method and two examples are shown. The magnetic flux line visualization helps us to interpret the magnetic field and the phenomenon.

V. REFERENCES

- [1] V. Cingoski, et al., "Analytical calculation of magnetic flux lines in 3-D space," *IEEE Trans. on Magnetics*, 30(5): 2912-2915, 1994.
- [2] S. Noguchi, et al., "Analytical computation and visualization of magnetic flux lines in 3-D space from hexahedral edge finite element results," *IEEE Trans. on Magnetics*, 41(5): 1820-1823, 2005.
- [3] K. Shimada, "Physically-based automatic mesh generation," *Journal of the Japan Society for Simulation Technology*, 12(1): 11-20, 1993.
- [4] T. Ykoyama, et al., "3-D Automatic Mesh Generation for FEA Using Dynamic Bubble," *IEEE Trans. on Magnetics*, 35(3): 1318-1321, 1999.
- [5] M. Hirahatake, et al., "Allocation Method of Magnetic Flux Lines Using Bubble System for Magnetic Field Visualization," *Proc. COMPUMAG 2007*, 1: 81-82, 2007.

A Weakly Coupled Parallel 2D Delaunay Refinement Algorithm

Mauro Massayoshi Sakamoto, José Roberto Cardoso, Marcelo Facio Palin, Maurício Barbosa de Camargo Salles
 LMAG - PEA - EPUSP - Av. Prof. Luciano Gualberto, trav. 3 - n. 158 - 05508-900 - São Paulo/SP - Brazil
 Email: mauro@pea.usp.br; cardoso@pea.usp.br; palin@pea.usp.br; mausalles@pea.usp.br

Fabio Henrique Pereira
 Universidade Nove de Julho – Rua Vergueiro, 235 - 01504-001 – São Paulo/SP – Brasil
 Email : fabiohp@uninove.br

Abstract – A strategy for the parallel 2D Delaunay refinement algorithm is proposed in this work. The implementation approach is based on the decomposition of the initial coarse mesh into smaller subdomains which are refined in parallel. The developed parallel method presents few message-passing operations and low communication costs due to application of a preresinement and a discretization of the segments along the boundaries.

I. INTRODUCTION

Nowadays, the immense technological progress provides access to powerful computers for problem resolution, mainly in areas such as Computational Fluid Dynamics (CFD) and Computational Electromagnetics (CEM) that require larger meshes [1].

Methods such as Delaunay Algorithm [2], [3] or Advancing Front [4] can be applied for 2D quality grid generation. Nevertheless, the mesh generation grows with the problem size, thus the triangulation produces very large meshes with millions of elements, increasing the processing time and, in some cases, exceeding the memory capacity.

The advent of the cluster brought a new programming strategy: the parallel programming. Parallel mesh refinement decomposes the initial mesh into smaller submeshes which are refined in parallel. However, this induces unpredictable communication costs with degree of dependency or synchronization [5].

An alternative to overcome this problem is the application of two strategies in order to minimize the synchronization between the subdomains.

First of all, the initial coarse mesh is preresefined by eliminating the extremely obtuse triangles generating a less poor “initial mesh” [6]. Second, the discretization of the boundary segments along neighboring partitions decrease the coupling between them [5].

II. PARALLEL 2D DELAUNAY REFINEMENT

Typically, a Delaunay mesh refinement finds an initial mesh starting from a collection of vertices and segments, also known as *Planar Straight Line Graph* (PSLG). In a triangulation, only the half-lines of the input PSLG will be considered segments, while the other ones are edges [3].

This work was supported in part by the CNPQ under Grand No. 140226/2002-8

The next stage is to decompose the coarse grid into smaller subdomains using METIS, a popular partitioning program from the University of Minnesota [7].

The partitions are distributed over the nodes of the cluster, where each submesh is refined concurrently. If a boundary segment is split, the neighboring subdomains are updated for this split by means of messages [8], ensuring the conformity of the mesh along the interfaces.

However, this synchronization strategy has high coupling, presenting high communication costs.

III. COMMUNICATION STRATEGY

The main insight of this algorithm is to attempt to reduce the communication and synchronization, through improvements in the initial mesh, resulting in submeshes nicely subdivided with minimal interaction among processors, which enables a weak coupled between shared subsegments.

The algorithm does not divide the initial coarse mesh; firstly, a preresinement, method developed by the authors [6], was used to try to eliminate triangles whose apex angle is extremely obtuse, generating an “initial mesh” with fewer small angles, instead.

Therefore, the preresinement strategy improves the coarse grid allowing the METIS to get submeshes with few extremely obtuse triangles in the boundary segments, decreasing the encroached subsegments and, consequently, less refinement is necessary in these places [6].

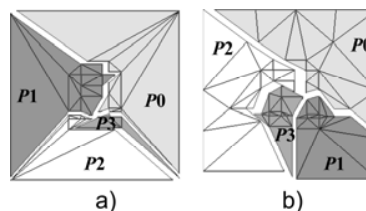


Fig. 1. Traditional domain decomposition (a) and with reduced communication strategy (b).

Another important optimization is the discretization of the segments along their common boundary. The goal of this step is to anticipate the addition of the necessary vertices to guarantee a boundary conforming along the shared segments, decreasing more and more the number of the message-passing between them.

The discretization proposed differs from others in that, instead of generating a constrained Delaunay triangulation, it ensures that all elements are Delaunay.

As Fig. 1a shows, the submeshes have very small angles in boundary segments due partition of the initial coarse mesh of an electromagnet. In Fig. 1b, a few small angles are generated by prerenement application.

IV. RESULTS

The examples approach the final parallel mesh of an electromagnet with 4 partitions. In Fig. 2 a traditional parallelism is accomplished, while Fig. 3 illustrates the mesh with low synchronization obtained by the developed method, i.e., with weakly coupled parallelism.

The comparison of the traditional algorithm and the communication strategy execution for an electromagnet with 4 partitions is shown in Tables I and II. Table I summarizes the number of message-passing for the traditional parallel refinement. Similarly, Table II presents the results for the method proposed.

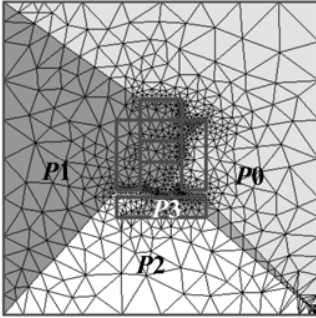


Fig. 2. Parallel mesh of an electromagnet without reduced communication strategy.

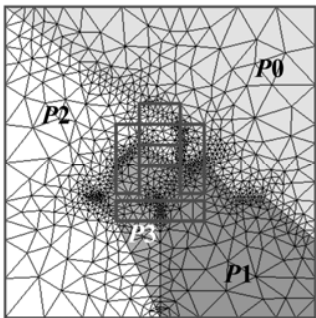


Fig. 3. Parallel mesh of an electromagnet with reduced communication strategy.

TABLE I: PARALLEL REFINEMENT WITHOUT COMMUNICATION STRATEGY.

Process	No of triangles	No of sent messages	No of received messages	Time (s)
P_0	386	9	35	<2
P_1	313	6	9	<2
P_2	170	9	36	<2
P_3	208	65	9	<2

TABLE II: PARALLEL REFINEMENT WITH COMMUNICATION STRATEGY.

Process	No of triangles	No of sent messages	No of received messages	Time (s)
P_0	578	2	2	<1
P_1	367	2	7	<1
P_2	637	4	5	<1
P_3	392	11	5	<1

V. CONCLUSIONS

The presented strategies provided substantial improvements in the communication reduction in parallel 2D Delaunay refinement. The experimental results showed that the algorithm is weakly coupled or even decoupled according to the problem.

The prerenement generates a less poor “initial mesh”, so supplying quality submeshes with low degree of dependency, by decreasing the number of encroached subsegments. In addition, the discretization of the common boundary “predicts” the local of futures vertices, thus minimizing or eliminating the amount of necessary communication to ensure the conformity along the shared segments.

Another possibility to reduce more and more the communication is to smoothing the boundary between the subdomains, i.e., if an element has more neighbors in a neighboring partition, then the element is transferred from original partition to this neighboring subdomian.

Future works intend to smooth the boundaries, and, besides, to extend the developed strategies to a three-dimensional version. The key idea is to apply the diametral sphere and equatorial sphere techniques [2] to extend the prerenement process for 3D.

REFERENCES

- [1]. R. Said, N. P. Weatheril, K. Morgan, and N. A. Verhoeven, “Distributed parallel Delaunay mesh generation”, *Comput. Meth. Appl. Mech. Engrg*, 177, pp. 109-125, 1999.
- [2]. J. R. Shewchuk, “Delaunay refinement mesh generation”, Ph.D. dissertation, School Comput. Sci., Carnegie Mellon Univ., Pittsburg, PA, May 1997.
- [3]. J. Ruppert, “A Delaunay refinement algorithm for quality 2-dimensional mesh generation”, *J. Algorithms*, vol. 18, no 3, pp. 548-585, May 1995.
- [4]. R. Löhner and P. Parikh, “Generation of three-dimensional unstructured grids by the advancing-front method”, *Int. J. of Num. Meth. in Fluids*, vol. 8, pp. 1135-1149, 1988.
- [5]. A. N. Chernikov and N. P. Chrisochoides, “Algorithm 872: Parallel 2D constrained Delaunay mesh generation”, *ACM Transactions on Mathematical Software*, vol. 34, no. 6, 2008.
- [6]. M. M. Sakamoto, J. R. Cardoso, J. M. Machado, and M. B. C. Salles, “A 2-D Delaunay refinement algorithm using an initial prerenement from the boundary mesh”, *IEEE Transactions on Magnetics*, vol. 44, no. 6, pp. 1418-1421, June 2008.
- [7]. G. Karypis and V. Kumar, *METIS* A Software Package for Partitioning Unstructured Graphs, Partitioning Meshes, and Computing Fill-Reducing Orderings of Sparse Matrices*. Minneapolis: Univ. Minnesota, Dept. Comput. Sci./Army HPC Res. Center, 1998.
- [8]. P. Pacheco, *Parallel Programming with MPI*. San Francisco, CA: Morgan Kaufmann, 1996.
- [9]. C. O. Moretti, T. N. Bittencourt, “Uma técnica paralela para geração de malhas tridimensionais”, Technical report, Escola Politécnica da Universidade de São Paulo, 2001, vol. 0109, pp. 1-12.

The Broad Sense Chain-Making and Chain-Coupling Theorems of Element Grid in 2-D Problems

Nan Xiong^{1*}, Kexun Jiang²

¹ Institute of Electrical Engineering Chinese Academy of Sciences, Beijing, 100190, China

² Department of Electrical Engineering, Chongqing University, Chongqing, 400044, China
Email: xiongnan@mail.iee.ac.cn

Abstract-The purpose of these papers is to answer a basic problem of finite element method that is how do the elements which have determined shapes form the element grid which has determined structure. In order to study this problem, a method called chain-making and chain-coupling is established. Through this method the quantitative relationships between the geometric structures of the element grid and the geometric structures of its elements are founded. This problem is studied both in 2-D and 3-D cases and here is the second part of 2-D case conclusions.

I. INTRODUCTION

In order to answer the problem of how do the elements which have determined shapes form the element grid which has determined structure, a method called chain-making and chain-coupling is established. In the method, the relationships between elements in an element grid are classified according to their topological relationships. Then through defined steps the element grid which has complicated relationships between its elements can be disassembled to another element grid which just has a single kind of 0-dimension relationship between its elements. The disassembled element grid is called chain, and the disassemble procedure is called chain-making.

In a chain, elements have simple relationships of 0-dimension, so the quantitative relationships between the geometric structures of the chain and the geometric structures of its elements can be found relatively easily.

On the other hand, the 0-dimension relationships between the elements in a chain are inherited from the original element grid, so the original element grid can be reassembled from its chain. The procedure about how does the original element grid to be reassembled from its chain is called chain-coupling. By studying the chain-coupling procedure, basic properties about how do the elements in a chain form the original element grid are found, and the quantitative relationships between the geometric structures of the element grid and the geometric structures of its elements are found. So the problem of how do the elements which have determined shapes form the element grid which has determined structure are answered

II. NARROW SENSE CHAIN-MAKING AND CHAIN-COUPLING THEOREM OF 2-D GRID

Definition 2-1: Vertex Chain

On a set N which consists of elements with a number of n , a function f can be defined as following:

1. The first element e_1 just has one 0-dimension relationship with the second element e_2 through a common vertex v_{12} ;
2. The i th ($1 < i < n$) element e_i has one 0-dimension relationship with the $(i-1)$ th element e_{i-1} through a common vertex $v_{(i-1)i}$, and it has one 0-dimension relationship with the $(i+1)$ th element $e_{(i+1)}$ through a common vertex $v_{i(i+1)}$;
3. The n th-element e_n just has one 0-dimension relationship with the $(n-1)$ th element $e_{(n-1)}$ through a common vertex $v_{(n-1)n}$;

Thus the elements in set N are mapped to a vertex chain through function f .

Theorem 2-1: The first chain-making theorem in 2-D grid

In a 2-D triangle grid, if there are not cut-vertex, cut-edge and interior boundary in it, this triangle grid can be made into a vertex chain.

Theorem 2-2: The second chain-making theorem in 2-D grid

In a 2-D rectangle grid, if there are not cut-vertex, cut-edge and interior boundary in it, this rectangle grid can be made into a vertex chain.

Theorem 2-3: In a 2-D vertex chain, if the element number is n , the edge number of every element is m , then the total edge number in the chain is $l_c = n \times m$ and the total vertex number in the chain is $v_c = (n \times m) - (n - 1)$.

Theorem 2-4: Narrow sense chain-coupling theorem in 2-D grid

In a narrow sense chain-makeable 2-D grid among the number of elements: n , the edges of every element: m , total number of edges of the grid: l , number of boundary edges: l_b , number of interior edges: l_i ; total number of vertexes of the grid: v , number of interior vertexes: v_i , the following quantitative relationships hold:

$$l_i = (n \times m - l_b) / 2 \quad (1)$$

$$l = (n \times m + l_b) / 2 \quad (2)$$

$$v = l - (n - 1) \quad (3)$$

$$v_i = l - (n - 1) - l_b \quad (4)$$

The concern concepts and the demonstration of these theorems can be found in reference [1].

III. BROAD SENSE CHAIN-MAKING THEOREM

As shown in reference [1], the condition and procedure for narrow sense chain-making and chain-coupling are quite strict

and complicated. At the same time, along with these discussions, a very important property of chain-making and chain-coupling can be found, that is when the chain-coupling property of the n th element on a vertex chain is studied, the continuity of the n th element in the $(n-1)$ th order chain-making grid and n th order chain-coupling grid are required. But when this continuity is satisfied, it is not required that the original element grid could be made into a entire vertex chain, and there could be some branches in the making out vertex chain.

Definition 3-1: Branched Vertex Chain

A function f can be defined on a set N which consists of elements with a number of n , if it makes the i th ($i \leq n$) element e_i in the j th ($j \geq 1$) branch has one 0-dimension relationship with the $(i-1)$ th element e_{i-1} through a common vertex $v_{(i-1),j}$, then the elements in set N are mapped to a branched vertex chain through function f .

Definition 3-2: Branching Element in a Branched Vertex Chain

If branches appear on an element of a branched vertex chain, this element is called a branching element of the branched vertex chain.

Theorem 3-1: Chain-making Theorem in 2-D Grid

A 2-D grid can be made into one branched vertex chain at least.

IV. BROAD SENSE CHAIN-COUPLING THEOREM

Theorem 4-1: Theorem of Branched Chain-coupling

Branches in a branched vertex chain have no influence on the result of chain-coupling.

Theorem 4-2: In a 2-D branched vertex chain consist of elements of m edges and with element number of n , there are n element, $l_c = n \times m$ edges and $v_c = (n \times m) - (n - 1)$ vertexes in it.

Theorem 4-3: If there are x class touch vertexes with order of d_u ($1 \leq u \leq x$) and number of n_u ($1 \leq u \leq x$) for each class, in a 2-D grid with boundary edge number of l_b , then number of

boundary vertex in it is $v_b = l_b - \sum_{u=1}^x n_u \times d_u$.

Theorem 4-4: Chain coupling theorem in 2-D grid

In a 2-D grid if there are x class touch vertexes in it, among the number of elements: n , the sides of every element: m , the number of interior boundary i , the order of the x class touch point d_u ($1 \leq u \leq x$), the number of d_u order touch point: n_u ($1 \leq u \leq x$), total number of sides of the grid: l , number of boundary sides: l_b , number of interior sides: l_i ; total number of vertexes of the grid: v , number of interior vertexes: v_i , the following quantitative relationships hold:

$$l_i = (n \times m - l_b) / 2 \quad (1)$$

$$l = (n \times m + l_b) / 2 \quad (2)$$

$$v = l - (n - 1) - i \quad (3)$$

$$v_i = l - n - i + \sum_{u=1}^x n_u \times d_u - l_b + 1 \quad (4)$$

The concern concepts and the demonstration of these

theorems would be given in full paper.

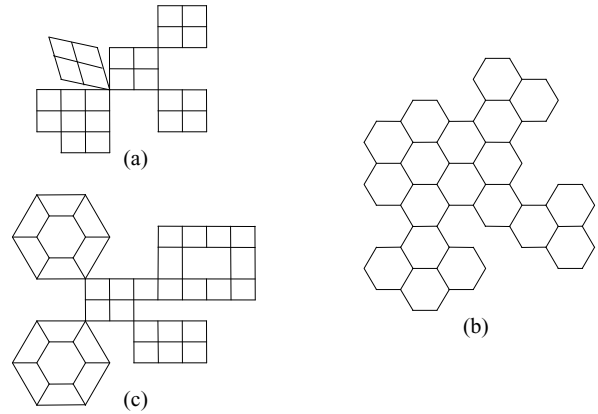


Fig.1. Sample grid in 2-D case

In fig.1 three sample grids are shown. In fig1(a) $n=24, m=4, l_c=96, v_c=73, i=0, \sum_{u=1}^x n_u \times d_u=4, l_b=44, l_i=26, l=70, v=47, v_i=7$. In fig1(b) $n=19, m=6, l_c=114, v_c=96, i=0, l_b=52, l_i=31, l=83, v=65, v_i=13$. In fig1(c) $n=33, m=4, l_c=132, v_c=100, i=3, \sum_{u=1}^x n_u \times d_u=3, l_b=62, l_i=35, l=97, v=62, v_i=3$.

V. CONCLUSIONS

The goal of our work is to find out the numerical relationships among the number of geometric structures of the FEM grid and its elements. This task is rather difficult and interesting in 3-D case and the results can be used to verify FEM grid directly especially for automatic FEM grid generation.

On the other hand, during the analysis topological relationship between FEM elements in a FEM grid is studied thoroughly. Thus many further researches and application can be performed. In the end an unified description of FEM procedure based on these numerical relationships can be gained, and this is especially effective for large FEM software programming.

REFERENCES

- [1] Nan Xiong, Kexun Jiang, "Narrow Sense Chain-making and Chain-coupling Theorems of Element Grid in 2-D Problem", Proceedings of ICEMS2008 (electronic publication).
- [2] Ziqi Chen, Graph Theory, 1st ed., Higher Education Press, 1990.
- [3] Yiqi Dai, Graph Theory and Algebra Structure, 1st ed., Tsinghua University Press, 1995.
- [4] Jitai Cheng, Set Theory, 1st ed., National Defense Industry Press, 1985
- [5] Chengshu Yan, Guidance of Set Theory, 1st ed., China Social Science Press 1994.
- [6] Xiaoling Zuo, Weijian Li, Discrete Mathematics, 1st ed., Shanghai Science and Technology Literature Press, 1982.
- [7] Tianfa Hang, Discrete Mathematics, 1st ed., Press of University of Electronic Science and Technology of China, 1995.

Analyse of different programming solutions adapted to block matrix type in electromagnetic modelling

L. Santandréa, Y. Choua, A. Ospina Y. Le Bihan and C. Marchand
 Laboratoire de Génie Électrique de Paris
 CNRS UMR8507; SUPELEC; UPMC Univ Paris 06; Univ Paris-Sud 11
 11 rue Joliot-Curie, Plateau de Moulon, F-91192 Gif-sur-Yvette Cedex
 santandrea@lgep.supelec.fr

Abstract—Block matrix type linear systems often appear in many numerical resolution of electromagnetic problems and coupling problems. This paper deals with the evaluation of some adapted programming solutions for building and for inverting this kind of algebraic systems. One pays a particular attention to three criteria : development time, computation time and facility of use.

I. INTRODUCTION

BLOCK matrix is a current structure of linear system obtained when a numerical resolution is applied for an electromagnetic problems or more generally for multiphysics problems. For example, this kind of algebraic system appears in the implementation of the dual magnetodynamic potential finite element formulations, the mortar method implementation, a piezoelectric problem solved with finite elements method, the introduction of shell finite elements, or mixed formulations using boundary elements and finite elements, etc... In the last case, according of the nature of matrix blocks, different mode storages can be used full and sparse. In this paper three programming solutions are evaluated to implement this kind of linear systems in a finite element context. First by a MATLAB approach is presented on the 2D mortar method. The second solution is the use of a compiled language based on an oriented object approach. Finally an alternative solution based on a combined Python and C++ approach is proposed.

II. MATLAB APPROACH

The Matrix based languages such as commercial software MATLAB, or equivalent Open Source Free Software such as OCTAVE or SCILAB seem to be the more adapted solution. No type declaration is necessary and they don't need compilation.

In Matlab environment, once the blocks are made, the language allows great flexibility for manipulating block matrix. In particular, the user has two options to perform conjugate gradient method. As an example we can consider a 2D rotating electrical motor simulation with a mortar method approach [1]. The first option consists to assemble blocks to form a single global matrix. This option allows indifferently the use of iterative or direct solvers (based on the Gauss method) for the inversion of the linear system.

```
MatMortar = [A2ii CrossMortarBlock' Block0
             CrossMortarBlock DiagBlock A1Gammai
             tBlock0 A1iGamma A1ii];
Sol = pcg(MatMortar,SdMembre);
```

with the direct solver the resolution line becomes

```
Sol=MatMortar \ SdMembre;
```

The previous example shows the synthetic and digest writing of Matlab. The block matrix are manipulated as scalar variables.

A second option is to call the iterative method directly with the function defining how the matrix-vector product must be performed "MulMortar".

```
Sol = pcg(@MulMortar,SdMembre);
```

But Matlab code is interpreted during runtime and the computing time depends directly of the vectorization capability of the algorithm. If the different parts of the elements loop can be easily vectorized in a finite elements program, this operation is impossible for the elements loop itself. This drawback may be critical for a large 3D problem. It can be solved by the use of compiled subprograms (Fortran or C++ for example) directly interfaced with MATLAB through the dedicated interface process named mex-files or indirectly through files exchange cross the hard disk. This approach come to the loss of two main advantages of MATLAB as program readability and portability. One other critic is the poverty of the C++ interface.

III. OBJECT ORIENTED APPROACH

To reduce computational time for the resolution of important 3D problems, a compiled code is developed. An Object Oriented Programming (OOP) approach well adapted to finite element method is used with the C++ language. The time performance of this language is closed to Fortran one of the most popular and most efficiency language in scientific computing. A lot of libraries for scientific computing using this language already exist. For example in the code developed, the Array Class RNM of the free Open Source Software Freefem++ is used for managing multidimensional arrays [2]. The main goal of our code architecture is to guarantee no anticipation on the matrix structure of the algebraic system and its mode of

associated storage. The matrix can be an one block or a multi-block matrix with different storage modes for each block. The resolution of the algebraic system is based on iterative method as one of the most popular : the conjugate gradient. These methods are well adapted to this matrix structure because the iterative product can be performed for each block independently. Furthermore using specify functionality of the C++ language as the mechanism of "template", the implementation of the iterative resolution function can be made only once. The mechanism of "template" make the implementation of algorithms independent of data types. This is not possible in Fortran. The figure below presents a simplified scheme of the software architecture. The linear system resolution part uses the same principle seen previous with the definition of the function MulMortar in the Matlab example.

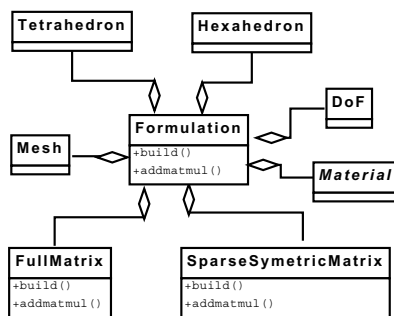


Fig. 1. Class aggregation

Each storage mode has its own class with its associated methods like constructors, pointers building, assembling, take into account boundary conditions, and obviously how performs the matrix-vector product.

To illustrate the code performance, a classical 3D Non Destructive Testing Problem (air Coil over a conducting plate) [3] is considered. Using a finite element modelling with combined potential formulation A-V (570 000 degrees of freedom), the computation time is about 420 s CPU on a pentium 2.66 GHz Processor. For the linear system resolution, the method of conjugate gradient is used with a Jacobi preconditionner (615 iterations). It can be observed that computation time is reduced of a factor 10 comparing to a Matlab Program. In the other hand, time for developement can be more disavantageous than in Matlab language. Furthermore the introduction of the problem data is more difficult.

IV. PYTHON APPROACH

An alternative solution is the use of the Python language developed in the 90s. It is a dynamic object-oriented programming language that can be used for many kinds of software development. Like Matlab, it has tools dedicated to a specific domain named "modules". In the last years, Scientific module (SciPy) for scientific functions and linear algebra, numerical module (NumPy) for multidimensional arrays management or a module for sparse matrix management (PySparse) have been developed. But the fundamental difference with Matlab is the number of solutions to encapsulate compiled languages [4]. Most languages offer the possibility to call programs written

in other languages but in Python this is particularly easy and smooth process. One reason is that Python was initially designed for being integrated with C and extended with new C codes. Several very powerful tool such as Swig, f2Py or Python Weave have been developed in this aim. It allows particularly to preserve existing Fortran, C or C++ solvers and to nest different codes in a multiphysics context [5]. Using Python script with NumPy, SciPY and PySparse modules for finite element method implementation, a computational time similar to the Matlab code is obtained. But using C++ encapsulation tool such as Swig allows to reduce computation time by a factor of more than 10. A complete example using several techniques to interface C++ with Python will be detailed and compared in the final paper. The Python script below shows that using dedicated modules for scientific computing, finite element method can have a Python implementation close to the Matlab implementation.

```

# element loop
for ielt in range(nbelt) :
    .....
    # Computation of the Elementary Stiffness matrix (analytic integration)
    MatElmt = (Grad.transpose()*InvJac.transpose()*InvJac)*Grad*double(DetJac/2./mu[idom])
    RHSElmt = ones(3,double)*J[idom]*DetJac/6.
    .....
# end of the element loop
.....
# inversion.
S = MatMef.to_sss().
K_ssr = precon_ssr(S, 1.9)
info, iter, relres = itsolvers.pcg(S, RHS, Az, tol, 100, K_ssr)
  
```

Fig. 2. Python script example

V. CONCLUSION

Recent numeric tools developed in Python make that this Free Open Source language can be a good alternative to Matlab for very fast numerical methods evaluating. Furthermore it seems to be very efficiency to encapsulate compiled language. These properties will be developed in the final paper to prove Python performance. Actually, it is more and more used in an agile programming process in software engineering and in numerical modelling.

REFERENCES

- [1] F. Rapetti, L. Santandrea, F. Bouillault, A. Razek, "Calculation of eddy currents in moving structures using a finite element method on non-matching grids", *COMPTEL*, vol 19 n 1 2000
- [2] F. Hecht, O. Pironneau, A. Le Hiaryc, K.Ohtsuka "FreeFem++", *FreeFem Documentation*, www.freefem.org
- [3] M. Bensetti, Y. Choua, L. Santandrea, Y. Le Bihan and C. Marchand, "Adaptive mesh refinement and probe signal calculation in eddy current NDT by complementary formulations", *IEEE Trans. on Magn.*, vol. 44, no. 6, pp. 1646–1649, 2008.
- [4] H.P. Langtangen, "Python scripting for computational science", *Springer*, 2008.
- [5] "Salome Platform", *website*, www.salome-platform.org/

Simulation of Electric Field Distribution in Polymeric Insulators

Rosemeri C. Fagundes¹, Walmor C. Godoi¹, Marco A. A. Vasco², Andre E. Lazzaretti¹, Vitoldo Swinka-Filho¹ and Klaus de Geus³

¹Instituto de Tecnologia para o Desenvolvimento – LACTEC
BR116 - Km 98 - S/Nº - Centro Politécnico UFPR, PO box 19.067, Brazil.
tiameri@yahoo.com.br, (walmor, lazzaretti, vitoldo)@lactec.org.br

²Faculdade de Odontologia de Ribeirão Preto – USP – Av. do Café s/nº - Ribeirão Preto, SP, Brazil
maavasco@gmail.com

³Companhia Paranaense de Energia – Copel, Rua Emiliano Perneta, 390, Curitiba, PR, Brazil.
klaus@copel.com

Abstract – This work aims to present a visualization based simulation methodology of potentials and electric fields distribution applied to a pin-type polymeric insulators used in electric power distribution lines. The methodology is based on obtaining a three dimensional tomography of the part, generating three dimensional surfaces by the Marching Cubes algorithm, generating a STL (Stereolithography) file and, from it, obtaining the solid in order to simulate the electric field and potential applied on it. The advantage of this methodology is in the obtainment of the defect volumes such as they were produced in the parts, making the simulation closer to the use conditions.

I. INTRODUCTION

The use of polymeric insulators in the electric power distribution and transmission lines has constantly grown in the last years [1]. These components have advantages such as resistance to hydrophobicity in the presence of saline mist and rain, reduced mass, low cost and contamination resistance. On the other hand, we can cite the existence of defects in its interior, originated from the manufacture process as the main disadvantage [1]-[2]. A test used to verify these defects is the X-ray tomography [2]. It can provide a view of the forms of the object internal structure, such as the forms of the defects in the tested components.

Tomographic measurements techniques have their origin in the medical applications from the 60's. Nowadays, it has been used widely in engineering and science [2]-[3].

Reconstructions of three dimensional surfaces of objects offer a valuable diagnostic tool such as the anatomic form of the reconstructed object and volume measurements or surface area [2]. Knowing the volume of a defect, for instance, may help in the decision making regarding the suitable measurements in relation to the tested part (change or not).

The aim of this work is to present a methodology that uses the three dimensional tomography to create the real volume of polymeric insulators used in distribution lines to simulate and measure the electric field in these components.

II. GENERATION OF THE THREE DIMENSIONAL TOMOGRAPHY

The acquisition of the tomographic slices was carried out in the Instituto de Tecnologia para o Desenvolvimento – LACTEC, through an industrial tomography system

(Gilardoni). The images of the reconstructed surfaces are generated from multiples two-dimensional slices that compose the volume to be reconstructed. The Marching Cubes algorithm [4] was used in the tomographic images (slices in the bitmap format) for the generation of the three dimensional surfaces. The algorithm implementation was done in Java with the Open Source VTK (Visualization Toolkit) library in Linux 64 Bits platform. The Marching Cubes algorithm is based on two steps: (i) Surface detection corresponding to the assigned value as the parameter, (ii) normal calculation [4].

The surfaces generated by the algorithm are generally represented by a considerable number of triangles. The quantity of these triangles, presented in meshes, determines the quality and the processing time of the geometric model. However, meshes that present a high number of triangles are not adequate to real time applications. Thus, before generating the STL file, the number of polygons present in the 3D tomography must be reduced. In this work, the `vtkDecimatePro` class from the VTK library was used. The Decimation, proposed by Schroeder et al. [5], is a process that reduces the number of triangles in a mesh, preserving its characteristics as much as possible.

III. SOLID GENERATION FOR THE FINITE ELEMENTS SIMULATION

The finite elements method requires a solid for the generation of the simulation mesh. The model generated by the tomography in STL mesh (Stereolithography, 3D Systems, Valencia, California) was transferred to a CAD software type Solidworks (Solidworks Corporation, Dassault Systems, France) and through the “Scan to 3D” supplement, the model was edited and reconstructed from the STL file to a file of solid in the parasolid format (Siemens PLM Software, Berlin, Germany). This transformation was necessary in order to enable the processing of the model by the Comsol Multiphysics[®] analysis software.

This conversion enabled the removal of undesirable geometries resultant from noises in the computerized tomography, such as tips and other anomalies, as well as the reduction of processing computational costs, and the promotion of the discretization process in the future simulation

10. Software Methodology

by the transformation of a mesh surface in a solid model. The mesh surfaces are constituted of poly faces that have triangular borders and are exclusively flat, while the surfaces of solid models can be round and register protuberances or other geometry irregularities in the same face. In the present insulator model, it was possible to transform 270842 poly faces in a solid model with 1200 faces, with a minimal geometric distortion, as seen in Fig. 01 and Fig. 02.

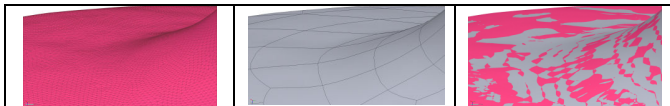


Fig. 1. Left: Mesh with poly faces, Center: reconstructed solid model and Right: overlapping of the mesh with the solid model showing a low distortion of the process.

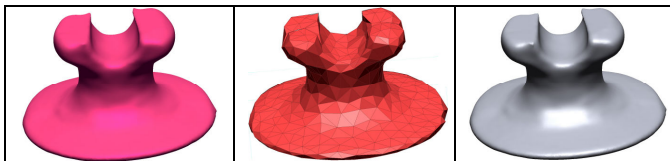


Fig. 2. Comparison of different models. Left: mesh with 270842 poly faces, Center: mesh with 1200 poly faces and Right: solid body with 1200 faces.

IV. SIMULATIONS WITH THE COMSOL MULTIPHYSICS® SOFTWARE

In order to identify electric field concentration on critical points, computational simulations using the Comsol Multiphysics® software were made, using the file generated from the three dimensional tomography of an insulator with bubble. The simulations are represented through a decreasing chromatic scale where the red color represents the highest intensity of the electric and potential field.

The configuration used for the simulations of the pin type polymeric insulator is shown in Fig. 3.

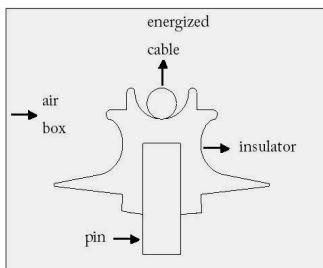


Fig. 3. Configuration used for the simulations of the pin type polymeric insulator.

The material of the pin type polymeric insulator is the high density polyethylene (HDPE), which must have maximum ϵ permissivity equal to 3. The electric potential applied to the cable was 8 kV. The metallic pin is grounded. Involving the system, it was inserted a box with air of $\epsilon = 1$ permissivity, in order to compose the limits of the considered system. The air bubble (defect) inside the insulator has $\epsilon = 1$ permissivity.

The simulation of electric potential applied to the insulator is shown in Fig. 4. Fig. 5 illustrates the distribution of the electric field. The black arrow points to the bubble.

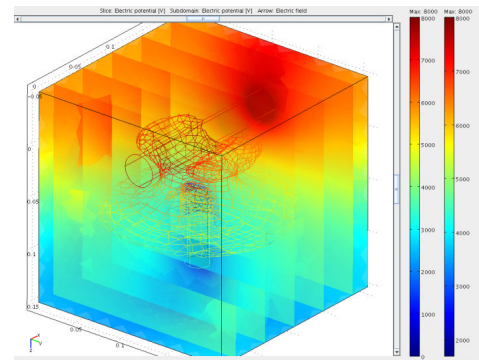


Fig 4. Simulation of the electric potential distribution.

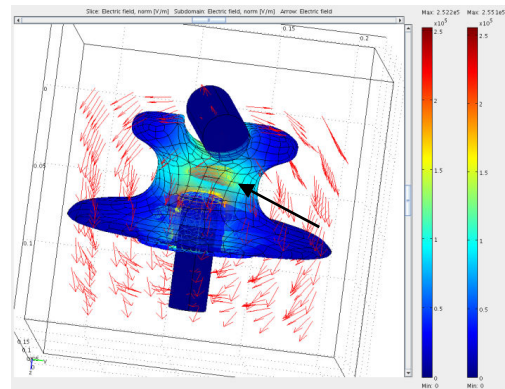


Fig 5. Simulation of the electric field distribution.

The simulated potential has a higher value in the region of the insulator that is near to the energized cable. The value of the electric field found inside the largest bubble is 114 kV/m. This value is above the electric field of the points that surround it, indicating the highest electric field concentration in this area. The existence of heterogeneity of the materials permissivity that composes the simulated system generates the electric field concentration in certain points. This electric field concentration may lead to the occurrence of internal partial discharges that erode the cavities inside the dielectric until its perforation [6].

V. REFERENCES

- [1] W C Godoi, R R da Silva and V Swinka-Filho, *Pattern recognition in the automatic inspection of flaws in polymeric insulator*, Insight (Northampton), vol. 47, n.10, p. 608-614, October 2005
- [2] W C Godoi, K de Geus, V. Swinka-Filho, R R da Silva. *Volume and surface measurements of flaws in polymeric insulators using X-ray computed tomography*. Insight (Northampton), vol. 50, p. 554-559, 2008.
- [3] M Behling and D Mewes, *Process Tomography: Development and Application of Non-intrusive Measuring Techniques for Multiphase Flows*, Computerized Tomography for Scientists and Engineers, New Delhi, Anamaya Publishers, 2007.
- [4] W E Lorensen and H E Cline *Marching Cubes: A high resolution 3D Surface Construction Algorithm*, Computer Graphics, vol. 21, n.4, 1987.
- [5] W Schroeder, J Zarge and W Lorensen *Decimation of Triangle Meshes*. Computer Graphics, vol. 26, n.2, p.65-70, Chicago, 1992.
- [6] R. C. Fagundes, *Avaliação de acessórios poliméricos de redes compactas protegidas por meio de ensaio de multiestressamento e simulação computacional*. MSc Thesis, Universidade Federal do Paraná. Curitiba, Brazil, 2008.

The Cross-Entropy Method and its Application to Inverse Problems

S. L. Ho¹, and Shiyou Yang^{1,2}

¹Department of Electrical Engineering, The Hong Kong Polytechnic University, Hong Kong

²College of Electrical Engineering, Zhejiang University, Hangzhou, 310027, China

Abstract—This paper explores firstly the potential of a new evolutionary method - the Cross-Entropy (CE) method in solving continuous inverse problems. For this purpose, a CE based metaheuristic algorithm is proposed and evaluated on both low- and high-frequency engineering problems with promising results.

I. THE CROSS-ENTROPY METHOD

In the study of inverse problems, the evolutionary algorithm plays an important role because of the multimodal nature of the objective functions of inverse problems. In this regard, the simulated annealing, genetic, tabu search, particle swarm optimization, and ant colony algorithms have all been developed and applied in the computational electromagnetics community to solving typical inverse problems. Nevertheless, there is no universal algorithm according to the no-free-lunch theorem. Consequently, it is essential to guarantee the diversity of available evolutionary algorithms. In this regard, the cross-entropy (CE) method is worthy of further studies.

The CE method is firstly developed by Rubinstein for estimating the probabilities of rare events as an adaptive importance sampling algorithm [1], and soon it is extended to solve both combinatorial and continuous optimal problems [2]. The significance of the CE method is that it defines a precise mathematical framework for deriving fast and yet ‘optimal’, to a certain extent, updating/learning rules which are based on advanced simulation theory [3]. In finding the global optimum f^* of the following maximization problem

$$\max f(x): X \in R^n \rightarrow R, \quad (1)$$

the CE method will firstly randomize the problem according to a family of *probability density functions* (pdf) $\{g(\cdot; \mathbf{v}), \mathbf{v} \in \mathcal{V}\}$ on X , and (1) is then transformed to the so-called *associated stochastic problem* (ASP) to estimate the following probability

$$I(\gamma) = P_u(f(\mathbf{X}) \geq \gamma) = E_u I_{\{f(\mathbf{X}) \geq \gamma\}} \quad (2)$$

where, E_u denotes the corresponding expectation operator, \mathbf{X} is a random n -dimensional vector with the pdf of $g(\cdot; \mathbf{u})$ for some $\mathbf{u} \in \mathcal{V}$, γ is an adaptively updating parameter.

For the ASP problem, the CE method adaptively updates $g(\cdot; \mathbf{u})$ based on the Kullback-Leibler cross entropy, resulting in a set of degenerated pdfs $g(\cdot; \mathbf{u}), g(\cdot; \mathbf{v}_1), g(\cdot; \mathbf{v}_2) \dots$, which will quickly converge to the global optimal probability density function $g(f^*; \mathbf{v}^*)$. Consequently, the CE method comprises generally of the following two phases:

- (1) Generate a set of candidate solutions according to a predefined probability density function;
- (2) Update the parameters of this pdf by using only the

elite solutions to steer the search towards the global optimal in subsequent iterations.

In this paper, the normal distribution function $N(\mu, \sigma^2)$ with its mean μ and standard deviation σ is selected as the pdf of $g(\cdot; \mathbf{u})$. For the conditions as described, μ and σ will converge, respectively, to the global optima f^* and zero efficiently; and the corresponding iterative procedures of the proposed CE method are summarized as:

Algorithm based on CE method for Continuous Optimizations

1. Initialize: Set: N -size of the population, ρ -rarity parameter (which are small constant thresholds of the elite solutions for updating the parameters of pdf), $\mu_0, \sigma_0, \alpha_0, t = 0$.

2. Repeat

- 2.1 $t = t + 1$, Generate a population of feasible solutions according to the normal distribution pdf $N(\mu_{t-1}, \sigma_{t-1}^2)$;

- 2.2 Select elites, let \mathbf{I} be the indices of the ρN best samples (elites);

- 2.3 Update μ and σ . For all $j=1, \dots, n$, compute

$$\mu_{ij} = \sum_{i \in \mathbf{I}} x_{ij} / (\rho N), \quad \sigma_{ij}^2 = \sum_{i \in \mathbf{I}} (x_{ij} - \mu_{ij})^2 / (\rho N)$$

- 2.4 Smooth

$$\mathbf{u}_t = \alpha_t \mathbf{u}_t + (1 - \alpha_t) \mathbf{u}_{t-1}, \quad \boldsymbol{\sigma}_t = \alpha_t \boldsymbol{\sigma}_t + (1 - \alpha_t) \boldsymbol{\sigma}_{t-1}$$

- 2.5 Test for the stop criterion. If the stop criterion is satisfied, set the Stop-criterion:='true';

3. Until Stop-criterion:='true'.

The CE programming algorithm is very simply in code programming. Only a few parameters such as the size of the population and the rarity parameter need to be predefined and most of the key parameters are adaptively updated in the iterative process. For example, the performance parameter γ as used in (2) is automatically designated to the worst solution of the ρN best elites. On the other hand, the smoothing parameter α is updated automatically from its minimal to maximal values as the iterative number increases. Also, some small values of perturbations are deliberately and randomly added to σ to enhance the global search ability of the proposed CE method.

II. APPLICATIONS

A. Case Study One

The proposed CE method is firstly used to optimize a completely non-uniform antenna array, as depicted in Fig. 1, with the minimal number of elements being exploited to produce a satisfactory or acceptable pattern of the desired field, which is a shaped beam with a cosecant variation, as defined in [4]: the field will vary following a cosecant function in the

interval $\cos \theta \in [0.1, 0.5]$ and has a Maximum SideLobe Level (MSLL) of less than -25 decibel in the residual intervals. Mathematically, the desired pattern is expressed as:

$$F_{desired}(\cos \theta) = \begin{cases} \text{cosecant}(\cos \theta) & (0.1 \leq \cos \theta \leq 0.5) \\ 0 & (\text{elsewhere}) \end{cases} \quad (3)$$

$$MSLL_{desired} \leq -25 \text{ dB}$$

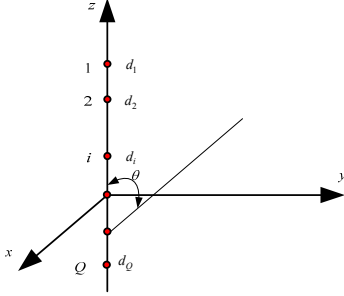


Fig.1. The schematic diagram of a linear antenna array of Q punctiform and omnidirectional elements along the z axis.

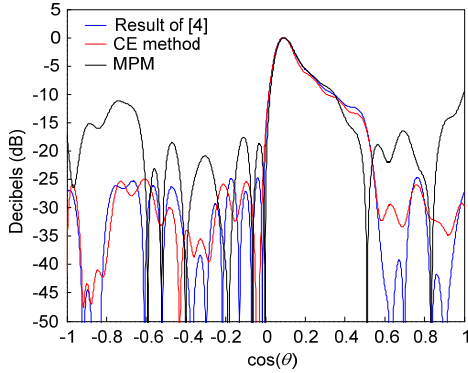


Fig.2. Comparison of the field patterns of the optimized (non-)uniform arrays by using different optimal algorithms

To optimize the non-uniform antenna array, the following objective function is defined and used:

$$\min f = \sqrt{\frac{\sum_{i=1}^N [f_{desired}^{norm}(\theta_i) - f_{designed}^{norm}(\theta_i)]^2}{\sum_{i=1}^N [f_{desired}^{norm}(\theta_i)]^2}} \quad (4)$$

where, $f_{desired}^{norm}(\theta_i)$ is the value of the normalized desired radiation pattern at the sampling point θ_i , $f_{designed}^{norm}(\theta_i)$ is the value of the radiation pattern produced by a designed array of Q elements.

To produce a field pattern which is close enough to the desired one using the proposed method (CE), a 19 element non-uniform antenna array is selected and used to optimize the complex excitations and locations of each element in order to find the global optimal solutions of these decision parameters. For performance comparison purpose, the matrix pencil method (MPM) [5] is also employed in this case study. The final solutions of the location (given in relative values with reference to the wavelength λ), amplitude (Ampl) and phase (Phas in degree) of each element of the optimized array by using the CE method are tabulated in Table I. The radiation patterns for the optimized arrays obtained using different algorithms as well as the results of a 30 uniformly spaced antenna array, which has been optimized using a modified tabu search algorithm [4], are depicted in Fig. 2.

From these numerical results it is obvious that a non-uniform antenna array with a minimal number of 19 elements optimized using the proposed CE method can produce a satisfactory radiation pattern which is almost the same as that of a 30 element uniform array obtained using the tabu search method, whereas the results for the same non-uniform array optimized using available MPM technique are not acceptable.

B. Case Study Two

As a last example, the Team Workshop problem 22 of a superconducting magnetic energy storage (SMES) configuration with 8 free parameters as reported in [6] is solved by using the proposed CE method. Table II gives the performance comparison of the proposed CE algorithm and the best ones searched so far by IGTE [6]. Again, this case study confirms positively the feasibility of the proposed algorithm in solving low frequency inverse problems.

III. REFERENCES

- [1] R. Rubinstein, "Optimization of computer simulation with rare events," *Journal of Operations Research*, vol. 99, pp.89-112, 1997.
- [2] R. Rubinstein, "The cross entropy method for combinatorial and continuous optimizations," *Methodology and Computing in Applied Probability*, vol. 2, pp.127-190, 1999.
- [3] P. T. De Boer, D. P. Kroese, S. Mannor, and R. Y. Rubinstein, "A tutorial on the cross-entropy method," *Annals of Operations Research*, vol. 134, pp.19-67, 2005.
- [4] A. Akdagli, and K. Guney, "Shaped-beam pattern synthesis of equally and unequally spaced linear antenna arrays using a modified tabu search algorithm," *Microwave Opt. Technol. Lett.*, vol. 36, no. 1, pp. 16-20, 2003.
- [5] Yanhui Liu, Zaiping Nie, and Qing Huo Liu, "Reducing the number of elements in a linear antenna array by the matrix pencil method," *IEEE Trans. Antennas Propagat.*, vol. 56, pp. 2955-2962, 2008.
- [6] *TEAM optimization benchmark problem 22* [online], available at: www.igte.tugraz.at/archive/team/index.htm.

TABLE I

THE OPTIMIZED POSITIONS, AMPLITUDES AND PHASES OF THE 19 ELEMENT NON-UNIFORMLY SPACED ARRAY BY THE PROPOSED METHOD

d_i/λ	7.314	6.495	5.597	4.726	3.813	2.958	2.098	1.215	0.458	-0.202	-0.938	-1.746	-2.636	-3.438	-4.294	-5.075	-5.852	-6.702	-7.452
Ampl	0.0175	0.0209	0.0340	0.0459	0.0557	0.0845	0.0893	0.1521	0.2164	0.2418	0.1778	0.1014	0.0862	0.0664	0.0441	0.0370	0.0268	0.0188	0.0161
Phas	160.7	-175.1	-165.3	-145.7	-125.6	-109.1	-91.3	-73.4	-32.3	14.8	61.4	84.6	99.0	127.5	129.4	151.6	173.5	-178.6	-155.0

TABLE II

PERFORMANCE COMPARISON OF THE PROPOSED METHOD AND THE IGTE SOLUTION FOR THE SMES CONFIGURATION

Results	R_1 (m)	R_2 (m)	$h_1/2$ (m)	$h_2/2$ (m)	d_1 (m)	d_2 (m)	J_1 (MA/m ²)	J_2 (MA/m ²)	f_{obj}	No. iterations
PROPOSED	1.5702	2.1017	0.7845	1.4201	0.6002	0.2574	17.3402	-12.9653	6.7238×10^{-3}	2543
By IGTE	1.5703	2.0999	0.7846	1.4184	0.5943	0.2562	17.3367	-12.5738	5.5203×10^{-3}	/

Scalability of Higher-Order Discontinuous Galerkin FEM Computations for Solving Electromagnetic Wave Propagation Problems on GPU Clusters

N. Gödel¹, *Student Member, IEEE*, N. Nunn, T. Warburton² and M. Clemens¹, *Senior Member, IEEE*

¹Helmut-Schmidt-University, University of the Federal Armed Forces Hamburg, Faculty of Electrical Engineering, Chair for Theory of Electrical Engineering and Computational Electromagnetics, P.O. Box 700822, D-22008 Hamburg, Germany

²Computational and Applied Mathematics, Rice University, 6100 Main Street MS-134, Houston, TX, USA

Abstract—A Graphics Processing Unit (GPU) cluster optimized implementation of Maxwell’s equations discretized with a higher-order Discontinuous Galerkin Finite Element Method (DG-FEM) in the time domain is presented. DG-FEM is used because its characteristics are matching the parallelization design aspects of the NVIDIA Compute Unified Device Architecture (CUDA) programming model. Asynchronous file transfer is introduced to minimize parallelization overhead and improve scalability.

Index Terms—GPU-computing, GPGPU, CUDA, Discontinuous Galerkin, FEM, High Order.

I. INTRODUCTION

Efficient numerical simulation of electromagnetic devices strongly depends on short simulation time, which requires efficient solvers running on fast hardware. In addition to multicore parallelization, GPU computing has gained attention for accelerating volume based simulation methods. In [1] and [2], FDTD and FEM computations on GPUs are presented. First DG-FEM simulations on GPUs are reported in [3]. First multi-GPU configurations for the DG-FEM solution of Maxwell’s equations in time domain are considered in [4]. In this paper, the performance of DG-FEM discretized Maxwell’s equations computed on a NVIDIA GPU cluster is analyzed. A 3-level parallelization strategy is presented using the NVIDIA CUDA programming model as well as a linux pthread implementation [5] on the CPU level. The focus of this publication is the CUDA adapted DG-FEM discretization and its scalability when using more than a single GPU.

II. DISCRETIZATION

Electromagnetic wave propagation in lossless medium can be described using Maxwell’s curl equations

$$\frac{\partial \vec{D}}{\partial t} = \nabla \times \vec{H}, \quad (1)$$

$$\frac{\partial \vec{B}}{\partial t} = -\nabla \times \vec{E}. \quad (2)$$

Here, \vec{D} and \vec{B} denote the electric and magnetic flux density, respectively, whereas \vec{H} and \vec{E} identify the magnetic and the electric field strength. A nodal variational form of Maxwell’s equations is derived in [6], where the unknown field vectors are approximated using local high-order multi-dimensional

Lagrange polynomials. The DG-discretization of (1), (2) leads to a system of ordinary differential equations, reading

$$\frac{d}{dt} \varepsilon \mathbf{E} = \mathbf{M}^{-1} \mathbf{S} \mathbf{H} + \mathbf{M}^{-1} \mathbf{F} (\hat{\mathbf{n}} \times (\mathbf{H}^* - \mathbf{H}^-)), \quad (3)$$

$$\frac{d}{dt} \mu \mathbf{H} = -\mathbf{M}^{-1} \mathbf{S} \mathbf{E} - \mathbf{M}^{-1} \mathbf{F} (\hat{\mathbf{n}} \times (\mathbf{E}^* - \mathbf{E}^-)). \quad (4)$$

A special characteristic of DG-FEM is that the DG-operators \mathbf{M} , \mathbf{S} and \mathbf{F} , leading to mass-, stiffness and flux-matrices, respectively, have compact support only within each element’s boundary. As a consequence, \mathbf{M} is locally defined on the reference element and can be inverted without much numerical effort. This provides the opportunity of using explicit time integration schemes, e.g. the 4th order low storage explicit Runge-Kutta scheme or local timestepping schemes. Furthermore, the first term of the right-hand side (RHS) is purely local, i.e. each element can be computed separately. This part of the RHS can be specified as volume kernel since it refers to the volume integration of the curl operator applied on the degrees of freedom inside each element. The second term in the RHS identifies the fluxes from one element to its adjacent elements. Fluxes combine all local element solutions to a global solution and control unphysical components. Here, not all values are element-local since the flux terms \mathbf{H}^* and \mathbf{E}^* are a linear combination of face values at neighboring elements. Regarding elementwise parallelization, these adjacent values have to be supplied additionally.

III. PARALLELIZATION STRATEGY

The NVIDIA CUDA programming model incorporates two parallelization levels. The computational work is associated with a CUDA grid. In the coarse level, this grid is divided into CUDA blocks, which are computed in parallel on the multi-processors (MP). The fine grained level is associated with CUDA threads which are computed on the streaming processors (SP) cores of each MP. Regarding DG-FEM discretization, the computational domain is an unstructured mesh, divided into finite elements. On these finite elements, degrees of freedom are defined. Consequently, to match CUDA design aspects for DG-FEM implementation, it is a natural approach to associate the CUDA grid with the DG unstructured mesh and to map each DG-element to a CUDA block and each degree of freedom to a cuda thread. For detailed information

about CUDA parallelization of DG-FEM discretization, see [3]. In case of multiple GPUs, a further top layer parallelization level can be introduced with help of a METIS domain decomposition of the set of finite elements, [7]. Each subdomain can be computed on one of the GPUs as the computational data of all subdomains are independent of each other, except for the flux data at the METIS boundaries. These flux terms have to be synchronized after each timestep. The overhead of the flux gathering can be minimized using the asynchronous file transfer feature of current Nvidia TESLA GPUs. It provides concurrent CUDA kernel and CUDA memcopy execution. Since the volume kernel execution is numerically expensive and purely element-local, flux gathering can be hidden behind the volume kernel execution, at least for a small amount of METIS subsets compared to the global amount of elements.

IV. FIRST NUMERICAL RESULTS

As a first numerical benchmark, the enclosure of a mac-mini has been discretized using 201 765 tetrahedra.

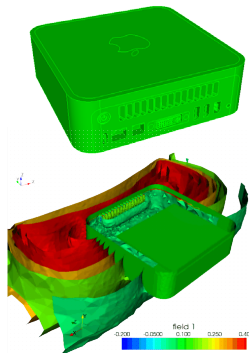


Fig. 1. Mac-mini model hit by a wave front

The coupling of a TEM wave into the device via its ventilation slots as presented in Fig. 1 has been computed on hardware listed in Table I. In Fig. 2, the GPU performance is compared to a floating point single precision CPU computation for different polynomial orders. In summary, 4 GPUs can

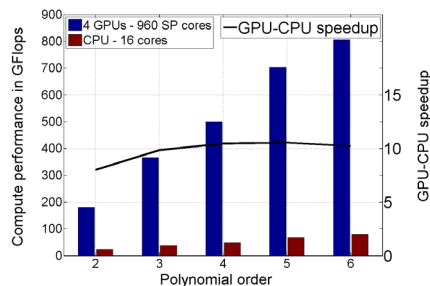


Fig. 2. Comparison of the computational performance

perform about one order of magnitude faster than a current CPU setup with four quad cores. Regarding hardware costs, a 4 GPU setup can be realized much cheaper than a 4 CPU configuration, at almost the same power consumption, including host computer. The resulting performance per cost ratio is considerably higher using graphics hardware. Regarding further upgrades of GPU based clusters, scalability is an important factor. The scalability of the parallelization

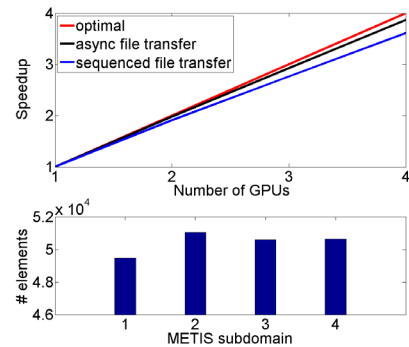


Fig. 3. Scalability and METIS element distribution of a 4 GPU setup. 201 765 elements with 4th order basis functions.

as well as the METIS element distribution is presented in Fig. 3 resulting in 96.75% and 90.2% with and without the asynchronous file transfer feature, respectively. The benefits of the asynchronous file transfer result in better scalability, since the complete flux transfer could be hidden behind the execution of the volume kernel which took 11.56 ms on average, whereas the transfer process needed approximately 4.4 ms per timestep. The gap between these two times shows that further parallelization can be beneficial. Furthermore, since the work distribution of the METIS domain decomposition is not perfectly balanced, further improvement in scalability converging towards 100% is possible.

V. CONCLUSION

A multilevel parallelization strategy for solving DG-FEM discretized Maxwell's equations on a GPU cluster was presented. The suitability of DG-FEM for GPU computations using the CUDA programming model was described. With help of asynchronous file transfer, good scalability for up to four GPUs was demonstrated. Further improvements in scalability can be achieved by using work-balancing METIS functions, also on more than four GPUs, depending on the element distribution.

ACKNOWLEDGMENT

The authors gratefully acknowledge the support of AFOSR under grant number FA9550-05-1-0473. The opinions expressed are the views of the authors. They do not necessarily reflect the official position of the funding agencies.

REFERENCES

- [1] S. Krakowsky, L. Turner, and M. Okoniewski, "Acceleration of finite-difference time-domain (FDTD) using graphics processor units (GPU)," *Microwave Symposium Digest, 2004 IEEE MTT-S International*, vol. 2, pp. 1033–1036, June 2004.
- [2] D. Göddeke, R. Strzodka, and S. Turek, "Accelerating double precision FEM simulations with GPUs," in *18th Symposium of Simulation Technique Erlangen, 2005*. SCS Publishing House e.V., 2005, pp. 139–144.
- [3] A. Kloeckner, T. Warburton, J. Bridge, and J. Hesthaven, "Nodal discontinuous galerkin methods on graphics processors," *Journal of computational physics - preprint*, 2009.
- [4] N. Gödel, T. Warburton, and M. Clemens, "GPU accelerated discontinuous Galerkin FEM for electromagnetic radio frequency problems," *IEEE APS - Full paper accepted for publication*, 2009.
- [5] B. Nichols, D. Buttlar, and J. P. Farrell, *Pthreads Programming*. 101 Morris Street, Sebastopol, CA 95472: O'Reilly, 1998.
- [6] J. S. Hesthaven and T. Warburton, *Nodal Discontinuous Galerkin Methods*. Springer, 2008.
- [7] G. Karypis and V. Kumar, "A fast and high quality multilevel scheme for partitioning irregular graphs," *Conference on Parallel Processing*, pp. 113–122, 1995.

EMC Modeling of an Industrial Variable Speed Drive with an Adapted PEEC Method

Vincent ARDON^{1,2}, Jérémie AIME^{1,3}, Olivier CHADEBEC¹, Edith CLAVEL¹,
Jean-Michel GUICHON¹, Enrico VIALARDI²,

¹Grenoble Electrical Engineering Lab., Université J. Fourier / Grenoble-INP / CNRS, 38402 Grenoble, France

²Cedrat, Technological Department-Software, 38246 Meylan, France

³Schneider and Toshiba Inverter Europe, 27120 Pacy sur Eure, France

vincent.ardon@g2elab.grenoble-inp.fr

Abstract—This paper presents an adapted PEEC-based (Partial Element Equivalent Circuit) methodology applied to the modeling of interconnections of power electronics devices. Although this method is known, the originality of this work is its use to model a device presenting an industrial complexity. To make possible this modeling, two adapted integral methods, based on two different meshings are presented. They compute respectively parasitic inductances and capacitances and lead to an equivalent circuit of the system. From a time-domain simulation of this circuit, current and voltage sources can be extracted and used to compute the radiated near magnetic field. This approach has been applied to model a real industrial static converter, a variable speed drive.

I. INTRODUCTION AND STATE OF THE ART

Today power electronics devices are more and more compact and small and the working frequency range is rising. Consequently the compliance to EMC standards is not guarantee. That is why power interconnections need accurate modeling that takes into account some magnetic constraints (i.e., the skin and proximity effects) and the most important electric couplings between the conductors of the device. According to the sizes of the typical industrial application, the propagation phenomena can still be neglected because the frequency range is from 150kHz to 200MHz and the longest conductor size is around 10cm ($\lambda/10=15$ cm).

To model such industrial devices, constituted of complex conductors (multi-layer tracks close to each others), the finite element method would be few adapted regarding the difficulty of volume air region meshing and conductors discretization to properly take into account skin/proximity effects. On the contrary, the PEEC method (i.e. extraction of equivalent circuit components thanks to integral approach) is known to be well adapted to model complex geometries with an important surrounded air region [1]. However, the full-PEEC approach, based on dual inductive and capacitive meshings (and a 3D meshing of dielectrics), would be also very memory consuming and not adapted.

Thus, in the next part, we propose an adapted PEEC formulation where two integral methods lying on two separated meshes are combined to build a parasitic equivalent circuit of the power interconnections. In the last section, this approach is tested by modeling an industrial variable speed drive and comparisons between simulations and measurements are carried out: the behavior of the harmonic response and the emitted near magnetic field.

II. EXTRACTION OF (R-L-M-C) EQUIVALENT CIRCUIT

By considering the integral form of the Maxwell's equations and by assuming quasi-static conditions and surface location of the free-charges ρ in a medium of permittivity ϵ and permeability μ , the external applied electric field \mathbf{E} in a point \mathbf{r} of space can be rewritten as:

$$\begin{aligned}\mathbf{E}(\mathbf{r}) &= \frac{\mathbf{J}(\mathbf{r})}{\sigma} + j\omega\mathbf{A}(\mathbf{r}) + \nabla\phi(\mathbf{r}) \\ &= \frac{\mathbf{J}(\mathbf{r})}{\sigma} + j\omega\mu \iiint_V G(\mathbf{r}, \mathbf{r}') \mathbf{J}(\mathbf{r}') dV + \frac{1}{\epsilon} \nabla \iint_S G(\mathbf{r}, \mathbf{r}') \rho(r') dS\end{aligned}\quad (1)$$

where \mathbf{J} is current density, σ the conductivity of conductors, \mathbf{A} the magnetic vector potential, ϕ the electric potential and $G=1/(4\pi\|\mathbf{r}-\mathbf{r}'\|)$ the Green function. The three parts of (1) are respectively due to resistive, inductive and capacitive effects.

In our adapted PEEC approach, these effects are modeled by using two different meshings of conductors and dielectrics (Fig. 1). Parasitic resistances, inductances and mutual-inductances (R-L-M) are computed from a volume meshing of conductors, and capacitances (C), from a non-necessarily conformal surface meshing of conductors and dielectrics.

A. Extraction of resistive and inductive elements (R-L-M)

Each mesh element presents a resistance and a self inductance (analytical formulas). Mutual inductances between different elements are numerically computed thanks to a Galerkin method [1-2], which consists in integrating the magnetic vector potential created by one volume element on the other.

Depending on the directions of the flowing current, conductors can be either unidirectional (thin or long tracks) or bidirectional (large tracks and ground planes). The conductors belonging to the first type are meshed in the skin depth but not in their length (gain in number of elements), whereas the bidirectional ones are discretized in two directions. These meshes are adapted to model skin and proximity effects from which an inductive dense and square matrix and a resistive

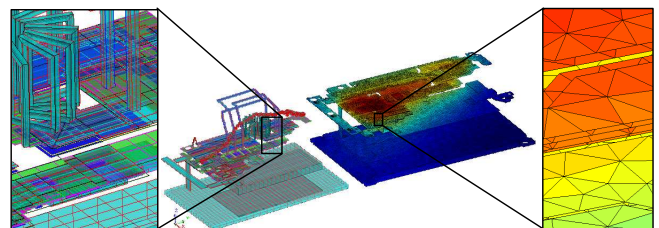


Fig. 1. Resistive-inductive (left) and capacitive (right) meshings

diagonal matrix are extracted. The number of mesh elements is equal to the size of the (R-L-M) matrix.

B. Extraction of capacitive elements (C)

For the modeling of capacitive effects, an electrostatic formulation is used and consequently the meshing is adapted to the surface free-charge distribution (side effects). Thinner mesh elements than the inductive ones are required to take into account accurate spatial variation of surface charges which is due to the uniform surface distribution of electric potentials.

Unlike the use of a Galerkin method, a 0-order point matching method is sufficient to accurately compute the potential coefficients $P_{i,j}$ and the normal field coefficients $E_{i,j}$. These coefficients are respectively calculated between each conductor or dielectric elements and all (conductor and dielectric) elements of the meshing. Consequently, they compose the square and dense interaction matrix P/E [3].

The $N*N$ capacitance matrix ($N \ll$ number of elements) which models the electric couplings between the N conductors of the device (or part of conductors) is computed by properly adding free-charge sets. These ones (Q) are obtained by performing N resolutions of the linear system $V=[P/E]*Q$ with N different potential distributions V (0 or 1V on each mesh). The worst inconvenience of this method is the storage of the matrix and the integration time which increases in $O(n^2)$.

To overcome this issue of modeling large devices, the algorithm AMLFMM [4] is used: in fact, it accelerates the computation of interaction coefficients ($O(n.log(n))$) and is low-memory consuming thanks to the use of a truncated multipole decomposition of interactions. This method subdivides the geometry in cubes of different levels with an adaptive octree algorithm which controls the interaction computations and leads to a compact matrix-vector product. Finally, the problem is solved with an iterative solver, a left preconditioned GMRESR(m) algorithm [5].

III. APPLICATION TO AN INDUSTRIAL VARIABLE SPEED DRIVE

A. Extraction of the equivalent circuit

This methodology has been applied to obtain an equivalent circuit of an industrial static converter: a marketed variable speed drive. This complex device is composed of four copper-track layers. Figure 1 shows the two different meshings used to extract the lumped elements. The square resistive-inductive matrix (6,800*6,800 elements) is computed with InCa3D [6]. The capacitive matrix (27*27 elements) is computed with AMLFMM and 27 GMRESR(m) solvings of a linear system of 48,500 unknowns (the conductor charges).

The complete PEEC circuit of the interconnections of this device is built in a system-level software (Saber) and is composed of an (R-L-M) macroblock and all the capacitances which are manually linked themselves.

B. Harmonic response and near magnetic field studies

The supply chain, the load (a three-phase motor) and the command circuit are then added to the previous PEEC circuit. Thanks to time-domain simulations and Fourier transforms of the results, it is possible to analyse the parasitic equivalent circuit by means of a harmonic response study in the

conducted frequency range (150kHz-30MHz). This study has validated our method because the frequency resonances obtained by simulation and measurement are the same (detailed results of this analysis will be reported in the final version of the paper).

Then, a second analysis of the emitted near magnetic field, just over the static converter, has been led. The Fourier transform of currents and voltages of the circuit, which have been obtained by a time-domain simulation, have been introduced as sources in our model and the emitted magnetic field has been computed at a given frequency by means of the Biot and Savart law. Figure 2 shows the comparison between the vertical component of the magnetic field H_z at 32kHz simulated and measured and a good adequation between the two color shades can be appreciated. It means that the current loops are correctly modeled.

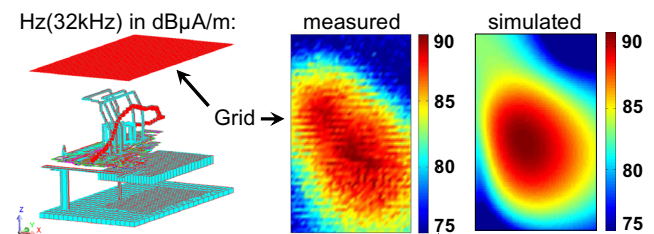


Fig. 2. Radiated near magnetic field H_z measured and simulated at 32kHz

IV. CONCLUSIONS

In this paper, it has been presented the coupling between two adapted integral methods from two adapted meshings allowing, respectively, the extraction of resistive-inductive and capacitive equivalent elements of power interconnections of industrial complexity.

It has also been highlighted that the complete (R-L-M-C) equivalent circuit can be exported into a SPICE-like tool where time-domain analysis can be performed. Then, the obtained Fourier transforms of the currents and voltages have been introduced as sources in the 3D geometric representation of the interconnections for analyzing the EMC performances of the system on a wide frequency range. The harmonic response and the emitted near magnetic field comparisons with measurements have validated this approach on a real industrial variable speed drive.

V. REFERENCES

- [1] A. E. Ruehli, "Survey of computer-aided electrical analysis of integrated circuit interconnections," *IBM J. Res. Develop.*, vol. 23, pp. 626-639, Nov. 1979.
- [2] J. Aimé, J. Roudet, E. Clavel, O. Aouine, C. Labarre, F. Costa, J. Ecrabey, "Prediction and measurement of the magnetic near field of a static converter", *IEEE International Symposium on Industrial Electronics*, Jun. 2007.
- [3] K. Nabors, J. Withe, "Multipole-Accelerated Capacitance for 3-D Structures with Multiple Dielectrics", *IEEE Transactions on Circuits and Systems*, vol. 39, N°11, Nov. 1992.
- [4] J. Carrier, L. Greengard, and V. Rokhlin, "A fast adaptive multipole algorithm for particle simulations, *SIAM J. Sci. Statist. Comput.*, 1988.
- [5] Y. Saad and M. H. Schultz, "GMRES: A generalized minimal residual algorithm for solving nonsymmetric linear systems," *SIAM J. Scientific and Statistical Computing*, vol. 7, pp. 856-869, July 1986
- [6] InCa3D software, Cedrat, www.cedrat.com

Calculation of Equivalent Circuit Parameters for a High-Frequency RFID Transponder

T. Bauernfeind¹, K. Preis¹, O. Bíró¹ and F. Hämmerle²

¹Institute for Fundamentals and Theory in Electrical Engineering, Graz University of Technology
Kopernikusgasse 24, 8010 Graz, Austria
t.bauernfeind@tugraz.at

²Research Centre for Microtechnology, Vorarlberg University of Applied Sciences
Hochschulstraße 1, 6850 Dornbirn, Austria

Abstract — A method for specifying the electrical parameters of a High-Frequency (HF) Radio-Frequency-Identification (RFID) transponder loop antenna is presented. It is based on a quasi-static or a full wave field analysis of the subjacent eddy-current problem. A comparison between two- and three-dimensional computations is given. Additionally, the results obtained by in-house software tools are compared with those from calculations using a commercial code. Finally, initial results of measurements carried out on a given HF-RFID transponder tag are presented.

I. INTRODUCTION

HF-RFID transponders, usually working at 13.56 MHz in the near field of the reader antenna are operating like resonant networks since the energy extraction from the emerging reader field can thereby be maximized [1]. Due to the resonance condition, it is of major importance that the electric parameters of the antenna structure and the analog input stage of the HF-RFID transponder chip are well specified [2].

In order to enhance the reading range the induced voltage has to be raised, this can be attained by increasing the number of windings of the loop antenna or the antenna area or the magnetic field strength \mathbf{H} of the reader at the given frequency. Since the reader field strength is limited by regulations, the only way to increase the induced voltage is to build efficient antennas considering the limitations given by the application. The loop antenna which is investigated in the present work is shown in Fig. 1 and a variation in terms of antenna size is not possible. Table I gives an overview of the structure of the transponder antenna.

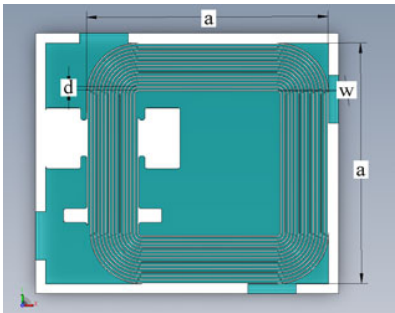


Fig. 1. Geometry of the transponder antenna

In general, the input stage of an RFID transponder chip is a multi-stage charge pump structure with an effective input capacitance which mainly defines the silicon area of the chip [2], so the input capacitance is limited to a certain value in the small pF-domain. Hence, to enable the resonance condition of

the transponder, an additional capacitance C_{Res} as shown in Fig. 2 is necessary.

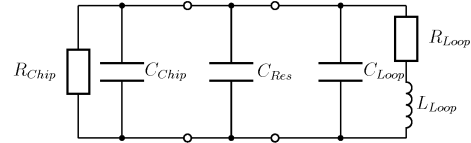


Fig. 2. Equivalent electrical circuit of the HF-RFID transponder

To determine the value of the resonance capacitor, the electrical parameters of the transponder chip as well as the electrical parameters of the given antenna structure have to be specified.

TABLE I
STRUCTURE OF THE TRANSPONDER LOOP

Number of windings n	1, 2, 14
Outer dimension a (mm)	6
Distance between turns d (μm)	90
Width of wire w (μm)	30
Relative permittivity of the substrate	4.1
Relative permittivity of the photoresist	3
Conductivity of the Nickel (Ni) trace (S/m)	$1.5625 \cdot 10^7$
Relative permeability of the Ni trace	1240

II. PROBLEM TYPE

Using the conditions for electrically small loop antennas in [3] valid for circular loop antennas and adapting them to a flat spiral loop of square shape leads to

$$k_0 \left(4 \cdot a + \sum_{i=1}^n 4 \cdot (a - 2i \cdot d) \right) \ll 1. \quad (1)$$

With the given dimensions of the loop and the phase constant for free space k_0 the condition (1) is certainly satisfied. Hence, one can assume a constant current along the circumference of the loop and, therefore, a quasi static approximation of the subjacent problem is allowed [4]. For the numerical simulation, the following equations in the time harmonic case applied in the eddy current region have to be solved [5]

$$\nabla \times \mathbf{E} = -j\omega \mathbf{B}, \quad \nabla \times \mathbf{H} = \mathbf{J} \quad \text{and} \quad \mathbf{J} = \sigma \mathbf{E}. \quad (2)$$

In the non-conducting domain

$$\nabla \times \mathbf{E} = -j\omega \mathbf{B} \quad \text{and} \quad \nabla \cdot \mathbf{B} = 0 \quad (3)$$

characterize the problem. The problem described in (2) and (3) is referred to as a quasi static magnetic field (QSMF) problem in the following. Note that in (2) the displacement

current is neglected. To get the stray capacitance of the loop one can either solve a full wave problem with

$$\nabla \times \mathbf{H} = \mathbf{J}_{tot} \text{ and } \mathbf{J}_{tot} = (\sigma + j\omega\epsilon)\mathbf{E} \quad (4)$$

or solve in addition to the QSMF problem a quasi static electric field (QSEF) problem and assuming a complex current flow:

$$\nabla \times \mathbf{E} = 0, \nabla \cdot (\mathbf{J} + j\omega\epsilon\mathbf{E}) = 0. \quad (5)$$

III. NUMERICAL MODELS

To get a reference point for the loop antenna's input impedance, a 2D analysis of the given antenna structure is considered first.

A. 2D simulations

The real 3D structure has been transformed to a rotationally symmetric arrangement by assuming an equal mean circumference of the innermost winding. Since a full wave simulation is not implemented in the 2D in-house code, the results given in Table II are limited to the resistance and inductance of the loop antenna.

B. 3D simulations

The equivalent circuit parameters according to Fig. 2 can be obtained from a field simulation by evaluating the mean power loss P_l , the magnetic energy W_m and the electric energy W_e . If the voltage, U , of the circuit is prescribed, the following relationships are valid for the resistance R_{Loop} , the inductance L_{Loop} and the capacitance C_{Loop} :

$$R_{Loop} + j\omega L_{Loop} = \frac{U^2}{P_l - j2\omega W_m}, \quad (6)$$

$$C_{Loop} = \frac{2 \cdot W_e}{U^2}. \quad (7)$$

If, on the other hand, the current, I , of the circuit is prescribed, R_{Loop} and L_{Loop} can be obtained as

$$R_{Loop} + j\omega L_{Loop} = \frac{P_l + j2\omega W_m}{I^2}. \quad (8)$$

1) Full wave simulations

The full wave simulations have been carried out with the voltage given and the circuit parameters have been obtained by (6) and (7). The results for full 3D models like the one shown in Fig. 3 are given in Table II. Since the convergence for the full wave simulation using an iterative solver is weak, only results for loops with one and two windings are available.

2) QSMF- and QSEF-simulations with full model

The QSMF simulations have been done with the current prescribed and the QSEF simulations with the voltage prescribed. QSMF simulations have yielded R_{Loop} and L_{Loop} from (8) and QSEF analyses C_{Loop} by (7). The results are presented in Table II, too.

3) QSMF-simulations with quarter model

An approximate way to determine the equivalent circuit is to assume two symmetry planes and analyze only a quarter of the problem. Influences of the contact areas on the ohmic part and the inductance of the loop antenna's input impedance are thereby neglected. The results are again shown in Table II.

The results obtained by the commercial code are also based on a QSMF simulation of the quarter problem to obtain R_{Loop} and L_{Loop} . These results are also given in Table II.

A detailed comparison of the efficiency and accuracy of the various approaches will be carried out in the full paper.

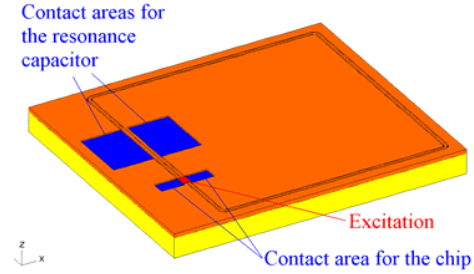


Fig. 3. Full 3D model of the transponder with two windings

C. Antenna measurement

As a first approach, a vector network analyzer measurement has been carried out [6]. Initial results for the resistance and the inductance are also given in Table II. Improvements in terms of more suitable test fixtures are matter of the running activities and the corresponding results will also be presented in the full paper.

TABLE II
COMPARATIVE RESULTS

Type	n	R_{Loop} (Ω)	L_{Loop} (nH)	C_{Loop} (fF)
2D	1	7.1	104.5	-
Full wave	1	8.6	94.7	330.7
QSMF+QSEF	1	6.5	118.7	330.3
QSMF 1/4-model	1	7.3	113.1	-
2D	2	14	238.9	-
Full wave	2	17.5	223.7	615.9
QSMF+QSEF	2	13.4	280.5	620.8
QSMF 1/4-model	2	14.3	255.2	-
2D	14	82.5	2654.3	-
QSMF+QSEF	14	79.8	2568.6	350.9
QSMF 1/4-model	14	77.7	2531.8	-
Com. code	14	82.1	2416.6	-
Measurement	14	57.5	2457.0	-

IV. REFERENCES

- [1] K. Finkenzeller, *RFID Handbook*, 2nd ed., Chichester: John Wiley & Sons Ltd., 2003
- [2] L. W. Mayer and A. L. Scholtz, "A dual-band HF/UHF antenna for RFID Tags", *2008 IEEE 68th Vehicular Technology Conference*, 2008.
- [3] G. S. Smith, *An Introduction to Classical Electromagnetic Radiation*. Cambridge: Cambridge University Press, pp. 482-485, 1997
- [4] M. Bensetti et al., "A hybrid finite-element method for the modeling of microcoils", *IEEE Trans. on Magnetics*, 41(5): 1868-1871, 2005
- [5] O. Biro, "Edge element formulations of eddy current problems", *Computer methods in applied mechanics and engineering*, vol. 169, pp. 391-405, 1999
- [6] Agilent Technologies, *Impedance Measurement Handbook*, 2008

Planar Coil Model using Shell Elements Applied to an Eddy-Current Non-Destructive Testing

A. Ospina, L. Santandrea, Y. Le Bihan and C. Marchand

Laboratoire de Génie Electrique de Paris, CNRS UMR8507; SUPELEC; UPMC Univ. Paris 06; Univ. Paris-Sud 11; 11 Rue Joliot-Curie, Plateau de Moulon, 91192 Gif-sur-Yvette Cedex, France

alejandro.ospina@lgep.supelec.fr

Abstract — This paper deals with a original kind of planar coil model developed in the finite element method for non destructive testing applications. The model is constructed by the use of degenerated elements (shell elements). An example is implemented with two well known electromagnetic formulations in 2D. The accuracy of the model is established with analytical equations.

I. INTRODUCTION

Planar printed coils are increasingly used in eddy-current (EC) non-destructive testing (NDT) applications such as detection or material characterization [1-2]. The use of planar printed coils offers many advantages in NDT applications: capability to improve spatial resolution, sensitivity and if it is constructed on a flexible substrate, adaption to complex geometries.

Numerical methods are adapted for the study of electromagnetic problems in EC-NDT applications with complex geometries. Among the numerical methods for the study of planar coils in NDT the finite element method (FEM) is one of the most adapted. However, in the discretization stage, the FEM make a considerable increase in the number of unknowns and, in consequence, in the computation time. These difficulties are related to the meshing process, such as for example, a strong density of elements (increase in the unknown number) or deformed elements in the thin area and its vicinity (ill-conditioned system). In order to eliminate these problems a kind of degenerated elements (shell elements) is used in this paper [3-4].

In the meshing process, the planar coil is considered as a surface, since increase and deformation of elements are avoided. Then, in the stage problem formulation, the degenerated elements are introduced in order to model the planar coil. Finally, a linear equation system is solved and the fields are calculated in the “real” geometry.

II. PROBLEM DESCRIPTION

The basic geometric configuration is a classical problem in EC NDT: a coil placed above a metallic material (Fig. 1). The problem domain Ω is decomposed in three regions: the target material (conducting and/or ferromagnetic) Ω_c , the planar coil domain Ω_0 and the air region. The planar coil domain has a current density j_0 and a thickness denoted by d .

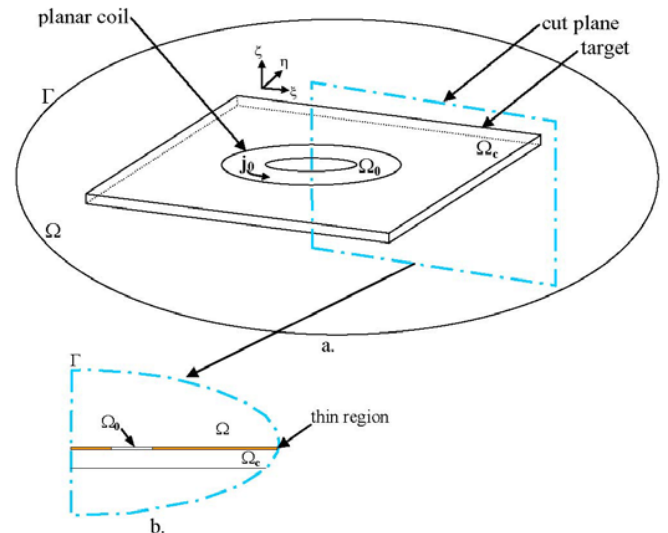


Fig. 1. a. Problem description. b. 2D cut plane

The planar coil is geometrically characterized by an aspect ratio L between its thickness d and a characteristic geometrical quantity L_g (in this case L_g is the inner radius):

$$L = \frac{d}{L_g} . \quad (1)$$

In the proposed example, the target material is conductive. Thus the field produced by the coil induces EC in the target. The thickness of the coil, d , vary between about 1 micron to 10 millimeters.

III. MAGNETODYNAMIC FORMULATIONS

The physical model of the EC problem is performed by the Maxwell reduced equations (without displacement currents: the capacitance effect is not significant). Among the models of EC problems, an approach based on dual formulations has been proposed by Ren and Razek [5]: the electric and the magnetic formulations.

In the electric formulation, the electric field \mathbf{e} is associated to a modified magnetic vector potential \mathbf{a}^* , in the form

$$\mathbf{a}^* = - \int_t \mathbf{e} dt . \quad (2)$$

The weak formulation is based on the Ampere's law, for $t > 0$ in the harmonic regime.

In the magnetic formulation, the magnetic field \mathbf{h} is decomposed in two potentials, the electric vector potential \mathbf{t} and the scalar magnetic potential ϕ , with

$$\mathbf{h} = \mathbf{t} - \mathbf{grad} \phi. \quad (3)$$

The weak form is based on the Faraday's law applied in the conducting regions and completed by $\text{div } \mathbf{b} = 0$ for all domains.

IV. SHELL ELEMENTS

The shell elements are a space degeneration of the finite elements. They are geometrical objects that have a $D-1$ geometrical dimensions, where D is the model geometrical dimension (usually $D=3$ or 2). In the first stage of the discretization process (meshing) since the shell elements are 1 dimensional geometrical objects (lines), the thin region is represented by a middle line (Γ_{sh}). Then, the edge and the nodes in Γ_{sh} are projected on two "virtual" lines (Γ_{sh}^+ and Γ_{sh}^-). The physical behavior inside the planar coil is represented by the shape functions in these lines. Additionally, these projections can be repeated many times in order to stratify the thin region. Using these approximations the formulations are transformed in linear systems in which, the unknowns are the vector circulation along the edges and the scalar quantities at the nodes.

In the first stage of the modeling process, a triangular mesh is constructed. This mesh is highly refined to reduce the error originated by triangular elements. After that, the shell elements are inserted in the thin region. In the example the thin region is stratified in four layers in order to obtain a better approximation of the fields. In this way the error is strongly dependent on the shell elements.

V. RESULTS

The spatial distribution of the real part of magnetic field lines is shown in Fig. 2. A good agreement is observed with the physical behavior: the magnetic field lines encircle the currents. The resistance and reactance of the coil are calculated in the dual formulations and compared with Dodd and Deeds model [6]. The results are shown in Fig. 3.

The field approximation which is made by the linear shape functions in the shell elements explain the different levels of

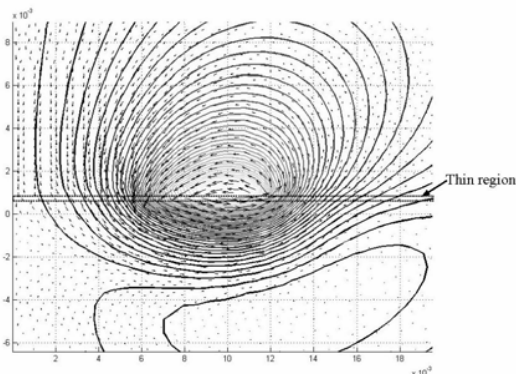
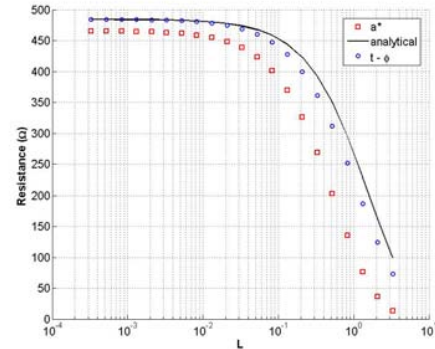


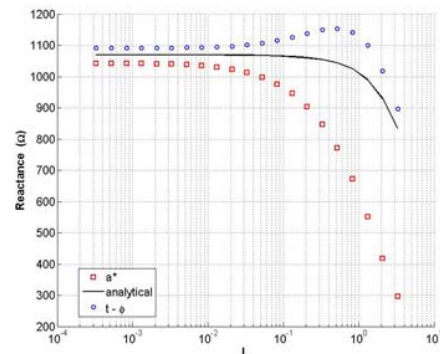
Fig. 2. Spatial distribution of the real part of magnetic flux density vectors and field lines obtained in the \mathbf{a}^* formulation.

accuracy in the results. The use of the \mathbf{a}^* formulation implies a linear variation of the electrical field. The magnetic field \mathbf{h} ,

calculated by the curl operator, is then constant and the error is quite important on the reactance (Fig 3b.). In the $\mathbf{t} - \phi$ formulation, the behavior of shell elements is analogue: the magnetic field \mathbf{h} has a linear variation across the thickness. The variation is more realistic, and the relative error on the



a.



b.

Fig. 3. a. Resistance vs aspect ratio (L). b. Reactance vs aspect ratio (L).

reactance is less important (Fig 3b.).

The example developed in this digest show that the application of the shell elements in the simulation of planar coils for EC-NDT applications represents an interesting solution when meshing with classical elements is impossible to realize or requires a high number of elements. In the extended paper more details will be provided about the 2D model and a 3D model of the planar coil will be presented.

VI. REFERENCES

- [1] Fava J.O. Ruch, M. C. Calculation and simulation of impedance diagrams of planar rectangular spiral coils for eddy-current testing. NDT & E International 39, pp 414-424, 2006.
- [2] Ditchburn R. J, Burke, S. K, Planar rectangular spiral coils in eddy-current non-destructive inspection, . NDT & E International 38, pp 690-700, 2005.
- [3] Z. Ren, Degenerated Whitney Prism Elements – General Nodal and Edge shell Elements for Field Computation in Thin Structures, IEEE Transactions on Magnetics, vol. 34, no. 5, (Sept 1998), pp. 2547-2550.
- [4] A. Ospina Vargas, Y. Le Bihan, L. Santandrea C. Marchand , Electromagnetic field computation in magnetic and conductive thin sheets, Proceedings of the European Magnetic Sensors and Actuators, Caen, 2008.
- [5] Z. Ren, A. Razek, Computation of 3D electromagnetic field using differential forms based elements and dual formulations, Int. J. Numer. Model., vol. 9, no. 3, (1996), pp. 81-98.
- [6] Dodd C. V, Deeds W.E, Analytical Solutions to eddy-current probe-coil problems. J. Appl Phys. 1968; 39(6)2829-38.

Numerical Field Calculation in Support of the Hardware Commissioning of the LHC

Bernhard Auchmann*, Stephan Russenschuck*

*CERN/TE, Geneva, Switzerland, Email: bernhard.auchmann@cern.ch

Abstract—The hardware commissioning of the Large Hadron Collider (LHC) required the testing and qualification of the cryogenic and vacuum system, as well as the electrical systems for the powering of more than 10000 superconducting magnets. Non-conformities had to be resolved within a tight schedule. In this paper we focus on the role that electromagnetic field computation has played in the treatment of these non-conformities which have required analysis of magnet quench, electromagnetic force calculations in busbars and splices, as well as field-quality predictions for the optimization of powering cycles.

Index Terms—Superconductors, Quench Calculation, Persistent Currents

I. INTRODUCTION

WITH the Large Hadron Collider (LHC), the particle physics community aims at testing various grand unified theories by studying collisions of counter-rotating proton beams with a center-of-mass energy of 14 tera electron volts (TeV). Physicists hope to prove the popular Higgs mechanism for generating elementary particle masses of quarks, leptons, and the W and Z bosons. The LHC reuses civil engineering infrastructure at CERN with a tunnel of 3.8 m in diameter and a circumference of about 27 kilometers that straddles the Swiss French border near Geneva. With a given radius of the accelerator tunnel, the maximum achievable particle momentum is proportional to the operational field in the bending magnets. Superconducting dipole magnets cooled to 1.9 kelvin with a nominal field of 8.33 tesla, allow energies of up to 7 TeV per proton beam.

During the design and construction of the LHC, an undertaking of more than 20 years, various challenges had to be met in all domains of physics and engineering. They are, among others, material science for superconducting wires and cables, mechanical engineering challenges for the construction of magnets weighing up to 20 tons, the physics of superfluid helium, vacuum technology for insulation and beam vacuum, and electrical engineering challenges for power supplies, current leads using high- T_c superconductors, superconducting busbars, diodes operating at cryogenic temperatures, magnet protection systems, etc. The requirements of field uniformity in the superconducting magnets have also posed a challenge to numerical field computation and optimization techniques. Motivated by the magnet design, the CERN field computation program ROXIE [1] has been developed which was also used to trace manufacturing errors during magnet production.

After an ambitious hardware commissioning phase a first beam was circulated on September 10, 2009. In this paper we

review the role that numerical field computation plays during the hardware commissioning phase.

II. QUENCH SIMULATION

Above a certain limit on the temperature, current density or magnetic flux density, the superconductor shows a transition between the superconducting and normal conducting state which is known as resistive transition or quench.

Quench detection and magnet protection against overheating and voltages peaks during a quench is an important issue in the design of superconducting magnets. We will show that it is important to treat all involved phenomena (thermal, electrical, and magnetic) in a coupled way. The integrated numerical model allows to study the impact of different effects such as quench-back, normal zone propagation, quench heater performance, local field distribution, and iron saturation.

The simulation of thermal processes at cryogenic temperatures is an intricate problem. Material properties at cryogenic temperatures and under pressure are often difficult to know to adequate precision. The highly nonlinear behavior of these parameters lead to an ill-conditioned numerical problem in quench simulations. Moreover the problem generally is ill-posed, as there are more model parameters than validation criteria such as measurements of the current decay and signals at the voltage taps or quench antenna [2].

In the commissioning phase of the LHC a quench heater developed an open circuit after the cool-down of the magnet to the operation temperature. The aim of quench simulations was to determine the best powering scheme for the remaining quench heater circuits, while activating redundant heaters in the low field region of the coil. In another case a quench occurred in both apertures of a dipole magnet. The coincidence caused significant delays in the quench detection. Simulation efforts were directed at determining the worst-case scenario of heat deposition inside the magnet, under which the measured voltage signals could be reproduced.

III. 3-D FORCE- AND PEAK-FIELD-CALCULATIONS

Electromagnetic forces on interconnection busbars were identified during commissioning to be an important issue for the long-term reliability and the electro-mechanical integrity of the machine. While field-quality calculations for long accelerator magnets can be carried out to highest precision in 2-D calculations, the interconnect regions between magnet coils and neighbouring magnets require a 3-D approach. Applying the BEM-FEM technique, the finite-element modeling could

be restricted to the nonlinear ferromagnetic yoke. The involved layout of cosine-theta-type coilends and the busbar routing was captured in a Biot-Savart type model built from straight line-current segments.

The Biot-Savart model was generated from basic building blocks such as easy- and hardway bend and twists. The twist-pitch of the Rutherford-type cable is neglected. An automatic connection routine computes the transformations that are required for a continuous interconnection of individual components. The complete BEM-FEM model consists of about 600,000 line-current segments in the BEM domain, and only about 60,000 finite elements. The calculation of forces on the interconnection busbars takes approximately two hours on a 2.8 GHz Xeon processor machine.

Despite the relatively low number of finite elements in the model, the accuracy of peak-field calculations on the superconducting cable exceeds by far the precision that could be achieved in a pure finite-element model. The reason is that the local field distribution in the cables is determined by the current flow in individual strands, which cannot be adequately represented in a FEM approach. Among the results that will be presented in the full paper, we note that the forces pulling in longitudinal direction (along the magnet axis) on the so-called half-moon interconnects, see Fig. 1 (left) that connect individual coils in a magnet assembly are on average 240 N.

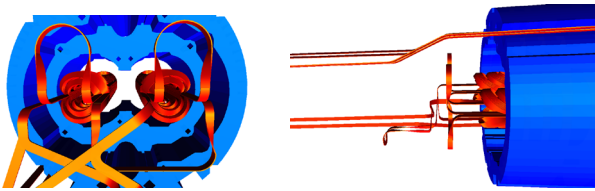


Fig. 1. Electromagnetic model of the interconnections at the end regions of the main-bending dipoles of the LHC.

IV. FIELD-QUALITY SIMULATION

The operation of the LHC requires that all field errors in the superconducting magnets are compensated for by dedicated corrector magnets, so that the integrated field error as seen by the particle beam remains below a tolerated limit. Beam-based measurements can serve as a feedback on the field quality and as an input for automated controls of the corrector magnets. Yet, for a large scale machine like the LHC, operators cannot rely solely on feedback systems. For this reason, the Field Description of the LHC (FiDeL) program collects measurement data of all components in the the LHC and extracts a fast online model, that yields the field quality at a given time, magnet operating current, magnet ramp rate, magnet temperature, and magnet powering history [3]. The modeling is especially critical at very low currents, where the persistent current magnetization of superconducting strands has a large influence on the field quality. The FiDeL model is based on measurements that were performed for quality assurance during the production of the LHC magnets. Simulation is performed if required for three reasons: 1) validation of the FiDeL mathematical model; 2) counter-check measurement data; 3) supply data where measurements are not available.

The FiDeL model is based on the identification and physical decomposition of the effects that contribute to the total field in the magnet aperture. Each effect is modeled by an appropriate mathematical model. The physical behavior of the models can be tested over the entire parameter space by means of simulation. At the exception of decay- and snap-back effects, the ROXIE software comprises all relevant effects. A database of electromagnetic models of all LHC superconducting magnets is used to compare model- and measurement results. Suspicious measurement data can be tested and validated by comparison. In the low-field region, where the persistent-current effects on field quality are dominant, the ROXIE model [4] can yield data for powering cycles that have not previously been measured. Most demanding in this respect are nested corrector magnets, where the persistent-current magnetization depends strongly on the powering cycle of each of the nested coil assemblies. In May 2009 the ROXIE vector-hysteresis model [4] for persistent currents will be validated for the first time by measurements of the MCBX corrector magnets, see Fig. 2. Results will be presented in the full paper.



Fig. 2. Left: Cross-section through the nested MCBX corrector magnet. Right: Persistent-current magnetization due to a rotating field in the magnet aperture.

V. CONCLUSION

Numerical field computation is indispensable in the design and manufacturing phase of accelerator magnets. Challenging computations, however, are carried out through the commissioning phase, in order to understand measured behaviour or to work out fall-back solutions. As a side-effect of an additional measurement campaign in 2009 we will be able to validate the ROXIE vector-hysteresis model for persistent currents.

REFERENCES

- [1] S. Russenschuck. *Electromagnetic Design and Mathematical Optimization Methods in Magnet Technology*. eBook at <http://cern.ch/russ>, 3rd edition, February 2006.
- [2] N. Schwerg, B. Auchmann, and S. Russenschuck. Validation of a coupled thermal-electromagnetic quench model for accelerator magnets. *IEEE Transactions on Applied Superconductivity*, 18(2):1565–1568, June 2008.
- [3] N. Sammut, L. Bottura, and J. Micallef. Mathematical formulation to predict the harmonics of the superconducting large hadron collider magnets. *Phys. Rev. STAB* 9, 1(012402), 2006.
- [4] M. Aleksa, B. Auchmann, S. Russenschuck, and C. Voellinger. A vector hysteresis model for superconducting filament magnetization in accelerator magnets. *IEEE Transactions on Magnetics*, 40(2):864–867, March 2003.

Fault Classification and Detection by Wavelet Based Magnetic Signature Recognition

Carlos A. F. Sartori, Francisco X. Sevegnani

Dep. de Eng. de Energia e Automação Elétricas da Escola Politécnica da Universidade de São Paulo PEA/EPUSP
Av. Luciano Gualberto, trav. 3, N° 158 – 05508-900 – São Paulo–SP – Brasil.

Centro das Ciências Exatas da Pontifícia Universidade Católica de São Paulo CCET/PUC/SP.
R. Marquês Paranaguá, N° 111. 01303-050 – São Paulo–SP – Brasil.
sartori@pea.usp.br; fransev@pucsp.br

Abstract — A non-invasive methodology to evaluate and classify the electrical system failures is presented in this work. It is based on the electrical system magnetic signature recognition using the wavelet signal decomposition and the resulting variance spectrum evaluation, respectively. The validation of the proposed methodology is carried out by comparison between theoretical and experimental results. The Finite Element Method is used in the numerical simulations of the magnetic flux density, and a post-processing approach is adopted in the signal decomposition and analyses. An experimental setup was built to obtain the magnetic signature regarding some pre-selected faults configurations.

I. INTRODUCTION

A methodology concerning the theoretical evaluation of fault detection in electrical systems was presented in the previous paper [1]. The proposed method is a non-invasive one based on the evaluation of the resulting magnetic signature of the electrical systems after applying the wavelet transform [2]-[3]. In this theoretical study, simulations were carried out, in order to obtain the fault current and the resulting magnetic field. In the present work, a new development is shown, including the fault classification approach and the validation based on an experimental setup.

II. METHODOLOGY

A brief description of the methodology used in this work is presented in this item. This methodology consists of two phases: The first is the experimental data acquisition (fault current and resulting magnetic flux density). Various kinds of faults were evaluated. Fig. 1 shows the experimental setup used. On the other hand, the fault waveforms are also introduced as current sources on corresponding electric circuit, and used to simulate the resulting magnetic flux density. The Finite Element Method is applied [4]. On the second phase, the decomposition of the magnetic flux signal through Wavelet Transform (WT), and the evaluation of the variance spectrum by the signals post-processing are carried out [5]-[7]. Critical analysis and discussion of the results are made, aiming to evaluate the suitability of the method for detecting and classifying the faults in electrical systems.

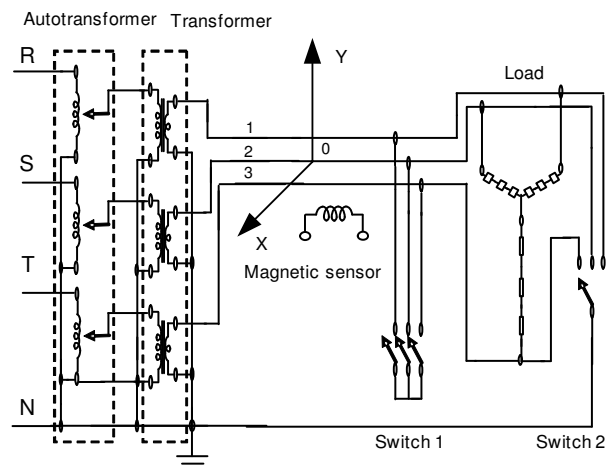


Fig. 1 – Sketch of the experimental setup

III. THEORETICAL ASPECTS

The information about both time and frequency domain can be obtained by applying the WT. This is an intrinsic and suitable WT characteristic concerning the signal decomposition accuracy. The details on the theoretical and practical aspects of WT are carefully described in the literature, e.g., [2], [3]. In general, the decomposed signal $x(t)$ can be expressed in a discrete form by:

$$x(t) = \sum_{k=-\infty}^{\infty} \sum_{j=-\infty}^{\infty} a_{jk} \psi_{jk} \quad (1)$$

In (1), j and k are integer numbers, and ψ are the Mother-Wavelet functions. The so-called *Daubechies Wavelet* was assumed as the base function in this work. This function was chosen, based on previous studies that support its robustness and suitability for fault detection evaluation. Concerning the signal decomposition process, Multiple Resolution Analysis (MRA) was applied [5]-[9]. The variance spectrum can be obtained based on Parseval's Theorem. It states that the distorted signal energy may be divided in terms of expansion coefficients [9]:

$$\int_{-\infty}^{\infty} |x(t)|^2 dt = \sum_{k=-\infty}^{\infty} |c(k)|^2 + \sum_{j=0}^{\infty} \sum_{k=-\infty}^{\infty} |d_j(k)|^2 \quad (2)$$

The variance can be considered as a measure of the average signal energy. Thus, the variance of the decomposed signal related to different resolution levels is proposed as merit index to the fault classification. The number of levels is selected according to the considered frequency range.

IV. APPLICATIONS AND RESULTS

In order to illustrate the proposed methodology, some theoretical and experimental results related to mono-phase faults are presented. The experimental setup (Fig.1) is a 220/1V (Y/Y) three-phase circuit, in which the secondary of the transformer was designed to obtain current peak values around 60 A (Fault conditions). The conductors (16 mm²) have a length equal to 4m, and are spaced by 0.50m. The clearance to the floor of the lab is 1.7m. The conductor phases are indicated by numbers 1, 2 and 3. By combining the switches 1 and 2, different sorts of faults can be reproduced. A specially designed coil probe was calibrated, and used as magnetic sensor. The Cartesian system adopted, regarding the evaluated points, is represented in Fig.1. As an example, Fig. 2 presents the results related to the magnetic flux density at P (-0.5, -0.25) m, for the Phase1-Ground faults. By inspecting the figure, besides the resulting peak values of the flux density, the fault durations can be noticed.

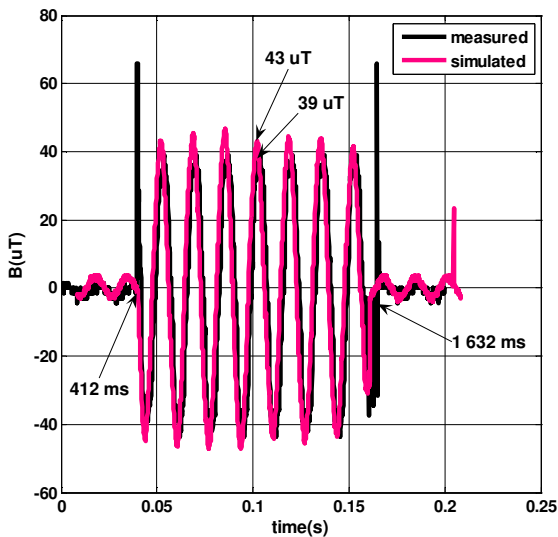


Fig.2 – Comparison between the simulated and measured magnetic flux densities Bx, at point P (-0.5;-0.25) m, for Phase 1-Ground fault (FIT).

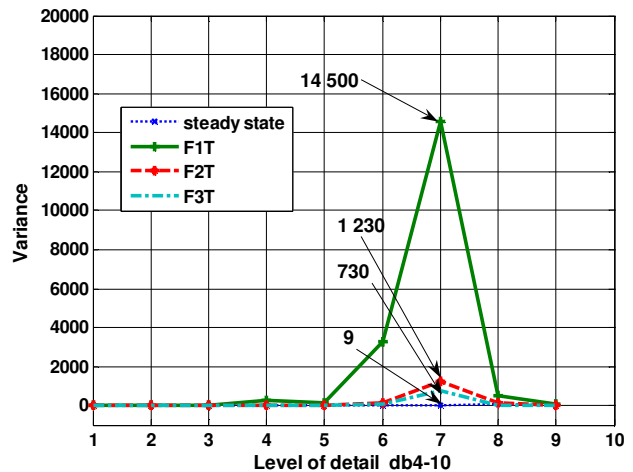


Fig.3 – Experimental Results: Magnetic flux density variance spectrum for mono-phase faults - P (-0.50;-0.25) m.

Fig. 3 shows the wavelet variance spectrum of the magnetic flux density for the experimental mono-phase fault values at P(-0.5;-0.25) m.

It should be mentioned that the same variance spectrum profile can be observed when the theoretical approach is taken into account. Additional results will be presented in the full paper in order to illustrate and show the details of the method regarding fault detection and their classification.

IV. REFERENCES

- [1] M.G. Pelegrina, C.A.F. Sartori and F.X. Sevegnani. "A Hybrid fault detection approach based on the resulting magnetic signature and wavelets". Compumag 2007 – 16th International Conference on the Computation of Electromagnetic Fields- Aachen- Germany, 2007.
- [2] I. Daubechies. "Ten Lectures on Wavelets" CBMS-NSF Regional Conference Series in Applied Mathematics (Philadelphia: SIAM), 1992.
- [3] O.Poisson,et. at al., "Detection and Measurement of Power Quality Disturbances Using Wavelet Transform". IEEE Transactions on Power Delivery, v.15, n.3, p.1039-1044, july 2000.
- [4] Flux 2D User's Guide, Vol. 3, "Physical Properties, Parametrization solving and Results". CEDRAT, France, 2001.
- [5] C.H.Kim , R. Aggarwal. "Wavelet transforms in power systems: Part 1 General introduction to the wavelet transforms. Power Engineering Journal, v.14,n.2,p. 81-87, Apr.2000.
- [6] Kim,C.H.; Aggarwal ,R. Wavelet transforms in power systems: Part 2 Examples of application to actual power system transients. Power engineering Journal, p. 193-202, Aug. 2001.
- [7] D.Hanselman and B.Littlefield, *Mastering Matlab 7*, Pearson Higher Education, 2004.
- [8] P.S.,ADDISON,"The Illustrated Wavelet Transform Handbook", Institute of Physics Publishing , Bristol and Philadelphia, 2002.
- [9] A.M.,Gaouda et. al., "Power Quality Detection and Classification using Wavelet-Multiresolution Signal Decomposition".IEEE Tranactions on power Delivery, 14,4, 1469 – 1476, O.,1999.

Modeling the dynamic behavior of magnetostrictive actuators

Oriano Bottauscio, Paolo E. Roccatò, and Mauro Zucca
 Istituto Nazionale di Ricerca Metrologica
 Strada delle Cacce 91, 10135 Torino, Italy
o.bottauscio@inrim.it, p.roccato@inrim.it, m.zucca@inrim.it

Abstract — This paper deals with the modeling and design of magnetostrictive devices in dynamic regime. It starts from an approach which couples a physical model of magnetostriction with finite element electromagnetic field analysis of the entire device. A first study, developed under simplifying hypothesis of steady-state working conditions, is here extended to arbitrary supply conditions, including the mechanical coupling. A comparison between computed and measured results is presented.

I. INTRODUCTION

Magnetostrictive (MST) devices exhibit interesting electro-magneto-mechanical properties for applications like the micro positioning and the active control of mechanical vibrations. Compared with piezoelectric devices, they show higher forces and have significant advantages (e.g. higher dynamic), avoiding the need of heavy electrical insulations, required by high voltages, which reduce the cooling efficiency.

The prediction of the dynamical performances of MST devices is a fundamental step, both in the design phase and in the successive development of efficient algorithms for their real-time control [1-3]. To avoid a complex and wide experimental characterization, numerical tools are welcomed, allowing analysis under various working conditions (working frequency, excitation current, mechanical load, etc.). The modeling approach should be able to account for the electromagnetic phenomena arising in the device, as well as the complex magnetoelastic behavior of the active MST element.

First approaches to the modeling of MST devices have been proposed in [4, 5], where the magnetoelastic models of the MST rod have been coupled with finite element tools, enabling the analysis of the main phenomena affecting the macroscopic behavior of these devices. Anyway, the aforementioned works were developed under the simplifying hypothesis of steady-state working conditions, enabling the study and design of a new device, but making not possible their use as computational engine in real-time control. In the present work, the coupled finite element – magnetoelastic model has been extended to work under arbitrary supply conditions, also including the coupling with simplified mechanical equations. In the following, some aspects of the modeling approach are detailed, considering both the physical model for describing magnetostriction, as well as their

coupling with the finite element electromagnetic field analysis.

II. MODELING APPROACH

To accurately modeling the MST rod, both magnetic and mechanical hysteresis has to be properly taken into account. The mechanical effects are introduced in the magnetic properties through an effective field H_e , which depends on the applied stress σ [6]. Magnetic flux density B is expressed as:

$$B = \Psi(H) = \mu_0 H + J = \mu_0 H + \zeta(H_e) \quad (1)$$

where the magnetic polarisation J , including reversible and irreversible contributions, depends on H_e . Hysteretic function ζ is described through the classical Preisach model (CPM). The effective field H_e depends on the applied field H , tuned by a corrector term $\xi(J, \sigma)$, function of the mechanical stress σ :

$$H_e = H + \xi(J, \sigma) \quad (2)$$

At a given instant, the computation of magnetic flux density evolution by Eqn. (1) is performed by an iterative procedure based on Fixed Point (FP) technique. Assumed the applied stress σ and field H to be known, the effective field is written as:

$$H_e = H + \psi(H_e, \sigma) = \upsilon H_e + S(H_e, \sigma) \quad (3)$$

where function ψ is written as the sum of a linear term (with constant υ) plus a residual S . The constant υ is determined by the maximum and minimum slopes of ψ for the considered value of σ , and the nonlinear residual $S(H_e, \sigma)$ is updated during the iteration process, starting from a trial value. At the generic iteration ($m-1$), the sequence of operations is:

$$\begin{aligned} H_e^{(m)} &= \frac{H + S^{(m-1)}}{1 - \upsilon} \\ J^{(m)} &= \zeta(H_e^{(m)}) \\ S^{(m)} &= \xi(J^{(m)}, \sigma) - \upsilon H_e^{(m)} \end{aligned} \quad (4)$$

The magnetoelastic model of a MST rod is coupled with a step-by-step finite element computational scheme, accounting for the electromagnetic phenomena within all the device. Taking advantage of the geometrical structure of these kind of devices (Fig. 1), the computations are performed in an axial-symmetric domain with cylindrical coordinates $\{r, \theta, z\}$. By employing the FP iterative technique to handle the magnetic nonlinearities, the weak formulation becomes:

$$\int_{\Omega} \nabla \text{curl} \mathbf{A} \cdot \text{curl} w ds = - \int_{\Omega} \mathbf{R} \cdot \text{curl} w ds + \sum_k \left[\int_{\Omega_k} \frac{N_k \dot{A}_k}{S_k} w ds - \frac{1}{\rho_k} \int_{\Omega_k} \dot{A} w ds + \frac{1}{\rho_k} \int_{\Omega_k} \mathbf{M}_{\Omega_k}(\dot{A}) w ds \right] \quad (5)$$

where \mathbf{A} is the magnetic vector potential, w is the test function, and Ω is the full domain. In (4) k indicates a generic conductor of resistivity ρ_k having trace Ω_k , area S_k and turn number N_k , \mathbf{R} is the FP residual and $\mathbf{M}_{\Omega_k}(\dot{A})$ is the mean of \dot{A} over Ω_k . For the sake of simplicity, the dependency of the field quantities on time has been omitted.

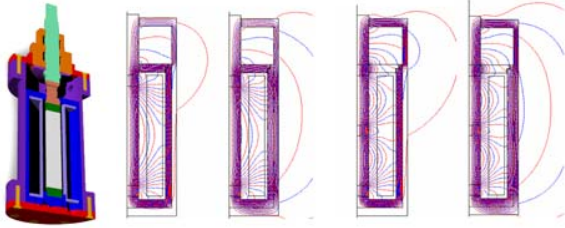


Fig. 1. MST device structure and simulations of the magnetic field distribution inside the device for different configurations.

At each time step, nonlinear problem (5) is iteratively computed, starting from a trial value of the residual. At iteration j , the residual update is performed in two steps:

$$\begin{aligned} \tilde{\mathbf{H}}^{(j)} &= \nabla \mathbf{B}^{(j)} + \mathfrak{R}^{(j-1)} \\ \mathfrak{R}^{(j)} &= \tilde{\mathbf{H}}^{(j)} - \nabla \Psi(\tilde{\mathbf{H}}^{(j)}) \end{aligned} \quad (6)$$

where Ψ describes the relationship between magnetic field and magnetic flux density, here in bold type being vector quantities, and $\tilde{\mathbf{H}}^{(j)}$ represents a magnetic field estimate.

The Preisach distribution function, which defines CPM model described in (1) by ζ , and function ξ are identified starting from a set of static B - H cycles measured at different stresses, following the approach described in [4]. Known the time waveform of J , the local strain λ of the magnetostrictive rod is approximated by the function:

$$\lambda(J, \sigma) = \lambda_0 - \frac{\lambda_0}{e} \frac{|J| - J_0}{\Delta J} \quad (7)$$

where J_0 depends on stress σ and constants λ_0 , ΔJ , $J_{0,1}$, $J_{0,2}$, and $J_{0,3}$ are determined by a nonlinear minimisation algorithm.

The computation of the local value of strain λ within the rod by (7) enables the determination of the total rod elongation. The coupling with a simplified mass-spring mechanical model enables the determination at each time step of the new value of the mechanical stress σ .

III. ANALYSIS OF A MST DEVICE

The coupled FEM-MM approach has been applied to the simulation of a device equipped with a Terfenol-D rod. A prototype of actuator is available for laboratory

measurements, allowing the measurements of local and global electromagnetic and mechanical quantities. In the results reported in Fig. 2, the prediction of the total rod elongation, determined as average value of the local deformations over the entire rod, is plotted versus the excitation current and compared with experiments, showing discrepancies lower than 22%.

The dynamic response of the MST actuator is evidenced by the plots of Fig. 3, where the time evolution of the total rod elongation is plotted versus the supply current, for the rod with negligible preload and with a 13 MPa preload. Due to dynamic phenomena, simulations evidence how the area of the loop increases and the maximum elongation slightly decreases with frequency.

The modeling details and its complete validation by comparison with experiments will be presented at the Conference.

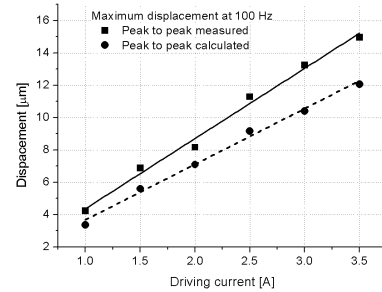


Fig. 2. Comparison between computed and measured total rod elongation.

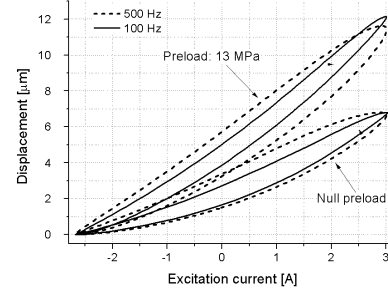


Fig. 3. Dynamic response of the MST actuator. Plots of the total elongation versus supply current for the unloaded and preloaded rod.

IV. REFERENCES

- [1] F. Stillesjö, G. Engdahl, A. Bergqvist, "A design technique for magnetostrictive actuators with laminated active materials", IEEE Trans. Magn., vol. 32, pp. 2141-2143, 1998.
- [2] S. Mandayam, L. Udpa, S.S. Udpa, Y.S. Sun, "A fast iterative finite element model for electrodynamic and magnetostrictive vibration absorbers", IEEE Trans. Magn., vol. 30, pp. 3300-3303, 1994.
- [3] S.C. Cao, B. Wang, J. Zheng, W. Huang, Y. Sun, Q. Yang, "Modeling dynamic hysteresis for giant magnetostrictive actuator using hybrid genetic algorithm", IEEE Trans. Magn., vol. 42, pp. 911-914, 2006.
- [4] O. Bottauscio, M. Chiampi, A. Lovisolo, P.E. Roccatto, M. Zucca, "Dynamic modelling and experimental analysis of Terfenol-D rods for magnetostrictive actuators", J. Appl. Phys., Vol. 103, 07F121/1-3, 2008.
- [5] O. Bottauscio, A. Lovisolo, P.E. Roccatto, M. Zucca, C. Sasso, R. Bonin, "Modelling and experimental analysis of magnetostrictive devices: from the material characterisation to their dynamic behaviour", IEEE Trans. Mag., Vol. 44, No. 11, 2008, pp. 3009-3012.
- [6] M.J. Sablik, D.C. Jiles, "Coupled magnetoelastic theory of magnetic and magnetostrictive hysteresis", IEEE Trans. Magn., vol. 29, pp. 2113-2123, 1993.

Determination of d-q Axis Parameters of Interior Permanent Magnet Machines

P. Zhou, D. Lin, G. Wimmer and Z.J. Cendes
Ansoft LLC, 225 W. Station Square Dr, Pittsburgh 15219 USA
ping@ansoft.com

Abstract — In this paper, a new approach is presented for extracting saturated parameters L_d , L_q and permanent-magnet flux linkage λ_{md} for interior permanent magnet machines. The procedure starts with the parameter extraction in actual abc reference frame based on transient finite element analysis in time-domain. Then the parameters in abc reference frame are transformed to $d-q$ axis reference frame. This approach is able to provide better accuracy and allow easy implementation because the parameters are derived from a realistic physical representation and the effects of the slot leakage and phase-spread harmonic fields are included in the simulation.

I. INTRODUCTION

Interior permanent magnet (IPM) machines are widely used in various electrical devices due to their high torque-to-current and power-to-weight ratios, and their high efficiency. The transient finite element analysis (FEA) coupled with driven circuits can provide a powerful design tool to take geometric complexity, high local magnetic saturation, induced eddy currents, dynamic core loss and mechanical movement into account [1]-[2]. However, the extraction of saturated $d-q$ axis parameters is still highly desirable because in addition to providing good insight into the feasibility of a design [3], $d-q$ axis parameters are also fundamental parameters to many vector control algorithms in the $d-q$ reference frame for fast and accurate response with quick recovery from a disturbance [4].

For computation of saturated $d-q$ axis parameters, the conventional method considers neither the change of winding induced voltage with load nor the cross effects on field saturation between the d -axis and q -axis [5]-[6]. A method called the loading method was developed in [7] to consider the cross effects of d - and q -axis load currents on field saturation with improved accuracy. This method computes the $d-q$ axis parameters based on the fundamental air-gap fluxes from two field solutions in terms of a specific load current and a small current increment at a fixed rotor position. However, this procedure may cause some uncertainty due to the arbitrary choice of a small displacement from the operating point, or the arbitrary alignment of the rotor pole center with the stator slot center, the tooth center, or in between. In addition, the effects of stator slot leakage and phase-spread harmonic leakage are not directly taken into account in the field simulation.

In this paper, the saturated parameters and the flux linkage produced by permanent magnet (PM) at various load conditions are first directly extracted in actual (natural) abc reference frame based on the frozen method from the transient FEA solution. Then they are transformed to $d-q$ axis reference in terms of the average values over one steady-state cycle. Thus, the extracted $d-q$ parameters have taken into account the

effects of the slot leakage and phase-spread harmonic field. This approach is able to provide better accuracy.

II. PARAMETER EXTRACTION IN ABC REFERENCE FRAME

The saturated parameters in the abc reference frame vary with the load conditions. When the three-phase windings are excited with constant three-phase AC voltages, these parameters can be extracted and expressed as a function of torque angle δ . Because the torque angle is the displacement by which the induced voltage phasor lags the applied voltage phasor, this modeling request can be easily realized in transient FE analysis by the following steps: 1) rotate the rotor to the initial position θ_0 at which the negative d -axis aligns with the positive phase-A axis as shown in Fig. 1; 2) apply three-phase voltages in terms of a specific torque angle as

$$\begin{cases} v_a = \sqrt{2}V_1 \sin(\omega t + \delta) \\ v_b = \sqrt{2}V_1 \sin(\omega t + \delta - 2\pi/3) \\ v_c = \sqrt{2}V_1 \sin(\omega t + \delta - 4\pi/3) \end{cases} \quad (1)$$

where ω is the angular frequency. With such scheme, phase-A will have the negative maximum flux linkage produced by PM at the initial position, which corresponds to zero crossing from negative to positive of the induced voltage in phase-A.

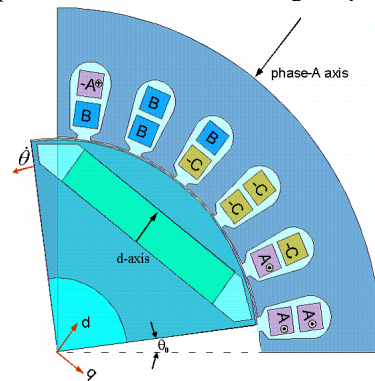


Fig. 1 Initial rotor position where d -axis oppositely aligns with phase-A axis

After solving transient FEA under a specific load condition at each time step, the FEA system's coefficient matrix is frozen, which is equal to freezing the permeability of each element. Then the field is resolved with the frozen coefficient matrix together with different right-hand sides corresponding to the excitation of 1A current in turn in each winding with the exclusion of magnets and all other winding excitations. As a result, the calculated flux linkages provide the self and mutual inductances for all windings. Similarly, by enabling the excitation of magnets alone with zero currents in all windings, the flux linkage due to magnets for each winding is obtained.

III. PARAMETERS IN DQ REFERENCE FRAME

The transformation matrix from abc reference frame to $d-q$ reference frame is

$$[C] = \sqrt{\frac{2}{3}} \begin{bmatrix} \cos\theta & \cos(\theta - 2\pi/3) & \cos(\theta - 4\pi/3) \\ \sin\theta & \sin(\theta - 2\pi/3) & \sin(\theta - 4\pi/3) \\ 1/\sqrt{2} & 1/\sqrt{2} & 1/\sqrt{2} \end{bmatrix} \quad (2)$$

where θ , which is equal to $\omega t + \pi$ at the synchronous speed, is the angle from the phase-A axis to the d -axis in electrical radians. It can be verified that this transformation is able to keep the power and torque invariant, as well as to have identical transformation for both current and voltage. Therefore, the transformation of impedance is

$$\begin{bmatrix} L_d & 0 & 0 \\ 0 & L_q & 0 \\ 0 & 0 & L_0 \end{bmatrix} = [C] \cdot \begin{bmatrix} L_{aa} & L_{ab} & L_{ac} \\ L_{ab} & L_{bb} & L_{bc} \\ L_{ac} & L_{bc} & L_{cc} \end{bmatrix} \cdot [C]^T \quad (3)$$

where superscript T denotes the transpose of $[C]$. The transformation of flux linkage produced by PM alone is

$$\begin{bmatrix} \lambda_{md} \\ \lambda_{mq} \\ \lambda_{m0} \end{bmatrix} = [C] \cdot \begin{bmatrix} \lambda_{ma} \\ \lambda_{mb} \\ \lambda_{mc} \end{bmatrix} \quad (4)$$

The $d-q$ axis inductances L_d and L_q , and flux linkages λ_{md} and λ_{mq} are computed for each time step. Figs. 2 and 3 show the variations of average values of these parameters over one steady-state cycle with the torque angle δ for the application example to be discussed in the next section.

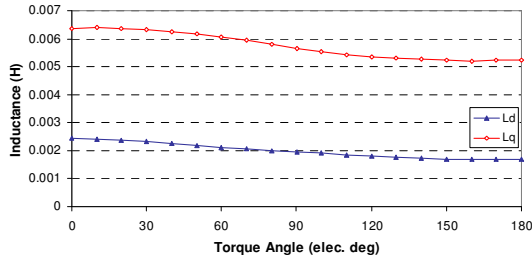


Fig. 2 L_d and L_q profiles with torque angle

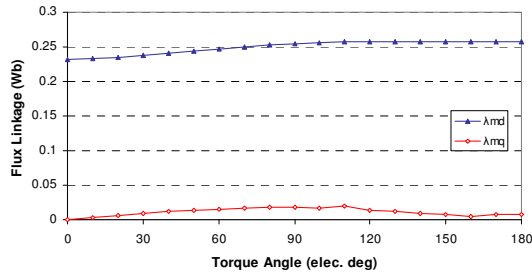


Fig. 3 λ_{md} and λ_{mq} profiles with torque angle

IV. NUMERICAL VALIDATION

As an application example, the proposed approach is applied to simulate the performance of 8-pole, 48-slot Toyota Prius IPM motor [8]. The rating of the prototype is 50kW at 200V phase peak voltage and 3000 rpm.

In order to validate the effectiveness of the proposed approach, let us to compare the torque value between two cases: the first one is that the torque value is obtained directly from transient FEA simulation; the other one is that the torque

value is derived in terms of the above extracted parameters shown in Figs. 2 and 3 based on the lumped parameter model. From (1) and (2), the $d-q$ voltage at the synchronous speed is

$$\begin{bmatrix} v_d \\ v_q \\ v_0 \end{bmatrix} = [C] \cdot \begin{bmatrix} v_a \\ v_b \\ v_c \end{bmatrix} = \begin{bmatrix} -\sqrt{3}V_1 \sin\delta \\ -\sqrt{3}V_1 \cos\delta \\ 0 \end{bmatrix} \quad (5)$$

The voltage equation in the $d-q$ reference frame is

$$\begin{bmatrix} v_d \\ v_q \end{bmatrix} = \begin{bmatrix} 0 \\ -\dot{\theta}\lambda_{md} \end{bmatrix} + \begin{bmatrix} R_1 & \dot{\theta}L_q \\ -\dot{\theta}L_d & R_1 \end{bmatrix} \cdot \begin{bmatrix} i_d \\ i_q \end{bmatrix} \quad (6)$$

where $\dot{\theta}$ is the synchronous speed in electrical radians per second, and R_1 is the resistance of the phase winding. Thus

$$\begin{bmatrix} i_d \\ i_q \end{bmatrix} = \frac{1}{R_1^2 + \dot{\theta}^2 L_d L_q} \begin{bmatrix} R_1 v_d - \dot{\theta} L_q (v_q + \dot{\theta} \lambda_{md}) \\ \dot{\theta} L_d v_d + R_1 (v_q + \dot{\theta} \lambda_{md}) \end{bmatrix} \quad (7)$$

and the torque is

$$T_e = p \left[-(L_d - L_q) i_d i_q - \lambda_{md} i_q \right] \quad (8)$$

where p is the number of pole pairs. Fig. 4 shows the torque characteristics computed by (8) using the extracted lumped parameters, compared with the results directly from FEA transient simulation. It can be seen they match very well.

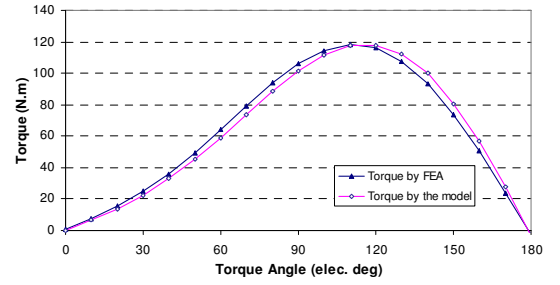


Fig. 4 Torque characteristics from the lumped parameter model, compared with the FEA transient simulation results

V. REFERENCES

- [1] P. Zhou, D. Lin, W.N. Fu, B. Ionescu, and Z.J. Cendes, "A general co-simulation approach for coupled field-circuit problems," *IEEE Trans. Magn.*, vol. 42, no. 4, pp. 1051-1054, Apr. 2006.
- [2] D. Lin, P. Zhou, W.N. Fu, Z. Badics, and Z.J. Cendes, "A dynamic core loss model for soft ferromagnetic and power Ferrite materials in transient finite element analysis," *IEEE Trans. Magn.*, vol. 40, no. 2, pp. 1318-1321, Mar. 2004.
- [3] T.J.E. Miller, "Method of testing permanent magnet ac motors," *IEEE Ind. Appl. Soc. Annu. Rec.*, pp. 494-499, 1981.
- [4] M.A. Rahman, R.M. Milasi, C. Lucas, B.N. Araabi, and T.S. Radwan, "Implementation of emotional controller for interior permanent-magnet synchronous motor drive," *IEEE Trans. Ind. Appl.*, vol. 44, no. 5, pp. 256-267, Apr. 2008.
- [5] S.F. Gorman, C. Chen, and J.J. Cathey, "Determination of permanent magnet synchronous motor parameters to use in a brushless dc motor drive analysis," *IEEE Trans. Energy Convers.*, vol. 3, no. 3, pp.674-681, 1988.
- [6] P.H. Mellor, F.B. Chaban, and K.J. Binns, "Estimation of parameters and performances of rare-earth permanent-magnet motors avoiding measurement of load angle," in *Proc. IEE*, vol. 138, pt. B., no. 6, 1991, pp. 322-330.
- [7] M.A. Rahman and P. Zhou, "Determination of saturated parameters of PM motors using loading magnetic fields," *IEEE Trans. Magn.*, vol.27, no. 5, pp.3947-3950, Sept.1991.
- [8] J.S. Hsu, C.W. Ayers, C.L. Coomer, R.H. Wiles, S.L. Campbell, and K.T. Lowe, "Report on toyota/prius motor torque capability, torque property, no-load back EMF, and mechanical losses", Oak Ridge Institute for Science and Education, ORNL/TM-2004/185.

Simulation of the Winding Overhangs in Permanent Magnet Synchronous Machines

B. Funieru, and A. Binder

Technische Universitaet Darmstadt
Landgraf-Georg-Str. 4, D-64283 Darmstadt, Germany
bfunieru@ew.tu-darmstadt.de

Abstract — The stator winding overhangs of two permanent magnet (PM) synchronous machines are simulated using a 3D simulation program dedicated for calculation of special end effects in electrical machines. The main issues with simulation of the stator winding ends and the adopted solutions are presented in this paper. Two models with different type of winding overhangs are calculated to demonstrate the program functionality.

I. INTRODUCTION

Numerical simulation of electrical machines is widely used especially by the calculation and optimization of PM machines. Often in the daily use, specialized 2D programs [1], which allow fast deploying of the model and offer the necessary results in a convenient manner, are preferred to a multipurpose general program, which may not be so time efficient. In order to expand the capabilities of an established 2D FEM code, a special 3D program is developed for considering only 3D end effects in electrical machines. The program uses as the base for the mesh generation the established 2D mesh, which is extruded to create the three dimensional meshes. For solving the 3D numerical problems an open source software [2] is used.

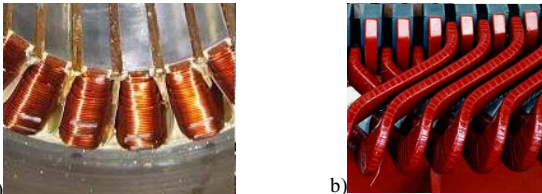


Fig. 1. a) Tooth wound coil b) Two layers distributed coil (Source a) TU Darmstadt, b) VA Tech Andritz)

Simulation of electrical machines with 3D models is usually avoided due to the complicated model construction and increased calculation time. For many cases a 2D calculation is considered sufficient. However, if the simulated machine is relatively short like the disc type machines, or if the stator and rotor have big differences in length in the axial direction or the effects of the winding overhang are important, a 2D solution is not sufficient. In this paper the generation of the winding overhang as a special example of a 3D problem is discussed. The winding overhang can be complicated to implement, depending on the machine type. The tooth wound coils (Fig. 1 a)) are easy to implement, but the high voltage two layer distributed winding (Fig. 1 b)) features a complicated 3D structure, which must be considered by a special mesh generation. The developed 3D FEM code provides the user with an automatic generation of the winding

overhangs in order to reduce the time, needed to prepare the simulation.

II. WINDING OVERHANG MESH GENERATION

For the treatment of end effects the mesh is generated mostly by extrusion from the original 2D mesh of the previously investigated machine. The same procedure is applied also for the winding overhangs, where the extrusion path is chosen to be found in the center of the coil cross section. Thus the extrusion path is a 3D curve that needs to follow the winding overhang shape. One problem that arises during extrusion is that the coil can get skewed and the lateral cross section areas are not planar anymore. That requires the use of second order elements which are not supported by the used open source software. For this reason the winding overhangs mesh is not done with hexahedral or triangular based prisms, but with first order tetrahedral elements, which due to their triangular faces have always plane faces. A small geometrical discretization error (Fig. 2) appears for strong twisting, which can be reduced by an increase of the mesh density.

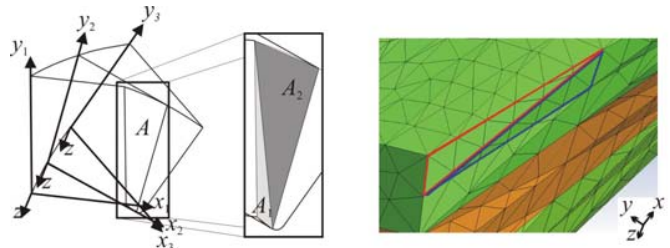


Fig. 2. Skewed geometry with the non-planar quadrilateral surface A approximated by two planar triangular surfaces A_1 and A_2

The extrusion path contains straight segments and circle arcs. In order to avoid unnatural deformation of the mesh during extrusion, straight segments are not usually connected directly, if they are forming an angle different of 180° . A procedure that connects two neighboring segments with an arc of a given radius is used to maintain a valid mesh. A simple application is a tooth wound coil, which only contains two straight segments and an arc, all found in the same plane. The example is an outer rotor PM machine, used as a fan motor (Fig. 3 a)). For this example the simulation of a 3D model is interesting, because the outer rotor is longer than the stator.

III. TWO LAYER DISTRIBUTED WINDING

Distributed windings are used instead of tooth wound coils, because they are decreasing the harmonic content of the

stator field and so decrease the losses in the machine. The complicated manufacturing increases the manufacturing costs. Two layers distributed winding with a constant coil span are used as form wound coils in large machines. The coils are connected between the upper and the lower layer coil side without intersecting each other in the overhang region and having a regular arrangement of the end connections (Fig. 3 b)). The presented example is a linear machine. In the case of rotating machines an additional bending is necessary to follow the machine cylindrical shape.

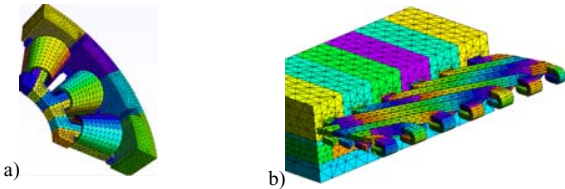


Fig. 3. a) One pole pair of the tooth wound coil outer rotor PM synchronous machine b) One pole of the two layers distributed winding linear PM machine

TABLE I
MAIN MOTOR PARAMETERS FOR SIMULATION

Parameter\Motor	Tooth-coil	Distributed winding
Phase number	3	3
Turns / Phase	100	5
Iron stack length	5 mm	60 mm
Magnet length	15 mm	60 mm
Overhang length	12 mm	67 mm
Iron relative permeability	1000 (rotor) 10000 (stator)	1000

The modeling of this type of machine is difficult, when the symmetry is exploited and periodical boundary conditions are used to limit the calculation domain. For example, in Fig. 3 b) the mesh for only one pole of the motor is used and the winding must pass through the boundary. That can happen at an arbitrary angle and so care must be taken that the elements remain valid. Furthermore, the periodical boundary conditions require that the mesh on both sides (left and right in Fig. 3 b)) is identical. The solution adopted was to generate the entire preformed coil and to cut the part that surpasses the model boundary. The parameters used for the simulations are given in Table I.

IV. CALCULATION RESULTS AND COMPARISON WITH 2D RESULTS

For validation of the results the calculations were done using the 2D software [1]. The model for the 3D software was based on an extruded mesh similar to the 2D model (a). For this purpose the end windings and end region were not simulated, and at the two boundaries in longitudinal direction (minimum and maximum z) a parallel flux *Dirichlet* boundary condition was used. The results of the 2D and 3D model are directly comparable in this case (Table II). All presented simulations are no-load calculations without excitation current in the stator winding only the PM field of the rotor is considered. Due to yet limited post processing capabilities the only integral value available is the flux linkage Ψ integrated according to (1), where \mathbf{A} is the magnetic vector potential, N

is the number of turns per phase and C is the curve on which the coil is extruded.

$$\Psi = N \int_C \mathbf{A} \cdot d\mathbf{s} \tag{1}$$

The full 3D simulation (b) considers also the winding overhang (Fig. 4). For the tooth wound coil PM machine the flux linkage increases about three times due to the longer magnets on the rotor. The length of the magnets is about 3 times bigger than the stator iron stack. Also due to the linear calculation, which neglects the iron saturation. For the distributed winding machine the full 3D model uses the same magnet volume. The flux linkage decreases due to the fact that a part of the magnetic flux lines closes in the air at the motor end without contributing to the winding flux.

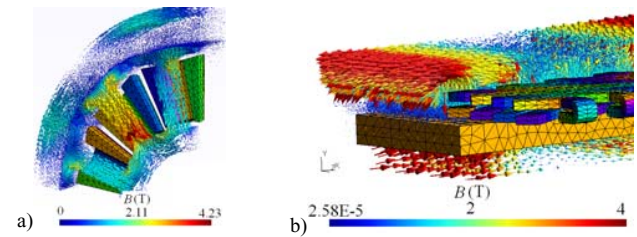


Fig. 4. Vector plot of magnetic flux density of: a) Tooth coil PM machine b) The distributed winding PM linear machine

TABLE II
COMPARISON OF CALCULATED FLUX LINKAGE IN WINDINGS FOR 2D AND 3D SIMULATION (IN $10^{-3} \cdot \text{V} \cdot \text{s}$)

Program\Motor	Tooth-coil			Distributed winding		
	U	V	W	U	V	W
2D	0.181	0.181	0.362	29.2	-43.0	9.8
a) 3D as 2D	0.183	0.183	0.365	29.0	-42.8	9.8
b) 3D	0.494	0.493	0.986	23.7	-34.6	7.8

The results of the 2D model and the first 3D model are in good concordance and so the results of the 3D program are validated.

V. CONCLUSIONS

The first results obtained with a 3D electrical machines oriented program were presented in this paper. The generation of the winding overhangs model is done using the extrusion of the 2D mesh of the coil along an arbitrary path. Periodical boundary conditions require a special treatment of the mesh generation to ensure identical mesh on the master and slave sides of the boundary condition.

VI. REFERENCES

- [1] K. Reichert, "Steady-state Finite-Element Methods to Permanent Magnet Motor Characteristics Determination" International Symposium on Power Electronics, Electrical Drives, Automation and Motion SPEEDAM 2008, Ischia, Italy, pp. 1306-1308.
- [2] P. Dular, C. Geuzaine, F. Henrotte, W. Legros, "A general environment for the treatment of discrete problems and its application to the finite element method", *IEEE Trans. on Magnetics*, 34(5): pp. 3395-3398, 1998.
- [3] A. Mocanu, "Computation of winding ends leakage inductance", IEEE International Electrical Machines and Drives Conference 1997, Milwaukee, USA, pp. TB2/10.1-TB2/10.3
- [4] R. Sikora et al., "Magnetic Field Computation in the End-Region of Electric Machines using Various Boundary Conditions on Iron Surfaces" *IEEE Trans. on Magnetics*, 22(3): pp. 204-207, 1986 .

Dynamic Analysis Method of Spiral Resonant Actuator Using 3-D FEM

Satoshi Suzuki¹, Yoshihiro Kawase¹, Tadashi Yamaguchi¹, Shuhei Kakami¹,
Katsuhiro Hirata² and Tomohiro Ota³

¹Department of Information Science, Gifu University, Japan

e-mail: sato@fem.info.gifu-u.ac.jp

²Department of Adaptive Machine Systems, Graduate School of Engineering, Osaka University, Japan

e-mail: k-hirata@ams.eng.osaka-u.ac.jp

³Advanced Technologies Development Laboratory, Panasonic Electric Works, Ltd., Japan

e-mail: t_oota@panasonic-denko.co.jp

Abstract— This paper proposes a dynamic analysis method for a novel spiral resonant actuator with two-degree-of-freedom employing the 3-D finite element method (FEM). The effects of the slit structure on the performance of the actuator are quantitatively clarified using this method.

I. INTRODUCTION

We have been developing a novel spiral resonant actuator with two-degree-of-freedom based on the linear resonant actuator with active vibration absorber [1][2].

In this paper, we propose a dynamic analysis method for the actuator, in which motion equations of linear and rotation are simultaneously solved employing the 3-D finite element method (FEM). Consequently, the effects of the slit structure on the performance of the actuator are quantitatively clarified using this method.

II. BASIC STRUCTURE AND PRINCIPLE OF OPERATION

Fig. 1 shows the proposed spiral resonant actuator. It mainly consists of an armature (yoke A and shaft) and a stator (coil, permanent magnet, yoke B and case). The armature is connected to the resonance spring. The active vibration absorber, which decreases the vibration of case, is connected to the armature.

Fig. 2 shows the magnetic circuit at the x-z section. The thrust is not generated on the armature when the coil is not excited because the magnetic flux by the magnet is balanced in two gaps. On the other hand, when the coil is excited, the thrust is generated on the armature because the total magnetic flux by the magnet and current becomes unbalanced.

Fig. 3 shows the magnetic circuit at the x-y section. In order to achieve the spiral motion, both of the armature and the stator have slits (pitch θ_p , width w , depth d), and the upper and lower slits of the armature are shifted with θ_s and $-\theta_s$ against the stator slit. The clockwise torque is generated on the armature when the armature moves in the positive direction of

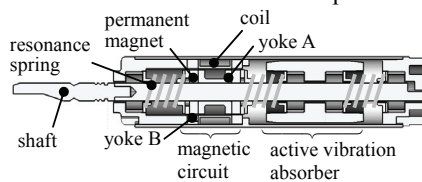


Fig. 1. Spiral resonant actuator.

z-axis because the torque generated on the upper part of the armature is dominant. On the other hand, the counterclockwise torque is generated on the armature when the armature moves in the negative direction of z-axis because the torque generated on the lower part of the armature is dominant.

III. ANALYSIS METHOD

A. Magnetic Field Analysis

The equations of the magnetic field and the electric circuit are coupled using the 3-D FEM, which are given by the magnetic vector potential \mathbf{A} and the exciting current I_0 as follows [3]:

$$\text{rot}(\nu \text{rot } \mathbf{A}) = \mathbf{J}_0 + \nu_0 \text{rot } \mathbf{M} \quad (1)$$

$$E = V_0 - RI_0 - \frac{d\Psi}{dt} = 0 \quad (2)$$

$$\mathbf{J}_0 = \frac{n_c}{S_c} I_0 \mathbf{n}_s \quad (3)$$

where ν is the reluctivity, \mathbf{J}_0 is the exciting current density, ν_0

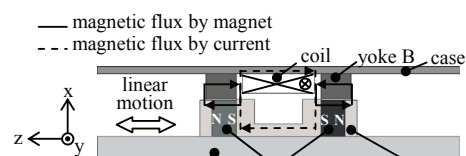


Fig. 2. Magnetic circuit (x-z section).

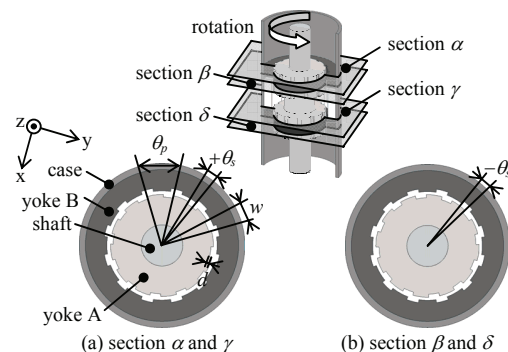


Fig. 3. Magnetic circuit (x-y section).

is the reluctivity of the vacuum, \mathbf{M} is the magnetization of permanent magnet, V_0 is the applied voltage, R is the effective resistance, Ψ is the interlinkage flux of exciting coil, n_c and S_c are the number of turns and the cross-sectional area of the coil respectively and \mathbf{n}_s is the unit vector along with the direction of exciting current.

The kinetic model of this actuator is shown in Fig. 4.

The linear motions of the armature, the active vibration absorber and the case are described as follows [3]:

$$m_1 \frac{d^2 z_1}{dt^2} = F + k_1(z_3 - z_1) + k_2(z_2 - z_1) + c_1 \left(\frac{dz_3}{dt} - \frac{dz_1}{dt} \right) + c_2 \left(\frac{dz_2}{dt} - \frac{dz_1}{dt} \right) \quad (\text{armature}) \quad (4)$$

$$m_2 \frac{d^2 z_2}{dt^2} = k_3(z_3 - z_2) + k_2(z_1 - z_2) + c_3 \left(\frac{dz_3}{dt} - \frac{dz_2}{dt} \right) + c_2 \left(\frac{dz_1}{dt} - \frac{dz_2}{dt} \right) \quad (\text{active vibration absorber}) \quad (5)$$

$$m_3 \frac{d^2 z_3}{dt^2} = -F + k_1(z_1 - z_3) + k_3(z_2 - z_3) + c_1 \left(\frac{dz_1}{dt} - \frac{dz_3}{dt} \right) + c_3 \left(\frac{dz_2}{dt} - \frac{dz_3}{dt} \right) \quad (\text{case}) \quad (6)$$

where m_i , z_i , k_i and c_i ($i=1,2,3$) are the mass, displacement, spring constant and viscous damping coefficient of the armature, active vibration absorber and case, respectively. F is the electromagnetic force acting on the armature.

The rotation of the armature is described as follows [3]:

$$I \frac{d^2 \theta}{dt^2} = T_m + k' \theta + c' \frac{d\theta}{dt} \quad (\text{armature}) \quad (7)$$

where I is the moment of inertia of the armature, θ is the rotation angle, T_m is the torque acting on the armature, k' is the spring constant for rotation and c' is the viscous damping coefficient for rotation.

B. Dynamic Analysis Method

In order to simulate the dynamic behavior of the actuator, it is necessary to solve the motion equations of linear and rotation simultaneously.

The detail of the procedure is shown as follows:

- (i) The meshes are modified according to the displacement of the armature for linear motion analysis.
- (ii) The meshes are modified according to the rotation angle of the armature for rotation analysis.
- (iii) The 3-D magnetic field analysis is conducted.
- (iv) The displacement of the armature, the active vibration absorber and the case are calculated by solving (4)-(6).

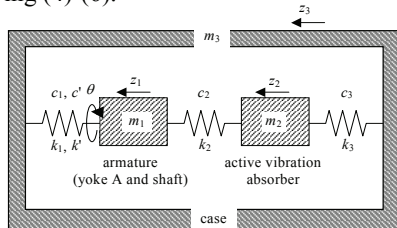


Fig. 4. Kinetic model of spiral resonant actuator.

- (v) The rotation angle of the armature is calculated by solving (7).

IV. ANALYZED MODEL AND ANALYSIS CONDITIONS

The magnetic circuit of the actuator is analyzed using the 3-D FEM (Ref. Figs. 2 and 3). The analyzed region is 1/12 of the whole region because of the symmetry. The slit pitch θ_p , the slit depth d and the slit shift θ_s are 30.0° , 0.3mm and 7.5° , respectively.

V. RESULTS AND DISCUSSION

Fig. 5 shows the waveforms of current, thrust and torque in steady state. From this figure, the maximum thrust and the maximum torque are 2.9N and $1.8\text{mN}\cdot\text{m}$, respectively. Fig. 6 shows the amplitude and rotation of the armature in resonance. From this figure, the resonance is synchronized with the rotation. The maximum amplitude and the maximum rotation angle are 0.36mm and 6.6° , respectively. The effectiveness of the calculated results will be confirmed through the comparison with the measured ones in the full paper.

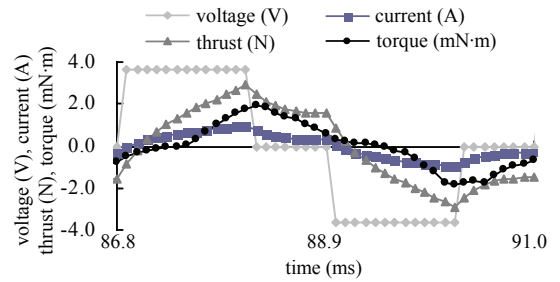


Fig. 5. Waveforms of current, thrust and torque.

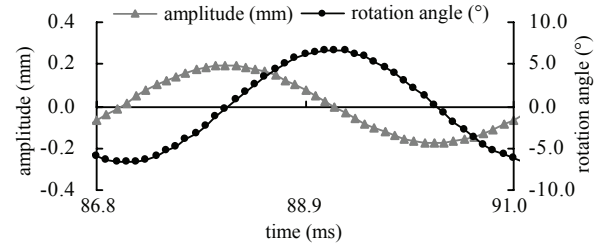


Fig. 6. Amplitude and rotation of the armature.

REFERENCES

- [1] S. Suzuki, Y. Kawase, T. Yamaguchi, S. Kakami, K. Hirata, T. Ota and Y. Hasegawa: "Dynamic Analysis of Spiral Resonant Actuator Using 3-D Finite Element Method", Proceedings of the 18th International Conference on Electrical Machines, Paper ID 1483, September 2008.
- [2] S. Suzuki, T. Ota, Y. Kawase, T. Yamaguchi, S. Kakami and K. Hirata: "Enhanced Torque and Rotation Angle of Spiral Resonant Actuator", The Papers of Technical Meeting on Linear Drives, IEE Japan, LD-09-10, 2009. (in Japanese)
- [3] Y. Kawase and S. Ito: "New Practical Analysis of Electrical and Electronic Apparatus by 3-D Finite Element Method", Morikita Publishing Co., Tokyo, Japan, 1997. (in Japanese)

Field Reconstruction Method in the Optimal Design of Doubly Fed Induction Generators

Wei Wang, Babak Fahimi

Renewable Energy and Vehicular Technology Lab, University of Texas at Arlington
416 S. Yates St., Arlington, TX, 76019, USA.

Email: wei.wang@mavs.uta.edu

Abstract—Doubly fed induction generator is attracting attention among options in distributed wind energy harvest. Traditional design and analysis of Doubly Fed Induction Generator (DFIG) dominantly rely on lump-parameters and Finite Element models. Although Finite Element Analysis (FEA) method is available, the computational time limits its application in iterative optimal design practices of DFIG. This paper is based on the use of Field Reconstruction Method (FRM) which can greatly reduce the computation cost while maintaining acceptable accuracy. In order to conduct efficiency optimization the procedure to calculate flux density and core losses are described. Finally, an optimal design method of DFIG towards maximum annual energy production in a given area with available wind speed information is presented.

I. FIELD RECONSTRUCTION METHOD IN DFIG

A. Field reconstruction model of machine

FEA is the mainstream tool in the design and analysis of electric machines. However, an optimal and iterative design of an electrical machine, using FEA, typically requires much more computation cost than lump-parameter model. In the absence of magnetic saturation, Field Reconstruction (FR) method [1] can offer the distribution of the flux density with acceptable accuracy using superposition of two pre-existing magneto-static FE field solutions. It is understood that distributed wind generators that are grid connected should not operate under saturated conditions to avoid emission of undesirable harmonics. Therefore, with the linearity assumption, the normal and tangential flux density in the airgap of DFIG can be viewed as the superposition of the stator and rotor contributions

$$B_n = B_{ns} + B_{nr} \quad (1)$$

$$B_t = B_{ts} + B_{tr} \quad (2)$$

In (1) and (2), B_{ns} , B_{nr} , B_{ts} , B_{tr} denote the normal and tangential components of flux density generated by stator and rotor excitations respectively. In particular, B_{ns} , B_{ts} can be obtained by adding the flux components created by 3 phases stator current I_{as} , I_{bs} and I_{cs} . This can be expressed as

$$B_{ns} = B_{nas} + B_{nbs} + B_{ncs} \quad (3)$$

$$B_{ts} = B_{tas} + B_{tbs} + B_{tcs} \quad (4)$$

Where B_{nas} , B_{tas} can be defined as

$$B_{nas} = I_{as} f_{ns}(\phi_{sm}) \quad (5)$$

$$B_{tas} = I_{as} f_{ts}(\phi_{sm}) \quad (6)$$

In which, $f_{ns}(\phi_{sm})$, $f_{ts}(\phi_{sm})$ are the basis functions only related with the geometry parameters of DFIG. The angle ϕ_{sm} refers to angular position relative to stator axis. Due to the symmetry of stator, the flux component of stator can be expressed as

$$B_{ns} = I_{as} f_{ns}(\phi_{sm}) + I_{bs} f_{ns}(\phi_{sm} - \theta) + I_{cs} f_{ns}(\phi_{sm} - 2\theta) \quad (7)$$

$$B_{ts} = I_{as} f_{ts}(\phi_{sm}) + I_{bs} f_{ts}(\phi_{sm} - \theta) + I_{cs} f_{ts}(\phi_{sm} - 2\theta) \quad (8)$$

Where θ is equal to 120 degree divided by number of pole pairs. Since the structure of rotor is similar to stator in DFIG, B_{nr} , B_{tr} can be defined as

$$B_{nr} = I_{ar} f_{nr}(\phi_{rm}) + I_{br} f_{nr}(\phi_{rm} - \theta) + I_{cr} f_{nr}(\phi_{rm} - 2\theta) \quad (9)$$

$$B_{tr} = I_{ar} f_{tr}(\phi_{rm}) + I_{br} f_{tr}(\phi_{rm} - \theta) + I_{cr} f_{tr}(\phi_{rm} - 2\theta) \quad (10)$$

B. Basis functions

Magneto static Finite Element Analysis of DFIG Model in commercial Maxwell is used to compute the basis functions $f_{ns}(\phi_{sm})$, $f_{ts}(\phi_{sm})$, $f_{nr}(\phi_{rm})$, $f_{tr}(\phi_{rm})$. By setting the $I_{as} = 1A$ while other phases of stator and rotor are kept open, basis functions $f_{ns}(\phi_{sm})$ and $f_{ts}(\phi_{sm})$ can be obtained using a single FE field solution. Similarly, the basis functions of rotor flux density can be calculated. Fig. 1 and Fig. 2 show the normal and tangential flux density of one 4 poles, 3 phases DFIG calculated by FR and FEA methods when the excitation is 30AT, -15AT, -15AT at stator phase a, b, c respectively. The rotor excitation is the same with stator. Our results show that FRM is typically two orders of magnitude faster than FEA and can have a high impact on computational time and resources.

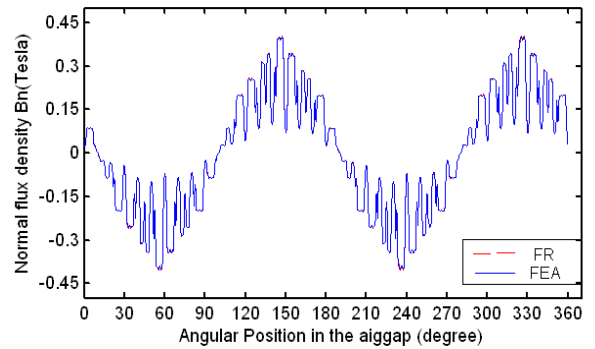


Fig. 1. Normal flux density in the airgap calculated by FR method and FEA

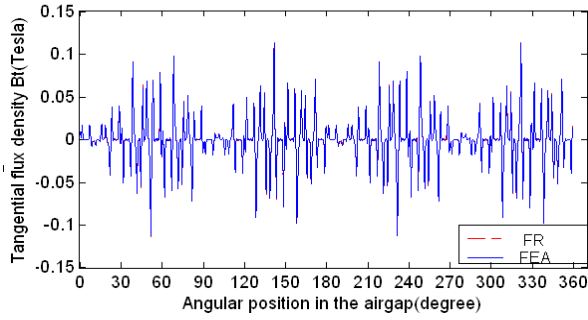


Fig. 2. Tangential flux density in airgap calculated by FR method and FEA

II. FLUX AND CORE LOSS CALCULATION

Starting from the knowledge of flux distribution in the middle of the airgap the flux at various parts of the DFIG is calculated by integration of flux density over the area of various stator teeth. Once the flux distribution is known, the core loss model of the ferromagnetic materials is applied to calculate the core loss. Since the normal and tangential component of magnetic field is already computed by FR method, the calculation of core loss distribution is straight forward according to (11).

$$P_v = K_h f B_m^2 + K_c (f B_m)^2 + K_e (f B_m)^{1.5} \quad (11)$$

In which, K_h , K_c , K_e refer to the hysteresis loss, eddy current loss and excess loss coefficients respectively, which only related with material properties and B_m is the magnitude of flux density. Fig. 3 shows core loss of the DFIG model used in this paper when fed by 5A current at both stator and rotor.

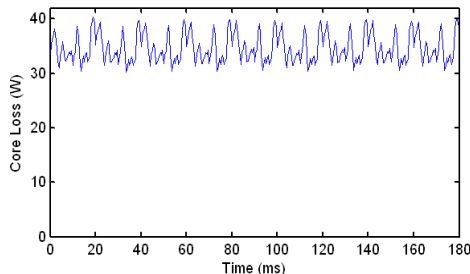


Fig. 3. Core Loss of the DFIG

III. OPTIMAL DESIGN OF DFIG ACCORDING TO WIND SPEED DISTRIBUTION

A. Wind Speed Distribution

One drawback of the wind energy is that the available power relies heavily on the weather condition. There would be large fluctuation in wind energy due to the uncertainty of wind speed. To facilitate the optimal design, the Rayleigh distribution showed in Fig. 4, which has reasonable approximation of real wind speed condition, is applied in this paper. The probability density function is given by

$$f(v) = (\pi v / 2u_a) \exp(-\pi v^2 / 4u_a^2) \quad (12)$$

In which, v is the wind speed, u_a is average wind speed.

However, in the practical design, it is better to take advantage of specific site wind speed distribution data if it is accessible.

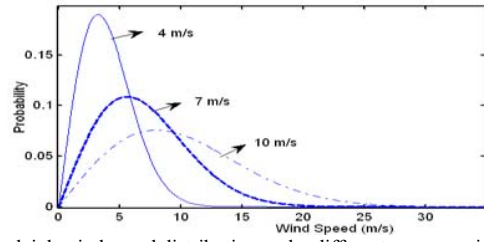


Fig. 4. Rayleigh wind speed distribution under different average wind speeds

B. Optimal design

Typically, the electric machines are designed to have the maximum efficiency at the rated operation condition. Nevertheless, DFIG always works at points apart from the rated condition due to the uncertain wind condition. The total output power of DFIG based on such design may not be the maximum in unit period. Actually, it is more straightforward if the optimal design aims at highest overall efficiency or total annual power output. However, accurate simulation based on FEA is time consuming. Fig. 5 shows the proposed optimal design procedure of DFIG which only requires one single magneto statistic FEA evaluation in one optimization circle when new geometry parameters generated. This can be much less time consuming than optimal design based on FEA.

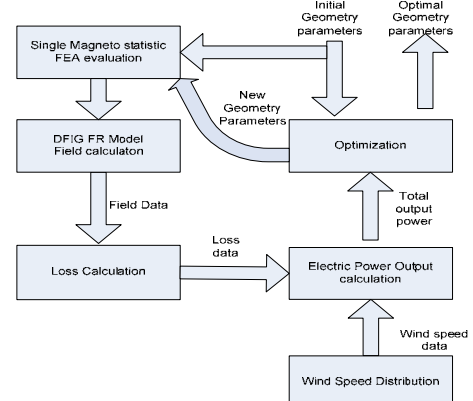


Fig. 5. Magnetization as a function of applied field

IV. CONCLUSION

An optimal design method of DFIG based on FR and FEA, aimed at maximum annual energy production, is proposed in this paper. Using the proposed method, optimal design can be achieved while the computation cost would be significantly reduced with reasonable accuracy compared to FEA. An optimal design case will be presented in the full version of the paper.

V. REFERENCES

- [1] W. Zhu, B. Fahimi, and S. Pekarek, "A Field Reconstruction Method for Optimal Excitation of Permanent Magnet Synchronous Machines," *IEEE Trans. on Energy Conversions*, 21(2): 305-313, June, 2006.
- [2] S. Jung, H. Jung, W. Jeon, H.K. Jung, S. Hahn, C. Lee, "Optimal Design of Direct-Driven PM Wind Generator for Maximum Annual Energy Production," *IEEE Trans. on Magnetics*, 44(6):1062-1065, June, 2008.
- [3] D.S. Zinger and E. Muljadi, "Annualized Wind Energy Improvement Using Variable Speeds," *IEEE Trans. On Ind. Appl.*, 33(6):1444-1447, Nov, 2008.

Analysis of Harmonic Iron Losses for IPMSM Considering the Rotating Field

Jang-Ho Seo and Hyun-Kyo Jung

School of Electrical Engineering, Seoul National University, Shillim-dong, Kwanak-gu, Seoul, 151-742, Korea
jangoho78@elecmech.snu.ac.kr.

Abstract— In this paper, we investigated the iron loss of interior permanent magnet machines for high-speed operation. In the analysis, to consider the harmonic magnetic field and the rotational variation of flux vectors in the core of the machine effectively, we proposed a new harmonic iron loss calculation method based on variable loss coefficients due to their flux density and frequency. In order to verify the performance of the proposed method, we calculated the iron loss in interior-permanent magnet synchronous machine (IPMSM) with conventional methods. Then, the estimated iron losses were compared with the experimental data. It was clarified that the proposed method is more effective than conventional methods at high-speed operation.

I. INTRODUCTION

With the increasing demand on high efficiency and high power density for energy saving, it is important to estimate iron loss of electrical machines accurately [1]-[5]. Until now, several models for harmonic iron loss in rotating machines using both Fourier transform and Epstein test have been developed [1]-[2].

In [1] the authors showed an iron loss evaluation method (*Conv. Method-1*) considering elliptically rotating field and harmonic flux density distribution. The method used the constant loss coefficient which is acceptable for line-fed machines with magnetic circuit loaded at 1.5-1.8T. However, such strategy based on constant loss coefficients is not suitable for the machine using field-weakening control in which the frequency and the flux density of flux waveform are varied remarkably according to its driving condition [3]-[5].

In [2] the authors showed a simple iron loss calculation method (*Conv. Method-2*) without using loss coefficients. However, the method needs experimental data curves very much because the model can't define the arbitrary loss curve used to calculate harmonic iron losses.

In this study, we proposed a new iron loss model adopting the variable loss coefficients concept [3], [4]. In order to verify the performance of the proposed method, we calculated the iron loss in IPMSM with conventional methods. Then, the estimated iron losses were compared with the experimental data.

II. PROPOSED MODEL

A. Adaptive Loss Coefficients

The conventional iron loss model with constant coefficients give rise to substantial error in specific frequency range and flux density, we adopt the concept of variable coefficients [3]-[5]. The iron loss model using the variable coefficients can be expressed as follows:

$$w_i = K_e(f, B)f^2 B^2 + K_h(f, B)f B^2. \quad (1)$$

The coefficients of K_e and K_h are variables with f and B . To attain the variable coefficients (K_e and K_h) with small relative error, we divided overall frequency range into two parts. One is low frequency (50-1000 Hz), the other is high frequency (1000-10000 Hz). And the determination of loss coefficients is shown in Fig. 3.

The following fifth-order polynomials were employed for curve fitting of K_e and K_h :

$$K_e = k_{e0} + k_{e1}B + k_{e2}B^2 + k_{e3}B^3 + k_{e4}B^4 + k_{e5}B^5, \quad (2)$$

$$K_h = k_{h0} + k_{h1}B + k_{h2}B^2 + k_{h3}B^3 + k_{h4}B^4 + k_{h5}B^5. \quad (3)$$

B. Rotational Iron Loss Evaluation

Generally, the loss data obtained from Epstein test has been widely used to calculate iron loss [1]-[5]. The Epstein test is performed in alternating field conditions and the method give good precision in predicting iron loss in transformers where the alternating field is dominant. However, in case of the rotating machines, there exist rotational flux density variations with different degrees of polarization. In addition, it has been reported that the iron loss occurring in the rotational field is much larger than that of the alternating one [1].

The additional iron loss caused by the rotational field is assumed to be proportional to the circular degree of flux vector loci expressed by the short-axis-to-long-axis rate c ($0 \leq c \leq 1$). The evaluation of this additional iron loss can be expressed as follows [1]:

$$W_i = \begin{aligned} &= P_{hys-rot} + P_{eddy-rot} \\ &= P_{hys-alt} + P_{eddy-alt} + P_{add_rot} \end{aligned}, \quad (4)$$

$$P_{add-rot} = \gamma \frac{L_{short}}{L_{long}} (P_{hys-alt} + P_{eddy-alt}), \quad (5)$$

$$= \gamma c (P_{hys-alt} + P_{eddy-alt})$$

where $P_{hys-rot}$ and $P_{eddy-rot}$ is hysteresis and eddy-current loss respectively when rotational field considered, P_{add_rot} is the additional iron loss caused by rotational field, L_{short} and L_{long} is the short and long axis of the flux vector trajectory ellipse, γ is the rate of iron loss increment under the circular rotational field to the loss in alternating field. The constant ' γ ' varies with flux density and the kind of core material. For simplicity, γ is fixed to 1.

Using FEM analysis, the flux density waveform at each element can be obtained. And then, Fourier transform is

performed to get fundamental and harmonics components. According to (4), total iron loss considering rotating field can be estimated as follows [1]:

$$W_i = \int_{iron} \sum_n \left(K_e D \cdot (nf)^2 B_{m,n}^2 + K_h D \cdot (nf) B_{m,n}^a \right) \cdot (1 + \gamma C_n) dv, \quad (6)$$

where C_n is the short-axis-to-long-axis rate of the flux vector locus at harmonic order n .

Since using the constant coefficients may induce the large computational error, (6) is not suitable for the machine using field-weakening control in which the frequency and the flux density of flux waveform are varied dramatically according to its driving condition.

Based on the equation (1), (2), and (3), we proposed a new iron loss model that employs the variable loss coefficients. The proposed model, based on (6), can be formulated as follows:

$$W_i = \int_{iron} \sum_n \left(K_e(nf, B_{m,n}) D \cdot (nf)^2 B_{m,n}^2 + K_h(nf, B_{m,n}) D \cdot (nf) B_{m,n}^a \right) \cdot (1 + \gamma C_n) dv \quad (7)$$

III. SIMULATION RESULTS AND DISCUSSION

To verify our proposed method, an IPMSM having 3[kW] power rating prototype machine was selected. For validation of our proposed method, the estimated iron loss was compared with the measurements. In the experiment, the open-circuit iron losses were measured with an input-output test. Fig. 2 shows the experimental equipments for measuring of iron loss. Fig. 3 shows the FE model and iron loss distribution of the machine at open-circuit operation.

The comparison of computational results is presented in Fig. 4. From the figure, we can see that our method agree well with the experimental ones compared with the conventional methods.

IV. REFERENCES

- [1] L. Ma, M. Sanada, S. Morimoto, and Y. Takeda, "Prediction of iron loss in rotating machines with rotational loss included", *IEEE Trans. Magnetics*, 39(4): 2036-2041, 2003.
- [2] H. Nam, K. H. Ha, J. J. Lee, and J. P. Hong, "A study on iron loss analysis method considering the harmonics of the flux density waveform using iron loss curves tested on Epstein samples", *IEEE Trans. Magnetics*, 39(3): 1472-1475, 2003.
- [3] D. M. Ionel, M. Popescu, S. J. Dellinger, T. J. E. Miller, R. J. Heideman, and M. I. McGilp, "On the variation with flux and frequency of the core loss coefficients in electrical machines", *IEEE Trans. Ind.*, 42(3): 658-667, 2006.
- [4] D. M. Ionel, M. Popescu, M. I. McGilp, T. J. E. Miller, S. J. Dellinger, and R. J. Heideman, "Computation of core losses in electrical machines using improved models for laminated steel", *IEEE Trans. Ind. Appl.*, 43(6): 1544-1564, 2007.
- [5] J. H. Seo, S. Y. Kwak, S. Y. Jung, C. G. Lee, T. K. Chung, and H. K. Jung, "A Research on Iron Loss of IPMSM With a Fractional Number of Slot Per Pole", *IEEE Trans. on Magnetics*, 45(3): 1824-1827, 2009.

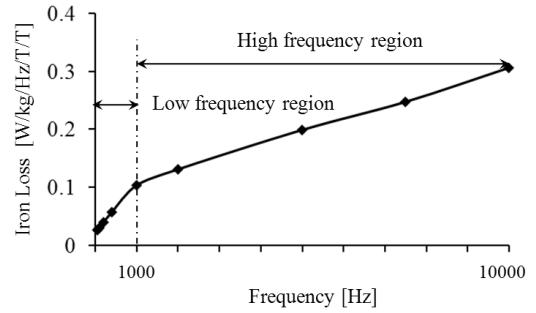


Fig. 1. Determination of coefficients of iron loss.

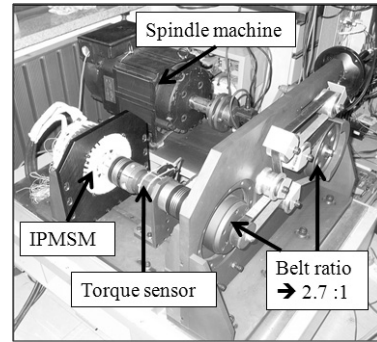


Fig. 2. Measuring equipments.

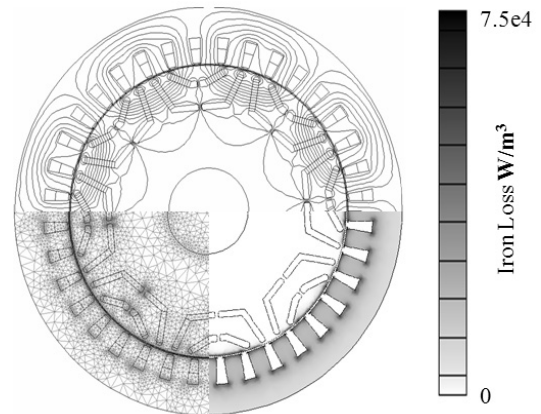


Fig. 3. FE model of IPMSM operating in open circuit at 5000 [rpm]. The distribution of iron loss is shown in shades of gray.

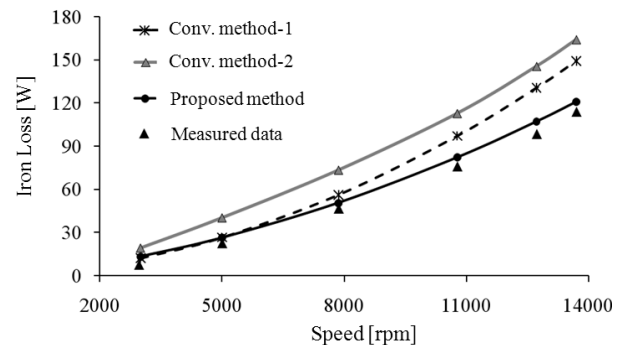


Fig. 4. Calculated and measured iron loss at open-circuit condition.

Characteristic Analysis & Optimum Design of Permanent Magnet Assisted Synchronous Reluctance Motor for Premium Efficiency Performance

Jung Ho Lee, *Member, IEEE*, Tae Won Yun, Sung Ju Mun
 Dept. of Electrical Engineering, Hanbat National University
 Dukmyung-Dong Yuseong-Gu, Daejeon, 305-719, KOREA
 komosin@nate.com

Abstract — This study deals with the characteristics analysis and optimum design of Permanent Magnet Assisted Synchronous Reluctance Motor (PMASynRM) using Finite Element Method (FEM) and Response Surface Methodology (RSM). The focus of this paper is finding of optimum design solutions due to the characteristics analysis of d, q axis inductance according to the size and magnetizing quantity of interior permanent magnet for PMASynRM. Investigation on nonlinear characteristic of machine is performed by Preisach's theory application. The proposed optimum design procedure (RSM) & characteristics analysis allow to define the rotor geometric dimensions performed premium efficiency starting from an existing motor or a preliminary design.

I. INTRODUCTION

The performance of a synchronous reluctance motor (SynRM) in terms of torque and power factor depends on the two-axis inductance L_d and L_q of the machine. The large difference of $(L_d - L_q)$ and L_d / L_q ratio are good for the machine's properties. Unless the high saliency ratio L_d / L_q is reached, the torque density, power factor and efficiency remain well below those of induction motors with an identical stator. Considerable attention has been paid in the past to improve rotor design of SynRM [1]-[3].

By adding a proper quantity of permanent magnets the torque density and power factor of SynRM can be greatly increased. It is called Permanent Magnet Assisted mSynchronous Reluctance motor (PMASynRM).

However, when a proper quantity of P.M. is chosen to counteract the quadrature mmf as shown in Fig. 1, 2 rotor ribs must be saturated by means of an additional magnet quantity. The effects of saturation and iron losses are often important issues in the performance of PMASynRMs. The saturation effect in the daxis of the rotor is very different from that of the q-axis because the nature of the magnetic paths is different. In the case of d-axis excitation, the saturation is the combined effect of saturation in the stator yoke, stator teeth, and rotor ribs, and can reduce the L_d inductance by as much as 50%. [4],[5]

In high speed applications, iron losses can become the major cause of power dissipation. Therefore, whereas in other kind of machines a rough estimation of iron losses is acceptable, their importance in PMASynRM justifies a greater effort in calculating them more precisely.

Finite element methods have the abilities to model the

complicated internal structure within PMASynRM and to model magnetic saturation to a high degree of accuracy.

This study deals with the characteristics analysis and optimum design of Permanent Magnet Assisted Synchronous Reluctance Motor (PMASynRM) using Finite Element Method (FEM) and Response Surface Methodology (RSM). The focus of this paper is finding of optimum design solutions due to the characteristics analysis of d, q axis inductance according to the size and magnetizing quantity of interior permanent magnet for PMASynRM.

Investigation on nonlinear characteristic of machine is performed by Preisach's theory application.

The proposed optimum design procedure (RSM) & characteristics analysis allow to define the rotor geometric dimensions performed premium efficiency starting from an existing motor or a preliminary design.

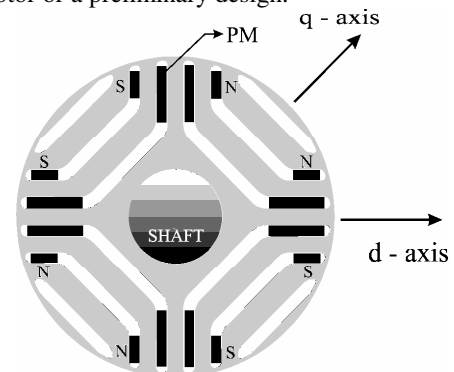


Fig.1 Rotor cross-section of PMASynRM

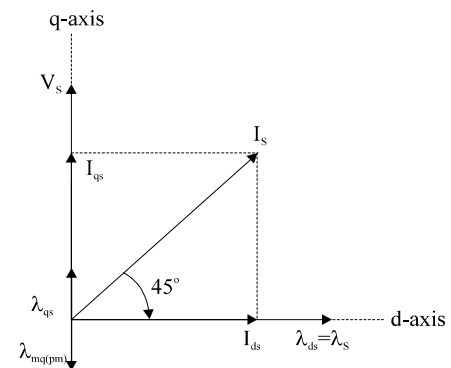


Fig.2 Phasor diagram corresponding to PMASynRM

II. CONCEPT OF RESPONSE SURFACE METHODOLOGY

The RSM seeks to find the relationship between design variable and response through statistical fitting methods, which are based on the observed data from system.

The response is generally obtained from real experiments or computer simulations. Therefore finite element analysis (FEA) is performed to obtain the data of SynRM in this paper.

There are many experimental designs for creation of response surface. In this paper the central composite design (CCD) is chosen to estimate interactions of design variables and curvature properties of response surface in a few times of experiments. The CCD has been widely used for fitting a second-order response surface. [6]

TABLE I
ANALYSIS OF VARIANCE

Source of Variation	Degree of Freedom	Sum of Squares	Mean Square	F_0
Regression	k	SS_R	$SS_R / k = MS_R$	MS_R / MS_E
Residual	$n-k-1$	SS_E	$SS_E / (n-k-1) = MS_E$	
Total	$n-1$	S_{yy}		

It is always necessary to examine the fitted model to ensure that it provides an adequate approximation to the true response and verify that none of the least squares regression assumptions are violated. In order to confirm adequacy of the fitted model, analysis-of-variance (ANOVA), shown in Table I is used in this paper. In Table I, n is the total number of experiments and k is the number of parameters in the fitted model.

III. OPTIMIZATION PROCEDURE

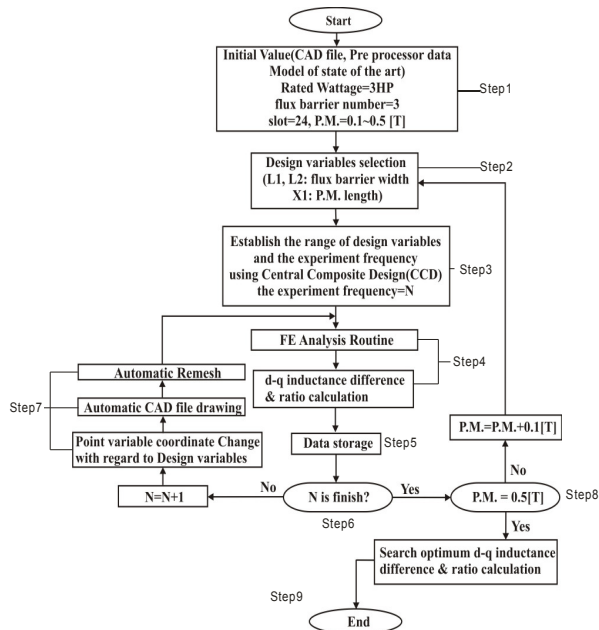


Fig. 3 the flow chart of optimum design procedure

Fig3. shows the flow chart of total design strategy.

Design procedure according to the flow chart is as follows;
Step1 : Set the initial value (CAD file, Pre-processor data). And the initial model is assigned to Rated Wattage=3HP, flux barrier=3, slot=24, P.M.=0.1~0.5[T]

Step2 : flux barrier width (L1,L2) in rotor are adopted the design variables related to torque density in the SynRM.

However, the ribs have a fixed value due to inherent manufacturing limitations.

Step3 : The range of design variables and experiment frequency is established by using the central composite design (CCD). The experiment frequency is N.

Step4 : Finite element analysis (FEA) is performed and Ld-Lq is calculated.

Step5 : The Ld-Lq obtained from FEA, are stored.

Step6 : The experiment frequency (N) is finish?

► Yes:P.M.=0.5[T]. ► No: N=N+1

Step7 : When the rotor shape according to variables (L1,L2) is varied, they have a difficulty in performing a lot of the pre-processor for FEA. For this reason, the new CAD file is redrawn with regard to the change of the design variables automatically. Next the process of automatic mesh generation follows. In mesh generation, mesh data doesn't change the node number, element number, region, boundary condition, etc., but only x, y coordinate data of the design variables. In this way, the proposed pre-processor procedure can be performed in a short period of time.

Step8 : P.M.=0.5[T]

► Yes: Finite element analysis (FEA) is performed and Ld-Lq is calculated.

► No: P.M.=P.M.+0.1[T]

Step9 : The response surface model is created by data obtained from FEA according to an established range.

Therefore, it is possible to get optimum torque density

More detailed results and discussion will be given in final paper. And the mathematical expressions for response surface methodology and optimum design procedures will be also given in extended version.

IV. REFERENCES

- [1] V. B. Honsinger, "The Inductances Ld and Lq of Reluctance Machines," *IEEE Trans.*, PAS-90, (1), pp. 298-304, 1971
- [2] J. H. Lee, J. C. Kim, D. S. Hyun, "Effect of Magnet on Ld and Lq Inductance of Permanent Magnet Assisted Synchronous Reluctance Motor", *IEEE Transaction on Magnetics*, Vol. 35, No. 5, pp. 1199-1202, May 1999.
- [3] J. H. Lee, "Efficiency Evaluations of Synchronous Reluctance Motor Using Coupled FEM and Preisach Modeling", *IEEE Transaction on Magnetics*, Vol. 39, No. 5, pp 3271~3274, September, 2003
- [4] J. H. Lee, "Design Solutions to Minimize Iron Core Loss in Synchronous Reluctance Motor using Preisach Model and FEM" *IEEE Transaction on Magnetics*, Vol. 38, No. 5, pp 3276~3278, September, 2002.
- [5] J. H. Lee, D. S. Hyun, "Hysteresis Analysis for Permanent Magnet Assisted Synchronous Reluctance Motor by Coupled FEM & Preisach Modelling", *IEEE Transaction on Magnetics*, Vol. 35, No. 5, pp. 1203-1206, May 1999.
- [6] J. M. Park, S. I. Kim, J. P. Hong, J. H. Lee, "Rotor design on Torque Ripple Reduction for a synchronous reluctance motor with concentrated winding using response surface methodology", *IEEE Transactions on Magnetics*, vol. 42, No. 10, pp.3479-3481. Oct 2006.

Characteristic Analysis Method of Irreversible Demagnetization in Single-phase LSPM Motor

B. H. Lee¹, S. O. Kwon¹, J. J. Lee¹, L. Fang¹, J. P. Hong¹ and H. Nam²

¹Department of Automotive Engineering, Hanyang University, ²LG Electronics Inc.

¹Haengdang-dong, Seongdong-gu, Seoul 133-791, Korea, ²Gaeumjeong-dong, Changwon 641-773, Korea
lbhwa@hanyang.ac.kr, hongjp@hanyang.ac.kr

Abstract—This paper presents the effective analysis method of irreversible demagnetization for line-start permanent magnet (LSPM) motor considering magnetic field produced by secondary conductor bars. By using Finite Element Analysis (FEA) in transient magnetic field, currents in primary and secondary conductors are estimated and used for demagnetization analysis in magneto-static field. Therefore closer condition to actual situation can be achieved. General demagnetization analysis using primary currents only and presented analysis methods are compared and verified by experiments.

I. INTRODUCTION

LSPM motors have both conductor bars and permanent magnet (PM) in the rotor. Accordingly, line-start of induction motor (IM) is possible and operation in synchronous speed is possible at steady state by magnetic torque and reluctance torque. Therefore position sensor of general permanent magnet motor for starting and operation is not necessary, and conductor loss of general induction motor is small since LSPM motor operates at synchronous speed in steady state. Consequently, LSPM motor provides lower production cost than general permanent magnet motors and higher efficiency than general induction motors. The application of LSPM motor is suitable for home appliances which require low cost and high efficiency [1]. However, the large current at starting causes irreversible demagnetization of PM [2]. Generally the irreversible demagnetization of PM is decided by the operating point in B - H or M - H curve of PM when only primary part is excited. However, LSPM motor is operated as IM at starting and magnetic field by secondary conductors produced. This results in the reduced magnetic field acting on PM to be reduced. Therefore general demagnetization analysis leads to the over estimation of magnetic field acting on PM, and results in excessive PM usage.

This paper deals with demagnetization of LSPM motor by considering magnetic field by secondary conductor bars. By using FEA in transient magnetic field, currents in primary and secondary conductors are estimated and used for demagnetization analysis in magneto-static field. Therefore closer condition to actual situation can be achieved. General demagnetization analysis using primary currents only and presented analysis methods are compared and verified by experiments.

II. STRUCTURE OF SINGLE-PHASE LSPM MOTOR

The configuration and winding connection of a single-phase LSPM motor with rare-earth PM are shown in Fig. 1(a) and

(b) respectively. As shown in Fig. 1, both consist of main and subsidiary windings in the stator and conductor bars to produce the starting torque in the rotor. Starting capacitance C_s , running capacitance C_r , and positive temperature coefficient (PTC) are connected with the subsidiary windings to increase the starting torque and power factor. Accordingly, it could be considered as a two-phase motor. The motor has 2-pole rotor with 28-slot stator for household appliance.

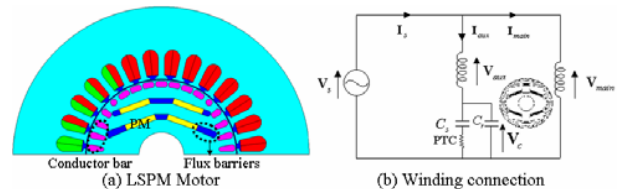


Fig. 1. Single-phase LSPM motor and their stator winding connection

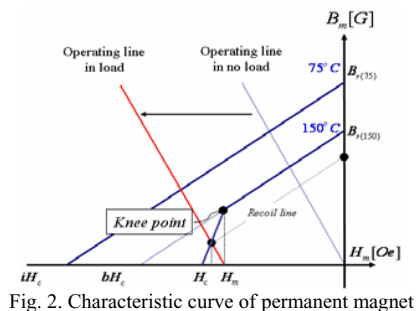


Fig. 2. Characteristic curve of permanent magnet

III. DEMAGNETIZATION OF PM

A. Nonlinear analysis of PM

The demagnetization analysis considers not only nonlinear characteristics of the core but also that of the PM on the B - H curve. Fig.2 shows an irreversible demagnetization curve of rare earth PM magnet each temperature. The equation (1) is approximate equation for Magnetization M [3].

$$M = B - \mu_0 f(B) = h(B). \quad (1)$$

Where H is $f(B)$ and μ_0 is permeability.

B. Calculation of demagnetizing current

On designing the thickness of PM, demagnetizing current is calculated in equation (2).

$$I \leq h_m \frac{2}{m} \cdot \frac{\pi}{4} \cdot \frac{2pH_c}{\sqrt{2}Nk_w}. \quad (2)$$

Where H_c is coercive force, m is phase number, h_m is PM thickness, p is pole-pair, k_w is a winding factor and N is turn number.

C. Analysis process

General demagnetization analysis method (Method1) using primary currents only and presented analysis method (Method2) for LSPM motor are compared. Initially, irreversible demagnetization current of Method1 is calculated using equation (2) at the TABLE I, and then identical current is used to Method2 in order to consider the effect of secondary conductor bars current on the irreversible demagnetization of PM.

As shown in fig. 3, the analysis process of demagnetization for LSPM motor is as following. Firstly, using transient analysis, currents in primary and secondary conductor bars are estimated. Then calculated currents by transient analysis are applied to irreversible demagnetization analysis in every rotor position considering not only nonlinear characteristic of the core but also that of the PM on the *B-H* curve. When the operating point of PM is below its knee point, the residual flux density of the PM is renewed. Finally, with renewed flux density of the PM elements, no-load back-EMF is calculated. By comparing no-load back-EMF before and after demagnetization field, irreversible demagnetization of PM is determined.

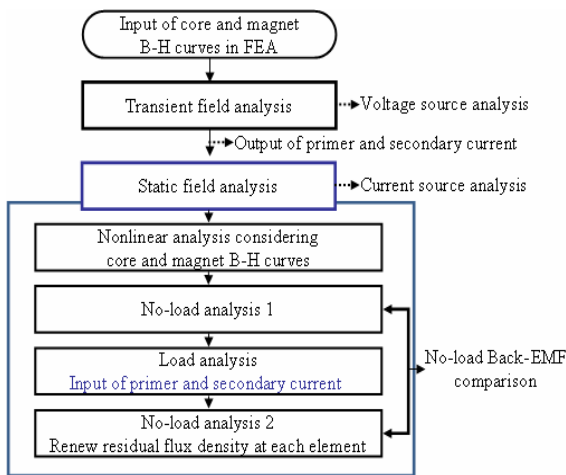


Fig. 3. The process of Method 2

TABLE I
INPUT CURRENT AT THE ROCKED-ROTOR STATE

Temperature [°C]	Magnetizing current [A]	Magnetization ratio [%]
120	60	8.20
150	28	12
165	15	8.81

IV. RESULT AND DISCUSSION

Fig. 4 shows comparison of magnetic flux density from Method1 and Method2 when external demagnetization field is applied. Using Method2, magnetic field by primary current reduced by secondary conductor current can be observed. Experiments are conducted under identical current and temperature conditions. To verify results according to analysis method by the test, DC current is excited in Method1 and AC current is excited in Method 2. Fig. 5 shows the input current and temperature of conductor bars and PM at experiments. As seen in Fig. 6 and TABLE II, using Method1, 8.8% of PM is

irreversibly demagnetized from analysis and experimental results. Meanwhile, no irreversible demagnetization occurs with Method2.

The effect of reduced primary field by secondary conductor field is clearly shown, therefore Method2 is closer to actual situation. Using presented analysis method 2, effective estimation of irreversible demagnetization of PM and cost reduction of LSPM motor reasonably can be achieved.

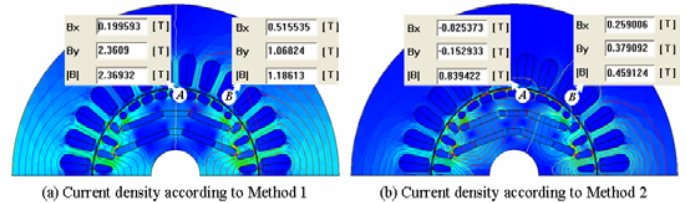


Fig. 4. Current density by Method1 and Method 2

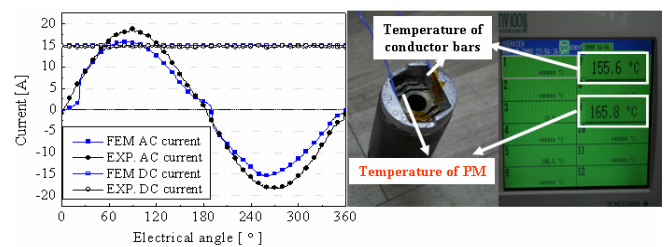


Fig.5. Input current and temperature of PM and conductor bar

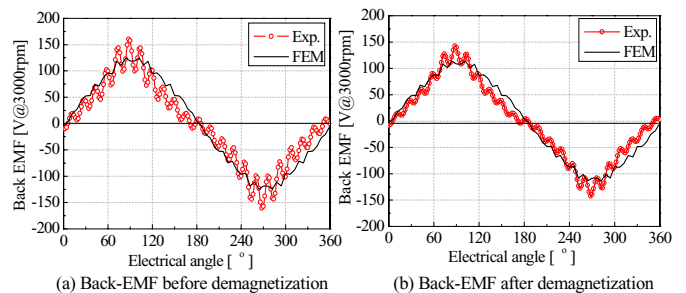


Fig.6. Back EMF comparison of analysis and experiment result

TABLE II
BACK EMF COMPARISON OF ANALYSIS AND EXPERIMENTAL RESULT

	FEM result		Experiments result	
	Method1	Method2	Method1	Method2
Back EMF after demagnetization [V _{rms}]	81.99	81.99	78.42	78.42
Back EMF before demagnetization[V _{rms}]	74.77	81.99	72.35	78.41
Demagnetization ratio [%]	8.80	0.00	7.74	0.00

V. REFERENCES

- [1] Timothy J. E. Miller, "Single-Phase Permanent-Magnet Motor Analysis", IEEE Trans. On Indus. Appl., Vol. IA-21, No. 4, May/June 1985.
- [2] G. H. Kang, J. Hur, H. Nam, J. P. Hong, and G. T. Kim, "Analysis of Irreversible Magnet Demagnetization in Line-Start Motors based on Finite Element Method," IEEE Trans. Magn., vol.39, no.3, pp. 1488-1491, May 2003.
- [3] J. P. Hong, H. Nam, T. H. Kim, "A study on the Irreversible Magnet Demagnetization in Single-Phase Line-Start Permanent Magnet Motor," J. Appl Phys. 105, 07F108, 2009

Pre-Processing of Inductances for Intercell Transformer Optimization

Bernardo Cougo*, Thierry Meynard*, François Forest**, and Eric Labouré***

*LAPLACE (Laboratoire Plasma et Conversion d'Énergie)

2, rue Charles Camichel, 31071, Toulouse. FRANCE.

cougo@laplace.univ-tlse.fr

Abstract— This paper presents a method to speed up an accurate optimization of intercell transformers (ICTs). ICT design strongly relies on its associated leakage inductance, which is usually calculated by 3D or 2D FEM simulation. In an optimization procedure, introducing 3D or even 2D FEM simulation in the main loop considerably slows down the process. In order to speed up an accurate ICT optimization process, we use intensive 2D FEM simulation to generate an N-dimensional matrix containing the values of the leakage inductance related to N parameters which define the ICT geometry. In this way, the optimization loop simply performs an N-dimensional interpolation of the N-dimensional matrix to find the leakage inductance required in the design development.

I. INTRODUCTION

Intercell Transformers (ICTs) are used mainly in interleaved converters to reduce conduction losses in the switches and copper losses in the inductors [1]. Depending on the application, the design of such transformers specially relies on the calculation of the leakage inductance. Analytical formulation of the field distribution inside the window is easily obtained under the assumption that the window is rectangular and its depth is infinite. However, some real components are far from this assumption, and the field outside the window (which cannot be easily modeled) has a very significant contribution to the overall leakage inductance. Consequently, the use of 3D FEM simulation is necessary to precisely predict the leakage inductance.

The use of 3D FEM simulation may result on accurate calculation of the leakage inductance, but it is very time consuming. 2D FEM simulation can be considered [2] if the procedure used in the simulation takes into account 3D effects.

Even though 2D FEM simulations are much faster than 3D, it is sometimes impractical to make use of them inside an optimization process. The time necessary to the main optimization algorithm to call the FEM software, draw the 2D model, simulate it and acquire the resulting inductance values is enormous when comparing to a simple equation resolution or table reading.

The idea is to speed up the process of obtaining the desired leakage inductance by simply interpolating pre-simulated values of such inductances. These values are stored in an N-dimensional matrix where N is the number of geometrical parameters of the magnetic device which may modify the leakage inductance.

II. SIMULATION OF SIMPLE INTERCELL TRANSFORMERS

Let's analyze the proposed method by taking as an example the transformer on Fig. 1a. The leakage inductance is due to the energy stored in the air inside the core window and also outside it. The energy outside the core may be simulated using 2D FEM simulation. On the other hand, the energy inside the core window may be easily analytically calculated by making some assumptions which are acceptable for most of industrial transformers. In our analysis we will just deal with the energy outside the core and we will assume that the calculation inside the core is possible. When the calculation of the energy inside the core window cannot be done analytically, the proposed method may be used.

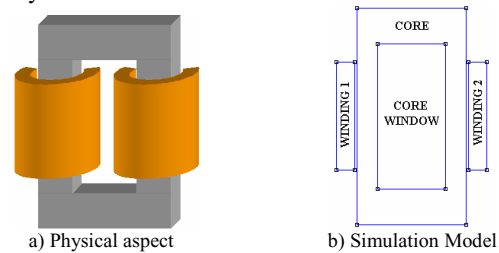


Fig. 1. Simple model for the simulation of the energy outside the window of an intercell transformer

Concerning the leakage inductance related to the energy outside the core window, we may simulate it by using the model represented in Fig. 1b [3]. Note that both windings are represented only outside the core window and that, independently of the number of turns and conductor cross-section shape, it is represented by a rectangular conductor with P turns.

In Fig. 2 all the parameters which may change the leakage inductance are represented. By simulation, 3 conclusions could be stated:

1. If we shrink or expand the transformer, maintaining the ratios between all parameters shown in Fig. 2, the leakage inductance per unit length remains the same.
2. Parameter F (core leg width) has a negligible influence on the leakage inductance if it is greater than 8% of A (core width). This is usually the case for regular transformers and cores available on the market.
3. Leakage inductance is proportional to the square of the number of turns in the winding, independently of the shape of the core and winding.

By conclusions 2 and 3, we assume that parameters F and P are not essential parameters when creating the N-dimensional matrix containing the pre-calculated leakage inductance values. By conclusion 1, we observe that we just

need to simulate a transformer normalized in geometry. We did it by fixing parameter A as the reference parameter. The other parameters (B , C , D , E) should be related to A , which lead us to a matrix with 4 dimensions (B/A , C/A , D/A , E/A).

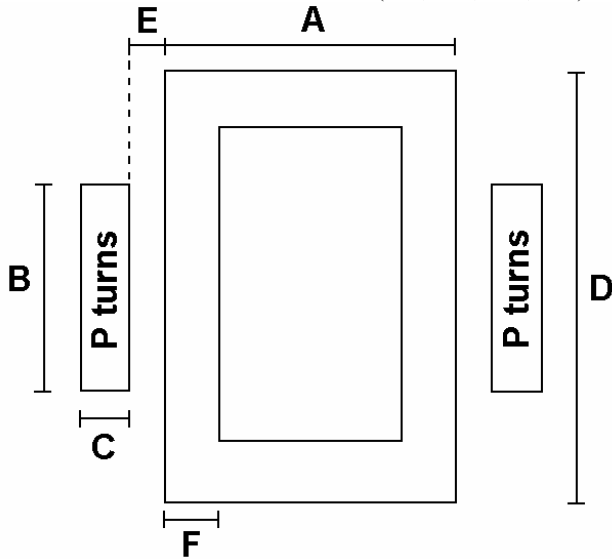


Fig. 2. Transformer parameters

A. Number of Points

The number of points needed in each dimension must be wisely chosen in order to minimize the interpolation error and the size of the 4-dimensional matrix. For this purpose, simulations were performed by varying each parameter at once (starting from a standard shape) and using small steps. The result is shown in Fig. 3. Note that in fact parameter F does not significantly modify the leakage inductance. Also, since the other curves have a soft shape, a small number of points is needed to reliably represent the leakage inductance behavior related to the transformer geometry.

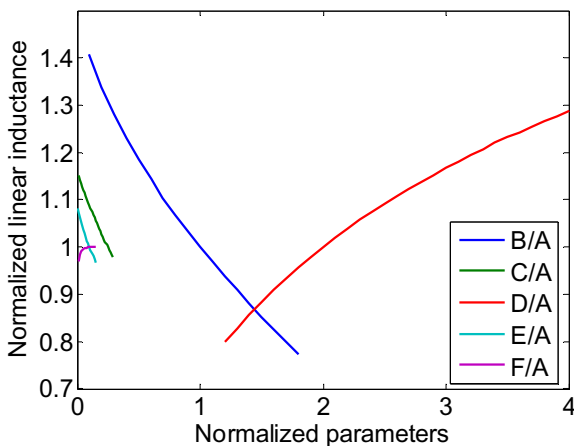


Fig. 3. Variation of the normalized linear inductance

The number of points in each dimension was chosen to be equal to 10, which makes a 4-dimensional matrix with 10000 values. The number of simulations needed is the same as the number of values in the matrix, and so the simulation mesh must be carefully chosen. A study about the mesh generation in this case will be shown in the full paper.

III. SIMULATION RESULTS

The 4-dimensional matrix was created and it took about 16 hours to be completed with 10000 values. In order to compare the advantages of using this matrix in an optimization process instead of inserting the FEM simulation inside the optimization loop, the time consumed by the FEM simulation (using the software FEMM) and the multidimensional interpolation must be compared. This comparison is shown in Table I, where there is also an evaluation of the maximum error observed for each type of interpolation used in software MATLAB. The computer used has Windows Vista operational system and Pentium dual-core (1.46GHz) processor.

TABLE I
TIME AND ERROR COMPARISON

	Direct FEM Simulation	Interpolation Method		
		linear	cubic	spline
Time (ms)	12527	7.57	570	604
Max Error (%)	0	1.07	1.24	1.24

Note that the greatest maximum error exists when using cubic and spline interpolations and this error is only 1.24%. By this table we can see the great advantage of the proposed method. The fastest interpolation method (which is the most accurate) is 1655 times faster than direct FEM simulation.

IV. CONCLUSION

Accurate prediction of leakage inductance is necessary in ICT design since its current ripple strongly depends on the inductance. The lack of analytical formulas to describe leakage inductance due to the energy outside the core makes necessary the use of 2D or 3D FEM simulation. The use of this type of simulation in an optimization process is impractical given that it very time-consuming task.

In this paper, a method was proposed to speed up this process. It is based on the pre-processing of the desired leakage inductances and the storage of the essential values in an N-dimensional matrix. By multidimensional interpolation of this matrix, the desired leakage inductance value is found in few milliseconds. We showed that the slowest and the fastest interpolation methods are, respectively, 20.74 and 1655 times faster than 2D FEM simulation and they are both accurate.

The proposed method can also be used to predict leakage inductance inside the core window when 2D and 3D effects are predominant and when the use of well-known 1D analytical formulas is not possible.

V. REFERENCES

- [1] Pit-Leong Wong, Peng Xu, P. Yang, and F.C. Lee, "Performance improvement of interleaving VRMs with coupling inductors," *IEEE Trans. on Power Electronics*, vol.16, pp 499-507. 2001
- [2] R. Prieto, J. Cobos, V. Bataller, O. Garcia and J. Uceda, "Study of toroidal transformers by means of 2D approaches," *IEEE Power Electronics Specialist Conference (PESC) 1997*.
- [3] B. Cougo, T. Meynard, F. Forest and E. Laboure "Calculation of Inductances in Intercell Transformers by 2D FEM Simulation," *COMPUMAG2009*, submitted for publication.

Hysteresis Torque Analysis of PM Motor Using Initial B-H curve and Tested Core Loss

Jeong-Jong Lee¹, Soon-O Kwon¹, Jung-Pyo Hong¹, Hong-Soon Choi²

¹ Department of Automotive Engineering, Hanyang University, Seoul 133-791, Korea

² School of Electronic and Electrical Engineering, Kyungpook National University, Sangju 742-711, Korea
motor@hanyang.ac.kr, hongjp@hanyang.ac.kr

Abstract — This paper presents the hysteresis torque analysis method for the permanent magnet rotary motor using hysteresis loss separated from the measured core loss data. Principally, hysteresis torque is defined by hysteresis loss. In this paper, hysteresis loss to get the torque is computed flux density of each element of FEM which is used of the initial magnetizing curve. And the core-loss is calculated considering hysteresis model and tested material core loss. In this case, core-loss data is provided by manufacturing companies. And this method is tested in electric motor with lower cogging. The calculated hysteresis torque is compared to the experimental result.

I. INTRODUCTION

Hysteresis phenomenon is become important in many areas of science and technology, such as magnetic recording, permanent magnets, hysteresis motor and so forth. Many models are known in literatures about hysteresis modeling [1]-[2]. The Preisach model is general and provides precise prediction of magnetization in the various models for scalar hysteresis models [3]-[4]. Hysteresis phenomenon is inevitable in general electric machines and occurs even without electrical input in permanent magnet motor. Hysteresis loss produces loss torque and called hysteresis torque, and hysteresis torque is assumed to be maintained constant force like a mechanical friction. In order to analyze the hysteresis torque, the use of measured hysteresis loop using the Preisach model is reasonable and efficient, however, the method and process are complicate. Therefore, a simple calculation method of hysteresis loss torque is presented using hysteresis loss data separated from measured core loss data. The hysteresis torque causes the breaking torque in electric motor. In order to compute the hysteresis torque, FEM is used. After calculation of $B(t)$ (magnetic flux density) in each element of core, hysteresis loss is calculated. The hysteresis loss data is separated from core loss by using Steinmetz Equation. At the result, analysis results are compared to experimental results.

This method is more convenient than the method using Preisach model and easy to understand the theoretical background. A surface permanent magnet motor for electric power steering system (EPS) is used for the hysteresis torque analysis and measurement of cogging torque.

For the EPS motor, the effect of cogging torque is very important due to driving comforts, therefore, the cogging torque and hysteresis are important factors in EPS system[4].

In order to verify the accuracy of simulation result, hysteresis torque is tested.

The experimental method of electric motor hysteresis torque is similar with cogging torque test. From the cogging torque test result, the offset of dc-bias component is defined hysteresis torque and friction torque. As a result, hysteresis torque is measurable considering cogging and friction in shaft torque.

II. MODEL AND ANALYSIS METHOD

A. B-H curve and Hysteresis Loss

In this paper, FEM simulation is used with initial b-h curve, also hysteresis curve are used for computation hysteresis loss.

Fig. 1 shows the b-h model and Fig. 2 shows the process of hysteresis torque analysis. This method can include some errors of magnetizing curve, but it is much simpler than Preisach model.

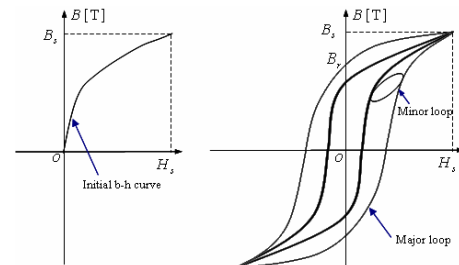


Fig. 1. Initial B-H curve and hysteresis curve

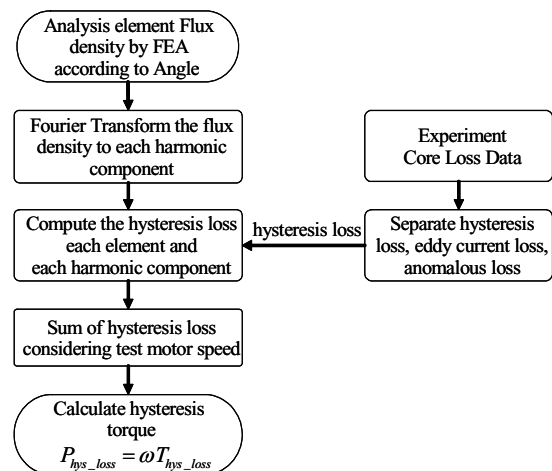


Fig. 2. Process of hysteresis torque analysis

B. Magnetic Field Analysis

The static field FEM is used for the analysis of the magnetic field. The governing equation for 2-D FE analysis is given by (1).

$$\frac{\partial}{\partial x} \left(\frac{1}{\mu} \frac{\partial A}{\partial x} \right) + \frac{\partial}{\partial y} \left(\frac{1}{\mu} \frac{\partial A}{\partial y} \right) = -J_0 - J_m \quad (1)$$

where, A is the z-component of magnetic vector potential, μ is the permeability, J_0 is electrical input current density and J_m is magnetizing current density. The input current J_0 is not exists in hysteresis torque analysis. Therefore, J_0 is equal to zero.

C. Hysteresis loss data

Core loss data is provided by manufacturer. The data are measured with sinusoidal input source. But the magnetic field \mathbf{H} is not sinusoidal in each element. Therefore, hysteresis loss is calculated by each harmonic component of each element. And hysteresis loss data is separated from the tested core loss data using Steinmetz equation as in (2). In this paper,

$$P_{core} = k_h f B^2 + k_e f^2 B^2 + k_a f^{1.5} B^{1.5} \quad [\text{W/kg}] \quad (2)$$

where k_h , k_e , k_a is coefficient of hysteresis loss, eddy current loss, anomalous loss respectively.

D. Analysis Model

Fig. 1 and Table I shows the cross-section and brief specifications of the analysis model.

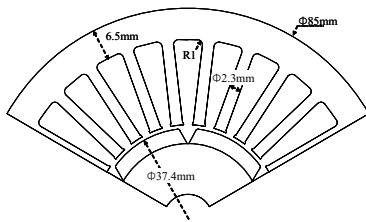


Fig. 3. Cross-section view of 3-phase brushless motor

TABLE I
BRIEF SPECIFICATIONS OF 3-PHASE BRUSHLESS MOTOR

Item	Value	Item	Value
Pole number	6	Magnet Br (T)	1.2
Slot number	27	Recoil Perm.	1.05
Stator outer dia. (mm)	85	Core-Material	S60 (0.5t)
Airgap (mm)	0.8	PM direction	Radial
Stack length (mm)	26	Voltage (Vdc)	12

III. RESULT AND DISCUSSIONS

Fig. 4 shows the FEM result and FFT result of flux density in P1. Hysteresis loss distribution is shown in Fig. 5. High density hysteresis losses exist in tooth. And hysteresis loss of rotor is almost zero because there is few flux variation. Fig. 6 shows comparison between the experimental result and simulation result. In the test result, cogging torque is very small about 2.5mNm and the offset of torque is 13.8mNm, the mechanical friction is included in the offset. The simulated hysteresis torque is 13.4 mNm. The difference between simulation result and tested result are expected to the friction torque.

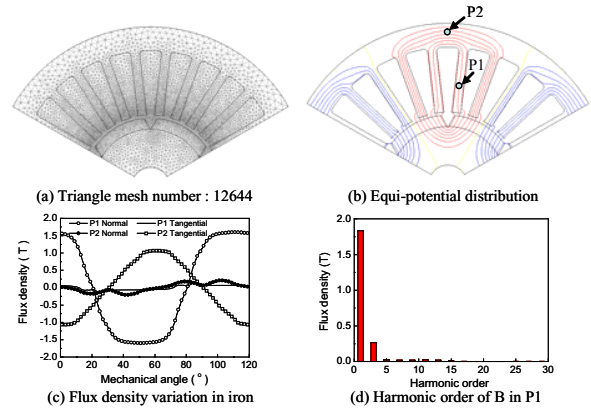


Fig. 4. FEM Result and Hysteresis loss distribution

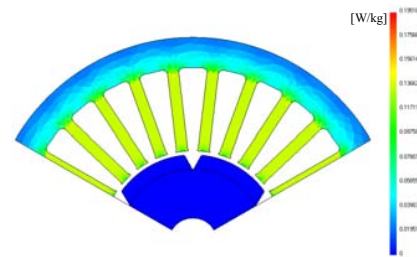


Fig. 5. Hysteresis loss distribution of permanent magnet motor

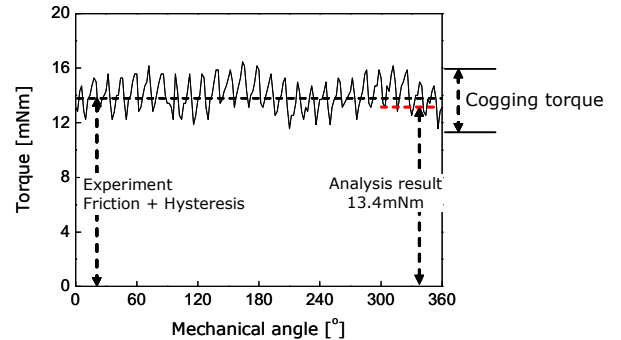


Fig. 6. Comparison experiment and analysis result

IV. CONCLUSION

In this work, hysteresis torque is obtained from hysteresis loss which is separated from the core-loss experiment. This method is much simple than Preisach model and the result is similar experiment and analysis result. The proposed analysis method and experimental results will be reported in extend paper in detail.

V. REFERENCES

- [1] Edward Della Torre, "Existence of magnetization-dependent Preisach models," *IEEE Trans. on Magnetics*, vol. 27, no. 4, July 1991, pp. 3697-3699
- [2] O. Bottauscio, M. Chiampi, D. Chiarabaglio, M. Repetto, "Preisach-typ hysteresis models in magnetic field computation," *Physica B* 275, 2007, pp.34-39
- [3] E. Dlala, A. Arkkio, "Measurement and analysis of hysteresis torque in a high-speed induction machine," *IET Electr. Power Appl.*, 2007, 1, (5), pp 737-742
- [4] A. Yoneda, T. Miyoshi, Y. Shimizu, "Cogging Torque Target and Design of Motor for EPS.," SAE Technical Paper, 2006.

Contactless Torque Transmission by a Magnetic Gear

Veronika Reinauer, Jan Albert, Remus Banucu, Wolfgang Hafla, Christian Scheiblich,
Andreas Weinläder* and Wolfgang M. Rucker

Universitaet Stuttgart, Institute for Theory of Electrical Engineering

* Universitaet Stuttgart, Institute of Power Transmission and High Voltage Technology
Pfaffenwaldring 47, 70569 Stuttgart, Germany
e-mail: veronika.reinauer@ite.uni-stuttgart.de

Abstract— A progressive type of contactless torque transmission is effectuated by the innovation of a magnetic gear. The torque is purely transmitted by a selectable gear ratio via the magnetic fields inside the magnetic gear. Therefore, the assembly, the operating mode, the generation of the torque, and numerical field analyses by means of a FEM are presented, discussed and proven.

I. INTRODUCTION

An efficient design of the several components to obtain high torque and avoid harmonics in the torque is the main challenge. For lower rotational frequencies, the magnetic gear possesses a significantly higher efficiency than a mechanical gear due to no friction losses at all. The only occurring losses in the magnetic gear are caused by eddy currents that are only increasing by the frequency.

The magnetic gear is above all a very good alternative to mechanical gears. Also the weight and treatment of the magnetic gear are advantageous as no attendance is needed. The magnetic gear holds an overload protection by the physical effects. For overloading forces it acts like a slipping clutch and no teeth can ever blockate or even never break.

II. COMPOSITION OF THE MAGNETIC GEAR

The magnetic gear consists of three major parts, a rotor, a modulator, and a stator, that are separated by air gaps. The rotor and the stator possess a specific number of magnetic poles (p_R and p_S respectively) while the modulator consists of a specific number of modulator segments (p_M) that are composed of a magnetizable material e.g. iron. The rotor contains a ferrous core.

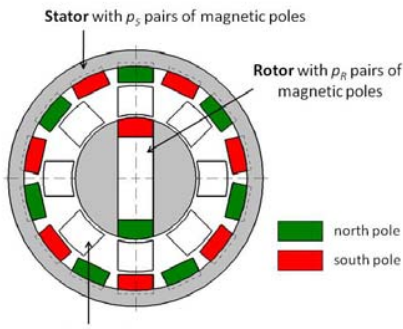


Fig. 1. Setup of the magnetic gear

Figure 1 shows the schematical setup of the magnetic gear with its rotor, modulator and stator.

The gear ratio is fixed and depends on the number of modulator segments and the number of magnetic poles in the rotor and the stator.

III. THEORY OF THE OCCURING FIELDS AND WAVES INSIDE THE GEAR AND GENERATION OF THE TORQUE

A torque is generated if the occurring waves in the magnetic gear are reacting with each other. One wave is effected by the permanent magnets of the rotor and another one by the magnets of the stator. The modulator's ferrous segments are modulating the frequencies of the existing waves.

A. Magnetomotive Force of the Stator

The magnetomotive force Θ_S of the stator is calculated via Ampere's Law. It leads to a $2\pi/p_S$ -periodic rectangular function with the amplitude Θ_S' as shown in Fig 2.

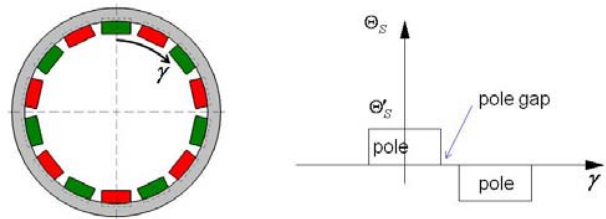


Fig. 2. Magnetomotive Force of the Stator

The Fourier analysis of this rectangular function leads to

$$\Theta_S = \hat{\Theta}_S \left[\cos(p_S \gamma) + \frac{1}{3} \cos(3p_S \gamma) + \frac{1}{5} \cos(5p_S \gamma) + \dots \right] \quad (1)$$

with the fundamental wave

$$\Theta_S = \hat{\Theta}_S \cdot \cos(p_S \gamma) \quad (2)$$

and the amplitude $\hat{\Theta}_S$ [1].

B. Magnetic Permeance of the Modulator

For the modulator the modus operandi is similar, however instead of the magnetomotive force the magnetic permeance of the modulator segments is examined. Figure 3 shows that also the magnetic permeance in the modulator follows a rectangular function; hence the period is $2\pi/p_M$ now.

The Fourier analysis of this rectangular function leads to

$$\Lambda = \Lambda_0 + \Lambda_{p_M} \cos(p_M(\gamma + \omega_M t)) + \Lambda_{2p_M} \cos(2p_M(\gamma + \omega_M t)) + \dots \quad (3)$$

where ω_M is the angular speed of the modulator.

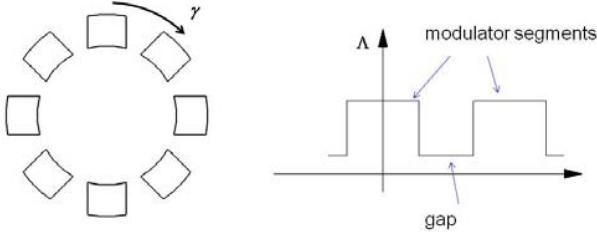


Fig. 3. Magnetic permeance of the modulator segments

C. Magnetomotive Force of the Rotor

Similar to the computation of the magnetomotive force of the stator the fundamental wave of the magnetomotive force of the rotor can be specified as

$$\Theta_R = \hat{\Theta}_R \cdot \cos(p_R(\gamma + \omega_R t)) \quad (4)$$

where ω_R is the angular speed of the modulator.

D. Magnetic Air Gap Induction, Stator's Part

The magnetic poles of the stator are causing a part of the total air gap induction, calculated via

$$B_S = \Theta_S \cdot \Lambda. \quad (5)$$

As this is only a consideration of how the torque is generated, the harmonics can be neglected and the formula is simplified to

$$B_S = \hat{\Theta}_S \cdot \Lambda_0 \cdot \cos(p_S \gamma) + \frac{1}{2} \cdot \hat{\Theta}_S \cdot \Lambda_{p_M} \cdot \cos(\gamma(p_S + p_M) + p_M \omega_M t) + \frac{1}{2} \cdot \hat{\Theta}_S \cdot \Lambda_{p_M} \cdot \cos(\gamma(p_S - p_M) - p_M \omega_M t) \quad (6)$$

E. Generation of the Torque

For generating the torque, the magnetic air gap induction of the stator is reacting with the magnetomotive force of the rotor. The comparison of the relevant waves leads to the following interrelationships between the number of poles or segments respectively of stator, modulator and, rotor:

$$p_L = p_S - p_M. \quad (7)$$

the gear ratio is simply calculated via

$$gr = \frac{\omega_M}{\omega_R} = \frac{p_M}{p_L}. \quad (8)$$

The torque can be calculated via the transverse strain $\tau(\gamma)$ [1] but therefore it is important to take into account that the magnetic induction B is only in rough approximation the sum of B_S and B_R as the whole system is not linear.

IV. OPTIMIZATION

For optimizing the magnetic gear, that means maximizing the transmittable torque, the harmonics of the torque waves have to be minimized. For erasing the seventh harmonic for example, the pole coverage of the rotor of 6/7 is used [2]. The geometric dimensions of the gear like radii, dimensions of magnets, air gaps and segments can be adjusted to ameliorate the performance of the magnetic gear.

V. SIMULATION

The development of the magnetic gear is based on numerical simulations. Therefore, the FEM software Ansys is used. A quasi-static analysis is performed while eddy currents are not considered.

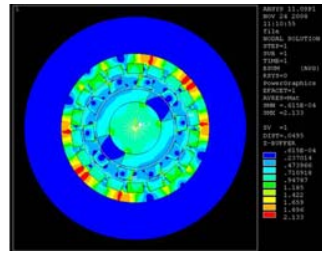


Fig. 4. Magnetic field

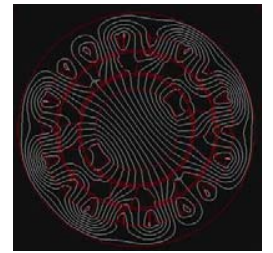


Fig. 5: Magnetic fluxlines

VI. CONCLUSION

A prototype of the magnetic gear has been manufactured and is in use in a machine tool. It is in an endurance test and performs satisfying results. Another illustrative model prototype is available and will be presented in an augmented reality session with a camera-notebook setup.



Fig. 6. Picture of the illustrative model (the black and white papers are markers for the visualization system)

VII. REFERENCES

- [1] G. Müller, K. Vogt, B. Ponick, *Berechnung elektrischer Maschinen*, 6th ed., WILEY-VCH Verlag GmbH&Co. KGaA, Weinheim, 2008.
- [2] G. Müller, *Elektrische Maschinen*, 2nd ed., VEB Verlag Technik, Berlin, 1998.

Tests and simulation results of the static torque characteristics of a brushless DC permanent magnet motor

P. P. de Paula and P. S. Ulian

Technological Centre of the Brazilian Navy
Av. Prof. Lineu Prestes, 2468, São Paulo, SP, 05598-000, Brazil
pedro.pereira@ctmsp.mar.mil.br

Abstract — This paper shows the simulation and tests activities developed to study some design aspects of a brushless permanent magnet motor regarding the torque production using the finite-element method and static torque tests.

I. INTRODUCTION

This paper regards a prototype of a converter fed brushless permanent magnet motor designed and manufactured at the Technological Centre of the Brazilian Navy. This prototype has similar characteristics to the drives presented in [1], [2] and [3]. An analytical method to get the main dimensions of the machine was used at the design stage. Several tests and simulations were already done with the prototype showed in [4], [5], and [6]. The full paper will show the simulations and tests results of the static torque characteristics which are very important to improve the efficiency and to minimize the noise and vibrations due to the cogging torque. The skewing of the stator slots are also taken into account in the simulations. The comparisons of the simulations and tests results have a good agreement, which assures the improvement of the design methods of this kind of drive.

II. THE MOTOR PROTOTYPE

This variable speed drive prototype consists of a brushless permanent magnet motor with electronic commutation. The motor is fed by a DC lin by 6 PWM inverters and each phase has its own converter and the main characteristics are showed in Table 1.

TABLE I
MAIN CHARACTERISTICS OF THE PROTOTYPE

Rated power	75 kW
Maximum speed	600 rpm
Number of phases	6 phases
Number of poles	12 poles
Rated voltage – DC link	600 volts
Maximum current	29 A (peak per phase)
Permanent magnets	Sm2Co17
Power converter type	H bridge

The prototype is an interior rotor motor with surface mounted permanent magnets and radially oriented magnetic field in the air gap. The magnetic induction waveform in the air gap is trapezoidal due to the configuration of assembling the permanent magnets.

The stator stack laminations are of the silicon steel type and has 72 slots. The winding is distributed on the stator slots as a lap winding, single layer and full-pitch, with 6 slots/pole. The signals to switch the phases is generated by an incremental encoder attached to the machine axis. Fig. 1

shows the cross section of the machine. This figure was depicted through the software FLUX2D [7], which is used in the simulations of this work, and shows also the flux distribution on the machine due to the permanent magnets. One can notice in this figure that the rotor of the machine has some pieces to guide the flux.

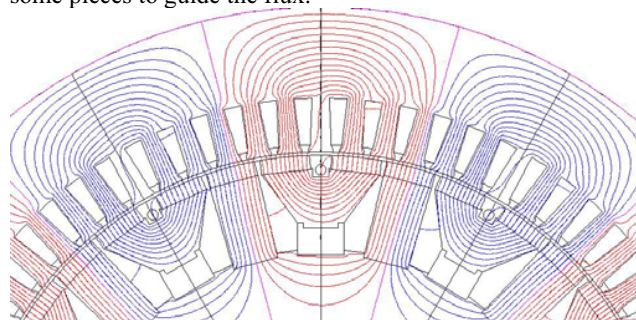


Fig. 1. Machine cross-section

III. STATIC TORQUE SIMULATIONS

The FLUX2D software solves complex electromagnetic field problems by using the finite-elements method. In this paper the problem is a bi-dimensional magnetostatic problem. The domain of study comprehends 30 degrees of the motor cross section, which corresponds to one pole of the motor. A 2D n-slice model, with $n=10$, was used to take into account the skewed slots of the stator. The axial length of the stator laminations is 160 mm and the simulations were done with a model of 16 mm length. The total torque is then calculated taking into account the angular displacements of the several slices of the model. The slots are skewed by the equivalent of one slot pitch, which means a skewing of 5 degrees regarding the longitudinal axis of the machine.

The static torque characteristic of the machine is the torque obtained from the machine for one or a set of phases energized with constant DC current as a function of the rotor position. The simulations were done for one phase energized and for a set of 5 phases energized. The details will be discussed in the full paper.

IV. STATIC TORQUE TESTS

The torque transducer and a special device designed and manufactured for these tests are showed in Fig. 2. The details of the equipments, devices and test methods will be presented in the full paper.

The static torque tests were developed with one phase energized by the following values of constant DC currents: 5,

11. Electric Machines and Drives

10, 15 and 20 ampères. Another set of tests were done with 5 phases connected in series for the same current values.



Fig. 2 – Torque transducer and special device

V. RESULTS

Fig. 3 shows the tests results for one phase fed with the currents values of 5, 10, 15 and 20 ampères. The lower curve corresponds to the test results with no current in the phase. The other curves corresponds to the torques obtained to increasing values of the currents, the maximum torque regards the maximum current. One may notice that the waveform of the torque characteristic is the same of the magnetic induction in the air gap.

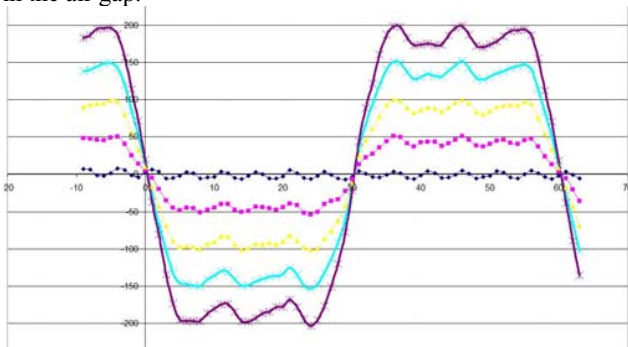


Fig. 3 – Tests results for one phase energized

Fig. 4 shows the test and simulation results of the static torque characteristic for one phase energized with a current value of 10 A and the good agreement between these results. The skewing was taken into account as explained before which assures the good agreement of the results. The full paper will show the details of these achievements.

Fig. 5 shows the test and simulation results of the static torque characteristic for five phases energized with a current value of 10 A and the good agreement between these results. The skewing was taken into account as explained before which assures the good agreement of the results. The full paper will show the details of these achievements.

Fig. 6 shows the simulation results for five phases energized for three different skewing values, which shows the importance of this feature on the performance. The full paper will discuss these achievements.

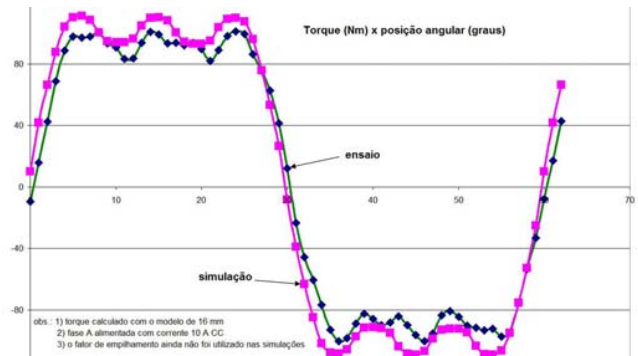


Fig. 4 – Tests and simulation results for one phase energized

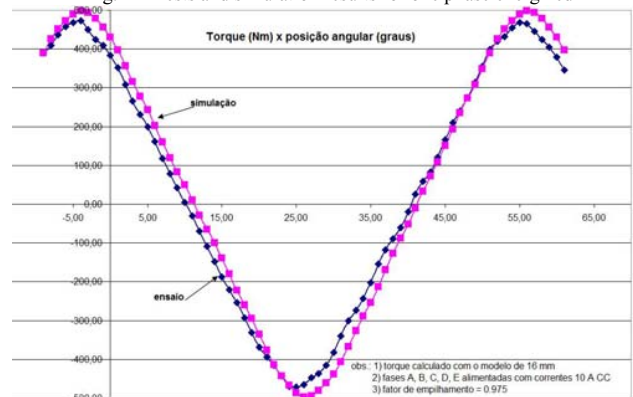


Fig. 5 – Tests and simulation results for five phases energized

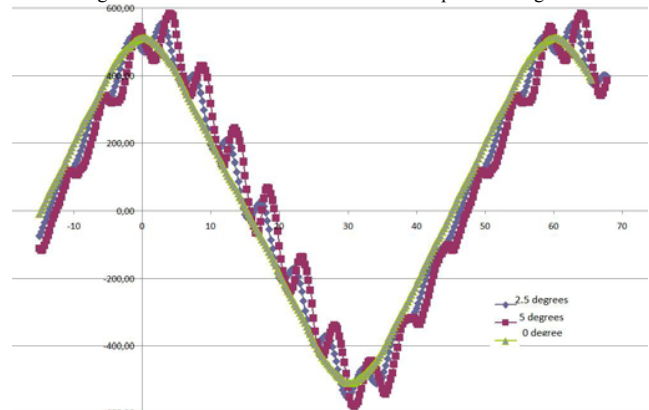


Fig. 6 – Simulation results for some different skewing values

VI. REFERENCES

- [1] H. Fürsich et al, "New converter fed permanent field motor", *ICEM'86*, Munich, Germany, 1986.
- [2] J. Saint Michel et al, "Propulsion by electronic motor", *EPE'89*, 1989.
- [3] K. H. Soyk, "The MEP motor with PM excitation for ship propulsion", in *EDS'90*, Capri, Italy, 1990.
- [4] P. P. de Paula et al, "Modeling of a 100 HP PM brushless DC motor prototype by using the finite-element method," *IMACS'96*, Saint Nazaire, France.
- [5] P. P. de Paula et al, "Influences of the self and mutual inductances of a 100 HP PM brushless DC motor prototype" *ICEM'96*, Vigo, Spain.
- [6] P. P. de Paula et al, "An aspect of modeling a PM motor by using the finite-element method coupled with circuit equations," *IEEE IEMDC'99*, Seattle, USA.

An Improved Calculation Model for Core Losses of Soft Magnetic Composite Motors

Yunkai Huang¹, Jianguo Zhu², Youguang Guo²

¹School of Electrical Engineering, Southeast University, Nanjing, Jiangsu 210096, China

²Faculty of Engineering, University of Technology, Sydney, NSW 2007, Australia

huangyunkai@gmail.com, joe@eng.uts.edu.au, youguang@eng.uts.edu.au

Abstract—The soft magnetic composite (SMC) is a new type of soft magnetic material made of insulated iron powders. Core loss is very important to SMC motor design. For accurate prediction, the rotational core losses model should be used. But rotational core loss coefficients derived from rotational loss data are difficult to get for most designers, because two dimensional core loss tester isn't popular as 25cm Epstein frame. This paper presents an improved calculation model for core losses of SMC motors, which only uses alternating core loss coefficients. Compared under different standard loci, such as alternating, circular, and elliptical ones, the new model shows the sufficiently accuracy. Finally, the model is testified by experiments on a high speed motor with SMC material.

I. INTRODUCTION

Made of insulated iron powders, the SMC is both magnetically and mechanically isotropic, and therefore is suitable for making electrical machines of 3D flux, such as the claw pole and transverse flux machines, which introduces many new design flexibilities in machine topologies and performance. To make the best use of the material for design, it's important to calculate core loss accurately.

There is an increasing need to develop high efficiency electrical machine nowadays for energy saving and the protection of the environment, which requires a more accurate prediction of core losses in the stage of design. Epstein test or single sheet test is performed with alternating fields where the core loss versus flux density is obtained. Designers use these data to calculate core loss of each part of the machine. This method has been proved to have a good consistence in the calculation of core loss in transformers, where the alternating field is dominant. In rotating machines, this method has a relative worse accuracy because the flux variation pattern is more complicated than in transformers. There exists a rotational flux component with different degrees of polarization besides the alternating components of flux observed in transformers. The loci of the flux in rotating machines may be line, circle, ellipse or other complicated pattern depending on location. It has been reported that core loss under a rotational field has a much larger value than that in an alternating field. In calculation of core loss in rotating machines, ignoring such additional loss caused by the rotational field will result in an excessively large value of error [1, 2].

Experience coefficients derived from a long-term production were used to modify the calculation of core loss. It is commonly used in the design of asynchronous machines, and gets good effects. But, for machines which have new materials or new structures, especially SMC motors, the

experience coefficient is very difficult to get. Many researchers [3-5] used the three term model for alternating core losses and time-stepped finite element method. There is about 20% difference because the rotational core loss is neglected. As the occurring of two-dimensional core loss tester, more and more researches have been conducted in the area of rotational core loss in electrical machines. Zhu et al. [1, 6, 7] studied core losses of core materials under 2-D and 3-D magnetic excitations, and proposed the rotational core loss model in electrical machines by combing FEA results with physical models of core loss. Stranges and Findlay[2] described direct approaches for coupling rotational core loss measurements with FEA results that yield the distribution of rotational flux in induction motor cores. Because the two-dimensional core loss tester exists only several research institute, and the international standard is in draft, it makes the rotational core loss model is difficult to use widely. Nowadays, although it has been realized that a considerable amount of the total core loss of a rotating electrical machine is caused by the rotating magnetic field, alternating core loss models were generally employed due to the lack of rotational core loss data.

This paper presents an improved calculation model for core losses, which only uses alternating core loss coefficients. Through theoretic calculation and experiments on high speed SMC motor, it shows good accuracy.

II. CORE LOSS MODE

A. Rotational core loss model

Corresponding to various types of magnetizations and soft magnetic materials, a core loss model was developed[6]. In a soft magnetic material, the core loss with various typical magnetic flux patterns can be calculated by:

Alternating flux:

$$P_{alt} = K_{ah} f B_m^h + K_{ae} (f B_m)^2 + K_{aa} (f B_m)^{3/2} \quad (1)$$

Circular rotating flux:

$$P_{rot} = P_{rh} + K_{re} (f B_m)^2 + K_{ra} (f B_m)^{3/2} \quad (2)$$

Elliptical rotating flux:

$$P_{fe} = R_B P_{rot} + (1 - R_B)^2 P_{alt} \quad (\text{W/kg}) \quad (3)$$

where $R_B = B_{min}/B_{maj}$ is the axis ratio; B_{maj} and B_{min} are the major and minor axes of the elliptical \mathbf{B} locus.

B. Improved model

The elliptical \mathbf{B} locus can be expressed as:

$$\mathbf{B} = e_{maj} B_{maj} \cos(\omega t) + e_{min} B_{min} \sin(\omega t) \quad (4)$$

where, e_{maj} and e_{min} are unit vector along the major and minor axes of the elliptical locus.

Eddy current loss under the elliptical B locus:

$$\begin{aligned} P_{e_ell} &= K_{ae} \int_0^T \left(\frac{d\mathbf{B}}{dt} \right)^2 dt \\ &= K_{ae} (fB_{maj})^2 + K_{ae} (fB_{min})^2 \end{aligned} \quad (5)$$

Anomalous loss under the elliptical B locus:

$$\begin{aligned} P_{a_ell} &= K_{aa} \int_0^T \left| \frac{d\mathbf{B}}{dt} \right|^{3/2} dt \\ &= K_{aa} \int_0^T \left[\left(\frac{dB_{maj}(t)}{dt} \right)^2 + \left(\frac{dB_{min}(t)}{dt} \right)^2 \right]^{3/4} dt \end{aligned} \quad (6)$$

Hysteresis loss under the elliptical B locus:

$$P_{h_ell} = K_h f (B_{maj})^h + \alpha_h K_h f (B_{min})^h \quad (7)$$

where, when $B_{maj} < B_s$, $\alpha_h = 1 \sim 1.2$, and $B_{maj} > B_s$, $\alpha_h = -1$

The total core loss under the elliptical B locus:

$$P_{fe} = P_{h_ell} + P_{e_ell} + P_{a_ell} \quad (\text{W/kg}) \quad (8)$$

The detail will be presented in the full paper.

The calculation flow can be seen form fig. 1.

Compared under different loci ($f=50\text{Hz}$, $B_{maj}=0.7\text{T}$), such as alternating ($R_B=0$), circular ($R_B=1$), and elliptical ones, as shown in Table 1, the improved model shows the sufficiently accuracy.

TABLE I
COMPARED RESULT UNDER DIFFERENT LOCI

R_B	Rotational model	Improved model	Error (%)
0	3.68	3.68	0
0.2	3.89	4.01	3.12
0.4	4.39	4.66	5.7
0.6	5.19	5.51	5.8
0.8	6.28	6.54	3.9
1	7.67	7.72	0.7

III. EXPERIMENT

Fig.2 compares the calculated and measured core losses of the high speed claw pole PM motor. As shown the maximum error is about 20%. This can be attributed to that the core loss coefficients were deduced from the core loss data of SMC measured up to 100 Hz while the operation frequency of this machine is 666.67 Hz, and the eddy current loss is under estimated. More results will be presented in the full paper.

IV. CONCLUSION

In this paper, an improved model is proposed to calculate core losses of SMC motor, which only uses alternating core loss coefficients. Compared with the rotational core loss model and experiment results on a high speed SMC motor, it shows the sufficiently accuracy, and it can be also used to calculate core losses of motors which have special structure or materials.

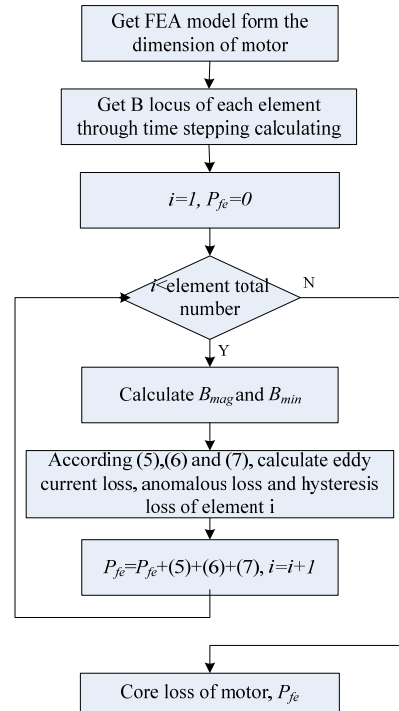


Fig. 1 Calculation flow chart of the improved model

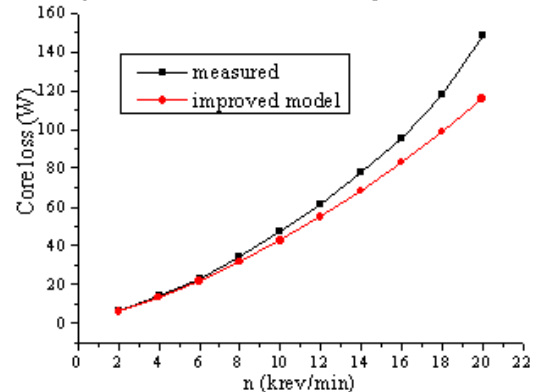


Fig. 2 Comparison of calculated and measure core losses in the high speed (20,000 rev/min) claw pole PM motor

V. REFERENCES

- [1] J. G. Zhu and V. S. Ramsden, "Improved formulations for rotational core losses in rotating electrical machines," *IEEE Trans. On Magnetics*, vol. 34, pp. 2234-2242, July 1998.
- [2] N. Stranges and R. D. Findlay, "Methods for Predicting Rotational Iron Losses in Three Phase Induction Motor Stators," *IEEE Trans. On Magnetics*, vol. 36, No.5, pp. 3112-3114, SEPTEMBER 2000.
- [3] C. T. Mi, G. R. Slemon, and R. Bonert, "Modeling of Iron Losses of Permanent-Magnet Synchronous Motors," *IEEE Trans. On Industry Applications*, vol. 39, NO. 3, pp. 734-742, MAY/JUNE 2003.
- [4] W. Roshen, "Iron Loss Model for Permanent-Magnet Synchronous Motors," *Magnetics, IEEE Transactions on*, vol. 43, NO. 8, pp. 3428-3434, Aug. 2007.
- [5] D. M. Ionel, M. Popescu, M. I. McGilp, and T. J. E. Miller, "Computation of Core Losses in Electrical Machines Using Improved Models for Laminated Steel," *IEEE Trans. On Industry Applications*, vol. 43, NO.6, pp. 1554-1564, NOV./DEC. 2007.
- [6] J. G. Zhu, J. J. Zhong, V. S. Ramsden, and Y. G. Guo, "Power losses of composite soft magnetic materials under two dimensional excitations," *Journal of Applied Physics*, vol. 85, pp. 4403-4405, April 1999.
- [7] J. G. Zhu, J. J. Zhong, Z. W. Lin, and J. D. Sievert, "Measurement of Magnetic Properties Under 3-D Magnetic Excitations," *IEEE Trans. On Magnetics*, vol. 39, No.5, pp. 3429-3431, 2003.

An Extended B - H Curve Modeling of 2D Magnetic Properties of Silicon Steel and Its Influences on Motor Performances

Hee Sung Yoon, Pan-seok Shin*, and Chang Seop Koh, *Senior Member, IEEE*
 College of ECE, Chungbuk National University *Dept. of EE, Hongik University
 San 48, Gaesin-dong, Cheongju, Chungbuk 361-763, KOREA
 hsyoon@chungbuk.ac.kr

Abstract — This paper investigates the influences of the two-dimensional (2D) magnetic properties of silicon steel sheet on the performance of a very large-scale permanent magnet brushless DC motor. The 2D magnetic properties of a non-oriented silicon steel (50A1300) are measured by using 2D single sheet tester and modeled by using an extended B - H curve method to be applied to finite element method. Through the finite element analysis the influences of the two-dimensional magnetic properties of silicon steel on the motor performance are investigated.

I. INTRODUCTION

Recently, very-large scale permanent magnet brushless DC (BLDC) motors of which rating power is few MW have been employed for the propulsion system of electric trains, vessels [1]. The performances such as iron loss, back-emf and torque characteristics of the large scale motors are a lot affected by the magnetic properties of silicon steel sheets employed. A non-oriented silicon steel sheet for motor, conventionally, has been assumed to have independent magnetic characteristics on the direction of the applied magnetic flux density (B), i.e. the magnitude of magnetic field intensity (H) has been modeled as a function of only that of B , and the direction of H has been assumed to be exactly same with that of B without regard to the direction of B . With the development of two-dimensional (2D) single sheet tester (SST), however, it is found that even a non-oriented silicon steel has different magnetic properties according to the direction of B [2]. Fig. 1 compares the measured H -waveforms when constant magnitude (1.3T) of alternating magnetic flux density is applied in the directions of 0° , 15° , and 75° . The H -waveforms are measured at 50Hz by using 2D single sheet tester (SST) having waveform control function with the specimen of non-oriented silicon steel 50A1300. It can be seen that both the magnitude and direction of H strongly depend on the direction of B . The 2D magnetic properties of silicon steel sheet, therefore, should be considered in finite element analysis (FEA) for more precise performance analysis such as iron loss and cogging torque.

In this paper, the 2D magnetic properties of non-oriented silicon steel sheet (50A1300) are measured by using 2D SST and numerically modeled with independent variables of the magnitude and direction of magnetic flux density to be applied to FEA of a large-scale permanent magnet BLDC motor.

II. MAGNETIC RELUCTIVITY MODEL

In this paper, the hysteretic H -waveform corresponding to an alternating B -waveform of which maximum magnitude and

direction are B_m and θ_B , respectively, is measured by using 2D SST with B -waveform control, and the relationship between B and H is represented, as shown in Fig. 2, as (B_m, θ_B) - (H_m, θ_H) where H_m and θ_H are magnitude and direction of H corresponding to (B_m, θ_B) [3]. For various B_m and θ_B , by repeating this procedure, the relationships between (B_m, θ_B) and (H_m, θ_H) are obtained as shown in Fig. 3. It is observed that the silicon steel has the smallest magnetic permeability around 50° - 55° , and the biggest phase difference between B and H around 30° from its rolling direction. Since the B -waveform is represented as (B_m, θ_B) , this approximation is referred to, hereinafter in this paper, (B_m, θ_B) model, and this is a natural extension of the conventional B - H curve method.

Through the measured 2D magnetic properties shown in Fig. 1 and Fig. 3, it can be seen that the catalog data which is measured along rolling direction ($\theta_B=0$) and provided by manufacturer is not enough for precise modeling of the 2D magnetic properties even in non-oriented silicon steels. The 2D magnetic properties should, therefore, be considered for accurate performance analysis of the motors.

The magnetic reluctivity tensor for describing the relationship between B and H considering the modeled 2D magnetic

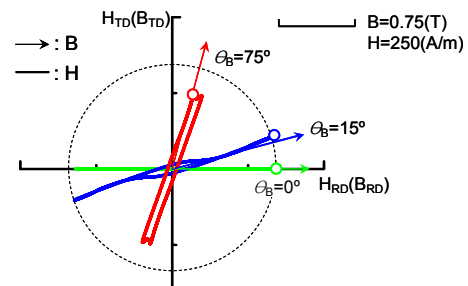


Fig. 1. Measured H -waveforms for different directions of the applied magnetic flux density when $B_m=1.3$ (T).

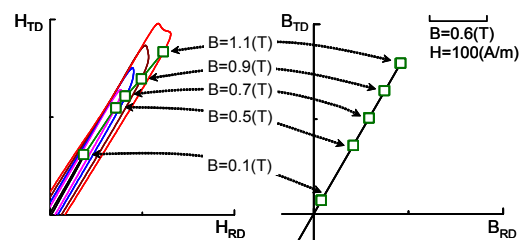


Fig. 2. B - H relationships approximated from measured H -waveforms corresponding to alternating B -waveforms when $\theta_B=60^\circ$.

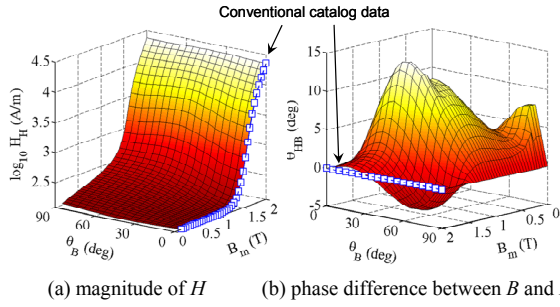


Fig. 3. Measured 2D magnetic properties for non-oriented silicon steel sheet 50A1300, where line marked by empty rectangular is catalog data.

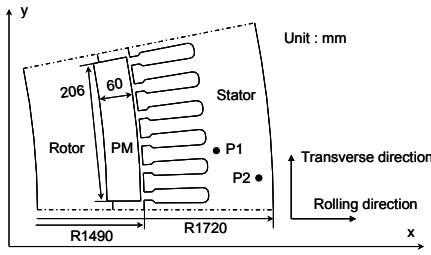


Fig. 4. Specifications of 6MW PM BLDC motor (1/32 model).

properties is derived based on the effective anisotropic reluctivity as follows [3], [4]:

$$[v] = \begin{bmatrix} v_x & 0 \\ 0 & v_y \end{bmatrix} = \begin{bmatrix} H_x(B_m, \theta_B)/B_x & 0 \\ 0 & H_y(B_m, \theta_B)/B_y \end{bmatrix} \quad (1)$$

During the non-linear finite element analysis, in an element, if (B_m, θ_B) is found, then the corresponding reluctivities can be obtained using (1) and Fig. 3.

Using (1), the weighted residual and its derivative required in Newton-Raphson formulation for non-linear analysis is derived as follows:

$$R_i^{(e)} = v_x B_x d_i / 2 - v_y B_y c_i / 2 - J_0 \Delta / 3 \quad (2)$$

$$\frac{\partial R_i^{(e)}}{\partial A_j} = (v_x d_i d_j + v_y c_i c_j) / 4 \Delta + 0.5 B_x d_i \frac{\partial v_x}{\partial A_j} - 0.5 B_y c_i \frac{\partial v_y}{\partial A_j} \quad (3)$$

where Δ is the area of an element (e), c_i and d_i are the functions of coordinates of nodal points, and A and J_0 are magnetic vector potential and applied current density, respectively. The derivatives of the magnetic reluctivities in (3) are function of B_m , θ_B , H_m and θ_H , and expressed as follows:

$$\frac{\partial v_k}{\partial A_j} = c_1^k \frac{\partial H_m}{\partial B_m} + c_2^k \frac{\partial H_m}{\partial \theta_B} + c_3^k \frac{\partial \theta_H}{\partial B_m} + c_4^k \frac{\partial \theta_H}{\partial \theta_B}, \quad k = x, y \quad (4)$$

where c^k is calculated from B_m , θ_B , H_m and θ_H , and the derivatives are calculated by using Bezier surface spline of the measured data [5].

III. ANALYSIS RESULTS OF 6MW BLDC MOTOR

Fig. 4 shows a 6MW permanent magnet BLDC motor of which rating voltage is 720(V). The rolling direction of the stator and rotor is coincident with x -axis initially, and that of rotor rotates. Fig. 5 compares the distributions of the magnetic flux density obtained from the conventional and proposed

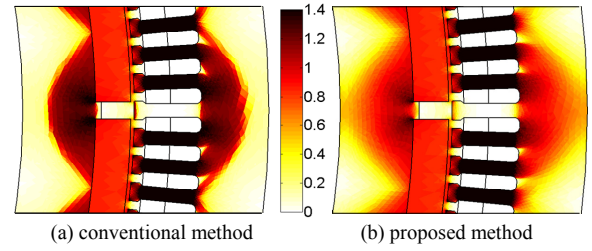


Fig. 5. Comparison of magnetic flux density distributions.

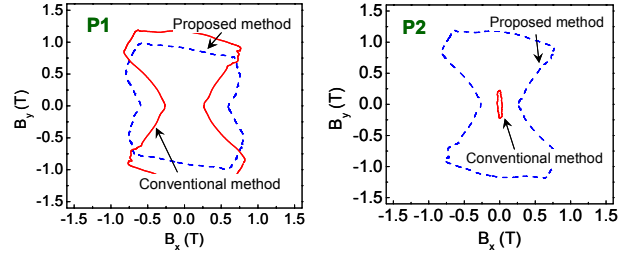


Fig. 6. Comparison of B -waveforms at the points P1 and P2 shown in Fig 4.

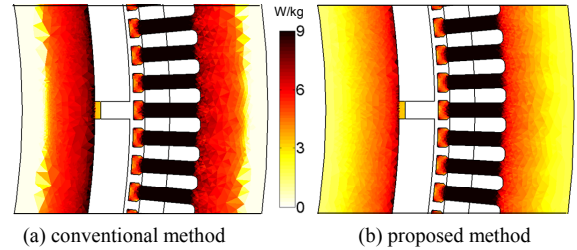


Fig. 7. Comparison of iron loss distributions.

analyses. It is observed that the proposed analysis distributes the magnetic flux more extensively with smaller maximum magnetic flux density than the conventional one. Fig. 6 shows the B -waveforms at the points P1 and P2 shown in Fig. 4. It is found that the two analyses give a lot different B -waveforms. Fig. 7 shows quite different distributions of iron loss between conventional B - H curve method and proposed method.

In the version of full paper, the influences on the other characteristics such as cogging torque and Back-emf waveforms will be investigated.

IV. REFERENCES

- [1] P. S. Shin, S. H. Woo, Y. Zhang, and C. S. Koh, "An application of Latin hypercube sampling strategy for cogging torque reduction of large-scale permanent magnet motor," *IEEE Trans. on Magn.*, vol. 44, no. 11, pp. 4421-4424, Nov. 2008.
- [2] H. J. Kim, C. S. Koh, S. K. Hong, and P. S. Shin, "Double-excitation type single sheet tester for the measurement of the magnetic characteristics of the electrical steel sheets," *Trans. of KIEE*, vol. 54-B, no. 10, pp. 461-469, Oct. 2005.
- [3] H. S. Yoon, Y. H. Eum, Y. Zhang, P. S. Shin, and C. S. Koh, "Comparison of magnetic reluctivity models for FEA considering two-dimensional magnetic properties," *IEEE Trans. on Magn.*, vol. 45, no. 3, pp. 1202-1205, Mar. 2009.
- [4] M. Enokizono and N. Soda, "Finite element analysis of transformer model core with measured reluctivity tensor," *IEEE Trans. on Magn.*, vol. 33, no. 5, pp. 4110-4112, Sep. 1997.
- [5] K. Fujiwara, T. Adachi, and N. Takahashi, "A proposal of finite-element analysis considering two-dimensional magnetic properties," *IEEE Trans. on Magn.*, vol. 38, no. 2, pp. 889-892, Mar. 2002.

Computation on Electromagnetic Torque of Solid Rotor Induction Motor

Yan HU, Jinzhe CHEN

School of Electric Engineering, Shenyang University of Technology
Shenyang, 110178, China
E-mail: huyansy@163.com

Abstract—A finite element method, coupled field-circuit, is applied to compute on electromagnetic torque of a solid rotor induction motor in this paper. And a field-circuit coupled model has been set up for considering the velocity effect, eddy current effect and non-linear property. A new end-region coefficient is presented to correct the effect of end region. It makes performance calculation more accurate. The method makes the period of design short and saves hardware from computing three-dimensional non-linear model. The comparison between tested and computed results proves that the method has higher accuracy and validity.

I. INTRODUCTION

Since having high starting torque and small starting current, solid rotor induction motor is suitable for starting with heavy load. Its quality factor of starting is better than that of common squirrel-cage induction motor. But the low efficiency and power factor has limited its development. For a long term, in order to solve this problem, many scholars have been working on it. Due to so many hypotheses and approximate treatments, analytical methods are incapable of calculating rotor parameters accurately. So the analytical methods will result in huge error in design of solid rotor induction motor.

In recent years, with the development of numerical arithmetic, finite element method has been used to compute the electromagnetic field in motor. Since the electromagnetic field in solid rotor is typically three-dimensional non-linear eddy field, there too many unknown quantities to be solved. And this will be restricted by the capability of computers. Actually, in the case of having no huge differences in structure and field distribution in axial direction, computing a two-dimensional model will get satisfied results. So a two-dimensional coupled-circuit method is adopted to design and analyze solid rotor induction motor. Because of taking voltage source directly as the known quantity and it is unnecessary to calculate rotor parameters separately, the error caused by calculating rotor parameters has been avoided. But the effect of end region still exists and being ignored in this method, so a new end-region coefficient is presented to consider the effect caused by end region in this paper. The level of designing has been improved greatly.

II. MATHEMATICAL MODEL

Considering saturation, the mathematical model of two-dimensional non-linear sinusoidal eddy field can be written as

$$\begin{cases} \nabla \times (\nu \nabla \times \dot{A}_z) = js\omega_1 \sigma \dot{A}_z - J_s \\ \dot{A}_z|_{\Gamma_1} = 0 \end{cases} \quad (1)$$

where ν is magnetic resistivity, Γ_1 is the boundary of model, s is slip ratio, ω_1 is angular velocity of stator current, σ is conductivity, J_s is current density of stator windings, $js\omega_1 \sigma \dot{A}_z$ is eddy current density of rotor. And the unknown quantity J_s , which varies with different loads, can be obtained by the expression^[1] as follows.

$$J_s = K \frac{N_{s1} \dot{I}_1}{S_a} \quad (2)$$

where N_{s1} is number of conductors in one slot, \dot{I}_1 is stator phase current, S_a is effective area of conductors in one slot, K is coefficient represented the direction of current, it is 1 along positive z-direction and -1 along negative z-direction.

Voltage equation for one phase can be expressed as

$$U_1 = -\dot{E}_1 + \dot{I}_1 R_1 + j\omega_1 L_1 \dot{I}_1 \quad (3)$$

where U_1 is voltage of one phase, R_1 is resistance of one phase, L_1 is leakage inductance of end region, \dot{E}_1 is back electromotive force and can be obtained by \dot{A}_z ^[2].

There is no need to solve \dot{I}_1 directly, the first step is to solve electromagnetic field by finite element method to get z-component magnetic potential \dot{A}_z , and then \dot{E}_1 will be obtained by \dot{A}_z . At last, \dot{I}_1 can be obtained by equation (3). So all we have to do is to apply actual sinusoidal voltage source to the finite model^[2].

III. ELECTROMAGNETIC TORQUE AND END-REGION EFFECT

A. Electromagnetic Torque

Z-component magnetic potential has been solved, and electromagnetic force and torque can be computed by Virtual work. The basal expression to calculate electromagnetic torque can be written as

$$F = -\frac{\partial W_m}{\partial s} \quad (4)$$

where W_m is stored energy of magnetic field. The air elements adjacent to rotor surface are effective in this method^[3]. In order to calculate the total magnetic force, it is

necessary to summarize the force acting on each element by the expression as follows.

$$F_e = \int_{V_e} (\mathbf{B}^T \frac{\partial \mathbf{B}}{\partial s} - \frac{\partial}{\partial s} \int_0^H \mathbf{B}^T d\mathbf{H}) dV \quad (5)$$

where F_e is s-component force acting on element e , s is displacement at x, y and z direction respectively^[4], V_e is the volume of each element. For two-dimensional analysis, electromagnetic torque can be written as

$$T_{em} = \sum_{e=1}^{E_a} F_t r = \sum_{e=1}^{E_a} (F_x \sin \theta_e - F_y \cos \theta_e) r \quad (6)$$

where F_t is tangential magnetic force acting on element e , F_x is x-component magnetic force, F_y is y-component magnetic force, E_a is the number of air elements selected, θ_e and r are the angle and radius location in coordinate system respectively.

B. End-Region Effect

By the rotor field analysis, it can be seen that as slip increases, rotor eddy current increases correspondingly. But the axial length of rotor is finite, and the direction of eddy current gradually changes from axial to tangential in end region. As a result, tangential current in end region increases greatly, skin effect becomes more intense and heat generation caused by power loss increases enormously. All these changes will have significant influence on performances of solid rotor induction motor. Therefore, the influence of slip should be included in the computation of end-region coefficient.

All kinds of end-region coefficients^[5] are given in Fig.1.

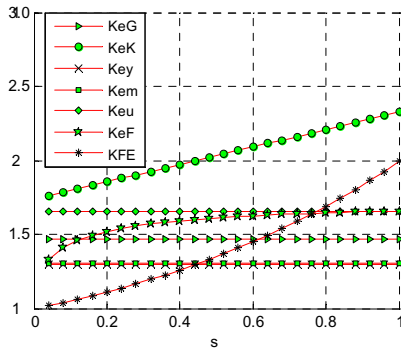


Fig.1 All kinds of end-region coefficients versus slip

None of them but K_{eK} and K_{eF} varies with slip, moreover, K_{ey} , K_{em} , K_{eG} and K_{eu} are constant and have nothing to do with slip.

As a matter of fact, none of them is suitable for the method used in this paper. So based on lucubrating of all kinds of end-region coefficient and the variation with slip, a new end-region coefficient is proposed. And it can be written in terms of slip:

$$K_{FE} = \left(\frac{K_T}{2} \right)^s \quad (7)$$

where

$$K_T = K_{eG} + K_{eF} \quad (8)$$

It is used to correct the performances of solid rotor induction motor influenced by end region. The curve of K_{FE} versus slip is shown in Fig.1.

IV. COMPUTED RESULTS

By the proposed method, a solid rotor induction motor, rated power is 7.5kW, has been designed. Rated data are given in table I. Computed values and tested results are given in table II. Comparison between the computed values and tested results shows that the computed values have very high accuracy.

TABLE I
DATA OF SOLID ROTOR INDUCTION MOTOR

Rated voltage	connection	pole	stator slot	Core length	rotor steel	rotor radius	air gap
380V	Δ	4	36	145 mm	10#	210 mm	0.6 mm

TABLE II
COMPARISON BETWEEN TESTED AND COMPUTED RESULTS

slip	performances	tested	computed	error
s=1	I_{st}/A	31.5	30.78	2.28 %
	$T_{st}/N \cdot m$	74	75.02	1.37 %
s=0.0067 (no-load)	I_0/A	5	5.084	1.68 %

V. CONCLUSION

Field-circuit coupled method based on finite element theory is applied to design solid rotor induction motor. This method can not only consider velocity effect, but also the non-linear property. Since there's no need to calculate parameters of rotor separately, the errors caused by calculating parameters of rotor are avoided. At the same time, a new end-region coefficient is proposed to correct the influence of end region in this paper. It makes the performances computation more accurate and improves the level of designing. And the tested results prove the accuracy and validity of the proposed method.

VI. REFERENCES

- [1] BI Daqiang, WANG Xiangheng, Li Decheng. "Magnetic analysis and design method for solid rotor induction motors based on directly coupled field-circuit". *Power Electronics and Motion Control Conference*.2000, 3(15-18): 1323-1327.
- [2] Tang Renyuan, Hu yan et al. "Computation of transient electromagnetic torque in a turbogenerator under the cases of different sudden short circuits". *IEEE Transactions on Magnetics*, 1990,26(2): 1042-1045.
- [3] L. T. Ergene, S. J. Salon. "Determining the equivalent circuit parameters of canned solid-rotor induction motors". *IEEE Trans. on Magnetics*, 1990,26 (2): 548-550.
- [4] M. E. Zaim. "Non-linear models for design of solid rotor induction machines". *IEEE Trans. on Machines*, 1999, 35(3): 1310-1313.
- [5] Fengli FU, Xiaogao TANG. Handbook for induction motor design. Beijing: China machine press,2006.

Dynamic Characteristics Analysis in A Pole Changing Memory Motor Using Coupled FEM & Preisach Modeling

Jung Ho Lee, *Member, IEEE*, Yong Hyun Cho, Il Kyo Lee
 Dept. of Electrical Engineering, Hanbat National University
 Dukmyung-Dong Yuseong-Gu, Daejeon, 305-719, KOREA
 E-mail: legend213@hanmail.net

Abstract — This paper deals with the PM performance evaluations in a pole changing memory motor (PCMM) using a coupled transient finite element method (FEM) and Preisach modeling, which is presented to analyze the magnetic characteristics of permanent magnets. The focus of this paper is the dynamic characteristics evaluation relative to magnetizing direction and the pole number of machine on re-, demagnetization condition in a pole changing memory motor.

I. INTRODUCTION

Electric drives in which discrete speed control is required are today equipped exclusively with squirrel-cage induction motors, due to the property of the squirrel cage to always have the same number of poles as the stator winding. Conventional permanent-magnet (PM) machines have a constant number of poles and can be operated from a constant frequency source only at one speed. If a PM machine is built after the principles of memory motors, one can change its number of poles as simply as in a squirrel-cage machine.

The operation of a memory motor is based on its ability to change the magnetization of its magnets with a low amount of stator current. It is illustrated how the magnetization of rotor magnets can be continually varied by applying a short pulse of stator current [1], [2].

If the rotor of a memory motor is built following the same sandwich principle shown in [1], but with more than one magnet per pole one can group equally magnetized magnets in various manners. As a consequence, the number of rotor poles changes. This is the basic principle of operation of a pole-changing memory motor, as illustrated in Figs. 1 and 2.

In Fig. 1, the cross-sectional view of a pole-changing memory motor with 32 tangentially magnetized magnets is shown. On the rotor side there are four magnets per pole, all of them being magnetized in the same direction. PMs along with iron segments build the rotor wreath which is mechanically fixed to a nonmagnetic shaft. After the stator winding is reconnected into six-pole configuration, a short pulse of stator current changes the rotor eight-pole magnetization into a six-pole one, as shown in Fig. 2. Since the number of magnets per pole is not any more an integer ($32/6=5.333\dots$), some magnets can remain demagnetized.

Issues such as magnetizing direction and quantity are important in evaluating the performance of the memory motor.

Such characteristics depend upon the characteristic of material and, therefore, require a numerical evaluation.

Whereas in other kinds of machines a rough estimation of hysteresis and magnetizing characteristics can be accepted, their importance in a memory motor justifies a greater effort in calculating them more precisely. The Preisach model is now generally accepted to be a powerful hysteresis model, and is therefore intensively studied [3], [4].

In this paper, a coupled finite element analysis and Preisach modeling for a PCMM are presented and dynamic characteristics analysis are performed under the situations of pole changing due to short pulse current.

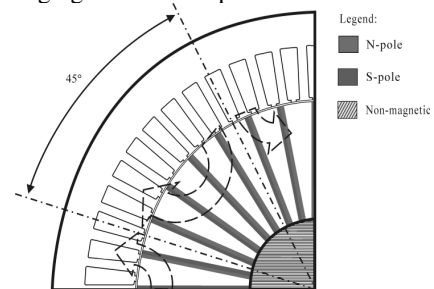


Fig. 1 8-pole magnetized PCMM

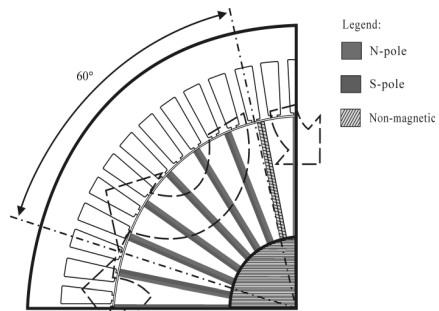


Fig. 2 6-pole magnetized PCMM

II. COUPLED FEM AND PREISACH'S MODELING

A. Governing Equation of PCMM

Maxwell's equations can be written as

$$\nabla \times \vec{H} = \vec{J}_0 \quad (1)$$

$$\nabla \cdot \vec{B} = 0 \quad (2)$$

$$\vec{B} = \frac{1}{\nu_0} \vec{H} + \vec{M} \quad (3)$$

where, \vec{M} is the magnetization of magnetic material with

respect to the magnetic intensity \vec{H} . The magnetic vector potential \vec{A} and the equivalent magnetizing current \vec{J}_m are expressed as follows:

$$\vec{B} = \nabla \times \vec{A} \quad (4)$$

$$\vec{J}_m = \nu_0 (\nabla \times \vec{M}) \quad (5)$$

The governing equation derived from (1)-(5), is given by

$$\nu_0 (\nabla \times \nabla \times \vec{A}) = \vec{J}_0 + \vec{J}_m \quad (6)$$

When the moving coordinate system is used, the governing equation in 2D is given as follows:

$$\frac{\partial}{\partial x} \nu_0 \left(\frac{\partial A_z}{\partial x} \right) + \frac{\partial}{\partial y} \nu_0 \left(\frac{\partial A_z}{\partial y} \right) = -J_z - J_m \quad (7)$$

$$J_m = \nu_0 \left(\frac{\partial M_y}{\partial x} - \frac{\partial M_x}{\partial y} \right) \quad (8)$$

Where, A_z : z component of magnetic vector potential

J_z : current density

ν_0 : magnetic resistivity

M_x, M_y : Magnetization of magnetic material

with respect to the magnetic intensity H_x, H_y

B. System Matrix

The circuit equation is written as:

$$\{V\} = [R]\{I\} + [L_0] \frac{d}{dt} \{I\} + \{E\} \quad (9)$$

Where, $\{E\}$: E.M.F. vector in the winding

$\{V\}$: supplying voltage vector

$\{I\}$: phase current vector

$[L_0]$: leakage inductance

To solve (7), we used the Galerkin finite element method. For the time differentiation in (9), a time stepping method is used with backward difference formula. Coupling (7), (8) and (9), the system matrix is given as follows:

$$\left[\begin{array}{cc} \nu_0 [S] & -[N] \\ [0] & [R] \end{array} \right] + \frac{1}{\Delta t} \left[\begin{array}{cc} [0] & [0] \\ [LG]^T & [L_0] \end{array} \right] \left\{ \begin{array}{c} \{A\} \\ \{I\} \end{array} \right\}_t = \frac{1}{\Delta t} \left[\begin{array}{cc} [0] & [0] \\ [LG]^T & [L_0] \end{array} \right] \left\{ \begin{array}{c} \{A\} \\ \{I\} \end{array} \right\}_{t-\Delta t} + \left\{ \begin{array}{c} \{M\} \\ \{V\} \end{array} \right\}_t \quad (10)$$

Where, $[LG]$ is coefficient matrix related to emf, the magnetization $\{M\}$ is calculated by preisach modeling

C. Application of Preisach's Model

The magnetization M can be expressed as a scalar model, because the rotor rotates according to the input current angle θ synchronously. Therefore, it can be supposed that the domain in stator is an alternating field with reference to x axis and y axis. B and H of the domain in rotor is constant and is a rotating field, but it is an alternating field with reference to x axis and y axis, also [5]-[7]. It is natural that M, H which is calculated on the same axis has a same vector direction.

$$M(t) = \iint_{\alpha\beta} \mu(\alpha, \beta) \gamma_{\alpha\beta}(H(t)) d\alpha d\beta \quad (11)$$

$$= \iint_{S^+(t)} \mu(\alpha, \beta) d\alpha d\beta - \iint_{S^-(t)} \mu(\alpha, \beta) d\alpha d\beta$$

A more convenient treatment of this model is also to substitute the Everett plane for Preisach's one as shown in (12).

$$E(\alpha, \beta) = \iint_{\alpha\beta} \mu(\alpha, \beta) \gamma_{\alpha\beta}(H(t)) d\alpha d\beta \quad (12)$$

In the Everett plane, the distributions of M , which is accepted from experimental data of material S40 and ferrite magnet, are Gaussian ones.

III. ALGORITHM OF COMPUTING

Fig. 3 shows the block diagram of whole analysis mechanism.

The field-oriented control algorithm with PWM fed inverter is applied to the proposed analysis model for the example of dynamic characteristics and magnet characteristic due to PWM input source, as shown in Fig. 3.

Through the more detailed analysis, the variable performance of the pole changing memory motor will be represented in next extended version.

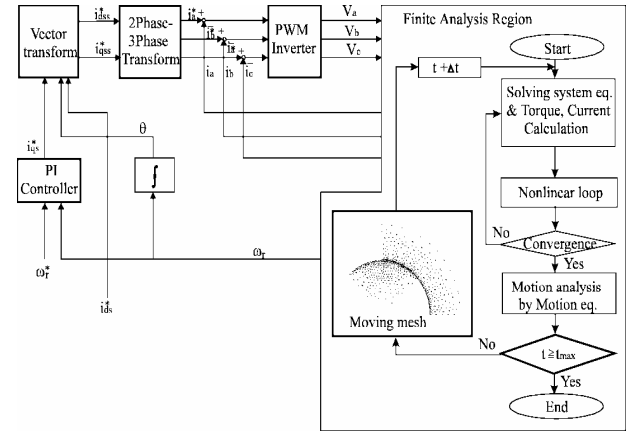


Fig3. Block diagram of analysis system

REFERENCES

- [1] V. Ostovic, "Memory motor-A new class of controllable flux PM machines for a true wide speed operation," in Conf. Rec. IEEE-IAS Annu. Meeting, 2001, pp. 2577-2584.
- [2] V. Ostovic, "Pole changing permanent magnet machines," *IEEE Trans. On Industry Applications*, Vol. 38, No.6, pp.1493-1499 Dec. 2002
- [3] A. Ivanyi, Hysteresis Models in Electromagnetic Computation, AKADEMIAI KIADO, BUDAPEST
- [4] J. H. Lee, D. S. Hyun, "Hysteresis Characteristics Computation on PWM Fed Synchronous Reluctance Motor Using Coupled FEM & Preisach Modeling," *IEEE Transaction on Magnetics*, Vol. 36, No. 7, pp 1209-1213, July 2000.
- [5] J. H. Lee, D. S. Hyun, "Hysteresis Analysis for permanent Magnet Assisted Synchronous Reluctance Motor by Coupled FEM & Preisach Modelling", *IEEE Transaction on Magnetics*, Vol. 35, No. 5, pp. 1203-1206. May 1999.
- [6] J. H. Lee, J. C. Kim, D. S. Hyun, "Effect of Magnet on Ld and Lq Inductance of Permanent Magnet Assisted Synchronous Reluctance Motor", *IEEE Tranl.on Magn* Vol.35, No. 5, pp. 1199-1202, May 1999.
- [7] J. H. Lee, J. C. Kim, D. S. Hyun, "Dynamic Characteristic Analysis of Synchronous Reluctance Motor Considering Saturation and Iron Loss by FEM", *IEEE Transaction on Magnetics*, Vol. 34, No. 5, pp. 2629-2632, Sep. 1998

Improvement in accuracy of thermal FEM model partition wall with the use of optimization algorithm

Peter Kitak¹, Igor Ticar¹, Joze Pihler¹, Oszkar Biro², Kurt Preis²

¹Faculty of Electrical Engineering and Computer Science
Smetanova 17, SI-2000 Maribor, Slovenia

peter.kitak@uni-mb.si

²Graz University of Technology
Kopernikusgasse 24, A-8010 Graz, Austria
biro@TUGraz.at

Abstract— this paper describes thermal analysis of eddy currents phenomena in a switchgear partition wall and determination of input parameters of numerical FEM model with particle swarm optimization (PSO) algorithm. The main intension of presented procedure is to fully calibrate numerical model, respectively calculate all necessary input parameters for analysis of eddy currents and thermal analysis. The goal of the optimization procedure is to achieve even better agreement between results of the numerical analysis and measured results (with thermovision camera). Numerical analysis presents a coupled problem of eddy currents phenomena through a thermal field observation. Both analyses are based on finite element method.

I. INTRODUCTION TO THE NUMERICAL MODEL

Partition wall is located between two medium voltage switchgear cells, where conductors (bus bars) go through. Partition wall consists of a metal plate and three bushing elements that go through it (model is shown in Fig. 3, which presents results). Beside insulation, the bushing elements contain cylindrical brass mesh (brass is any alloy of copper and zinc). Conductive areas, such as cylindrical brass meshes and metal plate, have an affinity towards eddy currents occurrence that cause Joule losses and affect temperature increase.

Constants that present some material properties (for example, conductivity, permeability, heat transfer coefficient) are obtained from tables and are given under certain boundaries. For the exact calculation of the temperature values it is necessary to calibrate the numerical model. The calibration is carried out with an optimization algorithm, which estimates the correct input parameters of numerical model for the thermal calculation.

Since the calculation is based on finite element method, it is crucial to define a proper numerical model. The numerical model consists of two components. First component considers eddy current density and magnetic field [1], meanwhile the other one takes into consideration thermal properties [2]. Finite element method is separately applied to eddy currents and thermal analysis, which means that the model is coupled [3].

Eddy currents are not uniformly distributed since the origin of the phenomena is based on proximity effect. Due to

the non-uniform eddy currents distribution, a numerical postprocessor is designed to calculate the average eddy current density value in each finite element, which belongs to the metal plate or cylindrical meshes. Joule losses are obtained from previous calculations, and are applied further on in the second part of the process (thermal analysis) [4].

II. DETERMINATION OF FEM MODEL PARAMETERS WITH PARTICLE SWARM OPTIMIZATION ALGORITHM

The complete procedure of calibration of the numerical model with measured parameter values is based on particle swarm optimization (PSO) algorithm [5]. Detailed analysis of the process is shown as a pseudo-code in Fig. 1. Numerical calculations evolve inside the optimization algorithm and compose the objective function. The objective function f_t of the optimization algorithm is a sum of square differences (Euclidian norm) between calculated and measured temperature values in different points of interest:

$$f_t = \mathbf{e}_t^T \mathbf{e}_t, \quad (1)$$

where the difference \mathbf{e}_t in n points between measured and calculated results is given by

$$\mathbf{e}_t = \mathbf{t}_m - \mathbf{t}_c \quad [n \times 1] \quad (2)$$

Temperature field distribution was firstly calculated by using initial parameters presented in Table 1.

TABLE I
Initial FEM model parameters

Parameter	index	value
Conductivity of metal partition wall	σ	$6 \cdot 10^6$ S/m
permeability	μ	300
heat transfer coefficient (in air)	h_a	0.024 W/(m ² K)
heat transfer coefficient (in metal partition wall)	h_{pv}	64 W/(m ² K)
heat transfer coefficient (in cylindrical brass mesh)	h_m	80 W/(m ² K)

The complete numerical model is built with two parametric preprocessors, numerical postprocessor and a graphic postprocessor. The preprocessors are written in Matlab and FEM calculations are carried out with EleFAnT3D

solver [6]. The numerical model consists of 45,100 finite elements, which are 20-nodal isoparametric hexahedrals.

```

Temperature measurements obtained with thermovision camera
Parametrically written FEM model of partition wall
Create initial population for particle swarm optimization (PSO)
While the stopping criterion is not reached Do
  Create preprocessor_1 (materials, boundary conditions,
    effective current 630 A in conductors)
  Solve the eddy current problem (current density in each FE)
  Create preprocessors_2 (materials, boundary conditions,
    Joule losses in each FE)
  Solve the thermal field (temperature distribution)
  Evaluate the objective function  $f_i$  (norm between calculated and
    measured temperature values in  $n$  points)
  If ( $f_i <$  required condition) Then
    The numerical model is calibrated.
  Else
    Use of particle swarm optimization (PSO) algorithm
    New values of optimization parameters (conductivity,
      permeability, heat transfer coefficient)
  EndIf
EndIf
End

```

Fig. 1. Pseudo-code of the whole process for calibration of numerical model parameters.

Temperature measurements of real metal partition wall were obtained with thermovision camera InfraTec VarioCam.

III. RESULTS

This digest describes results of the numerical analysis. Fully described results will be presented in the full paper.

Eddy currents are caused when a moving or changing magnetic field intersects conductive areas, or when conductive areas move throughout magnetic field. The relative motion causes a circulating flow of particles or current. These circulating eddies of current create electromagnets with magnetic fields that is opposite to the main magnetic field. The stronger the applied magnetic field, or greater the electrical conductivity of the conductor, or greater the relative velocity of motion, the greater the currents developed and the greater the opposite field is.

Eddy currents indirectly affect warming of medium voltage cell. They occur in metal plate and cylindrical brass meshes, because of the proximity of source conductors, which are placed in the middle of the bushing elements and carry 630 A of effective current. Depending on conductivities and permeabilities of the metal plate and cylindrical meshes, eddy current density varies. The whole physical process could be explained with proximity effect. The source conductors generate time-harmonic magnetic field, which is assessed with Biot-Savart law. Variable magnetic field has an amount of influence on conductive materials. According to Faraday's Law time-harmonic magnetic field that crosses materials induces voltage and consequently the current. The closer the source conductors are, the greater is the influence on the rest of the conductive materials. Effective current value of conductors is the second significant parameter that determines magnetic field impact on the conductive areas located near the source (bus bars). Values of eddy current density calculated on axis that go through all three conductors are shown on Fig. 2a.

Power losses in every finite element are a direct input in the numerical preprocessor for thermal analysis. Distribution (histogram) of the power losses magnitudes inside the finite element model is shown in figure 2b.

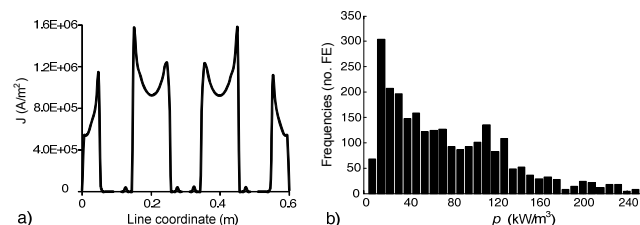


Fig. 2. a) Distribution of the eddy currents effective values in the metal plate, b) Histogram of the average power loss values in finite elements.

Temperature distribution, which occurs because of the eddy currents, is shown in Fig. 3. For the fully presented problem, it is important to take into consideration effective conductors' current of 630 A, which contributes to the total temperature increase. The temperature increases in the metal plate for 0.3 °C extra.

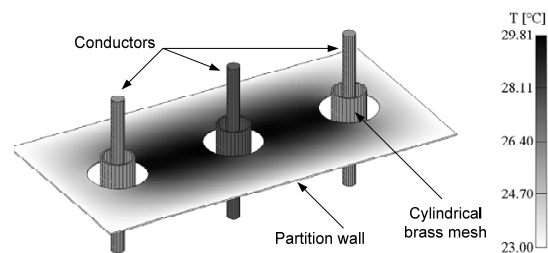


Fig. 3. Temperature of the metal partition wall as a consequence of eddy currents.

IV. CONCLUSION

The aim of this research is to improve parameters of the numerical thermal model. Numerical model is calibrated when calculated and measured results achieve good agreement. Determined parameters (conductivity, permeability, heat transfer coefficients) can be used in further analysis and other calculations for medium voltage cell.

V. REFERENCES

- [1] J.P.A. Bastos, N. Sadowski, *Electromagnetic Modeling by Finite Element Methods*, Marcel Dekker Inc., New York, 2003.
- [2] I.C. Popa, I. Cautil, D. Florica, "Electro-thermal Numerical Model for Optimization of High Currents Dismountable Contacts," *Proceedings of the 8th WSEAS International Conference on Mathematical Methods and Computational Techniques in Electrical Engineering*, Bucharest, 2006, pp. 103-106.
- [3] K. Hamayer, J. Driesen, H.D. Gersem, R. Belans, "The Classification of Coupled Field Problems," *IEEE Transactions on Magnetics*, vol. 35, no. 3, 1999, pp. 1618-1621.
- [4] K. Preis, O. Biro, G. Buchgraber and I. Tičar, "Thermal-Electromagnetic Coupling in the Finite-Element Simulation of Power Transformers," *IEEE Transactions on Magnetics*, vol. 42, no. 4, 2006.
- [5] J. Kennedy, R. C. Eberhart, "Particle swarm optimization," *Proc. IEEE int'l conf. on neural networks*, Vol. IV, Piscataway, NJ, pp. 1942-1948, 1995.
- [6] Program tools ELEFANT. Graz, Austria: Inst. Fundam. Theory Elect. Eng., Univ. Technol. Graz, 2000.

Field Computation and Performance of a Series-Connected Self-Excited Synchronous Generator

T. F. Chan¹, Weimin Wang¹, and Loi Lei Lai²

¹Department of EE, The Hong Kong Polytechnic University, Hung Hom, Hong Kong, China

²Energy Systems Group, School of Mathematics and Engineering Sciences, City University London, UK
eetfchan@polyu.edu.hk

Abstract— This paper presents the field computation and the operating characteristics of a series-connected self-excited synchronous generator. Modeling for time-stepping coupled field–circuit analysis is explained. The proposed method is vigorously tested on a three-phase, 1.8-kW induction generator for various operating conditions. The computed results obtained by the FEA are found to be in good agreement with experimental results.

I. INTRODUCTION

Series-connected self-excited synchronous generator (SCSESG) is a wound-rotor induction machine in which the stator and rotor windings are connected in series, the phase sequences of the stator being opposite to that of the rotor. When driven by an external prime mover and a suitable capacitance is connected across the stator terminals, the machine will self-excite and deliver electrical power at a frequency equal to half of the rotor angular frequency. Steady-state and transient D-Q theory have been used for analyzing the performance [1]–[3]. Performance of this type of machine based on field analysis, however, has not been attempted before. In this paper, we briefly address the field computation aspects with reference to the SCSESG and then, we present a comparison between the experimental results and the computed results based on FEA in order to verify the feasibility of the proposed approach.

II. COMPUTATION METHOD

In order to simulate the operating conditions of this generator the computation method presents the following features:

- Due to the existence of magnetic circuits with saturated magnetic materials a nonlinear FEA was adopted.
- The anti-periodic boundary condition was applied to the field analysis to decrease computation time.
- Time-stepping FEM was employed in order to correctly evaluate the transient characteristic of the generator's voltage and current changes due to its rotation.

A. Governing Equations

The governing system of equations for 2-D FEA is derived from the Maxwell equations

$$\nabla \times (\mathbf{v} \nabla \times \mathbf{A}) - \nabla \mathbf{v}_e \nabla \cdot \mathbf{A} = -\sigma \frac{\partial \mathbf{A}}{\partial t} - \sigma \nabla V \quad (1)$$

where \mathbf{A} is the magnetic vector potential, \mathbf{v} is the reluctivity tensor, σ is the conductivity tensor, and \mathbf{v}_e is defined as one third of the trace of reluctivity tensor. In the analysis, the winding is assumed to be composed of stranded coils, each

having many fine turns in series and with eddy current effect ignored. For a stranded coil, (1) becomes:

$$\nabla \times (\mathbf{v} \nabla \times \mathbf{A}) - \nabla \mathbf{v}_e \nabla \cdot \mathbf{A} = \mathbf{J} \quad (2)$$

with the current density given by

$$\mathbf{J} = i_n \frac{n}{s} i(t) \mathbf{z} \quad (3)$$

where S_c is the coil cross sectional area, n is the number of turns and $i(t)$ is the current per turn. i_n is a unit to stand for the coil current in the z (axial) direction.

B. Field Coupling to External Circuit with Periodic Boundary Condition

Modeling of the external electric circuit was achieved by using the connectivity patterns between various circuit elements such as resistors, capacitor and inductors. Such elements consist of nodes having voltage potential DOF (degree of freedom). The stranded coil nodes possess magnetic potential A_z , EMF and current DOFs in field region. The stranded coil represents a current source in the circuit loop, and it has three nodes. Two nodes carry the voltage potential DOF and these are used for connection with other circuit elements; the third node is any node in the field region for the stranded coil, and so this node carries current and EMF information. Since anti-periodic boundary condition is applied to the field region, the current source for the conductor regions in the remaining $\frac{3}{4}$ of the machine cross-section can be coupled to the modeling conductors' nodes directly.

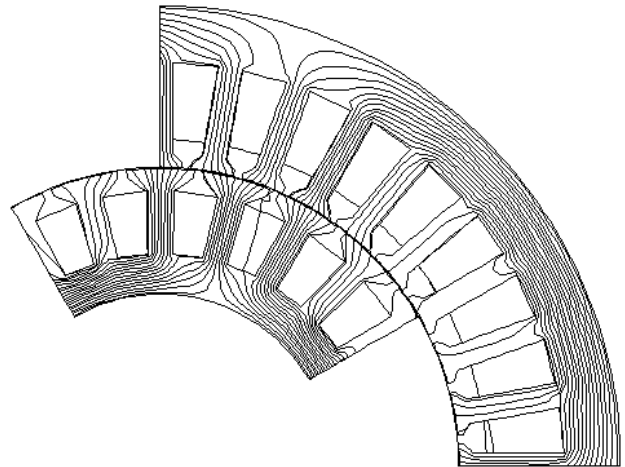


Fig. 1. Computed flux line distribution at a rotor position of 60 electrical degrees under no load condition ($C=120 \mu\text{F}$, speed = 1143 rpm)

C. Initial Conditions for Field Computation

Modeling of the residual flux in the FEA computation presents some difficulties as the residual flux cannot be easily incorporated into the material properties in the machine model. To overcome this problem the initial current is specified instead. Computations showed that the initial current DOF value for the conductor region is important for successful simulation of voltage build up. It was found that the residual current magnitude should be about 1 A and its electrical angle should be approximately the phase difference between the stator and rotor current vector directions.

III. RESULTS

A. Field Computation Results

The stator end-winding leakage inductance L_{es} of the prototype SCSESG is 0.154mH, and the rotor end-winding leakage inductance L_{er} is 0.025mH, determined using an analytical method [4].

Fig. 1 shows the computed no-load flux line distribution for a rotor position of 60 electrical degrees when $C=120 \mu\text{F}$ and the rotor speed is 1143 rpm. Fig. 2 shows the computed radial flux density distribution for the same rotor position when the generator is under no load and when supplying a resistance load of 131.7Ω per phase. It can be seen that the air gap flux density decreases when the generator is loaded.

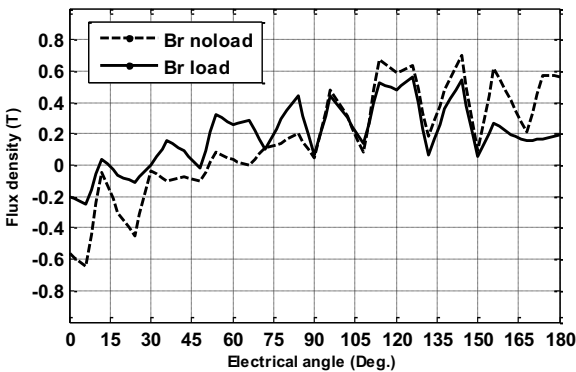


Fig. 2. Computed radial flux density distribution at a rotor position of 60 electrical degrees under no load and loaded conditions ($C=120 \mu\text{F}$, speed = 1143 rpm)

B. Performance Characteristics

The experimental slip-ring induction machine has the following ratings: 1.8 kW, 380/220V, Y/ Δ , four-pole 50Hz. TABLE I shows the number of unknowns and total computation time for a computation task. The computed and measured no load voltage versus speed is given in Fig. 3 when the excitation capacitance is $120 \mu\text{F}$, $200 \mu\text{F}$ and $280 \mu\text{F}$. It can be observed that the voltage increases with generator speed, and higher voltages are produced by a larger capacitance. For a given capacitance, the SCSESG cannot maintain the excitation below a certain cutoff speed. The load characteristic of the SCSESG is shown in Fig. 4. A fair agreement between computed and experimental results is observed.

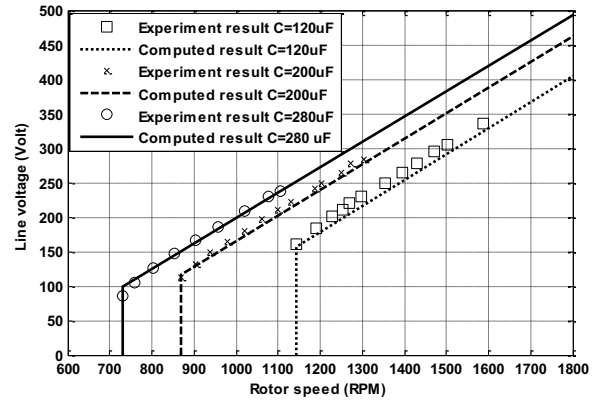


Fig. 3. Variation of no-load voltage of SCSESG with speed with different excitation capacitances

TABLE I
COMPUTATIONAL COST PER ANALYSIS

Total number of unknowns (Points) \times Time Steps	Computation time
(9606) \times 360=3,458,160	about 10 hours

(Based on Sun Microsystems Sun-Fire E6900 CPU 4x 900 MHz 64 bits Processor Memory 4 GB)

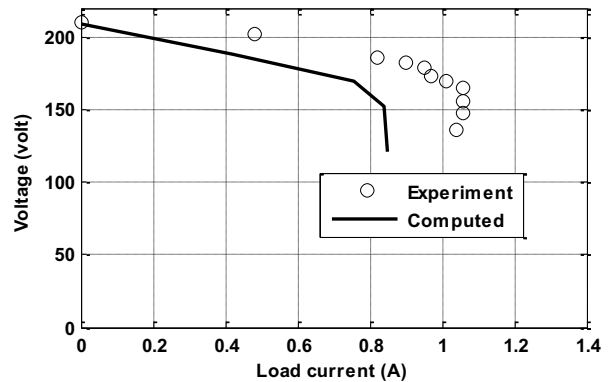


Fig. 4. Computed and experimental load characteristics at a speed of 1100 rpm when $C = 200 \mu\text{F}$

IV. ACKNOWLEDGMENT

The work described in this paper was fully supported by the Hong Kong Polytechnic University under grant G-U487.

V. REFERENCES

- [1] A. L. Mohamadein, H. A. Yousef and Y. G. Dessouky, "Series-connected self-excited synchronous generator: steady state and transient behaviors", *IEEE Trans. Energy Convers.*, 14(4), pp. 1108-1111, 1999.
- [2] A. L. Mohamadein and E. A. Shehata, "Theory and performance of series connected self-excited synchronous generators", *IEEE Trans. Energy Convers.*, 10(3), pp. 508-515, 1995.
- [3] A. S. Mostafa, A. L. Mohamadein and E. M. Rashad, "Analysis of series-connected wound-rotor self-excited induction generators", *IEE Proceedings Electric Power Applications*, 140(5), pp. 329-336, 1993.
- [4] J. F. Gieras, *Permanent-magnet motor technology*, 2nd ed., Marcel Dekker: New York, 2002.

Power Factor Calculation by the Finite Element Method

Claudia A. da Silva¹, Francis Bidaud², Philippe Herbet², Jose R. Cardoso³.

¹Tecumseh do Brasil, R&D, Electrical Motor, São Carlos, SP, Brazil

²Tecumseh Europe, R&D, Electrical Motor, Barentins, France

³São Paulo University, LMAG-PEA, São Paulo, SP, Brazil

claudia.silva@tecumseh.com

Abstract — The use of finite element analysis (FEA) to design electrical motors increased significantly last years due the better performance of modern computers. Even though the analytical software remains the most used tool, the FEA is widely used to refine the analysis and gives the final design to be prototyped. The power factor, a standard data of motor manufactures data sheet is important because it shows how much reactive power is consumed by the motor. This data became important when the motor is connected to network. However, the calculation of power factor is not an easy task. Due the saturation phenomena the input motor current has a high level of harmonics that cannot be neglected. In this work the FEA is used to evaluate the power factor of a small single-phase induction motor.

I. INTRODUCTION

The analytical methodology remains as the most important daily work tool of motor designers at industry. The use of analytical tools is important to reduce calculation time especially during optimization. However some important phenomena cannot be evaluated in these methodology and then numerical methods are used. The use of finite element analysis is very important because it provides detailed simulation and it is more accurate regarding saturation and field distribution. Even though demanding more calculation time the use of FEA to simulate electromagnetic devices increased significantly last years due the better performance of modern computers. The literature is full of valuable works that finite element analysis to evaluate the performance of electrical motors [2][3]. Some of these works use software developed at academy and others use the available commercial software. No matter the software used the understanding of basic phenomena are required to make a good work. If motor designers do not know very well the theory of electrical motor they cannot evaluate correctly the results and may take wrong decisions.

Induction motors consume alternative power and then consume both real power (P) and reactive power (Q). The vector sum of real and reactive power is the apparent power (S). The power factor of an electric motor is defined as the ratio of its real power P in Watts to the apparent power S in VA. The presence of reactive power causes the real power (or useful power) to be less than apparent power, consequently induction motors have power factor less than 1. Motors with low power factor are undesirable load in the network [1]. Even though the power factor of an induction motor can be easily obtained by tests, this is not true for simulations carried by the finite element method because it is not obtained directly at the end of calculation. The level of saturation can also

distort the current curve and leads to false values of power factor.

In this work the finite element method is used to evaluate the performance of a small industrial capacitor run, single-phase induction motor. A method to extract the input power of a motor calculated from post-treatment of a finite element model, including consideration of saturation and harmonics, is proposed hereafter. The power factor is then deducted and calculated, but might be considered as an indicative value due observed distortion.

Results of simulation are compared to experimental ones and the problem of power factor calculation discussed is. The analysis presented in this paper may be not new for skilled engineers that are used to run the finite element method in motor design. However, it is useful for the fresh ones that look for information normally not available in the literature.

II. POWER FACTOR ANALYSIS

To analyze the problem of calculation of power factor by the finite element method the single-phase run capacitor motor of 100W, 60 Hz, 2 poles of Fig.1 is used. The coupled electric circuit is shown in Fig.2.

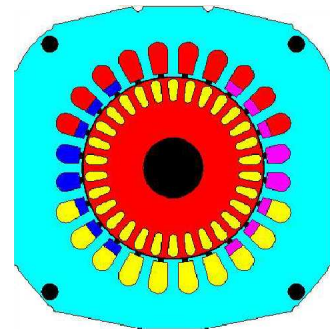


Fig.1. Design of analyzed single-phase motor

The basic theory of single-phase induction motor shows that, the mean input power P_{IN} of a run capacitor single-phase induction motor can be obtained by the equation (1). The V_{source} , I_{main} , I_{aux} are the applied voltage, the current of main winding and the current of auxiliary winding, taken in one period of the time T respectively. The time T of calculation corresponds to one cycle (1/f) of input power where f is the frequency of applied voltage.

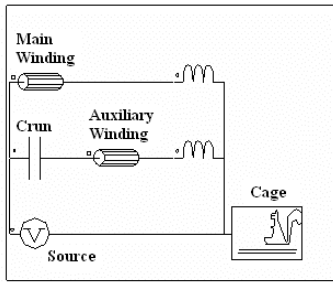


Fig. 2. Coupled electric circuit

$$P_{IN} = \frac{1}{T} \int_t^{t+T} (V_{source} \times (I_{main} + I_{aux})) dt \quad (1)$$

It is known that the input power of induction motors has several harmonics and they are more pronounced in saturated motors where the input current is strongly distorted as shown in Fig. 3. The high level of harmonics in the total current affects the correct calculation of power factor.

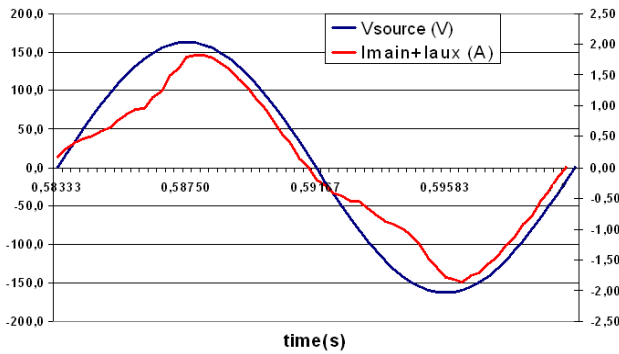


Fig. 3. Curves of V_{source} and I_{total} at steady state

In the finite element method two ways are normally used to calculate the power factor $\cos\phi$. The first way is the direct one where the values of V_{source} and I_{total} ($I_{main} + I_{aux}$) are taken at each time of one analyzed cycle at steady state. This methodology requires a calculation with a very small time step. The time where the V_{source} and I_{total} became positive (or negative) is taken. The difference between them gives the angle of displacement and consequently the value of power factor $\cos\phi$. Even though this academic method is easy and fast it may be avoided in analysis of saturated motors because the current curves are distorted. Additionally, as the time step increases the real time where the curves change the direction is lost as shown in Table I. This easy method is useful only in non-saturated motors and simulated with a very small time step ($\Delta t < T/180$).

TABLE I
POWER FACTOR FOR DIFFERENT TIME STEP CALCULATION

Time step (ms)	Cos ϕ
0.092	1
0.185	1.
0.277	0.994

The second way to calculate the power factor is by the use of equation (2). In this equation the power factor is deduced from the input power mean value P_{IN} and the rms total current and rms V_{source} . To have the input mean value P_{IN} at first we calculate the $P_{IN}(t)$ by use of equation (3). Here the V_{source} , I_{main} and I_{aux} versus time are exported from Flux2D. Next, the main value of P_{IN} is obtained directly at Flux2D with $Mean_{value}(P_{IN}(t)) = P_{IN}$.

As shown in Fig. 3 the harmonic content of total current is high. From a Fourier point of view, the result obtained with equation (2) is not correct because P_{IN} it is not limited to first harmonic. The value of power factor is then only an approximated value.

$$\cos\phi = \frac{P_{IN}}{V_{SOURCE} \text{eff} \times (I_{main} + I_{aux}) \text{eff}} \quad (2)$$

$$P_{IN}(t) = V_{source}(t) \times (I_{main}(t) + I_{aux}(t)) \quad (3)$$

As the power factor is only an approximated value the motor efficiency is calculated directly with equation (4). The output power is deduced from the shaft torque mean value T_N (N.m) and speed mean value ω_R (rad/s), that is $P_{OUT} = \omega_R \times T_N$.

$$\text{eff} = \frac{P_{OUT}}{P_{IN}} \quad (4)$$

In the full paper results of simulations with a capacitor run single-phase motor will be presented. The complete analysis will show the power factor value obtained by the different methods discussed above. The final paper will also discuss more deeply the effect of time step in power factor calculation and compare the calculated and measured motor efficiency.

III. REFERENCES

- [1] Li Kai, Cheng Xing Lin, Tang Qiang, "Studies on efficiency and power factor optimizing of IM using soft computing", Vehicle Power and Propulsion Conference, pp. 1-6, September, 2008. DOI 10.1109/VPPC.2008.4677597.
- [2] C.A. da Silva, N. Sadowski, R. Carlson, N.Lajoie-Mazenc, Y. Lefevre, "Analysis of the Effect of Inter-Bar Currents on the Performance of Polyphase Induction Motors", IEEE Transaction on Industry Applications, v.39, no.6, pp. 1674-1680, 2003.
- [3] T. Chevalier, A. Kedous-Labouc, B. Cornut, C. Cester, "Estimation of Magnetic Loss in an Induction Motor fed with Sinusoidal Supply using a Finite Element Software and a new Approach to Dynamic Hysteresis", IEEE Transaction on Magnetics, v.35, no.5, Part 2, pp. 3400-3402, September 1999.

Comprehensive Research on Stator Shapes and Frames in Switched Reluctance Motor: Electromagnetic, Thermal and Vibration Analyses

Jian Li, Xueguan Song, Dawoon Choi, Yunhyun Cho
 Dong-A University
 Hadan 2 Dong, #840, Saha-gu, Busan, 604-714, South Korea
 lijian613@gmail.com

Abstract—The vibrations of electric motors are mainly determined radial force excitation and stiffness of stator and frame. Stator shapes have a large influence on vibration performance. In this paper four different stator shapes were analyzed by using transient magnetic and thermal analysis and it was found that the “V” shape has the best thermal effect. Modal analysis was carried out on precise mechanical models of prototype motor in three dimensional finite element method (3D FEM) software to study the structure borne transfer function.

the motor to environment, whereas the square shape has the worst one.

I. INTRODUCTION

The switched reluctance motor (SRM) has raised significant interest among the industry for several reasons, including a mechanically and thermally robust rotor, simple stator windings and ease of manufacture. The study of acoustic noise in SRM has attracted much attention due to the ever-increasing consciousness of environmental noise pollution.

II. STUDY ON STATOR SHAPES

Based on the same inner structure of stator (inner side stator yoke diameter, pole and winding) and utilization of lamination, four shapes as proposed in [1] were used to design stators. The stator outer diameter is largest diameter of stator in ‘V’ ‘T’ shape model and the side in square shape. Modal analysis was also carried out. Comparing the modal frequency and modal shape, same conclusion could be obtained as [1], so it is skipped here. Dynamic finite element analysis of the motors with different stator shapes were carried out. The flux density distributions are shown in Fig. 1. With the same turn on angle 1°, turn off angle 16° and rotating speed 3600rpm, the square shape and ‘V’ shape model have a lower efficiency whereas ‘T’ shape has highest efficiency.

For a simple comparison of thermal effect of stators, a transient thermal analysis was carried out. During simulation, the environmental temperature and initial stator temperature was assigned to be 22°C. At t=0, the inside surface was assigned with a temperature of 80°C and the temperature of outside surface was checked after 5s. The temperature distributions are shown in Fig. 2. Performances were summarized in Table II. Comparing the heat exchange rate of four models, it could be concluded that ‘V’ shape stator has the best thermal effect which dissipate the heat generated in

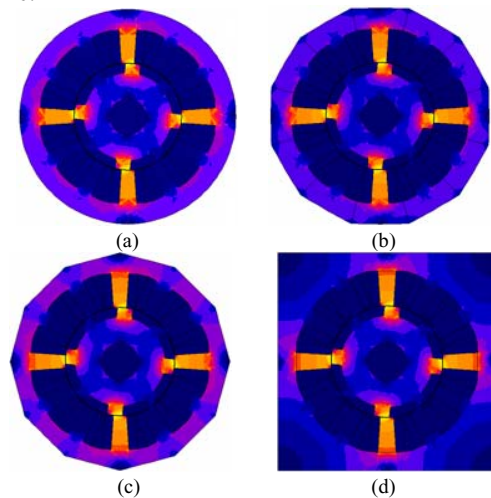


Fig. 1. Flux density distribution of different stators: (a) circle shape; (b) ‘T’ shape; (c) ‘V’ shape; (d) square shape.

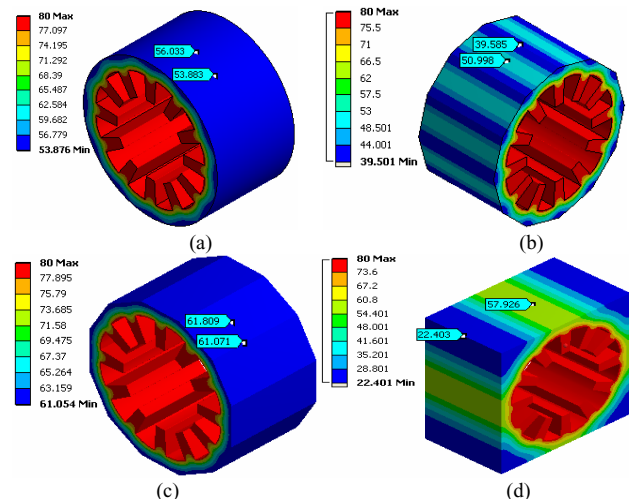


Fig. 2. Temperature distribution of different stators: (a) circle; (b) ‘T’; (c) ‘V’; (d) square shape.

TABLE II
MOTOR'S PERFORMANCE ACCORDING TO STATOR SHAPE

Stator shape	Circle	'T'	'V'	Square
RMS current (A)	6.16	6.30	6.24	6.18
Copper loss (W)	141.4	143.2	140.2	137.4
Iron loss (W)	166	163	170	178
Power (W)	1748	1763	1733	1763
Efficiency	85.0%	85.2%	84.8%	84.8%

III. MODAL ANALYSIS OF FRAMES

A modal analysis, or a free vibration analysis, is performed to obtain the natural frequencies and mode shapes of a structure. For a modal analysis, the natural circular frequencies ω_i and mode shapes ϕ_i are obtained from the matrix equation:

$$([\mathbf{K}] - \omega_i^2 [\mathbf{M}])\{\phi\} = \{0\} \tag{1}$$

where the structure stiffness matrix $[\mathbf{K}]$ and the inertia matrix $[\mathbf{M}]$ are formed from elementary stiffness inertia matrix stiffness inertia matrix, respectively [6]. Equation (8) has a nontrivial solution when the determinant of the coefficients vanishes, i.e.

$$\det([\mathbf{K}] - \omega_i^2 [\mathbf{M}]) = 0 \tag{2}$$

The polynomial equation has n eigenvalues, which corresponds to n natural frequencies.

After the stator core was studied, five frames with different structure and material to study the structure borne transfer function. The five models with same stator are shown in Fig. 3. The traditional circle shape stator is still used since the emphasis is frame in this part. Model I has an axial ribbed aluminum frame with 2.5mm thickness. In Model II, the thickness of frame increases to 5 mm. Model III has the same shape with Model II but uses gray iron cast. Model IV has a radial ribbed aluminum frame, 5 mm thickness. The material of frame in Model V is changed to structural steel and there are no ribs on frame because manufacture of ribbed steel frame is a big problem. The end bells in these models are made of aluminum and have the same dimensions. The in-plane flexural modes play important roles in electromagnetic vibrations while the bending, tensional, and out-of-plane flexural modes contribute to vibrations under unbalanced or fault situations [2], so only the in-plane flexural mode shapes are presented graphically in Fig. 4(a)-(e), which shows the 2nd mode shapes and their associated frequencies.

IV. CONCLUSION

This paper investigated the influence of stator shapes and frames to motor's performance. Modal analysis of stator shapes was described in literature, electromagnetic and thermal analysis of stator shapes are the new contribution of this paper. Comprehensive study of frames with different shapes and materials using modal analysis is firstly proposed in this paper. Since the paragraph limitation, more results and experimental verification will be reported in full paper.

V. ACKNOWLEDGEMENT

This work is the outcome of a Manpower Development Program for Energy & Resources supported by the Ministry of Knowledge an Economy (MKE)

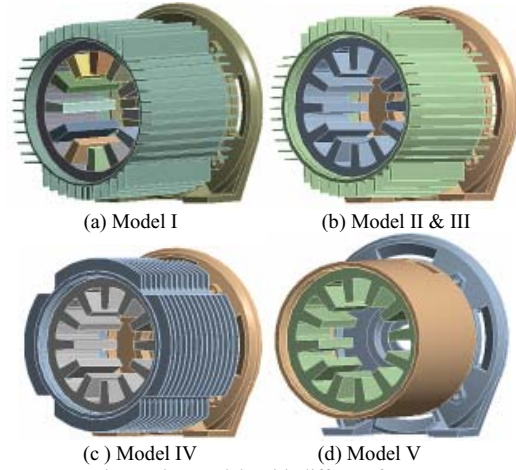


Fig. 3. Five models with different frames.

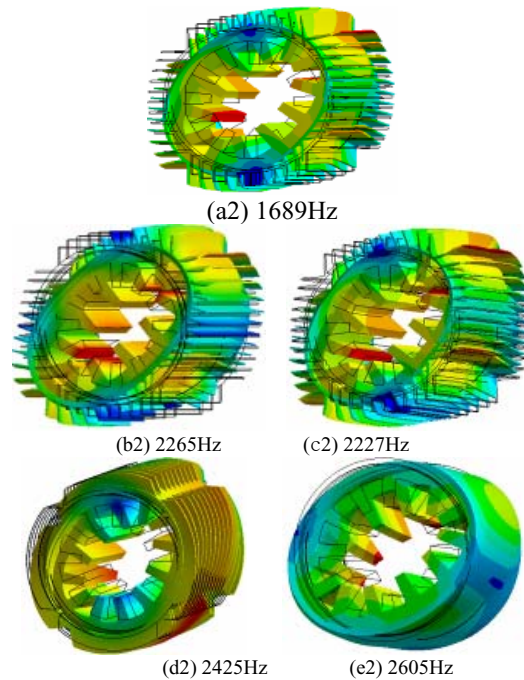


Fig. 4. Second mode shapes and mode frequencies of different frames

VI. REFERENCES

[1] W.Cai and P. Pillay, "Resonant frequencies and mode shapes of switched reluctance motors," *IEEE Trans. Energy Conversion.*, vol. 16, pp. 43-48, March. 2001. P. Pillay and W. Cai, "An investigation into vibration in switched reluctance motors," *IEEE Trans. Ind. Applicat.* vol. 35, pp.589-596, May/June. 1999.

[2] W.Cai and P. Pillay, "Resonant frequencies and mode shapes of switched reluctance motors," *IEEE Trans. Energy Conversion.*, vol. 16, pp. 43-48, March. 2001.

Investigation of System Efficiency in Nd-Fe-B and Ferrite Magnet Synchronous Motors with Coupled Field-Circuit Analysis

Tao Sun, Soon-O Kwon, and Jung-Pyo Hong
 Department of Automotive Engineering, Hanyang University
 Haengdang-dong, Seongdong-gu, Seoul, 133-971, Korea
 laplace_sun@hotmail.com, hongjp@hanyang.ac.kr

Abstract — This paper studies the influence of permanent magnet (PM) on the total motor system efficiency. Two PM synchronous motors with Nd-Fe-B and ferrite magnets which have the same Back electromotive force and output power have been designed. An indirect coupled field-circuit analysis is used in this paper to calculate motor losses and inverter losses. First, the electric circuit domain simulation is performed with the parameters of the semiconductor devices and these two motors. The current waveforms, copper losses and inverter losses can be evaluated in this process. And then, by means of the current waveforms, numerical methods and Epstein Frame, the iron losses of these two motors will be calculated. Finally, the sum of the inverter losses, copper losses and iron losses can be used to reflect the influence of the magnet on the total system efficiency. The analysis results will be verified by the experiment to show the validation of this analysis method.

I. INTRODUCTION

Ferrite magnet has been widely used in permanent magnet synchronous motors (PMSM) for a few decades. Recently, due to the superior remanent flux density and coercively force, the Nd-Fe-B magnet is gradually replacing the application of ferrite magnet. By using Nd-Fe-B magnet, the high efficiency and size reduction can be easily achieved. Considering the cost difference between the Ferrite magnet and Nd-Fe-B magnet, however, it is necessary to investigate the influence of magnet on the total motor system performance. As the same back electromotive force (Back-EMF) and output power, the motor with ferrite magnet may have higher inductance and resistance than the motor with the Nd-Fe-B magnet because of its larger number of winding turns and dimension. The different inductance and resistance may lead to the different time constant, which seriously affects the switching efficiency of the motor drive and current waveforms. Furthermore, the different current waveforms will produce different copper losses and iron losses in motors.

In order to solve this coupled field-circuit problem, [1]-[3] proposed several methods. These methods can be classified into direct coupled field-circuit method and indirect coupled field-circuit method. In the direct coupled field-circuit method, the field governing equations are combined with the circuit state space equations, and solved simultaneously [1]. To obtain the accurate current waveforms, the computation step of this method should be small enough. Although [3] proposed a computation step optimization method, the convergence of each step still is in both field and circuit equations. The indirect coupled field-circuit method solved the time consuming problem of the direct coupled

field-circuit method [2]. In the circuit domain calculation, the steady state could be achieved more quickly. Therefore, it does not need to spend much time into the transient process.

Based on the mentioned above, an indirect coupled field-circuit method is used to evaluate the motor and inverter losses in this paper. Two PMSMs have been designed with the same Back-EMF and output power using the ferrite magnet and Nd-Fe-B magnet, respectively. First, the parameters of these two motors including magnet flux linkage, phase resistance and nonlinear inductance profiles are calculated by the magneto-static field finite element method (FEM). Then, using the parameters of the inverter and motors, the losses of the switching devices, current waveforms, and the copper losses of motors are calculated by an electric circuit domain simulation program considering pulse width modulated (PWM) current regulation. Next, a magneto-static FE model is computed with the current waveforms obtained from the circuit domain simulation. The obtained flux densities of all elements are decoupled into the temporal and spatial components by the Discrete Fourier transforms (DFT), and used to index the iron losses with the Epstein frame. Finally, the iron losses of motor can be calculated by summing the losses of all elements in the all harmonics. An experiment will be done to verify the validation of this method. The analysis results will give more suggestions to the application of ferrite and Nd-Fe-B magnets.

II. MODELING IN CIRCUIT DOMAIN

A. Modeling of PMSM

According to the Park's transformation, the state space equations of the PMSM can be described as (1)-(3). And the corresponding d- and q-axis equivalent circuits are shown in Fig. 1 (a) and (b), respectively. [4]

$$\begin{bmatrix} v_d \\ v_q \end{bmatrix} = R_a \begin{bmatrix} i_{od} \\ i_{oq} \end{bmatrix} + \left(1 + \frac{R_a}{R_c}\right) \begin{bmatrix} v_{od} \\ v_{oq} \end{bmatrix} + P \begin{bmatrix} L_d & 0 \\ 0 & L_q \end{bmatrix} \begin{bmatrix} i_{od} \\ i_{oq} \end{bmatrix} \quad (1)$$

$$\begin{bmatrix} v_{od} \\ v_{oq} \end{bmatrix} = \begin{bmatrix} 0 & -\omega L_q \\ \omega L_d & 0 \end{bmatrix} \begin{bmatrix} i_{od} \\ i_{oq} \end{bmatrix} + \begin{bmatrix} 0 \\ \omega \psi_a \end{bmatrix} \quad (2)$$

$$T = P_n \left[\psi_a i_{od} + (L_d - L_q) i_{od} i_{oq} \right] \quad (3)$$

The parameters required in PMSM state space equations could be calculated in the numerical methods which have been introduced in [4].

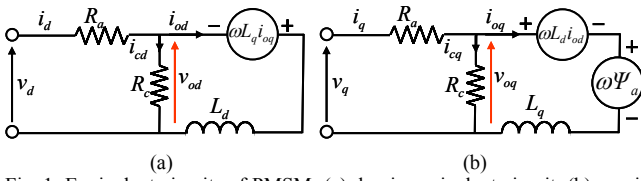


Fig. 1. Equivalent circuits of PMSM: (a) d-axis equivalent circuit, (b) q-axis equivalent circuit

B. Modeling of Inverter

The voltage source inverter is modeled by using of the switch function concept which is introduced in [5]. As the transistors switching-on or switching-off, four kinds of losses are produced [6]. They are current flowing losses and switching losses in transistors and freewheeling diodes, respectively. The calculation equations of these four losses are shown in (4)-(7).

$$P_{IO} = I_{MP} V_{CES} \left(\frac{1}{8} + \frac{M}{3\pi} \cos \theta \right) \quad (4)$$

$$P_{DO} = I_{MP} V_F \left(\frac{1}{8} - \frac{M}{3\pi} \cos \theta \right) \quad (5)$$

$$P_{IS} = (E_{on} + E_{off}) f_{sw} \frac{1}{\pi} \quad (6)$$

$$P_{DS} = \frac{1}{4} f_{sw} Q_{rr} V_{DC} \quad (7)$$

where all variables will be explained in the extended paper.

III. MODELING IN MAGNETIC FIELD DOMAIN

A. Magneto-static Field FEM

The 2D magneto-static field FEM is used to calculate the magnetic field distribution with the known current waveforms and time steps. Its governing equation, i.e. the nonlinear Poisson equation, is described in (8).

$$\nabla \times \nu (\nabla \times \mathbf{A}) = \mathbf{J} + \nabla \times (\nu \mu_0 \mathbf{M}) \quad (8)$$

where all variable will be explained in the extended paper.

B. Iron Losses Calculation

The iron losses calculation is consisted of three processes, which is simplified in Fig. 2. The detail introduction of this method is presented in [4].

IV. ANALYSIS MODEL AND RESULTS

Two PMSMs with ferrite and Nd-Fe-B magnets have been designed to have the same Back-EMF and output power. Their d- and q-axis inductances are shown in Fig. 3 (a) and (b), respectively. Additionally, at 25°C the motor with ferrite magnet has 1.16Ω phase resistance and 32.13V_{rms}/krpm line-to-line Back-EMF, while the motor with Nd-Fe-B magnet has 1.09Ω phase resistance and 30.475V_{rms}/krpm line-to-line Back-EMF.

The circuit domain calculation has been processed to both motors. And the current waveforms at 2000rpm and 0.35Nm operation condition are shown in Fig. 4. It is obvious that the current of the motor with Nd-Fe-B magnet is regulated more frequently, while the current of the other motor has more sm-

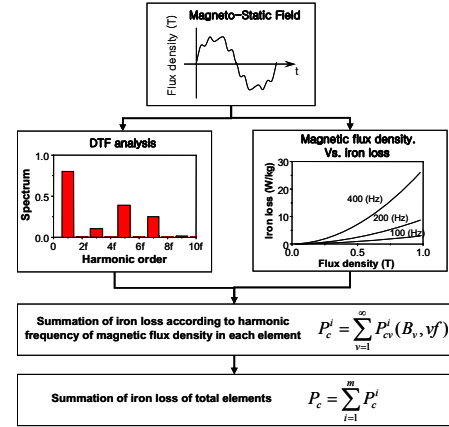


Fig. 2. Iron losses calculation process

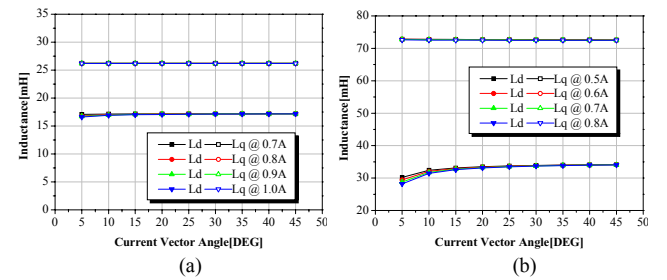


Fig. 3. Inductance profiles: (a) inductances of Nd-Fe-B magnet motor, (b) inductances of ferrite magnet motor

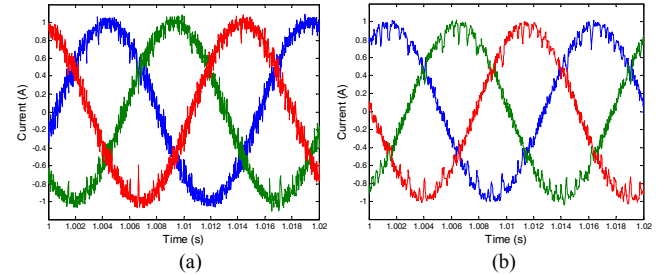


Fig. 4. Calculated current waveforms: (a) current waveforms of Nd-Fe-B magnet motor, (b) current waveforms of ferrite magnet motor

ooth waveforms. The motor specifications, more analysis results, experiment results and discussion will be presented in the full paper.

V. REFERENCES

- [1] L. Xu, and Ruckstadter E, "Direct modeling of switched reluctance machine by coupled field-circuit method," *IEEE Trans. on Energy Convers.*, Vol. 10, No. 3, pp.446-454, Sept. 1995.
- [2] P. Zhou, D. Lin, etc., "A General Cosimulation Approach for Coupled Field-Circuit Problems," *IEEE Trans. on Magn.*, Vol. 42, No. 4, pp.1051-1054, April 2006.
- [3] J. J. Lee, J. P. Hong, etc., "Loss distribution of three phase induction motor fed by pulsewidth-modulated inverter," *IEEE Trans. on Magn.*, Vol. 40, No. 2, pp.761-765, March 2004.
- [4] Tao. Sun, J. P. Hong, etc., "Determination of Parameters of Motor Simulation Module Employed in ADVISOR," *IEEE Trans. on Magn.*, Vol. 44, No. 6, pp.1578-1581, June 2008.
- [5] W. T. Lee, J. P. Hong, etc., "Object oriented modeling of an Interior Permanent Magnet Synchronous Motor Drives for Dynamic Simulation of Vehicular Propulsion," *IEEE Vehicle Power and Propulsion Conference, VPPC '06*, Sept. 2006.
- [6] Application Note of SEMiX-703GB126HD by SEMIKRON, www.semikron.com

Minimizing Torque Ripple of a BLDC Motor by Offsetting Cogging Torque with Voltage Control

Jin-seok Jang and Byung-taek Kim
 Dept. of Electrical Eng., Kunsan National University
 San68, Myrongsong, 573-701, Korea
 sadimy@kunsan.ac.kr

Abstract — This paper deals with reduction of torque ripple in a brushless DC motor with input voltage control. The commutation torque ripple can be controlled with varying input voltage, although cogging torque is independent on it. So, in this paper a strategy for minimizing torque ripple is proposed by offsetting the cogging torque with deliberate voltage control. The optimal condition is determined with various voltage levels and lead angles. As results, it is shown that the method causes 71% decrease of torque ripple.

I. INTRODUCTION

Torque ripple of a brushless DC (BLDC) motor consists of one produced by a voltage commutation and the other due to magnetic cogging. Numerous studies have been proposed for reduction of the torque ripple [1]~[3]. Of these studies, a method reducing the ripple by a various voltage instead of DC voltage was presented [3]. It focused on eliminating the current ripple, however, strangely the method was not applied to a BLDC motor but to a sinusoidal wave motor, so it was not possible to look into the effect of cogging torque ripple.

In this paper, reduction of a net ripple including cogging torque is focused. Since a cogging torque is inherent and unavoidable, we propose a method offsetting it with an input voltage control. For a given BLDC motor, equations to achieve a certain commutation ripple are analytically induced, and cogging torque is obtained with FE-analysis. With variance of voltage lead angle and commutation ripple, the net torque ripples are calculated in order to find the best voltage condition.

II. PROPOSED METHOD FOR TORQUE RIPPLE MINIMIZATION

A. Components of Torque Ripple in a BLDC motor

A 3-phase, concentrated wounded, surface PM BLDC motor is shown in Fig. 1. When it is driven with a DC voltage, the phase currents are obtained by using circuit analysis as shown in Fig. 2. The phase currents produce a commutation torque through interaction with a back EMF as given by

$$T_{com} = \frac{I_a E_a + I_b E_b + I_c E_c}{\omega_m} \quad (1)$$

, where ω_m is mechanical angular velocity and E is back-EMF. Using (1) the commutation torque can be calculated as shown in Fig. 2. Both Fig. 1 and Fig. 2 show that the commutation torque ripple is due to current ripples and it is deeply related with falling time t_f of each phase current.

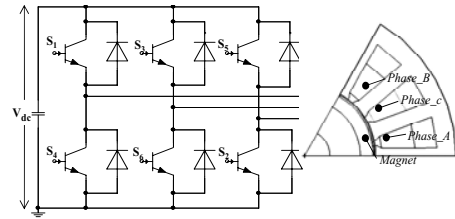


Fig.1. Circuit of BLDC motor

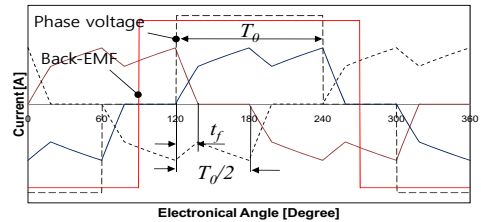


Fig. 2. Current, voltage and back-EMF waveforms

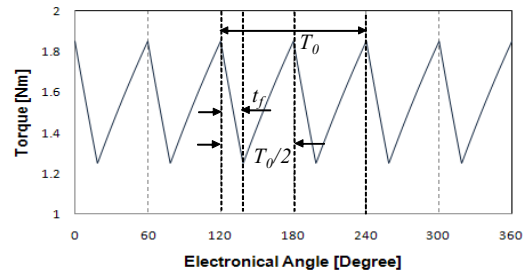


Fig. 3. Commutation torque (equivalent circuit analysis)

The actual net torque is obtained through FE-analysis as shown in Fig. 4. Since it includes both commutation and cogging torque ripples simultaneously, only a cogging torque is again analyzed by using FEM as shown in Fig. 4. The commutation torque is obtained by subtracting cogging torque from a net torque and represented in Fig. 5. It shows that the simulation results in Fig. 3 are very similar to the actual commutation ripples therefore, the analytic approach is valid.

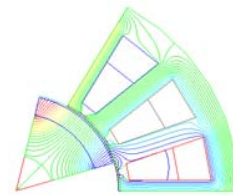


Fig. 4. Magnetic flux lines in BLDC motor (FE-analysis)

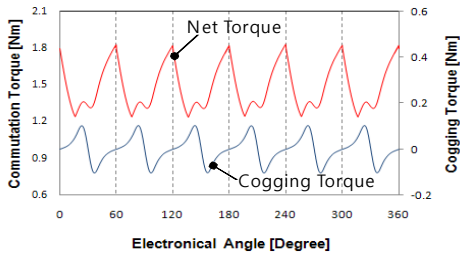


Fig. 5. Torque waveforms (FE-analysis)

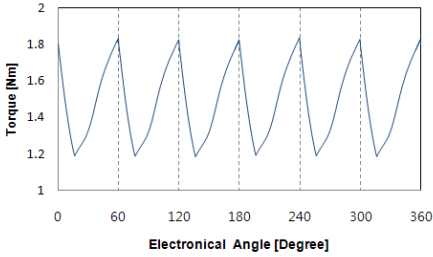


Fig. 6. Commutation torque (FE-analysis)

B. Cogging Torque Offset with Commutation Ripple

The commutation ripples in current and torque can be controlled by adjusting the input voltage V_1 and V_2 as shown in Fig. 7. Especially the falling time of a phase current t_f is expressed in terms of V_1 and V_2 , given by

$$t_f = \frac{(1 - 2e^{-\tau t_0/2})V_1 + \frac{3}{2}V_2 - E(1 - 2e^{-\tau t_0/2})}{(1 - 2e^{-\tau t_0/2})V_1 + \frac{3}{2}e^{-\tau t_0/2}V_2 + E(2 - e^{-\tau t_0/2})} \quad (2)$$

, where τ is the time constant of a circuit, that is R/L

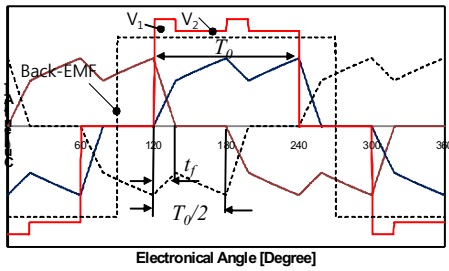


Fig. 7. Waveforms in voltage control

As previously shown in Fig. 2 and Fig. 3, the falling time t_f of each phase fairly affects the torque ripple. Therefore, the V_1 and V_2 are obtained by using (2) for various t_f , and the commutation torques are calculated and depicted in Fig. 8. It shows that comparing with the cogging torque, the magnitude of commutation ripple changes so abruptly that it is very difficult to offset the cogging torque. Thus we select a lead angle of voltage as well as a falling time t_f for control variables. From -30° to 30° for lead angle, the magnitudes of ripple in net torque are calculated according to variation of falling time, and the calculated results are plotted in Fig. 9. It shows that the best lead angle is 9.5° at which V_1 and V_2 are

respectively 434.2[V] and 170.4[V]. The net torque produced by the determined voltage conditions is shown in Fig. 10 which is reduced by 71% of that of a conventional DC input voltage.

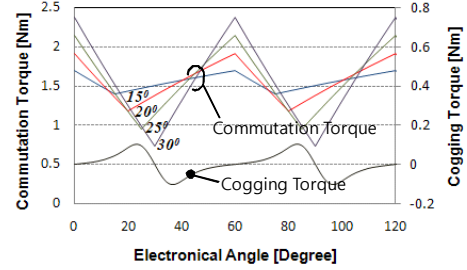


Fig. 8. Cogging torque and commutation torque for various t_f

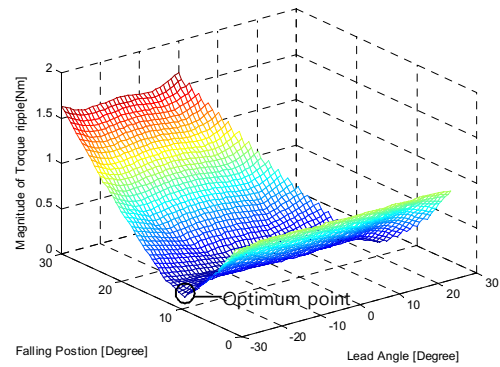


Fig. 9. Magnitude of torque ripple for various t_f and lead angle

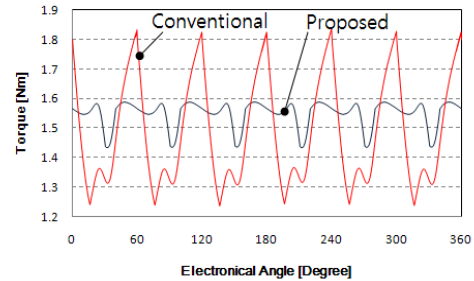


Fig. 10. Comparison of torque waveforms

ACKNOWLEDGMENT

This work is the outcome of a Manpower Development Program for Energy & Resources supported by the Ministry of Knowledge and Economy (MKE) and a second stage BK21 project of Korean Research Foundation.

REFERENCES

- [1] Keun-Young Yun, Byoung-Yull Yang, Byng-il Kwon "Reducing Cogging Torque by Flux-Barriers in Interior Permanent magnet BLDC Motor", *Trans. of KIEE*, 55B(10): 491-497, 2006.
- [2] Mahdi Ashabani, Ali Kashеfi Kaviani, Jafar Milimonfared, Babak Abdi, "Minimization of Commutation Torque Ripple in Brushless DC Motors with Optimized Input Voltage Control", *International Symposium on SPEEDAM*, pp. 250-255, 2008
- [3] Ki-Yong Nam, Woo-Taik Lee, Choon-Man Lee, Jung-Pyo Hong, "Reducing Torque Ripple of Brushless DC Motor by Varying Input Voltage", *IEEE Trans. On Magnetics*, 42(4): 1307-1310, 2006

A Novel Transverse Flux Linear Motor for Direct Drive Applications

Junghwan Chang*, Jiwon Kim**, Dohyun Kang** and Deokje Bang***

* Department of electrical engineering, Dong-A University, Saha-gu, Busan, 604-714, Korea

** Industry application Laboratory, KERI, Changwon-city, 641-120, Korea

*** Electric power processing Laboratory, Delft University of technology, 2628 CD Delft, The Netherlands

* cjhwan@dau.ac.kr

Abstract— This paper describes the development of a novel transverse flux linear motor (TFLM) excited by permanent magnets. It produces high thrust force with reduced normal force by combining the advantages of two different kinds of TFLMs. Magnetic field is analyzed by combining three-dimensional equivalent magnetic circuit network (EMCN) method with two-dimensional finite element analysis. The experimental results of prototyped motors are in good agreements with the analysis ones, and show the possibility of the new suggested motor as a direct drive requiring relatively long displacement of a mover.

I. INTRODUCTION

In direct drive applications, the main issue is to increase the force and power density of the machine by improving constructional design of stator and mover constituents. This normally requires careful considerations in the designing of the magnetic topologies, which promotes significant weight reduction in the magnetic mass as well as improvement in the form factor of the magnetic design [1]. A number of novel forms of permanent magnet machines have been developed for such applications and transverse flux machines are considered as one of the candidates to achieve the highest force densities among them, especially at a low speed. In this research, two different kinds of TFLMs with PM excitation are compared, and a novel transverse flux machine is suggested by combining the advantage of the two structures.

Fig. 1 shows the one phase of two different kinds of TFLM with PM excitation [2]. In each mover, the permanent magnets are fitted between the iron cores and magnetized with alternating polarity facing to each other. These arrangements produce a high air gap flux density in the air gap region compared to other permanent magnet motor types. The ends of the mover are skewed by one pole pitch each other, and form the path for three-dimensional flux flow with the adjacent teeth of the stator. With these features, it can produce unidirectional thrust force at the entire region by reversing the polarity of the applied current. The major differences between models are the positions of the armature windings and the presence of normal force. The first model has armature windings in the stator and the mover is inserted between the poles of the stator. In this case, normal force does not exist and lateral forces existing in the two air gaps between the teeth of stator and mover are cancelled out each other. However, some applications require long stroke of mover, and it is not practical to mount armature windings in the long stator considering the effective utilization

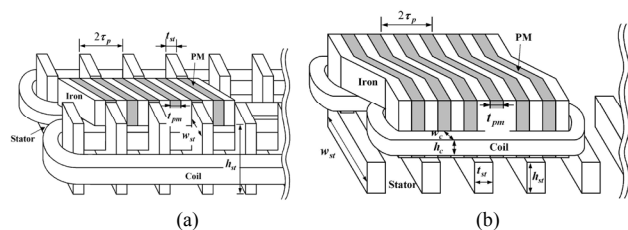


Fig. 1. Conventional design of TFLMs (a) I-shaped mover core type (b) U-shaped mover core type

of windings and significant loss of flux linkage. The second model has U-shaped mover cores and the armature windings are inserted into the poles of the mover. This feature seems to be suitable for the applications requiring relatively long displacement of the mover comparing I-shaped mover core type. However, this type of motor produces much bigger normal force than the thrust force. This can limit the use of it due to the friction loss caused by the normal force.

In the stocker system, which is used for transferring glasses in the LCD industry, there are great demands for linear direct drives to avoid drawbacks of traditional drives having rotary motor and mechanical motion conversion devices. In this application, the stator is installed up to 100 m and system requires thrust force of 10,000N. Thus, it is difficult to apply the I-shaped mover core type alone due to the leakage flux caused by long stator. Of course, U-shaped mover core type can be applied to this application, but it has also drawbacks of huge normal force.

Fig. 2 shows the conceptual development process of the new model and Fig. 3 shows the one phase of it. It is developed by combining the advantage of the previous two models; non-existent normal force of the I-shaped mover core type and effective coil arrangement of U-shaped mover core type. Basically, it can produce two times higher thrust force than the U-shaped mover core type by jointing it in parallel way. However, the normal force is just increased by 50% comparing the U-shaped mover core type that can produce the same thrust force. This is due to the fact that the extruding pole arrangement of E-shaped core type at the both ends of the mover provides only thrust force, and the attractive forces between stator and mover are cancelled out each other. It can also reduce almost 50% of the copper for windings. This implies that winding losses of the suggested motor can be substantially decreased.

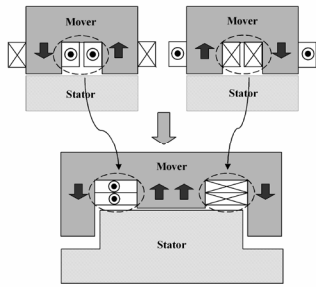


Fig. 2. Development process of new type TFLM

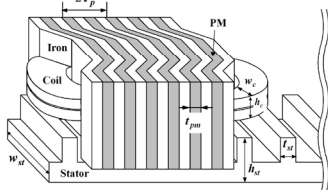


Fig. 3. Newly designed TFLM having E-shaped mover cores

II. ANALYSIS AND EXPERIMENT RESULTS OF TFLMS

Magnetic field is analyzed by three-dimensional equivalent magnetic circuit network (EMCN) method using a symmetry condition of flux distribution. Two-dimensional finite element analysis is also used to find the influence of the end effect of mover on the performance of TFLMs [2]. Fig. 5 shows the thrust and normal forces of TFLMs having U and E-shaped mover cores. For comparison, each value is corresponding to one-pole pair of each model when applying different magnitude of MMF. The E-shaped core type produces almost two times of the thrust force than the U-shaped core type at the all applied MMFs. But, in case of normal force, they have almost same peak levels due to the cancellation of attractive force between mover and stator at the both sides of mover in the E-shaped core type. The ratio of normal force to thrust force is decreasing with the increase of the applied MMF.

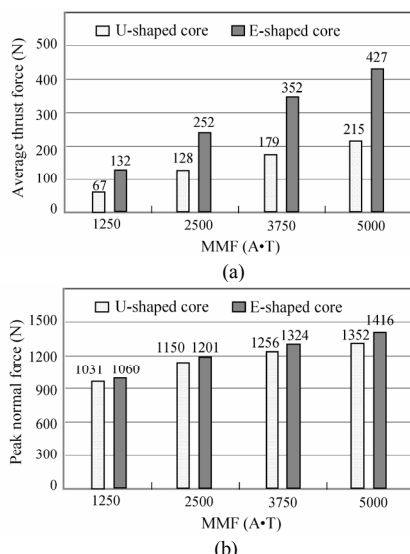


Fig. 4. Comparison of thrust and normal force (a) average thrust force (b) peak normal force

Fig. 5 and Fig. 6 show movers and stators of the U and E-shaped core type TFLM for static experiments, respectively. Fig. 7 shows the comparison of the thrust force profiles for different MMFs during the displacement of the mover between stable and unstable equilibrium positions. The averaged thrust forces are in good agreement with experimental ones. At 50% and 100% of the rated MMFs, experiment shows that the average thrust force of E-shaped core type is 2.12 and 2.15 times higher than that of U-shaped core type, respectively.

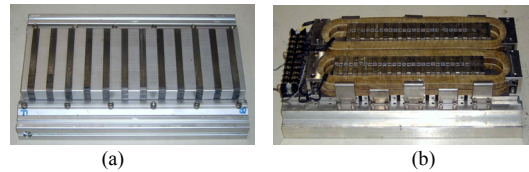


Fig. 5. U-shaped mover core type TFLM (a) stator (b) mover

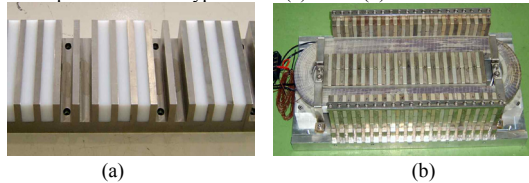


Fig. 6. E-shaped mover core type TFLM (a) stator (b) mover

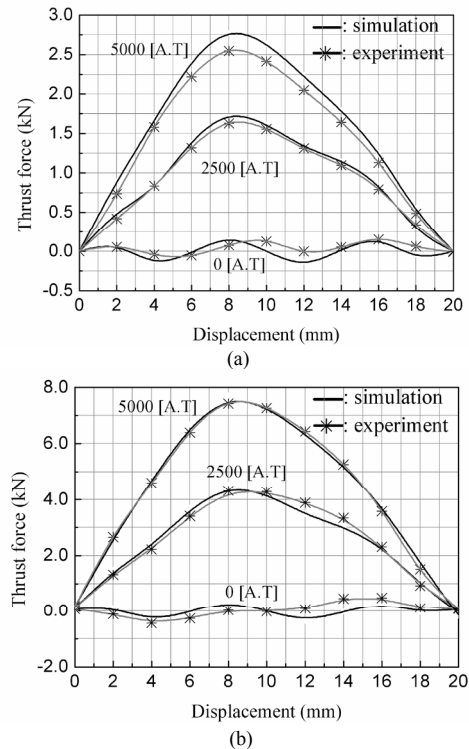


Fig. 7. Thrust force profile (a) U-shaped mover core type (b) E-shaped mover core type

III. REFERENCES

- [1] Z. Soghomonian, Z. Rahman, and K. Martin "New excitation methods for direct drive DC brushless motors with complex electromagnetic core designs", 23th Annual Conference on Properties and Applications on Magnetic Materials, 2004.
- [2] Junghwan Chang, Dohyun Kang, "Development of a stocker system using transverse flux linear motor with permanent magnet," *Journal of Electromotion*, vol.12, no. 2-3, pp.99-105, 2005

Design Strategy of Interior Permanent Magnet Synchronous Motor for Electric Power Steering Considering Cogging Torque and Torque Ripple using Current Harmonics

Soon-O Kwon¹, Jeong-Jong Lee¹, Tao Sun¹, Young-Kyun Kim², Geun-Ho Lee¹, and Jung-Pyo Hong¹

¹ Department of Automotive Engineering, Hanyang University, Seoul 133-791, Korea

² Korea electronics technology institute, Bucheon-si, Gyeonggi-Province, Korea
Hongjp@hanyang.ac.kr

Abstract — This paper presents the design strategy of interior permanent magnet synchronous motor for electric power steering (EPS) considering cogging torque and torque ripple using current harmonics. For the EPS motor, cogging torque and torque ripple reduction are important design factors. In order to reduce cogging torque and torque ripple, optimal design methodology, such as response surface methodology (RSM) can be used and design parameters can be pole angle, slot opening, notch, etc. However, it is shown that optimal design satisfying cogging torque and torque ripple does not exist by response surface methodology in the presented design. In order to satisfy both cogging torque and torque ripple, design parameters minimizing cogging torque is determined by RSM and torque ripple is reduced by harmonic current. Therefore, minimization of both cogging torque and torque ripple can be achieved. Presented design strategy is verified by finite element analysis (FEA) and experiments.

I. INTRODUCTION

Interior permanent magnet synchronous motors have higher torque density per volume than induction motor and reluctance motor with wide operating speed range with the help of field weakening control. Therefore, it is widely applied from small power to large power such as traction motor for electric vehicles.

For the application of EPS, high power density, low torque ripple, and low cogging torque are required. To reduce cogging torque and torque ripple, various design topologies can be applied. Choice of fractional pole/slot combination or optimal geometry design etc. can be one of choice. Fractional pole/slot combination provides low cogging torque and torque ripple, however, unbalanced radial forces in air gap leads to high vibration and noise. For optimal shape design of magnetic circuit, even though computer system developed highly, huge computation time and efforts are required. Because many motor geometry parameters closely related to torque ripple and cogging torque. In addition, reduction of cogging torque and torque ripple simultaneously with shape optimization is difficult because minimum cogging torque design does not guarantee minimum torque ripple and vice versa. Therefore there should be compromise between cogging torque reduction and torque ripple reduction design. In addition, sometimes other motor characteristics should be sacrificed to satisfy cogging torque and torque ripple since both are the main constraints for comfortable driving.

On the other hand, output torque ripple can be reduced by control strategy [1, 2]. By applying appropriate current, torque ripple can be reduced. Therefore, both geometrical optimization to reduce cogging torque and current harmonic injection are used in this paper.

II. HARMONIC CURRENT ESTIMATION

The input current of synchronous motor is assumed to sinusoidal wave and correspondent output torque is produced by interaction between magnetic field by permanent magnet and armature reaction. Due to non-linear characteristics of magnetic material, output torque and torque ripple are not proportional to input current. Therefore, output torque waves for various inputs current are estimated FEA and instantaneous current which provides constant torque are calculated. Calculated current wave is composed of various harmonic components, represented by a set of function of input current and harmonic order. Therefore, in ideal case of high response speed of microprocessors, nearly 0% of torque ripple can be achieved. The results of harmonic current are firstly examined by FEA. The main process of estimation of harmonic currents is summarized as follow;

1. Calculation of output torque wave form by FEA for various sinusoidal input currents
2. Instantaneous current for required constant torque are calculated.
3. Harmonic analysis for instantaneous input current
4. Development of function of harmonic current

III. OPTIMAL DESIGN USING RSM

Table 1 shows the main specification of analysis model. The model has 10pole and 15slots with concentrated windings.

Fig. 1 shows the design variables for optimal design, and optimal design results. The IPMSM is chosen and 2 design variables of pole angle and rotor eccentricity are chosen. Like general IPMSM, permanent magnets are buried in the rotor core. To reduce cogging torque and torque ripple, notch and eccentricity are applied to stator teeth and rotor respectively. The model is optimized for cogging torque. Unlike general EPS motor, the developed motor has no skew for research purpose.

TABLE 1 BASIC INFORMATION OF DESIGN MODEL

Motor type	IPMSM
Phase number	3
Pole number	10
Slot number	15
Stator outer diameter (mm)	90
Stack length (mm)	40
Parallel circuit number	5

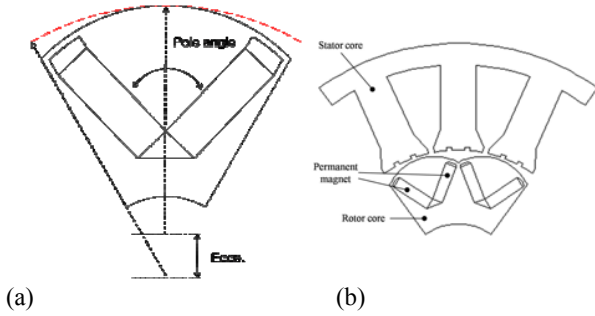


Fig. 1 (a) design variables, (b) optimal design result

Fig. 2 shows the effect of design variables on cogging torque and torque ripple. As shown in the figure, it is impossible with geometry design satisfying both cogging torque and torque ripple. The optimal value of pole angle and eccentricity are around 37 and 7mm respectively.

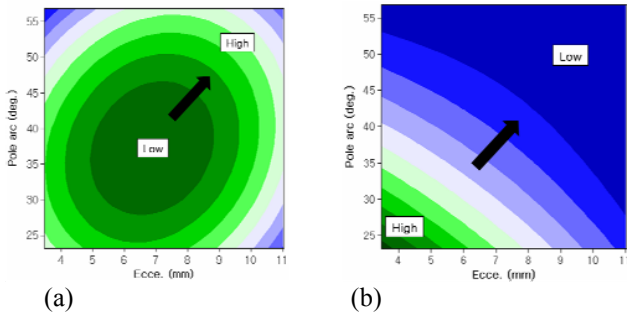


Fig. 2 Equi-plot of (a) cogging torque and (b) torque ripple.

Fig. 3 shows the output torque wave according to sinusoidal input current from 48 to 52Arms. In the figure, it is shown that the torque ripple varies with input current and rotor positions. In order to get constant torque, a straight line is drawn and current at each crossing point is estimated and overall current wave of one phase is shown in Fig. 3 (b). Unlike general current controlled synchronous motors, input current is distorted and contains large harmonic components and this is shown in Fig. 4 (a)

In Fig. 4 (b), comparison of output torque wave form between general current control and harmonic current injection is shown. In the figure, 8% of torque ripple is obtained with general current control and 0.7 % of torque ripple is obtained with harmonic current injection. The average torque is slightly reduced but the ratio is not significant and it is caused by calculation error of input current. It is expected that the current step in Fig. 3 is smaller, 0% of torque ripple can be achieved without decrease of average torque.

Fig. 5 shows the fabricated EPS motor. In the full paper, detailed design process and test results and verification will be included.

IV. CONCLUSION

This paper presented the design strategy of IPMSM for EPS to minimize both cogging torque and torque ripple. Cogging torque is minimized by optimal design of motor geometry and torque ripple is minimized by harmonic current. Presented design results are verified by experiments and could be effectively applied to the EPS motor design. In the full paper, motor control strategy, experimental verification, and other motor characteristics will be presented.

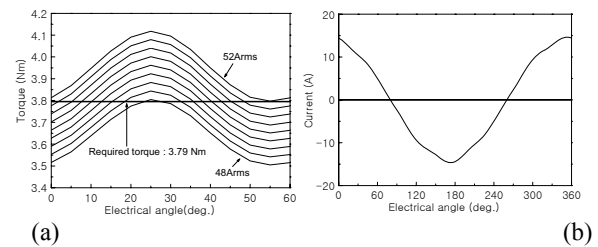


Fig. 3 (a) output torque wave for various input currents (b) input current wave form for constant torque

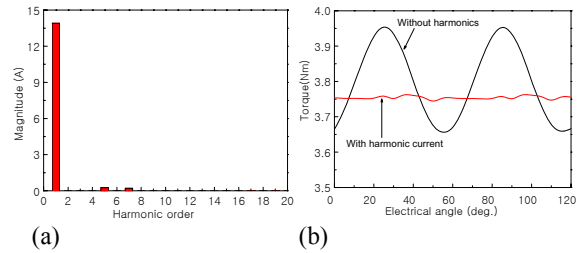


Fig. 4 (a) input current THD, (b) resultant torque from with and without harmonic current



Fig. 5 Fabricated EPS motor

REFERENCES

- [1] Geun-Ho Lee, Sung-Il Kim, Jung-Pyo Hong, Ji-Hyung Bahn, "Torque Ripple Reduction of Interior Permanent Magnet Synchronous Motor Using Harmonic Injected Current", *IEEE Trans. Magn.*, Vol. 44, No. 6, June 2008
- [2] Haifeng Lu, Lei Zhang, and Wenlong Qu, "A New Torque Control Method for Torque Ripple Minimization of BLDC Motors With Un-Ideal Back EMF", *IEEE Trans. Power electronics*, Vol. 23, No. 2, March 2008
- [3] Ji-Young Lee, Sang-Ho Lee, Geun-Ho Lee, Jung-Pyo Hong, "Determination of parameters considering magnetic nonlinearity in an interior permanent magnet synchronous motor", *IEEE Trans. Magn.*, Vol. 42, No. 4, Apr. 2006

Calculate the Parameters of IPMSM according to distance of PM and Magnetic saturation.

Ik Sang Jang, Chang Sung Jin, Seung Joo Kim, and Ju Lee
 Hanyang University
 17 Haengdang-dong, Seongdong-gu, Seoul, 133-791, Korea
 coldest@hanyang.ac.kr

Abstract — Interior Permanent Magnet Synchronous Motor (IPMSM) produces two kind of torque that Magnetic and Reluctance torque. The permanent magnet linkage flux Ψ_a and d-axis and q-axis inductances have an important influence on the torque characteristic of IPMSM. Thus their accurate prediction is essential for predicting performance aspect such as the torque and flux-weakening capabilities. In this paper, in many causes which affect the characteristic parameters, effect of distance of Permanent Magnets will be inquired. Nonlinear characteristic of inductances is considered as calculating inductances using finite element method.

I. INTRODUCTION

Permanent magnet synchronous motor (PMSM) has many advantages, such as high torque density, high power density, high efficiency, among others. Advances in PMSM manufacturing and technology are primarily responsible for lowering the cost and increasing the applications of PMSMs. PMSMs are classified into sinusoidally fed PMSMs and rectangular fed brushless PM motors (BLDC). The magnets are either mounted on the surface of the rotor, called surface mount permanent magnet synchronous motors (SPMSM), or placed inside the rotor, called interior permanent magnet synchronous motor (IPMSM). Because the magnets of the IPMSMs are embedded inside the rotor, magnets are protected from flying away from the rotor surface from the centrifugal force. IPMSMs produce not only the magnetic torque, but also the reluctance torque, which is due to the difference between the d-axis and q-axis inductance L_d, L_q by geometrical rotor structure. Therefore, it is possible to control the machine in the wide speed range control by means of flux-weakening control method. The air-gap flux can be weakened by applying large demagnetizing current in the d-axis of the permanent magnets. The steady-state performance analysis and precise control of the IPMSM greatly depend on determining the parameters accurately. The three essential parameters of the IPMSMs are armature flux linkage of PM (Ψ_a), d-axis and q-axis inductances (L_d, L_q). The magnet flux linkage is usually estimated from the back electromotive force (EMF). It is possible to estimate accurate value of magnet flux linkage as long as rotor speed and induced voltage are measured precisely. However, estimation of d-axis and q-axis inductances needs more careful approach as it involves saturation and cross-coupling effects. There are various approaches to estimate d-axis and q-axis inductances

such as analytical methods, finite-element analysis, and experimental measurements.

This paper studies whether the distance of PM affects characteristic parameters. The inductances were estimated from the finite element method and measured by current vector control method considering saturation and cross-saturation effects.

II. INDUCTANCE COMPUTATION

The voltage equation of IPMSM which is got to be transformed into d, q axis coordinate system can be written as

$$\begin{bmatrix} v_d \\ v_q \end{bmatrix} = \begin{bmatrix} R_a + pL_d & -\omega L_q \\ \omega L_d & R_a + pL_q \end{bmatrix} \begin{bmatrix} i_d \\ i_q \end{bmatrix} + \begin{bmatrix} 0 \\ \omega \Psi_a \end{bmatrix} \quad (1)$$

Where,

$$\Psi_a = \sqrt{\frac{3}{2}} \Psi_f = \sqrt{3} \Psi_e$$

Ψ_e : the effective value of armature linkage flux of u-phase by permanent magnets

v_d, v_q : d, q elements of armature voltage

i_d, i_q : d, q elements of armature current

R_a : winding resistance

In the steady state, the differential terms are eliminated in Eq. 1.

The inductance parameters were computed from the finite element method. The finite element method is considered to be a very powerful tool to predict and estimate machine parameters. It can also give good insight into the saturation and leakage of flux inside the machine. It is available to estimate the d-, q-axis inductances in following procedure from flux linkage vector diagram shown in Fig. 3.1

1) Assuming that the motor is driven by load, open the motor terminals and rotate the rotor by FEM. Calculate the variation of flux linkage or induced voltage on phase U winding.

2) Assuming that current with magnitude i_a and phase angle β is applied. Rotate the rotor in same way like 1), calculate the variation of flux linkage or induced voltage on phase U winding.

3) Calculate the phase difference and effective values Ψ_{ua} , Ψ_{uo} of fundamental wave component for the waveform obtained through.

4) Using the equation (2)~(4), compute parameters with values obtained through 3).

$$i_d = -I_a \sin\beta \quad i_q = I_a \cos\beta \quad (2)$$

$$\Psi_a = \sqrt{3}\Psi_{ua} \quad \Psi_o = \sqrt{3}\Psi_{uo} \quad (3)$$

$$L_d = \frac{\Psi_o \cos\alpha - \Psi_a}{i_d} \quad L_q = \frac{\Psi_o \sin\alpha}{i_q} \quad (4)$$

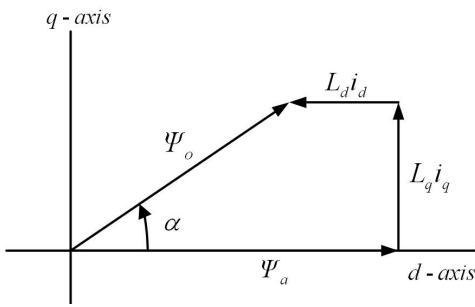


Fig. 1. Flux linkage vector diagram of IPMSM

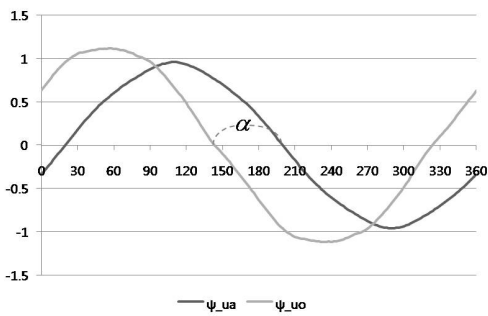


Fig. 2. Flux linkage waveform of phase U

III. ANALYSIS MODELS

Each Analysis model has same amount of PM. But it has different that distance of two magnets. Magnetic flux path of each model is different to each other. Thus it has different saturation region of rotor.

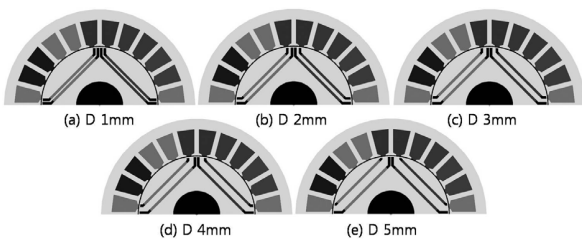


Fig. 3. Analysis Models

IV. TORQUE MECHANISM OF IPMSM

In IPMSM, besides magnetic torque in SPMSM, also reluctance torque by saliency arc produced. If balanced 3-

phase currents flow through stator coils distributed by 120 degree in space, rotating magnetic field is created with stator. The mathematical model of torques in IPMSM can be attained by the vector product between current vector \mathbf{i}_a and armature linkage flux vector Ψ_a .

$$T = P_n \Psi_a i_q + P_n (L_d - L_q) i_d i_q \quad (5)$$

IPMSM produce not only magnetic torque but also reluctance torque. Therefore, using flux-weakening control, IPMSMs can be driven at higher speed than surface mount permanent magnet synchronous motors (SPMSMs).

V. RESULTS

Fig. 2 shows inductance parameters of each model. Model (b), which has 2mm distance, has the largest L_d , L_q . But model (d) has the largest inductance difference $L_q - L_d$ that produce reluctance torque. As shown in Fig. 3 model (e) has the largest torque because of it has the largest linkage flux between outer PM and stator coil. Model (d) has the largest $L_q - L_d$. Thus it has the largest reluctance torque and maximum speed is high.

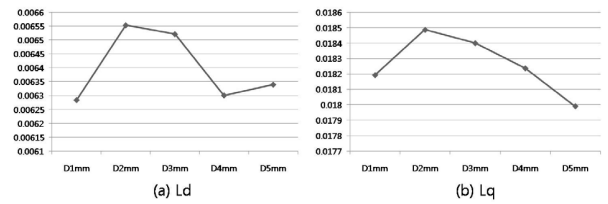


Fig. 2. d-axis, q-axis inductances

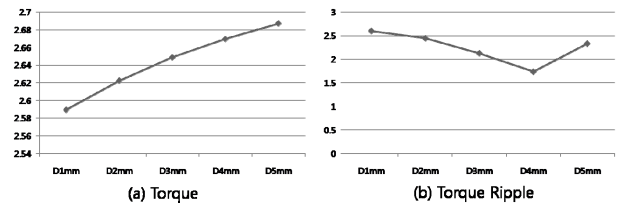


Fig. 3. Torque and torque ripple of IPMSM

VI. REFERENCES

- [1] P.H.Mcellor, F.B. Chaaban, and K.J.Binns, "Estimation of parameters and performance of rare-earth permanent-magnet motors avoiding measurement of load angle," in Proc. Inst. Elect. Eng.- B, vol. 138, 1991, pp.322-330.
- [2] Hanyang Univ. Energy Conversion Lab. Trans, "Design and Control of IPMSM", Inter Vision, 2007.
- [3] Rukmi Dutta and M. F. Rahman, "A Comparative Analysis of Two Test Methods of Measuring d- and q-Axes Inductances of interior permanent-Magnet Machine", IEEE TRANSACTIONS ON MAGNETICS, VOL. 42, NO 11, p. 3712~3718, 2006.
- [4] Khwaja M. Rahman and Silva Hiti, "Identification of machine Parameters of a Synchronous Motor," IEEE Transactions on Industry Applications, Vol. 41, No. 2, pp. 557-565, March/April 2005.

Axial Magnetic Flux and Eddy-Current Loss in Core Ends of a Large Induction Machine

Ranran Lin, Ari Haavisto, and Antero Arkkio

Department of Electrical Engineering, Faculty of Electronics, Communications and Automation,
Helsinki University of Technology, Espoo, Finland

ranran.lin@tkk.fi, ari.haavisto@tkk.fi, and antero.arkkio@tkk.fi

Abstract—The axial magnetic induction in the core ends of a large induction machine, caused by the leakage flux of the end winding, was analyzed. The analysis is based on 3-D finite element method (FEM), involving the anisotropic property of the core ends as well as the use of the standard impedance boundary condition (SIBC) to model the eddy current in the end shield and frame. The 3-D model is validated by measuring the axial magnetic induction on the end surface of the core as well as the induced electromotive force along a search coil. The analysis results show that the eddy current, which flows in the radial-circumferential planes of the laminations, is induced in the core ends due to the presence of the axial magnetic induction. The corresponding eddy-current loss is small and most of the loss occurs within 50 mm from the end surface of the core in the axial direction. In addition, the axial magnetic induction near the tooth tips and the bottoms of the slots of the core ends is much stronger than in the yoke.

I. INTRODUCTION

In the numerical analyses of electric machines, a 2-D cross-section model is quite common because the magnetic field in the core centre is basically parallel to the radial-circumferential plane. However, due to the leakage flux caused by the end winding, the magnetic field in the end region is definitely 3-D [1]. The core ends may be affected by the leakage as well, so the axial component of the magnetic induction may occur there. The direct effect of the axial magnetic induction is the eddy current in the laminations of the core ends. Under some fault conditions, the eddy current may be large and lead to considerable loss, which affects the efficiency of the machine and goes further to cause hot spots in the structures [2, 3].

II. METHODS

A. 3-D Numerical Model and Finite Element Analysis

A 3-phase, 4-pole, 2.24-MW squirrel-cage induction machine with a form-wound two-layer diamond winding was studied. Since it was impossible to test this machine at full load in the laboratory, the rotor parts were taken away and the stator parts were tested at the rated current 830 A.

The skin depth of the end shield and frame is 1 mm at the rated frequency 50 Hz. However, if a mesh included such small elements to model the eddy current in the end shield and frame, it would be impossible to solve the large equation system by the computer. Therefore, the standard impedance boundary condition (SIBC), also called the Leontovich boundary condition, was imposed to model the eddy current in these parts. The model of the anisotropic, 150-mm-long (axial

length) core end was cut into 15 slices in the axial direction, and the axial thickness of each slice was 10 mm. Fig. 1 shows the 3-D numerical model of the induction machine.

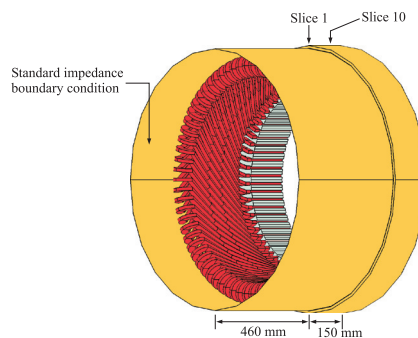


Fig. 1. The 3-D numerical model of the induction machine (without the air region and end shield). Only the first 10 slices of the total 15 slices are used in the calculation and slice 1 is the one nearest to the end surface of the core.

A series of time-harmonic numerical analyses were carried out. The governing equation was

$$\nabla \times [\boldsymbol{\nu} \cdot (\nabla \times \underline{\mathbf{A}})] + j\omega\boldsymbol{\sigma}\underline{\mathbf{A}} - \underline{\mathbf{J}}_s = \mathbf{0}, \quad (1)$$

where $\underline{\mathbf{A}}$ and $\underline{\mathbf{J}}_s$ are complex vectors of magnetic vector potential and source current density, respectively; $\boldsymbol{\nu}$ and $\boldsymbol{\sigma}$ are tensors of reluctivity and conductivity, respectively; ω is an angular frequency; and j is the imaginary unit.

The SIBC, as shown in Fig. 1, was imposed according to

$$\underline{\mathbf{E}} - (\mathbf{n} \cdot \underline{\mathbf{E}})\mathbf{n} = Z_s \mathbf{n} \times \underline{\mathbf{H}}, \quad (2)$$

where $\underline{\mathbf{E}}$ and $\underline{\mathbf{H}}$ are complex vectors of electric field strength and magnetic field strength, respectively; \mathbf{n} is the outward-directed normal unit vector on the surface; Z_s is the standard surface impedance of a medium.

The mesh of the core end was made into many layers and the axial thicknesses of the three layers close to the end surface were 0.25 mm, 0.45 mm, 0.9 mm, to model the skin effect. Galerkin's method was used in the weak form of the method of weighted residual to construct the finite element discretization.

B. Validation of 3-D Numerical Model

To validate the model, two types of measurement were done. Firstly, a search coil was built along a coil end, and the induced electromotive force (EMF) was measured and compared. The rms value of the measured EMF was 0.61 V, and the simulation gave 0.59 V. Secondly, the magnetic induction on the end

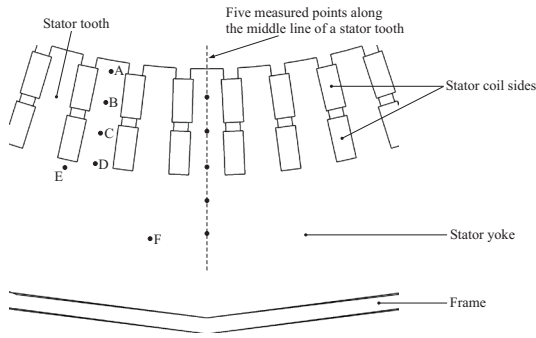


Fig. 2. The five measured points used in the validation are distributed evenly along the middle line (dash line) of each tooth. In addition, the six positions used in the calculation are marked as A, B, C, D, E, and F.

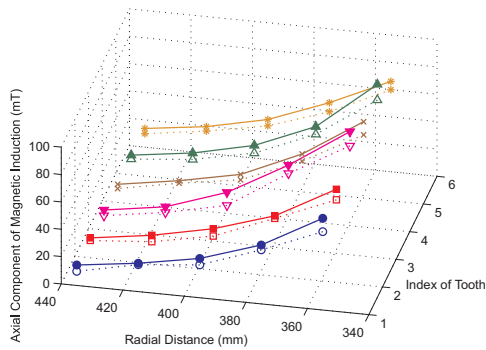


Fig. 3. The rms values of the axial components of the magnetic induction. Dash lines: simulation results; solid lines: measurement results.

surface of the core was measured. Six successive teeth in one phase belt were chosen to be measured. Along the middle line of each tooth, five points were measured. Fig. 2 illustrates the positions of the five measured points along the middle line (dash line). The results are shown in Fig. 3. The measured values are consistent with the simulated ones. Therefore, the measurement validated the numerical model.

III. RESULTS OF FINITE ELEMENT ANALYSIS

To fully analyze the axial component of the magnetic induction in the core ends, different positions were chosen. They were A, B, C, and D in the tooth between two successive phase belts, and E near the bottom of a slot and F in the middle of the yoke, respectively, as marked in Fig. 2. Because the core end was cut into 15 slices of equal length in the axial direction, the axial magnetic induction was calculated in the middle of the axial thickness of each slice. The corresponding results in slices 1–10, as marked in Fig. 1, are shown in Fig. 4.

In addition, the eddy-current loss caused by the axial magnetic induction was calculated in each slice by

$$\overline{P}_{Ft}^{calc} = \frac{1}{2} \int_{\Omega} \text{Re} \left\{ \frac{1}{\sigma_x} \underline{J}_x \underline{J}_x^* + \frac{1}{\sigma_y} \underline{J}_y \underline{J}_y^* \right\} dV, \quad (3)$$

where \overline{P}_{Ft}^{calc} is the time average value of the eddy-current loss over a period; \underline{J}_x and \underline{J}_y are the phasors of the components of the eddy current; σ_x and σ_y mean conductivity. Fig. 5 shows the eddy-current loss, calculated by (3), in slices 1–10.

The total eddy-current loss in one core end was calculated as 144.2 W. In the core end within the skin depth 1.6 mm in

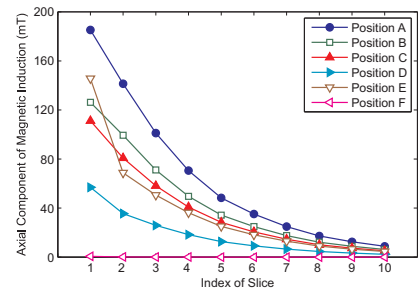


Fig. 4. The maximum values of the axial magnetic induction in slices 1–10 of the core end.

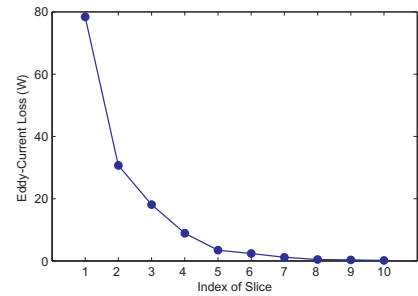


Fig. 5. The time average values of the eddy-current loss in slices 1–10 of the core end.

the axial direction, the loss was 30.2 W. Besides, in Fig. 5, most of the loss is concentrated in slices 1–5, that is, 50 mm from the end surface of the core in the axial direction.

IV. CONCLUSIONS

The axial magnetic flux and the eddy-current loss in the core ends of a 2.24-MW induction machine, caused by the end winding leakage flux, was studied. The anisotropic property of the core ends was taken into account and the eddy current in the end shield and frame was modelled as well.

The analysis results show that under the normal working condition, the total eddy-current loss in the core ends is small, by comparison with, for example, the stator copper loss, 5.4 kW. The stator end winding leakage causes the axial magnetic induction in the core ends, and it is enough to cause some loss within 50 mm from the end surface of the core in the axial direction. In the radial-circumferential planes of the laminations, relatively large axial magnetic induction occurs in the core ends near the tooth tips and the bottoms of the slots (positions A and E in Fig. 2). Moreover, there is a slight difference in the axial magnetic induction among different teeth in a phase belt. By the validation, the 3-D model proves to be feasible in analyzing both the end region and core ends.

REFERENCES

- [1] D. Ban, D. Žarko, and I. Mandić, "Turbogenerator end-winding leakage inductance calculation using a 3-D analytical approach based on the solution of Neumann integrals," *IEEE Trans. Energy Convers.*, vol. 20, no. 1, pp. 98–105, Mar. 2005.
- [2] Y. Yao, H. Xia, G. Ni, X. Liang, S. Yang, and P. Ni, "3-D eddy current analysis in the end region of a turbogenerator by using reduced magnetic vector potential," *IEEE Trans. Magn.*, vol. 42, no. 4, pp. 1323–1326, Apr. 2006.
- [3] M. Fujita, T. Tokumasu, H. Yoda, H. Tsuda, K. Ito, and S. Nagano, "Magnetic field analysis of stator core end region of large turbogenerators," *IEEE Trans. Magn.*, vol. 36, no. 4, pp. 1850–1853, Jul. 2000.

Double-layer Interior-PM Design in Single-Phase Line-Start Motor For Reducing Magnet

Liang Fang¹, Byeong-Hwa Lee¹, Jung-Pyo Hong¹, Hyuk Nam²

¹Department of Automotive Engineering, Hanyang University. ²LG Electronics Inc.

¹Haengdang-dong, Seongdong-gu, Seoul 133-791, Korea. ²Gaeumjeong-dong, Changwon 641-773, Korea
fangliang@hanyang.ac.kr, hongjp@hanyang.ac.kr

Abstract—This paper present a study on magnet reduction in a single-phase line-start permanent magnet motor(LSPMM) by utilizing the advantage of multi-layer rotor structure. Based on an existing single-layer interior-PM design LSPMM, a double-layer interior-PM rotor design is adopted for reducing the buried PM material without deteriorating motor torque and efficiency performances. The double-layer interior-PM rotor can create higher rotor saliency that benefits to reluctance torque generation, which is utilized to compensate the decreasing of magnet torque production since the PM usage reduction. The unique hybrid torque attribute benefits to torque and efficiency improvement are emphasized in this study. Finite element analysis and test results confirmed the validity of the presented analysis method.

I. INTRODUCTION

The single-phase line-start permanent magnet motors (LSPMM) are widely used in household appliance, such as the compressor of air-condition, due to its feature operating characteristics that fed directly from the commercial electricity, without additional power electronic switching devices and position sensor [1].

Due to the conductor bars and assisted PMs buried inside rotor core, the LSPMM has the beneficial attribute of high starting torque by means of a line-start induction motor and high efficiency, high torque performance at steady state as an interior-PM synchronous motor(IPMSM).

From a cost standpoint, the reduction of magnetic material in PM motor is desired on the premise of keeping the main machine performances, such as torque and motor efficiency. In this study, the falling of machine performance of a prototype single-layer LSPMM caused by the PM usage reduction is predicted to be improved by adopting double-layer IPM rotor structure. For maintaining the maximum torque and efficiency performances, the hybrid torque characteristic is enhanced by changing the balance ratio of the hybrid torque components generated from the IPM rotor, that the reluctance torque production increased by creating a higher rotor saliency is utilized to compensate the decreasing of magnetic torque production due to less magnet usage[2].

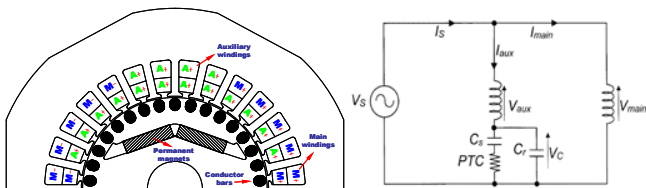


Fig. 1. Prototype single-phase LSPMM model and its stator winding circuit

With the help of response surface methodology(RSM) simulation, an optimized double-layer IPM rotor structure is built and almost 30% PM is saved. The equivalent circuit method(ECM) coupled with finite element analysis(FEA) is performed, and the torque and efficiency performance can be predicted. The experiment results of prototype single-phase LSPMM confirmed the validity of presented analysis method.

II. MODEL AND ANALYSIS METHOD

A. Prototype Single-phase LSPMM

In this study, an existing single-phase LSPMM used as air compressor is given as prototype model, in Fig. 1 shows. The single-phase LSPMM has main and auxiliary winding arranged in the stator slot regions. In the rotor part, the conductor bars and PM segments are buried in the iron core.

TABLE I
SPECIFICATION OF PROTOTYPE SINGLE-PHASE LSPMM MODEL

Item	Value	Unit
Pole / Slot number	2 / 28	
B_r [75 °C]	1.168	[T]
Magnet volume/pole	$(4.7 \times 19.0) \times 2$	[mm ³]
Stack length	90	[mm]
Air gap length	0.5	[mm]
Input voltage	220	[V _{rms}]
Rate Speed	3000	[Rpm]
Rated torque	6.5	[Nm]

B. ECM coupled with FEA in Single-phase LSPMM

In Fig. 1, the stator windings circuit shows the single-phase LSPMM taking a time difference by capacitance and spatial phase difference of main and auxiliary windings, generating an unbalanced magnetic field, which can be considered to be a two phase motor. The FEA is performed by converting single-phase LSPMM to an ideal two-phase motor that has equal turns orthogonally on d - q plane[1].

C. PM Reduction Design

The reduction of PM usage results in the decreasing of machine performances, such as torque and motor efficiency. On the other hand, the motor performance can be improved by taking advantage of unique rotor structure, such as multi-layer IPM design. In this study, a double-layer IPM rotor design is chosen for simple manufacture. In steady state, the single-phase LSPMM is dealt with a classical IPMSM. Therefore, hybrid torque characteristic can be expressed as following[2]:

$$T_e = P_n \{ \lambda_d i_q - \lambda_q i_d \} = P_n \{ \psi_a i_q + (L_d - L_q) i_d i_q \} = T_m + T_r \quad (1)$$

The torque equation above emphasizes that the hybrid torque is composed of magnet T_m torque and reluctance torque T_r , as Fig. 2 illustrates, in which the same amplitude of hybrid torque T_{e_Max} is achieved with different balance ratio of reluctance torque and magnet torque production, in term of $\beta(=T_m/T_r)$. The increase of β suggests the higher rotor saliency effect. It is predicted that the “New” LSPMM model with ratio $\beta(7:6)$ can saving almost 30% PM material compare to the prototype LSPMM with ratio $\beta(10:3)$. In another words, the higher rotor saliency of IPM rotor helps to reduce the PM usage for achieving the identify torque performance.

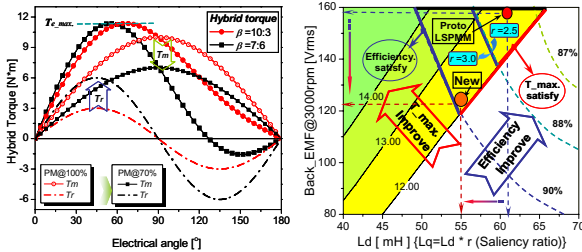


Fig. 2. Hybrid torque generation Fig. 3. Torque-Efficiency map

By performing ECM, the motor torque-efficiency is mapped with different saliency ratio(L_q/L_d). The torque and motor efficiency performances are predicted according to the variation of the significant motor parameters Back-EMF and d -axis inductance, as Fig. 3 shows. It is found that the closed triangle region satisfying both torque and efficiency enlarged with the increasing of saliency ratio. According to the predicted higher saliency ratio, the design objectives of Back-EMF(line-to-line) and d -axis inductance are determined for the double-layer IPM design with less PM material.

III. OPTIMIZATION OF DOUBLE-LAYER LSPMM

RSM is a collection of statistical and mathematical techniques used for developing, improving and optimizing process[2]. It is applied to determine an optimum structure of double-layer IPM rotor for PM reduction in LSPMM.

As the torque-efficiency map prediction, the rotor saliency ratio enhance from 2.5 to 3.0, corresponding to the decrease of Back-EMF and inductance. Therefore, the double-layer design of LSPMM model is built for satisfying the predicted “New” point characteristics. Fig. 5 illustrates the basic model of double-layer IPM rotor structure with design variables and their experiment ranges are given in Fig. 4. The Back-EMF (line-to-line) and rotor saliency ratio in steady operating condition(@3000rpm, $I_m=8A, \beta=40^\circ$) are chosen as objective functions in RSM. The optimal double-layer LSPMM is obtained, as Fig. 5 shows. The main machine characteristics of prototype and optimized models are confirmed by FEA.

Optimal design model	Hi	LPM_1	LPM_2	α	Prototype LSPMM model
	Lo	9.50	18.00	26.0	
		[7.60]	[17.50]	[22.5]	
		7.50	13.00	18.0	
Back-EMF [L-to-L@3000rpm] Y1=123[Vrms]					Back-EMF [L-to-L@3000rpm] Y=160[Vrms]
Saliency ratio [Lm=8A, $\beta=40^\circ$] Y2=3.0					Saliency ratio [Lm=8A, $\beta=40^\circ$] Y=2.54

Fig. 4. Optimization of Back-EMF and saliency ratio by RSM

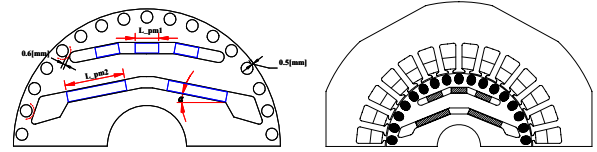


Fig. 5. Double-layer IPM design model and optimized double-layer LSPMM

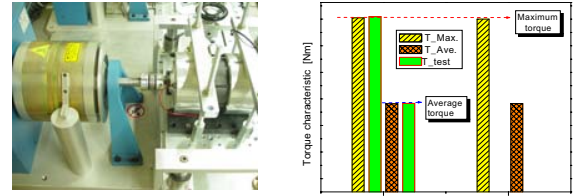


Fig. 6. Torque performance of single-phase LSPMM by test

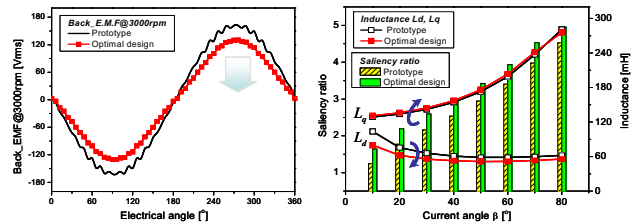


Fig. 7. Back-EMF (line-to-line @3000rpm) and rotor saliency characteristic

TABLE II
COMPARISON BETWEEN PROTOTYPE MODEL AND OPTIMAL DESIGN MODEL

Model	Back-EMF @3000(rpm) L-to-L[Vrms]	Saliency ratio [Lm=8(A), $\beta=40^\circ$]	Max. Torque [N*m]	Motor Efficiency [%]
Prototype [100%]PM	160.0	2.54	13.1	89.0
Optimal design [70%]PM	123.1	3.0	13.0	88.8

IV. RESULT ANALYSIS

The torque performance of prototype single-layer LSPMM is tested and well proved the validity of presented analysis, in Fig. 6. The optimized double-layer LSPMM model has lower Back-EMF and higher rotor saliency characteristics, in Fig. 7, but almost same torque and efficiency performances are achieved with saving 30% PM, as TABLE II compared.

V. CONCLUSION

This paper studied on the PM reduction design in a single-phase LSPMM. By improving the reluctance torque generation to compensate magnet torque production, the dependency of magnet usage is lowered. The optimized double-layer design LSPMM model is built with using 70% of PM used in prototype LSPMM, but achieving similar torque and efficiency performances. In conclusion, the double-layer IPM rotor design is an effective approach for improving IPM motor performance, further to realize magnet usage reduction.

VI. REFERENCES

[1] Timothy J. E. Miller, "Single-Phase Permanent-Magnet Motor Analysis", *IEEE Trans. On Indus. Appl.*, Vol. 1A-21, No. 4, May/June 1985.
 [2] Liang Fang; Jae-woo Jung; Jung-Pyo Hong; Jung-Ho Lee, "Study on High-Efficiency Performance in Interior Permanent-Magnet Synchronous Motor With Double-Layer PM Design," *IEEE Trans. Magn.*, vol. 44, Issue 11, Part 2, Nov. 2008.

Study on Partial Discharge Location in Oil Based on Ultrasonic Phased Array and Wideband Array Signal Processing

Xie Qing¹, Li Yan-qing¹, Lu Fang-cheng¹, Li Cheng-rong², Wang Nan¹
 North China Electric Power University, Baoding 071003, Hebei Province, China
 E-mail auto.ok@163.com

Abstract: A new partial discharge (PD) location method in oil is presented based on ultrasonic phased array and wideband array signal processing in this paper. Firstly, a set of partial discharge detection system based on ultrasonic phased array is built. And the wideband array ultrasonic signals of PD are received directly and formatted through this system. Secondly, the method of RSS (Rotational Signal Subspace) is used to focusing processing to the wideband array ultrasonic signals of PD. The focused processing is to search the focusing matrix T_j and convert the signal direction matrix

$A(f_i)$ under different frequencies to the same one center frequency, which can realize the information accumulation of wideband signal. Then we can realize estimating of direction of arrival (DOA) and locating of PD source by MUSIC (Multiple Signal Classification) only for narrow band signals processing. Lastly, the results of experimental research indicate the method is correct with smaller errors.

I. BACKGROUND

The partial discharge (PD) is an important reason for the insulation deterioration of electric power equipments. The accurate PD location can provide scientific information and guidance for the state maintenance and is favorable to rapidly remove the fault, avoid the occurrence of fatal accident, reduce the losses by blackout accident and cut down the maintenance cost, so great attentions have been paid by the electric power operation departments.

At present, the PD location methods adopted at home and abroad mainly include ultrasonic method, electric method and UHF method, which have been deeply studied [1]. Xi'an Jiaotong University has firstly brought forward the ultrasonic phased array technology based on 256 array elements and beam-forming algorithm for PD location, which has improved the low sensitivity deficiency of traditional single sensor, but this method needs too many array elements to cause the great difficulty in hardware implementation and the beam-forming algorithm is restricted by the "Rayleigh limit" with poor location

accuracy. North China Electric Power University has brought forward the PD location based on MUSIC algorithm, which can prevent the restriction of "Rayleigh limit" in the beam-forming location algorithm and improve the location accuracy. Based on this, a new PD location method based on 4×4 ultrasonic plane phased array and wideband array signal spectrum estimation algorithm is brought forward in this paper.

II. PARTIAL DISCHARGE DETECTION SYSTEM OF ELECTRICAL EQUIPMENT BASED ON ULTRASONIC PHASED ARRAY

The PD detection system of electrical equipment based on ultrasonic phased array is mainly consisted of ultrasonic phased array sensor, preamplifier, high-speed synchronous data acquisition device and laptop computer (as in fig. 1).



Fig.1 PD detection system



Fig.2 The model of 16-array elements ultrasonic phased array

The ultrasonic phased array sensor[2] is 16-array element and 4-row×4-column plane structure (as in fig. 2), the single array element is 4×4×15mm cuboid column, the space between the array elements is 5mm, the material is piezoelectric ceramics and the center frequency of its received signal is designed as 150kHz. A charge preamplifier is adopted in this paper, which is a wideband sensor with frequency covering 3 kHz~10MHz and gain of

up to 40dB. The signal detected by the sensor is accessed into the acoustic emission preamplifier through the BNC interface and is output through BNC interface after being amplified. The amplifier is supplied by 12V DC power supply. The high-speed data acquisition system integrates the computer control (program-controlled amplification and band pass filtering), data acquisition and high-speed serial data transmission functions. The high-speed data acquisition device has 16 channels and the amplification factor of single channel is 1 to 256 times controlled by the software in 16 shifts. The cut-off frequency of band pass filter is 20 kHz to 300 kHz and the sampling frequency is 512 kHz to 10MHz. The high-speed data acquisition device is connected with the computer via USB interface to realize the high-speed data transmission.

III. LOCATION ALGORITHM OF ULTRASONIC WIDEBAND ARRAY SIGNAL OF PARTIAL DISCHARGE

The focused processing is the precondition for the DOA of wideband array signal and essentially is to search the focusing matrix T_j and convert the signal direction matrix $A(f_i)$ under different frequencies to the same one center frequency. The RSS [3] is to derive the focusing matrix based on the least-error principle between the directional matrix after focusing and the directional matrix of the center frequency point.

Then, the MUSIC [3] algorithm is adopted for the direction-of-arrival estimation of the acquired narrowband signal. The MUSIC algorithm builds the spatial spectrum function with the orthogonality of signal subspace and noise subspace and detects the DOA of signal through the search of spectrum peak.

Finally, on the basis of the accurate estimation of the direction-of-arrival of single PD source, the accurate single PD source location is realized through the crossing of two directions of arrival in the space with the spatial information of PD source received by two ultrasonic phased array sensors A and B.

IV. EXPERIMENTAL STUDY

The pin-to-plate discharge model is adopted in the experiment, which is put into an oil tank full of mineral oil with dimensions of 100cm×100cm×120cm to simulate the PD situation in oil and generate the ultrasonic signal. The phased array sensor is placed on the outer wall of the oil tank and is close to the outer wall with the butter. The 16-array element ultrasonic signal acquired by the data acquisition device is shown as in Fig.3 and the direction finding spectrogram is shown as in Fig.4. With the PD source location error of less than 10cm, the experimental results verify the correctness of the method in this paper.

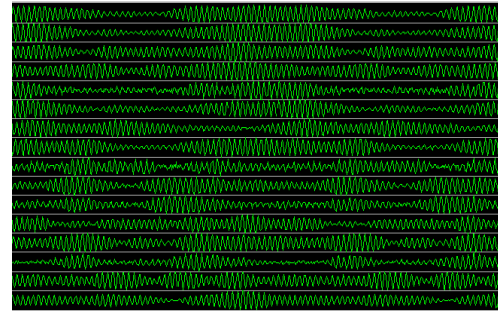


Fig3. Signal wave

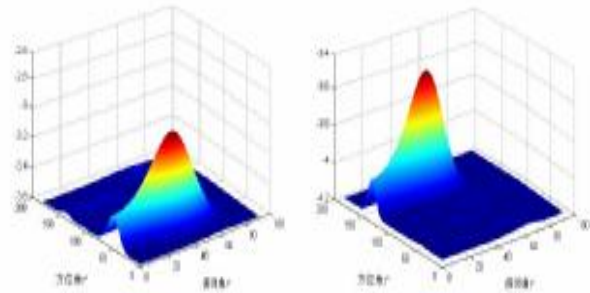


Fig.4 spectra of sensor arrays A spectra of sensor arrays B

V. CONCLUSION

A pair of plane ultrasonic phased array sensors are developed, which can directly detect and generate the ultrasonic wideband array signal of partial discharge in oil.

The RSS algorithm, MUSIC algorithm and crossover location principle are combined to realize the focusing processing, DOA estimation and geometric location of the wideband ultrasonic array signal of PD and overcome the limitation that the traditional algorithm can not directly process the actual wideband ultrasonic array signal of partial discharge.

The experimental platform for partial discharge location in oil is built for the experimental study. The location error is less than 10cm in the experiment, which verifies the correctness of the location method and provide perfect foundation for the further engineering application.

VI. REFERENCES

- [1] Sun Caixin , Luo Bing , Gu Leguan , et al. Research on locating partial discharge sources in transformer with electric-supersonic method and supersonic method and evaluation on each[J] . Transactions of CES , 1997 , 12(5) : 49-52, 60.
- [2] Luan Guidong, Zhang Jinyi, Wang Renqian. Piezoelectric Transducer and Transducer Array [M]. Beijing, Peking University Press, 2004.
- [3] Wang Yongliang, ChenHui, PengYining,etl. Spatial Spectrum Estimation Theory and Algorithms[M]. Beijing: Tsinghua University Press, 2004.

A Study on the Relation between Deformation of Stator Yoke and Acoustic Noise in Interior Permanent Magnet Motor

Do-Jin Kim, Sang-Ho Lee, Jeong-Jong Lee, Ji-Min Kim, Jung-Pyo Hong
Department of School of Mechanical Engineering, 17 Haengdang-dong, Seongdong-gu, 133-791, Seoul, Korea
k641170@hanyang.ac.kr, hongjp@hanyang.ac.kr

Abstract— In order to analyze noise of interior permanent magnet (IPM) motor, this paper deals with relation between deformation of stator and noise from motor. The resonance frequency is calculated by Ansys P/G and resonance frequency band based on 1/3 octave band is determined. In order to calculate deformation of stator, current considering load condition is calculated from dynamic simulation and normal and tangential force which affects on the tooth are computed by equivalent magnetizing current (EMC). After harmonic analysis for the computed forces is performed, the harmonic component of each force in the resonance frequency band put in the surface of tooth, respectively. And then, the quantity of deformation of stator is calculated and compared. Finally, the relationship between the quantity of deformation of stator yoke and noise spectrum is analyzed.

I. INTRODUCTION

Noise of motor can be classified into three sections. First of all, there are higher space and time harmonics eccentricity, phase unbalance, slot opening, magnetic saturation, and magnetostrictive expansion of the core laminations in electrical noise. Secondly, there are mechanical noises associated with the mechanical assembly. Thirdly, there are aerodynamic noises associated with flow of ventilating air through or over the motor [1].

The noise and vibration of the motor structure are the direct response of the excitation by these forces. For example, if the frequency of the radial magnetic force is close to one of the natural frequencies of the stator system and the factor order r is the same as the circumferential vibrational mode m of the stator system, significant vibration and acoustic noise can be produced [2].

For studying on the relation between deformation of stator yoke and acoustic noise in IPM motor, modal analysis, this paper deals with calculation of exciting force which is composed of tangential and normal force on the tooth, harmonic analysis for the exciting force, the quantity of deformation of stator yoke, and the comparison between calculated the quantity of deformation of stator yoke and acoustic noise.

In order to calculate electrical exciting forces which affect on the acoustic noise, the current is calculated by dynamic simulation considering load condition. The tangential and normal forces which affect on tooth of stator are calculated using finite element method (FEM). Especially, equivalent magnetizing current (EMC) method uses magnetizing current which exists on element boundary and it can directly calculate

the electromagnetic force which affects the surface of tooth [3].

The exciting forces are put in the surface of tooth of stator and the quantity of deformation of stator yoke is calculated. Finally, the tendency of calculation of the quantity of deformation of stator yoke and measured acoustic noise of analysis model is compared.

II. THEORY

A. Equivalent magnetizing current (EMC)

The differentia of tangential component of field intensity between two materials is equal to the magnetizing current on element boundary. On the element boundary, magnetizing current is calculated by eq (1).

$$I_m = \frac{1}{\mu_0} \int \nabla \times \vec{M} \cdot d\vec{s} = \frac{1}{\mu_0} (M_{1t} - M_{2t}) l_{ij} \quad (1)$$

where, M_{1t} and M_{2t} are the tangential components of magnetization on element boundary, l_{ij} is the distance on element boundary.

The electromagnetic force f_{ij} which affect on i, j element on the element boundary is written as [4]

$$\vec{f}_{ij} = \vec{I}_{ij} \times \vec{B}_{ext} \quad (2)$$

Flux density value of \vec{B}_{ext} is given as the average value for each element.

B. Spectrum analysis

The noise near the resonant frequencies, which affect harmonics of electrical exciting forces, is larger than other natural frequencies. Therefore, modal analysis for stator is performed and then center frequencies for 1/3 octave band based on the resonant frequencies of stator is designated. The center frequencies is defined by eq. (3)

$$f_c = \sqrt{f_u \cdot f_l} \quad (3)$$

where f_c is center frequency, f_u and f_l are the upper and lower half-power frequencies.

III. ANALYSIS MODEL

The specifications of analysis model are shown as Table I. The analysis model which consists of 4-pole/6-slots and concentrated windings is driven by BLAC operation and rated speed and torque are 1800rpm and 1.0 Nm, respectively. In

addition, pulse width modules (PWM) frequency is 4.0 kHz, respectively.

TABLE I
Specifications and resonant frequencies of stator

Contents	Values
Number of poles slots	4/6
Rated current (A_{rms})	1.5
Series turn number per phase (turns)	65
Rated speed (rpm)	1800
Rated torque (Nm)	1.0
PWM frequency (kHz)	4.0

IV. ANALYSIS METHOD AND RESULTS

In order to study on the relation between deformation of stator and acoustic noise, analysis method is divided into 4 steps.

Firstly, modal analysis for the stator of analysis model is performed. Fig. 1 shows that circumferential mode (m) 2 and 3 of the stator with resonant frequency. And then, center frequencies and band widths for 1/3 octave band based on modal analysis for stator are designated.

Secondly, exciting forces, which are composed of tangential and normal force, on the stator tooth versus rotor position are calculated by using the equivalent magnetizing current (EMC). And then, the harmonic components of exciting forces are calculated through harmonic analysis. It is shown in Fig. 2.

Thirdly, harmonic component of tangential and normal force versus harmonic order is assigned at the surface of tooth, respectively. It is shown in Fig. 3. It should be considering phase difference because each the harmonic component according to the change of rotor position is changed such as sinusoidal.

Finally, the quantity of deformation of stator yoke is calculated by harmonic analysis using the harmonic components of exciting force and the result of deformation of stator yoke as shown in Fig. 4. And then, the quantity of deformation of stator yoke in the band widths is summated.

The analysis results and comparisons of measured acceleration and acoustic noise will be presented in extended paper.

V. REFERENCES

- [1] M. N. Anwar and Iqbal Husai, "Radial Force Calculation and Acoustic Noise Prediction in Switched Reluctance Machines." *IEEE Trans., on Ind. Applicat.*, Vol. 36, No. 6, pp. 1589-1597, Nov./Dec. 2000
- [2] Jacek F. Gieras, Chong Wang, Joseph Cho Lai, *Noise of Polyphase Electric Motors*, CRC press, 2006.
- [3] Sang-Ho Lee, Jung-Pyo Hong, Sang-Moon Hwang, Ji-Young Lee, Young-Kyoun Kim "Optimal Design for Noise Reduction in Interior Permanent Magnet Motor," *Industry Applications Society 41th Annual Conference Paper*, Oct., 2006.
- [4] Matthew N. O. Sadiku, *Elements of Electromagnetics*, Oxford Univ. press, 2001

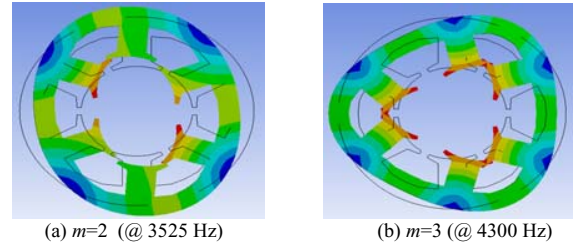


Fig. 1. Circumferential mode $m=2, 3$ of the stator

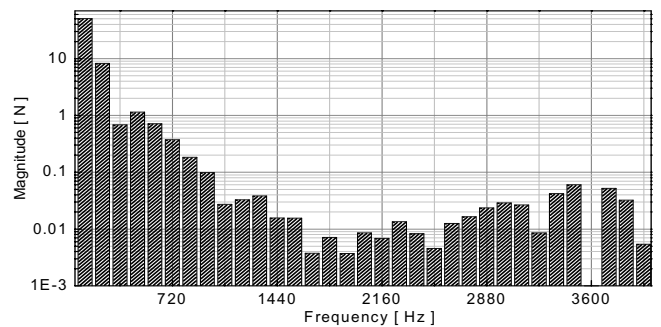


Fig. 2. The harmonic components of normal force

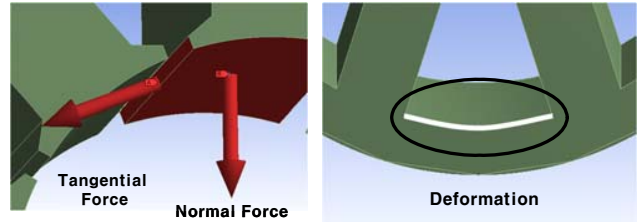


Fig. 3. Parts which is assigned exciting force and is calculated the quantity of deformation of stator yoke

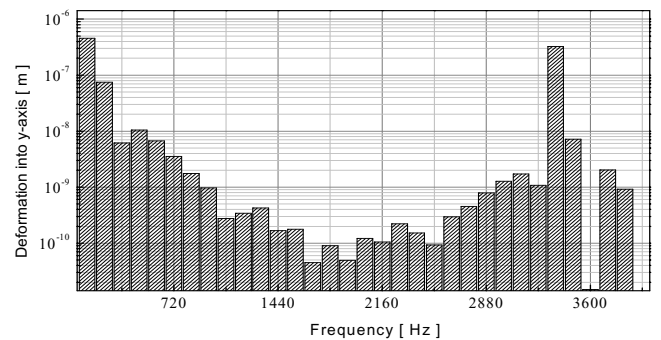


Fig. 4. The quantity of yoke deformation versus the harmonic components of normal force

Analysis of Vibration and Music Scale of Brushless DC Motor with Surface Permanent Magnets

Takeo Ishikawa, Satoshi Azami, and Ryo Ataka
 Gunma University
 1-5-1 Tenjin-cho, Kiryu, Gunma, 376-8515, Japan
ishi@el.gunma-u.ac.jp

Abstract — This paper investigates the vibration and musical scale emitted from the brushless DC motor by introducing the d-axis current with a sound frequency. First we analyze the vibration acceleration of the motor and verify the calculation method by comparing with the measured ones. Next, we clarify the vibration characteristics by changing the sound frequency, the motor speed and the output power.

I. INTRODUCTION

Brushless DC motors with permanent magnets are widely used in industrial applications and computer peripheral devices, and they become smaller size and higher power by use of high-grade magnet. Since the permanent magnet is higher grade and the encasing is less stiff, the motor becomes more sensitive to the vibration and acoustic noise. Several papers have been published on the vibration and acoustic noise emitted from the brushless DC motor. For example, the vibration and noise of the interior permanent magnet motor have been analyzed by finite element method [1], [2], and an active noise control have been proposed to cancel the acoustic noise by adding the other noise with a phase shifted by π [rad] [3]. However, the perfect reduction of noise is very difficult.

The authors have proposed a method to convert the meaningless electromagnetic noise into a comfortable melody, and have emitted experimentally a desired melody by sequentially generating the musical scale from a brushless DC motor [4]. This paper investigates numerically the vibration and musical scale emitted from the brushless DC motor fed by a PWM inverter. First we analyze the vibration acceleration of the motor, and compare with the measured vibration acceleration and musical scale. Next, we clarify the vibration characteristics by changing the sound frequency, the motor speed and the output power.

II. ANALYSIS METHOD

The d-axis current of the brushless DC motor with surface permanent magnets (SPM) is usually controlled to be 0, because the output torque can be linearly controlled by the q-axis current. However, the sinusoidal d-axis current can generate the sinusoidal flux density, resulting in the sinusoidal radial magnetic force and then the sinusoidal vibration. Therefore, the authors have proposed the generation method of the musical scale from the brushless DC motor with SPM by controlling the d-axis current as follows,

$$i_d = I_s \sin(2\pi f_s t) \quad (1)$$

where f_s is a sound frequency.

In this paper, we investigate theoretically the vibration and musical scale emitted from the brushless DC motor. First, the magnetic field in an experimental brushless DC motor is calculated by 2D non-linear finite element method, and the electromagnetic force is calculated by the Maxwell's stress tensor method. Next, the vibration acceleration of the motor is calculated by solving the following equation with 2D finite element method.

$$[\mathbf{M}]\{\ddot{x}\} + [\mathbf{C}]\{\dot{x}\} + [\mathbf{K}]\{x\} = \{f\} \quad (2)$$

where, $\{x\}$ is the node displacement, $\{f\}$ is the electromagnetic force, and $[\mathbf{M}]$, $[\mathbf{C}]$ and $[\mathbf{K}]$ are the global mass matrix, viscous friction matrix and stiffness matrix, respectively.

III. SIMULATION AND MEASUREMENT

The experimental motor used for verification purpose has 1kW power, 4 pole-pairs and 7.8A stator current. Fig.1 shows the calculated vibration acceleration when $f_s = 349\text{Hz}$ corresponding to a music scale of "fa", and the motor speed is 675min^{-1} , that is, the rotating frequency $f_m = 90\text{Hz}$. There are big vibration accelerations at the frequency of $2pf_m$, f_s and $f_s \pm 2pf_m$, where p is the number of pole pairs. Fig.2 shows the measured vibration acceleration and sound. The vibration acceleration was measured with a piezoelectric accelerometer placed at the top of the stator and a preamplifier and a signal analyzer. The sound was measured with a noise level meter and the signal analyzer. Fig.2 (a) shows the measured vibration acceleration when $i_d = 0$. There are many peaks at npf_m and mf_{source} , where f_{source} is the frequency of the line source 50Hz and n and m are the integer. Fig.2 (b) shows the vibration acceleration when $i_d = I_s \sin(2\pi \times 349t)$. We can find the big vibrations at $f_s = 349\text{Hz}$ and 481Hz. The frequency of 481Hz is $f_s + 12f_m$, therefore it is the frequency of rotor vibration, which is produced by the number of stator slots 12 and the sound frequency. It is shown from fig.2(c) that there is a big sound at the frequency of "fa". Therefore, the simulation has verified that the d-axis current with a sound frequency generates the musical scale.

Fig.3 shows the vibration acceleration by changing the sound frequency f_s . It is shown that this motor can generate bigger vibration acceleration and thus bigger sound at higher sound frequency. Fig. 4 shows the vibration acceleration by changing the motor speed. It is shown that the vibration acceleration does not depend on the motor speed very much, if

the rotating frequency does not match or close to the sound frequency.

IV. CONCLUSIONS

This paper has analyzed the vibration acceleration of the brushless DC motor, and has verified that the d-axis current with sound frequency generates the musical scale. In addition, a desired melody can be generated by sequentially generating the musical scale, and the generation of musical scale does not affect the speed response of the brushless DC motor with SPM.

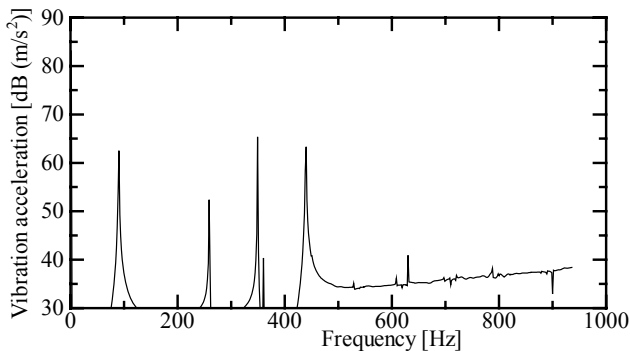


Fig. 1. Spectrum of the calculated vibration acceleration when $i_d = I_s \sin(2\pi \times 349t)$

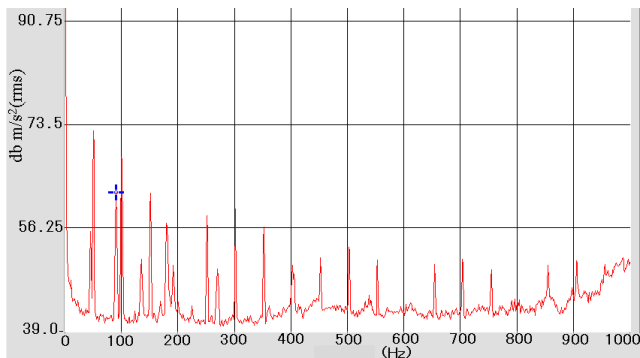


Fig. 2 (a). Spectrum of the measured vibration acceleration when $i_d = 0$

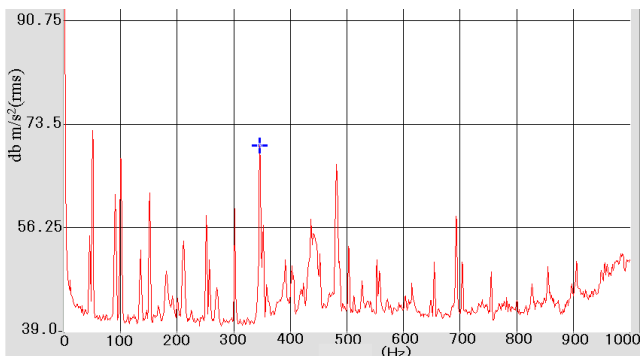


Fig. 2 (b). Spectrum of the measured vibration acceleration when $i_d = I_s \sin(2\pi \times 349t)$

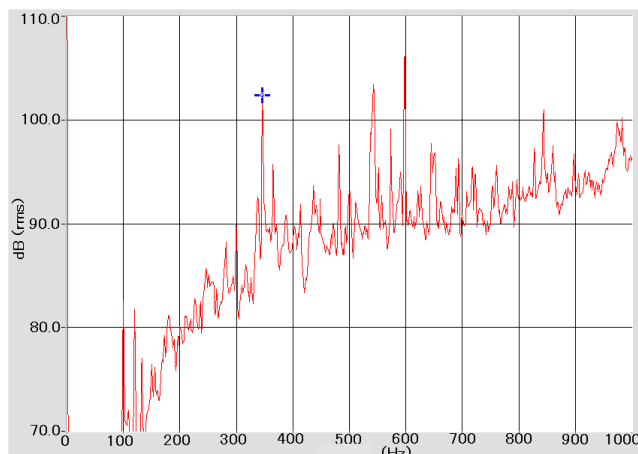


Fig. 2 (c). Spectrum of the measured sound when $i_d = I_s \sin(2\pi \times 349t)$

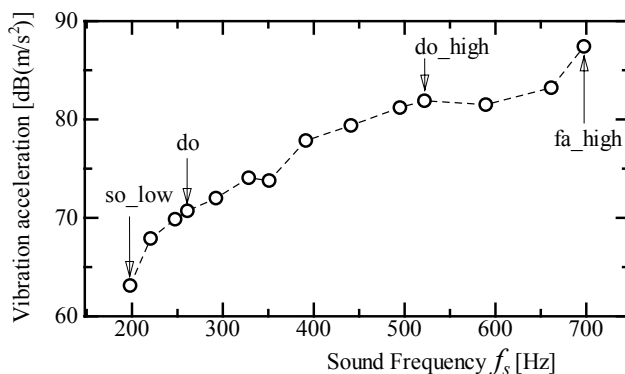


Fig. 3. The vibration characteristics by changing the sound frequency

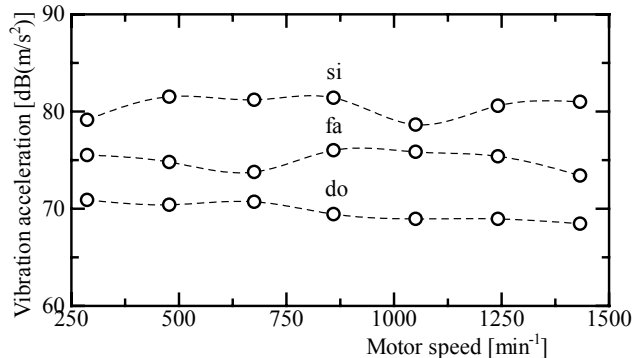


Fig. 4. The vibration characteristics by changing the motor speed

V. REFERENCES

- [1] H. Inaba, T. Ishikawa, M. Matsunami, "Comparison of Vibration Characteristics of Several Interior Permanent Magnet Synchronous Motors", *The 2008 Annual Meeting Record IEE Japan* [5], pp.48-49, 2008.
- [2] H.S. Ko, K.J. Kim, "Characterization of Noise and Vibration Sources in Interior Permanent-Magnet Brushless DC Motors", *IEEE Trans on Mag*, 40 (6), pp.3482-3489, 2004.
- [3] Nishimura, *Journal of INCE/J*, 27 (4), pp.223-225, 2003.
- [4] R. Ataka, T. Ishikawa, and M. Matsunami, "Generation method of a music scale by brushless DC motor", *J. of the Japan Society of Applied Electromagnetics and Mechanics*, to be published.

Internal Faults Simulation and Analysis for Linear Synchronous Motor

Fang Yu¹, Haitao Yu¹, S.L. Ho² and Minqiang Hu¹

¹School of Electrical Engineering, Southeast University, Nanjing, 210096, P.R. China

²Department of Electrical Engineering, Hong Kong Polytechnic University, Hong Kong
htyu@seu.edu.cn

Abstract—A novel model based on winding function theory are presented for the simulation of major internal faults in the long-stator linear synchronous motor (LSM) of maglev train. The potential internal faults of LSM generally contain single-phase, double-phase short circuit and single-phase open circuit, etc. When different fault occurs, the impedance matrix related to inductance is accurately computed with winding function. Through the comparison of the simulation results under different fault conditions, the proposed method has showed that it is useful to diagnosis of internal faults.

Index Terms—Winding function, linear synchronous motor, internal faults.

I. INTRODUCTION

High-speed maglev train system is a new transportation system which first appeared in Shanghai for the commercial use in 2003. The advantages over its high speed, low noise and non-pollution make it suitable to long distance transportation. However, as the critical technology of maglev train system, the internal faults of long stator linear synchronous motor will cause serious consequences of endangering the passengers on the trains. So quickly simulating and diagnosing the faults of LSM become very important to prevent from extensive failure and make preparations for further uses.

In order to establish an appropriate mathematical model for LSM, a more accurate method, for calculation of the inductances of windings in the stator and moving parts, is very necessary. Most of the literature introduces the traditional dq0 model, but it's not suitable for the stator internal faults modeling. So this paper presents a new method based on winding function theory, which can take into account of the effect of all space harmonics and the asymmetry armature windings in case of internal faults of LSM. In the fault conditions, the faulty armature phase can be separated into two or three parts to simulate the effects brought by faults so that the fault models can easily be established.

The paper is arranged as follows. In section II, a new formulation for inductances calculation is derived and the voltage equations under normal condition are set up based on the winding function theory. In section III, the current waveforms under three kinds of internal faults are obtained by calculating the corresponding inductance matrix and linear equations. The results show that electromagnetic forces are not stabilized under internal fault conditions.

II. SIMULATION MODEL

A. Winding function theory

In a conventionally rotational machine, the mutual inductance of two armature windings a and b can be written, using winding function, as follows [1]-[4]:

$$L_{ab} = \mu_0 r l \int_0^{2\pi} g^{-1}(\varphi, \theta) N_a(\varphi, \theta) N_b(\varphi, \theta) d\varphi \quad (1)$$

where μ_0 is the permeability of air, r is the average radius of the air-gap, l is the axial stack length of the armature, and $g^{-1}(\varphi, \theta)$ is the inverse air-gap length function, $N(\varphi, \theta)$ is the winding function. In the case of LSM, equation (1) should be modified, because the winding function of LSM isn't the function of the rotor angle any more but the function of the relative position of the secondary. It can be expressed as $N(x, x')$, which is the function of displacement of the stator and mover, the inverse air-gap function should be modified accordingly. The modified formula is used to calculate the self inductances of LSM and the mutual inductances between stator and excitation windings, shown in fig.1.

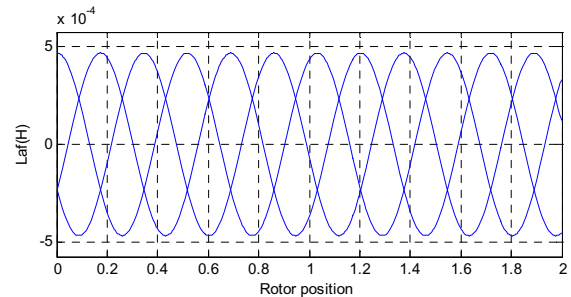


Fig. 1 The mutual inductances between stator and excitation windings

B. Voltage equation

For the purpose of establishing the exact coupled mathematical model for LSM, we need to make some appropriate simplifications such as neglecting the effects of iron saturation and magnetic hysteresis. Under the normal condition, the LSM is usually described as a system with three-phase circuit loops in stator and an excitation loop in the secondary. The voltage equations of LSM can be written as:

$$[U] = [R][I] + [L] \frac{d}{dt} [I] + \frac{d}{dt} [L][I] \quad (2)$$

And

$$L = \begin{bmatrix} L_{aa} & L_{ab} & L_{ac} & L_{af} \\ L_{ab} & L_{bb} & L_{bc} & L_{bf} \\ L_{ac} & L_{bc} & L_{cc} & L_{cf} \\ L_{af} & L_{bf} & L_{cf} & L_{ff} \end{bmatrix}, \quad R = \begin{bmatrix} r & 0 & 0 & 0 \\ 0 & r & 0 & 0 \\ 0 & 0 & r & 0 \\ 0 & 0 & 0 & r_f \end{bmatrix}, \quad I = \begin{bmatrix} i_a \\ i_b \\ i_c \\ i_f \end{bmatrix}$$

where the inductance matrix contains the self and mutual inductances between the armature windings and the mutual inductances between armature and excitation windings.

Equation (2) can also be written as:

$$\frac{dI}{dt} = -[L^{-1}(R + \frac{dL}{dt})]I + L^{-1}U \quad (3)$$

With substituting the corresponding calculated inductance and resistance parameters into (3), the differential equation can be solved by using the numerical integration method, and hence the current waveforms, the propulsion and the levitation forces can all be obtained. When the internal fault occurs, we only need to recalculate the inductance and resistance matrix according to the different fault type and the short circuit ratio, but the mathematical model keeps the same, the simulation results in section III are derived from this method.

III. SIMULATION RESULTS

It's likely to occur three typical types of internal fault in LSM, single-phase and double-phase short circuit and single phase open circuit. As an example, the double-phase short circuit is discussed here. The internal fault voltage equation can be described as:

$$[U'] = [R'] [I'] + [L'] \frac{d[I']}{dt} + \frac{d[L']}{dt} [I']$$

$$\text{where } [U'] = [U_a, U_{b1}, U_{b2}, U_{c1}, U_{c2}, U_f]^T \quad (4)$$

$$[I'] = [I_a, I_{b1}, I_{b2}, I_{c1}, I_{c2}, I_f]^T$$

An equivalent circuit of the faulty coil is formed. The corresponding inductance matrix should be recalculated due to the short circuit ratio of phase bc .

Fig.2 shows us the current waveforms, the propulsion and the levitation forces under 50% double-phase short circuit. And with the increment of short circuit ratio, the amplitude of the waveforms increases and the harmonic components also strengthen. The more the number of short turns is, the more differences can be observed between normal phase and faulty phase. These simulation results are the basis of analysis of further fault diagnosis.

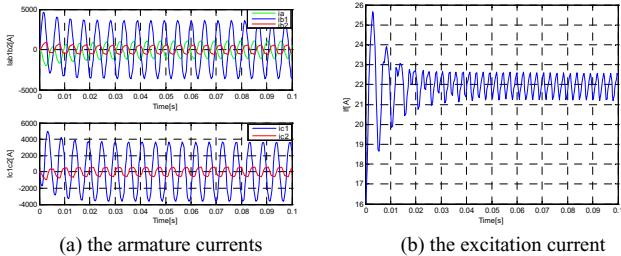


Fig .2 The simulation results of the 50% ratio of double-phase short circuit currents

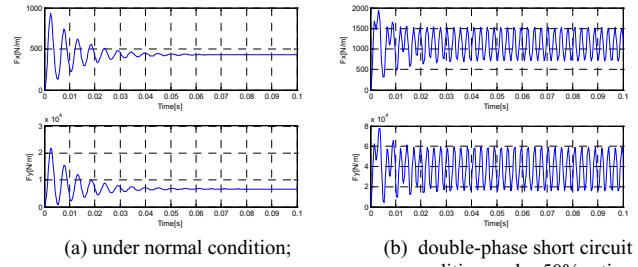


Fig .3 The simulation results of the propulsion and levitation forces

In Fig.3 (a), it can be seen that when the maglev train system operates in steady-state, that is to say the speed and the system power angle keep constant, the propulsion and levitation forces also tend to stabilize. However, the electromagnetic force can't keep stable when double-phase short circuit occurs shown in Fig.3 (b).

According to the simulation results of LSM under normal and internal faults conditions, the fault law can easily be found. Whatever the fault happens, the waveforms of fault currents and electromagnetic forces all appear a certain extent oscillation. Through specific wavelet packet transforming, the harmonic components can be obtained, which can also be used for fault diagnosis.

IV. CONCLUSIONS

In this paper, a useful internal fault model is proposed based on the winding function theory. This method has distinctive advances compared to the previous ones. The calculation of the impedance matrix mainly including inductances under normal and internal fault conditions is not only simpler but also accurate. Furthermore, the programmed software package for LSM internal fault simulation and analysis can realize the man-machine conversation.

V. REFERENCE

- [1] Xiaoping Tu, Louis-A.Dessaint, Nicolas Fallati, etal. "Modeling and Real-Time Simulation of Internal Faults in Synchronous Generators With Parallel Connected Windings" [J]. *IEEE Trans on industrial electronics*. Vol, 54. No.3, Jun 2007,pp:1400-1409
- [2] Iman Tabatabaei, Jawad Faiz, Lesani, et.al. "Modeling and Simulation of a Salient-Pole Synchronous Generator With Dynamic Eccentricity Using Modified Winding Function Theory". *IEEE Trans on magnetics*. Vol, 40. No. 3, May 2004,pp:1550-1555
- [3] N. A. Al-Nuaim H.A. Toliyat, "Simulation and Detection of Dynamic Air-Gap Eccentricity in Salient-Pole Synchronous Machines"[J].*IEEE Trans. on Industry Applications*, Vol. 35, No. 1, Jan/Feb 1999,pp. 86-93.
- [4] Hamid A. Toliyat, Shailesh P. Waikar, Thomas A. Lipo, "Analysis and Simulation of Five-Phase Synchronous Reluctance Machines Including Third Harmonic of Airgap MMF".*IEEE Trans. on Industry Applications*, Vol. 34, No. 2, Mar/Apr 1998,pp. 332-339.
- [5] V.A.Kinisty. " Calculation of Internal Fault Currents in Synchronous Machines".*IEEE Trans PAS*, Vol.84, No.5, 1965: 381~389
- [6] N. L. Shmitz and D.W. Novotny, *Introductory Electromechanics*[M]. New York: Roland, 1965.

Effects of Magnetic Saturation on Spindle Motor Characteristics

Jaenam Bae, Seung-Joo Kim, Sung-Chul Go, Dong-Woo Kang, Sang-Hwan Ham, and Ju Lee
 Hanyang University
 17 Haengdang-dong, Sungdong-gu, Seoul, 135-111, South Korea
 Baejn81@hanyang.ac.kr

Abstract — In spindle motor for disk memory devices, constant torque is very important. There are three kinds of source for the torque ripple viz. harmonics, cogging torque, reluctance torque. Because the motor has uniform airgap and a permanent magnet for the motor is magnetized on the special fixture, the effect of harmonics and reluctance torque is not considerable but cogging torque is the most influence to the torque ripple. However, when the ferromagnetic material is saturated, we get unexpected results such as torque fluctuation. In this paper, effect of magnetic saturation on spindle motor is presented. FPM is used to consider the saturation in FEA simulation.

I. INTRODUCTION

M brushless DC motors are widely used for the spindle motor in disk memory devices such as a CD-ROM drive system. In current disk drive system, the motor with slotted laminations and NdFeB magnets is the most common for use as the spindle motor [1]. Because an ODD speed and torque characteristics depends on spindle motor, it is very important the spindle motor has constant torque independent of the rotor position.

There are three sources for torque pulsation. First is the field harmonic torque due to non-ideal spatial distribution of flux density in the airgap and another is cogging torque or detent torque and third is reluctance torque, produced due to unequal reluctances of the d- and q- axis [2]–[4]. Because a magnet for the spindle motor is magnetized very sinusoidal, spatial distribution of flux density in the airgap is also sinusoidal. Moreover most of them have a fractional pole-slot combination which results in filtering high frequency component of induced voltage. Besides it has uniform airgap and equal reluctances of the d- and q-axis therefore it doesn't have reluctance torque. In conclusion, the most important source in the spindle motor is cogging torque in three of them.

There are several researches about cogging torque reduction in [5][6]. However they don't take into account magnetic saturation. As known, an important part of electrical machines is made of ferromagnetic materials. These materials consist of nonlinear magnetic characteristics. When the total magnetic motive force in the machine increases saturation of the ferromagnetic parts appears [7]. The result of the saturation effects is a variation of the stator and rotor inductances. For an optimized design of electrical machines, it needs designing the machines near the saturation point. Therefore the magnetic saturation effects should be considered.

Kwak et al. suggests Fixed Permeability Method (FPM) to get more accurate motor parameters (d- and q-axis inductance,

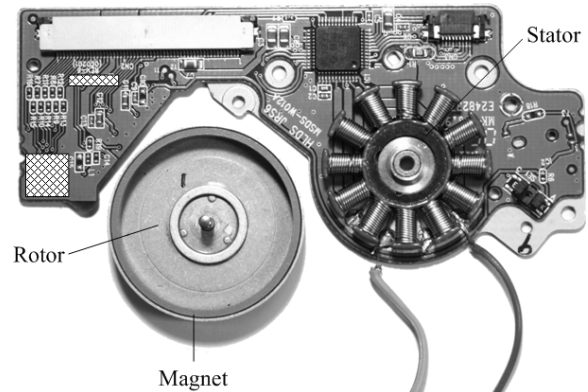


Fig. 1. Spindle motor for the study. It has 16 poles and 12 slots

back-EMF constant) by dividing the total magnetic flux linkage into the flux linkage due to the PM and to the stator current in [8]. The method can be also applied in a magnetic saturation effects. In this paper, an effect of the magnetic saturation on the motor characteristics is investigated using the FPM.

II. STUDY MODEL

Fig. 1 shows the spindle motor for the study. The motor has 16 poles and 12 slots and the NdFeB bonded magnet is mounted on the rotor inner surface. Ring magnet is used for cost reduction and it is magnetized on a special magnetizing fixture for sinusoidal distribution. Actually the magnet has both of radial and tangential components on its body, but only radial component is considered in the study because influence of the tangential component is very lower than that of the radial component. The radial component of the magnetization is defined as (1)

$$M_r = \frac{B_r}{\mu_0 \mu_r} \cos\left(\frac{N_p}{2} \theta\right) \quad (1)$$

where μ_0 and μ_r is permeability of the free space and relative permeability of the magnet respectively, B_r is residual flux density of the magnet and N_p is the number of poles.

III. TORQUE CONSIDERING MAGNETIC SATURATION

Voltage equation for a phase is given by

$$v = Ri + e$$

$$\therefore e = \frac{d\lambda}{dt} = \frac{d\lambda}{d\theta} \frac{d\theta}{dt} + \frac{d\lambda}{di} \frac{di}{dt} \quad (2)$$

where e is back-EMF, R is a resistance of the phase and λ is a flux linkage.

The flux linkage λ is varying to the rotor position but not to the current when magnetic saturation is not considered. However, in condition of saturation, λ is varying to the current and it makes distortion of back-EMF. Output power is a product of back EMF and input current thus it makes torque ripple. The effects of saturation can be considered by fixed permeability method (FPM). The procedure is presented below.

1. Calculating permeability when motor operates in given condition.
2. Calculating torque remaining only field excitation sources with the permeability calculated previously.

Fig. 2 shows torque waveform considering magnetic saturation. In the figure, torque produced by input current is not considered but only represent torque by permanent magnet with saturation core. Negative torque is produced when the core is saturated by input current. This can be explained with the Fig. 3. In the figure, the rotor is positioned to the 3.75 deg and therefore the tooth in a circle is aligned to the center of two poles. In the condition of unsaturated, the tooth has symmetric flux distribution.

Force on an object is calculated by

$$F = \left. \frac{dW(s,i)}{ds} \right|_{i=const} = \frac{\partial}{\partial s} \left[\int_V \left(\int_0^H \mathbf{B} \cdot d\mathbf{H} \right) dV \right] \quad (3)$$

where $W(s,i)$ is the magnetic coenergy of the system. The current, i , is held constant.

Calculating force on the rotor including permanent magnet, it is canceled by symmetry condition. But in case of saturated condition, the distribution is not symmetric. Right side of the tooth is more saturated than left side therefore the rotor has attraction force to the right direction and negative torque is produced.

IV. REFERENCES

- [1] C. C. Hwang, S. B. John and S. S. Bor, "The Analysis and Design of a NdFeB Permanent-Magnet Spindle Motor for CD-ROM Drive", IEEE Transactions on Energy Conversion, Vol. 14, No. 4, pp.1259-1264, December 1999.
- [2] T. L. Skvarenina, The Power Electronics Handbook. West Lafayette, IN: Purdue University, CRC Press, 2002.
- [3] S. Meier, "Theoretical design of surface-mounted permanent-magnet motors with field-weakening capability," M.S. thesis, Royal Inst. Technol., Stockholm, Sweden, 2002.
- [4] T. M. Jahns and W. L. Soong, "Interior permanent-magnet synchronous motors for adjustable-speed drives," IEEE Transactions on Industry Applications, vol. IA-22, no. 4, pp. 738-747, Jul./Aug. 1986.
- [5] D. H. Kim et al., "Optimal shape design of iron core to reduce cogging torque of IPM motor," IEEE Transactions on Magnetics, vol. 39, no. 3, pp. 1456-1459, May 2003.

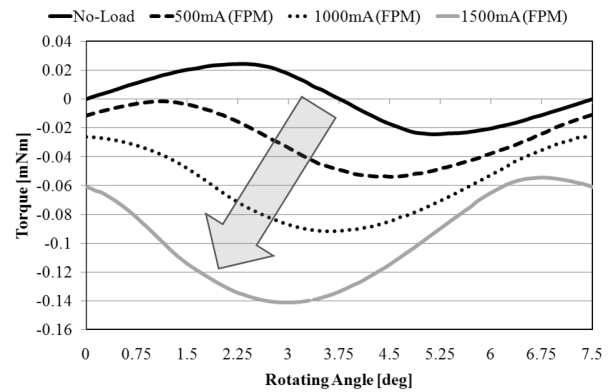


Fig. 2. Torque waveforms considering magnetic saturation. The effects of external current are not considered but only torque by the magnet with saturated core is represented.

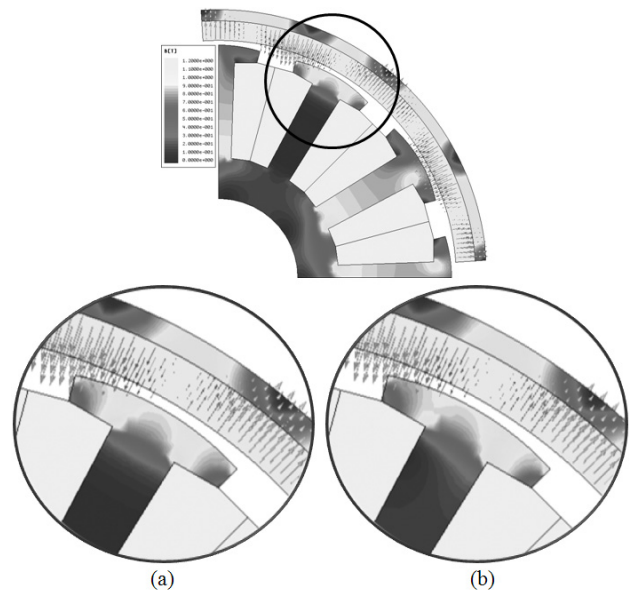


Fig. 3. Flux distribution under the condition of (a) unsaturated and (b) saturated

- [6] J. H. Lee et al., "Minimization of higher back-EMF harmonics in permanent magnet motor using shape design sensitivity with B-spline parameterization," IEEE Transactions on Magnetics, vol. 39, no. 3, pp. 1269-1272, May 2003.
- [7] Thierry Lubin, Hubert Razik, Member, IEEE, and Abderrezak Rezzoug, "Magnetic Saturation Effects on the Control of a Synchronous Reluctance Machine", IEEE TRANSACTIONS ON ENERGY CONVERSION, VOL. 17, NO. 3, pp.356-362, SEPTEMBER 2002
- [8] Sang-Yeop Kwak et al., "Characteristic Analysis of Multilayer-Buried Magnet Synchronous Motor Using Fixed Permeability Method," IEEE Transactions on energy conversion, vol. 20, no. 3, pp.549-555, Sep. 2005.

The Optimal Design of the Secondary Reaction Plate Shape of Single-Sided Linear Induction Motor for Urban Maglev Train

Sang-Hwan Ham, Sung-Gu Lee, Su-Yeon Cho, Chang-Sung Jin, and Ju Lee
 Department of Electrical Engineering, Hanyang University
 17 Haengdang-dong, Seongdong-gu, Seoul, 133-791, Korea
 goodhami@hanmail.net

Abstract — The edge effect of the secondary reaction plate is influenced on performances of single sided linear induction motor (SLIM). Considering shapes of the secondary reaction plate, it will be optimized thrust force and efficiency-power factor product of SLIM. Thickness and overhang length of reaction plate are weighty design factors for optimal design. For the optimal design, magnetic equivalent circuit is used [1]. Two and Three dimensional finite element analysis is applied for validation of design parameter. And SLIM testing machine is used for validity of design optimization.

Introduction

In recent decades, there have been many researches for a linear motor in urban maglev. And single-sided linear induction motor (SLIM) with reaction plate that covered the secondary solid or laminated core is widely used for propulsion in urban maglev because of its linear motion characteristics [2]. SLIM for railroad system can provide higher efficiency of the total system and smaller construction cost in tunnel than traditional system.

Conventional trains using a rotational motor are faced with difficulty for complicated structure of power transmission from rotational torque to linear thrust force. As rapid development of power electronics and switching devices, SLIM replace the rotating motors with a gear. However SLIM have unique characteristics like a longitudinal end effect and a transverse edge effect. Because of these reasons, the optimal design of SLIM is very difficult. In this paper, we will archive the optimal design for high thrust force and efficiency-power factor product by reducing a transverse edge effect. Main influence of a transverse edge effect is increasing the equivalent resistance of secondary reaction plate. And in general, length of reaction plate is longer than length of primary core. Eddy current of surface on secondary reaction plate is non-uniform by transverse edge effect (Fig.1).

I. METHODS FOR OPTIMIZATION

Many methods for optimization of SLIM are existed. Among of them, we analyze the characteristics by changing shapes of the secondary reaction plate. Shape of reaction plate affects performance through changes in the effective secondary impedance [3]. The secondary impedance, consist of impedances both reaction plate and secondary core, is determined from the electromagnetic field distribution at the surfaces of that [4]-[5]. Thrust force and efficiency – power

factor product of SLIM are usually the most important performances in urban maglev train, thus the optimal design is focused on these two characteristics by changing of reaction plate shape. Thickness and overhang length of reaction plate are important design factors for optimal design..

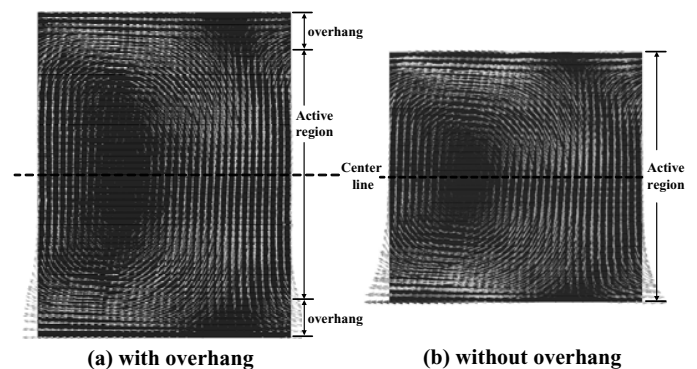


Fig. 1 Overhang effect on secondary reaction plate

And Using single-stator test, no-load test, and blocked-rotor test by 2D FEM analysis, we estimated the parameters of equivalent circuit of a common induction motor. Winding resistance and leakage reactance of primary is calculated by single-stator test. By no-load test, magnetizing reactance is estimated. And winding resistance and leakage reactance of secondary is calculated by blocked-rotor test.

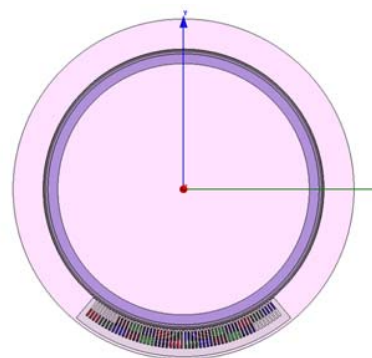


Fig. 2 2D FEM model of LIM

And design of experiments is applied for optimizing design factors. Design specifications of LIM are shown in table I. For analyzing the equivalent circuit, 2D FEM model (Fig.2) is applied.

II. VARIATION OF DESIGN PARAMETER

For validation of design parameters, the two dimensional (2D) and the three dimensional (3D) finite element analysis (FEM) is applied. The 2D FEM is used for analyzing the influence by changing the thickness of reaction plate, because the 3D FEM is very complicated and time consuming. Arc type model is used for matching the testing machine [6]. The 3D FEM is employed to analyze the overhang effect by changing the shape. Fig.3 is the 3D FEM model and this model has only one pole for reducing calculation time. Fig. 4 is shown the LIM testing machine for validity of design optimization. And LIM testing machine is a reduction model in the ratio of ten to one for retrenching the cost and the space. An experiment using LIM testing machine is going in progress with Korea Railroad Research Institute (KRRRI). In the course of time, the results of experiment will be derived and then we will compare the result with simulation.

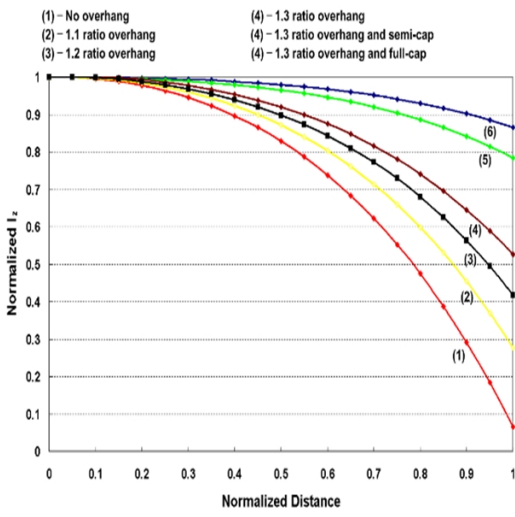
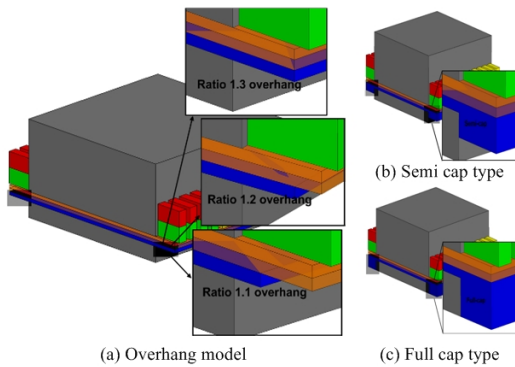


Fig. 3 Three dimensional analysis model of SLIM using different overhang ration and its characteristics

TABLE I
DESIGN SPECIFICATIONS OF LIM

Item	Value	Unit
Continuous rated power of LIM	110.6	kW
Rated frequency	21.2	Hz
Rated Speed	8.333	m/s
Rated slip	0.22	-
Number of phases	3	-
Number of poles	8	-
Length of primary	2181,5	mm
Laminated width	250	mm

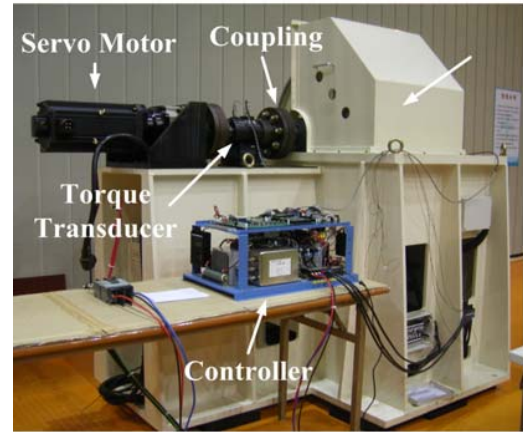


Fig. 4 Testing Machine of LIM

III. REFERENCES

- [1] A. Hassanpour Isfahani, B. M. Ebrahimi, and H. Lesani, " Design Optimization of a Low-Speed Single-Sided Linear Induction Motor for Improved Efficiency and Power Factor", IEEE Transaction on Magnetics, Vol. 44, No. 2., pp 266-272, February 2008.
- [2] S. A. Nasar, and I. Boldea, "Linear motion electric machines", John Wiley & Sons, 1976.
- [3] J. F. Gieras, A.R. Eastham, and G. E. Dawson, "The influence of conductive cap thickness on the performance of single-sided linear induction motors", Electric Machines and Power Systems, pp 125-136, November, 1986.
- [4] J. F. Gieras, A. R. Eastham, and G.E. Dawson, "Performance calculation for single-sided linear induction motor with a solid steel reaction plate under constant current excitation", Electric Power Applications, IEE Proceedings B, pp 185-194, July, 1985.
- [5] E. M. Freeman, "Travelling waves in induction machines : Input impedance and equivalent circuit", Proceeding IEEE, vol. 115, no. 12, pp. 1772-1776, 1968.
- [6] J. Mukolera, and G. R. Slemon, "Calculation of pitch torque for an arc-type linear induction motor", Electric Machines and Electromechanics: An International Quarterly, 4, pp 285-289, November, 1979.

The impact of static eccentricity on rotor bar current distribution in case of one broken bar in Induction Motor

H. Razik, and F.M. Sargos
GREEN, BP 239

F-54506 Vandoeuvre-lès-Nancy, Cedex, France

E-mail: Hubert.Razik@green.uhp-nancy.fr, Francois.Sargos@ensem.inpl-nancy.fr

Abstract — This paper deals with the effect of static eccentricity on the rotor current dispersion when the motor operates with a broken rotor bar. Even if the induction motor has the reputation to be a world-beater for its robustness, such a defect sometimes occurs. Moreover, it presents a natural asymmetry due to the construction of the machine. It can accelerate the damage of the motor, leading it to the breakdown of a process. We only focus our attention on the alteration depending on the eccentricity severity. The study of this type of faulty condition is significant for the condition monitoring of induction motors and for better understanding the ageing acceleration of the motor.

I. INTRODUCTION

Even if the induction motor has been studied for a long time either in healthy or faulty conditions, as far as we know, few or none researches have been made considering the presence of broken bar and static eccentricity. In that case, the induction motor operates in strongly environment. Many researches have been made for the last two decades on the analysis of particular faults, but none on the simultaneous faults. It is obvious that faults generate specific signatures allowing the diagnosis and the estimation of the *State Of Health* (SOH) of the induction motor. They are generally well known in case of an individual fault but the conjunction of two or more faults is actually a huge challenge.

The monitoring of the SOH of the induction motor has been based on the *Motor Current Signature Analysis* (MCSA) for a long time [1]. This is a passive technique in comparison with specific signals injections in the stator current. Nevertheless, all techniques outline on the electric signals due to the magnetic disturbance or magnetic asymmetry in faulty conditions [2-3].

In this paper, we point out the distribution of the rotor bar currents when the motor operates under one broken bar and a static eccentricity. The main idea is to highlight the growing rate of ageing due to the dispersion of the rotor bar currents which depends on the static eccentricity severity.

II. STATIC ECCENTRICITY AND BROKEN BAR

For this study, the induction motor operates at nominal load condition and has one pair pole. The magnetic field distribution is evaluated thanks to the FEMM 4.0 software. It depends on the mechanical dimension of the electric motor and on the material used. The static eccentricity is one of the

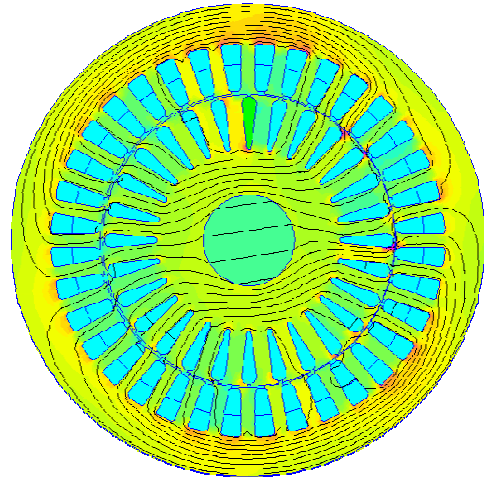


Fig. 1. Magnetic field distribution: the 8th rotor bar is broken and the static eccentricity is equal to 90%

three types which are: static, dynamic and mixed. In case of static eccentricity, the rotational axis of the rotor is a little bit displaced from the stator axis. Consequently, the air-gap is not constant (Fig. 1). The broken bar is showed in green. The entire machine is considered as to obtain the magnetic field because there is no geometrical symmetry.

The diffusion equations for the stator and for the rotor are respectively:

$$j\omega\sigma A + \nabla \times \frac{1}{\mu_r} (\nabla \times A) = \mu_0 J \quad (1)$$

$$j\omega s\sigma A + \nabla \times \frac{1}{\mu_r} (\nabla \times A) = 0 \quad (2)$$

where: μ_r is the relative magnetic permeability, A is the magnetic vector potential, σ is the conductivity of the material, ω is the supply frequency and J is the complex current density. The slip s is considered as equal to 4.6% at the nominal load. A broken rotor bar is considered as an increased value of its resistance. So its conductivity is characterized as being equal to the healthy case divided by a huge scalar. In case of healthy consideration, σ is equal to 4.45Ms/M for the aluminum. The currents flowing in the stator are as follows:

$$i_{A,B,C}(t) = I \cos(\omega t + \varphi_{(0, 2\pi/3, 4\pi/3)}) \quad (3)$$

III. SIMULATION RESULTS

The model of the induction motor as it was established allows an accurate estimation of the magnetic field in the case of mechanical and electrical rotor asymmetry. Moreover, the rotor current distribution clearly appears whatever the rotor fault severity is.

In order to highlight the impact of the eccentricity, we present some relevant figures. The first one (Fig. 2) shows the magnitude of all the 28 rotor bar currents in function of the static eccentricity, which varies from 0% to 95% of the air-gap. The first consequence of the broken bar is the modification of the rotor current distribution at its neighborhood (Fig. 3). Moreover, when static eccentricity occurs, all the rotor current distribution is modified. The greater the eccentricity is, the greater the dispersion is. The dispersion of all rotor bar currents is represented in Fig. 4. It shows that the dispersion could be close to 10% at 95% of static eccentricity. Figure 5 illustrates the dispersion under a different angle of view. As a consequence, rotor bars at the neighborhood of the broken one have higher current and the static eccentricity modifies their values as well. The results obviously depend on the broken bar relatively to the rotating field. There are given here for a quadrature position, which corresponds to the 8th bar.

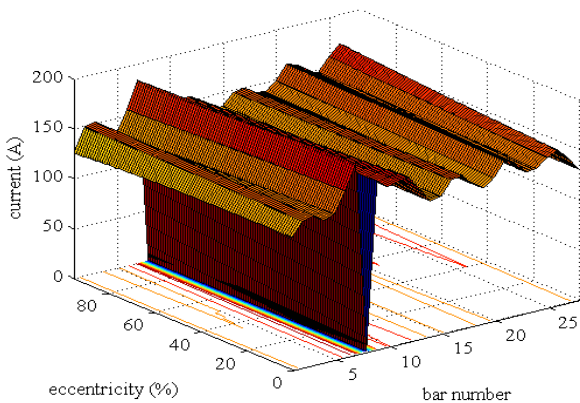


Fig. 2. Module of the rotor bar currents in function of the eccentricity

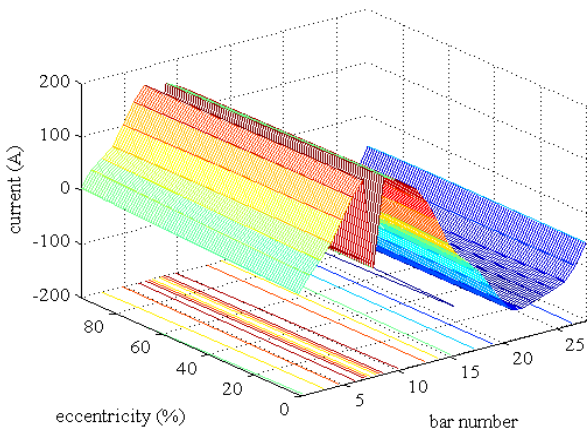


Fig. 3. The rotor bar currents in function of the eccentricity

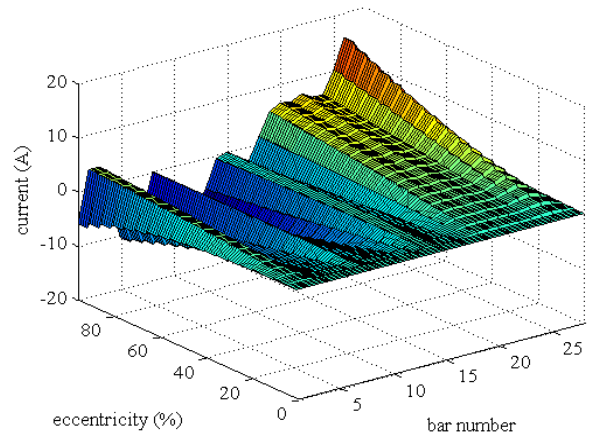


Fig. 4. Dispersion of the rotor bar currents in function of the eccentricity

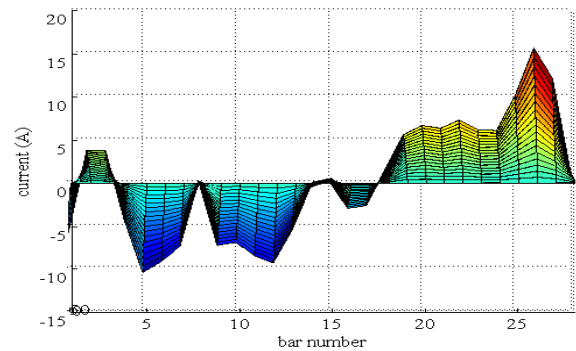


Fig. 5. Dispersion of the rotor bar currents in function of the eccentricity

IV. CONCLUSION

This study emphasizes the influence of the static eccentricity on the currents flowing in each rotor bar in the presence of one broken bar. The magnitude of the current in all rotor bars are altered and more especially at the neighborhood of the broken bar. This study used the software FEMM 4.0 in order to estimate the magnetic field inside the motor and the rotor bar currents. This approach, without discussion, shows that the dispersion of each rotor bar currents is important. As a consequence, the magnetic field distribution and the asymmetric rotor current dispersion in case of static eccentricity accelerate the ageing of induction motor. Thus, other rotor bars will be defective earlier. Consequently, early fault detection is necessary in order to prevent from disastrous failures.

V. REFERENCES

- [1] S. Nandi, R. Bharadwaj, H.A. Toliyat and A.G. Parlos, "Study of Three Phase induction motors with incipient rotor cage faults under different supply conditions", *Proceedings of the IEEE-IAS 1999 Annual Meeting*, vol. 3, pp. 1922-1928.
- [2] R. Fiser and S. Ferkolj, "Magnetic Field Analysis of Induction Motor with rotor Faults", *Proc. ISEF'97*, Gdansk, Poland, pp. 53-56.
- [3] J. Faiz and B.M. Ebrahimi, "Mixed Fault Diagnosis in three-phase squirrel cage induction motor using analysis of air-gap magnetic field", *Progress In Electromagnetics Research*, PIER 64, 239-255, 2006.

Optimum LIM Interval Selection of Vector Controlled Moving Secondary Plate Conveyor System Using FEM & SUMT

Jung Ho Lee, *Member, IEEE*, Tae Hoon Lee, Yong Hyun Cho
 Dept. of Electrical Engineering, Hanbat National University
 Dukmyung-Dong Yuseong-Gu, Daejeon, 305-719, KOREA
 lth5557@naver.com

Abstract — It is necessary to modify the state-of-the-art of speed control theory because of the phase asymmetry in the Linear Induction Motor (LIM) and in order to the constant speed control of mover (aluminum plate) using single vector control inverter system, it is important that primary stack is located in appropriated intervals in the 3D conveyer system using LIM because of control parameters are varied.

The dynamic characteristic analysis method of the vector controlled LIM using coupled FEM and control algorithm taking into account the movement is proposed.

Moreover, in order to obtain the detailed intervals, optimization algorithm, sequential unconstrained minimization technique (SUMT) is used.

The focus of this paper is the analysis relative to selecting primary stack intervals in order to constant speed control in the 3D conveyer system using LIM.

To prove the propriety of the proposed method, the Digital Signal Processor (DSP) installed experimental devices are equipped and the experiment is performed.

I. INTRODUCTION

Linear Induction Motor (LIM) has been developed for use in the industry, transportations, OA, FA, because of the merits of direct drive and simple structure.

This paper deals with the three dimensional conveyer systems for light objects out of the auto conveyer systems.

In this system, since LIM is turn on only when carrier is over it, it can be reduced much energy and obtained many merits of high speed, automation (acceleration and deceleration control, the control of precision position), and removing the power supply cable or lead wire.

For the constant speed control of mover using single vector control inverter system, it is important that primary stack is located in appropriated intervals. And for a LIM, the constants of each phase are different due to the motor structure.

Thus, it is difficult, especially in moving secondary plate system, for the accurate speed control of LIM by the state-of-the-art of rotating machine theory.

The finite element approach has been gaining progressively greater importance than the equivalent circuit method in solution of non-linearity, anisotropy characteristic and motion analysis, especially selecting appropriated motor intervals of this paper, etc.

These approaches, which are coupled with control algorithm and

numerical analysis method, have an interest for researchers now [1]-[3].

In this paper the dynamic characteristic analysis method of the controlled LIM sets of 3D conveyer system using coupled FEM and control algorithm taking into account the movement is proposed and it has been selected a appropriated interval of primary motors in order to constant speed control through the optimization algorithm (SUMT).

II. ANALYSIS MODEL

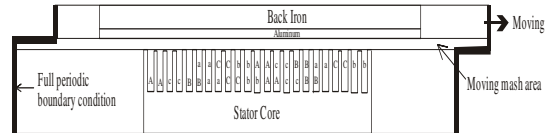


Fig. 1 Analysis model of LIM

The two dimensional model of LIM is shown in Fig.1

The primary stack intervals increasing (2m, 1.6m, 1.2m, 0.8m, 0.6m, 0.4m) are considered by enlarging full boundary condition of both sides to x direction.

The mesh should be changed according to the movement of the mover in moving mesh area. A moving line is introduced to save computing time and to perform the process efficiently in FE analysis.

III. ANALYSIS METHOD

Fig. 2 shows the block diagram of system. Asymmetrical slip angular velocity algorithm is applied to the control logic for the comparison with flux angle of FEM.

The proposed analysis method is applied to the step velocity command (2.0 m/sec) in the vector control logic part using 10(μ sec) sampling time.

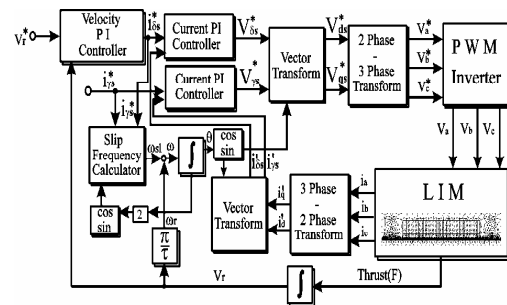


Fig. 2. Block diagram of the system

IV. SIMULATION & DISCUSSION

Fig.3 show the flux plot of analysis model example considered movement out of numerous data.

Fig 4 (a) – (e) shows the primary stack intervals (2m, 1.6m, 1.2m, 0.8m, 0.6m, 0.4m) due to the enlarging full periodic boundary condition of both side.

In the case of each primary stack intervals, it is observed that whereas speed responses highly oscillate as motor intervals is wider, speed responses in the 0.4m and 0.6m motor interval is nearly match constant speed commend 2 m/sec as shown in Fig. 5.

Fig. 6, Fig.7 represents forward-reverse speed response characteristics of each primary stack intervals.

It is observed that whereas speed responses in the 0.4m motor interval is nearly match constant speed commend, others highly delayed as motor intervals is wider and constant speed responses (2 m/sec) in 0.6m motor interval is nearly match, but especially, forward-reverse speed response is delayed as shown in Fig. 6, Fig. 7.

Therefore stator stack interval between 0.4m and 0.6m can be defined as the optimum ones for the speed vector control of the 3D conveyor system.

Moreover, in order to obtain the detailed intervals, optimization algorithm, sequential unconstrained minimization technique (SUMT) is used as shown in Fig. 8.

The more detailed optimum procedure and discusses will be represented in next extended version.

To prove the propriety of the proposed method, the Digital Signal Processor (DSP) installed experimental devices are equipped and the experiment is performed.

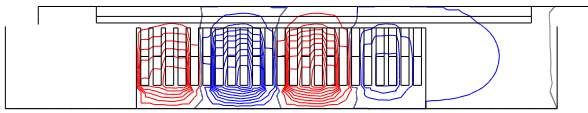


Fig.3. Flux plot example of analysis model considering movement

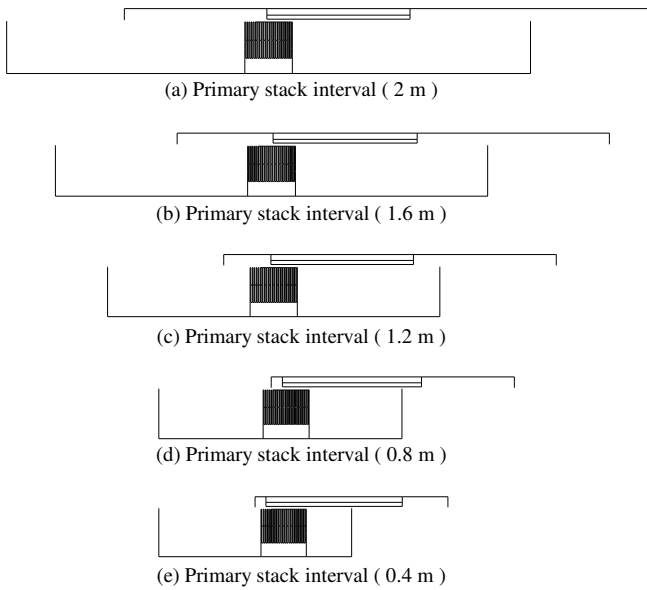


Fig.4. Primary stack interval increasing considering periodic boundary

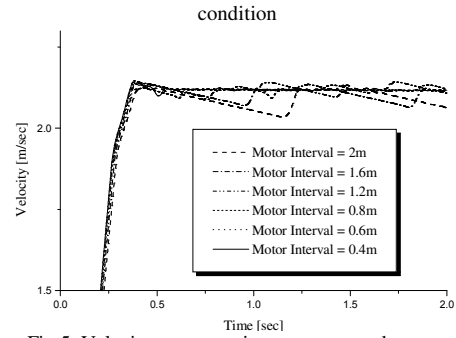
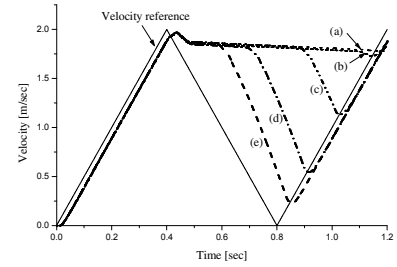


Fig.5. Velocity responses in constant speed commend



(a) Motor interval = 2m (b) Motor interval = 1.6m
(c) Motor interval = 1.2m (d) Motor interval = 0.8m
(e) Motor interval = 0.6m

Fig. 6. Velocity responses in forward-reverse speed commend

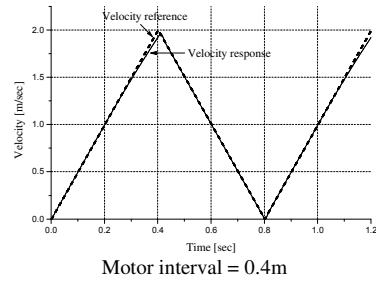


Fig. 7. Velocity responses in forward-reverse speed commend

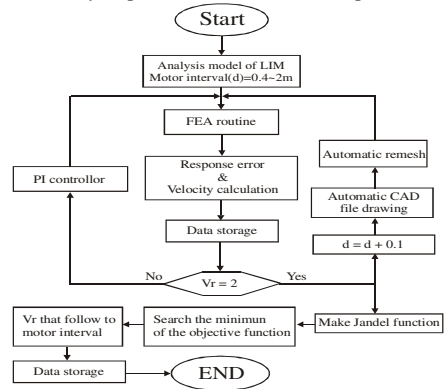


Fig. 8. Flow chart of total design procedure

V. REFERENCES

- [1] D. H. Im and J. H. Lee, "Dynamic characteristics analysis of LIM's vector control using FEM," *Proceedings of LDIA'95*, pp. 307-310, 1995.
- [2] D. H. Im, and C. E. Kim, "Finite element force calculation of a linear induction motor taking account of the movement," *IEEE Trans. on Magnetics*, Vol. 30, No. 5, pp. 3495-3498, 1994.
- [3] J. H. Lee, D. S. Hyun, "Dynamic Characteristic Analysis of LIM Using Coupled FEM & Control algorithm," *IEEE Trans. on Magnetics*, Vol. 36, No. 7, pp 1876-1879, July 2000.

Novel method for analyzing the Permanent Magnet Motors

Sung-Hong Won¹, Cheol-Jick Ree², and Ju Lee³

¹Dept. of Electrical System, Dongyang Technical College
62-160, Gocheck-dong, Guro-gu, Seoul, 152-714, South Korea
sagewide@dongyang.ac.kr

³Dept. of Electrical Engineering, Hanyang University, Seoul, 133-791, SouthKorea
julee@hanyang.ac.kr

²Dept. of Electrical Engineering, Daelim University College, Kyung-gi Do, 431-715, SouthKorea
chjree@daelim.ac.kr

Abstract — This paper suggest a novel magnetic circuit method for simualting permanent magnet motors without time-consuming numerical methods. Generally, because the conventional magnetic circuit method gives us period average values like average torque, average power, getting instantanious characteristics like cogging torques, torque ripples are very hard with the magnetic circuit method. But the convolution operations according to relative angle variations of stator magnetic circuits and rotor magnetic circuits can make considering instantanious values possible. The authors compare the novel mothod with the finite element method and verify the simulation results with the measured cogging torque profile.

I. INTRODUCTION

Since permanent magnets were adopted in motors, many researchers have been studied on the analysis method of motors and the methods can be divided into two ways roughly. The first one is so-called “lumped-sum parameter method” in which method, the magnetic system is considered as a circuit and average magnetic flux values per pole are calculated for obtaining the average torque or power. This method is very convenient and simple to calculate but not easy to get instantaneous torque or back-emf values.

The other method is the distributed parameter methods like finite element method (FEM). This method is suitable for analyzing instantaneous values and can consider the magnetic saturation effect of the iron steel core so that the analysis of motors using this method is getting popular these days. But the method takes a lot more times than the lumped-sum parameter method and needs experiences of experts in the industry[1][2].

For improving these methods, some researchers have studied several new methods like Electro-Magnetic Circuit Network (EMCN) method but this improved method has same problems of taking a lot of times to obtain the results[3].

II. METHOD DESCRIPTION

In this study, the authors proposed a novel method for analyzing permanent magnet motors using divided magnetic circuits and convolution method. This new method can calculate permanent magnet motor characteristics like cogging torque and back-emf values which were considered as very

difficult characteristics to get without using some special methods or techniques.

This method is very powerful because the finite element analysis of the permanent magnet motors which is a laborious and time-taking job cannot be finished in minutes while this method can be done in several minutes.

A pole-pair structural period of motor rotor is divided into several parallel magnetic circuits and the stator magnetic circuits of one tooth period including various airgap permeances are also composed as parallel circuits. The convolution calculation of these two groups of parallel circuit values can give us the motor characteristics of cogging torques or back-emf values.

Fig. 1 shows the HDD spindle motor which uses outer-rotor type permanent ring magnet and back-yoke outside of the magnet.

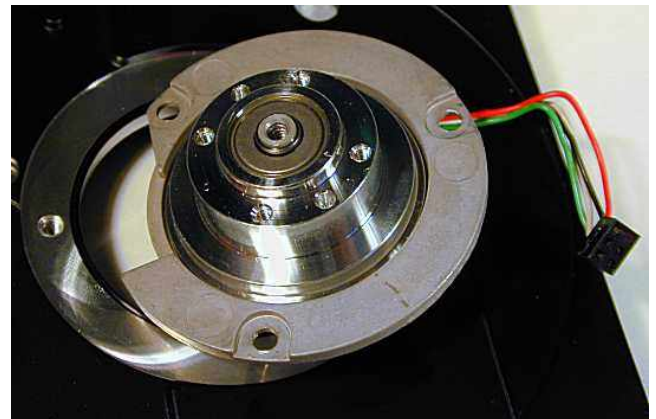


Fig. 1. HDD spindle motor

Fig.2 shows the inside of the spindle motor. There are the stator teeth and the ring-type magnet and backyoke rotor in the spindle motor. To strengthen the mmf of the magnetic circuit and prevent the leakage flux, the backyoke is supposed to be outside of the magnet.

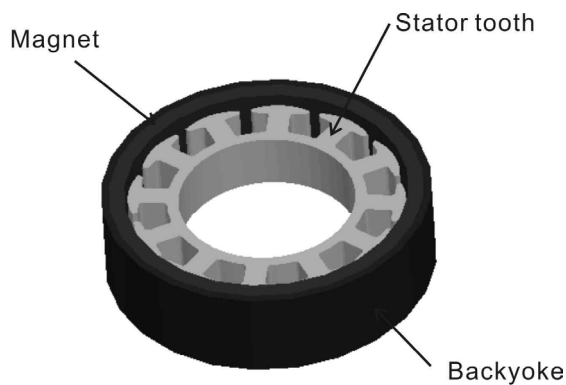


Fig. 2. The stator teeth and the ring-type magnet and backyoke rotor of the spindle motor

Fig.3 shows the stator and rotor magnetic circuits of the spindle motor and concept of convolution method. Because the magnet is not segmented, there are dead-zone between magnet poles and these dead-zone must be considered in analyzing the motor characteristics also.

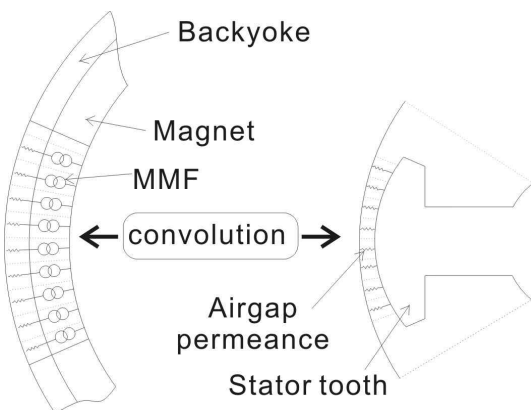


Fig. 3. Stator and rotor magnetic circuits of the spindle motor and concept of convolution method

The most strong point of this method is that when the design parameters are changed, the design result can be obtained very easily. For an example, the cogging torque profile changes can be easily checked out instantaneously when the slot open width(length between a tooth and neighbor tooth) is changed from 1mm to 1.5mm. Fig. 4 shows the calculated cogging torque when the slot open is 1mm and fig. 5 shows the result when the slot open is 1.5mm.

The changes in the magnetization profile and the changes in tooth shape are also can be considered by this method very easily.

The extended paper will contain more detail method and the comparison with the finite element analysis and the measured values.

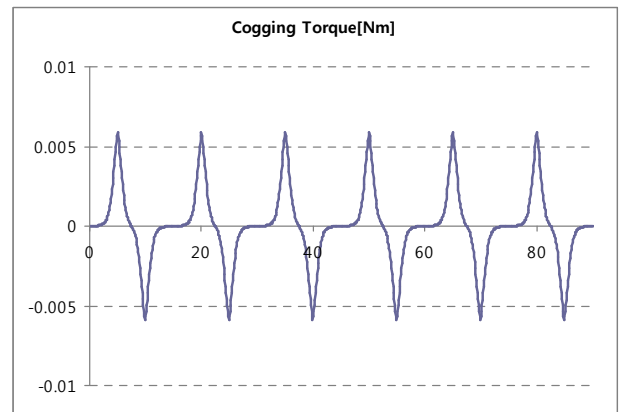


Fig. 4. Calculated cogging torque when the slot open is 1mm.

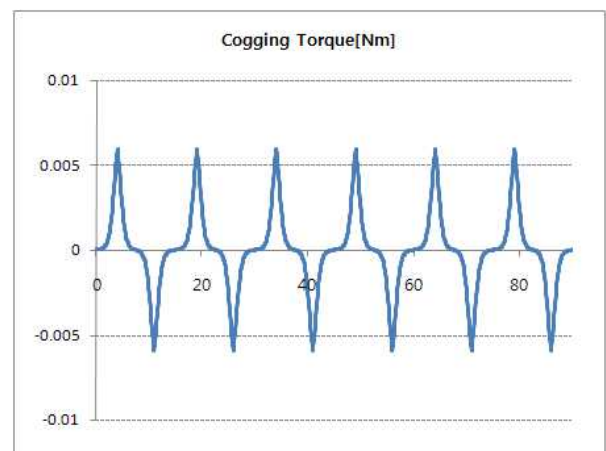


Fig. 5. Calculated cogging torque when the slot open is 1.5mm.

III. CONCLUSION

The permanent magnet motors are very important devices in modern industry. So, it is important to find out new method of predicting the performance of the permanent magnet motors much faster than finite element analysis. This paper is very useful to the researchers who search the method to analyze the permanent magnet motors.

IV. REFERENCES

- [1] Seung-Chan Park, Byung-Il Kwon, Hee-Soo Yoon, Sung-Hong Won, Young-Gyu Kang, "Analysis of Exterior-rotor BLDC Motor Considering the Eddy Current Effect in the Rotor Steel Shell", *IEEE Trans. Magn*, vol. 35, no. 3, pp.1302-1305, May, 1999.
- [2] Seung-Chan Park, Tae-Ho Yoon, Byung-Il Kwon, Hee-Soo Yoon, Sung-Hong Won, "Influence on Brushless DC Motor Performance Due to Unsymmetric Magnetization Distribution in Permanent Magnet", *Trans.on Magentics*, vol.36, no.4, pp.1898-1901, Jun. 2000.
- [3] Yon Do Chun, Jae-Eung Oh, Yasushi Fujishima, Shinji Wakao, Yun-Hyun Cho, Ju Lee, "Comparison between three-dimensional 3D equivalent magnetic circuit network method and 3D finite element method for magnetic-field computation", *Journal of Applied Physics*, vol. 97, no. 10, pp.10E105-10E105-3, May, 2005.

Design of copper die-cast rotor bar of single phase induction motor for high starting torque

Kwangsoo Kim, Jong-Bin Im, Seung-Joo Kim, Won-Ho Kim and Ju Lee, Senior Member, IEEE
 Dept. of Electrical Engineering, Hanyang University
 17 Haengdang-dong, Seongdong-gu, Seoul, 133-791, South Korea
 nicekwangsoo@naver.com

Abstract — This paper describes design of rotor slot of single phase induction motor with copper die-cast rotor cage for high starting torque. We applied die-cast copper rotor cage to single phase induction motor for premium level high efficiency. But Efficiency increases slightly and starting torque is extremely reduced due to higher conductivity of copper rotor bar. Therefore we design the optimal shape of copper rotor bar of single phase induction motor for high starting torque and high efficiency. This study is base on the FEM analysis.

I. INTRODUCTION

Recently the oil price is continuously increasing and the natural resources are getting reducing so that the attention of the energy saving and environmental protection is getting higher. Therefore, it is not a future problem for us to make the motors have a high efficiency. The single phase induction motor is used widely by all the industrial, residential and commercial applications in the present day and we need to develop high efficiency induction motor [1].

In recently, there has been an effort to make high efficiency induction motor. The copper die-cast rotor bar has been also applied to high efficiency induction motor for higher efficiency [2, [3]. In case of single phase induction motor, it needs to have high starting torque as well as high efficiency. But there is trade-off between efficiency and starting torque. Therefore we study design shape of rotor slots of the single phase induction motor using FEM analysis for high efficiency and high starting torque.

II. COPPER DIE-CAST MOTOR

First, we design high efficiency single phase induction motor with aluminum die-cast rotor bar. The specification of motor is 1.12 kW, 4 pole and capacitor - run & start type. To make premium efficiency level motor, copper die-cast rotor bar is applied this motor. It is important to note that the improvements in motor performance by substituting copper for aluminum in this rotor were made without re-design for the copper die-cast. Table I. shows characteristics of aluminum die-cast motor and copper die-cast motor using FEM analysis and experiment result.

TABLE I
 EFFICIENCY AND STARTING TORQUE OF TWO TYPES SPIM

Material of die-cast	Efficiency [%]	Starting torque [Nm]
Aluminum (FEM)	85.4	11.39
Aluminum(Exp.)	84.2	11.5
Copper (FEM)	86.4	8.09

Though just only experiment of aluminum die-cast motor is performed but we can estimate results of copper die-cast motor from FEM analysis. The copper die-cast motor has higher efficiency but far lower torque than the aluminum die-cast motor. This motor should be satisfied twice of rate torque, 6[Nm]. Figure 1 shows that adjustment starting capacitance has limit to improve starting torque. Therefore, to improve starting torque, the double cage bar is chose for copper die-cast rotor bar. Because we can achieve both of high starting torque and high efficiency using double cage rotor bar [4].

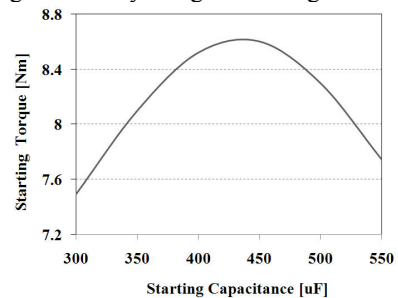


Fig. 1. Starting torque according to start capacitance

III. DESIGN PROCESS OF SPIM WITH COPPER DIE-CAST ROTOR BAR

Figure 2 show design process of SPIM with copper die-cast bar for high efficiency and starting torque. First, the stator and basic rotor shape of high efficiency SPIM is designed using magnetic equivalent circuit. Next, we should choose and design the basic shape of double cage bar using numerical method. Finally, we can obtain optimal shape of double cage bar through parametric analysis using FEA.

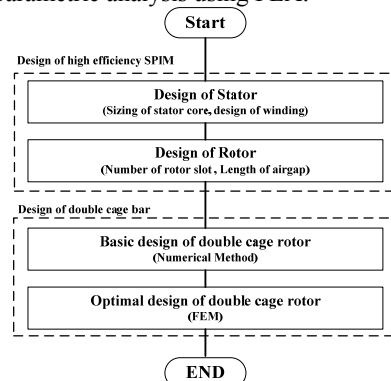


Fig. 2. Design process of double cage bar for premium efficiency level SPIM

IV. BASIC DESIGN OF DOUBLE CAGE ROTOR BAR

There are various types of double cage rotor. Among them, the basic model is shown in Figure 3. First, the basic shape of model is designed considering of rotor resistance and leakage reactance [4]. The starting resistance is at start

$$(R_r)_{s=1} = \frac{t_{LR} P_n}{3 \cdot 0.95 \cdot I_{LR}^2} \quad (1)$$

And from the equivalent circuit at start, rotor leakage inductance at start(S=1) is

$$(L_r)_{s=1} = \left(\sqrt{\left(\frac{V_{ph}}{I_{LR}} \right)^2 - (R_s + (R_r)_{s=1})^2} - L_{ls} \right) \frac{1}{\omega_1} \quad (2)$$

Using (1), (2), the resistances of working bar and starting bar can be calculated. And we can calculate working bar and starting bar cross section as following equation (3).

$$A_{w,s} = \frac{\rho_{Co} L}{R_{be}} \quad (3)$$

Here, L is length of stack, $R_{be,bs}$ is working bar and starting bar approximate resistance. The middle bar is designed using parametric analysis in chapter V.

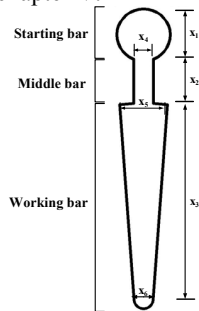


Fig. 3. Basic shape of double cage bar and design parameter for optimization

V. OPTIMAL DESIGN OF ROTOR SLOT OF SPIM WITH COPPER DIE-CAST BAR

Figure 3 shows design parameter for optimization using parametric analysis. Also, main effects of design parameters are analyzed for starting torque and efficiency by FEM analysis in shown figure 4.

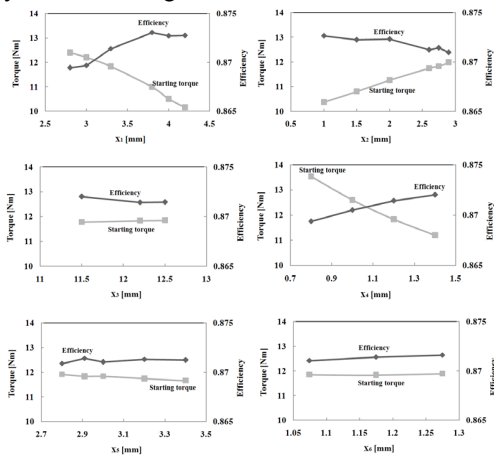


Fig. 4. Parametric analysis of design variable

Through the parametric analysis, we may choose the design main parameters x_1, x_2, x_4 . Other variables are fixed at their optimal values. The selected parameters are optimized by parametric analysis again. Through the design process, we can obtain the optimized model shown Figure 4.

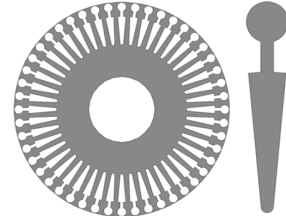


Fig. 4. Optimal shape of double cage rotor slot

Finally, we need to adjust the starting capacitor to make higher starting torque. Through adjustment of starting capacitance, starting torque increases by 11.8 Nm. Figure 5 shows experiment instrument of load test. And table III shows FEA result and experiments result. The optimized motor has higher efficiency and starting torque. Here, there is the difference of efficiency between two methods due to copper die-cast skill.

In this paper, we designed premium level high efficiency single phase induction motor with high starting torque using FEA method.

TABLE II
THE RESULTS OF OPTIMIZED DOUBLE CAGE BAR SPIM WITH COPPER DIE-CAST BAR

Method	Efficiency [%]	Starting torque [Nm]
FEA method	87.59	11.8
Experiments	89.2	12.01



Fig. 5 Experiment instrument of load test

VI. REFERENCES

- [1] Malinowski, J., McCormick, J., Dunn, K., "Advances in construction techniques of AC induction motors preparation for super-premium efficiency levels", *Industry Applications, IEEE Transactions on*, Vol 40, pp1665 - 1670, 2004.
- [2] Cowie, J.G., Brender, D.T, "Die-cast copper rotors for improved motor performance", *Electric Machines and Drives Conference 2003 vol.2*. pp1265 - 1271, June 2003
- [3] Peters, D.T., Cowie, J.G., Brush, E.F., Jr., Van Son, D.J., "Copper in the squirrel cage for improved motor performances," *Electric Machines and Drives Conference 2003 vol.2*. Page(s):1265 - 1271, June 2003
- [4] Ion Boldea, Syed A. Nasar "The induction machine handbook", CRC Press, 2001, pp 559-566.

A Study on Performance Simulation of Interior Permanent Magnet Synchronous Motor for Electric Vehicle considering Nonlinearity

Ki-Chan Kim, and Ju Lee, *senior member, IEEE*
 Dept. of Electrical Engineering, Hanbat National University
 Dukmyung-dong, Yuseong-gu, Daejeon, 305-719, South Korea
 Email : kckim@hanbat.ac.kr

Abstract — In this paper, we proposed a simulation algorithm for driving characteristics considering nonlinear parameters of interior permanent magnet synchronous motor (IPMSM) for electric vehicle such as d-axis and q-axis inductances. D-axis and q-axis inductances are changed according to both current magnitude and current angle between q-axis and current axis because of nonlinearity of magnetic flux density in rotor core. Therefore, the calculation of d-axis and q-axis inductances with nonlinearity of magnetic flux density is performed by using FEM. We can get precise driving performance of traction motor for electric vehicle adopting nonlinear d-axis and q-axis inductance table. Finally driving performance by proposed algorithm was verified by experiment of proto type.

I. INTRODUCTION

It is important to calculate the exact value of d-axis and q-axis inductances at the design step of interior permanent magnet synchronous motor (IPMSM) because these parameters are related to torque and speed characteristics of IPMSM closely if it is controlled by flux weakening control mode [1], [2]. It is very difficult to calculate the exact d-axis and q-axis parameters in an application area which is needed for compact and high power density design owing to magnetic flux saturation effect in its core. Analytical method by using equivalent magnetic circuit makes the error of d-axis and q-axis inductance values maximize under the extreme magnetic saturation area [3]. Therefore, d-axis and q-axis inductances considering nonlinear characteristics according to current angle between q-axis and current axis as well as magnitude of armature current should be analyzed by FEM.

In the paper, a simulation algorithm for driving performance of IPMSM considering nonlinearity of d-axis and q-axis inductances according to current angle and current magnitude is studied. Moreover, the algorithm is very effective for performance analysis with field weakening control which needs the information on the d-axis and q-axis inductances according to current angle. The driving performance considering constant value of d-axis and q-axis inductances is compared with proposed one. Finally, the validity of proposed algorithm is verified through the experiment of proto type.

II. INDUCTANCE CALCULATION

Fig. 1 shows analysis model of IPMSM for the paper. It is a 4kW traction motor of small automobiles whose power source is 48V battery.

There are several methods for the calculation of d-axis and q-axis inductances [4]. In the paper, we adopted the inductance calculation method derived from two-axis vector diagram of IPMSM as shown in Fig. 2. In the figure, we can calculate d-axis and q-axis inductances by using following equations, respectively.

$$L_d = \frac{\Psi_0 \cos \alpha - \Psi_a}{i_d} \quad (1)$$

$$L_q = \frac{\Psi_0 \sin \alpha}{i_q} \quad (2)$$

where, Ψ_0 is linkage flux of phase winding at load operation, Ψ_a is linkage flux of phase winding at no load operation and α is angle between Ψ_0 and Ψ_a .

D-axis and q-axis inductances are changed according to both input current magnitude and current angle between q-axis and current axis. The inductance calculation results by using FEM are showed in Fig. 3(a) and Fig. 3(b), respectively. The conditions for the analysis of Fig. 3(a) are fixed load angle δ and variable input current i_a . On the other hand, the conditions for the analysis of Fig. 3(b) are variable load angle δ and fixed input current i_a which is rated current at continuous mode, 46.5A.

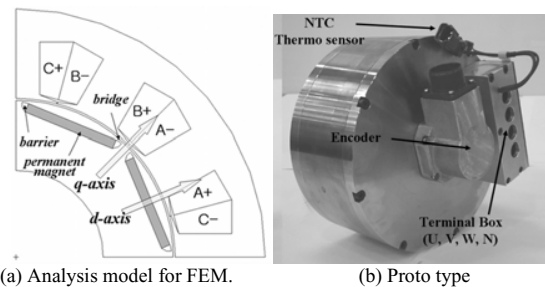


Fig. 1. Analysis model and proto type of IPMSM for electric vehicle.

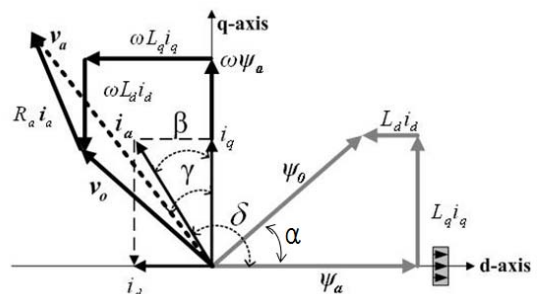
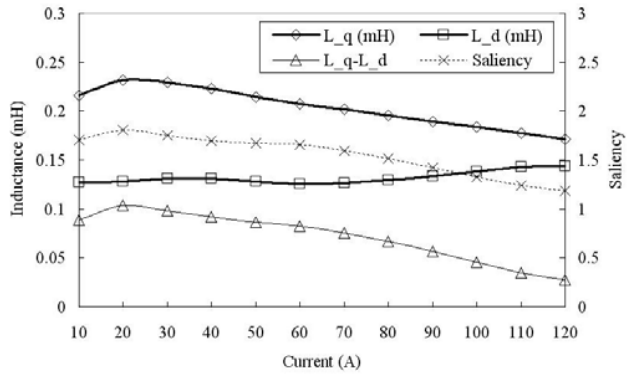
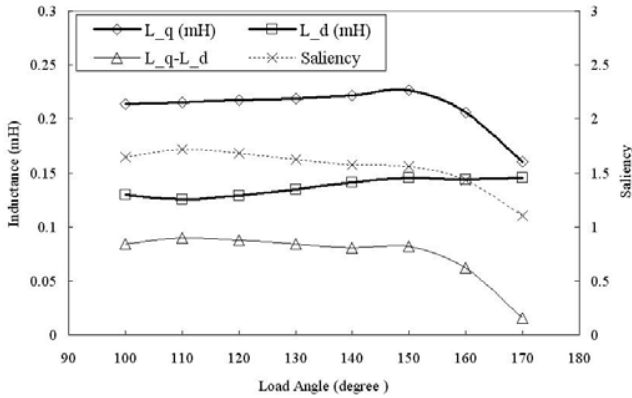


Fig. 2. 2-axis Vector Diagram of IPMSM for the calculation of inductances.



(a) Inductance characteristics according to input current.



(b) Inductance characteristics according to load angle (or current angle)
Fig. 3. The analysis results of d-axis and q-axis inductances by FEM.

III. ALGORITHM FOR DRIVING PERFORMANCE OF TRACTION MOTOR FOR ELECTRIC VEHICLE

In general, IPMSM for electric vehicle is controlled with maximum power control mode. However, d-axis and q-axis inductances have nonlinearity due to magnetic saturation in the core. Therefore, we proposed driving performance algorithm of IPMSM considering nonlinear d-axis and q-axis inductances in the paper. Fig. 4 shows the flowchart for driving performance algorithm which is divided into two control modes of constant torque and constant power. It is important to deal with inductance table between load angle and current magnitude in order to consider nonlinearity of d-axis and q-axis inductances. From the algorithm, we can calculate voltage, current, efficiency, power factor, torque, output power according to motor speed.

If we ignore nonlinearity according to load angle, we have remarkable errors, especially near high speed region. The comparison results of driving performance considering between linear value of inductances and nonlinear ones are shown in Fig. 5. It corresponds to the torque and power characteristics according to motor speed in case of intermittent operation with input current, 120A.

IV. CONCLUSION

In the paper, FEM analysis method of nonlinear d-axis and q-axis inductances of IPMSM and the algorithm of driving performance with maximum power control mode considering the nonlinear d-axis and q-axis inductances are proposed and

verified through experiment. The proposed algorithm can make efficiency map of IPMSM with ease which is main design target of traction motor for electric vehicle.

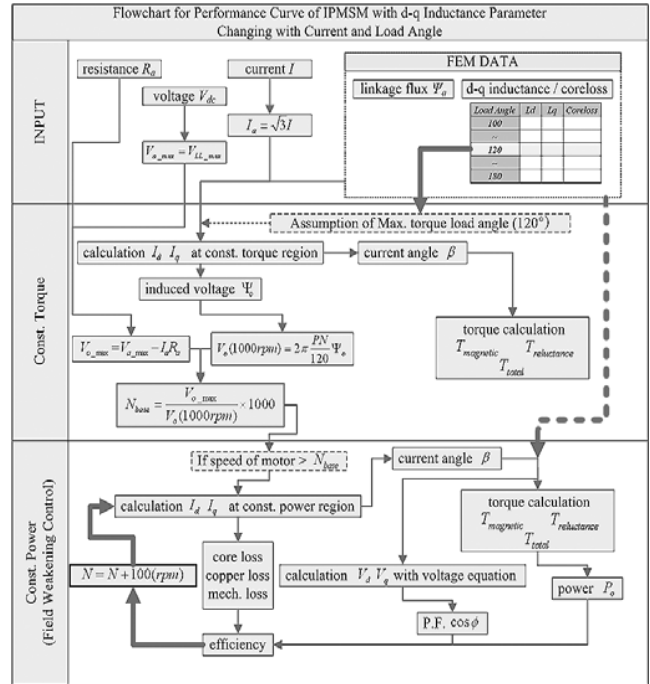


Fig. 4. Algorithm for driving performance of IPMSM according to control modes (constant torque and constant power modes)

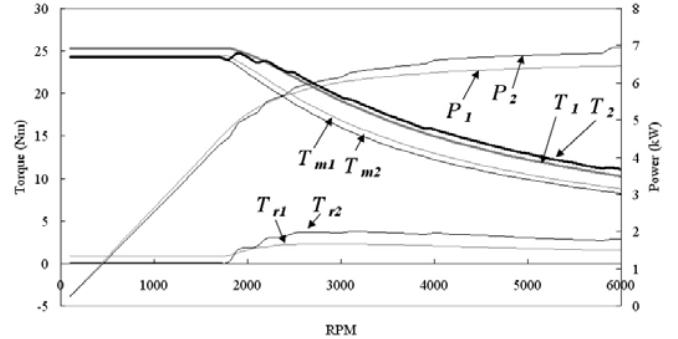


Fig. 5. Comparison results of torque and power parameters calculated with linear value of inductances and with nonlinear table of inductances at intermittent mode.

V. REFERENCES

- [1] M. N. Uddin, T. S. Radwan and M. A. Rahman, "Performance of Interior Permanent Magnet Motor Drive over Wide Speed Range", *IEEE Transactions on Energy Conversion*, vol. 17, no. 1, pp. 79-84, March 2002.
- [2] J. S. Moghani, J. F. Eastham, "Field Weakening Performance of a Linear Brushless AC Machine," *IEEE Transactions on Magnetics*, vol. 32, no. 5, pp. 5007-5009, Sept. 1996.
- [3] S. Y. Kwak, J. K. Kim and H. K. Jung, "Characteristic Analysis of Multilayer-Buried Magnet Synchronous Motor using Fixed Permeability Method", *IEEE Transactions on Energy Conversion*, vol. 20, no. 3, pp. 549-555, Sept. 2005.
- [4] K. C. Kim, J. S. Ahn, S. H. Won, J. P. Hong, and J. Lee, "A Study on the Optimal Design of SynRM for the High Torque and Power Factor," *IEEE Transactions on Magnetics*, vol. 43, no. 6, pp. 2543-2545, June 2007.

Characteristics Analysis & Optimum Design of Anisotropy Rotor SynRM Using Coupled FEM & RSM

Jung Ho Lee, *Member, IEEE*, Il Kyo Lee, Yong Hyun Cho
Dept. of Electrical Engineering, Hanbat National University
Dukmyung-Dong Yuseong-Gu, Daejeon, 305-719, KOREA
82donin@naver.com

Abstract — This paper deals with the characteristics analysis & optimum design of Synchronous Reluctance Motor (SynRM) with anisotropy rotor using a coupled Finite Element Method (FEM) & Response Surface Methodology (RSM). The focus of this paper is the characteristics analysis & optimum design relative to the output power on the basis of rotor materials of a SynRM. The coupled Finite Elements Analysis (FEA) & Preisach model have been used to evaluate nonlinear solutions. Comparisons are given with characteristics of normal synchronous reluctance motor and those of anisotropy rotor SynRM (ANISO-SynRM), respectively. The feasibility of using RSM with FEM in practical engineering problem is investigated with computational examples and comparison between the fitted response and the results obtained from an analytical solution according to the design variables of rotor in anisotropy rotor SynRM.

I. INTRODUCTION

The performance of a synchronous reluctance motor (SynRM) in terms of torque and power factor depends on the two-axis inductance L_d and L_q of the machine. The large difference of (L_d-L_q) and L_d/L_q ratio is good for the machine's properties. Therefore, Considerable attention has been paid in the past to improve rotor design of SynRM [1] – [3].

However the mechanical problems related to a segmented type of rotor have been disregarded up to now. A relevant advantage of the segmented structure (with respect to the axially laminated one, for example) is the rotor laminations can be punched, as in an induction motor: of course, thin ribs have to be left between adjacent segments.

The presence of these ribs introduces an additional q-axis flux and the torque performance is lowered.

In construction, the simplest way is to accept this loss of performance and to reduce it by accurately proportioning and positioning the rib width. Another solution is to proceed as before (punching), then cast the rotor of a suitable material and, finally, machine-out the ribs. The casting material should be non-conduction in order to avoid eddy currents and related effects. A plastic material can be used but some problems arise because of the low elasticity module.

By adding a proper quantity of permanent magnets the torque density and power factor of SynRM can be greatly increased. It is called Permanent Magnet Assisted Synchronous Reluctance Motor (PMASynRM) [4]-[5].

New solution is to use as anisotropy materials, then wire cut the rotor of a suitable material and, finally, removed flux of the ribs.

This paper deals with the characteristics analysis & optimum design of Synchronous Reluctance Motor (SynRM) with anisotropy rotor using a coupled FEM & RSM.

II. ANALYSIS MODEL

The approximation consists of a priori imposing the working flux density of the rib iron B_s : this depends on the applied mmf and on the rib length, of course, but cannot increase beyond a certain (practical) limit because of the iron saturation.

Moreover, equal width ribs can be supposed as shown in Fig. 1. Each width would follow from the mechanical (finite element) design; however, a practical limit exists in cutting very thin ribs, and an equal width seems a reasonable hypothesis, at least for small machines.

Owing to the above hypotheses, the flux flowing in a rib is given by (1). The torque equation is modified, in this case, as in (3), showing the torque loss due to rib flux of (2)

$$\phi_{wk} = B_s w l \quad (1)$$

$$\lambda_r = \frac{4}{\sqrt{3}} w l N B_s \quad (2)$$

$$T = \frac{3}{2} \frac{P}{2} (k_{dq} \lambda_{md} i_q - \lambda_r i_d) \quad (3)$$

By using a proper anisotropy material of rotor the torque density and power factor of SynRM (removed second term of (3)) can be greatly increased as shown in Fig. 2.

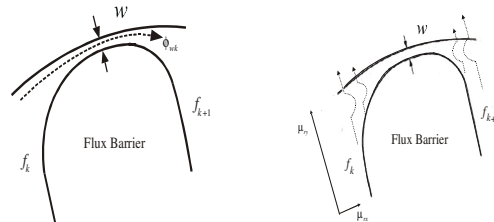


Fig. 1. Rib profile & path of rib flux

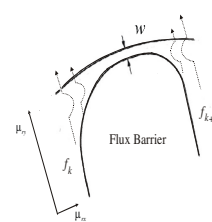


Fig. 2. Rib flux path of anisotropy model

III. ANALYSIS USING COUPLED FEM AND PREISACH MODELING

Fig. 3, 4. show the effects of anisotropy rotor structure that the q axis rib flux is assumed to completely cancel at some positions (except ribs from 0 degree to 5 degree and from 175 degree to 180 degree, no all rib) as shown in Fig. 5, 6. Flux distribution for q-axis excitation, for the normal SynRM and ANIRO-SynRM with a conventional stator having 24 slots and two poles, are shown in Fig. 5, 6.

Whereas the rotor rib tangential flux is appeared in a normal SynRM, the rotor rib tangential flux would have nearly zero since the spatial anisotropy in an ANIRO-SynRM is constructed, resulted in Fig. 3, 4.

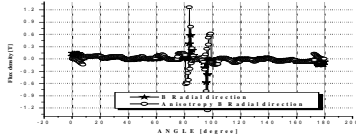


Fig. 3. Radial rib flux density distribution of SynRM and ANIRO-SynRM

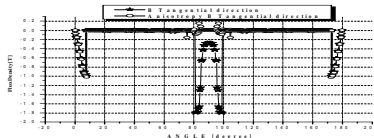


Fig. 4. tangential rib flux density distribution of SynRM and ANIRO-SynRM

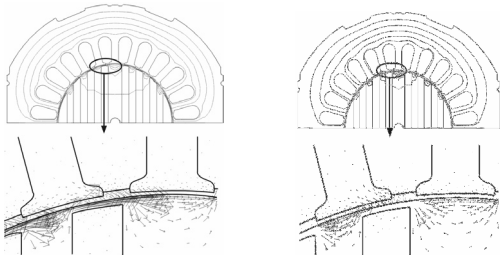


Fig. 5. q-axis plots of SynRM

Fig. 6. q-axis plots of ANIRO-SynRM

IV. OPTIMIZATION PROCEDURE

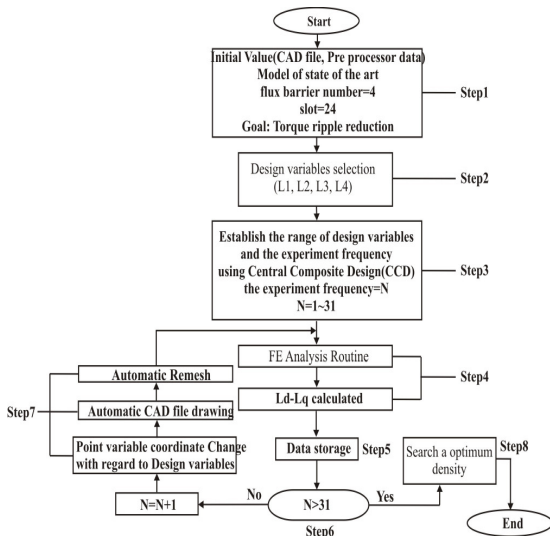


Fig. 7. The flow chart of design procedure

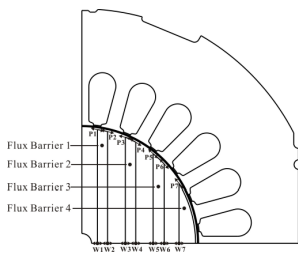


Fig. 8. Design variables and variation direction of the SynRM

Fig. 7 shows the flow chart of total design strategy.

Fig. 8 shows design variables and variation direction for the shape transformation according to flux barrier width.

Design procedure according to the flow chart is as follows;

Step1. : Set the initial value (CAD file, Pre-processor data). And the initial model is assigned to flux barrier=4, slot=24.

Step2. : flux barrier width (L1~L4) in rotor are adopted the design variables related to torque density in the SynRM. However, the ribs have a fixed value due to inherent manufacturing limitations.

Step3. : The range of design variables and experiment frequency is established by using the central composite design (CCD). The experiment frequency (N) is 31th.

Step4. : Finite element analysis (FEA) is performed and Ld-Lq is calculated.

Step5. : The Ld-Lq obtained from FEA, are stored.

Step6. : The experiment frequency (N) > 31?

► Yes: Search a optimum torque density. ► No: N=N+1

Step7. : The example of the point variables and variation direction of flux barrier rotor is well shown Fig. 9.

When the rotor shape according to variables (L1~L4) is varied, they have a difficulty in performing a lot of the pre-processor for FEA. For this reason, the new CAD file is redrawn with regard to the change of the design variables automatically. Next the process of automatic mesh generation follows. In mesh generation, mesh data doesn't change the node number, element number, region, boundary condition, etc., but only x, y coordinate data of the design variables. In this way, the proposed pre-processor procedure can be performed in a short period of time. In this way, this procedure goes on until N=31.

Step8. : The response surface model is created by data obtained from FEA according to an established range. Therefore, it is possible to get optimum torque density.

The RSM seeks to find the relationship between design variable and response through statistical fitting methods, which are based on the observed data from system.

More detailed results and discussion will be given in final paper. And the mathematical expressions for response surface methodology will be also given in extended version

V. REFERENCES

- [1] S. B. Kwon, S. J. Park, J. H. Lee, "Optimum Design Criteria Based on the Rated Watt of a Synchronous Reluctance Motor Using a Coupled FEM and SUMT", IEEE Transactions on Magnetics, Vol.41, No.10, pp 3970~3972, Oct. 2005.
- [2] J. H. Lee, "Efficiency Evaluations of Synchronous Reluctance Motor Using Coupled FEM and Preisach Modeling", IEEE Transaction on Magnetics, Vol. 39, No. 5, pp 3271-3274, September, 2003.
- [3] J. H. Lee, "Design Solutions to Minimize Iron Core Loss in Synchronous Reluctance Motor using Preisach Model and FEM", IEEE Transaction on Magnetics, Vol. 38, No. 5, pp 3276-3278, September, 2002.
- [4] Y. J. Jang, J. H. Lee, "Characteristic Analysis of Permanent Magnet-assisted Synchronous Reluctance Motor for High Power Application", Journal of Applied Physics, Vol.97, No.10, 10Q503, May, 2005.
- [5] J. H. Lee, D. S. Hyun, "Hysteresis Analysis for Permanent Magnet Assisted Synchronous Reluctance Motor by Coupled FEM & Preisach Modelling", IEEE Transaction on Magnetics, Vol. 35, No. 5, pp. 1203-1206, May 1999.

Irreversible Demagnetization on Permanent Magnet Motors

Luiz von Dokonal, Flavio J. H. Kalluf
Whirlpool S.A. – Embraco Compressors Unit
Rua Rui Barbosa, 1020, Caixa Postal 91, Joinville – SC, Brazil
ldokonal@embraco.com.br

Abstract — Permanent magnet electromagnetic devices generate induced voltages (EMF) at any electrical conductor submitted to its magnetic field. These induced voltages are proportional in module and frequency to the rotational speed.

Low impedance circuits crossing this magnetic field can generate high induced currents, and, since the direction of the field is always opposed to the source field, in some cases the magnet can be irreversibly demagnetized.

The irreversible demagnetization degenerates the startability, reduces the efficiency and overheats the motor, so it must be avoided by all means.

The main goal of this study is the evaluation of this phenomenon, trying to reproduce it by analytical and FEA analysis.

I. INTRODUCTION

The electrical motors can be classified in terms of quality mainly by its performance, cost, robustness and reliability. It means the product attractiveness cannot be measured only by its performance, but also for how good it can cope with overloads, voltage fluctuations, high or low temperatures and other environmental issues. Also, the reliability is related to the product ability to predict and prevent possible problems, which can come from an external source or even a not previewed fail mode of the motor and its control.

Regarding permanent magnet motors, many fail mode are covered by the control, and most of them are easy to be detected since the current can be monitored. In the other hand, some problems can occur internally on the motor, generating closed loops that are difficult to be detected by the control.

The specific fail mode to be analyzed by this study is the stator closed loop generated by a short circuit between the stator turns. At first, an analytical approach will be suggested for didactic reasons and, finally, a FEA analysis example will be presented.

II. DEMAGNETIZATION BASICS

A permanent magnet as show in Fig.1a has a demagnetization curve as shown in Fig.1b.

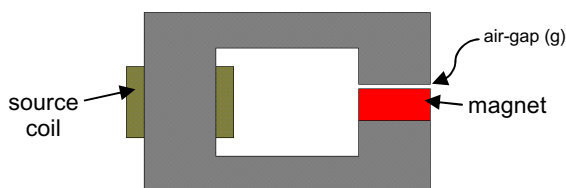


Fig. 1a - Example of magnetic circuit with magnet and source coil

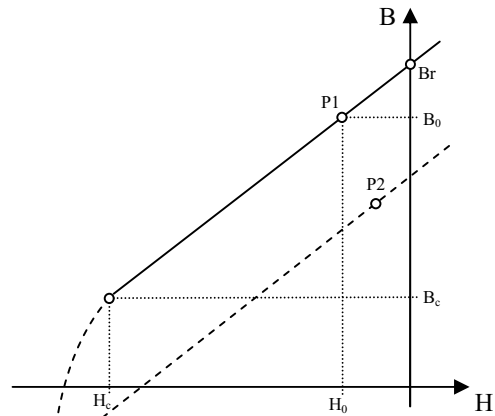


Fig. 1b - Magnetization curve for Fig.1a circuit

The effective air gap g in Fig.1a represents the magnet thickness plus the air gap thickness. B_0 is the magnetic induction in the air gap generated by the magnet at operation point. N is the number of turns and I is the demagnetization current.

The demagnetization can take place when is applied a current to the winding so as to generate a reverse field to the magnet, moving the magnet operation point beyond H_c ($H_c = H(P1) - N \cdot I / g$). In this case, even when the source current is removed, the magnet original remanent induction will not be restored (point $P2$ in Fig.1b). The new $P2$ point location will depend on how severe was the demagnetization. The induction value at this point can even be zero or lower (reverse magnetization). The solid line in Fig.1b shows the normal operation region and the dashed curve shows the behavior of the magnet during the demagnetization procedure, caused by the reverse field.

The demagnetization phenomenon depends on the following factors:

- Magnet class (H_c and B_r are related only to the magnet class);
- Demagnetizing field magnitude;
- Effective air gap thickness (magnet thickness + air gap thickness).

B_0 and H_0 values (which are constant at any point of the magnet, since rectangular magnets do not have significant flux fringing) depend on the magnet thickness, air gap thickness and B_r (remanent induction), according to the following relations:

$$B_0 = B_r \cdot L_m / (L_m + g)$$

$$H_0 = (B_r - B_0) / \mu_0$$

where,

$$L_m = \text{magnet thickness}$$

$$\mu_0 = 4 \cdot \pi \cdot 10^{-7}$$

For permanent magnets which have radial field orientation, mounted externally on rotor surface, the B_0 value varies as a function of the magnet radius. In the full version of the paper the equations that describe the variation of B_0 will be shown in a simplified form. These simplified equations lead to a good precision for almost all cases where the magnet thickness is less than 30% of the rotor radius.

III. GENERATED EMF AND DEMAGNETIZATION CURRENT

Now let us suppose a short-circuit coil is placed on the circuit as shown in Fig.2

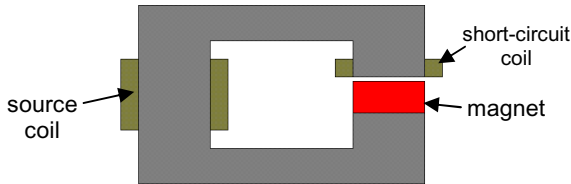


Fig. 2 - Example of magnetic circuit with with a short-circuit coil

The short-circuit coil, which is linking the alternating flux generated by the source coil will produce an induced voltage, proportional to the frequency and magnitude of the flux. This voltage will generate currents which setups a magnetic flux in opposed direction to the source field (Lenz's Law). Fig. 3a and fig. 3b shows the field map for both cases.

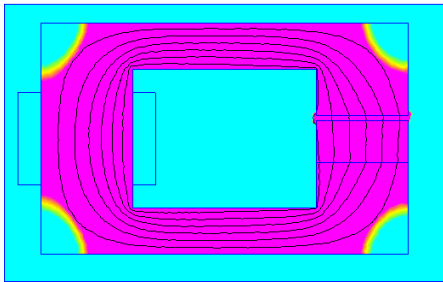


Fig. 3a - Field map for fig.1a circuit

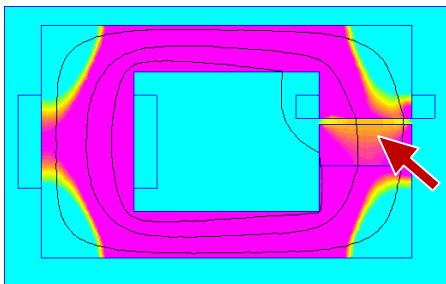


Fig. 3b - Field map for fig.2 circuit

Note that in fig.3b, the demagnetizing effect is clearly seen (red arrow). Note only the pink color denotes a magnetic induction above B_c (minimum induction to prevent demagnetization). By the same principle, the demagnetization can take place on most permanent magnet motors, as can be seen on figs.4a, 4b and 4c.

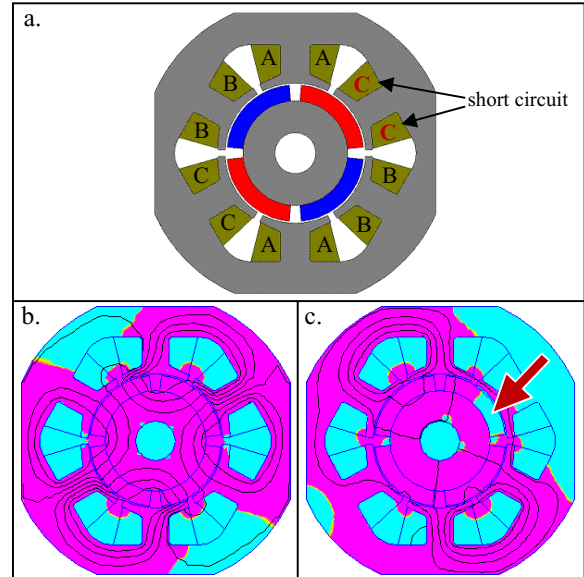


Fig. 4 - Demagnetization effect on a brushless-DC motor

IV. CONCLUSION

The previous examples show how a short-circuit fail can lead to demagnetization in permanent magnet devices. In the full paper version a theoretical approach will be used to calculate the minimum induction value, in order to quantify the risk of demagnetization on a didactic motor.

V. REFERENCES

- [1] G. R. Slemon, Magnetic Equipment: Transducers, Transformers and Machines, vol. 1, LTC, Sao Paulo: 1974, p. 32.
- [2] FEMM, Finite Elements Method Magnetics v. 4.02: <http://femm.foster-miller.net>
- [3] L.V. Dokonal, Research on Actuators, Universidade do Estado de Santa Catarina, Joinville: 2001, pp. 50-56.
- [4] RODRIGUES, Daniel, LANDGRAF, Fernando J.G. and TEIXEIRA, Julio Carlos. "Magnets: Applications, Process and Properties", IPT.
- [5] L. V. Dokonal, C. Pompermaier. "Study on non-uniformity of remanent flux density in ferrite magnets", Induscon, Joinville, 2004

Improved FE Post-Processors for Design of PM Fractional-Slot Machines

Jérôme Cros, Mehdi Taghizadeh and Philippe Viarouge

LEEPCI, Electrical & Computer Eng. Dept., Laval University,
1065 Ave de la Médecine, Québec (PQ) G1V 0A6, CANADA

E-mails: cros@gel.ulaval.ca, mehdi.taghizadeh.1@ulaval.ca, viarouge@gel.ulaval.ca.

Abstract — This paper presents useful improvements of FE Post-processors for machine designer, specially in the case of PM fractional slot machines with sinusoidal current supply. The computation of maximal flux densities on each stator mesh during one half of electrical period provides more information than instantaneous values of magnetic fields. Implementation method is detailed for linear and non-linear solving process to perform fast analysis of iron losses with flux weakening operations and efficiency optimization. As an example, a 12 slot-10 pole PM machine with concentrated winding is presented to illustrate this method and compare different iron loss models.

I. INTRODUCTION

Design of electrical machines is often based on an analytical method with an estimation of no-load flux densities in the air-gap to calculate the dimensions of the magnetic circuit. Next step is to perform a Finite Element Analysis (FEA) to optimize geometry, to compute the equivalent circuit parameters and to validate performances of the machine for rated operation. Well-known post-processors [1] can be applied for conventional machines, but some improvements are required to study fractional slot machines because the magnetic field pattern under load is not repetitive for each rotor pole. Indeed, the distribution of magnetic flux densities for a given rotor position or a given simulation time step does not provide useful information for designer and is not significant. It's better to compute the maximal flux densities in each stator mesh on a half electrical period, with movement of the rotor and sinusoidal rated current supply. The method is efficient to investigate possible stator modifications, to compare different winding configurations and to analyze the effect of different supply current control angles for flux weakening operation. Same approach is used to investigate iron loss.

II. MACHINES WITH FRACTIONAL SLOT WINDING

Some synchronous machines have a fractional number of slots per pole and per phase to reduce the EMF harmonic content (hydraulic alternators [2]), to simplify winding realization (machines with concentrated winding [3]) or to minimize cogging torque ripple (permanent magnet machines [3]). In such a case, the phase coil arrangement in the stator is not repetitive under every pole of the rotor and this generates some MMF sub-harmonics when the machine is fed by sinusoidal currents [2]. This phenomenon is very important in PM machines with concentrated windings because there is only a single coil per pole. When the stator magnetic reaction is

greater than 0.5 pu, there are local magnetic saturation zones in the yoke that increase the magnetic losses and torque ripple. The distribution of the flux densities is very different from that obtained during no-load operation and this modification must be taken into account in the design of the machine. However, saturated zones are difficult to identify when one uses drawings and computations from instantaneous values of magnetic field.

III. POST-PROCESSOR IMPROVEMENTS

The calculation of the values of maximal flux densities is very easy to implement with a non-linear solving approach, as illustrated by Fig.1. However, very fast analysis can be performed with post-processors using results from linear solving method and a single matrix inversion. It is possible to calculate separately, the field of permanent magnets for different rotor positions and the field of stator phase windings using a constant value of current density. Linear combinations of these results with a post-processor is particularly powerful to simulate flux weakening with sinusoidal current waveforms and compute a large number of steady state operation points to perform efficiency analysis. This method also permits to estimate the magnetic losses in each mesh with an analytical expression for the specific magnetic losses density [4]. In this case, one can apply a constant value of maximal flux density limit to simulate magnetic saturation effect. Generally this assumption is valid during flux weakening operation of a surface mount PM machine if magnetic circuit is not saturated during a maximal torque control ($I_d=0$). These methods will be detailed in the final paper.

IV. ANALYSIS OF A 12 SLOT-10 POLE MACHINE WITH CONCENTRATED WINDINGS

We have selected a 3 phase, 12 slot and 10 pole PM machine to illustrate analysis of flux weakening operation using post-processing approach. Fig. 2 shows the distribution of full-load instantaneous magnetic flux densities for a given rotor position and a given supply current with a small amount of flux weakening. This data is difficult to use in design process because of variable values of flux densities in each stator part. Fig. 3 shows the distribution of the maximal values of the magnetic flux densities computed with results from several rotor positions, during no-load operation. In this case, it is easier to measure maximal flux densities in any part of the machine (tooth tips, teeth, yoke) for a validation of magnetic saturation effect. Fig.4 shows the distribution of maximal

values of full-load flux densities calculated by the same approach for the same machine with a single layer winding. One can see important modifications of flux density pattern in the yoke compared to Fig.3. Stator magnetic reaction decreases maximal flux densities in the teeth and tooth tips but increases flux densities in some parts of the stator yoke. This is a particularity of fractional slot machine revealed by maximal flux densities drawings. Fig.5 shows the distribution of the local magnetic loss densities with conventional laminated material. The combined hysteresis and eddy current losses per kg are calculated using following equation [4]:

$$P_{mag_{i,j}} = k_h \cdot f \cdot B_{Maxij}^2 + k_e \cdot f^2 \cdot B_{Maxij}^2 \quad (1)$$

The loss density distribution is similar to maximal flux density pattern. Some parts of stator yoke have high losses and it will be interesting to increase the section of magnetic circuit in these regions and decrease sections in the others. Table I shows a comparison of iron losses in different parts of magnetic circuit with no load and flux weakening operation.

V. REFERENCES

- [1] P.A. Bastos, N. Sadowski, Electromagnetic modeling by finite element methods, Marcel Dekker, New York, 2003, ISBN 0824742699
- [2] M. Liwschitz-Garik, C. C. Whipple, *Alternating-current machines, Second ed.*, D. Van Nostrand Company, Inc, Princeton (NJ), 1961.
- [3] J. Cros, P. Viarouge, "Synthesis of high performance PM motors with concentrated windings", *IEEE Energy conversion*, Vol.17-2, Jun. 2002.
- [4] H. Domeki and al. "Investigations of benchmark model for estimating Iron loss in rotating machine", *IEEE Magnetics*, Vol. 40 (2), Mar. 2004.

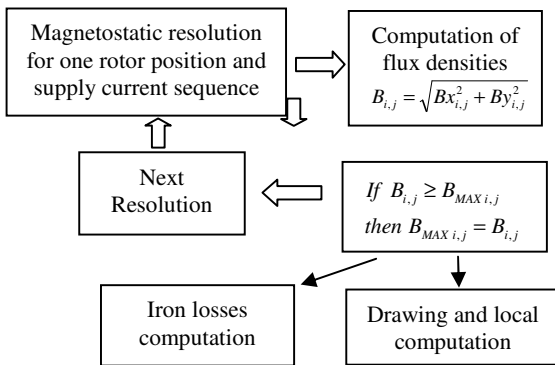


Fig.1 : Flowchart of maximal flux density calculation

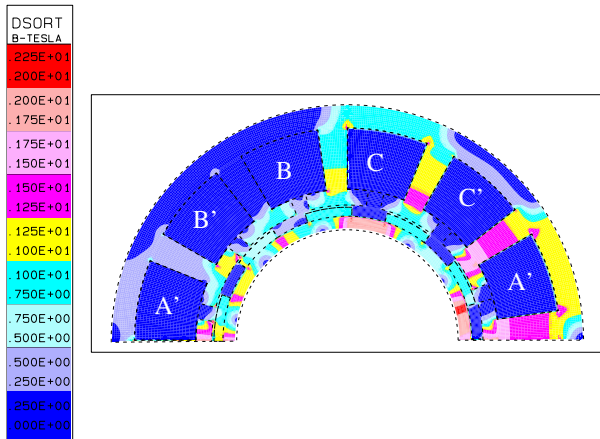


Fig.2: Distribution of instantaneous full-load flux densities (Flux weakening operation with $I_d=0.577.I_q$)

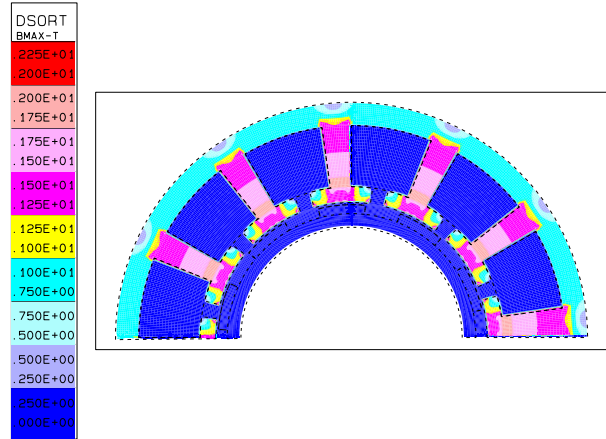


Fig.3 : Maximal no-load flux densities computed on a half electrical period

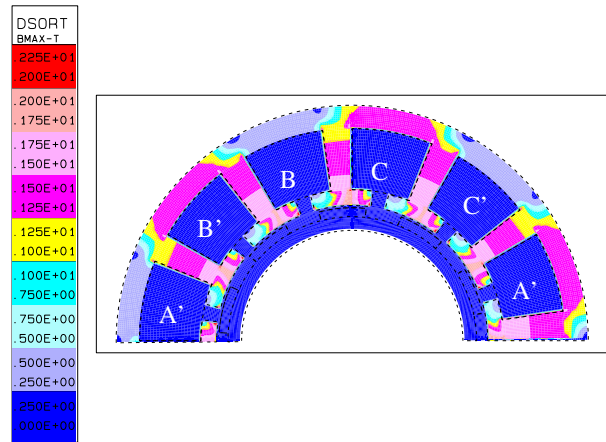


Fig.4 : Maximal flux densities with a single layer stator winding (Flux weakening operation with $I_d=0.577.I_q$)

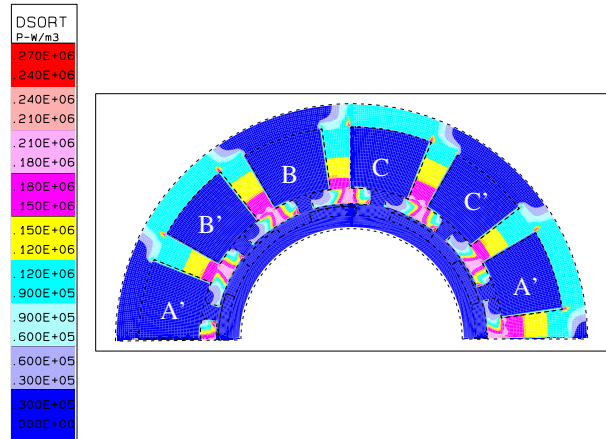


Fig.5 : Iron Losses with a single layer stator winding (Flux weakening operation with $I_d=0.577.I_q$)

	Torque (N.m)	Yoke (W)	Teeth (W)	Tooth tips (W)	Total (W)
<i>No-load</i>	-	39	72	27	138
<i>I_d=0.268.I_q</i>	47.6	51	75	30	156
<i>I_d=0.577.I_q</i>	44.7	46	63	28	137
<i>I_d=I_q</i>	38.4	39	49	25	113

Novel DTC Based on SVM with Adaptive stator Flux Observer for Induction Motors

Zhifeng Zhang, Renyuan Tang, and Baodong Bai

National Engineering Research Center for Rare-earth Permanent Magnet Machines
Shenyang University of Technology, Shenyang, 110178, China
imdtc@126.com

Abstract—This paper describes a combination of Direct Torque Control (DTC) and Space Vector Modulation (SVM) for an adjustable speed sensorless induction motor (IM) drive. The motor drive is supplied by a two level SVPWM inverter. The inverter reference voltage is obtained based on input-output feedback linearization control, using the IM model in the stator d-q axes reference frame with stator current and flux vectors components as state variables. Moreover, a robust full-order adaptive stator flux observer is designed for a speed sensorless DTC-SVM system and a new speed-adaptive law is given. By designing the constant observer gain based on LMI, the stability of the observer systems is ensured. Finally, the effectiveness and validity of the proposed control approach is verified by computer simulation results.

I. INTRODUCTION

Direct torque control based on space vector modulation (DTC-SVM) preserve DTC transient merits, furthermore, produce better quality steady-state performance in a wide speed range. At each cycle period, SVM technique is used to obtain the reference voltage space vector to exactly compensate the flux and torque errors. The torque ripple of DTC-SVM in low speed can be significantly improved.

In this paper, SVM-DTC technique based on input-output linearization control scheme for induction machine drives is developed. Furthermore, a robust full-order speed adaptive flux observer is designed for a speed sensorless DTC-SVM system and a speed-adaptive law is given. The constant observer gain, which is obtained by solving two bilinear matrix inequalities (BMIs) using LMI Toolbox in MATLAB [1], can overcome the real-time computational complexity of the adaptive observer gain in [2]. The stability of the speed adaptive stator flux observer is also guaranteed by the constant gain in very low speed. The proposed control algorithms are verified by extensive simulation results.

II. DTC-SVM BASED ON INPUT-OUTPUT LINEARIZATION

The DTC-SVM scheme is developed based on the IM torque and the square of stator flux modulus as the system outputs; stator voltage components defined as system control inputs and stator currents as measurable state variables.

Define the controller objectives e_1 and e_2 as

$$e_1 = T_e - T_{\text{eref}} \quad (1)$$

$$e_2 = |\psi_s|^2 - |\psi_{\text{sref}}|^2 \quad (2)$$

where, T_{eref} , T_e , ψ_{sref} , ψ_s are reference and real value of electromagnetic torque, stator flux respectively.

According the model of induction, the time derivative of e

is as (3),

$$\begin{bmatrix} \dot{e}_1 \\ \dot{e}_2 \end{bmatrix} = \begin{bmatrix} g_1 \\ g_2 \end{bmatrix} + \mathbf{D} \begin{bmatrix} u_D^* \\ u_Q^* \end{bmatrix} \quad (3)$$

where, $g_1 = p_n \left[c(\psi_D i_Q - \psi_Q i_D) + \omega_m (\psi_D i_D + \psi_Q i_Q) - \frac{\omega_r}{\sigma L_s} |\psi_s|^2 \right]$,

$$g_2 = -2R_s (\psi_D i_Q + \psi_Q i_D), \quad \mathbf{D} = \begin{bmatrix} (i_Q - \frac{\psi_Q}{\sigma L_s}) & -(i_D - \frac{\psi_D}{\sigma L_s}) \\ 2\psi_D & 2\psi_Q \end{bmatrix}$$

where ψ_D , ψ_Q , u_D , u_Q , i_D , i_Q are respectively the d-q axes of the stator flux, stator voltage and stator current vector components, ω_m is the rotor electrical angular speed, L_s , L_r , L_m are the stator, rotor, and magnetizing inductances, respectively, $\sigma = 1 - (L_m^2 / L_s L_r)$ and R_s , R_r are the stator and rotor resistances, respectively. $c = -1 / (\sigma(R_s / L_s + R_r / L_r))$

According to $i_s = \frac{\psi_s}{\sigma L_s} - \frac{L_m}{\sigma L_s L_r} \psi_r$, the characteristic

determinant of \mathbf{D} is as follows

$$\det(\mathbf{D}) = -\frac{4L_m}{\sigma L_r} p_n |\psi_r| \cdot |\psi_s| \cos(\psi_r, \psi_s) \quad (4)$$

From (4), \mathbf{D} is a nonsingular matrix since the inner product of stator flux vector and rotor flux vector can not be physically zero.

Based on input-output feedback linearization, the following control inputs are introduced.

$$\begin{bmatrix} u_D^* \\ u_Q^* \end{bmatrix} = \text{inv}(\mathbf{D}) \begin{bmatrix} -g_1 + u_x \\ -g_2 + u_y \end{bmatrix} \quad (5)$$

where, u_x , u_y are the auxiliary control inputs and are defined based on the pole placement concept of the linear control systems so that

$$u_x = -c_1 e_1, \quad u_y = -c_2 e_2 \quad (6)$$

where, c_1 and c_2 are positive constants.

III. SPEED ADAPTIVE STATOR FLUX OBSERVER

The state observer, which estimates the state current and the stator flux together, is given by the following equation[2].

$$\frac{d\hat{x}}{dt} = \hat{\mathbf{A}}\hat{x} + \mathbf{B}u + \mathbf{G}(\hat{i}_s - i_s) \quad (7)$$

$$\hat{i}_s = \mathbf{C}\hat{x} \quad (8)$$

where $\hat{\cdot}$ denotes the estimated values and \mathbf{G} is the observer gain matrix which is chosen so that the stability of the flux observer can be guaranteed. In order to derive the adaptive scheme, Lyapunov theorem is utilized. Now, let us define the following Lyapunov function

$$V = \mathbf{e}^T \mathbf{P} \mathbf{e} + (\hat{\omega}_r - \omega_r)^2 / \lambda \quad (9)$$

The time derivative of V along error equation (4) becomes:

$$\frac{dV}{dt} = \mathbf{e}^T \left[(\mathbf{A}_1 - \mathbf{G}\mathbf{C})^T \mathbf{P} + \mathbf{P}(\mathbf{A}_1 - \mathbf{G}\mathbf{C}) + \omega_r (\mathbf{A}_\omega^T \mathbf{P} + \mathbf{P}\mathbf{A}_\omega) \right] \mathbf{e} - (\hat{\mathbf{x}}^T \Delta \mathbf{A}^T \mathbf{P} \mathbf{e} + \mathbf{e}^T \Delta \mathbf{A} \hat{\mathbf{x}}) + \frac{2}{\lambda} (\hat{\omega}_r - \omega_r) \frac{d\hat{\omega}_r}{dt} \quad (10)$$

Let

$$-(\hat{\mathbf{x}}^T \Delta \mathbf{A}^T \mathbf{P} \mathbf{e} + \mathbf{e}^T \Delta \mathbf{A} \hat{\mathbf{x}}) + \frac{2}{\lambda} (\hat{\omega}_r - \omega_r) \frac{d\hat{\omega}_r}{dt} = 0, \quad (11)$$

if we select observer gain matrix \mathbf{G} so that the validity of the inequality

$$(\mathbf{A}_1 - \mathbf{G}\mathbf{C})^T \mathbf{P} + \mathbf{P}(\mathbf{A}_1 - \mathbf{G}\mathbf{C}) + \omega_r (\mathbf{A}_\omega^T \mathbf{P} + \mathbf{P}\mathbf{A}_\omega) < 0 \quad (12)$$

can be guaranteed, the state observer is stable.

The adaptive scheme for speed estimation is given by

$$\hat{\omega}_r = \left(K_p + \frac{K_i}{p} \right) (\hat{\psi}_s^T) \mathbf{J} (\mathbf{i}_s - \hat{\mathbf{i}}_s) \quad (13)$$

By the Lyapunov stability theory, the state observer is asymptotically stable if there is symmetric positive definite matrix \mathbf{P} and matrix \mathbf{G} such that (12) hold.

Suppose ω_{\max} is upper bound of permitted rotor speed. For ensuring system with a certain reliability and robustness, ω_{\max} is selected larger than rated speed of IM in general.

When the speed changed in the interval $[-\omega_{\max}, \omega_{\max}]$, the state observer is stable can be guaranteed by the following two matrix inequalities:

$$(\mathbf{A}_1 - \mathbf{G}\mathbf{C})^T \mathbf{P} + \mathbf{P}(\mathbf{A}_1 - \mathbf{G}\mathbf{C}) + \omega_{\max} (\mathbf{A}_\omega^T \mathbf{P} + \mathbf{P}\mathbf{A}_\omega) < 0 \quad (14)$$

$$(\mathbf{A}_1 - \mathbf{G}\mathbf{C})^T \mathbf{P} + \mathbf{P}(\mathbf{A}_1 - \mathbf{G}\mathbf{C}) - \omega_{\max} (\mathbf{A}_\omega^T \mathbf{P} + \mathbf{P}\mathbf{A}_\omega) < 0 \quad (15)$$

Inequality (14) and (15) are bilinear matrix inequalities (BMIs) about matrix variables \mathbf{P} and \mathbf{G} . Noticing that if fixed matrix \mathbf{G} , BMIs (14) and (15) will become linear matrix inequalities (LMIs) about matrix variable \mathbf{P} ; and if fixed \mathbf{P} , BMIs (14) and (15) will become linear matrix inequalities (LMIs) about matrix variable \mathbf{G} . So, the feasible solution of BMIs (14) and (15) can be obtained by LMI toolbox in MATLAB [1].

IV. SIMULATIONS

To verify the DTC-SVM scheme based on input-output linearization and adaptive observer, simulations are performed in this section. The block diagram of the proposed system is shown in fig.1. The speed and torque response curves of conventional DTC and DTC-SVM are shown fig. 2. The command speed value is 5 rpm in both two systems. At startup, the system is unloaded, the load torque is changed to 17Nm at $t=1s$, then the load torque is changed from 17Nm to 10Nm at $t=1.5s$. In order to highlight validity of the sliding-mode observer, the stator resistance and rotor resistance are set to twice of the rated value in simulation. The stator flux observer curve is shown in fig.3. Compared with conventional DTC,

the DTC-SVM has much smaller torque ripple. From fig.3, it can be seen that the adaptive observer can estimate the stator flux well and truly.

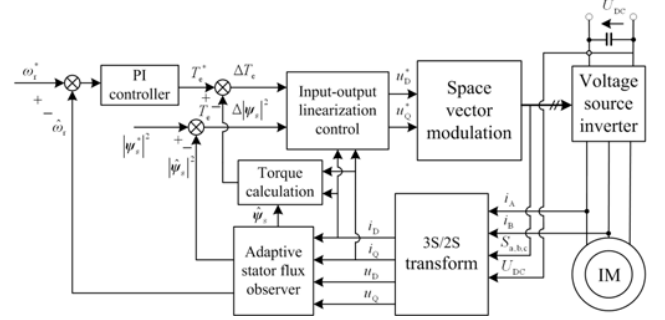
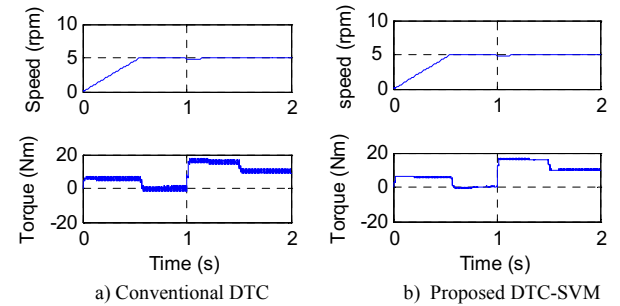


Fig.1 The block diagram of the DTC-SVM system



a) Conventional DTC b) Proposed DTC-SVM

Fig.2 Speed and torque response curve

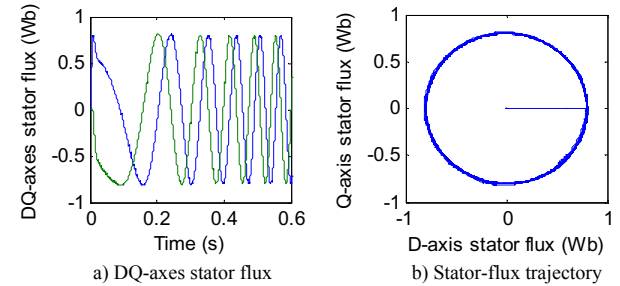


Fig.3 Stator flux curve

V. CONCLUSIONS

A new DTC-SVM scheme has been presented for the IM drive system, which is on the basis of input-output linearization control. In this control method, a SVPWM inverter is used to feed the motor, the stator voltage vector is obtained to fully compensate the stator flux and torque errors. Furthermore, a robust full-order adaptive flux observer is designed for a speed sensorless DTC-SVM system. By designing the constant observer gain based on LMI, the stability of the observer systems is ensured. Compared with the conventional DTC, the proposed drive system has much smaller torque ripple in very low speed and exhibits good dynamic and steady-state performance.

VI. REFERENCES

- [1] Xiaohong Nian, Tao Wang, Jian Wang, et al. "Adaptive stator resistance estimation method for speed sensorless DTC controlled IM drives", *APEC' 2007*, pp. 214-221, 2007
- [2] XI Guo-hua, GAO Hong-yang, XU Wei, et al. "A method to determine gain matrix of stator flux full order observer." *J.Cent.South Univ.(Science and Technology)*, vol.39, no4, pp.793-798, 2008

A New Anisotropic Bonded NdFeB Permanent Magnet and Its Application to a Small DC Motor

Hyo Jun Kim, Hee Sung Yoon*, and Chang Seop Koh*, *Senior Member, IEEE*

R&D Center of Jahwa Electronics Co. Ltd., 7-6 Hyeonam-ri, Buki-myeon, Cheongwon-gun, 363-922, KOREA
hjkim2@jahwa.co.kr

*College of ECE, Chungbuk National University, San 48, Cheongju, Chungbuk 261-763, KOREA
kohcs@chungbuk.ac.kr

Abstract— This paper presents an application of a new permanent magnet MAGFINE, *polar anisotropic bonded NdFeB PM*, to a small size DC motor. The new PM gives very high residual magnetic flux density and energy product with lower cost than a sintered NdFeB PM. An application of this PM to a small size DC motor shows it can reduce the volume and weight of a motor up to fifty percent.

I. INTRODUCTION

DC motors employing sintered ferrite permanent magnets (PMs) have, so far, been widely used in automotive applications such as seat, blower and sunroof. These days, PM motors are required to have higher efficiency for energy saving, better performance with smaller volume and lighter weight, and even higher power density. In the design of DC motor, therefore, PMs having high energy density, such as NdFeB, are more attractive to get high power to volume ratio [1].

The NdFeB magnets are usually classified into *sintered* and *bonded* PMs according to their manufacturing process, and also *isotropic* and *anisotropic* PMs by their microstructure. The popular types, however, are limited to *isotropic bonded* PMs having $(BH)_{\max}$ of $80(\text{kJ}/\text{m}^3)$ and *anisotropic sintered* PMs of $400(\text{kJ}/\text{m}^3)$ due to some technical difficulties. Conventionally, for small size DC motors, *isotropic bonded* NdFeB PM, made by compression process of the NdFeB powder and binders, is preferred to a sintered one because it gives lower assembling costs and more flexibility.

Very recently, *anisotropic bonded* NdFeB PM, named MAGFINE having high energy product up to $200(\text{kJ}/\text{m}^3)$, has been developed by Aichi Steel Corporation and Jahwa Electronics [2]. Comparing with a sintered NdFeB PM, the MAGFINE gives little bit lower residual magnetic flux density (1.0T) and costs around 40(%) cheaper. Since the *anisotropic bonded* NdFeB PM has high energy product and residual magnetic flux density and is cheaper than the sintered NdFeB PM, it is expected to give higher air-gap magnetic flux density and power density with low cost when it is applied to a DC motor. The PM, furthermore, gives precise dimensions, roundness and concentricity after housing assembly process. The research on its application to PM motor, however, is still in early stage, and more discussions and researches are strongly required.

In this paper, a ring-type *anisotropic bonded* NdFeB PM is applied to a small size DC motor by replacing the conventional segment-type sintered ferrite PM to achieve a high power to volume ratio of the motor. In the application, *anisotropic* directions of each part of the ring-type *anisotropic*

bonded NdFeB PM were investigated, and the shape of rotor teeth are optimized.

II. 4 POLE POLAR ANISOTROPIC BONDED NDFEB PM

A 2-pole 10 slot ferrite PM DC motor, of which maximum output is 25(W) and specifications are shown in Table I, for the sunroof of a car is taken as a model. In order to develop a high power density motor, the *anisotropic bonded* NdFeB PM, JHMF23 made by Jahwa Electronics Co. Ltd., KOREA, of which magnetic performances are $B_r=1.0(\text{T})$, $iH_c=0.96(\text{MA}/\text{m})$, $bH_c=0.6(\text{MA}/\text{m})$ and $(BH)_{\max}=175(\text{kJ}/\text{m}^3)$, respectively, is selected. It is a ring-type 4 pole *polar anisotropic* PM as shown in Fig. 1. The PM is manufactured as follows:

Step 1. The *anisotropic bonded* NdFeB compound containing 2(wt%) of resin is prepared through the blending process under Ar atmosphere.

Step 2. With the compound, a mold for compression with magnetic fields is filled with a filling density of $4000(\text{kg}/\text{m}^3)$ as shown in Fig. 1(a). In order to align the magnetic particles in *polar anisotropic* directions, the magnetic powder is exposed to a magnetic field of 1200 (kA/m) while keeping the mold temperature in the range of 120~150 °C, and then compressed under the pressing pressure of 4 (ton/cm²). Fig. 1(b) shows the distribution of the magnetic flux density, obtained from a transient FEM analysis at moment of peak current, and Fig. 1(c) the maximum applied magnetic field intensities, during the compression process, at the compound. The final directions of the magnetic particles, obtained from that of magnetic fields, are shown in Fig. 1(d), and the *anisotropic bonded* NdFeB compound is ready to be magnetized in 4-pole *polar anisotropic* PM.

Step 3. The PM, compressed compound, is magnetized by

TABLE I
SPECIFICATIONS OF FERRITE PM AND PROPOSED MOTORS

Section	Item	Ferrite PM motor	Anisotropic bonded PM motor
PM	Number of pole	2	4
	B_r (T)	0.4	1.0
	Outer diameter (mm)	36.6	25.8
	Inner diameter(mm)	26	23.8
Armature	Axial length(mm)	54	27
	Outer diameter(mm)	25	23.2
	Number of slots(mm)	10	10
Return yoke	Axial length(mm)	44	25
	Thickness(mm)	1.7	2

using magnetizing fixture.

III. CONSTRUCTION OF A MOTOR AND TESTS

A DC motor employing the proposed PM is initially designed with air-gap of 0.3(mm) as shown in Fig. 2, and its specifications are compared, in Table I, with those of a model motor. Fig 3 shows the distributions of the magnetic flux density generated by the proposed *polar anisotropic bonded NdFeB PM* with and without an armature core where teeth width and slot opening are set to 2.2 (mm) and 1.6 (mm), respectively.

In order to decide the teeth width (Tw) and slot opening (So) optimally, the parametric analyses using FEM are performed over the range of $1.3(\text{mm}) \leq Tw \leq 2.2(\text{mm})$ and $1.2(\text{mm}) \leq So \leq 3.0(\text{mm})$, respectively. The upper limit of the teeth width is decided considering an enough winding space. During the analyses the air-gap between the PM and armature is fixed to 0.3(mm).

Fig. 4 shows that the torque constant increases as the teeth width increases. It is partially because the armature core is easily saturated in the narrow teeth, and means the proposed PM provides sufficient magnetic flux. With regard to the slot opening, the optimum condition is found at 1.6(mm). Through these analyses, the thickness of PM, teeth width and slot opening are decoded as 1(mm), 2.2(mm) and 1.6(mm), respectively.

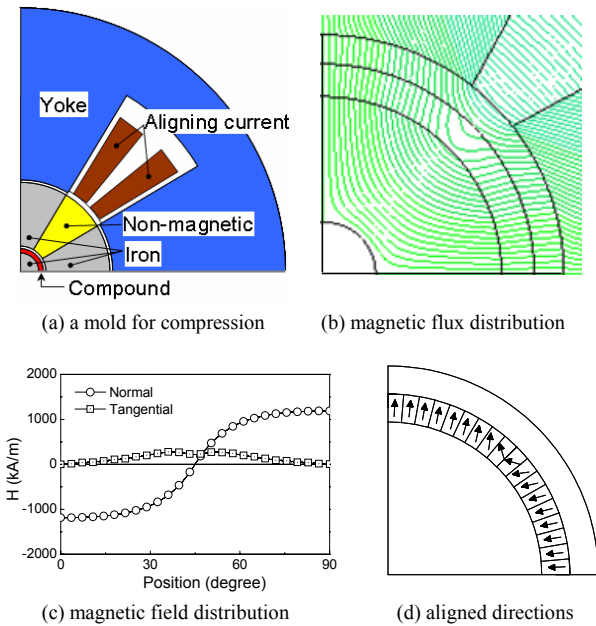


Fig. 1. Analysis results.

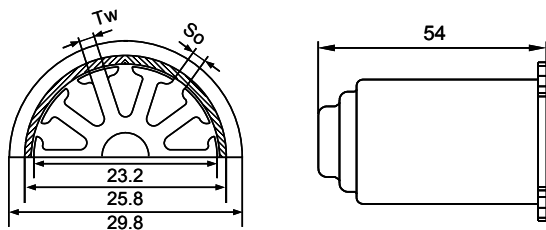


Fig. 2. Design of 4-pole polar anisotropic NdFeB PM motor.

Fig. 5(a) shows a comparison of the motor performances, measured at supplied voltage of 12(V), and sizes between the proposed 4-pole *polar anisotropic bonded NdFeB PM* motor and 2-pole conventional Ferrite DC one. It can be seen, from Table I and Fig. 5, that the proposed motor gives almost same performances with 50% reduced volume and weight.

IV. REFERENCES

[1] V. S. Ramsden, "Application of rare-earth magnets in high performance electric machines", *Proc. 15th Int. Workshop on REM and Their Applications*, pp. 623-625, 1998.
 [2] N. Hamada, C. mishima, H. Mitarai, and Y. Hunkura, "Development of Nd-Fe-B anisotropic bonded magnet with 27 MGOe", *IEEE Trans. on Magn.*, Vol. 39, No.5, pp. 2953-12955, September 2003.

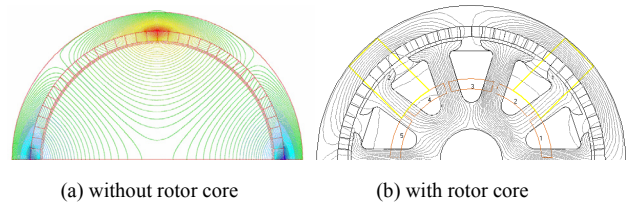


Fig. 3. Magnetic flux distributions.

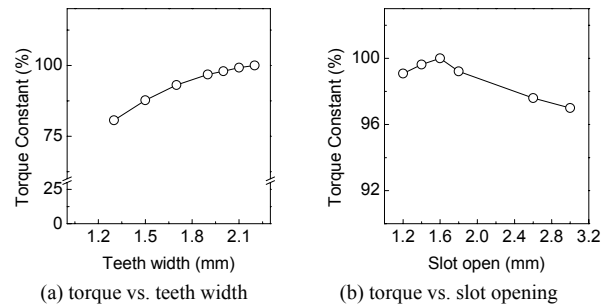


Fig. 4. Torque constants.

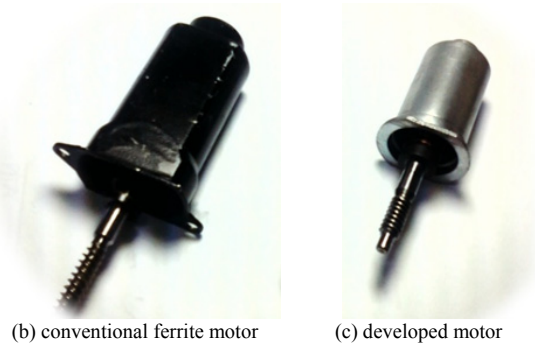
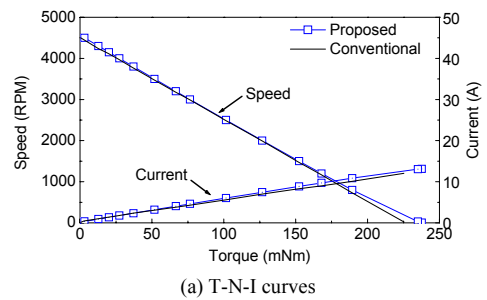


Fig. 5. Comparison of the proposed motor with conventional ferrite PM motor.

Optimum Design For Premium Efficiency of 250 kW Traction Induction Motor Using Response Surface Methodology & FEM

Jung Ho Lee, *Member, IEEE*, Sung Ju Mun, Tae won Yun
 Dept. of Electrical Engineering, Hanbat National University
 Dukmyung-Dong Yuseong-Gu, Daejeon, 305-719, KOREA
 E-mail: lucasmsj@nate.com

Abstract —This paper deals with optimum design criteria for premium efficiency of 250kW traction induction motor using response surface methodology (RSM) & finite element method (FEM). The RSM has been achieved to use the experimental design method in combination with Finite Element Method and well adapted to make analytical model for a complex problem considering a lot of interaction of design variables.

The proposed procedure allows to define the rotor copper bar shape, stator slot and stator, rotor dimensions starting from an existing motor or a preliminary design.

I. INTRODUCTION

Recently, saving energy is a most important task in the world. Thus, obtaining high efficiency electrical machines and apparatus is a very important task.

Induction Motors are very important in industry. For many years, the efficiency of three-phase induction motors has been the subject of numerous investigations aimed at increasing efficiency values by minimizing losses during the operation.

Induction motor design principles have not changed dramatically over the years, whereas the tools and the knowledge of engineers have improved considerably.

This better understanding has led to continuous improvements for reducing losses in electric motors.

Systematically analyzing the root causes of losses and the possibilities for improvements requires a complete and new approach, looking into not only the electrical area but also mechanical areas such as cooling, temperature levels, and outer diameter (OD) versus length ratio, etc. In this article, we apply a systematic and optimized new design approach for 250 kW Traction Induction Motor.

The electromagnetic factors for improving efficiency are as follows:

- 1) increase the amount of active material
- 2) utilize high-performance lamination materials
- 3) optimize the stator/rotor geometries
- 4) optimize the air gap dimensions

All the factors have to be carefully looked at and investigated, because most of them are not independent from each other and may negatively influence the efficiency gains in one case or the other. Secondly, the commercial impacts have to be strongly considered, since with higher efficiency the premium paid may limit the savings seen.

The RSM has been achieved to use the experimental design method in combination with Finite Element Method and well

adapted to make analytical model for a complex problem considering a lot of interaction of design variables [1]-[3].

The focus of this paper is found firstly a design solution through the comparison of torque and losses according to rotor bar shape and stator, rotor dimensions variations and, Secondly, a mixed resolution with central composite design (CCD) is introduced and analysis of variance (ANOVA) is conducted to determine the significance of the fitted regression model.

II. DESIGN ALGORITHM AND MODEL

The variables for optimization design are shown in Fig. 1.

In Fig. 1, design variables that are slot depth and width of stator, slot depth and width of rotor and air gap width, are determined to improve torque performance of 250kW traction induction motor.

Analysis data is obtained through finite element method based on central composite design mostly used in RSM, and optimum point is determined through analysis of the data.

Finally, it can be obtained the maximum torque density & minimum loss of 250kW traction induction motor.

Fig. 1 shows the point variables and variation direction example for the shape change according to slot depth and width of stator and rotor.

Points of W1-W8 and P1-P8 move as a condition that slot depth and width.

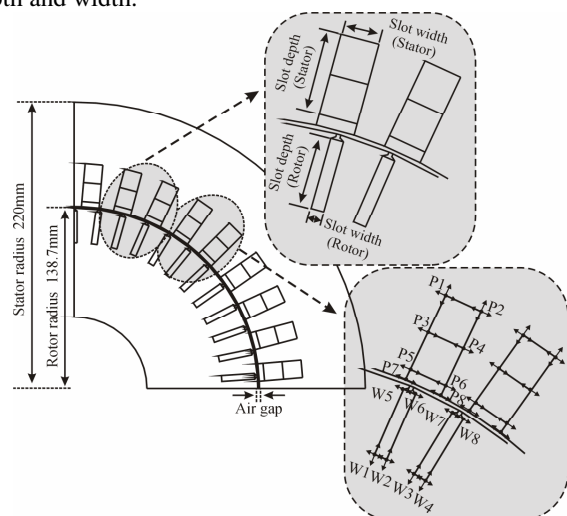


Fig. 1. The initial model, design variables and variation direction of 250kW traction induction motor

III. CONCEPT OF RESPONSE SURFACE METHODOLOGY

TABLE I
ANALYSIS OF VARIANCE

Source of Variation	Degree of Freedom	Sum of Squares	Mean Square	F_0
Regression	k	SS_R	$SS_R / k = MS_R$	MS_R / MS_E
Residual	$n-k-1$	SS_E	$SS_E / (n-k-1) = MS_E$	
Total	$n-1$	S_{yy}		

It is always necessary to examine the fitted model to ensure that it provides an adequate approximation to the true response and verify that none of the least squares regression assumptions are violated. In order to confirm adequacy of the fitted model, analysis-of-variance (ANOVA), shown in Table I is used in this paper. In Table I, n is the total number of experiments and k is the number of parameters in the fitted model.

IV. OPTIMIZATION PROCEDURE

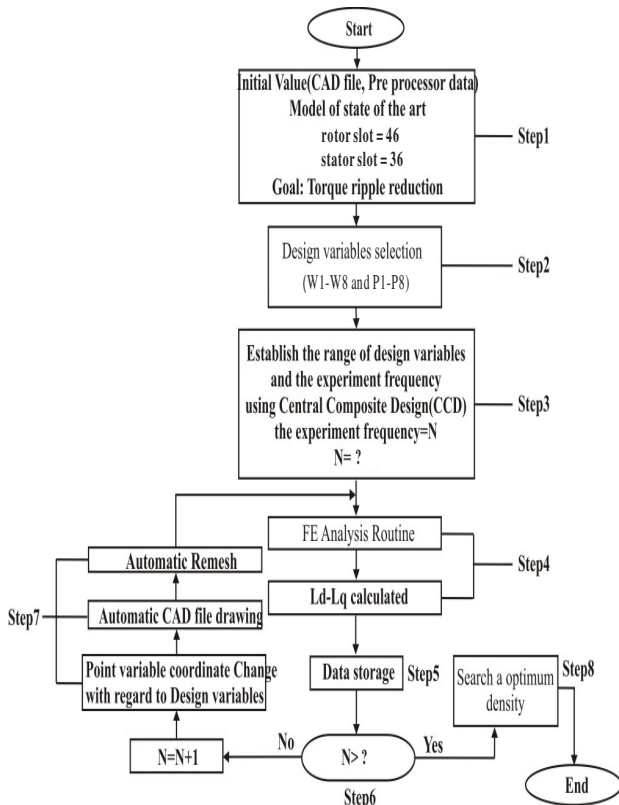


Fig. 2. Flow chart of design procedure

Fig. 2 shows the Flow chart of design procedure.

Design procedure according to the flow chart is as follows;

Step1 : Set the initial value (CAD file, Pre-processor data). And the initial model is assigned to rotor slot=46, stator slot=36.

Step2 : Width and depth in rotor and stator are adopted the design variables related to torque density in 250kW traction

induction motor. However, the ribs have a fixed value due to inherent manufacturing limitations.

Step3 : The range of design variables and experiment frequency is established by using the central composite design (CCD) shown Table I and II. The experiment frequency (N) is 2^k .

Step4 : Finite element analysis (FEA) is performed and Ld-Lq is calculated.

Step5 : The Ld-Lq obtained from FEA, are stored.

Step6 : The experiment frequency (N) > ?.

► Yes : Search a optimum torque density.

► No : $N=N+1$.

Step7 : The example of the point variables and variation direction of flux barrier rotor is well shown Fig. 2.

When the rotor and stator shape according to variables is varied, they have a difficulty in performing a lot of the pre-processor for FEA. For this reason, the new CAD file is redrawn with regard to the change of the design variables automatically. Next the process of automatic mesh generation follows. In mesh generation, mesh data doesn't change the node number, element number, region, boundary condition, etc., but only x, y coordinate data of the design variables. In this way, the proposed pre-processor procedure can be performed in a short period of time. In this way, this procedure goes on until $N=?$.

Step8 : The response surface model is created by data obtained from FEA according to an established range. Therefore, it is possible to get optimum torque density.

The RSM seeks to find the relationship between design variable and response through statistical fitting methods, which are based on the observed data from system.

The response is generally obtained from real experiments or computer simulations. Therefore finite element analysis (FEA) is performed to obtain the data of 250kW traction induction motor in this paper.

There are many experimental designs for creation of response surface. In this paper the central composite design (CCD) is chosen to estimate interactions of design variables and curvature properties of response surface in a few times of experiments. The CCD has been widely used for fitting a second-order response surface. [4]

More detailed results and discussion will be given in final paper. And the mathematical expressions for response surface methodology will be also given in extended version.

REFERENCES

- [1] J. M. Park, S. I. Kim, J. P. Hong, J. H. Lee, "Rotor design on Torque Ripple Reduction for a synchronous reluctance motor with concentrated winding using response surface methodology", *IEEE Transactions on Magnetics*, vol. 42, No.10, pp.3479-3481, Oct. 2006.
- [2] F. Gillon and P. Brochet, "Shape optimization of a permanent magnet motor using the experimental design method," *IEEE Trans. Magn.*, Vol.35, no. 3, pp. 1278-1281, 1999.
- [3] A. I. Khuri and J. A. Cornell, *Response Surface: Designs and Analysis*. New York, NY: Marcel Dekker, Inc., 1996.
- [4] Y. C. Choi, H. S. Kim, J. H. Lee, "Design Criteria for Maximum Torque Density & Minimum Torque Ripple of SynRM according to the Rated Wattage using Response Surface Methodology", *IEEE Transactions on Magnetics*, vol. 44, No. 11, pp.4135-4138. Nov 2008.

Optimal PM Design of PMA-SynRM for Wide Constant-Power Operation and Torque Ripple Reduction

Won-Ho Kim, Kwang-Soo Kim, Seung-Joo Kim, Jong-Bin Im, and Ju Lee, *Senior Member, IEEE*
 Department of Electrical Engineering, Hanyang University, Seoul, Korea
 wonho79@nate.com

Abstract— This paper presents the design process of permanent magnets to enable a wide range of constant-power operation and reduce the torque ripple by using analytical and numerical methods in PMA-SynRM. For a wide range of constant-power operation, the minimum d-axis flux-linkage of the permanent magnet is designed to be close to zero. Moreover, the unbalanced flux density in each segment is adjusted by changing the size of each permanent magnet to reduce the torque ripple. Finally, control simulations and experiments will be conducted to prove the validity of the suggested process.

I. INTRODUCTION

Existing permanent magnet designs, such as the BLDC and IPM, were designed after the D²L method to determine the outer diameter of the rotor first. However, for the permanent magnet assisted synchronous reluctance motor (PMA-SynRM) design, in which the permanent magnet is inserted into the existing SynRM, many parameters have been designated, and therefore the existing methods can't be applied.

This paper presents the design process of permanent magnets to enable a wide range of constant-power operation and reduce the torque ripple by using analytical and numerical methods in PMA-SynRM.

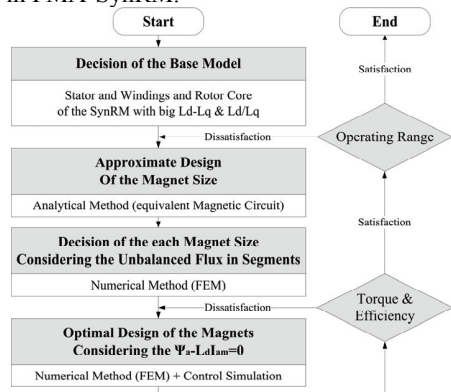


Fig. 1. Flowchart for the magnet design of PMA-SynRM

II. PERMANENT MAGNET DESIGN PROCESS

The most important factors when converting the existing SynRM into PMA-SynRM are the magnet location and designing the size. For wide constant-power operation, the magnet designing process is divided into three steps in this thesis. Prior to designing the magnet, the SynRM model was selected and the stator, windings, and rotor core were considered as the base models. After the base models were selected, the equivalent magnetic circuit method is used to largely design the permanent magnet. Additionally PM design is conducted for the correction of the unbalanced flux density in segments. Finally, in order to meet the ideal condition to

acquire no power limit, maximum power scope and constant-power operation scope, optimized designing for the permanent magnet is conducted. Follow contents give a full detail of three steps. The designing process is shown in Fig. 1.

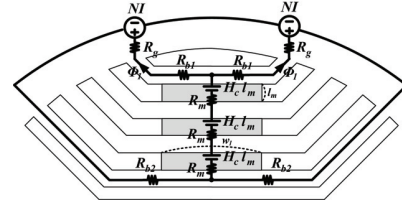


Fig. 2. Equivalent magnetic circuit of the PMA-SynRM

III. EQUIVALENT MAGNETIC CIRCUIT METHOD

The location of the permanent magnet can be limited upon the shape of barriers because the permanent magnet is inserted to the existing SynRM, therefore, the thickness of the permanent magnet is limited to the thickness of the barriers. Thus, width designing of the permanent magnet is focused in this thesis. For the model of this thesis, the shapes that allow inserting three magnets in the center were adopted and magnetic circuit of this model is shown in Fig. 2.

$$w_1 = \frac{3\Phi_g \cdot l_m}{\{3H_c l_m - NI - \frac{(R_{b1} + R_{b2} + R_g)\Phi_g}{2}\} \cdot \mu_{rec} \mu_0 L} \quad (1)$$

Formula (1) shows the equations related width of the permanent magnet by summarizing the magnetic circuit, and value is assumed by considering the machine parameters of existing SynRM and target specification and finally the approximate size of the permanent magnet is determined by applying the value on the formula.

IV. DESIGN CONSIDERING THE UNBALANCED FLUX

All the magnet sizes are assumed to be same in the above hypothesis. However, Fig. 3(a), which shows the flux density distribution calculated through FEM, shows that segment-1, -4 have saturation but there is almost no magnetic flux in the segment-2, -3. This phenomenon increases the use of permanent magnet unnecessarily and also can cause problems such as torque ripple due to the unbalanced flux in each segment. To solve this problem, the width of the permanent magnet located in the layer-2 was increased and the width of the permanent magnet located in the layer-1, -3 were decreased to balance the flux in the overall segments. During this process, the sum of magnet sizes were maintained as same as the existing. Fig. 3(b) shows the flux density distribution of the model with the optimized ratio of permanent magnets. In addition, torque ripple decreased significantly compared to the existing model in Fig. 4.

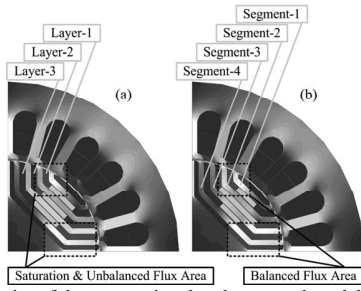


Fig. 3. Flux density of the conventional and proposed model at 15A, 500rpm

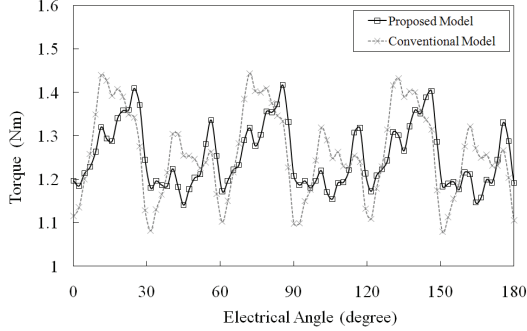


Fig. 4. Torque of the proposed model and conventional model@500rpm, 15A

V. PM DESIGN FOR WIDE CONSTANT-POWER OPERATION

If the voltage and current limitation are considered, the maximum power scope can be acquired by properly controlling the current vector. In order to broaden the scope of the constant-power operation, the optimized design for permanent magnet is conducted to meet $\Psi_a = L_d I_{am}$. [2] At this time, width ratio of the permanent magnet that was designed in the above is used.

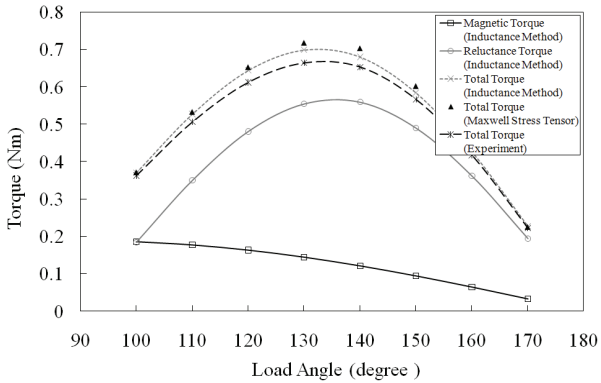


Fig. 5. Reluctance and magnetic and total torque@500rpm, 10.5A

A. FEM Analysis

In order to accurately calculate the inductance by considering the non-linear characteristics, RMS value of EMF and flux-linkage at no load, RMS value of flux-linkage when the current is applied, and phase difference between two flux-linkage were acquired through FEM.

In Fig. 5, reluctance torque and magnetic torque were calculated separately by means of the calculated inductance and result of Maxwell stress tensor method to prove the validity of the inductance calculation method in Fig. 5.

B. Maximum Power Control Simulation

The parameters that considered the calculated non-linear characteristics were used to conduct the maximum power control simulation. Constant-torque mode is controlled by means of Maximum Torque / Current Control Method and the formula for the reference current is shown in Formula (2).

$$i_{d_cr} = \frac{\Psi_a}{4(L_q - L_d)} - \sqrt{\frac{\Psi_a^2}{16(L_q - L_d)^2} + \frac{I_{am}^2}{2}} \quad (2)$$

In the constant-power torque, the Flux-Weakening Control Method is used to control and the current vector formula that is required during the flux-weakening is shown in Formula (3).

$$i_{d_cp} = \frac{\Psi_a L_d - \sqrt{(\Psi_a L_d)^2 + (L_q^2 - L_d^2) \left\{ (L_q I_{am})^2 - \left(\frac{V_{om}}{\omega} \right)^2 \right\}}}{L_q^2 - L_d^2} \quad (3)$$

Based on this, the locus of the current phase angle according to the speed of the final model is expressed in Fig. 6 as well as the limitation for voltage and current. Fig. 7 shows the torque and power versus speed.

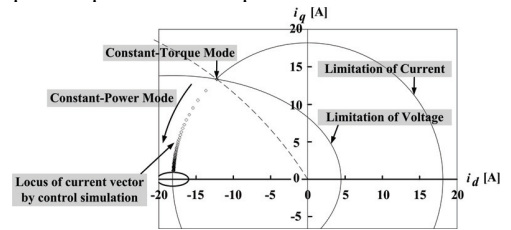


Fig. 6. Locus of the current phase angle in proposed model

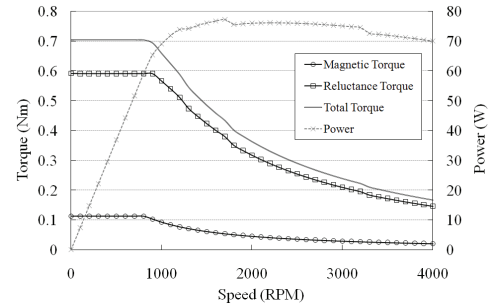


Fig. 7. Torque and power versus speed of proposed model

VI. EXPERIMENT AND CONCLUSION

The final model is manufactured for experiment and evaluation. The experiment results are shown Fig. 5 to prove the validity of the simulation. Finally, this model has simulated parameter $\Psi_{dmin}=0.003$ and measured parameter $\Psi_{dmin}=0.004$. This results shows the validity of the proposed design method.

VII. REFERENCES

- [1] I.S. Jacobs and C.P. Bean, "Fine particles, thin films and exchange anisotropy," in *Magnetism*, vol. III, G. T. Rado and H. Suhl, Eds. New York: Academic, 1963, pp. 271-350.
- [2] Shigeo Morimoto, Masayuki Sanada, and Yoji Takeda, "Performance of PM-Assisted Synchronous Reluctance Motor for High-Efficiency and Wide Constant-Power Operation", *IEEE Trans. Ind. Applicat.*, vol. 37, no. 5, pp. 1234-1240 SEP/OCT. 2001.

Study of Static and Dynamic Eccentricities of a Synchronous Generator Using 3D FEM

B. A. T. Iamamura¹, Y. Le Menach², A. Tounzi², N. Sadowski³, E. Guillot¹
EDF R&D¹, L2EP-LAMEL², GRUCAD³

EDF Electricité de France, 1 Av. Général de Gaulle 92141 Cedex, Clamart, France
L2EP University of Lille Nord de France, Cité Scientifique 59655, Villeneuve d'Ascq, France
GRUCAD/UFSC, CP. 476, 88040-900, Florianópolis-SC, Brazil
ba.tanno-iamamura@ed.univ-lille1.fr

Abstract — This paper deals with the study of static and dynamic rotor eccentricities of a synchronous generator using 3D FEM. First, both eccentricity cases are introduced as well as the used approach. Then, the model of the structure, based on the vector potential formulation is presented. Results obtained for magnetostatic case related to both defects and their combination are presented and discussed. The saturation effect is highlighted.

I. INTRODUCTION

Synchronous generators are widely used in high power conversion plants and their predictive maintenance constitutes a very important task in order to avoid an interruption of production. Therefore, the forecast and/or the detection of eventual defects are essential.

A very common defect in the rotor of such generators is eccentricity. Many techniques for diagnosis of this type of failure have been proposed, including analysis of the current in parallel windings [1], analysis of the rotor and stator vibrations [2], analysis of the shaft voltage, use of capacitive sensors [3] and use of flux probes in the stator iron stack [4]. Another approach is based on the measure of the magnetic field density in the air gap of the machine [5]. The last method is employed in this work. Thus, it is useful to arrange signatures of eccentricity defects to detect them.

In this paper, we present the study of the rotor static and dynamic eccentricities of a synchronous generator using 3D finite element analysis. Once both defects and the detection method presented, we introduce the used 3D-FEM model which is based on the potential vector formulation. Finally results for a specific synchronous generator are given for both defects and their combination. The effects of the steel saturation in the machine are highlighted.

II. ECCENTRICITY CASES AND MEASUREMENT METHOD

Generally, we can distinguish two eccentricity cases. In the static case, the rotor rotates around its own rotation axis but this one is displaced with regard to the stator axis (Fig. 1.a).

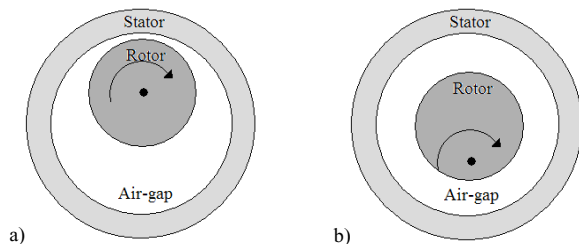


Fig. 1: Eccentricities: a) static b) dynamic.

In the case of dynamic eccentricity the center of the rotor axis is the same as the center of the stator one but it does not correspond to the rotation axis of the rotor (Fig. 1.b). These cases can be found alone or combined. When they are combined, the center of the rotor is not the same as the center of the stator and the rotor rotation axis is displaced.

It must be noticed that, in the experimental detection of these defects, when measuring the induction signal on only one point of the machine air-gap, it is impossible to verify whether there is a static eccentricity or not, because there is no variation of the radial flux in only one point. To overcome this problem, two 90° spatially shifted signals are subtracted and a Fast Fourier Transform (FFT) of the obtained waveform is analyzed.

III. FINITE ELEMENT METHOD APPROACH

To study the structure, we use three dimensional finite element method. In the magnetostatic case, the computation is carried out with the magnetic vector potential A formulation:

$$\text{rot} \frac{1}{\mu} \text{rot} A = J \quad (1)$$

with μ the magnetic permeability and J the current density. For the conductive region (damper windings), A - φ formulation is used to compute the eddy current:

$$\text{rot} \frac{1}{\mu} \text{rot} A + \sigma \left(\frac{\partial A}{\partial t} + \text{grad} \varphi \right) = 0 \quad (2)$$

with σ the electrical conductivity and φ the electrical scalar potential. Furthermore, the magnetic materials are modeled taking into account the non-linear $B(H)$ curve. At last, the movement is implemented through the locked step method.

To take into account the static eccentricity, all the nodes inside the slip surface (i.e. the nodes of the rotor, of the inner part of the air gap and the ones on the slip surface) must be moved (Fig. 2.b) with the same distance. In the case of the dynamic eccentricity, only the nodes of the rotor have to be moved while the slip surface remains at its initial position (Fig. 2.c).

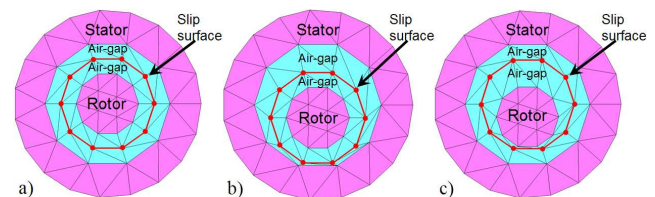


Fig. 2: Eccentricities techniques: a) healthy machine b) static c) dynamic.

To simulate the combined eccentricities (static and

dynamic) the slip surface and the node of the rotor must be moved but not with the same distance.

IV. APPLICATION

A. Description of the machine

To validate the approach, we study a turbo-generator of small size, similar to a French nuclear plant generator. This machine, of about 26.7 kVA at 50 Hz, has four poles, 48 slots in the stator and 36 slots in the rotor. Besides, the rotor has 36 short-circuited damping bars. The constant air-gap thickness is 1,5mm. The used mesh is constituted of 29160 nodes and 29014 elements. A cross section view is given in Fig. 3.

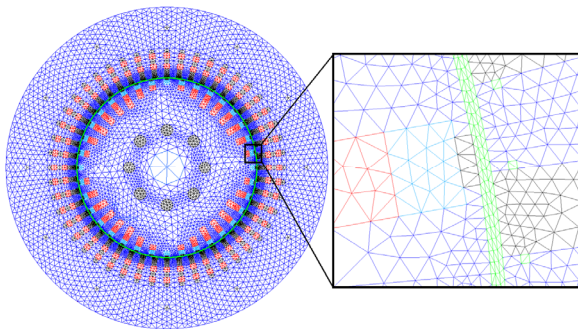


Fig. 3. Cross section view of the turbo-generator mesh.

B. Results

For each type of eccentricity, with the same 0.3 mm magnitude, simulations are carried out at no load conditions. Two cases are investigated: a non-saturated case with an excitation current I_{ex} of 5A and a very saturated case with $I_{ex}=30$ A.

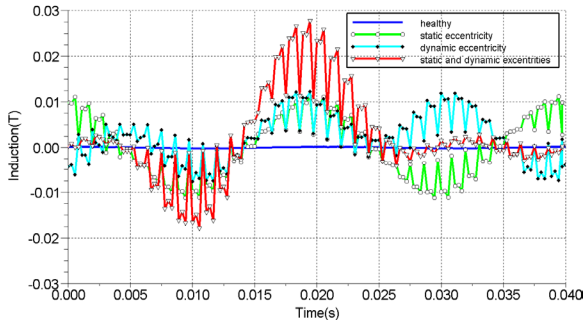


Fig. 4. Subtraction of the two signals in the air-gap, $I_{ex} = 5$ A.

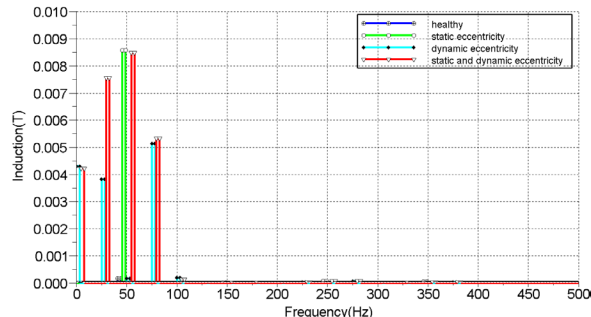


Fig. 5. FFT of the subtraction of the two signals in the air-gap, $I_{ex} = 5$ A.

Figures 4 and 6 show the subtraction of the two signals in air-gap for $I_{ex}=5$ A (Fig.4) and $I_{ex}=30$ A (Fig.6). In figures 5

and 7, the FFT of these signals are shown. While the signals of the healthy machine are harmonic free, for both cases, the static eccentricity induces a significant 50Hz-harmonic while dynamic eccentricity yields harmonics of 25 Hz and 75 Hz. Furthermore, the saturation introduces much more harmonics than those present in the linear case.

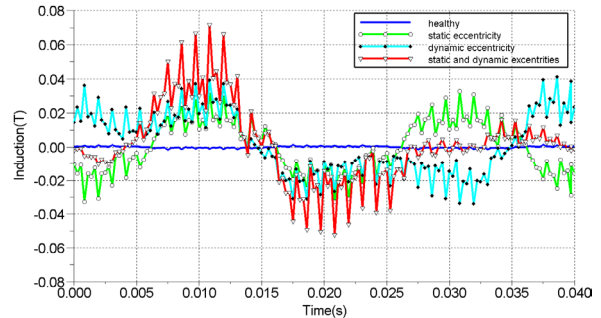


Fig. 6. Subtraction of the two signals in the air-gap, $I_{ex} = 30$ A.

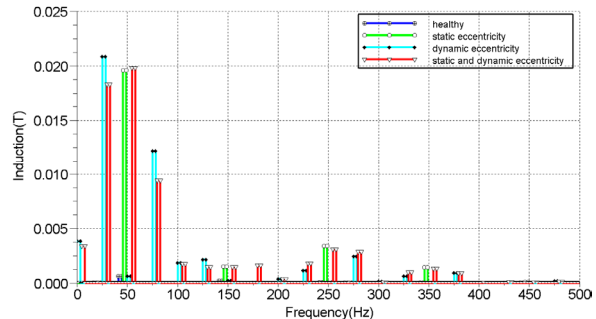


Fig. 7. FFT of the subtraction of the two signals in the air-gap, $I_{ex} = 30$ A.

V. CONCLUSIONS

In this paper, we studied the static and dynamic eccentricities at no load using 3D-FEM. Two 90° shifted magnetic induction signals in the air gap, can lead to the detection of the eccentricities and to differentiate their type by studying their harmonic content.

In the final paper, more details related to the numerical model will be given. Furthermore, results in magnetodynamic case will be presented and discussed in order to quantify the effect of the damper windings currents.

VI. REFERENCES

- [1] A. Foggia, J. Torlay, C. Corewinder, A. Audoli et J. Hérigault, "Circulating current analysis in the parallel-connected windings of synchronous generators under abnormal operating conditions", *IEMD International Conference on Electric Machines and Drives*, pp 634-636, Seattle, 1999.
- [2] D. Canha, W. Cronje, A. Meyer et S. J. Hoffe, "Methods for diagnosing static eccentricity in a synchronous 2 pole generator", *IEEE Power Tech*, pp 2162-2167, Lausanne, 2007.
- [3] G. B Pollock. et J. F. Lyles, "Vertical hydraulic generators experience with dynamic air gap monitoring", *IEEE Transactions on Energy Conversion*, vol. 7, n° 4, pp 660-668, 1992.
- [4] J. J. Simond, M. Tu Xuan et R. Wetter, "An innovative inductive air-gap monitoring for large low-speed hydro-generators", *ICEM International Conference on Electrical Machines*, Vilamoura, 2008.
- [5] R. L. Stoll et A. Hennache, "Method of detecting and modelling presence of shorted turns in DC field windings of cylindrical rotor synchronous machines using two airgaps search coils", *IEE Proceedings - Electric Power Applications*, vol. 135, pp 281-294, 1988.

FE-Circuit Coupled High Frequency Model of Electric Machines for Simulation and Evaluation of EMI Issues in Motor Drives

O. A. Mohammed

Florida International University

ECE Department, Energy Systems Research Laboratory, Miami, FL, USA

mohammed@fiu.edu

Abstract—An FE-circuit coupled high frequency model is proposed to simulate electromagnetic interference (EMI) due to terminal overvoltage and ground current of electric machines and their driving circuits. The high frequency effects due to PWM drive were considered in the transient FE-circuit coupled model of the motor using a two-step procedure. First, the resistance in each individual winding turn is evaluated by time harmonic FE analysis considering skin and proximity effects. The capacitances between the winding were calculated by an electrostatic FE analysis to form a distributed parameter model of the winding in each conductive region. Second, a lumped parameter model for the conductive regions was obtained through matrix reduction technique. The lumped models of the distributed coils were connected in series to form a per phase winding model. The FE-circuit coupled model of the motor is laboratory tested in a motor drive to evaluate the terminal over voltages and ground currents. The numerical results were successfully verified by laboratory testing.

I. INTRODUCTION

High frequency motor models play important roles in the evaluation of EMI in an integrated motor drive system. In earlier work by these authors, the high frequency phase variable model of PM synchronous motor was developed and implemented in Simulink environment [1]. In this model, the per phase distributed winding circuit was developed considering the high frequency effects and then lumped to form the high frequency winding branch. This branch was connected in parallel to the low frequency phase variable model to form the high frequency phase variable model which can be used for dynamic simulations.

In this paper, the full FE model was used directly to couple the driving circuit rather than creating the phase variable model first. This can be used when the high frequency interactions are needed to evaluate EMI issues without the need for including low frequency effects. The model can also be used for new motor design development when the motor is utilized in a developmental driving circuit as Hardware-in-the-loop. This model can be used to further verify the accuracy of the previously developed high frequency phase variable

The model is coupled to an external circuit to include various capacitances dominant under high frequency operation. The circuit is excited by an external voltage source modeled in Simulink. To simplify the circuit, the machine windings were divided into several sections. Each coil represents one section. A 2D magnetodynamic analysis was performed to find the resistance of each turn of the coil as a function of frequency while an electrostatic analysis was performed to find the capacitance between the various

parts of the coil. The coupled circuit-FE model was exported to Simulink environment for use in the integrated drive system.

II. DISTRIBUTED PARAMETER MODEL OF THE COIL

Simulations were performed on a small 3-phase, 42-V, 10-pole, 0.28-HP, 3600-rpm, 7.8-A PM synchronous motor. The simulated motor model was built based on its actual geometry information. The individual turns in each coil were considered. The motor has double layer windings with random winding arrangement. There are four coils per phase; each coil has 13 turns. Therefore, each half slot contains 13 conductors. Each turn is made of wire gauge number 22. All the slots were modeled so that the effects of geometrical variation in the magnetic circuit on the machine circuit parameters can be considered. The machine was modeled to take into consideration the conductor skin and proximity effects. The resistance value at high frequency can be much higher than the low frequency value. The inductance value decreases with an increase in the operating frequency while the capacitance effect comes into effect at high frequencies.

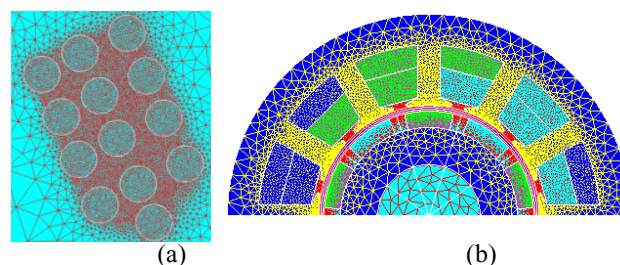


Fig. 1 Mesh details (a) in individual turn (b) in half geometry model

Fig. 1(a) shows the FE mesh inside each individual turn used to solve magnetodynamic analysis while fig. 1 (b) shows the FE mesh inside the half geometry model used to solve the transient FE analysis. The current is supplied to each individual turn in a coil with a set of frequency value ranging from 5 kHz to 1 MHz. The voltage of each turn was obtained to provide the impedance. Using the impedance, the resistance was calculated at the corresponding applied frequency. The same procedure was repeated for the turns in all other coils. The frequency range mentioned above covers the PWM practical switching frequencies and their associated harmonic components. Since the capacitances are dependent only on the geometry of the motor and less dependent on the covered PWM frequency range, an electrostatic analysis was performed

for its calculation. The machine's core was considered as ground for the calculation of capacitance values to ground.

Fig. 2 shows the distributed parameter model a coil where N represents the number of turns in the coil. The self and mutual capacitances between the various turns of the coil were considered. Each turn has a self capacitance and mutual capacitances with other turns in the coil. The lumping of the turns parameters in each coil was performed to reduce the order of the model [2]. The lumped winding model for each phase is shown in fig.3. In this figure, A1, A2, A3, A4 represent the coils in each phase. These coils were assigned to the FE domain to consider the high frequency effects in the coupled FE-circuit model.

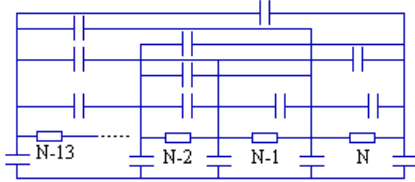


Fig. 2. The distributed parameter model of a coil

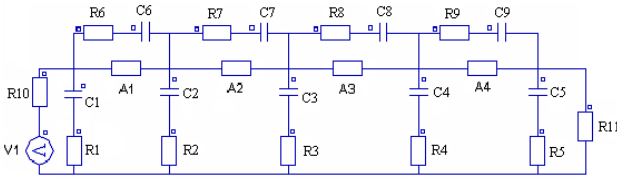


Fig.3 Lumped winding model for each phase

The coupled field and circuit equations were solved simultaneously during the magnetodynamic and transient problems. The equations used for the coupled problem are as follows:

$$\nabla \times H = J_s + J_e \quad (1)$$

$$[E_m] = [R_m][I_m] + [L_m] \frac{d}{dt}[I_m] + (1/C_m) \int I_m dt + [\gamma_m] \quad (2)$$

Where, H is the magnetic field intensity, J_s is the source current density, J_e is the induced current density. In equation (2), R_m represents the resistances matrix, L_m is the inductances matrix, C_m is the capacitances matrix, γ_m is the matrix of non-linear voltage drops, I_m is the matrix of currents. E_m is the matrix of voltage sources.

The resistance value of the coils was obtained from the FE solutions to account for the skin and proximity effects of each turn in the lumped model. Small value resistances were added to capacitances for numerical stability.

The capacitances C1 to C5 represent the coil to ground capacitance while C6 to C9 represent mutual capacitances between different coil sections. The coil capacitances were obtained by lumping the turn capacitance network. The matrix reduction technique was used for lumping the parameters [2]. The resulting matrix is of the order 2N following a process of shifting internal capacitances towards pre-established section nodes. Once the capacitances are moved to section nodes, the conductor

resistances were lumped. Similar winding model was formed for each phase.

III. EXPERIMENTAL AND SIMULATION RESULTS

A real time distributed simulation environment with the actual motor and drive implemented on PC-cluster was used for performing the experimental verification. Results for overvoltage and ground current were obtained and compared with the simulation results.

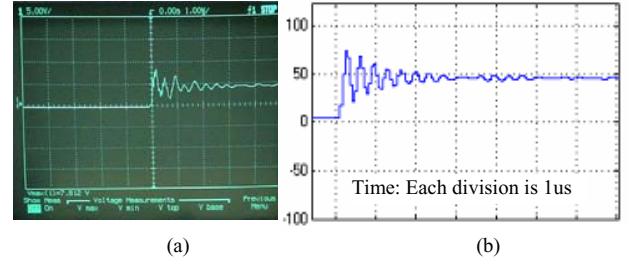


Fig. 4. (a) Experimental overvoltage (b) simulation overvoltage

For simulation, the high frequency models of the integrated system components including inverter and cable in addition to the motor were built and implemented in Simulink. The model was tested for the motor terminal overvoltage and ground current. During transient simulation, the FE model, drive and control equations were solved simultaneously with the same time step. Fig. 4 shows a comparison between experimental and simulation results of overvoltage. The magnitude of overvoltage is about 75 volts. The time period of $2\mu s$ shows the same number of oscillations. Thus the results show good agreement in terms of magnitude and frequency of oscillations. Both results are captured with different time steps since the same time step can not be maintained in experiment and simulation and at different instants of time. However, the correspondence between two is satisfactory. Complete results will be given in full paper.

IV. CONCLUSION

The coupled FE-circuit electric machine model for simulating EMI issues in a motor drive was presented. The model can accurately predict the EMI caused by ground current and motor terminal overvoltage. Use of this procedure could prove economical as it would help designers develop new motor designs for low and high frequency operating conditions numerically. Using the proposed model, this is achieved without the need for repeated build and test procedures in the development stage.

V. REFERENCES

- [1] O. A. Mohammed, S. Ganu, N. Abed, S. Liu and Z. Liu, "High frequency PM synchronous motor model determined by FE analysis," IEEE Transactions on Magnetics, April 2006, pp.1291-1294.
- [2] F. D. Leon, A. Semlyen, "Reduced order model for transformer transients," IEEE Transactions on Power Delivery, Vol.7, No.1, Jan.1992, pp. 361-369.

A New Scheme for Detecting Longitudinal Defects in Conductive Tubes by EC Testing

[†]F. Ferraioli, ^{*}A. Formisano, ^{*}F. Iacotucci and ^{*}R. Martone.

(+)Ansaldo Ricerche S.p.A. Via Nuova Delle Breccie 260, I-80147 Naples, Italy

(*) Dipartimento di Ingegneria dell'Informazione, Seconda Università di Napoli, Italy

Via Roma 29, I-81031 CE Aversa, Italy, E-mail: raffaele.martone@unina2.it

Abstract — The inducting coils typically used in Eddy Current Testing (ECT) of tubular structures, dominated by longitudinal dimensions, are much more effective for *azimuthal* than for *longitudinal* defects. This paper shows how *azimuthal* inducting currents are well suited for *longitudinal* defects. In addition, the paper proposes a new concept of exciting coils, *azimuthally* shaped, longitudinally displaced and suitably powered; it is showed how, by suitably driving the coils current, the resulting excitation field can be controlled in position, shape and speed in such a way to optimize the defect searching and sizing.

I. INTRODUCTION

Eddy current testing is one of the most diffused methods for nondestructive inspection of metallurgical products. It uses a time varying magnetic field, designed to induce in the sample a suitable current pattern. Of course, the actual current distribution is affected by defects, eventually located in the sample. As a consequence, the analysis of either the resulting magnetic field or the impedance of the coils could provide useful information for the defect characterization.

A relevant field of application of ECT is the testing of tubular metallic structures. The practical solution firstly proposed was based on the use of rotating components [1], or encircling coils [2]. Successively, fixed systems generating rotating fields have been proposed [3]-[8], and finally multi-frequency currents have been introduced [9].

Most of the proposed layouts were based on the use of *longitudinal* currents, whose shape match the main direction of the tube. Such driving systems are well suited to localize *azimuthal* defects, because the currents they induce are in the longitudinal directions.

In this paper an *azimuthal* induction system is illustrated and its effectiveness for catching *longitudinal* defects is investigated. In addition, a flexible strategy is proposed to drive the inducting currents with the aim of patrolling the suspected region, to try to localize the defect and to identify its main characteristics.

It is well known that a rotating field can be created by driving a suitable set of *longitudinal* coils with a poliphase set of currents [11]; in similar way, here it is shown that a sort of *traveling* field can be easily produced by a poliphase set of currents driving a suitable set of *azimuthal* coils. Of course, each actual coil has to include both *longitudinal* and *azimuthal* coils, because of the needs for current closure. In the full paper a suitable 3D short “saddle” coil, able to highlight *azimuthal* effects, will be analyzed, while in this short version, a simplified 2D *azimuthal* coil system is used to assess the effectiveness of the method.

II. PRELIMINARY RESULT

The mathematical formulation of the problem has been previously reported, and can be considered rather standard [3]. Therefore, its description with some details will be given in the full version while reserving here a larger room for the system description and for the discussion of the preliminary results.

In order to assess the proposed technique, a conductive non-magnetic tubular structure has been considered and a set of 18 *circular* coils has been introduced to induce eddy current maps in the tube (see Table I and Fig. 1)

TABLE I
GEOMETRICAL AND ELECTROMAGNETICAL CHARACTERISTIC

Parameter	Value
Tube length	10 m
Tube diameter	0.3 m
Tube thickness	0.03 m
Tube conductivity	6.0e7 S/m
Tube permeability	1.27 10 ⁻⁷ H/m
Number of coils	18
Coils cross section	12 cm ²
Coil distance	0.1 m
AC current frequency	200 Hz
Current amplitude	65 A

It should be noticed that the tube is long enough to neglect the effect of *longitudinal* boundary effects. In addition, the frequency has been fixed in such a way to provide a penetration depth (in order of 0.15 m) much higher than the tube thickness.

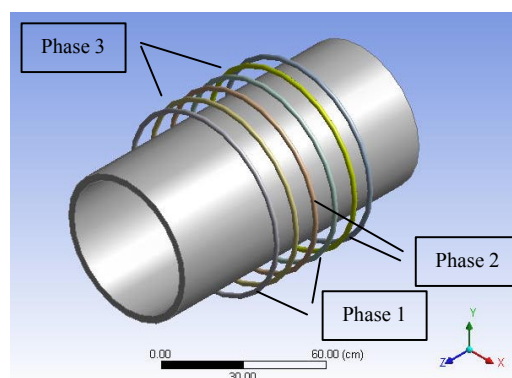


Fig. 1. – Overview of the excitation system. The phase of each coil is also shown.

When connected in opposite series, three couples of coils form a “three phase *longitudinal* polar couple”. Of course several polar couples can be generated by juxtaposing suitable

sets of six coils. In the case here described, the 18 coils are combined to create three *longitudinal* polar couples (in Fig.1 just one of them is reported). Such a system, if driven with a symmetric three-phase currents system, is able to generate a magnetic field *traveling* in *longitudinal* direction.

In order to evaluate the capability of such a system to perform an effective ECT, the Ohmic power density related to the eddy currents induced in the tube has been calculated in a number of tube positions (Fig. 2), and it is reported in Fig. 3 for each evaluation point. Of course, the power density shows a doubled frequency, because of the square of the current density in the power expression, and reaches its maximum just near the coils. Note that the higher the power density is at the suspected defect location, the more sensible the detection system becomes to perturbations induced by defects.

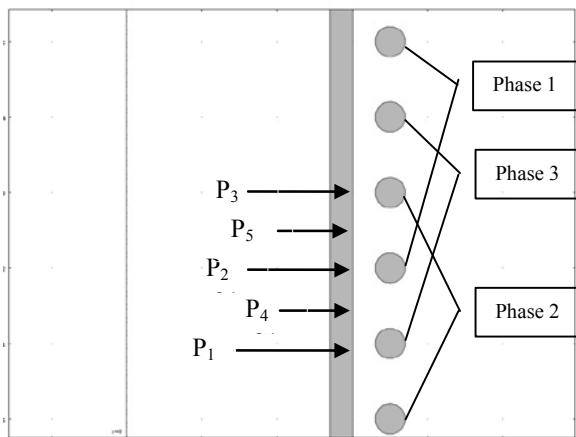


Fig. 2 Test points in the tube.

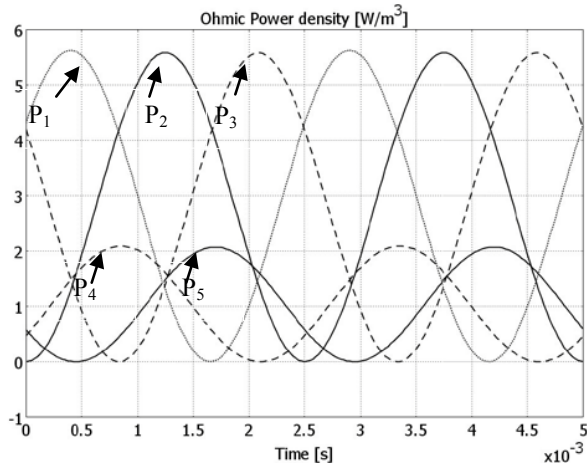


Fig. 3 Ohmic power density in the test points for a *travelling* field

However, a more general power supply system can generate a magnetic field distribution characterized by different shape and velocity. For example, the *traveling* field can be *stopped* if, instead of a set of three-phase currents, three *in-phase* currents are used with suitable amplitudes, and the actual position of the *stopped* field depends only on such current amplitudes. As an example, in Fig. 4 the power density time variation is shown for a field *stopped* in correspondence of the point P₂ (see for comparison Fig. 3).

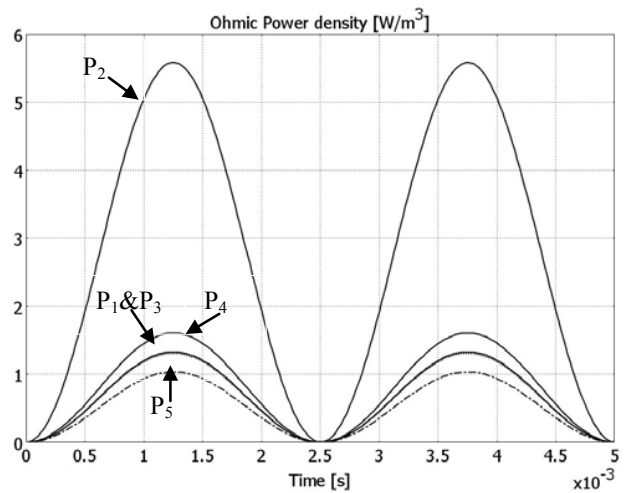


Fig. 4 Ohmic power density in the test points for a *stopped* field

III. CONCLUSION

An effective use of longitudinal and azimuthal inducting currents combined with independent control of the driving currents allows to increase the ECT performance in testing tubular structure. In the full paper, a detailed description of the mathematical model for the proposed excitation system will be given, and 3D saddle coils will be used.

IV. REFERENCES

- [1] P. Xiang, S. Ramakrishnan, X. Cai, P. Ramuhalli, R. Polikar, S.S. Udpa and L. Udpa, "Automated analysis of rotating probe multi-frequency eddy current data from steam generator tubes", IJAEM., vol. 12, pp. 151–164, 2000.
- [2] B. Bisiaux, C. Reboud, D. Premel, G. Pichenot, D. Lesselier, "Simulation of 3D Eddy Current Testing Of Tubes with External Probes: Modelling Approach and Experimental Validations", Proceedings ECNDT 2006, 25-29 Sept. 2006, Berlin (G).
- [3] A. Savin, R. Grimberg, and O. Mihalache "Analytical Solutions Describing the Operation of a Rotating Magnetic Field Transducer", IEEE T-MAG, vol. 33, no.1, pp. 697-702, 1997
- [4] R. Grimberg, I. Olteanu, T. Cristea, M. Goia, D. Gradinariu, R. Plavanescu, T. Bacanu, A. Andreescu, and D. Apavaloie, "Eddy current examination of steel wires," NDTInt., vol. 23, no. 4, pp. 201-206, 1990.
- [5] R. Grimberg, Adriana Savin, O. Mihalache, N. Rezlescu, Elena Bradu, S. Chifan, V. Iftimi and A. Andreescu, "Reliability of automatic eddy-current equipment with a rotating magnetic field", NDT&E International, vol. 28, no. 5, pp. 297-301, 1995
- [6] F. Ferraioli, A. Formisano, and R. Martone, "A Novel Eddy Current Diagnostic Technique For Tubular Structures", Proceeding IGTE Symp. 2006, 17-20 Sept. 2006, Graz (AC)
- [7] R. Grimberg et al., "Eddy current method for characterizing the tubes under pressure", Proceedings ISCS2007, Timisora, Romania, 20-21 Nov 2007
- [8] R. Grimberg, L. Udpa et al., "Eddy Current Examination Of Steam Generator Tubes From Phwr Power Plants Using Rotating Magnetic Field Transducer" November 07–09, 2007, pp 87-96 Prague, Czech Republic
- [9] E. Goldstein and S. A. Kalganov, "Eddy-Current Nondestructive Testing of Long Cylindrical Components Using Spatial Magnetic Field Components of Different Frequencies", Russian Journal of Nondestructive Testing, vol. 36, no. 5, pp. 360-365, 2000
- [10] A. Formisano, R. Martone, F. Ferraioli and F. Iacotucci, Virtual positioning and Shaping of Source Fields for ECT of Tubes, EMF 2009, Mondovi (TO), Italy, accepted for presentation.

A Study on the FE Analysis of a Flux-Reversal Machine under 4-switch converter

Hyun-Soo Kang¹, Tae Heoung Kim², and Byoung-Kuk Lee¹

School of Information and Communication Engineering, Sungkyunkwan University
Suwon-si, 440-746, Korea

Department of Electrical Engineering, Engineering Research Institute, Gyeongsang National University
Jinju-si, 660-701, Korea
Ktheoung@gnu.ac.kr

Abstract— Many different converter topologies have been developed to reduce the converter construction cost by using minimum number of switches. Among of the solutions, four-switch converter topology with a novel PWM control technique based on the current controlled PWM method is treated as a good solution. In this paper, one introduces a two dimensional time-stepped voltage source finite-element method (FEM) to analyze the characteristics of a Flux-Reversal Machine (FRM) with the 4-switch converter. To prove the proposed computational method, the digital signal processor (DSP) installed controller and the prototype FRM are built and experiments are performed.

I. INTRODUCTION

Because the principle of operation is similar to the brushless DC machine (BLDCM), 3-phase Flux-Reversal Machine (FRM) needs quasi-square current waveforms, which are synchronized with the back-EMF to generate constant output torque and have 120° conduction and 60° non-conducting regions. Also, at every instant only two phases are conducting and the other phase is inactive. This control action can be realized using 6-switch converter topology. However, these days, many different converter topologies have been developed to reduce the converter construction cost by using minimum number of switches. One of them is 4-switch converter topology, which is shown in Fig. 1 with a novel PWM control technique based on the current controlled PWM method [1]. However, the FRM under 4-switch converter is supplied by different voltage level, so that the load current are reduced by $\sqrt{3}$ with respect to the current obtained when the same voltage and the 6-switch converter is used. Also, due to supplying voltage irregularity and lack of a phase control freedom, the phase current can be much more fluctuated, resulting in torque ripple. Therefore, when the 4-switch FRM is used for a certain application, one should understand and analyze the overall performance with respect of torque ripple and iron losses, compared with 6-switch FRM.

In this paper, the authors introduce the computational method to analyze the characteristics of the FRM under the 4-switch converter using a two dimensional time-stepped voltage source finite-element method (FEM). To produce the 4-switch converter and perform the experiment, the digital signal processor (DSP) installed controller and the prototype FRM are built. From the analysis and experimental results, it can be verified that the proposed analysis method is suitable to

analyze a FRM under 4-switch converter.

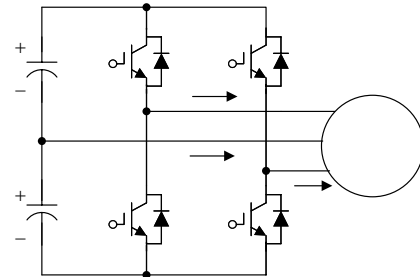


Fig. 1. 4-switch 3-phase FRM drive system

II. FINITE ELEMENT FORMULATIONS

At each instant, the interaction between the 4-switch converter circuitry and electromagnetics is achieved by defining the winding current in terms of the electrical circuit parameters [2]. The actual phase currents of the 4-switch FRM are controlled by hysteresis current controller. Therefore, the detailed voltage equations taking account of the current regulation using hysteresis controller should be derived.

A. Voltage Equation when current is flowing through phases B and C

With reference to Fig 1, consider a 60-degree period when current is flowing through phases B and C. The switch S4 is turned on and off according to the current regulation in this mode, so that the flow of current can be categorized into four cases as shown in Figs. 2. Fig. 2(a) and (b) show the current flows at the commutation instant when switch S4 is turned on and off, respectively. In these cases, the current continues to flow in open phase A due to its inductance L . As the result, two voltage equations can be derived as:

$$R_c i_c + L_{lc} \frac{di_c}{dt} + \frac{d\Phi_c}{dt} + R_b i_b + L_{lb} \frac{di_b}{dt} - \frac{d\Phi_b}{dt} = V_1 \quad (1)$$

$$R_c i_c + L_{lc} \frac{di_c}{dt} + \frac{d\Phi_c}{dt} + R_a i_a + L_{la} \frac{di_a}{dt} - \frac{d\Phi_a}{dt} = V_2 \quad (2)$$

where R is the resistance of phase winding, L_l is the leakage inductance of the stator coil ends and Φ is the flux linkage of phase winding. V_1 and V_2 represent voltage and Table II shows there values. V_{CE} and V_F are the forward

voltage drop across the transistor and the diode, respectively.

If the current in the open phase A decays to zero and switch S4 is turned on and off, only the main voltage equation exists as shown in Figs. 2(c) and 2(d). In these cases, the voltage equations are identical to (1).

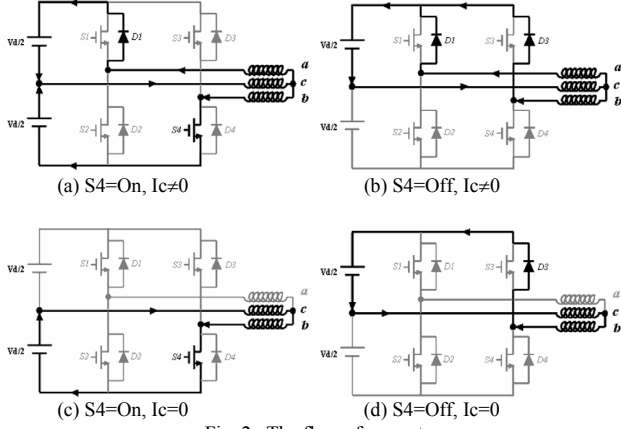


Fig. 2. The flow of current

B. System Matrix

After deriving the circuit voltage equations at each Mode, the backward difference method is adopted to treat the time derivative terms and to construct system matrix.

In the case there is one current loop as shown in Figs. 2(c) and (d), the system matrix can be expressed as (3). In the case of having two circuit voltage equations as shown in Figs. 2(a) and (b), the system matrix can be obtained as (4).

$$\begin{aligned} & \begin{bmatrix} [S] & \{Q\} \\ [F]/\Delta t & 2R + 2L_l/\Delta t \end{bmatrix} \begin{bmatrix} \{A\}^{t+\Delta t} \\ I_1^{t+\Delta t} \end{bmatrix} \\ & = \begin{bmatrix} [0] & \{0\} \\ [F]/\Delta t & 2L_l/\Delta t \end{bmatrix} \begin{bmatrix} \{A\}^t \\ I_1^t \end{bmatrix} + \begin{bmatrix} \{G\}^{t+\Delta t} \\ V_1^{t+\Delta t} \end{bmatrix} \end{aligned} \quad (3)$$

$$\begin{aligned} & \begin{bmatrix} [S] & \{Q_1\} & \{Q_2\} \\ [F_1]/\Delta t & 2R + 2L_l/\Delta t & R + L_l/\Delta t \\ [F_2]/\Delta t & R + L_l/\Delta t & 2R + 2L_l/\Delta t \end{bmatrix} \begin{bmatrix} \{A\}^{t+\Delta t} \\ I_1^{t+\Delta t} \\ I_2^{t+\Delta t} \end{bmatrix} \\ & = \begin{bmatrix} [0] & \{0\} & \{0\} \\ [F_1]/\Delta t & 2L_l/\Delta t & L_l/\Delta t \\ [F_2]/\Delta t & L_l/\Delta t & 2L_l/\Delta t \end{bmatrix} \begin{bmatrix} \{A\}^t \\ I_1^t \\ I_2^t \end{bmatrix} + \begin{bmatrix} \{G\}^{t+\Delta t} \\ V_1^{t+\Delta t} \\ V_2^{t+\Delta t} \end{bmatrix} \end{aligned} \quad (4)$$

where, S is the stiffness matrix, Q and F are the matrix related to the stator winding and back-EMF, respectively. G is the forcing term by a magnet.

III. RESULTS AND DISCUSSIONS

Fig. 3 compares the measured and the calculated current in each phase. It is noted that the experimental results closely match the simulation ones of the proposed analysis method. As phases A and B are activated, these phases are supplied by the full of dc-link voltage, so that during one PWM period, the

current is increased more than the other operating modes. Moreover, independent control of phases A and B results in current ripple in phase C during the silent periods, resulting from the difference between the phase A and phase B currents. Even though it contains more current ripple than case of the six-switch converter, it can be acceptable and also can be reduced by controlling the hysteresis band size. From the detailed investigation of the experimental results, it is noted that the authors successfully utilize the four-switch converter topology to drive the 3-phase FRM and the validity of the developed direct current controlled PWM is fully verified.

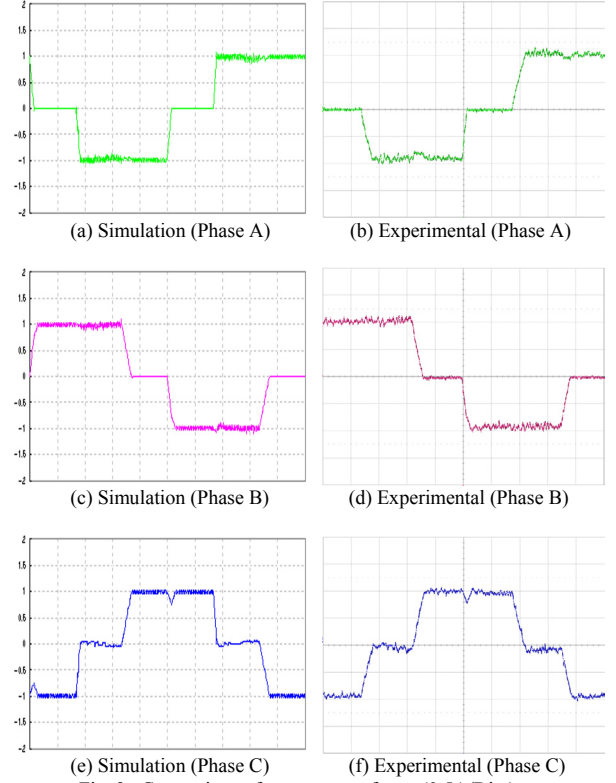


Fig. 3. Comparison of current waveforms (0.5A/Div.)

IV. CONCLUSION

In this paper, a 2-dimensional time-stepped voltage source finite element method in 4-switch converter system has been proposed. To prove the propriety of the proposed analysis method, the prototype FRM and a DSP installed experimental devices were equipped and the experiment has been performed. As a result, accurate solutions can be obtained by the proposed method and the 4-switch converter topology with a direct current controlled PWM can be successfully utilized to drive the 3-phase FRM.

V. REFERENCES

- [1] B. K. Lee, T. H. Kim, and M. Ehsani, "On the feasibility of four-switch bldc motor drives for low cost commercial applications: topology and control," *IEEE Trans. on Power Electronics*, vol. 18, no. 1, pp. 164-172, 2003.
- [2] T. H. Kim and J. Lee, "Influences of PWM mode on the performance of flux reversal machine," *IEEE Trans. on Magn.*, vol. 41, no. 5, pp. 1956-1959, May 2005.

EEG inverse problem solution with minimal influence of the conductivity

Bertrand Russel Yitembe¹, Guillaume Crevecoeur², Roger Van Keer¹, and Luc Dupré²

¹Dept. of Mathematical Analysis, Ghent University, Galglaan 2, B-9000 Ghent, Belgium

²Dept. of Electrical Energy, Systems & Automation, Ghent University, Sint-Pietersnieuwstraat 41, B-9000 Ghent, Belgium

Abstract—In this paper, we propose a novel method that improves the accuracy of the estimation of neural electrical dipoles when solving the EEG inverse problem. A spherical head model is used where we limit the influence of the unknown conductivity brain-skull ratio on the inverse problem. We redefine the cost function that is used in the EEG problem where only relevant information is taken as input in the inverse problem. In contrast to previous approaches, weighting factors are used so that the impact in the inverse problem of each electrode is strategically chosen in order to reduce the error made on EEG dipole source localization. The proposed method enhances the source localization accuracy from approximately 9mm to 1mm for dipoles near the edge and from 2.1mm to 0.4mm for dipoles near the center of the brain.

I. INTRODUCTION

ELECTROENCEPHALOGRAPHY (EEG) is a medical imaging technique that neurologists use to investigate neurological disorders. Using metal electrodes, brain activity can be recorded non-invasively. EEG source analysis is particularly useful in the diagnosis of neurological disorders like epilepsy. Indeed, the determination of the origin of specific EEG waveforms helps neurologists to pinpoint the origin of the epilepsy and to evaluate the patient for resective surgery. However, when coupling the non-invasive EEG measurements to a numerical method, inaccuracies in the neural source localization are introduced. Indeed, the accuracy of EEG source analysis is mainly determined by the noise in the measurement and the accuracy of the numerical head model parameters. Also, the source modelling of the brain activity introduces an error. Since the brain electrical activity of patients suffering from epilepsy are characterized by a limited number of electrical dipoles [1], we do not investigate the influence of the used source model. The head model on the other hand has a large impact on the solution of the EEG inverse problem where important errors are introduced by the uncertainties of the values of the electrical conductivity of the brain and the skull. The quantitative values of the electrical conductivity of the brain and the skull remain a very important parameter that attract a lot of debates in EEG source analysis field, see e.g. [2], [3]. In numerical methods, the brain to skull ratio of the conductivity is the important parameter and may vary between 1/9 to 1/60. This paper presents a novel numerical scheme, the so-called Reduced Conductivity Dependence (RCD) method, that minimizes the influence of the conductivity uncertainty on the localization errors. This method introduces a selection procedure of the EEG electrodes

that are minimally influenced by the conductivity values. We validate the method onto a widely-used approximation of the head: the semi-analytical spherical head model. Comparisons are made with traditional least-squares minimization methods. For simplicity of analysis, we impose that the neural activity is represented by a single electrical dipole.

II. EEG SOURCE ANALYSIS

A. Forward problem

The forward problem starts from a given electrical dipole and calculates the potentials at the electrodes. For this, the brain to skull ratio of the conductivity X needs to be provided. The spherical head model is a widely-used approximation of the head where the head is represented by three spheres: the inner sphere represents the brain, the intermediate layer represents the skull and the outer layer represents the scalp. The forward problem needs to solve the Poisson's equation:

$$\nabla \cdot (\sigma(\mathbf{r})\nabla V(\mathbf{r})) = \mathbf{d} \delta(\mathbf{r} - \mathbf{r}_d) \quad (1)$$

with $\sigma(\mathbf{r})$ the place dependent conductivity determined by X , $V(\mathbf{r})$ the place dependent potential, \mathbf{d} the dipole orientation vector (with intensity $I = \|\mathbf{d}\|$) and \mathbf{r}_d the dipole location vector. $\delta(\cdot)$ is the three-dimensional delta Dirac function. An analytical expression for the potential values can be calculated using [4]. In this study, a standard configuration of $m = 27$ electrodes is used. For given \mathbf{r}_d and dipole orientation \mathbf{d} , the electrical potential values at the given electrodes can be calculated: $\mathbf{V}_m(\mathbf{r}_d, \mathbf{d}) \in \mathbb{R}^{m \times 1}$. The potential values are a linear function of the dipole orientation: $\mathbf{V}_m = \mathbf{L}(\mathbf{r}_d) \cdot \mathbf{d}$ with $\mathbf{L} \in \mathbb{R}^{m \times 3}$ the so-called lead field matrix.

B. Traditional solution of EEG inverse problem

The aim of the EEG inverse problem is to start from measured EEG potentials $\mathbf{V}_{\text{meas}} \in \mathbb{R}^{m \times 1}$ and to recover the neural dipole location \mathbf{r}_d^* and orientation \mathbf{d}^* . This is carried out by minimizing a cost function, the so-called relative residual energy (RRE):

$$\{\mathbf{r}_d^*, \mathbf{d}^*\} = \arg \min_{\mathbf{r}_d, \mathbf{d}} \text{RRE}(\mathbf{r}_d, \mathbf{d}) \quad (2)$$

with

$$\text{RRE}(\mathbf{r}_d, \mathbf{d}) = \frac{\|\mathbf{V}_{\text{meas}} - \mathbf{V}_m(\mathbf{r}_d, \mathbf{d})\|}{\|\mathbf{V}_{\text{meas}}\|} \quad (3)$$

where $\|\cdot\|$ is the L_2 norm. The number of parameters in this least-squares cost function can be reduced by considering

the optimal dipole components: $\mathbf{d}_{\text{opt}} = \mathbf{L}^\dagger \cdot \mathbf{V}_{\text{meas}}$ with \mathbf{L}^\dagger the Moore-Penrose pseudo inverse of the lead field matrix. Equation (3) becomes then, see e.g. [5]:

$$\text{RRE}(\mathbf{r}_d) = \frac{\|\mathbf{V}_{\text{meas}} - \mathbf{L}(\mathbf{r}_d)\mathbf{L}(\mathbf{r}_d)^\dagger\mathbf{V}_{\text{meas}}\|}{\|\mathbf{V}_{\text{meas}}\|}. \quad (4)$$

The widely Nelder-Mead simplex method is used here to find the global minimum of the Relative Residual Energy (RRE).

III. REDUCED CONDUCTIVITY DEPENDENCE (RCD) METHOD

A. Description of the method

The RCD method proposes an alternative cost function that needs to be minimized for EEG source analysis. The main idea lies in the selection of electrodes that provide useful information in the sense that the electrodes which are selected, are minimally affected by the unknown conductivity in the forward model. Indeed, depending on the location of the electrical dipole and its orientation, some potentials are highly affected by X and others are not. The selection procedure needs to be performed in each iteration k of the minimization scheme, in this case the Nelder-Mead simplex method. In the following, we explain the basic steps taken by the RCD method.

Step 1: Start value $\mathbf{r}_d^{(0)}$ is evaluated in the forward model, yielding the lead field matrix $\mathbf{L}(\mathbf{r}_d^{(0)})$, and simulated potential values $\mathbf{V}_m(\mathbf{r}_d^{(0)}) = \mathbf{L}(\mathbf{r}_d^{(0)})\mathbf{L}(\mathbf{r}_d^{(0)})^\dagger\mathbf{V}_{\text{meas}}$. Initialize $k = 0$.

Step 2: Calculate the sensitivity \mathbf{W} and the normalized sensitivity \mathbf{w} of the simulated electrode potentials to the conductivity for a certain conductivity ratio X_0 :

$$\mathbf{W} = \frac{\partial \mathbf{V}_m(\mathbf{r}_d^{(k)})}{\partial X} \Big|_{X=X_0}, \quad \mathbf{w} = \frac{|\mathbf{W}|}{\|\mathbf{W}\|} \quad (5)$$

In the case of the spherical head model, \mathbf{W} and \mathbf{w} can be calculated analytically. When considering more complex realistic head models, this can be calculated by numerical differentiation.

Step 3: Selection of least sensitive electrodes, based on (5). Largest values are not considered in the EEG inverse problem, since their potential values are affected by the conductivity. A new set of potential values are obtained: $\mathbf{S}_m \in \mathbb{R}^{N \times 1}$ and the corresponding set of measured EEG potentials are considered $\mathbf{S}_{\text{meas}} \in \mathbb{R}^{N \times 1}$. N is the number of selected potentials.

Step 4: Calculation of RCD cost function:

$$\text{RCD}(\mathbf{r}_d^{(k)}) = \frac{\|\mathbf{S}_{\text{meas}} - \mathbf{S}_m(\mathbf{r}_d^{(k)})\|}{\|\mathbf{S}_{\text{meas}}\|} \quad (6)$$

Step 5: Based on (6), the next iterate $\mathbf{r}_d^{(k+1)}$ can be calculated. If the termination criteria of the minimization procedure are met, i.e. $\text{RCD}(\mathbf{r}_d^{(k)})$ reaches tolerance, then stop the algorithm. Otherwise, go to step 2.

B. Results and discussion

The efficiency of the RCD method is illustrated by performing Monte Carlo simulations. Starting from known dipole locations $\tilde{\mathbf{r}}$ and a given conductivity ratio X_0 , we compute EEG

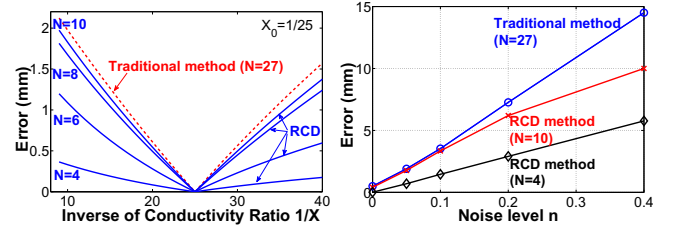


Fig. 1. Plot of Conductivities vs Error with $X_0 = 1/25$ (left) and for several noise levels (right) at $X=1/40$, for dipoles located near the center of the head.

potentials. Gaussian noise is added to these potentials in order to simulate real measured EEG potentials. Dipole locations $\hat{\mathbf{r}}$ are then estimated using the traditional method, i.e. solution of (2), and estimated using the RCD method, explained in III.A. The accuracy of both methods is determined by the error $E = \|\tilde{\mathbf{r}} - \hat{\mathbf{r}}\|$ for different values X and noise levels. The white zero mean Gaussian noise with standard deviation Σ has a noise level defined as $n = \frac{\Sigma}{\mathbf{V}_{RMS}}$ with \mathbf{V}_{RMS} the root mean square of \mathbf{V} . Fig. 1 illustrates the decrease in localization error due to the use of the RCD method (with varying number of selected potentials $N=4, 6, 8, 10$ in step 3 of III.A.) compared to the traditional method ($N=27$). A reduction of the error is introduced due to the use of the RCD method.

For dipoles located near the center of the head, the localization error can be reduced from 2 mm to 0.4 mm, while for dipoles located near the edge of the head from 9 mm to 1 mm. These results are obtained when using $X_0 = 1/25$ for constructing the “measured” electrode potentials and when assuming $X = 1/40$ for solving the inverse problem. The influence of noise has almost no effect on the relative localization error between the RCD and the traditional RRE method.

IV. CONCLUSION

This paper proposes a method that decreases the error introduced by the uncertainties of the conductivity. The results show that the EEG inverse problem can be solved with considerably improved quality, as compared to the traditional inverse solutions.

ACKNOWLEDGMENT

B. Yitembe is supported by the Belgian Science Policy through IUAP project B/0784 at Ghent University.

REFERENCES

- [1] J. de Munck, B. Van Dijk, and H. Spekreijse, “Mathematical dipoles are adequate to describe realistic generators of human brain activity,” *IEEE Transactions on Biomedical Engineering*, vol. 35, pp. 960-965, 1988.
- [2] L.A. Geddes, and L.E. Baker, “The specific resistance of biological material—a compendium of data for the biomedical engineer and physiologist,” *Medical and Biological Engineering*, vol. 5, pp. 271-293, 1967.
- [3] D. Gutiérrez, A. Nehorai, and C.H. Muravchik, “Estimating brain conductivities and dipole source signals with eeg arrays,” *IEEE Transactions on Biomedical Engineering*, vol. 51, no. 12, pp. 2113-2122, 2004.
- [4] Y. Salu, L. Cohen, D. Rose, S. Sato, C. Kufta, and M. Hallett, “An improved method for localizing electric brain dipoles,” *IEEE Transactions on Biomedical Engineering*, vol. 37, pp. 699-705, 1990.
- [5] J. Mosher, R. Leahy, “Source localization using recursively applied and projected (RAP) MUSIC,” *IEEE Transactions on Signal Processing*, vol. 47, pp. 332-340, 1999.

Modeling and Extraction of Parasitics in IGBT Modules

Zarife Cay, Olaf Henze, Stephan Koch, and Thomas Weiland
 Institut fuer Theorie Elektromagnetischer Felder
 Schlossgartenstrasse 8, 64289 Darmstadt, Germany
 cay@temf.tu-darmstadt.de

Abstract — One of the most dominant parasitics causing even fatal problems in PWM inverters is the parasitics of IGBT modules. In this paper, the parasitic parameters of a high-power multi-chip IGBT module are modeled and extracted. The extraction approach is verified by comparing the S-parameters of the proposed network model with the S-parameters of the electromagnetic model of the module.

I. INTRODUCTION

PWM inverters are nowadays the most commonly used adjustable speed drives (ASDs) mainly because of superior, dynamic performance benefit of low cost, fast switching insulated gate bipolar transistors (IGBTs). High switching speed of IGBTs, however, induces high rates of change of voltage and current with respect to time (dv/dt , di/dt) which, in turn, increase the action of parasitic components in printed circuit boards (PCBs) and packages of power inverters. These parasitics are reported to have severe negative effects on the electrical efficiency and electromagnetic compatibility of ASDs [1]. Therefore, it is necessary to obtain high frequency (HF) electrical models of ASDs including dominant parasitics at the early design stage.

Parasitic elements of IGBT modules are one of the major parasitics deteriorating the good performance of PWM inverters. In this paper, these parasitics are modeled for an IGBT module.

II. MODELING AND EXTRACTION OF PARASITICS

A. Six-pack IGBT Module

An IGBT module consisting of six chips, three IGBTs and three anti-parallel diodes, is studied. Fig. 1 shows a picture of the module.

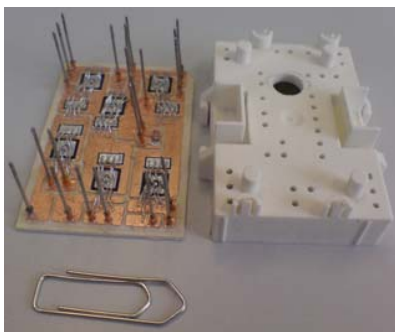


Fig. 1. Six-pack IGBT module

B. High Frequency Electromagnetic Analysis

The electromagnetic (EM) analysis is conducted using the

frequency domain solver of CST MW Studio® capturing the 3D geometrical effects and the high frequency effects, such as skin and proximity effects, of the design. Table I summarizes the details of the computational analysis. The simulation model is illustrated in Fig. 2.

TABLE I
HIGH FREQUENCY ELECTROMAGNETIC ANALYSIS

MICROWAVE STUDIO®	
Solver Type	Frequency Domain Solver
Mesh Type	Tetrahedral Mesh
Adaptive Mesh Refinement	Yes
Number of Mesh Cells	$\approx 9e + 5$
Frequency Range	from 0.1 MHz to 10 MHz

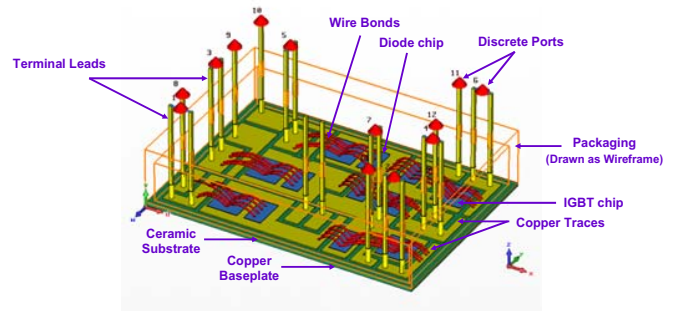


Fig. 2. EM model of the IGBT in CST MW Studio®

C. Modeling and Parasitic Extraction Approach

The parameter extraction tool of CST MW Studio® based on the transmission line method is employed to compute the parasitics of the structure. This tool extracts a SPICE-compatible network model consisting of lumped R, L, C, G, M elements from previously calculated S-parameters [2]. As S-parameters represent the high frequency behavior of a 3D EM model equivalently, it is expected that the derived circuitry responses nearly the same as physical device at the input/output terminals. The proposed network model of the module is depicted in Fig. 3. Table II gives the extracted parasitics. The typical values of the two circuit parameters reported in the data sheet of the module are displayed in Table III [3]. The computed inductances are consistent with the typical value of the stray module inductance. The typical lead resistance is obviously smaller than the extracted ones. The HF effects can lead to such large differences in the ac resistance as the frequency increases.

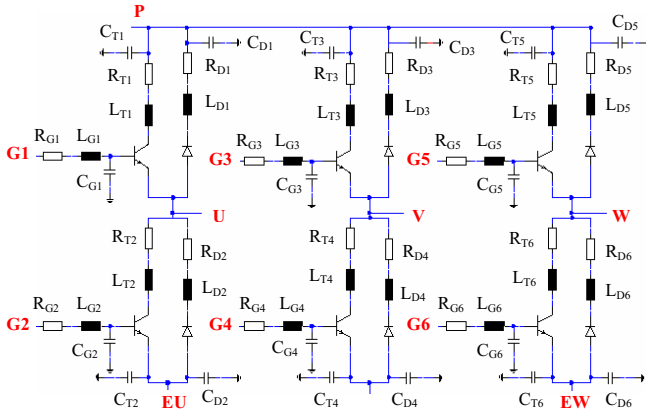


Fig. 3. Parasitic network model

 TABLE II
 PARASITIC PARAMETERS COMPUTED AT 1 MHz

First Phase Leg		Second Phase Leg		Third Phase Leg	
R_{T1}	$1.94e-2 \Omega$	R_{T3}	$6.94e-3 \Omega$	R_{T5}	$1.38e-2 \Omega$
L_{T1}	$3.21e-8 \text{ H}$	L_{T3}	$2.45e-8 \text{ H}$	L_{T5}	$2.92e-8 \text{ H}$
C_{T1}	$4.43e-11 \text{ F}$	C_{T3}	$4.93e-11 \text{ F}$	C_{T5}	$4.97e-11 \text{ F}$
R_{D1}	$2.02e-2 \Omega$	R_{D3}	$7.26e-3 \Omega$	R_{D5}	$1.44e-2 \Omega$
L_{D1}	$3.37e-8 \text{ H}$	L_{D3}	$2.60e-8 \text{ H}$	L_{D5}	$3.09e-8 \text{ H}$
C_{D1}	$4.43e-11 \text{ F}$	C_{D3}	$4.93e-11 \text{ F}$	C_{D5}	$4.97e-11 \text{ F}$
R_{G1}	$9.83e-3 \Omega$	R_{G3}	$8.49e-3 \Omega$	R_{G5}	$1.06e-2 \Omega$
L_{G1}	$2.59e-8 \text{ H}$	L_{G3}	$2.48e-8 \text{ H}$	L_{G5}	$2.69e-8 \text{ H}$
C_{G1}	$9.21e-11 \text{ F}$	C_{G3}	$10.2e-11 \text{ F}$	C_{G5}	$10.3e-11 \text{ F}$
R_{T2}	$3.42e-2 \Omega$	R_{T4}	$3.11e-2 \Omega$	R_{T6}	$4.65e-2 \Omega$
L_{T2}	$3.72e-8 \text{ H}$	L_{T4}	$3.64e-8 \text{ H}$	L_{T6}	$3.95e-8 \text{ H}$
C_{T2}	$1.78e-11 \text{ F}$	C_{T4}	$2.34e-11 \text{ F}$	C_{T6}	$2.4e-11 \text{ F}$
R_{D2}	$3.44e-2 \Omega$	R_{D4}	$3.15e-2 \Omega$	R_{D6}	$4.63e-2 \Omega$
L_{D2}	$3.81e-8 \text{ H}$	L_{D4}	$3.76e-8 \text{ H}$	L_{D6}	$3.97e-8 \text{ H}$
C_{D2}	$1.78e-11 \text{ F}$	C_{D4}	$2.34e-11 \text{ F}$	C_{D6}	$2.4e-11 \text{ F}$
R_{G2}	$1.82e-2 \Omega$	R_{G4}	$1.21e-2 \Omega$	R_{G6}	$9.73e-3 \Omega$
L_{G2}	$3.34e-8 \text{ H}$	L_{G4}	$2.75e-8 \text{ H}$	L_{G6}	$2.57e-8 \text{ H}$
C_{G2}	$1.12e-11 \text{ F}$	C_{G4}	$1.04e-11 \text{ F}$	C_{G6}	$0.38e-11 \text{ F}$

 TABLE III
 LUMPED ELEMENT PARAMETERS OF THE IGBT MODULE UNDER CONSIDERATION

Stray inductance module	L_{sCE}	35 nH
Chip module lead resistance, terminals	R_{CC+EE}	4 m Ω

A. Verification of Parasitic Extraction Approach

As the analytical calculation of parasitics for such a complex geometry is too complicated, the constructed parasitic circuit model is verified numerically. For this

purpose, the circuit model is implemented in CST Design Studio™. The S-parameters for the case, when the transistor labeled as T1 is on and the current flows from the power supply to the AC motor, are computed. These results are presented in Fig. 4 together with the S-parameters of the EM model for the same case. The network parameters extracted at 1 MHz are used. Thus, the agreement between the results is best at 1 MHz. At higher frequencies, the agreement is less good due to the frequency dependence of the extracted lumped element parameters.

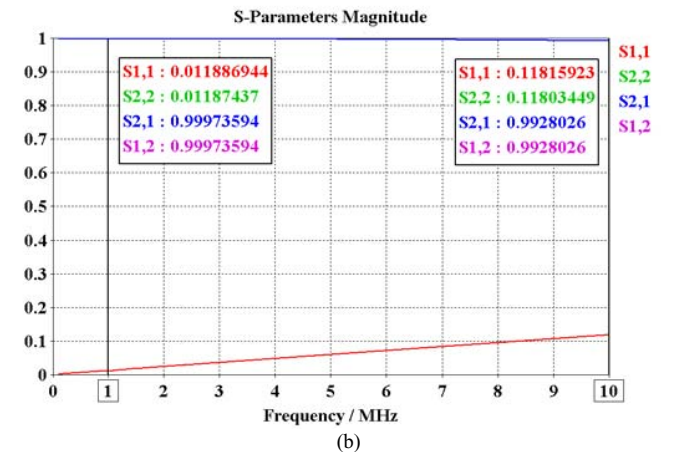
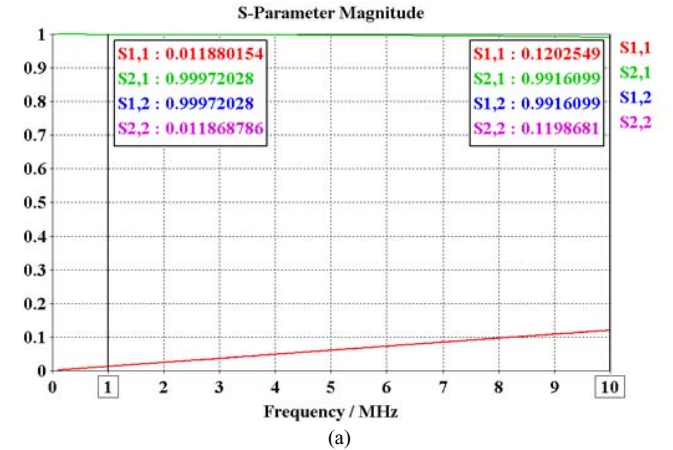


Fig. 4. S-Parameters of (a) the EM model and (b) the parasitic network model

III. CONCLUSIONS

A parasitic network model of an IGBT module is developed using the network parameter extraction tool of CST MW Studio® based on transmission line models. The electrical model and the extracted parameter values are verified by comparing the S-parameters of both the electromagnetic and the circuit model. A more detailed discussion of the parasitic extraction technique and further results will be presented in the full paper.

IV. REFERENCES

- [1] X. Huang, *Frequency domain conductive electromagnetic interference modeling and prediction with parasitics extraction for inverters*, Ph.D. Thesis, Virginia Polytechnic Institute and State University, 2004.
- [2] Computer Simulation Technology (CST), *User manual of CST Microwave Studio®*, 2008.
- [3] EUPEC, *Data sheet of IGBT module FS35R12YT3*.

Modelling Motion, Stiffness and Damping of a Permanent-Magnet Shaft Coupling

A. Niemenmaa¹, L. Salmia¹, A. Arkkio¹, J. Saari²

¹Helsinki University of Technology, P.O. Box 3000, FIN-02015 TKK, Finland

²Hamilton Sundstrand Associate Fellow
asko.niemenmaa@tkk.fi

Abstract— Different methods for modelling the motions, torques and losses in a permanent-magnet shaft coupling are studied. The containment shroud of the coupling is a homogeneous conducting cylinder. Its motion can be modelled using the motional electromotive force, i.e. the $v \times B$ term. The moving-band technique is used for modelling the relative motion of the magnet cylinders of the coupling. Using the motional electromotive force for the shroud gives reliable results while the computational effort is kept at minimum. The stiffness and damping coefficients of the coupling are obtained from a numerical impulse response test.

I. INTRODUCTION

Fig. 1 show a cross-sectional view of a magnetic shaft coupling. These couplings are used when pumping a reactive fluid and absolutely hermetic handling is required. The outermost cylinder is composed of a ferromagnetic yoke, permanent magnets and a stainless steel cover over the magnets for their protection. Typically, the outer part is mechanically connected on the shaft of an electrical motor and rotated say at 1500 rpm. The thin stationary cylinder in the middle is the containment shroud. It makes the hermetic seal. The shroud material is stainless steel resistant to the aggressive fluid. It should also have a large specific resistance to reduce the eddy-current loss. The innermost cylinder is a mirror image of the outermost one and made of the same materials. The inner part is typically connected on a rotor shaft of a pump. The field from the permanent magnets provides the magnetic coupling and torque transfer from the electrical motor to the pump. The magnets are either of NdFeB or SmCo type depending on the operation temperature of the coupling.

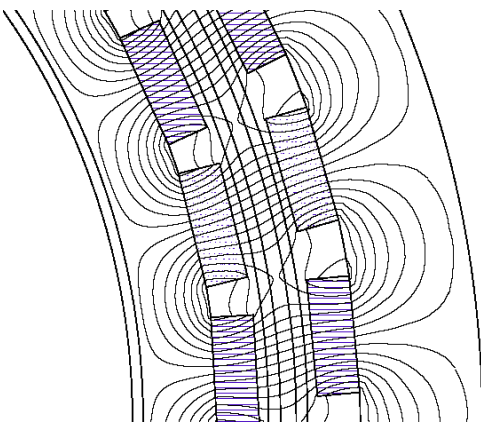


Fig. 1. Cross-sectional view of a permanent-magnet coupling. The thin shroud in the middle is moving with respects to the other parts at a speed of 13 m/s (downwards).

This cylindrical coupling arrangement has some challenge from the modelling point of view as all the three cylinders may be in relative rotation with respect to each other. The shroud is a simple homogeneous cylinder, and there are several ways of modelling its motion. Davat et al. [1] have studied motion within finite element analysis, and Sadowski et al. [2] have studied the torque computation, among others. Similar methods are also studied in the present paper in association with the permanent-magnet shaft coupling.

The aim is to find the most efficient methods of magnetic field analysis for the structural optimisation of this type of a coupling. In addition, the torsion oscillations of the coupling and the passive electromagnetic damping of these oscillations are studied.

II. METHODS OF ANALYSIS

A. Magnetic field analysis

The length to pole-pitch ratio of the coupling studied is about 16. Thus, the magnetic field of the coupling can be assumed to be two-dimensional. The magnetic vector potential A and finite element method are used.

B. Modelling motion and computing the torques

The motion of the shroud is modelled either by using the motional electromotive force $v \times B$ or by applying the moving-band technique [1] in the air gaps on both sides of the shroud.

Fig. 2 shows a finite element mesh for the moving-band technique. It is built up of five sub-meshes, rigid ones for the three cylinders and changeable ones for the two air gaps. The vector potentials of the sub-meshes are coupled through periodic boundary conditions. Thus, the field of each sub-mesh region is modeled in its own frame of reference and the vector potential is forced to be continuous from mesh to mesh by the periodic boundary conditions. The air gaps on both sides of the shroud are discretised in two layers of elements. One of the element layers is used for the rotation, the other one for torque computation.

The torques are calculated applying the equation [3]

$$T = \frac{l}{\mu_0(r_o - r_i)} \int_{S_{ag}} r B_r B_\phi dS \quad (1)$$

on the non-changing finite element layers chosen for the purpose (Fig. 2). l is the axial length, r_o the outer radius and r_i the inner radius of the air gap. B_r and B_ϕ are the radial and circumferential components of the flux density and r is the radius. S_{ag} is the cross-sectional area of the air gap.

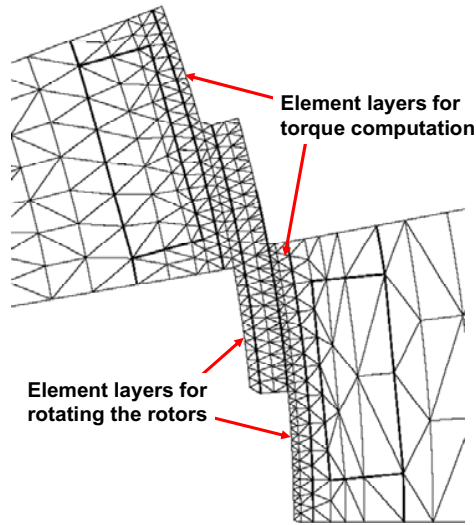


Fig. 2. Second-order isoparametric elements were used for the analysis.

C. Analysis of losses

The eddy-current losses induced in the conducting structures of the coupling are obtained by integrating the eddy-current loss density

$$p_e = \frac{1}{\sigma} \mathbf{J}^2 = \sigma \left(-\frac{\partial \mathbf{A}}{\partial t} + \mathbf{v} \times \mathbf{B} \right)^2 \quad (2)$$

over the conducting volume. The eddy-current loss is the only component of loss included in the present analysis.

D. Torque stiffness and damping

To study the damping characteristics of the coupling within numerical analysis one can either apply harmonic torsion-angle excitation or a numerical impulse response test [4]. In the harmonic excitation, the inner magnet cylinder is forced to torsion oscillation at a single frequency. In the impulse test, the innermost cylinder is displaced from its stationary position for a short period of time and returned back to its original position. The excitation and response signals are recorded and Fourier transformed, and when the transformed signals are divided frequency by frequency, a frequency response function based on numerical analysis is obtained. The advantage of the impulse response test is that a wide range of frequencies is excited and modelled in a single simulation. The harmonic excitation test has to be repeated for each frequency of interest.

The stiffness of the coupling K (spring constant) is related to the real part of the frequency response function and the damping coefficient C to the imaginary part [4].

III. RESULTS

Table 1 shows the results computed for the rated steady-state operation point of the coupling. In a reference frame fixed to the outer cylinder, the field is a dc field and it can be solved by a dc solver using the motional electromotive force for the shroud. In addition, both the electromotive-force formulation and moving-band technique can be used within time-discretised analysis. The three methods give almost similar results. The power balance seems to be fulfilled

slightly better by the two cases in which the motional electromotive force is used. The time step used was 0.1 ms. The power balance of the moving-band technique can be improved by using a shorter time step but the simulation time increases accordingly.

Fig. 3 shows the frequency response function obtained from the numerical impulse test. This type of a coupling has very little dynamics within the range of its potential torsion oscillations. The stiffness coefficient K is about 8000 Nm/rad and the damping coefficient C is only 0.17 Nms/rad².

TABLE I
RESULTS FOR THE RATED STEADY-STATE OPERATION OF THE COUPLING.

	dc solution	time-discretised	time-discretised
	motional emf	motional emf	moving band
Torque in the outer air gap [Nm]	320.58	320.58	320.65
Torque in the inner air gap [Nm]	298.73	298.73	298.67
Shaft power on the shroud [W]	3431.98	3431.98	3452.87
Resistive loss in the shroud [W]	3432.1	3432.1	3411.44
Error in power balance [W]	-0.12	-0.12	41.43
Error percent [%]	0.00	0.00	1.21

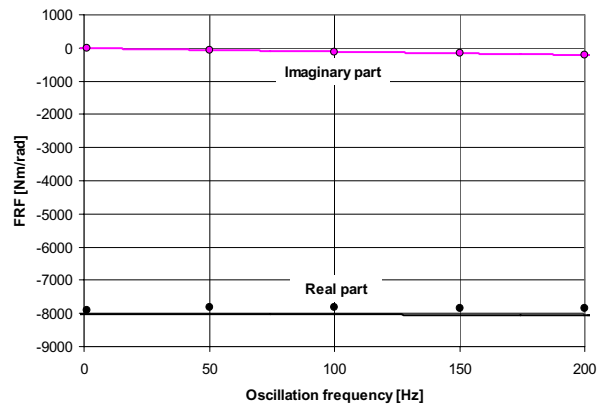


Fig. 3. Frequency response between the torque transmitted by the coupling and the torsion angle. The continuous curves are from the numerical impulse test, the dots from time-harmonic torsion-angle excitation.

IV. CONCLUSION

The motional electromotive-force formulation gives good results when modelling the motion of the shroud of a magnet coupling while the computational effort is kept at minimum. The results from the moving-band technique, a method validated by measurements in several other problems, verify the results of the motional electromotive-force formulation.

V. REFERENCES

- [1] Davat B., Ren Z., Lajoie-Mazenc M., "The movement in field modeling," *IEEE Trans. Magnetics*, 21 (6): 2296-2298. 1985.
- [2] Sadowski N.; Lefevre Y.; Lajoie-Mazenc M.; Cros J., "Finite element torque calculation in electrical machines while considering the movement". *IEEE Trans. Magnetics*, 28 (2): 1410-1413. 1992.
- [3] Arkkio A., "Finite element analysis of cage induction motors fed by static frequency converters". *IEEE Trans. Magnetics*, 26(2): 551-554. 1990.
- [4] Repo A.-K., Rasilo P., Niemmaa A., Arkkio A., "Identification of electromagnetic torque model for induction machines with numerical magnetic field solution". *IEEE Trans. Magnetics*, 44 (6):1586-1589. 2008.

Discrete geometric approach to modeling the cathodic region in a PEM fuel cell

Paolo Bettini¹, Ruben Specogna¹, Andrea Stella², and Francesco Trevisan¹

¹Dipartimento di Ingegneria Elettrica, Gestionale e Meccanica, Università di Udine,
Via delle Scienze 208, 33100 Udine, Italy,

²Dipartimento di Ingegneria Elettrica, Università di Padova,
Via Gradenigo 6/A, 35100 Padova, Italy

bettini@uniud.it, ruben.specogna@uniud.it, stella@unipd.it, trevisan@uniud.it

Abstract—We present a model of the cathodic region in a Proton Exchange Membrane (PEM) fuel cell, where a segmented electrode is considered. The model, based on the discrete geometric approach, couples a discrete formulated steady state current conduction problem in a non isotropic medium with electrochemical reaction at the catalyst layer described by means of the Butler-Volmer equation. The model allows to analyze either the constant voltage operation or the constant current operation of the fuel cell.

Index Terms—PEM fuel cells, Steady state current conduction, Discrete geometric approaches.

I. INTRODUCTION

During the last decade the idea of a sustainable development based on eco-compatible technologies has taken more and more relevance, with particular attention to the energy production by clean, efficient and low impact processes, such as the chemical processes within the fuel cells, [1], [2]. These devices produce electric power by direct conversion of hydrogen or an aqueous solution of methanol. Fuel cells are an important technology for a potentially wide variety of applications including auxiliary power, transportation power, and stationary power for buildings and other distributed generation applications. These applications are encountered in a large number of industries worldwide. Among a variety of fuel cells available, proton exchange membrane (PEM) fuel cells are considered to be most suitable for transportation and portable applications due to attractive features like low operation temperature, high energy density and efficiency. In this context, a correct acquisition in situ of the parameters that determine their functioning, requires the implementation of mathematical models that could remarkably contribute to the interpretation of experimental results and to the determination and optimization of useful geometric configurations to further optimize their performance.

One of the aspects that needs to be improved in a typical PEM fuel cell is to achieve an higher average current density at any given operating cell voltage. On the other hand, uniformity of current density distribution across the entire active area is crucial for performance optimization.

In the electrochemical reactions of the PEM fuel cells, hydrogen (or methanol) at the anode provides protons, freeing electrons in the process that must pass through an external circuit to reach the cathode. The protons, which remain solvated

with a number of water molecules, migrate, through the membrane, to the cathode to react with oxygen and the returning electrons. Water is subsequently produced at the cathode. In a PEM, Nafion is used as the membrane placed between the anode and the cathode. Furthermore, it is also employed as an important component of the active layer, where the catalyst is present.

The aim of this paper is to develop a numerical simulation model, based on Discrete Geometric Approach, [3], [4], [5], of the electronic conduction in the so called Gas Diffusion Layer (GDL) region of the PEM fuel cell attached to a segmented graphite current collector region, concurring to analyze the potential distribution in the cathodic region, [6], [7]. From the potential distribution it is straightforward to compute the current density distribution in order to estimate its degree of uniformity through the entire active area of the electrodes. In this way, it is possible to increase the current density for a given working cell potential.

II. A DISCRETE GEOMETRIC MODEL

We propose a 2D discrete geometric model of the cathodic region, where electronic conduction occurs; we model a portion of the periodic structure corresponding to a segmented electrode fuel cell. We denote with D the domain of interest, consisting of a GDL region D_{GDL} and one half of two adjacent graphite current collectors plates D_a, D_b respectively separated by an insulating region D_i , Fig. 1. The upper part of the boundary of D_{GDL} region is in contact with the catalyst layer, where electrons react with protons during the electrochemical reaction; the catalyst layer is modeled here as a zero-thickness region. We introduce in $D_{GDL} \cup D_a \cup D_b$ a pair of interlocked grids, one dual of the other, where the primal grid consists of nodes n , edges e , faces f and volumes v , [4], [5]; the volumes are prisms with a triangular base. The dual grid is obtained from the primal by means of the barycentric subdivision and it consists of dual volumes \tilde{v} , dual faces \tilde{f} , dual edges \tilde{e} and dual nodes \tilde{n} . Since the problem is 2D and electric E and current density J vector fields are in a plane, we consider the projection on a plane of such a pair of interlocked grids; therefore the primal volumes coincide with the triangles of the mesh and the primal faces coincide with the edges of the mesh.

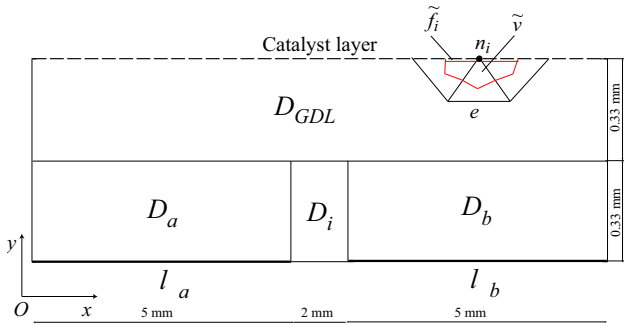


Fig. 1. Geometry of the 2D model of a portion of the periodic structure corresponding to a segmented electrode fuel cell; the draw is not to scale.

The electron current I_n^s across a dual face \tilde{f}_n , in a one to one correspondence with node n in the catalyst layer (refer to Fig. 1), can be modeled according to Boutler-Volmer equation¹ [6], [7]

$$I_n^s(V_n) = -|\tilde{f}_n|J_0(10^{[(V_n - E^0)/\eta_c]} - 10^{[-(V_n - E^0)/\eta_c]}), \quad (1)$$

where E^0 is the equilibrium potential characteristic of the electrochemical reaction, η_c is the cathode Tafel slope at 30 C, J_0 is the apparent exchange current density and $|\tilde{f}_n|$ is the area of the dual face \tilde{f}_n ; $I_n^s(V_n)$ is a non linear function of the electric potential V_n in a neighborhood of node n .

Next, we can formulate the steady state current conduction problem according to the Discrete Geometric Approach, [8], [9] as

$$-(\mathbf{G}^T \boldsymbol{\sigma} \mathbf{G} \mathbf{V})_i - (\mathbf{I}_s(\mathbf{V}))_i = 0, \quad (2)$$

where \mathbf{V} is the array of the electric scalar potentials V_i associated with a primal node n_i , \mathbf{G} is the incidence matrix between the orientations of the a primal edge and a primal node, $\boldsymbol{\sigma}$ is a square matrix of dimension $N^2 - N$ being the number of primal nodes— representing a discrete counterpart of the constitutive relation at continuous level $\mathbf{J} = \boldsymbol{\sigma} \mathbf{E}$, [8], [9], [10]; in the case of D_{GDL} region, it is important to note that the conductivity tensor $\boldsymbol{\sigma}$ is diagonal, but it represents an anisotropic conductivity along orthogonal directions ($\sigma_{xGDL} = 0.785$ S/cm, $\sigma_{yGDL} = 3.14$ S/cm), while the conductivity of the bulk graphite collector regions D_a, D_b is isotropic, $\sigma_{D_{a,b}} = 670$ S/cm. The subscript $(\mathbf{x})_i$ denotes the i -th entry of the array \mathbf{x} , in a one-to-one correspondence with the node n_i ; if the node n_i belongs to the catalyst layer, then $(\mathbf{I}_s(\mathbf{V}))_i$ is the current crossing the dual face \tilde{f}_i corresponding to the node n_i ; the entries of $(\mathbf{I}_s(\mathbf{V}))$ are null for any node not belonging to the catalyst layer. Boundary conditions must be considered in addition along the l_a, l_b lines, Fig. 1; the potential is unknown along the catalyst layer. Symmetry boundary conditions on the pair of lateral sides of D are considered in addition.

III. NUMERICAL RESULTS

We will analyze the potential distribution in the cathodic region of a segmented electrode cathode of a PEM fuel cell, by

¹This model accounts for various factors like local membrane hydration state, reactant and product concentration, temperature, etc. affecting the electrochemical reactions in a fuel cell.

considering a portion D of the periodic current collector structure with the geometry given in Fig. 1. We solved the non-linear system (2) by means of a Newton-Raphson method. As boundary condition we implemented the so called constant voltage operation of the fuel cell, where the potential of the primal nodes on l_a, l_b is imposed as $V_{l_a} = V_{l_b} = 0.695$ V. In the full paper, we will also show the so called constant current operation, where the total current crossing dual faces along l_a, l_b are imposed and consequently the potential V_{l_a}, V_{l_b} of the equipotential interfaces l_a, l_b is computed.

The final potential distribution in $D_{GDL} \cup D_a \cup D_b$ is shown in Fig. 2. The obtained results are in a good agreement with those reported in literature, but obtained by means of a finite difference method, [7].

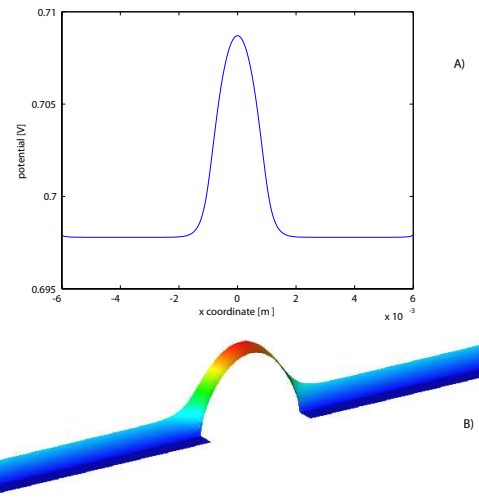


Fig. 2. Part A): The resulting potential distribution along the catalyst layer is shown. Part B): the resulting overall potential distribution in the 2D region $D_{GDL} \cup D_a \cup D_b$ is depicted.

REFERENCES

- [1] James Larminie, Andrew Dicks, "Fuel Cell Systems Explained," J. Wiley, England, 2003.
- [2] S. Gottesfeld, "Polymer Electrolyte Fuel Cells", Advances in Electrochemical Science and Engineering, Vol. 5, Wiley-VCH, 1997.
- [3] T. Weiland, "Time domain electromagnetic field computation with finite difference methods," Int. J. Numer. Model. vol. 9, , 1996, pp. 295-319.
- [4] E. Tonti, "Finite Formulation of the Electromagnetic Field," IEEE Trans. Mag. Vol. 38, No. 2, 2002, pp. 333-336.
- [5] A. Bossavit, L. Kettunen, "Yee-like Schemes on Staggered Cellular Grids: A synthesis Between FIT and FEM Approaches," IEEE Trans. Mag. Vol. 36, No. 4, 2000, pp. 861-867.
- [6] K. Scott, P. Argyropoulos, "A current distribution model of a porous fuel cell electrode," Journal of Electroanalytical Chemistry, Vol. 567, 2004, pp. 103-109.
- [7] Dilip Natarajan, Trung Van Nguyen, "Effect of electrode configuration and electronic conductivity on current density distribution measurements in PEM fuel cells," Journal of Power Sources, Vol. 135, 2004, pp.95-109.
- [8] F. Trevisan, L. Kettunen "Geometric interpretation of finite dimensional eddy current formulations," Int. Jou. for Numerical Methods in Engineering, Vol. 67, Iss. 13, 2006, pp. 1888-1908.
- [9] R. Specogna, F. Trevisan, "Discrete constitutive equations in $A - \chi$ geometric eddy-currents formulation," IEEE Trans. Magn. Vol. 41, No. 4, 2005, pp. 1259-1263.
- [10] L. Codecasa, R. Specogna, F. Trevisan, "Symmetric Positive-Definite Constitutive Matrices for Discrete Eddy-Current Problems", IEEE Trans. Mag., Vol. 43, pp. 510-515, 2007.

Modeling of a current sensor with a FE-tuned MEC: Parameters identification protocol

F. Sixdenier^a, M.-A. Raulet^a, B. Lefebvre^b

a: Université Lyon 1, CNRS UMR5005 Ampere, 43, Bld du 11 Novembre 1918 Villeurbanne F-69622, France,
fabien.sixdenier@univ-lyon1.fr, marie-ange.raulet@univ-lyon1.fr

b : ABB France, Automation Products Division, Protection & Control Activity, 10, rue Ampère, ZI, BP 114,
F-69685, Chassieu Cedex, France
bruno.lefebvre@fr.abb.com

Abstract — This paper presents a magnetic circuit modeling of closed loop Hall-effect current sensors based on a magnetic equivalent circuit which could be simulated with a circuit type simulator software (PSPICE model). First, the principle of measurement of the closed loop Hall-effect current sensors is presented. Then, the magnetic equivalent circuit (MEC) modeling justified by the engineers' model needs is elaborated. Finally the parameters identification protocol based on 3D Finite-Elements (FE) simulations and simplex optimization method is explained.

I. INTRODUCTION

The closed loop Hall-effect current sensors [1] can measure all kinds of current from DC to several tens of kHz with a galvanic insulation between the primary current and the measuring signal. The current sensor must have a measuring signal directly proportional to the current to be measured. In order to improve current sensors accuracy, frequency bandwidth or magnetic immunity, engineers require specific models able to reproduce signals with a good accuracy in a short time in order to test many improvement ideas. A specific model which can be implemented in circuit-type simulator software has been created in order to help engineers to improve the sensors performances.

II. PRINCIPLE OF MEASUREMENT

The current sensor main parts are represented in Fig. 1.

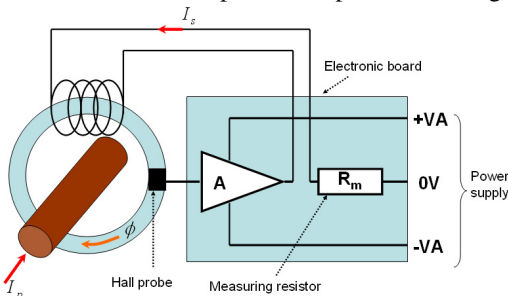


Fig. 1 : Current sensor main parts

The primary current (I_p) passing through the sensor creates a magnetic flux ϕ . This magnetic flux is concentrated by the magnetic core. The Hall probe placed inside the air-gap of the core provides a voltage proportional to the magnetic flux density. The electronic board converts this voltage into a secondary current. This secondary current is then, at any time,

proportional to the primary current following (1), (N_p, N_s : primary and secondary coil number of turns respectively):

$$N_p I_p = N_s I_s \quad (1)$$

III. MAGNETIC CIRCUIT MODELING

A. Engineers' needs

The electronic board, necessary to create the secondary current proportional to the primary one, contains many electronic components (diodes, resistors, capacitors...). In order to test the whole system (magnetic circuit and electronic board), engineers need a model of the magnetic circuit able to be implemented in a circuit-type simulator software. The magnetic behavior non-linearities (hysteresis and dynamic effects) excludes a linear electric equivalent model (R,L,C model). A magnetic equivalent circuit or reluctance network model offers a good compromise between accuracy and rapidity. The final model must take into account all the phenomena (geometric effects, hysteresis, dynamic effects) that can create signal distortion. These different phenomena occurred by the magnetic circuit can be studied separately.

B. Modeling of "geometric effects"

The air-gap, where the hall probe is placed, induces flux leakages which lead to local saturation of the magnetic circuit. The Fig. 2 shows the results of a 3D finite elements simulation in magnetostatic. It can be seen that the modulus flux density B inside the magnetic circuit is greatly inhomogeneous. This means that there are a lot of flux leakages.

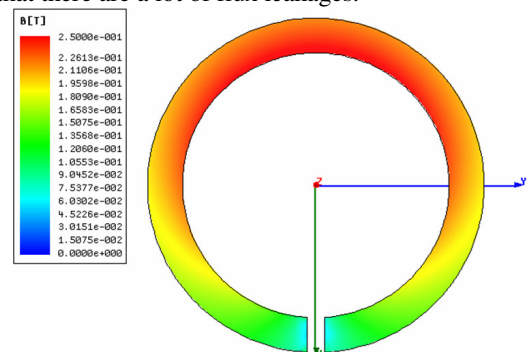


Fig. 2: Flux density modulus inside the magnetic circuit.

The model must take into account these flux leakages, so the magnetic circuit is decomposed into several flux tubes like shown on Fig. 3

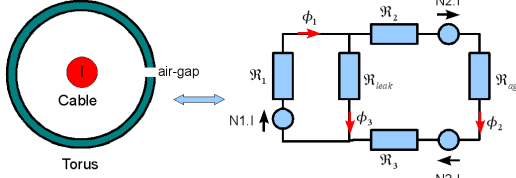


Fig. 3: Magnetic equivalent circuit scheme

With:

- $\mathfrak{R}_1, \mathfrak{R}_2, \mathfrak{R}_3$: magnetic circuit flux tubes
- \mathfrak{R}_{leak} : leakage flux tube
- \mathfrak{R}_{ag} : air-gap flux tube
- $N1.I, N2.I, N3.I$: fictitious magnetomotive force sources
- ϕ_1, ϕ_2, ϕ_3 : magnetic fluxes.

After analysis, and in order to represent accurately the geometric effects (flux leakages, air-gap), three specific parameters that can not be identified analytically have to be determined. These three parameters are: α , the angular position of the leakage flux tube, S_{ag} the cross-section of the air-gap flux tube, S_{leak} , the cross-section of the leakage flux tube.

In order to identify these parameters, an optimization algorithm [2] based on the simplex method is used. The criterion used here is the mean quadratic error between the flux density modulus calculated by a 3D FE simulation in magneto static and the flux density modulus calculated by the magnetic equivalent circuit along the mean length of a half of the magnetic circuit. In order to find constant parameters and make a compromise between linear and saturated behavior, two objective functions (OF_1, OF_2) are evaluated. Then, these two objective functions are used to make a single objective function OF so as to:

$$OF = \sqrt{(OF_1)^2 + (OF_2)^2} \quad (2)$$

OF is the simplex optimization algorithm criterion to minimize. Results of the optimization are shown on Fig. 4.

C. Magnetic material dynamic effects modeling

The magnetic material dynamic effects are represented with a differential equation. This model is based on (3).

$$H_{app} - H_{stat}(B) = \gamma \frac{dB}{dt} \quad (3)$$

H_{app} is the applied excitation field, $H_{stat}(B)$ represents a fictitious static excitation field for a given flux density B and γ is a constant coefficient that represents the whole dynamic effects (eddy currents, wall motion). Assumption, limits and rules of use are described in [3]. This model can

easily be introduced in the MEC seen before. γ is determined by comparing simulated and measured hysteresis loops.

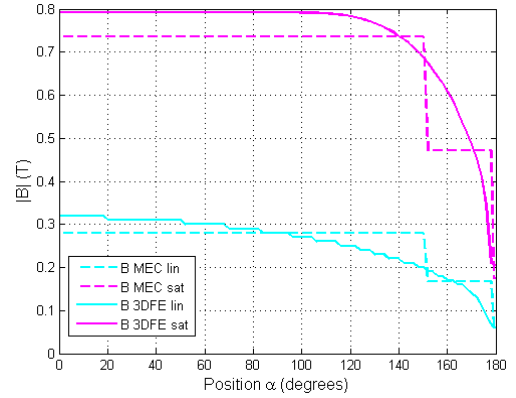


Fig. 4: flux density modulus versus position angle for a half magnetic circuit and air-gap. (MEC: Magnetic equivalent circuit, 3DFE: 3 dimensions finite elements, lin: linear, sat: saturated)

IV. RESULTS

After identification of all the parameters, the model is tested without the electronic card (the measuring resistor is directly linked to the secondary coil) for different current amplitudes and frequencies. Fig.5 shows an example for a current of amplitude 800A and frequency 100Hz. The measured primary current is imposed to the simulation, and the measured and simulated secondary currents are in good agreement.

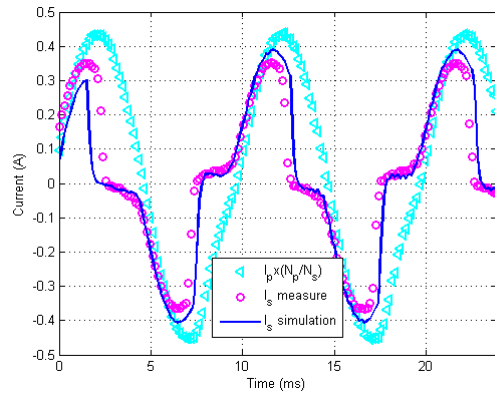


Fig. 5: imposed primary current and secondary current

V. CONCLUSION

In the extended paper, more details about the parameters identification protocol will be given. The present protocol will be applied for different magnetic circuit sizes and different materials.

VI. REFERENCES

- [1] T. Waeckerlé et al., *Journal of Magnetism and Magnetic Materials*, Volume 304, Issue 2, September 2006, Pages e850-e852
- [2] Lagarias, J.C. et al., *SIAM Journal of Optimization*, Vol. 9 Number 1, pp. 112-147, 1998
- [3] Rault M.-A. et al., *COMPEL Int J for Computation and Maths in Electrical and Electronic Eng* 27, 1 (2008) 256-265.

Study of Three Dimensional Flux Distribution in Nonlinear Core of Power Transformers Based on 3-D FEM Modeling

Mousavi S. A, Faridi M. and Nabaei V.
Azad University of Khodabadeh
Iran-Transfo Co., Zanjan, Iran
ali.sam2006@gmail.com

Abstract— In this study, we examined three dimensional magnetic flux distributions in the case of single and three phase power transformers. The method of flux distribution inside every packet and also between them has been studied. However, total flux which passes through core limbs may be sinusoidal, but local flux density in some regions of core is distorted and has higher additional harmonics along with fundamental one. In this work, local harmonic flux density is identified. The three dimensional, time-stepped edge-based finite element method is used for modeling power transformer cores. Anisotropy and nonlinear of Laminated steel have been considered in this analysis. The accuracy of this method have examined by experimental results.

I. INTRODUCTION

Power transformers have a very important role in transmission of electrical energy in power systems. The quality of core has large effect on transformer performance and efficiency. Therefore, many researches have been done for investigation of flux distribution in core and improving its characteristics [1, 2]. In previous works, studies are performed by experimental method on a scaled sample core [1] or by numerical two dimensional methods [2]. The disadvantage of experimental methods is that by changing core material or its dimensions, the early results will not be valid. In addition, the test sample is a scale of large power transformer cores and thus its results are not completely correct for actual one. In most cases, core cross section tends to be of roughly circular or semi-circular shape. For this purpose, core is made of several packets that have different widths and depths. In numerical two dimensional methods, we can not model this packet design and the core is taken as one packet with rectangular cross section.

In this paper, we modeled single and three phase three-limbs power transformer cores with 3-dimensional geometry (Fig.1). In order for analyzing, we applied 3-dimensional time-stepped edge-based finite element method. Packet design, nonlinear and anisotropy characteristics of laminated steel has been considered in this model. The skin effects in very thin laminated steels which core is made from are completely negligible in power frequency conditions [3].

We examined 2, 3 and 4 limbs single phase and 3 and 5 limbs three phase power transformers and compared them together.

II. FINITE ELEMENT METHOD

Analysis of flux distribution in power transformer cores is a complex electromagnetic problem. Since the core has a three dimensional structure and its medium is anisotropy and nonlinear, therefore, in this paper we used 3-D finite element method (FEM) with edge based vector potential formulation. Inaccuracies in FEM analysis of 3-D magnetic field problems with nodal based continuous vector potential in present inhomogeneous media are shown in [5]. These shortcomings can be eliminated by applying edge element method. In this method, we considered both anisotropy and nonlinear B_H curve.

For arbitrary voltage supply, first total magnetic flux must be pass through the winding is calculated in term of time. Then in each time step a magneto static analysis is done in such a way that total passed flux across winding equals with calculated one in same time. The current flow from windings in each time step is computed by an iterative algorithm.

After doing this analysis in a time period, we could determine the distribution of magnetic flux density in terms of time and place.

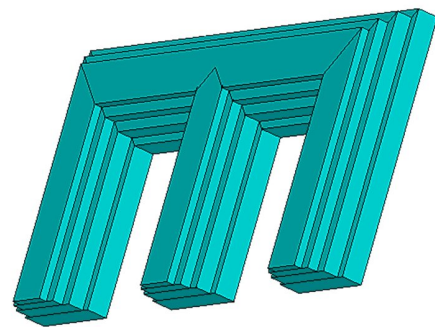


Fig. 1. Three dimensional geometry model of a three phase, three limbs power transformer core with $\frac{1}{4}$ symmetry

III. RESULTS

Generally, the flux and loss profiles showed a trend to exhibit the following features:

The magnetic flux in limbs and yokes of each packet has higher density near core window; by increasing flux and reaching to saturation state, the flux distribution tends to take uniform shape in limbs and yokes.

In low flux densities, flux distributions between packets have great variety, but by reaching to saturation state, distribution would be uniform.

For example, flux distribution in low and high average flux densities for a 4-limbs single phase power transformer are shown in Figs. 2 and 3, respectively.

The most flux distortion is observed in T-joint region.

In core types that have return path, the total flux distortion can be seen in return limbs, too.

The detailed findings and results of modeling the commercial power transformers will be presented in our complete article.

We examined 2, 3 and 4 limbs single phase and 3 and 5 limbs three phase power transformers and compared them together. Furthermore, the results of flux distribution obtained from modeling, is compatible with the results of measurement which is reported in [1] for a sample core.

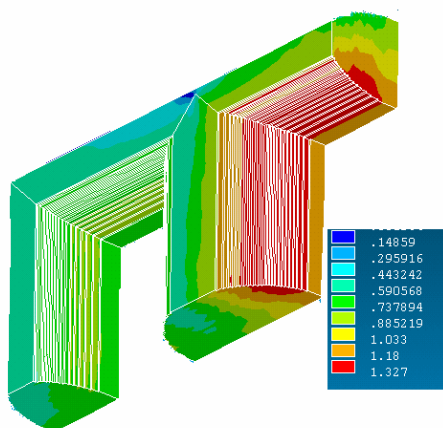


Fig. 2. Flux distribution in low average flux density for single phase, 4-limbs power transformer in 1/8 symmetry

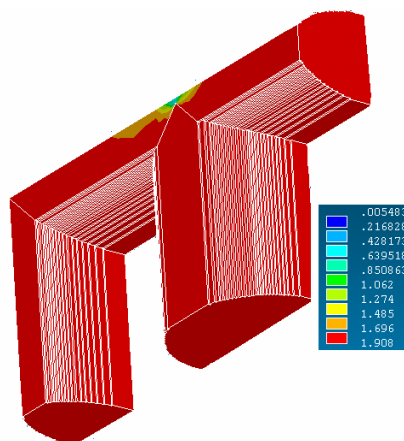


Fig. 3. Flux distribution in high average flux density (near to saturation) for single phase, 4-limbs power transformer in 1/8 symmetry

IV. REFERENCES

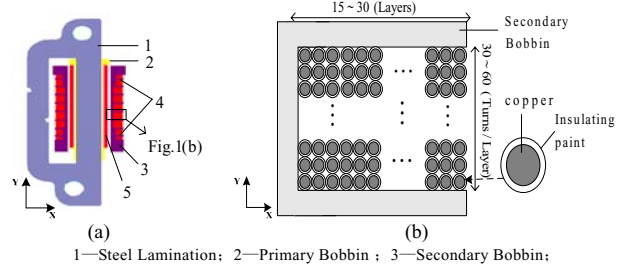
- [1] A. Basak and A. A. Qader, "Fundamental and harmonic flux behaviour in a 100 KVA distribution transformer core", IEEE Transactions on Magnetics, Vol. 19, No. 5, Sep 1983, pp. 2100-2102.
- [2] E. G. Tenyehuis, G. F. Mechler and R. S. Girgis, "Flux distribution and core loss calculation for single phase and five limb three phase transformer core designs", IEEE Transactions on Power Delivery, Vol. 15, No. 1, Jan 2000, pp. 204-209.
- [3] J. Gyselincx, L. Vandeveld, J. Melkebeek, P. Dular, F. Henrotte and W. Legros, "Calculation of eddy currents and associated losses in electrical steel laminations", IEEE Transactions on Magnetics, Vol. 35, No.3, May 1999, pp. 1191-1194.
- [4] IEC 404-2.
- [5] O. Biro, K. Preis, C. Magele, W. Renhart, K. R. Richter and G. Vrist, "Numerical Analysis of 3D Magnetostatic Fields", IEEE Transaction on Magnetics", Vol. 27, No. 5, Sep 1991, pp. 3798-3803.
- [6] E. Barbisio, F. Fiorillo and C. Ragusa, "Predicting loss in magnetic steels under arbitrary induction waveform and with minor hysteresis loops", IEEE Transactions on Magnetics, Vol. 40, No. 4, July 2004, pp. 1810-1819.

Wideband Equivalent Circuit Model for Automotive Ignition Coil

JIA Jin, YU Ji-hui, WANG Quan-di, ZHENG Ya-li

The Key Laboratory of High Voltage Engineer and Electric New Technology under the State ministry of Education, Chongqing University, Chongqing 400030, China
E-mail:twoj1985-163.com@163.com

Abstract—automotive ignition coil acts as a transient voltage transformer in spark process. A lumped circuit model is proposed in this paper to predict the wideband characteristics of ignition coil. This model separates the winding into individual sections that simulate winding impedance quality. The parameter capacitance and inductance in circuit are derived from Finite Element Method (FEM) analysis. Calculated results are compared with the measured data in frequency and time-domain and the reliability of the presented model in this paper is verified.



1—Steel Lamination; 2—Primary Bobbin ; 3—Secondary Bobbin;
4—Secondary Winding; 5—Primary Winding

Fig.1 Physical model of ignition coil

I. INTRODUCTION

The basic function of an ignition coil is to convert low-voltage DC source into very fast high voltage at the spark plug gap [1]. Due to primary and secondary coil inductance, stray capacitance, core eddy current loss, the ignition coil terminal characteristics become more sophisticate than stationary state.

The objective of this paper is to predict the wideband characteristic of ignition coil. A wideband, lumped equivalent circuit model topology for ignition coil is proposed. And the parameters in the circuit model are calculated using FEM. The measured and the simulated frequency- and time-domain results are presented. These results show that the proposed model accurately predicts the ignition coil terminal responses in the 100Hz to 10MHz frequency range.

II. COMPUTATION MODEL

Ignition coil 2D cross-section is described in the Fig.1 (a). Fig.1 (b) shows a single section in secondary winding, which consists of hundreds of coated copper wires.

Fig.2 shows equivalent circuit model. This model separates the winding into individual sections. Each section of the circuit consists of capacitance C , inductance L and resistance R . Ten sections were used in this paper.

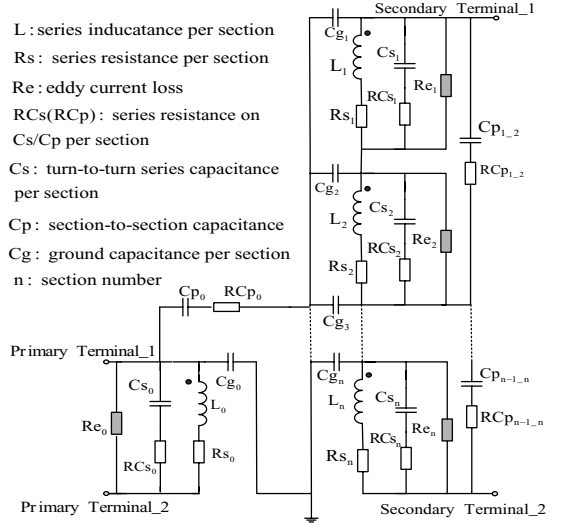


Fig.2 Equivalent circuit model of ignition coil

III. PARAMETER CALCULATION

A. Capacitance

For calculating the ground capacitance C_g and the section-to-section capacitance C_p , simplified solid winding substitutes the virtual winding section, as shown in Fig.3 (a). The capacitance matrix can be obtained from the electrostatic 3D FEM analysis, which is based on (1). Fig.4 (a) shows the 3D meshes of ignition coil.

$$W = \frac{1}{2} \sum_{i=1}^n \sum_{j=1}^n C_{ij} U_i U_j \quad (1)$$

Where W is electrostatic energy; C_{ij} is capacitance between section i and j ; U_i , U_j is voltage to ground of section i , j ; n

is the number of sections. For calculating the turn-to-turn series capacitance C_s , simplified sheet winding substitutes the virtual winding section, as shown in Fig.3 (b). Capacitance matrix is derived from electrostatic 2D FEM analysis. Fig.4 (b) shows the 2D meshes of single section when sheet winding layers number is 20. Then using the matrix data, the capacitance C_s can be calculated with (2).

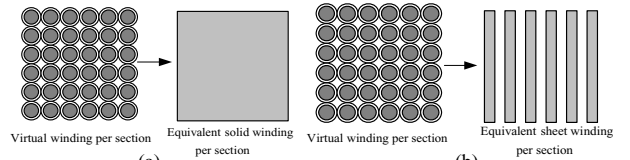
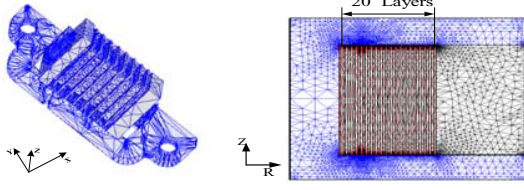


Fig.3 simplified model of virtual winding

$$C_s(N) = \frac{\sum_i \sum_j ij C_{ij}}{(N-1)^2} \quad (2)$$

Where C_s is turn-to-turn series capacitance; C_{ij} is capacitance between sheet i and j ; N is the number of sheet winding layers.



(a) Fig.4 2D/3D mesh in FEM analysis (b)

B. Inductance

In this work, for converting nonlinear problem to linear, the varying relative permeability μ_r of steel lamination was substituted by the constant and magnetic saturation phenomenon was also ignored. The inductance matrix can be extracted from the magnetostatic 3D FEM analysis, which is based on (3).

$$L_{ij} = N_i N_j \int \vec{B}_i \cdot \vec{H}_j d\Omega \quad (3)$$

L_{ij} is mutual inductance between section i, j ; N_i, N_j is the number of winding turns in section i, j .

Inductance value follows the frequency varying, because of skin effect. Hence, steel lamination $\mu_r=2800$ is adopted for low frequency range, and in this case the inductance matrix is defined as L_L ; $\mu_r=0.001$ is for high frequency range, and the inductance matrix is L_H , as shown in Fig.5.

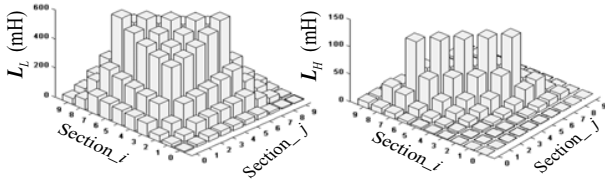


Fig.5 Inductance Matrix in low-frequency (left) range and high-frequency range (right)

C. Resistance

In circuit model, R_s represents the winding resistance; RC_s/RC_p represents the capacitance dielectric loss and their calculation methods are presented in [2]; R_e represents the steel eddy current loss and its calculation method is proposed in [3].

IV. SIMULATION AND EXPERIMENT

A. Frequency-domain

To invest the secondary winding terminal impedance response from 100Hz to 10MHz, the following simulation cases are studied: Case A-the inductance matrix L_L is adopted as series inductance L; Case B-the inductance matrix L_H is adopted as series inductance L; Case C-ignoring the turn-to-turn series capacitance C_s . As shown in Fig.6, in case A, the simulation matches well with the calculation from 100Hz to 10MHz; and in the other two cases, the simulations only partly agree with measurement.

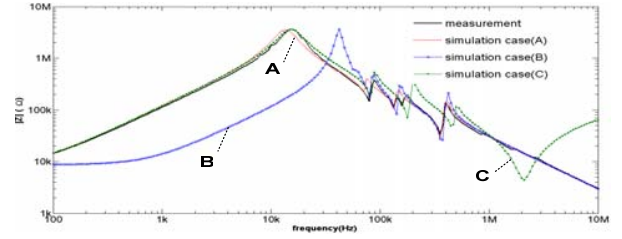


Fig.6 measured and simulated magnitudes of secondary winding impedance

B. Time-domain

Fig.7 shows the transient voltage test circuit principle. In time-domain test, the above-mentioned case A is performed. The primary winding current and secondary winding voltage are measured and calculated, and the results show a reasonable agreement, as shown in Fig.8

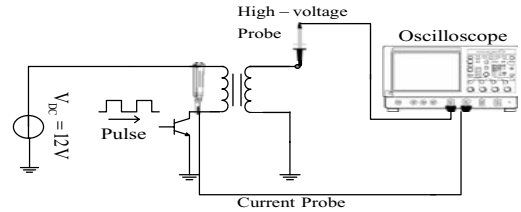


Fig.7 time-domain test circuit principle for ignition coil

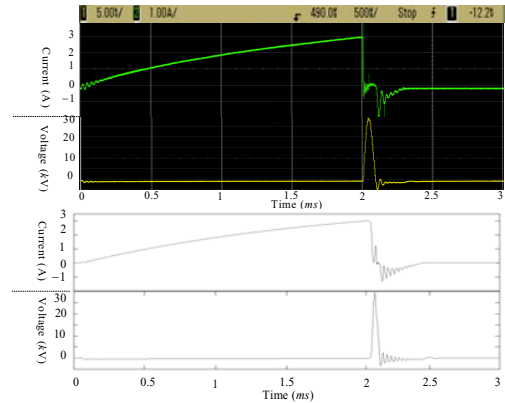


Fig.8 measured (upper-part) and calculated (under-part) current of primary winding and voltage of secondary winding

V. CONCLUSION

This paper has presented an equivalent lumped circuit model for predicting wideband characteristics of automotive ignition coil. The main parameters in the circuit are calculated with FEM field analysis. This circuit model was validated by experiment in both frequency and time domains.

VI. REFERENCES

- [1] Rohwein, Babcock, Buttram, Camilli. Advanced automotive ignition system, Digest of Technical Papers-IEEE international Pulsed Power Conference, 1: 40-45, 1995
- [2] Yoshikazu, Shibuya, Shigeto F. High frequency model and transient response of transformer Windings [C]. IEEE/PES Transmission and Distribution Conference and Exhibition Asia Pacific, Yokohama, 3: 1839-1844, 2002
- [3] Jens Benecke, Stefan Dickmann. Analytical HF Model for Multipole DC Motors. Proceedings of the 18th international Zurich Symposium on Electromagnetic Compatibility, EMC, pp. 201-204, 2007

Factors Affecting Eddy Current Losses of Segmented Nd-Fe-B Sintered Magnets without Insulation

Norio Takahashi¹, Hirofumi Shinagawa¹, Daisuke Miyagi¹, Yuhito Doi² and Koji Miyata²

¹ Dept .Electrical and Electronic Eng., Okayama University,
3-1-1 Tsushima, Okayama 700-8530, Japan (E-mail: norio@elec.okayama-u.ac.jp)

² Magnetic Materials R&D Center, Shin-Etsu Chemical Co.,Ltd,
Echizen, Fukui 915-8515, Japan

Abstract- In large permanent magnet motors, the permanent magnet in the motor is segmented into parts in order to reduce the eddy current loss in permanent magnet. It is reported that the insulation between sintered Nd-Fe-B magnets is possible only by contacting the segmented permanent magnets without insulation. But the mechanism for such a phenomenon has not been clear. We have already reported that the analysis considering the resistance of the contact part is possible by defining the contact resistance coefficient K . In this paper, the effects of number of segments of magnet, exciting frequency, contact resistance between magnets and the permeance of magnetic circuit on the eddy current loss of a magnet are investigated. It is shown that the property of eddy current loss in a magnet at high frequency is different from that at low frequency, and the tendency is changed by the contact resistance and the permeance (surrounding iron core).

I. INTRODUCTION

It is reported that the eddy current loss of the segmented Nd-Fe-B sintered magnet can be reduced even if magnets are not insulated[1]. We measured the resistance between magnets under various compressive stresses, then, the effect of stress on the contact resistance between magnets is clarified. Moreover, the eddy current analysis is performed using the 3-D finite element method by considering a contact resistance between magnets. But, the examination was limited to one kind of frequency (=10kHz) and a case of six segmented magnet in an open circuit. As the carrier frequency of the inverter used for the control of PM motor is sometimes more than 10 kHz, and the magnet in a motor is surrounded by the iron core, a systematic investigation of the effects of the exciting frequency etc. is required.

In this paper, the effects of the number of segments of magnet, the exciting frequency, the contact resistance between magnets etc. on the eddy current loss are investigated.

II. MEASUREMENT AND EXAMINATION OF CONTACT RESISTANCE

We measured the resistance of the contact part between magnets by putting two magnets in a vice and by impressing a compressive stress. As the length ΔL of the contact part is unknown, the following contact resistance coefficient K is defined:

$$K = \rho^* \Delta L = SR' \quad (1)$$

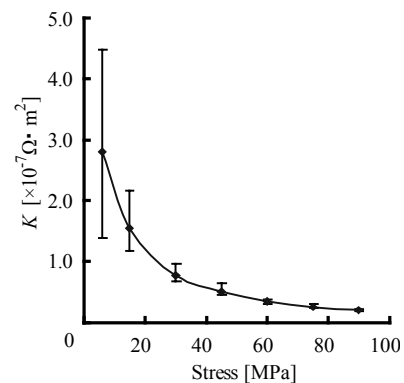


Fig.1 . Relationship between contact resistance coefficient K and stress.

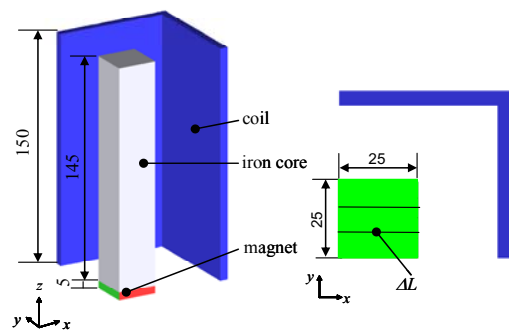


Fig.2. Analysis model of eddy current loss.

where ρ^* is the resistivity of contact part, S is the cross sectional area of the contact region, R' is the resistance of the contact part. The relationship between K and the stress is shown in Fig.1. The figure denotes that the contact resistance coefficient is decreased with the stress.

III. EFFECT OF SEGMENTS, FREQUENCY AND CONTACT RESISTANCE

The eddy current analysis considering the resistance of the contact part is carried out. Fig.2 shows the examined model. A large magnet (50mm×50mm×10mm) is segmented into n

7. Material Modelling

parts. The magnetic field is impressed in the z-direction. The magnetic flux density is 13.5mT when there is no magnet.

Fig.3 shows the relationship among the eddy current loss, the exciting frequency (10kHz, 40kHz), the number of segments (n=1-6), and the contact resistance (compressive stress) when there is no iron core. The figure denotes that the eddy current loss W_e decreases with the decrease of contact resistance (with the increase of stress) at 40kHz. This is, because most of eddy current flows along the edge of magnet due to the remarkable skin effect, and the length of eddy current path is decreased when the contact resistance is decreased (when the stress is increased) as shown in Fig. 4. On the contrary, the eddy current losses W_e at $n=3-6$ are

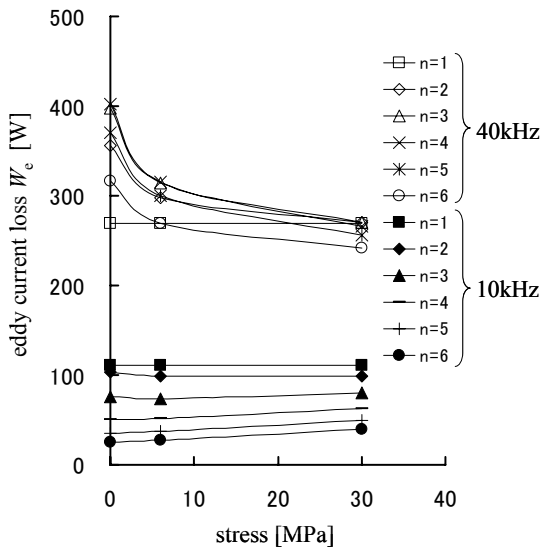


Fig.3. Effect of frequency, number of segments and contact resistance on eddy current loss (compressive stress).

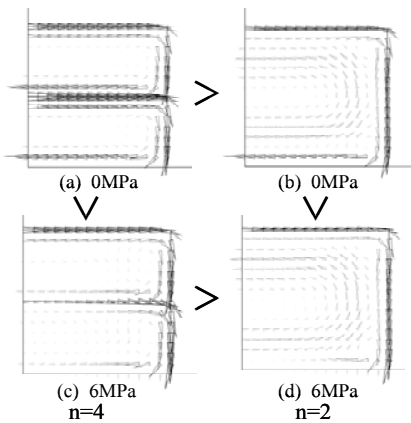
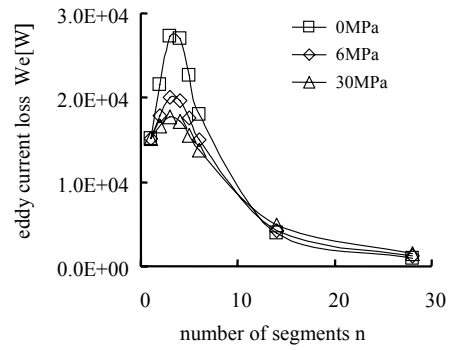


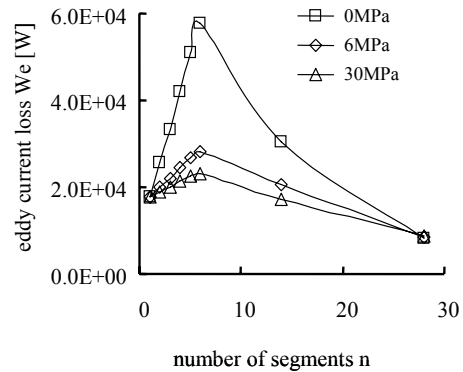
Fig.4. Eddy current distribution (40kHz).

increased with the decrease of contact resistance at 10kHz.



(a) 10kHz

This is, because the amplitude of eddy current density at 6MPa is increased compared with that at 0MPa as the



(b) 40kHz

Fig.5 Relationship among W_e , n and contact resistance.

apparent area of magnet is increased due to the decrease of contact resistance. From the above-mentioned results, it can be found that the eddy current loss is not always reduced when the contact resistance is increased (or magnets are insulated).

Fig.5 shows the eddy current loss W_e when iron cores are put in both sides of magnet as shown in Fig.1. As the skin effect is remarkable when iron cores are put, W_e increases with n and has a peak value due to the same reason discussed in the case of 40kHz in Figs. 3 and 4. When n is larger than about eight, W_e at 10kHz is decreased by segmenting the magnet at 10kHz, but W_e at 40kHz is increased by the segmenting. The figure denotes that W_e can be reduced if adjacent segments are connected by the contact resistance. Therefore, the segmented magnet without insulation has an advantage that W_e at a high frequency of more than the carrier frequency can be reduced.

REFERENCE

[1]N. Takahashi, H. Shinagawa, D. Miyagi, Y.DoI, and K.Miyata, " Analysis of eddy current losses of segmented Nd-Fe-B sintered magnets considering contact resistance", IEEE Trans. Magn., vol.45, no.3, pp.1234-1237, 2009.

Electromagnetic Analysis of Umbilical Cables with Complex Configurations

Salles¹, M. B. C., Costa¹, M. C., Filho², M. L. P., Cardoso¹, J. R., Marzo¹, G. R.

¹Applied Electromagnetism Laboratory (LMAG) – PEA – EPUSP, São Paulo - Brazil

²Institute for Technological Research – IPT, São Paulo - Brazil

E-mail: mausalles@pea.usp.br; mcosta@electromag.com.br

Abstract — these studies will describe the electromagnetic analyses of different configurations of the so called “Integrated Production Umbilical” (IPU), or simply umbilical cables. Modern IPU can have more than 4 independent 3-phase power circuits as well as steel tubes physically inside the same cable. There is no 2-D symmetry for these cable configurations and the 3-D simulations are very undesirable since they can have more than 10 km. The adopted methodology is a combination of 2D-finite element analyses (coupled with electric circuit) and the transposition technique. The cable performance (voltage drops and modulation) will be investigated to determine the appropriate configuration.

I. INTRODUCTION

The oil exploration on offshore platforms represents an activity of high investment, where the risk of fails must be minimized. On the oil exploration process, there are cables composed by hydraulic steel tubes, independent 3-phase power circuits, signal conductors, etc., integrating an “Umbilical Cable” (UC). Nowadays, the new concept of umbilical cables requires more than only one independent power circuit. The power circuits are required to operate in a wide range of voltage and frequency levels, with strong power quality requirements. The UC configuration aspects can affect the magnetic coupling between the UC components derating the ampacity of the UC [1]-[3] and also degraded the power quality on the load terminals. The main objective of the electromagnetic analysis presented in this paper is to calculate mutual coupling effects between power conductors, power shields, metal tubes and armors (metallic parts inside the cable) to determine the terminal voltage at the load terminals. Moreover, an original combined methodology was developed to make the simulations less time consuming than the 3D-model.

The sections are organized as follows. In section II, one presents the main geometric and electrical characteristics of the analyzed configuration of UC. The original methodology is presented in section III. In section IV, partial results are shown.

II. DESCRIPTION OF THE UC’S SYSTEMS

The configuration of the analyzed umbilical cables consists of four 3-phase power circuits (Circuit #1, Circuit #2, Circuit #3 and Circuit #4). Each circuit feeds independently one submerged oil pump. The main electrical characteristics of the variable voltage supplied by the converters (C1, C2, C3 and C4) are: frequency range ($F = 30\text{-}80$ Hz); supply voltage ($V = 1200\text{-}3200$ V); V/F constant; constant current ($I = 280$ A).

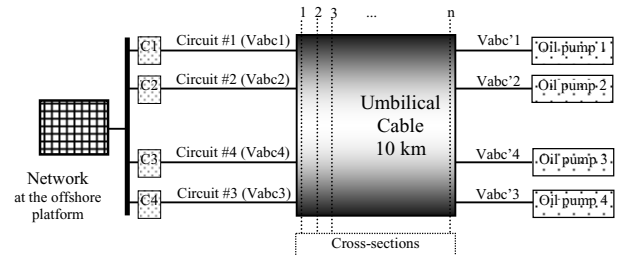


Fig. 1. Unifilar diagram of the 3-phase system

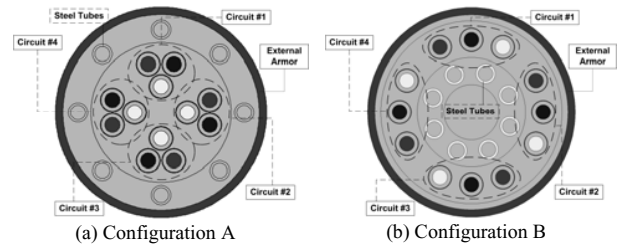


Fig. 2. Cross-sections number 1 of the two analyzed UC configurations.

The cross-sections number 1 of the two analyzed UC configurations are shown in Fig. 2. One can see the 4 power circuits on the inner layer (configuration A) and in the outer layer (configuration B) of the cables with their respective phases A (dark grey), B (black) and C (white). Each power conductor has its own copper shield. There are 8 steel tubes in the outer layer (configuration A) and in the inner layer (configuration B) used to transport fluid. Both have an external metallic armor mainly used for mechanical purposes. The outer diameter of both configurations is 280 mm and its length is 10 km.

For better structural resistance, the internal structure of the UC must rotate in relation to the center along its length. In this specific case, the entire inner layer rotates in anticlockwise direction (1 turn every 1000 mm), while the entire outer layer rotates in clockwise direction (1 turn every 1500 mm). As can be seen, these cables have only 3D model. In addition, a configuration C is derived from the configuration A including the rotation of each power circuit in relation to its own center completing one turn every 750 mm. The full paper will evaluate the power quality of the supply voltage at the oil pump terminals for all the three configurations by a developed methodology to represent the 3D characteristics of the UC’s using a combination of 2D finite element analysis and the transposition technique [1],[4].

III. THE COMBINED METHODOLOGY

As indicated in section II, the analyzed cables has no 2D symmetry, once the metallic elements (conductors, shields, tubes and armors) of the UC change their relative position along the cable length, performing an helicoidally path. Therefore, it is not possible to represent the cables performance simulating only one cross section presented in Fig. 2. In order to avoid the use of the 3D models, one has developed a combined methodology using 2D models and the transposition technique.

As described in section II, the inner layer of these UC's completes 1 turn every 1000 mm while its outer layer completes 1 turn every 1500 mm. The Least Common Multiple (LCM) between layer lengths is then 3000 mm. This means that at each 3000 mm, the cable pattern repeats. The concept of transposition is addressed in classical 3-phase high voltage transmission line (TL) theory [4]. More details will be given in the full paper.

IV. PARTIAL RESULTS

The evaluation of the UC performance regarding to the power quality was performed using the methodology described in section III for two configurations: A (the power circuits do not turn around their own centers) and C (the power circuits turn around their own centers). The configuration B will be analyzed in the full paper. The supplied voltage of the circuits consider one of the worst operation conditions considering the modulation criteria: 3 circuits (#1, #2 and #3) were supplied on 80 Hz, while 1 circuit (#4) was supplied on 30 Hz. These two cases were analyzed to verify the impact of circuit rotation on modulation results.

A. Induced Voltage at the Load Terminal

Fig. 3 (a) shows the equipotential lines obtained from the steady-state analysis of the circuits #1, #2 and #3 supplied on 80 Hz, while Fig. 3 (b) shows the other separately analysis of the circuit #4 on 30 Hz, both for the cross section number 1 of 50. These two separately analyses are necessary to analyze the power quality. For each cross section, the real and the imaginary components of terminal voltage in the pump connected to circuit (#4) were kept separately. As in the transposition technique, the average values of real and imaginary components were calculated. The terminal voltage of case A and C obtained by the 2D FE steady-state analysis are discussed below.

In Fig. 4, the average of voltage values is used to compute the power quality characteristics. Moreover, one can verify that the values are almost constant because of the fact that the power circuits do not rotate around their own centers resulting on a fixed relative position between them with almost constant induced voltage. From Fig. 5, one can verify that these values are not constants. The rotation of the power circuits around their own centers results on a variable induced voltage that compensates itself.

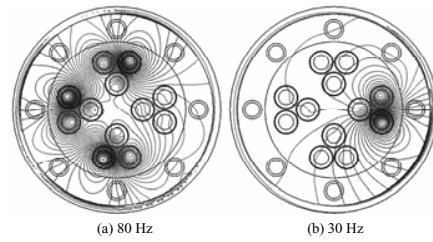


Fig. 3. Equipotential lines of magnetic potential obtained in the cross section number 1 of configuration A.

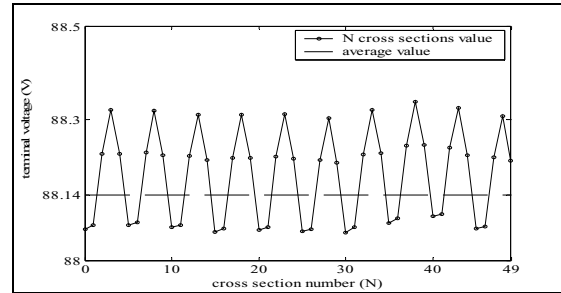


Fig. 4. RMS real components of induced voltage (80 Hz) in phase C of circuit #4 - configuration A

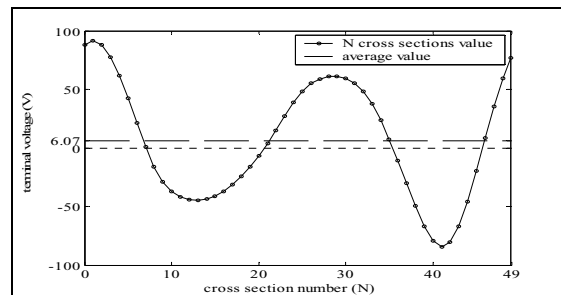


Fig. 5. RMS real components of induced voltage (80 Hz) in phase C of circuit #4 - configuration C

B. Power Quality Analysis

The induced voltage on the oil pump terminal of circuit (#4) by the 80 Hz circuits were computed and compared with its terminal voltage feed on 30 Hz. Configuration A presents the highest modulation values of 7,2 % over the phase C while configuration C only 0,45 %.

The full paper will present more specific results and will include the analysis of the configuration B. This configuration can be built physically in a less complex machine than configuration A and C.

V. REFERENCES

- [1] Petterson P., Schönborg, N., "Reduction of Power System Magnetic Field by Configuration Twist"; *IEEE Transactions on Power Delivery*, vol. 12, n. 4, pp. 1678-1683, 1997.
- [2] Demoulias, C., Labridis, D.P., Dokopoulos, P.S., Gouramanis, K., "Ampacity of Low-Voltage Power Cables Under Nonsinusoidal Currents"; *IEEE Transactions on Power Delivery*, vol. 22, n. 1, pp. 584-594, 2007.
- [3] de Leon, F., Anders, G.J., " Effects of Backfilling on Cable Ampacity Analyzed With the Finite Element Method"; *IEEE Transactions on Power Delivery*, vol. 23, n. 2, pp. 537-543, 2008.
- [4] William D. Stevenson, *Elements of Power System Analysis*, McGraw-Hill, 1982.

Signal-to-noise ratio analysis of radio frequency coils in low-field MRI systems

Ye Li and Xiaohua Jiang

Department of Electrical Engineering, Tsinghua University, 100084 Beijing, China
jiangxiaohua@mail.tsinghua.edu.cn

Abstract—An approach to analyze signal-to-noise ratio of radio frequency coils in low-field magnetic resonance imaging systems is presented. The integral equation method (IEM) is proposed and used to calculate with high accuracy the coil self-resistance that accounts for much higher percentage of the equivalent noise resistance in low field MRI than that in high field MRI. A two dimensional model is built and the analysis of a simple surface RF coil for a 0.3T permanent MRI system is performed. The results show that the coil self-resistance is comparable with the sample resistance, which indicates the importance of accurate coil self-resistance analysis. With IEM for calculating the coil self-resistance, the coil geometries can be easily optimized to obtain the optimal SNR in the region of view.

I. INTRODUCTION

The performance of radio frequency (RF) coils, which are used to pick up magnetic resonance signal, is significant for imaging quality [1]. The signal-to-noise ratio (SNR) and sensitive distribution of RF coils are the targets to optimize coil structure for better imaging quality and higher imaging speed.

The noise voltage picked up by RF coils is proportional to the equivalent noise resistance, which consists of coil self-resistance, sample resistance and dielectric loss in the sample [2, 3]. In low-field magnetic resonance imaging (MRI) system, the dielectric loss can be reduced remarkably by using distributed tuning capacitors and neglected due to the quasi-static assumption. The equivalent noise resistance is therefore dominant by coil self-resistance and sample resistance, which are closely related to current distribution in the conductor and induced current in the sample respectively.

The finite difference time domain (FDTD) method is a widely used numerical method to calculate RF field distributions, power dissipation and tuning capacitor value of the RF coils in high-field MRI because the sample resistance is much larger than the coil self-resistance at 64MHz and above [4]. However, in low-field situation when the coil self-resistance is comparable with the sample resistance, the accuracy of the current density distribution in the conductor calculated by the FDTD method is limited by the Cartesian grid. Although the finite element method (FEM) can achieve accurate results of RF field distribution in both coil conductor and imaging sample, it is limited by the calculation efficiency when used to optimize coil geometries.

This work proposes an approach to calculate coil SNR in low-field MRI system, in which coil self-resistance is calculated by the integral equation method (IEM) and both coil sensitivity and sample resistance are calculated by the magnetic vector potential. In addition, an optimization design approach to improve the SNR of a RF surface coil is presented

as example. The geometry of the circular coil is optimized to achieve the highest SNR with sensitivity homogeneity constraint in the region of interest.

II. ANALYSIS APPROACH

According to the concept of reception, the SNR of RF coils is defined by the following equation [3]

$$SNR = \omega |M_{xy} \cdot B_I| / \sqrt{4kT\Delta f R_e} \quad (1)$$

where M_{xy} is the magnetization vector, B_I is the magnetic field generated by RF coil, R_e is the equivalent noise resistance, T is the temperature, k is the Boltzmann constant and Δf is the band width. Coil self-resistance and sample resistance are proportional to current density integration and the power absorbed by the sample respectively. Generally,

$$SNR \propto |B_I| / \sqrt{R_{coil} + R_{sample}} \quad (2)$$

where R_{coil} and R_{sample} are coil self-resistance and sample resistance respectively.

The magnetic field B_I and electric field $E(r)$ can be calculated by Biot-Savart's law and magnetic vector potential respectively [5]. Coil self-resistance is estimated by current density in conductor at resonance frequency, which is given by

$$\mathbf{J} = -\sigma \cdot (\partial \mathbf{A} / \partial t + \nabla \cdot \varphi) \quad (3)$$

where \mathbf{J} is the current density, \mathbf{A} is the vector potential and φ is the scalar potential. Since the conductivity of the conductor is much higher than that of the sample, the influence of eddy current in the sample on current density in the conductor is neglected. Under the quasi-static assumption, the variation of current density along current direction is neglected. Thus, the two dimension current density distribution is given by [6]

$$\dot{\mathbf{J}} = -j\sigma\mu f \iint_S \dot{\mathbf{J}} \ln r ds - \dot{J}_0 \quad (4)$$

where σ and μ are the conductivity and the permeability of the conductor respectively, f is the resonance frequency, r respects to the distance between ds , S is the cross section, and $\dot{J}_0 = \sigma \cdot \partial \varphi / \partial z$ is a constant in this case.

This integral equation is solved by numerical method which changes integral equations to matrix equations [6]. The cross section of conductor is discretized on an $M \times N$ grid. Assuming the current density of each cell on the grid is constant, (3) is expressed as following linear integral equations

$$\begin{aligned} \mathbf{J}_i + j\sigma\mu f \iint_S \mathbf{J}_i \ln r ds = -\mathbf{J}_0 \\ \sum_{i=1}^{M \times N} s_i \mathbf{J}_i = \mathbf{I} \end{aligned} \quad (5)$$

where J_i and s_i are current density and area of the i^{th} element respectively, and I is the current in conductor. The above $M \times N + 1$ equations can be represented in the matrix-vector form.

The proximity effect can be analyzed as well as the skin effect by this method. All the cross sections of conductor are meshed by the same way, which is shown in Fig. 4. The scale of integral equations shown in (5) increases to $(M \times N + 1) \times n$, including all the elements in the conductors.

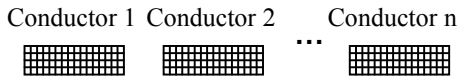


Fig. 1. The cross section mesh for proximity effect analysis

The current density distribution is obtained by solving the above linear equations. AC resistance coefficient k_{ac} is defined as (6) to describe skin effect and proximity effect on coil self-resistance.

$$k_{ac} = R_{ac}/R_{dc} = S \cdot \sum_{i=1}^{M \times N} s_i |\mathbf{J}_i|^2 / I^2 \quad (6)$$

In order to obtain homogeneous images, the sensitivity homogeneity S in the region of interest should be considered as constraint. S is related to the magnetic field generated by RF coil, which is defined as

$$S = 1 - 2 \times (|\mathbf{B}_f|_{\max} - |\mathbf{B}_f|_{\min}) / (|\mathbf{B}_f|_{\max} + |\mathbf{B}_f|_{\min}) \quad (7)$$

where $|\mathbf{B}_f|_{\max}$ and $|\mathbf{B}_f|_{\min}$ are the maximum and minimum magnetic field of the RF coil in the region of interest.

III. EXAMPLES

The imaging sample is human body, which is simplified as a cylinder ($\sigma = 0.5$ S/m and $\mu = \mu_0$) with length $L=15$ cm, diameter $D=30$ cm. The conductor is copper tape with a 1.2 cm width, a 0.018 cm thickness and $\sigma = 5.3 \times 10^8$ S/m. The region of interest is a 2 cm diameter sphere of which the center is 4cm from the right end of the cylinder. The RF coil is a circular surface coil and the gap between the RF coil and the cylinder sample is 1 cm. The geometries of model are shown in Fig. 2. The coil is designed for a 0.3T permanent MRI system of which the resonant frequency is 12.72 MHz.

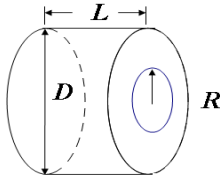


Fig. 2. The geometries of sample and RF coil

A. Current Density Distribution Analysis

The penetration depth at 12.72 MHz is 0.023 mm. As shown in reference [6], the current density in centre region of conductor is much more uniform than that of edge region. The mesh of the conductor is formed by a non-uniform rectilinear grid with higher densities in the edge region.

The current density distribution is obtained by the IEM. The contour of current density on cross section is shown in Fig. 3.

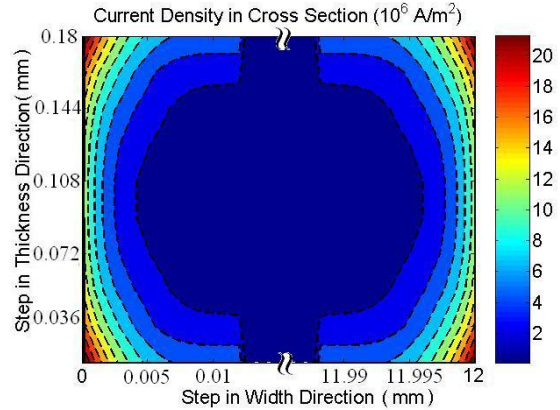


Fig. 3. Contours of current density.

B. Coil Geometry Optimization

The geometry variable of the surface coil is the radius R shown in Fig. 2, which is optimized to achieve the highest SNR in the region of interest with the homogeneity constraint.

The optimized radius R is 4.0 cm. In this case, the sensitivity homogeneity in the region of interest is 81.7%. The coil self-resistance and the sample resistance are 43.8 m Ω and 45.1 m Ω respectively.

IV. CONCLUSION

In the present paper a method to analyze SNR of RF coils in low-field MRI systems is presented. By using IEM, the calculation efficiency of coil self-resistance analysis is improved with good accuracy. Also, it is relatively easy to combine the proposed approach with the optimization problem to improve coil performance.

The results of the sample analysis show that the coil self-resistance of a surface RF coil for a 0.3T permanent MRI system is comparable with the sample resistance, which indicates the importance of accurate coil self-resistance analysis.

V. REFERENCES

- [1] Darrasse, L. and J. C. Ginefri, "Perspectives with cryogenic RF probes in biomedical MRI," *Biochimie*, Vol. 85, 915–937, 2003.
- [2] Hoult D. I. and R. E. Richards, "The Signal-to-Noise Ratio of the Nuclear Magnetic Resonance Experiment," *Journal of Magnetic Resonance*, Vol. 24, 71–85, 1976.
- [3] Wang, J., A. Reykowski and J. Dickas, "Calculation of the Signal-to-Noise Ratio for Simple Surface Coils and Arrays of Coils," *IEEE Transaction on Biomedical Engineering*, Vol. 42, No. 9, 908–917, 1995.
- [4] Christopher M Collins, "Numerical field calculations considering the human subject for engineering and safety assurance in MRI", *NMR Biomed*. 2008, published online in Wiley InterScience: 2008
- [5] Jianming Jin, "Electromagnetic analysis and design in magnetic resonance imaging", New York: CRC Press, 1998.
- [6] Li, J., Niu, Z., Fang, D. and Shi, Y., "Numerical Analysis of the Skin Effect in Long Rectangle Conductor", *Journal of Information Engineering University*, Vol. 7, No. 2, 167–171, 2006.

Time Domain Analysis Of Compact Lumped Element Circulators

Robert Stonies, Dirk Schulz
 High Frequency Institute
 Friedrich Wöhler Weg 4, 42277 Dortmund, Germany
 schulz@hft.e-technik.uni-dortmund.de

Abstract — A symmetrical 3-port lumped element circulator is designed by the use of a numerical time domain method. It is shown, that the application of the numerical time domain method is essential for the numerical analysis of very compact circulator devices built by using thin film technology.

The circulator performance is numerically calculated and optimized to some extent, providing valuable information about important device performances. A comparison with measured scattering parameters shows good agreement with the numerical simulation.

I. INTRODUCTION

Nowadays circulators and isolators are very important components in radio frequency and microwave systems due to their unique non-reciprocal characteristics. Their design and principles of operation have been discussed in some detail for many years now. Among the various kinds of realizations the lumped element approach shows the most promising properties for miniaturization.

However, in opposite to most other types of circulators and isolators, to the knowledge of the authors a lumped element circulator will not be examined with numerical methods in detail. One reason may be the difficulties arising from the adverse aspect ratios of the structure features. With the availability of powerful solvers for EM problems this is no longer an obstacle.

The simulation results presented in this paper are obtained from the commercial numerical tool MICROWAVE STUDIO (CST), because the necessary algorithms for gyromagnetic media are included using the finite integration technique, a time domain approach based on solving the integral form of Maxwell's equations by discretization in time and space. Complex media such as ferrites can be included. This is a prerequisite to model the circulators in discussion.

Numerical results are compared with measurements to proof the results. For the experimental setup a hybrid setup is chosen due to the advantage of using a standard industrial process for the production of printed circuit boards to realize the coupling network, which is essential for the device operation.

II. DESIGN CONSIDERATIONS

In opposite to commonly used distributed circulators, lumped element types are independent from the wavelength to some extent. The only prerequisite is that the wavelength is much larger than the element.

For lumped element circulators, a size-reduction of a factor of 5-10 [1] can be achieved with adequate performance. Distributed devices have been examined in detail inter alia by Bosma [2] and Fay [3]. For them it is necessary to satisfy the condition $kR=1.84$ [2], [4] for the normal mode excitation of a ferrite disc with its radius R . k is the wave number within the ferrite [2]. The most interesting part of a lumped element circulator certainly is the magnetic circuit.

II. DEVICE UNDER TEST

Two different technological concepts are used for the time domain simulation and described in the following. The first one is a double sided standard process printed circuit board process with drilled via-holes. The second one is a sequential layer build-up process allowing for a very thin insulation layer between the conductor layers. The device structure under test is shown in Fig. 1.

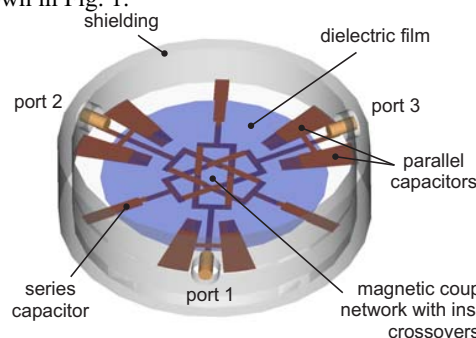


Fig. 1. Three dimensional view of the device showing the interwoven conductor structure, ports and some additional lumped capacitors

A. Double Sided Standard Process

The substrate materials used for in this case, FR4 glass reinforced epoxy ($140\ \mu\text{m}$) or MylarTM (DuPont) polyester film ($175\ \mu\text{m}$), is drilled ($250\ \mu\text{m}$ diameter) to form the necessary via-holes first. Thin layers of titanium and copper are sputtered on both sides. Furthermore, the vias are activated for later electroplating implicitly. A $25\ \mu\text{m}$ dry film photoresist FP325 (Elga Europe) is laminated on both sides and structured with a MA56 mask aligner (Suess). Electroplating is now used to grow copper into the resist grooves and form the conductors. After electroplating, the resist is stripped and the seed layers are removed through chemical etching.

B. Sequential Layer Build-Up Process

First, the substrate is coated with titanium and copper on one side through sputtering to provide a seed layer for later

electroplating. Then, the FP325 dry film resist is laminated and structured. Copper is electroplated to a height of 15 μm into the grooves. The resist is stripped and the seed layers are etched. Now, a second layer of FP325 is laminated on top. It is structured by the via and feed-line pattern before the surface is completely sputter-coated with titanium and copper again. An additional electroplating process enhances the layer thickness to 15 μm . Finally, AZ-3210 (ALLRESIST), a thick film positive photo resist, is spin-coated onto the sample and structured to protect the later bridges and vias of the top layer from being etched. In contrast to the first example interdigital lumped capacitors are used for matching and tuning.

III. SIMULATION AND OPTIMIZATION

The parasitics appear to influence the characteristics in particular. Especially the crossover capacities are responsible for a significant decrease of the operating frequency. To speed up the calculation, the lumped capacitors may be substituted through idealized capacitors, virtually connected between two mesh points. Once the necessary capacity is evaluated, a separate parametric simulation model including single capacitor model is used to obtain the exact geometries. To be more exact with that capacitors, a full three-dimensional electrodynamic calculation can be performed at the design center frequency. Finally, the geometries of all simulations are combined into one CAD-file and masks are generated. As can be concluded from Fig. 3 and is expected, fringing fields tend to increase the capacity to an amount that does not allow to neglect them. Another interesting observation, already predicted in [7] is, that the magnetic field is not at all homogeneously distributed in the ferrites. It is rather clearly concentrated around the conductors (Fig. 2). The ferrites bulk shows a magnetic field that is less than 10 percent of the field close to the conductor.

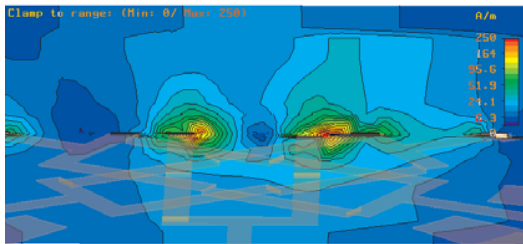


Fig. 3. Magnetic field (in a plane) concentrating in the vicinity of conductors, normalized to 1 W input power at 2.5 GHz

IV. VERIFICATION

To verify the calculated performance, the structures are mounted into a jig containing the ferrites and providing the SMA connectors to the interface of a vectorial network analyzer. The dc magnetic field is generated by a current-controlled electromagnet with a slitted yoke.

For the double sided processed structure including drilled vias, Fig. 4 shows a comparison between the calculated and measured performance. It ought to be reminded that the layout for the structure only consists of the isoductor conductors.

No capacitors are included and hence there is only the small parasitic capacity of the line crossings that act as a tuning element for the device. This leads to a much higher

resonance frequency close to the gyromagnetic resonance frequency. This reduces bandwidth and implies higher insertion losses. The inclusion of explicit lumped tuning elements is no problem at all and similar to the sequential layer build up.

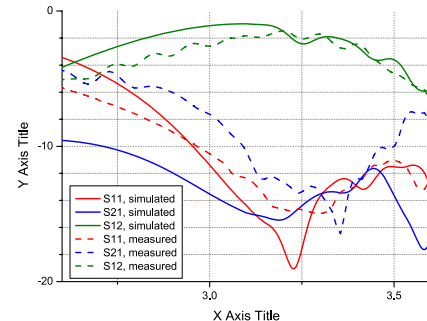


Fig. 4. Calculated and measured scattering parameters

For the second structure the scattering parameters are also measured and compared with the calculated ones. In evidence from Fig. 5, the measured data agree well with the data resulting from a numerical calculation but the center frequency is slightly shifted to lower frequencies. The authors assume that the reasons for this shift are inaccuracies in the calculation and in the technological process. First, the ferrite is treated as to be completely homogenous magnetized, which is not true in reality. Magnetostatic calculations show, that the magnetic field is much stronger close to the circumference than it is in the middle of the thin disc. Second, thin layers are represented by one mesh-cell in height to keep the time for calculation short. This may lead to some inaccuracies, especially concerning the field distribution at edges.

Nevertheless, the comparison shows a quite good agreement and with some correction and modifications it will be possible to predict the behaviour of a lumped element circulator with high accuracy by use of numerical calculations.

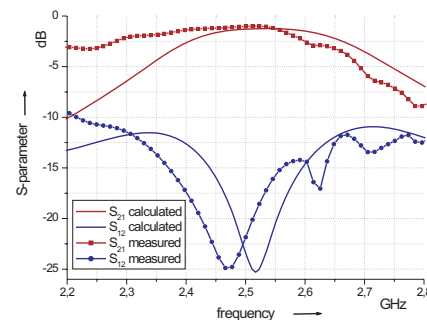


Fig. 5. Calculated and measured scattering parameters

V. REFERENCES

- [1] C. E. B. R. H. Knerr and F. Bosch, "A compact broad-band thin-film lumped-element l-band circulator," *IEEE Transactions on Microwave Theory and Techniques*, 18(12): 1100–1108, 1970.
- [2] H. Bosma, "On stripline y-circulation at uhf," *IEEE Transaction on Microwave Theory and Techniques*, 12: 61–72, 1964.
- [3] C. E. Fay and R. L. Comstock, "Operation of the ferrite junction circulator," *IEEE Transactions on Microwave Theory and Techniques*, 13: 15–27, 1965.

12. DEVICES AND APPLICATIONS

- [4] J. Helszajn, *Principles of Microwave Ferrite Engineering*. Wiley-Interscience, 1969.
- [5] I. Ikushima and M. Maeda, "A temperature-stabilized broad-band lumped-element circulator," *IEEE Transactions on Microwave Theory and Techniques*, 22: 1220–1225, 1974.
- [8] H. Katoh, "Temperature-stabilized 1.7-ghz broad-band lumped-element circulator," *IEEE Transactions on Microwave Theory and Techniques*, 23: 689–696, 1975.
- [12] R. H. Knerr, "A compact thin film lumped element circulator using a capacitor, common to all three arms, for broadbanding or switching," *International Microwave Symposium*: 393–396, 1970.

Determination of a correction factor due to joints for core losses in power transformers by 2D FEA

W.V. Calil¹, V.C. Silva²

¹ABB Asea Brown Boveri Brasil, Av. Monteiro Lobato, 3411, 07190-904 Guarulhos SP Brazil

²Universidade de São Paulo, Av. Prof. Luciano Gualberto, T.3/158, 05508-900 São Paulo SP Brazil

wilson.calil@br.abb.com

Abstract — We present an approach to determine a correction factor for core losses due to joints in power transformers. Its determination is carried out by finite element analysis in two dimensions. The influence of two kinds of joints, namely with and without *step-lap*, are investigated, as well as three airgaps. Results are validated by comparison with other authors, and also by experimental data.

I. INTRODUCTION

The determination of core losses in power transformers is usually carried out with the aid of the curve W/kg versus T for a given frequency, provided by the steel manufacturer. This curve includes both hysteresis and eddy current losses.

However, other effects not predicted by those curves, which are mainly due to core manufacturing process, such as burr, localized poor insulated lamination, airgaps due to joints and so on, also give rise to additional, not-predicted losses and local heating in transformer cores. Most of those effects are of difficult estimation, owing to their randomness. Therefore, the estimation of actual core losses is always a troublesome, difficult task.

Manufacturers of power transformers make use of a *building factor* (BF) to correct the calculated core losses. This BF is obtained statistically from historical, experimental data sets, which can lead to either an over or an underestimation of the losses, with resulting cost penalization [1].

This work thus proposes a correction in the BF in order to improve the estimation of the total core losses by means of a *correction factor* (CF). This CF takes into account the increase in the core losses due to the presence of joints in the core of power transformers.

It is well known that core losses in transformer can be considerably reduced by an improved joint design, which can be achieved by an accurate knowledge of the local flux density distribution, both in the corners and in the limbs. Then, the proposed approach to calculate this CF is based on two-dimensional (2D) finite element analysis (FEA). The methodology is outlined in the following sections.

II. TRANSFORMER CORE JOINT CONFIGURATIONS

Two configurations of core transformer joints will be analyzed. Fig. 1 depicts a typical transformer core, in which regions of joints appear dark-grayed. Fig. 2 illustrates the two joint configurations, with and without *step-lap*, used in the analysis.

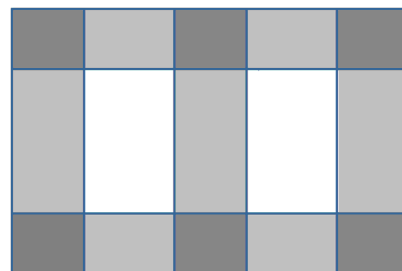


Fig. 1 A 3-phase transformer core showing regions with joints (in dark gray).

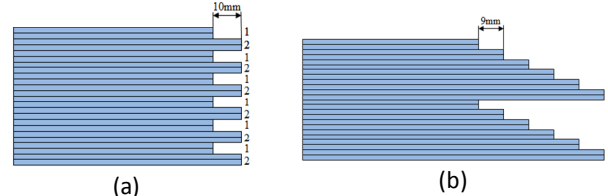


Fig. 2 Transformer core joints: (a) without *step-lap*; (b) with *step-lap*.

III. FEA OF CORE JOINTS

To estimate the increase in no-load core losses due to the core joints, a CF, k_c , has been defined, as follows:

$$k_c = P_{0j} / P_0, \quad (1)$$

where P_{0j} and P_0 stand for losses in cores with and without joints, respectively. These core losses are determined through a FE modeling of the joint regions.

Two FE simulations were carried out with the aid of a trial edition of commercial FE-package for electromagnetic design. By means of a 2D magnetostatic simulation, the package calculates the power losses from the computed flux density distribution in the domain.

In order to overcome the modeling restrictions of this FE-package, the joint regions are modeled as a 2D periodic domain, excited by a hypothetical current source coil.

The 2D FE models are illustrated in Fig. 3. No simplification was adopted in the core model, such as shell elements or stack-homogenization, since no such facilities were available in the package. Therefore, all steel sheets of the laminated stack, as well as their insulations, have been represented in the geometrical model of the core. Two simulations were performed, for the two configurations (with and without joint), to calculate P_0 and P_{0j} .

The magnitude of the current to excite the hypothetical source coil was determined by trial and error, in order to yield, close to the periodic boundaries, the required, typical average values of peak flux density, present in joint-free parts of the core (i.e. limbs and yoke).

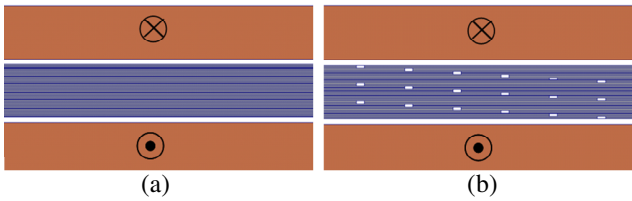


Fig. 3 2D FE domains with laminated core (cyan) and source coil (brown) to model the transformer core joints. (a) Without joint. (b) With joint.

The adjusted no-load core loss, including the correction factor, can then be estimated as follows:

$$P_0 = m_{Fe} \cdot \left[\frac{W}{kg} \right] \cdot \left[(F_j \cdot k_c) + (1 - F_j) \right] \quad (2)$$

In (2) the factor F_j was introduced in order to correct the losses only in the joint-parts of the transformer core (see Fig. 1) and is given by the ratio between two areas: the total area of the joint regions (sum of dark-grayed areas in Fig. 1) and total area of transformer core (sum of light- and dark-grayed areas in Fig. 1). The quantities m_{Fe} and $[W/kg]$ stand for the core mass and the core loss density, respectively.

IV. RESULTS

A set of FE simulations were performed with the following values of airgaps and average peak flux densities: 0.5/1.0/1.5 mm and 1.0/1.2/1.4/1.73/1.77 T.

Figs. 4 and 5 show color maps of flux densities in non-step-lap and step-lap joints, respectively, where it can be seen that the latter exhibits a significant reduction in saturated spots, and hence iron losses, as expected. These results were obtained with a 1.73T flux density and a 1.5mm airgap.

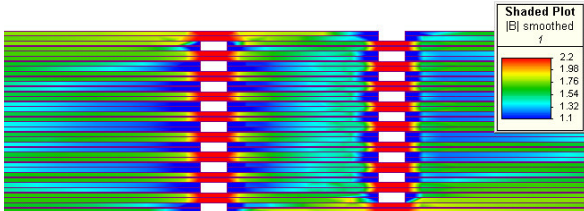


Fig. 4. Color map of flux-density distribution in a *non-step-lap* joint (1.5mm airgap, 1.73 T).

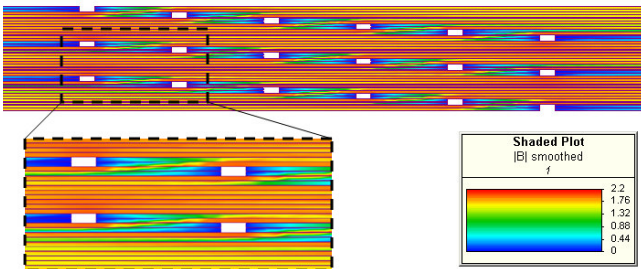


Fig. 5. Color map of flux density distribution in *step-lap* joint (1.5-mm airgap).

A comparison of the computed CFs for joints without and with step-lap is presented in Fig. 6.

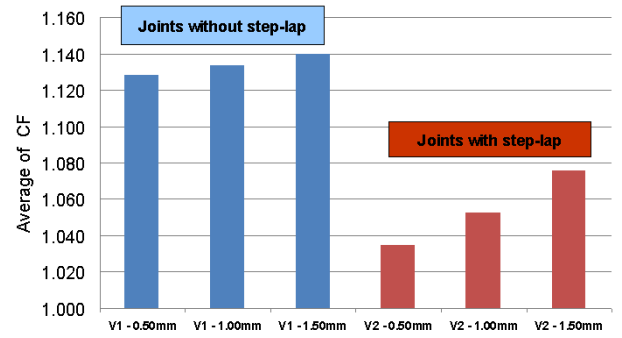


Fig. 6. CF determined by FEA for joints without (V1) and with (V2) *step-lap*.

These results are in accordance with other authors [1],[4]-[5], since they confirm the reduction in the CF yielded by the step-lap joint with respect to that without step-lap.

The methodology was applied in the transformers of a manufacturer data set. The newly estimated core losses, with the proposed correction, led to a better agreement with the measured losses than those adjusted by the original, conventional BF.

V. CONCLUSION

A correction factor was proposed to account for the increase in no-load transformer core losses due to core joints, thereby improving its estimation. This more accurate adjustment was accomplished by applying a 2D FEA of a reduced, equivalent model of core joint region. The effectiveness of *step-lap* joints in reducing core losses was confirmed, when compared to *non-step-lap* joints, although the latter proved to be less sensitive to variations in the airgap. Additional experimental verification and results are intended to be presented in an extended version of this digest.

VI. REFERENCES

- [1] R. S. Girgis, Ed G. teNijenhuis, K. Gramm, and J. E. Wrethag, "Experimental Investigations On Effects Of Core Production Attributes On Transformer Core Loss Performance," *IEEE Trans. on Power Delivery*, 13(2): 526-531, 1998.
- [2] G. F. Mechler, R. S. Girgis, "Calculation of Spatial Loss Distribution in Stacked Power and Distribution Transformer Core," *IEEE Trans. on Power Delivery*, 13(2): 532-537, 1998.
- [3] Ed G. teNijenhuis, R. S. Girgis, and G. F. Mechler, "Other Factors Contributing to the Core Loss Performance of Power and Distribution Transformers," *IEEE Trans. on Power Delivery*, 16(4): 648-653, 2001.
- [4] D. Pavlik, D. C. Johnson, and R. S. Girgis, "Calculation and Reduction of Stray and Eddy Losses in Core-Form Transformers Using a Highly Accurate Finite Element Modelling Technique," *IEEE Trans on Power Delivery*, 8(1): 239-245, 1993.
- [5] G. F. Mechler and R. S. Girgis, "Magnetic Flux Distribution in Transformer Core Joints," *IEEE Trans. on Power Delivery*, 15(1): 198-203, 2000.

Effects of a remanent magnetization on the detection signals of the metal loss in Magnetic Flux Leakage type NDT

Kang Seo, Gwan Soo Park and Jae Min Kim

School of Electrical Engineering, Pusan National University, Busan 609-735, South Korea

E-mail: kalam@pusan.ac.kr

Abstract—Because of a strong magnetic field in magnetic flux type NDT system, the object itself is magnetized so that it shows a hysteresis characteristics during the sensing, which might cause a distortion of the defect signals. In this research, the magnetization characteristics of a pipeline in the magnetic flux leakage type non-destructive testing are analyzed. Effects of a magnetic hysteresis of a pipeline are analyzed. Magnetic flux density due to a remanent magnetization of gas pipeline is computed and verified by real measurement.

Index Terms—magnetic flux leakage, magnetic sensor, non destructive testing, nonlinear finite element analysis

I. INTRODUCTION

The magnetic flux leakage type non-destructive testing system is widely used to detect metal losses of the underground pipe in gas pipelines [1]. In the system, the sensor modules are consisted of permanent magnet, magnetic yoke and Hall sensors to detect the metal loss, corrosion defect and any other damages of the gas pipeline. The object pipeline is magnetically saturated by a magnetic system with permanent magnet and yokes as in Fig. 1. Hall sensors detect the stray leakage fields in the metal loss region.

In the system, a magnetization level is designed to be high enough to saturate the pipeline in order to increase the sensitivities of the systems [2]-[3]. So, in most cases, pipes are to have remanent magnetizations that have distorted the sensing signals to reveal the metal losses [4]-[6]. To detect the defects precisely, the sensing signals need to be compensated to eliminate the distortions coming from the media hysteresis. In this paper, the magnetizations of the pipeline in MFL type NDT are analyzed by 3 dimensional finite element analysis and the distortions of the sensing signals are compared with measurement.

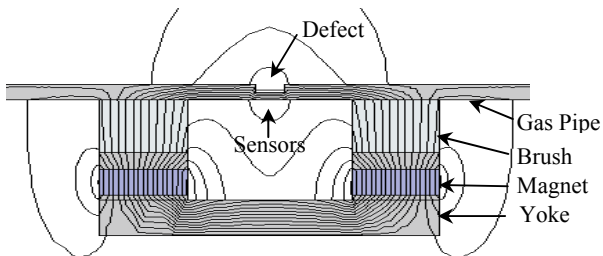


Fig. 1 Diagram of a MFL type NDT

II. MAGNETIZATION IN MFL TYPE NDT

The relations between magnetic field intensity H , magnetic flux density B and magnetization M of the magnetic material could be represented as follows,

$$B = \mu_0(H + M') \quad (1)$$

$$B = \nabla \times A \quad (2)$$

$$\nabla \times H = J \quad (3)$$

The main source of the magnetic field in this system is permanent magnet so the magnetization M' is represented by the sum of reversible component (χH) and irreversible component (M) as in (4).

$$M' = \chi H + M \quad (4)$$

The magnetic field in this case is represented as follows,

$$H = \nu B - \nu_r M \quad (5)$$

where $\nu = 1/\mu$, $\mu = \mu_0 \mu_r$, $\nu_r = 1/\mu_r$, $\mu_r = 1 + \chi$.

From substituting these equations into (1) and (3), Coulomb gauge and vector relation gives

$$\nabla \times (\nu \nabla \times A) = J + \nu_r \nabla \times M \quad (6)$$

$$-(\nabla \cdot \nu \nabla) A = J + \nu_r \nabla \times M \quad (7)$$

In this equation, M is not constant in hysteresis problems. The classical Preisach modeling [3] is adopted in this system.

$$M(t) = \iint_{u,v} P(u,v) \cdot H(t) du dv \quad (8)$$

where $P(u,v)$ is Preisach density function. To solve the hysteresis problem, this modeling is solved with finite element solution simultaneously. Finite element analysis gives the final matrix equation as follows,

$$[K_v] \{A\} = \{f\} + \{f_m\} \quad (9)$$

In this equation, $[K_v]$ includes the geometry and material constant information whereas $\{f_m\}$ includes the magnetic hysteresis characteristics of the materials. The iterative algorithm to solve the scalar Preisach modeling is included in the computations.

III. HYSTERESIS EFFECTS ON THE SENSING SIGNALS

To measure this, we made a measuring coil in the pipeline as in Fig. 2. The magnetization level of the pipeline could be measured from the flux linked in the coil. As the PIG passing again, the remanent magnetization level becomes decreased as in Fig. 3. Fig. 4 shows the decrease of the sensing signals of a defect $2t \times 2t \times 0.8t$. The remanent magnetic field according to the remnant magnetization of the object could be summarized as in Fig. 5. So, the compensating data as a function of pigging events are successfully obtained. For the exact estimation of the defects, the sensing signals needs to be corrected by using this data according to the numbers of sensing events.

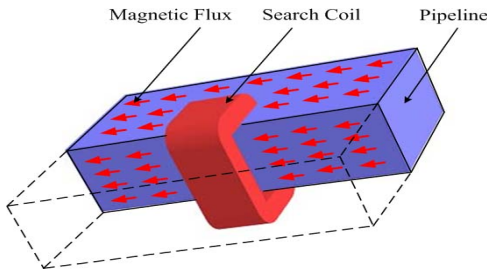


Fig. 2 Search coil for the measurement of remanent magnetic flux

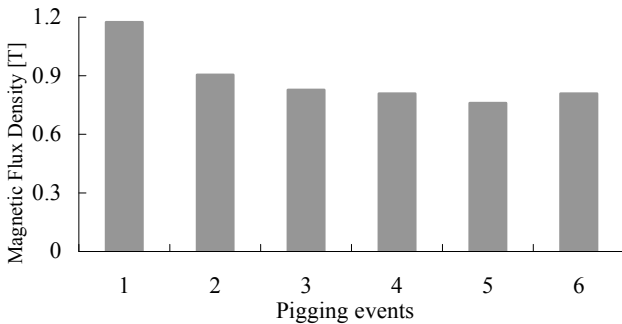


Fig. 3 Remanent magnetization according to the pigging events

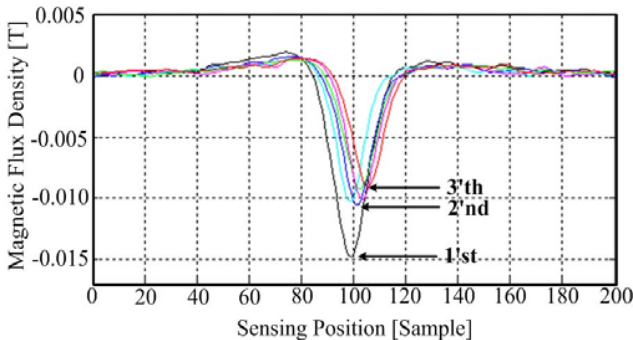


Fig. 4 Decrease of sensing signals according to the pigging events

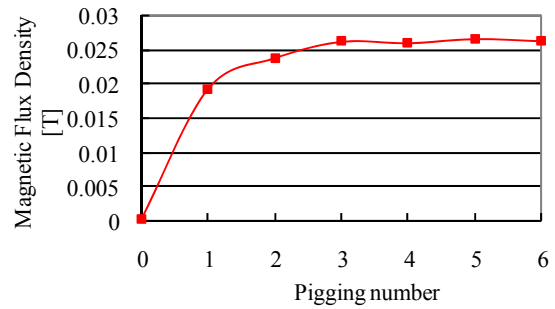


Fig. 5 Remanent magnetic fields according to the pigging numbers

IV. CONCLUSIONS

In MFL type NDT system, a magnetization level is designed to be high enough to saturate the pipeline in order to increase the leakage field under the defect region. So, in most cases, pipeline is to have remanent magnetizations according to the movement of the PIG so that the sensing signals are distorted to reveal the metal losses. In this research, the dynamic characteristics of magnetization in MFL type NDT system are analyzed. Effects of a remanent magnetization is computed by using 3 dimensional finite element analysis including hysteresis characteristics. The results show that the effects of axial components of magnetization are increasing the MFL signals. In case of re-magnetization, the magnitudes of magnetization level become increased because of magnetic hysteresis, which are agreed well with measurement. So, it is necessary to include the magnetic hysteresis of the pipeline for the precise analysis of the MFL type NDT.

REFERENCES

- [1] Jim Cordell, C.Eng, M.I.Mech.E, F.Inst.Pet and Hershel Vanzant, "In-line inspection pigging", All about pigging., chapter 8, pp. 1-28, 1999.
- [2] H. Haines et. Al., "Advanced MFL signal analysis aids pipe corrosion detection", Pipeline & Gas Industry, pp. 49-63, March 1999.
- [3] J. Bruce Nestleroth, Steven W. Rust, and David A. Burgoon, "Determining Corrosion Defect Geometry from Magnetic Flux Leakage PIG Data", The NACE International Annual Conference and Exposition CORROSION 96, Paper No. 44, pp. 1-11, 1996.
- [4] G.S.Park, P.W.Jang, Y.W.Rho, "Optimum Design of a Non-Destructive Testing System to Maximize Magnetic Flux Leakage", Journal of Magnetism, vol.6, no. 1, pp. 31-35, March 2001.
- [5] G.S.Park, Eun Sik Park, "Improvement of the Sensor System in Magnetic Flux Leakage type NDT", IEEE Trans. On Magn., vol. 38, no. 2, pp. 1277-1280, March 2002
- [6] G.S.Park, Sang Ho Park, "Analysis of the Velocity Induced Eddy Current in MFL type NDT", IEEE Trans. On Magn., vol. 40, no. 2, pp. 663-666, March 2004

Force Computation in a MEMS Structure Using Adaptive Mesh Refinement

F. Bölöni¹, A. Benabou¹, G. Krebs² and A. Tounzi¹

¹ L2EP – USTL, Bât. P2, Cité Scientifique, 59655, Villeneuve D’Ascq, France

² LGEP - CNRS / SUPELEC - 11, rue Joliot Curie - Plateau de Moulon - 91192 Gif sur Yvette, France
mounaim.tounzi@univ-lille1.fr

Abstract — This paper investigates the effect of an adaptive mesh refinement strategy for the force computation in Micro Electro Mechanical Systems (MEMS). First, the error is estimated in the whole domain and then the refinement is applied in specific regions of the system. The results given by the refinement are compared with those of a reference problem issued from a system with a fine mesh.

I. INTRODUCTION

Micro Electro Mechanical Systems (MEMS) consist mostly of movable and fixed parts subjected to an electric potential difference to create an electrostatic force. Thus, to describe such systems, an electro-mechanical model can be useful [1]. In the case of a weak coupling between electrostatic and mechanical models, the coupling term is the electrostatic force which must be determined with accuracy. To this purpose, the finite element method (FEM) is a useful tool but it requires a suitable mesh construction, especially for high field gradient regions.

In this paper, the electrostatic force involved in a simple MEMS structure is computed for different positions of the movable part. The approach consists in an adaptive mesh refinement strategy. This one is based on the error due to the discontinuity of the normal component of the electrical flux density when using the scalar electric potential formulation in the FEM. As a result, the refined mesh will have higher granularity where it is needed.

A common MEMS actuator is the *linear comb drive* that consists of interlocking teeth on which a voltage is applied. To study this type of actuator, a unit cell, i.e. a segment representative of the entire system, is defined.

First, we present the FE formulation. Then, we introduce the chosen error estimator. Some results are presented for the studied device.

II. MATHEMATICAL MODEL

Considering an electrostatic problem with free charge region, the distribution of the electric field in a domain D of boundary Γ is given by the Maxwell’s equations such as,

$$\operatorname{div} \mathbf{D} = 0 \quad \text{with } \mathbf{D} \cdot \mathbf{n} = 0 \quad \text{on } \Gamma_D \quad (1)$$

$$\operatorname{curl} \mathbf{E} = 0 \quad \text{with } \mathbf{E} \times \mathbf{n} = 0 \quad \text{on } \Gamma_E \quad (2)$$

with \mathbf{E} the electric field, \mathbf{D} the electric flux density and Γ_D , Γ_E complementary boundaries of the studied domain D . The electric behavior law of the material is given by,

$$\mathbf{D} = \varepsilon \mathbf{E} \quad (3)$$

with ε the electric permittivity. To solve the problem constituted by the relationship (2), the scalar electric

potential (φ) formulation can be used and the electric field can be written such as,

$$\mathbf{E} = -\operatorname{grad} \varphi - \nabla \operatorname{grad} \alpha \quad \text{with } \varphi=0 \quad \text{on } \Gamma_E \quad (4)$$

where φ is the scalar electric potential and α a scalar function defined in order to take into account the imposed voltage V [2]. In the case of numerical discretization, Whitney’s elements can be used to discretize the potential φ and the function α in the nodal element space.

Using equations (1), (3) and (4), the weak form of the scalar potential formulation is written as,

$$\int_D \varepsilon \operatorname{grad} \varphi \operatorname{grad} \varphi' dD = -V \int_D \varepsilon \operatorname{grad} \alpha \operatorname{grad} \varphi' dD \quad (5)$$

with φ' a test function verifying the same boundary condition as the potential φ . Using the Galerkin’s method, the interpolation functions are used as test function in (5).

III. ADAPTIVE MESH REFINEMENT

In this formulation, the electric field \mathbf{E} obtained by the FEM has a continuous tangential component on the whole domain as it is derived from the gradient of the scalar potential φ . The electric flux density \mathbf{D} is continuous in each element but its normal component continuity at the interface between elements is not verified. In fact, these discontinuities of boundary conditions between elements are due to the FEM approximation of the scalar potential. The evaluation of the numerical error due to this unphysical discontinuity is used as criterion for the mesh refinement.

Let f be a facet of an element of the mesh. On each facet f an error ε_f is defined such that,

$$\varepsilon_f = (\Phi_f^+ - \Phi_f^-)^2 \quad (6)$$

where Φ_f^+ and Φ_f^- are the fluxes of \mathbf{D} calculated from, respectively, both elements associated to the facet f . Then, the error associated to an element e of the mesh is obtained by summing the errors calculated on its facets,

$$\varepsilon_e = \sum_{f \in e} \varepsilon_f \quad (7)$$

At this point, an error distribution map can be defined for the studied domain. Using this error distribution, one can use a mesh refinement tool according to an error criterion defined by the user.

In our case, we used HOMARD® which is a mesh refiner from EDF R&D [3]. It is based on the refinement, and eventually the unrefinement, of meshes by cutting the elements. The criterion of the refinement has been fixed such that the elements with an error greater than the average

error are refined while the others remain untouched. The refinement can be done either in the whole domain or in a chosen part of the domain.

IV. APPLICATION

The application chosen to emphasize the presented approach is a unit cell of an electrostatically actuated MEMS comb drive [4]. The geometry of the studied system is depicted in Fig. 1. Its dimensions are $L=10\ \mu\text{m}$, $g=1\ \mu\text{m}$, $b=1\ \mu\text{m}$, $t=2\ \mu\text{m}$, $ts=0.5\ \mu\text{m}$, $gs=1\ \mu\text{m}$, $Ls=20\ \mu\text{m}$.

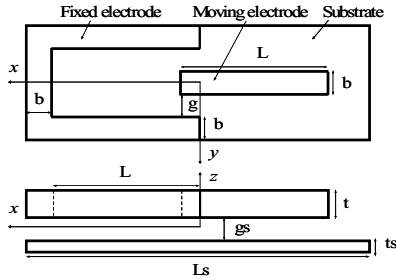


Fig. 1: Geometry of the studied system

A voltage of 30V is applied between the fixed and the moving electrodes, leading to an attractive electrostatic force in the x direction. First, a reference system is considered, which consists in solving the problem with 3D-FEM using a very fine mesh (~ 300000 elements, Fig. 2).

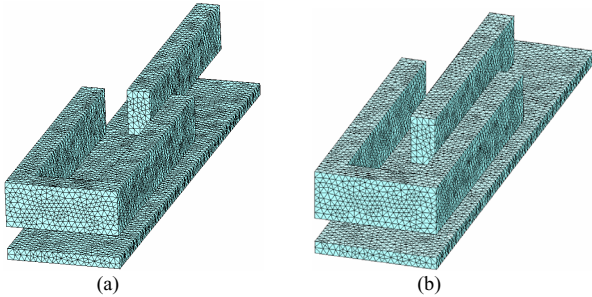


Fig. 2: Reference meshes for positions $0\ \mu\text{m}$ (a) and $5\ \mu\text{m}$ (b)

Then, starting from an initial coarse mesh, the same problem is solved and the mesh is refined according to the calculated error distribution using the previously mentioned criterion. The mesh size for several positions and refinement steps are given in Table I.

TABLE I
MESH SIZE FOR THREE POSITIONS AND REFINEMENT STEPS

Refinement step	Number of elements		
	Position $0\ \mu\text{m}$	Position $1\ \mu\text{m}$	Position $2\ \mu\text{m}$
Initial mesh	21349	20644	20708
1	52298	52576	52007
2	64896	69126	65028
3	95054	100937	96484

In this study, the error was considered on the whole domain and the refinement was applied in a region surrounding the movable part. The meshes for two refinement steps are shown in Fig. 3. The electrostatic force is computed using a method based on the virtual work principle.

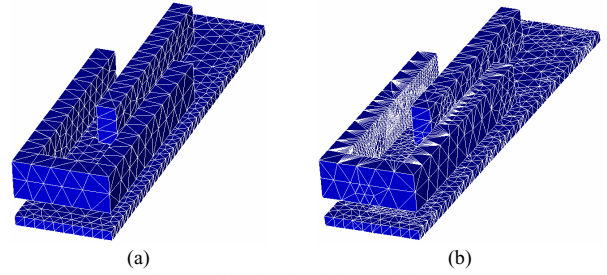


Fig. 3: Initial (a) and final refined (b) mesh for position $5\ \mu\text{m}$

In Fig. 4, we present a comparison between the results obtained by the reference system and after 1, 2 and 3 refinement steps for the coarse mesh. At step 2, the results are already in good agreement with the reference.

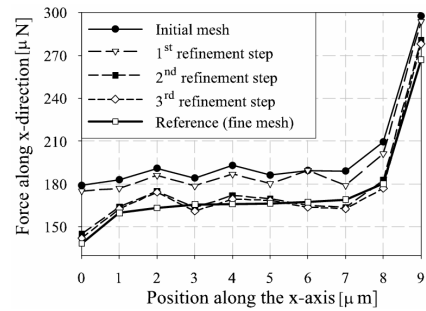


Fig. 4: Force comparison between the reference and refinement

The relative error between the forces obtained from the reference, the coarse mesh and its last step refinement are given in Fig. 5.

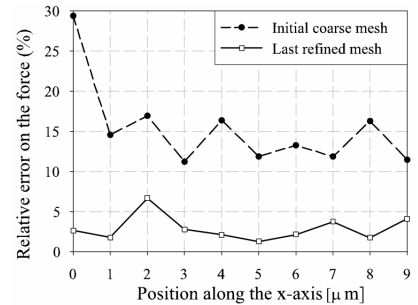


Fig. 5: Relative error for the force calculation

The results obtained with the average error criterion and the refinement in a specific part of the domain, give satisfactory results. Nevertheless, the accuracy can be further improved. In the extended version, other error estimation techniques and refinement strategies will be presented.

V. REFERENCES

- [1] J.R. Gilbert, R. Legtenberg and S.D. Senturia, '3D coupled electro-mechanics for MEMS : application of CoSolve-EM', in *Proc. IEEE MEMS Workshop*, pp. 122-127, 1995.
- [2] T. Henneron, S. Clénet, S., P. Dular and F. Piriou, 'Discrete finite element characterisations of source fields for volume and boundary constraints in electromagnetic problems', *Journ. of Comp. and Applied Math.*, Elsevier, Vol. 215, No. 2, pp. 438-447, 2008.
- [3] <http://www.code-aster.org/outils/homard/>
- [4] M. Boutaayamou, R.V. Sabariego and P. Dular, 'Electrostatic Analysis of Moving Conductors Using a Perturbation Finite Element Method', *IEEE Trans. Magn.*, Vol. 45, No. 3, pp. 1004-1007, 2008.

A Methodology for Applying Three Dimensional Constrained Delaunay Tetrahedralization Algorithms on MRI Medical Images

Feras AbuTalib and Dennis Giannacopoulos
Department of Electrical and Computer Engineering, McGill University
3480 University Street, Montreal (QC), H3A 2A7, Canada
feras.abutalib@mail.mcgill.ca, dennis.giannacopoulos@mcgill.ca

Abstract— This paper addresses the problem of producing three-dimensional constrained Delaunay tetrahedral meshes from sequential two dimensional MRI medical image slices. The approach is to generate the volumetric meshes of the scanned organs as a result of several low-level tasks: image segmentation, connected component extraction, isosurfacing, image smoothing, mesh decimation and constrained Delaunay tetrahedralization. The proposed methodology produces a portable application that can be easily adapted, evaluated, and extended by the researchers. Experimental results are presented to validate the new approach and characterize its performance.

I. INTRODUCTION

Finite element (FE) analysis of MRI medical data depends heavily on the quality of the mesh representation of the scanned organs. Most medical applications available in the market today are commercial and very expensive. Moreover, they are designed for specific hardware architectures that limit their portability [1]. This paper proposes an architecture that can be used to transfer the medical images into meshes that can be utilized by FE software such as ANSYS, and NASTRAN. A set of different quantitative measures is also compiled in order to be able to evaluate the implementations of such applications. The paper also presents experimental test results that illustrate how the different operations performed during the process can affect the quality of the final mesh.

II. THE SYSTEM ARCHITECTURE

The functional features of the proposed system are: (1) ability to process MRI images in their native format; (2) capability of providing the various image processing services needed during the various steps to generate the mesh such as the segmentation, isosurface creation, smoothing, and decimation techniques; and, (3) ability to generate volume adaptive Delaunay meshes when seeded with an initial surface mesh. The non-functional features include: (1) performance (the proposed system is designed to maximize speed while minimizing the memory as much as possible); (2) usability; (3) expandability; and, (4) portability.

The approach to build the proposed system is to integrate the minimum number of developed compatible open-source software components/libraries of which each would be able to achieve a sub-set of the functional requirements while not breaking the overall non-functional requirement. Fig 1. shows the various steps needed in this process and the chosen components/libraries needed to accomplish each task.

The overall functionalities are achieved by combining the different software libraries and components together after defining the interfaces between the different components as shown in Fig 2.

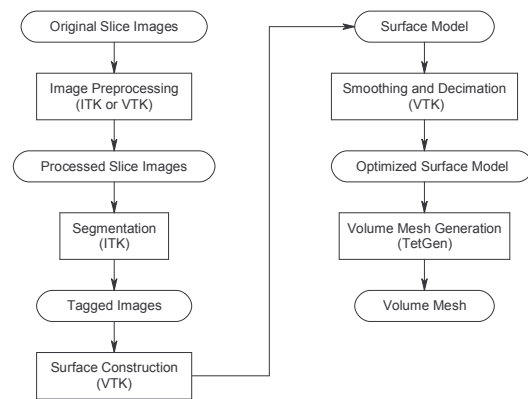


Fig. 1: The proposed object design process with the data flow

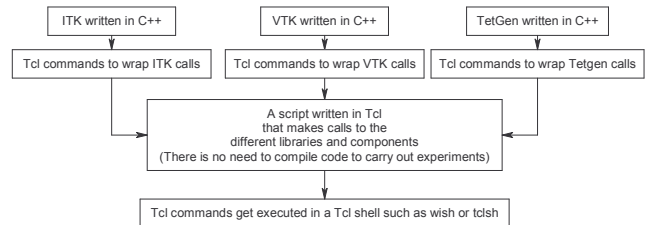


Fig. 2: The proposed interfaces used between the software components.

III. EXPERIMENTAL SETUP

This section provides a set of criteria which can be employed to compare and evaluate the experimental results of such systems. These can be summarized into three categories: (A) geometric mesh quality measures; (B) mesh surface approximation measures; and, (C) performance measures.

A. Geometric Mesh Quality Measures

It is well known that the accuracy and efficiency of the FE method can be directly affected by very poor quality elements [2]. Geometric mesh quality measures evaluate the shape of the produced tetrahedra based on purely geometric characteristics. Most of these measures are usually presented in the form of quantities such as volume, edge lengths and radii of the spheres associated with the tetrahedral elements.

Both α and β_{Baker} measures are considered among the most commonly used measures [2].

$$\alpha = \frac{3R_i}{R_c} \quad (1)$$

$$\beta_{Baker} = 2\sqrt{6} \frac{R_i}{l_{max}} \quad (2)$$

R_i is the radius of the insphere inscribed in a tetrahedron such that each face of the tetrahedron is tangent to the sphere, R_c is the circumsphere radius of the sphere passing through all four vertices of the tetrahedron, and l_{max} is the length of the largest edge in a tetrahedron. Both ratios achieve a value of one for equilateral tetrahedra [3]. Elements having a lower value considered poorer quality.

B. Mesh Surface Approximation Measures

One of the most important properties of a tetrahedral mesh is that it must completely fill the region being simulated. In the proposed methodology, this heavily depends on the surface approximation of the anatomical object. The quality of the surface approximation can be evaluated using the Hausdorff distance mean error $d_m(S, S')$ [4] between the approximated surface (S') and the original surface (S).

$$d_m(S, S') = \frac{1}{|S|} \iint_{p \in S} d(p, S') dS \quad (3)$$

$|S|$ donates the area of the surface S and $d(p, S')$ is the distance between a surface S' and a point p belonging to surface S and it can be computed as

$$d(p, S') = \min_{p' \in S'} \|p - p'\|_2 \quad (4)$$

C. Mesh Performance Measures

Performance measures include both the modeling time and the memory needed during the process. Also, the mesh produced from such systems should lead to as few computations as possible in a finite element simulation. Both the bad quality and the large number of the mesh elements can negatively affect the execution time of a FE simulation. The number of the mesh elements should be small enough to keep the computation time reasonable [5]; however, the number of elements cannot be very small as this would lead to mesh elements with large sizes. Mesh elements with large sizes are reported to produce less accurate FE results than the smaller ones [6]. Therefore, in order to evaluate the performance of such systems, the system should report the time needed for the various tasks to be executed, the number of mesh elements that were generated, the sizes of these elements, and the memory needed during the process.

IV. EXPERIMENTAL RESULTS

Mesh quality is a pre-requisite for successful FE analysis. The implementation of the proposed architecture and the measures described above were utilized to study the affect of some individual operations executed during the process to

transform the medical images into volumetric meshes. The experimental results are summarized qualitatively in Table 1.

TABLE I
SUMMARY OF THE EXPERIMENTAL RESULTS

1) Effect of the Decimation Operation	
a) Decimation Reduction Rate Effect	By changing this factor, there was low impact on the geometric measures. The impact was clearer on the performance measures as higher reduction rates caused better performance. However, the rate of improvement slowed down with higher reduction rate because of the restriction to maintain the topology of the object.
b) Different Decimation Implementation	Similar results were obtained as in 1a. The algorithm used had less restriction in maintaining the topology and more performance was achieved with higher reduction rate.
2) Effect of the Smoother Operation	
a) Effect of the Weight Factor of the Smoother Operation	By increasing the value of this factor, there was a clear positive change in the geometric measures. There was improvement in the performance measures as well.
b) Effect of the Number of Iterations of the Smoother Operation	Similar results were obtained as in 2a which suggests that both parameters have similar effect on the quality of the final mesh.
c) Combined Effect of Both Parameters of the Smoother	Achieved very similar results as in 2a but by using only half the values used in 2a and 2b.
3) Effect of Adding a New Operation	
The operation added was applying the Gaussian Smooth on the initial nodes before the surface construction operation. By introducing this new pre-processing operation in the middle of the tasks, it was possible to get improvement in the performance measures. There was no clear change introduced in the geometric measures for the final mesh though.	

Quantitative results corresponding to the experiments summarized in Table I will be presented in the long version paper along with detailed descriptions of the MRI data used. Full details of the proposed architecture as well as the novel features of the low-level operations described will also be presented at the conference and in the long version paper.

A very interesting possible future work is to extend the current design and implementation to support parallelism. Both VTK and ITK software components can be utilized to provide a parallel solution; however, TetGen component doesn't support parallelism and therefore it is possible to be modified or replaced with a different component.

V. REFERENCES

- [1] A. Coronato, G. De Pietro, and I. Marra, "An Open-source Software Architecture for Immersive Medical Imaging," Proceedings of 2006 IEEE International Conference. July 2006, pp. 166-170.
- [2] M. Dorica and D. Giannacopoulos, "Towards Optimal Mesh Quality Improvements for Adaptive Finite Element Electromagnetics with Tetrahedra," IEEE Transactions on Magnetics, 2004, 40(2).
- [3] V.N. Parthasarathy, "A Comparison of Tetrahedron Quality Measures," Finite Elements in Analysis and Design, 1993, 15:255-261.
- [4] N. Aspert, D. Santa-Cruz, and T. Ebrahimi, "MESH: Measuring Errors Between Surfaces Using the Hausdorff Distance," IEEE International Conference on Vol. 1, 2002, pp. 705-708.
- [5] M. Sermesant, C. Forest, H. Delingette, and N. Ayache, "Biomechanical Model Construction from Different Modalities: Application to Cardiac Images," MICCAI 2002: 5th International Conference, Tokyo, Japan, September 25-28, 2002, Proceedings, Part I, pp. 714-721.
- [6] Jonathan Richard Shewchuk, *Lecture Notes on Delaunay Mesh Generation*, Department of Electrical Engineering and Computer Science, University of California, Berkeley, CA, 1999.

Analysis of copper losses in resistance spot welding transformer windings with Dowell method and numerical approach

J. Popović, D. Dolinar, *Member, IEEE*, G. Štumberger, *Member, IEEE*, I. Tičar, *Member, IEEE* and B. Klopčič

University of Maribor, Faculty of Electrical Engineering and Computer Science
Smetanova ulica 17, 2000 Maribor, Slovenia
jelena.popovic@uni-mb.si

Abstract— This paper describes calculation of copper losses in resistance spot welding transformer (RSW) windings with two different methods, Dowell method and finite element method. The advantage of Dowell method, as an analytical method is inclusion of proximity effect influence in calculations and possibility of further use in determining of minimal copper losses by an optimization algorithm. The second part of the research gives a comparison between analytical results, numerical results and experimentally obtained ones. The main objective of this research is to evaluate the agreement between analytical and numerical results and to compare them with experimental results. It has also been proven that Dowell method is applicable on this particular type of transformer.

I. INTRODUCTION

This paper describes resistance spot welding (RSW) transformer and numerical, analytical and experimental analysis of copper losses in the windings. An algorithm to achieve minimal copper losses in windings by proper conductors design is fully described in the full paper. The real RSW transformer consists of two laminated iron cores, four layers of primary turns and two layers of secondary turns. Primary winding consists of four layers with total number of turns 55. Secondary winding consists of two layers and each one has a single turn. Primary winding of RSW transformer is supplied by a pulse width modulated voltage, which gives characteristic pulse form of primary current with a peak value 100 A. Secondary current is 55 times higher and it retains a pulse form. Due to the rectifier mounted onto the secondary windings of RSW transformer, only one secondary layer (turn) is active during each half of a primary current period. At the load side (rectifier output) first half of a period gives 5500 A and the second as well. Together, two secondary turns give 11000 A of DC peak value current at rectifier output. Nominal power at 80% duty cycle is 75 kVA.

II. NUMERICAL MODEL

Numerical model is based on finite element method [1]. Modelling, magnetic transient analysis and post-processing are carried out with programme package Maxwell3D.

It has already been mentioned in introduction that during each half of a period of primary current only one secondary layer (turn) is active. It means that number of total active layers in one half of a period equals five. Number of layers and turns is significant for Dowell method [2].

Each primary and secondary turn is separately modelled, which contributes to the preciseness of the numerical model. Transient analysis is necessary to obtain instantaneous power time behaviour and determine copper losses in each time instant. Instantaneous losses time behaviour enables calculation of average copper losses. Minimal average copper losses can represent an objective function and winding's dimensions can be optimization parameters. It is possible to create a parametric numerical model and apply an optimization algorithm in the case of numerical calculation. Numerical calculation of copper losses is based on current density calculation, which is determined with Helmholtz equation (1):

$$\nabla^2 \mathbf{J} - j\omega\mu_0\sigma\eta\mathbf{J} = 0, \quad (1)$$

where \mathbf{J} is current density vector, j is defined as $j = \sqrt{-1}$, ω represents angular frequency, μ_0 is permeability of free space, σ is electrical conductivity and η is conductor spacing factor, respectively.

III. DOWELL METHOD

The magnetic field strength in the vicinity of the transformer winding can be easily determined by using MMF (magneto motive force) diagrams [3]. These diagrams are constructed by application of Ampere's law, following the closed paths of the magnetic field lines which pass near the winding conductors. Dowell method is generally based on Fourier analysis of current and MMF diagrams. Fourier analysis is used to include the influence of higher harmonics from primary and secondary current, while MMF diagrams determine magnetic field strength. For this particular case, MMF diagrams are non-symmetric functions. The construction of the MMF diagram for the first half-period of the primary and secondary current is shown in Fig. 1. Total copper losses, without DC losses, according to Dowell method are given by the following expression (2):

$$\sum_{n=1}^{harm.layers} \sum_{k=1} P_{nk} = \sum_{n=1}^{harm.layers} \sum_{k=1} I_{nk}^2 R \varphi_n \left[\left(2m_k^2 - 2m_k + 1 \right) G_1(\varphi_n) - 4m_k (m_k - 1) G_2(\varphi_n) \right], \quad (2)$$

where n signifies the n^{th} harmonic, k is the layer number in transformer windings, $harm$ is total number of harmonics, $layers$ is total number of layers, P_{nk} is copper loss caused by the n^{th} harmonic in the k^{th} winding layer, I_{nk} is Fourier coefficient obtained from Fourier analysis of the primary or secondary current, R is ohmic resistance at the given operation temperature, φ_n is obtained from conductor spacing factor and skin depth at the given frequency, m_k represents real part of the magnetic field ratio and $G_1(\varphi_n)$, $G_2(\varphi_n)$ are expressions containing trigonometric and hyperbolic functions. The last two are obtained from the solution for the current density from relevant Helmholtz equation (1). Factors φ_n and m_k refer to proximity effect.

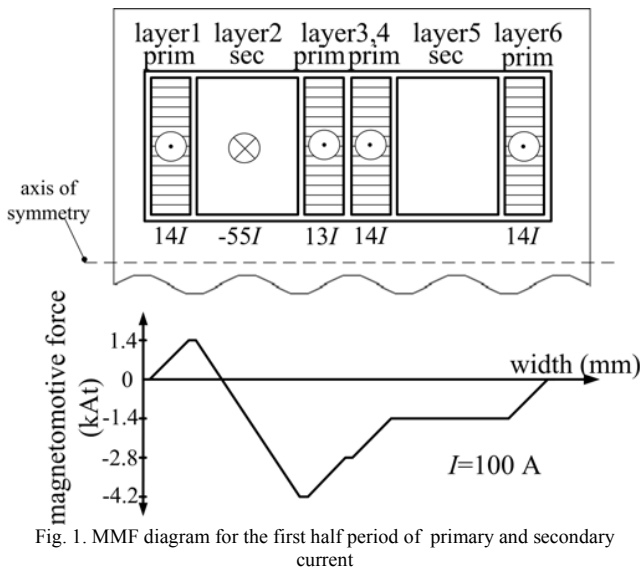


Fig. 1. MMF diagram for the first half period of primary and secondary current

It is necessary to note that Dowell method encompasses copper losses caused by higher harmonics and skin effect.

IV. RESULTS

Results are obtained with analytical calculations (Dowell method) and finite element method in Maxwell3D. Numerically calculated copper losses vary from analytical ones for approximately 10%. Table 1 contains results for only one case of dimension of windings and the differences between numerical, analytical and experimental results for this particular case are minor. Note that only preliminary experimental results are given here due to the space limit. More completed experimental, numerical and analytical results will be presented in the full paper. For now, analytical results distinguish from existing experimental results for approximately 8%.

Finite element method results strongly depend on accuracy of the numerical model and time discretization. Instantaneous power time behaviour (Fig. 2) contains irregular increases of values because of the questionable accuracy of the finite element method.

TABLE I
SUMMARY OF DATA AND SOME OBTAINED RESULTS

Physical Quantity	Value
Primary Current Peak Value	100 A
Secondary Current Peak Value	11000 A
Primary Winding Temperature	130°C
Secondary Winding Temperature	50°C
Primary Winding Electrical Conductivity	$38 \cdot 10^6$ S/m
Secondary Winding Electrical Conductivity	$56 \cdot 10^6$ S/m
Nominal Power	75 kVA
Copper Losses Obtained Numerically	2.058 kW
Copper Losses Obtained With Dowell Method	2.154 kW
Copper Losses Obtained With Measurements	2.326 kW

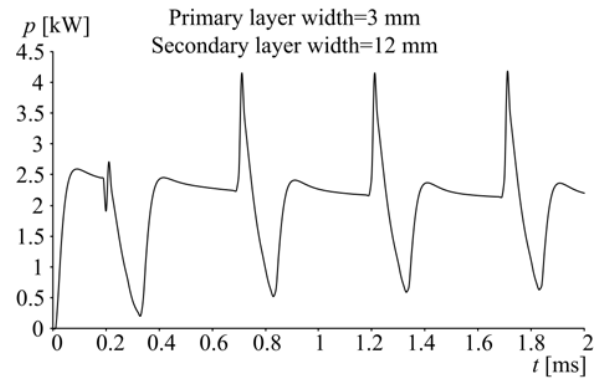


Fig. 2. Instantaneous power time behaviour for primary layer width 3 mm and secondary layer width 12 mm obtained with Maxwell3D

According to Fig. 2, total average copper losses, calculated with finite element method, given in Table 1, are obtained with (3):

$$P = \frac{1}{t} \int_0^t p(\tau) d\tau = \frac{1}{2 \cdot 10^{-3}} \int_0^{2 \cdot 10^{-3}} p(\tau) d\tau, \quad (3)$$

where $p(\tau)$ is instantaneous power and t is time interval (in this case $t = 2$ ms).

V. CONCLUSION

The objective of this research is to analyze copper losses in RSW transformer windings. Three different methods are used to obtain results. Analytical approach (Dowell method) gives results, which are very close to so far experimentally obtained values, while numerical approach gives less accurate results.

VI. REFERENCES

- [1] J. P. A. Bastos, N. Sadowski, *Electromagnetic Modeling by Finite Element Methods*, Marcel Dekker Inc., New York, 2003.
- [2] J. Vandelaç, P. D. Ziogas, "A novel approach for minimizing high-frequency copper losses", *IEEE Transactions on Power Electronics*, Vol. 3, No.3, pp. 266-277, July 1988.
- [3] R. W. Erickson, D. Maksimović, *Fundamentals of Power Electronics*, Second edition, Springer Science + Business Media. Inc., New York, 2001.

Lightning Induced Voltage on the Underground Pipeline near Overhead Transmission Line

Lei Qi, Xiang Cui, Yan Wu and Zhaonan Luo

Beijing Key Laboratory of High Voltage & EMC, North China Electric Power University

No.2 Beinong Road, Changping District, Beijing 102206, China

Qilei@ncepu.edu.cn

Abstract— As China's economy continued to grow, the electromagnetic influence on oil/gas pipeline near transmission line becomes increasingly prominent. In this paper, firstly, the transient simulation of the currents along ground wire and tower is performed by EMTP when the lightning strikes the tower of the transmission line. The results show that the currents along the ground wire and tower dramatically decrease and can be ignored after 5 spans (about 2 km). Secondly, based on the method of moment, the coating stress voltage on the oil/gas pipeline parallel to or across the transmission line is investigated and the approximate expression for the crossing situation is obtained, which involves the lightning current, pipeline type, earth resistivity and the distance between the pipeline and tower grounding structure. Eventually, with the lightning electrical strengths of different coatings, the safety distances between the pipeline and tower grounding structure for different lightning current peaks are suggested.

I. INTRODUCTION

With the fast development of economy in China, energy demand is gradually pressing and the power transmission lines and oil/gas pipelines are in the construction of rapid development. Ultra High Voltage (UHV) and West-East gas projects are the national key projects in recent years. Because of the similarity of transmission path selectivity in the power industry and oil/gas industry, the situations of parallelism, oblique approach and crossing between the transmission lines and pipelines have frequently happened. Therefore, the electromagnetic influence on oil/gas pipelines near the transmission lines becomes increasingly prominent [1].

The pipelines are subject to interference arising from three parts, capacitive, inductive and resistive coupling. Capacitive coupling only affects the aboveground pipeline since it has both a capacitance to the transmission line and to earth. And the pipeline buried below ground is shielded by the ground and cannot be affected by capacitive coupling. Inductive coupling is caused by the time-varying magnetic field produced by the transmission line currents. The induced voltage at the pipeline ends will vary as a function of length of parallelism, earth resistivity, distance between the pipeline and transmission line, and so on. Aerial and underground pipelines are both affected by inductive coupling. Resistive coupling between the transmission line and pipeline is only relevant during the grounding fault and lightning strike when significant level of current flows into the earth. And this will raise the potential of the tower base and of the neighboring soil with regard to the remote earth, and result in a considerable stress voltage across the coating of the pipeline, which can lead to arcing that damages the coating, or even the

pipeline itself. When the lightning strikes the transmission line, both the inductive and resistive coupling will take place and put the pipeline at severe risk.

The electromagnetic influence on the underground pipeline near transmission line is chiefly concerned with the personal safety, pipeline safety, alternating current (ac) corrosion of pipeline and normally operating of pipeline cathodic protection system. Some research work has been carried out and the limits of electromagnetic influence are released in [2]-[4]. These studies mainly focus on the inductive and resistive coupling modeling during the normally operating and ground fault of the transmission line. The switching and lightning transient induced voltages on the aerial and buried pipelines are simulated and some conclusions are obtained in [5].

In this paper, firstly, the transient simulation of the currents along ground wire and tower is performed by EMTP when the lightning strikes the tower of the transmission line. Secondly, based on the method of moment (MoM) [6], the coating stress voltage on the pipeline parallel to or across the transmission line is investigated and the approximate expression for the crossing situation is put forward. Finally, with the lightning electrical strengths of different coatings, the safety distances between the pipeline and tower grounding structure can be obtained for different lightning current peaks.

II. LIGHTNING CURRENTS ALONG GROUND WIRE AND TOWER

In this section, the transient simulation of the currents along ground wire (shield wire) and tower is carried out making use of EMTP when the lightning strikes the tower of the transmission line, which involves different voltage levels (330kV, 500kV, 750kV and 1000kV), different configurations of the transmission line (horizontal-single-circuit, triangular-single-circuit and vertical-double-circuit) and different earth resistivity (100Ωm, 500Ωm, 1000Ωm and 2000Ωm). The detailed results are not listed here. As illustrated in Fig.1, the EMTP simulation model includes 24-span ground wires and 25-base towers, which is symmetrical with regard to the lightning point. The ground wires are symmetrically numbered from 1 to 12 while the towers are from 0 to 12, where the No.0 tower represents the location of lightning current injection. During the simulation, the lightning current is with the amplitude of 100kA, waveform of 2.6/50μs and wave impedance of 250Ω. The tower is modeled as the transmission line with single wave impedance, the grounding impedance of the tower takes the lightning impulse impedance, and the ground wires are modeled as the overhead transmission line. One thing worthy of note is that both the so-

called back-flashover toward phase conductors and the spark discharge of the grounding conductors of the tower are not involved when the lightning strikes the tower of the transmission line.

Based on the above simulations, the conclusions can be listed as follows: (1) the currents along the ground wires dramatically decrease, i.e. 20%-25% of the intruding lightning current peak for the 1st span, 10%-15% for the 2nd span, 5%-10% for the 3rd span, and the currents can be ignored after the 5th span; (2) the currents along the towers dramatically decrease, i.e. 80%-90% of the intruding lightning current peak for the No.0 base where the lightning current is injected, 15%-20% for the 1st base, 5%-10% for the 2nd base, and the currents can be ignored after the 3rd base; (3) the currents along the ground wire and tower slightly depend on the voltage levels and configurations of the transmission line, namely, the height of tower is not very important during the simulation; (4) the higher the earth resistivity, the greater the lightning impulse impedance of the tower grounding structure, the higher the current along the ground wire, and the lower the current along the tower. In general, the earth resistivity has little effect on the lightning current distribution of the ground wire and tower. These conclusions turn out contrary to those of the ground fault of the transmission line.

As a result, for the situation of parallelism or oblique approach between the transmission line and pipeline, both the inductive and resistive coupling are considered, and the simplified transmission line model is suggested, which only includes 5 spans on each side of the lightning current injection point (10 spans in total). While for the situation of crossing, only the resistive coupling of the current in the earth through two towers adjacent to the pipeline is considered and the inductive coupling of the current along the overhead ground wire is ignored during the simulation.

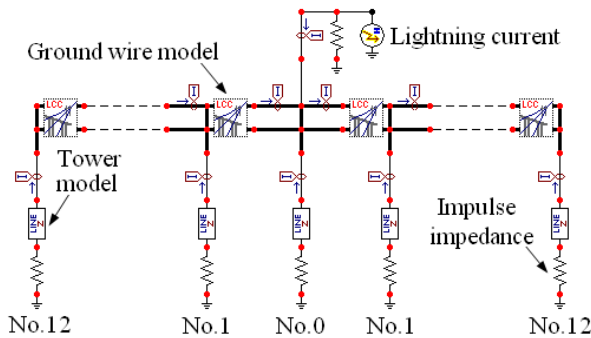


Fig. 1. Simulation model for EMTP

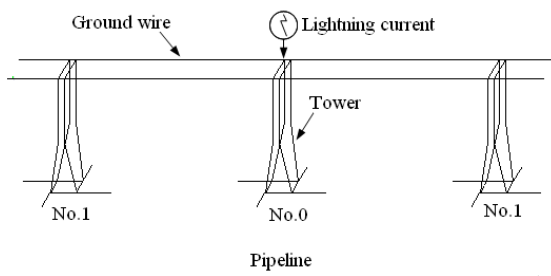


Fig. 2. Simulation model for the method of moment

III. COATING STRESS VOLTAGE FOR PARALLELISM

As shown in Fig.2, the simulation model for the method of moment includes 10-span ground wires and 11-base towers. Both the two ground wires of the 1000kV double-circuit ac transmission line and the tower grounding structure shown in Fig.3 are modeled by the thin conductors according to the actual size of the configuration. The tower is approximately modeled by 4 vertical thin conductors. The underground pipeline is modeled by the hollow conductors with insulation coating. Combined the method of moment with the Fourier transform, the transient coating stress voltage along the pipeline parallel to transmission line is investigated for different approach distances.

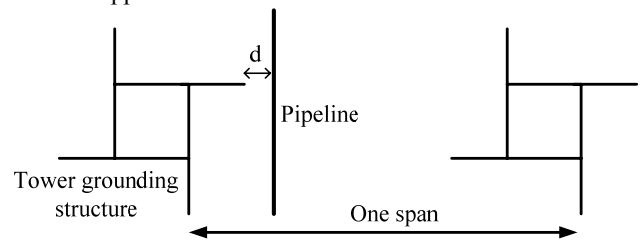


Fig. 3. Configuration of the pipeline and tower grounding structure

IV. COATING STRESS VOLTAGE FOR CROSSING

In this section, the proposed method is applied to the evaluation of the coating stress voltage along the pipeline across transmission line shown in Fig.3 and the corresponding approximate expression is put forward, which involves the lightning current, pipeline type, earth resistivity and the distance between the pipeline and tower grounding structure. Finally, with the lightning electrical strengths of different coatings, the safety distances between the pipeline and tower grounding structure for different lightning current peaks are suggested.

ACKNOWLEDGEMENT

This work was supported by the National Natural Science Foundation of China (no. 50707008).

V. REFERENCES

- [1] China Electric Power Research Institute, *Influence and mitigation of 1000kV UHVAC double-circuit transmission line on metallic pipeline*, China: China Electric Power Research Institute, 2009.
- [2] CIGRE, *Guide on the influence of high voltage ac power systems on metallic pipelines*, France: CIGRE, 1995.
- [3] EPRI, *Power line fault current coupling to nearby natural gas pipelines*, Canada: EPRI, 1987.
- [4] F.P. Dawalibi, R.D. Southey, "Analysis of electrical interference from power lines to gas pipelines Part I: computation methods," *IEEE Trans. on Power Delivery*, 4(3): 1840-1846, 1989.
- [5] K. Kopsidas, I. Cotton, "Induced voltages on long aerial and buried pipelines due to transmission line transients," *IEEE Trans. on Power Delivery*, 23(3): 1535-1543, 2008.
- [6] B. Zhang, Z. Zhao, X. Cui, "Diagnosis of breaks in substation's grounding grid by using electromagnetic method," *IEEE Trans. on Magnetics*, 38(2): 473-476, 2002.

A Development on the Analysis Method of Synchronous Reluctance Motor Using FEM Coupled Electromagnetic Field of Thermal Field

Jung Ho Lee, *Member, IEEE*, Tae Hoon Lee, Sung Ju Mun
Dept. of Electrical Engineering, Hanbat National University
Dukmyung-Dong Yuseong-Gu, Daejeon, 305-719, KOREA
lth5557@naver.com

Abstract — This paper deals with the development of analysis method in a synchronous reluctance motor (SynRM) using finite element method (FEM) coupled electromagnetic field of Preisach model, which is presented to represent the additional thermal source due to hysteresis loss, & thermal field. The focus of this paper is the thermal analysis relative to hysteresis loss and copper loss in a SynRM.

I. INTRODUCTION

Issues such as efficiency and torque/ampere are important in evaluating the performance of an electric machine.

Such characteristics depend mostly upon the losses behavior of the machine and therefore the study of heating problems of electric machines and the prediction of temperature rises of magnetic core, teeth, insulation, conductor etc. are necessary for sophisticated design, yet extremely complex.

Accurate solution is important to maintain design integrity, assure high performance and optimize costs.

For this purpose, it is essential that the temperature distribution and its gradient in the electric machines are predicted more accurately.

The heat losses of SynRM mainly consist of the Joule effect resulting from copper winding and the hysteresis loss of magnetic materials.

The heat generated by copper windings could be obtained from the results of a general process used in the heat transfer analysis method [1].

However hysteresis component in the internal thermal source have traditionally been obtained by analytical techniques, with many simplifying assumptions with respect to geometry and manufacturer material data.

The Preisach model is now generally accepted to be a powerful hysteresis model, and is therefore intensively studied [2]-[4].

With the advent of Preisach model, numerical technique for modeling the additional thermal source J_m in the magnetic material can be obtained.

In this paper, a finite element analysis coupling electromagnetic field of Preisach model & thermal field for a SynRM are presented and dynamic characteristic analyses are performed under the effect of Joule and hysteresis loss.

The focus of this paper is the development of thermal analysis method in a SynRM for Joule and hysteresis loss.

II. FINITE ELEMENT METHOD COUPLED ELECTROMAGNETIC FIELD OF PREISACH MODEL & THERMAL FIELD

A. Governing Equation of SynRM in Electromagnetic Field

When the moving coordinate system is used, the governing equation in 2D is given as follows:

$$\frac{\partial}{\partial x} \nu_0 \left(\frac{\partial A_z}{\partial x} \right) + \frac{\partial}{\partial y} \nu_0 \left(\frac{\partial A_z}{\partial y} \right) = -J_z - J_m \quad (1)$$

$$J_m = \nu_0 \left(\frac{\partial M_y}{\partial x} - \frac{\partial M_x}{\partial y} \right) \quad (2)$$

Where, A_z : z component of magnetic vector potential
 J_z : current density, ν_0 : magnetic resistivity

B. System Matrix

The circuit equation is written as:

$$\{V\} = [R]\{I\} + [L_0] \frac{d}{dt} \{I\} + \{E\} \quad (3)$$

Where, $\{E\}$: E.M.F. vector in the winding, $\{V\}$: supplying voltage vector, $\{I\}$: phase current vector, $[L_0]$: leakage inductance

To solve (1), we used the Galerkin finite element method. For the time differentiation in (3), a time stepping method is used with backward difference formula. Coupling (1), (2) and (3), the system matrix is given as follows:

$$\begin{aligned} & \left[\begin{array}{cc} \nu_0[S] & -[N] \\ [0] & [R] \end{array} \right] + \frac{1}{\Delta t} \left[\begin{array}{cc} [0] & [0] \\ [LG]^T & [L_0] \end{array} \right] \begin{Bmatrix} \{A\} \\ \{I\} \end{Bmatrix}_t \\ & = \frac{1}{\Delta t} \left[\begin{array}{cc} [0] & [0] \\ [LG]^T & [L_0] \end{array} \right] \begin{Bmatrix} \{A\} \\ \{I\} \end{Bmatrix}_{t-\Delta t} + \begin{Bmatrix} \{M\} \\ \{V\} \end{Bmatrix}_t \end{aligned} \quad (4)$$

Where, $[LG]$ is coefficient matrix related to emf, the magnetization $\{M\}$ is calculated by preisach modeling [5].

C. Finite element formulation in thermal field

In the thermal field, the finite element model corresponding to variational formulation of the heat conduction problem with convective boundary conditions and thermal sources, for typical element, is given by the

following matrix equation.

$$[M^e] \frac{d}{dt} [T^e] + ([S^e] + [H^e] + [G^e]) [T^e] = [F^e] + [F_m^e] + [P^e] + [R^e] \quad (5)$$

where,

$\frac{d}{dt} [T^e]$: time derivative temperature vector, $[M^e]$:

thermal capacity matrix, $[S^e]$: thermal conductivity matrix ,

$[H^e]$: convection matrix, $[G^e]$: resistivity temperature dependency matrix , $[T^e]$: temperature vector, $[F^e]$:

Heating sources vector due to the copper winding, $[F_m^e]$:

Heating sources vector due to hysteresis of materials, $[P^e]$:

convective vector, $[R^e]$: Boundary vector

$$[M^e] = \rho c \Delta \frac{1}{2} \begin{bmatrix} 2 & 1 & 1 \\ 1 & 2 & 1 \\ 1 & 1 & 2 \end{bmatrix}, [S_{ij}^e] = \frac{k}{4\Delta} (c_i c_j + d_i d_j)$$

$$[H^e] = \frac{h_{ij} l_{ij}}{6} \begin{bmatrix} 2 & 1 & 0 \\ 1 & 2 & 0 \\ 0 & 0 & 0 \end{bmatrix} + \frac{h_{jk} l_{jk}}{6} \begin{bmatrix} 0 & 0 & 0 \\ 0 & 2 & 1 \\ 0 & 1 & 2 \end{bmatrix} + \frac{h_{ki} l_{ki}}{6} \begin{bmatrix} 2 & 0 & 1 \\ 0 & 0 & 0 \\ 1 & 0 & 2 \end{bmatrix}$$

$$[G^e] = -\rho_0 \alpha l^2 \Delta \frac{1}{12} \begin{bmatrix} 2 & 1 & 1 \\ 1 & 2 & 1 \\ 1 & 1 & 2 \end{bmatrix},$$

$$[F^e] = \frac{\rho_0 J_0^2 (1 - \alpha T_0) \Delta}{3} \begin{bmatrix} 1 \\ 1 \\ 1 \end{bmatrix}, [F_m^e] = \frac{\rho_0 J_m^2 (1 - \alpha T_0) \Delta}{3} \begin{bmatrix} 1 \\ 1 \\ 1 \end{bmatrix}$$

$$[P^e] = \frac{h_{ij} l_{ij} T_f}{2} \begin{bmatrix} 1 \\ 1 \\ 0 \end{bmatrix} + \frac{h_{jk} l_{jk} T_f}{2} \begin{bmatrix} 0 \\ 1 \\ 1 \end{bmatrix} + \frac{h_{kj} l_{ki} T_f}{2} \begin{bmatrix} 1 \\ 0 \\ 1 \end{bmatrix}$$

$$[R^e] = \frac{l_{ij} T_0}{2} \begin{bmatrix} 1 \\ 1 \\ 0 \end{bmatrix} + \frac{l_{jk} T_0}{2} \begin{bmatrix} 0 \\ 1 \\ 1 \end{bmatrix} + \frac{l_{ki} T_0}{2} \begin{bmatrix} 1 \\ 0 \\ 1 \end{bmatrix}$$

Where

ρ_0 : electric resistivity at T_0 temperature [$\Omega \cdot m$], α : linear expansion coefficient [$1/K$], T_f : undisturbed fluid temperature [K], l : length between node [m]

The convective heat transfer coefficient is calculated from the following experimental expression [5].

$$h = h_f = h_n (1 + 1.3 \sqrt{v_f})$$

Where

h_f : forced convective heat transfer coefficient [$W/(m^2 \cdot K)$]

h_n : natural convective heat transfer coefficient [$W/(m^2 \cdot K)$]

v_f : average fluid velocity [m/s]

III. SIMULATION AND DISCUSSION

Fig.1 is the flow chart of transient thermal analysis of a SynRM using coupled electromagnetic of Preisach model & thermal finite element method taking into account the rotation.

Current density J_0 and equivalent magnetizing current density J_m , which were calculated previously in electromagnetic field, are used as a heating source of thermal field. The variation of stator resistance and conductivity, which are caused by temperature rise, are returned to electromagnetic field. Fig.2 represents the isothermal line of analysis model.

Through the proposed method, the characteristics of variable thermal analysis will be observed for a SynRM in next extended version

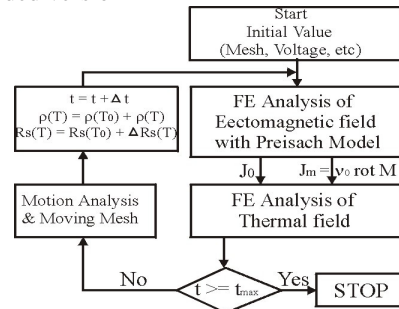


Fig. 1 Flowchart of analysis

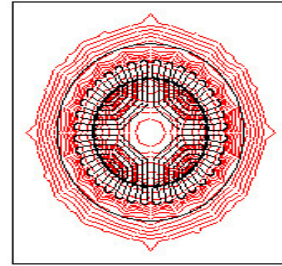


Fig. 2 Isothermal line of analysis model

IV. REFERENCES

- [1] K. H. Huebner, E. A. Thornton, T. G. Byron, The Finite Method For Engineers, John Wiley & Sons, Inc., Newyork, 1995.
- [2] A. Ivanyi, Hysteresis Models in Electromagnetic Computation, AKADEMAI KIADO, BUDAPEST
- [3] J. H. Lee, D. S. Hyun, " Hysteresis Analysis for the Permanent Magnet Assisted Synchronous Reluctance Motor by Coupled FEM & Preisach Modelling", *IEEE Trans. on Magn.*, Vol. 35, No. 3, pp1203-1206, May, 1999.
- [4] I. D. Mayeroyz, "Mathematical Models of Hysteresis," *IEEE Trans. In Magnetics*, Vol. MAG-22, No.5, pp.603-608 Sept. 1986
- [5] J. A. D. Pinto, A. P. B. Coimbra and C. F. R. L. Antunes, "Transient Heating and Cooling Analysis in an Electromagnetic Device", *IEEE*

Novel Preconditioning in Finite Element Analysis of Electromagnetic Field: A - ϕ Block IC Preconditioning

Y. Takahashi, T. Mifune, and T. Iwashita

Kyoto University

Yoshida-Honmachi, Sakyo-ku, Kyoto 606-8501 JAPAN

E-mail ytakahashi@i.kyoto-u.ac.jp

Abstract — This paper proposes a novel preconditioning based on the incomplete Cholesky (IC) factorization and the concept of the explicit error correction (EEC) method for finite element electromagnetic field analyses: A - ϕ block IC preconditioning. The A method using the proposed method has the same convergence characteristic as the A - ϕ method with block IC preconditioning. The effectiveness of the proposed method is investigated in high-frequency and quasi-static field analyses comparing conventional preconditioning.

I. INTRODUCTION

In electromagnetic field analyses by the edge-based finite-element method (FEM), it is well known that the A - ϕ method has an advantage over the A method in convergence characteristic of iterative solvers such as the incomplete Cholesky conjugate gradient (ICCG) method [1]. The A method is superior to the A - ϕ method in terms of the number of unknowns. However, the improvement of the condition number is more significant and therefore the A - ϕ method is much faster than the A method.

On the other hand, the explicit error correction (EEC) method and the implicit error correction (IEC) method were proposed as the novel frameworks for linear iterative solvers [2][3]. For example, the A - ϕ method can be regarded as an implicit error correction with the redundant unknowns ϕ . If the EEC method attains nearly the same convergence property as the IEC method by appropriately devising the auxiliary matrix, the EEC method is generally superior to the IEC method in terms of computational costs. This feature is noticeable in the case of the multigrid method which executes error correction at multiple levels [4]. These imply the possibility that the convergence characteristic of the A method can be improved by the concept of the EEC method. In fact, the folded preconditioning, which has a strong relationship to the EEC and IEC methods, especially in the case of folded Gauss-Seidel preconditioner, has been proposed [5].

In this paper, from a different perspective, we develop the novel preconditioning for the A method based on the IC factorization by using the concept of the EEC method. The application of the IC smoother to the ordinary EEC procedure cannot derive the effective preconditioning because the preconditioner becomes nonsymmetric and cannot treat the off-diagonal blocks of the coefficient matrix obtained from the A - ϕ method, which represents the relationship between A and ϕ . Because preconditioning only needs the approximate solution, we propose omitting the off-diagonal blocks in the EEC procedure, which results in the novel preconditioning: the A - ϕ block IC preconditioning. We clarify the relationship

between the proposed method and the folded preconditioning. To investigate the effectiveness of the proposed method, we compare the performance of the standard ICCG method, the folded ICCG method and the A - ϕ block ICCG method.

II. A - ϕ BLOCK IC PRECONDITIONING

A. EEC Method for the A method

Consider solving the following linear system of equations derived from the A method

$$K\mathbf{x} = \mathbf{b}. \quad (1)$$

Here, K is the coefficient matrix, \mathbf{x} is the unknown vector, and \mathbf{b} is the right-hand-side vector. Similarly, the linear system derived from the A - ϕ method is given by

$$\begin{pmatrix} K & KG \\ G^T K & G^T KG \end{pmatrix} \begin{Bmatrix} \mathbf{y}_1 \\ \mathbf{y}_2 \end{Bmatrix} = \begin{Bmatrix} \mathbf{b} \\ G^T \mathbf{b} \end{Bmatrix}, \quad (2)$$

where G is the discrete gradient operator. The procedure of the EEC method corresponding to (2) is as follows [3]:

- (i) Update the approximate solution $\tilde{\mathbf{x}}$ by a sweep for (1).
- (ii) Compute vector \mathbf{p} by solving $G^T KG \mathbf{p} = G^T (\mathbf{b} - K\tilde{\mathbf{x}})$.
- (iii) Update the approximate solution by $\tilde{\mathbf{x}} \leftarrow \tilde{\mathbf{x}} + G\mathbf{p}$.

The above procedure can also be used as the preconditioning.

B. A - ϕ Block IC Preconditioning

In order to develop the effective preconditioning for the A method which has nearly the same convergence characteristic as the A - ϕ method, we use the IC smoother for a sweep in the EEC procedure. The preconditioning for (1) with the IC smoother in the EEC procedure can be written as follows.

$$M^{-1} = \left((L_1 L_1^T)^{-1} + G (L_2 L_2^T)^{-1} G^T (I - K (L_1 L_1^T)^{-1}) \right). \quad (3)$$

where M indicates the preconditioner, the superscript T means transpose, and the lower triangular matrix L_1 and L_2 are given by (4) by using IC factorization

$$\begin{pmatrix} K & KG \\ G^T K & G^T KG \end{pmatrix} \approx \begin{pmatrix} L_1 & O \\ L_3 & L_2 \end{pmatrix} \begin{pmatrix} L_1 & O \\ L_3 & L_2 \end{pmatrix}^T. \quad (4)$$

The preconditioning (3) is nonsymmetric and the effective preconditioner cannot be derived if a post sweep is added to the EEC procedure. Preconditioning generally needs only the approximate solution. Additionally, (3) does not include the off-diagonal block L_3 . Therefore, we propose omitting the off-diagonal blocks KG and $G^T K$ in (2) when the EEC procedure is used as the preconditioning. In this case, the step (ii) is modified as

- (ii)' Compute vector \mathbf{p} by solving $G^T KG \mathbf{p} = G^T \mathbf{b}$.

This modification derives the novel preconditioner as follows:

$$M^{-1} = (L_1 L_1^T)^{-1} + G(L_2 L_2^T)^{-1} G^T. \quad (5)$$

We term this method the A - ϕ block IC preconditioning because it only treats the diagonal blocks in (2).

C. Relationship between A - ϕ Block IC and Folded IC

The folded IC preconditioner for (1) is given by

$$M^{-1} = L_1^{-T} L_1^{-1} + (G - L_1^{-T} L_3^T) L_2^{-T} L_2^{-1} (G^T - L_3 L_1^{-1}). \quad (6)$$

Preconditioner (5) can be derived from (6) by regarding L_3 as zero matrix, which indicates the A - ϕ block IC is a special case of the folded IC. For any preconditioned Krylov subspace (KS) method for a redundant linear system of equations, a mathematically equivalent KS method for the redundancy-reduced linear system of equations can be constructed by using the folded preconditioner [5]. Thus, the CG method preconditioned by the A - ϕ block IC for the A method is mathematically equivalent to the CG method preconditioned by the block IC for the A - ϕ method. The convergence characteristic of the A - ϕ block ICCG method for the A method can be deteriorated slightly compared with the standard ICCG method for the A - ϕ method because of the omission of the off-diagonal blocks. However, the optimal acceleration factor [6] of two diagonal blocks of (5) can be decided independently, which leads to the compensation for the deterioration. Furthermore, the operation counts for one iteration step and memory requirement can be reduced because of the decrease of the number of unknowns. Therefore, the total performance of the A - ϕ block ICCG method for the A method is expected to be superior to the standard ICCG method for the A - ϕ method.

III. NUMERICAL EXAMPLES

A. Rectangular-Iris Coupled Circular-Waveguide Filter

The performance of the proposed method is examined in the high-frequency electromagnetic field analysis of the rectangular-iris coupled circular-waveguide filter shown in Fig. 1(a). The quarter part of the whole model is analyzed because of the symmetry. The convergence criterion for the iterative solvers is set to 10^{-8} and computations are executed on a Xeon X5472 with 8 GB RAM.

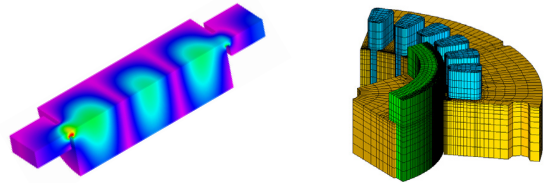
Table I shows the computational results obtained from 4 kinds of methods. The convergence characteristic of the folded ICCG method for the A method is almost the same as that of the standard ICCG method for the A - ϕ method, and the folded ICCG method has better performance. Meanwhile, the application of the A - ϕ block IC preconditioner does not deteriorate the convergence property due to the appropriate acceleration factors which vary by block. Thus, the proposed method can reduce the elapsed time by about 47 % and 37 % compared with the standard ICCG method and the folded ICCG method, respectively. From the above results, the effectiveness of the proposed method can be confirmed with respect to both elapsed time and memory requirement.

B. Surface Permanent Magnet Motor

The effectiveness of the proposed method is investigated in the nonlinear eddy-current analysis of the surface permanent magnet (SPM) motor shown in Fig. 1 (b). The one-

eighth part of the whole model is analyzed because of the symmetry and periodicity. To model the laminated iron core, the homogenization method is utilized. Table II shows the computational results at the first time step. The number of nonlinear iterations is 12 in all the cases. In eddy-current problems, the region where ϕ is defined is small compared with high-frequency problems. However, even in the case of eddy-current analyses of the practical electric machine, the A - ϕ block IC preconditioning is fairly effective.

More numerical results and detailed discussion about the proposed method will be included in the full paper.



(a) Circular-waveguide (95,256 elements) (b) SPM motor (94,316 elements)
Fig. 1. Magnetization as a function of applied field

TABLE I
Performance of iterative solves for circular-waveguide filter

Solver	ICCG (A - ϕ)	ICCG (A)	Folded ICCG (A)	A - ϕ block ICCG (A)
Number of unknowns	366,950	276,392		
Number of iterations	225	1357	224	184
Elapsed time (s)	53.0	143.9	43.9	27.8
Maximum memory consumption (MB)	492	269	393	324

TABLE II
Performance of iterative solvers for SPM motor

Solver	ICCG (A - ϕ)	ICCG (A)	Folded ICCG (A)	A - ϕ block ICCG (A)
Number of unknowns	304,347	280,180		
Total number of CG iterations	2496	14,587	2494	2321
Elapsed time (s)	266.8	923.7	262.4	217.5
Maximum memory consumption (MB)	197	167	190	178

IV. REFERENCES

- [1] K. Fujiwara, T. Nakata, and H. Ohhashi, "Improvement of convergence characteristic of ICCG method for the A - ϕ method using edge elements," *IEEE Trans. Magn.*, vol. 32, no. 3, pp. 804-807 (1996).
- [2] T. Iwashita, T. Mifune, and M. Shimasaki, "Similarities Between Implicit Correction Multigrid Method and A-phi Formulation in Electromagnetic Field Analysis," *IEEE Trans. Magn.*, vol. 44, no. 6, pp. 946-949 (2008).
- [3] T. Mifune, S. Moriguchi, T. Iwashita, and M. Shimasaki, "Convergence Acceleration of Iterative Solvers for the Finite Element Analysis Using the Implicit and Explicit Error Correction Methods," *IEEE Trans. Magn.*, vol. 45, no. 3, pp. 1104-1107 (2009).
- [4] T. Iwashita, T. Mifune, and M. Shimasaki, "New multigrid method: basic concept of implicit correction multigrid method," *IPSSJ Trans. Advanced Computing Systems*, vol. 48, pp. 1-10 (2007) (in Japanese).
- [5] T. Mifune, Y. Takahashi, and T. Iwashita, "Folded Preconditioner: a New Class of Preconditioners for Krylov Subspace Methods to Solve Redundancy-Reduced Linear Systems of Equations," *IEEE Trans. Magn.*, to be published.
- [6] K. Fujiwara, T. Nakata, and H. Fusayasu, "Acceleration of Convergence Characteristic of the ICCG Method," *IEEE Trans. Magn.*, vol. 29, no. 2, pp. 1958-1961 (1993).

\mathcal{H} -Matrix Based Operator Preconditioning For Full Maxwell At Low Frequencies

Jörg Ostrowski

ABB Switzerland Ltd., Corporate Research
Email: joerg.ostrowski@ch.abb.com

Mario Bebendorf

Institut für Numerische Simulation
Universität Bonn

Ralf Hiptmair and Florian Krämer

Seminar for Applied Mathematics
ETH Zürich

Abstract—A robust formulation for the computation of combined resistive, capacitive and inductive effects in time-harmonic low frequency applications has been introduced in [1]. The Galerkin discretization with conforming finite elements leads to a sparse system matrix. Large jumps in the material coefficients may cause severe ill-conditioning of the matrix. In this paper we investigate how *operator preconditioning* can be used to construct an efficient preconditioner. The approach can be treated with almost linear complexity by making use of *hierarchical matrices*.

I. INTRODUCTION

Finite element based discretization of time-harmonic full Maxwell or eddy current problems in realistic industrial applications requires a huge number of degrees of freedom (d.o.f.) in order to guarantee sufficient precision. Thus, the application of iterative solvers is desirable. It is often realized by employing algebraic multigrid methods, see [2] and [3]. A novel alternative is preconditioners that are based on *hierarchical matrices*. This yields a robust method even in the presence of large jumps in the material coefficients [4].

II. ROBUST FULL MAXWELL AT LOW FREQUENCIES

If neither capacitive nor inductive effects can be neglected in a low frequency application then quasi-static models cannot be used and the solution of the full Maxwell's equations is necessary. An example is shown in figure 1. We consider the case where field computation is confined to an artificially bounded domain $\Omega \subset \mathbb{R}^3$ of simple topology. Inside Ω there are ohmic conductors occupying the region Ω_c , and the non-conducting region is $\Omega_e := \Omega \setminus \overline{\Omega_c}$. Note that the non-conducting domain may not only consist of air, but also of other parts like the high-permeable core in figure 1. Voltage boundary conditions are imposed at the contacts at $\partial\Omega \cap \partial\Omega_c$. The stationary limit $\omega \rightarrow 0$ of the full Maxwell's equations has been addressed in [1]. There it has been described how standard potential based formulations of full Maxwell lack stability at low frequencies. A robust formulation can be achieved by coupling Gauss' law in the non-conductive domain Ω_e . This extra condition has to be balanced by an extra unknown that results from the non-direct splitting of the electric scalar potential φ into two parts $\varphi = \tilde{\varphi} + \psi$, with $\psi = \text{constant}$ in Ω_e . The final stable formulation

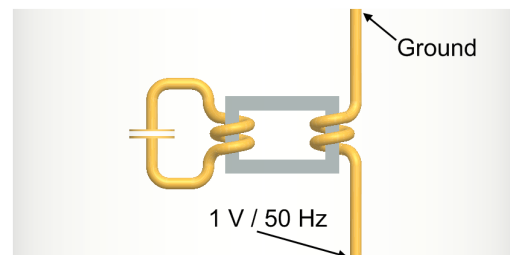


Fig. 1. Arrangement of an inductively coupled capacitor. A time-harmonic voltage-drop of 1 V / 50 Hz is imposed at the contacts. The conductors are made of copper and have cylindrical shape with diameter of 2.5 cm. The core is a non-conductor with relative permeability of 2000.

in strong form is given by:

$$\begin{aligned} \operatorname{curl} \frac{1}{\mu} \operatorname{curl} \mathbf{A} - (\omega^2 \epsilon - i\omega\sigma) \mathbf{A} \\ + (i\omega\epsilon + \sigma) \operatorname{grad}(\tilde{\varphi} + \psi) = 0 \quad \text{in } \Omega, \\ \operatorname{div}(\epsilon \mathbf{A}) = 0 \quad \text{in } \Omega, \\ \operatorname{div}(\epsilon \operatorname{grad}(\tilde{\varphi} + \psi)) = 0 \quad \text{in } \Omega_e. \end{aligned} \quad (1)$$

Herein μ , ϵ , σ are the material coefficients and ω is the angular frequency. The matrix \mathbf{M} that results from Galerkin discretization of the system (1) with conformal finite elements is singular. This becomes obvious by applying the divergence on the first equation, because of the linear dependency of the resulting equations in the non-conducting domain. An iterative preconditioned BiCGstab succeeded in solving the unsymmetric system. A preliminary preconditioner \mathbf{P}_p was obtained by applying the direct solver Pardiso [5] to (1) after setting $\omega \leftarrow \max\{\omega, 1 \text{ Hz}\}$, $\sigma(\mathbf{x}) \leftarrow \max\{\sigma(\mathbf{x}), 10 \Omega \text{ m}^{-1}\}$. This measure removes the linear dependence of the equations and regularizes the system. Nevertheless, this procedure provides a good approximation of (1), because of the continuity with respect to frequency and conductivity. Fig. 2 shows the results of the computation on a mesh that consists of 250,000 curved tetrahedral first order finite elements.

III. OPERATOR PRECONDITIONING

An alternative preconditioner for \mathbf{M} can be derived by using the idea of operator preconditioning that has been introduced in [6, Sect. 3]. It makes use of the stability of the variational problem related to (1) with respect to suitably chosen norms on

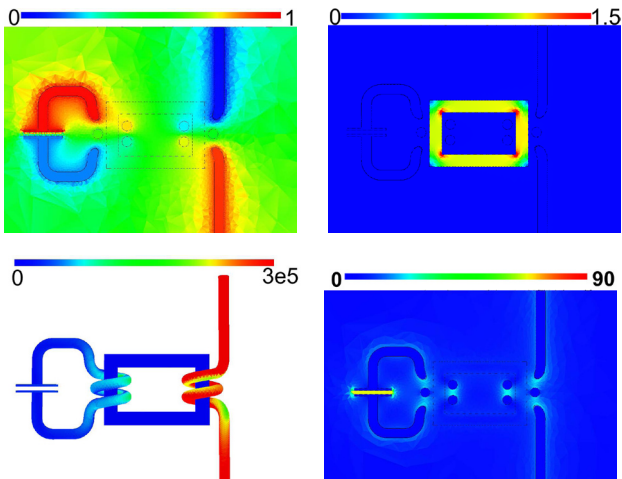


Fig. 2. Simulation results of the arrangement described in figure 1. The upper left illustration shows the real part of the electric potential in [V], the upper right picture shows the rms-value of the magnetic induction in [T], the lower left picture shows the rms-value of the current density in [A/m²], and the lower right picture shows the rms-value of the electric field in [V/m].

the function spaces. The inverse of the operator inducing these norms will then furnish a preconditioner which is robust with respect to discretization parameters. In the concrete setting of (1) the novel preconditioner is given by inverting a finite element discretization of

$$\mathbf{P} := \begin{pmatrix} \operatorname{curl} \frac{1}{\mu} \operatorname{curl} \mathbf{A} + \omega \sigma \mathbf{A} & 0 & 0 \\ 0 & \Delta \tilde{\varphi} & 0 \\ 0 & 0 & \Delta \psi \end{pmatrix}, \quad (2)$$

with \mathbf{A} , φ functions on Ω , and ψ supported in Ω_e . In (2) we also impose lower bounds for frequency and conductivity, that is, we set $\omega \leftarrow \max\{\omega, 1 \text{ Hz}\}$, $\sigma(\mathbf{x}) \leftarrow \max\{\sigma(\mathbf{x}), 10 \Omega \text{ m}^{-1}\}$. First tests with a direct solver applied to \mathbf{P} demonstrated strongly improved efficiency of a preconditioned BiCGstab iteration, see table I. The computations were carried out on a 4 core 2,5 GHz / 16 GB RAM Intel Xeon.

Number of complex d.o.f.	Time old min	Memory old GB	Time new min	Memory new GB
199 000	4.2	6.0	0.6	1.4
405 000	16.8	15.3	1.4	3.3
708 000	-	-	3.3	6.3
1 074 000	-	-	7.0	10.4
1 564 000	-	-	10.6	15.1

TABLE I

TOTAL MEMORY AND TIME CONSUMPTION FOR THE COMPUTATION OF THE PROBLEM OF FIGURE 1 WITH OLD \mathbf{P}_p AND NEW PRECONDITIONER \mathbf{P} .

Note that each block of the block-diagonal matrix \mathbf{P} is real, symmetric and positive definite. This is a great advantage compared to other preconditioners. Memory and time consumption of the applied direct solver Pardiso could drastically be reduced by using a Cholesky decomposition.

IV. HIERARCHICAL MATRICES (\mathcal{H} -MATRICES)

We have to overcome the fill-in problems of direct solvers if the problem size is further enlarged. Fast summation

methods have considerably attracted attention during the last two decades. The introduction of *hierarchical matrices* (\mathcal{H} -matrices) [7], [8] has paved the way to methods which have almost linear complexity and which are robust; see also [9]. Their efficiency is gained from representing sub-blocks from an appropriate matrix partition P by low-rank matrices; see Fig. 3. The set of hierarchical matrices on the partition P and

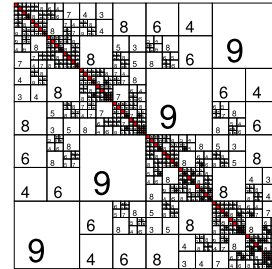


Fig. 3. A hierarchical matrix with its rank distribution.

blockwise rank k is defined as

$$\mathcal{H}(P, k) = \{A \in \mathbb{C}^{M \times N} : \operatorname{rank} A_b \leq k \text{ for all } b \in P\}.$$

The elements of this set can be stored with logarithmic-linear complexity and hence provide data-sparse representations of fully populated matrices. Additionally, exploiting the hierarchical structure of the partition, an approximate algebra can be defined which is based on divide-and-conquer versions of the usual block operations. These approximate operations also have logarithmic-linear complexity and can be used to define substitutes for higher level matrix operations such as inversion and LU factorization. Our aim is to construct approximate preconditioners for (1) by computing \mathcal{H} -matrix approximations to the factors of the Cholesky decomposition of (2). This has not yet been implemented, but will be accomplished and presented at the conference.

REFERENCES

- [1] R. Hiptmair, F. Krämer, and J. Ostrowski, "A robust Maxwell formulation for all frequencies," *IEEE Transactions on magnetics*, vol. 44, no. 6, pp. 682–685, 2008.
- [2] S. Reitzinger and J. Schöberl, "An algebraic multigrid method for finite element discretizations with edge elements," *Numer. Linear Algebra Appl.*, vol. 9, no. 3, pp. 223–238, 2002.
- [3] S. Zaglmayr, "High order finite element methods for electromagnetic field computation," Ph.D. dissertation, Johannes Kepler University, Linz, Austria, 2006.
- [4] M. Bebendorf and J. Ostrowski, "Parallel hierarchical matrix preconditioners for the curl-curl operator," *to appear in J. of Comp. Math.*, 2009.
- [5] O. Schenk, "Pardiso website, http://www.computational.unibas.ch/computer_science/people/schenk/software/."
- [6] R. Hiptmair, "Operator preconditioning," *Computers and Mathematics with Applications*, vol. 52, no. 5, pp. 699–706, 2006.
- [7] W. Hackbusch, "A sparse matrix arithmetic based on \mathcal{H} -matrices. Part I: Introduction to \mathcal{H} -matrices," *Computing*, vol. 62, no. 2, pp. 89–108, 1999.
- [8] W. Hackbusch and B. N. Khoromskij, "A sparse \mathcal{H} -matrix arithmetic. Part II: Application to multi-dimensional problems," *Computing*, vol. 64, no. 1, pp. 21–47, 2000.
- [9] M. Bebendorf, *Hierarchical Matrices: A Means to Efficiently Solve Elliptic Boundary Value Problems*, ser. Lecture Notes in Computational Science and Engineering (LNCSE). Springer, 2008, vol. 63, ISBN 978-3-540-77146-3.

The hybrid numerical integration algorithm of Hankel transform for magnetic induction tomography

He wei, Luo Haijun, Xu zheng, Li Qian, Wang Junfeng

State Key Laboratory of Power Transmission Equipment & System Security and New Technology, The Electrical Engineering College, Chongqing University, Chongqing 400044, P. R. China
Email: xuzheng@cqu.edu.cn, hewei@cqu.edu.cn

Abstract—In the forward problem of multi-layer medium magnetic induction tomography and geological electromagnetic field, the integration including dual Bessel function should be calculated. Because of the serious oscillation and slow decay of the product term, it is difficult to use ordinary numerical integration method. This paper provide a hybrid numerical integration algorithm, which divide the integral interval $[0, \infty)$ into two regions: $[0, \lambda_0)$ and $[\lambda_0, \infty)$. In $[0, \lambda_0)$, the integration can be calculated through Gauss-Legendre numerical integral method, while in $[\lambda_0, \infty)$, we convert the integration into Fourier transform and calculate it by polygonal approximation algorithm. Finally, add the two results. This algorithm is proved to have better convergence characteristic and higher precision.

Index Terms—hybrid numerical integration, Gauss-Legendre method, polygonal approximation

I. Introduction

In the forward problem of magnetic induction tomography and geological electromagnetic field, the integration including dual-Bessel function of the following form should be calculated:

$$\int_0^{\infty} F(\lambda) \cdot J_1(\lambda\rho) \cdot J_1(\lambda\rho') \cdot d\lambda \quad (1)$$

where $\rho > 0$, $\rho' > 0$, $F(\lambda)$ is the kernel function. $J_1(\lambda\rho), J_1(\lambda\rho')$ are the first order Bessel functions of first kind. It is also called as Hankel transform.

Due to the serious oscillation and slow decay of the dual Bessel function product term (as shown in Fig.1), it is difficult to use ordinary numerical integration method. Referring to the research of Chave^[1] and Huajun^[2], a new numerical integration algorithm is introduced.

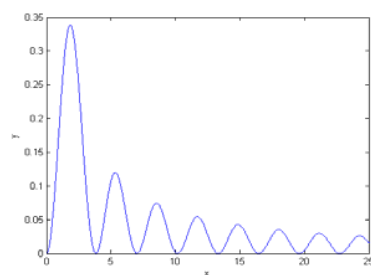


Fig.1. The plot of two one-order and first kind Bessel functions multiplying

II. Algorithm Description

According to the gradually changed attenuation characteristic of Bessel function, the integral interval $[0, \infty)$ can be divided into two regions: $[0, \lambda_0)$ and $[\lambda_0, \infty)$. In these two regions, the integration be calculated by different methods. The result is the sum of the two results.

A. Integration in Region $[0, \lambda_0)$

First, find the distribution of zero points for the dual Bessel function product term in this interval. Then, use Gauss-Legendre integral method between the adjacent two zeros in turns. We get 5 zero points of five-order Legendre polynomials as the Gauss points in $[-1, 1]$. Arbitrary integral interval $[a, b]$ could be converted into interval $[-1, 1]$ by coordinate transform^[3].

B. Integration in region $[\lambda_0, \infty)$

The Hankel transform can be written as fourier transformation using the mass-argument approximate expression of Bessel function, and calculated by polygonal approximation algorithm. The mass-argument approximate expression of one-order Bessel function is:

$$J_1(x) \approx \sqrt{\frac{2}{\pi x}} \cos\left(x - \frac{3\pi}{4}\right) \quad (x \rightarrow \infty) \quad (2)$$

Taking (2) into (1), substituting the integral region with $[\lambda_0, \infty)$ yields:

$$\begin{aligned} & \int_{\lambda_0}^{\infty} F(\lambda) \cdot J_1(\lambda\rho) J_1(\lambda\rho') \cdot d\lambda = \\ & \int_{\lambda_0}^{\infty} F(\lambda) \cdot \frac{-\sin[\lambda(\rho+\rho')]}{\pi\lambda\sqrt{\rho \cdot \rho'}} \cdot d\lambda \quad (3) \\ & + \int_{\lambda_0}^{\infty} F(\lambda) \cdot \frac{-\cos[\lambda(\rho-\rho')]}{\pi\lambda\sqrt{\rho \cdot \rho'}} \cdot d\lambda \end{aligned}$$

The Hankel transform has been convert into the sum of two fourier transforms. Polygonal approximation algorithm is employed to calculate these two fourier transforms:

$$\begin{aligned} & \int_a^b F(\lambda) \cdot \cos(\lambda\rho) d\lambda = \frac{1}{\rho} F(\lambda) \sin(\lambda\rho) \Big|_{\lambda=a}^b \\ & + \frac{1}{\rho^2} \sum_{i=0}^n \frac{F(\lambda_{i+1}) - F(\lambda_i)}{\lambda_{i+1} - \lambda_i} [\cos(\lambda_{i+1} \cdot \rho) - \cos(\lambda_i \cdot \rho)] \end{aligned} \quad (4)$$

$$\begin{aligned} & \int_a^b F(\lambda) \cdot \sin(\lambda\rho) d\lambda = -\frac{1}{\rho} F(\lambda) \cos(\lambda\rho) \Big|_{\lambda=a}^b \\ & + \frac{1}{\rho^2} \sum_{i=0}^n \frac{F(\lambda_{i+1}) - F(\lambda_i)}{\lambda_{i+1} - \lambda_i} [\sin(\lambda_{i+1} \cdot \rho) - \sin(\lambda_i \cdot \rho)] \end{aligned} \quad (5)$$

Notes that, the integrating region of Polygonal approximation algorithm is finite, namely, $[a, b]$. But the integrating region in expression(3) is infinite: $[\lambda_0, \infty)$, the infinite interval should be truncated according to the convergence characteristic of $F(\lambda)$ at infinity.

III. Experiment of the test function

We used the following expression as the test function.

$$F(x) = \int_0^{\infty} \lambda \cdot e^{-\lambda^2 x^2} \cdot J_1(\lambda\rho) \cdot J_1(\lambda\rho') \cdot d\lambda \quad (6)$$

This integration has an analytical solution:

$$f(x) = \frac{1}{2x^2} e^{-\frac{\rho_1^2 + \rho_2^2}{4x^2}} \cdot I_1\left(\frac{\rho_1 \cdot \rho_2}{2x^2}\right) \quad (7)$$

where I_1 is the first kind of one-order modified Bessel function.

The result of the numerical algorithm and the analytical solution are drawn in the Fig.2:

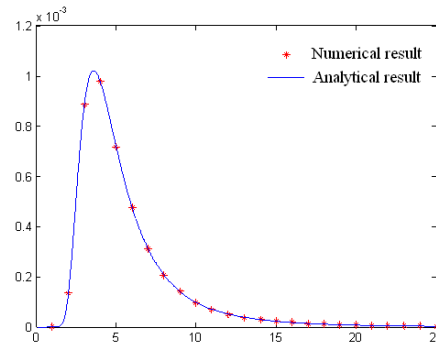


Fig.2. Comparison between function analytical solution and numerical solution

As Fig.2 shown, we can see that the numerical solutions are coincide with the analytical ones.

IV. Conclusion

The algorithm solves the problem of numerical integration of Hankel transform. The calculation of the test function shows that this algorithm has better convergence characteristic, higher precision and efficiency. The algorithm can be used in the solution of the forward problem in magnetic inductive imaging and geological electromagnetism exploration.

Acknowledge

This work is supposed by the National 863 Foundation of China (2006AA02Z4B7), National Natural Science Foundation of China (50877082), Specialized Research Fund for the Doctoral Program of Higher Education of China (20070611035) and International S&T Cooperation Program of China (2007DFR30080).

Reference

- [1]Chave A D. Numerical integration of related Hankel transformations by quadrature and continued fraction expansion [J]. Geophysics, 1983, 48 (12):1671-1686.
- [2]Hua jun, Jiang yansheng, Wangwenbing, The numerical integration of dual hankel transformation, [J], Goal geology and exploration, 2001, pp29 (3):58-62.
- [3]Xu Shiliang, "The numerical mathematic and computation realization", Tsinghua University Press, pp:295-297, 2006

A New Multilevel Smoothing Method for the Wavelet-Based Algebraic Multigrid

Fabio Henrique Pereira^{1,2} and Silvio Ikuyo Nabeta²

¹Industrial Engineering Post Graduation Program – UNINOVE, São Paulo, SP, Brazil

²Electrical Machine and Drives Lab – GMACq – USP, Escola Politécnica, São Paulo, SP, Brasil

fabiohp@uninove.br; nabeta@pea.usp.br

Abstract — In contrast to the standard algebraic multigrid, the Wavelet-based Algebraic Multigrid method relies more strongly on the smoothing method because the coarse spaces are chosen a priori. So, it is very important to develop new smoother methods, especially for those cases where the classical Gauss-Seidel smoothing method does not give good results. This paper proposes a new multilevel smoothing approach based on projection technique. The proposed smoothing method was applied to smoothing the error in a linear systems issued from finite element solutions of the elliptic equation and the results compared with those obtained from the Gauss-Seidel method.

I. INTRODUCTION

THE WAVELET-BASED Algebraic Multigrid method (WAMG) was proposed for the solution of linear systems issued from Finite Element applications in Electromagnetic Field problems [1]. In this method an incomplete discrete wavelet transform is applied in order to generate an approximation of the original matrix in each level of a multiresolution process. The same approach is also used to transfer the vectors between the different grids in the multigrid scheme. In contrast to the standard algebraic multigrid, that uses some simple relaxation scheme and enforces the interaction between the smoother and the coarse-grid correction by choosing the coarser levels and the transfer operators appropriately [2],[3], the WAMG relies more strongly on the smoothing method because the coarse spaces are chosen a priori. So, the WAMG selects a suitable smoothing method to ensure an accurate error representation in the coarsest level.

In face of this, it is very important to develop new smoothing methods that are suitable for the case where the classical Gauss-Seidel smoothing method does not give good results as, for example, for the global systems resulting from FEM–BEM formulations which the common smoother types do not work properly [4].

This paper proposes a new multilevel smoothing approach based on projection techniques which search an approximation in the high frequency subspace created by the high-pass filters in the discrete wavelet transform.

II. THE REQUIREMENTS OVER THE SMOOTHER IN WAMG

In order to analyze the requirements over the smoothing methods in WAMG, we have to understand the DWT behavior and the effects of the use of this technique in the algebraic multigrid context.

Usually in the literature, the discrete wavelet transform is

defined using the concept of filter bank [5]. In such cases low-pass and high-pass filters are chosen to obtain the low frequency and the high frequency terms of the input signal, respectively. In this procedure, if the discrete input signal $x = \{x[n]\}_{n \in \mathbb{Z}}$ is sufficiently smooth then the high frequency terms are close to zero and the output low frequency component will be a good approximation of the signal.

To better understand the effects of this technique in the WAMG context, we will suppose that there are only two grids: the original grid and a coarse grid.

The WAMG method uses only the low-pass filters to produce an approximation of the original coefficient matrix. This approximation will represent the system of equation in the coarse grid and it will be used to solve the residual equation on the coarse grid. Then, the residual equation solution is used in the correction of the error in the original grid.

As the WAMG coarse grid is created by the low-pass filters, the coarse grid error correction will only be accurate if the error is smooth. The fact that the error is smooth means that the high frequency components become small after a few stationary iterative iterations whereas the low frequency components hardly change [2]. Therefore, the smoothing method should be able to remove or, at least, to lessen the high frequency components of the error.

III. THE PROPOSED MULTILEVEL SMOOTHER METHOD

In a projection process an approximation for the solution of a linear system is extracted from a subspace \mathcal{K} which is the subspace of candidate approximations, or search subspace. If m is the dimension of \mathcal{K} , then the residual vector $b - Ax$ is constrained to be orthogonal to m linearly independent vectors in order to obtain such an approximation. This orthogonal condition defines another subspace \mathcal{L} , of dimension m , called the subspace of constraints [6].

Mathematically, if we know an initial guess, $x_0 \in \mathcal{K}$, the approximate solutions can be defined as

$$\tilde{x} = x_0 + \delta, \quad \delta \in \mathcal{K} \quad (1)$$

$$(r_0 - A\delta, w) = 0, \quad \forall w \in \mathcal{L} \quad (2)$$

in which $r_0 = b - Ax_0$.

As an ideal smoother should remove the high frequency error component it is interesting that this smoother search an approximation to the linear system solution in a high frequency subspace.

In other hand, the multiresolution analysis in discrete wavelet transform decompose the original grid (space) V in two subspaces V_1 and W_1 such that

$$V_1 = \text{span} \{ \phi(2^{-1}x - k) \}_{k \in \mathbb{Z}}, \quad (3)$$

$$W_1 = \text{span} \{ \psi(2^{-1}x - k) \}_{k \in \mathbb{Z}}, \quad (4)$$

and

$$V_1 \oplus W_1 \quad (5)$$

where ϕ and ψ are the scaling and wavelets function, respectively. Therefore, we can develop a smoothing method based on a projection approach with,

$$\mathcal{K} = \mathcal{L} = W_1 \quad (6)$$

which will search the approximations to the solution in the high frequency subspace W_1 . As result the obtained error should be smooth in the sense of the Discrete Wavelet Transform.

In a matrix representation, denoting by $W = [w_1, \dots, w_m]$ an $n \times m$ matrix whose column-vectors form a basis of W_1 , a two-level smoothing method based on projection technique can be represented by the following algorithm:

Algorithm: Two-level smoothing method

1. Get the current approximation x_i
2. $r^h = b - Ax_i$
3. $r^{2h} = W^T r^h$
4. $e^{2h} = (W^T AW)^{-1} r^{2h}$
5. $x_{i+1} = x_i + We^{2h}$
6. Return x_{i+1}

The recursion of this two-level process produces a new multilevel smoothing method which has shown to be efficient in smoothing the high frequency error.

IV. DESCRIPTION OF THE TEST PROBLEM

In order to analyze the efficiency of the proposed smoother the method was applied to smoothing the error in the linear systems with 5041 rows and 56911 nonzero elements, issued from finite element solutions of the elliptic equation.

For analyzing the smoothing method behavior we assume that the exact solution \bar{x} is known,

$$\bar{x}_i = \sin(2i \times 200\pi / n) + \sin(2i \times 600\pi / n) + \sin(2i \times 1200\pi / n) \quad i=1, \dots, 5041, \text{ and we use it to supply the right hand side vector } b.$$

The error is analyzed after one, two and three smoother iterations. As in the WAMG context is supposed to there is no predefined geometric grids the error is analyzed in an algebraic sense, in which an error is smooth if it is slow to converge with respect to the smoothing method [2]. The classical Gauss-Seidel was used for comparison.

V. RESULTS

The error after one, two and three smoothing iterations are shown in Fig. 1. As a zero initial guess was adopted the initial error is equal to the exact solution \bar{x} .

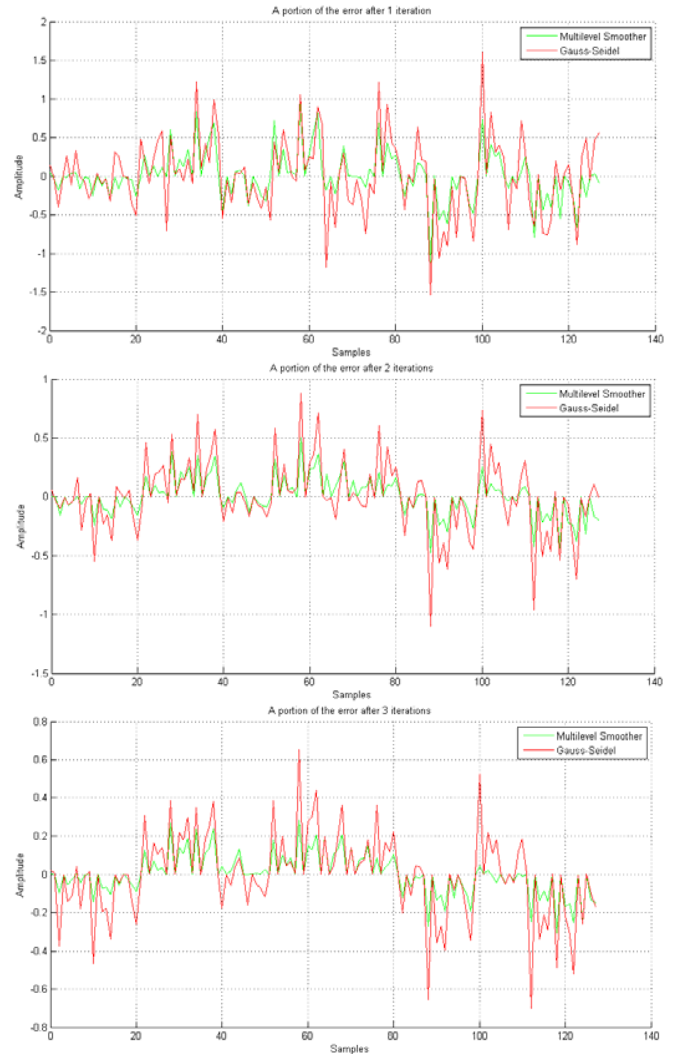


Fig. 1. A portion of the error after one (top), two (middle) and three smoothing iterations

VI. CONCLUSIONS

The proposed method seems to be very efficient in smoothing the high frequency error. The results in Fig. 1 show that the errors produced by the multilevel approach appear less oscillatory than those created by the classical Gauss-Seidel method in the three first iterations.

VII. REFERENCES

- [1] F. H. Pereira, et. al., "A Wavelet-based Algebraic Multigrid Preconditioning for Iterative Solvers in Finite Element Analysis". *IEEE Trans. on Magn.*, 43(4): 1553-1556, 2007.
- [2] U. Trottenberg, C. W. Oosterlee, and A. Schuller, *Multigrid*, Academic Press, New York, 2001, pp. 45-56.
- [3] W. L. Briggs, V. E. Henson, and S. F. McCormick, *A Multigrid Tutorial*, 2nd. ed, SIAM, California, 2000.
- [4] F. H. Pereira, M. M. Afonso, and S. I. Nabeta, "An Efficient Two-Level Preconditioner for FEM-BEM Equations based on Lifting", submitted for *17th International Conference on the Computation of Electromagnetic Fields*, Compumag 2009, Florianópolis, Brazil.
- [5] A. Jensen, A. la Cour-Harbo, *The Discrete Wavelet Transform*, Ripples in Mathematics, Springer, Berlin, 2001.
- [6] Y. Saad, *Iterative Methods for Sparse Linear Systems*, 2nd ed, SIAM, Philadelphia, 2003.

Analysis of Omnidirectional Compact Dual-reflector Antenna

S. R. Zang^{#1}, and J. R. Bergmann^{#1}

[#]PUC-Rio, CETUC

Rua Marques de São Vicente 225, 22453-900, Rio de Janeiro, Brazil

¹sandro@cetuc.puc-rio.br, bergmann@cetuc.puc-rio.br

Abstract—This work shows the use of a hybrid numerical technique to fully analyze circularly symmetric omnidirectional antennas fed by coaxial horn. Mode Matching technique is employed to analyze the interior region of the coaxial horn. The Electric and Magnetic Field Equations (EFIE/HFIE) are employed to related the horn aperture fields and the induced currents on the reflectors and outer surfaces of the feed. Method of Moments (MoM) is used to solve the Field Integral Equations. The analysis yields the accurate prediction of the antenna radiation pattern and return loss at the feed connector. Due to the numerical efficiency of the scheme, the analysis can be associated with optimization methods to design the feed horn in order to minimize the antenna return loss.

I. INTRODUCTION

Last-mile broadband access has been considered as an alternative wireless technology to attend the growing interest on high-speed Internet access, as it can show lower costs, rapid deployment, and lower maintenance when compared with cable technologies. For the antenna in the hub station, compact single and dual reflector omnidirectional antennas have been considered [1,2]. The reflector surfaces are bodies of revolution obtained by rotating the generating curves about a symmetry axis, as illustrated in Figure 1 for dual reflector systems. The vertical polarization is obtained by employing a coaxial TEM feed horn, placed on the central opening of the main reflector, as indicated in Figure 1.

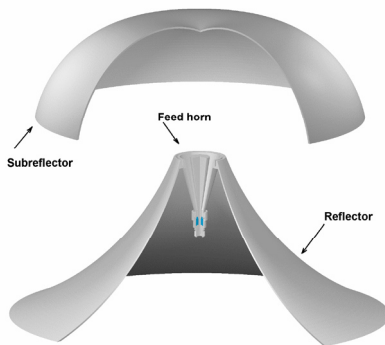


Figure 1 - Circular symmetric reflector surfaces.

Besides the control of the radiation pattern in the elevation plane and the reduction of the return loss at the feed input, the design of the reflector these omnidirectional antennas has to provide compact configurations to make them attractive.

However, the design for compact geometries implies on diminishing the distance between the elements and increasing the coupling effects between feed and reflectors. In order to estimate electrical performance of these compact omnidirectional antennas, a full-wave stepped-waveguide model and MoM/HFIE method are combined to analyse both the fields in the interior region and the contributions of the induced currents on the reflector, subreflector, and the exterior wall of the feed horn [3,4]. The interaction is accurately analysed by using the EFIE on the exterior surfaces of the coaxial horn. The equivalence currents principle is introduced to formulate the HFIE on the radiating aperture which combines the interior field transition problem with the exterior radiation. The procedure is similar to those described in [3,4] and applied in the electromagnetic analysis of conical feed horns excited by the TE₁₁ mode. Here, the procedure is adapted to include the reflectors and a coaxial feed horn excited by the TEM mode. As a consequence of the TEM mode excitation, only the TEM and TM modes are considered at the transition region, as the TE mode do not couple with the TEM excitation.. The application of the analysis technique yields the antenna radiation pattern as well as the antenna return loss at the end of the N-type connector. The numerical scheme is particularly efficient in the optimization of the antenna feed horn.

II. ANTENNA ANALYSIS

The analysis is separated in two parts. First, the horn is represented as series of stepped coaxial waveguides sections and Mode Matching is performed by rigorously enforcing the boundary conditions at each step. It results a scattering matrix [S] for the entire transition region:

$$\begin{bmatrix} b^C \\ b^A \end{bmatrix} = \begin{bmatrix} S_{11} & S_{12} \\ S_{21} & S_{22} \end{bmatrix} \begin{bmatrix} a^C \\ a^A \end{bmatrix} \quad (1)$$

The scattering matrix relates the reflected modes at the two extremes of the transition region. In (1), the vectors $[a^C]$ and $[a^A]$ contain the amplitudes of incident modes at the region 'C' and 'A', respectively, whereas the vectors $[b^C]$ and $[b^A]$ contain the amplitudes of reflected modes at the connector 'C' and aperture 'A', respectively (see Figure 2). The matrix [S] depends on the geometrical parameters and on the wavelength as well as the number of modes considered to ensure continuity of the electric and magnetic throughout the transition region. Part of the power of the modes reaching the

aperture, region A, is radiated into the space while the rest is reflected back into the horn.

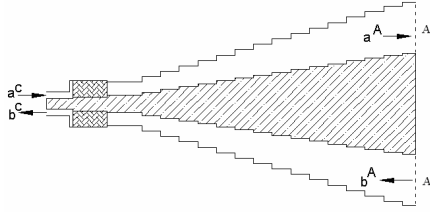


Figure 2 - Horn represented as series of stepped coaxial waveguides sections

In the second part of the analysis scheme, to calculate the radiate fields and the amplitude of the reflected modes $[b^A]$, MoM is employed to solve the EFIE and MFIE, as described in [4]. To apply the above strategy, an equivalent to the actual electromagnetic problem is defined by replacing the feed radiating aperture by a sheet of perfect conductor with an equivalent magnetic current density

$$\vec{M}([a^A], [b^A]) = -\sum_{l=1}^{N_M} (a_l^A + b_l^A) (\hat{n} \times \vec{e}_l^A) \quad (2)$$

where \hat{n} is the unit vector normal to the aperture, \vec{e}_l^A is the electric field of the modes internal to the aperture and N_M is the number of modes used in the expansion. The magnetic current density \vec{M} radiates into the space and induces an electric surface current \vec{J} on the metallic wall of the equivalent problem, as described in Figure 3. These currents ensure the continuity of the tangential magnetic field across the aperture and zero tangential electric field on the metallic surface at the aperture and reflectors:

$$\begin{aligned} \hat{n} \times [\vec{E}^S(\vec{J}) + \vec{E}^S(\vec{M})] &= 0 \\ \hat{n} \times [\vec{H}^S(\vec{J}) + \vec{H}^S(\vec{M})] &= \hat{n} \times \vec{H}^A \end{aligned} \quad (3)$$

where \vec{E}^S and \vec{H}^S are electromagnetic field scattered by the currents \vec{M} and \vec{J} .

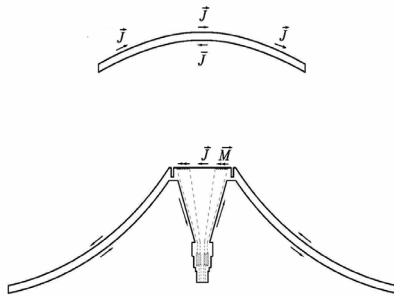


Figure 4 - Surface currents outside the feed horn

To apply the MoM solution, the current densities \vec{M} and \vec{J} are expanded by sub sectional roof-top patch modes \vec{P}_j^J and \vec{P}_k^M respectively. In this way, a conversion matrix is introduced to transform the roof-top patch modes into eigenmodes of the aperture fields. By testing the EFIE with \vec{P}_i^J and the HFIE with $\hat{n} \times \vec{e}_i^A$, it leads to two systems of matrix

equations. By combining them with (1), it is possible to define a relation between the vector $[a^C]$ and the vectors $[b^C]$, $[a^A]$ and $[b^A]$.

III. RESULTS

The analysis algorithm was applied to calculate the antenna radiation pattern and the antenna return loss of a dual reflector omnidirectional system. The antenna is generated by an axis displaced confocal conics of ADE type where the parameters are described in [2]. The antenna radiation pattern and return loss are depicted in Figures 4 and 5 (dotted line), respectively. In order to minimize the peak of the antenna return loss over the operation band (7.5-10.0 GHz), the analysis was embedded in an optimization scheme to shape the feed horn profile. The results after the shaping are show by the lull line in Figure 3, where can e observed a 2 dB reductio in the peak. As the shaping may modify the feed radiation pattern, Figure 4 shows the antenna radiation pattern after optimization (full line). Measured results will be available for comparison.

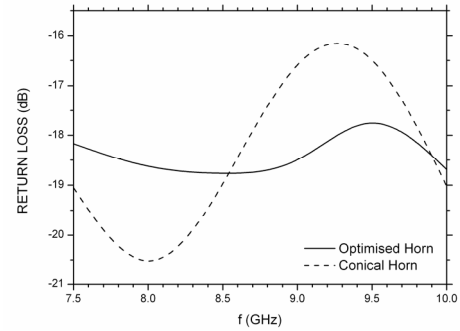


Figure 3 -Antenna Return Loss at the N-Type Connector

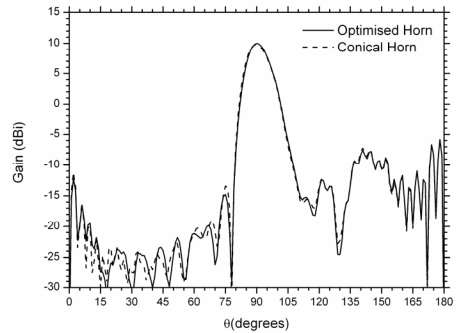


Figure 4 -Antenna Radiation Pattern

REFERENCES

- [1] A. P. Norris and W. D. Waddoup, "A millimetric wave omnidirectional antenna with prescribed elevation shaping," in Proc. ICAP—4th Int. Conf. Antennas and Propagation, 1985, pp. 141–145.
- [2] F. J. S. Moreira and J. R. Bergmann, "Classical Axis-Displaced Dual-Reflector Antennas for Omnidirectional Coverage", IEEE Transactions on Antennas and Propagation, Nova York, v. 53, n. 9, pp. 2799-2808, 2005.
- [3] E. Kuhn, V. Hombach, "Computer-aided analysis of corrugated horns with axial or ring-loaded radial slots", Proc. ICAP 83, Part 1, pp.127-131, 1983.
- [4] Kefeng Lui, C. Balanis, C. Birtcher, and G. Barber, "Analysis of Pyramidal Horn Antennas Using Moment Methods", IEEE Trans. Antennas Propagat., vol. 41, no. 10, pp. 1379–1389, Oct. 1993.

Mixed Fault Diagnosis of Squirrel Cage Induction Motor by Winding Function Approach

Daesuk Joo

Kyungil Woo

Pukyong National University, Yongdang-Dong, Nam-Gu, Busan, South Korea
cogging@pknu.ac.kr

Abstract — This paper studies on the mixed fault diagnosis of 3-phase squirrel cage induction motor with the broken rotor bar and rotor static eccentricity at steady state. The fault model is presented by the winding function approach and the coupled magnetic circuit theory. Fast Fourier transform of the stator current is used to diagnose faults. Individual and mixed fault characteristic caused by the broken rotor bar and the rotor static eccentricity are analyzed. From the individual fault analysis result it is shown that there are sidebands due to the broken rotor bar and the rotor static eccentricity respectively. Examination of the mixed fault analysis result shows that one fault characteristic made by the broken rotor bar does not affect the other fault characteristic cause by the rotor static eccentricity.

I. INTRODUCTION

The induction motor is the most important one because of its simplicity, low cost and ease of operation. Asymmetrical operation of the induction motor results in poor efficiency which eventually leads to the failure of the motor. The analysis of the induction motor is important for diagnose failures in the motor. The conventional d-q model of the induction motor is based on the assumption that distribution of the stator windings is sinusoidal. This implies that the harmonics of the winding distribution are neglected in the analysis of the motor. This model is not suitable for motor analysis and simulation under rotor eccentricity or the broken rotor bars. However a model based on the winding function theory is more convenient for such conditions.

This paper focuses on the mixed fault analysis of 3-phase squirrel cage induction motor with the rotor static eccentricity and the broken rotor bars at steady state. The fault model is presented by the winding function theory and the coupled magnetic circuit method. Self and mutual inductances for the induction motor are calculated by using the winding function theory. The stator current is obtained by means of the coupled magnetic circuit method and Park's transformation. Individual and mixed fault characteristic caused by the broken rotor bar and the rotor static eccentricity are analyzed. The analysis results are identified by the special frequency component obtained by the spectrum analysis of the stator current.

II. MODELING OF INDUCTION MACHINES

The voltage equations of m -phase induction machine with n rotor bars for the stator loops in vector-matrix form can be written as

$$V_s = R_s I_s + \frac{d\Lambda_s}{dt} \quad (1)$$

$$\Lambda_s = L_{ss} I_s + L_{sr} I_r \quad (2)$$

where V_s is the stator voltage matrix, R_s is an m dimensional diagonal matrix consisting of resistances of each stator phase, I_s is the stator current matrix, Λ_s is the stator flux linkage matrix, L_{ss} is the $(m \times m)$ matrix of stator inductance, L_{sr} is an $(m \times n)$ matrix comprised of the mutual inductances between the stator phases and the rotor loops, and I_r is the rotor current matrix.

The voltage equations for the rotor loops are

$$V_r = R_r I_r + \frac{d\Lambda_r}{dt} \quad (3)$$

$$\Lambda_r = L_{rs} I_s + L_{rr} I_r \quad (4)$$

where V_r is the rotor voltage matrix. In case of a cage rotor, the rotor loop voltages, $V_r = 0$. R_r is n symmetric matrix consisting of resistances of each rotor bar, Λ_r is the rotor flux linkage matrix, L_{rs} is a $(n \times m)$ matrix consisting of the mutual inductances between the rotor loops and the stator phases, and L_{rr} is $(n \times n)$ matrix of rotor inductances.

III. CALCULATION OF INDUCTANCES

The winding function is defined by

$$N(\phi) = n(\phi) - \frac{1}{2\pi} \int_0^{2\pi} n(\phi) d\phi \quad (5)$$

The function $n(\phi)$ is called the turns function. The second term is clearly the average value of the turns function.

Fig. 1 shows an important example of continuous winding distribution and such a winding is said to be uniformly distributed. Here, the N_t turns are assumed to be uniformly distributed over β radians. The function $n(\phi)$ is

$$n(\phi) = \frac{N_t}{\beta} \phi \quad (6)$$

where $\phi_1 - \frac{\beta}{2} \leq \phi \leq \phi_1 + \frac{\beta}{2}$. Hence, $n(\phi)$ changes linearly over this region. The other quantity changes same manner. The turns function $n(\phi)$ remains fixed at $N_t/2$ until reaches ϕ_2 at which point negative turns start being enclosed.

According to winding function theory, the calculation of winding inductance between any two windings "A" and "B" in any electric machine can be computed by

$$L_{AB}(\theta_r) = \mu_0 \ell \int_0^{2\pi} r(\theta_r, \phi) \frac{N_A(\theta_r, \phi) \cdot N_B(\theta_r, \phi)}{g_e(\theta_r, \phi)} d\phi \quad (7)$$

where θ_r is the angular position of the rotor with respect to some stator reference, ϕ is a particular position along the stator inner surface, g_e is effective air-gap function, ℓ is the length of the stack, and r is the average radius of the air-gap.

The term $N_A(\theta_r, \phi)$ and $N_B(\theta_r, \phi)$ are called the winding function.

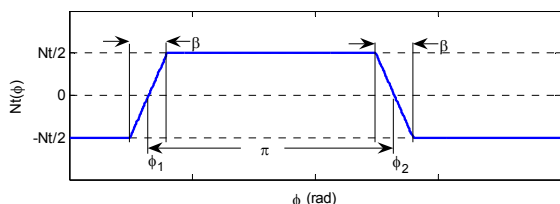


Fig. 1. Winding function, $n(\phi)$ changes linearly over the slot

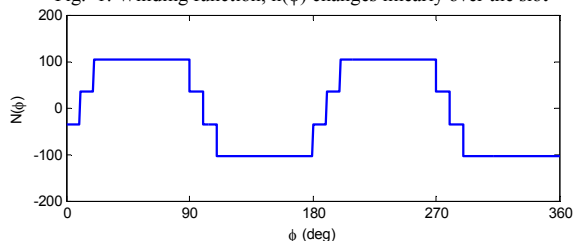


Fig. 2. Winding function of phase "a" not considering effect of slot width

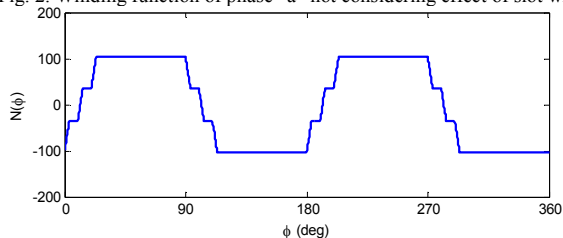


Fig. 3. Winding function of phase "a" considering effect of slot width

Fig. 2 shows the winding function of the phase "a" not considering the slot width of the induction motor. In this figure, it is shown that the distribution of current over a slot pitch has been neglected in the computation of the winding function. Fig. 3 shows the winding function of phase "a" considering the slot width. As the width of the slot increases, the winding function changes linearly across the slot.

The specific machine studied in this paper is a three-phase, 1-hp, 60-Hz, 4-pole, 380-V induction motor. The motor has 36 stator slots and 44 rotor bars with one coils per stator phase.

IV. SIMULATION RESULTS

Motor current signature analysis is a noninvasive, on-line monitoring technique for the diagnosis of problems in induction motors.

Fig. 4 is a fast Fourier transform(FFT) zoom current spectra for 3 broken rotor bars. In Fig. 4, Fig. 5 and Fig. 6 a solid line and a dashed line represent a faulty motor and a healthy motor respectively. The motor was operating at full-load slip of 0.05, and the predicted twice slip frequency sideband " $(1-2s)f$ " for a supply frequency of 60 Hz are ± 6 Hz. As in Fig. 4 there is sideband at -6 Hz around the supply frequency by broken rotor bar. This is referred to as a twice slip frequency due to broken rotor bars.

Fig. 5 is a FFT zoom current spectra for 50% rotor static eccentricity. In this figure there is only a frequency components " $\pm f_{ec}$ " which are a function of rotor eccentricity.

Fig. 6 is a FFT zoom current spectra for 3 broken rotor bars and 50% rotor static eccentricity. In this figure there are

sideband and frequency component together. From these result, we know that one fault characteristic made by the broken rotor bars does not affect the other fault characteristic cause by the rotor static eccentricity.

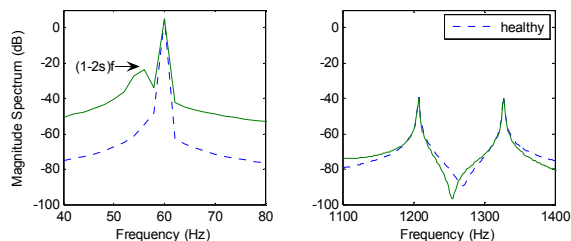


Fig. 4. FFT zoom stator current spectra for 3 broken rotor bars.

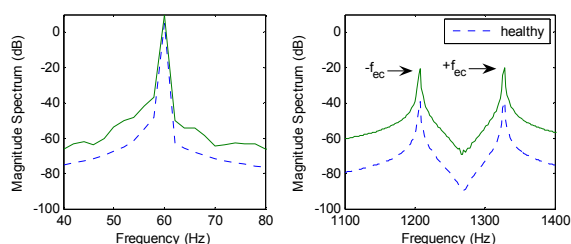


Fig. 5. FFT zoom stator spectra for 50% rotor static eccentricity.

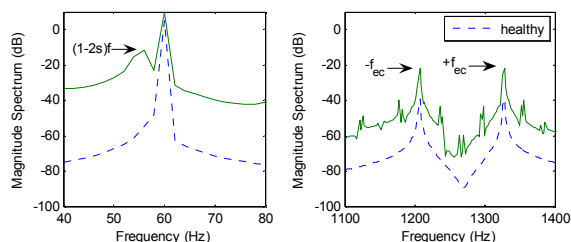


Fig. 6. FFT zoom stator spectra for 3 broken rotor bars and 50% rotor static eccentricity.

V. REFERENCES

- [1] Toliyat, H.A.; Lipo, T.A., "Transient analysis of cage induction machines under stator, rotor bar and end ring faults," *Energy conversion, IEEE transactions on*, vol.10, no.2, pp.241-247, Jun 1995
- [2] Toliyat, H.A.; Arefeen, M.S.; Parlos, A.G., "A method for dynamic simulation of air-gap eccentricity in induction machines," *Industry Applications, IEEE Transactions on*, vol.32, no.4, pp.910-918, Jul/Aug 1996
- [3] Gojko, J.M.; Momir, D.D.; Aleksandar, O.B., "Skew and linear rise of MMF across slot modeling-winding function approach," *Energy conversion, IEEE transactions on*, vol.14, no.3, pp.315-320, Sep 1999
- [4] Thomson, W.T.; Fenger, M., "Current signature analysis to detect induction motor faults," *Industry Applications Magazine, IEEE*, vol.7, no.4, pp.26-34, Jul/Aug 2001
- [5] Lipo, T.A., "Theory and control of Synchronous Machines," Lecture Notes for ECE 511, Department of Electrical and Computer Engineering, University of Wisconsin, Madison, 2002
- [6] Mohamed B.; Mohamed Y. K.; Abdelmalek K., "Park model of squirrel cage induction machine including space harmonics effects," *Journal of Electrical Engineering*, vol.57, no.4, pp.193-199, 2006

Simple Parallelization Strategy for Mesh Refinement Algorithms

Thiago E. A. Macêdo, Adriano C. Lisboa, and Renato C. Mesquita
 Department of Electrical Engineering, Universidade Federal de Minas Gerais
 Av. Antônio Carlos 6627, 31270-901, Brazil
 th.emmanuel@gmail.com, adriano@cpdee.ufmg.br

Abstract—This paper presents a simple implementation strategy for parallelizing mesh refinement algorithms that, besides performance improvements, requires only a few changes in the refinement algorithm. Furthermore, its fundamental structure allows a generic implementation for reusable code. It is applied and further analyzed in the instance of a Delaunay refinement algorithm for curved complexes.

I. INTRODUCTION

The clock frequency of processors seems to have reached an upper bound. This achievement has put parallelization as an ever so important way to speed up computational applications. A new programming paradigm has come up: algorithms must allow parallel processing.

Parallelizing an algorithm may require great changes, or even be impractical. A parallelization strategy that is less intrusive in the sequential algorithm may be considered preferable. Common strategies to parallelize a mesh refinement algorithm include a fine grain parallel cavity expansion, a medium grain parallel expansion of multiple cavities, and a coarse grain parallel refinement of geometry subregions [1]. A fine granularity must consider specific algorithm behavior, and it is justified only when the cavity inclusion predicate is computationally expensive. At coarser granularity levels, it is possible to develop strategies that are less dependent on a specific refinement algorithm. This paper proposes a simple medium grain implementation pattern.

The proposed strategy is used to parallelize a Delaunay refinement algorithm for curved complexes [2]. Despite the unique cavity expansion and remeshing of this refinement algorithm, the parallelization strategy can be implemented seamlessly.

II. IMPLEMENTATION PATTERN

The implementation pattern considers a refinement algorithm that takes an element from the refinement queue, marks up extra elements to be remeshed (cavity expansion algorithm), remeshes the cavity, and finally updates the refinement queue. The refinement queue contains full identification of elements that must be refined according to some refinement criteria. The parallelization strategy requires the following interventions in the mesh generation algorithm:

- the refinement algorithm is embedded in a thread;

This work was supported by FAPEMIG under grant 13180, Brazil.

- the refinement queue becomes a global refinement queue whose access is protected;
- the cavity expansion algorithm must detect and treat cavity conflicts;
- the selection of an element to refine is only taken from the global refinement queue when the thread's local refinement queue is empty.

Two extra data structures are used in the implementation pattern. The first one is a local refinement queue for each thread with elements that must exclusively be refined by its thread. The second one is a localizing vector where threads mark up elements of their cavity, and query to detect conflicts. The localizing vector is indexed by element identification numbers, and contains the respective owner thread. The following subsections describes the behavior of the implementation pattern. Further details will be given in the final paper.

A. Non-conflicting Cavity Expansion

Each thread selects an element to refine and start expanding its cavity from it (see Fig. 1). A thread marks up an element with their identification number in the localizing vector as soon as the cavity membership is verified. After completing its cavity expansion, a thread remeshes the cavity and updates the global refinement queue: cavity elements are removed from the queue, and new elements that do not satisfy the refinement criteria are inserted into the queue. Before selecting another element to refine, the thread unmarks its cavity elements in the localizing vector and clears its cavity.

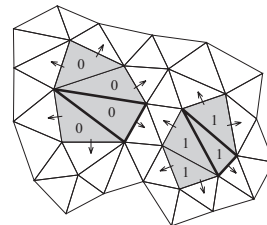


Fig. 1. Threads 0 and 1 concurrently expand their cavities marking up member elements in the localizing vector. The cavity expansion starts from the bold border element. They are non-conflicting since no neighbor of one cavity belongs to the other cavity.

B. Handling Conflicts

The cavity expansion goes through neighbor elements. Before testing the membership of a neighbor element, a thread

checks, in the localizing vector, whether the element has already been marked up by another thread. If so, a conflict is confirmed. The conflicted thread then unmarks all its cavity elements and pushes the start cavity element identification into the local refinement queue of the conflicting thread, as shown in Fig. 2. Using local refinement queues avoids another conflict with the same thread when starting from the same element. The conflicted thread takes another element to refine, and the conflicting thread continues its cavity expansion.

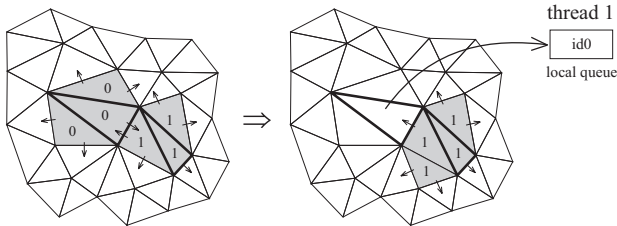


Fig. 2. Threads 0 and 1 concurrently expand their cavities marking up member elements in the localizing vector (left). The cavity expansion starts from the bold border element. Thread 0 detects a conflict with thread 1, then unmarks all elements of its cavity and pushes its start element identification into thread 1 local refinement queue (right). Thread 1 continues its cavity expansion.

Each thread checks, in the localizing vector, whether the start element of its cavity, which is taken from a refinement queue, has already been marked up by another thread. If so, a conflict is confirmed. In this case, the thread can simply discard the refinement element, since it will be removed by the conflicting thread after reshaping its cavity. The conflicted thread takes another element to refine, and the conflicting thread continues its cavity expansion.

C. Synchronization

To avoid inconsistencies with multiple threads changing, at the same time, the global refinement queue or the localizing vector, a binary semaphore for each data structure guarantees exclusive access. The synchronization on the global refinement queue is trivial: a thread claims the exclusive access to the queue through its respective semaphore, and releases it after changing it. The synchronization on the localizing vector deserves some remarks.

When a thread detects a conflict, it owns the exclusive access to the localizing vector. At this time, it unmarks all elements of its cavity, and also pushes the start element into the conflicting thread local refinement queue, before releasing the access. The conflicting thread would have to own the semaphore to detect a conflict with the same thread, so that it always continues expanding its cavity without realizing what happened. Furthermore, the conflicting thread only access its local refinement queue after unmarking elements of its cavity. That is why local refinement queues do not need their own semaphores to guarantee exclusive access.

D. Preventing Conflicts

The local refinement queues were introduced to handle conflicts. However, delegating elements to be refined by a specific

thread can be used to prevent conflicts in a more general sense. For instance, if it is possible to define disconnected refinement locations for each thread, then elements to be refined from one location can be pushed into the local refinement queue of a specific thread. Notice that it does not matter the strategy used to assign an element to a thread, and that intermediate strategies are also possible, where unassigned elements are obviously pushed into the global refinement queue. However, if a thread becomes allowed to assign an element to another one, the exclusive access to local refinement queues must be guaranteed. Preventing conflicts imbues features of a coarse grain parallelization.

III. INSTANTIATION

This section describes the instantiation of the parallelization strategy for a Delaunay refinement algorithm for curved geometries.

The cavity expansion comes from an extension of the Bowyer-Watson algorithm, which may contain simplices of different dimensions. Fortunately, the parallelization strategy does not depend on expansion rules. It only interferes where new cavity simplices are identified. Notice that neighbor simplices can also be lower dimensional.

The refinement queues in Delaunay refinement algorithms are usually actually priority queues, in order to reduce the output mesh cardinality. However, only the exclusive access guaranteed by a semaphore is required by the parallelization strategy, which is independent on how elements to be refined are removed/pushed from/into the queues.

It is possible to detect conflicts a priori and to efficiently determine non-conflicting sets of elements to be refined for Delaunay refinement algorithms [3], [4]. Although, they have not been tested on curved geometry constraints.

Timings and practical behavior of the parallel Delaunay refinement algorithm for curved geometries, with and without strategies for preventing conflicts, will be shown in the final paper. Further details of the instantiation will also be included.

IV. CONCLUSION

This paper presents a simple and general parallelization strategy for mesh refinement algorithms. The parallelization is typically medium grain, but allows to introduce features of coarse grain ones by preventing conflicts.

REFERENCES

- [1] C. D. Antonopoulos, X. Ding, A. Chernikov, F. Blagojevic, D. S. Nikolopoulos, and N. Chrisochoides, "Multigrain parallel Delaunay mesh generation: challenges and opportunities for multithreaded architectures," *Proceedings of the 19th International Conference on Supercomputing*, pp. 367–376, 2005.
- [2] A. C. Lisboa, "Delaunay refinement for curved complexes," Ph.D. dissertation, Universidade Federal de Minas Gerais, 2008.
- [3] A. N. Chernikov and N. P. Chrisochoides, "Parallel guaranteed quality delaunay uniform mesh refinement," *SIAM Journal on Scientific Computing*, vol. 28, pp. 1907–1926, 2006.
- [4] D. A. Spielman, S. hua Teng, and A. Ungor, "Parallel Delaunay refinement: algorithms and analyses," *Proceedings of the 11th International Meshing Roundtable*, 2002.

Magnetic Field Analyses of Architectural Components Using Homogeneous Technique

Shunya Odawara¹, Yu Haraguchi¹, Kazuhiro Muramatsu¹, Keita Yamazaki², and Shigetaka Hirotsato²

¹Dept. of Electrical and Electronic Engineering, Saga Univ., Saga, Saga 840-8502, Japan

²Research & Development Institute, Takenaka Corporation, Inzai, Chiba 270-1395, Japan
05236023@edu.cc.saga-u.ac.jp

Abstract — When the magnetic field analyses of architectural components, in which magnetic materials are distributed complicatedly, are carried out, huge efforts toward the modelling are required. In this paper, a homogeneous technique is applied to the magnetic field analysis of the architectural components in order to reduce the effort and computer costs. The suitable region, where the homogeneous technique is applied, is investigated in the analysis of magnetic disturbance of a building model. Moreover, the effectiveness is shown in the analysis of the shielding performance of an open-type magnetically shielded room for MRI. It is shown that the homogeneous technique should be applied to not only the magnetic materials with complicated structure but also the air region surrounding them.

I. INTRODUCTION

For example, when the magnetic disturbance due to buildings is calculated by the magnetic field analysis with the finite element method (FEM) [1, 2], huge efforts toward modelling complicatedly distributed magnetic materials in buildings are required. Moreover, the huge memory requirements and CPU time are also required due to large number of the finite elements. Recently, the homogeneous technique, in which the complicatedly distributed magnetic materials are replaced to the homogeneous body with the equivalent permeability, was proposed [3]. In this technique, the equivalent permeability is determined so that the energy of homogeneous body is equal to be that in the region of distributed magnetic materials.

In this paper, the technique is applied to the magnetic field analysis of architectural components, in which magnetic materials are distributed complicatedly. First, the suitable region, where the homogeneous technique is applied, is investigated in the calculation of the magnetic disturbance of a simple building model. Next, the technique is applied to the analysis of the shielding performance of an open-type magnetically shielded room (MSR) [4] with square cylinders made of magnetic materials for a magnetic resonance imaging (MRI) in order to investigate the effectiveness.

II. HOMOGENEOUS TECHNIQUE

The homogeneous technique [3] using a simple building model composed of only iron bars shown in Fig. 1 used in this paper is described. In the homogeneous technique, the iron bars distributed complicatedly in the building are replaced to the homogeneous body with equivalent permeability μ_h . The subscript h denotes the value for the homogeneous model. The equivalent permeability μ_h is determined by using the cell model which is a part of building as shown in Fig. 2. For example, the x -component μ_{hx} of μ_h is determined so that the energy of the homogeneous body is equal to be that of the cell model obtained by FEM as the following equation, in the case

the same average flux density B_x is applied in the x -direction for both models;

$$\sum_{ie=1}^{ne} \frac{B^{(ie)^2} \cdot V^{(ie)}}{2 \mu^{(ie)}} = \frac{B_x^2 \cdot V_h}{2 \mu_{hx}} \quad (1)$$

where left and right hand side correspond to energies of cell and homogeneous models, respectively. The superscript ie denotes the value for each element in cell model. ne and V are the number of elements and the volume, respectively.

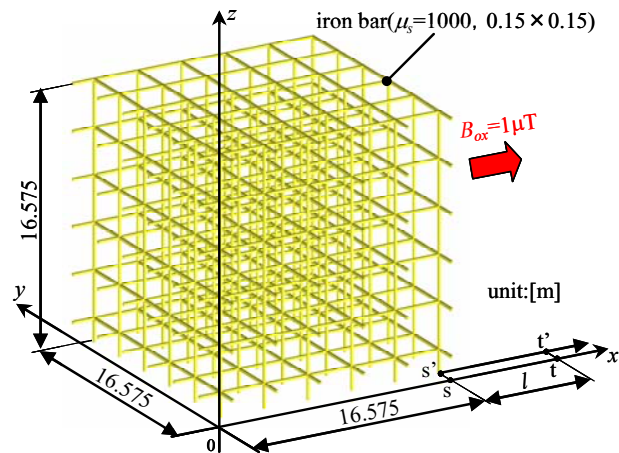


Fig. 1. A simple building model (1/8 region).

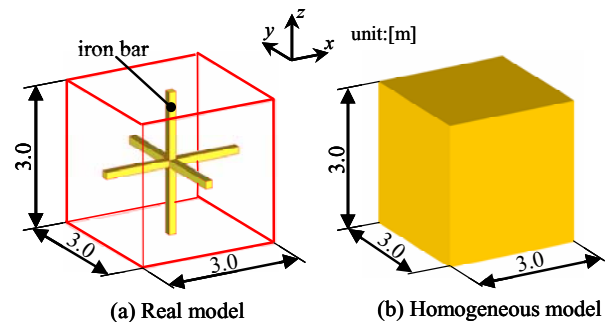


Fig. 2. Homogeneous technique.

III. ANALYSIS OF MAGNETIC DISTURBANCE DUE TO BUILDING

The magnetic disturbance due to the simple building model shown in Fig. 1, when the uniform flux density $B_{ox} = 1 \mu\text{T}$ is applied in the x -direction, is analyzed by the homogeneous techniques with the following treatments:

Method 1: One homogeneous model determined by the cell model shown in Fig. 2 (a) is applied to the whole region of buildings.

Method 2: The homogeneous model determined by the different cell model is applied on the side of building because the shape configuration of cell model shown in Fig. 2(a) is different from that on the side of the real model.

Method 3: The homogeneous model determined by the cell model adding that of Method 2 to the air region is applied on the side of building.

Fig. 3 shows the distributions of the magnetic disturbances ΔB_x ($\Delta B_x = B_{cx} - B_{ox}$, B_{cx} : the flux density obtained from calculation), obtained from the calculation using the real model and the several homogeneous techniques, on the line s-t which exists on the position between iron bars and the line s'-t' which exists at the position on the extension line of the iron bar, shown in Fig. 1. In the homogeneous techniques, the ΔB_x 's on the lines s-t and s'-t' are almost the same, whereas the ΔB_x on the line s'-t' becomes larger than that on the line s-t in the real model because the flux concentrates near the iron bar. The results obtained from the homogeneous techniques should be close to the average values of those on lines s-t and s'-t' in the real model. However, the results obtained from Methods 1 and 2 are close to that on the line s'-t' in the real model. This is because the flux distribution in the air region near the building becomes uniform and the increase of the energy due to the concentration of the flux density near the iron bar can not be taking into account in Methods 1 and 2. On the other hand, the result obtained from Method 3 becomes appropriate. As a conclusion, the homogeneous technique should be applied to not only the magnetic materials but also the air region surrounding them.

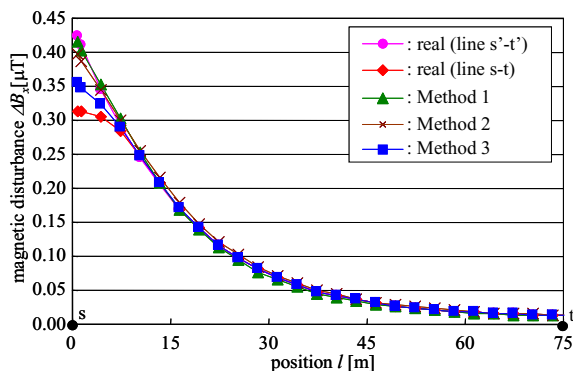


Fig. 3. Distributions of magnetic disturbance ΔB_x on lines s-t and s'-t'.

IV. ANALYSIS OF OPEN TYPE OF MSR FOR MRI

The homogeneous technique is also applied to the analysis of the shielding performance for an open-type MSR with the square cylinders made of magnetic material for MRI [4] shown in Fig. 4. The enlarged view of the square cylinder is shown in Fig. 5. The square cylinder is divided into two parts by the large slit in order to obtain the higher shielding performance.

Two homogeneous techniques are examined: one is that each magnetic cylinder is replaced to the homogeneous body (Method A). The other is that both magnetic cylinders including the slit are replaced to the homogeneous body (Method B).

Fig. 6 shows the distributions of the leakage flux densities on the line L shown in Fig. 4, obtained from the real model and the homogeneous techniques. The flux distribution

obtained from Method A is much different from that of the real model. This is because the increase of the energy due to the non-uniformity of the flux distribution in the slit can not be represented in Method A. The result obtained from Method B is in good agreement with that of the real model.

The homogeneous technique is effective for the magnetic field analyses of architectural components when the cell model including air region near the magnetic material is used.

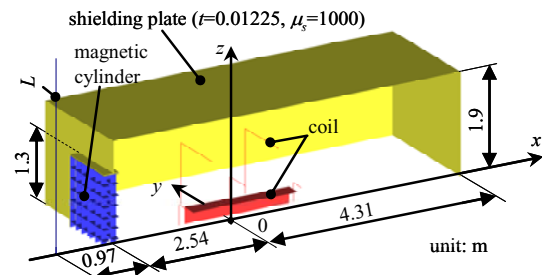


Fig. 4. Open-type MSR and MRI model (1/4 region).

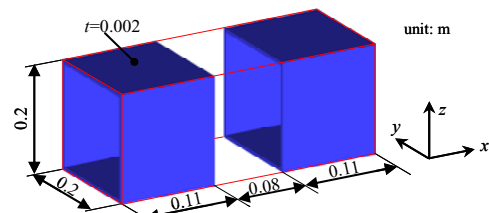


Fig. 5. Magnetic cylinders.

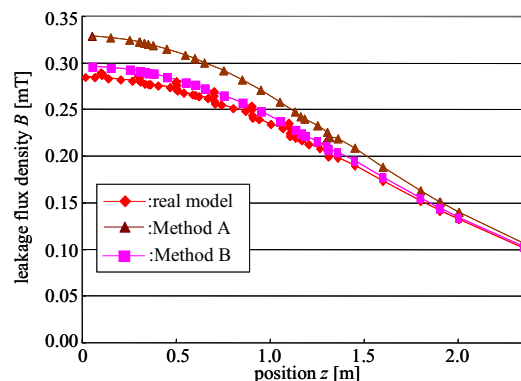


Fig. 6. Distribution of leakage flux density on line L.

V. REFERENCES

- [1] K. Yamazaki, K. Kato, K. Ono, H. Saegusa, K. Tokunaga, Y. Iida, S. Yamamoto, K. Ashiho, K. Fujiwara, and N. Takahashi, "Analysis of magnetic disturbance due to buildings," *IEEE Trans. on Magn.*, vol. 39, no. 5, pp. 3226–3228, Sep. 2003.
- [2] K. Yamazaki, K. Kato, K. Muramatsu, M. Uchida, K. Fujiwara, M. Miyamoto, H. Kaneko, and H. Saegusa, "A practical method for evaluating magnetic disturbance due to buildings for the design of a magnetic testing site," *ibid.*, vol. 41, no. 5, pp.1856-1859, 2005.
- [3] H. Waki, H. Igarashi, and T. Honma, "Analysis of magnetic shielding effect of layered shields based on homogenization," *ibid.*, vol. 42, no. 4, pp. 847-850, 2006.
- [4] K. Yamazaki, S.Hirosato, K. Kamata, K. Muramatsu, K. Kobayashi, and A. Haga, "Open-type magnetically shielded room combined with square cylinders made of magnetic and conductive materials for MRIs," *ibid.*, vol. 44, no. 11, pp.4183-4186, 2008.

Finite Element Method Coupled with Delaunay Refinement for Curved Geometries

Adriano C. Lisboa¹, Renato C. Mesquita¹, Rodney R. Saldanha¹, and Ricardo H. C. Takahashi²

¹Department of Electrical Engineering, Universidade Federal de Minas Gerais

²Department of Mathematics, Universidade Federal de Minas Gerais

Av. Antônio Carlos 6627, 31270-901, Brazil

adriano@cpdee.ufmg.br, renato@cpdee.ufmg.br

Abstract—An adaptive mesh for the finite element method is problem dependent and, hence, unlikely to be defined a priori in complex problems. The usual strategy to reach it is starting with a coarse mesh and then solving the problem to define where the mesh must be refined according to an error estimation. This process goes on iteratively until a given accuracy is met. Under this procedure, pre-discretization of curved parts of the geometry clearly seems to be inefficient. This paper highlights improvements and challenges when a finite element method is coupled with a Delaunay refinement algorithm for curved geometries.

I. INTRODUCTION

DELAUNAY refinement algorithms were first developed for meshing piecewise linear complexes [1], [2], [3], [4], and they were mainly motivated by the finite element method. They already enjoy good theoretical guarantees in quality, size and grading for arbitrary bidimensional piecewise linear complexes. Unfortunately, for higher dimensional inputs, they still lack meaningful theoretical guarantees, specially when considering small input dihedral angles. Fortunately, Delaunay refinement algorithms perform better in practice than in theory.

The Ruppert's Delaunay refinement algorithm has been extended [5], [6] to deal with curved bidimensional geometries. This extension carries out all theoretical guarantees of Ruppert's algorithm, except size optimality that must be further analyzed for curved geometries. Recently, Cheng et al. [7], [8] have proposed a new Delaunay refinement algorithm to cope with curved tridimensional geometries, based on a Delaunay criterion over manifolds [3], [9]. Despite its ability to mesh a large class of geometries, its queries on curved surfaces are very complex and time consuming. This paper is based on a simpler and faster, though less general, Delaunay refinement algorithm for curved geometries [10].

II. DELAUNAY REFINEMENT FOR CURVED COMPLEXES

The Delaunay refinement algorithm for curved complexes used in this paper [10] extends the fundamental ideas of Ruppert refinement and Bowyer-Watson incremental insertion algorithms. Every strongly Delaunay simplex is part of a Delaunay simplicial complex. Hence, pre-defined circumscribed balls of conforming simplices do not enclose any other vertex throughout the refinement. If any of them is encroached by

the insertion point, the insertion point is projected on the respective piece, just like as in Ruppert algorithm. The new simplices created by connecting the new vertex to the cavity boundary, just like as in Bowyer-Watson algorithm, will have empty circumscribed balls as long as the cavity simplices are all those encroached by the projected insertion point. However, for curved pieces, the empty circumscribed balls may not be the pre-defined ones, so that some vertices may have to be removed to ensure that. The creation of the initial mesh is also changed. Homeomorphic simplices are created from lower to higher dimensions. Lower dimensional simplices are guaranteed, by refinement until they become strongly Delaunay, to be part of connected higher dimensional meshes. In this process, an input constraint piece only defines its own parametric space. All boundary or constraint information comes from lower dimensional connected simplices.

III. FINITE ELEMENT METHOD ON CURVED GEOMETRIES

Throughout this section, the improvements and challenges of coupling finite element method and Delaunay refinement for curved geometries will be highlighted in a simple electromagnetic analysis of a micromotor [11], whose geometry is shown in Fig. 1.

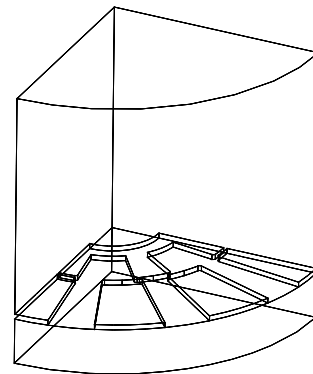


Fig. 1. Point and line constraints of the micromotor geometry.

The first and most notable improvement when using Delaunay refinement for curved geometries is the efficient use of coarse meshes, as the one shown in Fig. 2, and, naturally, fine meshes. An adaptive strategy could start with such a

This work was supported by FAPEMIG under grant 13180, Brazil.

coarse mesh and then refine it wherever needed, without recreating the mesh after re-discretizing curves and surfaces as an ordinary Delaunay refinement algorithm for piecewise linear complexes would do.

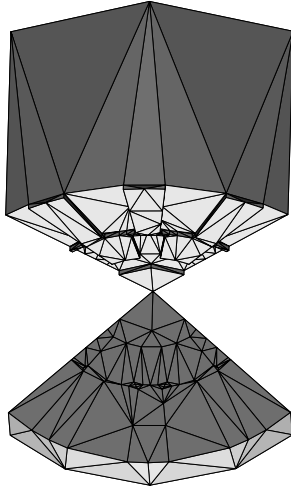


Fig. 2. Coarse mesh for the micromotor (dielectric board and air meshes are shown separately to ease visualization).

When the Delaunay refinement algorithm can handle curved geometries, it becomes clear what is mesh generation, and what is modeling, because no intermediate steps are needed to create linear approximations of curved pieces. For instance, the mesh generator itself truly refined the coarse mesh, shown in Fig. 2, into a finer mesh with better geometry representation, as shown in Fig. 3. During this refinement, new vertices were inserted into curves and surfaces as needed.

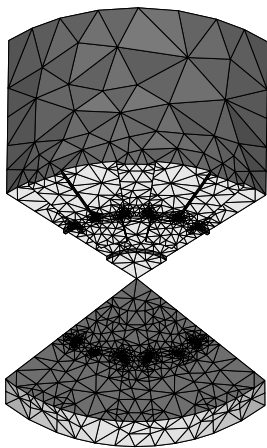


Fig. 3. Refinement of the coarse mesh for the micromotor (dielectric board and air meshes are shown separately to ease visualization).

The refinement timing difference, between the Delaunay refinement for curved geometries used in this paper and one for piecewise linear complexes, comes almost exclusively from the computation of the point on piece that is equidistant to the vertices of a conforming simplex. Whenever this computation is fast (e.g. pieces are spheres, cylinders), or vertices are rarely

inserted on curved pieces (e.g. uniform refinement), the timing difference is negligible.

Unfortunately, the Delaunay refinement for curved geometries used in this paper requires strongly Delaunay simplices conforming the input pieces, unique point on piece that is equidistant to the vertices of a conforming simplex, and that each curved piece is entirely contained in the circumscribed balls of its conforming simplices. These requirements must be satisfied throughout the refinement since the initial mesh. In order to meet them, either artificial features could be inserted into the input geometry, or more complex approaches [7], [8] could be used to generate the initial mesh. Both result in a higher computation cost and in a finer initial mesh.

Another challenging open problem in Delaunay refinement for tri or higher dimensional curved geometries, is the treatment of small input dihedral angles. Slivers can still be removed in practice with a refinement criterion on minimum (typically 15°) or maximum (typically 165°) dihedral angle, although without any theoretical guarantee.

More details about the tetrahedral mesh quality and grading, and refinement timing, will be given in the final paper, as well as electromagnetic solutions of the micromotor problem.

IV. CONCLUSION

The Delaunay refinement for curved geometries has shown to be very competitive when some requirements on the initial mesh are verified. However, it is still a great challenge to cope with small input dihedral angles and with arbitrarily complex curved geometries. Its application to finite element method seems to be rather promising, specially as a key feature in adaptive and efficient mesh generation.

REFERENCES

- [1] L. P. Chew, "Guaranteed quality triangular mesh," Cornell University, Tech. Rep., 1989.
- [2] J. Ruppert, "A Delaunay refinement algorithm for quality 2-dimensional mesh generation," NASA Ames Research Center, Tech. Rep., 1994.
- [3] L. P. Chew, "Guaranteed-quality mesh generation for curved surfaces," *Proceedings of the 9th Symposium on Computational Geometry ACM*, pp. 274–280, 1993.
- [4] J. R. Shewchuk, "Delaunay refinement mesh generation," Ph.D. dissertation, Carnegie Mellon University, 1997.
- [5] C. Boivin and C. Ollivier-Gooch, "Guaranteed-quality triangular mesh generation for domains with curved boundaries," *International Journal for Numerical Methods in Engineering*, vol. 55, no. 10, pp. 1185–1213, 2002.
- [6] S. Gosselin and C. Ollivier-Gooch, "Revisiting Delaunay refinement triangular mesh generation on curve-bounded domains," *Proceedings of the 14th Conference of the Computational Fluid Dynamics Society of Canada*, 2007.
- [7] S.-W. Cheng, T. K. Dey, and E. A. Ramos, "Delaunay refinement for piecewise smooth complexes," *Proceedings of the 18th Annual ACM-SIAM Symposium on Discrete Algorithms*, pp. 1096–1105, 2007.
- [8] S.-W. Cheng, T. K. Dey, and J. A. Levine, "A practical Delaunay meshing algorithm for a large class of domains," *Proceedings of the 16th International Meshing Roundtable*, 2007.
- [9] H. Edelsbrunner and N. R. Shah, "Triangulating topological spaces," *Proceedings of the 10th Annual Symposium on Computational Geometry*, pp. 285–292, 1994.
- [10] A. C. Lisboa, "Delaunay refinement for curved complexes," Ph.D. dissertation, Universidade Federal de Minas Gerais, 2008.
- [11] U. Beerschwinger, N. Milnes, J. Yang, R. Reuben, A. Sangster, and H. Ziad, "Coupled electrostatic and mechanical fea of a micromotor," *Journal of Microelectromechanical Systems*, vol. 3, no. 4, pp. 162–171, 1994.

Impact of Tetrahedral Mesh Quality for Electromagnetic and Thermal Simulations

Julien Dardenne*[†], Nicolas Siauve*, Sébastien Valette[†], Rémy Prost[†] and Noël Burais*

*University of Lyon, University Lyon 1, AMPERE, CNRS UMR 5005

[†]University of Lyon, INSA-Lyon, CREATIS-LRMN, CNRS UMR 5220, Inserm U630

julien.dardenne@creatis.insa-lyon.fr

Abstract—Finite element simulation can be directly affected by mesh quality. The accuracy of finite element calculations is dependent upon of the mesh quality. Previously, we have introduced a novel approach to the construction of high-quality, isotropic tetrahedral meshes from segmented medical imaging data. This article proposes an experimental evaluation of the impact of our tetrahedral meshes on electromagnetic and thermal simulations with finite elements.

I. INTRODUCTION

In this paper, we show the impact of the geometrical modelling on the numerical simulation of electromagnetic and thermic phenomena in the human body exposed to radiofrequency field. We present the electromagnetic [1] and thermal Finite Element Models (FEM). The time harmonic formulation is directly written in term of total electric field \mathbf{E} (1). It is obtained by applying the Galerkin method to the wave equation. Coupling to a first order Engquist-Majda Absorbing Boundary Conditions (ABC) taking into account the open boundary:

$$-\int_{\mathcal{V}} \nabla W \times \nabla \times \mathbf{E} \cdot d\mathbf{v} - \int_{\mathcal{V}} W k_0^2 \varepsilon_t^* \mathbf{E} \cdot d\mathbf{v} + \int_{\mathcal{V}} W g_{ABC}(\mathbf{E}) \cdot d\mathbf{s} = -j\omega\mu_0 \int_{\mathcal{T}} \mathbf{J}_e \cdot d\mathbf{v} \quad (1)$$

with $g_{ABC}(\mathbf{E}) = jk_0 \mathbf{E}_t$, where \mathbf{E}_t is the tangential field, k_0 is the propagation constant of the electromagnetic field, W the weight function, ε_t^* the tissue complex permittivity values and \mathbf{J}_e the electric current density. Space discretization is performed using incomplete first order edge elements.

Temperature calculation is based on the solution of the instationary Pennes bio-heat equation (2) with \mathbf{E} as source term.

$$\rho C \frac{\delta T}{\delta t} = \nabla \cdot (k \nabla T) - C_b \omega_b (T - T_a) + \frac{1}{2} \sigma |\mathbf{E}|^2 + Q_m \quad (2)$$

with ρ , the tissue density, C the specific heat of the tissue, k the thermal conductivity, ω_b the blood flow, C_b the specific heat of the blood, T_a the temperature of the arteries, σ the electrical conductivity and Q_m the amount of heat produced by metabolism. Thermal modelling is carried out with classic nodal FEM. We use conjugate gradient solver with various preconditioning techniques: diagonal, SSOR and Gauss.

II. TETRAHEDRAL MESHES GENERATION

A. State of the Art

There are basically three approaches for tetrahedral meshing: greedy approaches, Delaunay-based methods and hierar-

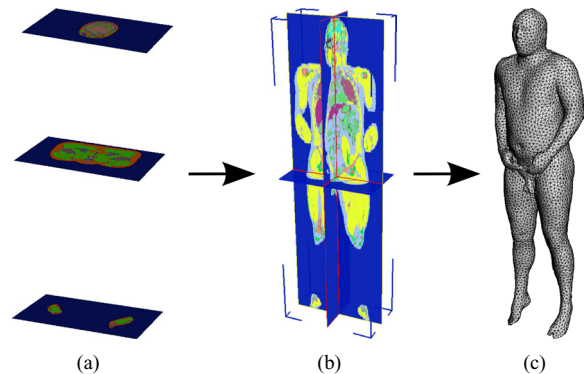


Fig. 1. Meshing process: the segmented "Visible Human" Male Dataset (a), tridimensional discrete set (b), tetrahedral meshing (c) of (b) with our approach.

chical decomposition approaches. The greedy approaches start from a boundary and move a front from the boundary towards the empty space within the domain. Delaunay approaches generate triangulations using Delaunay criteria. Unfortunately, in 3D and higher dimensions, the Delaunay property alone is insufficient to guarantee well-shaped elements. Finally, hierarchical decomposition approaches recursively subdivide the cube containing the geometric model until the desired resolution is reached. Elements that lie outside the meshing domain, and the elements inside the domain are split into tetrahedra. Most of the previously cited approaches share a common point: they take an input surface and enrich it with new vertices to generate the tetrahedra. This can be problematic around the objects boundaries, as the vertices of the input surface can be an important constraint for the resulting mesh, and induce tetrahedra with bad aspect ratio.

B. The Proposed Approach

We have proposed a novel tetrahedral mesh generation algorithm in [2]. Our algorithm directly processes voxels of segmented volumes coming from Tomographic Scanners or Magnetic Resonance Images (MRI) (Fig. 1). No polygonal input surface is needed. Our approach provides a robust mesh design tool for discrete data that can accommodate requirements on the final budget of vertices and on the mesh gradation, for arbitrary domain complexity.

C. Tetrahedra Quality Measure

In our case, the ideal isotropic tetrahedral element is the equilateral tetrahedron. An important parameter in this study

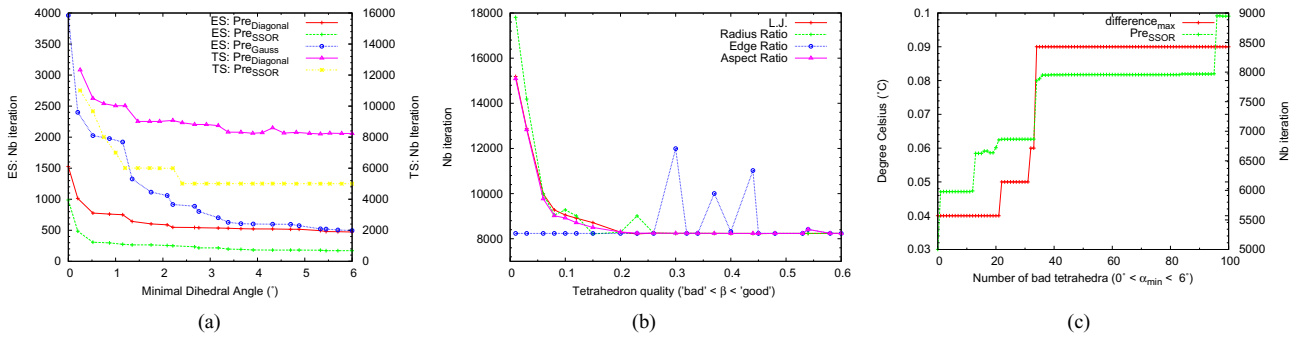


Fig. 2. Effect of the tetrahedral quality: (a) on the electromagnetic and thermal simulations, respectively ES and TS, for several preconditioning techniques; (b) on the thermal simulation for several quality criteria; (c) on the difference between the thermal problem simulation and the analytical solution.

is the choice of the quality criterion. Several quality measures are available in the literature. In this paper, we use five quality criteria : The first criterion is the Minimal Dihedral Angle (MDA) α_{min} of a tetrahedron, which has a maximal value of $\arccos(1/3) = 70,5^\circ$, for a regular tetrahedron. Table I tabulates several quality measures for tetrahedral elements quality evaluation.

Criteria	MDA	L.J.	Radius ratio	Edge ratio	Aspect ratio
Formula	α_{min}	$\frac{12\sqrt[3]{9V^2}}{\sum l_{i,j}^2}$	$3\frac{r_{in}}{r_{out}}$	$\frac{l_{min}}{l_{max}}$	$\frac{12}{\sqrt{6}}\frac{3V}{l_{max}\sum A_i}$

TABLE I
QUALITY MEASUREMENT FACTORS

In this Table I, l is the length of the edges, A the areas of the faces of a tetrahedron, r_{in} the radius of its inscribed sphere, r_{out} the radius of its circumscribed sphere and V its volume. The criterion L.J. is cited in [3]. The criteria are normalized between 0 and 1 (excepted MDA), where 0 denotes a bad element and 1 an equilateral tetrahedron.

III. EFFECT OF THE TETRAHEDRAL QUALITY

A. Theoretical Impact

The quality of geometric discretization is crucial for the effectiveness of these applications [4]. Coarse discretization and poor shape of the elements can introduce incorrect results and numerical errors. Degenerate elements with small volumes and small dihedral angles may lead to large local errors of the solution. Small dihedral angles can have a negative effect on the condition number of the stiffness matrix and large dihedral angles cause large interpolation errors. The worst impact results in an unsolvable system of equations.

B. Numerical Impact

The calculations are realized on a spherical geometry generated by our approach. The minimal dihedral angle is of 16.31° . Figure 2.a shows the impact of the addition of a single bad tetrahedron on the electromagnetic (incident wave at 433 MHz) and thermal (temporal model for convection transfer heat) simulations for several preconditioning techniques. Figure 2.b presents the impact of the addition of a bad tetrahedron on the thermal simulation for several quality criteria. Figure 2.c shows the difference between the thermal problem simulation and the analytical solution [5] when several bad elements are

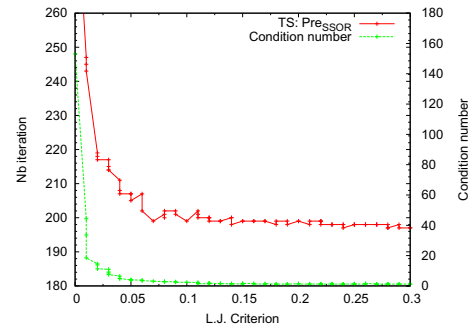


Fig. 3. Influence of the poor quality elements on the condition number for the thermal simulation.

added. The condition number for a positive definite matrix is defined by the ratio of the maximum eigenvalue to the minimum eigenvalue. Figure 3 shows the condition number and the number of iterations are highly correlated.

IV. DISCUSSION AND CONCLUSIONS

Certain geometrical quality measures are not adapted to evaluate the shape of an element. As an example, a bad-quality tetrahedron has a too great radius-edge ratio and a sliver has a good radius-edge ratio but nearly zero volume (slivers). The radius-edge ratio is not a proper measure for slivers. We have shown in a practical way the impact of the quality of tetrahedral meshes on electromagnetic and thermal finite element models. Our results clearly show that the FEM accuracy can be directly affected by mesh quality. Experimental findings suggest dramatic run time reductions using our high-quality mesher. According to this study, we chose the criteria based on the MDA and cited in [3] for the evaluation and the optimization of our mesh generation algorithm.

REFERENCES

- [1] N. Siauve, L. Nicolas, C. Vollaire, A. Nicolas and J.A. Vasconcelos, "Optimization of 3D SAR distribution in local hyperthermia", *IEEE Transactions on Magnetics*, 40(2):1264-1267, 2004.
- [2] J. Dardenne, S. Valette, N. Siauve, N. Burais and R. Prost, "Variational tetrahedral mesh generation from discrete volume data", *The Visual Computer*, in press, DOI: 10.1007/s00371-009-0323-7, 2009.
- [3] A. Liu and B. Joe, "On the shape of tetrahedra from bisection", *Math. of Computation*, 63(207):141-154, 1994.
- [4] J. R. Shewchuk, "What Is a Good Linear Element? Interpolation, Conditioning, and Quality Measures", *In Eleventh International Meshing Roundtable*, 115-126, 2002.
- [5] H. Dubbel, "Taschenbuch für den Maschinenbau", *Springer*, 1999.

Parallel Computing of Magnetic Field for Rotating Machines on PC Cluster

Tomohito Nakano¹, Yoshihiro Kawase¹ and Tadashi Yamaguchi¹

¹Department of Information Science, Gifu University, Gifu 501-1193, Japan E-mail: nakan@fem.info.gifu-u.ac.jp

Abstract—We have developed a parallel computation method of the magnetic field for rotating machines by using the 3-D FEM with edge elements, which can run on PC clusters. In the developed method, the block ICCG method is adopted as the linear solver. The performance of the developed method running on a PC cluster is quantitatively clarified.

I. INTRODUCTION

From the viewpoint of the fields of the industrial applications, the parallel computing of the magnetic field for practical rotating machines on a reasonable PC cluster is desired.

We have developed a parallel computing method of the three-dimensional finite element method (3-D FEM) with the edge elements for PC clusters in which the block ICCG method is adopted as the linear solver [1].

In this paper, we describe the outline of developed method and the performance of the developed method running on a PC cluster.

II. DOMAIN DECOMPOSITION METHOD

In the parallel computing, the domain decomposition method (DDM) is adopted. Using the DDM, the analyzed domain is divided into multiple subdomains, and the subdomains are calculated in parallel while doing appropriate data communications between those subdomains.

Fig. 1 illustrates the DDM for FEM with edge elements. This figure shows that one domain is divided in two subdomains.

The number of edges in each subdomain is almost the same to split the CPU power into subdomains evenly. The divided domain has the overlap elements. By using the overlap elements, the data communication between subdomains becomes unnecessary when the element coefficient matrix is created.

The overlap element has two kinds of edges, one is called ‘boundary edges’ and another is called ‘external edges’. In Fig. 1 (b), the boundary edges are drawn as the bold lines (edge 7 in *Subomain I*, and edges 8 and 9 in *Subdomain II*), and the external edges are drawn as the dotted lines (edges 8 and 9 in *Subdomain I*, and edge 7 in *Subdomain II*). The boundary edge in one subdomain is the external edge in another subdomain.

III. BLOCK ICCG METHOD

In the ICCG method, the calculation in the forward and backward substitutions occupies around 50% of the total computing time. Therefore, these calculations should be parallelized in order to compute efficiently.

The block ICCG method is one of the parallel processing techniques of the ICCG method [2]. Fig. 2 shows the coefficient matrix and vectors of Fig. 1 in the block ICCG method. The external edges in each subdomain are ignored in calculation of the IC decomposition in the block ICCG method to calculate the forward and backward substitutions in parallel.

Fig. 3 shows the algorithm of block ICCG method. The upper subscripts k is the iteration count, the lower subscripts n is the subdomain number, and N is the number of subdomains. The communications are required in the calculation of inner product in line (a) and in the matrix-vector product in line (b). Other calculations in the method can be independently carried out in each subdomain.

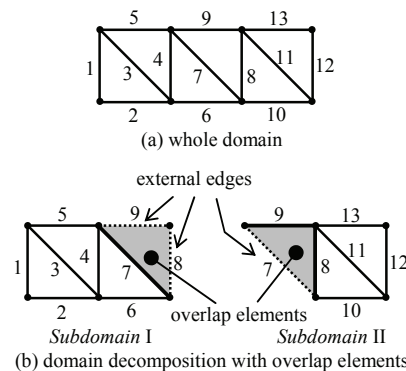


Fig. 1 Domain decomposition method for finite element method with edge elements.

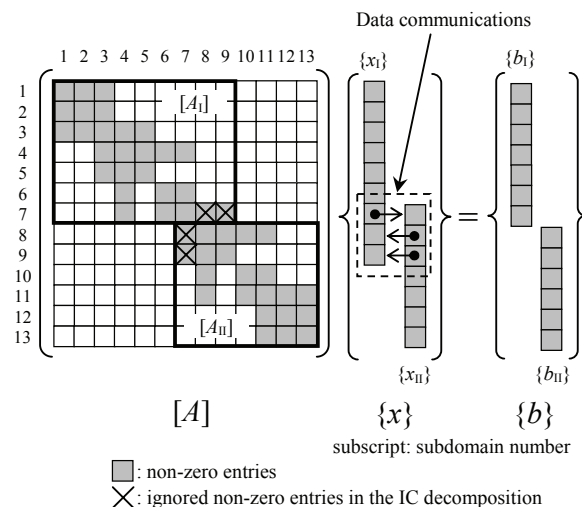


Fig. 2. Coefficient matrix and vectors in block ICCG method.

```

 $\mathbf{r}_n^{(0)} = \mathbf{b}_n - A_n \mathbf{x}_n^{(0)}$ 
for  $k = 1, 2, \dots$ 
  solve  $(L_n D_n L_n^T) \mathbf{z}_n^{(k-1)} = \mathbf{r}_n^{(k-1)}$ 
   $\rho^{(k-1)} = \sum_{n=1}^N (\mathbf{r}_n^{(k-1)}, \mathbf{z}_n^{(k-1)}) \leftarrow (a)$ 
  if  $k = 1$ 
     $\mathbf{p}_n^{(1)} = \mathbf{z}_n^{(0)}$ 
  else
     $\beta^{(k-1)} = \rho^{(k-1)} / \rho^{(k-2)}$ 
     $\mathbf{p}_n^{(k)} = \mathbf{z}_n^{(k-1)} + \beta^{(k-1)} \mathbf{p}_n^{(k-1)}$ 
  endif
   $\mathbf{q}_n^{(k)} = A_n \mathbf{p}_n^{(k)} \leftarrow (b)$ 
   $\alpha^{(k)} = \rho^{(k-1)} / \sum_{n=1}^N (\mathbf{p}_n^{(k)}, \mathbf{q}_n^{(k)}) \leftarrow (a)$ 
   $\mathbf{x}_n^{(k)} = \mathbf{x}_n^{(k-1)} + \alpha^{(k)} \mathbf{p}_n^{(k)}$ 
   $\mathbf{r}_n^{(k)} = \mathbf{r}_n^{(k-1)} - \alpha^{(k)} \mathbf{q}_n^{(k)}$ 
  check convergence
end

```

Fig. 3. Algorithm of block ICCG method

IV. NUMERICAL RESULTS AND DISCUSSION

A. Fundamental Equation of Magnetic Field

The fundamental equation of magnetic field is given by the magnetic vector potential \mathbf{A} as follows:

$$\text{rot}(\nu \text{rot} \mathbf{A}) = \nu_0 \text{rot} \mathbf{M} + \mathbf{J}_0 + \mathbf{J}_e \quad (1)$$

where ν is the reluctivity, ν_0 is the reluctivity of the vacuum, \mathbf{M} is the magnetization of permanent magnet, \mathbf{J}_0 is the exciting current density, \mathbf{J}_e is the eddy current density.

B. System configuration of PC cluster

The PC cluster used in this study is composed of 16 PCs that have an Intel Core 2 Duo processor (2.66GHz) and 4GB memory. Each PC is connected by the 1 gigabit local area network. Because the PC cluster system has the distributed memory, not only speed-up but also a very large-scale analysis can be performed.

C. Analyzed Model

Fig. 4 shows the analyzed model of a motor for Blu-ray disc drive. In order to understand the analyzed model easily, the motor case is shown in only 1/3 region. The number of the unknown variables of this model is 19,430,514.

In the full paper, other rotating machines are also studied.

D. Performance of Proposed Method

Fig. 5 shows the contour of flux density. The contour agrees completely with that calculated on a single PC.

Table I shows the performance evaluation of the developed method. The performance of a single PC, which has the Intel Xeon processor (3.0GHz) and 16 GB memory, is also shown in order to evaluate the influence of the number of CPU on the iterations of CG. The elapsed time is evaluated in

one time step. This calculation requires about 144 hours on a single PC. However, using the PC cluster, the calculation has been done in about 9 hours. The increase of CG iterations is due to the ignored non-zero entries in the block ICCG. It is expected that the convergence of CG becomes worse as the number of CPU becomes large. The convergence of Newton-Raphson method doesn't depend on the number of CPU.

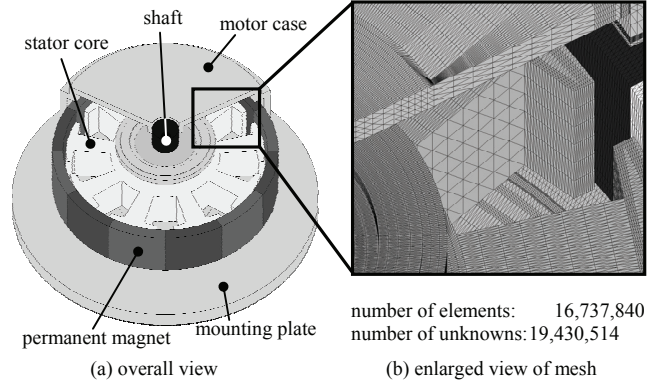


Fig. 4. Analyzed model

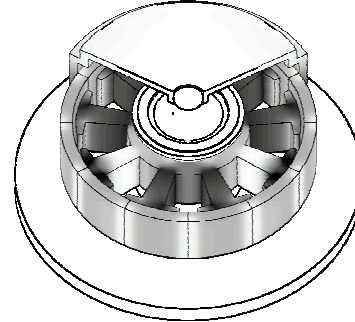


Fig. 5. Contour of flux density

TABLE I
PERFORMANCE EVALUATION OF THE DEVELOPED METHOD

number of CPU	elapsed time (hours)	iterations of CG	iterations of Newton-Raphson
1 ^{*1}	144.1	111,279	21
16 ^{*2}	8.8	144,114	21

^{*1}Computer used Intel Xeon (3.00GHz) PC.

^{*2}Computer used Intel Core2 Duo (2.66GHz) PC.

V. CONCLUSION

We have developed a parallel computation method of the magnetic field for rotating machines by using the 3-D FEM with edge elements, which can run on PC clusters. The very large-scale analysis can be performed by the PC cluster that has a distributed memory.

In the full paper, other practical rotating machines are also computed on the PC cluster system.

VI. REFERENCES

- [1] T. Nakano, Y. Kawase, T. Yamaguchi and S. Ukai, "Fundamental study of parallel computation for rotation machines", The Papers of Technical Meeting on Static Apparatus and Rotating Machinery, IEE Japan, SA-09-27/RM-09-27, 2009 (in Japanese).
- [2] K. Nakajima and H. Okuda, "Parallel iterative solvers with Localized ILU Preconditioning for Unstructured Grids on Workstation Cluster", International Journal for Computational Fluid Dynamics, vol.12: pp.315-322, 1999.

Mesh Refinement in Eddy Current Testing with Separated T-R probes

Y. Choua, Y. Le Bihan, L. Santandréa and C. Marchand

Laboratoire de Génie Électrique de Paris

CNRS UMR8507; SUPELEC; UPMC Univ Paris 06; Univ Paris-Sud 11

11 rue Joliot-Curie, Plateau de Moulon, F-91192 Gif-sur-Yvette Cedex

choua@lgep.supelec.fr

Abstract—A local error estimator used for *a posteriori* h-type finite element mesh refinement is presented in eddy current testing with separated T-R probes. The proposed technique combines the solutions obtained by feeding alternatively the source and the measurer. The obtained results are compared to the Ligurian approach.

I. INTRODUCTION

EDDY current testing (ECT) is widely used to check the integrity of conducting parts. The finite element method (FEM) is well fitted to the modelling of this kind of problems due to its large flexibility which allows to deal with complex probe and part configurations. However it requires much attention to get a reliable result. In most case, the signal variations in ECT due to a flaw are very low. In this context, the quality of the mesh for a finite element simulation is crucial. Creating a such mesh is delicate and requires expertise from the user. In particular, a user of a finite element software must pay attention to have a sufficient number of elements in the skin depth of the part, in the vicinity of the probe and of the flaw, etc. . . . To obtain accurate result, a slolution is to use a mesh adaptation. In [1] the authors proposed an adaptive mesh refinement procedure in ECT with double fonction probe: a single coil that is used to induce the eddy currents and sense changes in the test material. This procedure does not require deep expertise from the user about the mesh construction. Furthermore, only the required regions are refined to improve the results in an automatic way.

In this paper we are interesting in mesh adaptation in ECT problems with separated T-R probes (Transmitter and Receiver probes). The last ones are constituted at least from two coils, one (Transmitter :T-coil) is used to generate the source field and the other (Receiver: R-coil) is used to sense changes in the test material. The application of a mesh refinement procedure using a “standard” approach like the Ligurian [1] [2] for example, leads to refine the mesh around the T-coil whereas the refinement mesh in the vicinity of the R-coil is ignored. Consequently, inaccuracies in the response calculation of the probe can be induced. In this context, an error estimator for T-R separated probes is developed and compared to the Ligurian approach.

II. DESCRIPTION OF THE PROBLEM

Fig. 1 shows an ECT arrangement. It includes a probe constituted of two coils and a conducting material Ω_c in which exists a flaw.

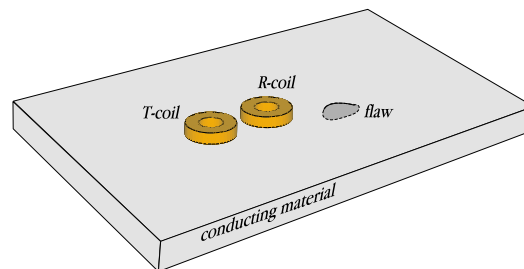


Fig. 1. ECT configuration

The ECT problem can be solved by FEM using either a magnetic formulation in terms of the combined vector-scalar potentials $\mathbf{t} - \phi$ where, \mathbf{t} is the electric vector potential and ϕ is the magnetic scalar potential, or an electric formulation in terms of $\mathbf{a} - \psi$ where \mathbf{a} and ψ are the magnetic vector potential and a time primitive of the electric scalar potential, respectively [3].

Considering a sinusoidal excitation, the transimpedance Z_{21} of the probe is calculated from Φ_{21} the flux in the R-coil due to I_1 the T-coil current and is obtained as:

$$Z_{21} = j\omega \frac{\Phi_{21}}{I_1} \quad (1)$$

where $j = \sqrt{-1}$ and ω denotes the pulsation.

A. Error estimators

Two error estimators are studied in this part. Both are based on the minimization of the error in the respect of the magnetic constitutive law which describes the relationship between \mathbf{B} and \mathbf{H} , where \mathbf{B} and \mathbf{H} are determined by the $\mathbf{a} - \psi$ and $\mathbf{t} - \phi$ formulations, respectively. Indeed, the magnetic formulation strongly verifies the Ampere law whereas the electric formulation strongly verifies the Faraday law. It follows that the errors appear in the way of a nonrespect of the constitutive laws. A two criteria for error estimation in harmonic linear case are presented in the following.

1) *1st approach*: This error estimator is called Ligurian. It corresponds to a magnetic energy characterizing the difference between the two formulation results [4]. For an element k of the mesh, the magnetic Ligurian estimator is given by the following equation:

$$\lambda_k(\mathbf{H}, \mathbf{B}) = \int_{\Omega_k} \frac{1}{2\mu_k} \|\mu_k \mathbf{H} - \mathbf{B}\|^2 d\Omega_k \quad (2)$$

where \mathbf{B} is the complex magnetic induction field obtained by the electric formulation $\mathbf{a} - \psi$ and \mathbf{H} the complex magnetic field obtained by the magnetic formulation $\mathbf{t} - \phi$.

Experiences have shown that the application of the mesh adaptation procedure using the Ligurian as error estimator leads to refine the mesh around the T-coil and in the skin depth of the conducting material whereas the mesh in the vicinity of the R-coil is not refined. This can introduces inaccuracy in the calculation of probe transimpedance (equation 1). To overcome this effect, an error estimator is developed in what follow.

2) *2nd approach*: The idea is based on the Lorentz-reciprocity relation in the calculation of the separated T-R probe response [5]. It involves the product of fields obtained by feeding alternatively the T-R coils. When the R-coil is fed and T-coil is turned off, two admissible solutions \mathbf{B}_R and \mathbf{H}_R are obtained by using the two dual formulations $\mathbf{a} - \psi$ and $\mathbf{t} - \phi$ respectively. Vice-versa, when the T-coil is fed and the R-coil is turned off, we get two admissible solutions \mathbf{B}_T and \mathbf{H}_T by the two formulations. Let's define an error estimator such as:

$$\lambda_k^{TR} = \sqrt{\lambda_k(\mathbf{H}_T, \mathbf{B}_T) \lambda_k(\mathbf{H}_R, \mathbf{B}_R)} \quad (3)$$

The criterion (3) allows to locate simultaneously the errors in the mesh around the T-R coils which can lead to have a good accuracy on the response of the probe.

III. NUMERICAL EXAMPLE

It consists in two identical circular air-cored coil (inner radius of 6.15 mm, outer radius of 12.4 mm, lift-off of 0.88 mm, thickness of 6.15 mm and 3790 turns) which are placed on an unflawed aluminum alloy plate (12.22 mm thick) with a conductivity of 30.6 MS/m. The frequency is of 900 Hz. Fig. 2 presents the initial mesh for the considered configuration. The distance between the two coils is of 24.8 mm.

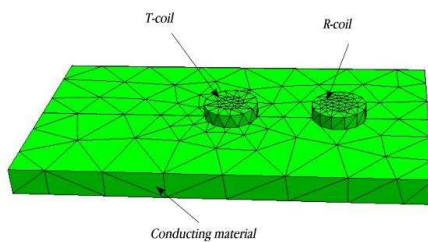


Fig. 2. Initial mesh

An iterative procedure of mesh refinement is applied using the two error estimators described above.

Fig. 3 shows the imaginary and real parts of the transimpedance of the probe versus the iterations number.

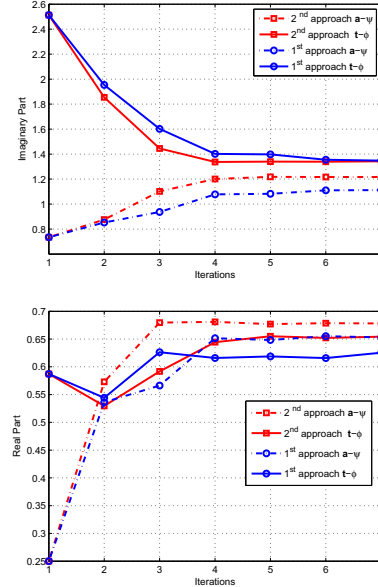


Fig. 3. Imaginary and real parts of the probe transimpedance

IV. CONCLUSION

It can be observed that the results obtained by using the second approach are effectively better than those obtained by the Ligurian approach : the results converge quickly to each others for the second approach than the first one. More details will be presented in the final paper (about accuracy, computation time and the response of the probe in presence of a thin crack [6] ...).

REFERENCES

- [1] M. Bensetti, Y. Choua, L. Santandrea, Y. Le Bihan and C. Marchand, "Adaptive mesh refinement and probe signal calculation in eddy current NDT by complementary formulations", *IEEE Trans. on Magn.*, vol. 44, no. 6, pp. 1646–1649, 2008.
- [2] J. Rikabi, C. F. Bryant and E. M. Freeman, "An error-based approach to complementary formulations of static field solutions", *Int. J. Numer. Meth. Eng.*, vol. 26, pp. 1963–1987, 1988.
- [3] Z. Ren et A. Razek, "Computation of 3-D electromagnetic field using differential forms based elements and dual formulations", *Int. J. Numer. Model.*, vol. 9, pp. 81–98, 1996
- [4] C. Li, Z. Ren and A. Razek, "An approach to adaptive mesh refinement for three-dimensional eddy-current computations", *IEEE Trans. on Magn.*, Vol. 30, no 1, pp. 113–117 1994.
- [5] B. A. Auld and J. C. Moulder, "Review of advances in quantitative eddy current nondestructive evaluation", *Journal of Nondestructive evaluation*, Vol. 18, no 1, pp. 3–36 1999.
- [6] Y. Choua, L. Santandrea, Y. Le Bihan et C. Marchand, "Thin Crack Modeling in ECT with Combined Potential Formulations", *IEEE Trans. on Magn.*, vol. 43, no. 4, pp. 1789–1792, 2007.

Demagnetized Permanent-Magnet Fault Recognition in Synchronous Motors

Bashir Mahdi Ebrahimi and Jawad Faiz

University of Tehran

Faculty of Engineering, Campus #2, University of Tehran, Kargar Shomali, Tehran, Iran, P.O. Box 14395-515

ebrahimibm@ut.ac.ir

Abstract — In this paper, a novel approach is demonstrated to detect demagnetization of permanent-magnet in synchronous motors. For this, an efficient criterion is introduced based on processing of developed torque using time series data mining method. This criterion function can be utilized to diagnose demagnetization fault occurrence and determine its percentage precisely. Meanwhile, impacts of load variation on the proposed criterion are investigated. Then the ability of the proposed criterion for the demagnetization fault detection and estimation of its severity is evaluated. For this, the relation between the nominated criterion and demagnetization percentage is computed by mutual information criterion. So, the percentage of the demagnetization is predicted using a support vector machine (SVM) as the classifier. The classification results illustrate that the proposed criterion can recognize fault percentage accurately. Finally, a white Gaussian noise is added to the simulated torque and robustness of the proposed criterion is analyzed with respect to the noise variance. Since, the accuracy of the calculated torque from modeled motor, has considerable impacts on precise fault recognition, time stepping finite element method (TSFEM) is used to model the healthy and faulty PMSM.

I. INTRODUCTION

Protection and maintenance of permanent magnet synchronous motors (PMSMs) as efficient motors in different industries are necessary. Faults in PMSMs are classified into three parts: magnetic, electrical and mechanical faults. Due to having access to the stator of the motor, detection of electrical fault in faulty PM is much easier in magnetic or mechanical faults [1]-[2]. Albeit lots of researches have been published to investigate impacts of demagnetization in PMSMs [3], there are a few documents which introduce an approach to detect this fault precisely [2]. A comprehensive fault recognition approach includes punctual modeling of faulty motor, selection of an appropriate signal for processing and a proper index. Proposed approach in this paper is illustrated in Fig. 1.

II. MODELING OF FAULTY PMSM USING FINITE ELEMENT

According to Fig. 1, exact model of faulty PMSM is the first stage of any reliable fault recognition algorithm. Therefore, in developed model practical conditions of the faulty motor should be considered. Modeling methods which are based on the magnetic field computation and regard different aspects of the machine can be selected as an efficacious manner to evaluate required signals and parameters for processing and feature extraction. In this paper, healthy and faulty PMSM under demagnetization is modeled using TSFEM. In this modeling, geometrical complexities of all parts of the motor including stator, rotor and shaft are included. Moreover, spatial distribution of the stator windings,

non-uniform air-gap, physical conditions of the stator conductors, rotor, shaft and air-gap, and non-linearity of the core materials are taken into account. Three-phase sinusoidal voltage applied to the terminals of the motor is the input. The transient equations of the external circuit and circuit elements are combined with the magnetic field equations. In addition, the motion equations are combined with the magnetic field equations in the FEM in which the motion equations are combined with these equations. Solving the set of equations gives the stator phase currents, magnetic flux density distribution, torque and speed as required variables for analyzing, processing and feature extraction (see Fig. 1). Fig. 2 depicts the magnetic flux density distribution of the healthy and faulty motor under partial demagnetization of a PM. It depicts that the demagnetization distorts magnetic flux density wave forms. Distortion of magnetic flux density makes asymmetrical the torque profile. Fig. 3 demonstrates developed torque of the healthy and faulty motor. Fig. 3, represents that demagnetization causes torque ripples to increase. Since the variation rate of the faulty motor torque is considerable, time series data mining method (TSDM) is utilized for torque signal processing and feature extracting for demagnetization fault diagnosis.

III. TIME SERIES DATA MINING METHOD

TSDM attitude is employed to elicit efficacious criterion functions from the torque signal produced by the TSFEM. Based soundly in dynamical systems theory, the TSDM method reveals hidden patterns in time series data [4]. In this paper, time series data is time domain torque profile. A process called time-delay embedding is used to transform the torque profile into reconstructed state spaces, also called phase-spaces. Nominated the torque time series, $T_{em} = \{T(k), k=1, \dots, M\}$, where k is a time index, M is the number of observations, a two dimensional (2-D) phase-space is generated by plotting $T(k-10)$ on the x - y plane's abscissa and $T(k)$ on the ordinate. Then, $\Delta T = T(k) - T(k-1)$ which is calculated by applying the time delay embedding process to the time series of the torque profile. Fig. 4 presents the phase-space of the torque first difference time series for the healthy and faulty motor.

IV. INTRODUCING A NOVEL CRITERION FUNCTION FOR DEMAGNETIZATION FAULT DIAGNOSIS

Radius of geration around the center of mass [5] of the points in the phase-space mass is proposed as an efficient criterion for demagnetization fault detection. It should be noted that

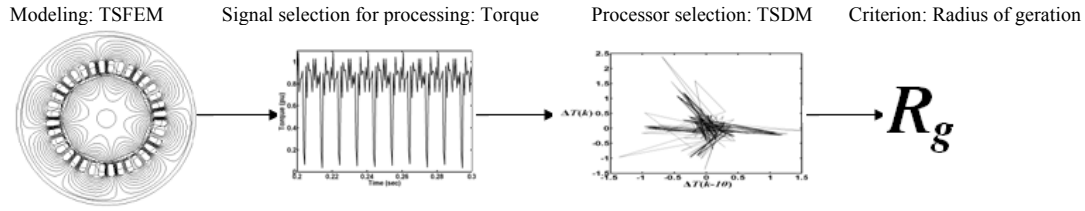


Fig. 1. Algorithm for static eccentricity fault diagnosis in a PMSM

each point in the phase-space is given a unit mass. The radius of gyration R_g is computed as follows [4]:

$$R_g = \sqrt{\frac{\sum_{k=1+l}^M d(k)^2}{M-l}} \quad (1)$$

Where l is the time lag of the phase space, M is the number of observations and the distance $d(k)$ between the center of mass and the k^{th} point in the phase space is as follows:

$$d(k)^2 = (x(k) - \mu_0)^2 + (x(k-l) - \mu_l)^2 \quad (2)$$

where μ_0 and μ_l , the centers of mass for their respective dimensions, are as follows:

$$\mu_n = \frac{\sum_{k=1+l}^{M-l+n} x(k)}{M-l} \quad (3)$$

Where $x(k)$ is the time series observations at time index k . It is noticeable that $d(k)$ is the distance of the k^{th} phase-space "point" from the center of mass of the phase-space "points". Table I. shows the evaluated R_g for different partial and full demagnetization of one PM in the motor. Referring to Table I exposes that demagnetization occurrence causes to rise the R_g which can be utilized as a proper criterion for precise demagnetization fault diagnosis.

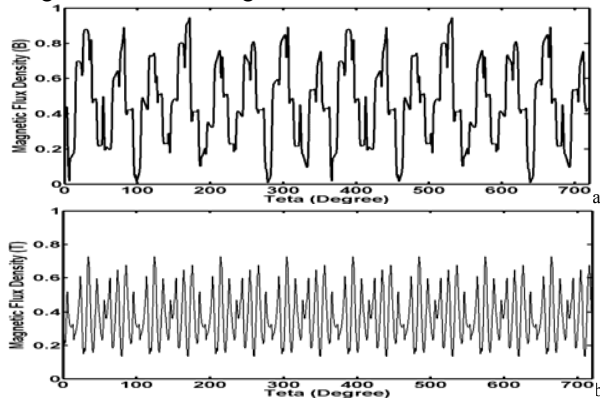


Fig. 2. Magnetic flux density distribution in PMSM air gap, (a) healthy and (b) with 25% demagnetization of one PM

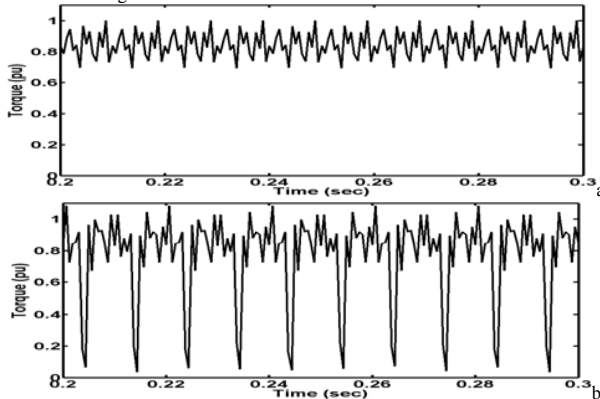


Fig. 3. Time variation of the developed torque (a) healthy and (b) faulty motor with 25% demagnetization of one PM

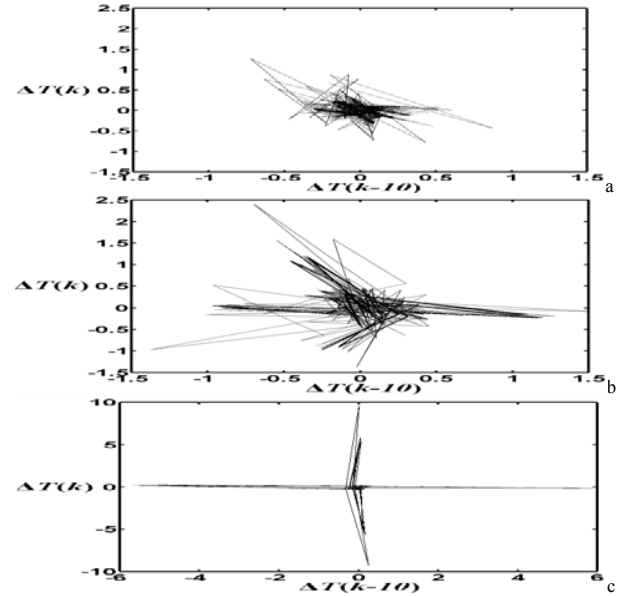


Fig. 4. Torque first difference phase-space, (a) Healthy, (b) 25% demagnetized and (c) full demagnetized

Meanwhile, it illustrates that develops of the demagnetization increases the R_g which can be employed to determine the percentage of the demagnetization. Estimation of the demagnetization percentage is so important to predict motor performance and fixing necessity.

TABLE I.
RADIUS OF GERATION FOR DIFFERENT PERCENTAGE OF DEMAGNETIZATION

Operating Mode	Radius of Geration
Healthy	0.25
25% Demagnetization	0.61
50% Demagnetization	0.86
75% Demagnetization	1.24
100% Demagnetization	2.82

V. REFERENCES

1. B. M. Ebrahimi, J. Faiz, M. J. Roshtkhari and A. Z. Nejhad, "Static Eccentricity Fault Diagnosis in Permanent Magnet Synchronous Motor using Time Stepping Finite Element Method", *IEEE Transaction on Magnetics*, Vol. 44(11), Dec, 2008, pp. 4297-4300.
2. W. L. Roux, R. G. Harley and T. G. Habetler, "Detection rotor faults in low power permanent magnet synchronous machines", *IEEE Trans on Power Electronics*, Vol. 22(1), Jan, 2007, pp. 322-328.
3. J. H. Lee and J. P. Hong, "Permanent Magnet Demagnetization Characteristic Analysis of a Variable Flux Memory Motor Using Coupled Preisach Modeling and FEM", *IEEE Transactions on Magnetics*, Vol. 44(6), June 2008, pp. 1550 - 1553.
4. J. F. Bangura, R. J. Povinelli, N. A. O. Demerdash, R. H. Brown, "Diagnostics of eccentricities and bar/end-ring connector breakages in poly phase induction motors through a combination of time series data mining and time-stepping coupled FE-state-space techniques Industry Applications", *IEEE Transactions on Industry Applications*, Vol. 39(4), July-Aug.2003, pp. 1005 - 1013
5. P. A. Tipler, physics, 2nd ed. New York: Worth, 1982, Vol. 1.

Induction motor analysis using optimal torque predictor and massive conductor approach

Sławomir Stepień

Poznan University of Technology
 Chair of Computer Engineering
 Piotrowo 3a, 60-965 Poznan, Poland
 Slawomir.Stepien@put.poznan.pl

Abstract — This research presents a method for the simulation of the magneto – mechanical system dynamics taking motion and eddy currents into account. The major contribution of this work leans on the coupling the field – motion problem considering windings as current forced massive conductors, rotor motion with two conductive materials and the torque calculated by the modified Maxwell stress tensor method and predicted by special stochastic algorithm. 3D model of the device is analyzed by time stepping finite element method. Mechanical motion of the rotor is determined by solving second order motion equation. Both magnetic and mechanical equations are coupled in iterative solving process. Presented method is verified by solving TEAM Workshop Problem 30.

I. INTRODUCTION

The improvement of numerical methods in the numerical analysis of electromechanical systems deals with development of the modeling techniques. In case of the analysis of field – motion coupled problems, beside field or motion mathematical description and numerical implementation, also coupling effects should be precisely determined [3-6,8]. That is why researchers pay special attention to obtain the best force or torque numerical approach and construct most optimal predictors. This is the necessary condition to construct useful model for analysis devices such as electromagnetic actuators, AC motors, permanent magnet DC or BLDC drives, etc [2,4,8].

This paper presents a consistent numerical method to analyze the AC induction motor described in TEAM Workshop Problem 30 [1], i.e., time – stepping finite – element analysis of the magnetic field considering motor windings as massive conductors and time – stepping model of the mechanical motion considering modified Maxwell stress tensor method combined with optimal torque predictor [9].

II. THE MODEL

The model of the problem is described by magnetic vector potential \mathbf{A} and electric scalar potential V [7]. The problem is defined in three regions: Ω_c^i - conducting region of immovable conductor, Ω_c^m - conducting region of movable conductor and Ω_n - non-conducting region. The alternating current flows by the massive conductor generates magnetic field rotation in region Ω_n and eddy current in movable conductor Ω_c^m .

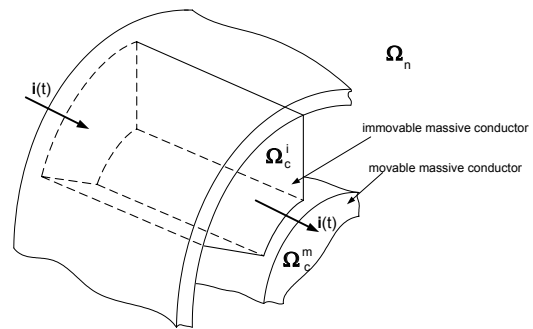


Fig. 1. Model of induction motor part

The total current $i(t)$ is connected to the boundary surfaces of immovable massive conductor. The boundary value problem will be described widely in full paper.

The magnetic torque is calculated using modified Maxwell stress tensor method. The global torque is determined from surface stresses combination caused by electromagnetic field. In case of the presented problem, the electromagnetic torque is calculated by the relationship:

$$T \approx r \times \sum_k P_{12,k} \Delta S_{2,k}, \quad (1)$$

and is evaluated along a surface placed in the airgap between rotor and immovable massive conductor.

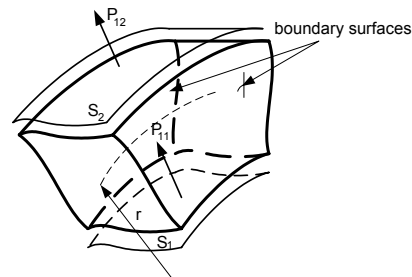


Fig. 2. Illustration of the torque calculation

Fig. 2 shows stress tensors P and radius r used to determine global torque. As a new contribution, the obtained torque value in each time step of the calculation is combined with optimal predictor [9]:

$$\hat{T}(t + \Delta t) = -\alpha_1 c \hat{T}(t) + \alpha_2 (c + 1) T(t) + \alpha_3 \Delta t \frac{dT(t)}{dt}. \quad (2)$$

where T is a torque value obtained from Maxwell stress tensor, \hat{T} is a prediction of T . The term $\frac{dT(t)}{dt}$ is obtained from spline cubic approximation of $T(t)$. The predictor (2) minimizes value of the expectation $E[T(t) - \hat{T}(t)]^2$. A new predicted value $\hat{T}(t + \Delta t)$ is used to solve numerically the mechanical motion equation

$$J \frac{d\omega}{dt} = \hat{T} \quad (3)$$

where ω is an angular velocity and J is a inertia of the rotor. In the full article will be presented wide description of adopted prediction technique.

III. NUMERICAL EXPERIMENT

To demonstrate the effectiveness of the method, a single phase induction motor is tested. The motor geometry and its excitation is detailed in description of the TEAM Problem 30 [1]. There is examined 3D problem in which the eddy currents in the rotor composed of two different materials are induced by time harmonic current on the massive windings and rotation of the rotor.

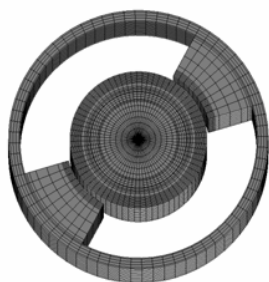


Fig. 3. The mesh of analyzed motor

The massive conductors are excited current 2045,175 A at 60 Hz. The rotor is made from aluminum and steel, so for the experiment purpose, assumed following specific gravity values: 2700 kgm^{-3} and 7800 kgm^{-3} . The presented model has been tested with initial torque $\hat{T}(0) = 10^{-5} \text{ Nm}$, considering dynamic characteristics: speed and torque-speed relationship.

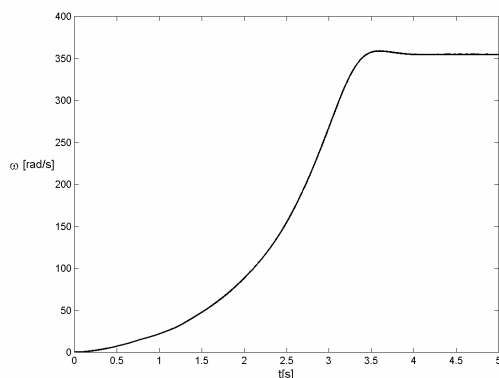


Fig. 4. Speed profile of the rotor

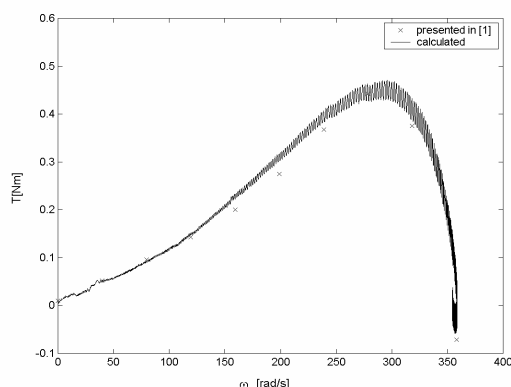


Fig. 5. Torque – speed relationship of AC motor

Fig. 4 shows the computed angular speed profile. In steady state the speed is about 360 rad/s, in accordance to the field rotating speed.

Fig. 5 shows the torque - speed mechanical characteristic. Obtained curve during computations in comparison with [1] shows good agreement and usefulness of presented model.

IV. CONCLUSION

A method of analysis of the AC motors including the massive conductors approach and optimal torque predictor is presented. This method, thanks to adopted predictor technique, allows an exact analysis of electrical machines dynamics. Also the windings can be successfully represented as massive conductors with known prescribed currents for the very low frequency analysis. The comparison of simulated results and results given in description [1] shows a good agreement.

V. REFERENCES

- [1] K. Davey, "Induction Motor Analysis, International TEAM Workshop Problem 30", available at www.compumag.co.uk.
- [2] A. Demenko, D. Stachowiak, "Orthogonal transformation of moving grid model into fixed grid model in the finite element analysis of induction machines", *COMPEL*, 23(4): 1015-1022, 2004.
- [3] H. De Gersem and K. Hameyer, "Finite element simulation of a magnetic brake with a soft magnetic solid iron rotor", *COMPEL*, 21(2): 296-306, 2002.
- [4] G. Jang, J. Chang, D. Hong and K. Kim, "Finite element analysis of an electromechanical field of a BLDC motor considering speed control and mechanical flexibility", *IEEE Trans. Mag.*, 38(2), pp. 945-948, 2002.
- [5] D. H. Kim, D.A. Lowther and J.K. Sykulski, "Efficient Force Calculations Based on Continuum Sensitivity Analysis", *IEEE Trans. on Mag.*, 41(5), pp. 1404-1407, 2005.
- [6] P. Kuo-Peng, J. Roel O., N.Sadowski, N.J. Batistela, J.P.A.Bastos, "Coupling static converter with control loop and non-linear electromagnetic devices", *IEEE Trans. on Mag.*, 37(5), pp. 3514-3517, 2001.
- [7] A. Patecki, G. Szymański and S. Stepień, "Power losses analysis in the windings of electromagnetic gear", *COMPEL*, 23(3), pp. 748-757, 2004.
- [8] A. de Oliveira, R. Antunes, P. Kuo-Peng, N. Sadowski and P. Dular, "Electrical machine analysis considering field – circuit – movement and skewing effects", *COMPEL*, 23(4), pp. 1080-1091, 2004.
- [9] P. Stoica, A. Nehorai, "On the uniqueness of prediction error models for systems with noisy input – output data", *Automatica*, 23, pp. 541-543, 1987.

FD-TD Calculations of SAR Validated Through Measurements

Ana de Oliveira Rodrigues, Juliano Junio Viana,
Alisson Henrique Quemel de Souza, Eduardo Aparecido dos Santos

Abstract—This paper presents the validation of Copacabana v1.0, a Java based software that calculates Specific Absorption Rate (SAR) using the Finite-Difference Time-Domain method (FD-TD). Measurements were performed at the Laboratório de Absorção e Dosimetria (LAD) of the Centro de Pesquisa e Desenvolvimento em Telecomunicações (CPqD) using a DASY4 system. The half-wavelength dipole was validated by comparing the field of this dipole with measurements and analytical solutions. SAR calculation was validated using a three-dimensional model described in international standards [3]. It is concluded that the software Copacabana v1.0 was validated for SAR calculations with maximum error of 14%.

keywords — SAR, FD-TD, measurements

I. INTRODUCTION

The Specific Absorption Rate (SAR) must be measured to evaluate the thermal effect of high frequency electromagnetic fields in the human body. SAR indicates the energy or power absorbed by one mass unity, usually expressed in Watts per kilogram of biological tissue (W/kg), and is proportional to the peak value of the electric field $|E_0|$ irradiated by the source, and tissue density (ρ [Kg/m³]) and conductivity (σ [S/m]). SAR calculated using Eq.(1) [3]. SAR is usually an indication of the temperature rise in the tissue induced by the electromagnetic field.

$$SAR = \frac{\sigma |E_0|^2}{2\rho} [W/kg] \quad (1)$$

Simulation software is necessary to calculate the SAR that will be obtained by equipment under development to guarantee that "spatial peak SAR values (should not exceed) 1.6 W/kg, as averaged over any 1 g of tissue (defined as a tissue volume in the shape of a cube)"[2]. Direct measurements allow certification of equipment developed. This work presents a software, Copacabana v.1.0, developed to calculate SAR in three-dimensional (3D) models, using the Finite-Difference Time-Domain (FD-TD) Method, and validation of the software through direct measurements.

II. METHODS

A. FD-TD Calculations

Copacabana v1.0. is a Java based software that implements the Finite-Difference Time-Domain Method (FD-TD) [7] in 3D with Mur boundary conditions [5]. These boundary conditions present expected error of 10%. The software calculates peak value of electric field, peak SAR, SAR for 1g and SAR for 10g in each point of the domain.

Dr. Ana de Oliveira Rodrigues is a professor at Centro Universitário de Belo Horizonte UNI-BH. ana.rodrigues@acad.unibh.br.

Juliano Junio Viana is a software developer at Logic Style Serviços de Informática. juliano@logicstyle.com.

Alisson Henrique Quemel de Souza is a graduate student of Telecommunication Engineering at Centro Universitário de Belo Horizonte UNI-BH.

Eduardo Aparecido dos Santos is an electronics Technician at Centro de Pesquisa e Desenvolvimento em Telecomunicações (CPqD). t_826361@cpqd.com.br.

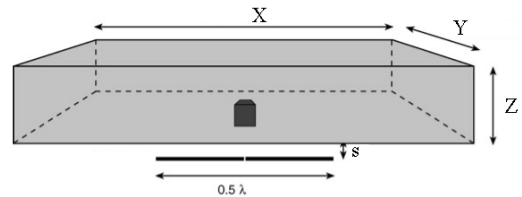


Fig. 1. "Flat Phantom" (adapted from [3]).

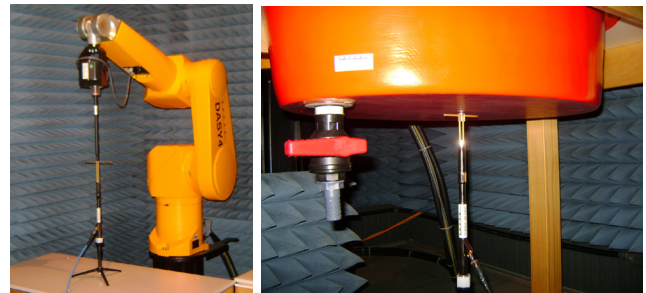


Fig. 2. Measurements: Dipole in Air and Flat Phantom

The model developed, shown in Fig.1, was a "flat phantom" [3] for 1.8GHz. The model is composed of 119, 122 and 89 cubes with 2mm side in x, y and z directions (total of 1,292,102 cubes). Simulation was run for 1,000 time steps of 2ps. The model tissues are: air around the phantom ($\epsilon_R = 1, \sigma = 0$); a 2mm plastic shell ($\epsilon_R = 3.7, \sigma = 0$); and the internal liquid ($\epsilon_R = 40, \sigma = 1.40$).

The source was modeled as a half wavelength dipole, with a radiated power (P_r) of 1W.

B. Measurements

All measurements were performed in the Laboratório de Absorção e Dosimetria (LAD) do Centro de Pesquisa e Desenvolvimento em Telecomunicações (CPqD). Fig2 shows the dipole in air and the "flat phantom", filled with a liquid with $\epsilon_R = 38, 11$ and $\sigma = 1, 43$. Expected error of measurements is 25%.

III. RESULTS

A. Dipole in Air

The electromagnetic field irradiated by a half wavelength dipole in air were obtained through analytical solution [1], measurements, and FD-TD simulations using Copacabana v.1.0. The RMS value of the electric field ($|E|$) in air were calculated and measured for a 2D plane of 12cm using a 2mm grid. Fig.3 shows the results.

As the analytical solution is provided for the far field, it can be observed that its values are not compatible with the measurements and simulation in the near field points (0,02m to 0,08m). Measurements show a better agreement to the results of the simulation in these points than the analytical solution.

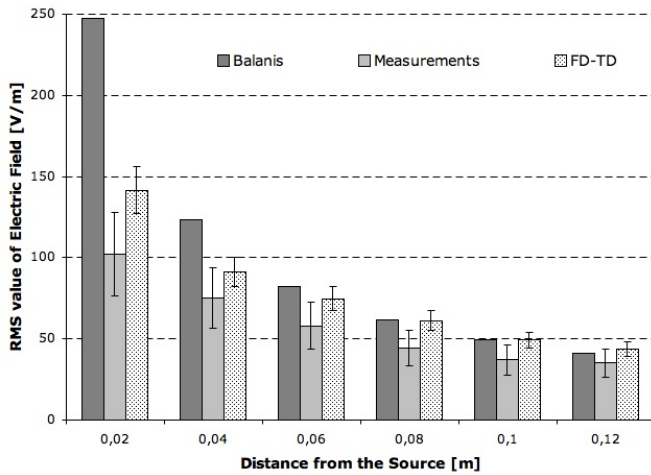


Fig. 3. Results of electric field calculated with analytical solution from Balanis [1], measurements and calculated with FD-TD. Vertical bars show simulation (10%) and measurement (25%) expected errors.

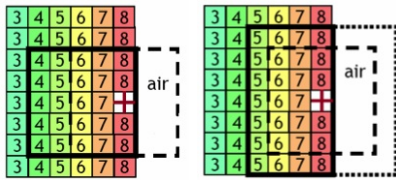


Fig. 4. Left: Average SAR calculation using [4]. Right: Average SAR calculation using [6]. Figure adapted from [6]

TABLE I
FD-TD CALCULATIONS OF SAR

Method	Peak SAR [W/kg]	SAR 1g [W/kg]	SAR 10g [W/kg]
Standard [3]	69.5	38.1	19.8
FD-TD [4] (error)	50.8 (27%)	32.8 (14%)	17.0 (13%)
FD-TD [6] (error)	50.8 (27%)	33.0 (14%)	17.8 (8%)

B. SAR

1) *FD-TD Calculation*: SAR averaged in 1g and 10g were calculated using Copacabana v.1.0 in the "flat phantom" described. Two different methods were used, presented in Fig.4. In [4], the 1g averaged cube is centered in the material and contains the peak SAR value. In [6], the peak SAR value is considered in the centre of the cube, and air cubes are not considered. Results are shown in Table I. These results are compared to those presented in international standards [3].

The percentual error in Peak SAR is relatively high (27%). However, this value is directly dependent of the cell size used in the simulations. A smaller grid will necessarily result in a higher peak SAR value. SAR averaged in 1g and 10g, on the other hand, are similar for [3] and both methods, with a maximum error of 14% for [4] and [6]. The method described in [4] requires that either all cubes are calculated, which is a large burden computationally, or that the user indicates the point where the cube must be calculated. The method described in [6], on the other hand, presents the advantage of being model independent, because it does not require the knowledge of where the peak SAR occurs. The calculation can be performed using ever increasing cube sizes until the 1g or 10g SAR is achieved. This algorithm can be automatic and does not require user intervention.

2) *Measurements*: Peak SAR, SAR 1g and SAR 10g were measured inside the phantom shown in Fig.2. Measurements were performed in a cube with sides of 3cm, divided in a 2mm x 2mm x 6mm

TABLE II
MEASUREMENTS OF SAR

SAR 16dBm [W/kg]			SAR 1W [W/kg]		
Máx	1g	10g	Máx	1g	10g
1.68	1.50	0.787	41.33	36.91	19.37

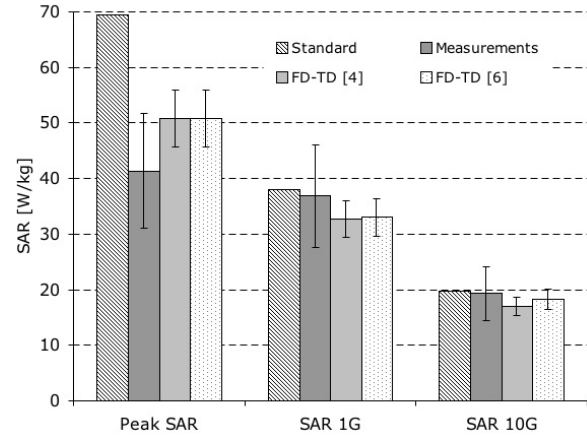


Fig. 5. SAR results from international standard [3], measurements and FD-TD calculations using [4] and [6]. Vertical bars show simulation (10%) and measurement (25%) expected errors.

grid. Table II presents SAR measurements for the maximum power irradiated of 16.09dBm (40.64mW), then normalized to 1W.

IV. CONCLUSIONS

This work presented the comparison of SAR calculated by Copacabana v.1.0 Java based software with measurements. The electric field of a dipole in air was calculated was compared to measurements and analytical solution, presenting a good agreement. Fig.5 resumes the results obtained for peak SAR, SAR 1g and SAR 10g in the international standard [3], measurements and FD-TD simulations. Peak SAR shows an error of 27%, a significant difference that is due to differences in cell size. SAR 1g and SAR 10g, that do not depend on cell size, present error of 14%. It is concluded that the Copacabana v.1.0 software was validated for SAR calculations using FD-TD, with a maximum error of 14%.

REFERENCES

- [1] C. A. Balanis. *Antenna Theory - analysis and design*. Wiley Interscience, 2005.
- [2] ANSI/IEEE C95.1-1992. *American National Standard-Safety Levels with Respect to Exposure to Radio Frequency Electromagnetic Fields, 3 kHz to 300 GHz*. New York: IEEE, 1992.
- [3] IEEE. *IEEE STD 1528 Recommended Practice for Determining the Peak Spatial-Average Specific Absorption Rate (SAR) in the Human Head from Wireless Communications Devices: Measurement Techniques*. Institute of Electrical and Electronics Engineers, Inc., 2003.
- [4] IEEE. *IEEE C95.3 Recommended Practice for Measurements and Computations of Radio Frequency Electromagnetic Fields With Respect to Human Exposure to Such Fields, 100 kHz-300 GHz*. Institute of Electrical and Electronics Engineers, Inc., 2006.
- [5] G. Mur. Absorbing boundary conditions for the finite-difference approximation of the time-domain electromagnetic-field equations. *IEEE Transactions on Electromagnetic Compatibility*, 23(4):377-382, 1981.
- [6] Nan QI, Min ZHANG, Tilmann WITTIG, and Alexander PROKOP. Application of cst time domain algorithm in the electromagnetic simulation standard of the sar for mobile phone. *Microwave and Millimeter Wave Technology, 2008. ICMMT 2008. International Conference on*, 4:1717 - 1720, 2008.
- [7] A. Taflov. *Computational Electrodynamics - The Finite-Difference Time-Domain Method*. Artech House, Norwood, MA., 2000.

Finite Element Method Model Improvement for the Conducted Emission Analysis of a Lighting Fixture

Yoshihiko Namba^{#1}, Tomoyuki Kida^{#2}, Katsuhiro Hirata^{#1}, Shohei Ikejiri^{#1}, Fuminao Obayashi^{#1}

^{#1} Graduate School of Engineering, Osaka University, 2-1 Yamadaoka, Suita-shi, Osaka 565-0871, Japan

¹yoshihiko.namba@ams.eng.osaka-u.ac.jp, ¹k-hirata@ams.eng.osaka-u.ac.jp, ¹shohei.ikejiri@ams.eng.osaka-u.ac.jp, ¹fuminao.obayashi@ams.eng.osaka-u.ac.jp

^{#2} Panasonic Electric Works Analysis Center Co., Ltd., 1048, Kadoma, Kadoma-shi, Osaka 571-8686, Japan

²kida.tomoyuki@panasonic-denko.co.jp

Abstract — This paper describes a technique for the multi-scale numerical modelling of conducted emissions for the inverter lighting fixture placed in a large space of a shielded room. The analysis employs the 3-D finite element method. It is experimentally understood that conducted emissions are mainly generated by the common mode current, therefore the displacement current is also taken into consideration in the model. That is, precise FEM model is employed only for the region displacement current influences. The validity of the computation was confirmed by a comparison with measured results of a lighting fixture.

I. INTRODUCTION

Electromagnetic waves caused by electric and electronic equipment are a serious problem because of interference to other equipment. Conducted emission, superimposed onto the power line, flow into other equipment and cause malfunctions. For this reason, electric and electronic devices are required to reduce conducted emissions. It is experimentally understood that conducted emissions are mainly generated by the common mode current.

On lighting fixtures, a driving method for the inverters commonly used in such fixtures comparatively generates more noise than conventional lighting methods. Therefore the establishment of simulation technology to predict the noise is required during the design of such lighting fixtures. The authors have been studying an analysis technique [1], however, the common mode current has not been considered precisely because of the CPU time.

In this paper, some parts, those thought to be influenced by the common mode current, are modeled in detail and other parts are modeled roughly to get highly accurate analyzed results within reasonable CPU time. The 3-D finite element method is employed for the numerical modelling of conducted emissions from the inverter in the frequency range from 10 to 30 MHz. The validity of this numerical model is confirmed by comparing with the measured results.

II. ANALYSIS METHOD

In this analysis, 3-D finite element method [2] is employed. By considering displacement current, the fundamental

equations of the electromagnetic field in frequency domain can be expressed as follows.

$$\text{rot}(\nu \text{rot} \mathbf{A}) = \mathbf{J}_0 + \mathbf{J}_e + j\omega \mathbf{D} \quad (1)$$

$$\mathbf{J}_e = -\sigma(j\omega \mathbf{A} + \text{grad} \phi) \quad (2)$$

where, ν is reluctivity, \mathbf{A} is vector potential, \mathbf{J}_0 is forced current density, \mathbf{J}_e is eddy current density, \mathbf{D} is dielectric flux density, σ is conductivity, ν , \mathbf{A} , \mathbf{J}_0 , \mathbf{J}_e and \mathbf{D} are complex numbers. In this analysis, the displacement current $j\omega \mathbf{D}$ in equation (1) is taken into consideration, whereas eddy current density \mathbf{J}_e is not calculated since the displacement current is more dominant than the eddy current around this frequency. ω is the angular frequency.

III. BASIC ANALYZED MODEL

The calculation model of analyzed region is shown in Fig. 1. The LISN (Line Impedance Stabilization Network) is placed on the Ground reference plane and all the 6 faces of the shielded room are supposed to be perfect conductor as ground. The number of elements of this model is 690,609 and that of unknown variables is 645,577.

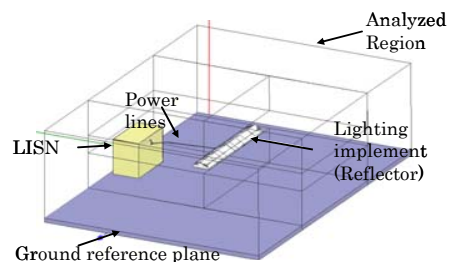


Fig. 1 Position of the implement model in the whole analyzed region

IV. EXPERIMENTAL VERIFICATION METHOD

A method of verifying analyzed results is to compare with the measured conducted emission from the lighting implement. The measurements are conducted in the shielded room. The lighting implement is set on a mounting table whose height is 0.4 m and the power line of 0.8m is wired straight towards the

LISN as shown in Fig.2. The LISN ESH2-Z5 manufactured by Rohde & Schwarz, whose operating frequency is from 9kHz to 30MHz, is set on the ground reference plane and conducted emission, common mode voltage, are measured with a spectrum analyzer 8542E produced by Hewlett-Packard, whose operating frequency is from 9 kHz to 29 GHz.

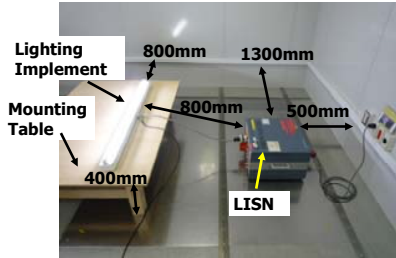


Fig. 2 Conducted emission measurement in the shielded room

V. IMPROVEMENT OF FEM MODEL

Powerline, that is thought to be influenced by the common mode current, is modeled in detail to calculate displacement current. Basic model of the power line is shown in Fig. 3. Precise model is shown in Fig. 4.

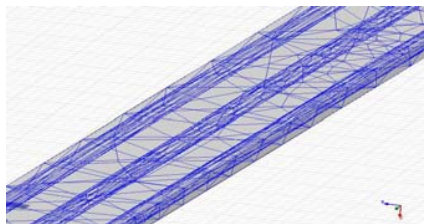


Fig. 3 Basic model of the power line

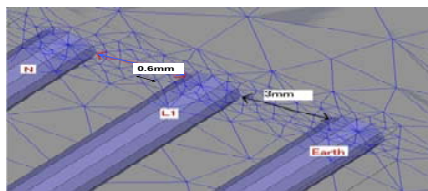


Fig. 4 Precise model of the power line

VI. ANALYZED RESULTS AND DISCUSSION

Fig. 5 shows the comparison of analyzed and measured conducted emission noise. Analyzed results of precise model of the power line better agree with the measured results than those of the basic model. Displacement current distribution around the power line is shown in Fig. 6. These figures indicate that the accuracy of the analysis is improved with the detailed mesh of the area thought to be influenced by the common mode current. The calculation error of about 5 to 10dB is observed. One of the reasons is considered that the mesh size between lamp line inside the lighting implement and the implement itself is not adequate to calculate the displacement current. The number of elements of these

models, unknown variables and CPU time are shown in Table. I.

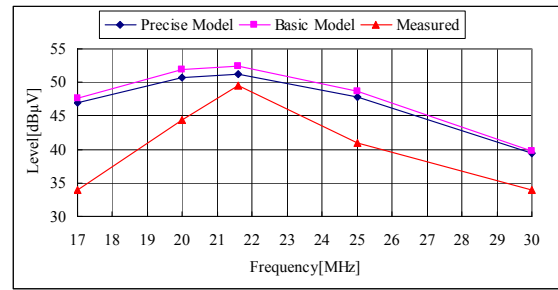


Fig. 5 Comparison of analyzed and measured results when the power line modeling is improved

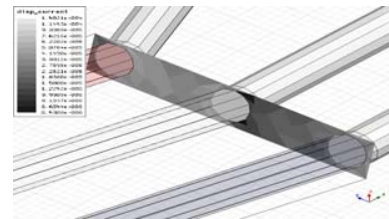


Fig. 6 Displacement current distribution around the power line

TABLE I DISCRETIZATION DATA AND CPU TIME

	Basic Model	Precise Model
Number of elements	229,795	2,807,128
Unknown variable	288,338	3,147,214
CPU Time	43min	10h14min

VII. CONCLUSION

This paper described the technique of multi-scale numerical modelling of conducted emission for the inverter lighting implement placed in a large space of a shielded room employing the 3-D finite element method. The validity of the analysis was clarified through the measurement. The following conclusions were obtained.

- 1) The common mode current flows mainly on power line.
- 2) The power line should be modeled with the proper element size to be able to calculate displacement current.

Consequently, the calculated results using this model were in better agreement with the measurement than those of the previous model in the frequency range from 10 to 30 MHz, thereby showing the validity of the model.

VIII. REFERENCES

[1] Y. Namba, T. Kida, Y. Mitsutake and K. Hirata, "Conducted Emission Analysis of A Lighting Implement Employing the 3-D Finite Element Method," COMPEL, vol.27, No.4, pp.855-860, 2008

[2] K. Hirata, Y. Mitsutake and Y. Tamai, "Dynamic Performance Analysis of Rapid-Start Ballast using 3-D Finite Element Method", Trans. IEE of Japan, vol. 122-D, no. 3, pp.241-246, March 2002

Reduced Thermal Model for Stator Slot

L. Idoughi¹, X. Mininger¹, F. Bouillault¹ and E. Hoang²

¹LGEp (CNRS(UMR 8507) ; SUPELEC ; Univ Paris-Sud ; UPMC Paris 6),
Plateau de Moulon, 11 rue Joliot-Curie ; F-91192 Gif sur Yvette Cedex ; France
name@lgep.supelec.fr

²SATIE, ENS Cachan, CNRS UMR 8029, UniverSud, 61 av President Wilson, F-94230 Cachan Cedex, France

Abstract—This paper presents a method to get a reduced thermal model simplifying the calculation of different temperatures in an electrical machine winding. The equivalent thermal conductivity is deduced from a homogenization of the winding, and a discretization is achieved using the Finite Integration Technique. The model is then reduced, and the corresponding results are compared with finite element simulations.

I. INTRODUCTION

A current tendency in electrical engineering is the use of electrical actuators in rough conditions, particularly in high temperature. For such applications, precise thermal models integrating thermal material (electric insulates and magnetic materials) properties are necessary to describe the system behavior. Thus, one of the main points in the thermal study of electrical machines concerns their winding, where the temperature rises to the maximum. However, the use of numerical tools like finite element methods to estimate the hot spot in the slot can lead to excessive simulation time, due to the heterogeneous structure and the presence of electrical conductors with small geometric dimensions compared to the machine ones. In this paper, a reduced thermal model is proposed to determine different temperatures (maximal, average...) in the slot. The first step corresponds to an thermal homogenisation of a simple geometry slot. Next, the Finite Integration Technique (FIT) is used to establish the reduced thermal model.

II. EQUIVALENT THERMAL CONDUCTIVITY OF THE SLOT

In this study, we consider a slot, made up of only two materials. The first one corresponds to the copper conductors (thermal conductivity λ_1), randomly distributed, and placed in a second material, that can be air or resin (thermal conductivity λ_2). Considering an isotropic distribution of 2D cylindrical conductors, [1] have shown that an estimation of the effective conductivity can be obtained with the estimation of Hashin and Shtrikman. The equivalent thermal conductivity λ_{eq} is expressed:

$$\lambda_{eq} = \lambda_2 \cdot \frac{(1 + \tau)\lambda_1 + (1 - \tau)\lambda_2}{(1 - \tau)\lambda_1 + (1 + \tau)\lambda_2} \quad (1)$$

with τ the occupancy rate of the conductors in the slot. Fig. 1 presents the corresponding results, considering either resin or air in the slot.

The increase of the equivalent thermal conductivity with the occupancy rate is important with the resin, because of its high thermal conductivity comparing to the air one. In the next parts, an occupancy rate of 55% is considered, with resin around the copper ($\lambda_{eq} = 0.87$).

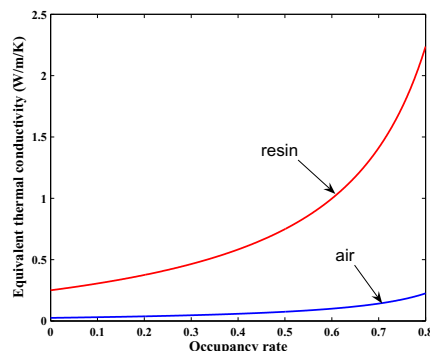


Fig. 1. Equivalent thermal conductivity as a function of the occupancy rate

III. REDUCED THERMAL MODEL OF THE SLOT

A usual solution to get simple thermal models of electrical machines is the nodal approach, considering the elementary volume as isotherm at the temperature of the associated node. The thermal models often consider only one node in the slot, giving one temperature of the winding [2]. The main difficulty of this problem is the determination of the conductance between the two nodes, which depends on geometrical dimensions and thermal material properties, with the choice of the length and surface that have to be considered to get a correct representation of the thermal flux distribution. Fig. 2 shows a static finite element simulation corresponding to the thermal problem (2, with φ the thermal flux, P the heat losses), where Dirichlet boundary condition ($T = 0$) is imposed on the upper side of the structure, and Neumann boundary condition on the other sides.

$$\begin{cases} \text{div}(\vec{\varphi}) = P \\ \vec{\varphi} = -\lambda \cdot \overrightarrow{\text{grad}}T \end{cases} \quad (2)$$

Due to the high iron conductivity, the corresponding part of the machine is quite isotherm, and can therefore be right represented with only one node. On the other hand, the temperature gradient is important in the slot, where the maximum temperature is reached. Thus, the model has to be more detailed in this area.

To treat this problem, we use the FIT method, which is well adapted to highlight the concept of thermal resistances of the different parts of the slot. The FIT method transforms the thermal equations in their integral form into a set of matrix equations on dual grids pair [3]:

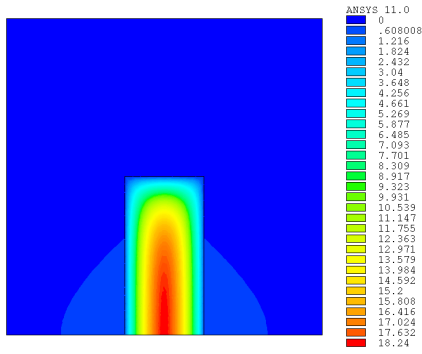


Fig. 2. Temperature distribution, FE method

$$C\Phi = P \text{ and } H = C^T T \quad (3)$$

where C is the discrete divergence matrix and $-C^T$ the gradient one. Φ is the thermal flux vector through the facets of the dual mesh, H the thermal grid voltage and T the temperature at the nodes of the primary mesh. To complete the system, we add a behavior law ($H = M\Phi$). In the case of orthogonal grids, the M matrix is diagonal and m_{ii} is equal to:

$$m_{ii} = \frac{1}{S_L} \int_{L_i} \frac{1}{\lambda} \vec{\tau} \cdot d\vec{\gamma} \quad (4)$$

where λ is the local thermal conductivity, S_i the surface of facet i , L_i the length of edge i , $\vec{\tau}$ the unit tangent vector along the edge i . From (3) and the behavior law, the system becomes:

$$[C][M]^{-1}[C^T][T] = [G][T] = [P] \quad (5)$$

If the domain relative to the thermal fluxes is the slot, the unknown temperatures near the boundary are linked to those in the iron, supposed to be at the same temperature T_f .

If we suppose that Joule losses P_0 are uniform in the slot, P can be expressed as $[P] = P_0[D]$ with $D_i = S_i/S$, S being the total surface of the slot.

Equation 5 can be written

$$[T_s] = -T_f[G_s]^{-1}[G_f] + P_0[G_s]^{-1}[D] \quad (6)$$

Due to the property of matrix $[G]$, $[G_s]^{-1}[G_f]$ is a vector $[I]$ with all elements equal to 1, and the system becomes:

$$[T_s] = -[I]T_f + P_0[R] \quad (7)$$

R is the column vector giving the equivalent thermal resistance between the considered point in the slot and the one in the iron. The different equivalent thermal models of the devices using two nodes are represented Fig. 3.

The resistance R_f includes the effect of conduction in the core and the convection exchange with the exterior, supposed to be at temperature T_e . Considering a 9-nodes model for a half slot, the resulting nodal locations are shown Fig. 4.

Depending on the choice for the node i , the temperature T_i can have different meanings:

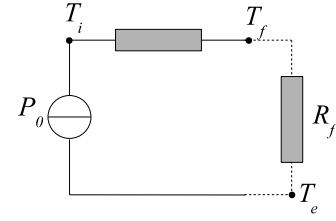


Fig. 3. Reduced thermal model

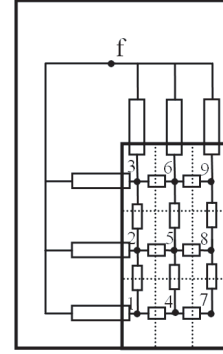


Fig. 4. Nodal discretization of a half slot

- maximum temperature in the slot (node 7)
- mean temperature of the slot (obtained by the mean of all the equivalent thermal conductances)

The corresponding results are presented in table I, with a comparison with FE ones. The relative error is lower than 5 %.

TABLE I
COMPARISON OF ANALYTICAL AND FEM RESULTS

	ΔT_{max} ($^{\circ}\text{C}$)	ΔT_{mean} ($^{\circ}\text{C}$)
Reduced model	18.02	10.96
FE Method	18.24	11.43
Relative error (%)	1.2	4.3

IV. CONCLUSION

The results obtained in the static case with the reduced model presents a good accuracy, with low computation needs. In the full paper, an extension of the model for transient analyses will be established in order to get the temperature variations versus time. Ongoing works will concern the adaptation of this reduced model to structures more similar to usual electrical machines.

REFERENCES

- [1] L. Daniel, and R. Corcolle, *A note on the effective magnetic permeability of polycrystals*, IEEE Trans. on Magnetics, vol. 43, no. 7, pp. 3153-3158, July 2007.
- [2] P.H. Mellor, D. Roberts, and D.R. Turnerpoulos, *Lumped parameter thermal model for electrical machines of TEFC design*, Proc. Inst. Elect. Eng., pt. B, vol. 138, no. 5, pp. 205-218, Sep. 1991.
- [3] T. Weiland, *A discretization method for the solution of Maxwell's equations for six-component fields*, Electron. Commun. AEU, vol. 31, no. 3, pp. 116-120, Sep. 1977.

Distributed Processing Management using ROME

Nancy Miekko Abe, Claudio Dias Marins and Angelo Passaro
 Virtual Engineering Laboratory, Institute for Advanced Studies - IEAv
 Rodovia dos Tamoios, km 5,5, 12228-001, Brazil
 nancy@ieav.cta.br

Abstract — This work presents new features of the system named ROME, developed at the Virtual Engineering Laboratory of the Institute for Advanced Studies of Brazilian Air Force, and the analysis of its application on optimization problems. ROME was developed based on Java and RMI technology and aims to manage distributed processing in non-dedicated heterogeneous clusters. The system provides robust mechanisms for self-adjusting load balancing and fault tolerance during the execution of parallel processing.

I. INTRODUCTION

Load balancing, fault-tolerance and scalability are the problems commonly encountered when performing parallel and/or distributed computing. A different approach to the parallelization of systems was developed at the Virtual Engineering Laboratory (LEV) of the Institute for Advanced Studies [1]. The system, named ROME, was developed in Java and uses the remote method invocation (RMI), a mechanism that provides the ability to remotely invoke a method of an object in another Java Virtual Machine (JVM)[2]. The major focus of the project was to develop a system which provides native load balancing and run-time failure recovery. Due to the characteristics of Java, the system is inherently multiplatform allowing its use in clusters composed by computers with different hardware and operating system configurations. It is more appropriate for coarse-grain parallel processing.

The system was developed based on the object oriented programming (OOP) paradigm and designed to be used as a class library, allowing its use with low level of additional programming. The description of classes, their functionalities and an evaluation of the system behavior when managing a optimization problem were presented in [1].

II. BASIC DESCRIPTION OF THE SYSTEM AND NEW FEATURES

Table I presents the main features of system ROME, compared with two of the most popular packages widely used to perform calculations and simulations in the area of parallel scientific computing: the Message Passing Interface (MPI) [3] and Parallel Virtual Machine (PVM) [4].

ROME follows a master/slave model, in the sense that there is an application (master) responsible for dividing the global problem in small tasks, sending the tasks to be solved by the slave applications and gathering back the results. It is composed basically by two main programs: a master machine and a slave machine. However, unlike the traditional master/slave model, the master machine is set to a passive mode, behaving most like a “server application”: the master waits for a “request for a task” of a slave application before

sending a task to it.

The operation using the "request for a task" mode allows implicit load balancing, since the slave application executed in an environment that presents higher performance will call for more tasks than other in a lower performance environment. A slave requests for a task only when the percentage of use of its processor is below a certain value defined by the user.

The system allows configuring the total number of slave machines connected per master machine as well as the number of slave machines for each user's parallel application managed by the master machine.

Two methods for identifying slave application faults are available: the direct detection method and the time estimation method. In the time estimation method, a estimative of the response time of a slave machine is calculated during run-time. If the response time of the slave machine exceeds the estimative (expires), the tasks attributed to it is sent to another slave.

TABLE I
MPI, PVM and ROME CHARACTERISTICS

Characteristics	MPI	PVM	ROME v.1	ROME v.1.1
Heterogeneous architectures	•	•	•	•
Multiplatform	• ⁱ	• ⁱ	•	•
Slaves intercommunication	•	•	•	•
Fault tolerant		• ⁱⁱ	•	•
Native load balancing			•	•
Dynamic identification of slaves			•	•
Native slave redundancy			•	•
Object transmission			•	•
Dynamic identification of multiple core processors				•
Native master redundancy				•
Additional user's programming	High	High	Low	Lower
Programming languages	C, C++, Fortran	C, C++, Fortran	Java ⁱⁱⁱ (C, C++, Fortran, etc)	Java ⁱⁱⁱ (C, C++, Fortran, etc)

ⁱ requires compilation for each operating system, ⁱⁱ requires implementation to recover lost data ⁱⁱⁱ the system is implemented in Java language but the applications can be implemented in any language because they can be executed as processes.

The usage of the system requires the implementation, in Java, of two methods of an abstract class, responsible for the master process, and of two other methods of the slave process class. These methods should be implemented in derived classes. The user's application can be developed either in Java, or be executed as processes. In the last case, the user's application can be developed in any desired language.

9. NUMERICAL TECHNIQUES

In the new version (v1.1), changes were made to further enhance the reliability (fault-tolerance) of the system with the identification of failures in the master machine, allowing a second machine to take control of the parallel processing without losing data of the tasks already computed. Other feature included is the possibility of communication among slaves, i.e., tasks running on different machines or processors can exchange information among themselves. Communication between nodes was made only between master and slaves in the previous version.

The new version also allows using computers that have multiple processors cores, automatically identifying the number of processors available. The system allows to add all or part of them in the processing cluster.

III. RESULTS

In a previous work, ROME was submitted to tests using codes for the optimization of electrooptic modulator devices by using a genetic algorithm (GA) [5]. Figures of merit of each individual generated by the GA are computed by a code based on the Finite Element Method. In this case, each task submitted to a given slave presents almost the same execution time. Fig. 1 shows the relative performance of the slaves used in the parallel processing and the automatic load balancing achieved. The cluster was composed by computers with very different hardware configurations and operating systems. Slave 1 and 10 run in a dual core processor. Slave 10 joined the computation later, by manual interference of the operator.

Fig. 2 illustrates the behavior of the response time estimative of one slave. After five tasks were completed, the system began to compute the estimative using the historical data. For the referred slave the value changed to 400s and remained almost constant for all the computed tasks.

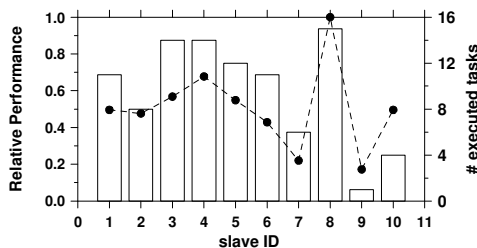


Fig. 1. The dots indicate the relative performance of each processor (left axis) and the histogram represents the number of the processes distributed to each processor (right axis)

In a recent test, ROME was used in a study of doped multi-quantum well (MQW) semiconductor structures [6], involving an optimization process. A MQW can be composed by several wells with different doping concentrations. In this problem, when the doping concentration in the wells is low (less than $5.0 \times 10^{16} \text{cm}^{-3}$), the convergence of the self-consistent computation is fast. However, for high values of doping concentration the convergence process can be much more costly. A homogeneous cluster composed by four multi-core computers was used to carry out the optimization. Fig. 3 shows the adaptation of one processing core of the system to tasks of different response time. In this case, the method for estimating the response time was able to adapt the system to the response

time of the slave. The master machine invalidates a task that do not answer in the predicted time and includes it back in the list of tasks waiting for a free processor. However, the system accepts results of a task whose response time has expired, provided that the task has not been sent to other slave yet. It should be pointed out that, in some cases, the submission of tasks of very different execution time to a processing core can result in a dead-lock. Because the process is invalidated, the estimative of response time is not updated. This procedure continues, occupying all processors.

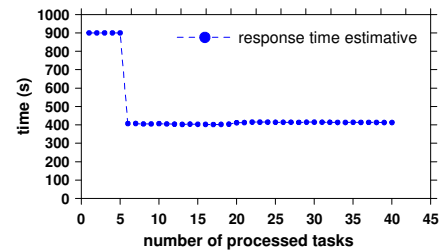


Fig. 2. Estimative response time of a slave.

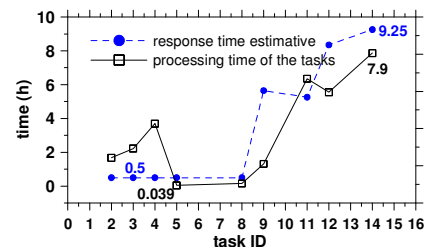


Fig. 3. Estimative response time for tasks with a very different response time

IV. FINAL COMMENTS

This work presents new features of system ROME, a robust management system for distributed processing, developed using Java language and the RMI resource.

The system is in testing with the execution of applications developed at LEV. New methods for adapting the system to applications in which the execution time of the tasks executed in the slaves are too different are about to be defined and implemented. In principle, the system allows the identification of slaves connected in LAN or WAN and is a powerful tool for parallel processing in a distributed and heterogeneous environment.

V. REFERENCES

- [1] A. Passaro, C. D. Marins, O. F. Lima and N. M. Abe, "ROME-RMI: A Robust Management Environment for Distributed Processing based on RMI", *IEEE Transactions on Parallel Distributed Systems*, submitted for publication.
- [2] Sun Microsystems, *Java™ Remote Method Invocation Specification: Revision 1.10, Java™ 2 SDK*, Std Ed, v1.5.0, 2004.
- [3] Peter S. Pacheco, *Parallel Programming with MPI*, Morgan Kaufmann Publishers, Inc. 1997.
- [4] A. Geist et. al, *PVM Parallel Virtual Machine: A Users Guide and Tutorial for Networked Parallel Computing*, MIT Press, 1994.
- [5] A. Muraro Jr, A. Passaro, N. M. Abe, A. J. Preto, and S. Stephany, "Design of Electrooptic Modulators Using a Multiobjective Optimization Approach", *J. Lightwave Technology*, 26 (16): 2969-2976, 2008.
- [6] R. Y. Tanaka, A. Passaro, N. M. Abe, G. S. Vieira, and S. Stephany, "Self-Consistent Analysis of Quantum Well Based Structures." *Proc. 13th Biennial IEEE Conference on Electromagnetic Field Computation, CEFC2008*, pp.550, 2008.

Simple Evaluation of Solution Accuracy on FEA by calculating Magnetic Flux Lines

So Noguchi, Hajime Igarashi and Hideo Yamashita*
Hokkaido University, N14 W9 Kita-ku, Sapporo 060-0814, Japan
E-mail: noguchi@ssi.ist.hokudai.ac.jp

*Hiroshima Institute and Technology, 2-1-1 Miyake, Saeki-ku, Hiroshima 731-5193, Japan

Abstract — In common, the accuracy of FEA result is a strong relation to the mesh characteristics, such as the number of elements, the element shape, the mesh density and so on. However, it is difficult to clarify whether the mesh is suitably generated, and whether the accuracy is sufficient enough. We have proposed the method to simply evaluate the characteristics of mesh and FEA result by using the magnetic flux lines, which are analytically calculated from the FEA result.

I. INTRODUCTION

Often, in order to increase the accuracy of FEA and to shorten the computation time, the graded mesh is employed. However, it may contain the poor-shaped elements causing long computation time and inaccuracy. Sometimes, in order to increase the accuracy, the excessively small elements are generated, therefore the computation time is wasted. The result accuracy and the speed of FEA are a strong relation to the mesh characteristics, such as the number of elements, the element shape and the mesh density. However, we cannot easily judge which mesh characteristics is the most important factor to increase the accuracy of FEA results. Also, we cannot know whether the obtained FEA result has enough accuracy. Usually, the error estimation method [1] is used. However, to estimate the error all over the domain is a labor task, and it is difficult to estimate the error since the true value is unknown. Consequently, another result with more fine mesh is necessary to estimate the error.

In this paper, we have proposed the way to simply and roughly evaluate the mesh characteristics and the result accuracy from the magnetic flux lines calculated from only one FEA result. The actual magnetic flux line in a closed domain is closed. The magnetic flux line analytically calculated from the FEA result [2], [3] is also closed in the domain, but the locus is unrealistically long and complex when the result accuracy is poor. Therefore, the characteristics of the result and the mesh are easily evaluated by drawing a few magnetic flux lines.

II. EVALUATION FROM MAGNETIC FLUX LINE

The methods to analytically calculate magnetic flux lines from tetrahedral and hexahedral edge FEA results were proposed [2], [3]. Surely, the calculated magnetic flux lines in a closed domain are closed and do not go outside the domain, since the result of FEA satisfies $\text{div } \mathbf{B} = 0$. However, when the accuracy is poor, some calculated magnetic flux lines are not simply closed, as shown in Fig. 1(b). The unrealistic magnetic flux lines are generated from the FEA result with poor mesh quality, i.e. bad-shaped elements exist, number of elements is

insufficient, and so on. On the other hand, the magnetic flux line in Fig. 1(a) is actual and it is obtained from the FEA result with good mesh quality. Consequently, by drawing the magnetic flux lines of FEA result, it is possible to judge whether the mesh is suitable for the FEA and whether the accuracy is sufficient enough. It is, however, impossible to obtain the exact value of the accuracy in this method. Of course, the true value of the magnetic field is also unknown.

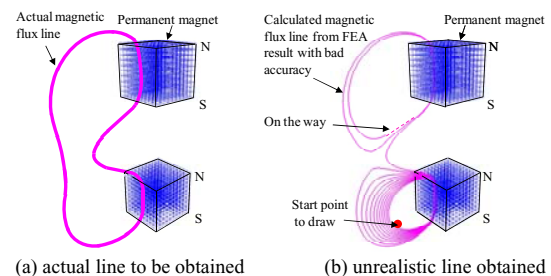


Fig. 1. Actual and unrealistic magnetic flux lines

We have investigated the relation between the calculated magnetic flux lines and the mesh quality. The gap distance generated by drawing round the magnetic flux line obtained from the FEA result is defined as an error indicator, as shown in Fig. 2. The simple test model, as shown in Fig. 3, consists of a permanent magnet in a closed domain, and six different meshes generated by the mesh generator in [2] are prepared. The properties of six meshes are shown in Table I.

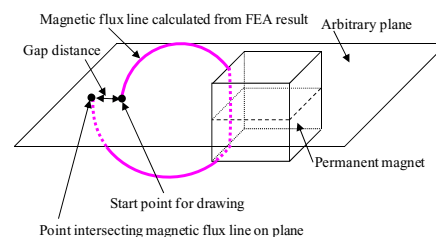


Fig. 2. The definition of the gap distance occurring from inaccurate result.

III. RESULTS OF EVALUATION

The gap distances of 6 magnetic flux lines on each mesh are plotted in Fig. 4, and the loci of the magnetic flux lines on Mesh I, III, V and VI are visualized in Fig. 5. In Figs. 4 and 5, the solutions in the cases of Mesh II and III have the high accuracy, since the magnetic flux lines are almost single loop. On the other hands, the Mesh I is too rough though the computation time and the ICCG convergence reveal good

TABLE I
PROPERTIES OF MESHES

Mesh No.	I	II	III
No. of Elements	29,791	226,9981	531,441
No. of Edges	95,232	703,452	1,633,932
No. of unknowns	83,700	658,800	1,555,200
Solver Time [s]	8.0	11.0	323.5
No. of ICCG Iteration	134	269	338
Mesh Characteristic	Regular Hexahedron	Regular Hexahedron	Regular Hexahedron
Mesh No.	IV	V	VI
No. of Elements	202,153	367,817	620,827
No. of Edges	613,196	1,113,788	1,854,374
No. of unknowns	600,128	1,093,616	1,824,374
Solver Time [s]	3,265.5	19,368.3	60,873.1
No. of ICCG Iteration	6,643	24,595	42,296
Mesh Characteristic	Graded Hex. Mesh	Graded Hex. Mesh	Graded Hex. Mesh

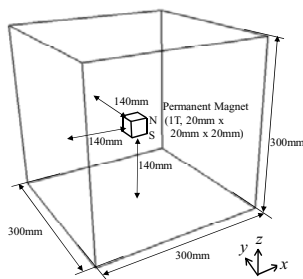


Fig. 3. Simple test model consisting of a permanent magnet.

performance. The Meshes IV, V and VI contain some bad-shaped elements, even though Mesh VI has the largest number of elements. The magnetic flux line 1 in Fig. 5(d) shifts to y -direction, therefore the gap distance is large.

The graded mesh is, often, used to shorten the computation time while keeping the high accuracy. However, the graded hexahedral mesh contains some distorted elements, as the result, the accuracy becomes poor. On the Fig. 5 (c), the loci of the magnetic flux line 1, the most outer line, are multiple-looped, since the line 1 passes through the distorted elements with poor quality on changing mesh density. The magnetic fields B_z and B_y on the $+x$ -direction line from the center of the permanent magnet are plotted in Fig. 6. The magnetic fields about B_z agree well, but the magnetic field B_y of the Mesh VI is obviously wrong since $B_y = 0$. The large gap distance results from such small error.

When the property of the magnetic flux lines is good, the ICCG convergence and the accuracy are good enough. Therefore, by drawing the magnetic flux lines using the method [2] from only one FEA result, it is possible to judge whether the properties of the mesh is good or poor, without computing the exact value of the error.

IV. CONCLUSION

In this paper, the method to roughly judge the accuracy of the edge FEA result has been proposed. In the method, it is checked whether the magnetic flux line calculated from the FEA result with good property is closed or not.

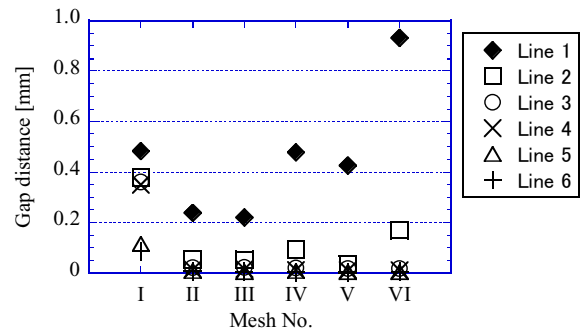


Fig. 4. Gap distance of magnetic flux lines.

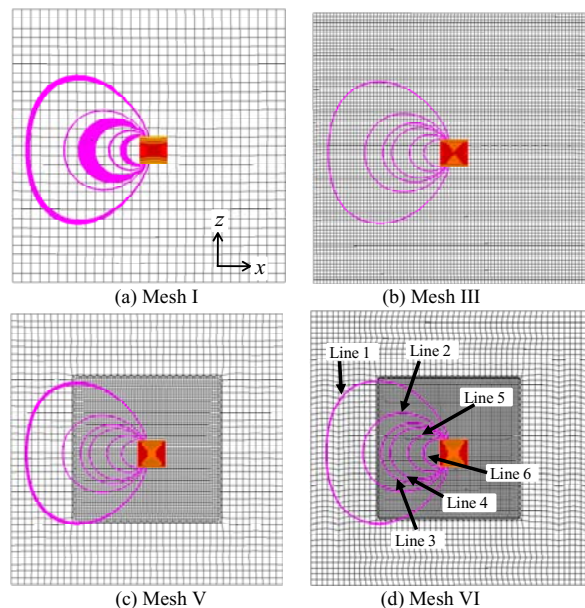
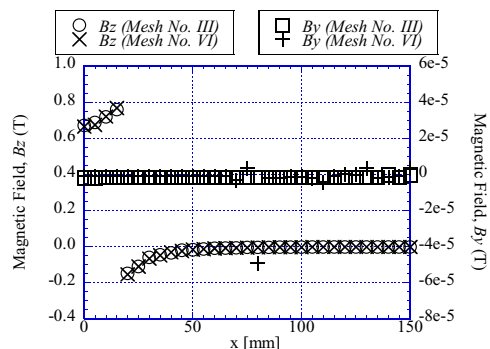


Fig. 5. Visualization of loci of magnetic flux lines.

Fig. 6. Magnetic field B_z and B_y of Meshes III and VI.

V. REFERENCES

- [1] O. C. Zienkiewicz and J. Z. Zhu, "A simple error estimate and adaptive procedure for practical engineering analysis," *Int. J. Numer. Meth. Eng.*, 24: 337-357, 1987.
- [2] V. Cingoski, et al., "Analytical calculation of magnetic flux lines in 3-D space," *IEEE Trans. on Magnetics*, 30(5): 2912-2915, 1994.
- [3] S. Noguchi, et al., "Analytical computation and visualization of magnetic flux lines in 3-D space from hexahedral edge finite element results," *IEEE Trans. on Magnetics*, 41(5): 1820-1823, 2005.

Performance Analysis of Inductive Coil Gun Based on Field-Circuit Method

Liu Shoubao, Ruan Jiangjun, Zhang Yu, Peng Ying and Du Zhiye
 School of Electrical Engineering, Wuhan University
 No.8, South Road of Eastern Lake, 430072, China
 Liushoubao1983@126.com

Abstract—Inductive coil gun's performance analysis is very important for experimental research and its electromagnetic optimization design. Circuit simulation is carried out based on current filament model (CFM), the governing equations of CFM may boil down to initial value problem of non-linear variable coefficient ordinary differential equations, which can be solved by numerical method and is easy to program. From circuit simulation, the dependence of system performance on variable parameter can be found. Field model is built based on composite grid method (CGM). CGM uses two sets of mutual independent grids to discrete solution region, the coarse grids discrete the global region and the fine grids discrete the moving part, so the trouble of remeshing in normal finite element technique based on one set of grid is overcome. In this paper performance analysis of three stages coaxial inductive coil gun is carried out based on field-circuit method. Three dimensional moving conductor eddy current (MCEC) field simulation of coil gun is realized, field variables distribution in the launching process is obtained. By comparing the results of circuit model and field model validity of the two models is proved.

I. INTRODUCTION

Coil launcher commonly constitutes by five parts: pulse power, high-speed switch, exciting coil, armature and projectile [1]. The pulse power loads electromagnetic energy on exciting coil after pulsed on. Transient magnetic field produced by the exciting coils induces circumferential eddy current in the armature. The circumferential eddy current interacts with radial component of the magnetic field which produces Lorentz force to drive the armature and projectile in the direction of muzzle. When armature arrives at an appropriate position, the next stage is fired, this process continues until the projectile is out of bore.

Coil gun's launching is a complex electromagnetic transient process; to obtain main performance parameters is not easy. Compared with expensive prototype experiments, numerical simulation can save design cost and improve work efficiency greatly in the optimized design of coil gun. Numerical simulation model for coil gun can be divided into two types: circuit model and multi-physical field model [2]. The circuit model has the virtue of simple and easy realization. According to the circuit model, dependence of variable parameters on result can be found easily. The multi-physical field model solves the problem from partial differential equation or integral equation, and can obtain various field quantities accurately, such as magnetic flux density and eddy current density [3].

In the analysis of coil gun only use circuit model can't get the field distribution, so precise analysis is impossible [4];

only use field model can't complete the whole analysis procedure, since the current of exciting coils which is material property in field model doesn't know in advance. So it is absolutely essential to analyze coil gun based on field and circuit combined model.

II. BASIC PRINCIPLES OF CIRCUIT MODEL AND FIELD MODEL

A. Current Filament Model

There are two types of circuit model: current sheet model (CSM) [5] and current filament model (CFM) [6]. CSM replaces the currents in an actual barrel and in a cylindrical tubular projectile (sleeve) with two equivalent current sheets located at their equivalent radius; by computing the magnetic field produced by the two current sheets the Lorentz force applied on projectile can be obtained. CFM divides massive conductive parts of the system into elementary volume elements, in which uniform distribution of current is assumed, a current filament is associated with every volume element, and its electrical parameters are calculated, the electrical and mechanical equations governing the behaviors of the system are formulated on the basis of the adopted equivalent network (schematic diagram of CFM is shown in Fig. 1.). Considering the definite physical meaning and simple solving process of CFM, this paper uses it to establish circuit model.

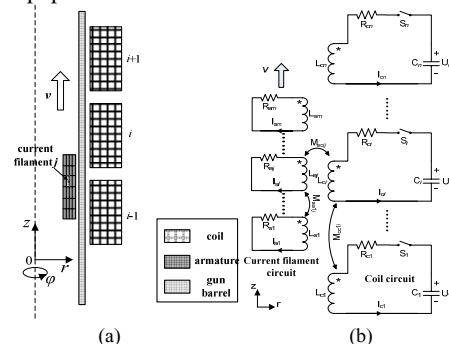


Fig. 1. Schematic diagram of CFM (a. CFM of coil gun; b. equivalent circuit)

B. Composite Grid Method

Launching process of coil gun is a complex moving conductor eddy current (MCEC) problem. In order to solve the problem, this paper applies a novel method — composite grid method (CGM). CGM developed from the conventional multi-grid method uses two grid sets: one coarse grid for the global region and one fine grid for the local region [7], as shown in Fig. 2. The results of the coarse mesh are interpolated onto the boundary of the fine mesh as its Dirichlet condition. Then fine mesh region is solved and reaction force

on its boundary is obtained, the reaction force reacts on the coarse mesh and global region is re-solved. The iteration continues until result convergence. The calculation procedure of CGM is shown in Fig. 3. Since the two grid sets are created independently, CGM overcomes the trouble caused by only one set of grid and it is very convenient to handle with MCEC problems [8].

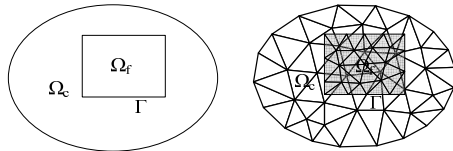


Fig. 2. Solution region and discrete grids of CGM

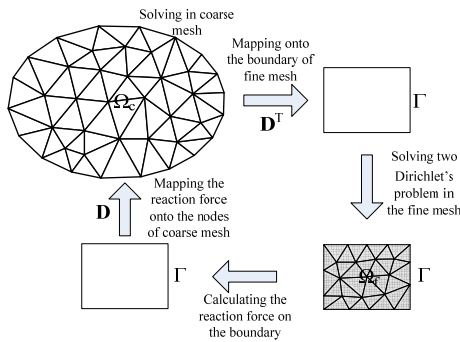


Fig. 3. Calculation procedure of CGM

III. COUPLE THE TWO METHOD IN ANALYSIS OF COIL GUN

A three-stage coaxial inductive coil gun simulation model according to field-circuit technique is built in this paper. First, we use circuit model to simulate launching process. The structure diagram of coil gun and division of current filament is shown in Fig. 4. Current waveform of exciting coils and current filaments obtained from circuit simulation are shown in Fig. 5.

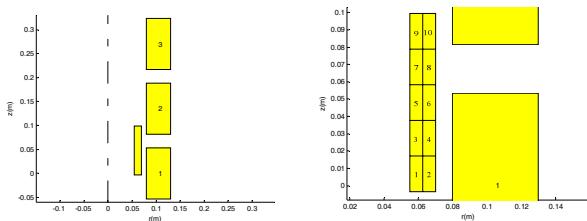


Fig. 4. Structure diagram of coil gun and division of current filament

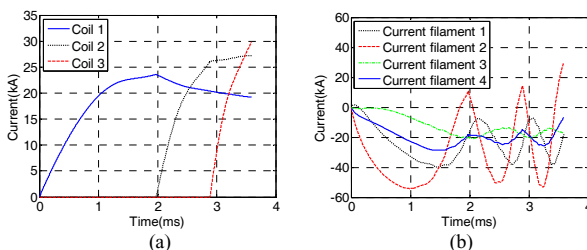


Fig. 5. Current waveform of circuit model (a. Current of exciting coil; b. Current of the first four current filaments)

Then the 3D field model based on CGM is built as shown in Fig. 6. The currents got by circuit model are loaded in field model as material properties of exciting coils and the field model is solved. Field quantities such as eddy current field,

magnetic flux density are displayed in Fig. 7. Results of the two models are compared (as shown in Fig. 8.) and the agreement of the two methods is proved.

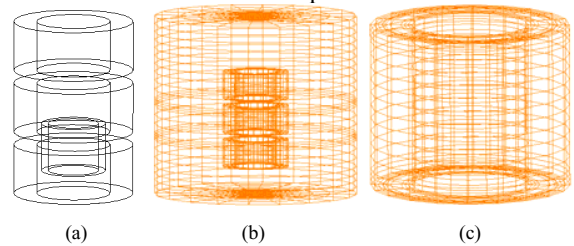


Fig. 6. Field model and domain mesh (a. 3D view; b. global region meshed in coarse grids; c. armature meshed in fine grids)

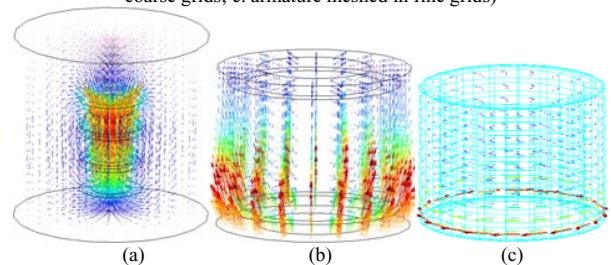


Fig. 7. Field quantities distribution at 3.1ms (a. flux density in coarse mesh; b. flux density in armature; c. eddy in armature)

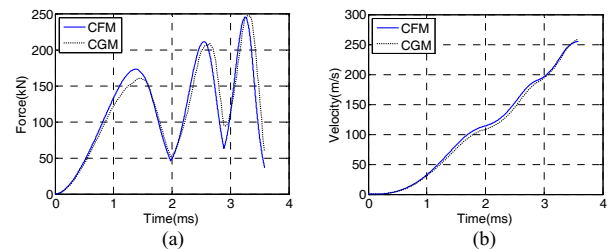


Fig. 8. Results comparison of CFM and CGM (a. force; b. velocity)

IV. REFERENCES

- [1] R Haghmaram., A Shoulaie, "Literature review of theory and technology of air-core tubular linear induction motors [electromagnetic launcher applications]," Universities Power Engineering Conference 2004, 2004:517-5221.
- [2] M. S. Aubuchon, T. R. Lockner, B. N.Turman et al, "Results from Sandia National Laboratories / Lockheed Martin Electromagnetic Missile Launcher (EMML)," IEEE Pulsed Power Conference 2005, 2005:75-78.
- [3] K. Yamazaki, S.Watari and A. Egawa , "Adaptive finite element meshing for eddy current analysis of moving conductor.," IEEE Transactions on magnetics, 2004, 40(2):993-996.
- [4] Liu ruifang,Yan, Dengjun, and Hu Minqiang, "Field circuit and movement coupled time stepping finite element analysis on permanent magnet brushless DC motors," Proceedings of the CSEE, 2007, 27(12): 59-64.
- [5] J. L He., E. Levi, Z. Zabar et al, "Analysis of induction-type coilgun performance based on cylindrical current sheet model," IEEE Transactions on magnetics, 1991, 27(1): 579-584.
- [6] D. G. Elliott, "Mesh-matrix analysis method for electromagnetic launchers," IEEE Transactions on magnetics, 1989, 25(1):164-169.
- [7] Peng Ying, Ruan Jiangjun, Zhang Yu, et al. "A composite grid method for moving conductor eddy-current problem," IEEE Transactions on magnetics, 2007, 43(7): 3259- 3265.
- [8] Zhang Yu, Ruan Jiangjun, Gan Yan et al. "Application of a Composite Grid Method in the Analysis of 3-D Eddy Current Field Involving Movement," IEEE Transactions on magnetics , 2008, 44(6):1298-1301.

Finite Element Magnetic Models via a Coupling of Subproblems of Lower Dimensions

P. Dular^{1,2}, R.V. Sabariego¹, C. Geuzaine¹, M. V. Ferreira da Luz³, P. Kuo-Peng³ and L. Krähenbühl⁴

¹ University of Liège, Dept. of Electrical Engineering and Computer Science, ACE, B-4000 Liège, Belgium

² F.R.S.-FNRS, Fonds de la Recherche Scientifique, Belgium

³ GRUCAD/EEL/UFSC, Po. Box 476, 88040-970 Florianópolis, Santa Catarina, Brazil

⁴ Université de Lyon, Ampère (UMR CNRS 5005), École Centrale de Lyon, F-69134 Écully Cedex, France

Abstract— Model refinements of magnetic circuits are performed via a subdomain finite element method based on a perturbation technique. A complete problem is split into subproblems, some of lower dimensions, to allow a progression from 1-D to 3-D models. Its solution is then expressed as the sum of the subproblem solutions supported by different meshes. The procedure simplifies both meshing and solving processes, and quantifies the gain given by each model refinement on both local fields and global quantities.

I. INTRODUCTION

The perturbation of finite element (FE) solutions provides clear advantages in repetitive analyses and helps improving the solution accuracy [1]-[4]. It allows to benefit from previous computations instead of starting a new complete FE solution for any variation of geometrical or physical data. It also allows different problem-adapted meshes and computational efficiency due to the reduced size of each subproblem.

A subproblem FE method is herein developed for coupling solutions of various dimensions, starting from simplified models, based on ideal flux tubes defining 1-D models, that evolve towards 2-D and 3-D accurate models. It is an extension of the method proposed in [2]-[4], applied to refinements up to 3-D models. From the so calculated field corrections, the associate corrections of global quantities inherent to magnetic models, i.e. fluxes, magnetomotive forces (MMFs), currents and voltages, are also evaluated. The developments are performed for the magnetic vector potential FE magnetostatic and magnetodynamic formulations, paying special attention to the proper discretization of the constraints involved in each subproblem. The method is illustrated and validated on test problems.

II. COUPLING OF MAGNETIC MODELS OF VARIOUS DIMENSIONS

A. Series of coupled subproblems

Instead of solving a complete problem, generally with a 3-D model, it is proposed to split it into a sequence of subproblems, some of lower dimensions, i.e. 1-D and 2-D models. Its solution is then to be expressed as the sum of the subproblem solutions.

Each subproblem is defined in its own domain, generally distinct from the complete one. At the discrete level, this aims to decrease the problem complexity and allow distinct meshes with suitable refinements. Each subproblem approximates at best its contribution to the complete solution. The domains of

the subproblems can overlap [2], [3] or not [1], [4]. Herein, non-overlapping subdomains are considered. They are separated by interfaces $\Gamma_{f,p}$, through which a sequence of boundary conditions (BCs) or interface conditions (ICs) is to be defined.

B. Canonical magnetostatic or magnetodynamic problems

Each subproblem p is defined in a domain Ω_p , with boundary $\partial\Omega_p = \Gamma_p = \Gamma_{h,p} \cup \Gamma_{b,p}$. It is governed by magnetostatic or magnetodynamic equations with volume and surface sources or constraints. Classical volume sources fix remnant inductions in magnetic materials and current densities in stranded inductors. Similar volume sources can also express changes of permeability and conductivity from one problem to another [3]. Also, the usually homogeneous surface sources, i.e. BCs or ICs on the traces of the magnetic field \mathbf{h}_p and flux density \mathbf{b}_p , respectively $\mathbf{n} \times \mathbf{h}_p|_{\Gamma_{f,p}}$ and of $\mathbf{n} \cdot \mathbf{b}_p|_{\Gamma_{f,p}}$, with \mathbf{n} the unit exterior normal, can be extended to non-zero constraints calculated from previous problems. ICs have the general forms

$$[\mathbf{n} \times \mathbf{h}_p]_{\gamma_p} = \mathbf{j}_{f,p}, \quad [\mathbf{n} \cdot \mathbf{b}_p]_{\gamma_p} = \mathbf{b}_{f,p}, \quad (1a-b)$$

where the notation $[\cdot]_{\gamma} = \cdot|_{\gamma^+} - \cdot|_{\gamma^-}$ expresses the discontinuity of a quantity through an interface γ (with sides γ^+ and γ^-) in Ω_p . The associated surface fields $\mathbf{j}_{f,p}$ and $\mathbf{b}_{f,p}$ are generally zero, defining classical ICs for the physical fields, i.e. the continuities of the tangential component of \mathbf{h}_p and of the normal component of \mathbf{b}_p . If nonzero, they define possible surface sources that account for particular phenomena occurring in the idealized thin region between γ^+ and γ^- .

C. Sources at subproblem interfaces

Portions of a 3-D structure satisfying a translational or rotational symmetry can be first studied via 2-D models. This consists in neglecting some end effects, zeroing either $\mathbf{n} \times \mathbf{h}_p|_{\Gamma_{f,p}}$ or $\mathbf{n} \cdot \mathbf{b}_p|_{\Gamma_{f,p}}$. Besides, if the field is chosen to be zero out of Ω_p , a discontinuity of one of its traces is then voluntarily defined through $\Gamma_{f,p}$.

With such assumptions, two subproblems 1 and 2 with adjacent non-overlapping subdomains Ω_1 and Ω_2 share a common interface $\Gamma_{f,1} = \Gamma_{f,2}$ through which a field discontinuity occurs. A third subproblem, 3-D, serves then to correct the field distribution in a certain neighborhood Ω_3 on both sides of the interface, then denoted $\Gamma_{f,3}$. This is done via ICs

$$[\mathbf{n} \times \mathbf{h}_3]_{\Gamma_{f,3}} = \mathbf{j}_{f,3}, \quad [\mathbf{n} \cdot \mathbf{b}_3]_{\Gamma_{f,3}} = \mathbf{b}_{f,3}. \quad (2a-b)$$

with the surface sources

$$\mathbf{j}_{f,3} = -(\mathbf{n} \times \mathbf{h}_1|_{\Gamma_{f,1}} - \mathbf{n} \times \mathbf{h}_2|_{\Gamma_{f,2}}), \quad \mathbf{b}_{f,3} = -(\mathbf{n} \cdot \mathbf{b}_1|_{\Gamma_{f,1}} - \mathbf{n} \cdot \mathbf{b}_2|_{\Gamma_{f,2}}). \quad (3a-b)$$

This work was supported by the F.R.S.-FNRS (Belgium), the CNPq (Brazil), the Belgian Science Policy (IAP P6/21) and the Walloon Region.

These sources compensate the traces 1 and 2 to recover the continuity of the total solution. Note that $\Gamma_{f,1}$, $\Gamma_{f,2}$ and $\Gamma_{f,3}$ are similar and only differ at the discrete level due to their different supporting meshes.

The ICs (2a) and (2b) in a magnetic vector potential (\mathbf{a}) FE formulation are considered via natural and essential constraints respectively [3]. The essential constraint strongly fixes the discontinuity of the trace of \mathbf{a} through $\Gamma_{f,3}$ (continuity if $\mathbf{b}_{f,3}=0$), whereas the natural constraint weakly acts via a surface integral term in the FE formulation. This surface term, with (2a) and (3a), involves the traces of previous solutions, each one being actually involved in similar surface terms in the associated previous FE formulations, thus linked with their other volume integrals. At the discrete level, these surface integrals must be substituted with those volume integrals, limited to one single layer of FEs touching the interface [1]-[4]. Because each solution is calculated in a different mesh, mesh-to-mesh projections of solutions are necessary. They can be profitably limited to the single layers of FEs. This procedure is of key importance for ensuring consistency between all the formulations and their coupling. It will be detailed in the extended paper and it will be shown to allow the accurate calculation of the global quantities (flux, MMF, current, voltage) at each step of the series, in particular the correction due to the end effects.

III. APPLICATION EXAMPLES

As a primary illustration, two flux tubes are first separately considered before being connected in series (Fig. 1). The solutions in each separate tube are simply calculated via 1-D models. When the tubes are connected, their junction surface acts as an interface $\Gamma_{f,3}$, with continuity of the normal magnetic flux density ($[\mathbf{n} \cdot \mathbf{b}_3]_{\Gamma_{f,3}} = 0$) and discontinuity of the tangential magnetic field ($[\mathbf{n} \times \mathbf{h}_3]_{\Gamma_{f,3}} \neq 0$). This gives the requested source for a 2-D model, calculating the field correction limited to a certain neighborhood Ω_3 on both sides of the interface, with a locally refined mesh.

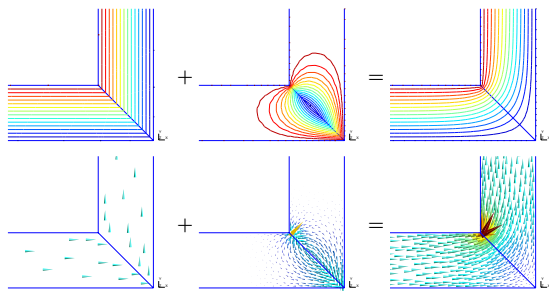


Fig. 1. Field lines (top) and magnetic flux density (bottom) of the initial problem with two ideal flux tubes in series (\mathbf{b}_1 and \mathbf{b}_2 in both tubes *left*), its local correction at the junction (\mathbf{b}_3 , *middle*) and the complete solution (\mathbf{b} , *right*).

A stranded inductor is then studied via the coupling of a 2-D plane model for its portion with a translational symmetry, a 2-D axisymmetrical model for its end winding and a 3-D model for the 3-D correction on both sides of the interface separating the portions (Figs. 2 and 3). Because the correction is local to the interface, the associated 3-D mesh only needs to be refined in its vicinity.

Various results and discussions will be given in the extended paper, in particular regarding the correction of both local and global quantities, the way to consider additional regions (e.g. the magnetic or conducting plate below the inductor in Fig. 2; based on [1] and [3] for magnetostatic and magnetodynamic models), the way the fields decrease at infinity

with the different models and the adaptation of the domain of each subproblem with its effect on the convergence of the complete solution. Parameterized analysis modifying some subproblems (e.g. end windings) while keeping the others constant will be shown to benefit from the developed method.

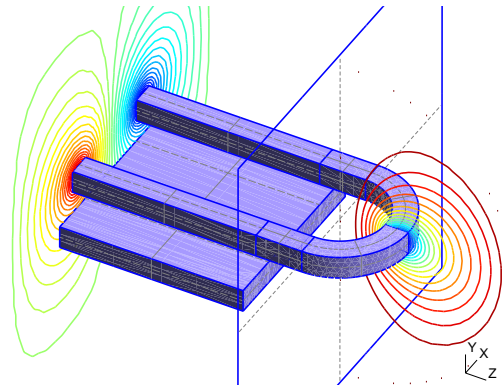


Fig. 2. Field lines generated by a stranded inductor (half geometry): solution of a 2-D plane model in the XY plane ($z=0$) (\mathbf{b}_1 , portion on the *left*) and of a 2-D axisymmetrical model in the YZ plane ($x=0$) (\mathbf{b}_2 , portion on the *right*); the interface between the two portions is shown.

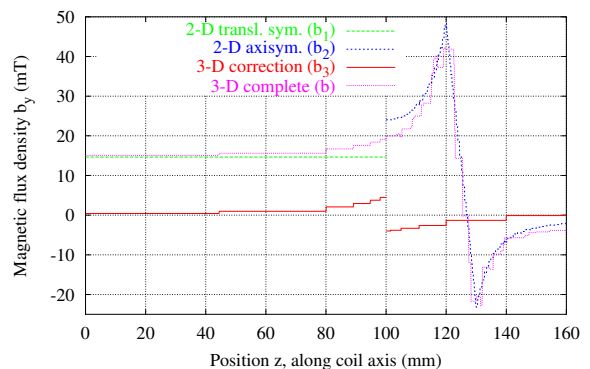


Fig. 3. Magnetic flux density along the coil axis in the 3-D system: \mathbf{b}_1 for the 2-D plane model (implicitly extended as a constant up to $z=100$ mm), \mathbf{b}_2 for the 2-D axisymmetrical model, \mathbf{b}_3 for the 3-D correction and \mathbf{b} for the complete 3-D model. The solution $\mathbf{b}_1+\mathbf{b}_2+\mathbf{b}_3$ is generally obtained with a higher accuracy than \mathbf{b} for a lower computational cost thanks to the coupling of meshes, some of lower dimensions.

IV. CONCLUSIONS

The developed subdomain FE method allows to split magnetic models into subproblems of lower complexity with regard to meshing operations and computational aspects. A natural progression from simple to more elaborate models, from 1-D to 3-D geometries, is thus possible, while quantifying the gain given by each model refinement on both local and global quantities.

REFERENCES

- [1] P. Dular, R. V. Sabariego, J. Gyselinck and L. Krähenbühl, "Sub-domain finite element method for efficiently considering strong skin and proximity effects," *COMPEL*, Vol. 26, No. 4, pp. 974-985, 2007.
- [2] P. Dular, R. V. Sabariego, M. V. Ferreira da Luz, P. Kuo-Peng and L. Krähenbühl, "Perturbation Finite Element Method for Magnetic Model Refinement of Air Gaps and Leakage Fluxes," *IEEE Trans. Magn.*, Vol. 45, No. 3, pp. 1400-1403, 2009.
- [3] P. Dular, R.V. Sabariego, M.V. Ferreira da Luz, P. Kuo-Peng and L. Krähenbühl, "Perturbation finite-element method for magnetic circuits," *IET Science, Measurement & Technology*, Vol. 2, No. 6, 2008.
- [4] P. Dular, R.V. Sabariego and L. Krähenbühl, "Magnetic Model Refinement via a Perturbation Finite Element Method - From 1-D to 3-D," *COMPEL*, Vol. 28, 2009, *in press*.

Improved Bacterial Foraging Strategy Applied to TEAM Workshop Benchmark Problem 22

Leandro dos Santos Coelho¹, Camila da Costa Silveira¹,
Cezar Augusto Sierakowski¹, and Piergiorgio Alotto²

¹Automation and Systems Laboratory, LAS/PPGEPS, Pontifical Catholic University of Paraná
Rua Imaculada Conceição, 1155, Zip code 80215-901, Curitiba, Paraná, Brazil
E-mail: leandro.coelho@pucpr.br, camila.silveira@gmx.de, cezars@positivo.com.br

²Dip. Ingegneria Elettrica, Università di Padova
Via Gradenigo 6/A, 35131, Italy
E-mail: alotto@die.unipd.it

Abstract— During the course of evolution living organisms have developed sophisticated behavior, intricate communication capabilities, decentralized colony control, group foraging strategies and a high degree of cooperation when tackling tasks. Bio-inspired optimization techniques, which operate in analogy to the swarming and social behavior found in nature, have been adopted to solve a variety of engineering problems. In this paper an optimization strategy based on an improved bacterial foraging strategy based on Gaussian distribution is proposed. The validity of the given algorithm is tested on the TEAM workshop benchmark problem 22.

Index Terms— TEAM workshop benchmark problem 22, optimization, swarm intelligence, electromagnetic optimization, bacterial foraging algorithm.

I. INTRODUCTION

Recently, great efforts have been devoted to the application of optimization metaheuristics inspired by swarm intelligence approaches, and in this context the development of bio-inspired swarm intelligence methodologies based on bacteria colony behavior is an emergent research area [1],[2].

A particularly interesting group behavior has been demonstrated for several motile species of bacterial colonies, where intricate stable spatio-temporal patterns based on stimuli of cell-cell signaling and foraging are formed in semi-solid nutrient media. Defining chemotaxis as a bias of movement according to the gradient of a chemical agent, chemotactic signaling is a response to an agent emitted by the bacteria [3]. Basically, chemotaxis is a foraging behavior that implements a type of optimization where bacteria try to climb up the nutrient concentration and avoid noxious substances. Relying on these biological concepts, an optimization method based on the foraging of *Escherichia coli* can be defined [4].

In this work, an improved approach based on a bacterial foraging strategy using a variable speed with Gaussian probability distribution function is proposed and tested on the TEAM workshop problem 22 in comparison with the classical foraging strategy proposed in [1].

II. FUNDAMENTALS OF BACTERIAL FORAGING OPTIMIZATION

Natural selection tends to eliminate animals with poor foraging strategies and to favor gene propagation of those with

good foraging strategies, since these have higher chances of succeeding in reproduction.

Bacterial colonies have developed sophisticated modes of cooperative behavior which enable them to respond to adverse growth conditions and it has been shown that this behavior manifests itself in the formation of complex colonial patterns. This phenomenon can be modeled by four simple and distinct behaviors (steps): chemotaxis, swarming, reproduction, and elimination and dispersal.

The presence of a flagellum allows the bacteria to move in two different forms: they might run (swim for a period of time), movement achieved by the flagellum rotation counter clockwise, or they can tumble, achieved by the flagellum rotation clockwise. Bacteria switch between these two modes of operation during their entire lifetime (rarely the flagellum stops rotating).

After a run period, a bacterium tumbles, and the tumble interval is about 0.14 ± 0.19 s, according to Passino [2]. After the tumble, the bacterium is pointed in a random direction. When the flagellum are rotated counter clockwise, the bacterium will move towards the direction it's turned, at an average speed of 10–20 $\mu\text{m/s}$, meaning, about 10 times its length by second, for a mean interval of 0.86 ± 1.18 s.

The local environment where bacteria live might change, either gradually or suddenly. Therefore, bacteria can suffer a process of elimination, through the appearance of a noxious substance, or a process of dispersion, through the action of other substances.

A bacterium position after a tumble can be determined through equation (1), where the position in that instant is calculated in terms of the position in the previous instant and the step size $C(i)$ applied in a random direction $\phi(j)$, generated by the bacterium tumble,

$$\theta'(j+1, k, l) = \theta'(j, k, l) + C(i) * \phi(j, k, l). \quad (1)$$

where i indicates the bacterium, j the chemotactic step, k the reproductive step and l the elimination and dispersal step.

To adapt such strategy to optimization problems, an equation to determinate the cost of each position is needed, to generate the comparison between the position and the

environment. In standard BFS notation, the cost is determined by the equation,

$$J(i, j, k, l) = J(i, j, k, l) + J_{cc}(\theta'(j, k, l), P(j, k, l)). \quad (2)$$

In which the cost (fitness) of a position $J(i, j, k, l)$ is also affected by the attractive and repulsive forces existing among the bacteria of the population, $J_{cc}(\theta'(j, k, l), P(j, k, l))$.

After a determined number of chemotactic steps (steps including the movement and the cost determination of each bacterium position), a reproductive step occurs. In this reproductive step bacteria are sorted in decreasing order by their cumulative cost. The lower half of the list dies, these are the bacteria that couldn't gather enough nutrients during the chemotactic steps, and the upper half divide themselves into two new bacteria, located in the same position.

Summarizing, the locomotory response of a cell to its environment is such that the cell responds by changing both the direction and the duration of the next movement step. This response requires some directional information from the environment that bacteria obtain by comparing an environmental property at two different time steps.

A. Improved bacterial foraging strategy

The parameter $C(i)$, $i=1,2,\dots,S$ regulates the speed of the movement taken in one step of bacteria colony, where S is population size (total number of bacteria). In this work, new approaches for the setup of parameter $C(i)$ are proposed.

In this paper, the an improved bacterial foraging strategy (IBFS) is proposed based on the studies of mutation operators in fast evolutionary programming [5], [6] and fast particle swarm optimization [7]-[8] for the setup of speed parameter $C(i)$ of bacteria.

The aim is to modify the constant $C(i)$ in conventional bacterial foraging strategy proposed by Passino [2] by a Gaussian distribution which can improve local searches. The IBFS approach tested is based on the following configuration: $C(i)=0.01 \cdot |\text{Gauss}| \cdot (ub-lb)$, $i=1,2,\dots,S$, where $\text{Gauss}(\cdot)$ are random numbers generated according to a Gaussian probability distribution with zero mean, and ub and lb are upper and lower bound of search space.

The simulation results of the IBFS method are compared with the classical bacterial foraging strategy (CBFS) approach with constant velocity, where $C(i)=0.01 \cdot (ub-lb)$, $i=1,2,\dots,S$.

III. OPTIMIZATION RESULTS

The TEAM workshop problem 22 concerns the optimal design of a superconducting magnetic energy storage (SMES) device in order to store a significant amount of energy in the magnetic field with a fairly simple and economical coil arrangement which can be rather easily scaled up in size. The benchmark consists in a continuous, constrained, eight-parameter problem and all details are given in [9].

In the TEAM 22 problem study, the following control parameters have been adopted for both the IBFS and CBFS approaches: population size $S=20$, number of chemotactic steps $N_c = 10$, maximum number of steps for bacterium

movement in a turn $N_s = 5$, number of reproductions $N_{re} = 5$, number of elimination-dispersals events $N_{ed} = 5$, and elimination-dispersal probability $p_{ed} = 0.3$. The stopping criterion was 10,000 evaluations of objective function.

The experiments were conducted for 30 independent runs.

Table I reveals that IBFS is clearly superior to CBFS for this benchmark problem.

TABLE I
ANALYSIS OF RESULTS (30 RUNS) FOR TEAM WORKSHOP PROBLEM 22

Optimization Approaches	Objective Function OF in 30 Runs			
	Maximum (Worst)	Mean	Minimum (Best)	Std. Dev.
CBFS	8.7454	3.4360	0.8333	3.5638
IBFS	2.7362	1.3107	0.0917	0.9529

IV. CONCLUSION AND FUTURE RESEARCH

In this paper, the CBFS and IBFS approaches are compared on the basis of the TEAM 22 benchmark problem. In the extended version of the papers both techniques will be compared with other families of stochastic optimizers and more details regarding the implementation and the tuning of the control parameters of both CBFS and IBFS approaches will be given.

Ongoing research is aimed at designing an IBFS for multiobjective problems.

ACKNOWLEDGMENTS

This work was partially supported by the National Council of Scientific and Technologic Development of Brazil — CNPq — under Grant 309646/2006-5/PQ.

REFERENCES

- [1] L. S. Coelho and V. C. Mariani, "Use of chaotic sequences in a biologically inspired algorithm for engineering design optimization," *Expert Systems with Applications*, vol. 34, no. 3, pp. 1905-1913, 2008.
- [2] K. M. Passino, "Biomimicry of bacterial foraging for distributed optimization and control," *IEEE Control Systems*, vol. 22, no. 3, pp. 52-67, 2002.
- [3] E. O. Budrene. and H. C. Berg, "Dynamics of formation of symmetrical patterns by chemotactic bacteria," *Nature*, vol. 376, pp. 49-53., 1995.
- [4] L. S. Coelho and C. A. Sierakowski, "Path planning optimization for mobile robots based on bacteria colony approach," In: A. Abraham; B. De Baets; M. Köppen; B. Nickolay. (Org.). *Applied Soft Computing Technologies: The Challenge of Complexity*. London, UK: Springer, pp. 185-196, 2006.
- [5] K. Chellapilla, "Combining mutation operators in evolutionary programming," *IEEE Transactions on Evolutionary Computation*, vol. 2, no. 3, pp. 91-96, 1998.
- [6] X. Yao and Y. Liu, "Fast evolutionary programming," *Proc. of 5th Annual Conference on Evolutionary Programming*, San Diego, CA, USA, pp. 451-460, 1996.
- [7] B. R. Secrest, and G. B. Lamont, "Visualizing particle swarm optimization - Gaussian particle swarm optimization," in *Proc. of the IEEE Swarm Intelligence Symposium*, Indianapolis, IN, USA, pp. 198-204, 2003.
- [8] N. Higashi and H. Iba, "Particle swarm optimization with Gaussian mutation," in *Proceedings of the IEEE Swarm Intelligence Symposium*, Indianapolis, IN, USA, pp. 72-79, 2003.
- [9] P. Alotto, A. V. Kuntsevich, C. Magele, G. Molinari, C. Paul, M. Repetto, and K. Richter, "Multiobjective optimization in magnetostatics: a proposal for a benchmark problem," *IEEE Trans. on Magnetics*, vol. 32, no. 3, pp. 1238-1241, 1996.

A Population Based Incremental Learning Method for Robust Optimal Solutions

S. L. Ho¹, and Shiyou Yang^{1,2}

¹Department of Electrical Engineering, The Hong Kong Polytechnic University, Hong Kong

²College of Electrical Engineering, Zhejiang University, Hangzhou, 310027, China

Abstract—A Population Based Incremental Learning (PBIL) method is proposed to search the robust optimal solution of an inverse problem in which some tolerances or small perturbations on the decision variables are inevitable. The numerical results serve to demonstrate the advantages and disadvantages of the proposed algorithm and the necessity to devote efforts in the development of robust oriented optimal algorithms.

I. A PBIL METHOD FOR ROBUST OPTIMAL SOLUTIONS

Traditionally, the main goal of most optimization studies is to find the global optimal solutions of a single or multiple objective function(s). In real engineering applications, uncertainties and tolerances are inevitable, hence if the global solution being found is very sensitive to design variables, small variation or perturbation on the optimized decision variables will give rise to significant performance degradation of the ‘global optimal design’. Therefore, the preferred design solution is probably not the global optimal solution, but the ‘optimal’ one that has a high tolerance or robustness against small variation of the decision parameters [1]. Consequently, it is necessary to develop techniques which identify the robust optimal solutions of a design problem.

To evaluate the robust performance of a solution, an expected fitness function as defined below is commonly used.

$$f_{\text{exp}}(x) = \int_{-\infty}^{\infty} f(x + \delta) p(\delta) d\delta \quad (1)$$

where, δ is the disturbance on the design variable x distributed based on a probability function $p(\delta)$, $f(x)$ is the original objective function of the design problem.

The expected fitness function defined in (1), rather than the original one, is proposed to be used in the iterative process of a robust algorithm to assess the solutions. Since there is no close form for the probability function $p(\delta)$, the expected fitness value of a solution x is generally determined from

$$f_{\text{exp}}(x) = \frac{1}{n} \sum_{i=1}^n f(x_i) \quad (2)$$

where n is the number of sampling points generated in a small neighborhood of the specific point x .

Obviously, a set of additional function evaluations are required to determine the expected fitness of a specific solution. However, the function evaluations in inverse problems are nontrivial and hence are computationally heavy.

A. The PBIL Method

The proposed PBIL method is developed by combining genetic algorithm (GA) and competitive learning so as to reduce the difficulties of crossover and mutation operations in GA, whilst retaining the stochastic search nature of a GA

[2],[3]. The PBIL method therefore is similar to GA in using a binary encoded representation of an optimal problem. The salient feature of this algorithm is the introduction of a real valued probability vector. The length of this real valued probability vector is identical to that of the encoded chromosome of a feasible solution in optimal problems. The value of each element of the vector is the probability of having a ‘1’ in that particular bit position of the encoded chromosome. In every generation, this probability vector is used to generate a new population in such a way that the probability for the i^{th} bit of a chromosome to become ‘1’ is proportional to the value of the i^{th} element of this probability vector. After evaluating the objective functions of the new population, this probability vector is updated using only the best individual of the current population and shifts it towards the chromosome of the best individual.

B. Mechanism for Expected Fitness Assignment

Generally speaking, the robust optimal solutions of a multimodal objective function are either those of the local (global) optima or those distributed on the boundaries of the parameter space. For an idea robust oriented optimizer, the expected fitness assignment procedure of the aforementioned solutions instead of all the intermediate ones are activated in order to reduce unnecessary computational burdens without scarifying the solution quality. Based on this argument, only the best two elites and boundary solutions in the current population are proposed to be designated with the expected fitness values. Obviously, the implementation of such a mechanism will save a huge amount of computation costs, which are otherwise required by available robust optimal methods, in which the expected fitness values for all the solutions are uniformly assigned.

C. Generation of Additional Sample Points

As formulated in (2), to evaluate the expected fitness of a potential robust solution, some additional sampling points and their objective function evaluations are generally required. Since the function evaluation is computationally heavy due to the involvement of numerical simulation such as finite element analysis, it would be desirable if the individuals in the current population could be used for determining the expected fitness value of a potential solution. However, the precondition for the current individuals to be designated a fitness value of a specified solution is that the distances between these individuals and the solution in question will not exceed a small threshold. In this regard, the intrinsic mechanism for generating a new population of the PBIL method is such that the whole population is generated by

using a single probability vector and satisfies this precondition absolutely (this is also the reason why PBIL method is being proposed in this study for robust optimizations). Consequently, the application of the mechanism for generating new populations of the proposed PBIL method eliminates the additional computation burden for generating additional samples and function evaluations.

D. Formulation to Compute Expected Fitness

To consider the effect of the distribution of neighborhood points on the expected fitness value, a distance-weighted formula for fitness computations of a solution x_i is proposed as

$$f_{\text{exp}}(x) = \frac{\sum_{i=1}^n w_i f(x_i)}{\sum_{i=1}^n w_i} \quad (3)$$

where, $w_i = 1/\|x - x_i\|^\alpha$ is the distance-weighted factor of the i^{th} sampling point of x , α is a positive constant, n is the number of the total sampling points.

II. APPLICATIONS

A. Application One

This is a high frequency inverse problem. The problem is to exploit the minimal number of elements to optimize a completely non-uniform antenna array to produce a satisfactory or acceptable field pattern. The desired field pattern is a shaped beam with a cosecant variation and the details about this problem are referred to [4].

To produce a field pattern which is close enough to the desired one using the proposed method, a 19 element non-uniform antenna array is selected and used to optimize the complex excitations and locations of each element so as to find the robust solution of this inverse problem. Also, for performance comparison purpose, a general purpose PBIL algorithm is employed to find the global optimal of the same problem. After 43655 iterations, the proposed algorithm finds a robust solution with an objective function value of 0.09044. These are compared to 40102 iterations of the general purpose PBIL for the global solution with an objective function value of 0.079049. The array factors of the final solutions of the proposed and the general purpose PBIL methods are compared in Fig. 1, and the robustness of these two optimal solutions against some small tolerances are shown in Fig. 2. From these numerical results it can be seen that although the final solution of the general purpose PBIL algorithm is better than that of the proposed robust optimal method, the robustness of the optimal solution of the latter is considerable stronger than that of the former, as the maximum sidelobe level of the final design of the general purpose PBIL, when subject to a small perturbation, exceeds the predefined limit of -25 decibel. Moreover, the higher iteration numbers with the proposed algorithm compared with those of other available robust optimizers is not an issue as almost all of the intermediate solutions of available optimizers are required to be assigned a fitness value, whereas the proposed one assigns the fitness values intelligently.

B. Application Two

The geometry optimization of the multi-sectional arcs of

the pole shoe of a large salient pole hydro-generator [5] is then solved. For performance comparison purpose, a general purpose PBIL algorithm is also used in this case study. The final numerical results are given in Table I. Similar conclusions as those for application example one are also observed.

Moreover, the numerical results as reported serve to demonstrate that it is essential to conduct robust optimal designs for an inverse problem in which uncertainties are inevitable.

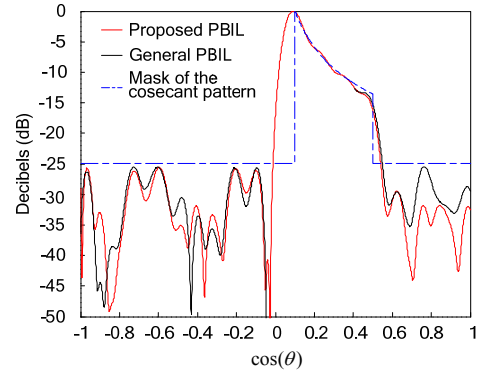


Fig. 1 Comparison of the array factors of the optimized antenna arrays by using different optimal methodologies.

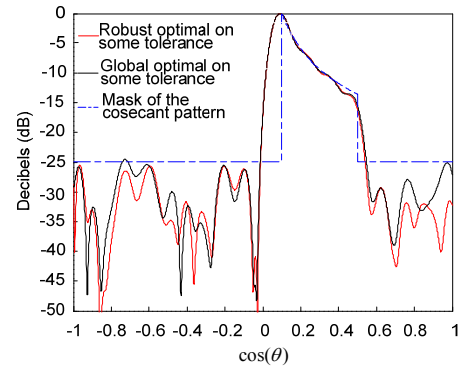


Fig. 2. Robustness of the final solutions of different optimal methodologies.

TABLE II
PERFORMANCE COMPARISON ON APPLICATION TWO

Algorithm	Iterative No.	B_{fl} (Tesla)	$(B_{fl})_{\text{exp}}$ Tesla)
General PBIL	2415	1.085	1.001
Proposed PBIL	3146	1.056	1.043

III. REFERENCES

- [1] Gerald Steiner, Daniel Watzenig, Christian Magele, and Ulrike Baumgartner, "Statistical robust design using the unscented transformation," *COMPEL*, vol. 24, pp. 606-619, 2005.
- [2] S. Baluja, and R. Caruana, "Removing the genetics from the standard genetic algorithm," *Proc. of ICML95*, 1995, pp. 38-46.
- [3] Marcus Gallagher, and Marcus Frean, "Population-based continuous optimization, probabilistic modelling and mean shift," *Evolutionary Computation*, vol. 13, pp. 29-42, 2005.
- [4] A. Akdagli, and K. Guney, "Shaped-beam pattern synthesis of equally and unequally spaced linear antenna arrays using a modified tabu search algorithm," *Microwave Opt. Technol. Lett.*, vol. 36, no. 1, pp. 16-20, 2003.
- [5] S. Y. Yang, G. Z Ni, Yan Li, B. Tian, and R. Li, "A universal tabu search algorithm for global optimization of multimodal functions with continuous variables in electromagnetics," *IEEE Trans. Magn.*, vol. 34, pp. 2901 - 2904, 1998.

Krylov-based algebraic multigrid for edge elements

François Musy¹, Artem Napov², Yvan Notay², Ronan Perrussel³ and Riccardo Scorretti³

¹ Institut Camille Jordan, CNRS UMR5208; ³ Laboratoire Ampère, CNRS UMR5005
Université de Lyon, École Centrale de Lyon, F-69134 Écully, France

² Service de Métrologie Nucléaire, Université Libre de Bruxelles, B-1050 Brussels, Belgium
mail to: ronan.perrussel@ec-lyon.fr

Abstract—This work tackles the evaluation of a multigrid cycling strategy using inner flexible Krylov subspace iterations. It provides a valuable improvement to the Reitzinger and Schöberl algebraic multigrid method for systems coming from edge-element discretizations.

I. INTRODUCTION

In finite element method libraries, the linear system solvers play a key role in terms of performances in the computing time and in the memory consumption. Multigrid methods are among the most efficient iterative linear system solvers for elliptic problems [1]. In this work, we focus on the discretization with the lowest order edge element of a curl-curl equation

$$\operatorname{curl} \delta \operatorname{curl} \mathbf{U} + \gamma \mathbf{U} = \mathbf{f} \text{ on } \Omega \subset \mathbb{R}^d \ (d = 2 \text{ or } 3), \quad (1)$$

which gives rise to a linear system $Ax = f$. Several Algebraic MultiGrid (AMG) algorithms have been proposed for “efficiently” solving this system [2]–[7]. We use the main ideas of the algorithm proposed by Reitzinger and Schöberl (RS), who were the first to propose an edge prolongation matrix satisfying a *commutativity property* [3]. Our motivation comes from the fact that this algorithm has the fastest setup time and gives the sparsest prolongation and coarse grid matrices among the available methods. However, it also gives the poorest rate of convergence, leading, in the literature, to a non-optimal multigrid solver. We combine the RS algorithm ideas with a Krylov-based multigrid cycle in order to recover classical multigrid performance. Numerical experiments are performed on 2D problems.

II. COMPONENTS OF THE ALGORITHM

A. Recursive Krylov-based multigrid cycle

The multigrid preconditioning algorithm on grid k (denoted by MGp) is given by *Algorithm 1* where matrix A_k represents the discrete problem on grid k (grid 0 is the coarsest) and P_k is the prolongation matrix from grid $k - 1$ to grid k .

Algorithm 1: INPUT r_k , OUTPUT $z_k = \text{MGp}(r_k)$

- 1) Relax using smoother M_k : $z_k \leftarrow M_k^{-1} r_k$.
- 2) Restrict residual: $r_{k-1} \leftarrow P_k^T (r_k - A_k z_k)$.
- 3) Compute an approximate solution $\tilde{\theta}_{k-1}$ to:

$$A_{k-1} \tilde{\theta}_{k-1} = r_{k-1}. \quad (2)$$

- 4) Prolongate coarse-grid correction: $z_k \leftarrow z_k + P_k \tilde{\theta}_{k-1}$.
- 5) Relax using smoother M_k : $z_k \leftarrow z_k + M_k^{-1} (r_k - A_k z_k)$.

If $k - 1$ is zero, the solution of (2) is exact. If not, a common strategy is to perform once $\text{MGp}(r_{k-1})$ (V-cycle) or twice (W-cycle) to approximately solve (2). Following [8], we propose to consider a K_2 -cycle which is a W-cycle completed by the two first iterations of a flexible Krylov subspace method. An example with the flexible conjugate gradient is given by *Algorithm 2*.

Algorithm 2: INPUT r_{k-1} , OUTPUT $\tilde{\theta}_{k-1} = \text{CS}(r_{k-1})$

- 1) First iteration:

$$d_{k-1} \leftarrow \text{MGp}(r_{k-1}); \alpha_{k-1} \leftarrow \frac{r_{k-1}^T d_{k-1}}{d_{k-1}^T A_{k-1} d_{k-1}};$$

$$\tilde{\theta}_{k-1} \leftarrow \alpha_{k-1} d_{k-1}; r_{k-1} \leftarrow r_{k-1} - \alpha_{k-1} A_{k-1} d_{k-1}.$$

- 2) Second iteration:

$$c_{k-1} \leftarrow \text{MGp}(r_{k-1});$$

$$d_{k-1} \leftarrow d_{k-1} - \frac{c_{k-1}^T A_{k-1} d_{k-1}}{d_{k-1}^T A_{k-1} d_{k-1}} c_{k-1};$$

$$\tilde{\theta}_{k-1} \leftarrow \tilde{\theta}_{k-1} + \frac{r_{k-1}^T d_{k-1}}{d_{k-1}^T A_{k-1} d_{k-1}} d_{k-1}.$$

The iteration cost in time and memory of both K_2 - and W-cycle is roughly equivalent. Moreover, their convergence rate are *theoretically similar* [8]. Nevertheless, in practice the K_2 -cycle has a better convergence rate than the W-cycle [8].

B. Prolongation matrix and smoother

Reitzinger and Schöberl proposed to construct an edge prolongation matrix P^{edg} satisfying a commutativity property:

$$P^{\text{edg}} G^H = G^h P^{\text{nod}}. \quad (3)$$

In this equality, P^{nod} is a nodal prolongation matrix obtained from a nodal auxiliary matrix and G^h and G^H are respectively fine and coarse edge-node incidence matrix.

At the finest level, G^h is given by the relation between vertices and edges on the finite element mesh. At the same level, the nodal auxiliary matrix B , following the proposition in [9], contains information about the edge-node incidence, the lengths of the edges and coefficient δ from (1). The construction of P^{nod} is then performed by the double pairwise-aggregation algorithm proposed in [10]. Once P^{nod} is known, the definition of the coarse edge incidence matrix G^H and the edge prolongator P^{edg} are straightforward. To apply the construction recursively, coarse grid matrices are obtained by Galerkin product:

$$A^H = (P^{\text{edg}})^T A P^{\text{edg}}, \quad B^H = (P^{\text{nod}})^T B P^{\text{nod}}. \quad (4)$$

The smoother is a symmetric version of the smoother proposed in [11] in a geometric multigrid context. It uses on each grid the corresponding edge-node incidence matrix.

III. NUMERICAL RESULTS

The behavior of the method with an increasing size of the problem and several kinds of parameters δ and γ is studied.

A. Structured mesh

The examples are taken from [12]. The domain is a unit square and Dirichlet boundary conditions are enforced. The mesh with triangles is structured but this fact is not used by the solver. For the parameters, three situations are considered:

- 1) Homogeneous parameters: $\delta = \gamma = 1$.
- 2) Oscillating with discontinuities for $\delta = f(x, y)$ and $\gamma = 1$. Function f have the following definition:

$$f = C(2 + \sin(40\pi x))^2(2 + \cos(40\pi y))^2$$

$$\text{with } C = \begin{cases} 10 \text{ in }]0, 0.5[\times]0, 0.5[, \\ 10^4 \text{ in }]0.5, 1[\times]0, 0.5[, \\ 10^{-1} \text{ in }]0, 0.5[\times]0.5, 1[, \\ 10^2 \text{ in }]0.5, 1[\times]0.5, 1[. \end{cases}$$

- 3) Oscillating with discontinuities for $\delta = f(x, y)$ and for $\gamma = f(y, x)$.

The behavior of the iterative method is evaluated by computing the average convergence rate σ_{est} in energy norm:

$$\sigma_{\text{est}} = \left(\frac{\text{er}_k^t \text{Aer}_k}{\text{er}_0^t \text{Aer}_0} \right)^{1/(2k_f)}$$

with er_k the error at the k -th iteration and k_f the iteration where the stopping criterion is reached.

An examination of the convergence rate of the two-grid algorithm provides information to predict the behavior of the multigrid cycle. In Table I, the two-grid convergence rate is quasi-independent of the size of the problem and is bounded away from 1. Case 3 is the worst situation probably because the aggregation does not take into account variation of γ ; it may explain the bad convergence rate for one particular mesh in this case (in bold). The number of unknowns is divided roughly by 4 between fine and coarse grids which is the best trade-off between coarsening and the overall arithmetic complexity.

With such convergence rates for the two-grid solver, it is illustrated in Table II that the convergence rates of the W-cycle (and of course of the V-cycle) deteriorates as the number of grids increases. On the contrary, the convergence rate of the K_2 -cycle has a remarkable stability.

TABLE I
RESULTS OBTAINED WITH A TWO-GRID SOLVER.

	d.o.f. fine grid	736	3008	12160	48896
Case 1	d.o.f. coarse grid	184	751	3040	12224
	σ_{est}	0.62	0.68	0.70	0.71
Case 2	d.o.f. coarse grid	187	788	3087	12404
	σ_{est}	0.64	0.72	0.69	0.69
Case 3	d.o.f. coarse grid	187	788	3087	12404
	σ_{est}	0.61	0.72	0.87	0.68

TABLE II

COMPARISON BETWEEN A W-CYCLE AND A K_2 -CYCLE SOLVER. CASE 3 ON THE MESH WITH 48896 D.O.F.

# grids	3	4	5	6	7
d.o.f. coarsest grid	3279	844	216	55	11
K_2 -cycle, σ_{est}	0.68	0.68	0.68	0.68	0.68
W-cycle, σ_{est}	0.83	0.89	0.93	0.95	0.97

B. Unstructured mesh

Coefficients δ and γ are those defined in Case 3. The domain is still a unit square but an unstructured mesh, refined at the center of the square, is considered. Table III confirms the results obtained for the structured meshes.

TABLE III

COMPARISON BETWEEN A TWO-GRID, A W-CYCLE AND A K_2 -CYCLE SOLVER.

d.o.f. finest grid	2043	8988	36717
two-grid, σ_{est}	0.64	0.61	0.61
# grids	5	6	5
d.o.f. coarsest grid	6	9	216
K_2 -cycle, σ_{est}	0.64	0.62	0.61
W-cycle, σ_{est}	0.90	0.80	0.95

The change of cycling proposed for the RS algorithm seems to make this algorithm robust and optimal in 2D. The proposed algorithm can be straightforwardly extended to 3D problems but our actual Matlab implementation does not enable us to propose results on challenging problems and also to discuss computational time and memory requirements. We are working on an implementation in Fortran90 in order to propose valuable comparisons on realistic problems.

REFERENCES

- [1] D. W. Hackbusch, *Multi-Grid Methods and Applications*, 1985.
- [2] R. Beck, "Algebraic multigrid by components splitting for edge elements on simplicial triangulations," *Preprint SC 99-40, ZIB*, Dec. 1999.
- [3] S. Reitzinger and J. Schöberl, "An algebraic multigrid method for finite element discretizations with edge elements," *Numerical Linear Algebra with Applications*, vol. 9, no. 3, pp. 223–238, 2002.
- [4] J. J. Hu, R. S. Tuminaro, P. B. Bochev, C. J. Garasi, and A. C. Robinson, "Toward an h-independent algebraic multigrid method for Maxwell's equations," *SIAM Journal on Scientific Computing*, vol. 27, no. 5, pp. 1669–1688, 2006.
- [5] T. Boonen, G. Delière, and S. Vandewalle, "On algebraic multigrid methods derived from partition of unity nodal prolongators," *Numerical Linear Algebra with Applications*, vol. 13, no. 2-3, pp. 105–131, 2006.
- [6] R. Hiptmair and J. Xu, "Nodal auxiliary space preconditioning in H(curl) and H(div) spaces," *SIAM J. Numer. Anal.*, vol. 45, no. 6, pp. 2483–2509, 2007.
- [7] F. Musy, L. Nicolas, and R. Perrussel, "Compatible coarse nodal and edge elements through energy functionals," *SIAM Journal on Scientific Computing*, vol. 29, no. 3, pp. 1315–1337, 2007.
- [8] Y. Notay and P. S. Vassilevski, "Recursive krylov-based multigrid cycles," *Numerical Linear Algebra with Applications*, vol. 15, p. 473–487, 2008.
- [9] M. Kaltenbacher and S. Reitzinger, "Algebraic multigrid methods for nodal and edge based discretizations of maxwell's equations," *International Compumag Society Newsletter*, vol. 9, no. 2, pp. 15–23, 2002.
- [10] Y. Notay, "An aggregation-based algebraic multigrid method," Université Libre de Bruxelles, Brussels, Belgium, Tech. Rep. GANMN 08–02, 2008, <http://homepages.ulb.ac.be/~ynotay>.
- [11] R. Hiptmair, "Multigrid method for Maxwell's equations," *SIAM Journal on Numerical Analysis*, vol. 36, no. 1, pp. 204–225 (electronic), 1999.
- [12] J. Jones and B. Lee, "A multigrid method for variable coefficient maxwell's equations," *SIAM Journal on Scientific Computing*, vol. 27, no. 5, pp. 1689–1708, 2006.

A p -adaptive scheme for scalar fields, using high-order, singular finite elements

J. P. Webb

McGill University, Department of Electrical and Computer Engineering
3480 University Street, Montreal, H3A 2A7, Canada
jon.webb@mcgill.ca

Abstract — For problems with sharp edges, where the electric or magnetic field is singular, p -adaptive finite-element analysis loses some of its effectiveness. This can be remedied by including singular elements which are better able to model the potentials near such edges. The singular elements are hierarchical and the p -adaption takes places over the combined set of singular and regular elements. Results show that a greatly improved adaptive convergence is obtained.

I. INTRODUCTION

The adaptive finite element (FE) method is generally accepted as being an effective technique for computing electromagnetic fields [1]. In p -adaption, the elements of the starting mesh are not changed in shape or size, but instead more basis functions are added to elements in which the unknown field is thought to need improvement. Since most finite elements use polynomial basis functions, this is usually done by increasing the polynomial order of the elements. For this to work, a range of element orders must be available, and they must be hierarchical, so that two neighboring elements can be of different orders without causing a discontinuity in the field.

P -adaption has the advantage over h -adaption that it does not require mesh refinement, which can be costly and unreliable. In smooth regions, away from material interfaces, p -adaption is known to provide exceptional accuracy. However, near sharp corners and edges, where the electric or magnetic field is mathematically singular, p -adaption loses some of its effectiveness. It can be improved by combining it with mesh refinement in hp methods, e.g. [2]. An alternative, which avoids mesh refinement entirely, is proposed here. In the elements connected to the singular corners and edges, the usual polynomial basis functions of the hierarchal elements are replaced by singular basis functions that are better able to represent the field behavior in those regions. The singular elements are also hierarchical and can support p -adaption, which then proceeds on the entire mesh of regular and singular elements.

II. REGULAR AND SINGULAR HIERARCHICAL ELEMENTS

The proposed method computes a scalar potential in 3D, e.g., the magnetic or electric scalar potential. The regular elements are the scalar, hierarchical tetrahedra described in [3]. The p^{th} -order element can represent all polynomials of degree p in 3D.

The singular elements are built from these by a process of transformation. This is explained more fully in [4], but the

main steps are as follows. First, two kinds of singular element are identified: those with just one vertex on a sharp edge (“Point” elements) and those with just two vertices on a sharp edge (“Line” elements). All other elements are assumed to have no vertices on a sharp edge and are regular. New local coordinates are introduced in the Point and Line elements and in both cases, one of the coordinates, ρ , represents the normalized distance from the sharp edge. Next, the polynomial basis functions are re-expressed in the new coordinates. Each then takes the form of a polynomial in ρ .

This polynomial is transformed by replacing each term ρ^k by ρ^{ν_k} , where ν_k are singularity indices. These are non-integer in general and are obtained from the analytic expression for the scalar potential near a sharp edge. They depend on the geometry and materials at the edge. For example, if two zero-potential plates meet at an interior angle $\alpha > \pi$, forming a sharp edge, the indices are $\nu_k = k\pi/\alpha$.

The transformation produces a set of new basis functions that are much better at modeling the potential near the singularity. Moreover, the p^{th} -order singular element has the same number of basis functions as the p^{th} -order regular element, and the Line, Point and regular elements may all be set to any orders without introducing discontinuities in the potential.

III. ERROR INDICATOR AND THE ADAPTION SCHEME

At each adaptive step, the order of element e is increased or not depending on the value of an error indicator. The indicator used in this work exploits the hierarchical nature of the elements and is based on the approach taken in [5], though that work described an indicator specifically for the scattering parameters of a microwave device.

Suppose the discrete, weighted-residual problem solved at any stage of the adaption is to find the unknown potential u belong to a discrete space V :

$$a(u, w) = b(w) \quad \forall w \in V \quad (1)$$

where a and b are bilinear and linear forms, respectively, and w is a weight function. Let V_e be the slightly larger function space in which the order of element e has been increased by 1, and let u_e be the discrete solution in this larger space. The error indicator is an estimate of the square of the energy norm of the difference between u and u_e :

$$a(u_e - u, u_e - u) \quad (2)$$

It can be shown that expression (2) is exactly equal to

$$b(u_e - u) - a(u_e - u, u) \quad (3)$$

but that (3) is more accurate than (2) when u_e is approximated, which it must be because it would be too expensive to obtain u_e exactly. It is approximated by $u + \Delta u_e$, where u is the solution to (1), as before, and Δu_e is a linear combination of just the *new* basis functions added to element e when its order is increased. Let ΔV_e be the space spanned by these new basis functions. To determine Δu_e , we solve:

$$a(u + \Delta u_e, \Delta w_e) = b(\Delta w_e) \quad \forall \Delta w_e \in \Delta V_e \quad (4)$$

This results in a local matrix problem, equal in dimension to the number of extra basis functions added to element e . It is solved for each element in the problem. From (3), the indicator is:

$$I_e = |b(\Delta u_e) - a(\Delta u_e, u)| \quad (5)$$

At each adaptive step, the elements are ranked according to (5) and a specified fraction of them with the highest errors have their orders increased by 1. This fraction is set to 25% for the results below.

IV. TEST CASE

The adaptive algorithm is applied to the geometry shown in Fig. 1, which shows a gap between two stripline transmission lines. Half the geometry is shown: there is a plane of symmetry at $x=0$. The gap capacitance is found by setting the electric potential on the narrower strip to 1V, and on the wider strip to 0V. The box walls at $y=0$, $y=b$ and $x=0$ are left unconstrained, and the other three box walls are constrained to 0V. Solving this electrostatic problem by the FE method gives the potential throughout the box, from which the stored energy and capacitance can be found.

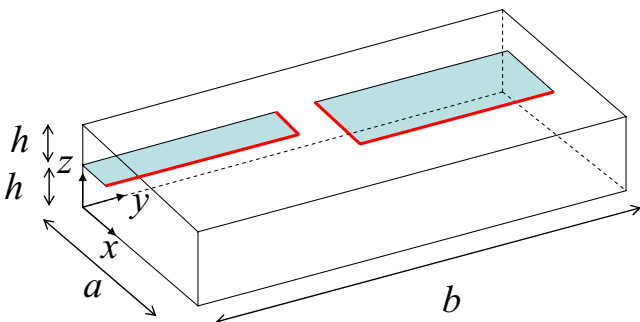


Fig. 1. A gap between two stripline transmission lines. $b=11a/5$, $h=a/5$. The strips are of equal length and the gap between them is $a/5$. The wider strip has a half-width (shown) of $2a/5$ and the narrower strip has a half-width of $a/5$.

The volume is subdivided into a coarse, unstructured mesh of 160 tetrahedra. For the case “**Singular adaption**” in Fig. 2, the tetrahedra touching the sharp edges (shown with thick red lines in Fig. 1) are made into singular Line or Point elements. In the “**Regular adaption**” case, all the elements use polynomial basis functions. Each point shows the result of one FE solution in the adaptive iteration, starting with all element orders equal to 1. The highest element order allowed is 4. The sharp edges have an interior angle $\alpha = 2\pi$, so $\nu_k = k/2$. Nothing special is done about the two sharp *corners* that are present, where the behavior of the potential is different.

A reference value of the stored energy is obtained by using independent FE software [6] with an h -adapted mesh of 116,803 third-order tetrahedra. The reference value is estimated to be within 0.1% of the true energy.

Fig. 2 clearly shows the limitation of traditional p -adaption. Using only regular elements, the error cannot be made smaller than about 5%. On the other hand, by including singular elements, not only does the error fall more swiftly as the adaption proceeds, but the final accuracy is about 0.6%.

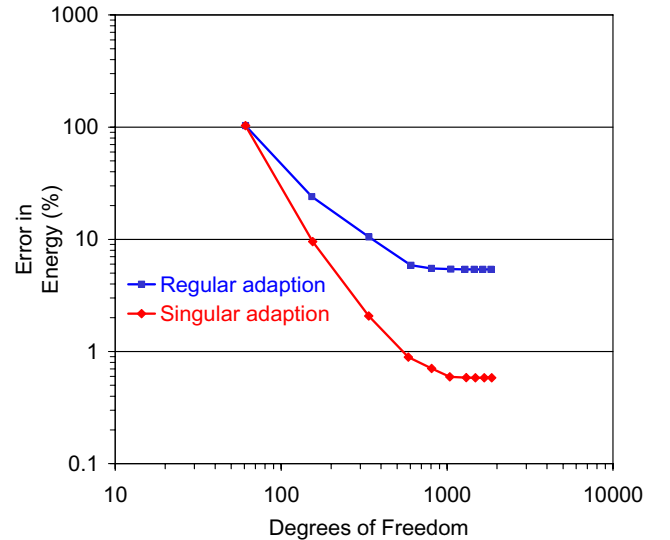


Fig. 2. Error in computed energy versus the number of degrees of freedom for the stripline example, during an adaptive solution using either regular elements alone, or a combination of regular and singular elements.

V. REFERENCES

- [1] J. Lang and D. Teleaga, “Towards a fully space-time adaptive FEM for magnetoquasistatics,” *IEEE Transactions on Magnetics*, vol. 44, pp. 1238-1241, Jun 2008.
- [2] I. Gomez-Revuelto, L. E. Garcia-Castillo, D. Pardo, and L. F. Demkowicz, “A two-dimensional self-adaptive hp finite element method for the analysis of open region problems in electromagnetics,” *IEEE Transactions on Magnetics*, vol. 43, pp. 1337-1340, Apr 2007.
- [3] J. P. Webb, “Hierarchical vector basis functions of arbitrary order for triangular and tetrahedral finite elements,” *IEEE Trans. on Antennas and Propagation*, vol. 47, no. 8, pp.1244-1253, August 1999.
- [4] J. P. Webb, “Singular tetrahedral finite elements of high order for scalar magnetic and electric field problems,” *IEEE Transactions on Magnetics*, vol. 44, pp. 1186-1189, Jun 2008.
- [5] D. Nair and J. P. Webb, “P-Adaptive computation of the scattering parameters of 3-D microwave devices,” *IEEE Transactions on Magnetics*, vol. 40, pp. 1428-1431, Mar 2004.
- [6] ElecNet 6.17, 2007, Infolytica Corporation, Montreal, Canada, <http://www.infolytica.com/>.

A Discrete (2+1)-D Formulation for 3-D Field Problems with Continuous Symmetry

Bernhard Auchmann*, Bernd Flemisch†, and Stefan Kurz‡

*CERN/TE, Geneva, Switzerland, Email: bernhard.auchmann@cern.ch,

†Universität Stuttgart, IWS, Stuttgart, Germany, ‡ETAS GmbH, Stuttgart, Germany

Abstract—We describe a general formalism that allows to reduce the spatial dimension of a field problem from 3-D to (2+1)-D. Subsequently we identify conditions under which the third dimension can be eliminated. Eventually we see that the resulting 2-D field problems only decouple if an orthogonality criterion is fulfilled. The approach is based solely on differential-form calculus and can therefore be easily transferred into a discrete setting. As a numerical example we compute the fields of twisted wires.

Index Terms—Continuous Symmetries, Dimensional Reduction, Discrete Electromagnetism

I. DIMENSIONAL REDUCTION

DIMENSIONAL reduction occurs in different contexts: Relativistic 4-D field problems are reduced, mostly implicitly, to 3-D problems with time as a parameter. 3-D problems with symmetries (axi-symmetry, symmetry along a Cartesian axis) are reduced to 2-D problems. This paper constitutes a step in the endeavor to unite all different aspects in a single, differential-form based framework.

We denote by \mathcal{X}^p the space of p -vector fields of tangent vectors on a 3-dimensional Riemannian manifold M , and by \mathcal{F}^p the space of differential p -forms on M . We use the *generalized contraction operator* $i : \mathcal{X}^q \times \mathcal{F}^p \rightarrow \mathcal{F}^{p-q} : (\mathbf{v}, \omega) \mapsto i_{\mathbf{v}}\omega$, $p \geq q$, which is induced from the standard contraction with a 1-vector according to the rule $i_{\mathbf{w}\wedge\mathbf{u}} = i_{\mathbf{u}}i_{\mathbf{w}}$ for $\mathbf{u} \in \mathcal{X}^1$, $\mathbf{w} \in \mathcal{X}^{q-1}$. Moreover we define the *multiplication operator* as $j : \mathcal{F}^1 \times \mathcal{F}^p \rightarrow \mathcal{F}^{p+1} : (\boldsymbol{\mu}, \omega) \mapsto j_{\boldsymbol{\mu}}\omega = \boldsymbol{\mu} \wedge \omega$. The operators i and j are defined in the obvious way on the respective dual spaces, [2]. The duality product is denoted by $\cdot | \cdot$.

Let $\boldsymbol{\mu} \in \mathcal{F}^1$ be an exact 1-form $\boldsymbol{\mu} = d\lambda$ that defines a (codimension one) foliation of the 3-dimensional manifold M . $\varphi : U \rightarrow M$ denotes the embedding of the 2-dimensional manifold U in M at $\lambda = \text{const}$. We define the horizontal (w.r.t. the foliation) component of a differential form by the introduction of a directional vector field $\mathbf{u} \in \mathcal{X}^1$ that is transversal to the foliation so that $i_{\mathbf{u}}\boldsymbol{\mu} = 1$. We denote $\mathcal{F}_{\mathbf{u}}^p := \{\omega \in \mathcal{F}^p | i_{\mathbf{u}}\omega = 0\}$ the space of horizontal differential forms and $\mathcal{X}_{\boldsymbol{\mu}}^p = \{\mathbf{v} \in \mathcal{X}^p | i_{\boldsymbol{\mu}}\mathbf{v} = 0\}$ the space of horizontal vector fields. The horizontal component $\omega_{\parallel} \in \mathcal{F}_{\mathbf{u}}^p$ of a form ω is defined by the relation $\omega_{\parallel} | \varphi_*\mathbf{v} = \varphi_*\omega | \mathbf{v}$, $\mathbf{v} \in \mathcal{X}^p(U)$. It can be shown that $\omega_{\parallel} = i_{\mathbf{u}}j_{\boldsymbol{\mu}}\omega$. Moreover, each $\omega \in \mathcal{F}^p$ can be uniquely represented by a pair of horizontal forms $(\omega_{\parallel}, \omega_{\perp}) = (i_{\mathbf{u}}j_{\boldsymbol{\mu}}, i_{\mathbf{u}})\omega \in \mathcal{F}_{\mathbf{u}}^p \times \mathcal{F}_{\mathbf{u}}^{p-1}$. Conversely, $\omega = \omega_{\parallel} + j_{\boldsymbol{\mu}}\omega_{\perp}$.

For all relevant operators of exterior calculus on M we introduce counterparts (denoted by a hat) that are defined on

the horizontal subspaces. On the other hand, these operators are defined on U as well (subscripted by U), either intrinsically or induced by the embedding. For example, for the *horizontal exterior derivative* $\hat{d} := i_{\mathbf{u}}j_{\boldsymbol{\mu}}d : \mathcal{F}_{\mathbf{u}}^p \rightarrow \mathcal{F}_{\mathbf{u}}^{p+1}$ it can be shown that $\varphi^* \circ \hat{d} = d_U \circ \varphi^*$.

Let $g : \mathcal{X}^p \rightarrow \mathcal{F}^p$ denote the Riesz isomorphism of the metric on M . We define $\hat{g} : \mathcal{X}_{\boldsymbol{\mu}}^p \rightarrow \mathcal{F}_{\mathbf{u}}^p$ such that $\hat{g}\mathbf{v} | \mathbf{w} = g\mathbf{v} | \mathbf{w} \forall \mathbf{v}, \mathbf{w} \in \mathcal{X}_{\boldsymbol{\mu}}^p$. If g_U denotes the Riesz isomorphism of the induced metric on U , then $g_U = \varphi^* \circ \hat{g} \circ \varphi_*$.

Let $\Omega \in \mathcal{F}^3$ denote the normalized and $\hat{\Omega} := i_{\mathbf{u}}\Omega \in \mathcal{F}_{\mathbf{u}}^2$ the *horizontal volume form* on M , $\hat{\Omega} | \hat{g}^{-1}\hat{\Omega} = 1$. Then $\Omega_U = \pm \varphi^*\hat{\Omega}$, depending on the orientation of U . We assume that U is oriented such that the positive sign holds.

The explicit definition of the Hodge operator on M reads $* : \mathcal{F}^p \rightarrow \mathcal{F}^{3-p} : \alpha \mapsto i_{\hat{g}^{-1}\alpha}\hat{\Omega}$. The *horizontal Hodge operator* is defined analogously, $\hat{*} : \mathcal{F}_{\mathbf{u}}^p \rightarrow \mathcal{F}_{\mathbf{u}}^{2-p} : \alpha \mapsto i_{\hat{g}^{-1}\alpha}\hat{\Omega}$, and again $\varphi^* \circ \hat{*} = *_U \circ \varphi^*$.

II. CONTINUOUS SYMMETRY

We use the above definitions to decompose the magnetic vector potential A , the electric current density J , and eventually the curl-curl equation of magnetostatics, $d \frac{1}{\mu} * dA = J^1$:

$$\begin{pmatrix} \hat{d} & 0 \\ \mathcal{L}_{\mathbf{u}} & -\hat{d} \end{pmatrix} \frac{1}{\mu} \hat{*} \begin{pmatrix} -\eta i_{\mathbf{v}} & \eta \\ \frac{1}{\eta}(1 + \eta^2 j_{\boldsymbol{\nu}} i_{\mathbf{v}}) & -\eta j_{\boldsymbol{\nu}} \end{pmatrix} \begin{pmatrix} \hat{d} & 0 \\ \mathcal{L}_{\mathbf{u}} & -\hat{d} \end{pmatrix} \begin{pmatrix} A_{\parallel} \\ A_{\perp} \end{pmatrix} = \begin{pmatrix} J_{\parallel} \\ J_{\perp} \end{pmatrix}, \quad (1)$$

where $\eta = \|\boldsymbol{\mu}\|$, $\boldsymbol{\nu} = (g\mathbf{u})_{\parallel}$, and $\mathbf{v} = \hat{g}^{-1}\boldsymbol{\nu}$. The 2x2 block representation of the exterior derivative and the Hodge operator in terms of the horizontal operators has been derived in [1], eq. (19) and (46)², respectively.

Continuous symmetry means that \mathbf{u} denotes a direction in which the Lie derivatives $\mathcal{L}_{\mathbf{u}}$ vanish, i.e. no variation of fields, material parameters and metric (\mathbf{u} is a Killing field) along \mathbf{u} .

For the system (1) to be decoupled, we need the symmetry direction \mathbf{u} to be orthogonal to the foliation, thus $\boldsymbol{\mu} \wedge g\mathbf{u} = 0$, or, equivalently $\boldsymbol{\nu} = \mathbf{v} = 0$. Since $g\mathbf{u}$ is not an integrable form in general, a foliation that ensures decoupling does not generally exist.

¹ μ denotes the linear magnetic permeability, not to be confused with the 1-form $\boldsymbol{\mu}$.

²Note that the parameters \mathbf{v} and $\boldsymbol{\nu}$ are defined slightly differently in [1]. \mathbf{v} in [1] has to be replaced by $-\xi\eta^2\mathbf{v}$, and $\boldsymbol{\nu}$ by $-\frac{1}{\xi}\boldsymbol{\nu}$.

III. DISCRETIZATION

A mimetic discretization of the pulled-back version of (1) requires discrete counterparts of each of the operators. For this paper we restrict ourselves to 2-D triangular meshes and first-order approximation of p -forms by p -cochains. The derivative operators are well-known to be discretized by incidence matrices. For a discrete Hodge operator we refer to [3], among several possibilities.

The vector-field \mathbf{v} can be discretized by a 1-chain v , see [4]. The 1-form ν and the right-hand side forms are discretized by the de Rham map. The multiplication operator can be derived from the discrete cap product [5] that approximates the continuous wedge product.

A discrete contraction operator has been proposed in [4]. We give a brief outline of the basic concept. The continuous contraction fulfills $i_v \beta | s = \lim_{t \rightarrow 0} t^{-1} \beta | \text{extr}(s, \mathbf{v}, t)$ for a 2-form β , a 1-vector-field \mathbf{v} , and a 1-chain s ³. The extrusion of s in the 2-manifold U is done by transporting the points of s by the flow of the vector-field \mathbf{v} , parameterized by t .

On the discrete level we wish to contract a 2-cochain β by a 1-chain v which stems from the discretization of \mathbf{v} . To this end we extrude all edges e_i in the complex by edges e_j , $j \neq i$. If the edges i and j coincide in a node, the result of the extrusion is a triangle spanned by the two edges which can be approximated by a 2-chain. The extrusion is the empty point-set otherwise. Next the extrusion 2-chain is mapped to the reals by the 2-cochain β . Eventually the above limit process yields

$$i_v \beta | e_i = \sum_j \sum_k \frac{|\mathbf{e}_i \wedge \mathbf{e}_j|}{|\mathbf{f}_k|} v^j \lambda_{ij}^k \beta_k \quad (2)$$

which defines the i -th coefficient of the 1-cochain $i_v \beta$. The factor λ_{ij}^k equals the orientation $\text{or}(\mathbf{e}_i \wedge \mathbf{e}_j)$ if the triangle formed by e_i and e_j has a nonzero intersection with the positively oriented face f_k , and 0 otherwise. Bold-font letters denote the 1- and 2-vectors for edges and faces, and v^j and β_k are the chain and cochain coefficients of v and β , respectively.

This result has been validated by numerical experiments, it differs however from the formulae given in [4], [6].

IV. HELICOIDAL SYMMETRY - NUMERICAL EXAMPLE

In the axi-symmetric case we use cylindrical coordinates (r, φ, z) and set $\boldsymbol{\mu} = d\varphi$, $\mathbf{u} = \partial_\varphi$, and hence $\eta = \frac{1}{r}$. For $\mathcal{L}_{\partial_\varphi} = 0$ we find with $\boldsymbol{\nu} = 0$ and $\mathbf{v} = 0$

$$-\hat{d} \frac{1}{r} \frac{1}{\boldsymbol{\mu}} \hat{*} \hat{d} A_\perp = J_\parallel, \quad -\hat{d} r \frac{1}{\boldsymbol{\mu}} \hat{*} \hat{d} A_\parallel = J_\perp, \quad (3)$$

as the dimensionally reduced representation of the curl-curl equation.

As an example of a non-orthogonal splitting, we use helicoidal coordinates (R, ϕ, Z) , $R = r$, $Z = z$ and $\phi = \varphi - \alpha z$, to represent thin wires along $\mathbf{u} = \partial_Z$. The foliation is given by $\boldsymbol{\mu} = dZ$. We compute $\eta = 1$, $\boldsymbol{\nu} = \alpha R^2 d\phi$, and $\mathbf{v} = \alpha \partial_\phi$.

With this information at hand we proceed to a mimetic discretization of (1). The kernel of the system matrix is

³This is essentially the same as requiring $i_v \beta | \mathbf{w} = \beta | j_v \mathbf{w}$.

composed from the space of constant 0-cochains (A_\perp part) and the image of the discrete gradient (A_\parallel part). A regularization scheme $S' = S + KK^T$ is employed, where S is the system matrix, K is a basis of the kernel of S , and S' is the regularized matrix. This approach is feasible despite the asymmetry of S since $\text{kern} S = \text{kern} S^T$.

As an example we calculate the fields of three twisted wires for vanishing sum of the three currents through the 2-D cross-section U , see Fig. 1.

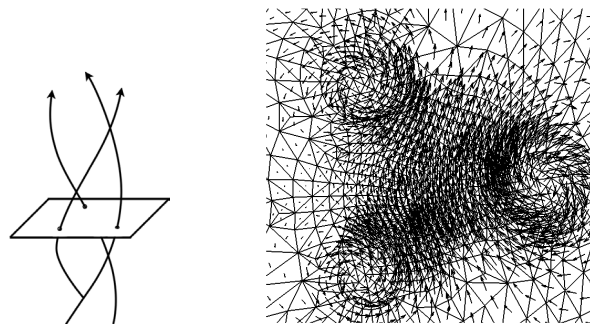


Fig. 1. Left: Currents flowing along helicoidal paths through a 2-D cross-section U . Right: Vector proxies of the parallel magnetic induction in U .

V. CONCLUSION

We have given a (2+1)-D formulation of 3-D magneto-static field problems. Continuous symmetry along a transversal direction eliminates the third dimension. In case there exists a foliation that is orthogonal to the symmetry direction, the equations can be decoupled, resulting in two independent 2-D field problems.

We have applied the theory to a field problem with helicoidal symmetry and successfully produced first results. A thorough validation will follow in the full paper. During the process we have had to reopen the question how to properly discretize the contraction operator. Additional work is required to provide an answer in more general cases, including an analysis of the mimetic properties of the discrete contraction. We will get back to this matter in the full paper as well.

REFERENCES

- [1] S. Kurz, B. Auchmann, and B. Flemisch. Dimensional reduction of field problems in a differential-forms framework. *COMPEL*, accepted for publication, 2009.
- [2] W. H. Greub. *Multilinear Algebra*. Springer-Verlag, Berlin/Heidelberg/New York, 1967.
- [3] B. Auchmann and S. Kurz. A geometrically defined discrete Hodge operator on simplicial cells. *IEEE Transactions on Magnetics*, 42(4):643–646, April 2006.
- [4] A. Bossavit. Extrusion, contraction: their discretization via Whitney forms. *COMPEL*, 22(3):470–480, 2003.
- [5] S. O. Wilson. *On the Algebra and Geometry of a Manifold's Chains and Cochains*. PhD thesis, Stony Brook University, New York, August 2005.
- [6] A. Bossavit. Private Communication, 2009.

Electromagnetic Field Computation in 2D Using the Discrete 1D Green's Function

Do Wan Kim

Department of Applied Mathematics
Hanyang University
Ansan, Republic of Korea
Email: dokim@hanyang.ac.kr

Young-Cheol Yoon

Department of Civil Engineering
The abstract goes here. Myongji College
Seoul, Republic of Korea
Email: ycyeon@mjc.ac.kr

Abstract—A discrete 1D Green's function for accurately computing the 2D electromagnetic field in complicated domains is introduced. The key advantages of the proposed method is laid on the accuracy as well as the availability on complex domains. The 2D Green's function for solving electromagnetic field computations in a 2D domain is strongly depend on the geometry of the domain. The boundary element method uses only the fundamental solution instead of the Green's function itself since it is even easier to find the fundamental solution than to do the Green's function. In this case, however, attentions must be paid, due to the singularity of the fundamental solution, to the singular integrals on the boundary of the domain. It is another merit of our method to circumvent such a singular integral.

I. INTRODUCTION

Green's function methods for solving electromagnetic field computations in 2D strongly depend on problem domains. The boundary element method [1], [2] is well known technique using only the fundamental solution instead of the Green's function since it is even easier to find the fundamental solution than to do the Green's function itself. However, attentions must be paid in this case to the singular integrals over the boundary since the fundamental solution has the blow-up singularity at a singular point. To avoid the singular integral and accurately compute the 2D electromagnetic field in complicated domains, we introduce a discrete 1D Green's function for a 1D differential operator separated from the 2D differential one to govern the electromagnetic field in a 2D domain.

The first attempt has been made to solve the higher dimensional elliptic boundary value problems using the axial Green's function method (AGM) [3]. As a matter of fact, although the AGM is an accurate approach in a complicated domain, it needs the numerical integration on parallel lines to each axis in 2D to solve the elliptic type of boundary value problems since the axial Green's function is found in an integral form due to variable coefficient. In case of the static electromagnetic field, the governing equation has the type of Poisson problem which is elliptic with constant coefficient, so that we can find the discrete 1D Green's function simpler than the axial Green's function of AGM. It has nothing to do with numerical integrations. Since the numerical integrations is in general a time consuming work, it becomes more efficient way to use the discrete 1D Green's function proposed in this paper instead using the axial Green's function in [3]. Through the static

electromagnetic field computation, we show the efficiency and accuracy of the method using the discrete 1D Green's function.

II. DISCRETE 1D GREEN'S FUNCTION METHOD

Let us first consider the following Dirichlet problem in 1D which can describe the 1D electrostatic potential:

$$L_t(u) \equiv u''(t) = f(t) \quad \text{in } \Omega = [a, b] \quad (1)$$

$$u(a) = u_a, u(b) = u_b. \quad (2)$$

Assume $P_n = \{a = t_0 < t_1 < \dots < t_n = b\}$ is an arbitrary partition of the interval $[a, b]$. If $\bar{u}_h(t)$ is a piecewise linear interpolation for a given function $u(t)$ on P_n , then it is readily obtained that

$$\bar{u}_h(t) = \sum_{k=1}^{n-1} \frac{1}{2} \left(\frac{u(t_{k+1}) - u(t_k)}{\Delta t_{k+1}} - \frac{u(t_k) - u(t_{k-1})}{\Delta t_k} \right) |t - t_k| + At + B \quad (3)$$

for some constants A and B where $\Delta t_k = t_k - t_{k-1}$ is the length of k -th subinterval on $[a, b]$. Applying the boundary conditions (2) and then rearranging terms, the interpolation in (3) can be translated into

$$\bar{u}_h(t) = \sum_{k=1}^{n-1} \frac{1}{2} \beta_k(u) G(t, t_k; a, b) + u^B(t; a, b, u_a, u_b) \quad (4)$$

provided we define

$$\beta_k(u) \equiv \frac{u(t_{k+1}) - u(t_k)}{\Delta t_{k+1}} - \frac{u(t_k) - u(t_{k-1})}{\Delta t_k}, \quad (5)$$

$$G(t, \tau; a, b) \equiv |t - \tau| - \left[\frac{b-t}{b-a} |a - \tau| + \frac{t-a}{b-a} |b - \tau| \right], \quad (6)$$

$$u^B(t; a, b, u_a, u_b) \equiv u_a \frac{b-t}{b-a} + u_b \frac{t-a}{b-a}. \quad (7)$$

As a matter of fact, the coefficient $\beta_k(u)$ can be written as follows for $k = 1, 2, \dots, n-1$,

$$\beta_k(u) = u''(t_k) \frac{\Delta t_k + \Delta t_{k+1}}{2} + \frac{1}{6} (u'''(t_k^+) \Delta t_{k+1}^2 - u'''(t_k^-) \Delta t_k^2) \quad (8)$$

for some t_k^\pm with $t_{k-1} < t_k^- < t_k < t_k^+ < t_{k+1}$.

Based on the interpolation (3) and the approximation (8), the inverse differential operator approximated with second order accuracy for the 1D problem in (1) and (2) is obtained as the form

$$u_h(t) = \sum_{k=1}^{n-1} \frac{1}{2} h_k f(t_k) G(t, t_k; a, b) + u^B(t; a, b, u_a, u_b) \equiv \langle f, G_t \rangle + u_t^B = L_t^{-1}(f) \quad (9)$$

where $h_k = \frac{1}{2}(\Delta t_k + \Delta t_{k+1})$ implies the average length of adjacent subintervals at t_k for $k = 1, 2, \dots, n-1$.

It can be proved that the approximate solution in (9) has $O(h^2)$ -convergence for arbitrary subintervals due to (8). We call $\frac{1}{2}G$ in (9) the discrete 1D Green's function since it acts as a Green's function in a discrete sense.

III. OPERATOR DECOMPOSITION FOR 2D ELECTROSTATIC POTENTIAL PROBLEM

The electrostatic potential problem in 2D is expressed in the Poisson problem. Assume Ω is an open bounded domain in \mathbb{R}^2 and $\mathbf{x} = (x, y)$ a point in Ω . Using the 1D inverse operator in (9), our aim is to solve the 2D Poisson problem defined by

$$L_x(u) + L_y(u) = u_{xx} + u_{yy} = f \quad \text{in } \Omega, \quad (10)$$

$$u = u^{\partial\Omega} \quad \text{on } \partial\Omega. \quad (11)$$

Introducing a new variable ϕ enables us to decompose the Poisson equation into two equations

$$L_x(u) = \phi \quad \text{in } \Omega, \quad (12)$$

$$L_y(u) = f - \phi \quad \text{in } \Omega, \quad (13)$$

$$u = u^{\partial\Omega} \quad \text{on } \partial\Omega. \quad (14)$$

As a result of elimination of u (see [3]) from (12), (13), and (14) at the cross point $(x_i, y_j) \in \Omega$ of x -axial line(X_{y_j}) and y -axial line(Y_{x_i}) illustrated in fig 1(left), we can write

$$L_x^{-1}(\phi) = L_y^{-1}(f - \phi) \quad \text{at } (x_i, y_j) \in \Omega, \quad (15)$$

provided (x_i, y_j) is a cross point of x -axial line X_{y_j} and y -axial line Y_{x_i} . Equivalently, from the definitions of the bracket $\langle \cdot, \cdot \rangle$ and the boundary value operator u^B in (9), the formulation for ϕ becomes

$$\langle \phi, G_x \rangle + u_x^B = \langle f - \phi, G_y \rangle + u_y^B \quad \text{at } (x_i, y_j) \in \Omega. \quad (16)$$

After discretizing and solving the resultant linear system in (16) by the BiCGM, we obtain ϕ and then by inserting it into (9) instead of f the numerical solution u_h can be calculated. Moreover, directly differentiating it, the first order derivatives are estimated on any cross point.

IV. NUMERICAL RESULTS AND CONCLUSION

Fig 1, the error decay of u_h is of order $O(h^2)$ and its first derivatives have the convergence rate faster than $O(h)$. The uniform axial lines are used in this case and it is also checked that the same convergence order can be achieved even in non-uniformly distributed axial lines. Fig 2 shows the numerical solution for the electrostatic potential problem on L -shaped

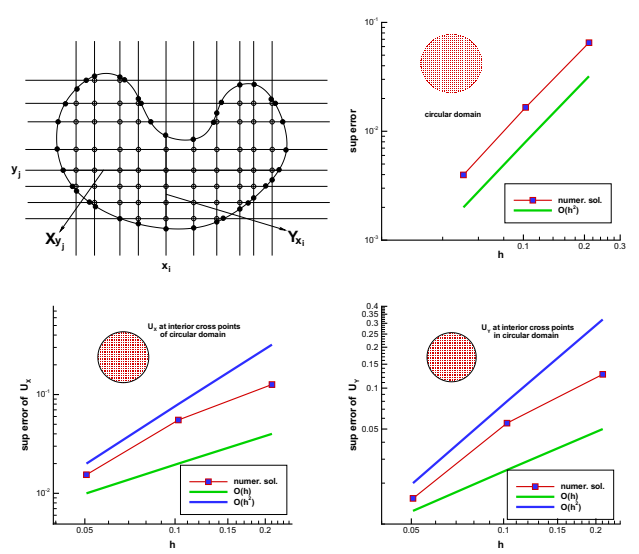


Fig. 1. Schematic diagram for axial lines X_{y_j} and Y_{x_i} which meet at (x_i, y_j) (top left), $O(h^2)$ convergence rates of the numerical solution $U = u_h$ (top right) and its first derivatives U_x (bottom left) and U_y (bottom right): Exact solution $u(x, y) = \cos(xy)$ in $(x-3)^2 + (y-3)^2 < 1.5^2$.

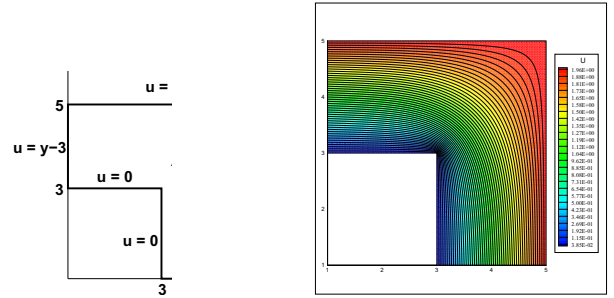


Fig. 2. 2D electrostatic potential problem: Domain configuration(left) and the numerical solution u_h (right)

domain. Although the exact solution u is known to have a derivative singularity at the corner, the discrete 1D Green's function method for the 2D electrostatic problem yields an accurate numerical solution. As we anticipated from the fact that there is no numerical integrations at all, this method is far faster than the original AGM in [3] particularly for the Poisson problem. Our method is not a difference scheme but rather close to the integral one, so that it helps the method stable and accurate.

REFERENCES

- [1] A. Sutradhar and G.H. Paulino, *A simple boundary element method for problems of potential in nonhomogeneous media*, International Journal for Numerical Methods in Engineering, 60:2203-2230, 2004.
- [2] L.C. Wrobel and M.H. Aliabadi, *The Boundary Element Method*, Wiley, New Jersey, 2002
- [3] D.W. Kim, S.-K. Park, and S. Jun, *Axial Green's function method for multi-dimensional elliptic boundary value problems*, International Journal for Numerical Methods in Engineering, 76:697-726, 2008.

Load Scheduling for Power Aware Matrix Multiplication on CPU-GPU Multiprocessing Platform

Da Qi Ren and Reiji Suda

Department of Computer Science, the University of Tokyo
7-3-1 Hongo, Bunkyo ku, Tokyo, 113-0033, Japan
dren@is.s.u-tokyo.ac.jp, reiji@is.s.u-tokyo.ac.jp

Abstract— we introduce a parallel programming method to solve massive matrix multiplications on multi-core and multi-GPU platform with CUDA. Based on the different power features of each power-related processing element (PE) including CPUs and GPUs, we provide a load scheduling approach to adjust the workload distribution among each PE in order to optimize the overall power efficiency of the system during the matrix computation. On GPU kernel programming, some memory management methods have been implemented for enhancing the utilities of GPU shared memories therefore accelerating computation speed. The timing and power consumptions have been measured when the above methods have been implemented. Comparing with non load scheduling program, it can save up to 25% of energy; also the multi GPU timing performance has enhanced 40% than single GPU.

Index Terms—Software Methodology: (g) programming techniques, (h) massively parallel algorithms.

I. INTRODUCTION

An optimal way of multiplying matrices is a fundamental operation in solving electromagnetic problems requiring large numbers of elements for high-accuracy solutions. Faster matrix multiplication would give more efficient algorithms for many standard linear algebra problems, such as solving systems of linear equations and finding determinants. The performance of matrix multiplication is highly dependent on the underlying computational algorithm as well as the system architecture. The Graphics Processing Units (GPU) are now considered as serious challengers for high-performance computing solutions because of its suitability for massively parallel processing and vector computations. However they have power consumptions up to 300W. Power efficiency investigation is also required by program design because a large scale computation may need hundreds hours of continuous execution, the program design strategies will significantly affect the overall energy expense. [1]

We introduce in this paper (1) Parallel matrix multiplication by Parallel CUDA kernel on multi-GPUs.to reach a very high GFLOPS. (2) A load balancing approach to adjust the workload distribution therefore minimizing the power consumption. (3) The performance results. [2], [3]

II. LARGE MATRIX MULTIPLICATION ON CPU-GPU MULTIPROCESSING PLATFORM

For given matrices $A \in R^{m \times n}$ and $B \in R^{n \times m}$, there are various algorithms to implement $C = AB$ in parallel. Here we partition the matrix A, let $A = (A_1^T, A_2^T \dots A_n^T)^T$, where $A_i \in R^{1 \times n}$ ($i = 1, 2, \dots, n$) is each row in matrix A. We calculate $C = AB$ follow the procedure, as shown in Fig 1.

- (1) Assign computations $(A_{im/p+1}, \dots, A_{(i+1)m/p})B$ to GPU i ($i = 0, 1, \dots, p-1$);
- (2) Run local computation on each GPU $(C_{im/p+1}, \dots, C_{(i+1)m/p}) = (A_{im/p+1}B, \dots, A_{(i+1)m/p}B)$;
- (3) Write the result in matrix C to CPU memory.

GPU is viewed as a compute device operating as a processor to the main CPU (host). Data-parallel, compute intensive functions should be loaded to the GPU device. Also a different level of parallelism is applied on CPU side with OpenMP to parallelize applications in a coherent and efficient way. A CUDA kernel can be called by any of the CPUs running OpenMP. To well utilize the GPU shared memory in one block, we schedule the workload segment as same size as the shared memory, this can significantly improve GPU efficiency. The usage of Multi-GPU can gain 40% speedup than single GPU. (The programming details will be provided in the long paper).

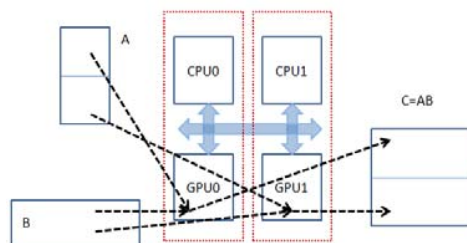


Fig.1 Parallel Matrix Multiplication on Multi CPU-GPU platform

III. POWER AWARE

In a multiprocessing system, power can be defined at various levels of granularity such as system, cores, and components, represented as P_{system} , P_{core} , $P_{component}$. the overall system power consumption can be defined as (1)

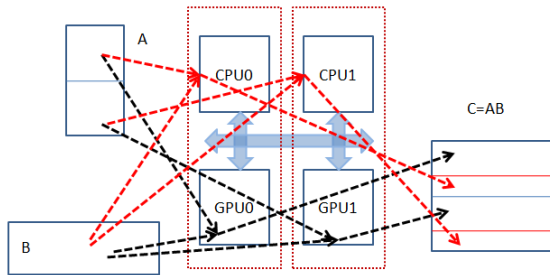


Fig.2. Scheduled workload for Matrix Multiplication on Multi CPU-GPU platform

$$P_{system}(w) = \sum_{i=1}^N P_{CPU}^i(w^i) + \sum_{j=1}^M P_{GPU}^j(w^j) + P_{comm} + P_{heat} \quad (1)$$

Where N is the number of CPU cores, M is the number of GPUs, w is the workload, w^i and w^j represent the workload assigned to the CPU i and GPU j , respectively. If a core i is composed by k components and a GPU is composed by l components, their power consumption can be represent as

$$P_{CPU}^i = \sum_{n=1}^k P_{CPU}^{(i,k)}(w^i) \text{ and } P_{GPU}^j = \sum_{n=1}^l P_{GPU}^{(j,l)}(w^j), \text{ respectively.}$$

A basic principle for power aware load scheduling is to (1) try to move workloads to low-power component; (2) minimize the number of used high-power component; (3) try to reduce the working time, in order to save system power.

In this work, (1) and (3) have been implemented. In detail we schedule the portion of the computations to be run on CPUs by using multi threads, then the CPU utilization is enhanced, and the overall time performance is improved, finally the total energy consumption is reduced. We change

- (1) Assign computations ($A_{im/p+1}, \dots, A_{(i+1)m/p-k}$) B to GPU i ($i = 0, 1, \dots, p-1$);
- (2) Assign computations ($A_{(i+1)m/p-k}, \dots, A_{(i+1)m/p}$) B to CPU i ($i = 0, 1, \dots, p-1$);
- (3) Run local computation on each CPU and GPU, and then write the result in matrix C to CPU memory.

Where k is the number of vectors to be assigned to CPU, also in above algorithm, we assume the number of CPU and GPU are same. (We will provide detailed approach in the long paper).

IV. RESULTS

We provide the results from DELL M1730 with duo cores platform composed by 2 Intel(R) Core(TM) 2 Extreme CPU X9000 @ 2.80GHz, and two Nvidia GeForce graphic cards 8800MGTX. One thing need to be noted that, the double precise in CPU is 64bits; however GPU can only use float which is 32bits. We use Kahan Summation Formula to improve the precision for the multiplication result.

We calculated $m \in [1000, 10000]$ and $n \in [2000, 20000]$ double precise matrix multiplication on above CPU-GPU platforms utilizing the GPU programming method in (I) and power aware load scheduling method in (II). The peak performance for one GPU can reach 654.82 GFLOPS. The timing result is shown in Fig.1. When applying load scheduling, we have 20-30% speedup than without load scheduling. (Detail analysis will be in the long paper)

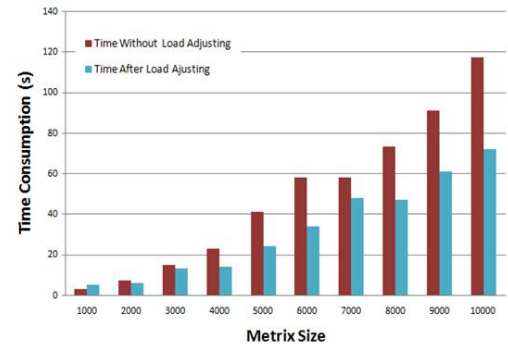


Fig.3. Timing Performance

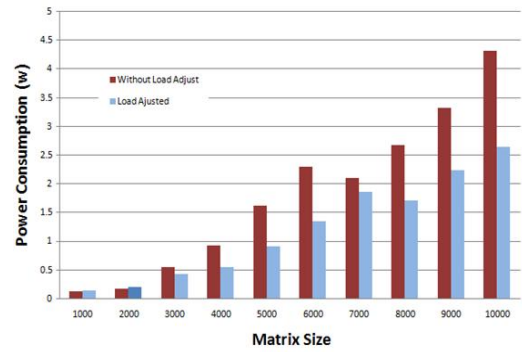


Fig.4. Power Performance

We have measured the power consumption of the computation by using power analyzer from AC power input, and without AC power by measure the battery. The power consumption values measured from the program are shown in Fig. 4. The Load balancing approach can improve power performance around 5 -30% depending on the problem size and working environment (in this DELL M1730).

V. CONCLUSION

A CPU-GPU programming method for large- scale matrix multiplication on multi-core platform has been proposed. Power aware load scheduling approach are introduced to the algorithm model for timing and power performance improving.

VI. REFERENCES

- [1] David C. Snowdon, Stefan M. Petters, Gernot Heiser, Power measurement as the basis for power management, Work Shop on Operating System Platforms for Embedded Real-Time applications, 2005.
- [2] Intel® 64 and IA-32 Architectures Software Developer's Manual, Volume 1: Basic Architecture, Order Number: 253665-028US September 2008.
- [3] www.nvidia.com/object/cuda_develop.html, CUDA 2.0 Programming Guide,

Finite element sparse matrix vector multiplication on graphic processing units

Maryam Mehri Dehnavi, David M. Fernández, and Dennis Giannacopoulos, *Members, IEEE*

Department of Electrical & Computer Engineering, McGill University

3480 University Street, Montreal, Quebec H3A 2A7, Canada

maryam.mehridehnavi@mail.mcgill.ca, david.fernandezbecerra@mail.mcgill.ca, dennis.giannacopoulos@mcgill.ca

Abstract— A wide class of finite element electromagnetic applications require computing very large sparse matrix vector multiplications (SMVM). Due to the sparsity pattern and size of the matrices, solvers can run relatively slowly. The rapid evolution of graphic processing units (GPUs) in performance, architecture and programmability make them very attractive platforms for accelerating computationally intensive kernels such as SMVM. This work presents a new algorithm to accelerate the performance of the SMVM kernel on the NVIDIA graphic cards.

I. INTRODUCTION

The performance of finite element (FE) electromagnetic applications can be dominated by the iterative solvers used, such as conjugate gradient (CG) based methods. As problems become larger and more complex, the computation overhead of these kernels dramatically increases the execution time of such solvers on single core CPUs. Thus the development of efficient methods to improve the performance of iterative solvers on parallel processors is almost inevitable.

One of the most important kernels in iterative solvers such as the CG method is the sparse matrix vector multiplication (SMVM). This operation is performed at each iteration and often consumes a majority of the computation time. The main objective of the SMVM kernel is to calculate Ax where A is a sparse matrix and x is a dense vector. Major limitations of SMVM computation involving FE matrices are large memory storage and bandwidth requirements as well as indirect and irregular memory accesses.

Graphic Processing Units (GPUs) have recently evolved into very attractive commodity data-parallel coprocessors. Easy to learn programming interfaces such as CUDA [1] have allowed massive multithreading and increased utilization of large numbers of cores on the GPU, making them cost efficient highly parallel platforms to solve computationally intensive scientific problems [2].

The main objective of this work is to accelerate the performance of finite element SMVM kernels on the NVIDIA GT 8800 graphic cards using a new algorithm, namely PCSR (Prefetch-Compressed Row Storage).

II. GPU ARCHITECTURE

The NVIDIA GT 8800 graphic card (Fig. 1) consists of 12 *streaming multiprocessors* (SMs), each containing eight *scalar processors* (SPs), or processors cores running at 1.5GHz. Each of the SMs access a separate 16KB shared Memory and a total of 8192 registers. The 12 SMs are connected via 512MB of off-chip device memory.

Using the CUDA programming model, the GPU is viewed as a compute device capable of executing a large number of threads in parallel. While the main core of the code is run on the CPU, parts of the applications that exhibit rich data parallelism are implemented as kernel functions on the device

(GPU). Data required by the kernel is transferred to the GPU global memory and the parallel portion of the application is then executed on the device using many different threads. The programmer divides the threads into threads blocks which are distributed amongst the SMs allowing each multiprocessor to run a maximum of 8 blocks. Thread blocks allocated to one SM communicate via fast shared memory, but blocks from different SMs can only communicate through global memory with a memory access latency of up to 600 cycles. Every 32 threads in a block execute the same instruction and are called a warp. When threads in the same warp follow different paths of control flow, we say that these threads *diverge* in their execution. Thread divergence forces the threads in a warp to execute sequentially thus reduces the execution speed of the application and should be avoided [1].

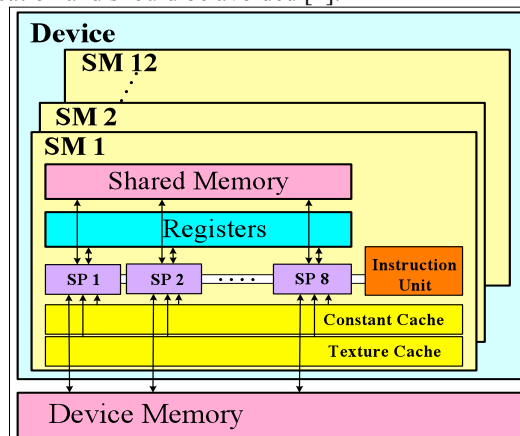


Fig. 1. The GT8800 underlying architecture.

III. SMVM IMPLEMENTATION ON GPUS

The SMVM kernel is one of the most popular operations in finite element simulations. One of the most commonly used data structures for solving such kernels is the Compressed Row Storage (CSR) format. CSR stores the nonzero elements of the sparse matrix into a value vector (VAL) while a corresponding array (INDX) holds the column index of each entry. The format also uses a pointer array (PTR), which points to the first entry of each row in VAL and INDX [3].

Although the computation capabilities of GPUs are very promising (up to 250GFLOPS for GT8800), many challenges exist in optimizing the performance of scientific applications such as the SMVM kernel on such platforms. Some are as follows: global memory access latency, limited shared memory, thread synchronizations, thread divergence, inadequate number of threads and limited global memory bandwidth. The way the programmer addresses these issues differs depending on the application [1].

Since the release of CUDA in 2007, few works have investigated the SMVM kernel optimization on the GPUs.

Buatois *et al.* [4] investigated the performance of Blocked-CSR on the G80 series of NVIDIA graphic cards. Their method does not address thread divergence and is not efficient for sparse matrices with small average non-zeros per row. Sengupta *et al.* [5] proposed the use of segmented scan for calculating SMVM on GPUs. Wiggers *et al.* [6] reorders the matrix rows to increase parallelism in the SMVM kernel. Compared to previous work, our proposed algorithm introduces new methods to hide global memory access latency (data prefetch) and also introduces a new partitioning scheme that enables the programmer to achieve maximum performance by changing the size of the partitions for each block and thread. Detailed description of the methods and its major contributions are described in the next section.

IV. THE PREFETCH-CSR ALGORITHM

The proposed algorithm, PCSR (Prefetch-Compressed Row Storage), is composed of a novel partitioning scheme and a kernel implementation strategy. The partitioning scheme determines the number of threads per block (n) and blocks per kernel (m) during execution. The VAL and INDX vectors in the CSR format are first padded with zeros to be divisible into m equal sections, each sent to a separate block. As shown in Fig. 2, each block then calculates their allocated section of the value vector in n iterations. While some threads are prefetching the required data for iteration $x+1$ from global memory into shared memory, the remaining threads proceed with the addition and multiplications required to calculate the result vector related to rows uploaded in the previous iteration. Major advantages and contributions of the new algorithm in overcoming some of the GPU programming limitations for the SMVM kernel are as follows:

- Pre-fetching the required data for the next iteration in each thread block hides much of the global memory access latencies; thus, while many threads are waiting on global memory accesses, other threads proceed with the necessary calculations for the current data in shared memory.
- Unlike previous techniques, in the new algorithm the threads only need to be synchronized once, minimizing the number of idle threads throughout execution.
- Simultaneous upload of required values of the x vector for each iteration into the shared memory regularizes the accesses to the x vector, enables parallel uploading of the x vector values, and decreases the memory access overhead by loading it into fast shared memory.
- Rows split by iterations in each block can communicate through the very fast on-chip register file avoiding excessive global memory accesses.
- By varying m and n in the proposed partitioning scheme, maximum performance can be determined via changing the number of threads executing per SM while considering the register and shared memory limitations of each multiprocessor.
- Thread divergence is also decreased by allocating the calculations for the result vector to consecutive threads in a warp while threads in other warps upload data into shared memory.

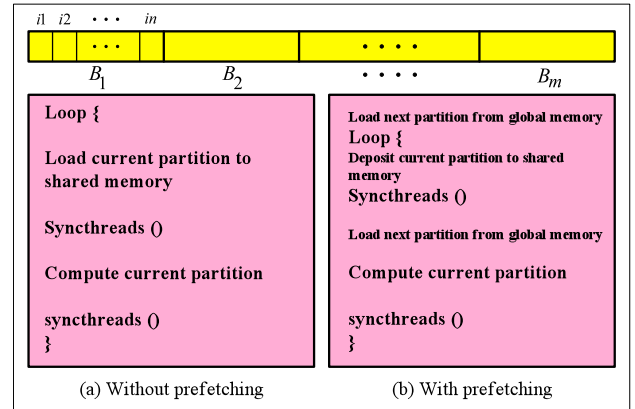


Fig. 2. The Prefetch-CSR Algorithm.

Sample results of PCSR for the *bcsstk* matrix from [6] are shown in Table I. The speedups demonstrated show the performance of the PCSR algorithm vs. the non-prefetch CSR on the GPU (m and n are the same in both methods). As n increases the number of iterations per block increase, allowing the prefetch algorithm to hide more of the memory access latency. Although the performance of PCSR compared to non-prefetch CSR further increases for values of m below 12, the general performance compared to CPUs of both algorithms for $m < 12$ decreases due to having idle SMs (full details in long version paper). Speedups of up to 1.5 with full utilization of all SMs, shows the importance of prefetching data in CSR using GPUs. Since previous non-prefetching CSR algorithms [3] on the GPU have shown up to 10 times speedup compared to the CPU, speedup increases of 1.5 for PCSR compared to previous algorithms can accelerate CSR on the GPUs up to 15 times compared to the CPU (PCSR speedup results compared to the CPU will be presented in the long version paper).

TABLE I
PCSR ALGORITHM SPEEDUP COMPARED TO NON-PREFETCH CSR
ON GT 8800

Partitioning values	$n=1$	$n=12$	$n=15$	$n=30$
	$m=180$	$m=15$	$m=12$	$m=6$
Speedup	1	1.3	1.5	1.9

In the long version of the paper we will propose a technique to minimize thread divergence in the SMVM algorithm and increase the instruction mix, and m and n partitioning values will also be varied to achieve maximum performance.

V. REFERENCES

- [1] NVIDIA CUDA, <http://developer.nvidia.com/object/cuda.html>.
- [2] J. D. Owens, *et al.*, "A survey of general-purpose computation on graphics hardware," *Computer Graphics Forum*, 2007, pp. 80–113. 34.
- [3] Saad Yousef, "Iterative Methods for Sparse Linear Systems," *SIAM*, 2003, pp. 528.
- [4] L. Buatois, G. Caumon, B. Lévy, "Concurrent Number Cruncher: An Efficient Sparse Linear Solver on the GPU," *HPCC*, 2007, pp. 358–371.
- [5] S. Sengupta, M. Harris, Y. Zhang, J. D. Owens, "Scan primitives for GPU computing," *Graphics Hardware*, 2007, pp. 97–106.
- [6] W.A. Wiggers, V. Bakker, A.B.J. Kokkeler, A.B.J. and G.J.M. Smit, "Implementing the conjugate gradient algorithm on multi-core systems." *Proc. International Symposium on System-on-Chip*, 2007, pp. 11–14.
- [7] Matrix market, March 2007 [Online]. Available: <http://math.nist.gov/MatrixMarket/>.

AUTHOR'S INDEX

- Abdellatif, Miraoui 420
Abdesslem, Djerdir 420
Abed, Nagy Y 177
Abe, Nancy Mieko 412
Abe, Nancy Mieko 326, 1060
Abi Rached, Lena 438
Abou-Elyazied Abdallah, Ahmed 316
Abu Talib, Feras 1018
Ackermann, Wolfgang 670, 825
Adriano, Ricardo Luiz 518
Afonso, Marcio Matias 835
Afonso, Márcio Matias 516
Agheb, Edris 767
Aguglia, Davide 197
Aiello, Giovanni 27, 43
Aimé, Jérémie 881
Akduman, Ibrahim 466
Al-Aawar, Nizar F. 271
Albanese, Raffaele 77, 642
Albert, Jan 57, 773, 911
Albuquerque, Maria Rosa M. L. 456
Alfonzetti, Salvatore 27
Alfonzetti, Salvatore 43
Aliferov, Alexandr 155
Alípio, Rafael Silva 516
Allag, Hicham 574
Almeida, Andre A. 494
Alotto, Piergiorgio 97, 303, 454, 719, 1068
Alvarenga, Leonardo Lopes Santos 518
Alvarez-Mariño, Casimiro 372
Alves, Francisco 438
Amara, Yacine 127, 799
Amoiralis, Eleftherios Ioannis 99
Andjelic, Zoran 141
Andjelic, Zoran 63, 161, 666
Andrade, André de 185
Antczak, Marcin 213, 622
Araújo, Laís Martins 426
Araújo, Lincoln Machado de 364
Ardon, VinCent 881
Arjona, Marco 85, 195, 283
Arkadan, Abdul Rahman A. 271
Arkkio, Antero 71, 87, 209, 219, 568, 600, 941
Arkkio, Antero 191, 993
Artaserse, Giovanni 77
Asai, Yasuyoshi 149
Assumpção Bastos, João Pedro 717
Ataka, Ryo 949
Aubertin, Mathieu 29

Auchmann, Bernhard 887, 1076
 Außerhofer, Stefan 69
 Ayala, Helon Vicente Hultmann 303
 Azami, Satoshi 949
 Baatar, Nyambayar 588
 Babaie, Mojtaba 785
 Badics, Zsolt 5
 Bae, Jaenam 953
 Baek, Myung Ki 400
 Baggio Filho, Nolvi Francisco 201
 Bai, Baodong 973
 Bai, Baodong 725
 Bandelier, Bernard 715
 Bandlow, Bastian 548
 Bang, Deokje 935
 Banucu, Remus 57, 773, 911
 Barakat, Georges 127, 799
 Barbosa, Leandro Zavarez 245
 Bartel, Andreas 227
 Bastos, João Pedro Assumpção 133, 739
 Batista, Lucas de Souza 295
 Batistela, Nelson Jhoe 137
 Batoun, Bachir 620
 Baudrand, Henri 490, 823
 Bauernfeind, Thomas 358, 883
 Baumgarten, Daniel 275
 Baumgartner, Ulrike 584
 Bebendorf, Mario 1028
 Beghou, Lotfi 500
 Belahcen, Anouar 87, 568, 578, 600, 727
 Belakehal, Soltane 620
 BeLkadi, Mohamed 89
 Benabou, Abdelkader 11, 737, 739, 741, 1016
 Benalla, Hocine 620
 Benderskaya, Galina 825
 Beniakar, Minos E. 179
 Benoit, Delinchant 7
 Benoit, Delinchant 83
 Bentounsi, Ammar 620
 Berbecea, Alexandru Claudiu 312
 Berger, Kévin 512
 Bergmann, José Ricardo 1034
 Bernard, Laurent 187, 237
 Bertoli, Sávio Leandro 857
 Bettini, Paolo 25, 995
 Bezerra, Diego Souza 462
 Bidaud, Francis 927
 Bilicz, Sandor 432
 Bilicz, Sandor 3
 Binder, Andreas 895
 Bird, Jonathan 121
 Biro, Oszkar 358, 883, 923
 Bíró, Oszkàr 472

Bíró, Oszkár 69, 113, 398
Bíró, Oszkár 81, 552, 584
Bittencourt, Helio Radke 51
Boesing, Matthias 596
Bölöni, Francisc Attila 1016
Bonisoli, Elvio 173
Borzi, Giuseppe 43
Bossavit, Alain 223
Bottauscio, Oriano 646, 891
Bouillault, Frederic 576
Bouillault, Frédéric 187, 564
Bowen, David 171
Brauer, Hartmut 644
Braunstein, J. 285
Brisset, Stephane 536, 865
Brochet, Pascal 312, 865
Brochet, Pascal 536
Buffa, Annalisa 366, 807
Burais, Noël 1044
Buzaid, Antonio Carlos 51
Byun, Jin-Kyu 540
Byun, Jin-Kyu 273, 289
Cabral, Emanuela 486
Cabral, Sérgio Henrique Lopes 857
Calà, Enrica 530
Calil, Wilerson Venceslau 1012
Calvano, Flavio 277, 546
Caminiti, Ida Maria Vincenza 634
Campelo, Felipe 324, 410
Campos, Antonio Luiz Pereira de Siqueira 364
Canova, Aldo 49, 173
Carcangiu, Sara 255
Cardelli, Ermanno 193, 544
Cardona, Augusto 51
Cardoso, Jose Roberto 498
Cardoso, Jose Roberto 1005
Cardoso, José Roberto 927
Cardoso, José Roberto 514
Cardoso, José Roberto Cardoso 869
Carlos, Sartori 506
Cauffet, Gilles 15
Cauffet, Gilles 145
Cay, Zarife 991
Cazacu, Emil 855
Cedens, Zoltan 893
Cendes, Zol 572
Cendes, Zoltan 386
Cervený, Jakub 101
Chadebec, Olivier 15, 293, 512, 881
Chang, Junghwan 416, 935
Chaniotis, Antonios 95
Chan, Tze-Fun 217, 586, 757, 925
Chari, Mvk 285

Charmoille, Vincent 115
 Chebak, Ahmed 111
 Chen, Chao 398
 Cheng, K.W.E 672
 Cheng, Zhiguang 731
 Cheng, Zhiguang 861
 Chen, Jiaxin 793
 Chen, Liang 628
 Chen, Mingyou 125
 Chen, Qingming 572
 Chen, Shuiming 520
 Chen, Shuiming 157
 Chen, Yu 584
 Chen, Zhenmao 328
 Cheong, Hee Jun 787
 Chiampi, Mario 646
 Choi, Dawoon 929
 Choi, Hong Soon 159
 Choi, Hong-Soon 17, 588, 909
 Choi, Jong-Ho 630
 Choi, Myoung-Hyun 189
 Choi, Nak-Sun 540
 Cho, Su-Yeon 955
 Choua, Yahya 873, 1048
 Cho, Yong Hyun 921, 967
 Cho, Yonghyun 959
 Cho, Yunhyun 181, 606, 929
 Chung, Shi-Uk 759
 Ciric, Ioan R. 119
 Cisneros-Gonzalez, Merit 195
 Ciuperca, Ionel 13
 Ciuprina, Gabriela 392
 Clavel, Édith 881
 Clemens, Markus 123
 Clemens, Markus 390, 879
 Clenet, Stephane 61, 404, 681
 Coco, Salvatore 314, 530
 Coco, Salvatore 33, 488, 554, 819
 Codecasa, Lorenzo 65, 376, 721
 Coelho, Leandro dos Santos 452
 Coelho, Leandro dos Santos 245, 440
 Colin, Arnaud Christophe Pierre Marie 518
 Corcolle, Romain 564
 Corrêa, Bruno Carvalho 380
 Cortes, André 326
 Costa, Emanuel 464
 Costa, François 500
 Costa, Karlo Queiroz 470
 Costa, Mauricio Caldora 1005
 Cougo, Bernardo 624, 803, 907
 Coulomb, Jean-Louis 145
 Coulomb, Jean-Louis 15, 293
 Cranganu-Cretu, Bogdan 538

Crevecoeur, Guillaume 297, 316, 989
 Cros, Jérôme 111, 197
 Cros, Jérôme 971
 Crozier, Stuart 299
 Cruz, Rossana M. S. 354, 422
 Cruz, Vanessa Gomes 841
 Cugat, Orphée 656
 Cui, Xiang 528
 Cui, Xiang 31, 348, 1022
 Cunha Pinto, José Kleber 514
 Cvoric, Dalibor 167
 da Costa Silveira, Camila 1068
 Daikoku, Akihiro 205
 da Luz, Mauricio Valencia Ferreira 137, 741
 D'amore, Marcello 508
 Daniel, Laurent 103, 187, 564
 Dantas, Alberto Lisboa 514
 Dardenne, Julien 334, 1044
 da Silva, Claudia Andréa 927
 da Silva, José Patrocínio 362
 Das, Rajeev 9
 D'Assunção, Adaildo Gomes 364
 D'assunção, Adaildo Gomes 354, 422, 456
 D'assunção Jr, Adaildo Gomes 490
 Davidovich, Michael V. 839
 de Doncker, Rik W. 596
 de Farias, José Ewerton P. 823
 de Gersem, Herbert 117, 227, 699
 de Gersem, Herbert 19
 de Haan, Sjoerd W.H. 167
 Dehez, Bruno 301
 Dekeyser, Jean-Luc 408
 Delinchant, Benoit 574
 Della Torre, Edward 544
 Demenko, Andrzej 213, 622, 677
 Demillier, Laurent 15
 de Paula, Pedro Pereira 913
 de Santis, Valerio 370, 508
 de Souza, Alisson Henrique Quemel 1054
 Di Barba, Paolo 305
 Dilettoso, Emanuele 43
 Dilettoso, Emanuele 418
 Ding, Kai 672
 Ding, Wen 37, 203
 Di Rienzo, Luca 73
 Djeghloud, Hind 620
 Djennah, Mohammed 524
 Djonny, Weinzierl 506
 Dlala, Emad 219, 568, 578, 600, 727
 Dlotko, Pawel 109
 Dmitriev, Victor 374, 470, 484
 Dohlus, Martin 390
 Doi, Yuhito 1003

Dokonal, Luiz Von 969
Dolean, Victorita 241, 338
Dolezel, Ivo 101, 175
Dolinar, Drago 1020
Dorrell, David G. 594, 761
Dorrell, David George 207, 781
Dosopoulos, Stylianos 703
dos Santos Coelho, Leandro 454
dos Santos Coelho, Leandro 303, 1068
dos Santos, Eduardo Aparecido 1054
do, Thai Phuong 560
Douine, Bruno 687
Duarte, Jorge 616
Dubas, Frédéric 211, 859
Dubcova, Lenka 101
Duchesne, Stéphane 562
Ducreux, Jean Pierre 11
Dughiero, Fabrizio 305, 510
Dular, Patrick 297
Dular, Patrick 65, 135, 137, 344, 721, 1066
Dular, patrick 1
Dupré, Luc 316
Dupré, Luc 297, 989
Du Terrail Couvat, Yves 151
Du, Zhiye 628
Dyck, Derek 592
Ebrahimi, Bashir Mahdi 775, 785, 1050
Ehrich, Matthias 713
Ehsan, Hashemi 999
Eichardt, Roland 251
Ekram, Samsul 594, 761
El Alami, Nabil 715
El Bouajaji, Mohamed 241
Emmanuel, Hoang 1058
Encica, Laurentiu 616
Enciu, Petre 249
Espanet, Christophe 211, 859
Esposito, Vincenzo 193
Esquerre, Vitaly Felix Rodriguez 462
Ewald, Hartmut 47
Faba, Antonio 193, 544
Fabrice, Auzanneau 340
Fabrice, Duval 492
Fagundes, Rosemeri C 875
Fahimi, Babak 899
Fahs, Hassan 338
Faiz, Jawad 775, 1050
Faiz, Jawad 785
Fang, Liang 795, 905, 943
Fang, Shuhua 660
Fang, Xu 632
Fanni, Alessandra 255
Faridi, Mohsen 767

Faridi, Mohsen 999
Feliachi, Mouloud 831
Feliziani, Mauro 508
Feliziani, Mauro 370
Feng, Han 31
Fernandes, Leandro Carísio 460
Fernández, David M. 827, 1082
Ferraioli, Fabrizio 985
Ferraioli, Fabrizio 634
Ferreira, Antonio Carlos 791
Ferreira da Luz, Mauricio V. 1066
Ferreira, J. Abraham 167
Fezoui, Loula 338
Figuroa, Hugo Enrique Hernandez 462
Filho, Mario Leite Pereira 1005
Filipowicz, Stefan Franciszek 436, 851
Firmino, Luciana 502
FLemisch, Bernd 1076
Flores Filho, Ály Ferreira 201
Fonseca, Alexandre Ramos 380
Fontchastagner, Julien 257
Fonteyn, Katarzyna Anna 87
Fontgalland, Glauco 490, 823
Forest, François 624, 803, 907
Forghani, Behzad 861
Formisano, Alessandro 634, 751, 985
Forzan, Michele 155, 510
Fouladgar, Javad 89, 570
Fraga, Fabio. N. 494
Franck, David 801
Frédéric, Bouillault 1058
Fresa, Raffaele 77
Freschi, Fabio 281
Freschi, Fabio 49, 173, 480, 719
Fujino, Chiyo 205
Fujita, Masafumi 813
Fujiwara, Koji 566
FujiWara, Koji 382, 749, 845
Fukuchi, Shigemasa 749
Fukushima, Noriaki 743
Fulginei, Francesco Riganti 554
Funieru, Bogdan 895
Furno Palumbo, Maurizio 642
Fu, Weinong 793
Fu, Zhengcai 705
Gagnoud, Annie 151
Gaignaire, Roman 61, 297, 344
Gao, Yanhui 566, 749
Gati, Azzedine 668
Gerard, Meunier 7
Gerbaud, Laurent 249, 560
Geus, Klaus de 875
Geuzaine, Christophe 233

Geuzaine, Christophe 297, 344, 1066
 Geuzaine, Christophe 1
 Ghassemi, Majid 139
 Ghassemi, Majid 21
 Giaccone, Luca 49
 Gianluca, Mazzucco 91
 Giannacopoulos, Dennis D. 1018, 1082
 Giannacopoulos, Dennis D. 827
 Gilbert, Geoff 592
 Gillon, Frédéric 312
 Giovara, Vittorio 480
 Glineur, François 301
 Glotic, Adnan 424
 Godard, Pierre 342
 Goddard, Kevin 310
 Gödel, Nico 550
 Gödel, Nico 879
 Godoi, Walmor C 875
 Golosnoy, Igor O. 229
 Golshayan, Maryam 650
 Gong, Weizhi 632
 Go, Sung-Chul 789, 953
 Gotman, Jean 723
 Gotoh, Yuji 67, 542, 747
 Greaves, Simon 235
 Gross, Warren J. 827
 Grubisic, Stevan 486
 Grzywacz, Tomasz Marek 809
 Guarnieri, Massimo 91, 97
 Guerin, Christophe 115
 Guerin, Pierre 29
 Gu, Huanhuan 723
 Guibert, Arnaud 293
 Guichon, Jean-Michel 881
 Guillot, Eilin 981
 Guimaraes, Frederico Gadelha 295
 Guo, Youguang 582, 915
 Guo, Youguang 153, 163, 215, 259, 434, 632, 729, 793
 Guyomarch, Frédéric 847
 Guyomarc'h, Frédéric 408
 Gyimothy, Szabolcs 432
 Gyimothy, Szabolcs 3
 Gyselinck, Johan 1
 Gyselinck, Johan 135
 Gysen, Bart 616
 Gysen, Bart. L.J. 769
 Haavisto, Ari 941
 Habjanic, Anton 131
 Hafla, Alexander 773
 Hafla, Wolfgang 911
 Hafner, Martin 213, 622, 801
 Haguët, Vincent 636
 Haijun, Luo 1030

Hameyer, Kay 213, 394, 622, 801, 811
 Hämmerle, Florian 883
 Ham, Sang-Hwan 953, 955
 Han, Kyuyoung 416
 Hantila, Florea I. 75
 Hantila, Florea I. 119
 Haraguchi, Yu 1040
 Hashemi, Ehsan 767
 Haueisen, Jens 251, 275
 He, Bo 386
 He, Jinliang 157
 He, Jinliang 45, 520
 Henaux, Carole 35
 Henneron, Thomas 29, 739
 Henrotte, Francois 843
 Henrotte, François 394, 811
 Henze, Olaf 991
 Herbet, Philippe 927
 Hernandez, C 85
 Hernandez, Concepcion 283
 HernaNdez, Concepcion 195
 Heumann, Holger 394
 He, Wei 53, 125
 Hihat, Nabil 556
 Hijazi, Toufic M. 271
 Hiptmair, Ralf 1028
 Hirata, Katsuhiko 662, 664
 Hirata, Katsuhiko 149, 165, 777, 897, 1056
 Hirata, Katuhiko 805
 Hirosato, Shigetaka 1040
 Hofer, Matthias 658
 Honegger, Thibault 636
 Hong, Jong-Pyo 905
 Hong, Jung-Pyo 221, 590, 608, 612, 763, 795, 931, 937
 Hong, Jung-Pyo 909, 943
 Hong, Jungpyo 947
 Hong, Sun-Ki 580, 733
 Ho, Siu-Lau 660
 Ho, S.L. 261, 877, 1070
 Hsieh, Min-Fu 594, 761
 Huang, Hongxia 679
 HuaNg, Yunkai 915
 Hubert, Olivier 103
 Huf, Alexander 773
 Hulusi, Acikgoz 640
 Hu, Yan 919
 Hwang, Sang-Moon 759
 Iacotucci, Francesco 985
 Iamamura, Bruno Akihiro Tanno 981
 Ida, N. 336
 Ida, Nathan 61
 Igarashi, Hajime 324, 406, 410, 476, 837
 Igarashi, Hajime 695

Iijima, Yosuke 324
 Ikejiri, Shohei 1056
 Ikuno, Soichiro 652
 Ikuno, Soichiro 701
 Im, Jong Bin 765, 963
 Im, Jongbin 979
 Ioan, Daniel 392
 Ionita, Valentin 855
 Ishibashi, Kazuhisa 63
 Ishiguro, Hiroshi 664
 Ishihara, Yoshiyuki 382
 Ishihara, YoshiyuKi 749, 845
 Ishikawa, Takeo 949
 Islam, Mohammad Jahirul 209
 Itoh, Taku 711
 Iwashita, Takeshi 1026
 Iwashita, Takeshi 813
 Jaendl, Michael 243, 430, 538
 Jang, Ik Sang 939
 Jang, Jin Seok 933
 Jassal, Anoop 199
 Jean Louis, Coulomb 83
 Jean-Michel, Guichon 7
 Jeong, Young Woo 614
 Jesenik, Marko 131
 Jeung, Giwoo 534, 540
 J. Gulo, Carlos Alex Sander 691
 Jia, Jin 526
 Jiangjun, Ruan 1064
 Jiang, Kexun 871
 Jiang, Xiaohua 1007
 Jiang, Youming 163
 Ji-Hui, Yu 1001
 Jin, Chang Sung 939
 Jin, Chang-Sung 955
 Jin, Jia 1001
 Jin, Ping 660
 Joo, Daesuk 1036
 José, Cardoso 506
 Junfeng, Wang 1030
 Jung, Hyun-Kyo 330, 630, 901
 Kagimoto, Hiroyuki 745
 Kahng, Sungtek 428
 Kaimori, Hiroyuki 813
 Kakami, Shuhei 777, 897
 Kalluf, Flavio Jorge Haddad 969
 Kameari, Akihisa 813
 Kameni, Abelin 687
 Kaminski, Grzegorz 191
 Kamitani, Atsushi 701, 711
 Kamitani, Atsushi 652
 Kanai, Yasushi 356
 Kanai, Yasushi 235

Kanayama, Hiroshi 360
 Kanayama, Hiroshi 23
 Kang, do-Hyun 608
 Kang, Dohyun 935
 Kang, Dong-Woo 789, 953
 Kang, Hyun-Soo 987
 Kanou, Yuji 388
 Kaper, Knut A. 596
 Karaguler, Turhan 478
 Karban, Pavel 101, 175
 Kashiwa, Tatsuya 356
 Kasumovic, Mensur 424
 Kauffmann, Paul 636
 Kawanaka, Keiji 745
 Kawanaka, Keiji 450
 Kawano, Kenji 324
 Kawase, Yoshihiro 777, 821, 897, 1046
 Kefalas, Themistoklis D. 179
 Kenmoe-Fankem, Eric D. 225
 Keshtkar, Asghar 21
 Kettunen, Lauri 546
 Khang, Huynh Van 209
 Kher, Sameer 386
 Kida, Tomoyuki 1056
 Kienesberger, Markus 243
 Kim, Byongkuk 606
 Kim, Byung-Taek 189
 Kim, Byung-Taek 610
 Kim, Byung Teak 933
 Kim, Dae-Kyong 610
 Kim, Dojin 947
 Kim, Dong-Hun 273, 287, 534, 540
 Kim, Dong Sok 279, 320
 Kim, Dong-Wook 534
 Kim, do Wan 384
 Kim, do Wan 1078
 Kim, Heung-Geun 17, 534
 Kim, Hyeong-Seok 273, 287, 289, 428
 Kim, Hyo Jun 975
 Kim, Jae Min 279
 Kim, Jae Min 320
 Kim, Jimin 947
 Kim, Jinho 416
 Kim, Ji-Won 759, 763
 Kim, Jiwon 935
 Kim, Ki-Chan 598, 965
 Kim, Koon-Tae 428
 Kim, Kwang Soo 765
 Kim, Kwangsoo 963, 979
 Kim, Seung Joo 765, 939, 963
 Kim, Seung-Joo 953
 Kim, Seungjoo 979
 Kim, Tae Heoung 987

Kim, Won Ho 765, 963
 Kim, Won-Ho 789
 Kim, Wonho 979
 Kim, Yong Hyun 602
 Kim, Youngkyoun 221
 Kim, Young-Kyun 937
 Kim, Young Sun 105, 159, 332, 400, 755
 Kim, Young-Sun 17
 Kim, Yung Hyun 626
 Kiss, Imre 432
 Kitak, Peter 923
 Kiya, Atsushi 67
 Kladas, Antonios 95
 Kladas, Antonios 99
 Kladas, Antonios G. 179, 618
 Kluess, Daniel 47
 Knight, Andrew M. 446
 Koch, Stephan 19, 991
 Koczka, Gergely 113
 Koestinger, Alice 538
 Koh, Chang Seop 247, 580, 614, 733, 735, 787, 863, 917
 Koh, Chang Seop 588, 975
 Ko, JAe-Hyeong 287, 289
 Koltermann, Paulo Irineu 853
 Komeza, Krzysztof 556
 Kong, Li 308
 Konrad, A. 683
 Korecki, Julien 11, 847
 Kost, Arnulf 713
 Köstinger, Alice 243, 430
 Koterias, Dariusz 771
 Kouhia, Reijo 87
 Koyama, Kazuya 235
 Krafft, Charles 171
 Krahenbuhl, Laurent 498
 Krähenbühl, Laurent 512, 1066
 Krämer, Florian 1028
 Krebs, Guillaume 681, 843, 1016
 Kreuawan, Sangkla 312
 Krischan, Klaus Krischan 552
 Kropik, Petr 175
 Kuo-Peng, Patrick 135, 185
 Kuo-Peng, Patrick 137, 1066
 Kurose, Hiroaki 745
 KuRz, Stefan 1076
 Kustov, Mikhail 656
 Kutschera, Ralph 430
 Kwon, Byung-Il 610
 Kwon, Soon-O 590, 612, 905, 909, 931, 937
 Labbé, Thibaut 301
 Labie, Patrice 115
 Labouré, Eric 624, 803, 907
 Ladas, Dimitrios 143

Lahaye, Domenico 199
 Lahaye, Domenico 167
 Laid, Idoughi 1058
 Lai, Loi Lei 217, 757, 925
 Lai, Loi Lei 586
 Lambert, Marc 3
 Lange, Enno 394, 811
 Lanteri, Stéphane 241, 338
 Laskaris, Konstantinos I. 618
 Laudani, Antonino 33, 314, 488, 530, 554, 819
 Laurent, Krahenbuhl 506
 Lavers, J. D. 259, 683
 LaZZaretti, Andre E 875
 Lebensztajn, Luiz 245, 841
 Lebensztajn, Luiz 291, 452, 604
 Leber, Gerald 584
 Le Bihan, Yann 438
 Le Bihan, Yann 873, 885, 1048
 Lecointe, Jean Philipe 556
 Lee, Byeong-Hwa 905, 943
 Lee, Byoung-Kuk 987
 Lee, Chany 330, 630
 Lee, Geon-Ho 937
 Lee, Geun-Ho 612
 Lee, Hong-Ju 759
 Lee, Ho-Young 17
 Lee, Hyang-Beom 273, 287
 Lee, Il Kyo 626, 921, 967
 Lee, Jeong-Jong 590, 612, 795, 905, 909, 937
 Lee, Jeongjong 947
 Lee, Jin-Fa 378, 703
 Lee, Ji-Young 608, 763
 Lee, Ju 598, 765, 789, 939, 953, 955, 961, 963, 965, 979
 Lee, Jung Ho 602, 626, 903, 921, 967
 Lee, Jungho 959, 1024
 Lee, Sang-Ho 763
 Lee, Sangho 947
 Lee, Se-Hee 17, 231, 675, 755
 Lee, Sung-Gu 955
 Lee, Taehoon 959, 1024
 Lefebvre, Bruno 997
 Lefevre, Yvan 257
 Lei, Gang 259
 Leite, Jean V. 741
 Leite, Jean Vianeí 133
 Leite, Jean Vianeí 737
 Le Menach, Yvonnick 408
 Le Menach, Yvonnick 11, 847, 981
 Lessa, Moisés Ferber de Vieira 426
 Lévêque, Jean 59, 687
 Liang, Deliang 37, 203
 Liao, Dan 163
 Li, Cheng-Rong 945

Li, Jian 181, 606, 929
Li, Jinbiao 689
Li, Lin 31, 679
Li, Lin 348
Li, Min 253
Lin, Dingsheng 386, 572, 893
Lin, Heyun 660
Liniger, Markus 464
Lin, Mingyao 779
Lin, Ranran 941
Lin, Zhiwei 729
Lionel, Pichon 640
Lionel, Pichon 340, 492
Lisboa, Adriano Chaves 41, 269, 532, 1038, 1042
Liu, Dikai 434
Liu, Feng 299
Liu, Lei 352
Liu, Qilin 731
Liu, Xiaoming 689
Li, Wei 45, 614, 863
Li, Xin 779
Li, Yan-Qing 945
Li, Ye 1007
Li, Yongjian 582
Lomonova, Elena 616
Lomonova, Elena A. 769
Lopes, Bruno Marciano 426
Lopez-Fernandez, Xose M. 372
Lormel, Corine 334
Lounes, Mokhtari 83
Lowther, David 9, 253, 263, 444, 707
Lowther, David A. 267, 592
Lowther, David A. 534
Lowther, David Alister 709
Luan, Feng 630
Lu, Fang-Cheng 945
Lu, Haiyan 729
Luiz, Lebensztajn 506
Lu, Jiang 614, 863
Lu, Junwei 705
Lu, Junwei 352, 504
Lukasik, Bartosz 310
Luo, Zhaonan 1022
Lu, Tiebing 348
Lu, Tiebing 31
Mac, Duy Hung 404
Macêdo, Thiago Emanuel Alves 1038
Machado, Jose Marcio 691
Machado, Vitor Malo 107
Magele, Christian 243, 430, 468, 538
Majorana, Carmelo 91
Malé, Gaël 59
Malo Machado, Vitor 372

Maniçoba, Robson Hebraico Cipriano 364
 Maradei, Francescaromana 370
 Marchand, Claude 873, 885, 1048
 Marc, Lambert 340
 Marc, Olivas 340
 Mariani, Viviana Cocco 440
 Maricaru, Mihai 119
 Marini de Almeida, Antonio 514
 Marins, Claudio Dias 1060
 Marion, Romain 334
 Mario, Santos Jr 506
 Marques, Gleber Nelson 691
 Martinho, Lucas Blattner 291
 Martins, Éder Rodrigues 853
 Martins, Tiago Carvalho 374
 Martone, Raffaele 634, 751
 Martone, Raffaele 985
 Marzo, Giuseppe Renato Di 1005
 Masse, Alain 636
 Matsuo, Tetsuji 239, 458, 558, 845
 Matsuo, Tetsuji 324
 Mayergoyz, Isaak 171
 Mazauric, Vincent 143, 753
 Mazauric, Vincent 79
 Mcfee, Steve 650
 Medeiros, Luiz Henrique Alves de 494
 Meessen, Koen 616
 Meessen, Koen J. 769
 Mehri Dehnavi, Maryam 1082
 Meibody-Tabar, Farid 225
 Mellor, Phil 783
 Melo, Marcos T. de 494
 Menana, Hocine 831
 Meng, Xiangjun 434
 Mereu, Anna 255
 Mesquita, Renado Cardoso 1042
 Mesquita, Renato Cardoso 380, 1038
 Mesquita, Renato Cardoso 350, 709
 Messine, Frederic 257
 Meunier, Gerard 79
 Meunier, Gerard 115
 Meynard, Thierry: 185
 Meynard, Thierry 624, 803, 907
 Mezani, Smail 59, 687
 Mifune, Takeshi 324, 1026
 Mininger, Xavier 187
 Mipo, Jean Claude 29
 Mipo, Jean-Claude 404
 Miwa, Masahiko 147, 318
 Miyagi, Daisuke 265, 322
 Miyagi, Daisuke 450, 745, 1003
 Miyasaka, Fumikazu 805
 Miyata, Koji 1003

Moghnieh, Hussein 707
 Mohamed Rachid, Mekideche 420
 Mohammad Etemad Rezaie, Mohammad 775
 Mohammed, Osama A 983
 Mohammed, Osama A 177
 Monebhurrun, Vikass 496, 522
 Monebhurrun, Vikass 668
 Montisci, Augusto 255
 Montrucchio, Bartolomeo 480
 Moon, Seung-Ryul 608, 759
 Moos, Sandro 173
 Moreau, Olivier 61, 404
 Moreira, Fernando 817
 Moreira, Fernando José da Silva 350
 Morel, Laurent 560
 Morin, Eric 560
 Moro, Federico 97
 Moro, Federico 91
 Mostafa Kamel, Smail 340
 Motooka, Yuichiro 406
 Motta, Cláudio Costa 55
 Moulin, Renaud 59
 Mousavi, Ali 767
 Mousavi, Seyed Ali 999
 Moussouni, Fouzia 536
 Mühlen, Sérgio 514
 Müller, Juliana Luisa 739
 MUn, Sung Ju 977
 Mun, Sung Ju 903
 Mun, Sungju 1024
 Muramatsu, Kazuhiro 566, 749, 1040
 Muraoka, Hiroaki 235
 Muraro Jr, Ademar 326
 Muraro Jr., Ademar 412
 Murayama, Toshio 815
 Musy, François 685, 1072
 Nabaei, Vahid 999
 Nabeta, Silvio Ikuyo 402, 835, 1032
 Nakamura, Masanori 821
 Nakano, Tomohito 821, 1046
 Nakata, Yoshihiro 664
 Nakazaki, Shunsuke 265, 450
 Namba, Hideyuki 450
 Namba, Yoshihiko 1056
 Nam, Hyuk 905, 943
 Nam, Ki-Yong 590
 Napieralska-Juszczak, Ewa 556
 Napieralski, Piotr 556
 Napov, Artem 1072
 Nassira, Ferkha 420
 Nazarzadeh, Jalal 785
 Netter, Denis 687
 Neumayer, Markus 414

Niayesh, Kaveh 767
 Nicolas, Laurent 685
 Nicolet, Andre 342
 Nicolet, Andre 233
 Nicomedes, Williams Lara 350
 Niemenmaa, Asko 191, 993
 Ni, Guangzheng 352
 Nishikawa, Noriaki 821
 Nishishita, Akira 747
 Nogarede, Bertrand 35
 Noguchi, So 406, 867, 1062
 Nogueira, Antônio Flavio 849
 Notay, Yvan 1072
 Nunes, Cássia Regina Santos 709
 Nunes Freire, Marcílio 362
 Nunn, Nigel 879
 Nyambayar, Baatar 247
 Obayashi, Fuminao 1056
 ODawara, Shunya 1040
 Ofner, Georg Ofner 552
 Ogino, Masao 23, 360
 Ohtani, Tadao 356
 Okamoto, Yoshifumi 382, 845
 Okaue, Yu 805
 Okutani, Tamio 318, 648
 Oliveira, Diogo 295
 Oliveira, Diogo Batista 169
 Oliveira, José de Ribamar S. 456
 Oliveira, Luciana Oliveira 51
 Oliveira, Rosemari Teresinha 51
 Olivier, Chadebec 7
 Olivier, Meyer 640
 Onda, Kazuhiko 318
 Oonishi, Atsurou 165
 Ortega, Jéferson Meneguín 853
 Ospina, Alejandro 873, 885
 Ostrowski, Joerg 396
 Ostrowski, Jörg 1028
 O'sullivan, Francis 231, 675
 Oswald, Alexander Thomas 448
 Otake, Asuka 318, 648
 Ota, Tomohiro 149, 777, 897
 Ota, Tomohiro 662
 Ouyang, Jun 263, 444
 Ovando-Martínez, R.B.B 85
 Palade, V. 336
 Palade, Vasile 269
 Palin, Marcelo Facio Palin 869
 Palmaccio, Roberto 642
 Panek, David 175
 Parise Jr., Orlando 51
 Park, Gwan Soo 320, 1014
 Park, Gwan Soo 279, 482

Park, Il Han 105, 159, 332, 400, 755
Park, Il-Han 231, 675
Park, Il Hwan 482
Park, Joon-Goo 540
Passaro, Angelo 1060
Passaro, Angelo 326, 412
Patsios, Charalampos 95
Paulides, Johan 616
Paulides, Johannes J.H. 769
Paulino, José Osvaldo 518
Paul, Prakash 346
Pavo, Jozsef 3, 432
Peng, Ying 628
Peng, Zhen 378
Pereira Carpes Junior, Walter 486
Pereira, Fabio Henrique 402, 835, 1032
Pereira, Fabio Henrique Pereira 869
Pereira Filho, Mário Leite 514
Pereira, Jonas Alves de Almeida 426
Pereira, Valmir Machado 853
Perotoni, Marcelo 514
Perrussel, Ronan 241, 685
Perrussel, Ronan 13, 498, 512, 1072
Peyrade, David 636
Pham, Minh-Trien 247
Pham, Pascale 636
Pichon, Lionel 237
Pichon, Lionel 500
Pihler, Joze 424, 923
Pinciuc, C. M. 683
Pippuri, Jenni 578, 727
Pippuri, Jenni Elina 568
Piriou, Francis 11, 847
Piriou, Francis 29, 739
Pirmohammadi, Mohsen 21, 139
Poignard, Clair 13
Polinder, Henk 199
Pollicino, Giuseppe 488
Pollicino, Giuseppe 33, 819
Poole, Michael 299
Potratz, Carsten 47
Preda, Gabriel 75
Preis, Kurt 923
Preis, Kurt 358, 883
Preis, Kurt Preis 552
Preto, Airam J. 326
Prost, Rémy 1044
Pusch, David 63
Pusch, David 141, 396, 666
Qian, Li 1030
Qi, LEi 528, 1022
Qiu, Jie 163, 434, 632
Quan-Di, Wang 1001

Qu, Hui 129
 Qu, Hui 308
 Ragusa, Carlo 480
 Raharijaona, Jacques 799
 Rainer, Siegfried 81, 552
 Raizer, Adroaldo 502
 Raizer, Adroaldo 500
 Ramdane, Brahim 89
 Ramirez, Jaime Arturo 295
 Ramirez, Jaime Arturo 410
 Ramos, Airton 829
 Rannou, Corinne 293
 Rapetti, Francesca 338
 Rasilo, Paavo 71
 Raulet, Marie-Ange 997
 Raumonon, Pasi 546
 Rawart, Vineet 378
 Razik, Hubert 957
 Rebbahi, Fares 620
 Rebbah, Redem 620
 Rebican, Mihai 75
 Ree, Cheol-Jick 789, 961
 Reghem, Pascal 127
 Reinauer, Veronika 57, 773, 911
 Reinhold, Christian 670
 Remy, Ghislain 843
 Ren, Daqi 1080
 Renhart, Werner 430
 Renhart, Werner 243, 468, 538
 Ren, Zhe 163
 Ren, Zhiqiang 731
 Ren, Zhuoxiang 308
 Ren, Zhuoxiang 129
 Repetto, Maurizio 49, 719
 Repetto, Maurizio 173, 480
 Repo, Anna-Kaisa 209
 Resende, Ursula 817
 Reyne, Gilbert 636, 656
 Rezzoug, Abderrezak 59
 Rhyu, Se-Hyun 221
 Riganti Fulginei, Francesco 314
 Righi, Luiz Antônio 853
 Rioux-Damidau, Françoise 715
 Rioux, Françoise 524
 Rizzo, Santi Agatino 418
 Robertson, Nick 93
 Roccato, Paolo E. 891
 Rodrigues, Ana de Oliveira 1054
 Rodrigues, Wendell O. 408
 Rodriguez Velandia, Elkin Ferney 791
 Roger, Daniel 562
 Roger, Jean-Yves 739
 Rondot, Loïc 79, 143

Rotaru, Mihai 310
 Rotaru, Mihai Dragos 638
 Rouve, Laure-Line 15, 145
 Ruan, Jiangjun 628
 Rubinacci, Guglielmo 546
 Rubinacci, Guglielmo 77, 277, 366, 642, 693
 Rucker, Wolfgang M. 57, 911
 Rucker, Wolfgang M. 773
 Russenschuck, Stephan 887
 Rymarczyk, Tomasz 436, 851
 Saari, Juha 993
 Sabariego, Ruth 344
 Sabariego, Ruth V. 137, 1066
 Sabariego, ruth V. 1
 Sabioni, Claret Laurente 426
 Sadowski, Nelson 717, 737, 741
 Sadowski, Nelson 133, 135, 185, 981
 Sahinturk, Hulya 466
 Saitoh, Ayumu 711
 Saito, Masahiko 648
 Sakamoto, Mauro Massayoshi 869
 Saldanha, Rodney R. 269, 532
 Saldanha, Rodney Rezende 41, 1042
 Salerno, Nunzio 27, 43, 418
 Salles, Mauricio Barbosa de Camargo 1005
 Salles, Maurício Barbosa de Camargo Salles 869
 Salmia, Lauri 993
 Salon, Sheppard 285
 Salvini, Alessandro 314, 554
 Sanchez Lopez, Hector 299
 Santandrea, Laurent 187, 873, 885
 Santandréa, Laurent 1048
 Santisteban Larrea, Jose Andres 791
 Santos, Claudio Henrique Gomes 518
 Santos Jr, Mario Alves dos 498
 Sarajlic, Nermin 424
 Sargos, Francois. M. 225
 Sargos, François-Michel 957
 Sartori, Carlos A.F. 889
 Sartori, Carlos Antonio França 498, 514
 Sasaguri, Nobuya 542, 747
 Satiramatekul, Thitipong 576
 Sawicki, Bartosz 654
 Schanen, Jean-Luc 512
 Scheiber, Christian 472
 Scheiblich, Christian 57, 773, 911
 Schmidt, ErIch 658, 797
 Schoenen, Timo 596
 Schoeps, Sebastian 227
 Scholz, Eike Michael 390
 Scholz, Peter 670
 Schomann, Steffen 368
 Schöning, Marc 213, 622

Schroeder, Marco Aurélio de Oliveira 516
 Schuhmann, Rolf 548
 Schulz, Carl A. 562
 Schulz, Dirk 474, 1009
 Scorretti, Riccardo 1072
 Selvaggi, J. 285
 Seo, Jang-Ho 330, 901
 Seo, Kang 482, 1014
 Sérgio, Avila 506
 Serres, Alexandre 823
 Sevegnani, Francisco Xavier 889
 Shao, Keran 259
 Shao, K.R. 153
 Shinagawa, Hirofumi 1003
 Shin, Eunchul 428
 Shin, Pan Seok 787
 Shin, Pan-Seok 917
 Shiyou, Yang 672
 Shoubao, Liu 1064
 Siauve, Nicolas 334, 1044
 Sieni, Elisabetta 305, 510
 Sierakowski, Cezar Augusto 1068
 Sievers, Denis 548
 Sikora, Jan 809, 851
 Sikora, Jan 436
 Silva, Anderson Oliveira 484
 Silva, Elson Jose 169
 Silva, Elson Jose 295
 Silva, Elson José da 380
 Silva, Fabio R. L. 494
 Silva, Jose Patrocínio da 462
 Silva, Marco Aurélio Nunes da 464
 Silva, Paulo H. da F. 354, 422
 Silva, Sandro Gonçalves 456
 Silva, Selênio Rocha 426
 Silva, Viviane Cristine 1012
 Silva, Viviane Cristine 291
 Simkin, John 93
 Sirois, Frédéric 687
 Sixdenier, Fabien 334
 Sixdenier, Fabien 560, 997
 Smajic, Jasmin 538
 Smajic, Jasmin 141
 Soares, Antonio José Martins 460
 Solin, Pavel 101
 Song, Jungtae 181
 Song, Xueguan 929
 Souffrant, Robert 47
 Souflaris, Athanassios 99
 Specogna, Ruben 25, 65, 109, 376, 721, 995
 Staszewski, Pawel 191
 Steiner, Gerald 414
 Steinmetz, Thorsten 123

Stella, Andrea 995
Stephany, Stephan 326
Stepien, Slawomir 1052
Stermecki, Andrej 552
Štumberger, Gorazd 1020
Suda, Reiji 1080
Sugimoto, Shin-Ichiro 23, 360
Sun, Tao 612, 931, 937
Sun, Wei 163
Susic, Marko 797
Suuriniemi, Saku 546
Suzuki, Daniela O.H. 829
Suzuki, Satoshi 662, 777, 897
Swinka-Filho, Vitoldo 875
Sykulski, Jan 677
Sykulski, Jan K. 229, 310, 534, 638
Taghizadeh, Mehdi 971
Taguchi, Kenji 356
Takahashi, Norio 67, 542, 747
Takahashi, Norio 265, 322, 450, 745, 861, 1003
Takahashi, Ricardo Hiroshi Caldeira 1042
Takahashi, Yasuhito 147, 318, 648, 813, 1026
Takahata, Tetsumi 749
Takayama, Teruou 652, 701
Takayasu, Kenta 318, 648
Takei, Amane 360
Takorabet, Nouredine 225
Tamburrino, Antonello 277, 366, 693
Tanai, Masahiro 318
Tanaka, Roberto Yuji 412
Tanaka, Toshinori 205
Tang, Renyuan 973
Tani, Yoshihiro 205
Tarik, Hacib 640
Tatsuishi, Takuya 147
Taylor, Simon 93
Teixeira, Rodrigo Stanziola 969
Telló, Marcos 51
Tesanovic, Majda 424
Testoni, Pietro 642
Thiel, David 504
Thierry, Chevalier 83
Ticar, Igor 358
Ticar, Igor 923
Tinzefté, Abdellatif 847
Tirrò, Paola 33, 819
Tokumasu, Tadashi 813
Tomczuk, Bronislaw 771
Tomczuk, Bronislaw Zbigniew 39, 183
Tornincasa, Stefano 173
Torrado, Ruben 237
Tounzi, Abdelmounaim 1016
Tounzi, Abdelmounaïm 981

Toyoda, Akihisa 648
 Tran, Tuan-Vu 536, 865
 Travassos, Lucas 336
 Trevisan, Francesco 25, 65, 109, 376, 721, 995
 Trichet, Didier 89, 570
 Trlep, Mladen 131
 Tsambouris, Evangelos 95
 Tsili, Marina Antonios 99
 Tsukamoto, Toshio 235
 Tsukerman, Igor 681
 Tuerk, Christian 468
 Tung, Le Duc 7
 Tymburski, Marek 436
 Uchida, Naoki 450, 745
 Uehara, Hitoshi 821
 Ueki, Manabu 235
 Ulian, Paulo Sérgio 913
 Valente Jr., Wilson 502
 Valette, Sébastien 1044
 Van Keer, Roger 989
 Van Rienen, Ursula 47
 Vasco, Marco A A 875
 Vasconcelos, Christianne F. L. 456
 Vasconcelos, Joao Antônio 518
 Vasconcelos, João Antônio 426
 Vazquez, Emmanuel 3
 Vázquez, Rafael 807
 Vialardi, Enrico 881
 Viana, Antoine 145
 Viana, Juliano Junio 1054
 Viarouge, Philippe 971
 Viarouge, Philippe 111, 197
 Vichos, Anastasios G. 618
 Vieira, D. A. G. 336
 Vieira, Douglas Alexandre Gomes 41
 Vieira, Douglas Alexandre Gomes 269, 532
 Vieira, Gustavo S. 412
 Vilamot, Raphael 35
 Villone, Fabio 642
 Villone, Fabio 77
 Vincent, Benjamin 512
 Vincent, Jean-Noël 562
 Viola, Bruno 77
 Vollaire, Christian 498
 Voyer, Damien 498
 V. Sabariego, Ruth 135
 Vuillermet, Yannick 15
 Waindok, Andrzej 39, 183
 Wakao, Shinji 147, 813
 Wakao, Shinji 318, 648
 Wamkeue, René 197
 Wang, Li 328
 Wang, Linda 267

Wang, Nna 945
Wang, Qiuwang 163
Wang, Quan-Di 526
Wang, Shuhong 729
Wang, Shuhong 163, 215, 434, 632
Wang, Wei 899
Wang, Weimen 757
Wang, Weimin 217, 925
Wang, Xianbing 660
Wang, Xiaoyan 731
Wang, Yi 163, 215, 434, 632
Warburton, Tim 879
Wasselynck, Guillaume 570
Watanabe, Kota 695
Watanabe, Kota 324, 476, 837
Watanabe, Yuta 476
Webb, Jon 346, 723, 1074
Weida, Daniel 123
Wei, He 1030
Weiland, Thomas 19, 825, 991
Weiland, Thomas 670
Weilharter, Bernhard 81
Weinzierl, Djonny 498
Wiak, Slawomir Jan 556
Wiert, Joe 668
Wimmer, Georg 893
Winkler, Gunter 243
Wissem, Yahyaoui 492
Wojciechowski, Rafal 677
Wong, Man-Fai 668
Won, Hyuk 279, 482
Won, Sung-Hong 789, 961
Woo, Byung-Chul 759, 763
Woo, Dong-Kung 330
Woo, Kyungil 1036
Woo, Sung Hyun 787
Wrobel, Rafal 783
Wurtz, Frederic 249, 560
Wu, Yan 528, 1022
Xavier, César Candido 55
Xavier, Mininger 1058
Xiaobo, Yang 161
Xiao, Dongping 53
Xiao, Dongping 125
Xiao, Hongli 632
Xie, Baochang 480
Xie, Dexin 689, 731, 735
Xie, Qing 945
Xin, Ying 632
Xiong, Nan 871
Xu, Wei 163, 215, 434
Xu, Wei 632
Xu, Xiaoyu 308

Ya-Li, Zheng 1001
 Yamada, Takaya 322
 Yamaguchi, Shinichi 205
 Yamaguchi, Tadashi 1046
 Yamaguchi, Tadashi 777, 821, 897
 Yamashita, Hideo 867, 1062
 Yamazaki, Katsumi 388, 743
 Yamazaki, Keita 1040
 Yang, Fan 125
 Yang, Fan 53
 Yang, Guangyuan 153
 Yang, Liu 442
 Yang, Qingxin 582
 Yang, Shiyou 261, 877, 1070
 Yang, Shiyou 352
 Yang, Xiaobo 666
 Yan, Lie Tong 586
 Yann, Le Bihan 640
 Yapar, Ali 466
 Yeh, Yu-Han 594, 761
 Ying, Peng 1064
 Yitembe, Bertrand Russel 989
 Yoneta, Kenji 837
 Yonnet, Jean-Paul 574
 Yoo, Byungjin 165
 Yoon, Hee Sung 975
 Yoon, HeE Sung 580, 588, 917
 Yoon, Young-Cheol 1078
 Yoon, Young-Cheol 384
 Yoshida, Everton S. 604
 Yoshida, Kazuetsu 235
 Yoshikawa, Gaku 805
 Yoshimura, Shinobu 23, 815
 Yoshimura, Shinobu 360
 Yuan, Haiyan 705
 Yuan, Jingguo 735
 Yuen, Cherry 161
 Yu, Gwang-Jun 755
 Yu, Haitao 779, 833, 951
 Yu, Ji-Hui 526
 Yun, Tae Won 602, 903
 Yun, Yuxin 53
 Yu, Zhang 1064
 Yves, Lembeye 7
 Zahn, Markus 231, 675
 Zakrzewski, Kazimierz 771
 Zanella, Rodrigo 51
 Zang, Sandro Rogério 1034
 Zeng, Haiquan 725
 Zeng, Jianbin 725
 Zeng, Rong 45
 Zeng, Rong 157, 520
 Zhang, Bo 45, 157, 520

Zhang, Lei 779
Zhang, Mingxia 348
Zhang, Xiaoyang 632
Zhang, Yang 697
Zhang, Yanli 731, 735
Zhang, Zhifeng 973
Zhang, Zichi 73
Zhan, Yang 446
Zhao, Chun 628
Zhao, Jian 23
Zhao, Zhibin 31, 348
Zheng, Xu 1030
Zheng, Ya-Li 526
Zhiye, Du 1064
Zhong, Jinjiang 729
Zhou, Limin 163
Zhou, Ping 386, 572, 893
Zhuang, Chijie 157
Zhu, Boyuan 504
Zhu, Jian Guo 163, 434, 632
Zhu, Jianguo 153
Zhu, Jianguo 215, 259, 582, 729, 793, 915
Zilberti, Luca 646
ZimOn, Jan 39, 183
Ziolkowski, Marek 644
Zolla, Frederic 233, 342
Zucca, Mauro 891